

Andreas Jess, Peter Wasserscheid

WILEY-VCH

Chemical Technology

An Integral Textbook



Andreas Jess and Peter Wasserscheid

Chemical Technology

Related Titles

Baerns, M., Behr, A., Brehm, A., Gmehling, J., Hinrichsen, K.-O., Hofmann, H., Onken, U., Palkovits, R., Renken, A.

Technische Chemie

2013

ISBN: 978-3-527-33072-0

Arpe, H.-J., Hawkins, S

Industrial Organic Chemistry

2010

978-3-527-32002-8

Hagen, J.

Industrial Catalysis

A Practical Approach

2005

ISBN: 978-3-527-31144-6

Green, M. M., Wittcoff, H. A.

Organic Chemistry Principles and Industrial Practice

2003

ISBN: 978-3-527-30289-5

Weissert, K., Arpe, H.-J.

Industrial Organic Chemistry

2003

ISBN: 978-3-527-30578-0

Froment, G. F. / Bischoff, K. B. / De Wilde, J.

Chemical Reactor Analysis and Design

2010

ISBN: 978-0-470-56541-4

Moulijn, J. A., Makkee, M., van Diepen, A.

Chemical Process Technology

2001

ISBN: 978-0-471-63062-3

Levenspiel, O.

Chemical Reaction Engineering

1998

ISBN: 978-0-471-25424-9

Rothenberg, G.

Catalysis

Concepts and Green Applications

2008

ISBN: 978-3-527-31824-7

Andreas Jess and Peter Wasserscheid

Chemical Technology

An Integral Textbook



WILEY-VCH Verlag GmbH & Co. KGaA

The Authors

Prof. Dr.-Ing. Andreas Jess

Universität Bayreuth
Lehrstuhl für Chemische Verfahrenstechnik
Universitätsstraße 30
95447 Bayreuth
Germany

Prof. Dr. Peter Wasserscheid

Universität Erlangen-Nürnberg
Lehrstuhl für Chemische Reaktionstechnik
Egerlandstraße 3
91058 Erlangen
Germany

All books published by Wiley-VCH are carefully produced. Nevertheless, authors, editors, and publisher do not warrant the information contained in these books, including this book, to be free of errors. Readers are advised to keep in mind that statements, data, illustrations, procedural details or other items may inadvertently be inaccurate.

Library of Congress Card No.: applied for

British Library Cataloguing-in-Publication Data

A catalogue record for this book is available from the British Library.

Bibliographic information published by the Deutsche Nationalbibliothek

The Deutsche Nationalbibliothek lists this publication in the Deutsche Nationalbibliografie; detailed bibliographic data are available on the Internet at <http://dnb.d-nb.de>.

© 2013 Wiley-VCH Verlag & Co. KGaA, Boschstr. 12, 69469 Weinheim, Germany

All rights reserved (including those of translation into other languages). No part of this book may be reproduced in any form – by photoprinting, microfilm, or any other means – nor transmitted or translated into a machine language without written permission from the publishers. Registered names, trademarks, etc. used in this book, even when not specifically marked as such, are not to be considered unprotected by law.

Cover Design Adam-Design, Weinheim

Typesetting Thomson Digital, Noida, India

Printing and Binding Markono Print Media Pte Ltd, Singapore

Print ISBN: 978-3-527-30446-2

ePDF ISBN: 978-3-527-67062-8

ePub ISBN: 978-3-527-67061-1

mobi ISBN: 978-3-527-67060-4

Printed in Singapore

Printed on acid-free paper

Cover Picture Ethylene plant in Secunda/
Southafrica; with kind permission of Linde AG

*To our wives Christina and Talke and our children
Antonia, Friederike, Jonathan, Karolin, Lukas, and Theresa.*

Contents

Preface	XVII
Notation	XXI
1	Introduction 1
1.1	What is Chemical Technology? 1
1.2	The Chemical Industry 2
2	Chemical Aspects of Industrial Chemistry 7
2.1	Stability and Reactivity of Chemical Bonds 7
2.1.1	Factors that Influence the Electronic Nature of Bonds and Atoms 7
2.1.2	Steric Effects 8
2.1.3	Classification of Reagents 9
2.2	General Classification of Reactions 10
2.2.1	Acid–Base Catalyzed Reactions 11
2.2.2	Reactions via Free Radicals 11
2.2.3	Nucleophilic Substitution Reactions 13
2.2.4	Reactions via Carbocations 14
2.2.5	Electrophilic Substitution Reactions at Aromatic Compounds 15
2.2.6	Electrophilic Addition Reactions 17
2.2.7	Nucleophilic Addition Reactions 17
2.2.8	Asymmetric Synthesis 17
2.3	Catalysis 19
2.3.1	Introduction and General Aspects 20
2.3.2	Homogeneous, Heterogeneous, and Biocatalysis 26
2.3.3	Production and Characterization of Heterogeneous Catalysts 29
2.3.4	Deactivation of Catalysts 32
2.3.5	Future Trends in Catalysis Research 35
3	Thermal and Mechanical Unit Operations 39
3.1	Properties of Gases, Liquids, and Solids 40
3.1.1	Ideal and Real Gas 40
3.1.2	Heat Capacities and the Joule–Thomson Effect 45
3.1.3	Physical Transformations of Pure Substances: Vaporization and Melting 48
3.1.4	Transport Properties (Diffusivity, Viscosity, Heat Conduction) 52
3.1.4.1	<i>Basic Equations for Transfer of Heat, Mass, and Momentum</i> 52
3.1.4.2	<i>Transport Coefficients of Gases</i> 57
3.1.4.3	<i>Transport Coefficients of Liquids</i> 61
3.2	Heat and Mass Transfer in Chemical Engineering 65
3.2.1	Heat Transport 66
3.2.1.1	<i>Heat Conduction</i> 66
3.2.1.2	<i>Heat Transfer by Convection (Heat Transfer Coefficients)</i> 67

3.2.1.3	<i>Boiling Heat Transfer</i>	78
3.2.1.4	<i>Heat Transfer by Radiation</i>	79
3.2.1.5	<i>Transient Heat Transfer by Conduction and Convection</i>	80
3.2.2	<i>Mass Transport</i>	84
3.2.2.1	<i>Forced Flow in Empty Tubes and Hydrodynamic Entrance Region</i>	84
3.2.2.2	<i>Steady-State and Transient Diffusive Mass Transfer</i>	85
3.2.2.3	<i>Diffusion in Porous Solids</i>	89
3.3	Thermal Unit Operations	93
3.3.1	<i>Heat Exchangers (Recuperators and Regenerators)</i>	94
3.3.2	<i>Distillation</i>	97
3.3.2.1	<i>Distillation Principles</i>	98
3.3.2.2	<i>Design of Distillation Columns (Ideal Mixtures)</i>	101
3.3.2.3	<i>Azeotropic, Extractive, and Pressure Swing Distillation</i>	106
3.3.2.4	<i>Reactive Distillation</i>	108
3.3.3	<i>Absorption (Gas Scrubbing)</i>	108
3.3.3.1	<i>Absorption Principles</i>	108
3.3.3.2	<i>Design of Absorption Columns</i>	113
3.3.4	<i>Liquid–Liquid Extraction</i>	116
3.3.4.1	<i>Extraction Principles</i>	116
3.3.4.2	<i>Design of Extraction Processes</i>	118
3.3.5	<i>Adsorption</i>	120
3.3.5.1	<i>Adsorption Principles</i>	120
3.3.5.2	<i>Design of Adsorption Processes</i>	130
3.3.6	<i>Fluid–Solid Extraction</i>	136
3.3.6.1	<i>Principles of Fluid–Solid Extraction</i>	136
3.3.6.2	<i>Design of Fluid–Solid Extractions</i>	139
3.3.7	<i>Crystallization</i>	140
3.3.7.1	<i>Ideal Binary Eutectic Phase System</i>	140
3.3.7.2	<i>Ideal Binary Phase System with Both Solids Completely Soluble in One Another</i>	141
3.3.8	<i>Separation by Membranes</i>	144
3.3.8.1	<i>Principles of Membrane Separation</i>	144
3.3.8.2	<i>Applications of Membrane Separation Processes</i>	147
3.4	Mechanical Unit Operations	151
3.4.1	<i>Conveyance of Fluids</i>	152
3.4.1.1	<i>Pressure Loss in Empty Tubes</i>	152
3.4.1.2	<i>Pressure Loss in Fixed, Fluidized, and Entrained Beds</i>	156
3.4.1.3	<i>Compressors and Pumps</i>	159
3.4.2	<i>Contacting and Mixing of Fluids</i>	161
3.4.3	<i>Crushing and Screening of Solids</i>	163
3.4.3.1	<i>Particle Size Reduction</i>	163
3.4.3.2	<i>Particle Size Analysis</i>	164
3.4.3.3	<i>Screening and Classification of Particles (Size Separation)</i>	166
3.4.3.4	<i>Solid–Solid Separation (Sorting of Different Solids)</i>	167
3.4.4	<i>Separation of Solids from Fluids</i>	168
3.4.4.1	<i>Filtration</i>	168
3.4.4.2	<i>Separation of Solids from Fluids by Sedimentation</i>	168
3.4.4.3	<i>Screening and Classification of Particles (Size Separation)</i>	171
4	Chemical Reaction Engineering	175
4.1	Main Aspects and Basic Definitions of Chemical Reaction Engineering	176
4.1.1	<i>Design Aspects and Scale-Up Dimensions of Chemical Reactors</i>	176
4.1.2	<i>Speed of Chemical and Biochemical Reactions</i>	177
4.1.3	<i>Influence of Reactor Type on Productivity</i>	178

4.1.4	Terms used to Characterize the Composition of a Reaction Mixture	179
4.1.5	Terms used to Quantify the Result of a Chemical Conversion	179
4.1.6	Reaction Time and Residence Time	180
4.1.7	Space Velocity and Space–Time Yield	181
4.2	Chemical Thermodynamics	182
4.2.1	Introduction and Perfect Gas Equilibria	183
4.2.2	Real Gas Equilibria	190
4.2.3	Equilibrium of Liquid–Liquid Reactions	193
4.2.4	Equilibrium of Gas–Solid Reactions	195
4.2.5	Calculation of Simultaneous Equilibria	197
4.3	Kinetics of Homogeneous Reactions	200
4.3.1	Rate Equation: Influence of Temperature and Reaction Order	200
4.3.1.1	<i>First-Order Reaction</i>	204
4.3.1.2	<i>Reaction of n-th Order</i>	204
4.3.1.3	<i>Second-Order Reaction</i>	205
4.3.2	Parallel Reactions and Reactions in Series	206
4.3.2.1	<i>Two Parallel First-Order Reactions</i>	206
4.3.2.2	<i>Two First-Order Reactions in Series</i>	207
4.3.3	Reversible Reactions	210
4.3.4	Reactions with Varying Volume (for the Example of a Batch Reactor)	213
4.4	Kinetics of Fluid–Fluid Reactions	216
4.4.1	Mass Transfer at a Gas–Liquid Interface (Two-Film Theory)	217
4.4.2	Mass Transfer with (Slow) Homogeneous Reaction in the Bulk Phase	219
4.4.3	Mass Transfer with Fast or Instantaneous Reaction near or at the Interface	220
4.5	Kinetics of Heterogeneously Catalyzed Reactions	226
4.5.1	Spectrum of Factors Influencing the Rate of Heterogeneously Catalyzed Reactions	227
4.5.2	Chemical Reaction Rate: Surface Kinetics	231
4.5.2.1	<i>Sorption on the Surface of Solid Catalysts</i>	231
4.5.2.2	<i>Rate Equations for Heterogeneously Catalyzed Surface Reactions</i>	231
4.5.3	Reaction on a Solid Catalyst and Interfacial Transport of Mass and Heat	235
4.5.3.1	<i>Interaction of External Mass Transfer and Chemical Reaction</i>	235
4.5.3.2	<i>Combined Influence of External Mass and Heat Transfer on the Effective Rate</i>	239
4.5.4	Chemical Reaction and Internal Transport of Mass and Heat	247
4.5.4.1	<i>Pore Diffusion Resistance and Effective Reaction Rate</i>	247
4.5.4.2	<i>Combined Influence of Pore Diffusion and Intraparticle Heat Transport</i>	252
4.5.5	Simultaneous Occurrence of Interfacial and Internal Mass Transport Effects	254
4.5.5.1	<i>Irreversible First-Order Reaction</i>	254
4.5.5.2	<i>Reversible First-Order Reaction with the Influence of External and Internal Mass Transfer</i>	256
4.5.6	Influence of External and Internal Mass Transfer on Selectivity	259
4.5.6.1	<i>Influence of External Mass Transfer on the Selectivity of Reactions in Series</i>	259
4.5.6.2	<i>Influence of External Mass Transfer on the Selectivity of Parallel Reactions</i>	262
4.5.6.3	<i>Influence of Pore Diffusion on the Selectivity of Reactions in Series</i>	263
4.5.6.4	<i>Influence of Pore Diffusion on the Selectivity of Parallel Reactions</i>	267

4.6	Kinetics of Gas–Solid Reactions	268
4.6.1	Spectrum of Factors Influencing the Rate of Gas–Solid Reactions	269
4.6.2	Reaction of a Gas with a Non-porous Solid	270
4.6.2.1	<i>Survey of Border Cases and Models for a Reaction of a Gas with a Non-porous Solid</i>	270
4.6.2.2	<i>Shrinking Non-porous Unreacted Core and Solid Product Layer</i>	270
4.6.2.3	<i>Shrinking Non-porous Unreacted Core and Gaseous Product(s)</i>	273
4.6.3	Reaction of a Gas with a Porous Solid	276
4.6.3.1	<i>Survey of Border Cases and Models for a Reaction of a Gas with a Porous Solid</i>	276
4.6.3.2	<i>Basic Equations for the Conversion of a Porous Solid with a Gaseous Reactant</i>	277
4.6.3.3	<i>General Closed Solution by Combined Model (Approximation)</i>	277
4.6.3.4	<i>Homogeneous Uniform Conversion Model (No Concentration Gradients)</i>	280
4.6.3.5	<i>Shrinking Unreacted Core Model (Rate Determined by Diffusion Through Product Layer)</i>	280
4.7	Criteria used to Exclude Interphase and Intraparticle Mass and Heat Transport Limitations in Gas–Solid Reactions and Heterogeneously Catalyzed Reactions	282
4.7.1	External Mass Transfer Through Boundary Layer	282
4.7.2	External Heat Transfer	283
4.7.3	Internal Mass Transfer	284
4.7.4	Internal Heat Transfer	284
4.8	Kinetics of Homogeneously or Enzyme Catalyzed Reactions	287
4.8.1	Homogeneous and Enzyme Catalysis in a Single-Phase System	287
4.8.2	Homogeneous Two-Phase Catalysis	290
4.9	Kinetics of Gas–Liquid Reactions on Solid Catalysts	291
4.9.1	Introduction	291
4.9.2	High Concentration of Liquid Reactant B (or pure B) and Slightly Soluble Gas	295
4.9.3	Low Concentration of Liquid Reactant B and Highly Soluble Gas and/or High Pressure	295
4.10	Chemical Reactors	296
4.10.1	Overview of Reactor Types and their Characteristics	296
4.10.1.1	<i>Brief Outline of Ideal and Real Reactors</i>	296
4.10.1.2	<i>Classification of Real Reactors Based on the Mode of Operation</i>	298
4.10.1.3	<i>Classification of Real Reactors According to the Phases</i>	299
4.10.2	Ideal Isothermal Reactors	305
4.10.2.1	<i>Well-Mixed (Discontinuous) Isothermal Batch Reactor</i>	306
4.10.2.2	<i>Continuously Operated Isothermal Ideal Tank Reactor</i>	307
4.10.2.3	<i>Continuously Operated Isothermal Ideal Tubular Reactor</i>	308
4.10.2.4	<i>Continuously Operated Isothermal Tubular Reactor with Laminar Flow</i>	309
4.10.2.5	<i>Continuously Operated Isothermal Cascade of Tank Reactors</i>	311
4.10.2.6	<i>Ideal Isothermal Tubular Recycle Reactor</i>	311
4.10.2.7	<i>Comparison of the Performance of Ideal Isothermal Reactors</i>	313
4.10.3	Non-isothermal Ideal Reactors and Criteria for Prevention of Thermal Runaway	316
4.10.3.1	<i>Well-Mixed (Discontinuously Operated) Non-isothermal Batch Reactor</i>	317
4.10.3.2	<i>Continuously Operated Non-isothermal Ideal Tank Reactor (CSTR)</i>	322
4.10.3.3	<i>Continuously Operated Non-isothermal Ideal Tubular Reactor</i>	328

4.10.3.4	<i>Optimum Operating Lines of Continuous Ideal Non-isothermal Reactors</i>	332
4.10.4	Non-ideal Flow and Residence Time Distribution	336
4.10.5	Tanks-in-Series Model	340
4.10.5.1	<i>Residence Time Distribution of a Cascade of Ideal Stirred Tank Reactors</i>	340
4.10.5.2	<i>Calculation of Conversion by the Tanks-in-Series Model</i>	342
4.10.6	Dispersion Model	343
4.10.6.1	<i>Axial Dispersion and Residence Time Distribution</i>	343
4.10.6.2	<i>Calculation of Conversion by the Dispersion Model</i>	348
4.10.6.3	<i>Dispersion and Conversion in Empty Pipes</i>	349
4.10.6.4	<i>Dispersion of Mass and Heat in Fixed Bed Reactors</i>	352
4.10.6.5	<i>Radial Variations in Bed Structure: Wall Effects in Narrow Packed Beds</i>	354
4.10.7	Modeling of Fixed Bed Reactors	355
4.10.7.1	<i>Fundamental Balance Equations of Fixed Bed Reactors</i>	355
4.10.7.2	<i>Criteria used to Exclude a Significant Influence of Dispersion in Fixed Bed Reactors</i>	357
4.10.7.3	<i>Radial Heat Transfer in Packed Bed Reactors and Methods to Account for This</i>	363
4.10.8	Novel Developments in Reactor Technology	370
4.10.8.1	<i>Hybrid (Multifunctional) Reactors</i>	370
4.10.8.2	<i>Monolithic Reactors</i>	372
4.10.8.3	<i>Microreactors</i>	373
4.10.8.4	<i>Adiabatic Reactors with Periodic Flow Reversal</i>	376
4.11	Measurement and Evaluation of Kinetic Data	379
4.11.1	Principal Methods for Determining Kinetic Data	380
4.11.1.1	<i>Microkinetics</i>	380
4.11.1.2	<i>Macrokinetics</i>	380
4.11.1.3	<i>Laboratory Reactors</i>	380
4.11.1.4	<i>Pros and Cons of Integral and Differential Method</i>	382
4.11.2	Evaluation of Kinetic Data (Reaction Orders, Rate Constants)	382
4.11.3	Laboratory-Scale Reactors for Kinetic Measurements	385
4.11.4	Transport Limitations in Experimental Catalytic Reactors	388
4.11.4.1	<i>Ideal Plug Flow Behavior: Criteria to Exclude the Influence of Dispersion</i>	389
4.11.4.2	<i>Gradientless Ideal Particle Behavior: Criteria to Exclude the Influence of Interfacial and Internal Transport of Mass and Heat</i>	390
4.11.4.3	<i>Criterion to Exclude the Influence of the Dilution of a Catalytic Fixed Bed</i>	392
4.11.5	Case Studies for the Evaluation of Kinetic Data	392
4.11.5.1	<i>Case Study I: Thermal Conversion of Naphthalene</i>	392
4.11.5.2	<i>Case Study II: Heterogeneously Catalyzed Hydrogenation of Hexene</i>	394
4.11.5.3	<i>Case Study III: Heterogeneously Catalyzed Multiphase Reaction</i>	395
4.11.5.4	<i>Case Study IV: Non-isothermal Oxidation of Carbon Nanotubes and Fibers</i>	400
5	Raw Materials, Products, Environmental Aspects, and Costs of Chemical Technology	407
5.1	Raw Materials and Energy Sources	408
5.1.1	Energy Consumption, Reserves and Resources of Fossil Fuels and Renewables	408
5.1.1.1	<i>Global and Regional Energy Consumption and Fuel Shares</i>	408
5.1.1.2	<i>World Energy Consumption and World Population</i>	410

5.1.1.3	<i>Economic and Social Aspects of Energy Consumption</i>	410
5.1.1.4	<i>Conventional and Non-conventional Fossil Fuels</i>	418
5.1.1.5	<i>Nuclear Power</i>	420
5.1.1.6	<i>Renewable Energy</i>	421
5.1.1.7	<i>Energy Mix of the Future</i>	422
5.1.1.8	<i>Global Warming</i>	425
5.1.1.9	<i>Ecological Footprint and Energy Consumption</i>	425
5.1.1.10	<i>Energy Demand and Energy Mix to Reconcile the World's Pursuit of Welfare and Happiness with the Necessity to Preserve the Integrity of the Biosphere</i>	428
5.1.2	Composition of Fossil Fuels and Routes for the Production of Synthetic Fuels	431
5.1.3	Natural Gas and Other Technical Gases	433
5.1.3.1	<i>Properties of Natural Gas and Other Technical Gases</i>	433
5.1.3.2	<i>Conditioning of Natural Gas, Processes and Products Based on Natural Gas</i>	435
5.1.4	Crude Oil and Refinery Products	437
5.1.4.1	<i>Production, Reserves, and Price of Crude Oil</i>	437
5.1.4.2	<i>Properties of Crude Oil</i>	440
5.1.4.3	<i>Properties of Major Refinery Products</i>	442
5.1.4.4	<i>Refinery Processes</i>	443
5.1.5	Coal and Coal Products	445
5.1.5.1	<i>Properties of Coal and Other Solid Fuels</i>	445
5.1.5.2	<i>Processes and Products Based on Coal</i>	447
5.1.6	Renewable Raw Materials	450
5.1.6.1	<i>Base Chemicals from Renewable Raw Materials</i>	450
5.1.6.2	<i>Fats and Vegetable Oils</i>	451
5.1.6.3	<i>Carbohydrates</i>	453
5.1.6.4	<i>Extracts and Excreta from Plants</i>	455
5.2	Inorganic Products	457
5.3	Organic Intermediates and Final Products	459
5.3.1	Alkanes and Syngas	460
5.3.2	Alkenes, Alkynes, and Aromatic Hydrocarbons	464
5.3.3	Organic Intermediates Functionalized with Oxygen, Nitrogen, or Halogens	472
5.3.3.1	<i>Alcohols</i>	472
5.3.3.2	<i>Ethers</i>	477
5.3.3.3	<i>Epoxides</i>	478
5.3.3.4	<i>Aldehydes</i>	478
5.3.3.5	<i>Ketones</i>	481
5.3.3.6	<i>Acids</i>	481
5.3.3.7	<i>Amines and Nitrogen-Containing Intermediates</i>	484
5.3.3.8	<i>Lactams, Nitriles, and Isocyanates</i>	486
5.3.3.9	<i>Halogenated Organic Intermediates</i>	488
5.3.4	Polymers	491
5.3.4.1	<i>Polyolefins and Polydienes</i>	492
5.3.4.2	<i>Vinyl-Polymers and Polyacrylates</i>	493
5.3.4.3	<i>Polyesters, Polyamides, and Polyurethanes</i>	497
5.3.5	Detergents and Surfactants	500
5.3.5.1	<i>Structure and Properties of Detergent and Surfactants</i>	500
5.3.5.2	<i>Cationic Detergents</i>	501
5.3.5.3	<i>Anionic Detergents</i>	502
5.3.5.4	<i>Non-ionic Detergents</i>	504
5.3.6	Fine Chemicals	505

5.3.6.1	<i>Dyes and Colorants</i>	506
5.3.6.2	<i>Adhesives</i>	506
5.3.6.3	<i>Fragrance and Flavor Chemicals</i>	506
5.3.6.4	<i>Pesticides</i>	506
5.3.6.5	<i>Vitamins, Food, and Animal Feed Additives</i>	508
5.3.6.6	<i>Pharmaceuticals</i>	508
5.4	Environmental Aspects of Chemical Technology	509
5.4.1	Air Pollution	510
5.4.2	Water Consumption and Pollution	512
5.4.3	“Green Chemistry” and Quantifying the Environmental Impact of Chemical Processes	515
5.5	Production Costs of Fuels and Chemicals Manufacturing	517
5.5.1	Price of Chemical Products	517
5.5.2	Investment Costs	518
5.5.3	Variable Costs	521
5.5.4	Operating Costs (Fixed and Variable Costs)	522
6	Examples of Industrial Processes	525
6.1	Ammonia Synthesis	525
6.1.1	Historical Development of Haber–Bosch Process	525
6.1.2	Thermodynamics of Ammonia Synthesis	528
6.1.3	Kinetics and Mechanism of Ammonia Synthesis	529
6.1.4	Technical Ammonia Process and Synthesis Reactors	531
6.2	Syngas and Hydrogen	536
6.2.1	Options to Produce Syngas and Hydrogen (Overview)	536
6.2.2	Syngas from Solid Fuels (Coal, Biomass)	542
6.2.2.1	<i>Basic Principles and Reactions of Syngas Production from Solid Fuels</i>	542
6.2.2.2	<i>Syngas Production by Gasification of Solid Fuels</i>	543
6.2.2.3	<i>Case Study: Syngas and Hydrogen by Gasification of Biomass</i>	544
6.2.3	Syngas by Partial Oxidation of Heavy Oils	552
6.2.4	Syngas by Steam Reforming of Natural Gas	555
6.3	Sulfuric Acid	558
6.3.1	Reactions and Thermodynamics of Sulfuric Acid Production	558
6.3.2	Production of SO ₂	559
6.3.3	SO ₂ Conversion into SO ₃	560
6.3.4	Sulfuric Acid Process	566
6.4	Nitric Acid	568
6.4.1	Reactions and Thermodynamics of Nitric Acid Production	568
6.4.2	Kinetics of Catalytic Oxidation of Ammonia	572
6.4.2.1	<i>Catalytic Oxidation of Ammonia on a Single Pt Wire for Cross-Flow of the Gas</i>	573
6.4.2.2	<i>Catalytic Oxidation of Ammonia in an Industrial Reactor, that is, on a Series of Pt Gauzes</i>	579
6.4.3	NO Oxidation	583
6.4.4	Nitric Acid Processes	584
6.5	Coke and Steel	587
6.5.1	Steel Production (Overview)	587
6.5.1.1	<i>Steel Production Based on the Blast Furnace Route</i>	588
6.5.1.2	<i>Steel Production based on Scrap and Direct Reduced Iron (DRI)</i>	589
6.5.2	Production of Blast Furnace Coke	589
6.5.2.1	<i>Inspection of Transient Process of Coking of Coal</i>	591
6.5.2.2	<i>Case I: Negligible Thermal Resistance of Coal/Coke Charge</i>	591
6.5.2.3	<i>Case II: Negligible Thermal Resistance of Heated Brick Wall</i>	592

6.5.2.4	<i>Case III: Thermal Resistances of Brick Wall and Coal Charge have to be Considered</i>	594
6.5.3	Production of Pig Iron in a Blast Furnace	595
6.5.3.1	<i>Coke Consumption of a Blast Furnace: Historical Development and Theoretical Minimum</i>	599
6.5.3.2	<i>Residence Time Distribution of a Blast Furnace</i>	601
6.6	Basic Chemicals by Steam Cracking	604
6.6.1	General and Mechanistic Aspects	605
6.6.2	Factors that Influence the Product Distribution	608
6.6.2.1	<i>Influence of Applied Feedstock</i>	608
6.6.2.2	<i>Influence of the Temperature in the Cracking Oven</i>	608
6.6.2.3	<i>Influence of Residence Time</i>	608
6.6.2.4	<i>Influence of Hydrocarbon Partial Pressure in the Cracking Oven</i>	609
6.6.3	Industrial Steam Cracker Process	610
6.6.4	Economic Aspects of the Steam Cracker Process	615
6.7	Liquid Fuels by Cracking of Heavy Oils	616
6.7.1	Thermal Cracking (Delayed Coking)	616
6.7.2	Fluid Catalytic Cracking (FCC Process)	620
6.8	Clean Liquid Fuels by Hydrotreating	624
6.8.1	History, Current Status, and Perspective of Hydrotreating	624
6.8.2	Thermodynamics and Kinetics of Hydrodesulfurization (HDS)	625
6.8.3	Hydrodesulfurization Process and Reaction Engineering Aspects	629
6.9	High Octane Gasoline by Catalytic Reforming	633
6.9.1	Reactions and Thermodynamics of Catalytic Reforming	633
6.9.2	Reforming Catalyst	636
6.9.3	Process of Catalytic Reforming	637
6.9.4	Deactivation and Regeneration of a Reforming Catalyst	638
6.9.4.1	<i>Coke Burn-Off within a Single Catalyst Particle</i>	639
6.9.4.2	<i>Regeneration in a Technical Fixed Bed Reactor</i>	645
6.10	Refinery Alkylation	652
6.10.1	Reaction and Reaction Mechanism of Refinery Alkylation	652
6.10.2	Alkylation Feedstock and Products	654
6.10.3	Process Variables	655
6.10.3.1	<i>Reaction Temperature</i>	655
6.10.3.2	<i>Acid Strength and Composition</i>	656
6.10.3.3	<i>Isobutane Concentration</i>	656
6.10.3.4	<i>Effect of Mixing</i>	656
6.10.4	Commercial Alkylation Processes	657
6.10.4.1	<i>Commercial Processes using Hydrofluoric Acid as Liquid Catalyst</i>	657
6.10.4.2	<i>Commercial Processes Using Sulfuric Acid as Liquid Catalyst</i>	658
6.10.4.3	<i>Comparison of Commercially Applied Alkylation Processes</i>	661
6.11	Fuels and Chemicals from Syngas: Methanol and Fischer-Tropsch Synthesis	662
6.11.1	Fischer-Tropsch Synthesis	664
6.11.1.1	<i>Reactions and Mechanisms of Fischer-Tropsch Synthesis</i>	664
6.11.1.2	<i>Intrinsic and Effective Reaction Rate of Fischer-Tropsch Synthesis</i>	668
6.11.1.3	<i>History, Current Status, and Perspectives of Fischer-Tropsch Synthesis</i>	670
6.11.1.4	<i>Fischer-Tropsch Processes and Reactors</i>	674
6.11.1.5	<i>Modeling of a Multi-tubular Fixed Bed Fischer-Tropsch Reactor</i>	677
6.11.2	Methanol Synthesis	685
6.11.2.1	<i>Thermodynamics of Methanol Synthesis</i>	686
6.11.2.2	<i>Catalysts for Methanol Synthesis</i>	689
6.11.2.3	<i>Processes and Synthesis Reactors</i>	692

6.12	Ethylene and Propylene Oxide	695
6.12.1	Commercial Production of Ethylene Oxide	695
6.12.1.1	<i>Chlorohydrin Process</i>	696
6.12.1.2	<i>Direct Oxidation of Ethylene</i>	696
6.12.1.3	<i>Products Made of Ethylene Oxide</i>	699
6.12.2	Commercial Production of Propylene Oxide	700
6.12.2.1	<i>Chlorohydrin Process</i>	700
6.12.2.2	<i>Indirect Oxidation of Propylene</i>	702
6.12.2.3	<i>Products Made of Propylene Oxide</i>	705
6.13	Catalytic Oxidation of o-Xylene to Phthalic Acid Anhydride	706
6.13.1	Production and Use of Phthalic Anhydride (Overview)	707
6.13.2	Design and Simulation of a Multi-tubular Reactor for Oxidation of o-Xylene to PA	708
6.14	Hydroformylation (Oxosynthesis)	716
6.14.1	Industrial Relevance of Hydroformylation	717
6.14.2	Hydroformylation Catalysis	718
6.14.3	Current Hydroformylation Catalyst and Process Technologies	722
6.14.4	Advanced Catalyst Immobilization Technologies for Hydroformylation Catalysis	730
6.14.4.1	<i>Immobilization of Homogeneous Hydroformylation Catalysts on Solid Surfaces by Covalent Anchoring</i>	731
6.14.4.2	<i>Catalyst Separation by Size Exclusion Membranes</i>	732
6.14.4.3	<i>Catalyst Immobilization in Liquid–Liquid Biphasic Reaction Systems using Fluorous Phases, Supercritical CO₂ or Ionic Liquids</i>	733
6.14.4.4	<i>Supported Liquid Hydroformylation Catalysis</i>	736
6.15	Acetic Acid	739
6.15.1	Acetic Acid Synthesis via Acetaldehyde Oxidation	741
6.15.2	Acetic Acid Synthesis via Butane or Naphtha Oxidation	742
6.15.3	Acetic Acid Synthesis via Methanol Carbonylation	743
6.15.3.1	<i>BASF High-Pressure Process</i>	743
6.15.3.2	<i>Monsanto Low-Pressure Process</i>	744
6.15.3.3	<i>Cativa Process</i>	747
6.15.4	Other Technologies for the Commercial Production of Acetic Acid	747
6.15.4.1	<i>Direct Ethylene Oxidation</i>	747
6.15.4.2	<i>Acetic Acid Production by Ethane and Methane Oxidation</i>	748
6.16	Ethylene Oligomerization Processes for Linear 1-Alkene Production	749
6.16.1	Industrial Relevance of 1-Olefins	749
6.16.2	Aluminum-alkyl-based “Aufbaureaktion” (Growth Reaction)	750
6.16.3	Nickel-Catalyzed Oligomerization – Shell Higher Olefins Process (SHOP)	753
6.16.4	Metallacycle Mechanism for Selective Ethylene Oligomerization	757
6.17	Production of Fine Chemicals (Example Menthol)	763
6.17.1	Menthol and Menthol Production (Overview)	763
6.17.2	Thermodynamics and Kinetics of Epimerization of Menthol Isomers	764
6.17.3	Influence of Mass Transfer on the Epimerization of Menthol Isomers	766
6.17.4	Epimerization of Menthol Isomers in Technical Reactors	771
6.18	Treatment of Exhaust Gases from Mobile and Stationary Sources	773
6.18.1	Automotive Emission Control	773
6.18.1.1	<i>Emission Standards and Primary Measures for Reduction of Engine Emissions</i>	773
6.18.1.2	<i>Catalytic Converters for Reduction of Car Engine Emissions</i>	775

6.18.2	Selective Catalytic Reduction (SCR) of NO _x from Flue Gas from Power Plants	778
6.18.2.1	<i>Treatment of Flue Gas from Power Plants (Overview)</i>	778
6.18.2.2	<i>Formation of Nitrogen Oxides during Fuel Combustion in Power Plants</i>	779
6.18.2.3	<i>Catalysts and Reactors for Selective Catalytic Reduction of NO_x</i>	780
6.18.2.4	<i>Reaction Chemistry of Selective Catalytic Reduction of NO_x</i>	781
6.18.2.5	<i>Reaction Kinetics and Design of SCR Reactor</i>	781
6.19	Industrial Electrolysis	786
6.19.1	Electrochemical Kinetics and Thermodynamics	786
6.19.1.1	<i>Faraday's Law and Current Efficiency</i>	786
6.19.1.2	<i>Electrochemical Potentials</i>	787
6.19.1.3	<i>Galvanic and Electrolysis Cells, Nernst's Law</i>	788
6.19.1.4	<i>Standard Electrode Potentials</i>	789
6.19.1.5	<i>Electrical Work and Thermoneutral Enthalpy Voltage</i>	789
6.19.1.6	<i>Overpotentials</i>	791
6.19.2	Chlorine and Sodium Hydroxide	791
6.19.2.1	<i>Applications of Chlorine and Sodium Hydroxide</i>	791
6.19.2.2	<i>Processes of Chlor-Alkali Electrolysis</i>	792
6.19.2.3	<i>Diaphragm Process</i>	793
6.19.2.4	<i>Mercury Cell Process</i>	795
6.19.2.5	<i>Membrane Process</i>	796
6.19.3	Electrolysis of Water	797
6.19.4	Electrometallurgy (Purification of Metals by Electrorefining)	800
6.19.4.1	<i>Electrolytic Refining in Aqueous Solution</i>	800
6.19.4.2	<i>Fused Salt Electrolysis (Production of Aluminum)</i>	801
6.20	Polyethene Production	803
6.20.1	Polyethene Classification and Industrial Use	803
6.20.2	General Characteristics of PE Production Processes	805
6.20.2.1	<i>Exothermicity of the Reaction and Thermal Stability of Ethene</i>	805
6.20.2.2	<i>Purity of Ethene</i>	805
6.20.3	Reaction Meachanism and Process Equipment for the Production of LDPE	806
6.20.4	Catalysts for the Production of HDPE and LLDPE	809
6.20.4.1	<i>Ziegler Catalyst Systems</i>	809
6.20.4.2	<i>Phillips Catalyst Systems</i>	810
6.20.4.3	<i>Single-Site Metallocene Catalyst Systems</i>	811
6.20.5	Production Processes for HDPE and LLDPE	812
6.20.6	PE Production Economics and Modern Developments in PE Production	815
	References	817
	Index	833

Preface (and Guidelines how to Use this Textbook)

This textbook tries to marry the four disciplines of chemical technology, namely, chemistry (key reactions, catalysis), thermal and mechanical unit operations (distillation, absorption/adsorption, mixing of fluids, separation of solids from fluids, etc.), chemical reaction engineering (thermodynamics, kinetics, influence of heat and mass transfer, reactor modeling), and general chemical technology, that is, the pedigree of routes from raw materials via intermediates to final products and environmental aspects chemical technology.

The development and understanding of chemical processes relies on knowledge of all four disciplines. This book is an approach to integrating these disciplines and to enlivening them by problems and solutions of industrial practice. The book intends to enable students of chemical engineering as well as of chemistry (especially those with a focus on technical chemistry) to understand industrial processes and to apply these fundamental disciplines for the design of reactors, including pre- and post-treatment of feedstocks and products.

We emphasize that the depth of specialist literature cannot and should not be reached; but students who want to study certain aspects in more detail will find further references.

The book is organized into three main parts:

- The first half provides a comprehensive examination of the fundamental disciplines of chemical technology: After a short introduction, the subsequent chapters survey chemical aspects (Chapter 2), thermal and mechanical unit operations (Chapter 3), and chemical reaction engineering (Chapter 4).
- Chapter 5 gives an overview of raw materials and energy sources (fossil fuels, renewable energy), in which economical, ecological and social aspects of energy consumption are also covered. Thereafter, the routes from fossil fuels (natural gas, oil and coal) to fuels, petrochemicals, bulk chemicals, and final products are described, and the main inorganic intermediates and final products are also given. Finally, some main environmental aspects of chemical technology (air and water pollution), and the costs of manufacturing fuels and chemicals are discussed.
- In the last part (Chapter 6), 20 industrial chemical processes and their design are analyzed, exemplifying the inherent applied nature of chemical technology. By this means the reader can recapitulate, deepen, and exercise the chemical and engineering principles and their interplay (hopefully learned in Chapters 1–5), and will extend them to industrial practice. The processes have been selected such that they all differ with respect to at least one important aspect like the type and design of the reactor, the chemistry involved, or the separation process used.

The book is supplemented by a brief survey of selected modern trends such as microreactors, and new solvents for catalysis like ionic liquids, which should convince the reader that chemical technology is not a “completed” discipline, but a

developing field with huge future challenges such as, for example, with regard to solving the energy problems for generations to come.

Several chapters are based on Bachelor and Master Courses the authors have taught students of chemistry and of chemical engineering at different Universities for many years (Aachen, Bayreuth, Erlangen, Karlsruhe). We have tried to consider the challenges specific to instructing chemists and engineers in chemical technology; for example, the problems both groups have in integrating the different disciplines: According to our experience, chemists tend to be too anxious with regard to chemical engineering methods (and most notably with the mathematics involved). In contrast, engineers often feel uncomfortable if chemical aspects have to be examined and come to the fore.

We hope that students both of (technical) chemistry and chemical engineering will appreciate this book, and that chemical engineers will acquire a sufficient feeling for chemistry and, likewise, chemists for the principles of chemical engineering.

To facilitate learning, the reader will find many instructive figures, examples, and rules of thumb for estimations of parameters and data of chemical media, many examples utilizing data from industrial processes, and in some cases partly the results of the authors' research. Complicated mathematical operations will only be used if mandatory. Numerous literature references are cited to guide the reader, where certain aspects are documented in more detail.

To simplify consultation of this textbook, several equations are accentuated by two types of exclamation marks:

- ! • In our opinion, chemical engineers and technical chemists should know these important equations by heart.
- ▽ ° These equations are useful and often used (without the need to memorize them in detail).

To illustrate certain aspects in more detail and to facilitate the use of the derived equations, several insertions marked either as "topics" or "examples" have been added.

At the end of each main chapter, a summary with "take-home messages" is given.

This book cannot, and is not intended to, compete with specialized textbooks, but hopefully gives a comprehensive and integrated outline of the fascinating subject of chemical technology and all its facets. It intends to be of value to all students of chemical engineering and technical chemistry, as well as to researchers and people from industry needing a concise book that covers all main aspects of industrial chemistry.

A book such as this could not have appeared without the sustainable help of a number of people. Only a few of them can be mentioned by name.

Our understanding of chemical technology owes much to having been fortunate in working and discussing the subject with Professor Wilhelm Keim, Professor Kurt Hedden, and Prof. Gerhard Emig, and we are grateful to all three of them.

We would like to thank our students, who followed our courses and/or did their PhD thesis in our institutions. They provided us with plenty of feedback.

We express special gratitude to Dr. Christoph Kern, Dr. Wolfgang Korth, and Professor Bastian Etzold for fruitful discussions, ideas and critiques, Michael Gebhardt and Dr. Stephan Aschauer for all the work and care invested in preparing numerous figures, Dr. Eva Öchsner and Dr. Sebastian Willmes for their assistance in preparing Chapters 6.9, 6.11.2, 6.12, 6.15, Prof. Udo Kragl for his assistance in preparing Chapter 2.3, and Markus Preißinger and Andreas Hofer for proofreading.

We would also like to thank the production team at Wiley-VCH, particularly Waltraud Wüst and Karin Sora.

Finally, we would like to express our appreciation to our wives and children, who witnessed the writing of this book in so many evening and weekend hours,

continuously encouraged us, and patiently allowed us to spend a considerable amount of time during the last eight years on the preparation of this book.

If you like this book, please recommend it to others. If you have suggestions for improvements or discover faults (inevitable despite of all our efforts) please send us an e-mail¹⁾.

Prost! (Latin: it may be useful)

Andreas Jess (jess@uni-bayreuth.de)

Peter Wasserscheid (Peter.Wasserscheid@crt.cbi.uni-erlangen.de)

Bayreuth/Erlangen, October 2012

¹⁾The corresponding author for the chapters 3, 4, 5.1, 5.4, 5.5, 6.1- 6.5, 6.7-6.9, 6.11.1, 6.13, and 6.17-6.19 is Andreas Jess; the responsible author for the chapters 2, 5.2, 5.3 and 6.6, 6.10, 6.11.2, 6.12, 6.14-6.16, and 6.20 is Peter Wasserscheid.

Notation

The International System of Units (abbreviated SI from the French *Système international d'unités*) developed in 1960 is the modern form of the metric system. This system is nowadays used in many countries both in everyday life and in science. Unfortunately, the popular use of SI units is still limited in important countries like the USA and the UK, although this may lead to mathematical mismatches with disastrous consequences (see Section “Critical units” at the end of this chapter).

As listed in Table 1, the SI defines seven base units, namely, meter, kilogram, second, ampere, kelvin, mole, and candela. All other units can be derived from these base units. Frequently used SI derived units are newton (N), the unit of force ($1\text{ N} = 1\text{ kg m s}^{-2}$), pascal (Pa), the unit of pressure ($1\text{ Pa} = 1\text{ N m}^{-2} = 1\text{ kg m}^{-1}\text{s}^{-2}$), joule (J), the unit of energy ($1\text{ J} = 1\text{ N m} = 1\text{ kg m}^2\text{s}^{-2}$), and watt (W), the unit of power ($1\text{ W} = 1\text{ J s}^{-1} = 1\text{ N m s}^{-1} = 1\text{ kg m}^2\text{s}^{-3}$).

Throughout this book, all equations (and the respective symbols listed in Table 2) are related to SI units. As a consequence and a general rule for this book: insert all variables in SI units into the equations and you will always get the correct result of a certain quantity in SI units. Nevertheless, the results of calculations are sometimes given in “handier” units, for example, with a prefix such as kJ or MJ instead of 1000 J or 1 000 000 J, or the well-known unit bar (= 10^5 Pa) is used for the pressure instead of Pa.

Simple abbreviations or subscripts such as A and B to denote the components as well as n and m as variables for reaction orders, or integration constants, are subsequently not listed.

Comments on the Symbols Used in this Book

Throughout this book, we have tried to use available standards for all our symbols. Hence, most of our symbols agree with common practice. Unfortunately, there is yet no standard set of symbols in chemical engineering. Most notably, there are still differences between European and American practice. For the reader's convenience, Table 3 summarizes some important deviations of our symbols from the practice of others.

Presentation of Measured Values and Confidence Limits

Presentation of Measured Values

In general, the result of a measurement is represented exactly by the measured (mean) value x , the measurement error Δx , and the unit $[x]$:

$$x = (x \pm \Delta x)[x]$$

For example the measured value of a length is correctly represented by:

$$L = (5.81 \pm 0.005)\text{ m.}$$

Table 1 The seven base units of the SI.

Name	Symbol	Quantity	Definition
Meter	m	Length	Length traveled by light in vacuum during the time interval of 1/299 792 458 s.
Kilogram	kg	Mass	Mass of the <i>prototype kilogram</i> , a Pt-Ir cylinder kept at the Bureau International des Poids et Mesures in Paris. The kilogram is the only base unit with a prefix and is still not defined by a fundamental physical property, but there are ongoing efforts to introduce a new definition based on such properties.
Second	s	Time	Duration of 9 192 631 770 periods of the radiation of the transition between two hyperfine levels of the ground state of the caesium-133 atom at a temperature of 0 K.
Ampere	A	Electrical current	Constant current which if maintained in two straight parallel conductors of infinite length and negligible cross-section, placed one meter apart in vacuum, would produce a force between the conductors of 2×10^{-7} newton per meter length.
Kelvin	K	Thermodynamic temperature	The thermodynamic (or absolute) temperature is the fraction 1/273.16 of the absolute triple point temperature of water.
Mole	mol	Amount of substance	Quantity that contains the same number of entities (atoms, molecules, etc.) as there are atoms in 12 g of carbon-12. This number – Avogadro's number N_A – is about 6.022×10^{23} .
Candela	Cd	Luminous intensity	Luminous intensity in a given direction of a source that emits monochromatic radiation with a wavelength of 555 nm and a radiant intensity in that direction of 1/683 watt per steradian.

Table 2 Symbols and abbreviations used in this book.

Symbol	Meaning	Unit
Latin letters		
a	Activity	—
α	Thermal diffusivity	$\text{m}^2 \text{s}^{-1}$
a_{cat}	(Remaining) activity of catalyst	—
A	Van der Waals constant	$\text{Pa m}^6 \text{mol}^{-2}$
A	Thermal diffusivity, conductivity of temperature	$\text{m}^2 \text{s}^{-1}$
A	Area	m^2
A_{ads}	Cross sectional area of adsorption bed	m^2
A_{BET}	Internal surface area per mass of catalyst or solid measured by BET analysis	$\text{m}^2 \text{kg}^{-1}$
A_e	Electrode surface area	m^2
A_h	Area for heat transfer	m^2
A_i	Interfacial area	m^2
$A_{\text{int,V}}$	Internal surface area per volume of solid (catalyst)	$\text{m}^2 \text{kg}^{-1}$
$A_{i,m}$	Specific interfacial area per mass of catalyst	$\text{m}^2 \text{kg}^{-1}$
$A_{i,V}$	Specific interfacial area per volume of reactor	$\text{m}^2 \text{m}^{-3}$
$A_{m,\text{ex}}$	External surface area per mass of catalyst or solid	$\text{m}^2 \text{kg}^{-1}$
A_p	External surface area of particle	m^2
$A_{\text{pore,ex}}$	Cross-sectional area of pore	m^2
A_{pore}	Internal (mantle) area of pore	m^2
A_R	Cross sectional area of reactor	m^2

A_t	Cross sectional area of tube	m^2
A_V	External surface area per volume of catalyst or solid	$\text{m}^2 \text{ m}^{-3}$
$A_{V,s}$	Surface area per volume of solid	$\text{m}^2 \text{ m}^{-3}$
A_{wall}	Area of wall for heating or cooling	m^2
B	Van der Waals constant	$\text{m}^3 \text{ mol}^{-1}$
C	Production capacity	kg s^{-1}
C_{BET}	BET constant (in the equation for multilayer adsorption)	—
$C_{\text{calorimeter}}$	Heat capacity of calorimeter	J K^{-1}
$C_{\text{Sutherland}}$	Sutherland constant	K
c	Heat capacity of a fluid or solid with negligible small thermal expansivity and compressibility, that is, $c_p = c_v$	$\text{J mol}^{-1} \text{ K}^{-1}$ or $\text{J kg}^{-1} \text{ K}^{-1}$
c	Concentration	mol m^{-3}
\bar{c}	Mean concentration (in a porous particle)	mol m^{-3}
c_s	Concentration at the (external) surface	mol m^{-3}
c_{cat}	Concentration of catalyst	kg m^{-3} or mol m^{-3}
c_p	Molar heat capacity of fluid at constant pressure	$\text{J mol}^{-1} \text{ K}^{-1}$
$c_{p,m}$	Heat capacity related to mass	$\text{J kg}^{-1} \text{ K}^{-1}$
$c_{p,m}$	Heat capacity of fluid related to mass at constant pressure	$\text{J kg}^{-1} \text{ K}^{-1}$
c_v	Molar heat capacity of fluid at constant volume	$\text{J mol}^{-1} \text{ K}^{-1}$
c_s	Concentration at the surface	mol m^{-3}
c_s	Heat capacity of solid	$\text{J kg}^{-1} \text{ K}^{-1}$
d, D	Diameter, distance	m
d_h	Hydraulic diameter	m
D	Diffusion or dispersion coefficient (always diffusion coefficient if no specifying subscript or just a subscript denoting a component is used)	$\text{m}^2 \text{ s}^{-1}$
D_{ax}	Axial dispersion coefficient	$\text{m}^2 \text{ s}^{-1}$
D_{eff}	Effective diffusion coefficient (in a porous solid)	$\text{m}^2 \text{ s}^{-1}$
D_{Knu}	Knudsen diffusion coefficient	$\text{m}^2 \text{ s}^{-1}$
D_{mol}	Molecular diffusion coefficient	$\text{m}^2 \text{ s}^{-1}$
D_{pore}	Diffusion coefficient in a pore	$\text{m}^2 \text{ s}^{-1}$
D_{rad}	Radial dispersion coefficient	$\text{m}^2 \text{ s}^{-1}$
E	Electromotive force, cell voltage, electrode potential	V
E^0	Standard value of electrode potential at 1.013 bar	V
E_{th}^0	Standard value of thermoneutral enthalpy voltage (at 1.013 bar)	V
E	E-function of residence time distribution	s^{-1}
E	Enhancement factor	s^{-1}
E_A	Activation energy	J mol^{-1}
$E_{\text{A,app}}$	Apparent activation energy	J mol^{-1}
E_{kin}	Kinetic energy	J mol^{-1}
E_θ	Dimensionless E-function of residence time distribution	—
F	Friction factor	—
F	Fugacity	—
F	Faraday constant (96 485)	A s mol^{-1}
F	F-function of residence time distribution	—
F_θ	Dimensionless F-function of residence time distribution	—
G	Acceleration of gravity	m s^{-2}
G	Gibbs function	J mol^{-1}
$GHSV$	Gas hourly space velocity	$\text{m}^{-3} \text{ h m}^{-3}$

(continued)

Table 2 (Continued)

Symbol	Meaning	Unit
Greek letters		
g	Gravitational acceleration (9.81)	m s^{-2}
$HETP$	Height equivalent of one theoretical plate	m^{-1}
$HETS$	Height equivalent of one theoretical stage	m^{-1}
H	Enthalpy	J mol^{-1}
H_x	Henry coefficient related to the molar content	$\text{Pa mol}_{\text{liq}} \text{mol}_{\text{gas}}^{-1}$
H_c	Henry coefficient related to the concentration	$\text{Pa m}_{\text{liq}}^3 \text{mol}_{\text{gas}}^{-1}$
HTZ	Height of transfer zone	m
HR	Heating rate	K s^{-1}
i	Current density	A m^{-2}
I	Current	A
I	Investment costs	$\$\text{ or } \epsilon$
k	Boltzmann constant (1.38×10^{-23})	J K^{-1}
k	Reaction rate constant (depends on reaction order)	for 1st order: $\text{mol m}^{-3} \text{s}^{-1}$
k_{ads}	Rate constant of adsorption	$\text{s}^{-1} \text{Pa}^{-1}$
k_A	Reaction rate constant related to external surface area of solid or catalyst (depends on reaction order)	for 1st order: $\text{m}^3 \text{m}^{-2} \text{s}^{-1}$
k_{cool}	Reaction rate constant for $T = T_{\text{cool}}$	s^{-1}
k_{crit}	Reaction rate constant for $T = T_{\text{crit}}$	s^{-1}
k_{des}	Rate constant of desorption	s^{-1}
$k_{\text{M,mol}}$	Permeability of membrane related to molar flux	mol s kg^{-1}
$k_{\text{M,V}}$	Permeability of membrane related to volumetric flux	$\text{m}^3 \text{s kg}^{-1}$
k_m	Reaction rate constant related to mass of catalyst or solid (depends on reaction order)	for 1st order: $\text{m}^3 \text{kg}^{-1} \text{s}^{-1}$
k_s	Reaction rate constant related to overall (mostly internal) surface area of a catalyst	$\text{mol m}^{-2} \text{s}^{-1}$
k_s	Roughness equivalent to a grain of sand	m
k_V	Reaction rate constant related to volume of reaction	$\text{m}^3 \text{m}^{-3} \text{s}^{-1}$
k_0	Pre-exponential factor (depends on reaction order)	for first order: $\text{mol m}^{-3} \text{s}^{-1}$
K_1	Equilibrium constant	$\text{mol s}^2 \text{kg}^{-1} \text{m}^{-2}$
K_2	Equilibrium constant	—
K_3	Equilibrium constant	—
K_p	Equilibrium constant with regard to partial pressures	—
K_{ads}	Equilibrium constant of adsorption	Pa^{-1}
K_c	Equilibrium constant with regard to molar concentrations	—
K_{ext}	Distribution ratio or partition coefficient of extraction related to molar content	$\text{mol mol}^{-1}/(\text{mol mol}^{-1})$
$K_{\text{ext,m}}$	Distribution ratio or partition coefficient of extraction related to mass content	$\text{kg kg}^{-1}/(\text{kg kg}^{-1})$
K_f	Equilibrium constant with regard to fugacities	—
K_{GL}	overall gas-liquid mass transfer coefficient	$\text{m}^{-3} \text{m}^{-3} \text{s}^{-1}$
K_M	Michaelis–Menten constant	mol m^{-3}
K_p	Equilibrium constant with regard to partial pressures	—
K_R	Universal equilibrium constant (also denoted reaction quotient)	—
K_x	Equilibrium constant of a liquid phase reaction with regard to molar fractions	—
K_y	Equilibrium constant of a gas phase reaction with regard to molar fractions	—
K_ϕ	Equilibrium term considering the fugacity coefficients	—

K_γ	Equilibrium term considering the activity coefficients	—
L_p	Length of perimeter	m
L	Length	m
$LHSV$	Liquid hourly space velocity	$\text{m}^3 \text{ h m}^{-3}$
LUB	Length of unused bed	m
M	Mass	kg
\dot{m}	Mass flow	kg s^{-1}
m_{ads}	Mass of adsorbent	kg
M	Molar mass	kg mol^{-1}
N	Rotational frequency	s^{-1}
N	Number of moles	mol
n_{stirrer}	Stirrer speed	s^{-1}
N	Number of moles	mol
n_e	Number of electrons	mol
n_{max}	Maximum number of layers	—
\dot{n}	Molar flux	mol s^{-1}
N	Number of tanks of a cascade	—
N	Number of molecules	—
N_{act}	Number of active sites (relative to the initial number)	—
N_A	Avogadro or Loschmidt number, 6.022×10^{23}	mol^{-1}
\dot{p}	Flux of momentum	kg m s^{-2}
P	Pressure, total pressure	Pa
$P_{\text{projection, area}}$	Projection area	m^2
p^*	Saturation vapor pressure	Pa
p_0	Standard pressure ($1.01\ 325\ \text{bar} = 1\ \text{atm}$)	Pa
p_{sat}	Saturation vapor pressure (of a pure liquid)	Pa
p_{vap}	Vapor pressure (of a pure liquid)	Pa
P	Power	W
q	Energy consumption	J kg^{-1}
\dot{q}	Heat flux per unit of volume	$\text{J m}^{-3} \text{ s}^{-1}$
\dot{q}_{HP}	Heat production per unit mass	$\text{J kg}^{-1} \text{ s}^{-1}$
\dot{q}_{HR}	Heat removal per unit mass	$\text{J kg}^{-1} \text{ s}^{-1}$
Q	Amount of heat	J
\dot{Q}	Heat flux	W, J s^{-1}
Q_R	Reaction quotient	—
R	Radius	M
R	(Equivalent) reaction rate	$\text{mol m}^{-3} \text{ s}^{-1}$
r_A	Reaction rate per unit (internal) surface area	$\text{mol m}^{-2} \text{ s}^{-1}$
r_c	Radius of the unreacted core	M
r_m	Reaction rate per unit of mass of catalyst or solid	$\text{mol m}^{-3} \text{ s}^{-1}$
r_v	Reaction rate per unit of volume of reactor or catalyst	$\text{mol m}^{-3} \text{ s}^{-1}$
R	Ideal gas law constant (8.314)	$\text{J mol}^{-1} \text{ K}^{-1}$
R	Dimensionless radial coordinate	—
R	Reflux ratio	—
R	Reaction rate	$\text{mol m}^{-3} \text{ s}^{-1}$
S	Differential (instantaneous) selectivity	$\text{J mol}^{-1} \text{ K}^{-1}$
S	Entropy	—
S	(Integral) selectivity	—
STY	Space–time yield	$\text{mol m}^{-3} \text{ s}^{-1}$
SV	Space velocity	s^{-1}
t	(Reaction) time	s
t_b	Breakthrough time	s
t_{sat}	Saturation time	s
t_{st}	Stoichiometric time	s
T	Temperature	$^{\circ}\text{C}, \text{K}$
T_g	Gas temperature (bulk phase)	$^{\circ}\text{C}, \text{K}$
T_h	Cooling/heating temperature	$^{\circ}\text{C}, \text{K}$
T_s	Surface temperature	$^{\circ}\text{C}, \text{K}$
TOF	Turn over frequency	$\text{mol mol}^{-1} \text{ s}^{-1}$

(continued)

Table 2 (Continued)

Symbol	Meaning	Unit
Latin letters		
TON	Turn over number	mol mol^{-1}
\bar{u}	Mean velocity (of atoms and molecules)	m s^{-1}
U	Velocity	m s^{-1}
u_s	Superficial fluid velocity (related to empty reactor)	m s^{-1}
U	(Cell) voltage	V
U	Internal energy	J or J mol^{-1}
U_h	Overall heat transfer coefficient, thermal transmittance	$\text{W m}^{-2} \text{K}^{-1}$
v_{mol}	Molar volume	$\text{m}^3 \text{mol}^{-1}$
V	Volume	m^3
\dot{V}	Volumetric flow rate	$\text{m}^3 \text{s}^{-1}$
V_m	Specific volume of particle (related to mass)	$\text{m}^3 \text{kg}^{-1}$
w	Weight fraction	kg kg^{-1}
W	Weight	Kg
W	Work	J
WHSV	Weight hourly space velocity	kg h m^{-3}
X	Coordinate	M
X	Liquid volume fraction, molar content	mol mol^{-1}
X	Loading of a solid or liquid	kg kg^{-1} or mol mol^{-1}
X	Dimensionless length	—
X	Conversion	—
γ	Gas volume fraction, molar content	mol mol^{-1}
Y	Yield	—
Y	Loading of a gas	mol mol^{-1}
z	Electron transfer number	—
Z	Real gas factor, compressibility factor	—
Z	Coordinate	M
Z	Dimensionless axial coordinate	—
Greek letters		
α	Heat transfer coefficient	$\text{W m}^{-2} \text{K}^{-1}$
α_{Bu}	Bunsen absorption coefficient	$\text{m}^3 \text{Pa}^{-1}$
α	Relative volatility	—
β	Mass transfer coefficient	m s^{-1}
β_{LS}	Liquid–solid mass transfer coefficient	m s^{-1}
γ	Activity coefficient	—
γ	Angle	—
δ	Thickness of boundary layer, film thickness	M
$\delta_{0.99}$	Film thickness defined as the distance from a surface where $\Delta T = 0.99 \Delta T_{\max}$ (or $\Delta c = 0.99 \Delta c_{\max}$)	M
ΔG	(Absolute) change of Gibbs enthalpy	J
$\Delta_F G$	Gibbs enthalpy of formation	J mol^{-1}
$\Delta_R G$	Gibbs enthalpy of reaction	J mol^{-1}
$\Delta_F H$	Enthalpy of formation	J mol^{-1}
$\Delta_{\text{ads}} H$	Enthalpy of adsorption	J mol^{-1}
$\Delta_R H$	(Molar) reaction enthalpy (heat of reaction for constant pressure) according to the stoichiometric equation	J mol^{-1}
Δp_t	Pressure drop in an empty tube	Pa
Δp_b	Pressure drop in tube filled with particles (fixed bed etc.)	Pa
ΔS_{sys}	Change of (absolute) entropy of system	J K^{-1}
ΔS_{surr}	Change of (absolute) entropy of surrounding	J K^{-1}
$\Delta S_{\text{overall}}$	Overall change of (absolute) entropy	J K^{-1}
$\Delta_R S$	(Molar) reaction entropy	$\text{J mol}^{-1} \text{K}^{-1}$
ΔU	Change of (absolute) internal energy	J

$\Delta_R U$	Change of molar internal energy by reaction	J mol^{-1}
ΔS	Change of entropy	$\text{J mol}^{-1} \text{K}^{-1}$
ΔT_{ad}	Adiabatic temperature increase	$^{\circ}\text{C}, \text{K}$
$\Delta T_{\text{arith,mean}}$	Arithmetic mean temperature difference	$^{\circ}\text{C}, \text{K}$
$\Delta T_{\text{ln,mean}}$	Logarithmic mean temperature difference	$^{\circ}\text{C}, \text{K}$
ΔT_{max}	Maximum adiabatic temperature increase	$^{\circ}\text{C}, \text{K}$
$\Delta_{\text{ads}} H$	(Molar) enthalpy of adsorption	J mol^{-1}
$\Delta_{\text{vap}} H$	(Molar) enthalpy of vaporization	J mol^{-1}
$\Delta_{\text{vap}} S$	(Molar) entropy of vaporization	$\text{J mol}^{-1} \text{K}^{-1}$
$\Delta\varphi$	Electrochemical potential	V
$\Delta\varphi^0$	Electrochemical standard potential at 1.013 bar	V
ε	Porosity (voidage of packed bed)	—
ε_V	Fractional change of reaction volume	—
ε	Fraction of liquid phase (gas-liquid system)	—
ε_p	Porosity of particle	—
ε	Surface emissivity	—
ζ	Factor considering the particle shape	—
η	Dynamic viscosity	Pa s^{-1}
η_{current}	Current efficiency, yield of charge	—
η_{ex}	Effectiveness factor related to external diffusion resistance	—
η_{overall}	Overall particle effectiveness factor	—
η_{pore}	Pore effectiveness factor	—
$\eta_{\text{pore,0}}$	Initial pore effectiveness factor	—
θ	Dimensionless temperature	—
θ	Surface coverage (relative to monolayer capacity)	—
λ	Wavelength	M
λ	Thermal conductivity	$\text{W m}^{-1} \text{K}^{-1}$
λ	Lambda value	—
λ_p	Thermal conductivity of particle	$\text{W m}^{-1} \text{K}^{-1}$
λ_{ax}	Axial dispersion coefficient of heat (effective axial heat conductivity in a packed bed)	$\text{W m}^{-1} \text{K}^{-1}$
λ_p	Effective thermal conductivity of particle	$\text{W m}^{-1} \text{K}^{-1}$
λ_{rad}	Radial dispersion coefficient of heat (effective radial heat conductivity in a packed bed)	$\text{W m}^{-1} \text{K}^{-1}$
λ_s	Thermal conductivity of (porous) solid	$\text{W m}^{-1} \text{K}^{-1}$
Λ	Mean free path	M
μ	Chemical potential	$\text{Pa s, kg m}^{-1} \text{s}^{-1}$
μ_{JT}	Joule–Thomson coefficient	K Pa^{-1}
ν	Stoichiometric coefficient (reactants < 0, products > 0)	—
ν	Frequency	$\text{Hz (s}^{-1}\text{)}$
ν	Kinematic viscosity	$\text{m}^2 \text{s}^{-1}$
ξ	Dimensionless friction number	—
ρ	Density	kg m^{-3}
ρ_b	Bulk density (of packed bed)	kg m^{-3}
ρ_c	Density (concentration) of reactant in the core	kg m^{-3}
ρ_g	Density of gas phase	kg m^{-3}
ρ_{mol}	Molar fluid density	mol m^{-3}
ρ_p	Density of particle	kg m^{-3}
σ	Surface tension	N m^{-2}
σ	Collision cross section	m^2
σ	Stefan–Boltzmann constant (5.67×10^{-8})	$\text{W m}^{-2} \text{K}^{-4}$
τ	(Mean) residence time (related to empty reactor)	s
τ_D	Characteristic time of diffusion	s
τ_m	Modified residence time (mean residence time related to mass of catalyst or solid reactant)	kg s m^{-3}
τ_M	Tortuosity of a membrane	—

(continued)

Table 2 (Continued)

Symbol	Meaning	Unit
Greek letters		
τ_p	Tortuosity of particle	—
τ_R	Characteristic reaction time	s
φ	Fugacity coefficient	—
φ_{12}	Specific dissipation of energy	$m^2 s^{-2}$
Φ	Ratio of two Thiele moduli	—
ω	Acentric factor	—
χ	Association parameter	—
χ	Heat capacity ratio (c_p/c_v)	—
Subscripts		
∞	Infinity	
0	Related to initial condition	
A	Related to activity	
ad	Adiabatic	
ads	Adsorption, adsorbent	
app	Apparent	
approx	Approximated	
ax	Axial	
b, bed	Related to fixed or packed bed	
b	Bulk phase	
b	Bottom of separation column	
B	Breakthrough	
boil	Boiling	
BET	Method of Brunauer, Emmett and Teller	
bulk	Bulk phase of fluid	
C	Core	
cap	Capillary	
cat	Catalyst	
con	Convective	
charac	Characteristic	
comp	Compression, compressor	
cool	Cooling	
cp	Condensation point	
crit	Critical (pressure or temperature)	
cyl	Cylinder	
c	Cylindrical vessel	
CSTR	Continuously stirred tank reactor	
d	Distillate	
deact	Deactivation	
dis	Discharge	
eff	Effective	
eq	Equivalent	
ex	External	
ext	Extraction	
f	Fluid	
fin	Final	
g	Gas phase	
GL	Gas-liquid	
h	Heat, hydraulic	
HP	Heat production	
HR	Heat removal	
HW	Hougen-Watson (type of kinetic equation)	
i	Initial	
i	Interphase	
i	Component i	
in	Inlet of reactor	
int	Internal	
kin	Kinetic	
Knu	Knudsen (diffusion)	

L	Liquid, liquid phase
lam	Laminar (flow)
liq	Liquid
LH	Langmuir–Hinshelwood (type of kinetic equation)
LS	Liquid–solid
M	Related to mass, membrane
max	Maximum
melt	Melting
min	Minimum
mol	Molecular
mon	Monolayer
n	Related to reaction order $n \neq 1$
ori	Orifice
out	Outlet of reactor
P	Particle
P	Perimeter
pore	Pore of solid or catalyst
proj	Projection screen
PFR	Plug flow reactor
R	Reaction
R	Reactor
rad	Radial
red	Reduced dimensionless variable (related to critical p or T)
ref	Reference
s	Solid
s	Surface
sat	Saturation
st	Stoichiometric
surr	Surrounding
sys	System
t	Tube
t	Total
turb	Turbulent (flow)
V	Related to volume
vap	Vaporization
W	Wall
x	Related to the coordinate x

Superscripts

0	Standard conditions (1.013 bar, 273 K)
*	Saturation (vapor pressure), equilibrium

Dimensionless numbers**Definition and comments**

Bi_h	Biot number for heat transfer with L as ratio of volume to external surface)	$\frac{a L}{\lambda}$
Bi_m	Biot number for mass transfer with L ratio of volume to external surface	$\frac{\beta L}{D_{\text{eff}}}$
Bo	Bodenstein number	$\frac{u L}{D_{\text{ax}}}$ (for a packed bed use $u = u_s/\varepsilon$)
Da	Damkoehler number	Depends on reaction order and reactor type, for example, for batch reactor and first order: $Da = kt$
Fo	Fourier number	$\frac{at}{L_{\text{charac}}^2} = \frac{\lambda}{c_p \rho} \frac{t}{L_{\text{charac}}^2}$
Gr	Grashoff number	$\frac{g d_p^3 \Pr \rho_s - \rho_b}{\nu^3} \frac{\rho_s}{\rho_s}$
Ha	Hatta number	$\frac{\sqrt{k_{A,V} D_{A,l}}}{\beta_{A,l}}$
Hi	Hinterland ratio	$Hi = \frac{V_1}{V_{\delta,l}} = \frac{\beta_{A,l}}{A_{i,V} D_{A,l}}$

(continued)

Table 2 (Continued)

Symbol	Meaning	Unit
Dimensionless numbers		Definition and comments
N_{ad}	Dimensionless number accounting for adiabatic temperature rise	$\frac{\Delta T_{ad} E_A}{R T_{cool}^2}$
Ne	Newton number of a stirrer (often termed power number)	$\frac{P}{\rho n_{stirrer}^3 d_{stirrer}^5}$
N_C	Dimensionless number of cooling capacity	$\frac{U_h \frac{A_h}{V_R} \Delta T_{ad}}{k_{cool} (-\Delta_R H) c_{A,o}}$
Nu	Dimensionless number of heat transfer	$\frac{ad_{charc}}{\lambda}$
$Pe_{h,ax}$	Peclet number for axial dispersion of heat	$\frac{u_s c_p \rho_{mol} d_p}{\lambda_{ax}}$
$Pe_{h,rad}$	Peclet number for radial dispersion of heat	$\frac{u_s c_p \rho_{mol} d_p}{\lambda_{rad}}$
$Pe_{m,ax}$	Peclet number for axial dispersion of mass	$\frac{u_s d_p}{\varepsilon D_{ax}}$
$Pe_{m,rad}$	Peclet number for radial dispersion of mass	$\frac{u_s d_p}{\varepsilon D_{rad}}$
Pr	Prandtl number	$\frac{\rho c_p \nu}{\lambda}$
Re	Reynolds number (related to diameter of tube)	$\frac{ud_t}{\nu}$ (for a packed bed u: superficial velocity)
Re_p	Reynolds number (related to particle diameter)	$\frac{ud_p}{\nu}$ (for a packed bed u: superficial velocity)
$Re_{p,bed}$	Reynolds number (related to particle diameter of particles in a fixed bed)	$\frac{ud_p}{\varepsilon \nu}$ (u: superficial velocity, ε: porosity of bed)
$Re_{stirrer}$	Reynolds number of stirrer	$\frac{n_{stirrer} d_{stirrer}^2}{\nu}$
Sc	Schmidt number	$\frac{\nu}{D}$
Sh	Sherwood number	$\frac{\beta L_{charac}}{D}$ (L_{charac} : characteristic length, e.g., d_p)
β_{ex}	Prater number for external diffusion	$\frac{D_{A,g} (-\Delta_R H) c_{A,g}}{\lambda_g T_g}$ (reactant A)
β_{int}	Prater number for internal diffusion	$\frac{D_{A,eff} (-\Delta_R H) c_{A,s}}{\lambda_p T_s}$ (reactant A)
γ_{ex}	Arrhenius number for external diffusion	$\frac{E_A}{RT_g}$
γ_{int}	Arrhenius number for internal diffusion	$\frac{E_A}{RT_s}$
ϕ	Thiele modulus (first order reaction)	$\frac{V_p}{A_{p,ex}} \sqrt{\frac{k_m \rho_p}{D_{i,eff}}}$
ϕ_n	Thiele modulus (n^{th} order reaction)	$\frac{V_p}{A_{p,ex}} \sqrt{\left(\frac{n+1}{2}\right) \frac{k_m \rho_p c_{i,s}^{n-1}}{D_{i,eff}}}$
ψ	Weisz modulus (first order reaction)	$\left(\frac{V_p}{A_{p,ex}}\right) \left(\frac{n+1}{2}\right) \frac{k_{m,eff} \rho_p c_{i,s}^{n-1}}{D_{i,eff}}$
ψ_n	Weisz modulus (n^{th} order reaction)	$\left(\frac{V_p}{A_{p,ex}}\right) \left(\frac{n+1}{2}\right) \frac{k_{m,eff} \rho_p c_{i,s}^{n-1}}{D_{i,eff}}$

Abbreviations

AAS	Atomic absorption spectroscopy
AES	Auger electron spectroscopy
AFM	Atomic force microscopy
ALI	Adult literacy index
a.u.	Arbitrary units
BET	Analysis of (internal) surface area according to Brunauer, Emmett, and Teller (Section 3.3.5)
CGER	Combined gross enrollment index
CSTR	Continuously stirred tank reactor
CT	Computed tomography
DLS	Dynamic light scattering
DTA	Differential thermal analysis
EDX	Energy dispersive X-ray spectrometer
EI	Education index
EO	Ethylene oxide
ESR	Electron spin resonance spectroscopy
ETM	Electron tunneling spectroscopy
EXAFS	Extended X-ray absorption fine structure
GER	Gross enrollment index
GNP	Gross national product
GDP	Gross domestic product
GHSV	Gas hourly space velocity
HDI	Human development index
HTZ	Height of transfer zone
IR	Infrared spectroscopy
ISS	Ion scattering spectroscopy
LEI	Life expectancy index
LHSV	Liquid hourly space velocity
LPG	Liquefied petroleum gases (mainly butane and propane)
LUB	Length of unused bed
Mtoe	Million tonnes of oil equivalent
MTZ	Mass transfer zone
NMP	N-Methylpyrrolidone
NMR	Nuclear magnetic resonance
NTP	Normal temperature and pressure (20 °C, 1.013 bar)
Ox	Oxidant, oxidizing agent
pc	Per capita
PFG	Pulsed field gradient (NMR)
PFR	Plug-flow reactor
PO	Propylene oxide
PPP	Purchasing power parity
QSDFT	Quenched solid density functional theory
Red	Reducant, reducing agent
RTD	Residence time distribution
rts	Rate depending step
SATP	Standard ambient temperature and pressure (25 °C, 1.013 bar)
SEM	Scanning electron microscopy
SIMS	Secondary ion spectroscopy
STM	Scanning tunneling microscopy
STP	Standard temperature and pressure (0 °C, 1.013 bar)
STY	Space-time yield
SWB	Subjective well-being index
TEM	Transmission electron microscopy
TGA	Thermal gravimetric analysis
toe	Tonnes of oil equivalent
TOF	Turn over frequency
TON	Turn over number
TPD	Temperature programmed desorption
TPO	Temperature programmed oxidation
TPR	Temperature programmed reduction
WHSV	Weight hourly space velocity

(continued)

Table 2 (Continued)

Symbol	Meaning	Unit
Abbreviations		
UPS	Ultraviolet photoelectron spectroscopy	
XPS	X-ray photoelectron spectroscopy	
XRD	X-ray diffraction	
XRF	X-ray fluorescence	
Miscellaneous		
\bar{x}	mean value of quantity x	

Nevertheless, in most cases, the measured value is only given with the respective unit. For the above given example, a value of $L = 5.81 \text{ m}$ would indicate that the true value is somewhere between 5.805 and 5.815 m. Thus a rough indication and crude way to represent the error is also provided by the number of significant figures (also called significant digits). Rounding to significant digits is a more general technique than rounding to n decimal places, since it handles numbers of different scales in a uniform way.

Table 3 Meaning and definition of symbols.

Meaning (name in this book)	Symbol and definition used in this book	Other symbols and definitions (most notably in American practice)
Thermal diffusivity	$a = \lambda / (\rho c_p)$	α
Pre-exponential factor	k_0	A, k_∞
Molar flow rate	\dot{n}	F
Volumetric flow rate	\dot{V}	V
Liquid volume content	x	f
Gas volume content	y	f
Heat transfer coefficient	α	h
Mass transfer coefficient	β	k
Thermal conductivity	λ	k
Peclet number for axial dispersion of heat	$Pe_{h,ax} = \frac{u_s c_p \rho_{\text{mol}} d_p}{\lambda_{\text{ax}}}$	No name
Peclet number for radial dispersion of heat	$Pe_{h,rad} = \frac{u_s c_p \rho_{\text{mol}} d_p}{\lambda_{\text{rad}}}$	No name
No name	$Re \times Pr$	Peclet number $Pe = Re \times Pr = ud/a$ (a = thermal diffusivity)
Peclet number for axial dispersion of mass	$Pe_{m,ax} = \frac{u_s d_p}{\varepsilon D_{\text{ax}}}$ with $D_{\text{ax}} = \text{axial dispersion coefficient}$	No name
Peclet number for radial dispersion of mass	$Pe_{m,rad} = \frac{u_s d_p}{\varepsilon D_{\text{rad}}}$ with $D_{\text{rad}} = \text{radial dispersion coefficient}$	No name
Bodenstein number	$Bo (= u L / D_{\text{ax}})$ with $D_{\text{ax}} = \text{axial dispersion coefficient}$	Reciprocal of vessel Dispersion number
No name	$Re \times Sc$	Bodenstein number $Bo = u L / D$ with $D = \text{molecular diffusion coefficient}$

For example, if rounding to 3 significant figures:

- 19.341 becomes 19.3
- 0.034 567 8 becomes 0.034 6
- 34 560 becomes 34 600.

One issue with rounding to significant digits is that the value of n is not clear if the last digit(s) is (are) zero. For example in the final example above, n could be anything from 3 to 5, that is, the value may lie in between 34 500 and 34 700.

The number of significant digits is particularly important with regard to *spurious accuracy*, as revealed by the following example. In September 2011, the Kenyan long-distance runner Patrick Makau broke the marathon world record in 2:03:38 h (7418s). If we use a calculator, which is usually equipped with ten decimal places, and divide the distance (42,195 m) by the time, we get an average speed of 5.688 190 887 m s⁻¹ which is equivalent to 5 688 190 887 nm s⁻¹. Quite evidently, the speed of the runner is not known with an accuracy of nm s⁻¹, and so it is probably more sensible to report it only to four significant digits (5.688 m s⁻¹) as the time is also only measured to four significant digits (s).

Experimental results are also frequently evaluated by a pocket calculator or a computer, for example, the electrical resistance of a wire may be derived by dividing the adjusted voltage by the measured current. As a general rough rule as to how to present experimental results we may state that the last but one digit should be really accurate and be secured by the experimental method used. In other words, you are not accountable for the last but for the last but one digit.

A general rule of how to handle additions, subtractions, multiplications, and divisions of experimental values is that the number of significant digits of the result of such operations is never greater than the smallest value of all significant figures. For example, the product of 1.142 and 2.345 678 should be given as 2.679 (and not as 2.6 787 642 764 ...), or the sum of 1.142 and 2.345 678 should be given as 3.488 (and not as 3.487 678).

Mean Value and Confidence Limits

Usually, we carry out experiments where we measure the value of a certain quantity n times. Now we want to know the *mean value* μ and the *confidence interval*. The confidence limits for μ are given by:

$$\mu = \bar{x} \pm t \frac{s}{\sqrt{n}} \quad \text{with} \quad s = \sqrt{\frac{\sum x^2}{n-1} - \frac{(\sum x)^2}{n(n-1)}} \quad \text{and} \quad \bar{x} = \frac{\sum x}{n}$$

The factor t depends on the *significance level* and on the number of measurements (Table 4). For the significance level, values of 5% or 1% are typically chosen, which

Table 4 The “ t ” table.

Number of measurements n	t values for confidence coefficient		
	90%	95%	99%
2	6.314	12.71	63.66
3	2.920	4.303	9.925
4	2.353	3.182	5.841
5	2.132	2.776	4.604
6	2.015	2.571	4.032
7	1.943	2.447	3.707
8	1.895	2.365	3.499
9	1.860	2.306	3.355
10	1.833	2.262	3.250
100	1.660	1.980	2.626
∞	1.645	1.960	2.576

Table 5 Example of how to determine the mean value and confidence interval.

Number of measurement	Measured reaction rates x (e.g., in $\text{mol m}^{-2} \text{s}^{-1}$)	x^2
1	2.05	4.20
2	2.33	5.43
3	1.98	3.92
4	2.05	4.20
5	2.29	5.24
6	2.10	4.41
7	1.97	3.88
8	1.96	3.84
9	2.21	4.88
10	1.94	3.76
$n = 10$	$\bar{x} = 2.088$	$\sum x^2 = 43.78$
	$(\sum x)^2 = 436.0$	

is equivalent to a *confidence coefficient* of 95% and 99%, respectively. In most cases, the confidence coefficient is set to 95%.

Example: The reaction rate (at constant reaction conditions, i.e., constant concentration, temperature, etc.) is measured 10 times ($n = 10$, Table 5). The confidence coefficient is set to 95%, and the t value is then 2.262 (see Table 4 above). Thus we get:

$$\mu = \bar{x} \pm 2.262 \frac{s}{\sqrt{n}}$$

Here we obtain for the standard deviation:

$$s = \sqrt{\frac{43.78}{9} - \frac{436}{90}} = 0.141$$

and thus we, finally, have:

$$\mu = 2.088 \pm 2.262 \frac{0.141}{\sqrt{10}} = 2.088 \pm 0.101.$$

In other words, at 95% confidence, we have a true mean value of the reaction rate lying between the 2.189 and 1.987.

Problem of Outlier

It sometimes occurs in a series of $n + 1$ measurements that one value (x_{n+1}) lies far from the other values. A criterion as to whether this so-called outlier can be omitted is:

$$|x_{n+1} - \bar{x}_n| > ks$$

The value of k depends on the number of measurements n . For $n > 10$, $k = 4$, and for lower values of n , k increases (e.g., for $n = 4$, k is about 7).

For the given example (with $k = 4$ and $s = 0.141$) we get:

$$|x_{n+1} - \bar{x}_n| > 0.564$$

and thus if the value of the rate of the outlier would be more than 2.65 (= 2.088 + 0.564) or less than 1.54 (= 2.088 - 0.564) it can be omitted.

Critical Units

Conversions from one unit to another are very important. Two examples may illustrate this (found and adopted in/from S. S. Zumdahl (2009) Chemical principles. Brooks/Cole, Belmont, USA).

- If you ask the National Aeronautics and Space Administration (NASA), such conversions are very important. In 1999 NASA lost the \$ 125 million *Mars Climate Orbiter* just as it was approaching the red planet. The problem? Unit conversion. NASA's scientists and engineers in Pasadena worked in metric units, and assumed that the thrust data for the rockets on the orbiter they received from Lockheed Martin Aeronautics in Denver, which built the spacecraft, were in metric units. In reality, the units were imperial (pounds, miles, etc.), and the lack of conversion meant that the orbiter approached Mars from an altitude of 60 kilometers instead of 150 kilometers. As the result the friction from the atmosphere caused the craft to burn up. The root cause of the failure was that the flight system written to take thrust instructions used the metric unit newton (N), while the software on the ground, which generated those instructions used the imperial measure pound-force (lbf). As a result, the thruster firings were underestimated by a factor of 4.45 ($1 \text{ lbf} = 4.45 \text{ N}$).
- The *Gimli Glider* is the nickname of an Air Canada aircraft that was involved in an aviation incident in 1983. At an altitude of 12,500 m it ran out of fuel halfway through its flight from Montreal to Edmonton via Ottawa. The crew was able to glide the aircraft safely at a former Canadian Air Force base in Gimli, Manitoba. The subsequent investigation revealed that someone pumped 22,300 pounds of kerosene into the aircraft instead of 22,300 kilogramms.

The moral of both stories: remember to watch your units!

Piping and Instrumentation Symbols Used in Flow Schemes (Table 6)

Symbols Used in Measuring and Control Technology

Measurement and control devices in flow schemes of chemical plants are denoted by a combination of up to four letters:

First letter (measured variable):

- D: density
- E: electricity
- F: flow
- L: level
- M: moisture
- Q: quality (e.g., concentration)
- S: speed, rotational frequency
- T: temperature
- W: weight

Supplement letter:

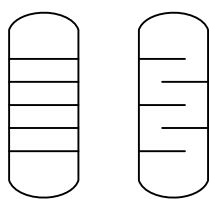
- D: difference
- F: fraction
- Q: quantity (e.g., total flow rate)

Consecutive letters (measured data processing):

- I: indication
- R: recording
- C: control

Table 6 Flow scheme symbols.

		Valve
		Heat exchanger
		Pump
		Compressor
		Multistage compressor
		Filter
		Cyclone
		Turbine
		Generator
		Oven
		Combustor furnace chamber
		Condenser
		Separator (gas/liquid)



Column with traps
(distillation, absorption)



Distillation column



Absorption/extraction column



Fixed-bed reactor
adsorption column

S: switch

A: alarm

+ (or H): upper limit (high)

- (or L): lower limit

Examples:

PI: pressure indicator

PICA +: pressure indicator and controller with alarm if an upper limit is exceeded

TIR: temperature indication and registration

1**Introduction****1.1****What is Chemical Technology?**

The field of *chemical technology* stands between:

- **classical chemistry**, which is the science concerned with the composition, behavior, and properties of matter, and with the changes it undergoes during chemical reactions and
- **chemical engineering**, which is the branch of engineering that deals with the application of chemistry, physics, life sciences, and mathematics to processes of converting raw materials or chemicals into more useful or valuable forms or to environmental processes, and involves the design of large-scale processes and also of laboratory-scale plants. Modern chemical engineering is also concerned with the design and synthesis of new materials, new techniques such as nanotechnology, and is one of the major disciplines related to energy technology such as the development of efficient fuel cells, energy storage systems, and the use of solar energy and other renewables.

In the chemical industry, natural scientists (primarily chemists, but also biologists and physicists), engineers, and also business men form a team, and the following questions may, for example, be important:

- What is the amount and purity of the product that the client would like to have?
- What apparatus are suitable to produce a certain chemical?
- How can the heat be provided for an endothermic reaction and how can we cool a reactor in the case of an exothermic reaction?
- Is the process safe and economic?
- How can a current process be improved?
- What type of equipment is needed to separate a reaction mixture?
- Which catalyst is the best and for how long is the catalyst still active?
- Is the process environmentally benign?

Chemical technology should give answers to all these questions, and relies mainly on knowledge of the following four key disciplines and on their application and integration:

- 1) (physical) **chemistry** with a focus on key reactions, kinetics, and catalysis;
- 2) **thermal and mechanical unit operations** to design processes like distillation, absorption, adsorption, extraction, pumping and compressing of liquids and gases, filtration, and so on;
- 3) **chemical reaction engineering**, that is, knowledge of how to measure kinetic data for industrially relevant conditions, of the influence of heat and mass transfer on chemical reactions, and of all aspects of reactor design and modeling;
- 4) **general chemical technology**, that is, the pedigree of routes from raw materials such as crude oil, natural gas, coal, and biomass via intermediates to final products and environmental aspects of chemical technology.

This book covers all four disciplines: chemical aspects in Chapter 2, thermal and mechanical unit operations (Chapter 3), reaction engineering (Chapter 4), and general chemical technology (Chapter 5). In addition, 20 industrial processes are inspected in detail (Chapter 6).

1.2 The Chemical Industry

For all industrialized countries the chemical industry is an important part of the economy. However, compared to the oil, gas, and coal industries – which are equally reliant on chemical technology – the chemical industry is relatively small. In 2011, six of the ten (and ten of the 20) most important companies by revenue were primarily oil and gas companies, and the biggest chemical company (BASF) was ranked only 62 (Table 1.2.1). Thus the chemical industry, which produces chemicals ranging from base chemicals to fine chemicals mainly from crude oil derivatives, such as naphtha and liquefied petroleum gases (LPG), is still has a “free ride” in terms of energy consumption, which is still mainly driven by crude oil.

The ten largest chemical companies (without pharmaceuticals) by sales and a geographic breakdown of world chemicals sales are listed in Tables 1.2.2 and 1.2.3, respectively. In recent years the role of the chemical industry in the European Union (EU-27) and in North America has decreased; for example, in 2000 the EU-27 share of the global production of chemicals was about 29%, whereas the value for 2010 is only 21%. The share of Asia (without Japan) has increased in this period from 21% to 42%. Table 1.2.4 lists the top ten pharmaceutical companies.

Table 1.2.1 List of the 20 most important companies by revenues in 2011. Data from http://en.wikipedia.org/wiki/List_of_companies_by_revenue (accessed on 04.09.2012).

Rank	Company	Primary industry	Revenue in billion US \$	Employees in 1000	Country
1	ExxonMobil	Oil and gas	486	82	USA
2	Royal Dutch Shell	Oil and gas	470	90	UK/NL ^{a)}
3	Wal-Mart	Retailing	447	2150	USA
4	BP	Oil and gas	386	98	UK
5	Vitol	Commodities	297	–	SW/NL ^{b)}
6	Sinopec	Oil and gas	102	401	China
7	Chevron	Oil and gas	254	61	USA
8	ConocoPhillips	Oil and gas	251	30	USA
9	Toyota	Automotive	137	316	Japan
10	Samsung	Electronics	136	275	South Korea
11	State Grid	Electric utility	227	1564	China
	Corporation of China				
12	PetroChina	Oil and gas	222	464	China
13	Total	Oil and gas	220	111	France
14	Volkswagen	Automotive	211	502	Germany
15	Japan Post Holdings	Conglomerate	204	229	Japan
16	Glencore	Commodities	186	52	Switzerland
17	Saudi Aramco	Oil and gas	182	54	Saudi Arabia
18	Gazprom	Oil and gas	158	432	Russia
19	Fannie Mae	Financial services	154	7	USA
20	General Motors	Automotive	150	284	USA
62	BASF	Chemical industry	95	109	Germany

a) UK/NL = United Kingdom/Netherlands.

b) SW/NL = Switzerland/Netherlands.

Table 1.2.2 The 10 largest chemical companies by sales in 2007 and 2010 (without pharmaceuticals. Data for 2007 from Behr, Agar, and Joerissen [2010] and for 2010 from International Chemical Information Service, www.icis.com (accessed on 04.09.2012).

Company	Country	Sales in 2007 in billion US \$ (rank)	Sales in 2010 in billion US \$ (rank)
BASF	Germany	85 (1)	85 (1)
Dow	USA	54 (2)	54 (2)
Chemical			
Exxon Mobil	USA	54 (3)	54 (3)
Shell	United Kingdom/Netherlands	46 (4)	40 (7)
LyondellBasell	Netherlands	45 (5)	41 (4)
Ineos	United Kingdom	41 (6)	35 (9)
SABIC	Saudi-Arabia	34 (7)	41 (6)
Sinopec	China	33 (8)	49 (4)
Mitsubishi Chem.	Japan	30 (9)	38 (8)
DuPont	USA	29 (10)	32 (10)

Table 1.2.3 Geographic breakdown of world chemicals sales in 2010 (production of chemicals excluding pharmaceuticals; data from www.cefic.org/facts-and-figures, accessed 18.09.2012).

Country/region	Sales in billion €		Share of world sales in %	
	2000	2010	2000	2010
China	92	575	6.4	24.4
EU-27 ^{a)}	421	491	29.2	20.9
NAFTA ^{b)}	404	455	28.1	19.3
Japan	172	153	12.0	6.5
Rest of Asia	210	419	14.6	17.8
Latin America	68	128	4.7	5.4
Rest of Europe	39	87	2.7	3.7
Rest of the world	33	45	2.3	2.0
Total	1437	2353	100	100

a) EU-27: Austria, Belgium, Bulgaria, Cyprus, Czech Republic, Denmark, Estonia, Finland, France, Germany, Greece, Hungary, Italy, Ireland, Latvia, Lithuania, Luxembourg, Malta, Netherlands, Poland, Portugal, Rumenia, Slovak Republic, Slovenia, Spain, Sweden, and United Kingdom.

b) USA, Canada, and Mexico.

Table 1.2.4 The 10 largest pharmaceutical companies by 2011 sales. http://de.wikipedia.org/wiki/Pharmaunternehmen-Gro.C3.9Fe_Pharmaunternehmen (accessed on 04.09.2012).

Company	Country	Sales in 2011 in billion US \$
Pfizer	USA	58
Novartis	Switzerland	54
Merck & Co.	USA	41
Sanofi-Aventis	France	37
Hoffmann-La Roche	Switzerland	35
GlaxoSmithKline	United Kingdom	34
AstraZeneca	United Kingdom	34
Johnson & Johnson	USA	24
Abbott	USA	22
Eli Lilly	USA	22

Table 1.2.5 gives the annual global production of important chemicals in 2003. In general, the structure of the chemical industry is characterized by a small number of base chemicals such as ammonia, ethylene, and chlorine, which are further converted into many intermediates such as ethylenoxide, styrene and vinyl chloride and

Table 1.2.5 World production of important chemicals in 2003 (Baerns *et al.*, 2006).

Product	Million tonnes	Billion €
Inorganic base chemicals		
Sulfuric acid (100%)	170	
Ammonia	111	
Nitrogen-fertilizers (counted as N)	90	
Chlorine	43	
Phosphor-fertilizers (counted as P ₂ O ₅)	37	
Potassium salts (counted as K ₂ O)	28	
Organic chemicals		
Ethylene	100	
Propylene	56	
Benzene	32	
Methanol	29	
Polymers	202	
Pharmaceuticals		466
Pesticides		25

Table 1.2.6 Important products of the German chemical industry for 2007 (Behr, Agar, and Joerissen, 2010).

Products	Share of total production value (%)
Organic base chemicals	18
Inorganic base chemicals	8
Polymers and rubber	18
Chemical fibers	2
Fine and specialty chemicals	26
Pharmaceuticals	20
Soaps, detergents, and cosmetics	8

Table 1.2.7 Sales of the oil & gas industry (only oil and gas business) and sales of the chemical and pharmaceutical industry in 2008 (estimations based on various sources).

Product group	Sales (billion €)	Share of total sales (%)	Share of sales only of chemical and pharmaceutical industry (%)
Oil business	2000 ^{a)}	38	Not counted
Natural gas business	800 ^{b)}	15	Not counted
Basic chemicals ^{c)}	900	17	36
Life sciences ^{d)}	750	14	30
Fine chemicals ^{e)}	600	11	23
Consumer products ^{f)}	250	5	11
Total	5300	100	100

a) Calculated based on the global oil consumption (2008) of 29 billion barrel and an oil price of €70 per barrel.

b) Calculated based on the global consumption of natural gas (2008) of about 3200 billion m³ and a gas price of €250/1000 m³.

c) Petrochemicals, intermediates, fertilizers, and polymers.

d) Mainly pharmaceuticals, but also animal health products, vitamins, and crop protection.

e) Electronic chemicals, catalysts, coating, adhesives, and so on.

f) Soaps, detergents, and cosmetics.

finally into a huge number of chemical consumer goods such as pharmaceuticals or polymers (Table 1.2.5).

Today, bulk chemicals are increasingly produced in Asia and in the Middle East and not in Europe, Japan, and North America. For example, in Germany, the most

important chemicals are fine chemicals and pharmaceuticals, with a share of 46%, whereas the role of organic and inorganic base chemicals is comparatively small (26%) (Table 1.2.6).

Global sales in the oil and gas industry are of the same order of magnitude as those of the world's chemical and pharmaceutical industry (Table 1.2.7). If the global oil and gas consumption and the respective average prices are taken as an estimation of sales, we obtain values of these two businesses of €2000 and €800 billion a⁻¹, respectively, compared to sales for the global chemical and pharmaceutical industry of €2500 billion a⁻¹ (basic chemicals, life sciences, fine chemicals, and consumer products, see Tab. 1.2.7). Within the chemical and pharmaceutical industry, the share of the sales of basic chemicals (including polymers) is 36% followed by life science products (mainly pharmaceuticals) with 30%, and fine chemicals and consumer products with 23% and 11%, respectively.

2

Chemical Aspects of Industrial Chemistry

2.1

Stability and Reactivity of Chemical Bonds

Chemical reactions proceed by the linking and/or cleaving of chemical bonds. If we take the molecule A-B, for example, the covalent bond between A and B can be broken homolytically or heterolytically. In the first case each atom A and B receives one unpaired electron to form radicals, in the second case both electrons of the chemical bond go with either A or B, forming charged species (Scheme 2.1.1).

Radicals and charged species play a very important role as reactive intermediates in various organic transformations. Even if they may be present only in small quantities and for a short time (and thus are difficult to measure analytically), they play a crucial role in the mechanism of the ongoing reaction.

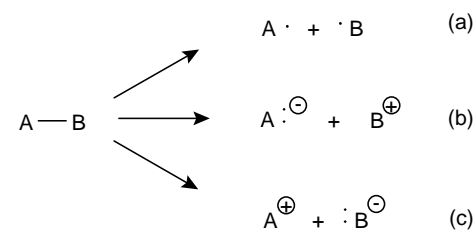
Note that the reverse reactions to those shown in Scheme 2.1.1 play a very important role for the formation of new covalent bonds. In addition, radicals or charged species can attack neutral compounds to form different radicals and charged species involving new chemical bonds. Scheme 2.1.2 gives examples of some practical relevance in chemical technology. In transformation (a), a methyl radical attacks a chlorine molecule to form chloromethane and a chlorine radical. This reaction is one of the key steps in technical methane chlorination. In transformation (b), an isopropyl carbocation attacks water to form isopropanol with the release of a proton, the key mechanism in the technical production of isopropanol and all higher secondary and tertiary alcohols. In transformation (c), an anionic methanolate ion acts as starter for an anionic polymerization reaction – one possible starting step in technical anionic polymerization.

Note that the reactivity of radicals, carbocations, or carbanions (the negative charged counterpart of carbocations), is not always the same but depends strongly on the surrounding neighboring groups with their specific electronic and steric effects. As the influence of electronic and steric factors on the reactivity of molecules is also of key importance for many transformations in chemical technologies we will devote the following sub-sections to introducing these phenomena. For a more detailed treatment of the reactivity of organic molecules – that is certainly indispensable for all research efforts into new chemical transformations – excellent textbooks in organic chemistry can be recommended (Sykes, 1988; March, 1992; Sykes, 1996; Walter and Francke, 1998; Fanghänel, 2004).

2.1.1

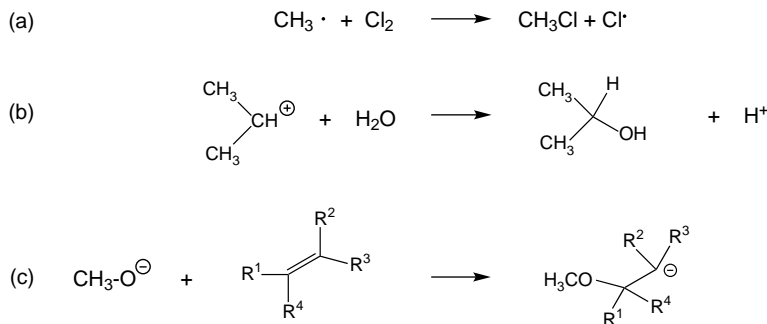
Factors that Influence the Electronic Nature of Bonds and Atoms

All effects that influence the electron density in a specific part of a molecule strongly affect the chemical reactivity of that part. While – for example – electron-rich parts show hardly any reactivity against HO^- , electron-poor parts will easily react with this strong electron-donor.



Scheme 2.1.1 Different modes of breaking the covalent bond in molecule A-B, forming either radicals (a) or charged species (b, c).

Scheme 2.1.2 Reactivity of radicals, carbocations, and carbanions exemplified for reactions of relevance in chemical technology: reaction of (a) the methyl radical with chlorine (key-step in methane chlorination); (b) the isopropylum ion with water (key-step in isopropanol synthesis from propene); (c) methanolate with an alkene to form a carboanion (key-step in the start-up of an anionic polymerization reaction).



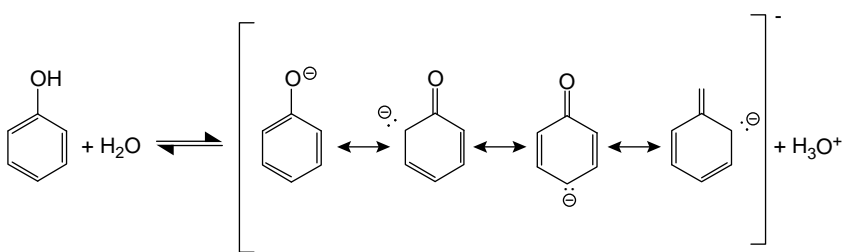
The most important effects that influence the electron density of specific parts of a molecule are the inductive and conjugative effects.

Inductive effects on electron density originate from the fact that the electron pair in a covalent σ -bond that links two different atoms (e.g., carbon and oxygen in a C—O bond) are never shared evenly. The more electronegative atom (in our example oxygen) will always receive more electron density, which leaves the carbon with some lack of electron density. Thus, a carbon atom attached to an oxygen atom (or any other strongly electronegative atom) always shows increased reactivity against strong electron-donor reagents relative to a carbon attached to another carbon. If the C—O bond is incorporated in a larger molecule, the carbon attached to the oxygen will also influence its immediate neighborhood by its ability to compensate for part of its electron deficiency by taking electron density from the surrounding atoms. Most groups attached to a carbon atom exert an inductive effect that pulls electrons away from the carbon (so-called $-I$ -effect) because most atoms are more electronegative than carbon. Important exceptions are alkyl groups and metal atoms such as lithium (i.e., in organolithium reagents) or magnesium (i.e., in Grignard reagents of the type RMgX). A carbon linked to these groups receives more electron density than usual (so-called $+I$ -effect) and becomes an electron-rich reagent that searches for electron-deficient partners for reaction. Note that all inductive effects on electron density are based on the permanent polarization of bonds and, therefore, these effects are also expressed in the physicochemical properties of the molecules, for example, their dipole moment.

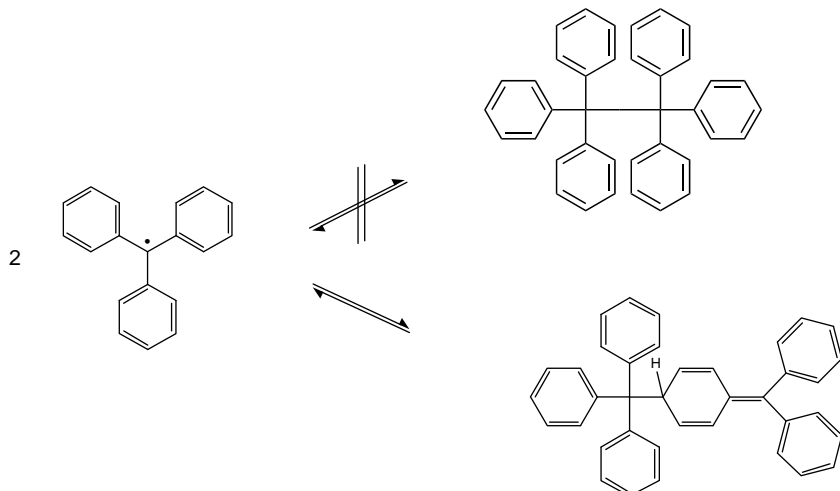
Conjugative effects on electron density are based on the high degree of polarizability of π -electrons in unsaturated and, especially, in conjugated systems (systems with alternating single and double bonds, such as butadiene). In contrast to inductive effects, conjugative or mesomeric effects influence the electron density distribution in a molecule over large distances in expanded conjugated systems. Moreover, the conjugative effects result in atoms of alternating and fluctuating polarization and electron density in these systems. It is of great practical relevance that the possibility of stabilizing a positive or negative charge in a π -electron system by conjugative or mesomeric effects leads directly to a large increase in stability of such species. For example, the much stronger acid character of phenol compared to methanol can be understood as a direct consequence of the mesomeric stabilization of the phenolate ion after proton transfer (Scheme 2.1.3). Of course a similar kind of stabilization is not possible with any saturated aliphatic alcohol. Conjugative electronic effects are also permanent and they influence strongly the physicochemical properties of molecules with unsaturated bonds and conjugated π -electron systems.

2.1.2 Steric Effects

Sometimes two molecules do not react even though they are expected to on the basis of the electronic nature of their reactive centers. In most cases, steric effects account for this reduced reactivity. To understand the nature of steric effects we simply have to consider that two molecules have to approach each other very closely



Scheme 2.1.3 Stabilization of the phenolate ion by conjugative (or mesomeric) effects – note the two different notations of the arrows, indicating a reversible chemical reaction (left-hand side) and different mesomeric structures of the phenolate ion (three arrows in brackets).



Scheme 2.1.4 Reactivity of two trityl radicals – due to steric reasons the expected combination of two radicals is suppressed and instead a less sterically demanding dimerization takes place.

to enable the formation of a new covalent bond. If the reactive centers of both molecules are surrounded by bulky, inflexible, or geometrically restricted groups, the repulsive interaction of these surrounding groups can prevent the two reactive centers from approaching in the required way. As a consequence, the two molecules do not react or if they do the formed bond is very unstable and can be cleaved easily by heating or by reaction with a less sterically demanding other reagent. Scheme 2.1.4 shows the unusual reactivity of two trityl radicals, which originates from the fact that the simple recombination of two trityl radicals is sterically too demanding to take place.

2.1.3

Classification of Reagents

Strong electron donating reagents, such as HO^- , search for electron-deficient counterparts to lower their energy by forming a stable covalent bond. Therefore, these species are called nucleophiles or nucleophilic reagents. In an analogous manner there also exist reagents that themselves are very poor in electron density and, therefore, search for electron-rich counterparts for reactions. The latter are called electrophiles or electrophilic reagents. Table 2.1.1 gives an overview of technically

Table 2.1.1 Technically important nucleophiles and electrophiles – atoms in bold refer to the atoms that transfer or accept electrons to the substrate according to their nucleophilic or electrophilic nature (R represents an alkyl or aryl group, X represents a halide).

Technically important nucleophiles	Technically important electrophiles
H^- , HO^- , RO^- , RS^- , CN^- , RCO_2^- , $\text{R}'\text{-O-R}''$, $\text{R}'\text{-S-R}''$, $\text{R}'_3\text{N}$, RMgX , RLi	H^+ , H_3O^+ , NO_2^+ , NO^+ , R_3C^+ , SO_3 , CO_2 , BF_3 , AlCl_3 , Br_2 , O_3

important nucleophiles and electrophiles. Note that the electronic character of these species can be very much understood using the arguments discussed in Section 2.1.1. Note further that to establish an order of strength among different nucleophiles one can take their basicity as a rough first approximation. An important difference, however, is that the terms “electrophilicity” and “nucleophilicity” are derived from kinetic experiments (therefore aspects like steric arguments can play a very important role) while the terms “acidity” and “basicity” are derived from a thermodynamic evaluation of the acid–base equilibria.

2.2 General Classification of Reactions

Organic reactions can be grouped into four basic types of transformations that all play very important roles in chemical technology. These four types will be briefly presented here and each type will be exemplified using one technically relevant example:

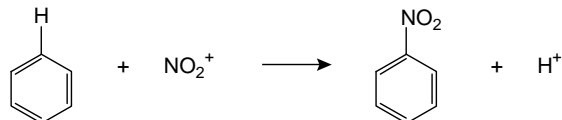
- substitution reactions
- addition reactions
- elimination reactions
- rearrangement or isomerization reactions.

Substitution reactions are characterized by the fact that a substrate reacts with a second molecule by incorporating the second molecule in its structure and by releasing a part of the substrate. Substitution reactions can take place as electrophilic (see Section 2.2.5 for details), nucleophilic (Section 2.2.3), or radical substitution reactions (Section 2.2.2) depending on the nature of the attacking reagent. Scheme 2.2.1 shows the electrophilic substitution of a hydrogen atom at benzene by the nitronium electrophile NO_2^+ . This technically relevant reaction liberates a proton and forms nitrobenzene. It represents an important step in the synthesis of nitrobenzene, the key-intermediate for the production of aniline.

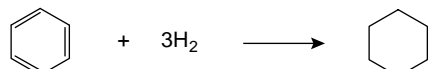
Addition reactions proceed typically at unsaturated bonds such as $\text{C}=\text{C}$, $\text{C}=\text{O}$, $\text{C}=\text{N}$, $\text{C}\equiv\text{N}$ or carbon–carbon triple bonds. A molecule is added to the substrate and the product forms without release of any another molecule. With all substrates becoming part of the product, the atom economy of addition reactions is very favorable. Because today’s chemical technology is largely based on unsaturated base chemicals obtained in the steam cracker process (e.g., ethylene, propylene, butenes, benzene, see Chapter 6.6), addition reactions are of the highest relevance in the whole petrochemistry. Scheme 2.2.2 shows as one important example, namely, the addition of hydrogen to benzene to form cyclohexane, a key intermediate in the production of, for example, adipinic acid or caprolactam (nylon).

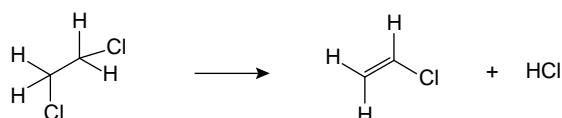
Elimination reactions can be regarded as the reverse of addition reactions. One substrate is converted into at least two molecules, with dehydrogenation, dehydration, dehalogenation, and dehydrohalogenation reactions being of highest technical

Scheme 2.2.1 Electrophilic substitution of a hydrogen atom at benzene to form nitrobenzene.



Scheme 2.2.2 Addition of hydrogen to benzene to form cyclohexane.





relevance. Scheme 2.2.3 shows, as an example of a technically relevant elimination reaction, the dehydrochlorination of dichloroethane, a key step in the production of vinyl chloride.

Rearrangement or isomerization reactions proceed typically at carbocations or other electron-deficient positions of a molecule. In rearrangement reactions the substrate stabilizes itself by rearranging its structure without changing the number and type of its atoms. Thus, rearrangement reactions proceed without addition/release of molecules other than substrate and product. Rearrangement reactions of technical importance are the isomerization of linear alkanes to branched alkanes (important to increase the quality of fuels) and the rearrangement of cyclohexanone oxime to ϵ -caprolactam (Scheme 2.2.4).

The following sub-sections highlight important mechanistic aspects of organic reactions. They focus on the question of how a certain organic transformation proceeds and how it can be influenced beneficially, for example, by the use and choice of a catalyst, the choice of solvent, or reaction parameters. Of course, a certain understanding of the type of reaction mechanism is also very helpful in choosing the right kinetic model for kinetic investigations in the context of process development studies.

2.2.1

Acid–Base Catalyzed Reactions

Acid-catalyzed reactions are characterized by the fact that either a proton (in the case of Brønsted acid catalysis) or a strongly electron-deficient catalyst (in case of Lewis acids) interacts with the substrate, typically by the intermediate formation of a carbocation ion. The latter is highly activated and undergoes transformations, for example, in the form of substitution, addition, or rearrangement reactions. After reaction the acid catalyst is liberated from the product. Technically important examples of all three types of transformation are (i) Lewis acid (here typically AlCl_3) catalyzed electrophilic substitution to form ethylbenzene from benzene (the key-step in styrene production), (ii) Brønsted acid catalyzed addition of water to ethene to form ethanol, and (iii) isomerization of *n*-hexane to iso-hexane catalyzed by strong Brønsted acids to improve the quality of fuel for Otto engines.

In the case of base-catalyzed reactions the substrate comes into contact with either HO^- or any other highly electron-rich catalyst (e.g., alcoholates, strongly basic amines, metal alkyls). Again, the substrate is activated, typically via the intermediate formation of carbanion species. A technically important example of base catalysis is the transesterification of natural oils to fatty acid methyl esters (FAME, better known as “biodiesel”), a process typically catalyzed by methanolate salts.

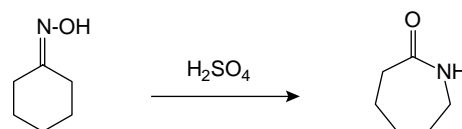
2.2.2

Reactions via Free Radicals

As mentioned in Chapter 2.1, the formation of radicals requires the homolytic cleavage of a covalent bond. Energetically such homolytic cleavage is particularly favorable in gas-phase reactions and for liquid-phase reactions in nonpolar solvents. In polar solvents, however, the energy contribution from the solvation of ionic species formed in heterolytic cleavage reverses the picture and heterolytic cleavage becomes more favorable.

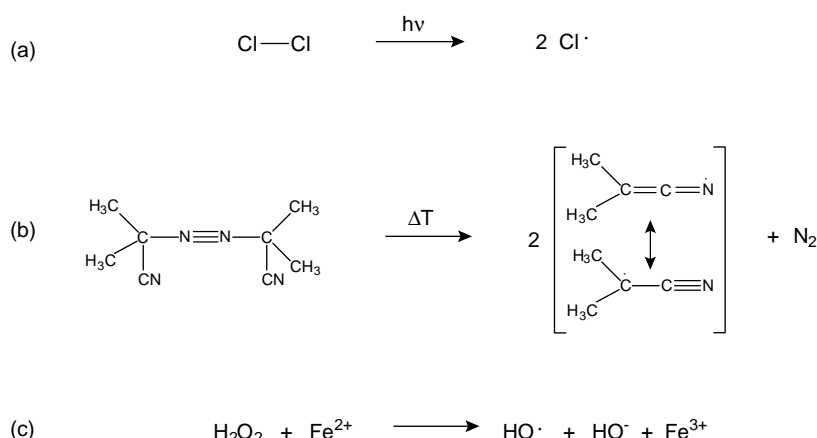
Radical reactions are of greatest importance in chemical technologies. The combustion of hydrocarbons – surely the most important organic reaction in volumetric terms – involves the formation of radicals in the same way as most oxidation

Scheme 2.2.3 Elimination of HCl from dichloroethane to form vinyl chloride.



Scheme 2.2.4 Rearrangement of cyclohexanone oxime to form ϵ -caprolactam.

Scheme 2.2.5 Different ways of forming radicals exemplified for reactions of technical importance: (a) photochemical cleavage of chlorine to form a chlorine radical as applied in the sulfochlorination of alkanes; (b) thermal cleavage of bis- α -azobisisbutyronitrile as applied in the radical polymerization of styrene; (c) formation of OH radicals from hydrogen peroxide as applied in radical oxidation reactions.



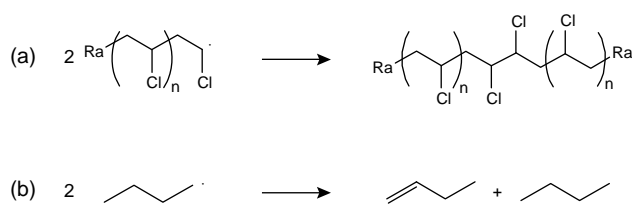
reactions for the production of chemicals (e.g., oxidation of cyclohexane to cyclohexanol). Other very important radical reactions include thermal cracking of hydrocarbons [e.g., in the steam cracker process (Chapter 6.6) or in the delayed coker process], radical substitution reactions (e.g., alkane chlorination or alkane sulfoxidation), and radical polymerization reactions [for the production of, for example, polystyrene, poly(vinyl chloride), or polymethacrylate)]. The latter reactions involve formally the addition of a radical to the monomer alkene followed by chain propagation to form the polymer.

All radical reactions start with the initial formation of radicals in the reaction mixture. This decisive step can proceed either photochemically (as, for example, in the technical sulfoxidation and sulfochlorination processes) or thermally (as in all technical oxidation and cracking reactions as well as in most radical polymerizations). A third important type of radical formation proceeds via redox reaction with a one-electron transfer either using metal salts (e.g., $\text{Fe}_2^+/\text{Fe}_3^+$ or $\text{Cu}^+/\text{Cu}^{2+}$) or via electrolysis. Scheme 2.2.5 gives examples of technical relevance for all three radical formation mechanisms.

Radicals are very reactive due to their unpaired electron. Once formed, they typically react very quickly with organic molecules in addition, substitution, or rearrangement reactions. If radicals react with neutral molecules, new radicals form and the reaction can quickly propagate as low energy barriers are characteristic for this kind of radical reactions. Note that, as a consequence of their high reactivity, radicals react in most cases in a less selective manner than carbocations or carbanions.

A radical reaction or radical chain propagation (such as in alkene polymerization) is terminated by either the reaction of two radicals or by disproportionation of the radical into alkane and alkene (Scheme 2.2.6). The latter reaction plays the dominant role in petrochemical cracking processes. Alternatively, a radical reaction can be stopped by adding to the reaction mixture substances that react very easily with radicals by forming very stable radicals themselves so that the propagation reaction is terminated. Examples of such radical scavenger molecules are phenols, quinones, and diphenylamines.

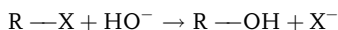
Scheme 2.2.6 Chain termination in radical reactions by either (a) reaction of two radicals, exemplified for poly(vinyl chloride) synthesis, Ra = initial radical, or (b) disproportionation, exemplified for the reaction of two butyl radicals relevant in steam cracking.



2.2.3

Nucleophilic Substitution Reactions

In a nucleophilic substitution, one substituent of a saturated carbon atom is exchanged with another substituent. A typical example is the reaction of a haloalkane R—X with the hydroxide ion HO[−] to form the respective alcohol:



Kinetic studies of numerous nucleophilic substitution reactions have demonstrated that there exist two borderline cases. In the first case, also referred to as an S_N2 reaction, the reaction rate is proportional to the concentration of both R—X and HO[−] [Eq. (2.2.1)], in the second case, called an S_N1 reaction, the reaction rate is only dependent on the concentration of R—X [Eq. (2.2.2)]:

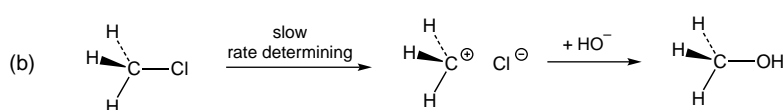
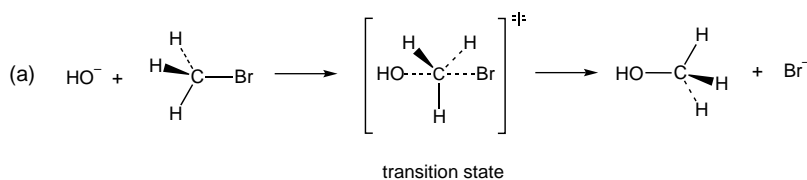
$$r \sim [\text{R—X}][\text{HO}^-] \quad (2.2.1)$$

$$r \sim [\text{R—X}] \quad (2.2.2)$$

A more detailed mechanistic analysis reveals that in the case of an S_N2 reaction both R—C and HO[−] are involved in the rate-determining step (formation of the transition state), while in an S_N1 reaction heterolytic cleavage of the C—X bond is the rate-determining step, and, thus, only the concentration of R—X influences the kinetics. Scheme 2.2.7 displays the two different borderline cases and their rate-determining steps.

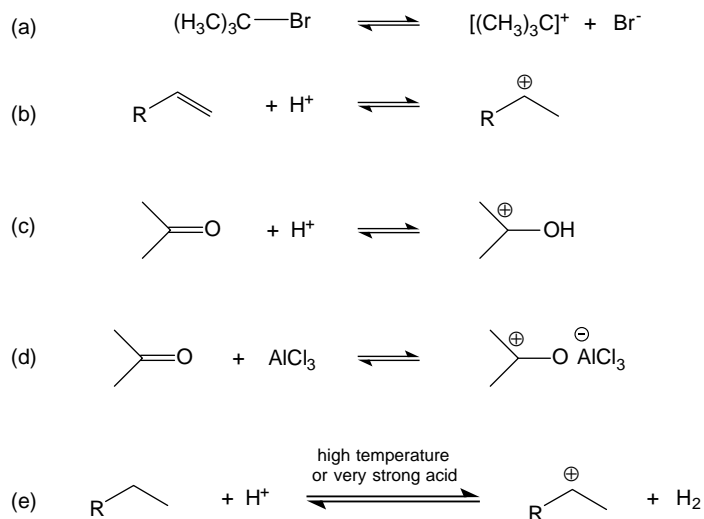
Several important factors influence whether a given nucleophilic substitution reaction proceeds more according to the S_N1 or the S_N2 mechanism:

- **Choice of solvent:** The higher the dielectric permittivity ϵ of the solvent the better is the solvation of the ion pair in the S_N1 mechanism, leading to increasing probability of an S_N1 mechanism. Note that nucleophilic substitution according to the S_N1 mechanism is typically not found in gas-phase reactions.
- **Groups surrounding the carbon atom at which the substitution reaction proceeds:** The higher the steric demand of the remaining substituents at the carbon atom the more difficult it is to realize the transition state required by the S_N2 route. Note that the S_N2 mechanism requires an attack of the nucleophile from the opposite site of the leaving, weaker nucleophile. In addition, the groups surrounding the carbon atom also affect the probability of S_N1 versus S_N2 mechanism by means of their electronic influence. If the groups attached to the carbon atom exert an electron donating inductive effect, such as, for example, in the case of a carbon atom attached to three methyl groups, then the carbocation formed in the S_N1 reaction is greatly stabilized and this mechanistic path becomes more probable.
- **Nature of the incoming group:** For obvious reasons the strength of the incoming nucleophile does not influence the rate of a S_N1 reaction, the incoming nucleophile is not involved in the rate determining step. For S_N2 reactions the reaction rate increases with increasing nucleophilic character of the incoming group.



Scheme 2.2.7 Mechanistic borderline cases in nucleophilic substitution reactions: (a) S_N2 reaction with formation of the transition state being the rate-determining step; (b) S_N1 reaction with heterolytic cleavage of the C—Cl bond being the rate-determining step.

Scheme 2.2.8 Important routes for carbocation formation: (a) heterolytic bond cleavage as observed in S_N1 reactions; (b) addition of acids to alkenes – key step in alcohol formation from alkenes; (c) addition of protons to carbonyl bonds; (d) addition of Lewis acids to carbonyl bonds; (e) hydride abstraction.



- **Nature of the leaving group:** The nature of the leaving group influences both the rate of S_N1 and S_N2 reactions. The relative tendency of a leaving group X to leave the molecule R—X is influenced by the strength and polarization of the R—X bond as well as by the stability and solvation of the leaving group X.

2.2.4

Reactions via Carbocations

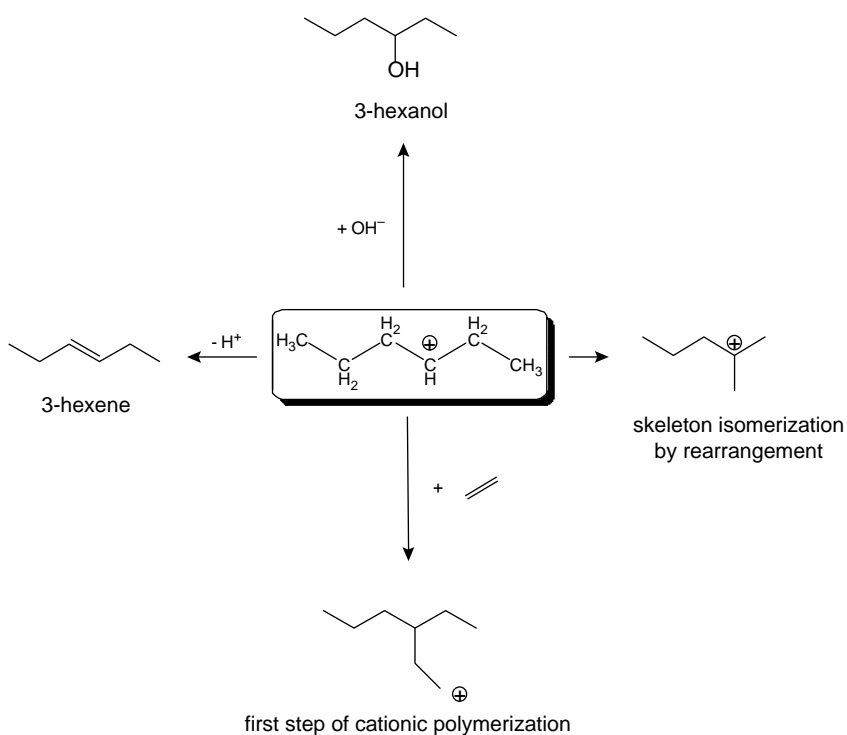
Carbocations are formed by several reactions. One example has been discussed already in the context of the S_N1 reaction (Scheme 2.2.8a). Other important options include the addition of protons to double bonds, for example, the addition of a Brønsted acid to an alkene or ketone (Scheme 2.2.8b and c, respectively). The addition of a Lewis acid to a carbonyl group can also lead to a type of carbocation, an effect that is exploited in all kinds of technical Friedel–Crafts acylation reactions (Scheme 2.2.8d). Finally, in high-temperature refinery processes, the formation of carbocations from alkanes is of highest relevance. Here acidic catalysts are usually applied that abstract a hydride from the alkane to form hydrogen and a carbocation at the alkane substrate (Scheme 2.2.8e).

The stability of carbocations increases for alkyl cations with the number of alkyl groups that surround the positive charge and thereby stabilize it by their inductive effects. Thus, a methyl carbocation CH_3^+ is the most unstable and reactive one while the *tert*-butyl cation $[(\text{CH}_3)_3\text{C}]^+$ is the most stable and least reactive. This stability order is also the reason why carbocations frequently undergo isomerization and rearrangement reactions after formation, a reactivity that is very important for all isomerization reactions in refineries (here branched hydrocarbons are highly desired due to their higher octane number – see Chapters 6.9 and 6.10).

Carbocations can – once formed – undergo in principle the following transformations:

- combination with a nucleophile
- abstraction of a proton
- addition to an unsaturated bond
- rearrangement.

Scheme 2.2.9 demonstrates these different options for a C₆-carbocation that carries its positive charge at carbon number 3 (C3). While the reaction with the nucleophile HO^- leads to 3-hexanol, abstraction of a proton will produce 3-hexene. Addition of ethylene or any alkene would result in an addition reaction forming a new, very reactive carbocation. As a consequence, cationic polymerization would



Scheme 2.2.9 Reactivity of carbocations exemplified for a hexyl ion carrying the cationic charge at carbon number 3 (C3).

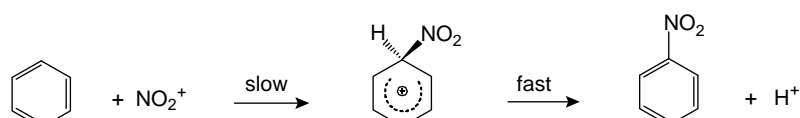
result from the addition of this alkene. Finally, the cation tends to rearrange itself to a more stable carbocation, for example, the 2-methylpentyl cation if no other reactant is around for reaction and the conditions are appropriate. The technical relevance of these different options is obvious for alcohol production from alkenes, for catalytic cracking (where significant amounts of alkenes are formed under specific, applied reaction conditions by proton abstraction from carbocations), for cationic polymerization processes, and for fuel reforming.

2.2.5

Electrophilic Substitution Reactions at Aromatic Compounds

Aromatic compounds are characterized by their π -electron systems, which create a high electron density above and below the planar six-membered ring of carbon atoms. Consequently, aromatic compounds are easily attacked by electrophiles and the reconstitution of the energetically favored aromatic character leads to replacement of one substituent at the carbon ring with the attacking electrophile. In total, an electrophilic substitution reaction takes place. By the same argument, nucleophilic substitution reactions at aromatic rings are much more difficult, but are possible if strong nucleophiles and activated aromatic substrates (e.g. nitrobenzol or pyridine) are used (see Sykes, 1988; March, 1992 for details). In the following paragraphs we focus solely on the technically very relevant electrophilic substitution reactions.

Scheme 2.2.10 displays the general mechanism of an electrophilic substitution reaction for the important example of nitrobenzene synthesis from nitric



Scheme 2.2.10 Nitration of benzene using HNO_3/H_2SO_4 – an example of an electrophilic substitution reaction of technical relevance.

acid/sulfuric acid and benzene. This reaction is a key step in the industrial synthesis of aniline, which is obtained subsequently by nitrobenzene hydrogenation.

While in the case of the nitration reaction the attacking electrophile NO_2^+ is generated from the $\text{HNO}_3/\text{H}_2\text{SO}_4$ mixture, in other electrophilic substitution reactions a Lewis-acid catalyst plays a very important role in generating the reactive electrophile. Examples are the Lewis-acid catalyzed chlorination or bromination of aromatic compounds (typical catalysts: FeCl_3 or FeBr_3) and Friedel-Crafts alkylation with alkyl halide or alkenes (typical catalyst: AlCl_3). In each case, interaction of the Lewis acid with the approaching non-aromatic substrate leads to a large increase in the electrophilicity of the attacking reagent. Another technically important example of a non-catalyzed electrophilic substitution reaction is the sulfonation of benzene and other aromatic compounds. The reaction proceeds quickly in mixtures of SO_3 and sulfuric acid, in which SO_3 acts as a strong electrophile.

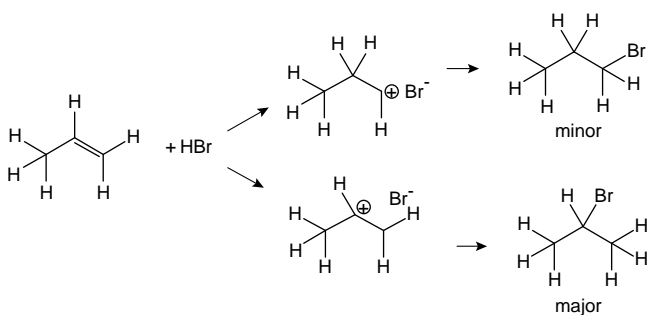
A question of high practical relevance for all electrophilic substitution reactions is the influence of an already existing substituent Y on the aromatic ring on the reactivity and regioselectivity of a second substitution reaction with the electrophile X. Comparing substitution reactions with X for different aromatic starting materials (with Y = H for benzene as the reference), two distinctive patterns can be distinguished:

- The second substitution is comparably fast or even faster than in the case of benzene and the second substituent is found preferably at the 2-(*ortho*) or 4-(*para*) position of the product (with respect to the substituent present in the aromatic substrate defining the 1-position).
- The second substitution is slower than in the case of benzene and the second substituent is preferably found at the 3-(*meta*) position.

To explain these patterns, electronic influences are most relevant. In addition, steric factors play a certain role for substitution at the 2-(*ortho*) position. Substituents Y with a free electron pair on the atom that is to be attached to the aromatic ring (e.g. OCOR, NHCOR, OR, OH, NH₂, NR₂) provide this electron pair for conjugative stabilization of the cationic transition state formed after attack of the electrophile. This leads to an acceleration of the reaction (lowering of the energetic level of the transition state) and to preferable electrophilic substitution at *ortho*- and *para*-positions. For these positions, stabilization involving the free electron pair of Y is more favorable than for the *meta*-position.

In contrast, substituents Y with no free electron pair at the atom attached to the aromatic ring (e.g. R₃N⁺, Cl₃C, NO₂, CHO, COOH) provide no electron pair for conjugative stabilization of the cationic transition state. Without this conjugative stabilization only the stronger electron-withdrawing effect of this group of higher electronegativity affects the reaction mechanism. These substituents exert an electron-withdrawing effect and thus the electrophilic substitution is slowed down compared to the reaction with benzene. However, the ability to stabilize the positive charge of the transition state is greater for substitution at the *meta*-position than for the other two positions, leading to a preferred nucleophilic substitution at this position.

So far, our discussion has always referred to kinetic arguments. It has to be considered, however, that most reaction systems that undergo electrophilic substitution reaction can also promote intra- or even intermolecular exchange of substituents. In the case of intermolecular exchange, this results in an isomerization reaction of the different regioisomers with the relative thermodynamic stabilities of the different isomers as the driving force. As a consequence we can obtain in short-term experiments kinetic product mixtures (depending on the above-mentioned arguments) and if we apply longer reaction times these kinetic mixture transform into the thermodynamic mixture of regioisomers. Detailed knowledge of the substitution and isomerization kinetics as well as of the temperature-dependent equilibria allows us to adjust the obtained product mixture to a certain degree to meet market needs.



2.2.6

Electrophilic Addition Reactions

The technically most important electrophilic addition reactions proceed at alkenes and alkynes. The reactive π -electrons of these compounds are attacked by electrophiles, resulting in the formation of a positively charged reaction intermediate. Stabilization of this positive charge plays a very important role in the regioselectivity of electrophilic addition reactions. This is demonstrated in Scheme 2.2.11 for the addition of HBr to propene, a reaction that produces almost uniquely the product 2-bromopropane and almost no 1-bromopropane as a consequence of the inductive stabilization of the secondary propyl cation compared to the cation with the charge at C1. This selectivity, where the proton becomes attached to the carbon with fewer alkyl substituents, is known as Markovnikov's rule.

Besides the addition of halides and hydrogen-halide acids to alkenes or alkynes, other industrially relevant electrophilic addition reactions involve hydration reactions (addition of water to alkenes and alkynes, forming alcohols), cationic polymerization (addition of carbocation to an alkene), hydrogenation (addition of hydrogen to alkenes to form alkanes), and Diels–Alder reactions (addition of an alkene to a conjugated diene to form complex, unsaturated hydrocarbon structures).

2.2.7

Nucleophilic Addition Reactions

Nucleophilic addition reactions are mainly of technical interest in the context of further reactions at C=O groups present in aldehydes or ketones. The electronic nature of a carbonyl group is characterized by the greater electronegativity of the oxygen atom compared to the carbon atom. Thus, the carbon atom is the preferred place of nucleophilic attack, that is, of reaction with an electron-rich reagent. Scheme 2.2.12 gives as an example the technically important cyanohydrin reaction. Other important nucleophilic additions are the reaction of carbonyl compounds with alcohols and water, bisulfite and metal hydrides.

2.2.8

Asymmetric Synthesis

A compound possessing a carbon atom that is surrounded by four different substituents exists in two stereoisomers that are like image and mirror image and are, therefore, not superimposable. Such a compound is said to be “chiral” and both stereoisomers are called “enantiomers.” Figure 2.2.1 shows the two enantiomers of 2-butanol. The central carbon is also called “asymmetric” and a synthesis that produces selectively one stereoisomer is therefore called an asymmetric synthesis.

Scheme 2.2.11 Electrophilic addition of HBr to propene – due to the higher stability of the secondary carbenium ion there is hardly any 1-bromopropane found in the product.

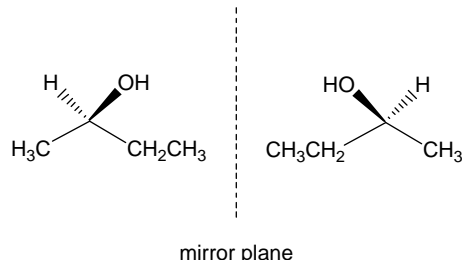
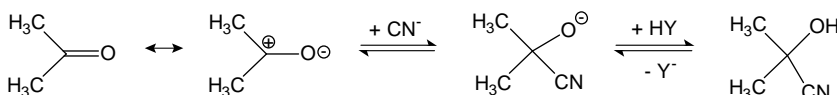


Figure 2.2.1 The two enantiomers of 2-butanol.



Scheme 2.2.12 Nucleophilic addition of CN^- to acetone in the cyanohydrin synthesis.

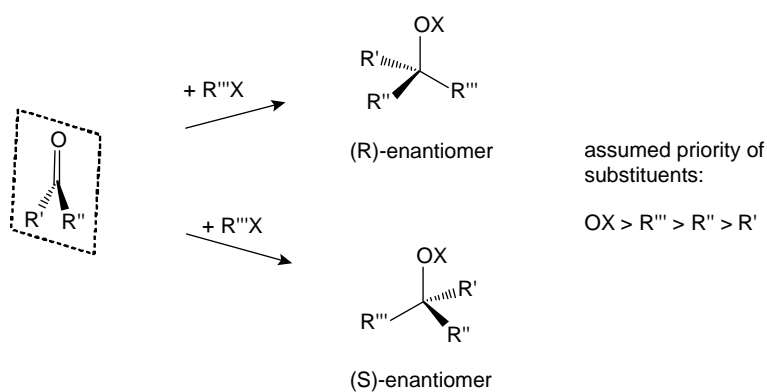
The two enantiomers of a chiral compound have the same chemical and physicochemical properties in an achiral environment. Nevertheless, asymmetric synthesis is a very important field in preparative organic synthesis and fine chemicals production because nature is full of chiral receptors, catalysts, and reactants. Thus, the different enantiomers of chiral products typically exhibit very different performance and properties when applied as agrochemical, fragrance, or pharmaceutical in the chiral biological environment.

For compounds with more than one asymmetric carbon atom there exist enantiomers and diastereomers. In detail, a compound with n asymmetric carbon atoms can be formed in 2^n different configurations. Some of these behave like image and mirror image – these are pairs of enantiomers. However, there are also pairs of stereoisomers that are not mirror images of each other. These are called diastereomers. Note that diastereomers differ in their physicochemical and chemical properties even in an achiral environment.

Synthesis of a chiral compound from an achiral compound requires a prochiral substrate that is selectively transformed into one of the possible stereoisomers. Important prochiral substrates are, for example, alkenes with two different substituents at one of the two C-atoms forming the double bond. Electrophilic addition of a substituent different from the three existing ones (the two different ones above and the double bond) creates a fourth different substituent and, thus, an asymmetric carbon atom. Another class of important prochiral substrates is carbonyl compounds, which form asymmetric compounds in nucleophilic addition reactions. As exemplified in Scheme 2.2.13, prochiral compounds are characterized by a plane of symmetry that divides the molecule into two enantiotopic halves that behave like mirror images. The side from which the fourth substituent is introduced determines which enantiomer is formed. In cases where the prochiral molecule already contains a center of chirality, the plane of symmetry in the prochiral molecules creates two diastereotopic halves. By introducing the additional substituent diastereomers are formed.

The most important nomenclature for enantiomers is the so-called CIP system introduced by Cahn, Ingold, and Prelog (Cahn, Ingold, and Prelog, 1966; Prelog and Helmchen, 1982). It is based on a priority rule for substituents at an asymmetric center – the higher the atomic number in the periodic table of elements the greater the priority – beginning with the atoms bonded directly to the asymmetric center. If the atoms directly bonded to the asymmetric center are identical, atoms in the second sphere are considered. If those are identical, too, then the third bonding sphere is ranked. To determine the correct nomenclature for an enantiomer with an asymmetric C-atom according to the CIP system we turn the molecule in such a way that the tetrahedron around the asymmetric C-atom points the substituent with the lowest priority (e.g., a hydrogen atom) away from the plane that is formed by the other three substituents. By looking at this plane, we identify the substituent with the highest priority. For the order of the substituents in the plane we can now distinguish two cases: (i) the order decreases clockwise – the enantiomer is then

Scheme 2.2.13 Nucleophilic addition to a prochiral carbonyl compound to form a new asymmetric C-atom with two enantiomers.



called a “(R)-enantiomer” (from the Latin *rectus*, right); (ii) the order decreases anticlockwise – the enantiomer is called a “(S)-enantiomer” (from the Latin *sinister*, left). Scheme 2.2.13 shows an example of this nomenclature.

In an achiral environment, both enantiotopic halves of the prochiral compound are even, which means the addition reaction in the case depicted in Scheme 2.2.13 would lead to a 1:1 mixture of the (R)- and (S)-enantiomers. Such a mixture is called a racemic mixture.

In chemical technology there are two ways to produce only one enantiomer in pure form: racemic resolution and steroselective synthesis.

In racemic resolution processes a racemic mixture of the desired product is produced first. There are several techniques by which this mixture can be separated into its two enantiomers. A favorable option is to react the racemic mixture with another chiral compound to form diastereomers. The latter have different physicochemical properties and thus they can be separated, for example, by chromatographic or crystallization processes. After separation of the diastereomers the chiral auxiliary compound is split-off and separated to re-obtain the desired compound as pure enantiomer. In an alternative concept, called kinetic racemic resolution, the initial racemic mixture is reacted with a chiral reactant or in the presence of a chiral catalyst (e.g., an enzyme) and only one of the two enantiomers of the desired product is transformed into a new compound. The reacted and non-reacted enantiomers are usually easily separated. All processes of racemic resolution have the common disadvantage that both enantiomers, the desired and the undesired one, have to be synthesized initially. Consequently, half of the initial racemic mixture is the undesired enantiomer, which usually has no or very little commercial value. This problem is partially solved by applying racemization processes in which after separation the pure “wrong” enantiomer is re-converted into the racemic mixture. The latter is then applied in another round of racemic resolution again to increase the final yield of the desired enantiomer.

In a chiral environment the two enantiotopic halves of a prochiral compound behave differently. Thus, the addition of a reactant proceeds in a selective manner. The higher the degree of differentiation between the two halves, the higher the selectivity. The chiral information necessary to create stereochemically uneven halves at the prochiral center is called chiral induction. Typical ways to introduce chiral induction into a system to realize steroselective syntheses are:

Substrate induction: Here the substrate already contains a chiral center so that this creates uneven diastereotopic halves. The reaction proceeds via diastereomeric intermediates with different energies. The product resulting from the diastereomeric intermediate with the lowest energy is kinetically favored.

Auxiliary induction: Here the prochiral substrate is reacted first with a chiral auxiliary to form, basically, the starting point for a substrate induction. After the reaction the auxiliary is split-off, isolated, and can be re-used often.

Reagent induction: In this case, the prochiral substrate is reacted in the presence of a chiral reagent to give a chiral product. The stereochemical information can be transferred either stoichiometrically or – very important in chemical technology – catalytically. In the latter case a chiral catalyst (e.g., a chiral transition metal complex, an organocatalyst, an enzyme, or a catalyst surface modified with chiral compounds) has to be applied.

2.3 Catalysis

Here we discuss catalysis and its relevance for chemical technology. Catalysis is applied industrially in the form of heterogeneous catalysis, homogeneous catalysis, and biocatalysis. All three forms follow the same general principles. However, the

nature of the catalytically active center is different in all three cases, varying from an active site that is part of a solid (heterogeneous catalysis), an active site that is part of a dissolved chemical compound (homogeneous catalysis), or an active site that is part of an enzyme or whole cell (biocatalysis).

Catalysts:

- accelerate the reaction rate (kinetics) but do not influence the chemical equilibrium (thermodynamics) of a reaction;
- are not consumed during reaction and undergo catalytic cycles during operation;
- are characterized in their technical performance by their activity (expressed as turnover frequency), selectivity, and lifetime (expressed as overall turnover numbers);
- can produce different reaction products from the same feedstock depending on their specific nature and composition.



Photograph of the drying step in the production of a heterogeneous catalyst.
Courtesy of Süd-Chemie, Germany.

2.3.1

Introduction and General Aspects

Catalysis is of greatest relevance for chemical technology. It is assumed that about 90% of all chemical processes work with the help of at least one catalyst. It is further assumed that 80% of the added value of the chemical industry and about 20% of the world economy depend directly or indirectly on catalysis. The catalyst market (the value of traded catalysts) was about €10⁹ in 2007, but at the same time the value of the goods produced by these catalysts was at least 100 times higher [$>\text{€}1 \times 10^{12}$ Weitkamp and Glaeser, 2003]. A recent article forecasts that the value of traded catalysts will reach \$17.2 billion in 2014 with an actual rise of 6% per year (Hydrocarbon Processing, 2011)

Industrial catalysts are found, to about the same extent (with respect to catalyst market value), in four different application areas: (i) environmental catalysts, with catalysts for exhaust gas cleaning in automotive applications and power plants being the most important examples; (ii) catalyst for refinery applications, for example, cracking catalysts, desulfurization catalysts, isomerization catalysts, and hydrogenation/dehydrogenation catalysts; (iii) catalysts for the production of polymers, such as Ziegler or metallocene catalysts for the production of polyethylene; (iv) catalysts for transformations in the chemical and petrochemical industry, including catalysts for C-C-coupling reactions, oxidations, hydrogenations, functionalizations, isomerizations, and many other reactions.

Our world would look very different without the catalysts that have been developed over the last 100 years. For example, supplying food for about 6 billion people on earth would be impossible without the catalytic transformation of nitrogen from air into ammonia, as only the latter allows the production of fertilizers for food production on today's scale. Without refinery catalysts we would certainly have much higher energy prices and would run out of oil much earlier.

One can calculate that the annual consumption of crude oil would be more than 400 Mio per year higher, due solely to the lower efficiency of our refineries without the catalysts used today (for comparison, annual crude oil consumption was about 3×10^9 tons per year in 2005). Materials would be very different as many plastics cannot be produced without catalysts that promote the polymerization process or that are needed for the production of monomers. Incidentally, we should not forget that nature is also full of biocatalysts that accelerate important processes like photosynthesis or the metabolism in our bodies and thus provide the fundamentals of life on earth.

Catalysis is of major socio-economic importance. To solve future problems connected with limited resources and energy, as well as environmental protection, there is no way around catalysis. In fact, we can regard catalysis as *the* key technology for the sustainable production of chemicals since efficient catalysis saves raw materials and energy and avoids waste formation.

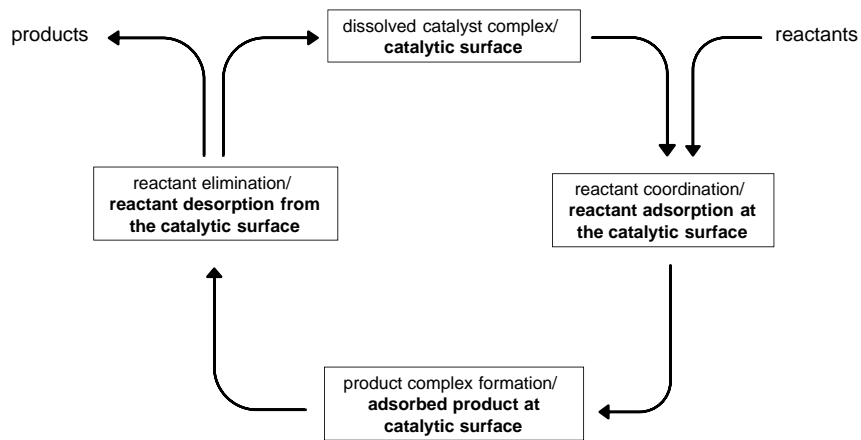
The term “catalysis” originates from the Greek word *καταλιστός*, which means “to dissolve, to loosen, to unfix.” Berzelius (1779–1848) introduced the term in 1836. Other pioneers of the concept of catalysis were Döbereiner (1780–1849), Mitscherlich (1794–1863), and Liebig (1803–1873). These first catalyst researchers observed in many cases that two substances that do not show a tendency for reaction do in fact react quickly in contact with a third substance that is not consumed in the reaction. Wilhelm Ostwald (see box) made a very significant contribution to the modern physicochemical understanding of catalysis.

Wilhelm Ostwald (1853–1932) was born in Riga and studied chemistry in Dorpat (now Tartu, Estonia). After his PhD thesis and habilitation, he worked as professor in Riga and Leipzig. Ostwald is regarded as the founder of physical chemistry in Germany. In 1909, he was awarded the Nobel Prize for his achievements in catalysis and his studies on chemical equilibria and kinetics. Notably, since Ostwald’s time many more Nobel Prizes have been awarded to catalyst researchers (Table 2.3.1), underlining the tremendous relevance of catalysis for the whole field of chemistry.

Table 2.3.1 Nobel Prizes in Chemistry awarded for achievements in catalysis research.

Year	Name	Achievement
1907	Eduard Buchner (Germany)	“for his biochemical researches and his discovery of cell-free fermentation”
1909	Wilhelm Ostwald (Latvia)	“in recognition of his work on catalysis and for his investigations into the fundamental principles governing chemical equilibria and rates of reaction”
1912	Paul Sabatier (France)	“for his method of hydrogenating organic compounds in the presence of finely disintegrated metals whereby the progress of organic chemistry has been greatly advanced”
1918	Fritz Haber (Germany)	“for the synthesis of ammonia from its elements”
1929	Arthur Harden (UK) and Hans v. Euler-Chelpin (Germany)	“for their investigations on the fermentation of sugar and fermentative enzymes”
1931	Carl Bosch (Germany) and Friedrich Bergius (Germany)	“in recognition of their contributions to the invention and development of chemical high pressure methods”
1932	Irving Langmuir (USA)	“for his discoveries and investigations in surface chemistry”
1956	Sir Cyril N. Hinshelwood (UK)	“for researches into the mechanism of chemical reactions”
1963	Karl Ziegler (Germany) and Giulio Natta (Italy)	“for their discoveries in the field of the chemistry and technology of high polymers”
1972	Stanford Moore (USA) and William H. Stein (USA)	“for their contribution to the understanding of the connection between chemical structure and catalytic activity of the active center of the ribonuclease molecule”
1975	John Warcup Cornforth (UK)	“for his work on the stereochemistry of enzyme-catalyzed reactions”
1997	Paul D. Boyer (USA) and John E. Walker (UK)	“for their elucidation of the enzymatic mechanism underlying the synthesis of adenosine triphosphate (ATP)”
2001	William S. Knowles (USA), Ryoji Noyori (Japan), and K. Barry Sharpless (USA)	“for their work on chirally catalyzed hydrogenation and oxidation reactions”
2005	Yves Chauvin (France), Robert H. Grubbs (USA), and Richard R. Schrock (USA)	“for the development of the metathesis method in organic synthesis”
2007	Gerhard Ertl (Germany)	“for his studies of chemical processes on solid surfaces”
2010	Richard F Heck (USA), E. Negishi (Japan), and A. Suzuki (Japan)	“for Pd-catalyzed cross couplings in organic synthesis”

Figure 2.3.1 Representation of a catalytic cycle. Expressions in bold reflect heterogeneous catalysis and expressions in normal print reflect homogeneous catalysis and enzyme catalysis.



Ostwald realized that a catalyst only influences kinetics, leaving the thermodynamics unaffected. Thus, the equilibrium is reached faster, but the position of the equilibrium is not changed. Ostwald also found that the accelerating effect of the catalyst is linked to an active participation of the catalyst in the reaction mechanism, although the catalyst is not consumed during the reaction and thus does not appear in the stoichiometric equation.

Catalytic reactions are characterized by a reaction sequence in which one reactant (the catalyst) is re-formed in the final reaction step in the same stoichiometric amount as it was added. This behavior leads to a closed reaction cycle, the so-called catalytic cycle (as schematically shown in Figure 2.3.1). A catalyst is characterized (in contrast to a stoichiometric additive) by the fact that it undergoes more than one cycle.

Technically relevant catalysts undergo during their operational lifetime millions of cycles; therefore, a large number of product molecules can be formed with a small number of catalytic centers. The number of cycles that a catalyst can undergo prior to its deactivation is a very important performance criterion in catalysis. This dimensionless characteristic number for each catalyst is called the turnover number (TON) and describes the catalyst's stability and lifetime. The TON, which originates from the field of enzymatic catalysis, is defined as the maximum amount of reactant (in moles) that a certain number of catalytically active centers (in moles) can convert into a certain product. For a $A \rightarrow B$ reaction we obtain:

$$\text{TON} = \frac{n_{A,\text{converted,max}}}{n_{\text{cat}}} = \frac{n_{B,\text{produced,max}}}{n_{\text{cat}}} \quad (2.3.1a)$$

For a batch process we obtain:

$$\text{TON} = \frac{n_{A,0} - n_{A}(t_{\text{deactivation}})}{n_{\text{cat}}} \quad (2.3.1b)$$

where $n_{A,0}$ is the molar amount of reactant A at the start of the reaction, $n_A(t_{\text{deactivation}})$ is the actual remaining molar amount of A, and n_{cat} is the molar amount of dissolved catalyst (in the case of homogeneous catalysis) or catalytic centers on the surface (in case of heterogeneous catalysis). To obtain a reasonable quantity for the TON, the experiment has to be carried out to complete catalyst deactivation ($t_{\text{reaction}} = t_{\text{deactivation}}$).

While TON indicates the overall catalyst lifetime it is not an indicator of the catalyst activity per unit time. To compare the number of catalytic cycles per unit time the turnover frequency (TOF) has been introduced [Eq. (2.3.2)] for a batch process

and reactant (A). TOF values of industrial catalysts are typically of the order of 1 s^{-1} or higher:

$$\text{TOF} = \frac{1}{n_{\text{cat}}} \left(-\frac{dn_A}{dt} \right) \quad (2.3.2)$$

For enzymatic and homogeneous catalysis, in which well-defined catalyst molecules are generally present in solution, the TON and TOF can be directly determined. For heterogeneous catalysis, this is generally difficult because the activity depends on the size of the catalyst surface, which does not have a uniform structure. The number of active sites per unit mass and so on can be determined indirectly by chemisorptions measurements, but such measurements require great care, and the results are often not applicable to process conditions (Hagen, 1999). Although the TON and TOF are attractive values due to their molecular simplicity, they should be used advisedly for solid catalysts in special cases. Alternatively, the catalyst activity can be given by the reaction rate of a catalytic reaction r referenced to some characteristic catalyst property, such as the mass of the applied heterogeneous catalyst (for details see Section 4.5.1, Topic, 4.5.3):

$$r = \frac{1}{m_{\text{cat}}} \left(-\frac{dn_A}{dt} \right) \quad (2.3.3)$$

In catalytic reactions with very expensive catalyst metals, for example, ruthenium, iridium, or platinum, it is of special interest to know how much mass of product, m_{product} , can be produced with a given mass of the precious catalyst metal, $m_{\text{cat, metal}}$, per reaction time t . This important aspect leads to the definition of catalyst productivity according to Eq. (2.3.4):

$$\text{Productivity} = \frac{m_{\text{product}}}{m_{\text{cat,metal}} t} \quad (2.3.4)$$

The productivity is sometimes also related to the total mass of the catalyst, that is, to support plus active metal, but we recommend the definition according to Eq. (2.3.4) as the price of a catalyst is dominated by the metal that is used. The price of metals varies strongly over time. Thus, for a comparison, the actual prices should be used. In September 2010, the prices for some precious metals were $\text{€}41\text{ g}_{\text{Pt}}^{-1}$, $\text{€}14\text{ g}_{\text{Pd}}^{-1}$, $\text{€}20\text{ g}_{\text{Ir}}^{-1}$, $\text{€}59\text{ g}_{\text{Rh}}^{-1}$, and $5\text{ € g}_{\text{Ru}}^{-1}$.

Finally, it is also important to know how much volume of a catalyst bed or a catalytic reactor is needed to produce a certain amount of product, m_{product} (in kg) or n_{product} (in mol). This knowledge is important as the size of the reactor determines largely the investment costs for the whole production plant. In Eq. (2.3.5) the space-time yield (STY) is introduced that reflects exactly this kind of information. Typical space-time yields of commercial catalytic reactors are in the range $0.5\text{--}10\text{ tons}_{\text{product}}\text{ m}^{-3}\text{ h}^{-1}$:

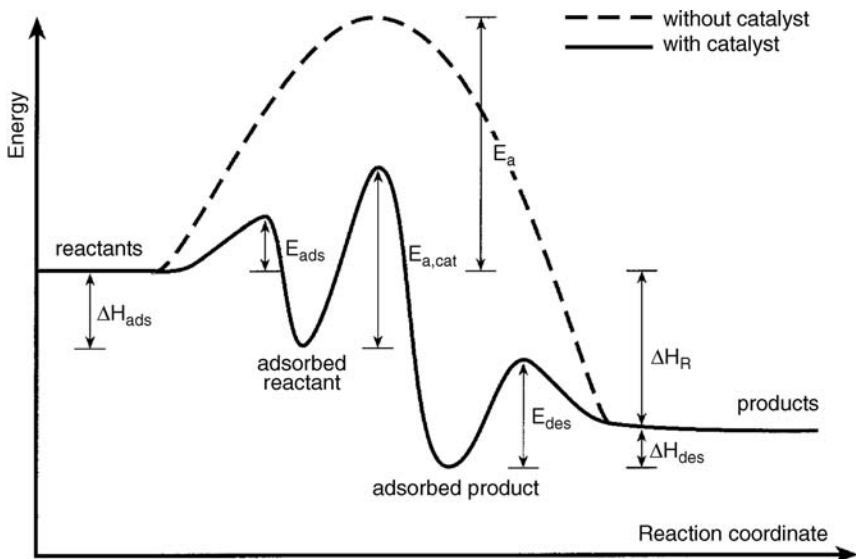
$$\text{STY} = \frac{m_{\text{product}}}{V_{\text{cat,reactor}} t} \quad (2.3.5)$$

The STY may also be expressed in terms of mol of product per volume of reactor and time [see Eqs. (4.1.21) and (4.1.22) in Section 4.1].

As mentioned above, one important characteristic property of a catalyst is its ability to enhance the rate of a chemical reaction. How can this be explained? As shown schematically in Figure 2.3.2, the interaction of reactants with the catalyst during a reaction opens up an alternative reaction pathway.

The latter is characterized by the fact that the energies of the transition states are generally lowered by interaction with the catalyst. Importantly, this leads to a lower maximum energy barrier that has to be overcome by the system on its way to product formation. As this maximum energy barrier is directly linked to the reaction rate, a lower maximum energy barrier results directly in a higher rate r and rate constant k .

Figure 2.3.2 Schematic energy profiles of a catalyzed (terms refer here to a heterogeneously catalyzed reaction) and a non-catalyzed reaction (see also Topic 4.3.2 in Section 4.3.1 for a further explanation of the term *reaction coordinate*).



Another very important feature of a catalytic reaction is that its energy profile should not have any deep throughs. Such a low-energy intermediate would reflect a stable “resting-state” from which a huge energy barrier would prevent the successful closing of the catalytic cycle. Note that the value of the energy barrier schematically drawn in Figure 2.3.2 is not the same as the activation energy introduced in Section 4.3.1 with the Arrhenius law. The Arrhenius law is within the technically used temperature regime a very good approximation but it is not a physically exact equation. For most Arrhenius activation energies derived from kinetic experiments all temperature influences on the system are “summarized” within the parameter of the activation energy.

Technical reactions can profit in different ways from the higher reaction rate enabled by a catalyst. Obviously, a higher reaction rate leads to higher space–time yield and thus the same amount of product can be produced in a smaller reactor. This leads directly to lower investment necessary for the reactor inventory. For exothermic reversible reactions, such as, for example, methanol synthesis, ammonia synthesis, SO_2 oxidation, or the water-gas shift reaction, a catalyst of higher activity allows us to obtain the same reaction rate at a lower temperature, which leads to higher equilibrium conversion (see also Section 4.2.1 and Example 4.2.4). In addition, endothermic reversible reactions can also profit from a highly active catalyst that provides the same reaction rate at lower temperature. Even if the equilibrium conversion is lower at lower temperature here, the benefit in this case results from the fact that the catalyst helps to operate below a technically critical temperature, for example, the decomposition temperature of the product or a temperature that would require special reactor equipment. A typical example of the latter is steam reforming of methane to produce syngas.

Even more important than the rate-accelerating effect of a catalyst is its ability to favor one specific reaction pathway in the cases with more than one thermodynamically possible pathway. From an industrial perspective selectivity is generally more important than activity. This becomes understandable in view of the economic damage caused by converting a valuable feedstock into a worthless product. Figure 2.3.3 shows for the specific example of the heterogeneous catalyzed oxidation of propylene the influence of different catalysts on the main product formed.

In terms of the energy profile diagram in Figure 2.3.2 the catalyst’s influence on the selectivity means that more than one energy profile for the catalyzed reaction is found, with each profile leading to different products. For different catalysts the relative energies of the transition states on the way to the different products differ.

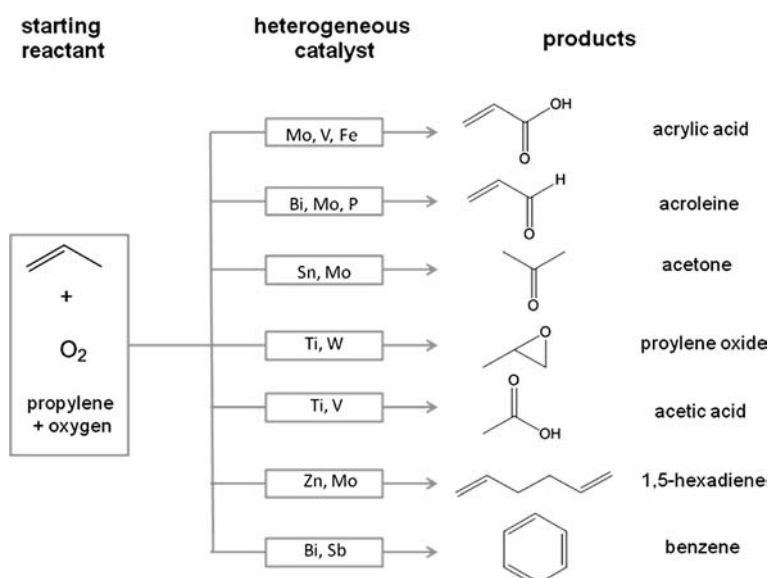


Figure 2.3.3 Main products formed in the oxidation of propylene depending on the active metal of the applied heterogeneous catalyst.

A selective catalyst accelerates one specific pathway and slows all other possible pathways down. The resulting relative rate constants of the different pathways determine the selectivity, as exemplified by Eq. (2.3.6) for the least complicated case of a parallel reaction in which feedstock A is converted into product B or product C, with both reactions being of the same reaction order, with k_1 as rate constant for conversion into B and k_2 as rate constant for conversion into C (see Section 4.3.2 for details):

$$S_B = \frac{k_1}{k_1 + k_2}, \quad S_C = \frac{k_2}{k_1 + k_2} \quad (2.3.6)$$

Owing to the enormous relevance of rate acceleration and selectivity enhancement for the industrial production of chemicals, tremendous research efforts have been devoted over the last 100 years to developing improved catalysts and optimized catalytic processes. Table 2.3.2 shows an overview of important discoveries in catalysis research that have led to major technical applications. Given the great advances in spectroscopic and analytic techniques, in modeling, and in materials synthesis in the last ten years, many more success stories and innovations can be expected from the “art of catalysis” in the years to come.

Table 2.3.2 Important discoveries in catalysis that led to major technical applications.

Year	Discovery
1913	Synthesis of ammonia from N ₂ and H ₂ (Haber–Bosch process)
1915	Oxidation of ammonia (Ostwald process)
1923	Methanol synthesis from CO/H ₂
1935	<i>Acetobacter suboxydans</i> for selective oxidation for vitamin C production
1936	Catalytic cracking of heavy oil fractions
1938	Liquid fuels from CO/H ₂ (Fischer–Tropsch synthesis)
1939	Hydroformylation
1962	Synthesis gas from methane
1969	Immobilized acylase for optically pure amino acids
1975	Catalytic cleaning of automotive exhaust gases
1977	Higher olefins from ethylene (Shell Higher Olefin Process)
1984	Enantioselective catalysis for menthol and others
1985	Enzymes are active in organic solvents
1993	Genetic engineering for improvement of enzymes
1996	Enantioselective hydrogenation for (S)-metolachlor production

2.3.2

Homogeneous, Heterogeneous, and Biocatalysis

Many different compounds can act as a catalyst. For different reasons – that will be treated in more detail below – the use of solid materials as catalysts (so-called heterogeneous catalysis) plays the most important role in chemical technology. Solid contacts catalyze about 80% of all catalytic processes. Compounds that are dissolved in the reaction phase (so-called homogeneous catalysts) catalyze about 15% of all catalytic processes. Biocatalysts contribute the remaining 5%. They are applied as a soluble enzyme or as whole cell. Both types may be immobilized on a support, forming a heterogenous catalyst with slightly different properties than the heterogeneous catalyst described below.

When it comes to industrial catalysis easy processing is the characteristic strength of heterogeneous catalysis compared to homogeneous catalysis. This advantage concerns mainly the isolation of a catalyst-free product combined with an easy recovery and recycling of the precious catalyst (note that catalytically active metals are usually rare and expensive). In the case of heterogeneous catalysis, the separation and isolation step is usually straightforward. Catalyst and products are already present in two different phases; separation by simple filtration is the method of choice.

Heterogeneous catalysis is a surface phenomenon. Therefore, a highly active heterogeneous catalyst requires a large specific surface area. As compact particles have specific surface areas below $1\text{ m}^2\text{ g}^{-1}$, most heterogeneous catalysts are porous in nature. Note that, in theory, the specific surface of compact materials could reach higher values for very small particles (about $100\text{ m}^2\text{ g}^{-1}$ for $d_p > 100\text{ nm}$, see Figure 4.5.1). However, it is very difficult and mostly impossible to handle such small particles in a catalytic reactor due to the resulting high pressure drop. Therefore, compact, non-porous catalyst are only found in applications where specific selectivity problems linked to the formation of consecutive reaction products make it unfavorable to realize longer residence times of the desired intermediate product in a porous solid, or where the external mass transfer dominates the effective reaction rate, and thus the reactant concentration is nearly zero at the external surface (and also in the pores, if a porous catalyst would be used). A particular important example of the latter kind is ammonia oxidation to NO (Section 6.4).

Typical porous catalysts are characterized by specific surfaces of $100\text{--}1000\text{ m}^2\text{ g}^{-1}$. An important class of porous materials for heterogeneous catalysis is zeolites. These crystalline, hydrated aluminosilicates consist of a very regular three-dimensional, polyanionic network of SiO_4 and AlO_4 tetrahedra linked through oxygen atoms. The void spaces in zeolite networks have dimensions on the scale of the reactant and product molecules, which allow selective diffusion of molecules into the catalyst pores (“form selectivity”). Zeolites play a very important role in refinery and petrochemical processes, such as, for example, catalytic cracking, isomerization or alkylation. While in catalysis with pure zeolites the porous material acts itself as catalyst, other important classes of catalysts use porous materials, such as, for example, alumina or silica to load it with the catalytically active transition metal. By a fine dispersion of the active metal crystallites (ideally in their most active size) on the supporting porous solid, a very effective usage of the expensive metal component can be realized.

In contrast to heterogeneous catalysis, classical homogeneous catalysis takes place in the bulk of a solvent. However, due to the lack of a phase boundary it is much more complicated in this case to isolate the fully dissolved transition metal complex from the desired reaction product. Often, distillation fails due to the thermal instability of the dissolved catalyst or the fact that unselective reactions occur in the bottom of the distillation column. Catalyst recovery and recycling strategies for homogeneous catalytic processes can therefore sometimes be rather complicated

Table 2.3.3 Homogeneous versus heterogeneous catalysis.

	Homogeneous catalysis	Heterogeneous catalysis
Selectivity	High, molecularly defined active centers	Variable, often undefined active sites
Reaction conditions	Mild, $T < 200^\circ\text{C}$	Often harsh
Sensitivity towards poisons	Low	High
Variability of steric and electronic properties	Possible by ligand effects	Difficult
Understanding	Plausible under random conditions	Often very difficult (<i>pressure & material gap</i>)
Catalyst/product separation	Difficult, often expensive	Straightforward
Robustness, thermal stability, service life	Often low	Often high

and involve steps like chemical treatment of the catalyst, salt precipitation, co-solvent addition, and solvent distillation steps. However, these difficult aspects of catalyst separation/recycling and thermal lability should not hide the fact that homogeneous catalysis offers several important advantages compared to heterogeneous catalyzed reactions. The applied catalyst complex is usually molecularly defined and can be rationally optimized by ligand modification. In principle, every metal atom is active in the reaction and displays the same reactivity. This allows mild reaction conditions (T usually $<200^\circ\text{C}$), leading often to high selectivities. Table 2.3.3 displays in a generalized manner the specific advantages and disadvantages of homogeneous and heterogeneous catalysts.

These points become understandable given that it is still somewhat impossible to synthesize a catalytic solid of technical relevance in which each active center is exactly in the same steric environment and has exactly the same electronic properties. In technical catalysis, the support is not an ideal surface but the product of a more or less defined precipitation, particle growth, or particle agglomeration process during its synthesis. Thus, the support is not uniform and contains many different sites at which the catalytic metal ends after the metal loading process (e.g., by impregnation, infiltration; see Section 2.3.3 for details of the catalyst preparation process). Of course these different sites at the faces, edges, or corners of the support will provide a different “ligand effect” to the supported metal. The situation is even more complex as very often defects, kinks, or other irregularities of the solid surface exert a very strong influence on the electronic properties of a catalytic metal deposited nearby. In the light of all these aspects it is not surprising that in many heterogeneous catalysts only a minor part of the metal loading is responsible for the largest part of the catalytic activity observed.

In contrast, homogeneous catalysts are in most cases transition metal complexes, purified by washing, crystallization, or chromatography steps and used as pure compounds. These complexes are applied in a homogeneous and uniform solvent environment during catalysis. Consequently, every metal atom experiences, in principle, exactly the same electronic and steric effects, leading to an extremely well-defined reactivity. This is why homogeneous catalysis is usually applied in cases where high selectivity is needed (e.g., due to high feedstock value) and the selectivity pattern is complex (e.g., complex regio- or stereoselective reactions). Table 2.3.4 displays important examples of homogeneous catalyzed processes. Figure 2.3.4 displays the different chemical natures of typical homogeneous and heterogeneous catalysts for the examples of a chiral Ni-complex for homogeneous catalyzed, asymmetric C—C linkage reactions and a schematic representation of a heterogenous, precious metal on a support catalyst.

An elegant way to combine the advantages of homogeneous catalysis with an efficient strategy for catalyst recycling is liquid–liquid biphasic catalysis: Only one phase contains the dissolved catalyst, allowing easy product separation by phase

Table 2.3.4 Important examples of homogeneous catalysis in the chemical industry.

Process	Catalyst	Capacity (kt a ⁻¹)
Hydroformylation	HRh(CO) _n (PR ₃) _m HCo(CO) _n (PR ₃) _m	3690 2445
Hydrocyanation	Ni[P(OR) ₃] ₄	~1000
Ethene oligomerization (SHOP)	Ni(P ^o O)-chelate complex	870
Acetic acid (Eastman Kodak)	HRhI ₂ (CO) ₂ /HI/CH ₃ I	1200
Acetic acid anhydride	HRhI ₂ (CO) ₂ /HI/CH ₃ I	227
Metolachlor (Novartis)	[Ir(ferrocenyldiphosphine)] I/H ₂ SO ₄	10
Citronellal (Takasago)	[Rh(binap)(cod)]BF ₄	1.5
Indenoxyde (Merck)	Chiral Mn(salen) complex	0.6
Glycidol (ARCO, SIPSY)	Ti(O _i Pr) ₄ /diethyl tartrate	Several tons

separation (Figure 2.3.5). After decantation, the catalyst phase can be recycled without further treatment.

However, the right combination of catalyst, catalyst solvent, and product is crucial for the success of biphasic catalysis (Drießen-Hoelscher, 1998). The catalyst solvent has to provide excellent solubility for the catalyst complex for full catalyst immobilization but must not compete with the substrate for the free coordination sites at the catalytic center. Furthermore, a reaction system providing a miscibility gap throughout the whole conversion range is required. Finally, another prerequisite of liquid–liquid biphasic catalysis is the provision of a catalyst solvent with enough solubility for the feedstock to allow sufficient reactant concentration in the reaction phase and thus sufficient reaction rate. A technical example of liquid–liquid biphasic catalysis is given in Section 6.15. The same section discusses modern aspects of solvent development and advanced solvents for the application in liquid–liquid multiphase catalytic processes.

Biocatalytic processes have been used for centuries, especially in the preparation of food and beverages. In the last century, biocatalysis were introduced into industrial production processes as well (Table 2.3.5). When speaking about biotechnological processes one has to distinguish between fermentation processes where products are synthesized by microorganisms (bacteria, yeasts) or higher cells (animal cells, plant cells) from components in the fermentation broth such as carbohydrates, amino acids, and trace elements. Product examples are amino acids, vitamins, pharmaceuticals, or recombinant pharma proteins such as erythropoietin or Factor VIII. On the other hand, the term biocatalysis or biotransformation is used for processes where a starting material is converted into the desired product in one step only. This can be done using either (partly) purified enzymes or whole cells. Product examples range from bulk chemicals such as acrylamide, fine chemicals, and chiral synthons such as chiral alcohols to food ingredients such as high fructose corn syrup. In addition, in daily life enzymes play an important role: they are ingredients in washing powders, “stone washed jeans” are obtained by bio-bleaching, and citrus fruits are peeled with the help of pectinases.

Figure 2.3.4 Typical transition metal complex for homogeneous catalysis (a); schematic view of the surface of a real precious metal on a catalyst support (b).

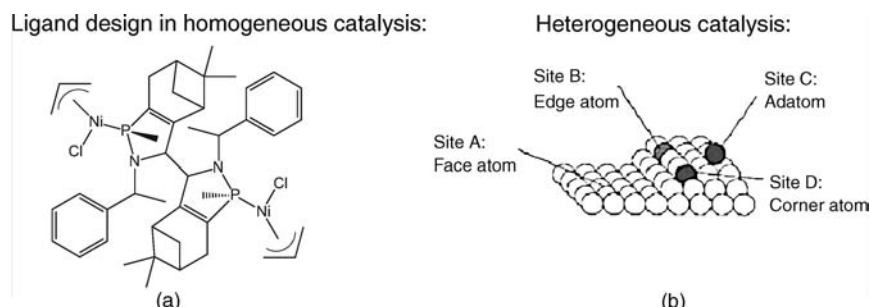


Table 2.3.5 Important examples of biocatalysis in the chemical industry.

Process/product	Catalyst	Capacity (kt a ⁻¹)
Kinetic resolution of amino acids	Amino acylase	>1
Hydrocyanation	Hydroxynitrile lyase	0.01
Kinetic resolution of amines	Lipase	>1
6-Aminopenicillanic acid	Penicillin amidase	10
Acrylamide	Nitrile hydratase	>30
High fructose corn syrup	Glucose-fructose isomerase	>1000

Owing to evolutionary processes biocatalysts function at low temperatures (10–70 °C), ambient pressure, and in an aqueous environment at a neutral pH. This may require different handling than for a heterogeneous or homogeneous catalyst as described above. However, enzymes in native form can be applied in liquid–liquid biphasic catalysis, normally with water or buffer as the phase containing the biocatalyst. Zaks and Klibanov demonstrated in the 1980s that enzymes also work in almost water-free organic solvents. A minimum amount of water – best described by the physicochemical water activity – has to be present to maintain the enzyme's structure and activity. However, enzymes do not dissolve in organic solvents and are used either adsorbed or coupled to an insoluble support, mostly organic polymers. When an immobilized enzyme is used, mass transport limitations may occur and must be treated accordingly. The so-called Michaelis–Menten kinetics is a form of saturation kinetics found for most enzymes, but is also observed for other homogeneously soluble catalysts.

2.3.3

Production and Characterization of Heterogeneous Catalysts

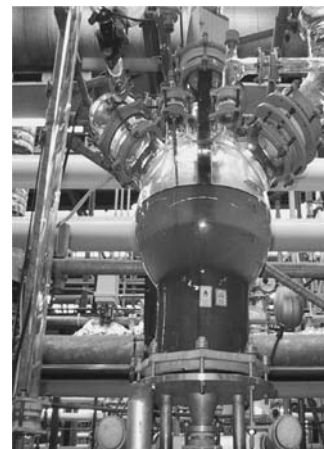
In principle, solids found in nature can display activity as heterogeneous catalysts (e.g., iron ores are applied in high temperature Fischer–Tropsch catalysis). However, after 100 years of intense research in catalysis it has been found that in most cases synthetic materials are more suitable as the reproducibility of their synthesis is higher and their specific properties can be adjusted by the synthetic procedure.

The most important method to produce catalyst supports or solid catalysts is *precipitation*. The precipitation process is realized by controlled addition of a precipitation reagent (very often a change of pH by addition of acid or base). Depending on the desired composition of the catalyst material, co-precipitation of more than one component is frequently applied. An alternative process is the precipitation of metal salts onto preformed support particles.

Precipitation is a complex sequence of supersaturation, seeding, and coagulation. All three steps determine particle size and size distribution of the obtained particles. The process is strongly dependent on the exact precipitation conditions and is still difficult to model. Table 2.3.6 displays examples of technically important catalysts or catalyst supports produced by precipitation.

A few industrial important heterogeneous catalysts are prepared by *melt processes*. Examples are the Fe-catalyst for the Haber–Bosch process and the Pt/Rh-net for the ammonia oxidation in the Ostwald process (see also Section 6.4). Melting is also the initial process step for the preparation of Raney-nickel and Raney-copper catalysts. For these catalysts an alloy of Ni/Cu and Al is prepared by melting. This alloy is later treated with NaOH to dissolve the Al from the solid to create pores and reactive surface sites. Raney-Ni and Raney-copper are very important hydrogenation catalysts.

For the synthesis of zeolites and related compounds, *hydrothermal synthesis* and *sol–gel* processes are of importance. In the hydrothermal synthesis a hydrogel is prepared from the Si- and Al-sources in an aqueous medium. The latter often



Photograph of a homogeneously catalyzed, liquid–liquid biphasic reaction.

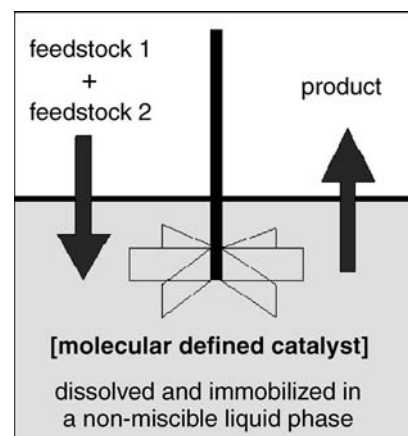


Figure 2.3.5 Schematic view of a liquid–liquid biphasic catalytic reaction; note that the diagram shows the stirrer when it is switched off for phase separation.

Table 2.3.6 Important examples of catalysts or catalyst supports produced by precipitation.

Material	Application examples in catalysis
$\gamma\text{-Al}_2\text{O}_3$	Support for $\text{CoO}\text{-MoO}_3$ in the catalytic dehydrosulfurization of refinery cuts; catalyst in the Claus process; catalyst for the dehydratization of alcohols
SiO_2	Support for V_2O_5 in the oxidation of SO_2 ; support for Pt, Pd, and Ni for catalytic hydrogenation reactions
Fe_2O_3	Catalyst for Fischer-Tropsch synthesis; catalyst component for the ethylbenzene dehydrogenation catalyst
TiO_2	Catalysts component for the reduction of nitrogen oxides with NH_3
$\text{Cu-ZnO/Al}_2\text{O}_3$	Catalyst for low pressure MeOH synthesis
$(\text{VO})_2\text{P}_2\text{O}_7$	Catalyst for the selective oxidation of <i>n</i> -butane to maleic acid anhydride
$\text{Bi}_2\text{O}_3\text{-MoO}_3$	Catalyst for the selective oxidation of propene to acrolein

contains ammonium salts and detergents as structural modifiers. This gel is later transferred to an autoclave and crystallized at temperatures of up to 200 °C.

In a *sol-gel process*, metal organic starting materials like triisopropylaluminium, tetrabutoxytitan, and tripropoxysirconium are applied as starting materials of a controlled hydrolysis and condensation process. In contrast to precipitation sol-gel processes are more complex and more expensive. However, sol-gel processes allow the preparation of oxide catalysts in higher purity and with better control of the pore system.

Many catalysts use a precious metal as active component. Owing to the high price of these metals, it is of great importance to prepare a support/catalyst system in such a manner that all metal atoms are fully available at the surface for the reaction (=100% dispersion, 10% of atoms are surface atoms and available for catalysis = 10% dispersion). The most important process by which to achieve a suitable metal loading on a support of choice is *impregnation*. During impregnation, the support is typically contacted with an aqueous solution of a suitable precious metal salt or precursor. After adsorption of the metal component, the solid is isolated, thermally treated, and (often) reduced. Important technical catalysts prepared by impregnation are the $\text{CoO}\text{-MoO}_3/\gamma\text{-Al}_2\text{O}_3$ catalyst for the desulfurization of fuels (Section 6.8) and the $\text{Pt-Re}/\gamma\text{-Al}_2\text{O}_3$ catalyst for the isomerization/dehydrogenation of fuels in the platforming process (Section 6.9).

If the catalyst support is an ion-exchange material (e.g., in the case of zeolites) *ion exchange* is another suitable process to load a catalytic active compound on a support. For zeolites, the Na^+ form of the material is often prepared by hydrothermal synthesis. This material is contacted with an electrolyte containing the salt of the intended active compound. By solid isolation, thermal treatment, and often reduction the active supported catalyst is obtained.

All the processes mentioned above are characterized by the fact that a support is treated with a suitable solution of the precious metal. An alternative preparation method in which a solid react with a metal precursor from the gas phase is *metal-organic vapor deposition* (MOCVD). In this process, a volatile metal organic precursor strikes the hot surface of the support. This contact leads to the immediate thermal decomposition of the surface with formation of a metal species on the support that can be further treated thermally, often under reducing gas atmospheres.

For scientific studies and quality control, detailed characterization of the produced catalytic material is necessary. A key method to test a catalytic material is of course to study its performance in a reaction by a detailed analysis of its reactivity, selectivity, and lifetime. Note in this context that the observable kinetics of a heterogeneous catalyst or a catalyst in any multiphase reaction system is usually a complex interplay of diffusion and reaction processes (for details see Chapter 4).

Apart from catalyst characterization by kinetic investigations, modern catalyst research has a plethora of spectroscopic methods at hand to determine the size,

Table 2.3.7 Important spectroscopic and analytic techniques used to characterize heterogeneous catalysts (for definition of abbreviations see Notation).

Probed property	Technique or method
Chemical composition	AAS, AES, XRF
Phases, phase transitions	XRD, SEM, TGA, DTA, TPR/TPO
Size and form of catalytic particles	SEM, TEM, DLS
Nature, size, and form of metal clusters within the catalyst particles	SEM, TEM, chemisorption (H_2 , O_2 , CO), magnetism, XRD
Internal surface and porosity	Physisorption (N_2 , Ar, He, CO_2 , noble gases) evaluated, for example, via the BET or QSDFT method, Hg-porosimetry, thermoporometry, micro-CT
Functionality/active centers:	
• local structure (averaged over particle)	IR, Raman, UV/Vis, NMR, ESR, EXAFS, Mössbauer
• surface structure and composition	XPS, UPS, ISS, SIMS, ETM, AFM
• reactivity	TPD, adsorption of probe molecules (including spectroscopic characterization of adsorbats), catalytic test reactions

shape, specific surface, porosity, chemical composition, surface composition, and chemical functionality of a heterogeneous catalyst. An overview of the most important methods is given in Table 2.3.7 (Weitkamp, 2003). A detailed description of these methods is found in Ertl (2008).

In the context of this textbook only a few important methods will be described briefly to give an impression of their different measuring principles, the type of information provided, and potential interplay. These short descriptions may also illustrate that the comprehensive characterization of a heterogeneous catalyst is a complex task and requires – along with the researcher's expertise – highly sophisticated and often expensive equipment.

Atomic absorption spectroscopy (AAS) is used to determine the chemical composition of the metal loading of a supported catalyst. In a sample preparation procedure the catalyst is treated with very strong and often oxidizing acids to extract all metal atoms as ions in solution. This solution is injected into a spectrometer that gives a quantitative analysis of all metal components in the solution based on the spectral absorption (or emission in the case of Auger electron spectroscopy, AES) in a flame. Note that in this method all dissolvable metal atoms are analyzed not only the catalytic active surface atoms.

X-ray diffraction (XRD) is the method of choice to analyze the crystalline structure of a catalyst or catalyst support. For example, it is the standard procedure used to determine and check the structure of crystalline zeolites after synthesis.

Owing to the importance of the catalyst pore structure for the performance of a catalyst, its determination is also highly important. Total surface area, total pore volume, and pore size distribution are directly connected values. According to IUPAC (International Union of Pure and Applied Chemistry) pores are defined with respect to their pore diameters d_{pore} as micropores ($d_{\text{pore}} < 2.0 \text{ nm}$), mesopores ($2.0 \text{ nm} \leq d_{\text{pore}} \leq 50 \text{ nm}$), and macropores ($>50 \text{ nm}$).

Surface analysis via physisorption is the appropriate technique to analyze the specific surface of a catalyst. The catalyst sample is contacted at different pressures (normally from vacuum to atmosphere) with a gas that physisorbs under appropriate temperature conditions (normally N_2 at 77 K) in a defined manner on its surface. Owing to this physisorption process the pressure in the sample chamber changes. From this pressure drop, the physisorbed amount of gas per sample mass is determined. The adsorbed amount versus the applied pressure is called the sorption isotherm and with different models, such as, for example, the most common BET (Brunauer, Emmett, and Teller) model, the available surface can be calculated from the isotherm. Other models like the BJH (Barrett, Joyner, and

Table 2.3.8 Typical conditions and catalyst lifetimes for important heterogeneous catalysts.

Process	Catalyst	Reaction conditions	Catalyst lifetime (years)
NH ₃ synthesis	Fe-K ₂ O/Al ₂ O ₃	450–550 °C 200–500 bar	5–15
Steam reforming of natural gas	Ni-CaO/Al ₂ O ₃	500–850 °C 30 bar	2–4
NH ₃ combustion	Pt nets	800–900 °C 1–10 bar	0.1–0.5
Catalytic reforming	Pt/Al ₂ O ₃	450–550 °C 5–50 bar	0.01–0.5 (coke formation; reversible deactivation) 2–15 (irreversible deactivation)
Catalytic cracking	Zeolites	500–600 °C 1–3 bar	10 ⁻⁵ (coke formation; reversible deactivation.) 0.1 (irreversible deactivation)

Halenda) or modern DFT (density functional theory) methods also allow to evaluate the pore size distribution from the same data. Sample preparation, highly defined experimental conditions, and very precise pressure measurements are the key factors for accurate surface analysis. While sorption experiments probe pores in the size range from approximately 0.3 to 100 nm, *mercury porosimetry* is the method of choice to determine the total pore volume and the pore size distribution from 5 nm up to 500 µm. The method pushes liquid mercury under high pressure into the porous material and the Hg volume accommodated in the solid is monitored as a function of pressure. Following the Kelvin equation, a higher pressure is necessary to push the mercury into smaller pores. Therefore, from the amount of mercury infiltrated into the solid as a function of pressure the pore size distribution can be obtained.

X-ray photoelectron spectroscopy (XPS) is an ultrahigh vacuum spectroscopic technique used to investigate the surface composition and surface structure of a catalyst. X-ray irradiation hits the sample and, by energy absorption of the surface elements, photoelectrons are emitted. The kinetic energy of the latter is determined in an analyzer. The energetic difference between the energy of the incoming X-ray irradiation and the kinetic energy of the photoelectrons determined in the analyzer gives a direct indication of the binding energy the electrons experienced in the element they originate from. In this way, XPS is a quantitative, element specific, oxidation state specific, and surface sensitive characterization method for solid catalysts.

2.3.4

Deactivation of Catalysts

During the operational lifetime of most catalysts, their activity decreases. Interestingly, the time period of economic operation can be very different even for commercial catalysts and ranges from a couple of seconds to many years. Table 2.3.8 gives an overview of some important heterogeneous catalyzed reactions, their reaction conditions, deactivation mechanism, possible regeneration options, and lifetime. It can be seen from the table that there is no direct correlation between thermal stress and lifetime.

In most cases, the deactivation of heterogeneous catalysts can be attributed to one of the four processes displayed in Figure 2.3.6.

Poisoning is a deactivation pathway in which at least one component of the reaction mixture adsorbs in a very strong – often irreversible – manner to the catalytic active center (Figure 2.3.6a). Kinetically speaking, the number and concentration of catalytic sites for this process reduces over time. In cases in which the catalytic material is characterized by different catalytic centers of different reactivity the poisoning process can be selective for one sort of center. By selective poisoning

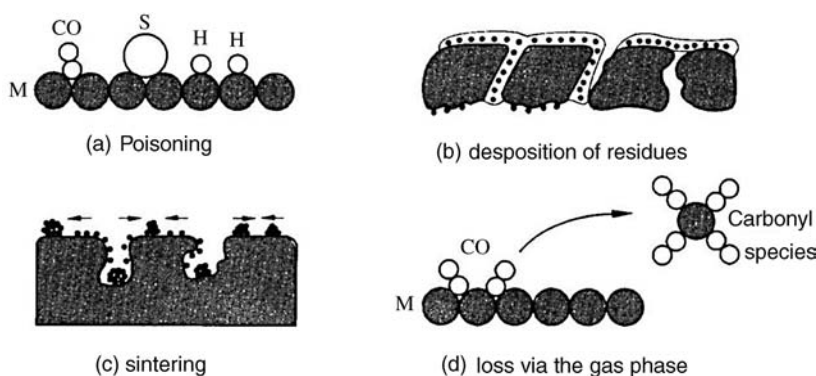


Figure 2.3.6 Schematic view of the four main processes leading to deactivation.

experiments it is possible to learn more about the chemical nature of the different catalytic sites in a material. In technical catalysis, selective poisoning is sometimes used to eliminate unwanted side reactions caused by catalytic sites that are too active, for example, in the case of reforming of heavy fuels (Forzatti and Lietti, 1999). Owing to the different reactivities of technical catalysts, the chemical nature of poisoning components can also be very different. Typical poisons for technical important heterogeneous catalysts are displayed in Table 2.3.9 (Weitkamp and Glaeser, 2003; Kern and Jess, 2006).

Deposition of residues or coking is a process in which process components form a solid, non-porous layer on the catalyst surface that prevents the reactants reaching the active sites or even entering the porous structure of the catalyst (Figure 2.3.6b). In terms of kinetic, coking is again a process in which the number of accessible catalyst centers reduces over time. It is frequently observed in high temperature operations with hydrocarbon feedstocks, for example, in refinery or petrochemical processes. Depending on the temperature, coke is a hydrogen-rich carbon material (“soft coke” formed at low temperatures) or a polycyclic, hydrogen-poor material (“hard coke” formed at high temperatures). In some refinery and petrochemical processes coke deposits of up to 20% with respect to the catalyst mass have been reported.

A convenient strategy to reduce coke formation is the addition of hydrogen or water vapor to the reactor. Hydrogen hydrogenates coke precursors to fluid hydrocarbons. This is the reason why in the reforming of heavy fuels (platforming) the reactor is operated at H_2 pressures of up to 40 bar even though a low pressure would be favorable to shift the dehydrogenation equilibrium to the desired aromatic products (see also Section 4.2).

Once the catalyst is deactivated by coke it is usually possible to perform an oxidative regeneration step to remove the carbon from the catalytic surface. Special care is necessary in this process, however, to keep the temperature in this strongly exothermic step ($\Delta_R H = -393 \text{ kJ mol}^{-1}$) below the critical temperature at which the catalyst starts to suffer from the sinter processes (e.g., T_{sinter} is 550 °C in the case of the Pt/Al₂O₃ catalyst for heavy fuel reforming). Therefore, the engineering of an optimized catalyst regeneration process requires detailed knowledge of the kinetics of coke combustion and the development of quantitative models for the prediction

Table 2.3.9 Examples for typical catalyst poisons in industrial catalytic processes.

Reaction	Catalyst	Typical poison
$N_2 + 3H_2 \rightarrow 2NH_3$	Fe	CO
$CH_4 + H_2O \rightarrow CO + 3H_2$	Ni/α-Al ₂ O ₃	H ₂ S
$CO + 2H_2 \rightarrow CH_3OH$	Cu-ZnO/Al ₂ O ₃	H ₂ S, AsH ₃ , PH ₃ , HCl
$C_2H_4 + 0.5O_2 \rightarrow C_2H_4O$	Ag/Al ₂ O ₃	C ₂ H ₂
Automotive exhaust gas cleaning	Pt-Rh	Pb, P, SO ₂

of concentration and temperature profiles in the reactor [see Section 6.9.3 and Kern and Jess, 2006 for details].

Sintering describes a thermally induced surface diffusion process in which the number of active catalytic centers reduces by an agglomeration process (Figure 2.3.6c). Sintering is mainly observed for supported metal or oxide catalysts. Two different mechanisms have been suggested for sintering (Forzatti, 1999): the migration of single metal atoms that are captured by particles, leading to particle growth, and the migration of small particles followed by agglomeration to bigger particles. As a rule of thumb, metal particles can start to undergo sintering at temperatures of $0.3\text{--}0.5T_{\text{melt}}$, depending on their particle size. Stabilizers in the catalyst formulation have been found to prevent or slow down sintering. In most cases, sintering is irreversible and the sintered catalyst has to be replaced by a fresh one.

Loss via gas phase occurs only if at least one of the catalyst species on the surface shows a relevant vapor pressure under the reaction conditions (Figure 2.3.6d). Note that during a catalytic operation, for example, in the presence of impurities, volatile catalyst species may form that are not part of the catalytic cycle. Typical volatile complexes that can form under catalytic conditions in technical reactors are metal carbonyls. Another important example of catalyst loss via the gas phase is the catalytic oxidation of ammonia in the Ostwald process (Section 6.4). Here the catalyst, a non-porous Pt/Rh net, reacts at the very high reaction temperatures of 900°C with O_2 to give PtO_2 which is volatile enough under these harsh conditions to leave the reactor via the gas phase (Hagen, 1999). By installation of Pd/Au wires behind the Pt/Rh net, up to 60% of the volatile precious metal vapor can be recondensed.

Catalyst deactivation also occurs in homogeneous catalysis. Here, similarly, catalyst poisoning means that one component from the reaction mixture coordinates in a very strong or even irreversible manner to the dissolved catalytic center. A major catalyst deactivation route in homogeneous catalysis is also thermal degradation of the active metal complex. To understand this phenomenon we have to take into account that hardly any organometallic transition metal complex is stable beyond 200°C , with many interesting complexes showing slow degradation even at much lower temperatures. Another very important deactivation route is the reaction of components and impurities with the ligand in a way that affects the ligand's ability to remain coordinated to the metal (e.g., the oxidation of phosphine complexes by traces of oxygen in the reaction system). Coking, sintering, and evaporation of catalyst components are irrelevant in most homogeneously catalyzed reactions, mainly due to the much lower temperature level in these catalytic reactions.

The deactivation of a catalyst with activity a_{cat} (here dimensionsless, that is, relative to the initial activity) occurs over time. To obtain manageable equations to describe in a quantitative manner catalyst deactivation it is useful to define a rate of deactivation r_{deact} (dimensionless, i.e., the ratio of the actual reaction rate to the initial rate) that may be equivalent to the reduction of the number of active sites N_{act} (relative to the initial number) over time, Eq. (2.3.7). Note that t' is the time on stream of the catalyst, which may be different to the reaction time:

$$r_{\text{deact}} = \frac{da_{\text{cat}}}{dt'} = \frac{dN_{\text{act}}}{dt'} \quad (2.3.7)$$

In most cases r_{deact} will depend on the temperature T , the concentration of deactivating components c_{deact} , and/or on the activity a_{cat} itself (with k_{deact} , $k_{0,\text{deact}}$, and $E_{A,\text{deact}}$ as rate constant, pre-exponential factor and activation energy, respectively, of the deactivation). Consequently, r_{deact} may be expressed in quantitative terms as:

$$r_{\text{deact}} = k_{\text{deact}} f(a_{\text{cat}}, c_{\text{deact}}) \quad \text{with} \quad k_{\text{deact}} = k_{0,\text{deact}} e^{-\frac{E_{A,\text{deact}}}{RT}} \quad (2.3.8)$$

In the least complicated case, a power law rate expression can be applied:

$$r_{\text{deact}} = -\frac{da_{\text{cat}}}{dt'} = k_{\text{deact}} a_{\text{cat}}^n c_{\text{deact}}^m \quad (2.3.9)$$

For example, in a pure sintering process, no deactivating component is considered ($m = 0$) and the deactivation is first order with regard to the (actual) remaining activity. Thus we obtain after integration for $a_{\text{cat}}(t')$:

$$a_{\text{cat}}(t') = e^{-k_{\text{deact}} t'} \quad (2.3.10)$$

To determine the reaction rate r of a reaction of interest we can use $a_{\text{cat}}(t')$ as a multiplicative term, with r_0 being the initial rate of the fresh catalyst:

$$r = r_0 a_{\text{cat}}(t') \quad (2.3.11)$$

For an irreversible reaction of reactants A and B [with the initial relative activity $a_{\text{cat}}(t' = 0) = 1$], and assuming power law first-order kinetics regarding both reactants A and B, we obtain for this example of a catalytic reaction under deactivation by a sintering process the following expression (with k as the initial rate constant of the reaction and k_{deact} as the rate constant of deactivation):

$$r = k c_A c_B e^{-k_{\text{deact}} t'} \quad (2.3.12)$$

Of course, depending on the assumption for the underlying catalyst deactivation mechanism, the parameters n and m of Eq. (2.3.9) may have different values and, consequently, quite different equations can occur. Note that in the case of catalyst poisoning by a reaction the situation in the reactor can become rather complicated. For example, in a tube reactor, the catalyst deactivation process becomes then a function of the position in the tube.

2.3.5

Future Trends in Catalysis Research

Future trends in catalysis research can be related to the relevant application areas for industrial catalysts. New challenges arise from, for example, changing raw material availability and quality, new economic and even political boundary conditions, or new customer needs. These developments promote in many cases the search for new and better catalysts, which makes catalyst research highly important for sustainable economic growth. Important research topics within the actual catalyst development and optimization efforts are given below (Beller, 2010). The examples have been grouped according to the four main application areas of industrial catalysts (see also Section 2.3.1):

Environmental catalysis:

- better catalysts for cleaning water (e.g., nitrates from groundwater, catalytic degradation of pharmaceuticals from hospital wastewaters);
- better catalysts for the degradation/decomposition of toxic and dangerous molecules (e.g., hydrodechlorination of chlorinated hydrocarbons, catalytic oxidation of toxic waste);
- better catalysts for the decomposition of greenhouse gases (e.g., CH₄, N₂O) and hydrocarbons from industrial flue gas streams;
- reduction of the precious metal content in automotive exhaust gas catalysts;
- reduction of the start-up temperature of exhaust gas oxidation catalysts;
- long-term stable NO_x storage catalysts with a wide temperature window of operation.

Catalysts for refinery and energy applications:

- catalytic refinery technologies (cracking, isomerization, dehydrosulfurization, hydrogenation, etc.) that can work efficiently with poor crude qualities (very heavy, high in sulfur, high contents of N, P, and metals);

- development of catalysts for the direct conversion of alkanes (e.g., methane into aromatics or olefins; alkane oxidation, alkane dehydrogenation);
- development of catalysts for the efficient transformation of components from coal (e.g., more efficient coke hydrogenation catalysts, S-resistant catalysts for coal gasification);
- development of efficient catalysts for biorefinery concepts (e.g., depolymerization of cellulose, depolymerization of lignin, selective de-functionalization and re-functionalization of biogenic raw materials; note that biomass is rich in potential catalyst poisons, such as S, N, P);
- better catalysts for the selective transformation of syngas (CO/H_2) into fuels, olefins, and alcohols and development of catalysts for the transformation of CO_2 into fuels or fuel equivalents (e.g., methane, methanol);
- improvement of catalysts for the decentralized production of hydrogen from gas, oil, coal, and biomass (by reforming and water-gas-shift catalysis) or water (by electrolysis or by photoelectrocatalysis).

Catalysts for the production of polymers and materials:

- development of catalysts and catalytic processes for monomer production from gas, coal or biomass;
- better catalysts for the production of polymers, for example, higher tolerance against feedstock impurities and polar functional groups and better control of microstructure and morphology;
- catalysts for the manufacture of biodegradable polymers.

Catalysts for chemical synthesis:

- new catalyst technologies for sustainable and selective functionalization of aromatic compounds, for example, introduction of hydroxyl, amino, carbonyl, and carboxyl groups;
- catalytic technologies that combine the advantages of homogeneous and heterogeneous catalysis;
- catalytic technologies that combine chemo- and biocatalytic steps;
- catalytic technologies for chemical synthesis from renewable feedstocks.

Apart from these application related aspects, there are also several new methodologies in modern catalysis research that have already demonstrated their importance for the development of more efficient catalysts or processes. These include the following technologies:

- high-throughput experimentation;
- multifunctional reactors (catalytic membrane reactor, reactive distillation);
- catalytic microreactor technology;
- advanced solvents and materials in catalytic systems (e.g., ionic liquids, sc CO_2 , metal organic frameworks, nanostructures as catalyst supports, hierarchical materials as catalyst supports);
- *in situ* methods for catalyst monitoring or characterization;
- multi-scale modeling and simulation in catalysis.

Summary of Section 2.3 (take-home messages):

- **Catalysis** is of greatest relevance for chemical technology because about 90% of all chemical processes work with the help of at least one catalyst.
- Catalytic reactions are characterized by a **reaction sequence** in which one reactant (the catalyst) is re-formed in the final reaction step in the same stoichiometric amount as it was added (**catalytic cycle**). The number of cycles that a catalyst can undergo prior to its deactivation is a very important performance criterium in catalysis. This dimensionless characteristic number for each catalyst is called the **turnover number** (TON) and describes the catalyst's stability and lifetime.

- An important property of a catalyst is also its **ability to enhance the reaction rate** of a chemical reaction (activity). This can be characterized (mainly for enzymatic and homogeneous catalysis) by the number of cycles per time, the **turn-over frequency** (TOF). Alternatively, the catalyst activity can be given by the **reaction rate** referenced to some characteristic catalyst property, for example, the mass of a solid catalyst.
- More important than the rate accelerating effect is the ability to **favor a specific reaction pathway** (selectivity) in the case of several thermodynamically possible pathways.
- Many different compounds can act as a catalyst. The use of solid catalysts (**heterogeneous catalysis**) plays the most important role in chemical technology. Solid contacts catalyze about 80% of all catalytic processes. Compounds that are dissolved in the reaction phase (**homogeneous catalysts**) catalyze about 15% of all catalytic processes. **Biocatalysts** contribute the remaining 5%.
- Heterogeneous catalysis is a **surface phenomenon**. Therefore, a highly active heterogeneous catalyst requires a large specific surface area. Typical porous catalysts have specific surface areas of $100\text{--}1000\text{ m}^2\text{ g}^{-1}$.
- Homogeneous catalysis and biocatalysis take place in the bulk of a solvent, which makes it complicated to separate the dissolved transition metal complex from the desired product. An elegant way to combine the advantages of homogeneous catalysis with an efficient way of catalyst recycling is **liquid–liquid biphasic catalysis**.
- During the operational lifetime of most catalysts, their activity decreases by **deactivation**. The time period of economic operation can be very different even for commercial catalysts and ranges from a couple of seconds to many years. Catalyst deactivation of heterogeneous catalysts can be attributed four processes:
 - **poisoning**, in which a component of the reaction mixture adsorbs strongly;
 - **coking**, whereby a solid carbon-rich layer is formed on the catalyst surface under high temperature operations with hydrocarbon feedstocks;
 - **sintering**, where the number of active centers is reduced by agglomeration;
 - **loss via gas phase**, if one of the catalyst species shows a relevant vapor pressure under the reaction conditions. Typical volatile complexes that can form under catalytic conditions are metal carbonyls.

3

Thermal and Mechanical Unit Operations



Distillation towers of ethylene plant in Secunda, South Africa. Courtesy of SASOL.



Control valve of a urea plant. Courtesy of Uhde, Germany.

In Chapter 3, the following thermal and mechanical unit operations will be examined:

3.1 Properties of Gases, Liquids, and Solids

Ideal and real gas, heat capacity, Joule–Thomson effect, physical transformations of pure substances, and transport properties.

3.2 Heat and Mass Transfer in Chemical Engineering

Heat conduction, convection, boiling heat transfer, radiation, transient heat transfer, forced flow in pipes and packed beds, mass transfer by diffusion, and diffusion in porous solids.

3.3 Thermal Unit Operations

Heat exchangers, distillation, absorption, liquid–liquid extraction, adsorption, liquid–solid extraction, crystallization, and membranes

3.4 Mechanical Unit Operations

Conveyance of fluids, pressure loss in tubes, fixed, fluidized and entrained beds, compressors and pumps, mixing of fluids, and separation of solids from fluids.

Physical data of pure substances such as the phase behavior or the properties for transport of mass and heat are needed in many areas of chemical technology, ranging from thermal unit operations such as distillation up to catalytic processes that are frequently influenced by diffusion and heat transfer. In this chapter the following data on chemical media will be covered:



Typical technical gases. Courtesy of Linde Engineering, Germany.

- Real gases deviate from ideal gas behavior at higher pressures and lower temperatures, which has to be accounted by real gas equations and the real gas factor z .
- The heat capacity is important, for example, to calculate the increase of temperature, if energy is released by a chemical reaction.
- During adiabatic expansion of a real gas the temperature may decrease (*Joule-Thomson effect*), which is used for liquefaction of gases, for example, for air separation.
- Depending on pressure and temperature, phase transitions such as vaporization, liquefaction, and melting take place.
- If p and T exceed certain critical values, an isothermal change of p or an isobaric change of T no longer leads to a change of aggregation (supercritical stage).



Plant for liquefaction of natural gas in Kollsnes, Norway. Courtesy of Linde Engineering, Germany.

- Gradients of temperature or concentration lead to heat and mass transfer by conduction and diffusion. Thus it is important to know the transport properties of gases and liquids such as the diffusivity and thermal conductivity.
- For velocity gradients in fluids, the flow of momentum is determined by the viscosity.

3.1 Properties of Gases, Liquids, and Solids

3.1.1

Ideal and Real Gas

The kinetic theory of gases assumes that gas molecules or atoms occupy a negligible fraction of the total volume of the gas and that the forces of attraction between gas molecules are zero. Such a gas is called a perfect or ideal gas, and the equation of state is the “ideal gas law:”

$$\bullet \quad pV = nRT \quad (3.1.1)$$

which was developed based on the experiments of Robert Boyle, Edme Mariotte, and Joseph Gay-Lussac and later by calculations made by Amedeo Avogadro (see box). This equation relates the absolute pressure p (N m^{-2}), the volume V (m^3), the amount of substance n (mol), the temperature T (K, not $^\circ\text{C}$), and the ideal gas constant R ($8.314 \text{ J mol}^{-1} \text{ K}^{-1}$).

■ Originators of the ideal gas law

Robert Boyle (1627–1691), an Irish chemist, physicist, and inventor who discovered the inverse relationship of volume and pressure in gases (*Boyle's law*, $V \sim 1/p$) and was the first to publish it in 1662. He made investigations into the expansive force of freezing water, on crystals, on electricity, and on hydrostatics, studied the chemistry of combustion, and conducted experiments in physiology.

Edme Mariotte (1620–1684), a French physicist and priest, discovered *Boyle's law* independently of *Boyle* in 1676, so the law is also known as *Boyle–Mariotte's law*. In 1660, *Mariotte* also discovered the eye's blind spot. He worked on many subjects, such as the motion of fluids, the nature of color, the notes of the trumpet, the barometer, the fall of bodies, and the freezing of water.

Joseph Louis Gay-Lussac (1778–1850) was a French chemist and physicist. He is known mostly for two laws related to gases. In 1802, *Gay-Lussac* formulated the law that at constant pressure the volume of a gas increases by the same factor as its temperature ($V \sim T$). This law was first published by *Gay-Lussac*, but he referenced an unpublished work of **Jacques Charles** (1746–1823, French scientist and balloonist) from around 1787. This reference has led to the law being also known as *Charles's Law*. The second law of *Gay-Lussac* states that the pressure of a gas at fixed volume is directly proportional to its temperature ($p \sim T$). *Gay-Lussac* is also well-known for his hot-air balloon ascent with *Jean-Baptiste Biot* (Section 3.2.1.5) to a height of 6 km in an early investigation of the Earth's atmosphere (1804). In 1805, together with his friend and scientific collaborator *Alexander von Humboldt*, he also discovered that the composition of the atmosphere does not change with decreasing pressure and increasing altitude, respectively.

Amedeo Carlo Avogadro (1776–1856) was an Italian chemist, most noted for his contributions to the theory of molarity and molecular weight. In 1811, he declared the hypothesis of what we now call *Avogadro's law*: Equal volumes of gases, at the same temperature and pressure, contain the same number of molecules. Hence, the gas laws of *Boyle*, *Mariotte* and *Gay-Lussac* in combination with *Avogadro's Law* can be generalized by the ideal gas law. The *Avogadro* constant N_A , that is, the number of molecules in one mol is $6.022 \times 10^{23} \text{ mol}^{-1}$, is named in his honor. The numerical value of N_A was first estimated in 1865 by **Johann Josef Loschmidt** (1821–1895), an Austrian scientist.

N_A is related to the universal gas constant R by $R = N_A k$ with k (and R , respectively) as the fundamental constant relating temperature to energy (Section 3.1.4). **Max Planck** (1858–1947) first introduced k and gave an accurate value for it in his derivation of the law of black body radiation in 1900. The constant k , although **Ludwig Boltzmann** himself never introduced it, was named the Boltzmann constant, as he was the first (1877) who stated that the entropy of a gas is proportional to the logarithm of the number of microstates a gas can occupy with k as the factor of proportionality.

Equation (3.1.1) may also be written in terms of the molar volume, v_{mol} ($\text{m}^3 \text{ mol}^{-1}$), as:

$$p v_{\text{mol}} = RT \quad (3.1.2)$$

No gas is truly ideal, but many gases follow the predictions of the ideal gas law at normal temperature and pressure (1.013 bar, 0 °C) within 5% deviation. At lower temperatures or higher pressures, the behavior of a real gas may significantly deviate from that of an ideal gas, as shown in Figure 3.1.1 for the example of CO₂ by the plot of $p v_{\text{mol}}$ versus p . The ideal gas equation predicts that this plot should give horizontal lines that only depend on temperature, but we see by the experimental data that this is not the case (see also Example 3.1.1).

In 1873, Johannes van der Waals (see box) proposed a modification of the ideal gas law:

$$\left(p + \frac{a}{v_{\text{mol},\text{real}}^2} \right) (v_{\text{mol},\text{real}} - b) = RT \quad (3.1.3)$$

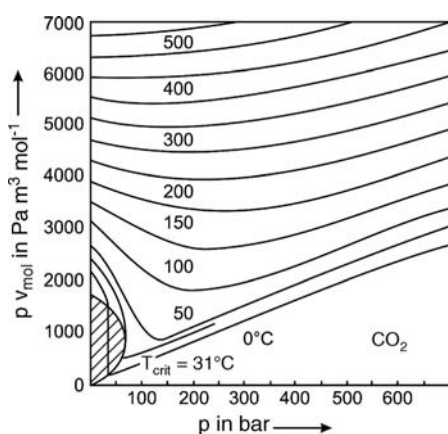


Figure 3.1.1 $p v_{\text{mol}}$ versus p plot for CO₂ (dashed area: liquid). Values from Jakubith (1998).

Johannes Diderik van der Waals (1837–1923) was a Dutch scientist famous for his work on the relationship between the pressure, volume, and temperature of gases. He was the first to realize the necessity of taking into account the volume of molecules and the intermolecular forces, now generally named after him as van der Waals forces. His career was quite unusual: After he had studied mathematics and physics, he became at first “only” director of a secondary school (1866). In 1873, he obtained a doctoral degree for his thesis “*On the continuity of the gas and liquid state*,” for which he got the Nobel Prize in Physics (1910). In 1876, he was appointed the first professor of physics at the University of Amsterdam.

Table 3.1.1 Van der Waals constants of selected gases. Data from Jakubith (1998).

Gas	a (Pa m ⁶ mol ⁻²)	$10^{-5}b$ (m ³ mol ⁻¹)
He	0.003	2.38
H ₂	0.025	2.67
N ₂	0.141	3.92
CO	0.151	4.00
O ₂	0.138	3.19
CH ₄	0.229	4.30
CO ₂	0.365	4.28
NH ₃	0.422	3.71

The van der Waals equation can describe the real gas behavior in sufficient approximation over a wide range of temperatures and pressures. It takes into account the molecular size as well as the molecular interaction forces by the introduction of two additional terms: (i) As the attractive forces tend to hold the molecules together, the pressure is lower than the ideal value. To account for this, the pressure is augmented by an attractive force term a/v_{mol}^2 , the internal pressure (where a is a constant). (ii) Likewise real molecules have a volume, and the interaction of molecules is strongly repulsive in close proximity. This is represented by the constant b , which is subtracted from the real volume to account for the fact that gases are not as compressible at high pressures as an ideal gas. Table 3.1.1 gives values of both van der Waals constants.

Example 3.1.1: Magnitude of deviation from ideal gas behavior (example CO₂)

The magnitude of deviation from ideal gas behavior can be illustrated by comparing the results using the *ideal gas law* and the van der Waals equation for 1 mol of CO₂ at 50 °C. For a volume of 0.0269 m³, the pressure would be exactly 1 bar according to the ideal gas equation, Eq. (3.1.1). With the data of Table 3.1.1, we obtain 0.997 bar according to the van der Waals equation [Eq. (3.1.3)]. Thus, both equations give essentially the same result for ambient pressure. But if the CO₂ is then compressed isothermally so that it fills a vessel that is 100 times smaller (0.000269 m³), a pressure of 100 bar is predicted by the ideal gas equation whereas the van der Waals equation yields a pressure of only 68.4 bar to achieve the same result.

For comparison: If we neglect the forces of attraction ($a=0$), we get 119 bar, and if we neglect the covolume ($b=0$), we obtain 49 bar. Thus, as the pressure increases, the van der Waals equation initially gives pressures that are lower than predicted by the ideal gas law because of the forces of attraction. However, at very high pressures, we finally end up with pressures that are higher than the ideal values. The influence of the volume of the CO₂ molecules (repulsive force) then dominates, for example, for 100 °C at $p > 600$ bar (Figure 3.1.1).

The deviation of a real gas from an ideal gas can also be expressed by only one parameter, the real gas or compressibility factor z , based on a simple extension of the ideal gas law:

$$\bullet \quad p v_{\text{mol,real}} = z RT \quad (3.1.4)$$

Comparison with the ideal gas law [Eq. (3.1.2)] leads to:

$$z = \frac{v_{\text{mol,real}}}{v_{\text{mol,ideal}}} \quad (3.1.5)$$

Figure 3.1.2 shows the influence of pressure on z for different gases (Figure 3.1.2a) and the influence of temperature and pressure for the example of nitrogen (Figure 3.1.2b). At moderate temperatures z initially decreases with increasing pressure for most gases as the influence of the attractive forces dominates. Exceptions are H₂ and He, where even at room temperature z increases with p as the parameter for the attractive force (value of constant a in Table 3.1.1) is very small. At high pressures, the influence of the covolume has an increasingly strong influence for all gases – as for H₂ already at

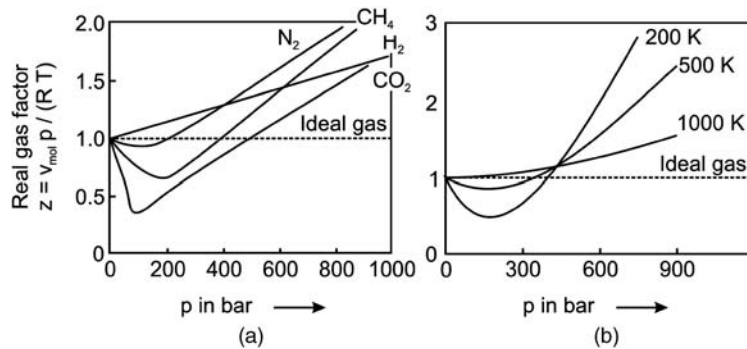


Table 3.1.2 Values of critical temperature and critical pressure of selected substances.

Gas	T_{crit} (K)	p_{crit} (bar) (10^5 Pa)	a calculated by Eq. (3.1.7) ($\text{Pa m}^6 \text{ mol}^{-2}$)	$10^{-5}b$ calculated by Eq. (3.1.8) ($\text{m}^3 \text{ mol}^{-1}$)
He	5.2	2.3	0.003	2.35
H_2	33.2	13	0.025	2.65
N_2	126.2	33.9	0.137	3.87
CO	132.9	35.0	0.147	3.95
O_2	154.6	50.5	0.138	3.18
CH_4	190.9	46.0	0.231	4.31
CO_2	304.2	73.8	0.366	4.28
NH_3	405.6	112.8	0.425	3.74
H_2O	647.3	216.9	0.563	3.10

ambient conditions – and the repulsive forces lead to values of z that are greater than unity.

The deviation from ideal gas behavior is very significant near the boiling temperature (Figure 3.1.1) and decreases with increasing temperature (Figure 3.1.2b).

Based on the van der Waals equation, Eq. (3.1.3), the compressibility factor z is given by:

$$z = \frac{v_{\text{mol},\text{real}}}{v_{\text{mol},\text{real}} - b} - \frac{a}{v_{\text{mol},\text{real}} RT} \quad (3.1.6)$$

as deduced from Eq. (3.1.3) by multiplying with v_{mol} , subsequent rearrangement, and comparison with Eq. (3.1.4). As shown by Example 3.1.2 and Tables 3.1.1 and 3.1.2, the van der Waals constants can be calculated based on the critical temperature and critical pressure (explained below) as follows:

$$a = \frac{27}{64} \frac{R^2 T_{\text{crit}}^2}{p_{\text{crit}}} \quad (3.1.7)$$

$$b = \frac{1}{8} \frac{RT_{\text{crit}}}{p_{\text{crit}}} \quad (3.1.8)$$

The van der Waals equation does not account adequately for real gas behavior at high pressures and low temperatures (Figure 3.1.3). Thus, for accurate calculations

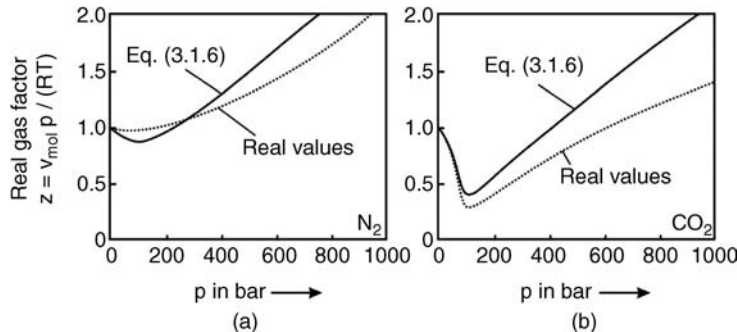


Figure 3.1.3 Real gas factor versus pressure of (a) N_2 (273 K) and (b) CO_2 (313 K): comparison of real values and calculations by the van der Waals equation [Eq. (3.1.6), with a and b as in Table 3.1.1].

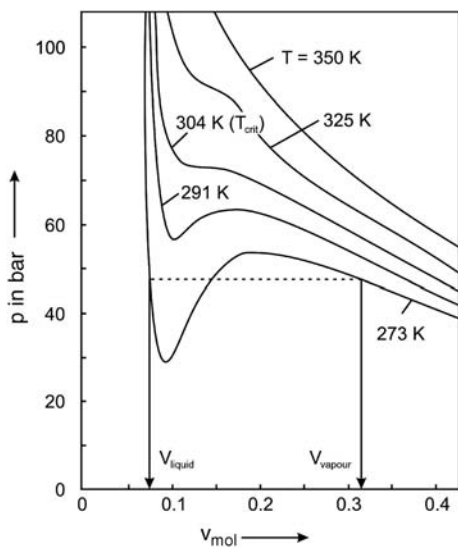


Figure 3.1.4 Isotherms of CO_2 according to the van der Waals equation.

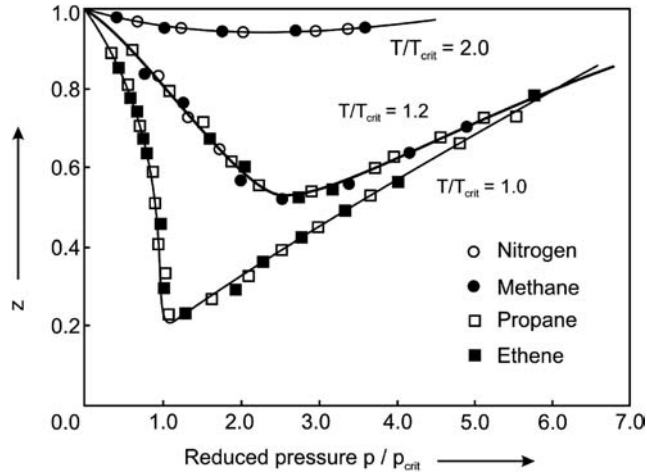
other real gas equations with, usually, more than two parameters [like a and b in Eq. (3.1.3)] should be used, for example, the Redlich–Kwong equation (1949), the Soave–Redlich–Kwong equation (1972), and the Peng–Robinson equation (1976) [details in Atkins and de Paula (2002) and Gmehling and Brehm (1996)].

The van der Waals equation does also not consider condensation. For example, Figure 3.1.4 shows isotherms of CO_2 according to the van der Waals equation. The oscillations, the van der Waals loops, are unrealistic – for example, an increase in pressure cannot lead to an increase in volume. Thus, we have to replace the loops with horizontal lines representing condensation.

At a certain critical value of temperature and pressure, for example, 304 K and 74 bar for CO_2 , the two-phase region vanishes (Figure 3.1.4). Now an isothermal compression or an isobaric decrease in temperature no longer leads to a change of state of aggregation. The corresponding critical values, p_{crit} , T_{crit} , and $v_{\text{mol,crit}}$, can be calculated by the van der Waals equation in approximation (Example 3.1.2). Experimental values of p_{crit} and T_{crit} are given in Table 3.1.2.

The critical constants are characteristic properties, and dimensionless reduced variables obtained by dividing p , T , and v_{mol} by the critical values are commonly used to produce to plots that are general and almost independent of the sort of gas. An example is shown in Figure 3.1.5, indicating that this method, called the “principle of corresponding states,” works well for spherical molecules. For non-spherical and polar molecules, deviations are stronger and the method fails.

Figure 3.1.5 Compressibility factor z in terms of reduced pressure and temperature (Atkins, 2002).



Example 3.1.2 Estimation of critical data based on the van der Waals equation

Figure 3.1.4 shows that at the critical point we have a flat inflection, so the first and the second derivative of the van der Waals equation:

$$p_{\text{crit}} = \frac{a}{27b^2} \quad (3.1.10)$$

$$T_{\text{crit}} = \frac{8a}{27Rb} \quad (3.1.11)$$

$$p = RT/(v_{\text{mol}} - b) - a/v_{\text{mol}}^2$$

must be zero:

$$\frac{dp}{dv_{\text{mol}}} = -\frac{RT}{(v_{\text{mol}} - b)^2} + \frac{2a}{v_{\text{mol}}^3} = 0 \quad \text{and} \quad \frac{d^2p}{dv_{\text{mol}}^2} = \frac{2RT}{(v_{\text{mol}} - b)^3} - \frac{6a}{v_{\text{mol}}^4} = 0$$

Combination of these two equations leads to:

$$v_{\text{mol,crit}} = 3b \quad (3.1.9)$$

and by rearrangement we obtain Eqs. (3.1.7) and (3.1.8). The critical compressibility factor according to the van der Waals equation of state is:

$$z_{\text{crit}} = \frac{p_{\text{crit}} v_{\text{mol,crit}}}{RT_{\text{crit}}} = \frac{3}{8} = 0.375 \quad (3.1.12)$$

Real values are mostly approximately 0.3 and so the discrepancy is gratifying small.

3.1.2

Heat Capacities and the Joule–Thomson Effect

The change in internal energy U of a closed system is described by the first law of thermodynamics:

$$\Delta U = Q + W \quad (3.1.13)$$

where W is the work done on the system and Q is the heat supplied to it. If we only consider the work involved in compressing or expanding a gas (and not electrical work and also not work involved with a change of surface area or length), Eq. (3.1.13) leads to:

! $\Delta U = Q - p\Delta V \quad (3.1.14)$

For a constant volume of the system (no work is done by or on the system) we obtain:

$$\Delta U = Q \quad (\text{for constant volume}) \quad (3.1.15)$$

Therefore the heat supplied to the system at constant volume equals the change of internal energy, and with the molar heat capacity at constant volume, c_v , we find:

! $\Delta U = nc_v\Delta T \quad (3.1.16)$

If we now consider that heat is supplied at constant pressure and assume that the gas is confined by a mass-less and frictionless perfect fitting piston (Figure 3.1.6), we have:

$$\Delta U = U_2 - U_1 = Q - p(V_2 - V_1) \quad (\text{for constant pressure}) \quad (3.1.17)$$

Equation (3.1.17) can be simplified by the introduction of a new quantity, the enthalpy H :

$$H = U + pV \quad (3.1.18)$$

and we obtain by insertion of Eq. (3.1.18) into Eq. (3.1.17):

! $\Delta H = \Delta U + p\Delta V = Q \quad (\text{for constant pressure}) \quad (3.1.19)$

Introduction of the molar heat capacity at constant pressure, c_p , then leads to:

! $\Delta H = Q = nc_p\Delta T \quad (\text{for constant pressure}) \quad (3.1.20)$

For an ideal gas, the difference between the two heat capacities c_p and c_v can now be readily calculated. Since $p\Delta V = nR\Delta T$ for $p = \text{constant}$ we obtain from Eq. (3.1.19):

$$\Delta H = \Delta U + nR\Delta T \quad (3.1.21)$$

and insertion of Eq. (3.1.16) and (3.1.20) into Eq. (3.1.21) leads to:

! $c_p = c_v + R \quad (3.1.22)$

Table 3.1.3 gives selected c_p values. At 298 K we have c_p values of about $30 \text{ J mol}^{-1} \text{ K}^{-1}$ and thus c_v is about $22 \text{ J mol}^{-1} \text{ K}^{-1}$ [Eq. (3.1.22), $R = 8.314 \text{ J mol}^{-1} \text{ K}^{-1}$].

Table 3.1.3 Molar heat capacity^{a)} and Joule–Thomson coefficient μ_{JT} (298 K, 1 bar).

Gas	$c_p (\text{J mol}^{-1} \text{ K}^{-1})$		$\mu_{JT} (\text{K bar}^{-1}) [\text{Eq. (3.1.27)}]$ (positive value: cooling on expansion)
	298 K	1000 K	
H_2	28.8	30.2	-0.03
He	20.8	20.8	-0.06
H_2O (steam)	33.6	41.2	6.6 (100 °C, 1 bar), 2.4 (200 °C, 1 bar)
N_2	29.1	32.7	0.25
CO	29.1	33.2	0.25
CO_2	37.1	54.3	1.11
CH_4	35.8	72.0	0.44

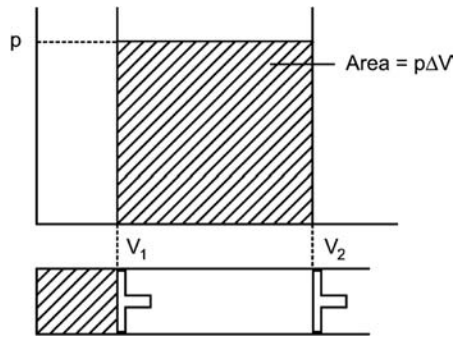


Figure 3.1.6 Work done by a gas during expansion against a constant external pressure p .

a) For solids and liquids, the thermal expansivity and compressibility is small, that is, in most cases $c_p = c_v$, for example, for water (at 25 °C) c_p is $75.3 \text{ J mol}^{-1} \text{ K}^{-1}$ and c_v is $74.8 \text{ J mol}^{-1} \text{ K}^{-1}$. For details see textbooks of physical chemistry, for example, Atkins and de Paula (2002).

For noble gases, c_p is independent of temperature and equals $(5/2)R$, but for other gases we have to consider the influence of temperature, usually by a power series in T :

$$c_p(T) = A + BT + CT^2 + DT^3 \dots \quad (3.1.23)$$

The tabulated so-called virial coefficients A , B , C , D , and so on are specific for each gas.

The enthalpy H of an ideal gas depends only on temperature and not on pressure because of the absence of intramolecular forces. In a real gas these forces cannot be neglected, and H depends on pressure. In most cases this leads to a decrease in temperature if a real gas is adiabatically expanded (Joule–Thomson effect, named after *James Prescott Joule* and *William Thomson*, see boxes). This property is relevant for many practical applications, for example, for refrigerators, heat pumps, and for the cooling and liquefaction of gases (*Linde* process).

James Prescott Joule (1818–1889): An English physicist who discovered the relationship of heat to mechanical work (theory of conservation of energy, first law of thermodynamics). He collaborated from 1852 to 1856 with *William Thomson* (see box below). They developed the absolute scale of temperature and discovered the Joule–Thomson effect. *Joule* also found the relationship between the flow of current through a resistance and the dissipated heat, now called *Joule's law*.

William Thomson, later Lord Kelvin (1824–1907): An Irish–Scottish mathematical physicist and engineer. He carried out important work in the mathematical analysis of electricity and thermodynamics, and unified the emerging discipline of physics in its modern form. He was also a telegraph engineer and inventor. *Thomson* studied in Glasgow and Cambridge, where he graduated in 1845. One of the examiners is said to have declared to another examiner “*You and I are just about fit to mend his pens.*” *Thomson* was also active in sports and rowed in the winning boat at the Oxford and Cambridge boat race. In 1846, *Thomson* was appointed to the chair of natural philosophy of University of Glasgow at the age of only 22. In 1848, he was the first to propose an absolute temperature scale. *Thomson* also became famous to the general public by his engagement in the first laying of a transatlantic cable. After several disasters *Thomson* sailed in 1866 on the finally successful cable-laying expedition of the *SS Great Eastern*. Along with others of the project, he was knighted in 1866. The title *Lord Kelvin* came from the river Kelvin, which flows past his university in Glasgow.

To understand the change of temperature of a real gas during adiabatic expansion, we consider a throttling experiment as shown in Figure 3.1.7. No heat is exchanged with the surrounding (perfect insulation, $Q=0$). Now an arbitrary volume of gas, V_1 , at a temperature T_1 and pressure p_1 is forced through a plug and then emerges at a lower constant pressure p_2 .

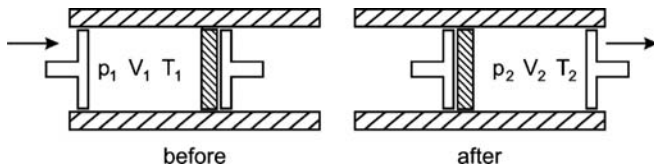
The total work is the sum of the work done on the gas in pushing through the plug and the work done by the gas on the surroundings during expansion at p_2 :

$$W = - \int_{V_1}^0 p_1 dV - \int_0^{V_2} p_2 dV = p_1 V_1 - p_2 V_2 \quad (3.1.24)$$

For $Q=0$, Eqs. (3.1.13) and (3.1.24) lead to:

$$U_2 - U_1 = p_1 V_1 - p_2 V_2 \quad (3.1.25)$$

Figure 3.1.7 Joule–Thomson throttling process.



and with the definition of the enthalpy, Eq. (3.1.18), we obtain:

$$\Delta H = 0 \quad (3.1.26)$$

Thus we conclude that in a Joule–Thomson throttling process the enthalpy is conserved. Therefore, the temperature of an ideal gas does not change as the heat capacity c_p and thus the enthalpy H do not depend on pressure. The change of temperature of a real gas during such an isenthalpic expansion is characterized by the Joule–Thomson coefficient μ_{JT} :

! $\mu_{JT} = \left(\frac{dT}{dp} \right) \Big|_H \quad (3.1.27)$

As explained in detail in many textbooks on physical chemistry, for example, in Atkins and de Paula (2002) and Wicke (1980), the Joule–Thomson coefficient μ_{JT} can be calculated by:

$$\mu_{JT} = \frac{1}{c_p} \left[T \left(\frac{dv_{mol}}{dT} \right) \Big|_p - v_{mol} \right] \quad (3.1.28)$$

Equation (3.1.28) has to be solved based on the respective equation of state. For example, for a “van der Waals gas,” Eq. (3.1.3), we obtain a good approximation for large molar volumes v_{mol} :

$$\begin{aligned} RT &= \left(p + \frac{a}{v_{mol}^2} \right) (v_{mol} - b) = pv_{mol} + \frac{a}{v_{mol}} - pb - \frac{ab}{v_{mol}^2} \Rightarrow v_{mol} \\ &\approx \underbrace{\frac{ap}{RT}}_{\gg 0 \text{ for high values of } v_{mol}} \quad \gg 0 \text{ for high values of } v_{mol} \\ &\approx \frac{RT}{p} - \frac{a}{RT} + b \end{aligned} \quad (3.1.29)$$

Differentiation yields:

$$\left(\frac{dv_{mol}}{dT} \right) \Big|_p \approx \frac{R}{p} + \frac{a}{RT^2} \quad (3.1.30)$$

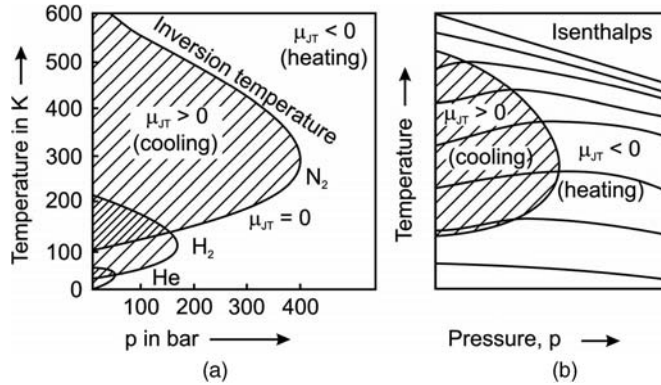
By insertion of Eqs. (3.1.30) and (3.1.29) into Eq. (3.1.28) we finally get:

! $\mu_{JT} = \frac{1}{c_p} \left[\frac{2a}{RT} - b \right] \quad (\text{approximation for a van der Waals gas}) \quad (3.1.31)$

For example, Eq. (3.1.31) leads to a value of 0.26 K bar^{-1} (cooling) for the Joule–Thomson coefficient of nitrogen at 298 K, if we use the values of a , b , and c_p as given in Tables 3.1.1 and 3.1.3, which is quite reasonable compared to the measured value of 0.25 K bar^{-1} .

The values of μ_{JT} given in Table 3.1.3 indicate that at ambient conditions most gases cool on expansion to overcome the forces of attraction. Exceptions are He and H₂, where even at ambient conditions the influence of the volume of the atoms and molecules (repulsive forces) dominates. The value and sign of μ_{JT} depends on the specific gas as well as on pressure and temperature as shown in Figure 3.1.8a for N₂, He, and H₂. The boundary at a given pressure is the inversion temperature. Inside the boundary, μ_{JT} is positive and expansion leads to cooling. A reduction of pressure under adiabatic conditions moves the system along constant enthalpy curves (Figure 3.1.8a), and $T_{inversion}$ is reached when the isenthalps change the sign of their slope. Thus, if cooling during expansion is required, the temperature must be below a certain value, for example, below 500 K for N₂ at 200 bar (Figure 3.1.8a). If the temperature becomes too low (at 100 bar about 120 K for N₂) the boundary is crossed again and heating occurs.

Figure 3.1.8 Sign of Joule–Thomson coefficient: (a) T – p plot for N_2 , H_2 , and He ; (b) schematic T – p plot with isenthalps.



Note that for most liquids at temperatures well below their critical temperature, the Joule–Thomson coefficient is negative, and a decrease in p raises the temperature (Example 3.1.3).

Example 3.1.3: Joule–Thomson coefficient of liquids (example water)

If we consider water as an incompressible liquid, Eqs. (3.1.25) and (3.1.16) lead to:

$$\begin{aligned}\Delta U_{\text{H}_2\text{O},\text{l}} &= V_{\text{H}_2\text{O},\text{l}}(p_1 - p_2) \\ &= n_{\text{H}_2\text{O},\text{l}} c_{\text{H}_2\text{O},\text{l}}(T_2 - T_1) \left(\text{for } \frac{dV}{dp} \approx 0 \right)\end{aligned}\quad (3.1.32)$$

and rearrangement gives:

$$\begin{aligned}\left. \frac{(T_2 - T_1)}{(p_2 - p_1)} \right|_{\text{H}_2\text{O},\text{l}} &= \left. \left(\frac{dT}{dp} \right) \right|_{\text{H}} = \mu_{\text{JT},\text{H}_2\text{O},\text{l}} = -\frac{V_{\text{H}_2\text{O},\text{l}}}{n_{\text{H}_2\text{O},\text{l}} c_{\text{H}_2\text{O},\text{l}}} \\ &= -\frac{v_{\text{mol},\text{H}_2\text{O}}}{c_{\text{H}_2\text{O},\text{l}}}\end{aligned}\quad (3.1.33)$$

and with $c_{\text{H}_2\text{O},\text{l}} = 74.4 \text{ J mol}^{-1} \text{ K}^{-1}$ and $v_{\text{mol},\text{H}_2\text{O}} = 18.08 \text{ cm}^3 \text{ mol}^{-1}$ we get:

$$\mu_{\text{JT},\text{H}_2\text{O},\text{l}} = -0.0243 \text{ K bar}^{-1} \quad (3.1.34)$$

of an incompressible fluid does not depend on pressure and thus the heat of friction leads to a heating of a liquid. (Conversely, the temperature of an ideal gas is constant as the heat of friction increases the entropy, $\Delta S = Q_{\text{friction}}/T$.)

Equation (3.1.34) may also be derived by rearrangement of Eq. (3.1.28):

$$\mu_{\text{JT},\text{H}_2\text{O},\text{l}} = \frac{v_{\text{mol},\text{H}_2\text{O},\text{l}}}{c_{\text{H}_2\text{O},\text{l}}} \left[T \left(\frac{1}{v_{\text{mol},\text{H}_2\text{O},\text{l}}} \frac{dv_{\text{mol}}}{dT} \right) \Big|_p - 1 \right] \quad (3.1.35)$$

The term $1/v_{\text{mol}} (dv_{\text{mol}}/dT)$ is called the isobaric thermal expansivity. For water (300 K, 1 bar) we have a value of 0.00028 K^{-1} , and the first term in the bracket of Eq. (3.1.35) is very small, which is in general true for liquids. For water we get for 300 K:

$$\mu_{\text{JT},\text{H}_2\text{O},\text{l}} = \frac{v_{\text{mol},\text{H}_2\text{O},\text{l}}}{c_{\text{H}_2\text{O},\text{l}}} (0.08 - 1) = -0.0224 \text{ K bar}^{-1} \quad (3.1.36)$$

Thus the temperature of liquid water increases during adiabatic and isenthalpic expansion (although the value is rather small). This fact can also be interpreted in terms of the entropy (Section 3.1.3). The entropy

which almost equals the literature value of $-0.0220 \text{ K bar}^{-1}$ at 300 K and 1 bar (National Institute of Standards & Technology, 2007).

3.1.3

Physical Transformations of Pure Substances: Vaporization and Melting

The general starting point to calculate the equilibrium state is the *Clausius inequality*:

$$\Delta S_{\text{overall}} = \Delta S_{\text{sys}} + \Delta S_{\text{surr}} \geq 0 \quad (3.1.37)$$

named after Rudolf Clausius (see box). Equation (3.1.37) states that any change of the absolute entropy (J K^{-1}) of the system, ΔS_{sys} , for example, during vaporization generated by heat transfer to the vaporizing system, is accompanied by a change of the entropy in the surrounding, ΔS_{surr} [All natural processes lead to a chaotic dispersal of the total energy, and the entropy is a measure to quantify this by the second law of thermodynamics, as described in many textbooks, for example, by Atkins and de Paula (2002).] The overall change of the entropy is greater than zero

in general, as the change might be irreversible. Only if the heat Q is reversibly transferred is $\Delta S_{\text{overall}}$ zero. If we use the convention that Q is positive, if energy is supplied to the system, for example, for vaporization, it follows that ΔS_{surr} equals the term $-Q/T$. So for vaporization we obtain from Eq. (3.1.37):

$$\begin{aligned}\Delta S_{\text{overall}} &= 0 = \Delta S_{\text{sys}} \\ &\quad - \frac{Q_{\text{vap}}}{T} \quad (\text{2nd law of thermodynamics for the case of vaporization})\end{aligned}\quad (3.1.38)$$

For a constant pressure, the work done by the system on the surrounding (e.g., by a piston) is $p(V_{\text{vap}} - V_{\text{liquid}}) = p\Delta V$, so we obtain a positive term for an expansion of the system:

$$Q_{\text{vap}} = \Delta_{\text{vap}} U + p\Delta V \quad (\text{for } p = \text{const.}) \quad (3.1.39)$$

Introduction of the enthalpy H , Eq. (3.1.18), leads to:

$$Q_{\text{vap}} = \Delta_{\text{vap}} H \quad (\text{for } p = \text{const.}) \quad (3.1.40)$$

If we now use $\Delta_{\text{vap}} S$ instead of ΔS_{sys} , we get from Eq. (3.1.38) and Eq. (3.1.40):

$$\Delta_{\text{vap}} S = S_{\text{vap}} - S_{\text{l}} = \frac{\Delta_{\text{vap}} H}{T} \quad (3.1.41)$$

The entropy of a liquid is approximately independent of pressure and can be expressed by the standard value S_{l}^0 at $p_0 = 1.013$ bar. For the vapor phase (ideal gas) we have to consider the change of entropy if the pressure changes from p_0 to p by:

$$S_{\text{vap}} = S_{\text{vap}}^0 - \int_{p_0}^{p_{\text{vap}}} \frac{v_{\text{mol}}}{T} dp = S_{\text{vap}}^0 - R \int_{p_0}^{p_{\text{vap}}} \frac{1}{p} dp = S_{\text{vap}}^0 - R \ln \frac{p_{\text{vap}}}{p_0} \quad (3.1.42)$$

Thus we can rewrite Eq. (3.1.41) as:

$$\Delta_{\text{vap}} H = T \left(S_{\text{vap}}^0 - R \ln \frac{p_{\text{vap}}}{p_0} - S_{\text{l}}^0 \right) = T \Delta_{\text{vap}} S^0 - RT \ln \frac{p_{\text{vap}}}{p_0} \quad (3.1.43)$$

Rearranging yields the vapor pressure equation in its simplest form:

$$\ln \frac{p_{\text{vap}}}{p_0} = - \frac{\Delta_{\text{vap}} H}{RT} + \frac{\Delta_{\text{vap}} S^0}{R} \quad (3.1.44)$$

Values of the enthalpy and standard entropy of vaporization are tabulated in reference books [e.g., *Landolt–Boernstein* (Martienissen *et al.*, 1976–1997), *CRC Handbook* (Lide, 2003/04)]. A small selection is given in Table 3.1.4. For the measurement of p_{vap} of high boiling liquids see Example 3.2.9.

Table 3.1.4 Some values of vaporization enthalpy, boiling temperature, and Trouton's constant.

Substance	$\Delta_{\text{vap}} H^0 \text{ (kJ mol}^{-1}\text{)}$	$T_{\text{boil}}^0 \text{ (K) at 1.013 bar}$	$\Delta_{\text{vap}} H^0 / T_{\text{boil}}^0 = \Delta_{\text{vap}} S^0 \text{ (J mol}^{-1} \text{ K}^{-1}\text{)}$
H ₂	0.9	20	44.3
N ₂	5.6	77	72.1
O ₂	6.8	90	75.7
NH ₃	23.4	240	97.4
C ₃ H ₈	25.8	309	83.4
C ₆ H ₆	30.8	353	87.2
C ₂ H ₅ OH	38.7	352	110.1
H ₂ O	40.7	373	109.1
Zn	114.7	1180	97.2
Pb	179.5	2025	88.6
Cu	304.0	2868	106.0

Rudolf Julius Emanuel Clausius (1822–1888), a German physicist and mathematician, was one of the founders of thermodynamics. By his restatement of *Carnot's principle*, he put the theory of heat on a sounder basis. His most important paper “On the mechanical theory of heat” (1850) first stated the ideas of the second law of thermodynamics. In 1865, he introduced the concept of entropy. He also contributed to the kinetic theory of gases by including translational, rotational, and vibrational molecular motions, and introduced the mean free path of a particle. *Clausius deduced the Clausius–Clapeyron relation* – see Eq. (3.1.45) below – based on thermodynamic considerations. This law on phase transition had originally been developed in 1834 by *Émile Clapeyron*.

Differentiation of Eq. (3.1.44) leads to the influence of temperature on the vapor pressure, the *Clausius–Clapeyron* equation (*Rudolf Clausius*, *Benoit Clapeyron*, see boxes):

$$\frac{d\left(\ln \frac{p_{vap}}{p_0}\right)}{dT} = \frac{\Delta_{vap}H}{RT^2} \Rightarrow \ln\left(\frac{p_{vap,T_2}}{p_0}\right) - \ln\left(\frac{p_{vap,T_1}}{p_0}\right) = \ln\left(\frac{p_{vap,T_2}}{p_{vap,T_1}}\right) \approx \frac{\Delta_{vap}H(T_2 - T_1)}{R\left(\frac{T_2+T_1}{2}\right)^2} \quad (3.1.45)$$

If we take water at 50 °C (T_1) as an instructive example ($\Delta_{vap}H \approx 41 \text{ kJ mol}^{-1}$) we calculate by Eq. (3.1.45) that the vapor pressure of water increases by about a factor of two for a rise in temperature of 15 K, which is a helpful rule of thumb in the temperature range 0–100 °C.

If we use Eq. (3.1.44) for the special case of $p_{vap} = p_0 = 1.013 \text{ bar}$, we get:

$$\nabla_o 0 = \frac{\Delta_{vap}H^0}{RT_{boil}^0} - \frac{\Delta_{vap}S^0}{R} \Rightarrow \frac{\Delta_{vap}H^0}{T_{boil}^0} = \Delta_{vap}S^0 \approx 90 \text{ J mol}^{-1} \text{ K}^{-1} \quad (3.1.46)$$

This ratio of the standard vaporization enthalpy $\Delta_{vap}H^0$ to the normal boiling temperature (at 1 bar), that is, the standard vaporization entropy $\Delta_{vap}S^0$, is called Trouton's constant (*Frederick Trouton*, see box). Table 3.1.4 indicates that the values of $\Delta_{vap}S^0$ are in the range $70\text{--}110 \text{ J mol}^{-1} \text{ K}^{-1}$, and we can use $90 \text{ J mol}^{-1} \text{ K}^{-1}$ as a mean value for $\Delta_{vap}S^0$. Thus for a rough estimation of $\Delta_{vap}H^0$ we only have to multiply the normal boiling temperature (at 1 bar) by $90 \text{ J mol}^{-1} \text{ K}^{-1}$. This rule of thumb (Trouton's rule) has the advantage that usually T_{boil} at 1 bar (but not necessarily $\Delta_{vap}H^0$) is well known or can easily be measured.

Benoit Paul Émile Clapeyron (1799–1864): A French engineer and physicist and one of the founders of thermodynamics. In 1843, *Clapeyron* further developed the idea of a reversible process, already suggested by *Carnot*, and made a definitive statement of *Carnot's principle*, which is now known as the second law of thermodynamics. *Clapeyron* also worked on the characterization of perfect gases, the calculation of the statics of continuous beams, and on phase transitions, Eq. (3.1.45).

Frederick Thomas Trouton (1863–1922): An Irish engineer and physicist. In 1883 he discovered Trouton's rule, Eq. (3.1.46). He also worked on osmotic pressure, adsorption, and rheology. More details on his life and work are given in a recent publication of Wisniak (2000).

Equation (3.1.44) is an approximation as we have assumed a constant value of the vaporization enthalpy, a negligible influence of pressure on the entropy of a liquid, and ideal gas behavior of the vapor. More sophisticated equations use more than two parameters to account for these factors. For example, the *Antoine* equation uses three parameters:

$$\nabla_o \ln(p_{vap}) = A - \frac{B}{C + T} \quad (3.1.47)$$

The values of A , B , and C are tabulated. Note that, depending on the reference book, the temperature has to be inserted in K or °C, and sometimes we get the vapor pressure in units like Torr. For mixtures, p_{vap} is denoted as p_{sat} , the saturation vapor pressure of a component.

Figure 3.1.9 shows the general location of the phase boundaries between the solid, the liquid, and the gas phase and the respective diagram for water. Note the small decrease of the melting temperature with increasing pressure, which is the result of the anomaly of water by which the liquid phase has a higher density than ice. All three phases are in equilibrium at the triple point. If the temperature and pressure exceed the so-called critical values, 374 °C and 218 bar for water, the phase boundary between liquid and vapor vanishes. For this supercritical state, a

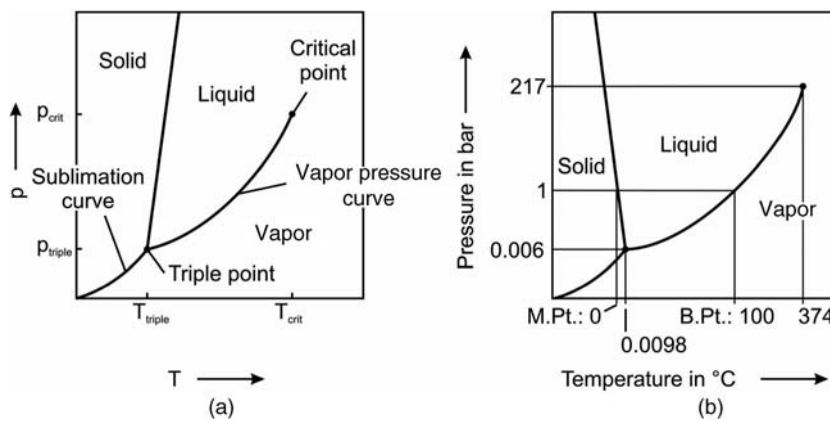


Figure 3.1.9 Phase boundaries between solid, liquid, and gas (a) and phase diagram of water (b) (M.Pt.: melting point; B.Pt.: boiling point).

change of pressure and temperature no longer leads to a change of the state of aggregation. This is the reason why air separation by distillation is only possible at very low temperatures, as N_2 and O_2 have values of T_{crit} of -147°C and -118°C , respectively (Table 3.1.2). Thus, we have to cool air to a very low temperature before we can separate the liquid O_2 from the more volatile N_2 , in industrial practice typically at moderate pressures of about 6 bar.

Table 3.1.5 lists values of the melting enthalpy and melting point of selected liquids. Comparison with Table 3.1.4 indicates that the vaporization enthalpy is higher than the melting enthalpy, for example, for benzene and water by a factor of 3 and 7, respectively. In contrast to vaporization, where we have an almost constant vaporization entropy for a given pressure [Trouton's constant, Eq. (3.1.46) and Table 3.1.4)], such regularity does not occur for melting, as we see by comparison of the values of $\Delta_{\text{melt}}H^0/T_{\text{melt}}^0$ given in Table 3.1.5.

Compared to vaporization, the influence of pressure on the melting point is small. In general, the influence of pressure on a phase transition process is given by the Clapeyron equation:

$$\frac{dp}{dT} = \frac{\Delta S_{\text{phase transition}}}{\Delta \nu_{\text{mol, phase transition}}} = \frac{\Delta H_{\text{phase transition}}}{T \Delta \nu_{\text{mol, phase transition}}} \quad (3.1.48)$$

For vaporization, the molar volume of a gas is much higher than that of a liquid, typically by a factor of 1000 at ambient conditions, and for an ideal gas $\Delta \nu_{\text{mol, phase transition}}$ is almost equivalent to $\nu_{\text{mol, gas, phase transition}} = RT/p_{\text{vap}}$. Hence, rewriting Eq. (3.1.48) yields:

$$\left. \frac{dp_{\text{vap}}}{dT} \right|_{\text{ideal gas}} = \frac{p_{\text{vap}} \Delta_{\text{vap}} H}{RT^2} \quad (3.1.49)$$

and rearrangement of Eq. (3.1.49) [by using $d(\ln p_{\text{vap}}) = dp_{\text{vap}}/p_{\text{vap}}$] again leads to Eq. (3.1.45).

Note that the vapor pressure over curved surfaces is dependent on the radius of curvature. This involves modifications to the vapor pressure relationships for highly curved systems like rain drops or liquids confined in small capillaries (Topic 3.1.1).

Table 3.1.5 Melting enthalpy and melting point of selected liquids (at 1.013 bar).

Substance	$\Delta_{\text{melt}}H^0 (\text{kJ mol}^{-1})$	$T_{\text{melt}}^0 (\text{K})$	$\Delta_{\text{melt}}H^0/T_{\text{melt}}^0 (\text{J mol}^{-1} \text{ K}^{-1})$
C_6H_6	9.8	278	35.3
CH_3OH	3.0	175	17.1
H_2O	6.0	273	22.0
NaCl	28.8	234	26.8
Fe	14.4	1807	8.0

For melting, we derive an approximate solution of Eq. (3.1.48), if we assume that the melting enthalpy and the change of volume are insensitive to p and T . Integration then yields:

$$\int_{p_1}^{p_2} dp_{\text{melt}} = \left(\frac{\Delta_{\text{melt}} H}{\Delta v_{\text{mol,melt}}} \right) \int_{T_{\text{melt},1}}^{T_{\text{melt},2}} \frac{dT_{\text{melt}}}{T_{\text{melt}}} \Rightarrow T_{\text{melt},2} = T_{\text{melt},1} e^{\frac{(p_2-p_1)\Delta V_{\text{mol,melt}}}{\Delta_{\text{melt}} H}} \quad (3.1.50)$$

For example, the molar volume of water decreases during melting by about $1.64 \text{ cm}^3 \text{ mol}^{-1}$ ($v_{\text{mol,H}_2\text{O,liquid}} = 18.02 \text{ cm}^3 \text{ mol}^{-1}$, $v_{\text{mol,ice}} = 19.66 \text{ cm}^3 \text{ mol}^{-1}$ at 1 bar and 0°C), and the melting enthalpy is 6 kJ mol^{-1} . Thus, an increase of pressure from 1 to 1000 bar leads to a reduction of T_{melt} from 0°C to -7°C . This confirms the anomaly of water, as shown in Figure 3.1.9b.

Topic 3.1.1 Vapor pressure over curved surfaces

Based on surface thermodynamic principles [e.g., see Atkins and de Paula (2002)], the vapor pressure over a curved surface relative to that over a plane surface is given by:

$$\frac{p_{\text{vap,curvature}}}{p_{\text{vap,plane}}} = e^{\frac{\sigma v_{\text{mol}}}{RT} \left(\frac{1}{r_1} + \frac{1}{r_2} \right)} \quad (3.1.51)$$

where σ is the surface tension, v_{mol} the molar volume, and r_1 and r_2 the principal radii of the surface. Lord Kelvin was the first to analyze the problem of the vapor pressure over curved surfaces, and therefore Eq. (3.1.51) is known as the *Kelvin* equation. For a spherical surface like a droplet for which $r_1 = r_2 = d/2$ (d = droplet diameter) we have:

$$\frac{p_{\text{vap,curvature}}}{p_{\text{vap,plane}}} = e^{\frac{4\sigma v_{\text{mol}}}{dRT}} \quad (3.1.52)$$

For droplets of water with a diameter of 20 nm and of 200 nm the ratios $p_{\text{vap,curvature}}/p_{\text{vap,plane}}$ are about 1.1 and 1.01, respectively. Hence for $d > 200 \text{ nm}$, the normal vapor pressure is not affected (deviation $< 1\%$), whereas for $d < 20 \text{ nm}$ there is an appreciable increase in vapor pressure (deviation $> 10\%$) (Figure 3.1.10).

Thus, very small droplets already vaporize at a lower temperature than expected, for example, at a temperature of 95°C and a pressure of 1 bar [$\sigma_{\text{H}_2\text{O,air}} = 0.0718 \text{ N m}^{-1}$ (95°C), $p_{\text{vap,plane}} (95^\circ\text{C}) = 0.85 \text{ bar}$], droplets with a diameter of less than about 10 nm already vaporize.

The situation is reversed for the vapor pressure of liquids confined in small capillaries or pores of a solid. Now, we find capillary condensation, that is, condensation occurs at pressures below the vapor pressure of a plane surface (see Section 3.3.5.1, Example 3.3.8).

3.1.4

Transport Properties (Diffusivity, Viscosity, Heat Conduction)

3.1.4.1 Basic Equations for Transfer of Heat, Mass, and Momentum

The equation for one-dimensional stationary heat conduction is the first of Fourier's laws (*Jean Fourier*, see box):

$$\dot{Q} = -\lambda A \frac{dT}{dx} \quad (3.1.53)$$

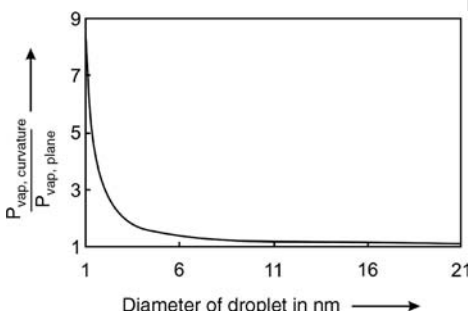


Figure 3.1.10 Vapor pressure of water droplets in air relative to the vapor pressure over a plane surface versus diameter of droplet [$\sigma_{\text{H}_2\text{O,air}} = 0.0718 \text{ N m}^{-1}$ (25°C), $V_{\text{mol,H}_2\text{O}} = 1.8 \times 10^{-5} \text{ m}^3 \text{ mol}^{-1}$].

Table 3.1.6 Transport properties in liquids and solids (Broetz and Schoenbucher, 1982; Jakubith, 1992; Cengel, 2002).

Substance	D ($\text{m}^2 \text{s}^{-1}$)	λ ($\text{W m}^{-1} \text{K}^{-1}$)	η (Pa s)
Solids			
Gold	2×10^{-13} (in lead at 100°C)	310 (20°C)	—
H_2 in iron	3×10^{-13} (20°C)	—	—
Carbon in iron	5×10^{-15} (500°C)	—	—
Hydrogen in iron	2.6×10^{-13} (25°C)	—	—
Glass	—	1 (20°C)	10^5 (700°C)
Liquids			
Benzene	1.3×10^{-9} (in <i>n</i> -heptane, 25°C)	0.15 (50°C)	—
Water	2.2×10^{-9} (in H_2O , 25°C)	0.61 (50°C)	1×10^{-3} (0°C)
Hexane	—	0.14 (50°C)	0.4×10^{-3} (0°C)
Methanol	1.8×10^{-9} (in H_2O , 25°C)	0.19 (50°C)	0.8×10^{-3} (0°C)
Hydrogen	6.3×10^{-9} (in H_2O , 25°C)	—	—

Table 3.1.7 Transport properties and density of selected gases ($1.013 \text{ bar}, 0^\circ\text{C}$).

	$10^5 v$ ($\text{m}^2 \text{s}^{-1}$)	$10^5 \eta$ (Pa s)	$10^5 D$ ($\text{m}^2 \text{s}^{-1}$)	λ ($\text{W m}^{-1} \text{K}^{-1}$)	ρ (kg m^{-3})
CO	1.33	1.66	1.70	0.023	1.25
H_2	9.33	0.84	12.00	0.171	0.09
CH_4	1.42	1.02	1.84	0.030	0.72
N_2	1.33	1.66	1.71	0.024	1.25
O_2	1.34	1.92	1.72	0.024	1.43
H_2O	1.25	1.00	1.55	0.025	0.8 (as ideal gas)
CO_2	0.70	1.37	0.91	0.015	1.97

The analogous equations for mass transport of species A by diffusion (Fick's first law; *Adolf Fick*, see box) and for transport of momentum (Newton's law, *Isaac Newton*, see box) are:

$$\mathbf{!} \quad \dot{n}_A = -D_A A \frac{dc_A}{dx} \quad (3.1.54)$$

$$\nabla \quad \dot{p} = -\eta A \frac{du}{dx} \quad (3.1.55)$$

Thus the flow rate of energy, matter, and momentum is proportional to the area perpendicular to the flow and to the gradients of temperature, concentration, and velocity. The connecting links are the transport coefficients, thermal conductivity λ , diffusion coefficient D , and the dynamic viscosity η . All three properties depend on the material, the state of aggregation, the temperature and, for gases, on the pressure (for λ only at extreme low pressures) as discussed below in more detail for gases and liquids. Selected values of the transport properties are given in Table 3.1.6 for solids and liquids and in Table 3.1.7 for gases.

■ Eponyms of the laws of energy, matter, and momentum

Jean Baptiste Joseph Fourier (1772–1837): A French mathematician and physicist. His masterpiece was the theory of heat conduction that marked an epoch in the field of applied mathematics, for in it he developed the theory of the series known by his name and applied it to the solution of partial differential equations. *Fourier* was the first to apply the concept of dimension to physical magnitudes (van Brakel, 2002). He also recognized dimensionless groups in his equations, but did not see the consequences that were drawn out later. **James Clerk Maxwell** (1831–1879) acknowledged *Fourier's* work and expressed the requirement of dimensional homogeneity more precisely. The first dimensionless number to gain acceptance was *Reynolds* number. An excellent review of the historical development of the theory of stationary and non-stationary heat transfer ranging from early works of *Newton*, *Fourier* and *Biot* until the 1950s is given by Cheng (1999).

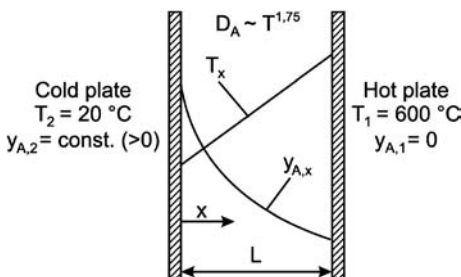


Figure 3.1.11 Model system to demonstrate the influence of a temperature gradient on mass transfer through a gas confined by two parallel plates (fast reaction at hot plate).

Adolf Eugen Fick (1829–1901): A German physiologist, who introduced in 1855 *Fick's law* of diffusion. *Fick* is also credited with the invention of contact lenses.

Sir Isaac Newton (1643–1727): One of the greatest scientists in history. He described universal gravitation and the three laws of motion, laying the groundwork for classical mechanics. By deriving *Kepler's* laws of planetary motion, he showed that the motion of objects on Earth and of celestial bodies is governed by the same laws. The unifying and deterministic power of his laws led to the scientific revolution and the advancement of heliocentrism. Among other scientific discoveries, he realized that the spectrum of colors observed if white light passes through a prism is inherent in the white light, and argued that light is composed of particles. He also developed a law of cooling, describing the rate of cooling of bodies exposed to air, and studied the speed of sound in air. *Newton* played a major role in the development of calculus, sharing credit with *Gottfried Leibniz*.

Equation (3.1.54) represents the usual form of *Fick's* first law of mass transport, but this equation is not correct if a temperature gradient exists (Westerterp, van Swaaij, and Beenackers, 1980; Cengel, 2002, Topic 3.1.2). For example, a temperature difference of $\Delta T = T_1 - T_2$ in an ideal gas, that is, $c_A = p_A/(RT) = \gamma_A p/(RT)$, leads to a concentration difference $\Delta c_A = \gamma_{A,1}p/(RT_1) - \gamma_{A,2}p/(RT_2)$. Nevertheless, this will not lead to a mass flux of species A if the mole fractions are equal ($\gamma_{A,1} = \gamma_{A,2}$), although a concentration gradient exists for $T_1 \neq T_2$. Thus, the general and correct form of Eq. (3.1.54) is:

$$\dot{n}_A = -D_{AA}\rho_{\text{mol}} \frac{dy_A}{dx} \quad (\text{for } \rho_{\text{mol}} \neq \text{const.}) \quad (3.1.56)$$

whereby ρ_{mol} is the molar density of the fluid (mol m^{-3}) and y_A the mole fraction of species A (denoted as y_A for a gas and x_A for a liquid in mol mol^{-1}). Note that for heat transport such an interplay with mass transfer does not exist, that is, heat transfer is not affected by diffusion.

Topic 3.1.2 Influence of a temperature gradient on mass transfer by diffusion

The general form of *Fick's* first law is Eq. (3.1.56). To show the impact of a temperature gradient on mass transport in a gas by diffusion, we use the following system (Figure 3.1.11):

- A stagnant gas mixture with component A (content y_A) is located between two parallel plates with different but constant temperatures (600 °C and 20 °C). The temperature increases linearly if we assume that the thermal conductivity of the gas is constant.
- The diffusion coefficient D_A is proportional to $T^{1.75}$, and thus increases for the given example from $D_{A,2}$ (cold plate) to $D_{A,1}$ (hot plate); $D_{A,1} = D_{A,2} (T_1/T_2)^{1.75}$.
- The molar density ρ_{mol} is proportional to $1/T$ (ideal gas) and decreases from $\rho_{\text{mol},2}$ (cold plate) to $\rho_{\text{mol},1}$ (hot plate); $\rho_{\text{mol},1} = \rho_{\text{mol},2} (T_2/T_1)$.
- The molar fraction of A (y_A) is zero at the hot plate, if we assume a very fast chemical reaction at the surface, and has a certain constant value $y_{A,2}$ at the cold plate.

For a further inspection of this system, we transform Eq. (3.1.56) into the dimensionless form. If we take the cold plate as the point of reference we get:

$$\frac{\dot{n}_A}{\left(\frac{D_{A,2} A y_{A,2} \rho_{\text{mol},2}}{L} \right)} = \dot{N}_A = - \left(\frac{D_{A,x} \rho_{\text{mol},x}}{D_{A,2} \rho_{\text{mol},2}} \right) \frac{d\left(\frac{y_{A,x}}{y_{A,2}}\right)}{d\left(\frac{x}{L}\right)} = -Z \frac{dY_A}{dX} \quad (3.1.57)$$

The stationary flux of component A must be constant:

$$-Z \frac{dY_A}{dX} = \dot{N}_A = \text{const.} \quad (3.1.58)$$

whereby the term combining the gas density and the diffusivity of A can be expressed as:

$$Z = \frac{D_{A,x} \rho_{mol,x}}{D_{A,2} \rho_{mol,2}} = \left(\frac{T_x}{T_2}\right)^{1.75} \left(\frac{T_2}{T_x}\right)^{0.5} = \left(\frac{T_x}{T_2}\right)^{0.75} = \left(1 + \frac{(T_1 - T_2)}{T_2}x\right)^{0.75} \quad (3.1.59)$$

The combination of Eqs. (3.1.58) and (3.1.59) leads to:

$$-\dot{N}_A \left(1 + \frac{T_1 - T_2}{T_2}x\right)^{-0.75} dx = dY_A \quad (3.1.60)$$

and by integration we obtain:

$$Y_A = 1 - 4\dot{N}_A \left(\frac{T_2}{T_1 - T_2}\right) \left[\left(1 + \frac{T_1 - T_2}{T_2}x\right)^{0.25} - 1 \right] + C_1 \quad (3.1.61)$$

The first boundary condition is $Y_A = 1$ for $X = 0$, and thus $C_1 = 0$. The second condition is $Y_A = 0$ for $X = 1$, and thus \dot{N}_A , the ratio of the real flux and the flux at isothermal conditions, is:

$$\dot{N}_A = \frac{1}{4} \left(\frac{T_1 - T_2}{T_2}\right) \left[\left(\frac{T_1}{T_2}\right)^{0.25} - 1 \right]^{-1} \quad (3.1.62)$$

By insertion of $C_1 = 0$ and Eq. (3.1.62) in Eq. (3.1.61) we finally obtain:

$$Y_A = 1 - \left[\left(1 + \frac{T_1 - T_2}{T_2}x\right)^{0.25} - 1 \right] \left[\left(\frac{T_1}{T_2}\right)^{0.25} - 1 \right]^{-1} \quad (3.1.63)$$

Figure 3.1.12 presents the solution for $T_2 = 20^\circ\text{C}$ and $T_1 = 600^\circ\text{C}$. \dot{N}_A here is 1.59, that is, the flux is by about 60% higher than without a temperature gradient. Note that the local gradient of Y_A decreases to the same degree as Z increases, and thus \dot{N}_A is constant, whereas for the isothermal case we simply get a linear profile of Y_A , and Z would be unity. In general, we may use the following equation to approximate the influence of temperature:

$$\begin{aligned} \dot{n}_A &= -D_A A \rho_{mol} \frac{dy_A}{dx} \approx -D_{A,T_{mean}} A \rho_{mol,T_{mean}} \left(\frac{dy_A}{dx}\right)_{T_{mean}} \\ &\approx -D_{A,T_{mean}} A \rho_{mol,T_{mean}} \frac{\Delta y_{A,\text{total}}}{L} \end{aligned} \quad (3.1.64)$$

Here, the mean temperature is 583 K, which leads to an enhancement of mass transfer by the factor $(583/293)^{0.75} = 1.67$ (as $D\rho \sim T^{0.75}$), which almost equals the exact value of 1.59.

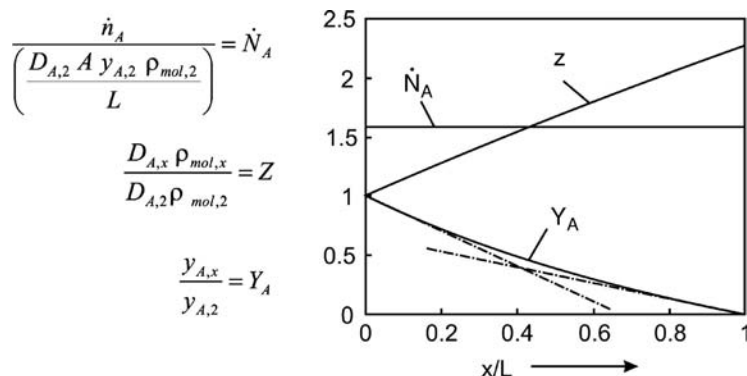


Figure 3.1.12 Profiles of molar fraction (of component A), the factor Z [Eq. (3.1.59)], and of the flux of A in a gas confined by two plates of different temperature (see Figure 3.1.11).

Figure 3.1.13 Enhancement and decrease of molar flux compared to the isothermal case for different values of temperature T_2 for $T_1 = 873$ K (Figure 3.1.11).

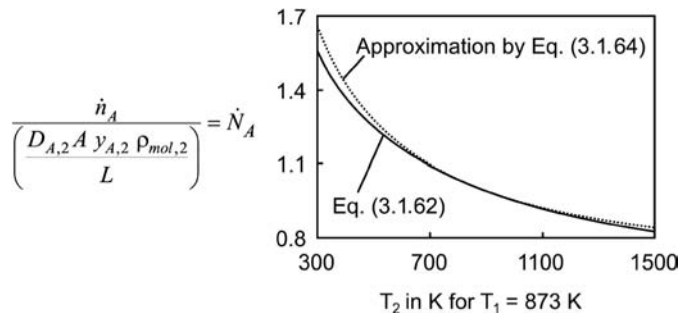


Figure 3.1.14 Dimensionless molar concentration C_A and molar content Y_A of species A in a gas confined by two plates of different T : (a) small ΔT , small ΔY_A ; (b) high ΔT , $\Delta Y_{A,\max}$.

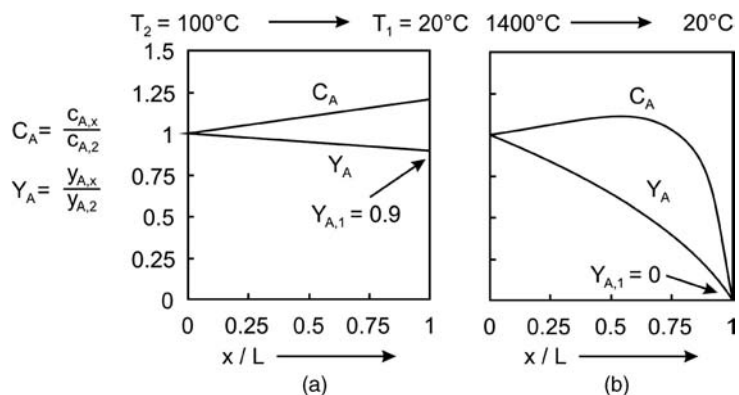


Figure 3.1.13 shows the enhancement and decrease, respectively, of the (dimensionless) flux compared to the isothermal case for different values of T_2 for a fixed value of T_1 (873 K). As expected, the flux from plate 1 to plate 2 is enhanced for $T_1 > T_2$ and decreases for $T_1 < T_2$.

In principle, even a diffusional flux against a concentration gradient is possible in non-isothermal systems, if the temperature decreases in the direction of flux. Figure 3.1.14 shows two respective examples for a gas phase confined by two plates of different temperature. For a small difference of the molar content between both plates, a small ΔT already leads to an increase of the molar concentration in the direction of flow. For a high ΔY_A , extremely high values of ΔT are needed to “create” this effect, and thus the example shown in Figure 3.1.14b is more of a mind game as we have neglected any influence of free convection that is always induced by temperature gradients and may superimpose this effect.

The influence of temperature on diffusion should not be confused with thermal diffusion, which leads to a separation of components with different molar masses (*Soret effect*). The theory is complicated but can be explained as follows: At a warmer location, all gas molecules gain the same kinetic energy ($m/2v^2$) but the impulse of heavier molecules is higher (mv). Thus, at collisions, they penetrate deeper into the direction of the lower temperature than lighter ones. The separation causes a concentration gradient parallel (heavy molecules) or antiparallel with respect to the temperature gradient. Thermal diffusion is very slow and mostly negligible compared to ordinary diffusion, but is relevant for polymer characterization and enrichment of isotopes, for example, for uranium isotopes.

Example: The diffusion coefficient in a liquid benzene/cyclohexane mixture (D_{mol}) is $1.4 \times 10^{-9} \text{ m}^2 \text{ s}^{-1}$ (300 K), whereas the thermal coefficient D_{thermal} is about $5 \times 10^{-12} \text{ m}^2 \text{ s}^{-1} \text{ K}^{-1}$ (Zhang, 2006). For steady state, the fluxes (in the z-direction) by thermal and ordinary molecular diffusion are equal:

$$D_{\text{mol}} \frac{dx_{\text{benzene}}}{dz} = D_{\text{thermal}} x_{\text{benzene}} (1 - x_{\text{benzene}}) \frac{dT}{dz} \quad (3.1.65)$$

[Note that the factor x_{benzene} ($1 - x_{\text{benzene}}$) is introduced by convention to account for the fact that the thermal diffusion becomes zero for pure substances, that is, for $x_{\text{benzene}} = 1$ or $x_{\text{benzene}} = 0$.] For $x_{\text{benzene}} = 0.5$, we obtain $\Delta x_{\text{benzene}}/x_{\text{benzene}} \approx (D_{\text{thermal}}/D_{\text{mol}}) 0.5 \Delta T = \Delta T/560 \text{ K}$. Thus the Soret effect only plays a role for strong temperature gradients, for example, for $\Delta T = 100 \text{ K}$ we find $\Delta x_{\text{benzene}}/x_{\text{benzene}} = 0.18$.

3.1.4.2 Transport Coefficients of Gases

For ideal gases, we have according to the kinetic theory of gases (for rigid spheres of very small molecular dimensions):

$$\lambda_g = \frac{1}{3} \bar{u} \Lambda \rho_{g,\text{mol}} c_v \quad (3.1.66)$$

$$D_g = v_g = \frac{\eta_g}{\rho_g} = \frac{1}{3} \bar{u} \Lambda \quad (3.1.67)$$

Experience and detailed theoretical calculations show that more accurate values are given by:

$$\lambda_g = 1.2 \bar{u} \Lambda \rho_{g,\text{mol}} c_v \quad (3.1.68)$$

$$D_g = 0.7 \bar{u} \Lambda \quad (3.1.69)$$

$$v_g = 0.5 \bar{u} \Lambda \quad (3.1.70)$$

The mean velocity of the molecules, \bar{u} , and the mean free path, Λ , are:

$$\bar{u} = \sqrt{\frac{8RT}{\pi M}} \quad (3.1.71)$$

$$\Lambda = \frac{1}{\sqrt{2} \sigma p} \quad (3.1.72)$$

with k as Boltzmann constant ($1.38 \times 10^{-23} \text{ J K}^{-1}$, Ludwig Boltzmann, see box) and σ as the collision cross-section of the molecules ($\sigma = \pi d^2$ for hard spheres with d as diameter). The velocity of molecules in a gas varies according to the Maxwell–Boltzmann distribution (Topic 3.1.3), but the mean value [Eq. (3.1.71)] sufficiently describes the macroscopic behavior with regard to the transport properties λ_g , D_g , and v_g .

At 20°C and 1 bar, the mean velocity of air molecules is about 500 m s^{-1} and the mean free path Λ 70 nm ($0.07 \mu\text{m}$). Thus, the diffusion coefficient and the kinematic viscosity are about $0.2 \text{ cm}^2 \text{ s}^{-1}$. Table 3.1.7 indicates that the values of D , λ , v , and ρ for H_2 deviate by a factor of more than 10 from those of other gases (low value of M of H_2 and thus of \bar{u} and D and λ).

For an ideal gas, Eqs. (3.1.68) to (3.1.72) lead to the influence of T and p on the transport properties (if we neglect the influence of T on c_v and σ):

$$\lambda_{g,\text{ideal gas}} \sim \sqrt{T} \frac{p}{T} \sim \sqrt{T} \quad (3.1.73)$$

$$D_{g,\text{ideal gas}} \approx v_{g,\text{ideal gas}} \sim \sqrt{T} \frac{T}{p} \sim \frac{T^{1.5}}{p} \quad (3.1.74)$$

Experimental values deviate from those calculated by the simple rigid-sphere theory. For example, for N_2 (273 K , 1 bar), Eqs. (3.1.68)–(3.1.72) yield $\lambda = 0.0086 \text{ W m}^{-1} \text{ K}^{-1}$ and $D = v = 0.093 \text{ cm}^2 \text{ s}^{-1}$, whereas measured values are by a factor of about two higher (factor 1.8 for D , 1.4 for v , and 2.8 for λ , Table 3.1.8). Based on experimental data, better approximations are:

$$\lambda_g \sim T^{0.75} \quad (3.1.75)$$

$$D_g \text{ and } v_g \sim \frac{T^{1.75}}{p} \quad (3.1.76)$$

Ludwig Eduard Boltzmann (1844–1906): An Austrian physicist famous for his work in the field of statistical thermodynamics. His most important contributions were in kinetic theory, the Maxwell–Boltzmann distribution for molecular speeds in a gas and the Boltzmann energy distribution. Much of the physics establishment rejected his thesis about the reality of atoms and molecules, and he had a long-running dispute with the editor of a German physics journal, who refused to let him refer to atoms and molecules as anything other than theoretical constructs. Tragically, in 1906, he committed suicide during an attack of depression. Only three years after Boltzmann's death, Perrin's studies of colloidal suspensions confirmed the values of the Avogadro number and the Boltzmann constant.

Table 3.1.8 Binary gas diffusion coefficients $D_{AB,g}$ (in cm^2s^{-1} , 1.013 bar, 0 °C) (self-diffusion coefficients are in bold). Data from Baerns *et al.* (2006).

	CH₄	CO	CO₂	H₂	N₂	H₂O
CH ₄	0.18	0.19	0.15	0.63	0.18	0.24
CO	0.19	0.17	0.14	0.65	0.18	0.22
CO ₂	0.15	0.14	0.09	0.55	0.12	0.16
H ₂	0.63	0.65	0.55	1.20	0.65	0.83
N ₂	0.18	0.18	0.12	0.65	0.17	0.21
H ₂ O	0.24	0.22	0.16	0.83	0.21	0.16

as Eqs. (3.1.75) and (3.1.76) consider that σ decreases with temperature:

$$\sigma(T) = \sigma_\infty \sqrt{1 + \frac{C_{\text{Sutherland}}}{T}} \quad (3.1.77)$$

with the *Sutherland* constant $C_{\text{Sutherland}}$ (*W. Sutherland*, see box), for most gases being 50 to 500 K.

Note that for extremely low pressures the mean free path becomes the order of magnitude of the vessel diameter, which is then limiting and has to be used instead of Λ in Eqs. (3.1.68)–(3.1.70). For air (at 20 °C), a pressure of less than 10^{-3} mbar is needed to obtain a mean free path of the order of magnitude of a cm [Eq. (3.1.72)]; λ_g is then proportional to p , and thus this effect is used for superinsulations by highly evacuated casings. In addition, note that the diffusivities given in Table 3.1.7 are only valid for pure gases (self-diffusion coefficients). In binary gas mixtures, the binary coefficient $D_{AB,g}$ has to be used (Table 3.1.8). Note that in a binary gas mixture the diffusion coefficient is independent of the content of both components and that the diffusion coefficient of A in B is equal to the diffusion coefficient of B in A.

Calculation of binary diffusion coefficients based on Eqs. (3.1.69),(3.1.71),(3.1.72) and (3.1.79) is limited because estimations of the collision cross-section of the molecules σ (and of the influence of the temperature on σ) are not available for all gases. A more accurate but also more complicated equation is given by Hirschfelder, Curtiss, and Bird (1967) based on the *Chapman–Enskog* kinetic theory of gases. The so-called *Hirschfelder* equation is frequently presented in many textbooks and used in the literature, but values of parameters such as the collision diameters of the molecules and characteristic energies are needed. Instead, many authors have developed empirical relations. For non-polar gas pairs, $D_{AB,g}$ is in good approximation (deviation <10%) given by the equation of Slattery and Bird (1958):

$$D_{AB,g} \approx \frac{4 \times 10^{-8} (p_{A,\text{crit}} p_{B,\text{crit}})^{0.333} (T_{A,\text{crit}} T_{B,\text{crit}})^{0.417} \left(\frac{M_A + M_B}{M_A M_B}\right)^{0.5}}{p} \left[\frac{T}{(T_{A,\text{crit}} T_{B,\text{crit}})^{0.5}} \right]^{1.823} \quad (3.1.78a)$$

with $D_{AB,g}$ as the binary diffusion coefficient in $\text{m}^2 \text{s}^{-1}$, p as the total pressure in Pa, M in kg mol^{-1} , T_{crit} as the critical temperature in K, and p_{crit} as the critical pressure in Pa.

Another effective equation to predict binary diffusion coefficient of gases was derived by Fuller, Schettler, and Giddings (1966):

$$D_{AB,g} \approx \frac{3.16 \times 10^{-8} T^{1.75} \left(\frac{M_A + M_B}{M_A M_B}\right)^{0.5}}{p \left[\left(\sum_A v_{i,\text{FSG}}\right)^{\frac{1}{3}} + \left(\sum_B v_{i,\text{FSG}}\right)^{\frac{1}{3}} \right]^2} \quad (\text{with } v_{i,\text{FSG}} \text{ as listed in Table 3.1.9}) \quad (3.1.78b)$$

In Eq. (3.1.78b), $D_{AB,g}$ is the binary diffusion coefficient in $\text{m}^2 \text{s}^{-1}$, p the total pressure in Pa, M the molar mass in kg mol^{-1} , T the temperature in K, and $v_{i,\text{FSG}}$ the special diffusion volume (increments) according to Fuller, Schettler and

William Sutherland (1859–1911), an Australian physicist, was born in Scotland and emigrated in 1859 as a child with his family to Australia. He derived an equation to describe Brownian motion and diffusion, and presented his work at a conference in New Zealand in 1904 and published it in 1905 (Sutherland, 1904, 1905). At about the same time, *Albert Einstein*, an unknown patent clerk in Bern (Switzerland), published the results of his thesis on the same topic (Einstein, 1905). The *Einstein* equation for diffusion in liquids is $D = kT/(6\pi\eta r_{\text{molecule}})$ and was obtained by *Sutherland* one year earlier but, unfortunately, the proceedings of the 1904 conference had an unfortunate misprint in the key equation. Thus, in truth it should be named *Sutherland–Einstein* Equation. *Sutherland* never held a permanent university position. In 1889, he applied for the *Chair of Natural Philosophy* at Melbourne University, in those days still through London, but was not appointed. Instead, he received a letter that his application for the *Chair of Music* was unsuccessful (McKellar, 2005). He was an excellent pianist and violinist so the mistake is not as strange as it seems at first sight. As a private researcher he investigated the viscosity of fluids, molecular attraction, and the electronic theory of matter. Based on studies of the influence on temperature on the viscosity of gases, he derived Eq. (3.1.77).

Table 3.1.9 Special diffusion volumes derived by Fuller, Schettler, and Giddings (1966) (parenthesis indicate that the value is uncertain).

Atomic and structural diffusion volume increments ν_i for organic vapors	Diffusion volume $\Sigma \nu_i$ for simple molecules	
	$10^6 \nu_i$ ($\text{m}^3 \text{ mol}^{-1}$)	$10^6 \Sigma \nu_i$ ($\text{m}^3 \text{ mol}^{-1}$)
C	16.5	H ₂ 7.07
H	1.98	He 2.88
O	5.48	N ₂ 17.9
(N)	5.69	O ₂ 16.6
(Cl)	19.5	Air 20.1
(S)	17.0	CO 18.9
Aromatic or heterocyclic ring	-20.2	CO ₂ 26.9
		N ₂ O 35.9
		NH ₃ 14.9
		H ₂ O 12.7
		(Cl ₂) 37.7
		(SO ₂) 41.1

Giddings in $\text{m}^3 \text{ mol}^{-1}$ (Table 3.1.9). The term for diffusion volumes here parallels the collision cross section in Eq. (3.1.72).

A comparison of experimental values of binary diffusion coefficients in gases with the values estimated by Eqs. (3.1.78a) and (3.1.78) indicates that both equations are suitable (Table 3.1.10), but Eq. (3.1.78b) is slightly more successful. Equation (3.1.78a) should not be used for polar molecules like ethanol or water.

Owing to practical relevance, the diffusion of water vapor in air has been the topic of many studies. The following correlation is given by Marrero and Mason (1972):

$$D_{\text{H}_2\text{O-air,g}} \approx 1.89 \times 10^{-5} \frac{T^{2.072}}{p} \quad (\text{for } 280 < T < 450 \text{ K, } T \text{ in K, } p \text{ in Pa}) \quad (3.1.79)$$

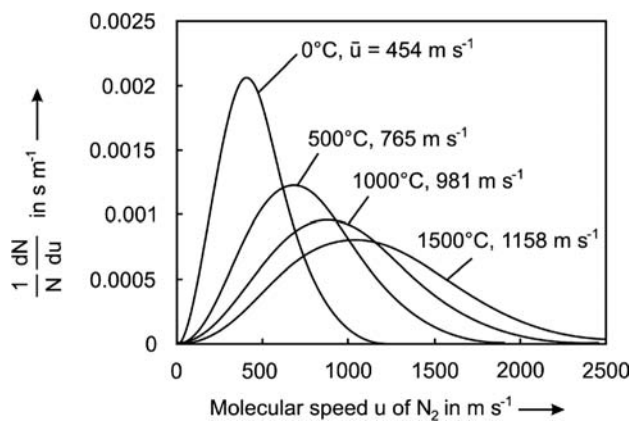
For a gas mixture consisting of more than three components, the approximation of Wilke (1986) based on the binary diffusion coefficients and the molar content γ is useful:

$$\bar{\nu}_o = D_{k,m} = \frac{1 - \gamma_k}{\sum_{i=1, i \neq k}^N \frac{\gamma_i}{D_{ki}}} \quad (\text{with } k \text{ as the component that diffuses in the gas mixture m}) \quad (3.1.80)$$

Table 3.1.10 Binary gas diffusion coefficients (and selected self-diffusion coefficients) at 1 bar: comparison of experimental values (Baerens *et al.*, 2006) and estimations by Eqs. (3.1.78a) and (3.1.78b).

System	Temperature (°C)	D_{AB} ($\text{cm}^2 \text{ s}^{-1}$)		
		Experimental value	Equation (3.1.78a)	Equation (3.1.78b)
H ₂ /H ₂	0	1.20	1.30	1.24
N ₂ /N ₂	0	0.17	0.18	0.18
H ₂ /N ₂	0	0.65	0.68	0.65
CO ₂ /N ₂	0	0.12	0.13	0.14
Air/SO ₂	341	0.47	—	0.45
O ₂ /N ₂	43	0.23	0.23	0.23
CO ₂ /C ₂ H ₅ OH	0	0.069	0.104	0.086
CO ₂ /C ₆ H ₆	45	0.072	0.074	0.080
N ₂ /CH ₄	43	0.24	0.24	0.24
H ₂ /NH ₃	25	0.78	0.68	0.83
H ₂ /C ₃ H ₈	27	0.45	0.50	0.44
H ₂ /H ₂ O	35	0.26	0.10	0.28

Figure 3.1.15 Maxwell–Boltzmann distribution of molecular speed u in N_2 for different temperatures [mean velocity \bar{u} as calculated by Eq. (3.1.71)].



Topic 3.1.3 Distribution of molecular speed and energy in a gas

The distribution of molecular speeds in a gas is given by the Maxwell–Boltzmann equation:

$$\frac{1}{N} \frac{dN}{du} = \frac{4}{\sqrt{\pi}} \left(\frac{M}{2RT} \right)^{1.5} u^2 e^{-\frac{Mu^2}{2RT}} \quad (3.1.81)$$

where N is the number of molecules or atoms with molar mass M , and dN/N is the portion with velocities between u and $(u + du)$. Figure 3.1.15 shows this distribution for nitrogen.

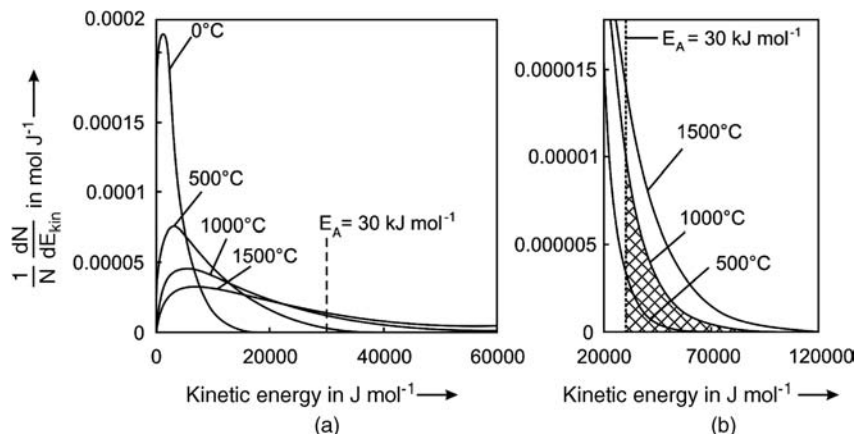
With regard to the kinetics of chemical reactions, the influence of temperature on the portion of molecules exceeding a certain kinetic energy is important. Thus we need the Maxwell–Boltzmann distribution of kinetic energy. If we use $E_{\text{kin}} = Mu^2/2$ (in J mol^{-1}) and $dE_{\text{kin}} = Mu du$, Eq. (3.1.81) yields the distribution of the kinetic energy (in three dimensions) as shown in Figure 3.1.16:

$$\frac{1}{N} \frac{dN}{dE_{\text{kin}}} = \left(\frac{2}{\sqrt{\pi}(RT)^{1.5}} \right) \sqrt{E_{\text{kin}}} e^{-\frac{E_{\text{kin}}}{RT}} \quad (3.1.82)$$

Note that Eq. (3.1.82) and Figure 3.1.16 are independent of the molar mass and are thus valid for all gases.

In the collision theory of gas-phase reactions, an activation energy E_A is assumed for a collision to be effective, and only molecules with a kinetic energy exceeding E_A react. The respective portion of molecules for an arbitrarily chosen value of E_A of 30 kJ mol^{-1} and a temperature of 1000°C is indicated in Figure 3.1.16b (hatched area).

Figure 3.1.16 (a) and (b) Boltzmann distribution of kinetic energy (in three dimensions) according to Eq. (3.1.83) for different temperatures [hatched area in (b): solution of Eq. (3.1.83) for 1000°C].



area). The value of this portion is calculated by integration of Eq. (3.1.82):

$$\left. \frac{\Delta N}{N} \right|_{E_{\text{kin}} > E_A} = C_1 \int_{E_A}^{\infty} \sqrt{E_{\text{kin}}} e^{-\frac{E_{\text{kin}}}{RT}} dE_{\text{kin}} \quad \left[\text{with } C_1 = \frac{2}{\sqrt{\pi(RT)^{1.5}}} \right] \quad (3.1.83)$$

either by graphical methods, a spreadsheet, or by solution of Eq. (3.1.83) by a series expansion:

$$\int x^n e^{ax} dx = 1/a x^n e^{ax} - n/a \int x^{n-1} e^{ax} dx$$

to give:

$$\int_{E_A}^{\infty} \sqrt{E_{\text{kin}}} e^{-\frac{E_{\text{kin}}}{RT}} dE_{\text{kin}} = RT \sqrt{E_A} e^{-\frac{E_A}{RT}} \left[1 + \frac{1}{2} \frac{RT}{E_A} - \frac{1}{4} \left(\frac{RT}{E_A} \right)^2 + \frac{3}{8} \left(\frac{RT}{E_A} \right)^3 \dots \right] \quad (3.1.84)$$

For a value of the term RT/E_A of less than 0.5 (e.g., for $E_A = 30 \text{ kJ mol}^{-1}$ and $T < 1500^\circ\text{C}$), the series in the brackets of Eq. (3.1.84) may be terminated after the term $(1/2)RT/E_A$, and Eqs. (3.1.83) and (3.1.84) lead to the following simplified solution of Eq. (3.1.82):

$$\left. \frac{\Delta N}{N} \right|_{E_{\text{kin}} > E_A} \approx \left[RTC_1 \sqrt{E_A} \left(1 + \frac{1}{2} \frac{RT}{E_A} \right) \right] e^{-\frac{E_A}{RT}} \quad (\text{for } RT/E_A < 0.5) \quad (3.1.85)$$

For the given example, the deviation of the approximation by Eq. (3.1.85) and the correct value according to Eq. (3.1.84) are within less than 4%.

The influence of temperature on the exponential term is much stronger than on the pre-exponential term in the square brackets of Eq. (3.1.85). Hence an even simpler solution of Eq. (3.1.83) is derived by introducing a mean temperature \bar{T} and a respective mean value of C_1 for the temperature range from T_1 to T_2 that is under consideration:

$$\bar{C}_1 = \frac{2}{\sqrt{\pi(R\bar{T})^{1.5}}} \quad \left(\text{with } \bar{T} = \frac{T_1 + T_2}{2} \right) \quad (3.1.86)$$

Insertion of \bar{T} and \bar{C}_1 in Eq. (3.1.85) leads to the so-called Arrhenius equation:

$$\begin{aligned} \left. \frac{\Delta N}{N} \right|_{E_{\text{kin}} > E_A} &\approx \left[\sqrt{\frac{E_A}{\pi R \bar{T}}} \left(2 + \frac{R\bar{T}}{E_A} \right) \right] e^{-\frac{E_A}{R\bar{T}}} \\ &= \text{const.} \times e^{-\frac{E_A}{R\bar{T}}} \quad (\text{for } R\bar{T}/E_A < 0.5) \end{aligned} \quad (3.1.87)$$

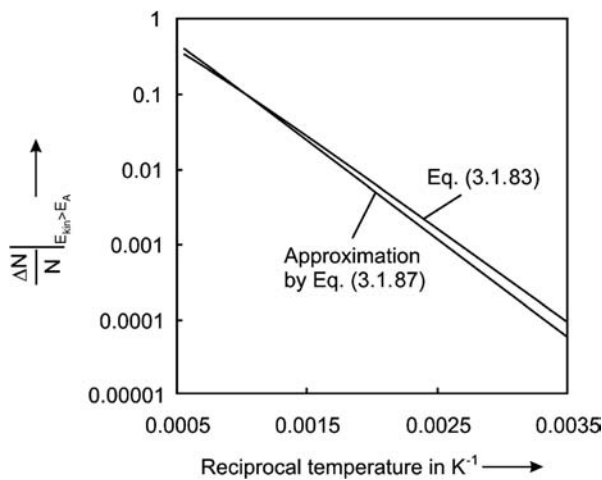
Figure 3.1.17 shows that the deviation of Eq. (3.1.87) for $E_A = 30 \text{ kJ mol}^{-1}$ and a temperature range of 0–1500 °C ($\bar{T} = 1023 \text{ K}$) from the exact equation (3.1.84) is small, which is the reason why in chemical kinetics the Arrhenius equation based on a constant pre-exponential factor is frequently used (Section 4.3.1). Moreover, the values of the pre-exponential factor and of the activation energy are determined based on the best fit to experimental kinetic data, which compensates for the disregard of the weak influence of temperature on the pre-exponential factor.

3.1.4.3 Transport Coefficients of Liquids

The thermal conductivity of a liquid can be found from the *Bridgman* equation (Bridgman, 1923):

$$\lambda_l \approx 2.8 \times 10^{-7} u_{\text{sound}} \left(\frac{\rho_l}{M_l} \right)^{0.67} \quad (3.1.88)$$

Figure 3.1.17 Arrhenius plot: portion of molecules with energy exceeding 30 kJ mol^{-1} according to the Maxwell–Boltzmann distribution of kinetic energy (in three dimensions).



where λ_l is in $\text{W m}^{-1} \text{K}^{-1}$, u_{sound} is the velocity of sound in the liquid in m s^{-1} , ρ is density in kg m^{-3} , and M is the molar mass in kg mol^{-1} . For example, for water ($u_{\text{sound}} = 1484 \text{ m s}^{-1}$), Eq. (3.1.88) yields a value of $0.59 \text{ W m}^{-1} \text{K}^{-1}$ compared to the measured value of $0.60 \text{ W m}^{-1} \text{K}^{-1}$ (20°C).

The influence of temperature on the viscosity of a liquid is approximately given by:

$$\eta_l = C e^{\frac{E}{RT}} \quad (3.1.89)$$

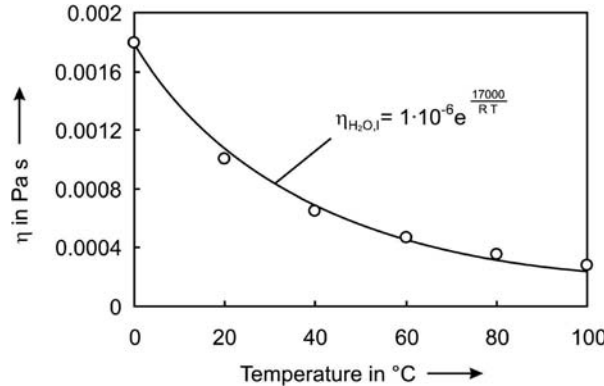
The constants C and E in Eq. (3.1.89) have to be measured and up to now cannot be calculated based on a theory or by semi-empirical equations. E represents the energy needed to create a cavity in the dense packing of the liquid, that is, to push the molecules apart. Typically, E is of the order of magnitude of 10 kJ mol^{-1} , for example, for water about 17 kJ mol^{-1} in the range $0\text{--}100^\circ\text{C}$. The strong decrease of η with temperature is shown in Figure 3.1.18 for the example of water.

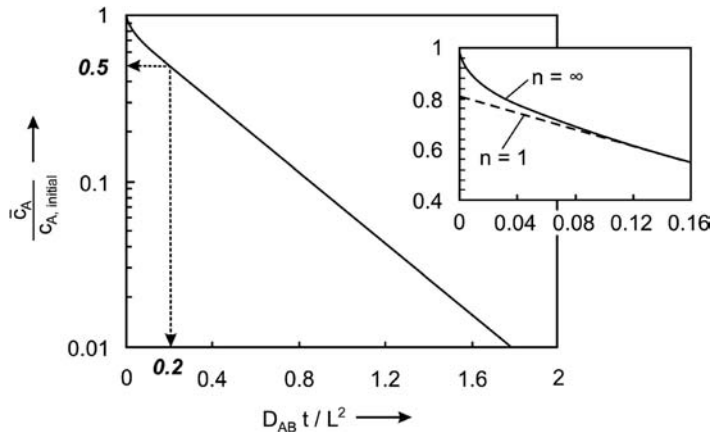
The diffusion coefficient in liquids (solute A in solvent B) can be calculated for dilute solutions with errors of usually less than 20% by the *Wilke–Chang equation* (Wilke and Chang, 1955):

$$D_{AB,l} = 5.88 \times 10^{-17} \frac{T \sqrt{\chi_B M_B}}{\eta_B (\nu_{\text{mol, cp},A})^{0.6}} = C \frac{T}{\eta_B} \sim T e^{-\frac{E}{RT}} \quad (3.1.90)$$

where $D_{AB,l}$ is in $\text{m}^2 \text{s}^{-1}$, χ is an association parameter (2.6 for water, 1.9 for methanol, 1.5 for ethanol, 1 for non-polar organic liquids), M is the molar mass in kg mol^{-1} , $\nu_{\text{mol, cp}}$ is the molar volume of solute at the condensation point at 1 bar in $\text{m}^3 \text{mol}^{-1}$, and η is in $\text{kg m}^{-1} \text{s}^{-1}$. $D_{AB,l}$ is inversely proportional to η_{solvent} , and thus strongly (almost exponentially) increases with temperature.

Figure 3.1.18 Temperature dependence of the viscosity of (liquid) water [measured values and correlation according to Eq. (3.1.89)].





Methods for measuring diffusion coefficients in liquids are described in Topic 3.1.4.

Topic 3.1.4 Methods to measure diffusion coefficient in liquids

Capillary Method

The capillary method is a suitable method for the measurement of diffusion coefficients in liquids (Cussler, 2009). It uses a small capillary tubing as diffusion cell. One end of the capillary is sealed shut. The cell is filled with a solution of known concentration, for example, a certain amount of component A in B. The diffusion cell is then dropped into a large, stirred, thermostated solvent bath (filled with B). After a certain time, the capillary is removed and the (mean) concentration of the solute (here A) within the cell is measured. The diffusion coefficient D_{AB} can then be calculated by the following equation (Cussler, 2009):

$$\frac{\bar{c}_A}{c_{A,\text{initial}}} = \frac{8}{\pi^2} \sum_{n=1}^{\infty} \frac{1}{(2n-1)^2} e^{-\pi^2(n-\frac{1}{2})^2 \frac{D_{AB} t}{L^2}}$$

$$\approx \frac{8}{\pi^2} e^{-\frac{\pi^2 D_{AB} t}{4 L^2}} \quad \left(\text{for } \frac{D_{AB} t}{L^2} > 0.1, \text{ deviation} < 5\% \right) \quad (3.1.91)$$

in which \bar{c}_A is the average concentration in the cell (capillary) at time t , $c_{A,\text{initial}}$ is the initial concentration at time zero, and L the length of the capillary.

The power series in Eq. (3.1.91) converges rapidly, and for a value of the dimensionless term $D_{AB}t/L^2$ of more than 0.1 ($\bar{c}_A/c_{A,\text{initial}} < 0.3$) we can base the analysis on the first term of the series ($n=1$, deviation $< 5\%$). Figure 3.1.19 shows the plot of Eq. (3.1.91).

Example: A mixture of methanol and water is filled into a capillary with length 4 cm. The cell is then dropped into a large well-mixed water bath of 25 °C. The diffusion coefficient of methanol in water is $1.8 \times 10^{-9} \text{ m}^2 \text{ s}^{-1}$ (Table 3.1.6). The mean concentration in the capillary is half of the initial value for $D_{AB}t/L^2 = 0.2$. Thus we get $t = 49.4 \text{ h}$ (for $\bar{c}_A/c_{A,\text{initial}} = 0.5$).

The capillary method can only hardly be used for gases, in particular as the experimental time is rather short. For example, the diffusivity of CO₂ in N₂ (1 bar, 0 °C) is $1.2 \times 10^{-5} \text{ m}^2 \text{ s}^{-1}$ (Table 3.1.8). Thus the mean concentration in the capillary would already be half of the initial value after only 27 s, and even for a mean concentration of only 5% of the initial value ($D_{AB}t/L^2 = 1.13$), only 2.5 min would be needed.

Magnetic Suspension Balance (Diffusion of Dissolved Gases in Liquids)

The diffusion coefficient (as well as the solubility) of a gas in a liquid may be measured by a magnetic suspension balance (Figure 3.1.20). At the start of a

Figure 3.1.19 Change of mean concentration of solute A in capillary tubing after dropping into a large, stirred, thermostated solvent bath filled with solvent B [Eq. (3.1.91)].

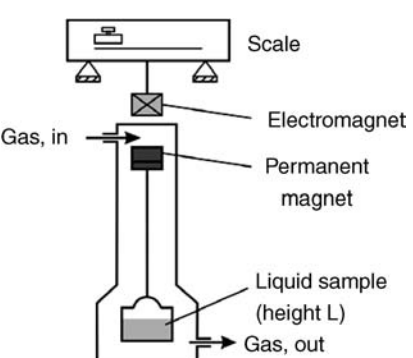
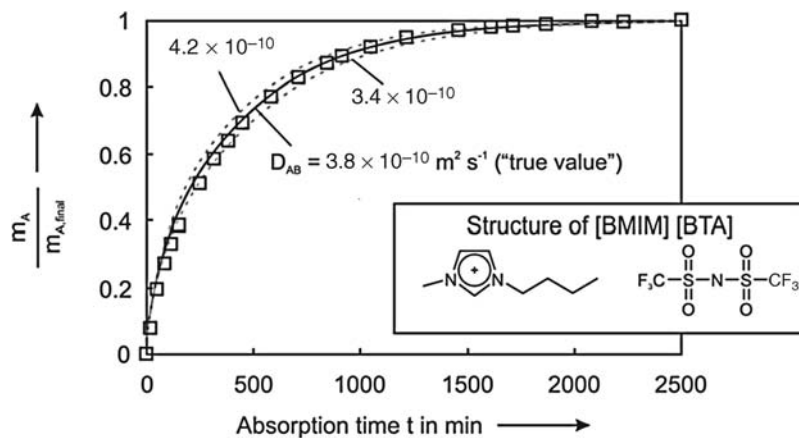


Figure 3.1.20 Simplified scheme of a magnetic suspension balance (see also Figure 4.11.7).

Figure 3.1.21 Increase of mass of a liquid sample with time upon uptake (absorption) of a gas; $L = 5 \text{ mm}$, 25°C , A = H_2S , B = [BMIM][BTA], pressure = 28 bar (argon with 2.5 vol.% H_2S).



measurement a sample of a liquid with known mass is placed in the measuring cell, which is evacuated until the liquid is completely degassed. The cell is then filled with the gas with a designated pressure and temperature. By absorption of the gas in the liquid the sample weight increases with time until the liquid is completely saturated. From the final value of the gain of mass reached at saturation the gas solubility (Henry coefficient) is calculated.

To determine the diffusion coefficient of a dissolved gas (e.g., of gas A in liquid B), the weight versus time curve during absorption is analyzed by comparison with modeled curves calculated on the basis of the second Fickian law. According to Crank (2003), the diffusion of a dissolved gas A in a solvent B for a one-dimensional diffusion in a slab with height L and constant concentration at the surface of the slab is described by:

$$\frac{m_A}{m_{A,\text{final}}} = 1 - \frac{8}{\pi^2} \sum_{n=0}^{\infty} \frac{1}{(2n+1)^2} e^{-\pi^2(n+\frac{1}{2})^2 \left(\frac{D_{AB} t}{L^2}\right)} \\ \approx 1 - \frac{8}{\pi^2} e^{-\frac{\pi^2}{4} \left(\frac{D_{AB} t}{L^2}\right)} \quad \left(\text{for } \frac{D_{AB} t}{L^2} > 0.1\right) \quad (3.1.92)$$

where m_A is the measured increase of mass of the liquid sample (= mass of dissolved A) at time t , and $m_{A,\text{final}}$ is the maximum final mass of A dissolved at infinite time.

Example: The diffusion of H_2S in the ionic liquid butylmethylimidazolium bis(trifluoromethylsulfonylimide) ([BMIM][BTA]) was measured in a magnetic suspension balance. [Ionic liquids are low melting salts ($< 100^\circ\text{C}$) with negligible vapor pressure, see Section 4.8 for more details.] Figure 3.1.21 shows the result of the experiment. Analysis of the experiment by Eq. (3.1.92), that is, the best fit, leads to $D_{\text{H}_2\text{S}, \text{BMIM BTA}} = 3.8 \times 10^{-10} \text{ m}^2 \text{ s}^{-1}$. For comparison, the calculated curves for a lower and higher coefficient are also shown, which indicate that the accuracy is limited to about $\pm 10\%$.

Summary of Section 3.1 (take-home messages)

- No gas is truly ideal, but many gases follow the predictions of the **ideal gas law** at normal temperature and pressure ($p v = R T$).
- The van der Waals equation describes sufficiently the real gas behavior:

$$\left(p + \frac{a}{v_{\text{mol,real}}^2}\right)(v_{\text{mol,real}} - b) = RT$$

- The change in internal energy U and the enthalpy H of a closed system by work and heat is described by the first law of thermodynamics ($\Delta U = Q + W$), and we obtain $\Delta U = Q - p\Delta V$ and $\Delta H = \Delta U + p\Delta V = Q$ for $p = \text{const.}$ and $\Delta U = Q$ for $V = \text{const.}$
- The temperature of an ideal gas remains constant during adiabatic expansion. The change of temperature of a real gas during expansion is characterized by the **Joule–Thomson coefficient**. In most cases this leads to a decrease in temperature.
- All natural processes lead to a chaotic dispersal of the total energy, and the **entropy** S is a measure to quantify this (second law of thermodynamics). Any change of the entropy of a system is accompanied by a change of the entropy in the surrounding. The overall change of the entropy is greater than zero in general. Only if the heat Q is reversibly transferred, does the overall change of the entropy become zero.
- The **phase diagram** shows the location of the phase boundaries between the solid, liquid, and gas phases. All three phases are in equilibrium at the **triple point**. If the temperature and pressure exceed the so-called critical values, the phase boundary between liquid and vapor vanishes. For this **supercritical state**, a change of pressure and temperature no longer leads to a change of the state of aggregation. The influence of pressure on a phase transition is given by the **Clapeyron equation**.

$$\frac{dp}{dT} = \frac{\Delta H_{\text{phase transition}}}{T \Delta v_{\text{mol,phase transition}}}$$

The ratio of the standard vaporization enthalpy to the normal boiling temperature ($\Delta_{\text{vap}}H^0/T_{\text{boil}}^0$) equals the standard vaporization entropy $\Delta_{\text{vap}}S^0$. For an estimation of $\Delta_{\text{vap}}H^0$ based on T_{boil}^0 we may use $\Delta_{\text{vap}}S^0 \approx 90 \text{ J mol}^{-1} \text{ K}^{-1}$ (**Trouton's rule of thumb**).

- The vapor pressure over curved surfaces is dependent on the radius of curvature. This involves modifications to the vapor pressure relationships for highly curved systems like rain drops or liquids confined in small capillaries.
- The basic equations for stationary **transport of heat, mass, and momentum** are the first laws of *Fourier*, *Fick*, and *Newton*, respectively. The flow rate of energy, matter, and momentum is proportional to the area perpendicular to the flow and to the gradients of temperature, concentration, and velocity. The connecting links are the transport coefficients, thermal conductivity λ , diffusion coefficient D , and dynamic viscosity η . For gases, these quantities can be estimated by the kinetic theory of gases.

3.2

Heat and Mass Transfer in Chemical Engineering

In virtually every process of chemical technology (and also in many processes of everyday life) the transport of mass and heat is involved. The fundamental equations of (steady) heat and mass transfer and values of the thermal conductivity and of the diffusion coefficient of gases, liquids, and solids have been treated in Section 3.1.4. Building on that, this sub-chapter dedicates itself to the following heat and mass transfer processes, which are particularly relevant for chemical engineering:

- The mechanisms of heat transport can be divided into heat conduction, heat transfer by natural or forced convection, and radiation heat transfer. If two of the named processes take place simultaneously, we use overall heat transfer coefficients.

$$\dot{Q} = U_h A \frac{T_1 - T_2}{d}$$

$$Nu = \frac{\alpha d_{\text{charac.}}}{\lambda}$$



Wound heat exchanger. Courtesy of Linde Engineering, Germany.

$$\frac{dT}{dt} = \frac{\lambda}{c_p \rho_{\text{mol}}} \frac{d^2T}{dx^2}$$

$$= a \frac{d^2T}{dx^2}$$

$$\dot{n} = \beta A(c_{\text{fluid}} - c_s)$$

$$Sh = \frac{\beta d_{\text{charac}}}{D}$$

$$\frac{dc}{dt} = D \frac{d^2c}{dx^2}$$

- For transient heat conduction, which is, for example, important to heat up or cool down a body, we have to consider the variation of temperature with time as well as with local position.
- The mechanisms of mass transport can be divided into convective and molecular flow processes. Convective flow is either forced flow, for example, in pipes and packed beds, or natural convection induced by temperature differences in a fluid. For diffusive flow we have to distinguish whether we have molecular diffusion in a free fluid phase or a more complicated “effective” diffusion in porous solids. Like heat transport, diffusion may be steady-state or transient.

“Operating manual” for beginners and intermediate learners:

Start with Sections 3.2.1.1–3.2.1.4, which deal with steady-state heat transfer. Then study the basic mechanism of mass transfer (Sections 3.2.2.1 and 3.2.2.2).

“Operating manual” for advanced learners:

Advanced learners should also study transient heat conduction processes (Section 3.2.1.5) and the special problems encountered with diffusion in porous solids (Section 3.2.2.3).

3.2.1

Heat Transport

3.2.1.1 Heat Conduction

The equation for the one-dimensional steady heat conduction is *Fourier’s first law*, Eq. (3.1.53). For a plane wall with thickness d and a temperature T_1 on one side and a lower temperature T_2 on the opposite side we obtain:

! $\dot{Q}_{\text{wall}} = \lambda_{\text{wall}} A \frac{T_1 - T_2}{d}$ (3.2.1)

Figure 3.2.1 gives typical values of the thermal conductivity of solids, liquids, and gases.

For heat conduction through the wall of a tube with an externally cooled surface and an internal and external diameter of d_{int} and d_{ex} , respectively, and a length L we have:

$$\dot{Q}_{\text{tube}} = \lambda_{\text{wall}} A_{\text{int}} \frac{(T_{\text{int}} - T_{\text{ex}})}{\frac{d_{\text{int}}}{2} \ln\left(\frac{d_{\text{ex}}}{d_{\text{int}}}\right)} = \lambda_{\text{wall}} 2\pi L \frac{(T_{\text{int}} - T_{\text{ex}})}{\ln\left(\frac{d_{\text{ex}}}{d_{\text{int}}}\right)} \quad (3.2.2)$$

For a thin wall, the term $d_{\text{int}}/2\ln(d_{\text{ex}}/d_{\text{int}})$ almost equals $(d_{\text{ex}} - d_{\text{int}})/2$ [as $\ln(d_{\text{ex}}/d_{\text{int}}) \approx d_{\text{ex}}/d_{\text{in}} - 1$ for $d_{\text{ex}}/d_{\text{in}} \approx 1$], and thus we then use Eq. (3.2.1) with d as the wall thickness ($d = d_{\text{ex}} - d_{\text{int}}$).

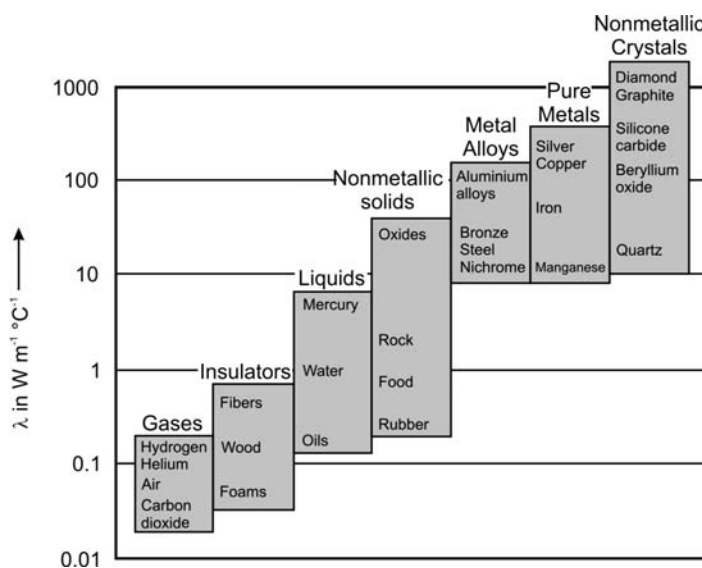


Figure 3.2.1 Thermal conductivity of gases, liquids, and solids ; for exact values and equations for the thermal conductivity of gases and liquids see Section 3.1.4. (adapted from Cengel, 2002)

For heat conduction in a spherical shell (internal and external diameter d_{int} and d_{ex}) we have:

$$\dot{Q}_{\text{sphere}} = \lambda 2\pi \frac{(T_{\text{int}} - T_{\text{ex}})}{\frac{1}{d_{\text{int}}} - \frac{1}{d_{\text{ex}}}} \quad (3.2.3)$$

Equation (3.2.3) leads to an interesting border case if the external diameter becomes infinitely large. The specific heat flux per unit surface area, $\dot{Q}_{\text{sphere}}/(\pi d_{\text{int}}^2)$, then equals the term $\lambda 2\Delta T/d_{\text{int}}$, which corresponds to the minimum heat loss of a sphere (with diameter d_{int}) to the surroundings with thermal conductivity λ . In principle, every finite body has such a limiting value of heat loss.

3.2.1.2 Heat Transfer by Convection (Heat Transfer Coefficients)

For heat transfer from a stagnant or a flowing fluid to a solid we have to use the following equation instead of Eq. (3.2.1):

$$\dot{Q} = \lambda_{\text{fluid}} A \frac{T_{\text{fluid}} - T_s}{\delta} \quad (3.2.4)$$

Here δ is the thickness of the boundary layer if the real trace of the temperature curve is approximated by a straight line with the slope corresponding to the gradient directly at the surface (Figure 3.2.2). More details on this definition of δ are given in Topic 3.2.1.

The terms λ and δ are combined by introduction of the heat transfer coefficient α and we obtain:

$$\dot{Q} = \frac{\lambda_{\text{fluid}}}{\delta} A (T_{\text{fluid}} - T_s) = \alpha A (T_{\text{fluid}} - T_s) \quad (3.2.5)$$

For estimations, the α values in Table 3.2.1 are useful, indicating that α is high for liquids compared to gases and that high values are reached with boiling liquids (Section 3.2.1.3).

Table 3.2.1 Rough estimations of heat transfer coefficients (α). Data from Emig and Klemm (2005).

Case	α (water) ($\text{W m}^{-2} \text{K}^{-1}$)	α (air) ($\text{W m}^{-2} \text{K}^{-1}$)
Turbulent flow in a tube	1000–4000	30–50
Turbulent transversal flow against a tube	2000–7000	50–80
Laminar flow	250–350	3–4
Natural convection	250–700	3–20
Boiling water	1500–15 000	—

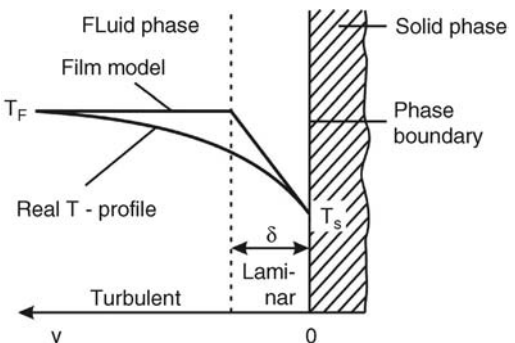


Figure 3.2.2 Temperature curve at the boundary of a fluid to a solid.

The heat transfer coefficient α is calculated by equations for the Nusselt number Nu (Wilhelm Nusselt, see box) based on a characteristic length (diameter of a sphere or tube etc.):

$$\bullet \quad Nu = \frac{\alpha d_{\text{charac.}}}{\lambda} \quad (\text{see Topics 3.2.2 and 3.2.3 for further insights into } Nu) \quad (3.2.6)$$

Combining the definition of Nu [Eq. (3.2.6)] with Eq. (3.2.5) leads to:

$$Nu = \frac{d_{\text{charac.}}}{\delta} \quad (3.2.7)$$

and thus Nu corresponds to the ratio of the characteristic length to the thickness of the boundary layer. For different geometries (particles of different shape, tube, plane wall) and flow conditions (against or through tubes, laminar or turbulent flow) different equations for Nu were deduced based on numerous experimental data. Here we only specify some cases frequently needed in chemical engineering; other correlations are given in Cengel (2002) and VDI (1997).

Wilhelm Nusselt (1882–1957), a German engineer, published in 1915 his pioneering work “The basic law of heat transfer” (Nusselt, 1915), in which he derived the dimensionless numbers directly from the differential equations of fluid flow and heat transfer. In this paper he states (see Topic 3.2.2):

It is often claimed in the literature that heat transmission from a body is based on three mechanism, radiation, conduction, and convection. This subdivision of heat transmission in conduction and convection gives the impression as if we have two independent phenomena. From this one had to conclude, that heat might also be transferred by convection without any contribution of conduction. This, however, is not true.

Other studies by him were concerned with condensation of steam on surfaces, coal combustion, and the analogy between heat and mass transfer in evaporation.

Topic 3.2.1 Definitions used for the thickness δ of the thermal boundary layer

Two definitions of the thickness δ of the thermal boundary layer (but also of the boundary layer of concentration in mass transport and velocity in hydrodynamics) are mostly used:

- 1) The thermal boundary layer $\delta_{0.99}$ is defined as the distance from the surface for which $\Delta T/\Delta T_{\max} = 0.99$, for example, for temperatures of the surface and the free stream of 100 °C and 20 °C this position corresponds to a temperature of 99.2 °C.
- 2) One may also use (as throughout this book) the distance from the surface, where the temperature of the free stream is reached, if the temperature gradient would be hypothetically constant and equal to the initial value at the surface (linearized film model, Figure 3.2.2). This definition is mostly used in (chemical) engineering, for example, in Eq. (3.2.5).

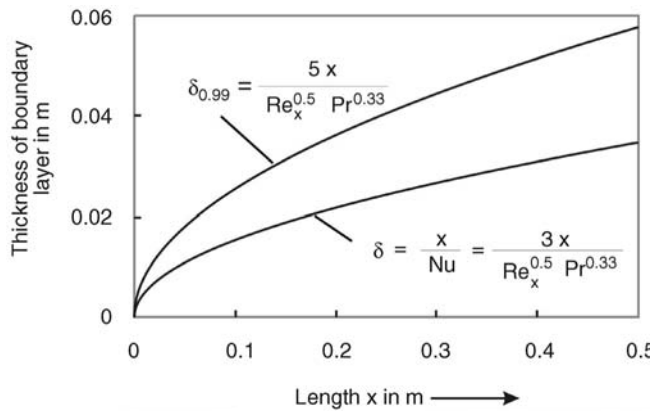
The values of $\delta_{0.99}$ and of the thickness according to the linearized film model δ differ, typically by a factor of about two, as shown in Figure 3.2.3 for a laminar flow over a flat plate.

Topic 3.2.2 Nusselt number Nu and heat transfer through a fluid between two parallel plates (see also Cengel, 2002)

To understand the physical significance of the Nusselt number Nu , consider a fluid layer of thickness L confined by two plates maintained at different temperatures (Figure 3.2.4).

Assuming no fluid motion, heat is only transferred by conduction, and we have [Eq. (3.2.4)]:

$$\dot{q}_{\text{conduction}, u=0} = \frac{\dot{Q}_{\text{conduction}, u=0}}{A} = \frac{\lambda_{\text{fluid}}}{L} (T_1 - T_2) \quad (\text{no fluid motion})$$



If a fluid is flowing between the two plates, heat transfer is enhanced since energy is now also carried to the cold plate by fluid motion and not only by conduction. To describe this situation we have to consider that the fluid in motion comes to a complete stop at the surface of the plates; thus the fluid layers in direct contact with the plates “stick” to the surface (no-slip condition, Section 3.2.2). An implication of this effect is that the heat transfer to the cold plate from the hot fluid layer adjacent to the cold surface (and vice versa from the hot plate to the cooler fluid at $z=L$) is only by pure conduction through the fluid and can be expressed by the thermal conductivity and the respective temperature gradient at $z=0$ (surface of cold plate). Thus we have for steady state conditions:

$$\dot{q}_{\text{conduction}, u>0} = \lambda_{\text{fluid}} \left(\frac{dT}{dz} \right)_{z=0} = \dot{q}_{\text{convection}} = \alpha(T_1 - T_2)$$

Note that now the temperature gradient is higher than without fluid motion (Figure 3.2.4), and thus the heat transfer is enhanced.

The ratio of the convective heat flux to the heat flux by pure conduction *without* fluid motion gives the Nusselt number (here with the distance L between the two plates as characteristic length):

$$Nu = \frac{\dot{q}_{\text{convection}}}{\dot{q}_{\text{conduction}, u=0}} = \frac{\alpha(T_1 - T_2)}{\lambda_{\text{fluid}} \frac{(T_1 - T_2)}{L}} = \frac{\alpha L}{\lambda_{\text{fluid}}}$$

Hence for the given example, a minimal Nusselt number of $Nu = 1$ represents heat transfer by pure conduction (no fluid motion), and the larger Nu the more effective the convection.

Topic 3.2.3 Presentation of experimental results by dimensionless numbers

The advantage of the use of dimensionless numbers can be seen by a typical heat transfer process based on the example and data given by Polifke and Kopitz (2009). Let us assume two groups of researchers have measured the convective heat transfer between the top surface of a plate and a gas that flows over the plate.

Figure 3.2.3 Thickness of the thermal boundary for laminar flow ($Re_x \ll 5 \times 10^5$) over a plate [air, $T_{\text{plate}}: 100^\circ\text{C}$, $T_{\text{bulk-phase}}: 20^\circ\text{C}$, gas velocity: 0.1 m s^{-1} , v (60°C): $0.019 \text{ cm}^2 \text{ s}^{-1}$, $Re_x = 2600$ for $x = 0.5 \text{ m}$, correlations from Cengel (2002); for definition of Pr see Eq. (3.2.10)].

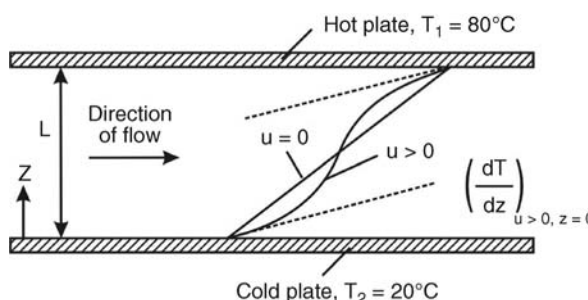
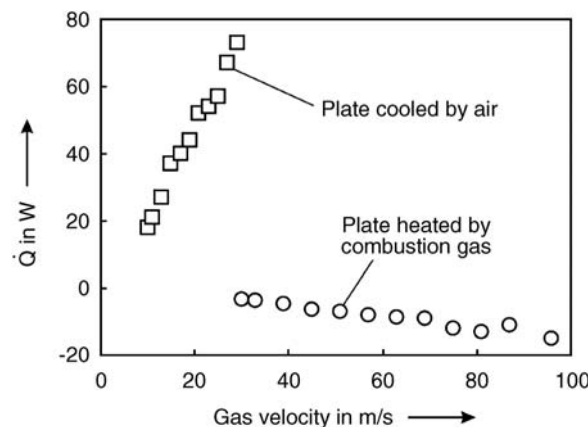


Figure 3.2.4 Temperature profiles for heat transfer through a fluid confined by two parallel plates (schematically, plates are assumed to have a constant but different temperature).

Figure 3.2.5 Heat flux from a cooled and from a heated plate to a gas (see text).



Group A carried out experiments with an electrically heated plate (length L in direction of flow = 1 m, area $A = 0.5 \text{ m}^2$) cooled by forced air with a velocity of 10 to 30 m s^{-1} . The plate has a very high heat conductivity and thus a uniform temperature. A constant temperature difference between the plate (with temperature 302 K) and the main stream of air of 2 K is established by adjusting the electrical power. The heating power is then measured as a function of the gas velocity (Figure 3.2.5).

Group B performed measurements with hot combustion gas, at a pressure of 6 bar and a temperature of 800 K, that flows with a velocity of $30\text{--}90 \text{ m s}^{-1}$ over a cooled plate (length $L = 0.4 \text{ m}$, area $A = 0.2 \text{ m}^2$) with a constant temperature of 600 K. Now the cooling power is measured (Figure 3.2.5), for example, by the increase of the temperature of the cooling medium (which should be small to keep the plate at an almost constant temperature).

Figure 3.2.5 shows that there is obviously no coherence between the experiments and even the algebraic sign is different (positive for flow into the gas).

The heat flux by convection is given by:

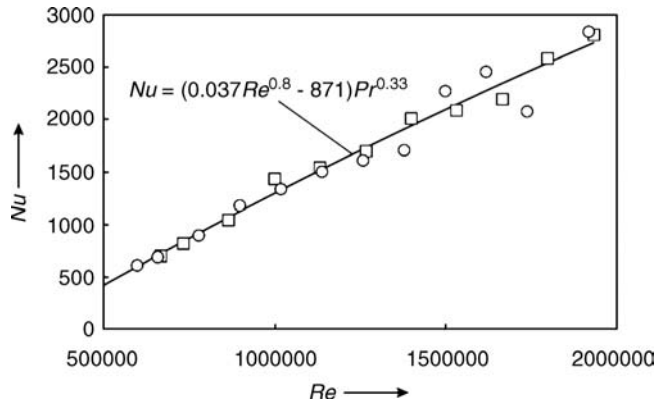
$$\dot{Q} = \alpha A (T_{\text{plate}} - T_{\text{gas}})$$

and with the definition of the Nusselt number [Eq. (3.2.6)] we get:

$$Nu = \frac{\alpha L}{\lambda} = \frac{\dot{Q}L}{A(T_{\text{plate}} - T_{\text{gas}})\lambda}$$

If we now use the dimensionless plot of Nu versus the Reynolds number ($Re = uL/\nu$), we obtain good coherence of both experimental data (Figure 3.2.6). Thus, we can derive a general correlation, which reflects that the physical background of both experiments is the same.

Figure 3.2.6 Nu versus Re for heat flux from a cooled (○) and from a heated (□) plate to a gas [kinematic viscosity: air (300 K, 1 bar) = $0.15 \text{ cm}^2 \text{s}^{-1}$, combustion gas (mean temp. of 700 K, 6 bar) = $0.2 \text{ cm}^2 \text{s}^{-1}$; thermal conductivity λ : air (300 K) = $0.026 \text{ W m}^{-1} \text{K}^{-1}$, combustion gas (700 K) = $0.053 \text{ W m}^{-1} \text{K}^{-1}$]. The correlation ($Pr = 0.7$) was taken from Polifke and Kopitz (2009).



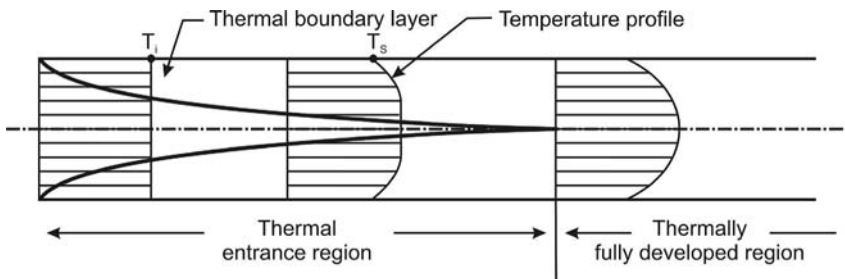


Figure 3.2.7 Thermal boundary layer of a fluid flowing in an empty tube if the fluid is cooled.

Heat Transfer between a Fluid and the Internal Surface of an Empty Tube Liquid or gas flow through pipes is commonly used in heating and cooling applications. When a fluid is heated or cooled as it flows through a tube, the temperature at any cross section changes from T_s at the internal surface of the tube wall to a maximum value (or minimum in case of heating) at the tube center. In fluid flow it is convenient to work with an average or mean temperature T_{mean} that remains uniform within a cross section. Unlike the mean fluid velocity, the mean temperature T_{mean} will change in flow direction whenever the fluid is heated or cooled. (The value of T_{mean} is determined from the requirement of conservation of energy. The respective equation to determine T_{mean} is available in the literature, e.g., Cengel, 2002.)

Consider a fluid at a uniform initial temperature T_i that enters a tube whose surface is adjusted to a constant but different temperature T_s (Figure 3.2.7). The fluid in the layer that is in direct contact with the surface immediately adopts the surface temperature. This initiates a heat transfer within the tube and leads to the development of a thermal boundary layer along the tube. The thickness of this layer increases in the direction of flow until the layer reaches the tube center and fills the entire tube. The region where the thermal boundary layer develops is called the thermal entrance region. The length of this region is the thermal entry length L_{thermal} , and the region beyond the thermal entrance region is called the *thermally fully developed region*.

For laminar flow, the thermal entry length is approximately given by (Cengel, 2002):

$$L_{\text{thermal}} = 0.05 Re \times Pr \times d_t \quad (\text{for } Re < 2300) \quad (3.2.8)$$

where Re is the Reynolds number, named after *Osborne Reynolds* (see box):

$$Re = \frac{ud_t}{\nu} \text{ with } u = u_{\text{mean}} = \frac{\dot{V}_{\text{fluid}}}{A_t} \quad (3.2.9)$$

and Pr as the *Prandtl* number (*Ludwig Prandtl*, see box):

$$Pr = \frac{\nu}{\alpha} = \frac{\nu c_p \rho_{\text{mol}}}{\lambda} \quad (3.2.10)$$

For gases, Pr is around 0.7 and is almost independent of temperature and pressure, as we can deduce from the Eqs. (3.2.10), (3.1.68), and (3.1.70) and the correlation $c_p/c_v \approx 1.4$ or by the values given in Tables 3.1.7 and 3.1.3. Thus, for $Re < 30$, the thermal entry length is less than the tube diameter [Eq. (3.2.8)], and reaches in the limiting case of $Re = 2300$ a value of $80d_t$. For liquids, the value of L_t is higher, for example, for water ($Pr = 7$ for 20°C), L_{thermal} is then $800d_t$ for $Re = 2300$. For turbulent flow, the entry length is much shorter and given by:

$$L_{\text{thermal}} \approx 10d_t \quad (\text{for } Re > 2300) \quad (3.2.11)$$

Within the thermal entrance region, the local value of the heat transfer and the local Nusselt number Nu_x steadily decreases as the thermal boundary layer increases until in the thermally fully developed region Nu_x reaches a constant value (Example 3.2.4). However, the value of the local Nusselt number is of little value in

Ludwig Prandtl (1875–1953): A German physicist famous for his work in aeronautics. In 1904, he “discovered” the “boundary layer” that adjoins the surface of a body moving in a fluid (or a fluid flowing around a body), which led to an understanding of skin friction drag and of the way streamlining reduces the drag of airplane wings. Thus, *Prandtl’s* work became the basics of aeronautics.

Osborne Reynolds (1842–1912), an English engineer and physicist, is best known for his work in the field of hydrodynamics. His studies on condensation and heat transfer between solids and fluids brought about a revision in boiler and condenser design. He formulated the theory of lubrication, and also investigated the transition from laminar to turbulent flow.

heat transfer calculations since the average Nu number over the entire surface of the tube is needed. Thus, the correlations given in the following always refer to the average value of Nu .

For fully developed laminar flow (Section 3.2.2.1), the average Nu number for the heat transfer to the internal surface of the tube with uniform temperature, length L , and diameter d_t is (Schluender, 1970; VDI, 1997, see Example 3.2.1):

$$Nu = \frac{\alpha d_t}{\lambda} = \left\{ \underbrace{3.66^3}_{\text{Asymptotic value for large values of } L/d_t} + \underbrace{0.7^3 + \left[1.615 \left(\frac{Re \times Pr \times d_t}{L} \right)^{\frac{1}{3}} - 0.7 \right]^3}_{\text{Contribution of thermal entrance region}} \right\}^{0.33} \quad (\text{for } Re < 2300) \quad (3.2.12)$$

For long tubes the average Nu number approaches 3.66 and the thermal entrance region has a negligible influence on Nu . Conversely, we get higher Nu values for short tubes, where the contribution of the entrance region is not negligible. For example, for $L = 10 d_t$ and a value of the term $Re \times Pr$ of 1000, we obtain a Nu number of 7, but for $L = 100 d_t$ we have $Nu = 4.1$ and so we already approach the limiting value of 3.66. In general, we may use as an approximation:

$$Nu \approx 3.66 \quad (\text{for } Re \times Pr \times d_t/L < 10, \text{laminar flow}) \quad (3.2.13)$$

For turbulent flow we can almost neglect the influence of thermal entrance region and get:

$$Nu = \frac{\frac{(0.79 \ln(Re) - 1.64)^{-2}}{8} (Re - 1000/Pr)}{1 + 12.7 \sqrt{\frac{(0.79 \ln(Re) - 1.64)^{-2}}{8} (Pr^{\frac{2}{3}} - 1)}} \quad (\text{for } Re > 2300, 0.5 < Pr < 2000) \quad (3.2.14)$$

where the term $(0.79 \ln(Re) - 1.64)^{-2}$ is called friction factor f_t (Section 3.4.1.1).

For fully developed turbulent flow in smooth tubes ($L/d_t > 10$), we may also use the following simple relation instead of Eq. (3.2.14), if an error of up to 25% is acceptable (Cengel, 2002):

$$Nu = 0.023 Re^{0.8} \times Pr^{\frac{11}{3}} \quad (\text{for } Re > 10000, 0.7 < Pr < 160) \quad (3.2.15)$$

Example 3.2.1: Local and average Nu number for laminar flow in a circular tube

According to VDI (2002), the local Nusselt number Nu_x for laminar flow in a circular tube is:

$$Nu_x = \frac{\alpha_x d_t}{\lambda} = \left\{ 3.66^3 + 0.7^3 + \left[1.077 \left(\frac{Re \times Pr \times d_t}{x} \right)^{\frac{1}{3}} - 0.7 \right]^3 \right\}^{\frac{1}{3}} \quad (\text{for } Re < 2300) \quad (3.2.16)$$

The average Nu number is defined as:

$$Nu = \frac{1}{L} \int_0^L Nu_x dx \quad (3.2.17)$$

and insertion of Eq. (3.2.16) into Eq. (3.2.17) and numerical integration leads to Eq. (3.2.12).

Figure 3.2.8 shows Nu and Nu_x as a function of the dimensionless length $x/(d_t Re Pr)$, indicating that for values > 0.1 , both numbers approach a constant value of 3.66.

Comments:

- The equations given in this chapter for Nu are only valid for a fully developed laminar flow, that is, without a hydrodynamic entrance region. Similar considerations can be made for the heat transfer in a tube with both a thermal and a hydrodynamic entrance region, whereby the differences in the values of Nu and Nu_x are mostly small (VDI, 2002).

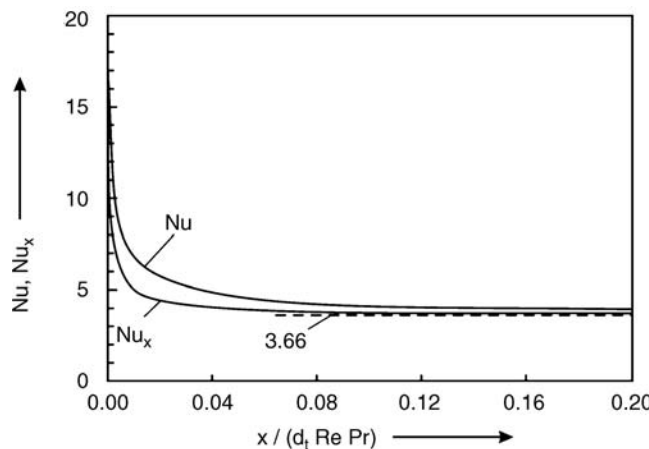


Figure 3.2.8 Local and average Nusselt number (Nu_x , Nu) for laminar flow in a tube (fully developed laminar flow, that is, without hydrodynamic entrance region, see Section 3.2.1.2.1).

- For pure heat transfer problems, the value of the Nu_x is not needed, and knowledge of an average Nu number is sufficient. However, Nu_x may be important for a heated or cooled tube if a chemical reaction takes place in the tube. Then the behavior (and the modeling) of the reactor depends on Nu_x as the (local) reaction rate r strongly depends

on temperature (typically an increase of r by a factor of two for $\Delta T = +10$ K).

- For turbulent flow, both the thermal and the hydrodynamic entrance region (Section 3.2.2.1) are small [Eq. (3.2.11)], and thus Nu and Nu_x are almost equal.

Heat Transfer between a Fluid and the External Surface of a Tube (Cylinder) Heat transfer by forced convection from a fluid to the surface of a cylinder for cross flow is given by the following empirical correlation (Cengel, 2002):

$$Nu = C Re^m Pr^{\frac{1}{3}} \quad (\text{with } Re = u d_{\text{cylinder}} / v) \quad (3.2.18)$$

with:

$$\begin{aligned} C &= 0.989 \text{ and } m = 0.330 \quad (\text{for } 0.4 < Re < 4) \\ C &= 0.911 \text{ and } m = 0.385 \quad (\text{for } 4 < Re < 40) \\ C &= 0.683 \text{ and } m = 0.466 \quad (\text{for } 40 < Re < 4000) \\ C &= 0.193 \text{ and } m = 0.618 \quad (\text{for } 4000 < Re < 40000) \\ C &= 0.027 \text{ and } m = 0.805 \quad (\text{for } 40000 < Re < 400000) \end{aligned}$$

The fluid properties are evaluated at the film temperature, which is the average of the free-stream and the surface temperature. Correlations for non-cross flow and non-circular tubes are given in VDI (2002) and Cengel (2002).

Figure 3.2.9 shows a graphical presentation of Eq. (3.2.18) for gases ($Pr = 0.7$). For comparison, two other correlations given in the literature are also shown. The deviations are small (<20%); in most cases, Eq. (3.2.18) is sufficient.

The Nu number determined by Eq. (3.2.18) or by the two other equations given in Figure 3.2.9 represents the average heat transfer that is required for heat transfer calculations. The local heat transfer along the circumference of a cylinder is not needed in practical applications, but discussion of the local Nusselt number is insightful (Example 3.2.2).

Example 3.2.2: Local heat transfer for the flow of a fluid across a cylinder

The variation of the local Nu number along the circumference of a cylinder in cross flow of air ($Pr = 0.7$) for low and high Reynolds number is shown in Figures 3.2.10 and 3.2.11, respectively. The reason for the local variation of Nu is that the cross flow over a cylinder (and also over other bodies) exhibits complex flow characteristics. The fluid approaching the cylinder at the front stagnation point (angle $\gamma = 0$) branches out and

encircles the cylinder. For subcritical flow ($Re < 200000$), a laminar boundary layer forms on the front of the cylinder and grows with angle γ . For $Re < 5$, the fluid completely wraps around the cylinder, and the boundary layer increases on the rear part of the cylinder. Thus, the heat transfer coefficient and the Nusselt number, respectively, continuously decrease along the circumference of a cylinder (Figure 3.2.10, $Re = 1$

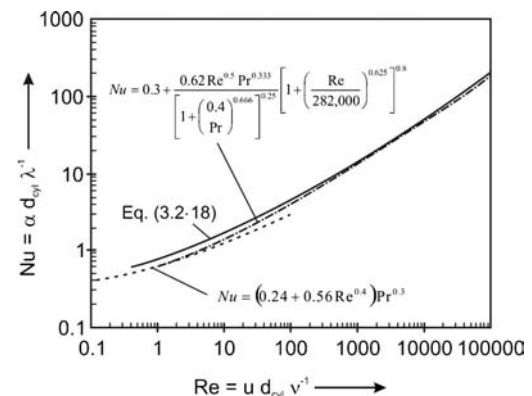
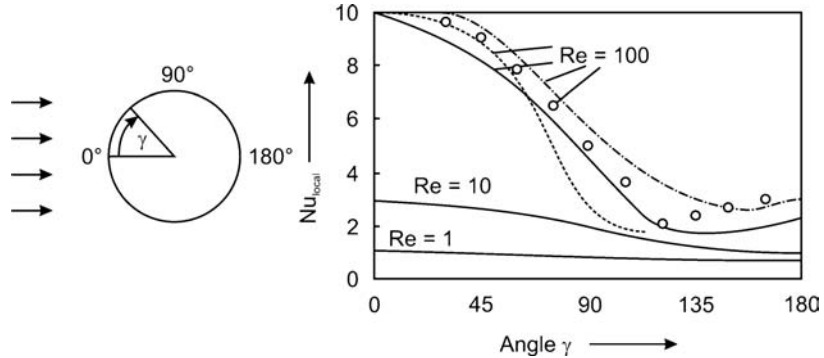


Figure 3.2.9 Average Nu number for the cross-flow of a gas ($Pr = 0.7$) over a cylinder according to Eq. (3.2.18). For comparison, two other equations proposed by Churchill and Bernstein (for $Re \times Pr > 0.2$, dotted-dashed line, Cengel, 2002) and by Collis and Williams (for $0.02 < Re < 44$, dotted line, Fand and Keswani, 1972; Collis and Williams, 1959) are also shown.

Figure 3.2.10 Variation of local Nusselt number along the circumference of a cylinder for cross flow of air ($Pr = 0.7$) for low Reynolds numbers $Re = ud_{cyl}/v$ [Sucker and Brauer, 1976, short-dash line: values of Khan, Culham, and Yovanovich (2005) for 0° (front stagnation point) $< \gamma < 120^\circ$; dotted-dashed line and circles: computed and experimental values of Krall (1969), Eckert and Soehngen (1952), and Krall and Eckert (1966, 1970)].



and 10). At about $Re = 10$, the fluid still hugs the frontal side, but at the top of the cylinder ($\gamma = 90^\circ$) the fluid is too fast to remain attached to the surface. Separation then starts on the rear side of the cylinder, and a wake region characterized by random vortices is formed, which leads to an increase of the heat transfer coefficient and the Nusselt number, respectively, on the rear part (Figure 3.2.10 for $Re = 100$ and Figure 3.2.11). For very high Re numbers, the intense mixing in the turbulent wake region at the rear part of the cylinder leads to a sharp increase of Nu at about $\gamma = 130^\circ$ (Figure 3.2.11).

Figure 3.2.12 shows that the contribution of the heat transfer from the rear part of the cylinder to the overall heat transfer decreases with increasing Re number until a value of Re of about 1000 is reached. Then the share of the rear part increases again as expected with regard to the highly turbulent flow in the wake region. For $Re > 60\,000$, the contribution of the rear part of the cylinder is even higher than that of the front part.

As discussed in Section 6.4 for ammonia oxidation at a single Pt wire, that is, where the cylindrical wire is heated by an exothermic chemical reaction, the variation of temperature around a cylinder can nowadays be modeled by computer programs, for example, by the finite element method. The geometric structure is approximated by a meshing procedure that is used to define and break the model up into small elements. The differential equations of heat transfer and of the fluid dynamics (Navier–Stokes equations) are then numerically solved. The temperature gradients at the surface of the cylinder ($T_{cyl} = \text{const.} = T_s$ at $r = d_{cyl}/2$) are then used to calculate the local Nu number as a function of the angle γ by:

$$Nu_{\text{local}} = \alpha_{\text{local}} \frac{d_{\text{cyl}}}{\lambda} = \frac{\dot{q}}{(T_s - T_{\text{surr}})} \frac{d_{\text{cyl}}}{\lambda} = \frac{\lambda \left(\frac{dT}{dr} \right)_{r=\frac{d_{\text{cyl}}}{2}, \gamma} d_{\text{cyl}}}{(T_s - T_{\text{surr}}) \lambda} = \left(\frac{dT}{dr} \right)_{r=\frac{d_{\text{cyl}}}{2}, \gamma} \frac{d_{\text{cyl}}}{(T_s - T_{\text{surr}})}$$

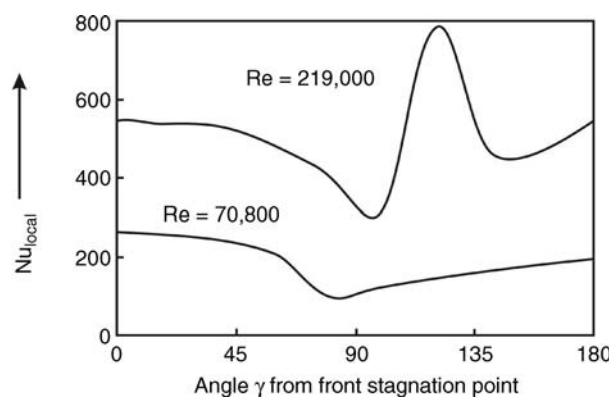
The respective plot is shown in Figure 3.2.13 together with experimental data determined by a Mach–Zehnder interferometer (Eckert and Soehngen, 1952), and data from Sucker and Brauer (1976) who also solved the differential equations numerically but with the simplifying assumption of a constant viscosity and a constant thermal conductivity.

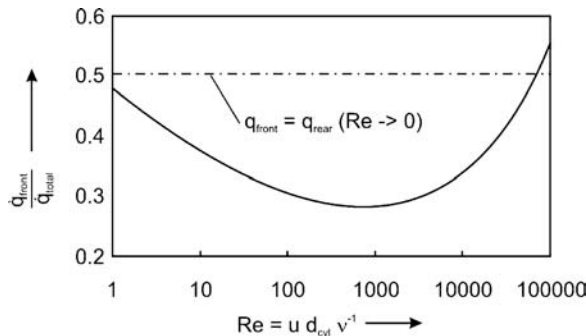
Inspection of the heat transfer (and of the local Nusselt number) along the circumference of a cylinder leads to the following conclusion. The overall heat transfer from cylinders (and other bodies) consists of three parts: (i) the convective heat transfer in the laminar boundary layer of the front part, (ii) heat transfer from the rear part, where – depending on Re – separation and turbulences occur, and (iii) a constant and small part representing the limit case of minimum heat loss to a stagnant surrounding [$Re = 0$, see text below Eq. (3.2.3)]. Hence, the mean Nu number can be expressed by a correlation equation of the form:

$$Nu = \underbrace{C_1}_{\text{Factor for minimum heat loss (about 0.3 for a cylinder)}} + \underbrace{C_2 Re^{0.5} Pr^{0.3}}_{\text{Convective laminar heat transfer in the front part}} + \underbrace{C_3 f(Re, Pr)}_{\text{Convective heat transfer in the rear part}}$$

Regrettably, this approach leads to complicated equations (e.g., Fand and Keswani, 1972) and in practice the overall range of Re is subdivided into sub-intervals with the corresponding simpler approximated correlations for the Nu number, see, for example, Eq. (3.2.18).

Figure 3.2.11 Variation of local Nusselt number along the circumference of a cylinder for cross flow of air ($Pr = 0.7$) for high $Re = ud_{cyl}/v$ (Giedt, 1949, see also Cengel, 2002).





Heat Transfer between a Fluid and a Single Particle The Nusselt number for heat transfer from a fluid to a spherical particle is given (Schluender, 1986; VDI, 2002) by:

$$Nu_{\text{single particle}} = \frac{\alpha d_p}{\lambda} = 2 + \sqrt{Nu_{\text{lam}}^2 + Nu_{\text{turb}}^2} \quad (3.2.19a)$$

with the laminar and turbulent Nu numbers:

$$Nu_{\text{lam}} = 0.664 \sqrt{Re_p} \sqrt[3]{Pr} \quad (3.2.19b)$$

$$Nu_{\text{turb}} = \frac{0.037 Re_p^{4/5} Pr}{1 + 2.44(Pr^{2/3} - 1) Re_p^{-0.1}} \quad \left(\text{with } Re_p = \frac{ud_p}{v} \right) \quad (3.2.19c)$$

Equations (3.2.19b) and (3.2.19c) yield the ratio of Nu_{turb} to Nu_{lam} for gases with $Pr \approx 0.7$:

$$\frac{Nu_{\text{turb}}}{Nu_{\text{lam}}} \approx \frac{0.044 Re_p^{0.3}}{1 - 0.52 Re_p^{-0.1}} \quad (\text{for gases and } Pr \approx 0.7) \quad (3.2.20)$$

Thus for $Re_p < 50$, we have values of this ratio of less than 0.2 and Eq. (3.2.19a) leads to:

$$Nu_{\text{single particle}} \approx 2 + \sqrt{Nu_{\text{lam}}^2} = 2 + 0.664 \sqrt{Re_p} \sqrt[3]{Pr} \quad (\text{for } Re_p < 50) \quad (3.2.19d)$$

Some additional remarks on the minimum value of the Nusselt number, Nu_{\min} :

- According to Eq. (3.2.19a), Nu_{\min} is 2 for very small particles ($Re_p \rightarrow 0$) and α is given by the term $2\lambda/d_p$. Thus α is proportional to $1/d_p$ and we may conclude that α becomes very high for very small particles. For example, for a particle with a diameter of 1 μm cooled or heated by air ($\lambda = 0.026 \text{ W m}^{-1} \text{ K}^{-1}$ at 25 °C), α is $50\,000 \text{ W m}^{-2} \text{ K}^{-1}$. But for even smaller particles, α can hardly exceed this value as the maximum heat flux is limited by the molecular transport. To calculate the maximum value for α , we take a distance of 2Λ (with Λ as mean free path) as the minimum value for the energy exchange by heat conduction. (Molecules coming from the position $x + \Lambda$ and $x - \Lambda$ collide and balance their energies at the position x .) Thus we get $\alpha_{\max} = \lambda/(2\Lambda)$, and for gases [Eq. (3.1.66)] α_{\max} approaches $(1/6)\bar{u}\rho_{g,\text{mol}}c_v$. For air at 1 bar and 25 °C [$\bar{u} = 470 \text{ m s}^{-1}$, Eq. (3.1.71), $\rho_{g,\text{mol}} = 40 \text{ mol m}^{-3}$, $c_v = 21 \text{ J mol}^{-1} \text{ K}^{-1}$] this corresponds to α_{\max} (1 bar) = $66\,000 \text{ W m}^{-2} \text{ K}^{-1}$.
- Nu_{\min} was already deduced in Section 3.2.1.1 by the inspection of heat conduction from a spherical particle to an infinitely large surrounding with thermal conductivity λ . This minimal conductive heat flux per unit surface area is given by $2\lambda\Delta T/d_p$ [see text below Eq. (3.2.3)]. Thus α is $2\lambda/d_p$ and Eq. (3.2.19a) leads to $Nu_{\min} = 2$.
- Eq. (3.2.19) considers forced convection but not the contribution of natural convection. The contribution of fluid motion by natural means (buoyancy) on the overall heat transfer is represented by the *Grashof* number Gr :

$$Gr = \frac{g d_p^3 |\rho_s - \rho_b|}{\nu^2} \quad (3.2.21)$$

Figure 3.2.12 Crossflow of air around a cylinder: fraction of heat transfer from the rear part ($0 < \gamma < 90^\circ$) of the total heat transfer. Data from Fand and Keswani (1972).

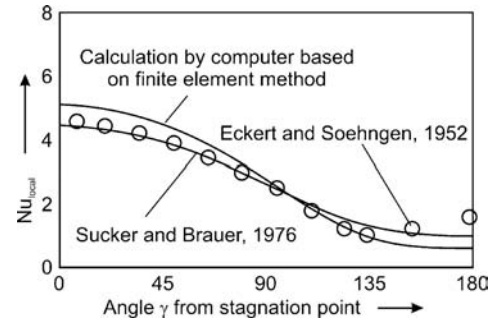


Figure 3.2.13 Variation of local Nusselt number along the circumference of a cylinder for cross flow of air ($Pr = 0.7$) and $Re = 23$: comparison of experimental data (Eckert and Soehngen, 1952), a numerical solution (Sucker and Brauer, 1976), and results of a calculation by the finite element method [$T_s = 600^\circ\text{C}$, $T_{\text{surr}} = 500^\circ\text{C}$, $\lambda_{\text{air}} = 0.063 \text{ W m}^{-1} \text{ K}^{-1}$ (600°C), $\nu_{\text{air}} = 2.4 \times 10^{-5} \text{ m}^2 \text{ s}^{-1}$ (600°C), $\nu \sim T^{1.75}$, $\lambda \sim T^{0.75}$, program COMSOL PHYSICS, FEMLAB Company, Göttingen, Germany].

where g is the gravitational acceleration (9.81 m s^{-2}) and ρ_s and ρ_b represent the density of the fluid at the surface and sufficiently far from the surface (bulk phase), respectively. Equations (3.2.19a)–(3.2.19c) are still valid, if we determine the so-called resulting Reynolds number by the following equation and use $Re_{p,\text{res}}$ instead of Re_p , that only represents the contribution of forced convection (Example 3.2.3):

$$Re_{p,\text{res}} = \sqrt{Re_p^2 + 0.4Gr} \quad (3.2.22)$$

Example 3.2.3: Contribution of free convection to overall heat transfer

The influence of natural convection on the overall convective heat transfer for typical conditions of chemical engineering problems (e.g., heterogeneous catalysis) can be estimated as follows: Let us assume a particle diameter of 5 mm and a fluid velocity of 0.1 m s^{-1} . For gases and liquids, the kinematic viscosity ν (at 20°C) is $15 \times 10^{-6} \text{ m}^2 \text{s}^{-1}$ (air, 1 bar) and $1 \times 10^{-6} \text{ m}^2 \text{s}^{-1}$ (water). Thus Re_p is 33 (air) and 500 (water). The value of the term $\Delta\rho/\rho_b$ depends on the volumetric expansion, and is given for ideal gases by the term $\Delta T/T_s$ ($= 34 \times 10^{-4} \text{ K}^{-1} \Delta T$ for

20°C). For water, we get $2 \times 10^{-4} \text{ K}^{-1} \Delta T$ (at 20°C). Equation (3.2.21) then leads to $Gr = 245 \text{ K}^{-1} \Delta T$ for water and $Gr = 19 \text{ K}^{-1} \Delta T$ for air. Thus, according to Eq. (3.2.22) the contribution of natural convection can be neglected (5% deviation, that is, $Re_{p,\text{res}} < 1.05 Re_p$), if the temperature difference would be less than about 260 K (water) and 15 K (air). Natural convection, therefore, only plays a role for gases at low values of Re_p and for fluids with a low viscosity compared to water (20°C), for example, for liquid hydrocarbons at high temperatures.

For non-spherical particles Eqs. (3.2.19)–(3.2.22) are also valid if an equivalent particle diameter is used, which is defined as the diameter of a sphere with the same surface area (VDI, 2002):

$$d_{p,\text{equivalent}} = \sqrt{\frac{A_{\text{ex}}}{\pi}} \quad (\text{for non-spherical particles, e.g., short cylinders}) \quad (3.2.23)$$

As shown in Topic 3.2.4, Eq. 3.2.19 in a slightly modified form can also be used for the average Nusselt number for cross flow over a long cylinder (low diameter-to-height ratio and thus a negligible contribution of both end planes).

Topic 3.2.4 Nusselt number for cross flow over a long cylinder (beware of the exact definition of dimensionless numbers, here the Reynolds and Nusselt numbers)

When correlations of dimensionless numbers are compared, it is important to take a close look at the definition of the characteristic length. For example, the correlations given in Figure 3.2.9 for the Nu number for cross flow of a long cylinder are only valid if the diameter of the cylinder is used for Nu and Re (subsequently named Nu_d and Re_d). According to VDI (2002), a modified form of Eq. 3.2.19 can also be used:

$$Nu_L = \frac{\alpha L_{\text{cyl}}}{\lambda} = 0.3 + \sqrt{Nu_{L,\text{lam}}^2 + Nu_{L,\text{turb}}^2} \quad (3.2.24a)$$

with the laminar and turbulent Nu numbers:

$$Nu_{L,\text{lam}} = 0.664 \sqrt{Re_L} \sqrt[3]{Pr} \quad (3.2.24b)$$

$$Nu_{L,\text{turb}} = \frac{0.037 Re_L^{4/5} Pr}{1 + 2.44(Pr^{2/3} - 1)Re_L^{0.1}} \quad (\text{with } Re_L = \frac{u}{\nu} L_{\text{cyl}} = \frac{u \pi}{\nu} d_{\text{cyl}}) \quad (3.2.24c)$$

Thus, instead of the diameter of the cylinder, the length of overflow (half of the perimeter) is used. If we now want to compare Eq. (3.2.24a) with the correlation as given by Figure 3.2.9, we need to rewrite Eq. (3.2.24a) into the form based on the diameter (or vice versa):

$$Nu_d = \frac{\alpha d_{\text{cyl}}}{\lambda} = \frac{2}{\pi} \left(0.3 + \sqrt{Nu_{d,\text{lam}}^2 + Nu_{d,\text{turb}}^2} \right) \quad (3.2.24d)$$

$$Nu_{d,\text{lam}} = 0.664 \sqrt{\frac{\pi}{2} Re_d} \sqrt[3]{Pr} \quad (3.2.24\text{e})$$

$$Nu_{d,\text{turb}} = \frac{0.037 \left(\frac{\pi}{2} Re_d \right)^{\frac{4}{5}} Pr}{1 + 2.44 \left(Pr^{\frac{2}{3}} - 1 \right) \left(\frac{\pi}{2} Re_d \right)^{-0.1}} \quad \left(\text{with } Re_d = \frac{ud_{\text{cyl}}}{v} \right) \quad (3.2.24\text{f})$$

Figure 3.2.14 indicates that the correlation of Eq. (3.2.24d–f) is in good agreement with other correlations given in the literature (e.g., with the correlation of Churchill and Bernstein, Figure 3.2.9), whereas the deviation becomes pronounced for low Re numbers, if “accidentally” Eq. (3.2.24a–c) was used without considering the difference between L_{cyl} and d_{cyl} .

Heat Transfer between a Fluid and Particles of a Packed Bed For the heat transfer between a fluid and spheres of a packed bed (porosity $\varepsilon \approx 0.4$) we have (Schluender, 1986; VDI, 2002):

$$Nu_{\text{bed}} = [1 + 1.5(1 - \varepsilon)] Nu_{\text{single particle}} \approx 1.9 Nu_{\text{single particle}} \quad (\text{for } \varepsilon \approx 0.4 \text{ and spheres}) \quad (3.2.25)$$

The Reynolds number needed to determine $Nu_{\text{single-particle}}$ by Eqs. (3.2.19)–(3.2.23) is now based on the interstitial velocity, which is the ratio of the superficial velocity to the bed porosity, $Re_{p,\text{bed}} = ud_p/(\varepsilon v)$. For $Re_{p,\text{bed}} < 100$, we may have lower Nu_{bed} values as calculated by Eq. (3.2.25), which is attributed to inhomogeneities of the bed and channeling.

Heat Transfer between a Body and a Fluidized Bed High heat transfer coefficients are reached for the heat transfer between a fixed solid body, for example, a cooling coil, and a fluidized bed (Figure 3.2.15).

Note: do not mistake this with heat transfer between the fluid and the solid particles of a fluidized bed. In this case, α is much lower and calculated by Eq. (3.2.25) by the discharging velocity and the porosity of the fluidized bed (Section 3.4.1.2) (see Schluender and Martin, 1995).

Overall Heat Transfer through Plane Walls and Cylindrical Shells Surrounded by Fluids The combination of conduction and convection may be characterized by the thermal transmittance U_h . For a plane wall surrounded by fluids of different temperature (Figure 3.2.16) we have:

$$\dot{Q} = U_h A \frac{T_1 - T_2}{d} \quad (3.2.26)$$

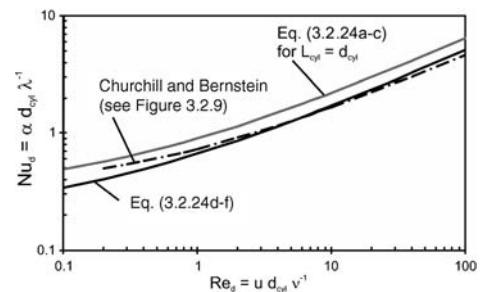


Figure 3.2.14 Nu for cross-flow over a cylinder ($Pr = 0.7$) according to Eq. (3.2.24d–f) (see text). For comparison, the equation of Churchill and Bernstein (Figure 3.2.9) is also shown.

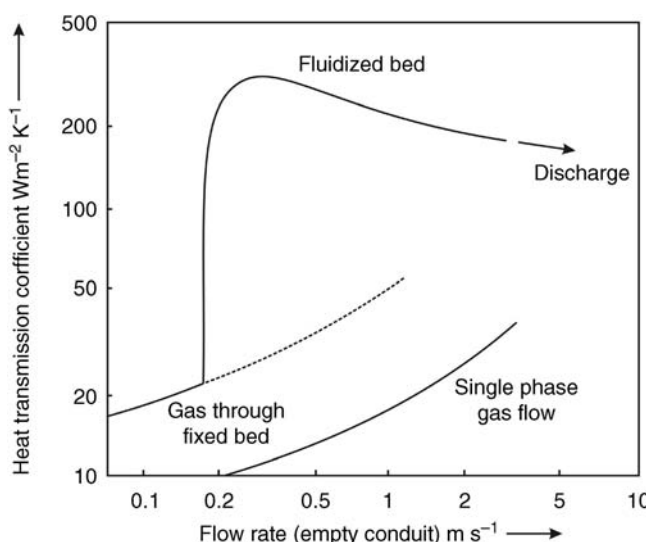


Figure 3.2.15 Heat transfer coefficient in a packed and in a fluidized bed for the heat transfer from the bed to a vertical cylinder. Adapted from Gmehling and Brehm (1996).

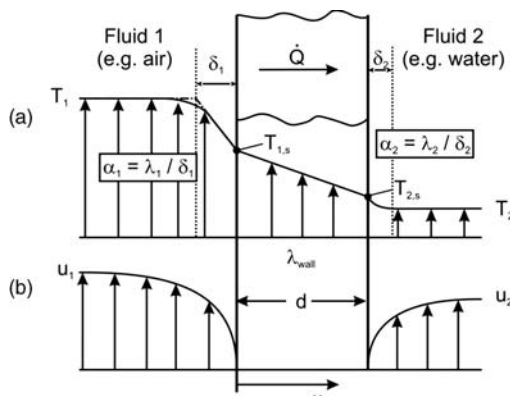


Figure 3.2.16 Steady-state heat transport through a plate with a flowing fluid on each side:
(a) temperature profile; (b) velocity profile.

We now use Eq. (3.2.5) to calculate the temperatures at each side of the wall:

$$T_{1,s} = T_1 - \frac{\dot{Q}}{\alpha_1 A} \quad (3.2.27)$$

$$T_{2,s} = T_2 + \frac{\dot{Q}}{\alpha_2 A} \quad (3.2.28)$$

Insertion of Eqs. (3.2.27) and (3.2.28) into Eq. (3.2.1) leads to:

$$\begin{aligned} \dot{Q} &= \lambda_{\text{wall}} A \frac{T_{1,s} - T_{2,s}}{d} = \lambda_{\text{wall}} A \frac{\left(T_1 - \frac{\dot{Q}}{\alpha_1 A} \right) - \left(T_2 + \frac{\dot{Q}}{\alpha_2 A} \right)}{d} \Rightarrow \dot{Q} \\ &= \frac{A(T_1 - T_2)}{\frac{1}{\alpha_1} + \frac{d}{\lambda_{\text{wall}}} + \frac{1}{\alpha_2}} \end{aligned} \quad (3.2.29)$$

and thus the thermal transmittance or overall heat transfer coefficient is given by:

$$U_h = \left(\frac{1}{\alpha_1} + \frac{d}{\lambda_{\text{wall}}} + \frac{1}{\alpha_2} \right)^{-1} \quad (3.2.30)$$

For steady-state heat transfer through a cylindrical shell of a pipe with an internal and external diameter d_{int} and d_{ex} , respectively, and a length L we get:

$$U_h = \frac{\dot{Q}}{A_{\text{int}}(T_1 - T_2)} = \frac{\dot{Q}}{\pi d_{\text{int}} L (T_1 - T_2)} = \left[\frac{1}{\alpha_{\text{int}}} + \frac{d_{\text{int}}}{2\lambda_{\text{wall}}} \ln \left(\frac{d_{\text{ex}}}{d_{\text{int}}} \right) + \frac{1}{\alpha_{\text{ex}}} \frac{d_{\text{int}}}{d_{\text{ex}}} \right]^{-1} \quad (3.2.31)$$

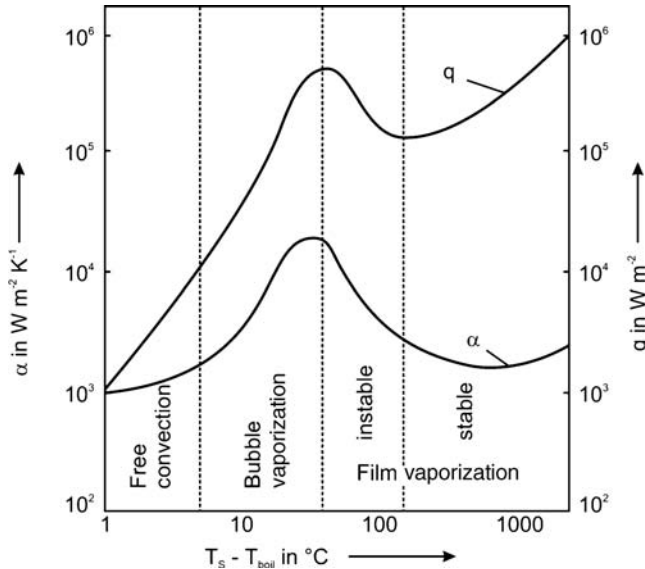
if we use the internal surface, A_{int} , and the internal diameter, d_{int} as references.

3.2.1.3 Boiling Heat Transfer

Extremely high values of the heat transfer coefficient of more than $10^5 \text{ W m}^{-2} \text{ K}^{-1}$ are reached with boiling liquids, as depicted for water in Figure 3.2.17. Depending on the difference between the surface temperature T_s and the boiling temperature T_{boil} we have to distinguish four regions:

- 1) For $\Delta T = (T_s - T_{\text{boil}}) < 6 \text{ K}$ (H_2O , 1 bar), we are in the region of convective boiling, and α increases only slightly with temperature ($\alpha \sim \Delta T^{1/3}$).
- 2) For $6 \text{ K} < \Delta T < 30 \text{ K}$, we have nucleate boiling, and α strongly increases ($\alpha \sim \Delta T^{7/3}$), which is the result of the intensification of the liquid circulation by steam bubbles.

Figure 3.2.17 Heat transfer α as a function of the temperature difference between the wall and the boiling temperature of water (here at 1 bar 100°C).



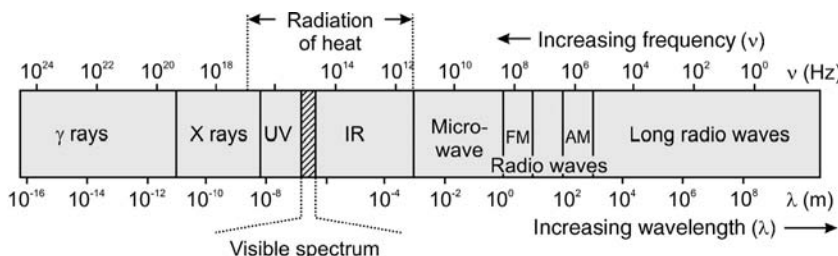


Figure 3.2.18 Electromagnetic spectrum.

- 3) For $\Delta T > 30$ K, we get film boiling. The bubbles become so numerous that the surface is partially blanketed with them. If the surface temperature continues to increase, the heat transfer decreases due to the insulating effect of the steam blanket. Thus, this region is characterized by an increase in ΔT but nevertheless a decrease in heat flux.
- 4) A further increase in ΔT then causes total film boiling ($\Delta T > 100$ K), and the steam completely blankets the heat transfer surface. The heat transfer coefficient is then approximately constant, and the heat flux again increases in proportion to ΔT .

In practice, the transition from nucleate boiling to film boiling occurs suddenly, and the temperature difference rapidly rises. The heat flux associated with that point of transition is commonly denoted as the critical heat flux, which is an important critical parameter in many applications.

3.2.1.4 Heat Transfer by Radiation

All objects emit electromagnetic waves, because of their temperature, and absorb thermal radiation from their surrounding. If an object is hotter than the surrounding it emits more radiation than it absorbs, and tends to cool. In thermal equilibrium the rate of absorption equals the rate of emission. The spectrum of thermal radiation from a hot body is continuous over a rather large range of wavelengths or frequencies (Figure 3.2.18). At room temperature, the dominant portion of radiation is in the infrared part of the spectrum and is not visible. If the temperature is increased, radiation increases and becomes visible to humans.

The wavelengths of thermal radiation follow a probability distribution depending only on temperature, which is given for a black-body by *Planck's law*. The most likely wavelength of the emitted radiation is given by *Wien's law* [Wilhelm Wien (1864–1928), λ_{\max} in $\mu\text{m} = 2898/T$].

Radiation heat transfer must account for incoming and outgoing thermal radiation. Incoming radiation is either reflected, absorbed, or transmitted, and for the relative fractions we have:

$$1 = \epsilon_{\text{reflected}} + \epsilon_{\text{absorbed}} + \epsilon_{\text{transmitted}} \quad (3.2.32)$$

Since most solid bodies are opaque to thermal radiation, transmission is negligible in most cases. To account for a body's outgoing radiation, we make a comparison with a perfect body that emits as much radiation as possible, known as a black-body. The ratio of the actual heat flow to the heat flow of a black-body is defined as the surface emissivity ϵ_s , and ranges from about 0.05 for polished metal surfaces to more than about 0.7 for ice, cast iron, corroded iron, rubber, and brick. The surface emissivity equals the absorption fraction (*Kirchhoff's law*):

$$\epsilon_s = \epsilon_{\text{absorbed}} \quad (3.2.33)$$

The radiated power of a body is given by the *Stefan-Boltzmann law* (Joseph Stefan, see box below, and Ludwig Boltzmann, see box in Section 3.1.4):

$$\dot{Q} = \epsilon_s \sigma A T^4 \quad (\text{with } \sigma \text{ as Stefan-Boltzmann constant, } 5.67 \times 10^{-8} \text{ W m}^{-2} \text{ K}^{-4}) \quad (3.2.34)$$

Joseph Stefan (1835–1893), a Slovene-Austrian physicist, is best known for originating the law that the radiation from a black-body is proportional to the fourth power of temperature. In 1884, this law was theoretically derived by his student *Ludwig Boltzmann* and is known as the *Stefan-Boltzmann law*. *Stefan's* electromagnetic equations are also important, as his work on the kinetic theory of heat. He was among the first physicists who understood *Maxwell's* electromagnetic theory.

For two parallel plates of equal size but different temperature we get for the net heat flux:

$$\bullet \quad \dot{Q}_{12} = \frac{A}{\frac{1}{\varepsilon_1} + \frac{1}{\varepsilon_2} - 1} \sigma (T_1^4 - T_2^4) = \varepsilon_{12} \sigma A (T_1^4 - T_2^4) \quad (3.2.35)$$

For a body (index 1) surrounded by an area (index 2) we have:

$$\dot{Q}_{12} = \frac{A_1}{\frac{1}{\varepsilon_1} + \frac{A_1}{A_2} \left(\frac{1}{\varepsilon_2} - 1 \right)} \sigma (T_1^4 - T_2^4) \quad (3.2.36)$$

and thus ε_{12} equals the emissivity of the body, ε_1 , if the body (A_1) is small and the surrounding area (A_2) is large. For other geometries, we refer to respective textbooks. Estimations of the heat loss by radiation compared to convection are given in the Examples 3.2.4 and 3.2.5.

Example 3.2.4: Estimation of the heat loss of a human body

A clothed person with a surface temperature of 28°C is standing in a room of 20°C . The surface area is about 1.5 m^2 and the emissivity 0.9.

Based on Eq. (3.2.34) we find:

$$\dot{Q}_{\text{human body, radiation}} \approx 0.9 \sigma 1.5 \text{ m}^2 \left[(301 \text{ K})^4 - (293 \text{ K})^4 \right] \approx 64 \text{ W}$$

which is equivalent to the power of a light bulb. The heat transfer coefficient by natural convection is about $6 \text{ W m}^{-2} \text{ K}^{-1}$, and the additional convective heat loss is then:

$$\begin{aligned} \dot{Q}_{\text{human body, convection}} &\approx 6 \text{ W m}^{-2} \text{ K}^{-1} \times 1.5 \text{ m}^2 (28^\circ\text{C} - 20^\circ\text{C}) \\ &\approx 72 \text{ W} \end{aligned}$$

For comparison: The metabolic heat generated in a human body varies from about 100 W for office work up to about 1000 W for heavy physical work. Note that heat loss by evaporation of water from the skin (perspiration) and in the lungs, which may considerably contribute to the overall heat transfer, is not considered here.

Example 3.2.5: Heat loss of a hot wire by radiation and convection

Two hot wires of 300°C are placed in a large room (20°C). The wires have diameters of 0.1 and 1 mm, respectively, are 2 m long, and have an emissivity of 0.8. The convective heat transfer coefficient α_{cyl} is given by $Nu_{\min} \lambda_{\text{air}} / d_{\text{wire}} \approx 0.3 \lambda_{\text{air}} / d_{\text{wire}}$ (Figure 3.2.9). We now compare the heat loss by convection ($\lambda_{\text{air}} = 0.037 \text{ W m}^{-1} \text{ K}^{-1}$ at T_{mean} of 160°C) and radiation (assuming a negligible heat loss via the end planes). The convective heat loss of both wires is:

$$\begin{aligned} \dot{Q}_{\text{con}} &= \alpha_{\text{cyl}} \pi d_{\text{wire}} L_{\text{wire}} (T_{\text{wire}} - T_{\text{surrounding}}) \\ &\approx 0.3 \lambda_{\text{air}} \pi L_{\text{wire}} (T_{\text{wire}} - T_{\text{surrounding}}) = 19.5 \text{ W} \end{aligned}$$

For $A_{\text{wire}}/A_{\text{surrounding}} \approx 0$, the heat loss by radiation is given by Eq. (3.2.36):

$$\begin{aligned} \dot{Q}_{\text{rad}} &= \varepsilon_{\text{wire}} \pi d_{\text{wire}} L_{\text{wire}} \sigma (T_{\text{wire}}^4 - T_{\text{surrounding}}^4) \\ &= 28.6 \text{ W} \text{ (for 1 mm)} \text{ and } 2.86 \text{ W} \text{ (0.1 mm)} \end{aligned}$$

Thus, even at relatively low temperatures, radiation is not negligible. Note that the contribution of radiation to the overall heat loss strongly decreases with decreasing wire diameter.

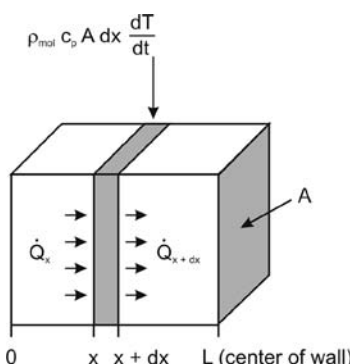


Figure 3.2.19 Transient one-dimensional heat conduction in a large plane wall (thickness $2L$).

3.2.1.5 Transient Heat Transfer by Conduction and Convection

For a transient heat transfer process, for example, for heating up or cooling down a body, we have to consider the variation of temperature with time as well as with position. For a large plane wall of thickness $2L$, the heat conduction perpendicular to the (almost infinite) area A of the plate is one-dimensional. To derive the respective differential equation, we use the energy balance for a small slice with thickness Δx and volume $A \Delta x$ (Figure 3.2.19):

$$\underbrace{\dot{Q}_x}_{\text{Rate of heat conduction at } x} = \underbrace{\rho_{\text{mol}} c_p A \Delta x \frac{dT}{dt}}_{\text{Rate of change of energy content of element}} + \underbrace{\dot{Q}_{x+\Delta x}}_{\text{Rate of heat conduction at } (x+\Delta x)} \quad (3.2.37)$$

Rewriting with the first of Fourier's law, Eq. (3.1.53), leads to:

$$-\lambda A \left(\frac{dT}{dx} \right)_x = \rho_{\text{mol}} c_p A \Delta x \frac{dT}{dt} - \lambda A \left(\frac{dT}{dx} \right)_{x+\Delta x} \quad (3.2.38)$$

and by rearranging we obtain:

$$\lambda \frac{\left(\frac{dT}{dx} \right)_{x+\Delta x} - \left(\frac{dT}{dx} \right)_x}{\Delta x} = \rho_{\text{mol}} c_p \frac{dT}{dt} \quad (3.2.39)$$

Taking the limit of an infinitesimal small value of $\Delta x = dx$ we obtain:

$$\lambda \frac{d^2 T}{dx^2} = \rho_{\text{mol}} c_p \frac{dT}{dt} \quad (3.2.40)$$

We also arrive at Eq. (3.2.40) by using Eq. (3.2.38) for a differentially small slice:

$$-\lambda A \left(\frac{dT}{dx} \right)_x = \rho_{\text{mol}} c_p A dx \frac{dT}{dt} - \lambda A \left(\frac{dT}{dx} \right)_{x+dx} \quad (3.2.41)$$

For the T-gradient at the position $x + dx$ we use the Taylor series:

$$\begin{aligned} \left(\frac{dT}{dx} \right)_{x+dx} &= \left(\frac{dT}{dx} \right)_x + \frac{d^2 T}{dx^2} dx + \frac{1}{2!} \frac{d^3 T}{dx^3} dx^2 + \frac{1}{3!} \frac{d^4 T}{dx^4} dx^3 \dots \\ &\quad + \frac{1}{(n-1)!} \frac{d^n T}{dx^n} dx^{n-1} \end{aligned} \quad (3.2.42)$$

For small values of dx , we terminate the series after the second term, and insertion of Eq. (3.2.42) into Eq. (3.2.41) yields Eq. (3.2.40).

Introduction of the thermal conductivity $a (= \lambda / (\rho_{\text{mol}} c_p))$, which represents how fast heat is transported through a material, yields the common form of the Fourier's second law for a one-dimensional heat transfer in a plane wall:

$$! \quad \frac{dT}{dt} = \frac{\lambda}{c_p \rho_{\text{mol}}} \frac{d^2 T}{dx^2} = a \frac{d^2 T}{dx^2} \quad (3.2.43)$$

Typical values of a (in $\text{cm}^2 \text{s}^{-1}$) at ambient conditions are 0.001–0.01 for non-metallic solids, 0.1–1 for solid and liquid metals, 0.001 for non-metallic liquids, and 0.1 for most gases.

If we know the boundary conditions, for example, a constant surface temperature or a constant heat transfer coefficient from a surrounding fluid to the plate, Eq. (3.2.43) can be solved using advanced mathematical techniques. The solution involves infinite series that are inconvenient and time-consuming to evaluate [for details see, for example Cengel (2002)]. Thus, there is motivation to present solutions in tabular or graphical form. However, this involves many parameters: the local position x , the half-thickness of the plate L , the time t , the thermal diffusivity a , the surface temperature T_s , the initial temperature of the plate T_0 , and depending on the boundary conditions also the heat transfer coefficient α and the temperature of the surrounding T_{surr} . Thus, we have too many parameters to make graphical presentations practical. To reduce the number, we non-dimensionalize the problem by defining dimensionless quantities:

$$\text{Dimensionless distance from the center : } X = \frac{x}{L} \quad (3.2.44)$$

$$\begin{aligned} \text{Dimensionless temperature : } \theta_{\text{center}} &= \frac{T_{\text{center}}(t) - T_{\text{surr}}}{T_0 - T_{\text{surr}}} \quad \text{or} \\ \theta_X &= \frac{T(X, t) - T_{\text{surr}}}{T_{\text{center}}(t) - T_{\text{surr}}} \end{aligned} \quad (3.2.45)$$

Jean Baptiste Biot (1774–1862), a French physicist, is best known for his work on the polarization of light. Although younger than Fourier, he worked on the analysis of heat conduction even earlier (1802/03). He attempted unsuccessfully to deal with the problem of incorporating external convection in heat conduction analysis in 1804. Fourier read Biot's work and solved the problem in 1807. In 1804, Biot accompanied Gay-Lussac on the first balloon ascent undertaken for scientific purposes.

! Dimensionless time (Fourier number) : $Fo = \frac{at}{L^2}$ (3.2.46)

! Dimensionless heat transfer coefficient (Biot number) : $Bi_h = \frac{\alpha L}{\lambda}$ (3.2.47)

Based on the numbers θ , X , and Fo , we rewrite Eq. (3.2.43) in the dimensionless form as:

$$\frac{d\theta}{dFo} = \frac{d^2\theta}{dX^2} \quad (3.2.48)$$

Beside the assumption of symmetry for the center of the plate ($dT/dx=0$ for $x=L$), we use as the second boundary condition the situation at the surface of the plate:

$$-\lambda \frac{dT}{dx} \Big|_{x=0} = \alpha(T_s - T_{\text{surr}}) \quad (3.2.49)$$

and introduction of the dimensionless surface temperature:

$$\theta_s(X=0, t) = \frac{T_s - T_{\text{surr}}}{T_0 - T_{\text{surr}}} \quad (3.2.50)$$

and of the *Biot* number Bi_h , Eq. (3.2.47), leads to the dimensionless boundary condition:

$$\frac{d\theta_s}{dX} \Big|_{X=0} = \left\{ \frac{L}{(T_0 - T_{\text{surr}})} \frac{dT}{dx} \right\} \Big|_{x=L} = -\frac{\alpha L (T_s - T_{\text{surr}})}{\lambda (T_0 - T_{\text{surr}})} = -Bi_h \theta_s \quad (3.2.51)$$

By the non-dimensionalization the dimensionless temperature (θ) is presented in terms of three parameters only: X , Bi_h , and Fo . Apart from this advantage of practicable presentation of solutions by tables and figures, the use of dimensionless numbers has an additional advantage: regardless of the concrete solution of the differential equations, we always reach the same status of heating of a body (i.e., value of θ), if the dimensionless numbers – here Bi and Fo – are constant, as examined by the Examples 3.2.6 and 3.2.7.

Example 3.2.6: Transient heating of a plate for $Bi_h < 0.1$ (lumped body model)

The simplest case of transient heating of a plate is the *lumped body model*, which only considers the heat transfer between the plate and the surrounding fluid. The main assumption is that the plate has a uniform temperature and thus a high thermal conductivity (low value of Bi_h). Furthermore, the surrounding fluid must be large enough so that its temperature remains constant throughout. This approximation is reasonable for $Bi_h = \alpha L / \lambda \ll 1$.

During the interval dt , the temperature of the plate (heated from both sides) with mass m , half-thickness L , and initial temperature $T_{\text{plate},0}$ rises by dT . The energy balance is given as:

$$\underbrace{\alpha 2A(T_{\text{surr}} - T_{\text{plate}}) dt}_{\text{Heat flux to the plate during } dt} = \underbrace{\rho c_{p,m} 2LA dT}_{\text{Change of energy of the plate during } dt} \quad (3.2.52)$$

If we use the dimensionless temperature:

$$\theta_{\text{plate}} = \frac{T_{\text{plate}}(t) - T_{\text{surr}}}{T_{\text{plate},0} - T_{\text{surr}}} \quad (3.2.53)$$

Equation (3.2.52) leads to:

$$\begin{aligned} \frac{d\theta_{\text{plate}}}{dt} &= \frac{dT}{T_{\text{plate},0} - T_{\text{surr}}} = -\frac{\alpha}{\rho c_{p,m} L} \frac{[T_{\text{plate}}(t) - T_{\text{surr}}]}{(T_{\text{plate},0} - T_{\text{surr}})} dt \\ &= -\frac{\alpha}{\rho c_{p,m} L} \theta_{\text{plate}} dt \end{aligned} \quad (3.2.54)$$

Rearrangement and insertion of the Fourier and Biot numbers, Eqs. (3.2.46) and (3.2.47), yields:

$$\frac{d\theta_{\text{plate}}}{\theta_{\text{plate}}} = -\frac{\alpha dt}{\rho c_{p,m} L} = \left(\frac{\alpha L}{\lambda} \right) \left(\frac{a}{L^2} dt \right) = -Bi_h dFo \quad (3.2.55)$$

For cylinders, spheres, and so on, the ratio of the volume to the surface area perpendicular to the flow is used instead of the half-thickness of the plate L . Integration of Eq. (3.2.55) yields:

$$\theta_{\text{plate}} = e^{-Bi_h Fo} \quad (3.2.56)$$

Note that even if we would not know the solution of Eq. (3.2.55) we can calculate the time needed for the heat transfer process based on the dimensionless numbers if we have experimental data. For example, let us assume we have made an experiment with plate 1 with a half-thickness L_1 , thermal diffusivity α_1 , thermal conductivity λ_1 , and heat transfer coefficient α_1 . After a time t_1 we have a measured θ_{plate} of, for example, 0.5. We now want to calculate the time t_2 to reach $\theta_{\text{plate}} = 0.5$ for a second plate 2 with $L_2 = 2L_1$, $\alpha_2 = 1/4\alpha_1$, $\lambda_2 = 1/4\lambda_1$, and $\alpha_2 = 5\alpha_1$. According to the condition

that we need a constant value of $Bi_h Fo$ we have:

$$Bi_h Fo = \left(\frac{\alpha L}{\lambda} \right) \left(\frac{a}{L^2} t \right) = \frac{\alpha a}{\lambda L} t \quad (= \text{constant for } q = \text{constant}) \quad (3.2.57)$$

and:

$$t_2 = t_1 \frac{\alpha_1 a_1 \lambda_2 L_2}{\alpha_2 a_2 \lambda_1 L_1} \quad (\text{for } q = \text{constant}) \quad (3.2.58)$$

For the given example we obtain:

$$t_2 = t_1 \frac{1412}{5141} = 0.4t_1$$

Example 3.2.7: Transient heating of a plate for any value of Bi_h

For Bi_h numbers >0.1 , the thermal conductivity of the plate is not high enough and T -profiles develop in the plate during the transient heating (or cooling). Therefore, we have to solve the differential equation (3.2.48) for the boundary condition given by Eq. (3.2.51). For $Fo > 0.2$, the solution for the center of the plate ($x=L$, i.e., $X=1$) is to a good approximation:

$$\theta_{\text{center,plate}} = C_1 e^{-C_2 Fo} \quad (3.2.59)$$

[with C_1 and $C_2 = f(Bi_h)$ and for $Fo > 0.2$]

where the constants C_1 and C_2 are both functions of the Bi_h number only [values are tabulated elsewhere, e.g., in Cengel (2002)]. Once Bi_h is known, the above equation can be used to determine the temperature in the center of the plate. This again shows the advantage of dimensionless numbers, as we can now use charts based on θ_{plate} , Bi_h , and Fo . These charts depict, for example, the dimensionless temperature $\theta_{\text{center,plate}}$ for given values of Fo and Bi_h (Figure 3.2.20). Figure 3.2.21 shows

the local distribution of $\theta_{X,\text{plate}}$ – now with $\Delta T_{\max} = T_{\text{center,plate}} - T_{\text{surr}}$ as the reference – to obtain a chart that is independent of time for $Fo > 0.2$. For other bodies (cylinders, spheres, etc.), similar charts are valid (Cengel, 2002).

For $Bi_h = \alpha L / \lambda = \infty$ ($\alpha \rightarrow \infty$), the surface temperature T_s equals the temperature of the surrounding T_{surr} at all times after the plate is brought into contact with the surrounding fluid. With the respective values of C_1 and C_2 for an infinite Bi number, Eq. (3.2.59) leads to:

$$\theta_{\text{center,plate}} = 1.27 e^{-2.47 Fo} \quad (\text{for } Fo > 0.2 \text{ and } Bi_h \rightarrow \infty) \quad (3.2.60)$$

Note that Eqs. (3.2.59) and (3.2.60) are only good approximations for $Fo > 0.2$, that is, if the initial time needed for the development of a pronounced T -profile in the whole plate is negligible.

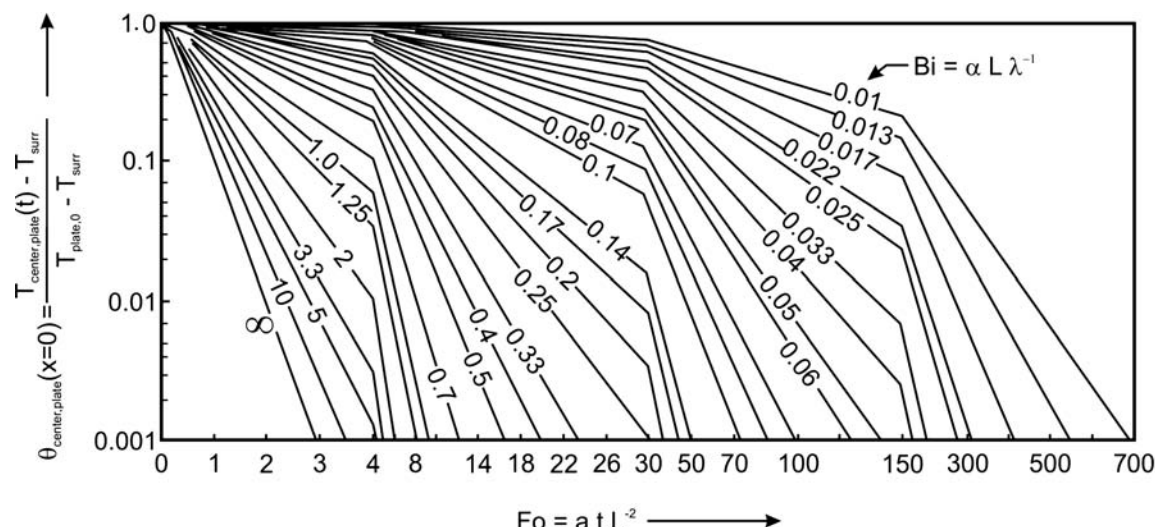
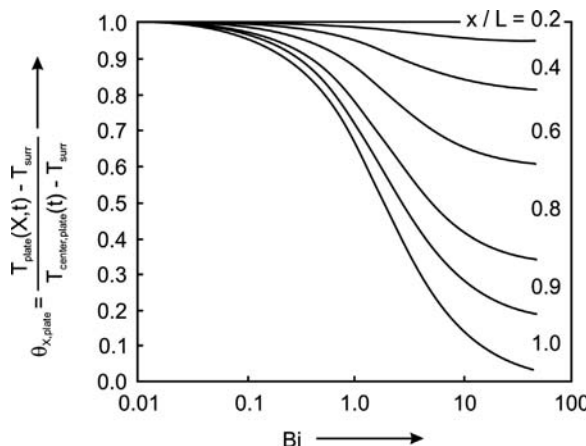


Figure 3.2.20 Transient chart for midplane temperature of a plane with half-thickness L initially at a uniform temperature $T_{\text{plate},0}$ subjected to convection from both sides to a surrounding fluid with constant T_{surr} ($\theta_{\text{center,plate}}$ with $\Delta T_{\text{initial}}$ as reference; chart valid for $Fo > 0.2$).

Figure 3.2.21 Temperature distribution in a plane (half thickness L) subjected to convection ($T_{\text{surf}} = \text{const.}$, $\theta_{x,\text{plate}}$ with $\Delta T_{\max} = T_{\text{center,plate}} - T_{\text{surf}}$ as reference; chart is valid for $Fo > 0.2$).



For $Bi_h \ll 1$ ($\lambda/L \alpha \rightarrow \infty$), the resistance of convective heat transfer dominates. The T -gradient in the plane is then negligible, and we get a uniform change of temperature with time. This is the border case of the lumped body model (Example 3.2.7). For $Bi_h \rightarrow 0$, C_1 and C_2 converge to 1 and Bi_h , respectively, and Eq. (3.2.59) equals Eq. (3.2.56).

In contrast to the lumped body model, the general case, which includes T -gradients in the plane and in the boundary layer around the plane, implies that two systems are only equal if the Bi_h and the Fo number are identical.

3.2.2 Mass Transport

The mechanisms of mass transport can be divided into convective and molecular-flow processes. Convective flow is either forced flow by pumps and compressors, for example, in pipes and packed beds, or natural convection driven by density gradients that are induced by temperature gradients in a fluid. For molecular flow we have to distinguish whether we have diffusion in a free fluid phase or in porous solids. These processes are examined below.

3.2.2.1 Forced Flow in Empty Tubes and Hydrodynamic Entrance Region

If a fluid flows through an empty tube with a smooth surface and a cross-section A_t , we have to distinguish different flow regimes (Figure 3.2.22) that depend on the Reynolds number:

$$Re = \frac{ud_t}{\nu} \quad \text{with } u = u_{\text{mean}} = \frac{\dot{V}_{\text{fluid}}}{A_t} \quad (3.2.61)$$

For Re below a critical value of about 2300, we have laminar flow with a parabolic velocity profile. The maximum velocity in the center of the tube is twice as much as the mean value u_{mean} defined by Eq. (3.2.61). The radial velocity profile for laminar flow in a round tube is given by:

$$\nabla_o \quad u(r) = u_{\text{max}} \left(1 - \frac{4r^2}{d_t^2} \right) = u_{\text{mean}} \left(2 - \frac{8r^2}{d_t^2} \right) \quad (3.2.62)$$

(laminar flow, $r = 0$ at center of tube)

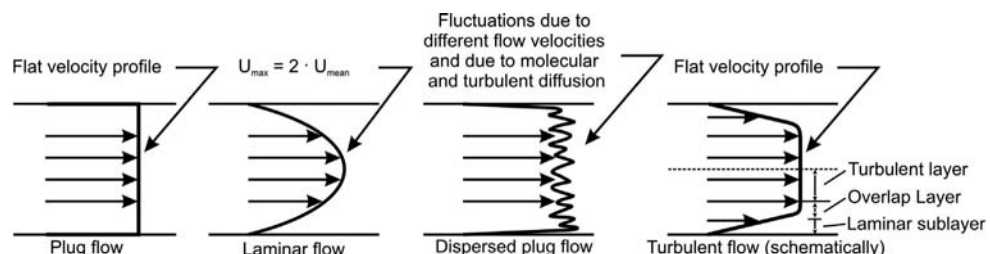
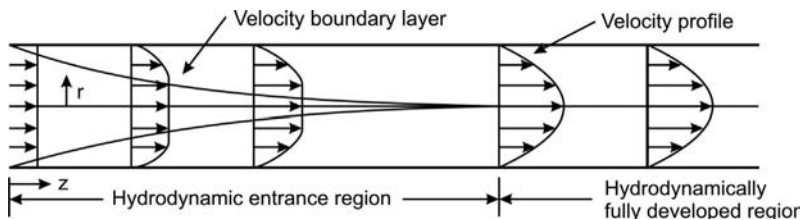


Figure 3.2.22 Flow regimes for flow of a fluid through an empty tube.



For $Re > 10\,000$, we have turbulent flow with an almost constant velocity in the main part of the tube and a small laminar sublayer near the wall where the velocity goes down to zero (no-slip condition). For $2300 < Re < 10\,000$, we have a transition regime. Any disturbances, for example, surface roughness or particles of a packed bed, lead to a lower value of the critical Re number.

The driving force is the pressure, and the friction leads to a pressure loss in empty tubes as well as in fixed, fluidized, and entrained beds (Sections 3.4.1.1 and 3.4.1.2).

The velocity profiles shown in Figure 3.2.22 do not represent the situation at the entrance of the tube, and we have to examine the entrance region more closely. Consider a fluid entering a circular tube with a uniform radial velocity profile. The fluid layer directly in contact with the surface of the tube will come to a complete stop. This layer causes the fluid in the adjacent layers to slow down gradually as a result of friction. This leads to an increased velocity in the midsection of the tube to keep the mass flow through the tube constant, and thus a velocity boundary layer develops along the tube. The thickness of this layer increases in flow direction until the layer reaches the tube center and fills the entire tube (Figure 3.2.23).

The region from the tube inlet to the point at which the boundary layer reaches the centreline is called hydrodynamic entrance region, and the length of this region is the hydrodynamic entrance length $L_{\text{hydrodynamic}}$. The region beyond the entrance region in which the velocity profile is fully developed and remains unchanged is called the hydrodynamically fully developed region.

The hydrodynamic entry length is usually taken as the distance from the tube entrance where the friction factor (pressure loss coefficient, see Section 3.4.1.1) reaches within 2% deviation the fully developed value. In laminar flow, the hydrodynamic entry length is (Cengel, 2002):

$$L_{\text{hydrodynamic}} = 0.05 Re d_t \quad (\text{for } Re < 2300) \quad (3.2.63)$$

For $Re < 20$, the hydrodynamic entry length is less than the tube diameter, and reaches in the limiting case of $Re = 2300$ a value of $115d_t$.

The entry length is much shorter in turbulent flow and its dependence on Re is weaker. According to the literature (Cengel, 2002), $L_{\text{hydrodynamic}}$ is $11d_t$ for $Re = 10\,000$, and increases to $40d_t$ at $Re = 10^5$. Usually, the entry length for turbulent flow is approximated by:

$$L_{\text{hydrodynamic}} \approx 10d_t \quad (\text{for } Re > 2300) \quad (3.2.64)$$

3.2.2.2 Steady-State and Transient Diffusive Mass Transfer

The one-dimensional steady-state transport of mass by diffusion is given by Fick's first law [Eq. (3.1.54)], and for a liquid or gaseous slab of constant density with thickness d we obtain:

$$\dot{n} = DA \frac{c_1 - c_2}{d} \quad (3.2.65)$$

For a one-dimensional transient diffusion process, we have to use Fick's second law:

$$! \quad \frac{dc}{dt} = D \frac{d^2 c}{dx^2} \quad (3.2.66)$$

Figure 3.2.23 Development of the velocity boundary layer of a fluid flowing in an empty tube. The velocity profile in the hydrodynamically fully developed region is parabolic in laminar flow (as shown) and somewhat blunt in turbulent flow (see Figure 3.2.22).

Note the similarities of Eqs. (3.2.65) and (3.2.66) to the respective equations for heat transfer by conduction, Eqs. (3.2.1) and (3.2.43).

For mass transfer from a fluid phase to a solid surface, the characteristic length of diffusion is the film thickness δ , and by introduction of the mass transfer coefficient β we obtain:

$$\dot{n} = \frac{D}{\delta} A(c_{\text{fluid}} - c_s) = \beta A(c_{\text{fluid}} - c_s) \quad (3.2.67)$$

This situation is shown by Figure 3.2.2, if we replace the temperatures by concentrations.

The value of β is calculated based on the dimensionless *Sherwood number* Sh , which is the counterpart to the Nu number, but is used for convective mass transport and not – as Nu – for heat transport. Sh is also defined based on a characteristic length (diameter of a sphere or tube etc.) as:

$$Sh = \frac{\beta d_{\text{charac.}}}{D} \quad (\text{named after Thomas K. Sherwood}) \quad (3.2.68)$$

As a good approximation, we can use the equations for the Nu number (Section 3.2.1.2) to calculate the Sh number, if we replace the *Prandtl number* Pr by the *Schmidt number*:

$$Sc = \frac{\nu}{D} \quad (\text{named after Ernst Schmidt, see box}) \quad (3.2.69)$$

For gases Sc is around 0.7 and independent of temperature and pressure as we can deduce from Eqs. (3.1.69), (3.2.69), and (3.1.70). Furthermore, $Sc \approx Pr$, and thus the approximation $Sh = Nu$ is valid [$Sh/Nu \approx (Sc/Pr)^{1/3}$, see Eqs. (3.2.18) and (3.2.19b)]. For example, for mass transfer to the surface of a single particle we have for $Re_p < 50$:

$$Sh_{\text{single particle}} \approx 2 + 0.664 \sqrt{Re_p} \sqrt[3]{Sc} \quad (\text{for } Re_p = ud_p/n < 50) \quad (3.2.70)$$

and for a fixed bed we have in analogy to Eq. (3.2.25):

$$Sh_{\text{bed}} = [1 + 1.5(1 - \varepsilon)] Sh_{\text{single particle}} \approx 1.9 Sh_{\text{single particle}} \quad (\text{for } \varepsilon \approx 0.4 \text{ and spheres}) \quad (3.2.71)$$

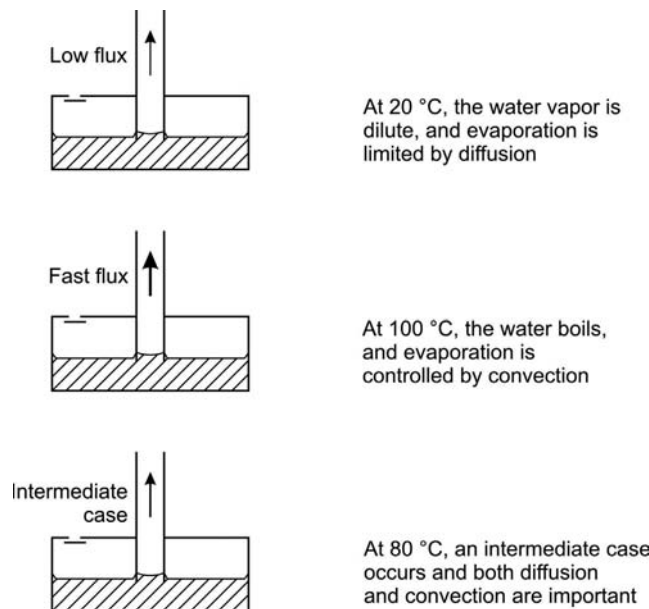
whereby $Re_{p,\text{bed}}$ [= $ud_p/(\varepsilon\nu)$] is now used in Eq. (3.2.70) instead of Re_p (= ud_p/ν) with u as superficial velocity. For natural convection mass transfer the analogy between Nu and Sh still holds and thus we may use the equations (3.2.22) and (3.2.23) if natural convection has to be considered (buoyancy by temperature gradients between surface and bulk phase).

Note that diffusion may cause convection (*Stefan flow*). Figure 3.2.24 shows an example to illustrate this for the case of evaporation. Further quantitative details are given in Topic 3.2.5.

The system consists of a large reservoir of water connected to a large volume of air by a capillary tube. At low temperatures, for example, at room temperature, the vapor pressure and thus the volume content is low (23 mbar, i.e., a content of 2% at 1 bar total pressure). In such a dilute solution, the process is dominated by the diffusion of water vapor through the capillary into the surrounding air. Thus the flux of the vapor can be determined by Eq. (3.2.65), and the concentration profile is linear. At the boiling point (100 °C at 1 bar) we enter a completely different situation. The water now boils, and the vapor rushes through the capillary into the surrounding air. This process has little to do with diffusion. At intermediate temperatures, and thus in concentrated solution of vapor in air, both diffusion and convection are important, and the total flux of water vapor is now higher as if we would only consider the diffusion flux [see Topic 3.2.5; further details are also given by Cussler (2009)].

Thomas Kilgore Sherwood (1903–1976): an American chemical engineer whose primary research area was mass transfer and its interaction with flow and with chemical reaction.

Ernst Schmidt (1892–1975): a German scientist in the field of heat and mass transfer who measured the radiation properties of solids and developed the use of aluminum foils as radiation shields. He was the first to measure velocity and temperature fields in free convection boundary layers and discovered the large heat transfer coefficients occurring in condensation. A paper on the analogy between heat and mass transfer caused the dimensionless quantity involved to be called the *Sc* number.



Topic 3.2.5 Interrelation of diffusion and convection (Stefan flow)

Figure 3.2.25 depicts the evaporation of water through a gas-filled capillary of length L and cross section A . We assume a large reservoir of water and thus a constant value of L . We also assume that the capillary is connected to a large volume of well-stirred air, so that the vapor content at the outlet of the tube is zero. The total pressure p is 1 bar and the temperature throughout the system is constant. At the water-air interphase ($z=0$), the vapor pressure of water is established ($p_{\text{H}_2\text{O}} = p_{\text{H}_2\text{O,vap}}$), and the content of vapor is given by the ratio of the saturation vapor pressure and the total pressure ($y_{\text{sat}} = p_{\text{H}_2\text{O,vap}}/p$).

Because we are dealing with rapid evaporation – at least for higher temperatures – we must consider both diffusion and convection. At steady state, the total flux of water (with $D_{\text{H}_2\text{O}} \approx D_{\text{air}} = D$) is constant ($= C_1$) and given by:

$$\frac{\dot{n}_{\text{H}_2\text{O}}}{A} = -Dc \frac{dy_{\text{H}_2\text{O}}}{dz} + u_{\text{con}} y_{\text{H}_2\text{O}} c = C_1 \quad (3.2.72)$$

(with u_{Stefan} as velocity of convective flux)

in which $y_{\text{H}_2\text{O}}$ is the content of vapor in the capillary, c the total concentration of the gas (mol m^{-3}), and u_{con} the velocity (in m s^{-1}) of the convective flux, also denoted as the *Stefan flux*.

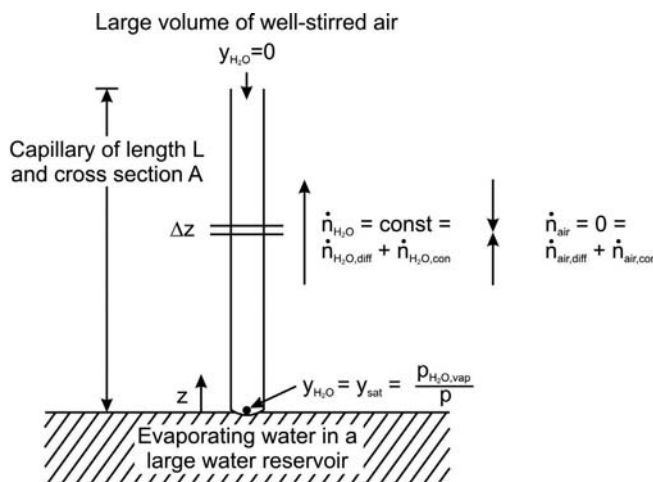


Figure 3.2.24 Evaporation of water as an example of the interrelation of diffusion and convection in dilute and concentrated solutions.

Figure 3.2.25 Evaporation of water in a capillary.

The total pressure p and the total concentration c are constant [$c = p/(RT)$]. Thus we get a gradient of the air content that corresponds to the respective gradient of the vapor:

$$\gamma_{\text{air}} = 1 - \gamma_{\text{H}_2\text{O}} \Rightarrow \frac{dy_{\text{air}}}{dz} = -\frac{dy_{\text{H}_2\text{O}}}{dz} \quad (3.2.73)$$

Consequently, we obtain a diffusion flux of air in the opposite direction of the flow of the vapor. If the air is not absorbed by the water, the net total flux of air must be zero, that is, the diffusion flux is compensated by a convective flux in the opposite direction (Figure 3.2.25):

$$\frac{\dot{n}_{\text{air}}}{A} = 0 = -Dc \frac{dy_{\text{air}}}{dz} + u_{\text{con}} \gamma_{\text{air}} c \quad (3.2.74)$$

The combination of Eqs. (3.2.74) and (3.2.73) leads to:

$$u_{\text{con}} = -\frac{D}{(1 - \gamma_{\text{H}_2\text{O}})} \frac{dy_{\text{H}_2\text{O}}}{dz} \quad (3.2.75)$$

and by insertion into Eq. (3.2.72) and rearrangement we obtain:

$$\frac{dy_{\text{H}_2\text{O}}}{(1 - \gamma_{\text{H}_2\text{O}})} = -\frac{C_1}{cD} dz \quad (3.2.76)$$

Integration for the boundary condition $\gamma_{\text{H}_2\text{O}} = \gamma_{\text{sat}}$ for $z = 0$ yields:

$$\ln\left(\frac{1 - \gamma_{\text{H}_2\text{O}}}{1 - \gamma_{\text{sat}}}\right) = \frac{C_1}{cD} z \quad (3.2.77)$$

and the constant C_1 (= total flux of vapor) is determined by the second boundary conditions $\gamma_{\text{H}_2\text{O}} = 0$ for $z = L$:

$$\frac{\dot{n}_{\text{H}_2\text{O}}}{A} = C_1 = \frac{cD}{L} \ln\left(\frac{1}{1 - \gamma_{\text{sat}}}\right) \quad (3.2.78)$$

and insertion into Eq. (3.2.77) finally yields the concentration profile:

$$\gamma_{\text{H}_2\text{O}} = 1 - (1 - \gamma_{\text{sat}})^{(1-\frac{z}{L})} \quad (3.2.79)$$

Note that for a low value of γ_{sat} we get [as $\ln(1/(1-a)) \approx a$ for $a \ll 1$]:

$$\frac{\dot{n}_{\text{H}_2\text{O}}}{A} = Dc \frac{\gamma_{\text{sat}}}{L} \quad (\text{for } \gamma_{\text{sat}} \ll 1) \quad (3.2.80)$$

that is, the solution becomes dilute, convection is negligible, and the concentration profile becomes linear. Figure 3.2.26 shows the influence of temperature on the concentration profiles of air and water vapor during evaporation of water in a capillary at 1 bar. For high values of the saturation vapor pressure and thus of γ_{sat} (e.g., 0.83 for 95 °C), the concentration profile is exponential, and the contribution of convection is not negligible.

Figure 3.2.27 shows the ratio of the total flux of steam [Eq. (3.2.78)] to the flux assuming a dilute solution [Eq. (3.2.80)]. The error that would be caused by neglecting convection is:

$$\text{Error} = \frac{\dot{n}_{\text{H}_2\text{O}} - \dot{n}_{\text{H}_2\text{O},\text{diff}}}{\dot{n}_{\text{H}_2\text{O},\text{diff}}} = \frac{-\ln(1 - \gamma_{\text{sat}}) - \gamma_{\text{sat}}}{\gamma_{\text{sat}}} \leq 5\% \quad \text{for } \gamma_{\text{sat}} \leq 10\% \quad (3.2.81)$$

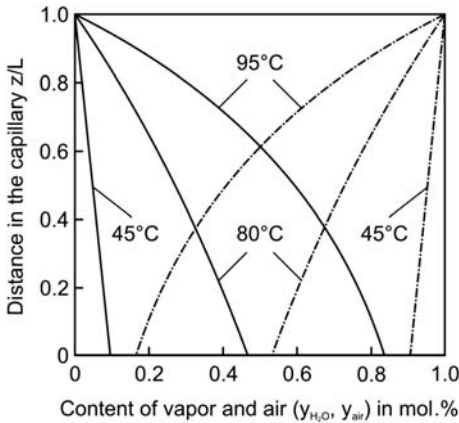


Figure 3.2.26 Concentration profiles of air and water vapor during evaporation of water in a capillary at different temperatures (1 bar; dotted-dashed lines: air; solid lines: water vapor).

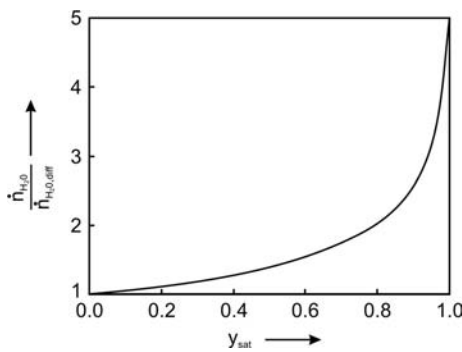


Figure 3.2.27 Ratio of total flux of steam [Eq. (3.2.78)] to the flux assuming a dilute solution (case of evaporation as shown in Figure 3.2.25).

3.2.2.3 Diffusion in Porous Solids

The molar flux of a component i diffusing in a single pore of a porous solid, for example, a solid catalyst or a solid reactant like coke, coal, or an ore, is given by:

$$\dot{n}_i = D_{\text{pore}} A_{\text{pore}} \frac{dc_i}{dz_{\text{pore}}} \quad (3.2.82)$$

where A_{pore} and z_{pore} are the pore cross section and the diffusion path length along the pore, respectively. For an actual solid with a complicated pore structure both terms are unknown, and the concept of an effective diffusion coefficient is used, defined by:

$$\dot{n}_i = D_{\text{eff}} A \frac{dc_i}{dz} \quad (3.2.83)$$

where A and z denote the well-defined external surface area and the radial coordinate of the porous particle. Equating Eq. (3.2.82) with Eq. (3.2.83) leads to:

$$D_{\text{eff}} = D_{\text{pore}} \frac{A_{\text{pore}}}{A} \frac{z}{z_{\text{pore}}} \quad (3.2.84)$$

Thus, D_{eff} has to consider the following three factors:

- 1) Only a portion of the particle is permeable, so the ratio of surface holes to the total area, A_{pore}/A , has to be considered, which approximately equals the porosity, ε_p . Typically, the porosity of porous catalysts is about 0.5.
- 2) The path through the particle is random and tortuous. The correction factor for z , the tortuosity, τ_p , approximately equals the ratio z_{pore}/z , but has also to consider dead end pores. Typical values for the tortuosity are in the range 2–7 for $0.3 < \varepsilon_p < 0.7$ as depicted in Figure 3.2.28 by values and correlations given in the literature.
- 3) Finally, we may have to consider that if the free path of a molecule is of the order of magnitude of the pore diameter, collisions with the pore wall cannot be neglected.

Summarizing these factors we obtain:

! $D_{\text{eff}} = \frac{\varepsilon_p}{\tau_p} D_{\text{pore}} \quad \text{with} \quad D_{\text{pore}} = \left(\frac{1}{D_{\text{mol}}} + \frac{1}{D_{\text{Knu}}} \right)^{-1} \quad (3.2.85)$

Thus, depending on the pore diameter, the diffusivity in a pore is the combined diffusivity of the molecular and Knudsen diffusivity, whereby the latter is calculated by:

! $D_{\text{Knu}} = \frac{1}{3} \bar{u} d_{\text{pore}} = \frac{1}{3} \sqrt{\frac{8RT}{\pi M}} d_{\text{pore}} \quad (3.2.86)$

which is named after the Danish physicist Martin Hans Christian Knudsen (1871–1949). More details on the diffusion in small pores/capillaries are given in Topic 3.2.6.

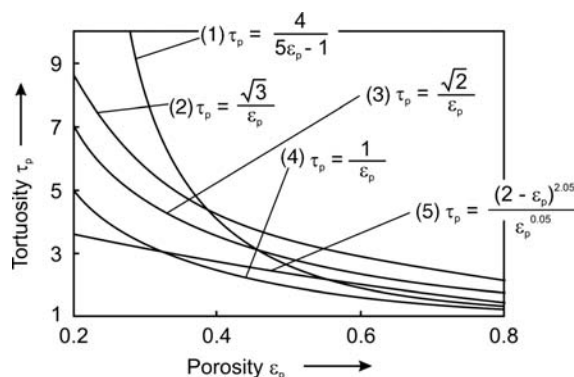


Figure 3.2.28 Influence of the porosity of a porous solid on the tortuosity according to correlations given in the literature: (1) Hugo (1974), (2) Weisz and Schwartz (1962), (3) Wheeler (1955), (4) Froment and Bischoff (1990), and (5) Probst and Wohlfahrt (1979).

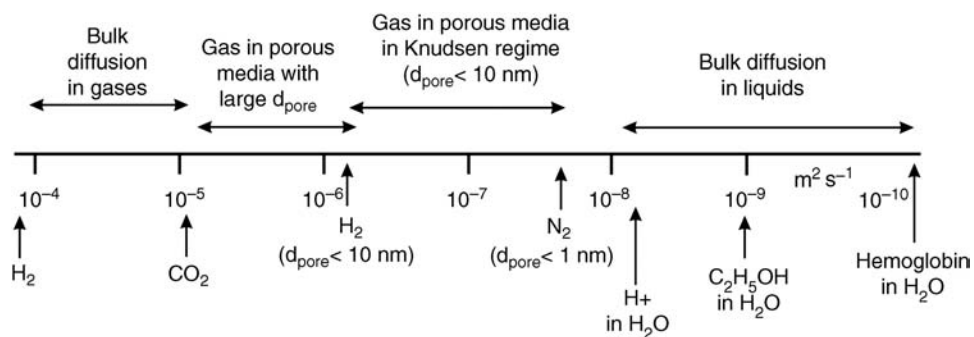


Figure 3.2.29 Diffusion coefficients for bulk diffusion in fluids and effective diffusion in porous media (1 bar, 0 °C; not considered: surface and configurational diffusion in porous media).

An important example in chemical engineering, where pore diffusion is relevant, is a solid catalyst. If the influence of Knudsen diffusion is negligible, the effective diffusion coefficient is then typically, by a factor of about 6, lower than the molecular diffusivity ($\epsilon_p \approx 0.5$, $\tau_p \approx 3$).

Finally, three special cases should be mentioned without giving further details:

- 1) If adsorption leads to a sufficiently large accumulation this must be included in the mass balance. This leads to a formal decrease of the (apparent) pore diffusivity (see Topic 3.3.4 in Section 3.3.5). However, for hydrocarbon gases in usual catalysts, this effect is mostly negligible, but for microporous solids it may have an influence, especially for liquids (Froment and Bischoff, 1990).
- 2) If the adsorbed molecules are mobile on the surface, this may lead to an additional surface diffusion flux with the concentration of the adsorbed species in the adsorbate as driving force. However, surface diffusivities of small molecules (at 20 °C) are of the order of magnitude of only 10^{-3} to $10^{-5} \text{ cm}^2 \text{ s}^{-1}$ (Baerns *et al.*, 2006) and are thus small compared to molecular diffusivities of gases of the order of magnitude of $0.1 \text{ cm}^2 \text{ s}^{-1}$.
- 3) If the molecular dimensions are of the order of magnitude of the pore diameter, we may also have to consider the so-called configurational diffusion. However, configurational diffusivities are of the order 10^{-6} – $10^{-14} \text{ cm}^2 \text{ s}^{-1}$, and are therefore only relevant in solids with pore diameters of less than 1 nm (Baerns *et al.*, 2006; Froment and Bischoff, 1990).

Typical values of diffusion coefficients for bulk diffusion in fluids and effective diffusion in porous media are given in Figure 3.2.29 without consideration of surface and configurational diffusion in porous media (see also values given in Tables 3.1.6 and 3.1.7).

Topic 3.2.6 Knudsen diffusion and related phenomena

Knudsen diffusion and related phenomena are shown in Figure 3.2.30 for the example of two (well-mixed) volumes separated by a capillary or an orifice. Each volume contains a gas. Depending on the size of the capillary and orifice, the transport mechanisms are different.

We first consider normal diffusion in a capillary (Figure 3.2.30a). The diameter of the capillary is much larger than the mean free path (Λ) of the gases (here H₂ and N₂), and molecular diffusion takes place in the capillary between both volumes until the concentrations are equal in both volumes. The fluxes of H₂ and N₂ are equal and depend on the binary diffusion coefficient, which is proportional to the square root of the reciprocal of the harmonic average of the molecular weights [Eq. 3.1.78]:

$$\dot{n}_{N_2} = D_{N_2/H_2} A_{\text{cap}} \frac{\Delta c_{N_2}}{l_{\text{cap}}} = \dot{n}_{H_2} = D_{H_2/N_2} A_{\text{cap}} \frac{\Delta c_{H_2}}{l_{\text{cap}}} \quad (d_{\text{cap}} \gg \Lambda, D_{N_2/H_2} = D_{H_2/N_2}) \quad (3.2.87)$$

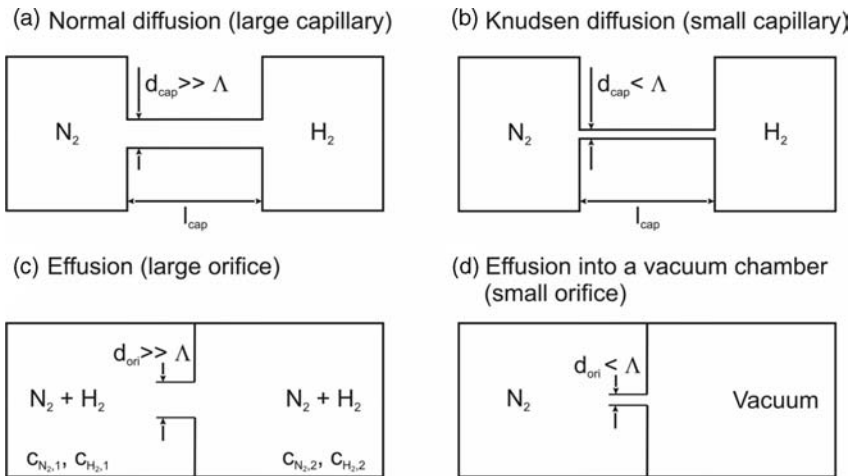


Figure 3.2.30 Knudsen diffusion and related phenomena (flux in capillaries and orifices).

Secondly, we consider the case of Knudsen diffusion, that is, the diameter of the capillary is smaller than Λ (Figure 3.2.30b). According to Eq. (3.1.72), this condition is fulfilled for:

$$d_{\text{cap}} < \Lambda = \frac{1}{\sqrt{2}} \frac{kT}{\sigma p} \quad (\text{condition for Knudsen diffusion}) \quad (3.2.88)$$

To give an idea of the orders of magnitude: at 300 K and 1 bar, Λ of air is 0.07 μm. Thus the capillary must be smaller to get into the Knudsen regime. Alternatively, we may use a low pressure, for example, for a capillary of 0.1 mm, the pressure must be lower than 70 Pa. The molecules now collide much more frequently with the capillary walls than with other diffusing molecules. The (Knudsen) diffusion coefficient for each species is proportional to the inverse square root of its molecular weight, and the flux through the capillary is:

$$\dot{n}_{N_2} = D_{Knu,N_2} A_{\text{cap}} \frac{\Delta c_{N_2}}{l_{\text{cap}}} = \frac{1}{3} \sqrt{\frac{8RT}{\pi M}} d_{\text{cap}} A_{\text{cap}} \frac{\Delta c_{H_2}}{l_{\text{cap}}} \quad (d_{\text{cap}} < \Lambda) \quad (3.2.89)$$

The ratio of the fluxes of the two gases (here N₂ and H₂) is given by:

$$\frac{\dot{n}_1}{\dot{n}_2} = \sqrt{\frac{M_2}{M_1}} \quad (\text{Knudsen diffusion, } d_{\text{cap}} < \Lambda) \quad (3.2.90)$$

Thus we may use Knudsen diffusion experiments to determine relative molar masses.

In the third case (Figure 3.2.30c), the capillary is extremely short compared to the diameter, that is, we have an orifice and thus no concentration gradient in the orifice itself. The diffusion is now not one-dimensional and narrows down to pass through the orifice followed by an extension into the gas phase behind the orifice. We assume that the diameter of the orifice is large compared to Λ , and that the diffusion coefficient is equal in both chambers, for example, we start with (different) N₂/H₂ mixtures such as 50%/50% and 40%/60% and can use the binary diffusion coefficient. The flux is now (Cussler, 2009):

$$\dot{n}_{N_2} = D_{N_2/H_2} A_{\text{ori}} \left(\frac{4l_{\text{ori}}}{\pi d_{\text{ori}}} \right) \frac{\Delta c_{N_2}}{l_{\text{ori}}} = D_{N_2/H_2} A_{\text{ori}} \frac{4}{\pi} \frac{\Delta c_{N_2}}{d_{\text{ori}}} \quad (\text{for } d_{\text{ori}} \gg \Lambda) \quad (3.2.91)$$

For an ideal gas, an interesting correlation can be derived by rewriting of Eq. (3.2.91):

$$\dot{n}_i = \frac{dm_i}{dt} \frac{1}{M_i} = D_i \frac{A_{\text{ori}}}{d_{\text{ori}}} \frac{4 \Delta p_i}{\pi RT} \Rightarrow \frac{dm_i}{dt} = \left(\frac{D_i d_{\text{ori}} M_i}{RT} \right) \Delta p_i \quad (3.2.92)$$

Equation (3.2.92) can be used to determine the vapor pressure of a high boiling liquid by measuring the (constant) mass loss of a liquid in a closed small containment. The vapor can only escape to the surrounding (e.g., air) through a small hole (orifice). For a given molecular weight of the liquid, the mass loss is directly related to the vapor pressure, Eq. (3.2.92), that is, Δp_i can be replaced by p_{vap} if the vapor content in the gas phase surrounding the containment is negligible. Such a measurement can be carried out, for example, by thermogravimetry (Section 4.11.5.4). (Note that the mass loss through the orifice must be small so that the partial pressure or vapor pressure, respectively, in the containment is constant.)

In the fourth case (Figure 3.2.30d), one chamber is evacuated. Now the molecules simply fly through the orifice without collision with other molecules or the orifice (mean free path of the molecules \gg diameter of the orifice). This mechanism is called effusion and the flux is:

$$\dot{n}_i = \frac{1}{4} \bar{u}_i c_i A_{\text{ori}} = \frac{1}{4} \sqrt{\frac{8RT}{\pi M_i}} c_i A_{\text{ori}} \quad (\text{for } d_{\text{ori}} \ll \Lambda) \quad (3.2.93)$$

where \bar{u}_i is the mean velocity of the molecules, Eq. (3.1.71). Note that the term $0.25\bar{u}_i c_i$ represents the number of collisions of gas molecules with a wall [see, for example Atkins and de Paula (2002)], for example, for 1 bar and 300 K we have 3×10^{23} collisions $\text{s}^{-1} \text{cm}^{-2}$.

As in case of Knudsen diffusion [Eqs. (3.2.89) and (3.2.90)] we get for the ratio of the fluxes:

$$\frac{\dot{n}_1}{\dot{n}_2} = \sqrt{\frac{M_2}{M_1}} \quad (\text{diffusion through orifice into vacuum with for } d_{\text{ori}} \gg \Lambda) \quad (3.2.94)$$

This law is also called *Graham's law* and coincides with Eq. (3.2.81) for Knudsen diffusion through a capillary. Thus, different mass transfer mechanisms can give similar results, showing the subtlety of the apparently simple mechanism of diffusion.

Summary of Section 3.2 (take-home messages)

- For heat transfer, we have to consider heat conduction, convection, and radiation.
- To calculate the heat transfer by convection, for example, from a plate to a fluid, the heat transfer coefficient and the respective dimensionless Nusselt number Nu is used.
- Extremely high values of the heat transfer coefficient are reached with boiling liquids, above all in the regime nucleate boiling. If the surface temperature is too high, the heat transfer decreases due to the insulating effect of the vapor blanket (film boiling).
- For calculations of the transient heat transfer by conduction and convection, for example, heating up a body, the *Fourier's second law* is used, and we need to know the *Fourier number* Fo and *Biot number* Bi_h . The advantage of these numbers is that we can use charts, which depict the dimensionless temperature for given values of Fo and Bi .
- If a fluid flows through an empty tube, we have to distinguish different flow regimes. For a Reynolds number below 2300, we have laminar flow with a parabolic velocity profile and a velocity in the center of the tube that is twice as much as the mean value. For $Re > 10\,000$, we have turbulent flow with an almost constant velocity in the main part of the tube and a small area near the wall where the

velocity goes down to zero (laminar sublayer, no-slip condition). For $2300 < Re < 10\,000$, we have a transition regime. Any disturbances of the flow – for example, by surface roughness, fixtures, or particles of a packed, fluidized, or entrained bed – leads to a lower value of the critical Re number. The driving force is the pressure, and the friction leads to a pressure loss in empty tubes as well as in fixed, fluidized, and entrained beds.

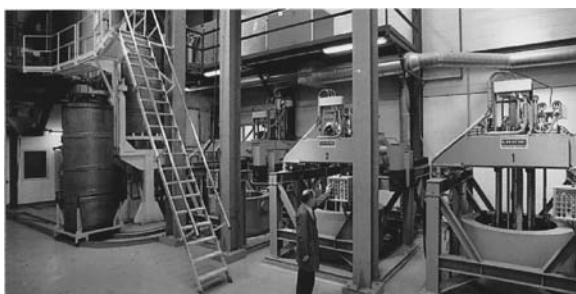
- The equations for the steady-state and transient diffusive mass transfer are analogous to those used for heat transfer. Here, we use as mass transfer coefficient and the dimensionless *Sherwood number* Sh , which is the counterpart to the Nusselt number.
- For diffusion in porous solids, an effective diffusion coefficient is used that has to consider the three factors:
 - Only a portion of the particle is permeable, so the ratio of surface holes to the total area has to be considered, which approximately equals the **porosity**.
 - The path through the particle is random and tortuous. The correction factor is the **tortuosity**, which also has to consider dead end pores.
 - For gases, we may also have to consider that, if the free path of a molecule is of the order of magnitude of the pore diameter, collisions with the pore wall cannot be neglected (**Knudsen diffusion**). Thus, depending on the pore diameter, the diffusivity in a pore is the combined diffusivity of the molecular and Knudsen diffusivity.

3.3

Thermal Unit Operations

Although the reactor where chemical reactions take place is the heart of a process, we have to keep in mind that for industrial processes the pretreatment of feedstocks and the separation of products are highly important. In this chapter the following thermal unit operations will be examined with regard to the physicochemical principles and to the process design:

- Heat exchangers are important for heat transfer from one fluid to another, and are needed for an efficient use of energy in a chemical plant.
- Distillation is the most common separation technique for liquid mixtures. Industrial distillation is performed by stepwise condensation and reboiling in columns with many separation stages.
- Absorption is used for scrubbing gas streams that contain components such as CO_2 , H_2S , and NH_3 . Scrubbers are applied for emission control as well as for the separation of valuable products.
- Liquid–liquid extraction is a useful technique to separate components of a mixture if separation by distillation is impossible or hard to achieve.
- Adsorption removes unwanted impurities or valuable substances from gases and liquids.
- Other separation processes are liquid–solid extraction with supercritical fluids, crystallization, and separation by membranes.



Extraction plant of tea. Courtesy of Uhde, Germany.



Distillation column (cold box) for air separation. Courtesy of Linde Engineering, Germany.



Adsorption plant for H_2 production in Antwerp, Belgium. Courtesy of Linde Engineering, Germany.

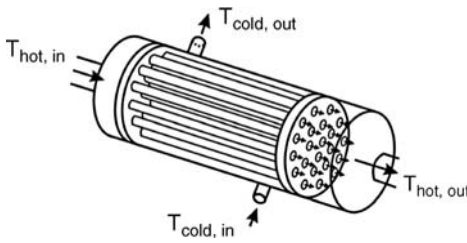


Figure 3.3.1 Tube bundle heat exchanger.
Tube bundle heat exchanger.

“Operating manual”:

Beginners and intermediate learners should leave out the complicated Section 3.3.2.2 about the design of adsorption processes, which only advanced learners should study.

3.3.1

Heat Exchangers (Recuperators and Regenerators)

Common heat exchangers are recuperatively operated tube bundles consisting of many tubes through which one fluid runs. The second fluid flows around the tubes and is heated or cooled, and vice versa the fluid in the tube is cooled or heated (Figure 3.3.1). For efficiency, heat exchangers are designed to maximize the surface area that separates the two fluids.

Heat exchangers are classified according to their flow arrangement. In parallel-flow heat exchangers, both fluids enter the exchanger at the same end, and flow in parallel to one another. In counter-flow exchangers the fluids enter the exchanger from opposite ends. In a cross-flow heat exchanger, the fluids travel perpendicular to one another.

A serious problem of heat exchangers is fouling, for example, biological debris enter the heat exchanger via cooling water from rivers or sea and build layers that decrease the heat transfer. Chemical deposits such as calcium carbonate may also be formed, and therefore heat exchangers must be cleaned periodically, for example, by acid or bullet cleaning.

Typical temperature profiles of heat exchangers are shown schematically in Figure 3.3.2.

The temperature in both fluids changes along the local position of a heat exchanger. To account for this, a logarithmic mean temperature difference $\Delta T_{ln,mean}$ (Topic 3.3.1) is used:

$$\Delta T_{ln,mean} = \frac{\Delta T_1 - \Delta T_2}{\ln\left(\frac{\Delta T_1}{\Delta T_2}\right)} \quad (3.3.1)$$

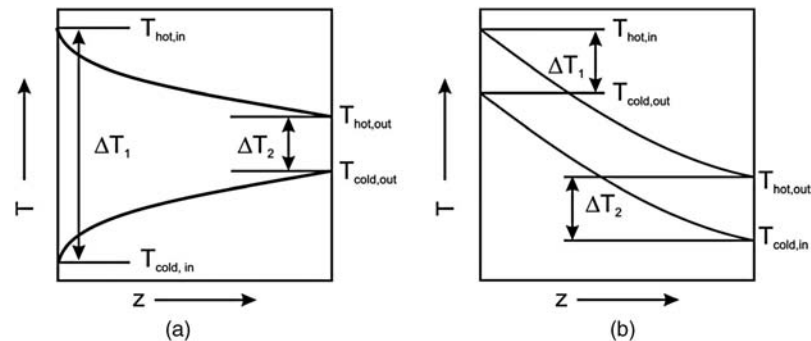
where ΔT_1 and ΔT_2 represent the temperature difference between the hot and cold medium at both ends of the heat exchanger (Figure 3.3.2). Equation (3.3.1) is valid for both parallel and counter flow. The amount of heat transferred in a heat exchanger between medium 1 and 2 is:

$$\dot{Q} = U_h A \Delta T_{ln,mean} \quad (3.3.2)$$

where U_h is the thermal transmission coefficient according to Eq. (3.2.30) and A represents the exchange area. The definition of U_h depends on the choice of the reference area, which is either the internal or the external area of the tubes (Section 3.2.1.2). However, in most cases tubes with a thin wall are used and the difference between both areas is negligible.

The fluids are heated or cooled, and the heat flux and the temperature differences are linked by the following energy balance (if heat losses to the surrounding

Figure 3.3.2 Temperature profiles in a parallel (a) and a counter-flow heat exchanger (b).



are negligible):

$$\dot{Q} = \dot{m}_{\text{cold}} c_{p,\text{m},\text{cold}} (T_{\text{cold,out}} - T_{\text{cold,in}}) = \dot{m}_{\text{hot}} c_{p,\text{m},\text{hot}} (T_{\text{hot,in}} - T_{\text{hot,out}}) \quad (3.3.3)$$

By insertion of Eqs. (3.3.1) and (3.3.2) into Eq. (3.3.3) we get:

$$\begin{aligned} \Delta T_{\text{cold}} &= \frac{\dot{m}_{\text{hot}} c_{p,\text{m},\text{hot}}}{\dot{m}_{\text{cold}} c_{p,\text{m},\text{cold}}} \Delta T_{\text{hot}} = \frac{\dot{Q}}{\dot{m}_{\text{cold}} c_{p,\text{m},\text{cold}}} = \frac{U_h A \Delta T_{\text{ln,mean}}}{\dot{m}_{\text{cold}} c_{p,\text{m},\text{cold}}} \\ &= \frac{U_h A}{\dot{m}_{\text{cold}} c_{p,\text{m},\text{cold}}} \frac{\Delta T_1 - \Delta T_2}{\ln\left(\frac{\Delta T_1}{\Delta T_2}\right)} \end{aligned} \quad (3.3.4)$$

Hence, the temperature difference in both fluids is identical, if the terms $\dot{m}_i c_{p,\text{m},i}$ are equal.

The temperature difference at the entrance of a parallel-flow heat exchanger is higher than for counter-current flow (Figure 3.3.2), but the mean temperature difference is lower. As shown by Example 3.3.1, the heat exchange area of a counter-current heat exchanger needed for the transfer of a certain amount of heat per unit time is therefore lower than for parallel flow; vice versa, more heat can be transferred for a given exchange area. Therefore, parallel flow is only used if rapid cooling of a medium is needed (e.g., for thermally unstable products of a chemical reactor) as we then have the need of a high temperature difference between the cooling medium and the hot fluid at the entrance of the heat exchanger (rapid cooling).

Topic 3.3.1 Logarithmic mean temperature difference in a heat exchanger

For parallel flow (Figure 3.3.2a), the energy balance for a differential section with area dA is given by:

$$d\dot{Q} = \dot{m}_{\text{cold}} c_{p,\text{m},\text{cold}} dT_{\text{cold}} = -\dot{m}_{\text{hot}} c_{p,\text{m},\text{hot}} dT_{\text{hot}} = U_h (T_{\text{hot}} - T_{\text{cold}}) dA$$

If we use the definition $\Delta T = T_{\text{hot}} - T_{\text{cold}}$, rearrangement leads to:

$$\begin{aligned} \frac{dT_{\text{hot}} - dT_{\text{cold}}}{(T_{\text{hot}} - T_{\text{cold}})} &= -\frac{U_h dA}{\dot{m}_{\text{hot}} c_{p,\text{m},\text{hot}}} - \frac{U_h dA}{\dot{m}_{\text{cold}} c_{p,\text{m},\text{cold}}} \Rightarrow \frac{d\Delta T}{\Delta T} \\ &= -U_h dA \left(\frac{1}{\dot{m}_{\text{cold}} c_{p,\text{m},\text{cold}}} + \frac{1}{\dot{m}_{\text{hot}} c_{p,\text{m},\text{hot}}} \right) \end{aligned}$$

Integration from the inlet to the outlet temperature difference of the heat exchanger yields:

$$\ln\left(\frac{T_{\text{hot,out}} - T_{\text{cold,out}}}{T_{\text{hot,in}} - T_{\text{cold,in}}}\right) = \ln\left(\frac{\Delta T_2}{\Delta T_1}\right) = -U_h A \left(\frac{1}{\dot{m}_{\text{cold}} c_{p,\text{m},\text{cold}}} + \frac{1}{\dot{m}_{\text{hot}} c_{p,\text{m},\text{hot}}} \right)$$

and insertion of Eq. (3.3.3) leads to:

$$\ln\left(\frac{\Delta T_2}{\Delta T_1}\right) = -U_h A \left(\frac{\Delta T_{\text{cold}}}{\dot{Q}} + \frac{\Delta T_{\text{hot}}}{\dot{Q}} \right) = -U_h A (\Delta T_{\text{cold}} + \Delta T_{\text{hot}}) \frac{1}{\dot{Q}}$$

which can be rearranged to Eq. (3.3.4):

$$\begin{aligned} \dot{Q} &= U_h A \frac{(T_{\text{cold,out}} - T_{\text{cold,in}}) + (T_{\text{hot,in}} - T_{\text{hot,out}})}{\ln\left(\frac{\Delta T_1}{\Delta T_2}\right)} \\ &= U_h A \frac{(T_{\text{hot,in}} - T_{\text{cold,in}}) - (T_{\text{hot,out}} - T_{\text{cold,out}})}{\ln\left(\frac{\Delta T_1}{\Delta T_2}\right)} \\ &= U_h A \frac{\Delta T_1 - \Delta T_2}{\ln\left(\frac{\Delta T_1}{\Delta T_2}\right)} = U_h A \Delta T_{\text{ln,mean}} \end{aligned}$$

Table 3.3.1 $\Delta T_{\text{arithm,mean}}$ and $\Delta T_{\text{ln,mean}}$ for different values of ΔT_2 and $\Delta T_1 = 100$ K.

$\Delta T_2 (\Delta T_1 = 100 \text{ K}) (\text{K})$	$\Delta T_{\text{arithm,mean}} (\text{K})$	$\Delta T_{\text{ln,mean}} (\text{K})$	Deviation (%)
70	85	84.1	1
45	72.5	68.9	5
10	55	39.1	29
5	52.5	31.7	40
1	50.5	21.5	57

Table 3.3.1 compares the logarithmic mean temperature difference $\Delta T_{\text{ln,mean}}$ and the arithmetic mean temperature difference $\Delta T_{\text{arithm,mean}} = 0.5 (\Delta T_1 + \Delta T_2)$ for different values of ΔT_2 for a constant ΔT_1 of 100 K. Note that $\Delta T_{\text{ln,mean}}$ is always less than $\Delta T_{\text{arithm,mean}}$. If ΔT_2 differs from ΔT_1 by less than about 55%, the error in using $\Delta T_{\text{arithm,mean}}$ is less than 5%.

Example 3.3.1: Comparison of counter-flow and parallel-flow heat exchangers

For comparison of a cross-flow and a parallel-flow heat exchanger we assume the following conditions:

- The inlet temperatures of the hot and the cold medium are 350 and 300 K, respectively.
- The term $\dot{m}_i c_{p,m,i}$ of both fluids is 4200 W K^{-1} (e.g., water with a flow rate of 1 kg s^{-1}). Thus we have:

$$\begin{aligned} T_{\text{hot,in}} - T_{\text{hot,out}} &= T_{\text{cold,out}} - T_{\text{cold,in}} \Rightarrow T_{\text{cold,out}} \\ &= 650 \text{ K} - T_{\text{hot,out}} \end{aligned}$$

- The overall heat transfer coefficient is $500 \text{ W m}^{-2} \text{ K}^{-1}$.

Equation (3.3.4) leads to the following equations for the heat exchange area:

Parallel-flow heat exchanger:

$$A_{\text{parallel flow}} = \frac{\dot{m} c_{p,m}}{U_h} \frac{(T_{\text{hot,in}} - T_{\text{hot,out}}) \ln \left(\frac{T_{\text{hot,in}} - T_{\text{cold,in}}}{T_{\text{hot,out}} - T_{\text{cold,out}}} \right)}{(T_{\text{hot,in}} - T_{\text{cold,in}}) - (T_{\text{hot,out}} - T_{\text{cold,out}})}$$

Counter-flow heat exchanger:

$$A_{\text{counter flow}} = \frac{\dot{m} c_{p,m}}{U_h} \frac{(T_{\text{hot,in}} - T_{\text{hot,out}}) \ln \left(\frac{T_{\text{hot,in}} - T_{\text{cold,out}}}{T_{\text{hot,out}} - T_{\text{cold,in}}} \right)}{(T_{\text{hot,in}} - T_{\text{cold,out}}) - (T_{\text{hot,out}} - T_{\text{cold,in}})}$$

and for the given case of $T_{\text{hot,in}} - T_{\text{hot,out}} = T_{\text{cold,out}} - T_{\text{cold,in}}$ we obtain [note that $\ln(a/b)/(a-b) = 1/a$ for $a=b$]:

$$A_{\text{counter flow}} = \frac{\dot{m} c_{p,m}}{U_h} \frac{(T_{\text{hot,in}} - T_{\text{hot,out}})}{(T_{\text{hot,in}} - T_{\text{cold,out}})}$$

With the conditions given above we have:

$$A_{\text{parallel flow}} = 8.4 \text{ m}^2 \frac{(350 \text{ K} - T_{\text{hot,out}}) \ln \left(\frac{50 \text{ K}}{2T_{\text{hot,out}} - 650 \text{ K}} \right)}{(700 \text{ K} - 2T_{\text{hot,out}})}$$

$$A_{\text{counter flow}} = 8.4 \text{ m}^2 \frac{(350 \text{ K} - T_{\text{hot,out}})}{(T_{\text{hot,out}} - 300 \text{ K})}$$

Figure 3.3.3 depicts the heat exchange area needed in both cases to reach a certain outlet temperature of the hot stream, which clearly shows the advantage of counter flow:

- The exchange area needed to reach a certain exit temperature of the hot medium is smaller.
- Only for counter flow does $T_{\text{hot,out}}$ approach $T_{\text{cold,in}}$ for high heat exchange areas. For parallel flow the minimum value of $T_{\text{hot,out}}$ is higher, for example, for the given conditions ($\dot{m}_i c_{p,m,i} = \text{constant}$) we approach a limiting value of $(T_{\text{hot,in}} + T_{\text{cold,in}})/2 = 325 \text{ K}$.

Figure 3.3.3 Comparison of the heat exchange area of a parallel and a counter-flow heat exchanger (conditions: see Example 3.3.1).

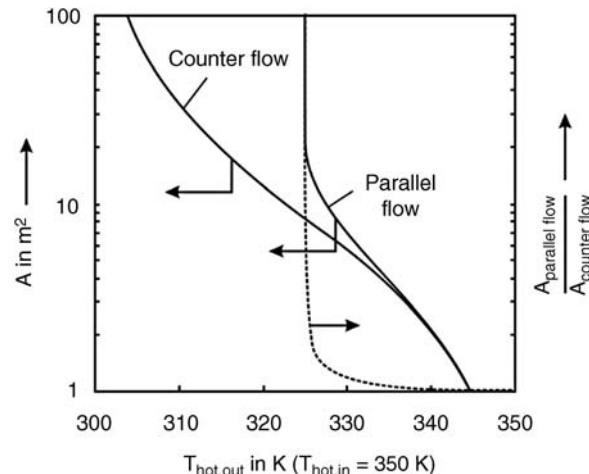


Table 3.3.2 Physical data of heat transfer fluids. Data from Broetz and Schoenbucher (1982).

Property	Water (liquid)	High-temperature melt	Mineral oils (mean values)
Melting point (pour point) ($^{\circ}\text{C}$)	0	142	-20
Limit of stability ($^{\circ}\text{C}$)	—	480	300
Range of application temperature ($^{\circ}\text{C}$)	0–90	<480	0–250
Heat capacity ($\text{kJ kg}^{-1} \text{K}^{-1}$)	4.2	1.6	2.2
Density (kg m^{-3})	959	1860	870
Thermal conductivity ($\text{W m}^{-1} \text{K}^{-1}$)	0.68	0.39	0.12
Dynamic viscosity (mPa s)	0.28 (300 $^{\circ}\text{C}$) 1.00 (20 $^{\circ}\text{C}$)	3.2 (300 $^{\circ}\text{C}$)	1.5–6.0 (300 $^{\circ}\text{C}$)

The most important heat transfer medium is water, which can be used in principle up to the critical temperature of 373 $^{\circ}\text{C}$, but then we reach very high pressures of more than 200 bar ($p_{\text{crit}} = 221$ bar). If steam is used, we have to desalinate the water by ion exchange to avoid deposits. For higher temperatures, liquid metals, high-temperature molten salts, and, for specific applications, mineral oils are applied. Table 3.3.2 lists data of these heat transfer media.

Another group of heat exchangers are non-stationary operated thermal regenerators in which heat is stored and released alternately by a heat storage matrix, for example, two fixed beds, a rotary regenerator, or systems with a circulating solid (Figure 3.3.4).

3.3.2

Distillation

Distillation is a very common technique used to separate a liquid mixture of two or more substances, based on differences in their volatility, to a desired purity by the supply of heat to the component fractions. The vapor of the boiling mixture is richer in the component with the lower boiling point and if the vapor is cooled and condensed, the condensate contains more components of higher volatility. [Note that for mixtures forming a so-called azeotrope this may be different, that is, no or even an enrichment of the (as a pure substance) higher boiling component in the vapor phase may occur (see Sections 3.3.2.1 and 3.3.2.3)].

In *industrial* practice, distillation is done by stepwise condensation and reboiling, and columns consisting of many separation stages are used to achieve an efficient separation. Distillation consumes enormous amounts of energy both in terms of cooling and heating requirements, and may contribute to more than 50% of the operating costs of a chemical plant. Thus a thorough understanding of distillation is essential. To focus on the main principles, the following simplifications are assumed throughout the next two sections:

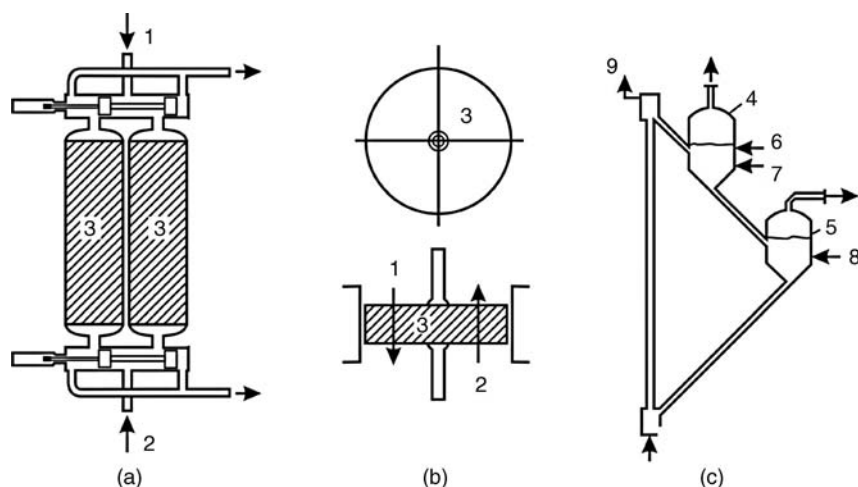


Figure 3.3.4 Thermal regenerators: (a) fixed bed, (b) rotary regenerator, and (c) system with circulating solid; (1) hot gas, (2) cold gas, (3) storage matrix, (4) regenerator, (5) reactor, (6) fuel, (7) air, (8) charge, and (9) medium for transport. Adapted from Broetz and Schoenbucher (1982).

- The vapor is considered as an ideal gas.
- To derive simple equations for the description of the vapor–liquid equilibrium and for the design of distillation columns, the liquid is considered as an ideal mixture, that is, the forces of attraction between molecules of the pure components equal those in the mixture.

Non-ideal systems are only briefly treated in Sections 3.3.2.3 and 3.3.3.1; details of non-ideal systems are given in other textbooks (Gmehling and Brehm, 1996; Ruthven, 2001).

3.3.2.1 Distillation Principles

Consider, for example, a liquid mixture of benzene and toluene heated in a typical laboratory-scale one-step distillation unit (Figure 3.3.5). The initial distillate collected after condensation of the vapor, which evolves as soon as the initial boiling point of the mixture is reached, contains the highest portion of the lower-boiling benzene. Conversely, the final distillate has the lowest content of benzene and practically consists of pure toluene, if the process is carried out carefully. Between these two extremes the composition of the distillate and the remaining liquid gradually change with time and increasing boiling temperature. This is shown in Figure 3.3.6a for a pressure of 1 bar by the temperature–composition diagram that represents the molar content of benzene in the liquid (lower line), x_{benzene} , and in the vapor (upper line), y_{benzene} , at different temperatures.

At the boiling point of pure benzene (80°C at 1 bar), the molar fraction x_{benzene} is 1, and at the boiling point of toluene (111°C) x_{benzene} is 0. The upper curve in Figure 3.3.6a is the dew-point curve, T versus y_{benzene} , representing temperatures where the saturated vapor condenses. The lower curve is the bubble-point curve, T versus x_{benzene} , and represents where the liquid starts to boil. The regions above the dew-point curve and below the bubble-point curve (boiling line) represent superheated vapor and subcooled liquid, respectively.

For example, if a subcooled liquid toluene–benzene mixture with a molar fraction of benzene of 50% is heated (point A in Figure 3.3.6a) its composition remains constant until the boiling point (B) is reached. Now evaporation starts, and the initial vapor evolved, that is, the first droplet collected after condensation (point C), contains about 70 mol.% benzene, and is therefore richer in benzene than the original liquid mixture. Further heating of the mixture leads to an increase of the boiling temperature, and the composition of the distillate and of the remaining liquid gradually changes along the bubble-point and the dew-point curve, respectively. Finally, almost pure toluene evaporates and condenses as the last droplet.

The vapor–liquid diagram (Figure 3.3.6a) relates the composition of the vapor and the liquid phase for each boiling temperature. Thus we can deduce the vapor–liquid equilibrium plot (Figure 3.3.6b), which represents the molar fraction of benzene in the vapor phase (y) as a function of the molar content in the liquid mixture (x). This diagram can also be derived based on the relative volatility α , which is an

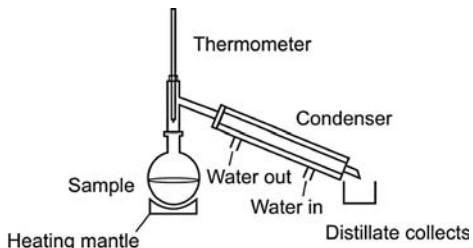


Figure 3.3.5 Simple distillation apparatus.
Simple distillation apparatus.

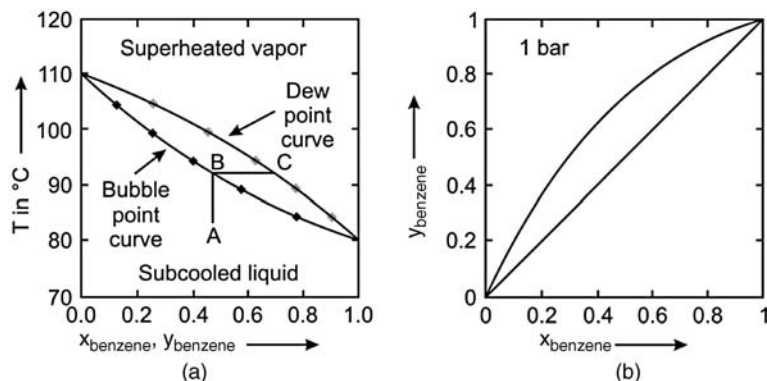


Figure 3.3.6 Isobaric vapor liquid equilibrium of a toluene–benzene mixture at 1 bar: (a) T versus x,y plot and (b) y versus x plot.

indication how easy or difficult the separation is. For a mixture of benzene and toluene α is defined as:

$$\alpha_{\text{benzene,toluene}} = \frac{(y_{\text{benzene}}/x_{\text{benzene}})}{(y_{\text{toluene}}/x_{\text{toluene}})} \quad (3.3.5)$$

For an ideal mixture of two liquids, the vapor pressures are related to the composition in the liquid mixture by Raoult's law (*François-Marie Raoult*, see box):

$$p_{\text{benzene}} = x_{\text{benzene}} p_{\text{sat,benzene}} \text{ and } p_{\text{toluene}} = x_{\text{toluene}} p_{\text{sat,toluene}} \quad (3.3.6)$$

with p_{sat} as the saturation vapor pressure of the component (at T).

According to Dalton's law (*John Dalton*, see box), the molar fractions in the vapor phase of a benzene–toluene mixture are related to the partial pressures and the total pressure, p , by:

$$y_{\text{benzene}} + y_{\text{toluene}} = \frac{p_{\text{benzene}}}{p} + \frac{p_{\text{toluene}}}{p} = 1 \quad (3.3.7)$$

Based on Eqs. (3.3.6) and (3.3.7), the relative volatility defined by Eq. (3.3.5) is given for an ideal mixture by:

$$\alpha_{\text{benzene,toluene}} = \left(\frac{y_{\text{benzene}}}{y_{\text{toluene}}} \right) \left(\frac{x_{\text{toluene}}}{x_{\text{benzene}}} \right) = \left(\frac{\frac{p_{\text{benzene}}}{p}}{\frac{p_{\text{toluene}}}{p}} \right) \left(\frac{\frac{p_{\text{toluene}}}{p_{\text{sat,toluene}}}}{\frac{p_{\text{benzene}}}{p_{\text{sat,benzene}}}} \right) = \frac{p_{\text{sat,benzene}}}{p_{\text{sat,toluene}}} \quad (3.3.8)$$

If we use the vapor pressure equation, Eq. (3.1.44), we can rewrite Eq. (3.3.8) as:

$$\alpha_{\text{benzene,toluene}} = \left(\frac{e^{-\frac{\Delta_{\text{vap}} S^0_{\text{benzene}}}{R}}}{e^{-\frac{\Delta_{\text{vap}} S^0_{\text{toluene}}}{R}}} \right) \frac{e^{\frac{\Delta_{\text{vap}} H^0_{\text{benzene}}}{RT}}}{e^{\frac{\Delta_{\text{vap}} H^0_{\text{toluene}}}{RT}}} \approx \text{constant} \times e^{\frac{(\Delta_{\text{vap}} H^0_{\text{benzene}} - \Delta_{\text{vap}} H^0_{\text{toluene}})}{RT}} \quad (3.3.9)$$

Thus strictly speaking, the relative volatility is always a function of temperature as the vaporization enthalpies are unlikely to be identical. However, if the values of $\Delta_{\text{vap}} H^0$ are approximately the same, we can use an average value for α . For example, $\alpha_{\text{benzene,toluene}}$ is 2.61 at 80 °C (boiling point of pure benzene at 1 bar) and 2.32 at 111 °C (boiling point of toluene), so we may use a mean value of 2.46. A stronger variation of α with the composition of the mixture is discussed in Example 3.3.2 for a mixture of methanol and water.

A useful simple equation for the vapor–liquid equilibrium can be derived as follows. Combination of the laws of Raoult and Dalton, Eqs. (3.3.6) and (3.3.7), yields:

$$p(y_{\text{benzene}} + y_{\text{toluene}}) = x_{\text{benzene}} p_{\text{sat,benzene}} + x_{\text{toluene}} p_{\text{sat,toluene}} \quad (3.3.10)$$

For the given binary system with $(y_{\text{toluene}} + y_{\text{benzene}}) = 1$ and $x_{\text{toluene}} = (1 - x_{\text{benzene}})$, the combination of Eq. (3.3.10) with Dalton's law [Eq. (3.3.7)] and Raoult's law [Eq. (3.3.6)] leads to:

$$\begin{aligned} y_{\text{benzene}} &= \frac{p_{\text{benzene}}}{p} = \frac{x_{\text{benzene}} p_{\text{sat,benzene}}}{x_{\text{benzene}} p_{\text{sat,benzene}} + (1 - x_{\text{benzene}}) p_{\text{sat,toluene}}} \\ &= \frac{x_{\text{benzene}} \frac{p_{\text{sat,benzene}}}{p_{\text{sat,toluene}}}}{1 + x_{\text{benzene}} \left(1 - \frac{p_{\text{sat,benzene}}}{p_{\text{sat,toluene}}} \right)} \end{aligned} \quad (3.3.11)$$

For a constant relative volatility, insertion of Eq. (3.3.8) into Eq. (3.3.11) finally yields:

$$y_{\text{benzene}} = \frac{\alpha_{\text{benzene,toluene}} x_{\text{benzene}}}{1 + x_{\text{benzene}} (\alpha_{\text{benzene,toluene}} - 1)} \quad (3.3.12)$$

François-Marie Raoult (1830–1901): A French chemist who discovered the depression of the freezing point of liquids by the presence of dissolved substances and found that the diminution of the vapor pressure of a solvent, caused by a substance dissolved in it, is proportional to the molecular weight of the substance dissolved. He also worked on phenomena of the voltaic cell.

The law of partial pressures, Eq. (3.3.7), was observed in 1801 by **John Dalton** (1766–1844), a British chemist and physicist. He worked on the constitution of mixed gases, on the vapor pressure of liquids, and on the thermal expansion of gases. His most important investigations are those concerned with the atomic theory in chemistry, which can be summarized as follows: (i) Elements are made of tiny particles called atoms. (ii) Atoms of a given element are identical and different from those of other elements. (iii) Atoms of one element can combine with atoms of other elements to form compounds that always have the same relative numbers of types of atoms. (iv) Atoms cannot be created, divided into smaller particles, or destroyed in the chemical process. These statements of *Dalton's theory* are to a large extent still true. Today we know that his statement "Atoms cannot be created, divided . . ." is inconsistent with nuclear fusion and fission, and his statement "All atoms of a given element are identical" is also not precisely true, as there are different isotopes of an element. *Dalton* also did research into color blindness, which is sometimes called *Daltonism* in his honor.

Figure 3.3.6 shows the exact solution of Eq. (3.3.12) with $\alpha_{\text{benzene, toluene}}$ varying from 2.61 to 2.32. Figure 3.3.7 gives solutions for different but constant values of α . For $\alpha < 1$, the plot represents the component that is less volatile.

Example 3.3.2: Vapor–liquid equilibrium curve for the system methanol and water

At a total pressure of 1 bar, a mixture of methanol and water boils in a range of 64.5 °C (pure methanol) to 100 °C. At a mean temperature of 82 °C, the vapor pressures of pure methanol and pure water are 194 and 51 kPa, respectively. Thus, the mean relative volatility $\alpha_{\text{methanol,water}}$ is 3.8, and by Eq. (3.3.12) we get the vapor–liquid equilibrium curve:

$$\gamma_{\text{methanol}} = \frac{3.8x_{\text{methanol}}}{1 + 2.8x_{\text{methanol}}} \quad (\text{for } p = 1 \text{ bar})$$

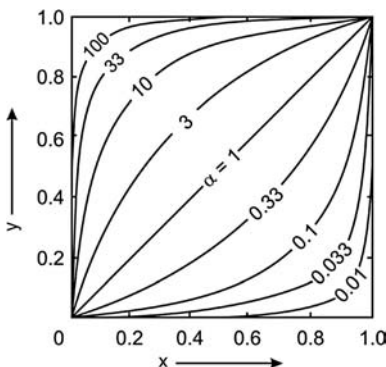


Figure 3.3.7 Liquid–vapor equilibrium for different values of the relative volatility.

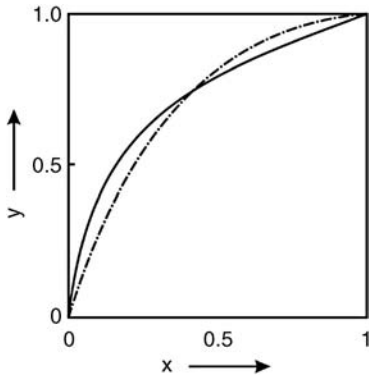


Figure 3.3.8 Vapor–liquid equilibrium data of the system methanol and water (1 bar, x and y are related to methanol as the reference component). Data from Gmehling and Brehm (1996); dashed line: approximation by Eq. (3.3.12) and $\alpha = 3.8$.

which is shown in Figure 3.3.8 (dashed curve). Table 3.3.3 gives the respective values of γ_{methanol} at different values of x_{methanol} and the corresponding boiling temperatures. For comparison, the true values considering real solution behavior are also given, indicating higher true values of γ_{methanol} for $x_{\text{methanol}} < 0.5$ and lower values for $x_{\text{methanol}} > 0.5$, but this effect is still not so significant as for mixtures that form an azeotrope, as discussed below.

For real mixtures and thus for deviations from ideality by dissimilar liquids, Raoult's law is obeyed only for the component in excess as it approaches purity. Note that "ideal solution" means something different than gas ideality. In a liquid mixture, there are always interactions, but in an ideal solution the A–B interactions are the same as the A–A and B–B interactions, as is almost the case for a mixture of benzene and toluene. Many systems deviate from ideal mixtures because the interactions of the molecules all differ. For marked deviations, this may completely upset the distillation process (azeotropic mixtures).

If, for example, the A–B interactions are stronger than the A–A and B–B interactions of the pure components, this leads to a stabilization of the liquid mixture and to a decrease of the vapor pressure for a given temperature compared to the ideal case. This in turn leads to a higher boiling point of the mixture, and we may even get a maximum in the bubble point curve. Such a system is called a high-boiling azeotrope [from the Greek words α (negation) $\zeta\sigma$ (boiling) $\tau\rho\pi\sigma\sigma$ (change), meaning "no change on boiling"], as shown in Figure 3.3.9c for the example of acetone and chloroform. Conversely, if the mixture is destabilized relative to an ideal solution, we may get a minimum in the boiling point curve (low-boiling azeotrope), as shown in Figure 3.3.9a for the example of a mixture of isopropyl alcohol and isopropyl ether.

The consequence for a distillation process is that if the azeotropic composition is reached (starting with a mixture with a composition either on the right- or left-hand side of this point) the vapor has the same composition as the liquid. Evaporation then occurs without any change in composition, and distillation can no longer separate the two liquids. In Section 3.3.2.3 we will learn how we can deal with azeotropes and still attain a separation.

Table 3.3.3 Vapor–liquid equilibrium of the binary mixture of methanol and water (1 bar). Data from Gmehling and Brehm (1996).

Molar content in the liquid phase (x_{methanol})	$T_{\text{boil}} (\text{°C})$	Molar content in the vapor phase γ_{methanol}	
		Exact solution considering real solution behavior	Approximation by Eq. (3.3.12) assuming an ideal mixture with $\alpha = 3.8$
0.1	88	0.41	0.30
0.3	78	0.67	0.62
0.5	73	0.79	0.79
0.7	69	0.88	0.90
0.9	66	0.96	0.97

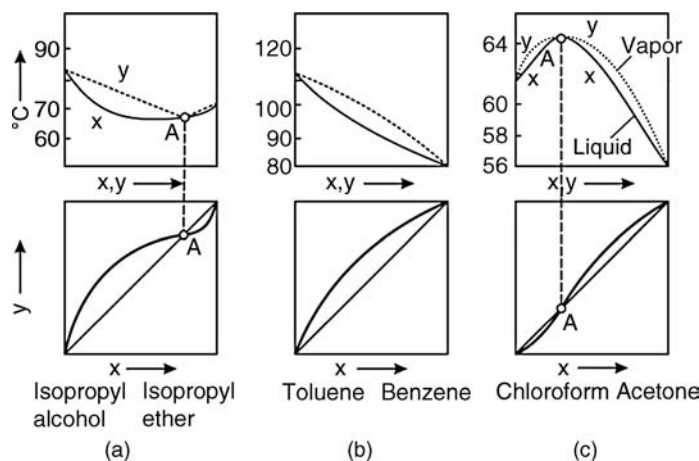


Figure 3.3.9 Isobaric liquid–vapor equilibrium of a low-boiling azeotrope (a) and a high-boiling azeotrope (c) at 1.013 bar; (b) an almost ideal solution for comparison.

3.3.2.2 Design of Distillation Columns (Ideal Mixtures)

A typical distillation column, as shown in Figure 3.3.10, is divided by trays into subsequent separation steps. In the ideal case, equilibrium is reached on each tray. The feed mixture with a certain molar content of the low-boiling component A ($x_{A,\text{feed}}$, for simplicity abbreviated as x_{feed} in Figure 3.3.10) is separated stepwise, and a vapor enriched in A ($y_{A,5}$) leaves the top of the column. After condensation, the distillate flow \dot{n}_d (with $x_{A,d} = y_{A,5}$) leaves the distillation unit, while a certain part is pumped back into the column as reflux, \dot{n}_{reflux} . The liquid flows down the column by gravity, and after intensive contact with the countercurrent upward flow of vapor (\dot{n}_g), a liquid product with flow \dot{n}_b and a certain remaining content of A, $x_{A,b}$, leaves the column at the bottom. The bottom section below the feed supply is called the stripping section of the column and the upper section is called rectification or enriching section.

The common design procedure of a distillation column is the McCabe–Thiele approach that was developed in 1925 by Warren L. McCabe and Ernest. W. Thiele by the combination of graphical methods with experimental data (McCabe and Thiele, 1925). The main parameter calculated by this graphical method is the number of theoretical equilibrium stages required for fractionating. The method is based on the assumption that the flow rates of the up-flowing vapor and down-flowing liquid in the stripping and in the rectification section are constant (although mostly different from each other). This implies that (i) the molar heats of vaporization of the components are the same and that (ii) heat effects (heats of solution, heat losses) are negligible, and thus for every mole of vapor condensed, 1 mol of liquid is vaporized.

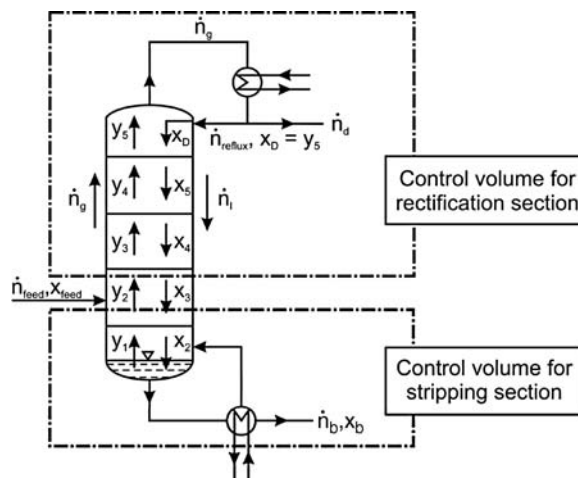


Figure 3.3.10 Distillation column and control volumes for the rectification and stripping section (x and y refer to lower-boiling feed component A, i.e., to x_A and y_A in the text).

The feed that enters a distillation column can be a vapor, a partially vaporized liquid, a saturated liquid, or a subcooled liquid. Here we only derive the respective mass balances by assuming that the feed is a saturated liquid, and thus the composition of the feed equals precisely the composition of the liquid in the column at the feed supply. For other cases, the vapor and liquid portions have to be considered in the mass and heat balances, and we refer to textbooks that specialize in thermal operation units.

The McCabe–Thiele approach for a binary mixture can be described as follows. First, we take the vapor–liquid equilibrium diagram (y/x plot). Then we draw the operating lines based on the mass balance for the liquid and the vapor phase. There is one operating line for the stripping section and one for the top (rectification or enriching) section. The assumption of (in each case) constant molar flows of liquid and vapor ensures strictly straight operating lines.

The operating line for the rectification section is derived as follows. The mass balance of liquid and vapor is (see control volume for rectification section in Figure 3.3.10):

$$\begin{aligned}\dot{n}_g &= \dot{n}_{\text{reflux}} + \dot{n}_d \\ &= \dot{n}_l + \dot{n}_d \quad (\text{for a constant heat of vaporization and no heat losses})\end{aligned}\quad (3.3.13)$$

where \dot{n}_g is the flow of the up-streaming vapor, \dot{n}_{reflux} the flow of liquid that is returned back to the column as reflux, and \dot{n}_d is the distillate flow that leaves the unit as top product (Figure 3.3.10). As we have assumed that the heat of vaporization does not depend on the composition of the liquid phase, the amount that vaporizes at every stage of the rectification section equals the amount that condenses. Thus \dot{n}_l , the flow of the down-streaming liquid, is constant and equals the reflux of the liquid (\dot{n}_{reflux}). For a mixture consisting of A and B, we rewrite Eq. (3.3.13) for the lower-boiling reference component A as follows:

$$y_A \dot{n}_g = x_A \dot{n}_l + x_{A,d} \dot{n}_d \Rightarrow y_A = x_A \frac{\dot{n}_l}{\dot{n}_g} + x_{A,d} \frac{\dot{n}_d}{\dot{n}_g} \quad (3.3.14)$$

The reflux ratio R is defined as the ratio of the reflux flow to the distillate flow:

$$R = \frac{\dot{n}_{\text{reflux}}}{\dot{n}_d} = \frac{\dot{n}_l}{\dot{n}_d} = \frac{\dot{n}_g - \dot{n}_d}{\dot{n}_d} = \frac{\dot{n}_g}{\dot{n}_d} - 1 \Rightarrow \frac{\dot{n}_d}{\dot{n}_g} = \frac{1}{R+1} \quad \text{and} \quad \frac{\dot{n}_l}{\dot{n}_g} = R \frac{\dot{n}_d}{\dot{n}_g} = \frac{R}{R+1} \quad (3.3.15)$$

and insertion of Eq. (3.3.15) into Eq. (3.3.14) yields the equation for the operating line of the rectification section:

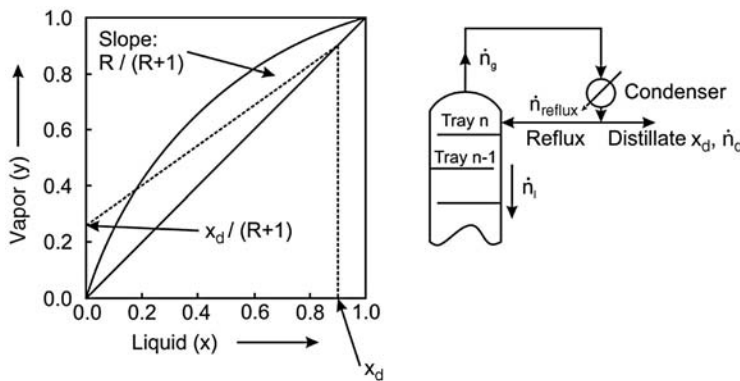
$$! \quad y_A = \frac{R}{R+1} x_A + \frac{1}{R+1} x_{A,d} \quad (3.3.16)$$

As shown by Figure 3.3.11, this operating line is represented for a given desired top product composition ($x_{A,d}$) and reflux ratio R by a line that intersects the diagonal line that splits the vapor–liquid equilibrium plot in half at a value of $y_A = x_{A,d}$, as required by Eq. (3.3.16) for $x_A = x_{A,d}$. The slope is $R/(R+1)$ – see Eq. (3.3.16) – and the operating line of the rectification section intersects the y-axis ($x_A = 0$) at $y_A = x_{A,d}/(R+1)$.

The operating line for the stripping section is constructed in a similar manner. The overall mass balance of liquid and vapor is (Figure 3.3.10):

$$\dot{n}_{\text{feed}} + \dot{n}_l = \dot{n}_g + \dot{n}_b \quad (3.3.17)$$

where \dot{n}_{feed} is the flow of feed entering the column, and \dot{n}_l is flow of the liquid coming from the rectification section. Thus the flow of liquid in the stripping section is by \dot{n}_{feed} higher than in the rectification section, \dot{n}_g is the flow of vapor that



streams upwards into the rectification section, and \dot{n}_b is the flow of the liquid leaving the column at the bottom (Figure 3.3.10).

With the assumption that the feed enters the column as saturated liquid with a composition equal to the liquid at the feed supply ($x_{A,\text{feed}} = x_A$), Eq. (3.3.17) can be rewritten for the lower-boiling compound A, and we obtain the equation for the operating line of the stripping section:

$$x_A(\dot{n}_{\text{feed}} + \dot{n}_l) = y_A \dot{n}_g + x_{A,b} \dot{n}_b \Rightarrow y_A = \frac{\dot{n}_l + \dot{n}_{\text{feed}}}{\dot{n}_g} x_A - \frac{\dot{n}_b}{\dot{n}_g} x_{A,b} \quad (3.3.18)$$

For $x_A = x_{A,b}$, Eq. (3.3.18) leads to:

$$y_A = x_{A,b} \frac{\dot{n}_l + \dot{n}_{\text{feed}} - \dot{n}_b}{\dot{n}_g} = x_{A,b} \quad (\text{for } x_A = x_{A,b}) \quad (3.3.19)$$

For $x_A = x_{A,\text{feed}}$, Eq. (3.3.18) yields:

$$y_A = \frac{x_{A,\text{feed}} \dot{n}_l + x_{A,\text{feed}} \dot{n}_{\text{feed}} - x_{A,b} \dot{n}_b}{\dot{n}_g} \quad (\text{for } x_A = x_{A,\text{feed}}) \quad (3.3.20)$$

With the insertion of the overall mass balance of the column:

$$x_{A,\text{feed}} \dot{n}_{\text{feed}} = x_{A,d} \dot{n}_d + x_{A,b} \dot{n}_b \quad (3.3.21)$$

into Eq. (3.3.20), we obtain:

$$! y_A = x_{A,\text{feed}} \frac{\dot{n}_l}{\dot{n}_g} + x_{A,d} \frac{\dot{n}_d}{\dot{n}_g} \quad (\text{for } x_A = x_{A,\text{feed}}) \quad (3.3.22)$$

For construction of the operating line of the stripping section, we take the desired bottom product composition as the starting point, and then draw a vertical line to the diagonal line as required by Eq. (3.3.22) ($y_A = x_{A,b}$ for $x_A = x_{A,b}$). From this point we draw a line with slope $(\dot{n}_l + \dot{n}_{\text{feed}})/\dot{n}_g$ according to the equation for the operation line of the stripping section [Eq. (3.3.18), see Figure 3.3.12].

At the point of feed supply ($x_A = x_{A,\text{feed}}$), Eq. (3.3.22) for the stripping section equals Eq. (3.3.14) for the rectification section, and the intersection is the point of transition between both sections.

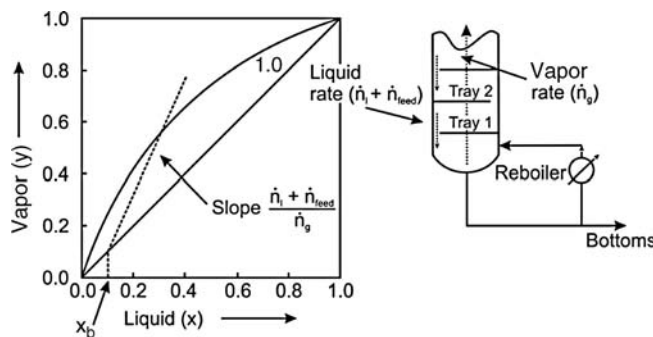


Figure 3.3.11 Construction of the operating line for the rectification section of a distillation column (x and y refer to lower-boiling feed component A, i.e., to x_A and y_A in the text).

Figure 3.3.12 Construction of the operating line for the stripping section of a distillation column (x and y refer to lower-boiling feed component A, i.e., to x_A and y_A in the text).

Figure 3.3.13 Details of the operating and equilibrium line (rectification section).

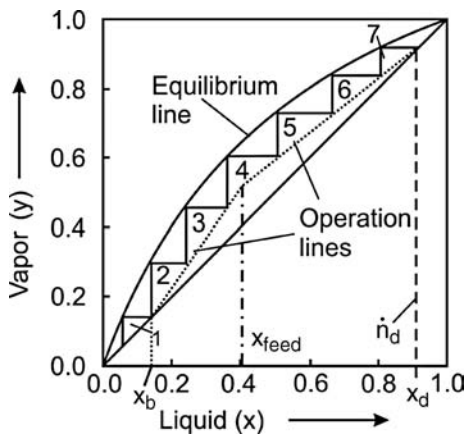
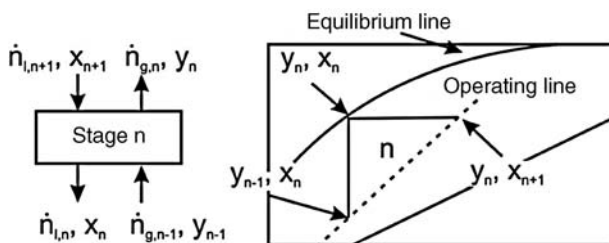


Figure 3.3.14 Graphical method to determine the number of theoretical stages of a column.

The McCabe-Thiele method assumes that the liquid on each tray and the vapor above it are in equilibrium, and that between the trays the molar composition of the down-flowing liquid and the up-flowing vapor are related by the operation lines, Eq. (3.3.16) for the rectification section and Eq. (3.3.18) for the stripping section (Figure 3.3.13).

Carrying out the graphical construction repeatedly leads to a number of corner sections, and each section is equivalent to a distillation stage. This McCabe-Thiele graphical design method is shown schematically in Figure 3.3.14 and examined in Example 3.3.3 for the separation of methanol from water. For the example shown in Figure 3.3.14, seven theoretical stages are required. The number of trays (as opposed to stages) is one less than the number of stages since the graphical construction includes the contribution of the reboiler (Figure 3.3.12, right-hand side).

The actual number of trays is the ratio of the number of theoretical trays to the tray efficiency:

$$n_{\text{tray}} = \frac{n_{\text{tray, theo}}}{\eta_{\text{tray}}} \quad (3.3.23)$$

The tray efficiency typically ranges from 0.5 to 0.7 and depends on several factors, such as the type of tray and the liquid and vapor flow conditions.

To characterize a distillation process, two border cases are often considered and calculated, namely, the minimum number of theoretical stages and the minimum reflux ratio:

- The minimum number of stages is achieved at total reflux, that is, when all the overhead vapor is condensed and returned. Consequently, the reflux ratio R is infinite. This, in turn, makes the operating lines equal to the diagonal line, and Eq. (3.3.16) reduces to:

$$y_A = x_A \quad (\text{for } R = \infty, \text{i.e. total reflux}) \quad (3.3.24)$$

- The minimum reflux condition represents the opposite of total reflux, and thus an infinite number of ideal separation stages.

The graphical procedure to determine the minimum number of stages and the minimum reflux ratio is examined in Example 3.3.3 for the system of methanol and water.

Figure 3.3.15 shows the internals of a typical distillation column.

Example 3.3.3: Reflux ratio and number of theoretical stages (for methanol and water)

A methanol–water mixture with 30 mol.% methanol needs to be separated by distillation at 1 bar. The vapor–liquid equilibrium is given in Example 3.3.2 by Figure 3.3.8. The boundary conditions are a content of 98 mol.% methanol in the distillate and 2 mol.% in the bottom product. What is the minimum reflux ratio R_{\min} and the minimum number of theoretical stages N_{\min} ? What is the number of theoretical stages for a reflux ratio of $1.4 R_{\min}$?

The minimum number of stages is reached for an infinite reflux ratio. With the operating line on the diagonal, we are as far as possible

from the equilibrium curve, which minimizes the number of stages. By graphical construction using the diagonal and the equilibrium curve, we find a minimum number of stages of five (four trays plus reboiler) (Figure 3.3.16a, dashed steps).

For R_{\min} , the operating line crosses the equilibrium curve for a molar methanol content in the liquid of x_{feed} . Thus, the distance between the equilibrium curve and the operating line is at its minimum. The stepping triangles become very small, there is no gap between the equilibrium curve and the intersection point, and thus

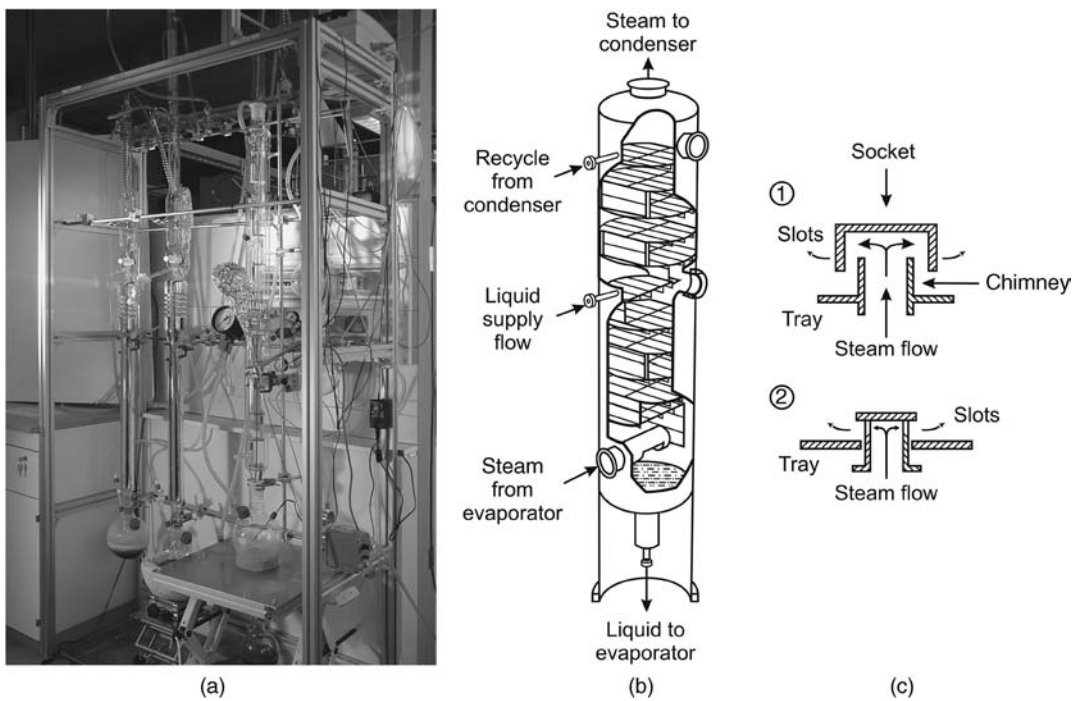


Figure 3.3.15 Distillation columns: (a) laboratory-scale, (b) industrial column, and (c) internals of a column (1: bubble cap trays, 2: valve trays. Adapted from Gmehling and Brehm (1996).

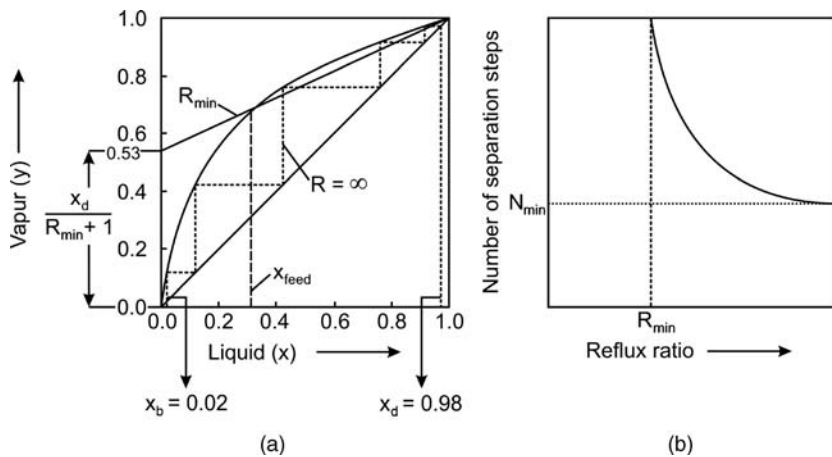


Figure 3.3.16 Graphical determination of (a) minimum reflux ratio and (b) minimum number of stages for the separation of methanol and water; x and y are related to methanol as the lower boiling point reference component. Data from Gmehling and Brehm (1996).

we cannot step past the feed point ($x = x_{\text{feed}}$). For our example, we obtain a value for the intercept with the y -axis at $y = 0.53$, and thus with the target value of x_d of 0.98 we have a minimum reflux ratio R_{\min} of 0.85. The general influence of the reflux ratio R on N is shown schematically in Figure 3.3.16b.

When designing columns, we have to choose a reflux ratio that is higher than R_{\min} . Depending on the operating costs (particularly energy costs) and investment costs, the cost optimum reflux ratio is typically in the range 1.1 to 1.5 R_{\min} . Figure 3.3.17 shows the principle of the method used to determine the optimum cost. For R_{\min} , the operating costs are low, but the investment costs would be infinite (infinite number of stages). For a high reflux ratio, we have the

opposite. Experience shows that a reflux R of about $1.2R_{\min}$ is a good design value.

In our example we have assumed a reflux ratio of $1.4R_{\min}$ ($= 1.19$). The respective diagram needed to determine the number of theoretical stages is given in Figure 3.3.18, from which we obtain eleven theoretical stages. As a rule of thumb, we take a value of 0.6 for the stage (tray) efficiency and by Eq. (3.3.23) we would finally calculate a practical number of stages of 18.

Table 3.3.4 gives typical numbers of stages of important distillation processes. The values show that more than 100 stages are seldom utilized in commercial processes.

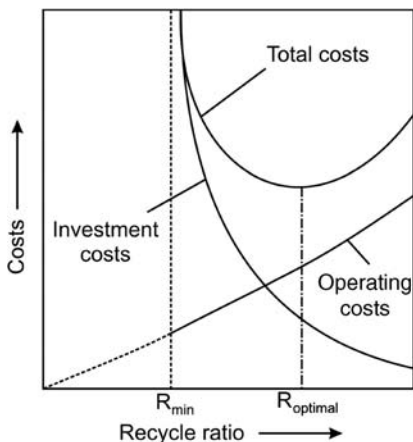


Figure 3.3.17 Principle of the method used to determine the cost optimum reflux ratio of a distillation.

Table 3.3.4 Typical numbers of stages of industrially important distillation processes. Data from Stichlmair and Fair (1976).

Components	Typical number of stages	Boiling points (at 1 bar)
Nitrogen/oxygen	100	-196/-183 °C
Crude oil (atmospheric column)	30 (100 including side columns)	0 to more than 500 °C
Ethylene/ethane	73	-104/-89 °C
Propylene/propane	138	-48/-42 °C
Benzene/toluene	40	80/111 °C
Toluene/xylanes	45	111/138-144 °C ^{b)}
<i>o</i> -Xylene/ <i>m</i> -xylene	130	144/138 °C
Methanol/formaldehyde	23	65/-21 °C
Acetic acid/water	40	118/100 °C
Ethanol/water	60	78/100 °C
Ethylene glycol/water	16	197/100 °C ^{a)} 1,2-Dimethylbenzene (<i>o</i> -xylene): 144 °C, 1,3-dimethylbenzene (<i>m</i> -xylene): 139 °C, 1,4-dimethylbenzene (<i>p</i> -xylene): 138 °C.

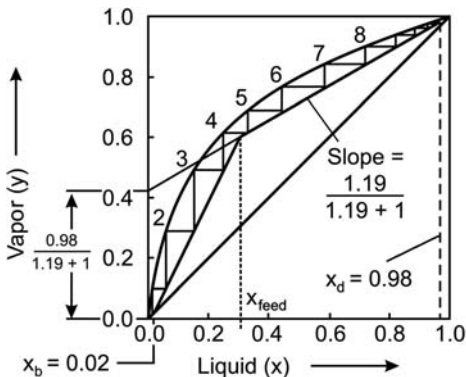


Figure 3.3.18 Graphical determination of the number of theoretical stages for a reflux ratio R of 1.19 ($= 1.4R_{\min}$) (distillation of a methanol–water mixture).

3.3.2.3 Azeotropic, Extractive, and Pressure Swing Distillation

The three methods used to break an *azeotrope* by means of distillation are azeotropic distillation, extractive distillation, and pressure swing distillation.

Azeotropic Distillation In azeotropic distillation, an entrainer is added to generate a new low-boiling azeotrope by changing the molecular interactions. The drawback is that at least one additional separation step is needed to remove the entrainer, which is recycled into the azeotropic distillation column. To ensure a simple separation of the entrainer, the new azeotrope should form two immiscible phases after condensation (heterogeneous azeotrope). For a homogeneous azeotrope, separation by extraction in combination with distillation is frequently needed.

An example of homogeneous azeotropic distillation is the system benzene and cyclohexane with acetone as entrainer (Figure 3.3.19). A binary mixture of benzene and cyclohexane forms an azeotrope at approximately equimolar composition (Figure 3.3.19a, dotted curve). By the addition of acetone, a new homogeneous azeotrope consisting of acetone and cyclohexane is formed as the distillate, and benzene is left as the bottom product (Figure 3.3.19a, dashed curve). Note that the values of $y_{C_6H_{12}}$ and $x_{C_6H_{12}}$ given in Figure 3.3.19 still refer to the binary system without counting the entrainer acetone. The new azeotrope is separated by extraction with water, whereby acetone is dissolved in water and simultaneously a cyclohexane phase is formed. The acetone–water mixture is separated by distillation and acetone and water are recycled into the azeotropic distillation column and into the extraction unit, respectively.

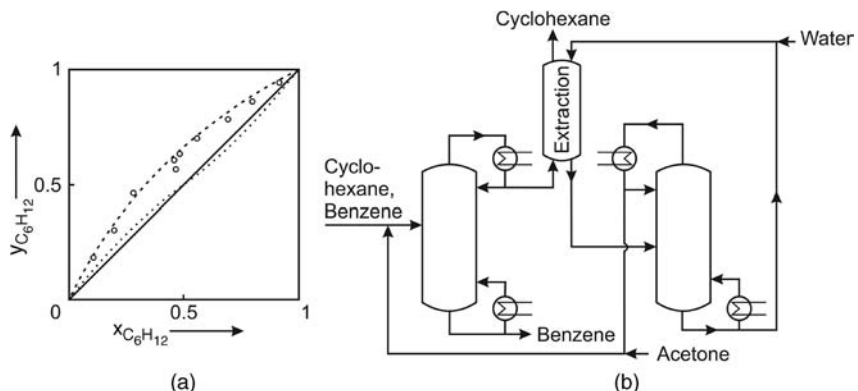


Figure 3.3.19 Homogeneous azeotropic distillation of cyclohexane and benzene at 1 bar: (a) y - x -diagram in mol.% without (dotted line) and with (short-dashed line) addition of 50 mol.% acetone; note that the content of acetone is not counted, that is, $x_{C_6H_6} = 1 - x_{C_6H_{12}}$. Adapted from Emmons *et al.* (1974). (b) Typical process configuration. Adapted from Gmehling and Brehm (1996).

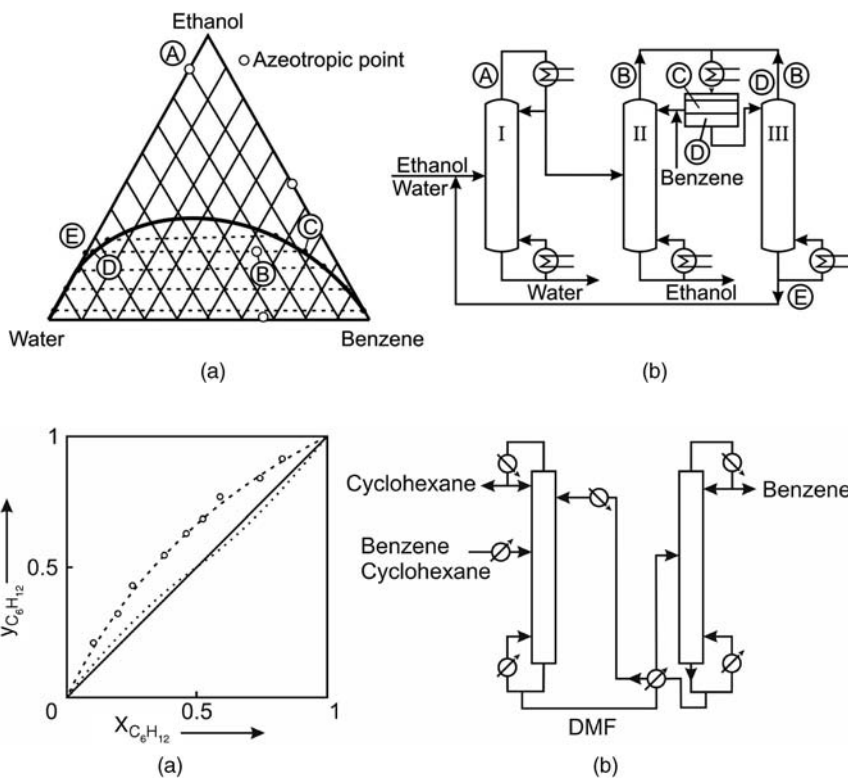


Figure 3.3.20 Heterogeneous azeotropic distillation of ethanol and water at 1 bar with benzene as entrainer (concentration in molar content). Adapted from Gmehling and Brehm (1996).

An example of heterogeneous azeotropic distillation is the system ethanol and water with benzene as entrainer (Figure 3.3.20). In a first column (without entrainer, column I in Figure 3.3.20b), the binary ethanol–water mixture is separated by normal distillation. An azeotrope with about 90 mol.% ethanol (96 wt%) leaves the column on top (A) while water forms the bottom product. The azeotrope is fed to a second column where benzene (recycle of a phase rich in benzene from the separator of the top products of column II and III) is added as entrainer. A new low-boiling heterogeneous azeotrope (B) leaves column II as distillate, and pure ethanol remains as bottom product. After condensation, the heterogeneous azeotrope separates into two phases rich in either benzene (C) or water (D). The phase rich in benzene is recycled back into column II while the phase rich in water is reconditioned in a third column by distillation. The small amount of benzene is separated as top product (azeotrope B), and a mixture of ethanol and water (E) is recycled into column I.

Extractive Distillation For extractive distillation, a miscible high-boiling solvent is added that interacts with the components of the mixture and changes their relative volatilities as shown in Figure 3.3.21a, again for the example of a mixture of cyclohexane and benzene. The equilibrium curve is shifted and the azeotropic point vanishes. The component with the higher volatility (here cyclohexane) leaves the column as distillate. The bottom product consists of the solvent and the second component (benzene), which is separated by distillation (Figure 3.3.21b).

Pressure Swing Distillation The third method to break an azeotrope is pressure swing distillation, which relies on the fact that the location of the azeotropic point depends in some cases relatively strongly on the total pressure. In contrast to extractive or azeotropic distillation, the azeotrope is not broken by a solvent, but is jumped over by altering the pressure, and thus the distillation can continue. For example, the system tetrahydrofuran (THF) and water is at first distilled at 1 bar up to approximately 80% THF (Figure 3.3.22a), that is, just before the azeotropic point is reached. The distillate rich in THF with a composition close to the azeotropic

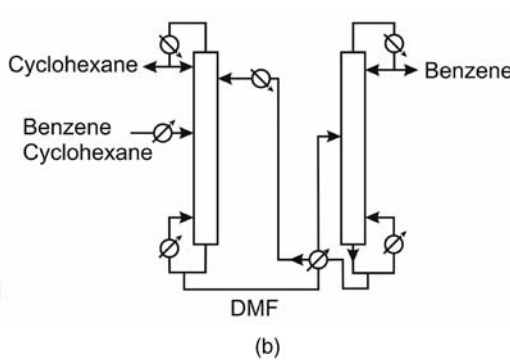


Figure 3.3.21 Extractive distillation of the azeotropic system cyclohexane and benzene at 1 bar: (a) y - x diagram without (dotted line) and with (short-dashed line) addition of 50 mol.% dimethylformamide (DMF); note that the content of DMF is not counted, that is, $x_{C_6H_{12}} = 1 - x_{C_6H_{12}}$; (b) typical process configuration. Adapted from Gmehling and Brehm (1996).

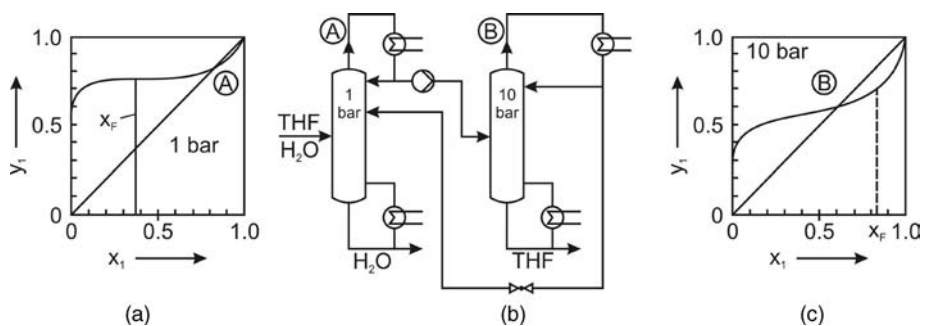


Figure 3.3.22 (a)–(c) Pressure swing distillation of the system tetrahydrofuran (1, THF) and water (2) (Gmehling and Brehm, 1996).

point at 1 bar is then sent to a second distillation column that operates at 10 bar, which shifts the azeotropic point down to about 60% (Figure 3.3.22c). Since the mixture is already above this new azeotropic point, the distillation continues, and water can be distilled to whatever concentration is needed, that is, almost pure THF leaves the column as bottom product.

3.3.2.4 Reactive Distillation

In reactive distillation, both the chemical reaction and the distillative separation of the product mixture are carried out simultaneously. This integrative strategy allows us to overcome chemical equilibrium limitations. For an exothermic reaction, the heat of reaction can be used directly for distillation. The term catalytic distillation is also used for such systems where a catalyst (homogeneous or heterogeneous) is used to accelerate the reaction. The synthesis of methyl acetate and MTBE (methyl tertiary butyl ether) are the two most prominent examples, where reactive distillation is used on an industrial scale (for MTBE see Section 4.10.8.1). It is beyond the scope of this textbook to discuss more details of this technology. Details can be found in the literature (Sundmacher and Kienle, 2002; Harmsen, 2007; Taylor and Krishna, 2000; Krishna, 2002; Stankiewicz, 2003).

3.3.3

Absorption (Gas Scrubbing)

3.3.3.1 Absorption Principles

During absorption, a gas component is selectively dissolved by contact with a liquid in which the component is soluble. Absorption is used for scrubbing gas streams from components such as CO_2 , H_2S , SO_2 , and NH_3 . Gas scrubbers are not only applied for emission control and separation of unwanted gas components but also to separate valuable products selectively from a gas stream, for example, SO_3 in sulfuric acid production.

Absorption may be either physical or chemical (or a combination of both). Physical absorption involves the solubility and the vapor-pressure relationships. Chemical absorption involves a reaction of the primarily physically absorbed solute with the absorbing medium. Thus, chemical absorption always combines with physical absorption, as visualized in Figure 3.3.23 for the chemical absorption of CO_2 and H_2S in an amine solution.

The influence of the partial pressure of the solute on its equilibrium content in the solvent, the loading X_{abs} , is shown in Figure 3.3.24 for a physical absorption of CO_2 in water and methanol and a chemical absorption in an aqueous solution of monoethanolamine (MEA).

Chemical solvents are used if the partial pressure of the undesired component is low as a high loading of the solvent is then already reached (Figure 3.3.24a for monoethanolamine). Thus, in a continuous scrubbing process with a

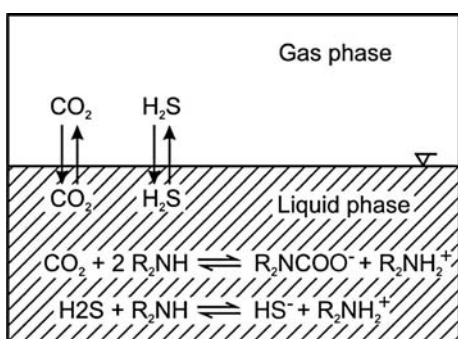


Figure 3.3.23 Equilibria of chemical absorption of CO_2 and H_2S in an amine solution.

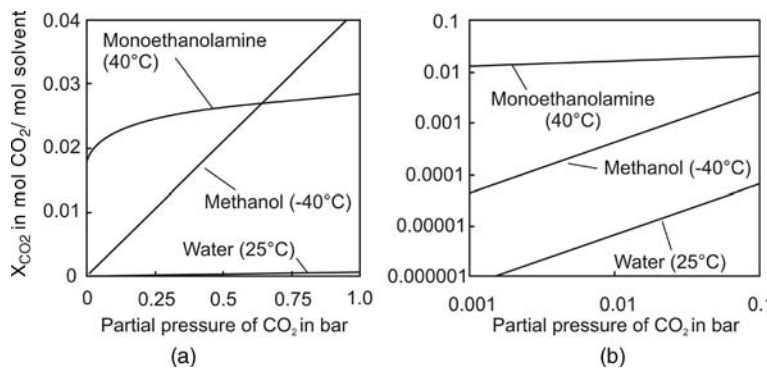


Figure 3.3.24 Comparison of equilibria of physical absorption (a) of CO₂ in water and methanol and chemical absorption (b) in an aqueous solution of monoethanolamine (MEA) with 2 kmol MEA m⁻³.

countercurrent flow of gas and liquid, a very low outlet content of the unwanted component in the gas stream can be reached. For a high partial pressure of the undesired compound, physical solvents are advantageous, as shown in Figure 3.3.24 for the absorption of CO₂ in methanol, but the outlet content in the scrubbed gas is then limited to about 0.1 vol.%.

For physical absorption of a gaseous component A, *Henry's law* is mostly used, named after *William Henry* (see box):

$$p_A = H_{A,x} x_A = H_{A,x} \frac{n_{A,\text{dissolved}}}{n_{\text{liquid}}} = H_{A,x} \frac{n_{A,\text{dissolved}}}{n_{\text{solvent}} + n_{A,\text{dissolved}}} = H_{A,x} \frac{X_A}{1 + X_A} \quad (3.3.25)$$

whereby x_A is the molar content of the solute in the liquid (consisting of solvent and solute) and $H_{A,x}$ is the Henry coefficient in Pa or bar. Strictly speaking, Henry's law is only valid if the concentration of the solute is small, that is, if we approach infinite dilution and the molar content of the solute in the liquid x_A approaches the loading of the solvent with solute X_A (see Example 3.3.4 for more details). Table 3.3.5 gives selected values of $H_{A,x}$.

Table 3.3.5 Henry coefficients for different gases. Data for SO₂–water and SO₂–H₂SO₄ from Simecek *et al.* (1969) and for CO₂/H₂S–methanol or N-methylpyrrolidone from Schmidt (1970).

Gas	Liquid solvent	T (°C)	H_x [Eq. (3.3.25)] (bar mol _{liq} mol _{gas} ⁻¹)
He	Water	25	152 000
H ₂			71 000
N ₂			87 000
O ₂			44 000
CO			59 000
CO ₂			1600
H ₂ S			600
CH ₄			42 000
C ₂ H ₆			31 000
C ₂ H ₄			12 000
H ₂	Benzene	25	3700
N ₂			2400
CO ₂			100
CH ₄			600
H ₂	Hexane	25	1400
CO ₂	Methanol	20	153
CO ₂		-40	25
H ₂ S		20	34
H ₂ S		-40	6
CO ₂	N-Methylpyrrolidone	20	57
H ₂ S		20	6
SO ₂	Water	20	33
	H ₂ SO ₄ (50 wt%)		38
	H ₂ SO ₄ (84.5 wt%)		32
	H ₂ SO ₄ (100 wt%)		16

William Henry (1775–1836), an English chemist who studied medicine at Edinburgh, but when ill-health interrupted his practice as a physician he devoted his time to chemical research. One of his best-known papers describes experiments on the quantity of gases absorbed by water at different temperatures and under different pressures. His results are known today as Henry's law. Other works deal with gas-analysis, fire-damp, illuminating gas, and the composition of hydrochloric acid and of ammonia.

Example 3.3.4: Absorption of CO₂ in water and subsequent bicarbonate formation

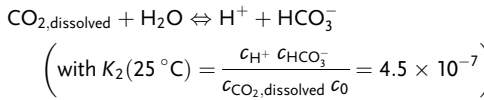
Henry's law is only valid if we approach infinite dilution, but is still in many cases a good approximation even for higher concentrations, typically up to a molar content of the solute of 20%. For a higher content, we increasingly approach Raoult's law (Figure 3.3.25). In addition, chemical reactions occurring in the liquid are not considered by Henry's law. We may inspect this for CO₂ absorption in pure water (25 °C), which can be described by:



$$\left(\text{with } K_1 = \frac{c_{\text{CO}_2,\text{dissolved}}}{p_{\text{CO}_2}} \approx \frac{1}{H_{\text{CO}_2,\text{H}_2\text{O}} v_{\text{mol},\text{H}_2\text{O}}} \right)$$

The molar volume of water $v_{\text{mol},\text{H}_2\text{O}}$ is $1.8 \times 10^{-5} \text{ m}^3 \text{ mol}^{-1}$, and the Henry coefficient of CO₂ in water (25 °C) is 1600 bar. Thus K_1 is $34.7 \text{ mol m}^{-3} \text{ bar}^{-1}$.

Some of the dissolved CO₂ reacts (via the unstable H₂CO₃) to bicarbonate (HCO₃⁻):



Combination of these equations ($c_0 = 1 \text{ mol l}^{-1}$, $c_{\text{HCO}_3^-} = c_{\text{H}^+}$) leads to:

$$c_{\text{HCO}_3^-} = \sqrt{K_1 K_2 c_0 p_{\text{CO}_2}} = 0.125 \text{ mol m}^{-3} \text{ bar}^{-0.5} \sqrt{p_{\text{CO}_2}}$$

For example, a CO₂ partial pressure of 10 bar leads to a bicarbonate concentration of only about 0.4 mol m^{-3} compared to the concentration of physically dissolved CO₂ (according to Henry's law) of 347 mol m^{-3} . Thus the portion of CO₂ in water that exists in the form of bicarbonate is only about 0.1% and, therefore, is negligible. Note that this changes for a low partial pressure, for example, for ambient air in contact with water.

Then the CO₂ partial pressure is only 0.37 mbar, and the bicarbonate concentration is $0.0024 \text{ mol m}^{-3}$ compared to the concentration of physically dissolved CO₂ of 0.013 mol m^{-3} . Thus the portion of CO₂ in water that exists as bicarbonate is then about 16% [$= 0.0024 / (0.013 + 0.0024)$].

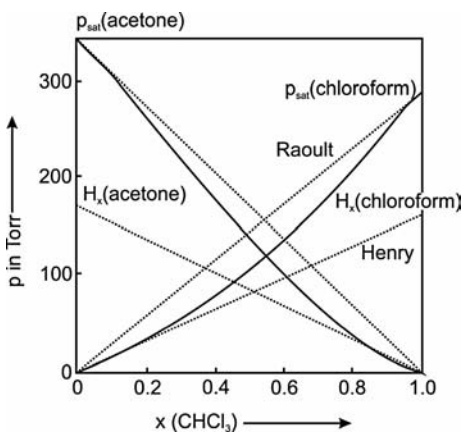


Figure 3.3.25 Partial vapor pressures of a mixture of chloroform and acetone (Atkins, 2002).

In most cases, the gas solubility decreases with increasing temperature, that is, H_x increases. An exception is hydrogen, where the solubility in hydrocarbons increases with temperature.

Note that Henry's constant is expressed in various other units, for example, in conjunction with kinetic equations for gas–liquid systems (Section 4.4). If the gas phase concentration is denoted in pressure units (Pa) and the liquid phase concentration in molarity (mol m⁻³), a different unit for Henry's constant is obtained ($H_{A,c} = p_A/c_A, \text{ Pa m}^3 \text{ mol}^{-1}$). If both the liquid and the gas phase concentrations are expressed as molar fractions, a dimensionless value is obtained for Henry's constant. Therefore, be careful in noting the correct units obtained from the literature. In addition, note that in older literature an absorption coefficient is frequently used, for example, the *Bunsen* absorption coefficient α_{Bu} (in $\text{m}^3 \text{ m}^{-3} \text{ bar}^{-1}$) defined as the volume of gas (at 1.013 bar and 0 °C) absorbed by one volume of liquid at a certain pressure, for example, 1 bar. Thus α_{Bu} is inversely proportional to H_x and equivalent to the term $\rho_{\text{mol,liq}} 0.0224 \text{ m}^3 \text{ mol}^{-1} / H_x$.

For the rare case of an ideal mixture, the forces of attraction between solute and solvent equal the attractive forces in the mixture. Then Raoult's law, Eq. (3.3.6), is even valid for a high dilution, and the vapor pressure of the pure solute $p_{A,\text{sat}}$ (also denoted as $p_{A,*}$) equals $H_{A,x}$:

$$p_A = x_A p_{A,\text{sat}} = x_A H_{A,x} \Rightarrow p_{A,\text{sat}} = H_{A,x} \quad (\text{for ideal systems}) \quad (3.3.26)$$

In reality, we mostly have strong deviations from Eq. (3.3.26), as shown in Figure 3.3.25 for the example of chloroform and acetone at 35 °C (Table 3.3.6).

The deviation from non-ideal behavior of solute and solvent is discussed in Topic 3.3.2.

Table 3.3.6 Activity and activity coefficients of chloroform in acetone at 35 °C both on the basis of Raoult's law and of Henry's (see also Figure 3.3.25). Data from Atkins (2002).)

Molar fraction of chloroform $x_{\text{chloroform}}$	Raoult's law activity a_{Raoult}	Raoult's law activity coefficient γ_{Raoult}	Henry's law activity a_{Henry}	Henry's law activity coefficient $\gamma_{\text{Henry}}^{\text{a}}$
0	0	—	0	1
0.2	0.12	0.6	0.21	1.05
0.4	0.28	0.7	0.50	1.25
0.6	0.49	0.82	0.86	1.43
0.8	0.75	0.94	1.33	1.66
1.0	1.00	1.00	1.78	1.79

^aNote that the combination of Eq. (3.3.27) and (3.3.28) yields $\gamma_{\text{Henry}} = \gamma_{\text{Raoult}}(p_{\text{sat}}/H_A)$.

Topic 3.3.2 Solvent and solute activity

For non-ideal mixtures, the activity is used, a kind of effective molar fraction. Thereby, we have to distinguish between the activity of the solvent and activity of the solute.

Solvent Activity

In the case of a component that is in excess, all solvents obey Raoult's law [Eq. (3.3.6)] increasingly closely as they approach purity (for a solvent A this means $x_A \rightarrow 1$), as shown in Figure 3.3.25 for the example of chloroform. For $x_A < 1$, a convenient way to express the deviation from Raoult's law is to introduce an activity a_A and an activity coefficient γ_A , and instead of Raoult's law for ideal mixtures we use:

$$p_A = a_A p_{A,\text{sat}} = \gamma_A x_A p_{A,\text{sat}} \quad (3.3.27)$$

For $x_A \rightarrow 1$ (pure solvent), $a_A \rightarrow x_A$ and $\gamma_A \rightarrow 1$.

Solute Activity

In the case of a component being present only in a very low concentration, all solutes obey Henry's law [Eq. (3.3.26)] increasingly closely as they approach a molar fraction of zero (e.g., for a solute B $x_B \rightarrow 0$), as also shown in Figure 3.3.25 for the example of chloroform. For $x_A > 0$, a convenient way to express the deviation from Henry's law is to introduce an activity a_B and an activity coefficient γ_B for the solute, and instead of Henry's law we get:

$$p_B = a_B H_{B,x} = \gamma_B x_B H_{B,x} \quad (3.3.28)$$

For $x_B \rightarrow 0$ (infinite dilution), $a_B \rightarrow x_B$ and $\gamma_B \rightarrow 1$.

For practical applications, the loading X_A in mol solute per mol solvent (liquid phase *without* dissolved A) is frequently used instead of the molar content x_A (mol of dissolved A per mol liquid consisting of solvent *and* dissolved A). Analogously, the loading of the gas Y_A (mol A per mol of gas *without* A) is used instead of the molar content y_A (mol of gaseous A per mol of *total* gas phase). Rewriting Eq. (3.3.25) leads to:

$$p_A = \frac{n_{A,g}}{n_{A,g} + n_{g,\text{without } A}} p = \frac{Y_A}{1 + Y_A} p = H_{A,x} \frac{X_A}{1 + X_A} \Rightarrow X_A = \frac{p_A}{H_{A,x} - p_A} \quad (3.3.29)$$

and by rearrangement we get Y_A as a function of X_A and vice versa:

$$Y_A = \frac{X_A H_{A,x}}{p(1 + X_A) - X_A H_{A,x}} \quad (3.3.30a)$$

$$X_A = \frac{Y_A p}{H_{A,x}(1 + Y_A) - Y_A p} \quad (3.3.30b)$$

Figure 3.3.26 Physical absorption of CO₂ in methanol (-40°C): comparison of molar content x_{CO_2} and loading X_{CO_2} .

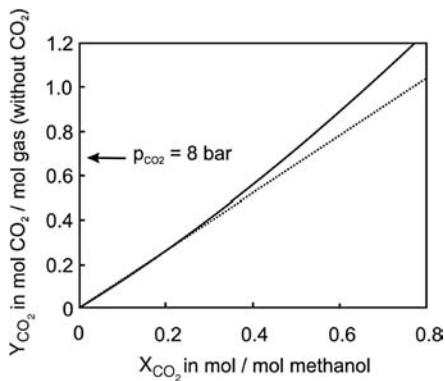
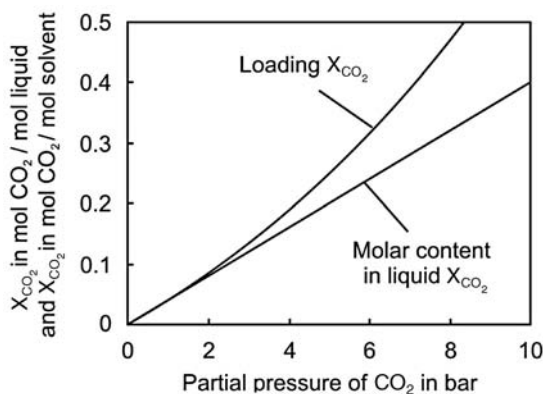


Figure 3.3.27 Loading diagram of physical CO₂ absorption in methanol (-40°C , $p_{\text{total}} = 20$ bar).

If p_A is low compared to $H_{A,x}$ [Eq. (3.3.27)], the plot of X_A versus p_A gives a straight line. This is shown in Figure 3.3.26 for the example of physical absorption of CO₂ in methanol. For a partial pressure of CO₂ of less than about 2 bar, which is still low compared to $H_{\text{CO}_2, \text{methanol}}$ of 25 bar (-40°C), the molar content x_{CO_2} still almost equals X_{CO_2} (Figure 3.3.26, deviation <10%), but for higher partial pressures we get an increasingly stronger deviation.

The plot of Y_A versus X_A , which is frequently used for the design of an absorption process (Section 3.3.3.2), is in general also not a straight line (Figure 3.3.27), but deviation from the line representing the initial slope (dashed line in Figure 3.3.27) is smaller (here <10% up to p_{CO_2} of 8 bar) compared to the corresponding plot of X_{CO_2} versus p_{CO_2} (Figure 3.3.26).

Chemical absorption and its quantitative description are complicated compared to physical absorption as we have to consider physical absorption as well as the equilibria of chemical reactions. Here, only the example of chemical absorption of CO₂ is examined (Example 3.3.5).

Example 3.3.5: Chemical absorption of CO₂ in N-methyldiethanolamine (MDEA)

The absorption of CO₂ in an aqueous solution of *N*-methyldiethanolamine (MDEA, CH₃NH[(CH₃)₂OH]₂) can be described by the following overall reaction:



To describe this absorption system, we have to consider the following reaction steps with K_i as respective equilibrium constant:

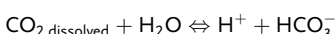
- 1) **Physical absorption of CO₂:** If we assume that the physical absorption in the aqueous solution is equivalent to absorption in pure water, we can use the Henry coefficient in water ($H_{\text{CO}_2, \text{H}_2\text{O}} = 2000$ bar at 40°C):



$$\left[\text{with } K_1(40^{\circ}\text{C}) = \frac{c_{\text{CO}_2, \text{dissolved}}}{p_{\text{CO}_2}} \approx \frac{1}{H_{\text{CO}_2, \text{H}_2\text{O}} v_{\text{mol}, \text{H}_2\text{O}}} \right]$$

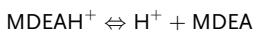
The molar volume of water $v_{\text{mol}, \text{H}_2\text{O}}$ is $1.8 \times 10^{-5} \text{ m}^3 \text{ mol}^{-1}$, and thus K_1 is $27.8 \text{ mol m}^{-3} \text{ bar}^{-1}$.

- 2) **Reaction of dissolved CO₂ (via the unstable H₂CO₃) to bicarbonate (HCO₃⁻):**



$$\left[\text{with } K_2(40^{\circ}\text{C}) = \frac{c_{\text{H}^+} c_{\text{HCO}_3^-}}{c_{\text{CO}_{2, \text{dissolved}}} c_0} = 5 \times 10^{-7}; c_0 = 1 \text{ mol l}^{-1} \right]$$

- 3) **Dissociation of MDEAH⁺ ions (formed by MDEA hydrolysis to MDEAH⁺ + OH⁻):**



$$\left[\text{with } K_3(40^{\circ}\text{C}) = \frac{c_{\text{H}^+} c_{\text{MDEA}}}{c_{\text{MDEAH}^+} c_0} \approx 5.6 \times 10^{-9}, \text{ Xu et al., 1998} \right]$$

Combination of all three equations leads to:

$$c_{\text{HCO}_3^-} = \frac{K_1 K_2 p_{\text{CO}_2} c_{\text{MDEA}}}{K_3 c_{\text{MDEAH}^+}}$$

If we consider that the overall concentration of MDEA, $c_{\text{MDEA, total}}$, is given by the term $(c_{\text{MDEA}} + c_{\text{MDEAH}^+})$ and that – according to the overall

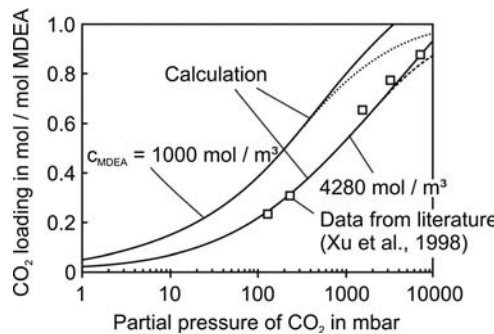


Figure 3.3.28 Chemical absorption of CO₂ in MDEA (methyldiethanolamine) (40 °C, c_{MDEA} = 1000 and 4280 mol m⁻³; dashed and dotted lines: calculation without physically dissolved CO₂).

reaction – equimolar amounts of bicarbonate and non-dissociated amine are formed ($c_{\text{HCO}_3^-} = c_{\text{MDEAH}^+}$), we get after rearrangement:

$$c_{\text{HCO}_3^-} = \sqrt{2C p_{\text{CO}_2} c_{\text{MDEA, total}} + C^2 p_{\text{CO}_2}^2} - C p_{\text{CO}_2} \quad (\text{with } C = \frac{K_1 K_2}{2K_3})$$

For the given system, the value of the constant C (at 40 °C) is 1240 mol m⁻³ bar⁻¹. Figure 3.3.28 shows the results of the calculation for $c_{\text{MDEA, total}} = 4280$ and 1000 mol m⁻³. For comparison, values given in

the literature (for 4280 mol m⁻³) are also shown, indicating that the calculation is quite accurate. Note that the contribution of the physically absorbed CO₂ to the overall absorption is rather negligible, for example, only about 280 mol m⁻³ = 0.06 mol CO₂ per mol MDEA for $p_{\text{CO}_2} = 10$ bar compared to about 0.9 mol CO₂ overall per mol MDEA. The same is true for the contribution of CO₃²⁻ ions (dissociation of HCO₃⁻) as well as for H₂CO₃, which is strongly unstable and practically completely dissociates to HSection 3.2.2.3 and HCO₃⁻.

3.3.3.2 Design of Absorption Columns

Table 3.3.7 lists examples of absorption processes. Absorption is usually carried out in columns (Figure 3.3.29), and the loaded solvent is regenerated in a desorber by an increase of temperature, decrease of pressure, or by stripping, and is then recycled to the absorber.

Gas scrubbers are operated in countercurrent flow and are typically equipped with structured packings or trays. The degree of removal of gaseous components depends on their solubility in the liquid absorption agent and thus on pressure and temperature, and on the liquid-to-gas ratio, which is defined as the ratio of the carrier fluid flow to the gas flow. For the design of an absorption column, the McCabe-Thiele approach is used, as already examined for distillation in Section 3.3.2.2.

Table 3.3.7 Examples of technical absorption processes.

Absorbed gas (solute)	Absorption agent (solvent)
Chemical absorption	
CO ₂	Hot potash solution (K ₂ CO ₃)
CO ₂ , H ₂ S (syngas, natural gas)	Mono-, di- and triethanolamine (MEA, C ₂ H ₇ NO; DEA, C ₄ H ₁₁ NO ₂ ; TEA, C ₆ H ₁₅ NO ₃); diisopropanolamine (DIPA, C ₆ H ₁₅ NO ₂); N-Methyldiethanolamine (MDEA, C ₇ H ₁₃ NO ₂); mixture of DIPA and sulfolane (C ₄ H ₈ O ₂ S)
Physical absorption	
CO ₂ , H ₂ S (syngas, natural gas)	Methanol, N-methylpyrrolidone (C ₅ H ₉ NO)
HCl	Water
NH ₃ (coke oven gas, syngas)	Di- and triethylene glycol (C ₄ H ₁₀ O ₃ , C ₆ H ₁₄ O ₄)
Ethylene oxide	
Water vapor (drying of natural gas)	
NO ₂ (production of nitric acid)	Water
SO ₃ (production of sulfuric acid)	Sulfuric acid

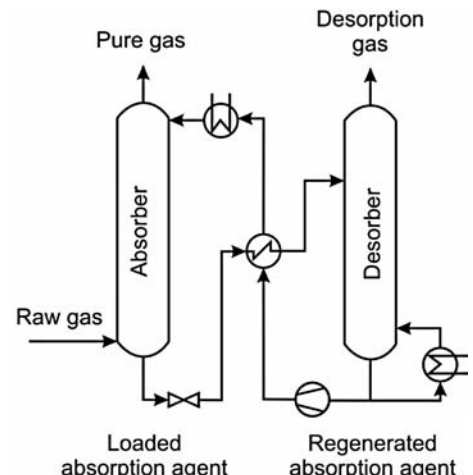


Figure 3.3.29 Typical absorption process. Adapted from Gmehling and Brehm (1996).

To derive the operating line and the number of separation stages, we make the following simplifying assumptions and definitions:

- Only one component is absorbed. Thus the flow rate of the carrier gas, \dot{n}_g , which is the total gas flow minus the usually small flow of the absorbed component, is constant.
- The vapor pressure of the absorption agent and thus a transfer into the gas phase is negligible, and the flow of liquid (without absorbed gas), \dot{n}_l , is constant.
- Y_A is the loading of the carrier gas with the absorbed gaseous component A (mol mol^{-1}), and X_A is the loading of the liquid absorption agent (mol mol^{-1}). Note that in contrast to distillation, where the molar content in the total vapor (y_A) and in the total liquid phase (x_A) is used, loadings are typically used for absorption. However, the differences of Y_A and X_A compared to y_A and x_A are negligible if the content of the absorbed component is small.

Contrary to distillation, only one single operating line is needed for design of the absorption column. The gas enters the column at the bottom and the absorption agent is supplied on top, so we do not have to consider two sections with different flow rates of gas and liquid as in case of distillation. Hence in total, we need two lines, the equilibrium and the operating line.

The equilibrium line (or curve) of the physical or chemical absorption is either known, as shown in Figure 3.3.27 for the example of physical absorption of CO_2 in methanol, or can be calculated for physical absorption by the Henry coefficient [Table 3.3.5, Eq. (3.3.25)], or by respective equations for the case of chemical absorption (Example 3.3.5).

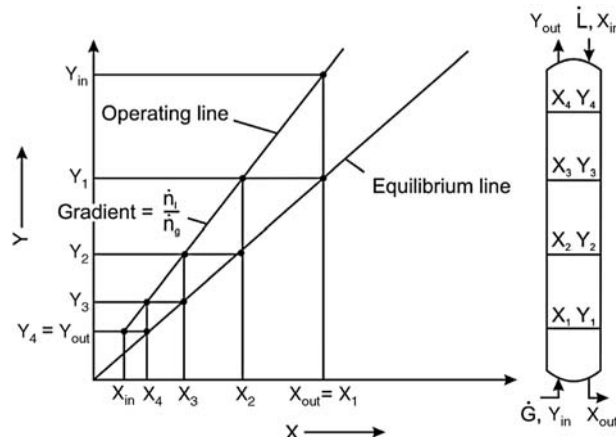
The operating line is derived by a mass balance for the absorbed gas component A:

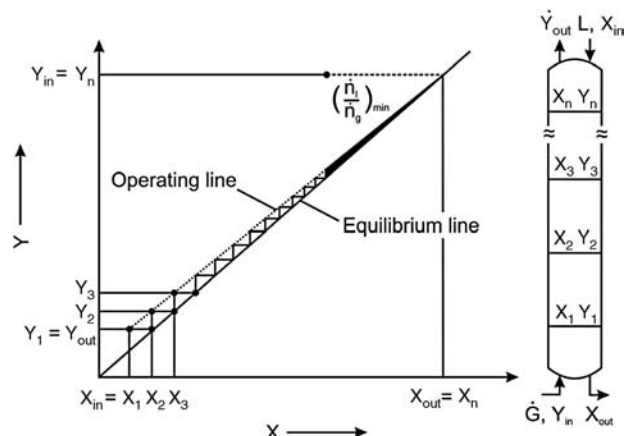
$$\bullet \quad (Y_{A,\text{in}} - Y_{A,\text{out}})\dot{n}_g = (X_{A,\text{out}} - X_{A,\text{in}})\dot{n}_l \Rightarrow Y_{A,\text{out}} = Y_{A,\text{in}} - \frac{\dot{n}_l}{\dot{n}_g}(X_{A,\text{out}} - X_{A,\text{in}}) \quad (3.3.31)$$

The values of $Y_{A,\text{in}}$ and $Y_{A,\text{out}}$ are fixed by the initial loading of the gas and by the target of separation, that is, by the desired purity of the treated gas, respectively. $X_{A,\text{in}}$, the initial loading of the absorption agent, is also fixed and depends on the quality of the regeneration of the liquid by desorption. In the ideal case, $X_{A,\text{in}}$ should be zero. Thus only the loading of the solvent leaving the column at the bottom, $X_{A,\text{out}}$, is a variable and depends on the gas-to-liquid ratio [Eq. (3.3.30)]. Thus the operating line starts at point $Y_{A,\text{out}} = X_{A,\text{in}}$ and the slope is given by the liquid-to-gas ratio [Figure 3.3.30, Eq. (3.3.31)].

The number of theoretical separation stages is determined based on the operating line and the equilibrium curve with the corresponding construction of the step function between both lines. For the example shown in Figure 3.3.30, we get four theoretical stages. The number of stages decreases with increasing liquid-to-gas

Figure 3.3.30 McCabe–Thiele diagram of an absorption process (adapted from Gmehling and Brehm, 1996) (Y and X refer to absorbed component A, i.e., to Y_A and X_A in the text).





ratio as the upper operating point ($Y_{A,in} = X_{A,out}$) shifts to the left. (Similarly, the value of $Y_{A,out}$ would decrease for a fixed number of stages.)

The minimum liquid-to-gas ratio is determined by the intercept of the operating line with the equilibrium curve at point $Y_{g,in} = X_{l,out}$ (Figure 3.3.31). The stepping triangles then become infinitely small, which corresponds to an infinite number of stages.

In industrial practice, the liquid-to-gas ratio is by a factor of 1.3–1.6 higher than the minimum value of the liquid-to-gas ratio (Gmehling and Brehm, 1996) (see also Example 3.3.6).

Industrial absorption (and also distillation) columns are equipped either with trays, located about every 0.3–1 m up the column, or packed columns are used. The most widely used trays are sieve or valve trays. Sieve trays are simple flat plates with a large number of holes. The gas phase flows up through the holes, preventing the liquid from falling through. The liquid phase flows across each tray, passes over a weir, and drops into a downcomer that provides liquid for the tray below. Valve trays are built with a cap that fits over the hole in the tray and that can move up and down, providing more or less space as the gas flow rate changes.

For packed columns, the height equivalent of one theoretical stage (HETS) – also called the height equivalent of one theoretical plate (HETP) – is needed to calculate the length of the column for a given number of theoretical stages determined by the McCabe–Thiele approach. The HETS must be determined experimentally, depends on the system (density, viscosity, diffusivity, flow rates) and the size and form of the packing material (pall and Raschig rings, spherical particles, saddles), and may vary in the range 0.3–1 m (Lohrengel, 2007).

For the liquid and gas flow we have to consider minimum and maximum values (Figure 3.3.32):

- If the gas velocity becomes too large, the column experiences an overload (flooding). The liquid from one tray is then transported to the one above, and the

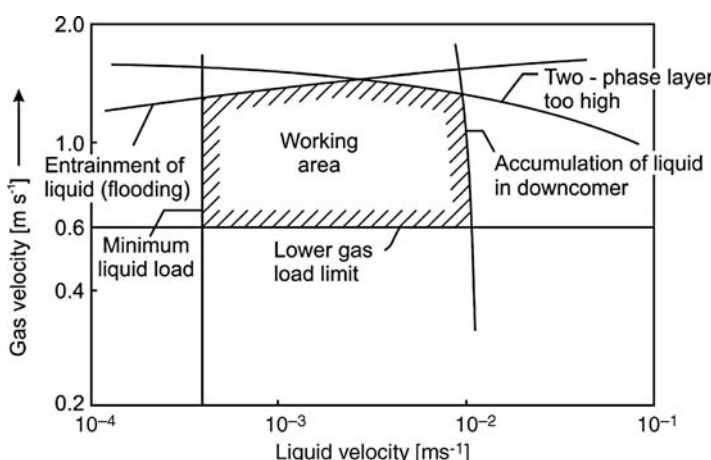
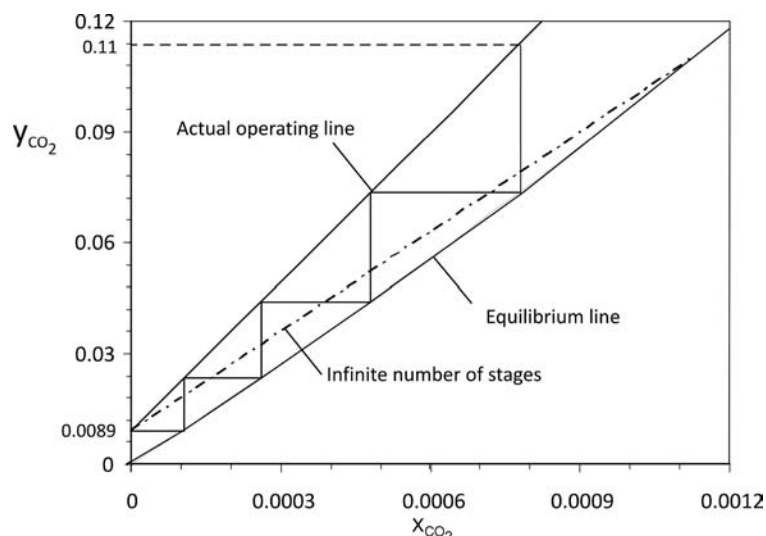


Figure 3.3.32 Preferable operation conditions of a sieve tray. Adapted from Dittmeyer *et al.* (2003).

Figure 3.3.33 McCabe–Thiele diagram for absorption of CO₂ in cold water (5 °C).



efficiency of the separation strongly decreases. On the other hand, the gas velocity should not be reduced too much: If the gas pressure drop through the openings in the tray becomes too small the liquid flows down through the channels that are meant for the gas (weeping). If this occurs gas–liquid contact is also poor and the separation suffers.

- If the liquid velocity becomes too large, the liquid accumulates in the downcomer, and if the velocity is reduced too much we get inequalities of the flow on the tray. Then it becomes difficult to hold enough liquid on the tray to enable sufficient gas–liquid contact, and the efficiency decreases.

Example 3.3.6: Basic design data of a column for absorption of CO₂ in water

A gas stream of 44 kmol h⁻¹ (1000 m³ h⁻¹ at 1 bar and 0 °C) containing 90 mol.% N₂ and 10% CO₂ is passed through an absorber at 10 bar, in which pure water at 5 °C is used as a solvent. The liquid flow rate is 1.5 times the minimum liquid flow rate. What is the number of theoretical separation stages needed to absorb 92% of CO₂ (= 4.05 kmol h⁻¹). The Henry coefficient is 880 bar mol_{liq} mol_{gas}⁻¹. First, we determine the equilibrium curve in terms of the loading of the gas and liquid with CO₂ (Y, X) by using Henry's law [see Eq. (3.3.30a)]:

$$X = \frac{Yp}{H_{CO_2,x}(1+Y) - Yp}$$

This equilibrium curve is shown in Figure 3.3.33. The inlet loading of the gas (Y_{in}) is 0.11 (= 0.1/0.9), and Y_{out} is 0.0089 [= (1-0.92) 0.1/0.9]. Since pure water is used as solvent, X_{in} = 0, the origin of the operating line is the point (X_{in} = 0, Y_{out} = 0.0089). The minimum liquid flow rate line (infinite number of separation stages) is the operating line that

touches the equilibrium line at Y_{in} = 0.11 and X_{out} = 0.0011, and the slope is 89.7 (Figure 3.3.33). The slope of the actual operating line is 1.5 times higher. Since Y_{in} = 0.11 is still the same, we can calculate the corresponding value of X_{out} by the slope of the actual operating line:

$$\text{Slope} = 134.6 = \frac{Y_{in} - Y_{out}}{X_{out} - X_{in}} = \frac{0.11 - 0.0089}{X_{out} - 0} \Rightarrow X_{out} = 0.00075$$

The step function, starting from the point (0, 0.0089) to the point where X = X_{out} = 0.00075 yields the number of separation stages as about 4. Finally, we calculate the volume rate of water:

$$(X_{out} - X_{in})\dot{n}_{H_2O} = (Y_{in} - Y_{out})\dot{n}_{N_2} \Rightarrow \dot{n}_{H_2O} = \frac{0.101}{0.00075} 39.6 \text{ kmol h}^{-1} \\ = 5333 \text{ kmol h}^{-1}$$

So the volume rate of water is 96 m³ h⁻¹ and almost equals the gas rate (100 m³ h⁻¹ at 10 bar).

3.3.4 Liquid–Liquid Extraction

3.3.4.1 Extraction Principles

Liquid–liquid extraction is used to separate components of a liquid mixture, if separation by distillation is hard to achieve – for example, for liquids with similar boiling points or for temperature-sensitive substances with a high boiling point. Extraction is used to separate a valuable substance as well as to remove unwanted

impurities, and thus we find extraction processes in refineries, in the petrochemical industry, as well as in the production of fine chemicals.

Extraction depends upon the difference in solubility of a compound in two immiscible liquids, and is based on the interfacial transfer of a solute. The liquid remaining after treatment with an extracting agent is called raffinate, forming a two-phase system with the extracting agent.

A distribution ratio is often quoted as a measure of how extractable a species is. The distribution ratio, K_{ext} , called *Nernst's partition coefficient* (*Walther Nernst*, see box), is equal to the content of a solute i in the first liquid phase 1 (usually the extracting agent) divided by its content in the second liquid phase (phase 2), usually the raffinate:

$$! K_{\text{ext}} = \frac{x_{i,\text{phase 1}}}{x_{i,\text{phase 2}}} \quad (3.3.32a)$$

The distribution ratio may also be related to the masses of solute i and of both liquid phases:

$$K_{\text{ext,m}} = \frac{\frac{m_{i,\text{phase 1}}}{m_{\text{phase 1}}}}{\frac{m_{i,\text{phase 2}}}{m_{\text{phase 2}}}} \quad (3.3.32b)$$

Depending on the system, the distribution ratio is a function of temperature, concentration of the involved species, and other factors such as the unwanted solubility of the extracting agent in the raffinate and vice versa. The properties of an ideal extracting agent are:

- high selectivity for the solute (high value of partition coefficient);
- low or no solubility in the raffinate;
- non-toxic and a high chemical and thermal stability;
- low viscosity with regard to the energy needed for the mixing of both phases;
- low volatility;
- regeneration of the extracting agent (separation of the solute) should be easy with respect to re-use in a continuous extraction process.

In addition to the value of the partition coefficient, the recovery of the solute depends on the ratio of the amount of the extracting agent to the amount of liquid treated by extraction. This can be explained by the following example. Imagine we have water containing 1 wt% of a solute, and for a given extracting agent a distribution ratio related to mass of 1. If a 1-kg aqueous solution is mixed with 1 kg of extracting agent and stirred until equilibrium is reached, 5 g of solute are transferred, leaving behind 5 g in the aqueous raffinate (thus $K_{\text{ext,m}} = 1$). The degree of separation would be 50%. In a second experiment, the aqueous mixture is treated with 2 kg of extracting agent. The ratio of the content of solute in both phases is still 1, but as the ratio of extracting agent to aqueous solution is now twice as much, the extracting agent would contain 6.67 g of solute and the raffinate 3.33 g. Hence, the degree of separation would be 67%.

A concise depiction of the extraction is a triangular diagram, as shown in Figure 3.3.34 for a mixture of A and B with B as the solute and A as the component that accumulates in the raffinate. The liquid C represents the extracting agent. In the equilateral triangle, the sum of the length of the perpendiculars from a point within the triangle to the three sides is equal to the height of the triangle. This height is set equal to 100% (molar content x_i or content by weight or volume), so each corner represents one of the three pure components. The lines between two corners (e.g., line A–B) represent binary systems.

For extraction, the extracting agent (C) is added to a binary mixture (E). The ternary mixture is represented by a point within the triangle (e.g., D in Figure 3.3.34a). For extraction, this point must lie in the two-phase region that is separated from the

Walther Hermann Nernst (1864–1941, Nobel Prize in Chemistry in 1920), a German chemist, is one of the founders of modern physical chemistry. He worked on thermodynamics, electrochemistry, solid state and photochemistry, osmotic pressure, and electroacoustics. In 1887 he invented the *Nernst* lamp by using an incandescent ceramic rod (a precursor of the incandescent lamp). He established the third law of thermodynamics that describes the behavior of matter as the temperature approach absolute zero (1905). In association with the companies *Bechstein* and *Siemens*, he also invented the electric piano (1930) to produce electronically modified sound in the same way as an electric guitar.

Figure 3.3.34 Triangular diagram of a ternary liquid–liquid system (ideal system where the bimodal curve coincides with the triangle's axes).

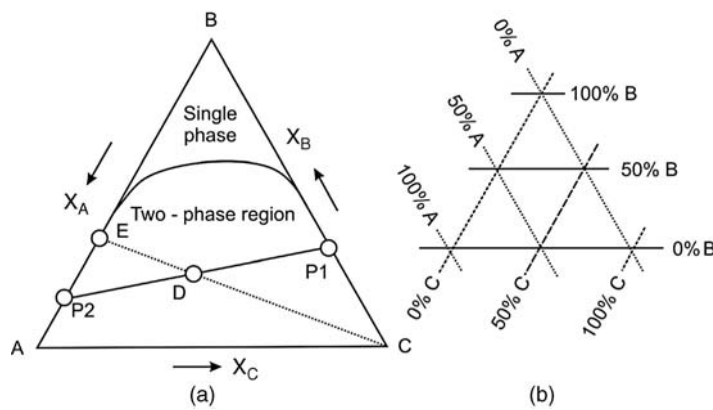
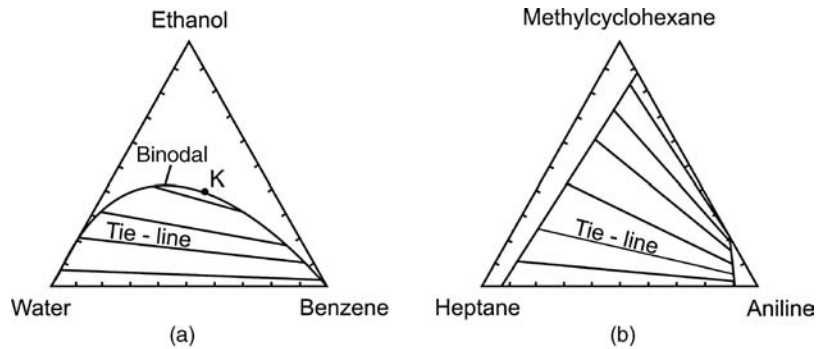


Figure 3.3.35 Triangular diagrams of ternary liquid–liquid systems based on molar content: (a) closed system and (b) open system. Data from Gmehling and Brem (1996).



single-phase region by the binodal curve (coexistence curve) (see Figures 3.3.34 and 3.3.35). This is the case for the mixture D in Figure 3.3.34, and disaggregation in two immiscible phases would start if agitation is stopped. The composition of these two phases is given by tie-lines, indicating pairs of partially miscible liquids, for example, P1 and P2 for the mixture D in Figure 3.3.34.

For an ideal extraction process, as depicted in Figure 3.3.34, only the solute B is transferred between both phases. Thus, only binary systems such as P1 and P2 in Figure 3.3.34 can exist. The raffinate P2 consists only of component A and a certain remaining amount of solute B, whereas the extract P1 consists of the extracting agent C and the solute A.

For such ideal two-phase systems with regard to extraction, the triangular diagram is not needed to design the extraction as the system is simply represented by the distribution ratio, Eqs. (3.3.32a) and (3.3.32b), which is constant for an ideal mixture.

However, in many ternary systems, all compounds have a degree of solubility in both phases (Figure 3.3.35). Typically, such ternary triangular phase diagrams are characterized by two liquid pairs that are completely miscible in all proportions, for example, water–ethanol and ethanol–benzene (Figure 3.3.35a), or by two pairs that are only partially miscible, for example, heptane–aniline and aniline–methylcyclohexane (Figure 3.3.35b).

3.3.4.2 Design of Extraction Processes

Technically, continuously operated extraction processes are conducted in a mixer-settler cascade (Figure 3.3.36b) or in countercurrent columns (Figure 3.3.36a) equipped with pulsating or rotating internals or with packings to ensure a good agitation and a high interfacial surface area between both immiscible fluids.

For an ideal ternary system where practically only the solute is soluble in both phases, the design of an extraction process is straightforward. As shown by

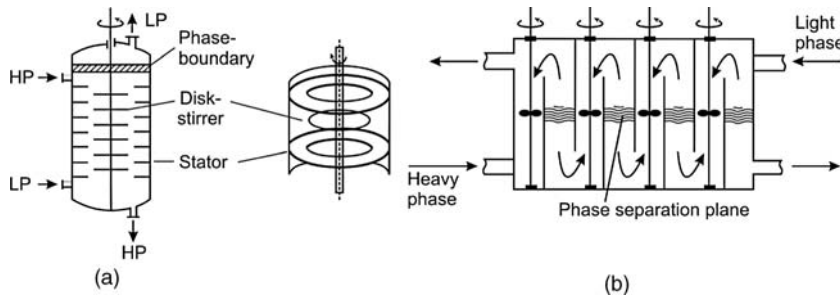


Figure 3.3.36 Typical technical extraction units:
(a) rotating disc contactor and (b) mixer-settler unit;
HP: heavy phase, LP: light phase. (a) Adapted from Sattler (2001) and (b) adapted from Gmehling and Brehm (1996).

Example 3.3.7, the McCabe–Thiele approach – already examined for distillation (Section 3.3.2) and absorption (Section 3.3.3) – is the common technique used to design an extraction process:

- If the equilibrium data are given or if in the simplest case we even have a constant distribution ratio, we can construct the x_{extract} (content of solute in extract phase) versus $x_{\text{raffinate}}$ (content of solute in raffinate) equilibrium diagram.
- Based on the material balances we construct the operating curve (Example 3.3.7).
- Once the equilibrium and the operating line are available, they can be stepped off into triangles, and we finally determine the number of theoretical separation stages, $n_{\text{stage, theo}}$.

The actual number of extraction stages required is given by the ratio of the theoretical number of stages to the stage efficiency:

$$n_{\text{stage}} = \frac{n_{\text{stage, theo}}}{\eta_{\text{stage}}} \quad (3.3.33)$$

For packed columns or columns with rotating or pulsating internals, the height equivalent to one stage (*HETS*) is commonly used, and the total column height is determined by:

! $H_{\text{column}} = n_{\text{stage}} HETS \quad (3.3.34)$

The value of *HETS* must be determined experimentally and depends both on the apparatus and the ternary system used for the extraction.

For non-ideal systems with two ternary phases, the triangular phase diagram must be used for the design of an extraction process; for details we refer to textbooks such as Ruthven (2001), Sattler (1986), and Gmehling and Brehm (1996).

The main parameters that characterize an extraction apparatus are (Example 3.3.7):

- For an ideal system that consists only of two binary mixtures (two-phase region in Figure 3.3.34a), there is a minimum solvent-to-feed ratio for a given feed composition, required degree of extraction, and choice of extracting agent (Example 3.3.7). This corresponds to an infinite number of stages, which is comparable to the minimum reflux and infinite number of stages in the case of distillation.
- For non-ideal systems, there is a minimum and sometimes also a maximum solvent-to-feed ratio, for example, for the ternary system shown in Figure 3.3.35b. If too little solvent (aniline) is added ($<\approx 10\%$) the two phase region is not reached, and if too much aniline is added ($>\approx 90\%$) a single-phase region is entered again. In both cases, it is impossible to divide the mixture into two phases and no separation is achieved. The minimum and maximum solvent-to-feed ratio therefore corresponds to the respective mixtures on the binodal.

Example 3.3.7: Number of theoretical separation stages of extraction [separation of phenol from sewage water by butyl acetate, data as given by Gmehling and Brehm (1996)]

Sewage water containing phenol (100 kmol h^{-1} , 0.002 mol phenol per mol water) is to be cleaned by extraction with butyl acetate; 90% of the phenol should be extracted. What is the amount of the extracting agent butyl acetate needed to achieve this goal with two and with three theoretical stages? What is the minimum solvent-to-feed ratio (corresponding to an infinite number of stages)? We may assume an ideal system consisting only of binary phases and neglect the fact that a small amount of butyl acetate is dissolved in water and vice versa.

To solve this problem, we use the x_{extract} (phenol in the extract phase) versus $x_{\text{raffinate}}$ (phenol in the raffinate phase) diagram and the corresponding equilibrium curve (Figure 3.3.37). $x_{\text{extract,in}} = 0$.

One point of the operating line can be determined directly based on the boundary condition that the content of phenol at the outlet of the extractor, $x_{\text{raffinate}}$ ($0.0002 \text{ mol mol}^{-1}$), corresponds to the content in the fresh extracting agent (pure butyl acetate, $x_{\text{extract,in}} = 0$). We then have to find the slopes of the operating line, where we get exactly two and three stages. As shown in Figure 3.3.37, $x_{\text{extract,out}}$ is 0.28 for two stages and 0.39 for three stages.

The mass balance for phenol based on the flow rates of solvent and raffinate (\dot{S}, \dot{R}) yields:

$$(x_{\text{extract,out}} - x_{\text{extract,in}})\dot{S} = (x_{\text{feed}} - x_{\text{raffinate,out}})\dot{R} \quad (3.3.35)$$

For the given data we obtain:

$$\begin{aligned} (x_{\text{extract,out}} - 0)\dot{S} &= (0.002 - 0.0002)100 \text{ kmol h}^{-1} \Rightarrow \dot{S} \\ &= \frac{0.18 \text{ kmol h}^{-1}}{x_{\text{extract,out}}} \end{aligned} \quad (3.3.36)$$

and thus for two and three separation stages ($x_{\text{extract,out}}$ is 0.28 and 0.39) we obtain flow rates of butyl acetate of 0.64 and 0.46 kmol h^{-1} , respectively.

The minimum solvent-to-feed ratio is determined by the intercept of the operating line and equilibrium curve (dot-dashed line, $x_{\text{extract,out}} = 0.53$). Here we obtain a flow rate of $0.34 \text{ kmol solvent h}^{-1}$ and a minimum solvent-to-feed ratio of 0.0034.

3.3.5

Adsorption

Impurities in gases are removed by:

- absorption in liquids (Section 3.3.3),
- condensation, for example, to separate higher hydrocarbons from natural gas,
- adsorption on solids as examined in this chapter.

Adsorption can also be used to remove unwanted impurities or valuable substances from liquids, and is therefore an alternative to liquid–liquid extraction (Section 3.3.4). In general, adsorption is advantageous if the impurity concentration is low and high purity is needed.

3.3.5.1 Adsorption Principles

Adsorption of fluids is based on the selective binding of components on the surface of a solid. In catalysis, adsorption is the essential first step followed by a chemical transformation of the adsorbed species (Section 4.5). In purification of gases and liquids, no further chemical reaction takes place, and the loaded solid, the

Figure 3.3.37 Extraction of phenol from sewage water with butyl acetate (solid line: three separation stages, dotted line: two stages, dot-dashed line: infinite number of stages).

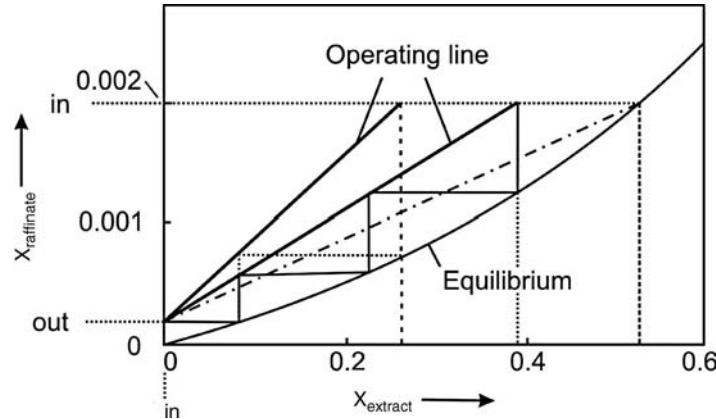


Table 3.3.8 Surface areas of selected adsorbents. Data from Gmehling and Brehm (1996).

Adsorbent	Surface area ($\text{m}^2 \text{ g}^{-1}$)
Activated carbon	300–2500
Silica	300–350
Aluminum oxide	300–350
Zeolites	500–800

adsorbent, is regenerated from time to time, whereby the adsorbed substance, the adsorbate, reversibly desorbs.

To reach a high adsorption capacity, adsorbents must provide a large surface area (Table 3.3.8). This can only be achieved by highly porous adsorbents with very small pore diameters, of the order of magnitude of less than 1000 nm (Figure 3.3.38). To reach extremely high values of more than $100 \text{ m}^2 \text{ g}^{-1}$, a mean pore diameter of less than about 10 nm is needed, as inspected in more detail in Section 4.5 with regard to porous solid catalysts.

Zeolites (minerals mainly based on Si- and Al-oxide) even have pores of the order of magnitude of the size of molecules (Figure 3.3.39). Only small molecules can enter the pores, which are used for shape selective adsorption, for example, to separate *n*-from *i*-paraffins (no. 3, Figure 3.3.39).

If a gas is in contact with a solid, equilibrium is established between the molecules in the gas phase and the corresponding adsorbed species. An approach to

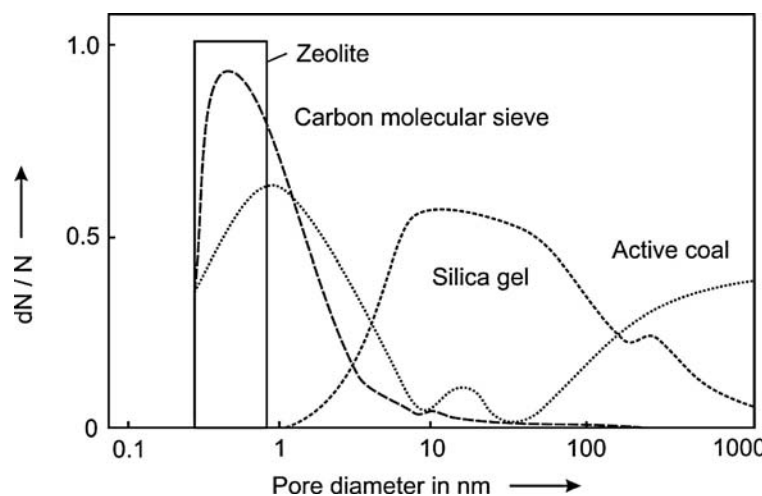


Figure 3.3.38 Pore diameter distribution of selected adsorbents (adapted from Gmehling and Brehm, 1996).

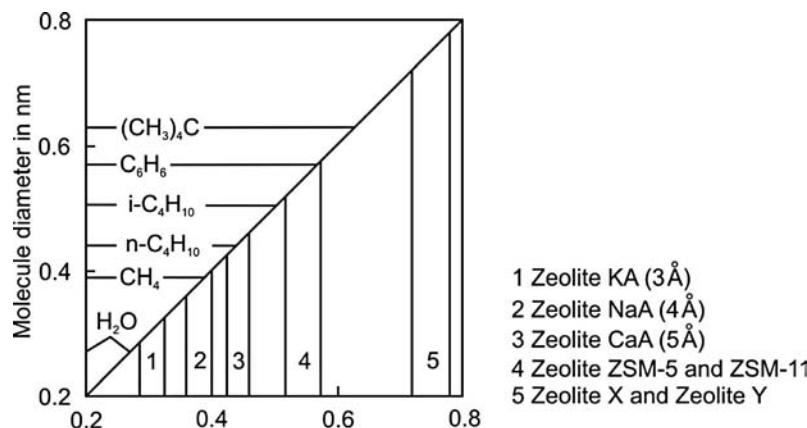


Figure 3.3.39 Comparison of mean pore diameter of different zeolites with the diameter of selected molecules (adapted from Gmehling and Brehm, 1996).

describe this equilibrium is the so-called Langmuir isotherm (Irving Langmuir, see box). (For liquids this is similar, but subsequently gas adsorption is used as an example to derive the basic equations of adsorption.)

We derive the Langmuir isotherm by treating the adsorption process like any other chemical equilibrium, except that it is established between gas molecules (species A), vacant surface sites of number n_{vacant} , and species adsorbed on the surface (number n_A). For a non-dissociative adsorption of species A, adsorption is represented by the following chemical equation:



The total number of surface sites, n_t , is equivalent to the sum of n_{vacant} and n_A , and so we inherently have assumed a fixed number of localized surface sites. We now formally define an equilibrium constant (e.g., here with n/A as a measure of the surface concentration in mol m^{-2}):

$$K_{\text{ads},A} = \frac{\frac{n_A}{A}}{p_A \frac{n_{\text{vacant}}}{A}} = \frac{n_A}{p_A n_{\text{vacant}}} = \frac{n_A}{p_A (n_t - n_A)} \quad (3.3.38)$$

Equation (3.3.38) leads to the surface coverage θ_A relative to the monolayer capacity:

$$\theta_A = \frac{n_A}{n_t} = \frac{K_{\text{ads},A} p_A}{1 + K_{\text{ads},A} p_A} \quad (3.3.39)$$

According to Eq. (3.3.39), the surface coverage approaches unity for high partial pressures of the adsorbate, and a complete monolayer is established. The equilibrium constant of adsorption depends on temperature and is related to the adsorption enthalpy by:

$$K_{\text{ads},A} = K_{\text{ads},A,0} e^{\frac{-\Delta_{\text{ads}}H}{RT}} \quad (3.3.40)$$

Equation (3.3.40) and thus Eq. (3.3.39) are only correct if the enthalpy of adsorption is independent of the coverage.

Equation (3.3.39) is also derived based on kinetic suggestions. In equilibrium, the rate of adsorption (in $\text{mol m}^{-2} \text{s}^{-1}$) equals the rate of desorption, which is justified as sorption is an almost instantaneous chemical process (the potential influence of mass transfer is discussed below):

$$k_{\text{ads},A} \frac{n_{\text{vacant}}}{A} p_A = k_{\text{des},A} \frac{n_A}{A} \quad (3.3.41)$$

Introduction of the surface coverage, Eq. (3.3.39), leads to:

$$k_{\text{ads},A} (1 - \theta_A) p_A = k_{\text{des},A} \theta_A \quad (3.3.42)$$

and rearrangement yields:

$$\theta_A = \frac{\frac{k_{\text{ads},A}}{k_{\text{des},A}} p_A}{1 + \frac{k_{\text{ads},A}}{k_{\text{des},A}} p_A} \quad (3.3.43)$$

By comparison of Eq. (3.3.43) with Eq. (3.3.39) we obtain:

$$K_{\text{ads},A} = \frac{k_{\text{ads},A}}{k_{\text{des},A}} \quad (3.3.44)$$

which is the condition of the dynamic equilibrium of adsorption and desorption.

For practical applications, the loading $X_{\text{ads},\text{sat}}$ in $\text{kg adsorbate per kg of adsorbent}$ (m_{ads}) is frequently used instead of the surface coverage, and Eq. (3.3.39) may be

Irving Langmuir (1881–1957), an American chemist and physicist, who developed in 1916 the theory that describes the dependence of the surface coverage on the partial pressure of the adsorbed gas, named after him as the Langmuir isotherm. He was awarded the 1932 Nobel Prize in Chemistry for his work on surface chemistry. Langmuir improved vacuum techniques by the invention of the high-vacuum tube. He discovered that the lifetime of a tungsten filament was greatly lengthened by filling the bulb with an inert gas, which is an important part of the modern day incandescent light bulb. He was one of the first to work with plasmas and the first to call these ionized gases by that name, as they reminded him of blood plasma.

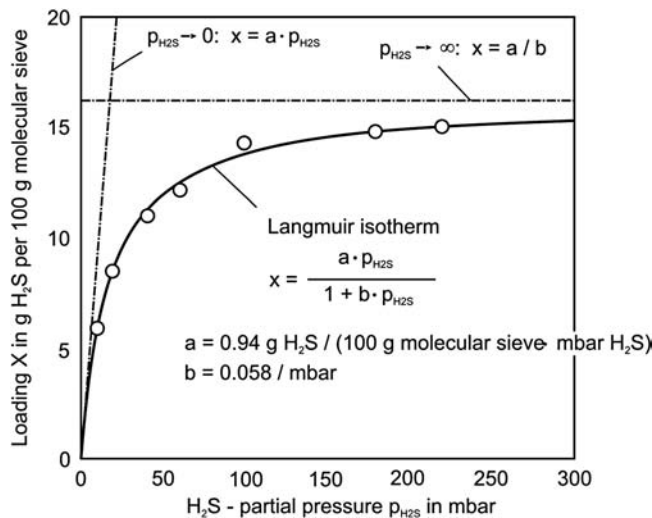


Figure 3.3.40 Adsorption isotherm of pure H_2S on a molecular sieve (20°C). Data from Groninger, Hedden, and Rao (1987).

re-written as:

$$X_{\text{ads},A,\text{sat}} = \frac{m_A}{m_{\text{ads}}} = \frac{n_A M_A}{m_{\text{ads}}} = \frac{\theta_A n_t M_A}{m_{\text{ads}}} = \frac{\left(K_{\text{ads},A} M_A \frac{n_t}{m_{\text{ads}}} \right) p_A}{1 + K_{\text{ads},A} p_A} = \frac{ap_A}{1 + bp_A} \quad (3.3.45)$$

An example showing that this form of the Langmuir isotherm fits well real systems is illustrated by Figure 3.3.40 for the adsorption of H_2S on a molecular sieve.

Adsorption of H_2S is an important process, for example, for natural gas purification. In this process, not pure H_2S but a mixture of methane and H_2S (and also other components like CO_2 and hydrocarbons such as ethane and propane) come into contact with the adsorbent, and competitive adsorption has to be considered. As shown in Figure 3.3.41b, the loading of the molecular sieve by H_2S (for a given partial pressure of H_2S) is reduced by about 20% if we increase the total pressure to 60 bar by the addition of CH_4 . Even if methane is only weakly adsorbed compared to H_2S (Figure 3.3.41a), the high partial pressure of methane in natural gas considerably reduces the loading with H_2S , since H_2S is partly replaced by methane by competitive adsorption. This phenomenon has to be considered in many adsorption processes, as examined below in more detail.

In some cases, the adsorption cannot be described by the Langmuir theory, and the isotherms have a quite different shape (Figure 3.3.42). In the literature, several types of isotherms are discussed that differ in one or more of the assumptions made to derive the Langmuir isotherm (monolayer, constant adsorption enthalpy, constant

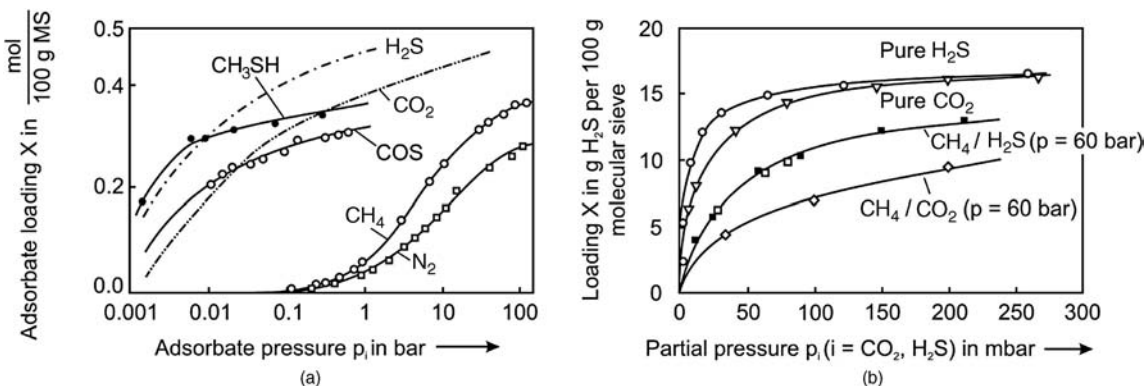


Figure 3.3.41 (a) Comparison of equilibrium loading (adsorption isotherm) for different (pure) gases; (b) adsorption isotherms of H_2S and CO_2 for pure H_2S and CO_2 and for mixtures of H_2S or CO_2 with CH_4 (molecular sieve, 20°C). Data from Groninger, Hedden, and Rao (1987).

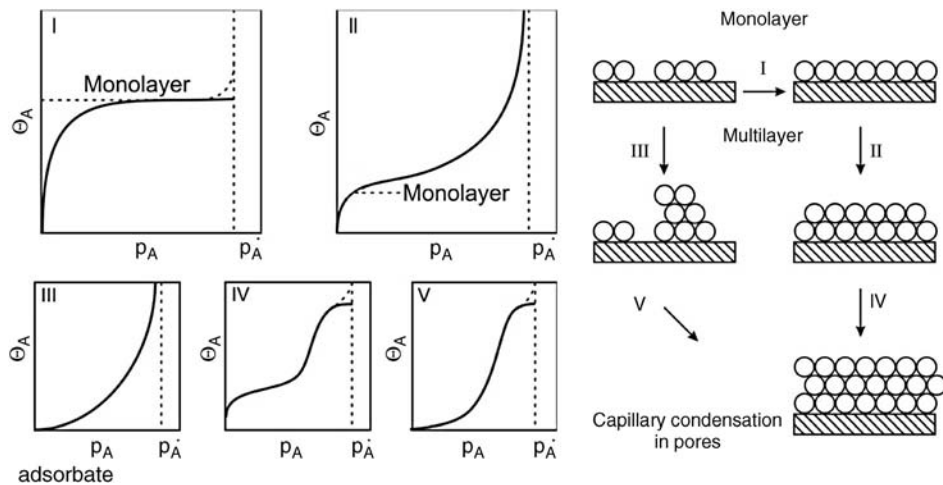


Figure 3.3.42 Typical shapes of adsorption isotherms; p_A : partial pressure of adsorbate A, p_A^* : vapor pressure of liquid A, θ_A = coverage relative to monolayer capacity; type I: Langmuir adsorption, for example, benzene on silica gel, NH_3 on charcoal, or H_2S on molecular sieve (Figure 3.3.40); type II: multilayer BET type of adsorption, for example, water on Al_2O_3 , N_2 on silica; type III: multilayer adsorption, for example, bromine on silica, type IV and V: multilayer adsorption and capillary condensation in pores, for example, water on silica or benzene on Fe_2O_3 (IV) and water on charcoal (V).

Table 3.3.9 Important adsorption isotherms (θ_A = coverage relative to monolayer capacity).

Originator(s)	Isotherms	Area of application
Langmuir	$\theta_A = \frac{K_{\text{ads},A} p_A}{1 + K_{\text{ads},A} p_A} \quad (3.3.39)$	Physisorption, chemisorption
Freundlich	$\theta_A = K_{\text{ads},A} p^n \quad \text{with } n \leq 1 \quad (3.3.46)$	Physisorption, chemisorption
Brunauer, Emmett, Teller (BET)	$\theta_A = \frac{C_{\text{BET}} \frac{p_A}{p_A^*}}{\left[1 - \frac{p_A}{p_A^*}\right] \left[1 + (C_{\text{BET}} - 1) \frac{p_A}{p_A^*}\right]} \quad \text{with } \theta_A = \frac{n_A}{n_{A,\text{monolayer}}} \quad (3.3.47a)$	Multilayer physisorption

number of sites that are identical with regard to the strength of adsorption). Thus, other equations are needed to describe the coverage (Table 3.3.9). For elucidation, three cases beyond non-dissociative Langmuir adsorption are subsequently examined: multilayer, dissociative, and competitive adsorption.

BET Isotherm The Langmuir isotherm does not consider adsorption beyond a monolayer. Multilayer adsorption was treated by Stephen Brunauer, Paul Emmett, and Edward Teller (Brunauer, Emmett and Teller, 1938, see box) and named after the initials of their surnames as the BET theory. The BET theory is an extension of the Langmuir theory to multilayer adsorption with the following hypotheses: $\Delta_{\text{ads}}H_{\text{mon}}$ is the enthalpy of adsorption for the first monolayer, $\Delta_{\text{ads}}H_L$ is that for the second and higher layers, and the Langmuir theory can be applied to each layer. We then have:

$$\theta_A = \frac{n_A}{n_{A,\text{monolayer}}} = \frac{C_{\text{BET}} \frac{p_A}{p_A^*}}{\left[1 - \frac{p_A}{p_A^*}\right] \left[1 + (C_{\text{BET}} - 1) \frac{p_A}{p_A^*}\right]} \quad (3.3.47a)$$

where p_A^* is the saturation vapor pressure of the adsorbed component and C_{BET} the BET constant:

$$C_{\text{BET}} = e^{-\frac{\Delta_{\text{ads}}H_{\text{mon}} + \Delta_{\text{ads}}H_L}{RT}} \quad (3.3.48)$$

C_{BET} is usually higher than unity as the (absolute) value of the enthalpy of adsorption for a monolayer is higher than for subsequent layers, $\Delta_{\text{ads}}H_L$, which is the

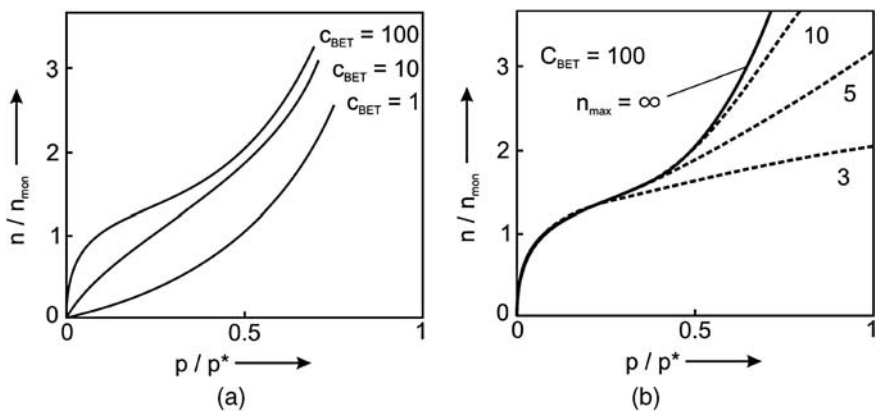


Figure 3.3.43 Shapes of adsorption isotherms according to the BET (Brunauer, Emmett, and Teller) theory for various values of C_{BET} (not considering capillary condensation and surface inhomogeneities): (a) Equation (3.3.47a) for an unlimited number of layers; (b) n -layer BET equation for $C_{\text{BET}} = 100$, if the number cannot exceed n_{max} , that is, for adsorption in a limited space such as a capillary, Eq. (3.3.47b).

enthalpy of condensation (-5.6 kJ mol^{-1} for N_2). Typical adsorption isotherms for various C_{BET} values are shown in Figure 3.3.43a. For $C_{\text{BET}} > 2$, we get a type II isotherm and for the reverse type III (Figure 3.3.42).

With increasing pressure, n_A exceeds $n_{A,\text{monolayer}}$ and θ_A is higher than unity (Figure 3.3.43a). The BET isotherm, Eq. (3.3.47a), is well-known for being used to determine the surface area of porous solids by physisorption, usually of N_2 . Rewriting Eq. (3.3.47a) leads to:

$$\frac{\frac{p_A}{p^*}}{n_A \left[1 - \frac{p_A}{p^*} \right]} = \frac{1}{n_{A,\text{monolayer}} C_{\text{BET}}} + \frac{(C_{\text{BET}} - 1)}{n_{A,\text{monolayer}} C_{\text{BET}} p^*} \quad (3.3.49)$$

A plot of the term on the left-hand side of Eq. (3.3.49) versus p_A/p_A^* leads to a straight line, and we obtain the amount of A needed for a monolayer by the slope $(C_{\text{BET}} - 1)/(C_{\text{BET}} n_{A,\text{monolayer}})$ and by the intercept $1/(C_{\text{BET}} n_{A,\text{monolayer}})$. Thus, $n_{A,\text{monolayer}}$ is equivalent to the term $1/(\text{slope} + \text{intercept})$.

The specific internal surface, A_{BET} ($\text{m}^2 \text{ kg}^{-1}$), is then easily calculated by:

$$A_{\text{BET}} = \frac{A_{\text{sample}}}{m_{\text{sample}}} = \frac{n_{A,\text{monolayer}} A_A N_A}{m_{\text{sample}}} \quad (3.3.50)$$

where N_A is the Avogadro constant (or Loschmidt number), $6.022 \times 10^{23} \text{ mol}^{-1}$, and A_A the required space of the probe molecule A ($1.62 \times 10^{-19} \text{ m}^2$ for N_2). In practice, we should limit the range of pressure relative to the saturation vapor pressure of the adsorbed component to $0.05 < p_A/p_A^* < 0.5$. For values of p_A/p_A^* higher than 0.5 we are limited by capillary condensation, which is not covered by the BET theory, as inspected in more detail in Topic 3.3.3. For $p_A/p_A^* < 0.05$ we also get deviations from the theory, through inhomogeneities of the surface.

Usually, the value of C_{BET} is in the range 20–300 for physisorption and higher than 500 for chemisorption. For such high values of C_{BET} , Eq. (3.3.49) can be simplified to:

$$n_{A,\text{monolayer}} = n_A \left[1 - \frac{p_A}{p_A^*} \right] \quad (\text{for } C_{\text{BET}} > 20) \quad (3.3.51)$$

This simplified equation in combination with Eq. (3.3.51) is used for single-point BET analysis (in contrast to the multi-point analysis described above) and only one measurement in the range $0.05 < \theta_A < 0.3$ is needed.

It might be of interest to know the coverage of the first layer, if the total amount of the adsorbed substance equals the amount needed to build a monolayer (Lowell *et al.*, 2004):

$$\theta_1 = 1 - \frac{1 - \sqrt{C_{\text{BET}}}}{1 - C_{\text{BET}}} \quad (\text{for } \theta_A = 1) \quad (3.3.52)$$

For example, for $C_{\text{BET}} = 10$, $\theta_1 = 0.79$, that is, the fraction of the surface that remains bare is 21%, and for $C_{\text{BET}} \rightarrow 1$ and $C_{\text{BET}} \rightarrow \infty$, θ_1 reaches the limiting values of 0.5 and 1, respectively.

Equation (3.3.47a) is only valid if the number of layers is unlimited. If the number of layers cannot exceed n_{\max} , the BET equation becomes (Lowell *et al.*, 2004; Allen, 1997):

$$\theta_A = \frac{C_{\text{BET}} \frac{p_A}{p_A^*} \left[1 - (n_{\max} + 1) \left(\frac{p_A}{p_A^*} \right)^{n_{\max}} + n \left(\frac{p_A}{p_A^*} \right)^{n_{\max}+1} \right]}{\left[1 - \frac{p_A}{p_A^*} \right] \left[1 + (C_{\text{BET}} - 1) \frac{p_A}{p_A^*} - C_{\text{BET}} \left(\frac{p_A}{p_A^*} \right)^{n_{\max}+1} \right]} \quad (3.3.47b)$$

Equation (3.3.47b) applies to adsorption in a limited space such as a very small capillary. Figure 3.3.43b represents this n -layer BET-equation for $C_{\text{BET}} = 100$ and different values of n_{\max} . For $n_{\max} > 10$, the n -layer BET-equation, Eq. (3.3.47b), almost leads to the same result (even for high relative pressures) as the BET-equation for an unlimited number of layers, Eq. (3.3.47a), see Figure 3.3.43b. Hence, Eq. (3.3.47b) is in most cases only relevant for very small pores with a diameter of less than about 20 molecular diameters of the absorbed compound. For nitrogen with a molecular diameter of around 0.4 nm, the limiting pore size is about 8 nm (micropores and small mesopores, see Tab. 4.5.2 in Section 4.5.1).

Topic 3.3.3: Capillary condensation and adsorption/desorption hysteresis

Capillary condensation in a porous solid is a secondary process since it can only occur after an adsorbed layer has been formed on the pore walls. According to the *Kelvin equation* the relative pressure p_A/p_A^* at which condensation occurs is:

$$\frac{p_A}{p_A^*} = e^{-\frac{\sigma v_{\text{mol,liq}}}{RT} \left(\frac{1}{r_1} + \frac{1}{r_2} \right)} \quad (3.3.53)$$

where r_1 and r_2 are the principal radii of the curvature, σ is the surface tension of the liquid condensate, and $v_{\text{mol,liq}}$ is its molar volume. By replacement of $(1/r_1 + 1/r_2)$ with $2/r_K$ we have:

$$\frac{p_A}{p_A^*} = e^{-\frac{2\sigma v_{\text{mol,liq}}}{RT r_K}} \quad (3.3.54)$$

where r_K is often referred to as *Kelvin radius*. For a cylindrical pore with an adsorbed liquid film, r_K equals $2r_{\text{pore}}$ as $r_1 = r_{\text{pore}}$ and $r_2 = \infty$. Thus if the relative pressure p_A/p_A^* during an adsorption experiment (e.g., the measurement of the BET surface area) is increased, capillary condensation will start in the smallest pores with a radius:

$$r_{\text{pore}} = \frac{2\sigma v_{\text{mol,liq}}}{RT \ln \left(\frac{p_A^*}{p_A} \right)} \quad (\text{condition for pore filling during adsorption}) \quad (3.3.55)$$

For a pore already filled with a liquid, r_K represents the curvature of a hemispherical meniscus ($r_1 = r_2 = r_K$). Thus if the relative pressure p_A/p_A^* is decreased from a high value (e.g., about 1) during a desorption experiment, draining of a pore will occur for:

$$r_{\text{pore}} = \frac{2\sigma v_{\text{mol,liq}}}{RT \ln \left(\frac{p_A}{p_A^*} \right)} \quad (\text{condition for pore draining during desorption}) \quad (3.3.56)$$

Nitrogen is generally considered as the most suitable adsorptive material with which to determine the surface area. At 77 K (boiling temperature at 1 bar), Eqs. (3.3.55) and (3.3.56) lead to ($\sigma_{N_2} = 6.3 \times 10^{-3} \text{ N m}^{-1}$, $v_{\text{mol,liq},N_2} = 3.3 \times 10^{-5} \text{ m}^3 \text{ mol}^{-1}$):

$$r_{\text{pore}} = \frac{3.3 \times 10^{-10} \text{ m}}{\ln \left(\frac{p_{N_2}^*}{p_{N_2}} \right)} \quad (\text{pore filling during N}_2\text{-adsorption at 77 K}) \quad (3.3.57)$$

$$r_{\text{pore}} = \frac{6.6 \times 10^{-10} \text{ m}}{\ln \left(\frac{p_{N_2}^*}{p_{N_2}} \right)} \quad (\text{pore draining during N}_2\text{-desorption at 77 K}) \quad (3.3.58)$$

For example, a mesopore with a radius of 10 nm is filled during adsorption for $p_{N_2}/p_{N_2}^* = 0.97$ and drained for a value of 0.94. For a micropore with a radius of 1 nm filling would already occur for $p_{N_2}/p_{N_2}^* = 0.72$ and draining for a value of 0.52. Thus during an adsorption and subsequent desorption experiment we see a hysteresis loop such as shown in Figure 3.3.44 for a pore with a radius of 1 nm and a C_{BET} of 100.

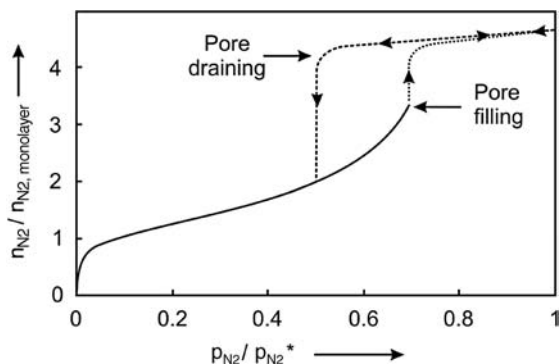


Figure 3.3.44 Hysteresis loop during adsorption and desorption of N_2 in a cylindrical pore with a radius of 1 nm [$C_{\text{BET}} = 100$, solid line calculated by Eq. (3.3.49) for $p_A/p_A^* < 0.7$, dashed curves represent, schematically, capillary condensation and pore draining].

■ Originators of the BET theory

Stephen Brunauer (1903–1986), a native of Hungary, came to the United States in 1921. In 1929, he completed his M.S. from *George Washington University*, where he met **Edward Teller** (see below). By that time he had already started work as a chemist for the U.S. Department of Agriculture and his long association with **Paul H. Emmett** had begun. In 1933 he was awarded his PhD with a thesis on N_2 adsorption on NH_3 catalysts. This work led eventually to the BET method for surface area determination. During the World War II (1942–1945) Brunauer became head of high explosives research and development for the US Navy. He recruited **Albert Einstein** as a Navy consultant – Einstein was evidently proud of his connection with the navy and relieved to find that this job did not require a navy haircut. In 1951, *Brunauer* became manager of the basic research of the *Portland Cement Association*, and from 1965 to 1973 he was head of the Chemistry Department of Clarkson University.

Paul Hugh Emmett (1900–1985), an American chemical engineer and close friend of **Linus Pauling** (American chemist and biochemist who was awarded the Nobel Prize in Chemistry in 1954). In 1937, *Emmett* became head of the Chemical Engineering Department at the *John Hopkins University*. In 1943 he joined the *Manhattan Project* for the development of the first nuclear weapons. The project, which was scientifically directed by the physicist **J. Robert Oppenheimer**, lasted from 1942 to 1946, and succeeded in developing three nuclear weapons in 1945, a test detonation on 16th July in New Mexico, and two bombs detonating on the 6th and 9th of August over Hiroshima and Nagasaki, respectively. Within this project, *Emmett* helped to develop the process for the separation of ^{235}U from ^{238}U . After the war, *Emmett* returned to research and university life. Beside his contribution to the BET theory, he worked on ammonia synthesis, the surface area of soils, and the porosity of coals.

Edward Teller (1908–2003), a Hungarian-born American nuclear physicist, is well-known as *the father of the hydrogen bomb*. He left Hungary in 1926 and received his higher education in Germany, where he graduated in chemical engineering at the University of Karlsruhe and received his PhD in physics under **Werner Heisenberg** in 1930 at the University of Leipzig. *Teller's* dissertation dealt with one of the first accurate quantum mechanical treatments of the hydrogen molecular ion. He spent two years at the University of Goettingen and left Germany in 1933 through the aid of the *Jewish Rescue Committee*. Passing through England, he moved for a year to Copenhagen, where he worked under **Niels Bohr**. In 1935, *Teller* was invited to the United States to become a Professor of Physics at the *George Washington University*, where he worked until 1941. In 1938, he made – in collaboration with *Brunauer* and *Emmett* – his important contribution to surface physics and chemistry, the BET isotherm. In 1941, his interest as a theoretical physicist turned to nuclear energy, both fusion and fission. *Teller* was an early member of the *Manhattan Project* (see above), and made a serious push to develop the first fusion-based weapons as well, but these were deferred until after World War II. In 1952, the first hydrogen bomb based on the concept of *Teller* and the Polish mathematician **Stanislaw Ulam** detonated and appeared to vindicate *Teller's* long-time advocacy for the hydrogen bomb. After *Teller's* controversial testimony in the security clearance hearing of his former Los Alamos colleague **Robert Oppenheimer**, *Teller* was ostracized by much of the scientific community. He was a co-founder of the *Lawrence Livermore National Laboratory*, and its director for many years. In

his later years he became especially known for his advocacy of controversial technological solutions to both military and civilian problems. He was a prominent advocate of *Ronald Reagan's Strategic Defense Initiative*, and was later accused of overselling the technical feasibility of the program. He was known both for his scientific ability and his difficult interpersonal relations. *Teller* is considered to be one of the key influences on the character *Doctor Strangelove* in the 1964 movie of the same name.

Dissociative Adsorption For dissociative adsorption, the following equation for the surface coverage θ_A is valid:

$$\theta_A = \frac{(K_{\text{ads},A} p_A)^{0.5}}{1 + (K_{\text{ads},A} p_A)^{0.5}} \quad (3.3.59)$$

Competitive Adsorption In practical systems, we may also have competitive adsorption of different species. The total coverage of the surface θ_t is then:

$$\theta_t = \sum_{i=1}^N \theta_i \quad (3.3.60)$$

If all components adsorb according to Langmuir's isotherm, the coverage of the surface with component 1, θ_1 , is given by:

$$\theta_1 = \frac{K_{\text{ads},1} p_1}{1 + \sum_{i=1}^N K_{\text{ads},i} p_i} \quad (3.3.61)$$

For two components A and B we obtain for the coverage with A:

$$\theta_A = \frac{K_{\text{ads},A} p_A}{1 + K_{\text{ads},A} p_A + K_{\text{ads},B} p_B} \quad (3.3.62)$$

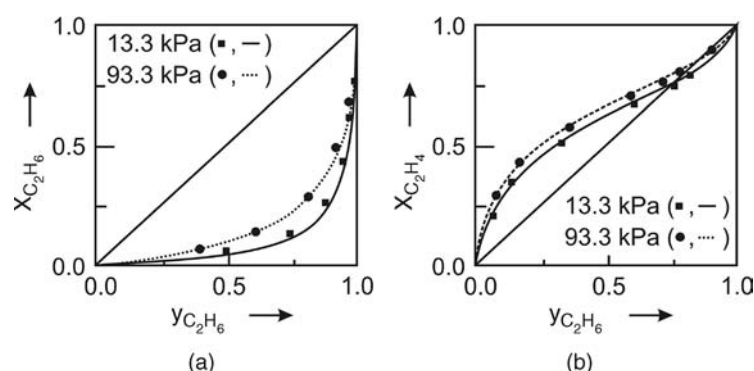
and the total coverage is given by:

$$\theta_t = \theta_A + \theta_B \quad (3.3.63)$$

Figure 3.3.45 shows two examples of competitive adsorption.

Up to now, we have only considered the thermodynamics of adsorption. However, in technical processes – for example, in a fixed bed – adsorption is a transient process until a particle or a zone of a fixed bed has reached the equilibrium loading. The intrinsic chemical process of adsorption can be regarded as instantaneous, and the mass transfer to and into the porous adsorbent determines how fast the equilibrium is reached. Experience teaches that the mass transfer resistance by film diffusion is mostly negligible, and so the adsorption is governed by pore diffusion (Topic 3.3.4). Pore diffusion can roughly be divided into macropore and micropore diffusion, for example, zeolites have macropores as well as micropores in the small crystallites, which form a sub-structure in a particle. The

Figure 3.3.45 Adsorption equilibrium of a binary system on zeolite 5 Å at 20 °C (y: molar content gas phase, x = molar content of adsorbed phase); (a) ethane–propane and (b) ethane–ethene. Adapted from Gmehling and Brehm (1996).



diffusion coefficient in micropores is much smaller than in macropores. However, the characteristic length for micropore diffusion (crystallite size about $1\text{ }\mu\text{m}$) is much lower than for macropore diffusion (particle size about 1 mm). Thus the characteristic time for micropore diffusion ($t_{\text{diff}} \sim L_{\text{diff}}^2/D$) may still be small compared to macropore diffusion, and the overall process may be dominated by macropore diffusion.

Topic 3.3.4: Adsorption kinetics (influence of pore diffusion)

The transient process of the loading of an adsorbent with an adsorbate A is described by *Fick's second law*, Eq. (3.2.66). For adsorption, we have to consider not only the change of the gas phase concentration in the pores with time (dc_A/dt) but also the change of the amount adsorbed on the internal surface of the solid ($dn_{\text{ads},A}/dt$). For a spherical particle and a constant effective diffusivity $D_{\text{eff},A}$ we find:

$$\varepsilon_p \frac{dc_A}{dt} + \frac{1}{V_p} \frac{dn_{\text{ads},A}}{dt} = D_{\text{eff},A} \frac{1}{r^2} \frac{d}{dr} \left(r^2 \frac{dc_A}{dr} \right) \quad (3.3.64)$$

According to Eqs. (3.2.75) and (3.2.76), $D_{\text{eff},A}$ is given by:

$$D_{\text{eff},A} = \frac{\varepsilon_p}{\tau_p} \left(\frac{1}{D_{\text{mol},A}} + \frac{1}{D_{\text{Knu},A}} \right)^{-1} \quad (3.3.65)$$

Rewriting Eq. (3.3.64) in terms of the loading $X_{\text{ads},A}$ ($= m_{A,\text{ads}}/m_{\text{ads}} = n_{A,\text{ads}}M_A/m_{\text{ads}}$), partial pressure p_A ($= c_A RT$), and particle density ρ_p ($= m_{\text{ads}}/V_p$) leads to:

$$\frac{\varepsilon_p}{RT} \frac{dp_A}{dt} + \frac{\rho_p}{M_A} \frac{dX_{\text{ads},A}}{dt} = \frac{D_{\text{eff},A}}{RT} \frac{1}{r^2} \frac{d}{dr} \left(r^2 \frac{dp_A}{dr} \right) \quad (3.3.66)$$

For the left-hand side of Eq. (3.3.66) we can also write:

$$\frac{\varepsilon_p}{RT} \frac{dp_A}{dt} + \frac{\rho_p}{M_A} \frac{dX_{\text{ads},A}}{dt} = \frac{dp_A}{dt} \left(\frac{\varepsilon_p}{RT} + \frac{\rho_p}{M_A} \frac{dX_{\text{ads},A}}{dp_A} \right) \quad (3.3.67)$$

and insertion of Eq. (3.3.67) into Eq. (3.3.66) and rearrangement lead to:

$$\frac{dp_A}{dt} = D_{\text{eff,ads},A} \frac{1}{r^2} \frac{d}{dr} \left(r^2 \frac{dp_A}{dr} \right) \quad \left[\text{with } D_{\text{eff,ads},A} = \frac{D_{\text{eff},A}}{\left(\varepsilon_p + \frac{RT\rho_p}{M_A} \frac{dX_{\text{ads},A}}{dp_A} \right)} \right] \quad (3.3.68)$$

where $D_{\text{eff,ads},A}$ represents an apparent effective diffusion coefficient that takes into account that the adsorption equilibrium has an influence on the adsorption rate. Equation (3.3.68) expresses that the adsorption rate – and thus formally $D_{\text{eff,ads},A}$ – decreases with increasing strength of adsorption, or more precisely with an increasing gradient of the loading with partial pressure p_A . The overall capacity for “storage” of A in the gas phase and at the surface of the pores is enhanced by adsorption, and therefore the amount of A diffusing into the particle during the transient process is higher. Thus the time needed for the adsorption increases, which is considered by the adsorption term in the denominator of Eq. (3.3.68).

It is interesting to examine two borderline cases. If the second term in the denominator of the expression for $D_{\text{eff,ads},A}$ [Eq. (3.3.68)] is much larger than the porosity of the particle (usually ε_p is about 0.5), we have a strong adsorption, and Eq. (3.3.68) leads to:

$$\frac{RT\rho_p}{M_A} \frac{dX_{ads,A}}{dt} = D_{eff,A} \frac{1}{r^2} \frac{d}{dr} \left(r^2 \frac{dp_A}{dr} \right) \quad \left(\text{for } \frac{RT\rho_p}{M_A} \left(\frac{dX_{ads,A}}{dp_A} \right) \gg \varepsilon_p \right) \quad (3.3.69)$$

Rearrangement of Eq. (3.3.69) yields:

$$\frac{1}{V_p} \frac{dn_{ads,A}}{dt} = D_{eff,A} \frac{1}{r^2} \frac{d}{dr} \left(r^2 \frac{dc_A}{dr} \right) \quad (3.3.70)$$

Equation (3.3.70) expresses that in this case we only have to consider the change of the amount of the adsorbed species of A and can neglect the change in the gas phase. [Hence Eq. (3.3.70) is equivalent to Eq. (3.3.64) for $\varepsilon_p (dc_A/dt) \ll (1/V_p) (dn_{ads,A}/dt)$.]

If the second term in the denominator of the expression for $D_{eff,ads,A}$ [Eq. (3.3.68)] is much smaller than the porosity of the particle (weak adsorption), Eq. (3.3.68) leads to:

$$\begin{aligned} \frac{dp_A}{dt} &= \frac{D_{eff,ads,A}}{\varepsilon_p} \frac{1}{r^2} \frac{d}{dr} \left(r^2 \frac{dp_A}{dr} \right) \quad \left[\text{for } \rho_p \frac{RT}{M_A} \left(\frac{dX_{ads,A}}{dp_A} \right) \ll \varepsilon_p \right] \\ &\Rightarrow \varepsilon_p \frac{dc_A}{dt} = D_{eff,A} \frac{1}{r^2} \frac{d}{dr} \left(r^2 \frac{dc_A}{dr} \right) \end{aligned} \quad (3.3.71)$$

Equation (3.3.71) expresses that if the amount of A is small compared to the amount present in the gas phase of the pores we have the “simple” case of an unsteady filling of the porous system by diffusion. Hence Eq. (3.3.71) is equivalent to Eq. (3.3.64) for $(1/V_p) (dn_{ads,A}/dt) \ll \varepsilon_p (dc_A/dt)$. {Note that Eq. (3.3.71) simply represents Fick’s second law [Eq. (3.2.66)] for a porous spherical particle.}

For a linear adsorption isotherm, $dX_{ads,A}/dp_A$ and hence $D_{eff,ads,A}$ are constant and Eq. (3.3.68) can be solved. Details are beyond the scope of this book. Here we only specify the approximation given by Kast (1988) for a loading of less than 90% of the equilibrium value:

$$\begin{aligned} \frac{\bar{X}_{ads,A}}{X_{ads,A,\infty}} &\approx \frac{6}{\sqrt{\pi}} \sqrt{\frac{D_{eff,ads,A} t}{r_p^2}} \\ &- 3 \frac{D_{eff,ads,A} t}{r_p^2} \quad \left(\text{for } \frac{D_{eff,ads,A} t}{r_p^2} < 0.2 \text{ and } \frac{\bar{X}_{ads,A}}{X_{ads,A,\infty}} < 0.9 \right) \end{aligned} \quad (3.3.72)$$

For example, the time taken to approach a mean particle load, $\bar{X}_{ads,A}$, corresponding to 50% of the maximum equilibrium value at infinite time is:

$$\frac{\bar{X}_{ads,A}}{X_{ads,A,\infty}} = \frac{1}{2} \Rightarrow \frac{D_{eff,ads,A} t_{ads,50\%}}{r_p^2} = 0.03 \Rightarrow t_{ads,50\%} = \frac{0.0075 d_p^2}{D_{eff,ads,A}} \quad (3.3.73)$$

If we take adsorption of water vapor on silica or on charcoal as an instructive example, we have according to Sattler (2001) a value of D_{eff,ads,H_2O} of approximately $10^{-10} \text{ m}^2 \text{s}^{-1}$. Thus we obtain a characteristic time t_{ads} for a particle diameter of 2 mm of 300 s.

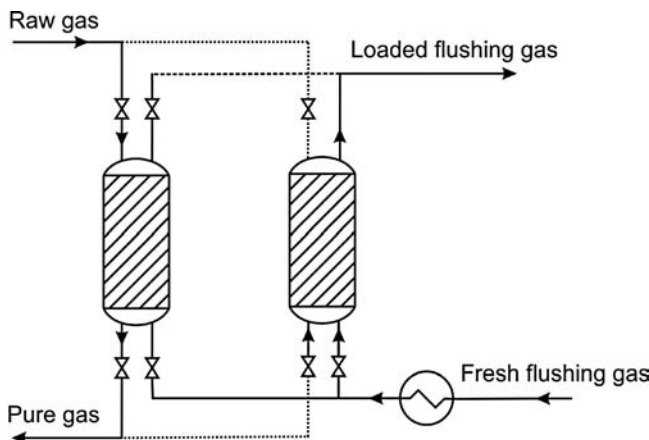
3.3.5.2 Design of Adsorption Processes

Table 3.3.10 lists application areas of gas and liquid phase adsorption. Figure 3.3.46 shows a typical process.

Adsorption is a transient process, and at least two adsorption beds are needed. The first bed (Figure 3.3.46, left-hand side) is utilized until or just before breakthrough of the adsorbed component(s) occurs, that is, a noticeable increase of concentration of adsorbed species is detected at the outlet of adsorber. Then the adsorbent is regenerated by desorption of the adsorbed gas(es), while a second, freshly regenerated bed, is now “on duty.”

Table 3.3.10 Application areas of adsorption of liquid and gaseous components.

Adsorbate	Adsorbent
Gas phase adsorption	
H_2S , CO_2 , water (steam)	$\gamma\text{-Al}_2\text{O}_3$, silica gel, molecular sieve
Hydrocarbons	Activated carbon
Solvents	Activated carbon, silica gel
Organic sulfur compounds	Fe_2O_3 , ZnO
<i>n</i> -Paraffins	Molecular sieve
Liquid phase adsorption	
Water softening and desalination	Ion exchanger
Dephenoxylation of sewage water	Activated carbon
Decoloration	Activated carbon
Separation of <i>n</i> -paraffins, olefins, <i>p</i> -xylene from organic mixtures	Molecular sieve

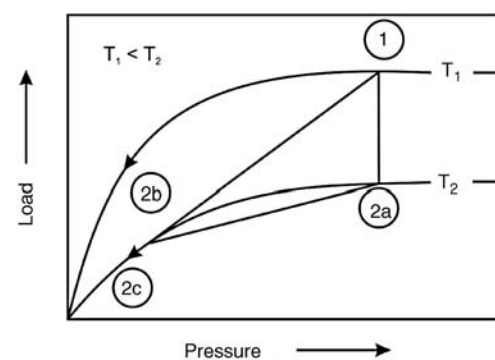
**Figure 3.3.46** Typical design of a fixed-bed adsorption process.

Regeneration of the loaded bed by purging is accomplished by pressure reduction and back-flushing, for example, with a small amount of the cleaned gas (Figures 3.3.46 and 3.3.47). Thus we reduce the partial pressure of the desorbing species, which has a similar effect as a reduction of total pressure (<1 bar) by vacuum. An additional increase in temperature may also help, as desorption is endothermic and thus favored by higher temperatures.

The concentration of the adsorbate, as well as the loading of the adsorbent, depends on the local position in the adsorption bed and on the time on stream (Figure 3.3.48). Initially, the fluid enters an unloaded bed and comes into contact with the first few layers of the adsorbent. The layers near the entrance of the bed are soon saturated and the adsorbate penetrates further into the bed. With increasing adsorption time the adsorption front moves through the bed, and if the end of the adsorber is reached, breakthrough occurs. The process is stopped at a predetermined maximum concentration in the gas, and the bed is regenerated. If the passage of the fluid is continued still further, the exit concentration continues to rise until the inlet concentration is reached (Figure 3.3.48).

Figure 3.3.49 depicts a snapshot of the adsorption front after a certain time on stream. The adsorption bed can be subdivided into three zones (for $t < t_{\text{breakthrough}}$):

- 1) In the front part of the adsorber, equilibrium loading corresponding to the inlet partial pressure of the adsorbate is achieved (area/zone of saturation in Figure 3.3.49).
- 2) Next follows the zone of adsorbate reduction, the so-called mass transfer zone (MTZ), as a certain length of the adsorber is required for the mass transfer of the adsorbate from the fluid phase to the internal surface of the porous adsorbent. The length of this section is designated as the height of transfer zone (HTZ,

**Figure 3.3.47** Desorption (regeneration) of an adsorbent by increase of temperature and/or decrease of pressure; 1–2a: isobaric increase of temperature; 1–2b: isothermal decrease of pressure; 1–2c: simultaneous increase of temperature and decrease of pressure; backflushing may lead to lower values of the loading beyond 2b and 2c. Adapted from Gmehling and Brehm (1996).

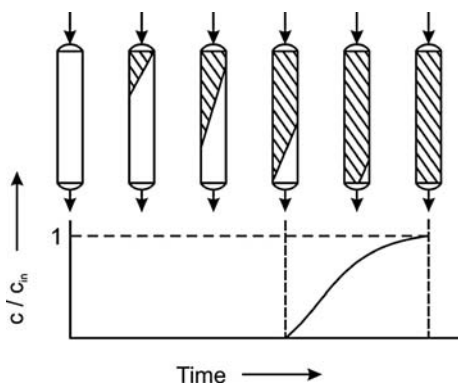


Figure 3.3.48 Typical adsorption front and breakthrough curve adapted from Gmehling and Brehm (1996).

Example 3.3.8: Estimation of the slope of the breakthrough curve

Exact calculation of the length and shape of breakthrough curve is rather complicated, but we may use the following correlation given by Kast (1981) to estimate the slope of the breakthrough curve at the point of inflection in approximation:

$$\frac{d\left(\frac{p_A}{p_{A,in}}\right)}{dt} = \sqrt{\frac{15D_{ads,eff,A} u_{front}}{\pi d_p^2 L_{ads}}} = \frac{\sqrt{15D_{ads,eff,A}}}{\sqrt{t_{front}}} \quad (\text{for } p_A = 0.5 p_{A,in}) \quad (3.3.74)$$

Thus Eq. (3.3.74) is only valid for the point where we reach a mean adsorption loading of approximately 50% of the maximum equilibrium value. In addition, Eq. (3.3.74) was deduced based on the assumption of a linear adsorption isotherm, and is therefore only a very rough estimation for a Langmuir isotherm and so on, as shown below.

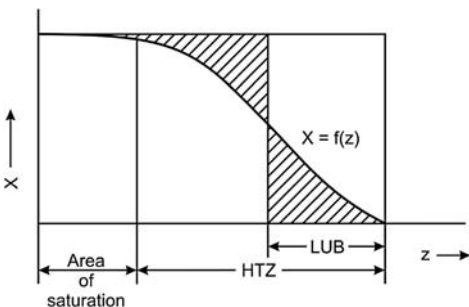


Figure 3.3.49 Height of mass transfer zone *HTZ* and length of unused bed *LUB* adapted from (Sattler, 2001).

Figure 3.3.50 Influence of pore diffusion on the form of the breakthrough curve for a residence time of the adsorption front (t_{front}) of 2000 s. Adapted from Kast (1988).

Figure 3.3.49). The value of the *HTZ* is determined by the competition of the rate of adsorption (which depends on the diffusivity of the adsorbate and on the adsorption isotherm, Example 3.3.8) with the flow rate of the fluid. In the *MTZ* with length *HTZ* the adsorbent is on average loaded only to half its maximum equilibrium capacity corresponding to the inlet partial pressure. The length of the unused bed (*LUB*) is therefore roughly equivalent to half of the *HTZ*. Both the *LUB* and the *HTZ* depend on the diffusivity and on the adsorption isotherm (Example 3.3.8).

- 3) The rear part of the bed beyond the *HTZ* is unloaded.

Calculation of the slope of the breakthrough curve and of the *LUB* and *HTZ* is complicated and, mostly, modeling by computer is needed (see Example 3.3.8 for an estimation of the slope).

Figure 3.3.50 shows the influence of mass transfer by pore diffusion on the slope and form of the breakthrough curve.

As a characteristic parameter we use here the term under the square root of the numerator of Eq. (3.3.74), and obtain:

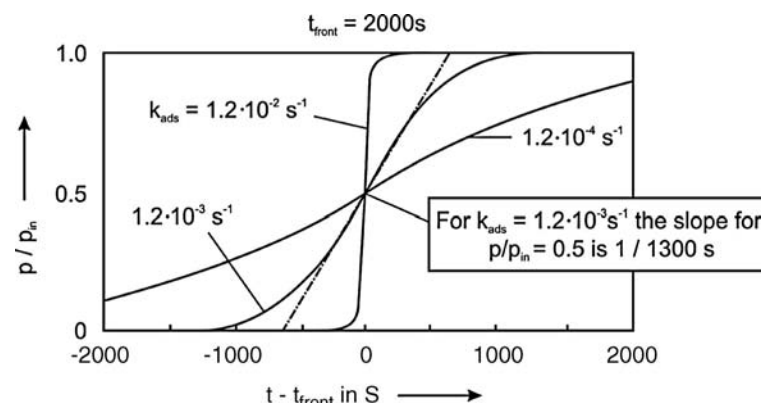
$$\frac{d\left(\frac{p_A}{p_{A,in}}\right)}{dt} = \sqrt{\frac{k_{ads}}{t_{front}}} \quad \left(\text{with } k_{ads} = \frac{15D_{eff,ads,A}}{\pi d_p^2}, \text{ valid for } p_A = 0.5 p_{A,in} \right) \quad (3.3.75)$$

The parameter k_{ads} can be regarded as the effective rate coefficient of adsorption.

We may now prove Eq. (3.3.75) by the data of Figure 3.3.50. For example, for a value of k_{ads} of $1.2 \times 10^{-3} \text{ s}^{-1}$ and a residence time of the adsorption front t_{front} of 2000 s we obtain a slope according to Eq. (3.3.75) of about $1/1300 \text{ s}^{-1}$, which is in agreement with Figure 3.3.50.

The shape of the adsorption front may change as the front moves through the bed, and the mass transfer zone may broaden or diminish. As described by Kast (1988), linear or concave isotherms tend to broaden, and convex Langmuir and Freundlich isotherms quickly achieve a constant pattern. This means that the shape of the front no longer changes during its motion through the adsorber, and that the *HTZ* is constant. For a constant pattern of behavior, measurements on a small scale apparatus can be used for the scale-up to a full-sized adsorber.

Figure 3.3.51 shows the breakthrough curves for the example of H_2S adsorption on a molecular sieve, where we have such a constant pattern behavior of the profiles



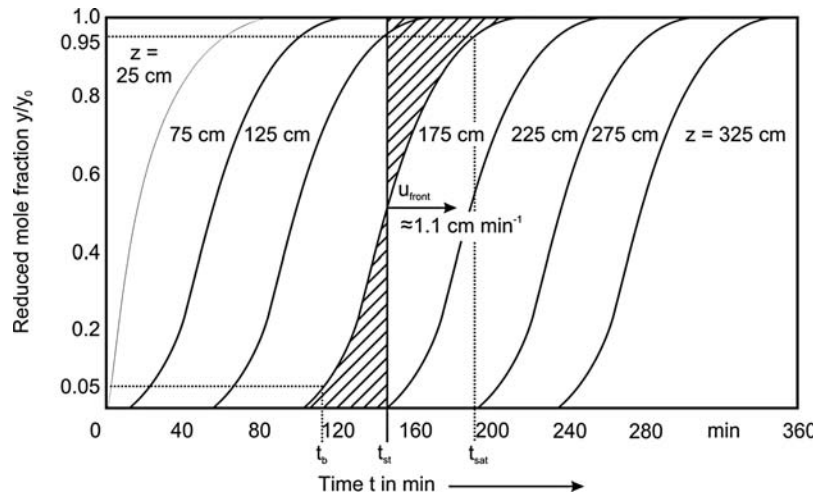


Figure 3.3.51 Breakthrough curves for the example of H_2S adsorbed on a molecular sieve ($d_p = 2.2 \text{ mm}$, $p = 60 \text{ bar}$, $p_{\text{H}_2\text{S,in}} = 43 \text{ mbar}$, $u_s = 15 \text{ cm s}^{-1}$). Data from Groninger, Hedden, and Rao (1987).

of the mole fraction of H_2S . To calculate HTZ and the LUB (Example 3.3.8) we may use for practical reasons 1% (and not 0%) of the inlet mole fraction for the breakthrough time t_B (i.e., $y_{\text{H}_2\text{S}}/y_{\text{H}_2\text{S,0}} = 0.01$) and, for reasons of symmetry, $y_{\text{H}_2\text{S}}/y_{\text{H}_2\text{S,0}} = 0.99$ for the saturation time t_{sat} . The stoichiometric time t_{ST} is defined by the equality of the hatched areas as shown in Figure 3.3.51 for $L = 175 \text{ cm}$.

For a given diameter, the key parameter of the design of an adsorber is the length of the bed needed for a given duty. Thus, the equilibrium loading and the adsorption kinetics are needed.

The total length required can be divided into (i) the (minimal) ideal length, $L_{\text{ads,ideal}}$, which is equivalent to the case that the adsorbent is fully utilized at each position in the bed corresponding to the equilibrium loading ($HTZ = 0$), and (ii) the length of the unused bed (LUB) that is left over at breakthrough (Figure 3.3.49). In turn, this implies that $L_{\text{ads,ideal}}$ is equal to the sum of the length of the bed where saturation is reached and the LUB (Figure 3.3.49).

Minimal Ideal Length of Adsorber $L_{\text{ads,ideal}}$ In contrast to the LUB and HTZ , calculation of $L_{\text{ads,ideal}}$ is straightforward based on the mass balance of the adsorbate A:

$$\dot{m}_{A,\text{in}} t_{\text{ads}} = m_{\text{ads,min}} X_{\text{ads,A,sat}} \quad (3.3.76)$$

Rewriting Eq. (3.3.76) leads to:

$$\underbrace{(u_s A_{\text{ads}})}_{\dot{V}_{\text{fluid}}} \underbrace{\left(\frac{p_{A,\text{in}} M_A}{RT} \right)}_{\dot{m}_{A,\text{in}}/\dot{V}_{\text{fluid}}} t_{\text{ads}} = \underbrace{(L_{\text{ads,ideal}} A_{\text{ads}})}_{V_{\text{ads,min}}} \underbrace{\left[(1 - \varepsilon) \rho_p \right]}_{\rho_{\text{bed}}} X_{\text{ads,A,sat}} \quad (3.3.77)$$

where ε is the porosity of the bed, ρ_p the particle density, A_{ads} the cross-sectional area of the bed, and u_s the superficial fluid velocity, usually $0.1\text{--}0.5 \text{ m s}^{-1}$. For a given adsorption time t_{ads} , the (ideal) minimum required length is obtained by rearrangement of Eq. (3.3.77):

$$\boxed{L_{\text{ads,ideal}} = L_{\text{ads,min}} = \left(\frac{M_A}{RT(1 - \varepsilon)\rho_p} \right) \left(\frac{p_{A,\text{in}}}{X_{\text{ads,A,sat}}} \right) u_s t_{\text{ads}}} \quad (3.3.78)$$

The first term in Eq. (3.3.78) is constant for a given temperature. For a certain adsorbent–adsorbate system and thus for a given relation of the loading of adsorbate and partial pressure of the adsorbate (adsorption isotherm), the second term ($p_{A,\text{in}}/X_{\text{ads,A,sat}}$) is also constant (for a given inlet partial pressure). Thus the minimum required length $L_{\text{ads,ideal}}$ increases proportionally with both superficial gas velocity and the required adsorption time, that is, the operating time before regeneration is needed and a second, freshly regenerated bed comes “on duty.”

Length of Unused Bed of an Adsorber LUB The height of the transfer zone is determined based on experimental data of the front velocity u_{front} and the difference between saturation time t_{sat} and breakthrough time t_b (Figure 3.3.51):

$$HTZ = u_{\text{front}}(t_{\text{sat}} - t_b) \quad (3.3.79)$$

In a similar manner, the length of unused bed LUB ($\approx 0.5 HTZ$) is calculated from u_{front} and the difference between stoichiometric time t_{st} and breakthrough time t_b (Figure 3.3.51):

$$\nabla_o \quad LUB = u_{\text{front}}(t_{\text{st}} - t_b) \quad (3.3.80)$$

The velocity of the adsorption front u_{front} is in many cases almost constant and given by:

$$u_{\text{front}} = \frac{\Delta L_{\text{st}}}{\Delta t_{\text{st}}} = \frac{L_{\text{st},n} - L_{\text{st},n-1}}{t_{\text{st},n} - t_{\text{st},n-1}} \quad (3.3.81)$$

where L represents the length where the stoichiometric concentration of the adsorbate (e.g., 50% of the inlet value) is reached after a certain time t and is, for example, determined based on experiments with two or more different bed lengths (Figure 3.3.51).

For a symmetric concentration profile we can also calculate u_{front} by rearrangement of Eq. (3.3.78):

$$\nabla_o \quad u_{\text{front}} = \frac{L_{\text{ads,ideal}}}{t_{\text{ads}}} = \left[\frac{M_A}{RT(1-\varepsilon)\rho_p} \right] \left(\frac{p_{A,\text{in}}}{X_{\text{ads},A,\text{sat}}} \right) u_s \quad (3.3.82)$$

Total Design Length of an Adsorber $L_{\text{ads,design}}$ For a technical adsorber, we have to stop the process at breakthrough, defined by a certain limiting value at the outlet of the adsorber, for example, 1% of the inlet content. Thus for the total design length we have to add the LUB to the minimum required ideal length:

$$\nabla_o \quad L_{\text{ads,design}} = LUB + L_{\text{ads,ideal}} \quad (3.3.83)$$

Hence, the overall time of adsorption before a breakthrough occurs is:

$$t_{\text{ads,design}} = \frac{(LUB + L_{\text{ads,ideal}})}{u_{\text{front}}} \quad (3.3.84)$$

Note that the (mean) velocity u_{front} of the adsorption front does not depend on the length and shape of the MTZ , and corresponds to the velocity of the movement of the centroid of the adsorption front through the bed, which is constant for a constant pattern behavior. In addition, note that u_{front} does not necessarily increase with increasing partial pressure of the adsorbent p_A , as we spuriously might expect on the basis of Eq. (3.3.82). We have to consider that the equilibrium loading $X_{\text{ads},A,\text{sat}}$ probably also depends on p_A , for example, for a Langmuir-type adsorption we have:

$$X_{\text{ads},A,\text{sat}} = \frac{ap_A}{1 + K_{\text{ads},A} p_A} \quad (3.3.45)$$

and insertion of Eq. (3.3.45) into Eq. (3.3.82) leads to:

$$u_{\text{front}} = \left[\frac{M_A u_s}{RT(1-\varepsilon)\rho_p a} \right] \left(1 + K_{\text{ads},A} p_{A,\text{in}} \right)$$

$$\Rightarrow \begin{cases} u_{\text{front}} \sim p_{A,\text{in}} & \text{for } K_{\text{ads},A} p_{A,\text{in}} \gg 1 \\ u_{\text{front}} = \text{constant} & \text{for } K_{\text{ads},A} p_{A,\text{in}} \ll 1 \end{cases} \quad (3.3.85)$$

Calculation of the parameters $L_{\text{ads,ideal}}$, HTZ , LUB , and so on based on breakthrough curves are explained by the example of H_2S adsorption on a molecular sieve in Example 3.3.9.

Example 3.3.9: Calculation of $L_{\text{ads, ideal}}$, HTZ, and LUB based on breakthrough curves

As an example of how to calculate the adsorption (breakthrough) time of a fixed bed adsorber, we use the breakthrough curves of H_2S during the adsorption on a molecular sieve (Figure 3.3.51). For the calculation, we use the following data (Groninger, Hedden, and Rao, 1987): adsorption temperature $T = 293 \text{ K}$, molar mass $M_{\text{H}_2\text{S}} = 34 \text{ g mol}^{-1}$, particle density $\rho_p = 1300 \text{ kg m}^{-3}$, porosity of bed $\varepsilon_p = 0.43$, and superficial gas velocity $u_s = 15 \text{ cm s}^{-1}$. The total length of the adsorber (fixed bed) should be 10 m. According to Figure 3.3.41b, the equilibrium loading $X_{\text{H}_2\text{S},\infty}$ for $p_{\text{H}_2\text{S,in}} = 43 \text{ mbar}$ and a total pressure of 60 bar is 0.07 kg kg^{-1} .

The velocity of the adsorption front u_{front} is calculated from the distances between two measuring points and between the corresponding stoichiometric times. According to Figure 3.3.51 and Eq. (3.3.81) we find here:

$$u_{\text{front}} = \frac{\Delta L_{\text{st}}}{\Delta t_{\text{st}}} = \frac{325 \text{ cm} - 175 \text{ cm}}{280 \text{ min} - 145 \text{ min}} = 1.11 \text{ cm min}^{-1}$$

The velocity of the adsorption front u_{front} may also be calculated by Eq. (3.3.82) and the data given above, which gives almost the same value of 1.04 cm min^{-1} .

The height of the transfer zone HTZ and the length of the unused bed LUB are calculated by Eqs. (3.3.79) and (3.3.80) and the values given in Figure 3.3.51; we obtain:

$$\begin{aligned} \text{HTZ} &= u_{\text{front}}(t_{\text{sat}} - t_b) = 1.1 \text{ cm min}^{-1}(40 \text{ min}) \\ &= 44 \text{ cm and LUB} = 2\text{HTZ} = 88 \text{ cm} \end{aligned}$$

Thus for the given length of the adsorber of 10 m, 9% (0.9 m) is needed for the unused bed. Based on the minimum length of an ideal adsorber (here 9.1 m) and Eq. (3.3.78) we can calculate the breakthrough time of adsorption, before we have to switch to a freshly regenerated adsorber:

$$t_{\text{ads}} = \frac{L_{\text{bed}} - L_{\text{UB}}}{u_{\text{front}}} = \frac{9.1 \text{ m}}{1.1 \text{ cm min}^{-1}} = 13.8 \text{ h}$$

To summarize: The main design parameter of an adsorber is the length needed for a given time on stream before breakthrough occurs as we

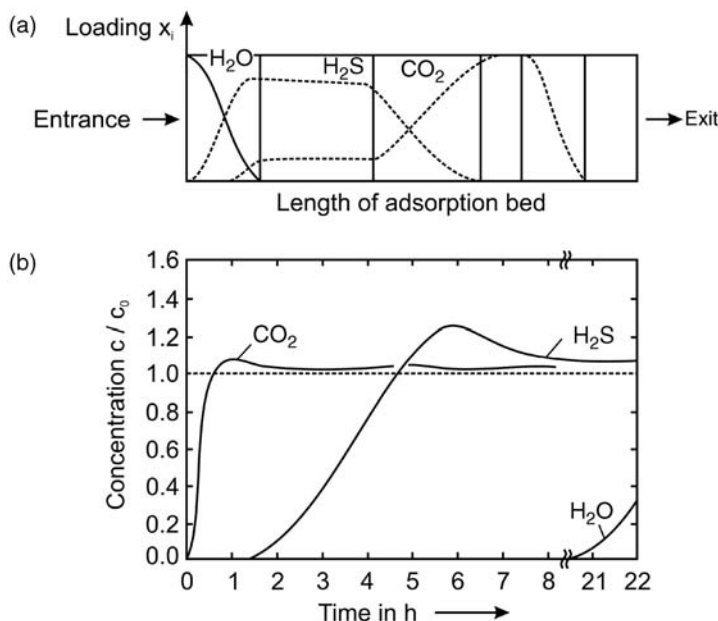


Figure 3.3.52 (a) Adsorption fronts (schematically shown for a time before breakthrough of CO_2 occurs); (b) breakthrough curves of the competitive adsorption of CO_2 , H_2S , and H_2O from natural gas (adapted from Gmehling and Brehm, 1996).

then we have to switch to a freshly regenerated bed. The overall length is the sum of the minimum length, which only depends on the equilibrium loading and the rate of fluid flow, Eq. (3.3.76), and a surcharge we have to pay for the kinetics, the length of the unused bed LUB, which is mostly governed by pore diffusion.

In principle, the concentration of the adsorbate in the effluent stream is zero before breakthrough, at least if we have no by-pass effects induced by very narrow packed beds with an aspect ratio d_{ads}/d_p of less than about 10 (Section 4.10.6.5). For laboratory-scale adsorbers, this effect is not negligible, but for technical adsorbers with a bed diameter of about 1 m and a particle diameter of about 1 mm (aspect ratio $d_{\text{ads}}/d_p \gg 10$) this effect is negligible.

The high purity of the effluent of adsorption is hardly achievable by other separations. Distillation (Section 3.3.2) is limited with regard to the effluent purity by the number of trays that can be installed in a column, which is usually not more than 100. The same is true for extraction (Section 3.3.4) and absorption (Section 3.3.3) with regard to the number of separation stages.

In many industrially operated adsorbers, several gas components are adsorbed simultaneously (competitive adsorption). For example, CO_2 , H_2S , and water vapor have to be separated from crude natural gas. Figure 3.3.52 shows the breakthrough curves of these three components. The CO_2 breakthrough curve is very steep and the breakthrough occurs early. Surprisingly at first sight, the CO_2 content at the adsorber outlet increases further after the breakthrough curve has reached the inlet content ($c_{\text{CO}_2,\text{out}} > c_{\text{CO}_2,\text{in}}$) but the explanation is straightforward. No more (or very little) CO_2 is adsorbed, and the adsorption front of the more strongly adsorbed H_2S moves through the reactor and displaces the already adsorbed CO_2 , which adds up to the inlet content of CO_2 . For H_2S we have a similar phenomenon as water vapor displaces adsorbed H_2S (and CO_2).

3.3.6

Fluid–Solid Extraction

3.3.6.1 Principles of Fluid–Solid Extraction

Fluid–solid extraction, also called leaching, is used to separate a substance from a solid matrix by solution into a suitable solvent. The solvent is either a liquid, for example, hot water or an organic solvent, or a supercritical fluid, most notably water or carbon dioxide.

Various solid ingredients are separated by extraction, for example, caffeine from coffee, vegetable oils from oilseeds, hop extract from hops, or drugs, fragrances, and flavors from plant materials. The feed material (e.g., a plant) frequently contains only very little valuable ingredients. Consequently, separation by pressing and squeezing is not possible, and certain ingredients such as fragrances or odors are too sensitive for distillation and denature on heating. Further examples are the extraction of sugar from sugar cane or of heavy oils from oil shale and tar sands. In addition, from everyday life, well-known liquid–solid extractions include dry-cleaning or percolated coffee from coffee powder.

Leaching is also widely used in extractive metallurgy since many metals form soluble salts in aqueous and non-aqueous acidic or basic liquids (lixivants). Compared to pyrometallurgical processes, leaching is easy to perform and less harmful as no gaseous pollution occurs. Typical feedstocks are metal oxides or sulfides, for example, acid leaching of zinc oxide to dissolve solid ZnO as soluble zinc sulfate ($\text{ZnO} + \text{H}_2\text{SO}_4 \rightarrow \text{ZnSO}_4 + \text{H}_2\text{O}$).

In some cases, extraction is not just a physical process but is also accompanied by a chemical reaction that initially converts the extract into a soluble form, for example, cellulose digestion.

The solid feed material is mostly porous, and the ingredient may be present in the raw material as a solid or a firmly bonded liquid. During extraction, the solvent penetrates into the pores and dissolves the extract. Ideally, the equilibrium solubility of the extract in the extraction solution is achieved. Total extraction is not possible, as a certain quantity of solvent, and thus also of extract, remains in the solid residue by adhesive forces.

In a technical process, the rate of extraction determines how closely and rapidly we reach the equilibrium solubility. This rate is the result of the interplay of mass transfer from the bulk phase of the solvent to the particle, pore diffusion, and dissolution into the solvent. Hence, depending on the value of the respective rate constants of these three processes, external and/or internal mass transfer may influence the effective extraction rate.

In general, the effective extraction rate is enhanced by the following factors:

- The feed material should be ground to increase the external surface area (enhancement of external mass transfer, Topic 3.3.5) and to reduce the diffusion length for the internal mass transfer by pore diffusion.
- A high flow rate ensures a high concentration gradient between the extract solution in the pores and in the solvent surrounding the particles.
- A temperature as high as possible should be adjusted to decrease the viscosity and thus to increase the diffusion coefficient. The solubility of many extracts thereby also increases. With regard to the pressure drop of fixed bed extraction, a low viscosity is also favorable.

An “ideal” solvent should satisfy the following requirements:

- a high solubility of the extract without dissolving of other components;
- a high chemical stability, non-flammable, non-toxic and non-corrosive;
- a low boiling point with regard to extract–solvent separation.

Table 3.3.11 Examples of products extracted using supercritical CO₂. Data from Goedecke (2006).

Feed material	Extract	p (bar)	T (°C)
Oil seeds	Vegetable oil	Up to 700	50
Pepper	Pepper oil	90	40
	Piperine	300–350	40–60
Coffee	Caffeine	300	80
Tobacco	Nicotine	Up to 1000	50
Paprika	Oleoresin	350	60
Hops	Hop extract	Up to 400	50
Cinnamon	Eugenol, cinnamon aldehyde	200	50
Chamomile	Matricine	90	40

Table 3.3.12 Critical data, density, diffusion coefficient, and viscosity of gases typically used for high-pressure fluid–solid extraction processes. Data from Sattler (1986).

Critical data			
Solvent	T _{crit} (°C)	p _{crit} (bar)	ρ _{crit} (kg m ⁻³)
Carbon dioxide	31.3	73.8	0.45
Propane	96.8	40.6	0.22
Toluene	320.8	41.6	0.26
Water	374.2	216.9	0.26
Order of magnitude of density, diffusion coefficient, and viscosity			
	Gas (1 bar, 0 °C)	Liquid	Supercritical
Density (kg m ⁻³)	1	1000	300
Diffusion coefficient (m ² s ⁻¹)	10 ⁻⁵	10 ⁻⁹	10 ⁻⁷
Viscosity (Pa s)	10 ⁻⁵	10 ⁻³	10 ⁻⁵

Important solvents are hydrocarbons, carbon disulfide (CS₂), ethers, and low boiling alcohols. Here only an overview of the technology of high-pressure extraction with supercritical fluids is given. For further details, see Voeste *et al.* (1998) or Goedecke (2006).

Table 3.3.11 lists examples of extraction products obtained with supercritical CO₂. Supercritical fluids such as water have also been studied for the production of fuels from coal and oil shale (Wilhelm and Hedden, 1950; Missal and Hedden, 1990). The oil extract can then be simply fractionated by means of a change of state.

Supercritical water and carbon dioxide are attractive for extractions as they are cheap (not always with regard to the operational costs), contaminant free, and cheaper to dispose of than organic solvents. In addition, supercritical extraction does not leave a chemical residue, which is an important aspect in the food industry. For CO₂, the critical parameters are rather low (31 °C and 74 bar) compared to water and many other gases (Table 3.3.12). This helps to prevent thermal degradation of components that are being extracted. For these reasons supercritical CO₂ is the solvent of choice, for example, to extract caffeine from green coffee beans.

Supercritical fluids have solvation properties similar to organic solvents, but a higher diffusivity and a lower viscosity, and these properties can be adjusted by pressure or temperature. An example is shown in Figure 3.3.53 for the system caffeine and carbon dioxide at 40 °C, which is just above the critical value of 31 °C. For elucidation, the phase diagram of CO₂ is also shown. As soon as we pass the critical pressure of 73.8 bar, the solubility increases by several orders of magnitude.

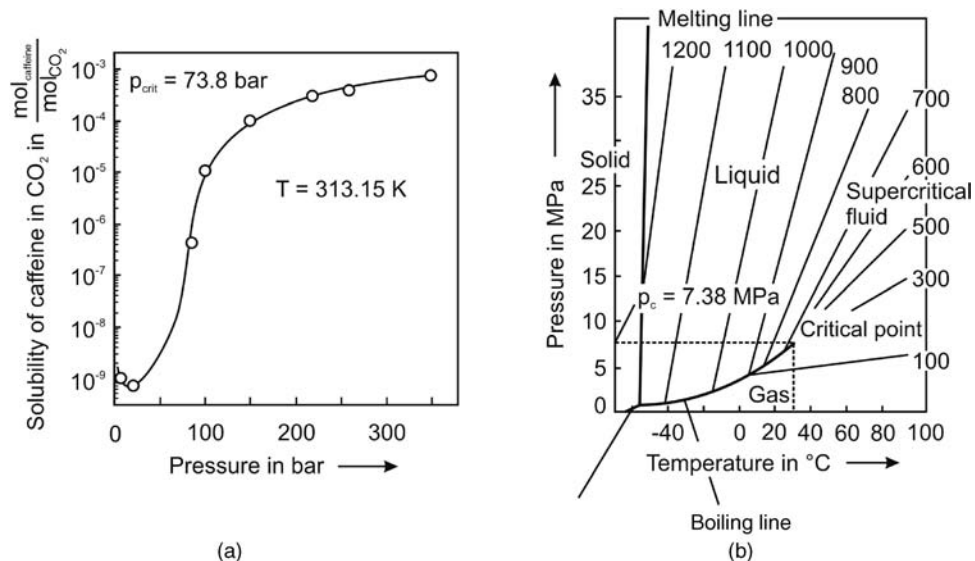


Figure 3.3.53 (a) Solubility of caffeine in CO_2 at 40°C (data from Xu *et al.*, 2000); (b) p - T diagram (densities in kg m^{-3} are given as third dimension) of CO_2 (adapted from Viani and Petracco, 2007).

Topic 3.3.5: Influence of particle size on rate of external mass transfer

To examine the influence of the particle size on the rate of external mass transfer (and thus potentially on the effective rate of extraction) we assume the following situation:

- Extraction is only determined by external mass transfer, that is, the effective dissolution rate within the porous particles (assumed to be spherical) is considered to be relatively high. Thus the concentration of the dissolved substance A at the external surface equals the equilibrium solubility ($c_{A,\text{equilibrium}}$). For the bulk phase concentration ($c_{A,\text{solvent}}$) we assume a value of zero (high surplus of solvent).
- The mass transfer coefficient β is given by Eq. (3.2.68), and according to Eq. (3.2.70) the minimal *Sherwood number* is 2 (no agitation of the liquid, single particle).

The mass transfer rate is given by Eq. (3.2.67), which reads for the given situation as:

$$\begin{aligned}\dot{n}_A &= \beta A_p (c_{A,\text{equilibrium}} - c_{A,\text{solvent}}) \approx Sh_{\min} \frac{D_A}{d_p} A_p (c_{A,\text{equilibrium}} - 0) \\ &\approx 2 \frac{D_A}{d_p} A_p c_{A,\text{equilibrium}}\end{aligned}\quad (3.3.86)$$

The external surface area ($A_{p,i}$) and the total volume of the spherical particles ($V_{p,i}$) depend on the number N_i of particles and on the particle diameter ($d_{p,i}$):

$$A_{p,i} = N_i \pi d_{p,i}^2 \quad (3.3.87)$$

$$V_{p,i} = N_i \frac{\pi}{6} d_{p,i}^3 \quad (3.3.88)$$

We now inspect the effect of grinding on the external mass transfer. Before grinding, we have particles (number N_1) with a diameter $d_{p,1}$. By grinding, the size is reduced ($d_{p,2} < d_{p,1}$) and the number increases to $N_2 > N_1$. As the total volume is constant, the number of ground particles is given by (if we assume that grinding leads to particles of equal size):

$$V_{p,1} = N_1 \frac{\pi}{6} d_{p,1}^3 = V_{p,2} = N_2 \frac{\pi}{6} d_{p,2}^3 \Rightarrow \frac{N_2}{N_1} = \left(\frac{d_{p,1}}{d_{p,2}} \right)^3 \quad (3.3.89)$$

Combination of Eqs. (3.3.86) to (3.3.89) yields:

$$\frac{\dot{n}_{A,2}}{\dot{n}_{A,1}} = \frac{2 \frac{D_A}{d_{p,2}} N_2 \pi d_{p,2}^2 c_{A,\text{equilibrium}}}{2 \frac{D_A}{d_{p,1}} N_1 \pi d_{p,1}^2 c_{A,\text{equilibrium}}} = \frac{N_2 d_{p,2}}{N_1 d_{p,1}} = \left(\frac{d_{p,1}}{d_{p,2}} \right)^3 \frac{d_{p,2}}{d_{p,1}} = \left(\frac{d_{p,1}}{d_{p,2}} \right)^2 \quad (3.3.90)$$

Thus the extraction rate is proportional to the square of the particle size (for the assumed case of complete control by external mass transfer), that is, enhanced by a factor of four for a size reduction by a factor of two.

3.3.6.2 Design of Fluid–Solid Extractions

Extraction is carried out batchwise or continuously. For batch extraction, rotating extractors are frequently used, serving both for extraction and the subsequent separation of the solvent from the extraction residue by distillation. Batch extractors are simple and robust, but have a limited capacity, and the periodic filling and emptying is time consuming. Consequently, for bulk materials continuous countercurrent extractors with a capacity of up to several 1000 t d^{-1} are widely used to process oilseeds, but they are also used for coffee and tea (Figure 3.3.54).

In the food industry, commercial plants with supercritical fluids have so far only been used with supercritical CO_2 as solvent. The first plant was opened in 1981 in Bremen (Germany) for decaffeination of coffee, by a process invented in the 1970s by Zosel (1973). Plants for the production of hop extract and for the decaffeination of tea are today also in operation, for example, in Germany, England, and Australia (Voeste *et al.*, 1997). Supercritical hydrocarbons such as propane are also used, for example, for deasphalting of heavy oils or for the removal of triglycerides from fish oils.

Countercurrent extraction with supercritical CO_2 is shown in Figure 3.3.55 for the extraction of caffeine from moist green coffee beans. After extraction, the supercritical CO_2 is separated from the extracted caffeine by water in a washing tower (Figure 3.3.55a) or the caffeine is adsorbed in a column by activated carbon, and the CO_2 is continuously recycled (Figure 3.3.55b).

To design such a process, the McCabe–Thiele method may be used to determine the number of theoretical separation stages, as examined in Sections 3.3.2–3.3.4 for distillation, absorption (gas scrubbing), and liquid–liquid-extraction. Thus, we obtain the number of theoretical extraction stages of a countercurrent extraction column based on the equilibrium curve (solubility of extract in the solvent for a given content in the solid) and the operating line. The latter depends on the extract content of the solid feed and residue, and on the in- and outlet extract concentration in the solvent. The extract content of the feed is fixed, and the value of the residue is specified by the required degree of extraction. The inlet content of the extract in the solvent is also fixed, as either pure solvent is used or the value is specified by separation of the extract from the used solvent after the extraction. Therefore, the only parameter that is left is the outlet concentration of the extract in the solvent, which depends on the ratio of the solvent flow to the feed rate of the solid feedstock (mass balance).

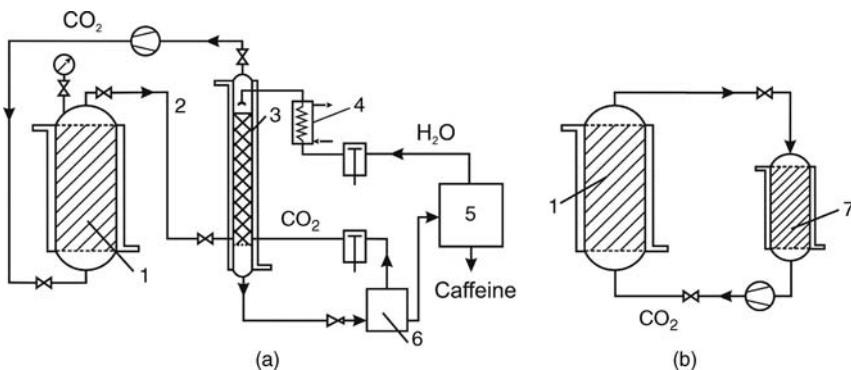


Figure 3.3.54 Typical column of a continuously operated high-pressure extraction (diameter: 800 mm, effective length: 12 m, operating pressure: 500 bar). Courtesy of Uhde, Germany.

Figure 3.3.55 Decaffeination with supercritical CO_2 (adapted from Viani and Petracco, 2007): (a) caffeine is washed off the fluid with water in a washing tower and recuperated; (b) caffeine is adsorbed on a column with activated carbon or resin, and the fluid is continuously recycled; (1) moist green beans, (2) $\text{CO}_2 +$ caffeine, (3) washing tower, (4) heat exchanger, (5) distillation column, (6) degassing chamber, and (7) active carbon or adsorbing resin column.

3.3.7

Crystallization

Crystallization is mainly used for separation as an alternative to distillation, if the involved compounds are thermally unstable (e.g., acrylic acid), have a low or practically no vapor pressure (like salts), if the boiling points are similar, or if the system forms an azeotrope. Crystallization is used for the production and purification of various organic chemicals ranging from bulk chemicals (*p*-xylene and naphthalene) to fine chemicals like pharmaceuticals (e.g., proteins). Further examples of industrial crystallization processes are sugar refining, salt production for the food industry, and silicon crystal wafer production.

The basic thermodynamic equation of crystallization for an ideal liquid and solid phase is:

$$\ln \frac{x_{i,\text{liq}}}{x_{i,s}} = -\frac{\Delta_{\text{melt}}H_i}{R} \left(\frac{1}{T} - \frac{1}{T_{\text{melt},i}} \right) \quad (3.3.91)$$

This equation is only valid if the activity coefficient of the liquid and the solid phase is 1.

Solid–liquid phase equilibria are typically shown in phase diagrams, usually by the temperature versus the composition of the liquid and the solid phase. Subsequently, only two cases are considered, which represent most binary systems.

3.3.7.1 **Ideal Binary Eutectic Phase System**

If the liquid phase is ideal, but the solid phase only consists of a pure crystalline component, we have a eutectic system. These phase systems allow crystallization of a pure component in a single step, until the point of eutectic composition is reached, where the solid and the liquid phase have the same composition. Hence, the yield is limited by the eutectic point.

In this case, Eq. (3.3.91) simplifies ($x_{i,s} = 1$ for the compound that crystallizes):

$$\ln x_{i,\text{liq}} = -\frac{\Delta_{\text{melt}}H_i}{R} \left(\frac{1}{T} - \frac{1}{T_{\text{melt},i}} \right) \quad (\text{ideal eutectic binary system}) \quad (3.3.92)$$

For a binary system, the composition of the liquid phase has to fulfill the condition:

$$x_{1,\text{liq}} + x_{2,\text{liq}} = 1 \quad (3.3.93)$$

if component 1 crystallizes and 2 remains in the liquid phase until the eutectic point is reached. Figure 3.3.56 shows the solution of Eqs. (3.3.92) and (3.3.93) for the example of *m*- and *p*-xylene (Table 3.3.13 gives values of melting enthalpies and melting points). For a mixture with 50 mol.% *m*-xylene and 50 mol.% *p*-xylene, pure *p*-xylene starts to crystallize at A. The yield is limited by the

Figure 3.3.56 Solidification temperature curves for *m*- and *p*-xylene [Eq. (3.3.92)].

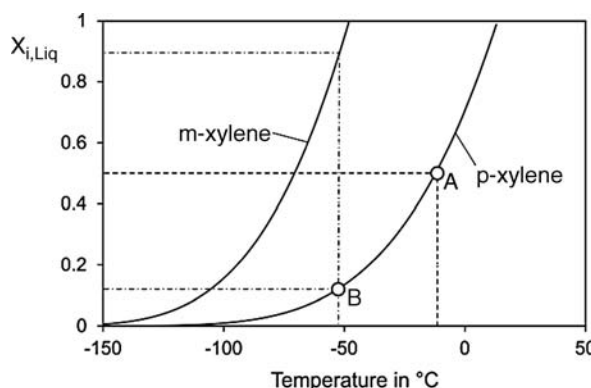
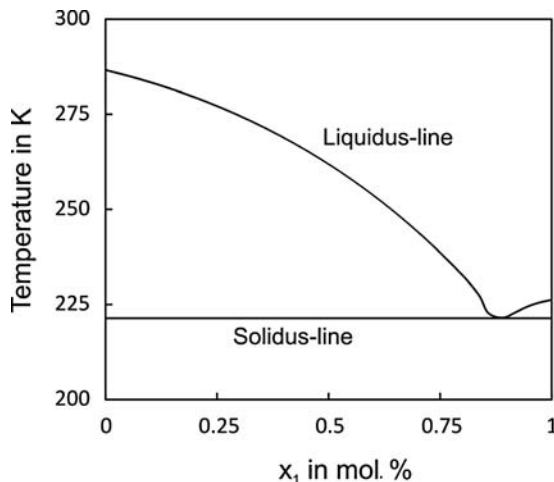


Table 3.3.13 Melting enthalpy and melting temperature of selected substances.

Substance	$\Delta_{\text{melt}}H \text{ [kJ mol}^{-1}\text{]}$	$T_{\text{melt}} \text{ [}^{\circ}\text{C]}$
Anthracene	28.86	216
Phenanthrene	18.64	96
<i>p</i> -Xylene	16.79	13
<i>m</i> -Xylene	11.54	-48

**Figure 3.3.57** Phase diagram of *p*- and *m*-xylene (1) as an example of a eutectic phase diagram.

eutectic point (B), where $x_{\text{liq},o\text{-xylene}} + x_{\text{liq},p\text{-xylene}} = 1$. Figure 3.3.57 gives the respective phase diagram.

3.3.7.2 Ideal Binary Phase System with Both Solids Completely Soluble in One Another

If both the liquid and solid phase are ideal, that is, both solids are completely soluble in one another, Eq. (3.3.91) is valid for both compounds:

$$\ln \frac{x_{1,\text{liq}}}{x_{1,s}} = - \frac{\Delta_{\text{melt}}H_1}{R} \left(\frac{1}{T} - \frac{1}{T_{\text{melt},1}} \right) = \ln C_1 \quad (3.3.94)$$

$$\ln \frac{x_{2,\text{liq}}}{x_{2,s}} = - \frac{\Delta_{\text{melt}}H_2}{R} \left(\frac{1}{T} - \frac{1}{T_{\text{melt},2}} \right) = \ln C_2 \quad (3.3.95)$$

For a binary system, the composition of the liquid and solid phase has to fulfill the conditions:

$$x_{1,\text{liq}} + x_{2,\text{liq}} = 1 \quad (3.3.96)$$

$$x_{1,s} + x_{2,s} = 1 \quad (3.3.97)$$

The solution of Eqs. (3.3.94) to (3.3.97) yields:

$$x_{1,\text{liq}} = \frac{(1 - C_2)}{\left(1 - \frac{C_2}{C_1}\right)} \quad (3.3.98)$$

$$x_{1,s} = \frac{x_{1,\text{liq}}}{C_1} \quad (3.3.99)$$

Figure 3.3.58 shows the solution of Eqs. (3.3.94) and (3.3.95) for the example of the system anthracene and phenanthrene (with data given in Table 3.3.13). Figure 3.3.59 depicts the respective phase diagram, calculated by Eqs. (3.3.98) and (3.3.99).

Industrial crystallization features generation of crystals by nucleation, crystal growth, and the recovery of crystals from the residual mother liquor. This can

Figure 3.3.58 System anthracene and phenanthrene as an example of an ideal phase diagram with both solids completely soluble in one another [Eq. (3.3.91)].

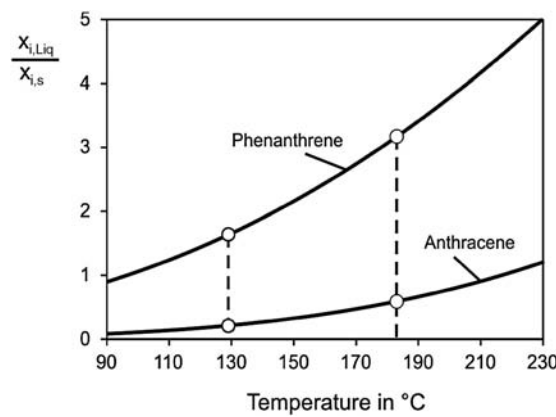
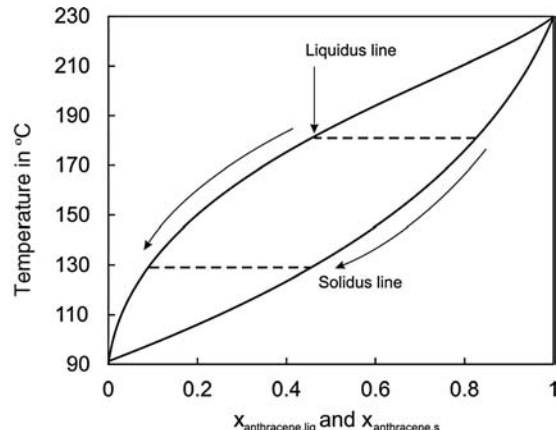


Figure 3.3.59 Phase diagram of anthracene (A) and phenanthrene (P) as an example of an ideal system with both solids completely soluble in one another [calculated by Eqs. (3.3.98) and (3.3.99)]. For a mixture of 50 mol.% A and 50 mol.% P, crystallization starts at 183 °C, and the first crystals consist of 84% A and 16% P. Further cooling decreases the anthracene concentration, for example, at 129 °C, 10% A is left in the liquid, and the crystals consist of 45% A (the rest is P).

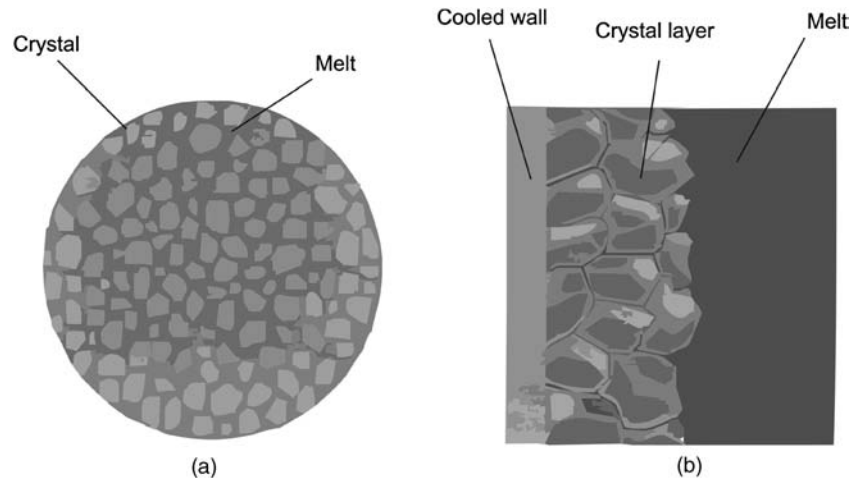


be achieved either by suspension crystallization or by layer crystallization (Figure 3.3.60).

In case of suspension crystallization, the crystals are freely suspended in the liquid, and crystallization proceeds by cooling the liquid below the saturation temperature. The crystals grow throughout the liquid phase with supersaturation as driving force (Figure 3.3.60a).

For layer crystallization (Figure 3.3.60b), the crystal mass is frozen onto a cooled surface, and crystallization proceeds by cooling the crystal mass. Typically, the crystal growth rate is 10–100 times faster than in suspension crystallization.

Figure 3.3.60 (a) Suspension crystallization and (b) layer crystallization.



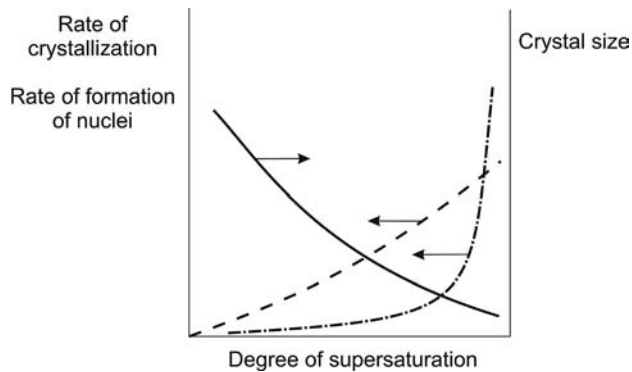


Figure 3.3.61 Influence of the degree of supersaturation on the rate of crystallization, the rate of formation of nuclei, and on the (average) crystal size. Adapted from Emons (1974).

The most important factor for the rate of crystallization and the average crystal size is the degree of supersaturation, which is the difference between the actual concentration and the respective equilibrium value. The rate of nuclei formation is given by:

$$r_{\text{nuclei}} \propto (c_{i,\text{liq}} - c_{i,\text{equilibrium}})^n \quad (3.3.100)$$

where the exponent n may vary in a range from 3 to 6, that is, the rate of formation of nuclei depends very strongly on the degree of supersaturation.

The rate of crystal growth is given by:

$$r_{\text{crystal growth}} \propto (c_{i,\text{liq}} - c_{i,\text{equilibrium}})^m \quad (3.3.101)$$

where the exponent m may vary in a range from 1 to 2, that is, (compared to the rate of nuclei formation) the rate of crystal growth is less dependent on the degree of supersaturation.

These two processes are in competition, which results in a strong influence of the degree of supersaturation on the mean crystal size (Figure 3.3.61), favoring small crystals at a high degree of supersaturation. To achieve a high production rate, a certain supersaturation is needed; but if the value is too high, only very small and thus poorly filtrable crystals are formed.

Figure 3.3.62 shows a simplified scheme of the process of crystallization in suspension. The liquid product (B) from the crystallizer is mixed with a concentrated solution (feed A). The mixture (M) is cooled in a heat exchanger to reach a supersaturation and finally fed into the crystallizer, where crystallization takes place.

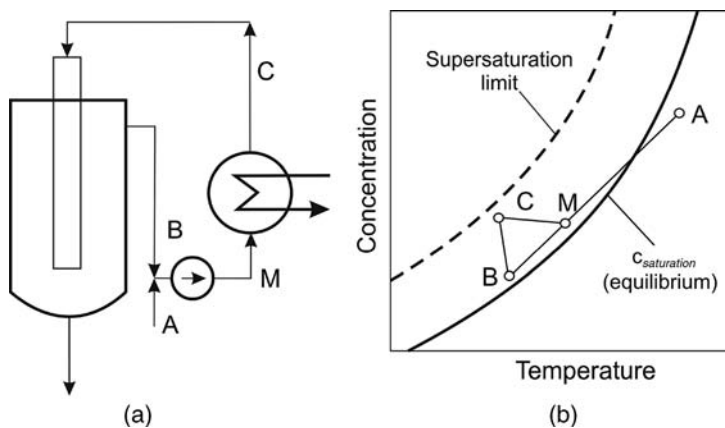
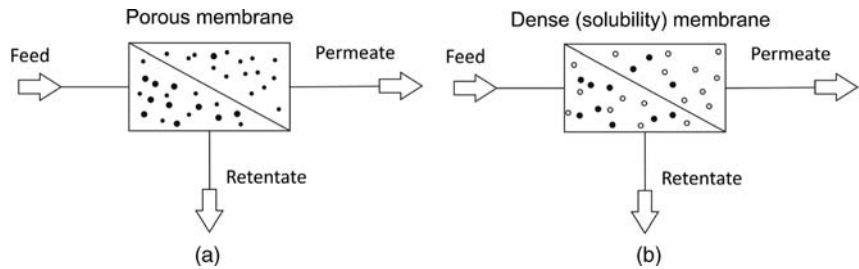


Figure 3.3.62 (a) and (b) Simplified scheme of process of crystallization in suspension (A: concentrated solution, B: liquid product from crystallizer, M: mixture of A and B, C: oversaturated system). Adapted from Baerns *et al.* (2006).

Figure 3.3.63 The two basic principles of membrane separation: (a) by porous membranes and (b) by dense (non-porous) membranes. Adapted from Baerns *et al.* (2006).



3.3.8 Separation by Membranes

3.3.8.1 Principles of Membrane Separation

Membranes separate particles and molecules on the basis of their molecular size or solubility by semipermeable membranes. The permeate is the fluid passing through the membrane, and the retentate (concentrate) is the fraction not passing through.

Two basic principles have to be distinguished (Figure 3.3.63):

- Porous membranes separate according to the size of particles/molecules. Depending on their size, membrane filtration systems have pore diameters from 1 nm to 1 μm (see Table 3.3.14 below).
- Dense (non-porous) membranes, for example, polymers, separate according to the difference in solubility and mobility (diffusion coefficient) of compounds present in the feed.

Both principles are combined in composite membranes, where a dense top layer, which is thin to achieve a high permeate flow, is located on a macroporous structure (for mechanical stability without transport resistance). Asymmetric membranes are similar, but the thin layer is not dense and has small pores (e.g., 1 nm), while the underlying porous structure has much bigger pores of, for example, 100 nm.

Depending on the membrane used and driving force (pressure, concentration, or electric field) involved, the basic equations of the flux through a membrane differ.

Table 3.3.14 Technically important applications of membrane separation technologies. Partly adapted from Baerns *et al.* (2006); details of these processes are found in Drioli and Giorno (2009), Nunes and Peinemann (1995), and Brueschke and Melin (2006).

Separation technology	Membrane structure (np: non-porous p: porous)	Driving force	Involved phases (s: solid, l: liquid, g: gas, v: vapor)	Technical applications
Microfiltration	p d_{pore} : 0.1–10 μm	Δp (<3 bar)	s/l	Separation of solid particles from suspensions; separation of bacteria and color particles; clarification of apple juice and wine
Ultrafiltration	p d_{pore} : 0.01–0.1 μm	Δp (<10 bar)	l/l	Drinking water purification; waste water treatment
Nanofiltration	p/np d_{pore} : 10^{-3} – 10^{-2} μm	Δp (<50 bar)	l/l	Water treatment; separation of homogeneous catalysts
Reverse osmosis	p/np d_{pore} : 10^{-3} – 10^{-4} μm	Δp (<200 bar)	l/l	Desalination of sea water; waste water treatment; concentration of fruit juices
Dialysis	p/np	Δc	l/l	Kidney dialysis
Electrodialysis	np	Electrical field	l/l	Separation of ions from aqueous solutions
Gas permeation	np	Δp	g/g	Gas separation, for example, N_2/O_2 , CO_2 , CH_4 , N_2/H_2 , $\text{N}_2/\text{C}_2\text{H}_4$, and $\text{C}_3\text{H}_6/\text{air}$; volatile hydrocarbons
Vapor permeation	np	Δp	v/v	Separation of azeotropic mixtures; removal of water from reaction mixtures (reversible reactions)
Pervaporation	np	Δp	l/v	Separation of azeotropic mixtures; solvent dehydration

Here, we only consider the basic equations describing the flux through porous membranes used for filtration and water treatment, and permeation through a dense membrane used for gas separation.

Mass Transport through a Porous Membrane If a membrane with thickness L consists of ideal parallel and cylindrical capillaries (pores) with uniform diameter d_{pore} , the velocity of flow in the pores is given by *Hagen–Poiseuille's law* for laminar flow, see Eq. (3.4.6) in combination with Eq. (3.4.15):

$$u_{\text{cap}} = \frac{\dot{V}}{A_{\text{pore}}} = \frac{d_{\text{pore}}^2}{32\rho_f v_f} \frac{\Delta p}{L} \quad (3.3.102)$$

(Capillaries of membranes are small, that is, $Re = u_{\text{cap}}d/\nu \ll 2300$, and the flow is laminar.)

Real pores are not ideal cylinders, and the so-called hydraulic diameter is used:

$$d_h = 4 \frac{A_{\text{pore,ex}}}{L_p} = 4 \frac{V_{\text{pore}}}{A_{\text{pore}}} \quad (3.3.103)$$

where $A_{\text{pore,ex}}$ is the cross-sectional area of a pore, L_p is the length of the perimeter of a pore, V_{pore} is the pore volume, and A_{pore} is the internal (mantle) area of pore. For cylindrical pores d_h equals d_{pore} .

For a real membrane, we have to consider the following additional factors.

The porosity of the membrane is defined as the ratio of pore volume and membrane volume:

$$\varepsilon = \frac{V_{\text{pore}}}{V_M} \quad (3.3.104)$$

Hence, the ratio of the membrane volume to the solid volume is given by:

$$\frac{V_s}{V_M} = 1 - \varepsilon \quad (3.3.105)$$

The definition of the surface area per volume of solid ($A_{V,s} = A_{\text{pore}}/V_s$), and insertion of Eqs. (3.3.104) and (3.3.105) into Eq. (3.3.103), yields:

$$d_h = 4 \frac{V_{\text{pore}}}{A_{\text{pore}}} = 4 \frac{V_{\text{pore}}}{V_M} \frac{V_M}{V_s} \frac{V_s}{A_{\text{pore}}} = \frac{4\varepsilon}{(1-\varepsilon)A_{V,s}} \quad (3.3.106)$$

When the membrane has a structure similar to that of a fixed bed of particles with diameter d_p , the hydraulic diameter is:

$$d_h = \frac{2\varepsilon}{3(1-\varepsilon)d_p} \quad (d_h \text{ of fixed bed}) \quad (3.3.107)$$

Similar to a solid (Section 3.2.2.3), the path through the pores of a membrane is tortuous, that is, the length (z_{pore}) exceeds the membrane thickness, which is considered by the tortuosity:

$$\tau_M = \frac{z_{\text{pore}}}{L} \quad (3.3.108)$$

The flux (in $\text{m}^3 \text{ m}^{-2} \text{ s}^{-1}$) through a porous membrane per unit cross-sectional area A_M ($= A_{\text{pore}}/\varepsilon$), which is also called the hydrodynamic permeability of a membrane, is defined as:

$$u_M = \frac{\dot{V}}{A_M} = \varepsilon u_{\text{cap}} \quad (3.3.109)$$

Insertion of Eq. (3.3.102) – but now with d_h instead of d_{pore} , Eq. (3.3.107), and $\tau_M L$ instead of L , Eq. (3.3.108) – into Eq. (3.3.109) finally yields:

$$u_M = \frac{\dot{V}}{A_M} = k_{M,V} \frac{\Delta p}{L} \quad (3.3.110)$$

with $k_{M,V}$ as the permeability of the membrane related to the volume rate:

$$k_{M,V} = \frac{\varepsilon^3}{2(1-\varepsilon)^2 A_{V,s}^2 \tau_M \rho_f v_f} \quad (3.3.111)$$

Equation (3.3.110) is also called Darcy's law. For a given fluid, $k_{M,V}$ (in $\text{m}^3 \text{s}^{-1} \text{m m}^{-2} \text{Pa}^{-1} = \text{m}^3 \text{s kg}^{-1}$) is constant for each porous membrane and has to be determined by experiments. If the flux of a certain component A (molar content x_A) is considered, Eq. (3.3.110) reads as:

$$\dot{n}_{M,A} = \frac{\dot{V}_A}{A_M} = x_A k_M \frac{\Delta p}{L} \quad (3.3.112)$$

For the case that only the flux of a certain component A (with molar content x_A) is taken into consideration, instead of Eq. (3.3.110) the molar flux may also be used (v_{mol} = molar volume):

$$\frac{\dot{n}}{A_M} = k_{M,\text{mol}} \frac{\Delta p}{L} = \frac{k_{M,V}}{v_{\text{mol}}} \frac{\Delta p}{L} \quad (3.3.113)$$

Note that the permeability of a membrane ($k_{M,\text{mol}}$ in $\text{mol m m}^{-2} \text{s}^{-1} \text{Pa}^{-1} = \text{mol s kg}^{-1}$) is most commonly given in the literature in Barrer, defined as $10^{-10} \text{ cm}^3 (\text{NTP}) \text{ cm} (\text{cm}^2 \text{s cm Hg})^{-1}$ and named after R.M. Barrer (1 Barrer = $0.33 \times 10^{-15} \text{ mol s kg}^{-1}$).

Mass Transport through a Non-porous Membrane The simplest model used to explain the permeation through a non-porous membrane (e.g., of a gas in a polymer membrane) is the solution-diffusion model. The concentration of a gas in the membrane matrix (mol A per m^3 membrane) is given by Henry's law:

$$c_A = \frac{p_A}{H_{A,c}} \quad (3.3.114)$$

The reciprocal value of the Henry coefficient is also denoted as gas solubility. For a given diffusion coefficient in the membrane material, the molar flux per unit cross-sectional area is:

$$\frac{\dot{n}_A}{A_M} = k_{A,M,\text{mol}} \frac{\Delta p_A}{L} = \frac{D_{A,M}}{H_{A,c}} \frac{\Delta p_A}{L} \quad (3.3.115)$$

Although the flux of a certain compound through the membrane should be as high as possible, the selectivity of the membrane for gas A relative to another gas B is equally, or even more, important, which is defined as the ratio of the respective permeabilities $k_{M,\text{mol}}$:

$$S_{AB} = \frac{k_{A,M,\text{mol},A}}{k_{B,M,\text{mol},B}} = \frac{D_{A,M}}{D_{B,M}} \frac{H_{B,c}}{H_{A,c}} \quad (3.3.116)$$

The ratio $D_{A,M}/D_{B,M}$ can be viewed as mobility selectivity and the ratio $(1/H_{A,c})/(1/H_{B,c})$ as solubility selectivity (Nunes and Peinemann, 2001). So for a given gas pair mobility and solubility, the selectivity depends on the chemical and physical properties of the membrane material.

Basic Principle of Reverse Osmosis If a salt (consisting of v ions) completely dissociates in solution with water, the osmotic pressure (Figure 3.3.64) is related to the molar concentration of the ions (mol m^{-3}) by:

$$p_{\text{osmosis}} = v c_{\text{salt}} RT \quad (3.3.117)$$

For example, the osmotic pressure of seawater (about $35 \text{ kg NaCl m}^{-3} = 0.6 \text{ kmol NaCl m}^{-3}$) is 30 bar (25°C). Hence, a higher pressure is needed for desalination of seawater by reverse osmosis (typically 55–68 bar) (Fritzmann *et al.*, 2007).

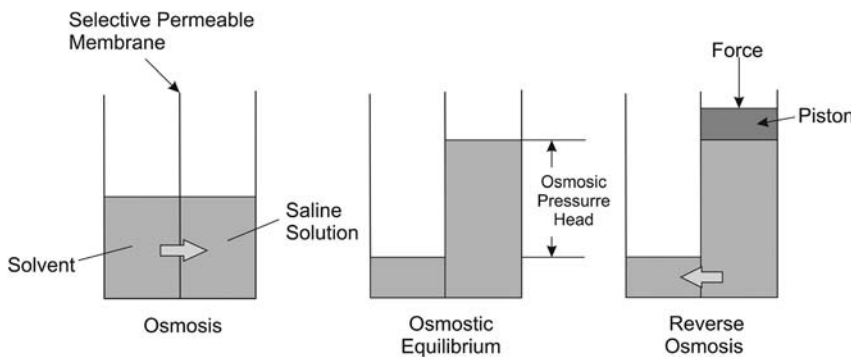


Figure 3.3.64 Illustration of osmosis and reverse osmosis.

3.3.8.2 Applications of Membrane Separation Processes

Table 3.3.14 gives an overview of the main membrane processes currently used. Subsequently, only two processes are inspected in more detail, desalination of seawater by reverse osmosis and gas separation.

Desalination of Sea Water Figure 3.3.65 shows the process scheme of a reverse osmosis seawater desalination plant. If a pressure exchange system is used, only part of the overall feed needs to be pressurized in the high pressure pump. Owing to pressure drop in the reverse osmosis system and piping, feed leaving the pressure exchanger needs additional pumping prior to the reverse osmosis stage.

Membranes installed in reverse osmosis desalination use hollow fiber membranes or flat membranes arranged in spiral-wound modules (Figure 3.3.66) because their packing densities are very high, $1000 \text{ m}^2 \text{ m}^{-3}$ for spiral-wound modules and up to $10\,000 \text{ m}^2 \text{ m}^{-3}$ for hollow fibers.

Table 3.3.15 shows that thermal desalination of sea water or brackish water by multistage flash distillation is more energy intensive than membrane desalination, but can better deal with more saline water and delivers even higher permeate quality, although reverse osmosis usually fulfills the requirements of drinking water (Table 3.3.16).

Gas Separation In general, a high selectivity is always obtained at the expense of an exponential reduction in gas permeability ($\log S = \text{const.} \times \log k_M$). A highly selective

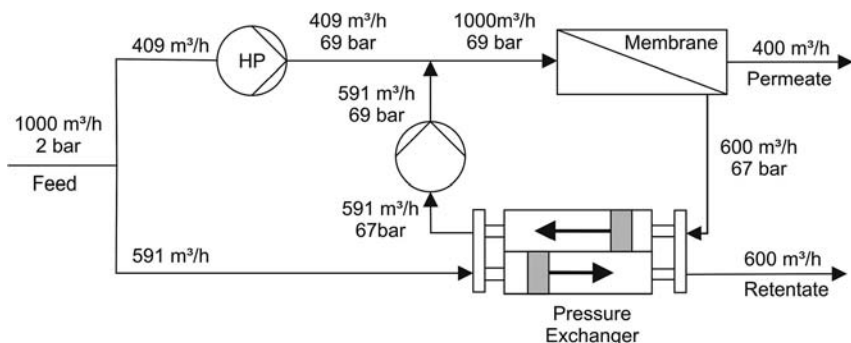


Figure 3.3.65 Seawater desalination process with pressure exchanger. Adapted from Fritzmann *et al.* (2007).

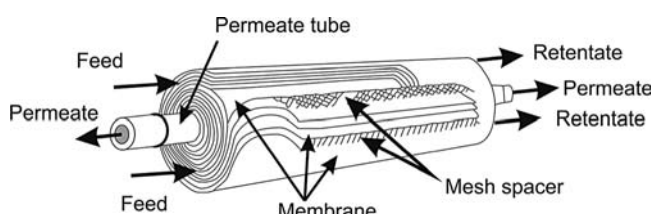


Figure 3.3.66 Schematic picture of a spiral-wound membrane element.

Table 3.3.15 Comparison of key operational data used in processes for desalination. Data from Fritzmann *et al.* (2007).

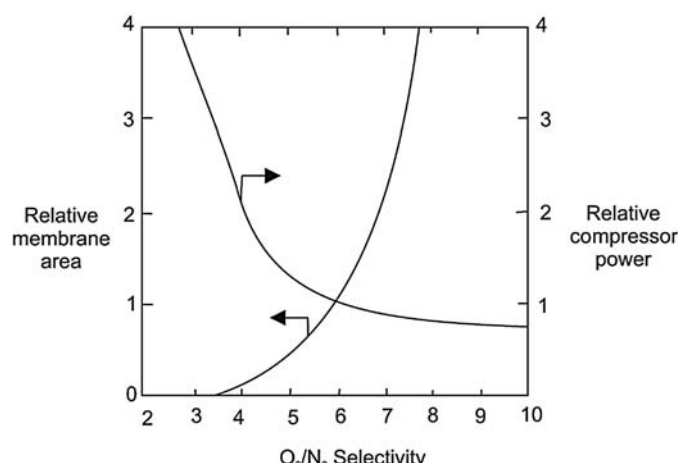
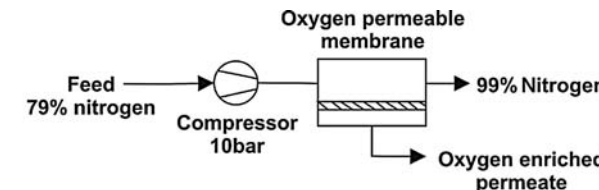
	Multistage flash distillation	Reverse osmosis	Electrodialysis
Thermal energy (kWh m^{-3})	12	—	—
Electrical energy (kWh m^3)	35	0.4–7	1
Typical salt content of raw water in total dissolved solids content (TDS) (mg l^{-1})	30 000–100 000	1000–45 000	100–3000
Typical salt content of product water in TDS (mg l^{-1})	<10	<500	<500

Table 3.3.16 Water characterization by salt content. Data from Fritzmann *et al.* (2007).

Feedwater and drinking water requirement	Salinity in total dissolved solids content (TDS) (mg l^{-1})
Seawater	15 000–50 000
Brackish water	1500–15 000
River water	500–1500
Pure water (WHO drinking water guidelines)	1000

membrane yields a good separation, and so the size of the compression costs per unit gas decrease. However, this decrease in compression costs is offset by an increase in the costs of the extra membrane area needed because of the lower membrane permeability (Drioli and Giorno, 2009). Figure 3.3.67 illustrates the trade-off between compression power and membrane area needed for various membrane units producing the same amount of nitrogen (99%). The base case is taken to be a membrane with an O_2/N_2 selectivity of 6 [details in Drioli and Giorno (2009)]. The compression power strongly decreases with increasing selectivity until a value of about 6 is reached. For higher selectivities the improvement is small. Conversely, the membrane area needed to produce the same amount of nitrogen increases sharply with increasing selectivity. For example, the O_2 permeability decreases by a factor of about

Figure 3.3.67 Process for N_2 membrane production: all numbers are shown relative to a membrane with an O_2/N_2 selectivity of 6 and an O_2 permeability of 0.8 Barrer. Adapted from Drioli and Giorno (2009).



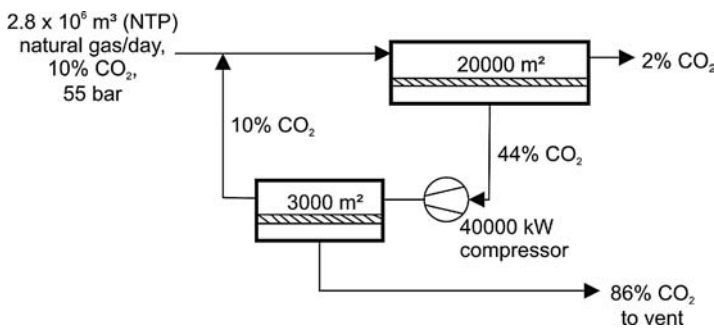


Figure 3.3.68 Process scheme for natural gas treatment by two-stage membrane separation of CO₂. Adapted from Drioli and Giorno (2009).

5, if the O₂/N₂ selectivity increases from 5 to 7 (Drioli and Giorno, 2009). Today's industrial membranes for gas separation therefore have a selectivity of 6–8.

Membrane gas separation processes can be improved by using multistage separation as depicted in Figure 3.3.68 for natural gas treatment with a two-stage membrane for the separation of CO₂. Traditionally, amine absorption is used to separate CO₂ from natural gas. Membrane plants require less operator attention and smaller units may even operate unattended. Hence, membrane separations are favored in remote locations like offshore platforms.

Summary of Section 3.3 (take-home messages)

- **Heat exchangers** are recuperatively operated tube bundles consisting of many tubes through which one fluid runs. The second fluid flows around the tubes and is heated/cooled, and vice versa the fluid in the tube is cooled/heated. Heat exchangers are classified according to their flow arrangement in parallel-, counter-, and cross-flow heat exchangers. The temperature in both fluids changes along the local position. To account for this, a logarithmic mean temperature difference is used.
- **Distillation** is a common technique used to separate a liquid mixture of two or more substances by the supply of heat into its component fractions, with the desired purity arising from differences in their volatility. For an ideal **mixture of liquids**, the vapor pressures are given by **Raoult's law**. A vapor–liquid equilibrium plot represents the molar fraction of a compound in the vapor phase as a function of the fraction in the liquid mixture. For ideal mixtures, this diagram can be derived based on the relative volatility. For **real mixtures** of dissimilar liquids, Raoult's law is obeyed only for the component in excess as it approaches purity. For marked deviations from ideality, this may completely upset the distillation process (azeotropic mixtures).
- **Distillation columns** are divided by trays into subsequent separation steps. In the ideal case, equilibrium is reached on each tray. The common design procedure is the **McCabe–Thiele approach** based on the vapor–liquid equilibrium diagram and operating lines for the top rectification section and the stripping section. The main parameter calculated by this method is the **number of theoretical equilibrium stages** required for fractionating. The actual number of trays is the ratio of the number of theoretical trays to the tray efficiency. When designing columns, we have to choose a reflux ratio that is higher than the **minimum reflux ratio** (infinite number of separation stages).
- To break an **azeotrope**, azeotropic, extractive, and pressure swing distillation can be used.
- During **absorption**, a gas component is selectively dissolved by contact with a liquid in which the component is soluble. Absorption is used for scrubbing gas streams to remove components such as CO₂, H₂S, SO₂ and NH₃. Absorption may be either physical or chemical (or a combination of both). Physical absorption involves the solubility (**Henry coefficient**). Chemical absorption involves a reaction of the primarily physically absorbed solute with the absorbing

medium, and thus always combines with physical absorption. Gas scrubbers are operated in countercurrent flow and are equipped with structured packings or trays. For the **design of an absorption column** (number of separation stages), the McCabe–Thiele approach is also used but, in contrast to distillation, only one single operating line is needed for the design of the absorption column.

- **Liquid–liquid extraction** is used to separate components of a liquid mixture if separation by distillation is hard to achieve, for example, for liquids with similar boiling points. Extraction depends upon the difference in solubility of a compound in two immiscible liquids. The liquid remaining after treatment with an extracting agent is called **raffinate** and forms a two-phase system with the extracting agent. A **distribution ratio** is often quoted as a measure of how well-extractable a species is (*Nernst's partition coefficient*). A concise depiction of the extraction is a triangular diagram. For extraction, we have to work in the two-phase region that is separated from the single-phase region by the **binodal curve**. Then disaggregation in two immiscible phases would start if agitation is stopped. The composition of these two phases is given by tie-lines, indicating pairs of partially miscible liquids. For an ideal extraction process only the solute is transferred between both phases. For such an ideal system, the triangular diagram is not needed to design the extraction as the system is simply represented by the distribution ratio, and again the McCabe–Thiele approach is the common design technique. Typical technical extraction units are rotating disc contactors or mixer-settler units.
- **Adsorption of fluids** is based on the selective binding of components on the surface of a solid. In purification of gases and liquids, the loaded solid, the **adsorbent**, is regenerated from time to time, whereby the adsorbed substance, the **adsorbate**, reversibly desorbs. In practical systems, we may also have a competitive adsorption of different species. To reach a high adsorption capacity, adsorbents must provide a **large surface area** of more than $100\text{ m}^2\text{ g}^{-1}$. An approach to describe this **adsorption equilibrium** is the **Langmuir adsorption isotherm**. Adsorption is a transient process until a particle or a zone of a fixed bed has completely reached equilibrium loading. The intrinsic chemical adsorption process is almost instantaneous, and mass transfer to and into the porous adsorbent determines how fast the equilibrium is reached. For a continuous adsorption process, at least two fixed beds are needed. The first is utilized until or just before breakthrough of the adsorbed component(s) occurs. Then the adsorbent is regenerated by desorption of the adsorbed gas(es), while a second, freshly regenerated bed is now "on duty." The main design parameter of an adsorber is the length needed for a given time on stream before breakthrough occurs and we have to switch to a freshly regenerated bed. The overall length of the adsorber is the sum of the minimum length, which depends only on the equilibrium loading and the rate of fluid flow, and a surcharge we have to pay for the kinetics, the **length of the unused bed**.
- **Fluid–solid extraction** is used to separate a substance from a solid matrix by solution into a suitable solvent. The solvent is either a liquid, for example, hot water or an organic solvent, or a **supercritical fluid**, most notably water or CO_2 . Various solid ingredients are separated by extraction, for example, caffeine from coffee, vegetable oils from oilseeds, hop extract from hops, or flavors from plant materials. Supercritical fluids have solvation properties similar to organic solvents, but a higher diffusivity and a lower viscosity. Fluid–solid extraction is carried out batchwise or continuously. In the food industry, commercial plants with supercritical fluids have so far only been used with supercritical CO_2 as solvent. Supercritical hydrocarbons such as propane are also used, for example, for deasphalting of heavy oils. For the process design, the McCabe–Thiele method may be used (number of theoretical separation stages etc.).

- **Crystallization** is mainly used for separation as an alternative to distillation, if the involved compounds are thermally unstable, have a low vapor pressure, if the vapor pressures and boiling points are similar, or if the system forms an azeotrope.
- **Membrane separation** is used for seawater desalination, ion separation, solvent dehydration, separation of azeotropic mixtures, and separation of gases.

3.4

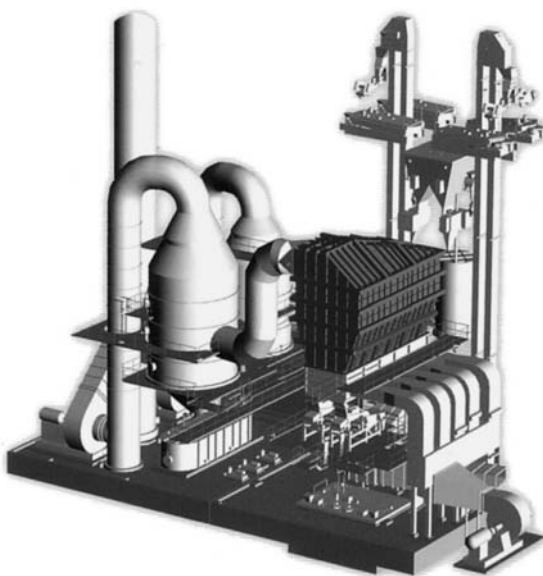
Mechanical Unit Operations

This chapter examines the following mechanical unit operations needed in chemical technology:

- Conveyance of fluids and the respective equations to determine the pressure loss in empty tubes as well as in fixed, fluidized and entrained beds will be derived.

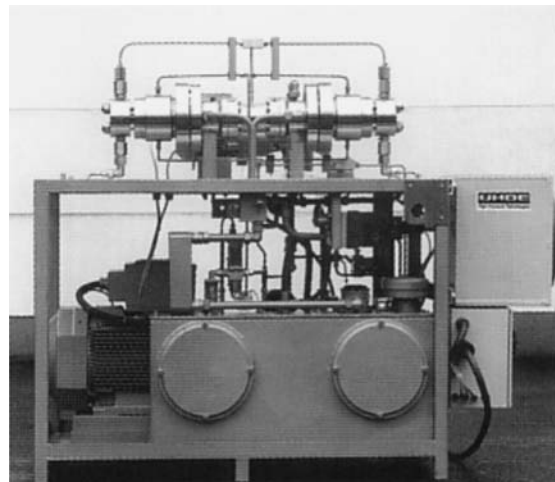


Pipeline bridge and cooling towers of a brown coal power station.
Courtesy of Linde Engineering, Germany.



Three-dimensional model of a fluid bed granulation plant.
Courtesy of Uhde, Germany.

- The main equations characterizing compressors and pumps are examined.



High-pressure pump for 10 000 bar and 20 l h⁻¹. Courtesy of Uhde, Germany.

- Contacting and mixing of fluids.
- Crushing and screening of solids (particle size reduction, classifying, and sorting).
- Separation of solids from fluids.

3.4.1

Conveyance of Fluids

3.4.1.1 Pressure Loss in Empty Tubes

Incompressible Fluids The basic equation of flow in a stream-tube is the Bernoulli equation (*D. Bernoulli*, see box), which is given for steady-state conditions and an incompressible fluid with internal friction by:

$$\frac{1}{2} u_1^2 + \frac{p_1}{\rho_f} + gh_1 = \frac{1}{2} u_2^2 + \frac{p_2}{\rho_f} + gh_2 + \varphi_{12} \quad (3.4.1)$$

[The respective equation for a compressible fluid (ideal gas) is discussed below in Topic 3.4.1.]

The first term on each side of Eq. (3.4.1) represents the kinetic energy ($\text{J kg}^{-1} = \text{m}^2 \text{s}^{-2}$), the second term the contribution of the static pressure, and the third term the specific potential energy with h as height above a reference height. The term φ_{12} is the specific energy dissipation (J kg^{-1}), that is, the ratio of the friction power, P_{friction} (J s^{-1}), to the flow of fluid, \dot{m} (kg s^{-1}):

$$\varphi_{12} = \frac{P_{\text{friction}}}{\dot{m}} = \frac{\Delta p_t}{\rho_f} \quad (\text{for an incompressible fluid and } \rho_f \text{ in } \text{kg m}^{-3}) \quad (3.4.2)$$

Experience shows that the specific dissipation φ_{12} is given by:

$$\varphi_{12} = \xi \frac{1}{2} u^2 \quad (3.4.3)$$

with ξ as the dimensionless friction number.

According to Eqs. (3.4.1) and (3.4.2) the total pressure loss is given by:

$$\Delta p_t = \frac{\rho_f}{2} \underbrace{(u_1^2 - u_2^2)}_{\text{Difference of kinetic pressure}} + \underbrace{(p_1 - p_2)}_{\text{Difference of static pressure}} + \underbrace{\rho_f g(h_1 - h_2)}_{\text{Difference of hydrostatic pressure}} \quad (\text{incompressible fluid, } \rho_f = \text{constant}) \quad (3.4.4)$$

Daniel Bernoulli (1700–1782): A Dutch-born mathematician who spent much of his life in Basel, Switzerland, where he worked on applications of mathematics to mechanics. He was a contemporary and intimate friend of *Leonhard Euler*. His main work is *Hydrodynamique* (1738), where he introduced the principle of conservation of energy. Bernoulli's principle states that the pressure in a fluid decreases as the speed of the fluid increases. Bernoulli was the first to formulate a kinetic theory of gases, and he applied this idea to explain the law of *Boyle and Mariotte* (Section 3.1.1).

For an incompressible fluid flowing in a horizontal tube ($h_1 = h_2$, for an altitude change see Example 3.4.1) with a constant cross-sectional area ($u_1 = u_2$), we simply obtain:

$$\Delta p_t = p_1 - p_2 \quad (3.4.5)$$

and for a tube with length L and diameter d_t , Δp_t is given by the Eqs. (3.4.2) and (3.4.3) as:

$$\Delta p_t = f_t \frac{L}{d_t} \frac{\rho_f}{2} u^2 \quad \left(\text{incompressible fluid, horizontal tube, } f_t = \xi \frac{d_t}{L}, u = \frac{\dot{V}_{\text{fluid}}}{A_t} \right) \quad (3.4.6)$$

Equation (3.4.6) is a very good approximation for all liquids as their compressibility is small, for example, for water an increase of pressure by 100 bar (at 20°C) causes a decrease of volume by only 0.045%. As inspected below, the friction factor f_t depends on the Re number and the surface roughness.

Compressible Fluids For compressible fluids like gases, we have to start with the differential form of Eq. (3.4.6):

$$dp_t = -f_t \frac{1}{d_t} \frac{\rho_g}{2} u^2 dL \quad (3.4.7)$$

To derive the equations for Δp_t , we now consider f_t to be constant and inspect the value later. If we use the index 1 for the initial values of pressure p (Pa), gas density ρ (kg m^{-3}), and velocity u (m s^{-1}), and if we assume ideal gas behavior ($u = u_1 p_1 / p$ and $\rho_g = \rho_{g,1} p / p_1$), we obtain:

$$dp_t = -f_t \frac{1}{d_t} \frac{\rho_{g,1} p}{2p_1} \left(\frac{u_1 p_1}{p} \right)^2 dL \Rightarrow p dp = -f_t \frac{1}{d_t} \frac{\rho_{g,1} p_1}{2} u_1^2 dL \quad (3.4.8)$$

Integration and rewriting leads to:

$$\frac{p_1^2 - p_2^2}{2} = f_t \frac{L}{d_t} \frac{\rho_{g,1} p_1}{2} u_1^2 \Rightarrow \Delta p_t = \left(\frac{2p_1}{p_1 + p_2} \right) f_t \frac{L}{d_t} \frac{\rho_{g,1}}{2} u_1^2 \quad (3.4.9)$$

Comparison with Eq. (3.4.6) shows that the term $2p_1/(p_1 + p_2)$ considers the change of density and velocity of a gas with decreasing pressure. This term is always higher than unity ($p_1 > p_2$). Hence, for gases – in general for compressible fluids – the pressure drop is higher, as calculated with Eq. (3.4.6). This is because the kinetic term $\rho_g/2u^2$ increases with decreasing pressure, for example, for ideal gases $\rho_g/2u^2 \sim 1/p$. Nevertheless, Eq. (3.4.6) can be used in most practical cases also for gases. The criterion for this is derived on the assumption that the deviation of calculation should be less than 5%. Hence we obtain:

$$\Delta p_{t,\text{Eq. (3.4.13)}} = 1.05 \Delta p_{t,\text{Eq. (3.4.6)}} \Rightarrow \left(\frac{2p_1}{p_1 + p_2} \right) = 1.05 \Rightarrow p_1 = 1.1p_2 \quad (3.4.10)$$

Thus, if Δp is lower than 10% of the total (initial) pressure, we can use the simple Eq. (3.4.6).

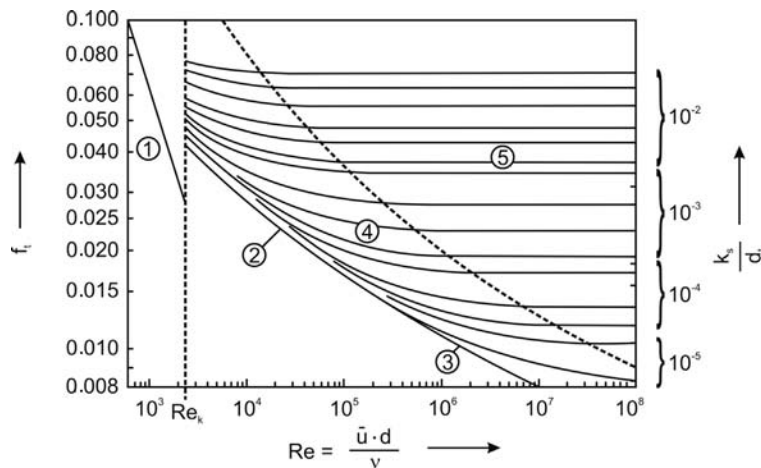
Correlations for Friction Factor f_t For tubes with a smooth surface, the friction factor f_t is calculated based on the Re number (ud_t/v) by:

$$f_t = \frac{64}{Re} \quad (\text{for } Re < 2300, \text{ Hagen-Poiseulle's law, see box}) \quad (3.4.11)$$

$$f_t = \frac{0.316}{Re^{0.25}} \quad (\text{for } 2300 < Re < 10^5, \text{ Blasius's law}) \quad (3.4.12)$$

$$\frac{1}{\sqrt{f_t}} = 2 \log \left(Re \sqrt{f_t} \right) - 0.8 \quad (\text{for } Re > 10^5 \text{ Prandtl's law}) \quad (3.4.13)$$

Figure 3.4.1 Influence of Re number on the friction factor for the flow of a fluid through an empty tube; 1: Eq. (3.4.11), 2: Eq. (3.4.12), 3: Eq. (3.4.13), 4: Eq. (3.4.15), 5: Eq. (3.4.16).



According to Petukhov (Petukhov, 2009), we may also use:

$$f_t = (0.79 \ln(Re) - 1.64)^{-2} \quad (\text{for } 10^4 < Re < 10^6, \text{ Petukhov's law}) \quad (3.4.14)$$

For tubes with a rough surface, the friction factor f_t is given by:

$$\frac{1}{\sqrt{f_t}} = 1.74 - 2 \log \left(\frac{2k_s}{d_t} + \frac{18.7}{Re \sqrt{f_t}} \right) \quad \left[\text{for } 2300 < Re < \left(\frac{225}{k_s/d_t} \right)^{8/7}, \text{ Colebrook's law} \right] \quad (3.4.15)$$

$$\frac{1}{\sqrt{f_t}} = 1.74 - 2 \log \left(\frac{2k_s}{d_t} \right) \quad \left[\text{for } Re > \left(\frac{225}{k_s/d_t} \right)^{8/7}, \text{ von Kármán's law, see box} \right] \quad (3.4.16)$$

with k_s/d_t as the ratio of the measurable roughness (equivalent to a grain of sand) to the tube diameter. Figure 3.4.1 shows a graphical presentation of f_t . Note that for a given volumetric flow rate and a high Re number the pressure loss in a tube is proportional to $1/d_t^5$ (Example 3.4.2), and thus a doubling of the tube diameter decreases Δp_t by a factor of 32!

Topic 3.4.1 Bernoulli equation for compressible fluids (example ideal gas)

For compressible fluids (e.g., a gas), the Bernoulli equation is given by:

$$\frac{1}{2} u_1^2 + \frac{p_1}{\rho_{g,1}} + g h_1 = \frac{1}{2} u_2^2 + \frac{p_2}{\rho_{g,2}} + g h_2 - \frac{1}{m} \int_1^2 p \, dV + \varphi_{12} \quad (3.4.17)$$

For an ideal gas, adiabatic expansion is isothermal (Section 3.1.2), that is, $pV = mRT/M = \text{constant}$. Hence, the specific work for volume change (J kg^{-1}) equals the term representing the change of entropy [Eq. (3.1.42)]:

$$\begin{aligned} -\frac{1}{m} \int_1^2 p \, dV &= -\frac{RT}{M} \int_1^2 \frac{1}{V} \, dV = \frac{RT}{M} \ln \left(\frac{V_1}{V_2} \right) = \frac{RT}{M} \ln \left(\frac{p_2}{p_1} \right) \\ &= \frac{T}{M} \Delta S_{12} \quad (\text{for } T = \text{const.}) \end{aligned} \quad (3.4.18)$$

For $T = \text{const.}$, $p_1/\rho_{g,1}$ equals $p_2/\rho_{g,2}$, and insertion of Eq. (3.4.18) into Eq. (3.4.17) yields:

$$\varphi_{12} = \frac{1}{2}(u_1^2 - u_2^2) + g(h_1 - h_2) + \frac{T}{M} \Delta S_{12} \quad (3.4.19)$$

For a horizontal tube ($h_1 = h_2$) and negligible change of the kinetic energy ($u_1 \approx u_2$) we get:

$$\varphi_{12} = \frac{T}{M} \Delta S_{12} = \frac{RT}{M} \ln\left(\frac{p_1}{p_2}\right) = \frac{p_1}{\rho_{g,1}} \ln\left(\frac{p_1}{p_2}\right) \approx \frac{\Delta p_t}{\rho_{g,1}} \left[\ln\left(\frac{p_1}{p_2}\right) \approx \frac{\Delta p_t}{p_1} \text{ for } \frac{p_1}{p_2} < 1.1 \right] \quad (3.4.20)$$

and thus the pressure loss corresponds to the increase in entropy of the gas.

■ Originators of equations for the pressure loss in a tube

Gotthilf Heinrich Ludwig Hagen (1797–1884) was a German physicist and hydraulic engineer. He studied at the University of Koenigsberg (where Immanuel Kant was a professor of philosophy at this time) mathematics, architecture, and civil engineering. In 1830, he became Director of the National Construction Works in Hydraulic Engineering, and inspected water and dock construction works in Prussia. Independently from Poiseuille, Hagen carried out in 1839 the first carefully documented friction experiments, from which the Hagen–Poiseuille law arose.

Jean Louis Marie Poiseuille (1799–1869), a French physician and physiologist, investigated the flow of human blood in narrow tubes. In 1828 he earned his doctoral degree with a dissertation entitled *Recherches sur la force du cœur aortique*. In the 1840s, he formulated Poiseuille's law, today named the Hagen–Poiseuille law in order to honor also Gotthilf Hagen.

Paul Richard Heinrich Blasius (1873–1970): a German fluid dynamics engineer and one of the first students of **Ludwig Prandtl** (see box in Section 3.2.1.2).

The Colebrook equation combines experimental results of studies of laminar and turbulent flow in pipes. It was developed in 1939 by the British physicist **Cyril Frank Colebrook** (1910–1997).

Theodore von Kármán (1881–1963), a Hungarian–American engineer, was responsible for many advances in aerodynamics. After studying engineering in Budapest he joined, in 1902, **Ludwig Prandtl** in Goettingen and received his doctorate in 1908. In 1912 he became director of the Aeronautical Institute in Aachen. He stayed there until 1930 (interrupted by service in the Austro-Hungarian army during WWI, where he designed a helicopter). Apprehensive about developments in Europe, in 1930 he accepted the directorship of the *Guggenheim Aeronautical Laboratory* at the *California Institute of Technology (Caltech)* and emigrated to the USA. In 1944, he left Caltech and worked as a consultant to the military, studying aeronautical technologies for the US Army Air Forces.

Example 3.4.1: Influence of the change of the altitude on Δp_{tube}

According to Eq. (3.4.4), the pressure loss of an incompressible fluid flowing in a tube with constant cross-sectional area (thus without change of the fluid velocity) is given by:

$$\Delta p_t = (p_1 - p_2) + \rho_f g(z_1 - z_2)$$

To compare the contributions of the static and hydrostatic pressure, we use water as example ($\rho = 1000 \text{ kg m}^{-3}$, $v = 10^{-6} \text{ m}^2 \text{s}^{-1}$). The velocity u should be 1 m s^{-1} and the diameter of the tube 0.1 m . For k_s/d_t (roughness) we use a value of 10^{-3} . Thus, Re is 100 000 and the friction factor

f_t is 0.03 (Figure 3.4.1). As a criterion for the negligible influence of the change of altitude on Δp_{tube} we assume that its contribution should be less than 5%:

$$\rho_f g(h_1 - h_2) < 0.05 \Delta p_t$$

Insertion of Eq. (3.4.6) and rearrangement lead to:

$$\frac{(h_1 - h_2)}{L} < \frac{0.05}{2g} f_t \frac{u^2}{d_t}$$

and thus for the given example the change of altitude should be less than 76 cm for a pipe 1 km long. (The pressure drop would then be 1.5 bar compared to the change in the hydrostatic pressure of 75 mbar.)

A similar calculation can be performed for a gas, if we assume for simplification that the change of density is negligible ($\Delta p_t \ll p$). As an instructive example we use the long-distance transport of natural gas in a pipeline. According to the literature (Konstantin, 2007)

typical values are a pipeline diameter of 1 m, total pressure of 75 bar, gas velocity of 5 m s^{-1} , and a friction factor f_t of 0.02. To neglect the influence of the hydrostatic pressure, the change of altitude should now be less than 1.3 m per km of gas pipeline. [The pressure drop would then be 130 mbar per km pipeline, if we use Eq. (3.4.6) and the density ρ of natural gas (methane) at 75 bar and 5°C of 52 kg m^{-3} .]

Example 3.4.2: Influence of tube diameter on the pressure loss of pipelines

To inspect the influence of tube diameter on the pressure loss in a pipeline for transport of gases and liquids, we consider a kinematic viscosity of $2 \times 10^{-7} \text{ m}^2 \text{s}^{-1}$ (methane, 75 bar) and $10^{-6} \text{ m}^2 \text{s}^{-1}$ (crude oil). For fluid velocities $> 1 \text{ m s}^{-1}$ and diameters $> 0.1 \text{ m}$, we get $Re > 10^6$ (gas) and $> 10^5$ (oil); thus the friction factor f_t is constant (Figure 3.4.1). For a negligible change of density ($\Delta p_t \ll p$), Eq. (3.4.6) yields the pressure loss per length of pipeline:

$$\frac{\Delta p_t}{L} = f_t \frac{\rho_f u^2}{2d_t} \sim \frac{u^2}{d_t} \quad (\text{for } f_t \text{ and } \rho_f = \text{constant})$$

Thus, if we have to transport a given volume rate of natural gas or crude oil, we obtain:

$$\frac{\Delta p_t}{L} \sim \left(\frac{\dot{V}}{A_t} \right)^2 \frac{1}{d_t} \sim \frac{1}{d_t^5} \quad \left(\text{for } \dot{V} = \text{constant and } A_t = \pi \frac{d_t^2}{4} \right)$$

This means that doubling the diameter decreases the pressure drop by a factor of 32, and the energy for compression (operational costs) decrease. On the other hand, we have to consider investment costs, for example, the amount of steel needed per length of pipeline is proportional to the square of the diameter as the wall thickness is almost proportional to the diameter:

$$(V_{\text{steel}}/L_{\text{pipeline}} = \pi d_t s_{\text{wall}} \sim d_t^2)$$

The economically optimum diameter is found by consideration of operational and investment costs (Figure 3.4.2). Note that for a more specified calculation we also have to consider the costs of laying the pipeline and the number of compressors needed along a pipeline that may be several thousand km long.

3.4.1.2 Pressure Loss in Fixed, Fluidized, and Entrained Beds

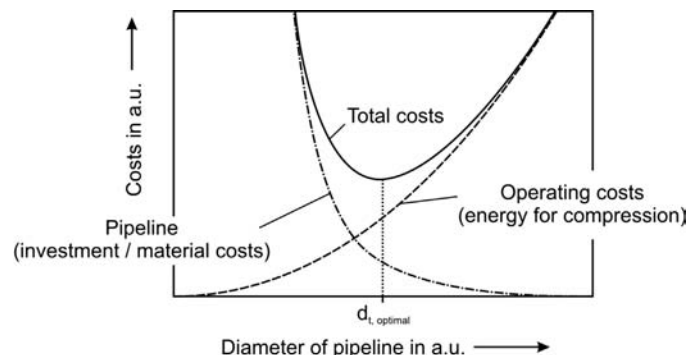
Pressure Drop in Fixed (Packed) Beds According to Ergun (1952), the pressure loss in a packed bed is given by:

$$\Delta p_b = f_b \frac{L \rho_f u_s^2}{d_p} \quad (3.4.21)$$

where u_s is the superficial velocity (empty tube) and f_b the friction factor of a packed bed, which is given by the following equation based on the particle Reynolds number, $Re_p = u_s d_p / v$:

$$f_b = \frac{(1 - \varepsilon)}{\varepsilon^3} \left[3.5 + (1 - \varepsilon) \frac{300}{Re_p} \right] \quad (3.4.22)$$

Figure 3.4.2 Influence of pipeline diameter on the costs of fluid transport.



For non-spherical particles we have to use an equivalent particle diameter defined as:

$$d_p = \frac{6V_p}{A_{ex}} \quad (3.4.23)$$

which is the diameter of a sphere with the same external surface area per unit volume as the actual particle.

For a packed bed of spheres (equal diameter, porosity $\varepsilon = 0.4$), Eq. (3.4.22) simplifies to:

$$f_b \approx 33 + \frac{1700}{Re_p} \quad (3.4.24)$$

The particle diameter and the fluid velocity have a strong influence on Δp_b . As we can see by insertion of Eq. (3.4.24) into Eq. (3.4.21), Δp_b is proportional to u_s/d_p^2 for low values of Re_p and to u_s^2/d_p^2 for high values (Example 3.4.3).

Example 3.4.3: Influence of particle size on the pressure drop of a fixed bed

Equations (3.4.24) and (3.4.21) lead to the following equation for the pressure drop of a fixed bed of spherical particles of equal size:

$$\frac{\Delta p_b}{L} \approx \left(33 + \frac{1700}{Re_p} \right) \frac{\rho_f u_s^2}{2d_p} \quad (3.4.25)$$

Thus we have:

$$\begin{aligned} \frac{\Delta p_b}{L} &\approx 17 \frac{\rho_f u_s^2}{d_p} & \left(\text{for } \frac{1700}{Re_p} \ll 33, \text{i.e. } Re_p \gg 50 \right) \\ \frac{\Delta p_b}{L} &\approx 850 \nu \frac{\rho_f u_s}{d_p^2} & \left(\text{for } \frac{1700}{Re_p} \gg 33, \text{i.e. } Re_p \ll 50 \right) \end{aligned}$$

Figure 3.4.3 shows the influence of the particle diameter on the pressure drop per meter length for a flow of air with a superficial velocity

of 0.01, 0.1 and 1 m s^{-1} at 20°C and 10 bar ($\nu_{\text{air}} = 1.5 \times 10^{-6} \text{ m}^2 \text{s}^{-1}$, $\rho_{\text{air}} = 11.9 \text{ kg m}^{-3}$). Note that the results shown in Figure 3.4.3 are only valid if the pressure drop is less than 1 bar (10% of the total pressure) as we then still can assume a constant fluid velocity, density, and kinematic viscosity. We also have assumed that the fixed bed is “frozen” (e.g., by a porous plate at the end of the bed) to avoid bed expansion for a high pressure drop (fluidized bed, see Figure 3.4.4 below).

For many technical processes (adsorption, gas-solid reactions, and heterogeneous catalysis) fixed beds are applied. The fluid velocity is typically in the range $0.1\text{--}1 \text{ m s}^{-1}$, and for a particle diameter of 1 mm we would get a pressure drop in the range $0.04\text{--}2 \text{ bar m}^{-1}$. This is the reason why smaller particles are rarely used in technical fixed bed processes, where the length of the bed is typically of the order of magnitude of 10 m.

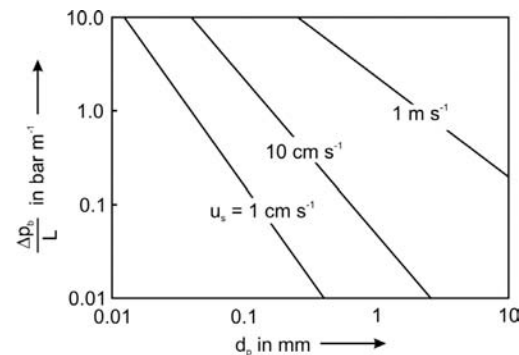


Figure 3.4.3 Influence of fluid velocity and particle diameter on the pressure drop per meter length of a fixed bed [air, 20°C , 10 bar (inlet), $\nu_{\text{air}} = 1.5 \times 10^{-6} \text{ m}^2 \text{s}^{-1}$, $\rho_{\text{air}} = 11.9 \text{ kg m}^{-3}$].

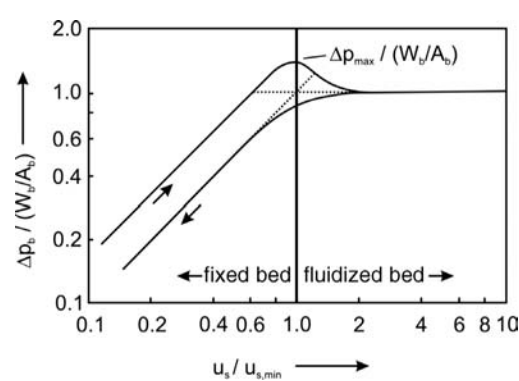


Figure 3.4.4 Influence of fluid velocity on the pressure drop of a fixed and a fluidized bed.



Insertion of Eq. (3.4.21) into Eq. (3.4.26) leads to:

$$(1 - \varepsilon_{mf}) (\rho_p - \rho_f) g = f_b \frac{1}{d_p} \frac{\rho_f u_{s,\min}^2}{2} \quad (3.4.27)$$

and by the appropriate equation for the friction factor [Eqs. (3.4.22) and (3.4.24)] the minimum fluidization velocity $u_{s,\min}$ can be calculated (Example 3.4.4). The porosity of the bed at the minimum fluidization velocity almost equals the value of the fixed bed as the bed expansion at this point is only about 10%. Thus we can still use as an approximation the value of the fixed bed with a typical porosity of 0.4. More details on ε_{mf} are given by Jakubith (1998).

Transition of Fluidized Bed into an Entrained Bed If the fluid velocity in a fluidized bed is continually increased we reach the discharging velocity, $u_{s,\text{dis}}$, and the fluidized bed switches over to an entrained bed. The discharging velocity is calculated based on a balance of forces on a single particle, that is, the weight of a particle (less the lifting force) equals the hydrodynamic resisting force of a single particle:

$$V_p \left(\rho_p - \rho_f \right) g = f_p \frac{\rho_f}{2} \left(\frac{u_{s,\text{dis}}}{\varepsilon_{\text{dis}}} \right)^2 A_{\text{proj}} \quad (3.4.28)$$

The porosity of the fluidized bed at the discharging velocity ε_{dis} is high – about 0.95 for fine particles and 0.98 for coarse particles, Froment and Bischoff (1990). Consequently we can use as approximation $\varepsilon_{\text{dis}} = 1$. The term A_{proj} is the projection screen of the particle, and f_p the friction factor of a single particle, as shown in Figure 3.4.5 for a spherical particle [$A_{\text{proj}} = \pi(d_p/2)^2$] and different Re_p numbers ($u_s d_p / \nu$). For Re_p values of less than 10^5 , the following equation is valid:

$$f_p = \frac{24}{Re_p} + \frac{4}{\sqrt{Re_p}} + 0.44 \quad (\text{for } Re_p < 10^5) \quad (3.4.29)$$

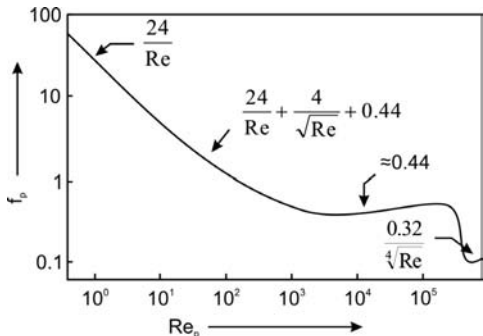


Figure 3.4.5 Influence of the Re_p number ($u_s d_p / \nu$) on the friction factor of a spherical particle.

By Eqs. (3.4.28) and (3.4.29), we calculate the discharging velocity (Example 3.4.4). In general, the ratio of the discharging velocity to the minimum fluidization velocity is about 10 for coarse particles and up to 100 for fine particles (Froment and Bischoff, 1990), that is, the regime of a fluidized bed with regard to the gas velocity is wider for fine particles.

Numerous correlations are given in the literature for the friction factor of a fixed bed, f_b , and for the friction factor of a single particle, f_p , of various shape (e.g., Jakubith, 1998). Both factors may also be linked; for example, f_b can be calculated as follows (Broetz and Schoenbucher, 1982):

$$f_b \approx \frac{\zeta}{\varepsilon^4} f_p \quad (3.4.30)$$

For spherical particles of equal size we have a porosity ε of 0.4. The factor ζ considers the particle shape and has a value in the range 1.5–8. For spherical particles, we have a value of about 2. The term ζ/ε^4 then equals 78, and Eqs. (3.4.30) and (3.4.29) yield:

$$f_b \approx 78 f_p = \frac{1870}{Re_p} + \frac{312}{\sqrt{Re_p}} + 34 \quad (\text{for spherical particles of equal size}) \quad (3.4.31)$$

Except for the factor $312Re_p^{-0.5}$, this equation is quite similar to Eq. (3.4.24), and only leads to slightly higher values of the pressure drop in a medium range of Re_p (10–1000). With regard to the limited accuracy of an exact calculation of a pressure drop this is an acceptable deviation, and thus we may use either Eq. (3.4.31) or Eq. (3.4.24) for spherical particles.

Example 3.4.4: Minimum fluidization velocity $u_{s,\min}$ of a packed bed and discharging velocity $u_{s,\text{dis}}$ (change of fluidized bed to an entrained bed)

As an example, we assume spherical particles ($\varepsilon_{mf} \approx 0.43$) with a diameter of 1 mm and a density of 1000 kg m^{-3} . The fluid (gas) has a density of 1 kg m^{-3} , so the lifting force can be neglected. The kinematic viscosity is $10^{-5} \text{ m}^2 \text{s}^{-1}$. Equations (3.4.24) and (3.4.27) lead to:

$$\left(33 + \frac{1700}{Re_p}\right) \frac{1}{d_p} \frac{\rho_g u_{s,\min}^2}{2} = 0.57 (\rho_p - \rho_g) g$$

By rearranging we obtain:

$$u_{s,\min}^2 + \frac{51.5\nu}{d_p} u_{s,\min} = \frac{(\rho_p - \rho_f)}{28.9\rho_g} d_p g$$

The solution of this equation leads to $u_{s,\min} = 0.39 \text{ m s}^{-1}$ (and $Re_p = 40$). Note that if we use Eq. (3.4.31) instead of Eq. (3.4.24) for f_b , we would get $u_{s,\min} = 0.27 \text{ m s}^{-1}$ (-30%), which shows the deviation we have to expect if we use different equations given in the literature.

To determine $u_{s,\text{dis}}$ (change from fluidized to entrained bed), we again neglect the lifting force and assume a porosity of almost 1. We then get

from Eq. (3.4.28) and Eq. (3.4.29):

$$\left(\frac{24}{Re_{p,\text{dis}}} + \frac{4}{\sqrt{Re_{p,\text{dis}}}} + 0.44 \right) \frac{\rho_g}{2} u_{s,\text{dis}}^2 \frac{\pi}{4} d_p^2 = \frac{\pi}{6} d_p^3 \rho_p g$$

Rewriting in terms of the Re number, $Re_{p,\text{dis}} = u_{s,\text{dis}} d_p / \nu$, leads to:

$$(24Re_{p,\text{dis}} + 4Re_{p,\text{dis}}^{1.5} + 0.44Re_{p,\text{dis}}^2) = \frac{4}{3} \frac{d_p^3 \rho_p}{\nu^2} g = 130\,800$$

Unfortunately, no term in the brackets on the left-hand side of this equation is negligible, but after some trial and error we obtain a value for $Re_{p,\text{dis}}$ of 436 and a value for $u_{s,\text{dis}}$ of 4.36 m s^{-1} .

3.4.1.3 Compressors and Pumps

Conveyance of Liquids by Pumps The delivery rate (power) needed to pump a liquid depends on the total delivery height, h_t , which is given by (Figure 3.4.6):

$$h_t = \frac{\Delta p_t}{\rho_f g} = (h_2 - h_1) + \left(\frac{u_2^2 - u_1^2}{2g} \right) + \left(\frac{p_2 - p_1}{\rho_f g} \right) + \frac{\Delta p_{\text{friction}}}{\rho_f g} \quad (3.4.32)$$

Thus we have to consider:

- the real lifting height, $h_2 - h_1$, which is zero for a horizontal tube;
- different fluid velocities on the suction and pressure side, if the cross-sectional areas of the respective pipes are different;
- the difference in the total (static) pressure, $p_2 - p_1$, which is zero if the pressure in both vessels is the same;
- the pressure drop provoked by friction in the pipe, valves, and so on ($\Delta p_{\text{friction}}$).

The delivery rate P_{pump} (power in W) is given by:

$$P_{\text{pump}} = \eta_{\text{pump}} \Delta p_t \dot{V}_1 = \eta_{\text{pump}} h_t \rho_f g \dot{V}_1 \quad (3.4.33)$$

where η_{pump} is the efficiency of the pump, which depends on the type of pump and the operation parameters, as shown in Figure 3.4.7 for the example of a rotary pump.

In many practical cases, the difference between the fluid velocities on the suction and pressure side is zero or negligible, and the difference in the total (static) pressure, $p_2 - p_1$, is zero, for example, if we pump a liquid from one reservoir into another reservoir, and both vessels are open to the atmosphere ($p_1 = p_2$ in Figure 3.4.6). We then obtain:

$$h_t = \frac{\Delta p_t}{\rho_f g} = (h_2 - h_1) + \frac{\Delta p_{\text{friction}}}{\rho_f g} \quad (\text{for } p_1 = p_2 \text{ and } u_1 = u_2) \quad (3.4.34)$$

The total delivery height is a function of the volume rate and starts at the lifting height for $\dot{V}_1 = 0$, and then increases almost proportionally to u_1^2 and \dot{V}_1^2 , respectively (Figure 3.4.7, see also Example 3.4.2). Thus, the operating point of a rotary pump is given by the intersection of this curve of operation with the respective characteristic curve of the pump that depends on the rotational frequency n . For a fixed value of n , the volume rate can be adjusted by using a choke valve, which increases the pressure drop and reduces the rate. For a piston pump, the characteristic curves are almost vertical lines, and the volume rate can only be adjusted by the rotational frequency.

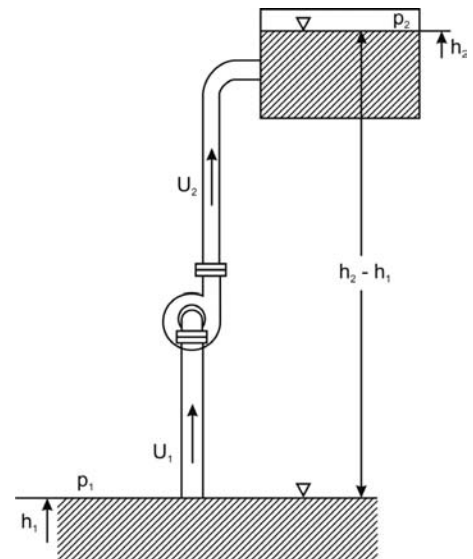
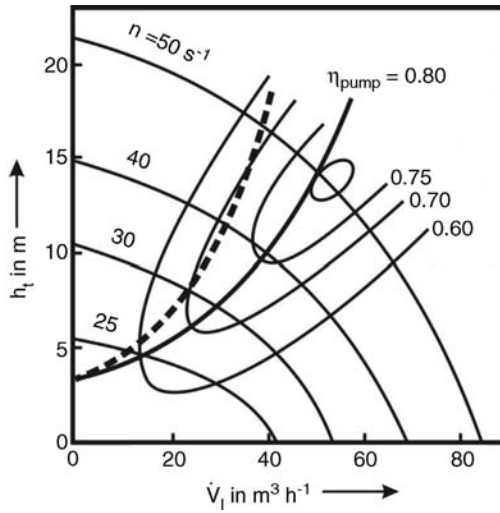


Figure 3.4.6 Terms that have to be considered for pumping a liquid.

Figure 3.4.7 Characteristic curves of a rotary pump and characteristic curves of operation for a lifting height, $h_2 - h_1$, of 3 m [see also Eq. (3.4.34); dashed line: example of the change of the characteristic curve of operation if a choke valve is used; η_{pump} is the efficiency of the pump].



Conveyance of Gases by Compressors The delivery rate (power in W) for the conveyance and compression of gases is given by:

$$P_{\text{comp}} = \eta_{\text{comp}} \int_1^2 \dot{V}_g dp \quad (3.4.35)$$

Thereby, we have to consider whether the compression is carried out under adiabatic or isothermal conditions (other situations in between these two border cases are not covered here).

For a perfectly cooled compressor ($T = \text{const.}$, and thus $\dot{V}_g p = \text{const.}$, i.e., $\dot{V}_g = \dot{V}_{g,1} p_1 / p$) and an ideal gas we obtain:

$$\begin{aligned} P_{\text{comp, isothermal}} &= \eta_{\text{comp}} \int_1^2 \dot{V}_{g,1} \frac{p_1}{p} dp = \eta_{\text{comp}} \dot{V}_{g,1} p_1 \int_1^2 \frac{1}{p} dp \\ &= \eta_{\text{comp}} \dot{V}_{g,1} p_1 \ln\left(\frac{p_2}{p_1}\right) \end{aligned} \quad (3.4.36)$$

For adiabatic compression we have to take into consideration that the temperature increases:

$$T_2 = T_1 \left(\frac{p_2}{p_1}\right)^{\frac{\kappa-1}{\kappa}} \quad \text{with} \quad \kappa = \frac{c_p}{c_v} \quad (3.4.37)$$

The delivery rate (power) is then given by ($pV^\kappa = \text{const.}$, $\kappa = c_p/c_v$):

$$P_{\text{comp, adiabatic}} = \eta_{\text{comp}} \dot{V}_{g,1} (p_1)^{\frac{1}{\kappa}} \int_1^2 \frac{1}{p^{\frac{1}{\kappa}}} dp = \eta_{\text{comp}} \frac{\kappa}{\kappa-1} \dot{V}_{g,1} p_1 \left[\left(\frac{p_2}{p_1}\right)^{\frac{\kappa-1}{\kappa}} - 1 \right] \quad (3.4.38)$$

For most gases, the heat capacity ratio κ is about 1.4, and the ratio of the power needed for adiabatic and isothermal compression is given by:

$$\frac{P_{\text{comp, adiabatic}}}{P_{\text{comp, isothermal}}} = \frac{\frac{\kappa}{\kappa-1} \left[\left(\frac{p_2}{p_1}\right)^{\frac{\kappa-1}{\kappa}} - 1 \right]}{\ln\left(\frac{p_2}{p_1}\right)} \approx \frac{3.5 \left[\left(\frac{p_2}{p_1}\right)^{0.29} - 1 \right]}{\ln\left(\frac{p_2}{p_1}\right)} \quad (3.4.39)$$

For example, for a pressure ratio $p_2/p_1 = 2$ and $T_1 = 20^\circ\text{C}$, the temperature increases during adiabatic compression by about 64 K [Eq. (3.4.37) for $\kappa = 1.4$], and the energy requirement is about 10% higher compared to isothermal compression.

Table 3.4.21 Energy requirement in kJ for the compression of 1 m³ air (1 bar, 20 °C)

	Compression from $p_1 = 1$ bar to p_2 (bar) of:				
	2	4	8	16	32
Energy for isothermal compression (kJ m ⁻³ air)	69	139	208	277	347
Energy for adiabatic compression (kJ m ⁻³ air)	77	170	284	423	592
Ratio of energy requirement for adiabatic compression to the requirement for isothermal compression	1.11	1.23	1.37	1.53	1.71
Temperature increase for adiabatic compression (K)	64	142	238	354	496

Values for other pressure ratios are given in Table 3.4.21, indicating that the temperature rise during adiabatic compression becomes very high for pressure ratios of more than about 4, which leads in turn to an excessive high energy input compared to isothermal compression.

In reality, isothermal compression is hard to realize, and so (almost adiabatic) compression is performed stepwise with intermediate cooling to avoid excessive high temperatures and energy requirements. Thus, in reality, gas compression is carried out somewhere in between the ideal case of isothermal compression and the “worst case” of adiabatic compression.

Figure 3.4.8 gives the power requirement for an isothermal reversible compression of air (starting from 1 bar) and the fields of application of compressors, blowers, and ventilators.

Importantly, for a given mass flow rate and pressure difference, the energy requirement for the conveyance of a liquid is much lower than for a gas (Example 3.4.5).

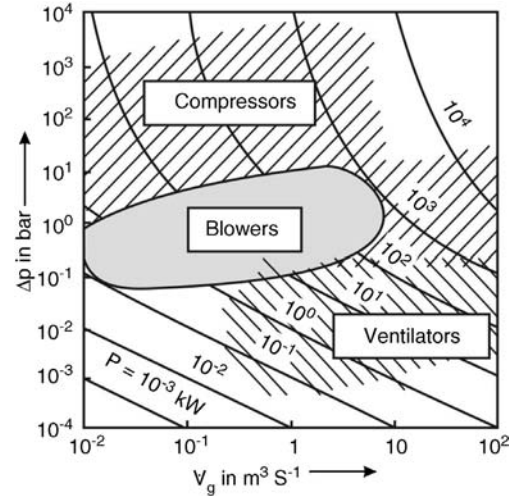


Figure 3.4.8 Power requirement for an isothermal reversible compression of air (starting from 1 bar) and fields of application of compressors, blowers, and ventilators.

Example 3.4.5: Estimation of energy requirement for the conveyance of fluids

Let us assume that we have to pump a liquid or to compress a gas from $p_1 = 1$ bar to $p_2 = 5$ bar. The flow rate should be 1 kg s^{-1} , so the volume rate (at p_1) would be about $1 \text{ m}^3 \text{ s}^{-1}$ (gas) and $0.001 \text{ m}^3 \text{ s}^{-1}$ (liquid). The energy requirement for the pump (for 100% efficiency, horizontal tube, constant liquid velocity) according to Eqs. (3.4.32) and (3.4.33) is:

$$P_{\text{pump}} = \dot{V}_l \Delta p_t = 0.001 \frac{\text{m}^3}{\text{s}} 4 \times 10^5 \text{ Pa} = 400 \text{ W}$$

For an ideal isothermal compressor (for 100% efficiency) we would get [Eq. (3.4.36)]:

$$\begin{aligned} P_{\text{comp, isothermal}} &= \dot{V}_{g,1} p_1 \ln \left(\frac{p_2}{p_1} \right) = 1 \frac{\text{m}^3}{\text{s}} 1 \times 10^5 \text{ Pa} \ln 5 \\ &= 161 \text{ kW} \end{aligned}$$

which is $300\times$ higher. For adiabatic compression we would have 204 kW (about 400× higher). Thus in most technical plants, the operating expenses of pumps are negligible compared to the expense of compressing gases.

3.4.2

Contacting and Mixing of Fluids

Contacting and mixing of fluids is an important factor in chemical engineering. It may be needed to homogenize different feedstocks before they enter a reactor and/or to ensure an almost constant temperature and concentration within a batch-wise or continuously operated stirred tank reactor. A controlled heat transfer is also essential in many processes, and an improved heat exchange can be obtained by a suitable mixing, because a flow along the heat transfer areas (vessel jackets etc.) improves the heat transfer coefficient and thereby the heat transfer to the cooling/heating medium. For details on industrial mixing see Paul, Atiemo-Obeng, and Kresta (1984).

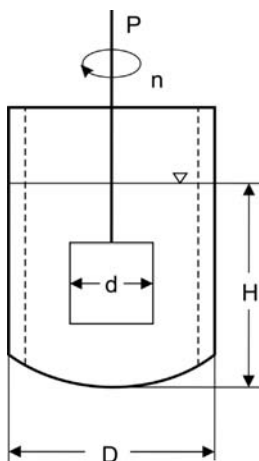


Figure 3.4.9 Sketch of a mixing vessel with blade stirrer and baffles (indicated by dashed lines).

Mixing can be achieved by dynamic or static mixers or a combination of both (e.g., by a blade stirred and baffles, Figure 3.4.9). Dynamic mixers are systems with moving stirrer tools. Static mixers are continuous systems, in which the mixing process is initiated by using the hydrodynamic energy of a fluid, which passes through a pipe with fixed settings.

The power consumption P of a stirrer of a certain type and geometry depends on four parameters:

- the stirrer diameter d_{stirrer} , which is mostly used as characteristic length of a stirrer;
- the stirred speed n_{stirrer} ;
- the density ρ and viscosity ν of the fluid.

Dimensionless analysis [see, for example, Zlokarnik (1973)] leads to two characteristic numbers, which determine the power requirements of a stirrer, the so-called Newton number Ne (often also termed power number) and the Reynolds number of a stirrer Re_{stirrer} :

$$Ne = \frac{P}{\rho n_{\text{stirrer}}^3 d_{\text{stirrer}}^5} \quad (3.4.40)$$

$$Re_{\text{stirrer}} = \frac{n_{\text{stirrer}} d_{\text{stirrer}}^2}{\nu} \quad (3.4.41)$$

In the range $Re_{\text{stirrer}} < 20$, the term $Ne \times Re_{\text{stirrer}}$ is constant (C_1), and the following equation applies:

$$P = C_1 \rho v n_{\text{stirrer}}^2 d_{\text{stirrer}}^3 \quad (3.4.42)$$

Hence for laminar flow, the power requirements are proportional both to the kinematic viscosity and density of the fluid. The value of C_1 depends on the type of stirrer (Table 3.4.22).

In the range $Re_{\text{stirrer}} > 50$ (baffled vessel) or $Re_{\text{stirrer}} > 5 \times 10^4$ (tank without baffles), Ne is constant (C_2), and we obtain:

$$P = C_2 \rho n_{\text{stirrer}}^3 d_{\text{stirrer}}^5 \quad (3.4.43)$$

The value of C_2 also depends on the type of stirrer (Table 3.4.22).

In unbaffled tanks an intermediate regime exists, in which both the density and the viscosity determine the power requirements. In this case $Ne = C_3 / Re_{\text{stirrer}}^{1/3}$ applies:

$$P = C_3 \nu^{1/3} \rho n_{\text{stirrer}}^{8/3} d_{\text{stirrer}}^{13/3} \quad (3.4.44)$$

Baffles have no effect in the laminar flow regime, but for high Reynolds numbers the effect is pronounced, as shown in Figure 3.4.10 for the example of a blade stirrer. In general, the power requirements increase if baffles are used.

Table 3.4.22 Values of C_1 [Eq. (3.4.42)] and C_2 [Eq. (3.4.43)] for different types of stirrers (for details see Zlokarnik, 1973; Baerns *et al.*, 2006).

Stirrer type	C_1	C_2	
		Baffled tank	Tank without baffles
Cross beam	110	3.2	0.4
Frame	110	5.5	0.5
Blade	110	9.8	0.5
Anchor	420	—	0.35
Turbine	70	5.0	—
Propeller	40	0.35	—
Impeller	85	0.75	0.2

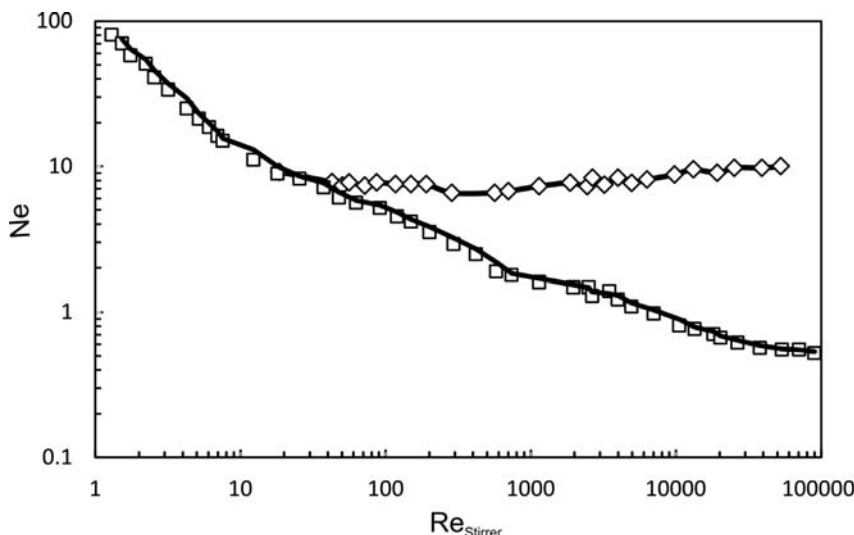


Figure 3.4.10 Power characteristic of a blade stirrer with a given geometry [data from Zlokarnik (1973)]; geometry (see Figure 3.4.9: $b/d = 1$ with b as blade height; $H/D = 1$. \diamond (upper curve): baffled tank, \square (lower curve): tank without baffles.

3.4.3

Crushing and Screening of Solids

3.4.3.1 Particle Size Reduction

In size-reduction equipment such as crushers and mills, the particles are stressed by contact forces, which leads to particle breakdown. The energetic effectiveness of crushers and mills is very small. Typically, only about 1% of the energy input is used for size reduction! Most of the input of electrical energy is consumed for interfacial work (frictional heat), deformation work, and working cycles without impact on crushing. Note that the global consumption of electrical energy for crushing and milling processes is enormous, about 600 TWh ($=600 \times 10^{12}$ Wh) (Hemming, 2008). This is about 9% of the electrical energy consumed worldwide by industry (≈ 7000 TWh = 41% of total global electricity consumption of $\approx 16\,000$ TWh in 2004).

A clearly defined boundary between crushers and mills does not exist. The term crusher is applied to devices that perform coarse size reduction, and the term mill is used for fine size reduction where the particle size of the feed is a few centimeters or less. Table 3.4.3 shows typical values of the maximum particle size of the charge treated by crushers and mills as well as the particle size reduction ratio, which is usually defined as the ratio of the maximum particle size before and after crushing and milling. Figure 3.4.11 shows a typical plant for a stepwise reduction of the particle size.

Crushers can be classified into jaw crushers, cone crushers, roll crushers (Figure 3.4.12), and impact crushers. Important mills are roller mills, cylindrical mills, and vibration mills. Cylindrical mills consist of a vessel containing a moving grinding medium, typically balls, rods, or short bars (Figure 3.4.13). In roller mills stress is applied to the feed in the gap between two counter-rotating rollers. In vibration mills, the mill vessel moves in a circular path, without rotating around its own axis, which sets the grinding medium in motion and produces a grinding action.

Table 3.4.3 Reduction ratios and maximum particle sizes (charge) of crushers and millers.

Equipment	Reduction ratio (ratio of max. particle size before and after crushing/milling)	Range of particle size (before crushing/milling)	Max. throughput ($t h^{-1}$)
Jaw crusher	3–6	100 mm–3 m	1200
Roll crusher	4–6	1 mm–1 m	1200
Cone crusher	4–6	25 mm–300 mm	600
Impact crusher	10–15	50–600 mm	300
Roller mill	10–50	60 μm –10 mm	10
Ball mill	10–50	30 μm –10 mm	10
Vibration mill	10–50	5 μm –1 mm	20

Figure 3.4.11 Plant for particle size reduction.
Adapted from Broetz and Schoenbucher (1982)

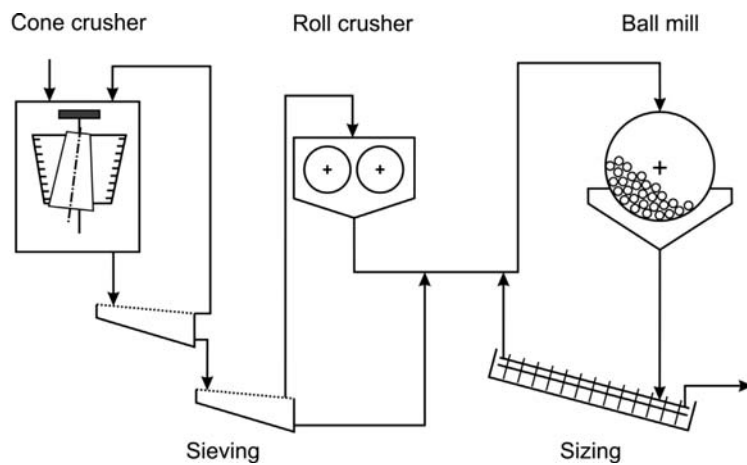


Figure 3.4.12 Important types of crushers: (a) jaw crusher, (b) cone crusher, and (c) roll crusher.
Adapted from Gmehling and Brehm (1996).

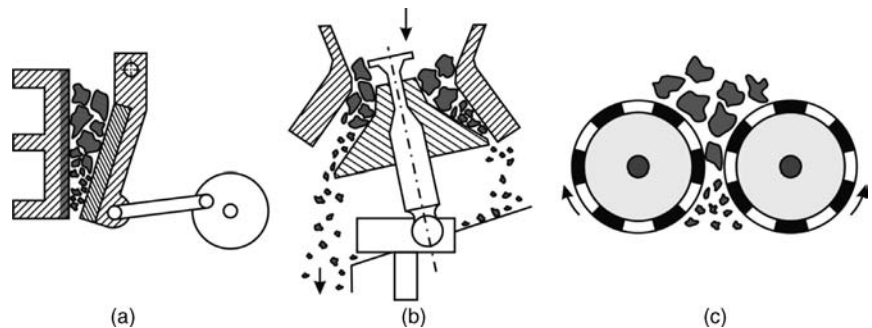
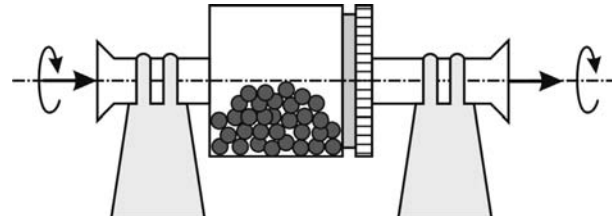


Figure 3.4.13 Cylindrical mill (ball mill)
(schematically with cogwheel for drive system).



3.4.3.2 Particle Size Analysis

Usually, we assume particles to be spherical for particle size analysis because a sphere is the only shape that can be described by one number, its diameter d . The precise shape of particles relevant for chemical and mechanical engineering (coal, catalysts, ores, cement, paint pigments etc.) differs, but we can easily convert the volume (V_p) or the mass of a particle (m_p) into the diameter of an equivalent sphere (equivalent sphere theory):

$$d_{eq} = \sqrt[3]{\frac{6V_p}{\pi}} \quad (3.4.45)$$

$$d_{eq} = \sqrt[3]{\frac{6m_p}{\pi\rho_p}} \quad (3.4.46)$$

The size of particles in a sample can be measured by microscope analysis or by the use of a set of sieves. Typically, a sample of particles is passed through a set of vibrating sieves arranged with downward decreasing mesh diameters. The mass of particles retained on each sieve is measured. This method is quick and sufficiently accurate for most purposes.

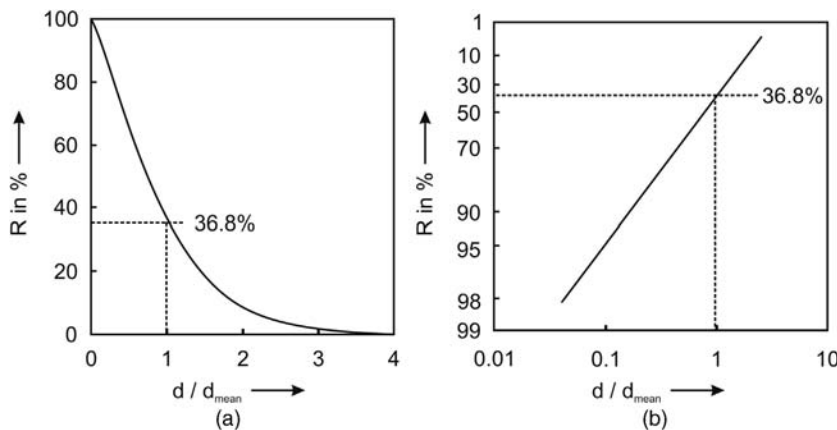


Figure 3.4.14 Example of an ideal particle size distribution curve according to the Rosin–Rammler–Sperling–Bennett (RRSB) function for $n = 1.3$:
 (a) Eq. (3.4.47) and (b) Eq. (3.4.48a).

To interpret sieve data, graphical and statistical methods of data presentation are used. The distribution curve that is widely used in industrial practice was developed by Rosin, Rammler, Sperling, and Bennett in the 1930s (Rosin, Rammler, Sperling, 1997; Rosin and Rammler, 1933; Bennett, 1936). They found out that the size distribution of coal dust and of other crushed and milled materials like cement follows a probability curve with a similar pattern as well-known physical functions such as the *Maxwell–Boltzmann* distribution (Section 3.1.4) of the speed of gas molecules (Schubert and Waechtler, 1969). The so-called Rosin–Rammler–Sperling–Bennett (RRSB) function is given by:

$$R = e^{-\left(\frac{d}{d_{\text{mean}}}\right)^n} \quad (3.4.47)$$

where d is the particle size, R the retained weight fraction, d_{mean} the mean particle size (defined below), and n is a measure of the spread of the function. Rearrangement of Eq. (3.4.47) leads to:

$$\log\left(\log\frac{1}{R}\right) = n \log\left(\frac{d}{d_{\text{mean}}}\right) + \log(\log e) \quad (3.4.48a)$$

which is the most common presentation of the RRSB distribution function, if log-probability paper (RRSB graphic paper) is used, or to:

$$\ln\left(\ln\frac{1}{R}\right) = n \ln\left(\frac{d}{d_{\text{mean}}}\right) \quad (3.4.48b)$$

The mean diameter d_{mean} represents the position where $R = 1/e = 0.368$ (36.8%), and the spread parameter n represents the slope of the straight line obtained when $\log[\log(1/R)]$ is plotted versus $\log(d/d_{\text{mean}})$, as shown in Figure 3.4.14 for an ideal RRSB function for $n = 1.3$.

Further insights into particle size distributions are given in Example 3.4.6.

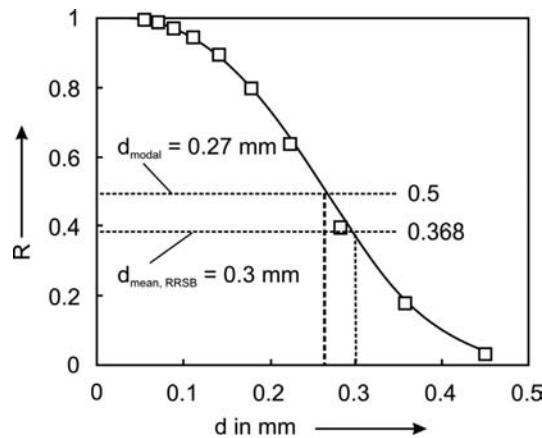
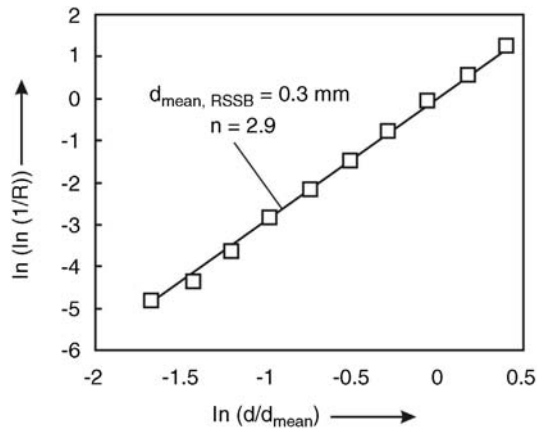
Example 3.4.6: Sieve analysis and particle size distribution of a granular material

Table 3.4.4 shows the result of a sieve analysis of natural sand from Drome, France (Besançon, Chastang, and Lafaye, 1993). Based on the values of the mean particle size and the respective values of the retained weight fraction, Figure 3.4.15, the mean particle diameter $d_{\text{mean,RRSB}}$ is determined by the RRSB method, and by the plot of $\ln[\ln(1/R)]$ versus $\ln(d/d_{\text{mean}})$ we obtain the parameter n (Figure 3.4.16). For the given example, the agreement between the measurement and RRSB theory is excellent (which is not the case for all crushed materials).

In some cases, the particle size distribution cannot be fitted by the RRSB function. Other approaches are then needed to characterize the mean diameter. One such approach is to use the median, that is, simply the mesh size and particle diameter where 50% of the particles are retained (Figure 3.4.15, Figure 3.4.17a). Alternatively, the so-called mode can be used that is gained from the density function, which is derived from the weight fraction distribution curve (Figure 3.4.17b). The mode is the maximum of the density function.

Table 3.4.4 Example of a sieve analysis of sand from France (Besançon, Chastang, and Lafaye, 1993).

Mesh size of sieve (mm)	Particle size interval Δs (mm)	Mean particle size d (mm)	Retained weight fraction R	Weight fraction r	Density function $r/\Delta s$ (mm $^{-1}$)
0.050	0–0.05	0.025	1.000	0.008	0.16
0.063	0.05–0.063	0.057	0.992	0.004	0.35
0.080	0.063–0.08	0.072	0.988	0.014	0.78
0.100	0.08–0.1	0.09	0.974	0.031	1.55
0.125	0.10–0.125	0.11	0.943	0.050	2.03
0.160	0.125–0.16	0.14	0.893	0.097	2.76
0.200	0.16–0.2	0.18	0.796	0.162	4.04
0.250	0.2–0.25	0.23	0.634	0.241	4.82
0.315	0.25–0.315	0.28	0.393	0.217	3.34
0.400	0.315–0.4	0.36	0.176	0.146	1.71
0.500	0.4–0.5	0.45	0.030	0.030	0.30

Figure 3.4.15 Result of sieve analysis of sand: retained weight fraction versus mean particle size [curve: Eq. (3.4.47) for $n = 2.9$].**Figure 3.4.16** Particle size distribution curve according to the Rosin–Rammller–Sperling–Bennett (RRSB) function as given by Eq. (3.4.48b).

3.4.3.3 Screening and Classification of Particles (Size Separation)

The two dominant industrial processes for size separation are screening and classification, which can be used for wet particles carried by water or other liquids or for dry particles that are free-flowing in gases. Industrial screening is carried out by

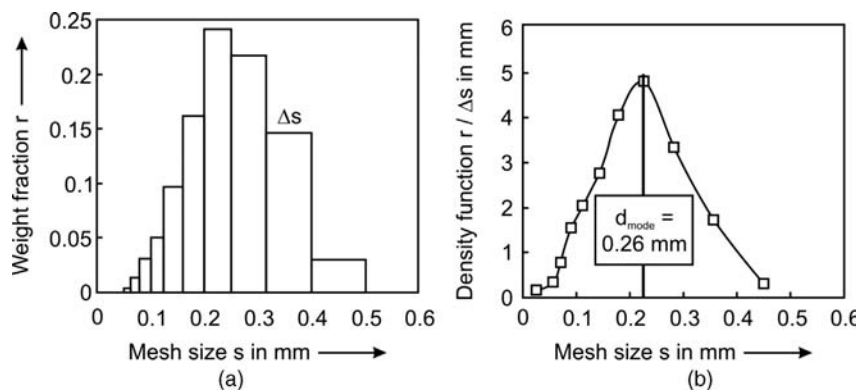


Figure 3.4.17 (a) Frequency distribution curve and (b) density function used to characterize the mean particle diameter by the mode, that is by the maximum of the density function.

vibrating sieves for coarse particles with sizes in the range of 1 m to 1 mm; in the laboratory, sieves down to about 10 μm are used.

Industrial classification for size separation of particles below 1 mm relies on different settling rates for particles of different sizes moving through fluids, usually air or water. Particles accelerating under the influence of gravity (or other forces) encounter increasing resistance from the enveloping medium. Terminal velocities are reached when the forces of acceleration and resistance are equal. Larger particles move away from smaller ones (of equal density) as the terminal velocity is higher (see *sedimentation in a gravitational field* in Section 3.4.4.2), and different size groups can be collected. In centrifugal classifiers, such as hydro- or aerocyclones, gravity is replaced by centrifugal forces to enhance the classification.

3.4.3.4 Solid–Solid Separation (Sorting of Different Solids)

The most important solid–solid separation processes are gravity separation, magnetic/electric separation, radiation sorting, and separation based on the wettability of surfaces:

- **Gravity separation:** (sink-float separation) employs a liquid that has a density that lies between those of the particles to be sorted.
- **Magnetic separation:** separates particles of different magnetic susceptibility, and can be carried out either dry or in liquid suspension.
- **Triboelectric separation:** is based on differences in electrical resistivity. Materials that are rubbed together, for example, in a rotating drum, may become positively or negatively charged and can be separated in an electrical field. This is, for example, used to separate polymer mixtures.
- **Radiation sorting:** relies on transmission, absorption, reflection, or emission of many types of radiation. For example, the reflection of visible light can be used to separate particles by color. Each particle, in free flight or traveling on a conveyor, is presented individually to a radiation source. The particle is inspected, and the information is analyzed to trigger an accept–reject signal that operates a sorting mechanism such as an air or water jet.
- **Separation processes based on the wettability:** make use of the effect that hydrophobic particles can be attached to air bubbles that transport them to the surface of the pulp, forming a froth that is collected as a concentrate. This process is known as flotation, and is an important method of solid–solid separation in the mineral industry. Various reagents are used to enhance the process. Flotation is used for the recovery of sulfides and oxides of various metals such as copper, lead, zinc, nickel, molybdenum, iron, titanium, tungsten, and tin.

3.4.4

Separation of Solids from Fluids

3.4.4.1 Filtration

Filtration is the separation of solid particles or of droplets from liquids and gases by a filter medium. The fluid separated from the solids is called the filtrate, effluent, or permeate. As in other separation processes, the separation of phases is never complete. Hence, the quality of the filtration operation is characterized by the liquid content of the separated solids (cake moisture) and by the content of solids in the filtrate (clarity).

In the simplest case, the fluid flows through the filter medium by gravity (hydrostatic filtration). More often, a pressure drop is imposed. In pressure filtration, the influent is under pressure. In vacuum filtration, a vacuum is applied to the effluent, while centrifugal filters employ centrifugal forces to drive and enhance filtration.

In cake filtration, most of the particles are larger than the openings in the filter medium. Therefore, the solids are retained as a cake of increasing thickness. In deep-bed filtration, the solids are retained in the interior of the filter medium. Here the effluent is the product, and because of the limited capacity of the filter bed to trap solids, only dilute slurries are treated.

More information on filtration (as well as on sedimentation, which is treated in the next section) are given for example in Perry and Chilton (1970), Broetz and Schoenbucher (1982), and Gmehling and Brehm (1996). Example 3.4.7 gives an instructive example.

Example 3.4.7: Filtration of a suspension of CaCO_3

The equation for the volumetric rate of the fluid during cake filtration is:

$$\dot{V}_{\text{fluid}} = \frac{dV_{\text{fluid}}}{dt} = \frac{A_{\text{filter}} \Delta p}{\eta (R_{\text{cake}} h_{\text{cake}} + R_{\text{filter}} h_{\text{filter}})} \quad (3.4.49)$$

with R_{cake} and R_{filter} as the specific resistance to flow of the cake and of the filter (in m^{-2}), respectively. For the filter, we have constant values of R_{filter} and h_{filter} . For the cake, we may also assume (for simplification) a constant value of R_{filter} , but the height h_{cake} changes with time and with the volume of the fluid that has passed the filter:

$$h_{\text{cake}} = \frac{V_{\text{cake}}}{A_{\text{filter}}} = \frac{m_{\text{solid}}}{\rho_{\text{cake}} A_{\text{filter}}} = \frac{\rho_{\text{fluid}} x_{\text{m,solid}} V_{\text{fluid}}}{\rho_{\text{cake}} A_{\text{filter}}} = C_1 \frac{x_{\text{m,solid}} V_{\text{fluid}}}{A_{\text{filter}}} \quad (3.4.50)$$

where $x_{\text{m,solid}}$ is the loading of the fluid with the solid ($\text{kg}_{\text{solid}} \text{ kg}_{\text{fluid}}^{-1}$).

Insertion of Eq. (3.4.50) into Eq. (3.4.49) yields:

$$\begin{aligned} \frac{dV_{\text{fluid}}}{dt} &= \frac{A_{\text{filter}} \Delta p}{\eta \left(C_1 R_{\text{cake}} \frac{x_{\text{m,solid}} V_{\text{fluid}}}{A_{\text{filter}}} + R_{\text{filter}} h_{\text{filter}} \right)} \\ &= \frac{A_{\text{filter}} \Delta p}{\eta \left(C_{\text{cake}} \frac{x_{\text{m,solid}} V_{\text{fluid}}}{A_{\text{filter}}} + C_{\text{filter}} \right)} \end{aligned} \quad (3.4.51)$$

and integration and rearrangement lead to:

$$\left(\frac{C_{\text{cake}} x_{\text{m,solid}}}{2 A_{\text{filter}}} \right) V_{\text{fluid}}^2 + C_{\text{filter}} V_{\text{fluid}} = \left(\frac{A_{\text{filter}} \Delta p}{\eta} \right) t \quad (3.4.52)$$

Table 3.4.5 gives the result of filtration with a suspension of CaCO_3 ($x_{\text{m,solid}} = 5 \text{ wt\%}$).

According to Eq. (3.4.52), a plot of t/V_{fluid} versus V_{fluid} should give a straight line, which for the given example is shown in Figure 3.4.18.

3.4.4.2 Separation of Solids from Fluids by Sedimentation

Sedimentation involves particle motion in gravitational, centrifugal, magnetic, and electrical fields, and is used in chemical, biological, and environmental processes

Table 3.4.5 Result of cake filtration experiment with a suspension of CaCO_3 [$x_{\text{m,solid}} = 5 \text{ wt\%}$, $\eta = 0.001 \text{ Pa s}$ (water, 20°C), $\Delta p = 13.3 \text{ kPa}$, $A_{\text{filter}} = 0.0074 \text{ m}^2$]. Data from Krypilo and Vogt (1993).

$V_{\text{fluid}} (\text{cm}^3)$	$t (\text{s})$	$V_{\text{fluid}} (\text{cm}^3)$	$t (\text{s})$
100	56	400	320
200	128	500	440
300	213	600	570

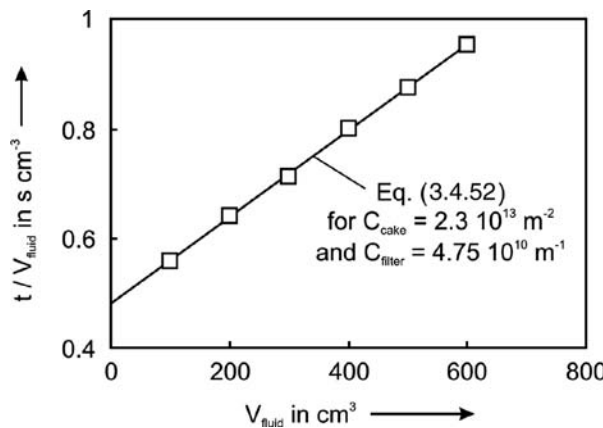


Figure 3.4.18 Result of cake filtration experiment with a suspension of CaCO₃ (other values used for the calculation are given in Tab. 3.4.5).

like wastewater treatment. Figure 3.4.19 gives an overview of processes used to separate solids from fluids.

Sedimentation in a Gravitational Field Usually, the acceleration phase until a constant sedimentation velocity is reached is negligible (Example 3.4.8). Thus particle sedimentation in a gravitational field is described by the balance of forces on a particle moving with constant velocity (steady-state), that is, the weight (less the lifting force) equals the hydrodynamic resistance. For spheres (Section 3.4.1.2) we have:

$$\nabla \text{ } V_p (\rho_p - \rho_f) g = f_p \frac{\rho_f}{2} (u_{\text{sedimentation}})^2 A_{\text{proj}} \quad (3.4.53)$$

where A_{proj} is the projection screen of the particle and f_p is the friction factor of a single particle (Figure 3.4.6). For a spherical particle [$A_{\text{proj}} = \pi(d_p/2)^2$] and Re_p numbers ($u_{\text{sedimentation}} d_p / \nu$) of less than about 2 (typical for sedimentation processes), the friction factor is given by *Stokes' law*:

$$f_p = \frac{24}{Re_p} \quad (\text{for } Re_p < 2) \quad (3.4.54)$$

Rearranging Eqs. (3.4.53) and (3.4.54) leads to the sedimentation velocity:

$$u_{\text{sedimentation}} = \frac{d^2}{18\nu} \frac{(\rho_p - \rho_f)}{\rho_f} g \quad (\text{for } Re_p < 2 \text{ and } \varepsilon_V < 0.05) \quad (3.4.55)$$

Example 3.4.9 shows how to estimate the size of a sand trap by Eq. (3.4.55).

Equation (3.4.55) does not consider that the sedimentation process may be hindered by the interactions of particles with each other. In case of a volume content of the particles (ε_V) of more than about 5%, the sedimentation velocity is substantially lower than calculated by Eq. (3.4.55). An empirical correlation to account for this effect is:

$$u_{\text{sedimentation}} = (1 - \varepsilon_V)^{4.65} \frac{d^2}{18\nu} \frac{(\rho_p - \rho_f)}{\rho_f} g \quad (\text{for } Re_p < 2 \text{ and } 0 < \varepsilon_V < 0.5) \quad (3.4.56)$$

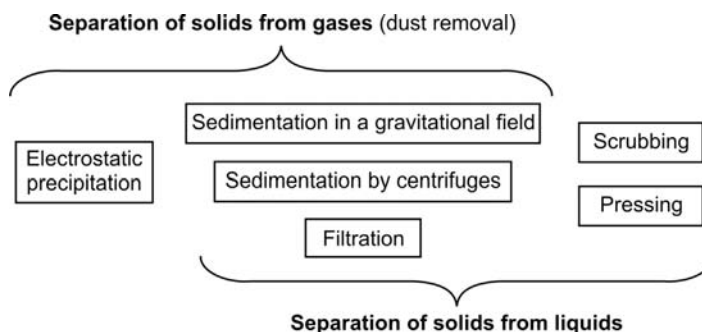


Figure 3.4.19 Technologies involved in the separation of solids from liquids and gases.

Figure 3.4.20 Influence of volume content on the sedimentation velocity in water (20°C) for the example of spheres with a diameter of 0.1 mm and particle density of 2000 kg m^{-3} .

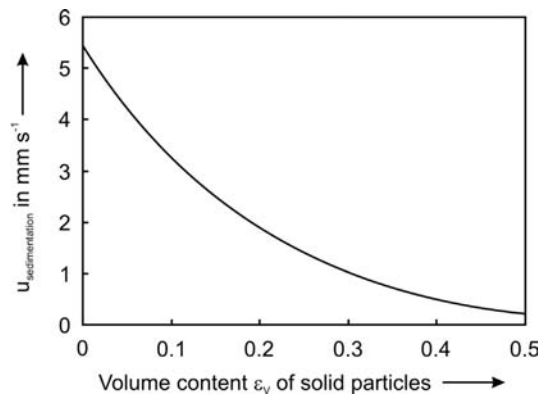


Figure 3.4.20 shows the strong influence of the volume content of the particles on the sedimentation for the case of water and spherical particles; for a volume content of more than about 50%, the sedimentation process practically comes to a standstill.

Example 3.4.8: Sedimentation of single sand particles in water

The sedimentation of single sand particles in a gravitational field is described by the balance of forces, that is, by the weight of a particle, the buoyancy force, the hydrodynamic resistance, and the inertial force [which is neglected if only the final constant sedimentation velocity is calculated by Eqs. (3.4.53) and (3.4.55)]. For spherical particles we obtain:

$$V_p \rho_p \frac{du}{dt} = V_p (\rho_p - \rho_f) g - f_p \frac{\rho_f}{2} u^2 A_{\text{proj}} \quad (3.4.57)$$

where $A_{\text{proj}} = \pi (d_p/2)^2$, $Re_p = ud_p/\nu$, and $f_p = 24/Re_p$ for $Re_p < 2$.

By rearrangement of Eq. (3.4.57) we obtain:

$$\frac{du}{dt} = \frac{(\rho_p - \rho_f)}{\rho_p} g - \frac{18\nu \rho_f}{d^2 \rho_p} u \quad (3.4.58)$$

Equation (3.4.58) is a differential equation of the form $du/dt = C_1 + C_2 u$, which can easily be solved by rearrangement [$du/(C_1 + C_2 u) = dt$] and subsequent integration. The solution for the boundary

condition of $u = 0$ for $t = 0$ is:

$$u = \left(1 - e^{-\frac{18\nu \rho_f}{d^2 \rho_p} t} \right) \left[\frac{d^2 g (\rho_p - \rho_f)}{18\nu \rho_f} \right] \\ = \left[1 - e^{-\frac{(\rho_p - \rho_f)}{\rho_p} \frac{g}{u_{\text{sedimentation}}} t} \right] u_{\text{sedimentation}} \quad (3.4.59)$$

where $u_{\text{sedimentation}}$ is the terminal sedimentation velocity according to Eq. (3.4.55).

Figure 3.4.21 depicts the course of the velocity of sand particles in water for two different particle diameters. Note that for the given example, Eq. (3.4.59) would not be valid for particle diameters of more than 0.2 mm, as the Reynolds number would then be higher than 2, that is, Stokes' law is no longer applicable. Figure 3.4.21 clearly indicates that the time needed to reach the terminal sedimentation velocity $u_{\text{sedimentation}}$ is very small (<20 ms). In addition, note that $u_{\text{sedimentation}}$ is proportional to d^2 .

Example 3.4.9: Estimation of the size of a sand trap of a sewage plant

Plants for sewage treatment use a sand trap to separate and remove sand. The tank should be large enough that the sand can settle. As an example we use a minimum particle size of 0.2 mm, a volume rate of the sewage water of $1 \text{ m}^3 \text{ s}^{-1}$, and a trap height of 3 m. What is the volume of the trap needed for sedimentation, if the acceleration phase is negligible (Example 3.4.8), and if the volume content of sand is less than 5%, that is, the sedimentation process is not hindered by the interactions of particles with each other? For the given conditions ($d = 0.2 \text{ mm}$, $\rho_p = 1500 \text{ kg m}^{-3}$, $\rho_f = 1000 \text{ kg m}^{-3}$, $\nu = 1 \times 10^{-6} \text{ m}^2 \text{ s}^{-1}$),

the (terminal) sedimentation velocity is given by Eq. (3.4.50), which leads to $u_{\text{sedimentation}} = 1.1 \text{ cm s}^{-1}$ (Figure 3.4.21 for $t > 15 \text{ ms}$). Thus the minimal residence time of the sewage water is given by:

$$\tau_{\text{water}} = \frac{h_{\text{trap}}}{u_{\text{sedimentation}}} = \frac{V_{\text{trap}}}{V_{\text{water}}} \quad (3.4.60)$$

which leads to a value of 273 s for τ_{water} and to a volume of the sand trap (V_{trap}) of 273 m^3 .

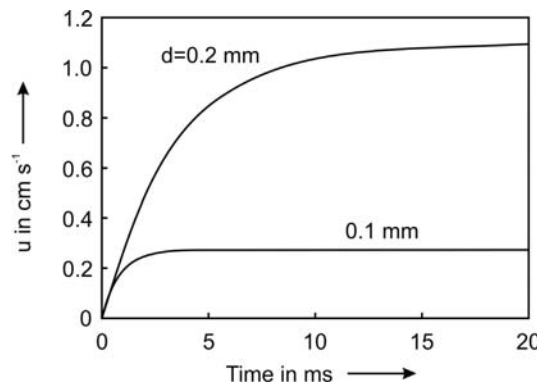


Figure 3.4.21 Velocity of sand particles in water for two different particle diameters d during the initial sedimentation period ($\rho_p = 1500 \text{ kg m}^{-3}$, $\rho_f = 1000 \text{ kg m}^{-3}$, $\nu = 1 \times 10^{-6} \text{ m}^2 \text{s}^{-1}$).

3.4.4.3 Screening and Classification of Particles (Size Separation)

Sedimentation in Centrifuges In a cylindrical vessel with a diameter d_{cyl} that rotates with a rotational frequency n (rotations per unit time), the centrifugal acceleration $a_{\text{centrifugal}}$ to which the particles are subjected is:

$$a_{\text{centrifugal}} = (2\pi n)^2 \frac{d_{\text{cyl}}}{2} \quad (3.4.61)$$

Separation by a centrifuge (Figure 3.4.22) is similar in principle to that achieved in a gravity separation process but the driving force is much higher.

The so-called centrifugational number is defined as the ratio of the centrifugal acceleration to the gravitational acceleration and may reach in technical centrifuges values of up to 4000 and in ultracentrifuges values of up to 10^6 .

Centrifuges can replace normal gravity in the sedimentation of suspensions and can also provide the driving force through a filter medium. The simplest device to use centrifugal forces to achieve separation is the cyclone, which is used for gas-solid as well as for liquid-solid separation. It is not really a centrifuge as the centrifugal separation is produced by the motion of the slurry, which is induced by the tangential introduction of the feed material.

Sedimentation in Electrical Fields (Electrostatic Precipitators) Electrostatic precipitation is typically a gas-phase process (although in some cases the particles are wetted by a water spray to enhance the separation), and is used, for example, to separate dust (flyash) from flue gases of power plants. The particulate loaded gas is passed through the passage between discharging (negative) electrodes and collecting (positive) electrodes. The particles receive a negative charge from the discharging electrodes and are attracted to the positively charged electrode and fasten onto it.

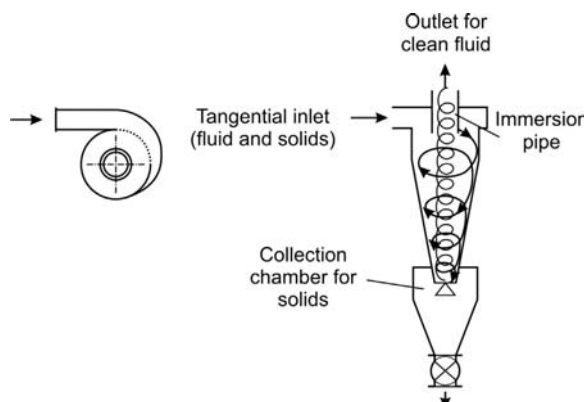


Figure 3.4.22 Cyclone for the separation of solid particles from gases or liquids.

Figure 3.4.23 Schematic of a plate-type electrostatic precipitator.

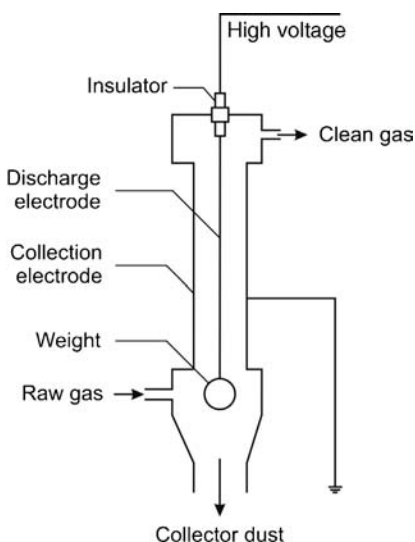
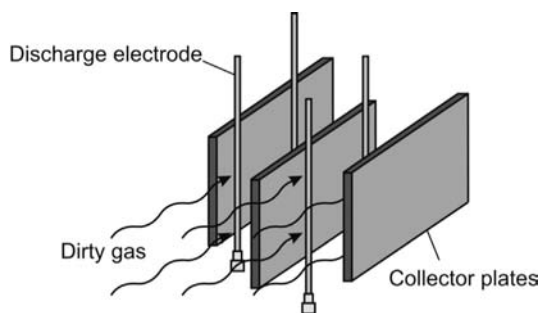


Figure 3.4.24 Tubular electrostatic precipitator.
Adapted from Gmehling and Brehm (1996).

Usually, either plate-type or tubular precipitators are used. Plate-type precipitators (Figure 3.4.23) consist of several grounded collecting plates, suspended parallel to one another with equal spacing (about 10 cm) and high voltage discharge electrodes (typically in a range of 10–80 kV) that are suspended vertically between the plates. The discharge voltage causes the air stream to ionize and the dust particles are negatively charged. As the negatively charged particles pass along the positively charged collection plates they adhere to them. The collecting electrode is cleaned, and the particles are collected in a hopper. With electrostatic precipitators, a very high separation degree (>99%) can be reached, and enormous gas throughputs of up to 10^8 m^3 gas per hour can be realized. Even for gas velocities of up to 5 m s^{-1} the pressure drop is still very low (only about 100 Pa = 1 mbar).

Tubular precipitators (Figure 3.4.24) have a discharge electrode placed in the center of the tube. The dust loaded air flows through the tube, becomes negatively charged and collects on the inside wall of the collecting tube. The dust is cleaned from the bottom of the tube.

Summary of Section 3.4 (take-home messages)

- The **pressure loss in empty tubes** depends on the **friction factor f_t** , which is a function of the Re number. For the **pressure drop in fixed beds**, which increases with decreasing particle diameter, the **Ergun equation** is used. For many processes (adsorption, gas–solid reactions, and heterogeneous catalysis) fixed beds are applied, and a particle size of more than 1 mm is used to avoid an excessive high pressure drop.
- If the fluid velocity is enhanced up to a certain critical value, a fixed bed expands and a **fluidized bed** is established. The **minimum fluidization velocity** needed for bed expansion mainly depends on the size and density of the particles, and on the viscosity of the fluid. If the fluid velocity in a fluidized bed is continuously increased we reach the **discharging velocity**, and the fluidized bed switches over to an **entrained bed**.
- **Conveyance of liquids and gases:** The delivery rate (power) needed to **pump** a liquid is proportional to the pressure drop provoked by friction in the pipe, valves, and so on. Conversely, the delivery rate for the conveyance and **compression** of gases is proportional to $\ln(p_2/p_1)$. The temperature increases during compression, which leads to an increase of energy requirement compared to isothermal conditions, which are hard to realize. Thus, (almost adiabatic) compression is carried out stepwise with intermediate cooling to avoid excessive high temperatures and energy requirements.
- For **particle size reduction** crushers and mills are used, and the particles are stressed by contact forces, which leads to a particle breakdown.
- **Particle size analysis** is performed by graphical and statistical methods. A widely used distribution curve is the *Rosin–Rammler–Sperling–Bennett* function.
- Industrial processes for size separation are screening and classification. **Screening** is carried out by vibrating sieves for coarse particles with sizes

below 1 mm. **Classification** of smaller particles relies on different settling rates for particles of different sizes moving through fluids under the influence of gravity or centrifugal forces.

- **Processes for sorting of different solids** are gravity separation, magnetic/electric separation, radiation sorting, and separation based on the wettability of surfaces.
- **Filtration** is used for the separation of solid particles or of droplets from liquids and gases. In the simplest case, the fluid flows through the filter medium by gravity (**hydrostatic filtration**). More often, a pressure drop is imposed (**pressure filtration**). Other filters use a vacuum or centrifugal forces.
- Separation by a **centrifuge** is similar to gravity separation but the driving force is higher.
- **Electrostatic precipitation** is typically used to separate dust from flue gases of power plants. The particulate loaded gas is passed through the passage between discharging (negative) electrodes and collecting (positive) electrodes. The particles receive a negative charge and are attracted to the positively charged electrode and fasten onto it.

4

Chemical Reaction Engineering

In this chapter emphasis is placed on chemical reaction engineering and the reactor design, although separation steps for product purification (examined in Section 3.3) are also important for the plant design (and in many cases have great visual impact, see figure below).



Syngas production by partial oxidation of heavy oil with CO₂-wash and pressure swing adsorption, Oberhausen, Germany. Courtesy of Linde Engineering, Germany.

4.1 Main Aspects and Basic Definitions of Chemical Reaction Engineering

4.2 Chemical Thermodynamics

What are the thermodynamic constraints of a reaction, and what temperature and pressure should be applied to maximize conversion and product yield(s)?

4.3–4.9 Kinetics of Various Non-catalytic and Catalytic Reactions

What is the size of reactor or amount of catalyst needed for a certain degree of reaction progress? Which processes determine the effective reaction rate? What are the differences between homogeneous, catalytic and gas-solid reactions? All these questions address the kinetics, and the equations for various reaction types will be derived, including the inspection of mass and heat transfer resistances.

4.10 Ideal and Real Reactors, Residence Time Distribution, and Reactor Modeling

What is the appropriate reactor and the optimal mode of operation for a certain conversion and product yield with a minimum effort (minimum reactor size and amount of catalyst)?

4.11 Evaluation of Kinetic Data

What has to be considered to determine kinetic data in laboratory reactors?

4.1

Main Aspects and Basic Definitions of Chemical Reaction Engineering

Chemical and biochemical processes such as dyeing, reduction of ore, or the manufacture of soap, wine, glass, pharmaceuticals, and – unfortunately – also of gunpowder have long been practiced, some of them since ancient times. However, these processes were developed empirically rather than based on theoretical guidelines and chemical engineering principles (Moulijn, Makkee, Van Diepen, 2004). Improvements were therefore slow until the eighteenth century when mystical interpretations were replaced by scientific theories. But it was still not until the beginning of the twentieth century that a systematic approach combining scientific and engineering disciplines became the foundation of process design. Only by this means has continuous large-scale production like ammonia synthesis became possible and common.

Although the reactor is the heart of each process, one has to keep in mind that industrial processes are often designed to produce desired products of high purity from various feedstocks and/or from a mixture of products. Therefore, pre-treatment such as the removal of impurities as well as product purification by distillation and so on (examined in Section 3.3) are also important (Figure 4.1.1).

4.1.1

Design Aspects and Scale-Up Dimensions of Chemical Reactors

The design of a chemical reactor uses knowledge and experience from various disciplines such as thermodynamics, chemical kinetics, fluid dynamics, material science, chemistry, catalysis, reaction engineering, and heat and mass transfer (Figure 4.1.2).

Only by integration of these disciplines, including economics, information science, and process control, are we able to design a reactor properly. This sometimes makes things complicated, for example, for students of chemical engineering or technical chemistry, but it is a fascinating challenge.

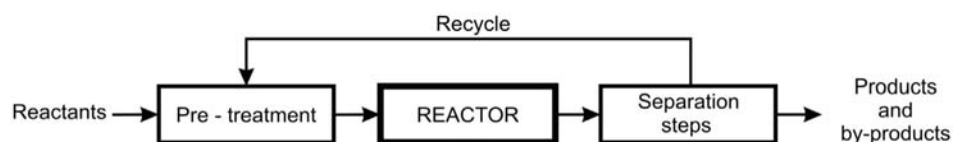
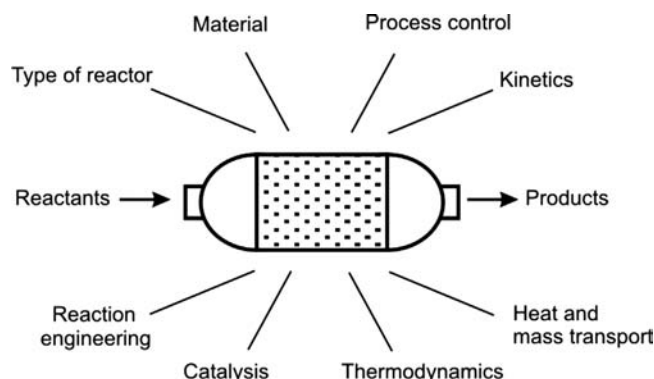


Figure 4.1.1 Structure of a chemical process.

Figure 4.1.2 Main disciplines needed for the design of a chemical reactor.



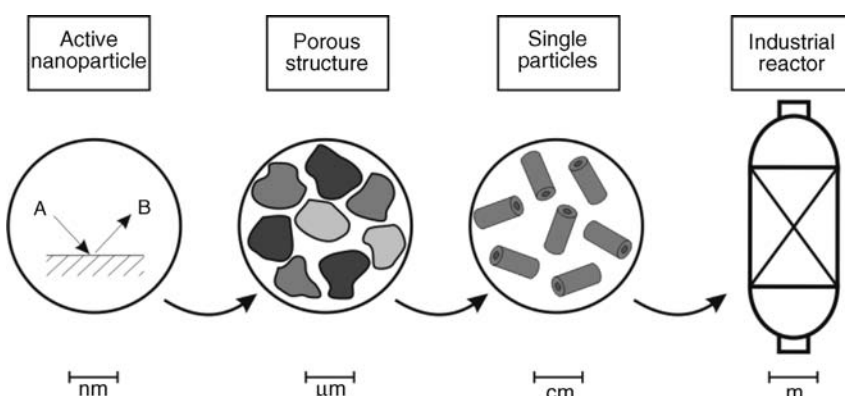


Figure 4.1.3 Scale-up dimensions of a chemical reactor: example fixed bed reactor.

Figure 4.1.3 underlines by the example of a heterogeneously catalyzed process that chemical reaction engineering has to consider a wide range of scale-up dimensions. Starting with molecules and active sites on the surface of a catalyst, having dimensions in the nanometer range, one has to consider the porous structure of catalytic particles and the mass and heat transfer processes involved on the micro- to millimeter range. In addition, finally, the design and scale-up of a reactor with a size of up to several hundred m³ has to be realized.

4.1.2

Speed of Chemical and Biochemical Reactions

Beside scale-up dimensions, we also have to keep in mind that the speed of reactions in terms of the amount of converted reactant per volume and reaction time may vary over several orders of magnitude (Figure 4.1.4). The kinetics of biochemical reactions are often slow (but not always) and take place on a time scale of hours and days, whereas industrially relevant chemical reactions proceed at rates usually more than two orders of magnitude higher (Weisz, 1982; Moulijn, Makkee, and Van Diepen, 2004). Taking microbial wastewater treatment as an example of a very slow biochemical process limited by the kinetics of O₂ metabolism, and NH₃ oxidation on a Pt-net as an example of an extremely fast heterogeneously catalyzed chemical process, we see that we have to deal with rates ranging from 10⁻⁴ to 10⁴ mol m⁻³ s⁻¹, which corresponds, for example, to a range of the characteristic reaction time of 1 day to 1 ms (Table 4.1.1). Needless to say that with such a large range, a case-specific design of reactors is needed.

Surprisingly, despite the large number of commercially attractive (mostly catalytic) reactions, the commonly encountered rates are in a quite narrow range (Figure 4.1.4). The practically relevant range of chemical reactions is rarely less than 0.1 and seldom more than 10 mol m⁻³ s⁻¹. The lower limit is set by economic constraints, as the reaction should proceed in a reasonable time and in a reasonably sized reactor in order to spend not too much money on space and hardware (vessels, catalyst). Reaction time and volume are expense-constrained parameters, which is the kineticist's proof that time is money (Weisz, 1982).

At first sight one might think that a rate exceeding the upper limit is something to be happy about. But, as for example discussed in the Sections 4.5–4.9 and for several industrial processes in Chapter 6, heat and mass transport may become limiting, if the intrinsic rate exceeds by far the upper limit. Consequently, we have to bring the specific

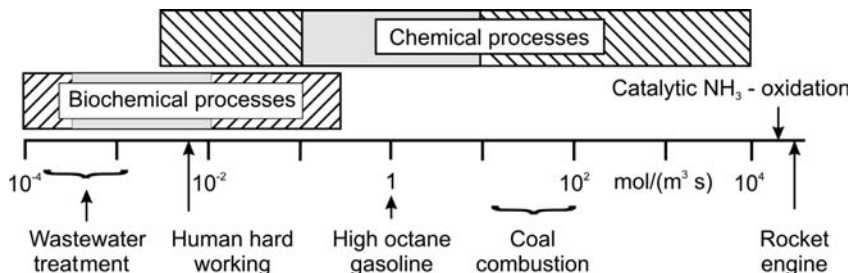


Figure 4.1.4 Windows of rates of biochemical and chemical processes (hatched areas: overall range; gray: majority of catalytic processes). Adapted from Weisz (1982) and Moulijn, Makkee, and Van Diepen (2004).

Table 4.1.1 Typical rates of reactions in mol-reactant per reaction volume and time.

Reaction	Reaction rate ($\text{mol m}^{-3} \text{s}^{-1}$)	Source
Biological wastewater treatment	$0.2\text{--}4 \times 10^{-3}$	Levenspiel (1999); Moulijn, Makkee, and Van Diepen (2004)
Human at rest and working hard ^{a)}	$3\text{--}7 \times 10^{-3}$	Own estimation
Desulfurization of diesel oil (with 300 ppmw S)	3×10^{-3}	Own estimation
Biological production of penicillanic acid ^{b)}	2×10^{-2}	Chmiel (2006)
Catalytic NO reduction (power plant, 1 g NO m^{-3})	0.1	Farrauto and Bartholomew (1997)
Biological production of amino acids (aspartic acid)	0.4	Praeve <i>et al.</i> (1987)
Catalytic oxidation of SO_2 (production of H_2SO_4)	0.5–4	Emig and Klemm (2005)
Production of high octane gasoline (reforming)	1	Own estimation
Production of blast furnace coke (coking of coal) ^{c)}	1	Own estimation
Gasoil cracking in a riser reactor	2	Froment and Bischoff (1990)
Three-way catalyst (CO conversion, 0.7 vol.% CO) ^{d)}	2	Farrauto and Bartholomew (1997)
Coal gasification (hydrogen production) ^{e)}	5	Own estimation
Syngas production (steam reforming of natural gas)	20	Froment and Bischoff (1990)
Ammonia synthesis	20	Appl (1999)
Coal combustion	10–100	Levenspiel (1999)
Catalytic oxidation of ammonia ^{f)} (production of HNO_3)	2×10^4	Own estimation
Rocket engine (combustion of H_2 with pure O_2)	3×10^4	Levenspiel (1999)
Recombination of ethyl radicals (1 bar, 400 °C)	1×10^{10}	Foersterling and Kuhn (1993)

a) Related to oxygen.

b) Many other industrial biotransformations are of the same order of magnitude (Liese, Seelbach, and Wandrey, 2006).

c) Related to carbon.

d) Related to CO.

e) Related to produced hydrogen.

f) Estimation for the reactor space where the first four Pt gauzes are located (details in Section 6.4).

activity of a catalyst back into the window of engineering reality (Weisz, 1982). For example, catalytic ammonia oxidation is a completely mass transfer controlled process; the extraordinary high (effective) reaction rate (Table 4.1.1) is only reached, because the wire diameter of the PtRh alloy gauze used as oxidation catalyst is exceptionally small (< 0.1 mm), which enhances the mass transfer. In the laboratory, such transport limitations may be negligible. For example, the particle size of an investigated catalyst may be very small, whereas in an industrial reactor, particle sizes in the range of several millimeters are needed to avoid an excessive high pressure drop. Hence, if transport processes are neglected, we may end up with an under-designed reactor. Transport limitations also can interfere with the selectivity and downstream processing units may be poorly designed.

4.1.3

Influence of Reactor Type on Productivity

For the productivity of a process, not only the reaction rate and for reversible reactions thermodynamic constraints but also the reactor type and operation mode (mixing, heating, cooling, etc.) play a decisive role. For example, the degree of mixing is an important factor for continuously operated reactors and, mostly, well-mixed systems lead to a low concentration and low reaction rate and, in turn, to a large reactor for a given duty (Example 4.1.1).

Example 4.1.1 Influence of mixing on the reactor size needed for 99% conversion

Consider a simple reaction A → B proceeding in an isothermal flow reactor with a degree of conversion X_A of 99%. For an inlet concentration $c_{A,\text{in}}$ of 1 mol m^{-3} we assume a reaction rate r_{inlet} of $1 \text{ mol m}^{-3} \text{s}^{-1}$. Therefore, if we further assume that the rate linearly depends on the concentration (a so-called first-order reaction), r will decrease within the reactor down to $0.01 \text{ mol m}^{-3} \text{s}^{-1}$ at the reactor outlet, where we have only a residual concentration $c_{A,\text{out}}$ of 0.01 mol m^{-3}

corresponding to $X_A = 99\%$. Thus, in a well-mixed vessel, we would have this low concentration and low reaction rate throughout the whole reactor ($r_{\text{inlet}} = r_{\text{outlet}}$), whereas in an unmixed system (e.g., in a thin, long tubular reactor) we would have a mean value somewhere between r_{in} and r_{out} . As we will learn more precisely in Section 4.10, the volume of the agitated vessel is then $20\times$ larger than the volume of an unmixed tube (for the given example of $X_A = 99\%$).

4.1.4

Terms used to Characterize the Composition of a Reaction Mixture

During a reaction, the reactants form products that can be sub-classified into principal (desired) products, coupled products (e.g., two principal products formed simultaneously), and (often undesired) by-products. Accompanying substances are inert gases, solvents, impurities, and so on. Basic terms for a quantitative description of the composition of a reaction mixture are the number of moles n_i or the masses m_i , linked by the molecular weight ($m_i = M_i n_i$).

During a chemical reaction the total mass remains constant, but the total number of moles, however, frequently varies. Thus, instead of these extensive terms, which depend on the system's size, intensive terms such as content and concentration, which are invariant in terms of size, are frequently used. If the reaction volume V is used as reference, the molar concentration c_i of a component i and the total concentration c_t in the reaction mixture are linked by:

$$c_t = \sum c_i = \sum \frac{n_i}{V} \quad (4.1.1)$$

V may change during a reaction, and the change in concentration is then no longer only proportional to a change in the number of moles.

Using the total number of moles n_t as reference leads to the molar fractions x_i and γ_i for liquid- and gas-phase reactions, respectively:

$$\sum x_i = 1 = \sum \frac{n_{i,l}}{n_{t,l}} \quad (4.1.2)$$

$$\sum \gamma_i = 1 = \sum \frac{n_{i,g}}{n_{t,g}} \quad (4.1.3)$$

For continuous (steady state) processes in flow reactors, molar fluxes and volumetric flow rates are used to calculate concentrations and molar fractions, and Eqs. (4.1.1)–(4.1.3) read as:

$$c_t = \sum c_i = \sum \frac{\dot{n}_i}{\dot{V}} \quad (4.1.4)$$

$$\sum x_i = 1 = \sum \frac{\dot{n}_{i,l}}{\dot{n}_{t,l}} \quad (4.1.5)$$

$$\sum \gamma_i = 1 = \sum \frac{\dot{n}_{i,g}}{\dot{n}_{t,g}} \quad (4.1.6)$$

For reactions involving gaseous phases, the partial pressure p_i is also taken as a measure for the concentration, and for ideal gases *Dalton's law* applies (with p as total pressure):

$$p_i = \gamma_i p \quad (4.1.7)$$

4.1.5

Terms used to Quantify the Result of a Chemical Conversion

Three quantities characterize the result of a chemical reaction: the conversion of reactant k (X_k) and the yields (Y_i) and selectivities (S_i) of the products i .

For a discontinuous mode of operation (batch reactors), these parameters are defined based on the initial number of moles $n_{i,0}$ and $n_{k,0}$, and the stoichiometric coefficients v (< 0 for reactants, > 0 for products):

$$X_k = \frac{n_{k,0} - n_k}{n_{k,0}} = 1 - \frac{n_k}{n_{k,0}} \quad (4.1.8)$$

$$Y_i = \frac{(n_i - n_{i,0}) |v_k|}{n_{k,0}} \quad (4.1.9)$$

$$S_i = \frac{(n_i - n_{i,0}) |v_k|}{(n_{k,0} - n_k) v_i} = \frac{Y_i}{X_k} \quad (4.1.10)$$

The yields and selectivities are thereby related to the limiting component, which is the reactant k with the lowest value of the ratio $n_{k,0}/|v_k|$.

For continuous processes in flow reactors, X_k , Y_i , and S_i are defined based on the molar fluxes:

$$X_k = \frac{\dot{n}_{k,\text{in}} - \dot{n}_{k,\text{out}}}{\dot{n}_{k,\text{in}}} = 1 - \frac{\dot{n}_{k,\text{out}}}{\dot{n}_{k,\text{in}}} \quad (4.1.11)$$

$$Y_i = \frac{(\dot{n}_{i,\text{out}} - \dot{n}_{i,\text{in}}) |v_k|}{\dot{n}_{k,\text{in}}} \quad (4.1.12)$$

$$S_i = \frac{(\dot{n}_{i,\text{out}} - \dot{n}_{i,\text{in}}) |v_k|}{(\dot{n}_{k,\text{in}} - \dot{n}_{k,\text{out}})} = \frac{Y_i}{X_k} \quad (4.1.13)$$

Note that the terms yield and selectivity are particularly important for parallel or consecutive reactions or reaction networks. For a single stoichiometrically independent reaction ($A \rightarrow B$), the conversion of A and the yield of B are identical and the selectivity to B is always one.

4.1.6

Reaction Time and Residence Time

For a batch reactor, the reaction time t is the natural performance measure. For flow reactors, the residence time τ is used, which is defined as the ratio of the reactor volume to the volumetric flow rate at reaction conditions (\dot{V} in $\text{m}^3 \text{s}^{-1}$):

$$\bullet \quad \tau = \frac{V_R}{\dot{V}(T, p)} \quad (4.1.14)$$

In mixed flow reactors, τ represents a mean value because the residence time of the fluid elements are distributed. Only for plug flow tubular reactors is the residence time the same for all fluid elements, which is of course an idealization as the fluid velocity becomes zero at the wall (no slip condition). Thus, the residence time of fluid elements near the wall is higher than the average, but for a reactor with a large diameter this effect is usually negligible.

For reactions with changing volume, it is conventional to define τ in terms of the inlet volumetric flow rate. The actual residence time (τ_{actual}) can then only be calculated, if the conversion and its influence on the volumetric rate (\dot{V}) is known. For example, for isothermal gas-phase reactions, \dot{V} may change proportionately with conversion, and the expansion or contraction can be expressed as:

$$\dot{V} = (1 + \varepsilon_V X_k) \dot{V}_{\text{in}} \quad (4.1.15)$$

where ε_V is the fractional change (also called expansion factor), for example, for a reaction $A \rightarrow 2B$, with pure A as feed, ε_V is 1.

For an ideal mixed flow reactor, that is, for the assumption that the volumetric flow changes immediately to \dot{V}_{out} upon entering the reactor, τ_{actual} is given by:

$$\tau_{\text{actual}} = \frac{V_R}{\dot{V}_{\text{out}}} = \frac{V_R}{\dot{V}_{\text{in}}(1 + \varepsilon_V X_k)} = \tau \frac{1}{(1 + \varepsilon_V X_k)} \quad (4.1.16)$$

For a plug flow tubular reactor, the actual residence time (τ_{actual}) is obtained by the differential term $d\tau_{\text{actual}} = dV_R/\dot{V}$, replacement of \dot{V} by Eq. (4.1.15), and subsequent integration:

$$\tau_{\text{actual}} = \frac{1}{\dot{V}_{\text{in}}} \int_0^{V_R} \frac{dV_R}{(1 + \varepsilon_V X_k)} \quad (4.1.17)$$

Substitution of dV_R by the cross-sectional area A_R and the differential length dz in the direction of flow leads to:

$$\tau_{\text{actual}} = \frac{A_R}{\dot{V}_{\text{in}}} \int_0^{L_R} \frac{dz}{(1 + \varepsilon_V X_k)} = \tau \frac{1}{L_R} \int_0^{L_R} \frac{dz}{(1 + \varepsilon_V X_k)} \quad (4.1.18)$$

To solve Eq. (4.1.18), the progress of conversion in the direction of flow (z) must be known, which may lead to a quite complicated solution of the integral. As examined in Section 4.10 (e.g., by Example 4.10.1 in Section 4.10.3), the performance equations of reactors therefore normally only interrelate the mean residence time τ (at inlet conditions), the inlet concentrations, the reaction rate [rate constant and reaction order(s)], and the conversion. Thus, τ_{actual} is not needed as we usually end up either with a closed-form solution, that is, with an equation $\tau = f[X_k, c_{i,\text{in}}, \text{reaction rate constant, reaction order(s)}, \varepsilon_V]$, or the mean residence time needed for a given duty is found by graphical or numerical integration.

For heterogeneously catalyzed or gas–solid reactions it is convenient to use a (mean) modified residence time τ_m (kg s m^{-3}) related to the mass of catalyst or solid with bulk density ρ_b :

$$! \quad \tau_m = \frac{m}{\dot{V}(T, p)} = \tau \rho_b \quad (4.1.19)$$

4.1.7

Space Velocity and Space–Time Yield

For flow reactors, the ratio of the volume rate [for gases usually at standard temperature and pressure (STP), that is, at 1.013 bar and 0°C] to the reactor volume is called the space velocity SV :

$$SV = \frac{\dot{V}_{\text{STP,in}}}{V_R} \quad (4.1.20)$$

The space velocity corresponds to the number of reactor volumes processed per unit time at specified conditions (normally STP), for example, a space velocity of 1 s^{-1} means that one reactor volume of feed (at STP) is being fed into the reactor per second.

The space velocity SV is in most cases not equivalent to the inverse of the (mean) residence time ($1/\tau$) as τ is usually the actual (mean) time spent by an element of fluid in the reactor and thus related to reaction conditions and not – as SV – to the standard state.

In industrial practice, the terms *WHSV* (weight hourly space velocity), *LHSV* (liquid hourly space velocity), and *GHSV* (gas hourly space velocity) are also used – defined as the ratio of the mass flow (*WHSV*) or volumetric flow (*LHSV* and *GHSV*, usually at STP) of the liquid or gaseous feed per volume of reactor.

The productivity of a reactor is frequently represented by the space–time yield (*STY*), which is defined as the amount of product i produced per unit time and unit volume (in $\text{mol m}^{-3} \text{ s}^{-1}$):

$$\begin{aligned} STY_i &= \frac{\dot{n}_{k,\text{in}} S_i X_k}{V_R} \frac{v_i}{|v_k|} = \frac{\dot{n}_{k,\text{in}} Y_i}{V_R} \frac{v_i}{|v_k|} = \frac{\dot{V}_{\text{in}} c_{k,\text{in}} Y_i}{V_R} \frac{v_i}{|v_k|} \\ &= \frac{c_{k,\text{in}} Y_i}{\tau} \frac{v_i}{|v_k|} \quad (\text{for flow reactors}) \end{aligned} \quad (4.1.21)$$

For a batch reactor, the ratio of the initial amount $n_{k,0}$ and the reaction time t is used instead of the molar flux of the reactant at the reactor inlet ($\dot{n}_{k,\text{in}}$) and the (mean) residence time τ :

$$STY_i = \frac{n_{k,0} S_i X_k}{t V_R} \frac{v_i}{|v_k|} = \frac{n_{k,0} Y_i}{t V_R} \frac{v_i}{|v_k|} = \frac{c_{k,0} Y_i}{t} \frac{v_i}{|v_k|} \quad (\text{for batch reactors}) \quad (4.1.22)$$

Remark: the space–time yield (*STY*) can also be defined based on the mass of the product, for example, as the mass of product that is produced per unit time and volume of catalyst. In any event it is important to mention the *exact* definition, for example, whether the volume of the catalytic fixed bed or the volume of the catalyst without the void space is used.

Summary of Section 4.1 (take-home messages)

- The **design of a chemical reactor** uses knowledge and experience from various disciplines such as thermodynamics, chemical kinetics, fluid dynamics, material science, chemistry, catalysis, reaction engineering, and heat and mass transfer.
- Chemical engineers have to consider a wide **range of scale-up dimensions** (e.g., for solid catalysts). Starting with molecules and active sites of a catalyst with dimensions in the nanometer range, one has to consider the porous structure of particles and the mass and heat transfer processes involved on the micro- to millimeter range. Finally, the design of a reactor up to several hundred m³ in size has to be realized.
- The **rate of reactions** in terms of the amount of converted reactant per volume of reactor and time may vary over several orders of magnitude. The kinetics of biochemical reactions are often slow, and take place on a time scale of hours and days, whereas chemical reactions proceed at rates that are orders of magnitude higher.
- For several industrial processes, **heat and mass transport** may become limiting, if the intrinsic rate exceeds by far the upper limit. Consequently, we have to bring the specific activity of a catalyst back into the window of engineering reality. Transport limitations can also interfere with the selectivity, and downstream processing units may be poorly designed.
- For the productivity of a process, not only the reaction rate and thermodynamic constraints but also the **reactor type** and **operation mode** (mixing, cooling, etc.) play a role.
- Terms used to characterize the composition of a reaction mixture are the content and **concentration**. The volume may change during a reaction, and the change in concentration is then no longer only proportional to a change in the number of moles. For flow reactors, **molar fluxes** are used to calculate concentrations. For reactions involving gases, the **partial pressure** is also taken as a measure of the concentration.
- **Terms used to quantify the result of a chemical conversion** are the conversion X, yield Y, and selectivity S.
- For a batch reactor, the **reaction time** *t* is the natural performance measure. For flow reactors, the **residence time** τ is used, which is defined as the ratio of the reactor volume to the volumetric flow rate at reaction conditions. In mixed flow reactors, τ represents a mean value because the residence time of the fluid elements is distributed. Only for plug flow tubular reactors is the residence time the same for all fluid elements. For heterogeneously catalyzed or gas-solid reactions it is convenient to use a (mean) modified residence time related to the mass of catalyst or solid.
- The **space velocity** corresponds to the number of reactor volumes processed per unit time under specified conditions. In industrial practice, the weight hourly space velocity, liquid hourly space velocity, and gas hourly space velocity are also used, and are defined as the ratio of the flow of the liquid or gaseous feed per volume of reactor.
- The productivity of a reactor is frequently represented by the **space-time yield**, which is defined as the amount of product *i* produced per unit time and unit volume.

4.2 Chemical Thermodynamics

Chemical reactions always move towards a dynamic equilibrium. The term “dynamic” expresses that a reactant A might still react to give a product B, but in an equilibrated system this conversion is exactly compensated by the reverse reaction

of B to A. More precisely, the reaction rate of $A \rightarrow B$ equals the rate of $B \rightarrow A$. Consequently, depending on the temperature, pressure, and initial concentrations we will end up with an equilibrium composition in which the net change of the system consisting of products and unconverted reactants is zero.

It is, thereby, important to note that the equilibrium composition of a reaction system only determines the maximum conversion and the respective maximum product yield(s), if we are not limited by the reaction time to reach this stage. For example, a piece of graphite in contact with oxygen is thermodynamically not stable with regard to the formation of CO_2 , but we know from experience that at temperatures below several hundred $^{\circ}\text{C}$ the reaction time needed to convert carbon with oxygen is almost infinite. Similar considerations are (luckily) true for the oxidation of organic substances such as hydrocarbons, which are also kinetically but not thermodynamically stable under moderate conditions, that is, they are metastable.

In some cases the equilibrium lies close to pure products, for example, the combustion of fuels like methane or crude oil fractions to carbon dioxide and steam. The reaction goes virtually to completion and we consider the reaction as irreversible. Conversely, we may consider a reaction as virtually impossible if the equilibrium lies close to pure reactants.

Many reactions are in between these two extreme cases. Thermodynamics then give a recipe to calculate the influence of reaction conditions on the tendency of a reaction to run in a particular direction, and to calculate and maximize the product yield(s) by proper choice of temperature and for gas-phase reactions also of the pressure.

“Operating manual” for beginners and intermediate learners

For a basic understanding of chemical thermodynamics, start with perfect gas equilibria (Section 4.2.1), (ideal) liquid–liquid systems (Section 4.2.3 until Example 4.2.5), and (ideal) gas–solid reactions [Section 4.2.4, ignoring Eq. (4.2.60)].

“Operating manual” for advanced learners

Advanced learners should then also study (after recapitulating the basic equations given in Sections 4.2.1 and 4.2.3 to become familiar with the nomenclature etc.) the more complex cases of real gas equilibria (Section 4.2.2), real liquid–liquid reactions (Example 4.2.6 in Section 4.2.3), and the calculation of simultaneous equilibria (Section 4.2.5).

4.2.1

Introduction and Perfect Gas Equilibria

The starting point to calculate the equilibrium state of a chemical reaction is the *Clausius inequality*, introduced in Section 3.1.3 for physical transformations of pure substances:

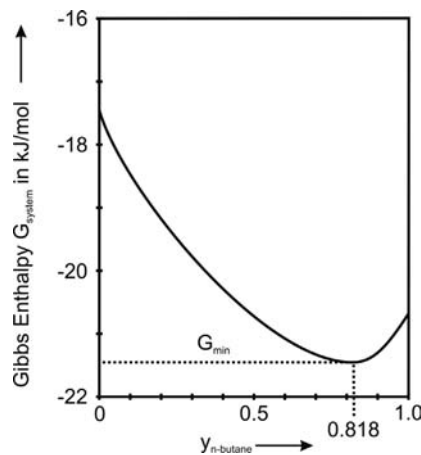
$$\Delta S_{\text{overall}} = \Delta S_{\text{sys}} + \Delta S_{\text{surr}} \geq 0 \quad (3.1.37)$$

For a chemical reaction, Eq. (3.1.37) states that any change of the entropy of the system provoked by a reaction is accompanied by a change of the entropy in the surrounding. The overall change is greater than zero in general, because the change might be irreversible.

For illustration, we consider a vessel where a chemical reaction takes place (the *system*), which is surrounded by a reservoir of a cooling (heating) medium (the *surrounding*). The vessel and the reservoir form a closed isolated system. We assume that both have the same temperature after the reaction has taken place, and that the generated (or consumed) heat Q_{reaction} is reversibly transferred from the vessel to the reservoir or vice versa. Thus we have:

$$\Delta S_{\text{overall, reversible}} = 0 \quad (4.2.1)$$

If we use the common convention that Q_{reaction} is negative, if energy has left the vessel (exothermic reaction), it follows that the change of the entropy of the



$$\Delta S_{\text{overall}} = \Delta S_{\text{sys}} + \Delta S_{\text{surr}} \geq 0$$

$$\Delta_R H^0 - T \Delta_R S^0 = -RT \ln K_p$$

surrounding is given by:

$$\Delta S_{\text{surr}} = -\frac{Q_{\text{reaction}}}{T} \quad (4.2.2)$$

Insertion of Eqs. (4.2.1) and (4.2.2) into Eq. (3.1.37) yields:

$$\Delta S_{\text{sys}} = \frac{Q_{\text{reaction}}}{T} \quad (4.2.3)$$

For an exothermic reaction, the entropy of the system decreases ($Q_{\text{reaction}} < 0$), and the entropy of the surrounding increases by the same amount.

For a constant volume, the system does not work on the surrounding, and Q_{reaction} equals the change of the internal energy ΔU :

$$Q_{\text{reaction}} = \Delta U \quad (\text{for } V \text{ and } T = \text{constant}) \quad (4.2.4)$$

For a constant pressure, we have to consider that the work done by (on) the system on (by) the surrounding is $p\Delta V$:

$$Q_{\text{reaction}} = \Delta U + p\Delta V \quad (\text{for } p \text{ and } T = \text{constant}) \quad (4.2.5)$$

and introduction of the enthalpy H , defined as $H = U + pV$ [Eq. (3.1.18)], leads to:

$$Q_{\text{reaction}} = \Delta H \quad (\text{for } p \text{ and } T = \text{constant}) \quad (4.2.6)$$

Insertion of Eq. (4.2.6) into Eq. (4.2.3) yields:

$$\Delta H - T\Delta S_{\text{sys}} = 0 \quad (\text{for } p \text{ and } T = \text{constant}) \quad (4.2.7)$$

This equation can also be expressed by the introduction of the free enthalpy, the Gibbs function ΔG , named after Josiah Willard Gibbs (see box):

$$\Delta G = \Delta H - T\Delta S_{\text{sys}} = -T(\Delta S_{\text{surr}} + \Delta S_{\text{sys}}) = -T\Delta S_{\text{overall}} = 0 \quad (4.2.8)$$

To derive the equations for a chemical equilibrium, the molar values associated with the stoichiometric equation for the conversion of one molar unit are used. Thus, instead of the absolute values of ΔG , ΔH , and ΔS_{sys} (in J for ΔG and ΔH and $J K^{-1}$ for ΔS), we will subsequently use the molar free (or Gibbs) enthalpy of reaction $\Delta_R G$ ($J \text{ mol}^{-1}$), the molar reaction enthalpy $\Delta_R H$ ($J \text{ mol}^{-1}$), and the molar reaction entropy $\Delta_R S$ ($J \text{ mol}^{-1} K^{-1}$). The condition for chemical equilibrium is then deduced from Eq. (4.2.8) as:

! $\Delta_R G = \Delta_R H - T\Delta_R S = 0 \quad (4.2.9)$

This condition of chemical equilibrium can also be expressed in terms of chemical potentials μ (the partial molar Gibbs functions), and, for example, for an $A \rightarrow B$ reaction we would obtain:

$$\Delta_R G = \mu_B - \mu_A = 0 \quad (4.2.10)$$

The Gibbs function expresses the direction of a spontaneous change: If $\Delta_R G < 0$, the reaction proceeds $A \rightarrow B$, and if $\Delta_R G > 0$, the reaction proceeds $B \rightarrow A$. The condition of equilibrium can be further developed by introduction of the standard reaction Gibbs function at the standard pressure of 1.013 bar and reaction temperature T , $\Delta_R G^0$:

$$\Delta_R G = \Delta_R G^0 + RT \ln K_R \quad (4.2.11)$$

The recommendation to take 1 bar as the standard pressure for reporting thermodynamic data is still not universally accepted. Many tabulated data still refer to the formerly used standard pressure of 1 atm (1.013 bar). Especially for liquids and solids, the differences in thermodynamic values are usually negligible. Here we use 1.013 bar for p_0 .

Different organizations have established a variety of definitions for standard reference conditions that should be used with care. It is always important to know

Josiah Willard Gibbs (1839–1903), an American mathematical physicist, contributed much to the foundation of chemical thermodynamics. He was the first in the USA to receive a PhD in engineering (Yale, 1863), and one of the earliest theoretical physicists in America and probably one of the earliest theoretical chemists. Gibbs can also be regarded as the inventor of vector analysis.

the reference temperature and pressure for the actual definition used. The following definitions are common:

- STP (standard temperature and pressure): 0 °C (273.15 K) and 1 atm (1.013 bar);
- NTP (normal temperature and pressure): 20 °C (293.15 K) and 1 atm (1.013 bar);
- SATP (standard ambient temperature and pressure): 25 °C (298.15 K) and 1.013 bar.

With $\Delta_R G = 0$, we obtain one of the most important equations in chemical thermodynamics:

!
$$\Delta_R G^0 = -RT \ln K_R \quad (4.2.12)$$

This equation is the link between tables of thermodynamic data (such as Table 4.2.1), which allow the evaluation of $\Delta_R G^0$, and the equilibrium constant K_R of the reaction (sometimes also denoted as reaction quotient Q_R), which is a function of the composition of the system in terms of concentration, molar fractions, and so on. The value and definition of K_R depends on the choice of the standard state and the ideality of the system, as shown subsequently for ideal and real gases, liquids, and gas–solid systems.

The standard reaction Gibbs function $\Delta_R G^0$ can easily be evaluated from tabulated values of the standard Gibbs functions of formation ($\Delta_F G^0$), as $\Delta_R G^0$ can also be expressed by the sum of the $\Delta_F G^0$ values of all products and reactants from the elements (and thus $\Delta_F G^0$ of elements is by definition zero):

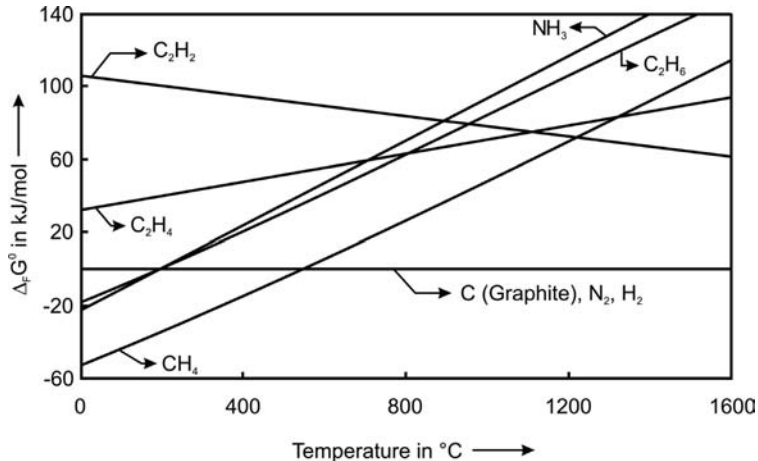
!
$$\Delta_R G^0 = \sum v_i \Delta_F G_i^0 \quad (v_i < 0 \text{ for reactants and } > 0 \text{ for products}) \quad (4.2.13)$$

The values of $\Delta_F G^0$ are tabulated for many species – a selection is given in Table 4.2.1 – or are given by respective $\Delta_F G^0$ –T charts (stability diagrams), as shown by Figure 4.2.1 for selected hydrocarbons and for ammonia.

Table 4.2.1 Thermodynamic data of selected species [at 298.15 K and 1.013 bar (= 1 atm)].

Substance and state (g: gas; l: liquid; s: solid)	$\Delta_F H_{298}^0$ (kJ mol ⁻¹)	S_{298}^0 (J mol ⁻¹ K ⁻¹)	c_p (J mol ⁻¹ K ⁻¹)	$\Delta_F G_{298}^0$ (kJ mol ⁻¹)	
H ₂	0	130.7	28.9	0	
O ₂	0	205.2	29.4	0	
H ₂ O	-241.8	188.9	33.6	-228.8	
H ₂ O	-285.9	70.0	75.4	-237.4	
N ₂	0	191.6	29.1	0	
NH ₃	-46.2	192.6	35.7	-16.7	
NO	90.4	210.8	29.9	86.8	
NO ₂	33.9	240.6	37.9	51.9	
S	s (graphite)	0	31.9	22.6	0
H ₂ S	-20.2	205.8	34.0	-33.0	
SO ₂	-297.1	248.7	39.8	-300.6	
SO ₃	-395.4	256.4	50.7	-370.6	
C	0	5.7	8.7	0	
CO	-110.6	198.0	29.1	-137.4	
CO ₂	-393.8	213.8	37.1	-394.7	
CH ₄	-74.9	186.3	35.8	-50.8	
C ₂ H ₂	226.9	201.0	44.0	209.3	
C ₂ H ₄	52.3	219.6	43.6	68.2	
C ₂ H ₆	-84.7	229.7	52.7	-32.9	
C ₃ H ₆	20.4	267.1	63.9	62.8	
C ₃ H ₈	-103.9	270.1	73.6	-23.5	
n-C ₄ H ₈	-0.1	305.8	85.7	71.6	
n-C ₄ H ₁₀	-126.2	310.3	97.5	-17.2	
CH ₃ OH	-201.3	237.8	45.1	-162.0	
C ₂ H ₅ OH	-235.5	282.2	73.7	-168.7	

Figure 4.2.1 Stability diagram: standard Gibbs functions of formation $\Delta_F G^0$ for selected species (for hydrocarbons, $\Delta_F G^0$ is related here to one carbon atom).



Alternatively, $\Delta_R G^0$ can also be determined in analogy to Eq. (4.2.9) by the standard enthalpies of formation $\Delta_F H^0$ and standard entropies S^0 :

$$\Delta_R G^0 = \Delta_R H^0 - T \Delta_R S^0 = \sum v_i \Delta_F H_i^0 - T \sum v_i S_i^0 \quad (4.2.14)$$

with $v_i < 0$ for reactants and > 0 for products.

For an ideal gas ($p v_{\text{mol}} = RT$), the influence of pressure on the entropy is given by:

$$S_i = S_i^0 - \int_{p_0}^p \left(\frac{d\nu_{\text{mol}}}{dT} \right)_p dp = S_i^0 - \int_{p_0}^p \frac{R}{p} dp = S_i^0 - R \ln \left(\frac{p}{p_0} \right) \quad (4.2.15)$$

and $\Delta_R H$ equals $\Delta_R H^0$. Thus Eqs. (4.2.15) and (4.2.9) lead to:

$$\begin{aligned} 0 &= \Delta_R H - T \Delta_R S \approx \Delta_R H^0 - T \left(\sum v_i S_i \right) \\ &= \Delta_R H^0 - T \Delta_R S^0 + RT \sum v_i \ln \left(\frac{p_i}{p_0} \right) \end{aligned} \quad (4.2.16)$$

and in combination with Eq. (4.2.14) we get:

$$\Delta_R G^0 = \Delta_R H^0 - T \Delta_R S^0 = -RT \sum v_i \ln \left(\frac{p_i}{p_0} \right) = -RT \sum \ln \left(\frac{p_i}{p_0} \right)^{v_i} \quad (4.2.17)$$

By comparison of Eqs. (4.2.17) and (4.2.12), we see that the equilibrium constant of a perfect (ideal) gas reaction, denoted as K_p , is given by:

$$\ln K_p = \sum \ln \left(\frac{p_i}{p_0} \right)^{v_i} = \ln \prod \left(\frac{p_i}{p_0} \right)^{v_i} \Rightarrow K_p = \prod \left(\frac{p_i}{p_0} \right)^{v_i} \quad (4.2.18)$$

Insertion of Eqs. (4.2.17) and (4.2.18) into Eq. (4.2.16) finally leads to the basic equation of chemical thermodynamics for ideal gas-phase reactions:

$$\Delta_R H^0 - T \Delta_R S^0 = \Delta_R G^0 = -RT \ln K_p = -RT \prod \left(\frac{p_i}{p_0} \right)^{v_i} \quad (4.2.19)$$

Replacing partial pressures with molar fractions ($y_i = p_i/p$ with p as total pressure) leads to:

$$\Delta_R G^0 = \prod \left(y_i \frac{p}{p_0} \right)^{v_i} = \left(\frac{p}{p_0} \right)^{\sum v_i} \prod y_i^{v_i} = \left(\frac{p}{p_0} \right)^{\sum v_i} K_y \quad (4.2.20)$$

The values of the standard reaction enthalpy $\Delta_R H^0$ and the standard reaction entropy $\Delta_R S^0$ still depend on temperature (but not on pressure!). If the influence of temperature on the heat capacity of each substance, Eq. (3.1.23), or a representative mean value $\bar{c}_{p,i}$ for a given temperature range is known, $\Delta_R H^0$ and $\Delta_R S^0$ can be

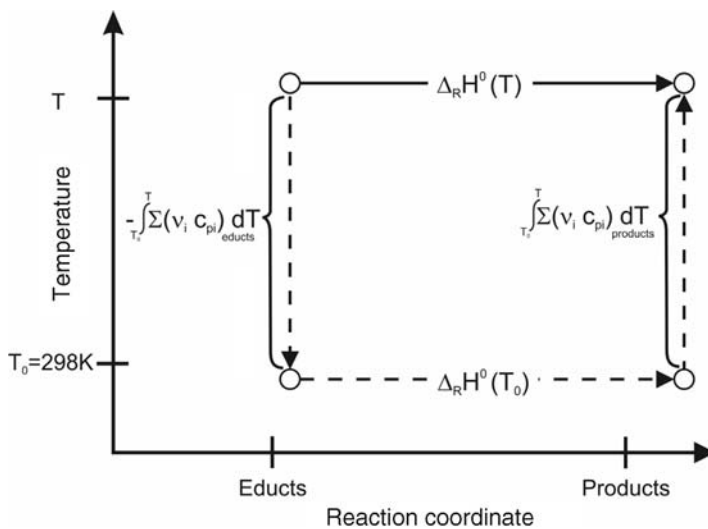


Figure 4.2.2 Illustration of the determination of $\Delta_R H^\circ(T)$ based on $\Delta_R H^\circ_{298}$ [Eq. (4.2.21)].

calculated based on the reference values at 298 K (often tabulated, see, for example, Table 4.2.1) as follows (Figure 4.2.2):

$$\nabla \quad \Delta_R H^\circ(T) = \Delta_R H^\circ_{298} + \int_{298}^T \sum v_i c_{p,i} dT \approx \Delta_R H^\circ_{298} + \sum v_i \bar{c}_{p,i} (T - 298 \text{ K}) \quad (4.2.21)$$

$$\nabla \quad \Delta_R S^\circ(T) = \Delta_R S^\circ_{298} + \int_{298}^T \frac{\sum v_i c_{p,i}}{T} dT \approx \Delta_R S^\circ_{298} + \sum v_i \bar{c}_{p,i} \ln\left(\frac{T}{298}\right) \quad (4.2.22)$$

Interestingly, $\Delta_R H^\circ$ is usually not measured directly. The most important device for measuring the heat released by a reaction is the bomb calorimeter, that is, at constant volume conditions. Thus the reaction energy $\Delta_R U^\circ$ is determined and has to be converted into the reaction enthalpy $\Delta_R H^\circ$ as examined in Topic 4.2.1.

Topic 4.2.1 Calorimetric measurements of $\Delta_R H$ and $\Delta_R U$

The adiabatic bomb calorimeter consists of a massive container (the bomb) and a stirred water bath surrounding the bomb (Figure 4.2.3). The whole device is immersed in a second water bath. The reaction is initiated inside the bomb, which contains the reactants (e.g., by ignition in case of oxidations). To ensure adiabaticity, the temperature of the external water bath is continuously readjusted to eliminate the heat loss to the external water bath.

The temperature change of the calorimeter is measured and the heat of reaction released at constant volume is calculated by the heat capacity of the calorimeter ($C_{\text{calorimeter}}$):

$$\Delta_R U = - \frac{\Delta T_{\text{calorimeter}} C_{\text{calorimeter}}}{n_{\text{reactant}}} \quad (\text{with } n \text{ as number of moles of reference substance})$$

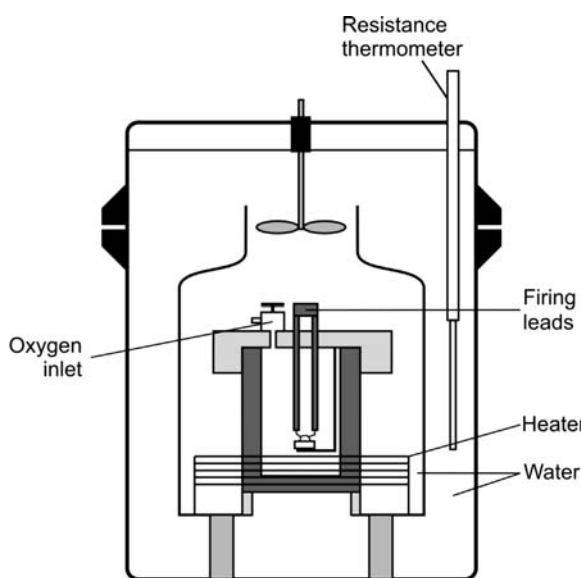
[$C_{\text{calorimeter}}$ (J K^{-1}) is known by calibration against a standard, for example, by combustion of benzoic acid.]

For example, the combustion of hydrogen (at 298 K) gives a value for $\Delta_R U_{298}$ of -282.2 kJ per mol H_2 , and Eq. (3.1.19) leads to:

$$\Delta_R H = \Delta_R U + \frac{p \Delta V}{n_{\text{H}_2}} = \Delta_R U + RT \frac{\Delta n}{n_{\text{H}_2}}$$

For combustion of hydrogen ($\text{H}_2 + 0.5\text{O}_2 \rightarrow \text{H}_2\text{O}_{\text{liquid}}$), $\Delta n/n_{\text{H}_2}$ is -1.5 , and we obtain a value of $\Delta_R H_{298} = -282.2 \text{ kJ mol}^{-1} - 1.5 \times 298 \times 8.314 \text{ J mol}^{-1} \text{ K}^{-1} = -285.9 \text{ kJ}$ per mol H_2 . Thus in this case less heat is released at constant pressure than at constant volume.

Figure 4.2.3 Constant volume bomb calorimeter (arrangement for oxidation of solid or liquid). Adapted from Atkins (2002).



To inspect how equilibrium responds to temperature, we differentiate Eq. (4.2.19):

$$R \frac{d(\ln K_p)}{dT} = +\frac{\Delta_R H^0}{T^2} - \frac{1}{T} \frac{d(\Delta_R H^0)}{dT} + \frac{d(\Delta_R S^0)}{dT} \quad (4.2.23)$$

According to Eqs. (4.2.21) and (4.2.22), the last two terms on the right-hand side of Eq. (4.2.23) are equivalent to $-\sum v_i c_{p,i}/T$ and to $+\sum v_i c_{p,i}/T$, respectively. Thus both terms nullify each other, which leads to the *van't Hoff equation* (*Jacobus van't Hoff*, see box):

$$\frac{d(\ln K_p)}{dT} = \frac{\Delta_R H^0}{RT^2} \quad (4.2.24)$$

Thus, endothermic reactions ($\Delta_R H^0 > 0$) favor the products with increasing temperature and exothermic reactions favor the reverse. An alternative form of Eq. (4.2.24) is obtained by recognizing that $d(1/T)/dT = -1/T^2$:

$$\frac{d(\ln K_p)}{d(1/T)} = -\frac{\Delta_R H^0}{R} \quad (4.2.25)$$

again showing that for an endothermic (exothermic) reaction, an increase (decrease) in temperature shifts the equilibrium towards the products. The gradient on the left-hand side of Eq. (4.2.25) is negative for $\Delta_R H^0 > 0$, and thus $\ln K_p$ decreases with $1/T$ and increases with T .

The equilibrium constant K_p depends only on $\Delta_R G^0$, defined at standard pressure p_0 , and thus K_p depends on temperature only but not on pressure. Formally, this is expressed as:

$$\frac{dK_p}{dp} = 0 \quad (4.2.26)$$

This does not mean that the amounts of the species at equilibrium, that is, the composition, do not depend on the total pressure p , if the reaction leads to a difference between the number of moles of the reactants and products (Example 4.2.1). Rewriting Eq. (4.2.20) leads to:

$$K_y = K_p \left(\frac{p_0}{p} \right)^{\sum v_i} \quad (4.2.27)$$

Jacobus Henricus van't Hoff (1852–1911): a Dutch physical and organic chemist (Nobel Prize in Chemistry in 1901). His research work concentrated on chemical kinetics, chemical equilibrium, osmotic pressure, and crystallography. He is one of the founders of the discipline of physical chemistry. He explained the phenomenon of optical activity by assuming that the chemical bonds between carbon atoms and their neighbors were directed towards the corners of a regular tetrahedron, applied the laws of thermodynamics to chemical equilibria, showed similarities between the behavior of dilute solutions and gases, and worked on the theory of the dissociation of electrolytes. In 1878, he became professor of chemistry at the University of Amsterdam, and in 1896 he became professor at the Prussian Academy of Science at Berlin, where he worked until his death.

and so an increase of the number of gas particles ($\sum v_i > 0$) leads to a decrease of K_y with increasing pressure ($K_y \sim 1/p^{\sum v_i}$). This is *Le Chatelier's principle* (Henri Le Chatelier, see box): A system at equilibrium, when subjected to a perturbation, responds in a way that tends to minimize the effect of the perturbation.

The equilibrium constants K_p or K_y are calculated based on the tabulated standard Gibbs functions of formation $\Delta_F G^0$ or based on the values of $\Delta_F H^0$ and S^0 of all products and reactants (Example 4.2.1). Alternatively, graphical $\Delta_F G^0-T$ presentations may be used (Figure 4.2.1, Example 4.2.2). Although the scale-reading precision might be limited, this method is advantageous in determining easily the temperature range where a reaction is favored or where a certain species is thermodynamically stable. Based on the equilibrium constants K_p or K_y we can then, finally, calculate the equilibrium composition of a reaction of ideal gases based on the stoichiometry and the mass balance, respectively, as shown by Example 4.2.3.

Henri Louis Le Chatelier (1850–1936): a French chemist of the late nineteenth and early twentieth century who is most famous for devising *Le Chatelier's principle* to predict the effect of a change in conditions (T and p) on a chemical equilibrium, presented in 1885. He also carried out research on metallurgy, and worked as consulting engineer for a cement company.

Example 4.2.1 Influence of pressure on the equilibrium of a gas reaction

We take the reaction $\text{CH}_4 + \text{H}_2\text{O} \leftrightarrow \text{CO} + 3\text{H}_2$ as an example to calculate the equilibrium constants K_p and K_y . (This reaction is important for syngas production from natural gas by steam reforming, Section 6.2.) The standard Gibbs function of reaction is:

$$\begin{aligned}\Delta_R G^0 &= \sum v_i \Delta_F G_i^0 = \Delta_F G_{\text{CO}}^0 + 3\Delta_F G_{\text{H}_2}^0 - \Delta_F G_{\text{CH}_4}^0 - \Delta_F G_{\text{H}_2\text{O}}^0 \\ &= \Delta_R H^0 - T\Delta_R S^0\end{aligned}$$

and we calculate $\Delta_R G^0$ based on the tabulated values of either $\Delta_F G^0$ or $\Delta_F H^0$ and S^0 :

$$\begin{aligned}\Delta_R H^0 &= \Delta_F H_{\text{CO}}^0 + 3\Delta_F H_{\text{H}_2}^0 - \Delta_F H_{\text{CH}_4}^0 - \Delta_F H_{\text{H}_2\text{O}}^0 \\ \Delta_R S^0 &= S_{\text{CO}}^0 + 3S_{\text{H}_2}^0 - S_{\text{CH}_4}^0 - S_{\text{H}_2\text{O}}^0\end{aligned}$$

If available, we use the values of $\Delta_F G^0$, $\Delta_F H^0$, and S^0 at the relevant temperature or calculate them by Eqs. (4.2.21) and (4.2.22) from the standard values at 298 K and the (mean) heat capacity of each substance in the relevant range of temperature.

For the given example, K_p [Eq. (4.2.18)] and K_y [Eq. (4.2.27)] are then determined by:

$$K_p = \frac{p_{\text{H}_2}^3 p_{\text{CO}}}{p_{\text{CH}_4} p_{\text{H}_2\text{O}} p_0^2} = e^{-\frac{\Delta_R G^0}{RT}} = e^{-\frac{\Delta_R H^0 + T\Delta_R S^0}{RT}}$$

$$K_y = \frac{y_{\text{H}_2}^3 y_{\text{CO}}}{y_{\text{CH}_4} y_{\text{H}_2\text{O}}} = K_p \left(\frac{p_0}{p} \right)^2$$

and therefore K_y (and thus the equilibrium conversion of methane) decrease with total pressure p .

For example, at 1000 K, K_p has a value of 26 ($\Delta_R H^0 = 226 \text{ kJ mol}^{-1}$, $\Delta_R S^0 = 253 \text{ J mol}^{-1}$). Thus K_y is 26 at atmospheric pressure ($p = p_0$) and only 0.03 at 30 bar. If we assume an equimolar ratio of methane to steam ($y_{\text{CH}_4} = y_{\text{H}_2\text{O}}$) and replace y_{H_2} by 3 y_{CO} , we get:

$$K_y = \frac{3^3 y_{\text{CO}}^4}{y_{\text{CH}_4}^2 y_{\text{CO}}^2} \Rightarrow \frac{y_{\text{CH}_4}}{y_{\text{CO}}^2} = \sqrt{\frac{27}{K_y}}$$

Further calculations considering the mass balance and stoichiometry (as shown by Example 4.2.3) lead to an equilibrium conversion of methane of 81% at atmospheric pressure and to a value of only 25% for a total pressure of 30 bar.

Example 4.2.2 Inspection of the equilibrium by $\Delta_F G^0-T$ charts

For dehydrogenation of ethane to give ethene and H_2 , we use Figure 4.2.1 to identify by the intersection of the $\Delta_F G^0$ functions ($T \approx 1050 \text{ K}$) where $\Delta_R G^0 = 0$ and thus $K_p = 1$:

$$\begin{aligned}\Delta_R G^0 &= \Delta_F G_{\text{C}_2\text{H}_4}^0 + \Delta_F G_{\text{H}_2}^0 - \Delta_F G_{\text{C}_2\text{H}_6}^0 \\ &= \Delta_F G_{\text{C}_2\text{H}_4}^0 + 0 - \Delta_F G_{\text{C}_2\text{H}_6}^0 \\ \Delta_R G^0 &= -RT \ln K_p = 0 \Rightarrow \Delta_F G_{\text{C}_2\text{H}_4}^0 = \Delta_F G_{\text{C}_2\text{H}_6}^0 \text{ and } K_p = 1\end{aligned}$$

$\Delta_R G^0$ is the difference between the $\Delta_F G^0$ values of C_2H_6 and C_2H_4 , and so ethane dehydrogenation is favored for $T > 800^\circ\text{C}$ ($\Delta_R G^0 < 0$, $K_p > 1$).

Figure 4.2.1 also shows that for $T > 1300^\circ\text{C}$, CH_4 is less stable than ethylene (C_2H_4), but unfortunately acetylene (C_2H_2) is thermodynamically even more favored. This is the main reason why C_2H_2 is industrially produced from natural gas (main component methane) in high

temperature processes, whereas C_2H_4 is not (or only indirectly via syngas and subsequent Fischer–Tropsch synthesis, Sections 6.2 and 6.11).

The stability diagram also indicates that with regard to decomposition to the elements C and H_2 , only methane and to some extent ethane are thermodynamically stable (for $T < 550^\circ\text{C}$ and 200°C , respectively). Both C_2H_2 and C_2H_4 (and all other alkenes, naphthalenes, aromatics, C_{3+} -paraffins) are unstable at temperatures of technical relevance ($T > 20^\circ\text{C}$).

We finally also learn from this diagram that NH_3 synthesis from N_2 and H_2 is favored for $T < 200^\circ\text{C}$, but this temperature is too low with respect to the activity of industrially used NH_3 catalysts (Section 6.1.3). Thus, we can already state based on the stability diagram that complete conversion of N_2 and H_2 per pass through an NH_3 reactor cannot be reached, and that we need a high total pressure to obtain realistic values of NH_3 yields.

Example 4.2.3 Equilibrium composition of SO₂ oxidation

SO₂ oxidation (SO₂ + ½O₂ ⇌ SO₃) is a good example by which to show how the equilibrium composition and conversion are calculated. We use the K_p value of 50 (500 °C, p = p₀) and an initial composition of 7.8% SO₂ and 10.8% O₂ (rest N₂). Equation (4.2.27) leads to:

$$K_y = \frac{\gamma_{SO_3}}{\gamma_{O_2}^{0.5} \gamma_{SO_2}} = K_p \left(\frac{p_0}{p} \right)^{-0.5} = 50 \Rightarrow \ln K_y = \ln \left(\frac{\gamma_{SO_3}}{\gamma_{O_2}^{0.5} \gamma_{SO_2}} \right) = 3.9$$

The mass balance for SO₂ in terms of conversion X_{SO₂} and the initial number of moles is:

$$n_{SO_2} = n_{SO_2,0} - X_{SO_2} n_{SO_2,0}$$

The total number of moles of the system n_t (initial value n_{0,t}) is given (for n_{SO₃,0} = 0) by:

$$\begin{aligned} n_t &= n_{SO_2} + n_{O_2} + n_{SO_3} + n_{N_2} = (n_{SO_2,0} - X_{SO_2} n_{SO_2,0}) \\ &\quad + (n_{O_2,0} - \frac{1}{2} X_{SO_2} n_{SO_2,0}) + X_{SO_2} n_{SO_2,0} + n_{N_2,0} \\ &= (n_{SO_2,0} + n_{O_2,0} + n_{N_2,0}) - \frac{1}{2} X_{SO_2} n_{SO_2,0} = n_{0,t} - \frac{1}{2} X_{SO_2} n_{SO_2,0} \end{aligned}$$

Combination of the last two equations leads to the molar content γ_{SO₂}:

$$\gamma_{SO_2} = \frac{n_{SO_2}}{n_t} = \frac{n_{SO_2,0} - X_{SO_2} n_{SO_2,0}}{n_{0,t} - \frac{1}{2} X_{SO_2} n_{SO_2,0}} = \frac{\gamma_{SO_2,0} - X_{SO_2} \gamma_{SO_2,0}}{1 - 0.5 X_{SO_2} \gamma_{SO_2,0}}$$

The term in the denominator considers the change of volume. For γ_{SO_{2,0}} = 0.078 we obtain:

$$\gamma_{SO_2} = \frac{0.078 - 0.078 X_{SO_2}}{1 - 0.039 X_{SO_2}}$$

Similar mass balances for SO₃ (for γ_{SO_{3,0}} = 0) and O₂ lead to:

$$\gamma_{SO_3} = \frac{\gamma_{SO_2,0} X_{SO_2}}{1 - 0.5 \gamma_{SO_2,0} X_{SO_2}} = \frac{0.078 X_{SO_2}}{1 - 0.039 X_{SO_2}}$$

$$\gamma_{O_2} = \frac{\gamma_{O_2,0} - 0.5 \gamma_{SO_2,0} X_{SO_2}}{1 - 0.5 \gamma_{SO_2,0} X_{SO_2}} = \frac{0.108 - 0.039 X_{SO_2}}{1 - 0.039 X_{SO_2}}$$

By insertion of these three mass balances into the K_y-term we obtain after rearrangement:

$$7.8 = \ln \left[\frac{(X_{SO_2})^2 (1 - 0.039 X_{SO_2})}{(1 - X_{SO_2})^2 (0.108 - 0.039 X_{SO_2})} \right]$$

Iteration or graphical solution leads easily to the solution X_{SO₂} = 0.93. The mass balances then yield γ_{SO₂} = 0.0057, γ_{SO₃} = 0.076, γ_{O₂} = 0.075, and γ_{N₂} = 0.843.

4.2.2

Real Gas Equilibria

For real gases, we have to consider the deviation from the ideal gas state, and the partial pressures p_i have to be replaced by the fugacities f_i. Hence Eq. (4.2.19) has to be modified:

$$\Delta_R G^0 = -RT \ln K_f = -RT \ln \left[\prod_i \left(\frac{f_i}{p_0} \right)^{v_i} \right] \quad (4.2.28)$$

The fugacities f_i and the partial pressures p_i are related by fugacity coefficients φ_i (Figure 4.2.3, unity for ideal gases):

$$\nabla_o \quad f_i = \gamma_i \varphi_i p = \varphi_i p_i \quad (4.2.29)$$

This leads to:

$$K_f = K_p \prod_i \varphi_i^{v_i} = K_p K_\phi = K_y K_\phi \left(\frac{p}{p_0} \right)^{\sum v_i} \quad (4.2.30)$$

K_φ is a measure for the deviation of K_p from K_f and thus for the deviation from ideal gas behavior. For example, for the reaction 2A + B → C + 3D, Eq. (4.2.30) yields:

$$K_f = \frac{\frac{f_C}{p_0} \left(\frac{f_D}{p_0} \right)^3}{\left(\frac{f_A}{p_0} \right)^2 f_B} = \frac{\frac{y_C \varphi_C p}{p_0} \left(\frac{y_D \varphi_D p}{p_0} \right)^3}{\left(\frac{y_A \varphi_A p}{p_0} \right)^2 \frac{y_B \varphi_B p}{p_0}} = \frac{y_D^3 y_C \varphi_D^3 \varphi_C p}{y_A^2 y_B \varphi_A^2 \varphi_B p_0} = K_y K_\phi \frac{p}{p_0}$$

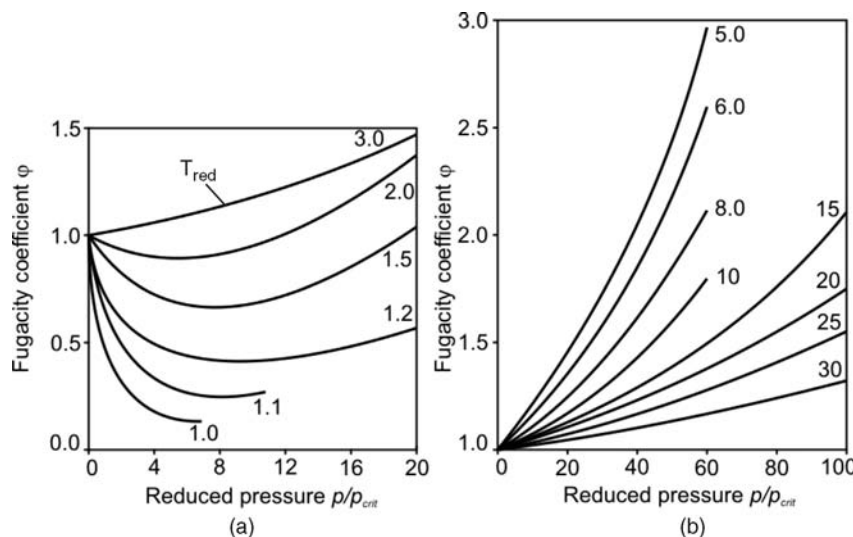


Figure 4.2.4 (a) and (b) Fugacity coefficient φ as function of the reduced pressure, p_{red} , and the reduced temperature, T_{red} . Adapted from Atkins (2002).

The fugacity coefficients φ_i can be approximated by the real gas factor z_i (Section 3.1.1), which is unity for ideal gases, and for real gases is defined as $z_i = p v_{\text{mol},i} / RT$. The equation to determine φ_i by z_i reads as:

$$\ln \varphi_i = \int_0^p \frac{z_i - 1}{p} dp \quad (4.2.31)$$

For the derivation of Eq. (4.2.31) see textbooks on physical chemistry, for example, Atkins and de Paula (2002). Note that z and thus also φ depend on temperature and pressure. Values of φ are given in Figure 4.2.4 for different reduced pressures and reduced temperatures ($p_{\text{red}} = p_i/p_{\text{crit}}$, $T_{\text{red}} = T_i/T_{\text{crit}}$). Exceptions are the gases He, Ne, and H₂, where a value of 8 (in bar and K, respectively) should be added both to p_{red} and T_{red} before such figures are used. Examples 4.2.4 and 4.2.5 illustrate how we have to account for the real gas behavior in thermodynamic calculations.

Example 4.2.4 Influence of pressure on fugacity

Table 4.2.2 lists the fugacity coefficients of N₂, H₂, and NH₃ (relevant for NH₃ synthesis) at different pressures and 400 °C, indicating that real gas behavior has to be considered for $p > 100$ bar. Note that the fugacity

coefficients in a mixture of N₂, H₂, and NH₃ might deviate from the values calculated for pure substances.

Table 4.2.2 Fugacity coefficients φ of N₂, H₂, and NH₃ at different pressures and 400 °C.

	Pressure (bar)	Pressure (bar)			
		50	100	200	600
N ₂ ($p_{\text{crit}} = 33.9$ bar, $T_{\text{crit}} = 126$ K, $T_{\text{red}} = 5.34$)	p_{red}	1.47	2.95	5.90	17.7
	φ_{N_2}	1.00	1.02	1.08	1.33
H ₂ ($p_{\text{crit}} = 13.0$ bar, $T_{\text{crit}} = 33.3$ K, $T_{\text{red}}^{\text{a)}} = 16.3$)	$p_{\text{red}}^{\text{b)}$	2.38	4.76	9.52	28.6
	φ_{H_2}	1.00	1.04	1.10	1.15
NH ₃ ($p_{\text{crit}} = 113.0$ bar, $T_{\text{crit}} = 405.6$ K, $T_{\text{red}} = 1.66$)	p_{red}	0.44	0.88	1.77	5.31
	φ_{NH_3}	0.98	0.95	0.90	0.82

a) $T_{\text{red}} = T/(T_{\text{crit}} + 8$ K).

b) $p_{\text{red}} = p/(p_{\text{crit}} + 8$ bar).

Example 4.2.5 Influence of real gas behavior on equilibrium of NH₃ synthesis

We take ammonia synthesis ($0.5\text{N}_2 + 1.5\text{H}_2 \leftrightarrow \text{NH}_3$) as an example to show the impact of real gas behavior on the equilibrium. Table 4.2.3 lists the results of different calculation methods with increasing degree of accuracy (for the example of 600 bar and 450 °C), indicating that for high pressures real gas behavior has to be considered, by the following methods:

Method I: The equilibrium constant K_p is calculated based on $\Delta_R H^0$ (25 °C), $\Delta_R S^0$ (25 °C), and Eq. (4.2.19), that is, we assume ideal gas behavior and $\Delta_R G^0 = \text{const.} = \Delta_R G^0$ (25 °C). The conversion X_{N_2} and the molar fractions y_i are determined based on a mass balance.

Method II: Refinement of method I by consideration of the exact value of $\Delta_R G^0$ at 450 °C.

Method III: Refinement of method II, as we now also consider real gas behavior by the fugacity coefficients of the *pure* compounds $\varphi_{i,\text{approx}}$ based on Figure 4.2.4, that is, we do not consider the interaction of all three species and its influence on φ_i .

Method IV: Refinement of method III. We now consider the exact values of the fugacity coefficients $\varphi_{i,\text{exact}}$ based on state equations considering the interaction of all three species.

The N₂ conversion is 60% if we make the oversimplifying assumption of ideal gas behavior (method II), and 68% and 67%, if we consider real gas behavior (method III and IV). The good agreement of the “exact” value (method IV, 67%) with the calculated value of 70% (method I) is accidental, and does not mean that method I can be recommended.

Table 4.2.3 Thermodynamic data of NH₃ synthesis ($0.5\text{N}_2 + 1.5\text{H}_2 \leftrightarrow \text{NH}_3$) at 600 bar.

Thermodynamic parameter	Value
Reaction enthalpy (kJ mol ⁻¹)	$\Delta_R H^0$ (25 °C) -45.8 $\Delta_R H^0$ (450 °C) -52.8
Reaction entropy (J mol ⁻¹ K ⁻¹)	$\Delta_R S^0$ (25 °C) -99 $\Delta_R S^0$ (450 °C) -115
Approximated fugacity coefficients $\varphi_{i,\text{approx}}$ (450 °C, 600 bar) based on Figure 4.2.4	$\varphi_{\text{NH}_3,\text{approx}}$ 0.85 $\varphi_{\text{N}_2,\text{approx}}$ 1.32 $\varphi_{\text{H}_2,\text{approx}}$ 1.15
Fugacity coefficients $\varphi_{i,\text{exact}}$ (450 °C, 600 bar) based on state equations considering the interaction of species (Gmehling and Kolbe, 1988)	$\varphi_{\text{NH}_3,\text{exact}}$ 1.03 $\varphi_{\text{N}_2,\text{exact}}$ 1.37 $\varphi_{\text{H}_2,\text{exact}}$ 1.25
Method I: K_p , N ₂ -conversion X_{N_2} , and mole fractions y_i based on $\Delta_R H^0$ (25 °C), $\Delta_R S^0$ (25 °C) and Eq. (4.2.19) [ideal gas, $\Delta_R G^0 = \text{const.} = \Delta_R G^0$ (25 °C)]	y_{NH_3} 0.54 y_{N_2} 0.12 y_{H_2} 0.34 X_{N_2} 0.70 K_p 0.013 K_φ 1 (ideal gas)
Method II: K_p , N ₂ -conversion X_{N_2} , and mole fractions y_i based on $\Delta_R H^0$ (450 °C), $\Delta_R S^0$ (450 °C) and Eq. (4.2.19) (ideal gas, influence of Ton $\Delta_R G^0$)	y_{NH_3} 0.43 y_{N_2} 0.14 y_{H_2} 0.43 X_{N_2} 0.60 K_p 0.0066 K_φ 1 (ideal gas)
Method III: K_p , K_φ , N ₂ -conversion X_{N_2} , and mole fractions y_i based on $\Delta_R G^0$ (450 °C) and Eqs. (4.2.28) to (4.2.30) (real gas, $\varphi_{i,\text{approx}}$)	y_{NH_3} 0.512 y_{N_2} 0.122 y_{H_2} 0.366 X_{N_2} 0.68 K_p 0.0110 K_φ 0.60
Method IV: K_p , K_φ , N ₂ -conversion X_{N_2} , and mole fractions y_i based on $\Delta_R G^0$ (450 °C) and Eqs. (4.2.28)–(4.2.30) (real gas, $\varphi_{i,\text{exact}}$)	y_{NH_3} 0.504 y_{N_2} 0.124 y_{H_2} 0.372 X_{N_2} 0.67 K_p 0.0105 K_φ 0.63

4.2.3

Equilibrium of Liquid–Liquid Reactions

For liquid–liquid reactions, the equilibrium constant K_R [Eq. (4.2.12)] is defined based on the activities a_i that represent “effective” molar fractions:

$$\nabla \quad \Delta_R G_l^0 = -RT \ln K_a = -RT \ln \prod a_i^{v_i} \quad (4.2.32)$$

The activities a_i are usually expressed by activity coefficients γ_i that represent the ratio of the fugacity f_i to the standard fugacity $f_{i,0}$:

$$\nabla \quad a_i = \gamma_i x_i = \frac{f_i}{f_{i,0}} \quad (4.2.33)$$

For the solvent (major component) the standard state is the pure solvent, so $\gamma \rightarrow 1$ for $x \rightarrow 1$, and for the solute (minor component) the standard state is a hypothetical state in which the solute is pure, but behaving as though it still obeyed Henry’s law (infinite dilution).

Equations (4.2.32) and (4.2.33) lead to:

$$K_a = \prod a_i^{v_i} = \prod (x_i \gamma_i)^{v_i} = K_x K_\gamma \quad (4.2.34)$$

where K_γ can be regarded as a measure for the deviation of a liquid system from the behavior of an ideal liquid mixture, where we have $K_\gamma = 1$.

Thus for liquid–liquid reactions, a similar approach is used as for real gas equilibria as discussed above in Section 4.2.2. For gas-phase reactions, we use the ratio of the fugacity f_i to the standard pressure p_0 ($= f_{i,0}$) instead of the activity a_i , and the fugacity coefficient φ_i ($= f_i/p_i$) instead of the activity coefficient γ_i ($= a_i/x_i$). Thus we have an ideal gaseous system for $f_i = p_i$, that is, $\varphi_i = 1$, and an ideal liquid system for $a_i = x_i$, that is, $\gamma_i = 1$.

If the mole fractions x_i are expressed by the concentrations c_i and the total concentration of the mixture c_t (usually in mol dm⁻³), Eq. (4.2.34) yields (for an ideal liquid phase):

$$K_a = K_x = \prod \left(\frac{c_i}{c_t} \right)^{v_i} = \prod c_i^{v_i} \prod \left(\frac{1}{c_t} \right)^{v_i} = K_c \left(\frac{1}{c_t} \right)^{\sum v_i} \quad (4.2.35)$$

It is sometimes easier to calculate the equilibrium of a liquid phase reaction based on the thermodynamic data of the corresponding gas-phase reaction (Example 4.2.6). To derive the respective equations, we assume ideal gas as well as ideal liquid phase behavior and a simple reversible A to B reaction as example. The standard Gibb’s enthalpy of the gas-phase reaction $\Delta_R G_g^0$ is:

$$\Delta_R G_g^0 = -RT \ln \left(\frac{p_B}{p_A} \right) \quad (4.2.36)$$

Introduction of the saturation vapor pressures of the pure liquids A and B, $p_{\text{sat},A}$ and $p_{\text{sat},B}$, according to *Raoult’s law*, Eq. (3.3.62), leads to the link of $\Delta_R G_g^0$ with the fractions in the liquid mixture, x_A and x_B , and with K_x , respectively (see also Example 4.2.6):

$$\Delta_R G_g^0 = -RT \ln \left(\frac{x_B p_{\text{sat},B}}{x_A p_{\text{sat},A}} \right) \Rightarrow K_x = \frac{x_B}{x_A} = \frac{p_{\text{sat},A}}{p_{\text{sat},B}} e^{-\frac{\Delta_R G_g^0}{RT}} \quad (4.2.37)$$

For a real liquid mixture of the components A and B ($K_\gamma \neq 1$), Eq. (4.2.34) leads to:

$$K_a = K_x K_\gamma = \frac{x_B}{x_A} \frac{\gamma_B}{\gamma_A} \quad (4.2.38)$$

and if in addition also the real gas behavior has to be considered we have to use the general form of Eq. (4.2.37):

$$\begin{aligned}\Delta_R G_g^0 &= -RT \ln \left(\frac{x_B \gamma_B \varphi_{B,\text{sat}} p_{\text{sat},B}}{x_A \gamma_A \varphi_{A,\text{sat}} p_{\text{sat},A}} \right) \Rightarrow K_x = \frac{x_B}{x_A} = \frac{e^{-\frac{\Delta_R G_g^0}{RT}}}{K_{p,\text{sat}} K_\gamma K_\phi} \\ &= \frac{p_{\text{sat},A}}{p_{\text{sat},B}} \frac{e^{-\frac{\Delta_R G_g^0}{RT}}}{\frac{\gamma_B \varphi_{B,\text{sat}}}{\gamma_A \varphi_{A,\text{sat}}}}\end{aligned}\quad (4.2.39)$$

The activity coefficients γ_i consider the deviation from an ideal liquid phase, and the fugacity coefficients $\varphi_{i,\text{sat}}$ the deviation of the pure vapor from an ideal gas. In Example 4.2.6, the equilibrium of a liquid phase reaction (esterification) of such a "real" system is examined.

Topic 4.2.2 Liquid–liquid equilibrium and link to gas-phase reaction

We can easily understand Eq. (4.2.37) if we consider that the standard Gibb's enthalpy of the liquid phase reaction $\Delta_R G_l^0$ (reaction A to B, ideal liquid, $\gamma \rightarrow 1$) is given by:

$$\Delta_R G_l^0 = -RT \ln \left(\frac{x_B}{x_A} \right) \quad (4.2.40)$$

and insertion into Eq. (4.2.37) yields:

$$-\frac{\Delta_R G_g^0}{RT} + \frac{\Delta_R G_l^0}{RT} = \ln \left(\frac{p_{\text{sat},B}}{p_{\text{sat},A}} \right) = -\frac{\Delta_R H_g^0 - T\Delta_R S_g^0}{RT} + \frac{\Delta_R H_l^0 - T\Delta_R S_l^0}{RT} \quad (4.2.41)$$

The vapor pressure of a liquid (here either reactant A or product B) is given by:

$$\ln \frac{p_{\text{sat},i}}{p_0} = -\frac{\Delta_{\text{vap}} H_i^0}{RT} + \frac{\Delta_{\text{vap}} S_i^0}{R} \quad (4.2.42)$$

and after some rearrangement, we finally get from Eqs. (4.2.41) and (4.2.42):

$$\begin{aligned}(\Delta_R H_l^0 - \Delta_R H_g^0) - T(\Delta_R S_l^0 - \Delta_R S_g^0) &= (\Delta_{\text{vap}} H_A^0 - \Delta_{\text{vap}} H_B^0) \\ &\quad - T(\Delta_{\text{vap}} S_A^0 - \Delta_{\text{vap}} S_B^0)\end{aligned}\quad (4.2.43)$$

Consequently, Eq. (4.2.39) and therefore also Eq. (4.2.37) are only fulfilled for:

$$\Delta_R H_l^0 = \Delta_{\text{vap}} H_A^0 + \Delta_R H_g^0 - \Delta_{\text{vap}} H_B^0 \quad (4.2.44)$$

$$\Delta_R S_l^0 = \Delta_{\text{vap}} S_A^0 + \Delta_R S_g^0 - \Delta_{\text{vap}} S_B^0 \quad (4.2.45)$$

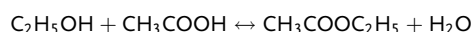
We can easily realize that Eq. (4.2.44) is correct if we recall *Hess's law* of the path-independence of ΔH : putting the right-hand side of Eq. (4.2.44) into words, this means that we start with evaporation of liquid A followed by a reaction of gaseous A to gaseous B and, finally, condensation to liquid B, that is, we have started with liquid A and have ended up with liquid B. Thus, the overall enthalpy of this process must equal the enthalpy of the reaction in the liquid phase [left-hand side of Eq. (4.2.44)]. A similar consideration is true for Eq. (4.2.45).

Table 4.2.4 Calculation of the equilibrium of a liquid-phase reaction based on the Gibb's enthalpy of the gas-phase reaction and thermodynamic data for the vapor and the liquid phase; example esterification of ethanol at 100 °C. Data from Gmehling and Kolbe (1988).

Thermodynamic parameter		Value
Gibb's enthalpy of reaction (kJ mol ⁻¹)	$\Delta_R G_g^0$ (373 K)	-9.99
Equilibrium constant (100 °C)	$K_a = \exp\left[\frac{-\Delta_R G_g^0(373 \text{ K})}{R(373 \text{ K})}\right]$	25.06
Fugacity coefficients of the compounds in the vapor phase	$\varphi_{\text{ethanol,sat}}$ $\varphi_{\text{acetic acid,sat}}$ $\varphi_{\text{water,sat}}$ $\varphi_{\text{ethyl acetate,sat}}$	0.95 0.36 0.99 0.93
Activity coefficients of the reactants in the liquid stage [$\gamma_i = f(x_i)$; determined by iteration]	γ_{ethanol} $\gamma_{\text{acetic acid}}$ γ_{water} $\gamma_{\text{ethyl acetate}}$	1.13 0.85 1.89 1.53
Vapor pressure (bar) of the pure liquid reactants (100 °C)	$p_{\text{ethanol,sat}}$ $p_{\text{acetic acid,sat}}$ $p_{\text{water,sat}}$ $p_{\text{ethyl acetate,sat}}$	2.26 0.57 1.01 2.04
Constant considering the fugacity coefficients	$K_f = \prod f_i^{v_i} = \frac{f_{\text{ethyl acetate,sat}} f_{\text{water,sat}}}{f_{\text{ethanol,sat}} f_{\text{acetic acid,sat}}}$	3.0
Constant considering the activity coefficients	$K_\varphi = \prod \varphi_{i,\text{sat}}^{v_i} = \frac{\varphi_{\text{ethyl acetate,sat}} \varphi_{\text{water,sat}}}{\varphi_{\text{ethanol,sat}} \varphi_{\text{acetic acid,sat}}}$	
Constant considering the vapor pressures	$K_p, \text{sat} = \prod p_{i,\text{sat}}^{v_i} = \frac{p_{\text{ethyl acetate, sat}} p_{\text{water,sat}}}{p_{\text{ethanol,sat}} p_{\text{acetic acid,sat}}}$	
Equilibrium constant with regard to molar fractions in the liquid phase	$K_x = \frac{x_{\text{ethyl acetate,sat}} x_{\text{water,sat}}}{x_{\text{ethanol,sat}} x_{\text{acetic acid,sat}}} = \frac{K_a}{K_\gamma K_\varphi K_p, \text{sat}}$	1.9
Final result: molar fractions in the liquid phase	$x_{\text{ethanol}} = x_{\text{acetic acid}}$ $x_{\text{water}} = x_{\text{ethyl acetate}}$	21% 29%

Example 4.2.6 Equilibrium of liquid phase esterification

We inspect the esterification of ethanol with acetic acid as an illustrative example for the equilibrium of a liquid phase reaction:



According to Eq. (4.2.39) the ratio of the molar fractions in the liquid phase is given by:

$$K_x = \frac{x_{\text{ethyl acetate}} x_{\text{water}}}{x_{\text{ethanol}} x_{\text{acetic acid}}} = \frac{K_a}{K_{p,\text{sat}} K_\gamma K_\varphi} = \frac{1}{K_{p,\text{sat}} K_\gamma K_\varphi} e^{-\frac{\Delta_R G_g^0}{RT}}$$

Table 4.2.4 shows the course of the calculation based on thermodynamic data and Eq. (4.2.39). Consequently, we can calculate the thermodynamic equilibrium based on the respective data of the gas-phase reaction and the thermodynamic data of vaporization of the reactants.

4.2.4

Equilibrium of Gas–Solid Reactions

The influence of pressure on the (molar) enthalpy and entropy of an *ideal* gas is given by:

$$\left(\frac{dH_g}{dp}\right)_T = v_{\text{mol, g}} - T \left(\frac{dv_{\text{mol, g}}}{dT}\right)_p = v_{\text{mol, g}} - T \frac{R}{p} = v_{\text{mol, g}} - v_{\text{mol, g}} = 0 \quad (4.2.46)$$

$$\left(\frac{dS_g}{dp}\right)_T = \left(\frac{dv_{\text{mol, g}}}{dT}\right)_p = T \frac{R}{p} = v_{\text{mol, g}} \quad (4.2.47)$$

Thus, for the functions at a pressure p in terms of their values at p_0 (1.013 bar) we have:

$$H_g(p) = H_g^0 \quad (4.2.48)$$

$$S_g(p) = S_g^0 - R \ln\left(\frac{p}{p_0}\right) \quad (4.2.49)$$

For solids, the volume changes only slightly with pressure and temperature, for example, for copper an isothermal compression from 1 to 100 bar only leads to a decrease of volume by 0.007%, and an isobaric increase of temperature by 100 K only to an increase of the volume by 0.5%. Thus, for solids we may state to a very good approximation:

$$\left(\frac{dH_s}{dp}\right)_T = v_{\text{mol},s} - T\left(\frac{dv_{\text{mol},s}}{dT}\right)_p \approx v_{\text{mol},s} \quad (4.2.50)$$

$$\left(\frac{dS_s}{dp}\right)_T = \left(\frac{dv_{\text{mol},s}}{dT}\right)_p \approx 0 \quad (4.2.51)$$

and the enthalpy and entropy of a solid at pressure p in terms of the values at p_0 are:

$$H_s(p) \approx H_s^0 + v_{\text{mol},s}(p - p_0) \quad (4.2.52)$$

$$S_s(p) \approx S_s^0. \quad (4.2.53)$$

By means of Eqs. (4.2.48), (4.2.49), (4.2.52) and (4.2.53), the Gibb's enthalpy of reaction [Eq. (4.2.9)] of a gas–solid reaction reads as:

$$\begin{aligned} \Delta_R G &= \Delta_R H - T\Delta_R S \approx \Delta_R H^0 - T\Delta_R S^0 + \sum \left[v_{i,g} RT \ln\left(\frac{p_{i,g}}{p_0}\right) \right] \\ &\quad + \sum [v_{\text{mol},i,s}(p - p_0)] \end{aligned} \quad (4.2.54)$$

The third term on the right-hand side of Eq. (4.2.54) accounts for the influence of the gaseous compound(s) on the pressure dependence of the Gibb's enthalpy of reaction and the fourth term accounts for the influence of the solid compound(s).

Insertion of Eq. (4.2.14) into Eq. (4.2.54) and the condition $\Delta_R G = 0$ [Eq. (4.2.9)] yields:

$$\Delta_R G^0 = \Delta_R H^0 - T\Delta_R S^0 = -RT \ln\left[\prod \left(\frac{p_{i,g}}{p_0}\right)^{v_{i,g}}\right] - \sum [v_{\text{mol},i,s}(p - p_0)] \quad (4.2.55)$$

For most pressures of technical relevance, the term $v_{\text{mol},s}(p - p_0)$ is small and negligible. For example, for the reaction of graphite with CO_2 to CO , $\Delta_R G^0$ is 171 kJ mol^{-1} , whereas even for 100 bar the term $v_{\text{mol},s}(p - p_0)$ is only 0.42 kJ mol^{-1} ($v_{\text{mol},\text{graphite}} = 43 \text{ cm}^3 \text{ mol}^{-1}$). Consequently, the influence of pressure on the Gibb's function can be neglected and Eq. (4.2.55) simplifies to:

$$\Delta_R G^0 = \Delta_R H^0 - T\Delta_R S^0 = -RT \ln\left[\prod \left(\frac{p_{i,g}}{p_0}\right)^{v_{i,g}}\right] = RT \ln K_p \quad (4.2.56)$$

with:

$$\Delta_R G^0 = \sum_{\text{gas}} v_{i,g} \Delta_F G_{g,i}^0 + \sum_{\text{solid}} v_{i,s} \Delta_F G_{s,i}^0 \quad (4.2.57)$$

$$\Delta_R H^0 = \sum_{\text{gas}} v_{i,g} \Delta_F H_{g,i}^0 + \sum_{\text{solid}} v_{i,s} \Delta_F H_{s,i}^0 \quad (4.2.58)$$

$$\Delta_R S^0 = \sum_{\text{gas}} v_{i,g} S_{g,i}^0 + \sum_{\text{solid}} v_{i,s} S_{s,i}^0 \quad (4.2.59)$$

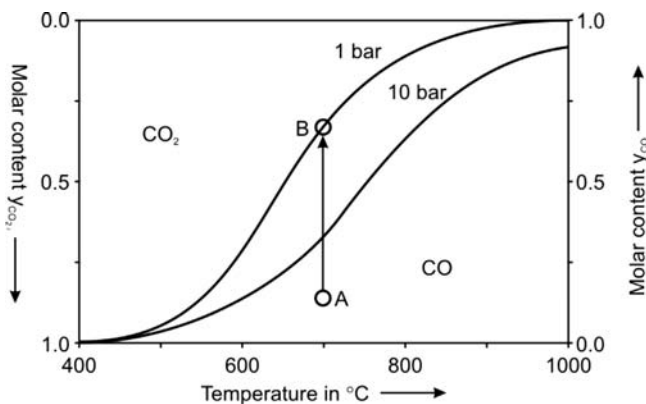


Figure 4.2.5 Equilibrium of the Boudouard reaction: CO and CO₂ in contact with graphite. For a mixture according to point A, carbon would react with CO₂ until point B is reached if enough carbon is present.

Hence the equilibrium gas composition is independent of the amount of solid (or liquid) present. For real gases, we have to use the general form of Eq. (4.2.56):

$$\Delta_R G = 0 = \sum_{\text{gas}} v_{i,g} \Delta_F G_{g,i}^0 + RT \ln \left[\prod \left(\frac{f_{i,g}}{p_0} \right)^{v_{i,g}} \right] + \sum_{\text{solid}} v_{i,s} \Delta_F G_{s,i}^0 \quad (4.2.60)$$

An example of a gas–solid equilibrium is given in Example 4.2.7 for the Boudouard reaction, which is important for coal gasification (Section 6.2.2) and the blast furnace (Section 6.5.2).

Example 4.2.7 Equilibrium of Boudouard reaction

For the (endothermic) Boudouard reaction (C + CO₂ ↔ 2CO), Eq. (4.2.56) reads as:

$$\begin{aligned} -\frac{\Delta_R G^0}{RT} &= \frac{\Delta_F G_{CO_2}^0 + \Delta_F G_C^0 - 2\Delta_F G_{CO}^0}{RT} = \frac{\Delta_F G_{CO_2}^0 - 2\Delta_F G_{CO}^0}{RT} \\ &= \ln K_p = \ln \left(\frac{p_{CO}^2}{p_{CO_2} p_0} \right) \end{aligned}$$

Introduction of the mole fraction of CO, γ_{CO} , and of the total pressure p leads to:

$$\frac{\gamma_{CO}^2}{(1 - \gamma_{CO})} = \frac{K_p}{p} \Rightarrow \gamma_{CO} = \frac{K_p}{2p} \left[\sqrt{1 + \frac{4p}{K_p}} - 1 \right]$$

Figure 4.2.5 depicts the influence of temperature.

For a mixture according to point A, carbon would react with CO₂ until point B is reached if enough carbon is present.

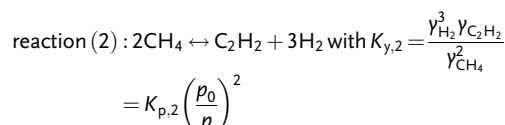
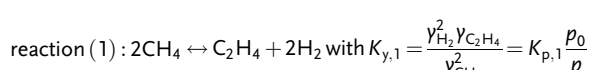
4.2.5

Calculation of Simultaneous Equilibria

For reaction systems consisting of several stoichiometrically independent reactions all values of K_p (or K_f or K_a) must be established (simultaneous equilibria). Calculation of the equilibrium composition is then not straightforward for more than two reactions (where a graphical solution is still possible based on the conversion of two reference reactants for both reactions as a function of $K_{p,1}$ and $K_{p,2}$), see Example 4.2.8.

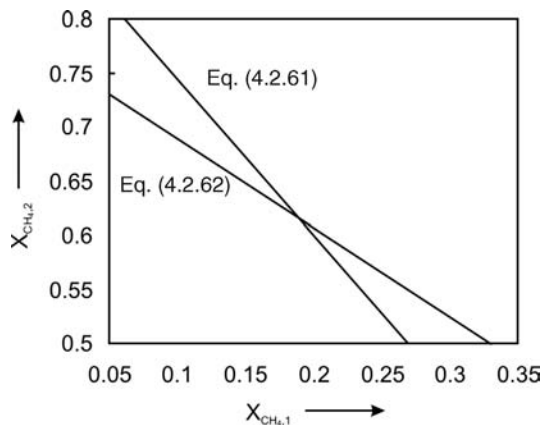
Example 4.2.8 Equilibrium of methane pyrolysis

A good example for the equilibrium of a system for which more than one reaction has to be considered is the pyrolysis of CH₄ to ethene (ethylene) and ethyne (acetylene):



In reality, methane pyrolysis is more complicated, for example, carbon (soot) is formed, which is not considered here. For a total pressure of

Figure 4.2.6 Methane pyrolysis: graph to determine the equilibrium conversion into ethylene (1, x-axis) and into acetylene (2, y-axis) for a total pressure of 1 bar; equilibrium conversion into ethylene is 17% and into acetylene 63.



1.013 bar and 1600 K we have:

$$K_{y,1} = K_p,1 = 1.6 \quad \text{and} \quad K_{y,2} = K_p,2 = 3.9$$

The molar equilibrium content of methane is given by:

$$\gamma_{\text{CH}_4} = \frac{(1 - X_{\text{CH}_4,1} - X_{\text{CH}_4,2})n_{\text{CH}_4,0}}{n_g} = \frac{(1 - X_{\text{CH}_4,1} - X_{\text{CH}_4,2})}{1 + 0.5X_{\text{CH}_4,1} + X_{\text{CH}_4,2}}$$

with n_g and $n_{\text{CH}_4,0}$ as the total and initial number of moles of CH_4 , and $X_{\text{CH}_4,1}$ and $X_{\text{CH}_4,2}$ as the conversion of CH_4 by reactions (1) and (2). The equations for the other components are:

$$\gamma_{\text{C}_2\text{H}_4} = \frac{0.5X_{\text{CH}_4,1}}{1 + 0.5X_{\text{CH}_4,1} + X_{\text{CH}_4,2}}, \quad \gamma_{\text{C}_2\text{H}_2} = \frac{0.5X_{\text{CH}_4,2}}{1 + 0.5X_{\text{CH}_4,1} + X_{\text{CH}_4,2}}, \quad \text{and}$$

$$\gamma_{\text{H}_2} = \frac{X_{\text{CH}_4,1} + 1.5X_{\text{CH}_4,2}}{1 + 0.5X_{\text{CH}_4,1} + X_{\text{CH}_4,2}}$$

and thus we obtain:

$$K_{y,1} = 1.6 = \frac{0.5X_{\text{CH}_4,1}(X_{\text{CH}_4,1} + 1.5X_{\text{CH}_4,2})^2}{(1 - X_{\text{CH}_4,1} - X_{\text{CH}_4,2})^2(1 + 0.5X_{\text{CH}_4,1} + X_{\text{CH}_4,2})} \quad (4.2.61)$$

$$K_{y,2} = 3.9 = \frac{0.5X_{\text{CH}_4,2}(X_{\text{CH}_4,1} + 1.5X_{\text{CH}_4,2})^3}{(1 - X_{\text{CH}_4,1} - X_{\text{CH}_4,2})^2(1 + 0.5X_{\text{CH}_4,1} + X_{\text{CH}_4,2})^2} \quad (4.2.62)$$

Figure 4.2.6 shows the graphical solution of Eqs. (4.2.61) and (4.2.62).

As an alternative to graphical solutions of simultaneous equilibria (which is a must for complicated systems consisting of several independent reactions), the Gibbs enthalpy of a system $G_{\text{system}}(T, p)$ consisting of several compounds (ideal gases) can be calculated:

$$\begin{aligned} G_{\text{system}}(T, p) &= \sum_i n_i \left[\Delta_F G_i^0 + R \ln \left(\frac{p_i}{p_0} \right) \right] \\ &= \sum_i \gamma_i \left[\Delta_F G_i^0 + R \ln \left(\frac{p_i}{p_0} \right) \right] \end{aligned} \quad (4.2.63)$$

Equilibrium is established for the minimum value of G_{system} :

$$\nabla \quad G_{\text{system}}(T, p) = G_{\min} \Rightarrow \frac{dG_{\text{system}}}{dy_i} = 0 \quad (4.2.64)$$

The minimization of $G_{\text{system}}(T, p)$ is usually performed by a computer program. Example 4.2.9 gives a simple example to show the principle of this method.

Example 4.2.9 Calculation of equilibrium by minimization of the Gibbs enthalpy of a reaction system (G_{system})

The isomerization of *n*-butane (1) to *i*-butane (2) at 25 °C and 1.013 bar [$p = p_0$; $\Delta_F G_1^0$ (25 °C) = −17154 J mol^{−1}; $\Delta_F G_2^0$ (25 °C) = −20878 J mol^{−1}] is an instructive example to show the method of calculation of simultaneous equilibria, although for this simple reaction the equilibrium calculation based on K_p would be straightforward. Equation (4.2.61) here leads to:

$$G_{\text{system}}(T, p) = \gamma_1 (\Delta_F G_1^0 + R \ln \gamma_1) + (1 - \gamma_1) [\Delta_F G_2^0 + R \ln(1 - \gamma_1)]$$

The graphical solution (Figure 4.2.7) yields an equilibrium fraction of *n*-butane of 0.818.

For the given, relatively simple system used here to demonstrate the method, the minimum value of G_{system} can also be directly calculated by Eq. (4.2.61):

$$\begin{aligned} \frac{dG_{\text{system}}}{d\gamma_1} &= 0 = \Delta_F G_1^0 - \Delta_F G_2^0 + RT \ln \frac{\gamma_1}{\gamma_2} \Rightarrow \frac{\gamma_1}{1 - \gamma_1} = e^{\left(\frac{-3724}{8.314298} \right)} \\ &= 4.492 \Rightarrow \gamma_1 = 0.818 \end{aligned}$$

Summary of Section 4.2 (take-home messages)

- For a chemical reaction, any change of the entropy of the system provoked by a reaction is accompanied by a change of the entropy in the surrounding. If the generated (or consumed) heat is reversibly transferred from or into the system, the change of the entropy becomes zero, which is expressed by the free enthalpy (**Gibbs function**) as:

$$\Delta G = \Delta H - T\Delta S_{\text{sys}} = 0$$

With $\Delta_R G = 0$, obtain one of the most important equations in chemical thermodynamics:

$$\Delta_R G^0 = -RT \ln K_R$$

This equation is the link between tables of thermodynamic data, which allow the evaluation of $\Delta_R G^0$, and the **equilibrium constant** K_R , which is a function of the composition of the system in terms of concentration, molar fractions, and so on. The value and definition of K_R depends on the choice of the standard state and the ideality of the system.

- The standard reaction Gibbs function $\Delta_R G^0$ can be evaluated from the standard Gibbs functions of formation ($\Delta_F G^0$):

$$\Delta_R G^0 = \sum v_i \Delta_F G_i^0 \quad (v_i < 0 \text{ for reactants and } > 0 \text{ for products})$$

Alternatively, $\Delta_R G^0$ can also be determined by:

$$\Delta_R G^0 = \Delta_R H^0 - T\Delta_R S^0$$

The values of $\Delta_R H^0$ and $\Delta_R S^0$ still depend on temperature (but not on pressure!).

- The equilibrium constant of a perfect (ideal) gas reaction, denoted as K_p , is given by:

$$K_p = \prod \left(\frac{p_i}{p_0} \right)^{v_i}$$

The equilibrium constant K_p depends only on $\Delta_R G^0$, defined at standard pressure p_0 , and thus K_p depends on temperature only and not on pressure. This does not mean that the amounts of the species at equilibrium, that is, the composition, do not depend on the total pressure p , if the reaction leads to a difference between the number of moles of the reactants and products. For example, an increase of the number of gas particles ($\sum v_i > 0$) leads to a decrease of K_p with increasing pressure (*Le Chatelier's principle*).

- For **real gases**, we have to consider the deviation from the ideal gas state, and the partial pressures p_i have to be replaced by the fugacities.
- For **liquid–liquid reactions**, the equilibrium constant K_R is defined based on the activities that represent “effective” molar fractions.
- For **gas–solid reactions**, the equilibrium constant K_p is based on the partial pressures of the gaseous compounds.
- For reaction systems consisting of several stoichiometrically independent reactions, calculation of the equilibrium composition is not straightforward, and the **minimum of the Gibbs enthalpy of a system** is then calculated, usually by computer programs.

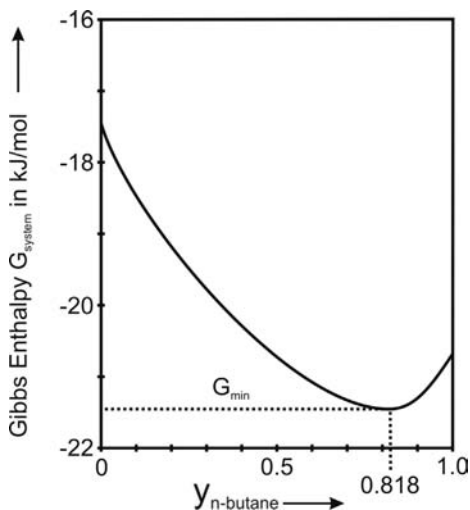
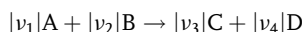


Figure 4.2.7 Gibbs enthalpy of the gas phase system of *n*-butane and *i*-butane as a function of the *n*-butane fraction y_1 (298 K, 1.013 bar). Adapted from Gmehling and Kolbe (1992).

4.3

Kinetics of Homogeneous Reactions

The quantitative description of the course of a chemical reaction with time is a relation between the reaction rate and the parameters influencing the rate, which are usually the temperature, concentrations (or partial pressures for gas reactions), and type and concentration of the catalyst in catalytic reactions. For simple reactions of the type:



only one equation is required. For complex reactions consisting of a network of parallel and/or consecutive reactions, the number of equations depends on the number of key components involved and the number of stoichiometric equations.

Subsequently, we will learn by the example of homogeneous non-catalytic reactions (and so without any influence of mass transport) how the rate is influenced by the temperature and the concentration of the reactants (Section 4.3.1). We then inspect simple systems consisting of two parallel or two series reactions (Section 4.3.2), reversible reactions (Section 4.3.3), and how to consider a change in volume of a system (Section 4.3.4).

4.3.1

Rate Equation: Influence of Temperature and Reaction Order

An exact kinetic description of the rate is only possible with knowledge of all elementary reactions. If unknown, formal kinetic estimates are used, for example, power law expressions:

$$xr = k c_1^{m_1} c_2^{m_2} \quad (4.3.1)$$

or more generally:

$$r = k \sum c_i^{m_i} \quad (4.3.2)$$

Equations (4.3.1) and (4.3.2) do not consider the reverse reaction (discussed in Section 4.3.3). Thus the rate r (e.g., in $\text{mol m}^{-3} \text{s}^{-1}$) depends on the concentration (s) c_i (mol m^{-3}), the rate constant k , and m_i , the partial reaction order with respect to reactant i . The orders may be positive or negative, integers, or numbers involving fractions. The overall order is:

$$m = \sum m_i \quad (4.3.3)$$

and thus the unit of k is $(\text{mol m}^{-3})^{1-m} \text{s}^{-1}$, for example, s^{-1} for $m=1$.

For an empirical model configuration, m_i cannot be interpreted physically. Only for elementary reactions does the order m_i correspond to the stoichiometric coefficient v_i (Topic 4.3.1).

Topic 4.3.1 Reaction mechanism: the view of chemist and chemical engineer

An illustrative example of the basic difference in the quantitative treatment of kinetics by a chemical engineer compared to a chemist is the chlorination of CH_3Cl . The mechanism used by the physical chemist is the description by a set of elementary reactions:

- 1) $\text{Cl}_2 \rightarrow \text{Cl}\cdot + \text{Cl}\cdot$
- 2) $\text{CH}_3\text{Cl} + \text{Cl}\cdot \rightarrow \text{CH}_2\text{Cl}\cdot + \text{HCl}$
- 3) $\text{CH}_2\text{Cl}\cdot + \text{Cl}_2 \rightarrow \text{CH}_2\text{Cl}_2 + \text{Cl}\cdot$
- 4) $\text{CH}_2\text{Cl}_2 + \text{Cl}\cdot \rightarrow \text{CHCl}_2\cdot + \text{HCl}$
- 5) $\text{CHCl}_2\cdot + \text{Cl}_2 \rightarrow \text{CHCl}_3 + \text{Cl}\cdot$
- 6) $\text{CHCl}_3 + \text{Cl}\cdot \rightarrow \text{CCl}_3\cdot + \text{HCl}$
- 7) $\text{CCl}_3\cdot + \text{Cl}\cdot \rightarrow \text{Cl}\cdot + \text{Cl}\cdot$

and so on.

The pattern of reactions used by a chemical engineer is much simpler, and usually only stable species (and no radicals) are involved:

- 1) $\text{CH}_3\text{Cl} + \text{Cl}_2 \rightarrow \text{CH}_2\text{Cl}_2 + \text{HCl}$
- 2) $\text{CH}_2\text{Cl}_2 + \text{Cl}_2 \rightarrow \text{CHCl}_3 + \text{HCl}$
- 3) $\text{CHCl}_3 + \text{Cl}_2 \rightarrow \text{CCl}_4 + \text{HCl}$

The mechanism based on the elementary reactions is of course closer to reality, but is as far as modeling is concerned too difficult to manage, and many reactions without relevance for the design and operation of a reactor are taken into account. The simple chemical engineering scheme is satisfactory to describe the distribution of products of di-, tri-, and tetrachloromethane with sufficient accuracy by means of a model.

Characteristic for a chemical reaction is the dependence of the rate constant on temperature, which is expressed according to *Arrhenius' law* (*Svante Arrhenius*, see box) as:

$$! k = k_0 e^{-E_A/(RT)} \Rightarrow \ln k = \ln k_0 - \frac{E_A}{RT} \quad (4.3.4)$$

where E_A is the activation energy in J mol^{-1} and k_0 the pre-exponential factor, the unit of which depends on the definition of the rate, for example, related to reaction volume or mass of catalyst, and on the overall reaction order. Strictly speaking, k_0 also depends (weakly) on temperature (see Section 3.1.4, Topic 3.1.3), but this is not considered here. A (simple) explanation of *Arrhenius' law* is given by the influence of temperature on the *Maxwell-Boltzmann* distribution of the energy of gas molecules (Section 3.1.4). *Arrhenius' law* [Eq. (4.3.4)] reflects the fact that the portion of molecules exceeding a certain kinetic energy needed to overcome the activation energy of a reaction (i.e., the probability that a collision is sufficiently energetic) increases exponentially with temperature (Figure 3.1.16). Topic 4.3.2 gives a more detailed illustration of the activation energy by energy/reaction coordinate diagrams.

Experimental determination of E_A and k_0 is carried out based on Eq. (4.3.4) by a plot of $\ln(k)$ versus $1/T$ (*Arrhenius plot*). As a rule of thumb, a rise in temperature by 10 K doubles k (e.g., for E_A of 100 kJ mol^{-1} and 140°C , see Topic 4.3.5 for more details). The common range of E_A values for catalytic and thermal processes is about $30\text{--}200 \text{ kJ mol}^{-1}$. Caution should be applied for $E_A < 30 \text{ kJ mol}^{-1}$, indicating that we may have mass transport limitations. Extrapolation of experimentally determined rates far outside the measured range is also problematic, as other mechanisms may prevail that result in different E_A values.

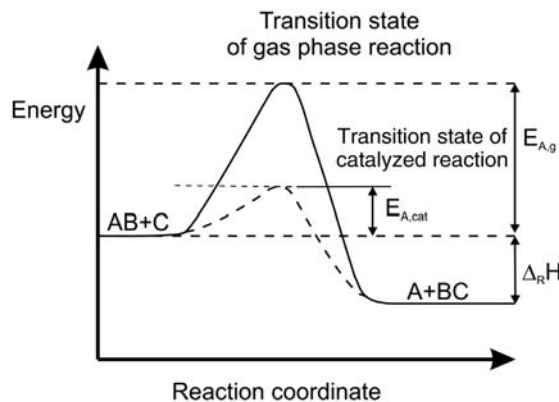
Topic 4.3.2 Illustration of the activation energy by energy/reaction coordinate diagrams [for details see e.g., Rothenberg, 2008, or Atkins and de Paula, 2002].

Let us assume a reaction: $\text{AB} + \text{C} \rightarrow \text{A} + \text{BC}$. The reaction may happen in the gas phase by the collision of AB with C or for a catalytic reaction via catalytic intermediates. This situation is typically represented by plotting the energy changes along the reaction coordinate (Figure 4.3.1). In this diagram we can identify the energy of the reactants and products and of the transition states of a thermal or catalyzed reaction. For the given example, we see that the activation energy is lower if a catalyst is used.

The traditional diagram of energy versus reaction coordinate is in fact only a "slice" of a multidimensional space. Going one dimension higher, we see that the transition state is not a "maximum" but a saddle point (Figure 4.3.2). R_{AB} and R_{BC} mark the equilibrium bond length of an AB and BC molecule, respectively. At the start of the collision the distance R_{BC} is high (strictly it relates to the arrangement when the

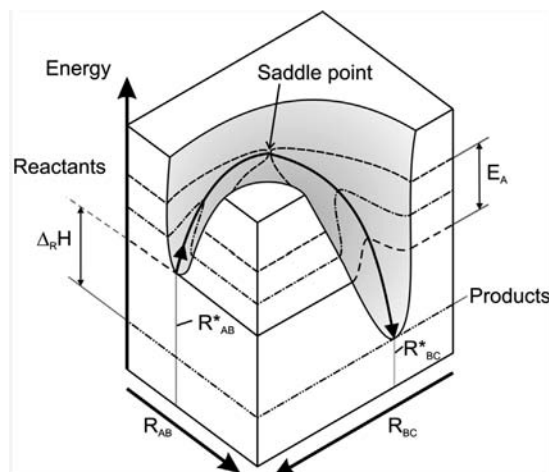
Svante August Arrhenius (1859–1927): A Swedish chemist and one of the founders of physical chemistry. At first, he worked on the conductivities of electrolytes. In 1884, he submitted a dissertation on electrolytic conductivity for the doctorate. It did not impress the professors, and he received the lowest possible passing grade. Later this work earned him the Nobel Prize (1903). *Arrhenius* made 56 theses in his dissertation, and most are still valid today with no or only minor modifications. The most important idea was his explanation of the fact that neither pure salts nor pure water are conductors, but solutions of salts in water are. In 1889, he also explained why most reactions require energy to proceed by formulating the concept of activation energy as the barrier that must be overcome before molecules react [Eq. (4.3.4), *Arrhenius*, 1889]. He also developed a theory to explain the ice ages, and was the first to formulate the idea that changes of CO_2 level in the atmosphere could alter the surface temperature by the greenhouse effect.

Figure 4.3.1 Traditional diagram of energy versus reaction coordinate for the exothermic reaction “ $AB + C \rightarrow A + BC$.” In this diagram the transition state is at the maximum. The influence of the catalyst is represented by a decrease of the activation energy.”



third partner C is at infinity) and R_{AB} is the AB equilibrium bond length. At the end of a successful reactive collision R_{BC} is equal to the bond length and the distance R_{AB} is high. The actual path of the atoms and molecules depends on their *total* energy, which depends on their kinetic energies as well as their potential energies. However, a general idea of the paths available to the system can be obtained by considering the potential energy surface alone, and looking for paths that correspond to least potential energy (Figure 4.3.2). For example, consider the changes in potential energy as H_a approaches an H_b-H_c molecule. The path corresponding to least potential energy is the one marked by the line with the arrows. It corresponds to R_{AB} lengthening as C approaches and begins to form a bond with B. The A–B bond relaxes at the demand of the incoming atom, and although the potential energy rises it climbs only as far as the saddle point. The reaction path involving least potential energy is the route up the floor of the valley, through the saddle point, and down the floor of the other valley as A recedes and the new B–C bond reaches to its equilibrium length. This path is the reaction coordinate shown in Figure 4.3.1. Thus, the traditional diagram of energy versus reaction coordinate is in fact only a “slice” of the multidimensional space, and the transition state is not a “maximum” but a saddle point between two bigger hills. Chemical reactions never climb to the tops of hills but always go via one or more saddle points. When a catalyst offers a faster reaction pathway, it is tantamount to an easier path through these mountains. The catalytic pathway may be longer and more tortuous, but its highest saddle point is lower than the highest saddle point along the non-catalytic pathway (Rothenberg, 2008).

Figure 4.3.2 Potential energy surface for the reaction “ $AB + C \rightarrow A + BC$.” The traditional diagram of energy versus reaction coordinate (a) is in fact only a “slice” of the multidimensional space, and represents just one of the degrees of freedom of the system. Going one dimension higher, we see that the transition state is not a “maximum” but a saddle point. R_{AB}^* and R_{BC}^* mark the equilibrium bond length of an AB and a BC molecule, respectively.



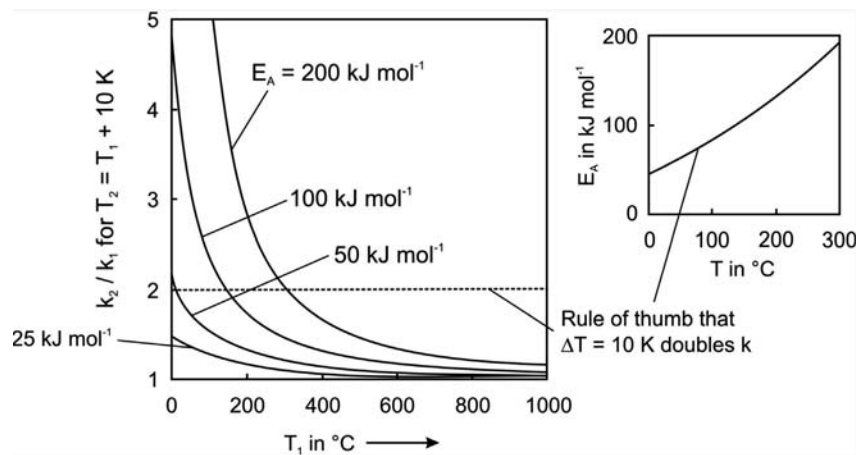


Figure 4.3.3 Influence of an increase in temperature by 10 K on the increase in rate constant: ratio of the rate constants (k_2/k_1) versus T_1 for $T_2 = T_1 + 10$ K.

Topic 4.3.3 Influence of activation energy on the increase of reaction rate constant

According to the *Arrhenius equation* [Eq. (4.3.4)], the ratio of the rate constants at two different temperatures with the second temperature (T_2) being 10 K higher than as T_1 is:

$$\frac{k_2}{k_1} = e^{\frac{E_A}{RT}\left(\frac{1}{T_1} - \frac{1}{T_1+10}\right)} \quad (\text{with } T_2 = T_1 + 10 \text{ K})$$

Figure 4.3.3 (left-hand side) shows the influence of an increase in temperature by 10 K on the increase of the rate constant by the ratio of the rate constants (k_2/k_1) versus T_1 for $T_2 = T_1 + 10$ K. Thus we see that the simple rule of thumb that a rise in temperature by 10 K doubles the rate constant k is of course not exact, but still reflects the order of magnitude for reaction temperatures below about 300 °C and activation energies in the range 50–200 kJ mol⁻¹ (Figure 4.3.3, right-hand side). The impact of temperature on k is slightly reduced with increasing level of reaction temperature, but has still a strong influence.

For a discontinuous batch process, the reaction rate of component i is usually defined as:

$$R_i = \frac{1}{V} \frac{dn_i}{dt} \quad (4.3.5)$$

and for a constant-volume reaction we have:

$$R_i = \frac{dc_i}{dt} \quad (4.3.6)$$

Thus, R_i is negative for an educt and positive for a product.

Quoting a rate only makes sense in conjunction with a stoichiometric equation. Consequently, throughout this book we will use the so-called equivalent reaction rate r_i instead of R_i :

$$! r_i = \frac{R_i}{v_i} = \frac{1}{v_i} \frac{1}{V} \frac{dn_i}{dt} \quad (4.3.7)$$

By convention, the stoichiometric coefficient v_i is negative for a reactant and positive for a product, and so the reaction rate r_i is always positive.

For example, for the reaction $|v_A|A + |v_B|B \rightarrow |v_C|C + |v_D|D$ we have:

$$r_i = \frac{R_A}{v_A} = \frac{R_B}{v_B} = \frac{R_C}{v_C} = \frac{R_D}{v_D} \quad (4.3.8)$$

For homogeneous reactions the volume V is taken as a reference. For gas-solid reactions or heterogeneously catalyzed reactions, it is more convenient to use the mass or the internal surface area of the catalyst, or of the solid reactant, as reference.

The definition of the reaction rate has to be combined with an appropriate expression for the rate in terms of the influence of concentration (reaction order) and temperature (rate constant), which are usually determined by measurements. Let us now consider a discontinuous batch experiment and an irreversible constant volume reaction for different reaction orders.

4.3.1.1 First-Order Reaction

For the rate of conversion of reactant A ($v_A = -1$) we then obtain:

$$\frac{1}{v_A} \frac{dc_A}{dt} = -\frac{dc_A}{dt} = r_A = kc_A \quad (4.3.9)$$

The final concentration c_A after the elapsed time t is determined by integration:

$$\int_{c_{A,0}}^{c_A} \frac{dc_A}{c_A} = -k \int_0^t dt \quad (4.3.10)$$

which leads to the change of concentration or of the conversion with reaction time:

$$\frac{c_A}{c_{A,0}} = e^{-kt} \quad (4.3.11)$$

$$X_A = 1 - \frac{c_A}{c_{A,0}} = 1 - e^{-kt} \quad (4.3.12)$$

A characteristic feature of reaction engineering is the introduction of dimensionless numbers to make reactions with different rates comparable. Here this is the Damkoehler number:

$$Da = kt \quad (\text{for } n = 1) \quad (4.3.13)$$

named after *Gerhard Damkoehler* (1908–1944), one of the founders of chemical engineering (Damkoehler, 1936–1939). Equations (4.3.11) and (4.3.12) may be rewritten as:

$$\frac{c_A}{c_{A,0}} = e^{-Da} \quad (4.3.14)$$

$$! X_A = 1 - e^{-Da} \quad (4.3.15)$$

For $Da = 1$, we get $c_A = c_{A,0}/e \approx 0.37 c_{A,0}$ and $X_A = 1 - 1/e \approx 0.63$. This leads to the typical definition of the characteristic reaction time (first-order reaction) as $\tau_R = 1/k$, that is, $Da = 1$ (see Topic 4.3.4 for more details on the characteristic reaction time).

4.3.1.2 Reaction of n -th Order

$$-\frac{dc_A}{dt} = r_A = kc_A^n \quad (4.3.16)$$

For $n \neq 1$ we obtain as solution for the remaining concentration and conversion:

$$\frac{c_A}{c_{A,0}} = \left[ktc_{A,0}^{n-1}(n-1) + 1 \right]^{\frac{1}{1-n}} \quad (4.3.17)$$

$$X_A = 1 - \left[ktc_{A,0}^{n-1}(n-1) + 1 \right]^{\frac{1}{1-n}} \quad (4.3.18)$$

With the definition of the Damkoehler number for an n -th order reaction:

$$Da = kc_{A,0}^{n-1} t \quad (4.3.19)$$

Equations (4.3.17) and (4.3.18) may be rewritten as:

$$\frac{c_A}{c_{A,0}} = [Da(n-1) + 1]^{\frac{1}{1-n}} \quad (4.3.20)$$

$$! X_A = 1 - [Da(n-1) + 1]^{\frac{1}{1-n}} \quad (4.3.21)$$

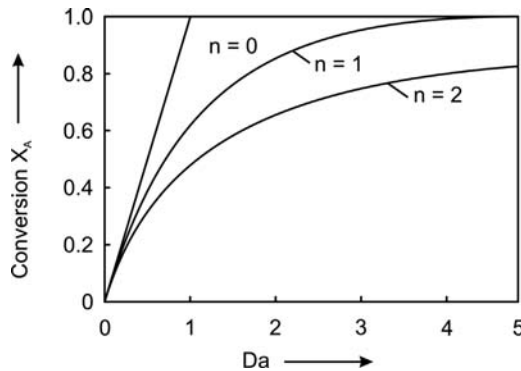


Figure 4.3.4 Influence of the Damköhler number Da on the conversion of reactant A for a zero-, first-, and second-order reaction [batch reactor; reaction order n ; for definition of Da see Eqs. (4.3.13) and (4.3.19)].

Figure 4.3.4 shows the influence of Da on the conversion for a zero-, first-, and second-order reaction. Note that for a reaction order $n \neq 1$ [Eq. (4.3.19)], Da depends on the initial concentration. Only for a first-order reaction are Da and thus the conversion independent of concentration [Eq. (4.3.13)]. The reason for this is that for $n = 1$ the rate increases not only proportionally to the concentration but also the amount of reactant A that has to be converted. These effects nullify each other. Figure 4.3.4 also indicates that the curvature flattens for an increasing order, that is, the expenditure (reaction time or reactor size) increases if a high conversion is needed.

4.3.1.3 Second-Order Reaction

Two cases frequently occur:

Case 1: $2A \rightarrow C$, for example, dimerization,

Case 2: $A + B \rightarrow C$, for example hydrogenation, chlorination, oxidation.

For case 1 we have:

$$-\frac{dc_A}{dt} = 2kc_A^2 \quad (4.3.22)$$

and by integration we get for the remaining concentration and the conversion of A:

$$\frac{c_A}{c_{A,0}} = \frac{1}{1 + 2ktc_{A,0}} = \frac{1}{1 + 2Da} \quad (4.3.23)$$

$$X_A = \frac{2Da}{1 + 2Da} \quad (\text{with } Da = kc_{A,0}t) \quad (4.3.24)$$

For case 2 ($A + B \rightarrow C$) we have:

$$-\frac{dc_A}{dt} = kc_A c_B \quad (4.3.25)$$

and for $c_{A,0} = c_{B,0}$ we obtain:

$$\frac{c_A}{c_{A,0}} = \frac{c_B}{c_{A,0}} = \frac{1}{1 + ktc_{A,0}} = \frac{1}{1 + Da} \quad (4.3.26)$$

$$X_A = \frac{ktc_{A,0}}{1 + ktc_{A,0}} = \frac{Da}{1 + Da} \quad (\text{with } Da = kc_{A,0}t) \quad (4.3.27)$$

For $c_{A,0} \neq c_{B,0}$ we have:

$$X_A = 1 - \frac{c_A}{c_{A,0}} = 1 - \frac{(c_{A,0} - c_{B,0})}{c_{A,0} - c_{B,0}} e^{(c_{B,0} - c_{A,0})kt} \quad (4.3.28)$$

Topic 4.3.4 Characteristic reaction time

The characteristic reaction time τ_R is a measure of the time scale over which the reaction takes place (seconds, minutes, hours, etc.), and is defined as the ratio of a reference concentration and a reference reaction rate:

$$\tau_R = \frac{c_{\text{reference}}}{r_{\text{reference}}}$$

It is convenient to use the initial values of the concentration and the reaction rate as reference. Thus, for an n -th order reversible $A \rightarrow B$ reaction we find:

$$\tau_R = \frac{c_{A,0}}{r_{A,0}} = \frac{c_{A,0}}{kc_{A,0}^n} = \frac{1}{kc_{A,0}^{n-1}}$$

If we compare this equation with the definition of the Damkoehler number [Eq. (4.3.19)], we see that Da can be regarded as the ratio of the reaction time and the characteristic reaction time:

$$Da = \frac{t}{\tau_R} = kc_{A,0}^{n-1} t$$

The characteristic reaction time τ_R can also be interpreted as the reaction time that would be (hypothetically) needed to reach full conversion, if the rate did not change with time and decreasing concentration. For an n -th order reaction, this hypothetical rate equals the maximum rate:

$$\left(-\frac{dc_A}{dt} \right)_{\max} = kc_{A,0}^n$$

Integration and rewriting leads to:

$$-\frac{\Delta c_A}{c_{A,0}} = \frac{c_{A,0} - c_A}{c_{A,0}} = X_A = kc_{A,0}^{n-1} t$$

Thus, for full conversion ($X_A = 1$), we obtain $t = \tau_R$. Self-evidently, in reality, that is, in case of a decreasing rate with time, we need a longer time to reach full conversion (with the exception of the rare case of a zero-order reaction, see Figure 4.3.4).

4.3.2

Parallel Reactions and Reactions in Series

In many practical cases, several reaction pathways are possible, and we may even have a complicated network of parallel and serial reactions. Here we only treat the simple cases of two parallel and two serial first-order reactions.

4.3.2.1 Two Parallel First-Order Reactions

For two first-order parallel reactions $A \xrightarrow{k_1} B$ and $A \xrightarrow{k_2} C$, the rate of depletion of reactant A is given by:

$$-\frac{dc_A}{dt} = (k_1 + k_2)c_A \quad (4.3.29)$$

Integration for the condition $c_A = c_{A,0}$ for $t = 0$ leads to:

$$\ln\left(\frac{c_A}{c_{A,0}}\right) = -(k_1 + k_2)t \quad (4.3.30)$$

or in terms of the conversion of A:

$$\overset{\nabla}{\underset{\circ}{\text{X}_A}} = 1 - e^{-(k_1+k_2)t} \quad (4.3.31)$$

For the yields of the products B and C we obtain for the condition $c_{B,0} = c_{C,0} = 0$:

$$\overset{\nabla}{\underset{\circ}{Y_B}} = \frac{k_1}{k_1 + k_2} \left[1 - e^{-(k_1+k_2)t} \right] \quad (4.3.32)$$

$$\nabla \quad Y_C = \frac{k_2}{k_1 + k_2} \left[1 - e^{-(k_1+k_2)t} \right] \quad (4.3.33)$$

According to Eq. (4.1.10) the selectivity for product B for a constant volume reaction is:

$$S_B = \frac{c_B}{c_{A,0} - c_A} \quad (4.3.34)$$

and by insertion of Eqs. (4.3.31) and (4.3.32) into Eq. (4.3.34) we obtain:

$$S_B = \frac{k_1}{k_1 + k_2} \quad (4.3.35)$$

Analogously, we get for the selectivity for product C:

$$S_C = \frac{k_2}{k_1 + k_2} \quad (4.3.36)$$

Consequently, for parallel first-order reactions, the selectivity depends solely on the ratio of the rate constants and not on the reaction progress and conversion of the reactant. This is also valid for parallel reactions of higher order, if all reactions are of the same order.

4.3.2.2 Two First-Order Reactions in Series

For two first-order reactions in series $A \xrightarrow{k_1} B \xrightarrow{k_2} C$, the reaction rate of reactant A is given by:

$$r_A = -\frac{dc_A}{dt} = k_1 c_A \quad (4.3.37)$$

Integration for $c_A = c_{A,0}$ for $t = 0$ leads to:

$$\ln\left(\frac{c_A}{c_{A,0}}\right) = -k_1 t \Rightarrow X_A = 1 - e^{-k_1 t} \quad (4.3.38)$$

For the yields of the products B and C we find for $c_{B,0} = c_{C,0} = 0$:

$$\nabla \quad Y_B = \frac{c_B}{c_{A,0}} = \frac{k_1}{k_1 - k_2} (e^{-k_2 t} - e^{-k_1 t}) \quad (4.3.39)$$

$$\nabla \quad Y_C = \frac{c_C}{c_{A,0}} = 1 + \frac{k_1}{k_2 - k_1} e^{-k_2 t} - \frac{k_2}{k_2 - k_1} e^{-k_1 t} \quad (4.3.40)$$

Figure 4.3.5 shows the residual content of reactant A and the product yields for different ratios k_1/k_2 as a function of $t/t_{1/2}$, chosen instead of t , with the definition $c_C(t_{1/2}) = c_{A,0}/2$. The yield of the intermediate B depends strongly on k_1/k_2 , and the yield of the final product C has a sigmoidal shape (pronounced in Figure 4.3.5 for $k_1/k_2 = 2$ and 1).

According to Eq. (4.1.10) the selectivity of the intermediate product B is given by ($c_{B,0} = 0$, constant volume, batch reactor):

$$S_B = \frac{c_B}{(c_{A,0} - c_A)} = \frac{Y_B}{X_A} \quad (4.3.41)$$

and together with Eqs. (4.3.38) and (4.3.39) we obtain:

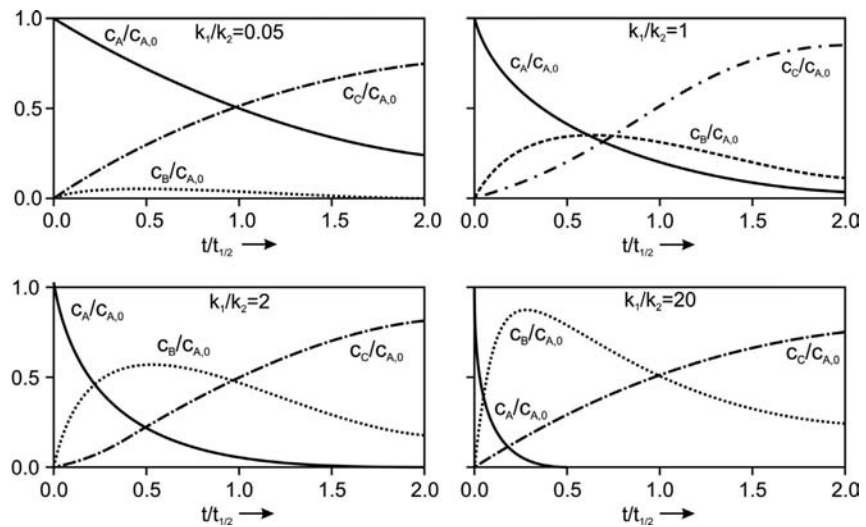
$$S_B = \frac{k_1 (e^{-k_2 t} - e^{-k_1 t})}{(k_1 - k_2)(1 - e^{-k_1 t})} \quad (4.3.42)$$

For the border cases of $k_1 \ll k_2$ and $k_1 \gg k_2$, Eq. (4.3.42) leads to:

$$S_B \rightarrow 0 \text{ for } k_1 \ll k_2 \quad (4.3.43)$$

$$S_B \rightarrow 1 \text{ for } k_1 \gg k_2 \quad (4.3.44)$$

Figure 4.3.5 First-order reactions in series ($A \xrightarrow{k_1} B \xrightarrow{k_2} C$): course of the concentrations of reactant A and products B and C for different ratios k_1/k_2 ($c_C = 0.5c_{A,0}$ for $t = t_{1/2}$; $c_{B,0} = c_{C,0} = 0$, constant volume, batch reactor). Adapted from Baerns *et al.* (2006).



Sometimes two kinds of selectivities are considered, namely, the integral (global) selectivity S defined by Eq. (4.3.41) and the so-called differential (instantaneous) selectivity s , which is the ratio of the rate of the formation of a product to the rate of conversion of the reactant:

$$s_B = \frac{r_B}{r_A} = -\frac{dc_B}{dc_A} = \frac{k_1 c_A - k_2 c_B}{k_1 c_A} = 1 - \frac{k_2}{k_1} \frac{c_B}{c_A} \quad (4.3.45)$$

Insertion of Eqs. (4.3.38) and (4.3.39) into Eq. (4.3.45) yields:

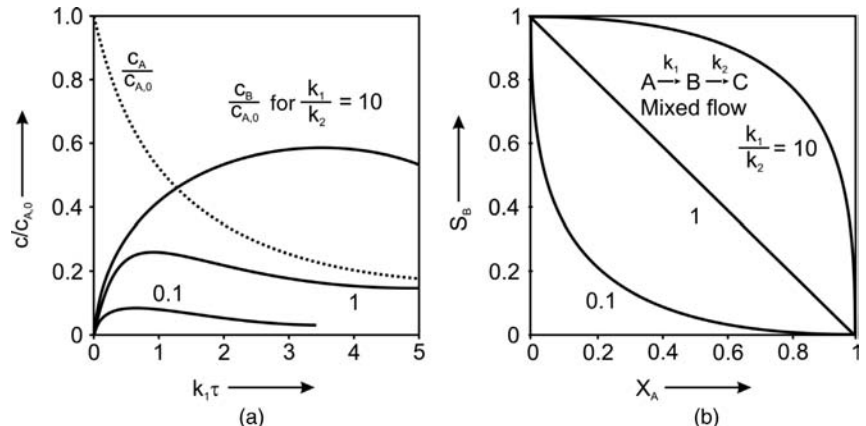
$$s_B = \frac{k_2 e^{(k_1 - k_2)t} - k_1}{k_2 - k_1} \quad (4.3.46)$$

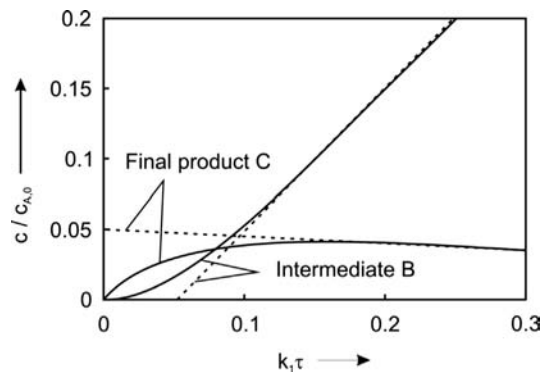
Figure 4.3.6a shows the course of the residual content of A and the yield of the intermediate product B as a function of $Da (= k_1 \tau)$ and Figure 4.3.6b shows the (integral) selectivity to the intermediate B as a function of the conversion of A for different ratios k_1/k_2 .

Thus, for consecutive reactions, the selectivity depends on the ratio of the rate constants as well as on the reaction progress and conversion of the reactant.

One specific case should be considered in more detail: For $k_1 \ll k_2$, the concentration and thus also the change of the concentration of the intermediate B with time is very low compared to the other two components, as depicted in Figure 4.3.5 for $k_1 = 0.05k_2$. Then the rate of consumption of reactant A approximately equals the rate of formation and consumption of the

Figure 4.3.6 First-order reactions in series ($A \xrightarrow{k_1} B \xrightarrow{k_2} C$): (a) conversion of reactant A and yield of intermediate B and (b) selectivity of the intermediate product B for different ratios of k_1/k_2 ($c_{B,0} = 0$, constant volume, batch reactor). Adapted from Levenspiel (1999).





intermediate B is almost zero:

$$\frac{dc_B}{dt} = k_1 c_A - k_2 c_B \approx 0 \quad (\text{for } k_1 \ll k_2) \quad (4.3.47)$$

For $k_1 \ll k_2$, Eqs. (4.3.39) and (4.3.40) yield:

$$Y_B \approx \frac{k_1}{k_2} e^{-k_1 t} \quad (\text{for } k_1 \ll k_2) \quad (4.3.48)$$

$$Y_C \approx 1 - \left(1 + \frac{k_1}{k_2}\right) e^{-k_1 t} \quad (\text{for } k_1 \ll k_2) \quad (4.3.49)$$

This method to derive approximate solutions for kinetic equations is called the *principle of quasi-stationarity* (first introduced by *Max Bodenstein*, see box), and is very helpful for the kinetic evaluation of complex reaction systems as the mathematical treatment of the kinetic systems becomes simpler. (Note that for the example discussed above the *Bodenstein principle* is not needed, as the exact equations (4.3.38)–(4.3.40) can be derived quite easily; this example was just chosen to show this principle.)

Figure 4.3.7 shows that the deviation of the exact solution (Eq. 4.3.39) and the approximation by Eq. (4.3.48) is small if the ratio k_1/k_2 is small (here 0.05). Only in the initial phase of the reaction [$k_1\tau < 0.1$, i.e., $X_1 = 1 - \exp(-k_1\tau) < 0.1$] should the approximation not be used.

Kinetics is not only important for chemical or biological processes, but also for everyday life, as inspected in Example 4.3.1 for the social process of the birth and death of a rumor with interacting subpopulations of ignorants, spreaders, and stiflers.

Figure 4.3.7 Yield of intermediate B and final product C for first-order reactions in series ($A \xrightarrow{k_1} B \xrightarrow{k_2} C$) for a ratio of k_1/k_2 of 0.05: comparison of exact solution [Eq. (4.3.39), solid lines] and approximation (dashed lines) by Eq. (4.3.48), that is, based on the *principle of quasi-stationarity* ($c_{B,0} = 0$, constant volume, batch reactor).

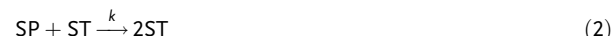
Max Bodenstein (1871–1942): a German physico-chemist and one of the founders of chemical kinetics. He introduced the *principle of quasi-stationarity*, which was named after him. He worked intensively on the reaction of hydrogen with chloride.

Example 4.3.1: Kinetics of the birth and death of a rumor

The social process of a propagation of a rumor is discussed by Hayes (2005) by means of statistical methods. This can also be carried out by the differential equations used to describe the kinetics of chemical reactions, if we use populations instead of concentrations. The model for the propagation of a rumor is as follows. The population is thoroughly mixed, so people encounter each other with uniform probability. We assume three interacting subpopulations, ignorants (I), spreaders (SP), and stiflers (ST). People always meet pairwise, never in larger groups, and the interactions are governed by a set of rules:

- Whenever a spreader meets an ignorant, the ignorant becomes a spreader, while the original spreader continues spreading.
- When a spreader meets a stifler, the spreader becomes a stifler.
- If two spreaders meet, we get one stifler and the other continues spreading.
- All other interactions (I-I, I-ST, ST-ST) have no effect on either party.

This system can be formally described by the following “reactions”:



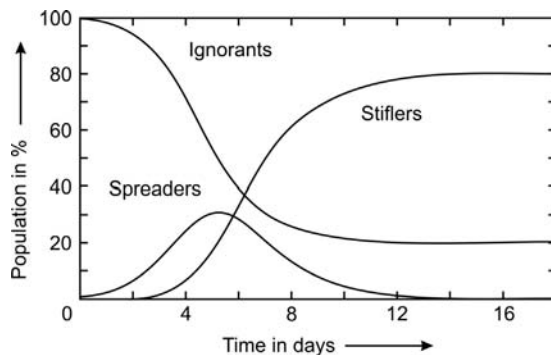
The corresponding differential equations for the change of the “concentrations” are then:

$$\frac{dc_{SP}}{dt} = kc_{SP}c_I - kc_{SP}c_{ST} - kc_{SP}^2 \quad (4)$$

$$\frac{dc_I}{dt} = -kc_{SP}c_I \quad (5)$$

$$\frac{dc_{ST}}{dt} = kc_{SP}c_{ST} + kc_{SP}^2 \quad (6)$$

Figure 4.3.8 Modeling of the propagation of a rumor by a “kinetic model.”



As boundary conditions we chose:

$$c_{ST,0} = 0 \quad (7)$$

$$c_{SP,0} \neq 0 = \frac{1}{100} c_{I,0} \quad (\text{initial population of } 1\% \text{ spreaders and } 99\% \text{ ignorants}) \quad (8)$$

$$c_{I,0} = \frac{99}{100} \quad (9)$$

$$c_I + c_{SP} + c_{ST} = c_{I,0} + c_{SP,0} \quad (10)$$

with:

c_i : “concentration” of subpopulation i (number of persons in subpopulation relative to total number),

k : “rate constant” (here arbitrarily chosen as one per day, e.g., for a population of, in total, 100 persons, we have 50 interactions per day).

Figure 4.3.8 shows the solution of the differential equations.

We see that rumors are self-limiting. Initially, spreaders are recruited from the reservoir of ignorants, and the rumor ripples through the population. However, as the spreaders proliferate, they start running into one another and become stiflers. The progression from ignorant to spreader to stifler is irreversible, and the rumor eventually dies out, as all spreaders end up as stiflers. What is not so obvious is that the last spreader disappears before the supply of ignorants is exhausted, and that the permanently clueless fraction equals 20% of the original population for the given boundary conditions. (For an initial population of 50% spreaders and 50% ignorants, we get a final clueless fraction of 15%).

4.3.3

Reversible Reactions

Any reaction is basically reversible, but in actual practice it is reversible only if the reverse reaction can be measured. Here we only consider a simple reversible $A \rightleftharpoons B$ reaction:



For the reaction rate of A the following term applies:

$$\frac{dc_A}{dt} = -k_1 c_A + k_{-1} c_B \quad (4.3.50)$$

The equilibrium is characterized by the equilibrium constant, and if we use c_A^* and c_B^* to denote the concentrations at equilibrium we have:

$$K_c = \frac{c_B^*}{c_A^*} \quad (4.3.51)$$

This equation can be used to derive a relation between kinetic parameters and thermodynamic principles (see Topic 4.3.5 for more details).

The dynamic condition for the equilibrium is that the rate becomes zero, and Eq. (4.3.50) yields:

$$\frac{dc_A}{dt} = 0 = -k_1 c_A^* + k_{-1} c_B^* \quad (4.3.52)$$

and by insertion of Eq. (4.3.51) we get:

$$\frac{c_B^*}{c_A^*} = K_c = \frac{k_1}{k_{-1}} \quad (4.3.53)$$

Combination of Eqs. (4.3.53) and (4.3.50) yields:

$$\bullet \quad \frac{dc_A}{dt} = -k_1 c_A + \frac{k_1}{K_c} c_B = -k_1 \left(c_A - \frac{c_B}{K_c} \right) \quad (4.3.54)$$

The term c_B/K_c is the “actual” (not the final) equilibrium concentration of A for a given degree of reaction progress and concentration of B. The reaction comes to a standstill, if c_A equals c_B/K_c , that is, $c_A = c_A^*$ and $c_B = c_B^*$. Thus, compared to the reactant concentration used for an irreversible reaction, the deviation from equilibrium ($c_A - c_B/K_c$) is utilized.

For a single reversible reaction (here we still use the example of an $A \rightarrow B$ reaction), we can derive an alternative expression to Eq. (4.3.54). For $c_{B,0}=0$ (pure A as feed) we can express c_B by Eq. (4.3.53) as follows:

$$c_B = c_{A,0} - c_A = c_A^* + c_B^* - c_A = c_A^*(1 + K_c) - c_A \quad (4.3.55)$$

and when solved for the concentration at equilibrium c_A^* we obtain:

$$c_A^* = \frac{c_{A,0}}{K_c + 1} \quad (4.3.56)$$

By insertion of Eq. (4.3.55) into Eq. (4.3.54) we get:

$$\frac{dc_A}{dt} = -k_1 c_A + \frac{k_1}{K_c} [c_A^*(1 + K_c) - c_A] = -k_1 \left(\frac{K_c + 1}{K_c} \right) (c_A - c_A^*) \quad (4.3.57)$$

Integration of Eq. (4.3.57) leads to:

$$\frac{(c_A - c_A^*)}{(c_{A,0} - c_A^*)} = e^{-k_1 \left(\frac{K_c + 1}{K_c} \right) t} \quad (4.3.58)$$

Insertion of Eq. (4.3.56) into Eq. (4.3.58) finally yields:

$$\frac{c_A}{c_{A,0}} = \frac{1}{K_c + 1} + \frac{K_c}{K_c + 1} \left[e^{-k_1 \left(\frac{K_c + 1}{K_c} \right) t} \right] \quad (4.3.59)$$

In terms of the conversion X_A , Eq. (4.3.59) is rewritten as:

$$X_A = 1 - \frac{c_A}{c_{A,0}} = \frac{K_c}{K_c + 1} \left[1 - e^{-k_1 \left(\frac{K_c + 1}{K_c} \right) t} \right] \quad (4.3.60)$$

If we use Eq. (4.3.56) to derive the equilibrium conversion X_A^* , we obtain:

$$X_A^* = 1 - \frac{c_A^*}{c_{A,0}} = \frac{K_c}{K_c + 1} \quad (4.3.61)$$

and rewriting of Eq. (4.3.60) finally yields:

$$X_A = X_A^* \left[1 - e^{-k_1 \left(\frac{K_c + 1}{K_c} \right) t} \right] = X_A^* \left[1 - e^{-\frac{k_1}{X_A^*} t} \right] \quad (4.3.62)$$

Note that all equations of this section are only valid if no other parallel or series reactions take place. In other words, the value of the final concentration or conversion at equilibrium c_A^* and X_A^* must be known in advance. Hence for the modeling of complex systems consisting of several parallel and/or consecutive reactions we should use equations such as Eq. (4.3.54) for each individual reaction. A good example of such a complex reaction system is the pyrolysis of CH_4 either to acetylene or in parallel to ethylene (Example 4.2.8).

For a single reaction (here the example of a simple A to B system) we may use either Eqs. (4.3.57) or (4.3.54) as shown by the following example: For a batch

process with an initial concentration $c_{A,0}$, a value of K_c of 3, and a conversion of 50% (as example) we find from Eq. (4.3.54):

$$\frac{dc_A}{dt} = -k_1 \left(0.5c_{A,0} - \frac{0.5c_{A,0}}{3} \right) = -\frac{1}{3} k_1 c_{A,0} \quad (\text{for } X_A = 0.5 \text{ and } K_c = 3)$$

The same result is obtained by Eq. (4.3.57) with $c_A^* = 0.25c_{A,0}$ [as calculated by Eq. (4.4.56) for the arbitrarily chosen value for K_c of 3]:

$$\begin{aligned} \frac{dc_A}{dt} &= -\left(k_1 + \frac{k_1}{3} \right) (0.5c_{A,0} - 0.25c_{A,0}) \\ &= -\frac{1}{3} k_1 c_{A,0} \quad (\text{for } X_A = 0.5 \text{ and } K_c = 3) \end{aligned}$$

Topic 4.3.5 Relationships of kinetics and thermodynamics of reversible reactions

Correlation between Activation Energy and Reaction Enthalpy

For a first-order reversible A to B reaction, the ratio of the rate constants of the forward and reverse reaction is given by the equilibrium constant K_C [Eq. (4.3.53)]:

$$\frac{k_1}{k_{-1}} = K_c \quad (4.3.53)$$

If we use the Arrhenius equation [Eq. (4.3.4)] for the rate constants and express K_C by the standard reaction enthalpy $\Delta_R H^0$ and entropy $\Delta_R S^0$ (Eqs. (4.2.12) and (4.2.14)), we get:

$$\frac{k_1}{k_{-1}} = \frac{k_{1,0} e^{-\frac{E_{A,1}}{RT}}}{k_{-1,0} e^{-\frac{E_{A,-1}}{RT}}} = K_c = e^{-\frac{\Delta_R H^0}{RT} + \frac{\Delta_R S^0}{R}} \Rightarrow \frac{k_{1,0}}{k_{-1,0}} e^{-\frac{(E_{A,1} - E_{A,-1})}{RT}} = e^{\frac{\Delta_R S^0}{R}} e^{-\frac{\Delta_R H^0}{RT}} \quad (4.3.63)$$

This leads to the ratio of the pre-exponential factors in terms of $\Delta_R S^0$:

$$R \ln \left(\frac{k_{1,0}}{k_{-1,0}} \right) = \Delta_R S^0 \quad (4.3.64)$$

and the difference of the activation energies in terms of $\Delta_R H^0$ is given by:

$$E_{A,1} - E_{A,-1} = \Delta_R H^0 \quad (4.3.65)$$

Equations (4.3.64) and (4.3.65) should be used with great care, as the values of $\Delta_R H^0$ and $\Delta_R S^0$ calculated by this means may deviate from those calculated based on the (tabulated) standard enthalpies of formation $\Delta_f H^0$ and the standard entropies S^0 [Eq. (4.2.14)].

What to do if the Experimental Reaction Orders Differ from Stoichiometric Coefficients

If the experimentally determined reaction orders differ from the stoichiometric coefficients, the following approach can be used in approximation. For example, we may have a reaction $A + B \rightarrow 2C$, and the following rate was determined for the forward reaction:

$$r_{A,\text{forward}} = -\frac{dc_A}{dt} = k_1 c_A^{0.5} c_B^{1.5} \quad (4.3.66)$$

As the reaction orders of the reverse reaction (n , m , and p) are unknown, we have:

$$r_A = -\frac{dc_A}{dt} = k_1 c_A^{0.5} c_B^{1.5} - k_{-1} c_C^n c_A^m c_B^p \quad (4.3.67)$$

The equilibrium constant is given by (with c_i^* as the concentration at equilibrium):

$$K_c = \frac{(c_C^*)^2}{c_A^* c_B^*} \quad (4.3.68)$$

At equilibrium the net rate change is zero, and Eq. (4.3.67) leads to:

$$0 = k_1(c_A^*)^{0.5}(c_B^*)^{1.5} - k_{-1}(c_C^*)^n(c_A^*)^m(c_B^*)^p \Rightarrow \frac{k_1}{k_{-1}} = \frac{(c_C^*)^n(c_A^*)^m(c_B^*)^p}{(c_A^*)^{0.5}(c_B^*)^{1.5}} \quad (4.3.69)$$

The equilibrium constant K_C and the ratio k_1/k_{-1} depend only on temperature and not on concentrations. Thus, we have to choose values for n and m in such a way, that Eq. (4.3.69) is not in contradiction to Eq. (4.3.68). This is only the case for $K_C = k_1/k_{-1}$, which yields:

$$K_C = \frac{(c_C^*)^2}{c_A^* c_B^*} = \frac{k_1}{k_{-1}} = \frac{(c_C^*)^n(c_A^*)^m(c_B^*)^p}{(c_A^*)^{0.5}(c_B^*)^{1.5}} \Rightarrow 1 = (c_C^*)^{n-2}(c_A^*)^{m+0.5}(c_B^*)^{p-0.5} \quad (4.3.70)$$

Equation (4.3.70) is only fulfilled if the terms $(n-2)$, $(m+0.5)$, and $(p-0.5)$ all become zero, and Eqs. (4.3.67) and (4.3.70) finally yield:

$$r_A = -\frac{dc_A}{dt} = k_1 c_A^{0.5} c_B^{1.5} - \frac{k_1}{K_C} c_C^{1/2} c_A^{-0.5} c_B^{0.5} = k_1 \left(c_A^{0.5} c_B^{1.5} - \frac{c_C^{1/2} c_A^{-0.5} c_B^{0.5}}{K_C} \right) \quad (4.3.71)$$

So for each compound, the difference of the reactions orders of the forward and reverse reaction must equal the stoichiometric coefficient, for example, for B we have $1.5 - 0.5 = 1$.

Relation between Equilibrium and Rate of Forward and Reverse Reaction

For a reversible A to B reaction, the rate constant of the forward reaction and the equilibrium constant are known ($K_C = 2$, $k_1 = 1 \text{ s}^{-1}$). What is the kinetic relation?

According to Eq. (4.3.53), the rate constant of the reverse reaction k_{-1} equals $k_1/K_C = 0.5$.

Thus the reaction rate of conversion of A is given by (with c_A and X_A as initial concentration and conversion of A, respectively):

$$-\frac{dc_A}{dt} = r_{\text{forward}} - r_{\text{reverse}} = k_1 c_A + \frac{k_1}{K_C} c_B = k_1 c_{A,0}(1 - X_A) + \frac{k_1}{K_C} c_{A,0} X_A \quad (4.3.72)$$

Figure 4.3.9 shows the rate of the forward and the reverse reaction for different degrees of conversion of A. At thermodynamic equilibrium ($X_A = \frac{2}{3}$), both rates are equal and the net change of the concentration of A and B becomes zero.

4.3.4

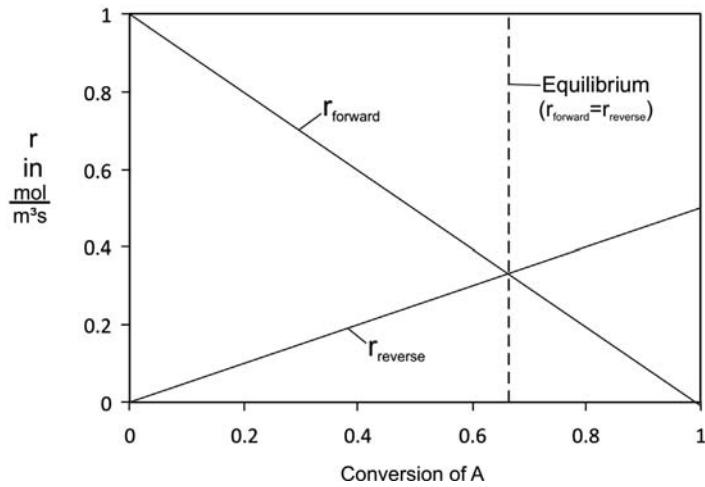
Reactions with Varying Volume (for the Example of a Batch Reactor)

For a reaction with varying volume, for example, a gas-phase reaction of A to 2B with initial volume V_0 , the change of volume is characterized by the fractional change ε_V for complete conversion ($X_A = 1$):

$$\varepsilon_V = \frac{V_{X_A=1} - V_0}{V_0} = \frac{V_{X_A=1}}{V_0} - 1 \quad (4.3.73)$$

Thus for the reaction A \rightarrow 2B and with pure A as feed, ε_V would be 1.

Figure 4.3.9 Rate of forward and reverse reaction as a function of conversion of A for a reversible reaction A into B ($K_C = 2$, $k_1 = 1 \text{ s}^{-1}$, $k_{-1} = k_1/K_C = 0.5$).



For a single reaction, the volume changes proportionally with conversion and we have:

$$V_{X_A} = (1 + X_A \varepsilon_V) V_0 \quad (4.3.74)$$

and the reaction rate in a batch reactor, Eq. (4.3.7), and the relation $dn_A = -dX_A n_{A,0}$ lead to:

$$\begin{aligned} r_A &= -\frac{1}{V_{X_A}} \left(\frac{dn_A}{dt} \right) = \frac{n_{A,0}}{V_{X_A}} \left(\frac{dX_A}{dt} \right) = \frac{n_{A,0}}{V_0(1 + X_A \varepsilon_V)} \left(\frac{dX_A}{dt} \right) \\ &= \frac{c_{A,0}}{(1 + X_A \varepsilon_V)} \left(\frac{dX_A}{dt} \right) \end{aligned} \quad (4.3.75)$$

(Here we examine only a batch process; for flow reactors see Example 4.10.1 in Section 4.10.3.) Integration of Eq. (4.3.75) yields the time needed for a certain conversion:

$$t = \int_0^{X_A} \frac{c_{A,0}}{r_A} \frac{dX_A}{(1 + X_A \varepsilon_V)} \quad (4.3.76)$$

and for a first-order reaction with rate constant k_1 (in s^{-1}) we obtain:

$$t = \int_0^{X_A} \frac{c_{A,0}}{k c_A} \frac{dX_A}{(1 + X_A \varepsilon_V)} \quad (4.3.77)$$

For reactions with changing volume ($\varepsilon_V \neq 0$), it is convenient to use X_A and not c_A to simplify the algebra. Based on Eq. (4.3.74), the concentration in terms of ε_V and X_A is given by:

$$c_A = \frac{n_A}{V_{X_A}} = \frac{(1 - X_A)n_{A,0}}{(1 + X_A \varepsilon_V)V_0} = \frac{(1 - X_A)c_{A,0}}{(1 + X_A \varepsilon_V)} \quad (4.3.78)$$

Substitution of c_A in Eq. (4.3.77) by Eq. (4.3.78) and integration (for T and $k = \text{const.}$) yields:

$$t = \frac{1}{k} \int_0^{X_A} \frac{1}{(1 - X_A)} dX_A \Rightarrow X_A = 1 - e^{-kt} \quad (4.3.79)$$

which is identical to the case of a constant volume reaction, Eq. (4.3.12).

Consequently, for a first-order reaction, the conversion in a batch reactor is not influenced by a change in volume. This can be explained by a simple thought experiment. Imagine that 1 mol of substance A is converted in a vessel with a volume of 1 m^3 . The reaction time t is 1 h and the rate constant k is 1 h^{-1} . Thus the

initial reaction rate ($t = 0$) is $1 \text{ mol m}^{-3} \text{ h}^{-1}$, and Eq. (4.3.15) leads to a conversion of 63%. Now we use two batch reactors (each with the size of the single reactor used before) and distribute the same amount of A equally. Now the initial concentration is only 0.5 mol m^{-3} and the initial rate in both vessels is also halved ($0.5 \text{ mol m}^{-3} \text{ h}^{-1}$). Nevertheless, after 1 h reaction time, we still reach a conversion of 63% as the lower rate is compensated for by the fact that the amount of A that has to be converted in each reactor is now also reduced by 50%.

The situation differs for non-first-order reactions; for example, for a zero-order reaction with rate constant k_0 (in $\text{mol m}^{-3} \text{ s}^{-1}$), Eq. (4.3.76) leads to:

$$t = \int_0^{X_A} \frac{c_{A,0}}{k_0} \frac{dX_A}{(1 + X_A \varepsilon_V)} \Rightarrow X_A = \frac{1}{\varepsilon_V} \left(e^{\frac{\varepsilon_V k_0 t}{c_{A,0}}} - 1 \right) \quad (4.3.80)$$

whereas for a constant volume zero-order reaction we get based on Eq. (4.3.18):

$$X_A = \frac{k_0 t}{c_{A,0}} \quad (\text{for } n = 0 \text{ and } \varepsilon_V = 0) \quad (4.3.81)$$

Equation (4.3.81) is also deduced from Eq. (4.3.80) as:

$$e^{\frac{\varepsilon_V k_0 t}{c_{A,0}}} = (1 + \varepsilon_V k_0 t / c_{A,0})$$

for $\varepsilon_V \rightarrow 0$.

For example, for a value of the term $k_0 t / c_{A,0}$ of 0.5 and $\varepsilon_V = 1$ (volume is doubled for full conversion), we obtain a conversion of 65% in a batch reactor. For a constant volume reaction, we would only get 50%. For a second-order reaction, the effect would be the reverse, and an increasing volume would lead to a lower conversion for a given reaction time.

Note that in flow reactors the change of volume has an influence on the conversion even for a first-order reaction because now we get a change of the (residence) time if the volumetric flow rate changes (Section 4.10.3, Example 4.10.1).

Summary of Section 4.3 (take-home messages)

- The exact kinetic description of a reaction rate is only possible if all **elementary reactions** are known; **formal kinetic estimates** are used, for example, power law expressions.
- Characteristic for a chemical reaction is the dependence of the rate constant on temperature, which is expressed according to **Arrhenius' law** as:

$$k = k_0 e^{-E_A/(RT)}$$

where E_A is the **activation energy** and k_0 the **pre-exponential factor**. An explanation of **Arrhenius' law** for gas-phase reactions is given based on the **Maxwell-Boltzmann** distribution of the energy of gas molecules. Arrhenius's law reflects the fact that the portion of molecules exceeding a certain kinetic energy needed to overcome the activation energy of a reaction (i.e., the probability that a collision is sufficiently energetic) increases exponentially with temperature.

- In a batch reactor experiment the rate of conversion of reactant A is given by:

$$X_A = 1 - e^{-kt} = 1 - e^{-Da} \quad (\text{with } Da \text{ as Damkoehler number})$$

In a continuous plug flow reactor we can use the same equation, if we use the residence time instead of the reaction time.

- In many practical cases, several reaction pathways are possible, and we may even have a complicated network of parallel and serial reactions. Simple cases are two parallel reactions $A \rightarrow B$ and $A \rightarrow C$, or two **reactions in series** ($A \rightarrow B \rightarrow C$). For **consecutive reactions**, the selectivity depends on the ratio of the rate constants as well as on the reaction progress and conversion of the reactant.

- Any reaction is basically reversible, but in actual practice it is reversible only if the **reverse reaction** can be measured. For the reversible reaction of A to B we obtain:

$$-\frac{dc_A}{dt} = k_1 \left(c_A - \frac{c_B}{K_c} \right)$$

The term c_B/K_c (with K_c as equilibrium constant) can be regarded as the “actual” (not the final) equilibrium concentration of A for a given degree of reaction progress.

Hence, the reaction comes to a standstill if c_A equals c_B/K_c , that is, $c_A = c_A^*$ and $c_B = c_B^*$. Thus, compared to the reactant concentration used for an irreversible reaction, the deviation of the concentration from the equilibrium ($c_A - c_B/K_c$) is utilized.

4.4

Kinetics of Fluid–Fluid Reactions

Fluid–fluid reactions can be divided into gas–liquid and liquid–liquid systems (Table 4.4.1). The relevance of fluid–fluid reactions will increase in the future, above all in the field of (waste)water treatment and in general for biotechnological processes.

In contrast to homogeneous single-phase reactions (Section 4.4), we now have to consider that the effective achievable reaction rate may be influenced by mass transfer steps to and within both phases. In the following, we derive first the equations for mass transport at a gas–liquid interface (Section 4.4.1). Then we discuss the interplay of mass transport both with a slow reaction (Section 4.4.2) and with a fast reaction (Section 4.4.3).

Table 4.4.1 Selected examples of industrial fluid–fluid reactions. Taken from Emig and Klemm (2005).

Reaction system	Examples	Reactor typically used
Gas–liquid reactions		
Oxidation	of ethane to acetaldehyde of <i>p</i> -xylene to terephthalic acid Wastewater treatment	Bubble column Bubble column Loop reactor (airlift)
Chlorination	of paraffins of benzene and benzene derivatives	Bubble column Packed column
Hydrogenation	of coal (emulsified in recycle oil)	Bubble column
Alkylation	of ethane and benzene	Bubble column
Absorption with reaction	Sulfuric acid production: SO ₃ in H ₂ SO ₄ Gas scrubbing: CO ₂ in H ₂ O/K ₂ CO ₃ Gas scrubbing: H ₂ S in ethanolamines Nitric acid production: NO ₂ in H ₂ O	Packed column Packed column Packed column Tray column
Liquid–liquid reactions		
Reactive distillation	Extraction of metal salts Extraction of acetic acid	Pulsated tray column Oscillating tray column
Production of derivatives of aromatic hydrocarbons	Nitration of aromatic hydrocarbons	Cascade of CSTRs ^{a)}
Miscellaneous	Sulfidation of alkylbenzene Furfural from xylose by diluted mineral acids Saponification and hydrolysis of esters	Cascade, batch reactor Batch reactor Spray tower

a) Continuous stirred tank reactor.

Most industrially relevant fluid–fluid reactions are gas–liquid systems, and only these systems will be treated here in some detail. The conclusions are directly transferable to liquid–liquid systems as long as the reactants are soluble in one of the two liquid phases. However, one has to bear in mind that the mass transfer resistance in the second liquid phase (without reaction) can often not be neglected, whereas for gas–liquid systems the mass transfer resistance on the side of the gas phase is often negligible.

4.4.1

Mass Transfer at a Gas–Liquid Interface (Two-Film Theory)

Interfacial mass transfer processes can be described by the two-film theory (Figure 4.4.1) based on the following assumptions:

- Both the gas and the liquid phase can be divided into a stagnant film (thickness δ_g and δ_l) located near the interface and well-mixed bulk phases without concentration gradients.
- The mass transfer is a steady-state process.

Other models such as the penetration model (surface renewal theory) developed by Higbie and Danckwerts (Westerterp, van Swaaij, and Beenackers, 1998) consider the mass transfer process to be essentially non-stationary, and the surface is assumed to consist of elements of different age at the surface, returning into the bulk phase while new elements originating from the bulk phase take their place. Results of calculations by the two-film theory and the surface renewal theory are similar. Thus, only the two-film theory, which is easier to understand and which is therefore used most, is considered here.

The mass transfer of a gaseous component A from the gas phase to the gas–liquid interface with surface area A_i and from the interface into the liquid phase can be written by the mass transfer coefficients β in the absence of a chemical reaction (see also Topic 4.4.1) as:

$$\dot{n}_{A,g} = D_{A,g} A_i \frac{\left(\frac{p_{A,g}}{RT} - \frac{p_{A,i}}{RT} \right)}{\delta_g} = \frac{D_{A,g} A_i}{\delta_g} \left(\frac{p_{A,g}}{RT} - \frac{p_{A,i}}{RT} \right) = \beta_{A,g} A_i \frac{(p_{A,g} - p_{A,i})}{RT} \quad (4.4.1)$$

$$\dot{n}_{A,l} = D_{A,l} A_i \frac{(c_{A,i} - c_{A,l})}{\delta_l} = \beta_{A,l} A_i (c_{A,i} - c_{A,l}) \quad (4.4.2)$$

Directly at the interface, there is no mass transfer resistance, so *Henry's law* is valid:

$$p_{A,i} = H_{A,c} c_{A,i} \quad (4.4.3)$$

The *Henry coefficient* $H_{A,c}$ in Eq. (4.4.3) is related to the molar concentration in the liquid phase ($H_{A,c} = p_A/c_A$ in $\text{Pa m}^3 \text{mol}^{-1}$). This definition is more convenient than the definition based on the molar fraction x_A [$p_A = H_{A,x}x_A$, Eq. (3.3.25)] that is frequently used for absorption processes without chemical reaction.

The two-phase theory is essentially a steady-state theory ($\dot{n}_{A,l} = \dot{n}_{A,g}$), and the combination of Eqs. (4.4.1)–(4.4.3) leads to:

$$\dot{n}_A = \dot{n}_{A,g} = \dot{n}_{A,l} = \beta_{A,g} A_i \frac{\left(\frac{p_{A,g}}{RT} - H_{A,c} c_{A,i} \right)}{RT} = \beta_{A,l} A_i (c_{A,i} - c_{A,l}) \quad (4.4.4)$$

Rearrangement leads to the unknown concentration in the liquid at the interphase (phase boundary):

$$c_{A,i} = \frac{\frac{\beta_{A,g}}{RT} p_{A,g} + \beta_{A,l} c_{A,l}}{\beta_{A,l} + \frac{\beta_{A,g}}{RT} H_{A,c}} \quad (4.4.5)$$

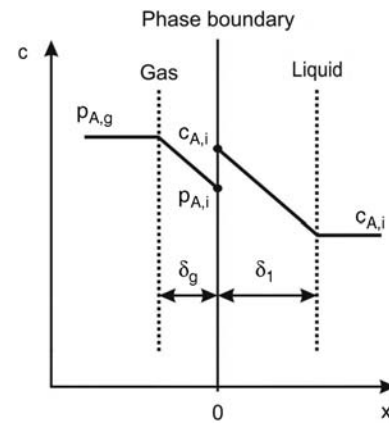


Figure 4.4.1 Two-film concept (stagnant film model) for gas–liquid mass transfer of component A.

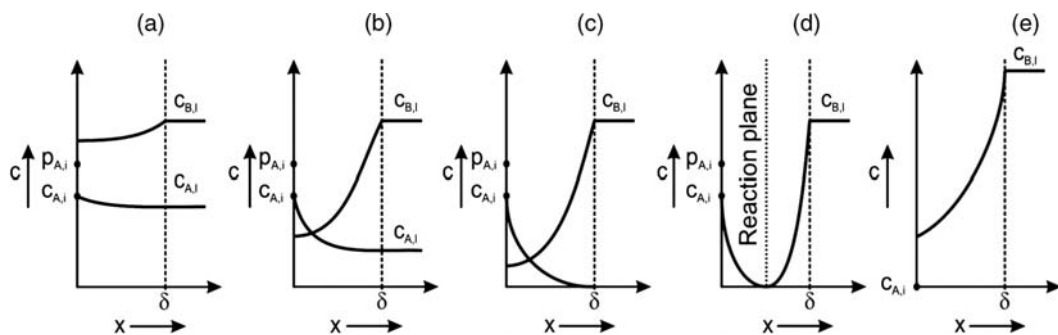


Figure 4.4.2 Reaction of gas A with liquid B: concentration gradients in the stagnant film of the liquid: (a) slow reaction rate, (b) medium reaction rate, (c) fast reaction, (d) instantaneous reaction at reaction plane in the liquid layer, and (e) instantaneous reaction at the interphase.

and by insertion of Eq. (4.4.5) into Eq. (4.4.2) we finally obtain:

$$\dot{n}_A = \beta_{A,l} A_i \left(\frac{\beta_{A,g} p_{A,g} + \beta_{A,l} c_{A,l}}{RT} - c_{A,l} \right) = A_i \left(\frac{\frac{p_{A,g}}{H_{A,c}} - c_{A,l}}{\frac{RT}{\beta_{A,g} H_{A,c}} + \frac{1}{\beta_{A,l}}} \right) \quad (4.4.6)$$

This equation formally describes the absorption process as if the mass transfer resistance were confined to the liquid phase. In many cases the mass transfer coefficient in the gas phase, β_g , is indeed much higher than the one in the liquid phase, β_l , or a pure gas is used and the vapor pressure of the liquid is negligible. For these two cases Eq. (4.4.6) reduces to:

$$\dot{n}_A = \beta_{A,l} A_i \left(\frac{p_{A,g}}{H_{A,c}} - c_{A,l} \right) \quad (\text{for } \beta_{A,g} \gg \beta_{A,l}) \quad (4.4.7)$$

The two-film theory certainly lacks physical reality in postulating the existence of stagnant films at the interface, but nevertheless contains the essential features of dissolution and diffusion prior to the transfer in the turbulent bulk of the fluid. It also describes quantitatively quite well the phenomena of mass transfer coupled with a chemical reaction, as discussed in the subsequent chapters. Thereby, the following cases, as depicted in Figure 4.4.2, will be inspected:

- The chemical reaction takes place mostly in the bulk phase of the liquid, and the reaction in the film can be neglected (Figure 4.4.2a, Section 4.4.2).
- The reactants react mostly within the liquid film or (for instantaneous reactions) in a reaction plane in the liquid film or at the interphase (Figure 4.4.2d and e, Section 4.4.3).

Topic 4.4.1 Equations of the two-film theory based on Fick's laws

The two-film theory assumes stagnant films where mass transfer takes place by molecular diffusion. For a planar interphase, each film can be considered as a plane wall with thickness δ . For steady-state conditions, *Fick's second law* leads to:

$$\frac{dc_A}{dt} = 0 = D_A \frac{d^2 c_A}{dx^2} \quad (4.4.8)$$

Twofold integration of Eq. (4.4.8) for the boundary conditions:

$$c_A = c_{A,i} \quad (\text{for } x = 0, i = \text{gas-liquid interphase}) \quad (4.4.9)$$

$$c_A = c_{A,bulk} \quad (\text{for } x = \delta, \text{bulk phase of gas or liquid}) \quad (4.4.10)$$

leads to:

$$c_A(x) D_A = D_A \frac{c_{A,bulk} - c_{A,i}}{\delta} x + D_A c_{A,i} \quad (4.4.11)$$

and differentiation with respect to the coordinate x gives:

$$D_A \frac{dc_A}{dx} = D_A \frac{c_{A,\text{bulk}} - c_{A,i}}{\delta} \quad (4.4.12)$$

Substitution of the term on the left-hand side of Eq. (4.4.12) by *Fick's law* [Eq. (3.1.54)] yields:

$$\frac{\dot{n}_A}{A_i} = D_A \frac{c_{A,i} - c_{A,\text{bulk}}}{\delta} \quad (4.4.13)$$

Comparison with Eq. (4.4.2) gives the mass transfer coefficient based on the film theory:

$$\beta_A = \frac{D_A}{\delta} \quad (4.4.14)$$

Equation (4.4.14) is valid for the gas and the liquid film, that is, $\beta_{A,g} = D_{A,g}/\delta_g$ and $\beta_{A,l} = D_{A,l}/\delta_l$, as already stated by Eqs. (4.4.1) and (4.4.2), respectively.

4.4.2

Mass Transfer with (Slow) Homogeneous Reaction in the Bulk Phase

We take an equimolar irreversible reaction of a gaseous reactant A with a liquid reactant B as an example to examine a slow chemical reaction taking place practically only in the bulk phase of the liquid (Figure 4.4.2a, and Figure 4.4.3):

To illustrate the features of this type of gas–liquid reaction, we assume a first-order reaction with respect to the absorbed gaseous reactant A (or a pseudo-first-order reaction, if the liquid reactant B is present in high excess, so that the concentration gradient of B vanishes). Consequently, the reaction rate of the chemical reaction in the liquid bulk phase is given by:

$$r_{A,V} = k_{A,V} c_{A,i} \quad (4.4.15)$$

For steady-state conditions $r_{A,V}$ expressed in terms of liquid volume ($\text{mol m}^{-3} \text{s}^{-1}$) equals the rate of transport of A through the liquid film for a given interfacial area $A_{i,V}$ ($\text{m}^2 \text{m}^{-3}$):

$$r_{A,V} = \beta_{A,l} A_{i,V} (c_{A,i} - c_{A,l}) \quad (4.4.16)$$

Combination of Eqs. (4.4.15) and (4.4.16) yields the concentration in the bulk phase:

$$c_{A,l} = \frac{\beta_{A,l} A_{i,V}}{k_{A,V} + \beta_{A,l} A_{i,V}} c_{A,i} \quad (4.4.17)$$

Insertion of Eq. (4.4.17) into Eq. (4.4.15) leads to:

$$r_{A,V,\text{eff}} = \frac{k_{A,V} \beta_{A,l} A_{i,V}}{k_{A,V} + \beta_{A,l} A_{i,V}} c_{A,i} = \frac{1}{\frac{1}{k_{A,V}} + \frac{1}{\beta_{A,l} A_{i,V}}} c_{A,i} \quad (4.4.18)$$

Hence, the process is governed by two serial resistances, $1/k_{A,V}$ for the reaction and $1/(\beta_{A,l} A_{i,V})$ for mass transfer, and we denote the rate as the effective rate $r_{A,V,\text{eff}}$ to distinguish it from the case of the absence of any mass transfer resistance ($\beta_{A,l} A_{i,V} \gg k_{A,V}$, i.e., $c_{A,l} \approx c_{A,i}$).

The concentration $c_{A,i}$ at the interface can be expressed by the partial pressure $p_{A,g}$. If the gas-phase transfer resistance can be neglected ($\beta_g \gg \beta_l$, $p_{A,g} \approx p_{A,i}$), *Henry's law* leads to:

$$c_{A,i} = \frac{p_{A,i}}{H_{A,c}} \quad \left(= \frac{p_{A,g}}{H_{A,c}} \text{ for a negligible mass transfer resistance} \right) \quad (4.4.19)$$

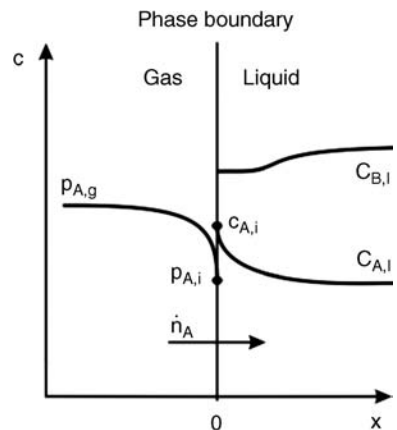


Figure 4.4.3 Two-film concept for a gas–liquid reaction with a relatively slow rate of chemical reaction (thus the reaction mainly takes place in the bulk phase of the liquid).

If the mass transfer resistance in the gas film cannot be neglected, $c_{A,i}$ has to be calculated based on the equations (4.4.1) and (4.4.2) and *Henry's law*:

$$c_{A,i} = \frac{\frac{\beta_{A,g} p_{A,g}}{RT} + \beta_{A,l} c_{A,l}}{\beta_{A,l} + \frac{\beta_{A,g} H_{A,c}}{RT}} \quad (4.4.20)$$

The reaction in the liquid film is negligible, if the characteristic time of diffusion τ_D is much smaller than the characteristic time for reaction τ_R :

$$\tau_D = \frac{\delta_l^2}{D_{A,l}} = \frac{D_{A,l}}{\beta_{A,l}^2} \ll \tau_R \approx \frac{c_{A,i} - c_{A,l}}{r_{A,V}} = \frac{1}{k_{A,V}} \quad (4.4.21)$$

4.4.3

Mass Transfer with Fast or Instantaneous Reaction near or at the Interface

If the chemical reaction is fast compared to the mass transfer of the gaseous reactant A from the gas phase into the liquid phase, the reaction in the liquid film has to be considered. In the border case of an instantaneous reaction, the reactants are converted in a reaction plane located in the liquid film or even directly at the gas-liquid interphase. For illustration, we limit ourselves to a first-order reaction with respect to the gaseous reactant A, for example, we may have a pseudo-first-order reaction if the liquid reactant B is in excess (negligible gradient of B). Initially, we also assume that the mass transfer resistance in the gas film can be neglected (Figure 4.4.4). The equation of the steady state two-film theory then leads to:

$$\frac{dc_A}{dt} = 0 = D_{A,l} \frac{d^2 c_A}{dx^2} - r_{A,V} \quad (4.4.22)$$

Note that Eq. (4.4.22) is derived from Eq. (4.4.8) by the addition of the reaction term.

The general solution of this differential equation is:

$$c_A = C_1 e^{\lambda x} + C_2 e^{-\lambda x} \quad (4.4.23)$$

with:

$$\lambda = \sqrt{\frac{k_{A,V}}{D_{A,l}}} \quad (4.4.24)$$

Introducing the dimensionless so-called Hatta number Ha leads to:

$$Ha = \delta_l \lambda = \delta_l \sqrt{\frac{k_{A,V}}{D_{A,l}}} = \frac{\sqrt{k_{A,V} D_{A,l}}}{\beta_{A,l}} \quad (4.4.25)$$

Ha reflects the ratio of the reaction rate to the rate of mass transfer.

With the boundary conditions [Eqs. (4.4.9) and (4.4.10)], the integration constants are:

$$C_1 = c_{A,i} - C_2 \quad (4.4.26)$$

$$C_2 = \frac{c_{A,i} e^{Ha} - c_{A,l}}{e^{Ha} - e^{-Ha}} \quad (4.4.27)$$

Equations (4.4.23), (4.4.26) and (4.4.27) lead to the course of the concentration of the absorbed gaseous reactant A in the liquid layer (relative to the value at the interphase):

$$\frac{c_A}{c_{A,i}} = \frac{\sinh\left(Ha - Ha \frac{y}{\delta_l}\right) + \frac{c_{A,l}}{c_{A,i}} \sinh\left(Ha \frac{y}{\delta_l}\right)}{\sinh(Ha)} \quad (4.4.28)$$

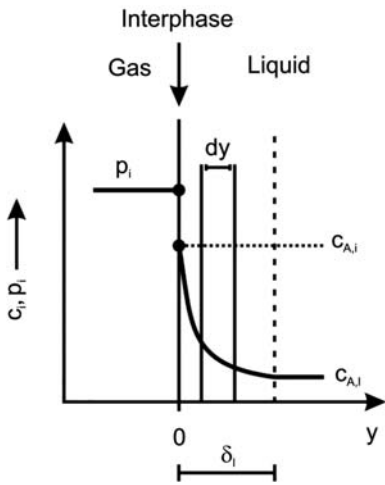


Figure 4.4.4 Illustration of a differential volume element in the liquid film (gas-liquid reaction with negligible mass transfer resistance in the gas film).

To calculate the effective rate $r_{\text{eff},A,V}$ related to the volume of liquid, a mass balance is needed. For an ideal mixed liquid bulk phase ($c_{A,l} = \text{const.}$), the flux of A (\dot{n}_A) from the gas to the liquid through the interface (at $y=0$, Figure 4.4.4) with the volumetric contact area (related to liquid phase) $A_{i,V}$ ($\text{m}^2 \text{ m}^{-3}$) equals the rate of the chemical reaction in the liquid:

$$r_{A,V,\text{eff}} = \frac{(\dot{n}_A)_{y=0}}{V_1} = -D_{A,l} A_{i,V} \left(\frac{dc_A}{dy} \right)_{y=0} \quad (4.4.29)$$

Differentiation of Eq. (4.4.28) with respect to y (for $y=0$, i.e., at the interphase) and insertion into Eq. (4.4.29) yields for the case of a negligible mass transfer resistance in the gas phase:

$$\begin{aligned} r_{A,V,\text{eff}} &= \frac{D_{A,l}}{\delta_{A,l}} A_{i,V} Ha \left[\frac{c_{A,i} \cosh(Ha) - c_{A,l}}{\sinh(Ha)} \right] \\ &= \beta_{A,l} A_{i,V} Ha \left[\frac{\frac{p_{A,g}}{H_{A,c}}}{\tanh(Ha)} - \frac{c_{A,l}}{\sinh(Ha)} \right] \end{aligned} \quad (4.4.30)$$

If the influence of the mass transfer in the gas phase has to be considered, we use:

$$r_{A,V,\text{eff}} = A_{i,V} \frac{Ha}{\tanh(Ha)} \left[\frac{\frac{p_{A,g}}{H_{A,c}} - \frac{c_{A,l} H_{A,c}}{\cosh(Ha)}}{\frac{RT}{\beta_{A,g}} + \frac{H_{A,c}}{\beta_{A,l}} \frac{\tanh(Ha)}{Ha}} \right] \quad (4.4.31)$$

For an infinitely slow chemical reaction rate, Ha approaches zero, and Eq. (4.4.31) equals the equation for the rate of physical absorption, Eq. (4.4.6).

The portion of the liquid phase that is utilized for reaction is defined as:

$$\eta_l = \frac{r_{A,V,\text{eff}}}{r_{A,V,\text{max}}} = \frac{r_{A,V,\text{eff}}}{k_{A,V} c_{A,i}} \quad (4.4.32)$$

Westerterp derived an equation for this degree of utilization η_l of the reaction (liquid) phase based on Ha and the dimensionless Hinterland ratio Hi (Westerterp, van Swaaij, and Beenackers, 1998):

$$\eta_l = \frac{1}{Ha Hi} \left[\frac{(Hi - 1)Ha + \tanh(Ha)}{(Hi - 1)Ha \tanh(Ha) + 1} \right] \quad (4.4.33)$$

with Hi as the ratio of the volume of the liquid phase to the liquid film volume:

$$Hi = \frac{V_1}{V_{\delta,l}} = \frac{V_{\text{bulk},l} + V_{\delta,l}}{V_{\delta,l}} = \frac{\beta_{A,l}}{A_{i,V} D_{A,l}} \quad (4.4.34)$$

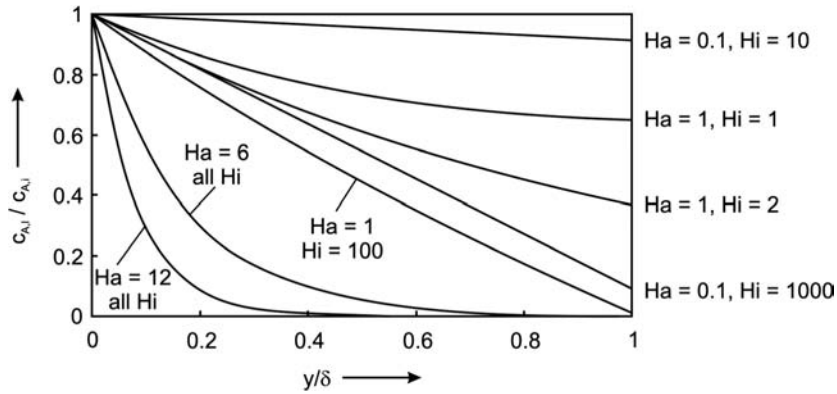
Westerterp, van Swaaij, and Beenackers (1998) also developed an equation for the ratio of the concentration at the interphase to that in the bulk phase (Westerterp, van Swaaij, and Beenackers, 1998):

$$\frac{c_{A,l}}{c_{A,i}} = \frac{1}{Ha(Hi - 1)\sinh(Ha) + \cosh(Ha)} \quad (4.4.35)$$

Combination of Eqs. (4.4.35) and (4.4.28) yields the concentration profile in the liquid film for reactant A, as depicted in Figure 4.4.5 for selected combinations of Ha and Hi .

The degree of utilization of the liquid phase is favored by good mixing (high value of Hi) and a slow rate of the chemical reaction (small value of Ha) (Figure 4.4.6).

Figure 4.4.5 Influence of the Hinterland ratio (Hi) and the Hatta number (Ha) on the concentration profile in the liquid mass transfer film for a first-order reaction of gaseous reactant A according to Eqs. (4.4.35) and (4.4.28).



For small values of Ha [<0.1 , i.e., $\tanh(Ha)/Ha \approx 1$], Eq. (4.4.33)) yields:

$$\eta_l = \frac{1}{Hi} \left[\frac{(Hi - 1) + \frac{\tanh(Ha)}{Ha}}{(Hi - 1)Ha^2 \frac{\tanh(Ha)}{Ha} + 1} \right] \approx \frac{1}{Hi} \left[\frac{(Hi - 1) + 1}{(Hi - 1)Ha^2 + 1} \right]$$

$$= \frac{1}{(Hi - 1)Ha^2 + 1} \quad (4.4.36)$$

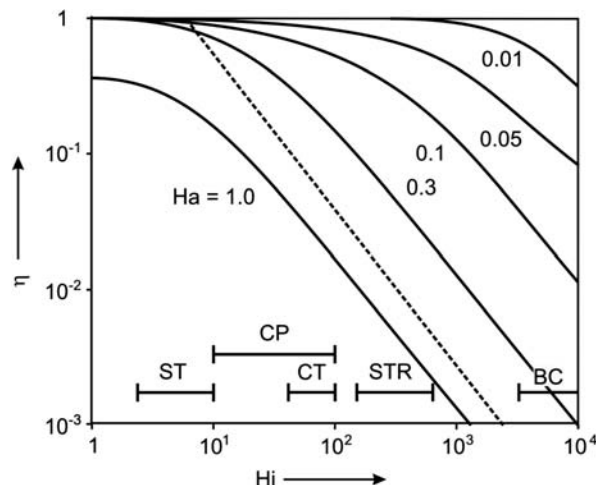
The utilization degree approaches unity, if the Hinterland ratio is less than about 10:

$$\eta_l \geq \frac{1}{(10 - 1)0.1^2 + 1} \approx 0.9 \quad (\text{for } Hi < 10 \text{ and } Ha < 0.1) \quad (4.4.37)$$

and then a better mixing by the use of a respective reactor (see Figure 4.4.6) is useless. To the contrary, Hi must be high for fast reactions (large Ha) to approach a utilization degree of unity, for example, adjusted by a large contact area. Hi depends strongly on the energy input per unit volume by the stirrer. Consequently, there is an optimization problem, as the costs of stirring usually exceed the costs of a larger reactor. Thus a larger reactor with poor utilization of the bulk phase is often cheaper than a smaller unit with intensive stirring.

We now determine the portion of conversion achieved in the liquid bulk phase $X_{A,bulk}$ compared to the total conversion $X_{A,t}$ in the bulk phase and in the liquid

Figure 4.4.6 Influence of the Hinterland ratio (Hi) and Hatta number (Ha) on the degree of utilization of the liquid phase (ST: spray tower, CP: column with packing, CT column with trays, STR: stirred tank reactor, BC bubble column; region above dashed line: more than 80% of conversion takes place in the bulk phase of the liquid). Adapted from Emig and Klemm (2005).



film ($= X_{A,\text{bulk}} + X_{A,\delta}$):

$$\begin{aligned} \frac{X_{A,\text{bulk},l}}{X_{A,t,l}} &= \frac{r_{A,\text{bulk}} V_{\text{bulk},l}}{\bar{r}_{A,V\delta} V_{\delta,l} + r_{A,\text{bulk}} V_{\text{bulk},l}} \approx \frac{k_{A,V} c_{A,l} V_{\text{bulk},l}}{k_{A,V} \left[\frac{c_{A,i} + c_{A,l}}{2} V_{\delta,l} + c_{A,l} V_{\text{bulk},l} \right]} \\ &= \frac{\frac{c_{A,l}}{c_{A,i}} (Hi - 1)}{\frac{1}{2} + (Hi - \frac{1}{2}) \frac{c_{A,l}}{c_{A,i}}} \end{aligned} \quad (4.4.38)$$

The expression for the total conversion [denominator of (Eq. (4.4.38)) and Eqs. (4.4.32) and (4.4.34) lead to:

$$\begin{aligned} \eta_l &= \frac{k_{A,V} \left[\frac{(c_{A,i} + c_{A,l})}{2} V_{\delta,l} + c_{A,l} V_{\text{bulk},l} \right]}{k_{A,V} c_{A,i} V_1} = \frac{\frac{1}{2} + \frac{1}{2} \frac{c_{A,l}}{c_{A,i}} + \frac{c_{A,l}}{c_{A,i}} (Hi - 1)}{Hi} \\ &\Rightarrow \frac{c_{A,l}}{c_{A,i}} = \frac{\eta_l Hi - \frac{1}{2}}{Hi - \frac{1}{2}} \end{aligned} \quad (4.4.39)$$

Insertion of Eq. (4.4.39) into Eq. (4.4.38) then finally yields:

$$\frac{X_{A,\text{bulk},l}}{X_{A,t,l}} = \frac{\left[\frac{2\eta_l Hi - 1}{2Hi - 1} \right] (Hi - 1)}{\frac{1}{2} + (Hi - \frac{1}{2}) \left[\frac{2\eta_l Hi - 1}{2Hi - 1} \right]} \quad (4.4.40)$$

Equation (4.4.40) determines η_l as a function of Hi for a given value of $X_{A,\text{bulk},l}$ compared to the overall conversion in the liquid $X_{A,t,l}$; for example, for a value of 80% this leads to:

$$\eta_l \geq \frac{5(Hi - 1)}{2Hi^2 - 6Hi} \quad \left(\text{for } \frac{X_{A,\text{bulk},l}}{X_{A,t,l}} \geq 0.8 \right) \quad (4.4.41)$$

This condition (always valid for $Hi \leq 5$) is depicted in Figure 4.4.6 as a dashed line.

If the reaction in the liquid film leads to an increase of dc_A/dy at the interface, the mass transfer of the absorbed gas from the interface into the liquid phase is enhanced compared to the absence of reaction. This effect is considered by the enhancement factor E :

$$E = \frac{(\dot{n}_A)_{\text{with reaction}}}{(\dot{n}_A)_{\text{without reaction}}} \quad (4.4.42)$$

For a negligible transfer resistance in the gas phase, Eqs. (4.4.16) and (4.4.30) yield:

$$E = \frac{\beta_{A,l} A_i H_a \left[\frac{c_{A,i} \cosh(H_a) - c_{A,l}}{\sinh(H_a)} \right]}{\beta_{A,l} A_i (c_{A,i} - c_{A,l})} = \frac{H_a \left[\frac{c_{A,i}}{\tanh(H_a)} - \frac{c_{A,l}}{\sinh(H_a)} \right]}{c_{A,i} - c_{A,l}} \quad (4.4.43)$$

The enhancement factor depends on the Hatta number and thus on the reaction rate:

For a **slow reaction** ($H_a < 0.3$, see Figure 4.4.2a), the mass transfer rate is not enhanced, and E approaches unity [$\sinh(H_a)$ and $\tanh(H_a) \approx H_a$ for $H_a < 0.3$].

For a **medium reaction rate** ($0.3 < H_a < 3$, see Figure 4.4.2b), the rate of mass transfer is enhanced, and E is given by [$c_{A,i} \gg c_{A,l}$ and $c_{A,l}/\tanh(H_a) \gg c_{A,l}/\sinh(H_a)$]:

$$\begin{aligned} E &\approx H_a \left[\frac{c_{A,i}}{\tanh(H_a)} \right] \frac{1}{c_{A,i}} \\ &= \frac{H_a}{\tanh(H_a)} \quad (\text{for } 0.3 < H_a < 3, \text{ medium reaction rate}) \end{aligned} \quad (4.4.44)$$

For a **fast reaction** ($3 < Ha < 10 E_{\max}$) the conversion mostly takes place in the liquid film (Figure 4.4.2c), and E is given by [$\tanh(Ha) \approx 1$ for $Ha > 3$]:

$$E = Ha \quad (\text{for } 3 < Ha < 10 E_{\max}, \text{ fast reaction}). \quad (4.4.45)$$

For an **instantaneous reaction**, the absorbed reactant A and the liquid reactant B do not coexist, and the conversion takes place at a reaction plane with a distance γ_{RP} ($< \delta_l$) from the interphase (Figure 4.4.2d). For a reaction $A(g) + B(l) \rightarrow C(l)$, the mass transfer rates are:

$$\dot{n}_A = A_i \frac{D_{A,l} c_{A,i}}{\gamma_{RP}} \quad (4.4.46)$$

$$\dot{n}_B = A_i \frac{D_{B,l} c_{B,l}}{\delta_l - \gamma_{RP}} \quad (4.4.47)$$

For steady-state conditions, both fluxes are equal, and γ_{RP} can be eliminated, which yields:

$$\dot{n}_B = \dot{n}_A = A_i \frac{D_{B,l} c_{B,l}}{\delta_l - \frac{D_{A,l} c_{A,i}}{\dot{n}_B}} \Rightarrow r_{V, \text{eff}} = \frac{\dot{n}_B}{V_1} = A_i v \frac{D_{B,l} c_{B,l} + D_{A,l} c_{A,i}}{\delta_l} \quad (4.4.48)$$

The definition of the enhancement factor [Eq. (4.4.42)] then yields:

$$E = E_{\max} = \frac{\frac{D_{B,l} c_{B,l} + D_{A,l} c_{A,i}}{\delta_l}}{\frac{D_{A,l} c_{A,i}}{\delta_l}} = 1 + \frac{D_{B,l} c_{B,l}}{D_{A,l} c_{A,i}} \quad (\text{for an instantaneous reaction}) \quad (4.4.49)$$

Figure 4.4.7 shows the overall picture of E for different values of Ha and E_{\max} .

In most cases the diffusion coefficients are of the same order of magnitude, and the maximum enhancement factor E_{\max} is then determined only by the ratio of the concentrations $c_{B,l}/c_{A,i}$. With increasing concentration of the liquid reactant ($c_{B,l}$), the reaction plane moves towards the interface, and the effective rate is then finally also influenced by the mass transfer on the side of the gas phase ($c_{A,i} < p_{A,g}/H_A$). For steady-state this leads to:

$$\dot{n}_A = \frac{\beta_{A,g}}{RT} A_i (p_{A,g} - p_{A,i}) = \frac{\beta_{A,g}}{RT} A_i (p_{A,g} - H_A c_{A,i}) = E_{\max} \beta_{A,l} A_i c_{A,i} \quad (4.4.50)$$

Figure 4.4.7 Influence of Ha on the enhancement factor E of gas–liquid reactions with negligible mass transfer resistance in the gas phase with $E_{\max} = 1 + D_{B,l} c_{B,l} / (D_{A,l} c_{A,i})$, Eq. (4.4.49), as parameter (to the right of dashed line: $E \approx E_{\max}$). Adapted from Emig and Klemm (2005).

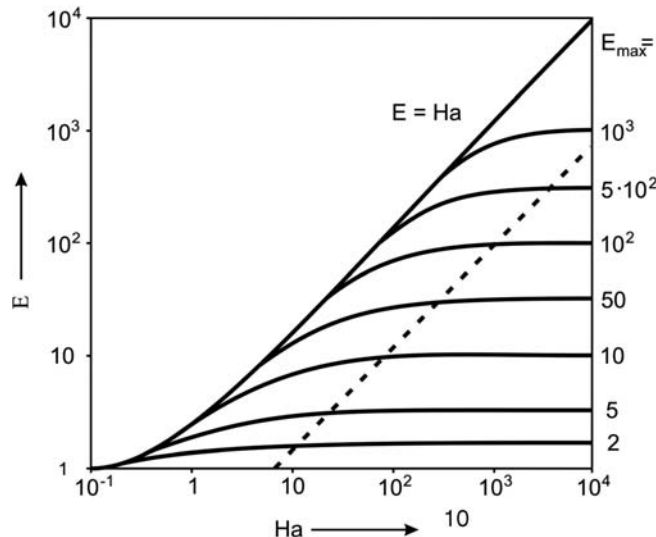


Table 4.4.2 Equations for gas–liquid reactions $A(g) + B(l) \rightarrow C(l)$ according to the two-film theory (first order in A, high excess of liquid reactant B).

Rate-determining step and assumptions	Equation for the effective reaction rate of the conversion of the gaseous reactant A expressed in terms of liquid volume ($\text{mol m}^{-3} \text{s}^{-1}$)
Slow homogeneous reaction in the bulk phase of the liquid	$r_{A,V} = \frac{1}{\frac{1}{k_V} + \frac{1}{\beta_{A,l} A_{i,V}}} \frac{p_{A,g}}{H_{A,c}}$ [Eqs. (4.4.18) and (4.4.19)]
Reaction in liquid film negligible	
Negligible mass transfer resistance in the gas film	
Slow homogeneous reaction in the bulk phase of the liquid	$r_{A,V} = \frac{\left(\frac{p_{A,g}}{RT} + \frac{\beta_{A,l}}{\beta_{A,g}} c_{A,l} \right)}{\left(\frac{1}{k_V} + \frac{1}{\beta_{A,l} A_{i,V}} \right) \left(\frac{\beta_{A,l}}{\beta_{A,g}} + \frac{H_{A,c}}{RT} \right)}$ [Eqs. (4.4.18) and (4.4.20)]
Reaction in liquid film negligible	
Influence of mass transfer in the gas film	
Reaction in the liquid film cannot be neglected	General solution [Eq. (4.4.30)]:
Negligible mass transfer resistance in the gas film	$r_{A,V,\text{eff}} = \beta_{A,l} A_{i,V} H_a \left[\frac{\frac{p_{A,g}}{H_{A,c}}}{\tanh(H_a)} - \frac{c_{A,l}}{\sinh(H_a)} \right]$
	$H_a < 0.3$ [$\sinh(H_a)$ and $\tanh(H_a) \approx H_a$]:
	$r_{A,V,\text{eff}} = \beta_{A,l} A_{i,V} \left(\frac{p_{A,g}}{H_{A,c}} - c_{A,l} \right)$
	$0.3 < H_a < 3$ [$p_{A,g}/H_a \gg c_{A,l}$ and $(p_{A,g}/H_a)/\tanh(H_a) \gg (c_{A,l})\sinh(H_a)$]:
	$r_{A,V,\text{eff}} = \beta_{A,l} A_{i,V} H_a \left[\frac{\frac{p_{A,g}}{H_{A,c}}}{\tanh(H_a)} \right]$
	$3 < H_a < 10 E_{\max}$ [$\tanh(H_a) \approx 1$ for $H_a > 3$]:
	$r_{A,V,\text{eff}} = \beta_{A,l} A_{i,V} H_a \frac{p_{A,g}}{H_{A,c}}$
Reaction in the liquid film cannot be neglected	General solution (Eq. (4.4.31)):
Influence of mass transfer in the gas film	$r_{A,V,\text{eff}} = A_{i,V} \frac{H_a}{\tanh(H_a)} \left[\frac{\frac{p_{A,g}}{RT} - \frac{c_{A,l} H_a}{\cosh(H_a)}}{\frac{H_{A,c}}{\beta_{A,g}} + \frac{H_{A,c} \tanh(H_a)}{\beta_{A,l} H_a}} \right]$
Instantaneous reaction at a plane in the liquid film	$r_{A,V,\text{eff}} = A_{i,V} (\beta_{B,l} c_{B,l} + \beta_{A,l} c_{A,l})$ [Eq. (4.4.48)]
Negligible mass transfer resistance in the gas film	

Solving Eq. (4.4.50) for the unknown concentration at the interphase ($c_{A,i}$) leads to:

$$\dot{n}_A = \frac{A_i p_{A,g}}{\left(\frac{RT}{\beta_{A,g}} + \frac{H_{A,c}}{E_{\max} \beta_{A,l}} \right)} \quad (4.4.51)$$

If the reaction plane is located at the interface (Figure 4.4.2e), that is, for high value of $c_{B,l}/c_{A,l}$ and thus of E_{\max} , the effective rate is only determined by the mass transfer through the gas film:

$$\dot{n}_A = \frac{\beta_{A,g}}{RT} A_i p_{A,g} \quad (\text{for } c_{B,l}/c_{A,l} \text{ and thus } E_{\max} \gg 1, \text{ i.e., } p_{A,i} \approx 0) \quad (4.4.52)$$

Table 4.4.2 summarizes the equations for the rate of gas–liquid reactions.

Summary of Section 4.4 (take-home messages)

- Interfacial mass transfer processes can be described by the **two-film theory**. Both the gas and the liquid phase can be divided into a stagnant film located near the interface and well-mixed bulk phases without concentration gradients. The two-film theory certainly lacks physical reality in postulating the existence

of stagnant films at the interface, but nevertheless contains the essential features of dissolution and diffusion prior to the transfer in the turbulent bulk of the fluid. It also describes quantitatively quite well the phenomena of mass transfer coupled with a chemical reaction.

- The reaction may take place mostly in the bulk phase of the liquid, and the reaction in the film can be neglected. Alternatively the reactants react mostly within the liquid film or (for **instantaneous reactions**) in a reaction plane in the liquid film or at the interphase.
- Gas–liquid reactions are governed by dimensionless numbers, namely, the **Hatta number** Ha , which reflects the ratio of the reaction rate to the rate of mass transfer, and the **Hinterland ratio** Hi , which is the ratio of the volume of the liquid phase to the liquid film volume.
- If the reaction in the liquid film leads to an increase in the concentration gradient of the reactant at the interface, the mass transfer of the absorbed gas from the interface into the liquid phase is enhanced compared to the absence of reaction. This effect is considered by the enhancement factor E , which depends on Ha . For a **slow reaction** (small Ha), the mass transfer rate is not enhanced. For a **fast reaction**, the conversion mostly takes place in the liquid film. For an **instantaneous reaction**, the absorbed reactant A and the liquid reactant B do not coexist, and conversion takes place at a reaction plane.

4.5

Kinetics of Heterogeneously Catalyzed Reactions

For a reaction to take place on the surface of a solid catalyst, the formation of a surface complex is essential, and the kinetic equation must account for this. In addition, mass and heat transport processes are involved, since the reactants, products, and heat of reaction must be transported to and removed from the surface site, where the reaction between adsorbed atoms or molecules takes place. This may lead to a decrease of the effective rate compared to the absence of any transport limitations.

An overview of the spectrum of factors influencing the rate of heterogeneously catalyzed reactions is given in Section 4.5.1. We will then study in detail the:

- chemical reaction rate on the surface of the catalyst (Section 4.5.2);
- interplay of the chemical reaction and interfacial mass and heat transport from the bulk phase of the fluid to the external surface of the catalyst (Section 4.5.3);
- interplay of chemical reaction and internal mass and heat transport within the porous structure of the catalytic particles (Section 4.5.4);
- simultaneous occurrence of interfacial and internal transport effects (Section 4.5.5);
- influence of mass transport on the selectivity (Section 4.5.6).

“Operating manual” for beginners and intermediate learners:

For a basic understanding of heterogeneously catalyzed reactions, start with the Sections 4.5.1 and 4.5.2, where the kinetics will be treated without the influence of mass and heat transfer. Then study the influence of external and internal mass transfer (Sections 4.5.3.1 and 4.5.4.1), and the situation when both phenomena occur simultaneously (Section 4.5.5).

“Operating manual” for advanced learners:

Heat and mass transfer to and within a porous particle are in many cases coupled processes. Consequently, advanced learners should also study the additional influence of heat transfer on the effective rate of a heterogeneously catalyzed reaction (Sections 4.5.3.2 and 4.5.4.2).



Various shaped solid catalysts. BASF, Germany, from Hagen, 1999.

Table 4.5.1 Specific surface areas of catalysts and support materials (Hagen, 1999) and typical prices (oral communication from Süd Chemie, 2010; for the Pt wire, the price of pure Pt from Sept. 2012 is given).

Catalyst/support	Surface area (m ² g ⁻¹)	Typical price (€ kg ⁻¹) (2010) ^{a)}
Zeolite for cracking processes	1000	
Activated carbon	200–2000	
Silica gel, aluminosilicates	200–700	
Al ₂ O ₃	50–350	
Ni/Al ₂ O ₃ (steam reforming, hydrogenation)	250	30
CoMo/Al ₂ O ₃ (hydrodesulfurization)	200–300	20
Fe-Al ₂ O ₃ -K ₂ O (NH ₃ synthesis)	10	20
V ₂ O ₅ (partial oxidation, e.g., phthalic anhydride synthesis)	1	40
Noble metal/support	0–10	For noble metal catalysts, the price may be up to several 100 € kg ⁻¹
Pt wire (NH ₃ oxidation)	0.003	50,000

a) Note that the volume of a fixed bed may reach values of some hundred m³, for example, for refinery processes like desulfurization (Chapter 6.8). Thus, the investment costs for the catalyst may be high, for example, €2 million for a fixed bed of 100 m³, a bulk density of 1000 kg m⁻³, and a catalyst price of €20 kg⁻¹.

4.5.1

Spectrum of Factors Influencing the Rate of Heterogeneously Catalyzed Reactions

The typical surface area of catalysts and support materials is in the range 10–1000 m² g⁻¹ (Table 4.5.1). If the term surface area is used in the context of solid catalysts, this concerns mostly only the internal surface. The external surface is usually negligible and is – if at all – only important for a particle size of less than 10 µm, as shown in Figure 4.5.1 by the plot of external area $A_{m,ex}$ versus diameter of spherical particles, where $A_{m,ex}$ is given by:

$$\nabla \quad A_{m,ex} = \frac{\pi d_p^2}{\frac{\pi}{6} d_p^3 \rho_p} = \frac{6}{d_p \rho_p} \quad (4.5.1)$$

Even for a still low value of the external surface area of 1 m² g⁻¹, a diameter of 6 µm would be needed for a particle density of 1000 kg m⁻³, but such small particles are technically mostly irrelevant with regard to the high pressure drop and adhesion of small particles. Thus, for most solid catalysts, the surface area is

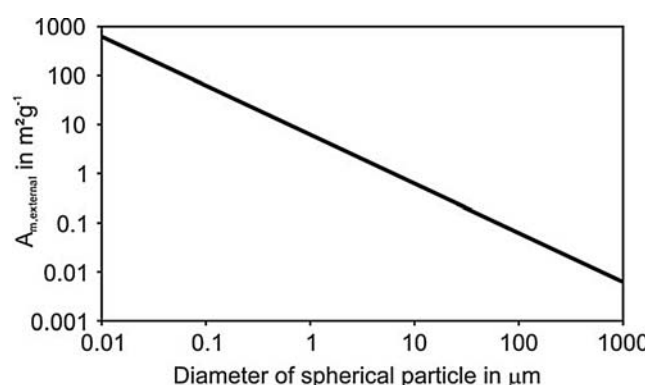


Figure 4.5.1 Specific external surface areas of spherical particles (with a density of 1 g cm⁻³).

Table 4.5.2 Classification of pores of a catalyst.

Notation	Pore diameter (nm)
Macropores	>50
Mesopores	2–50
Micropores	<2
Submicropores	<1

determined by the internal surface area of the porous structure, which consists of macro-, meso-, micro-, and submicropores (Table 4.5.2).

An exception where the surface area is generated solely by the external surface is NH₃ oxidation to NO, an important reaction step in the production of nitric acid (Section 6.4). In this case, a non-porous Pt-gauze with a wire diameter of 60 µm is used, and $A_{m,\text{ex}}$ is then given by $4/(d_{\text{wire}}\rho_{\text{Pt}}) = 4/(60 \mu\text{m} \times 23 \text{ g cm}^{-3}) = 0.003 \text{ m}^2 \text{ g}^{-1}$.

To get a better picture of the pore dimensions, it is interesting to calculate the mean pore diameter $d_{\text{pore,mean}}$ and the (hypothetical) overall pore length L_{pore} . Topic 4.5.1 shows that for a catalyst with 1000 m² g⁻¹ internal surface area we get impressive values of $d_{\text{pore,mean}}$ of only 2 nm and of L_{pore} of $160 \times 10^6 \text{ km g}^{-1}$. Thus the overall pore length of only 1 g of catalyst is equivalent to the distance between the earth from the sun (150 million km!).

Topic 4.5.1 Pore diameter and overall pore length of a porous solid (catalyst)

Assuming pores of cylindrical shape with a mean diameter $d_{\text{pore,mean}}$ we obtain:

$$\frac{V_{\text{pore}}}{A_{\text{pore}}} = \frac{L_{\text{pore}} \frac{\pi d_{\text{pore,mean}}^2}{4}}{L_{\text{pore}} \pi d_{\text{pore,mean}}} = \frac{d_{\text{pore,mean}}}{4}$$

Usually, the mass specific values of the internal surface area and pore volume (A_m and $V_{\text{pore,m}}$) are determined, and with the porosity ε_p and particle density ρ_p we obtain:

$$\frac{V_{\text{pore}}}{A_{\text{pore}}} = \frac{V_{\text{pore,m}}}{A_m} = \frac{\frac{\varepsilon_p}{\rho_p}}{\frac{\rho_p}{A_m}} = \frac{d_{\text{pore,mean}}}{4}$$

If we now take a catalyst (or a porous solid) with a porosity ε_p of 0.5, a particle density ρ_p of 1 g cm⁻³, and an internal surface area A_m of 1000 m² g⁻¹ as an example, we obtain a mean pore diameter $d_{\text{pore,mean}}$ of 2 nm. The specific pore length $L_{\text{pore,m}}$ (per unit mass) is:

$$\begin{aligned} L_{\text{pore,m}} &= \frac{V_{\text{pore,m}}}{A_{\text{pore}}} = \frac{4V_{\text{pore,m}}}{\pi d_{\text{pore,mean}}^2} \\ &= \frac{4 \frac{\varepsilon_p}{\rho_p}}{\pi d_{\text{pore,mean}}^2}, \text{ which yields a value of } 160 \times 10^6 \text{ km g}^{-1} \end{aligned}$$

Apart from the chemical (intrinsic) rate of reaction, the rate in a porous catalyst strongly depends on the accessibility of the active sites dispersed throughout the porous structure. Imagine a catalytic gas-phase reaction of A to B, where the following combined physical and chemical processes can be expected (Figure 4.5.2):

- 1) film diffusion of A from bulk phase through the boundary layer to the external surface;
- 2) diffusion of A into the pores (pore or intraparticle diffusion);
- 3) adsorption of A on the inner surface of the catalyst;
- 4) chemical surface reaction of adsorbed A to adsorbed product B;
- 5) desorption of B from the inner surface into the pores;
- 6) diffusion of B through the porous network structure to the external surface;
- 7) diffusion of B through the boundary layer into the gas phase.

Steps 3–5 are (physico-)chemical processes and depend nearly exponentially on temperature according to *Arrhenius's law* [Eq. (4.3.4)], typically with activation

energies of 20–200 kJ mol⁻¹. Steps 1, 2, 6, and 7 are mass transfer processes with a relatively small influence of temperature compared to chemical processes, for example, for gases the mass transfer is proportional to about $T^{1.75}$ (see Topic 4.5.2 for the influence of temperature on chemical reactions and diffusion).

Any of these steps can be sufficiently slow, relative to others, to control the overall reaction rate. The net (overall) kinetics is called effective kinetics or macrokinetics, in contrast to the kinetics of chemical processes, which is termed intrinsic kinetics or microkinetics.

Thus, by increasing the temperature, the intrinsic chemical rate is accelerated in a much more pronounced fashion than the rate of pore diffusion. Therefore, if the rate constants, which can be regarded as the reciprocal characteristic times, reach the same order of magnitude, the concentration inside the porous pellet starts to drop distinctly. Finally, external mass transfer may become rate controlling, and the reactant concentration already falls off steeply across the boundary layer. Consequently, mass (but also heat) transfer may strongly influence the effective rate of heterogeneously catalyzed reactions (and of gas–solid reactions, Section 4.6). As discussed in the following subchapters, this is considered by using the concept of effectiveness factors.

We can summarize the main aspects that influence the effective rate as follows:

- 1) The intrinsic rate of the chemical reaction is usually the maximum limiting value.
- 2) Pore diffusion resistance may lead to concentration gradients and causes the particle interior to be starved of reactant(s).
- 3) Film diffusion may lead to concentration gradients in the boundary layer. For example, the concentration becomes practically zero at the outer surface, if the intrinsic rate constant (more precisely the effective internal rate constant reflecting the interplay of intrinsic kinetics and pore diffusion) exceeds by far the external mass transfer coefficient.
- 4) Temperature gradients may occur within a particle in the case of a large heat release and limited heat transfer from the interior to the outer surface of the particle.
- 5) Temperature gradients may develop between the outer surface of the catalyst and the main stream of the fluid.

As a rule of thumb, slow reactions are influenced only by factor 1. With increasing intrinsic rate at first factor 2 and then factors 3 and 5 become important. Factor 4 can be omitted in most cases, and is only relevant for strong exothermic reactions. In liquid systems with a high thermal conductivity of the fluid, factor 5 is, mostly, also negligible.

Topic 4.5.2 Apparent activation energy of diffusion processes

If we want to compare the temperature dependence of a chemical reaction with that of diffusion, we have to reinterpret the influence of temperature on the diffusion coefficient in terms of Arrhenius's law with an apparent activation energy $E_{A,\text{app}}$:

$$D \sim e^{-\frac{E_{A,\text{app}}}{RT}}$$

Diffusion of gases: The diffusion coefficient of most gases is proportional to $T^{1.75}$, and so we have:

$$\begin{aligned} T^{1.75} &\sim e^{-\frac{E_{A,\text{app,g}}}{RT}} \Rightarrow \left(\frac{T_1}{T_2}\right)^{1.75} = e^{-\frac{E_{A,\text{app,g}}}{R} \left(\frac{1}{T_1} - \frac{1}{T_2}\right)} \\ &\Rightarrow E_{A,\text{app}} \approx 1.75 R \ln\left(\frac{T_1}{T_2}\right) \left(\frac{1}{T_2} - \frac{1}{T_1}\right)^{-1} \end{aligned}$$

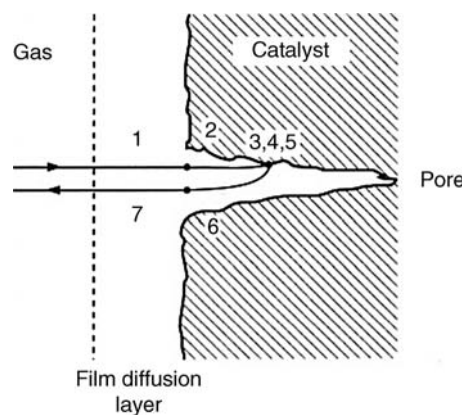


Figure 4.5.2 Steps of a heterogeneously catalyzed gas reaction (Hagen, 1999).

For 100 °C (373 K) ($=T_1$ and $T_2 = T_1 + 10$ K) as an example of a relatively low temperature for gas-phase reactions and 1100 °C (1373 K) as an example for a high temperature, we obtain values of the apparent activation energy $E_{A,\text{app}}$ of 5 and 20 kJ mol⁻¹, which is an order of magnitude lower than the intrinsic activation energies of chemical reactions.

Diffusion of liquids: The diffusion coefficient of liquids is proportional to T/μ , and the viscosity μ depends on temperature; for example, for octane we have (Gmehling and Brehm, 1996):

$$D_{\text{octane, liquid}} \sim \frac{T}{\mu_{\text{octane, liquid}}} \sim \frac{T}{e^{\frac{1070}{T}}} = Te^{-\frac{1070}{T}}$$

and in terms of an exponential function with an apparent activation energy $E_{A,\text{app}}$ we obtain:

$$\begin{aligned} Te^{-\frac{1070}{T}} &\sim e^{-\frac{E_{A,\text{app, octane, liquid}}}{RT}} \Rightarrow E_{A,\text{app, octane, liquid}} \\ &\approx R \ln\left(\frac{T_1}{T_2}\right) \left(\frac{1}{T_2} - \frac{1}{T_1}\right)^{-1} + 1070R \end{aligned}$$

Therefore, if we take temperatures of 0 °C (273 K) and 300 °C (573 K) ($=T_1$ and $T_2 = T_1 + 10$ K) to characterize the typical temperature range of liquid phase reactions, we obtain values of the apparent activation energy $E_{A,\text{app}}$ of octane diffusion in a range of 11 to 14 kJ mol⁻¹.

Usually, the rate of a catalyzed reaction is related to the mass of a catalyst, although one may also relate the rate to the volume or surface of a catalyst (Topic 4.5.3).

Topic 4.5.3 Different forms and units of reaction rates

For heterogeneously catalyzed reactions, the reaction rate may be related to the mass of the catalyst, to the surface area, or to the volume. It is, therefore, always important to use an exact definition, for example, if mass related and volume related reaction rates have to be compared. For illustration, we use a simple heterogeneously catalyzed first-order reaction of compound A taking place in a tubular fixed bed reactor with a continuous and constant throughput of A, that is, the flux of A (\dot{n}_A in mol s⁻¹) changes in the axial direction. The catalyst bed has a volume V_R , the total mass of the catalyst is m_{cat} , the (internal) surface area of the porous catalyst related to mass is A_m (m² kg⁻¹). If the catalyst consists of an inert support coated with an active compound (e.g., a noble metal), m_{act} represents the mass of the active species. We may now use the following definitions for the reaction rate:

$$r_{V,R} = -\frac{d\dot{n}_A}{dV_R} = k_{V,R} c_A \quad \text{with } r_{V,R} \text{ in mol m}_{\text{reactor}}^{-3} \text{s}^{-1} \text{ and } k_{V,R} \text{ in s}^{-1}$$

$$r_{V,\text{cat}} = -\frac{d\dot{n}_A}{dV_{\text{cat}}} = k_{V,\text{cat}} c_A \quad \text{with } r_{V,\text{cat}} \text{ in mol m}_{\text{cat}}^{-3} \text{s}^{-1} \text{ and } k_{V,\text{cat}} \text{ in s}^{-1}$$

$$r_{m,\text{cat}} = -\frac{d\dot{n}_A}{dm_{\text{cat}}} = k_{m,\text{cat}} c_A \quad \text{with } r_{m,\text{cat}} \text{ in mol kg}_{\text{cat}}^{-1} \text{s}^{-1} \text{ and } k_{m,\text{cat}} \text{ in m}^3 \text{ kg}_{\text{cat}}^{-1} \text{s}^{-1}$$

$$r_{m,\text{act}} = -\frac{d\dot{n}_A}{dm_{\text{act}}} = k_{m,\text{act}} c_A \quad \text{with } r_{m,\text{act}} \text{ in mol kg}_{\text{act}}^{-1} \text{s}^{-1} \text{ and } k_{m,\text{act}} \text{ in m}^3 \text{ kg}_{\text{act}}^{-1} \text{s}^{-1}$$

$$r_A = -\frac{d\dot{n}_A}{dA_{\text{cat}}} = k_A c_A \quad \text{with } r_A \text{ in mol m}^{-2} \text{s}^{-1}, k_A \text{ in m}^3 \text{ m}^{-2} \text{s}^{-1} \text{ and } A_{\text{cat}} = A_m m_{\text{cat}}$$

The different rate constants are then related by:

$$k_{V,\text{reactor}} = k_{V,\text{cat}} \frac{V_{\text{cat}}}{V_R} = k_{m,\text{cat}} \frac{m_{\text{cat}}}{V_R} = k_{m,\text{act}} \frac{m_{\text{act}}}{V_R} = k_A A_m \frac{m_{\text{cat}}}{V_R}$$

If we use the porosity (voidage) of the packed bed (ε), the bulk density (ρ_b), and the weight fraction of the active compound w_{act} ($= m_{\text{act}}/m_{\text{cat}}$ with $m_{\text{cat}} = m_{\text{act}} + m_{\text{support}}$) we obtain:

$$k_{V,\text{reactor}} = k_{V,\text{cat}}(1 - \varepsilon) = k_{m,\text{cat}}\rho_b = k_{m,\text{act}}w_{\text{act}}\rho_b = k_A A_m \rho_b$$

To characterize the activity of industrial catalysts, $k_{m,\text{cat}}$ is mostly used, whereas $k_{m,\text{act}}$ and k_A are mainly used in research; for example, to compare different catalysts with different internal surface area or mass fraction of active metal. The rate constant related to reactor volume ($k_{V,R}$) is usually not used in catalysis but, instead, for homogeneous reactions, while the rate constant related to catalyst (particle) volume $k_{V,\text{cat}}$ is mainly used to derive expressions accounting the influence of pore diffusion (Section 4.5.4).

4.5.2

Chemical Reaction Rate: Surface Kinetics

4.5.2.1 Sorption on the Surface of Solid Catalysts

The first step of the chemical reaction on a solid catalyst is always the sorption of at least one reactant, since this is the precondition for any reaction catalyzed by a solid. (Subsequently, we only consider gas-phase reactions, although the equations are also applicable to liquid-phase systems.)

It is necessary to discriminate between physisorption (*van der Waals* adsorption) and chemisorption, although there is somehow smooth transition and no strict borderline between both cases. Physisorption is considered as non-specific for a surface, comparable to condensation, whereas chemisorption is surface specific and comparable to a chemical reaction.

We have to realize that only the concentration in the bulk phase is measurable. Therefore, the relation between the unknown concentration at the surface and the measurable concentration in the fluid is needed to describe the surface reaction rate. These relations were surveyed in Section 3.3.5. In the following, we only recall Langmuir's adsorption isotherm as an important example of such a relationship. This isotherm describes the dimensionless coverage θ_A of the surface with species A relative to the coverage with a monolayer for a given partial pressure. If only reactant A is adsorbed we have:

!
$$\theta_A = \frac{K_{\text{ads},A} p_A}{1 + K_{\text{ads},A} p_A} \quad (3.3.39)$$

If two reactants A and B are adsorbed, Langmuir's adsorption isotherm becomes:

!
$$\theta_A = \frac{K_{\text{ads},A} p_A}{1 + K_{\text{ads},A} p_A + K_{\text{ads},B} p_B} \quad (3.3.62)$$

Adsorption isotherms – due to the assumptions made – are only coarse approximations but serve as a formal structure to establish rate equations. In most cases, the values of the constants $K_{\text{ads},i}$ are determined by adaptation to kinetic experiments.

4.5.2.2 Rate Equations for Heterogeneously Catalyzed Surface Reactions

The adsorbed reactant may react by itself, with other adsorbed reactants, or with reactants from the gas phase. For formulation of overall rate equations, the individual partial steps are considered as elementary reactions of an overall reaction scheme. It is difficult – frequently impossible – to derive from the rates of

adsorption, surface reaction, desorption, and so on a comprehensive analytic expression for the overall rate. We have to fall back on approximation, that is, to the concept of the rate-determining step to derive manageable rate equations. Assuming that sorption of all species is in equilibrium, the following equations are derived for mono- and bimolecular gas-phase reactions.

Monomolecular Mechanism This, the simplest, mechanism is based on the assumptions that we have a simple A-to-B reaction and that the reacting species A is adsorbed on the surface according to the *Langmuir isotherm*, which leads to the rate equation:

$$\bullet \quad r_A = k_s \theta_A = \frac{k_s K_{\text{ads},A} p_A}{1 + K_{\text{ads},A} p_A} \quad (4.5.2)$$

Of course, the concentration in the gas phase can also be used instead of the partial pressure. Note that the term $k_s K_{\text{ads},A}$ is an apparent rate constant, whereas the actual rate constant of the surface reaction (here the assumed rate-determining step) is k_s . Hence, the apparent activation energy is given by the term $E_A + \Delta_{\text{ads}}H$, and the apparent activation energy is lower than the actual one, if we consider that adsorption is exothermic ($\Delta_{\text{ads}}H < 0$):

$$k_s K_{\text{ads},A} = k_{s,0} e^{\left(\frac{-E_A}{RT}\right)} K_{\text{ads},A,0} e^{\left(\frac{-\Delta_{\text{ads}}H}{RT}\right)} = k_{s,0} K_{\text{ads},A,0} e^{\left[\frac{-(E_{A,s} + \Delta_{\text{ads}}H)}{RT}\right]} \\ = k_{A,0,\text{app}} e^{\left(\frac{-E_{A,\text{app}}}{RT}\right)} \quad (4.5.3)$$

The limiting cases of Eq. (4.5.2) lead to rate equations formally first- and zero-order:

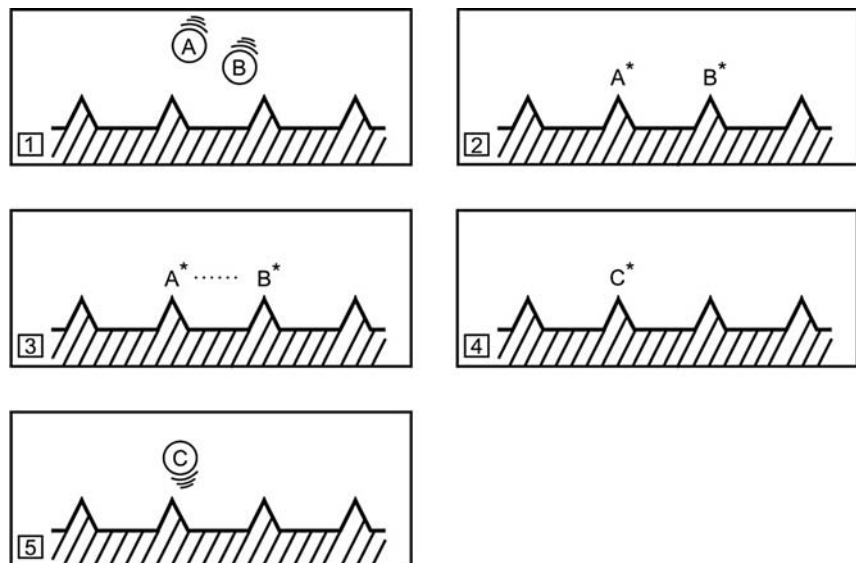
$$r_A \approx k_s K_{\text{ads},A} p_A \quad (\text{for } K_{\text{ads},A} p_A \ll 1) \quad (4.5.4a)$$

$$r_A \approx k_s \quad (\text{for } K_{\text{ads},A} p_A \gg 1) \quad (4.5.4b)$$

Therefore, experiments with varied pressures of the reactants lead to determination of the adsorption constant $K_{\text{ads},A}$ and of $\Delta_{\text{ads}}H$ (high partial pressure experiments) as well as of the actual rate constant k_s and the activation energy E_A (low partial pressure experiments), at least if the limiting cases are almost reached or can at least be reached accurately by extrapolation.

Langmuir–Hinshelwood Mechanism (1921) This bimolecular mechanism (Figure 4.5.3) is based on the assumption that both reactants (A and B) are adsorbed

Figure 4.5.3 Langmuir–Hinshelwood mechanism.
Adapted from Hagen (1999).



on the surface (equilibrium) according to *Langmuir*, Eq. (3.3.62), which leads to:

$$r_A = k_s \theta_A \theta_B = k_s \frac{K_{\text{ads},A} K_{\text{ads},B} p_A p_B}{(1 + K_{\text{ads},A} p_A + K_{\text{ads},B} p_B)^2} \quad (4.5.5)$$

For a constant partial pressure of one reactant, the rate passes a maximum, if the partial pressure of the second reactant is increased, as shown in Figure 4.5.4 for a variation of p_A and constant p_B . The maximum rate is reached if the whole surface is covered and if the value of the individual surface coverage is 0.5, which maximizes the term $\theta_A \theta_B$.

Eley–Rideal Mechanism (1943) If only one reactant A is adsorbed on the surface of the catalyst and reacts with the second species B coming from the gas phase (Figure 4.5.5), the following equation for the rate is derived:

$$r_A = k_s \theta_A p_B = k_s \frac{K_{\text{ads},A} p_A p_B}{1 + K_{\text{ads},A} p_A} \quad (4.5.6)$$

The limiting cases of Eq. (4.5.6) formally lead to second- and first-order rate equations:

$$r_A \approx k_s K_{\text{ads},A} p_A p_B \quad \begin{array}{l} \text{(first order in A and B, i.e. in total} \\ \text{second order for } K_{\text{ads},A} p_A \ll 1 \end{array} \quad (4.5.7a)$$

and:

$$r_A \approx k_s p_B \quad \text{(first order in B, zero order in A for } K_{\text{ads},A} p_A \gg 1\text{)} \quad (4.5.7b)$$

Therefore, for a constant partial pressure of reactant B (gas phase), the rate asymptotically approaches a constant maximal value, if the partial pressure of A is increased (Figure 4.5.6).

Langmuir–Hinshelwood–Hougen–Watson (LHHW) Rate Equations (1947) *Hougen* and *Watson* analyzed several types of catalytic reactions with different rate-determining steps (adsorption, surface reaction), different types of adsorption (one or more species, dissociative or molecular adsorption), and different types of reactions (mono- or bimolecular, reversible or irreversible). They derived a general rate equation based on three terms:

$$r = \frac{\text{(kinetic term)(driving force or displacement from equilibrium)}}{\text{(adsorption term)}^n} \quad (4.5.8)$$

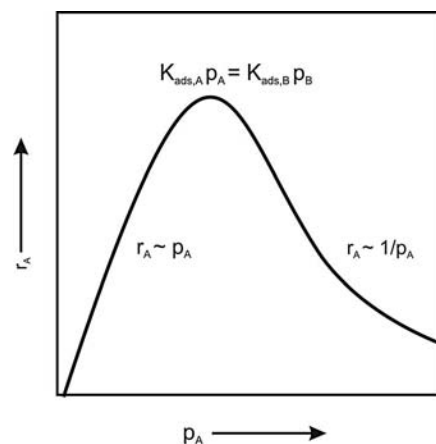


Figure 4.5.4 Influence of the partial pressure of reactant A on the rate of a catalyzed bimolecular reaction according to the Langmuir–Hinshelwood mechanism. (Note that for a constant partial pressure p_B , the maximum value of r_A is reached for the condition of $K_{\text{ads},A} p_A = 1 + K_{\text{ads},B} p_B$, that is, only for $K_{\text{ads},A} p_A \gg 1$, the condition for $r_{A,\max}$ reads as $K_{\text{ads},A} p_A \approx K_{\text{ads},B} p_B$.)

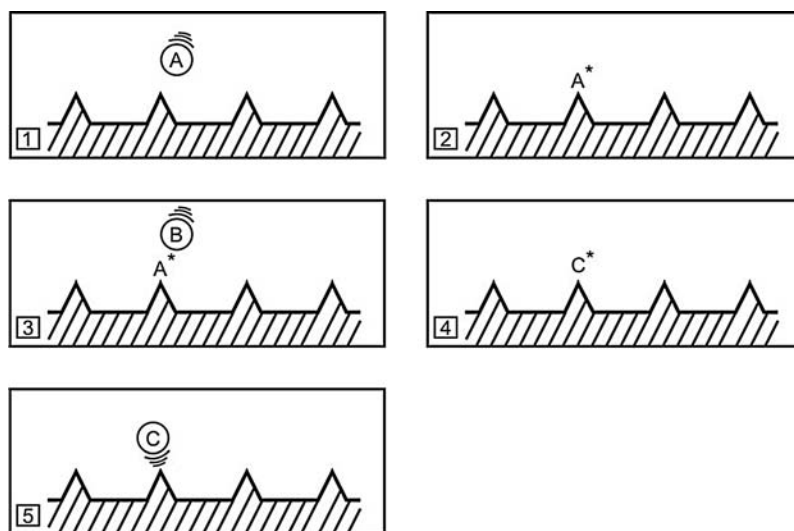


Figure 4.5.5 Eley–Rideal mechanism. Adapted from Hagen (1999).

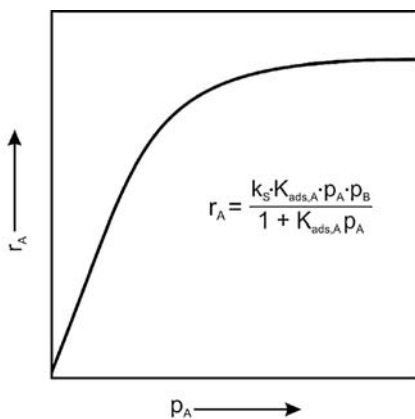


Figure 4.5.6 Influence of the partial pressure of the adsorbed reactant on the rate of a catalyzed bimolecular gas-phase reaction according to the Eley–Rideal mechanism.

The kinetic term considers the rate coefficient of the rate-determining step and the adsorption equilibrium constants. The driving force accounts for the displacement from equilibrium. For an irreversible reaction the driving force only considers the partial pressures of the reactants and the reaction order(s). For a reversible reaction, we have to consider the difference between the actual partial pressures and the values at equilibrium. The adsorption term considers the coverage of the active sites with adsorbed species and the number n accounts for the number of sites involved (details in Baerns *et al.*, 2006; Ertl, Knoezinger, and Weitkamp, 1997). Here we only consider the following case: (i) the surface reaction of the adsorbed reactants A and B to the product C is the rate-determining step; (ii) the reactants and the product are adsorbed; and (iii) the reaction is reversible (equilibrium constant K_p). Then Eq. (4.5.8) reads as:

$$r_A = \frac{\underbrace{(k_s K_{\text{ads},A} K_{\text{ads},B})}_{\text{Kinetic term}} \underbrace{\left(p_A p_B - p_C \frac{p_0}{K_p} \right)}_{\text{Driving force}}}{\underbrace{\left(1 + K_{\text{ads},A} p_A + K_{\text{ads},B} p_B + K_{\text{ads},C} p_C \right)^2}_{\text{Coverage of surface with adsorbed species}}} \quad (4.5.9)$$

The term for the driving force is derived based on the consideration that this term reflects the displacement from equilibrium partial pressure, which is given by:

$$p_A p_B - p_A^* p_B^* = p_A p_B - p_C \frac{p_0}{K_p} \quad \left(\text{with } K_p = \frac{p_C^* p_0}{p_A^* p_B^*} \right) \quad (4.5.10)$$

For illustration: the term $p_C p_0 K_p^{-1}$ represents the equilibrium partial pressures of the reactants A and B ($p_A^* p_B^*$) for the actual value of the partial pressure of the product C.

As pointed out by Levenspiel (2000), the usual procedure to study the kinetics of surface-catalyzed reactions is to propose a mechanism based on the Langmuir–Hinshelwood–Hougen–Watson (LHHW) model, derive the corresponding equation, and then fit it to the data at hand. If the fit is good, researchers often claim that they have found the actual mechanism. This procedure is questionable, as shown by Topic 4.5.4. It would be better to state that our experimental results are formally described (within the range of the investigated reaction conditions) by the selected kinetic equation (probably out of several possible others).

Topic 4.5.4 Comment on the proposal of a mechanism based on a Langmuir–Hinshelwood–Hougen–Watson (LHHW) model (partly literally from Levenspiel, 2000)

If we propose a reaction mechanism based on a good fit of our data with a LHHW model, we should consider the following suggestion given by Levenspiel (2000):

Spoil sports suggest that this procedure simply represents a curve-fitting exercise, and that before one can claim to have discovered the mechanism one must reject all other plausible mechanisms. Just finding a mechanism that fits the data is not good enough. In addition, with three to eight adjustable parameters, it is not surprising that one can fit the equation to a set of kinetic data. To add weight to their objections, these spoil sports like to quote the statement attributed to the great mathematician Friedrich Gauss which goes “Give me four parameters, and I will draw an elephant for you; with five I will have him raise and lower his trunk and his tail.” In mathematics there is a class of not-too-well-known expressions called animal functions. Here is the four-parameter elephant function:

$$f(\text{elephant}) = \sum_{i=1}^{12} (A + x_i, B + y_i, Cz_i, Dm_i, Dn_i) \quad (4.5.11)$$

in which A = longitude, B = latitude, C = size of elephant, and D = ± 1 .

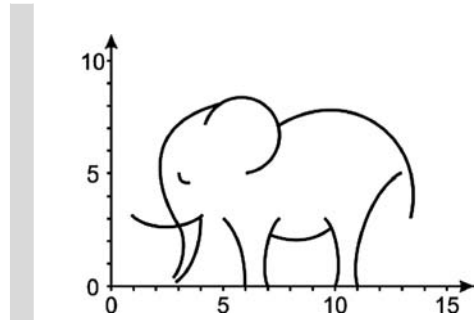
Table 4.5.3 Values of elephant function (x_i and y_i ; centers of arcs of circles with radius z_i ; m_i and n_i : angles at which the arcs begin and end, measured from 12 o'clock).

Arc no.	x_i	y_i	z_i	m_i (°)	n_i (°)
1	3.5	5.0	0.5	180	270
2	5.0	5.0	2.7	239	0
3	6.0	6.5	1.6	289	180
4	9.5	3.5	4.0	330	95
5	16.0	1.0	5.0	259	320
6	6.0	1.0	4.0	62	104
7	8.0	6.5	4.5	157	192
8	11.0	1.0	4.1	256	298
9	1.0	0.0	5.0	52	90
10	0.0	2.0	3.1	59	122
11	0.8	2.5	3.3	86	141
12	2.5	5.0	2.5	135	225

See Table 4.5.3 for the values of x_i , y_i , z_i , m_i and n_i .

With the four adjustable parameters A , B , C , and D , we can draw an adult ($C=1$) or baby ($C=\frac{1}{2}$) elephant facing left ($D=+1$) or right ($D=-1$). As an example, here is a papa elephant right in front of you ($A=0$, $B=0$) watching the sunset ($D=+1$).

Hence, proposal of the actual mechanism of the kinetics of catalyzed reactions simply by fitting experimental data with a set of parameters should be done with great care, and we should keep in mind that our results are only formally described, which is still highly valuable with regard to modeling a reaction system, a reactor, and so on.



4.5.3

Reaction on a Solid Catalyst and Interfacial Transport of Mass and Heat

Section 4.5.2 presented typical rate equations of heterogeneously catalyzed reactions. Now we inspect the influence of mass and heat transport on the achievable (effective) reaction rate. The effective rate is lower than what is possible with regard to the chemical kinetics, and only equals the intrinsic rate if transport resistances are negligible.

Subsequently, the rate of a catalyzed reaction is related to the mass of a catalyst (see Topic 4.5.3). To derive equations that are valid for gas and liquid phases we use concentrations c_i (mol m⁻³) instead of partial pressures p_i .

4.5.3.1 Interaction of External Mass Transfer and Chemical Reaction

The rate of diffusion through the boundary layer around a solid catalyst (mol kg_{cat}⁻¹ s⁻¹) is:

$$r_{m, \text{external diffusion}} = \beta A_{m,\text{ex}} (c_{A,g} - c_{A,s}) \quad (4.5.12)$$

whereby $c_{A,g}$ and $c_{A,s}$ are the concentrations of the reactant A in the bulk phase and at the external surface of the catalyst (Figure 4.5.7). The mass transfer coefficient β (m s⁻¹) depends on the particle size and geometry, and on the hydrodynamic conditions. Equations for β are given in Section 3.2.2.2. $A_{m,\text{ex}}$ is the external surface area per mass (m² kg_{cat}⁻¹), given for spherical particles with density ρ_p (kg m⁻³) by Eq. (4.5.1).

The reaction rate within the particle is given for a first-order reaction by:

$$r_{m, \text{eff}} = \eta_{\text{pore}} k_m c_{A,s} \quad (4.5.13)$$

The phrase “effective” considers that the rate within the particle may be diminished by intraparticle transport effects, if the rate of diffusion into the pores is small compared to the rate of reactant consumption by the reaction at the surface of the pores. This leads to a concentration profile within a porous particle and therefore

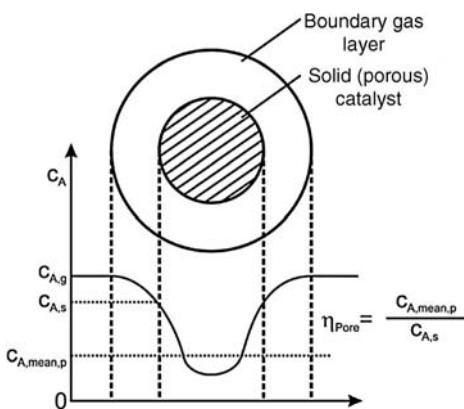


Figure 4.5.7 Concentration profiles of a gaseous reactant A during the reaction in a porous catalyst particle (η_{pore} is inspected in more detail in Section 4.5.4).

also to a decline of the rate (Figure 4.5.7). In anticipation of Section 4.5.4, we introduce here the effectiveness factor for pore diffusion, η_{pore} , as a measure of the deviation of the mean concentration of reactant A in the particle, $c_{A,\text{mean},p}$, from the value at the external surface, $c_{A,s}$. For subsequent inspection of the influence of external mass transfer only, we presume that the term $\eta_{\text{pore}}k_m c_{A,s}$ represents the mean rate of consumption of reactant A within a single particle. By this means we derive universally valid equations, and leave the survey of η_{pore} to Section 4.5.4.

For steady-state conditions, the rate of reactant consumption, $r_{m,\text{eff}}$, equals the flux through the boundary layer, $r_{m,\text{external diffusion}}$, and Eqs. (4.5.12) and (4.5.13) yield the unknown concentration at the surface:

$$\eta_{\text{pore}}k_m c_{A,s} = \beta A_{m,\text{ex}}(c_{A,g} - c_{A,s}) \Rightarrow c_{A,s} = \frac{\beta A_{m,\text{ex}}}{\beta A_{m,\text{ex}} + \eta_{\text{pore}}k_m} c_{A,g} \quad (4.5.14)$$

Combination of Eqs. (4.5.13) and (4.5.14) leads to the effective reaction rate for a porous particle (the rare case of an non-porous catalyst is inspected below):

$$! r_{m,\text{eff}} = \frac{1}{\frac{1}{\beta A_{m,\text{ex}}} + \frac{1}{\eta_{\text{pore}}k_m}} c_{A,g} = k_{m,\text{eff}} c_{A,g} \quad (4.5.15)$$

For $k_m \eta_{\text{pore}} \ll \beta A_{m,\text{ex}}$, the external mass transfer is rapid compared to consumption by the chemical reaction in the particle, and the concentration at the external surface almost equals the concentration in the bulk phase.

We may now define an external effectiveness factor η_{ex} as the ratio of the rate with external diffusion resistance to the rate without interfacial gradients:

$$\eta_{\text{ex}} = \frac{r_{m,\text{eff}}}{r_m(c_{A,s} = c_{A,g})} \quad (4.5.16)$$

If we use Eqs. (4.5.13) and (4.5.15), the definition by Eq. (4.5.16) leads to:

$$\eta_{\text{ex}} = \frac{\beta A_{m,\text{ex}}}{\beta A_{m,\text{ex}} + \eta_{\text{pore}}k_m} \quad (4.5.17)$$

For the rare case of a non-porous catalyst – for example, a metal wire gauze used for NH_3 oxidation (Section 6.4) – similar equations are valid. The rate of the chemical reaction is given by:

$$r_{m,\text{eff}} = k_A A_{m,\text{ex}} c_{A,s} \quad (4.5.18)$$

with k_A related to the external surface ($\text{m}^3 \text{ m}^{-2} \text{ cat s}^{-1}$). For steady-state conditions, the rate of reactant consumption equals the flux through the boundary layer, and Eqs. (4.5.18) and (4.5.12) lead to the concentration at the surface:

$$c_{A,s} = \frac{\beta}{\beta + k_A} c_{A,g} \quad (4.5.19)$$

By combination of Eqs. (4.5.18) and (4.5.19) we derive for the effective reaction rate:

$$r_{m,\text{eff}} = \left(\frac{1}{k_A} + \frac{1}{\beta} \right)^{-1} A_{m,\text{ex}} c_{A,g} \quad (4.5.20)$$

for a non-porous particle. For $k_A \ll \beta$, the concentration at the surface almost equals the value of the gas phase, and the concentration gradient in the boundary layer is almost zero. For the external effectiveness factor η_{ex} , which is the ratio of the effective rate [Eq. 4.5.20a] to the rate without interfacial gradients [Eq. (4.5.18) for the case $c_{A,s} = c_{A,g}$], we obtain:

$$\eta_{\text{ex}} = \left(1 + \frac{k_A}{\beta} \right)^{-1} \quad (4.5.21)$$

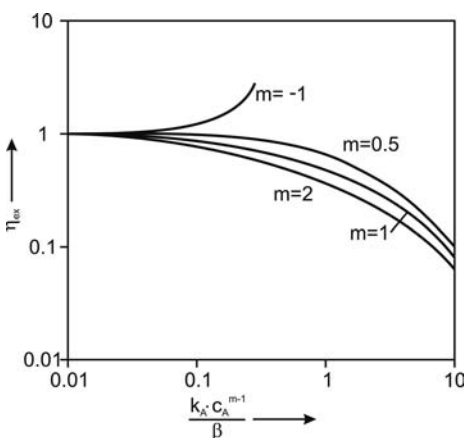


Figure 4.5.8 Effectiveness factor for external mass transfer as a function of $k_A c_A^{m-1} / \beta$ for a non-porous catalyst for different reaction orders (c_A = concentration in bulk phase, $T_p = T_g$).

An estimation of the minimal value of η_{ex} is given in Example 4.5.1. Note that for an exothermic (and thus non-isothermal) reaction η_{ex} may be >1 even for a first-order reaction (see end of Section 4.5.3.2). Figure 4.5.8 shows η_{ex} as a function of k_A/β according to Eq. (4.5.21) but also for reaction orders m that differ from unity. For a negative reaction order, the rate of the chemical reaction increases with decreasing concentration, and therefore we get the rare case that η_{ex} increases for a limitation of the rate by external diffusion (Example 4.5.2).

Example 4.5.1: Estimation of the minimal value of external effectiveness factor η_{ex}

For a packed bed of spheres, the minimum value of the *Sherwood number* for reactant A ($Sh = \beta d_p / D_{A,g}$) of 3.8 (for $Re_p \rightarrow 0$) can be used (Section 3.2.2.2). Thus we can estimate the minimum values of η_{ex} for porous and non-porous catalysts (first-order reaction). For porous particles we obtain based on Eq. (4.5.17):

$$\begin{aligned} \eta_{\text{ex}, \min} &= \frac{1}{1 + \frac{\eta_{\text{pore}} k_m}{\left(\frac{3.8}{d_p} D_{A,g}\right) A_{m,\text{ex}}}} = \frac{1}{1 + \frac{\eta_{\text{pore}} k_m}{\left(\frac{3.8}{d_p} D_{A,g}\right) \left(\frac{6}{d_p \rho_p}\right)}} \\ &\approx \frac{1}{1 + \frac{\eta_{\text{pore}} k_m d_p^2 \rho_p}{23 D_{A,g}}} \end{aligned} \quad (4.5.22)$$

For a packed bed of non-porous particles, we get based on Eq. (4.5.21):

$$\eta_{\text{ex}, \min} = \frac{1}{1 + \frac{k_A d_p}{3.8 D_{A,g}}} \quad (4.5.23)$$

Thus if the values determined by these equations are approximately unity, we can neglect the influence of external mass transfer without any further calculation of the exact value of the *Sherwood number*, which (in a fixed bed) can only be higher than 3.8.

Example 4.5.2: Effectiveness factor η_{ex} for a negative reaction order and for Langmuir–Hinshelwood kinetics (non-porous particle, only external mass transfer resistance)

As shown in Figure 4.5.9, we may find an effectiveness factor with regard to external diffusion exceeding unity if we have a reaction with a negative reaction order. For example, for an order of -1 , Eqs. (4.5.12) and (4.5.18) lead to:

$$r_A = \frac{k_A}{c_{A,s}} = \beta(c_{A,g} - c_{A,s})$$

This equation can be rewritten in dimensionless form if we use the rates relative to the maximum rate of mass transfer [$r_{A,\text{mass transfer, max}} = \beta(c_{A,g} - c_{A,s,\min}) \approx \beta c_{A,g}$]:

$$\left(\frac{k_A}{\beta c_{A,g}^2}\right) \frac{1}{c_{A,s}} = 1 - \frac{c_{A,s}}{c_{A,g}}$$

Figure 4.5.9 shows that only for a value of the term $k_A/(\beta c_{A,g}^2)$ of less than 0.25 do we obtain a solution for steady-state conditions; for higher values the rate of the chemical reaction would be (hypothetically) always higher than the rate of external diffusion, and we have no intersection point of the mass transfer line and the function representing the chemical reaction. For the borderline case of $k_A/(\beta c_{A,g}^2) = 0.25$, the intersection point leads to an effective rate that is by a factor of two higher than the rate without mass transfer resistance ($c_{A,g} = c_{A,s}$), as also shown by Figure 4.5.8.

In reality, a reaction order of -1 is unrealistic for low concentrations as we would get an infinite rate for $c_A \rightarrow 0$. Therefore, we now inspect as example a bimolecular reaction following a mechanism according to Langmuir–Hinshelwood kinetics (Section 4.5.2.2). For a constant partial

pressure of B, Eq. (4.5.5) reads as (with p_0 as standard pressure):

$$\begin{aligned} r_{A,\text{surface reaction}} &= k_s \frac{K_{\text{ads},A} K_{\text{ads},B} p_{A,s} p_{B,s}}{\left(1 + K_{\text{ads},A} p_{A,s} + K_{\text{ads},B} p_{B,s}\right)^2} \\ &= \frac{C_1 \frac{p_{A,s}}{p_0}}{\left(C_2 + C_3 \frac{p_{A,s}}{p_0}\right)^2} \quad (\text{for } p_B = \text{const.}) \end{aligned}$$

and for a high partial pressure of A we formally obtain a rate with order -1 .

The rate of external mass transfer is given by:

$$r_{A,\text{external mass transfer}} = \frac{p_0 \beta}{RT} \left(\frac{p_{A,g}}{p_0} - \frac{p_{A,s}}{p_0} \right) = C_4 \left(\frac{p_{A,g}}{p_0} - \frac{p_{A,s}}{p_0} \right)$$

and equals the rate of reaction for steady-state conditions, which leads to:

$$\left(\frac{p_{A,g}}{p_0} - \frac{p_{A,s}}{p_0} \right) = \frac{\frac{C_1 p_{A,s}}{C_4 p_0}}{\left(C_2 + C_3 \frac{p_{A,s}}{p_0} \right)^2}$$

Figure 4.5.10 shows the graphical solution of this equation. The intersections of the lines representing the mass transfer (for a given value of $p_{A,g}/p_0$) with the function for the rate of surface reaction are the solutions for steady-state conditions. Based on Figure 4.5.10, we can determine the effectiveness factor with regard to external diffusion, which is

Figure 4.5.9 Intrinsic reaction rate and mass transfer rate (relative to the maximum rate of mass transfer) as a function of the surface concentration (relative to the gas phase) for a reaction with an order of minus one.

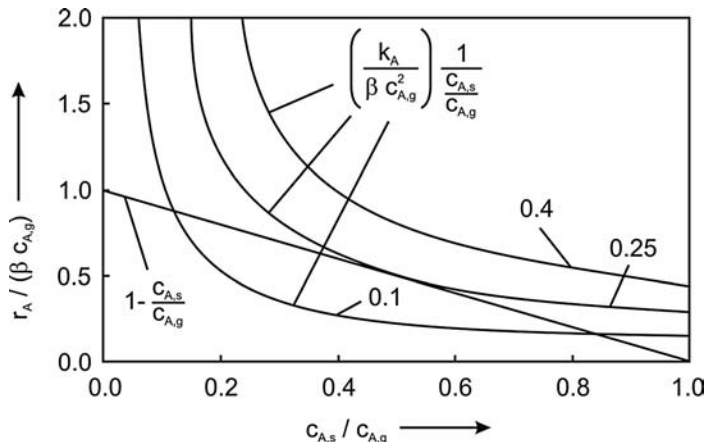


Figure 4.5.10 Dimensionless reaction rate and mass transfer rate for different gas phase concentrations $p_{A,g}$ as a function of the dimensionless partial pressure at the external surface for Langmuir–Hinshelwood kinetics ($C_1/C_4 = 80$, $C_2 = 1$, $C_3 = 20$, see text).

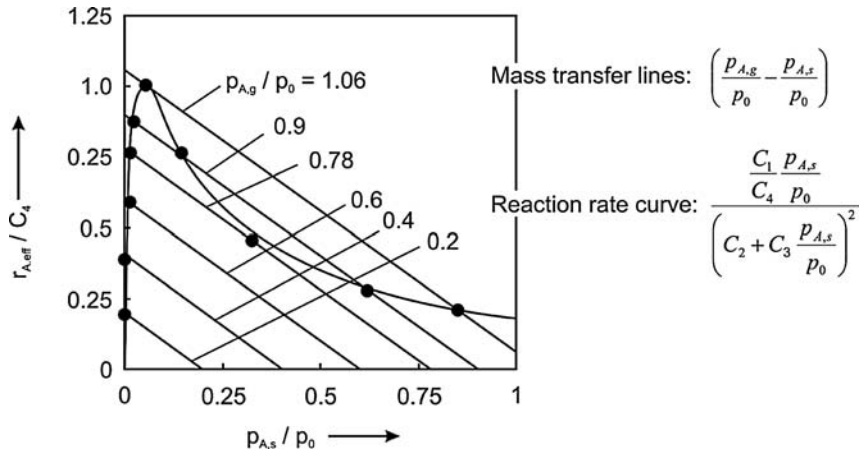
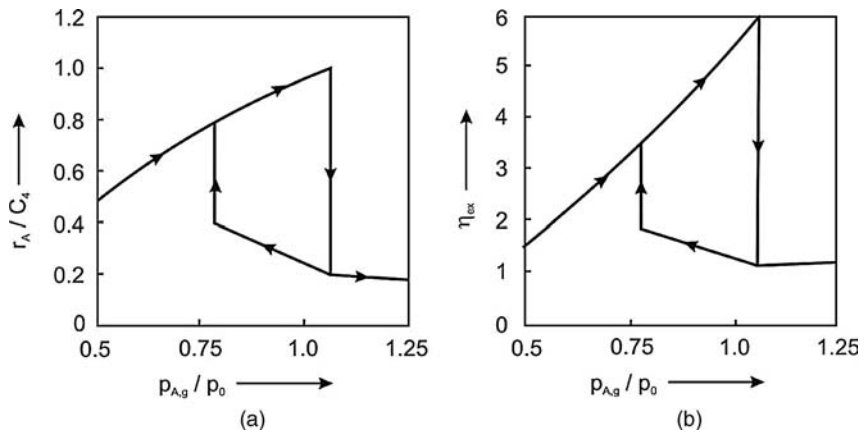


Figure 4.5.11 Influence of gas phase concentration on (a) the effective reaction and (b) the effectiveness factor (hysteresis loops of r_A and η_{ex} , see text).



defined as the ratio of the effective rate to the rate for $p_{A,s} = p_{A,g}$:

$$\eta_{ex} = \frac{r_{A,eff}}{r_A(p_{A,s} = p_{A,g})} = \frac{p_{A,s}}{p_{A,g}} \frac{\left(C_2 + C_3 \frac{p_{A,g}}{p_0}\right)^2}{\left(C_2 + C_3 \frac{p_{A,s}}{p_0}\right)^2}$$

Figure 4.5.11 shows the influence of partial pressure on the effectiveness factor and on the effective rate. Consequently, an increase and subsequent decrease of the gas phase concentration leads to the interesting phenomena of a hysteresis loop of η_{ex} and $r_{A,eff}$.

For processes controlled by external mass transfer, a reactor length of only about ten particle diameters is needed for almost complete conversion, as shown by Example 4.5.3. Technically relevant examples are catalytic ammonia oxidation on a platin gauze (Section 6.4) and the combustion of solid fuels like coal where we have the same interplay of mass transfer and chemical reaction as in heterogeneously catalyzed reactions.

Example 4.5.3: Estimation of the required length of a fixed bed reactor for a gas-phase reaction controlled completely by external mass transfer

As discussed in Section 3.2.2.2, the *Sherwood number* Sh for a gaseous reactant A in a packed bed of spherical particles is given (porosity of bed $\varepsilon \approx 0.4$, $Sc \approx 1$) by:

$$Sh = \frac{\beta d_p}{D_{A,g}} = 3.8 + 1.26 \sqrt{\frac{u_s d_p}{\varepsilon v_g}} \quad (4.5.24)$$

If the effective reaction rate is *controlled completely* by external mass transfer ($k_m \eta_{\text{pore}} \gg \beta A_m$ for porous catalysts or $k_A \gg \beta$ for non-porous systems), Eqs. (4.5.15) or (4.5.20) lead to the following equation of the effective reaction rate of consumption of A:

$$r_{m,\text{eff}} = -\frac{d\dot{n}_A}{dm_{\text{cat}}} = \beta A_{m,\text{ex}} c_{A,g} \quad (4.5.25)$$

By introduction of the volume rate \dot{V} we obtain with $\dot{n}_A = \dot{V} c_{A,g}$:

$$-\frac{dc_{A,g}}{c_{A,g}} = \beta A_{m,\text{ex}} \dot{V} dm_{\text{cat}} \quad (4.5.26)$$

Integration of Eq. (4.5.26) leads to:

$$-\ln\left(\frac{c_{A,g}}{c_{A,g,0}}\right) = \beta A_{m,\text{ex}} \dot{V} m_{\text{cat}} \quad (4.5.27)$$

Replacement of m_{cat} by the term $V_R \rho_p (1 - \varepsilon)$ and insertion of Eqs. (4.5.1) and (4.5.24) into Eq. (4.5.27) leads to:

$$-\ln\left(\frac{c_{A,g}}{c_{A,g,0}}\right) = \frac{V_R D_{A,g}}{\dot{V}} \left(3.8 + 1.26 \sqrt{\frac{u_s d_p}{\varepsilon v_g}} \right) \frac{6(1 - \varepsilon)}{d_p^2} \quad (4.5.28)$$

The term $V_R D_{A,g} / \dot{V}$ is equivalent to $L D_{A,g} / u_s$ and is independent of p and almost independent of T ($\sim T^{0.75}$ as $D_{A,g} \sim T^{1.75}$ and $u_s \sim T$). Hence, we can use the values at normal temperature and pressure (index n). If we also consider that $D_{A,g} \approx v_g$, we, finally, acquire the following expression for the reactor length:

$$L = \frac{u_{s,n} d_p^2 \left[-\ln\left(\frac{c_{A,g}}{c_{A,g,0}}\right) \right]}{D_{A,g,n} 6(1 - \varepsilon) \left(3.8 + 1.26 \sqrt{\frac{u_{s,n} d_p}{\varepsilon D_{A,g,n}}} \right)} \quad (4.5.29)$$

To estimate the reactor length (in terms of particle diameters) needed for a reaction controlled by external mass transfer we use the following data: $D_{g,n} = 2 \times 10^{-5} \text{ m}^2 \text{ s}^{-1}$, $\varepsilon = 0.4$, $u_{s,n} = 1 \text{ m s}^{-1}$. For a conversion of 99% ($c_{A,g}/c_{A,g,0} = 0.01$), Eq. (4.5.29) leads to:

$$\begin{aligned} \frac{L}{d_p} &= \frac{d_p 4.6}{2 \times 10^{-5} \times 3.6 \left(3.8 + 1.26 \sqrt{\frac{d_p}{0.8 \times 10^{-5}}} \right)} \\ &= \frac{16800 d_p}{1 + 117 \sqrt{d_p}} \quad (\text{with } d_p \text{ in m}) \end{aligned}$$

For a typical range of particle diameters in fixed beds from 1 mm to 2 cm, we obtain a reactor length ranging from 4 to 19 diameters. Thus, as a rule of thumb we can state that for processes controlled by external mass transfer we need a length for complete conversion that is ten times the characteristic length, which for packed beds is the particle diameter.

4.5.3.2 Combined Influence of External Mass and Heat Transfer on the Effective Rate

For steady-state conditions, the rate of heat production, \dot{q}_{HP} (W kg^{-1}), equals the rate of heat removal, \dot{q}_{HR} , which is governed by the heat transfer coefficient α ($\text{W m}^{-2} \text{ s}^{-1}$):

$$r_{m,\text{eff}} (-\Delta_R H) = \alpha A_{m,\text{ex}} (T_s - T_g) \quad (\text{with } T_s \text{ and } T_g \text{ as surface and gas temperature}) \quad (4.5.30)$$

In the following, we neglect temperature gradients within the particle ($T_p = T_s$), and Eqs. (4.5.30) and (4.5.15) lead to the steady state heat balance of a porous particle:

$$k_{m,\text{eff}} c_{A,g} (-\Delta_R H) = \alpha A_{m,\text{ex}} (T_s - T_g) \quad (4.5.31)$$

with:

$$k_{m,\text{eff}} = \frac{\eta_{\text{pore}} k_m \beta A_{m,\text{ex}}}{\beta A_{m,\text{ex}} + \eta_{\text{pore}} k_m} \quad (4.5.32)$$

(For a non-porous particle we use $k_A A_{m,\text{ex}}$ instead of $\eta_{\text{pore}} k_m$.)

The adiabatic temperature rise is given by:

$$\Delta T_{ad} = \frac{c_{A,g}(-\Delta_R H)}{c_p \rho_{mol}} \quad (4.5.33)$$

and then Eq. (4.5.31) reduces to:

$$k_{m, eff} \Delta T_{ad} c_p \rho_{mol} = \alpha A_{m, ex} (T_s - T_g) \quad (4.5.34)$$

An estimation of the maximum temperature difference is given in Example 4.5.4.

Example 4.5.4: Maximum temperature difference between particle and fluid

For the approximation $Nu = Sh$, the ratio β/α is given for gases by:

$$\begin{aligned} \frac{\beta}{\alpha} &= \frac{Sh \frac{D_{A,g}}{d_p}}{Nu \frac{\lambda_g}{d_p}} \approx \frac{D_{A,g}}{\lambda_g} = \frac{D_{A,g} \rho_{mol} c_p v_g}{\lambda_g \rho_{mol} c_p v_g} = \frac{D_{A,g} \rho_{mol} c_p v_g}{v_g \lambda_g \rho_{mol} c_p} \frac{1}{\rho_{mol} c_p} \\ &= \frac{Pr}{Sc} \frac{1}{\rho_{mol} c_p} \end{aligned} \quad (4.5.35)$$

if we use the definitions of the *Prandtl number*, Pr [Eq. (3.2.10)] and *Schmidt number*, Sc [Eq. (3.2.69)]. Equations (4.5.34) and (4.5.35) lead to the following estimation of the temperature difference between the particle and the bulk phase of the gas:

$$(T_s - T_g) = \frac{k_{m, eff} c_p \rho_{mol}}{\alpha A_{m, ex}} \Delta T_{ad} = \frac{Pr}{Sc} \frac{k_{m, eff}}{\beta A_{m, ex}} \Delta T_{ad} \approx \frac{k_{m, eff}}{\beta A_{m, ex}} \Delta T_{ad} \quad (4.5.36)$$

if we consider that the ratio Pr/Sc is almost unity for gases. (To prove this use the values of Table 3.1.7 and Table 3.1.3.) Thus, at

a low temperature, that is, $k_{m, eff} \approx \eta_{pore} k_m \ll \beta A_{m, ex}$, the particle temperature approximately equals the gas temperature. In the reverse case, that is, $\eta_{pore} k_m \gg \beta A_{m, ex}$, the effective rate constant $k_{m, eff}$ approaches $\beta A_{m, ex}$ [Eq. (4.5.32)], and the temperature rise in the boundary layer equals the adiabatic rise in temperature, which may easily lead to values of several hundred kelvin for strong exothermic processes.

For liquid phase reactions, the maximum temperature difference is usually much smaller. For complete control by external mass transfer ($k_{m, eff} = \beta A_m$), Eq. (4.5.36) leads to:

$$\begin{aligned} (T_s - T_g) &= \frac{\beta c_p, l \rho_{mol}}{\alpha} \Delta T_{ad} = \frac{Sh D_l c_p, l \rho_l}{Nu \lambda} \Delta T_{ad} = \frac{Sh D_l}{Nu a} \Delta T_{ad} \\ &= \frac{Sh Pr}{Nu Sc} \Delta T_{ad} \end{aligned} \quad (4.5.37)$$

The ratio Pr/Sc is typically only 0.01 for liquids ($D_l \approx 10^{-9} \text{ m}^2 \text{s}^{-1}$, $a \approx 10^{-7} \text{ m}^2 \text{s}^{-1}$). Thus, ΔT_{max} is about $0.01 \Delta T_{ad}$ for small values of Re ($Sh/Nu \approx 1$), and $0.05 \Delta T_{ad}$ for high values of Re [$Sh/Nu \approx (a/D_l)^{2/3}$, that is, $\Delta T_{max} = (D_l/a)^{2/3} \Delta T_{ad}$, see Eqs. (3.2.70) and (3.2.21)].

For exothermic reactions, the particle temperature may change drastically through small fluctuations of temperature or concentration. This ignition-extinction behavior can be analyzed for a porous particle by combining the steady-state heat balance [Eqs. (4.5.31) and (4.5.32)]:

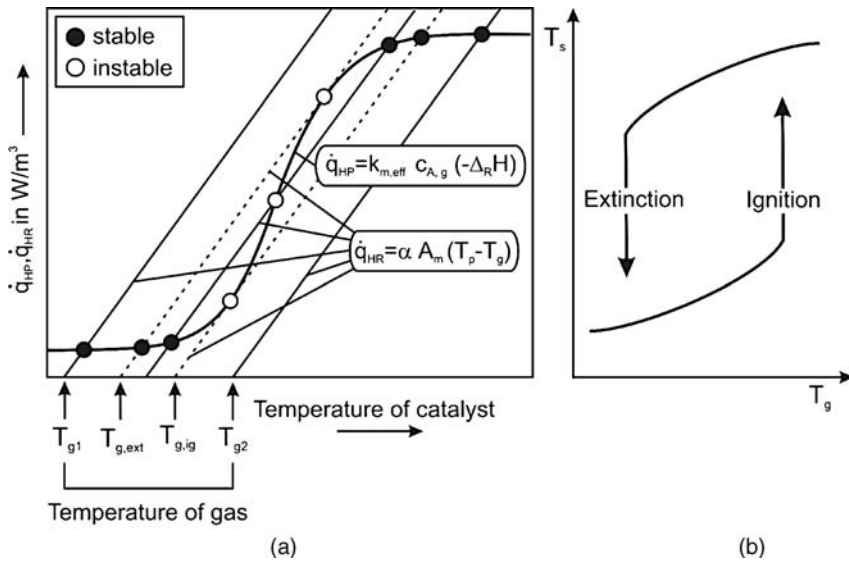
$$\frac{\eta_{pore} k_m \beta A_{m, ex}}{\beta A_{m, ex} + \eta_{pore} k_m} c_{A,g} (-\Delta_R H) = \underbrace{\alpha A_{m, ex} (T_s - T_g)}_{\text{Heat removal from external surface to the gas phase}} \quad (4.5.38)$$

If we use the temperature dependence of the rate constant k_m according to Arrhenius (and neglect here for simplification that η_{pore} also depends on temperature) we obtain:

$$\dot{q}_{HP} = \frac{\eta_{pore} k_{m,0} e^{-\frac{E_A}{RT_s}} \beta A_{m, ex}}{\beta A_{m, ex} + \eta_{pore} k_{m,0} e^{-\frac{E_A}{RT_s}}} c_{A,g} (-\Delta_R H) = \dot{q}_{HR} = \alpha A_{m, ex} (T_s - T_g) \quad (4.5.39)$$

Figure 4.5.12 shows the overall sigmoidal curve of the heat production function and selected lines representing the heat removal for different gas phase temperatures.

For a low gas temperature like T_{g1} in Figure 4.5.12a, the intersection point of the heat production function and the heat removal line (steady state) yields to a surface temperature that is only marginally higher than the gas temperature. $\beta A_{m, ex}$ is then



still much higher than $\eta_{pore}k_m$, and for low temperatures η_{pore} approaches unity (Section 4.5.4). Thus the heat production is only determined by the rate of chemical reaction, and Eq. (4.5.39) reduces to:

$$k_{m,0}e^{-\frac{E_A}{RT_s}}c_{A,g}(-\Delta_R H) = \alpha A_{m,ex}(T_s - T_g) \quad (\text{for } \beta A_{m,ex} \gg \eta_{pore}k_m \text{ and } \eta_{pore} \approx 1) \quad (4.5.40)$$

A further increase of the gas-phase temperature T_g leads to a steady increase of the surface temperature T_s until the ignition temperature $T_{g,ig}$ is reached. Then the system becomes unstable as small unavoidable fluctuations of the gas temperature (or concentration etc.) may lead to a small shift of the heat removal line to slightly higher temperatures. Now the stable operation point lies on the upper part of the heat production function, and T_s is much higher than the fluid temperature ($T_{g,ig}$). Here $\beta A_{m,ex}$ is much smaller than $\eta_{pore}k_m$, as the rate of the chemical reaction increases quasi-exponentially with temperature, whereas β can be regarded as comparatively constant ($\beta \sim D_g \sim T^{1.5}$). Thus the effective rate of heat production then depends only on the rate of external mass transport, and Eq. (4.5.38) reduces to:

$$\beta A_{m,ex} c_{A,g} (-\Delta_R H) = \alpha A_{m,ex} (T_s - T_g) \quad (\text{for } \beta A_{m,ex} \ll \eta_{pore}k_m) \quad (4.5.41)$$

and the temperature difference in the boundary layer equals the adiabatic temperature rise (Example 4.5.4). Consequently, gas temperatures exceeding $T_{g,ig}$ (e.g., T_{g2}) only lead to a proportional increase of the surface temperature ($T_s = T_g + \Delta T_{ad}$ for $T_g > T_{g,ig}$). If we now decrease T_g , the system will not become extinct before $T_{g,ext}$ (extinction temperature, Figure 4.5.12) is reached, which is lower than the ignition temperature $T_{g,ig}$. Consequently, an increase and subsequent decrease of the gas temperature leads to a hysteresis loop of the surface temperature, as shown schematically in Figure 4.5.12b.

For gas temperatures between $T_{g,ext}$ and $T_{g,ig}$, three solutions formally exist for the steady state (Figure 4.5.12). The midpoint is unstable, as a small increase (decrease) of T_g leads to ignition (extinction) because the increase in the rate of heat production (gradient in T) is higher (lower) than the increase of the rate of the heat removal. Thus, either the upper or lower point of stable operation is established, and in addition to the first criterion for a stable operation point given by Eq. (4.5.39) ($\dot{q}_{HP} = \dot{q}_{HR}$), the second criterion is mathematically given by:

$$\frac{d\dot{q}_{HR}}{dT} > \frac{d\dot{q}_{HP}}{dT} \quad (4.5.42)$$

Figure 4.5.12 (a) Ignition-extinction behavior of a single catalytic particle (schematically, HR: heat removal, HP: heat production by chemical reaction); (b) $T_{surface}$ versus T_{gas} .

Further insights into ignition behavior are given in Example 4.5.5 for the ignition of a platinum wire during the oxidation of ethylene. In this case ignition is induced by increasing the electrical power input and not by increasing the gas temperature.

Example 4.5.5: Ignition of a Pt-wire during oxidation of ethylene

The oxidation of ethylene in air on a Pt wire is a good example by which to demonstrate the ignition behavior of exothermic catalytic reactions. The experiment was conducted as follows (Table 4.5.4). A coil consisting of a thin Pt-wire is placed in a tubular reactor. Then an ethylene-air mixture of constant temperature and pressure (303 K, 1 bar) is fed into the tubular reactor. The wire is now electrically heated until ignition (jump in temperature) occurs. The current and the voltage is measured and, thus, also the temperature of the wire as the electrical resistance depends on temperature.

The intrinsic kinetics follow a Langmuir–Hinshelwood mechanism [Eq. (4.5.5)]:

$$r_{\text{ethylene}} = k_s \frac{K_{\text{ads}, \text{O}_2} K_{\text{ads}, \text{ethylene}} c_{\text{O}_2} c_{\text{ethylene}}}{(1 + K_{\text{ads}, \text{ethylene}} c_{\text{ethylene}} + K_{\text{ads}, \text{O}_2} c_{\text{O}_2})^2}$$

Ethylene is much more strongly adsorbed than oxygen, and for a surplus of oxygen we have:

$$r_{\text{ethylene}} \approx k_s \frac{K_{\text{ads}, \text{O}_2}}{K_{\text{ads}, \text{ethylene}}} \frac{c_{\text{O}_2}}{c_{\text{ethylene}}} = k_{\text{overall}} \frac{1}{c_{\text{ethylene}}}$$

and hence the heat production by the reaction (with $A_{\text{wire}} = \pi d_{\text{wire}} L_{\text{wire}}$ as wire surface) is:

$$\dot{Q}_{\text{HP}} = k_{\text{overall}} \frac{A_{\text{wire}}}{c_{\text{ethylene, surface}}} (-\Delta_{\text{R}} H) \quad (\text{with } k_{\text{overall}} = k_0, \text{overall} e^{-\frac{E_A}{RT}})$$

If external mass transfer (film diffusion) still has no influence on the effective reaction rate, $c_{\text{ethylene, surface}}$ equals the gas phase concentration $c_{\text{ethylene, gas}}$.

The maximum rate of heat production is limited by film diffusion:

$$\dot{Q}_{\text{HPmax}} = \beta A_{\text{wire}} c_{\text{ethylene, gas}} (-\Delta_{\text{R}} H) \quad (\text{for } c_{\text{ethylene, surface}} \approx 0)$$

For ethylene oxidation on the given Pt wire, film diffusion limits the effective rate of heat production at $T > 1000^\circ\text{C}$ (Figure 4.5.13). For $T < 900^\circ\text{C}$, the chemical kinetics are limiting, and for the range in between the effective rate is influenced by both factors.

Heat removal by convection is given by:

$$\dot{Q}_{\text{HR}} = \alpha A_{\text{wire}} (T_{\text{wire}} - T_{\text{gas}})$$

For the given experiments, the wire is not only heated by the reaction but also by the electrical current, and the overall heat balance reads as:

$$\dot{Q}_{\text{HR}} = \dot{Q}_{\text{HP}} + \dot{Q}_{\text{electrical}}$$

At low temperatures, the effective rate is controlled by the chemical (intrinsic) reaction rate ($c_{\text{ethylene, surface}} \approx c_{\text{ethylene, gas}}$), and the heat balance is given by:

$$\left\{ k_0, \text{overall} \frac{A_{\text{wire}}}{c_{\text{ethylene, gas}}} (-\Delta_{\text{R}} H) \right\} e^{-\frac{E_A}{RT_{\text{wire}}}} + \dot{Q}_{\text{electrical}} \\ = \alpha A_{\text{wire}} (T_{\text{wire}} - T_{\text{gas}}) \quad (\text{for } T < 900^\circ\text{C})$$

At high temperatures, the effective rate controlled by film diffusion ($c_{\text{ethylene, surface}} \approx 0$) is:

$$[\beta A_{\text{wire}} c_{\text{ethylene, gas}} (-\Delta_{\text{R}} H)] + \dot{Q}_{\text{electrical}} \\ = \alpha A_{\text{wire}} (T_{\text{wire}} - T_{\text{gas}}) \quad (\text{for } T > 1000^\circ\text{C})$$

If the input of electrical power is gradually increased, the stable operation point (intersection of heat removal and heat production curve) increases (Figure 4.5.14a) until ignition occurs at about 7 W (point A in Figure 4.5.14a and b). Thereafter, a new upper stable operation point is reached (point B in Figure 4.5.14a and c), whereby the power input decreases to 6 W as the resistance of the wire increases.

Table 4.5.4 Data for laboratory-scale ethylene oxidation on a Pt wire.^{a)}

Parameter	Value
Gas composition	1.5% C ₂ H ₄ in air
Reaction (combustion) enthalpy $\Delta_{\text{R}} H$	-1,400 kJ per mol ethylene
Wire diameter d and length L	0.25 mm, 0.21 m
Wire surface area A_{wire}	0.000165 m ²
Heat transfer coefficient α (convection, $Nu = 0.5 = \alpha d / \lambda$)	52 W m ⁻² K ⁻¹ (20 °C)
Mass transfer coefficient β ($Sh = 0.5 = \beta d / D_{\text{ethylene}}$)	0.032 m s ⁻¹ (20 °C)
Electrical power to initiate ignition $P_{\text{electrical, ignition}}$	7.1 W
Wire temperature at ignition T_{ignition}	839 K
T_{Wire} at upper operation point	1004 K
$P_{\text{electrical}}$ at upper operation point	6.1 W
Pre-exponential factor $k_{0,\text{overall}}$	5600 mol ² m ⁻⁵ s ⁻¹
Activation energy E_A	90 kJ mol ⁻¹

a) The experiment was conducted at the Department of Chemical Engineering (University of Bayreuth) during a practical course for students. The cooling of the wire is mainly governed by (forced) convection and to a low extent by radiation (<5%). The kinetic parameters were determined by experiments with varied C₂H₄ content.

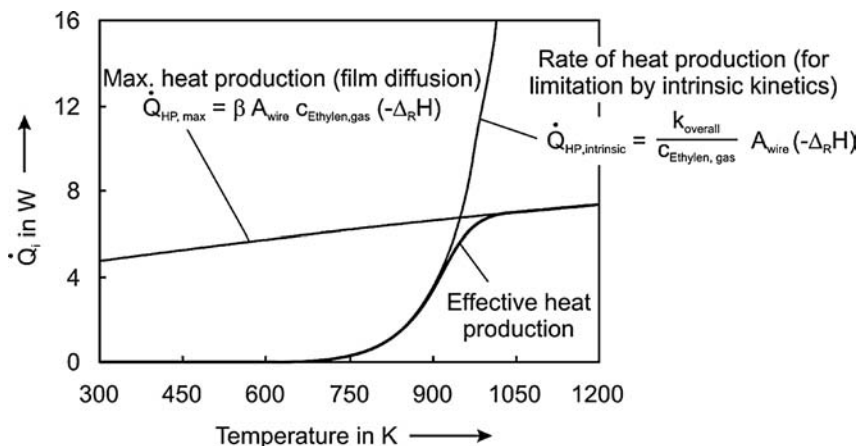


Figure 4.5.13 (a) Rate of heat production by oxidation of ethylene on a Pt wire for the two limiting cases of control by the intrinsic kinetics and by film diffusion.

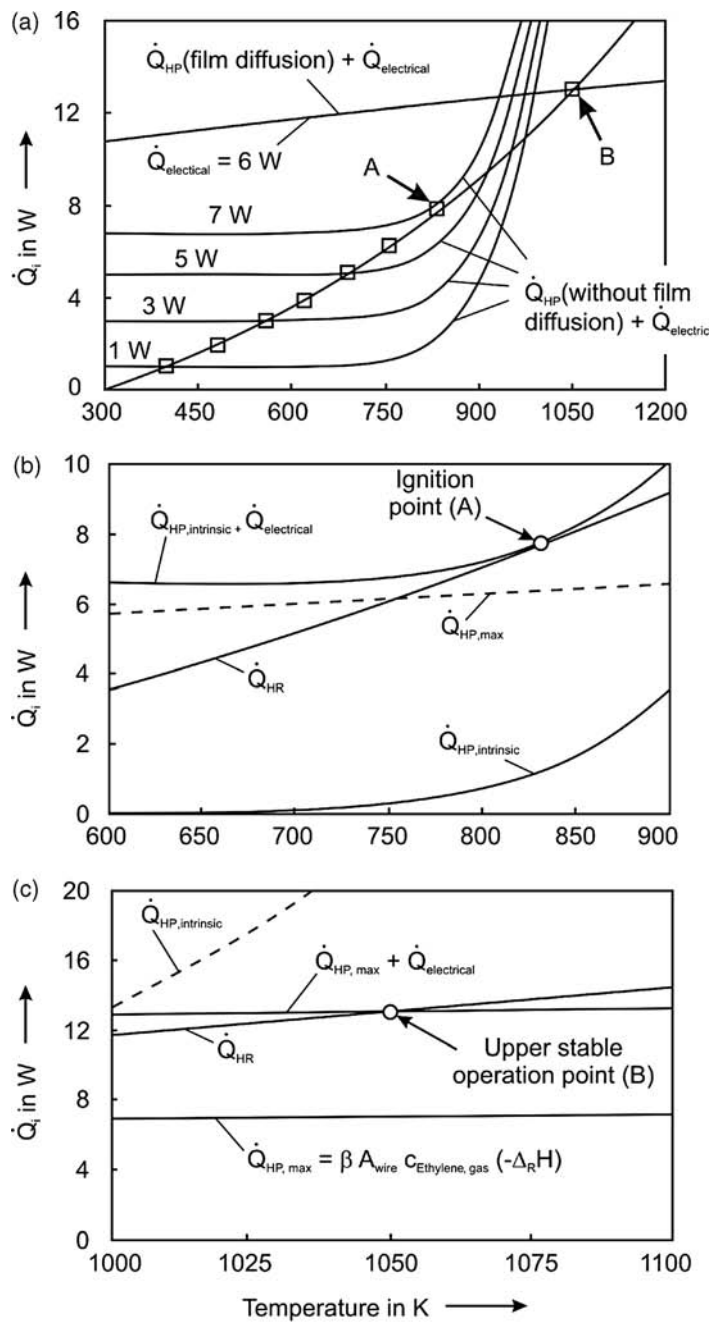


Figure 4.5.14 Ignition of a Pt-wire during oxidation of ethylene: (a) increase of operation point by stepwise increase of electrical power input; (b) ignition (rate still determined by chemical reaction, $P_{\text{electrical}} = 7 \text{ W}$); (c) stable upper operation point established after ignition (rate is then almost completely controlled by film diffusion, $P_{\text{electrical}} = 6 \text{ W}$).

Note that in case of an exothermic reaction the external effectiveness factor [defined by Eq. (4.5.21) for a first-order reaction] may be much higher than unity. This is because mass and heat transfer limitations lead to an interfacial concentration gradient *and* in most cases also to a temperature gradient in the boundary layer (overheating of the particle, that is, gas temperature T_g is much lower than particle temperature T_p). Thus, the effective rate (even under the strong influence of external mass transfer limitations) may exceed by far the rate without interfacial gradients, as this rate is by definition related to a probably much lower temperature. For example, for a non-porous catalyst η_{ex} for a first-order reaction is then given (if we neglect the relative small influence of temperature on β) by:

$$\eta_{ex} = \frac{r_{m,eff}(T_p)}{r_m(T_g)} = \frac{\left[\frac{1}{k_A(T_p)} + \frac{1}{\beta} \right]^{-1}}{\frac{1}{k_A(T_g)}} = \left[\frac{k_A(T_g)}{k_A(T_p)} + \frac{k_A(T_g)}{\beta} \right]^{-1} \quad (4.5.43)$$

Thus, if k_A (at T_g) is higher than β [or to be more precise $k_A(T_g) < k_{eff}(T_p) = (1/k_A(T_p) + 1/\beta)^{-1}$], η_{ex} is >1 (Topic 4.5.5). Details are given by, for example, Levenspiel (1996).

Topic 4.5.5 External effectiveness factor for an exothermic heterogeneously catalyzed gas reaction

To inspect the external effectiveness factor for an exothermic heterogeneously catalyzed first-order gas reaction (component A), we make the following assumptions:

- The particle is non-porous; thus the reaction rate is given by Eq. (4.5.18):

$$r_m = r_{m,eff} = k_m c_{A,s} = k_A A_{m,ex} c_{A,g} \quad (\text{index } s = \text{external surface})$$

The effective reaction rate is the result of the interplay of the chemical reaction at the external surface and external mass transfer, and we also have [Eq. (4.5.20)]:

$$r_{m,eff} = \eta_{ex} k_A(T_p) A_{m,ex} c_{A,g} = k_{m,eff} c_{A,g} = \left[\frac{1}{k_A(T_p)} + \frac{1}{\beta} \right]^{-1} A_{m,ex} c_{A,g}$$

- The heat balance (Eq. (4.5.30) yields:

$$r_{m,eff}(-\Delta_R H) = \beta A_{m,ex} (c_{A,g} - c_{A,s})(-\Delta_R H) = \alpha A_{m,ex} (T_p - T_g)$$

For gases, the Sherwood number almost equals the Nusselt number:

$$Sh \approx Nu \Rightarrow \frac{\alpha}{\beta} = \frac{\lambda_g}{D_{A,g}}$$

- The influence of temperature on the rate constant k_A [= $k_{A,o} \exp(-E_A/(RT))$] is strong, and so in the following the relatively weak influence of the temperature on the heat and mass transfer coefficients (α, β) is neglected.

With these assumptions, rearrangement of Eq. (4.5.43) leads to:

$$\eta_{ex} = \frac{1}{\frac{k_A(T_g)}{k_A(T_p)} \left[1 + \frac{k_A(T_p)}{\beta} \right]} = \frac{e^{-\frac{E_A}{RT_g} \left(\frac{T_g}{T_p} - 1 \right)}}{\left[1 + \frac{k_A(T_p)}{\beta} \right]} = \frac{e^{-\frac{E_A}{RT_g} \left(\frac{T_g}{T_p} - 1 \right)}}{\left[1 + \frac{k_A(T_p)}{\beta} \right]} \quad (4.5.44)$$

The denominator can be replaced by:

$$1 + \frac{1}{\beta} k_A(T_p) = 1 + \frac{1}{\beta} \left(\frac{1}{k_{m,eff}} - \frac{1}{\beta} \right)^{-1} = \left(1 - \frac{k_{m,eff}}{\beta} \right)^{-1} = \left(1 - \frac{r_{m,eff}}{r_{m,eff,max}} \right)^{-1} \quad (4.5.45)$$

and the heat balance and the assumption $Sh \approx Nu$ leads an expression for T_g/T_p :

$$\frac{T_g}{T_p} = \left\{ 1 + \frac{D_{A,g}(-\Delta_R H)c_{A,g}r_{m,eff}}{\lambda_g T_g \beta c_{A,g}} \right\}^{-1} = \left\{ 1 + \frac{D_{A,g}(-\Delta_R H)c_{A,g}}{\lambda_g T_g} \frac{r_{m,eff}}{r_{m,eff, max}} \right\}^{-1} \quad (4.5.46)$$

Introduction of the dimensionless *Prater number* β_{ex} and the *Arrhenius number* γ_{ex} gives:

$$\beta_{ex} = \frac{D_{A,g}(-\Delta_R H)c_{A,g}}{\lambda_g T_g} = \frac{\beta(-\Delta_R H)c_{A,g}}{\alpha T_g} \quad (\text{for } Sh = Nu) \quad (4.5.47)$$

$$\gamma_{ex} = \frac{E_A}{RT_g} \quad (4.5.48)$$

and insertion of Eqs. (4.5.46)–(4.5.48) into Eq. (4.5.44) finally yields:

$$\eta_{ex} = e^{-\gamma_{ex} \left(\frac{1}{1 + \beta_{ex} \frac{r_{m,eff}}{r_{m,eff, max}}} - 1 \right)} \left(1 - \frac{r_{m,eff}}{r_{m,eff, max}} \right) \quad (4.5.49)$$

For small values of the Prater number β_{ex} , Eq. (4.5.49) leads to:

$$\eta_{ex} = \left(1 - \frac{r_{m,eff}}{r_{m,eff, max}} \right) \quad (\text{for } \beta_{ex} \rightarrow 0) \quad (4.5.50)$$

The temperature difference between particle and gas phase is then negligible, and Eq. (4.5.49) yields the equation for η_{ex} for the isothermal case ($T_p = T_g$), Eq. (4.5.21):

$$\begin{aligned} \eta_{ex} &\approx \left(1 - \frac{r_{m,eff}}{r_{m,eff, max}} \right) = \left[1 - \frac{\eta_{ex} k_A(T_g) c_{A,g}}{\beta c_{A,g}} \right] \Rightarrow \eta_{ex} \\ &\approx \left(1 + \frac{k_A}{\beta} \right)^{-1} \quad (\text{for } \beta_{ex} \rightarrow 0) \end{aligned} \quad (4.5.51)$$

η_{ex} is then < 1 , and follows the function given in Figure 4.5.8 for $m = 1$ (first-order reaction).

Figure 4.5.15 shows η_{ex} as a function of the ratio of the (measurable) effective reaction rate to the maximum rate for complete control by external mass transfer for different values of β_{ex} and a constant γ_{ex} of 20, which represents the example of an activation energy of 78 kJ mol⁻¹ and a temperature of 473 K. As we can see, η_{ex} is > 1

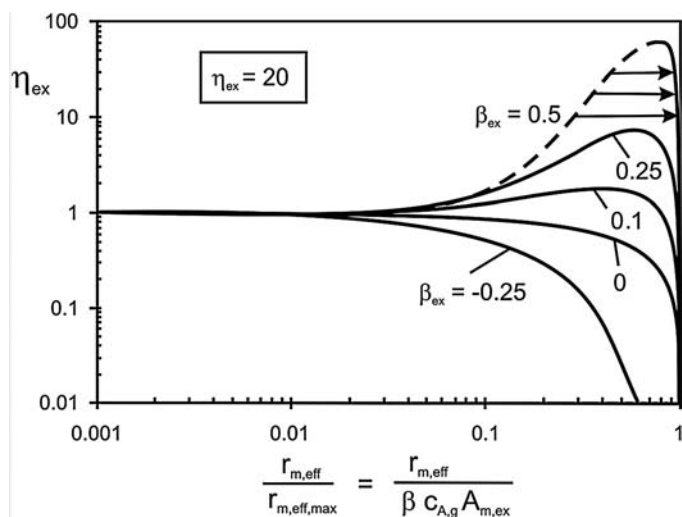


Figure 4.5.15 External effectiveness factor η_{ex} as a function of the ratio of the (measurable) effective reaction rate to the maximum rate (complete control by external mass transfer) for a constant Arrhenius number γ_{ex} of 20. For a Prater number $\beta_{ex} < 0$, the reaction is endothermic, for $\beta_{ex} > 0$ exothermic, and for $\beta_{ex} = 0$ we have isothermal conditions. Arrows and dashed line indicate ignition, as explained in the text.

for an exothermic reaction and β_{ex} is >0.1 , which is easily reached for gases: for example, for 1 bar, 500 K, and 10 mol.% A, $\beta_{\text{ex}} \approx -3 \times 10^{-6} \text{ mol J}^{-1} \Delta_{\text{R}}H$ [Eq. (4.5.47) for $D_{A,g} \approx 0.3 \text{ cm}^2 \text{ s}^{-1}$, $\lambda_g \approx 0.04 \text{ W m}^{-1} \text{ K}^{-1}$, and $c_{A,g} \approx 2 \text{ mol m}^{-3}$]. Thus, for $\Delta_{\text{R}}H \approx -30 \text{ kJ mol}^{-1} \text{ K}^{-1}$, $\beta_{\text{ex}} \approx 0.1$.

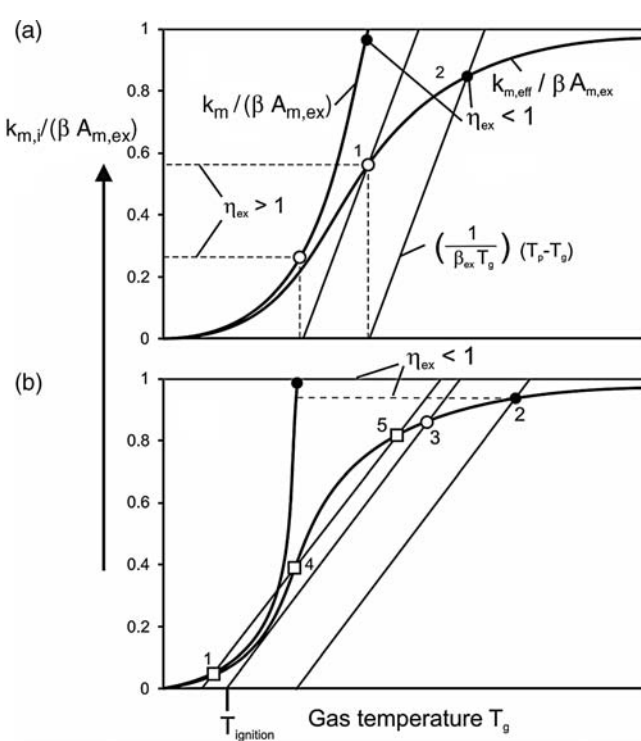
The system of an exothermic reaction at the surface of a solid catalyst can be also inspected with regard to the effective rate by rearranging the heat balance. For steady state, the effective rate (relative to the maximum rate in the case of complete control by external mass transfer) is deduced from Eqs. (4.5.31) and (4.5.47):

$$\frac{r_{m,\text{eff}}}{\beta A_{m,\text{ex}} c_{A,g}} = \frac{k_{m,\text{eff}}}{\beta A_{m,\text{ex}}} = \frac{\alpha(T_p - T_g)}{\beta(-\Delta_{\text{R}}H)c_{A,g}} = \frac{1}{\beta_{\text{ex}} T_g} (T_p - T_g)$$

The left-hand side of this equation leads to a sigmoidal curve in a plot of this term versus the temperature of the gas phase, while the right-hand side leads to lines as shown in Figure 4.5.16 for two different cases. In the first case (Figure 4.5.16a), the Prater number β_{ex} is small, ($<$ about 0.2) for example, the reaction is only weakly exothermic or cooling is efficient or the feed gas is diluted with inert gas. For a low gas temperature, η_{ex} is >1 , that is, $k_{m,\text{eff}}(T_p) > k_A(T_g) A_{m,\text{ex}}$ (state 1 in Figure 4.5.16a). If the temperature is increased, η_{ex} becomes < 1 (state 2 in Figure 4.5.16a).

In the second case (Figure 4.5.16b), the Prater number β_{ex} is higher, (>0.25 , see Fig. 4.5.15) and ignition may occur. As in the first case (Figure 4.5.16a), η_{ex} is >1 for a low temperature and η_{ex} is <1 for a (very) high temperature (states 1 and 2, respectively, in Figure 4.5.16b). Now, however, ignition occurs, if the gas temperature passes a certain value (T_{ignition} , state 3). For $T_g < T_{\text{ignition}}$, multiple states are possible. Certain states can then not exist (e.g., state 4), and for other multiple states (states 1 and 5), the actual state of a catalyst particle depends on its history, that is, did it start hot or cold. Note that in the case of such an ignition behavior, not all states shown in Figure 4.5.15 are possible, as indicated by the dashed line for the example of $\beta_{\text{ex}}=0.5$, where for $r_{m,\text{eff}}/r_{m,\text{max}} > 0.04$, ignition occurs (arrows in Figure 4.5.15). [Without further derivation, it should be mentioned that detailed analysis of the ignition behavior – as performed in Section 4.10.3 for chemical reactors – reveals that ignition is reached if $r_{m,\text{eff}}/r_{m,\text{max}}$ equals the term $(e\beta_{\text{ex}}\gamma_{\text{ex}})^{-1}$.]

Figure 4.5.16 Effective reaction rate constant relative to the maximum rate constant for complete control by external mass transfer for two different cases: (a) represents a moderate exothermic reaction/efficient cooling (low value of β_{ex}) and (b) the reverse.



4.5.4

Chemical Reaction and Internal Transport of Mass and Heat

4.5.4.1 Pore Diffusion Resistance and Effective Reaction Rate

In Section 4.5.3, we introduced effectiveness factors to derive universally valid equations for the interplay of the chemical reaction with the external and internal mass transfer. Now we inspect pore diffusion in more detail, first for a single pore and then for particles.

Single Cylindrical Pore In contrast to the interplay of chemical reaction with interfacial mass transfer, a reaction at the walls of the pores of a solid catalyst and the internal mass transfer by pore diffusion are not consecutive processes. For a single cylindrical pore of length L and a reactant A diffusing into the pore, where a first-order reaction takes place at the pore surface, we obtain:

$$r_A = -\frac{d\dot{n}_A}{dA_{\text{pore}}} = k_A c_A \quad (4.5.52)$$

The rate constant k_A ($\text{m}^3 \text{ m}^{-2} \text{ s}^{-1}$) is related to the surface of the pore A_{pore} (m^2). As shown by Figure 4.5.17, the steady state mass balance for a small slice with thickness Δz , cross-sectional area πr_{pore}^2 , and mantle area $2\pi r_{\text{pore}} \Delta z$ is given by:

$$\underbrace{-D_A \pi r_{\text{pore}}^2 \left(\frac{dc_A}{dz} \right)_z}_{\text{Input flux of A}} = \underbrace{k_A c_A 2\pi r_{\text{pore}} \Delta z}_{\text{Disappearance by reaction}} - \underbrace{-D_A \pi r_{\text{pore}}^2 \left(\frac{dc_A}{dz} \right)_{z+\Delta z}}_{\text{Output flux of A}} \quad (4.5.53)$$

if we use *Fick's first law* [Eq. (3.1.54)] for the flux of A into and out of the slice. D_A is the diffusion coefficient in the pore and equals the molecular diffusion coefficient, if the influence of *Knudsen diffusion* in very narrow pores is negligible (Section 3.2.2.3).

By rearrangement of Eq. (4.5.53) we obtain:

$$\frac{\left(\frac{dc_A}{dz} \right)_{z+\Delta z} - \left(\frac{dc_A}{dz} \right)_z}{\Delta z} = \frac{2k_A}{D_A r_{\text{pore}}} c_A \quad (4.5.54)$$

Taking the limit of an infinitesimal small value of Δz ($= dz$) we get:

$$\frac{d^2 c_A}{dz^2} = \frac{2k_A}{D_A r_{\text{pore}}} c_A \quad (4.5.55)$$

As boundary conditions we have:

$$c_A = c_{A,s} \quad (\text{for } z = 0, \text{ i.e., at the pore entrance, whereby the index "s" refers to the external surface of the pore that faces the bulk phase of the fluid}) \quad (4.5.56)$$

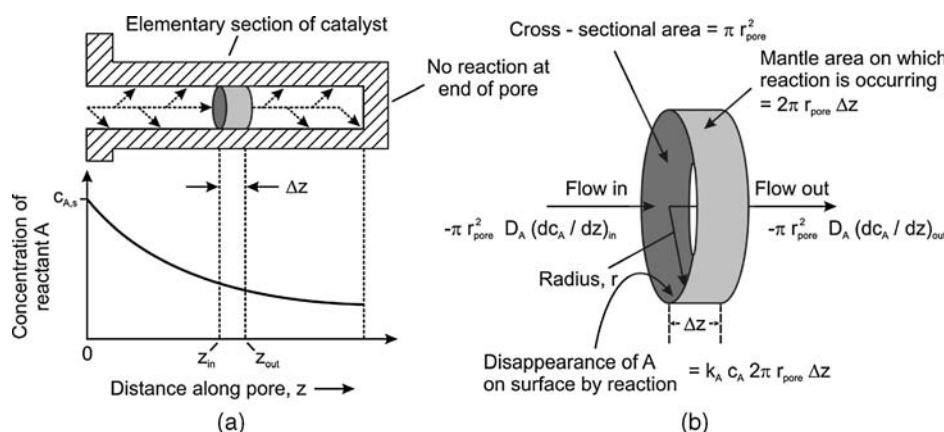


Figure 4.5.17 Representation of (a) a single cylindrical catalyst pore and (b) mass balance for an elementary slice of the pore. Adapted from Levenspiel (1999).

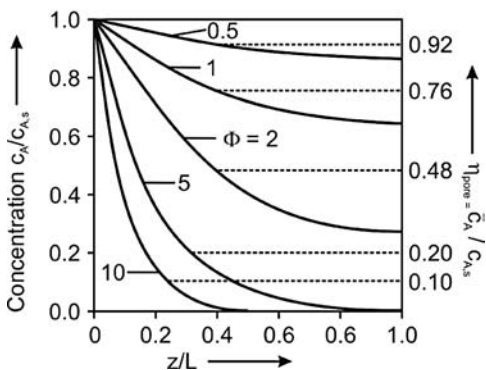


Figure 4.5.18 Influence of Thiele modulus ϕ on distribution and average value of concentration of reactant A in a single cylindrical pore (length L) as well as in porous slab (center at $z = L$) [for definition of η_{pore} see Eq. (4.5.62)].

Yakov Borisovich Zeldovich (1914–1987), a Russian physicist, played an important role in the development of Soviet nuclear weapons, and made important contributions to the fields of adsorption and catalysis, the theory of ignition and combustion, astrophysics, and general relativity.

Albert Einstein (1879–1955): a German physicist and one of the most important scientists of the twentieth century. He formulated the special and general theories of relativity, and made significant contributions to quantum mechanics, statistical mechanics, and cosmology. He was awarded the 1921 Nobel Prize in Physics for his explanation of the photoelectric effect.

Marian Smoluchowski (1872–1919): a Polish scientist and pioneer of statistical physics. He described Brownian motion, worked on the kinetic theory at the same time as *Albert Einstein*, and presented an equation that became the basis of the theory of stochastic processes.

$$\frac{dc_A}{dz} = 0 \quad (\text{for } z = L, \text{ i.e., at the interior closed end of the pore}) \quad (4.5.57)$$

The solution of the frequently met linear differential equation (4.5.55) is:

$$\frac{c_A(z)}{c_{A,s}(z=0)} = \frac{\cosh[\phi(1 - \frac{z}{L})]}{\cosh\phi} \quad (4.5.58)$$

where ϕ is the *Thiele modulus* of a single pore, named after *Ernst W. Thiele* (Thiele, 1939):

$$\phi = L \sqrt{\frac{2k_A}{D_A r_{\text{pore}}}} = L \sqrt{\frac{k_A A_{\text{int,V}}}{D_A}} \quad (4.5.59)$$

where $A_{\text{int,V}}$ ($\text{m}^2 \text{ m}^{-3}$) is the internal surface area per volume ($=2/r_{\text{pore}}$ for a cylindrical pore). The fall in concentration in the pore is shown in Figure 4.5.18 for different values of ϕ .

Notably, the Russian physicist *Zeldovich* (see box) derived the same equations and dimensionless modulus independently from Thiele in the same year (Zeldovich, 1939). Thus in truth ϕ should be named Thiele–Zeldowitch modulus.

Steep concentration profiles arise if the diffusion coefficient is low or if the length of the pore is high, or more precisely if the Thiele modulus ϕ exceeds a value of about 1. As a criterion for the development of distinct concentration gradients we may also state that the characteristic time for diffusion, τ_D , which equals the term $L^2/(2 D)$ according to the Einstein–Smoluchowski relation (see boxes), should be at least of the order of magnitude of the reaction time τ_R :

$$\tau_{D,\text{pore}} = \frac{L^2}{2D_A} \geq \tau_R = \frac{1}{k_A A_{\text{int,V}}} \quad (4.5.60)$$

This condition in terms of the Thiele modulus of a single pore [Eq. (4.5.59)] yields:

$$\phi = \sqrt{\frac{\tau_{D,\text{pore}}}{2\tau_R}} \geq 1 \quad (4.5.61)$$

In other words, the Thiele modulus is (almost) equivalent to the (square root) of the ratio τ_D/τ_R .

As a measure of how much the effective rate is lowered by the resistance of pore diffusion, the effectiveness factor η_{pore} is used, which is the ratio of the actual mean reaction rate in the pore to the maximum rate in the absence of pore diffusion limitation. For a first-order reaction, η_{pore} equals the ratio of the mean concentration to that at the pore entrance:

$$\eta_{\text{pore}} = \frac{r_{A,\text{eff}}}{r_{A,\text{max}}} = \frac{r_{A,\text{eff}}}{r_A(c_A = c_{A,s})} = \frac{k_A \bar{c}_A}{k_A c_{A,s}} = \frac{\bar{c}_A}{c_{A,s}} \quad (4.5.62)$$

The effective rate is obtained by the following integration:

$$r_{A,\text{eff}} = k_A \bar{c}_A = \frac{k_A}{L} \int_{z=0}^{z=L} c_A(z) dz = \frac{k_A c_{A,s}}{L} \int_{z=0}^{z=L} \frac{\cosh[\phi(1 - \frac{z}{L})]}{\cosh\phi} dz \quad (4.5.63)$$

The solution of this integral is:

$$r_{A,\text{eff}} = k_A \frac{\tanh\phi}{\phi} c_{A,s} = k_{A,\text{eff}} c_{A,s} \quad (4.5.64)$$

and insertion of Eq. (4.5.62) into Eq. (4.5.64) yields:

$$\eta_{\text{pore}} = \frac{\tanh\phi}{\phi} \approx \frac{1}{\phi} \quad (\text{for } \phi \geq 2) \quad (4.5.65)$$

Porous Catalyst Particles The results of inspection of the influence of pore diffusion on the effective rate in a single pore can be transferred to porous particles if we consider the following aspects:

- For a single cylindrical pore, the distance penetrated by the fluid is just the pore length. For catalyst particles of various shapes, like spheres, cylinders, and plates, we use the ratio of the particle volume V_p to the exterior surface $A_{p,\text{ex}}$ as the characteristic length.
- Instead of the molecular diffusion coefficient in a single pore, we have to use an effective diffusion coefficient $D_{A,\text{eff}}$ that considers the porosity of the porous particle and the tortuous nature of pores and pore constrictions. These two aspects (details in Section 3.2.2.3) lead to a value of $D_{A,\text{eff}}$ that is a factor of about 10 smaller than the molecular diffusivity. For Knudsen diffusion in narrow pores, this deviation is even higher.
- The rate constant can be expressed in different ways, for example, in terms of unit surface area (k_A in $\text{m}^3 \text{ m}^{-2} \text{ s}^{-1}$), particle mass (k_m in $\text{m}^3 \text{ kg}^{-1} \text{ s}^{-1}$), or particle volume (k_V in $\text{m}^3 \text{ m}^{-3} \text{ s}^{-1}$). Do not mistake k_V for the rate constant related to the volume of the catalyst bed, which has the same unit (s^{-1}) but is by the factor $(1 - \varepsilon)$ (ε = bed porosity) smaller than k_V . The relations between these rate constants and the respective Thiele moduli are:

$$k_V = k_m \rho_p = k_A A_{\text{int},V} \quad (4.5.66)$$

$$\phi = L \sqrt{\frac{k_A A_{\text{int},V}}{D_{A,\text{eff}}}} = L \sqrt{\frac{k_m \rho_p}{D_{A,\text{eff}}}} = L \sqrt{\frac{k_V}{D_{A,\text{eff}}}} \quad \left(\text{with } L = \frac{V_p}{A_{p,\text{ex}}} \right) \quad (4.5.67)$$

Let us now consider a first-order reaction in an isothermal porous flat plate (Figure 4.5.19).

The intrinsic reaction rate in terms of the mass of the catalyst particle ($\text{mol kg}_{\text{cat}}^{-1} \text{ s}^{-1}$) is:

$$r_m = -\frac{dc_A}{dm_{\text{cat}}} = k_m c_A \quad (4.5.68)$$

For a flat large plate, we only consider mass transfer in the z -direction perpendicular to the area A_{plate} . The mass balance for a small slice with thickness Δz and mass $\rho_p A_{\text{plate}} \Delta z$ is:

$$-D_{A,\text{eff}} A_{\text{plate}} \left(\frac{dc_A}{dz} \right)_z = k_m c_A \rho_p A_{\text{plate}} \Delta z - D_{A,\text{eff}} A_{\text{plate}} \left(\frac{dc_A}{dz} \right)_{z+\Delta z} \quad (4.5.69)$$

This equation is similar to the respective equation for a single cylindrical pore [Eq. (4.5.53)], and by a similar rearrangement we obtain the following differential equation:

$$D_{A,\text{eff}} \frac{d^2 c_A}{dz^2} = k_m c_A \rho_p \quad (4.5.70)$$

The solution of Eq. (4.5.70) for the boundary conditions:

$$c_A = c_{A,s} \quad (\text{for } z = 0 \text{ or } z = 2L, \text{ i.e., at both external surfaces}) \quad (4.5.71)$$

$$\frac{dc_A}{dz} = 0 \quad (\text{for } z = L, \text{ i.e., at the center line of the plate}) \quad (4.5.72)$$

is the same as already derived for a single pore [Eq. (4.5.58)]:

$$\frac{c_A(z)}{c_{A,s}(z=0 \text{ or } 2L)} = \frac{\cosh \left[\phi \left(1 - \frac{z}{L} \right) \right]}{\cosh \phi} \quad (4.5.73)$$

with ϕ as the Thiele modulus based on the rate constant related to the catalyst mass:

$$\phi = L \sqrt{\frac{k_m \rho_p}{D_{A,\text{eff}}}} \quad (4.5.74)$$

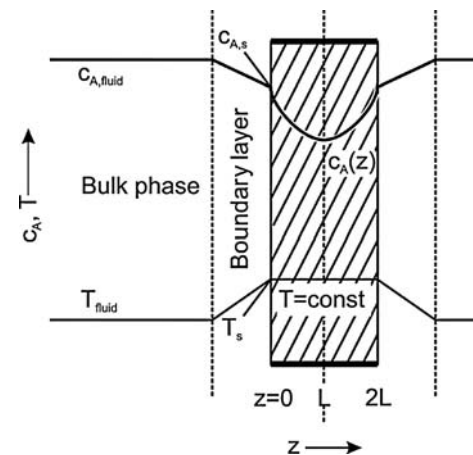


Figure 4.5.19 Concentration and temperature around and in a porous catalyst plate (external and internal gradients, although in this section only internal transport phenomena are inspected).

The concentration profiles according to Eq. (4.5.73) are shown in Figure 4.5.18.

Analogously to a single pore [Eq. (4.5.65)], the effectiveness factor in a flat plate is given by:

$$\eta_{\text{pore}} = \frac{r_{m,\text{eff}}}{r_m (c_A = c_{A,s})} = \frac{k_{m,\text{eff}}}{k_m} = \frac{\tanh \phi}{\phi} \approx \frac{1}{\phi} \quad (\text{for } \phi \geq 2) \quad (4.5.75)$$

It is interesting to take a closer look at the influence of temperature on the effective rate and rate constant, respectively. For a fully developed influence of pore diffusion ($\phi > 2$), we get based on Eqs. (4.5.74) and (4.5.75) and the Arrhenius equation [Eq. (4.3.4)]:

$$\begin{aligned} k_{m,\text{eff}} &= \frac{k_m}{\phi} = \frac{k_m}{L \sqrt{\frac{k_m \rho_p}{D_{A,\text{eff}}}}} = \frac{\sqrt{k_m}}{L \sqrt{\frac{\rho_p}{D_{A,\text{eff}}}}} = \frac{\sqrt{k_{m,0}}}{L \sqrt{\frac{\rho_p}{D_{A,\text{eff}}}}} e^{-\frac{E_A}{2RT}} \\ &\approx \text{const.} \times e^{-\frac{E_A}{2RT}} \quad (\text{for } \phi \geq 2) \end{aligned} \quad (4.5.76)$$

If we neglect the comparatively small influence of temperature on the diffusion coefficient, we obtain an apparent activation energy that is only half the value of the intrinsic constant.

The concept of an effectiveness factor of a porous slab can be extended to other geometries (solutions in Table 4.5.5). In contrast to some other textbooks ϕ is here always calculated based on the ratio of the particle volume to the external surface as characteristic length (L for a slab with thickness $2L$, $d_{\text{cyl}}/4$ for long cylinders, and $d_p/6$ for spheres):

$$\phi = \frac{V_p}{A_{p,\text{ex}}} \sqrt{\frac{k_m \rho_p}{D_{A,\text{eff}}}} \quad (4.5.77)$$

Figure 4.5.20 shows the effectiveness factor as a function of the Thiele modulus for a slab, a sphere, and a cylinder. It is apparent that all curves can be described with acceptable accuracy by the exact solution for a slab [$\eta_{\text{pore}} = \tanh(\phi/\phi)$; $\eta_{\text{pore}} = 1/\phi$ for $\phi > 2$]. Thus, Figures 4.5.21 and 4.5.22 derived for a flat plate can be used to a good approximation for any particle geometry (with $V_p/A_{p,\text{ex}}$ as characteristic length for ϕ).

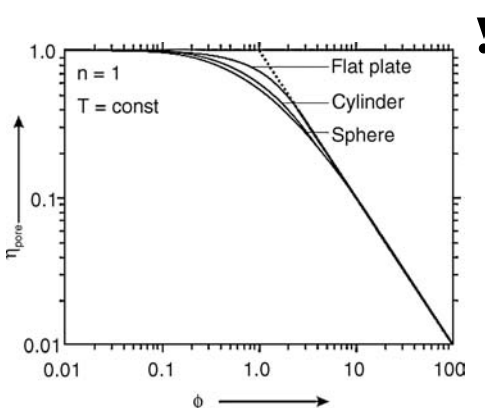


Figure 4.5.20 Effectiveness factor (pore diffusion) as a function of the Thiele modulus ϕ for a plate, sphere, and cylinder (first-order reaction).

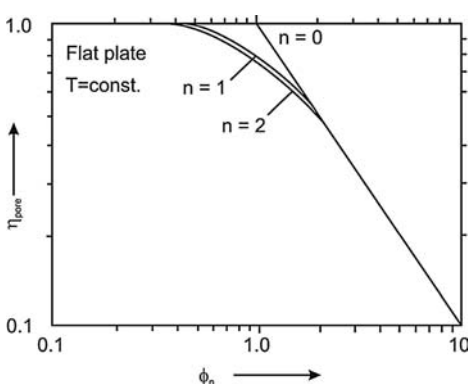


Figure 4.5.21 Effectiveness factor (pore diffusion) as a function of ϕ_n for an n th order reaction.

Table 4.5.5 Equations for the distribution of concentration of reactant A and effectiveness factor η_{pore} for pore diffusion (isothermal, irreversible first-order reaction).

Geometry	Thiele modulus ϕ	Distribution of concentration	Effectiveness factor η_{pore}
Flat plate (thickness $2L$)	$L \sqrt{\frac{k_m \rho_p}{D_{A,\text{eff}}}}$	$\frac{c_A(z)}{c_{A,s}} = \frac{\cosh[\phi(1 - \frac{z}{L})]}{\cosh \phi}$ with $c_A(z=0) = c_{A,s}$	$\frac{\tanh \phi}{\phi}$
Sphere (diameter d_p , radius r_p)	$\frac{d_p}{6} \sqrt{\frac{k_m \rho_p}{D_{A,\text{eff}}}}$	$\frac{c_A(r)}{c_{A,s}} = \frac{r_p}{r} \frac{\sinh\left(\frac{r}{r_p} 3\phi\right)}{\sinh(3\phi)}$ with $c_A(r=r_p) = c_{A,s}$	$\frac{1}{\phi} \left(\frac{1}{\tanh(3\phi)} - \frac{1}{3\phi} \right)$
Cylinder (diameter d_{cyl} , length L , $L \gg d_{\text{cyl}}$)	$\frac{d_{\text{cyl}}}{4} \sqrt{\frac{k_m \rho_p}{D_{A,\text{eff}}}}$	—	$\frac{1}{\phi} \left[\frac{I_1(2\phi)}{I_0(2\phi)} \right]$ $I = \text{Bessel function}^a$
All geometries (approximation)	$\frac{V_p}{A_{p,\text{ex}}} \sqrt{\frac{k_m \rho_p}{D_{A,\text{eff}}}}$	—	$\frac{\tanh \phi}{\phi}$

a) Values of $I_1(2\phi)/I_0(2\phi)$: 0.1 ($\phi = 0.1$), 0.45 ($\phi = 0.5$), 0.86 ($\phi = 2$), 0.98 ($\phi = 10$), ≈ 1 ($\phi > 10$).

The concept of an effectiveness factor can be further extended to other irreversible reactions with a reaction order $n \neq 1$ by the introduction of a modified Thiele modulus ϕ_n :

$$\phi_n = \frac{V_p}{A_{p,\text{ex}}} \sqrt{\left(\frac{n+1}{2}\right) \frac{k_m \rho_p c_{A,s}^{n-1}}{D_{A,\text{eff}}}} \quad (4.5.78)$$

Figure 4.5.21 shows the effectiveness factor as a function of ϕ_n for a slab (flat plate) and different reaction orders n . It is again obvious that except for a zero-order reaction ($n=0$), all curves are similar, and again the asymptotic solution $\eta_{\text{pore}} = 1/\phi$ is reached for $\phi_n > 2$.

For kinetics not described by power law equations, the calculation of η_{pore} is complicated and we refer to the literature (Hong, Hecker, and Fletcher, 2000; Levenspiel, 1999; Bischoff, 1965; Valdman and Hughes, 1976; Roberts and Satterfield, 1965, 1966). Here we only consider the reaction of a species adsorbed according to Langmuir and a first-order reversible reaction (Example 4.5.6). For a Langmuir type reaction [Eq. (4.5.2)] the rate related to the mass of catalyst is:

$$r_{m,A} = \frac{k_{m,A} c_A}{1 + K_{\text{ads},A} c_A} \quad (4.5.79)$$

For $K_{\text{ads},A} c_A \ll 1$, Eq. (4.5.79) approaches a first-order reaction and thus we have:

$$\eta_{\text{pore}} = \frac{\tanh \phi}{\phi} \quad \left(\text{with } \phi = \frac{V_p}{A_{p,\text{ex}}} \sqrt{\frac{k_{m,A} \rho_p}{D_{A,\text{eff}}}} \right) \quad (4.5.80)$$

For $K_{\text{ads},A} c_A \gg 1$, Eq. (4.5.79) approaches a zero-order reaction and we obtain by Eq. (4.5.78):

$$\eta_{\text{pore}} \approx \frac{\tanh \phi}{\phi} \quad \left(\text{with } \phi = \frac{V_p}{A_{p,\text{ex}}} \sqrt{\frac{k_{m,A} \rho_p}{2 K_{\text{ads},A} D_{A,\text{eff}} c_{A,s}}} \right) \quad (4.5.81)$$

Levenspiel (1999) proposed an approximated solution for all values of $K_{\text{ads},A} c_A$:

$$\eta_{\text{pore, Langmuir}} \approx \frac{\tanh \phi_{\text{Langmuir}}}{\phi_{\text{Langmuir}}} \quad \left[\text{with } \phi_{\text{Langmuir}} = \frac{V_p}{A_{p,\text{ex}}} \sqrt{\frac{k_{m,A} \rho_p}{D_{A,\text{eff}} (1 + 2 K_{\text{ads},A} c_{A,s})}} \right] \quad (4.5.82)$$

and thus we approach Eq. (4.5.80) for $K_{\text{ads},A} c_A \ll 1$ and Eq. (4.5.81) for $K_{\text{ads},A} c_A \gg 1$.

Example 4.5.6: Effectiveness factor (pore diffusion) for a reversible first-order reaction

The mass balance of a porous spherical particle and a reversible first-order reaction of A to B (with $k_{m,A}$ and $k_{m,B}$ as the rate constants for the reaction $A \rightarrow B$ and the reverse reaction, respectively) is:

$$D_{A,\text{eff}} \left(\frac{d^2 c_A}{dr^2} + \frac{2}{r} \frac{dc_A}{dr} \right) = (k_{m,A} c_A - k_{m,B} c_B) \rho_p \quad (4.5.83)$$

The equilibrium constant based on the molar equilibrium concentrations c_i^* is:

$$K_c = \frac{c_B^*}{c_A^*} = \frac{k_{m,A}}{k_{m,B}} \quad (4.5.84)$$

and together with the mass balance $c_A + c_B = c_A^* + c_B^*$ we obtain:

$$c_B = c_A^* + c_B^* - c_A = c_A^* (1 + K_c) - c_A \quad (4.5.85)$$

Insertion of Eqs. (4.5.84) and (4.5.85) into Eq. (4.5.83) leads to:

$$D_{A,\text{eff}} \left(\frac{d^2 c_A}{dr^2} + \frac{2}{r} \frac{dc_A}{dr} \right) = k_{m,A} \frac{(1 + K_c)}{K_c} (c_A - c_A^*) \rho_p \quad (4.5.86)$$

If we use the definition $\Delta c_A = c_A - c_A^*$ and thus $d(\Delta c_A) = dc_A$, Eq. (4.5.86) reads as:

$$D_{A,\text{eff}} \left(\frac{d^2 \Delta c_A}{dr^2} + \frac{2}{r} \frac{d\Delta c_A}{dr} \right) = k_{m,A} \frac{(1 + K_c)}{K_c} \Delta c_A \rho_p \quad (4.5.87)$$

The solution of this differential equation for the boundary conditions:

$$\Delta c_A = c_{A,s} - c_{A,s}^* \quad [\text{for } r = r_p \text{ (external surface of particle)}] \quad (4.5.88)$$

$$\frac{d\Delta c_A}{dr} = 0 \quad [\text{for } r = 0 \text{ (center of particle)}] \quad (4.5.89)$$

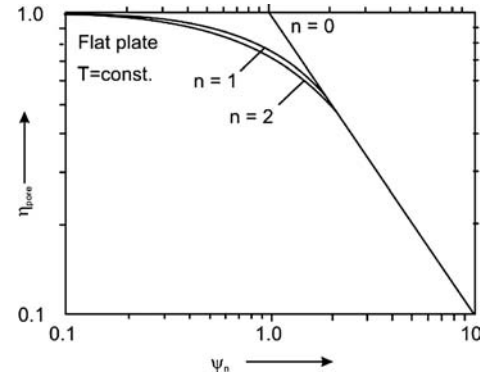


Figure 4.5.22 Effectiveness factor (pore diffusion) as a function of the Weisz modulus ψ_n [defined by Eq. (4.5.93)] for an irreversible reaction with reaction order n .

is:

$$\frac{c_A(r)}{c_{A,s}} = \frac{r_p}{r} \frac{\sinh\left(\frac{r}{r_p} 3\phi_{\text{reversible}}\right)}{\sinh(3\phi_{\text{reversible}})} \quad (4.5.90)$$

(with $\phi_{\text{reversible}} = \frac{d_p}{6} \sqrt{\frac{k_{m,A}\rho_p(1+K_c)}{D_{A,\text{eff}} K_c}}$)

Derivation of the effectiveness factor by Eq. (4.5.90) is similar to a reversible first-order reaction, as already derived for a single cylindrical pore [Eqs. (4.5.62)–(4.5.64)]:

$$\begin{aligned} \eta_{\text{pore}} &= \frac{k_{m,A,\text{eff}}}{k_{m,A}} = \frac{1}{\phi_{\text{reversible}}} \left[\frac{1}{\tanh(3\phi_{\text{reversible}})} - \frac{1}{3\phi_{\text{reversible}}} \right] \\ &\approx \frac{\tanh\phi_{\text{reversible}}}{\phi_{\text{reversible}}} \end{aligned} \quad (4.5.91)$$

The effective reaction rate is then given by (c_s = concentration at the external surface):

$$\begin{aligned} r_{A,\text{eff}} &= \eta_{\text{pore}} k_{m,A} \left(c_{A,s} - \frac{c_{B,s}}{K_c} \right) \\ &= \eta_{\text{pore}} k_{m,A} \frac{(1+K_c)}{K_c} \left(c_{A,s} - c_{A,s}^* \right) \end{aligned} \quad (4.5.92)$$

Note that for a reversible reaction the term $(1+K_c)/K_c$ is always higher than 1 and thus the Thiele modulus $\phi_{\text{reversible}}$ is higher (η_{pore} is smaller) than for an irreversible reaction.

The determination of η_{pore} still leads to the problem that rate constants are measured values and thus the question arises as to whether and to what extent the kinetic parameters are already influenced by transport processes. With the equations given so far, this question cannot be answered, since the Thiele modulus is defined based on the intrinsic constant k_m and not on $k_{m,\text{eff}}$. This problem can be solved by a modulus that contains only $k_{m,\text{eff}}$. This modulus is known as the *Weisz modulus* ψ and is defined for an arbitrary particle shape and order n as:

$$\nabla \quad \psi_n = \left(\frac{V_p}{A_{p,\text{ex}}} \right)^2 \left(\frac{n+1}{2} \right) \frac{r_{m,\text{eff}} \rho_p}{D_{A,\text{eff}} c_{A,s}} = \left(\frac{V_p}{A_{p,\text{ex}}} \right)^2 \left(\frac{n+1}{2} \right) \frac{k_{m,\text{eff}} \rho_p c_{A,s}^{n-1}}{D_{A,\text{eff}}} \quad (4.5.93)$$

The effectiveness factor as a function of the *Weisz modulus* ψ_n is depicted in Figure 4.5.22 for different reaction orders. This diagram is very useful since ψ_n only includes observables.

By recalling the Thiele modulus ϕ_n for an irreversible n -th order reaction and for particles of arbitrary shape, Eq. (4.5.78), we obtain the following relation:

$$\nabla \quad \psi_n = \eta_{\text{pore}} \phi_n^2 \quad (4.5.94)$$

For strong pore diffusion effects (approach to asymptotic solution $\eta_{\text{pore}} = 1/\phi_n$), we have:

$$\nabla \quad \eta_{\text{pore}} \approx \frac{1}{\phi_n} \approx \frac{1}{\psi_n} \leq 0.5 \quad (\text{for } \phi \text{ or } \psi_n \geq 2) \quad (4.5.95)$$

and for practically no resistance to pore diffusion we have:

$$\eta_{\text{pore}} \geq 0.95 \quad (\text{for } \psi_n \leq 0.15 \text{ or } \phi_n \leq 0.4) \quad (4.5.96)$$

For a first-order reaction and a plate of thickness $2L$ we obtain:

$$\psi = \eta_{\text{pore}} L^2 \frac{k_m \rho_p}{D_{A,\text{eff}}} = \eta_{\text{pore}} \phi^2 \quad (4.5.97)$$

4.5.4.2 Combined Influence of Pore Diffusion and Intraparticle Heat Transport

The solution of the differential equations for internal heat and mass transfer (details in Emig and Klemm, 2005; Levenspiel, 1996, 1999) lead to the temperature difference between the center and the outer surface of a particle with an effective thermal conductivity λ_p :

$$T_{\text{center}} - T_s = \frac{D_{A,\text{eff}} (-\Delta_R H)}{\lambda_p} (c_{A,s} - c_{A,\text{center}}) \quad (4.5.98)$$

Thus, for an exothermic reaction, the center of the particle is hotter than the external surface. The maximum temperature difference is established for $c_{A,\text{center}} = 0$, that is, for strong resistance to pore diffusion and a value of Thiele modulus of about more than 5, Figure 4.5.18:

$$\nabla T_{\text{center, max}} - T_s = \frac{D_{A,\text{eff}}(-\Delta_R H)}{\lambda_p} c_{A,s} \quad (4.5.99)$$

An estimation of the temperature gradient in a particle is given in Example 4.5.7, indicating that notable gradients can only occur for gas-phase reactions. For an exothermic reaction, overheating of the particle (to a certain mean temperature $\bar{T} > T_s$) leads to an increase in the intrinsic rate constant k_m compared to the one reached at the temperature of the external surface of the particle. This effect can overcompensate for the lower concentration compared to the bulk phase caused by diffusional limitations, and the effectiveness factor may reach values above unity:

$$\begin{aligned} \eta_{\text{pore}} &= \frac{r_{A,\text{eff}}(\bar{T}, \bar{c}_A)}{r_A(T_s, c_{A,s})} \\ &= \underbrace{\frac{k_{m,A}(\bar{T})}{k_{m,A}(T_s)}}_{> 1 \text{ (influence of heat transfer/overheating)}} \underbrace{\frac{\bar{c}_A}{c_{A,s}}}_{< 1 \text{ (influence of diffusion)}} \quad (\text{for an exothermic reaction}) \end{aligned} \quad (4.5.100)$$

To calculate η_{pore} , the mass and heat balances must be solved simultaneously. Analytical and numerical solutions are given by Petersen (1962), Tinkler and Pigford (1961), Carberry (1961), Tinkler and Metzner (1961), and Weisz and Hicks (1962). The behavior of a non-isothermal pellet in the regime of pore diffusion limitation is governed by the *Thiele modulus* ϕ (related to T_{surface}), the *Prater number* β_{int} , and the *Arrhenius number* γ_{int} :

$$\beta_{\text{int}} = \frac{T_{\text{center, max}} - T_s}{T_s} = \frac{D_{A,\text{eff}}(-\Delta_R H) c_{A,s}}{\lambda_p T_s} \quad (4.5.101)$$

$$\gamma_{\text{int}} = \frac{E_A}{RT_s} \quad (4.5.102)$$

as shown in Figure 4.5.23 for a spherical particle and an irreversible first-order reaction. The *Prater number* β_{int} accounts for the ratio of heat production to the dissipation by conduction, so a high value leads to an increase of the effectiveness factor for a given *Thiele modulus*. Negative values indicate an endothermic reaction. The *Arrhenius number* γ_{int} accounts for the temperature sensitivity, so a high value leads to an increase of the effectiveness factor.

For strong exothermic reactions multiple solutions may occur for $\phi < 1$ (Figure 4.5.23). Such a multiplicity results in the existence of several solutions for η_{pore} – usually up to three with an unstable midpoint. However, this phenomenon is rarely encountered in industrial practice.

Values of β_{int} , γ_{int} , and ϕ of selected reactions are listed in Table 4.5.6, which show that only for the dissociation of N_2O may the effectiveness factor $\eta_{\text{pore,max}}$ exceed unity (up to $\eta_{\text{pore,max}} = 100$ for $\phi = 1$, Figure 4.5.23). Thus, we conclude that η_{pore} is rarely influenced by heat transfer, and, only for control by external mass transfer, the overheating of a catalyst may enhance the effective rate constant compared to isothermal conditions (Topic 4.5.5).

Example 4.5.7: Intraparticle T-gradients for gas and liquid phase reactions

To estimate the intraparticle temperature rise, we use $D_{\text{eff}} \approx 0.1 D_{\text{mol}}$, $D_{\text{mol,gas}} \approx 2 \times 10^{-5} \text{ m}^2 \text{s}^{-1}$, $D_{\text{mol,liquid}} \approx 1 \times 10^{-9} \text{ m}^2 \text{s}^{-1}$, $c_{\text{gas}} (1 \text{ bar}, 600 \text{ K}) \approx 20 \text{ mol m}^{-3}$, $c_{\text{liquid}} \approx 10^4 \text{ mol m}^{-3}$, $\lambda_p \approx 0.2 \text{ W m}^{-1} \text{K}^{-1}$, and $\Delta_R H \approx -100 \text{ kJ mol}^{-1}$. Equation (4.5.99) then yields a maximum T -rise

of 20 K for gases and 0.5 K for liquids. As a rule of thumb, a relevant gradient is not expected for liquids, but may occur for gases, if the thermal conductivity of the pellet is poor.

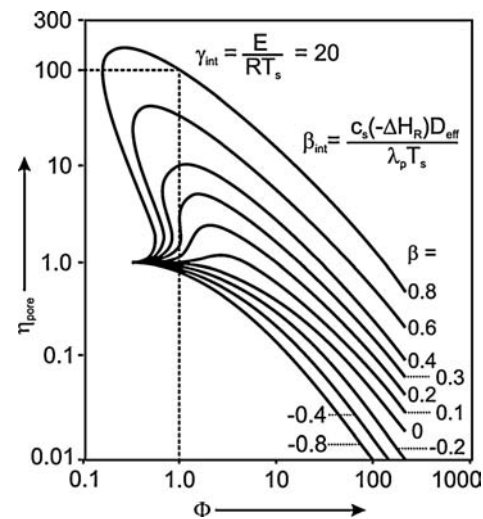


Figure 4.5.23 Effectiveness factor of a non-isothermal catalyst particle as a function of the Thiele modulus ϕ (at T_s) and the Prater number β_{int} for an Arrhenius number γ_{int} of 20 (for solutions for other γ_{int} values see Weisz and Hicks, 1962; Levenspiel, 1996).

Table 4.5.6 Values of Prater number β_{int} , Arrhenius number γ_{int} , and Thiele modulus ϕ [all related to T_s ; data from Murzin and Salmi (2005); Baerns *et al.* (2006); and Hlavacek, Kubicek, and Marek (1969)].

Reaction	β_{int}	γ_{int}	$\beta_{\text{int}} \times \gamma_{\text{int}}$	ϕ	$\eta_{\text{pore,max}}^{\text{a)}$
Dissociation of nitrous oxide (N_2O)	0.64	22	14	1–5	30
Hydrogenation of ethylene	0.07	23–27	1.6–1.9	0.2–2.8	≈1.2
Vinyl chloride from acetylene and HCl	0.25	7	1.8	0.27	≈1.1
Oxidation of ethylene to ethylene oxide	0.13	13	1.7	0.08	1
Oxidation of hydrogen	0.10	7–8	0.7–0.8	0.8–2	1
Hydrogenation of benzene	0.012	15	0.2	0.1–1.9	1
Oxidation of sulfur dioxide	0.012	15	0.2	0.9	1
Oxidation of methanol to formaldehyde	0.011	16	0.2	1.1	1
Ammonia synthesis	0.00006	29	0.002	1.2	1

a) Estimation based on the diagrams given by Weisz and Hicks (1962) and Levenspiel (1996).

4.5.5

Simultaneous Occurrence of Interfacial and Internal Mass Transport Effects

Based on the equations derived in Sections 4.5.3 and 4.5.4, we now define an overall effectiveness factor η_{overall} , which includes external and internal diffusion resistances. Here we only consider irreversible and reversible first-order isothermal reactions; for more complex cases see Baerns *et al.* (2006) or Westerterp, van Swaaij, and Beenackers (1998).

4.5.5.1 Irreversible First-Order Reaction

For an irreversible first-order reaction, the overall mass transfer resistance can be regarded as a serial connection of the two transport resistances by internal and external diffusion:

$$\eta_{\text{overall}} = \frac{r_{m,\text{eff}}}{r_m (c_A = c_{A,g})} = \frac{1}{k_m} \left(\frac{1}{\beta A_{m,\text{ex}}} + \frac{1}{\eta_{\text{pore}} k_m} \right)^{-1} = \eta_{\text{pore}} \left(1 + \frac{\eta_{\text{pore}} k_m}{\beta A_{m,\text{ex}}} \right)^{-1} \quad (4.5.103)$$

Comparison with Eq. (4.5.17) shows that η_{overall} equals $\eta_{\text{pore}} \eta_{\text{ex}}$. Example 4.5.8 gives a comparison of η_{overall} , η_{ex} , and η_{pore} both for a single particle and a fixed bed.

As a measure of the ratio of the external mass transfer to the mass transfer by pore diffusion, the *Biot number* for mass transfer, Bi_m , is frequently used:

$$Bi_m = \frac{\beta \frac{V_p}{A_{p,\text{ex}}}}{D_{\text{eff}}} = \frac{\beta \frac{d_p}{6}}{D_{\text{eff}}} \quad (\text{for a spherical particle}) \quad (4.5.104)$$

Insertion of this definition and of Eq. (4.5.77) into Eq. (4.5.103) leads to:

$$\eta_{\text{overall}} = \left(\frac{1}{\eta_{\text{pore}}} + \frac{\phi^2}{Bi_m} \right)^{-1} \quad (4.5.105)$$

Thus, for a high value of Bi_m , the overall effectiveness is dominated by the influence of pore diffusion ($\eta_{\text{overall}} \approx \eta_{\text{pore}}$). The minimum value of Bi_m can be roughly estimated as follows: The minimum mass transfer coefficient β_{min} equals the ratio of the molecular diffusivity D_{mol} to the maximum thickness of the boundary layer, δ_{max} [Eq. (3.2.67)]; for a single spherical particle, δ_{max} is about $d_p/2$ (for $Sh_{\text{min}} = 2$). D_{mol} is about ten-times higher than the effective diffusion coefficient D_{eff} in the porous structure (Section 3.2.2.3). Thus Eq. (4.5.104) yields:

$$Bi_{\text{min}} = \beta_{\text{min}} \frac{d_p}{6 D_{\text{eff}}} = \frac{D_{\text{mol}}}{\delta_{\text{max}}} \frac{d_p}{6 D_{\text{eff}}} = \frac{D_{\text{mol}}}{D_{\text{eff}}} \frac{1}{\delta_{\text{max}}} \frac{d_p}{6} \approx 10 \frac{2}{d_p} \frac{d_p}{6} \approx 3 \quad (\text{spherical particle}) \quad (4.5.106)$$

The influence of temperature on the role of external and internal diffusion on the effective reaction rate constant and on the apparent activation energy is discussed in Topic 4.5.6.

Example 4.5.8: Comparison of the overall effectiveness factor with those for pore diffusion and external mass transfer for a single spherical particle and a fixed bed

The effective rate may be influenced both by external and by pore diffusion. For a comparison of η_{overall} with η_{ex} and η_{pore} , we use the following assumptions:

- According to Eqs. (4.5.17) and (3.2.68), η_{ex} is given for a spherical particle by:

$$\begin{aligned}\eta_{\text{ex}} &= \frac{1}{1 + \frac{\eta_{\text{pore}} k_m}{\left(\frac{Sh}{d_p} D_{A,\text{mol}}\right) A_{m,\text{ex}}}} = \frac{1}{1 + \frac{\eta_{\text{pore}} k_m}{\left(\frac{Sh}{d_p} D_{A,\text{mol}}\right) \left(\frac{6}{d_p \rho_p}\right)}} \\ &= \frac{1}{1 + \frac{\eta_{\text{pore}} d_p^2 k_m \rho_p}{Sh 6 D_{A,\text{mol}}}}\end{aligned}\quad (4.5.107)$$

The effective pore diffusion coefficient is typically about 10% of the molecular diffusivity. Thus Eq. (4.5.107) can be rewritten in terms of ϕ (sphere, Table 4.5.5) by:

$$\begin{aligned}\eta_{\text{ex}} &\approx \frac{1}{1 + \eta_{\text{pore}} \frac{d_p^2 k_m \rho_p}{Sh 60 D_{A,\text{eff}}}} = \frac{1}{1 + \frac{\tanh \phi}{\phi} \frac{0.6}{Sh} \left(\frac{d_p}{6} \sqrt{\frac{k_m \rho_p}{D_{A,\text{eff}}}}\right)^2} \\ &= \frac{1}{1 + \frac{0.6}{Sh} \phi \tanh \phi}\end{aligned}\quad (4.5.108)$$

The effectiveness factor with regard to pore diffusion is given by Eq. (4.5.75), and insertion of Eqs. (4.5.75) and (4.5.108) into Eq. (4.5.107) finally yields:

$$\eta_{\text{overall}} = \eta_{\text{ex}} \eta_{\text{pore}} \approx \frac{\tanh \phi}{\phi + \frac{0.6}{Sh} \phi^2 \tanh \phi} = \frac{1}{\frac{1}{\eta_{\text{pore}}} + \frac{0.6}{Sh} \phi^2} \quad (4.5.109)$$

Figure 4.5.24 shows that for a low fluid velocity ($Re \rightarrow 0$), $Sh = Sh_{\min} = 2$ and 3.8 for a single particle and a fixed bed, respectively, Eqs. (3.2.70) and (3.2.71), η_{ex} has an influence on η_{overall} . Conversely, for a value of Sh of 19 (fixed bed, interstitial velocity of 1 m s^{-1} , N_2 , 1 bar, 25°C , $d_p = 2 \text{ mm}$), the influence of η_{ex} on η_{overall} is negligible ($\eta_{\text{overall}} \approx \eta_{\text{pore}}$) up to $\phi = 10$.

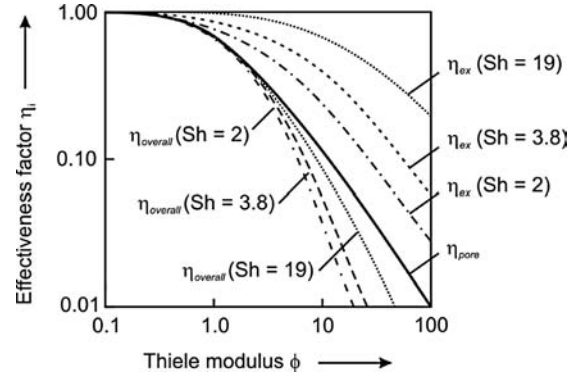


Figure 4.5.24 Effectiveness factors η_{overall} , η_{pore} , and η_{ex} for a single catalyst particle.

Topic 4.5.6 Influence of reaction temperature on the effective rate constant and on the apparent activation energy of a solid catalyzed reaction

According to Arrhenius, the chemical rate constant strongly depends on temperature:

$$k_m = k_{m,0} e^{-\frac{E_A}{RT}} \quad (4.3.4)$$

In contrast, the increase in effective pore diffusion coefficient with T is relatively small, for example, for gases it is "just" proportional to $T^{1.75}$. Thus with increasing temperature we enter the regime of the influence of pore diffusion. If we neglect this relatively small influence of temperature on the diffusion coefficient compared to the strong quasi-exponential influence on k_m , we obtain for a pronounced influence of pore diffusion ($\phi \geq 2$):

$$\begin{aligned}k_{m,\text{eff}} &= \eta_{\text{pore}} k_m = \frac{k_m}{\phi} = \frac{k_m}{L \sqrt{\frac{k_m \rho_p}{D_{\text{eff}}}} L \sqrt{\frac{\rho_p}{D_{\text{eff}}}}} \sqrt{\frac{k_{m,0}}{\rho_p}} e^{-\frac{E_A}{2RT}} \\ &\approx \text{const.} \times e^{-\frac{E_A}{2RT}} \quad (\text{for } \phi \geq 2)\end{aligned}\quad (4.5.76)$$

and the apparent activation energy is only half of the intrinsic “true” value (Figure 4.5.25).

If the temperature is increased further, external mass transfer becomes dominant, that is, the concentration at the external surface and within the porous particle is almost zero (for an irreversible reaction). According to Eqs. (4.5.25) and (3.2.68), we then get:

$$k_{m,\text{eff}} = \beta A_{m,\text{ex}} = Sh \frac{A_{m,\text{ex}}}{d_{\text{charac}}} D \approx \text{const.} \times D \sim T^{1.75} \quad (4.5.110)$$

As already shown in Example 4.5.2, the apparent activation energy is then determined simply by the relatively small influence of temperature on the diffusion coefficient and in terms of the Arrhenius’s law we get an apparent activation energy in the range of about 5 to 20 kJ mol⁻¹ (Figure 4.5.25).

4.5.5.2 Reversible First-Order Reaction with the Influence of External and Internal Mass Transfer

To derive the equations for the influence of internal and external mass transfer on a heterogeneously catalyzed reversible reaction of A to B, we use the following assumptions:

- The chemical rate of the forward reaction is first order and given by $k_{m,1}c_A$ and that of the reverse reaction by $k_{m,B}c_B$ (both in kmol kg⁻¹ s⁻¹).
- The internal surface area of the spherical catalyst particles is much higher than the external surface area A_m (m² kg⁻¹), and the reaction at the external surface is negligible.
- The mass transfer coefficient (β) and the effective diffusion coefficient (D_{eff}) are constants and have the same value for A and for B.
- The composition of the fluid in the bulk phase of the fluid (e.g., a gas) is given by $c_{A,g}$ and $c_{B,g}$; at the external surface of the porous particles we have $c_{A,s}$ and $c_{B,s}$.

For spherical particles, the mass balance for B for steady-state conditions and the definition of the equilibrium constant K_c [Eq. (4.5.84)] yields:

$$D_{\text{eff}} \left(\frac{d^2 c_A}{dr^2} + \frac{2}{r} \frac{dc_A}{dr} \right) = (k_{m,A} c_A - k_{m,B} c_B) \rho_p = k_{m,A} \rho_p \left(c_A - \frac{c_B}{K_c} \right) \quad (4.5.111)$$

The boundary conditions are:

$$r = \frac{d_p}{2} \text{ (center of spherical particle)} : \quad \frac{dc_A}{dr} = 0 \quad (4.5.112)$$

$$r = r_p \text{ (external surface of particle)} : \quad D_{\text{eff}} \frac{dc_A}{dr} = \beta(c_{A,g} - c_{A,s}) \quad (4.5.113)$$

The concentration of B can be expressed in terms of c_A :

$$c_A + c_B = c_{A,s} + c_{B,s} \quad (4.5.114)$$

and Eqs. (4.5.111) and (4.5.113) can be solved. The solution of the concentration distribution in the particle is found to be (Westerterp, van Swaaij and Beenackers, 1998):

$$c_A = c_{A,s} - \frac{K_c c_{A,s} - c_{B,s}}{K_c + 1} \left[1 - \frac{\frac{r_p}{r} \sinh \left(\frac{r}{r_p} 3\phi_{\text{reversible}} \right)}{\frac{D_{\text{eff}}}{\beta r_p} 3\phi \cosh(3\phi_{\text{reversible}}) + \left(1 - \frac{D_{\text{eff}}}{\beta r_p} \right) \sinh(3\phi_{\text{reversible}})} \right] \quad (4.5.115)$$

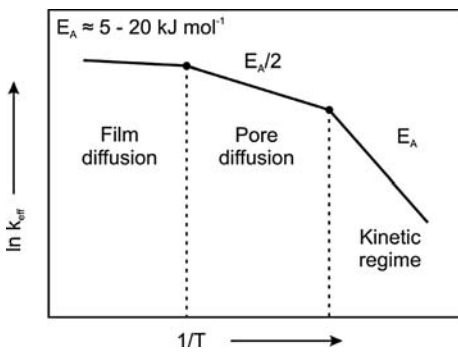


Figure 4.5.25 Arrhenius plot of effective rate constant for the three regimes of control by reaction, interplay of reaction and pore diffusion, and control by external diffusion.

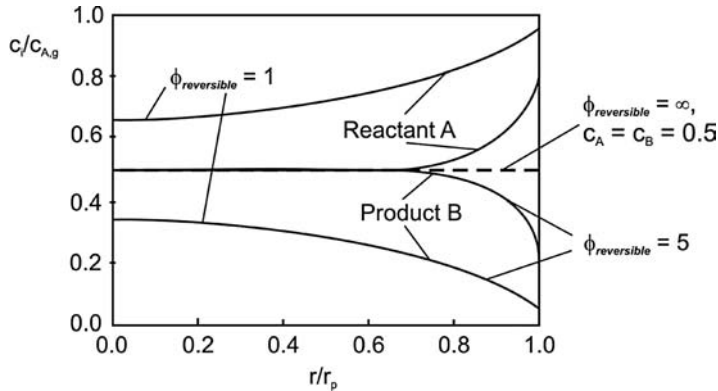


Figure 4.5.26 Radial concentration distribution in a porous spherical particle (diameter $2r_p$) for a first-order equilibrium reaction of $A \rightarrow B$ [$c_{B,g} = 0$; $D_{\text{eff}}/(\beta r_p) = 0.05$, that is, $Bi_m = 7$; $K_c = 1$; concentration in the film layer ($r > r_p$) is not shown].

where $\phi_{\text{reversible}}$ is given by Eq. (4.5.90), and $2D_{\text{eff}}/(\beta d_p)$ is a measure of the ratio of the external and internal mass transfer resistance, and equals $1/(3Bi_m)$, see Eq. (4.5.104).

Figure 4.5.26 shows the radial concentration distribution in a porous spherical particle with diameter $2r_p$ according to Eq. (4.5.115) for two values of the Thiele modulus $\phi_{\text{reversible}}$ for the example of a gas phase free of B ($c_{B,g} = 0$) and $D_{\text{eff}}/(\beta r_p) = 0.05$ and $K_c = 1$. Note that in the case of high values of $\phi_{\text{reversible}}$ ($\gg 5$ in Figure 4.5.26), the external mass transfer determines the effective reaction rate, that is, the equilibrium concentrations are almost reached within the porous particle (for the example of Figure 4.5.26, $K_c = 1$ and $c_{A,\text{equilibrium}} = c_{B,\text{equilibrium}} = 0.5c_{A,g}$), and the concentrations vary strongly in the boundary layer, for example, $\Delta c_{A,\text{external}} = c_{A,g} - c_{A,\text{equilibrium}}$.

The effective reaction rate (in $\text{kmol kg}^{-1} \text{s}^{-1}$) is given by (Westerterp, van Swaaij, and Beenackers, 1998):

$$r_{A,\text{eff}} = \beta A_m \left[\frac{3\phi_{\text{reversible}} - \tanh(3\phi_{\text{reversible}})}{3\phi_{\text{reversible}} + \left(\frac{\beta d_p}{2D_{\text{eff}}} - 1 \right) \tanh(3\phi_{\text{reversible}})} \right] \frac{K_c c_{A,g} - c_{B,g}}{K_c + 1} \quad (4.5.116)$$

For a fixed bed reactor with $c_{A,g,\text{in}}$ and $c_{B,g,\text{in}} = 0$ (and thus $c_{B,g} = c_{A,g,\text{in}} - c_{A,g}$) we obtain:

$$r_{A,\text{eff}} = \beta A_m \underbrace{\left[\frac{3\phi_{\text{reversible}} - \tanh(3\phi_{\text{reversible}})}{3\phi_{\text{reversible}} + \left(\frac{\beta d_p}{2D_{\text{eff}}} - 1 \right) \tanh(3\phi_{\text{reversible}})} \right]}_{k_{m,\text{eff, reversible}}} \left(c_{A,g} - \frac{c_{A,g,\text{in}}}{K_c + 1} \right) \quad (4.5.117)$$

Integration of Eq. (4.5.117) leads to the conversion of A (see also Section 4.3.3):

$$X_A = \frac{K_c}{K_c + 1} \left(1 - e^{-k_{m,\text{eff, reversible}} \tau_m} \right) \quad (4.5.118)$$

where X_A^* is the equilibrium conversion, $k_{m,\text{eff, reversible}}$ is defined by Eq. (4.5.117), and τ_m represents the (modified) residence time, that is, the ratio of the mass of catalyst to the volume rate (at reaction conditions).

Example 4.5.9 shows the influence of temperature on the conversion for a reversible exothermic reaction for different particle diameters, that is, for different strengths of the influence of the external and internal mass transfer.

Table 4.5.7 Kinetic parameters of an exothermic, heterogeneously catalyzed, reversible reaction of A to B.

Parameter	Value
Molecular diffusion coefficient $D_A (= D_B)$	$10^{-5} \text{ m}^2 \text{ s}^{-1}$
Effective diffusion coefficient $D_{A,\text{eff}} (= 0.1 D_A)$	$10^{-6} \text{ m}^2 \text{ s}^{-1}$
Density of catalyst particle ρ_p	1000 kg m^{-3}
Pre-exponential factor of forward reaction $k_{m,A}$	$0.5 \times 10^{11} \text{ m}^3 \text{ kg}^{-1} \text{ s}^{-1}$
Activation energy of forward reaction E_A	70 kJ mol^{-1}
External surface area A_m (spherical particle with diameter d_p)	$6/(d_p \rho_p) (\text{m}^2 \text{ kg}^{-1})$
Sherwood number mass $Sh = \beta_A d_p / D_A$	4
Equilibrium constant K_c	$10^{-8} \exp(12028/T)$
Modified residence time τ_m	5 kg s m^{-3}

Example 4.5.9: Influence of external and internal mass transfer on the conversion for an exothermic reversible first-order reaction of A to B

To calculate the conversion of component A for an exothermic reversible first-order reaction of A to B, we use the (arbitrarily chosen) data given in Table 4.5.7.

The conversion is given by Eq. (4.5.118), whereby $k_{m,\text{eff},\text{reversible}}$ is defined by Eq. (4.5.117) and τ_m is the (modified) residence time, that is, the ratio of the mass of catalyst to the volume rate (at reaction

conditions). Figure 4.5.27 shows the influence of temperature on the conversion of reactant A for different particle diameters, that is, for different strengths of the influence of mass transfer. For the given example, a particle diameter of less than about 0.1 mm would be needed to exclude an influence of mass transfer.

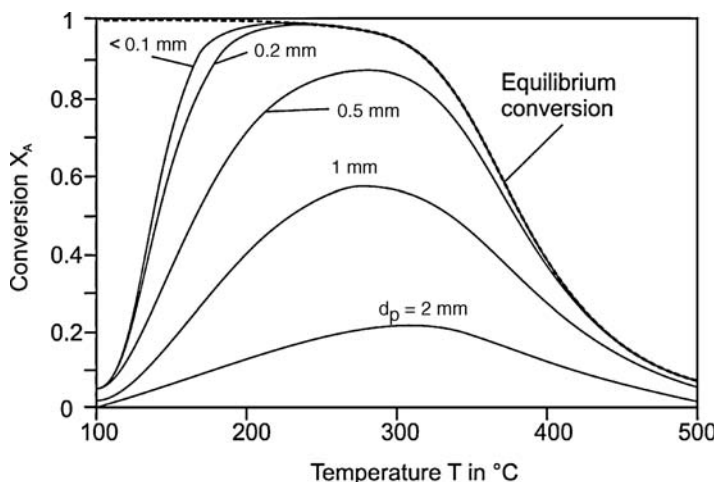
Equations (4.5.117) and (4.5.118) can be greatly simplified for some extreme values of certain parameters:

For a pronounced influence of pore diffusion and a negligible influence of external mass transfer ($3\phi_{\text{reversible}} \gg 1$, $\tanh(3\phi_{\text{reversible}}) \approx 1$, and $\beta d_p / (2D_{\text{eff}}) = 3Bi_m \gg 3\phi_{\text{reversible}}$), Eqs. (4.5.117) and (4.5.118) yield [if we consider that A_m is given by the term $6/(d_p \rho_p)$]:

$$\begin{aligned} r_{A,\text{eff}} &= \frac{k_{m,A}}{\phi_{\text{reversible}}} \left(\frac{K_c + 1}{K_c} \right) \frac{K_c c_{A,g} - c_{B,g}}{K_c + 1} \\ &= \frac{k_{m,A}}{\phi_{\text{reversible}}} \left(c_{A,g} - \frac{c_{B,g}}{K_c} \right) \quad (\text{for } Bi_m \gg \phi_{\text{rev.}} > 1) \end{aligned} \quad (4.5.119)$$

$$X_A = \frac{K_c}{K_c + 1} \left[1 - e^{-\frac{k_{m,A}}{\phi_{\text{reversible}}} \left(\frac{K_c + 1}{K_c} \right) \tau_m} \right] = X_A^* \left(1 - e^{-\frac{k_{m,A}}{\phi_{\text{reversible}} X_A^*} \tau_m} \right) \quad (4.5.120)$$

Figure 4.5.27 Influence of temperature on the conversion of reactant A (reversible first-order A → B reaction) for different particle diameters (parameters see Table 4.5.7).



[Note that Eq. (4.5.119) equals Eq. (4.5.92), which was already derived in Example 4.5.6, if we use $\eta_{\text{pore}} \approx 1/\phi_{\text{reversible}}$ for $\phi_{\text{reversible}} > 2$.]

If the external mass transfer determines the effective rate [$\beta d_p/(2D_{\text{eff}}) = 3Bi_m \ll 3\phi_{\text{reversible}}$], Eqs. (4.5.117) and (4.5.118) yield:

$$r_{A,\text{eff}} = \beta A_m \frac{K_c c_{A,g} - c_{B,g}}{K_c + 1} \quad (\text{for } Bi_m \ll \phi_{\text{reversible}}) \quad (4.5.121)$$

$$X_A = \frac{K_c}{K_c + 1} (1 - e^{-\beta A_m \tau_m}) = X_A^* (1 - e^{-\beta A_m \tau_m}) \quad (4.5.122)$$

Note that for $c_{B,g} = 0$ and $K_c = 1$, as assumed in Figure 4.5.24, Eq. (4.5.121) leads to $r_{A,\text{eff}} = \beta A_m c_{A,g}/2$, that is, the equilibrium concentrations ($= c_{A,g}/2$ for $K_c = 1$) are established at the external surface of the particle. In general, the term $(K_c c_{A,g} - c_{B,g})/(K_c + 1)$ is equivalent to the term $(c_{A,g} - c_{A,s}^*)$, where $c_{A,s}^*$ represents the actual equilibrium concentration at the external surface for the given values of $c_{A,g}$ and $c_{B,g}$, and $c_{B,s}^*$:

$$\begin{aligned} \frac{K_c c_{A,g} - c_{B,g}}{K_c + 1} &= c_{A,g} - \frac{(c_{A,g} + c_{B,g})}{K_c + 1} = c_{A,g} - \frac{(c_{A,s}^* + c_{B,s}^*)}{K_c + 1} \\ &= c_{A,g} - \frac{(c_{A,s}^* + K_c c_{A,s}^*)}{K_c + 1} = c_{A,g} - c_{A,s}^* \end{aligned}$$

In the case of a very slow chemical reaction rate, the effective rate is determined by the chemical (intrinsic) rate [$\phi_{\text{reversible}} \ll 1$, $\tanh(3\phi_{\text{reversible}}) \approx 3\phi_{\text{reversible}} - 9(\phi_{\text{reversible}})^3$, $\beta d_p/(2D_{\text{eff}}) = 3Bi_m \gg 3\phi_{\text{reversible}}$], and Eqs. (4.5.117) and (4.5.118) yield:

$$\begin{aligned} r_{A,\text{eff}} &\approx \frac{\beta A_m 9\phi_{\text{reversible}}^3}{3\phi} \frac{K_c c_{A,g} - c_{B,g}}{2D_{\text{eff}}} \\ &= k_m \left(c_{A,g} - \frac{c_{B,g}}{K_c} \right) \quad (\text{for } Bi_m \gg \phi_{\text{reversible}} \ll 1) \end{aligned} \quad (4.5.123)$$

$$X_A = \frac{K_c}{K_c + 1} \left[1 - e^{-k_m \left(\frac{1+K_c}{K_c} \right) \tau_m} \right] = X_A^* \left(1 - e^{-\frac{k_m}{X_A^*} \tau_m} \right) \quad (4.5.124)$$

Note that Eqs. (4.5.123) and (4.5.124) equal Eqs. (4.3.54) and (4.3.62), which we derived for a reversible reaction without any influence of mass transfer.

4.5.6

Influence of External and Internal Mass Transfer on Selectivity

Mass transfer resistances lead to a lower effective rate compared to the intrinsic chemical reaction, but may also significantly change the selectivity of parallel and consecutive reactions. In the following, this is discussed for two first-order reactions occurring in series or parallel. For simplification, the influence of external mass transfer is only discussed for a non-porous catalyst (to “exclude” pore diffusion), and the effect of pore diffusion is examined for a negligible influence of external mass transfer. Other more complicated cases are treated elsewhere (Baerns *et al.*, 2006; Levenspiel, 1999; Froment and Bischoff, 1990).

4.5.6.1 Influence of External Mass Transfer on the Selectivity of Reactions in Series

For two first-order reactions occurring in series on the external surface $A_{m,\text{ex}}$ ($\text{m}^2 \text{ kg}^{-1} \text{ cat}$) of a non-porous catalyst (reaction $A \xrightarrow{k_{A,1}} B \xrightarrow{k_{A,2}} C$), the effective reaction rate of reactant A $r_{m,\text{eff},A}$ ($\text{mol kg}_{\text{cat}}^{-1} \text{ s}^{-1}$) is given based on the rate constant $k_{A,1}$ ($\text{m}^3 \text{ m}^{-2} \text{ s}^{-1} = \text{m s}^{-1}$) by:

$$r_{m,\text{eff},A} = k_{A,1} A_{m,\text{ex}} c_{A,s} = \beta_1 A_{m,\text{ex}} (c_{A,g} - c_{A,s}) \quad (4.5.125)$$

since for steady-state the reaction rate on the surface equals the rate of transport from the bulk phase to the external surface. Equation (4.5.125) is valid for gas and

liquid reactions, but here we use a gas-phase process as example (index "g"). The rate of formation of intermediate B is:

$$r_{m,\text{eff}, B} = k_{A,1} A_{m,\text{ex}} c_{A,s} - k_{A,2} A_{m,\text{ex}} c_{B,s} = \beta_2 A_{m,\text{ex}} (c_{B,s} - c_{B,g}) \quad (4.5.126)$$

Rearrangement of Eq. (4.5.125) leads to Eq. (4.5.19), already derived in Section 4.5.3.1, as well as to the corresponding equation for the intermediate B:

$$c_{A,s} = \frac{\beta_1}{\beta_1 + k_{A,1}} c_{A,g} \quad (4.5.19)$$

$$c_{B,s} = \frac{c_{A,g}}{\left(\frac{\beta_2}{k_{A,1}} + \frac{\beta_2}{\beta_1}\right)\left(1 + \frac{k_{A,2}}{\beta_2}\right)} + \frac{c_{B,g}}{\left(1 + \frac{k_{A,2}}{\beta_2}\right)} \quad (4.5.127)$$

The fluxes of all three compounds are coupled by:

$$\beta_1 A_{m,\text{ex}} (c_{A,g} - c_{A,s}) = \beta_2 A_{m,\text{ex}} (c_{B,s} - c_{B,g}) + \beta_3 A_{m,\text{ex}} (c_{C,s} - c_{C,g}) \quad (4.5.128)$$

and thus for the case of equal diffusion coefficient (i.e., $\beta_1 = \beta_2 = \beta_3$) we obtain the following term for the surface concentration of the intermediate B and of the final product C:

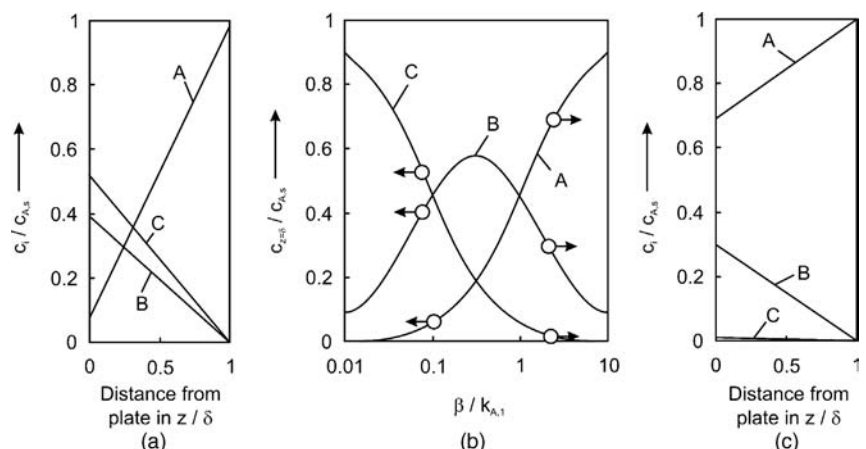
$$c_{B,s} = \frac{c_{A,g}}{\left(1 + \frac{\beta}{k_{A,1}}\right)\left(1 + \frac{k_{A,2}}{\beta}\right)} + \frac{c_{B,g}}{\left(1 + \frac{k_{A,2}}{\beta}\right)} \quad (4.5.129)$$

$$c_{C,s} = c_{C,g} + \frac{c_{A,g}}{\left(1 + \frac{\beta}{k_{A,1}}\right)\left(1 + \frac{\beta}{k_{A,2}}\right)} + \frac{c_{B,g}}{\left(1 + \frac{\beta}{k_{A,2}}\right)} \quad (4.5.130)$$

Figure 4.5.28b shows the influence of external mass transfer (parameter $\beta/k_{A,1}$) on the concentrations at the surface of a non-porous catalyst and the concentration profiles in the boundary gas layer for strong and weak influence of external mass transfer. For a strong influence of external mass transfer (Figure 4.5.28a, $\beta/k_{A,1} = 0.08$, $k_{A,2} = k_{A,1} = 0.1$), the final product C is formed to a large extent, although we have assumed that the gas phase is free of B, which corresponds to the entrance of a tubular reactor, where we start with a selectivity to B of 100%. For a weak influence of mass transfer (Figure 4.5.28c, with $\beta/k_{A,1} = 2.20$), very little C is formed. Note that for intermediate values of the parameter $\beta/k_{A,1}$ (about 0.3 for the case depicted in Figure 4.5.28b), we have the highest surface concentration ($c_{B,s}$) of the intermediate B (but not the highest selectivity). For higher values of $\beta/k_{A,1}$ the increasing rate of mass transport from the surface to the gas phase leads to a low value of $c_{B,s}$, and a low value of $\beta/k_{A,1}$ increases the reaction rate of the conversion of B (relative to mass transport).

Figure 4.5.28 Influence of external mass transfer on the concentration at the surface of a non-porous catalyst for a series reaction $A \xrightarrow{k_{A,1}} B \xrightarrow{k_{A,2}} C$:

(a) concentration profiles in the boundary gas layer for a strong influence of external mass transfer ($\beta/k_{A,1} = 0.08$); (b) concentrations at the external surface of the catalyst particles for various values of $\beta/k_{A,1}$ at the entrance of the reactor, that is, c_B and $c_C = 0$; (c) profiles for a small influence of external mass transfer ($\beta/k_{A,1} = 2.2$) ($c_{B,g} = c_{C,g} = 0$, $k_{A,2}/k_{A,1} = 0.1$, $\beta_1 = \beta_2 = \beta_3$). (Solution by the Eqs. (4.5.19), (4.5.129), and (4.5.130)).



The differential selectivity s [Eq. (4.3.45)] is defined as the ratio of the rate of formation of product B to the rate of consumption of A, and for a continuously operated tubular or a batch reactor we obtain:

$$\begin{aligned} s_B &= \frac{r_{m,\text{eff},B}}{r_{m,\text{eff},A}} = \frac{\frac{dc_{B,g}}{d\tau_m}}{-\frac{dc_{A,g}}{d\tau_m}} = -\frac{dc_{B,g}}{dc_{A,g}} \\ &= \frac{k_{A,1}A_{m,\text{ex}}c_{A,s} - k_{A,2}A_{m,\text{ex}}c_{B,s}}{k_{A,1}A_m c_{A,s}} = 1 - \frac{k_{A,2} c_{B,s}}{k_{A,1} c_{A,s}} \end{aligned} \quad (4.5.131)$$

where τ_m is the modified residence time (kg s m^{-3}), and is either the ratio of the mass of catalyst to the volume rate (tubular reactor) or the product of the concentration of the catalyst and the reaction time (batch reactor).

If we assume that the diffusion coefficients are equal, we can use β instead of β_1 and β_2 . Insertion of Eqs. (4.5.19) and (4.5.129) in Eq. (4.5.130) leads after rearrangement to:

$$s_B = -\frac{dc_{B,g}}{dc_{A,g}} = \left[1 - \frac{k_{A,2}}{k_{A,1}} \frac{\frac{k_{A,1}}{\beta}}{\left(1 + \frac{k_{A,2}}{\beta} \right)} \right] - \frac{k_{A,2}}{k_{A,1}} \frac{\left(1 + \frac{k_{A,1}}{\beta} \right)}{\left(1 + \frac{k_{A,2}}{\beta} \right)} \frac{c_{B,g}}{c_{A,g}} = a_1 - a_2 \frac{c_{B,g}}{c_{A,g}} \quad (4.5.132)$$

Equation (4.5.132) is a first-order linear differential equation with a_1 and a_2 as constants, and is solved by introduction of z for $c_{B,g}/c_{A,g}$ and thus $dc_{B,g}/dc_{A,g} = dz$. Integration from $c_{A,g,0}$ to $c_{A,g}$ and zero to z yields (for a feedstock free of B):

$$\begin{aligned} Y_B &= \frac{c_{B,g}}{c_{A,g,0}} \\ &= \frac{a_1}{(1 - a_2)} \left[\left(\frac{c_{A,g}}{c_{A,g,0}} \right)^{a_2} - \frac{c_{A,g}}{c_{A,g,0}} \right] \quad [a_1 \text{ and } a_2 \text{ as given by Eq. (4.5.132)}] \end{aligned} \quad (4.5.133)$$

Equation (4.5.133) is only valid for reactors with a successive decrease of the concentration with time (batch reactor) or residence time (tubular reactor); for a continuously stirred tank reaction (CSTR) see Levenspiel (1999).

Equation (4.5.133) can also be expressed in terms of the conversion of A as:

$$Y_B = \frac{c_{B,g}}{c_{A,g,0}} = \frac{a_1}{(1 - a_2)} [(1 - X_A)^{a_2} - (1 - X_A)] \quad (4.5.134)$$

The maximum yield of B, $Y_{B,\text{max}}$, is calculated by the condition $dY_B/dX_A = 0$, and thus differentiation of Eq. (4.5.134) leads to the conversion where $Y_{B,\text{max}}$ is just reached:

$$X_A|_{Y_B=Y_{B,\text{max}}} = 1 - \left(\frac{1}{a_2} \right)^{\frac{1}{a_2-1}} \quad (4.5.135)$$

Insertion of Eq. (4.5.135) into Eq. (4.5.134) yields:

$$Y_{B,\text{max}} = \frac{a_1}{(1 - a_2)} \left[\left(\frac{1}{a_2} \right)^{\frac{a_2}{a_2-1}} - \left(\frac{1}{a_2} \right)^{\frac{1}{a_2-1}} \right] \quad (4.5.136)$$

If the reaction is not influenced by the external mass transfer ($\beta \gg k_{i,A}$), the constant a_1 is 1 and a_2 reduces to $k_{A,2}/k_{A,1}$. Thus Eqs. (4.5.131), (4.5.134) and (4.5.136) simplify to:

$$s_B = -\frac{dc_{B,g}}{dc_{A,g}} = 1 - \frac{k_{A,2}}{k_{A,1}} \frac{c_{B,g}}{c_{A,g}} \quad (4.5.137)$$

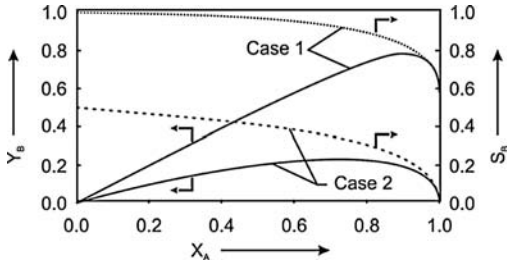


Figure 4.5.29 Influence of external mass transfer on the yield and selectivity of the intermediate product B for a series reaction on a non-porous catalyst in a batch or a plug flow reactor ($A \xrightarrow{k_{A,1}} B \xrightarrow{k_{A,2}} C$; case 1: no influence of external mass transfer ($\beta \gg k_{A,i}$, $k_{A,2}/k_{A,1} = 0.1$); case 2: influence of external mass transfer for $k_{A,2}/k_{A,1} = 0.1$, $k_{A,1}/\beta = 10$, $\beta_1 = \beta_2 = \beta$).

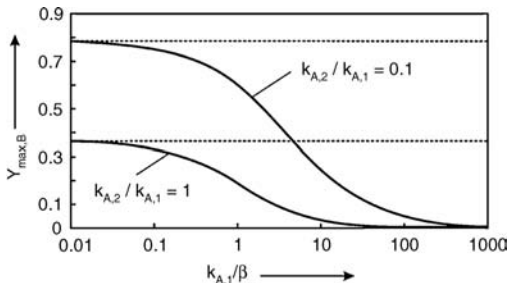


Figure 4.5.30 Influence of the ratio $k_{A,1}/\beta$ on the maximum yield of intermediate B for a series reaction on a non-porous catalyst ($A \xrightarrow{k_{A,1}} B \xrightarrow{k_{A,2}} C$) in a batch or plug flow reactor for two values of $k_{A,2}/k_{A,1}$ ($\beta_1 = \beta_2 = \beta$; dashed line: no external mass transfer resistance).

$$Y_B = \frac{1}{\left(1 - \frac{k_{A,2}}{k_{A,1}}\right)} \left[(1 - X_A)^{\frac{k_{A,2}}{k_{A,1}}} - (1 - X_A) \right] \quad (4.5.138)$$

$$\begin{aligned} Y_{B,\max} &= \frac{\left(\frac{1}{a_2}\right)^{\frac{a_2}{a_2-1}} - \left(\frac{1}{a_2}\right)^{\frac{1}{a_2-1}}}{(1-a_2)} = \left(\frac{1}{a_2}\right)^{\frac{a_2}{a_2-1}} \left[1 - \left(\frac{1}{a_2}\right)^{\frac{1-a_2}{a_2-1}} \right] = (a_2)^{\frac{a_2}{1-a_2}} \\ &= \left(\frac{k_{A,2}}{k_{A,1}}\right)^{\frac{1}{(k_{A,1}-k_{A,2})}} \end{aligned} \quad (4.5.139)$$

In general, the influence of external mass transfer leads to a lower yield and selectivity of the intermediate for a series reaction. This is shown in Figure 4.5.29 by comparison of the yield and the integral selectivity of the intermediate for the absence of an external mass transfer resistance (case 1) with the case of a strong influence of mass transfer (case 2).

Figure 4.5.30 shows that with increasing influence of external mass (increasing ratio $k_{A,1}/\beta$), the selectivity and thus the maximum yield of the intermediate decreases down to zero for complete control by film diffusion.

4.5.6.2 Influence of External Mass Transfer on the Selectivity of Parallel Reactions

For two parallel independent reactions ($A \xrightarrow{k_{A,1}} B$ and $A \xrightarrow{k_{A,2}} C$) with reaction orders of m and n occurring on the external surface $A_{m,\text{ex}}$ ($\text{m}^2 \text{kg}^{-1} \text{cat}$) of a non-porous catalyst the effective reaction rate of reactant A $r_{m,\text{eff},A}$ ($\text{mol kg}_{\text{cat}}^{-1} \text{s}^{-1}$) is given based on the rate constants $k_{A,1}$ and $k_{A,2}$ ($\text{m}^3 \text{m}^{-2} \text{s}^{-1}$) by:

$$r_{m,\text{eff},A} = k_{A,1} A_{m,\text{ex}} c_{A,s}^m + k_{A,2} A_{m,\text{ex}} c_{A,s}^n = \beta A_{m,\text{ex}} (c_{A,g} - c_{A,s}) \quad (4.5.140)$$

Equation (4.5.140) is valid for gas- and liquid-phase reactions, but again we only consider a gas-phase process (index “g”). For the rates of formation of products B and C we get:

$$r_{m,\text{eff},B} = k_{A,1} A_{m,\text{ex}} c_{A,s}^m \quad (\text{for a reaction order of } m) \quad (4.5.141)$$

$$r_{m,\text{eff},C} = k_{A,2} A_{m,\text{ex}} c_{A,s}^n \quad (\text{for a reaction order of } n) \quad (4.5.142)$$

The differential selectivity s is the ratio of the rate of formation of B (or C) to the rate of consumption of A, and for a continuously operated tubular reactor (or a batch reactor) we find:

$$s_B = \frac{r_{m,\text{eff},B}}{r_{m,\text{eff},A}} = \frac{k_{A,1} A_{m,\text{ex}} c_{A,s}^m}{\beta A_{m,\text{ex}} (c_{A,g} - c_{A,s})} \quad (4.5.143)$$

$$s_C = \frac{r_{m,\text{eff},C}}{r_{m,\text{eff},A}} = \frac{k_{A,2} A_{m,\text{ex}} c_{A,s}^n}{\beta A_{m,\text{ex}} (c_{A,g} - c_{A,s})} \quad (4.5.144)$$

The ratio of the differential selectivities is given by:

$$\frac{s_B}{s_C} = \frac{k_{A,1} c_{A,s}^m}{k_{A,2} c_{A,s}^n} = \frac{k_{A,1}}{k_{A,2}} c_{A,s}^{m-n} \quad (4.5.145)$$

and thus we obtain the following ratios for, respectively, the case of no limitation by external mass transfer (intrinsic rate, $c_{A,s} = c_{A,g}$) and with limitation by film diffusion (effective rate, $c_{A,s} < c_{A,g}$):

$$\left. \frac{s_B}{s_C} \right|_{\text{intrinsic}} = \frac{k_{A,1}}{k_{A,2}} c_{A,g}^{m-n} \quad (4.5.146)$$

$$\left. \frac{s_B}{s_C} \right|_{\text{eff}} = \frac{k_{A,1}}{k_{A,2}} c_{A,s}^{m-n} \quad (4.5.147)$$

and for the ratio of both quotients we get:

$$\frac{\left.\frac{s_B}{s_C}\right|_{\text{eff}}}{\left.\frac{s_B}{s_C}\right|_{\text{intrinsic}}} = \left(\frac{c_{A,s}}{c_{A,g}}\right)^{m-n} \quad (4.5.148)$$

If both reaction orders are equal, the selectivity is not influenced by external mass transfer, but for different orders the reaction with the lower order is favored, for example, for $m=1$ and $n=2$ the ratio given by Eq. (4.5.148) is >1 [$c_{A,s}/c_{A,g} < 1$, i.e., $(c_{A,s}/c_{A,g})^{-1} > 1$].

4.5.6.3 Influence of Pore Diffusion on the Selectivity of Reactions in Series

For two irreversible first-order reactions occurring in series in a porous catalyst with the intrinsic rate constants $k_{m,1}$ and $k_{m,2}$ ($\text{m}^3 \text{kg}^{-1} \text{cat s}^{-1}$) ($\text{A} \xrightarrow{k_{m,1}} \text{B} \xrightarrow{k_{m,2}} \text{C}$), the differential selectivity is given by:

$$\begin{aligned} s_B &= \frac{r_{m,\text{eff},B}}{r_{m,\text{eff},A}} = -\frac{dc_{B,s}}{dc_{A,s}} = \frac{1 - \left(\frac{\phi_2}{\phi_1}\right)^2 \left(\frac{\eta_{\text{pore},2}}{\eta_{\text{pore},1}}\right)}{1 - \left(\frac{\phi_2}{\phi_1}\right)^2} - \left(\frac{\eta_{\text{pore},2}}{\eta_{\text{pore},1}}\right) \left(\frac{k_{m,2}}{k_{m,1}}\right) \frac{c_{B,s}}{c_{A,s}} \\ &= b_1 - b_2 \frac{c_{B,s}}{c_{A,s}} \end{aligned} \quad (4.5.149)$$

if we assume for simplicity that pore, and not film, diffusion has an influence on the effective rate (for details see Levenspiel, 1999; Baerns, 2006, and also Example 4.5.10).

For equal effective diffusivities D_{eff} of A and B the effectiveness factors for pore diffusion and the Thiele moduli are given, respectively, by:

$$\eta_{\text{pore},i} = \frac{\tanh \phi_i}{\phi_i} \quad (\text{with } i = 1 \text{ for reaction A} \rightarrow \text{B and } 2 \text{ for reaction B} \rightarrow \text{C}) \quad (4.5.150)$$

$$\phi_i = \frac{V_p}{A_{p,\text{ex}}} \sqrt{\frac{k_{m,i} \rho_p}{D_{\text{eff}}}} \left(\text{all geometries, } \frac{V_p}{A_{p,\text{ex}}} = L \text{ for a plate and } \frac{d_p}{6} \text{ for a sphere} \right) \quad (4.5.151)$$

The structure of Eq. (4.5.149) equals Eq. (4.5.132). For a negligible influence of external mass transfer ($c_{A,g} = c_{A,s}$, $c_{B,g} = c_{B,s}$), and without B in the feed ($c_{B,g,0} = 0$), the solution for a batch or tubular flow reactor [see remarks below Eq. (4.5.132)] is:

$$Y_B = \frac{b_1}{(1 - b_2)} \left[\left(\frac{c_{A,g}}{c_{A,g,0}}\right)^{b_2} - \frac{c_{A,g}}{c_{A,g,0}} \right] \quad [\text{with } b_1 \text{ and } b_2 \text{ as given by Eq. (4.5.149)}] \quad (4.5.152)$$

Equation (4.5.152) can also be expressed in terms of the conversion of A as:

$$Y_B = \frac{b_1}{(1 - b_2)} \left[(1 - X_A)^{b_2} - (1 - X_A) \right] \quad (4.5.153)$$

The maximum yield of B is derived from the condition $dY_B/dX_A = 0$:

$$Y_{B,\text{max}} = \frac{b_1}{(1 - b_2)} \left\{ \left(\frac{1}{b_2}\right)^{\frac{b_2}{b_2-1}} - \left(\frac{1}{b_2}\right)^{\frac{1}{b_2-1}} \right\} \quad (4.5.154)$$

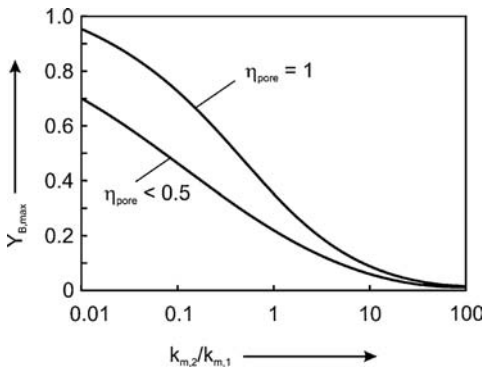


Figure 4.5.31 Influence of pore diffusion on the maximum intermediate yield in a batch or plug flow reactor for a reaction $A \xrightarrow{k_{m,1}} B \xrightarrow{k_{m,2}} C$ and different values of the ratio $k_{m,2}/k_{m,1}$; case 1: no influence of pore diffusion ($\eta_{\text{pore},1} = 1, \phi_i \ll 1$); case 2: strong resistance to pore diffusion ($\eta_{\text{pore},i} = < 0.5, \phi_i > 2$), equal diffusivities D_{eff} of reactant A and intermediate B.

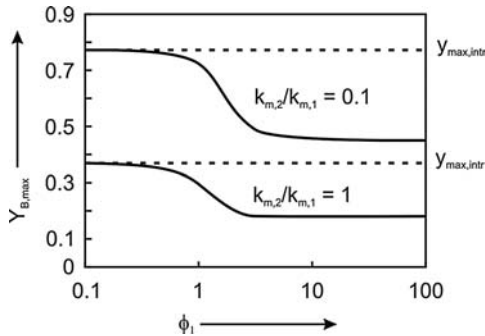


Figure 4.5.32 Influence of pore diffusion on the maximum yield of the intermediate B in a batch or plug flow reactor for a series reaction $A \xrightarrow{k_{m,1}} B \xrightarrow{k_{m,2}} C$ for different values of the Thiele modulus ϕ_1 and two different ratios $k_{m,2}/k_{m,1}$ (0.1 and 1), with equal effective diffusivities D_{eff} of A and B; dashed lines: absence of pore diffusion limitations.

If the reaction is not influenced by pore diffusion ($\eta_{\text{pore},i} = 1, \phi_i \ll 1$), b_1 is 1, b_2 reduces to $k_{m,2}/k_{m,1}$, and Eqs. (4.5.152)–(4.5.154) simplify to the case of control by the chemical reaction [Eqs. (4.5.137)–(4.5.139) with $k_{m,i}$ instead of $k_{A,i}$]. For strong resistance to pore diffusion we have:

$$\eta_{\text{pore},i} = \frac{1}{\phi_i} \quad (\text{for } \phi_i > 2) \quad (4.5.155)$$

$$\frac{\phi_2}{\phi_1} = \Phi_{21} = \sqrt{\frac{k_{m,2}}{k_{m,1}}} \quad (\text{for } D_{\text{eff},1} = D_{\text{eff},2}) \quad (4.5.156)$$

and Eqs. (4.5.149) and (4.5.152)–(4.5.154) lead to:

$$\begin{aligned} s_B &= \frac{r_{m,\text{eff},B}}{r_{m,\text{eff},A}} = -\frac{dc_{B,S}}{dc_{A,S}} \\ &= \frac{1}{1 + \Phi_{21}} - \Phi_{21} \frac{c_{B,S}}{c_{A,S}} \quad \left(\text{with } \Phi_{21} = \frac{\phi_2}{\phi_1} = \sqrt{\frac{k_{m,2}}{k_{m,1}}} \text{ for } D_{\text{eff},1} = D_{\text{eff},2} \right) \end{aligned} \quad (4.5.157)$$

$$Y_B = \frac{1}{(1 - \Phi_{21}^2)} \left[\left(\frac{c_{A,g}}{c_{A,g,0}} \right)^{\Phi_{21}} - \frac{c_{A,g}}{c_{A,g,0}} \right] \quad (4.5.158)$$

$$Y_B = \frac{1}{(1 - \Phi_{21}^2)} \left[(1 - X_A)^{\Phi_{21}} - (1 - X_A) \right] \quad (4.5.159)$$

$$Y_{B,\text{max}} = \frac{1}{(1 - \Phi_{21}^2)} \Phi_{21}^{\frac{\Phi_{21}}{(1 - \Phi_{21}^2)}} \quad (4.5.160)$$

In general, a resistance to pore diffusion decreases the yield of intermediates. This is depicted in Figure 4.5.31 for different ratios $k_{m,2}/k_{m,1}$ by comparison of the maximum yield of the intermediate B in the case where any influence of pore diffusion [Eq. (4.5.139) with $k_{m,i}$ instead of $k_{A,i}$] is absent and for a strong resistance to pore diffusion [Eq. (4.5.160)].

Figure 4.5.32 shows that with increasing influence of pore diffusion (increasing ϕ_1), selectivity to the intermediate decreases to a minimum value for a strong influence of pore diffusion. For example, for $k_{m,2}/k_{m,1} = 0.1$ and 1, $Y_{B,\text{max}}$ is 45% and 18%, respectively. The corresponding values in the absence of a mass transfer resistance are 77% and 37%.

Example 4.5.10: Effect of pore diffusional limitations on the concentration profiles in a porous catalyst with slab geometry in the case of consecutive first-order reactions

For two first-order reactions in series ($A \xrightarrow{k_{m,1}} B \xrightarrow{k_{m,2}} C$) taking place in a porous catalyst plate with thickness $2L$ [rate constants $k_{m,1}$ and $k_{m,2}$ ($\text{m}^3 \text{kg}^{-1} \text{cat} \text{s}^{-1}$)], the differential equations for the reactant A (feedstock) and the intermediate B are:

$$D_{A,\text{eff}} \frac{d^2 c_A}{dz^2} = k_{m,1} c_A \rho_p \quad (4.5.161)$$

$$D_{B,\text{eff}} \frac{d^2 c_B}{dz^2} = -k_{m,1} c_A \rho_p + k_{m,2} c_B \rho_p \quad (4.5.162)$$

Solutions of these equations with regard to the concentrations in the plate are:

$$c_A = c_{A,S} \frac{\cosh[\phi_1(1 - \frac{z}{L})]}{\cosh \phi_1} \quad \left(\text{with } \phi_1 = L \sqrt{\frac{k_{m,1} \rho_p}{D_{\text{eff},A}}} \right) \quad (4.5.163)$$

$$\begin{aligned} c_B &= \left[c_{B,S} + c_{A,S} \frac{D_{A,\text{eff}}}{D_{B,\text{eff}}} \frac{\phi_1^2}{(\phi_1^2 - \phi_2^2)} \right] \frac{\cosh[\phi_2(1 - \frac{z}{L})]}{\cosh \phi_2} \\ &\quad - c_{A,S} \frac{D_{A,\text{eff}}}{D_{B,\text{eff}}} \frac{\phi_1^2}{(\phi_1^2 - \phi_2^2)} \frac{\cosh[\phi_1(1 - \frac{z}{L})]}{\cosh \phi_1} \quad \left(\text{with } \phi_2 = L \sqrt{\frac{k_{m,2} \rho_p}{D_{\text{eff},B}}} \right) \end{aligned} \quad (4.5.164)$$

$$c_C = c_{\text{total}} - c_A - c_B \quad (4.5.165)$$

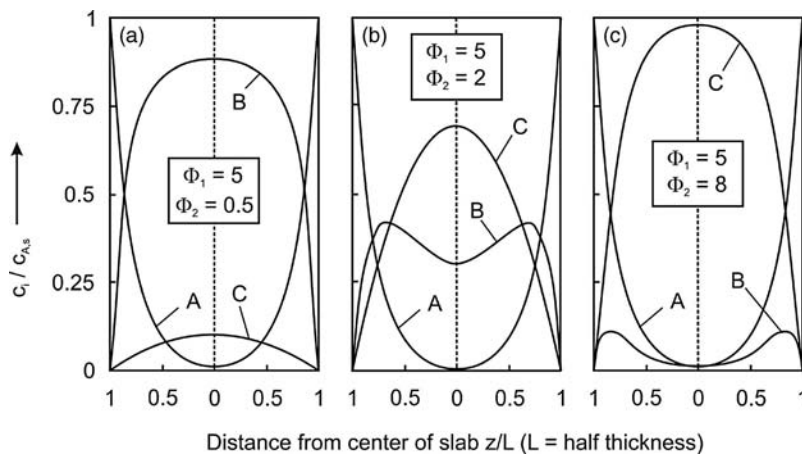


Figure 4.5.33 Concentration profiles in a catalytic porous plate for a series reaction $A \xrightarrow{k_{m,1}} B \xrightarrow{k_{m,2}} C$ ($\phi_1 = 5$, boundary conditions: $c_{B,s}$ and $c_{C,s} = 0$).

Differential selectivity to the intermediate B is given by:

$$s_B = \frac{r_{m,\text{eff},B}}{r_{m,\text{eff},A}} = \frac{r_{m,\text{eff},1} - r_{m,\text{eff},2}}{r_{m,\text{eff},1}} = 1 - \frac{\frac{1}{L} k_{m,2} \int_0^L c_{B,z} dz}{\frac{1}{L} k_{m,1} \int_0^L c_{A,z} dz} \quad (4.5.166)$$

where $c_{A,s}$ and $c_{B,s}$ are the concentrations at the external surface of the plate. Insertion of Eqs. (4.5.163) and (4.5.164) into Eq. (4.5.166) and integration yields Eq. (4.5.149).

Figure 4.5.33 shows concentration profiles in a porous plate for a value of ϕ_1 of 5, that is, a strong influence of pore diffusion on the effective reaction rate, and different values of ϕ_2 . For a slow reaction of B to C (Figure 4.5.33a), we reach a maximum concentration of the intermediate B in the center of the slab, whereas for a fast reaction (Figure 4.5.33c), the maximum of the concentration of B is reached somewhere in the plate.

Finally, two additional aspects should be mentioned without going into further details:

- For a high value of the Thiele modulus, we have to consider both external and internal concentration gradients (Section 4.5.5). The selectivity of an intermediate is then even lower, as if only one mass transfer resistance has to be taken into account.
- Up to now, we have only considered particles with one size of pore. In reality, we may have a wide spread of pore sizes or a micro-macroporous material (see Example 4.5.11 for the pore effectiveness factor in this case). Pellets are often prepared by compressing a porous powder, and thus we may get at least two pore sizes, large macropores between the agglomerated particles and small micropores within each particle. The micropores can be considered to be in series with the macropores and only the latter communicate with the external particle surface and the bulk phase of the fluid. For a strong resistance to both macro- and micropore diffusion, the following equation is obtained for the maximum selectivity of the intermediate, if external mass transfer limitations are neglected (Carberry, 1962; Froment and Bischoff, 1990; Levenspiel, 84,83):

$$Y_{B,\text{max}} = \frac{(1 - \sqrt{\Phi_{21}})}{(1 - \Phi_{21}^2)} \left(\sqrt{\Phi_{21}} \right)^{\frac{\sqrt{\Phi_{21}}}{1 - \sqrt{\Phi_{21}}}} \left(\text{with } \Phi_{21} = \frac{\phi_2}{\phi_1} = \sqrt{\frac{k_{m,2}}{k_{m,1}}} \right) \quad (4.5.167)$$

For example, for $k_{m,2}/k_{m,1} = 0.1$ we obtain a maximum yield of the intermediate of only 23% [Eq. (4.5.167)], whereas for one size of pores we have 45% (Figure 4.5.29). Thus, the selectivity decreases further for significant macro- and micropore diffusional limitations.

Example 4.5.11: Effectiveness factor for pore diffusion for macro- and micropores

To calculate the pore effectiveness factor of pellets that have macro- and micropores, we use the following simple model and respective assumptions:

- The spherical particles (diameter d_p) consist of small microporous grains with diameter d_{micro} and density ρ_{micro} . Between the agglomerated microporous grains we only have macropores that communicate with the external surface and the bulk phase.
- The porosity of the microporous grains is $\varepsilon_{\text{micro}}$ (ratio of volume of micropores to volume of grains), and the porosity of the macroporous structure is $\varepsilon_{\text{macro}}$ (ratio of volume of macropores to volume of particle). Here we assume a value of 0.4 for $\varepsilon_{\text{macro}}$. Thus, the overall porosity of the whole particle (ε_p) is given by the term $\varepsilon_{\text{micro}}(1 - \varepsilon_{\text{macro}}) + \varepsilon_{\text{macro}}$ (ratio of volume of micro- and macropores to volume of particle).
- The effective diffusion coefficients are [Eq. (3.2.75)]:

$$D_{\text{eff,macro}} = \frac{\varepsilon_{\text{macro}}}{\tau_{\text{macro}}} D_{\text{mol}} \quad (4.5.168)$$

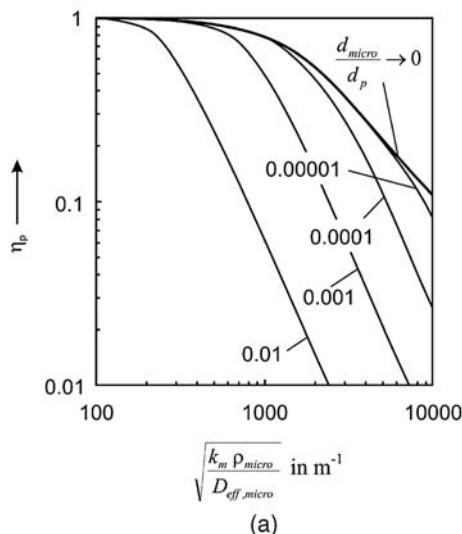
$$D_{\text{eff,micro}} = \frac{\varepsilon_{\text{micro}}}{\tau_{\text{micro}}} D_{\text{mol}} \quad (4.5.169)$$

For spherical microporous grains and an irreversible first-order reaction, the pore effectiveness factor is to a good approximation, see Table 4.5.5, given by:

$$\eta_{\text{pore,micro}} = \frac{\tanh(\phi_{\text{micro}})}{\phi_{\text{micro}}} \quad \left(\text{with } \phi_{\text{micro}} = \frac{d_{\text{micro}}}{6} \sqrt{\frac{k_m \rho_{\text{micro}}}{D_{\text{eff,micro}}}} \right) \quad (4.5.170)$$

For the macroporous system of the spherical pellet, we obtain a pore effectiveness factor of:

$$\eta_{\text{pore,macro}} = \frac{\tanh(\phi_{\text{macro}})}{\phi_{\text{macro}}} \quad \left(\text{with } \phi_{\text{macro}} = \frac{d_p}{6} \sqrt{\frac{\eta_{\text{pore,micro}} k_m \rho_{\text{micro}} (1 - \varepsilon_{\text{macro}})}{D_{\text{eff,macro}}}} \right) \quad (4.5.171)$$



where the factor $(1 - \varepsilon_{\text{macro}})$ considers that the particle density is by this factor lower than the density of the grains. The overall particle effectiveness factor is then given by:

$$\eta_p = \eta_{\text{pore,macro}} \eta_{\text{pore,micro}} \quad (4.5.172)$$

as the micropores can be considered to be in series with the macropores.

For strong limitation by diffusion $\eta_{\text{micro}} = (\phi_{\text{micro}})^{-1}$ and $\eta_{\text{macro}} = (\phi_{\text{macro}})^{-1}$, we get:

$$\eta_p = (\phi_{\text{micro}} \phi_{\text{macro}})^{-1} \quad (4.5.173)$$

Insertion of Eqs. (4.5.170) and (4.5.171) into Eq. (4.5.173) and rearrangement yields:

$$\eta_p = \frac{1}{\phi_{\text{micro}} \phi_{\text{macro}}} = \frac{6\sqrt{6}}{(1 - \varepsilon_{\text{macro}})^{0.5}} \frac{1}{d_{\text{micro}}^{0.5} d_p} \frac{D_{\text{eff,micro}}^{0.25} D_{\text{eff,macro}}^{0.5}}{(k_m \rho_{\text{micro}})^{0.75}} \quad (4.5.174)$$

Figure 4.5.34 shows the influence of the term $(k_m \rho_{\text{micro}} / D_{\text{eff,micro}})^{0.5}$ on the overall effectiveness factor η_p (Figure 4.5.34a) and on the factors for macro- and micropore diffusion for different values of d_{micro}/d_p , $D_{\text{eff,micro}}/D_{\text{eff,macro}} = 0.5$, and a particle diameter of 1 cm.

Often, micropores are short, that is, $\eta_{\text{micropores}} = 1$. Here, grains with a diameter $< 0.1 \mu\text{m}$ ($d_{\text{micro}}/d_p < 10^{-6}$) would be sufficiently small to suppress the mass transfer resistance of the micropores. Note that Eq. (4.5.174) indicates that the apparent activation energy is 0.25 of the intrinsic value for strong limitation by pore diffusion in micro- and macropores:

$$k_{\text{m,eff}} = \eta_p k_m \sim k_m^{0.75} k_m = k_m^{0.25} \sim e^{-\frac{E_A}{4RT}} \quad (\text{for both } \phi_{\text{micro}} \text{ and } \phi_{\text{macro}} \gg 1) \quad (4.5.175)$$

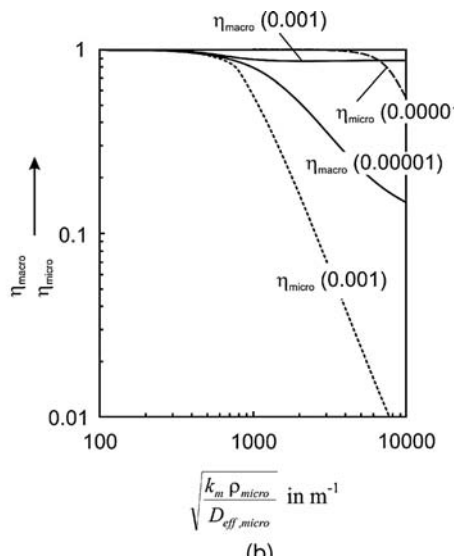


Figure 4.5.34 Effectiveness factors for pore diffusion of a pellet containing micro- and macropores ($D_{\text{eff,micro}}/D_{\text{eff,macro}} = 0.5$, $d_p = 1 \text{ cm}$).

4.5.6.4 Influence of Pore Diffusion on the Selectivity of Parallel Reactions

For two parallel independent reactions ($A \xrightarrow{k_{m,1}} B$ and $A \xrightarrow{k_{m,2}} C$) with reaction orders of m and n occurring in a porous catalyst with the rate constants $k_{m,1}$ and $k_{m,2}$ ($\text{m}^3 \text{kg}^{-1} \text{cat s}^{-1}$), the selectivity ratio is given by (Froment and Bischoff, 1990; Baerns *et al.*, 2006):

$$\frac{\left. \frac{s_B}{s_C} \right|_{\text{eff}}}{\left. \frac{s_B}{s_C} \right|_{\text{intrinsic}}} = \frac{\int_0^L k_{m,1} c_{A,s}^m}{\int_0^L k_{m,2} c_{A,s}^n} = \frac{k_{m,1} c_{A,g}^m}{k_{m,2} c_{A,g}^n} \quad (4.5.176)$$

For equal reaction orders ($m = n$), pore diffusion then has no influence on the selectivity. For $n \neq m$, the mathematical solutions are quite involved (Roberts, 1972). Selected results are shown in Figure 4.5.35 for a second- and first-order parallel reaction and a second- and zero-order parallel reaction for strong limitation by pore diffusion. The decrease in selectivity to product B (formed by the reaction with the higher order m) is larger for a larger difference in reaction order ($m - n$). An asymptotic minimum value of the effective selectivity to B relative to the intrinsic value is found for a low value of the ratio of the intrinsic reaction rates ($k_{m,1}/k_{m,2} c_{A,s}^{(m-n)} \ll 1$). This minimum value is given by (Roberts, 1972; Westerterp, van Swaaij, and Beenackers, 1998):

$$\left. \frac{s_B}{s_C} \right|_{\text{intrinsic}} \approx \frac{n+1}{2m-n+1} \quad (4.5.177)$$

(strong limitation by pore diffusion, $m > n$, $\frac{k_{m,1}}{k_{m,2}} c_{A,s}^{m-n} \ll 1$)

Figure 4.5.36 shows these asymptotic values of the maximum decrease of the selectivity of the formation of product B for different values of m and n .

Summary of Section 4.5 (take-home messages)

- The first step of the reaction on a solid catalyst is the sorption of at least one reactant. If two reactants are adsorbed, the rate follows the so-called **Langmuir–Hinshelwood mechanism**, which is based on the assumption that both reactants are adsorbed on the surface (equilibrium). If only one reactant is adsorbed on the surface of the catalyst and reacts with the second species coming from gas phase, the rate follows the **Eley–Rideal-mechanism**. Other more complex situations may be described by **Langmuir–Hinshelwood–Hougen–Watson (LHHW) rate equations**.
- Interaction of the **external and internal mass transfer** with the chemical reaction may lead to a concentration gradient of the reactant in the boundary layer surrounding a solid catalyst and within the porous structure. For a first-order reaction, this leads to the following equation for the effective reaction rate:

$$r_{m,\text{eff}} = \left(\frac{1}{\beta A_{m,\text{ex}}} + \frac{1}{\eta_{\text{pore}} k_m} \right)^{-1} c_{A,g} = k_{m,\text{eff}} c_{A,g}$$

where $c_{A,g}$ is the concentration of reactant A in the bulk phase, β the (external) mass transfer coefficient, $A_{m,\text{ex}}$ is the external surface area per mass, k_m the intrinsic rate constant, and η_{pore} the **effectiveness factor** with regard to internal pore diffusion, which can be calculated by the **Thiele modulus** ϕ . The simultaneous occurrence of interfacial and internal mass transport effects is characterized by the **Biot number** for mass transfer, Bi_m , which is a measure for the ratio of the external to the internal mass transfer.

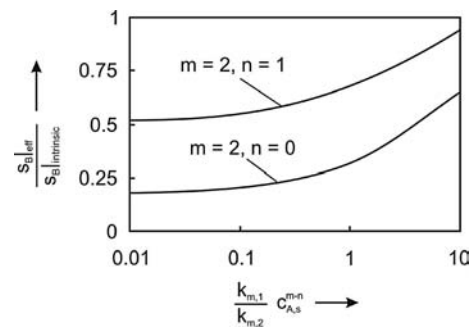


Figure 4.5.35 Influence of pore diffusion on the selectivity for two parallel reactions ($A \rightarrow B$, order m ; $A \rightarrow C$, order n) for $m = 2$ and $n = 0$ or 1 for strong limitation by pore diffusion.

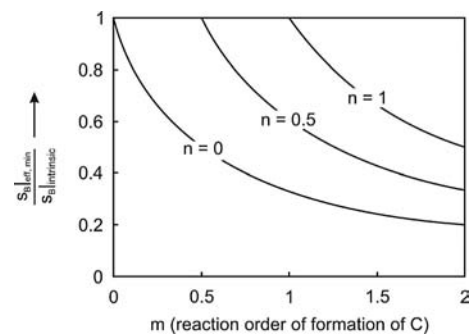


Figure 4.5.36 Influence of pore diffusion on the selectivity of two parallel reactions ($A \rightarrow B$, $A \rightarrow C$): asymptotic values of the minimum effective selectivity to B relative to the intrinsic value in the absence of diffusional effects for different values of m and n [Eq. (4.5.177)].

- For exothermic reactions, the particle temperature may be much higher than the bulk phase temperature. This **ignition-extinction behavior** can be analyzed for a porous particle by the steady-state heat balance:

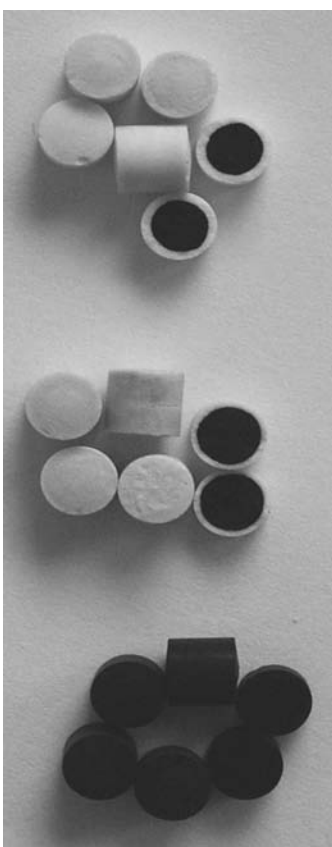
$$r_{m,\text{eff}}(-\Delta_R H) = \alpha A_{m,\text{ex}} (T_s - T_g)$$

measure for the ratio of the external mass transfer to the mass transfer by pore diffusion. Compared to external temperature differences, **intraparticle temperature gradients** are much smaller and in most cases negligible.

- Mass transfer resistances may also change the **selectivity** of parallel and consecutive reactions. For parallel reactions and equal reaction orders, pore diffusion and external mass transport have no influence on selectivity. For different orders, the reaction with the lower order is favored. For a series reaction, the influence of external and internal mass transfer leads to a lower yield and selectivity of the intermediate product.



Blast furnace coke just before stabilization by quenching with water. Courtesy of Uhde, Germany.



Partly regenerated coked catalyst. Details in Tang, Kern, and Jess, 2004.

4.6

Kinetics of Gas–Solid Reactions

Gas–solid reactions are important in many branches of the chemical and metallurgical industry. Examples are the reduction of iron ore in a blast furnace, roasting of sulfidic ores, coal combustion in a power plant, gasification of coal or biomass to produce syngas, regeneration of coked catalysts and limestone burning. Typically, fixed, fluidized, or entrained bed reactors are used. The following factors have to be considered with respect to the kinetics and the design of the reactor:

- The solid may be either porous or non-porous, that is, the reaction takes place internally or only at the external surface of the particles.
- A solid product or a solid inert residue and/or gases may be formed.
- The effective kinetics of gas–solid reactions are in many cases influenced by the internal and external mass transfer.

In contrast to heterogeneous catalysis, where we frequently also have to consider mass and heat transfer effects, the quantitative evaluation of a gas–solid reaction is much more complicated, because:

- the solid may change with respect to particle size;
- the mean value and the distribution of the solid reactant in the particle may also change during the reaction;
- additional mass transfer resistances may develop, for example, by a solid product layer.

“Operating manual” for beginners and intermediate learners:

For a basic understanding, start with Section 4.6.1, where the spectrum of factors influencing the effective rate of gas–solid reactions is discussed. Then study the border cases of non-porous and porous solids (Sections 4.6.2.1 and 4.6.3.1); in both sections the systems will be analyzed only qualitatively without any mathematics and equations.

“Operating manual” for advanced learners:

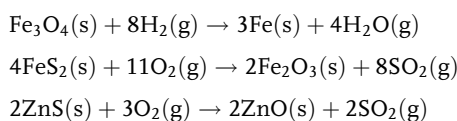
Advanced learners may also study the equations needed to describe quantitatively the progress of a gas–solid reaction in many different cases, for example, for a shrinking non-porous unreacted core with a solid product layer or gaseous products (Sections 4.6.2.2 and 4.6.2.3), or models to evaluate the reaction of a gas with a porous solid for a different strength of the mass transfer resistance (Sections 4.6.3.2–4.6.3.5).

4.6.1

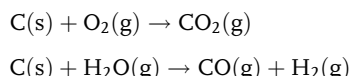
Spectrum of Factors Influencing the Rate of Gas–Solid Reactions

Some important examples of gas–solid (G/S) reactions are:

- Reduction of iron ore and roasting of sulfidic ore:



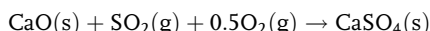
- Coal combustion and gasification, but also regeneration of coked catalysts:



- Limestone pyrolysis:



- Absorption of SO₂ (pollution control):



The solid may be porous or non-porous. In the first case, the reaction takes place practically only at the internal surface; the contribution of the external surface to the overall surface area is mostly negligible as the internal surface area is typically an order of magnitude larger for solid catalysts (up to several $100 \text{ m}^2 \text{ g}^{-1}$), and even for particles of $10 \mu\text{m}$ the external surface area is only about $1 \text{ m}^2 \text{ g}^{-1}$ (Figure 4.5.1). For non-porous particles, reaction can only take place at the shrinking external surface or at the surface of a reactive core if a solid product is formed. However, in most industrially relevant cases, solid reactants are porous or at least a porous structure is formed during the initial phase of the reaction.

For porous systems, the particle size can be mostly considered to be constant during the main part of the conversion, above all if a solid product is formed. If the solid is completely converted into gaseous products, the particle size may also change during the reaction.

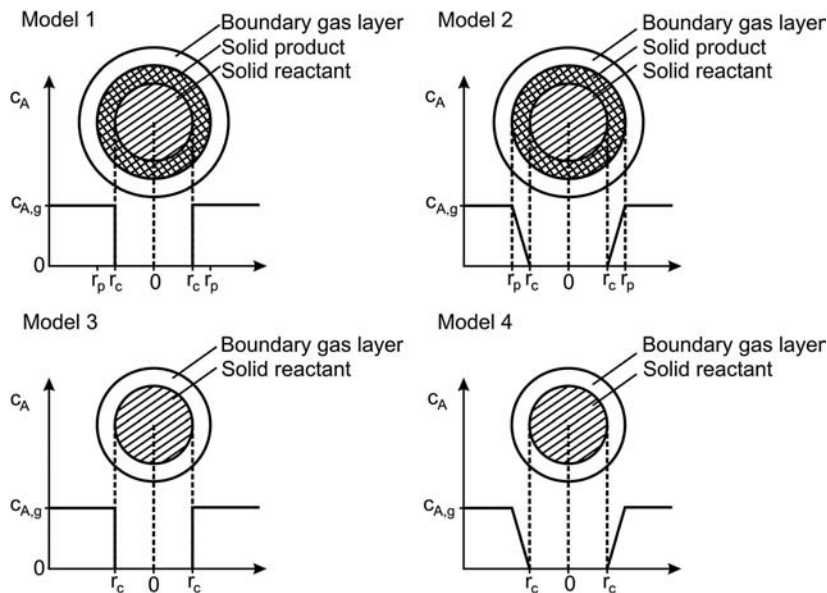
The influence of external and internal mass transfer is similar to heterogeneous catalysis (Section 4.6), but some aspects complicate the situation:

- G/S reactions are transient and the mass and sometimes the size of the solid change.
- Internal structural parameters – surface area, porosity, tortuosity, and pore size distribution – and thus the effective diffusion coefficient may also change during the reaction.
- A solid product or inert residue layer may lead to an additional mass transfer resistance.

For the quantitative description of G/S reactions, different models have been developed to derive equations that are not too complicated to describe the conversion of a solid reactant. These equations are based on simplifications. An example is the shrinking core model, which assumes that the reaction starts at the outer surface and that a sharp reaction zone moves into the particle. Subsequently, several cases are discussed based on the following assumptions:

- The reaction rate is first order both with regard to the solid and gaseous reactant.
- The internal porous structure remains constant (constant effective diffusivity).
- T-gradients are neglected, although they may occur between the external particle surface and the bulk phase of the gas if the reaction is strongly influenced by external mass transfer, as inspected for heterogeneous catalysts in Section 4.5.3.2.

Figure 4.6.1 Concentration of gaseous reactant A around and in a non-porous solid spherical particle if a solid product or residue layer (model 1 for control by chemical reaction rate and model 2 for control by diffusion through product layer) or a gaseous product (model 3 for control by chemical reaction rate and model 4 for control by film diffusion) is formed; simply hatched: solid reactant, crossed hatched: solid product or inert residue. Adapted from Baerns et al. (2006).



4.6.2

Reaction of a Gas with a Non-porous Solid

4.6.2.1 Survey of Border Cases and Models for a Reaction of a Gas with a Non-porous Solid

Four border cases can be distinguished for a non-porous particle (Figure 4.6.1).

- A solid product or an inert residue is formed and the reaction rate is slow (no influence of diffusion through boundary gas and solid product layer) (model 1 in Figure 4.6.1).
- A solid product or residue is formed, and the chemical reaction is fast, which leads to a control of the effective rate by pore diffusion through the outer layer free of solid reactant. The concentration of the gaseous reactant at the surface of the unreacted core is then negligibly small (model 2 in Figure 4.6.1).
- A gaseous product is formed and the rate of the chemical reaction is slow (no influence of external diffusion through the boundary gas layer) (model 3 in Figure 4.6.1).
- Only gases are formed, the chemical reaction is fast, and the effective rate is determined by external mass transfer to the surface of the shrinking particle (model 4 in Figure 4.6.1).

All these cases – including the general situation, where both mass transfer and chemical reaction influence the rate – are discussed in the following sections.

4.6.2.2 Shrinking Non-porous Unreacted Core and Solid Product Layer

We assume that the formation of a solid product or residue does not lead to a change of the particle size. Thus, the rate of transport of the gaseous reactant A by diffusion through the external boundary gas layer of a particle with an initial radius r_p is given by:

$$\dot{n}_A = 4\pi r_p^2 \beta (c_{A,g} - c_{A,s}) \quad (4.6.1)$$

The mass transfer coefficient β ($m s^{-1}$) depends on the particle size, geometry, and on the hydrodynamic conditions such as fluid viscosity and velocity. Equations to calculate β are given in Section 3.2.2.2 in combination with Section 3.2.1.2.

The rate of transport of the gaseous reactant A by diffusion through the product layer, which is established and increases during the conversion of the solid, is given by:

$$\dot{n}_A = 4\pi r_c^2 D_{A,\text{eff}} \frac{dc_A}{dr} \Big|_{r=r_c} \quad (\text{with } r_c \text{ as decreasing radius of unreacted core}) \quad (4.6.2)$$

For a certain concentration at the surface of the unreacted core, $c_{A,c}$, and rate constant k_A related to the surface area (m s^{-1}), the chemical reaction rate (first-order reaction) is given by:

$$\dot{n}_A = 4\pi r_c^2 k_A c_{A,c} \quad (4.6.3)$$

The general situation, where all three steps influence the rate, is shown in Figure 4.6.2.

The mass balance for the layer of the solid product or residue where reaction no longer takes place is given in spherical coordinates by:

$$0 = \frac{d^2 c_A}{dr^2} + \frac{2}{r} \frac{dc_A}{dr} \quad (4.6.4)$$

The solution of Eq. (4.6.4) by twofold integration for the boundary conditions:

$$c_A = c_{A,s} \quad (\text{for } r = r_p, \text{ i.e. at external surface of particle with constant radius } r_p) \quad (4.6.5)$$

$$c_A = c_{A,c} \quad (\text{for } r = r_c \text{ with } r_c \text{ as radius of unreacted core}) \quad (4.6.6)$$

leads to:

$$c_A = c_{A,c} + (c_{A,s} - c_{A,c}) \frac{\left(1 - \frac{r_c}{r}\right)}{\left(1 - \frac{r_c}{r_p}\right)} \quad (4.6.7)$$

Differentiation of Eq. (4.6.7) and insertion into Eq. (4.6.2) lead to the concentration gradient at the position $r = r_c$ and thus to the molar flux of A based on the still unknown concentration gradient of the gaseous reactant in the product layer:

$$\frac{dc_A}{dr} \Big|_{r=r_c} = \frac{(c_{A,s} - c_{A,c})}{r_c \left(1 - \frac{r_c}{r_p}\right)} \Rightarrow \dot{n}_A = 4\pi r_c D_{A,\text{eff}} \frac{(c_{A,s} - c_{A,c})}{\left(1 - \frac{r_c}{r_p}\right)} \quad (4.6.8)$$

Substitution of $c_{A,s}$ in Eq. (4.6.8) by (Eq. 4.6.1) and subsequent replacement of \dot{n}_A by Eq. (4.6.3) lead to the concentration at the surface of the unreacted core as a function of $c_{A,g}$:

$$c_{A,c} = \frac{c_{A,g}}{1 + \frac{r_c^2 k_A}{r_p^2 \beta} + \frac{k_A r_c}{D_{A,\text{eff}}} \left(1 - \frac{r_c}{r_p}\right)} \quad (4.6.9)$$

and by combination with Eq. (4.6.3) we finally get:

$$\dot{n}_A = \frac{4\pi r_c^2 k_A c_{A,g}}{1 + \frac{r_c^2 k_A}{r_p^2 \beta} + \frac{k_A r_c}{D_{A,\text{eff}}} \left(1 - \frac{r_c}{r_p}\right)} \quad (4.6.10)$$

For an equimolar reaction of the gaseous reactant A with the solid B (with density ρ_c) we obtain:

$$\dot{n}_A = -\frac{dm_B}{dt} \frac{1}{M_B} = -\frac{dV_c \rho_c}{dt} \frac{1}{M_B} = -\frac{d\left(\frac{4\pi}{3} r_c^3\right)}{dt} \frac{\rho_c}{M_B} = -\frac{dr_c}{dt} 4\pi r_c^2 \frac{\rho_c}{M_B} \quad (4.6.11)$$

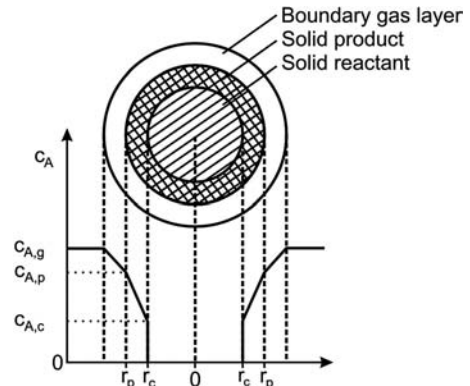


Figure 4.6.2 Concentration profiles of gaseous reactant A in a non-porous spherical particle and formation of a solid porous product, if film diffusion and diffusion through the product layer influence the rate; simply hatched: solid reactant, crossed hatched: solid product. Adapted from Baerns et al. (2006).

and insertion of Eq. (4.6.11) into Eq. (4.6.10) and rearrangement yields:

$$-\frac{dr_c}{dt} = \frac{k_A \frac{M_B}{\rho_c} c_{A,g}}{1 + \frac{r_c^2 k_A}{r_p^2 \beta} + \frac{k_A r_c}{D_{A,eff}} \left(1 - \frac{r_c}{r_p}\right)} \quad (4.6.12)$$

and integration finally leads to the time t as a function of the radius of the unreacted core (r_c):

$$t = \frac{\rho_c r_p}{k_A M_B c_{A,g}} \left\{ \left(1 - \frac{r_c}{r_p}\right) + \frac{k_A}{3\beta} \left[1 - \left(\frac{r_c}{r_p}\right)^3\right] + \frac{k_A r_p}{D_{A,eff}} \left[\frac{1}{6} - \frac{1}{2} \left(\frac{r_c}{r_p}\right)^2 + \frac{1}{3} \left(\frac{r_c}{r_p}\right)^3\right] \right\} \quad (4.6.13)$$

The conversion of the solid X_B is given by:

$$X_B = 1 - \frac{m_B}{m_{B,0}} = 1 - \left(\frac{r_c}{r_p}\right)^3 \Rightarrow \frac{r_c}{r_p} = (1 - X_B)^{\frac{1}{3}} \quad (\text{for } m_B = m_{B,0} \text{ for } t = 0) \quad (4.6.14)$$

and the combination of the last two equations leads to the relation between the reaction time and conversion (and vice versa):

$$t = \frac{\rho_c r_p}{k_A M_B c_{A,g}} \left\{ \left[1 - (1 - X_B)^{\frac{1}{3}}\right] + \frac{k_A}{3\beta} X_B + \frac{k_A r_p}{D_{A,eff}} \left[\frac{1}{6} - \frac{1}{2} (1 - X_B)^{\frac{2}{3}} + \frac{1}{3} (1 - X_B)\right] \right\} \quad (4.6.15)$$

If one reaction step is rate determining, Eq. (4.6.15) simplifies as follows:

Case I: slow chemical reaction ($k_A \ll \beta$; $k_A \ll r_p/D_{A,eff}$), (model 1, Figure 4.6.1):
For a slow reaction, Eq. (4.6.15) yields:

$$t = \frac{\rho_c r_p}{k_A M_B c_{A,g}} \left[1 - (1 - X_B)^{\frac{1}{3}}\right] \quad (4.6.16)$$

$$X_B = 1 - \left(1 - \frac{k_A M_B c_{A,g}}{\rho_c r_p} t\right)^3 \quad (4.6.17)$$

and for the final time (t_{fin}) for complete conversion we obtain:

$$t_{fin} = \frac{\rho_c r_p}{k_A M_B c_{A,g}} \quad (4.6.18)$$

Case II: rate limited by film diffusion and internal diffusion in the product layer (Figure 4.6.2 for $c_{A,c} = 0$, $k_A \gg \beta$ and $k_A \gg r_p/D_{A,eff}$):

Here, Eq. (4.6.15) simplifies to:

$$t = \frac{\rho_c r_p}{M_B c_{A,g}} \left\{ \underbrace{\frac{X_B}{3\beta}}_{\substack{\text{term that considers} \\ \text{film diffusion}}} + \underbrace{\frac{r_p}{D_{A,eff}} \left[\frac{1}{6} - \frac{1}{2} (1 - X_B)^{\frac{2}{3}} + \frac{1}{3} (1 - X_B)\right]}_{\substack{\text{term that considers diffusion through product layer}}} \right\} \quad (4.6.19a)$$

$$t_{fin} = \frac{\rho_c r_p}{3M_B c_{A,g}} \left(\frac{1}{\beta} + \frac{r_p}{2D_{A,eff}}\right) \quad (4.6.20)$$

During the initial stage of the conversion the product layer is small and thus so also is the diffusional resistance of the layer. With increasing conversion, this resistance is then no longer negligible. The conversion where this is the case (at the latest) can be estimated as follows:

For a single particle and a stagnant gas phase ($Re = 0$), the minimum value of β is $D_{A,g}/r_p$. The effective diffusion coefficient approximately equals $1/10D_{A,g}$, and Eq. (4.6.19) leads to an approximation of the time that we have to expect for this

minimum value of β :

$$t = \frac{\rho_c r_p}{M_B c_{A,g}} \frac{1}{3\beta_{\min}} \left[X_B + 5 - 15(1-X_B)^{\frac{2}{3}} + 10(1-X_B) \right] \quad (4.6.19b)$$

(for $\beta = \beta_{\min}$, i.e., $Re = 0$)

For example, for a conversion of only 6%, Eq. (4.6.20) already yields a reaction time that is 10% higher than without considering diffusion through the product layer [see Eq. (4.6.19b) without the term $5-15(1-X_B)^{\frac{2}{3}}$. . .]. Thus with increasing degree of conversion, the rate is increasingly dominated by the diffusional resistance of the product layer, and for complete conversion 83% of the total reaction time can be ascribed to this resistance [see Eq. (4.6.20) for $\beta = D_{A,g}/r_p$ and $D_{A,\text{eff}} = 0.1D_{A,g}$]. For many practical cases with $\beta > D_{A,g}/r_p$ (i.e., $Re > 0$), this effect is even more pronounced.

Case III: reaction and external mass transfer are fast compared to diffusion through the product layer (k_A and $\beta \gg D_{A,\text{eff}}/r_p$ model 2 in Figure 4.6.1):

Now Eq. (4.6.15) leads to:

$$t = \frac{\rho_c r_p^2 \left[3 - 2X_B - 3(1-X_B)^{\frac{2}{3}} \right]}{6M_B c_{A,g} D_{A,\text{eff}}} \quad (4.6.21)$$

$$t_{\text{fin}} = \frac{\rho_c r_p^2}{6M_B c_{A,g} D_{A,\text{eff}}} \quad (4.6.22)$$

Figure 4.6.3 clearly shows that by measurement of the conversion of the solid with time (dimensionless time t/t_{fin}) we can hardly decide whether the rate is controlled by the chemical reaction or by diffusion through the solid product layer/film diffusion. Therefore, we need more experimental data and further calculations. For example, the variation of the particle size is helpful, as the final time for conversion is proportional to the initial particle diameter for control by the chemical reaction, Eq. (4.6.18), whereas $t_{\text{fin}} \sim r_p^2$ if the rate is controlled by diffusion through the solid product layer, Eq. (4.6.22).

4.6.2.3 Shrinking Non-porous Unreacted Core and Gaseous Product(s)

For a gas–solid reaction with a gaseous product, the non-porous particle shrinks ($r = r_p$ for $t = 0$ and $r = r_c$ for $t > 0$) and thus so also does the external surface. The rate of transport of the gaseous reactant A through the boundary layer, Eq. (4.6.1), equals the reaction rate, Eq. (4.6.3):

$$\dot{n}_A = 4\pi r_c^2 \beta (c_{A,g} - c_{A,s}) = 4\pi r_c^2 k_A c_{A,s} \quad (4.6.23)$$

Note that the mass transfer coefficient β depends on the particle size and changes during the course of the reaction but, at first, this is not considered. Rewriting

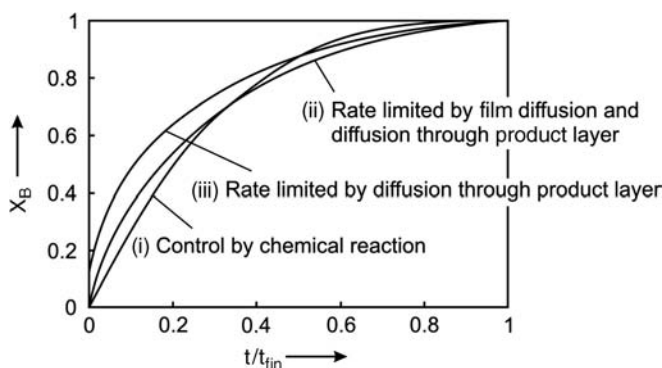


Figure 4.6.3 Conversion of a non-porous solid and formation of a layer of a solid product or solid residue for different cases: (i) slow chemical reaction, Eqs. (4.6.16) and (4.6.18), (ii) rate limited by film diffusion and diffusion through product layer, Eqs. (4.6.19b) and (4.6.20) for $Sh = 2$, $\beta = D_{A,g}/r_p$ and $D_{A,\text{eff}} = 0.1D_{A,g}$, and (iii) rate limited by diffusion through product layer, Eqs. (4.6.21) and (4.6.22).

Eq. (4.6.23) yields:

$$c_{A,s} = \frac{\beta}{(k_A + \beta)} c_{A,g} \quad (4.6.24)$$

$$\dot{n}_A = 4\pi r_c^2 \frac{k_A \beta}{\beta + k_A} c_{A,g} \quad (4.6.25)$$

Based on Eq. (4.6.11), we then obtain for an equimolar reaction of gas A with solid B:

$$-\frac{dr_c}{dt} = \frac{k_A \beta M_B}{(\beta + k_A) \rho_c} c_{A,g} \quad (4.6.26)$$

Integration of Eq. (4.6.26) yields the correlations for the radius of the unreacted core r_c (with initial radius r_p) and for the conversion of the solid (X_B):

$$r_c = r_p - \frac{k_A \beta M_B c_{A,g}}{(\beta + k_A) \rho_c} t \quad (4.6.27)$$

$$X_B = 1 - \left[1 - \frac{k_A \beta M_B c_{A,g}}{(\beta + k_A) \rho_c r_p} t \right]^3 \quad (4.6.28)$$

Case I: chemical reaction determines effective rate ($k_A \ll \beta$, model 3, Figure 4.6.1):

For this case Eq. (4.6.28) yields:

$$X_B = 1 - \left(1 - \frac{k_A M_B c_{A,g}}{\rho_c r_p} t \right)^3 \quad (4.6.29)$$

$$t_{fin} = \frac{\rho_c r_p}{k_A M_B c_{A,g}} \quad (4.6.30)$$

Case II: effective rate limited by external diffusion ($k_A \gg \beta$, model 4, Figure 4.6.1):

Now Eq. (4.6.28) leads to:

$$X_B = 1 - \left(1 - \frac{\beta M_B c_{A,g}}{\rho_c r_p} t \right)^3 \quad \left(\text{for } \beta = \text{constant} = \frac{Sh D_{A,g}}{2r_p} \right) \quad (4.6.31)$$

$$t_{fin} = \frac{2\rho_c r_p^2}{Sh D_{A,g} M_B c_{A,g}} \quad (\text{for } \beta = \text{constant}) \quad (4.6.32)$$

If we consider that the mass transfer coefficient β is a function of the declining value of r_c [$\beta = Sh \times D_{A,g}/(2r_c)$], then Eq. (4.6.26) leads to ($k_A \gg \beta \neq \text{const}$):

$$-\frac{dr_c}{dt} = \frac{\beta M_B}{\rho_c} c_{A,g} = \frac{1}{r_c} \frac{Sh D_{A,g} M_B c_{A,g}}{2\rho_c} \quad (4.6.33)$$

If we assume a constant value of Sh (but $\beta \sim 1/r_c$), which is more realistic than a constant value of β [Eqs. (4.6.31) and (4.6.32)], integration of Eq. (4.6.33) and insertion of Eq. (4.6.14) lead to:

$$X_B = 1 - \left(1 - \frac{Sh D_{A,g} M_B}{\rho_c r_p^2} c_{A,g} t \right)^{\frac{3}{2}} \quad \left(\text{for } \beta \sim \frac{1}{r_c} \right) \quad (4.6.34)$$

$$t_{fin} = \frac{\rho_c r_p^2}{Sh D_{A,g} M_B c_{A,g}} \quad \left(\text{for } \beta \sim \frac{1}{r_c} \right) \quad (4.6.35)$$

The final time is only half of the value according to Eq. (4.6.32), that is, for the assumption of a constant value of β . Thus, at least for a high conversion, Eq. (4.6.35) should be used.

Table 4.6.1 lists all equations for the conversion of a non-porous solid with solid or gaseous products. An instructive example is given in Example 4.6.1.

V

Table 4.6.1 Equations for the conversion of a non-porous solid B with a gaseous reactant A for different cases (isothermal, first-order irreversible reaction).

Case and product(s)	Rate-determining step (RDS), assumptions	Equations for the conversion X_B of the solid B with a gaseous reactant A for the reaction time t
Shrinking unreacted core; solid product layer	None (general solution)	$t = \frac{\rho_c r_p}{k_A M_B c_{A,g}} \left\{ \left(1 - \frac{r_c}{r_p}\right) + \frac{k_A}{3\beta} \left[1 - \left(\frac{r_c}{r_p}\right)^3\right] + \frac{k_A r_p}{D_{A,\text{eff}}} \left[\frac{1}{6} - \frac{1}{2} \left(\frac{r_c}{r_p}\right)^2 + \frac{1}{3} \left(\frac{r_c}{r_p}\right)^3\right] \right\}$ $\left[\text{with } \frac{r_c}{r_p} = (1 - X_B)^{\frac{1}{3}} \right]$
	Diffusion (boundary gas layer and product layer) $k_A \gg \beta$, $k_A \gg r_p/D_{A,\text{eff}}$	$t = \frac{\rho_c r_p}{M_B c_{A,g}} \left\{ \frac{1}{3\beta} \left(\frac{r_c}{r_p}\right)^3 + \frac{r_p}{D_{A,\text{eff}}} \left[\frac{1}{6} - \frac{1}{2} \left(\frac{r_c}{r_p}\right)^2 + \frac{1}{3} \left(\frac{r_c}{r_p}\right)^3\right] \right\}$ $\left(\text{with } \frac{r_c}{r_p} = (1 - X_B)^{\frac{1}{3}} \right)$
	Product layer diffusion k_A and $\beta \gg r_p/D_{A,\text{eff}}$	$t = \frac{\rho_c r_p}{M_j c_{A,g}} \left[\frac{r_p}{D_{A,\text{eff}}} \left(\frac{1}{6} - \frac{r_p^2}{2r_p^2} + \frac{r_p^3}{3r_p^3} \right) \right] \quad \left(\text{with } \frac{r_c}{r_p} = (1 - X_B)^{\frac{1}{3}} \right)$
Solid or gaseous product; homogeneous conversion	Chemical reaction (no gradients of solid and gaseous reactant) $k_A \ll \beta$, $k_A \ll r_p/D_{\text{eff}}$	$X_B = 1 - \left(1 - \frac{tk_A M_j c_{i,g}}{\rho_c r_p}\right)^3$
Shrinking unreacted core; gaseous product(s)	None (general solution)	$X_B = 1 - \left(1 - \frac{k_A M_B c_{A,g}}{(1 + k_A/\beta)\rho_c r_p}\right)^3$
	Chemical reaction $k_A \ll \beta$	$X_B = 1 - \left(1 - \frac{k_A M_B c_{A,g}}{\rho_c r_p}\right)^3$
	External mass transfer $k_A \gg \beta = \text{const.}$	$X_B = 1 - \left(1 - \frac{\beta M_B c_{A,g}}{\rho_c r_p}\right)^3$
	External mass transfer $k_A \gg \beta \neq \text{const.}$ $Sh = \text{const.}$	$X_B = 1 - \left(1 - \frac{Sh D_{A,g} M_B}{\rho_c r_p^2} c_{A,g} t\right)^{\frac{3}{2}}$

Figure 4.6.4 shows the plot of X_B versus t/t_{fin} for the boarder cases discussed before: (i) absence of any diffusional resistances, (ii) control by diffusion through the product layer, and (iii) control by external diffusion. These curves are helpful in analyzing experimental data, as the shape of the curve indicates which case we probably have. For comparison the time is normalized with the final time t_{fin} for complete conversion of the solid. The correlations are:

$$X_B = 1 - \left(1 - \frac{t}{t_{\text{fin}}}\right)^3 \quad (4.6.36)$$

if the chemical reaction is the rate-determining step [Eqs. (4.6.16), (4.6.17), (4.6.29), and (4.6.30)]:

$$\frac{t}{t_{\text{fin}}} = 3 - 2X_B - 3(1 - X_B)^{\frac{2}{3}} \quad (4.6.37)$$

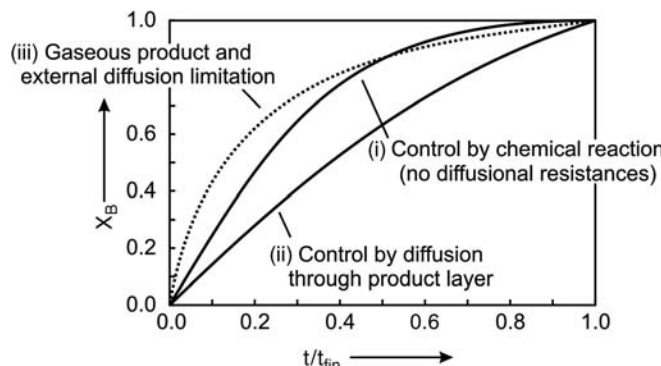


Figure 4.6.4 Conversion of a non-porous solid with a gas for different cases: (i) absence of any diffusional resistances, Eq. (4.6.36), (ii) control by diffusion through solid product layer, Eq. (4.6.37), and (iii) gaseous product and control by external diffusion, Eq. (4.6.38).

if the rate is controlled by diffusion through the solid product layer [Eqs. (4.6.21) and (4.6.22)], and:

$$X_B = 1 - \left(1 - \frac{t}{t_{\text{fin}}}\right)^{\frac{3}{2}} \quad (4.6.38)$$

if gases are formed and the rate is controlled by external diffusion [Eqs. (4.6.34) and (4.6.35)].

Figure 4.6.4 clearly shows that by the measurement of the conversion of the solid with time (the dimensionless time t/t_{fin}) we can decide whether the rate is controlled by diffusion through the solid product layer. However, we see that it is hard to distinguish between the other two cases depicted in Figure 4.6.4, and hence we then need more experimental data and further calculations. For example, the variation of particle size is helpful, as the final time for conversion is proportional to the initial particle diameter for control by the chemical reaction, Eq. (4.6.30), whereas $t_{\text{fin}} \sim r_p^2$ if a gaseous product is formed and the rate is controlled by external diffusion, Eq. (4.6.35). Additional calculations are also helpful, for example, to estimate the Thiele modulus or to compare the measured rate constant and the expected value, if external diffusion alone limits the rate.

Example 4.6.1: Combustion of hot blast furnace coke in contact with air

In a coking plant, the hot coke is discharged from the coking chamber at about 1000°C into a quenching car (see first page of this chapter), transported by train to a cooling tower and quenched with water. To estimate the loss of coke by combustion, we assume that before quenching the hot coke is in contact with air for 5 min. The particle diameter (sphere) is 0.1 m, and the density ρ_{coke} is 1200 kg m^{-3} . The diffusion coefficient of O_2 at 1 bar and a mean temperature in the boundary layer of 500°C is $1 \text{ cm}^2 \text{ s}^{-1}$, and the average O_2 concentration is 3 mol m^{-3} . For Sh we take a value of 3.8, which is the minimum value in a fixed bed of spheres ($Re \rightarrow 0$). The coke is considered to consist of pure carbon ($M = 12 \text{ g mol}^{-1}$) and to be non-porous, that is, the burn-off takes place at the external surface. At first, we assume that the combustion is controlled by external diffusion. By Eq. (4.6.35) we then obtain:

$$\begin{aligned} X_{\text{coke}} &= 1 - \left(1 - \frac{Sh D_{\text{O}_2} M_c}{r_p^2 \rho_{\text{coke}}} c_{\text{O}_2} t\right)^{\frac{3}{2}} \Rightarrow X_{\text{coke}} \\ &= 1 - (1 - 4.6 \times 10^{-6} \text{ s}^{-1} t)^{\frac{3}{2}} \end{aligned}$$

and thus for $t = 5 \text{ min}$, X_{coke} is only about 0.2%.

For comparison we now assume that the chemical reaction determines the rate. According to Hein (1999) the rate constant k_A of blast furnace coke is $6 \times 10^5 \text{ m s}^{-1} \times e^{-183000/RT}$. Thus, for 1000°C , k_A is 0.02 m s^{-1} and Eq. (4.6.29) yields for c_{oxygen} (1000°C) = 2 mol m^{-3} :

$$X_B = 1 - \left(1 - \frac{k_A M_c c_{\text{O}_2} t}{\rho_{\text{coke}} r_p}\right)^3 = 1 - (1 - 8 \times 10^{-6} \text{ s}^{-1} t)^3$$

For $t = 5 \text{ min}$, X_{coke} is 0.7%, which is more than three times higher than the value calculated for the assumption of control by external diffusion. This proves that for a particle diameter of 0.1 m the reaction is really controlled by mass transfer, but for smaller particles the effective rate would then be influenced by the rate of the chemical reaction.

4.6.3

Reaction of a Gas with a Porous Solid

4.6.3.1 Survey of Border Cases and Models for a Reaction of a Gas with a Porous Solid

In most practical cases, solid reactants are porous or at least a porous structure is formed during the reaction. Thus, in this chapter, the reaction of a gas with a porous solid is inspected. Compared to a non-porous solid, the equations are complicated. Subsequently, we assume a constant particle size. Then two cases have to be distinguished (Figure 4.6.5).

- The rate of the chemical reaction is fast, which leads to a gradient of the concentration of the gaseous reactant and with proceeding conversion also of the solid reactant.

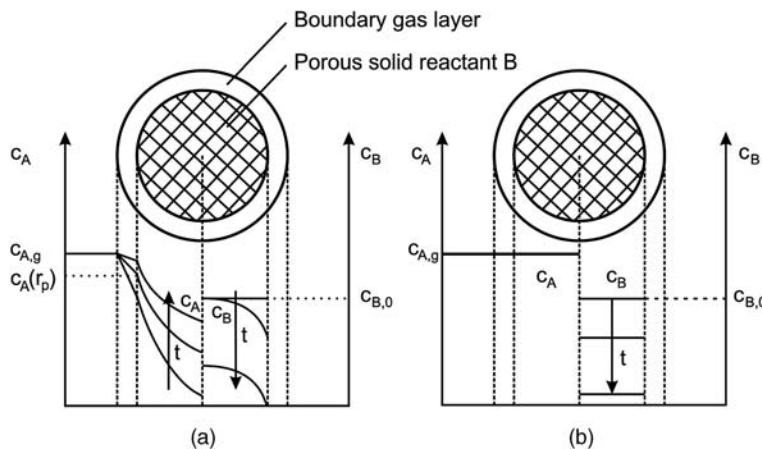


Figure 4.6.5 Concentration profiles of gaseous reactant A during the reaction with a porous particle (solid B) at different stages of the reaction (assumption of constant particle size, for example, a solid porous product or a scaffold rich in ash is formed): (a) influence of external mass transfer and pore diffusion; (b) no influence of mass transfer. Adapted from Baerns et al. (2006).

- The rate of the chemical reaction is slow compared to internal and external diffusion, and concentration gradients both of the solid and gaseous reactant are negligible.

Some border cases and also the general situation are discussed below.

4.6.3.2 Basic Equations for the Conversion of a Porous Solid with a Gaseous Reactant

During the conversion of a porous solid with a gas radial profiles of the gaseous and solid reactant occur. In the following, we assume (i) isothermal conditions, (ii) an equimolar irreversible reaction, (iii) a constant particle size, that is, a layer of solid product or residue (e.g., a scaffold rich in ash in the case of coal gasification/combustion or a metal for ore reduction), and (iv) no external mass transfer resistance. In contrast to Section 4.6.2, we consider (for the purpose of exercise) the case of cylindrical particles with length L_p and diameter d_p . Similar equations may be derived for spheres and so on. Assuming that axial concentration gradients of the solid reactant B (with density ρ_B in kg m^{-3}) and of the gaseous reactant A (c_A in mol m^{-3}) are negligible (high ratio L_p/d_p), the mass balance for a differential cylindrical shell with thickness dr yields:

$$\varepsilon_p \frac{dc_A}{dt} = \frac{1}{r} \frac{d}{dr} \left(D_{A,\text{eff}} r \frac{dc_A}{dr} \right) - r_m \rho_B \quad (4.6.39)$$

Note that the density of the solid reactant in the particle may change with time.

In contrast to a non-porous particle, the intrinsic rate of the chemical reaction r_m ($\text{mol kg}^{-1} \text{s}^{-1}$) is now expressed in terms of particle mass and not in terms of the external surface area, and for an equimolar first-order reaction with respect to solid B and gas A we have:

$$r_m = -\frac{dn_A}{dm_B} = k_m c_A \quad (4.6.40)$$

These differential equations can only be solved numerically for the boundary conditions:

$$\frac{dc_A}{dr} = 0 \quad (\text{for } r = 0, \text{ particle center}) \quad (4.6.41)$$

$$c_A = c_{A,g} \quad (\text{for } r = r_p, \text{ particle surface, no external mass transfer resistance}) \quad (4.6.42)$$

4.6.3.3 General Closed Solution by Combined Model (Approximation)

A closed solution, which can be used as an approximation, is the so-called “shrinking core model with the influence of the chemical reaction,” subsequently denoted

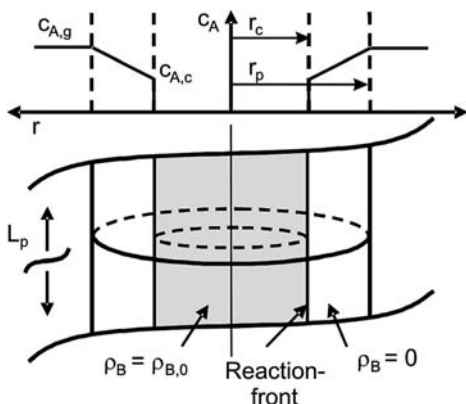


Figure 4.6.6 Combined model (shrinking core with influence of chemical reaction).

as the “combined model” (Kern, 2003; Kern and Jess, 2005, 2006). It is based on the assumption of two consecutive steps (Figure 4.6.6):

- 1) Diffusion of the gaseous reactant through an entirely converted shell (product layer) of the particle, ranging from the outer surface up to a defined reaction front at $r = r_c$:

$$\dot{n}_A = 2\pi r_c L_p D_{A,\text{eff}} \left(\frac{dc_A}{dr} \right)_{r=r_c} \quad (4.6.43)$$

- 2) Chemical reaction without pore diffusion resistance in the remaining core ($0 < r < r_c$) with a constant density of the solid reactant B, ρ_B :

$$\dot{n}_A = \pi r_c^2 L_p k_m c_{A,c} \rho_B \quad (4.6.44)$$

According to this model, the influence of diffusion is restricted to a shell free of solid reactant, whereas in reality the solid reactant is still present to a certain extent in this outer zone. This leads to an underestimation of the (mean) reaction rate. Conversely, the assumption of a constant solid concentration in the core (equivalent to the initial value) overestimates the (mean) rate as in reality the concentration of the solid and of the gaseous reactant decrease in the core. As shown in Section 6.9.4 by the example of the regeneration of a coked catalyst, these effects compensate each other quite well.

The concentration gradient at $r = r_c$ can be calculated based on the stationary mass balance for the outer shell free of the solid reactant:

$$0 = \frac{d^2 c_A}{dr^2} + \frac{1}{r} \frac{dc_A}{dr} \quad (4.6.45)$$

The boundary conditions are:

$$c_A = c_{A,c} \quad (\text{for } 0 < r \leq r_c) \quad (4.6.46)$$

$$c_A = c_{A,g} \quad (\text{for } r = r_p) \quad (4.6.47)$$

The latter condition implies that the external mass transfer resistance can be neglected.

The solution of Eq. (4.6.45) yields:

$$\frac{dc_A}{dr} = - \frac{(c_{A,g} - c_{A,c})}{\ln(r_c) - \ln(r_p)} \frac{1}{r_c} \quad (\text{for } r = r_c) \quad (4.6.48)$$

Based on Eqs. (4.6.48), (4.6.43) and (4.6.44), the concentration of the gaseous reactant A at $r = r_c$ (relative to the one in the gas phase) is given by:

$$\frac{c_{A,c}}{c_{A,g}} = \left[1 - \frac{r_c^2 k_m \rho_B \ln\left(\frac{r_c}{r_p}\right)}{2D_{A,\text{eff}}} \right]^{-1} \quad (4.6.49)$$

The correlation for the amount of solid B converted per unit time and the position of the reaction front r_c can be deduced from the consideration that the converted amount of the solid per unit time corresponds to the flux of the gaseous reactant diffusing into the particle:

$$\frac{dn_B}{dt} = -\dot{n}_A = \frac{1}{M_B} \frac{dm_B}{dt} = \frac{\rho_B}{M_B} \frac{dV_C}{dt} \quad (4.6.50)$$

where V_C is the volume of the core $V_c = 2\pi r_c^2 L_p$ and ρ_B the concentration of solid B, which stays constant according to the assumptions and equals the initial value. Thus we obtain:

$$-\dot{n}_A = \frac{\rho_B}{M_B} \frac{dV_C}{dt} = \frac{\rho_B}{M_B} 2\pi r_c L_p \frac{dr_c}{dt} \quad (4.6.51)$$

Based on Eqs. (4.6.44), (4.6.49), and (4.6.51), the velocity of the reaction front that moves towards the center of the particle is given by:

$$\frac{dr_c}{dt} = \frac{-0.5M_B c_{A,g}}{\frac{1}{k_m r_c} - \frac{r_c \rho_B}{2D_{A,eff}} \ln\left(\frac{r_c}{r_p}\right)} \quad (4.6.52)$$

The initial and the remaining mass of the solid reactant are:

$$m_{B,0} = \rho_B \pi r_p^2 L_p \quad (4.6.53)$$

$$m_B = \rho_B \pi r_c^2 L_p \quad (4.6.54)$$

and differentiation of Eq. (4.6.54) leads to:

$$\frac{dm_B}{dr_c} = \rho_B 2\pi r_c L_p \quad (4.6.55)$$

Substitution of r_c and dr_c in Eq. (4.6.52) by means of Eqs. (4.6.53)–(4.6.55) leads to:

$$\frac{dm_B}{dt} = \frac{-M_B c_{A,g}}{\frac{1}{k_m m_B} - \frac{\rho_B r_p^2}{4D_{A,eff} m_{B,0}} \ln\left(\frac{m_B}{m_{B,0}}\right)} \quad (4.6.56)$$

By integration of Eq. (4.6.56) we, finally, get:

$$t = C_1 \left(\frac{m_B}{m_{B,0}} \right) \ln\left(\frac{m_B}{m_{B,0}} \right) - \frac{1}{C_2} \ln\left(\frac{m_B}{m_{B,0}} \right) - C_1 \left(\frac{m_B}{m_{B,0}} \right) + C_1 \quad (4.6.57)$$

with:

$$C_1 = \frac{\rho_B r_p^2}{4D_{A,eff} M_B c_{A,g}} \quad (4.6.58)$$

$$C_2 = M_B k_m c_{A,g} \quad (4.6.59)$$

The effective reaction rate $r_{m,eff}$ according to the combined model is given by:

$$r_{m,eff} = -\frac{dm_B}{M_B dt} = k_{m,eff} m_B c_{A,g} \quad (4.6.60)$$

Insertion of Eq. (4.6.56) into Eq. (4.6.60) yields:

$$r_{m,eff} = \frac{c_{A,g}}{\frac{1}{k_m m_B} - \frac{\rho_B r_p^2}{4D_{A,eff} m_{B,0}} \ln\left(\frac{m_B}{m_{B,0}}\right)} \quad (4.6.61)$$

Note that the term $C_1 \times C_2$ equals the square of the Thiele modulus for a first-order reaction and a cylindrical particle, $\phi^2 = r_p^2 / (4(k_m \rho_B / D_{A,eff}))$ (see Table 4.5.5), and by insertion of Eq. (4.6.14) into Eq. (4.6.57) we can calculate the conversion for a given time:

$$t = \frac{1}{C_2} [\phi^2 (1 - X_B) \ln(1 - X_B) - \ln(1 - X_B) - \phi^2 (1 - X_B) + \phi^2] \quad (4.6.62)$$

For a negligible influence of pore diffusion (very low value of Thiele modulus ϕ) we obtain:

$$t = -\frac{1}{C_2} \ln(1 - X_B) \quad (\text{for } \phi \ll 1) \quad (4.6.63)$$

and for a strong limitation by pore diffusion (very high value of ϕ) we get:

$$t = C_1 - C_1 (1 - X_B) [1 - \ln(1 - X_B)] \quad (\text{for } \phi \gg 1) \quad (4.6.64)$$

4.6.3.4 Homogeneous Uniform Conversion Model (No Concentration Gradients)

If the chemical reaction is the rate-determining step, no concentration gradients of the solid and gaseous reactant will occur. Therefore, consumption of the gaseous and solid reactant is:

$$\dot{m}_A = -\frac{dm_B}{dt} \frac{1}{M_B} = \pi r_p^2 L_p k_m c_{A,g} \rho_B = k_m c_{A,g} m_B \quad (4.6.65)$$

and integration with $m_B = m_{B,0}$ for $t = 0$ and Eq. (4.6.14) leads to:

$$-\ln(1 - X_B) = M_B k_m c_{A,g} t \quad (4.6.66)$$

which corresponds to Eq. (4.6.63) if we consider that $M_B k_m c_{A,g} = C_2$.

4.6.3.5 Shrinking Unreacted Core Model (Rate Determined by Diffusion Through Product Layer)

If the transport of the gaseous reactant through the product layer of the cylindrical particle is the rate-determining step (fast chemical reaction, no mass transfer resistance by external diffusion), the concentration at the surface of the shrinking core almost reaches zero. Thus the reaction is confined to a front. In contrast to the shrinking core model with the influence of reaction (combined model, Section 4.6.3.3), the reactant concentration is zero at the reaction front, and no reaction occurs within the core. Equation (4.6.56) simplifies as we can assume a negligibly small value of the term $1/(k_m m_B)$, and we obtain:

$$\frac{dm_B}{dt} = \frac{M_B c_{A,g}}{\frac{\rho_B r_p^2}{4 D_{A,eff} m_{B,0}} \ln\left(\frac{m_B}{m_{B,0}}\right)} \quad (4.6.67)$$

Integration ($m_B = m_{B,0}$ for $t = 0$) and insertion of Eq. (4.6.14) results in:

$$(1 - X_B)[1 - \ln(1 - X_B)] = 1 - \frac{4M_B D_{A,eff} c_{A,g}}{\rho_B r_p^2} t \quad (4.6.68)$$

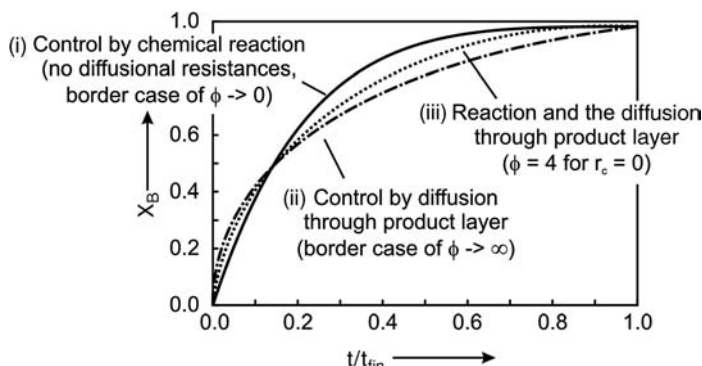
which corresponds to Eq. (4.6.64) if we consider the definition of C_1 [Eq. (4.6.58)].

The time for full conversion of the solid [left-hand side of Eq. (4.6.68) becomes zero] is given by:

$$t_{fin} = \frac{\rho_B r_p^2}{4M_B D_{A,eff} c_{A,g}} = C_1 \quad (4.6.69)$$

Analogously to a non-porous solid (Figure 4.6.4), Figure 4.6.7 shows the plot X_B versus t for three cases, (i) the absence of diffusional resistances, (ii) complete control by diffusion through the product layer, and (iii) both the chemical reaction and the diffusion through the product layer determine the effective rate for a value of the Thiele modulus $\phi = (C_1 C_2)^{0.5}$ of 4, Eq. (4.6.72).

Figure 4.6.7 Conversion of a porous solid with a gas for different cases: (i) absence of diffusional resistances, Eq. (4.6.70), (ii) control by diffusion through product layer, Eq. (4.6.71), and (iii) both the chemical reaction and the diffusion through the product layer determine the effective rate for a value of the Thiele modulus $\phi = (C_1 C_2)^{0.5}$ of 4, Eq. (4.6.72).



V
O**Table 4.6.2** Equations for conversion of porous solid B with gaseous reactant A (cylinder of constant size, isothermal, first order, irreversible, no influence of external diffusion).

Case and product(s)	Rate-determining step (RDS) and assumptions	Equation to determine the conversion X_B of solid B with gaseous reactant A; definitions: $C_1 = \frac{\rho_B r_p^2}{4M_B D_{A, \text{eff}} c_{A, \text{g}}}$; $C_2 = M_B k_m c_{A, \text{g}}$
Shrinking core; solid product (or inert residue) layer	No RDS (general solution) No RDS, but assuming: <ul style="list-style-type: none">• diffusion through layer free of solid reactant;• chemical reaction in the core with constant concentrations of solid and gaseous reactant Diffusion of gaseous reactant through product layer ($k_m \rho_B \gg D_{A, \text{eff}} / r_p^2$)	No closed solution (Section 4.6.3.1) $t = C_1(1 - X_B)\ln(1 - X_B) - \frac{1}{C_2}\ln(1 - X_B) - C_1(1 - X_B) + C_1$ $(1 - X_B)[1 - \ln(1 - X_B)] = 1 - \frac{t}{C_1}$
Solid product (or residue); homogeneous conversion	Chemical reaction ($k_m \rho_B \ll D_{A, \text{eff}} / r_p^2$)	$-\ln(1 - X_B) = C_2 t$

The time was normalized with the time t_{fin} to reach complete conversion. The respective correlations for these cases shown in Figure 4.6.7 are:

Case I: chemical reaction is the rate-determining step [Eqs. (4.6.63) and (4.6.66)]:

$$X_B = 1 - e^{-4.6 \frac{t}{t_{\text{fin}}}} \quad [\text{for } t(X_B = 0.99) \approx t_{\text{fin}}] \quad (4.6.70)$$

Case II: rate controlled by diffusion through solid product layer [Eqs. (4.6.64), (4.6.68) and (4.6.69)]:

$$\frac{t}{t_{\text{fin}}} = X_B + (1 - X_B)\ln(1 - X_B) \quad (4.6.71)$$

Case III: reaction and diffusion in product layer determines the rate [Eq. (4.6.57)]:

$$\frac{t}{t_{\text{fin}}} = \frac{X_B + (1 - X_B)\ln(1 - X_B) - \frac{1}{C_1 C_2} \ln(1 - X_B)}{0.944 + \frac{4.6}{C_1 C_2}} \quad [\text{for } t(X_B = 0.99) = t_{\text{fin}}] \quad (4.6.72)$$

Figure 4.6.7 shows that by looking at the measured conversion of the solid with time we cannot decide which case we have and what the rate-determining step is. Thus we need more data.

Table 4.6.2 summarizes the equations for the conversion of a porous solid.

Summary of Section 4.6 (take-home messages)

- Important examples of gas–solid (G/S) reactions are reduction of iron ore and roasting of sulfidic ore, coal combustion/gasification, limestone pyrolysis, and SO_2 absorption.
- The solid may be either porous or non-porous, but in most industrially relevant cases solid reactants are porous or at least a porous structure is formed during the initial phase of the reaction. Thus, the reaction takes place practically only at the internal surface, because the contribution of the external surface to the overall surface area is mostly negligible.
- The influence of external and internal mass transfer is similar to heterogeneous catalysis, but some aspects complicate the situation:
 - G/S reactions are transient and the mass and the size of the solid may change.
 - A solid product or inert residue layer may lead to an additional mass transfer resistance.

- For quantitative description of G/S reactions, different models have been developed to derive equations that are not too complicated to describe the conversion of a solid. These equations are based on simplifications. An example is the shrinking core model, which assumes that the reaction starts at the outer surface and then a sharp reaction zone moves into the particle.

4.7

Criteria used to Exclude Interphase and Intraparticle Mass and Heat Transport Limitations in Gas–Solid Reactions and Heterogeneously Catalyzed Reactions

As discussed in Sections 4.5 and 4.6, mass and heat transport may influence the effective rate of heterogeneously catalyzed and gas–solid reactions. External profiles of concentration and temperature may be established in the boundary layer around the outer surface of the particles, and internal gradients may develop in the particles. Deviations from the ideal zero-gradient situation are usually considered by effectiveness factors.

To predict significant transport effects, respective criteria are needed. This is particularly important for kinetic studies in laboratory reactors to minimize the intrusion of diffusion and heat conduction. Consequently, these criteria are deduced. The equations for the mass and heat transfer and the respective parameters such as α , β , and D_{eff} have already addressed in Sections 3.1 and 3.2, but some equations are subsequently repeated.

The concept used to derive such criteria is the following: Since gradients of concentration and temperature always exist in and around a particle (although sometimes they are negligibly small), an assumption has to be made about the deviation up to which the reaction can be considered to be uninfluenced by mass and heat transport. Commonly the criterion is that the deviation of the mean reaction rate from the zero-gradient rate should be within 5%.

4.7.1

External Mass Transfer Through Boundary Layer

The effective reaction rate is usually expressed in terms of particle mass ($\text{mol kg}^{-1} \text{ s}^{-1}$). Thus if we use the external surface ($\text{m}^2 \text{ kg}^{-1}$) and the mass transfer coefficient β (m s^{-1}) we obtain:

$$r_{\text{m, eff}} = \beta A_{\text{m, ex}} (c_{\text{A,g}} - c_{\text{A,s}}) \quad (4.7.1)$$

The term $c_{\text{A,g}}$ is the concentration in the gas phase but all equations derived here also apply for liquids. The criterion for a negligible influence of external mass transfer (i.e., a deviation of the mean rate from zero-gradient rate within 5%) equals the condition that the concentration gradient in the boundary layer should be less than 5% relative to the maximum gradient:

$$\frac{(c_{\text{A,g}} - c_{\text{A,s}})}{(c_{\text{A,g}} - 0)} = \frac{(c_{\text{A,g}} - c_{\text{A,s}})}{c_{\text{A,g}}} = \frac{r_{\text{m,eff}}}{\beta A_{\text{m,ex}} c_{\text{A,g}}} \leq 0.05 \quad (4.7.2)$$

For spherical particles with density ρ_p (kg m^{-3}), $A_{\text{m,ex}}$ is given by:

$$A_{\text{m,ex}} = \frac{\pi d_p^2}{\frac{\pi}{6} d_p^3 \rho_p} = \frac{6}{d_p \rho_p} \quad (4.7.3)$$

which finally leads to the criterion for exclusion of external mass transfer effects:

$$\frac{r_{\text{m,eff}} \rho_p d_p}{\beta c_{\text{A,g}}} \leq 0.3 \quad (4.7.4)$$

For a first-order reaction, this criterion is further simplified:

$$\frac{r_{m,\text{eff}} \rho_p d_p}{\beta c_{A,g}} = \frac{k_{m,\text{eff}} c_{A,g} \rho_p d_p}{\beta c_{A,g}} = \frac{k_{m,\text{eff}} \rho_p d_p}{\beta} \leq 0.3 \quad (4.7.5)$$

Note that $k_{m,\text{eff}}$ or $r_{m,\text{eff}}$ are the effective (measured) values of the rate constant and rate, respectively, which includes all internal and external mass transfer effects.

For a first rough estimation, the minimum *Sherwood number* in a packed bed can be used:

$$Sh_{\text{min, fixed bed}} = \frac{\beta d_p}{D_{A,g}} = 3.8 \quad (4.7.6)$$

and Eq. (4.7.5) leads to a simple criterion, indicating a strong influence of the particle size:

$$\frac{k_{m,\text{eff}} \rho_p d_p^2}{D_{A,g}} \leq 1.14 \quad (4.7.7)$$

The term $(k_{m,\text{eff}} \rho_p)^{-1}$ is the characteristic reaction time τ_R , that is, the time needed to reach a concentration of c_{initial}/e (63% conversion). If the thickness of the boundary layer δ ($= d_p/Sh = d_p/3.8$ for $Re_p \rightarrow 0$) is used as the length for the characteristic time for external diffusion $\tau_{D,\text{ext}}$ [Eq. (4.5.50)], the following relation for both times is derived from Eq. (4.7.7):

$$\frac{\tau_{D,\text{ext}}}{\tau_R} = \frac{\frac{\delta^2}{2D_{A,g}}}{\frac{1}{k_{m,\text{eff}} \rho_p}} = \frac{\left(\frac{d_p}{7.6}\right)^2 \frac{1}{D_{A,g}}}{\frac{1}{k_{m,\text{eff}} \rho_p}} \leq \frac{1.14}{7.6^2} = 0.02 \quad (4.7.8)$$

Thus this ratio almost equals the assumed limit of the decrease of the rate of 5%.

4.7.2

External Heat Transfer

For steady-state conditions, the heat production equals the heat removal, which is governed by the heat transfer coefficient α ($\text{W m}^{-2} \text{s}^{-1}$):

$$r_{m,\text{eff}} (-\Delta_R H) = \alpha A_{m,\text{ex}} (T_p - T_g) \quad (4.7.9)$$

The condition for a negligible effect of a temperature difference between the gas phase and the particle is given by (taking an exothermic reaction as example):

$$k_m(T_p) \leq 1.05 k_m(T_g) \quad (4.7.10)$$

In other words, the difference should be so low that the rate constant only increases by 5%:

$$e^{-\frac{E_A}{R} \left(\frac{1}{T_p} - \frac{1}{T_g} \right)} \approx e^{-\frac{E_A}{R} \left(\frac{T_g - T_p}{T_g^2} \right)} \leq 1.05 \quad (4.7.11)$$

Rewriting gives:

$$\frac{E_A (T_p - T_g)}{RT_g^2} \leq \ln(1.05) \approx 0.05 \quad (4.7.12)$$

Equations (4.7.3), (4.7.12), and (4.7.9) and $\alpha = Nu \lambda_g / d_p$ yield the criterion for a negligible influence of heat transfer:

$$\frac{r_{m,\text{eff}} (-\Delta_R H) \rho_p d_p E_A}{\alpha T_g^2 R} = \frac{r_{m,\text{eff}} (-\Delta_R H) \rho_p d_p^2 E_A}{Nu \lambda_g T_g^2 R} \leq 0.3 \quad (4.7.13)$$

For a rough estimation, the minimum Nu number of 3.8 (packed bed, $Re_p \rightarrow 0$) can be used:

$$\frac{r_{m,\text{eff}}(-\Delta_R H)\rho_p d_p^2 E_A}{\lambda_g T_g^2 R} \leq 1.14 \quad (4.7.14)$$

This leads for a first-order reaction to the criterion:

$$\frac{k_{m,\text{eff}} c_{A,g} (-\Delta_R H) \rho_p d_p^2 E_A}{\lambda_g T_g^2 R} \leq 1.14 \quad (4.7.15)$$

Notice the strong impact of the particle diameter.

4.7.3

Internal Mass Transfer

The effectiveness factor for pore diffusion is given by:

$$\eta_{\text{pore}} = \frac{r_{m,\text{eff}}}{r_m} = \frac{\tanh \phi}{\phi} \quad \left(\text{with } \phi = \frac{V_p}{A_{p,\text{ex}}} \sqrt{\frac{r_m \rho_p}{c_{A,s} D_{A,\text{eff}}}} \right) \quad (4.7.16)$$

If the decline of the reaction rate should be less than 5%, we find as criterion:

$$\eta_{\text{pore}} \geq 0.95 \Rightarrow \phi \leq 0.4 \quad (4.7.17)$$

and for spherical particles, Eqs. (4.7.16) and (4.7.17) lead to:

$$\frac{r_m \rho_p}{c_{A,s} D_{A,\text{eff}}} \left(\frac{V_p}{A_{p,\text{ex}}} \right)^2 = \frac{r_m \rho_p}{c_{A,s} D_{A,\text{eff}}} \left(\frac{d_p}{6} \right)^2 \leq 0.16 \quad (4.7.18)$$

For spherical particles, with a first-order reaction, and the approximation of $D_{A,\text{eff}}$ by $0.1 D_{A,g}$, this criterion can be further simplified:

$$\frac{k_m \rho_p d_p^2}{D_{A,g}} \leq 0.6 \quad (4.7.19)$$

With $d_p/2$ as the characteristic length for diffusion in a sphere, we get for the ratio of the characteristic times of pore diffusion and reaction:

$$\frac{\tau_{D,\text{in}}}{\tau_R} = \frac{\left(\frac{d_p}{2}\right)^2 \frac{1}{2D_{A,\text{eff}}}}{\frac{1}{k_{m,\text{eff}} \rho_p}} \leq 0.08 \quad (4.7.20)$$

Thus, this ratio again almost equals the assumed limit of the rate decrease of 5%.

4.7.4

Internal Heat Transfer

The equation for the temperature difference between the center and the external surface of the particle is (Section 4.5.4.2):

$$T_{\text{center}} - T_s = \frac{D_{A,\text{eff}} (-\Delta_R H)}{\lambda_p} (c_{A,s} - c_{A,\text{center}}) \quad (4.5.90)$$

This difference is maximized, if $c_{A,\text{center}}$ becomes zero. Figure 4.7.1 shows the influence of the Thiele modulus on the concentration of reactant A in the center of a spherical particle (first-order reaction), calculated by the equation in Table 4.5.5 [note that $\sinh(ax)/x = a$ for $x \rightarrow 0$]:

$$\frac{c_A(r)}{c_{A,s}} = \frac{r_p}{r} \frac{\sinh\left(\frac{r}{r_p} 3\phi\right)}{\sinh(3\phi)} \Rightarrow \frac{c_A(r=0)}{c_{A,s}} = \frac{3\phi}{\sinh(3\phi)} \quad \left(\text{with } \phi = \frac{d_p}{6} \sqrt{\frac{k_m \rho_p}{D_{A,\text{eff}}}} \right) \quad (4.7.21)$$

A simple linear approximation of the influence of the Thiele modulus ϕ on the concentration in the center of a spherical particle, that is, for $r=0$ (see also Figure 4.7.1) is given by:

$$\frac{c_{A,\text{center}}}{c_{A,S}} \approx 1 - 0.6\phi \quad \left(\text{for } \phi < \frac{5}{3} \right) \quad (4.7.22)$$

$$c_{A,\text{center}} \approx 0 \quad \left(\text{for } \phi > \frac{5}{3} \right) \quad (4.7.23)$$

Thus the maximum overheating of the particle corresponds to $\phi \approx 5/3$ ($c_{A,\text{center}} = 0$, Figure 4.7.1). The condition for a negligible effect of internal heat transfer is that the increase of the rate constant in the center should be less than 5%. For an exothermic reaction, this yields:

$$\frac{E_A(T_{\text{center}} - T_s)}{RT_s^2} \leq 0.05 \quad (4.7.24)$$

Combination of this condition with Eq. (4.5.90) for $c_{A,\text{center}} = 0$ leads to the criterion for exclusion of internal heat effects based on the *Prater number* β and *Arrhenius number* γ :

$$\frac{D_{A,\text{eff}}(-\Delta_R H)c_{A,S}}{\lambda_p T_s} \frac{E_A}{RT_s} = \beta\gamma \leq 0.05 \quad \left(\text{for } \phi > \frac{5}{3} \right) \quad (4.7.25)$$

For $\phi < 5/3$, we obtain by the insertion of Eqs. (4.7.22) and (4.7.24) into Eq. (4.5.90):

$$\frac{D_{A,\text{eff}}(-\Delta_R H)c_{A,S}}{\lambda_p T_s} \frac{E_A}{RT_s} 0.6\phi = 0.6\beta\gamma\phi \leq 0.05 \quad \left(\text{for } \phi < \frac{5}{3} \right) \quad (4.7.26)$$

The value of the terms $\beta\gamma$ (for $\phi > 5/3$) or $0.6\beta\gamma\phi$ (for $\phi < 5/3$) are only higher than the critical value 0.05 for very exothermic reactions and strong limitations by pore diffusion (Table 4.7.1). For industrial practice the influence of internal heat transfer can be neglected. This can also be demonstrated by an inspection of coke combustion (Example 4.7.1).

Based on the consideration that the maximum overheating of the particle corresponds to a Thiele modulus ϕ of about 5/3, an alternative equation to the criterion given by the Eqs. (4.7.25) and (4.7.26) can be derived as follows: the definition of ϕ (for a first-order reaction) and the condition $\phi = 5/3$ [thus $\eta_{\text{pore}} = \tanh(\phi/\phi) = 0.56$] leads to:

$$D_{A,\text{eff}} = \left(\frac{3}{5} \frac{d_p}{6} \right)^2 k_m \rho_p = \left(\frac{d_p}{10} \right)^2 \frac{k_{m,\text{eff}}}{\eta_{\text{pore}}} \rho_p = \frac{1}{56} d_p^2 k_{m,\text{eff}} \rho_p \quad \left(\text{for } \phi = \frac{5}{3} \right) \quad (4.7.27)$$

Table 4.7.1 Influence of internal heat transfer on the effective reaction rate: values of $\beta\gamma$ and Thiele modulus ϕ (see also Table 4.5.5) and parameter that should be less than 0.05 to exclude an influence of internal heat transfer.

Reaction	$\beta\gamma$	ϕ	Parameter that should be less than 0.05 (see text): $\beta\gamma$ (relevant for $\phi > 5/3$) or 0.6 $\beta\gamma\phi$ (relevant for $\phi < 5/3$)
Dissociation of nitrous oxide (N ₂ O)	14	1–5	8–14
Hydrogenation of ethylene	1.6–1.9	0.2–2.8	0.2–1.9
Oxidation of hydrogen	0.7–0.8	0.8–2	0.3–0.8
Vinyl chloride from acetylene and HCl	1.8	0.27	0.3
Hydrogenation of benzene	0.2	0.1–1.9	0.01–0.2
Oxidation of sulfur dioxide	0.2	0.9	0.1
Oxidation of methanol to formaldehyde	0.2	1.1	0.1
Oxidation of ethylene to ethylene oxide	1.7	0.08	0.08
Ammonia synthesis	0.002	1.2	0.001

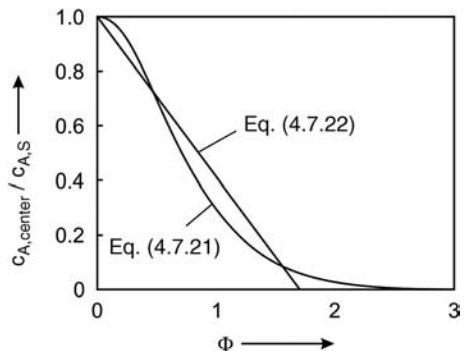


Figure 4.7.1 Influence of Thiele modulus ϕ on the concentration of reactant A in the center of a spherical particle relative to the concentration at the external surface (first-order reaction).

Table 4.7.2 Criteria for extra- and intraparticle mass and heat transfer limitations.

Transfer mechanism	General criterion	Simplified criterion (first-order reaction)
External mass transfer	$\frac{r_{m,\text{eff}} \rho_p d_p}{\beta c_{A,g}} \leq 0.3$	$\frac{k_{m,\text{eff}} \rho_p d_p^2}{D_{A,g}} \leq 1.14 \quad (\text{for } Sh_{\min} = 3.8)$
External heat transfer	$\frac{r_{m,\text{eff}} (-\Delta_R H) \rho_p d_p E_A}{\alpha T_g^2 R} \leq 0.3$	$\frac{k_{m,\text{eff}} c_{A,g} (-\Delta_R H) \rho_p d_p^2 E_A}{\lambda_g T_g^2 R} \leq 1.14 \quad (\text{for } Nu_{\min} = 3.8)$
Internal mass transfer	$\frac{r_{m,\text{eff}} \rho_p}{c_{A,s} D_{A,\text{eff}}} \left(\frac{V_p}{A_{p,\text{ex}}} \right)^2 \leq 0.16$	$\frac{k_m \rho_p d_p^2}{D_{A,g}} \leq 0.6 \quad (\text{for } D_{A,\text{eff}} \approx 0.1 D_{A,g})$
Internal heat transfer	—	$\frac{D_{A,\text{eff}} (-\Delta_R H) c_{A,s}}{\lambda_p T_s} \frac{E_A}{RT_s} \leq 0.05 \quad \left(\text{for } \phi > \frac{5}{3} \right)$ $\frac{D_{A,\text{eff}} (-\Delta_R H) c_{A,s}}{\lambda_p T_s} \frac{E_A}{RT_s} 0.6\phi \leq 0.05 \quad (\text{for } \phi < 5/3)$ ($C = 0.6\phi$ for $\phi < 5/3$)

Combination of this expression with Eq. (4.7.25) leads to the criterion:

$$\frac{d_p^2 k_{m,\text{eff}} \rho_p (-\Delta_R H) c_{A,g}}{\lambda_p T_s} \frac{E_A}{RT_s} \leq 3 \quad (4.7.28)$$

The advantage of Eq. (4.7.28) compared to Eqs. (4.7.25) and (4.7.26) is that the observable effective rate constant $k_{m,\text{eff}}$ is used instead of the mostly unknown value of $D_{A,\text{eff}}$. Note that this criterion is even stricter than those given by the Eqs. (4.7.25) and (4.7.26) as we have assumed the “worst case” of $\phi = 5/3$. Consequently, if Eq. (4.7.28) is fulfilled, we are “on the safe side.”

In summary: for many gas–solid and heterogeneously catalyzed reactions, external mass and heat transfer and internal mass transfer can not be neglected, but the influence of internal heat transfer is mostly marginal, except for highly exothermic reactions (Table 4.7.1). Table 4.7.2 summarizes the respective criteria.

Example 4.7.1: Overheating of coke particle during combustion with air

To inspect the internal overheating of a particle, we take coke combustion as an example of a very exothermic reaction. The data for air, 1000 °C, and 1 bar are as follows: The effective diffusion coefficient of O₂ is 0.2 cm² s⁻¹ (assumption of 10% of molecular diffusion coefficient), the O₂ concentration is 2 mol m⁻³, the activation energy E_a is 240 kJ mol⁻¹, $\Delta_R H$ is -400 kJ mol⁻¹, and λ_p is about 2 W m⁻¹ K⁻¹ (see also Section 6.5).

If we assume that external mass transport has no influence (thus the concentration of oxygen at the external surface equals the gas-phase concentration), we can use Eq. (4.5.99) to estimate the maximum temperature difference between the external surface and the center of the spherical coke particle:

$$\Delta T_{\max} = T_{\text{center,max}} - T_s = \frac{D_{O_2,\text{eff}} (-\Delta_R H)}{\lambda_p} c_{O_2,s}$$

Insertion of values given in the text leads to $\Delta T_{\max} \approx 8$ K. We now also estimate how this overheating may change the effective reaction rate. For a fully developed influence of pore diffusion the apparent activation is about half of the intrinsic value (see Example 4.5.11). The Arrhenius equation of the effective rate constant [Eq. (4.5.68)] yields:

$$\frac{k_{m,\text{eff}}(T_{\text{center}})}{k_{m,\text{eff}}(T_s)} = e^{-\frac{E_A}{2RT} \left(\frac{1}{T_{\text{center}}} - \frac{1}{T_s} \right)} \approx 1.07$$

(for $T_{\text{center}} = 1008$ °C and $T_s = T_g = 1000$ °C)

Thus, even for an extremely exothermic reaction, the influence of internal heat transfer is almost negligible, above all if we consider that the deviation of the mean rate representing the whole particle from the value at T_{surface} is even smaller than 7%.

Summary of Section 4.7 (take-home messages)

- **Mass and heat transport** may influence the effective rate of heterogeneously catalyzed and gas–solid reactions. **External profiles of concentration and temperature** may be established in the boundary layer between the surface of the particles and the fluid, and **internal gradients** may develop in the particles (although for industrial practice the influence of internal heat transfer can be usually neglected). Deviations from the ideal zero-gradient situation are usually considered by **effectiveness factors**.
- To predict significant transport effects, respective criteria are needed. This is particularly important for kinetic studies in laboratory reactors to minimize the intrusion of diffusion and heat conduction. The concept used to derive such criteria is the following: Since gradients of concentration and temperature always exist in and around a particle (although they are sometimes negligibly small), an assumption has to be made about the deviation up to which the reaction can be considered to be uninfluenced by mass and heat transport. Commonly, the criterion is that the deviation of the mean reaction rate from the zero-gradient rate should be within 5%.

4.8

Kinetics of Homogeneously or Enzyme Catalyzed Reactions

The following two sections give only a very brief introduction to the kinetics of homogeneously and enzyme-catalyzed reactions. For details see Bhaduri and Mukesh (2000), Behr (2008), Cornils and Herrmann (2002), Parshall and Ittel (1992), Cornils *et al.* (2005), Bommarius and Riebel-Bommarius (2004), Garcia-Junceda (2008), and Hou and Shaw (2008).

4.8.1

Homogeneous and Enzyme Catalysis in a Single-Phase System

In homogeneous catalysis and biocatalysis the catalyst molecules are present in solution. The reaction rate can therefore be directly determined by the turn over frequency *TOF*, which is defined as the number of reactant molecules (usually in mol) reacting per active center (amount of catalyst in mol) and time (s). For a batch reactor, we get for a reactant A:

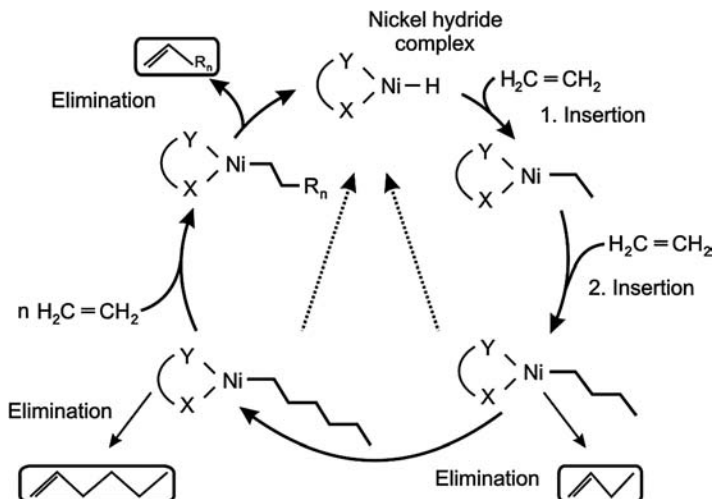
$$! \quad TOF = -\frac{dn_A}{n_{\text{cat}} dt} \quad (4.8.1)$$

The amount of A converted, that is, the absolute number of passes through the catalytic cycle before the catalyst becomes deactivated is called the turn over number (*TON*):

$$! \quad TON = -\frac{\Delta n_A}{n_{\text{cat}}} = \frac{n_{A0} - n_A(t)}{n_{\text{cat}}} \quad (4.8.2)$$

For industrial applications *TON* is 10^6 – 10^7 (Hagen, 2005). In heterogeneous catalysis, *TOF* and *TON* are seldom used as knowledge of the number of active sites is needed, for example, the number of active metal atoms dispersed over the surface of a catalyst. In principle, the number of sites per mass of a catalyst can be determined by means of chemisorption experiments, but such measurements require great care, and the results are often not applicable to process conditions. In addition, the catalyst surface is not uniform and hence the activity of different sites may vary. Although the *TON* is attractive due to its molecular simplicity, it should be used for solid catalysts with care. The kinetics of homogeneously catalyzed reactions can often be considered as a cyclic process consisting of insertion and elimination steps, as shown in Figure 4.8.1 for the oligomerization of ethene.

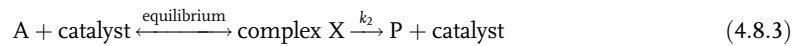
Figure 4.8.1 Typical mechanism of homogeneous catalysis – example of catalytic cycle of ethene oligomerization with a Ni catalyst. Adapted from Eichmann (1999).



Leonor Michaelis (1875–1947): a German biochemist and physician famous for his work with *Maud Menten* in enzyme kinetics. He studied medicine, and graduated and received his doctoral degree in 1897. In 1906 he started work as director of the bacteriology lab in Berlins *Charite hospital*, becoming Professor extraordinary at Berlin University in 1908. In 1922 he moved to the University of Nagoya (Japan) as Professor of biochemistry, in 1926 to *Johns Hopkins University* in Baltimore, and in 1929 to the *Rockefeller Institute of Medical Research* in New York City, where he retired 1941.

Maud Leonora Menten (1879–1960): a Canadian medical scientist who made significant contributions to enzyme kinetics and histochemistry. Her name is associated with the Michaelis–Menten equation. She studied medicine and was among the first women in Canada to earn a medical doctorate (1911, Chicago). In 1912 she moved to Berlin and worked with *Michaelis*. She worked as a pathologist at the University of Pittsburgh (1923–1950) and at the *British Columbia Medical Research Institute* (1951–1953). Her most famous work was on enzyme kinetics together with *Michaelis*. She also conducted the first electrophoretic separation of proteins in 1944, and worked on the properties of hemoglobin, regulation of blood sugar level, and kidney function.

Formally, the reaction rate of homogeneously catalyzed reactions can often be described by the following simple reaction mechanism:



It is, thereby, assumed that one reaction step is rate determining (e.g., for propene dimerization the second insertion, Figure 4.8.1). This reaction step can be subdivided into two steps, the formation of a complex X, which denotes a bound state of catalyst and reactant A, and the reaction of X to give the product P (or an intermediate, which quickly reacts further to P). This two-step reaction mechanism was proposed first by *Michaelis and Menten* (see boxes) in 1913 as a rate law for enzymatic sugar inversion (Michaelis and Meton, 1913), but is also frequently used to describe homogeneously catalyzed reactions. The basic assumption is a pre-equilibrium between reactant, catalyst, and complex.

The rate of a homogeneously or enzyme catalyzed reaction depends on the catalyst concentration c_{cat} even though the catalyst undergoes no net change. To relate c_X to c_{cat} , we use the steady-state approximation:

$$\frac{dc_X}{dt} = k_1 c_A c_{\text{cat}} - k_{-1} c_X - k_2 c_X \approx 0 \quad (4.8.4)$$

which leads to:

$$c_X = \frac{k_1 c_A c_{\text{cat}}}{k_2 + k_{-1}} \quad (4.8.5)$$

The concentrations c_A and c_{cat} refer to the free reactant and free catalyst, and $c_{\text{cat},0}$ is the initial (total) catalyst concentration with $c_{\text{cat}} + c_X = c_{\text{cat},0}$. Since the amount of the homogeneous catalyst or enzyme is small, the free reactant concentration is almost the same as the total reactant concentration ($c_A \approx c_{A,0}$), and Eq. (4.8.5) yields:

$$c_X = \frac{k_1 c_A (c_{\text{cat},0} - c_X)}{k_2 + k_{-1}} \Rightarrow c_X = \frac{k_1 c_A c_{\text{cat},0}}{k_2 + k_{-1} + k_1 c_A} \quad (4.8.6)$$

Hence, the reaction rate is given by:

$$r_A = -\frac{dc_A}{dt} = k_2 c_X = \frac{k_2 k_1 c_A c_{\text{cat},0}}{k_2 + k_{-1} + k_1 c_A} = \frac{k_2 c_A c_{\text{cat},0}}{\frac{(k_2 + k_{-1})}{k_1} + c_A} = \frac{k_2 c_A c_{\text{cat},0}}{K_M + c_A} \quad (4.8.7)$$

where K_M is called the Michaelis–Menten constant [= $(k_2 + k_{-1})/k_1$]. K_M values usually range from 10 to 0.01 mol m⁻³ (Liese, 2006). We can also derive Eq. (4.8.7) if we use the assumption that the preceding equilibrium (equilibrium constant K_c) is established:

$$K_c = \frac{k_1}{k_{-1}} = \frac{c_X}{c_A c_{\text{cat}}} = \frac{c_X}{c_A (c_{\text{cat},0} - c_X)} \Rightarrow c_X = \frac{K_c c_{\text{cat},0} c_A}{1 + K_c c_A} \quad (4.8.8)$$

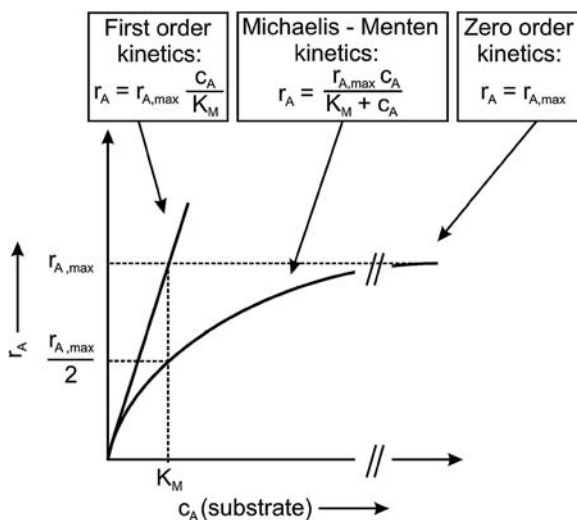


Figure 4.8.2 Typical Michaelis-Menten curve [$r_{\max} = k_2 c_{\text{cat},0}$, see Eq. (4.8.9)].

The reaction rate is then given by:

$$r_A = k_2 c_X = \frac{k_2 K_c c_A c_{\text{cat},0}}{1 + K_c c_A} = \frac{k_2 c_A c_{\text{cat},0}}{\frac{1}{K_c} + c_A} = (k_2 c_{\text{cat},0}) \frac{c_A}{K_M + c_A} \quad (4.8.9)$$

The Michaelis-Menten constant K_M is then given by the ratio $k_{-1}/k_1 (= 1/K_c)$, which equals the definition according to Eq. (4.8.7) for $k_{-1} \gg k_2$.

According to Eq. (4.8.9), the rate depends linearly on $c_{\text{cat},0}$, but in a more complicated way on the reactant concentration (Figure 4.8.2). For $c_A \gg K_M$, the rate reduces to $k_2 c_{\text{cat},0}$ and becomes zero order with respect to A. Now so much A is present that c_X reaches a constant maximal value and equals $c_{\text{cat},0}$ because the preceding equilibrium [Eq. (4.8.3)] is far on the right-hand side. For $c_A \ll K_M$, the rate is a first-order reaction with respect to the substrate A. If we use the maximum rate $r_{A,\max}$ for the term $k_2 c_{\text{cat},0} k_2$, Eq. (4.8.10) leads to:

$$r_A = r_{A,\max} \frac{c_A}{K_M + c_A} \quad (4.8.10)$$

Usually, industrial biotechnological processes are run in or near the zero-order regime (Figure 4.8.2) to maximize the rate. For biological sensors, the signal (rate) should be sensitive to concentration and, thus, the first order regime is desired. Biological processes in living systems (e.g., in our body) also run in the first-order regime, as the control of a reaction is more important than the speed. Diffusional problems are negligible for homogeneously or enzyme catalyzed reactions as long as the reactants, products, and catalyst form a single phase.

There are several ways of visualizing enzyme kinetic data. One approach is to plot the reciprocal rate of conversion of substrate A, $1/r_A$, against the reciprocal substrate concentration, $1/c_A$, which is known as the Lineweaver-Burk plot (Lineweaver and Burk, 1934):

$$\frac{1}{r_A} = \frac{1}{r_{A,\max}} + \frac{K_M}{r_{A,\max}} \frac{1}{c_A} \quad (4.8.11)$$

Plotting $1/r_A$ versus $1/c_A$ should give a straight line with a slope of $K_M/r_{A,\max}$ and intercept at $1/r_{A,\max}$ and $-1/K_M$ (Figure 4.8.3).

The Lineweaver-Burk plot can give useful information, but at low substrate concentrations (high $1/r_A$ values) small errors in the rate r_A will result in enormous errors in $1/r_A$. Conversely, the errors in $1/r_A$ at high substrate concentrations will be small (Rothenberg, 2008).

Alternatively, the Michaelis-Menten equation can be linearized by plotting r_A against r_A/c_A , which is known as the Eadie-Hofstee plot (Eadie, 1942; Hofstee, 1959):

$$r_A = r_{A,\max} - K_M \frac{r_A}{c_A} \quad (4.8.12)$$

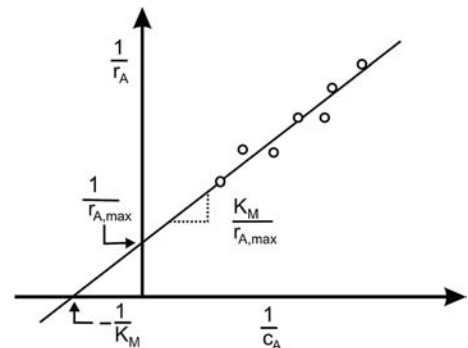


Figure 4.8.3 Plot of reciprocal rate of conversion of substrate A against reciprocal substrate concentration (known as a Lineweaver-Burk plot).

and should give a straight line with a slope of $-K_M$ and intercepts at $r_{A,\max}$ and $r_{A,\max}/K_M$. This approach is robust against error-prone data, but both the ordinate and the abscissa depend on r_A , so any experimental error will be present in both axes (Rothenberg, 2008).

Although linearized plots are useful for viewing the data, the best way of analyzing such kinetic data is to fit them directly to the Michaelis–Menten equation by using nonlinear regression, because today there are computers to do this.

4.8.2

Homogeneous Two-Phase Catalysis

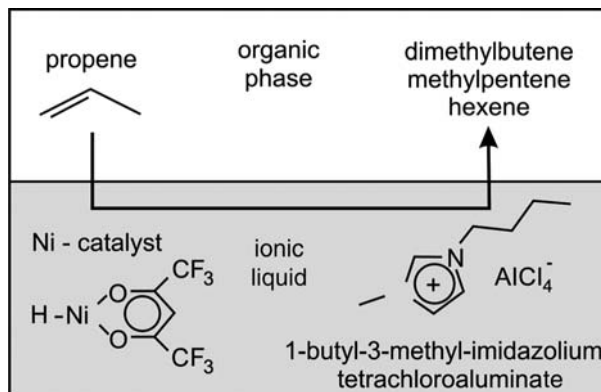
A general disadvantage of homogeneous catalysis compared to heterogeneous catalysis is the problematic separation of catalyst from the products. In this respect an interesting trend in homogeneous catalysis is the use of a biphasic system consisting of an organic phase, in which the catalyst is insoluble, and a second phase of a solvent with dissolved catalyst. This means that after reaction, for example, in an intensively mixed stirred reactor, the two phases can be separated, and the solvent (containing the catalyst) can be recycled.

Figure 4.8.4 depicts such a system for the Ni-complex catalyzed dimerization of propene. The solvent used for the catalyst in this case is an ionic liquid (IL), which is a low melting salt ($<100^\circ\text{C}$) with negligible vapor pressure. ILs are new promising solvents, particularly for catalytic and separation processes [see Wasser and Welton (2007)]. Thus the reaction takes place in the IL where the propene is partly soluble according to *Nernst's law* of partition. The products distribute among both phases (preferentially in the organic phase), and with respect to reaction engineering, diffusional problems, are now not negligible. This means that the effective reaction rate in a technical reactor does not depend only on the intrinsic chemical rate, and we have to consider at least two aspects:

- The concentration of the reactant(s) and product(s) at the interphase of both phases will depend on partition coefficients (according to *Nernst's law*).
- Diffusion from one phase to the other (e.g., of the reactant from the organic phase to the solvent containing the catalyst) may influence or even determine the overall reaction rate and thus the process.

This interplay of reaction, solution, and diffusion has already been discussed in Section 4.4 for fluid–fluid reactions. The equations derived there for gas–liquid systems (two-film theory) can be adapted directly for a homogeneously catalyzed liquid–liquid reaction if we use the partition coefficient for the reactant concentration in the reaction phase (here the solvent) instead of the *Henry coefficient* for the concentration of the gaseous reactant in the liquid. In this case there is an excess of A, and Eq. (4.9.14) is then more appropriate.

Figure 4.8.4 Example of homogeneous two-phase catalysis: propene dimerization with a homo Ni-catalyst and an ionic liquid as solvent. Adapted from Eichmann (1999).



Summary of Section 4.8 (take-home messages)

- In homogeneous catalysis and biocatalysis the catalyst molecules are present in solution. The rate is then usually determined by the **turn over frequency**, which is defined as the number of reactant molecules reacting per active center and time. For a batch reactor, the amount converted up to the time t is called the **turn over number**. (In heterogeneous catalysis, *TOF* and *TON* values are seldom used as knowledge of the number of active sites is usually limited.)
- The kinetics of homogeneously catalyzed reactions can often be considered as a **cyclic process** consisting of insertion and elimination steps.
- Formally, the reaction rate of homogeneously catalyzed reaction can often be described by the following the so-called **Michaelis–Menten mechanism**:



The basic assumption is a pre-equilibrium between reactant, catalyst, and complex.

- The **rate of a homogeneously or enzyme catalyzed reaction** depends on the initial catalyst concentration $c_{\text{cat},0}$ even though the catalyst undergoes no net change:

$$r_A = -\frac{dc_A}{dt} = k_2 c_{\text{cat},0} \frac{c_A}{K_M + c_A} = r_{\max} \frac{c_A}{K_M + c_A}$$

(with K_M as the Michaelis-Mentenconstant)

For $c_A \gg K_M$, the rate is maximized and zero order with respect to A. For $c_A \ll K_M$, we have a first-order reaction with respect to the substrate A. **Industrial biotechnological processes** are run in or near the zero-order regime to maximize the rate. For **biosensors**, where the signal should be sensitive to the concentration, the first-order regime is desired. Biological processes in living systems (e.g., our body) also run in the first-order regime, as the control of a reaction is more important than the rate.

- Diffusional problems** are negligible for homogeneously or enzyme catalyzed reactions, at least if the reactants, products, and catalyst form a single phase system.
- A general disadvantage of homogeneous catalysis compared to heterogeneous catalysis is the problematic **separation of catalyst** from the products. An interesting trend is the use of a biphasic system consisting of an organic phase, in which the catalyst is in insoluble, and a second phase of a solvent with dissolved catalyst. This means that after reaction, for example, in an intensively mixed stirred reactor, the two phases can be separated, and the solvent (containing the catalyst) can be recycled. Attractive solvents are **ionic liquids**, which are low melting salts ($<100^\circ\text{C}$) with negligible vapor pressure.

4.9

Kinetics of Gas–Liquid Reactions on Solid Catalysts

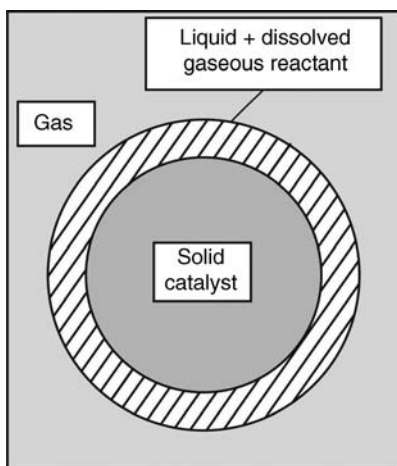
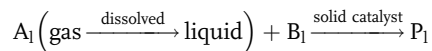
4.9.1

Introduction

Multiphase reactors, wherein gas and liquid reactants are contacted in the presence of a solid catalyst, are vitally important in many areas of industrial chemistry. They are not only used in refinery and petrochemical processes (hydrodesulphurization, hydrogenation, etc.) but also for the production of preliminary products (for polymers etc.) as well as of fine chemicals. Selected examples are examined in

Section 6.8 (clean fuels by hydrotreating) and in Section 6.17 (production of the fine chemical menthol).

Here, we will only examine the basic kinetic equations of gas–liquid reactions on solid catalysts, taking as example the simple reaction of a gaseous reactant A that reacts after dissolution in the liquid phase with a liquid reactant B ($v_A = v_B = -1$) to a liquid product P:



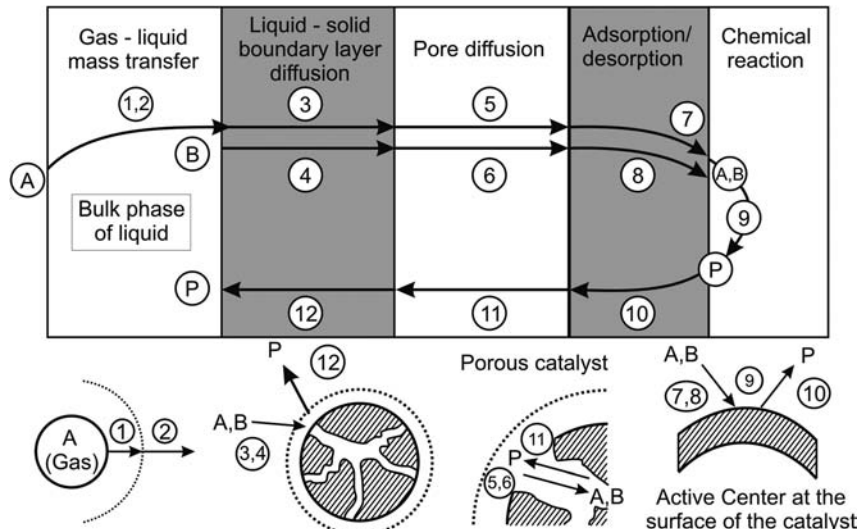
In common multiphase reactors mass transfer resistances frequently lead to a decrease of the effective reaction rate compared to the chemical (intrinsic) rate. In addition, many multiphase reactions like oxidations or hydrogenations are highly exothermic. Consequently, heat removal may also be important.

Thus, apart from the chemical rate of reaction, the following combined physical and chemical processes can be expected (Figure 4.9.1), which have been partly discussed already for fluid–fluid reactions without a solid catalyst (Section 4.4) and for heterogeneously catalyzed single phase reactions (Section 4.5):

1. mass transfer of gaseous reactant A from the main body of the gas phase (bubbles etc.) to the gas–liquid interphase and dissolution in the liquid phase;
2. mass transfer of dissolved gaseous reactant A into the bulk phase of the liquid;
3. and 4. mass transfer of dissolved A and of the liquid reactant B from the bulk phase of the liquid to the external surface of the catalyst particles;
5. and 6. diffusion of A and B into the pores by intraparticle (pore) diffusion;
7. and 8. adsorption of dissolved reactant A and/or liquid reactant B on the active surface;
9. chemical surface reaction of the reactants A and B to adsorbed product P;
10. desorption of product P;
11. diffusion of P through the porous network of the solid catalyst to the external surface;
12. diffusion of P through the boundary layer into the liquid phase.

As a rule of thumb, slow reactions are influenced only by the factors 7–10 (mostly only by factor 9). With increasing intrinsic rate and rate constant, respectively, the individual mass transfer resistances of both reactants have increasingly to be considered (Figure 4.9.2), particularly if large catalyst particles are used, such as in packed bed (trickle bed) reactors. For batch reactors or continuously operated slurry reactors with very fine suspended particles mass transfer resistances tend to play a

Figure 4.9.1 Individual steps of a heterogeneously catalyzed gas–liquid reaction.



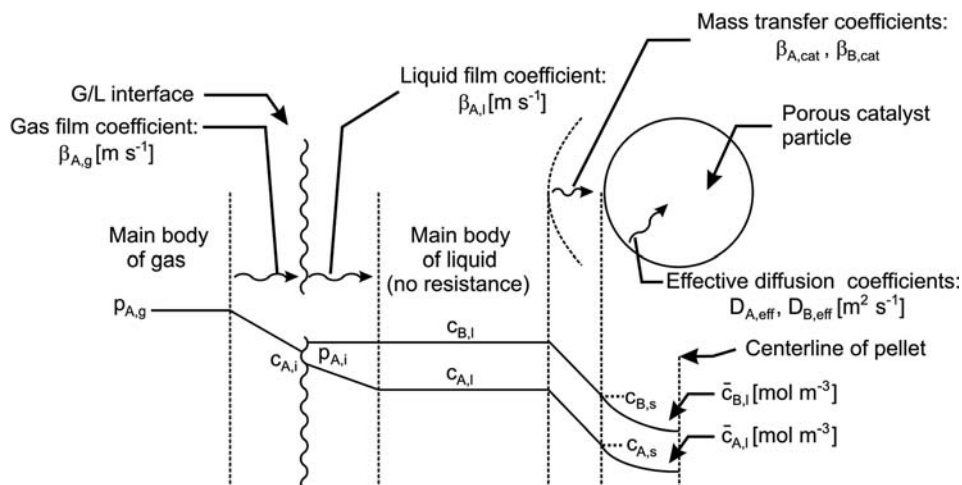


Figure 4.9.2 Mass transfer resistances of a heterogeneously catalyzed gas–liquid reaction. Adapted from Levenspiel (1999).

minor role. (Section 4.10.1.3 gives more information on reactor types for gas–liquid reactions on solid catalysts.)

As already outlined in Section 4.4, interfacial mass transfer processes can be described by the two-film theory. To recapitulate: this theory is based on the assumptions that (i) both the gas and liquid phase can be divided into a stagnant film near the interface and a well-mixed bulk phase without concentration gradients and that (ii) mass transfer is a steady-state process.

Mass transfer from the gas phase to the gas–liquid interphase (factor 1) can be omitted in the case of a pure gas phase (pure reactant A), and mostly also in other cases, as the rate of mass transfer from the gas phase to the gas–liquid boundary is generally high.

In simple cases, only one of the above-mentioned transport steps has an influence on the effective rate (e.g., pore diffusion of reactant A or B). The reaction system may also be simplified if the concentration of the dissolved gas is much higher than of the liquid reactant (or vice versa). Then the concentration of either A or B can be regarded as constant throughout the whole liquid phase (including the liquid filled pores), and at least all mass transfer resistances of one reactant are negligible.

To illustrate the specific features of a heterogeneously catalyzed gas–liquid reaction, we consider the simple case of a second-order reaction, that is, first order both with respect to the absorbed gaseous reactant A and to the liquid reactant B. Thus, the reaction rate related to the mass of catalyst ($\text{mol kg}_{\text{cat}}^{-1} \text{s}^{-1}$) is:

$$r_{\text{m,eff},\text{A}} = -\frac{d\dot{n}_\text{A}}{dm_{\text{cat}}} = -\frac{d\dot{n}_\text{B}}{dm_{\text{cat}}} = k_\text{m} \bar{c}_{\text{A},\text{l}} \bar{c}_{\text{B},\text{l}} \quad (4.9.1)$$

where $\bar{c}_{\text{A},\text{l}}$ and $\bar{c}_{\text{B},\text{l}}$ are the mean concentrations in the particles and k_m is the rate constant related to the mass of catalyst ($\text{m}^6 \text{mol}^{-1} \text{kg}_{\text{cat}}^{-1} \text{s}^{-1}$).

For a steady-state process, the consumption of A equals the mass transfer of the gaseous component A from the gas phase into the liquid phase [Eq. (4.4.6)]:

$$r_{\text{V,eff},\text{A}} = \frac{1}{\frac{1}{\beta_{\text{A},\text{l}} A_{\text{i,V}}} + \frac{1}{H_{\text{A,c}} \beta_{\text{A,g}} A_{\text{i,V}}}} \left(\frac{p_{\text{A,g}}}{H_{\text{A,c}}} - c_{\text{A},\text{l}} \right) \quad (4.9.2)$$

where $A_{\text{i,V}}$: interfacial area in $\text{m}^2 \text{m}^{-3}$ liquid, $H_{\text{A,c}}$ is the *Henry coefficient* related to the concentration in the liquid phase at the gas–liquid interface, $H_{\text{A,c}} = p_{\text{A,l}}/c_{\text{A},\text{l}}$, in $\text{Pa m}^3 \text{mol}^{-1}$.

In terms of the mass of catalyst, Eq. (4.9.2) can be rewritten with ρ_{cat} as the mass of catalyst per volume of liquid as:

$$r_{m,\text{eff},A} = \frac{1}{\rho_{\text{cat}}} r_{V,\text{eff},A} = \frac{1}{\frac{\rho_{\text{cat}}}{\beta_{A,l} A_{i,V}} + \frac{RT}{H_{A,c}} \frac{\rho_{\text{cat}}}{\beta_{A,g} A_{i,V}}} \left(\frac{p_{A,g}}{H_{A,c}} - c_{A,l} \right) \quad (4.9.3)$$

From the equations derived for heterogeneous single phase reactions we know the effective rate related to the mass of catalyst (in $\text{mol kg}_{\text{cat}}^{-1} \text{s}^{-1}$) (Section 4.5):

$$r_{m,\text{eff},A} = \frac{1}{\frac{1}{\eta_{\text{pore}} k_m \bar{c}_{B,l}} + \frac{1}{\beta_{A,\text{cat}} A_m}} c_{A,l} \quad (4.9.4)$$

The mass transfer coefficient $\beta_{A,\text{cat}}$ (m s^{-1}) refers to the diffusion of A through the boundary layer surrounding the particles, and A_m is the external surface per mass of catalyst ($\text{m}^2 \text{kg}_{\text{cat}}^{-1}$).

The effectiveness factor for pore diffusion of A is (Section 4.5):

$$\eta_{\text{pore},A} = \frac{r_{m,\text{eff},A}}{r_{m,A}(c_{A,l} = c_{A,s})} = \frac{\tanh \phi_A}{\phi_A} \quad (4.9.5)$$

with the Thiele modulus given here by:

$$\phi_A = \frac{V_p}{A_{p,\text{ex}}} \sqrt{\frac{k_m \bar{c}_{B,l} \rho_p}{D_{A,\text{eff}}}} \quad (4.9.6)$$

where ρ_p (kg m^{-3}) is the apparent density of the particles, $D_{A,\text{eff}}$ is the effective diffusion coefficient in the pores of the particles, and $\bar{c}_{B,l}$ is the mean concentration of the liquid reactant B in the particles. Consequently, the term $k_m \bar{c}_{B,l}$ ($\text{m}^3 \text{kg}_{\text{cat}}^{-1} \text{s}^{-1}$) is formally a first-order rate constant.

Combination of Eqs. (4.9.4) and (4.9.3) finally leads to (with $A_m = A_{i,V}/\rho_{\text{cat}}$):

$$r_{m,\text{eff},A} = \frac{1}{\frac{RT}{\beta_{A,g} A_m} + \frac{H_{A,c}}{\beta_{A,l} A_m} + \frac{H_{A,c}}{\beta_{A,\text{cat}} A_m} + \frac{H_{A,c}}{\eta_{\text{pore}} k_m \bar{c}_{B,l}}} p_{A,g} \quad (4.9.7)$$

For consumption of the liquid reactant B (where an interfacial mass transfer has not to be considered), we derive for an equimolar reaction the following correlation:

$$r_{m,\text{eff},B} = r_{m,\text{eff},A} = \frac{1}{\frac{1}{\beta_{A,\text{cat}} A_m} + \frac{1}{\eta_{\text{pore}} k_m \bar{c}_{A,l}}} c_{B,l} \quad (4.9.8)$$

The effectiveness factor for pore diffusion of B is now:

$$\eta_{\text{pore},B} = \frac{\tanh \phi_B}{\phi_B} \quad (4.9.9)$$

with the Thiele modulus:

$$\phi_B = \frac{V_p}{A_{p,\text{ex}}} \sqrt{\frac{k_m \bar{c}_{A,l} \rho_p}{D_{B,\text{eff}}}} \quad (4.9.10)$$

Note that $\bar{c}_{A,l}$ is now the mean concentration of the dissolved gaseous reactant A in the particles, so that now the term $k_m \bar{c}_{A,l}$ ($\text{m}^3 \text{kg}_{\text{cat}}^{-1} \text{s}^{-1}$) is formally a first-order rate constant. The reaction rate is given either by Eqs. (4.9.7) or (4.9.8), but unfortunately even if all parameters are known (β , A_m , k_m , etc.) we cannot solve the equations without trial and error or numerical calculations as the mean concentrations within the particles $\bar{c}_{B,l}$ and $\bar{c}_{A,l}$ are unknown. Only for $c_{A,l} \gg c_{B,l}$ (or vice versa) can we simplify the system.

4.9.2

High Concentration of Liquid Reactant B (or pure B) and Slightly Soluble Gas

If the concentration of B (high excess) is almost constant throughout the liquid phase and also within the pores of the catalyst, we obtain from Eq. (4.9.7):

$$r_{m,\text{eff},A} = r_{m,\text{eff},B} = \left(\frac{RT}{\beta_{A,g} A_m} + \frac{H_{A,c}}{\beta_{A,l} A_m} + \frac{H_{A,c}}{\beta_{A,\text{cat}} A_m} + \frac{H_{A,c}}{\eta_{\text{pore},A} k_m c_{B,l}} \right)^{-1} p_{A,g} \quad (4.9.11)$$

Thus the rate of consumption of the gaseous reactant A is then rate determining.

If the gas phase consists of pure A or the mass transfer resistance in the gas film can be neglected ($\beta_{A,g} \gg \beta_A$, $p_{A,g} \approx p_{A,i}$), Eq. (4.9.11) simplifies further:

$$r_{m,\text{eff},A} = r_{m,\text{eff},B} = \left(\frac{1}{\beta_{A,l} A_m} + \frac{1}{\beta_{A,\text{cat}} A_m} + \frac{1}{\eta_{\text{pore},A} k_m c_{B,l}} \right)^{-1} \frac{p_{A,g}}{H_{A,c}} \quad (4.9.12)$$

Further simplifications may be possible if one or more of the remaining mass transfer resistances (gas/liquid interface to bulk phase of liquid, liquid phase to external surface of catalyst particles, or the influence of pore diffusion) can be neglected. In the borderline case that only the (slow) rate of the chemical reaction has to be considered, Eq. (4.9.12) leads to:

$$r_{m,\text{eff},A} = r_{m,\text{eff},B} = k_m c_{B,l} \frac{p_{A,g}}{H_{A,c}} \quad (4.9.13)$$

4.9.3

Low Concentration of Liquid Reactant B and Highly Soluble Gas and/or High Pressure

If the concentration of the dissolved gaseous reactant A is high (high excess and/or high pressure), the concentration is almost constant throughout the liquid phase and within the pores of the catalyst. We then have a uniform concentration of A according to *Henry's law*, and Eq. (4.9.8) leads to:

$$r_{m,\text{eff},B} = r_{m,\text{eff},A} = \left(\frac{1}{\beta_{A,\text{cat}} A_m} + \frac{H_{A,c}}{\eta_{\text{pore},B} k_m p_{A,l}} \right)^{-1} c_{B,l} \quad (4.9.14)$$

and the rate of consumption of the liquid reactant B is rate determining.

It is important to note that the extremes reflected by Eqs. (4.9.11), (4.9.12), or (4.9.14) may also be reached in different axial local positions within a continuous fixed bed reactor (or at different reaction times in a batch reactor). For example, the reaction may start at the reactor inlet (or at reaction time zero) with pure liquid reactant [high excess and almost constant concentration of B throughout the liquid phase and within the pores, Eq. (4.9.11)]. However, if a certain degree of conversion has been reached after a certain length within a fixed bed reactor has been passed (or a certain reaction time has been reached in a batch process), the concentration of the dissolved gaseous reactant A now becomes higher than that of the remaining liquid reactant, and we increasingly run into the other extreme of an excess of A, and Eq. (4.9.14) is then more appropriate.

Summary of Section 4.9 (take-home messages)

- In **multiphase reactors** mass transfer resistances frequently lead to a decrease in the effective reaction rate compared to the chemical (intrinsic) rate. Apart from the chemical reaction, physical processes (absorption, mass transfer) are also present.
- The **interfacial mass transfer** processes can be described by the two-film theory. Mass transfer from the gas phase to the gas–liquid interphase (factor 1) can be omitted in the case of a pure gas phase (pure reactant A), and mostly also in

other cases, as the rate of mass transfer from the gas phase to the gas–liquid boundary is generally high.

- If the concentration of the liquid reactant is high (high excess), the rate of consumption of the gaseous reactant is **rate determining**. If the concentration of the dissolved gas is high, the rate of consumption of the liquid reactant is rate determining.

4.10 Chemical Reactors

In this chapter we discuss chemical reactor types and show how, despite the variety of reactions and the almost unlimited variety and possibilities for reactor design, only a few equations are needed to describe the reaction progress. Reactor modeling is, therefore, in many cases comparatively straightforward, and is facilitated by the classification into ideal reactors and real reactors.

To model a reactor we need:

- equations for the rate of the chemical reaction(s),
- equations for the transport of mass and heat,
- the laws of conservation for mass and energy (enthalpy),
- the law of conservation of impulse.

The reactor is either a concentrated system like a well-mixed stirred tank reactor, that is, parameters such as T and c do not vary within the whole reactor, or a distributed system, that is, the conditions depend on the local position, for example, a tubular reactor with axial gradients of c and often also of T .

“Operating manual” for beginners:

For a basic understanding of chemical reactor design, start with Sections 4.10.1 and 4.10.2, where different ideal and isothermal reactor types are introduced and the respective performance equations are derived. You should then study the behavior of real reactors (non-ideal flow and residence time distribution, Section 4.10.4) and the simplest model to account for deviations of real systems from ideal reactors, the tanks-in-series model (Section 4.10.5).

“Operating manual” for intermediate learners:

Intermediate learners should then also read Section 4.10.3, where non-isothermal ideal reactors and criteria for prevention of thermal runaway are discussed.

“Operating manual” for advanced learners:

Advanced learners should then also study the more complex aspects of reactor design and modeling (dispersion model, Section 4.10.6) and the modeling of fixed bed reactors (Section 4.10.7). Novel developments in catalytic reactor technology are discussed in Section 4.10.8.

4.10.1

Overview of Reactor Types and their Characteristics

4.10.1.1 Brief Outline of Ideal and Real Reactors

Both in research and in industrial practice, a large collection of different configurations of chemical and biotechnological reactors exist, and each reactor is designed and optimized for a specific chemical or biological task. The main reasons for this large variety are:

- The reaction parameters needed for chemical and also for biological reactions differ strongly, for example, the residence or reaction time (ranging from ms to



Laboratory-scale stirred tank reactor.



Reactor for production of ethylene by steam-cracking in Burghausen, Germany. Courtesy of Linde Engineering, Germany.

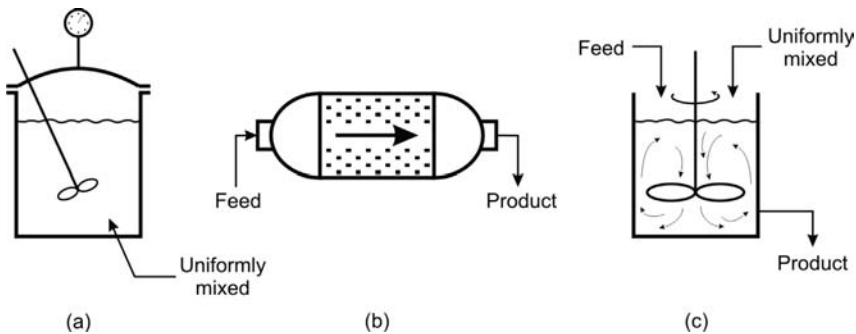


Figure 4.10.1 Ideal reactors: (a) batch reactor, (b) plug flow reactor (PFR), and (c) continuous stirred tank reactor (CSTR).

days), the pressure (up to 3000 bar), and temperature (typical ranges from 0 to 2000 °C).

- Cooling and heating is needed for strongly exothermic or endothermic reactions, respectively.
- The reaction may be single, bi-, or multi-phasic.
- The mode of operation may be discontinuous (batchwise) or continuous.
- The reaction is homogeneous or a catalyst may be needed.
- The temperature may be limited by thermodynamic constraints (reversible exothermic reaction) or by the stability of reactants, products, or the catalyst.

Reactors with idealized flow patterns are ideal reactors, and are simplified borderline cases. Three cases are of particular importance (Figure 4.10.1), the ideal, that is, uniformly mixed batch reactor, the ideal plug flow reactor (PFR), where no axial mixing and complete (radial) mixing across is assumed, and the continuous stirred tank reactor (CSTR). Ideal reactors are popular in chemical engineering as they are easy to treat with regard to their performance equations.

Real reactors are arbitrarily complicated but can be regarded as being composed of elements of ideal reactors. Modeling is possible, at least by approximation, if we know how to account for non-ideal flow.

Balancing is a condition precedent to describing the interaction between the reaction and transport processes for mass, energy, and impulse taking place simultaneously (Figure 4.10.2). To derive a reactor model based on these interactions we need:

- equations for the rate of chemical transformations;
- the law of conservation of mass with the variable concentration;
- the law of conservation of energy (enthalpy) with the variable temperature;
- equations for the physical transport processes of mass and heat;
- the law of conservation of impulse with the variable total pressure.

Depending on the specific case, not all of these equations are needed or have at least a different relevance:

- The equations for the rates of the chemical reactions and thus the mass balance are always needed.
- For an ideally mixed batch reactor, the equation for mass transport by convection is not needed but, apart from this exception, we have to account for convection and in many cases also for diffusion.

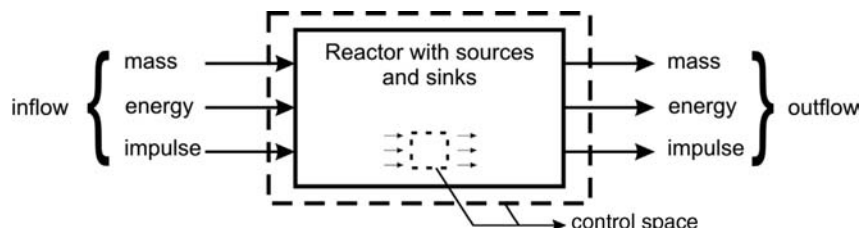


Figure 4.10.2 Balances to describe the interaction between reaction and transport processes.

- Isothermal operation makes the energy balance unnecessary. For non-isothermal reactors, the law of conservation of energy is essential. The link of the energy balance to the mass balance is the reaction rate, which is the reason for the consumption of reactants as well as for the accompanying generation or consumption of energy. For cooled or heated reactors, the equation for the heat transfer to or from the surrounding, internal cooling/heating devices, etc. is also needed.
- Contrary to the mass and the heat balance, the conservation equation of impulse mostly only serves to calculate the pressure drop in a reactor. It contains no source term and is thus not directly linked with the mass and heat balance, at least if the pressure drop does not have a pronounced influence on the concentrations of the reactants. Thus, the impulse balance is usually solved separately.

In any case, the definition of a suitable control space for balancing is important. In the simplest case, the variables describing the system, such as temperature and concentrations, are constant within the control space. This may be a single particle, if the gradients of c and T are negligible, or even the entire reactor for a well-mixed stirred tank with constant c and T (Fig. 4.10.2).

However, in many cases the system variables depend on the location and coordinates; for example, in the radial direction in a spherical particle, in the axial direction in an adiabatic tubular reactor, or in both the radial and axial direction in a cooled or heated tubular reactor. Then infinitesimal balances are needed and a control space must be selected that is so small that the variables involved are constant or linear variables with regard to the coordinates. Mathematically speaking, we have to solve the differential equations to obtain integral data such as the effective mean concentration in a particle or the conversion in a tubular reactor.

With the equations for the mass and heat balance and, if needed, for the pressure loss, every system can be (in principle) described mathematically. However, one still has to know which simplifications are suitable as the general equations are in many cases too complex and the effort for their solution is not justified by the result obtained. Thus, the equations for any type of chemical reactor have to be derived by more or less strong simplifications.

4.10.1.2 Classification of Real Reactors Based on the Mode of Operation

Discontinuous and Semicontinuous Mode of Operation (Batch Type Reactor) In discontinuous mode of operation, the reactants and any other additives such as catalysts are loaded into a stirred tank reactor (Figure 4.10.3), where the reaction mixture is homogenized and stays in the reactor for a well-defined reaction time to reach a certain conversion.

In many cases, the temperature in a batchwise operated reactor changes during the course of reaction and the evolution of the temperature can only be controlled by an appropriate cooling or heating. In the semicontinuous operation mode (semi-batch), some reactants are supplied batchwise while others are supplied continuously. Thus, beside cooling or heating, we then also have to consider an appropriate strategy of reactant addition as a second parameter to control the course of the reactor temperature and reactant concentration.

The advantage of the batch reactor is the high flexibility and high conversion as the reaction time may be arbitrarily long. Disadvantages are idle periods for loading, unloading, and heating, and the control and regulation of an unsteady process requires considerable instrumentation and effort. In the manufacture of fine chemicals and in the pharmaceutical industry, batch and semi-batch reactors are frequently used as small quantities are needed (drugs, dyes, cosmetic articles), and/or if the reactor is used to produce various products.

The stirred tank is the classic piece of equipment, and also well known to students of chemistry from practical courses. Heat exchange can take place through the wall, common practice in the laboratory, or by coils, an external heat exchanger in a recirculation loop, or by cooling with vapor phase condensation, as used in

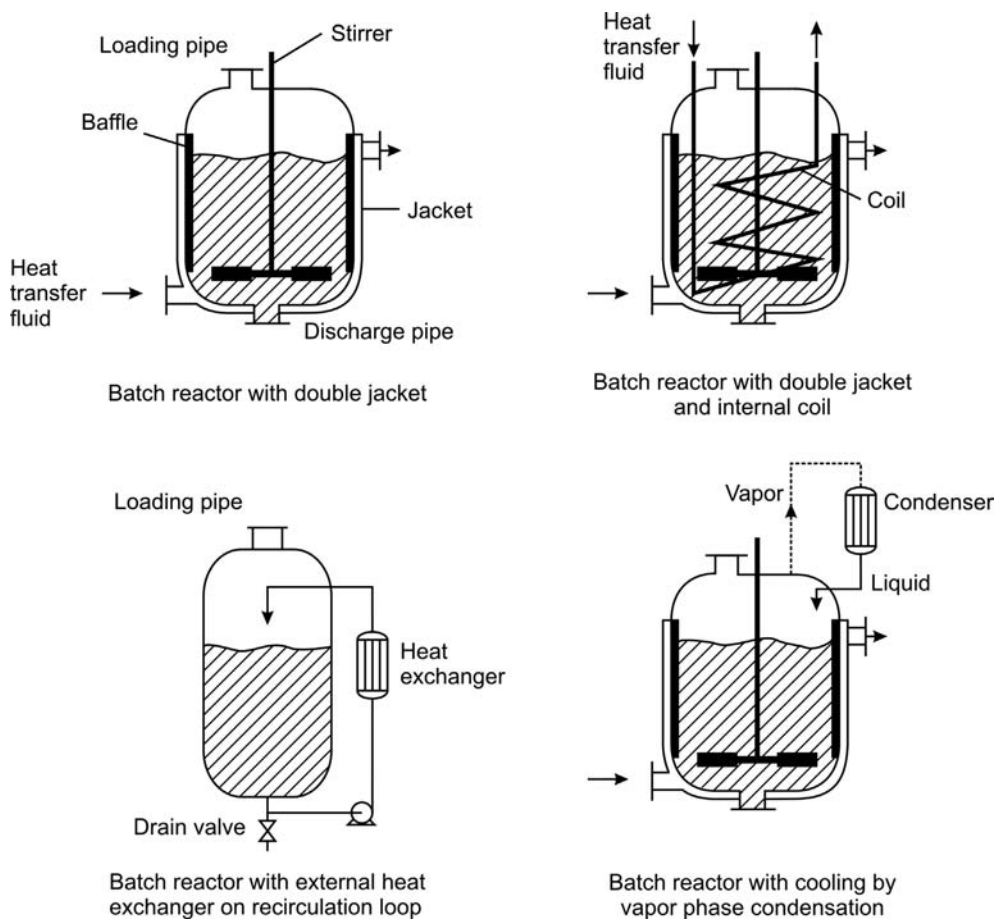


Figure 4.10.3 Batch reactor systems (adapted from Moulijn, Makkee, and Van Diepen, 2004).

technical reactors (Figure 4.10.3). Depending on the temperature level, liquid or vaporizing water, steam, oil, or molten salts are used as heat transfer media, which flow through a jacket or through a tubing welded onto the wall.

Continuous Mode of Operation In this type of production the reactants are continuously fed into the reactor and the products are likewise withdrawn with the same mass flow rate. Thus, after a certain start-up period, all parameters such as pressure, temperature, and concentrations are constant with respect to time (*steady state*). (In many practical cases of catalytic processes, this is strictly speaking not true, as the catalyst may lose activity by deactivation. But the characteristic time for deactivation is mostly much larger than the reaction time or residence time and, thus, we have pseudo-steady-state conditions.) Advantages of continuous processes are (i) a far-reaching automatization, (ii) a reduced volume of equipment at the same production rate compared to a batch reactor as the plant never runs idle, and (iii) a constant product quality as the operating conditions are constant. A disadvantage is the lower flexibility, as changes are laborious (catalyst). However, modern production is characterized by a continuous mode of operation, using various reactor types ranging from continuous stirred tank reactors to tubular reactors.

4.10.1.3 Classification of Real Reactors According to the Phases

Reactors for Non-catalytic Single-Phase Systems Classical reactors for single-phase reactions are stirred tank reactors for liquids (Figure 4.10.3) and flow tubes for fluids in all aggregation states. Ethylene and propylene synthesis from naphtha by thermal cracking in the presence of steam is a good example for a tubular reactor (Section 6.6). The tubes of a steam cracker have an internal diameter of 10 cm and

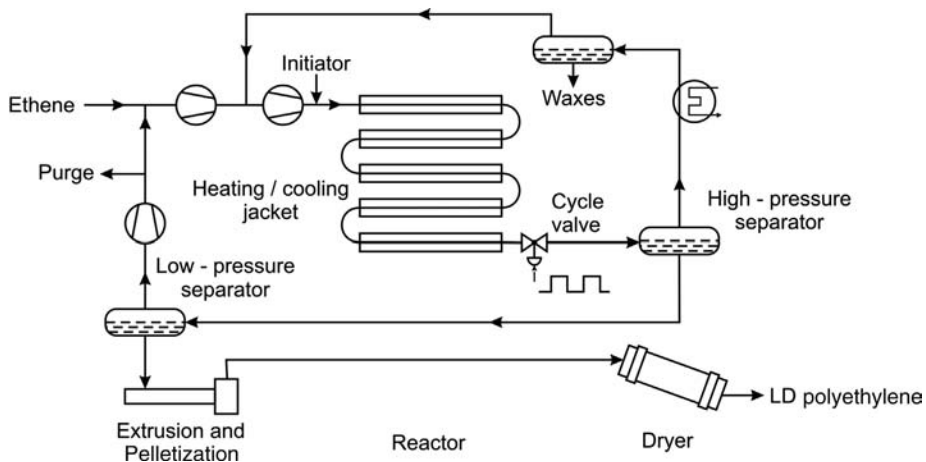


Figure 4.10.4 High pressure tubular reactor for synthesis of polyethylene (adapted from Moulijn, Makkee, and Van Diepen, 2004).

are between 50 and 200 m long. High-pressure polymerization of ethylene is likewise performed in tubular reactors ranging in length between 400 and 900 m (Figure 4.10.4, details in Section 6.20). The tubes have to be capable of withstanding a pressure of up to 3000 bar. The internal (external) diameter is typically 50 (120) mm.

Reactors for Heterogeneously Catalyzed Single-Phase Reactions During heterogeneously catalyzed reactions, the catalyst remains unchanged, if no or only a slow deactivation takes place. Transport of mass and heat play a critical role, and may have a strong influence on conversion and selectivity. The fixed-bed reactors shown in Figure 4.10.5a represent the design applied most frequently for heterogeneously catalyzed reactions and are the workhorse of heterogeneous catalysis. Reactors with

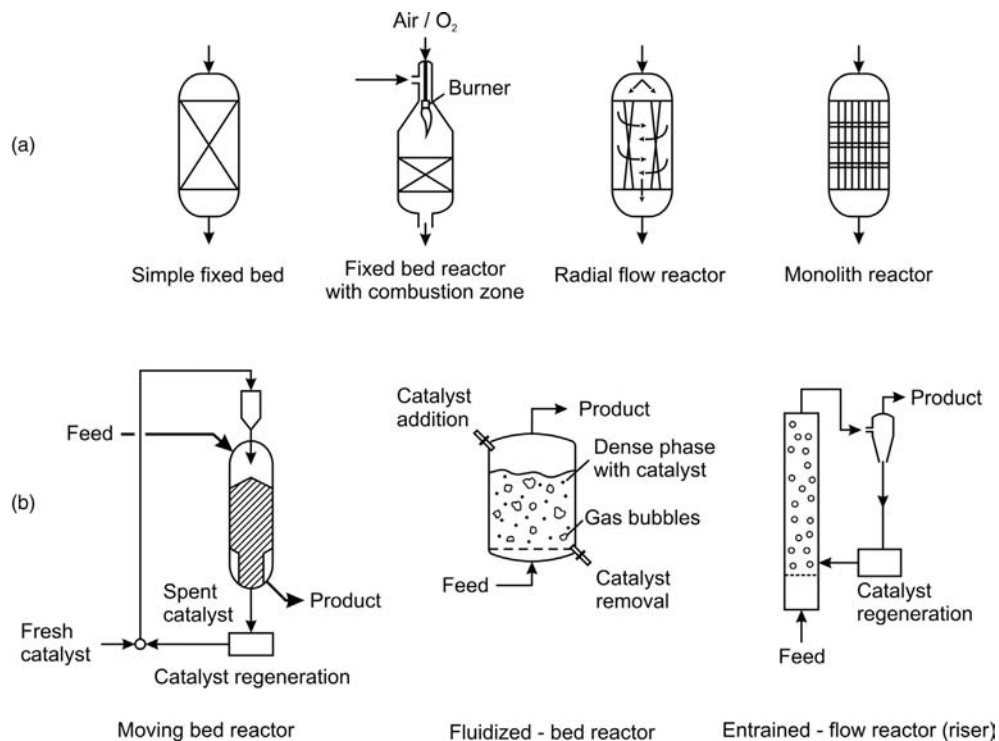


Figure 4.10.5 Reactors used for heterogeneously catalyzed reactions: (a) fixed bed reactors and (b) reactors with moving catalyst (adapted from Moulijn, Makkee, and Van Diepen, 2004).

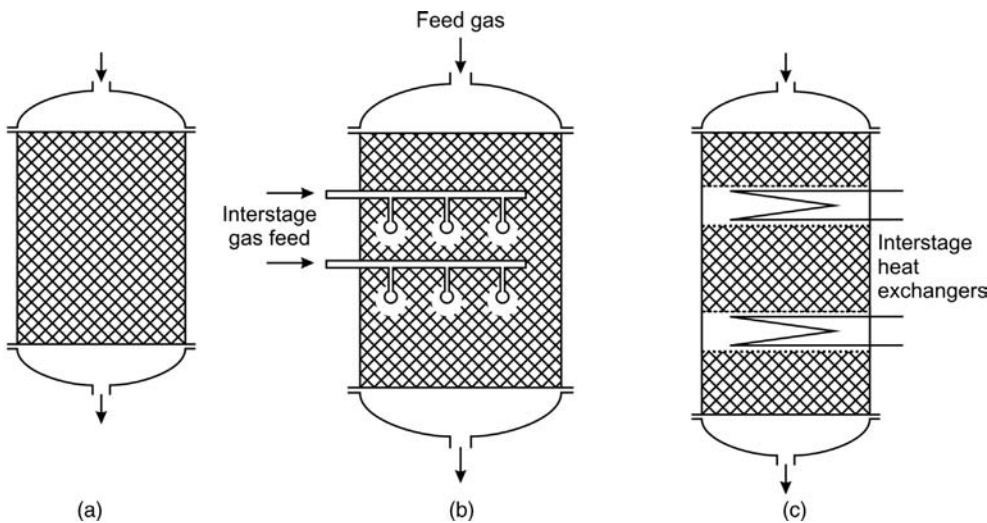


Figure 4.10.6 Adiabatic fixed bed reactors for gas–solid catalytic reactions: (a) simple fixed bed; (b) rack type reactor with interstage injection of gas; (c) rack type reactor with interstage cooling or heating (Ertl, Knoezinger, and Weitkamp, 1997).

an agitating catalyst (Figure 4.10.5b) are exceptions (e.g., fluidized catalytic cracking, Section 6.7) as abrasion and separation of the catalyst is problematic.

The technical design is largely determined by the extent of heat generated or consumed by the reaction and by the type of temperature control used. We have to distinguish between the rare case of isothermal operation, polytropic operated cooled or heated reactors, and adiabatic operation (ideal insulated reactor, no heat exchange with the surrounding). For isothermal and adiabatic operation, no radial profiles of temperature will develop inside the reactor.

In some cases, the temperature inside the reactor has to be limited; for example, to prevent overheating of the catalyst (deactivation by sintering) or to avoid cracking of thermally sensitive reactants and products. Other reasons are limitations of the conversion and yield in the case of exothermic reversible reactions (thermodynamic constraints), or the occurrence of unwanted side reactions at elevated temperatures (kinetic constraints).

Two types of fixed bed reactors are frequently used by the chemical industry, the rack type reactor (Figure 4.10.6) and the multi-tubular reactor (Figure 4.10.7). In a rack type reactor the fixed bed is divided into adiabatically operated racks where no heat exchange with the wall takes place. To limit the temperature, cooling is only provided between the racks by direct heat exchange by injecting cold gas or by indirect heat exchange via heat exchangers. A similar configuration with interstage heating is used for endothermic processes.

For strong exothermic or endothermic reactions with an adiabatic temperature rise of several hundred degrees, the rack type reactor is not sufficient. Then, a multi-tubular reactor is used, where the catalyst is located in up to 30 000 individual tubes, the outside of which is exposed to the flow of a heat transfer medium. In many cases, cooling is provided by boiling water, and the cooling temperature can easily be controlled by the pressure. For elevated temperatures molten salts can be employed as cooling or heating medium.

If the pressure drop is a limiting factor, monolith reactors are used, such as for automotive emission control or for NO_x-conversion in flue gases of power plants (Figure 4.10.5a, see Section 6.18).

Reactors for Gas–Solid Reactions Gas–solid reactions take place at the external solid surface and for porous solids more importantly at the internal surface. If not limited by the pressure drop, the particle size should be as small as possible to obtain a high effective reaction rate because of two aspects:

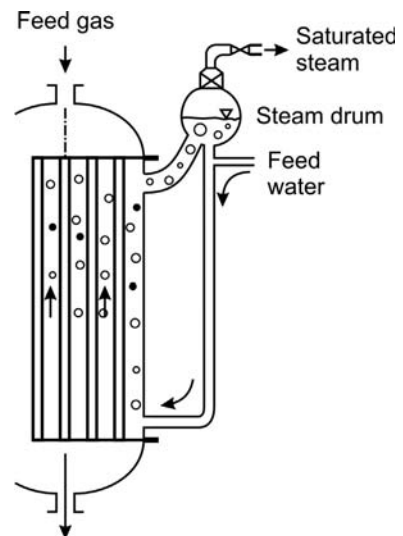


Figure 4.10.7 Multi-tubular fixed bed reactor cooled by boiling water.

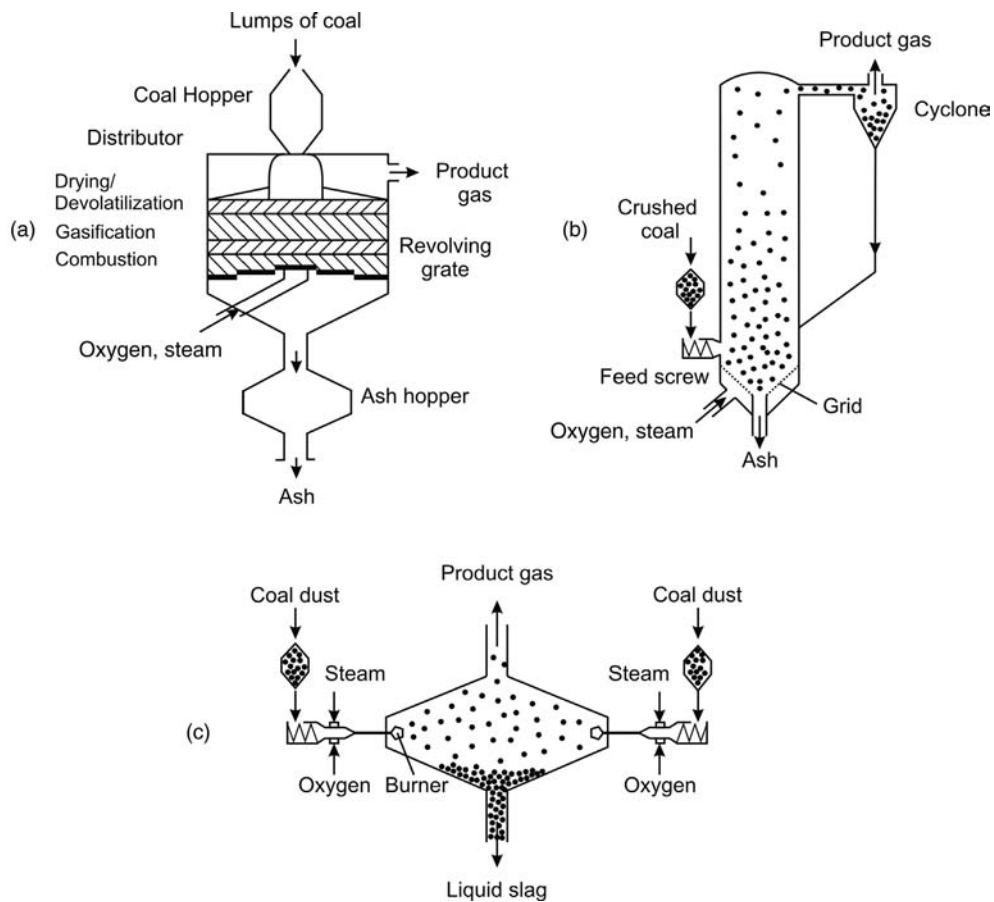


Figure 4.10.8 Reactors for gas–solid reactions, for example, coal gasification: (a) moving bed, (b) fluidized-bed, and (c) entrained-flow. Adapted from Moulijn, Makkee, and Van Diepen (2004).

- The external mass transport is strongly enhanced with decreasing particle size as the external surface area per mass of solid as well as (at least for $Sh \approx \text{constant}$) the mass transfer coefficient β (Eq. (3.2.68)) are inversely proportional to the particle diameter.
- Likewise, the resistance by pore diffusion also becomes smaller with both decreasing particle size and length for internal diffusion.

Figure 4.10.8 shows typical gas–solid reactors for coal gasification. Depending on the velocity of the gasifying agent, usually a mixture of oxygen and steam, we have to distinguish between fixed bed, fluidized bed, and entrained flow (Figures 4.10.8 and 4.10.9).

All three systems are used in industrial practice and have their specific advantages and drawbacks. For example, advantages of fluidized beds are:

- Radial and axial mixing of the solid is intensive, resulting in an even distribution of the solids and a uniform temperature pattern (no hot spots).
- The heat transfer coefficients to the reactor wall or a cooling coil are very large. For this reason, fluidized bed reactors are particularly suited for reactions with a large reaction enthalpy, and the reactor can easily be operated isothermally.

Disadvantages of fluidized bed gas–solid reactors are:

- The residence time distribution of the gas may deviate from plug-flow operation by dispersion and bypassing effects. (We will learn in the Section 4.10.3 why plug-flow operation is mostly advantageous compared to mixed flow.)

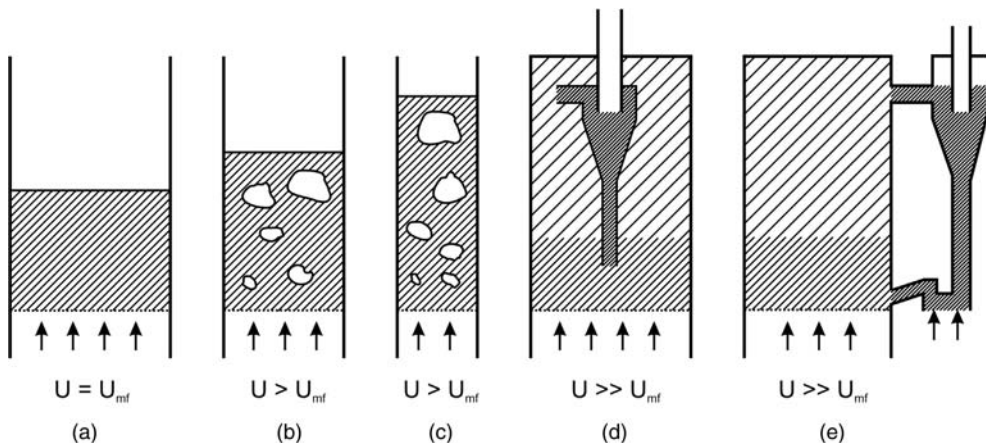


Figure 4.10.9 Forms of gas–solid reactors with regard to agitation of solid: (a) beginning of expansion of the bed (gas velocity = minimum fluidization velocity U_{mf}); (b) formation of solid-free gas bubbles; (c) formation of gas slugs; (d) turbulent impinging fluidized bed; and (e) expanded circulating fluidized bed with solid recycle system. Adapted from Ertl, Knoezinger, and Weitkamp (1997).

- Abrasion of the reactor vessel and attrition of the solid particles are very important properties to be considered in fluidized bed reactors.
- Modeling of fluidized bed reactors is difficult, and thus problems arise during scale-up.

Gas–solid reactions are sometimes also conducted in rotary furnaces; for example, for direct reduction of iron ore with coal or for the production of cement (Figure 4.10.10).

Reactors for Fluid–Fluid Reactions A fluid–fluid system either consists of two immiscible, or at least incompletely miscible liquids, or of a gas and a liquid. The reaction takes place in the liquid phase or in one of the two liquid phases only. For homogeneously catalyzed two-phase reactions (Section 4.8.2), the liquid catalyst is dissolved in one liquid phase, usually a solvent. In general, fluid–fluid reactions involve the mass transfer of at least one reactant into the liquid phase in which the reaction takes place. Thus, the transfer rate and interfacial area are crucial for a fluid–fluid reactor.

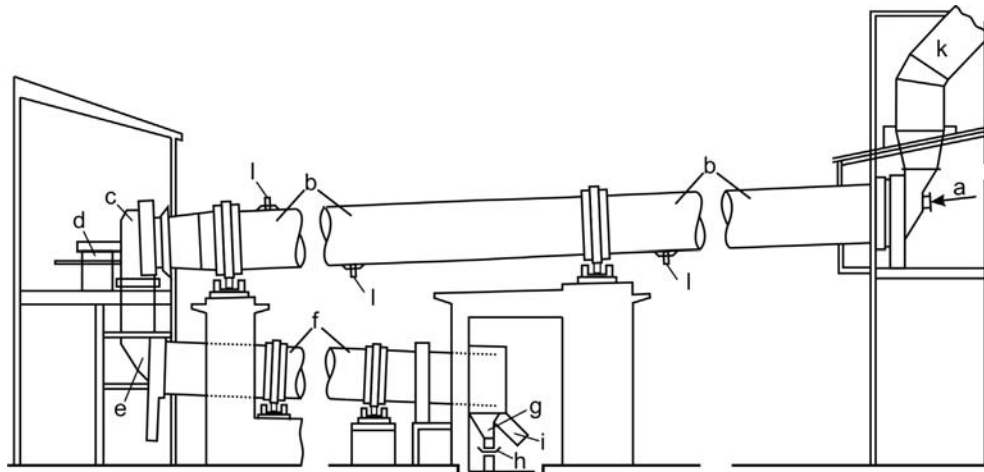


Figure 4.10.10 Reactor for direct reduction of iron ore with coal in a rotary furnace (a: inlet for ore and coal; b: reduction oven, c: outlet, d: main burner, e: inlet to cooling section, f: cooler for rotary furnace, g: product outlet, h: transport to magnetic separation, i: outlet for large particles, k: outlet for off-gas, l: burner. Adapted from Baerns, Hofmann, and Renken (1999).

Figure 4.10.11 Gas–liquid reactors. Adapted from Baerns *et al.* (2006).

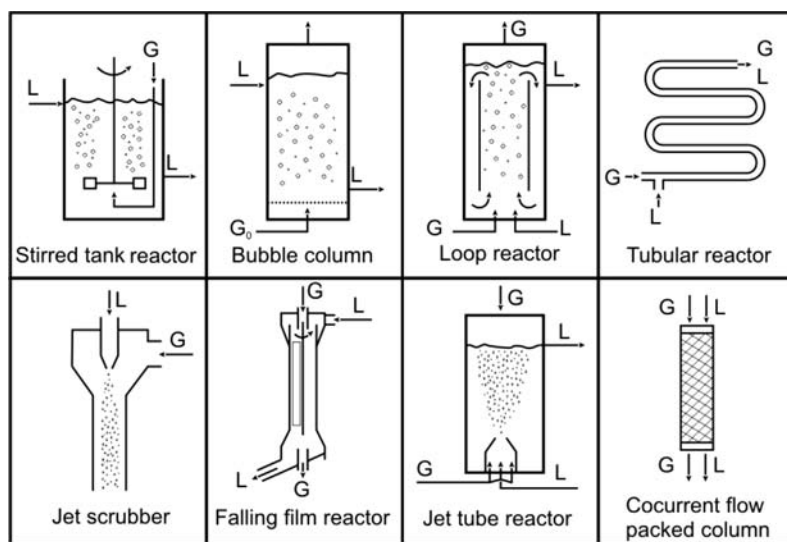


Figure 4.10.11 shows examples of gas–liquid reactors. Gas is usually dispersed in the liquid by a bubble column, tray column, or a stirring reactor with pressurized gas. Liquid is dispersed in the gas by means of a jet type washer or a spray tower. Liquid in the form of a thin film is exposed to a gas by a falling film reactor or a trickle reactor with filter elements. Details of the interplay of chemical reaction and mass transfer are given in Section 4.4.

Reactors for Heterogeneously Catalyzed Gas–Liquid Reactions (Multiphase Reactors)

Examples of multiphase reactors involving a liquid, a gas, and a solid catalyst are hardening of fat by hydrogenation and desulphurization of fuels. In a simpler case the solid substance may be inert and serves solely to increase the gas–liquid interface. The various three-phase reactors may be classified according to the mode of motion of the phases (Figure 4.10.12).

Fixed-bed reactors operated in co-current mode are so-called trickle bed reactors, where both the gas and the liquid are applied from above via distributor plates and the liquid trickles downwards over the packed bed (Figure 4.10.12a). Counter-current operation is not industrially applied except in special cases, although it may be preferable in some cases from a theoretical point of view, as examined by Moulijn, Makkee, and Van Diepen (2004) for the example of hydrodesulphurization of heavy oil fractions (Section 6.8). In industrial practice, it is impossible to operate

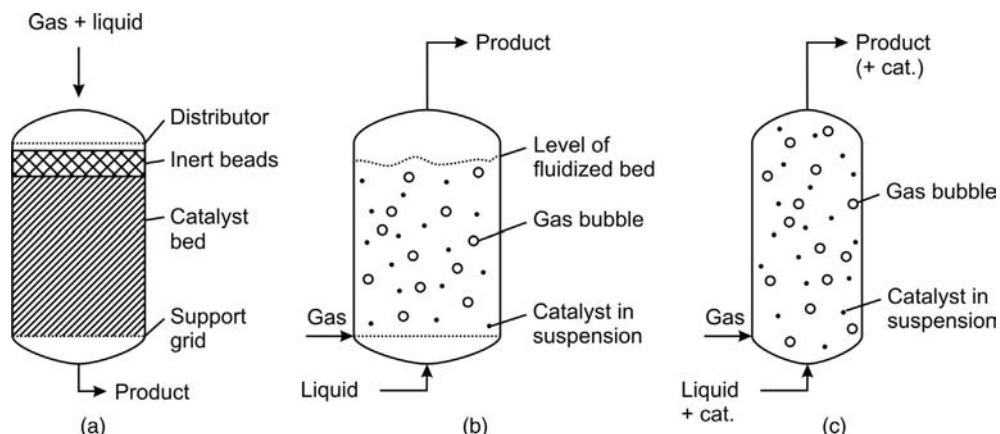


Figure 4.10.12 Continuously operated three-phase reactors: (a) fixed-bed reactor, (b) fluidized bed, and (c) slurry reactor (also called bubble column) (adapted from Moulijn, Makkee, and Van Diepen, 2004).

trickle-beds in countercurrent mode as the downward flow of liquid is impeded by the upward flow of gas, giving rise to flooding of the reactor.

In a three-phase fluidized-bed reactor, also called an ebullated bed reactor, the solid catalyst particles are kept in suspension by the gas and the liquid flowing upwards (Figure 4.10.12b). The particles are relatively large (1–5 mm) to keep them from being carried away. Fluidized beds are preferred for strongly exothermic reactions or if the catalyst must be frequently exchanged because of rapid deactivation.

Suspension reactors are frequently operated continuously as so-called bubble column or slurry reactors (Figure 4.10.12c). The liquid represents the continuous phase in which the gas and the solid catalyst are distributed. The particle size is much smaller than in other three-phase reactors (<0.1 mm). The solid concentration is merely 1%, to keep the energy required for suspension low. However, the small particles complicate the situation as the separation of the solid catalyst is essential. Batchwise operated suspension reactors (not shown in Figure 4.10.12) are mostly mechanically stirred to keep the particles in suspension.

Future Trends in Reactor Technology The technical reactors introduced here so far are those used today in common industrial processes. Of course, research and development activities in past decades have led to new reactor concepts that may have advantages with respect to process intensification, higher selectivities, and safety and environmental aspects. Such novel developments in catalytic reactor technology are, for example, monolithic reactors for multiphase reactions, micro-reactors to improve mass and heat transfer, membrane reactors to overcome thermodynamic and kinetic constraints, or multifunctional reactors combining a chemical reaction with heat transfer or with the separation in one instead of two units. It is beyond the scope of this textbook to cover all the details of these new fascinating reactor concepts, but for those who are interested in a brief outline we summarize important aspects in Section 4.10.8.

4.10.2

Ideal Isothermal Reactors

Reactors are mostly not isothermal, as heat is consumed or released, and perfect mixing or a perfect heat exchange with the surrounding is impossible. However, some reactors are almost isothermal, such as, for example, a well-mixed continuous stirred tank reactor (CSTR). In a batchwise operated stirred tank or in a plug-flow reactor (PFR), isothermal conditions with regard to reaction or residence time (axial position), respectively, are hard to realize. However, the assumption of an isothermal system is helpful for a first examination of reactor types as it simplifies the equations and we can focus on concentration and mixing effects only. Thus, here, we inspect isothermal reactors. Thermal effects are considered in Section 4.10.3.

If not otherwise stated, the following simplifications and assumptions are used:

- For homogeneous reactions, the reaction rate r ($\text{mol m}^{-3} \text{s}^{-1}$) and the rate constant k (s^{-1} for a first-order reaction) are typically related to the reactor volume. For heterogeneously catalyzed reactions or gas–solid reactions, the reaction rate r_m ($\text{mol kg}^{-1} \text{s}^{-1}$) and the rate constant k_m ($\text{m}^{-3} \text{kg}^{-1} \text{s}^{-1}$ for a first-order reaction) are usually related to the mass of the catalyst or solid reactant. To translate the equations derived in this chapter based on r and k , we simply have to substitute both parameters by the terms $r_m \rho_B$ and $k_m \rho_B$, respectively, where ρ_B is the bulk density of the catalyst or solid (kg m^{-3}).
- The reaction takes place without change in volume (rate).
- The density is constant and not a function of the changing composition.
- For continuous reactors (PFR, CSTR), steady-state conditions are assumed.

Solutions for deviating conditions are here only given for selected situations (e.g., reactions with changing volume are examined in Topic 4.10.1) and we refer to

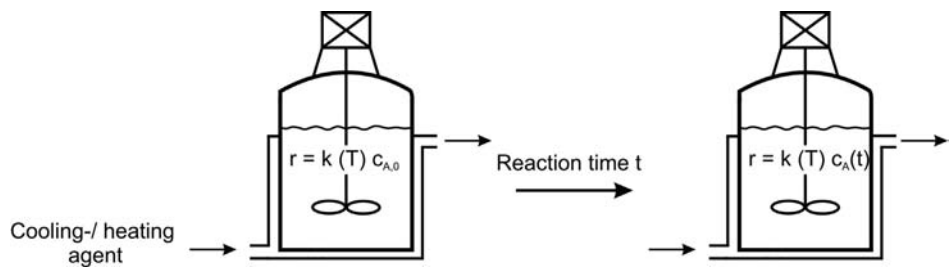


Figure 4.10.13 Ideally mixed batchwise operated stirred tank reactor.

other textbooks for further studies (Baerens *et al.*, 2006; Westerterp, van Swaaij, and Beenackers, 1998).

4.10.2.1 Well-Mixed (Discontinuous) Isothermal Batch Reactor

The ideally stirred tank reactor is perfectly uniform with regard to concentration and temperature. The general mass balance for such an ideally mixed reactor (either operated batchwise or in continuous mode) reads as:

$$\underbrace{V_R \frac{dc_i}{dt}}_{\text{Accumulation of } i} = \underbrace{\dot{V}_{in} c_{i,in}}_{\text{Flow of } i \text{ into reactor}} - \underbrace{\dot{V}_{out} c_{i,out}}_{\text{Flow of } i \text{ out of reactor}} + \underbrace{v_i r_i V_R}_{\text{Generation or consumption of } i} \quad (4.10.1)$$

For the specific case of a batchwise operated stirred tank reactor (Figure 4.10.13), the terms concerning convection (flow in and out) have to be omitted, and Eq. (4.10.1) simply reads as:

$$\frac{dc_i}{dt} = v_i r_i \quad (4.10.2)$$

Thus for a reactant A with $v_A = -1$ we get:

$$-\frac{dc_A}{dt} = r_A \quad (4.10.3)$$

Determination of the reaction time t required for a desired conversion is an important goal. In the following, we briefly recapitulate the respective equations already derived in Section 4.3.1.

For a first-order reaction with regard to reactant A and a rate constant k , Eq. (4.10.3) leads to:

$$-\frac{dc_A}{dt} = k c_A \quad (4.10.4)$$

and rearrangement and integration yields:

$$c_A = c_{A,0} e^{-kt} = c_{A,0} e^{-Da} \quad (4.10.5)$$

The term kt is called the *Damkoehler number* Da (of a first-order reaction).

Note that for a non-isothermal (batch) reactor, the energy balance has to be solved simultaneously with the mass balance, that is, both balances are strongly coupled. The rate constant k (which depends on temperature, typically a rise by a factor of two for an increase in T by 10 K) is not constant during the course of the reaction and a simple integration of Eq. (4.10.4) is not possible. This non-isothermal operation is considered in Section 4.10.3.1. For isothermal operation the conversion of A is given by:

$$\underbrace{X_A = 1 - \frac{c_A}{c_{A,0}}}_{\bullet} = 1 - e^{-Da} \quad (4.10.6)$$

For a reaction order $n \neq 1$, Eq. (4.10.3) leads to:

$$-\int_{c_{A,0}}^{c_A} \frac{dc_A}{c_A^n} = kt \quad (4.10.7)$$

and the solution of the integral and rearrangement yields:

$$\nabla \quad X_A = 1 - [1 + (n-1)Da]^{\frac{1}{1-n}} \quad (4.10.8)$$

with:

$$Da = kc_{A,0}^{n-1} t \quad (\text{for } n \neq 1) \quad (4.10.9)$$

For example, for a second- and a zero-order reaction we obtain:

$$X_A = \frac{Da}{1 + Da} \quad (4.10.10)$$

with:

$$Da = ktc_{A,0} \quad (\text{for } n = 2) \quad (4.10.11)$$

and:

$$X_A = Da \quad (4.10.12)$$

with:

$$Da = \frac{kt}{c_{A,0}} \quad (\text{for } n = 0) \quad (4.10.13)$$

Thus, for a given reaction time, the conversion increases with increasing initial concentration for an order $n > 1$, for example, for $n = 2$, see Eqs. (4.10.10) and (4.10.11), and decreases for $n < 1$, for example, for $n = 0$, see Eqs. (4.10.12) and (4.10.13). Only for a first-order reaction [Eq. (4.10.6)] does the conversion not depend on the initial concentration. This is because the increase in reaction rate with increasing concentration is matched by the reverse effect that the amount of reactant to be converted per unit time increases exactly by the same factor.

For more complex reactions, we may not even have a mathematical expression for r_A but, instead, measured data. Then we make use of the general integrated form of Eq. (4.10.3):

$$-\int_{c_{A,0}}^{c_A} \frac{dc_A}{r_A} = t \quad (4.10.14)$$

or in terms of conversion with $dX_A = -dc_A/c_{A,0}$ we use:

$$\nabla \quad c_{A,0} \int_0^{X_A} \frac{dX_A}{r_A} = t \quad (4.10.15)$$

By a plot of $1/r_A$ versus X_A , the reaction time needed to reach a certain conversion is easily determined by graphical integration (area below the curve) as schematically depicted in Figure 4.10.14. Of course, for an optimization of reactor design, it is always helpful to know the exact rate expression, but for a brief estimation the method outlined by Figure 4.10.14 is helpful.

4.10.2.2 Continuously Operated Isothermal Ideal Tank Reactor

For a continuously operated ideally stirred tank reactor (CSTR, Figure 4.10.15), the accumulation term dc/dt in the general mass balance of a stirred tank reactor [Eq. (4.10.1)] vanishes:

$$0 = \dot{V}_{in}c_{i,in} - \dot{V}_{out}c_{i,out} + v_i r_i V_R \quad (4.10.16)$$

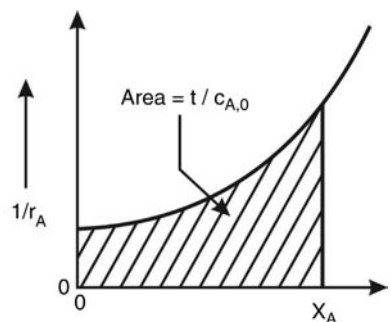


Figure 4.10.14 Determination of reaction time by $1/r_A - X_A$ plot (batch reactor, constant volume).

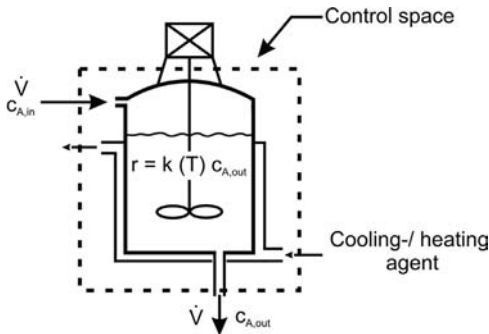


Figure 4.10.15 Ideally mixed continuous stirred tank reactor (CSTR).

The ideally stirred tank reactor is perfectly uniform with regard to concentration and temperature, and both parameters are identical to the values at the exit of the reactor.

For isothermal operation (for non-isothermal operation see Section 4.10.3.2) and a constant volume first-order reaction with respect to reactant A with $v_A = -1$, Eq. (4.10.16) leads to:

$$\dot{V}(c_{A,in} - c_{A,out}) = r_A V_R = k c_{A,out} V_R \quad (4.10.17)$$

Using the (mean) hydrodynamic residence time τ , defined as $\tau = V_R / \dot{V}$, we derive:

$$\frac{c_{A,out}}{c_{A,in}} = \frac{1}{1 + k \frac{V_R}{\dot{V}}} = \frac{1}{1 + k\tau} = \frac{1}{1 + Da} \quad (4.10.18)$$

and with the definition of the conversion we have:

! $X_A = 1 - \frac{c_{A,out}}{c_{A,in}} = \frac{Da}{1 + Da} \quad (\text{for } n = 1 \text{ with } Da = k\tau)$ (4.10.19)

Note that the volumetric rate \dot{V} and thus the residence time τ are related to the reaction conditions, that is, to the reaction temperature and reaction pressure.

For a reaction of n -th order with respect to the reactant A we obtain:

! $\frac{X_A}{(1 - X_A)^n} = k\tau c_{A,in}^{n-1} = Da \quad (4.10.20)$

and thus for a second- and a zero-order reaction we have:

$$\frac{X_A}{(1 - X_A)^2} = Da \quad (\text{for } n = 2 \text{ with } Da = k\tau c_{A,in}) \quad (4.10.21)$$

$$X_A = Da \quad \left(\text{for } n = 0 \text{ with } Da = \frac{k\tau}{c_{A,in}} \right) \quad (4.10.22)$$

For a zero-order reaction, the conversion in a batch reactor and in a CSTR (and in any other isothermal reactor) is equal for a given reaction rate constant and residence time. A detailed comparison of different ideal reactors is given below in Section 4.10.2.6.

4.10.2.3 Continuously Operated Isothermal Ideal Tubular Reactor

The ideal plug flow reactor PFR is a simplified picture of the motion of a fluid in a tubular reactor as it is assumed that all fluid elements move with a uniform velocity along parallel streamlines and thus have a fixed residence time τ . Strictly speaking, this assumption breaks the hydrodynamic rule that the velocity is zero at the wall (no slip condition, Figure 3.2.22). The steady-state mass balance of a PFR for a constant volume reaction can be deduced from the one-dimensional mass balance for a differential small element with thickness dz in direction of flow:

! $-d\dot{n}_A = \dot{V} dc_A = r_A dV_R \quad (4.10.23)$

Compared to a CSTR the ideal flow tube is recognized to be a non-back-mixed system, and the conversion and composition of the reaction mixture depends only on the axial coordinate z and not on the radial coordinate (Figure 4.10.16). With the residence time $\tau (= V_R / \dot{V} = L/u)$ and the conversion $X_A (= 1 - c_A / c_{A,in})$, that is, $dX_A = -dc_A / c_{A,in}$, rearranging of Eq. (4.10.23) yields:

$$\frac{dV_R}{\dot{V}} = d\tau = -\frac{dc_A}{r_A} = c_{A,in} \frac{dX_A}{r_A} \Rightarrow \tau = - \int_{c_{A,in}}^{c_A} \frac{dc_A}{r_A} = c_{A,in} \int_0^{X_A} \frac{dX_A}{r_A} \quad (4.10.24)$$

If Eq. (4.10.24) is compared with the corresponding Eqs. (4.10.14) and (4.10.15) for a batch reactor, it is easy to recognize that the course of the concentration in a

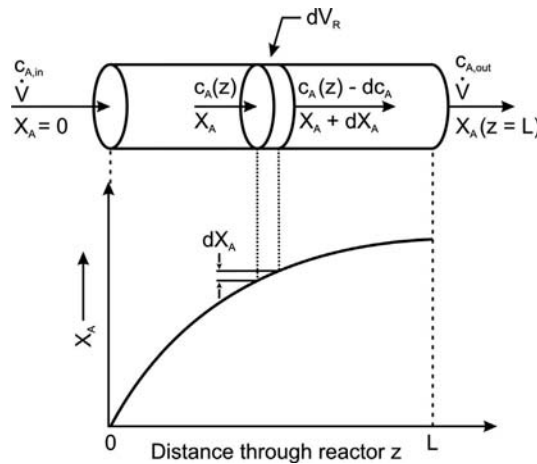


Figure 4.10.16 Ideal plug flow reactor.

plug flow reactor equals the course in an ideal batch reactor, if the reaction time t and the initial concentration $c_{A,0}$ ($t=0$) are replaced by the residence time τ and by the inlet concentration $c_{A,in}$. Thus the spacial succession in a PFR corresponds to the succession in time in a batch reactor.

For isothermal operation (for non-isothermal operation see Section 4.10.3.3), a first-order reaction with respect to reactant A ($r_A = kc_A$) and constant volume, Eq. (4.10.24) leads to:

$$! \quad \tau = - \int_{c_{A,in}}^{c_A} \frac{dc_A}{kc_A} = - \frac{1}{k} \int_{c_{A,in}}^{c_A} \frac{dc_A}{c_A} \Rightarrow \frac{c_{A,out}}{c_{A,in}} = e^{-k\tau} = e^{-Da} \Rightarrow X_A = 1 - e^{-Da} \quad (4.10.25)$$

For a reaction order of $n \neq 1$ we obtain:

$$\textcircled{v} \quad X_A = 1 - [1 + (n-1)Da]^{\frac{1}{(1-n)}} \quad (\text{with } Da = kc_{A,in}^{n-1} \tau) \quad (4.10.26)$$

If we compare the values of X_A calculated by Eqs. (4.10.19), (4.10.20), (4.10.25) and (4.10.26) for a given value of Da , we see that for a positive reaction order the conversion in a PFR is always higher than in a CSTR (see also Section 4.10.2.7). This effect can also be explained without any mathematics: The mean concentration in a PFR is somewhere between the in- and outlet value, whereas in a CSTR we have a constant but always lower reactor concentration that equals the outlet concentration. Thus for a positive value of the reaction order, the mean reaction rate in a PFR is higher. For a zero-order the difference in the reaction rate vanishes, and only for the rare case of a negative reaction order is the CSTR superior to a PFR.

4.10.2.4 Continuously Operated Isothermal Tubular Reactor with Laminar Flow

For a Re number of less than about 2300, we have laminar flow in a tubular reactor (Figure 3.2.22), and thus we can no longer use the assumption of ideal plug flow. Owing to the velocity profile a considerable spread in residence time occurs. In the center of the tube, we have a fluid velocity that is two times higher than the average velocity (and thus a residence time of 50% of the mean value). For the fluid elements in the region near the wall the reverse is true. This leads to a conversion in a reactor with laminar flow that is lower compared to turbulent flow (ideal PFR), and the Da number needed for a certain conversion is up to 50% higher.

The following simple model system may illustrate this situation. Let us assume we have two ideal PFRs, each with the same volume. Both reactors are run in parallel. If we assume a first-order reaction with a rate constant of 1 s^{-1} and a residence time in each reactor of 1 s we obtain a conversion of 63.2% in each reactor [Eq. (4.10.25)]. But if we divide the total volume rate unequally, the residence times

will be different. For example, if only 30% of the rate is fed to one reactor (which stands here for the region with low velocity near the wall of a tube with laminar flow), we have a residence time of 1.7 s. In contrast, we get 0.7 s in the second reactor with 70% of the total volume rate (which stands for the region near the tube center). We now find conversions of 81% and 51%, and the overall conversion in this model system is only 60% $[(0.7 \times 81\%) + (0.3 \times 51\%)] = 60\%$ compared to 63.2% for equal flow in both reactors.

In addition to the influence of the radial velocity profile, dispersion caused by molecular diffusion, which takes place in both axial and radial directions, may also play a certain role. The diffusion in radial direction tends to counteract the spreading effect of the velocity profile, while axial molecular diffusion increases the dispersion (details in Section 4.10.6.3). Instead of the simple differential mass balance of a plug flow reactor [Eq. (4.10.23)], the differential equation of a steady-state non-plug flow tubular reactor is:

$$\underbrace{-u(r) \frac{dc_A}{dz}}_{\text{Convection term with radial variation of } u} + \underbrace{D_{\text{mol}} \frac{d^2 c_A}{dz^2}}_{\text{Diffusion in axial direction } z} + \underbrace{D_{\text{mol}} \left(\frac{d^2 c_A}{dr^2} + \frac{1}{r} \frac{dc_A}{dr} \right)}_{\text{Diffusion in radial direction}} r = \underbrace{r_A}_{\substack{\text{Reaction term, e.g.,} \\ r_A = kc_A \text{ for first order}}} \quad (4.10.27)$$

If the influence of molecular diffusion is negligible (if not see Section 4.10.6.3), each fluid element of flow follows its own streamline without intermixing with neighboring elements. Then we only have to consider the influence of the velocity profile via $u(r)$, and for a laminar flow with the radial velocity profile according to Eq. (3.2.62) we obtain a simplified form of Eq. (4.10.27) for a first-order reaction:

$$-2u_{\text{mean}} \left(1 - \frac{4r^2}{d_t^2} \right) \frac{dc_A}{dz} = kc_A \quad [\text{for } D_{\text{mol}} \rightarrow 0, \text{ exact condition see Eq. (4.10.30)}] \quad (4.10.28)$$

The solution of Eq. (4.10.28) is:

$$X_A = 1 - \left(1 - \frac{Da}{2} \right) e^{-\frac{Da}{2}} - \left(\frac{Da}{2} \right)^2 \int_{Da/2}^{\infty} \frac{e^{-Da/2}}{Da/2} d\left(\frac{Da}{2}\right) \quad (\text{with } Da = k\tau) \quad (4.10.29)$$

As we always have a certain diffusivity (D_{mol}), the “exact” condition for a negligible influence of radial diffusion and, thus, for the validity of the Eqs. (4.10.28) and (4.10.29) is that the time constant for radial diffusion should be much longer than the average residence time:

$$\tau_D = \frac{r_t^2}{D_{\text{mol}}} \gg \tau = \frac{L}{u_{\text{mean}}} \Rightarrow \frac{L}{d_t} \ll \frac{u_{\text{mean}} d_t}{D_{\text{mol}}} = \frac{u_{\text{mean}} d_t}{\nu} \frac{\nu_t}{D_{\text{mol}}} = Re \times Sc \quad (4.10.30)$$

which is for example approached in short tubes with viscous liquids at low Re numbers.

The derivation of the rather complicated Eq. (4.10.29) is given in other textbooks (Westerterp, van Swaaij, and Beenackers, 1998; Levenspiel, 1996, 1999). Note that Eq. (4.10.29) is only valid for Newtonian fluids. The case of non-Newtonian fluids may also be important, such as, for example, in polymerization reactors, and is treated in the literature (Wen and Fan, 1975). Table 4.10.1 gives selected values of the exponential integral in Eq. (4.10.29). Figure 4.10.17 compares the conversion reached in a plug flow reactor with that in a tubular reactor with laminar flow.

As shown in Figure 4.10.17, we may use the PFR equation (4.10.25) for a conversion below 20%, and for higher conversions the following approximations instead of the complicated Eq. (4.10.29) may be helpful to estimate the conversion in a

Table 4.10.1 Selected values of the exponential integral in Eq. (4.10.29).

Da	$\int_{Da/2}^{\infty} \frac{e^{-Da/2}}{Da/2} d\left(\frac{Da}{2}\right)$	Da	$\int_{Da/2}^{\infty} \frac{e^{-Da/2}}{Da/2} d\left(\frac{Da}{2}\right)$
0.1	2.4679	1	0.5598
0.2	1.8229	2	0.2194
0.4	1.2227	4	0.04890
0.6	0.9057	10	0.00115

tubular reactor with laminar flow:

$$X_{A,\text{tube, laminar flow}} \approx 1 - e^{-\frac{Da}{C}} \text{ with } \begin{cases} C \approx 1 & \text{PFR} \\ C \approx 1.2 & \text{for } X_A < 0.2 \\ C \approx 1.4 & \text{for } X_A > 0.7 \end{cases} \quad (4.10.31)$$

4.10.2.5 Continuously Operated Isothermal Cascade of Tank Reactors

A cascade of stirred tanks (Figure 4.10.18) is the simplest combination of ideal reactors. This configuration is also used in the chemical industry since the principal disadvantage of a single stirred tank can be bypassed, namely, that a CSTR operates with a low conversion requiring a reactor with a large volume (Section 4.10.2.7). Thus it is helpful to use a sequence of reactors where only the last tank is operated at the final concentrations of the reactants. Furthermore, a cascade of CSTRs is useful to model real reactors as we will learn in Section 4.10.5.

In a simplifying assumption the reaction is again considered to take place under constant volume. For steady-state conditions and a first-order reaction ($r_N = kc_{A,N}$) the total conversion in a cascade of N CSTRs (each with a volume of $V_{R,N}$) can be calculated by back insertion up to the concentration $c_{A,0}$ at the entry to the cascade (for indices see Figure 4.10.18):

$$\nabla \quad X_A = \frac{\left(1 + \frac{k\tau}{N}\right)^N - 1}{\left(1 + \frac{k\tau}{N}\right)^N} = \frac{\left(1 + \frac{Da}{N}\right)^N - 1}{\left(1 + \frac{Da}{N}\right)^N} \quad (4.10.32)$$

where τ is the overall residence time in the cascade, defined as $\tau = NV_{R,N}/\dot{V}$.

In a PFR we have no axial and ideal radial mixing. A cascade consisting of an infinite number of CSTRs shows likewise behavior. Thus, depending on the number of tanks N , the cascade changes from a single CSTR ($N=1$) to a PFR for an infinite number of tanks.

4.10.2.6 Ideal Isothermal Tubular Recycle Reactor

It is sometimes advantageous to divide the product stream of a reactor and return a portion to the entrance, for example, to charge or discharge reaction heat outside of the reactor in the recycle line and thus limit the increase or decrease of temperature

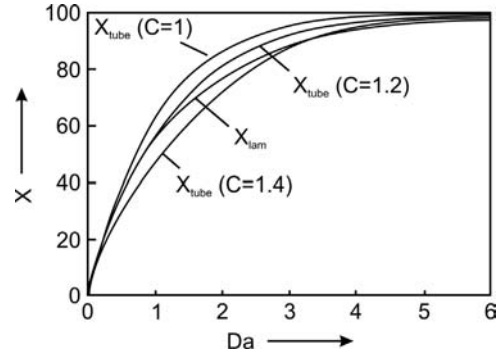
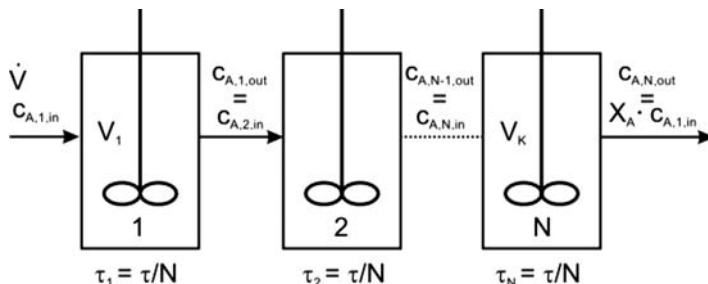
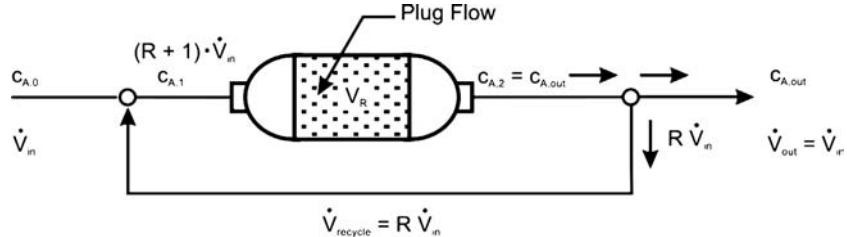


Figure 4.10.17 Conversion in an ideal plug flow reactor ($C = 1$) and in a tubular reactor with laminar flow (negligible molecular diffusion) for a first-order reaction ($Da = kt$); approximations for laminar flow as given by Eq. (4.10.31) are also shown.

Figure 4.10.18 Cascade of mixed stirred tank reactors.

Figure 4.10.19 Recycle reactor (in combination with an ideal plug flow).



in the reactor (Figure 4.10.19). Furthermore, the recycle reactor is an alternative to a cascade of CSTRs as a useful tool with which to model real reactors, as outlined briefly in Section 4.10.2.7.

The recycle ratio R is defined (for a constant volume reaction) as the ratio of the flow rate of fluid returned to the reactor entrance to the flow rate of the fresh feed entering the system:

$$R = \frac{\dot{V}_{recycle}}{\dot{V}_{out}} = \frac{\dot{V}_{recycle}}{\dot{V}_{in}} \quad (4.10.33)$$

Consequently, R may vary from zero (behavior of PFR) to infinity (CSTR). If we consider plug flow across the reactor itself (for nomenclature see Figure 4.10.19) we find based on Eq. (4.10.24):

$$-\int_{c_{A,1}}^{c_{A,2}} \frac{dc_A}{r_A} = \tau_{reactor} = \frac{V_R}{(\dot{V}_{recycle} + \dot{V}_{in})} \quad (4.10.34)$$

For a first-order reaction with respect to reactant A ($r_A = -1$) and constant volume, combination of Eqs. (4.10.33) and (4.10.34) leads to:

$$-\int_{c_{A,1}}^{c_{A,2}} \frac{dc_A}{kc_A} = \frac{V_R}{\dot{V}_{in}(1+R)} = \frac{\tau}{(1+R)} \quad (4.10.35)$$

where the residence time τ is only related to the volumetric flow of the fresh feed \dot{V}_{in} .

Integration of Eq. (4.10.35) for T and thus for $k = \text{constant}$ gives:

$$\ln \frac{c_{A,2}}{c_{A,1}} = \ln \frac{c_{A,out}}{c_{A,1}} = -\frac{k\tau}{(1+R)} \quad (4.10.36)$$

The concentration of reactant A at the entrance of the reactor ($c_{A,1}$) after mixing of the fresh feed ($c_{A,0}$) with the recycle stream ($c_{A,2} = c_{A,out}$) is given by:

$$c_{A,1} = \frac{c_{A,0} + Rc_{A,out}}{(1+R)} \quad (4.10.37)$$

and combination of Eq. (4.10.36) with Eq. (4.10.37) yields:

$$\begin{aligned} \nabla \ln \left[\frac{c_{A,0} + Rc_{A,out}}{(1+R)c_{A,out}} \right] &= \frac{k\tau}{(1+R)} = \frac{Da}{(1+R)} \Rightarrow X_A = 1 - \frac{c_{A,out}}{c_{A,0}} \\ &= \frac{1 + R - e^{\frac{Da}{(1+R)}}(1+R)}{R - e^{\frac{Da}{(1+R)}}(1+R)} \end{aligned} \quad (4.10.38)$$

For the first border case of a negligibly small recycle ratio ($R \rightarrow 0$), Eq. (4.10.38) approaches the equation for a plug flow reactor, Eq. (4.10.25):

$$X_A = \frac{1 + R - e^{\frac{Da}{(1+R)}}(1+R)}{R - e^{\frac{Da}{(1+R)}}(1+R)} = \frac{1 - e^{Da}}{-e^{Da}} = 1 - e^{-Da} \quad (\text{for } R \rightarrow 0) \quad (4.10.39)$$

For the second border case of an infinitely high recycle ratio ($R \rightarrow \infty$), Eq. (4.10.38) approaches the equation for a CSTR, Eq. (4.10.19). [Note that $e^a \rightarrow (1+a)$ for $a \rightarrow 0$.]:

$$\begin{aligned} X_A &= \frac{1+R - e^{\frac{Da}{(1+R)}}(1+R)}{R - e^{\frac{Da}{(1+R)}}(1+R)} = \frac{1+R - \left[1 + \frac{Da}{(1+R)}\right](1+R)}{R - \left[1 + \frac{Da}{(1+R)}\right](1+R)} \\ &= \frac{Da}{1+Da} \quad (\text{for } R \rightarrow \infty) \end{aligned}$$

4.10.2.7 Comparison of the Performance of Ideal Isothermal Reactors

The reactor type influences the conversion for a given reaction or residence time (or more precisely for a given Da number) as well as the selectivity and maximum yield that can be achieved for a given conversion degree. Subsequently, this is only examined for a first-order reaction without change of volume; details for other reaction types are given in the literature (e.g., Westerterp, van Swaaij, and Beenackers, 1998; Levenspiel, 1996, 1999). Some remarks on reactions with a change of volume are given in Topic 4.10.1.

Influence of Reactor Type on the Conversion for a given Da Number (or Vice Versa)

For an isothermal operation and a first-order reaction with respect to reactant A ($r_A = kc_A$) and constant volume, rearrangement of Eqs. (4.10.19) and (4.10.25) yields the residence time and Da number, respectively, needed to reach a certain conversion in a CSTR and a PFR:

$$Da = k\tau_{\text{CSTR}} = \frac{X_A}{(1-X_A)} \quad (\text{CSTR, isothermal first-order reaction}) \quad (4.10.19b)$$

$$\begin{aligned} Da &= k\tau_{\text{PFR}} = \int_0^{X_A} \frac{dX_A}{(1-X_A)} \\ &= -\ln(1-X_A) \quad (\text{PFR, isothermal first-order reaction}) \end{aligned} \quad (4.10.25b)$$

Figure 4.10.20a shows the graphical solution of both equations for the example of a conversion of 95%. The area under the function of $1/(1-X_A)$ versus X_A represents Da . For the given example, a value of 19 is needed in a CSTR (rectangle with area 20×0.95), whereas for the PFR the respective (dashed) area is only 3. For a cascade consisting of four CSTRs of equal size we get a Da value in between these two extremes of 4.4 (for $X_A = 95\%$).

Table 4.10.2 summarizes the equations for the conversion in ideal reactors and selected values for different *Damkoehler numbers*. As also shown in Figure 4.10.20b, the following trends can be identified:

- Deviation of the conversion in a PFR (and in a batch reactor, respectively) from the value obtained in a CSTR increases strongly with increasing Da . In turn, the value of Da needed in a CSTR is much higher compared to a PFR, if a high conversion is desired.
- A cascade with a number N of CSTRs of more than 10 can be approximately regarded as a PFR, as the difference in X_A for a given value of Da is small. Similarly, a recycle reactor with $R > 10$ can almost be regarded as a CSTR. For $N=2$ and $R=2$, a cascade and a recycle reactor exhibit almost the same behavior (Figure 4.10.20).
- For a constant volume reaction, a batch reactor performs as a PFR if the reaction time equals the residence time (for a reaction with a changing volume see Topic 4.10.1).

Figure 4.10.20 Comparison of ideal reactors: (a) method to determine graphically the Da number needed for a certain conversion X_A ; (b) X_A for a given Da (isothermal, first order, constant volume, N : number of CSTRs of a cascade, $Da = k\tau$).

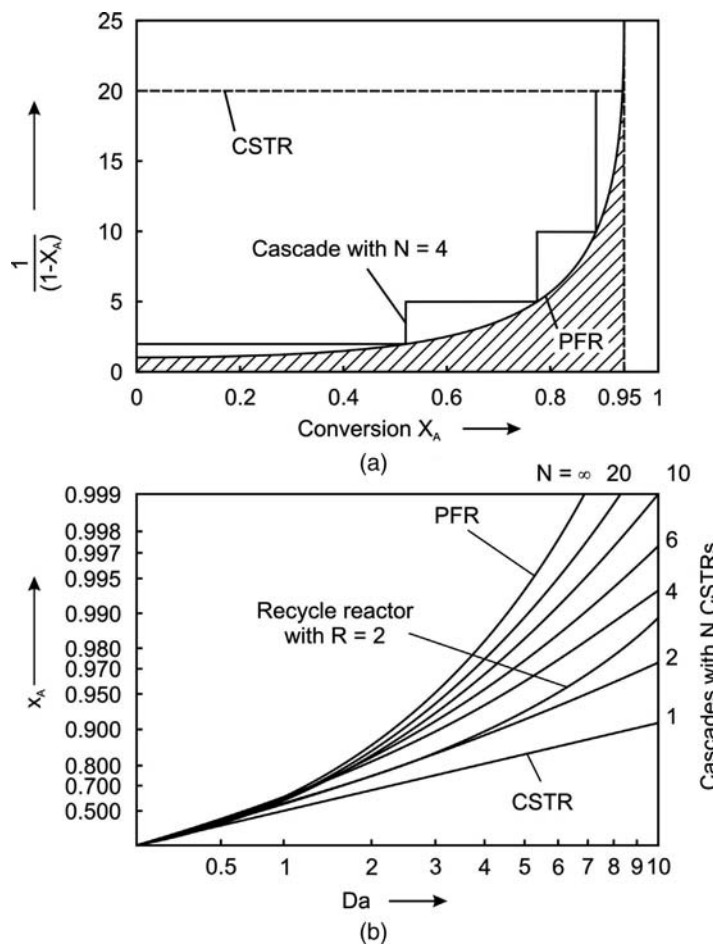


Table 4.10.2 Equations for the conversion of reactant A in ideal reactors (isothermal, first order, constant volume, $Da = k\tau$ for PFR, CSTR, and recycle reactor and $k\tau$ for a batch reactor).

Reactor type	Conversion X_A	X_A ($Da = 1$) (%)	X_A ($Da = 10$) (%)	Da ($X_A = 99\%$)																								
Ideal plug flow reactor (PFR)	$1 - e^{-Da}$	63.21	99.99	4.6																								
Tubular reactor with laminar flow, Newtonian fluid, negligible molecular diffusion	$1 - \left(1 - \frac{Da}{2}\right)e^{-\frac{Da}{2}} - \left(\frac{Da}{2}\right)^2 \int_{Da/2}^{\infty} \frac{e^{-Da/2}}{Da/2} d\left(\frac{Da}{2}\right)$	55.67	99.82	7.1																								
Ideally mixed batch reactor	$1 - e^{-Da}$	63.21	99.99	4.6																								
Ideal continuous stirred tank reactor (CSTR)	$\frac{Da}{1 + Da}$	50.00	90.91	99																								
Cascade of N stirred tank reactors	$\frac{\left(1 + \frac{Da}{N}\right)^N - 1}{\left(1 + \frac{Da}{N}\right)^N} \text{ with } \tau = \frac{N V_{R,N}}{\dot{V}}$	<table> <tr><td>$N = 1$</td><td>50.00</td><td>90.91</td><td>99</td></tr> <tr><td>$N = 2$</td><td>55.55</td><td>97.22</td><td>18</td></tr> <tr><td>$N = 4$</td><td>59.03</td><td>99.33</td><td>8.6</td></tr> <tr><td>$N = 10$</td><td>61.44</td><td>99.90</td><td>5.9</td></tr> <tr><td>$N = 100$</td><td>63.03</td><td>99.99</td><td>4.7</td></tr> <tr><td>$N = \infty$</td><td>63.21</td><td>99.99</td><td>4.6</td></tr> </table>	$N = 1$	50.00	90.91	99	$N = 2$	55.55	97.22	18	$N = 4$	59.03	99.33	8.6	$N = 10$	61.44	99.90	5.9	$N = 100$	63.03	99.99	4.7	$N = \infty$	63.21	99.99	4.6		
$N = 1$	50.00	90.91	99																									
$N = 2$	55.55	97.22	18																									
$N = 4$	59.03	99.33	8.6																									
$N = 10$	61.44	99.90	5.9																									
$N = 100$	63.03	99.99	4.7																									
$N = \infty$	63.21	99.99	4.6																									
Recycle reactor with recycle rate R	$\frac{1 - e^{Da/(1+R)}}{\frac{R}{1+R} - e^{Da/(1+R)}} \text{ with } R = \frac{\dot{V}_{\text{recycle}}}{\dot{V}_{\text{feed}}}$	<table> <tr><td>$R = 0$</td><td>63.21</td><td>99.99</td><td>4.6</td></tr> <tr><td>$R = 2$</td><td>54.27</td><td>98.78</td><td>10.6</td></tr> <tr><td>$R = 10$</td><td>51.14</td><td>94.22</td><td>25.3</td></tr> <tr><td>$R = 100$</td><td>50.12</td><td>91.31</td><td>69</td></tr> <tr><td>$R = \infty$</td><td>50.00</td><td>90.91</td><td>99</td></tr> </table>	$R = 0$	63.21	99.99	4.6	$R = 2$	54.27	98.78	10.6	$R = 10$	51.14	94.22	25.3	$R = 100$	50.12	91.31	69	$R = \infty$	50.00	90.91	99						
$R = 0$	63.21	99.99	4.6																									
$R = 2$	54.27	98.78	10.6																									
$R = 10$	51.14	94.22	25.3																									
$R = 100$	50.12	91.31	69																									
$R = \infty$	50.00	90.91	99																									

Topic 4.10.1 Influence of changing volume on the performance of isothermal ideal reactors (single first-order reaction)

In Section 4.3.4, we examined the influence of a varying volume on the performance of a batch reactor. To recall the result: For a first-order reaction, the performance of a batch is not influenced by the change of volume. This is different for flow reactors where the volumetric rate is given by Eq. (4.1.15) with ε_V as fractional change:

$$\dot{V} = (1 + \varepsilon_V X_k) \dot{V}_{in} \quad (4.1.15)$$

Plug flow reactor (PFR)

The differential mass balance [Eq. (4.10.24)] of a PFR for a first-order reaction leads to:

$$\tau = \frac{V_R}{\dot{V}_{in}} = - \int_{c_{A,in}}^{c_A} \frac{dc_A}{kc_A} = \int_0^{X_A} \frac{c_{A,in} dX_A}{kc_A} \quad (4.10.40a)$$

Rearrangement and insertion of Eq. (4.1.15) yields (for isothermal conditions):

$$\tau = \frac{c_{A,in}}{k} \int_0^{X_A} \frac{1}{c_A} dX_A = \frac{\dot{n}_{A,in}}{k \dot{V}_{in}} \int_0^{X_A} \frac{\dot{V}}{\dot{n}_A} dX_A = \frac{1}{k} \int_0^{X_A} \frac{(1 + \varepsilon_V X_A)}{(1 - X_A)} dX_A \quad (4.10.40b)$$

The solution of Eq. (4.10.40b) is given by:

$$k\tau = Da = -\ln(1 - X_A)^{(1+\varepsilon_V)} - \varepsilon_V X_A \quad (4.10.40c)$$

Mixed flow reactor (CSTR)

For an ideal CSTR, the volumetric flow changes immediately to \dot{V}_{out} , and the mass balance [Eq. (4.10.17)] for an isothermal first-order reaction leads to:

$$\dot{V}_{in} c_{A,in} - \dot{V}_{out} c_{A,out} = kc_{A,out} V_R \quad (4.10.40d)$$

Rearrangement and insertion of the term $(1 - X_A)/(1 + \varepsilon_V X_A)$ for $c_{A,out}/c_{A,in}$ yields:

$$\frac{\dot{V}_{in} c_{A,in} - \dot{V}_{out} c_{A,out}}{\dot{V}_{in} c_{A,in}} = X_A = \frac{kc_{A,out} V_R}{\dot{V}_{in} c_{A,in}} = k\tau \frac{c_{A,out}}{c_{A,in}} = Da \frac{(1 - X_A)}{(1 + \varepsilon_V X_A)} \quad (4.10.40e)$$

Thus, for the Damköehler number Da we obtain:

$$Da = \frac{X_A(1 + \varepsilon_V X_A)}{(1 - X_A)} \quad (4.10.40f)$$

Solutions for both types of flow reactors and reaction orders other than unity can be found in the literature (e.g., Levenspiel, 1996, 1999).

Table 4.10.3 gives the conversion in a batch reactor, a PFR, and a CSTR for different values of ε_V for the example of $Da = 1$. The data indicate that, in contrast to a batch reactor, X_A decreases for a reaction with increasing volume both in a CSTR and in a PFR, which is in general true for a reaction order > 0 [see Levenspiel (1996, 1999)]. For a reaction with decreasing volume rate, this is reversed. In both flow reactors (PFR, CSTR), the residence time changes compared to a constant volume reaction, while in a batch reactor the reaction time does not. Thus for reactions with changing volume, the batch and the plug flow performance equations are different.

Deviation of the conversion in a PFR/batch reactor and in a CSTR (for $Da = \text{const}$) is even stronger for reaction orders $n > 1$ and smaller for $n < 1$. For $n = 0$, the influence of the reactor type vanishes, and for a negative reaction order the trend reverses and the CSTR is superior to a batch reactor or PFR.

Table 4.10.3 Equations for conversion of reactant A in reactors with varying volume V ($T = \text{const.}$, first order, $Da = k\tau = k V_R / \dot{V}_{\text{in}}$ for a PFR and a CSTR and $k\tau$ for batch reactor).

Reactor type	Equation for conversion X_A	No change of volume (rate)	Increasing volume (rate)	Decreasing volume (rate)
		$\varepsilon_V = 0$	$\varepsilon_V = 1$	$\varepsilon_V = -0.5$
X_A for $Da = 1$ (%)				
PFR	$Da = -(1 + \varepsilon_V) \ln(1 - X_A) - \varepsilon_V X_A$	63.2	53.6	72.2
Batch reactor	$X_A = 1 - e^{-Da}$	63.2	63.2	63.2
CSTR	$Da = \frac{X_A(1 + \varepsilon_V X_A)}{1 - X_A}$	50.0	41.4	58.6

Influence of Reactor Type on Product Yields and Selectivity Let us consider two first-order reactions in series $A \xrightarrow{k_1} B \xrightarrow{k_2} C$. In batch and plug flow reactors, the yield of intermediate B is given by Eq. (4.3.39), derived in Section 4.3.2.1:

$$Y_B = \frac{c_B}{c_{A,\text{in}}} = \frac{k_1}{k_1 - k_2} (e^{-k_2\tau} - e^{-k_1\tau}) \quad (4.3.39)$$

The maximum value of the yield of B in a PFR is calculated by differentiation of Eq. (4.3.39), and we obtain the desired maximum value for the condition $dY_B/d\tau = 0$:

$$Y_{B,\text{max,PFR}} = \left(\frac{k_2}{k_1} \right)^{\frac{k_2/k_1}{(1-k_2/k_1)}} \quad (4.10.41)$$

For a CSTR, the yield of B is derived by the mass balance (for $c_{B,\text{in}} = 0$) as follows:

$$\frac{c_{B,\text{out}}}{\tau} = k_1 c_{A,\text{out}} - k_2 c_{B,\text{out}} \Rightarrow Y_B = \frac{c_{B,\text{out}}}{c_{A,\text{in}}} = \frac{k_1 \tau}{(1 + k_2 \tau)} \frac{c_{A,\text{out}}}{c_{A,\text{in}}} \quad (4.10.42)$$

The unknown concentration $c_{A,\text{out}}$ is given by Eq. (4.10.18), and insertion of this equation in Eq. (4.10.42) and differentiation leads to the maximum yield of the intermediate product B in a CSTR, as the condition for the maximum is again that the derivative $dY_B/d\tau$ vanishes:

$$\frac{dY_B}{d\tau} \Big|_{Y_B=Y_{B,\text{max}}} = \frac{d}{d\tau} \left[\frac{k_1 \tau}{(1 + k_1 \tau)(1 + k_2 \tau)} \right] = 0 \Rightarrow Y_{B,\text{max,CSTR}} = \left(1 + \sqrt{\frac{k_2}{k_1}} \right)^{-2} \quad (4.10.43)$$

The evolution of conversion and yields in an isothermal CSTR and PFR is compared in Figure 4.10.21 for the example of $k_2/k_1 = 0.1$. According to Eqs. (4.10.41) and (4.10.43), the maximum yield of B is 77% in a PFR and only 58% in a CSTR. This clearly shows that the PFR is superior to the CSTR, if the yield of the intermediate is to be maximized.

4.10.3

Non-isothermal Ideal Reactors and Criteria for Prevention of Thermal Runaway

The heat released or consumed by a reaction leads to a difference in reaction temperature compared to the inlet temperature of continuously operated reactors (CSTR, PFR) or to the initial temperature of a batch reactor. For a PFR, the temperature also changes with the local position in the reactor. Heat effects strongly influence the reactor behavior up to the danger of a thermal runaway, if we have an exothermic reaction and insufficient cooling. The reason for this unwanted behavior is straightforward (although we will learn in this chapter that the prediction is not so easy): According to Arrhenius's law the rate increases almost exponentially with temperature, whereas cooling only rises in proportion to the difference

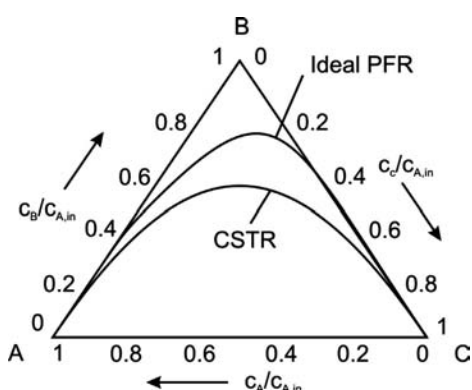


Figure 4.10.21 Typical evolution of conversion and product yields in an isothermal CSTR and PFR for a first-order reaction, $A \xrightarrow{k_1} B \xrightarrow{k_2} C$, for $k_2/k_1 = 0.1$.

between reaction and cooling temperature. Thus we may get a situation where an increase in temperature accelerates the heat production so strongly that this is no longer compensated by cooling.

Subsequently, mainly cooled non-isothermal reactors are examined, but all equations are also valid for heated reactors simply by replacing the cooling by the heating temperature. However, the operation of a heated reactor for an endothermic reaction is much less critical than of a cooled system with an exothermic reaction. A temperature runaway can never occur in case of an endothermic reaction, where in the worst case the reaction comes to a standstill.

The following simplifications were assumed to limit the complexity of the equations:

- The reaction is first-order with no change in volume.
- All data on chemical media (density, heat capacity, reaction enthalpy, etc.) are considered to be constant and not a function of temperature and changing composition.
- For the two continuous reactors (PFR, CSTR), which are examined in Sections 4.10.3.2 and 4.10.3.3, steady-state operation is assumed.
- The heat capacity of the reactor is negligible compared to the fluid phase(s).
- The cooling temperature is considered to be constant.

For more complicated situations we refer to other textbooks such as Westerterp, van Swaaij, and Beenackers (1998).

4.10.3.1 Well-Mixed (Discontinuously Operated) Non-isothermal Batch Reactor

Based on Eq. (4.10.4) the mass balance of a cooled batch reactor with a first-order reaction reads as follows, if we use Eq. (4.3.4) for the influence of temperature on the rate constant k :

$$\boxed{!} \quad -\underbrace{\frac{dc_A}{dt}}_{\text{Change of } c_A \text{ with time}} = \underbrace{\frac{dX_A}{dt} c_{A,0}}_{\text{Rate of chemical reaction of A}} = r_A = k c_A = k_0 e^{-\frac{E_A}{RT}} (1 - X_A) c_{A,0} \quad (4.10.44)$$

For the heat balance of a cooled batch reactor we consider the following heat flows \dot{Q} :

$$\boxed{!} \quad \underbrace{\rho_{\text{mol}} V_R c_p \frac{dT}{dt}}_{\dot{Q}_{\text{accumulation}}} = -\underbrace{U_h A_h (T - T_{\text{cool}})}_{\dot{Q}_{\text{cooling}}} + \underbrace{r_A (-\Delta_R H) V_R}_{\dot{Q}_{\text{reaction}}} \quad (4.10.45)$$

where U_h is the overall heat transfer coefficient ($\text{W m}^{-2} \text{K}^{-1}$), A_h the cooling area for heat transfer (m^2), T_{cool} the cooling temperature (assumed to be constant), T the reaction temperature, r_A the reaction rate of consumption of A ($\text{mol m}^{-3} \text{s}^{-1}$), ρ_{mol} the molar fluid density (mol m^{-3}), and c_p the molar heat capacity of the fluid ($\text{J mol}^{-1} \text{K}^{-1}$). Before we examine the situation of a cooled batch reactor further, we discuss first the simpler case of adiabatic operation.

Adiabatic Operation of a Batch Reactor For adiabatic operation, the cooling term $U_h A_h (T - T_{\text{cool}})$ vanishes, and combination of equations (4.10.44) and (4.10.45) leads to:

$$\rho_{\text{mol}} c_p \frac{dT}{dt} = c_{A,0} \frac{dX_A}{dt} (-\Delta_R H) \quad (4.10.46)$$

By rearrangement we get:

$$\frac{dT}{dX_A} = \frac{c_{A,0} (-\Delta_R H)}{\rho_{\text{mol}} c_p} = \frac{\Delta T}{X_A} \quad (4.10.47)$$

Thus for an exothermic reaction, the temperature increases proportionally with conversion X_A :

$$T - T_0 = X_A \left[\frac{c_{A,0} (-\Delta_R H)}{\rho_{\text{mol}} c_p} \right] = X_A \Delta T_{\text{ad}} \quad (4.10.48)$$

and for $X_A = 1$ we get the maximum adiabatic change ΔT_{ad} . To determine the time t to reach a certain conversion, we insert Eq. (4.10.48), the Arrhenius correlation $k = k_0[\exp(-E_A/RT)]$, and the correlation $c_A = (1 - X_A)c_{A,0}$ into Eq. (4.10.4) and by integration we obtain:

$$\begin{aligned} \int_0^t dt &= t = c_{A,0} \int_0^{X_A} \frac{1}{k} \frac{1}{c_A} dX_A = c_{A,0} \int_0^{X_A} \frac{e^{\frac{E_A}{RT}}}{k_0(1-X_A)} dX_A \\ &= \int_0^{X_A} \frac{e^{\frac{E_A}{R}(T_0+X_A\Delta T_{\text{ad}})}}{k_0(1-X_A)} dX_A \end{aligned} \quad (4.10.49)$$

Equation (4.10.49) can be solved graphically as shown in Example 4.10.1.

Example 4.10.1: Decomposition of H_2O_2 in an adiabatic batch reactor

The homogeneous catalytic decomposition of hydrogen peroxide (H_2O_2) (with Fe^{3+} ions as catalyst) in a batch reactor can be formally described by a first-order reaction:

$$-\frac{dc_{\text{H}_2\text{O}_2}}{dt} = k_0 e^{-\frac{E_A}{RT}} c_{\text{H}_2\text{O}_2}$$

For this example we use the data given by Baerns *et al.* (2006), that is, an activation energy of 105 kJ mol^{-1} and a pre-exponential factor k_0 of $2.73 \times 10^{15} \text{ s}^{-1}$. Equation (4.10.49) yields:

$$t = \int_0^X \frac{e^{\frac{E_A}{R}(T_0+X\Delta T_{\text{ad}})}}{k_0(1-X)} dX$$

The adiabatic rise in temperature is 58.4 K , and as initial temperature we use 29°C .

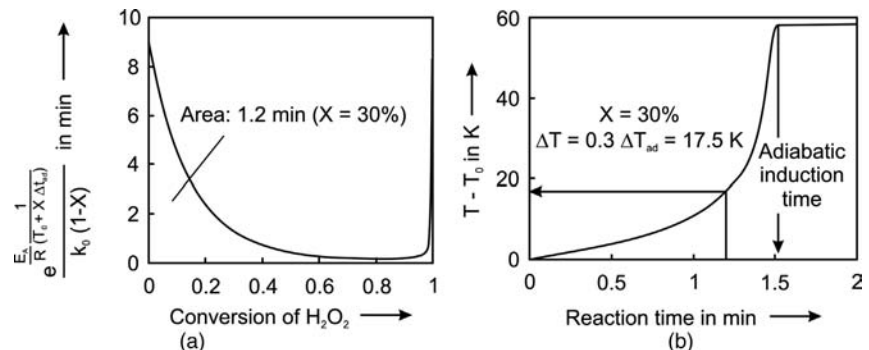
The plot of the integrand $e^{\frac{E_A}{R}(T_0+X\Delta T_{\text{ad}})} / [k_0(1-X)]$ versus X is shown in Figure 4.10.22. By graphical integration, that is, by evaluation of the area underneath the curve from 0 to X_A , we find the time needed to reach a certain conversion – for example, 1.2 min for 30% conversion. The reaction temperature and the temperature difference compared to the initial value T_0 is then easily determined as we know that $\Delta T = T - T_0 = X\Delta T_{\text{ad}}$ (Figure 4.10.22b).

Cooled Batch Reactor with Exothermic Reaction Based on the rate in terms of X_A , Eq. (4.10.44), and the adiabatic temperature rise, Eq. (4.10.48), the heat balance of a cooled batch reactor, Eq. (4.10.45), for $dc_A = -dX_A c_{A,0}$ reads as:

$$\frac{dT}{dt} = \frac{U_h A_h}{\rho_{\text{mol}} V_R c_p} (T_{\text{cool}} - T) + \Delta T_{\text{ad}} \frac{dX_A}{dt} \quad (4.10.50)$$

Figure 4.10.23 show typical devices used for the cooling of stirred tank reactors. The respective values of the overall heat transfer coefficient, the thermal

Figure 4.10.22 (a, b) Evolution of temperature in an adiabatic batch reactor during catalytic decomposition of H_2O_2 , $\Delta T_{\text{ad}} = 58 \text{ K}$; $T_0 = 302 \text{ K}$; data from Baerns *et al.* (2006).



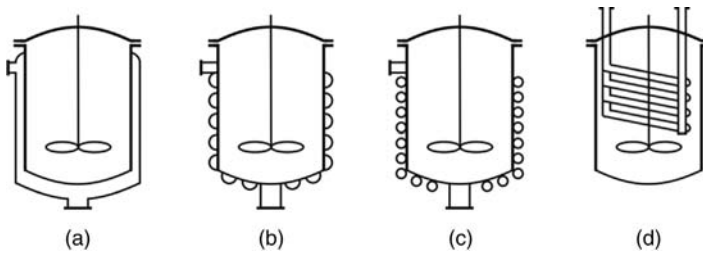


Figure 4.10.23 Typical devices for cooling stirred tank reactors: (a) double jacket, (b, c) half or full pipe welded on external surface, and (d) internal coil. Adapted from Dittmeyer *et al.* (2003).

Table 4.10.4 Typical values of the thermal transmission coefficient U_h in stirred tank reactors (see also Figure 4.10.21). Adapted from Dittmeyer *et al.* (2003).

$U_h (\text{W m}^{-2} \text{K}^{-1})$		
Double jacket	Liquid-to-liquid	150–300
	Steam-to-liquid	500–1500
Half pipe/full pipe	Steam-to-boiling liquid	700–1700
	Liquid-to-liquid	350–900
Internal coil	Steam-to-liquid	500–1700
	Steam-to-boiling liquid	700–2300
Internal coil	Liquid-to-liquid	500–1200
	Steam-to-liquid	700–2500
	Steam-to-boiling liquid	1200–3500

transmission coefficient U_h , are listed in Table 4.10.4 (for the definition of U_h see Section 3.2.1.2).

Equations (4.10.44) and (4.10.45) for mass and heat are coupled by the rate dX_A/dt and must be solved by numerical methods. A typical evolution of the temperature with time in a cooled batch reactor is shown in Figure 4.10.24 for the example of homogeneously catalyzed H_2O_2 -decomposition, which has already been examined in Example 4.10.1 for adiabatic operation.

Obviously, stepwise increase of the cooling temperature from 20 to 29 °C increasingly leads to a strong increase of the maximum temperature, and for 26 °C (curve 3 in Figure 4.10.24), the reactor becomes sensitive to a further rise of the cooling temperature. Such a sensitivity to small fluctuations of operational parameters (here T_{cool}) is unwanted for accurate reactor control. In addition, for reactions with a high adiabatic temperature rise, temperatures may be reached that are higher than the maximum allowable temperature with regard to stability of reactants and products, reactor material, and catalyst deactivation. [In the example given above for the decomposition of H_2O_2 (Figures 4.10.22 and 4.10.23), ΔT_{ad} is only 58 K, which is no problem with regard to these factors.]

This parametric sensitivity of a batch reactor for an exothermic reaction (runaway behavior) can be inspected by means of criteria developed by Barkelew (Barkelew,

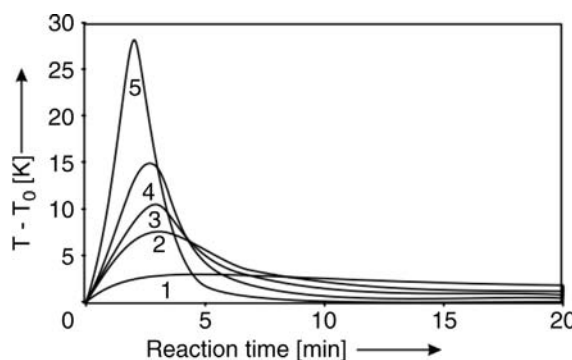


Figure 4.10.24 Typical evolution of reactor temperature in a cooled batch reactor; exothermic decomposition of H_2O_2 , $\Delta T_{ad} = 58 \text{ K}$; $T_0 = T_{cool}$; curves 1–5: $T_{cool} (\text{°C}) = 20, 25, 26, 27, \text{ and } 29$, which correspond $N_C/N_{ad} = 3.3, 1.7, 1.5, 1.3, \text{ and } 1$; $N_{ad} = 8.5$; data from Baerns *et al.* (2006).

1959), based on two dimensionless numbers, which are given for a first-order reaction as:

$$\nabla \quad N_c = \frac{U_h \left(\frac{A_h}{V_R} \right) \Delta T_{ad}}{k_{cool} c_{A,o} (-\Delta_R H)} \quad (\text{first-order reaction; for } n - \text{th use } c_{A,0}^n \text{ instead of } c_{A,0}) \quad (4.10.51)$$

$$\nabla \quad N_{ad} = \frac{\Delta T_{ad} E_A}{RT_{cool}^2} \quad (4.10.52)$$

N_c is a measure of the cooling capacity relative to heat production. N_{ad} accounts for the heat generation, and combines the dimensionless adiabatic temperature rise, $\Delta T_{ad}/T_{cool}$, and the temperature sensitivity, $E_A/(RT_{cool})$, also denoted as the *Arrhenius number* γ (introduced in Section 4.5.4.2). In practice, the values of N_{ad} are typically in the range 2–50; for example for a value of 20 with $T_{cool} = 200^\circ\text{C} = 473\text{ K}$, $E_A = 75\text{ kJ mol}^{-1}$ and $\Delta T_{ad} = 500\text{ K}$. Figure 4.10.25 shows the runaway diagram based on these two numbers and empirical correlations for N_c/N_{ad} as a function of N_{ad} as given in Baerns *et al.* (2006) for different reaction orders.

Barkelew arrived at this diagram by inspecting a large number of numerical integrations for a wide range of parameter values. The curves given in Figure 4.10.25 for four different reaction orders define bands that bound two regions, typically with an uncertainty of ± 0.15 in N_c/N_{ad} . If the conditions are such that they lead to a point above the curves, the reactor is insensitive to small fluctuations, but if situated under the curves then runaway is likely [details in Westerterp, van Swaaij, and Beenackers (1998); Baerns *et al.* (2006); Steinbach (1999)].

The numbers N_c and N_{ad} and the principle of the Barkelew diagram are derived as follows.

The critical reaction time during the course of reaction corresponds to the maximum temperature, such as that reached in the example of Figure 4.10.24 after about 2 min. Thus, a safety assessment has to focus on the prediction of the stability of this point in time, which is mathematically expressed by $dT/dt = 0$ for $T = T_{max}$.

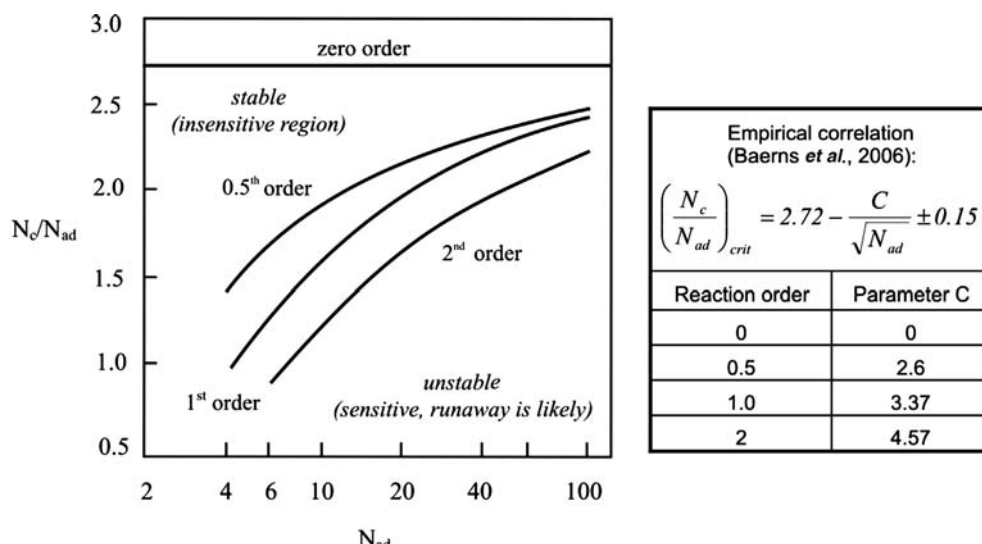


Figure 4.10.25 Runaway diagram according to Barkelew (1959) for $T_{cool} = T_0$ and correlations for different reactions orders [margin of deviation: 0.15; for an n -th order reaction use $c_{A,0}^n$ instead of $c_{A,0}$ in the denominator of N_c (Eq. (4.10.51)]. Adapted from Baerns *et al.* (2006).

Equations (4.10.44) and (4.10.50) then yield the first condition of a stable operation of a cooled batch reactor:

$$\frac{dT}{dt} = 0 \Rightarrow \frac{U_h A_h}{\rho_{\text{mol}} V_R c_p} (T_{\text{crit}} - T_{\text{cool}}) = \Delta T_{\text{ad}} k_0 e^{-\frac{E_A}{RT_{\text{crit}}}} (1 - X_A) \quad (4.10.53a)$$

Equation (4.10.53) expresses that if we reach the critical (maximum) reaction temperature, the heat released by the reaction just exactly equals the heat removed by cooling.

This safety requirement cannot be applied directly as an assessment criterion, as the time and conversion X_A at which T_{max} occurs is still unknown. For further inspection of the critical conditions, we set $X_A = 0$, that is, we neglect that in reality a conversion has taken place before T_{max} is reached. This simplifies the calculation and, furthermore, we are on the safe side, as the real heat release (for $X_A > 0$) is smaller at $T_{\text{max}} = T_{\text{crit}}$.

The second condition for a stable operation is then derived based on the consideration that if we reach T_{max} the increase of heat production with temperature (gradient with respect to T) must be lower than (and in the border case equal to) the gradient of the cooling term with T . In other words, a small rise in T should not increase the heat production more than the heat removal by cooling. If not, the temperature would rise further and a runaway would occur. For a batch reactor, this second condition of stable operation is mathematically derived by differentiation of Eq. (4.10.53) (with the simplifying assumption of $X_A \approx 0$):

$$\begin{aligned} \left. \frac{d\dot{Q}_{\text{removal}}}{dT} \right|_{T_{\text{crit}}} &= \left. \frac{d\dot{Q}_{\text{reaction}}}{dT} \right|_{T_{\text{crit}}} \Rightarrow \frac{d}{dT_{\text{crit}}} \left[\frac{U_h A_h}{\rho_{\text{mol}} V_R c_p} (T_{\text{crit}} - T_{\text{cool}}) \right] \\ &= \frac{d}{dT_{\text{crit}}} \left(\Delta T_{\text{ad}} k_0 e^{-\frac{E_A}{RT_{\text{crit}}}} \right) \end{aligned} \quad (4.10.54)$$

which leads to the second critical condition:

$$\frac{U_h A_h}{\rho_{\text{mol}} V_R c_p} = \Delta T_{\text{ad}} k_0 e^{-\frac{E_A}{RT_{\text{crit}}}} \left(\frac{E_A}{RT_{\text{crit}}^2} \right) = \Delta T_{\text{ad}} k_{\text{crit}} \left(\frac{E_A}{RT_{\text{crit}}^2} \right) \quad (4.10.55a)$$

Equation (4.10.55) cannot be solved exactly, as we do not know T_{crit} and thus also not the rate constant at T_{crit} . Thus, we need a solution by a further approximation (in addition to the simplification $X_A \approx 0$). At first, we derive an expression for k_{crit} as a function of k_{cool} :

$$\frac{k_{\text{crit}}}{k_{\text{cool}}} = \frac{k_0 e^{-\frac{E_A}{RT_{\text{crit}}}}}{k_0 e^{-\frac{E_A}{RT_{\text{cool}}}}} \Rightarrow k_{\text{crit}} = k_{\text{cool}} e^{-\frac{E_A}{R} \left(\frac{1}{T_{\text{crit}}} - \frac{1}{T_{\text{cool}}} \right)} = k_{\text{cool}} e^{\frac{E_A}{R} \left(\frac{T_{\text{crit}} - T_{\text{cool}}}{T_{\text{crit}} T_{\text{cool}}} \right)} \quad (4.10.56)$$

Secondly, we use an approximation for the term in brackets of the exponent in Eq. (4.10.56). Therefore, we insert Eq. (4.10.55) into Eq. (4.10.53) and assume that T_{crit}^2 approximately equals the term $T_{\text{crit}} T_{\text{cool}}$ and that $X_A \approx 0$. (e.g., for $T_{\text{crit}} = 650$ K and $T_{\text{cool}} = 600$ K, $T_{\text{crit}} T_{\text{cool}} = 390\,000$ K² T_{crit}^2 compared to $T_{\text{crit}}^2 = 422\,500$ K², with a deviation between the two values of only 8%). We then obtain:

$$! \quad (T_{\text{crit}} - T_{\text{cool}}) = \frac{RT_{\text{crit}}^2}{E_A} \approx \frac{RT_{\text{crit}} T_{\text{cool}}}{E_A} \Rightarrow \frac{(T_{\text{crit}} - T_{\text{cool}})}{T_{\text{crit}} T_{\text{cool}}} = \frac{R}{E_A} \quad (4.10.57)$$

By comparison of Eq. (4.10.56) with Eq. (4.10.57) we see that k_{crit} can be approximated by the term $e \times k_{\text{cool}}$ ($e = \text{Euler number, } 2.7183$). In other words, T_{crit} is reached if the reaction rate constant k_{crit} is 2.7 times higher than the value at T_{cool} . According to Eq. (4.10.57), this critical increase in temperature may be rather small, for example, only 40 K for a typical value of E_A for heterogeneously catalyzed reactions of 50 kJ mol⁻¹ and a temperature of 500 K.

Now we can derive an approximated solution of Eq. (4.10.55), if we (i) substitute k_{crit} by $e \times k_{\text{cool}}$, (ii) assume that T_{crit}^2 almost equals T_{cool}^2 , and (iii) use ΔT_{ad}

according to Eq. (4.10.48):

$$\underbrace{\frac{U_h \frac{A_h}{V_R} \Delta T_{ad}}{k_{cool}(-\Delta_R H) c_{A,0}}}_{N_c} \approx e \underbrace{\frac{\Delta T_{ad} E_A}{RT_{cool}^2}}_{e N_{ad}} \Rightarrow \frac{N_c}{N_{ad}} \approx e \quad (\text{for } X_{A,crit} \approx 0) \quad (4.10.58)$$

Comparison with the runaway diagram (Figure 4.10.25) shows that particularly for low values of N_{ad} (low value of E_A and/or of ΔT_{ad}) the criterion according to Eq. (4.10.58) is too strict, at least for reactions with a reaction order > 0 (see Topic 4.10.2). Hence, the reactor is already insensitive for values of N_c/N_{ad} of less than e , such as, for example, $N_c/N_{ad} = 1.5$ for $N_{ad} = 10$ (first-order reaction). This is because a negligible conversion ($X_A \approx 0$) up to the time when T_{max} is reached was assumed to derive Eq. (4.10.58). This assumption is of course an oversimplification, particularly with regard to low values of N_{ad} (and low values of E_A , respectively), as an increasing portion of conversion will already be achieved before the critical time and critical temperature are reached.

According to the runaway diagram (Figure 4.10.25), the first-order reaction system shown in Figure 4.10.24 with $N_{ad} = 8.5$ should be stable for $N_c/N_{ad} > 1.5$, which corresponds well to the curves 1–3. For the other curves, N_c/N_{ad} is already in the sensitive range (< 1.5), as also reflected by the temperature–time plot.

Topic 4.10.2 Critical condition for a thermal runaway for a zero-order reaction

For a zero-order reaction ($r_A = k^*$ in $\text{mol m}^{-3} \text{s}^{-1}$), the heat released by the reaction does not depend on the concentration and conversion. Thus the simplification of a negligible influence of the conversion on the runaway (to derive simple runaway criteria as shown above) is now not needed. Instead of Eqs. (4.10.53) and (4.10.55) we obtain for the first and second condition of a stable operation of a cooled batch reactor:

$$\begin{aligned} \frac{U_h A_h}{\rho_{\text{mol}} V_R c_p} (T_{crit} - T_{cool}) &= \Delta T_{ad} k_{crit}^* \frac{[(1 - X_A) c_{A,0}]^n}{c_{A,0}} \\ &= \Delta T_{ad} \frac{k_0^*}{c_{A,0}} e^{-\frac{E_A}{RT_{crit}}} \quad (\text{for } n = 0) \end{aligned} \quad (4.10.53b)$$

$$\frac{U_h A_h}{\rho_{\text{mol}} V_R c_p} = \Delta T_{ad} \frac{k_0^*}{c_{A,0}} e^{-\frac{E_A}{RT_{crit}}} \left(\frac{E_A}{RT_{crit}^2} \right) = \Delta T_{ad} k_{crit} \left(\frac{E_A}{RT_{crit}^2} \right) \quad (\text{for } n = 0) \quad (4.10.55b)$$

Both equations are valid for all values of conversion and not only for the simplification of $X_A \approx 0$ as in case of non-zero-order reactions. If we now follow the procedure given above to derive Eq. (4.10.58), we see that the critical condition $N_c/N_{ad} = e$ is the exact solution for a zero-order reaction for any value of N_{ad} (Figure 4.10.24). (Strictly speaking, we still have used as simplification that T_{crit}^2 approximately equals the terms $T_{crit} T_{cool}$ and T_{cool}^2 .)

4.10.3.2 Continuously Operated Non-isothermal Ideal Tank Reactor (CSTR)

For non-isothermal operation of a CSTR, the term “non-isothermal” only refers to the difference between the reaction temperature and the inlet temperature. For steady-state operation, the reaction temperature is constant at any time but higher (lower) than the feed temperature for an exothermic (endothermic) reaction. Thus, the heat and mass balances have to be examined simultaneously. The steady-state mass balance for an ideal CSTR, Eq. (4.10.17), for a first-order reaction with reactant A is given in terms of conversion and residence time as:

$$\mathbf{!} \quad r_A = \frac{(c_{A,in} - c_{A,out})}{\tau} = \frac{X_A c_{A,in}}{\tau} \quad (4.10.59)$$

The conversion given by Eq. (4.10.19) and the *Arrhenius equation* for the rate constant yield:

$$X_A = \frac{Da}{1 + Da} \quad \left(\text{with } Da = k\tau = k_0 e^{-\frac{E_A}{RT}} \tau \right) \quad (4.10.60)$$

The general steady-state heat balance of a CSTR with an exothermic reaction reads:

!

$$\underbrace{U_h A_h (T - T_{cool})}_{\dot{Q}_{cooling}} + \underbrace{\rho_{mol} c_p \dot{V} (T - T_{in})}_{\dot{Q}_{convection}} = \underbrace{r_A (-\Delta_R H) V_R}_{\dot{Q}_{reaction}} \quad (4.10.61)$$

$\underbrace{\dot{Q}_{cooling} + \dot{Q}_{convection}}_{\dot{Q}_{removal}}$

We will now discuss the two cases, adiabatic and cooled operation of a CSTR.

Adiabatic Operation of a CSTR For adiabatic operation, we have no cooling term, and Eqs. (4.10.59)–(4.10.61) yield:

$$\dot{Q}_{convection} = \rho_{mol} c_p \dot{V} (T - T_{in}) = \dot{Q}_{reaction} = \frac{Da}{1 + Da} c_{A,in} \dot{V} Z (-\Delta_R H) \quad (4.10.62)$$

or in dimensionless form, if we use the adiabatic temperature rise, Eq. (4.10.48), we obtain:

$$X_A = \frac{Da}{1 + Da} = \frac{\rho_{mol} c_p \dot{V}}{c_{A,in} \dot{V} Z (-\Delta_R H)} (T - T_{in}) = \frac{(T - T_{in})}{\Delta T_{ad}} \quad (4.10.63)$$

The graphical solution of Eq. (4.10.62) is shown in Figure 4.10.26. The reaction temperature T and the conversion X_A of the steady-state operation of the CSTR are characterized by the intersection of the sigmoidal heat production function and the heat removal line for a given value of T_{in} . This intersection yields the reaction temperatures for different inlet temperatures. Based on the value of T , we calculate the conversion, as X_A is given by the term $(T - T_{in})/\Delta T_{ad}$, Eq. (4.10.63), or by the term $\dot{Q}_{reaction}/\dot{Q}_{max, reactive}$, Figure 4.10.26.

For a low value of T_{in} (A in Figure 4.10.26), the increase in reaction temperature T and thus the conversion is small. If we now increase T_{in} up to a certain critical value (ignition temperature, B in Figure 4.10.26), a small increase in temperature would now lead to an increase in reaction temperature from C to a stable operation point according to point D, which is characterized by a high conversion and high temperature. For extinction, we have to decrease T_{in} to point F, which corresponds to the unstable point E, and the reaction temperature drops (to point H). Thus the reaction temperature passes through a hysteresis if we increase and subsequently decrease

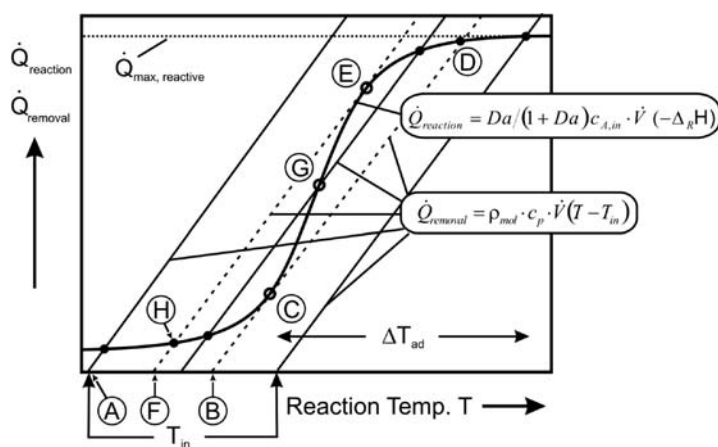


Figure 4.10.26 Heat production function (sigmoidal curve) and heat removal lines for an exothermic first-order reaction in an adiabatic CSTR.

T_{in} (CDEHC in Figure 4.10.26). Point G is unstable and never reached under normal circumstances as a small rise (decrease) in T would produce more (less) heat than is consumed by convection, and the mixture would heat up (cool down) further.

Examination of the unstable points C, E, and G leads to a general conclusion. The condition according to Eq. (4.10.62), $\dot{Q}_{reaction} = \dot{Q}_{removal}$, is necessary but not sufficient for a stable operation, and – analogously to a batch reactor and Eq. (4.10.54) – the second condition is:

$$\frac{d\dot{Q}_{removal}}{dT} \geq \frac{d\dot{Q}_{reaction}}{dT} \quad (4.10.64)$$

Cooled CSTR For a cooled CSTR, equations (4.10.59)–(4.10.61) lead to:

$$\underbrace{U_h A_h (T - T_{cool}) + \rho_{mol} c_p \dot{V} (T - T_{in})}_{\dot{Q}_{cooling}} + \underbrace{\dot{Q}_{convection}}_{\dot{Q}_{removal}} = \underbrace{\frac{Da}{1 + Da} c_{A,in} \dot{V} (-\Delta_R H)}_{\dot{Q}_{reaction}} \quad (4.10.65)$$

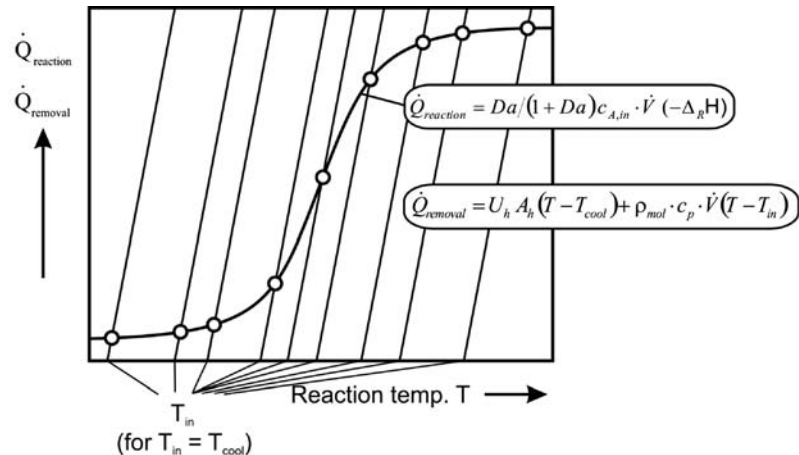
For the specific case of $T_{cool} = T_{in}$ we obtain:

$$(U_h A_h + \rho_{mol} c_p \dot{V}) (T - T_{in}) = \frac{Da}{1 + Da} c_{A,in} \dot{V} (-\Delta_R H) \quad (4.10.66)$$

The situation of an intensively cooled CSTR is shown in Figure 4.10.27 for different inlet temperatures. The slope of the heat removal lines was arbitrarily chosen to be so high that stable reaction temperatures T are reached for any value of T_{in} . In other words, the condition of Eq. (4.10.64) is always fulfilled, that is, the gradient of $\dot{Q}_{removal}$ is always higher than the corresponding gradient of $\dot{Q}_{reaction}$. Thus, if cooling is intensive enough, ignition can be avoided and all values of conversion can be realized by adjusting a respective value of T_{cool} .

Notably, the graphical method of analysis used above is only sufficient if the reactor operation can be regarded as a succession of pseudo-stationary states (static stability). The dynamic behavior and stability of a cooled CSTR, for example, after the onset of ignition, may lead to damped or undamped oscillations of T and c around a certain steady-state value (point D, Figure 4.10.26). In Topic 4.10.3, the static stability as well as the dynamic behavior is examined for the example of styrene polymerization. For mathematical details we refer to textbooks [e.g., Emig and Klemm (2005); Westerterp, van Swaaij, and Beenackers (1998)].

Figure 4.10.27 Heat production function (sigmoidal curve) and heat removal lines for an exothermic irreversible first-order reaction in a cooled CSTR.



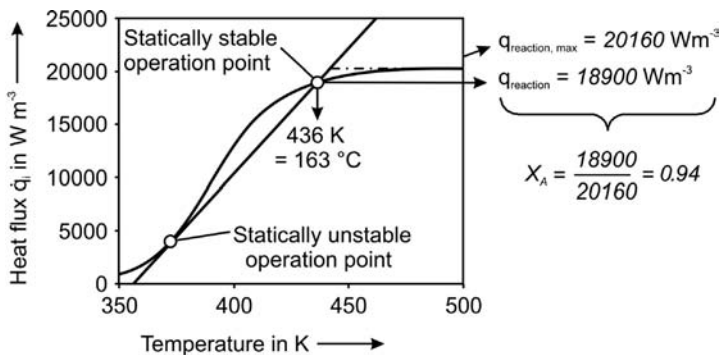


Figure 4.10.28 Static stability of a cooled CSTR for the example of styrene polymerization.

Topic 4.10.3 Static and dynamic stability of a cooled CSTR

The steady state heat balance of a cooled CSTR is given by Eq. (4.10.65):

$$\frac{U_h A_h}{V_R} (T - T_{\text{cool}}) + \rho_{\text{mol}} \frac{c_p \dot{V}}{V_R} (T - T_{\text{in}}) = \frac{Da}{(1+Da)} \frac{\dot{V} c_{A,\text{in}}}{V_R} (-\Delta_R H) \quad (4.10.65b)$$

and rewriting leads to:

$$\underbrace{\frac{U_h A_h}{V_R} (T - T_{\text{cool}}) + \frac{\rho_{\text{mol}} c_p}{\tau} (T - T_{\text{in}})}_{\dot{q}_{\text{removal}}} = \underbrace{\frac{k\tau}{(1+k\tau)} \frac{c_{A,\text{in}}}{\tau} (-\Delta_R H)}_{\dot{q}_{\text{reaction}}} \quad (4.10.65c)$$

Figure 4.10.28 shows the graphical solution for the example of styrene polymerization based on the data given in Table 4.10.5. For steady-state conditions, the reaction temperature is 436 K (163 °C) and the concentration and conversion of styrene are 540 mol m⁻³ and 94%, respectively.

Instead of the graphical solution (Figure 4.10.28), we can also calculate the critical reactor temperature T_{crit} by Eqs. (4.10.65c) and (4.10.64) as we know that T_{crit} is just reached for $d\dot{q}_{\text{removal}}/dT = d\dot{q}_{\text{reaction}}/dT$. Differentiation of Eq. (4.10.65c) and rearrangement yields:

$$\frac{Da_{\text{crit}}}{(1+Da_{\text{crit}})^2} = \frac{k(T_{\text{crit}})\tau}{[1+k(T_{\text{crit}})\tau]^2} \frac{\left(\frac{U_h A_h}{V_R} + \frac{\rho_{\text{mol}} c_p}{\tau}\right) RT_{\text{crit}}^2}{\frac{c_{A,\text{in}}}{\tau} (-\Delta_R H)} \frac{E_A}{(4.10.65d)}$$

With the values of Table 4.10.5 we get (after some trial and error) T_{crit} and Da_{crit} :

$$\frac{7.45 \times 10^{11} e^{-\frac{10719 \text{ K}}{T_{\text{crit}}}}}{\left(1 + 7.45 \times 10^{11} e^{-\frac{10719 \text{ K}}{T_{\text{crit}}}}\right)^2} = \frac{T_{\text{crit}}^2}{904370 \text{ K}^2} \Rightarrow T_{\text{crit}} = 372 \text{ K} \Rightarrow Da_{\text{crit}} = 0.23$$

Table 4.10.5 Parameters of styrene polymerization in a cooled CSTR (Wittmer *et al.*, 1965).

Parameter	Value
$c_{A,\text{in}}$	8689 mol m ⁻³
τ	32100 s
k_0	$2.32 \times 10^7 \text{ s}^{-1}$
E_A	89120 J mol ⁻¹
$U_h A_h/V_R$	$189 \text{ J K}^{-1} \text{ s}^{-1} \text{ m}^{-3}$
$\rho_{\text{mol}} c_p$	$1.56 \times 10^6 \text{ J K}^{-1} \text{ m}^{-3}$
$\Delta_R H$	$-74057 \text{ J mol}^{-1}$
T_{in}	303 K (30 °C)
T_{cool}	370 K (97 °C)

The conversion is 19% and the heat flux of 3.8 kW m^{-3} ($0.19 \times 20 = 160 \text{ W m}^{-3}$, Figure 4.10.28).

The equations governing the *dynamic* behavior of a CSTR and a first-order reaction with respect to reactant A are the mass balance:

$$\frac{dc_A}{dt} = \frac{(c_{A,\text{in}} - c_{A,\text{out}})}{\tau} - r_A = \frac{X_A c_{A,\text{in}}}{\tau} - k_0 e^{\frac{-E_A}{RT}} c_{A,\text{out}} \quad (4.10.67)$$

and the energy balance:

$$\begin{aligned} \rho_{\text{mol}} V_R c_p \frac{dT}{dt} = & -U_h A_h (T - T_{\text{cool}}) - \rho_{\text{mol}} \dot{V} c_p (T - T_{\text{in}}) \\ & + k_0 e^{\frac{-E_A}{RT}} c_{A,\text{out}} (-\Delta_R H) V_R \end{aligned} \quad (4.10.68)$$

Both equations are extensions of Eqs. (4.10.59) and (4.10.61) for non-steady-state conditions, that is, the accumulation terms for mass (dc_A/dt) and energy (dT/dt) are considered.

The numerical solution of the coupled differential Eqs. (4.10.67) and (4.10.68) is shown in Fig. 4.10.29. For the given example, the condition for dynamic stability is not met (details in Emig and Klemm, 2005; Westerterp, van Swaaij, and Beenackers, 1998; Wittmer *et al.*, 1965). Instead, the reactor operates in a fixed limit cycle around the statically stable point (Figures 4.10.29–31), and the temperature and concentration changes with a fixed frequency and amplitude around the respective values of the stable operating point.

If we start, for example, at point A (Figure 4.10.29b) c_A and T are higher than the statically stable values. Thus, the rate is too high, the mixture is heated up further, and the temperature increases and simultaneously c_A is reduced. When point B is reached, the rate has been reduced so much that the temperature starts to decrease by cooling, but the rate is still so high that the consumption of reactant A compensates the supply of fresh A by the feed. At point C, c_A reaches a minimum. The rate is now so low that the concentration starts to increase, and the mixture is further cooled by the cold feed and the cooling medium until point D is reached. Now sufficient A has been accumulated to increase the rate to an extent that heating starts again until point A is reached, and the cycle starts again.

Dynamic behavior and oscillations are also found in nature, such as predator-prey interactions. A classical example of interacting populations is shown in Figure 4.10.30 for the snowshoe hare and the Canadian lynx, a specialist predator. The lynx–hare

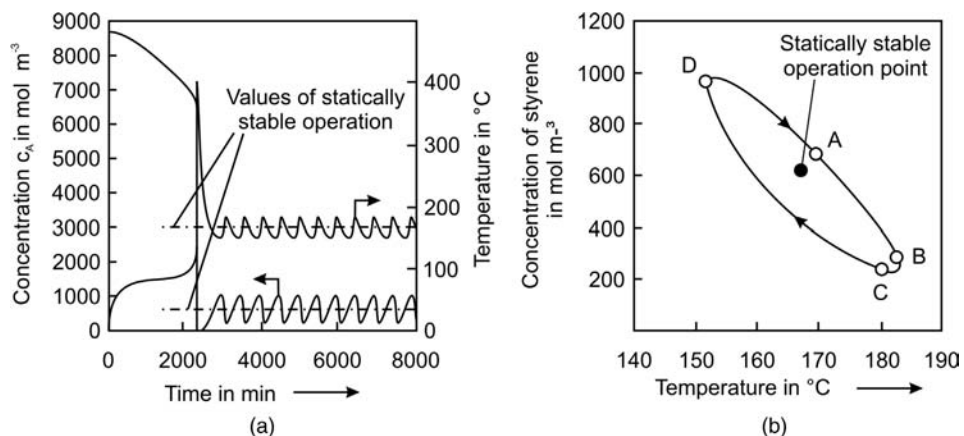


Figure 4.10.29 Dynamic behavior of a cooled CSTR for the example of styrene polymerization: (a) oscillations of T and c_A ; (b) limit cycle in a c_A - T plot.

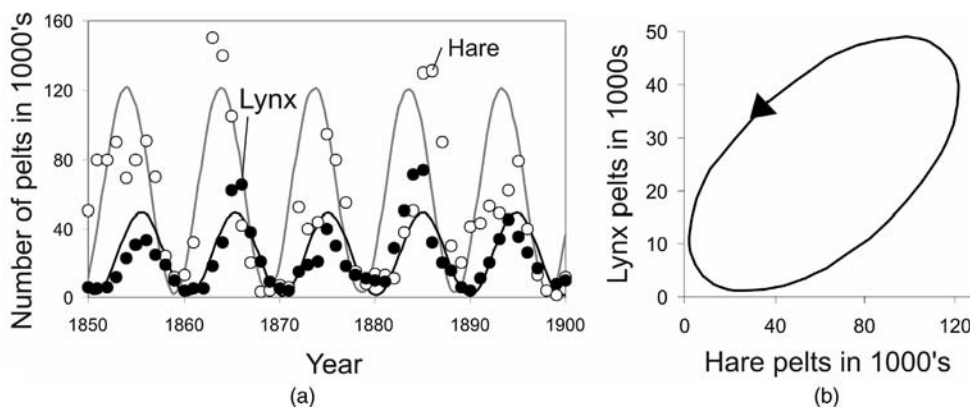


Figure 4.10.30 (a, b) Oscillations in population density: changes in the abundance of the lynx and snowshoe hare, indicated by the number of pelts (per year) received by the Hudson Bay Company from 1885–1900 [(a) oscillations of populations with time, (b) limit cycle].

cycle was first discovered from harvest records of the Hudson's Bay Company dating back to the early 1800s. The number of snowshoe hares peaks approximately every ten years and the number of lynxes follow the same pattern with a lag of typically 1–2 years. The fluctuations can be drastic, with hare abundance reaching 230 km^{-2} during the peaks and crashing to 12 km^{-2} during the lows.

The oscillations in the two populations result from the difference in phases between rabbit and lynx reproduction. The rabbits reproduce because their main food source (grassland) is plentiful. The lynx population will also increase, but only after the rabbit population has grown. Once the lynx population becomes too high, rabbits will be eaten more rapidly than new rabbits are born, and their population will begin to decrease, which in turn will lead to a decrease in the lynx population. The rabbit population can then begin to rise again. Thus there will be a time lag between changes in the two populations.

Vito Volterra (1860–1940), an Italian mathematician, and Alfred J. Lotka (1880–1949), an American mathematical biologist, formulated at about the same time the so-called Lotka–Volterra model of predator–prey population dynamics. The assumptions of this model are:

- The predator species is totally dependent on the prey species as its only food supply.
- The prey has an unlimited food supply and no threat to its growth other than the predator.

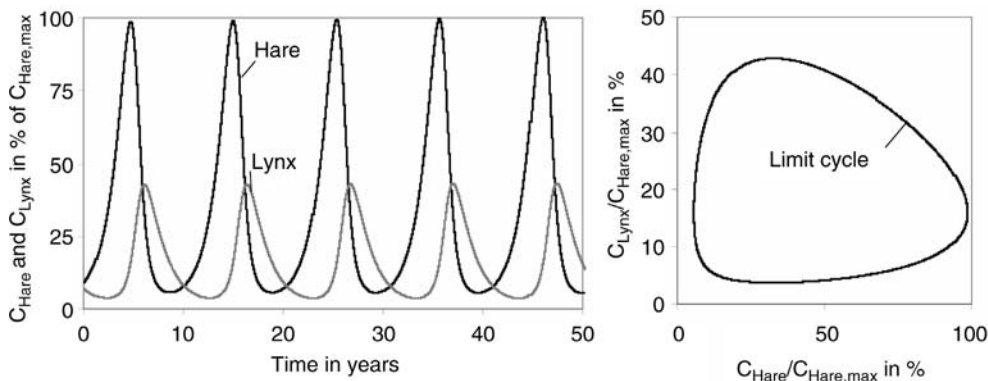


Figure 4.10.31 (a, b) Modeling of cyclic oscillations in population density by the Lotka–Volterra model of predator–prey population dynamics (example of changes in the abundance of the lynx and the snowshoe hare).

- If there were no predators, the prey species grows exponentially, that is, if c_{prey} is the size of the prey population at time t , then we would have $\frac{dc_{\text{prey}}}{dt} = Ac_{\text{prey}}$
- But there are predators, which must account for a negative component in the prey growth rate. The rate at which predators encounter prey is jointly proportional to the sizes of both populations, and a fixed proportion of encounters leads to the death of the prey.

These assumptions lead to changes of the prey (here e.g., hares) population:

$$\frac{dc_{\text{hare}}}{dt} = Ac_{\text{hare}} - Bc_{\text{hare}}c_{\text{lynx}}$$

Now we consider the predator (lynx) population. The natural growth rate is a composite of birth and death rates, both presumably proportional to population size. In the absence of food, there is no energy supply to support the birth rate and the population would die out at a rate proportional to its size, that is, we would find $\frac{dc_{\text{predator}}}{dt} = -Cc_{\text{predator}}$. But there is a food supply for the predator: the prey. Consequently, the energy to support the growth of the predator population is proportional to both the deaths of the preys and the number of (from the perspective of the lynx) "successful" encounters of lynxes and hares. So we have:

$$\frac{dc_{\text{lynx}}}{dt} = -Cc_{\text{lynx}} + Dc_{\text{hare}}c_{\text{lynx}}$$

Thus, the Lotka–Volterra model consists of these two linked differential equations that cannot be separated from each other and that cannot be solved in closed form. The numerical solution, which comes close to the real dynamics of the changes in the abundance of the lynx and snowshoe hare (Figure 4.10.30) is shown in Figure 4.10.31. For the arbitrarily chosen value of the maximum hare population of $c_{\text{hare,max}} = 100$ (a.u.), the parameters are (unit a^{-1}): $A = 0.8$, $B = 0.05$, $C = 0.6$, $D = 0.0184$, $c_{\text{hare},0} = 7$ (a.u.), $c_{\text{lynx},0} = 9$ (a.u.).

4.10.3.3 Continuously Operated Non-isothermal Ideal Tubular Reactor

The model of a non-isothermal wall-cooled ideal tubular reactor discussed in the following neglects radial gradients of temperature and concentration, and only considers axial gradients. The control space is a slab with the differential length dz in the direction of flow. For steady-state operation, the mass balance for a differential element $dV_R (= zdA_{t,int})$ and a constant volume reaction of reactant A is given by:

$$\bullet \quad \frac{d\dot{n}_A}{dV_R} = \dot{V} \frac{dc_A}{dV_R} = \frac{\dot{V}}{A_{t,int}} \frac{dc_A}{dz} = u_s \frac{dc_A}{dz} = \frac{dc_A}{d\tau} = -r \quad (4.10.69)$$

and for the heat balance we have to consider the following small differential values $d\dot{Q}$:

$$\underbrace{\rho_{\text{mol}} c_p \dot{V} dT}_{d\dot{Q}_{\text{convection}}} + \underbrace{U_h (T - T_{\text{cool}}) dA_{t,int}}_{d\dot{Q}_{\text{cooling}}} = \underbrace{(-\Delta_R H) r_A dV_R}_{d\dot{Q}_{\text{reaction}}} \quad (4.10.70)$$

Rewriting Eq. (4.10.70) with the internal surface per volume of reactor ($dA_{t,int}/dV_R = 4/d_{int}$), the superficial fluid velocity ($u_s = 4\dot{V}/\pi d_{int}^2$), and substitution of the rate r_A by $c_{A,\text{in}} dX_A/d\tau$ leads to the heat balance in terms of the heat flow per unit volume:

$$\bullet \quad \underbrace{\rho_{\text{mol}} c_p u_s \frac{dT}{dz}}_{d\dot{q}_{\text{convection}}} + \underbrace{\frac{4U_h}{d_{int}} (T - T_{\text{cool}})}_{d\dot{q}_{\text{cooling}}} = \underbrace{(-\Delta_R H) c_{A,\text{in}} \frac{dX_A}{d\tau}}_{d\dot{q}_{\text{reaction}}} \quad (4.10.71)$$

The cooling term U_h has to consider three parameters, (i) radial heat transfer from the fluid to the internal surface of the tube, (ii) conduction of heat through the wall, and (iii) heat transfer from the external surface to the cooling medium.

These three thermal resistances are combined in the thermal transmission coefficient U_h , already introduced in Section 3.2.1.2:

$$U_h = \left[\frac{1}{\alpha_{int}} + \frac{d_{int}}{2\lambda_{wall}} \ln \left(\frac{d_{ex}}{d_{int}} \right) + \frac{1}{\alpha_{ex} d_{ex}} \right]^{-1} \quad (3.2.31)$$

where α_{int} and α_{ex} are the internal and external heat transfer coefficients ($\text{W m}^{-2} \text{K}^{-1}$) and λ_{wall} is the thermal conductivity of the wall material ($\text{W m}^{-1} \text{K}^{-1}$). In most cases, the thermal resistance of the wall is negligible ($d_{int}/\lambda_{wall} \ll 1/\alpha_{int}$ or $1/\alpha_{ex}$), and for thin walls we obtain:

$$U_h \approx \left(\frac{1}{\alpha_{int}} + \frac{1}{\alpha_{ex}} \right)^{-1} \quad \left(\text{for } d_{ex} \approx d_{int} \text{ and } \frac{d_{int}}{\lambda_{wall}} \ll \frac{1}{\alpha_{int}} \text{ and } \frac{1}{\alpha_{ex}} \right) \quad (4.10.72)$$

In the following, we assume this case and denote the diameter of the reactor simply as d_R .

In many cases, the thermal resistance of internal heat transfer, $1/\alpha_{int}$, is dominant compared to external heat transfer, $1/\alpha_{ex}$, for example, if the tube is externally cooled by boiling water.

If we use Eq. (4.10.71), we have to keep in mind that pronounced radial temperature gradients may be present in cooled tubular reactors, even if the gradient is small or confined to a small region near the wall. Thus, Eq. (4.10.71) is strictly speaking only valid for an ideal PFR with a uniform radial temperature, but for the subsequent examination of the basic principles of the behavior of non-isothermal tubular reactors we neglect this aspect and use an overall heat transfer coefficient U_h . The more complicated radial heat transfer in the case of pronounced radial temperature gradients in tubular reactors such as packed bed reactors will be treated in Section 4.10.7.3. Subsequently, we inspect the adiabatic operation of a tubular reactor first. Thereafter, we take a closer look at a wall-cooled PFR.

Adiabatic Operation of a PFR For adiabatic operation, the term $4U_h/d_t(T - T_{cool})$ is zero, and Eq. (4.10.71) yields:

$$\rho_{mol} c_p u_s \frac{dT}{dz} = \rho_{mol} c_p \frac{dT}{d\tau} = (-\Delta_R H) c_{A,in} \frac{dX_A}{d\tau} \quad (4.10.73)$$

and by rearranging we obtain:

$$\frac{dX_A}{dT} = \frac{\rho_{mol} c_p}{(-\Delta_R H) c_{A,in}} \quad (4.10.74)$$

The term on the right-hand side of Eq. (4.10.74) is constant if we assume that the reaction enthalpy, $\Delta_R H$, the heat capacity, c_p , and the density of the reaction mixture, ρ_{mol} , are constant, that is, the influence of temperature and changing composition of the reaction mixture are negligible. We then obtain a linear relation between the rise in temperature and the conversion:

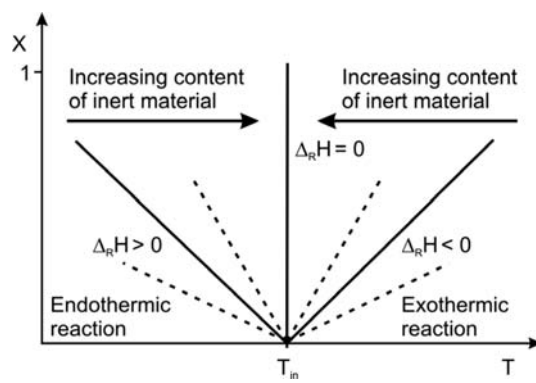
$$\frac{dX_A}{dT} \approx \frac{X_A}{(T - T_{in})} \Rightarrow X_A = (T - T_{in}) \frac{\rho_{mol} c_p}{(-\Delta_R H) c_{A,in}} \quad (4.10.75)$$

For complete conversion ($X_A = 1$), the temperature rise is maximized, denoted as adiabatic rise in temperature, ΔT_{ad} , and Eq. (4.10.75) may be rewritten as:

$$X_A = \frac{(T - T_{in})}{\Delta T_{ad}} \quad \left[\text{with } \Delta T_{ad} = \frac{(-\Delta_R H) c_{A,in}}{\rho_{mol} c_p} \right] \quad (4.10.76)$$

Conversion in an adiabatic PFR as a function of temperature is plotted in Figure 4.10.32 for different values of $\Delta_R H$. The slope of the lines (dX_A/dT) equals $1/\Delta T_{ad}$ [Eq. (4.10.76)]. For exothermic reactions, the adiabatic temperature rise can easily exceed values of several hundred degrees. Thus, for safety reasons, an efficient limit of the rise in temperature is essential such as, for example, by a reduction of the initial concentration or by using a cooled PFR.

Figure 4.10.32 Correlation of conversion and temperature for an exothermic and endothermic irreversible reaction in an adiabatic PFR ($T_{in} = T_0$). Adapted from Levenspiel (1999).



Wall-Cooled Ideal Tubular Reactor A simple form of the heat balance of a cooled PFR is derived by insertion of the adiabatic rise in temperature, Eq. (4.10.76), in Eq. (4.10.71):

$$\frac{dT}{dz} = \frac{4U_h}{\rho_{mol}c_p u_s d_R} (T_{cool} - T) + \frac{\Delta T_{ad}}{u_s} \frac{dX_A}{d\tau} \quad (4.10.77)$$

For subsequent discussion, we assume a first-order reaction with respect to the reactant A, and thus the differential mass balance in terms of conversion is:

$$\frac{dX_A}{d\tau} = k \frac{c_A}{c_{A,in}} = k_0 e^{-\frac{E_A}{RT}} (1 - X_A) \quad (4.10.78)$$

Figure 4.10.33 shows schematically typical conversion and temperature profiles of a tubular reactor for different cooling intensities.

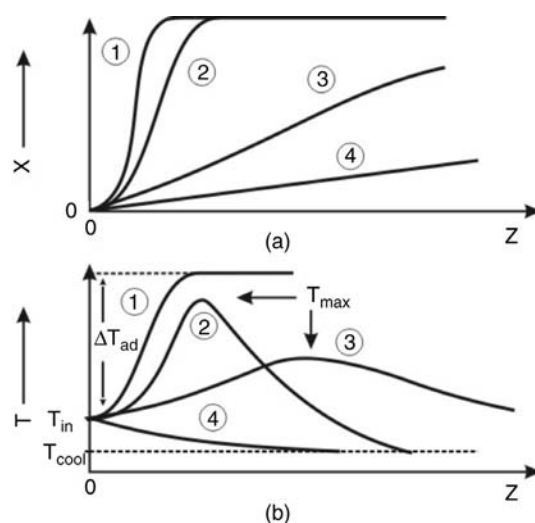
Analysis of the parametric sensitivity of a cooled PFR is exactly analogous to the analysis of a batch reactor (Section 4.10.3.1) if we replace the reaction time by the residence time.

The critical point in a tubular reactor corresponds to the axial position at which the maximum temperature is reached, and is characterized by the condition $dT/dz = 0$. This condition and the combination of the mass and heat balance, Eqs. (4.10.78) and (4.10.77), yields:

$$\left. \frac{dT}{dz} \right|_{T=T_{crit}} = 0 = \frac{4U_h}{\rho_{mol}c_p u_s d_R} (T_{cool} - T_{crit}) + \frac{\Delta T_{ad}}{u_s} k_0 e^{-\frac{E_A}{RT_{crit}}} (1 - X_A) \quad (4.10.79)$$

This equation shows that at the location of the critical maximum reaction temperature the heat released by the reaction equals the heat removal by wall-cooling. The

Figure 4.10.33 Evolution of temperature and conversion in a tubular reactor (1: adiabatic operation, 2–4: cooled reactor with increasing cooling intensity, for example, a decreasing diameter).



remaining problem to derive a safety criterion is that the location and, thus, the conversion at this critical position are unknown. However, to derive a criterion for runaway, we set $X_A \approx 0$, which simplifies the calculation. Furthermore, we are on the safe side, as for $X_A > 0$ the concentration at the critical point of T_{\max} is smaller and, thus, also the “real” rate of heat generation.

The second condition for stable operation derives from the condition that the increase of the heat generation with temperature must be lower than the increase of heat removal. Mathematically, this corresponds to the differentiation (d/dT) of Eq. (4.10.79) for $X_A \approx 0$:

$$\frac{4U_h}{\rho_{\text{mol}}c_p d_R} = k_0 e^{-\frac{E_A}{RT_{\text{crit}}}} \frac{\Delta T_{\text{ad}} E_A}{RT_{\text{crit}}^2} = k_{\text{crit}} \frac{\Delta T_{\text{ad}} E_A}{RT_{\text{crit}}^2} \quad (4.10.80)$$

Equation (4.10.80) cannot be solved exactly, as the critical temperature T_{crit} and, thus, also the value of the rate constant at the axial location of T_{crit} are unknown. Thus, we need a solution by approximation. This method has already been examined in Section 4.10.3.1 for a batch reactor, and we recall them here in a condensed form.

At first, we derive an expression for k_{crit} as a function T_{crit} and k_{cool} :

$$k_{\text{crit}} = k_{\text{cool}} e^{\frac{E_A}{R} \left(\frac{T_{\text{crit}} - T_{\text{cool}}}{T_{\text{crit}} T_{\text{cool}}} \right)} \quad (4.10.81)$$

Secondly, we derive an approximation for the term in brackets in Eq. (4.10.81) by insertion of Eq. (4.10.80) into Eq. (4.10.79) for $X_A \approx 0$, thereby assuming that T_{crit}^2 almost equals $T_{\text{crit}} T_{\text{cool}}$:

$$! \quad \frac{(T_{\text{crit}} - T_{\text{cool}})}{T_{\text{crit}} T_{\text{cool}}} = \frac{R}{E_A} \quad (4.10.82)$$

By comparison of Eq. (4.10.82) with Eq. (4.10.81) we see that k_{crit} can be approximated by the term $e k_{\text{cool}}$ ($e = 2.7183$). Now we can derive the final form of the approximated solution of Eq. (4.10.80), if we (i) substitute k_{crit} by $e k_{\text{cool}}$, and (ii) assume that $(T_{\text{crit}})^2$ is approximately $(T_{\text{cool}})^2$:

$$\underbrace{\frac{U_h}{k_{\text{cool}}(-\Delta_R H)c_{A,0}} \frac{4}{d_R} \Delta T_{\text{ad}}}_{N_c} \approx \underbrace{e \frac{\Delta T_{\text{ad}} E_A}{RT_{\text{cool}}^2}}_{e N_{\text{ad}}} \Rightarrow \frac{N_c}{N_{\text{ad}}} \approx e \quad (\text{for } X_{A,\text{crit}} \approx 0) \quad (4.10.83)$$

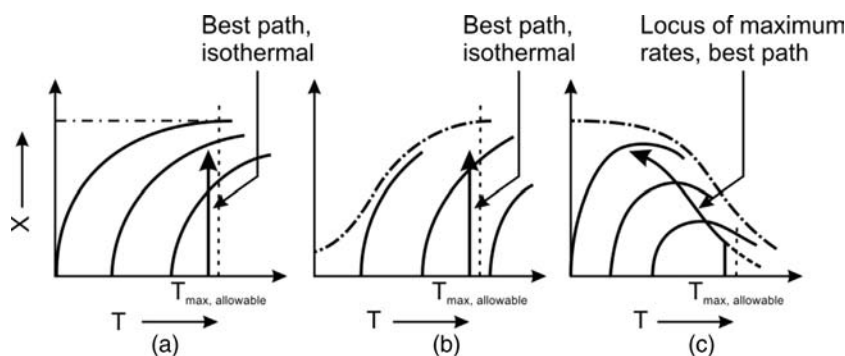
Recalling the corresponding term for N_c of a batch reactor:

$$N_c = \frac{A_h \frac{U_h}{V_R} \Delta T_{\text{ad}}}{k_{\text{cool}}(-\Delta_R H)c_{A,0}} \quad (4.10.51)$$

shows that both equations for N_c are identical, if we consider that the specific cooling area in a batch reactor is given by the term A_h/V_R and for a PFR by $4/d_R$. Note that for a heterogeneously catalyzed reaction we have to use the term $k_{m,\text{cool}} \rho_b$ instead of k_{cool} as the rate constant k_m ($\text{m}^3 \text{kg}^{-1} \text{s}^{-1}$) is related to the mass of catalyst and has to be converted with the bulk density of the fixed bed (ρ_b in kg m^{-3}) into a volume related rate constant.

Based on N_c and N_{ad} , we estimate the conditions of a safe and insensitive operation by the runaway diagram (Figure 4.10.25). For a high value of N_c , and thus for a safe operation, we need a high ratio of the cooling area to the reactor volume (for a tubular reactor $4/d_R$). For technical reactors with diameters in the range of meters, this term approaches zero, and the reactor operates in adiabatic mode. Thus wall-cooling only makes sense for a small tubular reactor, and then a sufficient production rate can only be realized by using multi-tubular reactors. Detailed discussion of the thermal stability of cooled multi-tubular reactors is given in Section 6.11 for Fischer-Tropsch synthesis and in Section 6.13 for the oxidation of *o*-xylene.

Figure 4.10.34 Operating lines for minimum reactor size for reactions: (a) irreversible, (b) reversible endothermic, and (c) reversible exothermic (lines indicate constant rates with increasing values from left to right, dash-dotted line: equilibrium). Adapted from Levenspiel (1999).



4.10.3.4 Optimum Operating Lines of Continuous Ideal Non-isothermal Reactors

The optimum temperature progression minimizes the residence time τ for a given conversion. This optimum may be achieved in some cases by isothermal operation and in others by changing the temperature, for example, along the length of a tubular reactor. Even if the optimal progression cannot be reached in a reactor with justifiable expenditure, knowledge of the ideal progression allows us to estimate how far the reactor departs from this ideal, as inspected in this chapter for adiabatic and non-adiabatic operation of a PFR and a CSTR.

For irreversible reactions, the rate always increases with temperature at any composition, so the highest rate is reached at the highest allowable temperature (Figure 4.10.34a). This temperature is set by the materials of construction, the thermal stability of reactants and products, and by the potentially increasing amounts of unwanted side products.

For reversible endothermic reactions, a rise in temperature increases both the equilibrium conversion and the rate of reaction (Figure 4.10.34b). Thus, as with irreversible reactions, the highest allowable temperature should be used.

The situation is different for exothermic reversible reactions (Figure 4.10.34c), as now two opposing factors are at work. The rate of the forward reaction speeds up with temperature but the maximum attainable conversion decreases. Consequently, we start at a high temperature and then reduce the temperature as conversion rises. The optimum operation line is found by connecting the maxima of the rate curves (Example 4.10.2).

Example 4.10.2: Conversion chart and locus of maximum rates (exothermic reversible reaction)

As an example, we take an exothermic reversible reaction with the following kinetics:

$$\begin{aligned} r_A &= k_1 c_A - k_{-1} c_B \\ k_1 &= 34 \times 10^6 \text{ min}^{-1} e^{-\frac{48900}{RT}} \\ k_{-1} &= 1.84 \times 10^{18} \text{ min}^{-1} e^{-\frac{124200}{RT}} \end{aligned}$$

For any combination of X_A and T we calculate the rate, for example, for $X_A = 0.5$, 50°C , and $c_{A,0} = 1 \text{ mol l}^{-1}$ we get $r_A = 0.2 \text{ mol l}^{-1} \text{ min}^{-1}$. The whole chart, as depicted in Figure 4.10.35, is prepared based on many of such calculations. If we then plot the lines with constant r_A , we obtain the locus of the maximum rates for a given X_A and the value of T_{opt} .

Optimum Operation Line for Adiabatic Operation The relations between conversion, temperature, and rate of reversible reactions in an adiabatic PFR and a CSTR are given schematically in Figure 4.10.36. For a constant value of c_p , we obtain:

$$X_A = \frac{\dot{n}c_p \Delta T}{\dot{n}_{A,\text{in}}(-\Delta_R H)} \quad (4.10.84)$$

and therefore straight lines in a plot of X_A versus T . Therefore, whatever X_A is at any point in the reactor, the temperature is at its corresponding value. For plug flow the fluid moves progressively along the operating line, for mixed flow we get an immediate jump to the final value.

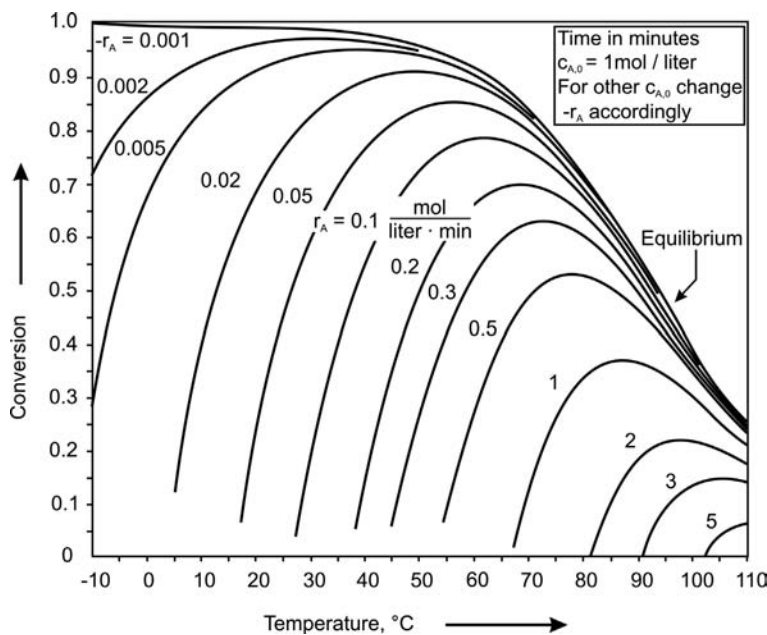


Figure 4.10.35 Rate conversion chart for a reversible reaction [based on the above given kinetic equations and $c_{A,0} = 1 \text{ mol l}^{-1}$; example taken from Levenspiel (1999)].

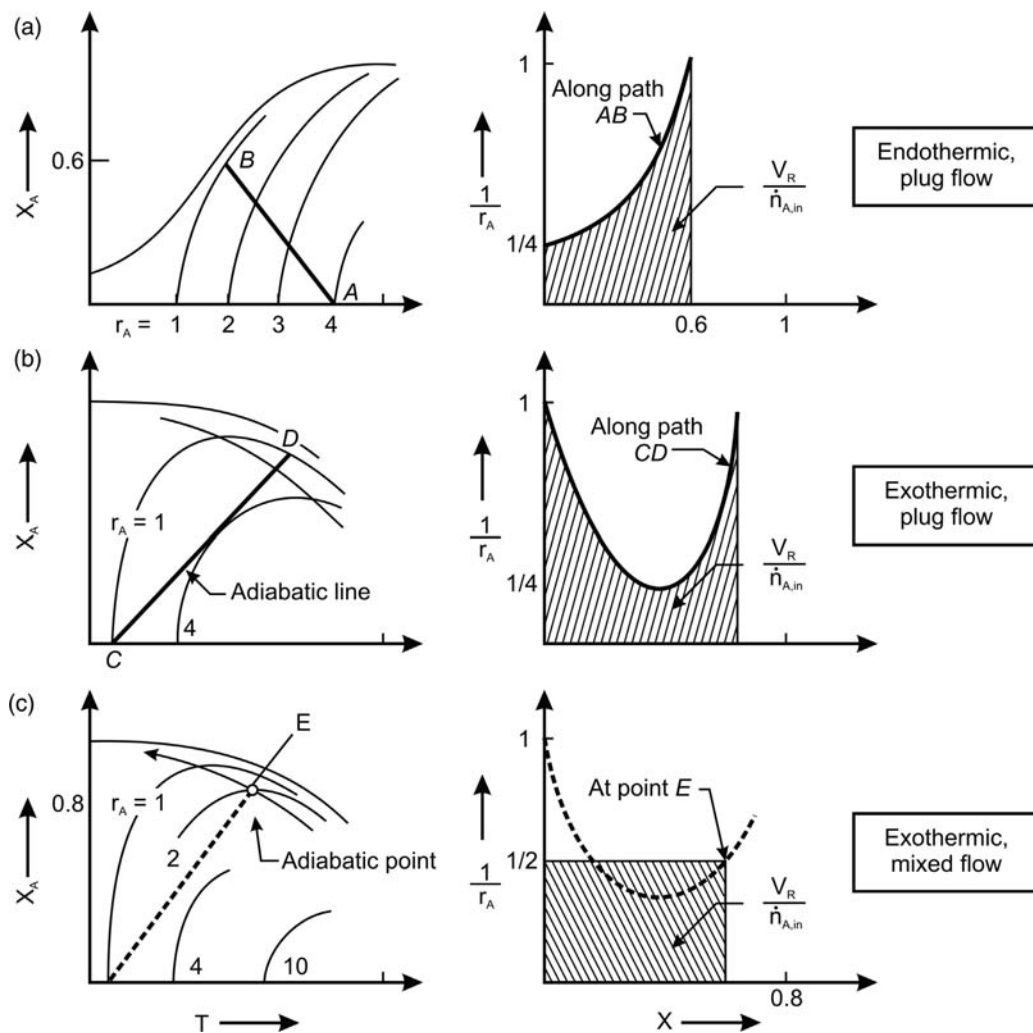
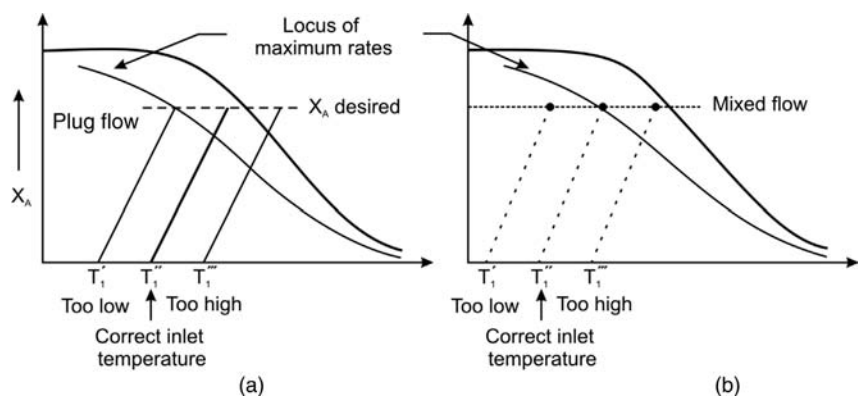


Figure 4.10.36 Calculation of reactor size for adiabatic operation of a PFR and a CSTR. Adapted from Levenspiel (1999).

Figure 4.10.37 Optimum adiabatic operation line to minimize the size of a PFR (a) and a CSTR (b). Adapted from Levenspiel (1999).



The size of a continuous reactor V_R and the residence time τ , respectively, needed for a given duty are found as follows (assuming steady state and conversion of reactant A). The ratio of the reaction volume to the feed rate of reactant A is deduced from:

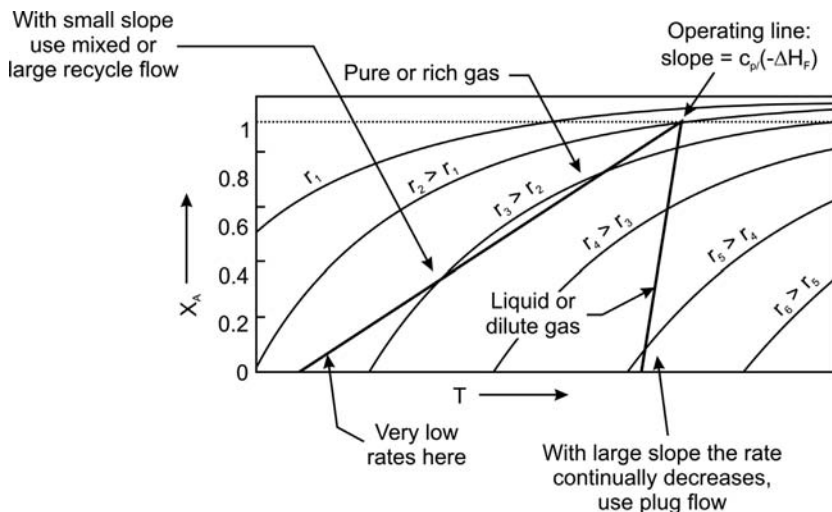
$$r_A = -\frac{dc_A}{d\tau} = c_{A,in} \frac{dX_A}{d\tau} \Rightarrow \int_0^{X_A} \frac{dX_A}{r_A} = \frac{\tau}{c_{A,in}} = \frac{V_R}{\dot{V}c_{A,in}} = \frac{V_R}{\dot{n}_{A,in}} \quad (4.10.85)$$

Hence, the integral of the function $1/r_A$ versus X_A is needed. For plug flow we calculate the rate for various X_A along the adiabatic operating line, prepare the $1/r_A$ versus X_A plot, and integrate graphically. For mixed flow we simply use the rate at the conditions in the reactor.

The best adiabatic operation of a PFR is found by shifting the operation line to the inlet temperature where the mean rate has the highest value. For endothermic reactions, we start at the highest allowable temperature (Figure 4.10.36a). For exothermic reactions a trial and error search is needed to find the optimal inlet temperature that minimizes the term $V_R/\dot{n}_{A,in}$, as shown schematically in Figure 4.10.37a. A CSTR with a uniform reaction temperature should be always operated on the locus of the maximum rates (Figure 4.10.37b).

The choice of the best reactor type to minimize $V_R/\dot{n}_{A,in}$ by $X_A - T$ graphs is explained by Example 4.10.3 for a reversible exothermic reaction. General rules are as follows. If the rate progressively decreases with X_A , then use plug flow. We have this situation for endothermic reactions (Figure 4.10.36a) and almost isothermal reactions. For exothermic reactions with a large temperature rise (low slope of X_A versus T), the temperature effect on the rate (increase of rate constant) initially compensates the decreasing concentration, but then the rate passes a maximum at some intermediate X_A and then falls (Figures 4.10.36b and 4.10.38). This effect may be even more pronounced if the reaction is reversible. Then a CSTR is the best

Figure 4.10.38 $X-T$ chart for exothermic reaction and adiabatic operation: mixed flow (CSTR) is best for a large temperature rise and plug flow for a small rise. Adapted from Levenspiel (1999).



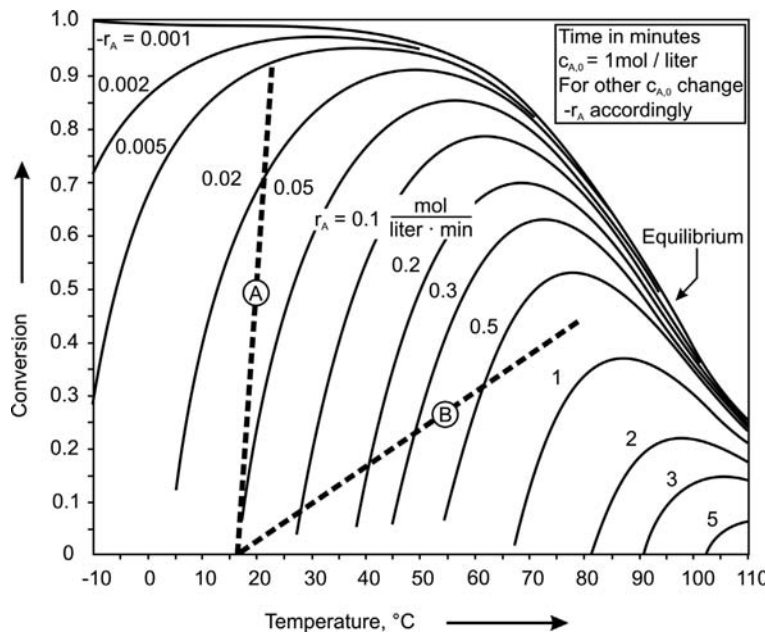


Figure 4.10.39 Conversion temperature chart for an exothermic reaction: mixed flow is best for a large temperature rise (B) and plug flow is best for a system close to isothermal conditions (A) [example taken from Levenspiel (1999)].

choice. Figure 4.10.38 shows this situation: one where plug flow is best and the other where mixed flow is best. The slope of the operation line determines which case one has at hand.

Example 4.10.3: Choice of best reactor type for adiabatic operation (reversible exothermic reaction)

The question of whether plug or mixed flow is best for an adiabatic operation can be shown by recalling the example already shown in Figure 4.10.32. In Figure 4.10.39 two cases are plotted. Case A stands for a large value of the slope, and the rate progressively decreases with increasing conversion, which favors plug flow. Case B stands for a

small value of the slope, and the rate progressively increases with X (at least if the distance to equilibrium is still large), which favors mixed flow. Therefore, for adiabatic operation, mixed flow is best for small values of $\dot{n}c_p / (\dot{n}_{A,in} |\Delta_R H|)$ and plug flow is best for large values (many inert etc.).

Optimum Operation Line for Non-adiabatic Operation of a PFR For a reversible exothermic reaction in a PFR, the optimum operating line (Figure 4.10.34c) can only be reached if we remove heat along the tube, as examined in Example 4.10.4.

Example 4.10.4: Optimum path to minimize the volume of a PFR (exothermic reversible reaction)

We take the reversible exothermic reaction with the kinetics given in Example 4.10.2, and assume an initial concentration of A of 4 mol l^{-1} , a maximum allowable temperature T_{\max} of 95°C , and 80% conversion as our goal. At first, we determine the locus of the maximum rates by Figure 4.10.35, whereby we have to consider that this figure was prepared for $c_{A,0} = 1 \text{ mol l}^{-1}$. Then we draw the optimum path starting with $T_{in} = T_{\max}$ (Figure 4.10.40a, line ABCDE), and calculate the ratio $\tau/c_{A,in}$ [Eq. (4.10.85)] by graphical integration of the $1/r_A - X_A$ plot (Figure 4.10.40b). This leads here to $\tau/c_{A,in} = 0.405 \text{ l min mol}^{-1}$, so τ is 1.62 min. Based on Figure 4.10.40 we can, finally, draw the axial evolution of temperature and conversion in the cooled PFR for the optimum path (Figure 4.10.41).

In industrial reactors, it is impractical to reach exactly this optimum temperature profile, as we would have to adjust appropriate locally adjusted values of the overall heat transfer coefficient and/or of the temperature gradient ($T_{reaction} - T_{cool}$).

Figure 4.10.42 shows ways to approach the ideal temperature path for a reversible exothermic reaction by heat exchange with the incoming fluid (Figure 4.10.42a) or multistage operation with interstage cooling between adiabatic sections (Figure 4.10.42b). For endothermic reactions, multistage operation with interstage heating is used to approach the ideal pathway (Figure 4.10.42).

Figure 4.10.40 Optimum path to minimize the reactor volume of a PFR for a reversible exothermic reaction (example taken from Levenspiel, 1999).

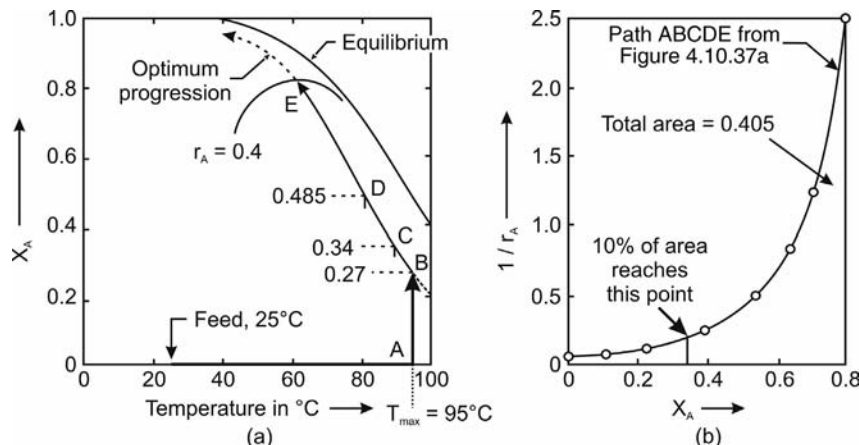
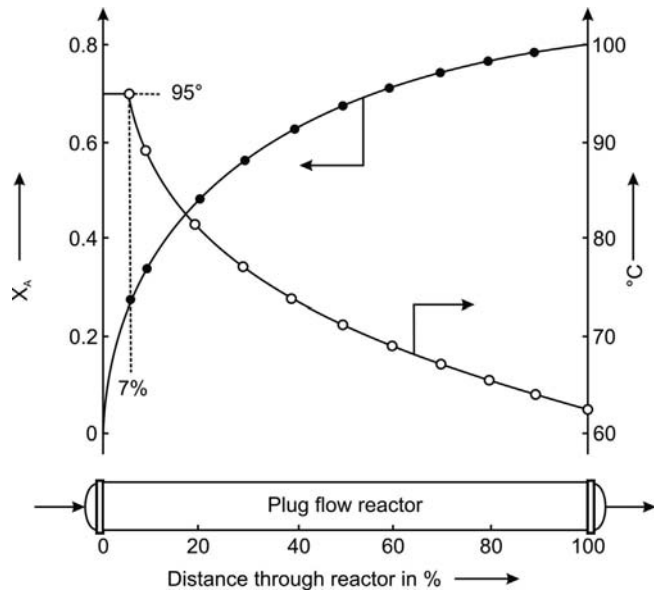


Figure 4.10.41 Evolution of temperature and conversion in a cooled tubular reactor for the optimum path to minimize the reactor volume for a reversible exothermic reaction (example taken from Levenspiel 1999).



4.10.4

Non-ideal Flow and Residence Time Distribution

In the previous sections we have only treated ideal flow patterns (PFR, CSTR), but real reactors always deviate from these ideals caused by stagnant zones, backmixing, channeling of fluid, short-circuiting, or imperfect mixing in a stirred tank reactor (Figure 4.10.43). The question is: How can this deviation be measured and how we can then account for this with regard to calculating the conversion and product yields for a given (mean) residence time?

The deviation of a real reactor from ideal systems is deduced by a widely used method of inquiry, the stimulus-response experiment with a nonreactive tracer. The goal is not knowledge of all the hydrodynamic details of the real flow, but to know how long the molecules stay in the reactor or, more precisely, determination of the residence time distribution (RTD). Based on the RTD and a respective link to the mass balance and conversion equation, respectively, the conversion of a reactant in a real reactor can then be calculated. We will learn this in Sections 4.10.5.2 and 4.10.6.2, limiting ourselves to the case of single-phase flow and steady-state operation.

There are two simple ways to identify the RTD, the pulse and the step experiment.

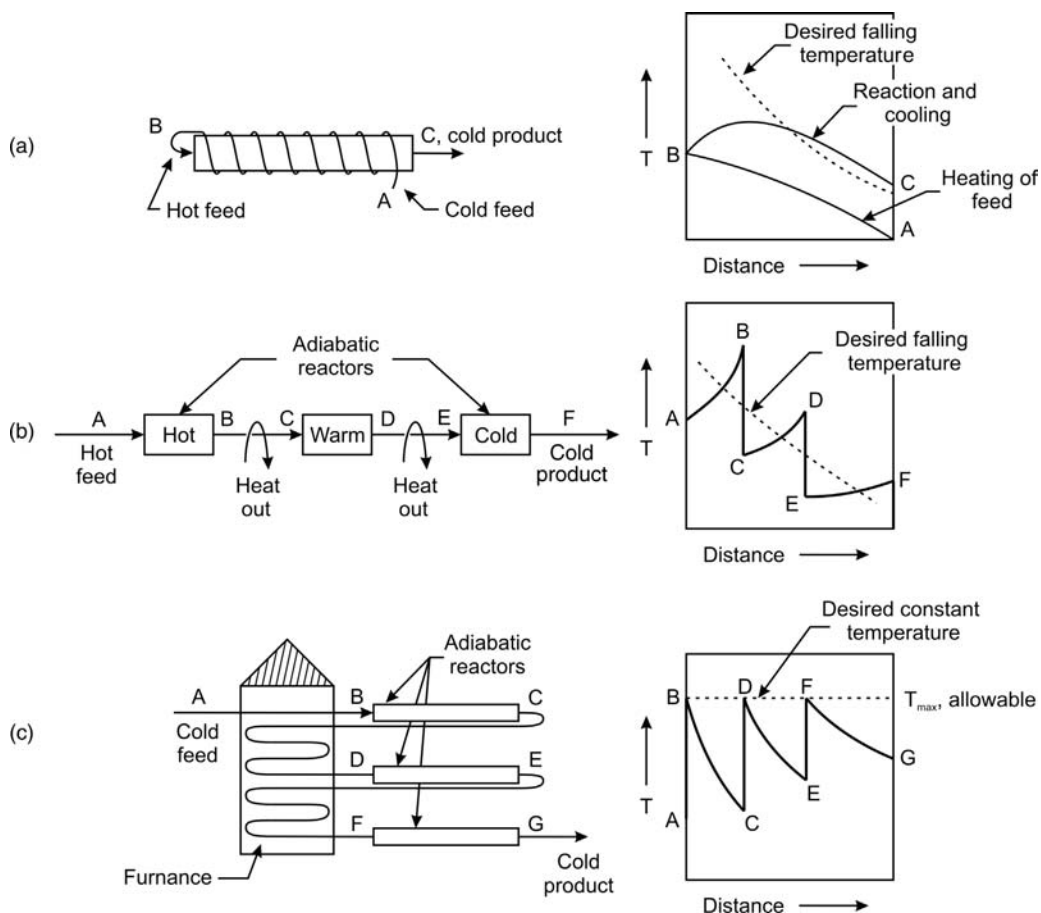


Figure 4.10.42 Ways to approach the ideal temperature profile by heat exchange for an exothermic reversible reaction (a, b) and an endothermic reaction (c). Taken from Levenspiel (1999).

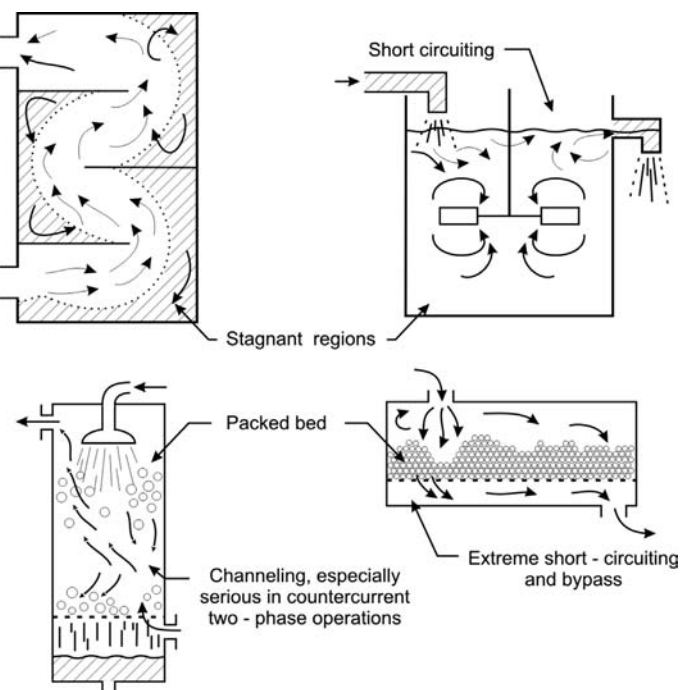
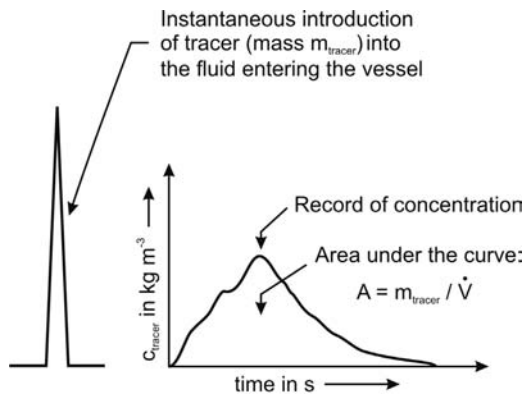


Figure 4.10.43 Non-ideal flow patterns of real reactors. Adapted from Levenspiel (1999).

Figure 4.10.44 Typical result of a pulse experiment.
Adapted from Levenspiel (1999).



Pulse Experiment At the inlet of the reactor with volume V_R a small amount of tracer (m_{tracer} in kg) is instantaneously introduced into the main stream of the fluid with volumetric rate \dot{V} , and the tracer concentration c_{tracer} (kg m^{-3}) at the exit is measured with time (Figure 4.10.44). The area A under this curve equals the term $m_{\text{tracer}}/\dot{V}$:

$$A = \int_0^{\infty} c_{\text{tracer}} dt = m_{\text{tracer}} \dot{V} \quad (4.10.86)$$

Different fluid elements may take different routes through the reactor and need a different time before they leave the vessel. The distribution of these times is the age distribution E (portion of the flow of tracer per unit of time, s^{-1}), and is found by dividing the actual tracer concentration at the exit by $m_{\text{tracer}}/\dot{V}$, that is, by the area under the curve of c_{tracer} versus time t :

$$E = \frac{c_{\text{tracer}} \dot{V}}{m_{\text{tracer}}} \quad (4.10.87)$$

where E represents the probability that a volume element that enters the reactor at $t=0$ leaves the reactor in the time interval $t+dt$. The integral of the E function from $t=0$ to $t=t_1$:

$$\int_0^{t_1} E dt$$

represents the fraction of the exit stream that is younger than t_1 , and the integral of the E function (zero to infinite) equals one:

$$\int_0^{\infty} E dt = 1 \quad (4.10.88)$$

Based on the dimensionless time $\theta = t/\tau$ we acquire the exit age distribution in dimensionless form:

! $E_{\theta} = \tau E = V_R \dot{V} \frac{c_{\text{tracer}} \dot{V}}{m_{\text{tracer}}} = \frac{V_R c_{\text{tracer}}}{m_{\text{tracer}}} \quad (4.10.89)$

with the mean residence time τ defined as:

$$\tau = V_R \dot{V} \quad (4.10.90)$$

where E_{θ} represents the ratio of the actual tracer concentration at the reactor outlet to the concentration if the tracer were instantaneously mixed throughout the reactor (and so E_{θ} equals unity in an ideal CSTR for $t=0$). Figure 4.10.45 shows the transformation of an E curve into an E_{θ} curve with the dimensionless time θ . The method to derive the E_{θ} curve based on a pulse experiment is also explained in Example 4.10.8 for the case of a CSTR.

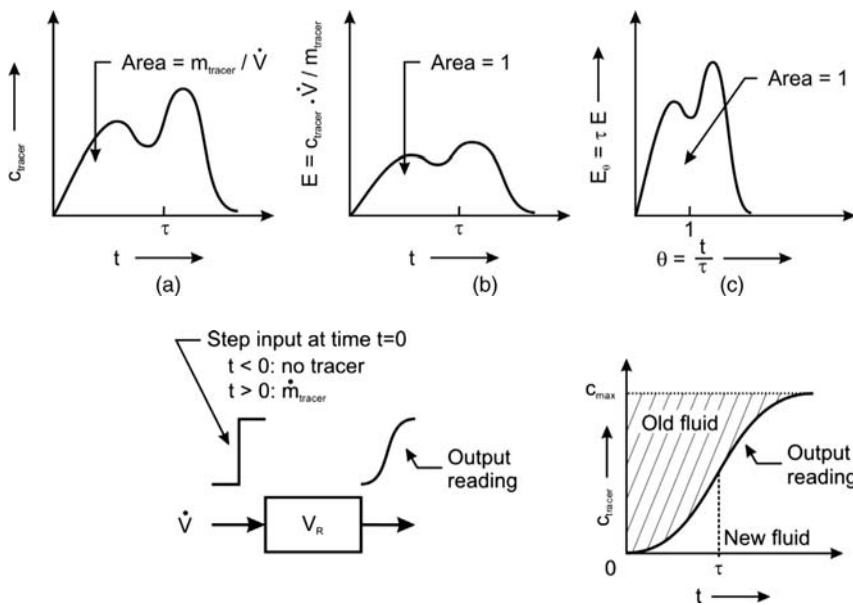


Figure 4.10.45 Transformation of \$c_{\text{tracer}}\$ curve (a) (pulse experiment) into an \$E\$ (b) and \$E_\theta\$ (c) curve.

Figure 4.10.46 Typical result of a step experiment. Adapted from Levenspiel (1999).

Step Experiment Instead of the pulse experiment, we can also use a *step experiment* to determine \$c_{\text{tracer}}\$ and \$E\$ curves (Figure 4.10.46). At time \$t=0\$ we switch from ordinary fluid to a fluid with a tracer of constant concentration \$c_{\text{max}} (\text{kg m}^{-3})\$ and measure the outlet tracer concentration \$c_{\text{tracer}}\$ versus \$t\$. With \$\dot{m}_{\text{tracer}}\$ as the flow rate of tracer (\$\text{kg s}^{-1}\$) and the volumetric rate of the total flow we obtain:

$$c_{\text{max}} = \frac{\dot{m}_{\text{tracer}}}{\dot{V}} \quad (4.10.91)$$

The dimensionless \$c_{\text{tracer}}\$ curve of a step experiment is the cumulative \$F(t)\$ function, and represents the fraction of elements in the exit stream with a residence time shorter than \$t\$:

$$! F(t) = \frac{c_{\text{tracer}}(t)}{c_{\text{max}}} \quad (4.10.92)$$

The mean (average) residence time can be calculated from:

$$\tau = \frac{1}{c_{\text{max}}} \int_0^{c_{\text{max}}} t \, dc_{\text{tracer}} = \text{shaded area in Figure 4.10.46 divided by } c_{\text{max}} \quad (4.10.93)$$

The \$E\$, \$E_\theta\$, and \$F\$ functions and thus step and pulse experiments are related by:

$$\nabla F = \int_0^t E \, dt \Rightarrow \frac{dF}{dt} = E \quad \text{or} \quad F_\theta = \int_0^\theta E_\theta \, d\theta \Rightarrow \frac{dF_\theta}{d\theta} = E_\theta \quad (4.10.94)$$

The tracer fraction at the exit at time \$t\$ (value of \$F\$) equals the fraction of the exit stream younger than age \$t\$ [Eq. (4.10.88)]. Figure 4.10.47 shows the graphical form of Eq. (4.10.94).

Derivation of the \$F\$ curve is also explained in Example 4.10.5 for the example of a CSTR.

Thus, we can use either a pulse or a step experiment to characterize the RTD (Figure 4.10.48). Should we use a pulse or step experiment? A comment from Levenspiel (1999) is helpful:

If we have a choice, the pulse method is preferred as it gives a more “honest” result. The \$F\$-curve integrates effects, and the smooth good-looking curve could hide real effects.

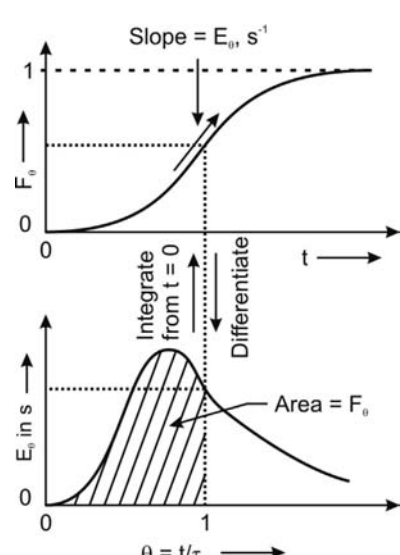


Figure 4.10.47 Relationship between \$E_\theta\$ and \$F_\theta\$ function. Adapted from Levenspiel (1999).

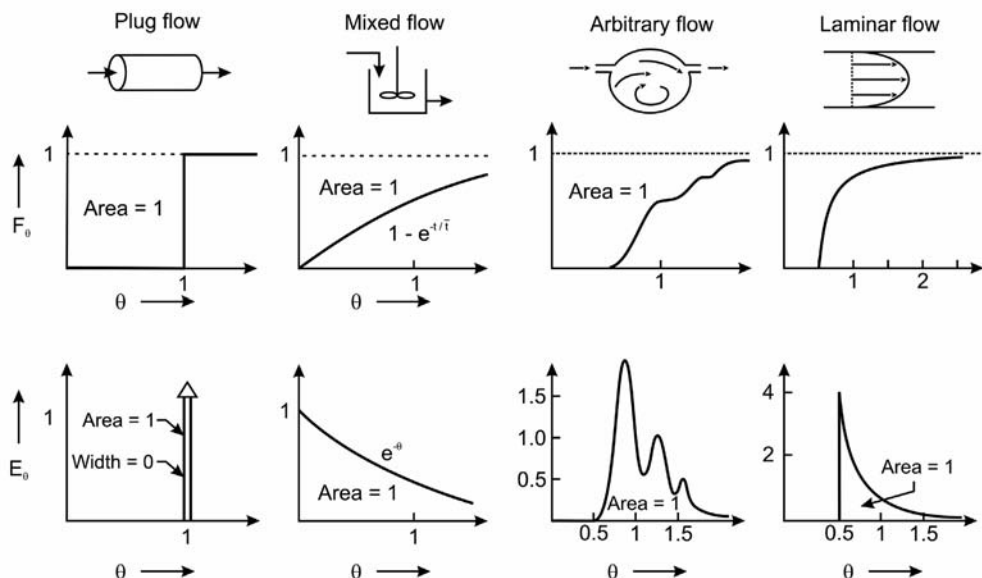


Figure 4.10.48 E_θ and F functions for various reactors in ordinary and dimensionless units. Partly adapted from Levenspiel (1999).

Example 4.10.5: Derivation of E_θ - and F -function of a CSTR

Pulse experiment and E_θ function: The mass balance of a pulse experiment with a tracer (m_{tracer} in kg, c_{tracer} in kg m^{-3}) is given by Eq. (4.10.1) (without reaction term):

$$-V_R \frac{dc_{\text{tracer}}}{dt} = \dot{V} c_{\text{tracer,out}}$$

In an ideal CSTR the tracer is instantaneously distributed throughout the reactor at $t=0$ (moment of injection), and the initial tracer concentration $c_{\text{tracer},0}$ equals m_{tracer}/V_R . Thus E_θ is given by $c_{\text{tracer}}/c_{\text{tracer},0}$ [Eq. (4.10.89)], and integration of the above equation leads to $E_\theta(\theta)$:

$$\begin{aligned} \int_{c_{\text{tracer},0}}^{c_{\text{tracer}}} \frac{dc_{\text{tracer}}}{c_{\text{tracer}}} &= - \int_0^t \frac{\dot{V}}{V_R} dt = - \int_0^t \frac{1}{\tau} dt \Rightarrow \ln\left(\frac{c_{\text{tracer}}}{c_{\text{tracer},0}}\right) \\ &= \ln(E_\theta) = -\frac{t}{\tau} = -\theta \Rightarrow E_\theta = e^{-\theta} \end{aligned}$$

Step experiment and F function: During a step experiment we change at $t=0$ from a tracer-free feed to a feed with a concentration of tracer $c_{\text{tracer,in}}$. By Eq. (4.10.1) (again without the reaction term) we obtain for the change of the tracer concentration with time:

$$V_R \frac{dc_{\text{tracer,out}}}{dt} = \dot{V}(c_{\text{tracer,in}} - c_{\text{tracer,out}})$$

Rearrangement and integration of this equation leads to the F function (Figure 4.10.47):

$$\begin{aligned} \int_0^{c_{\text{tracer,out}}} \frac{dc_{\text{tracer,out}}}{(c_{\text{tracer,in}} - c_{\text{tracer,out}})} &= \int_0^t \frac{dt}{\tau} = \int_0^\theta d\theta \Rightarrow \frac{c_{\text{tracer,out}}}{c_{\text{tracer,in}}} = F \\ &= 1 - e^{-\theta} \end{aligned}$$

which equals the integral of the E_θ function. Thus the development of the dimensionless concentration of a step experiment with time directly leads to the cumulative F function.

4.10.5 Tanks-in-Series Model

4.10.5.1 Residence Time Distribution of a Cascade of Ideal Stirred Tank Reactors

The tanks-in-series model considers the actual reactor as a system of N identical CSTRs with the same total volume as the actual reactor. The F_θ and E_θ functions of a cascade are shown in Figure 4.10.49 and are given by (with the dimensionless time $\theta = t/\tau$ and the mean residence time $\tau = V_R/\dot{V} = NV_{\text{tank}}/\dot{V}$):

$$\nabla \quad E_\theta = \frac{N}{(N-1)!} e^{-N\theta} (N\theta)^{N-1} \quad (4.10.95)$$

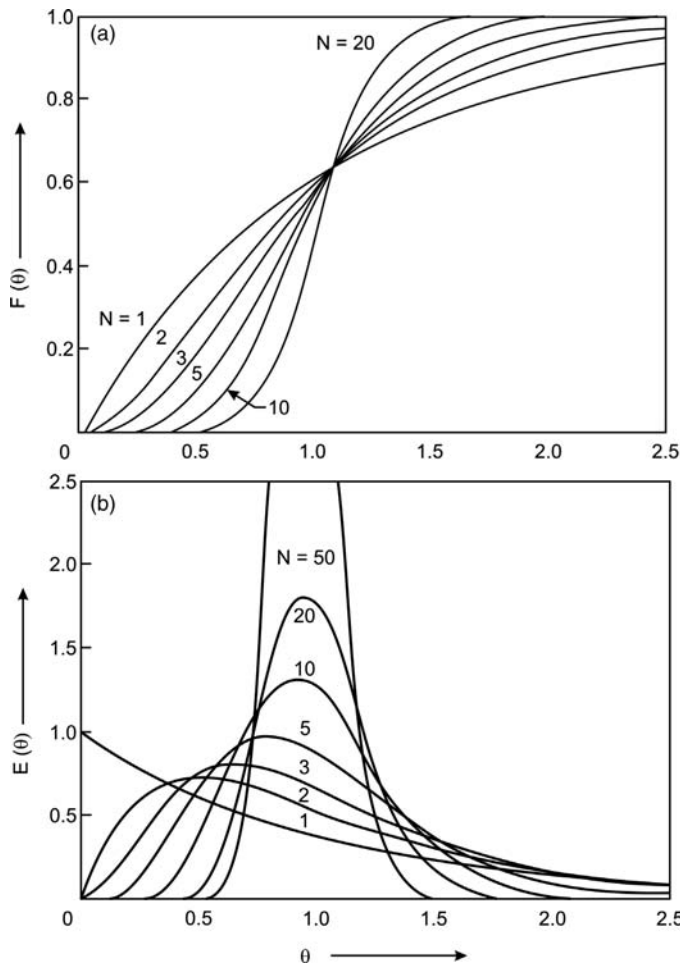


Figure 4.10.49 Dimensionless (a) F function and (b) E function of a cascade of CSTRs.

$$\nabla \quad F = 1 - e^{-N\theta} \left[1 + N\theta + \frac{(N\theta)^2}{2!} + \dots + \frac{(N\theta)^{N-1}}{(N-1)!} \right] \quad (4.10.96)$$

The RTD (E_θ function) is characterized by the variance σ_θ^2 and the standard deviation σ_θ , that is, by the spread of the curve (Figure 4.10.50). For a small deviation from plug flow ($N > 20$), σ_θ equals the width at the point of inflection ($E_\theta = 0.61 E_{\theta,\max}$), and the number of tanks is:

$$\nabla \quad N = \left(\frac{1}{\sigma_\theta} \right)^2 \quad (\text{for } N > 20) \quad (4.10.97)$$

Example 4.10.6 illustrates how to determine the number N based on a (measured) residence time distribution.

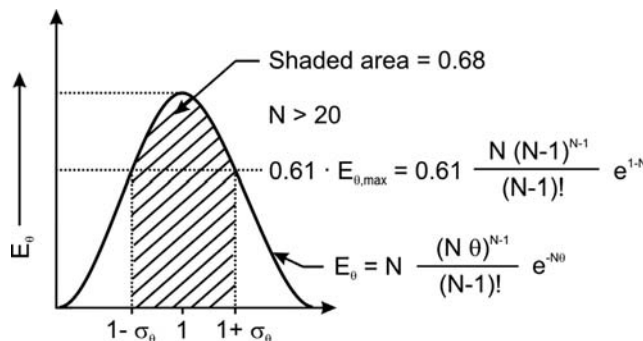
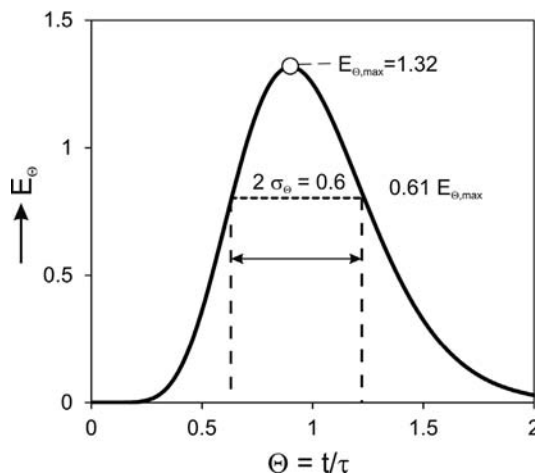


Figure 4.10.50 Dimensionless E_θ function and standard deviation σ_θ .

Figure 4.10.51 E_θ function, maximum value $E_{\theta,\max}$ and standard deviation σ_θ for $N = 10$.



Example 4.10.6: Derivation of the number of tanks-in-series by the E_θ function

To illustrate the method employed to determine the number of tanks-in-series by a measured residence time distribution, we use Figure 4.10.51, which shows the (exact) dimensionless E_θ function versus the dimensionless residence time θ for the example of $N = 10$. $E_{\theta,\max}$ is 1.32 and the standard deviation σ_θ about 0.3.

According to Eq. (4.10.97), we find a value for N of 11, which indicates that the value of N is still not accurate and is too low to use this correlation, but may be used as a rough estimation. The value of $E_{\theta,\max}$ as a function of the number of tanks-in-series N is given by (see formula in Figure 4.10.50) (see Figure 4.10.52):

$$E_\theta = \frac{N}{(N-1)!} e^{-N\theta} (N\theta)^{N-1}$$

Hence, for a given measured value of $E_{\theta,\max}$ the number can be estimated (Figure 4.10.52).

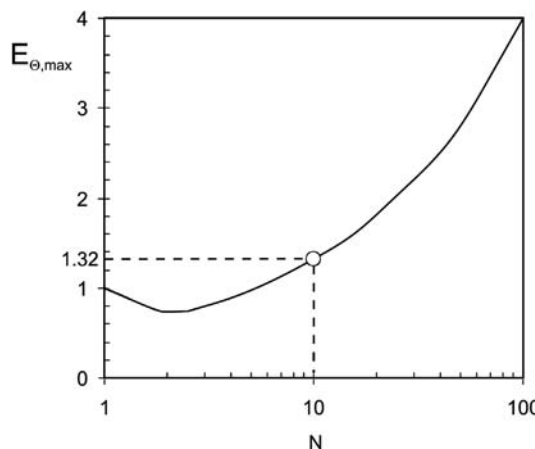
Therefore, we have three options to determine N by the residence time distribution (RTD):

- We compare the RTD with the solutions given in Figure 4.10.49 [or other solutions given by Eq. (4.10.95)]. The best fit then leads to the value for N ;
- we use $E_{\theta,\max}$ and Figure 4.10.52 to estimate N ;
- we use the standard deviation σ_θ and Eq. (4.10.97), if N is at least 10.

4.10.5.2 Calculation of Conversion by the Tanks-in-Series Model

Calculation of the conversion in a real isothermal reactor by means of the tanks-in-series model is straightforward. Based on a step or pulse input experiment, we get directly either the F or the E function of a real reactor. We just have to compare the measured function with the solutions given in Figures 4.10.49–4.10.52, and determine the hypothetical number N of CSTRs of our real system by the best fit of

Figure 4.10.52 $E_{\theta,\max}$ versus number of tanks-in-series N (formula in Figure 4.10.50).



the measured RTD signal with the theoretical solutions of an ideal cascade. Alternatively, we may use the value of the standard deviation σ_θ and Eq. (4.10.97) if the deviation from plug flow is small ($N > 20$) (see Example 4.10.10). The conversion for a first-order reaction is calculated by the equation already derived in Section 4.10.2.5:

$$X_A = \frac{\left(1 + \frac{k\tau}{N}\right)^N - 1}{\left(1 + \frac{k\tau}{N}\right)^N} = \frac{\left(1 + \frac{Da}{N}\right)^N - 1}{\left(1 + \frac{Da}{N}\right)^N} \quad (4.10.32)$$

(with τ as mean residence time of cascade)

Solutions for reaction orders $\neq 1$ are given by Westerterp, van Swaaij, and Beenackers (1998) and Levenspiel (1999). If the RTD does not satisfactorily fit with a curve of an ideal cascade (Figure 4.10.49), compartment models consisting of sequential/parallel ideal reactors and so on are used (Levenspiel, 1999).

4.10.6

Dispersion Model

4.10.6.1 Axial Dispersion and Residence Time Distribution

The dispersion model is an alternative to the tanks-in-series model to represent the flow in real, mostly tubular reactors. This model formally characterizes mass transport in radial and axial directions as a one-dimensional process in terms of an effective longitudinal diffusivity D_{ax} that is superimposed on the plug flow. The basic assumption is that the fluid velocity and reactant concentration are constant in the radial direction across the tube, which is a sound assumption for isothermal reactors and a negligible wall effect (Section 4.10.6.5). The magnitude of dispersion is assumed to be independent of the position in the vessel (no stagnant regions and no short-circuiting of fluid). If we consider a steady-state fluid flow but unsteady-state with respect to the tracer A passing through a reactor (without chemical reaction), the mass balance with regard to tracer A over a differential length dz of the reactor yields:

$$\nabla D_{ax} \frac{d^2 C_A}{dz^2} - u \frac{dC_A}{dz} = \frac{dC_A}{dt} \quad (4.10.98)$$

In dimensionless form, that is, with $\theta = t/\tau = t/(L/u)$ and $Z = z/L$, Eq. (4.10.98) leads to:

$$\left(\frac{D_{ax}}{uL}\right) \frac{d^2 C_A}{dZ^2} - \frac{dC_A}{dZ} = \frac{dC_A}{d\theta} \quad (4.10.99)$$

The dimensionless group $D_{ax}/(uL)$ is called the vessel dispersion number, and the reciprocal value is called the *Bodenstein number* Bo , which can be used in place of D_{ax} as the parameter for axial dispersion and represents the ratio of convective flux to diffusive (dispersed) flux.

The (axial) dispersion term $D_{ax}/(uL) = 1/Bo$ can be regarded as the product of two terms:

$$\nabla \frac{D_{ax}}{uL} = \frac{1}{Bo} = \left(\frac{D_{ax}}{ud}\right) \left(\frac{d}{L}\right) = \left(\frac{1}{Pe_{m,ax}}\right) \left(\frac{d}{L}\right) \quad (4.10.100)$$

= (intensity of mixing) × (geometric factor)

The dimensionless group ud/D_{ax} is called the axial *Peclet number* for mass $Pe_{m,ax}$ (named after *Jean Claude Peclet*, see box), and d is a characteristic length. For empty tubes, d is the tube diameter d_t , and for packed beds the particle diameter d_p is mostly used.

Jean Claude Eugene Peclet (1793–1857): a French physicist and a scholar of *Gay-Lussac* (Section 3.1.1). His famous book *Traite de la Chaleur et de ses Applications aux Arts et Aux Manufactures* (1829) was distributed worldwide. *Peclet* became professor of physical sciences in Marseille in 1816. In 1827, he was elected professor at the important *Ecole Centrale des Arts et Manufactures* in Paris. In 1840 he became *Inspecteur General de L'Instruction Publique* and retired in 1852 to devote himself exclusively to teaching. He continued lecturing until his death.

Correlations for axial dispersion coefficients in empty pipes and in packed beds are given in the Sections 4.10.6.3 and 4.10.6.4, respectively, so we can also calculate D_{ax} without the need of an experiment (or prove the results of measurements, respectively).

The dispersion coefficient D_{ax} ($\text{m}^2 \text{s}^{-1}$) and the dimensionless numbers Bo and $Pe_{m,ax}$ represent the spreading process of a pulse of tracer. Thus a large value of D_{ax} (low Bo and low $Pe_{m,ax}$) means rapid spreading of the tracer curve (mixed flow), and a low value of D_{ax} means slow spreading. For $D_{ax}=0$ we have no spreading and, hence, plug flow. Note that for a fixed bed we can still use Eqs. (4.10.98) and (4.10.99), but then Bo is related to the interstitial velocity (ratio of superficial velocity u_s in the empty reactor to the porosity ε of the packed bed with $\varepsilon \approx 0.4$).

Small Deviation from Plug Flow ($Bo > 80$) For an ideal pulse and a large value of Bo (>80), the tracer curve does not change its shape as it passes the reactor outlet. The solution of Eq. (4.10.99) is then:

$$E_\theta = \sqrt{\frac{uL}{4\pi D_{ax}\theta}} \exp\left[-\frac{uL}{4D_{ax}} \frac{(1-\theta)^2}{\theta}\right] = \sqrt{\frac{Bo}{4\pi\theta}} \exp\left[-\frac{Bo(1-\theta)^2}{4\theta}\right] \quad (4.10.101)$$

and gives a symmetrical Gaussian curve (normal curve) of the E_θ function (Figure 4.10.53).

For a small extent of dispersion ($Bo > 80$), the variance σ_θ^2 , which characterizes the width of the residence time distribution, is given by:

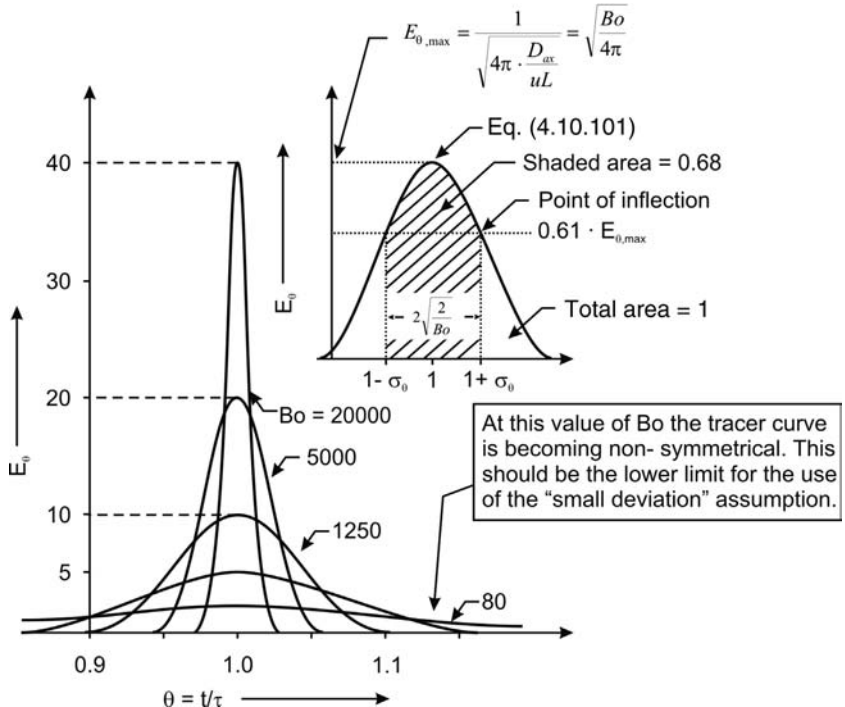
$$\nabla_o = \sigma_\theta^2 = 2 \frac{D_{ax}}{uL} = \frac{2}{Bo} \quad (4.10.102)$$

Note that the tracer spreads as it moves down the reactor. From Eq. (4.10.102) we find that σ^2 (square of the width of tracer curve in s^2) is proportional to L :

$$\sigma^2 = \sigma_\theta^2 \tau^2 = \left(2 \frac{D_{ax}}{uL}\right) \left(\frac{L}{u}\right)^2 = 2 \frac{D_{ax}L}{u^3} \sim L \quad (4.10.103)$$

Figure 4.10.53 shows that the width of the curve at the inflection point ($E_\theta = 0.61E_{\theta,\max}$) is given by $2\sigma_\theta = 2(2/Bo)^{0.5}$, which is the width that includes 68% of the area under the curve, that is, 68% probability for a fluid element to pass the exit. For 90% probability the width is $3.3\sigma_\theta$.

Figure 4.10.53 Dimensionless E_θ function for different values of $Bo = uL/D_{ax}$ for a small extent of dispersion ($Bo > 80$). Adapted from Levenspiel (1999).



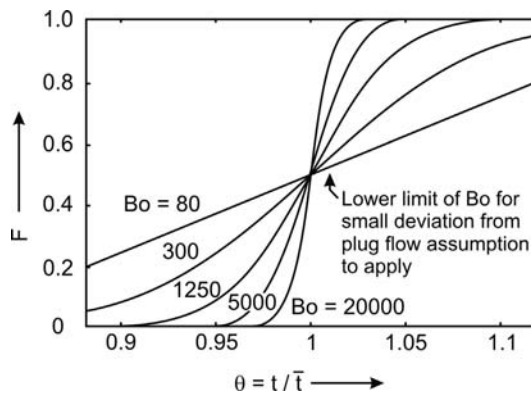


Figure 4.10.54 F functions (step response curves) for different values of $Bo = uL/D_{ax}$ for a small extent of dispersion (small deviation from plug flow). Adapted from Levenspiel (1999).

An example for the use of these values is given in Example 4.10.7. Figure 4.10.53 outlines two ways to determine D_{ax} and Bo from an experimentally determined E curve:

- We take the width of the curve at the point of inflection ($E_\theta = e^{-1/2} E_{\theta,\max} = 0.61 E_{\theta,\max}$), which equals $2\sigma_\theta$, and use the value of σ_θ to calculate D_{ax} and Bo by Eq. (4.10.102).
- Alternatively, we determine the maximum value $E_{\theta,\max}$ and calculate D_{ax} and Bo by:

$$\frac{D_{ax}}{uL} = \frac{1}{Bo} = \frac{1}{4\pi E_{\theta,\max}^2} \quad (4.10.104)$$

By comparison of Figures 4.10.49 and 4.10.53 we see that the E_θ functions of the tanks in series model and the dispersion model are similar. Matching the variances leads to:

! Number of tanks of a cascade $N = \frac{Bo}{2} = \frac{uL}{2D_{ax}}$ (for $Bo > 80$) (4.10.105)

and thus according to Eq. (4.10.102) the number of tanks is also given by $N = 1/\sigma_\theta^2$ as already stated by Eq. (4.10.97).

Figure 4.10.54 gives the corresponding F functions representing step response curves.

Fortunately, a small extent of dispersion simplifies the analysis of tracer curves as the shape is insensitive to the boundary condition (close or open vessel condition, Figure 4.10.55).

For a series of reactors the values of τ and σ_θ^2 of the individual reactors are additive:

$$\tau_{\text{overall}} = \sum \tau_i \quad (4.10.106)$$

$$\sigma_{\theta,\text{overall}}^2 = \sum \sigma_{\theta,i}^2 \quad (4.10.107)$$

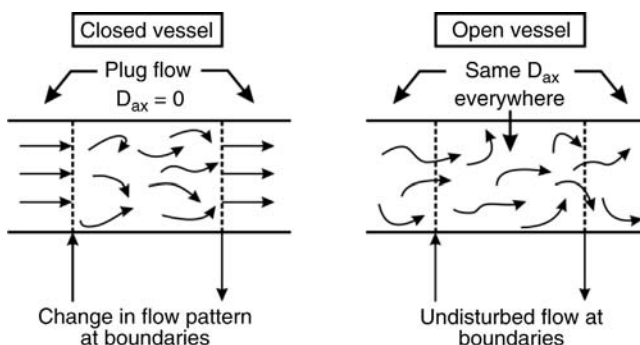


Figure 4.10.55 Various boundary conditions used for the dispersion model (Levenspiel, 1999).

This additivity property of σ_θ^2 allows us to treat any shape of tracer input, no matter how close the input approaches an ideal pulse, and to extract from it the variance:

$$\sigma_\theta^2 = \sigma_{\theta,\text{out}}^2 - \sigma_{\theta,\text{in}}^2 \quad (4.10.108)$$

Thus, the term D_{ax}/uL can be found independently of the shape of the input curve.

Example 4.10.7: Dispersion model and flow of two liquids in a pipeline

An interesting application of the dispersion model is to find the zone of intermixing – the contamination width – between two fluids flowing one after the other in a pipeline (Levenspiel, 1999). For a given D_{ax} – obtained by a tracer experiment or based on correlations given in the Section 4.10.6.3 the standard deviation σ (in s) is given by Eq. (4.10.103):

$$\sigma = \sqrt{2 \frac{D_{\text{ax}} L}{u^3}}$$

Example: kerosene and gasoline are successively pumped at 1 m s^{-1} through a 25-cm diameter pipeline that is 1000 km long (viscosity ν of a 50/50% mixture: $10^{-6} \text{ m}^2 \text{ s}^{-1}$, $Re = 2.5 \times 10^5$). What is the 5–95% contaminated width at the exit? The term $D_{\text{ax}}/(ud_i)$ is about 0.2 (Section 4.10.6.3), that is, $D_{\text{ax}} = 0.05 \text{ m}^2 \text{ s}^{-1}$. By Eq. (4.10.103) we obtain $\sigma = 316 \text{ s}^{-1}$. For a 5–95% contaminated width, we have to consider $3.3\sigma (= L_{\text{contaminated}}/u)$. Therefore, the width is 1 km. Finally, we calculate the Bo number to check whether we really have a small deviation from plug flow, and by Eq. (4.10.102) we find $Bo = uL/D_{\text{ax}} = 2 \times 10^7$, so $Bo \gg 80$.

Large Deviation from Plug Flow ($Bo < 80$) For $Bo < 80$, the tracer response curve is broad and passes the measuring point slowly, which leads to nonsymmetrical distribution curves (Figure 4.10.56a). Then the solutions of Eqs. (4.10.98) and (4.10.99) depend on the choice of the boundary conditions (open or closed vessel, closed-open, or open-closed vessel), which do not necessarily satisfy actual experimental conditions. A closed boundary condition at the inlet or outlet implies that the vessel is isolated in the sense of communication with the connecting pipe. An open boundary condition presumes that the same flow distribution occurs in the vessel and in the connecting pipe. It also implies that any tracer injected at the inlet can appear upstream of the inlet.

For a closed or open-closed vessel, an analytical solution for the E_θ and F functions is not available and numerical methods are needed. Only for an open vessel do we have an analytical solution, Eq. (4.10.101), but an open vessel also represents the commonly used experimental device. Figure 4.10.56 shows the respective E_θ

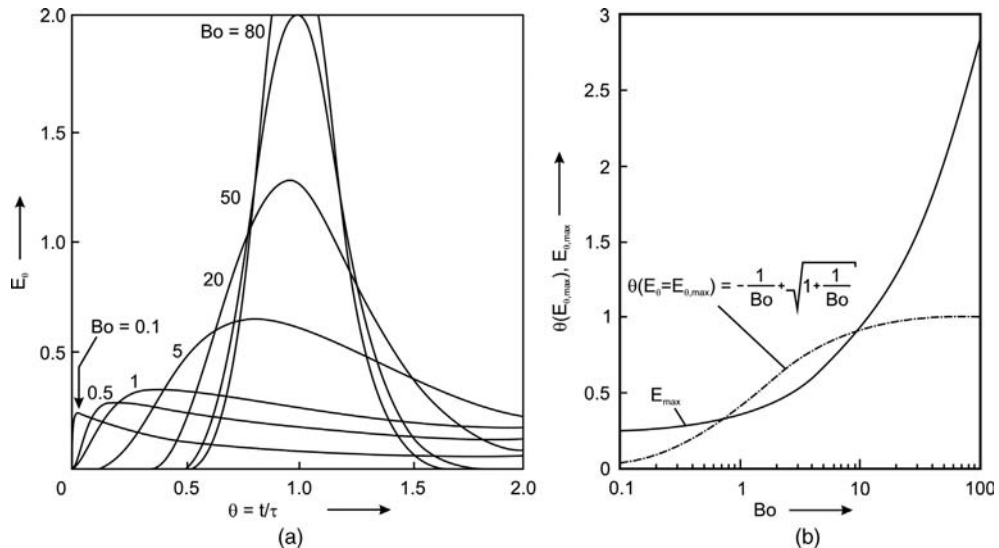


Figure 4.10.56 Dimensionless E_θ function (a), $E_{\theta,\text{max}}$ and θ for $E_\theta = E_{\theta,\text{max}}$ (b) for different values of $Bo = uL/D_{\text{ax}}$ for an open reactor and large extent of dispersion ($Bo < 80$).

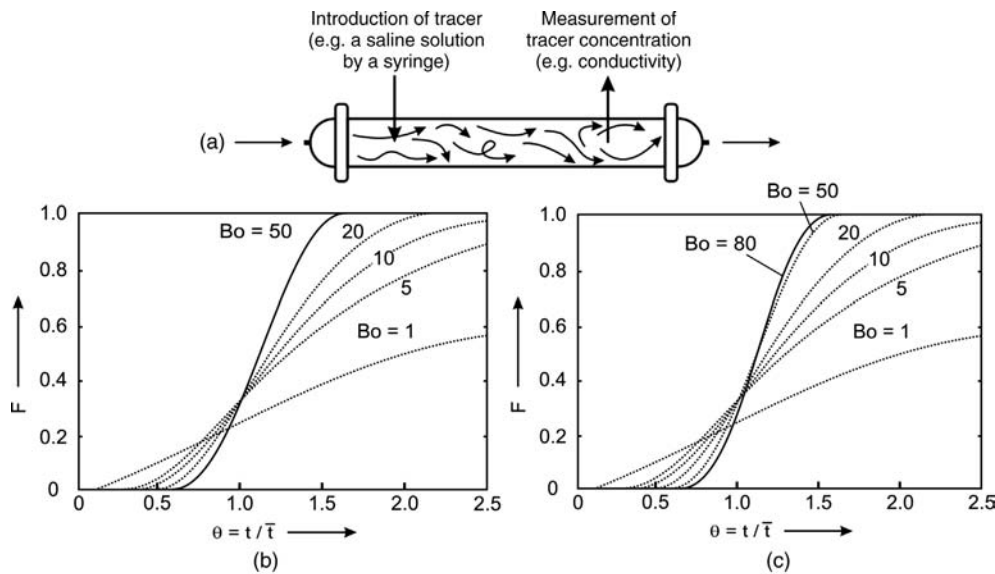


Figure 4.10.57 Experimental set-up for open vessel boundary condition (a) and F functions for a large extent of dispersion (high deviation from plug flow) for an open vessel (b) and closed vessel (c) for different values of $Bo = uL/D_{ax}$. Adapted from Levenspiel (1999).

functions for different values of Bo . Figure 4.10.57 depicts the F curves in the case of the open vessel and for comparison also for a closed vessel. For more details, see Levenspiel (1999, 1996) or Westerterp, van Swaaij, and Beenackers (1998).

For a large deviation from plug flow, Bo and D_{ax} are determined as follows (Example 4.10.8):

- The experimental curve is matched to the theoretical curves as given in Figure 4.10.56 (if we have an open vessel boundary condition).
- We calculate the variance, given in dimensionless terms by:

$$\sigma_\theta^2 = \int_0^\infty \theta^2 E_\theta d\theta - \left(\int_0^\infty \theta E_\theta d\theta \right)^2 \quad (4.10.109)$$

Because the experimental data are mostly discrete values of the tracer concentration at successive time intervals after introduction of the tracer, the intervals are normally replaced by summations in the analysis of actual data, and σ_θ^2 can be estimated by:

$$\sigma_\theta^2 = \sum \theta^2 E_\theta \Delta\theta - \left(\sum \theta E_\theta \Delta\theta \right)^2 \quad (4.10.110)$$

According to Levenspiel (1999), σ_θ^2 and the term $D_{ax}/(uL)$ are correlated by:

$$\sigma_\theta^2 = 2 \frac{D_{ax}}{uL} + 8 \left(\frac{D_{ax}}{uL} \right)^2 = \frac{2}{Bo} + \frac{8}{Bo^2} \quad (\text{for an open vessel}) \quad (4.10.111)$$

$$\begin{aligned} \sigma_\theta^2 &= 2 \frac{D_{ax}}{uL} - 2 \left(\frac{D_{ax}}{uL} \right)^2 \left(1 - e^{-\frac{uL}{D_{ax}}} \right) \\ &= \frac{2}{Bo} - \frac{2}{Bo^2} (1 - e^{-Bo}) \quad (\text{for a closed vessel}). \end{aligned} \quad (4.10.112)$$

Both equations simplify to Eq. (4.10.102) for high values of Bo .

- We may also use the measured value of $E_{\theta,\max}$ (or of θ at $E_\theta = E_{\theta,\max}$) and determine the value of Bo by Figure 4.10.56b and the given correlation for θ at $E_\theta = E_{\theta,\max}$.

By changing D_{ax} , one may vary the reactor performance from plug flow [$D_{ax}/(uL) = 0$ or $Bo = \infty$] to a CSTR [$D_{ax}/(uL) = \infty$ or $Bo = 0$]. At first sight, this simple model appears to account only for axial mixing effects. However, this approach not only compensates for problems caused by axial mixing but also for those related to radial mixing and non-uniform velocity profiles (Aris, 1956), as shown in Section 4.10.6.3 for laminar flow in tubular reactors.

4.10.6.2 Calculation of Conversion by the Dispersion Model

Calculation of the conversion of the reactant A (first-order irreversible reaction, $r_A = kc_A$) by means of the dispersion model is based on the mass balance for reactant A:

$$u \frac{dc_A}{dz} = D_{ax} \frac{d^2 c_A}{dz^2} - kc_A \quad (4.10.113)$$

In dimensionless terms this equation becomes:

$$\frac{dc_A}{dZ} = \frac{1}{Bo} \frac{d^2 c_i}{dZ^2} - k\tau c_A \quad (\text{with } Z = z/L, \tau = L/u, Bo = uL/D_{ax}) \quad (4.10.114)$$

The analytical solution (for details see, for example, Emig and Klemm, 2005) leads to:

$$\bullet \quad X_A = 1 - \frac{c_A}{c_{A,0}} = 1 - \frac{4Ce^{\left(\frac{Bo}{2}\right)}}{(1+C)^2 e^{\left(\frac{CB_0}{2}\right)} - (1-C)^2 e^{\left(-\frac{CB_0}{2}\right)}} \quad (4.10.115)$$

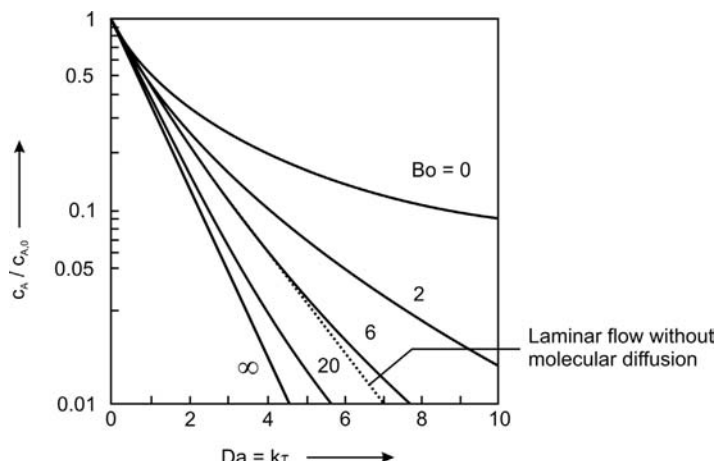
$$\left(C = \sqrt{1 + \frac{4Da}{Bo}}, Da = k\tau \right)$$

For $Bo = 0$, we have the behavior of a CSTR and Eq. (4.10.115) equals Eq. (4.10.19). For an infinite value of Bo we find the behavior of a PFR [Eq. (4.10.25)]. A tubular reactor with laminar flow without molecular diffusion is formally represented by $Bo \approx 6$ (Figure 4.10.58).

Based on a step or pulse experiment, we determine D_{ax} and Bo , see Section 4.10.6.1, and by Eq. (4.10.115) we calculate the conversion of a first-order reaction (Figure 4.10.58). Solutions for other orders are given by Westerterp, van Swaaij, and Beenackers (1998) and Levenspiel (1999).

The value of D_{ax} of this plug flow model with axial dispersion can also be calculated based on correlations given in Section 4.10.6.3. Example 4.10.8 gives an example to highlight the methods used to determine the conversion based on RTD measurements.

Figure 4.10.58 First-order reaction in a tubular reactor according to the dispersion model [Eq. (4.10.115); dotted line: laminar flow without molecular diffusion (Eq. (4.10.29))].



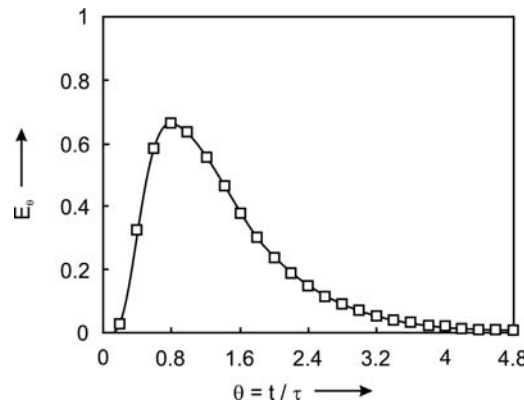


Figure 4.10.59 Example of an RTD (residence time distribution) curve (open vessel boundary condition, see Figures 4.10.55 and 4.10.57).

Example 4.10.8: Prediction of conversion based on residence time distribution

Figure 4.10.59 shows an example of a RTD curve (values in Table 4.10.6). The conversion can be predicted by the *axially dispersed plug flow* model or by the *tanks-in-series* model.

Dispersion model

Comparison of Figure 4.10.59 with Figure 4.10.53 shows that the width at $E_\theta = 0.61 E_{\theta,\max}$ cannot be used to determine the variance σ_θ (RTD curve not Gaussian, large deviation from plug flow, $Bo > 80$); σ_θ is derived by Eq. (4.10.110) and the values given in Table 4.10.7:

$$\begin{aligned}\sigma_\theta^2 &= \sum \theta^2 E_\theta \Delta\theta - \left(\sum \theta E_\theta \Delta\theta \right)^2 \\ &= 2.5 - 1.36^2 = 0.65 \Rightarrow \sigma_\theta = 0.81\end{aligned}\quad (4.10.116)$$

By the standard deviation $\sigma_\theta = 0.81$ and Eq. (4.10.111) we obtain for Bo :

$$\sigma_\theta^2 = 0.65 = \frac{2}{Bo} + \frac{8}{Bo^2} \Rightarrow Bo = 5.4$$

and Eq. (4.10.115) yields 58.6% conversion for $Da = 1$. We may also use $E_{\theta,\max}$ (or θ at $E_\theta = E_{\theta,\max}$) and determine Bo by Figure 4.10.56b, which yields $E_{\theta,\max} = 0.66$, $\theta = 0.82$ at $E_{\theta,\max}$, and an almost equal value for Bo of 5 and a conversion of 58.3% for $Da = 1$.

Tanks-in-series model

First we have to determine the number of tanks. For the given case we have to be aware of the fact that the RTD given in Figure 4.10.59 was determined by an open vessel arrangement. Thus we have to transfer this case to the RTD for a closed vessel arrangement. The value of $E_{\theta,\max}$ for a closed vessel and a value of Bo of 5 is ≈ 0.95 ($\theta \approx 0.6$) (Levenspiel, 1996). Figure 4.10.49 then leads to a number of tanks N of about 4.

If we know the number N of the tanks-in-series model, we calculate the conversion by Eq. (4.10.32); for example, for $Da = 1$ we obtain a conversion of 59.0%, which almost equals the values as determined by the axially dispersed plug flow model (58.6% and 58.3%).

4.10.6.3 Dispersion and Conversion in Empty Pipes

Axial Dispersion Model for Laminar Flow in Round Tubes The exact two-dimensional equation for laminar flow in tubes is given by Eqs. (4.10.27) and (4.10.28):

$$-2u_{\text{mean}} \left(1 - \frac{4r^2}{d_t^2} \right) \frac{dc_A}{dz} + D_{\text{mol}} \frac{d^2 c_A}{dz^2} + D_{\text{mol}} \left(\frac{d^2 c_A}{dr^2} + \frac{1}{r} \frac{dc_A}{dr} \right) = r_A \quad (4.10.117a)$$

If radial diffusion is relatively large and the radial concentration profile has a chance to stabilize, that is, if the length-to-diameter ratio is sufficiently large, the

Table 4.10.6 Values of the dimensionless RTD curve [$\theta = t / \tau$, $E_\theta = c_{\text{tracer}} / (m_{\text{tracer}} / V_R)$].

θ	E_θ	θ	E_θ	θ	E_θ	θ	E_θ
0.2	0.03	1.4	0.46	2.6	0.11	3.8	0.02
0.4	0.32	1.6	0.38	2.8	0.09	4.0	0.02
0.6	0.58	1.8	0.30	3.0	0.07	4.2	0.01
0.8	0.66	2.0	0.24	3.2	0.05	4.4	0.01
1.0	0.63	2.2	0.19	3.4	0.04	4.6	0.01
1.2	0.55	2.4	0.15	3.6	0.03	4.8	0.01

Table 4.10.7 Calculated values based on the RTD curve.

Interval $\Delta\theta$	Average θ_{interval}	Average E_θ , interval	$\theta_{\text{interval}} E_{\theta,\text{interval}}$	$\Delta\theta$	$(\theta_{\text{interval}})^2 E_{\theta,\text{interval}}$	$\Delta\theta$
0.2	0.1	0.015	0.0003		0.00003	
0.2	0.3	0.175	0.0105		0.0315	
0.2	0.5	0.45	0.0450		0.0225	
0.2	0.7	0.62	0.0868		0.0608	
0.2	0.9	0.65	0.1170		0.1053	
0.2	1.1	0.59	0.1298		0.1428	
0.2	1.3	0.51	0.1326		0.1724	
0.2	1.5	0.42	0.1260		0.1890	
0.2	1.7	0.34	0.1156		0.1965	
0.2	1.9	0.27	0.1026		0.1949	
0.2	2.1	0.22	0.0924		0.1940	
0.2	2.3	0.17	0.0782		0.1799	
0.2	2.5	0.13	0.0650		0.1625	
0.2	2.7	0.10	0.0540		0.1458	
0.2	2.9	0.08	0.0464		0.1346	
0.4	3.2	0.05	0.0640		0.2048	
0.4	3.6	0.03	0.0432		0.1556	
0.4	4.0	0.02	0.0320		0.1280	
0.4	4.5	0.01	0.0180		0.0812	
			$\sum \theta_{\text{interval}} E_{\theta, \text{interval}}$	$\Delta\theta = 1.36$	$\sum (\theta_{\text{interval}})^2 E_{\theta, \text{interval}}$	$\Delta\theta = 2.50$

dispersion model introduced in Section 4.10.6.2 can be used (with the radial mean concentration), and for a first-order reaction we acquire the following one-dimensional equation (Froment and Bischoff 1990):

$$-u_{\text{mean}} \frac{dc_{A,\text{mean}}}{dz} + D_{\text{ax}} \frac{d^2 c_{A,\text{mean}}}{dz^2} = kc_{A,\text{mean}} \\ \left(\text{for } \frac{L}{d_t} > 0.04 \frac{u_{\text{mean}} d_t}{D_{\text{mol}}} = Re \times Sc \right) \quad (4.10.117b)$$

This approach is different than if we were to neglect the influence of molecular diffusion as done in Section 4.10.2.4 to derive the equation for the conversion in a tube with laminar flow and negligible molecular diffusion, Eq. (4.10.29).

Equation (4.10.117) expresses that a tubular reactor is formally represented by axial dispersion superimposed on plug flow. The dispersion coefficient D_{ax} is then needed, for example, based on the measurement of the residence time distribution or based on correlations for D_{ax} . Note that D_{ax} considers axial convection, molecular diffusion, and the effect of the radial velocity profile.

According to Aris (1956) and Taylor (1954), D_{ax} for laminar flow in empty tubes is given by:

$$D_{\text{ax}} = D_{\text{mol}} + \frac{u^2 d_t^2}{192 D_{\text{mol}}} \quad \left(\text{for } 1 < Re = \frac{ud_t}{\nu} < 2000 \right) \quad (4.10.118)$$

or in terms of the axial *Peclet number*, *Reynolds* and *Schmidt number* ($Sc = \nu/D_{\text{mol}}$) by:

$$\bullet \quad \frac{1}{Pe_{m,\text{ax}}} = \frac{D_{\text{ax}}}{ud_t} = \frac{D_{\text{mol}}}{ud_t} + \frac{ud_t}{192 D_{\text{mol}}} = \frac{1}{Re \times Sc} + \frac{Re \times Sc}{192} \\ \left(\text{for } 1 < Re = \frac{ud_t}{\nu} < 2000 \right) \quad (4.10.119)$$

Figures 4.10.60 and 4.10.61 show the influence of the term $Re \times Sc$ on $Pe_{m,\text{ax}}$ and Bo , respectively, for laminar flow, that is, the graphical representation of Eq. (4.10.119). At a low flow rate, the dispersion is only driven by molecular

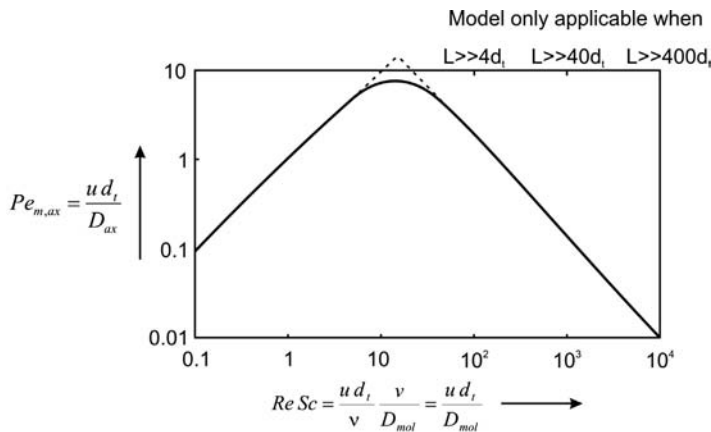


Figure 4.10.60 Axial dispersion for laminar flow in empty pipes (valid for $L/d_t > 0.04Re \times Sc$).

diffusion. At a higher flow rate the dispersion is caused by axial convection with radial diffusion and we have $D_{ax} = u^2 d_t^2 / (192 D_{mol})$.

Molecular diffusion strongly affects the dispersion rate in laminar flow. At a low flow rate (left arm in Figure 4.10.60), it promotes dispersion; at a higher rate the opposite is the case (right arm). This effect is used to find D_{mol} by measuring the axial dispersion in laminar flow (Example 4.10.9).

If the value of the Bo number is known (e.g., calculated by Figure 4.10.61) we can, finally, determine the conversion by Eq. (4.10.115).

For $Bo >$ about 80, we reach plug flow behavior, and the corresponding tube length-to-diameter ratio to fulfill this condition is given by:

$$\begin{aligned} Bo &= \frac{uL}{D_{ax}} = \frac{ud_t}{D_{ax} d_t} \frac{L}{d_t} = Pe_{m,ax} \frac{L}{d_t} \Rightarrow \frac{L}{d_t} \\ &= \frac{Bo}{Pe_{m,ax}} \quad \left(\text{thus for plug flow } \frac{L}{d_t} > \frac{80}{Pe_{m,ax}} \right) \end{aligned} \quad (4.10.120)$$

Figure 4.10.61 shows that this condition is fulfilled in a medium range of $Re \times Sc$, for example, for $L/d_t = 100$ for $1 < Re \times Sc < 250$, which is for a gas ($Sc \approx 1$) equivalent to the condition $1 < Re < 250$. For a liquid, for example, for water ($Sc \approx 450$), plug flow is reached for $L/d_t = 100$ for $0.002 < Re < 0.6$.

For comparison the case of a tubular reactor with laminar flow but without molecular diffusion is also shown in Figure 4.10.61, which is formally represented by $Bo \approx 6$, see also Figure 4.10.58. Values of Bo that are less than this value are only reached for very low values of $Re \times Sc$ and low L/d_t values, whereby we have to keep in mind that the model and thus Eqs. (4.10.117b) and (4.10.114) are only applicable for $L/d_t > 0.04Re \times Sc$.

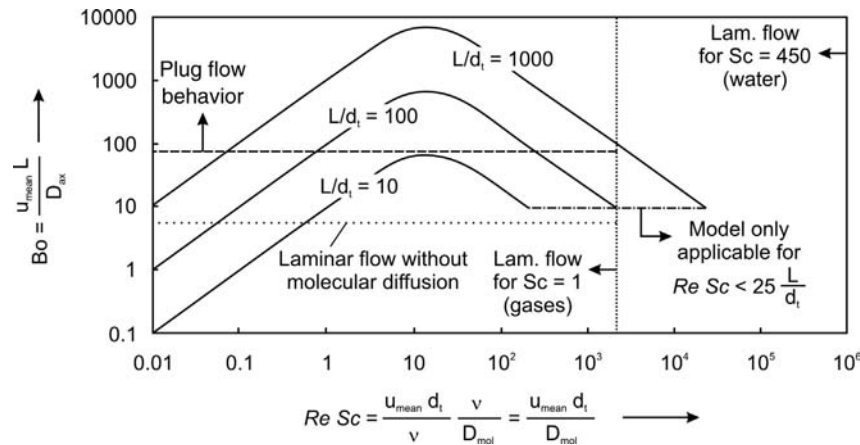


Figure 4.10.61 Bo number for laminar flow in an empty tube for different values of L/d_t (only valid for $L/d_t > 0.04Re \times Sc$).

Example 4.10.9: Determination of diffusion coefficients of fluids by dispersion measurements (Levenspiel, 1999)

We can also use Figure 4.10.61 to find D_{mol} of fluids by measuring the axial dispersion in laminar flow, which is quick, simple, and accurate. We simply determine the value of Bo based on the standard deviation σ_θ or based on $E_{\theta,\max}$, as outlined in Example 4.10.10. However, we will come up with two values of D_{mol} for a given value of Bo

(Figure 4.10.61), which give the same extent of axial dispersion. But if we know which arm of the curve we are on (a rough estimate of the term $Re \times Sc$ may help), we can find the correct value for D_{mol} ; if not, we need at least two runs at different velocities or two pipes with different sizes.

Axial Dispersion Model for Turbulent Flow in Round Tubes An empirical correlation given by Wen and Fan (1975) for turbulent flow in a round tube is:

$$\frac{1}{Pe_{m,\text{ax}}} = \frac{3 \times 10^7}{Re^{2.1}} + \frac{1.35}{Re^{1/8}} \quad (\text{for } Re = \frac{ud_t}{v} > 2000) \quad (4.10.121)$$

Figure 4.10.62 shows the influence of Re on $Pe_{m,\text{ax}}$. In the turbulent region a limiting value of about 5 is reached for $Pe_{m,\text{ax}}$, that is, plug flow behavior is usually achieved both for liquids and gases if the length-to-diameter ratio is higher than 20 [Eq. (4.10.120)].

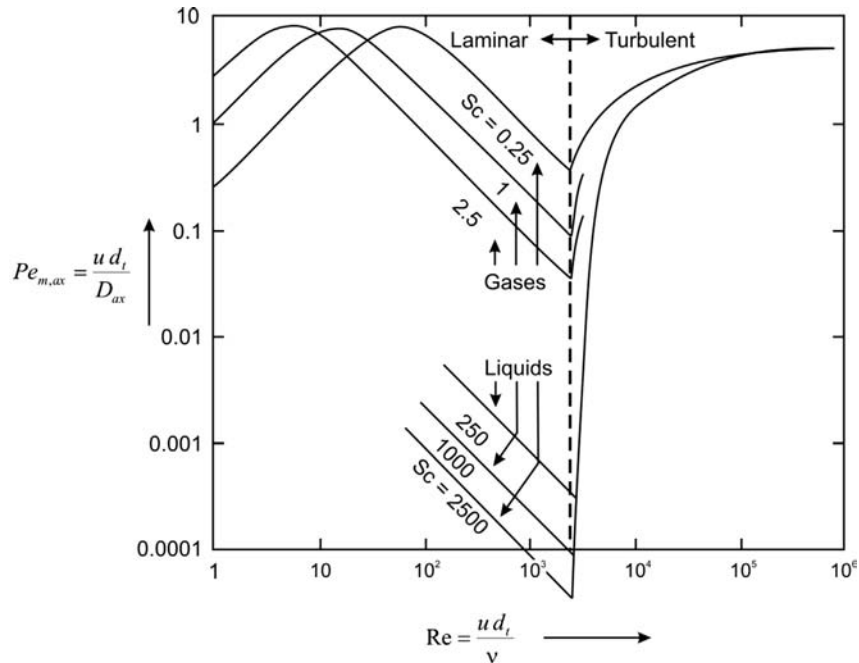
It follows from $Pe_{m,\text{ax}}$ in the laminar region that a negligible influence of dispersion and, thus, plug flow behavior can only barely be achieved for liquids as we get low values of $Pe_{m,\text{ax}}$ and thus low values of Bo ($= L/d_t Pe_{m,\text{ax}}$) unless L/d_t is not very high. For example, for $Pe_{m,\text{ax}} = 0.001$ a value of L/d_t of 80 000 would be needed to reach plug flow behavior.

For gases with $Sc \approx 1$, a much lower length-to-diameter ratio is needed to reach plug flow, as already discussed in conjunction with Figure 4.10.61, for example, for $Re = 1$, $L/d_t > 100$ for plug flow.

4.10.6.4 Dispersion of Mass and Heat in Fixed Bed Reactors

For packed beds, the axial Peclet number for mass $Pe_{m,\text{ax}}$ [$= u_S d_p / (\varepsilon D_{\text{ax}})$] is defined based on the interstitial velocity (ratio of superficial velocity and porosity, u_S/ε)

Figure 4.10.62 Axial dispersion of fluids in empty pipes (only valid for $L/d_t > 0.04 Re \times Sc$). Adapted from Levenspiel (1999).



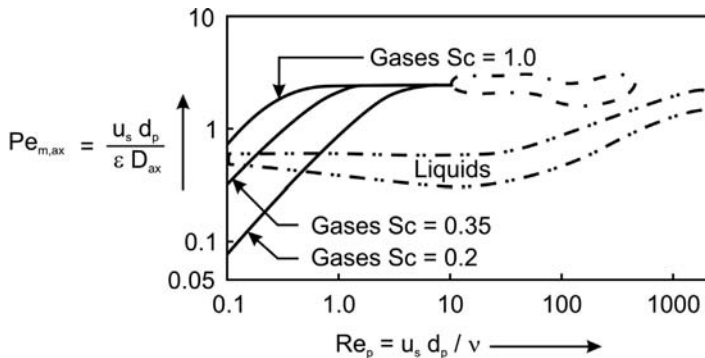


Figure 4.10.63 Axial dispersion of mass in a packed bed. Adapted from Levenspiel (1999).

and the particle diameter d_p as characteristic length. Figure 4.10.63 shows the experimental findings for $\text{Pe}_{m,\text{ax}}$ over a wide range of Re_p ($=u_s d_p/v$ with u as superficial velocity). For a small deviation from plug flow, a tubular reactor can be regarded as a cascade of N CSTRs, Eq. (4.10.105), and thus we have:

$$N = \frac{Bo}{2} = \frac{u_s L}{2\varepsilon D_{\text{ax}}} = \frac{\text{Pe}_{m,\text{ax}} L}{2d_p} \quad (\text{for } Bo > 80) \quad (4.10.122)$$

For high Re_p values we reach a value for $\text{Pe}_{m,\text{ax}}$ of 2 for gases and for liquids we have a value of 0.5 for $\text{Re}_p < 100$ (Figure 4.10.64). Thus we get the following rules of thumb:

! $N = \frac{\text{Pe}_{m,\text{ax}} L}{2d_p} \approx \frac{L}{d_p} \quad (\text{for gases, } \text{Re}_p > 10) \text{ and}$

$$N \approx \frac{L}{4d_p} \quad (\text{for liquids } \text{Re}_p < 100) \quad (4.10.123)$$

According to Eq. (4.10.123), the empty spaces of a packed bed with a gas flow can be regarded as ideal mixers, and each particle layer acts as one stirrer. Consequently, for a ratio of tube length to particle diameter of more than 40 (cascade with $N=40$), a fixed bed can be regarded as an ideal plug flow reactor (Section 4.10.2.3). For liquids, similar consideration leads to a tube length of 160 particle diameters to reach almost plug flow behavior.

The comparison of axial and radial dispersion in a packed bed is given in Figure 4.10.64 in terms of $\text{Pe}_{m,\text{ax}}$ [$u_s d_p / (\varepsilon D_{\text{ax}})$] and $\text{Pe}_{m,\text{rad}}$ [$u_s d_p / (\varepsilon D_{\text{rad}})$]. For high values of Re_p ($u_s d_p/v$), we reach a limiting value for $\text{Pe}_{m,\text{rad}}$ of about

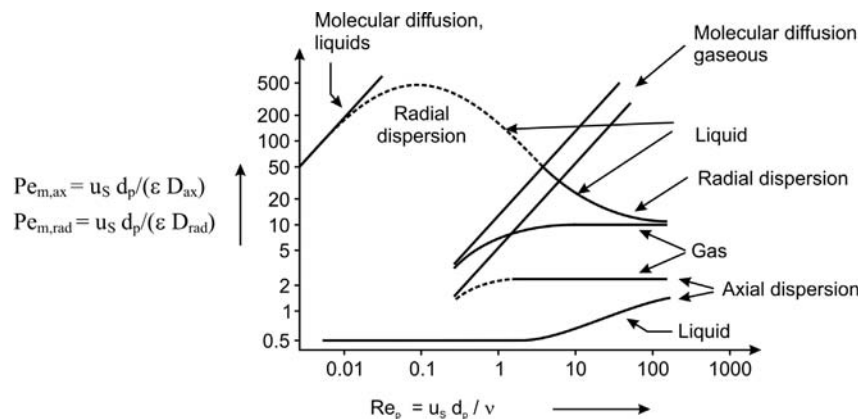


Figure 4.10.64 Comparison of axial and radial dispersion of mass (liquids and gases) in a packed bed. Adapted from Westerterp, van Swaaij, and Beenackers (1998).

10, which is by a factor of 5 higher than the value of $Pe_{m,ax}$. More details on dispersion of mass in packed beds may be found in Delgado (2006).

Dispersion of heat can be described in a similar manner as dispersion of mass if we use an effective thermal conductivity in the axial and radial direction (λ_{ax} , λ_{rad}). The corresponding dimensionless *Peclet numbers* are $Pe_{h,rad}$ ($= u_S c_p \rho_{mol} d_p / \lambda_{rad}$) and $Pe_{h,ax}$ ($= u_S c_p \rho_{mol} d_p / \lambda_{ax}$). Note that the superficial fluid velocity, u_S , and not the interstitial velocity, u_S/ϵ , is used in the definition of Pe_h , as the effective heat conduction (reflecting both the effective heat conduction in the gas and solid phase) is not limited to the empty space of the packed bed as in the case of dispersion of mass (see also differential equations of a fixed bed reactor in Section 4.10.7). As a rule of thumb, we can approximately use the same values for the *Peclet* number for dispersion of heat for high Re_p numbers (>100) as for the corresponding numbers for dispersion of mass, that is, $Pe_{h,rad} \approx 10$ and $Pe_{h,ax} \approx 2$. Details on the radial heat dispersion, which is important for wall-cooled reactors, are given in Section 4.10.7.3.

As we will learn in Section 4.10.7.2, radial dispersion of heat is by far the most important dispersion effect in fixed bed reactors. Thus, Section 4.10.7.3 gives some more accurate equations to determine the effective radial heat conductivity λ_{eff} .

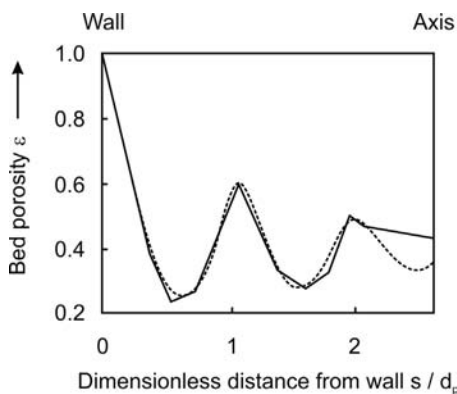


Figure 4.10.65 Calculated radial porosity profile (dashed line) for $d_R \approx 25$ mm and $d_p \approx 5$ mm (adapted from Delmas and Froment, 1988) and measured data (solid line) (Benenati and Brosilow, 1962).

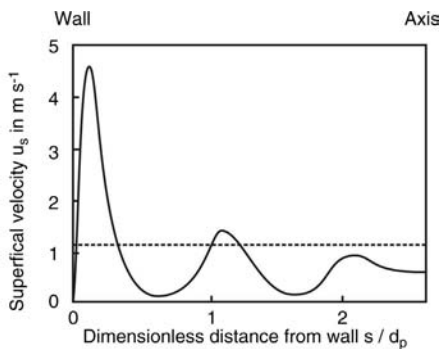


Figure 4.10.66 Calculated radial velocity profile for $d_R \approx 25$ mm and $d_p \approx 5$ mm [adapted from Delmas and Froment (1988)]; dashed line: average velocity.

4.10.6.5 Radial Variations in Bed Structure: Wall Effects in Narrow Packed Beds

Owing to the nonuniform radial distribution of voidage, permeability, and velocity in a critical region close to the wall, the ratio of the diameter of the tubular reactor (d_R) to the particle diameter (d_p), the aspect ratio, may influence transport properties in fixed-bed reactors. For uniform spheres with a smooth surface the interstitial bed porosity ϵ starts with a maximum value of unity at the reactor wall. Then ϵ displays damped oscillations with a period close to d_p over a distance of about $5d_p$ into the bulk of the bed until the void fraction reaches values typical for random close packings of about 40% (Benenati and Brosilow, 1962; Ridgway and Tarbuck, 1968). Examples of the radial void fraction profile and the corresponding radial velocity profile in a cross section of a narrow fixed bed with an aspect ratio of about 5 are shown in Figures 4.10.65 and 4.10.66. An empirical correlation for the average voidage is given by Jeschar (1964):

$$\epsilon = 0.375 + 0.34 \frac{d_p}{d_R} \quad (4.10.124)$$

The consequences of this geometrical wall effect for the flow heterogeneity, axial dispersion, and particle-to-fluid heat and mass transfer may be particularly severe for aspect ratios d_R/d_p below 15, where the wall region occupies a substantial fraction of the total reactor (Ahn, Zoulian, and Smith, 1986; Carbonell, 1980; Martin, 1978; Gunn and Price, 1969). Other values given in the literature for this limiting aspect ratio are 8 (Hsiang and Heynes, 1977) and 10 (Chu and Ng, 1989; Daszkowski and Eigenberger, 1992; Papageorgiou and Froment, 1995). Thus for aspect ratios higher than approximately 10, the dispersion in packed beds of spheres is within the limits of experimental precision independent of d_R/d_p , and wall effects are negligible. Unfortunately, small diameter packed beds are widely used in the case of strong exothermic reactions. The dispersion in these reactors may therefore be largely dependent on the ratio d_R/d_p , and influences the operation of packed bed reactors (Young and Finlayson, 1973).

4.10.7

Modeling of Fixed Bed Reactors

Fixed-bed tubular reactors are the most common reactors used for heterogeneously catalyzed reactions and are also applied for gas–solid reactions. Unfortunately, real fixed bed reactors may differ from plug flow reactors, for example, we may have radial profiles of concentration or temperature, dispersion of mass and heat, formation of channels and short circuit flow, or stagnant zones. Thus mass and heat transfer may significantly affect the reactor performance if temperature and concentration gradients are large. Thus, adequate modeling equations are needed, and criteria would be helpful to predict significant effects of mass and heat transfer. This is important for kinetic studies in laboratory-scale reactors to minimize the intrusion of dispersion effects as well as for the design of industrial reactors. Subsequently, these criteria and the modeling equations are deduced. Similar considerations may be deduced for other reactors, for example, a slurry or fluidized bed reactor, but are more complicated and are not considered here.

4.10.7.1 Fundamental Balance Equations of Fixed Bed Reactors

First, let us inspect the basic equations of a fixed reactor for a single reaction of reactant A and steady state, if the so-called pseudo-homogeneous two-dimensional model in its most complex form is used (for simplification, all data on chemical media and also the fluid velocity are considered to be constant throughout the reactor, that is, only the values of T and c change):

$$\boxed{!} \quad \underbrace{u_s \frac{dc_A}{dz}}_{\text{Change of concentration in axial direction}} = \underbrace{\varepsilon D_{ax} \frac{d^2 c_A}{dz^2} + \varepsilon D_{rad} \left(\frac{d^2 c_A}{dr^2} + \frac{1}{r} \frac{dc_A}{dr} \right)}_{\text{Dispersion of mass in axial and radial direction}} - \underbrace{r_{m,eff} \rho_b}_{\text{Chemical reaction}} \quad (4.10.125)$$

$$\boxed{!} \quad \underbrace{(\rho_{mol} c_p u_s) \frac{dT}{dz}}_{\text{Change of temperature in axial direction}} = \underbrace{\lambda_{ax} \frac{d^2 T}{dz^2} + \lambda_{rad} \left(\frac{d^2 T}{dr^2} + \frac{1}{r} \frac{dT}{dr} \right)}_{\text{Dispersion of heat in axial and radial direction}} - \underbrace{\Delta_R H r_{m,eff} \rho_b}_{\text{Heat production by chemical reaction}} \quad (4.10.126)$$

Equations (4.10.125) and (4.10.126) are extensions of the equations for an ideal plug flow reactor, Eqs. (4.10.69) and (4.10.70), to a tubular fixed bed reactor with radial gradients of temperature and concentration and hence include the factors considering the dispersion of mass and heat. (Note that we now use the term $r_{m,eff} \rho_b$ instead of r as used for homogeneous reactions.)

The effective reaction rate $r_{m,eff}$ (related to the mass of catalyst/solid) already considers all extra- and intraparticle mass and heat transfer effects (Sections 4.5–4.7). Thus the pseudo-homogeneous model does not distinguish between the conditions in the fluid and in the solid phase, as more sophisticated heterogeneous models do, as discussed, for example, in Baerns *et al.* (2006), Froment and Bischoff (1990), and Westerterp, van Swaaij, and Beenackers (1998). Thus, gradients of temperature and concentration within the particle and in the thermal and diffusive boundary layers are combined by the use of an overall effectiveness factor that enables the system of four equations (mass and heat balances for solid and fluid phase) to be replaced by just two equations, Eqs. (4.10.125) and (4.10.126).

These two equations may be rewritten in dimensionless form by introduction of the *Peclet numbers* for axial and radial dispersion of mass [$Pe_{m,ax} = u_s d_p / (\varepsilon D_{ax})$, $Pe_{m,rad} = u_s d_p / (\varepsilon D_{rad})$], and for heat dispersion [$Pe_{h,rad} = u_s c_p \rho_{mol} d_p / \lambda_{rad}$, $Pe_{h,ax} = u_s c_p \rho_{mol} d_p / \lambda_{ax}$] (see Section 4.10.6.4 for details). Together with the dimensionless axial and radial coordinates $Z = z/L$ and $R = r/r_R$, and the residence time with

respect to the empty reactor $\tau = L/u_s$, we then get:

$$\frac{dc_A}{dZ} = \frac{1}{Pe_{m,ax}} \frac{d_p}{L} \frac{d^2 c_A}{dZ^2} + \frac{1}{Pe_{m,rad}} \frac{L d_p}{r_R^2} \left(\frac{d^2 c_A}{dR^2} + \frac{1}{R} \frac{dc_A}{dR} \right) - \rho_b r_{m,eff} \tau s \quad (4.10.127)$$

$$\frac{dT}{dZ} = \frac{1}{Pe_{h,ax}} \frac{d_p}{L} \frac{d^2 T}{dZ^2} + \frac{1}{Pe_{h,rad}} \frac{d_p L}{r_R^2} \left(\frac{d^2 T}{dR^2} + \frac{1}{R} \frac{dT}{dR} \right) - \frac{\Delta_R H \tau}{\rho_m c_p} \rho_b r_{m,eff} \quad (4.10.128)$$

The adiabatic temperature rise is given by:

$$\Delta T_{ad} = \frac{c_{A,in} (-\Delta_R H)}{c_p \rho_{mol}} \quad (4.10.129)$$

and so we can simplify Eq. (4.10.128) further:

$$\frac{dT}{dZ} = \frac{1}{Pe_{h,ax}} \frac{d_p}{L} \frac{d^2 T}{dZ^2} + \frac{1}{Pe_{h,rad}} \frac{d_p L}{r_R^2} \left(\frac{d^2 T}{dR^2} + \frac{1}{R} \frac{dT}{dR} \right) + \frac{\Delta T_{ad} \tau}{c_{A,in}} \rho_b r_{m,eff} \quad (4.10.130)$$

Depending on the mode of reactor operation (adiabatic, wall-cooled etc.), these equations have to be complemented by respective boundary conditions (values at reactor inlet, symmetry considerations in the axis of a tubular reactor, radial heat transfer at the wall), as subsequently inspected in more detail in Section 4.10.7.3 for a wall cooled fixed bed reactor.

The two equations for the mass and heat balance, Eqs. (4.10.125) and (4.10.126) or the dimensionless forms represented by Eqs. (4.10.127), (4.10.128) and (4.10.130), consider that the flow in a packed bed deviates from the ideal pattern because of radial variations in velocity and mixing effects due to the presence of the packing. To avoid the difficulties involved in a rigorous and complicated hydrodynamic treatment, these mixing effects as well as the (in most cases negligible contributions of) molecular diffusion and heat conduction in the solid and fluid phase are combined by effective dispersion coefficients for mass and heat transport in the radial and axial direction (D_{ax} , D_{rad} , λ_{rad} , and λ_{ax}). Thus, the fluxes are expressed by formulas analogous to *Fick's law* for mass transfer by diffusion and *Fourier's law* for heat transfer by conduction, and Eqs. (4.10.125) and (4.10.126) superimpose these fluxes upon those resulting from convection. These different dispersion processes can be described as follows (see also the Sections 4.10.6.4 and 4.10.7.3):

- 1) **Radial (transverse) dispersion of mass:** During passage of the fluid through the fixed bed, the repeated lateral displacement combined with mixing of fluid elements of different streamlines lead to radial mixing perpendicular to the main flow in axial direction. This can be characterized by an apparent radial dispersion coefficient (effective radial diffusivity) D_{rad} , which is in most practical cases much higher than the molecular diffusion coefficient.
- 2) **Axial dispersion of mass:** The variations of local velocities in a packed bed and to a very small extent molecular diffusion cause an axial (longitudinal) dispersion in the direction of flow, which can be described by an axial dispersion coefficient or effective axial diffusivity D_{ax} , which is for high values of Re_p (>1 for gases and >100 for liquids) about 5 times higher than D_{rad} (Figure 4.10.64). The empty spaces of the packed bed can be regarded as ideal mixers, and so the number of mixers in series is roughly equals the ratio L/d_p . Hence, a reactor length of the order of magnitude of ten particles will almost lead to a plug flow behavior, because a cascade of ten CSTRs already approaches the behavior of a PFR.
- 3) **Axial dispersion of heat:** In the case of strong exothermic or endothermic reactions, axial temperature profiles will occur even in intensively cooled reactors, and axial (longitudinal) dispersion smoothens these profiles. This dispersion can be described by an effective axial thermal conductivity λ_{ax} that combines heat conduction via the gas and solid phase.
- 4) **Radial dispersion of heat:** In wall-cooled or heated reactors, the heat release or consumption leads to radial temperature gradients. Even for an adiabatic reactor such gradients may occur because of local radial differences of the fluid velocity

and thus of the residence time and local degree of conversion, but this effect is not of practical relevance. Analogously to axial heat dispersion, the radial heat transport is described by an effective radial thermal conductivity λ_{rad} , which is usually much higher than λ_{fluid} (Section 4.10.7.3).

- 5) **Radial variations in bed structure:** for a shallow reactor with a low ratio of the tube to particle diameter, undesirable wall effects (bypassing, slippage) may occur.

As a rule of thumb, axial dispersion of heat and mass (factors 2 and 3) only influence the reactor behavior for strong variations in temperature and concentration over a length of a few particles. Thus, axial dispersion is negligible if the bed depth exceeds about ten particle diameters. Such a situation is unlikely to be encountered in industrial fixed bed reactors and mostly also in laboratory-scale systems. Radial mass transport effects (factor 1) are also usually negligible as the reactor behavior is rather insensitive to the value of the radial dispersion coefficient. Conversely, radial heat transport (factor 4) is really important for wall-cooled or heated reactors, as such reactors are sensitive to the radial heat transfer parameters.

The model equations of the fixed bed reactor given by Eqs. (4.10.125) and (4.10.126) are still rather complicated. Thus, criteria would be helpful to decide whether and which of the different dispersion effects can be neglected. In Section 4.10.7.2, these criteria are examined. In Section 4.10.7.3, we will give deeper insight into the modeling of wall-cooled fixed bed reactors and the problems related to the modeling of radial heat transport.

4.10.7.2 Criteria used to Exclude a Significant Influence of Dispersion in Fixed Bed Reactors

Transport effects, occurring both radially and axially in the reactor as a whole are particularly difficult to evaluate and control. The equations used to derive the corresponding parameters D_{rad} , D_{ax} , λ_{ax} , λ_{rad} , and the dimensionless Pe numbers have already been addressed in Section 4.10.6.

The concept of criteria for exclusion of interparticle mass and heat transfer effects is the following. Since during a reaction non-zero gradients of concentration and/or of temperature always exist in the fixed bed reactor (albeit sometimes they are very small), a somewhat arbitrary assumption has to be made about the maximum deviation up to which the reaction can be considered not to be influenced by axial and radial mass and heat transport phenomena. The maximum deviation commonly used is 5%, for example, of the reaction rate compared to the zero-gradient rate or of the reactor length compared to the length of an ideal PFR.

Axial Dispersion of Mass The criterion for a negligible influence of axial dispersion of mass is (Mears, 1971, 1976):

$$\frac{L}{d_p} \geq 20 \frac{Da}{Pe_{m,\text{ax}}} \quad (4.10.131)$$

Mears derived this equation based on the assumption that the deviation of the required reactor length compared to an ideal plug flow reactor should be less than 5%. For a better understanding of this criterion we rewrite Eq. (4.10.131) for a first-order reaction as:

$$\frac{L}{d_p} \geq 20 \underbrace{\frac{\varepsilon D_{\text{ax}}}{u_s d_p}}_{1/Pe_{m,\text{ax}}} \underbrace{\left(k_{m,\text{eff}} \rho_b \tau \right)}_{Da} \Rightarrow \underbrace{\left(\frac{L}{u_s} \right)}_{\tau} \leq 0.05 \underbrace{\left(\frac{1}{k_{m,\text{eff}} \rho_b} \right)}_{\tau_R} \underbrace{\frac{1}{\tau}}_{\tau_{D,\text{ax}}} \underbrace{\left(\frac{L^2}{\varepsilon D_{\text{ax}}} \right)}_{\tau_{D,\text{ax}}} \quad (4.10.132)$$

and a more obvious criterion can be derived by the introduction of three characteristic times:

- the residence time $\tau = L/u_s$ (related to the empty tube with u_s as the superficial velocity);
- the time for axial dispersion in a reactor of length L , $\tau_{D,\text{ax}} = L^2/(\varepsilon D_{\text{ax}})$;

- the time for the reaction for a first-order reaction, $\tau_R = (k_{m,eff} \rho_b)^{-1} = \tau/Da$.
(Remark: For an n -th order reaction, use $r_{m,eff} \rho_b / c_A$ instead of $k_{m,eff} \rho_b k_{m,eff} \rho_b$)

Rewriting Eq. (4.10.132) by means of these characteristic times leads to:

$$\tau \leq 0.05 \frac{\tau_R}{\tau} \tau_{D,ax} = \frac{0.05}{Da} \tau_{D,ax} \cdot s \quad (4.10.133)$$

Equation (4.10.133) shows that the influence of axial dispersion is negligible if the residence time τ is by a factor of $0.05/Da$ smaller than the axial dispersion time $\tau_{D,ax}$.

Thus the value of τ that is needed to ensure that axial dispersion of mass affects the reactor length by less than 5%, depends on the *Damkoehler number* Da . For $Da=1$ this criterion is fulfilled if the residence time τ equals 5% of the dispersion time $\tau_{D,ax}$. For Da higher or lower than unity, the criterion is tightened ($\tau_{D,ax} < 0.05 \tau_{D,ax}$) or diminished ($\tau_{D,ax} > 0.05 \tau_{D,ax}$). This effect is easy to understand if we consider that deviation of the behavior of a back-mixed reactor compared to an ideal PFR increases with increasing conversion and value of Da – simply think of the case of a CSTR compared to a PFR – and thus the criterion for the minimal residence time compared to the axial dispersion time is stricter.

The axial *Peclet number* $Pe_{m,ax} = u_S d_p / (\varepsilon D_{ax})$ has a value of 2 for realistic *Reynolds numbers* Re_p (Section 4.10.6.4), and so the following simple criterion for a negligible influence of axial dispersion of mass can be derived based on Eq. (4.10.131):

$$\frac{L}{d_p} \geq 10Da \quad (\text{for a first-order reaction}) \quad (4.10.134)$$

Thus, even for a high conversion (e.g., 99% in a PFR, that is, $Da=5$), a length of 50 particle diameters is sufficient to exclude a significant influence of axial dispersion of mass.

Equation (4.10.134) can be also derived based on the following consideration: A real tubular reactor can be regarded as a cascade consisting of N CSTRs, and for a high value of N we approach plug flow behavior. Thus the condition of a negligible influence of backmixing is that the Da number needed to reach a certain conversion in the cascade should not deviate from the value of Da needed in an ideal PFR by more than 5%. For a first-order reaction, this condition and Eqs. (4.10.32) and (4.10.25) lead to:

$$\frac{(1 + 1.05 Da/N)^N - 1}{(1 + 1.05 Da/N)^N} = 1 - e^{-Da} \quad (4.10.135)$$

With increasing value of Da , the number N of CSTRs required to achieve this condition increases, which can be expressed by a factor f , that is, N is given by the term (fDa) . This leads to:

$$\frac{\left(1 + \frac{1.05}{f}\right)^{fDa} - 1}{\left(1 + \frac{1.05}{f}\right)^{fDa}} = 1 - e^{-Da} \Rightarrow f \ln\left(1 + \frac{1.05}{f}\right) = 1 \quad (4.10.136)$$

This condition, in turn, leads to a value for f of 10, that is, N for 5% deviation in Da is simply given by:

$$N \geq 10Da \quad (4.10.137)$$

As outlined in Section 4.10.6.4 each particle layer in a fixed bed acts as a stirrer, and the axial dispersion model and the tanks in series model are related by $N = L/d_p$ [Eq. (4.10.123)]. Thus, Eq. (4.10.123) in combination with Eq. (4.10.137) is equivalent to Eq. (4.10.134).

Radial Dispersion of Mass In contrast to axial dispersion in a tubular fixed bed reactor, mass transfer in the radial direction should be maximized to prevent

significant deviations from plug flow and thus a lower degree of conversion. A very strict criterion – too strict, as discussed below – for a negligible influence of radial dispersion of mass can be derived by assuming that the characteristic time for radial dispersion in the cross section of the tube (diameter d_R) should be below 5% of the characteristic time for reaction. For a first-order reaction, this condition for freedom from significant effects of radial dispersion of mass reads as:

$$\tau_{D,rad} \leq 0.05\tau_R \Leftrightarrow \frac{\left(\frac{d_R}{2}\right)^2}{\varepsilon D_{rad}} \leq \frac{0.05}{k_{m,eff} \rho_b} \quad (4.10.138)$$

For convenience, we rewrite Eq. (4.10.138) in terms of the radial *Peclet number* for mass $Pe_{m,rad} = u_S d_p / (\varepsilon D_{rad})$ and the *Damkoehler number* ($Da = k_{m,eff} \rho_b \tau = k_{m,eff} \rho_b L / u_S$):

$$\frac{\left(\frac{d_R}{2}\right)^2 Pe_{m,rad}}{u_s d_p} \leq 0.05 \frac{L}{Da} \quad (4.10.139)$$

and rearrangement leads to:

$$\frac{d_R}{d_p} \leq 0.2 \frac{L}{d_R Da} \frac{1}{Pe_{m,rad}} \quad (4.10.140)$$

Thus, for a high value of Da (conversion) and for a high value of $Pe_{m,rad}$ (low radial dispersion), a decrease of the reactor diameter is needed to avoid radial concentration profiles; $Pe_{m,rad}$ is about 10 for realistic *Reynolds* numbers Re_p (Section 4.10.6.4), and Eq. (4.10.140) yields:

$$\frac{d_R}{d_p} \leq 0.02 \frac{L}{d_R Da} \frac{1}{Pe_{m,rad}} \quad (4.10.141)$$

At first sight, Eqs. (4.10.139)–(4.10.141) presume that the criterion to exclude radial dispersion of mass depends on the reactor length L . This is not the case, as Da includes the residence time ($\tau = L/u_S$) and thus L , for example, for a first-order reaction [Eq. (4.10.141)] also reads as:

$$\frac{d_R}{d_p} \leq 0.02 \frac{u_S}{d_R k_{m,eff} \rho_b} \quad (4.10.142)$$

Thus, radial concentration profiles, for example, provoked by radial temperature profiles in cooled (or heated) reactors, are not completely smoothed, if Eqs. (4.10.141) and (4.10.142) are not fulfilled. In experimental reactors a typical value of the ratio L/d_R is 10 and Da is mostly smaller than unity (corresponding to a conversion of less than 60% in a PFR). Thus unrealistically small d_R -to- d_p ratios of less than unity are needed to exclude radial concentration gradients. Nevertheless, numerical simulations – for example, by Carberry and White (1969) on the oxidation of naphthalene in a cooled tubular catalytic fixed bed reactor – showed that even for a value of Da of 5, $L/d_R = 20$, and $d_R/d_p = 10$ the radial dispersion has no influence on the reactor performance, although the criterion of Eq. (4.10.141) is far from fulfilled. In other words, an insufficient radial mass transport may lead to a certain extent to an uneven radial concentration distribution, but the conversion and the yields are virtually the same as for a PFR.

Based on the above given values of Da , L/d_R , and d_R/d_p where radial dispersion still has no effect on the reactor performance, we can derive a new, more realistic and still conservative criterion for the exclusion of an influence of radial dispersion of mass:

$$\frac{d_R}{d_p} \leq 25 \frac{L}{d_R Da} \frac{1}{Pe_{m,rad}} \approx 2.5 \frac{L}{d_R Da} \quad (4.10.143)$$

Again taking typical values of experimental reactors ($L/d_R = 20$, $Da = 1$), we now get a d_R -to- d_p ratio of less than 50 to exclude radial concentration gradients. For technical wall-cooled or heated reactors, where radial concentration gradients may occur, the L -to- d_R ratio is even higher, and thus the d_R -to- d_p ratio needed to avoid an influence of radial dispersion of mass is higher.

Axial Dispersion of Heat According to Mears (1976), solution of the differential equations for the heat and mass balance (for a first-order reaction) lead to the following equation for the deviation of the axial temperature in a wall-cooled or heated fixed bed reactor from the corresponding value in an ideal plug-flow reactor:

$$(T - T_{PFR}) = \frac{k_{m,\text{eff}} c_{A,\text{in}} \rho_b d_p (-\Delta_R H)}{u_S c_p \rho_{\text{mol}}} \frac{\lambda_{\text{ax}}}{u_S c_p \rho_g d_p} \quad (4.10.144)$$

Introducing the axial *Peclet number* for heat $Pe_{h,\text{ax}} = u_S c_p \rho_g d_p / \lambda_{\text{ax}}$, the residence time τ with regard to the empty tube and the *Damkoehler number* $Da = k_{m,\text{eff}} \rho_b \tau = k_{m,\text{eff}} \rho_b L / u_S$ leads to (if an exothermic reaction is taken as example):

$$(T - T_{PFR}) = \frac{Da c_{A,\text{in}} d_p (-\Delta_R H)}{L c_p \rho_{\text{mol}}} \frac{1}{Pe_{h,\text{ax}}} \quad (4.10.145)$$

With the adiabatic temperature rise [Eq. (4.10.129)], Eq. (4.10.145) reduces to:

$$(T - T_{PFR}) = \frac{d_p Da \Delta T_{\text{ad}}}{L Pe_{h,\text{ax}}} \quad (4.10.146)$$

The criterion for negligible influence of axial dispersion of heat is that the rate (constant) is affected by less than 5%:

$$k_{m,\text{eff}}(T) \leq 1.05 k_{m,\text{eff}}(T_{PFR}) \quad (4.10.147)$$

Using the wall temperature T_W as a practical reference, this condition leads to:

$$e^{\frac{E_A}{R} \left(\frac{1}{T_{PFR}} - \frac{1}{T} \right)} \approx e^{\frac{E_A}{R} \left(\frac{T - T_{PFR}}{T_W^2} \right)} \leq 1.05 \quad (4.10.148)$$

Rewriting gives:

$$\frac{E_A}{R} \left(\frac{T - T_{PFR}}{T_W^2} \right) \leq \ln(1.05) \approx 0.05 \quad (4.10.149)$$

Combination of Eq. (4.10.149) with Eq. (4.10.146) finally leads to the criterion:

$$\frac{E_A}{RT_W} \frac{\Delta T_{\text{ad}}}{T_W} \frac{Da}{Pe_{h,\text{ax}}} \frac{d_p}{L} \leq 0.05 \quad (4.10.150)$$

or:

$$\frac{L}{d_p} \geq 20 \frac{E_A}{R T_W} \frac{\Delta T_{\text{ad}}}{T_W} \frac{Da}{Pe_{h,\text{ax}}} \quad (4.10.151)$$

The axial *Peclet number* for heat has about the same value as the corresponding value for dispersion of mass, that is, a value of 2 (Section 4.11.4), and so Eq. (4.10.151) simplifies to:

$$\frac{L}{d_p} \geq 10 Da \frac{E_A}{RT_W} \frac{\Delta T_{\text{ad}}}{T_W} \quad (4.10.152)$$

The term $E_A/(RT_W)\Delta T_{\text{ad}}/T_W$ is the well-known dimensionless number N_{ad} used in the analysis of the parametric sensitivity of reactors (Section 4.10.3):

$$N_{\text{ad}} = \frac{E_A}{RT_W} \frac{\Delta T_{\text{ad}}}{T_W} \quad (4.10.153)$$

The term N_{ad} accounts for the heat generation and combines the group for adiabatic temperature rise $\Delta T_{\text{ad}}/T_W$ with the temperature sensitivity of the reaction

$E_A/(RT_W)$, the so-called *Arrhenius number*. In many practical cases, N_{ad} reaches values of at least 5 – for example for $T = 600 \text{ K}$, $E_A = 50 \text{ kJ mol}^{-1}$, and $\Delta T_{ad} = 300 \text{ K}$. Comparison with the criterion for exclusion of a significant effect of axial dispersion of mass, Eq. (4.10.133), shows that the axial heat transfer becomes significant before the axial mass transfer does. Thus, the criterion of Eq. (4.10.152) is usually sufficient to exclude axial dispersion of heat *and* mass, and we obtain:

$$\frac{L}{d_p} \geq 10 \frac{k_{m,\text{eff}} L}{u_s} \frac{E_A}{RT_W} \frac{\Delta T_{ad}}{T_W} \quad (4.10.154)$$

Interestingly, the effects of axial dispersion of heat and mass oppose each other for an exothermic reaction (and are additive for endothermic reactions). With exothermic reactions the axial heat dispersion enhances the rate, whereas the axial dispersion of mass diminishes it. With endothermic reactions both effects act to diminish the rate. The combined criterion is:

$$\left| \left(\frac{d_p}{L} \frac{Da}{Pe_{m,\text{ax}}} \right) - \left(\frac{E_A}{RT_W} \frac{\Delta T_{ad}}{T_W} \frac{Da}{Pe_{h,\text{ax}}} \frac{d_p}{L} \right) \right| \leq 0.05 \quad (4.10.155)$$

Nevertheless, the opposing (or strengthening) effect of axial dispersion of heat and mass for exothermic (endothermic) reactions is in most cases negligible. For example, for an exothermic reaction, simplification with $Pe_{h,\text{ax}} \approx 2$ leads to:

$$\frac{L}{d_p} \geq 10 Da \left(\frac{E_A}{RT_W} \frac{\Delta T_{ad}}{T_W} - 1 \right) \quad (4.10.156)$$

The term $E_A \Delta T_{ad}/(RT_W^2)$ reaches values of at least 5 for exothermic reactions performed in wall-cooled tubular reactors, and so the term in brackets in Eq. (4.10.156) and thus the minimum L -to- d_p ratio according to Eq. (4.10.152) is only marginally diminished.

Radial Dispersion of Heat A criterion for negligible influence of radial dispersion of heat (negligible radial T -profile) can be derived by the simplified one-dimensional reactor model [Section 4.10.3.3, Eq. (4.10.70)], which reads for a differential segment of a fixed bed reactor with reaction temperature T_R and wall temperature T_W as:

$$\rho_{\text{mol}} c_p \dot{V} dT + U_h (T_R - T_W) dA_{t,\text{int}} = (-\Delta_R H) r_{m,\text{eff}} \rho_b dV_R s \quad (4.10.157)$$

if we neglect the convective term of the heat balance, that is, the term $u_s \rho_{\text{mol}} c_p dT$.

If we use the two-dimensional heat transfer parameters λ_{rad} (effective thermal conductivity in radial direction) and α_w (wall heat transfer coefficient at bed side), we can use the following approximation of the overall heat transfer coefficient U_h (Section 4.10.7.3):

$$\frac{1}{U_h} = \frac{d_R}{8\lambda_{\text{rad}}} + \frac{1}{\alpha_w} \quad (4.10.158)$$

(Note that if we neglect the convective term, the criterion derived is on the “safe side.”)

Analogously to axial heat dispersion, the condition for a negligible difference $T_R - T_W$ is:

$$(T_R - T_W) \leq 0.05 \frac{RT_W^2}{E_A} \quad (4.10.159)$$

Combination of Eqs. (4.10.157) and (4.10.159) leads to:

$$r_{m,\text{eff}} \rho_b d_R (-\Delta_R H) \leq 0.2 U_h \frac{RT_W^2}{E_A} \quad (4.10.160)$$

Introducing the radial *Peclet number* for heat $Pe_{h,\text{rad}} = u_s c_p \rho_{\text{mol}} d_p / \lambda_{\text{rad}}$, the adiabatic temperature difference ΔT_{ad} [Eq. (4.10.129)], the *Damkoehler number*

$Da = r_{m,eff}\rho_b\tau/c_A$, Eqs. (4.10.158) and (4.10.160) lead after some rearrangements to:

$$\frac{E_A}{RT_W} \frac{\Delta T_{ad}}{T_W} \frac{Pe_{h,rad} Da \times d_R^2}{d_p L} \leq \frac{1.6}{\left(1 + \frac{8\lambda_{rad}}{\alpha_W d_R}\right)} \quad (4.10.161)$$

The radial *Peclet number* for heat has about the same value as the corresponding value for dispersion of mass, that is, a value of about 10 (Figure 4.10.64), and so Eq. (4.10.161) leads to:

$$\frac{E_A}{RT_W} \frac{\Delta T_{ad}}{T_W} \frac{Da \times d_R^2}{d_p L} \leq \frac{0.16}{\left(1 + \frac{8\lambda_{rad}}{\alpha_W d_R}\right)} \quad (4.10.162)$$

or in terms of a minimum diameter to exclude significant effects of radial heat dispersion:

$$\frac{d_R}{d_p} \leq \frac{0.16}{\left(1 + \frac{8\lambda_{rad}}{\alpha_W d_R}\right)} \frac{L}{d_R} \frac{RT_W^2}{E_A \Delta T_{ad}} \quad (4.10.163)$$

This criterion for radial heat dispersion is independent of the length L (Da "includes" L); for example, for a first-order reaction, Eq. (4.10.163) reduces to:

$$\frac{d_R}{d_p} \leq \frac{0.16}{\left(1 + \frac{8\lambda_{rad}}{\alpha_W d_R}\right)} \frac{u_s}{d_R} \frac{RT_W^2}{k_{m,eff} \rho_b E_A \Delta T_{ad}} \quad (4.10.164)$$

The worst case is that the heat transfer resistance is only located in the packed bed and not at the wall ($\alpha_W \gg \lambda_{rad}/d_R$), which leads to:

$$\frac{d_R}{d_p} \leq 0.16 \frac{u_s}{d_R k_{m,eff} \rho_b} \frac{RT_W^2}{E_A \Delta T_{ad}} \quad (4.10.165)$$

The term $E_A \Delta T_{ad}/(RT_W^2)$ typically reaches values of at least 5; comparison of Eq. (4.10.165) with Eq. (4.10.142) leads to the conclusion that the radial temperature profile becomes significant before the radial concentration profile does.

Equation (4.10.157) may also be used to estimate the maximum temperature difference that we have to expect in the radial direction within the bed. Instead of the overall heat transfer coefficient to the wall, we then only have to consider the heat transfer in the bed and not the one located in the small region near the wall. If we use $8\lambda_{rad}/d_R$ instead of U_h in Eq. (4.10.158) we obtain:

$$\Delta T_{rad,max} = \frac{r_{m,eff} \rho_b d_R^2 (-\Delta_R H)}{32\lambda_{rad}} \quad (4.10.166)$$

For a typical value of the radial *Peclet number* ($u_s c_p \rho_{mol} d_p / \lambda_{rad}$) of 10, the adiabatic temperature difference, Eq. (4.10.129), and $Da = r_{m,eff} \rho_b \tau / c_A$, Eq. (4.10.166) leads to:

$$\Delta T_{rad,max} = \frac{Da \times c_A}{\tau} \frac{d_R^2}{32} \frac{\Delta T_{ad} c_p \rho_{mol}}{c_{A,in}} \frac{10}{u_s c_p \rho_{mol} d_p} = \frac{10}{32} Da \Delta T_{ad} \frac{d_R}{d_p} \frac{c_A}{c_{A,in}} \frac{d_R}{u_s \tau} \quad (4.10.167)$$

If we consider that the maximum value of c_A is $c_{A,in}$, and use the term L/u_s for the residence time τ we, finally, obtain:

$$\Delta T_{rad,max} = 0.3 Da \Delta T_{ad} \frac{d_R^2}{d_p L} \quad (4.10.168)$$

which is a useful equation to estimate the maximum radial temperature difference in a reactor.

Table 4.10.8 Criteria used to exclude dispersion of mass and heat in a fixed bed.

Effect responsible for deviation from ideal plug flow	General criterion used to exclude deviation from plug flow	Simplified criterion used to exclude deviation from plug flow
Axial dispersion of mass	$\frac{L}{d_p} \geq 20 \frac{Da}{Pe_{m,ax}}$	$\frac{L}{d_p} \geq 10 Da = 10 \frac{k_{m,eff} \rho_b L}{u_s}$ (for first order and $Pe_{m,ax} = 2$)
Radial dispersion of mass	$\frac{d_R}{d_p} \leq 25 \frac{L}{d_R} \frac{1}{Da Pe_{m,rad}}$	$\frac{d_R}{d_p} \leq 2.5 \frac{L}{d_R} \frac{1}{Da} = 2.5 \frac{u_s}{d_R k_{m,eff} \rho_b}$ (for first order and $Pe_{m,rad} = 10$)
Axial dispersion of heat	$\frac{L}{d_p} \geq 20 \frac{E_A}{R T_W} \frac{\Delta T_{ad}}{T_W} \frac{Da}{Pe_{h,ax}}$	$\frac{L}{d_p} \geq 10 Da \frac{E_A \Delta T_{ad}}{R T_W^2} = 10 \frac{k_{m,eff} \rho_b L}{u_s} \frac{E_A \Delta T_{ad}}{R T_W^2}$ (for first order and $Pe_{h,ax} = 2$)
Radial dispersion of heat	$\frac{d_R}{d_p} \leq \frac{1.6}{\left(1 + \frac{8\lambda_{rad}}{\alpha_w d_R}\right)} \frac{L}{d_R} \frac{RT_W^2}{E_A \Delta T_{ad}} \frac{1}{Da Pe_{h,rad}}$	$\frac{d_R}{d_p} \leq 0.16 \frac{RT_W^2}{E_A \Delta T_{ad}} \frac{L}{d_R} \frac{1}{Da} = 0.16 \frac{RT_W^2}{E_A \Delta T_{ad}} \frac{u_s}{d_R k_{m,eff} \rho_b}$ (first order, $\alpha_w d_R \gg \lambda_{rad}$, $Pe_{h,rad} = 10$)
Non-uniform radial porosity and velocity	$\frac{d_R}{d_p} \geq 10$	—

Radial Variations in Bed Structure As discussed in Section 4.10.6.4, radial variations in a packed bed occur in shallow reactors with a low ratio of the tube to particle diameter (<10). For lower values, a non-uniform radial velocity profile is induced and significant undesirable wall effects (bypassing, slippage) may occur. Consequently, the criterion for negligible influence of radial variations in bed structure is:

$$\frac{d_R}{d_p} \geq 10 \quad (4.10.169)$$

Summarizing Conclusions of the Influence of Dispersion in Fixed Bed Reactors Examination of the criteria for significant dispersion in fixed bed reactors shows that in practical cases of fixed bed reactor modeling, axial dispersion of mass and heat as well as radial dispersion of mass are negligible, which should be proven by the criteria summarized in Table 4.10.8. Then the mass and heat balance equations (4.10.125) and (4.10.126) simplify to:

$$u_s \frac{dc_A}{dz} = -\rho_b r_{m,eff} \quad (4.10.170)$$

$$(\rho_{mol} c_p u_s) \frac{dT}{dz} = \lambda_{rad} \left(\frac{d^2 T}{dr^2} + \frac{1}{r} \frac{dT}{dr} \right) - \Delta_R H \rho_b r_{m,eff} \quad (4.10.171)$$

or in dimensionless terms to:

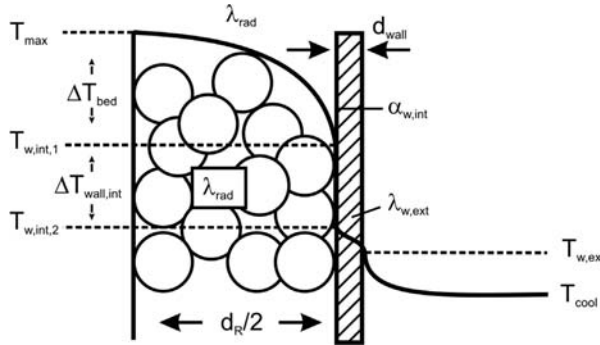
$$\frac{dc_A}{dZ} = -\rho_b r_{m,eff} \tau \quad (4.10.172)$$

$$\frac{dT}{dZ} = \frac{1}{Pe_{h,rad}} \frac{d_p L}{r_R^2} \left(\frac{d^2 T}{dR^2} + \frac{1}{R} \frac{dT}{dR} \right) - \frac{\Delta_R H \tau}{\rho_{mol} c_p} \rho_b r_{m,eff} \quad (4.10.173)$$

4.10.7.3 Radial Heat Transfer in Packed Bed Reactors and Methods to Account for This

Two-Dimensional Model of a Wall-Cooled Fixed Bed Reactor Radial heat transport is an important factor in wall-cooled (or heated) reactors, particularly if we have a strong exothermic reaction with the danger of a temperature runaway. Figure 4.10.67 shows a typical radial temperature profile in a cooled tubular fixed

Figure 4.10.67 Radial temperature profile in a cooled packed bed reactor according to the two-dimensional α_w model (consideration of radial and axial T -profiles).



bed reactor according to the frequently used two-dimensional α_w -model that is represented by Eq. (4.10.173). The boundary condition is that the heat flux from the bed to the internal side of the wall equals the flux by heat conduction through the wall and the heat transfer to the cooling medium:

$$\begin{aligned} \dot{q} &= \frac{\dot{Q}}{A_{\text{wall}}} = -\lambda_{\text{rad}} \frac{dT}{dr} \Big|_{r=d_R/2} = \alpha_{w,\text{int}} (T_{W,\text{int},1} - T_{W,\text{int},2}) \\ &= \frac{\lambda_{\text{wall}}}{d_{\text{wall}}} (T_{W,\text{int},2} - T_{w,\text{ex}}) = \alpha_{w,\text{ex}} (T_{w,\text{ex}} - T_{\text{cool}}) \end{aligned} \quad (4.10.174)$$

The bed and the fluid are considered as a pseudo-homogeneous medium, and the heat transfer in the bed up to the internal side of the wall is represented by two parameters, the radial effective conductivity λ_{rad} and the internal wall heat transfer coefficient $\alpha_{w,\text{int}}$. The introduction of $\alpha_{w,\text{int}}$ allows us to take into account a weaker heat transfer (smaller effective radial heat transfer coefficient λ_{rad}) close to the wall due to less mixing and a higher void fraction of the bed (Figure 4.10.64). Thus, $\alpha_{w,\text{int}}$ combines the interplay of convective flow at the wall and of conduction by contact between the bed and the heat exchange surface (internal wall), and assumes a jump in temperature directly at the wall. For relative simple modeling, the consequence of the introduction of $\alpha_{w,\text{int}}$ is also that we use a constant value of λ_{rad} within the bed.

For simplification, we have thereby also assumed a constant surface area A_{wall} and thus a constant heat flux per unit surface area as in most practical cases the internal and external surface area of the thin tube with thickness d_{wall} are almost equal, that is, $A_{\text{wall}} \approx L\pi d_R$, with L as length of tubular reactor.

For convenience we use an overall external wall heat transfer coefficient U_{wall} that combines the external heat transfer ($\alpha_{w,\text{ex}}$) and the heat transfer through the wall:

$$\dot{q} = U_{\text{wall}} (T_{W,\text{int},2} - T_{\text{cool}}) \quad (4.10.175)$$

U_{wall} is then given, based on Eqs. (4.10.174) and (4.10.175), by

$$\frac{\dot{q}}{U_{\text{wall}}} = (T_{W,\text{int},2} - T_{\text{cool}}) = (T_{W,\text{int},2} - T_{w,\text{ex}}) + (T_{w,\text{ex}} - T_{\text{cool}}) \quad (4.10.176)$$

By insertion of Eq. (4.10.174) into Eq. (4.10.176) we obtain:

$$\frac{\dot{q}}{U_{\text{wall}}} = \frac{\dot{q}}{\frac{\lambda_{\text{wall}}}{d_{\text{wall}}}} + \frac{\dot{q}}{\alpha_{w,\text{ex}}} \quad (4.10.177)$$

and thus the overall external wall heat transfer coefficient U_{wall} is given by:

$$U_{\text{wall}} = \left(\frac{d_{\text{wall}}}{\lambda_{\text{wall}}} + \frac{1}{\alpha_{w,\text{ex}}} \right)^{-1} \quad (4.10.178)$$

For the two-dimensional reactor modeling, we have to solve the heat and mass balances, Eqs. (4.10.170) and (4.10.171), in combination with Eqs. (4.10.174)–

(4.10.178). If axial dispersion of mass and heat is not negligible, we use Eqs. (4.10.125) and (4.10.126) instead of Eqs. (4.10.170) and (4.10.171).

Based on the effective kinetics and heat transfer parameters, solution of the differential equations by numerical integration in the radial and axial direction is carried out by programs, for example such as *Presto-Kinetics* (CiT, <http://www.cit-wulkow.de/>), which was frequently used in this book.

An alternative to the α_w -model discussed in the literature is the use of an effective radial heat conductivity λ_{rad} that depends on the radial position in the bed and decreases near the wall, and thus the rather arbitrarily assumption of $\alpha_{w,int}$ is not needed. Although this model comes closer to reality without the assumption of a temperature jump at the internal wall, it is complicated and rarely used, and for further information we refer to the literature (VDI, 2002).

One-Dimensional Model of a Wall-Cooled Fixed Bed Reactor In some cases, it may be convenient to use a simple one-dimensional model, for example, to get an initial insight into the reactor behavior by a less complicated model. This model also takes into account λ_{rad} and $\alpha_{w,int}$, but we now introduce a mean (constant) bed temperature T_{mean} and an overall heat transfer coefficient of the bed, the thermal transmittance U_{bed} , which collects the interplay of heat conduction in the bed (λ_{rad}) and the heat transfer at the wall ($\alpha_{w,int}$) (Figure 4.10.68). According to this model, heat transfer from a packed bed to a heat transfer medium that cools the outer surface of the wall of a tubular reactor is given by:

$$\dot{q} = U_{bed} (T_{mean} - T_{w,int,2}) = U_{wall} (T_{w,int,2} - T_{cool}) \quad (4.10.179)$$

with $1/U_{bed}$ as the thermal resistance of the packed bed:

$$\frac{1}{U_{bed}} = \underbrace{\frac{d_R}{8\lambda_{rad}}}_{\text{Thermal resistance of packed bed}} + \underbrace{\frac{1}{\alpha_{w,int}}}_{\text{Thermal resistance of heat transfer on the bed side of the wall}} \quad (4.10.180)$$

The factor 8 on the right-hand side of Eq. (4.10.180) is explained below.

Instead of the equations for the two-dimensional model, Eq. (4.10.171) in combination with Eqs. (4.10.174)–(4.10.178), the heat balance of the one-dimensional model reads as:

$$\begin{aligned} (\rho_{mol} c_p u_S) \frac{dT_{mean}}{dz} + \Delta R H \rho_b r_{m,eff} &= - \frac{U_{bed} A_{wall}}{V_R} (T_{w,int,2} - T_{mean}) \\ &= \frac{4U_{bed}}{d_R} (T_{w,int,2} - T_{mean}) \end{aligned} \quad (4.10.181)$$

combined with the boundary condition [Eq. (4.10.179)] that links the heat transfer in the bed with the transfer through the wall and to the cooling medium. Note that

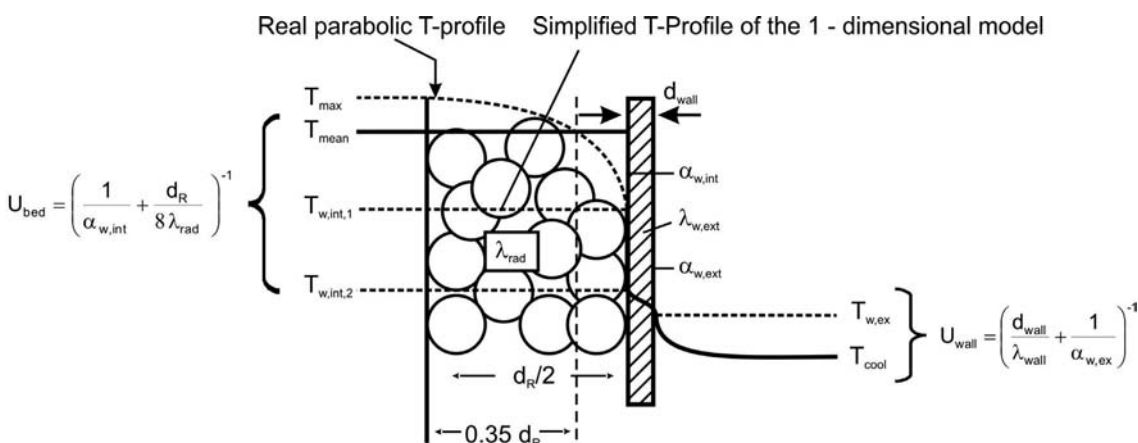


Figure 4.10.68 Radial temperatures in a cooled packed bed according to the simplified one-dimensional model with U_{bed} .

$r_{m,\text{eff}}$ is now constant in the radial direction as we assume a constant mean bed temperature, that is, $r_{m,\text{eff}} = r_{m,\text{eff}}(T_{\text{mean}})$.

The parameter for heat conduction through the wall is mostly negligible, as we usually have thin walls and the conductivity of the wall material, usually steel, is also high.

The heat transfer coefficient $\alpha_{w,\text{ex}}$ on the side of the cooling medium can be calculated based on empirical equations, for example, those given in Section 3.2.1.2 for cylinders in cross flow or by more sophisticated correlations given in the literature (VDI, 2002; Cengel, 2002).

If the tubular reactor is cooled by boiling water, we may reach values of $\alpha_{w,\text{ext}}$ of more than 1000 up to 10 000 W m⁻² K⁻¹ (Section 3.2.1.3), and then Eq. (4.10.181) can be simplified as:

$$(\rho_{\text{mol}} c_p u_S) \frac{dT_{\text{mean}}}{dz} + \Delta_R H \rho_b r_{m,\text{eff}} = - \frac{4 U_{\text{bed}}}{d_R} (T_{\text{mean}} - T_{\text{cool}}) \quad (\text{for } U_{\text{bed}} \ll U_{\text{wall}}) \quad (4.10.182)$$

that is, the temperature at the internal side of the tube wall almost equals the cooling temperature, as we can deduce from Eq. (4.10.179):

$$T_{w,\text{int},2} = \frac{U_{\text{bed}} T_{\text{mean}} + T_{\text{cool}} U_{\text{wall}}}{U_{\text{bed}} + U_{\text{wall}}} \approx T_{\text{cool}} \quad (\text{for } U_{\text{bed}} \ll U_{\text{wall}}) \quad (4.10.183)$$

Four questions still have to be answered with regard to use the above equations:

- 1) What is the exact meaning of the mean temperature of the one-dimensional model?
- 2) Can we use the one-dimensional model even if the criterion to neglect radial temperature gradients within the fixed bed is not met [Eqs. (4.10.164) and (4.10.165)]?
- 3) Why is the term $8\lambda_{\text{rad}}/d_R$ (particularly the factor 8) appropriate to describe the effective heat conduction in a cylindrical packed bed of spherical particles?
- 4) How do we determine the parameters λ_{rad} and $\alpha_{w,\text{int}}$?

To answers the first three questions, we start with the assumption that the radial temperature profile in a cylindrical wall-cooled packed bed with a chemical reaction has a parabolic curvature between the center of the tube (T_{max}) and the internal wall ($T_{w,\text{int},1}$). This assumption is supported by various measurements and calculations (Emig and Klemm, 2005; Westerterp, van Swaaij, and Beenackers, 1998; Froment and Bischoff, 1990). Thus, the temperature at any radial position is:

$$T_r = T_{w,\text{int},1} + (T_{\text{max}} - T_{w,\text{int},1}) \left[1 - \frac{r^2}{(0.5d_R)^2} \right] \quad (4.10.184)$$

For the mean temperature of the one-dimensional model we may take the value at the radial position r_{mean} , where the packed bed is radially divided into two parts with equal volume:

$$L\pi r_{\text{mean}}^2 = L\pi \left(\frac{d_R^2}{4} - r_{\text{mean}}^2 \right) \Rightarrow r_{\text{mean}} = 0.35d_R \quad (4.10.185)$$

Thus the radial position of the mean radial temperature that can be regarded as representative for the whole cross section is located at the radial position $r = 0.35d_R$ ($= 0.7r_R$). Thereby, we have to bear in mind that the reaction rate varies strongly with temperature, so the “purely geometrical” consideration of Eq. (4.10.185) is strictly speaking not exact but very convenient and therefore frequently used; other values recommended in the literature (Baerns *et al.*, 2006) are between $0.5r_R$ and $0.7r_R$, but this is not considered further here.

According to Eqs. (4.10.184) and (4.10.185), the mean temperature at $r_{\text{mean}} = 0.35d_R$ is given by

$$T_{\text{mean}} = \frac{T_{\max} + T_{w,\text{int},1}}{2} \quad (4.10.186)$$

To determine the heat flux from the bed to the wall, we use the derivation of Eq. (4.10.184) directly at the internal wall of the reactor, that is, for the radial position $r = 0.5d_R$:

$$\dot{q} = -\lambda_{\text{rad}} \frac{dT_r}{dr} \Big|_{r=0.5d_R} = \frac{4\lambda_{\text{rad}}}{d_R} (T_{\max} - T_{w,\text{int},1}) \quad (4.10.187)$$

Insertion of Eq. (4.10.186) into Eq. (4.10.187) then leads to:

$$\dot{q} = \frac{8\lambda_{\text{rad}}}{d_R} (T_{\text{mean}} - T_{w,\text{int},1}) \quad (4.10.188)$$

which proves that the term already used in Eq. (4.10.180) for the heat transfer resistance of the heat conduction within a packed bed is correct. Other authors give slightly different relations, for example, a factor of 6 instead of 8 in Eq. (4.10.188) (Crider and Foss, 1965).

We are now able to derive some characteristic temperature differences related to a cooled packed bed with chemical reaction. The temperature difference within the bed and the one directly at the internal wall are according to Eqs. (4.10.187) and (4.10.174) related by:

$$\begin{aligned} \dot{q} &= \frac{4\lambda_{\text{rad}}}{d_R} (T_{\max} - T_{w,\text{int},1}) = \alpha_{w,\text{int}} (T_{w,\text{int},1} - T_{w,\text{int},2}) \\ &\Rightarrow \frac{T_{\max} - T_{w,\text{int},1}}{T_{w,\text{int},1} - T_{w,\text{int},2}} = \frac{\alpha_{w,\text{int}} d_R}{4\lambda_{\text{rad}}} \end{aligned} \quad (4.10.189)$$

Thus for thin tubes (small values of d_R) the temperature difference in the bed is much lower than the temperature jump at the internal wall, and the temperature of the packed bed and the reaction rate in the radial direction can be regarded as almost constant.

For the ratio of the temperature difference within the bed and the whole remaining temperature difference between the internal wall and the cooling temperature we obtain according to the two-dimensional model and Eqs. (4.10.175)–(4.10.180):

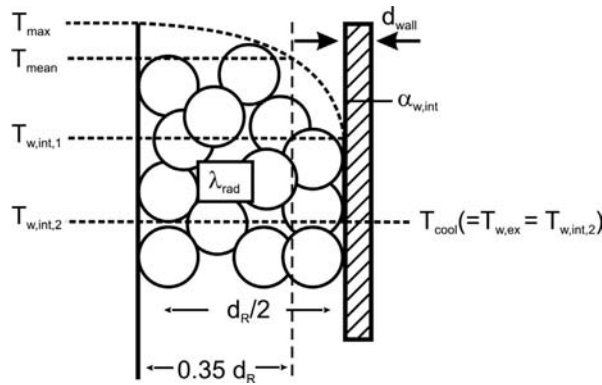
$$\begin{aligned} \frac{4\lambda_{\text{rad}}}{d_R} (T_{\max} - T_{w,\text{int},1}) &= \frac{(T_{w,\text{int},1} - T_{\text{cool}})}{\frac{1}{\alpha_{w,\text{int}}} + \frac{1}{U_{\text{wall}}}} \Rightarrow \frac{T_{\max} - T_{w,\text{int},1}}{T_{w,\text{int},1} - T_{\text{cool}}} \\ &= \frac{\frac{4\lambda_{\text{rad}}}{d_R}}{\left(\frac{1}{\alpha_{w,\text{int}}} + \frac{d_{\text{wall}}}{\lambda_{\text{wall}}} + \frac{1}{\alpha_{w,\text{ex}}} \right)} \end{aligned} \quad (4.10.190)$$

To characterize the non-uniformity of the temperature distribution, we use the mean temperature of the one-dimensional model. Insertion of Eq. (4.10.186) in Eq. (4.10.190) leads to the ratio of the difference between the maximum temperature in the center and the mean temperature to the difference between the mean and the cooling temperature:

$$\frac{T_{\max} - T_{\text{mean}}}{T_{w,\text{int},1} - T_{\text{cool}}} = \left[1 + \frac{8\lambda_{\text{rad}}}{d_R} \left(\frac{1}{\alpha_{w,\text{int}}} + \frac{d_{\text{wall}}}{\lambda_{\text{wall}}} + \frac{1}{\alpha_{w,\text{ex}}} \right) \right]^{-1} \quad (4.10.191)$$

In many cases, the thermal resistance of the reactor wall ($d_{\text{wall}}/\lambda_{\text{wall}}$) as well as the external heat transfer to the cooling medium ($1/\alpha_{w,\text{ex}}$) are negligible (the latter, for example, if the wall is cooled externally by boiling water). We then have a

Figure 4.10.69 Characteristic temperature differences in a cooled packed bed reactor with chemical reaction if the thermal resistances of the wall ($d_{\text{wall}}/\lambda_{\text{wall}}$) as well as of the external heat transfer to the cooling medium ($1/\alpha_{w,\text{ex}}$) are negligible.



uniform wall temperature T_{wall} ($= T_{w,\text{ex}} = T_{w,\text{int},2}$), and Eqs. (4.10.190) and (4.10.191) simplify:

$$\frac{T_{\text{max}} - T_{w,\text{int},1}}{T_{w,\text{int},1} - T_{\text{cool}}} = \frac{\alpha_{w,\text{int}} d_R}{4\lambda_{\text{rad}}} \quad \left(\text{for } \frac{1}{\alpha_{w,\text{int}}} \ll \frac{d_{\text{wall}}}{\lambda_{\text{wall}}} + \frac{1}{\alpha_{w,\text{ex}}} \right) \quad (4.10.192)$$

$$\frac{T_{\text{max}} - T_{\text{mean}}}{T_{\text{mean}} - T_{\text{cool}}} = \left(1 + \frac{8\lambda_{\text{rad}}}{\alpha_{w,\text{int}} d_R} \right)^{-1} \quad \left(\text{for } \frac{1}{\alpha_{w,\text{int}}} \ll \frac{d_{\text{wall}}}{\lambda_{\text{wall}}} + \frac{1}{\alpha_{w,\text{ex}}} \right) \quad (4.10.193)$$

Figure 4.10.69 shows some characteristic temperatures for this case.

Heat transport in packed tubes has been investigated and discussed in detail (Yagi and Kunii 1960; Yagi and Wakao, 1959; Calderbank and Pogorski, 1957; Demirel, Sharma, and Al-Ali, 2000; Dixon, 1985; Freiwald and Paterson, 1992; Li and Finlayson, 1977; Wen and Ding, 2006; Bey and Eigenberger, 2001; Froment and Bischoff, 1990, and further literature cited therein), and there are many correlations to calculate heat transport parameters. Here, only the probably most reliable correlations given in VDI (2002) are considered, which were deduced by the evaluation of numerous literature data including the influence of the aspect ratio d_R/d_p .

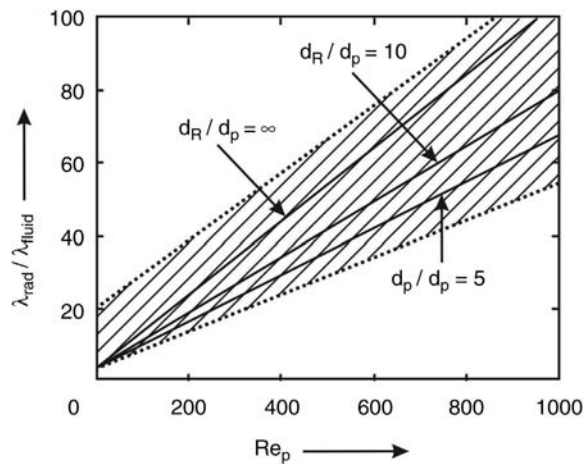
Effective Radial Conductivity λ_{rad} of a Packed Bed The effective radial conductivity λ_{rad} within a packed bed of spheres is given by (VDI, 2002):

$$\bullet \quad \frac{\lambda_{\text{rad}}}{\lambda_{\text{fluid}}} = \frac{\lambda_{\text{bed}}}{\lambda_{\text{fluid}}} + \frac{Re_p \times Pr}{7[2 - (1 - 2d_p/d_R)^2]} \quad (4.10.194)$$

with $Re_p = u_s d_p / v$ and $Pr = v/a = \nu c_p \rho_{\text{mol}} / \lambda_{\text{fluid}}$ (Figure 4.10.70).

For cylinders, a factor of 4.6 should be used instead of 7 in Eq. (4.10.194). The term λ_{bed} is the effective thermal conductivity of the bed without flow, and for the ratio of $\lambda_{\text{bed}}/\lambda_{\text{fluid}}$ we have values in the range 5–10, if the thermal conductivity of

Figure 4.10.70 Effective radial conductivity of a packed bed of spherical particles for different aspect ratios d_R/d_p , gases ($Pr = 0.7$), and high Re_p values ($Re_p = u_s d_p / v$); lines: correlation given in VDI (2002), see Eq. (4.10.194), for a value of the static contribution $\lambda_{\text{bed}}/\lambda_{\text{fluid}}$ of 4; area: range of literature data (Yagi and Kunii, 1960; Yagi and Wakao, 1959; Calderbank and Pogorski, 1957; Demirel, Sharma, and Al-Ali, 2000; Dixon, 1985; Li and Finlayson, 1977; Wen and Ding, 2006; Bey and Eigenberger, 2001; Froment and Bischoff, 1990, and literature cited therein).



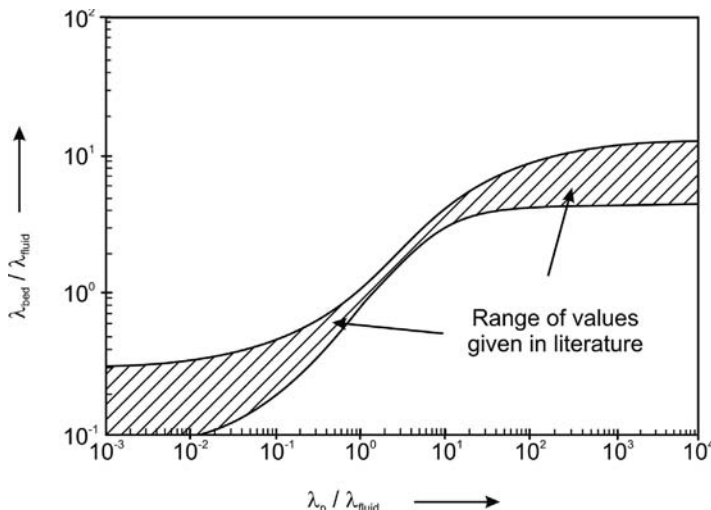


Figure 4.10.71 Effective radial conductivity of a packed bed without flow. Adapted from VDI (2002).

the particles is high compared to the fluid ($\lambda_p/\lambda_{\text{fluid}} > 10$, Figure 4.10.71). In general, values of the static contribution $\lambda_{\text{bed}}/\lambda_{\text{fluid}}$ given in the literature vary and a measurement of λ_{bed} is useful, if the contribution of this static term to the overall radial thermal conductivity of the bed is not negligible. Hofmann and Chao found that under reaction conditions $\lambda_{\text{bed}}/\lambda_{\text{fluid}}$ is smaller than those measured without reaction (Hofmann, 1979; Chao, Caban, and Irizarry, 1973). Apparently there exists an interaction between this static thermal conductivity and the kinetics (Westerterp *et al.*, 1998). For a rough estimation, a value for $\lambda_{\text{bed}}/\lambda_{\text{fluid}}$ of 4 should be used for the modeling of wall cooled chemical reactors (Figure 4.10.71). Thus, for a high aspect ratio d_R/d_p and high values of $\lambda_p/\lambda_{\text{fluid}}$, Eq. (4.10.194) simplifies to:

$$\frac{\lambda_{\text{rad}}}{\lambda_{\text{fluid}}} = 4 + \frac{Re_p \times Pr}{7} \quad (\text{for } Re_p > 10, d_R \gg d_p, \text{spherical particles}) \quad (4.10.195)$$

Equations (4.10.195) and (4.10.194) can now be compared with the estimations given in Section 4.10.6.4 for the dispersion in fixed beds. According to Figure 4.10.60 in combination with the assumption of the analogy of dispersion of mass and heat, the radial *Peclet number* is approximately 10 for high Re_p numbers. Thus we get:

$$Pe_{h,\text{rad}} = \frac{u_S d_p c_p \rho_{\text{mol}}}{\lambda_{\text{rad}}} = Re_p \times Pr \frac{\lambda_{\text{fluid}}}{\lambda_{\text{rad}}} \approx 10 \Rightarrow \frac{\lambda_{\text{rad}}}{\lambda_{\text{fluid}}} = \frac{Re_p \times Pr}{10} \quad (4.10.196)$$

which gives a quite similar result as Eqs. (4.10.194) and (4.10.195) for high Re_p numbers.

Heat Transfer Coefficient α_{rad} and Nu Number at the Internal Wall of a Packed Bed
For the heat transfer coefficient on the bed side we use the *Nu* number (VDI, 2002) (Figure 4.10.72):

$$Nu = \frac{\alpha_{\text{int}} d_p}{\lambda_{\text{fluid}}} = \left(1.3 + \frac{5d_p}{d_R} \right) \frac{\lambda_{\text{bed}}}{\lambda_{\text{fluid}}} + 0.19 Re_p^{\frac{3}{4}} Pr^{\frac{1}{3}} \quad (4.10.197)$$

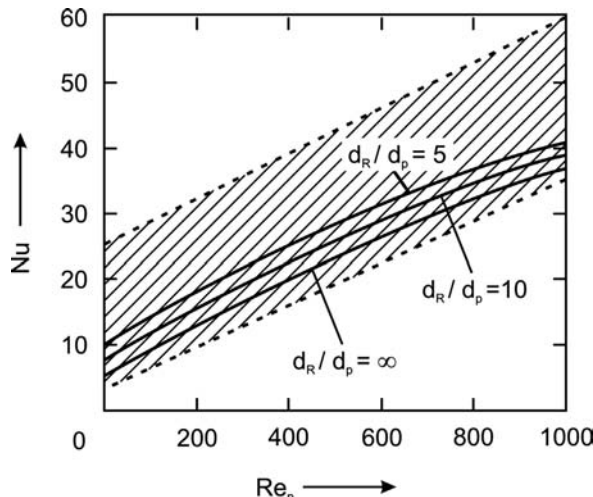
and for $\lambda_p/\lambda_{\text{fluid}} > 10$, gases ($Pr = 0.7$), $\lambda_{\text{bed}}/\lambda_{\text{fluid}}$ of 4, and a high d_R/d_p ratio we get:

$$Nu = 5 + 0.17 Re_p^{\frac{3}{4}} \quad (\text{for gases, } Re_p > 10 \text{ and } d_R \gg d_p) \quad (4.10.198)$$

The equations given above are also valid for non-spherical particles if we use the equivalent particle diameter:

$$d_{p,\text{eq}} = \sqrt[3]{\frac{6V_p}{\pi}} \quad (4.10.199)$$

Figure 4.10.72 Nu number [see Eq. (4.10.197)] for the heat transfer at the internal wall of a packed bed for different aspect ratios d_R/d_p , gases ($Pr = 0.7$), and high values of Re_p values ($Re_p = u_s d_p / \nu$), lines: correlation given in VDI, 2002, see Eq. (4.10.197), for $\lambda_{\text{bed}}/\lambda_{\text{fluid}}$ of 4; area indicates range of literature values (Yagi and Kunii, 1960; Yagi and Wakao, 1959; Demirel, Sharma, and Al-Ali, 2000; Dixon, 1985; Freivald and Paterson, 1992; Wen and Ding, 2006; Bey and Eigenberger, 2001; Froment and Bischoff, 1990 and literature cited therein).



which equals the diameter of a spherical particle with the same volume as of a non-spherical particle. For a cylinder with a length L_{cyl} and diameter d_{cyl} we obtain, for example:

$$d_{p,\text{eq},\text{cyl}} = \sqrt[3]{\frac{3L_{\text{cyl}} d_{\text{cyl}}^2}{2}} \quad (4.10.200)$$

4.10.8

Novel Developments in Reactor Technology

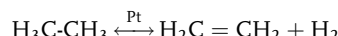
Research activities in past decades have produced new reactor concepts. For example, hybrid (multifunctional) reactors combining reaction and heat or mass transfer are an interesting new option. Progress has also been achieved with monolithic reactors, which are already used commercially in emission control systems. An overview of these developments is given by Moulijn, Makkee, and Van Diepen (2004). Details are given by Westerterp (1992) and Cybyulski and Moulijn (1997).

The use of miniaturized reactors with characteristic dimensions below about 1 mm, so-called microreactors, is also a currently interesting development. An overview of the basic principles of microreactors is given by Emig and Klemm (2005). Details are found in Hessel, Hardt, and Loewe (2004). Subsequently, short summaries of these new concepts based on the cited literature are given.

4.10.8.1 Hybrid (Multifunctional) Reactors

In hybrid systems different processes are coupled, for example, reaction and separation by membranes, adsorption, or distillation. This could lead to a reduction of the investment costs as two different functions are combined in one vessel, and one process step is eliminated. For example, a reactor with a catalyst and a membrane may be used or a distillation column with a catalytic packing, which could also lead to an optimal heat integration. Other benefits depend on the specific reaction. For example, equilibrium-limited reactions would benefit if a product is continuously removed *in situ*, which leads to an enhanced yield “beyond the equilibrium.”

Coupling Membranes and Reaction A catalytic membrane reactor combining catalysis and separation in one reactor is an excellent example of such a hybrid reactor (Figure 4.10.73), although this system is not yet used commercially. The potential of this concept has been demonstrated by the example of the catalytic dehydrogenation of ethane, which was investigated on the bench scale (Champagnie, Tsotsis, and Minet, 1990; Moulijn, Makkee, and Van Diepen, 2004):



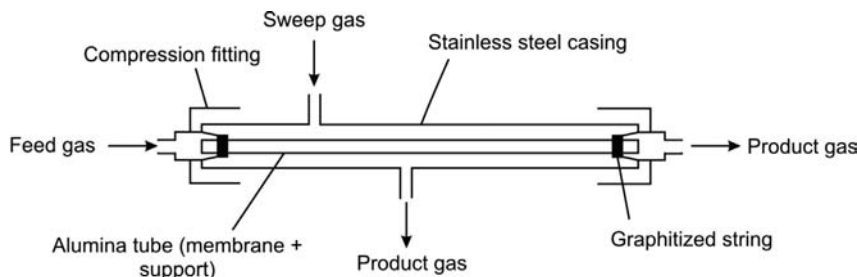


Figure 4.10.73 Membrane reactor for dehydrogenation of ethane. Adapted from Champagnie (1990); Moulijn, Makkee, and Van Diepen (2004).

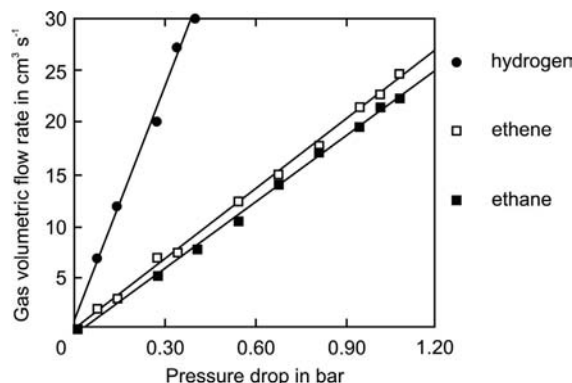


Figure 4.10.74 Flow of H₂, ethane, and ethene through a membrane at 400 °C. Adapted from Champagnie, Tsotsis, and Minet (1990).

The membrane reactor described by Champagnie, Tsotsis, and Minet (1990) consists of a porous membrane tube covered with Pt (Figure 4.10.73). The tube consists of a multilayered porous composite based on alumina. The first layer is only 5 µm thick and has a unimodal pore structure (4 nm). Successive layers are thicker with progressively larger pores and are supported on a layer (1.5 mm) with large pores of about 10 µm.

The H₂ transport is much faster than that of ethane and ethene (Figure 4.10.74). Hence, in principle it is possible to shift the equilibrium to the side of ethene by H₂ removal. Indeed, it was shown that conversions beyond thermodynamic equilibrium can be reached (Figure 4.10.75).

Although membrane reactors certainly open up opportunities, additional challenges have to be faced to design and produce robust modules that allow high rates of mass and heat transfer.

Coupling Reaction and Adsorption A multifunctional reactor may also combine reaction and adsorption. At the laboratory scale, this concept has been applied for a few reactions, for example, for ammonia and methanol synthesis. Although these processes have been optimized to a high degree of sophistication, improvements

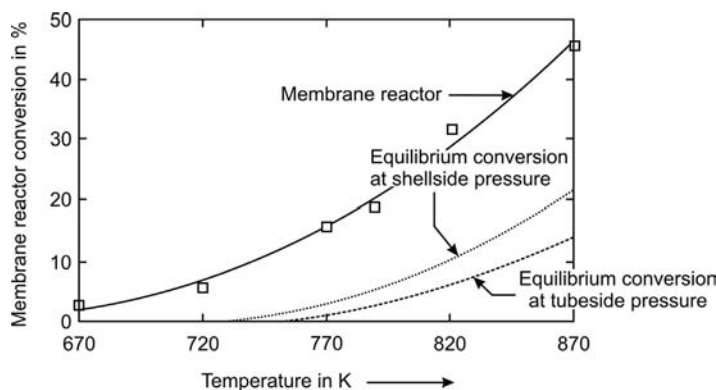


Figure 4.10.75 Dehydrogenation of ethane in a membrane reactor for a transmembrane pressure drop of about 0.7 bar and a tube side pressure of 1.7 bar (details in Champagnie, Tsotsis, and Minet, 1990).

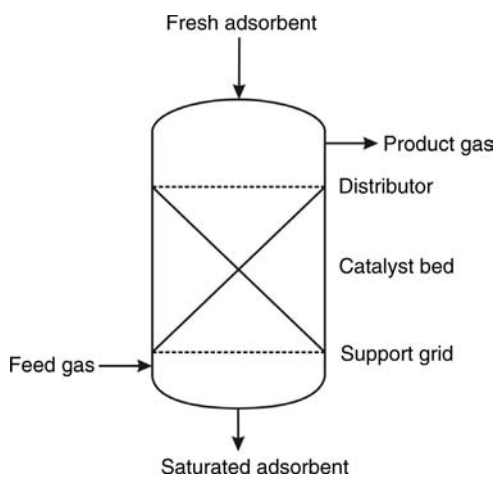


Figure 4.10.76 Hybrid reactor with a solid adsorbent. Adapted from Moulijn, Makkee, and Van Diepen (2004).

are still possible, for example, to decrease the energy loss by the syngas recycle due to the limited conversion per pass (ammonia and methanol synthesis are thermodynamically limited reactions, Sections 6.1 and 6.11, respectively). An additional disadvantage may occur from a kinetic origin as the product concentration increases along the fixed bed, which causes a drop of the rate by product inhibition, and the bed length and pressure drop increase.

It has therefore been suggested that adding a sorbent enables a higher conversion per pass. This reactor concept is called a gas-solid-solid trickle-flow reactor (Westerterp *et al.*, 1988; Westerterp, 1992). The reactor is a fixed-bed, with the sorbent and gas flowing countercurrently as shown in Figure 4.10.76 for methanol synthesis. A porous powder trickles over the catalytic fixed bed, adsorbs the methanol produced and hence the equilibrium is shifted towards methanol. Notably, adsorption is a function of temperature and not favored by high temperatures. Therefore, high temperatures imply a high flow rate of the adsorbent.

Catalytic Distillation Catalytic or reactive distillation is another example of the use of a hybrid reactor and combines catalysis and distillation in one column/reactor. Usually, we have a two-phase process with gas and liquid flowing in countercurrent mode. This requires special catalysts and packings, for example, monoliths, as in case of a fixed-bed flooding of the reactor would occur at high flow rates. In industry, catalytic distillation is already used for the production of MTBE (methyl *tert*-butyl ether), an important octane booster (Figure 4.10.77; DeGarmo, Parulekar, and Pinjala, 1992), cumene (DeGarmo, Parulekar, and Pinjala, 1992), and ethylbenzene (Podrebarac, Ng, and Rempel, 1997).

4.10.8.2 Monolithic Reactors

The use of structured catalysts has been considered in chemical engineering for years. Fixed-bed reactors, although most commonly used, have disadvantages such as the maldistribution of the catalyst and the fluids, a high pressure drop and possible plugging by dust. Structured catalysts are therefore promising as a means to solve these drawbacks. Two basic types have been investigated to date, monolithic catalysts and structured packings covered with the catalyst, analogous to the packings used in distillation and absorption columns.

Monoliths are continuous structures consisting of narrow parallel channels, typically with a diameter of 1–3 mm. A ceramic or metallic support is coated with a layer of material in which catalytically active components are dispersed (washcoat). The walls of the channels may be either permeable or impermeable. In the former case, the term membrane reactor (see above) is used. Figure 4.10.78 shows an example of a monolith. The shape of the monolith can be adapted to fit in the reaction chamber.

Monolithic reactors (Figure 4.10.79) have already found applications in automotive pollution control and for the treatment of power plant exhaust gases (Section 6.18). The main advantage of monolithic reactors over conventional fixed-beds is their low pressure drop, which is the result of the flow through straight channels instead through the tortuous path in a fixed bed.

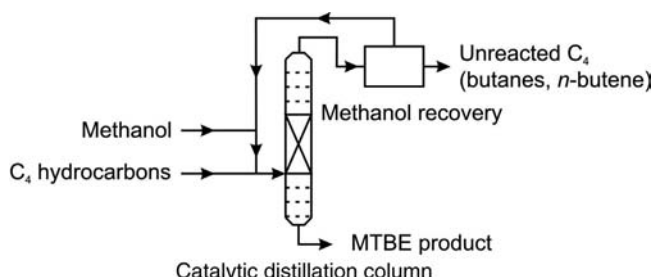


Figure 4.10.77 Catalytic distillation for MTBE production. Adapted from Moulijn, Makkee, and Van Diepen (2004); DeGarmo, Parulekar, and Pinjala (1992).

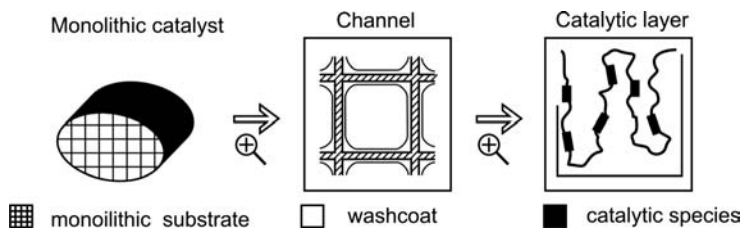


Figure 4.10.78 Example of a monolith with square channels. Adapted from Moulijn, Makkee, and Van Diepen (2004).

Other processes employing monolithic reactors, mostly still in the development stage, are catalytic combustion of fuels, oxidation of SO_2 and of NH_3 , and hydrogenations. In the last case, we have gas–liquid systems (Figure 4.10.79), and the feeding of the reactor is very important to ensure that all channels are equally wetted.

4.10.8.3 Microreactors

The use of miniaturized reactors with characteristic lateral dimensions below 1 mm has recently attracted great attention in chemical reaction engineering. The typical form of such confinement is microchannels. An excellent summary of the main aspects of microreactors is given by Emig and Klemm (2005). Microreactors offer the following advantages:

- For heat- and mass-transfer-limited reactions, large gradients in concentration and temperature are avoided by shrinking the characteristic dimensions down to the micro-scale.
- The high surface-to-volume ratio in microreactors give them far better heat exchange characteristics than those attainable in macroscopic batch or flow-through reactors, and hot spots can be suppressed.
- In addition to a better heat exchange, microreactors also intensify mixing and mass transport, which is particularly important in multiphase systems (gas–liquid or liquid–liquid).
- Greater safety is attained with toxic substances as a very small hold-up significantly decreases the expenditure for safety installations.
- A motivation to use microreactors arises also from safety considerations if explosive mixtures are used. Explosions can be suppressed by using microchannels with a hydraulic diameter below the quenching distance, which is usually (at room temperature) on the order of magnitude of a millimeter (Table 4.10.9). Hence, the microreactor may become inherently safe, although not necessarily the complete set-up. Even high-pressure reactions such as hydrogenations with pure H_2 seem to be possible with minor safety regulations.

Main drawbacks of microreactors are

- The uniform distribution of the fluids to a large number of small channels is problematic.
- The investment costs for a certain production rate may be high.

Table 4.10.9 Quenching distances of various flame barriers (at 1 bar, 20 °C, stoichiometric air–fuel mixture, that is, 9.5 vol.% CH_4 , 30 vol.% H_2 , or 4 vol.% C_3H_8 in air).

Quenching distance d_{quench}		
Parallel plate (d_{quench} : distance of plates) (mm)	Capillary (d_{quench} : diameter) (mm)	Fixed bed (beads) (d_{quench} : diameter of beads) (mm)
Methane	2	4
Hydrogen	0.7	1
Propane	1.8	3

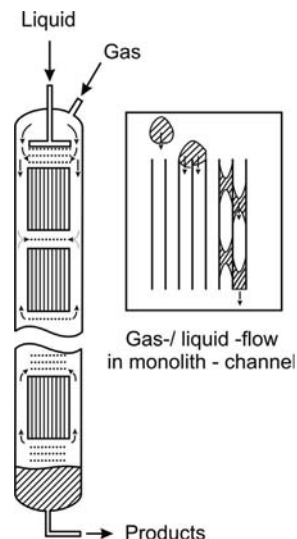


Figure 4.10.79 Monolith reactor with square channels for multiphase reactions (gas, liquid, solid catalyst). Adapted from Cybulski and Moulijn (1997).

Table 4.10.10 Typical values of characteristic parameters in microstructures (microreactors).

Radius r_t (μm)	Specific volumetric surface area a_V (m^{-1})	Characteristic time for diffusion τ_D (ms)		Characteristic time for heat transport τ_h (ms)	
		Nitrogen	Water	Nitrogen	Water
1000	2 000	100	10^6	33	6.900
100	20 000	1	10^4	0.3	69
10	200 000	0.01	100	0.003	0.7

- The uniform coating of the walls of the microchannels with a catalyst is not an easy task.
- Microreactors generally do not tolerate particles well (clogging).

For a closer look at heat and mass transfer in microstructures the characteristic times are helpful. The time constant of diffusion in a tube with circular cross-section is:

$$\tau_D = \frac{r_t^2}{D_{\text{mol}}} \quad (4.10.201)$$

and for the time constant of radial heat transfer by conduction in a tube we have:

$$\tau_h = \frac{r_t^2}{a} \quad (4.10.202)$$

Values of τ_D and τ_h and of the molecular diffusivity and conductibility of temperature are given in Tables 4.10.10 and 4.10.11, respectively, for gases (nitrogen) and liquids (water).

The characteristic time constants of heat and mass transfer strongly increase with decreasing tube diameter (Table 4.10.10), whereas the specific volumetric surface area a_V increases with decreasing tube radius, as a_V is inversely proportional to r_t :

$$a_V = \frac{2}{r_t} \quad (4.10.203)$$

Both effects are very helpful for an efficient mass and heat transfer, as discussed below.

Mass Transport and Residence Time Distribution in Microchannels In microchannels, we have a strong laminar flow as the Re number is typically in the range 10–500 (Emig and Klemm, 2005). Thus, at first sight, one could come to the conclusion that we have no plug flow behavior and a lower conversion compared to an ideal PFR (Section 4.10.2.7). However, this is not the case if molecular diffusion in the radial direction is relatively fast, that is, the time for radial diffusion is much shorter than the average residence time (Section 4.10.6):

$$\tau_D = \frac{r_t^2}{D_{\text{mol}}} \ll \tau = \frac{L}{u} \quad (4.10.204)$$

According to the values given in Table 4.10.10, the time constant for radial diffusion in microchannels is very short for gases (0.1–100 ms for a radius of 10 μm to 1 mm). For liquids, the values are much higher and thus radial diffusion may play only a minor role.

Table 4.10.11 Typical values of diffusivity (D_{mol}) and conductibility of temperature (a) of gases and liquids.

	D_{mol} ($\text{m}^2 \text{s}^{-1}$)	a ($\text{m}^2 \text{s}^{-1}$)
Gas (nitrogen)	10^{-5}	3×10^{-5}
Liquid (water)	10^{-9}	1.5×10^{-7}

To inspect the deviation from an ideal PFR, we use the axially dispersed plug flow model (Sections 4.10.6.1–4.10.6.3) and recall the equation for the term of axial dispersion:

$$\frac{D_{ax}}{uL_t} = \frac{1}{Bo} = \frac{D_{ax} d_t}{ud_t L_t} \quad (4.10.100)$$

as well as the correlation for D_{ax} for laminar flow in empty tubes:

$$D_{ax} = D_{mol} + \frac{u^2 d_t^2}{192 D_{mol}} \quad (4.10.118)$$

$\left(\text{valid for } 1 < Re = \frac{ud_t}{\nu} < 2000 \text{ and } \frac{L}{d_t} > 0.04 Re \times Sc \right)$

For Re less than about 10, we can almost neglect the first term on the right-hand side of Eq. (4.10.118) – see also Figures 4.10.63 and 4.10.64 – and the Bo number as a measure for the deviation from plug flow behavior reads as:

$$Bo = \frac{uL_t}{D_{ax}} \approx 192 \frac{L_t D_{mol}}{ud_t^2} \quad (\text{for } Re > 10) \quad (4.10.205)$$

The Bo number and the axial dispersion coefficient consider that the molecular diffusion in the radial direction tends to counteract the spreading effect of the laminar velocity profile, while in the axial direction the molecular diffusion increases the dispersion.

In terms of the residence time and the time for diffusion we can rewrite Eq. (4.10.205) as:

$$Bo = 192 \left(\frac{L_t}{u} \right) \left(\frac{D_{mol}}{4r_t^2} \right) = 192 \tau \frac{1}{4\tau_D} \approx 50 \frac{\tau}{\tau_D} \quad (4.10.206)$$

If we have values of $Bo > 80$, we almost have plug flow behavior, which is typically reached for a microreactor as shown in Figure 4.10.80. For example, for a Da number of 4 we get a conversion of 97.8% for $Bo = 80$ [first-order reaction, Eq. (4.10.115)] compared to 98.2% in an ideal PFR. Thus, according to Eq. (4.10.206), the residence time should be equal or higher than the characteristic time of diffusion τ_D . In microreactors τ_D is in the range of 0.1–100 ms (Table 4.10.10), and so we always obtain high values of Bo unless we do not operate with extremely low residence times. For liquids, we have values of τ_D of more than 100 ms (Table 4.10.10), and we only reach plug flow behavior for a residence time of the order of magnitude of the characteristic diffusion time.

For a gas–liquid reaction we may get *Taylor flow* (slug-flow, Figure 4.10.81).

The gas and the liquid phase are then separated but the influence of the wall friction, which leads to so-called *Taylor vortices*, and this annular flow leads to an intensified mass transfer.

Heat Transport in Microchannels The overall heat transfer coefficient, the thermal transmittance U_h , is mostly determined by the heat transfer coefficient from the

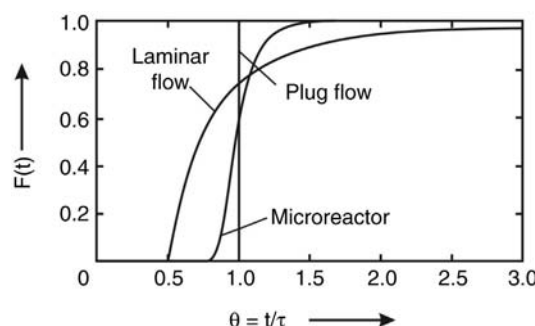
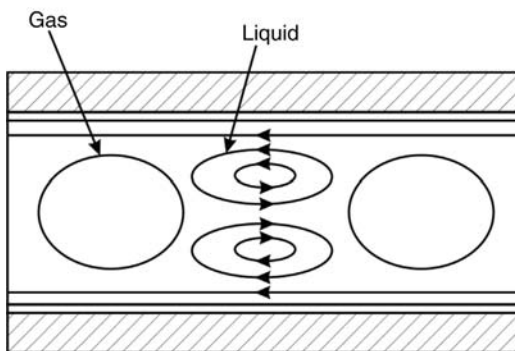


Figure 4.10.80 Typical residence time distribution in a microreactor (with a liquid phase) and a laminar tube without influence of molecular diffusion. Comparison with Figure 4.10.54 shows that the Bo number for the microreactor is >80 and, thus, we have almost plug flow. Adapted from Emig and Klemm (2005).

Figure 4.10.81 Gas–liquid reaction in a microchannel.



fluid flowing in the microchannel to the internal wall of the tube. For long round tubes and laminar flow the average Nu number approaches a value of 3.66 and the thermal entrance region has no influence on Nu . Thus we may use as approximation (Section 3.2.1.2):

$$Nu = \frac{\alpha d_t}{\lambda_{\text{fluid}}} \approx 3.66 \quad \left(\text{for } Re \times Pr \frac{d_t}{L} \geq 10, \text{ laminar flow} \right) \quad (3.3.12)$$

For gases with a thermal conductivity λ of about $0.02 \text{ W m}^{-1} \text{ K}^{-1}$ at normal conditions (Table 3.1.7) and a channel diameter of $100 \mu\text{m}$ we obtain a value for the heat transfer coefficient α of about $700 \text{ W m}^{-2} \text{ K}^{-1}$ compared to $30\text{--}50 \text{ W m}^{-2} \text{ K}^{-1}$ in a “macrotube” with turbulent flow (Table 3.2.1). For liquids with a thermal conductivity λ of at least $0.2 \text{ W m}^{-1} \text{ K}^{-1}$ (Table 3.1.6) we obtain (for a channel diameter of $100 \mu\text{m}$) a value for the heat transfer coefficient α of about $7000 \text{ W m}^{-2} \text{ K}^{-1}$, which is still higher compared to $1000\text{--}4000 \text{ W m}^{-2} \text{ K}^{-1}$ in a “macrotube” with turbulent flow (Table 3.2.1). Thus, microreactors can remove heat much more efficiently than macroreactors and hot spots due to exothermicity decrease remarkably. This is also very interesting for improved kinetic investigations, that is, at almost isothermal conditions, as local temperature gradients affecting reaction rates are much smaller than in any other usual laboratory-scale tubular reactor.

4.10.8.4 Adiabatic Reactors with Periodic Flow Reversal

Exothermic equilibrium reactions like methanol or ammonia synthesis have the disadvantage that a low temperature is needed to reach a favorable high equilibrium conversion of the reactants. Conversely, a sufficiently high temperature is required with respect to kinetics to carry out the reaction at an acceptable rate. Unfortunately, the temperature increases towards the exit of the fixed bed due to the exothermicity of the reaction (if we do not use intensive cooling), which additionally lowers the obtainable equilibrium conversion. Thus, the temperature profile is exactly the wrong way round, and the feed has to be preheated and the product stream has to be cooled, usually by feed-effluent heat exchangers. In addition, heat has to be removed between reaction stages, if the reaction temperature increases too much.

An alternative is the adiabatic fixed-bed reactor with periodic flow reversal (Borekov, Matros, and Kiselev, 1979; Matros, 1985, 1989; Matros and Bunimovich, 1996). Figure 4.10.82 shows the principle of such a system. The main idea is to utilize the heat of reaction within the catalyst bed itself.

Feeding a hot catalyst bed with relatively cold gas will cool the inlet side of the bed; on the other hand, the temperature at the exit of the bed will increase due to the heat produced by the reaction. By reversing the direction of flow the heat contained in the catalyst bed will bring the cold inlet stream to reaction temperature. The part of the bed that has now become the outlet zone is relatively cold, which is favorable for the reaction equilibrium. After some time the inlet has cooled again, while the outlet has become warmer. Then the flow is reversed again and a new

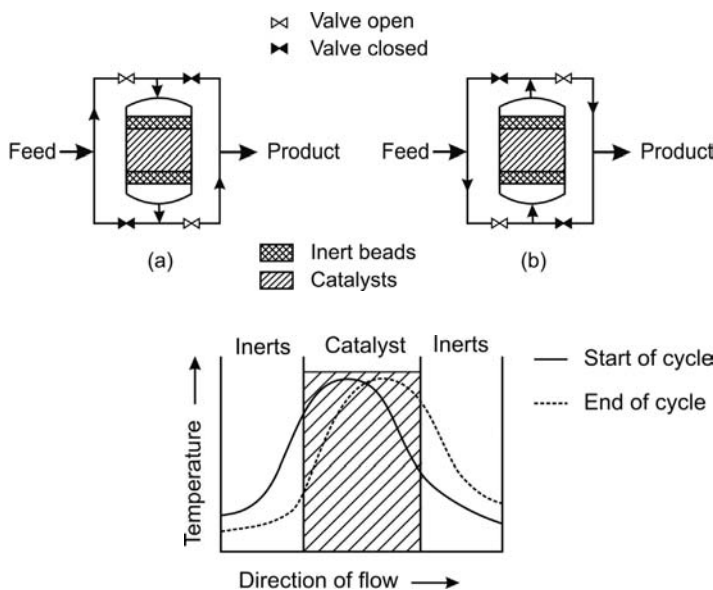


Figure 4.10.82 Principle of an adiabatic fixed-bed reactor with periodic flow reversal: (a) first half of the cycle; (b) second half of the cycle. Adapted from Moulijn, Makkee, and Van Diepen (2004).

cycle begins. After a sufficient number of flow reversals, an oscillating, but on average stationary, state is attained.

By reversing the flow at the right time heat can be kept in the reactor, and the temperature in the middle zone of the fixed bed remains above the ignition temperature. Once the process has been started up, the heat of reaction is sufficient to keep the process going; Figure 4.10.83 shows a typical temperature profile over the reactor as a function of time.

As only a sufficiently high temperature is maintained in the middle part of the reactor, part of the bed can consist of inert material, which should have a high heat capacity with regard to heat storage and heat release and a large particle diameter to lower the pressure drop.

The adiabatic fixed-bed reactor with periodic flow reversal has three commercial applications, oxidation of SO_2 for sulfuric acid production, oxidation of volatile organic compounds (VOCs) for purification of industrial exhaust gases, and NO_x reduction by ammonia in industrial exhaust gases. Other possible future applications are steam reforming and partial oxidation of methane for syngas production, synthesis of methanol and ammonia, and catalytic dehydrogenations (Matros and Bunimovich, 1996).

Summary of Section 4.10 (take-home messages)

- Ideal reactors have idealized flow patterns. Four cases are important, the **uniformly mixed batch reactor**, the **plug flow reactor (PFR)**, the **continuous stirred tank reactor (CSTR)**, and a **cascade of CSTRs**. Real reactors are arbitrarily complicated, but can be regarded as composed of elements of ideal reactors. Modeling is possible, if we know how to account for non-ideal flow.
- For the modeling of a reactor we need solutions of the equations of the **balances of mass, energy, and impulse**. For isothermal operation the energy balance is not needed. The impulse balance mostly only serves to calculate the pressure drop of a reactor. The definition of a suitable **control space** for balancing is important. In the simplest case, the variables – such as temperature and concentrations – are constant within the control space (stirred tank reactor). However, in many cases the system variables depend on the location, for example, in the axial direction in a tubular reactor. Then infinitesimal balances (differential equations) have to be solved to obtain integral data.

Figure 4.10.83 Temperature profiles in an adiabatic fixed-bed reactor with periodic flow reversal. Adapted from Moulijn, Makkee, and Van Diepen (2004).

- For **ideal isothermal reactors**, the conversion of a reactant A can be calculated by one parameter, the **Damkoehler number**. (For a cascade of CSTRs we also need the number of CSTRs.) For a reaction order n and a rate constant k , Da equals $kc_{A,\text{initial}}^{n-1} t$ for a batch reactor (t = reaction time) and $kc_{A,\text{in}}^{n-1} \tau$ (τ = residence time) for a continuous tank reactor and a plug flow reactor.
- For **non-isothermal ideal reactors** heat effects strongly influence the reactor behavior up to the danger of a **thermal runaway**, if we have an exothermic reaction and insufficient cooling. Then criteria for the **parametric sensitivity** are needed to prevent a runaway. For a non-isothermal CSTR, the reaction temperature (T_{reaction}) is constant at any time but higher (lower) than the feed temperature for an exothermic (endothermic) reaction. The steady state mass and heat balances lead to a graphical solution of T_{reaction} and conversion, which is characterized by the intersection of the sigmoidal heat production function and the heat removal line for a given inlet and cooling temperature ($T_{\text{in}}, T_{\text{cool}}$). In some cases, a small increase of T_{in} and T_{cool} leads to a strong increase of T_{reaction} (ignition), and T_{reaction} passes through a hysteresis, if we increase and decrease T_{in} and T_{cool} , respectively. For a **non-isothermal batch and a non-isothermal tubular reactor** the parametric sensitivity (runaway behavior) has to be inspected by means of criteria based on two dimensionless numbers, N_c and N_{ad} . N_c is a measure of the cooling capacity relative to heat production, and N_{ad} accounts for heat generation.
- The **optimum temperature progression** minimizes the residence time τ for a given conversion. For irreversible and reversible endothermic reactions, the rate always increases with temperature at any composition, so the highest rate is reached at the highest allowable temperature. The situation is different for exothermic reversible reactions, as now two opposing factors are at work. The rate of the forward reaction speeds up with temperature but the maximum attainable conversion decreases. Therefore we start at a high temperature and then reduce the temperature as the conversion rises. The optimum operation line is found by connecting the maxima of the rate curves.
- **Real reactors** deviate from ideal reactors because of stagnant zones, back-mixing, channeling of fluid, short-circuiting, or imperfect mixing. Thus, the question is: How can this deviation be measured and how we can then account for this with regard to calculating the conversion and product yields for a given (mean) residence time?
- The deviation of a real (continuously operated) reactor from ideal systems is deduced from the **residence time distribution** (RTD), which is measured by a pulse or by a step experiment. For a **pulse experiment**, a small amount of tracer is introduced into the feed stream, and the exit tracer concentration is measured with time (E function). For a **step experiment**, at time $t = 0$ we switch to a fluid with a tracer of constant concentration, and the exit tracer concentration versus time is measured (F function).
- Based on the RTD the conversion of a reactant in a real reactor is calculated by the **tanks-in-series model**, which considers the actual reactor as a system of N identical CSTRs. The F and E functions of a cascade are well known and, by comparison of the measured functions, N of our real system is estimated. Finally, the conversion is calculated based on Da and N .
- The **dispersion model** is an alternative to the tanks-in-series model. This model formally characterizes mass transport in the radial and axial direction as a one-dimensional process in terms of an **effective longitudinal diffusivity** D_{ax} that is superimposed on the plug flow. The dimensionless group $D_{\text{ax}}/(uL)$ is called the dispersion number, and the reciprocal value is the **Bodenstein number** Bo . Calculation of the conversion is possible by equations based on Da and Bo .
- **Fixed bed tubular reactors** are commonly used for heterogeneously catalyzed and gas–solid reactions. The **pseudo-homogeneous two-dimensional model**

does not distinguish between the fluid and solid phase, and considers extra- and intraparticle mass and heat transfer effects by the use of an effective reaction rate, that is, gradients of temperature and concentration within the particle and in the thermal and diffusive boundary layers are collected together by effectiveness factors, which enables the system of four equations (mass and heat balances for solid and fluid phase) to be replaced by two equations. The following dispersion processes account for deviations from an ideal plug flow: **radial dispersion of mass** (by an effective radial diffusivity), **axial dispersion of mass** (effective axial diffusivity), **axial dispersion of heat** (effective axial thermal conductivity), and **radial dispersion of heat** (effective radial thermal conductivity). As a rule of thumb, axial dispersion of heat and mass only has to be considered for strong variations in temperature and concentration over a length of a few particles. Radial mass transport effects are usually also negligible. Radial heat transport is important for wall-cooled or heated reactors. For a negligible influence of radial dispersion of heat, the **one-dimensional reactor model** can be applied.

- **Novel developments in reactor technology** are multifunctional reactors, which couple different processes such as reaction and separation by membranes, adsorption, or distillation, catalytic or reactive distillation, monolithic reactors, microreactors, and adiabatic reactors with periodic flow reversal.

4.11

Measurement and Evaluation of Kinetic Data

This chapter is important for anybody carrying out research in the field of kinetics or who is or will be involved in technical processes during his professional life in industry, because for process development the prime efforts on the laboratory level initially concentrate on the reaction, which usually represents the most important step in the entire process.

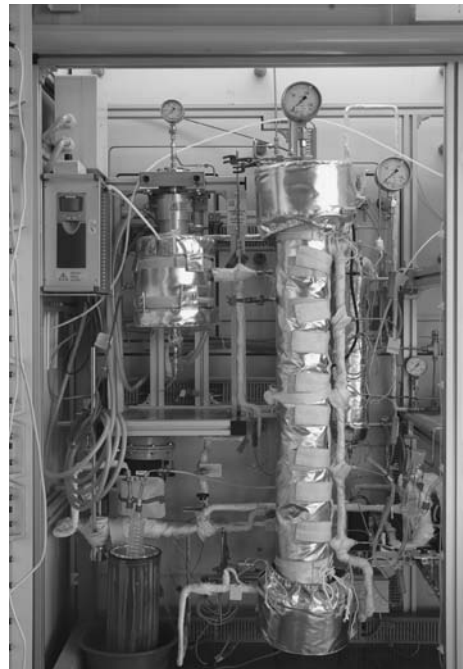
The goal of these efforts is a better understanding of the process and to achieve a scale-up-factor as large as possible. A direct transition from the development of a process at the laboratory level involving a few grams per hour of the particular product to the industrial process with yields of several tons per hour would be ideal. But this transition is difficult to achieve, as in the course of the scale-up many things may change:

- A laboratory-scale reactor may differ considerably from that of the technical reactor used in large-scale industrial production, for example, in terms of heating, dispersion, and mixing.
- The Re number and other dimensionless numbers encountered in technical reactors may strongly differ from laboratory reactors.

There are two approaches to overcome these difficulties. In the “classical” approach, many intermediate steps – for example, each with a small scale-up factor of around 10 – are used. Then no detailed study of the underlying processes is needed, but this is cumbersome, expensive, and purely empirical. The “modern” approach – on which we concentrate throughout this book – is the understanding of all processes in such detail as to allow their reliable description. In principle, this approach permits the scale-up in one single step up to any order of magnitude.

“Operating manual” for beginners and intermediate learners:

For a basic understanding of the methods used to determine kinetic data, start with Sections 4.11.1–4.11.3, which present the principal methods and different types of laboratory reactors. You should also read Section 4.11.5.1 as a relatively simple example of how to determine the reaction rate equation (thermal conversion of naphthalene).



Continuous fixed bed reactor.



“Operating manual” for advanced learners:

Advanced learners should then also study Section 4.11.4 (on transport limitations in experimental catalytic reactors) and Sections 4.11.5.2–4.11.5.4, where some more complex examples are given (heterogeneously catalyzed gas-phase reaction, catalytic multiphase reaction, and non-isothermal oxidation of carbon).

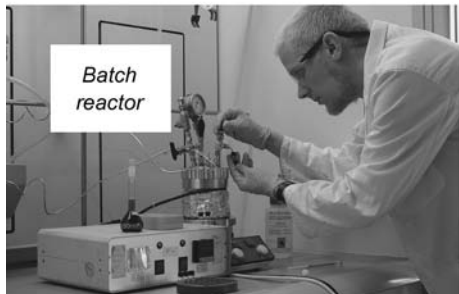
4.11.1

Principal Methods for Determining Kinetic Data

The objective of kinetic measurements is to discriminate between micro- and macrokinetics.

4.11.1.1 Microkinetics

As *microkinetics* we consider here the kinetics of the chemical reaction, that is, the (measured) reaction rate is not affected by transport processes of any kind (called *intrinsic kinetics*). Differentiation is necessary between largely comprehensive knowledge of underlying processes and simplifying assumptions about the particular reaction mechanism (Topic 4.3.1). Usually, complete knowledge about the reaction scheme cannot be obtained solely from kinetic measurements. Additional physicochemical measurements are needed, and considerable efforts are required for this purpose. Therefore, this approach is not suitable and is not necessary for the development of processes. Thus, in practice modeling of reactions starts with simplifying assumptions, applying formal kinetic equations as discussed in Section 4.4.



4.11.1.2 Macrokinetics

If the intrinsic chemical kinetics cannot be separated from transport processes at the conditions relevant for technical operation we speak of *macrokinetics* or effective apparent kinetics. Investigation of effective kinetics alone, that is, disregarding transport phenomena, sometimes also makes sense if the laboratory reactor intended for investigation of specific operating conditions is hydrodynamically similar to the technical reactor so that the transport parameters in both systems can also be assumed to be similar. For example, the response of a multi-tubular reactor (featuring up to 30 000 individual tubes) can easily be simulated in the laboratory, if a single tube is used, with which the response of the actual reactor under various conditions can be investigated. Unfortunately, this approach is in most cases not applicable, and so we have to determine all parameters of the micro- and macrokinetics.

4.11.1.3 Laboratory Reactors

Laboratory reactors should preferably be operated (for each experiment) isothermally to discriminate between temperature effects (activation energy) and concentration effects (reaction orders). The reaction conditions should be chosen in such a way that chemical and transport phenomena (microkinetic and macrokinetic effects), which are equally important in an industrial process, can be investigated separately.

Two types of laboratory reactors are most suitable for kinetic investigations:

Gradientless differential reactors allow evaluation of kinetic data practically free of distortion by heat/temperature effects. Depending on the flow, a distinction is made between reactors with outer and inner circulation (recycle reactor, continuous stirred tank reactor, Figure 4.11.1). Evaluation of kinetic measurements by means of the differential method is straightforward as the algebraic balance equation for a stirred tank reactor can be applied (prerequisite: high recycle ratio R). In practice it is found that recycle ratios of more than 10 are sufficient to achieve practically ideal

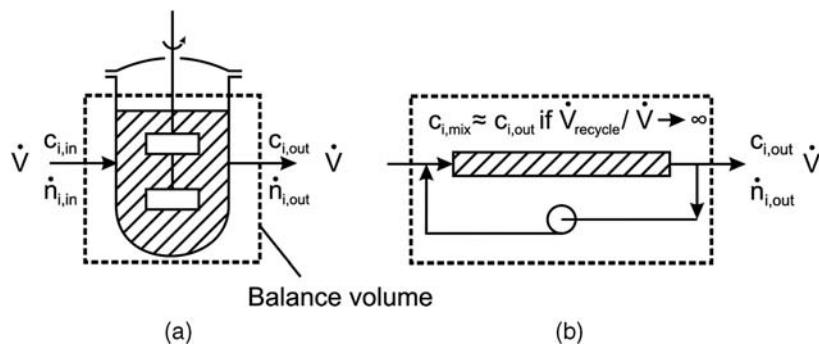


Figure 4.11.1 Gradientless laboratory reactors:
(a) continuous stirred tank reactor; (b) recycle reactor.

stirred tank behavior. The rate of conversion of a reactant A in a gradientless system is constant and simply given by the mass balance:

$$r_A = \dot{V} \frac{(c_{A,in} - c_{A,out})}{V_R} = \frac{X_A c_{A,in}}{\tau} \quad (4.11.1)$$

If, for example, the rate is first order with respect to A (which has to be proven by variation of the inlet concentration) the rate constant k is easily determined by:

$$r_A = \frac{X_A c_{A,in}}{\tau} = k c_{A,out} \Rightarrow k = \frac{X_A}{(1 - X_A)\tau} \quad (4.11.2)$$

as the outlet concentration is almost constant within the reactor and therefore determines the rate. Note that before a set of experiments is carried out, it has to be proven that the reactor is really suitable for kinetic investigations: (i) Deviations from ideal stirred tank behavior should be checked by residence time measurements, for example, by step or pulse tracer experiments (Section 4.10.4). (ii) Mass transfer resistances should be excluded by tests with different particle sizes and by calculations as subsequently summarized in Section 4.11.4.

In *integral reactors* the concentrations and the conversion vary either with the reaction time (batchwise operated stirred tank reactor) or locally with the residence time and axial position (tubular reactor). Figure 4.11.2 shows that both reactors are completely equivalent if the time required for the reaction in the batch type reactor is replaced by the residence time the substances spend in the tubular reactor $\tau = V_R / \dot{V}$.

Integral evaluation means that the measured data are compared with the integrated form of the rate equation, for example, for a constant volume first-order reaction of reactant A we have:

$$r_A = -\frac{dc_A}{dV_R} = -\dot{V} \frac{dc_A}{dV_R} = -\frac{dc_A}{d\tau} = k c_A(x) k \tau = -\ln(1 - X_A) \quad (4.11.3)$$

and a plot of $-\ln(1 - X_A)$ versus τ gives a straight line with slope k .

Differential evaluation of data from integral reactors means that the rates are determined based on concentration-time plots by differentiation (Figure 4.11.3a), that is, by the slope of the tangent of the conversion-time curve for different values of the residence time and residual reactant concentration, which corresponds to the

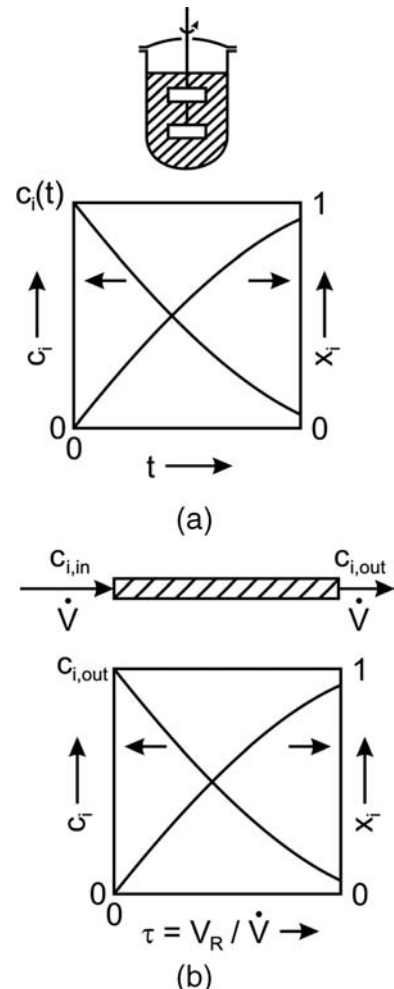


Figure 4.11.2 Integral laboratory reactors:
(a) batchwise operated stirred tank reactor;
(b) tubular (if possible plug flow) reactor.

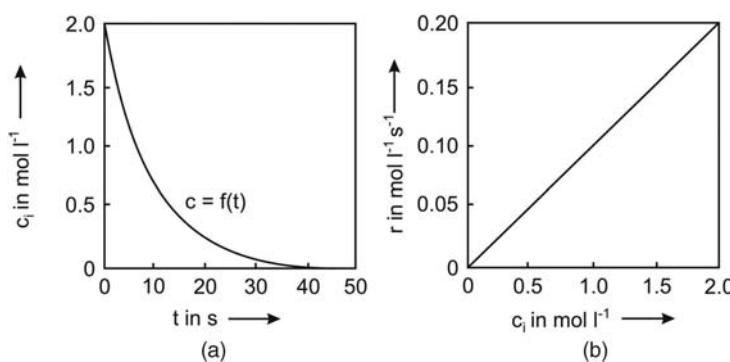


Figure 4.11.3 Evaluation of kinetic data by the differential method from data of an integral reactor (example of batch reactor).

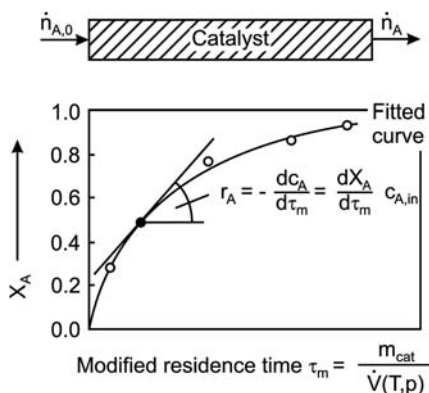


Figure 4.11.4 Evaluation of kinetic data from an integral reactor (Hagen, 2005).

momentary reaction rate. The rates at different stages of the reaction progress are then correlated with the respective concentrations to calculate the parameters (reaction orders) of the rate equation (first order for the example depicted in Figure 4.11.3b).

The differential and the integral method are compared in Figure 4.11.4 for a fixed bed reactor where, usually, the modified residence time (ratio of catalyst mass to total feed rate) is used.

If the conversion X in a (in principle integrally operated) reactor is differentially small (in practice below 10%), it is also possible to determine differentially the reaction rate directly from experiments. Such a reactor is then also called a differential reactor. For a constant volume reaction the following expression applies instead of Eq. (4.11.1):

$$r_A = -\frac{dc_A}{d\tau} \approx \frac{\Delta c_A}{\Delta \tau} \quad (\text{for } X_A \leq 10\%) \quad (4.11.4)$$

The rate can be attributed to the concentration at the reactor inlet, which is almost constant throughout the reactor, or to be even more accurate by the mean value $(c_{in} + c_{out})/2$:

$$r_A \approx \frac{\Delta c_{A,in}}{\Delta \tau} \approx kc_{A,in} \quad \text{or} \quad r_A \approx k \frac{(c_{A,in} + c_{A,out})}{2} \quad (\text{for } X_A \leq 10\%) \quad (4.11.5)$$

However, be careful as far as the differential mode of operation is concerned, for the differential expression $dc/d\tau$ (batch reactor: dc/dt) has to be replaced by the ratio of the differences $\Delta c/\Delta \tau$, since arbitrarily small differences cannot be determined analytically. Consequently, the reaction rate can no longer be attributed precisely to a specific concentration. Also for this reason, more accurate gradientless reactors are frequently used.

4.11.1.4 Pros and Cons of Integral and Differential Method

The least experimental problems are caused by integral reactors due to their simple construction and straightforward operation. Mostly the reactor consists of a flow tube 10–100 cm long and 1–5 cm in diameter, filled with catalyst or empty in the case of homogeneous reactions. By variation of the residence time by means of the flow rate (and/or the mass of catalyst), we can easily cover a wide range of conversion. A disadvantage of the integral reactor is that isothermal operation is hard to realize and that the measured conversion may be influenced by dispersion effects, so we have to inspect carefully whether we can consider the reactor as an ideal plug flow system (Section 4.11.4).

The integral method always involves comparing a model (fitted curve, Figure 4.11.4) with the measured data, which is a drawback compared to the differential method, where only moderate mathematical efforts are required. A disadvantage of a differential reactor is that the rate can only be determined directly by means of quite exhaustive experimental efforts (recycle reactor). The approximation according to Eqs. (4.11.4) and (4.11.5) may then be helpful.

4.11.2

Evaluation of Kinetic Data (Reaction Orders, Rate Constants)

Kinetic relationships, based on which a model can be formulated, are derived as follows:

- First, kinetic measurements are conducted at different temperatures, concentrations, and so on. The data are then evaluated by means of differential and/or integral methods.
- Choose a suitable function for the dependence of the rate from the concentrations (or from partial pressures for gas phase reactions) and temperature (Arrhenius equation).

- Determine the parameters of the kinetic model [order(s) of reaction, pre-exponential factor, activation energy].
- For complex systems, we additionally have to determine the structure of the scheme of all reactions involved (parallel and sequential reactions etc.).

Evaluation methods are presented here only for simple cases.

For an n -th order reaction with regard to reactant A (power law equation), we have:

$$r_A = -\frac{dc_A}{d\tau} = kc_A^n \quad (4.11.6)$$

and for the *differential method* the order n is obtained by the slope of the plot $\ln r_A$ versus $\ln c_A$:

! $\ln r_A = \ln k + n \ln c_A \quad (4.11.7)$

The intersection of the straight line with the ordinate yields the rate constant k . The values for the rate r_A may be determined either directly in a differential reactor or via differentiation of integral data. In practice attempts will be made to fit a straight line to the experimental points as closely as possible. Adapting the equation by the least-squares method to the experimental points to fit the equation would of course be more exact.

For the *integral method*, the concentrations of the products and reactants are measured as a function of reaction or residence time, respectively. The integrated form of the rate equation is then plotted as a diagram. For example, in the case of a tubular reactor, we obtain for a power law rate equation by integration of Eq. (4.11.6):

! $\left(\frac{c_{A,out}}{c_{A,in}}\right)^{1-n} = 1 + (n-1)k\tau c_{A,in}^{n-1} \quad (4.11.8)$

To determine the order n , we must check for which value of n the points representing the measured data are located on a straight line in the corresponding diagram. It is, thereby, helpful to choose a fixed point for the curve fitting (Section 4.11.5.2).

For a simple monomolecular *Langmuir type* of reaction rate – important for heterogeneously-catalyzed reactions (Section 4.5.2) – the rate expression may read as:

$$r_A = \frac{kp_A}{1 + Kp_A} \quad (4.11.9)$$

Rearrangement yields:

$$\frac{p_A}{r_A} = \frac{1}{k} + \frac{K}{k} p_A \quad (4.11.10)$$

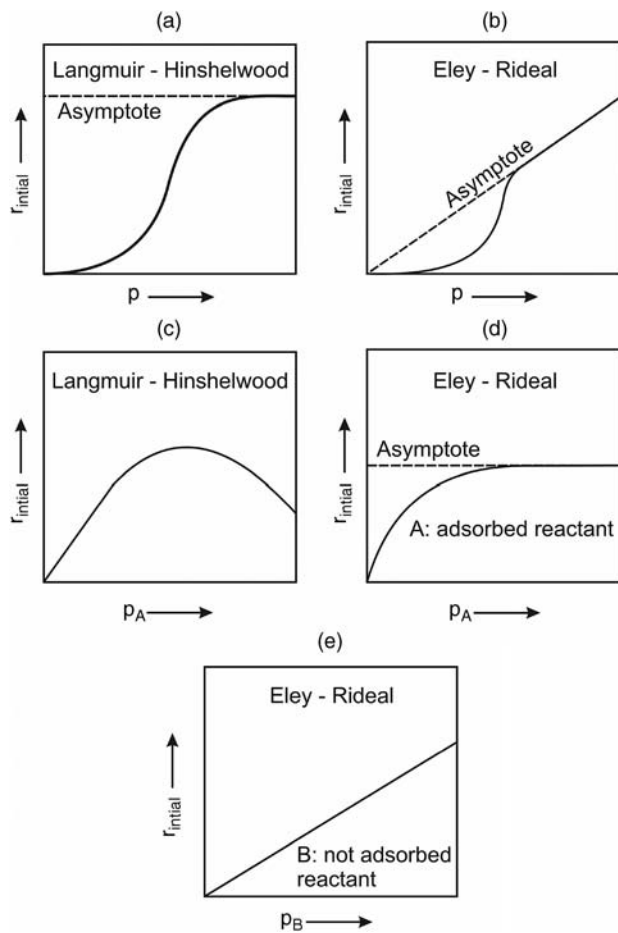
and a plot of p_A/r_A versus p_A gives a straight line with slope K/k and $1/k$ as intercept with the ordinate.

In many cases, the rate depends in a complicated way on the concentrations or partial pressures of reactants and products, and the data measured in the course of heterogeneously catalyzed reactions cannot be used directly to determine the rate law. Hence, depending on which reaction step constitutes the rate-determining step, numerous rate laws may apply. Model discrimination is then important, and the following strategy is frequently used.

First, we determine and use the initial reaction rates $r_{initial}$, that is, the conditions are adjusted such that the concentrations of the products still have no influence on the rate. This approach simplifies the rate equation considerably, since the corresponding terms with respect to the product concentrations can be canceled.

Particularly in heterogeneously catalyzed gas phase reactions, the initial reaction rate frequently depends on the total pressure as well as on the partial pressures of the reactants. Thus, by varying the total pressure p and the partial pressure p_i of one reactant a convenient form of the rate equation may be found, since (depending

Figure 4.11.5 (Pre)selection of the appropriate kinetic equation: influence of total pressure and partial pressure of one reactant on initial rate of a heterogeneously catalyzed bimolecular gas reaction of A and B: (a) Langmuir–Hinshelwood mechanism for variation of total pressure p ; (b) Eley–Rideal mechanism for variation of p ; (c) Langmuir–Hinshelwood for variation of partial pressure of one of the adsorbed reactants (e.g., p_A); (d) Eley–Rideal mechanism for variation of partial pressure of adsorbed reactant A (p_A); (e) Eley–Rideal mechanism for variation of partial pressure of reactant B (not adsorbed).



on the rate-determining steps) the initial rate depends on the total and partial pressure(s) in a characteristic way. This feature allows a (pre)selection of a suitable rate equation. Let us now inspect the characteristic plots of r_{initial} versus p or p_i by recalling two cases already examined in Section 4.5.2, a Langmuir–Hinshelwood and an Eley–Rideal mechanism for a bimolecular reaction of A with B. Figure 4.11.5 depicts how the initial rate depends on the total and partial pressure(s) for these two cases.

The Langmuir–Hinshelwood (LH) mechanism assumes that both A and B are adsorbed, and that the surface reaction of both adsorbed species is the rate-determining step, which leads to the following equation for the initial reaction rate if adsorption of products is negligible:

$$r_{A,\text{initial}} = \frac{k_A p_A p_B}{(1 + K_{\text{ads},A} p_A + K_{\text{ads},B} p_B)^2} \quad (\text{for LH mechanism}) \quad (4.5.5)$$

The Eley–Rideal (ER) mechanism assumes that only one reactant (A) is adsorbed on the surface and reacts with the second species B from the gas phase, which leads to:

$$r_{A,\text{initial}} = \frac{k_A p_A p_B}{1 + K_{\text{ads},A} p_A} \quad (\text{for ER mechanism}) \quad (4.5.6)$$

The first strategy for a (pre)selection of the kinetic equation is to vary the total pressure with an equimolar ratio of A and B in the feed, $p_A = p_B = p/2$. Equation (4.5.5) then leads to:

$$r_{A,\text{initial}} = \frac{k_A \frac{1}{4} p^2}{(1 + K_{\text{ads},A} \frac{1}{2} p + K_{\text{ads},B} \frac{1}{2} p)^2} = \frac{a_1 p^2}{(1 + b_1 p)^2} \quad (\text{for LH mechanism}) \quad (4.11.11)$$

Thus we should get a sigmoidal curve of the plot of $r_{A,\text{initial}}$ versus p , Figure 4.11.5a, and for a high total pressure p the rate becomes zero order with respect to p ($b_1 p \gg 1$).

For an Eley–Rideal mechanism, Eq. (4.5.6) leads to:

$$r_{A,\text{initial}} = \frac{k_A p_A p_B}{1 + K_{\text{ads},A} p_A} = \frac{k_A \frac{1}{4} p^2}{1 + K_{\text{ads},A} \frac{1}{2} p} = \frac{a_2 p^2}{1 + b_2 p}$$

(for ER mechanism) (4.11.12)

Thus, we should get a curve of the plot of $r_{A,\text{initial}}$ versus p that starts with $r_{A,\text{initial}} \sim p^2$ and then asymptotically converges to a straight line with $r_{A,\text{initial}} \sim p$ (Figure 4.11.5b).

The second strategy is to vary the partial pressure of one component (A), whereby we adjust a constant partial pressure of the second reactant B in the feed. This can be done either in approximation by a high surplus of B or we use a third inert component (nitrogen, argon) and reduce the partial pressure of this inert species according to the increasing pressure of A and constant pressure of B. Equations (4.5.5) and (4.5.6) then lead to:

$$r_{A,\text{initial}} = \frac{a_3 p_A}{(b_3 + p_A)^2} \quad \text{(for LH mechanism)} \quad \text{span style="float: right;">(4.11.13)}$$

$$r_{A,\text{initial}} = \frac{a_4 p_A}{b_4 + p_A} \quad \text{(for ER mechanism)} \quad \text{span style="float: right;">(4.11.14)}$$

For a Langmuir–Hinshelwood mechanism [Eq. (4.11.13)], we find an almost linear increase of $r_{A,\text{initial}}$ for low values of p_A , pass a maximum, and then the rate decreases for a further rise in p_A (Figure 4.11.5c).

For an Eley–Rideal mechanism [Eq. (4.11.14)], we also find a linear increase of r_A initial for low values of p_A , but then the rate becomes zero order for a further rise in p_A (Figure 4.11.5d). If the partial pressure of component B, which is not or only to a small extent adsorbed on the surface of the catalyst, is varied (at a constant pressure of A), Eq. (4.5.6) leads to:

$$r_{A,\text{initial}} = a_5 p_B \quad \left[\text{for ER mechanism with } a_5 = \frac{k_s K_{\text{ads},A} p_A}{1 + K_{\text{ads},A} p_A} \text{ in Eq. (4.5.6)} \right]$$

(4.11.15)

and thus the rate is directly proportionally to p_B (Figure 4.11.5e).

Other cases, for example, if adsorption of a reactant or desorption of a product are rate controlling, are discussed elsewhere [Baerns, Hofmann, and Renken (1999), Baerns *et al.* (2006), Emig and Klemm (2005), Froment and Bischoff (1990), Kapteijn and Moulijn (1999), Berger *et al.* (2001)].

Based on the results of these first two steps, selection among the remaining rate equations considering all terms (including product terms) can be performed. For this purpose the remaining rate equations are turned into a linear form by a suitable transformation and the measured values are plotted in a diagram. Now a search is made for the equation showing the minimum difference between the experiments and the calculation.

For the proper design of experiments, statistic-based methods of planning and evaluating are also used (factorial design). The purpose of planning experiments concerning kinetics is the layout of an experimental plan to obtain a maximum amount of information with a minimum effort. In this book this aspect – although important – is not considered, and we refer to well-known textbooks (e.g., Baerns, Hofmann, and Renken, 1999; Baerns *et al.*, 2006; Hagen, 2005; Hoffmann and Hofmann, 1971; Retzlaff, Rust, and Waibel, 1978).

4.11.3

Laboratory-Scale Reactors for Kinetic Measurements

Figures 4.11.6 and 4.11.7 show the classification of laboratory-scale reactors by their mode of operation. For liquid–liquid reactions, homogeneously catalyzed reactions

Figure 4.11.6 Classification of laboratory reactors according to their mode of operation (adapted from Kapteijn and Moulijn, 1999).

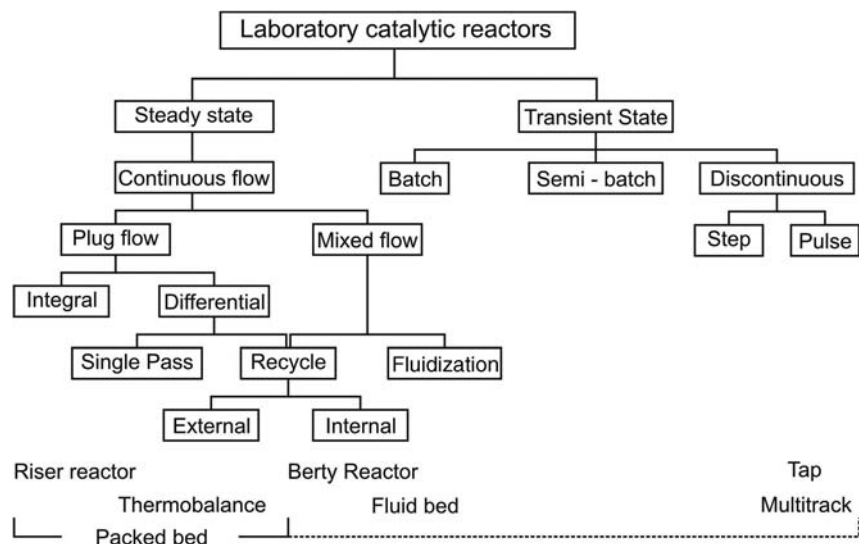
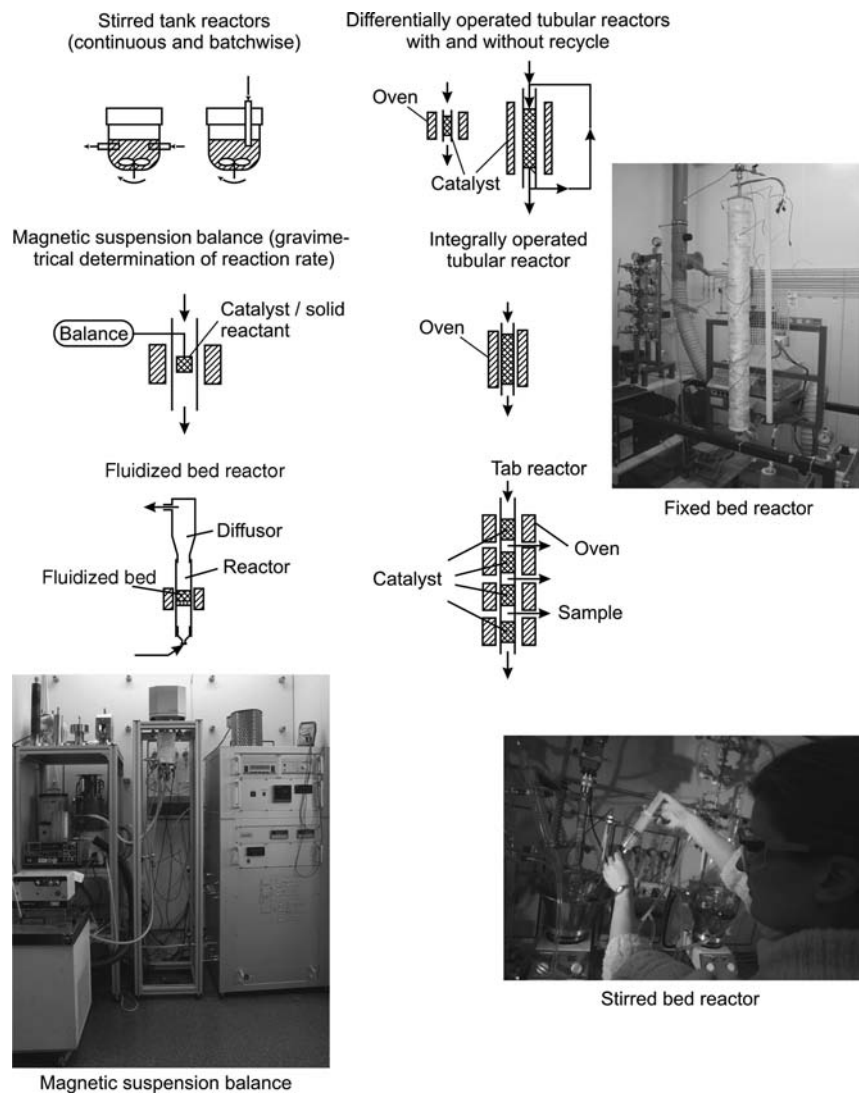
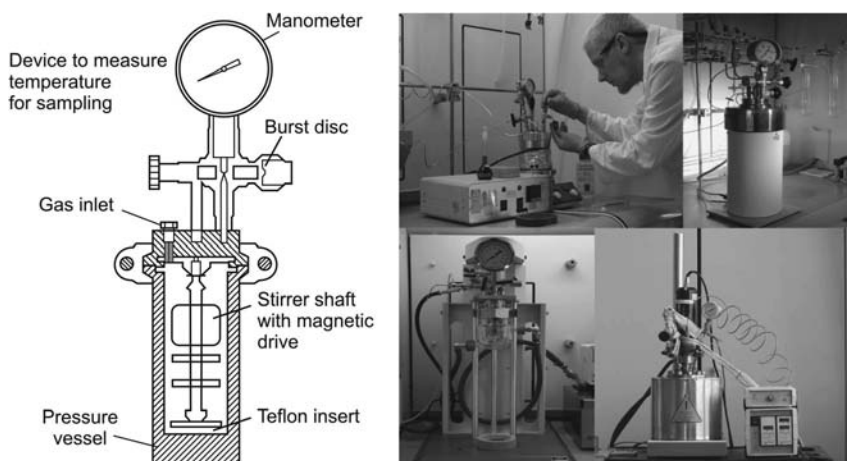


Figure 4.11.7 Typical laboratory reactors for kinetic measurements. Department of Chemical Engineering, University Bayreuth.





and heterogeneously catalyzed reactions in the slurry phase, a batchwise operated stirred tank reactor is frequently used (Figure 4.11.8).

More common for kinetic studies of heterogeneously catalyzed gas reactions are tubular reactors loaded with catalyst (fixed bed reactor). The tubular reactor displays a simple design and is easy to operate. A simultaneous integral and differential mode of operation can be achieved in a reactor with taps for measuring concentration and temperatures at defined axial positions (Figure 4.11.9). By using a tubular reactor, the density of information obtainable during experiments with fixed bed reactors is improved.

For strong exo- or endothermic reactions it is often difficult to operate the reactor isothermally. This makes modeling of the laboratory-type reactor more difficult. To keep the temperature gradients in the reactor as low as possible, the diameter of the reactor has to be minimized and the flow rate in the reactor maximized to achieve good heat transfer.

However, these provisions alone are often insufficient to achieve an appropriate isothermal mode of operation. The reactor can then be subdivided into several sections in which only a moderate axial temperature profile develops. The desired temperature for the reaction is then restored by heat exchange with the walls between the individual layers of catalyst. The rate of reaction then differs in the individual sections of the reactor. The catalyst may also be diluted with an inert material. This arrangement reduces the heat generated per unit volume; a criterion for the maximum dilution is given in Section 4.11.4.

Gradientless operation both with respect to temperature and concentration can be obtained by an external or internal recycle (Figure 4.11.10). In a recycle reactor the gas passes several times through the catalyst bed until the product gas leaves the reaction volume. This type of reactor is more elaborate in design, but evaluation is simpler as the rate can be determined directly. As there is a very high flow rate in

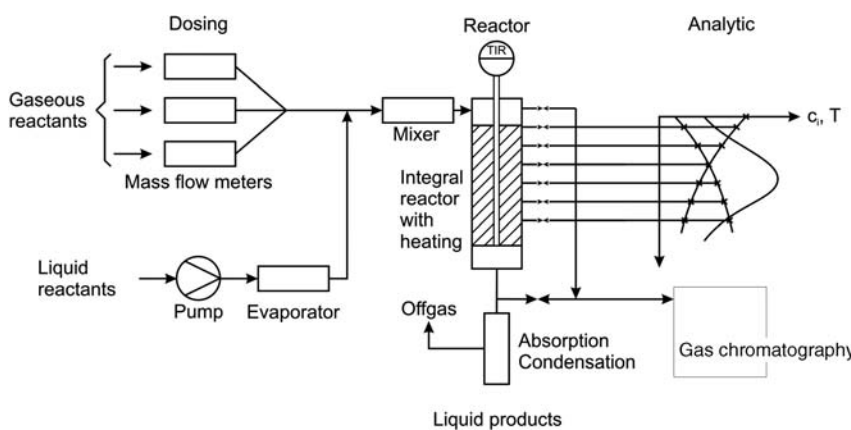


Figure 4.11.8 Batchwise operated stirred tank reactor. Department of Chemical Engineering, University Bayreuth.

Figure 4.11.9 Fixed bed reactor with taps for measuring axial concentration and temperature profiles in a fixed bed.

Figure 4.11.10 Gradientless reactor with internal recycle (so-called Berty reactor). Adapted from Baerns *et al.* (2006).

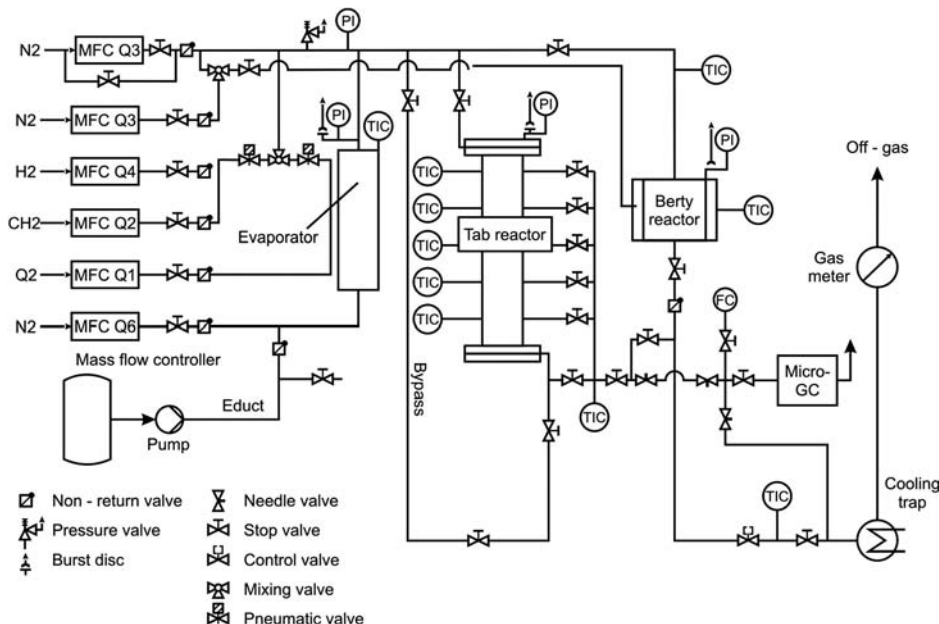
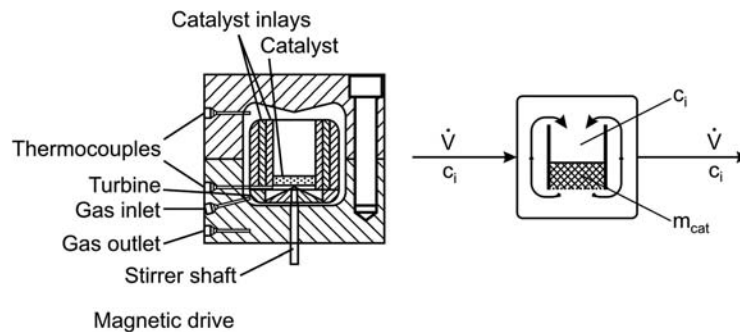


Figure 4.11.11 Laboratory apparatus (Department of Chemical Engineering, University Bayreuth) with fixed bed tab-reactor and fixed bed reactor with internal recycle (Berty reactor). Department of Chemical Engineering, University Bayreuth.

the reactor, the possibility of temperature gradients in the catalyst bed and an influence of film diffusion limitation are minimized. If possible, both differential and integral kinetic measurements should be carried out and combined to derive kinetic equations that hold for a wide range of conversion. Figure 4.11.11 shows a laboratory apparatus with a tab-reactor and a reactor with internal recycle (*Berty* reactor).

4.11.4

Transport Limitations in Experimental Catalytic Reactors

If we want to determine the “true” intrinsic rate of a heterogeneously catalyzed reaction in a laboratory fixed bed reactor, we have to consider two conditions to obtain reliable kinetic data (Figure 4.11.12):

- **Ideal plug flow behavior:** The behavior of the reactor (residence time distribution) should be such that we can consider the fixed bed as an ideal plug flow reactor (PFR). If this condition is fulfilled we can use the (relatively simple) equations valid for a PFR that correlate the conversion with the rate constant, residence time, and initial reactant concentration. For example, we can determine the rate constant for a reaction with order n by Eq. (4.10.26) if we have measured the conversion of reactant A at a given value of the residence time by:

$$k_{m,\text{eff}} = \frac{(1 - X_A)^{(1-n)} - 1}{(n-1)\rho_p \tau} \quad (\text{with } Da = k c_{A,\text{in}}^{n-1} \tau) \quad (4.10.26b)$$

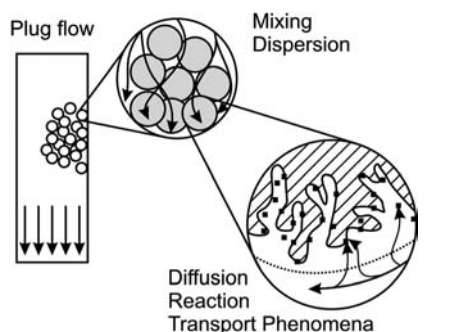


Figure 4.11.12 Transport phenomena in a catalytic fixed bed reactor on different levels (adapted from Kapteijn and Moulijn, 1999).

if we use the definition of the Da number for solid catalyzed reactions, that is, $Da = k_{m,\text{eff}}\rho_p\tau$. Note that $k_{m,\text{eff}}$ may still be influenced by inter- and intraparticle transport phenomena. To reach plug flow behavior, the influence of dispersion of mass and heat in the axial direction as well as radial variations in the bed structure (by-pass effects) should be minimized. Conversely, the dispersion of mass and heat in radial direction should be maximized to avoid radial gradients of temperature and concentrations.

- **Gradientless ideal particle behavior:** The second condition to assure that the intrinsic kinetics are measured is that gradients of temperature and concentration in the particles as well as in the boundary layer around the particles are negligible, that is, $k_{m,\text{eff}} = k_m$.

Hence we need respective criteria for the design and operation of a laboratory reactor to ensure negligible deviations from the ideal. Subsequently, we repeat these criteria, which were already derived in Sections 4.7, 4.10.6.5, and 4.10.7.2, and specify them for laboratory-scale experiments. In the next subsection, the criteria for *ideal plug flow behavior* (exclusion of an influence of axial and radial dispersion of mass and heat are covered), and in the subsequent subsection, the criteria for *gradientless deal particle behavior* (exclusion of an influence of interphase and intraparticle transport of mass and heat) are outlined.

4.11.4.1 Ideal Plug Flow Behavior: Criteria to Exclude the Influence of Dispersion

Radial Variations in Bed Structure The criterion for a negligible influence of *radial variations in the bed structure* is:

$$\frac{d_R}{d_p} \geq 10 \quad (4.11.16)$$

Axial and Radial Dispersion of Mass and Heat The criterion for a negligible influence of *axial dispersion of mass* (first-order reaction) is:

$$\frac{L}{d_p} \geq 10Da \quad (4.11.17)$$

Mass transfer in the radial direction should be maximized to prevent significant deviations from plug flow. The criterion for a negligible influence of *radial dispersion of mass* is:

$$\frac{d_R}{d_p} \leq 2.5 \frac{L}{d_R} \frac{1}{Da} \quad (4.11.18)$$

The criterion for a negligible influence of *axial dispersion of heat* is:

$$\frac{L}{d_p} \geq 10Da \frac{E_A \Delta T_{ad}}{RT^2} \quad (4.11.19)$$

The term $E_A \Delta T_{ad}/(RT^2)$ is in practical cases more than 5. Comparison with Eq. (4.11.17) shows that axial dispersion of heat becomes significant before axial mass transfer does.

Experimental fixed bed reactors are commonly heated electrically or cooled, and radial temperature gradients within the packed bed may occur. The criterion for exclusion of the influence of *radial heat dispersion* (negligible radial temperature profile) is:

$$\frac{d_R}{d_p} \leq 0.16 \frac{L}{d_R} \frac{1}{Da} \frac{RT^2}{E_A \Delta T_{ad}} \quad (4.11.20)$$

In contrast to fixed bed reactor modeling, see Section 4.10.7.2, we can neglect the influence of heat transfer at the internal reactor wall, as this induces a temperature jump directly at the wall. If the reaction temperature is measured in the bed, usually by a thermocouple located at the axis of the reactor, we only have to consider radial gradients in the bed itself.

Example 4.11.1 shows that the criterion to exclude radial dispersion of heat is the most severe problem of heat dispersion and dispersion in general. Thus, we have to limit ΔT_{ad} by dilution with inert, if the criterion according to Eqs. (4.11.19) and (4.11.20) are not fulfilled.

Example 4.11.1: Maximum adiabatic temperature rise to exclude axial and radial temperature gradients

We can use Eqs. (4.11.19) and (4.11.20) to estimate whether we have to limit the adiabatic temperature rise (ΔT_{ad}) by dilution with inert to avoid pronounced radial and axial temperature gradients in laboratory-scale reactors. As an example, we take a typical value for the term RT^2/E_A of 60 K (e.g., for 600 K and $E_A = 50 \text{ kJ mol}^{-1}$), a value for L/d_R of 10, a reactor length L of $50d_p$, and Da of 1. We also consider that the reactor diameter should be equivalent to at least 10 particle diameters, which is already needed to exclude wall effects [see Eq. (4.11.16)]. Therefore, according to Eq. (4.11.19) the influence of

axial dispersion of heat can be excluded for $\Delta T_{ad} < 600 \text{ K}$, which is a rather high value. Equation (4.11.20) yields a maximum ΔT_{ad} of only 10 K to avoid pronounced radial temperature gradients. Thus, the criterion to exclude radial dispersion of heat is the most severe problem of heat dispersion. For higher values of ΔT_{ad} , we have to dilute with inert to decrease ΔT_{ad} or we have to limit the conversion to decrease Da . For example, for 10% conversion, and thus a Da value of 0.1, we would then have a value of $\Delta T_{ad,max}$ of 100 K for the given example.

Comments

- Like any diagnostic test, the criteria given above must be used with caution. For example, the axial and radial Peclet numbers (2 and 10, respectively, see Sections 4.10.7.2 and 4.10.6.4) used to derive the criteria may deviate for $Re_p < 10$ to lower Pe values by factors of up to 5. This would lead to a more restrictive criterion.
- The basic assumption used to derive the criteria for negligible influence of dispersion of heat is that the rate is affected by less than 5%. According to Eq. (4.10.149), the corresponding allowable temperature difference ΔT_{max} is given by the term $0.05 RT^2/E_A$. For example, if RT^2/E_A is 20 K ($T = 350 \text{ K}$, $E_A = 50 \text{ kJ mol}^{-1}$), ΔT_{max} is 1 K, which is too restrictive with regard to the accuracy of temperature measurements.
- The axial temperature profile in an experimental fixed bed reactor and at least one value of the wall temperature should be measured. The value of the radial temperature difference can also be estimated by Eq. (4.10.168):

$$\Delta T_{rad} \approx 0.3 Da \Delta T_{ad} \frac{d_R^2}{d_p L} \quad (4.10.168)$$

Thus, the best method is to construct the reactor based on these criteria and to verify by measurements that radial gradients really are negligible.

- For trickle bed reactors, the Pe numbers are up to an order of magnitude lower. Thus, compared to a single-phase system, the reactor should be ten times longer for the same particle diameter.

4.11.4.2 Gradientless Ideal Particle Behavior: Criteria to Exclude the Influence of Interfacial and Internal Transport of Mass and Heat

Interfacial Mass Transfer (Concentration Gradients in the Film) For a first-order reaction and low Re numbers (for a fixed bed $Sh_{min} = 3.8$), the influence of film diffusion can be neglected, if the following condition is fulfilled (Section 4.7):

$$\frac{k_{m,eff} \rho_p d_p^2}{D_{A,g}} \leq 1.14 \quad (4.7.7)$$

For a fixed bed reactor, rearrangement of Eq. (4.7.7) with $Da = k_{m,eff} \rho_p \tau$ leads to:

$$d_p \leq 1.1 \sqrt{\frac{D_{A,g} \tau}{Da}} \quad (4.11.21)$$

Note that Da can be easily determined based on the conversion by $Da = -\ln(1 - X_A)$.

Interfacial Heat Transfer (Temperature Difference between Bulk Phase and Particle)

The condition for a negligible effect of a temperature difference between the gas phase and the surface of the particle is given by Eq. (4.7.14):

$$\frac{k_{m,\text{eff}} c_{A,g} (-\Delta_R H) \rho_p d_p^2 E_A}{\lambda_g T_g^2 R} \leq 1.14 \quad (4.7.14)$$

Rearrangement of Eq. (4.7.14) with $Da = k_{m,\text{eff}} \rho_p \tau$ leads to:

$$d_p \leq 1.1 \sqrt{\frac{\lambda_g RT^2}{E_A |\Delta_R H| Da c_{A,g}}} \quad (4.11.22)$$

Introduction of the adiabatic temperature rise, Eq. (4.10.76), the assumption of the “worst” case of $c_{A,g} = c_{A,g,\text{in}}$, and the use of the approximation that the diffusion coefficient of a gas equals the thermal conductivity divided by the term $c_p \rho_{\text{mol}}$ lead to:

$$d_p \leq 1.1 \sqrt{\frac{D_{A,g} \tau}{Da} \frac{RT^2}{E_A \Delta T_{ad}}} \quad (4.11.23)$$

The term $RT^2/(E_A \Delta T_{ad})$ is typically in the range 1–0.1. Thus, comparison of Eq. (4.11.23) with Eq. (4.11.21) shows that the external heat transfer becomes significant only if the external mass transfer does.

Internal Mass Transfer (Pore Diffusion) The simplified criterion for exclusion of an influence of internal mass transfer is given for spherical particles, a first-order reaction, and the assumption $D_{\text{eff}} = 0.1 D_{i,g}$ by Eq. (4.7.19):

$$\frac{k_{m,\text{eff}} \rho_p d_p^2}{D_{A,g}} \leq 0.6 \quad (4.7.19)$$

For a fixed bed reactor, rearrangement of Eq. (4.7.7) with $Da = k_{m,\text{eff}} \rho_p \tau$ yields:

$$d_p \leq 0.8 \sqrt{\frac{D_{A,g} \tau}{Da}} \quad (4.11.24)$$

Comparison of Eq. (4.11.24) with Eq. (4.11.21) shows that the internal mass transfer becomes significant before external mass transfer does.

Internal Heat Effects The criterion for exclusion of internal heat effects is given by Eq. (4.7.28):

$$\frac{d_p^2 k_{m,\text{eff}} \rho_p (-\Delta_R H) c_{A,g} E_A}{\lambda_p T_s RT_s} \leq 3 \quad (4.7.28)$$

Rearrangement yields:

$$d_p \leq 1.7 \sqrt{\frac{\lambda_p RT^2}{E_A |\Delta_R H| k_{m,\text{eff}} \rho_p c_{A,g}}} = 1.7 \sqrt{\frac{\lambda_p RT^2}{E_A |\Delta_R H| Da c_{A,g}}} \quad (4.11.25)$$

Example 4.11.2 shows that in most cases internal heat effects are negligible compared to external effects.

Example 4.11.2: Estimation of internal and external heat effects in porous particles

Comparison of Eq. (4.11.25) with Eq. (4.11.22) shows that the internal heat transfer is less significant than the external transfer. The ratio of the maximum particle diameter for exclusion of internal heat transfer effects to the value for external heat transfer is given by:

$$\frac{d_{p,\text{max,int}}}{d_{p,\text{max,ext}}} \approx 1.5 \sqrt{\frac{\lambda_p}{\lambda_g}} \approx 6 \quad (4.11.26)$$

as the effective heat conductivity in porous particles is about $0.3 \text{ W m}^{-1} \text{ K}^{-1}$, whereas the conductivity of a gas is $0.02 \text{ W m}^{-1} \text{ K}^{-1}$. Therefore, the critical diameter for the onset of an internal heat transfer resistance is by a factor of about 10 larger compared to external heat transfer.

4.11.4.3 Criterion to Exclude the Influence of the Dilution of a Catalytic Fixed Bed

Sometimes kinetic data are needed under conditions where concentration gradients exist, for example, in investigations under industrially relevant conditions or if pore diffusion effects should be studied. A method of avoiding dispersion effects is to dilute large catalytic particles with small inert particles. Such a dilution is also an option to obtain a sufficient bed length to exclude axial heat dispersion effects. However, if the dilution is too high, this may lead to an uneven particle distribution and to unwanted bypass effects. According to Berger *et al.* (2001), the criterion for a 5% deviation from the ideal situation is:

$$\frac{V_{\text{inert}}}{V_{\text{cat}}} \leq \frac{1}{10X_{\text{diluted}}} \frac{L_{\text{bed}}}{d_p} \quad (4.11.27)$$

(for $X < 0.8$ and deviation = $1 - X_{\text{diluted}}/X_{\text{undiluted}} < 0.05$)

where L_{bed} is the length of the diluted bed, and X is the conversion. For example, for a conversion of 0.5 (50%) and a length of 100 particle diameters, the maximum ratio of inert material to catalyst is 20. A combination of a high conversion and high dilution should be avoided.

4.11.5

Case Studies for the Evaluation of Kinetic Data

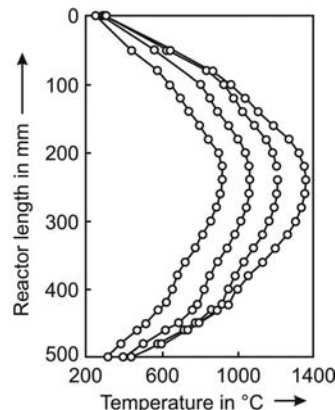
4.11.5.1 Case Study I: Thermal Conversion of Naphthalene

Concept of Effective Reaction Volume for Non-Isothermal Tubular Reactors The kinetics of thermal reactions of hydrocarbons in the presence of hydrogen and steam were studied in an empty ceramic tube (20 mm diameter and 500 mm long), which was heated by an electric resistance oven (Jess, 1995, 1996a, 1996b). Here we take naphthalene as an example. The axial temperature profiles measured in the center of the tube at different oven temperatures show that the reactor is, by far, not isothermal (Figure 4.11.13).

In contrast to investigations with solid catalysts, where we can place the catalyst in a small and almost isothermal zone, we have to accept non-isothermal operation in the case of a homogeneous gas phase reaction. It is, therefore, required to determine the kinetic parameters by means of an effective reaction volume. $V_{R,\text{eff}}$ is defined as the volume needed to reach the same conversion at a constant reference temperature T_{ref} as under the non-isothermal conditions with an axial temperature T_x . T_{ref} can be arbitrarily chosen, for example, the temperature at a fixed position in the middle of the tube. This definition leads to:

$$\int_0^{V_R} r_{N,T_x} dV = \int_0^{V_{R,\text{eff}}} r_{N,T_{\text{ref}}} dV \quad (4.11.28)$$

Figure 4.11.13 Axial temperature profiles during thermal cracking of naphthalene in an empty tubular reactor (Jess, 1995, 1996a, 1996b).



The rate r_N of naphthalene conversion depends on the concentrations of naphthalene, hydrogen, and steam, which may be expressed by a general function $f(c_i)$, as well as on the rate constant k_N , which strongly depends on the axial temperature T_x . Introduction of the cross-sectional area and length of the reactor, A_R and L_R , respectively, then leads to:

$$A_R \int_0^{L_R} k_{N,T_x} f(c_{i,T_x}) dx = A_R \int_0^{L_{R,\text{eff}}} k_{N,T_{\text{ref}}} f(c_{i,T_{\text{ref}}}) dx \quad (4.11.29)$$

In comparison to the strong influence of temperature on k_N according to Arrhenius's law, we may neglect the small change in concentrations with temperature, and Eq. (4.11.29) simplifies to:

$$V_{R,\text{eff}} = A_R L_{R,\text{eff}} = A_R \frac{\int_0^{L_R} k_{N,0} e^{-\frac{E_{A,N}}{RT_x} dx}}{k_{N,0} e^{-\frac{E_{A,N}}{RT_{\text{ref}}}}} \approx A_R \int_0^{L_{R,\text{eff}}} e^{-\frac{E_{A,N}}{R} \left(\frac{1}{T_x} - \frac{1}{T_{\text{ref}}} \right)} dx \quad (4.11.30)$$

The effective residence time is then defined as:

$$\tau_{\text{eff}} = \frac{V_{R,\text{eff}}}{\dot{V}(p, T_{\text{ref}})} \quad (4.11.31)$$

Note that radial temperature profiles in the thin reactor are not considered, and integration is only needed in the axial direction. [Detailed measurements show that radial temperature differences are less than 20 K (Kern, 1998).] The integral in Eq. (4.11.30) is determined graphically by the area under the respective function, as shown in Figure 4.11.14 for an activation energy of 300 kJ mol⁻¹ and a maximum temperature of 1200 °C.

To determine the value of $V_{R,\text{eff}}$ by the method described above, E_A is required, as $V_{R,\text{eff}}$ depends on E_A (Figure 4.11.15). To calculate τ_{eff} by Eq. (4.11.31), we must first derive E_A based on experiments with varied temperature. Figure 4.11.15 shows that for the given reactor and oven the effective reaction volume $V_{R,\text{eff}}$ luckily does not depend on the adjusted oven temperature (1000–1400 °C) and temperature level in the reactor, respectively.

Determination of Kinetic Parameters of Thermal Conversion of Naphthalene

Although different products (benzene, soot, C₂ hydrocarbons) are formed during the thermal conversion of naphthalene in the presence of hydrogen and steam, a simple power law equation can be used for the kinetic equation:

$$r_N = -\frac{d\dot{n}_N}{dV_{R,\text{eff}}} = k_N c_N^m c_{H_2O}^n c_{H_2}^p \quad \left(\text{with } k_N = k_{0,N} e^{-\frac{E_{A,N}}{RT}} \right) \quad (4.11.32)$$

Introduction of the residence time [Eq. (4.11.31)] and conversion ($dX_N = dc_N/c_{N,\text{in}}$) leads to:

$$c_{N,\text{in}} \frac{dX_N}{d\tau_{\text{eff}}} = k_N c_N^m c_{H_2O}^n c_{H_2}^p \quad (4.11.33)$$

Figure 4.11.16 shows the influence of the initial concentration of naphthalene on its conversion for different residence times and constant initial concentrations of hydrogen and steam. Although the reactor operates in integral mode, we can calculate the reaction order of naphthalene by the differential method, if we determine graphically the initial slopes of the $X_N - \tau_{\text{eff}}$ plot (Figure 4.11.16). Rearrangement of Eq. (4.11.33) for $\tau_{\text{eff}} \rightarrow 0$ ($c_N = c_{N,\text{in}}$) yields:

$$\ln \left(\frac{dX_N}{d\tau_{\text{eff}}} \right)_{\tau_{\text{eff}} \rightarrow 0} = (m-1) \ln(c_{N,\text{in}}) + \ln(k_N c_{H_2O,\text{in}}^n c_{H_2,\text{in}}^p) \quad (4.11.34)$$

and thus for constant inlet concentrations of H₂ and steam the plot $\ln(dX/d\tau)$ versus $\ln(c_{N,\text{in}})$ gives a straight line (Figure 4.11.17). The reaction order of naphthalene

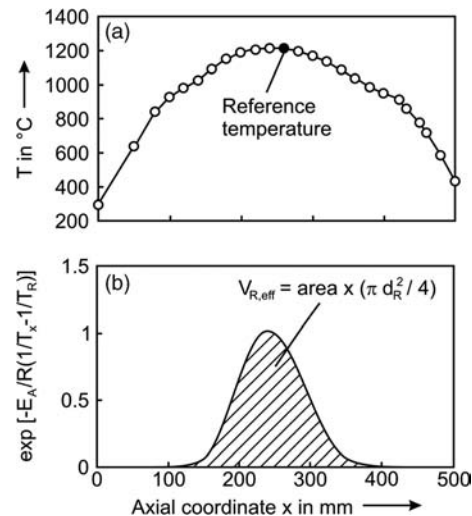


Figure 4.11.14 Method to determine the effective reaction volume (for the example of $E_A = 300 \text{ kJ mol}^{-1}$; see text). Taken from Jess (1995, 1996a, 1996b).

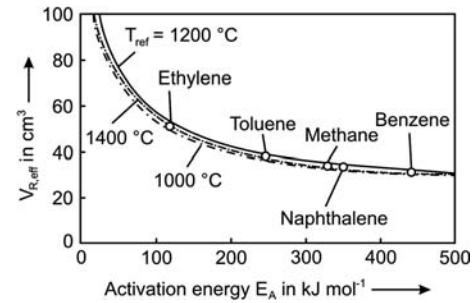


Figure 4.11.15 Effective reaction volume of the laboratory reactor (data from Jess, 1995).

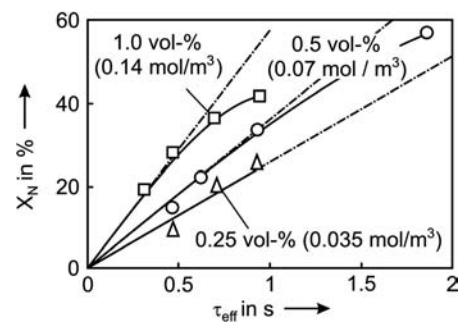


Figure 4.11.16 Influence of the concentration of naphthalene on the degree of conversion of naphthalene (dash-dotted lines: initial slope of conversion rate, 1100 °C, 1.6 bar, 48 vol.-% H₂, 16 vol.-% H₂O, 0.25–1 vol.-% C₁₀H₈, Rest: N₂). Taken from Jess (1995, 1996a, 1996b).

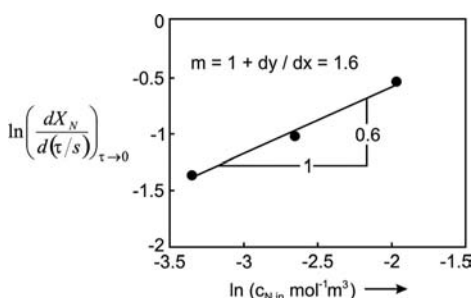


Figure 4.11.17 Influence on the inlet concentration of naphthalene on the initial rate of naphthalene conversion (conditions see Figure 4.11.16).

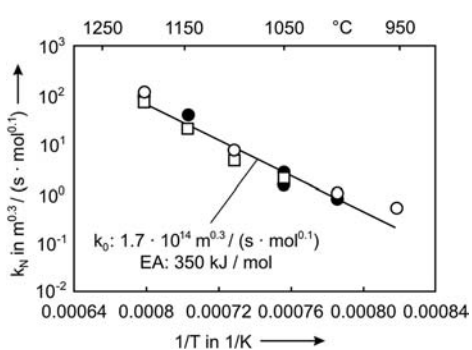


Figure 4.11.18 Rate constant of thermal conversion of $C_{10}H_8$ (τ_{eff} at 1100°C : □ 0.5 s, ● 1 s, ○ 2 s, 1.6 bar, 48 vol.% H_2 , 16 vol.% H_2O , 0.5 vol.% $C_{10}H_8$, rest: N_2). Taken from Jess (1996b).

calculated from the slope is 1.6. Experiments with varied concentrations of H_2 and steam lead to orders of 0 for steam and -0.5 for H_2 , which reflects the inhibition by H_2 (less formation of soot). Based on the orders, we determine the rate constant by the integral method by integration of Eq. (4.11.33), which leads for $m = 1.6$, $n = 0$, and $p = -0.5$ (and a surplus of H_2) to:

$$k_N = \frac{\tau_{\text{eff}} c_{H_2,\text{in}}^{0.5}}{0.6 c_{N,\text{in}}^{0.6}} \left[(1 - X_N)^{-0.6} - 1 \right] k_{N,0} \exp\left(-\frac{E_A}{RT_{\text{ref}}}\right) \quad (4.11.35)$$

The plot of $\ln(k_N)$ versus $1/T_{\text{ref}}$ gives a straight line (Figure 4.11.18), and we calculate E_A from the slope E_A/R and the pre-exponential factor $k_{N,0}$ from the intersection with the ordinate.

4.11.5.2 Case Study II: Heterogeneously Catalyzed Hydrogenation of Hexene

The kinetics of the heterogeneously catalyzed gas phase hydrogenation of 1-hexene on a Ni catalyst was studied in an almost isothermal (± 1 K) tubular fixed bed reactor (Pachow, 2005). Here we only look at the determination of the reaction order of hexene by the integral method and determine the influence of mass and heat transfer phenomena.

Determination of Reaction Order by the Integral Method If we have a high excess of hydrogen (and a reaction order of 1.2, as determined by experiments with varied hydrogen concentration), the conversion of hexene is given by:

$$X_{\text{hexene}} = 1 - \left[k_m c_{H_2,\text{in}}^{1.2} \tau(m-1) c_{\text{hexene,in}}^{m-1} + 1 \right]^{\frac{1}{(1-m)}} \quad (4.11.36)$$

As an alternative to the differential method (Section 4.11.1), the reaction order m for hexene can also be determined by the integral method. Therefore, we have to determine for which value of m we get the best fit of the calculated curve of X_{hexene} versus $c_{\text{hexene,in}}$ with the measured data. As shown in Figure 4.11.19, this is obviously the case for an order m of 0.3. The kinetic equation finally obtained based on the integral and the differential method is:

$$r_{m,\text{hexene}} = 1.83 \times 10^{11} \frac{m^{4.5}}{s \times kg \cdot mol^{0.5}} \cdot e^{-\frac{86.5 \text{ kJ mol}^{-1}}{RT}} \cdot c_{\text{Hexene}}^{0.3} c_{H_2}^{1.2} \quad (4.11.37)$$

Influence by Dispersion of Mass and Heat on the Performance of the Laboratory Reactor Now we will check whether dispersion and diffusion may have affected our measurement. Table 4.11.1 lists the conditions of the experiments.

The values given in Table 4.11.2 show that the influence of radial dispersion of heat, axial dispersion of mass and heat, and the influence of radial variations in the bed structure (wall effects) are negligible. However, radial dispersion of heat may have an influence, although the maximum radial temperature difference of 3 K still

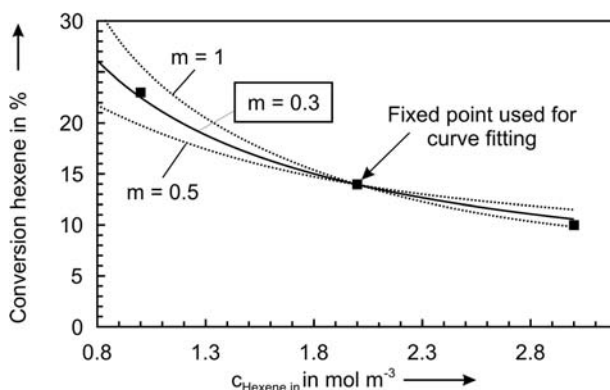


Figure 4.11.19 Determination of the reaction order with respect to hexene by means of the integral method (40°C , $1 \text{ mol m}^{-3} \leq c_{\text{Hexene}} \leq 3 \text{ mol m}^{-3}$, $c_{H_2} = 6 \text{ mol m}^{-3}$, $c_{N_2} \approx 79 \text{ mol m}^{-3}$, 72 l h^{-1} (NTP), 5 bar, $d_p = 125\text{--}250 \mu\text{m}$, $m_{SiO_2}/m_{\text{Kat}} = 75$, $m_{\text{cat}} = 009\,32 \text{ g}$).

Table 4.11.1 Experimental conditions used to determine the intrinsic kinetics of the heterogeneously catalyzed gas-phase hydrogenation of 1-hexene.

Parameter	Value
Particle diameter of catalyst d_p	About 250 μm
Dilution of catalyst with inert material	$V_{\text{inert}}/V_{\text{cat}} = 800$
Length of catalyst bed L , diameter of reactor d_R	1 m, 12 mm
(Maximum) temperature of kinetic study	80 °C
Adiabatic temperature rise (0.5 mol.% hexene)	21 K
$(\Delta_{\text{R}}H = -125 \text{ kJ mol}^{-1} \text{ and } c_{\text{p,gas}} = 30 \text{ J mol}^{-1} \text{ K}^{-1})$	
Activation energy	86.5 kJ mol^{-1}
Conversion of hexane, Da number (first-order reaction)	$X_{\text{hexene}} \leq 50\%, Da \leq 0.7$
Diffusion coefficient of 1-hexene D_h (5 bar and 80 °C)	0.023 $\text{cm}^2 \text{s}^{-1}$
Effective diffusivity D_h in the porous catalyst based on a particle porosity 0.4 and a tortuosity of 6	0.0014 $\text{cm}^2 \text{s}^{-1}$
Thermal conductivity of gas λ_g (5 bar, 80 °C)	0.018 $\text{W m}^{-1} \text{ K}^{-1}$
Thermal conductivity of catalyst λ_p	0.4 $\text{W m}^{-1} \text{ K}^{-1}$ (estimation)
Sherwood number Sh [$Re_p = u_e d_p / (\nu) = 1.4$; u_e = velocity in the empty tube; $Sc = \nu / D_h = 1.6$]	$1.9 (2 + 0.664 Re_p^{0.5} Sc^{0.33}) = 5.5$ (min. value of 3.8 was taken for subsequent analysis)

Table 4.11.2 Comparison of critical values according to the criteria for negligible influence of axial and radial dispersion of mass and heat (deviation from ideal plug flow behavior of the experimental reactor for 1-hexene hydrogenation for the conditions listed in Table 4.11.1).

	Relevant equation	Critical value according to relevant equation	Value for experimental reactor	Comment
Axial dispersion of mass	4.11.17	$L/d_p > 7$	$L/d_p = 4000$	Criterion fulfilled
Radial dispersion of mass	4.11.18	$d_R/d_p < 300$	$d_R/d_p = 48$	Criterion fulfilled
Axial dispersion of heat	4.11.19	$L/d_p > 13$	$L/d_p = 4000$	Criterion fulfilled
Radial dispersion of heat	4.11.20	$d_R/d_p < 10$	$d_R/d_p = 48$	Criterion not fulfilled
$\Delta T_{\text{rad,max}}$	4.10.168	—	$\Delta T_{\text{rad,max}} = 3 \text{ K}$	Value acceptable
Dilution of catalyst	4.11.27	$V_{\text{inert}}/V_{\text{cat}} < 800$	$V_{\text{inert}}/V_{\text{cat}} = 76$	Criterion fulfilled
Wall effect (bypassing)	4.11.16	$d_R/d_p > 10$	$d_R/d_p = 48$	Criterion fulfilled

seems to be an acceptable value. The dilution of the catalyst by inert material is low enough to avoid bypass effects.

Influence of Interfacial and Internal Transport of Mass and Heat The values given in Table 4.11.3 show that the influence of external and internal (pore) diffusion and heat transfer on the measured reaction rate is negligible.

4.11.5.3 Case Study III: Heterogeneously Catalyzed Multiphase Reaction

Multiphase fixed bed reactors have complex hydrodynamic and mass transfer characteristics (see also Section 4.9). Thus, the modeling and scale-up are difficult. As an instructive example, we inspect the catalytic 1-octene hydrogenation as a model reaction (Battsengel, Datsevitch, and Jess, 2002; Battsengel, 2002). Table 4.11.4 lists the characteristics of the commercial Ni-catalyst (NISAT, Südchemie) used for the experiments, data on chemical media, and the parameters that determine the mass transfer.

Kinetic studies on the catalytic hydrogenation of 1-octene to *n*-octane were performed in an agitated batch reactor with suspended catalyst. The primary result of the experiments is the curve of the octane concentration c_{oc} versus reaction time. By

Table 4.11.3 Comparison of critical values (d_p) according to the criteria for negligible deviation from an ideal gradientless particle with respect to temperature and concentration for 1-hexene hydrogenation and the conditions listed in Table 4.11.1.

Effect	Relevant equation	Critical value of d_p according to relevant equation (mm)	Value of d_p for experimental reactor (mm)	Comment
External mass transfer	4.11.21	<2.6	0.25 (250 μm)	Criterion fulfilled
External heat transfer	4.11.23	<1.5		Criterion fulfilled
Internal mass transfer	4.11.24	<1.4		Criterion fulfilled
Internal heat transfer	4.11.25	<16		Criterion fulfilled

Table 4.11.4 Characteristic data of the hydrogenation catalyst and of the chemical media used in the hydrogenation experiments (Battsengel, Datsevitch, and Jess, 2002; Battsengel, 2002).

Parameter	Value
Particle density of catalyst ρ_p (m_p/V_p)	1.5 g cm^{-3}
BET surface area A_{BET}	250 $\text{m}^2 \text{g}^{-1}$
Diffusion coefficient of octene D_{oc} (in the liquid octene/octane mixture)	$0.54 \times 10^{-4} \text{ cm}^2 \text{s}^{-1}$
Diffusion coefficient of hydrogen D_{H_2} (in the liquid octene/octane mixture)	$2.4 \times 10^{-4} \text{ cm}^2 \text{s}^{-1}$
Effective diffusivity $D_{\text{eff},i}$ ($i = \text{H}_2, \text{octene}$) based on particle porosity 0.5 and a tortuosity of 3	$0.16 D_{\text{liq},i}$
Mass transfer coefficient liquid to solid $\beta_{\text{LS},i}$	$Sh_i D_{\text{liq},i}/d_p$
Sherwood number Sh_i ($Re = ud_p/(\varepsilon v)$ with u = liquid velocity in the empty reactor; $Sc_i = v/D_i$)	$f(2 + 0.664 \times Re^{0.5} \times Sc_i^{0.33})$ with $f=1$ and $\varepsilon=1$ for a single particle and $f=1.9$ and $\varepsilon=0.4$ for a fixed bed
Solubility of H_2 in the liquid phase (100 °C)	$0.66 \times 10^{-5} \text{ mol cm}^{-3} \text{ bar}^{-1}$
Kinematic viscosity of liquid v (100 °C)	$3.9 \times 10^{-3} \text{ cm}^2 \text{s}^{-1}$

the slope of this curve the rate per volume of liquid (for any time and octene concentration) can be determined directly:

$$r_V = -\frac{dc_{\text{oc}}}{dt} \quad (4.11.38)$$

The reaction rate r_m related to the mass of catalyst is then given by the ratio of r_V to the concentration of the catalyst c_{cat} (kg m^{-3}). Depending on the reaction conditions, the following mass transfer resistances may have to be considered.

Gas–Liquid Mass Transfer of Hydrogen

$$r_V = K_{\text{GLH}_2} (c_{\text{H}_2,\text{sat}} - c_{\text{H}_2,\text{liq}}) \quad (4.11.39)$$

where $c_{\text{H}_2,\text{liq}}$ is the concentration in the liquid bulk phase, and $c_{\text{H}_2,\text{sat}}$ the saturation concentration at the gas–liquid interface, which according to Henry's law is proportional to the H_2 pressure (here approximately the total pressure). K_{GLH_2} is the overall gas–liquid mass transfer coefficient of H_2 ($=\beta_{\text{GL,H}_2} A_{\text{GL}}$). The mass transfer coefficient $\beta_{\text{GL,H}_2}$ and the specific interfacial area A_{GL} were not measured independently, and only K_{GLH_2} was determined.

Liquid–Solid Mass Transfer

$$r_m = \beta_{\text{LS},i} A_m (c_{i,\text{liq}} - c_{i,s}) \quad (i = \text{octane or hydrogen}) \quad (4.11.40)$$

where $c_{i,s}$ represents the concentration at the external surface of the catalyst, and A_m the external surface area per mass of catalyst. The decline in concentration of octene

and hydrogen from the bulk phase of the liquid to the external surface of the catalyst is given by:

$$\frac{c_{\text{oc,liq}} - c_{\text{oc,s}}}{c_{\text{H}_2,\text{liq}} - c_{\text{H}_2,\text{s}}} = \frac{\beta_{\text{LS,H}_2}}{\beta_{\text{LS,oc}}} \quad (4.11.41)$$

Interplay of Chemical Reaction and Pore Diffusion As shown below, the chemical (intrinsic) rate of octene hydrogenation is given by:

$$r_m = \frac{k_1 c_{\text{oc}} c_{\text{H}_2}}{1 + k_2 c_{\text{H}_2}} = \left(\frac{k_1 c_{\text{H}_2}}{1 + k_2 c_{\text{H}_2}} \right) c_{\text{oc}} = k_m c_{\text{oc}} \quad (4.11.42)$$

where k_m is the apparent first-order rate constant that still may depend on the pressure of H_2 . The reaction is first order with respect to octene and between 1 and 0 order with respect to H_2 . For $k_2 c_{\text{H}_2} \gg 1$, r_m is given by $k_1/k_2 c_{\text{oc}}$, and for $k_2 c_{\text{H}_2} \ll 1$, r_m is $k_1 c_{\text{oc}} c_{\text{H}_2}$.

If pore diffusion affects the effective reaction rate, the effectiveness factor η_{pore} has to be taken into account, which is related to the Thiele module ϕ by:

$$\eta_{\text{pore}} = \frac{\tanh \phi}{\phi} \quad (4.11.43)$$

If the H_2 concentration at the surface (and in the particle) is high, ϕ is given by:

$$\phi = \frac{d_p}{6} \sqrt{\frac{k_1 \rho_p}{k_2 D_{\text{eff,oc}}}} \quad (\text{for } c_{\text{H}_2,\text{liq}} \gg c_{\text{oc,liq}} \text{ and } k_2 c_{\text{H}_2,\text{s}} \gg 1) \quad (4.11.44)$$

In the reverse case, ϕ is given by:

$$\phi = \frac{d_p}{6} \sqrt{\frac{k_1 \rho_p c_{\text{oc,liq}}}{k_2 D_{\text{eff,H}_2}}} \quad (\text{for } c_{\text{oc,liq}} \approx c_{\text{oc,s}} \text{ and } c_{\text{H}_2,\text{liq}} \ll c_{\text{oc,liq}} \text{ and } k_2 c_{\text{H}_2,\text{s}} \ll 1) \quad (4.11.45)$$

If we also take into account the external diffusion to the outer surface of the catalyst we have, for example, for a high hydrogen pressure and/or low 1-octene concentration:

$$r_{m,\text{eff}} = \left(\frac{1}{\beta A_m} + \frac{k_2}{\eta_{\text{pore}} k_1} \right)^{-1} c_{\text{oc,liq}} = k_{m,\text{eff}} c_{\text{oc,liq}} \quad (\text{for } c_{\text{H}_2,\text{liq}} \gg c_{\text{oc,liq}} \text{ and } k_2 c_{\text{H}_2,\text{s}} \gg 1) \quad (4.11.46)$$

Based on these equations, the effective reaction rate $r_{m,\text{eff}}$ ($= k_{m,\text{eff}} c_{\text{oc,liq}}$) is calculated. The rate constant $k_{m,\text{eff}}$ takes into account not only the influence of pore diffusion and external diffusion but also the influence of H_2 on the chemical reaction. This leads to a simple first-order reaction with respect to octene, as $k_{m,\text{eff}}$ still includes the influence of H_2 .

To determine the intrinsic reaction rate, all mass transfer resistances have to be excluded by a proper adjustment of the reaction conditions. First we must determine the regime where the gas–liquid mass transfer of hydrogen has no influence on the effective rate. Figure 4.11.20 indicates that the effective rate in the batch reactor is limited by the gas–liquid mass transfer in case of high concentrations of the catalyst and/or high octene concentrations.

Further experiments show that even for a pressure of 25 bar, the initial rate (for $x_{\text{oc}} = 100\%$) is almost determined only by the gas–liquid mass transfer. For the succeeding experiments, the term $c_{\text{cat}} c_{\text{oc}}$ was minimized, such that the rate is unaffected by the gas–liquid mass transfer. For example, for $d_p = 50 \mu\text{m}$ and a catalyst concentration of $0.001 \text{ g}_{\text{cat}} \text{ cm}^{-3}$, an octane concentration of less than 10% was adjusted, that is, $c_{\text{cat}} c_{\text{oc}} < 6 \times 10^{-7} \text{ g}\text{-mol cm}^{-6}$, Figure 4.11.20.

Secondly, the influence of the liquid-to-solid mass transfer as well as of pore diffusion must be excluded by variation of the particle diameter. For $d_p < 100 \mu\text{m}$, the

Figure 4.11.20 Influence of concentration of the Ni catalyst and of 1-octene on the reaction rate of 1-octene hydrogenation (total pressure: 7 bar, partial pressure of hydrogen: 6.5 bar; batch reactor; 100 °C). Taken from Battsengel, Datsevitch, and Jess (2002) and Battsengel (2002).

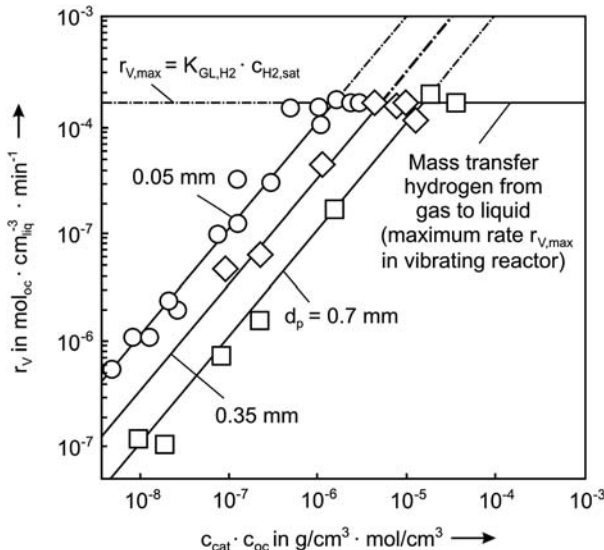


Figure 4.11.21 Influence of the H₂ pressure on the effective rate constant of catalytic 1-octene hydrogenation (100 °C, batch reactor, 0.0058 g_{cat} cm_{liq}⁻³ for d_p = 0.7 mm, 0.00 083 g_{cat} cm_{liq}⁻³ for 50 μm). Taken from Battsengel, Datsevitch, and Jess (2002) and Battsengel (2002).

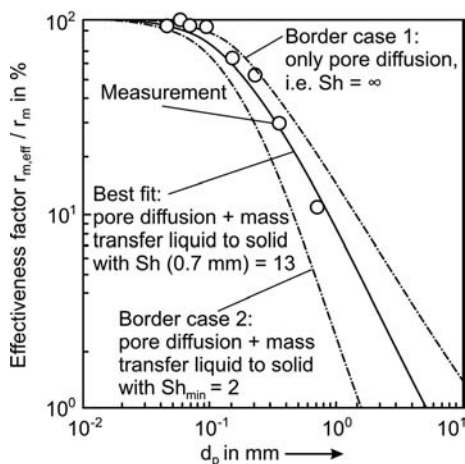
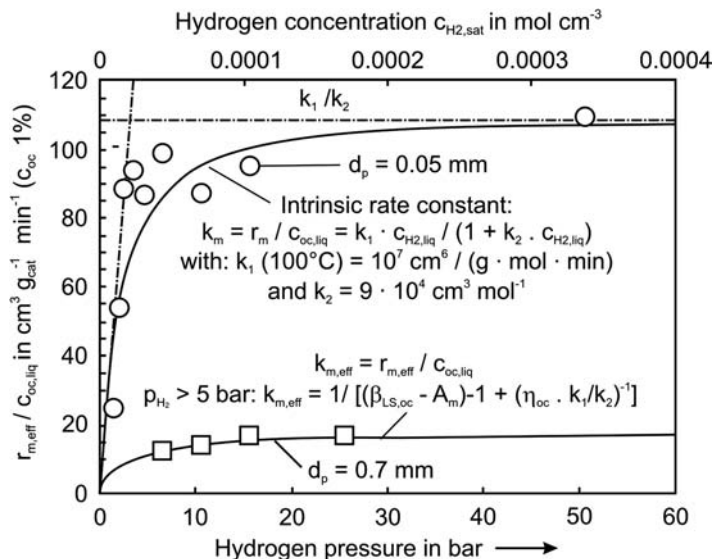


Figure 4.11.22 Effectiveness factor versus particle diameter (100 °C, batch reactor, 6 bar, c_{oc} < 1 mol.%). Taken from Battsengel, Datsevitch, and Jess (2002) and Battsengel (2002).

rate becomes independent of d_p, at least for c_{oc} < 10%; consequently, the intrinsic reaction rate is then measured. The experimental data (c_{oc} versus t) show that the rate of octene hydrogenation is first order with respect to octene, at least for the investigated concentration range (c_{oc} < 10%).

Figure 4.11.21 shows the influence of the partial pressure of H₂ on k_m (= r_m/c_{oc,liq}) for a particle diameter of 50 μm (c_{oc} < 1%). For H₂ pressures of more than 5 bar, the reaction rate is almost zero order with respect to H₂ (k_m = constant). For comparison, the results for particles of 0.35 and 0.7 mm are also shown in Figure 4.11.20, highlighting that the rate is lower due to the combined influence of liquid–solid mass transfer and pore diffusion.

Figure 4.11.22 shows the influence of particle size on the efficiency factor. For the given reaction conditions (p = 6 bar, 100 °C, c_{oc} < 1 mol.%), the influence of mass transfer is primarily initiated by pore diffusion. The best fit of experiment and calculation is obtained with Sh_{oc} = 13, which indicates that the liquid–solid mass transfer of octene is accelerated in the batch reactor compared to particles without any motion relative to the liquid (Sh = 2).

The influence of temperature on the effective rate constant η_{oc} × k₁/k₂ (see Figure 4.11.21 for the expression of the rate) is shown in Figure 4.11.23 for particle diameters of 0.7 mm and 50 μm. For particles <0.7 mm, the effective activation

energy $E_{A,\text{eff}}$ is lower than the true activation energy that was determined in the absence of diffusion limitations by using 50 μm particles. The measured value of $E_{A,\text{eff}}$ of 19 kJ mol^{-1} is similar to the value of 20.4 kJ mol^{-1} that was expected based on the interplay of pore diffusion and chemical reaction.

We may now calculate the situation in an industrial fixed bed reactor (trickle bed) based on the parameters for the chemical reaction, liquid–solid mass transfer, and pore diffusion, thereby assuming ideal plug flow behavior. In practice, the reaction rate in a trickle bed reactor will be lower because of imperfect wetting of the catalyst. As an example, a pressure of 10 bar, pure octene at the inlet of the reactor, and a constant temperature of 100 °C were assumed, although the latter assumption is unrealistic for a simple fixed bed reactor, as the reaction is highly exothermic. For simplification, the gas–liquid mass transfer is neglected ($c_{\text{H}_2,\text{liq}} \approx c_{\text{H}_2,\text{sat}}$), and for the liquid–solid mass transfer we take a value of 3.8 for Sh , which is the minimal value for spheres in a fixed bed.

Figure 4.11.24 indicates that for octene concentrations down to approximately 10% the effective rate constant $k_{m,\text{eff}}$ is relatively small. In this region the rate is limited by the H_2 consumption, and the H_2 concentration at the surface and within the particle is low, for example, with 100% octene (reactor entrance for hydrogenation of pure olefin), $c_{\text{H}_2,\text{s}}$ is only 6% of $c_{\text{H}_2,\text{liq}}$. The average H_2 concentration within the particle is even less ($\eta_{\text{H}_2} \times c_{\text{H}_2,\text{s}} = 0.1\%$ of $c_{\text{H}_2,\text{liq}}$). However, $c_{\text{oc},\text{s}}$ is still 95% of $c_{\text{oc},\text{liq}}$. Therefore, the reaction rate is independent of the octene concentration and, thus, $r_{m,\text{eff}} \approx \beta_{\text{H}_2 \text{ a.m.}} c_{\text{H}_2,\text{liq}}$. (Note that in Figure 4.11.24 k_m and not r_m is shown.)

For octene concentrations of less than approximately 10%, the situation is reversed. The mean H_2 concentration in the particle increases as such that the reaction is then zero order with respect to H_2 . In this region the reaction depends on the consumption of octene, that is, on the interplay of the chemical reaction, pore diffusion, and the liquid–solid mass transfer of octene.

Two general conclusions can be drawn based on the experiments and theoretical analysis of this model reaction:

- 1) If the concentration of the liquid reactant (here octene) is high compared to the dissolved gaseous reactant (here H_2), the effective rate is limited by the supply of the catalyst with gaseous reactant (gas–liquid and liquid–solid mass transfer). This is particularly true for fast chemical reactions and for particle diameters, which are of technical relevance for fixed bed reactors with respect to pressure drop ($>1\text{ mm}$). The mass transfer should therefore be increased by a high

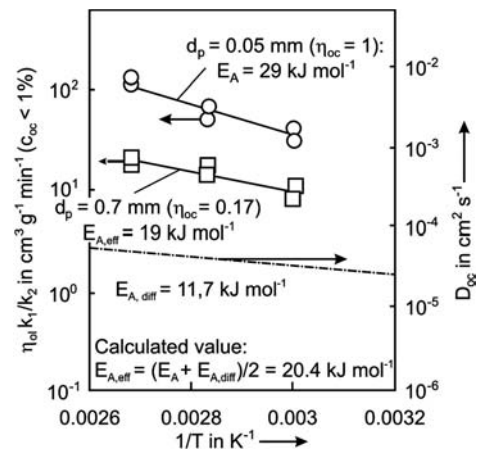


Figure 4.11.23 Arrhenius diagram for the catalytic hydrogenation of 1-octene (batch reactor; $p: 6\text{ bar}$; $0.0058 - 0.00083\text{ g}_{\text{cat}}\text{ cm}^{-3}\text{ liq}$; $d_p = 0.7\text{ mm} - 50\text{ }\mu\text{m}$, $c_{\text{oc}} < 1\%$; remark: the influence of temperature on k_2 is neglected). Taken from Battsengel, Datsevitch, and Jess (2002) and Battsengel (2002).

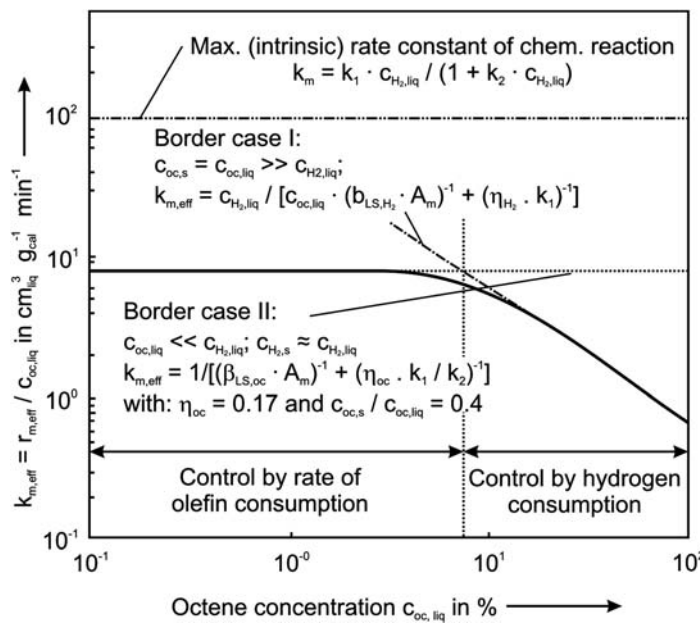


Figure 4.11.24 Calculation of catalytic hydrogenation of 1-octene in a catalytic fixed-bed reactor: effective rate versus octene concentration (25 bar, 100 °C, $Sh = 3.8$; assumptions see text). Taken from Battsengel, Datsevitch, and Jess (2002) and Battsengel (2002).

pressure and/or a recycle of the liquid (higher Sh) as the decrease of the liquid reactant concentration by the recycle has a minimal effect on the effective rate.

- 2) In case of a relatively low concentration of the liquid reactant, for example, in the rear part of the reactor or in processes like hydrodesulphurization of fuels (with a typical feed concentration of organic sulfur between 100 and 1000 ppm), the effective rate is limited by the concentration of the liquid reactant. The rate is determined by the interplay of the chemical reaction and the diffusion of the liquid reactant to and within the catalyst. Depending on the type of reaction, an increase in pressure may not help to improve the reaction rate, as demonstrated here for the hydrogenation of 1-octene. Then a liquid recycle would probably decrease the rate: Although the liquid–solid mass transfer coefficient is increased, this effect is more than compensated by the decrease of the liquid reactant concentration.

These two clearly different cases/reaction zones have to be considered in the modeling and improvement of multiphase reactors.

4.11.5.4 Case Study IV: Non-isothermal Oxidation of Carbon Nanotubes and Fibers

The kinetics of the oxidation of so-called carbon nanofibers and nanotubes (produced from an ethane/hydrogen mixture by chemical vapor deposition on catalytic particles in a fluidized bed, see Topic 4.11.1) were studied in an almost isothermal tubular fixed bed reactor and by thermogravimetric measurements in a commercial standard apparatus (Jung, 2005; Jess *et al.*, 2006; Schroegel, 2007). In the following, we consider only thermogravimetric (TG) measurements to introduce a non-isothermal method to determine kinetic data. TG is one of the oldest thermal analytical procedures and has been used extensively to study pyrolysis, combustion, and gasification of coal, coke, and polymers. The technique involves monitoring the weight loss (in some cases also weight gain) of a sample in a chosen atmosphere (usually N_2 or air) as a function of temperature, whereby the heating rate is kept constant. The usefulness of TG for analyzing kinetic processes is greatly enhanced if simultaneously the first derivative of the weight loss is recorded, which is referred to as derivative thermogravimetry (DTG).

Topic 4.11.1: Carbon nanotubes

Carbon nanotubes are fullerene-related structures, and consist of graphitic cylinders closed at either end with caps containing pentagonal rings; they were discovered in 1991 by Iijima. The term carbon nanofiber (Figure 4.11.25) summarizes a large family of different filamentous nanocarbons. They are distinguished according to the arrangement of the graphitic layers (platelet-like or herringbone substructure). Carbon nanofibers are typically grown by depositing carbon from a carbon-containing gas on fine metal catalyst particles, for example, in a fluidized bed (Figure 4.11.25). Depending on the kind of metal catalyst, different growth forms are found. Carbon nanomaterials have special electrical, mechanical, and thermal properties, and are therefore interesting new materials, for example, as additives in polymers, in the field of battery technology, catalysis and fuel cells, and gas storage and sorption. More information on these interesting materials is given in the literature (e.g., Reich, Thomsen, and Maultzsch, 2004; Bhushan, 2004).

Here we consider the carbon nanofibers simply as carbon that is oxidized by a first-order reaction with respect to carbon and oxygen:

$$r_m = -\frac{dm_C}{dt} = k_m c_{O_2} m_C M_C \quad \left[\text{with } k_m = k_{m,0} e^{-\frac{E_A}{RT}} \text{ in } m^3 \text{ kg}^{-1} \text{ s}^{-1} \right] \quad (4.11.47)$$

During the TG/DTG experiment, a small amount of the carbon nanomaterial (e.g., 0.1 g) is oxidized with a high surplus of O_2 and we can consider the O_2

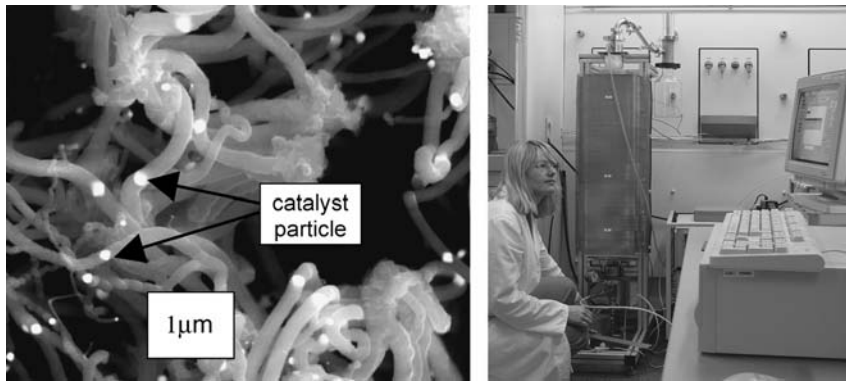


Figure 4.11.25 Energy-dispersive X-ray image of herringbone-carbon nanofibers synthesized by catalytic chemical vapor deposition in a fluidized bed reactor (Department of Chemical Engineering, University of Bayreuth) from an ethylene–nitrogen mixture (Jung, 2005).

concentration as constant. If we introduce the constant heating rate $H_R = dT/dt$, we can rewrite Eq. (4.11.47) as:

$$-\frac{dm_C}{dT} = \frac{k_{m,0} c_{O_2} M_C}{H_R} e^{-\frac{E_A}{RT}} m_C \quad (4.11.48)$$

and integration leads to:

$$-\int_{m_{C,0}}^{m_C} \frac{dm_C}{m_C} = \ln \frac{m_{C,0}}{m_C} = \frac{k_{m,0} c_{O_2} M_C}{H_R} \int_{T_0}^T e^{-\frac{E_A}{RT}} dT \quad (4.11.49)$$

The right-hand side of Eq. (4.11.49) has no exact integral and we use a series expansion as approximation:

$$\int_{T_0}^T e^{-\frac{E_A}{RT}} dT \approx \frac{RT^2}{E_A} e^{-\frac{E_A}{RT}} \left(1 + \frac{2!}{[-E_A/(RT)]} + \frac{3!}{[-E_A/(RT)]^2} + \dots \right) \Big|_{T_0}^T \quad (4.11.50)$$

The initial temperature T_0 is low enough (here 20 °C) for the lower limit to be negligible. Furthermore, the activation energy is here about 200 kJ mol⁻¹ (see below), thus $E_A/(RT)$ for experimentally relevant temperatures between 400 and 600 °C is 30. Consequently, the term $-2!RT/E_A$ is -0.067, but the term $3!(RT/E_A)^2$ is only 0.0067 and is thus negligible. This leads to:

$$\int_{T_0}^T e^{-\frac{E_A}{RT}} dT \approx \frac{RT^2}{E_A} e^{-\frac{E_A}{RT}} \left(1 - \frac{2RT}{E_A} \right) \quad (4.11.51)$$

Recommended simplifications for other values of $E_A/(RT)$ are given in Example 4.11.3.

Insertion of Eq. (4.11.51) into Eq. (4.11.49) yields the equation for the TG analysis:

!

$$\frac{m_C}{m_{C,0}} = \exp \left[-\frac{k_{m,0} c_{O_2} M_C}{H_R} \frac{RT^2}{E_A} e^{-\frac{E_A}{RT}} \left(1 - \frac{2RT}{E_A} \right) \right] \quad (4.11.52)$$

For DTG, we insert Eq. (4.11.52) into Eq. (4.11.48), which yields either:

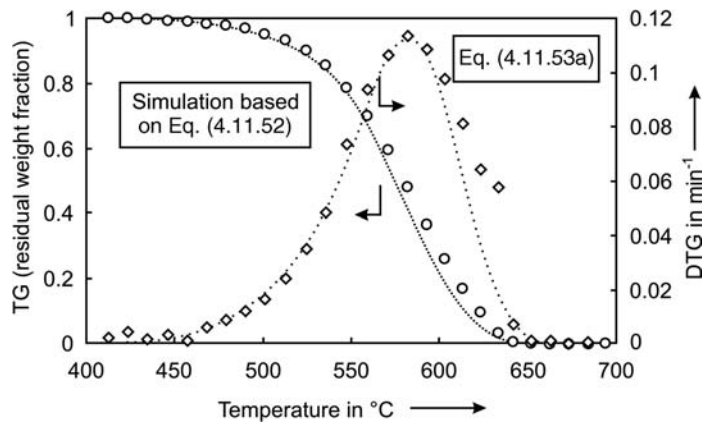
!

$$-\frac{1}{m_{C,0}} \frac{dm_C}{dt} = k_{m,0} c_{O_2} M_C \exp \left[-\frac{E_A}{RT} - \frac{k_{m,0} c_{O_2} M_C}{H_R} \frac{RT^2}{E_A} \left(1 - \frac{2RT}{E_A} \right) e^{-\frac{E_A}{RT}} \right] \quad (4.11.53a)$$

or:

$$-\frac{1}{m_{C,0}} \frac{dm_C}{dT} = \frac{k_{m,0}}{H_R} c_{O_2} M_C \exp \left[-\frac{E_A}{RT} - \frac{k_{m,0} c_{O_2} M_C}{H_R} \frac{RT^2}{E_A} \left(1 - \frac{2RT}{E_A} \right) e^{-\frac{E_A}{RT}} \right] \quad (4.11.53b)$$

Figure 4.11.26 Measured and simulated TG and DTG curves [3% O₂ in N₂, oxidation of herringbone carbon nanofibers; heating rate: 10 K min⁻¹; simulation based on Eqs. (4.11.52) and (4.11.53)]. Taken from Jung (2005).



For a high value of E_A , the term $(1 + 2RT/E_A)$ is almost one (e.g., 1.06 for $E_A = 200 \text{ kJ mol}^{-1}$ and $T = 500 \text{ }^\circ\text{C}$) and may be neglected for a first approximation.

Equation (4.11.53b) is the appropriate form to present DTG data in a *rate* versus *temperature* diagram if experiments at different heating rates are compared as the area under the DTG curves is then always unity. By Eq. (4.11.52) or (4.11.53a) and (4.11.53b), E_A and $k_{m,0}$ are evaluated by the best match of the experimental data with the simulation, which needs trial and error to find appropriate values for E_A and $k_{m,0}$ (Figure 4.11.26).

Comments

- Evaluation of the kinetic parameters based on DTG data should be preferred as it gives a more “honest” result. The TG signal is less sensitive and hides real effects, for example, if impurities consisting of amorphous carbon with a different reactivity are present. In the DTG signal this is more easily detected by double peaks and shoulders.
- To obtain the best fit of measurement and simulation, the following method is advisable to save time. Take the TG signal and determine for a fixed value of $m_C/m_{C,0}$ (e.g., 0.5) the respective value of the temperature $T_{0.5}$ (here about 575 °C). Based on Eq. (4.11.52), E_A and $k_{m,0}$ are then related by:

$$k_{m,0} = \left(0.69 \frac{H_R}{RT_{0.5}^2 c_{O_2} M_C} \right) E_A e^{\left(\frac{E_A}{RT_{0.5}} \right)} \quad (4.11.54)$$

During the procedure to find the best match, we only have to vary one parameter (choose E_A , as we know that the realistic range is between 50 and 200 kJ mol⁻¹ in most cases) step-by-step, and calculate the second parameter $k_{m,0}$ by Eq. (4.11.54). Thus, the simulation always matches at least the fixed point ($m_C/m_{C,0} = 0.5$ for $T_{0.5}$).

Example 4.11.3: Approximations for Eq. (4.11.50) by a series expansion

The approximation of Eq. (4.11.49) by a series expansion (Eq. (4.11.50)) leads to:

If, for example, we have a value of the term E_A/RT of about 30 (as we have here for the oxidation of nanofibers with $E_A \approx 200 \text{ kJ mol}^{-1}$ and a mean temperature of 800 K) we obtain:

$$\int_{T_0}^T e^{-\left(\frac{E_A}{RT}\right)} dT \approx \frac{RT^2}{E_A} e^{-\left(\frac{E_A}{RT}\right)} \left[1 - 2 \frac{RT}{E_A} + 6 \left(\frac{RT}{E_A}\right)^2 - 24 \left(\frac{RT}{E_A}\right)^3 + \dots \right] \quad (4.11.55)$$

(for $T \gg T_0$)

$$\int_{T_0}^T e^{-\left(\frac{E_A}{RT}\right)} dT \approx \frac{RT^2}{E_A} e^{-\frac{E_A}{RT}} (1 - 0.067 + 0.007 - 0.0009 \dots) \\ \approx \frac{RT^2}{E_A} e^{-\frac{E_A}{RT}} 0.94 \quad \left(\text{for } \frac{E_A}{RT} = 30 \right)$$

For E_A/RT values of 20 and 8 (here corresponding to $E_A \approx 130$ and 50 kJ mol^{-1}) we have:

$$\int_{T_0}^T e^{-\frac{E_A}{RT}} dT \approx \frac{RT^2}{E_A} e^{-\frac{E_A}{RT}} (1 - 0.10 + 0.015 - 0.003 \dots)$$

$$\approx \frac{RT^2}{E_A} e^{-\frac{E_A}{RT}} 0.91 \quad \left(\text{for } \frac{E_A}{RT} = 20 \right)$$

$$\int_{T_0}^T e^{-\frac{E_A}{RT}} dT \approx \frac{RT^2}{E_A} e^{-\frac{E_A}{RT}} (1 - 0.25 + 0.094 - 0.047 \dots)$$

$$\approx \frac{RT^2}{E_A} e^{-\frac{E_A}{RT}} 0.8 \quad \left(\text{for } \frac{E_A}{RT} = 8 \right)$$

For a further simplification of Eq. (4.11.55), we use a maximum deviation from the true value of 5% as a useful criterion. A more critical

limit is not justified as the accuracy of the TG method is limited, for example, if we consider the underlying assumption of a simple first-order reaction with respect to oxygen. We then arrive at the following rules of thumb:

$$\int_{T_0}^T e^{-\frac{E_A}{RT}} dT \approx \frac{RT^2}{E_A} e^{-\frac{E_A}{RT}} \quad \left(\text{for } \frac{E_A}{RT} > 30 \right) \quad (4.11.56)$$

$$\int_{T_0}^T e^{-\frac{E_A}{RT}} dT \approx \frac{RT^2}{E_A} e^{-\frac{E_A}{RT}} \left[1 - 2 \frac{(RT)}{E_A} \right] \quad \left(\text{for } 30 > \frac{E_A}{RT} > 8 \right) \quad (4.11.57)$$

For E_A/RT values of less than 8 the sensitivity of the TG/DTG-method is rather limited and should therefore not been used to determine kinetic data.

A comparison of the kinetic data with those determined by probably more accurate isothermal measurements are shown in Table 4.11.5 and Figure 4.11.27. The activation energies deviate, but the agreement of the absolute values of k_m is satisfactory.

Figure 4.11.28 shows the DTG curves for various carbonaceous materials, carbon nanotubes and carbon fibers, active charcoal, and graphite. Obviously, the nanotubes have the highest reactivity, followed by nanofibers, active charcoal, and graphite. It can also be seen that the nanomaterials are quite pure (ideal shape of the DTG signal), whereas a fraction of the charcoal is less reactive than the fraction that reacts first.

Table 4.11.5 Comparison of kinetic data obtained from isothermal measurements in a tubular fixed bed reactor with that from TG/DTG experiments (Jung, 2005).

	Activation energy E_A (kJ mol^{-1})	Pre-exponential factor $k_{m,0}$ ($\text{m}^3 \text{mol}^{-1} \text{s}^{-1}$)	Rate constant k_m at 550 °C ($\text{m}^3 \text{mol}^{-1} \text{s}^{-1}$)
TG/DTG method	188	3.5×10^9	4.0×10^{-3}
Isothermal method	231	3.0×10^{12}	6.5×10^{-3}

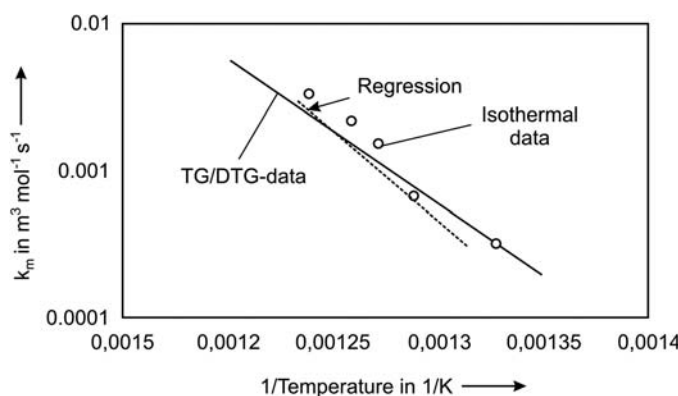
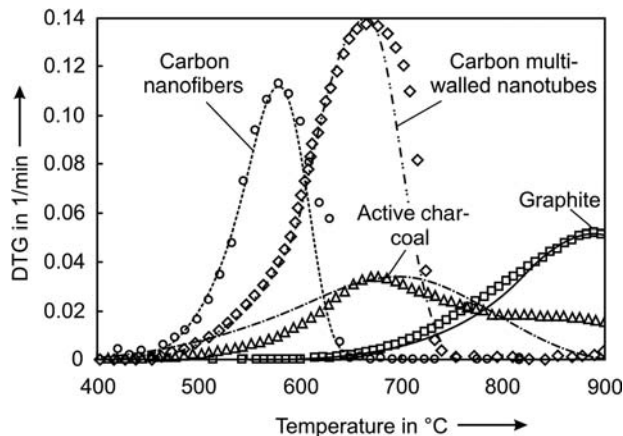


Figure 4.11.27 Arrhenius plot of the oxidation of carbon nanofibers based on isothermal and TG/DTG-measurements [3% O₂ in N₂, heating rate: 10 K min⁻¹; simulation based on Eqs. (4.11.51) and (4.11.52)]. Taken from Jung (2005).

Figure 4.11.28 DTG curves for different carbonaceous materials [3% O₂ in N₂, heating rate: 10 K min⁻¹, dashed lines: simulation, see Eqs. (4.11.47) and (4.11.48)], data of herringbone C-nanofibers from Jung (2005) and for the other materials from Schroegel (2004, 2007).



Summary of Section 4.11 (take-home messages)

- The objective of kinetic measurements is to discriminate between micro- and macrokinetics. As **microkinetics** we consider the kinetics of the chemical reaction, that is, the measured rate is not affected by transport processes (intrinsic kinetics). If the intrinsic kinetics cannot be separated from transport processes at the conditions relevant for technical operation we speak of **macrokinetics** or effective apparent kinetics.
- Laboratory reactors should be preferably operated isothermally to discriminate between temperature effects (activation energy) and concentration effects (reaction orders). The reaction conditions should be chosen in such a way that chemical and transport phenomena, which are equally important in an industrial process, can be investigated separately. Two types of laboratory reactors are most suitable for kinetic investigations, **gradientless differential reactors** and **integral reactors**, where the concentrations and the conversion vary either with the reaction time (batch reactor) or locally with the residence time and axial position (tubular reactor). **Integral evaluation** means that the measured data are compared with the integrated form of the rate equation. **Differential evaluation** of data from integral reactors means that the rates are determined based on concentration-time plots by differentiation, that is, by the slope of the tangent of the conversion-time curve for different values of the residence time and residual reactant concentration.
- Different **laboratory reactors** are used for kinetic studies. For studies of liquid–liquid reactions and homogeneously catalyzed reactions, a batchwise operated stirred tank reactor is frequently used. Tubular reactors loaded with catalyst (fixed bed) are more common for studies of heterogeneously catalyzed gas reactions. The tubular reactor displays a simple design and is easy to operate. A simultaneous integral and differential mode of operation can be achieved by a tap reactor for measuring concentration and temperatures at defined axial positions. Gradientless operation with respect to temperature and concentration can be obtained by an external or internal recycle.
- Thermogravimetry (TG)** is one of the oldest thermal analytical procedures and has been used extensively to study pyrolysis, combustion, and gasification of coal, coke, and polymers. The technique involves monitoring the weight loss of a sample in a chosen atmosphere as a function of temperature, whereby the heating rate is kept constant. The usefulness of TG for analyzing kinetic

processes is greatly enhanced if simultaneously the first derivative of the weight loss is recorded, which is referred to as derivative thermogravimetry (DTG). Evaluation of the kinetic parameters based on DTG data should be preferred as it gives a more “honest” result. The TG signal is less sensitive and hides real effects, for example, if impurities with a different reactivity are present. In the DTG signal this is more easily detected by double peaks and shoulders. Kinetic parameters such as the activation energy and the pre-exponential factor are obtained by the best fit between measurement and simulation.

5

Raw Materials, Products, Environmental Aspects, and Costs of Chemical Technology



Ammonia plant Jilin, China. Courtesy of Linde Engineering, Germany.



Ethylene dichloride via ethylene oxy-chlorination. Courtesy of Uhde, Germany.



Chlor-alkali electrolysis ($146\,000\,\text{t}\,\text{y}^{-1}$ caustic soda) based on membrane technology in Rafnes, Norway. Courtesy of Uhde, Germany.



Ethylene plant in Rayong, Thailand. Courtesy of Linde Engineering, Germany.

5.1 Raw Materials and Energy Sources

Reserves and resources of fossil fuels, renewable energy, natural gas and other technical gases, oil and refinery products, coal and coal products, renewable raw materials, and economic and social aspects of (future) energy consumption and mix.

5.2 Inorganic Products

Halogens, acids and bases, ammonia and fertilizers, and metals.

5.3 Organic Intermediates and Final Products

C_1 chemistry and syngas, olefins and aromatic hydrocarbons, organic components with oxygen, halogens and nitrogen, polymers, detergents, and fine chemicals

5.4 Environmental Aspects of Chemical Technology

Air pollution and flue gas cleaning and water pollution and treatment.

5.5 Production Costs of Fuels and Chemicals Manufacturing

Price of chemical products and investment and variable costs.



Syngas production by steam reforming of natural gas. Courtesy of Uhde, Germany.



Refinery Burghausen, Germany. Courtesy of Linde Engineering, Germany.

5.1

Raw Materials and Energy Sources

This chapter gives an overview of the main raw materials of the chemical industry as well as important energy sources with regard to the following aspects:

- global consumption, reserves and resources of fossil fuels, and renewable energy;
- natural gas and other technical gases such as biogas, coke oven gas, hydrogen and syngas, their properties and conditioning, and processes and products based on natural gas;
- crude oil, major refinery products and processes;
- coal and coal products like blast furnace coke;
- renewable raw materials for chemical and biological processes;
- resources of industrial inorganic chemistry.

5.1.1

Energy Consumption, Reserves and Resources of Fossil Fuels and Renewables

5.1.1.1 Global and Regional Energy Consumption and Fuel Shares

Today, global primary energy consumption is about 12 billion tonnes of oil equivalent (1 toe = 41.87 GJ). The three fossil fuels crude oil, coal, and natural gas make up about 80% of this supply (Table 5.1.1). Fossil fuels are relatively concentrated, pure energy sources, technically still easy to exploit, and to date provide cheap energy. (The history of fossil fuel prices is given in Section 5.1.4.1 for crude oil.) Crude oil products provide almost all of the world's transportation fuels and are the basis of most organic chemicals from bulk to fine chemicals (polymers, pharmaceuticals, dyes, etc.). Coal and natural gas mainly provide heat and electricity but also (although in a much small extent compared to oil) are a source of chemicals like NH₃, H₂, synthetic fuels via Fischer-Tropsch synthesis, and methanol. This dominant role of fossil fuels for fuels and chemicals will probably not change in the near future.

Table 5.1.1 2007 fuel shares of world total primary energy consumption (IEA, 2009, 2007).

Energy type	Share of world total primary energy consumption (%)
Crude oil	34.0
Coal	26.5
Natural gas	20.9
Nuclear ^{a)}	5.9
Total fossil fuels and nuclear	87.3
Hydro ^{b)}	2.2
Traditional biomass ^{c)}	6.5
Commercial biomass ^{c)}	3.3
Other (geothermal, wind, solar, tide) ^{b),d)}	0.7
Total renewables	12.7
Total energy consumption	12.0 billion toe (tonnes of oil equivalent)

a) Nuclear refers to the primary heat equivalent of the electricity produced by nuclear power plants with an average thermal efficiency of 33%, that is, 1 GWh = 3600 GJ electrical power = 3600 GJ/0.33 virtual primary energy input = 10 010 GJ/41.87 GJ per toe = 260 toe.

b) Hydro, wind, and tide refers to the energy content of the electricity produced in power plants, that is, 1 GWh = 3600 GJ electrical power = 3600 GJ/41.87 GJ per toe = 86 toe. The same is true for solar electricity. For geothermal electricity generation, 10% efficiency is assumed (1 GWh = 860 toe).

c) Traditional biomass is not traded for money and difficult to quantify. Here, an estimated ratio of traditional to commercial biomass of 2 to 1 is used (data from IEA for 2003).

d) In 2004, 0.41% geothermal, 0.06% wind, 0.04% solar, and 0.0004% tide (IEA, 2007). In recent years, the share of wind energy has considerably increased: In 2011, the share was around 0.3% (www.bp.com, accessed 10.09.2012).

Table 5.1.2 Regional distribution of consumption of primary energy 2007 (IEA, 2009, 2007).

Region	Consumption in Gtoe ^{a)} (2007)	Share of renewables in total energy (%) (2004)		
		Combustible renewables, waste	Hydro	Geothermal, solar, wind
OECD	5.50	3.0	2.0	0.7
China	1.97	13.5	1.9	—
Asia ^{b)}	1.38	29.4	1.3	1.1
Former USSR	1.02	0.8	2.1	0.04
Non-OECD Europe	0.11	5.8	4.6	0.3
Africa	0.63	47.6	1.3	0.2
Latin America	0.55	18.0	10.4	0.4
Middle East	0.55	0.2	0.3	0.2
World	12.03 ^{c)}	10.6	2.2	0.4

a) Billion tonnes of oil equivalent.

b) Excluding China.

c) Includes international aviation and international marine bunkers as well as electricity and heat trade (0.32 Gtoe).

The contribution of nuclear and hydro energy – which are both only used in power plants to produce electricity – to the global primary energy consumption is about 6% and 2%, respectively. The share of biomass in terms of the global energy supply is about 10%. The majority – about two thirds – is traditional biomass, which is not traded for money and therefore difficult to quantify. Other renewable energy sources such as geothermal, solar, wind, and tide energy currently do not play a remarkable role on a global basis (0.7%), but the application of renewable energy sources is increasing and is supported by some countries, which have now achieved relatively high levels of wind power penetration, such as 19% of stationary electricity production in Denmark, 11% in Spain and Portugal, and 7% in Germany in 2008.

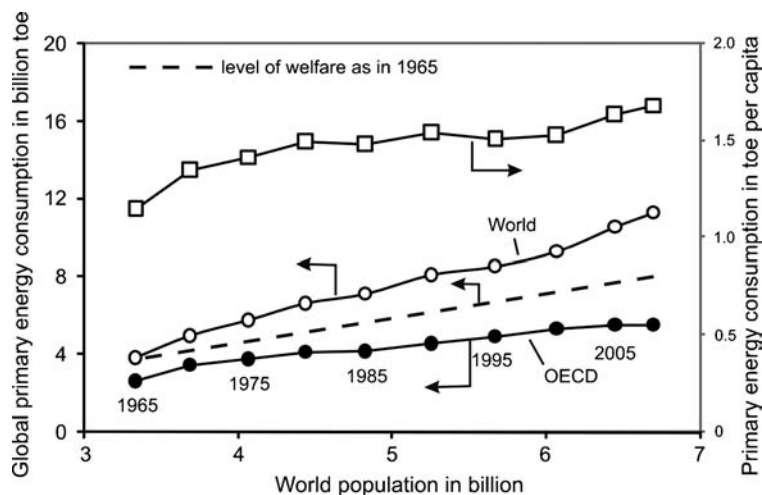
The regional distribution of primary energy consumption as well as the share of renewables differ considerably (Table 5.1.2). For example, in Africa, 48% is covered by traditional biomass with the severe problem of (currently) still negligible reforestation.

At present a relatively small part of the world's population consumes most of its resources. The OECD countries with a population of about 1.2 billion people, that is, 18% of the world's population, have a share of 47% of the global energy consumption and consume three-times as much energy as China with about the same population (Table 5.1.3). In Asia (excluding China) and Africa, the energy consumption per capita and year is only 0.6 toe (tonnes of oil equivalent), while the average OECD-value is 4.6 toe per capita and year.

Table 5.1.3 Regional distribution of population and specific energy need 2007 (IEA, 2009).

Region	Population in billion	Energy consumption (toe pc and a)
OECD	1.19	4.64
China	1.33	1.48
Asia (excluding China)	2.15	0.64
Former USSR & non-OECD Europe	0.34	3.34
Africa	0.96	0.66
Latin America	0.46	1.19
Middle East	0.19	2.86
World	6.62	1.82

Figure 5.1.1 Relationship between world primary energy consumption (without traditional biomass) and world population in the period 1965–2008 (Jess, 2010).



5.1.1.2 World Energy Consumption and World Population

An important driving force behind the world's energy demand is the world population. In 2009, the world's population was growing by 1.2% per year, and in the hypothetical case of an undamped demographic evolution the world population would double in 60 years. This population growth will certainly lead – at least in the near future – to a further rise in global energy consumption. Thus, it is instructive to examine the history of the world's global energy consumption and population, as shown in Figure 5.1.1 for the period 1965–2008.

The growth of the world population and average welfare has led to an increase in energy consumption from 3.8 billion toe in 1965 to 11.3 billion toe in 2008. The energy consumption has tripled during this period whereas the world population has "only" doubled. Thus, without increasing welfare in today's high-income and some developing countries the energy demand would have "only" grown to 7.6 billion toe (dashed line in Figure 5.1.1). In other words, the strong growth in energy consumption during the last four decades can be attributed in equal portions to the growth of welfare and of population. This more than proportional increase of energy demand with the growing world population is also reflected in the history of the average energy consumption per head, which has increased from 1.2 toe pc in 1965 to 1.7 toe pc in 2008 (Figure 5.1.1).

5.1.1.3 Economic and Social Aspects of Energy Consumption

Usually, the gross national product (*GNP*) [or the gross domestic product (*GDP*), see footnote 2 of Table 5.1.4] is used as a measure of a country's economic performance. For a comparison of countries, the purchasing power parity (*PPP*) should be used, that is, the *GNP* in international dollars with the same purchasing power as a US\$ in the United States. Values of selected countries are given in Table 5.1.4. The table also lists the land area per head, the population in 2009 (and prediction for 2050), and the energy consumption (pc).

Today, the mean global land area per capita is only two soccer fields (2 ha), which already includes areas that cannot, or only to a small extent, be used (Antarctica, deserts, etc.). Thus, in future, not only energy but also the available land area will be a limiting factor with regard to providing the world with energy, food, and so on, above all in countries with a high annual growth rate and an already limited area of less than one soccer field per head.

Other social aspects such as food, meat, fish and paper consumption, the share of Internet users in the population, life expectancy at birth, use of private cars per 100 people, and the annual consumption of motor gasoline and diesel oil are listed in Table 5.1.5 as these aspects are also linked to the energy demand and the standard of living.

Table 5.1.4 Population (2009, estimates for 2050), energy consumption (2007), land area, gross national product (2008), and poverty of some countries (World Bank, IEA, 2009).

Rank by population in 2009	Country	Population ^{a)} in million		Annual energy consumption in toe pc	Annual GNP PPP ^{b)} in international \$ per capita (pc)	Share of population living in poverty (%) ^{c)}	Land area in soccer fields ^{d)} pc (2009)
		2009	2050				
1	China	1339	1424	1.48	6020	47	1.0
2	India	1166	1656	0.53	2960	80	0.4
3	USA	307	439	7.75	46 970	Negligible	4.1
4	Indonesia	240	313	0.84	3830	52	1.1
5	Brazil	199	261	1.23	10 070	21	5.8
6	Pakistan	176	276	0.51	2700	74	0.5
7	Bangladesh	156	234	0.16	1440	83	0.1
8	Nigeria	149	264	0.72	1940	92	0.8
9	Russia	140	109	4.75	15 630	12	16.6
10	Japan	127	94	4.02	35 220	Negligible	0.4
11	Mexico	111	148	1.74	14 270	20	2.3
14	Germany	82	74	4.03	35 940	Negligible	0.6
15	Ethiopia	85	278	0.29	870	78	1.8
51	Australia	21	29	5.87	34 040	Negligible	50
149	Mongolia	3	4	1.11	2200	75	71
	World	6790	9320	1.82	7448	40	3.0

a) US Census Bureau, international database (<http://www.census.gov/>).

b) The gross national product (GNP) measures a country's economic performance and consists of the total value produced (gross domestic product GDP) together with its income received from other countries less similar payments made to other countries. For example, the profits of an Italian-owned company operating in France will count towards Italy's GNI. PPP is purchasing power parity, that is, an international \$ has the same purchasing power as a US\$ in the United States.

c) Share of population with less than 2 international \$ per capita and per day (for definition see footnote b).

d) Assumption: the typical area of a soccer field is 7 300 m² (= 0.7 ha).

Table 5.1.5 Annual energy consumption in tonnes of oil equivalent (toe) per capita (pc) (1 toe = 41.87 GJ), annual consumption of food, meat, and paper (including paperboard) pc (FAO, 2007, 2011), level of science and technology relative to the USA (see footnote a), share of Internet users in the population, life expectancy at birth (CIA, 2009), use of private cars per 100 people (World Bank, 2010), and annual consumption of motor gasoline and diesel oil (WRI, 2010) in selected countries.

Country	Annual energy consumption (2007) (toe pc)	Daily food consumption (2005) (kcal pc)			Annual paper consumption (2005) (kg pc)	Level of science & technology ^{a)} (2003)	Share of Internet users (2008) (%)	Life expectancy (2010) in years	Road traffic (2005)	
		Total	Meat	Fish					Number of cars ^{b)} (per 100 people)	Annual fuel consumption ^{c)} (liters pc)
USA	7.8	3850	462	34	297	Set to 100	75	78	45	2116
Germany	4.0	3510	344	41	232	74	75	79	57	698
Japan	4.0	2740	174	163	234	64	72	82	33	690
Russia	4.8	3160	234	44	38	15	21	66	21	337
China	1.5	2970	435	36	45	3	22	75	2	84
India	0.5	2350	21	8	5	1.6	7	66	1	21
Congo	0.3	1480	18	10	3	0.5	0.4	55	2	12
World	1.8	2800	219	50	55	15	24	66	10	291

a) As an indication of the level of science and technology the number of published scientific and engineering articles (relative to the USA) is used (World Bank, 2010). In the USA, the number is 7 per 10 000 people; this value is here set to 100. For Congo (Democratic Republic) the value is unknown and the average of Uganda, Kenya, and Nigeria is used as indication.

b) Privately owned cars with more than two wheels designed to seat no more than nine people (including driver).

c) Motor gasoline and diesel oil.

Figure 5.1.2 Gross national product in purchasing power parity per capita (2008) versus primary energy consumption pc (2007) (solid line with slope of current global average; dot-dash line indicates the development in countries with increased energy efficiency (Jess, 2010).

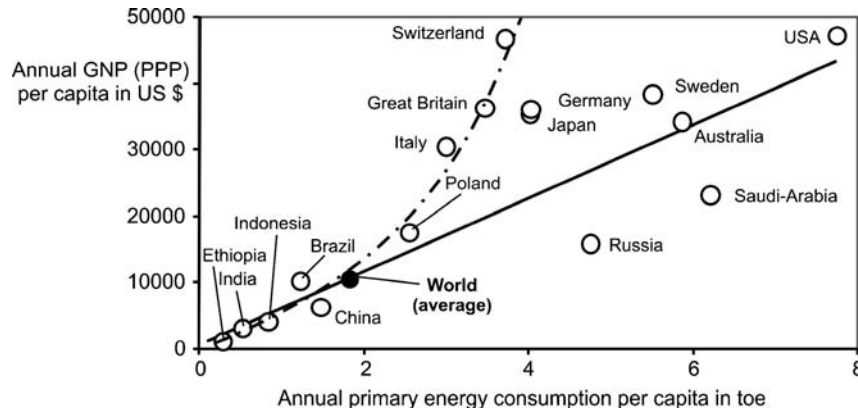
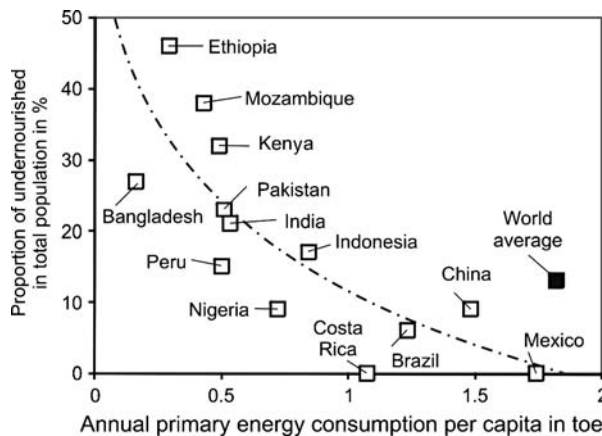


Figure 5.1.2 shows the GNP per capita (pc) versus the primary energy consumption (pc). Although there is a general trend that an increase of the GNP for the range below about US\$ 15 000 per head is associated with an increase in energy consumption, the development in certain high-income countries (Europe, Japan) gives rise to a certain optimism, which reflects the positive effect of efficient energy systems, lower consumption rates of transportation fuels like gasoline, diesel oil, and kerosene, etc. Nevertheless, more technical improvements are still needed in combination with restrictions of individual energy consumption in certain currently richer nations (e.g., in the USA). With regard to global energy consumption there is also a need for rapidly developing countries like China and India to also improve the efficiency of their energy systems (traffic, electricity, etc.).

A first indicator of what the minimum energy demand needed per capita might be is the proportion of undernourished in the total population. Figure 5.1.3 shows the respective correlation of this proportion versus the primary energy consumption per capita of selected underdeveloped and developing countries. For all countries with an annual energy consumption of more than 2 toe pc (e.g., OECD) the proportion of undernourishment is negligible. According to Figure 5.1.3, a minimum energy demand in the range of 1.5–2 toe pc and year is needed at the current status of technology to guarantee that starvation can be excluded, at least if the differences in income and welfare equality in a country are not too large.

The GNP per capita (pc) is an important indicator for measuring the average welfare of the population in a country or region. Countries with a higher GDP pc may be more likely to also score highly on other measures of welfare, such as life expectancy. However, there are serious limitations to the usefulness of GNP or GDP as a measure of welfare, even if the GNP per capita is measured at purchasing power parity:

Figure 5.1.3 Proportion of undernourished in total population (2003–2005) (FAO, 2009) versus primary energy consumption pc (2005). Note: for all countries with an annual energy consumption of more than about 1.5 toe pc the proportion of undernourishment is negligible (Jess, 2010).



- Measures of *GNP* exclude unpaid economic activity such as domestic work such as childcare.
- *GNP* takes no account of the working time needed to create a certain *GDP* (happiness of workers, leisure time).
- *GNP* does not measure the quality of life, such as the quality of the environment, security from crime, health care, and the population health and longevity.
- The *GNP* only reflects the average wealth, that is, a country may have a high average per-capita *GDP* but most of its citizens have a low level of income due to the concentration of wealth in the hands of a small fraction of the population. Such differences in income equality are measured by the *Gini coefficient*, which is a number between 0 and 1, where 0 corresponds to perfect equality – everyone has the same income – and 1 corresponds to perfect inequality (one person has all the income). In Japan and Central and Northern Europe, the inequality is low (e.g., in Denmark and Japan with $Gini < 0.25$), whereas in many countries in Africa and South America the inequality is high (e.g., in Brazil, Bolivia, Botswana, and Namibia, where $Gini > 0.55$), while the United States is a mid-fielder ($Gini = 0.41$) (data from *United Nations Development Programme*, human development report 2007/08).

Since 1990, the *Human Development Index (HDI)* has been published by the *United Nations* as an index to characterize the level of “human development” (purchasing power, life expectancy, literacy, educational attainment) as explained in Topic 5.1.1. As one may expect, the *HDI* is linked not only to the *GNP* (pc) (Figure 5.1.2) but is also strongly linked to the primary energy consumption (pc), but only up to a certain extent, that is, in poor countries. This is depicted by the graph of the *HDI* versus the annual primary energy consumption per capita (Figure 5.1.4).

In underdeveloped ($HDI < 0.5$) and developing countries ($0.5 < HDI < 0.8$), there is a relation between standard of living and energy consumption, but for developed countries ($HDI > 0.8$) the *HDI* is almost independent of the energy consumption. Thus, Figure 5.1.4 reflects a well-known law of economics, the so-called *diminishing marginal utility*, which states that as a person increases consumption of a certain product (here energy) there is a decline in the utility (here increase of *HDI*) that a person derives from consuming additional units of that product.

Some other important facts and conclusions can be also derived based on Figure 5.1.4:

- 1) Obviously, a minimum primary energy consumption of about 2 toe per capita (pc) is needed to reach the average *HDI* value (0.95) of high-income OECD countries. Thus, this value can be regarded as the minimum energy consumption to reach a high status of development. Remarkably (and by pure chance),

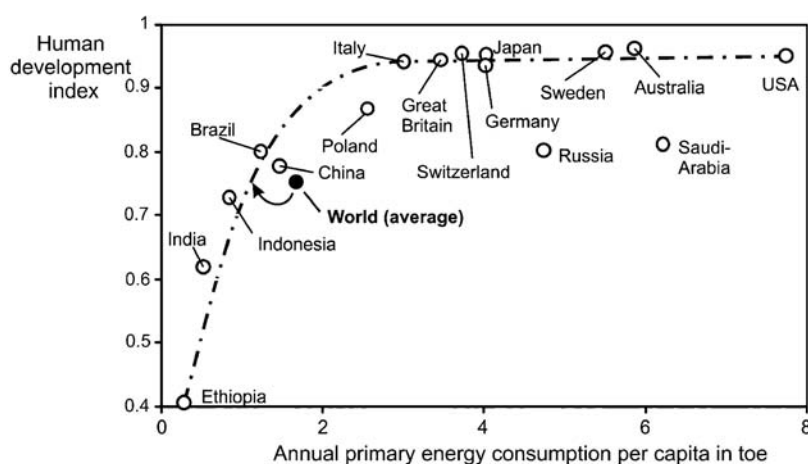


Figure 5.1.4 Human development index (*HDI*) versus energy consumption per capita. The *HDI* ranks countries by level of human development (2007, *HDI* from *UN Development Programme*, human development report 2007/08). Arrow indicates the theoretical decrease of global energy consumption pc to the minimum value that we could have today (2008) according to the trend (dot-dash curve) without change of global average *HDI* (Jess, 2010).

- this is almost the same value as the actual global average (1.8 toe pc and year, Table 5.1.5).
- 2) High-income OECD countries (Central/Northern Europe, USA, Japan, etc.) have in principle the chance to reduce their energy consumption without loss of welfare, whereas underdeveloped and developing countries like India and China inevitably need more energy to increase their current welfare until at least 2 toe pc is reached.
 - 3) Today, the global (average) *HDI* value is only 0.75 compared to 0.95 in high-income countries. In principle, this corresponds to a *minimum* global energy consumption of 1 toe (pc) and year (arrow in Figure 5.1.4) compared to the currently 1.8 toe (pc) and year. In other words, the global energy consumption could theoretically be reduced by 40% (from 1.8 to 1 toe pc) without changing today's global mean status of human development.
 - 4) According to UN estimates, the world population will be 9.2 billion in 2050 compared to 6.8 billion in 2009. Thus, if nothing changes – constant *HDI* and constant energy consumption per head in all countries – 35% more primary energy will be needed. This would almost completely consume the maximum potential savings we could reach (see point 3).
 - 5) Conversely, if the global average status of development increases in future, this will lead to an increase of the energy consumption, if we do not change our approach.

The following scenario for 2050 is instructive. Let us be very optimistic and assume that the current *HDI* value of high-income OECD countries (0.95) is then reached globally. Let us also assume that by means of advanced technologies and energy savings – first of all needed to reduce today's energy consumption of high-income countries – only 2 toe per head and year are consumed in 2050 on a global average. Thus, with a world population of 9.2 billion in 2050, we would then still need 18.4 billion toe, which is 50% more of what we consume today!

Some economists argue that although on average richer nations tend to be happier than poorer nations, beyond an average *GDP* per capita of about \$15 000 (PPP) a year there are studies that indicate the average income in a nation makes little difference to the average *happiness* of a nation (Layard, 2003; Ruckriegel, 2007; Inglehart *et al.*, 2008, see Topic 5.1.1). Although the *HDI* already includes elements that reflect the average *happiness* of a nation compared, it is still a matter of debate as to how to measure well-being even better and by this means give politicians better guidelines – hopefully not only with regard to winning elections. For example, the former French President *Nicolas Sarkozy* appointed a commission in 2008, chaired by the Nobel laureates *Amartya Sen* and *Joseph Stiglitz*, to come up with a better measure.

It is beyond the scope of this book to discuss all of the problems associated with future energy needs or the shares different fuels might have, but some aspects will be discussed in Sections 5.1.1.4–5.1.1.9, as one of the major global key questions beside the provision of clean water and enough food will be how to provide the growing world population with energy without damaging the planet Earth's ecological capacity and ecosystem. Let us hope that the following quotation is unfounded:

“Earth provides enough to satisfy every man's need, but not every man's greed”
(M. Gandhi, 1869–1948).

Topic 5.1.1 Human development index (HDI) and happiness of societies

The **human development index** is used to rank countries by level of “human development,” and combines normalized measures of life expectancy, literacy, educational attainment, and *GDP* per capita. To transform a raw variable x into a unit-free index between 0 and 1 (which allows different indices to be added together), the following formula is used:

$$(\text{unit free, i.e., normalized})x\text{-index} = \frac{x - x_{\min}}{x_{\max} - x_{\min}} \quad (5.1.1)$$

where x_{\min} and x_{\max} are the lowest and highest values, respectively, the variable x can attain.

The **HDI** combines three basic dimensions and the corresponding indices:

The **life expectancy index** is an index of population health and longevity:

$$\text{Life expectancy index (LEI)} = \frac{LE - LE_{\min}}{LE_{\max} - LE_{\min}} = \frac{LE - 25}{85 - 25} \quad (\text{with } LE \text{ in years}) \quad (5.1.2)$$

The **education index** is measured by the adult literacy rate (with two-thirds weighting) and the gross enrollment ratio (with one-third weighting):

$$\text{Education index (EI)} = \frac{2}{3} ALI + \frac{1}{3} GEI \quad (5.1.3)$$

with:

$$\text{Adult literacy index (ALI)} = \frac{ALR - 0}{100 - 0} \quad (\text{with } ALR \text{ as adult literacy rate in \%}) \quad (5.1.4)$$

$$\text{Gross enrolment index (GEI)} = \frac{CGER - 0}{100 - 0} \quad (5.1.5)$$

The **combined gross enrollment ratio CGER** (in %) incorporates different levels of education from kindergarten to postgraduate education.

The **standard of living** is measured by the natural logarithm of gross domestic product per capita at purchasing power parity (the reason for log-scale is given below):

$$\text{Gross domestic product (GDP)} = \frac{\log(GDP_{pc}) - \log(100)}{\log(40\,000) - \log(100)} \quad (\text{pc = per capita}) \quad (5.1.6)$$

This, finally, leads to the equation to calculate the **human development index**:

$$HDI = \frac{1}{3} LEI + \frac{1}{3} EI + \frac{1}{3} GDP \quad (5.1.7)$$

Figure 5.1.5 shows the human development index (HDI) versus the gross national product (GNP) in purchasing power parity (PPP) per capita. Obviously, the average welfare of a nation (as measured by the HDI) strongly increases as one moves from

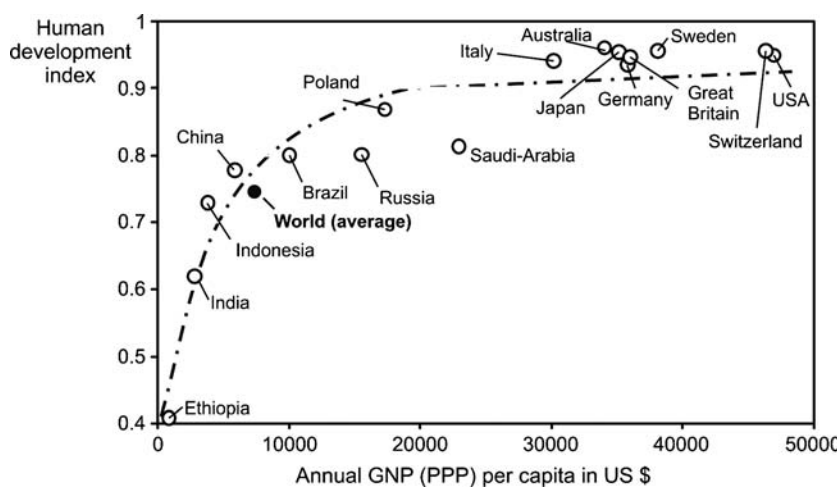


Figure 5.1.5 Human development index (HDI) in 2007 versus gross national product (GNP) in purchasing power parity (PPP) per capita in 2008 (JESS, 2010).

Table 5.1.6 Distribution of happiness in the USA in the period 1976–2010 (data from *General Social Survey* (NORC, 2012) and Layard, 2003).

	Average response (%)				
	1976	1986	1996	2006	2010
Very happy	35	33	32	32	29
Pretty happy	53	57	57	56	57
Not too happy	12	10	11	12	14

subsistence-level poverty to a modest level of economic security and then levels off at about \$15 000 per head (Figure 5.1.5). Among the high-income societies, a further increase in income is only weakly linked with higher levels of *HDI*, that is, further gains in income bring relatively little or no change in welfare. For underdeveloped and developing countries, however, there is a clear impact of income on welfare.

Happiness and Life Satisfaction of Nations Happiness is not easy to define – philosophers, economists, theologians, sociologists, and politicians have debated on this term since ancient times. In many societies, interest in happiness was brought to widespread attention with the moral philosophy that the purpose of politics should be to bring the greatest happiness to the greatest number of people. For example, in 1776 the American Declaration of Independence argued for “certain inalienable rights, that among these are life, liberty and the pursuit of happiness.” As such, nations have been formed on the basis of the search for happiness, and this desire has been put on a par with the right to life and the right to freedom.

The measurement and analysis of notions such as happiness, welfare, subjective well-being, and life satisfaction has a half-century history in the social sciences (Easterlin, 2001). In the USA the *General Social Survey* (National Opinion Research Center) has asked, since the early 1970s, the following question to measure happiness. “Taken all together, how would you say things are these days – would you say you are very happy, pretty happy or not too happy?” Table 5.1.6 shows the results for the period 1976–2010.

The distribution of happiness is practically unchanged over the period (1976–2010) although the *GNP (PPP)* per capita has more than doubled in that period. This finding is surprising since at any time within any community there is a clear relation between happiness and income (Table 5.1.7). Interestingly, though, happiness is directly proportional to the log of income rather than absolute income. In other words, the same proportional rather than absolute increase yields the same increase in happiness, which is why $\log(GDP)$ is used in Eq. (5.1.6).

Instead of happiness the respondents of surveys may be asked about their satisfaction with life as a whole. The happiness and the life satisfaction of a society are measured and combined by the *subjective well-being index (SWB)*, which has increasingly been used by economists in recent years. Typically, the value of the *SWB* is determined as follows.

Table 5.1.7 Percent distribution of population by happiness at various levels of income (USA, 1994, data from Easterlin, 2001).

Total household income (1994 dollars)	Mean happiness rating ^{a)}	Very happy	Pretty happy	Not too happy	Number of cases
75 000 and over	2.8	44	50	6	268
50–74 999	2.6	36	58	7	409
40–49 999	2.4	31	59	10	308
30–39 999	2.5	31	61	8	376
20–29 999	2.3	27	61	12	456
10–19 999	2.1	21	64	15	470
Less than 10 000	1.8	15	62	23	340

a) Based on score of “very happy” = 4, “pretty happy” = 2, “not too happy” = 0.

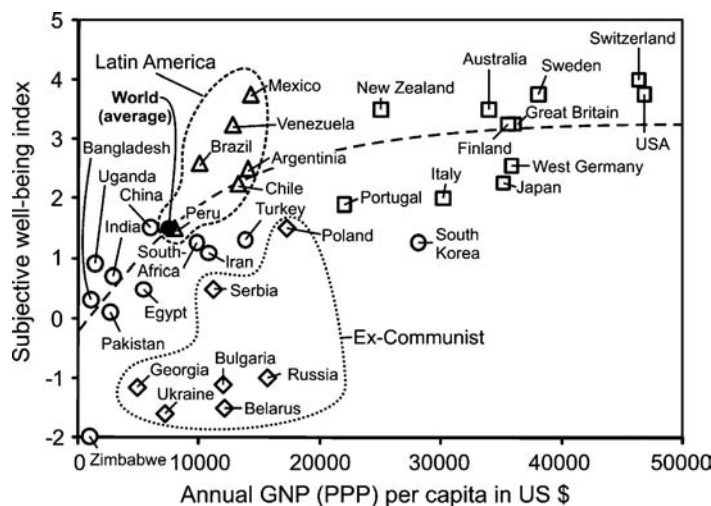


Figure 5.1.6 Subjective well-being index (SWB) (period 1995–2007) versus gross national product in purchasing power parity per capita (2008) [SWB from Inglehart *et al.* (2008); global average value based on 33 countries representing 68% of the world's population (Jess, 2010)].

Life satisfaction is assessed by asking respondents how satisfied they are with their life, using a scale from 1 (not at all satisfied) to 10 (very satisfied). Happiness is determined by asking how happy respondents are. For a composite measure of the *subjective well-being index*, the responses to both questions are combined with equal weight. Because life satisfaction is measured on a 10-point scale and happiness (according to the data published by Inglehart *et al.*, 2008) is measured on a 4-point scale ("very happy" = 1, "rather happy" = 2, "not very happy" = 3, "not at all happy" = 4), and because the two questions have opposite polarity, the SWB is calculated as follows: $SWB = \text{life satisfaction} - 2.5 \times \text{happiness}$. Thus, if 100% of people are very happy and extremely satisfied, a country gets the maximum score of 7.5. If more people are dissatisfied (for example an average score of only 4) or unhappy (for example an average value of 3 = "not very happy"), a country may even get a negative score (-3.5 for the given example = 4 - 2.5 × 3). Real values (Figure 5.1.6) vary in the range of -2 to 4.

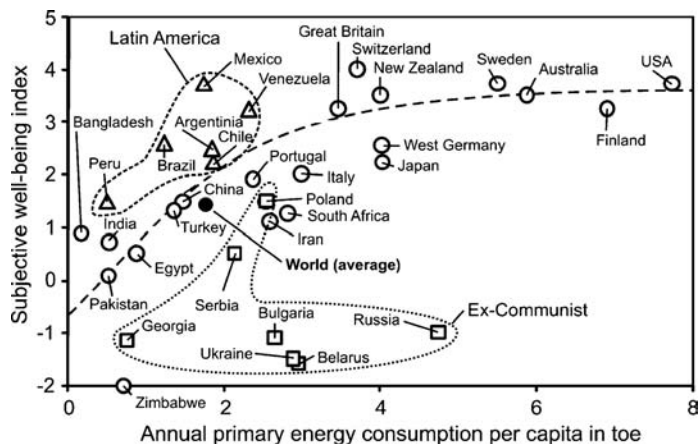
(Remark: It is far beyond the scope of this book to discuss philosophical aspects of happiness and welfare and so on in general. But, it should be mentioned that a certain but limited degree of unhappiness, lack of welfare, and income inequality is needed, for example, to create sufficient psychological strain to motivate people, especially for young people to do things better than their parents and others did. Each society should ensure the inalienable right of the pursuit of happiness but cannot guarantee happiness.)

Figure 5.1.6 shows the relationship between the SWB and the economic development (GNP in PPP per capita) in 33 countries that contain 68% of the world's population. The curve depicts a trend such that if the SWB of a society were determined by its level of economic development it would fall on this line. This trend-line is similar to the relationship of the human development index (HDI) and the GNP (PPP) per capita (Figure 5.1.5).

Happiness and life satisfaction rise steeply on moving from subsistence-level poverty to a modest level of economic security and then levels off. Among the richest societies, further increases in income are only weakly linked with higher levels of SWB, that is, further gains in income bring relatively little or no change in well-being. For poorer countries, however, there is a clear impact of income on happiness. Once a country has over about \$15 000 pc, its level of happiness appears to be independent of its income per head.

As Figure 5.1.6 indicates, the SWB of nations is closely related to economic development. The people of high-income countries are much happier and are more satisfied with life than people of low-income countries, and the differences are substantial. In Denmark, 52% of the public indicated that they were highly satisfied with their lives (placing

Figure 5.1.7 Subjective well-being index (SWB) in the period 1995–2007 versus primary energy consumption per capita in 2007 (Jens, 2010).



themselves at about 9 on the 10-point scale), and 45% said they were very happy. In Zimbabwe, only about 5% were highly satisfied with their lives as well as very happy.

Figure 5.1.6 reveals another interesting point. Some societies do a better job of maximizing their citizens' SWB than others. Latin American countries show higher levels of SWB than their economic levels would predict. Conversely, the ex-communist societies show lower levels of SWB than their economic levels would predict. Thus, Figure 5.1.6 tells us not only something about economics but also something about politics and mentality. The collapse of the political, economic, and belief systems in the Soviet Union (SU) has sharply reduced SWB in the ex-communist societies. The SU once played a prominent role in the world, which may have brought feelings of pride and satisfaction to many of its citizens.

The same trends can be derived from a plot of the subjective well-being index (SWB) versus the primary energy consumption per capita (Figure 5.1.7). About 2 toe per head are needed annually to make people happy, which corresponds to the value determined by the relationship of welfare (HDI) and energy consumption (Figure 5.1.4).

If more energy is consumed this brings no change in well-being, and there are substantial differences between this trend in ex-communist countries (less happy) and in Latin America where people obviously tend to be more happy than their energy consumption would predict.

To take stock: All indicators of prosperity, welfare, and happiness (*status of under-nourishment, GNP, HDI, SWB*) show that an annual energy consumption of not more than 2 toe pc is needed to ensure a sufficient standard of living. Thus, the quest for ever higher energy use has no justification in objective evaluations or subjective self-assessments.

5.1.1.4 Conventional and Non-conventional Fossil Fuels

For discussion of the availability of fuels, the following definitions are helpful: *Reserves* are currently technologically and economically recoverable, whereas *resources* are the additional quantities that cannot be recovered at current prices with current technologies but might be recoverable in future. Resources are difficult to assess and the tonnage given in the literature or by energy agencies varies strongly and depends on the definition, which may range from the "total amount present, whether or not recoverable at present" to the "amount in place that geological and engineering information indicates with reasonable certainty might be recovered in the future." For example, it is estimated that only 15% of coal resources can feasibly be extracted.

Beside conventional gas, oil, and coal resources, we also have to consider non-conventional resources (Table 5.1.8). Oil sands, extra heavy oils, and oil shale are

Table 5.1.8 Reserves and resources of fossil fuels 2008 (BGR, 2009).

Fuel type	Reserves ^{a)} (billion tonnes oil equivalent)	Resources ^{b)} (billion tonnes oil equivalent)
Crude oil	160 ^{c)}	92
Natural gas	171	217
<i>Conventional hydrocarbons^{c)}</i>	331	309
Oil sands and extra heavy oil	52	190
Oil shale	—	119
Non-conventional natural gas ^{d)}	5	2472
<i>Non-conventional hydrocarbons</i>	57	2781
Hard coal	431	9240
Soft brown coal	74	1177
<i>Coal (total)</i>	505	10.417
<i>Fossil fuels total</i>	<i>About 900</i>	<i>About 13.500</i>

a) Currently technologically and economically recoverable.

b) Geologically demonstrated and estimated quantities that cannot be recovered at current prices with current technologies but might be partly recoverable in the future.

c) The historical development of the crude oil reserves is discussed in more detail in Section 5.1.4.

d) Tight gas (25%), coal-bed gas (9%), aquifer gas (29%), and gas hydrates (37%).

estimated to contain three-times as much oil as the remaining conventional oil reserves, but (with the exception of Canadian oil sands) they are not yet economically recoverable, though this may change.

About 50% of the conventional natural gas reserves are located in countries far from consumers, for example, in the Middle East. In these regions, where movement by pipelines is not possible or not economical, natural gas can be transported as liquefied natural gas (LNG) by specially designed cryogenic sea vessels or cryogenic road tankers. The liquefaction process involves removal of certain components, such as dust, acid gases, helium, water, and heavy hydrocarbons, which could cause difficulties downstream, and subsequent condensation into a liquid at close to atmospheric pressure by cooling it to about -162°C . The reduction in volume makes it much more cost-efficient to transport over long distances where pipelines do not exist. The continued cost reduction of LNG transport has led to a strong increase of LNG production from 56 million tonnes (50 million toe, 4% of global natural gas demand) in 1990 to 165 million tonnes (147 million toe, 7% of the world's natural gas demand) in 2006. The three biggest LNG exporters in 2007 were Qatar (25 million million toe), Malaysia (20 million toe), and Indonesia (18 million million toe) and the three biggest LNG importers were Japan (58 million million toe), South Korea (30 million million toe), and Spain (21 million million toe). As an alternative to LNG transport, several companies have developed and built Fischer-Tropsch plants to enable exploitation of these so-called stranded gas reserves by conversion into liquid fuels (mainly diesel oil, see Section 6.11.1). The current capacity of Fischer-Tropsch plants based on natural gas is around 5 million toe (2009), but it is expected that this will grow to 30 million toe in the next decade.

There are large unconventional gas resources, like methane hydrate or aquifer gas, that could increase the amount of gas resources by a factor of ten or more. Methane hydrate is a clathrate, a crystalline form in which methane molecules are trapped. Hydrates are stable at high pressure and low temperatures (e.g., 100 bar at $T < 13^{\circ}\text{C}$), and are found at ocean depths $> 500\text{ m}$ as well as under permafrost conditions. Some experts argue that the quantities of methane hydrates exceed those of all other fossil fuels combined. However, technologies for extracting methane from hydrate deposits have not yet been developed.

Compared to oil and gas, coal reserves are huge (Table 5.1.9) as the resources are estimated to be about three-times larger than those of conventional and non-conventional gas and oil. In future, coal may increasingly be used as an energy

Table 5.1.9 Reserves and resources of fossil fuels 2008 (BGR, 2009).

Fuel type	Consumption (billion toe per year)	Reserves (billion toe)	Resources in billion toe	Reserves-to- production ratio in years	Resources-to- production ratio in years
Crude oil, oil sands, oil shale	3.8	212	401	56	About 100
Conventional and non- conventional natural gas	2.6	176	2689	68	About 1000
Coal total	3.3	505	10417	153	About 3000

source during oil and gas depletion, for example, by countries like India, China, and Australia. However, without storage of CO₂ in geological formations such as former oil or gas wells this will lead to an increase in CO₂ emissions.

The reserves-to-production ratios shown in Table 5.1.9 indicate that the current reserves will last about 60 and 70 years for oil and gas and 500 years for coal. Note that these numbers are static values based on current prices, technology, and energy consumption, for example, the ratios will increase if the oil price increases, and decrease if global consumption increases. If in future the resources are also partly used, oil, gas, and coal will last longer than 100 years (although not at current prices!). Nevertheless, fossil fuels are finite and we should use them with care for the sake of generations to come. If, to exercise our imagination, we did *not* use the majority of crude oil for the production of fuels like gasoline, jet fuel, diesel, and heating oil but only for chemicals then the reserves-to-production ratio would increase by a factor of about 10, that is, crude oil would then last for several hundred years! However, such a decoupling of feedstock and energy cannot be expected in the near future, and the chemical industry (petrochemistry) will remain the free-rider of oil consumption.

It is interesting to examine the regional distribution of the reserves and resources of conventional and non-conventional fossil fuels (Tables 5.1.10 and 5.1.11). More than 40% of current reserves of conventional natural gas and crude oil are located in the Middle East whereas the majority of coal reserves are located in North America, Australia, and Asia. This non-uniform distribution of reserves and resources of fossil fuels will play a strong role in future (struggle for resources etc.) and is a political risk. Most of the reserves and resources of non-conventional fossil fuels are located in North America and in the former USSR.

5.1.1.5 Nuclear Power

More than 400 nuclear power stations are in operation worldwide. Based on the current rate of use, the known low-cost uranium reserves will last for 50 years, but lower-grade sources could be used in future. An alternative could be thorium, which is three times more abundant than uranium. For example, India, which has large thorium reserves, may develop this technology.

The long-term radioactive waste storage problems have not yet been fully solved. Several countries are constructing underground repositories, and nuclear processing and fast breeder reactors are options to reduce the amount of waste.

The *Chernobyl accident* in Ukraine of 1986 and the Fukushima nuclear disaster in Japan of 2011 has caused massive public fear. Nevertheless, developing countries like India and China are growing rapidly, and with it their nuclear energy use too. In contrast, countries like Germany are abandoning nuclear power.

The use of nuclear energy is controversial. Critics believe nuclear power is uneconomic and dangerous. They claim that radioactive waste must be stored for indefinite periods, and are afraid of radioactive contamination by accident, natural disasters such as in Fukushima in 2011, or sabotage and of proliferation of nuclear

Table 5.1.10 Regional distribution of reserves and resources of *conventional* fossil fuels 2008 (BGR, 2009).

Fuel	Crude oil		Natural gas		Hard coal		Soft brown coal	
	Share of reserves (%)	Share of resources (%)	Share of reserves (%)	Share of resources (%)	Share of reserves (%)	Share of resources (%)	Share of reserves (%)	Share of resources (%)
Europe	1.5	4.5	3.1	3.6	2.7	3.0	24.6	7.1
Former USSR	10.8	26.2	31.9	49.7	17.0	18.4	34.9	31.6
Africa	10.2	10.8	7.9	4.7	4.5	0.3	—	—
Middle East	64.3	22.4	40.2	13.6	0.1	0.3	—	—
Asia, Australia	3.5	7.1	8.3	9.5	42.0	34.5	26.2	25.9
North America	4.0	18.5	4.4	14.7	32.6	42.3	12.4	34.9
Latin America	5.6	10.6	4.3	4.1	1.2	0.2	1.9	0.5
World in billion toe	160	92	171	217	431	9240	74	1177

a) Without oil shale and sand (Table 5.1.11).

b) Without non-conventional gas like tight gas and gas hydrates (Table 5.1.11).

weapons in politically unreliable countries. Proponents believe that the risks are small and can be reduced by advanced reactors. They also claim that, historically, coal power generation has caused more deaths than nuclear power, and that other kinds of energy infrastructure might also be attacked by terrorists, for example, hydropower plants and refineries.

Fusion power would not have the drawbacks associated with fission power, but no commercial fusion reactor is expected before 2050. In 2005, an international consortium consisting of the European Union, Japan, USA, Russia, South Korea, India, and China announced the €10 billion ITER (International Thermonuclear Experimental Reactor) project, which will be built in France to show within 30 years the technical feasibility of fusion power. Proposed fusion reactors use deuterium as fuel and in current designs also lithium. Assuming a fusion energy output equal to today's global need, the lithium reserves would last 3000 years.

5.1.1.6 Renewable Energy

Before the industrial revolution, renewable energy was the only energy source used, and biomass as wood is still an important power source in underdeveloped and developing countries.

At present, biomass is the most important renewable energy with a share of about 10% of the global energy consumption, but most biomass is still traditional biomass (Table 5.1.1), and the overuse of firewood leads to deforestation and desertification. Traditional biomass should, therefore, not be regarded as "renewable" and its share will, hopefully, fall if developing countries shift to modern forms of energy.

Commercial biomasses with a share of about 4% of the global energy are biofuels like ethanol obtained from fermenting biomaterials, biodiesel from rapeseed oil and so on, and biogas, from fermenting biological waste, which is a mixture of methane and carbon dioxide in about equal amounts. The largest increases will take place in OECD Europe and North America, driven by strong governmental policies to bring about the use of biofuels in road transportation (biodiesel etc.). It is questionable whether in future commercial biomass can play a significant role on a global basis as cultivable land is limited. As discussed below in Sections 5.1.1.7 and 5.1.1.10, the share of commercial biomass of the global energy production is not expected to increase sufficiently in the next few decades that fossil fuels could be significantly substituted.

Apart from biomass, hydroelectricity is the only other renewable energy that currently makes a considerable contribution to the world energy production (Tables 5.1.1 and 5.1.2). The long-term maximum technical potential is believed to be 10-times the current hydropower production, but environmental concerns also have to be considered.

Today, solar cells convert only about 20% of the energy of sunlight into electrical energy and can be, for example, placed on top of existing urban infrastructure. In addition, solar thermal collectors can capture solar energy to supply a house with hot water. However, the share of solar energy in the world's energy consumption is up to now less than 0.1% (Table 5.1.1), but this will probably change in future. Solar electricity generating capacity has grown strongly in the last decade (with average growth of 42% per year over the past ten years) from 0.4 GW in 1998 to 13.4 GW in 2008. Nevertheless, this is still very small compared to the electricity capacity installed worldwide of around 4000 GW (2006).

At present, wind power is the most rapidly growing form of alternative electricity generation. Thousands of wind turbines with a total capacity of about 60 MW are in operation, of which Europe accounts for 70% (31% Germany, 17% Spain, 5% Denmark), the USA for 16%, and India for 8% (2005). However, the share of wind energy in terms of global consumption of less than 0.1% is still marginal (Table 5.1.1).

On a global level, geothermal energy also plays a minor role (0.4% of the world's total primary energy consumption, Table 5.1.1), but there are local variations, for example, in Iceland with 17% of total electricity production and in New Zealand (7%). Moreover, geothermal energy is also used non-electrically by heat pumps, but there are no reliable data on this usage.

Tidal power is limited to special locations. Two noteworthy tidal power stations are in operation, the *Rance power plant* built as early as 1966 in France with 240 MW installed capacity, and the *Nova Scotia power plant* in Canada, operating since 1984, with 20 MW capacity.

In the short-term, renewable sources make most sense in less developed areas of the world, where the population density cannot economically support the construction of an electrical grid or a petroleum or gas supply network. Then small-scale electrical generation from renewables may be very useful and also even cheaper.

5.1.1.7 Energy Mix of the Future

It is generally accepted that fossil energy resources are limited, although it is a matter of debate as to how much is left (Table 5.1.9). Energy demand is rising worldwide, especially in countries undergoing economic booms like India and China. The future will show whether nuclear power will be abandoned in some countries or its share will increase as, at present, only hydroelectricity and nuclear power are the only significant alternatives to fossil fuels.

In the past, there have been alarming predictions by groups such as the *Club of Rome* that the world would run out of oil in the late twentieth century. Up to now, this is not the case, but in future the world will struggle to provide (cheap) oil and so costly and less productive methods such as deep sea drilling will have to be used. As discussed by *Schollnberger* (2006), the global pattern of primary energy consumption will change profoundly during the twenty-first century. In the long term this will create a new energy mix (Figure 5.1.8, Table 5.1.12).

Global energy demand might grow from today's value of 12 billion toe to 35 billion toe in 2100, and renewables may then make up 35% of the total. The share of nuclear power is expected to be 20%. Fossil fuels will still be important but with a smaller relative share of approximately 30% in 2100. The remaining 15% may be covered by other sources (waste, fuel cells, oil shale, etc.)

Table 5.1.13 shows one out of many published scenarios of the evolution of renewables up to 2030. The share of renewables in global energy consumption will remain unchanged in the next 25 years at around 14%. The share of traditional biomass (currently 7% of the world's energy demand) will fall as developing countries shift to modern forms of energy, but this will be compensated as renewable energy will play an increasing role in the field of electricity generation, as transportation fuel, and for heating purposes in buildings and in the industry (Table 5.1.13).

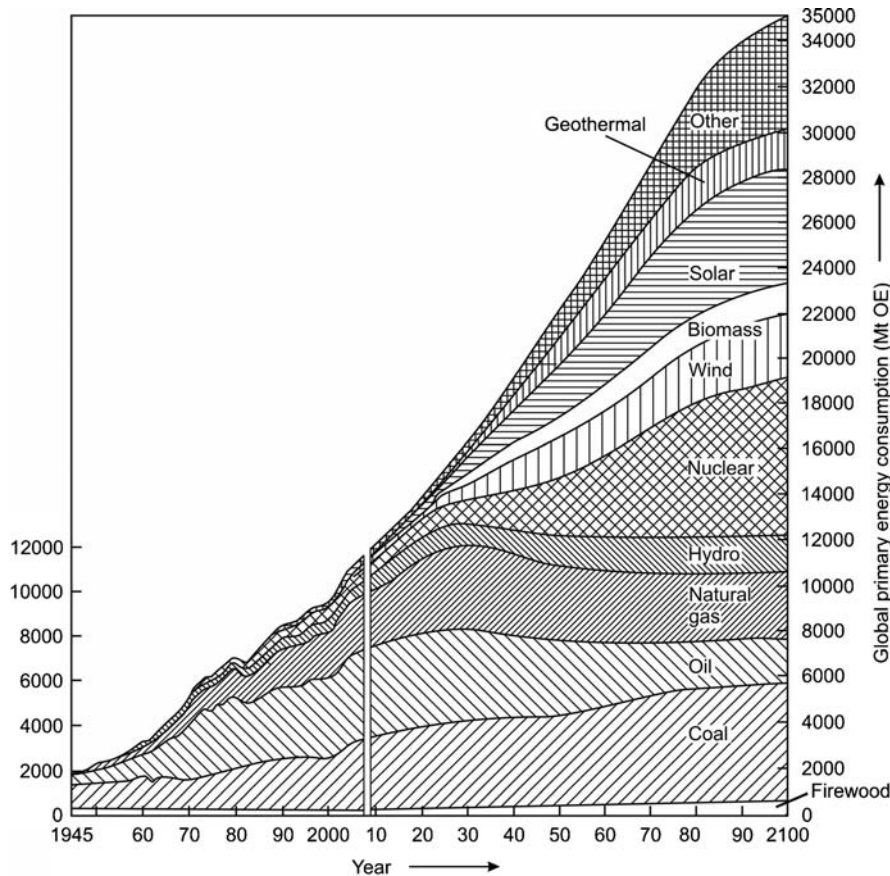


Figure 5.1.8 Global primary energy mix: history and outlook. The figure is based on weighing the component "strong economic growth" with 0.5, "security of energy supply" with 0.3, and "ecological precaution" with 0.2 throughout the twenty-first century (Tables 5.1.10 and 5.1.11); others: oil shale, H₂ fuel cells, waste incineration [data from Schollnberger (2006)].

Table 5.1.11 Regional distribution of reserves and resources of non-conventional fossil fuels 2008, without gas hydrates because the regional distribution is not known (BGR, 2009).

Fuel	Non-conventional oil (oil sand and oil shale)		Non-conventional natural gas (tight gas, coal-bed gas, aquifer gas)	
	Share of reserves (%)	Share of resources (%)	Share of reserves (%)	Share of resources (%)
Europe	0.1	1.7	2.7	5.1
Former USSR	34.3	22.7	—	15.1
Africa	0.4	1.9	—	5.3
Middle East	—	0.5	—	8.9
Asia, Australia	0.4	0.9	8.7	29.0
North America	52.5	55.5	88.6	22.5
Latin America	12.3	16.3	—	14.1
World in billion toe	52	309	5	1564

Table 5.1.12 History and outlook of global primary energy mix for the scenarios of "sustained strong economic growth" and "ecological precaution" (Schollnberger, 2006).

Year	Share of primary energy consumption (%)							
	Sustained strong economic growth				Ecologic precaution			
	Fire-wood	Fossil fuels	Nuclear	Renewables	Fire-wood	Fossil fuels	Nuclear	Renewables
1945	22	78	—	—	22	78	—	—
2006	3	83	6	8	3	83	6	8
2025	3	76	8	19	3	72	6	19
2050	2	53	12	33	2	36	7	55
2100	2	31	22	45	2	21	9	68

Table 5.1.13 Projected global increase of renewable energy until 2030 (IEA, 2006, 2007).

	2004	Share in 2004 (%)	2030	Share in 2030 (%) ^{a)}
Electricity generation (TWh)	3179^{b)}	18.2	7775	29.7
Hydropower	2810	16.4	4903	18.7
Biomass	227	1.0	983	3.8
Wind	82	0.5	1440	5.5
Solar	4	<0.1	238	0.9
Geothermal	56	0.3	185	0.7
Tide and wave	<1	<0.1	25	0.1
Biofuels (Mtoe)	15	1.0	147	4.6
Industry and Buildings (Mtoe)	272^{c)}	5.4^{c),d)}	539^{c)}	7.1^{c)}
Commercial biomass	261	5.2	450	5.9
Solar heat	7	0.1	64	0.8
Geothermal heat	4	0.1	25	0.3
Global primary energy consumption (Gtoe)	11.1	13^{e)}	16.5^{a)}	14^{e)}

a) Evaluation based on the assumption of an increase of total primary and final energy consumption in 2030 (compared to 2004) by 50%.

b) Total electricity production: 17 450 TWh.

c) Excluding traditional biomass that currently (2004) accounts for 7% of world energy demand.

d) Evaluation based on total final energy consumption excluding transport sector and non-energy use of about 5 Gtoe.

e) Including traditional biomass.

Scenarios of future energy consumption and energy mixes are needed, but we should keep in mind that they are probably uncertain, such as shown in Table 5.1.14 for global energy demand and in Table 5.1.15 for energy consumption in the USA, comparing forecasts from the 1970s for 2000 with the actual values.

To summarize: Energy generation using renewable energy is expected to become significant within the next 100 years. Competition between different fuels will be strong in the second half of the twenty-first century and will (hopefully) lead to continuous improvements in energy conversion efficiencies and in cost reductions. The anticipated energy mix for 2100 as predicted in most published scenarios (see, for example, Figure 5.1.8) could give future generations a chance to obtain the energy needed to prosper, but the level of fossil fuel consumption and thus of CO₂ emissions with the danger of an increasing global warming (see below) would then not have been reduced. Thus, the only option is to maintain (or even reduce) the current level of global energy consumption. To seize this opportunity, more excellent scientists and engineers are needed. Human ingenuity is boundless, and there is always the possibility that some previously unheard of technology may develop during this century.

Table 5.1.14 Forecast in 1977 of global primary energy consumption in 2000.

Energy source	Forecast in 1977 for 2000 ^{a)}		Real values 2000		Deviation of forecast (%) ^{b)}
	Consumption (Gtoe)	Share (%)	Consumption (Gtoe)	Share	
Coal	3.4	26	2.4	23	-30
Oil	4.5	35	3.6	35	-20
Natural gas	1.6	12	2.1	21	+30
Nuclear	1.9	12	0.7	7	-63
Renewables ^{c)}	1.9	15	1.4 ^{d)}	14	-26
Total primary energy	13	100	10.2	100	-21

a) World Energy Conference 1977.

b) Deviation of real consumption from predicted value.

c) Including non-commercial biomass.

d) 60–70% non-commercial biomass, rest hydro, commercial biomass, wind, and so on.

Table 5.1.15 Felix's forecast from 1974 of the energy consumption of the United States 2000 (Felix, 1974; Smil, 2003; BP, 2009).

Energy source	Forecast in 1974 for 2000		Real values 2000		Deviation of forecast (%) ^{a)}
	Consumption (Gtoe)	Share (%)	Consumption (Gtoe)	Share	
Coal	1.2	23	0.57	25	-48
Oil	0.9	18	0.90	39	—
Natural gas	0.5	9	0.60	26	+20
Nuclear ^{b)}	2.0	40	0.18	8	-91
Solar and geothermal ^{b)}	0.4	7	0.004	—	-99
Hydro ^{b)}	0.15	3	0.06	3	-60
Total primary energy	5.1	100	2.3	100	-55

a) Deviation of real consumption from predicted value.

b) Primary heat equivalent of the electricity produced with an average thermal efficiency of 38%.

5.1.1.8 Global Warming

Global warming caused by anthropogenic CO₂ emissions leads to the need to use alternative energy sources at a progressive rate. The major findings about global warming as for example compiled by *Rahmstorf* from the *Potsdam Institute for Climate Impact Research* in Germany are (for further details see for example Archer and Rahmstorf, 2010):

- The atmospheric CO₂ concentration has risen since about 1850 from 280 to 380 ppm (2011). This rise is entirely caused by humans and is primarily due to the burning of fossil fuels, with a smaller contribution due to deforestation.
- CO₂ is a gas that affects climate by changing the Earth's radiation budget. Since 1900, the global climate has warmed by 0.8 °C. Temperatures in the past ten years have been the highest since measured records started in the nineteenth century (Figure 5.1.9a).
- A further increase in CO₂ concentration will lead to a further rise in global mean temperature (Figure 5.1.9b). Compared to 1990, this rise will be in the range 1.4–5.8 °C.
- Risks are a rise in sea level, loss of ice sheets, and loss of ecosystems and species.

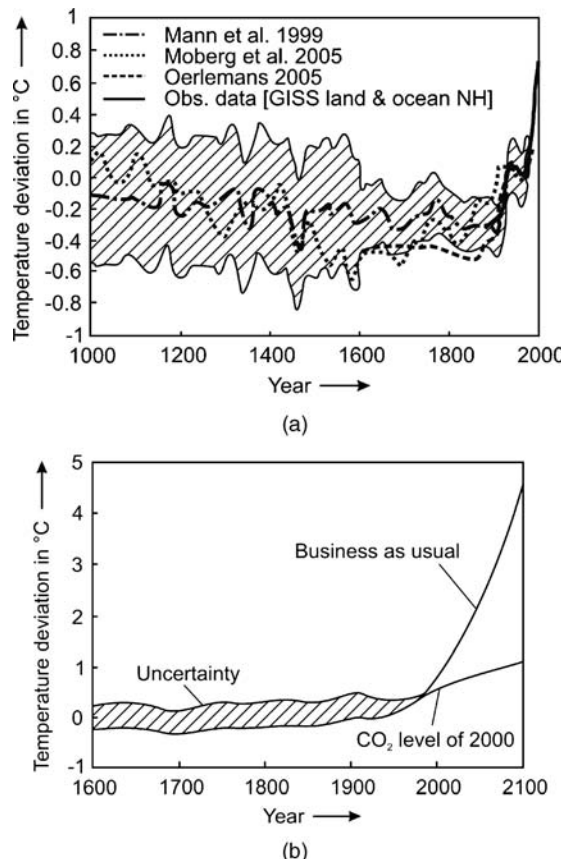
Figure 5.1.10 shows strategies and expenses (costs, efforts for research and development, and political efforts) involved in reducing CO₂ emissions. Without any structural change, the CO₂ emissions will rise by a factor of about two ("business as usual"). According to Matthes (2007, personal communication) from the Institute for Applied Ecology in Berlin, in the first place an increase in efficiency could decrease CO₂ emissions by 40%. Second, alternative energy sources (solar, wind, etc.) could be a further help, followed by nuclear power and CO₂ sequestration.

Although CO₂ is the main contributor to anthropogenic global warming (about 60%), CH₄ (20%), chlorofluorocarbons (14%), and N₂O (6%) also have to be considered. Note that CH₄ and N₂O have, respectively, about 20- and 300-times more impact per unit weight than CO₂. About 100 million tonnes of CH₄ are emitted per year from domesticated animals, which is about 25% of all CH₄ emissions. Thus cows, pigs, and sheep are one of the top greenhouse gas producers, contributing to man-made global warming by about 5%, which is of the order of magnitude of the contribution of all transportation fuels (10% of overall anthropogenic global warming).

5.1.1.9 Ecological Footprint and Energy Consumption

The *ecological footprint* is a measure of human demand on the Earth's ecosystems. It compares the demand with planet Earth's ecological capacity to regenerate, and represents the amount of biologically productive land and sea area needed to

Figure 5.1.9 (a) Temperature deviation in the northern hemisphere (NH) during the past millennium. The classic reconstruction of Mann, Bradley, and Hughes (1999) (with its uncertainty band) is shown as well as two new reconstructions including sediment data (Moberg *et al.*, 2005) and using glacier extensions (Oerlemans, 2005). Land and ocean observations in the northern hemisphere of the Goddard Institute for Space Studies (GISS) up to 2005 are also shown. (b) Projections of the Intergovernmental Panel on Climate Change for the global mean temperature in the twenty-first century (IPCC, 2007). Upper curve: worst case scenario ("business as usual"), lower curve: constant CO₂ content of 2000, reflecting the already generated but still not measurable increase of temperature.



regenerate the resources the human population consumes. Using this assessment, it is possible to estimate how much of the Earth (or how many planet Earths) it would take to support humanity if everybody in the world were to live a given lifestyle in a certain country. There are differences in the methodology used by various studies, for example, how sea area should be counted or how to account for fossil fuels and nuclear power. According to the *Global Footprint Network*, the ecological

Figure 5.1.10 Strategies and expenses to reduce CO₂ emissions. Adapted from Matthes (2007, personal communication, www.oeco.de); value of actual global CO₂ emission from 2009.

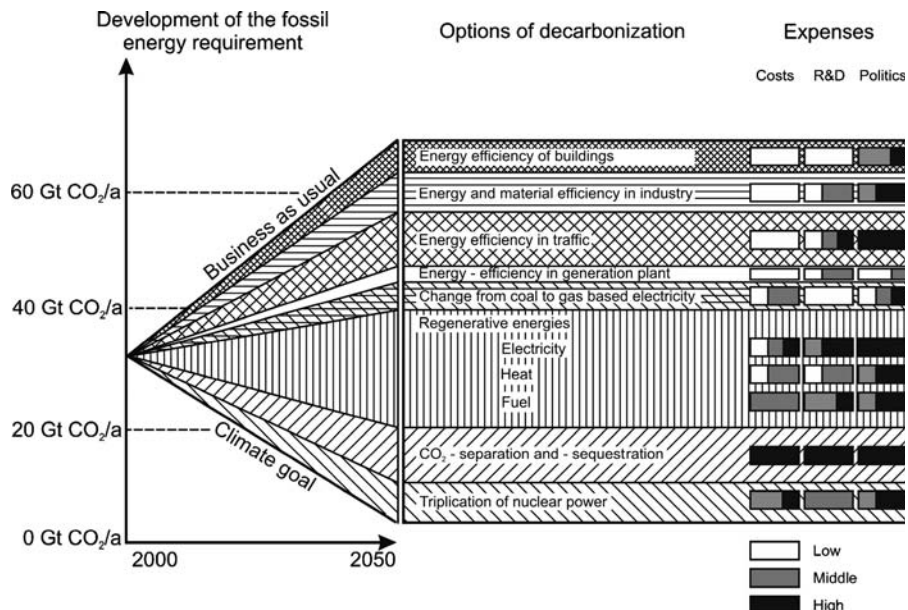


Table 5.1.16 Population, total ecological footprint, and footprint per person in 2005 in different regions (footprint data Global footprint network, 2009).

Region	Population (million)	Total ecological footprint (billion gha)	Ecological footprint per head in planet Earths
Africa	902	0.60	0.7
Middle East and Central Asia	366	0.84	1.1
Asia-Pacific	3562	5.70	0.8
Europe (EU)	487	2.29	2.2
Europe (non-EU)	240	0.84	1.7
Latin America and the Caribbean	553	1.33	1.1
North America	331	3.04	4.4
World	6476	17.5	1.3

footprint is defined as the sum of the area of all cropland, grazing land, forest, build-up land, and fishing grounds required to produce food, fiber, timber, and so on, and the carbon (CO_2) footprint that represents the biocapacity needed to absorb CO_2 emissions. In 2005, the total global footprint was 17.5 billion global hectares (gha) or 2.7 gha per head (a global hectare is a hectare with world-average ability to produce resources and absorb wastes). On the supply side, the total productive area was 2.1 gha per head. Thus, humanity's total ecological footprint equals 1.3 planet Earths. In other words, humanity uses ecological services 1.3 times as fast as Earth can renew them (Global footprint network, 2009). This value has grown over time from 0.55 planet Earths in 1960, 1 planet Earth in 1985, and 1.2 planet Earths in 2000. Without counteractions, a value of three planet Earths will be reached in 2050.

In 2005, the single largest demand humanity put on the biosphere was its carbon footprint (52%), followed by cropland (24%), grazing land (10%), forest (9%), fishing grounds (3%), and build-up land (2%). Tables 5.1.16 and 5.1.17 show some data for the population and ecological footprint in different regions and selected countries.

The USA and China had the largest total footprints, each using 21% of the planet's biocapacity, but China had a much smaller per capita footprint. India's total footprint was the next largest, although the per-person footprint is only 0.5 planet

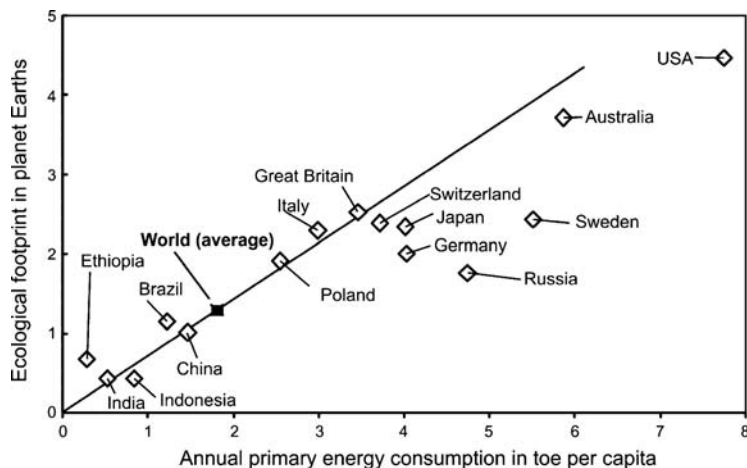
Table 5.1.17 Population, total ecological footprint (absolute and relative to own biocapacity), and footprint per head in selected countries (Global footprint network, 2009).

Country	Population (million) (2005)	Total ecological footprint (billion gha) (2005)	Ecological footprint (2005)	
			Per head in planet Earths ^{a)}	Total footprint relative to own total biocapacity
USA	298	2.80	4.5	1.9
Australia	20	0.16	3.3	0.5
Japan	128	0.63	2.3	8.1
Germany	83	0.35	2.0	2.2
Russia	143	0.53	1.8	0.5
Mexico	107	0.36	1.6	2.0
Brazil	186	0.45	1.1	0.3
China	1323	2.78	1.0	2.5
Nigeria	132	0.17	0.6	1.4
India	1103	0.99	0.4	2.2
Congo ^{b)}	58	0.03	0.3	0.2

a) Number of planet Earths, if everybody lived the lifestyle of named country.

b) Democratic Republic of Congo.

Figure 5.1.11 Ecological footprint (per capita) and primary energy consumption per capita in selected countries [footprint data from Global footprint network (2009)] (Jess, 2010).



Earths. As shown in Figure 5.1.11, the ecological footprint is strongly linked to the primary energy consumption per head.

As a rule of thumb, an increase in energy demand of 1.5 toe pc increases the ecological footprint by one planet Earth (Figure 5.1.11). In other words (as we only have one Earth), the maximum average annual primary energy consumption should only be 1.5 toe pc compared to today's value (2007) of 1.8 toe (pc). Thus we have to reduce the global energy consumption by about 15% to keep our planet "happy" (at current technologies and fuel shares). In future even this will be insufficient: If the world population grows to 9 billion in 2050 compared to today's population of 6.8 billion (2009), we would have to limit our annual energy consumption to around 1.1 toe (pc) at today's energy mix with a share of fossil fuels of more than 80%. This, however, is in contradiction with the moral philosophy and obligation to bring welfare and happiness to the greatest number of people: We need about 2 toe per head to reach the level of welfare and happiness that we have at the moment mostly realized only in high-income countries (Figures 5.1.4 and 5.1.7).

5.1.1.10 Energy Demand and Energy Mix to Reconcile the World's Pursuit of Welfare and Happiness with the Necessity to Preserve the Integrity of the Biosphere

Thus, the question inevitably arises as how to cut the Gordian knot of the conflict between a *happy planet* (stable ecosystems) and a *happy world population* (stable societies). For an answer, some (here optimistically chosen) assumptions and some estimations are needed:

- Most forecasts predict that the world population will continue to grow until 2050 and then peak at a population of 9 billion.
- High-income countries with currently more than 2 toe pc should reduce their energy consumption to this value, which could be possible without considerable loss of welfare, whereas currently low-income countries develop and increase their consumption until 2 toe pc is reached (scenario of a *happy world population*).
- Compared to today (1.8 toe pc, 6.8 billion people), this scenario (2 toe pc, 9 billion people) leads to an annual consumption of 18 billion toe compared to today's value of 12 billion toe. Thus, with current technologies and fuel shares the ecological footprint would increase to about 2 planet Earths ($18/12 \times 1.3$ planet Earths in 2005). This would be a disaster!
- The only way to implement an average energy consumption of 2 toe per head ("*happy population*") without increasing the ecological footprint ("*happy planet*") is to reduce the single largest demand humanity has put on the biosphere, which is the carbon (CO_2) footprint (with a share of currently 52% on the total ecological footprint). Only in the case of a complete shift from

Table 5.1.18 Today's and future global primary energy consumption [data from IEA, 43,42; forecast from Schollnberger (2006), see also Jess (2010)].

Energy type	World primary energy consumption (billion tonnes of oil equivalent)		
	Today (2007)	Forecast for 2100	Happy planet (stable ecosystems) and happy world population (stable societies)
Crude oil	4.0	2.1	
Coal	3.2	4.8	
Natural gas	2.5	2.8	
Traditional biomass (firewood)	0.8	0.7	—
Total fuels with CO ₂ footprint	10.6	10.4	1.5
Nuclear	0.7	7.0	
Hydro	0.3	1.4	
Commercial biomass	0.4	1.1	
Geothermal		1.8	
Wind	0.1	2.8	
Solar		5.6	
Waste, fuel cells, oil shale		4.9 ^{b)}	
Total fuels with no or negligible CO ₂ footprint	1.5	24.6	16.5
World energy consumption	12	35	18

a) 8% of the crude oil is used for petrochemicals (Moulijn, Makkee, and Van Diepen, 2004), which equals currently about 0.3 billion tonnes; 0.6 billion tonnes of coal are currently used for blast furnace coke (steel production). 0.1 Billion tonnes of ethane (separated from natural gas) are used for ethylene, and about 0.1 billion tonnes of fossil fuels are needed for ammonia production. Thus (if we only count these major chemical products), with a rising world population (from 6.8 to 9 billion people), about 1.5 billion tonnes of fossil fuels are needed for the chemical and metallurgical industry. At least, (organic) chemicals like polymers can in principle also be produced from renewables (e.g., via biomass gasification and subsequent Fischer-Tropsch synthesis to higher hydrocarbons, but this is not considered here).

b) Incineration, hydrogen, fuel cells, oil shale.

fossil fuels to renewables (except for the small amount probably still needed for chemicals and coke/steel production, see Table 5.1.17) would we halve the ecological footprint; and that is exactly what is needed to reach the desired footprint of 1 planet Earth.

Table 5.1.18 summarizes what has to be done in this century with regard to energy demand to reach a happy planet (stable ecosystems) and a happy population (stable societies).

Comparison of current forecasts of energy consumption and energy mix in 2100 (Schollnberger, 2006), with the goal of reconciling the world's unceasing demand for energy with the absolute necessity to preserve the integrity of the biosphere (Table 5.1.18), indicates that it will be a Herculean task to reach this goal, and that more, and excellent, scientists and engineers are needed. Although human ingenuity is boundless, and there is the possibility that some previously unheard of technology may develop during forthcoming decades, many steps are needed to change today's world energy mix and demand. Politicians should more than ever ensure framework requirements for an effective educational system and excellent conditions for (energy) research.

At present, there are few signs that politicians and societies are changing as required, but the pressure to do so will increase heavily in the decades ahead.

What are the alternatives ways we have to reach the goal of 2 toe per capita and year based on renewables? Table 5.1.19 shows estimations of the technical feasible potential of renewable energy in toe per capita and year for a world population of 9 billion based on the data given by MacKay (2008).

There is one clear conclusion: Non-solar renewables may be huge, but they are by far not huge enough. Even the technically feasible potential of wind, hydro, tide, wave, and geothermal energy would only cover 0.8 toe per capita and year compared to the goal of 2 toe. The contribution of biomass will be also very limited (probably <10%) as the land area available for energy generation from biomass in future will by far not be high enough (Table 5.1.20, Figure 5.1.12a and b).

Table 5.1.19 Estimation of the technically feasible potential of renewable energy in toe per capita and year (data from MacKay, 2008) and an energy plan for a “happy” world population of 9 billion.

Energy source	Energy potential and consumption (goal) (toe per capita)	
	Potential ^{a)} (estimation based on data from MacKay)	Scenario for a happy planet <i>and</i> a happy world population (2 toe per capita and year)
Wind	0.5	0.2 ^{b)}
Hydro	0.13	0.07 ^{c)}
Tide and wave	0.02	0.01
Geothermal	0.17	0.08
<i>Total non-solar renewable energy</i>	0.8	0.36
Solar for energy crops (biomass)	0.2 ^{d)}	0.1
Concentrated solar power ^{e)}	6	1.54
Nuclear (once-through reactor) ^{f)}	0.16	—
Nuclear (fast breeder) ^{f)}	9.5	—

a) The direct equivalence method was used as in an alternative world with relatively plentiful electricity and little oil, gas, and coal, we no longer use fossil fuels to produce electricity, and we might even use electricity to produce chemicals. The timeless and scientific way to summarize and compare energy is then a one to one conversion rate, that is, 1 kJ of electricity is 1 kJ of chemical energy (MacKay, 2008).

b) Although the technically feasible potential of wind energy is higher, the production of electrical power equivalent to 0.2 toe pc and year (2 TW) would already require the operation of 2 million state-of-the-art wind turbines.

c) This value is considered to be economically feasible hydropower and is reached if the currently installed capacity is increased by a factor of about 2.5 (MacKay, 2008).

d) Even the theoretical potential of energy crops, if all currently arable or crop land (27 million km²) would be used, is only about 0.8 toe per capita and year (world population of 9 billion, 33% losses in processing and farming, MacKay, 2008). This number of course cannot be far be reached, as we need agricultural land for food production. According to Heinloth (2003), the technically feasible potential of commercial biomass for heat (20%), fuels (25%), and electricity (55%) is in total about 0.2 toe per capita and year.

e) According to the DESERTEC plan, the use of concentrated solar power in sunny Mediterranean countries and high-voltage direct-current transmission lines could deliver power to Northern Europe. The economic potential adds up to 50 billion toe electricity (= 6 toe pc and year for a global population of 9 billion). It is also assumed that mirrors will remain cheaper than photovoltaic panels (MacKay, 2008), that is, photovoltaic was neglected.

f) Assumption that not only mined uranium can be used but also the uranium extracted from oceans, which is 98% of the total (MacKay, 2008). Comments on risks of nuclear energy and breeder technology are not given here.

With regard to the potential contribution of biomass/biofuels, the following statements of Burkhardt (2007) are instructive:

“Energy farming is an enemy of biodiversity. Any land taken away from wilderness destroys habitat and contributes to the mass extinction of species. The problems of large scale global use of biomass can be visualized by comparing it with food energy. A person needs some 2000 kcal per day (0.07 toe per year). Feeding the present world energy system with biomass power (1.82 toe pc and a in 2009) is equivalent to feeding an additional 27 ‘energy slaves’ for each person; it is quite obvious that a healthy World ecosystem cannot spare sufficient biomass production capacity to feed the equivalent of 180 billion human beings. Governments worldwide should place highest priority on research, development, and large scale implementation of technical solar energy conversion.”

To complete an energy plan that adds up, we must rely on one or more forms of solar power, or use nuclear power or both. One scenario (out of many one may think of) of a sustainable non-nuclear energy plan is given in Table 5.1.19 (right-hand column). It was thereby assumed that 50% of the technically feasible potential of solar power from energy crops and of wind, hydro, tide, wave, and geothermal power will be used, which reflects the economically visible potential (footnotes Table 5.1.19). Thus, 75% of the energy demand is covered by concentrated solar power.

In principle, it should also be possible not only to produce electricity from solar energy. In addition, “solar” methanol and other “solar” fuels like gasoline and diesel fuels can be produced with no or much less net CO₂ production compared to fossil

Table 5.1.20 Per capita balances for land area and maximum contribution of biomass to energy supply for the scenario “happy planet and happy world population,” that is, 2 toe pc and a population of 9 billion, see Table 5.1.19 [data of land areas partly from Pfennig (2007)].

	2009 (world population of 6.8 billion people)	2050 (9 billion, scenario of “happy planet and a happy world”)
	Land area per capita (m^2)	
Total land area (149 million km^2)	21 900	16 600
Desert, permafrost (30%)	-6600	-5000
Preserving nature (11%) ^{a)}	-2400	-1810
Living, traffic, production	-750	-750
Biomass as raw material	-400	-400
Managed forests (round-wood, fuel wood) ^{b)}	-2260 ^{b)}	—
Round-wood plantations ^{b),c)}	-180 ^{b)}	-440 ^{c)}
Food	-7600	-7600 (5100) ^{d)}
Remaining area for biofuels production	1710	600 (4400) ^{d)}
Maximum energy generation from biomass (contribution to global energy) ^{e)}	0.34 toe pc and year (19% of 1.82 toe pc)	0.12 (0.5 ^{d)} toe pc and year (6% (25% ^{d)} of 2 toe pc)

a) 30% of the total land area is covered by forests (2010, 40 million km^2), and 34% of the forest area (10% of total land area) is used for the production of roundwood and wood-fuel in about equal portions (FAO, 2007). According to Pfennig (2007), a minimum of 7% of the total land area should be reserved for untouched nature like primeval forests, which corresponds to today's rainforest area. According to the World Resources Institute (2010), 17 million km^2 of the forest area (11% of global land area) are unavailable for biomass production (protected, inaccessible). This value was used here to estimate the potential of biomass for energy generation.

b) Today, 34% of the forest area (14 million km^2) is used for the production of roundwood (1.6 billion m^3) and fuel-wood (1.8 billion m^3) (FAO, 2007). Plantations (1.2 million m^2), which have a higher productivity than managed forests, deliver only 22% of the world's roundwood supply (World Resources Institute, 2010).

c) If the probably severe problem of biodiversity is neglected, the world's current demand for roundwood (1.6 billion m^3 in 2007) could be met from plantations. Then an area of “just” 4.4 million km^2 would be needed. Another estimate is that only 1.5 million km^2 are needed, if a higher annual growth rate of 1000 m^3 roundwood per km^2 can be reached (World Resources Institute, 2010). Here we have assumed 3 million km^2 .

d) The area per capita (pc) needed for food production may be different in future mainly because of two factors, (i) the area specific yield of food and (ii) nutritional habits. For (i), during the last 40 years (1965–2005), the available agricultural area has decreased from 12 600 to 7600 m^2 per head, which is mainly the result of the increase in the world population from 3.3 to 6.5 billion. Nevertheless, the average consumption of food pc has increased from 2400 to 2800 kcal day $^{-1}$. This is the result of agricultural intensification (“green revolution”), which has led to an increase in the productivity of food production from 0.2 (1965) to about 0.4 kcal per m^2 and day (2005). In terms of (ii) nutritional habits are different. In India 92% of the caloric food consumption is covered by vegetal products, 7% by milk, butter, and eggs, and only 1% by fish and meat. In the United States, the shares are very different, 74% vegetal products, 13% milk, butter, and eggs, and 13% meat and fish. For purely plant-based nutrition only 3000 m^2 pc are needed compared to today's average of 7600 m^2 pc (Pfennig, 2007). To account for these two positive aspects, which would lower the area needed for food production, the values given in brackets are based on the assumption that 50% less area is needed per head until 2050.

e) Assuming that all of the remaining land area would be used for energy production from biomass. Efficiency of about 0.0002 toe (m^2 a) $^{-1}$ as reported by Pfennig (2007) and McCay (2008) for the overall global average.

fuels by the following steps (Behr, Vorholt, and Johnen, 2009; Centi and Perathoner, 2009; Saito *et al.*, 2000; Wolf and Scheer, 2005):

- 1) separation of CO₂ from flue gases (or even from the atmosphere),
- 2) hydrogen production by water electrolysis and non-fossil electricity ($H_2O \rightarrow H_2 + \frac{1}{2}O_2$),
- 3) CO production by reverse water gas shift (CO₂ + H₂ → CO + H₂O),
- 4) Fischer-Tropsch or methanol synthesis, CO + 3H₂ → -(CH₂)- + H₂O or CO + 2H₂ → CH₃OH.

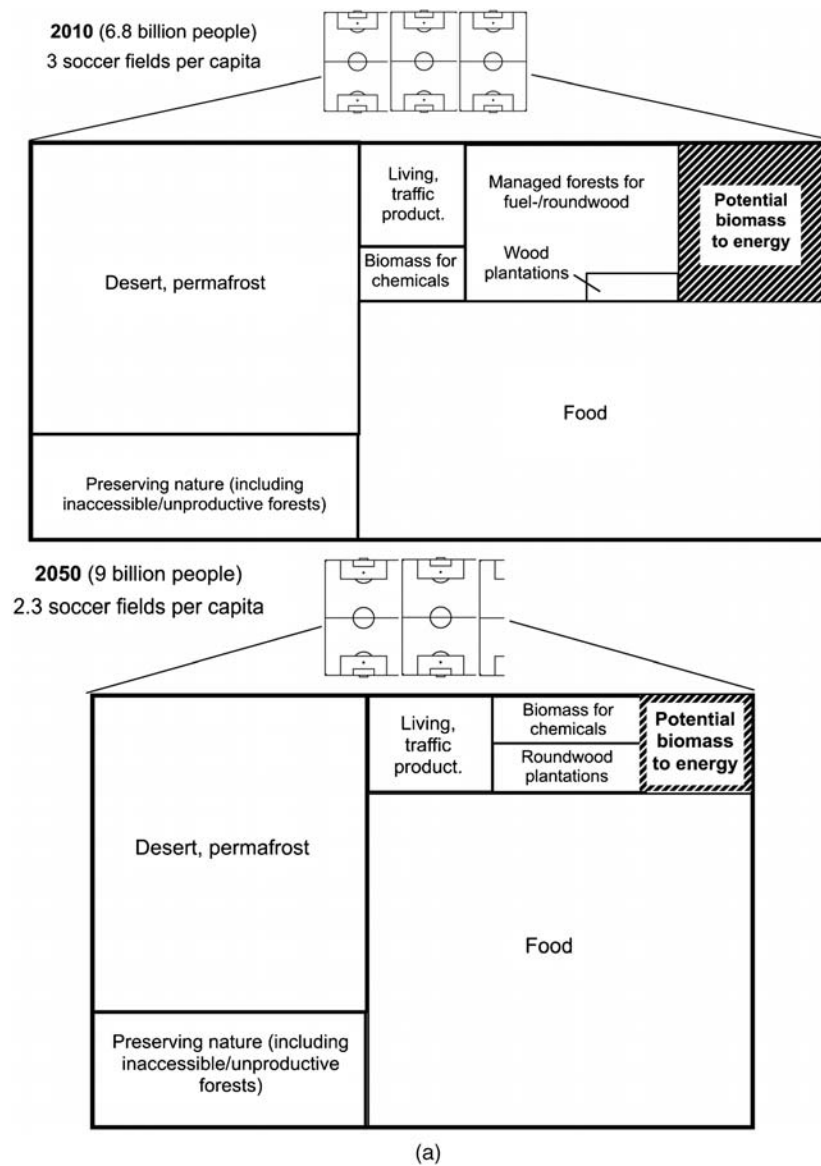
5.1.2

Composition of Fossil Fuels and Routes for the Production of Synthetic Fuels

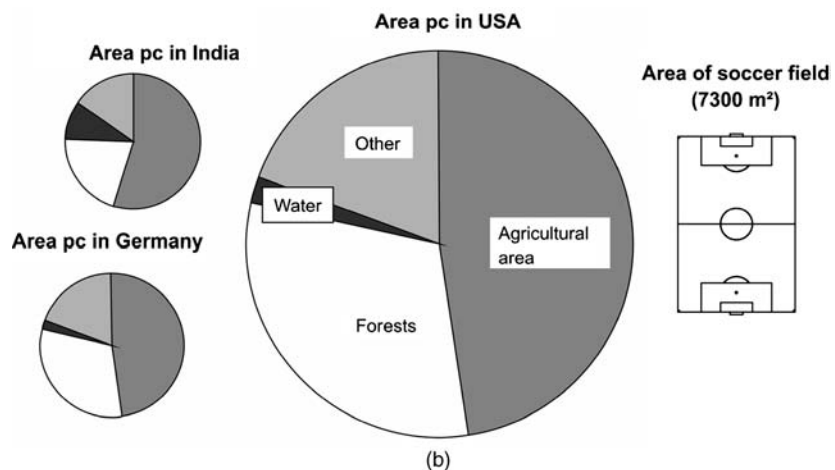
Figure 5.1.13 schematically shows the carbon, hydrogen, and oxygen content of fuels in a triangular diagram to illustrate routes for the production of synthetic fuels:

- *Route A* represents the direct conversion of coal into synthetic crude oil by hydrogenation, that is, mainly by hydrogen addition (Bergius–Pier process).

Figure 5.1.12 (a) Global average per capita balances for land area and maximum global contribution of biomass to energy supply for today and 2050 (soccer field: 7300 m^2 ; for details see Table 5.1.20). (b) Per capita land and inland water area in India, USA, and Germany.



(a)



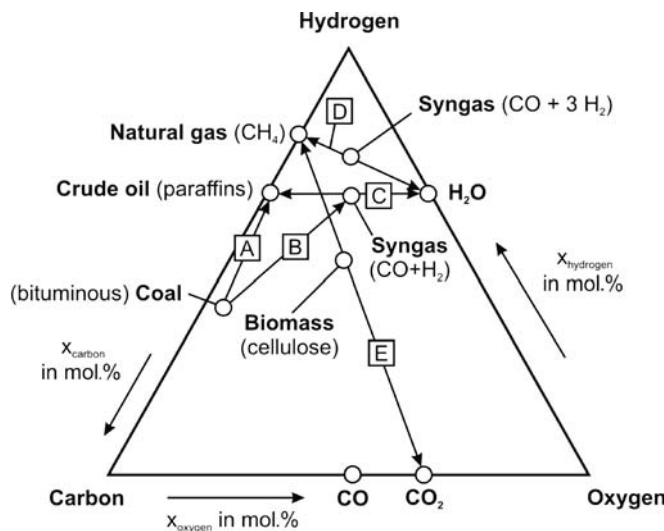


Figure 5.1.13 Triangular diagram of (molar) CHO content of fossil fuels and biomass and routes to produce synthetic fuels (A: direct coal liquefaction, B: coal to syngas, C: liquid fuels (paraffins) from syngas, D: synthetic natural gas from syngas, and E: biogas from biomass).

- *Route B* reveals the route from coal to syngas (mixture of CO and H₂), that is, oxygen and hydrogen are “added” by coal gasification with an appropriate mixture of O₂ and steam.
- *Route C* shows the route from syngas to liquid fuels (paraffins) with water as a byproduct. This synthesis is called Fischer–Tropsch synthesis.
- *Route D* represents syngas conversion into synthetic natural gas (again with water as a by-product), and vice versa syngas production by conversion of natural gas with steam.
- *Route E* displays the conversion of biomass into biogas ($\approx 50\%$ CH₄ and 50% CO₂).

All these routes represent technically important processes that will be discussed briefly in Sections 5.1.3–5.1.5 and partly in more detail in Chapter 6.2.

5.1.3

Natural Gas and Other Technical Gases

5.1.3.1 Properties of Natural Gas and Other Technical Gases

The use of natural gas was mentioned in China about 3000 years ago. In Europe, natural gas was discovered in England in 1659. However, since coal gas was already commercially available, natural gas remained unpopular. In 1815, natural gas was discovered in the United States, and commercially used in 1824 in the state of New York for illumination. At the end of the nineteenth century, larger industrial cities in the USA began to use natural gas, and the first pipelines were constructed to conduct gas to these areas. However, it was not until the early 1970s that the shortage of crude oil forced major industrial nations to seek alternatives. Since then, natural gas has become a central fossil fuel energy source. Today, the world natural gas production is 2.8 billion tonnes oil equivalent (21% of the global energy consumption, Table 5.1.1). The most important producers are the former Soviet Union and North America (Table 5.1.21).

Natural gas primarily consists of methane and is found in natural gas fields and as a by-product in oil fields and coal beds. It also contains hydrocarbons such as ethane, propane, and butane as well as sulfur components such as hydrogen sulfide, which must be removed.

Table 5.1.21 Regional distribution of worldwide production of natural gas 2008 (BP, 2009).

Region	Gas production (Mtoe)	2008 share of total (%)
North America (USA, Canada, Mexico)	740	26.7
Former Soviet Union ^{a)}	714	25.8
Total Asia Pacific	370	13.4
Middle East	343	12.4
Europe	264	9.6
Africa	193	7.0
Central and South America	143	5.2
World	2768	100

a) Azerbaijan, Kazakhstan, Russian Federation, Turkmenistan, Ukraine, and Uzbekistan.

The role of other important technical gases used as fuels or intermediates for the production of chemicals can be summarized as follows:

- Coke-oven gas is produced as a by-product of coke-making, and is mainly used for non-domestic purposes as an industrial fuel, for example, in the steel industry.
- The off-gas of a blast furnace with a relatively low heating value (about 60% nitrogen) is mainly used directly as fuel in the steel industry.
- Methane-rich gases are produced by the anaerobic decay of non-fossil organic matter (green waste, manure, sewage, plant material, municipal waste, etc.) and are – depending on their origin – referred to as biogas or landfill gas.
- Synthesis gas is produced from natural gas as well as from heavy oil and coal, and is used to produce liquid fuels and various chemicals (Section 6.2).

Table 5.1.22 gives the composition of these gases as well as of typical natural gases.

Table 5.1.23 lists the safety parameters of natural gas (methane) and other pure combustible gases. The most important parameters are the limits of flammability (upper and lower explosion limits). If gas concentrations reach explosive mixtures and are ignited this may result in powerful blasts. Interestingly, the lower limit, which is in most practical cases the value reached first (e.g., by a leakage), is identical in air and in pure oxygen. This is because at the lower limit we have a surplus of gaseous fuel, so the heat release is the same. Thus, the mixture is heated up to the same (ignition) temperature, as the molar heat capacities (Section 3.1.2) of nitrogen and oxygen are coincidentally the same, which leads to identical lower flammability limits.

Table 5.1.22 Composition of natural gases and other technically important gases (vol.%).

	H ₂	CO	CH ₄	C _m H _n	CO ₂	N ₂	H ₂ S
Natural gas (Groningen, The Netherlands)	—	—	81	4	1	14	—
Natural gas (Lacq, France)	—	—	69	6	10	—	15
Natural gas (Ekofisk, North Sea)	—	—	86	12	1	1	—
Coke oven gas (after treatment)	55	6	25	3	2	8	—
Blast furnace gas	2	31	—	—	9	58	—
Biogas, landfill gas	—	—	45–70	—	55–30	0.1–5	0–1
Synthesis gas (dry) produced from:							
(a1) Coal (fixed bed) ^{a)}	39	20	10	1	30	—	—
(a2) Coal (fluidized bed) ^{a)}	35	49	2	—	14	—	—
(a3) Coal (entrained bed) ^{a)}	36	57	—	—	7	—	—
(b) Heavy oil ^{a)}	45	49	—	—	5	1	—
(c) Natural gas (steam reforming)	68	10	8	—	10	4	—

a) Depending on the N- and S-content of the feedstock, a considerable amount of NH₃ and H₂S is present in the raw syngas, which is not counted here.

Table 5.1.23 Flame velocity, limits of flammability, and ignition temperature (Guenther, 1984).

Gas	Flame velocity (cm s ⁻¹)		Limits of flammability (vol.%)		Ignition temperature (°C) (air, 1 bar)
	Max.	Stoichiometric	in air	in O ₂	
CO	19.5	17.4	12.5–74	12.5–94	605
H ₂	346	237	4–75	4–95	560
CH ₄	43.0	42.0	5–15	5–60	540
C ₂ H ₆	48.7	47.6	2.9–12.5	—	515
C ₃ H ₈	47.2	46.0	2.1–9.5	2.3–45	450
C ₄ H ₁₀	45.2	43.4	1.5–8.5	—	365

5.1.3.2 Conditioning of Natural Gas, Processes and Products Based on Natural Gas

Figure 5.1.14 gives an overview of the processes employed for the use and conversion of natural gas. Before the crude natural gas can be used for transport in pipelines – and thus for heating, electricity production, or as a raw material for chemicals – it has to be treated (Figure 5.1.15):

- The content of water vapor has to be reduced so that the dew point of the gas is lower than the temperature during transport in pipelines. If not, solid methane hydrates are formed with condensing water, which would lead to a blockage of the pipeline. The simplest method of drying is cooling and subsequent separation of the liquid water. This can be obtained by pre-cooling in air and water coolers and subsequent expansion of the gas, which leads to a decrease of temperature by the Joule–Thomson effect (Section 3.1.2). This method is only possible if the pressure of the deposit is higher than the pressure needed for gas transport via pipelines (about 100 bar). If not, gas scrubbing with glycols or – if very low dew points are needed – adsorption processes are used.
- Natural gases containing appreciable quantities of H₂S or other sulfur compounds are called “sour” gases. Those with less sulfur are called “sweet.” With respect to corrosion of pipelines, toxicity of H₂S, environmental concerns (formation of SO₂ during gas combustion), and deactivation of catalysts in case of subsequent conversion into syngas (see below), H₂S is removed down to levels

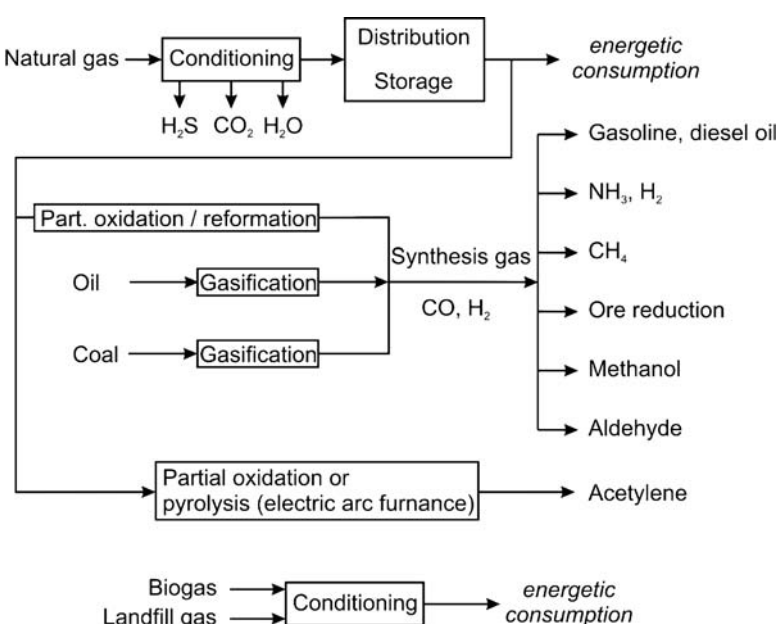


Figure 5.1.14 Overview of processes based on natural gas (and biogas and landfill gas).

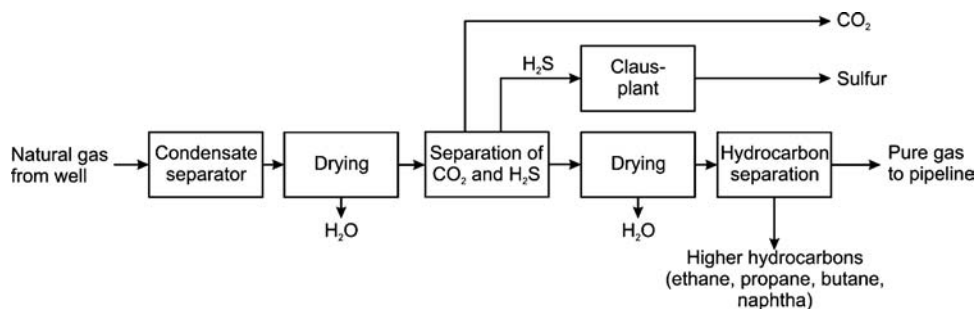


Figure 5.1.15 Processes of natural gas conditioning. Adapted from Keim, Behr, and Schmidt, (1986).

of a few ppm by absorption or adsorption. CO₂ may also be removed by this means so as to increase the caloric value. Processed natural gas is tasteless and odorless; however, before the gas is distributed to end-users it is odorized for safety reasons (leak detection) by adding small amounts of sulfur compounds such as tetrahydrothiophene.

Transportation of natural gas is sometimes difficult if consumers are far from gas fields. Overland pipelines are economical but are mostly impractical across oceans. Sometimes pipeline transport is also problematic for political reasons, for example, from the Middle East to Europe. Transportation of remote natural gas is then only possible as liquefied natural gas (LNG) or compressed natural gas (CNG), or, alternatively, the gas is converted into valuable (and easy to transport) liquid products such as methanol or diesel oil.

Moreover, gas associated with crude oil can mostly not be sold profitably and was in the past and is still today flared at the oil field. This practice is now illegal in many countries with regard to the greenhouse effect and waste of energy and, if transport is not viable, associated gas is now also re-injected into the formation for later recovery.

The domestic demand for gas varies and there are periods of high and low consumption (day and night, winter and summer). Consequently, gas is stored during periods of low demand and extracted during periods of higher demand. Large amounts of gas are stored in underground caverns formed inside depleted gas reservoirs from previous gas wells or synthetically formed in salt domes. Small amounts are also stored in tanks as LNG.

Natural gas is mainly used for heating and electricity:

- Some 40% of the world's natural gas production is used by industry for heating and to a small extent for the production of syngas as the basis for chemicals like ammonia or methanol or for synthetic fuels like diesel oil (DOE, 2005). Compressed natural gas is used as an alternative to other automobile fuels. In 2003, the countries with the largest number of natural gas vehicles were Argentina, Brazil, Pakistan, Italy, and India.
- Some 30% is used in power plants with a share of 16% of the total world's electricity production. Particularly high efficiencies can be achieved through combining gas turbines with steam turbines in combined cycle mode. Fuel cell technology may also be an option for converting natural gas into electricity, but as yet it is not price competitive.
- The rest, about 30%, is supplied to homes and is used for purposes such as cooking and heating.

Natural gas is also an important raw material for chemicals (Figure 5.1.14):

- Approximately 50% of the world's syngas production is based on natural gas. (The other 50% is based on coal, heavy oil, and biomass.) The numbers given in the literature differ, so this is only a rough estimation based on figures given for

Table 5.1.24 Production and application of hydrogen in 2009 [based on data given by Dueker (2010), Gerke *et al.* (2010), and own estimations for Fischer–Tropsch synthesis and coke-oven gas].

Use of hydrogen	H ₂ -consumption (million tonnes per a)	Section containing details
Ammonia production	25	6.1
Refineries ^{a)}	11	5.1.4, 6.2, 6.8, and 6.9
Methanol	7	6.11.2
Coke-oven gas ^{b)}	12	6.5.2
Reduction (mainly of ore)	3	—
Fischer–Tropsch synthesis	3	6.11.1
Acetic acid	0.5	6.15
Oxo alcohols	0.5	6.14
Fiber industry	0.5	—
Others	2	—
Total	About 65	

a) Refineries have established a H₂ network. The major consumers are hydrodesulfurization and hydrocracking. Main sources of H₂ are catalytic reforming of gasoline (with H₂ as important by-product) and H₂ production via steam reforming of natural gas or partial oxidation of heavy oil.

b) Estimation based on the following data: 440 Nm³ of (dry) coke oven gas (with 60 vol.% H₂) are released per tonne of blast furnace coke. In 2009, 520 million tonnes of coke were produced worldwide.

the production of hydrogen. According to DOE (2005) and Dueker (2010), about 50 Mio. tonnes of hydrogen are produced annually, with 48% based on natural gas, 30% based on oil, 18% based on coal (including hydrogen in coke-oven gas), and 4% based on electrolysis (mainly as by-product of chlor-alkali electrolysis, see Section 6.19). Table 5.1.24 gives numbers for the production and application of hydrogen in 2009. Syngas based on natural gas is mainly produced by catalytic conversion with steam (steam reforming, see Section 6.2.4), and to a minor extent by partial oxidation. Syngas is the basis for important chemicals like ammonia, aldehydes, and methanol (Section 6.11.2), for hydrogen and reduction gas, but in future also increasingly for the production of synthetic fuels like diesel oil by *Fischer–Tropsch* synthesis (Section 6.11.1).

- The only hydrocarbon produced directly from natural gas (methane) is acetylene (world production 1998 about 120 000 t a⁻¹, Talbiersky, 2006). Production is based on partial oxidation where about one-third of natural gas (methane) is converted into acetylene, while the rest is burned to reach a temperature of about 1500 °C. The entire process only takes a few milliseconds. Acetylene is also produced in arc furnaces. Up to the 1960s, acetylene was an important intermediate, but nowadays its relevance is small compared to olefins such as ethylene and propylene. Today, the most important product from acetylene is 1,4-butandiol, which is used for production of polyurethane and polyester plastics. Acetylene is also used for gas welding, as combustion with oxygen produces a flame of over 3000 °C.

5.1.4

Crude Oil and Refinery Products

5.1.4.1 Production, Reserves, and Price of Crude Oil

The petroleum industry began with the drilling of the first commercial oil well in 1859. The first refinery opened two years later, mainly producing petroleum as a cheaper and better source of light than whale oil. At the end of the nineteenth century, the development of combustion engines (Otto engine by Nicolaus August Otto in 1867, Diesel engine by Rudolf Diesel in 1897) and of the first petrol-powered automobile (Carl Benz, 1886) led to a strong increase in the production of gasoline

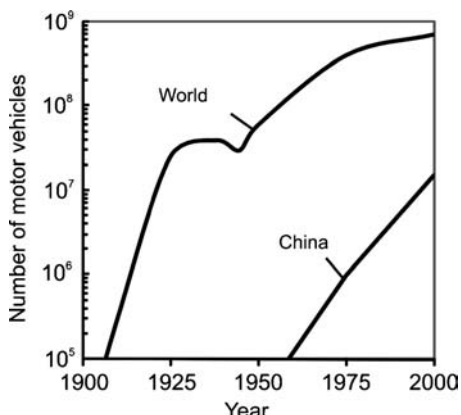


Figure 5.1.16 Development of the global and the Chinese fleet of vehicles (passenger cars, trucks, and buses) in the period 1900–2000 (data from Smil, 2003).

Table 5.1.25 Regional distribution of worldwide production of crude oil 2008 (BP, 2009).

Region	Crude oil production (million t)	2008 share of total (%)
Middle East	1254	31.9
North America (USA, Canada, Mexico)	619	15.8
Former Soviet Union	620	15.7
Africa	488	12.4
Total Asia Pacific	381	9.7
Central and South America	336	8.5
Europe	231	6.0

a) Azerbaijan, Kazakhstan, Russian Federation, Turkmenistan, and Uzbekistan.

and diesel fuels, and the evolution of the airplane created a need first for aviation gasoline and then for jet fuel, a sophisticated form called kerosene.

Figure 5.1.16 shows the strong increase in the number of vehicles during the last century. In 2000, the worldwide total of passenger cars and commercial vehicles (trucks and buses) surpassed 700 million, compared to less than 50 000 vehicles in 1900 (Smil, 2003). Today, in North America and Europe, automotive traffic shows signs of saturation, but continues to grow in developing countries as shown exemplarily in Figure 5.1.16 for China.

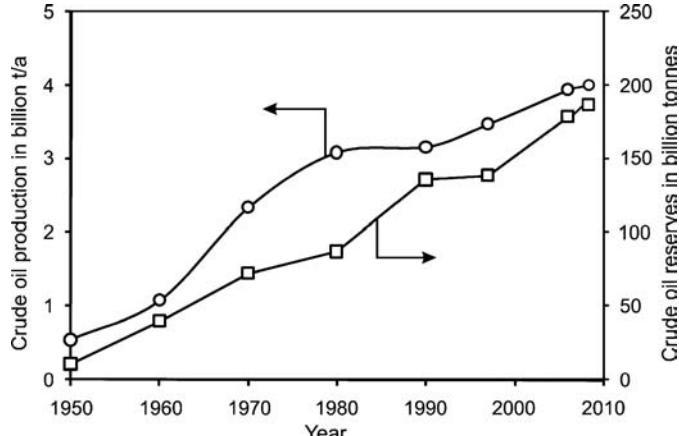
At present, worldwide crude oil production is 4 billion tones, with a share of transportation fuels of 60%. The most important region for crude oil production with a share of 32% is the Middle East, followed by North America, the former Soviet Union, and Africa (Table 5.1.25).

Figure 5.1.17 shows the production rate and the reserves (i.e., the amount currently technologically and economically recoverable) of crude oil in the period 1950–2009. Production has increased strongly in the last 60 years from 0.5 billion tonnes in 1965 to 4 billion tonnes in 2009, but this has (until now) not led to a decrease in the reserves-to-production ratio (about 50 years in 2009) because known reserves have increased to a similar extent.

Figure 5.1.18 shows the development and forecast of the production rate of crude oil in OPEC countries, non-OPEC countries, and the world based on estimations of Nashawi, Malallah, and Al-Bisharah (2010). Peak production is almost reached in non-OPEC countries, will be reached in OPEC countries by about 2026, and for the total world by about 2015.

Figure 5.1.19 shows the price of crude oil (adjusted for inflation) in the period 1865–2009. In general, the price of oil and thus of energy fluctuates strongly with time because of political and economic reasons (e.g., Arab oil embargo in 1974, Iranian revolution and Iran–Iraq war in 1979–80, Iraq war in 2003, and global

Figure 5.1.17 Production and reserves of crude oil in the period 1950–2009.



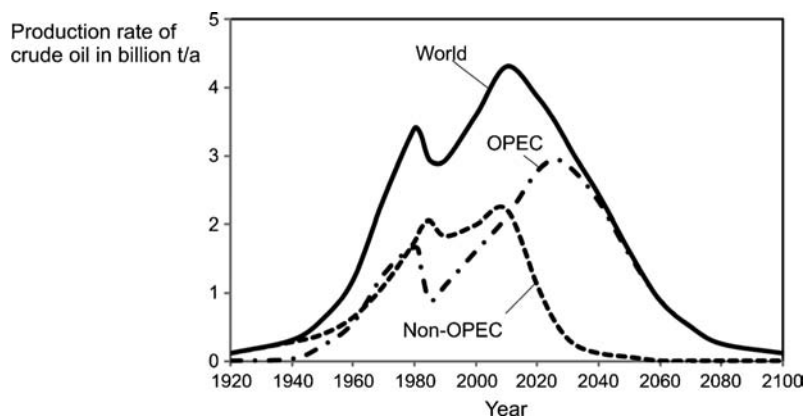


Figure 5.1.18 Development of the production rate of crude oil in OPEC countries, non-OPEC countries, and the world based on estimations of Nashawi, Malallah, and Al-Bisharah (2010).

recession and financial crisis starting in 2008). During the 20 year period 1989–2009, the oil price was lowest in 1999 (\$US 13 per barrel in money of 2009) and highest in 2008 with (monthly averaged) \$125 per bbl.

A graph of the year-to-year changes in world crude oil prices since 1950 gives us an impressive way to show that random swings make it impossible to forecast the oil price (Figure 5.1.19).

Refining is the processing of crude oil into a relatively small number of complex mixtures of hydrocarbons of high quality. The main products are fuels such as gasoline, diesel oil, jet fuel, and heating oil, but refineries also produce the major feedstocks (naphtha and LPG) for the petrochemical industry, and, therefore, crude oil is also the basis of industrial organic chemistry. The main objectives of a refinery can be briefly summarized as follows.

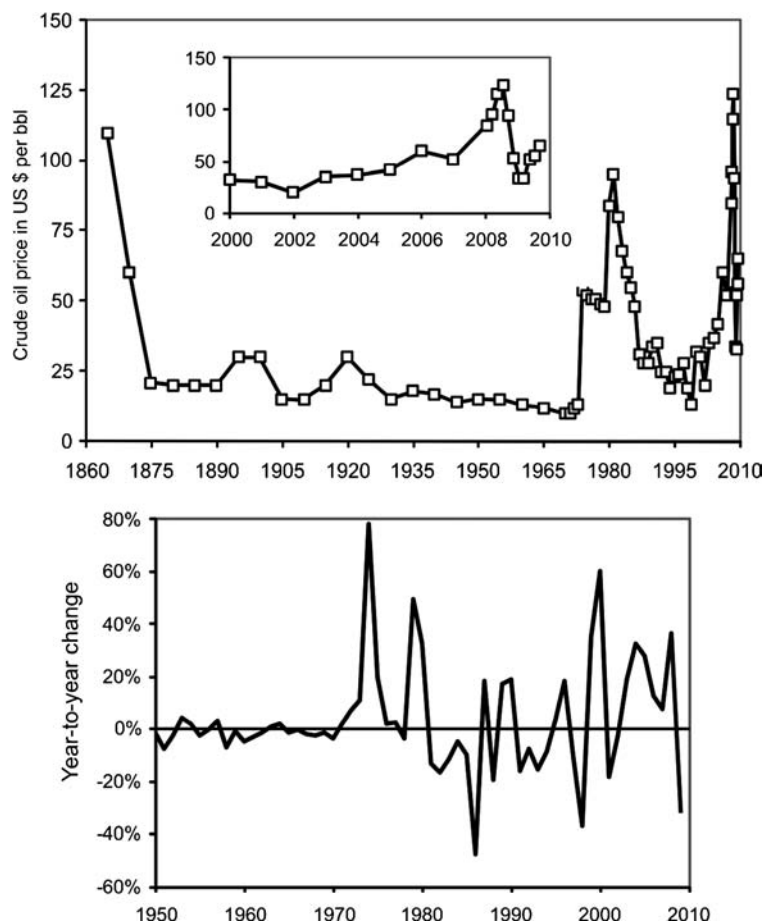


Figure 5.1.19 Crude oil price in the period 1865–2009 [prices are adjusted for inflation to 2009 and year-to-year changes in the period 1950–2009, 1 barrel (bbl) = 158.8 l].

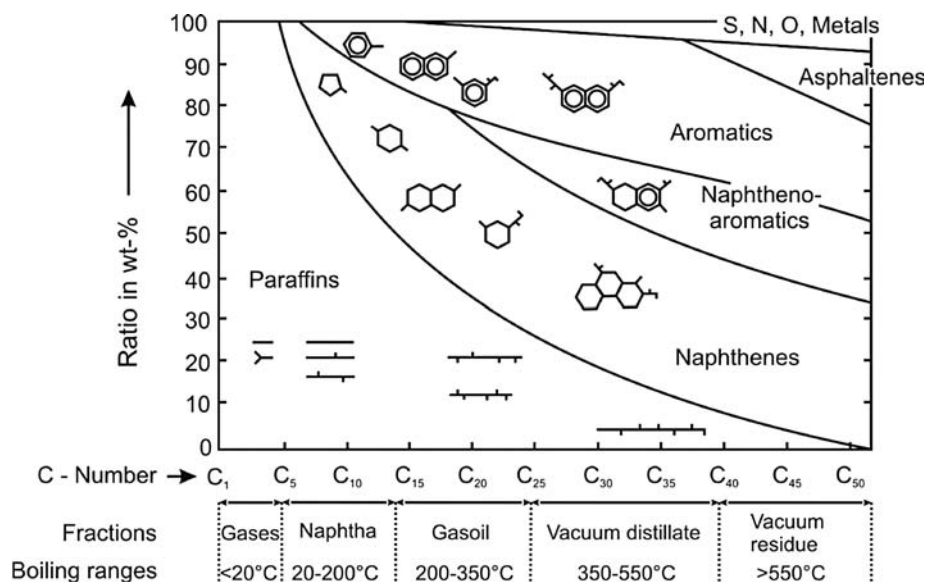


Figure 5.1.20 Composition of crude oil fractions. Adapted from Keim, Behr, and Schmidt (1986).

First, the crude oil is separated by distillation into fractions differing in the boiling-point range (Figure 5.1.20). Thereafter, the high boiling fractions (heavy oils) are converted by cracking into lighter ones to fulfill the needs of the market for gasoline, diesel, naphtha, and so on.

The quality of gasoline from distillation and cracking units is too low for proper combustion in modern engines, and chemical processes are needed to change the structure of the hydrocarbon molecules to enhance the octane number. With regard to environmental protection, nearly all refinery products have to be desulfurized.

5.1.4.2 Properties of Crude Oil

Crude oils are complex mixtures containing many different hydrocarbons that vary in appearance and composition between different oils. Crude oils range in consistency from water to tar-like solids. An average oil contains 84 wt% carbon, 14 wt% hydrogen, 1 wt% sulfur, and less than 1 wt% each of nitrogen, oxygen, metals, and salts. Hydrocarbons containing up to four carbon atoms are usually gases, those with 5–19 carbon atoms are usually liquids, and those with 20 or more are solids under normal conditions, as shown in Table 5.1.26 for *n*-alkanes.

Three groups of hydrocarbons occur naturally in crude oil (Table 5.1.27):

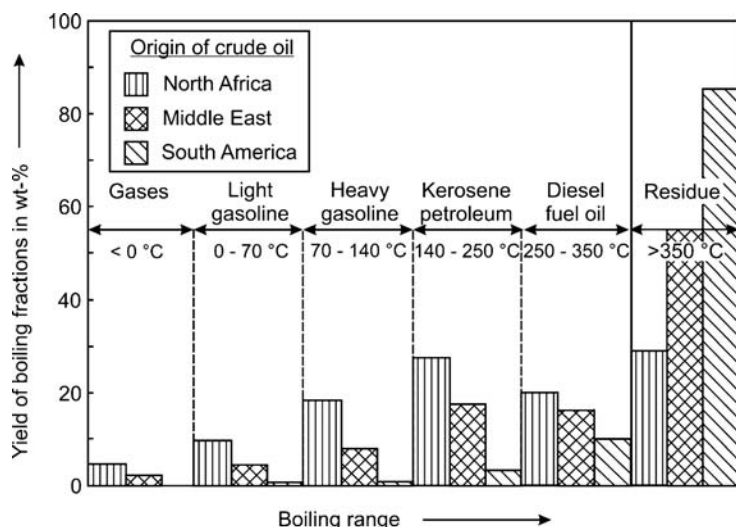
- *Paraffins* with the general formula C_nH_{2n+2} are either straight chains (normal) or branched chains (isomers). The latter have higher octane numbers.

Table 5.1.26 Boiling and melting points of *n*-alkanes (at 1 bar).

Name	Formula	$T_{\text{boiling}} \text{ (}^{\circ}\text{C)}$	$T_{\text{melting}} \text{ (}^{\circ}\text{C)}$	Crude oil fraction
Methane	CH_4	−164	−183	Refinery gas
Ethane	C_2H_6	−89	−183	
Propane	C_3H_8	−42	−189	Liquefied petroleum gas (LPG)
Butane	C_4H_{10}	−0.5	−138	
Pentane	C_5H_{12}	36	−130	Gasoline
Octane	C_8H_{18}	125	−57	
Decane	$\text{C}_{10}\text{H}_{22}$	174	−30	
Undecane	$\text{C}_{11}\text{H}_{24}$	196	−26	Jet fuel diesel oil, light heating oil
Pentadecane	$\text{C}_{15}\text{H}_{32}$	269	10	
Eicosane	$\text{C}_{20}\text{H}_{42}$	343	37	
Tricosane	$\text{C}_{23}\text{H}_{48}$	380	49	
Triacantane	$\text{C}_{30}\text{H}_{62}$	450	66	Heavy oil component

Table 5.1.27 Typical contents of paraffins, aromatics, and naphthenes in crude oils.

Crude source	Paraffins (vol.%)	Aromatics (vol.%)	Naphthenes (vol.%)
Venezuela-heavy	35	12	53
USA-Texas sour	46	22	32
North Sea-Brent	50	16	34
Saudi-light	63	19	18

**Figure 5.1.21** Yields of distillation fractions of different crude oils (atmospheric distillation).

- Aromatics** are unsaturated cyclic compounds, and have at least one benzene ring as part of their structure. Naphthalenes are aromatics with two rings. Polynuclear compounds have three or more aromatic rings, and are found in heavier fractions of the crude oil.
- Naphthenes** are saturated cyclic hydrocarbons with the general formula C_nH_{2n} , and are found in all fractions of crude oil except the very lightest. Single-ring naphthenes predominate, while two-ring naphthenes are found in heavier oil fractions.

Other hydrocarbons are only formed by refinery processes and are not present in crude oils:

- Alkenes** are mono-olefins with the general formula C_nH_{2n} , and contain one carbon–carbon double bond. Olefins are usually formed by thermal and catalytic cracking.
- Dienes and Alkynes**: Dienes are diolefins with two carbon–carbon double bonds, and alkynes have a carbon–carbon triple bond. They both have the formula C_nH_{2n-2} . An important diolefin is butadiene. Alkynes such as acetylene occur in light fractions of cracking units.

Olefins, diolefins, and alkynes are more reactive than paraffins or naphthenes and readily combine with other molecules such as hydrogen.

In a refinery, the different hydrocarbons are separated and grouped by distillation into fractions that differ in the range of boiling points (Figure 5.1.21). The yield of the different fractions depends strongly on the crude oil. For example, the yield of the atmospheric residue from distillation at almost normal pressure may range from about 30% up to 80%.

Non-hydrocarbons present in crude oil (fractions) can be characterized as follows:

- Typical **sulfur compounds** present in crude oils are shown in Figure 5.1.22. The S-content of crude oils and distillation fractions varies (Figure 5.1.23). As a general trend, heavy crude contains more sulfur than a lighter one. The combustion of S-containing fuels produces SO_2 . Thus the S-compounds are converted, and finally end up as elemental sulfur.

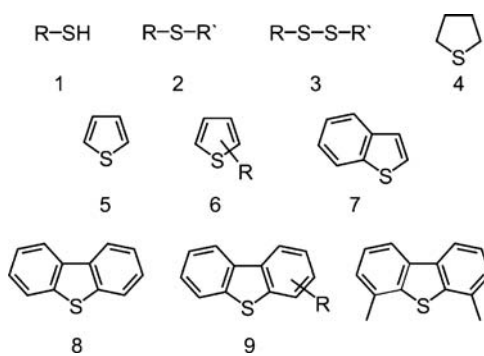
**Figure 5.1.22** Typical sulfur compounds in crude oil – 1: thiole, 2: sulfide, 3: disulfide, 4: tetrahydrothiophene, 5: thiophene, 6: alkylthiophene, 7: benzothiophene, 8: dibenzothiophene, 9: alkyl-dibenzothiophene, 10: 4,6-dimethylbibenzothiophene.

Figure 5.1.23 Sulfur content of crude oils and of distillation fractions.

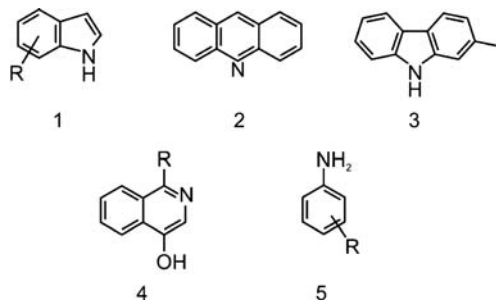
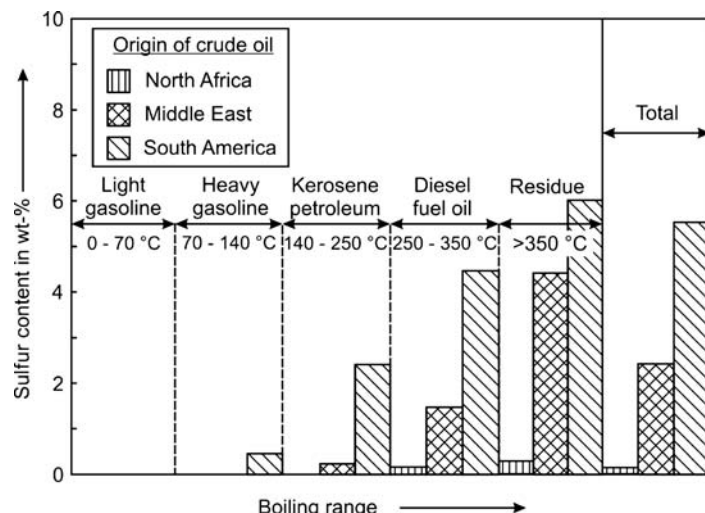


Figure 5.1.24 Typical nitrogen compounds in crude oil – 1: indole, 2: acridine, 3: methylcarbazole, 4: hydroxyquinoline, 5: aniline.

- Oxygen compounds are phenols, ketones, and carboxylic acids.
- Nitrogen compounds are found in lighter fractions of crude oil as basic compounds, and more often in heavier fractions of crude oil as non-basic compounds (Figure 5.1.24).
- Trace metals like Ni and V are present in small quantities as metal-organic species and are removed during the refining process, which is also needed as they poison catalysts.
- Crude oils contain inorganic salts such as sodium, magnesium, and calcium chlorides, which are removed before processing to prevent catalyst poisoning, corrosion, and fouling.

5.1.4.3 Properties of Major Refinery Products

Table 5.1.28 gives typical product spectra of crude oil refining. About 80% of all products account for gasoline, diesel fuel, jet fuel, and heating oil. Gasoline is the dominant transportation fuel in North America while in Europe the share of diesel fuel is higher:

- Gasoline:** On a global basis, the most important refinery product is motor gasoline, a blend of hydrocarbons boiling in a range from ambient temperature to

Table 5.1.28 Typical product spectra^{a)} of a European and an US refinery in 2008 ranked in the order of increasing boiling range (MWV, 2009 and IEA, 2009).

Product	Share of German refinery production (%)	Share of US-refinery production (%)
LPG (liquefied petroleum gas)	3	5
Naphtha (for petrochemicals)	8	2
Motor gasoline	23	34
Jet fuel	5	11
Diesel fuel	32	33 ^{b)}
Light heating oil	14	
Heavy fuel oil	9	5
Lubricants and waxes	2	2
Bitumen	3	3
Petrol coke	1	5

a) Products for sale, that is, without own fuel consumption (fuel gas, heavy oil, FCC coke), which is typically 7% (based on heating value of fuels for oil processing and heating value of crude oil, respectively).

b) About $\frac{2}{3}$ diesel, also including small amounts of oils used by the petrochemical industry (1% of total production).

about 180 °C. The important qualities for gasoline are the octane number (anti-knock), volatility/vapor pressure (starting, vapor lock, and environmental control), and the sulfur content (< 10 ppmw in OECD countries).

- **Diesel fuel and light heating oil** have boiling ranges from about 180 to 360 °C. Desirable qualities include controlled flash and pour points, clean burning, and for diesel fuel a high cetane rating for good starting and combustion. In most OECD countries, the statutory S-content is meanwhile about 10 ppmw for diesel fuel and 1000 ppmw for heating oil.
- **Naphtha**, consists mainly of C₅- and C₆-hydrocarbons, is produced for the manufacture of petrochemicals such as ethylene, propylene and butylenes by steam cracking (Section 6.6).
- **Kerosene** is a middle distillate with a boiling range of about 160–270 °C that finds considerable use as jet fuel. The most critical property of jet fuel is the freeze point as the temperature may reach –50 °C at flight altitudes of 10 000 m. Kerosene with less-critical specifications is used worldwide in lighting, cooking, and heating.
- **Liquefied petroleum gas (LPG)** consists of propane and butane and is produced for use as fuel and (as naphtha) as an intermediate for the manufacture of petrochemicals.
- **Heavy fuel oil** is used by marine vessels, power plants, and industrial facilities for heating and processing. The critical specifications are the viscosity and the sulfur content.
- **Coke and asphalt**: coke is almost pure carbon, with various uses from electrodes to charcoal briquettes. Asphalt is used for roads and roofing materials.
- **Lubricants** are produced mainly in specialized refineries. The critical parameter of motor oils and industrial greases is a high viscosity even under varying temperatures.
- **Oxygenates**: tetraethyl- and tetramethyl-lead are no longer used as additives to improve octane ratings, except in aviation gasoline. Today, ethers such as methyl tertiary butyl ether (MTBE), produced by conversion of olefins with methanol, are used to improve octane rating.

5.1.4.4 Refinery Processes

Refining starts with distillation; the different fractions are then converted into valuable products by changing the molecular size and structure and by the removal of undesirable compounds. The different units can be characterized as follows (Figure 5.1.25, Table 5.1.29).

Fractionation of crude oil is carried out in atmospheric and vacuum distillation towers. Gases from the atmospheric tower are separated further at a higher pressure, so that the LPG gases (propane and butane) are liquefied and separated from methane and ethane (so-called refinery fuel gas which is used for own consumption to cover the energy demand of the refinery processes). The two fractions from the vacuum tower, vacuum gas oil and vacuum residue, are cracked into lighter valuable products like gasoline and diesel oil. The vacuum residue is mostly cracked thermally rather by catalytic processes as the contents of metals (V, Ni) are too high and would lead to rapid deactivation of catalysts. Vacuum gas oil is catalytically cracked, which has the advantage (compared to thermal cracking) that more gasoline and diesel oil and less unwanted gases are formed. Two important cracking processes are examined in Section 6.7, namely, thermal cracking by delayed coking and fluid catalytic cracking.

Gasoline obtained either directly by crude oil distillation or from cracking processes has a low octane number. A structural change of the hydrocarbons is then needed. In the case of light gasoline, isomerization of the *n*-paraffins into branched, higher octane isomers is used. The heavy gasoline fraction is converted by reforming into a high octane reformate rich in aromatics. A valuable

Table 5.1.29 Main refinery processes (HCs = hydrocarbons).

Process group/name	Method and purpose	Feedstock(s)	Main product(s)
Fractionation processes			
Atmospheric distillation	Thermal separation of fractions	Desalted crude oil	Gas, gasoline, middle distillates, residual
Vacuum distillation		Atmospheric tower residual	Gas oil, lube stock, residual
Distillation at 5–15 bar		Top gas of atmospheric tower	Refinery gas LPG
Chemical conversion by decomposition (cracking)			
Fluid catalytic cracking (Section 6.7.2)	Catalytic cracking of long-chain hydrocarbons	Vacuum gas oil	Gasoline, petrochemical feedstocks (olefins)
Hydrocracking	Catalytic cracking/hydrogenation of long-chain hydrocarbons	Vacuum gas oil	Gasoline, jet fuel
Coking (Section 6.7.1)	Severe thermal cracking of long-chain hydrocarbons	Vacuum residue	Gasoline, diesel oil, coke, gases (by-product)
Visbreaking	Mild thermal cracking of long-chain hydrocarbons	Heavy oil with high viscosity	Heavy oil with lower viscosity
Chemical conversion by alteration and rearrangement			
Catalytic reforming (see Section 6.9)	Catalytic alteration and dehydrogenation of low-octane hydrocarbons	Heavy gasoline	High octane gasoline (aromatics)
Isomerization	Catalytic rearrangement of straight chain to branch HC	Light gasoline	High octane gasoline (isoparaffins)
Treatment processes			
Gas cleaning	Absorption to remove CO ₂ and H ₂ S	Sour gases	Acid-free gases
Hydrodesulfurization (Section 6.8)	Catalytic treatment of major streams to remove sulfur compounds	Gasoline, diesel oil, jet fuel, and so on.	Desulfurized fuels
Solvent deasphalting	Extraction of asphaltenes using paraffinic solvents (e.g., propane)	Vacuum tower residual, propane	Heavy lube oil, asphalt
Solvent dewaxing	Removal of wax from lube stocks	Lube oils	Dewaxed lube base-stock
Solvent extraction	Extraction of heavy aromatics with furfural or phenol	Lube oil based stocks	High-quality lubricating oil
Adsorptive separation	Extraction of aromatics by N-methyl-2-pyrrolidone or ethylene glycol Removal of n-paraffins by adsorption on molecular sieves	Kerosene	High-quality kerosene (low smoke point) Jet fuel with low freezing point
Production of hydrogen (needed for hydrotreating and hydrocracking)			
Steam reforming (Section 6.2.4)	Catalytic conversion	Desulfurized fuel gas, steam	Hydrogen (CO, CO ₂)
Partial oxidation (Section 6.2.3)	Thermal conversion	Heavy oil, oxygen and steam	Hydrogen (CO, CO ₂)

by-product is hydrogen, needed for hydrotreating and hydrocracking. The reforming process is examined in detail in Section 6.9. Other processes combine C₃- and C₄-olefins and paraffins by alkylation (Section 6.10) and oligomerization (called polymerization by refiners) into high octane gasoline compounds (not shown in Figure 5.1.25).

The most important treatment process to prepare finished products is hydrodesulfurization (Section 6.8). The organic S- and N-compounds (Figures 5.1.22 and 5.1.24) are catalytically converted with H₂ into the corresponding hydrocarbons, H₂S and NH₃, respectively. After separation, H₂S is converted into elementary sulfur by the Claus process.

Jet fuel with a high smoke point is not desirable. (The smoke point is the flame height under specified conditions at which a kerosene lamp begins to smoke. A high value indicates low smoke producing tendency.) Generally, the more aromatic the fuel the smokier the flame is. Thus, aromatics are extracted by N-methyl-2-pyrrolidone or ethylene glycol.

The freezing point (pour point, cloud point, cold filter plugging) of jet fuel and diesel is the lowest temperature at which the fuel remains free of solid hydrocarbon

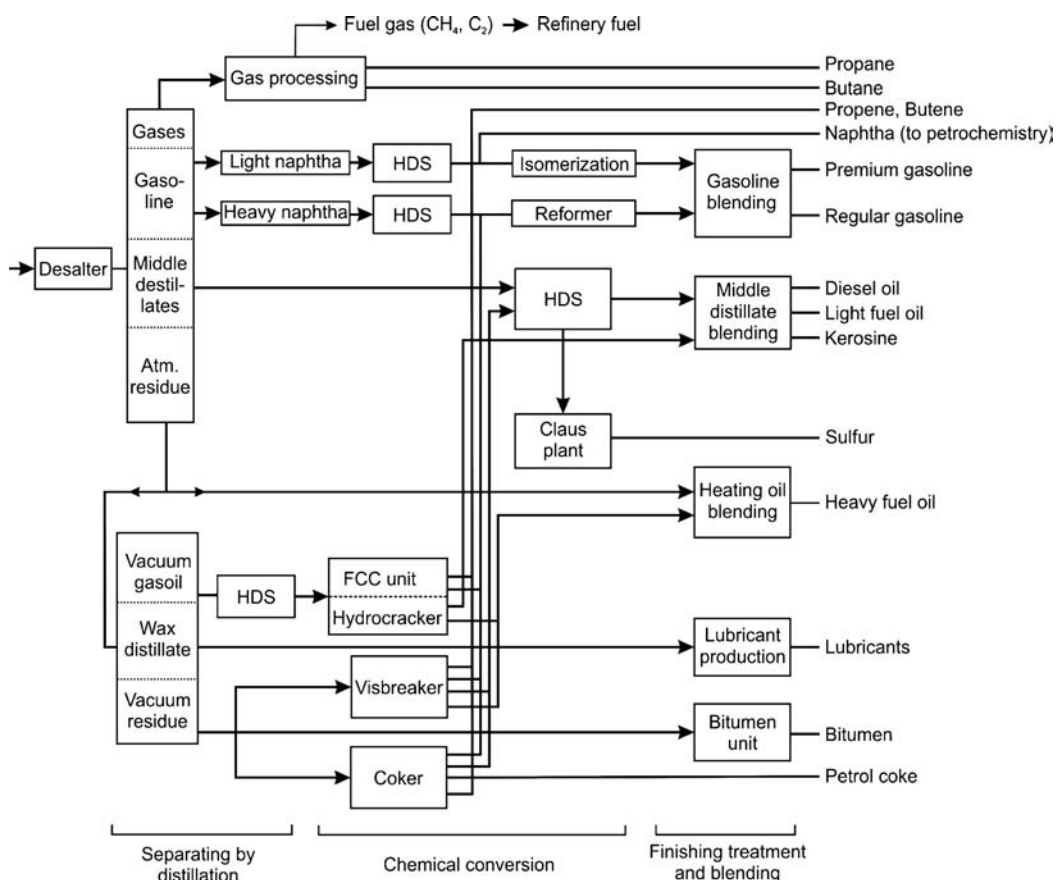


Figure 5.1.25 Simplified flow-sheet of a crude oil refinery.

crystals that can restrict the flow in the fuel system. This is especially important for jet fuel as the temperature in the tank falls during flight, depending on altitude, and may reach around -50°C . Straight-chain paraffins tend to crystallize first. One way of converting *n*-paraffin-containing feedstocks into high-grade products is by catalytic conversion (cracking, isomerization). Alternatively, the *n*-paraffins can be separated by adsorption using zeolite molecular sieves or by urea dewaxing, in which urea forms adducts with straight-chain paraffins.

In most cases, the amount of the hydrogen produced as by-product of gasoline reforming is sufficient and the balance comes out even. If not, for example if the amount of ultralow sulfur fuels is high and/or a hydrocracker is installed, hydrogen production based on heavy oil or refinery/natural gas is needed; for details see Section 6.2.

5.1.5

Coal and Coal Products

5.1.5.1 Properties of Coal and Other Solid Fuels

Coal has been used for centuries. Roman historians describe coal as a heating source, and coal was probably used in China 2000 years ago. Early coal mining was small scale and based on coal lying either on or very close to the surface. With the *Industrial Revolution* and the use of steam engines, coal became the preferred fuel and deep shaft mining became popular. Today, coal production has reached 3.3 billion tonnes oil equivalent (Table 5.1.30).

Table 5.1.30 Regional distribution of worldwide production of coal 2008 (BP, 2009).

Region	Coal production (Mtoe)	2008 share of total (%)
Total Asia Pacific ^{a)}	2031	56.1
North America (USA, Canada, Mexico)	638	19.2
Former Soviet Union ^{b)}	252	7.6
Europe	204	6.1
Africa	143 ^{c)}	4.3
Central and South America	56	1.7
World	3325	100

a) Mainly China (70% of total Asia/Pacific), Australia (11%), and India (10%).

b) Kazakhstan, Russian Federation, Ukraine.

c) Practically only South Africa (98% of total for Africa).

Interestingly, the share of coal in the consumption of fossil fuels has changed considerably during recent decades (Table 5.1.31), above all in Europe. In 1950, coal was by far still the dominant fossil energy, for example, in Europe with a share of 83%, and natural gas was almost not used. Today, the share of coal is only 21%, and natural gas has a share of 32%. Since the 1970s (and ten years earlier in the USA), crude oil has been the dominant fossil fuel.

Solid fuels like wood, peat, and coal contain more than 50 wt% carbon (Table 5.1.32). Higher rank coals contain less hydrogen and oxygen and up to 95% C. Wood, peat, and lignite usually contain a considerable amount of incidental moisture, more than 30%, while the content in bituminous coals is less than 10%. Another constituent is the mineral matter, usually as silicate or carbonate minerals. Methane is formed during coal mining and can cause explosions. It is, however, also a valuable by-product of some coal mining.

As geological processes applied pressure and temperature to plant matter over time, different coals were formed by carbonization (Figure 5.1.26 and Scheme 5.1.1), which leads to a lower H/C- and O/C-ratio with increasing time and/or more severe “reaction” conditions:

- Lignite – also referred to as brown coal, is the lowest rank of coal and used almost exclusively for steam-electric power generation.
- Sub-bituminous coal with properties ranging from lignite to bituminous coal is also primarily used as fuel for electric power generation.
- Bituminous coal – a dense coal, usually black, is used primarily as fuel for heat and power applications but also for the manufacture of blast furnace coke.
- Anthracite is the highest rank, used primarily for residential and commercial heating.

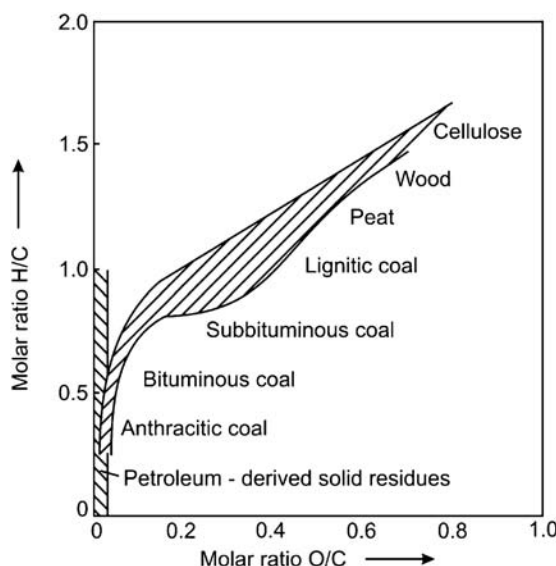
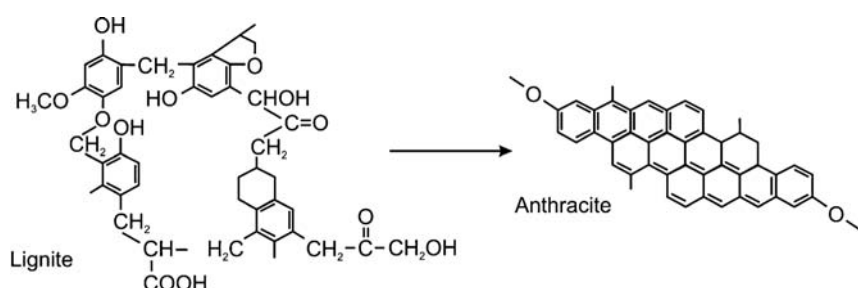
Table 5.1.31 Share of coal, oil, and gas in fossil fuel consumption in Europe (France, United Kingdom, Germany) and the USA in the period 1950–2008 (BP, 2009).

Fuel	Shares in fossil fuel consumption (%)									
	USA					France, UK, Germany				
	1950 ^{a)}	1965	1975	1985	2008	1950 ^{a)}	1965	1975	1985	2008
Coal	44	24	20	27	28	83	59	34	36	21
Crude oil	35	44	48	45	43	16	39	52	45	47
Natural gas	21	32	32	28	28	1	2	13	19	32
Total (billion toe)	0.84	1.24	1.59	1.61	2.05	0.16	0.55	0.66	0.64	0.62

a) Data from Winnacker-Kuechler (1970) for the whole of Europe and USA.

Table 5.1.32 Typical composition of solid fuels (Falbe, 1977).

	H_2O (wt%)	Volatile matter	C	H	O	N	S
			wt% (moisture- and ash-free)				
Wood, fresh	60–40	75–65	48–52	6.2–5.8	45–43	0.1–0.05	—
Peat, fresh	92–80	80–70	49–60	8–5	45–28	4–1	1–0.1
Lignite	63–30	60–47	65–73	8–5	30–16	1.5–0.5	3–0.5
Sub-bituminous (black) lignite	10–8	47–43	72–75	7–5.5	18–12	2–1	3–0.5
High volatile bituminous coal	8–3	45–35	75–85	6.6–5.6	12–7	1.8–1	1.8–0.5
Medium volatile bituminous coal	3–1	35–19	85–88	5.6–4.5	7–3.2	1.8–1	1.8–0.6
Low volatile bituminous coal	<1	19–14	88–90	4.5–4.0	3.2–2.8	1.7–1	1.7–0.6
Semi-anthracite coal	<1	14–12	90–91	4.0–3.8	2.8–2.5	1.7–1	1.7–0.6
Anthracite	<1	<10	>92	<3.8	<2.5	1.7–1	1.7–0.6

**Figure 5.1.26** Molar C-H-O ratio of solid fuels.**Scheme 5.1.1** Structure of lignite and anthracite formed by carbonization. Adapted from Keim, Behr, and Schmidt (1986).

5.1.5.2 Processes and Products Based on Coal

Figure 5.1.27 gives an overview of the use and conversion of coal.

The processes of coal utilization can be divided into four areas, pyrolysis, combustion, gasification to syngas, and liquefaction with high-pressure hydrogen.

Coal Pyrolysis Pyrolysis is the chemical decomposition by heating in the absence of oxygen or of any other reagent, whereby the volatile constituents of the coal – water, gases like H_2 , CO , and CO_2 , and hydrocarbons ranging from methane to tar – are driven off. Pyrolysis is not only important for coke making, but also as the

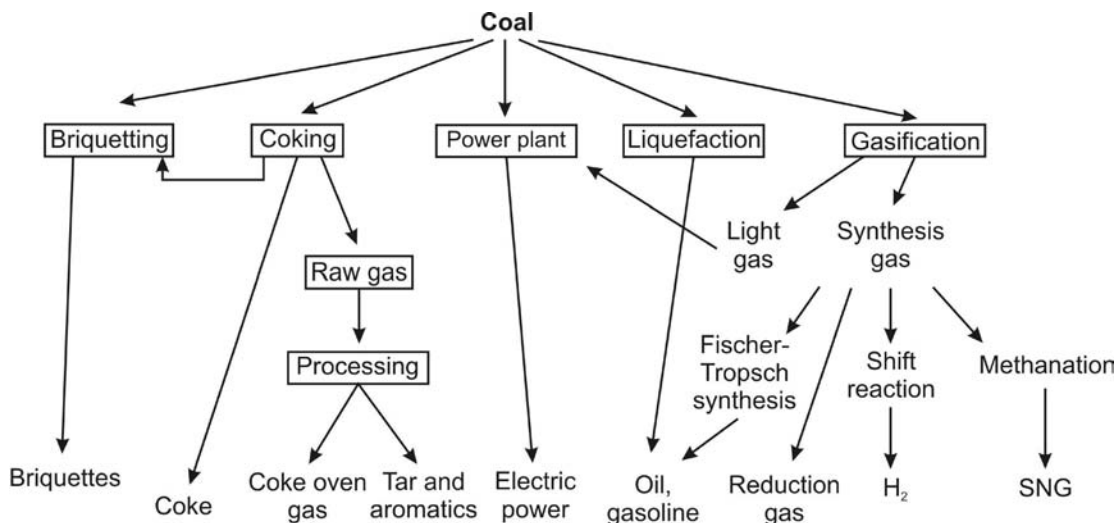
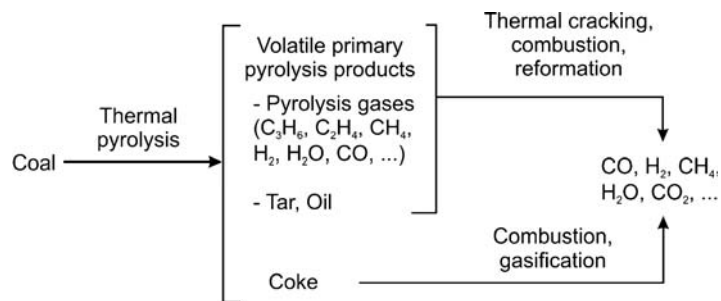


Figure 5.1.27 Processes and products based on coal. Adapted from Benthäus *et al.* (1978).

Figure 5.1.28 Main chemical reactions during pyrolysis, gasification, and combustion of coal.

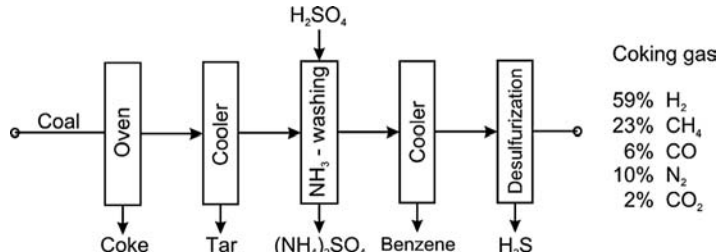


first step in any coal utilization process like combustion, gasification, or liquefaction (Figure 5.1.28).

Coal Combustion and Electricity Production World coal consumption is about 3.3 billion tonnes oil equivalent annually (2008), of which about 75% is used for to generate electricity. Coal currently supplies about 39% of the world's electricity, 4% based on lignite and 35% based on black (hard) coal (RWE, 2005). For electricity generation, coal is usually pulverized and burned in a furnace with a boiler to produce steam that is used in turbines to create electricity with about 40% efficiency for the entire process. In addition to electricity production, 13% of the global coal production is burned in the domestic and non-metallic industry, for example, for cement production.

Coal in Iron and Steel Production About 20% of the total global coal production is consumed by the steel industry in blast furnaces (Section 6.5), where coke made from coking coals is used (Figure 5.1.29). World steel production is 1.3 billion tonnes (2008), of which $\frac{2}{3}$ are made in blast furnaces, that is, about 0.9 billion

Figure 5.1.29 Process steps to produce blast furnace coke. Adapted from Keim, Behr, and Schmidt (1986).



tonnes of so-called pig-iron are currently produced annually. Coal and coke are essential for steel production as about 0.5 tonnes of blast furnace coke are needed per tonne of pig-iron. Some furnaces use pulverized coal injection to save coke (up to 25%) and costs. As a rough estimate, 0.65 billion tonnes of coal are needed for steel production, which equates to 0.45 billion tonnes of blast furnace coke (2008).

Coke is a carbonaceous residue derived from crushed bituminous coal from which the volatile constituents have been driven off by baking in a series of airless coke ovens at up to about 1200 °C. Thereby, the fixed carbon and residual ash are fused together. The released coke-oven gas is cleaned (Figure 5.1.29) and used as fuel (coking) gas, for example, in former times as town gas. Thereby, chemicals like tar, naphthalene, and benzene are separated, although the role of these products is small compared to crude oil based chemicals. Details on blast-furnace coke production are given in Section 6.5.2.

Coal Gasification The current high price of oil and gas has lead to an increased interest in coal gasification.

Coal gasification breaks down the coal into its components, usually by subjecting it to high temperature and pressure by using steam and sub-stoichiometric (with regard to total combustion) amounts of oxygen (for details on gasification see Section 6.2.2). This leads to the production of syngas, a mixture consisting mainly of CO and H₂, which can be used in the production of various products (ammonia, methanol, diesel oil etc.).

By 2004 world gasification capacity had grown to 45 GW thermal of syngas output at 117 operating plants in 24 countries with a total of 385 gasifiers (DOE, 2005; Talbiersky, 2006). Coal remains the predominant feedstock, accounting for 49% of syngas capacity generated from gasification, which corresponds to an annual consumption rate of 45 million tonnes of coal. Petroleum provides 37%, with the remaining 14% of gasifier feedstocks coming from natural gas (9%), petroleum coke, and biomass and waste. The primary product is syngas, which is used to obtain chemicals (37%), *Fischer-Tropsch* liquids (36%), power (19%), and gaseous fuels (8%). Additional plants, mainly in China, based on coal are forecasted to become operational in the next decade, with a capacity of at least 25 GW.

Coal Liquefaction Coal can also be converted directly into liquid fuels by the *Bergius-Pier* process by catalytic liquefaction by hydrogenation. This process was developed by Friedrich Bergius in 1913. Dry coal is mixed with heavy oil recycled from the process. A catalyst, typically based on iron, is added to the mixture. Liquefaction takes place at 450 °C and pressures up to 700 bar and proceeds in two steps, a liquid phase hydrogenation into raw coal oil and a subsequent catalytic gas-phase hydrogenation into gases, gasoline, and middle distillates. It can be regarded as a combination of hydrocracking and hydrotreating. Depending on the hydrogen pressure and consumption rate, different shares of liquid fuels are produced (Figure 5.1.30).

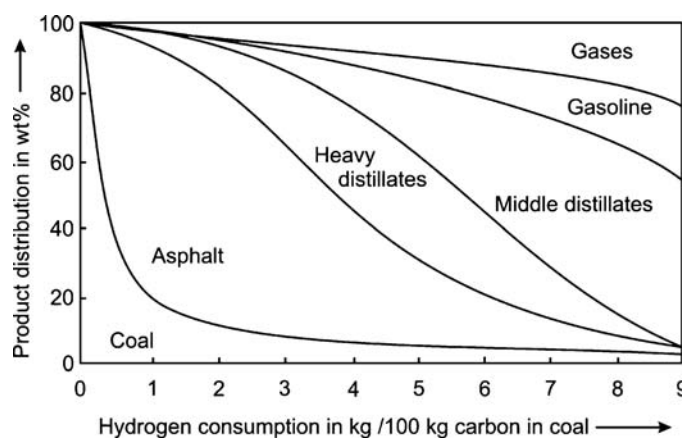
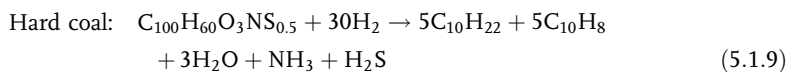
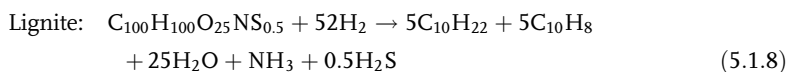


Figure 5.1.30 Product composition of direct coal liquefaction. Adapted from Keim, Behr, and Schmidt (1986).

The liquefaction of lignite and hard coal into liquid hydrocarbons can be represented by the following equations (dry and ash-free basis), if we take a 1 : 1 mixture of *n*-decane and naphthalene as representative for all produced hydrocarbons ranging from gases to heavy oil:



The theoretical H₂ consumption rate according to Eqs. (5.1.8) and (5.1.9) is 6 g per 100 g for lignite (= 8.6 g per 100-g carbon) and 4.5 g per 100 g for hard coal (5 g per 100-g carbon) (values on a dry and ash-free basis). Although compared to hard coal the H:C ratio of lignite is higher, more hydrogen is needed, mainly because lignite is richer in oxygen, which is converted into water.

Industrial coal liquefaction processes were until now only operated during World War II in Germany (for details see Section 6.11). Thereafter, no commercial plants were operated, but today this technology might undergo a renaissance. The Chinese energy corporation *Shenhua* announced the start of operation of the first post-war direct coal liquefaction plant in 2009. The plant is located in Inner Mongolia and the first production line should convert 3.5 million tonnes of coal to 1.1 million tonnes of gasoline, diesel, and LPG (Liu, Shi, and Li, 2010). The expected total capacity with three production lines is 3 million tonnes of fuels per year.

Miscellaneous Coal is also essential in manufacturing special products such as carbon fibers and activated carbon used as catalyst (support) or adsorbent for water/gas purification and kidney dialysis.

5.1.6

Renewable Raw Materials

5.1.6.1 Base Chemicals from Renewable Raw Materials

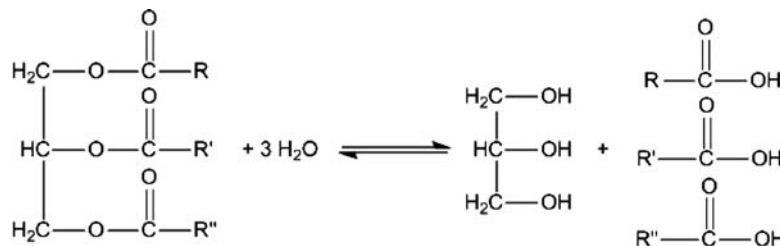
Table 5.1.33 shows the global production of important petrochemical base chemicals and base chemicals from renewable raw materials. The comparison shows that the orders of magnitude are similar. However, the use of renewable raw materials for the production of chemicals and biofuels is limited by the available land area and affects food production, respectively (Figure 5.1.12). Currently, 100 Mio. tonnes of biofuels are, globally, produced per year. This number is huge; however, one has to consider that the amount of liquid fuels produced from crude oil (gasoline, kerosene, diesel) is still much larger (about 2500 Mio. t a⁻¹).

Table 5.1.33 Comparison of global production of petrochemical base chemicals and base chemicals from renewable raw materials [data for 2005 from Behr, Agar, and Joerissen (2010) and for 2010 from OECD-FAO (2011); data for natural rubber from Ulber, Sell, and Hirth (2011)].

Raw material	Base chemical	Production (mio. t a ⁻¹)	Year	Price (2005) (€ t ⁻¹)
Renewable raw materials	Ethene	100	2005	1000
	Propene	64	2005	1000
	Benzene	23	2005	900
	Bioethanol	78	2010	650
	Biodiesel	18	2010	—
	Sugar	165	2010	250
	Cellulose	320	2005	500
	Starch	55	2005	250
	Vegetable oil	142	2010	—
	Natural rubber	10	2010	—

Table 5.1.34 Estimation of fossil and renewable raw materials of the chemical industry (i.e., without fuel and food production) in 2005 (Baerns *et al.*, 2006; Behr, Agar, and Joerissen, 2010).

Raw material	Raw material	Use for production of chemicals (mio. t a ⁻¹)
Fossil raw materials	Crude oil	135
	Natural gas	66
	Coal	25
Renewable raw materials	Carbohydrates/wood derivatives	9
	Fats and oils	10
	Proteins	0.2
	Plant extracts	6



Scheme 5.1.2 Hydrolysis of fatty acid esters into fatty acids and glycerol.

In 2005, 245 Mio. tonnes of fossil and renewable raw materials were used by the chemical industry, but only 10% stems from renewable resources, mainly plant material (Table 5.1.34).

5.1.6.2 Fats and Vegetable Oils

Fats and oils are esters, derived from reactions of fatty acids and glycerol, are often simply referred to as fatty acids since esters retain the basic long-chain structure of the parent acid. Triglycerides are hydrolyzed by water to give these two constituents (Scheme 5.1.2).

Naturally occurring triglycerides are esters with three long hydrocarbon chains, indicated as R, R' and R'' in Scheme 5.1.2. Each chain contains an even number of carbons, between 6 and 24, with varying degrees of saturation, up to three double bonds per chain. The C₁₈ fatty acids are the dominant components in vegetable oils (Table 5.1.35). The nomenclature used to designate the number of carbons and double bonds in the chain is C_n:*m*, where *n* designates the number of carbons and *m* the number of double bonds, for example, C18:2 indicates a fatty acid with 18 carbons and 2 double bonds. Examples of saturated fatty acids (FAs) are stearic FA (C18:0), palmitic FA (C16:0), myristic FA (C14:0), and lauric FA (C12:0). Unsaturated fatty acids are oleic FA (C18:1), linoleic FA (C18:2), linolenic FA (C18:3), and erucic FA (C22:1).

Table 5.1.35 Composition and production (2009) of important oils [adapted from Behr, Agar, and Joerissen (2010), production data from FAO (2011)].

Oil	Production (mio. t a ⁻¹)	Composition (%) (major fatty acids)								Remarks
		12:0	14:0	16:0	18:0	18:1	18:2	18:3	22:1	
Coconut	3.5	48	17	9	2	7	1	—	—	Used in soaps and cooking
Palm kernel	5.7	50	15	7	2	15	1	—	—	Seed of African palm tree
Palm	45.1	—	2	42	5	41	10	—	—	Tropical oil, also used for biofuel
Rapeseed “old”	21.2	—	1	2	1	15	15	7	50	Cooking oil, also used for biodiesel
Rapeseed “new”	—	1	4	1	60	20	9	2	—	—
Sunflower seed “old”	13.2	—	—	6	4	28	61	—	—	Cooking oil, also used for diesel
Sunflower seed “new”	—	—	4	4	84	5	—	—	—	—
Soybean	35.9	—	—	8	4	28	53	6	—	50% of global edible oil

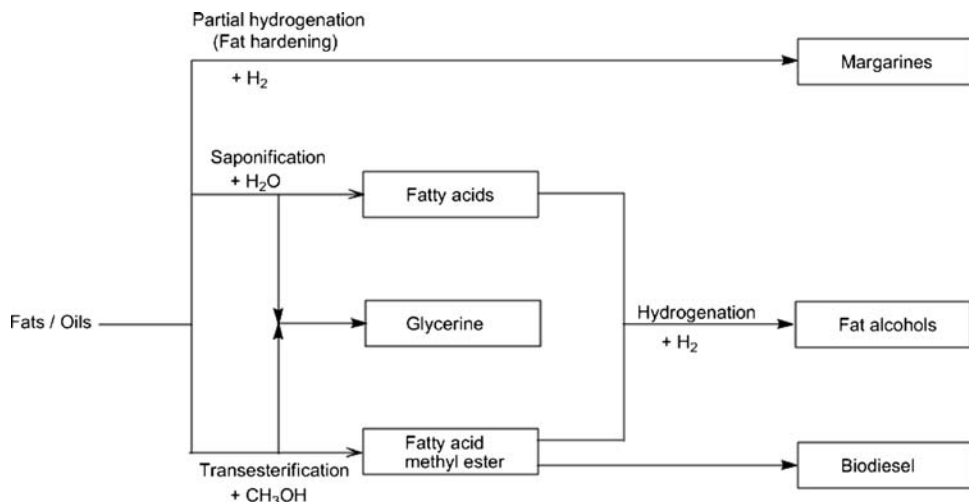
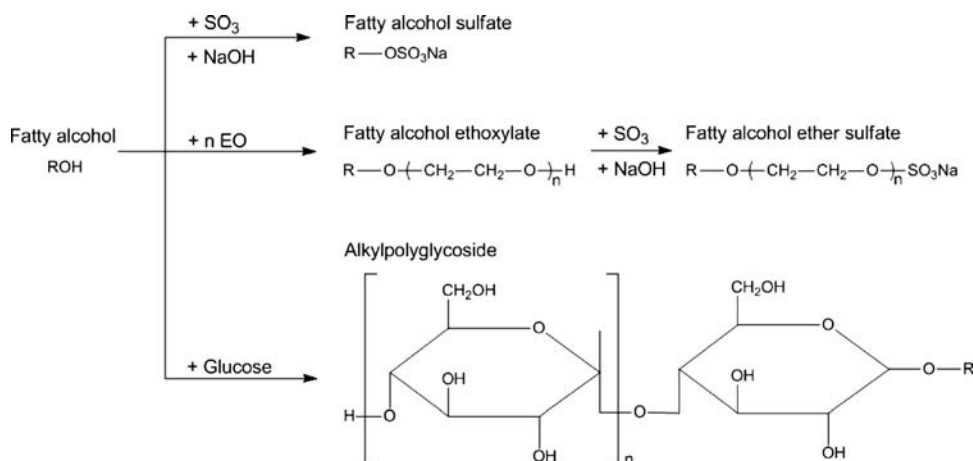


Figure 5.1.31 Industrial routes to convert fats and oils into base chemicals, margarines, and biodiesel. Partly adapted from Behr, Agar, and Joerissen (2010).

The melting point depends on the chain length and number of double bonds. T_{melt} increases with increasing degree of saturation (decreasing number of double bonds), for example, 73 °C for C18:0, 6 °C for C18:1, -13 °C for C18:2, and -24 °C for C18:3.

In 2009, 150 Mio. tonnes of natural oils and fats were produced worldwide (Rosillo-Calle, Pelkmans, and Walter, 2009). The lion's share is vegetable oils with 86%, and only 16% is animal fats (Gunstone, 2011). The main application and products of vegetable oils are (Figure 5.1.31):

- Most (70%, 90 Mio. t a⁻¹, Rosillo-Calle, Pelkmans, and Walter, 2009) is consumed directly or indirectly as ingredients in food – a role that they share with some animal fats like butter and ghee – for use in cooking, baking, salad dressings, and so on.
- Around 10 Mio. tonnes of vegetable oils (8%) are also used in the food industry and market as margarines (www.imace.org), that is, before use they are converted into fats and oils of higher melting point, which is achieved by catalytic hydrogenation of unsaturated vegetable oils. The process is usually conducted at about 150 °C and 10 bar. Complete hydrogenation is not desirable nutrition-wise. Saturated fats deposit as plaque on arterial walls (atherosclerosis, heart disease), whereas monosaturated and disaturated do not [for details on fat hardening see, for example, Farrauto and Bartholomew (1997)].
- Some 12% of all vegetable oils is used industrially (excluding biofuels) (Rosillo-Calle, Pelkmans, and Walter, 2009) for the production of detergents, cleaning agents, candles, and cosmetic products. The basic chemicals needed to produce surfactants are fatty alcohols (Figure 5.1.31). These are derived either by hydrolysis (no catalyst, 60 bar, 260 °C) to fatty acids or by transesterification of fats and oils to fatty acid methyl esters (240 °C, 90 bar, acidic catalyst). Both intermediates are finally hydrogenated to give the desired fat alcohols (CoCr-cat., 250 °C, 250 bar). Subsequently, the alcohols are converted into surfactants (Scheme 5.1.3).
- Today (2009), 10% of all vegetable oils such as palm, sunflower, rape seed, and soya bean oils are used for biodiesel (Rosillo-Calle, Pelkmans, and Walter, 2009), which is produced by transesterification of the oil with methanol to produce methyl esters (fatty acid methyl ester) and glycerol as by-product (Figure 5.1.31). The size of the large oil molecule is reduced to about 1/3 of its original size, which lowers the viscosity, making it similar to diesel.



Scheme 5.1.3 Conversion of fat alcohols into tensides. Adapted from Behr, Agar, and Joerissen (2010).

5.1.6.3 Carbohydrates

Wood and Cellulose Wood is a composite material consisting mainly of cellulose, hemicellulose, and lignin (Figure 5.1.32). Cellulose is a polysaccharide with a linear chain of several hundred to over ten thousand linked glucose units. Consequently, cellulose can also be regarded as a carbohydrate, $(\text{C}_6\text{H}_{10}\text{O}_5)_n$. Cellulose is obtained industrially from wood pulp and cotton and is mainly used to produce paper and paperboard wood.

Hemicellulose is also a polysaccharide but has a random amorphous structure. While cellulose is resistant to hydrolysis, hemicellulose is easily hydrolyzed by acids or bases.

Lignin is a complex three-dimensional compound and an integral part of the cell walls of plants. It is a polymer with a strong heterogeneity and no defined primary structure.

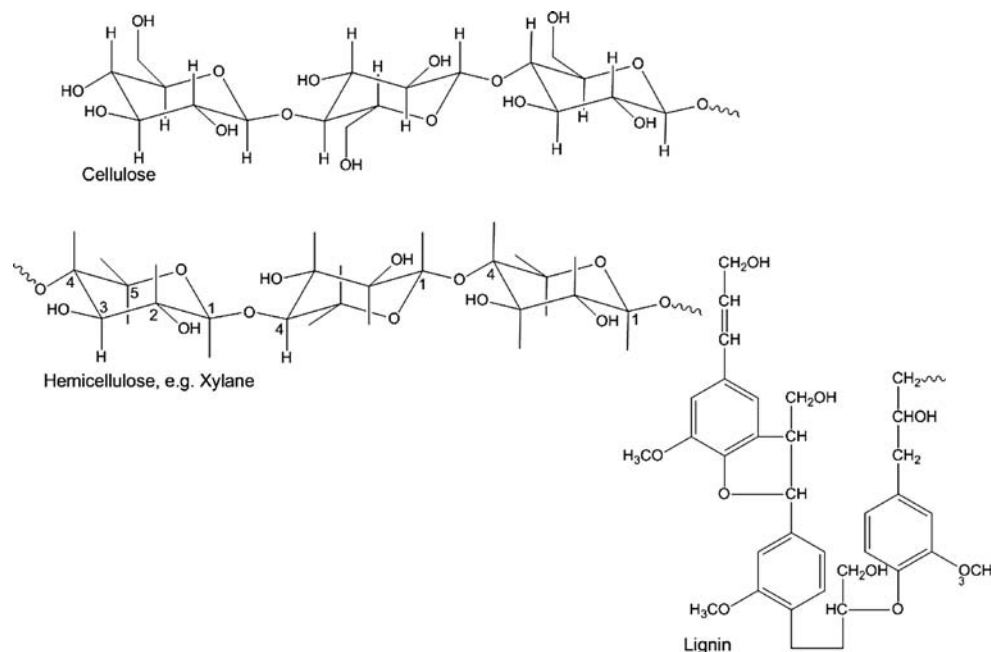
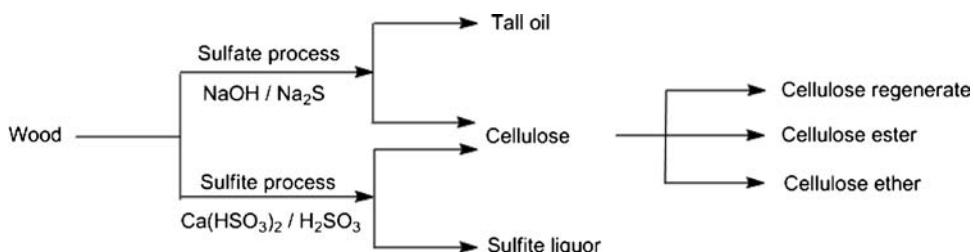


Figure 5.1.32 Main constituents of wood (typically 42–51 wt% cellulose, 24–40% hemicelluloses, 24–30% lignin, 1–10% extractives, and 0.2–0.8% minerals (adapted from Ulber, Sell, and Hirth, 2011).



Scheme 5.1.4 From wood to cellulose (derivatives). Adapted from Behr, Agar, and Joerissen (2010).

Table 5.1.36 World production of forest products in 2002 (Hillring, 2006; FAO, 2011).

	Global production of (mio. m ³ a ⁻¹) (2002)
Total volume of forestry production (if round-wood production is used as indicator)	3380
Products	
Wood fuel (31% Africa, 43% Asia)	1801
Char coal (51% Africa, 35% South America)	260 (42 Mio. t a ⁻¹)
Pulpwood (round and split)	484
Wood-based panels (plywood, veneer sheets, fiber boards, particle boards)	195
Sawn wood (lumber, furniture, etc.)	389
Wood residues	78
Other use, statistical difference	173

Scheme 5.1.4 shows the conversion of wood by chemical pulping (sulfate or sulfite process) into cellulose and cellulose derivatives. The lignin and hemicellulose are fragmented into small, water-soluble molecules that can be washed away from the cellulose fibers without depolymerizing the cellulose fibers.

Tables 5.1.36 and 5.1.37 give an overview of the current global status of production of forest products and of paper and paperboard. The total volume of forestry production (roundwood production) is about 3 billion m³ per year. The majority (about 60%) is used as fuel (wood fuel and char coal), mainly in developing countries. About 14% is used as pulpwood for the production of cellulose and paper. The rest (about 26%) is mainly used as sawn wood.

About half of the paper is freshly produced from wood by chemical or mechanical pulping. The rest is derived from recovered paper, which is recycled into the pulping process.

Starch Like cellulose, starch is a polysaccharide and carbohydrate, consisting of glucose units joined together by glycosidic bonds (Figure 5.1.33). Typically, starch contains about 20–25% amylose and 80–75% amylopectins. It is produced by all green plants as an energy store and is contained in large amounts in potatoes, corn, and rice. Most of the 55 Mio. tonnes of starch consumed each year is used in the food industry.

Sugar The global consumption rate of sugar is 165 Mio. tonnes per year. The term sugar usually refers to saccharose (“table sugar”), which is a disaccharide consisting of glucose and fructose (Figure 5.1.34). It is mostly obtained from sugar cane or sugar beet. Glucose – also known as dextrose or grape sugar – is the second most important form of sugar. It is a monosaccharide, and is industrially produced by hydrolysis of starch. An interesting option for the use of glucose is the production of non-ionic and biodegradable surfactants (“sugar based surfactants,” alkyl polyglycosides) by conversion with fatty alcohols (Scheme 5.1.5).

Table 5.1.37 World production of paper and paperboard 2009 (FAO, 2011; the total production of paper and paperboard was 376 Mio. tonnes).

Raw material	Share (%)
Chemical wood pulp	32
Mechanical wood pulp	8
Other fiber pulp (cotton etc.)	5
Semi-chemical wood pulp	3
Recovered paper	52

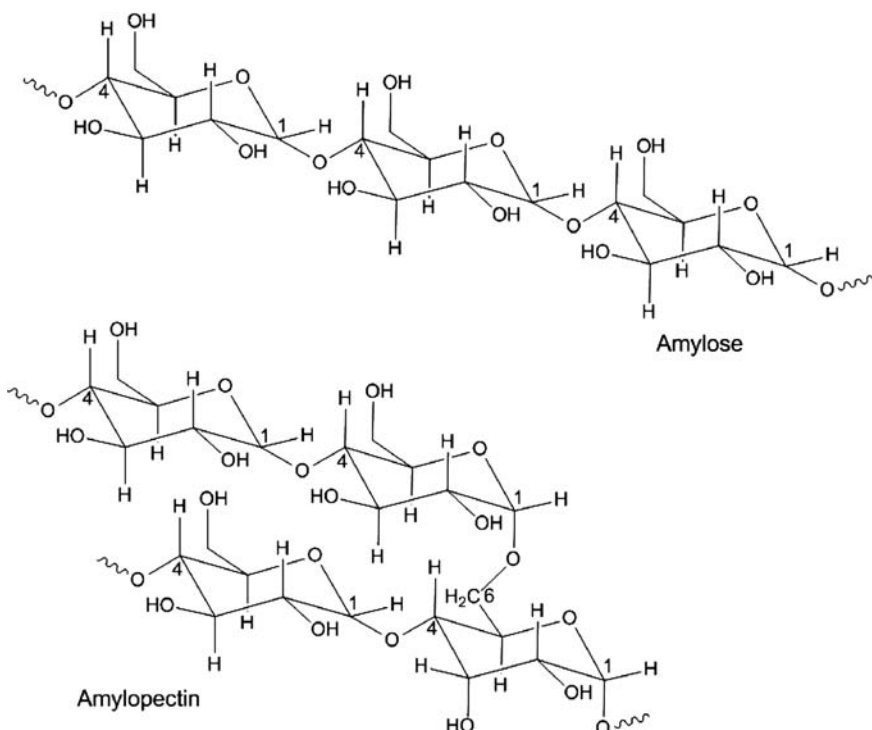
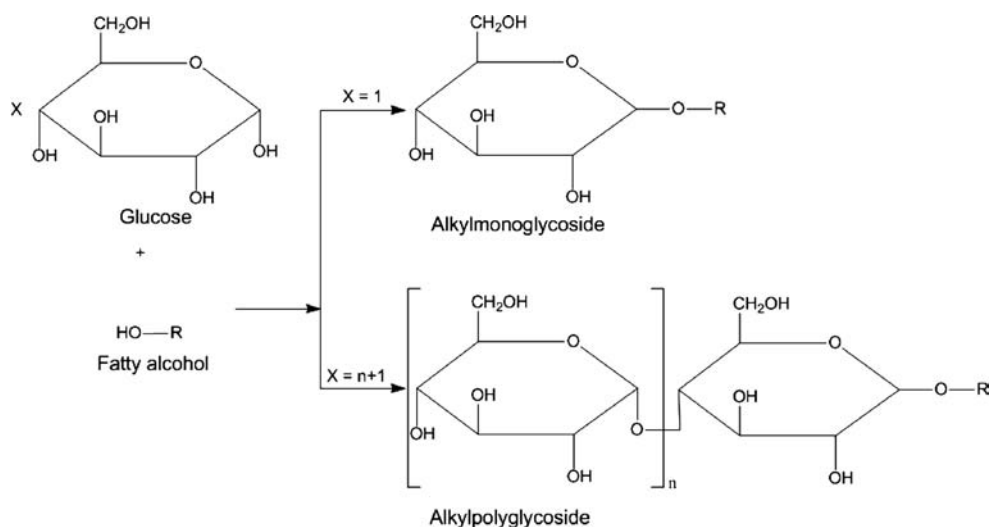


Figure 5.1.33 Molecular segments of two components of starch.

5.1.6.4 Extracts and Excreta from Plants

Natural Rubber Natural rubber, also called India rubber or caoutchouc, is an elastomer that is derived from latex, a milky colloid mainly extracted from rubber trees (Figure 5.1.35). The purified form of natural rubber is polyisoprene, which can also be produced synthetically. Natural rubber is used extensively in many applications and products, as is synthetic rubber. Today, the global annual production of natural rubber is 10 Mio. tonnes, which is about 40% of the total rubber production (natural and synthetic). The three largest producing countries of natural rubber are Thailand, Indonesia, and Malaysia.

Natural Dyes Natural dyes are mainly derived from plants like roots, berries, bark, or leaves, and also from invertebrates. One example is Tyrian purple



Scheme 5.1.5 Non-ionic surfactants based on fatty alcohols and glucose. Adapted from Baerns *et al.* (2006).

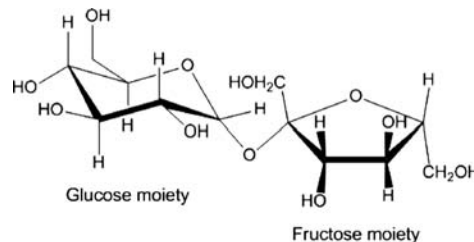


Figure 5.1.34 Saccharose (α -D-glucopyranosyl- β -D-fructofuranoside).

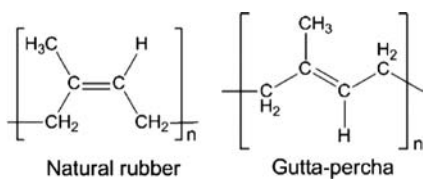


Figure 5.1.35 Molecular structure of natural rubber (*cis*-1,4-polyisoprene) and of gutta-percha (*trans*-1,4-polyisoprene), which has no importance for technical applications.

(6,6-dibromoindigo), which is extracted from sea snails and was highly prized in antiquity. An example of a famous plant-based dye is indigo (the blue of blue jeans), which is today practically only produced synthetically.

Natural Resins Resins are hydrocarbon secretions of many plants, particularly coniferous trees. They are used for the production of varnish, incense, and perfume.

Summary of Section 5.1 (take-home messages)

- Today's **global primary energy consumption** is 12 billion tonnes of oil equivalent (toe). At today's energy mix with a share of 80% fossil energy, the growth of world population and energy demand will lead to a conflict between stable ecosystems and global welfare. A complete shift from fossil fuels to renewables is needed for the desired **ecological footprint** of one planet. The capacity of non-solar renewables (wind, hydro, geothermal, tide) may be huge, but they are, by far, not huge enough. Thus, to complete an **energy plan** that adds up we must rely on solar power, which in the long run has to cover 75% of the energy demand, if fossil fuels are used only to produce chemicals.
- **Fossil fuel reserves** are currently technologically and economically recoverable, whereas **resources** are the additionally demonstrated quantities that cannot be recovered at current prices with current technologies but might be recoverable in future. Current reserves will last for about 70 years for oil and gas and 170 years for coal. If in future the resources are also partly used, fossil fuels will last for over 100 years. Nevertheless, they are finite and should be used with care for the sake of generations to come.
- **Natural gas** with an annual consumption rate of 3.3 billion toe is mainly used for heating and electricity, but is also an important raw material for chemicals via syngas.
- Global **crude oil** production is 4 billion tonnes with a share of fuels (gasoline, diesel fuel, jet fuel, heating oil) of about 80%. Only about 10% is used to produce basic chemicals like olefins and aromatics by steam cracking. **Refining** is the processing of oil into a small number of complex mixtures of hydrocarbons of high quality. Refining starts with distillation, and the fractions are then converted into valuable products by changing the molecular size (cracking, alkylation), structure (isomerization, aromatization), and by removal of undesirable compounds (hydrotreating).
- Today, **coal** production has reached 3.3 billion toe. The consumption of coal has changed considerably in recent decades. In 1950, coal was still by far the dominant fossil energy, for example, in Europe with a share of 83%. Today, the share of coal is only 21%. Industrial processes of coal utilization can be divided into three areas, pyrolysis to blast furnace coke and gaseous by-products, coal combustion for heat and electricity production, and coal gasification to syngas.
- The production of **renewable raw materials** (carbohydrates/wood derivatives, fats and oils, proteins, plant extracts), and petrochemical base chemicals is of the same order of magnitude are similar, but one has to consider that the use of renewable raw materials for the production of chemicals and biofuels is limited by the available land area and affects food production. Fats and oils are mainly consumed as food; 10% is used for production of surfactants, candles, and cosmetic products, and another 10% for biodiesel. Wood consists of cellulose, hemicellulose, and lignin. The majority is used as fuel, mainly in developing countries; 14% is used pulpwood for production of cellulose and paper. Other important renewable raw materials are starch and sugar, which are both mainly consumed as food. Extracts and excreta from plants are natural rubber, natural dyes, and natural resins.

5.2

Inorganic Products

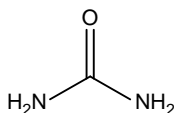
Inorganic products in chemical technology can be grouped as:

- inorganic nitrogen compounds (e.g., ammonia, nitric acid, urea);
- inorganic phosphorous compounds (e.g., phosphoric acids, phosphates);
- inorganic sulfur compounds (e.g., sulfur, sulfur oxide, sulfuric acid);
- products of electrolytic chloralkali production (chlorine, sodium hydroxide);
- soda (Na_2CO_3);
- products of the technical air separation (e.g., nitrogen, oxygen, argon, xenon) and other technically important gases, such as H_2 , CO , and CO_2 ;
- metals (e. g. Fe, Cu, Al).

Table 5.2.1 gives an overview of the most relevant inorganic products, their technical uses, and their production capacities.

Ammonia and **nitric acid** have been selected as process examples in this book and are treated in detail in Sections 6.1 and 6.4, respectively. **Urea** is produced industrially by reaction of ammonia and CO_2 via the intermediate product ammonium carbamate ($[\text{H}_2\text{N}-\text{COO}][\text{NH}_4]$). While the formation of the carbamate intermediate is exothermic and quantitative under the applied reaction conditions (200°C , 250 bar), urea forms from the intermediate by liberation of water in a slightly endothermic equilibrium reaction. Existing process technologies differ in their ways of carbamate decomposition as well as ammonia and CO_2 recycling. State-of-the-art urea plants produce up to 1.700 tons of urea per day and are often linked to ammonia plants as CO_2 is a by-product of NH_3 production from natural gas.

Table 5.2.1 Industrially important inorganic intermediates and final products.

Inorganic product	Structure	Major applications	World production (mio. t a ⁻¹)
Ammonia	NH_3	See Section 6.1	159 (2010, Section 6.1)
Nitric acid	HNO_3	See Section 6.4	55 (2005, Section 6.4)
Urea		Fertilizer, melamine for the production of resins	160 (2010) ^{a)}
Phosphoric acid	H_3PO_4	Metal treatment, phosphate salts as fertilizer, feed, and food ingredients	21 (1991) ^{a)}
Sulfur	S	Sulfuric acid	68 (2010) ^{b)}
Sulfuric acid	H_2SO_4	See Section 6.3	165 (2002) ^{a)}
Chlorine	Cl_2	See Section 6.19	9.1 (Europe, 2011) ^{c)}
Sodium hydroxide	NaOH	See Section 6.19	8.7 (Europe, 2011) ^{c)}
Hydrochloric acid	HCl	Chlorination and oxychlorination processes, chloride salts	15 (2000) ^{d)}
Soda ash	Na_2CO_3	Neutralization, sodium salts, glass, ceramics, paper, soaps, detergents	—
Oxygen	O_2	Oxidation processes, iron and steel production, welding, paper industry	—
Hydrogen	H_2	Hydrogenation, ammonia, methanol, Fischer-Tropsch, energy storage	65 (2009, see Section 5.1)
Iron	Fe	Steel, construction material	992 (steel, 2008) ^{e)}
Aluminum	Al	Light weight construction, alloys, reducing agent	39 (2008) ^{e)}
Copper	Cu	Electric/electronic equipment, alloys	31 (2008) ^{e)}

a) Wiley VCH (2012).

b) www.minerals.usgs.gov (accessed 18.09.2012)

c) Euro Chlor (2011).

d) Riedel and Janiak (2011); BGS (2010).

e) BGS (2010).

Phosphoric acid and **phosphate salts** are produced either by oxidation of elemental phosphorous or by extraction of the phosphate mineral $\text{Ca}_3(\text{PO}_4)_2$ (apatite) with sulfuric acid. Production from elemental phosphorous is energetically more demanding and therefore capacities are increasingly shifting towards the extraction process. However, the production of “food grade” phosphoric acid from the natural mineral apatite requires additional separation and purification steps to remove heavy metals (such as e.g., Cu or As) from the crude phosphoric acid. Precipitation techniques and countercurrent extraction with organic solvents, such as *n*-butanol or diisopropyl ether, are applied for this purpose.

The production of **sulfur** and **sulfur dioxide** serves mainly for the purpose of **sulfuric acid** production. Sulfur is obtained from the desulfurization of natural gas or fuels, from sulfidic ores (e.g., FeS_2 , Cu_2S , or ZnS), or from natural reservoirs of elemental sulfur. The production of sulfur from natural reservoirs is carried out by either direct mining or extraction of sulfur from the ground by hot water injection (Frasch process). The further processing of elemental sulfur to sulfuric acid is treated as a process example in this book (Section 6.3).

Chlorine and **sodium hydroxide** are the main products of the industrial chlor-alkali electrolysis that is described as a process example in Section 6.19. **Hydrochloric acid** is produced by reaction from the elements H_2 and Cl_2 or by the reaction of chloride salts such as, for example, NaCl or CaCl_2 , with sulfuric acid. Other important sources of HCl are industrial chlorination processes using Cl_2 as chlorination agent (e.g., chlorination of benzene to form chlorobenzene and HCl or the chlorination of methane to give chloromethane and HCl) or industrial dehydrochlorination processes (e.g., production of vinyl chloride and HCl from 1,2-dichloroethane). The main uses of hydrochloric acid are addition reactions to unsaturated compounds (by hydrochlorination or oxychlorination), formation of chlorine in the Deacon process, production of chloride salts from amines and other organic bases, dissolution of metals, regeneration of ion exchange resins, and the neutralization of alkaline products.

Industrial **soda ash (sodium carbonate)** is produced from natural reservoirs (e.g., in the USA) or by the Solvay process. The brutto reaction of the Solvay process is the conversion of NaCl and CaCO_3 into Na_2CO_3 and CaCl_2 . Figure 5.2.1 shows the process scheme and the number of unit operations. The key achievement in the historic development of the process (*E. Solvay*) was to realize a quantitative regeneration of ammonia. This point was essential for economic success as the price of ammonia is typically higher than the prize of soda ash.

Another group of inorganic base chemicals are the products of air separation, **nitrogen**, **oxygen**, and the **noble gases**. Air separation processes are carried industrially out by cryogenic distillation, adsorption, or membrane separation. For large industrial production plants cryogenic distillation is by far the most relevant. The process was developed in 1905 (*C. von Linde*) and makes use of the Joule–Thomson effect (cooling of a gas by decompression, see Section 3.1.2) in combination with cooling of the compressed gas.

Other technically important gases are **hydrogen**, **carbon monoxide** and **carbon dioxide**. Owing to their great relevance, Section 6.2 is devoted entirely to the processes of their production. Moreover, Sections 6.5, 6.8, 6.11 and 6.15 deal with processes applying these gases as feedstock.

Metals are industrially very important inorganic products. However, they are typically not produced by the chemical industry but by specialized companies. Typically, these companies focus on the production of one type of metal (including variations such as alloys and related technologies such as forming)

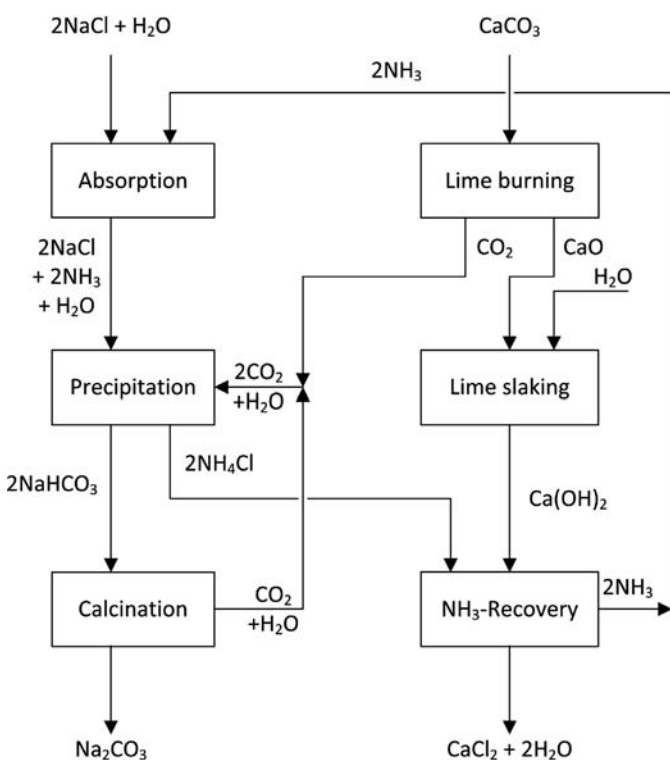


Figure 5.2.1 Process scheme of the Solvay process used to produce soda ash. Adapted from Onken and Behr, (1996).

or on one type of metallurgic process. The most important metals are *iron, aluminum, and copper*. The production of iron is described in detail in Section 6.5, and the electrometallurgical processes leading to Al and Cu are presented in Section 6.19.

Table 5.2.2 lists other inorganic products of technical relevance, together with literature references for more detailed reading.

5.3

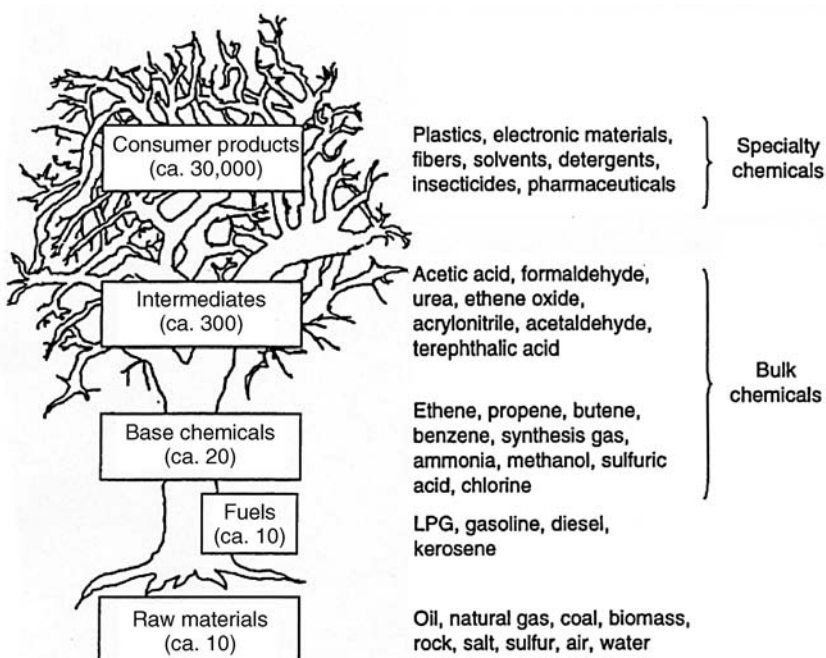
Organic Intermediates and Final Products

Today's industrial organic chemistry is still largely based on crude oil as primary feedstock. Crude oil has an inert, saturated hydrocarbon character that typically

Table 5.2.2 Further inorganic mass and specialty products.

Inorganic product	Main component(s)	Major applications	Reference for further reading
Fertilizer	[NH ₄] ₂ [SO ₄], [NH ₄][NO ₃], Ca[NO ₃] ₂ , Ca[CN] ₂ , Ca[H ₂ PO ₄] ₂ , [NH ₄][H ₂ PO ₄], [NH ₄] ₂ [HPO ₄], KCl, K ₂ [SO ₄]	Farming, agriculture	Mueller (1999)
Silicates	SiO ₂ , Na ₂ [SiO ₃], Na ₂ Si ₂ O ₅ , Na ₂ Si ₄ O ₉	Glass, zeolites	Vogel (2006)
Gypsum	Ca[SO ₄] ₂ , Ca[SO ₄] ₂ ·2H ₂ O	Construction material	Buechel <i>et al.</i> (2000)
Limestone	Ca[CO ₃]	Cement production	Boynton (1980)
Ceramics	Ba[TiO ₃], Al ₂ O ₃ , ZrO ₂ , BN, B ₄ C, Si ₃ N ₄ , SiC, TiC	Electric/electronic equipment, high temperature applications	Aldinger and Weberruss (2010)
Inorganic fibers	C, SiO ₂ , Al ₂ O ₃ , BN, B ₄ C	High temperature applications, composite materials	Buechel <i>et al.</i> (2000)
Silicones	[Si(CH ₃) ₂ -O-] _n ; n > 10.000	Silicone oils, silicone resins	Buechel <i>et al.</i> (2000)

Figure 5.3.1 The “chemis-tree” illustrating the origin of organic industrial chemicals from the main organic raw material resources oil, natural gas, coal, and biomass.



requires two process steps for its use to produce chemicals: (i) activation of the inert alkane by lifting the energy content of the molecule in an endothermic process step; (ii) selective functionalization of the activated organic molecule to generate the functionality in the molecule that is required for its end-use with the customer.

As illustrated in Figure 5.3.1 all organic industrial chemicals are based on a relatively small number of raw materials that are “activated” according to step (i) to around 20 base chemicals. The latter are functionalized according to step (ii) to around 300 intermediates that are applied in many thousands of consumer products.

This subchapter describes the most important products and product groups of industrial organic chemistry and presents their production routes, capacities, and main applications. Specific examples will be treated here only very briefly as they have been selected as process examples for much more detailed treatment in Chapter 6.

5.3.1

Alkanes and Syngas

Alkanes are saturated hydrocarbon compounds of the sum formula C_nH_{2n+2} ($n = 1-1000$; above 1000 the compounds are called “polymer”). Because the number of carbon atoms n and the degree of branching of the alkane chain offers an enormous structural diversity, the class of alkanes consists of a huge number of individual molecules. In chemical technology, alkanes are typically applied as mixtures; the natural alkane resource, crude oil, is also a mixture of alkanes. Only a few alkane representatives, in particular methane, ethane, propane, butane, and cyclohexane are of technical importance as pure compounds. Table 5.3.1 gives an overview of these industrially important alkanes, their main applications, and production capacities.

Methane is a major component of natural gas. An additional source of methane is the fermentation of biogenic waste, forming the so-called “biogas” that contains methane as a major component. Synthetic methane can be obtained by hydrogenation of CO ($\Delta H = -207 \text{ kJ mol}^{-1}$) over Ni/Al₂O₃ catalysts at 300–600 °C and

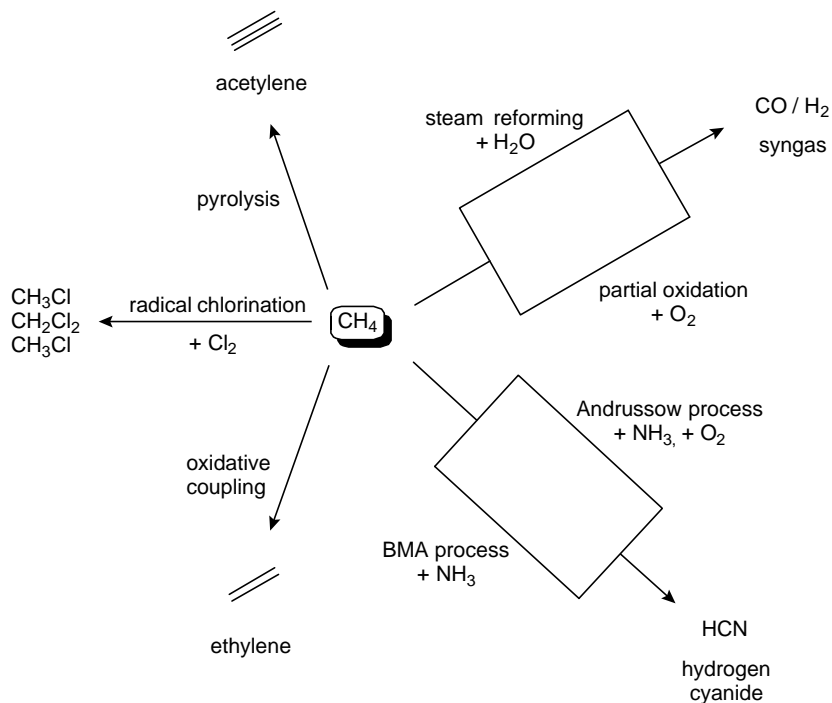
Table 5.3.1 Industrially important alkanes and their major applications.

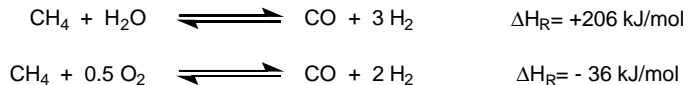
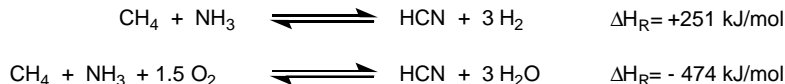
Alkane	Structure	Major applications	World production in 2010 (Wiley-VCH, 2012)
Methane	CH_4	See Figure 5.3.2	3.2 trillion $\text{m}^3 \text{a}^{-1}$ (3.2 billion t a^{-1})
Ethane		Ethylene	
Propane		Propylene	
Butane		Maleic acid anhydride	
Cyclohexane		ϵ -Caprolactam, adipinic acid, adipodinitrile, hexamethylene diamine, hexamethylene diiso-cyanate	4.6 mio. t a^{-1}

20–50 bar using fixed bed or fluidized bed reactors. Methane is applied mainly as heating gas in combustion devices to produce heat and electricity. Chemical applications of methane are summarized in Figure 5.3.2.

Chloromethane, dichloromethane, and chloroform are formed by radical chlorination of methane (Section 5.3.3.9). Acetylene is formed by the pyrolysis of methane, either in a strongly endothermic process producing hydrogen as coupling product (light arc process, 2000°C) or in an autothermic process with addition of O_2 and formation of acetylene and water (Sachsse–Bartholomé process). Methane is also used as feedstock to produce CO/H_2 mixtures that are usually referred to as “syngas.” Again, a strongly endothermic route and an autothermic process exist. As shown in Scheme 5.3.1, the first process converts water and CH_4 into CO and H_2 , while the second is a partial oxidation of methane resulting in a lower CO to H_2 ratio.

Production of hydrogen cyanide from methane is also possible using two process alternatives. The strongly endothermic BMA process (the name originates from the German “Blausäure aus Methan und Ammoniak,” 1200 – 1300°C , Pt contact)

Figure 5.3.2 Chemical products from methane.

Scheme 5.3.1 Syngas production from methane.**Scheme 5.3.2** Hydrogen cyanide production from methane.

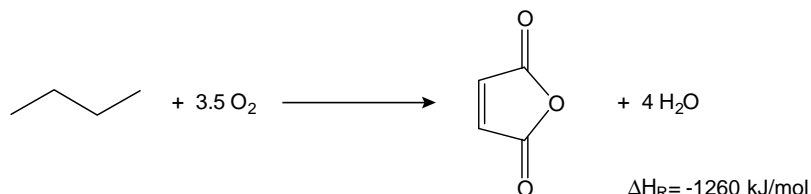
produces H_2 as the coupling product while in the strongly exothermic Andrussow process ($1000\text{--}1200^\circ\text{C}$, Pt/Rh-contact) these hydrogen equivalents are oxidized with the added oxygen to form water (Scheme 5.3.2).

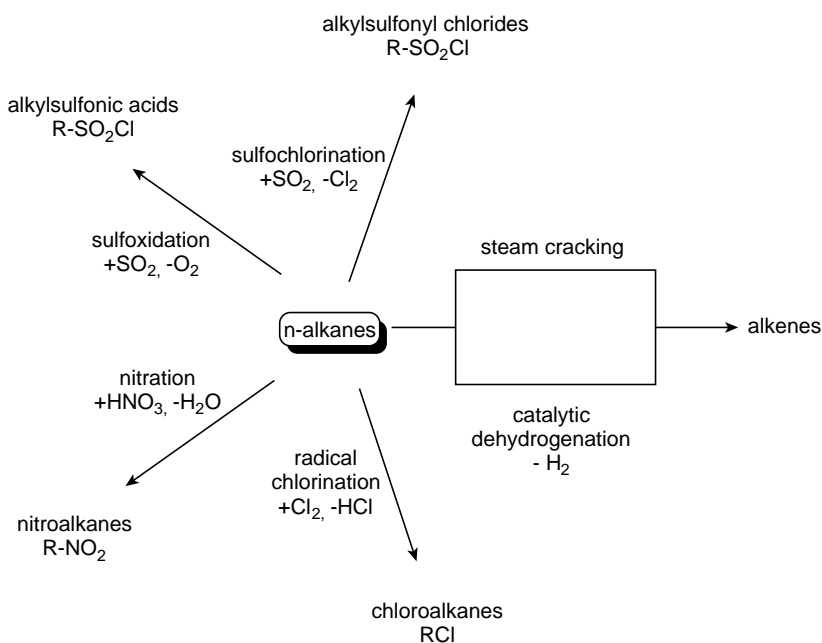
Hydrogen cyanide is an essential chemical for the production of methacrylic esters, adiponitrile, and some technical important amino acids, such as L-methionine. Alongside the two mentioned synthetic routes from methane, considerable amounts of HCN are also formed as a side product of acrylonitrile synthesis using the Sohio process (Section 5.3.3.8).

The production of ethylene by oxidative coupling of two molecules of methane and one molecule of oxygen (coupling product: water, $800\text{--}900^\circ\text{C}$, catalytic contact) is one of the younger and less well established routes to converting methane into useful chemicals. Significant research efforts are ongoing to improve the catalytic contacts for this reaction with the goal of further improving ethylene selectivity. In published reports the combined selectivities for ethane and ethylene reach 80%, which is close to the borderline of economic feasibility. However, 20% of the methane ends up in the undesired oxidation products CO and CO_2 .

Pure *ethane*, *propane*, and *butane* streams are isolated from wet natural gas. The main technical use of pure ethane and propane is catalytic dehydrogenation to ethylene and propylene, respectively. Alkane dehydrogenation is highly endothermic and, therefore, high temperatures are required to reach reasonable equilibrium conversions. The high process temperatures (e.g., $550\text{--}620^\circ\text{C}$ for the UOP Oleflex process; $590\text{--}650^\circ\text{C}$ for the ABB Lummus Catofin process) lead to significant cracking and coke formation in the reactor. Consequently, process concepts must be in place for frequent catalyst regeneration. There exist several different process variations for commercial catalytic dehydrogenation, which differ in the type of catalyst used (e.g., $\text{Pt}/\text{Al}_2\text{O}_3$ or $\text{Cr}/\text{Al}_2\text{O}_3$), reactor design (adiabatic moving bed reactors – Oleflex; parallel adiabatic fixed-bed reactors – Catofin; fluidized-bed reactor and regenerator – Snamprogetti), method of heat supply, and catalyst regeneration concept. Note that alkene yields are limited in catalytic dehydrogenation by thermodynamics and by the fact that the reaction conditions are chosen so as to minimize unfavorable side reactions. Typical single pass conversions in a commercial catalytic dehydrogenation plant are 20–40 wt%.

Butane can also be dehydrogenated to butenes, but even more important is its selective oxidation to maleic anhydride (Scheme 5.3.3). Butane oxidation is a highly exothermic catalytic process that is carried out in fluidized bed or multi-tubular

Scheme 5.3.3 Butane oxidation to produce maleic acid anhydride.



reactors. The reaction intermediates (e.g., 2-butene, butadiene, furan) are more reactive than the starting material butane, and the risk of overoxidation to CO₂ and water is very high if hot spots occur in the reactor.

Refinery alkylation, the reaction of isobutane (or isopentane) with light alkenes to produce high octane-number fuels, is a very important example of the technical use of branched light alkanes. This process is highlighted in Section 6.10.

Alkanes with five to eighteen carbons are isolated in the form of different distillation cuts from crude oil distillation in the refinery. Naphtha (C₅–C₁₄, boiling range: 20–200 °C) and light diesel fractions (C₁₅–C₁₈, boiling range: 200–280 °C) are converted into chemicals in different processes that are displayed in Figure 5.3.3.

A very important process for the use of higher alkanes in the chemical industry is steam cracking, which is also called “naphtha cracking” if naphtha is used as the main feedstock. Steam cracking is of great importance for the whole petrochemical industry as it is the key operation in producing the most important organic intermediates: ethylene, propylene, and butadiene as well as benzene, toluene, and xylenes. Owing to the importance of this process, steam cracking has been selected as an example in this textbook and the process is described in great detail in Section 6.6. Apart from steam cracking, which is a radical process, catalytic cracking (known as “fluid catalytic cracking” or “FCC-process”) of higher alkanes also produces a certain amount of alkenes (Section 6.7.2 for details). An alternative process option to convert higher alkanes into alkenes is the direct catalytic dehydrogenation of higher alkanes as described above for ethane, propane, and butane. Finally, a reaction sequence of radical alkane chlorination followed by a dehydrochlorination step can also convert alkanes into alkenes of the same C-number. However, this process requires expensive Cl₂ and produces HCl as stoichiometric coupling product which harms its economic attractiveness.

Apart from alkene production, n-alkanes are applied as feedstock in the technical production of alkyl sulfonate surfactants (see Section 5.3.5 for details about surfactants and their application). Two routes are established for the production of the alkyl sulfonate sodium salts [R-SO₃]Na from higher alkanes (for this application typical C-numbers are 12–18). In both routes, alkane activation proceeds via alkyl radicals, which are generated by UV-irradiation at room temperature. In the sulfochlorination route, the higher alkane is contacted with SO₂ and chlorine to form the alkylsulfonyl chloride, which is later neutralized with NaOH to give the

Figure 5.3.3 Important industrial processes for converting alkanes into chemicals.

corresponding alkyl sulfonate salt and NaCl. In the sulfoxidation route, the initial reaction of alkane, SO₂, and oxygen forms alkyl sulfonic acid which is also neutralized to form [R-SO₃]Na and water. The sulfoxidation route has the advantage that no chlorine is needed and that the NaCl coupling product is avoided.

The oxidation of higher alkanes leads to a large variety of oxidation products, including organic acids, aldehydes, ketones, and alcohols. In most cases the advantage of the cheap alkane feed is eliminated by the large effort required for the tedious separation and purification of the alkane oxidation product mix. This fact has restricted alkane oxidation processes in the chemical industry to few cases, such as, for example, butane oxidation to maleic acid anhydride.

The nitration of higher alkanes is of limited technical importance. It typically proceeds as a liquid-phase reaction at around 200 °C and produces the desired nitroalkanes together with significant amounts of oxidation and cracking product.

Cyclohexane is the most important cyclic alkane in industrial organic chemistry and plays a major role in the industrial production of important monomers, such as, for example, adipinic acid, adipodinitrile, hexamethylenediamine, hexamethylene diisocyanate, and ϵ -caprolactam (Sections 5.3.3.6, and 5.3.3.8 for details). For all these production processes cyclohexane is oxidized in the first step in a liquid-phase reaction to a mixture of cyclohexanol and cyclohexanone. Details about this process are given in Section 5.3.3.1.

“*Syngas*” is the technical term for gas mixtures of carbon monoxide and hydrogen. Syngas can be obtained by several processes from almost any carbon-containing feedstock, with natural gas, crude oil, coal, and biomass being the most relevant sources. Processes for the production of syngas are described in detail in Section 6.2. Major applications of syngas are also covered in specific examples, including ammonia synthesis (Section 6.1), methanol synthesis (Section 6.11.2), Fischer–Tropsch synthesis (Section 6.11.1), and hydroformylation (Section 6.15).

5.3.2

Alkenes, Alkynes, and Aromatic Hydrocarbons

Table 5.3.2 gives an overview of the industrially most relevant alkenes, alkynes, and aromatic compounds. Their most important industrial applications are also summarized.

Ethylene is obtained mainly by the steam-cracking process (Section 6.6) and by catalytic dehydrogenation of ethane (Section 5.3.1). Chemical transformations of ethylene to industrial relevant chemicals (Figure 5.3.4) can be classified in three main categories:

- 1) ethylene oligomerization to 1-alkenes and polymerization to different kinds of polyethylene products;
- 2) addition reactions to the ethylene double bound to yield, for example, ethanol, 1,2-dichloroethane, or styrene;
- 3) catalytic oxidation of ethylene for the production of ethylene oxide, acetaldehyde, and vinyl acetate.

Owing to their high industrial relevance, many of the processes named above have been selected as examples of this textbook. They are treated in detail in Sections 6.12 (ethylene oxide production), 6.15 (acetaldehyde production), 6.16 (ethylene oligomerization) and 6.20 (polyethylene production).

Propylene is also a product of the steam-cracking process (up to 15 wt% of the steam cracker product mix, Section 6.6). In addition, it is obtained by catalytic dehydrogenation of propane (Section 5.3.1) and as a by-product of the FCC process (Section 6.7.2). The technical relevance of propylene as a feedstock for the synthesis of industrial chemical processes has ever increased since the 1960s. The increasing value of propylene can be realized from the fact that propylene was seen in former times as an undesirable by-product of the steam-cracking process and as such it was

Table 5.3.2 Industrially important alkenes, alkynes, and aromatic compounds.

Compound	Structure	Major applications	World production (mio. t a ⁻¹) (unless specified, data from Wiley-VCH, 2012)
Ethylene		See Figure 5.3.4	120 (2008)
Propylene		See Figure 5.3.5	53 (2002)
Butadiene		Polybutadiene, copolymers, chloroprene, adipodinitrile, sulfolene	9 (2009)
Isobutene		Methyl <i>tert</i> -butyl ether (MTBE), polyisobutene, diisobutene, <i>tert</i> -butanol, copolymers, alkylate	14 isobutene + n-butenes (2008): 26 (for alkylate) 12 (MTBE) 4 (gasoline blendstock) 6 (chemical uses)
<i>n</i> -Butenes		See Figure 5.3.7	5
Benzene		See Figure 5.3.8	40 (2012) ^{a)}
Toluene		See Figure 5.3.9	20 (2008)
<i>o</i> , <i>m</i> , <i>p</i> -Xylene		Phthalic acid anhydride (<i>o</i> -xylene), isophthalic acid (<i>m</i> -xylene); terephthalic acid (<i>p</i> -xylene)	35 (2012) ^{a)}
Acetylene		Vinyl chloride, vinyl ester, vinyl ether, butanediol, processing of metals (welding) (Scheme 5.4.3)	0.7 in 1998 ^{b)} and 9 in 2012 ^{c)}

a) estimation based on various sources.

b) Weissermel and Arpe, 2003.

c) With the exception of 1,4-butanediol, the acetylene-based routes to chemicals (Fig. 5.3.10) were largely abandoned (starting in the 1960ties), see text below. However, in around 2000, these routes were revisited in China and exploded in growth, above all for vinyl chloride (VC) used to produce polyvinyl chloride (PVC). Today, about 85% of all China's VC capacity (22 mio. t/a in 2012) is via coal-derived acetylene, which is equivalent to about 8 mio. tonnes acetylene (www.icis.com/Articles/2012/04/16/9549986/china-invents-and-reinvents-coal-to-chemicals.html; accessed 19.09.2012). Hence, the estimated global capacity for production of acetylene in 2012 is around 9 mio. tonnes.

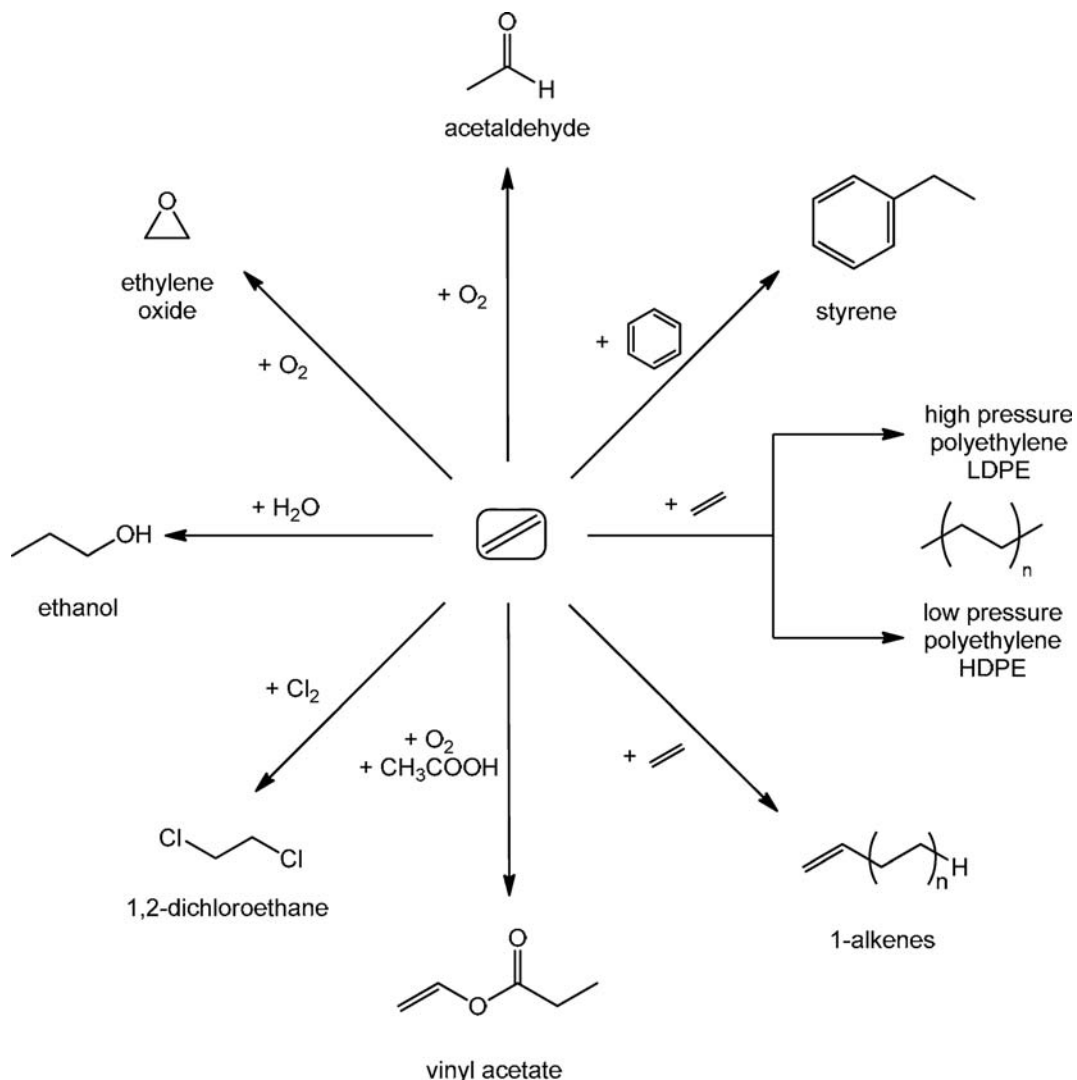


Figure 5.3.4 Important industrial products from ethylene.

burned as a fuel. In recent times, however, more and more processes have been developed and commercialized that convert ethylene and 2-butene into propylene by an alkene metathesis reaction.

Similar to ethylene, the main chemical transformations of propylene into industrial relevant chemicals (Figure 5.3.5) can be classified in three main categories:

- 1) propylene dimerization (to isohexene and high-octane C₆-fuel components) and propylene polymerization (to polypropylene, Section 5.3.4);
- 2) addition reactions to the propylene double bound to yield, for example, isopropanol, butanal, cumol, or allyl chloride;
- 3) catalytic oxidation of propylene to produce propylene oxide, acrylic acid, and acrylonitrile.

Chapter 6 highlights some of the most relevant processes named above. Propylene oxidation is described in Section 6.12 and propylene hydroformylation in Section 6.14.

Butadiene, isobutene, and butenes (1-butene, *cis*-2-butene, and *trans*-2-butene) are isolated from the C₄ cut of the steam cracker in a sequence of separation units that is depicted in Figure 5.3.6. In the first step, butadiene (representing roughly 50% of the cracker C₄ cut) is isolated from the other C₄ components by an extractive

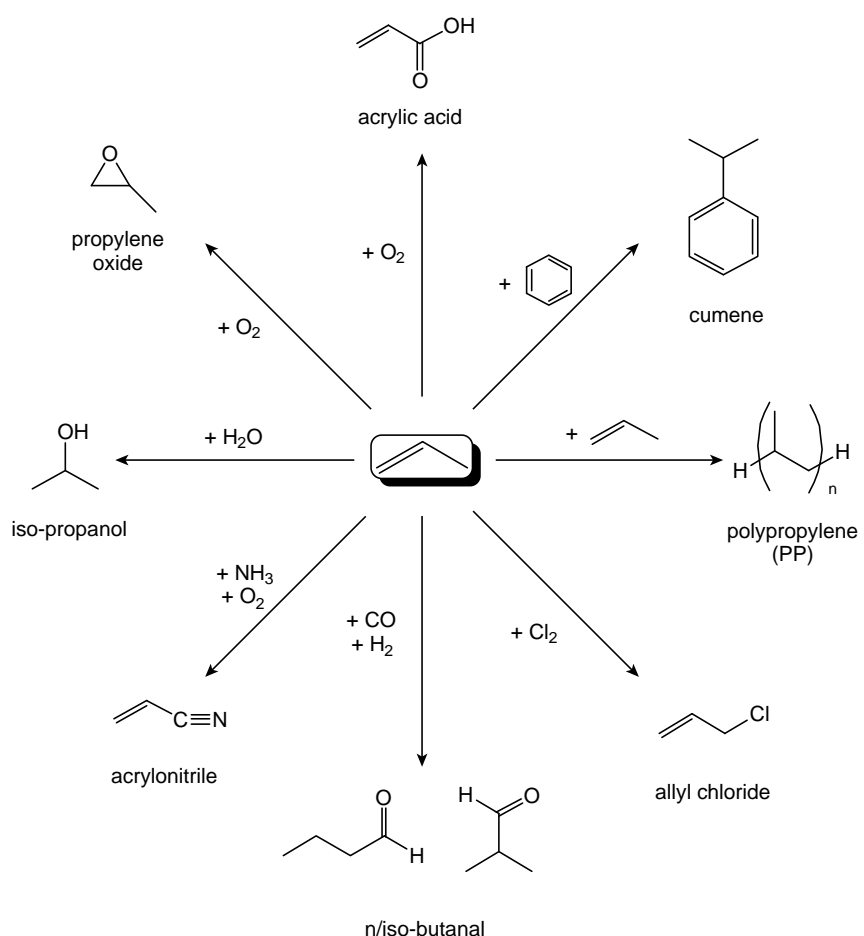


Figure 5.3.5 Important industrial products from propylene.

distillation process (see Section 3.3.2.3 for details). The added solvent [*N*-methylpyrrolidone (NMP), *N*-formylmorpholine, or dimethylformamide (DMF)] interacts strongly with butadiene and reduces greatly and selectively its vapor pressure, thus enabling distillation of the other C4 components from the butadiene–solvent mixture. The distilled mixture of C4 components leaving the extractive rectification step at the top of the column is called “Raffinate 1.” Typically, Raffinate 1 contains 45% iso-butene, 25% 1-butene, 9% *trans*-2-butene, 7% *cis*-2-butene, 11% butanes, 3% isobutane, and traces of 1,3-butadiene.

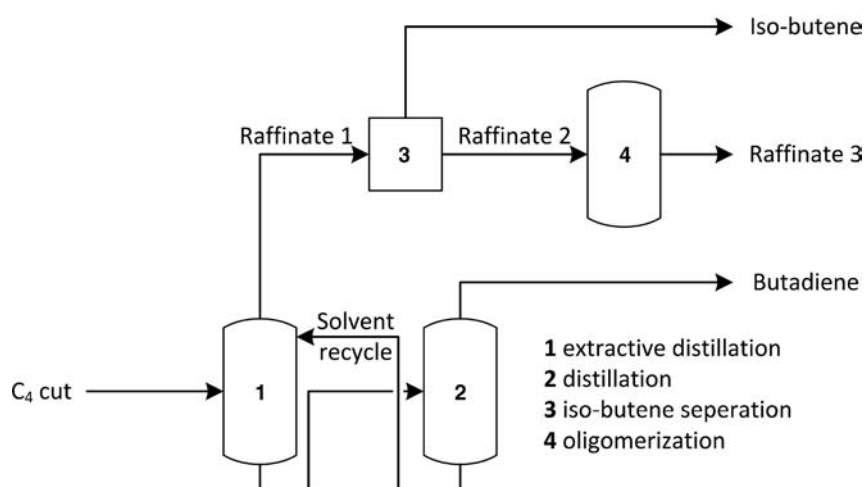


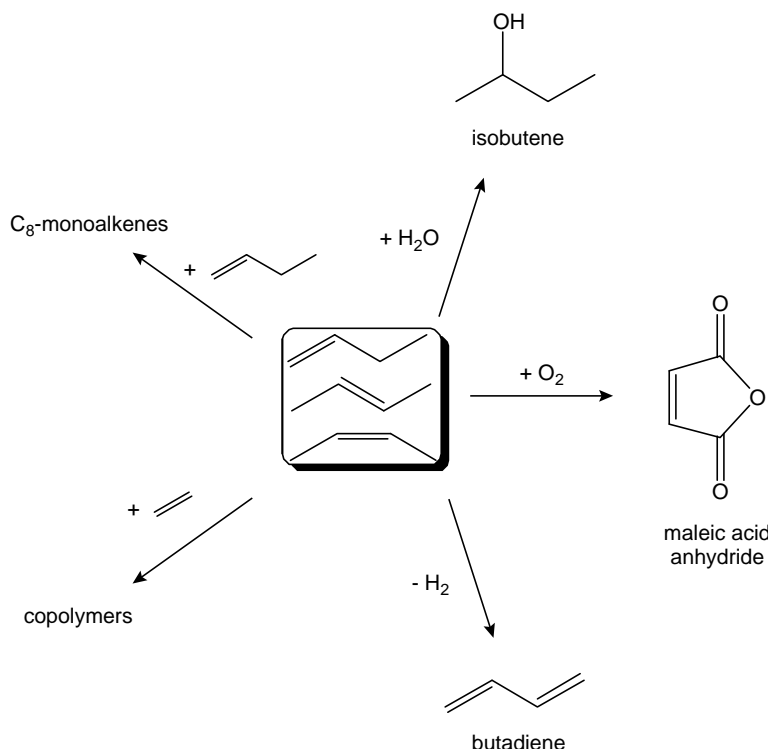
Figure 5.3.6 Technical processing of the steam-cracker C4-cut.

The next step in the cracker C4 treatment is the isolation of isobutene from Raffinate 1. To realize this step, Raffinate 1 is reacted with water or methanol to form *tert*-butanol or methyl-*tert*-butyl ether, respectively. Alternatively, Raffinate 1 can be treated with an acid catalyst to convert isobutene selectively into isoctene, an important fuel additive. All Raffinate 1 treatment processes have in common that isobutene reacts selectively from the mixture to form a compound of significantly lower vapor pressure. Thus, in the subsequent distillation process, the isobutene adduct is the low boiling component and remains at the bottom of the distillation column while the remaining C₄-compounds can be isolated at the top. The obtained distillate is called Raffinate 2 and consists typically of 45% 1-butene, 30% 2-butenes, 19% butanes, 6% isobutane, and traces of 1,3-butadiene. Raffinate 2 can be applied as feedstock for a distillation unit that isolates 1-butene from the mixture for copolymerization applications. Alternatively, Raffinate 2 can be fed into a dimerization unit where either a homogeneous (Dimersol-process) or a heterogeneous Ni-catalyst (Octol process) converts the butenes into C₈ dimers. Unconverted feedstock of this unit is called Raffinate 3. It typically contains around 70% butane and isobutane and 30% of remaining linear butenes. Raffinate 3 is recycled to the cracker to serve their as an addition to the cracker feed.

Apart from dimerization and copolymerization, linear butenes have a few other important applications, including hydration to isobutene, oxidation to maleic anhydride, and dehydrogenation to butadiene (Figure 5.3.7).

Benzene is produced together with toluene and xylenes via two major routes. One source is the C₅₊ product cut of the steam-cracking process (see Section 6.6 for details). It typically contains 30–45% benzene, 20% toluene, and 5–10% xylenes. The second production route is the reforming process in refineries (see Section 6.9 for details) with a typical product composition of 5–8% benzene, 20–25% toluene, and 30% xylenes. In former times, the production of aromatic compounds from coking plants also played a significant role but today 98% of benzene production is based on crude oil.

Figure 5.3.7 Important industrial products from *n*-butenes.



All technically relevant production routes for benzene, toluene, and xylenes are characterized by the fact that the aromatic compounds are formed in mixtures together with non-aromatic compounds of the same carbon numbers. To isolate individual aromatic compounds in pure form it is not only necessary to separate the different aromatics from each other, but – in most cases more difficult – to separate the aromatic compound from its non-aromatic counterpart with the same number of carbon atoms (e.g., cyclohexane from benzene or methylcyclohexane from toluene). Technical difficulties arise due to the very close boiling points and the formation of many different azeotropic mixtures among these mixtures. Consequently, special separation technologies had to be developed for these separation problems, leading to extractive distillation (Section 3.3.2.3) and liquid–liquid extraction processes. The decision among the latter two options is made according to the aromatics content in the feedstock mixture. For mixed feeds with low aromatic contents it is energetically unfavorable to use an extractive distillation process where the large share of light boiling non-aromatics has to be evaporated in the column. Therefore, diluted aromatic feeds are typically treated in extraction processes using solvents like dimethyl sulfoxide, sulfolane, or *N*-methylpyrrolidone/water mixtures as extraction medium. In contrast, for mixed feeds with high aromatics content it is advantageous to add an entrainer solvent (typically *N*-methylpyrrolidone) and to isolate the entrainer/aromatic mixture at the bottom of the distillation unit. This mixture is distilled later to obtain the pure aromatic product.

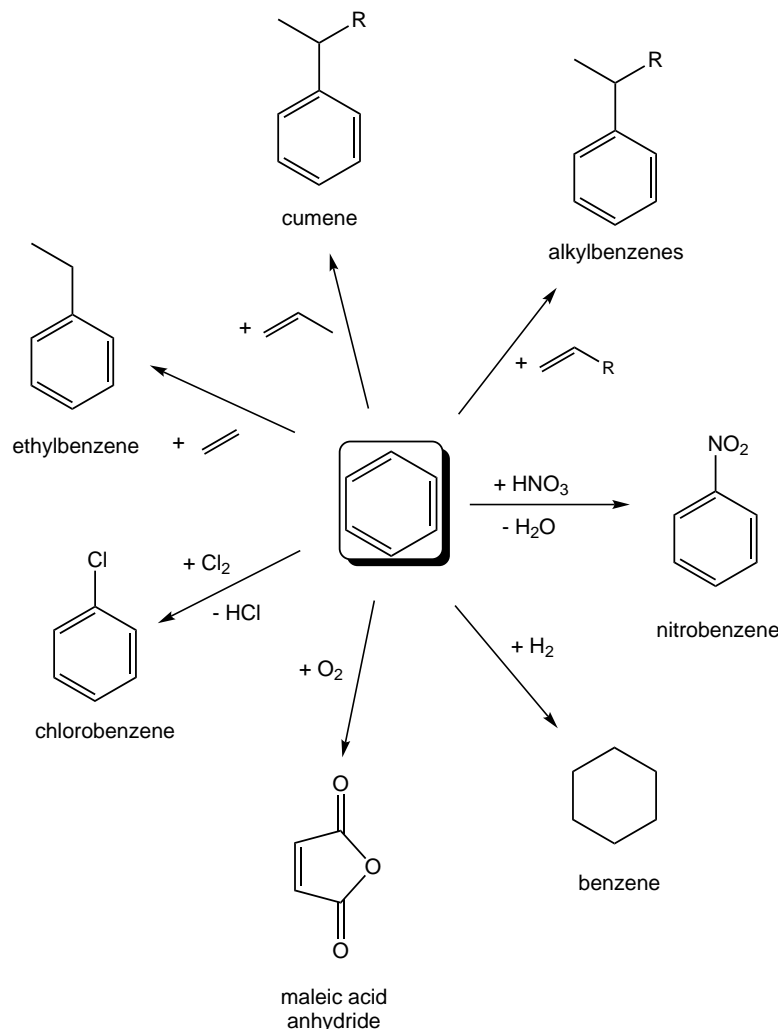
Note that the share of aromatic compounds obtained from industrial production processes does usually not correspond to the market need. Therefore, several transformation processes have been developed to convert a less desired aromatic compound into a more desired one. The most relevant are:

- hydrodealkylation, converting toluene and hydrogen into benzene and methane;
- disproportionation, converting two moles of toluene into benzene and xylene;
- transalkylation, converting toluene and trimethylbenzene into two moles of xylene;
- isomerization, converting pure *o*-, *m*-, or *p*-xylene (isolated, for example, by crystallization processes) into the thermodynamic mixture of xylenes (Octafining process).

Figure 5.3.8 shows the most important industrial applications of benzene. Ethylbenzene, cumene, and other alkylbenzenes are obtained in so-called “Friedel–Crafts alkylation” reactions (Section 2.2.5). In the Friedel–Crafts reaction an alkene or haloalkane reacts with an aromatic ring by replacing one or more ring-hydrogens with an alkyl group. The reaction is catalyzed by solid or dissolved acids and is usually carried out in bubble column reactors if benzene is contacted with gaseous reagents. Dehydrogenation of ethylbenzene leads to styrene, which is primarily used as monomer in polymer productions (Section 5.3.4). For cumene, the main further use is its conversion into phenol in an oxidation–rearrangement reaction sequence (see Section 6.14 for details). Higher alkylbenzenes are mainly used as intermediates for the production of detergents (in this case the alkyl group R contains typically 12–18 carbon atoms). Other important industrial applications include nitration to nitrobenzene, hydrogenation to cyclohexane, oxidation to maleic acid anhydride, and chlorination to chlorobenzene.

Figure 5.3.9 summarizes the most important technical applications of toluene. The fact that a very important reaction for toluene is its dealkylation to benzene (about 50% of industrial toluene use) indicates that more toluene is produced from steam cracking and reforming than industrially needed under typical market conditions. *o*-Xylene is mainly converted into phthalic acid anhydride, *m*-xylene into isophthalic acid, and *p*-xylene into terephthalic acid. While phthalic acid finds its most important use as a component in plasticizers, terephthalic acid is a key monomer for the production of polyesters (see Section 6.13 for details).

Figure 5.3.8 Important industrial products from benzene.



Acetylene is produced industrially from coal via calcium carbide (CaC_2), from crude oil, or from natural gas. In the synthesis of calcium carbide, calcium oxide (CaO) reacts with coal in an electrothermal oven to form the carbide. By reaction of the carbide with water, acetylene and calcium hydroxide are obtained. The synthesis of acetylene from crude oil or natural gas proceeds through a high-temperature pyrolysis reaction at 1400°C , using very short residence times in the millisecond range. The high temperature is required for thermodynamic reasons. The industrial processes in use differ by the way in which the high temperature is provided. The Hüls process uses a light arc, the Hoechst/Hüls process a plasma, and the Sachsse-Bartholomé process of BASF a flame provided by the incomplete combustion of methane or light fuel feedstock. Thus the Sachsse-Bartholomé process operates autothermally. Acetylene yields of around 20% are reached.

Figure 5.3.10 summarizes the most important industrial applications of acetylene. Note that acetylene produced from CaC_2 was the most important base chemical up to the 1960s and many important intermediates were produced at that time by addition reactions to the triple bond of acetylene. Since then acetylene has been increasingly replaced as key building block by ethylene. Ethylene production is significantly cheaper than acetylene production and technical chemists have learnt over the years to produce the same intermediate compounds from ethylene rather than from acetylene.

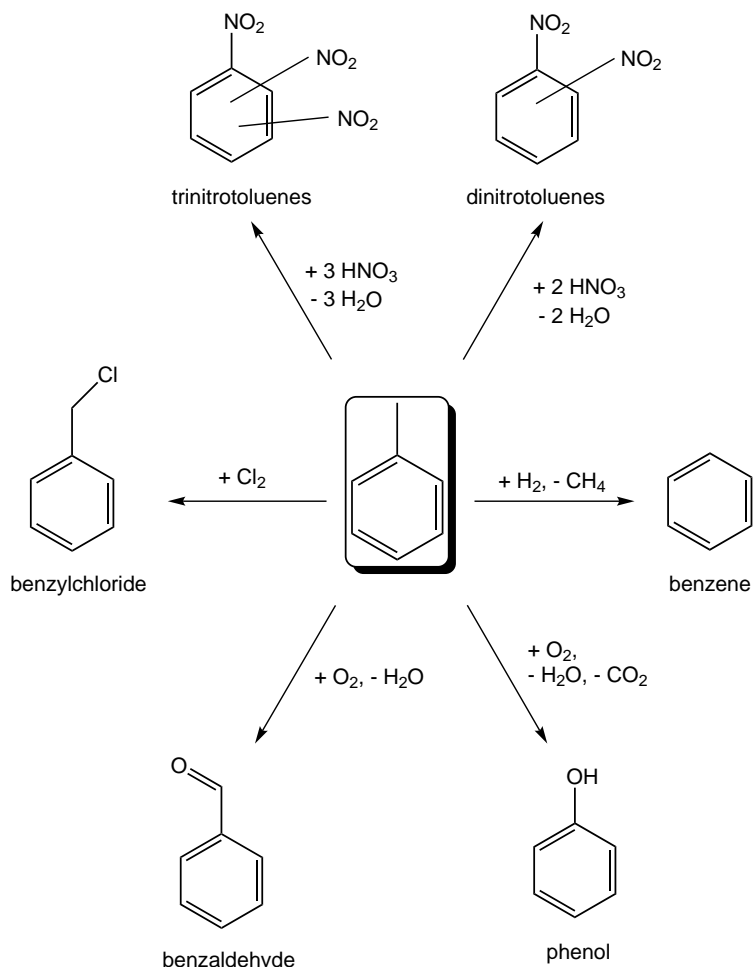


Figure 5.3.9 Important industrial products from toluene.

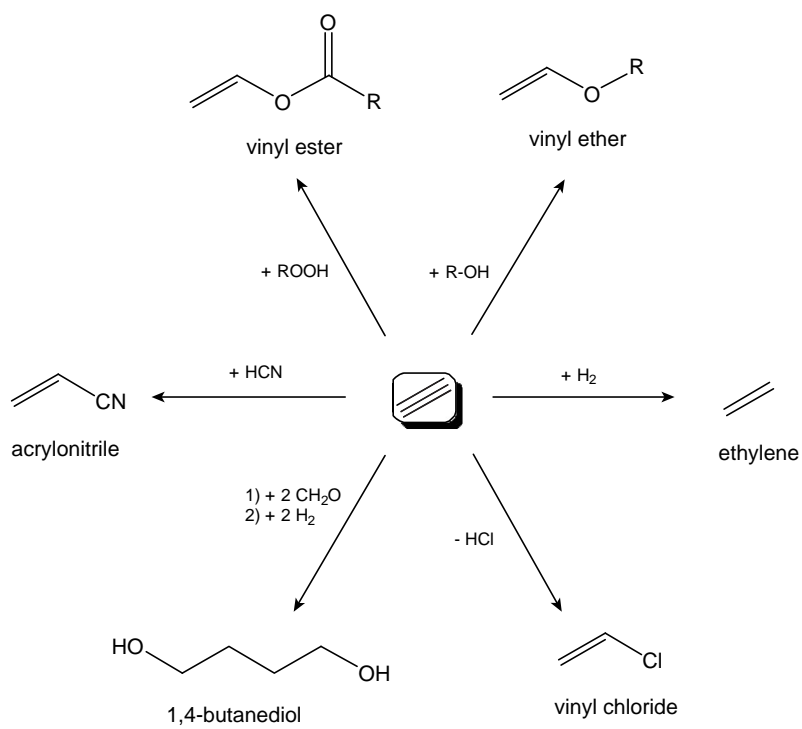


Figure 5.3.10 Important industrial products from acetylene.

5.3.3

Organic Intermediates Functionalized with Oxygen, Nitrogen, or Halogens

The production of organic intermediates from crude oil, natural gas, coal, and biomass (if converted into syngas in the first step) deals with the selective conversion and functionalization of the basic chemicals described in Sections 5.3.1 and 5.3.2. As organic intermediate we consider about 300 chemicals that are produced in large amounts ($>100\,000 \text{ tons yr}^{-1}$) but are not considered as final products for the end-user. Most organic intermediates contain at least one oxygen, nitrogen, or halogen functionality that is important for their chemical reactivity and, thus, for the range of their dedicated applications as building block, solvent, or part of product formulations.

The following subsections describe the state-of-the art in chemical technology for the production of the most relevant organic intermediates. Note that the production processes of some very important organic intermediates (methanol, ethylene oxide, propylene oxide, phthalic acid anhydride, phenol, butyraldehyde, 1-butanol, acetic acid, 1-olefins, adiponitrile, and vinyl chloride) have been selected in this textbook as “Examples of Industrial Processes” and will be treated in much more detail in Sections 6.11.2–6.19. These examples illustrate the complex interplay of thermodynamics, kinetics, chemical, mechanical, and economic aspects in developing and optimizing a chemical process. All intermediates treated in detail in Chapter 6 will be mentioned here only very briefly and in direct comparison to other representatives of the same product family. References to information in the specialized chapters are given wherever appropriate and helpful to the reader. Indeed, the same level of complexity as outlined in Chapter 6 can be expected for the production of almost all organic intermediates. For clarity and readability we have, however, restricted the detailed description at this higher level of complexity to a small selection of illustrative examples.

5.3.3.1 Alcohols

Alcohols that are industrially produced on a large technical scale consist of non-cyclic and cyclic and saturated and unsaturated representatives. Apart from monoalcohols, some diols and polyols are also of technical importance. Table 5.3.3 lists the most relevant examples together with their main applications areas and actual production capacities.

There are several ways to introduce selectively one or more hydroxyl functionalities into basic chemicals. The most important for the industrial production of monoalcohols are shown in Topic 5.3.1. Some of these routes are product specific (e.g., methanol synthesis from syngas), others can in principle be used for the production of a wide range of different alcohols [such as, for example, the reaction sequence of hydroformylation – see Section 6.14 – and hydrogenation – (c) in Example 5.3.1]. For a few alcohols, more than one industrial production route is in competition. This case either indicates similar production costs of the different competing routes [such as in the case of fatty alcohol production from either fatty acids – (f) in Example 5.3.1 – or by using the Alfol process – (g) in Example 5.3.1] or product specifications that are different enough to also justify the industrial use of a more expensive route [e.g., ethanol production by ethylene hydration – (c) in Example 5.3.1 – versus ethanol production by fermentation – (d) in Example 5.3.1].

Methanol production has been chosen as a process example of this textbook and is treated in detail in Section 6.11.2.

By far the largest part of *ethanol* is consumed in the form of alcoholic beverages or as biofuel and biogenic fuel additive. By law, this part of ethanol production is fully produced via fermentation [route (d) in Topic 5.3.1] from carbohydrates. Sugar mixtures (such as sugar cane or bagasse), starch-containing substrates (such as corn, potato, rice), and cellulosic substrates can be used in principle for the production of ethanol. In the case of starch-containing substrates, an enzymatic starch

Table 5.3.3 Industrially important alcohols and global production.

Alcohol	Structure	Major applications	World production (mio. t a ⁻¹) (unless specified, data from Wiley-VCH, 2012)
Methanol	CH ₃ OH	See Section 6.11.2	52 (2007) ^{a)}
Ethanol (chemical synthesis)		Acetaldehyde, ethyl acetate, ethylamine, fuel	
Ethanol (fermentation)		Beverages, ethylene	58 (2009) ^{b)}
<i>n</i> -Propanol		Solvent	
<i>iso</i> -Propanol		Solvent, fuel additive	2.4 (production capacity in 2003)
<i>n</i> -Butanol		Solvent, esters of carboxylic acids	
<i>iso</i> -Butanol		Solvent, esters of carboxylic acids	2.5 (total butanols, USA, W. Europe, Japan, 1999) ^{c)}
Fatty alcohols (C ₁₂ -C ₁₈)	e. g.	Non-ionic detergents	2.8 (2007)
2-Ethylhexanol		Plasticizer alcohol	2.9 (2004)
Cyclohexanol		Adipinic acid, ε-caprolactam	
Allyl alcohol		Glycerol, allyl ether, allyl ester	
Ethanediol		Poly(ethylene terephthalate) (PET), PE-glycols (PEGs), anti-frost agent	7 (2010)
1,3-Propanediol		Polyester	
1,4-Butanediol		Polyester, polyurethanes, γ-butyrolactone, THF, pyrrolidones	
Glycerol		Pharmaceuticals, cosmetics, anti-frost agent, sweetener	0.8 (1998)
Phenol		Phenolic resins, bisphenol A, alkylphenols	7 (2003)

a) Saade, 2009.

b) including chemical synthesis with a share of about 10%.

c) Weissermel and Arpe, 2003.

hydrolysis is needed prior to the fermentation process. For cellulosic substrates, a hydrolysis step to provide low molecular weight sugars is still important to reach reasonable fermentation rates.

Several kinds of yeasts and bacteria can be used as biocatalyst in this process. The yield in ethanol (with respect to the fermentable sugars) is 90–95%. The so-formed ethanol reduces the catalytic activity of the microorganisms (product inhibition), which leads to final ethanol concentrations of typically 6–8 mass% for yeast and 10 mass% for bacteria.

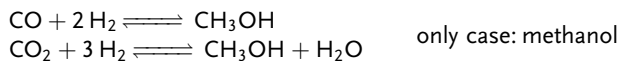
Ethanol isolation proceeds via distillative processes. Owing to the formation of an ethanol/water azeotrope (95.5 mass% ethanol at 1 bar), the production of water-free ethanol requires the application of extractive distillation (typical entrainer: benzene or cyclohexane, see Section 3.3.2.3). The isolation of water-free ethanol from fermentation is a relatively energy intense step. Even with a clever combination of several distillation columns working at different pressures, the energy input to produce 1 kg of bioethanol by fermentation is about 10 MJ (Baerns *et al.*, 2006). In a few countries, where the production of bioethanol is particularly cheap (e.g., Brazil), there have also been attempts to convert bioethanol into chemicals in commercial scenarios. The production of ethylene from bioethanol is a potential option in this context.

Chemical production routes for ethanol synthesis use mainly ethylene hydratization [route (c) in Topic 5.3.1]. The direct ethylene hydratization option uses solid acid catalysts (e.g., H₃PO₄ on kieselguhr, montmorillonite, or bentonite) in a continuous gas-phase reaction at 60–80 bar pressure and 250–300 °C. At an adjusted ethylene conversion of 5%, the selectivity to ethanol is 97%, with diethyl ether and acetaldehyde being the major side products.

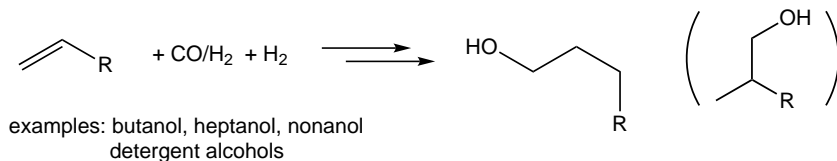
In the indirect ethylene hydratization process ethylene is contacted at 10–15 bar and 65–85 °C with concentrated sulfuric acid in a bubble column reactor. Mono and diethyl sulfate form and are hydrolyzed later (70–100 °C) to ethanol. Diethyl ether is the main side-product of the process (up to 10%). In the downstream of the reactor, ethanol and diethyl ether are distilled from the diluted sulfuric acid, neutralized, and separated by rectification. The diluted sulfuric acid produced in the process (45–60% sulfuric acid after water addition) is re-concentrated to 96%, a step that is energy intensive and problematic with respect to corrosion issues. Despite its relatively complex process scheme, the total ethanol yield in the indirect ethylene hydratization process is only 86%. One advantage of the indirect process, however, is that it also works with diluted ethylene feeds (e.g., feeds containing larger amounts of methane and ethane).

Topic 5.3.1 Important routes for the industrial production of saturated monoalcohols:

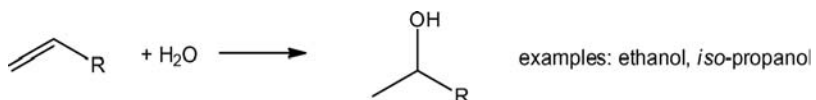
a) Alcohol synthesis directly from syngas (e.g., Cu/Zn catalyzed):



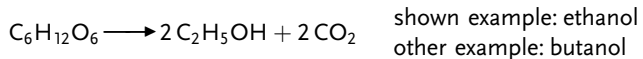
b) Alcohol synthesis from olefin and syngas (hydroformylation + hydrogenation – e.g., Co catalyzed):



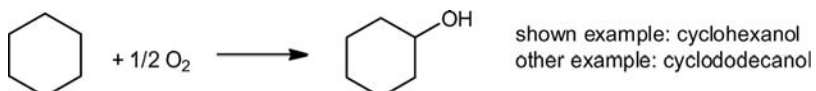
c) Alcohol synthesis by olefin hydration (acid catalyzed):



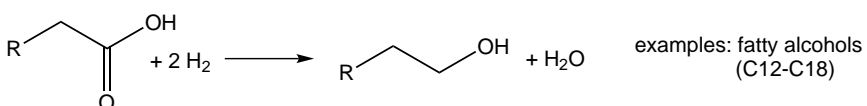
d) Alcohol synthesis by sugar fermentation (enzyme catalyzed):



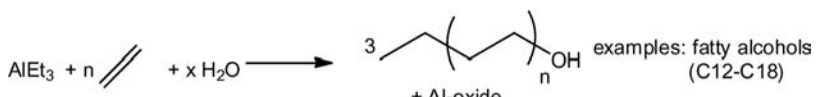
e) Alcohol synthesis by cycloalkane oxidation (e.g., Co-catalyzed):



f) Alcohol synthesis by fatty ester hydrogenation (e.g., Cu/Cr-oxide catalyzed):



g) Alcohol synthesis by ethylene oligomerization and Al-complex hydrolysis (Alfol process):



Among the propanols, *isopropanol* is of higher technical relevance. The compound is obtained in a very similar way to ethanol by acidic hydration (direct or indirect) of propene [route (c) in Topic 5.3.1]. *n*-Propanol is obtained from ethylene hydroformylation, followed by hydrogenation of the intermediate propanal.

Butanols exist as four isomers: *n*-butanol, isobutanol (2-methyl-1-propanol), 2-butanol, and *tert*-butanol (2-methyl-2-propanol). Both *n*- and isobutanol are obtained by propene hydroformylation followed by aldehyde hydrogenation [route (b) in Topic 5.3.1 and Section 6.14]. 2-Butanol and *tert*-butanol are industrially produced from hydration of 1-butene and isobutene, respectively [(route (c) in Topic 5.3.1)].

Fatty alcohols are industrially accessible by hydroformylation and hydrogenation of higher *n*-alkenes [route (b) in Topic 5.3.1]. Note that in this process, usually, fatty alcohols of uneven carbon number are obtained (as the original alkene has usually been produced on the basis of ethylene oligomerization processes – see Section 6.16 for details). Alternatively, fatty alcohols can be produced on the basis of ethylene using the so-called Alfol process, which has a great similarity to the “Ziegler growth reaction” discussed in Section 6.16 [route (g) in Topic 5.3.1]. Fatty alcohols can also be produced on the basis of a fatty methyl esters obtained by transesterification of biogenic oils and fats with methanol. At 200–300 bar hydrogen pressure and 350 °C these methyl esters can be hydrogenated using heterogeneous Cu-Cr-oxide catalysts to the corresponding fatty alcohol and water [route (f) in Topic 5.3.1].

Industrially important *cyclic alcohols* are cyclohexanol and cyclododecanol. Both products are obtained by a selective oxidation of the corresponding cycloalkane [route (e) in Topic 5.3.1]. Oxidation of cyclohexane to cyclohexanol is a radical reaction and proceeds in the presence of a cobalt naphthenate radical source that is

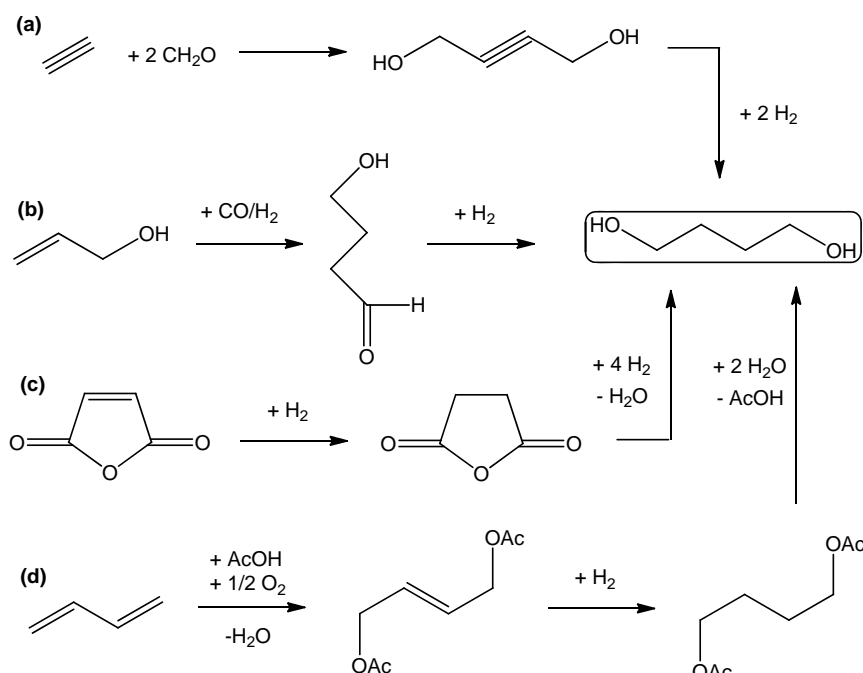
added to the reaction in ppm quantities. The reaction is carried out at 140–160 °C using air as oxidant. Cyclohexanone forms as the main by-product. Cyclododecanol is obtained by oxidation of cyclododecane (accessible by trimerization of butadiene followed by hydrogenation). Again, air is used as the oxidant to form the product at 150 °C in the presence of metaboric acid as the catalyst.

Allylic alcohol (2-propen-1-ol) is by far the most technically relevant *unsaturated alcohol*. The compound can be produced by different routes that all use propene as the starting point. However, direct production from propene is not possible. The viable alternatives include (i) hydroxylation of allyl chloride, (ii) selective hydrogenation of acrolein, (iii) ester hydrolysis of allyl acetate, and (iv) selective ring opening of propylene oxide.

Among the technically relevant diols and polyols, *ethylene glycol*, *1,3-propanediol*, *1,4-butanediol*, and *glycerol* are of special importance. Ethylene glycol is obtained by hydrolysis of ethylene oxide. To avoid the formation of higher glycols (diethylene glycol, triethylene glycol, etc.), hydrolysis is carried out in a ten-fold molar excess of water. The reaction can proceed in a catalytic manner (acid or base catalysis, 50–70 °C) or in a non-catalytic manner (150–200 °C, 20–40 bar). 1,3-Propanediol is produced industrially by hydrolysis of acrolein to 3-hydroxypropanal that is further hydrogenated to 1,3-propanediol. Alternatively, 3-hydroxypropanal can also be obtained by ethylene oxide hydroformylation. 1,4-Butandiol can be industrially produced from various feedstocks through different production routes (see Scheme 5.3.4 for an overview). The classical – but now less relevant route – uses the reaction of acetylene with two molecules of formaldehyde. The Cu-catalyzed reaction results first in the formation of 1,4-butyne diol that is hydrogenated to 1,4-butanediol [route (a) in Scheme 5.3.4]. To avoid the expensive acetylene feedstock, the following alternative routes are in technical use:

- hydroformylation of allyl alcohol (made in an indirect process from propene) to 4-hydroxybutanal followed by hydrogenation [route (b) in Scheme 5.3.4];
- hydrogenation of maleic anhydride (from butane oxidation) to butanoic acid anhydride followed by hydrolysis to and hydrogenation to 1,4-butanediol [route (c) in Scheme 5.3.4];

Scheme 5.3.4 Overview of alternative industrial production routes to 1,4-butanediol.



- catalytic conversion of butadiene and acetic acid into 1,4-diacetoxy-2-butene that is hydrogenated to 1,4-diacetoxylbutane and later hydrolyzed to 1,4-butandiol [route (d) in Scheme 5.3.4].

Glycerol can be produced from the petrochemical feedstock base of propene via allyl alcohol or epichlorohydrin as intermediates. Today, glycerol is mainly provided, however, by hydrolysis or transesterification of biogenic triglycerides, such as vegetable oils or fats. In the production of biodiesel, glycerol is a coupling product that is formed in stoichiometric amounts. Therefore, the availability and price of glycerol will largely depend in the coming years on the future of industrial biodiesel production.

Phenol production is typically carried out by acid induced conversion of cumene hydroperoxide to phenol and acetone (Hock process). Cumene hydroperoxide is obtained by oxidation of cumene. The cumene feedstock for the latter reaction is provided by Friedel-Crafts alkylation of benzene with propene. Alternative routes (chlorobenzene hydrolysis, cyclohexanol dehydrogenation, oxidative decarboxylation of benzoic acid) exist but are of much lower industrial relevance.

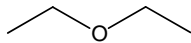
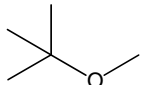
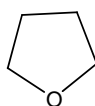
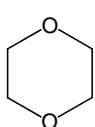
5.3.3.2 Ethers

Most industrial ether syntheses are carried out by condensation of two alcohol functionalities and liberation of water. If the two alcohol functionalities are attached to two different molecules, aliphatic ethers are formed. If the two alcohol functionalities are attached to the same molecule cyclic ethers are formed. Table 5.3.4 displays industrially important aliphatic and cyclic ethers, their main application areas, and their production capacity.

Dimethyl ether forms as condensation side product of the methanol synthesis from CO/H₂. Today, the greatly improved selectivity of modern methanol catalysts has reduced this side-product formation to such an extent that deliberate production of dimethyl ether from methanol at heterogeneous alumina or aluminosilicate contacts is carried out industrially.

In addition, *diethyl ether* forms as side product in ethanol production. If necessary, deliberate diethyl ether production is possible by dehydratization of ethanol using sulfuric acid or heterogeneous aluminum sulfate contacts.

Table 5.3.4 Industrially important ethers and their global production.

Ether	Structure	Major applications	Production (t a ⁻¹) (Wiley-VCH, 2012)
Dimethyl ether	CH ₃ -O-CH ₃	Blowing agent, dimethyl sulfate	50 000 (1998, Western Europe)
Diethyl ether		Solvent	
Methyl <i>tert</i> -butyl ether		Fuel additive	18 mio. (world, 2005)
Tetrahydrofuran		Solvent, poly(tetrahydrofuran)	439000 (world, 2006)
1,4-Dioxane		Solvent	

Other important aliphatic ethers include *ethylene and propylene glycol ether* that form from the respective epoxide by water addition (see Section 6.12 for details) and *methyl tert-butyl ether* (MTBE) that is obtained from condensation of methanol and isobutanol or by addition of methanol to isobutene.

Among the industrially relevant cyclic ethers *tetrahydrofuran* (THF) is by far the most important. THF is produced by condensation of 1,4-butandiol that is obtained from several feedstock basis (acetylene, propene, butadiene, and butane, see Scheme 5.3.4). *1,4-Dioxane* is obtained by condensation of diethylene glycol that itself is obtained by the addition of water to ethylene oxide. The reaction is catalyzed by sulfuric acid (homogeneous catalysis) or by acidic ion-exchange resins (heterogeneous catalysis) and proceeds at about 160 °C with continuous distillative removal of water.

5.3.3.3 Epoxides

Ethylene oxide and propylene oxide are by far the most important industrial epoxides. The production of these two compounds has been selected as a process example in this textbook and is described in detail in Section 6.12. Table 5.3.5 summarizes the most relevant applications of these important intermediates and gives the actual production capacities.

5.3.3.4 Aldehydes

Table 5.3.6 displays the most relevant aldehyde products in industrial chemistry together with their most important application areas and production capacities.

Formaldehyde is produced by oxidation of methanol or oxidative dehydrogenation of methanol. Oxidation of methanol [route (a) in Topic 5.3.2] is a strongly exothermic reaction ($\Delta H = -243 \text{ kJ mol}^{-1}$) that is carried out in a pressure-less oxidation with air in a multi-tubular reactor. The reaction is catalyzed by an iron/molybdenum oxide contact, with $\text{Fe}_2(\text{MoO}_4)$ being the active catalytic species. The oxidation is carried out at 350 °C with quantitative methanol conversion. The main side reaction is the total oxidation of methanol to CO_2 and water.

In contrast to methanol oxidation, oxidative dehydrogenation of methanol [route (b) in Topic 5.3.2] is an endothermic reaction ($\Delta H = +84 \text{ kJ mol}^{-1}$). Methanol is contacted at normal pressure with a heterogeneous silver at 500–700 °C. Owing to the kinetic instability of the formaldehyde product under the applied reaction conditions, the contact time at the catalyst is very short ($t < 0.01 \text{ s}$). This is realized by high flow rates in the reactor and a very effective quenching of the product flow leaving the reactor. The product gas is contacted with water to produce an aqueous

Table 5.3.5 Application areas and production of ethylene oxide and propylene oxide.

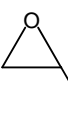
Epoxide	Structure	Major applications	World production (mio. t a ⁻¹) (Wiley-VCH, 2012)
Ethylene oxide		Ethylene glycol, glycol ethers poly(ethylene glycols), non-ionic tensides, ethanolamine	18 in 2005 (see Section 6.12)
Propylene oxide		Propylene glycol, glycol ethers, poly(propylene glycols) non-ionic tensides isopropanolamine	6 in 2005 (see Section 6.12)

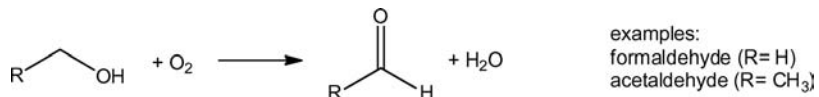
Table 5.3.6 Industrially important aldehydes and their production capacities.

Epoxide	Structure	Major applications	Production (mio. t a ⁻¹) (Wiley-VCH, 2012)
Formaldehyde	CH ₂ O	Polymers, 1,4-butandiol	9 (world production capacity in 1996)
Acetaldehyde		Acetic acid, ethyl acetate	1.3 (world, 2003)
<i>n</i> -Butyraldehyde (<i>n</i> -butanal)		2-Ethylhexanol, <i>n</i> -butanol, 2-ethylhexanoic acid, butanoic acid	see Section 6.14
Acrolein		Acrylic acid, acrylic acid esters, DL-methionine, 1,3-propanediol, pyridine	0.4 (Western Europe, USA, Japan, 2010)

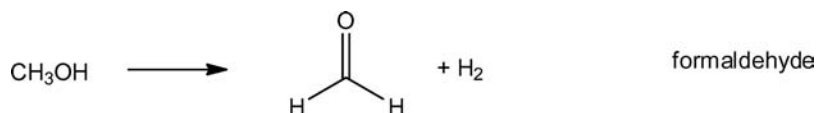
formaldehyde solution (37–44 mass% formaldehyde). The latter can be further concentrated by distillation. During this concentration process the formaldehyde hydrate converts into its trimer trioxane or into oligomeric forms (para-formaldehyde). All condensed forms can be reconverted into the monomeric form by addition of water.

Topic 5.3.2 Important routes for the industrial production of aldehydes:

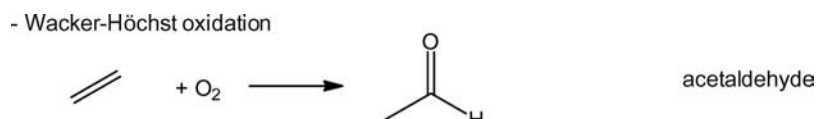
a) Alcohol oxidation:



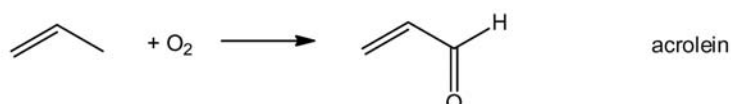
b) Oxidative dehydrogenation:



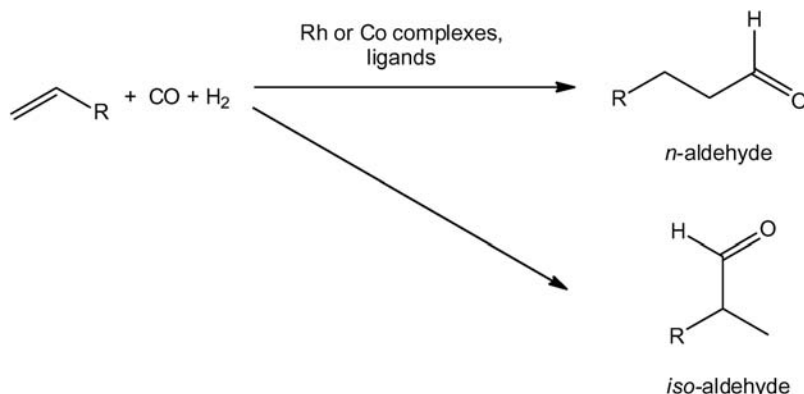
c) Alkene oxidation:



- Allylic oxidation



d) Hydroformylation:



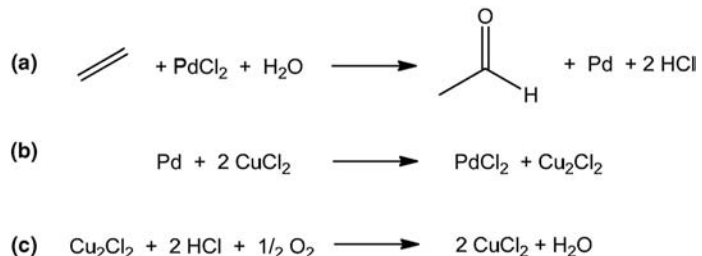
examples: *n*/*iso*-butanals, *n*/*iso*-nonanals, fatty aldehydes

Acetaldehyde (ethanal) used to be the most important intermediate for the production of acetic acid. However, since 1970 the production of acetaldehyde lost importance as acetic acid production switched increasingly to methanol carbonylation. The reason for this development has to do with the different feedstock base for both processes. While the production of acetaldehyde starts from ethylene, the synthesis of acetic acid via methanol carbonylation uses the significantly cheaper synthesis gas (CO/H_2) as feed, from which methanol is made first followed by a carbonylation step (see Section 6.15 for details).

The process of choice for acetaldehyde production is ethylene oxidation according to the so-called Wacker–Hoechst process [route (c) in Topic 5.3.2]. The reaction proceeds by homogeneous catalysis in an aqueous solution of HCl in the presence of palladium and copper chloride complexes. The oxidation of ethylene occurs in a stoichiometric reaction of PdCl_2 with ethylene and water that affords acetaldehyde, metallic palladium (oxidation state: 0), and HCl [step (a) in Scheme 5.3.5]. The elemental Pd is reoxidized in the process by Cu(II) chloride that converts in this step into Cu(I) chloride [step (b) in Scheme 5.3.5]. The Cu(II) chloride is regenerated by oxidation with air to finally close the catalytic cycle [step (c) in Scheme 5.3.5].

The technical realization of the Wacker–Hoechst process is particularly favorable in a one-step process that uses pure oxygen as oxidant. In a bubble column reactor the catalyst solution is contacted with a mixture of ethene and oxygen. Note that it is necessary to work with a significant excess of ethylene to stay outside of the explosion limits. Consequently, the degree of ethylene conversion is limited to 35–45%. The reaction proceeds at 120–130 °C and 3–5 bar pressure. The mixture leaving the bubble column at the top consists of the acetaldehyde product, non-converted ethylene, and the catalyst solution. In a first separator unit the catalyst solution is separated from gaseous acetaldehyde and the other volatile products and is recycled back to the reactor. The gaseous stream is contacted in an absorber with water, which dissolves the acetaldehyde product, allowing ethylene and other non-water-soluble volatiles to be vented over the top. The aqueous product solution is further

Scheme 5.3.5 Ethylene oxidation according to the Wacker–Hoechst process.



purified by distillation. Typical side-products of the Wacker–Hoechst process are methyl chloride, ethyl chloride, acetic acid, and chlorinated aldehydes. The total yield of acetaldehyde is around 95%.

Butyraldehyde production is technically carried out through propylene hydroformylation [route (d) in Topic 5.3.2]. The process is the key topic of Section 6.14.

Acrolein is produced via propene oxidation [route (c) in Topic 5.3.2]. The process uses bismuth and phosphorous molybdates as catalyst in a multi-tubular fixed bed reactor at reaction temperatures of 300–450 °C. The reaction is carried out by applying an excess of air to keep the degree of oxygen loading on the catalyst high. The process allows for propylene conversions of 96% and acrolein yields of 90%. The main side-products are acrylic acid, acetic acid, and acetaldehyde.

5.3.3.5 Ketones

The two most important industrial ketones are acetone and methyl ethyl ketone.

The most important source of *acetone* is the Hock process for phenol production. In this process acetone is obtained as stoichiometric coupling product. If acetone needs to be produced deliberately, it can be obtained by oxidative dehydrogenation or dehydrogenation of isopropanol. Oxidative dehydrogenation proceeds at 400–600 °C at silver or copper contacts, direct dehydrogenation is carried out at 300–400 °C using zinc contacts. Alternatively, acetone can also be obtained by a Wacker–Hoechst oxidation of propylene. Acetone is used industrially as solvent. Moreover, the aldol condensate products of acetone (diacetone alcohol) are used as solvents. Acetone is also converted in an acid catalyzed reaction with two moles of phenol for the synthesis of bisphenol A. Bisphenol A is an important feedstock for the production of epoxy resins and polycarbonates.

Methyl ethyl ketone is produced by dehydrogenation of 2-butanol. The reaction is carried out as either a gas-phase process (zinc or copper oxide contact, 400–500 °C) or liquid-phase process (Raney-nickel catalyst, 150 °C). Methyl ethyl ketone is mainly used as solvent in paints, coatings, or adhesives.

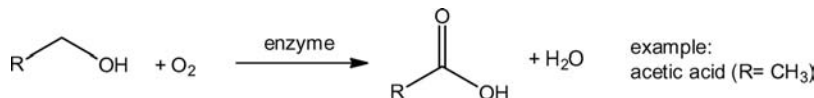
5.3.3.6 Acids

Table 5.3.7 displays the most important organic acids in industrial chemistry.

Formic acid is produced mainly by carbonylation of methanol to methyl formate followed by hydrolysis of this ester to formic acid and methanol [route (d) in Topic 5.3.3]. The applied reaction sequence represents formally the hydrolysis of carbon monoxide to formic acid. Owing to the growing worldwide interest in converting CO₂ into useful chemicals, the catalytic hydrogenation of CO₂ to formic acid has been investigated intensively but no commercial processes has been realized yet. Formic acid is also obtained as one of the side products in the catalytic oxidation of butane and light naphtha to acetic acid (see Section 6.15 for details).

Topic 5.3.3 Important routes for the industrial production of organic acids

a) Alcohol oxidation:



b) Aldehyde oxidation:

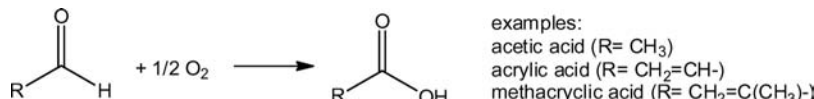
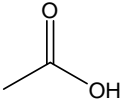
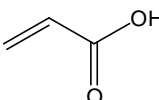
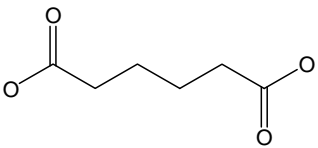
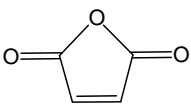
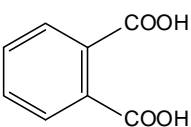
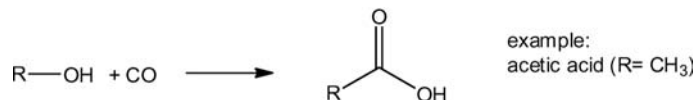


Table 5.3.7 Industrially important organic acids and their global production capacities.

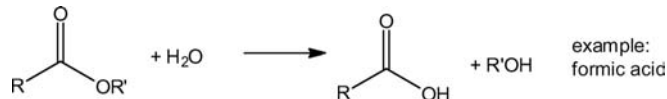
Acid	Structure	Major applications	World production (mio. t a ⁻¹) (unless specified, data from Wiley-VCH, 2012)
Formic acid	HCOOH	Animal nutrition, leather industry, formamide, dimethylformamide (DMF)	0.4 (2000)
Acetic acid		Solvent, vinyl acetate, esters,	11 (2008)
Acrylic acid		Acrylate polymers, acrylic esters,	3.4 (2002)
Adipic acid		Polyesters	2.1 (production capacity 1999)
Maleic acid anhydride		Unsaturated polyester, organic acids, 1,4-butandiol, furan, crop protection	1.4 (1999) ^{a)}
Terephthalic acid		Polyesters	24 (2000; Weisermel and Arpe, 2003)
Phthalic acid		Phthalate plasticizers	4.6 (2000)

a) Weisermel and Arpe, 2003.

c) Alcohol carbonylation:



d) Ester hydrolysis:



Acetic acid has been chosen as a process example of this textbook (Section 6.15 is fully devoted to this topic).

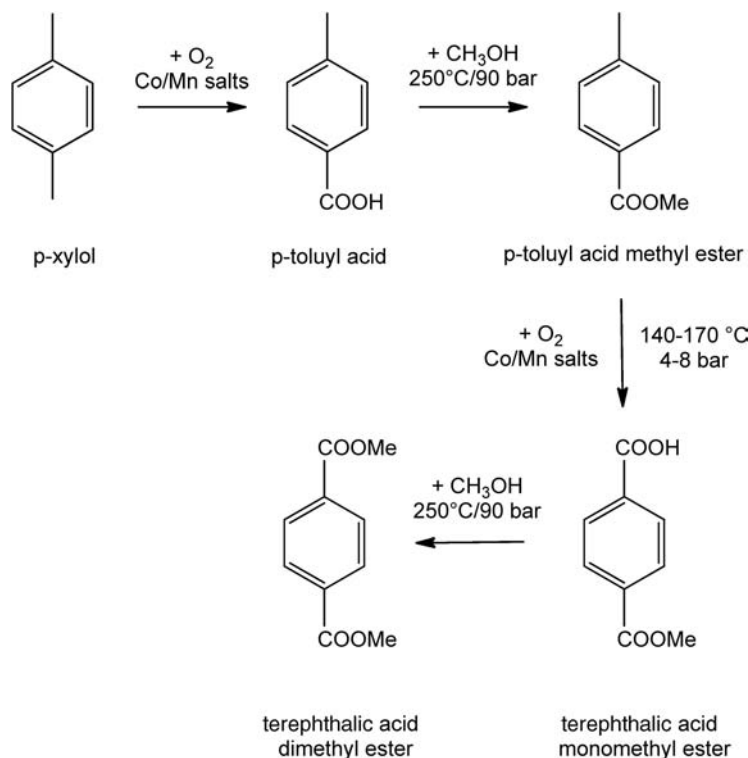
Acrylic acid is produced by aerial oxidation of acrolein according to route (b) in Topic 5.3.3. The reaction temperature is 260–300 °C and the catalyst is a molybdenum contact promoted with vanadium, tungsten, or iron.

Adipinic acid is produced industrially by oxidation of cyclohexane in a multistep oxidation process with cyclohexanol/cyclohexanone as important intermediates. The process operates at 125–165 °C and 8–15 bar and uses 50–65% nitric acid as the oxidant. As coupling product of the oxidation dinitrogen oxide (N_2O) is formed that has to be removed from the process flue gas due to its ozone layer depletion effect and its very high global warming potential (298 times that of CO_2). The reaction is catalyzed by vanadium and copper salts and reaches product yields of 96%.

Among the technically relevant unsaturated dicarboxylic acids, maleic acid is important, but even more relevant is its anhydride, *maleic acid anhydride*. The latter is produced by oxidation of *n*-butenes or butane. Typical process conditions are exemplified in the following for the case of butene oxidation. The highly exothermic reaction ($\Delta H = -1315 \text{ kJ mol}^{-1}$) proceeds at 350–500 °C and 3–5 bar pressure at vanadium oxide contacts (V_2O_5).

Terephthalic acid is of highest industrial relevance as its polyester with ethanediol, poly(ethylene terephthalate) (PET), plays a major role in the polymer industry, for example, for the bottling of beverages. To obtain high molecular weight polycondensates, terephthalic acid has to be produced in very high quality. The compound is industrially manufactured by oxidation of *p*-xylol (1,4-dimethylbenzol). Two process alternatives are industrially practiced. In the so-called Katzschmann process a multistep sequence is used as shown in Scheme 5.3.6.

The first oxidation step proceeds under conditions that lead only to the reaction of one methyl group and the monoacid is formed. To convert the second methyl group as well, it is necessary to form the monoacid methyl ester in the next step. After the second oxidation step the terephthalic dimethyl ester is formed under the same esterification conditions by reaction with methanol. Terephthalic dimethyl ester is later reacted directly with ethylene glycol to form the PET polymer with liberation of methanol. The total process provides a yield in terephthalic acid dimethyl ester of 85% with respect to *p*-xylene.



Scheme 5.3.6 Reaction sequence of the consecutive oxidation and esterification of *p*-xylol to produce terephthalic acid dimethyl ester—adapted from Baerns, 2006.

Alternatively, *p*-xylene can be oxidized to terephthalic acid in a direct manner in the so-called Amoco process. Here, the difficult oxidation of the second methyl group is enabled by a catalyst system that consists of Co or Mn salts dissolved in acetic acid together with a bromide source (HBr, NH₄Br). The bromide source acts as co-catalyst and provides bromine radicals in contact with oxygen that activate the second methyl group under the applied reaction conditions. The high corrosivity of the reaction mixture in the Amoco process (acetic acid solvent, bromide) requires the application of reactors made from Hastelloy C or titanium. The oxidation reaction proceeds at 200 °C and 25 bar. Under these conditions, terephthalic acid is produced in 90% yield with respect to *p*-xylene. The terephthalic acid product is finally isolated in polymer-grade purity by step-wise cooling and crystallization of the reactor effluent.

Phthalic acid is obtained from *o*-xylene by catalytic oxidation with air using a V₂O₅/TiO₂ contact. The applied multi-tubular reactor operates typically in the temperature range 375–410 °C. The reaction is cooled with molten salts to remove the significant exothermic reaction heat ($\Delta = -1110 \text{ kJ mol}^{-1}$) and the hot molten salt coolant is applied to produce high-pressure steam in a heat exchanger. The process allows a total phthalic acid yield of 87% with respect to *o*-xylene. Alternative process concepts using fluidized bed reactors are also known.

5.3.3.7 Amines and Nitrogen-Containing Intermediates

Aliphatic amines are classified in primary amines (RNH₂), secondary amines (R₂NH), and tertiary amines (R₃N), with R representing in this very general scheme an alkyl chain of any length and further functionalization. Technically interesting classes of amines are short-chain alkyl amines (primary, secondary, and tertiary), fatty amines, di- and polyamines, as well as aromatic amines. Table 5.3.8 highlights

Table 5.3.8 Industrially relevant amine compounds.

Amine	Structure	Major applications	World production (t a ⁻¹) (Wiley-VCH, 2012)
Methylamine, dimethylamine, trimethylamine	CH ₃ NH ₂ , (CH ₃) ₂ NH, (CH ₃) ₃ N	Solvents, fungicides, pharmaceuticals	Several 100 000
<i>tert</i> -Butylamine		pharmaceuticals, solvent applications	
Fatty amines	 n=10-16	Corrosion inhibitors, softener, special surfactants	
Ethylenediamine		Complexing agent, fungicides	
Hexamethylenediamine		Polyamides, hexamethylene diisocyanate, urethanes	1.6 mio. (2010)
Aniline		isocyanates, antioxidants, dyes, agrochemicals, pharmaceuticals	3.8 mio. (2008)

some of the most important individual structures together with their main fields of application and their production capacities.

Methylamine, *dimethylamine* and *trimethylamine* are produced by reaction of methanol with ammonia [route (a) in Topic 5.3.4]. The reaction proceeds as a continuous gas-phase catalysis using form-selective, acidic silicon/aluminum oxides (mordenite, chabasite) as catalyst contacts. This catalyst choice favors formation of the most desired product dimethylamine (<10% trimethylamine) in contrast to the earlier applied amorphous silicon/aluminum oxide contacts. The reactor temperature is kept between 250 and 300 °C and the reaction pressure is between 10 and 30 bar.

The production of *tert-butylamine* is interesting for the fact that this amine has been used to demonstrate the technical potential of hydroamination in commercial amine production [route (b) in Topic 5.3.4]. BASF introduced in the early 1990s the first process that operates with a zeolite catalyst and converts isobutene directly with ammonia. The reaction is carried out by contacting the supercritical reaction mixture with the catalyst at temperatures between 250 and 300 °C and at pressures between 200 and 350 bar. Under equilibrium conversion conditions *tert-butylamine* forms in 95% selectivity.

Fatty amines are manufactured industrially in most cases by hydrogenation of the fatty acid nitriles [route (c) in Topic 5.3.4]. The latter are formed before by reaction of fatty acids with ammonia in a catalytic dehydratization reaction. The fatty nitrile hydrogenation is preferentially carried out as a liquid-phase reaction using nickel or cobalt contacts as heterogeneous catalysts.

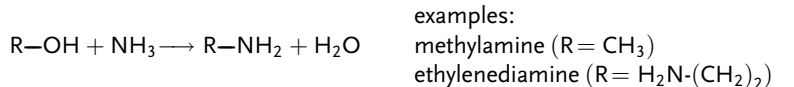
Ethylenediamine is produced technically by two different routes: The reaction of ammonia with dichloroethane [route (d) in Topic 5.3.4; for dichloroethane synthesis, see also Section 5.3.3.9] is still the most important production route. However, in this process 2 kg of NaCl is produced as stoichiometric coupling product per kg of ethylenediamine. For this reason an alternative process has been developed that converts ethanolamine and ammonia into ethylenediamine. Ethanolamine is obtained by reaction of ethylene oxide with ammonia.

Hexamethylenediamine is produced almost exclusively by catalytic hydrogenation of adiponitrile [route (e) in Topic 5.3.4]. The synthesis is carried out as a liquid-phase reaction and uses a heterogeneous iron contact at 100–200 °C and 200–400 bar hydrogen pressure.

Direct amination of benzene with ammonia to form aniline is not feasible. Therefore, aniline production is carried out technically by nitrobenzene hydrogenation. Nitrobenzene is produced in the first place by reacting benzene with a mixed acid composed of nitric acid (about 35 mass% of the mixed acid), sulfuric acid (about 55 mass%), and water (about 10%). The nitration of benzene is strongly exothermic ($\Delta H = -109 \text{ kJ mol}^{-1}$) and proceeds in a liquid–liquid biphasic reaction (benzene and the mixed acid show a miscibility gap). Owing to the thermal lability of nitroaromatic compounds (leading to the ability for spontaneous decomposition at elevated temperatures), safety aspects play an important role in the production of nitroaromatic compounds. The hydrogenation of nitrobenzene to aniline is performed industrially in liquid-phase (Huntsman), gas-phase (Bayer), or fluidized-bed (BASF) reactors. Typical reaction temperatures are 70–150 °C (liquid-phase process) or 250–480 °C (gas-phase processes). The applied heterogeneous catalysts are Ni- or Cu-contacts that are surface modified to moderate their catalytic activity. This catalyst modification is necessary to protect the product aniline against ring hydrogenation. Apart from aniline hydrogenation with hydrogen, some companies (Mobay, Bayer) also deploy the so-called Béchamp process. In this process the required hydrogen for nitrobenzene hydrogenation is formed *in situ* by the reaction of HCl with elemental iron. One important advantage of this process is the production of the valuable by-product iron oxide.

Topic 5.3.4 Industrial routes for production of amines

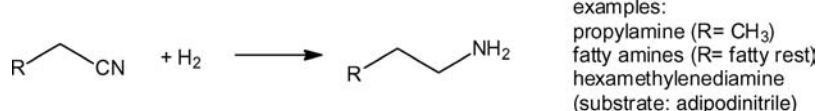
a) Alcohol + ammonia:



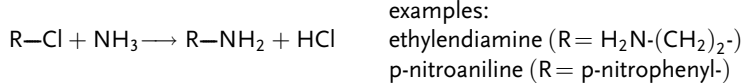
b) Hydroamination:



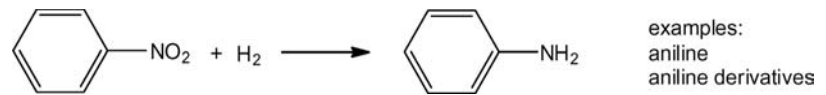
c) Nitrile hydrogenation:



d) Alkyl chloride + ammonia:



e) Hydrogenation of nitro compounds:



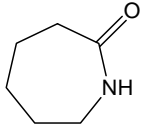
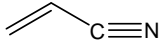
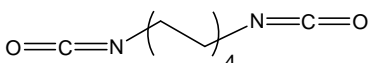
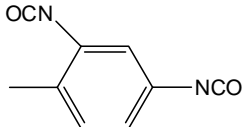
5.3.3.8 Lactams, Nitriles, and Isocyanates

Lactams, nitriles, and isocyanates are further important examples of N-functionalized bulk chemicals. Table 5.3.9 gives a selection of specific compounds, their structure, and applications.

Among the industrially produced lactams, ϵ -caprolactam has by far the highest production capacity due to its important role as monomer in the polyamide business. There exist several synthetic routes to produce ϵ -caprolactam. The most important one starts from benzene (Scheme 5.3.7). Benzene is hydrogenated in a first step to cyclohexane, followed by oxidation of the latter to a mixture of cyclohexanone and cyclohexanol. This mixture is then reacted with NH_2OH to give cyclohexanone oxime, which is converted under acid catalysis in a so-called Beckmann rearrangement reaction to ϵ -caprolactam. Alternative routes try to avoid the oxime intermediate (UCC peracetic acid process via ϵ -caprolactone), try to avoid the cyclohexanone intermediate (e.g., DuPont process converting cyclohexane directly into the oxime intermediate by reaction with nitric acid), or start from toluene (Snia-Viscosa process).

Acrylonitrile is produced today almost exclusively by ammonoxidation of propylene using the so-called Sohio process. “Sohio” stands for “Standard Oil of Ohio,” the first company to demonstrate successfully the process in 1960. The Sohio process reacts propylene, ammonia, and oxygen in a highly exothermic process ($\Delta H = -502 \text{ kJ mol}^{-1}$) at $400\text{--}500^\circ\text{C}$ to acrylonitrile and water. The process uses a fluidized bed reactor to operate the reactor as isothermally as possible. The catalyst is a Fe-modified bismuth-phosphorous molybdate contact. The Sohio process has

Table 5.3.9 Industrially relevant lactams, nitriles, and isocyanates.

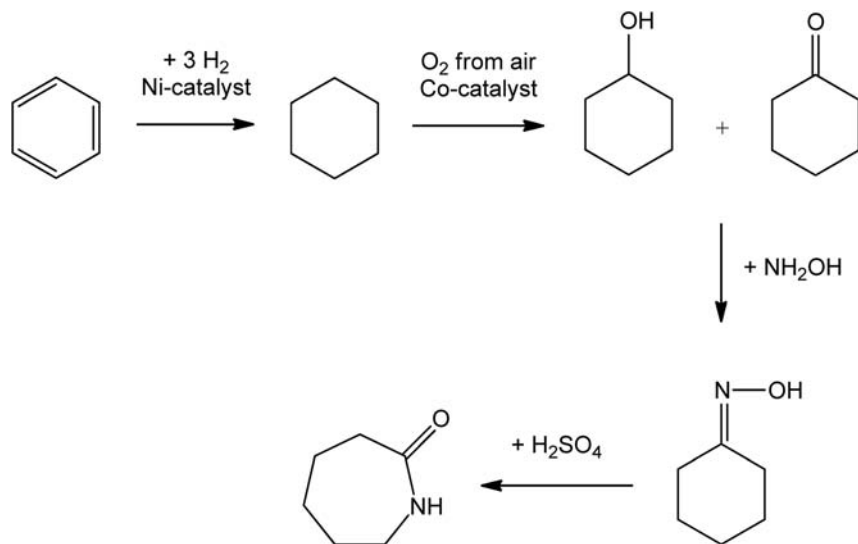
Compound	Structure	Major applications	World production (mio. t a ⁻¹) (unless specified, data from Wiley-VCH, 2012)
ϵ -Caprolactam		Polyamides	4 (2004)
Acrylonitrile		Acrylic fibers, acrylonitrile copolymers, acrylamide, adiponitrile	5.9 (production capacity in 2009)
Adiponitrile		Hexamethylene-diamine	1.4 (2000) ^{a)}
Aliphatic isocyanates	e.g. $\text{CH}_3\text{N}=\text{C}=\text{O}$, 	Herbicides, coatings, urethanes	
2,4-Toluene diisocyanate (TDI)		Polyurethanes	

a) Weissermel and Arpe, 2003.

the advantage of a one step access to acrylonitrile from base chemicals; however, its selectivity is not particularly good. From 1000 kg of propene feedstock, 900 kg acrylonitrile is formed, but so also is up to 100 kg acetonitrile and up to 200 kg HCN.

Adiponitrile is produced by a Ni-catalyzed reaction of butadiene with two mols of HCN. The process has been introduced by DuPont in the 1970ties.

Aliphatic isocyanates are produced by either phosgene-based processes or phosgene-free processes (note that the molecule named “phosgene” contains



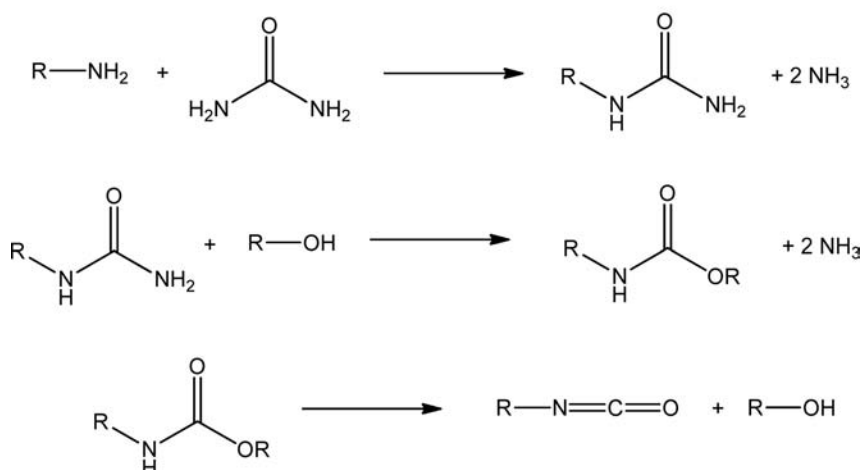
Scheme 5.3.7 Production route to ϵ -caprolactam via Beckmann-rearrangement of cyclohexanone oxime.

Scheme 5.3.8 Comparison of the phosgene-based route with the phosgene-free production of alkyl cyanates.

Phosgene-based route to alkyl isocyanates:



Phosgene-free route to alkyl isocyanates:



no phosphorous). Phosgene is a very dangerous chemical due to its volatility and its very high acute toxicity. However, its high reactivity enables synthetic transformations with very high selectivity. This general statement can be illustrated convincingly for the synthesis of aliphatic isocyanates as shown in Scheme 5.3.8.

While the use of phosgene allows direct conversion of the alkylamine into the isocyanate, the phosgene-free route requires for the same transformation three sequential reaction steps. First, the alkylamine is reacted with urea. The resulting urea derivative is then reacted with an alcohol to give the corresponding urethane. The urethane can then be cleaved in a third step to the desired isocyanate while liberating the applied alcohol again.

2,4-Toluene diisocyanate (*a*) is produced industrially together with its isomer 2,6-toluene diisocyanate in a three-step reaction sequence: First toluene nitration is carried out and from the obtained mixture of ortho-, meta-, and para-isomers only the ortho/para mixture is retained for further nitration. The resulting 2,4- and 2,6-dinitrotoluenes are then hydrogenated using nickel or palladium catalysts to the corresponding aromatic diamines. The latter are converted with phosgene into the technical TDI mixture, which is almost exclusively applied in combination with diols and triols to form polyurethane foam materials.

5.3.3.9 Halogenated Organic Intermediates

Table 5.3.10 summarizes industrially important halogenated organic compounds and their major applications. Topic 5.3.5 gives an overview of the most relevant production routes.

The production of *chloromethane* (methyl chloride), *dichloromethane* (methylene chloride), and *chloroform* is carried out in one process, the hot radical chlorination of methane [route (*a*) in Topic 5.3.5; for mechanistic details see Section 2.2]. The process yields a mixture of all the different chloromethanes including the least desired tetrachloromethane. The chlorination reaction is initiated at above 250 °C. This temperature represents the lower temperature limit for the formation of chlorine radicals Cl[•] by thermal decomposition of Cl₂ in sufficient quantity. During the

Table 5.3.10 Industrially relevant halogenated organic compounds.

Halogenated compound	Structure	Major applications	Production (mio. t a ⁻¹) (unless specified data from Wiley-VCH, 2012)
Chloromethane (methyl chloride)	CH ₃ Cl	Alkylation agent	
Dichloromethane (methylene chloride)	CH ₂ Cl ₂	Solvent	1.7 (all three chloromethanes in 2010) ^{a)}
Trichloromethane (chloroform)	CHCl ₃	Solvent, fluorochloromethanes	
Dichloroethane		Vinyl chloride	about 23 (2000) ^{b)}
Vinyl chloride		Poly(vinyl chloride) (PVC), copolymers	about 23 (2000) ^{b)}
Allyl chloride		Epichlorohydrin, allylamine, allyl alcohol, chloropropylsilanes	0.8 (1997)
Chlorobenzene		Agrochemicals, dyes, pharmaceuticals	
<i>o</i> -Dichlorobenzene		Solvent, agrochemicals, dyes	total chlorinated benzenes: 0.3 (1998) ^{c)}
<i>p</i> -Dichlorobenzene		Dyes, pharmaceuticals, polyphenylene sulfide	
1,1,1,2-Tetrafluoroethane (R134a)		Ozone-neutral refrigerants	

a) www.icis.com, accessed 18.09.2012.

b) Wiley-VCH, 2012.

c) Weissermel and Arpe, 2003.

chlorination process it is important to remove effectively the considerable reaction heat of methane chlorination from the reactor as temperatures above 500 °C would lead to irreversible product decomposition (formation of heavies and chlorinated charcoal). Typically, the process is carried out at between 400 and 450 °C in a loop reactor that allows both rapid heating of the reaction mixture at the reactor entrance and effective heat removal. Moreover, the process is operated at 2–4 bar with excess methane in the feed flow to avoid the explosive concentration range (mixtures with 12–58 mol.% CH₄ in Cl₂ are explosive). Under these process conditions the yield to chlorinated methanes is 98%. The different chloromethanes are separated in three consecutive distillation steps. Note, that the production capacities for all chloromethanes have decreased considerably during the last 20 years, which is mainly because their application as solvents has been increasingly restricted as a consequence of their toxicity, volatility, and lack of biodegradability (except for dichloromethane, which is biodegradable).

Dichloroethane is a key intermediate of all current processes to produce *vinyl chloride*. Dichloroethane is obtained by oxychlorination of ethylene [using HCl as chlorine source, route (b) of Topic 5.3.5] or by electrophilic addition of chlorine to ethylene [route (c) of Topic 5.3.5]. Dichloroethane is later converted into *vinyl chloride* by thermal elimination of HCl from dichloroethane.

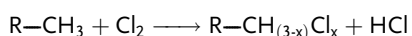
Allyl chloride is produced by hot radical chlorination [route (a) of Topic 5.3.5]. To achieve high selectivity of chlorine substitution versus chlorine addition to the double bond, high reaction temperatures of around 500 °C are needed. In addition, alternative process schemes using HCl as the chloride source under oxychlorination conditions are known.

Chlorobenzene and *dichlorobenzenes* are obtained by direct catalytic chlorination of benzene with chlorine. In the production process, gaseous chlorine is bubbled through a solution of the iron(III) catalyst FeCl₃ in benzene. All chlorination reactions at the aromatic core are highly exothermic (e.g., $\Delta H = -131.5 \text{ kJ mol}^{-1}$ for chlorobenzene formation from benzene and $\Delta H = -124.4 \text{ kJ mol}^{-1}$ for dichlorobenzene formation from chlorobenzene) and therefore appropriate reactor cooling (e.g., by internal cooling coils in the reactor) is required. Keeping the reaction temperature at a certain value is important to adjust the product distribution obtained from the process. For a high selectivity to monochlorobenzene the reaction temperature should be adjusted between 40 and 50 °C. Temperatures below 40 °C are unsuitable due to unfavorably low reaction rates. Temperatures above 50 °C, however, favor the formation of di- and even trichlorobenzenes. To maximize mono-chlorobenzene production it is, moreover, important to work with excess benzene such that the benzene conversion is limited to 65% at the desired full chlorine conversion.

1,1,1,2-Tetrafluoroethane (R134a) is an ozone-neutral refrigerant that was introduced around 1990 to replace chlorofluorocarbon compounds [CFCs, such as, for example, CClF₃ (R11)]. The latter had become known at that time for their potential to deplete the ozone layer. When reaching the stratosphere, CFCs decompose under UV-irradiation to give chlorine radicals that initiate rapid ozone decomposition. Based on these findings, an international convention, the so-called *Montreal Protocol*, was established in 1987. The protocol restricts drastically the industrial use of all chemicals with known ozone depletion potential. As a consequence of this agreement, substitutes for CFCs were introduced to the refrigerant markets. One of these substitutes is 1,1,1,2-tetrafluoroethane, which displays very similar thermodynamic properties to the banned CClF₃ (R11) and without the potential to release chlorine radicals under UV-irradiation. The compound is produced by reacting 1-chloro-2,2,2-trifluoroethane with HF in the presence of aluminum fluoride, chromium fluoride, or antimony fluoride in either gas-phase or liquid-phase reactions at between 100 and 150 °C.

Topic 5.3.5 Industrially relevant routes to halogenated compounds

a) Radical chlorination:



examples:

methyl chloride ($\text{R} = \text{H}$, $x = 1$)
methylene chloride ($\text{R} = \text{H}$, $x = 2$)
ethyl chloride ($\text{R} = \text{CH}_3$, $x = 1$)

b) Oxychlorination:

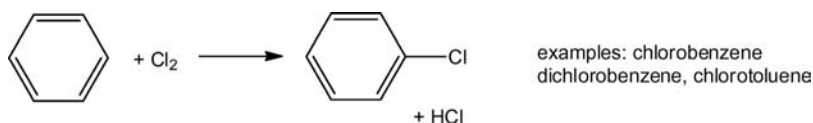


examples: dichloroethane

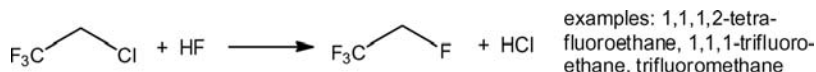
c) Chlorination of alkenes:



d) Chlorination of aromatic compounds:



e) Transformation of chlorinated alkanes with HF:



5.3.4

Polymers

Polymers are macromolecular substances built of repeating units, the so-called monomers. The synthetically produced polymers – that will be described here in more detail – are among the most important products of the chemical industry; naturally occurring polymers, such as cellulose, starch, or natural rubber are also technically very relevant.

The structure of a polymer determines its physicochemical and mechanical properties and with that its technical applicability. Typically, polymers contain a backbone, a long chain that goes through the whole molecule. This backbone can be formed only by one sort of atom (like in polyethylene) or by more than one sort of atoms (polyesters, polypeptides). It can be formed from one monomer only (homopolymers) or by different monomers (copolymers). In general terms the structure of a polymer is characterized by the following parameters:

- nature of the monomer (e.g., ethylene, styrene, adipinic acid);
- Sequence of the monomers (in cases where more than one monomer is involved in forming the polymer; the sequence can be statistically, alternating or in blocks);
- type and nature of branching (long versus short side chains);
- molar mass and molar mass distribution of the polymer;
- configuration of any asymmetric C-atoms contained in the polymer backbone; the most important example is polypropylene, where the configuration of the asymmetric carbon in the backbone leads to isotactic polypropylene (all asymmetric C atoms have the same configuration), syndiotactic polypropylene (subsequent asymmetric C-atoms show strictly alternating configurations), and atactic polypropylene (sequence of asymmetric C-atoms shows a random configuration).

Depending on processing options for the respective macromolecular material, polymers can be divided into several sub-classes. *Thermoplastic polymers* are mainly linear polymers that become flexible above a certain temperature and rigid again upon cooling below this temperature. In their flexible state they can be molded into shapes or can be drawn into fibers of technically attractive tensile strength and durability. *Thermoset resins* are three-dimensional network polymers that remain rigid at all temperatures until the temperature of their thermal decomposition. *Elastomers (synthetic rubber)* are macromolecules with double bonds remaining in their structure that can be deformed significantly on application of a small stress but regain their original shape when the stress is removed.

Table 5.3.11 Industrially relevant polyolefins and polydienes.

Polymer	Structure	Major applications	World production in mio. t a ⁻¹
Polyethylene (PE); low density PE; high density PE; linear low density PE	The structure shows a zigzag line representing a polymer chain segment, enclosed in brackets with a subscript 'n'. The first two segments are explicitly drawn as single bonds between carbon atoms.	Packaging, films, tubes, tanks, containers, plastic bags, sheathing for wires	66 (2005) ^{a)} 94 (production capacity in 2008) ^{b)}
Polypropylene (PP)	The structure shows a zigzag line representing a polymer chain segment, enclosed in brackets with a subscript 'n'. The second carbon atom is bonded to two methyl groups (CH3).	Packaging, tubes, tanks, containers, fibers	52 (2011) ^{c)}
Polytetrafluoroethylene (PTFE)	The structure shows a zigzag line representing a polymer chain segment, enclosed in brackets with a subscript 'n'. The two carbon atoms are each bonded to two fluorine atoms (F).	Corrosion protection, coatings, lubrication, insulation	0.06 (1999) ^{d)}
Polybutadiene (BR)	The structure shows a zigzag line representing a polymer chain segment, enclosed in brackets with a subscript 'n'. It features a conjugated diene unit (-CH2-CH=CH-CH2-) where the double bond is alternating between the second and third carbons.	Rubber for tires, tubes or belts, adhesives	2 (1998) ^{e)}
Polyisoprene (IR)	The structure shows a zigzag line representing a polymer chain segment, enclosed in brackets with a subscript 'n'. It features an isoprene unit (-CH2-C(CH3)=CH-CH2-) where the double bond is at the second position.	Rubber	1.3 (1989) ^{e)}

a) Behr, Agar, and Joerissen, 2010.

b) see Section 6.20.

c) www.plasteurope.com/news/plastics_markets_t221996, accessed 18.09.2012.

d) Weissermel and Arpe, 2003.

e) Wiley-VCH, 2012.

The following subsections give an overview of the most important types of technical polymers. Important additional information regarding the polymerization mechanism and about the most important polymer process technologies is in Topics 5.3.6 and 5.3.7, respectively. For more detailed information about the use and industrial production of polymers we refer to more specialized literature (e.g., Brazel 2012, Meyer 2005).

5.3.4.1 Polyolefins and Polydienes

The most important polyolefins (Table 5.3.11) are the different polyethylene qualities, polypropylene, and polybutadienes. Polyethylene is by volume the most important polymer. Therefore, its production has been chosen as a process example (Section 6.20).

Polypropylene (PP) is mostly produced by Ziegler–Natta polymerization (Topic 5.3.6) based on a titanium catalyst activated with alkyl-aluminum compounds. In this process isotactic PP is formed that is characterized by high crystallinity, high melting point ($mp = 165^\circ\text{C}$), and a low density ($d = 0.90 \text{ g cm}^{-3}$). New generations of zirconocene catalysts (activated with methylaluminoxane – MAO) produce PP either with high isotacticity or with high syndiotacticity depending on

the applied ligand system. Owing to its very attractive properties as a thermoplastic polymer of high stiffness and hardness, PP has gained increasing relevance in recent years. Most PP is produced either by suspension or by gas-phase polymerization (for different polymer production processes see Topic 5.3.7).

Polytetrafluoroethylene (PTFE) is the industrially most important fluoropolymer. Owing to its significant heat of polymerization ($\Delta H_R = -172 \text{ kJ mol}^{-1}$), PTFE is best produced by emulsion and suspension polymerization processes. The polymer is very resistant to organic solvents and chemicals, it shows very attractive properties as an electric insulator, and it displays excellent lubricating properties. However, the relatively high price of the monomer and the challenging polymerization technology restrict the technical use of PTFE to high-performance applications such as anticorrosion coatings, specialized process equipment, or sophisticated electronic applications.

Polybutadienes (BR) and *polyisoprenes* (IR) are the most important polydienes. Owing to the remaining olefinic double bound in the polymer (one double bound per monomer unit) these materials are characterized by reversible plasticity. The main application for polybutadiene is tires (ca 80% of the production capacity). Consequently, the development of industrial processes to replace natural rubber (mainly consisting of *cis*-1,4 polyisoprene) by synthetic polydiene production was strongly linked to the up-coming car manufacturing in the twentieth century. Polybutadienes and polyisoprenes are typically produced by polymerization in solution using cascade of two to four reactors. Ziegler–Natta systems or alkylolithium compounds are applied as catalysts. Depending on the catalyst, different shares of *cis*- and *trans*-polymers are obtained.

5.3.4.2 Vinyl-Polymers and Polyacrylates

Polystyrene (PS) (Table 5.3.12) is produced almost exclusively in-substance, for example, by using a production tower (see Topic 5.3.7 for details). The polymer is transparent and readily processable in molding techniques. However, pure PS is somewhat brittle and not very resistant to organic solvents. Therefore, copolymers with substantial shares of PS are of great industrial relevance. Examples are PS–acrylonitrile (SAN), PS–butadiene rubber (SBR), and PS–butadiene–acrylonitrile (ABS) copolymers. Another important application form of PS is PS foams (Styropor®). The latter are used for the thermal insulation of buildings as the air enclosed in the foam reduces the heat conductivity of the material to very small values.

Poly(vinyl chloride) is typically produced by radical polymerization processes. The reaction is carried out in-substance or by using suspension/emulsion technologies. By production volume, PVC is the most important polymer besides polyethylene and polypropylene. Its range of application is greatly extended by the use of plasticizers and other additives (such as heat stabilizers, lubricants, fillers). The most important group of plasticizers for PVC is phthalic acid esters, such as diethyl phthalates. Soft PVC qualities contain often more than 20 mass% of plasticizers. The presence of the plasticizer between the individual polymer chains reduces the hardness and the brittleness of PVC significantly and permits applications of the material in toys, transport belts, and packaging systems. PVC without plasticizer is called “hard PVC.” The material is hard and brittle but very resistant to hydrocarbons and acids and very robust against aging. Therefore, the material is applied in long-term applications, such as window frames, pipelines, or process equipment. Apart from plasticizers, a large range of other additives are applied in combination with PVC. These are added to the polymer to reduce flammability (phosphoric acid esters, chlorinated or brominated hydrocarbons) or to improve thermal stability (metal salts, metal-sulfur compounds) or color (pigments and dyes).

Poly(methyl methacrylate) (PMMA, “Plexiglas®”) is produced by radical polymerization of methyl methacrylate. The outstanding property of PMMA is its brilliant,

Table 5.3.12 Industrially relevant vinyl-polymers and polyacrylates.

Polymer	Structure	Major applications	World production in mio. t a ⁻¹
Polystyrene (PS)		Heat insulation, copolymers (SAN, SBR, ABS)	16 (2011) ^{a)}
Poly(vinyl chloride) (PVC)		Hard PVC: tubing, window frames; soft PVC: transport belts, toys, packaging systems	36 (2011) ^{a)}
Poly(methyl methacrylate) (PMMA)		Glass in buildings and vehicles, optic instruments and devices (lenses, prisms, reflectors)	1.6 (2010) ^{b)}
Polyacrylonitrile (PAN)		Fibers	2 (2009) ^{c)}

a) www.plasteurope.com/news/plastics_markets_t221996, accessed 18.09.2012.

b) M. Traexler (2011) Polymethyl methacrylat. Kunststoffe Intern. 10.

c) Wiley-VCH, 2012.

crystal clear appearance in combination with attractive mechanical properties. Moreover, PMMA is very robust against outdoor conditions and easy to coat and to color. To produce plates, objects, or devices from a PMMA, melt casting processes are applied.

Topic 5.3.6 Important mechanisms for the formation of polymers

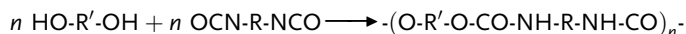
The different mechanisms of polymerization can be divided into two general groups, chain-growth polymerization and step-growth polymerization.

In a *step-growth reaction* the polymer forms by the reaction of bifunctional monomers. In this way at low conversion the molecular weight remains low as dimers and trimers form first. The degree of polymerization P_n depends on the conversion of reactive end groups X_{reg} by the equation $P_n = 1/(1 - X_{\text{reg}})$. Obviously, from this equation, for step-growth reactions only very high monomer conversions result in high molecular weights (Figure 5.3.11). An X_{reg} of 99% is required, for example, to realize a P_n of 100.

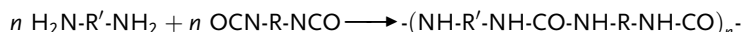
The two most important transformations that form polymers in step-growth reactions are *polyaddition* and *polycondensation*:

Examples of polyadditions:

a) Formation of polyurethanes:



b) Formation of polyurea from diamines and diisocyanates:



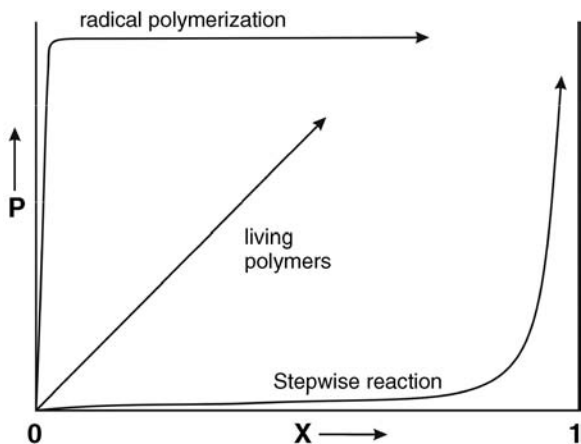
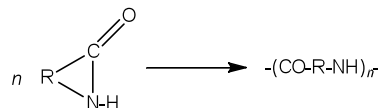


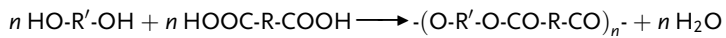
Figure 5.3.11 Degree of polymerization versus monomer conversion for different polymerization mechanisms. Adapted from Onken (1996).

c) Formation of polyamides by opening of lactams:

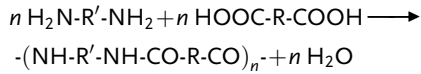


Examples of polycondensations:

a) Formation of polyesters from diols and dicarboxylic acids:



b) Formation of polyamides from diamines and dicarboxylic acids:



Important polymers that are produced by polyaddition are polyamide 6 (nylon) and all kinds of polyurethanes. In polycondensation one mol of a small molecule (typically H_2O) is liberated per step of chain growths. Important polymers that are produced by polycondensation are polyamide 6,6, poly(ethylene terephthalate) (PET), polycarbonate, polyarylate, and polysulfide. Step growth polymerization is usually slow, equilibrium limited and isothermal to slightly exothermic. Polyaddition and polycondensation reactions of monomers with three or more reactive end groups lead to three-dimensionally crosslinked resins.

Chain-growth polymerization reactions are characterized by the formation of an activated chain or monomer, rapid chain growth, and finally termination by transfer reactions or reactions of two activated chain ends. Chain growth polymerization is generally fast, irreversible, and moderately to highly exothermic. Chain-growth polymerization reactions proceed according to a radical, anionic, cationic, or transition metal catalyzed mechanism. The feasibility of these different mechanisms depends strongly on the monomer structure as the reactive end of the growing polymer chain is stabilized in a different manner by the polymer structure depending on the polymerization mechanism.

General information on radical reactions has been given in Section 2.2.2. In *radical polymerization reactions* a radical initiator $\text{I}\cdot\text{I}$ added to the monomer undergoes (through activation by temperature or irradiation) a homolytic bond cleavage to form two radicals $\text{I}\cdot$. Each radical $\text{I}\cdot$ reacts with a monomer M to form a new radical $\text{R-M}\cdot$ that continues to react with n further monomers to form a growing polymer $\text{R-(M)}_n\cdot$. Chain termination occurs by combination or disproportionation of two macro-radicals or by reaction of a macroradical with an initiator radical. It is characteristic

for radical polymerization that the formed polymers reach high degrees of polymerization even at relatively low monomer conversion. Owing to the balance of chain growth and termination reactions the degree of polymerization remains almost constant over a large range of monomer conversion (Figure 5.3.11). Typical initiators in radical polymerizations are dibenzoyl peroxide, cumene hydroperoxide, and *N,N*-azobisisobutyronitrile. Typical polymers that are produced industrially by radical polymerization are vinyl-polymers [polystyrene, poly(vinyl chloride), poly(vinyl acetate)], polyacrylates [poly(methyl methacrylate), polyacrylonitrile], or polydienes (polybutadiene, polyisoprene).

Anionic polymerization is initiated by a base B^- that reacts with the monomer M to provide $B\text{-M}^-$. The anionic product continues to react with n further monomer units to form the polymer $B\text{-}(M)_n^-$. Chain termination requires the addition of an acid. If no chain termination is induced, so-called living polymerization takes place. In living polymerization, every polymer chain grows without termination up to the point where all monomer is consumed. A reaction that has stopped in this way can be re-activated by the addition of further monomer. As a consequence, there is a linear correlation between the monomer conversion and the degree of polymerization (Figure 5.3.11). The degree of polymerization depends solely on the ratio of initiator and monomer. Anionic polymerization is particularly suitable if olefinic monomers with an electron-withdrawing substituent (e.g., methyl cyanoacrylate) or cyclic monomers with heteroatoms (e.g., ethylene oxide, caprolactam, caprolactone) are reacted in polar solvents (e.g., THF, glycol ethers, pyridine). Important initiators of anionic polymerization are alcoholates or organolithium compounds such as butyllithium. Amines or phosphines can also induce anionic polymerization by forming a zwitterion with the olefinic monomer; the anionic head group of the zwitterion then reacts with additional monomer.

Cationic polymerization reactions are initiated by an acid A^+ that reacts with the monomer M to furnish $A\text{-M}^+$. The cationic product grows by reacting with n further monomer units to the yield polymer $A\text{-}(M)_n^+$. Chain termination occurs by reaction with a base or by disproportionation of the carbenium ions to form alkane and alkene. Cationic polymerization requires monomers with strongly electron-donating substituents (e.g., isobutene, styrene, vinyl ether). Alternatively, polymerization of several cyclic monomers (e.g., cyclic ethers and imines) and monomers with polymerizable C=O bonds (e.g., trioxane, the cyclic trimer of formaldehyde) can proceed via the cationic mechanism. Important compounds that initiate cationic polymerization are strong Brønsted acids (e.g., sulfuric acid, triflic acid) or strong Lewis acids (e.g., BF_3 , AlCl_3). With Lewis acids acting as initiator for the cationic polymerization, addition of the acid to the olefinic monomer again forms a zwitterion, of which the cationic head group represents the reactive end for chain growth.

Transition metal catalyzed or insertion polymerization reactions are characterized by the fact that chain growth requires coordination of the monomer and of the growing polymer chain to a metal complex. At this metal complex the monomer inserts into the metal–polymer bond, thus elongating the coordinated polymer by one monomer unit. The most famous catalyst systems for insertion polymerization are the so-called Ziegler–Natta systems. The industrially most relevant systems of this kind are formed by *in situ* reaction of a transition metal compound of titanium, zirconium, or chromium with an alkyl-aluminium compound. Methylalumininoxane (MAO) – a partial hydrolysis product of AlMe_3 – is a particularly suitable choice. By ligand transfer this reaction creates the active transition metal alkyl species and a weakly coordinating aluminum compound. Note that the activated transition metal alkyl complex is typically a strong acid or even a cationic complex that has a very high affinity to the olefin. Systems that rapidly insert the coordinated olefin into their existing metal–carbon bond reach very high productivities. For MAO-activated zirconocene systems productivities of up to 40 tons of polymer per g Zr per hour have been reported. Interestingly, the stereocenter formed in the polymerization of higher 1-olefins

(C₃ and higher) can be influenced in insertion polymerization by the ligands attached to the transition metal complex. This gives controlled access to isotactic or syndiotactic polymers, an achievement that has drastically expanded the application fields of polypropylene in recent years. Insertion polymerization is particularly suitable for polymerization of ethylene (with or without higher 1-olefins as co-monomers), propene, butene, and styrene. Section 6.20 is devoted solely to processes for production of polyethylene, describing details of the mechanism of insertion polymerization and process parameters.

5.3.4.3 Polyesters, Polyamides, and Polyurethanes

Polyethylene terephthalate (PET) (Table 5.3.13) is obtained either by polycondensation of ethylene glycol and terephthalic acid or by transesterification of terephthalic acid dimethyl ester with ethylene glycol. The polymer has an unusually high melting point (260–270 °C) and very good mechanical properties. PET bottles and textile as well as industrial fiber applications are among the main applications of this polyester.

Table 5.3.13 Industrially relevant polyesters, polyamides, and polyurethanes.

Polymer	Structure	Major applications	World production in mio. t a ⁻¹
Poly(ethylene-terephthalate) (PET)		Bottles, containers, fibers	49 (2009) ^{a)}
Polycarbonate (PC) (Macrolon [®]) (e.g., bisphenol A + phosgene)		Tubing, containers, films, data storage (CD, DVD), safety glass	around 3 (2012) ^{b)}
Polyamide 6.6 (Nylon [®])		Fibers, slides, materials	4 (all polyamides in 2001) ^{c)}
Polyamide 6 (Perlon [®])		Fibers, slides, materials	
Polyurethane (PUR) [e.g., methylene diphenylene diisocyanate (MDI) + 1,6-hexadiol]		Linear PUR: fibers, textiles Crosslinked PUR: coatings, foams, elastomers	10 (2004) ^{c)}

a) www.chemmarket.info/en/home/article/2422/, accessed 18.09.2012.

b) estimation based on data given in www.mpmagazine.com/x/guideArchiveArticle.html?id=480, accessed 18.09.2012.

c) Wiley-VCH, 2012.

The industrially most relevant *polycarbonate* (PC) is formed by the reaction of the diol bisphenol A with diphenyl carbonate or phosgene. Formally, polycarbonates can be regarded as polyesters of the acid H_2CO_3 . Polycarbonates are transparent and display good mechanical and dielectric properties but are unstable against many organic solvents and strong bases.

Polyamides are produced by polycondensation of dicarboxylic acids and diamines, by polycondensation of amino acids, or by ring-opening polymerization of lactams. Polyamides are in general characterized by attractive mechanical properties, good heat resistance, and high stability against chemicals. *Polyamide 6.6 (nylon)* is produced from adipic acid and hexamethylene diamine in a polycondensation reaction. *Polyamide 6 (Perlon)* is obtained by ring-opening polymerization of ϵ -caprolactam.

Linear *polyurethanes* (PUR) are formed in a polyaddition reaction of diisocyanates [e.g. toluene diisocyanate (TDI) or methylene diphenyl diisocyanate (MDI)] and diols (e.g., 1,4-butanediol or 1,6-hexanediol). Crosslinking is introduced by either the reaction of triisocyanates or the reaction of triols instead of the corresponding difunctional monomer.

Topic 5.3.7 Important process options for the production of polymers

Polymerization processes are carried out in many different variations. Process selection depends on the monomer and, also, strongly on the desired product properties. Selection of the right polymerization process is also very important with regard to process safety. Polymerization reactions belong to the most dangerous processes in the chemical industry with respect to the risk of an uncontrollable thermal runaway in the reactor. The reasons for the special hazard potential caused by polymerization reactions are threefold:

- 1) many polymerization reactions are highly exothermic;
- 2) polymerization reactions do not slow down with monomer consumption as the product is also reactive and continues to react at the same rate;
- 3) during polymerization the viscosity of the reaction mixture increases, often drastically, and with that heat transfer onto the reactor wall becomes increasingly difficult.

It is important to note that problems to remove the heat from polymerization reactions are not only relevant in the case of thermal runaways. Local hot spots in the polymerization reactor can also cause undefined molecular mass distributions, product colorization, or decomposition reactions and result, in this way, in a lower product quality.

In general, we can distinguish homogeneous and heterogeneous polymerization processes. Homogeneous processes take place within the substance in question (with the monomer or the formed polymer acting as reaction medium) or in a solvent. Heterogeneous processes include precipitation, slurry phase, suspension, emulsion, or gas-phase polymerizations.

A strong point of *polymerization in-substance* is the fact that the whole reactor volume is used. This results in high space–time yields. Moreover, as no additional substance is added to the reaction mixture the resulting polymer is very pure. The main drawback is the high viscosity of the polymer melts and with this the difficulty in removing the reaction heat properly from the reacting mixture. Many technical polymerization reactions in-substance are stopped at monomer conversions of about 50% to limit the increase in viscosity to a manageable level. Typical examples of polymers that are produced in-substance are polystyrene, polymethacrylates, polyesters, polyamides, and high-pressure polymerization of ethylene to LDPE (low density polyethylene) (for details see Section 6.20).

Polymerization in solution uses an inert solvent to reduce the viscosity in the reactor and evaporation of the solvent to cool the reaction mixture. The process requires a solvent that dissolve both the monomers and the formed polymer. The homogeneous environment of the reaction allows defined polymer formation, for example,

with respect to the molecular mass of polymer by adjustment of the right monomer concentration. This way of processing is particularly suitable if the solution obtained after polymerization itself is the product, like, for example, in lacquer production. If the pure polymer is the commercial product additional efforts are necessary to remove the solvent from the polymer. Another drawback of polymerization in solution is its lower space–time yield (due to solvent taking up part of the reactor volume) and the slower kinetics due to lower monomer and polymer concentrations. Examples of polymers produced by polymerization in solution include ethene–vinyl acetate copolymers and ethene/propene/diene copolymerizations (EPDM).

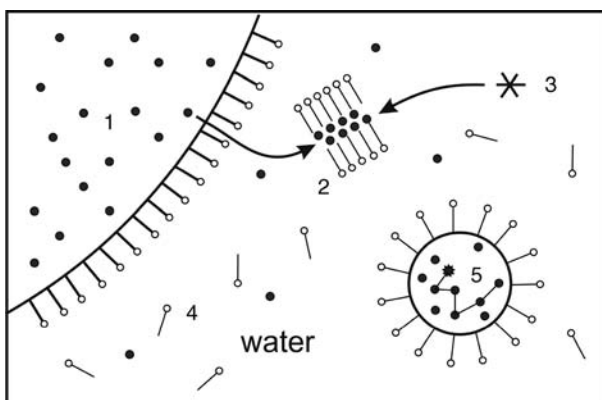
A special variation of solution polymerization is *precipitation polymerization*. The only difference here is that the polymer becomes more and more insoluble in the solvent as its molecular weight increases. The polymer precipitates from the solution and can be isolated by filtration. One interesting feature of precipitation polymerization is that the viscosity of the solution in the reactor remains almost constant. The production of polyacrylonitrile in water is an important example of this polymerization process.

Slurry-phase polymerization involves a solid from the beginning of the polymerization process. An important example is the production of high-density polyethylene (HDPE) using immobilized, solid Ziegler–Natta catalysts in a solvent (typically liquid alkanes). Slurry phase polymerization is carried out in stirred tank reactors or loop reactors where the three-phase system is pumped with high flow velocities to reduce the probability of reactor fouling (for details see Section 6.20).

In *suspension polymerization* the reaction mixture consists of a liquid–liquid biphasic system, one phase (typically water) of which is inert while the other phase is monomer. With intense mixing of the reactor, small droplets of monomer form in the aqueous phase. The added initiator is soluble in the monomer phase and starts the polymerization in the monomer droplets that are fully surrounded by the water, which acts as heat transfer fluid. The process results in spherical polymer beads of the size of the original monomer droplet if coagulation of the monomer droplets during mixing and polymerization can be avoided. In many suspension polymerization processes dispersants are added to achieve this. Important technical polymers produced by suspension polymerization are PVC and PMMA. In addition to these, spherical ion-exchange resins (typically polystyrene based) are also produced by suspension polymerization.

Emulsion polymerization is similar to suspension polymerization in the sense that the reaction also takes place in the presence of a water phase and the applied monomer forms a second liquid phase. However, in this case the added radical initiator is not soluble in the monomer droplets but in the water phase. To allow the monomer to come into contact with the initiator an emulsifier is added to the reaction mixture that creates micelles in the systems. By diffusion processes both monomer molecules and initiator molecules reach the micelle. Polymerization takes places and a polymer particle suspended in the water phase forms that is much smaller than the original monomer droplet (see Figure 5.3.12 for a graphical illustration of these steps). At the end of the overall emulsion polymerization process, all monomer droplets have been consumed by the polymerization reaction in the micelles. Typical emulsifiers for emulsion polymerization are natural or synthetic detergents, such as, for example, sodium palmitate or sodium alkyl sulfonates. Emulsion polymerization is very versatile and is applied for many polymers [e.g., PVC, styrene copolymers, poly(methacryl esters)] in batch, semi-continuous, and continuous processes. In some cases, the obtained polymer particles in water are directly applied as technical products for coatings, lacquer applications, or as adhesives. In other cases the formed product is further treated to obtain the dry polymer. Note that the aqueous phase in emulsion polymerization always contains some “isolated” emulsifier and also some monomer. Moreover, the formed polymer contains the emulsifier as impurity.

Figure 5.3.12 Relevant steps in emulsion polymerization: from the monomer droplet (1) monomer diffuses to a micelle (2), which also contains the radical initiator (3); the micelle is formed by added emulsifier (4); finally, a polymer particle forms in water (5) that is much smaller than the original monomer droplet.



It was stated at the beginning of this topic that heat management and safety aspects are important for the selection of the most suitable polymerization process. As the effectiveness of heat transfer is largely governed by the viscosity of the reaction mixture it is instructive to compare typical viscosities versus monomer conversion plots for the various polymerization processes that have been described above (Figure 5.3.13). Obviously, the most critical process with respect to heat removal is polymerization in-suspension, while suspension and emulsion polymerizations show only very small changes in viscosity and thereby allow proper heat transfer even at high monomer conversions.

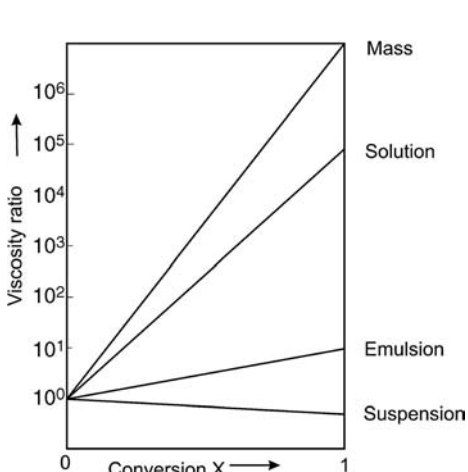


Figure 5.3.13 Viscosity of the reaction mixture versus monomer conversion for various polymerization processes.

5.3.5 Detergents and Surfactants

5.3.5.1 Structure and Properties of Detergent and Surfactants

Detergents and surfactants form an important class of chemical products (global production ca. 15 mio. t a⁻¹). All surface active molecules have the common structural feature that they combine in one molecule parts of very different polarity and hydrophilicity/hydrophobicity. Characteristically, one part of their molecular structure is highly nonpolar, hydrophobic, and lipophilic while the other part is highly polar, hydrophilic, and lipophobic (see Figure 5.3.14a). Owing to this special nature, detergents and surfactants can create compatibility among substances and surfaces of very different polarity and hydrophilicity/hydrophobicity.

Detergents and surfactants are water soluble. At low concentrations they enrich in multiphase systems (e.g., water/gas or water/solid) at the interphase, where they drastically influence important physicochemical properties, such as surface tension (in the case of water/gas interphase) or wettability (for water/solid interphases). With increasing detergent concentration in water, ensembles of detergent molecules form and this tendency leads at a characteristic

Figure 5.3.14 Schematic representation of the function of detergent molecules: (a) basic structure of a detergent molecule; (b) oil-in-water micelle; (c) water-in-oil micelle.

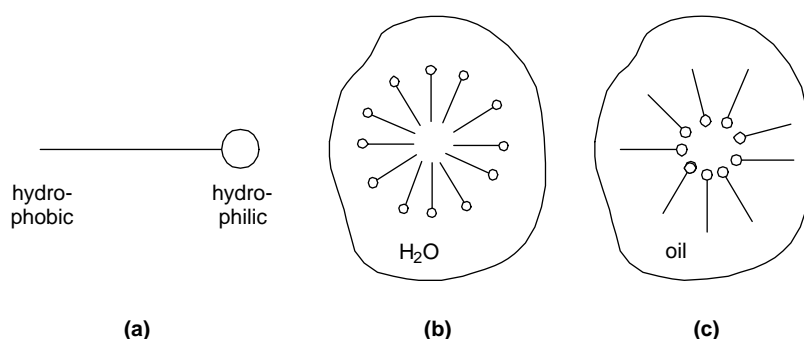


Table 5.3.14 Selection of important industrial applications of detergents and surfactants. Adapted from Baerns (2006).

Application field	Function of the detergent/surfactant
Crop science	Emulsifier/stabilizer in aqueous insecticide and herbicide solutions
Textile/leather industry	Cleaning agent for natural fibers and materials, antistatic agents for fiber spinning
Food industry	Emulsifiers, for example, for ice cream, mayonnaise, and dips
Paper industry	Deinking of scrap paper, foam regulators
Mining and oil drilling	Active agents in flotation processes, lubricant
Metal and galvanic industry	Cleaning agent, corrosion inhibitor, lubricant
Polymer production	Emulsion polymerization, polymer foam stabilizer
Coating and colorants	Dispersants

concentration, the so-called critical micelle concentration (CMC), to the formation of defined aggregates. Besides spherical micelles other shapes of detergent aggregates are also possible, including ellipsoids, cylinders, and bilayers. The shape and size of the formed micelle is a function of the molecular shape of its surfactant molecule, surfactant concentration, temperature, pH, and ionic strength of the surrounding medium.

When surfactants are present above their CMC they can allow a compound that is normally insoluble in the applied solvent to dissolve. This occurs, for example, by incorporating a nonpolar, water-insoluble oil or wax molecule into the nonpolar micelle core, which is itself solubilized in water by virtue of the polar head groups' favorable interactions with the solvent water. The formation of such an "oil-in-water micelle" (Figure 5.3.14b) forms the basis of the functionality of detergents in washing agent formulations. In a very similar manner, detergents can also help to disperse polar particles (such as metal particles or pigments) in oils by inverse micelle formation. In these "water-in-oil micelles" (Figure 5.3.14c) the polar head-groups of the surfactant point to the center, thereby enclosing a polar region, while the hydrophobic tails extend outward to solubilize the micelle in the continuous oil phase.

One of the main application fields of surfactants is their use as an essential part of household detergent formulations. A classical washing machine powder consists of about 10–20 mass% of detergents. Other major components are builders (e.g., zeolite A, 20–35 mass%) for the complexation of Mg^{2+} and Ca^{2+} ions, bleaching agents (e.g., perborates, 10–25 mass%), fillers (e.g., Na_2SO_4 , 0–20 mass%), as well as bleaching activators, sequestrants, foam regulators, anti-graying agents, detergent enzymes, optical brighteners, corrosion inhibitors, and fragrances. Liquid detergent formulation and compact powders consist of similar components albeit in a different composition (e.g., different detergent mixtures and builder systems). Moreover, they are manufactured by different production processes.

Besides these household applications, detergents and surfactant also find numerous important industrial uses. Table 5.3.14 gives an overview of some important fields and the specific function of the detergent therein.

In the following we describe the most important types of surfactants and detergents. These types can be classified according to the chemical nature of their polar head groups, which can be cationic, anionic, or neutral. The hydrophobic part of typical surfactant and detergent molecules is usually formed by a long-chain alkyl group with typically 12–18 carbon atoms.

5.3.5.2 Cationic Detergents

Table 5.3.15 gives an overview of the industrially most relevant cationic detergents and surfactants.

Cationic detergents are usually produced by alkylation of fatty amines (see Section 5.3.3.7 for details) with short-chain alkyl chlorides, dimethyl sulfate, or diethyl sulfate. Thus, a cationic detergent takes its fatty amine part from natural fats and oils while the alkylation agent is typically produced from fossil resources.

Table 5.3.15 Industrially relevant cationic detergents and surfactants.

Compounds	Structure ^{a)}	Major applications
Distearyl(dimethyl)ammonium chloride		Softener for laundry washing
Benzyl(dimethyl)dodecylammonium chloride		Disinfection
1-Alkoxyethyl-2-stearyl-3-methylimidazoliunium chlorides		Softener for laundry washing
Dialkoxoethyl(hydroxyethyl)methylammonium chlorides (ester quaternaries)		Softener for laundry washing

a) R = C₁₂-C₁₈ alkyl rest.

Cationic detergents are used to modify the surface properties of negatively charged surfaces, with important applications as softeners in washing formulations or as hydrophobic agent for metallic surfaces. In softener applications, distearyl (dimethyl)ammonium chloride is being increasingly replaced by ester quaternaries due to the better biological degradability of the latter. Shorter chain quaternary ammonium salts display bacteriostatic and biocidic properties leading to their use as disinfection agent. Of course, these biocidic structures are not applied in washing formulations due to their negative impact on the commonly used biological wastewater treatment plants.

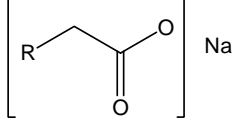
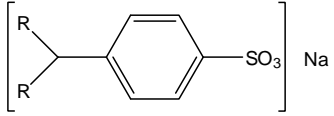
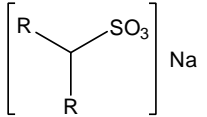
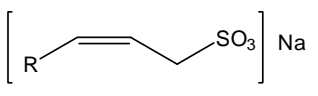
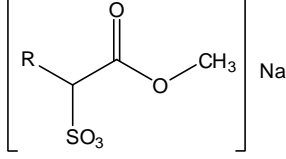
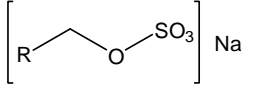
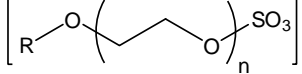
5.3.5.3 Anionic Detergents

As measured by the amount produced, anionic detergents are by far the most important class of surface active compounds. Table 5.3.16 gives an overview of the industrially most relevant representatives together with typical application fields.

Fatty carboxylates (soaps) were at one time the only known detergents. In recent times their importance has decreased, mainly due to problems with the formation of water-insoluble Ca and Mg salts if these cations are present in the washing water. Today, soaps are mainly applied as foam regulators in washing agents. The technical production of fatty carboxylates proceeds by treating vegetable or animal oils and fats with a strongly alkaline solution. In this process, also called “saponification,” the natural fat is hydrolyzed to the fatty carboxylate salt and glycerol (Scheme 5.3.9).

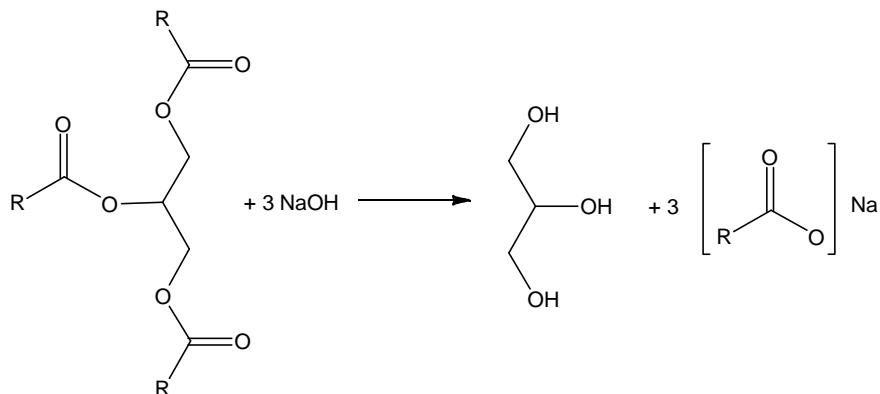
Alkylbenzene sulfonates form the most important single family of detergents. Their production is mostly based on fossil resources, starting from an acid-catalyzed Friedel–Crafts alkylation of benzene with linear alkenes followed by sulfonation of the aromatic ring and neutralization with NaOH. Note that it is crucial for the biological degradability of the resulting detergent that the applied alkene in the

Table 5.3.16 Industrially relevant anionic detergents and surfactants.

Compounds	Structure ^{a)}	Major applications
Fatty carboxylates		Soaps, liquid detergents
Alkylbenzene sulfonates		Washing powder formulations
Alkylsulfonates		Dish-washing formulations
Alkenyl sulfonates		Liquid soaps
Ester sulfonates		Washing powder formulations
Fatty alcohol sulfates		Washing powder formulations
Fatty alcohol ether sulfates		Shampoos, foam bath formulations

a) $R = C_9\text{--}C_{19}$ alkyl rest; $n = 3\text{--}15$.

first alkylation reaction has a linear structure. Owing to the importance of this structural property the whole class of alkylbenzene sulfonates is often referred to in the literature as “linear alkylbenzene sulfonates (LABS). LABS with alkyl chain lengths between C_{10} and C_{13} show the best compromise between biological degradability and washing performance.

**Scheme 5.3.9** Soap formation by basic ester cleavage (“saponification”) of natural oils and fats.

Alkylsulfonates are also important anionic detergents but less so for the production of solid washing powders as they cannot readily be processed in spray drying processes. For their production long-chain alkanes are treated with either SO_2/Cl_2 (sulfochlorination) or with SO_2/O_2 (sulfoxidation). Both processes require operation at low alkane conversion to avoid undesirable multi-sulfonation.

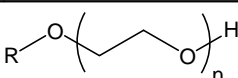
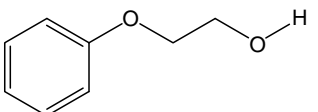
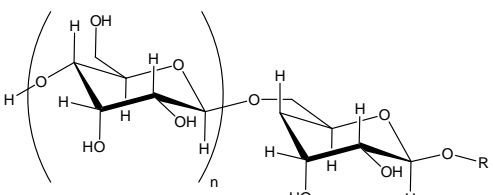
Alkenylsulfonates, *fatty alcohol sulfates* and *fatty alcohol ether sulfates* are produced today by contacting alkenes, fatty alcohols, or fatty alcohol ethers with gaseous SO_3 in multi-tubular falling film reactors. Typical reactor productivities reach up to 10 t of product per hour. An even temperature distribution throughout the reactor is an important prerequisite for optimum product quality in these processes.

5.3.5.4 Non-ionic Detergents

The most important families of non-ionic detergents are adducts of fatty alcohols or alkylphenol to ethylene oxide or propylene oxide oligomers. The hydrophilic part of these detergents is not formed by an ionic head group but results from the hydrogen-bond interactions between the ether oxygen functionalities and water. An alternative hydrophilic head group is formed by carbohydrates moieties. This family of detergents is called “alkylpolyglycosides” and consists typically of a sugar oligomer that acts as hydrophilic head group. The latter is linked to a fatty alcohol by an ether bridge. Alkylpolyglycosides have the advantage that both parts – hydrophilic head and hydrophobic tail – originate from biogenic resources. In contrast, typical fatty alcohol glycol ethers combine a biogenic part (fatty alcohol) and a petrochemical part (ethylene oxide, propylene oxide). Alkylphenol glycol ethers are fully petrochemical based. Table 5.3.17 gives an overview of the named important families of non-ionic detergents.

Fatty alcohol polyether glycals and *alkylphenyl polyether glycals* are produced by a catalyzed addition of ethylene oxide or propylene oxide to a fatty alcohol, fatty alcohol mixture, or alkylphenol. The properties of the resulting detergent can be tailored by the stoichiometry of epoxide and alcohol and by the nature of the fatty alcohol or alkylphenol applied. While a large excess of epoxide increases the hydrophilicity of the detergent, a longer alkyl chain of the applied alcohol increases its lipophilicity. In addition, the choice of catalyst influences the product spectrum obtained. Simple base catalysts lead to a very broad distribution of the ethylene glycol oligomers. In contrast, the use of heterogeneous contacts of the hydrotalcite type (e.g., $[\text{Mg}_4\text{Al}_2(\text{OH})_{12}][\text{CO}_3]x \cdot 4\text{H}_2\text{O}$) leads to a very narrow distribution of the poly(glycol ether) hydrophilic head group.

Table 5.3.17 Industrially relevant neutral detergents and surfactants.

Compounds	Structure	Major applications
Fatty alcohol poly(glycol ethers)		Detergents, tensides
Alkylphenol poly(glycol ether)		Detergents, emulsifiers
Alkylpoly-glycosides		Cosmetics, shampoos, dish-washing formulations

Alkyl-polyglycosides are produced by two different processes. In the two-step process glucose is first processed in a trans-acetalization with butanol to convert the sugar feedstock into a fatty alcohol-soluble derivative. In a second step, trans-acetalization with the fatty alcohol proceeds and butanol is recycled in the process. In the direct production route, an excess of fatty alcohol is contacted with glucose in a technical vacuum in the presence of an acid catalyst. The resulting alkylglucoside melt contains only minor amounts of the more volatile fatty alcohol. Remaining quantities of the latter are separated from the product in downstream purification steps. Alkyl-polyglycosides reach their optimum performance as detergents if the long alkyl chain contains 12–15 carbon atoms and the glucoside units make up about 65% of the detergent mass.

5.3.6

Fine Chemicals

The production of fine and specialty chemicals is characterized by several important and fundamental differences compared to producing bulk chemicals. These are summarized in Table 5.3.18. Many of these differences stem from the fact that the production volumes in fine and specialty chemicals manufacturing are much smaller. Moreover, the chemical complexity of these products is typically much higher. As a consequence, it is less the efficiency of the process that is in the focus but the quality and performance of the product itself. Characteristic for fine and specialty chemicals production is the fact that the products are formed in multistep syntheses (as demonstrated for the product Aspirin® in Topic 5.3.8). As each step provides the desired product in a certain selectivity, the overall ratio of by-product formation versus product formation is typically much higher than in bulk chemicals production. However, the added value in fine chemicals production is also very high as the customer appreciates the special performance of the product for their specific application.

While the production of fine chemicals is defined by a high added value and relatively low production volumes, specialty chemicals are formulations of several compounds containing one fine chemical or a mixture of several fine chemicals as active ingredients. Specialty chemicals are usually sold under brand names and are identified by their performance. For example, the active ingredients of a drug are fine chemicals, whereas the formulated drug itself is a specialty chemical.

Typical reaction equipment for fine and specialty chemicals production is a batch-wise operated multi-purpose plant (MPP). A common MPP set-up includes a stirred stainless-steel or glass-lined batch reactor with reflux condenser, feed systems for reactants and inert gases, as well as equipment for different, optional separation

Table 5.3.18 Characteristic differences in fine chemicals production versus petrochemicals and bulk chemicals production.

	Fine chemicals	Petrochemicals and bulk chemicals
Production volume	< 10 000 tons/year	> 10 000 tons year ⁻¹
Product price	> €8 kg ⁻¹	< €8 kg ⁻¹
Product life cycle	Short (<10 years)	Long (>30 years)
Chemical complexity, number of reaction steps, added value	High	Low
By-products (kg kg ⁻¹ product)	High	Low
Number of feasible routes	Many	Few
Process technology	Batch in multi-purpose facilities, increasing interest in continuous microreactor technologies	Continuous
Focus of R&D; patent protection	Product improvement	Process improvement

and purification operations (i.e. filters, driers, distillation equipment). MPPs are characterized by the fact that many different products are produced in the same piece of equipment over the year with, of course, extensive washing and cleaning procedures at each product change.

Here, different classes of industrially important fine and specialty chemicals are highlighted briefly. Table 5.3.19 presents important representatives and their chemical structures.

5.3.6.1 Dyes and Colorants

Dyes and colorants are complex organic molecules with conjugated or delocalized π -electron systems (chromophores). Based on the different relevant chemical functionalities that act as chromophores in specific dyes, the latter can be grouped into azo dyes, carbonyl dyes, methine dyes, and phthalocyanines. The dye "indigo" shown in Table 5.3.19 belongs to the group of carbonyl dyes.

5.3.6.2 Adhesives

Historically, adhesives have been produced from natural products, such as bones or starch. In the last 20 years, many synthetic adhesives have found important applications not only in furniture production but also in the manufacturing of cars, airplanes, microelectronic devices, and even in medical technologies. Typical synthetic adhesives are reactive polymers like polyurethanes, polydienes, polyamides, or polyacrylates.

5.3.6.3 Fragrance and Flavor Chemicals

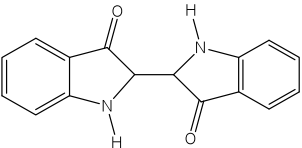
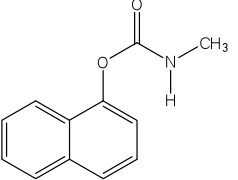
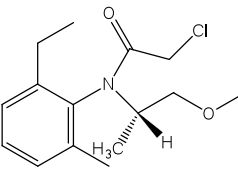
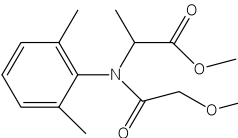
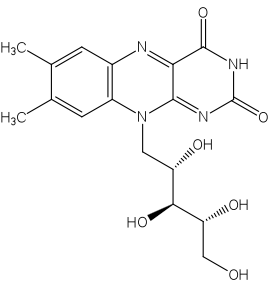
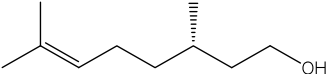
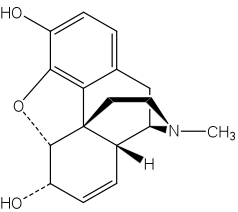
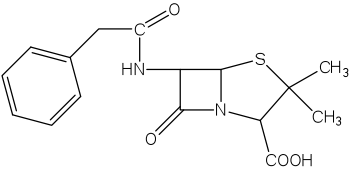
The role of fragrances since ancient times has been to cover unpleasant smell and to provide a pleasing impression (e.g., fruity, floral, marine etc.). Fragrance and flavor raw materials are obtained either from natural sources (e.g., terpenes, plant essential oils, animal secretions) or from chemical synthesis. As the enantiomers of many odorant molecules differ in strength and in odor/taste description, the selective (and often catalytic) synthesis of the more appreciated isomer is of great interest. This avoids the dilution effect by the non-desired isomer and reduces the amount of active ingredient in the final product. Table 5.3.19 shows the example of (*S*)-citronellol, an important perfumery raw material with a rose note.

5.3.6.4 Pesticides

Pesticides can be grouped into three categories according to their main targets. Insecticides protect plants against attack from insects, herbicides act against herbs, and fungicides are applied against plant damage by fungi.

Insecticides are not only relevant for plant protection but in addition (mainly in the developing countries) for fighting certain diseases, such as, for example, malaria. As many pathogens are transferred by insects, the use of insecticides can contribute significantly to minimizing the spread of these health problems. Important classes of insecticides include chlorohydrocarbons, pyrethroids, phosphoric acid esters, and carbamates. Table 5.3.19 shows the chemical structure of carbaryl (trade name "Sevin"), an important carbamate insecticide. Apart from its very wide use, this substance has received some special attention in the past for a very sad reason. One of the reaction steps to produce carbaryl requires the use of methyl isocyanate. In 1984, this extremely toxic chemical was released from a carbaryl production plant in Bhopal, India, causing the greatest chemical accident in history, with more than 2000 people being killed and more than 200 000 injured. The reason for this terrible accident was the unsafe storage of large amounts of methyl isocyanate in a 40 m³ storage tank. Therefore, modern production units prepare the methyl isocyanate needed for reaction just before its use in the synthesis, thus reducing drastically the stored quantities.

Table 5.3.19 Important examples of the different types of fine and specialty chemicals.

Chemical	Structure	Major applications
Indigo		Blue dye for coloring tissues and clothes
Carbaryl		Insecticide
(S)-Metolachlor		Herbicide for corn farming
Ridomil®		Fungicide in potato farming
Vitamin B ₂		Therapy, food, and animal feed additive
(S)-Citronellol		Rose note fragrance
Morphine		Strong anti-pain drug
Penicillin G		Anti-bacterial drug

Herbicides are used in many different forms. There are herbicides that are active against all herbs, while others show herb-selective action. Herbicides can be taken-up by the plant via roots or via leaves. Important chemical classes of herbicides are carbonic acid based, urea based, aniline based, and phosphonic or phosphoric acid based. The aniline-based herbicide (*S*)-metolachlor is shown as example in Table 5.3.19. This herbicide is used in corn farming and is one of the most important examples of products industrially synthesized by asymmetric synthesis using a chiral transition metal complex. The asymmetric synthesis was established after it was discovered that almost all the activity (95%) is caused by the (*S*)-metolachlor stereoisomer.

Fungicides prevent fungi from germinating and growing. In many applications, the seeds of agricultural crops are treated with fungicides to prevent detrimental influence of the fungi at the stage of seed storage. Inorganic fungicides were already developed in the nineteenth century and copper salts as well as sulfur suspensions proved to be successful against fungi that endangered vine farming at that time in Germany and France. Owing to their better biodegradability organic fungicides are preferred today. Important classes include organic sulfur compounds, arylamine derivates, and methoxyacrylates. The example Ridomil shown in Table 5.3.19 belongs to the class of the arylamine derivates and is used in potato farming.

5.3.6.5 Vitamins, Food, and Animal Feed Additives

Vitamins are organic compounds required as vital nutrients in small amounts by a given organism. Vitamins cannot be synthesized in sufficient quantities by the body and have to be provided with the diet to avoid characteristic diseases (e.g., scurvy in the case of human shortage of vitamin C). The three most important vitamins (by their industrial production capacities) are vitamin C, vitamin B₃ (nicotinic acid amide) and vitamin E (tocopherol). These three vitamins represent, from their structure and synthesis, typical fine chemicals. However, they are produced on a multi-10 000 ton-scale per year. To give an example that also fulfils the capacity criterion of fine chemicals, Table 5.3.19, shows vitamin B2 (riboflavin). The latter is produced both by chemical synthesis and fermentation on the order of 10 000 tons yr⁻¹. Riboflavin is required for a wide variety of cellular processes and is used for therapeutic purposes and as food additive.

The most relevant food additives, like glutaminic acid (flavor enhancer) or L-asparagine acid (Aspertame®, synthetic sweetener), are synthesized in much larger quantities than 10 000 tons yr⁻¹. The same is true for the most relevant animal feed additives, such as D,L-methionine and L-lysine, which are even produced on the multi-100 000 ton-scale in continuous plants in a quite similar manner to bulk chemicals.

5.3.6.6 Pharmaceuticals

The term “pharmaceutical” is used for chemicals that are produced for medical purposes. A pharmaceutical is typically composed of one or more active ingredients and many additional components (binder, stabilizers etc). The latter are present to provide a certain form of donation, for example, to integrate the active ingredient into a tablet, a powder, an ointment, or a solution. The active ingredients are produced using chemical synthesis, biological methods (such as fermentation or biocatalysis), or sequences of both. In addition, several active ingredients are obtained directly from plant extraction (e.g., morphine) or from chemical transformations of plant extracts (e.g., codeine).

Active ingredients in pharmaceuticals typically contain chiral atoms and their different enantiomers often show very different physiological effects. Therefore, the synthesis of many drugs requires asymmetric catalysis, with more and more biological methods and biocatalytic processes becoming used in the industry.

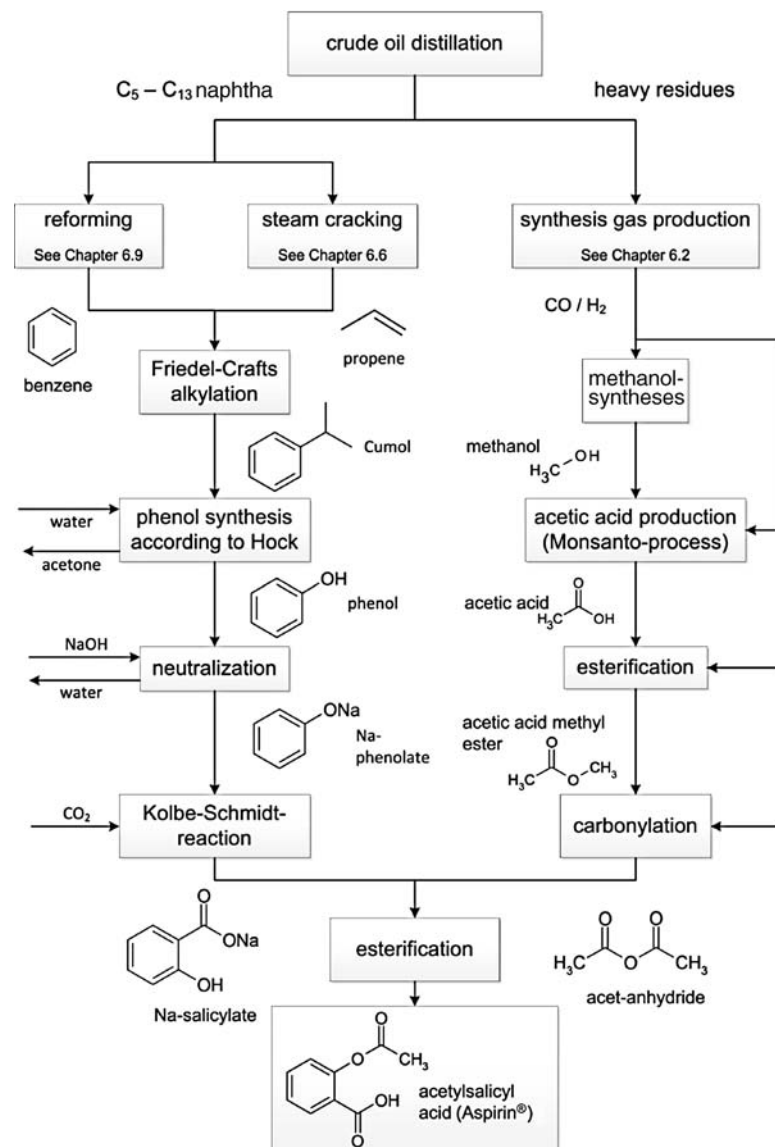


Figure 5.3.15 Schematic view on the multistep reaction sequence for producing the drug Aspirin® from crude oil.

For the production of pharmaceuticals it is of great importance that the feedstock purity is always the same and all synthetic and purifications steps are fully reproducible to guarantee that the final drug is of the highest quality.

Topic 5.3.8 Aspirin

Figure 5.3.15 illustrates the production process of the drug Aspirin® (which in fact is the fine chemical acetyl salicylic acid) from crude oil. The total reaction sequence involves 12 steps. Note that some of the basic chemical production processes that are exemplified in this book in Chapter 6 form the initial steps of the production process. Aspirin is among the most applied synthetic drugs.

5.4

Environmental Aspects of Chemical Technology

The pollution of air, water, and soil is a huge global problem, and environmental quality is not a simple, easy issue. The costs of environmental damages are high. For example, the annual costs of damage only from emissions of sulfur oxides

Table 5.4.1 Contributions (%) to various emissions by mobile sources (transport) and stationary sources in China (Wang *et al.*, 2005; Klimont *et al.*, 2002), USA (www.epa.gov), Germany, and Europe (www.bundesumweltamt.de).

Pollutant	China 2000		USA 2002		Germany 2006		Europe 2005	
	Transport	Stationary sources	Transport	Stationary sources	Transport	Stationary sources	Transport	Stationary sources
NO _x	30	70	38	62	50	50	44	56
SO ₂	50	50	1.8	98.2	0.3	99.7	3	97
HC	39	61	24	76	11	89	31	69
CO	15	85	58	42	38	62	56	44

and nitrogen oxides in North America are projected to be several billions of dollars (Farrauto and Bartholomew, 1997). Thus chemical and biological technologies – although also costly but probably in the long run not as costly as the environmental damages – are needed to avoid pollution and to clean wastewater or exhaust gases. Subsequently, some aspects of air and water pollution and of quantifying the environmental impact of chemical processes are discussed.

5.4.1 Air Pollution

Emissions of SO_x, NO_x (NO and NO₂), hydrocarbons (HCs), CO, and particulate matter from stationary and mobile combustion systems are serious hazards to human and animal health, and cause acid rain and smog, which leads to damage of property, agriculture, and forests. Mobile sources account for a large fraction of these emissions, especially of NO_x and CO. Stationary sources like coal-fired power plants are also major contributors, and account in most countries for most of the SO₂ and about half of the NO_x emissions (Table 5.4.1).

In view of these serious problems, it is no wonder that environmental issues have risen to the top of national and international agendas. For about the last three decades, control of NO_x, SO₂, HCs, and CO air emissions has been among the highest priorities, which is reflected by the worldwide increasingly restrictive standards on emissions (more details in Section 6.18).

As an example of the historical development of global emissions of air pollutants, Figure 5.4.1 presents the global SO₂ emissions for the period 1850–2000. The maximum was reached in 1989 with about 74 million tonnes of sulfur (as SO₂).

In 1850, Western Europe accounted for about 85% of the global SO₂ emissions (Figure 5.4.2). Today, the contribution of Western Europe to global SO₂ emissions is less than 10%, which reflects successful efforts to decrease SO₂ emissions (and also those of other pollutants). At the beginning of the

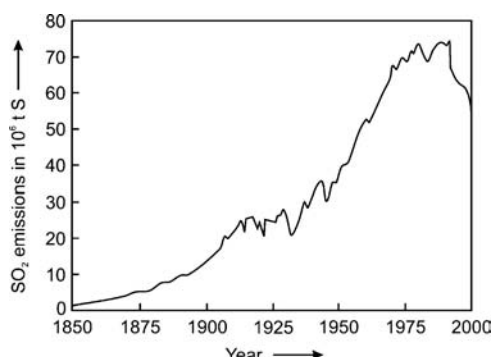


Figure 5.4.1 Global anthropogenic sulfur emissions (as SO₂) from 1850 to 2000 [data from Stern (2005)].

Figure 5.4.2 Shares of global anthropogenic SO₂ emission from 1850 to 2000 [data from Stern (2005)].

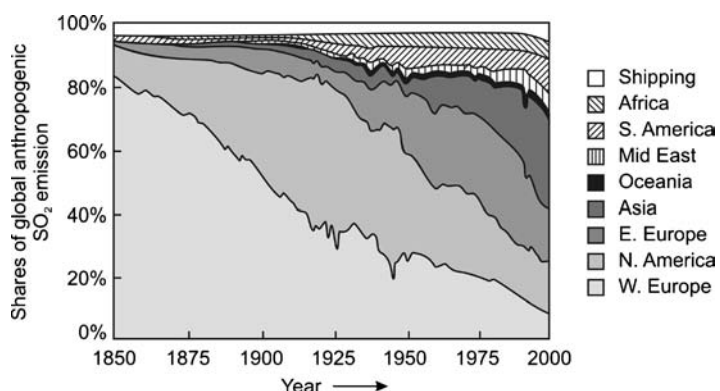


Table 5.4.2 Regional anthropogenic SO₂ peak emissions and emissions in 2000 (values do not include emissions from shipping) [data from Stern (2005)].

Region	Year of peak emissions	Peak emissions (10 ⁶ t S) (as SO ₂)	Emissions in 2000 (10 ⁶ t S) (as SO ₂)	Shares of global emissions in 2000 (%)
Western Europe	1974	13.7	3.8	7
North America	1974	17.6	8.6	17
Eastern Europe	1987	21.5	9.1	18
Asia	1996	≈20	≈17	≈32
South America	1999	6.2	5.7	11
Middle East ^{a)}	2000	3.8	3.8	7
Africa	1987	3.9	3.2	6
Oceania	2000	1.2	1.2	2

a) Excluding Kuwait oil fires during the Gulf War in 1990/91.

twentieth century, the locus of SO₂ emissions shifted from Western Europe to North America. About 50 years later, the share of Eastern Europe (including the former Soviet Union) increased followed by the strong rise of Asia as a substantial emitter. In the 1990s Asia became the largest source as Chinese SO₂ emissions overtook US emissions in 1987 to make China the largest single emitter. Chinese emissions peaked in 1996 and then fell as the Chinese government adopted various policies aimed at reducing emissions from cars, power plants, industry, and households. Table 5.4.2 lists the peak year of SO₂ emissions and the peak emissions in different regions as well as the regional anthropogenic SO₂ emissions and shares in 2000.

Globally, 56% of SO₂ emissions in 1990 were from coal, 24% from oil, 15% from industrial processes, and 3% from biomass burning (deforestation, savanna burning, and agricultural waste burning); the remaining 2% were from the use of traditional biomass as a source of residential fuel and from natural gas extraction, distribution, and use (Smith, Pitcher, and Wigley, 2001).

In 1990, the estimated global anthropogenic NO_x emissions were 31 million tonnes N per year. NH₃ and N₂O emissions in 1990 were 43 and 3.2 million tonnes N per year. Regional NO_x emissions are given in Table 5.4.3, indicating that in most industrialized countries they are decreasing, which shows the success of cleaning technologies in limiting emissions from cars and power plants. Notably, the values given in the literature for China and Asia vary by up to 50%, which is also true for SO₂ emissions.

There are two strategies to reduce air pollution: processes that produce fewer pollutants and efficient clean-up processes. Although both approaches also involve noncatalytic technologies, for example, combustion modifications or better scrubbers for removal of SO₂, environmental catalysis is contributing increasingly to both strategies. Two environmental catalytic processes are treated in Section 6.18,

Table 5.4.3 Anthropogenic NO_x emissions (excluding N₂O) in European countries (Vestreng *et al.*, 2008), China (Ohara *et al.*, 2007), and the USA (Olivier *et al.*, 1998 and <http://www.epa.gov/>).

Country	NO _x emissions (10 ⁶ t nitrogen)		
	1980	1990	2005
Russian Federation	1.00	1.09	0.85
United Kingdom	0.84	0.90	0.49
Germany	1.01	0.87	0.44
France	0.59	0.56	0.37
China	≈2	≈3	≈7
USA	8.3	7.3	5.8

namely, automotive emission control (Section 6.18.1) and the removal of NO_x from flue gases of power plants by catalytic reduction (Section 6.18.2).

5.4.2

Water Consumption and Pollution

Water is the most precious of all human resources. Fresh water is essential for household purposes (drinking, bathing, cooking, sanitation) but this only accounts to about 15% of the worldwide water use. Most fresh water is used for irrigation, that is, for agricultural use (70%), and 15% is needed for industrial use, for example, for cooling in power plants.

Unfortunately, 97% of the water on Earth is salt water, leaving only 3% as fresh water, of which more than two-thirds is frozen in polar ice caps and glaciers. The remaining unfrozen fresh water for direct use as a human resource is mainly found as groundwater (Table 5.4.4).

Usable freshwater comes from rainfall over land, about $120\,000 \text{ km}^3$ per year. Approximately 62% evaporates from the land surface into the atmosphere. The difference between precipitation and evaporation is the runoff of the rivers (95% of total runoff) and a small amount of groundwater runoff into the oceans. The total runoff is conventionally termed as renewable water resources, and is estimated at $43\,000 \text{ km}^3$ per year (Shiklomanov, 2000). The renewable water resources are very variable with space and time, and not all of the renewable water is accessible for use because part of it flows into remote rivers and seasonal flood waters that cannot be captured before they reach the oceans. According to the literature, 20–30% of the renewable water resources is all that is economically available for human use (Sophocleus, 2004), that is, today (2010) about 4 m^3 per capita and day on a global average.

Table 5.4.5 presents the distribution of the renewable water resources and the water availability by continent. The largest water resources are located in Asia and South America, and the smallest are found in Europe and Australia with Oceania. These absolute values do not reflect the water availability of the continents, as they differ much in area and population number. Hence, the specific water availability in cubic metres per year that fall on 1 km^2 of area and per person is also listed in Table 5.4.5. For example, Asia has the greatest total water availability but the lowest per capita availability because of the large population. Conversely, Australia and Oceania have the lowest water resources but by far the greatest per capita availability. The amount of fresh water is enough to meet human needs if it were evenly be distributed, but the freshwater supply and people are not evenly distributed around the globe, and two-thirds of the global population live in areas receiving only one-quarter of the world's annual rainfall (Sophocleus, 2004).

Table 5.4.4 Global water resources (Gleick, 1996).

Water source	Water volume (mio. km^3)	Percent of fresh water	Percent of total water
Salt water			
Oceans, seas, & bays	1338	—	96.5
Saline groundwater and lakes	13	—	0.9
<i>Total saline water</i>	1351	—	97.4
Fresh water			
Ice caps and glaciers	24.1	68.7	1.8
Fresh groundwater	10.5	30.1	0.8
Surface water (lakes, swamps, rivers)	0.1	0.3	0.01
Other freshwater sources (soil moisture, permafrost, atmosphere, biological water)	0.3	0.9	0.02
<i>Total fresh water</i>	35	—	2.6
<i>Total water</i>	1386	—	100

Table 5.4.5 Renewable water resources and water availability by continents in 1998 [data from Shiklomanov (2000) and Sophocleus (2004)].

Continent	Area (mio. km ²)	Population (millions)	Water resources (km ³ yr ⁻¹)	Potential water availability (1000 m ³ per year) ^{a)}	
				Per km ²	Per capita
Europe	10.46	685	2900	277	4.2
North America	24.3	453	7890	324	17.4
Africa	30.1	708	4050	134	5.7
Asia	43.5	3445	13510	311	3.9
South America	17.9	315	12030	672	38.2
Australia and Oceania	8.95	28.7	2404	269	83.7
World	135	5633	42785	317	7.6

a) Note that only about $\frac{1}{4}$ is economically available for human use (Sophocleus, 2004).

To characterize the water consumption of a country the water footprint concept developed in 2002 is useful (Hoekstra and Hung, 2002). The water footprint specifies the water needed as domestic water (drinking, washing, bathing, etc.) as well as for the production of agricultural and industrial goods. For the latter two consumption categories, the internal and the external water footprint, have to be considered. The internal footprint is the water needed for the production of goods in the national economy minus the virtual water export to other countries related to the export of domestically produced goods. The external footprint of a country (virtual water import) is defined as water used in other countries to produce goods and services consumed by the inhabitants of the country concerned.

Table 5.4.6 shows the water footprint of selected countries for the period 1997–2001, and Table 5.4.7 shows the domestic water consumption for the example of Germany. Compared to the global average value of the water footprint of about 3400 l per capita (pc) and day, the industrialized countries consume up to a factor of two more water, for example, about 6800 l pc and day in the USA, whereas developing countries consume much less. If only the consumption of domestic water is considered, the difference is even higher, for example, more than 900 l pc and day in Australia compared to only 71 l pc and day in China.

The virtual water content of agricultural and industrial goods is also of interest. Table 5.4.8 shows some examples.

The demand for fresh water already exceeds supply in many parts of the world, and as the world population continues to rise the present situation may intensify in future. In 2006, 13% of the global population lacked access to improved water sources, and 38% lacked access to improved sanitation (Figures 5.4.3 and 5.4.4).

Table 5.4.6 Water footprint of some countries (1997–2001, Hoekstra and Chapagain, 2007).

Country	Water consumption (liters per capita and per day)					
	Total water footprint	Domestic water	Water for agricultural goods		Water for industrial goods	
			Internal	External	Internal	External
USA	6801	595	3266	732	1668	540
Italy	6392	378	2271	2847	482	414
Russia	5087	268	3781	775	249	14
Germany	4234	181	1189	1655	625	584
Australia	3815	934	2016	112	175	578
Japan	3156	373	452	1682	296	353
India	2684	104	2485	38	52	5
China	1923	71	1548	110	178	16
Global avg.	3405	156	2485	438	216	110

Table 5.4.7 Domestic water consumption in industrialized countries (example Germany; data from www.bdew.de, accessed 29.10.2012).

Domestic water consumption (Germany, 2011)	
Component of water consumption	Daily consumption (liters per capita)
Bathing, showering	44
Toilet	33
Clothes washer	15
Dishwasher	7
Garden, cleaning	7
<i>Total</i>	122

Table 5.4.8 Global average virtual water content of some selected products (Hoekstra and Chapagain, 2007).

Product	Virtual water content (l)
1 Cup of coffee (125 ml)	140
1 Cup of tea (250 ml)	35
1 Glass of wine (125 ml)	120
1 Glass of milk	200
1 Egg (40 g)	135
1 Slice of bread (30 g)	40
1 Slice of bread (30 g) with cheese (10 g)	90
1 Hamburger (150 g)	2400
1 Apple (100 g)	70
1 Potato (100 g)	25
1 Tomato (70 g)	13
1 Orange (100 g)	50
1 Cotton T-shirt (250 g)	2000
1 Sheet of paper (80 g m^{-2})	10
1 Pair of shoes (bovine leather)	8000
1 Microchip (2 g)	32

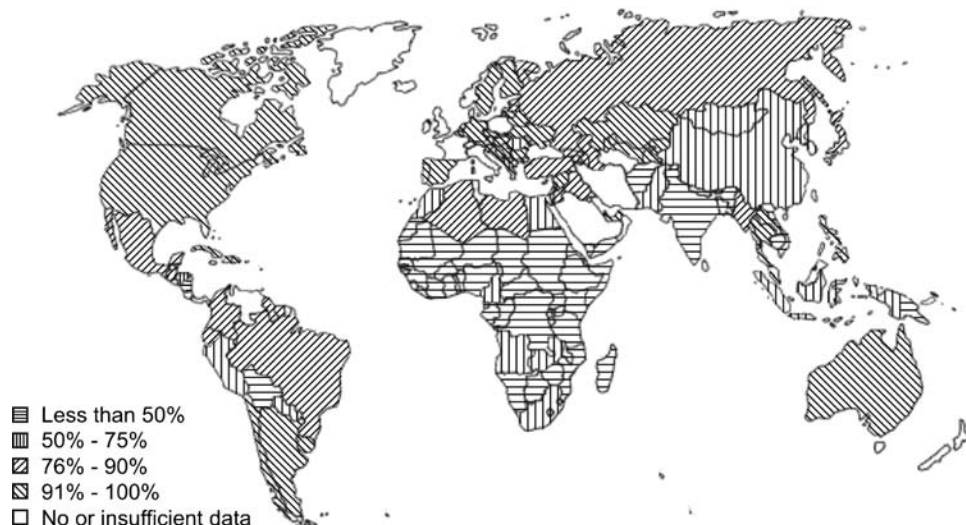


Figure 5.4.3 Global improved sanitation coverages in 2006 (improved sanitation ensures hygienic separation of human excreta from human contact) [data from WHO/UNICEF (2008)].

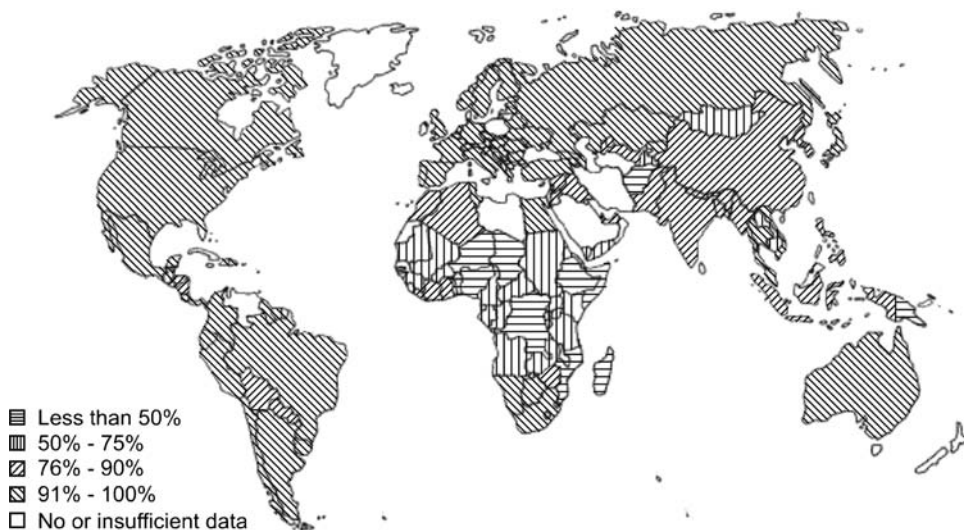


Figure 5.4.4 Global drinking water coverage in 2006 [data from WHO/UNICEF (2008)].

Many diseases are attributed to unsafe water supply, inadequate sanitation, and hygiene, mostly in developing countries: For example, in 2002, it was estimated that 1.8 million people die every year from diarrheal diseases (including cholera), 1.3 million people die of malaria each year, and there are 1.5 million cases of clinical hepatitis (www.who.int/water_sanitation_health/publications).

In many developing countries the bulk of domestic and industrial wastewater is discharged without any treatment or after primary treatment only. Thus, the global extension of domestic wastewater treatment is one of the main future challenges to supply the still growing global population with drinking water and improved sanitation. Wastewater treatment is needed to remove physical, biological, and/or chemical contaminants from wastewater, and includes physical, chemical, and biological processes.

5.4.3

“Green Chemistry” and Quantifying the Environmental Impact of Chemical Processes

It is beyond the scope of this textbook to discuss environmental aspects of chemical processes in detail, but some general aspects of “green chemistry” should be discussed. An excellent introduction into the field of green chemistry is given by Rothenberg (2008), and the main aspects outlined by him may be summarized as follows. “Green chemistry” deals with designing chemical processes that generate and use fewer (preferably no) hazardous substances. The green chemistry message is simple: “Seek prevention, not cure.” In 1998, Anastas and Warner formulated the following principles of green chemistry (Anastas and Warner, 2000):

- prevent waste instead of treating it;
- design atom-efficient synthetic methods;
- choose synthetic routes using nontoxic compounds where possible;
- design new products that preserve functionality while reducing toxicity;
- minimize the use of auxiliary reagents and solvents;
- design processes with minimal energy requirements;
- preferably use renewable raw materials;
- avoid unnecessary derivatization;
- replace stoichiometric reagents with catalytic cycles;
- design new products with biodegradable capabilities;

Table 5.4.9 Annual production and *E*-factors in the chemical industry (Rothenberg, 2008).

Industrial sector	Production (tonnes yr ⁻¹)	<i>E</i> -factor (kg _{waste} /kg _{product})
Petrochemicals	10 ⁶ –10 ⁸	<0.1
Bulk chemicals	10 ⁴ –10 ⁶	1–5
Fine chemicals	10 ² –10 ⁴	5–50
Specialties/pharmaceuticals	10–10 ³	20–100

- develop real-time and online process analysis and monitoring methods;
- choose feedstocks and design processes that minimize the chance of accidents.

Everyone agrees that green chemistry is a good thing, but how should we compare the environmental impact of processes? One method for quantifying a reaction's efficiency is by examining the conversion and the product selectivity and yield, which are all measures of the reaction efficiency, but not of the ecofriendliness of a process. As a measure of the "greenness" of processes, the *E*-factor was introduced by Sheldon in 1994. The *E*-factor is the quotient of the amount of waste and the amount of product (kg_{waste}/kg_{product}), whereby "waste" is everything formed in the reaction except the desired product. The waste can be gases, water, salts, and/or organic compounds. Table 5.4.9 compares the product rates and *E*-factors of various industrial sectors. The *E*-factor increases substantially on going from petrochemicals to bulk chemicals and finally to fine chemicals and specialties. The main reason is that fine-chemicals production often involves multistep syntheses.

The concept of atom economy, introduced by Barry Trost in 1992, is similar to that of the *E*-factor. Here one considers how many and which atoms of the reactants are incorporated into the products.

The *E*-factor and atom economy can be used to compare reaction alternatives, but the problem remains that there are different types of "waste." Obviously, water is "good waste," while, for example, heavy metal salts are "bad waste." To solve this problem, Sheldon introduced the environmental quotient *EQ* (Sheldon, 1994), which takes the amount as well as the nature of the waste by multiplying the *E*-factor by an arbitrarily assigned hazard factor *Q*. Assigning absolute *Q*-values to waste streams is difficult, because cases differ according to location and type of waste. Nevertheless, the *EQ* gives a better measure of the environmental impact of a process than the *E*-factor or the atom economy alone.

Summary of Section 5.4 (take-home messages)

- The **pollution of air, water and soil** is a huge global problem, and environmental quality is not a simple, easy issue. Air pollution by emissions of SO_x, NO_x, hydrocarbons (HCs), CO, and particulate matter from stationary and mobile combustion systems is a serious hazard to human and animal health, and causes acid rain and smog, which lead to damage of property, agriculture, and forests. Mobile sources account for a large fraction of these emissions, especially of NO_x and CO. Stationary sources like coal-fired power plants are also major contributors, and account in most countries for most of the SO₂ and about half of the NO_x emissions. For about the last three decades, control of NO_x, SO₂, HCs, and CO air emissions has been among the highest priorities, which is reflected by the worldwide increasingly restrictive standards on emissions.
- There are two **strategies to reduce air pollution**, the development of processes that produce fewer pollutants and efficient clean-up processes. Although both approaches also involve non-catalytic technologies, for example, combustion modifications or better scrubbers for removal of SO₂, environmental catalysis is contributing increasingly to both strategies. Two major environmental processes involving catalysis are **automotive emission control** (see also

Section 6.18.1) and the removal of NO_x from flue gases of power plants by selective catalytic reduction (Section 6.18.2).

- **Water** is a precious human resource. Fresh water is essential for household purposes (drinking, bathing, cooking, sanitation) but only accounts for 15% of the total global use.
- The majority of **fresh water** is used for irrigation, that is, for agricultural use (70%), and 15% is needed industrially. Unfortunately, 97% of water on the Earth is salt water, leaving only 3% as fresh water, of which more than two-thirds is frozen in polar ice caps and glaciers. The remaining unfrozen fresh water for direct use as a human resource is found mainly as groundwater. The demand for fresh water already exceeds supply in many parts of the world and, as the world population continues to rise, this situation may intensify in future. Today, 13% of the global population lacks access to improved water sources, and 38% lacks access to improved sanitation.
- In many developing countries the bulk of domestic and industrial wastewater is discharged without treatment or after primary treatment only. Thus, the global extension of domestic **wastewater treatment** is a main future challenge to supply the growing global population with drinking water and improved sanitation. Wastewater treatment is needed to remove physical, biological, and chemical contaminants from wastewater.
- The **environmental impact of a chemical process** can be characterized by the *E*-factor, which is the amount of waste (in kg) produced per kg of product, whereby “waste” is everything formed in the reaction except the desired product.

5.5

Production Costs of Fuels and Chemicals Manufacturing

Guidelines to calculate the investment and manufacturing costs are given in many textbooks (e.g., Baerns *et al.*, 2006; Emig and Klemm, 2005; Smith, 2005; Moulijn, Makkee, and Van Diepen, 2004). An excellent overview of production costs and prices of fuels and chemicals is given by Lange (2001). In the following, a short overview is given of the major cost contributions.

5.5.1

Price of Chemical Products

Product prices depend on at least three important factors: the structural demand for the product, the price of oil (and of other raw materials, for example in case of inorganic products the price of phosphorous, salts, metals, etc.), and the actual availability of the product. The structural demand determines the order of magnitude of the prices, and the impact of the oil price and the imbalance between supply and demand may affect the prices by a factor of about 2 (Lange, 2001; Sedriks, 1995).

The relationship between the structural demand and price of product is illustrated by Figure 5.5.1 for a large variety of (organic) products like crude oil and transportation fuels, organic chemicals, and polymers. According to Figure 5.5.1, the prices decrease as world demand increases. For example, the prices decrease by a factor of about two as the demand increases by a factor of ten. This relationship could even be extended to pharmaceuticals, which are characterized by world demands of $1\text{--}1000 \text{ kg a}^{-1}$ and prices (around the year 2000) of $\$1\text{--}1000 \text{ g}^{-1}$ (Figure 5.5.2). The relationship between price and demand is the result of competition between products. If a product becomes cheaper, it accesses new markets and can be used as feedstock for new production routes. This relationship also works in the opposite direction. Products with a smaller demand are manufactured at a smaller scale and therefore mostly at a lower efficiency, which results in higher production costs.

Figure 5.5.1 Average price and world demand of various fuels and organic chemicals at about 2001 (olefins, aromatics, oxygenated intermediates, polymers, biological chemicals, and others) [data from Lange (2001)].

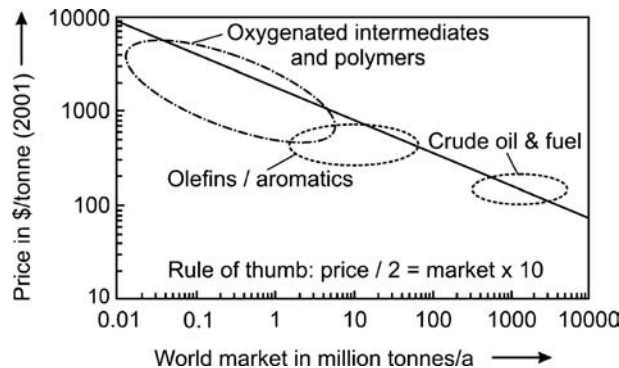
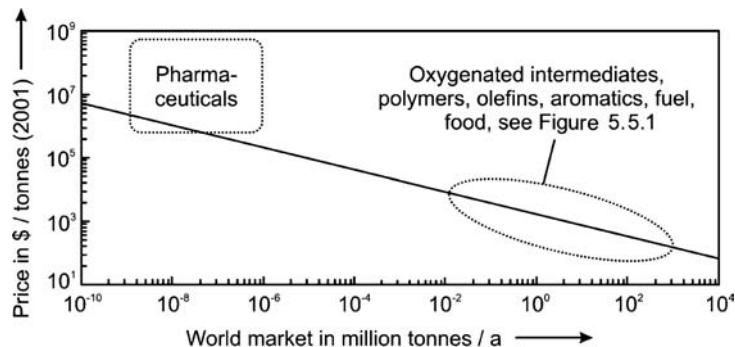


Figure 5.5.2 Average price and world demand of various fuels, organic chemicals, and pharmaceuticals [extension of Figure 5.5.1, data from Lange (2001)].



5.5.2

Investment Costs

If the delivered equipment costs (main items like reactors, heat exchangers, compressors, distillation columns . . .) are known, the total capital costs, which include additional direct and indirect costs for the erection, piping, engineering, and so on, can be estimated by the factors given in Table 5.5.1.

For a quick estimation of the total capital investment the overall factor method developed by Lang (1948) is helpful. The costs of each piece of equipment is estimated and summed and, finally, multiplied with the overall factor. Typically, the total costs are four times higher than the main items (Table 5.5.1). Values of this overall factor given in the literature vary in the range 3–6. According to Lang (1948),

Table 5.5.1 Typical factors used to calculate the capital costs based on the delivered equipment costs [data from Baerns *et al.* (2006)].

	Factor	Margin of deviation
Direct costs		
Equipment delivered costs (main items)	1	
Equipment erection	0.15	0.1–0.25
Piping	0.60	0.4–1.0
Instrumentation and control	0.35	0.2–1.2
Electrical	0.20	0.2–0.5
Buildings, foundations	0.65	0.3–1.0
Miscellaneous costs (fire protection, insulation, off-site investments, energy connections)	0.15	0.25–0.5
Indirect costs		
Engineering (design, construction)	0.40	0.25–0.5
Contingency (about 10% of total capital costs)	0.20	0.15–0.30
Total capital costs (investment costs)	4.0	3.0–5.0

Table 5.5.2 Typical values of the exponent n [Eq. (5.5.1)] used to calculate the capital costs based on the capital costs and production capacity of a given reference plant [data from Baerns *et al.* (2006); Emig and Klemm (2005); and Moulijn, Makkee, and Van Diepen (2004)].

Product(s)	Exponent n
Ammonia (based on natural gas)	0.70
Methanol (based on natural gas)	0.71
Polyethylene (low pressure process)	0.70
Sulfuric acid (based on sulfur)	0.64–0.67
Ethene oxide (oxidation of ethane)	0.69–0.78
Nitric acid (based on ammonia)	0.64
Electrolysis of NaCl	0.38

the overall factor for a plant for solid processing is 3.9 and for fluid processing 4.8. According to Smith, the factors are 4.4 and 5.8, respectively (Smith, 2005).

The investment costs of a plant for the production of fuel and chemicals vary from \$2 million for small plants of 10 000 tonnes annual capacity up to \$20 billion for refineries with a capacity of about 10 million tonnes (Lange, 2001; see reports published in the *European Chemical News* and the *Oil and Gas Journal*). Thus a 100-fold increase in investment is needed for a 1000-fold increase in capacity. The classical cost scaling rule is given by:

$$\nabla \quad I_i = I_j \left(\frac{C_i}{C_j} \right)^n \quad (\text{with } 0.4 < n < 0.8; \text{ typically } n = 2/3) \quad (5.5.1)$$

with I as the investment costs, C as the annual production capacity, and n as the exponent that considers the less-than-linear relationship. Typically n is about $\frac{2}{3}$, which corresponds exactly to a 100-fold increase in investment for a 1000-fold increase in capacity. This explains why fuel and chemical producers maximize the plant size (economy of scale, Table 5.5.2).

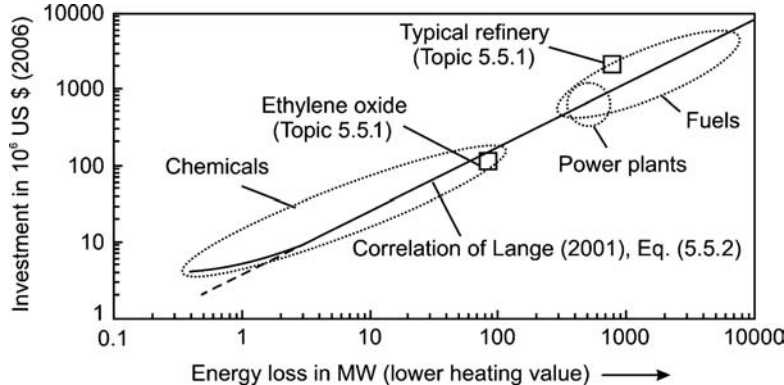
An accurate determination of investment costs is complicated and labor intensive. An estimation of $\pm 30\%$ accuracy requires an accurate identification and sizing of all of the large pieces of equipment. Hence, scientists and engineers need simple and crude methods to estimate investment costs. For this purpose, Lange (2001) identified the heat of reaction as a critical parameter that appears to affect the investment costs significantly. Reactions of interest to fuel and chemical manufacturing are characterized by widely differing heat of reactions, for example, 1–3 kJ g⁻¹ of total feed for endothermic reactions like dehydrogenations or dehydrations, to about 0 kJ g⁻¹ for skeleton isomerization, to 1–3 kJ g⁻¹ for hydrogenations and carbonylations, and –2 to –10 kJ g⁻¹ for exothermic oxidation reactions (Table 5.5.3).

Accommodating the heat of reaction requires equipment and costs. For example, exothermic reactions are often controlled by water cooling loops that withdraw the heat of reaction by boiling water at the wall of the reactor or in the effluent cooler.

Table 5.5.3 Heat of reaction for selected reactions of fuel and petrochemical manufacturing processes [data from Lange (2001)].

Reaction	$\Delta_{\text{R}}H$ (kJ per g total feed)
$\text{CH}_4 + \text{O}_2 \rightarrow \text{CO}_2 + 2\text{H}_2\text{O}$	–10
$\text{o-Xylene} + 3\text{O}_2 \rightarrow \text{phthalic anhydride} + 3\text{H}_2\text{O}$	–5.4
$\text{CO} + 2\text{H}_2 \rightarrow -\text{CH}_2 + \text{H}_2\text{O}$ (<i>Fischer-Tropsch synthesis</i>)	–4.5
$\text{C}_2\text{H}_4 + 0.5\text{O}_2 \rightarrow \text{ethylene oxide}$	–2.4
$\text{C}_6\text{H}_6 + 3\text{H}_2 \rightarrow \text{cyclohexane}$	–2.4
$\text{CH}_3\text{OH} + \text{NH}_3 \rightarrow \text{CH}_3\text{NH}_2 + \text{H}_2\text{O}$	–0.4
$n\text{-Butane} \rightarrow i\text{-butane}$	–0.1

Figure 5.5.3 Investment cost increase with energy loss on fuel and energy manufacturing plants (including power plants) for 2006 [energy loss = low heating value (LHV) of feed and fuel – LHV of product, calculated based on data of Lange, (2001)].



For endothermic reactions like cracking and dehydrogenation, the heat of reaction has to be supplied to the reactor as hot steam or via burners. Obviously, heat management affects the investment costs.

One way to account for the cost of heat management is to look at the total energy loss of a process, that is, to the difference between the lower heating values (LHV) of the plant intake (feed and fuel) and that of the product leaving the plant. The energy loss accounts for losses through heat of reaction, heat of fuel combustion, and heating value of purge streams. Typically, the heat of reaction accounts for the largest losses, except for endothermic processes, which lose most of their energy through fuel combustion. According to Figure 5.5.3, there is a clear relationship between the energy loss and investment costs of a plant.

Figure 5.5.3 was deduced by Lange (2001) based on data reported by Lange and Tijm (1996) and Chauvel and Lefebvre (1989). The correlation of Figure 5.5.3 follows (see Topic 5.5.1):

$$I (\text{in } 10^6 \text{ \$2006}) = 3.6(\text{Energy losses in MW})^{0.84} \quad (5.5.2)$$

Note that the costs deviate from the correlation at small energy loss and for batch processes used for manufacturing fine and specialty chemicals.

Topic 5.5.1 Calculation of investment costs based on the energy loss of a process

Let us consider the production of ethylene oxide to prove the accuracy of Eq. (5.5.2) developed by Lange (2001). According to Baerns *et al.* (2006), the following data are typical for an ethylene oxide (EO) plant with a capacity of 180 000 tonnes EO per year ($= 4.8 \cdot 10^6 \text{ GJ a}^{-1} = 152 \text{ MW}$ based on a LHV of EO):

- feed rate of ethylene: $142\ 000 \text{ t a}^{-1} = 6.7 \times 10^6 \text{ GJ (LHV) a}^{-1} = 212 \text{ MW}$;
- steam production: $18\ 000 \text{ t a}^{-1} = 0.06 \times 10^6 \text{ GJ a}^{-1} = 2 \text{ MW}$;
- production of ethylene glycol as by-product: $9000 \text{ t a}^{-1} = 0.15 \cdot 10^6 \text{ GJ a}^{-1} = 5 \text{ MW}$;
- consumption of electrical power: $108 \text{ GWh a}^{-1} = 12.3 \text{ MW}$, that is, for a typical efficiency of a power plant of 38%, about 32 MW primary energy.

Thus, for the energy loss (here: LHV of feed + LHV of fuel for power generation – LHV of EO as product and ethylene glycol as by-product – heating value of steam) we obtain a value of 85 MW ($= 212 \text{ MW} + 32 \text{ MW} - 152 \text{ MW} - 5 \text{ MW} - 2 \text{ MW}$). The estimation of the investment costs by Eq. (5.5.2) leads to a value of $\$150 \times 10^6$ which is well within the order of magnitude given by Baerns *et al.* (2006) of $\$112 \times 10^6$ (see also Figure 5.5.3).

As a second example we may take a refinery with investment costs of about \$2 billion for a capacity of 10 million tonnes of crude oil (Lange, 2001). The energy loss is typically about 8% of the LHV of the crude oil (LHV about 43 GJ t^{-1}), which is about 800 MW ($= 800\ 000 \text{ t a}^{-1} = 1.1 \text{ GW}$), which leads to investment costs of \$1.3 billion. Again, Eq. (5.5.2) leads to a value within an order of magnitude, with an accuracy of about 50% (Figure 5.5.3).

5.5.3

Variable Costs

Feedstock: The main component of the variable costs comes from the consumption and price of the feedstock. The consumption depends on the technology applied. However, it rarely exceeds 110% of the stoichiometric consumption in modern plants. As for feedstock and product prices, data are available in the literature and on various web sites.

Catalyst costs: According to Lange (2001), most catalysts applied for manufacturing fuels and commodity chemicals cost between \$1 and \$100 per kg, and are consumed at a rate of 0.01–1 kg per tonne of product. Thus, the catalyst costs may vary in a wide range of \$0.01–100 per tonne.

Energy costs: Manufacturing plants consume various utilities. In particular, they consume energy to run pumps and compressors or to heat process streams. According to Chauvel and Lefebvre (1989), the total energy consumption can amount to 25 GJ per tonne of product (25 kJ/g), which includes the consumption of fuel, steam, and electricity (Figure 5.5.4).

The energy requirements depend on the heat of reaction involved (Figure 5.5.4). Manufacturing shifts from being a net consumer of energy for endothermic and thermoneutral reactions to a net producer of energy for exothermic reactions. Older technologies tend to lie at the upper end of the consumption range, while modern best practice technologies tend to lie at the lower end. Some examples may illustrate Figure 5.5.4:

- NH₃ production from natural gas has a (released) reaction heat of -2 kJ per g-NH₃, whereas modern industrial plants consume (without natural gas as reformer feed) 7 kJ g^{-1} (Table 5.5.4, see also Section 6.1), which is the value expected by the correlation in Figure 5.5.4.
- For polyethylene (PE) this is similar: The (released) reaction heat is -3.6 kJ per g-PE, whereas modern industrial plants consume (without naphtha feed) 3.3 kJ g^{-1} for HDPE (high density polyethylene) and 6.4 kJ g^{-1} for LDPE (Table 5.5.4), which is also in the range expected by Figure 5.5.4.
- For phthalic acid anhydride (PSA) the (released) heat of reaction is theoretically -7.5 kJ per g-PSA, that is, for *o*-xylene oxidation with 100% selectivity to PSA (see Section 6.13). Industrial plants consume (without feed) 22 kJ per g-PSA, but according to Figure 5.5.4 this value should be around zero. The main reason for this difference is that the selectivity of catalytic *o*-xylene oxidation to PSA is less than 80%, and unwanted total oxidation to CO₂ takes place.

The cost of energy (Western Europe, 2007) typically varies from $\text{€}7 \text{ GJ}^{-1}$ for fuel to $\text{€}14 \text{ GJ}^{-1}$ for steam. At a rate of $\text{€}25 \text{ GJ}^{-1}$, power does not cover a large fraction of the energy need. Hence, the average energy price is $\text{€}10 \text{ GJ}^{-1}$, and typical energy costs are $\text{€}100 \text{ t}^{-1}$ product for thermoneutral reactions and an energy credit of up to $\text{€}100 \text{ t}^{-1}$ is found for exothermic reactions.

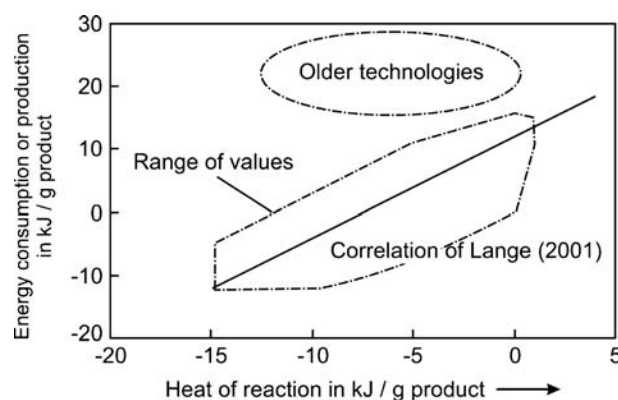


Figure 5.5.4 Energy consumption (or production for values < 0) of chemical manufacturing processes [data from Lange, (2001)].

Table 5.5.4 Specific energy consumption (best practice performance) in primary energy terms for the production of key chemicals [primary energy was calculated assuming a steam production efficiency of 90% and power generation efficiency of 40% (IEA, 2009b)]. 1 toe (tonnes of oil equivalent) = 41.9 GJ. Current average energy requirements are about 20% higher than best practice. Negative values for steam indicate surplus of steam. This steam may be "exported" and used in other processes.

Chemical and process	Energy consumption in final energy terms (feedstocks not included)			
	Electricity (GJ t ⁻¹)	Fuel (GJ t ⁻¹)	Steam (GJ t ⁻¹)	Total
				GJ t ⁻¹ toe t ⁻¹
Naphtha (refining of crude oil)				0.05
Ethylene, propylene, butane, butadiene, benzene (steam cracking of naphtha)	0.7	13.1	-1.5	12.3 0.29
Benzene (aromatic extraction)	0.1		2.2	2.3 0.05
Ethylbenzene	0.2		3.6	3.8 0.09
Ethylene oxide	2	2.5		4.5 0.11
Methanol from natural gas			9.4	9.4 0.22
Methanol from coal			16.1	16.1 0.38
Phenol	1.5		10.1	11.6 0.28
Phthalic anhydride	1.8	20		21.8 0.52
Propylene oxide	2.1		15.8	17.9 0.43
Polyethylene, high density (HDPE)	2.2		1.1	3.3 0.08
Polyethylene, low density (LDPE)	8.8		-2.4	6.4 0.15
Poly(ethylene terephthalate) (PET)	1.8	4.1		5.9 0.14
Polypropylene (PP)	2.2		0.1	2.3 0.05
Poly(vinyl chloride) (PVC)	1.6	0.5	1.4	3.5 0.08
Synthetic rubber	8.8		22.1	30.9 0.74
Ammonia from natural gas	0.7	10.9	-4.3	7.3 0.17
Ammonia from coal	9.3	17.3	-1.4	25.2 0.60
Ammonia from oil	0.7	16.1	-1.7	15.1 0.36
Oxygen	1.6			1.6 0.04
Chlorine (membrane process)	25		2.1	27.1 0.65

Energy consumption numbers in the case of best practice performance in terms of primary energy (without counting the feed) are listed in Table 5.5.4 for key chemicals. The calculation is based on the assumption of a steam production efficiency of 90% and a power generation efficiency of 40%. Average energy requirements are typically 20% higher. For example, 30 GJ t⁻¹ for Cl₂ are needed on a global average basis compared to 27 GJ t⁻¹ for best practise (membrane process), which reflects the fact that diaphragm processes (33% market share in 2006) and mercury cell processes (20%) are still used (IEA, 2009b).

Table 5.5.4 only reflects the energy requirements of a specific process. For example, the overall requirements to produce high density polyethylene (HDPE) are higher if the whole production chain is considered: crude oil refining to naphtha (0.05 toe t⁻¹) → ethylene production via steam cracking (0.29 toe t⁻¹) → HDPE production (0.08 toe t⁻¹). In total, 0.42 toe primary energy is need per t HDPE, which is 42% of the heating value of HDPE.

5.5.4

Operating Costs (Fixed and Variable Costs)

The costs for manufacturing fuels and chemicals consist of the variable costs such as feed, catalysts and energy. The variable costs depend on the actual consumption (and thus on the utilization degree) and also on the price of the various streams needed for production. The fixed costs include labor, maintenance, overhead, and above all the provision to recover the investment of the plant and lost interest (capital expenditure). Table 5.5.5 shows a breakdown of operating costs for the example of an ethylene oxide (EO) plant.

The total production costs are the sum of the variable and fixed costs. Assuming a linear increase of the variable costs with plant utilization, we obtain the cost diagram shown in Figure 5.5.5. According to Table 5.5.5, the production costs are determined mainly by the feed and costs related directly to the capital investment. The total fixed

Table 5.5.5 Fixed and variable costs of an ethylene oxide plant for a utilization degree of 100% (annual production rate of 180 000 t in 2006) [data from Baerns *et al.* (2006)].

	Portion (%)	mio. € a ⁻¹	€ per t product (% of total costs)
Fixed costs			
Personnel	100	1.5	8 (0.8)
Capital-related expenditures (see Table 5.5.6, here 23% of investment costs)	100	25.8	143 (14.6)
Selling	25	2.5	14 (1.4)
Administration	100	5.9	33 (3.3)
Other costs	50	2.3	13 (1.3)
Total annual fixed costs		38.0	211 (21.4)
Variable costs			
Feed costs (and other materials)	100	117.6	653 (66.3)
Energy	100	10.0	56 (5.7)
Royalties	100	2.0	11 (1.1)
Selling	75	7.4	41 (4.2)
Other costs	50	2.3	13 (1.3)
Total annual variable costs		139.3	774 (78.6)
Total production costs (100% utilization)		177.3	985 (100)

Table 5.5.6 Breakdown of capital-related fixed costs [data from Baerns *et al.* (2006)].

Capital-related fixed costs	Annual costs (% of total investment)
Depreciation (provision to recover investment)	10
Interest	6–8
Maintenance	3–5
Taxes and insurance	2
Overheads	1–3
Total capital-related fixed costs	22–28 (mean value: 25)

costs of a process depend on the plant complexity and on the total investment costs and the capital-related expenditures. The capital-related costs include the provision for recovering the investment, maintenance, and insurance (Table 5.5.6). A simple rule is that the annual fixed costs are 35% of total investment, 25% accounts for the capital-related expenditures, and 10% for other fixed costs.

The utilization degree where the production costs reach the revenues is the break-even point (for the given example shown in Fig. 5.5.5 65%). For projects with a certain risk of investment, the break-even point should be less than 70%. For detailed calculation of the influence of the utilization degree on the production costs, the assumption of a linear relationship between variable costs and utilization should no longer be used, and we obtain cost curves such as shown in Figure 5.5.6.

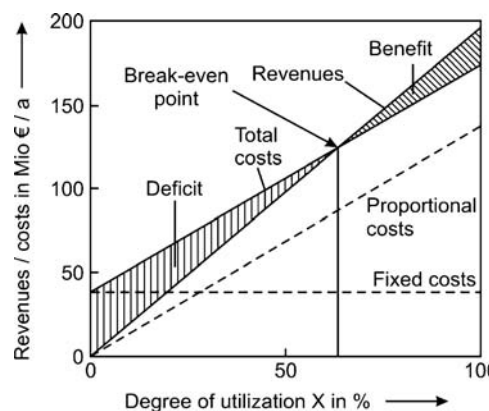
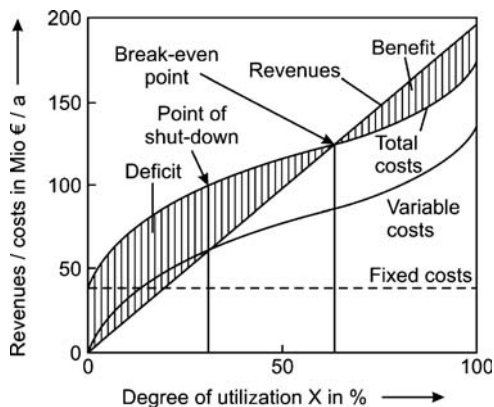


Figure 5.5.5 Influence of degree of utilization on the production costs and revenues of an ethylene oxide plant (annual production rate of 180 000 t) – a simplified diagram with a linear increase of variable costs with plant utilization. Adapted from Baerns *et al.* (2006).

Figure 5.5.6 Influence of degree of utilization on the production costs and revenues of an ethylene oxide plant (annual production rate of 180 000 t); nonlinear increase of variable costs with plant utilization. Adapted from Baerns *et al.* (2006).



Summary of Section 5.5 (take-home messages)

- The **price of chemical products** depends on at least three important factors: the structural demand for the product, the price of crude oil (energy), and the actual availability of the product. The structural demand determines the order of magnitude of the prices, and the impact of the oil price and the imbalance between supply and demand may affect the prices by a factor of about 2. Prices decrease as world demand increases. If a product becomes cheaper it accesses new markets and can be used as feedstock for new production routes. This relationship also works also in the opposite direction. Products with a smaller demand are manufactured at a smaller scale and at a lower efficiency, which results in higher production costs.
- Investment costs:** If the equipment delivered costs (main items like reactors, heat exchangers, compressors, distillation columns, etc.) are known, the total capital costs, which include additional direct and indirect costs for the erection, piping, engineering, and so on, can be estimated. For a quick estimation of the total capital investment the overall factor method is helpful. The costs of each piece of equipment is estimated and summed and, finally, multiplied by an overall factor of about four.
- The investment costs of a plant depend on the production capacity. The classical **cost scaling rule** is:

$$I_i = I_j \left(\frac{C_i}{C_j} \right)^n \quad (\text{with } 0.4 < n < 0.8; \text{ typically } n = \frac{2}{3})$$

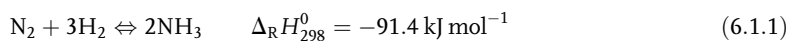
where I is the investment costs, C the annual production capacity, and n the exponent that considers the less-than-linear relationship. Typically, n is about $\frac{2}{3}$, which corresponds to a 100-fold increase in investment for a 1000-fold increase in capacity. This explains why fuel and chemical producers maximize the plant size (economy of scale).

- The operating costs for the manufacture of fuels and chemicals consist of the **variable costs** such as feed, catalysts, and energy, which depend on the actual consumption and on the price of the various streams needed for production. The **fixed costs** include labor, maintenance, overhead, and above all the provision for recovering the investment in the plant and lost interest (capital expenditure, i.e., provision for recovering the investment, maintenance, insurance, etc.). The total production costs are the sum of the variable and fixed costs, and depend on the plant complexity and capital-related expenditures. A simple rule is that the annual fixed costs are 35% of the total investment, 25% of which accounts for the capital-related expenditures and 10% for the other fixed costs.
- The utilization degree where the production costs reach the revenues is the **break-even point**.

6**Examples of Industrial Processes****6.1****Ammonia Synthesis****6.1.1****Historical Development of Haber–Bosch Process**

The synthesis of ammonia was the first large-scale synthesis in the chemical industry to work at high pressure, and the first process that was systematically developed based on chemical engineering concepts. We start with an overview of the history of the synthesis, from successful experiments in the laboratory to the start-up of the first industrial plant. For readers interested in details we refer to Appl (1999), Bakemeier *et al.* (1997), and Timm (1963).

Ammonia synthesis is based on the following reaction:

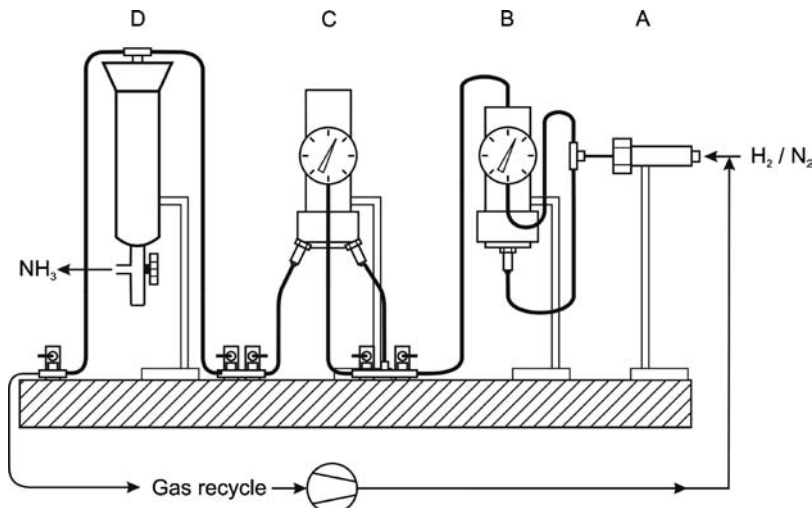


In the nineteenth century, the *Industrial Revolution* and the closely connected growth of the population generated a large demand for nitrogen fertilizers and (unfortunately) also of gunpowder ingredients, but the (natural) resources were at that time very limited:

- Potassium nitrate (KNO_3) is a naturally occurring mineral source of nitrogen with the common name *saltpeter* – from the Latin *sal petrae* (stone salt). It had been produced for gunpowder since the Middle Ages by decomposition and bacterial oxidation of organic material containing urea and other N-compounds or was harvested from bat guano in caves.
- Sodium nitrate (NaNO_3), also known as *Chile saltpeter* to distinguish it from ordinary saltpeter, KNO_3 , was mined at that time in South America, particularly in the *Atacama desert* of Chile. From about 1850 to 1920, Chile saltpeter was the main source for fertilizers and for KNO_3 to produce gunpowder (via $\text{NaNO}_3 + \text{KCl} \rightarrow \text{KNO}_3 + \text{NaCl}$). It was such a profitable business that at the end of the nineteenth century Chile, Peru, and Bolivia even fought during the *Saltpeter War* from 1879 until 1884 over the richest deposits.
- *Guano* from sea bird droppings consists of ammonia along with uric, phosphoric, oxalic, and carbonic acids, and has a high content of nitrates. *Guano* was an important fertilizer and gunpowder ingredient in the nineteenth century, and was mainly harvested in Chile, Peru, Bolivia, Namibia, and on some pacific islands like the Chincha Islands and Nauru.
- Synthetic ammonia was at that time only produced as a by-product of coke production, as raw coke oven gas released during coal pyrolysis contains about 1% NH_3 (Section 6.5.2).

Around the turn to the twentieth century it was recognized that these supplies would soon be insufficient for agricultural needs. Moreover, the explosives industry was developing due to the eve of the First World War.

Figure 6.1.1 Schematic presentation of laboratory apparatus of *Fritz Haber* and his assistant *Robert Le Rossignol* for ammonia synthesis; the original can be seen in the German museum (Deutsches Museum), Munich, Germany; A: catalytic oxidation of traces of oxygen by hydrogen present in the feed gas by a platinum catalyst; B: separation of steam formed in A; C: water cooled laboratory-scale NH₃ reactor; D: cooled vessel for separation of NH₃.



Already in the nineteenth century, various endeavors had been made to synthesize ammonia directly but these attempts remained unsuccessful. One of the main reasons was the limited knowledge of chemical thermodynamics. Around 1900 *Fritz Haber* (see box) began to investigate the ammonia equilibrium at atmospheric pressure and found very low NH₃ concentrations of less than 0.01% at 1000 °C. Based on subsequent experiments at pressures of up to 30 bar and theoretical calculations based on thermodynamic principles he concluded – in contradiction to other scientists like *Walther Nernst* (Topic 6.1.1) – that at pressures of more than 100 bar a technical process is visible. Perhaps equally important, *Haber* also proposed a recycle loop to overcome the problem that the syngas conversion in a single pass over the fixed bed catalyst is too small for an economical production. Hence in his laboratory apparatus (Figure 6.1.1), *Haber* separated NH₃ under pressure, and – after addition of fresh syngas – the gas was recirculated by a compressor to the reactor that contains the catalyst. This recycle method became the basis of industrial NH₃ production and was later applied to many other processes that are limited by thermodynamic constraints, for example, methanol production. *Haber* also pre-heated the syngas by heat exchange with the hot gas coming from the reactor, which is nowadays also a basic principle of chemical engineering in order to use the heat generated by an exothermic reaction, and he was one of the first to consider that not only the equilibrium but also the reaction rate is a determining factor for many industrial processes.

In July 1908, *Haber* convinced representatives of the *BASF* (*Badische Anilin & Soda Fabrik*), namely, *Carl Bosch* and *Alwin Mittasch* (see box), by a successful demonstration in his laboratory to support his work. During this performance, a production rate of 80 g-NH₃ h⁻¹ was reached with an osmium catalyst. In an unprecedented achievement, *Bosch* and his team succeeded in developing a commercial process, and the first plant started in 1913, with a capacity of 1.25 t of NH₃ per hour, that is, within five years a scale-up factor of 15 000 was reached.

Pioneers of ammonia synthesis: **Fritz Haber** (1868–1934) studied chemistry, and then worked as an assistant in Karlsruhe for *Hans Bunte* and *Carl Engler* in the fields of combustion and petrochemistry. In 1906 he became Professor of Physical Chemistry in Karlsruhe, and in 1911 Director of the *Institute for Physical and Electrochemistry* in Berlin. During his time in Karlsruhe, he and his English assistant **Robert Le Rossignol** developed the synthesis of NH₃. For this work, *Haber* received the Nobel Prize in Chemistry in 1918. He also (unsuccessfully) studied the separation of gold from sea water to enable Germany to meet war reparations, and made contributions to adsorption and electrochemistry. During World War I, he was a consultant for the German forces and organized gas attacks. Hence, he is also regarded as the “father of chemical warfare.” Despite all his contributions to the German war effort he was compelled to resign by the Nazis in 1933 because of his Jewish

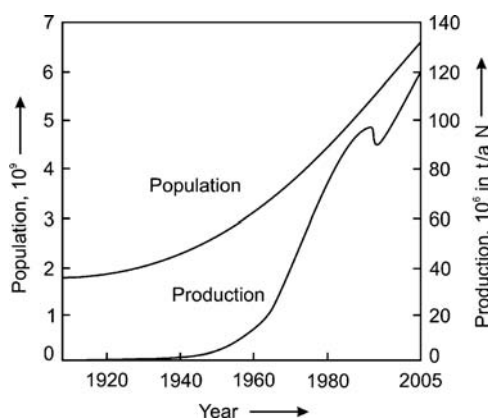


Figure 6.1.2 Evolution of the annual worldwide ammonia production (counted as N) and of the world population [data from Appl, 1999; data for NH₃ production for 2005 from IFA (2007)]. In 2010, production even reached ca. 130 mio. tonnes (counted as N) per year.

ancestry and had to emigrate. Tragically, many of his relatives were killed in concentration camps, gassed by Zyklon B, which he invented. *Haber* died in 1934 in Switzerland.

Carl Bosch (1874–1940) studied metallurgy, mechanical engineering, and chemistry. In 1899, he entered BASF and was at first active in the development of indigo synthesis. In 1908, he was given the task of developing ammonia synthesis on a large industrial scale. Thus he had to construct an apparatus that works at high pressures and high temperatures. The catalysts that were used by *Haber* such as the scarce and expensive osmium had to be replaced by a cheaper and more easily available catalyst. *Bosch's* coworker **Alwin Mittasch** (1869–1953) and various collaborators, therefore, carried 20 000 experiments with different materials and finally found the solution by using iron with certain additives (Mittasch, 1930). After World War I, *Bosch* also worked on high-pressure methanol synthesis. In 1931 he was awarded the Nobel Prize in Chemistry for the introduction of high-pressure chemistry.

Today, ammonia is one of the most important chemicals, with a production rate of about 130 million tonnes (counted as N) per year in 2010 (Figure 6.1.2). About 85% is used for fertilizers, and 15% is used in the chemical industry for various products such as nitric acid, plastics, fibers, and explosives.

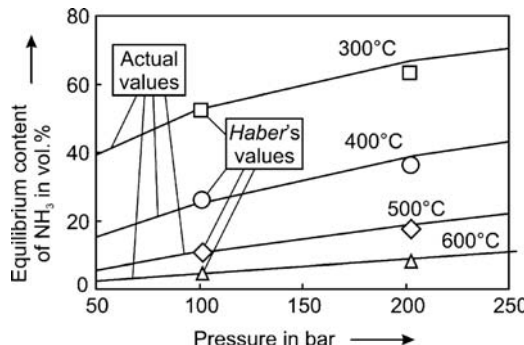
Topic 6.1.1 The Haber–Nernst dispute on ammonia equilibrium

During the first decade of the twentieth century, *Fritz Haber* and *Walther Nernst* (and their coworkers) had a long-standing dispute on the hydrogen–nitrogen–ammonia equilibrium and on the conclusions with regard to a technical ammonia synthesis. *Nernst* and his coworkers *Jost* and *Jellinek* concluded, based on their experiments, that commercial ammonia synthesis was not feasible in view of the low concentration they found at pressures of up to about 70 bar (*Jost*, 1908, see also *Maurer*, 1919, and *Appl*, 1999). To the contrary, *Haber* and his coworkers *Le Rossignol* and *Van Oordt* found higher NH₃ concentrations during their experiments at atmospheric pressures, see comparison of *Nernst's* and *Haber's* values in Table 6.1.1 (*Haber* and *Le Rossignol*, 1907; *Le Rossignol*, 1928). *Nernst*, who had at that time a much higher reputation than *Haber*, publicly challenged *Haber's* values at an important

Table 6.1.1 Content of ammonia in equilibrium with hydrogen and nitrogen (molar ratio of H₂-to-N₂ of 3, 1.013 bar): comparison of experimental values given by *Haber* and *Le Rossignol* (1907) with those given by *Jost* and *Nernst* (*Jost*, 1908).

Temperature (°C)	Equilibrium content of ammonia (vol.%)		
	<i>Haber</i> and <i>Le Rossignol</i>	<i>Jost</i> and <i>Nernst</i>	Correct values (own calculation)
700	0.0221	0.0174	0.0229
800	0.0108	0.0087	0.0121
930	0.0065	0.0043	0.0065
1000	0.0048	0.0032	0.0045

Figure 6.1.3 Comparison of calculated values of the equilibrium NH_3 content given by *Haber* and *Le Rossignol* in 1907 by extrapolation of their experimental values at pressures of up to 30 bar (*Haber* and *Le Rossignol*, 1907; review by *Le Rossignol*, 1928) with actual values (data from Appl, 1999; Gillespie and Beattie, 1930).



conference (Bunsentagung, 1907) and demanded “that Professor *Haber* should use a method that really gives precise values.” Deeply grieved, *Haber* and *Le Rossignol* repeated their experiments at atmospheric pressure as well as at higher pressures of up to 30 bar. Based on the results, which confirmed their former data, they calculated the ammonia content that could be expected at lower temperatures and higher pressures of up to 200 bar (Figure 6.1.3). In contradiction to *Nernst*, *Haber* concluded that a commercial synthesis is possible. He was after all correct, as clearly shown in Figure 6.1.3 by the comparison of data calculated by *Haber* around 1907 and modern actual data.

Epilogue: The deviations in experimental data of *Nernst* and *Haber* that gave rise to their acrimonious dispute were much smaller than both scientists thought. Already in 1919, *Maurer* showed by several calculations that the experimental values of *Nernst* also contained all the information needed to justify a technical high-pressure synthesis (*Maurer*, 1919). This was finally also realized by *Nernst* who told *Alwin Mittasch* in 1916 in a one-to-one interview “Unfortunately, I argued at that time (1907) that NH_3 synthesis is technically not possible” (*Mittasch*, 1951). In 1913, *Nernst* even acted as an appraiser for *Haber* and *BASF* in a claim of the Farbenwerke Hoechst against *BASF*’s ammonia patent. He appeared arm in arm with *Haber* before the court, and in a masterly speech successfully defended *Haber*’s inventive achievement. Side note: According to a contemporary, *Nernst* did not really want to support *Haber* but wished to provoke his colleague *Wilhelm Ostwald* (1853–1932), at that time one of the most famous chemists and who was the appraiser of the opposite side, the Hoechst company (Schindewolf, 2000).

6.1.2

Thermodynamics of Ammonia Synthesis

The equilibrium of NH_3 synthesis was examined in Example 4.2.5. As expected for an exothermic reaction with an increase of volume, favorable conditions are a low temperature and a high pressure (Figure 6.1.4). However, the minimum temperature is about 400°C , as at lower temperatures the reaction rate on commercially available catalysts is too low. Thus, the optimum pressure is a compromise between

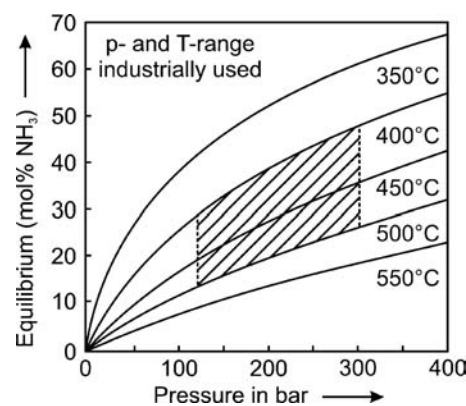


Figure 6.1.4 Influence of pressure and temperature on the equilibrium NH_3 content. (Dashed area indicates typical industrial reaction conditions.)

thermodynamically favorable conditions and operating costs. Typical industrial conditions are 400 °C (inlet) to 500 °C (exit) and 100–300 bar.

6.1.3

Kinetics and Mechanism of Ammonia Synthesis

Unsurprisingly, in view of the early technological significance of NH₃ synthesis, this synthesis was probably more intensively studied than any other catalytic reaction. A variety of literature addresses elementary steps as well as the reaction rate under industrial conditions, as, for example, reviewed by *Appl* (1999), *Farrauto* and *Bartholomew* (1997), *Nielsen* (1971), and *Aparicio* and *Dumesic* (1994). In the following, only main aspects are discussed.

According to *Gerhard Ertl* (born 1936, Nobel Prize in Chemistry in 2007), the reaction scheme of ammonia synthesis may be formulated by the following sequence of elementary steps:



The progress of NH₃ synthesis according to this reaction scheme may be described in the form of an energy profile (Figure 6.1.5). Mostly, dissociative N₂ adsorption [Eq. (6.1.4)] is regarded as rate determining. The subsequent hydrogenation steps are energetically “uphill,” but the energy differences can be overcome at technically relevant temperatures (>400 °C).

One of the first rate equation for engineering purposes was published by *Temkin* and *Pyzhev* (1940):

$$\frac{dp_{\text{NH}_3}}{d\tau} = k_1 \frac{p_{\text{N}_2} p_{\text{H}_2}^{1.5}}{p_{\text{NH}_3}} - k_2 \frac{p_{\text{NH}_3}}{p_{\text{H}_2}^{1.5}} \quad (6.1.9)$$

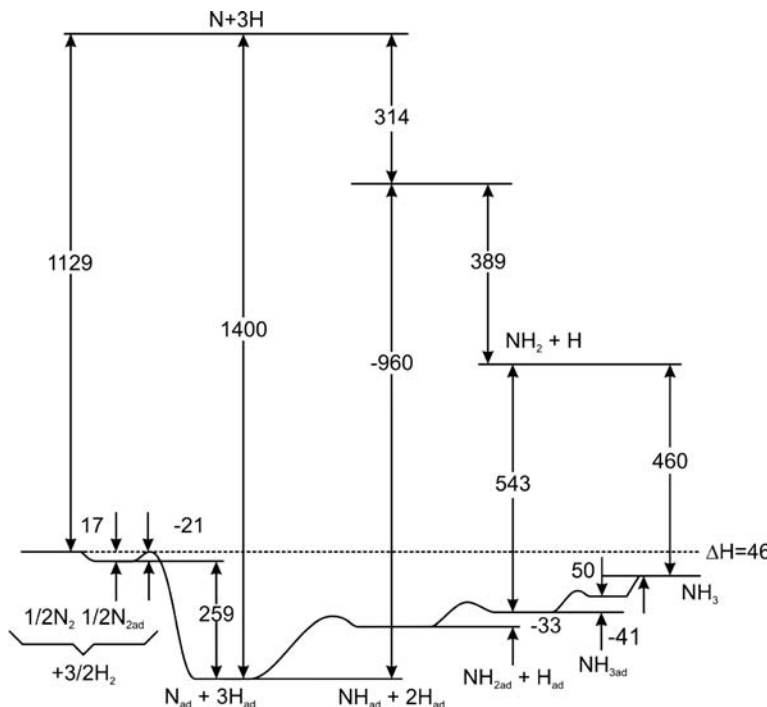
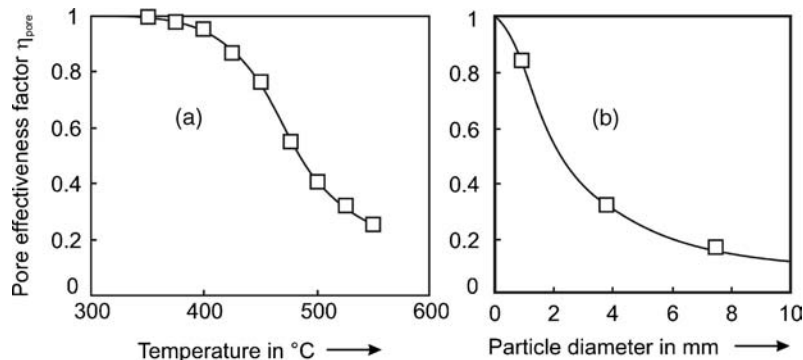


Figure 6.1.5 Schematic energy profile of NH₃ synthesis on Fe (energies in kJ mol⁻¹) (Ertl, 1991).

Figure 6.1.6 Influence of temperature and particle size on pore effectiveness factor: (a) 30 bar, particle diameter: 2.6 mm [data from Bokhoven and Raayen (1954)] (b) 100 bar, 500 °C, differential conversion, feed gas with 4% NH₃, H₂/N₂ = 3 [data from Jennings and Ward (1989)].



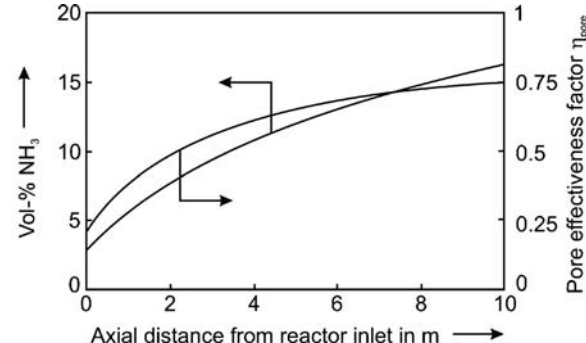
Based on this rate equation, several modifications were subsequently developed that describe even more accurate experimental results (Appl, 1999; Farrauto and Bartholomew, 1997). A problem with Eq. (6.1.9) – at least for laboratory studies where the syngas may be free of NH₃ – is the fact that the reaction rate becomes, formally, infinitely high for zero NH₃ concentration (reactor entrance). To avoid this, the following equation is often used:

$$\frac{dp_{\text{NH}_3}}{d\tau} \approx kp_{\text{H}_2}^{0.75} p_{\text{N}_2}^{0.25} \quad (\text{for } p_{\text{NH}_3} \rightarrow 0) \quad (6.1.10)$$

In industrial reactors, particle diameters in the range 1–10 mm are used (Appl, 1999). Thus, pore diffusion of the reactants and of ammonia may influence the effective rate as discussed by Akehata *et al.* (1961), Bokhoven and van Raayen (1954), and by Jennings and Ward (1989) [see also Appl (1999) and Nielsen, (1971)]. The ratio of the effective rate to the intrinsic (maximum) rate in the absence of internal mass transport restrictions is characterized by the pore effectiveness factor η_{pore} (Section 4.5.4). Figure 6.1.6 shows values of η_{pore} determined in a laboratory reactor at different temperatures and particle sizes. For technically relevant temperatures of 400–500 °C and particles up to 10 mm, η_{pore} is in a range of 1 down to 0.2.

As examined in Section 4.5.4, the effectiveness factor is only constant and independent of the degree of conversion if we have an irreversible first-order reaction (Tab. 4.5.5, Example 4.5.6). This is not the case for NH₃ synthesis, which is with regard to the kinetics much more complicated as we have a reversible *n*th order reaction according to the Eqs. (6.1.9) and (6.1.10). Hence, the effectiveness factor depends on the reactant (H₂ and N₂) and product (NH₃) concentrations and thus on the axial position in a fixed bed reactor. This leads to a decrease of the intrinsic rate along the bed (at almost constant effective diffusion coefficients), and in return to an increase of the effectiveness factor from the reactor inlet to the outlet as shown in Figure 6.1.7 for an isothermal and therefore hypothetical ammonia reactor; apart from the assumption of isothermality, the parameters used for the calculations correspond to an industrial reactor.

Figure 6.1.7 Content of NH₃ and pore effectiveness factor at different axial positions in a hypothetical (isothermal) fixed bed reactor [450 °C, 214 bar, 12% inert in feed gas, particle diameter: 5.7 mm, space velocity: 15 000 m³ gas (STP) h⁻¹ m⁻³ catalyst; data from Nielsen (1971)].



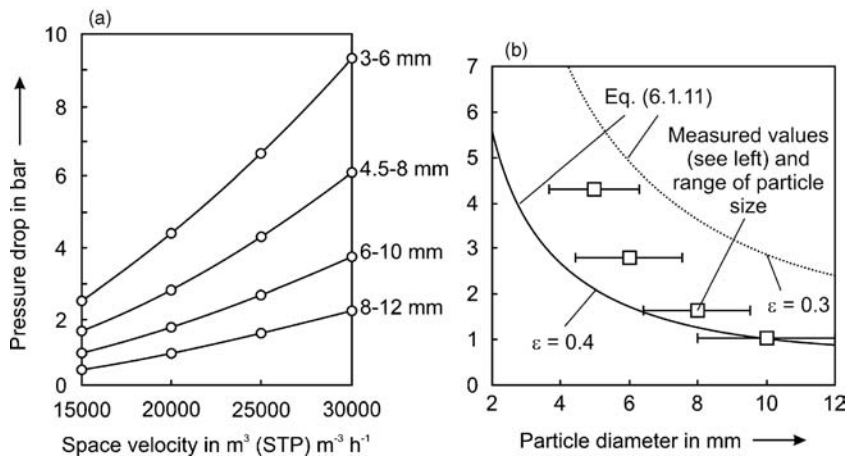


Figure 6.1.8 Pressure drop of NH_3 reactor at various particle sizes and space velocities SV (length: 7 m, 271 bar, 450°C) (a), values from Appl (1999); (b) measured values for $SV = 20\,000 \text{ h}^{-1}$ and calculation for spherical particles of equal diameter for $\varepsilon = 0.4$ and 0.3 (see text below).

External heat transfer effects (temperature difference between bulk gas phase and catalyst particles $< 1 \text{ K}$) and concentration gradients in the boundary gas layer are negligible (Appl, 1999).

From the standpoint of a high effective reaction rate, it is desirable to use very fine particles as we then have a pore effectiveness factor approaching unity. However, we have to consider the pressure drop in a technical reactor (Figure 6.1.8).

As an exercise, we can check the pressure drop given in Figure 6.1.8a. For this purpose, we recall Eqs. (3.4.21) and (3.4.22). For a bed of spherical particles of equal diameter we have:

$$\Delta p_b = \frac{(1 - \varepsilon)}{\varepsilon^3} \left[3.5 + (1 - \varepsilon) \frac{300}{Re_p} \right] \frac{L \rho_f u_s^2}{d_p} \quad (\text{with } Re_p = u_s d_p / \nu) \quad (6.1.11)$$

For the example of a space velocity of $20\,000 \text{ m}^3 \text{ h}^{-1} \text{ m}^{-3}$ and the conditions of Figure 6.1.8 we obtain $Re_p = 3.2 \times 10^5 d_p / m$ ($\nu \approx 0.15 \times 10^{-5} \text{ m}^2 \text{ s}^{-1}$, $u_s = 0.48 \text{ m s}^{-1}$) and a gas density ρ_f of 39 kg m^{-3} . For the bed porosity ε we use values of 0.3 and 0.4, which represents a typical range. The agreement between measurement and calculation [Eq. (6.1.11)] is satisfactory (Figure 6.1.8b), if we consider that ε is unknown and in reality we do not have spherical particles of equal size.

6.1.4

Technical Ammonia Process and Synthesis Reactors

Figure 6.1.9 shows a flow sheet of an NH_3 plant without syngas production. In Section 6.2, a plant based on natural gas is shown (Figure 6.2.3), but here we only consider NH_3 synthesis.

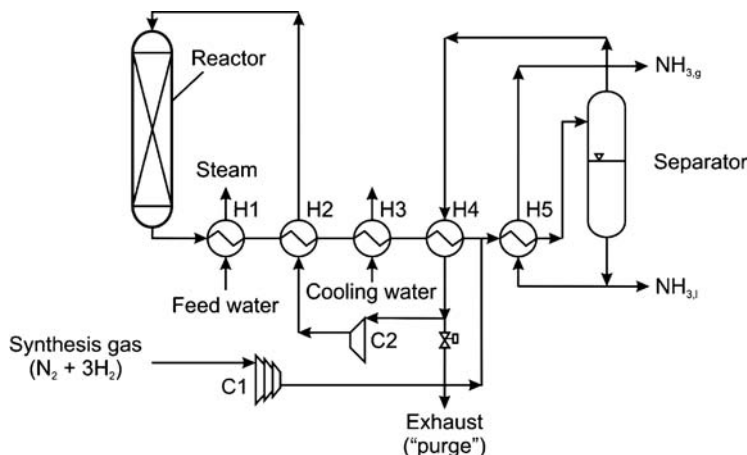


Figure 6.1.9 Flow sheet of an ammonia synthesis plant (H1–H5: heat exchangers, C1: compressor for fresh syngas, C2: recycle compressor). Adapted from Baerns *et al.* (2006). For syngas formation and an overview of a complete NH_3 plant see Section 6.2 (Figure 6.2.3).

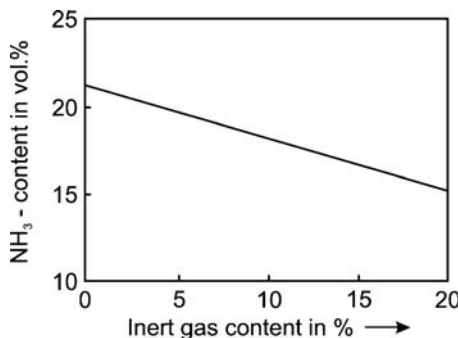
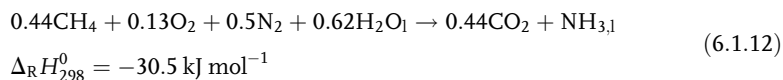


Figure 6.1.10 Influence of inert gas (CH_4 , Ar) on the performance of an ammonia reactor [SV: $20\,000 \text{ m}^3 \text{ gas (STP) h}^{-1} \text{ m}^{-3}$, 300 bar, inlet NH_3 content: 3.5%] (data from Appl, 1999).

The performance of an NH_3 reactor decreases with increasing inert gas content (Ar, CH_4 , NH_3) (Figure 6.1.10). Thus, for a high conversion, an effective syngas cleaning and separation of ammonia (low content of NH_3 at reactor entrance) should be adjusted.

Based on methane, the overall stoichiometric equation of NH_3 synthesis via steam reforming of natural gas (and the subsequent secondary reforming and water gas shift) is given by:



Equation (6.1.12) reflects the main route used today: In 2010, the world ammonia production was 131 million tonnes (N) in total (159 million tonnes ammonia; data from http://www.indexmundi.com/en/commodities/minerals/nitrogen/nitrogen_t12.html, accessed 27.10.2012). 77% of the production capacity is based on natural gas, followed by coal (13%), naphtha (6%), and heavy oil (4%) (numbers for 1998 from Appl, 1999).

Table 6.1.2 summarizes the energy requirement for ammonia production. The stoichiometric quantity of methane derived from Eq. (6.1.12) is 0.44 mol per mol NH_3 , corresponding to 20.7 GJ per t- NH_3 (lower heating value). If full recovery of the reaction heat ($30.5 \text{ kJ mol}^{-1} = 1.8 \text{ GJ t}^{-1} \text{ NH}_3$) is assumed, then the minimum energy requirement would be 18.9 GJ t⁻¹ NH_3 . Modern plants with a capacity of up to 2000 t- $\text{NH}_3 \text{ d}^{-1}$ have a consumption of natural gas as feed of 22.3 GJ per t- NH_3 , which is only 108% of the theoretical minimum; 7.3 GJ per t- NH_3 of additional primary energy is needed as fuel (mainly for steam reforming) and for the electricity consumed (details in Section 5.5, Table 5.5.4). Some 70% of the energy losses occur in the methane reforming section and 30% in the NH_3 synthesis section (Appl, 1999; Schloegl, 2003; Dybkjaer, 1995). Thus in a modern natural gas based plant, 29.6 GJ per t- NH_3 are needed, which is 157% of the theoretical minimum and 143% of the theoretical methane demand. This value is much lower than the demand of classical Haber–Bosch coal-based processes (85 GJ per t- NH_3) or of gas based plants in the 1950s (50 GJ per t- NH_3) (Appl, 1999).

As examined in Section 4.10.3, temperature control is a crucial factor for exothermic fixed bed processes like ammonia synthesis and the reaction heat needs to be removed:

- The equilibrium is favored by low temperatures.
- The NH_3 production rate depends on temperature and reaction progress. Figure 6.1.11 shows the optimum temperature pathway. (For the method used to determine this pathway see Section 4.10.3.)

In industrial ammonia converters, it is impractical to reach exactly this optimum temperature profile. Two methods are applied to get at least close to this optimum pathway:

- The catalyst bed is divided into several beds in which the reaction proceeds adiabatically. The heat is removed between the beds by injection of cold feed gas

Table 6.1.2 Energy requirements (including feed) for natural gas based NH_3 production [estimated based on data given by IEA (2009); Appl (1999)]. For electricity, primary energy was calculated assuming a power generation efficiency of 40%.

	Energy consumption (primary energy, lower heating value) (GJ per t- NH_3)
Classical Haber–Bosch plant based on coke	80–90
Natural gas based plants (1953–1955)	47–53
Value of a modern industrial plant	29.6 (22.3 as feed)
Minimum based on stoichiometric CH_4 demand	20.7
Reaction heat based on liquid NH_3 and liquid H_2O (feed), Eq. (6.1.12)	–1.8
Theoretical minimum (full recovery of reaction heat)	18.9

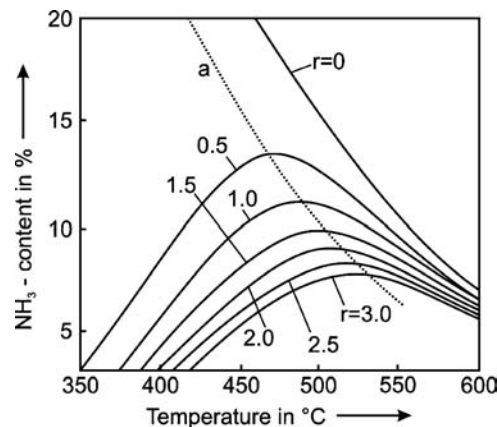


Figure 6.1.11 Rate of NH_3 synthesis (r) in $\text{m}^3 \text{NH}_3$ (STP)/(m^3 catalyst s) and optimal reaction pathway to maximize the rate at a given NH_3 content (dashed line a) at 200 bar and 11 vol.% inert in the inlet syngas [data from Appl (1999)].

(quench converter, Figure 6.1.12) or by heat exchangers cooled with syngas or water/steam (Figure 6.1.13).

- Alternatively, heat is removed from the bed by means of cooling tubes with co-current or countercurrent flow of the cooling medium (mostly feed gas) (Figures 6.1.14 and 6.1.15).

The power consumption of NH_3 synthesis (without syngas generation) depends on the following major aspects with regard to the total pressure (Appl, 1999):

- The energy required for compression of the fresh syngas increases with increasing pressure.

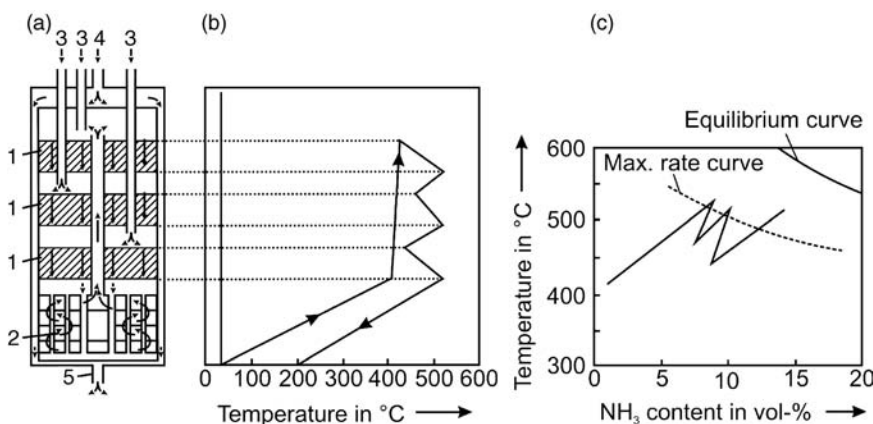


Figure 6.1.12 Multibed NH_3 reactor with quench cooling: (a) reactor, (1) catalyst, (2) heat exchanger, (3) quench gas inlets, (4) gas inlet, and (5) gas exit; (b) temperature profile through reactor; (c) NH_3 content versus temperature (adapted from Appl, 1999).

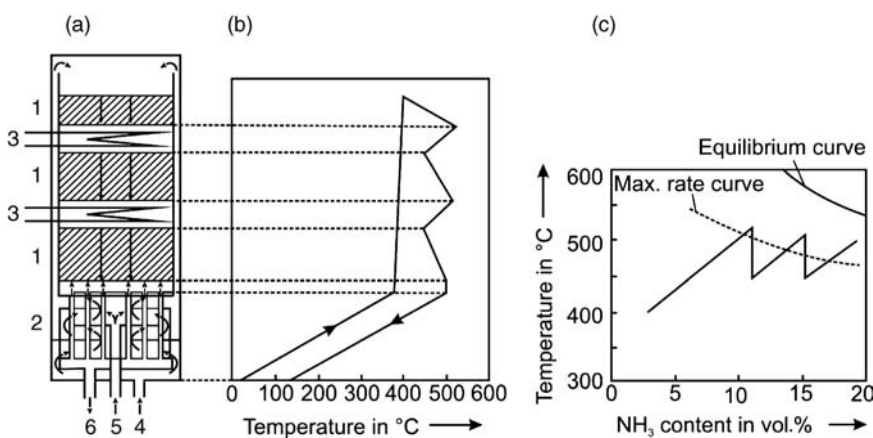


Figure 6.1.13 Multibed NH_3 reactor with indirect cooling: (3) cooling section, (5) inlet of temperature control gas (cold-shot), (6) gas exit; for other notation see Figure 6.1.12 (adapted from Appl, 1999).

Figure 6.1.14 Cocurrent-flow tube-cooled NH₃ reactor: (a) reactor, (1) catalyst, (2) heat exchanger, (3) cooling tubes, (4) gas inlet, (5) inlet of temperature control gas (cold-shot), and (6) gas exit; (b) temperature profile through reactor, (C) NH₃ content versus temperature (adapted from Appl, 1999).

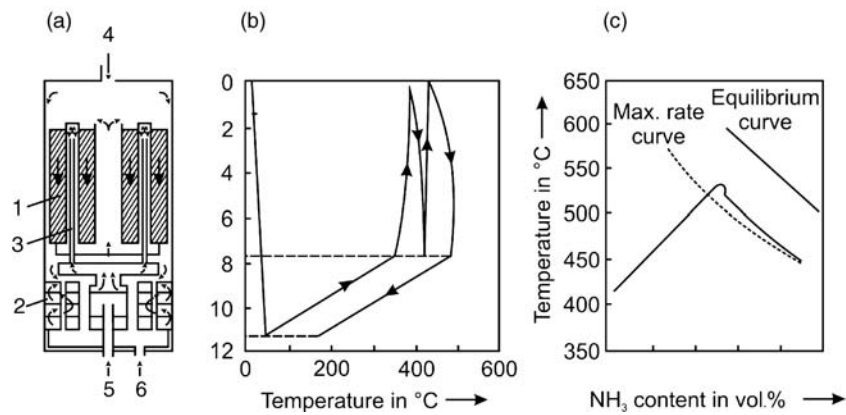
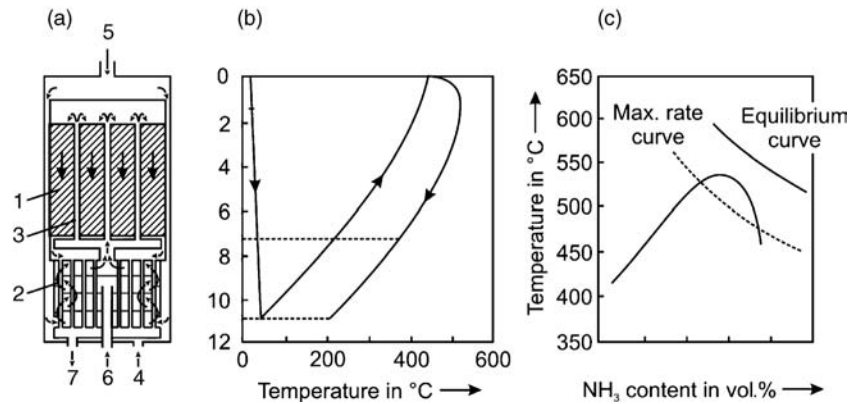
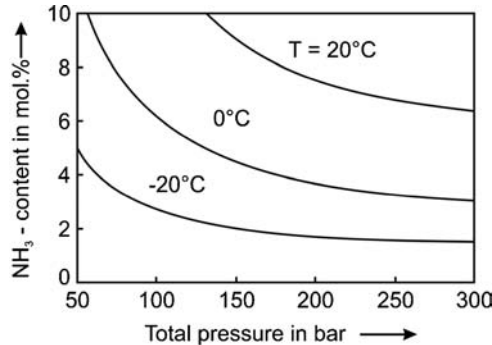


Figure 6.1.15 Countercurrent-flow tube-cooled NH₃ reactor: (5) vessel wall cooling gas inlet, (6) temperature control gas, and (7) gas exit; for other notation see Figure 6.1.14 (adapted from Appl, 1999).



- The energy needed for gas recycling decreases with increasing pressure: (i) for a given feed rate, the gas velocity and pressure drop decreases; (ii) even for a given pressure drop ($p_2 - p_1$), the compression work [Eq. (3.4.36) for isothermal compression] is proportional to $\ln(p_2/p_1) = \ln(1 + \Delta p/p_1) \approx \ln(1 + \Delta p/p)$ for $\Delta p \ll p_1$, which favors a high total pressure.
- The NH₃ content at the reactor exit is 20%. By water and air cooling, most of the NH₃ condenses for $p > 250$ bar; for example, for 300 bar and 20 °C, the residual NH₃ content is 6% (Figure 6.1.16). Refrigeration to condense more NH₃ reduces the recycle rate for a given production rate, as a high content of NH₃ at the reactor inlet decreases the conversion. For $p < 200$ bar, refrigeration is required to compensate the lower equilibrium NH₃ content and to reach a low residual content after cooling. Typically, refrigeration by a mechanical NH₃ refrigeration

Figure 6.1.16 Content of ammonia vapor in equilibrium with liquid ammonia in a 3 : 1 H₂/N₂ mixture [effect of methane and argon not counted; data from Jennings and Ward (1989)].



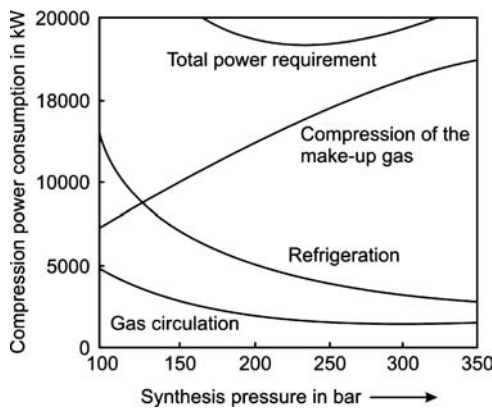


Figure 6.1.17 Influence of pressure on major power requirements for a typical ammonia plant [900 tonnes per day, data from Jennings and Ward (1989)].

cycle down to -25°C is used. The amount of NH_3 vaporized and reliquefied can be substantial; for example, at 150 bar, the reliquefied NH_3 may be twice the amount of NH_3 produced.

The influence of pressure on the power required for refrigeration, for the syngas loop, and compression of the fresh syngas (make-up gas) is shown in Figure 6.1.17, indicating that the overall energy consumption is the lowest at a pressure of around 250 bar.

Summary of Section 6.1 (take-home messages)

- In the nineteenth century, the **Industrial Revolution** and the growth of the population generated a large demand for nitrogen fertilizers and also for gunpowder ingredients, but the **(natural) resources** were at that time (KNO_3 , NaNO_3) very limited and synthetic ammonia was only produced as a by-product of coke production.
- The synthesis of ammonia was the **first large-scale synthesis** in the chemical industry working at **high pressure**, and the first process that was systematically developed based on chemical engineering concepts.
- Around 1900 **Fritz Haber** began to investigate the **ammonia equilibrium**, which favors low temperatures and high pressures. Based on experiments and calculations, he concluded that at pressures of more than 100 bar a technical process is possible. He proposed a recycle loop to overcome the problem that the syngas conversion in a single pass is too small, and he also considered that not only the equilibrium but also the **reaction rate** is a determining factor for many industrial processes.
- In 1913, **Carl Bosch** and **Alwin Mittasch** from BASF succeeded in developing the **first commercial process**. Today, ammonia is one of the most important chemicals, with a production rate of 120 million t a^{-1} . Of this, 85% is used for fertilizers and 15% for various other chemicals such as nitric acid, plastics, fibers, and explosives.
- The **minimum reaction temperature** is about 400°C as for lower temperatures the reaction rate is too low on commercially available catalysts. The **optimum pressure** of about 200 bar is a compromise between thermodynamically favorable conditions and operating costs.
- In industrial reactors, **particle diameters** in the range 1–10 mm are used, and pore diffusion of the reactants and of ammonia influence the effective rate; for example, at 500°C and with 10 mm particles, η_{pore} is about 0.2. From the standpoint of a high reaction rate, it is desirable to use fine particles as we then have a pore effectiveness factor approaching unity. However, we have to consider the **pressure drop** in a technical reactor.

- The performance of an ammonia reactor decreases with increasing **inert gas** content (Ar, CH₄, NH₃). Thus, for a high conversion, effective syngas cleaning and separation of ammonia (low content of NH₃ at reactor entrance) should be adjusted.
- In industrial ammonia converters, it is impractical to reach exactly this **optimum temperature profile** with regard to maximize the reaction rate. Two methods are applied to get at least close to this optimum pathway:
 - The catalyst bed is divided into several beds in which the reaction proceeds adiabatically. The heat is removed between the beds by **injection of cold feed gas** (quench converter) or by **heat exchangers** cooled with syngas or water/steam.
 - Alternatively, heat is removed from the bed by means of **cooling tubes** with co-current or countercurrent flow of the cooling medium (mostly feed gas).

6.2 Syngas and Hydrogen

The production of syngas, a mixture of carbon monoxide and hydrogen, is an important step for the manufacture of many chemicals such as methanol, higher alcohols, hydrogen, and ammonia (Chapter 5, Figures 5.1.14 and 5.1.28). In recent decades, syngas has also attracted increasing attention with regard to use natural gas, coal, and biomass for the production of fuels such as diesel oil and gasoline, via *Fischer-Tropsch* synthesis, which are currently practically only obtained from crude oil. Subsequently, an overview of syngas production and some details on selected processes are given. Further information can be found in the cited literature. In particular, figures and data given by Appl (1999) and Moulijn, Makkee, and Van Diepen (2004) in their excellent overviews on syngas production were used for the compilation of this chapter.

6.2.1 Options to Produce Syngas and Hydrogen (Overview)

Synthesis gas (syngas) is a general term for a mixture whose main constituents are hydrogen and carbon monoxide but also for a nitrogen–hydrogen mixture used for NH₃ synthesis. As shown in Figure 6.2.1, syngas may be produced from any fossil fuel and from biomass.

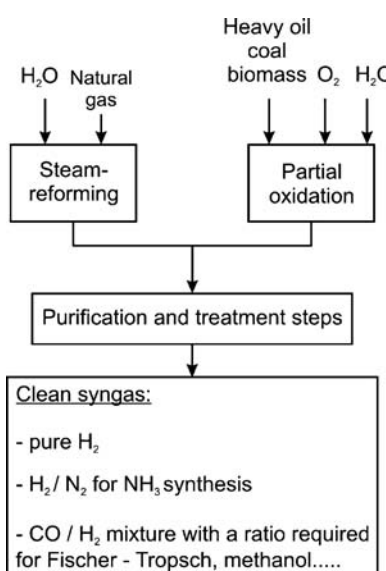


Figure 6.2.1 Production of syngas based on fossil fuels and biomass.

For heavy oils like vacuum gasoil and for solid feedstocks like coal and biomass, syngas production is always based on non-catalytic partial oxidation; for coal and biomass the term gasification is commonly used instead of partial oxidation. Natural gas or light hydrocarbons are catalytically converted with steam as these feedstocks can easily be desulfurized, and in contrast to coal and heavy oils other impurities like heavy metal compounds or inorganic matter that would lead to a rapid deactivation of the catalyst are not present. This catalytic process is called steam reforming and should not be confused with catalytic reforming of gasoline for improvement of the octane number (Section 6.9).

For natural gas, partial oxidation is usually not an economical option as the investment costs for the required cryogenic air separation are high. Only in cases where syngas with a high CO content is needed is partial oxidation of natural gas – mostly then in combination with a steam reformer – an option. Thus partial oxidation is mostly applied where steam-reformable feeds are not available and where local conditions provide relatively cheap heavy feedstocks such as coal or heavy oil.

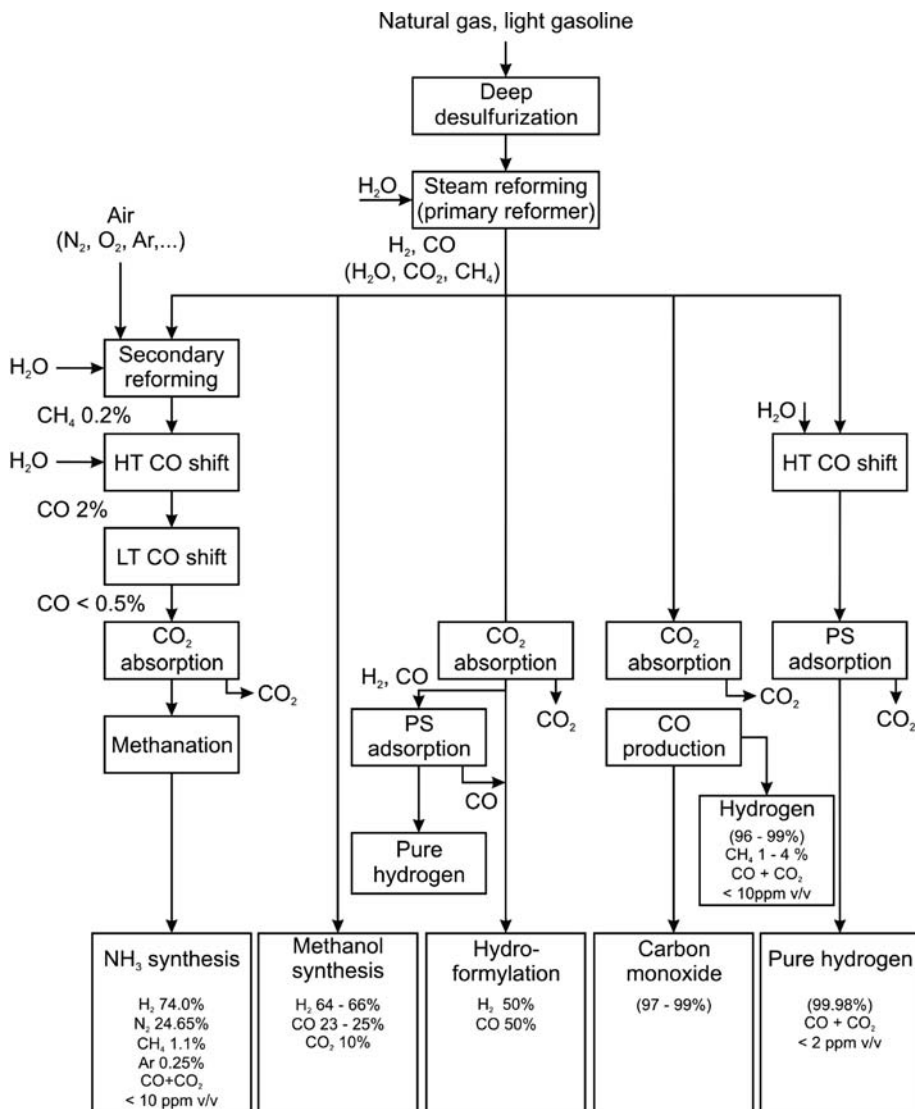


Figure 6.2.2 Production and treatment of syngas depending on the final use of the syngas for the example natural gas as feedstock. Adapted from Baerns *et al.* (2006).

Depending on the final use of the syngas, several additional treatment steps are still needed, primarily to remove unwanted impurities from the raw syngas such as H_2S and CO_2 and to adjust the required H_2 -to- CO ratio. As an example, Figure 6.2.2 shows a simplified block diagram of the main processes involved in syngas production based on light feedstocks (methane.....C₅-hydrocarbons).

The feed for steam reforming, typically natural gas, usually has to be desulfurized. If only small amounts of sulfur are present as H_2S , the reaction with ZnO (to ZnS) is used. For a high content of H_2S , scrubbing (absorption) with a solvent is usually the method of choice; if the feed also contains organic sulfur compounds, hydrotreatment is needed as the primary treatment step (Section 6.8).

For coal and heavy oil based syngas production, feedstock purification is, to date, not possible. Hence during partial oxidation the organic sulfur compounds are converted into H_2S as we have a reducing atmosphere, at least after the oxygen has been consumed. Thus, H_2S and other unwanted impurities like ash, tar, and solid carbon (soot) have to be separated from the raw syngas before it can be used further.

Even if all these unwanted impurities have been removed, extended treatment steps are still required such as the water-gas shift reaction, CO_2 removal, and

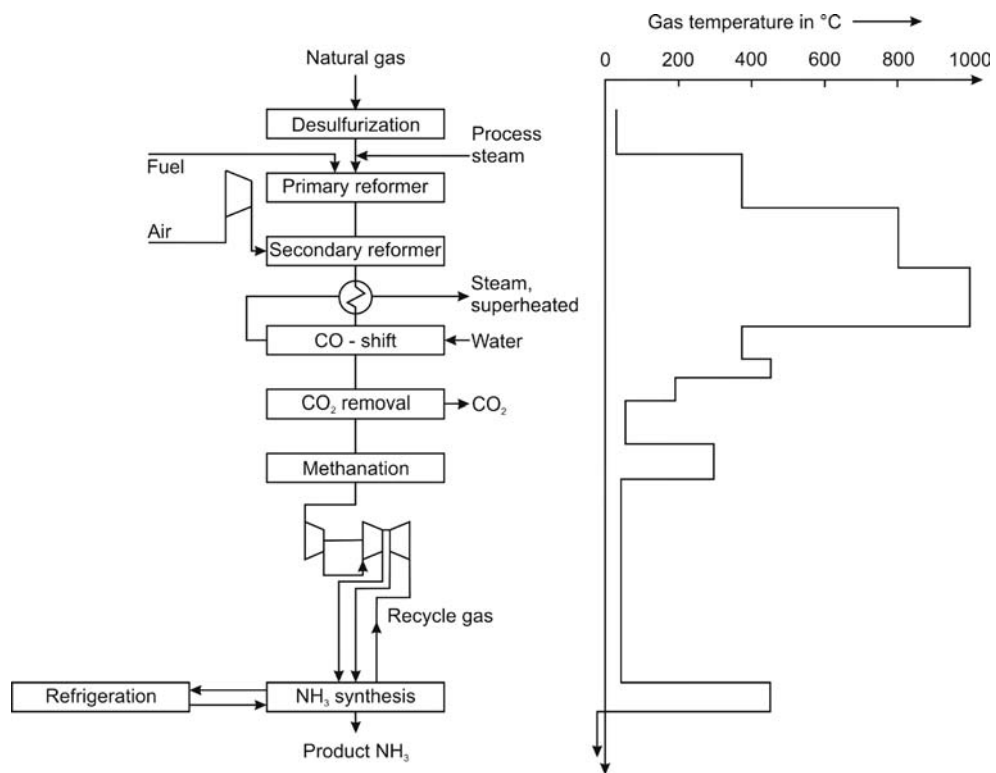


Figure 6.2.3 Block diagram and temperature profile for a steam reforming NH₃ plant. Adapted from Appl (1999).

methanation, for example, if pure H₂ or syngas for ammonia synthesis is needed. As an example of these treatment steps ammonia production based on natural gas (Figure 6.2.3) is discussed below. Table 6.2.1 gives the typical composition of syngas at different stages of syngas treatment.

Ammonia production requires a gas phase with hydrogen and nitrogen present in a ratio of 3 : 1 (Section 6.1), and the ammonia syngas must be free of CO and CO₂ because these compounds poison the iron catalyst used in the ammonia synthesis reactor.

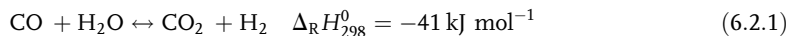
The two primary steps of (ammonia) syngas production from natural gas are steam reforming followed by autothermic (secondary) reforming where the residual methane of the syngas is converted with air by catalytic partial oxidation (Section 6.2.4). The syngas then contains hydrogen and nitrogen, but still also CO,

Table 6.2.1 Typical composition (vol.%) of syngas for NH₃ synthesis at different stages of syngas production and treatment for natural gas with 14% N₂ as feedstock [data from Bakemeier *et al.* (1997)].

Component	Primary reformer	Secondary reformer	High temperature shift	Low temperature shift	Methanation
H ₂	40.8	36.2	42.3	44.2	74
CO	6.4	8.2	2.1	0.2	<5 ppm
CO ₂	5.8	4.8	10.9	12.8	—
CH ₄	4.6	0.2	0.2	0.2	0.7
H ₂ O	39.8	36.0	29.9	28.0	—
N ₂	2.6	14.3	14.3	14.3	25
Ar	—	0.2	0.2	0.2	0.3

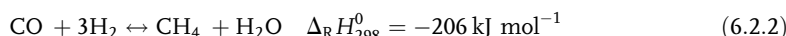
CO_2 , H_2O , and – in a very small quantity – still CH_4 (Table 6.2.1). Separation of these compounds is possible in principle, for example, by cryogenic processes, but this would be very costly. Therefore, the raw syngas is purified mainly by the following chemical conversion steps.

The syngas leaving the secondary reformer contains appreciable amounts of CO and CO_2 (Table 6.2.1). Separation of CO_2 by adsorption or absorption is relatively straightforward, but CO separation is not. Thus, CO is first converted into CO_2 by the water-gas shift reaction:



The shift reaction is exothermic and thus the equilibrium is favored by low temperatures (Figure 6.2.4). Thus, the reaction temperature should be kept as low as possible, but is limited by the activity of the catalyst. The Fe-Cr shift catalyst is sufficiently active only above about 300°C . Catalysts based on copper and zinc are active enough at about 200°C but these catalysts are very sensitive to poisoning and require extremely pure gases, typically with less than 1 ppm H_2S . In practice, the water-gas shift reaction is carried out in two adiabatic fixed-bed reactors with intermediate cooling between both converters. The first high-temperature shift reactor operates with a Fe-Cr catalyst, and the second low-temperature shift reactor contains the more active Cu-Zn system. At the exit of the second shift reactor, the CO_2 present in the converted syngas is removed in a gas scrubber, usually by chemical absorption in aqueous amine solutions, for example, mono- or diethanolamine (Section 3.3.3).

Although most of the CO originally present in the syngas is converted by the water-gas shift reaction into CO_2 there is still too much CO present as we are limited by thermodynamic constraints. If we take a typical temperature of about 240°C at the exit of the low-temperature shift reactor, we get a value for K_p ($= p_{\text{H}_2} p_{\text{CO}_2} / (p_{\text{H}_2\text{O}} p_{\text{CO}})$) of about 100 (Figure 6.2.4), which still corresponds to a CO content of about 0.2% (Table 6.2.1). This remaining CO is converted by methanation, which is the reverse of the steam reforming reaction:



The equilibrium favors methanation at low temperature and, therefore, a reaction temperature of about 450°C is used (whereas steam reforming is performed at about 800°C).

If syngas is produced by partial oxidation of heavy oils or gasification of solid fuels, oxygen is needed, which is produced by cryogenic air separation (Example 6.2.1). Hence, nitrogen is available and the CO separation is then conducted by a low temperature liquid nitrogen wash at about -190°C (83 K). By this means the N_2 needed for NH_3 synthesis is also added.

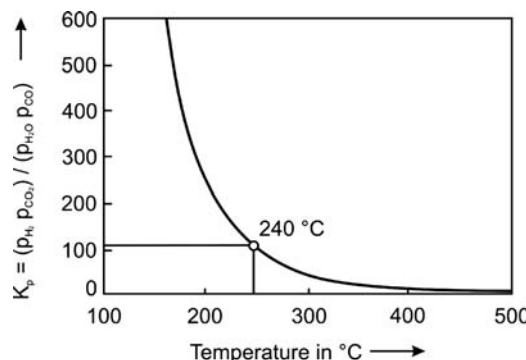


Figure 6.2.4 Influence of temperature on equilibrium constant of the water-gas shift reaction.

Example 6.2.1: Cryogenic air separation (Linde process)

Figure 6.2.5 shows a flow sheet of the *Linde* process for air separation by distillation. Air is compressed to about 6 bar, then cooled by water and/or air to remove water by condensation. In subsequent heat exchangers (E-1 to E-3 in Figure 6.2.5), the air is cooled countercurrently with cold N₂ and O₂ (coming from the distillation column) and is thereby partially liquefied. Water, CO₂, and other impurities such as hydrocarbons are removed by molecular sieve adsorbers, which are periodically switched from adsorption to regeneration and vice versa. The cooled and partially liquified air then goes to a double column for separation by distillation. In the first column (C-1), which has a top condenser, some N₂ is separated at a pressure of about 6 bar. The distillate of this column is used as reflux in the second column with a reboiler at the bottom (C-2) that operates at a lower pressure of about 1.3 bar. Since the reflux is provided by the first column, no top condenser is needed. The condenser of the first column and the reboiler of the second column are thermally coupled. Typically a temperature difference of 2.5 K is needed for heat transfer between reboiler and condenser, which is adjusted by the difference of pressure in both columns (Figure 6.2.6). The energy required for the separation is provided by a compressor and the low temperatures are generated by the expansion of some N₂ (about 12% of the feed, Stichlmair and Fair, 1998) in an expansion machine from 5.7 to 1.3 bar (Figure 6.2.5) or by the Joule-Thomson effect (Section 3.1.2), that is, the expansion machine is replaced by a valve, if the products are gaseous and less cooling energy is needed.

To determine the number of theoretical separation stages (Section 3.3.2.2), we need the relative volatility as defined by Eq. (3.3.8).

For air separation we have:

$$\alpha_{N_2,O_2} = \frac{p_{vap,N_2}}{p_{vap,O_2}} \quad (6.2.3)$$

and if we assume a constant value (= mean value at an average temperature in each column) we obtain [see Eq. (3.3.12)]:

$$\gamma_{N_2} = \frac{\alpha_{N_2,O_2} x_{N_2}}{1 + x_{N_2} (\alpha_{N_2,O_2} - 1)} \quad (6.2.4)$$

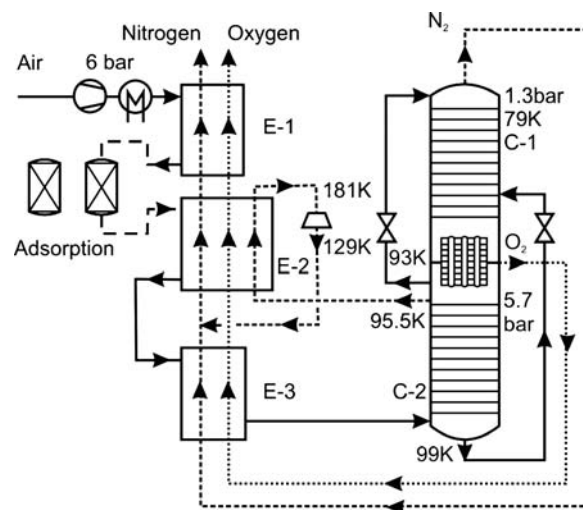
For air separation at 5.7 bar ($T_{mean} = 96$ K) and at 1.3 bar (86 K) α is 3 and 4, respectively, if we use the data of Figure 6.2.6. Figure 6.2.7 shows the plot of γ_{N_2} versus x_{N_2} .

As an example of the brief design of an air separation unit, we take a closer look at the lower distillation column ($p \approx 6$ bar). The minimum reflux ratio (infinite number of trays) is 0.5 (Figure 6.2.8, details on the method in Section 3.3.2.2). Thereby, notably, the high-pressure column consists only of a rectification section, and thus a line for the stripping section is not needed.

The cost optimum reflux ratio is typically in the range 1.1–1.5 R_{min} . Here we use a value of 1.5 and thus the reflux ratio is about 0.8 (Figure 6.2.9).

According to *Stichlmair and Fair*, the number of practical trays is about 40 in the high-pressure column and 60 in the low-pressure column. The stage efficiency in the high-pressure column is about 0.18 (Schlatterer, 1951), and thus Figure 6.2.9 leads to a calculated number of practical trays of 39, which is in agreement with plant data.

Figure 6.2.5 *Linde* process for air separation by distillation with a double column. Adapted from Stichlmair and Fair (1998) and Baerns *et al.* (2006); E: heat exchanger, C: column.



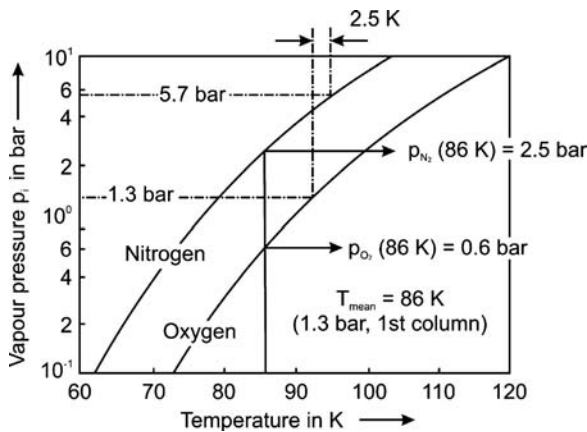


Figure 6.2.6 Vapor pressures of nitrogen and oxygen.

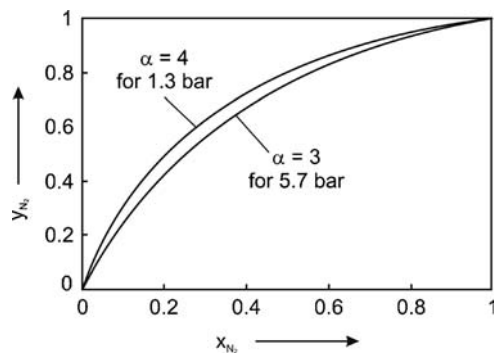


Figure 6.2.7 Liquid–vapor equilibrium of air at 1.3 and 5.7 bar (α = relative volatility).

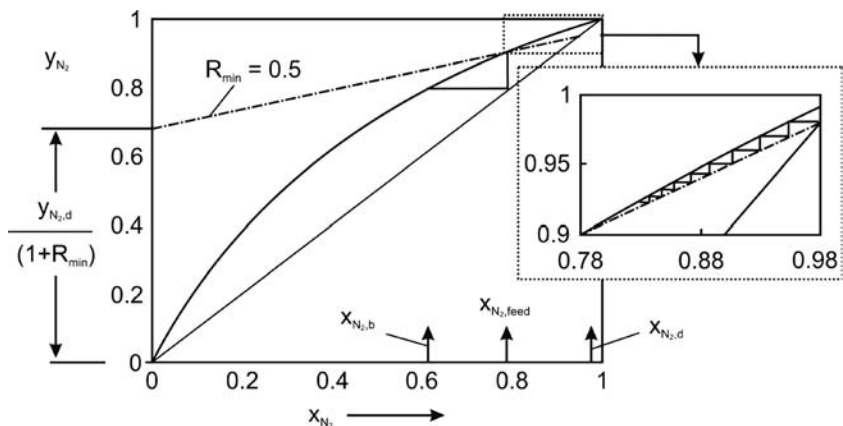


Figure 6.2.8 High-pressure column of air distillation unit: minimum reflux ratio (infinite number of trays in the stripping section, rectification section consists only of reboiler).

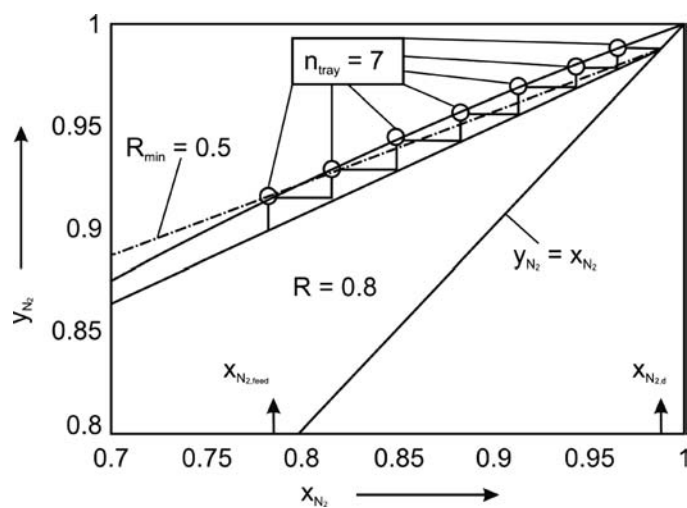
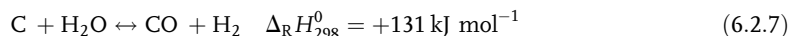
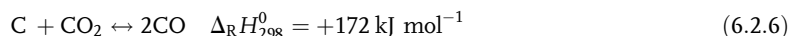
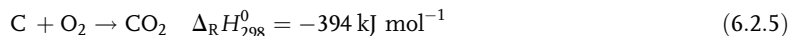


Figure 6.2.9 Determination of theoretical number of trays of the stripping section of the lower distillation column of an air distillation unit ($p = 6$ bar) for a reflux ratio of $0.8 = 1.5 R_{\min}$.

6.2.2

Syngas from Solid Fuels (Coal, Biomass)**6.2.2.1 Basic Principles and Reactions of Syngas Production from Solid Fuels**

Coal gasification to syngas is a complex network of parallel and consecutive reactions. Some basic aspects have already been examined in Section 5.1.5.2 and are treated in more detail in conjunction with the gasification of Chinese reed (Section 6.1.4.1) and the blast furnace process (Section 6.5). If we assume, for simplicity, that coal is represented by carbon ("C") the main reactions taking place are:



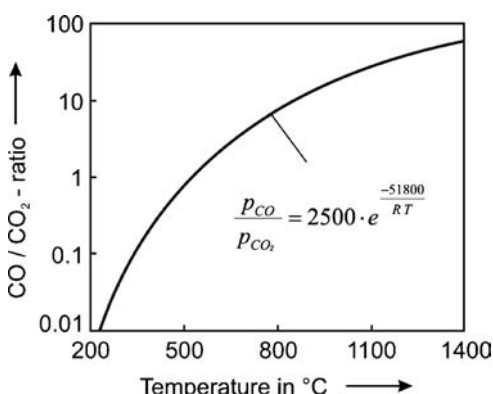
The direct oxidation of carbon to CO is not considered here because in technical processes the primarily formed CO is rapidly oxidized in a consecutive homogeneous reaction to CO₂. Thus Eq. (6.2.5) summarizes the oxidation of C to CO₂ (intrinsically only favored at low temperatures, Topic 6.2.1), and homogeneous CO oxidation.

Coal gasification is commonly conducted in autothermically, that is, gasification is carried out with a mixture of O₂ and H₂O, so that the combustion generates the heat needed to reach the high temperatures required for the endothermic gasification reactions [Eqs. (6.2.6) and (6.2.7)]. Beside these heterogeneous reactions, homogeneous reactions like the water-gas shift reaction also occur. In addition, coal is a complex mixture of organic and mineral compounds. Hence, if coal is heated various gases are evolved by pyrolysis (H₂, CH₄, CO, aromatics, tar, etc.) and the solid residue is transformed into a porous char. Depending on the process and reactor type, the volatile compounds and the char are further converted by thermal cracking and gasification reactions (Figure 5.1.28).

Topic 6.2.1 Intrinsic reactions between carbon and oxygen

If carbon or coke is combusted with oxygen, both CO and CO₂ are formed as primary products. Nevertheless, at temperatures relevant for industrial processes (>800 °C), CO₂ is the dominant (detectable) product as the primarily formed CO is further oxidized into CO₂. This reaction is catalyzed by H[•] and •OH radicals and thus normally always takes place as air contains some water vapor. Moreover, natural solid fuels like coal and coke always contain certain amounts of hydrogen and water. In the laboratory, homogeneous formation of CO₂ can be suppressed by the addition of the inhibitor phosphoryl chloride (POCl₃) to the oxidizing gas, as shown by Arthur (Arthur, 1951). This is because halogens are scavengers and POCl₃ captures H₂O. Based on the experiments performed by Arthur, the correlation for the primary CO/CO₂ ratio as shown in Figure 6.2.10 is valid. Thus, above 600 °C, CO is by far the dominant primary product but this cannot be used in technical processes (e.g., to oxidize coke directly to CO) without making a detour via the heterogeneous conversion of carbon with CO₂ [(Boudouard reaction, Eq. 6.2.7)].

Figure 6.2.10 Oxidation of carbon/coke: proportions of the carbon oxides primarily formed at various temperatures if conversion of CO with oxygen is inhibited by POCl₃ (data from Arthur, 1951).



6.2.2.2 Syngas Production by Gasification of Solid Fuels

Reactors for syngas production by gasification of solid fuels like coal and probably in future also of biomass are a moving bed, a fluidized-bed, or an entrained flow system as depicted in Figure 4.10.8 (Section 4.10). Table 6.2.2 lists the main characteristics. Depending on temperature of the gasifier the mineral matter is released as a liquid (slag) or a solid (ash).

The *fixed bed gasifier* (*Lurgi* reactor, Figure 4.10.8a) is operated countercurrently. The coal bed is supported on a rotating grate. Coal enters the gasifier at the top and is slowly heated, dried, and then pyrolyzed on its way down. Conversely, the product gas is cooled before it leaves the reactor. In the gasification zone the coal is partly gasified by steam and CO₂, until a reaction temperature of about 900 °C is reached, and the rate of both reactions become too low (Section 6.5). The remaining coal is finally combusted in the lowermost zone, where temperatures of 1200 °C are reached. The solid ash leaves the reactor at the bottom.

A disadvantage of the fixed-bed reactor is that a large amount of by-products is released as tar and oil. Only non-caking coals can be processed as they do not form agglomerates leading to an increased pressure drop or even plugging. A novel development is a slagging reactor with a higher temperature in the combustion zone of >1700 °C.

In the *fluidized-bed gasifier* (*Winkler* process, Figure 4.10.8b), the coal particles are well mixed, which leads to a moderate and uniform temperature. Char particles that leave the reactor together with the product gas are recovered in cyclones and are recycled. The ash is removed at the bottom. The solid phase is well mixed and is converted like in a CSTR, which leads to a lower carbon conversion compared to a plug flow system, and carbon is lost via the ash. The coal should therefore be reactive (e.g., brown coal) to permit a high conversion.

In the *entrained-flow gasifier* (*Koppers-Totzek* process, Figure 4.10.8c, see Section 6.2.2.3) the fine coal particles react cocurrently with steam and oxygen. The residence time is only a few seconds, and the temperature must be high to ensure a high coal conversion. The mineral matter is removed as molten slag. The entrained-flow reactor can handle all types of coal. The process was developed in 1939–1944 and initially worked at atmospheric pressure; to overcome this disadvantage, versions were developed in the 1970ties capable of operating at around 30 bar [Prenflow (pressurized entrained flow), Shell coal gasification process]. The Texaco coal gasification process is also an entrained bed gasifier operating at 20 to 40 bar and was departed from the process for partial oxidation of heavy oil (Section 6.2.3, Fig. 6.2.27); but instead of coal dust, an aqueous slurry containing 60–70% coal is fed to the gasifier.

Table 6.2.2 Typical conditions of coal gasification in different reactor types [various sources: Moulijn, Makkee, and Van Diepen (2004); Onken and Behr (1996); and Arpe (2007); Franck and Knop (1979); Falbe (1977)].

	Reactor type			
	Fixed bed	Fluidized bed	Entrained bed/Koppers-Totzek	Entrained bed/Texaco
Diameter of coal particles (mm)	6–40	1–8	<0.1	<0.1
Pressure (bar)	35	25	1	35
Suitable coal	Non-caking	Reactive	All	All (coal slurry)
Temperature (max./outlet) (°C)	1100/300	1000/900	2000/1000	2000/1000
Ash/slag removal	Solid	Solid	Liquid	Liquid
O ₂ consumption [m ³ (STP) per 10 MJ coal]	0.1–0.13	0.16–0.19	0.19–0.24	ca. 0.2
Steam consumption (kg per 10 MJ coal)	0.3–0.5	0.19–0.24	0–0.05	ca. 0.05
Typical composition of syngas (dry basis) for hard coal as feedstock (vol.%)				
H ₂	39	46	31	35
CO	22	30	58	50
CO ₂	28	22	10	14
CH ₄	10	1	<0.5	—
H ₂ S, COS, NH ₃	up to 1			
By-products	Tar, oil	None	None	None

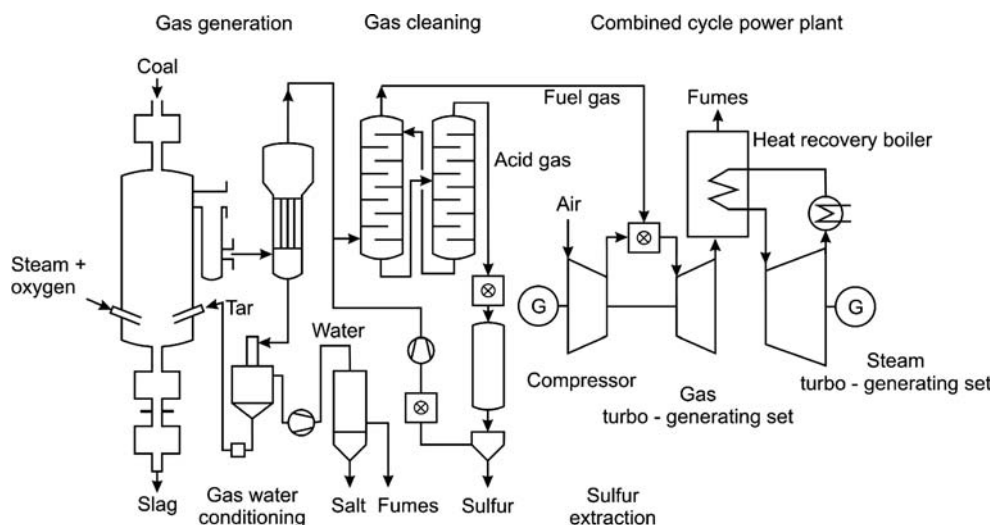


Figure 6.2.11 Combined cycle power plant based on coal gasification (adapted from Plass *et al.*, 1990).

These three reactor types differ with regard to the syngas composition (Table 6.6.2), which is the result of different operating temperatures and the amount of oxygen and steam used.

Besides syngas production for subsequent synthesis steps (methanol, *Fischer-Tropsch* etc.), coal gasification has recently also been considered as an attractive option for power generation. The so-called *combined cycle power plant* is shown in Figure 6.2.11 for the example of a fixed bed gasifier. First, fuel gas rich in H₂ and CO is produced by gasification. After cleaning, the fuel gas is combusted with compressed air in a gas turbine that drives the electricity generator and also the air compressor. The exhaust gas of the turbine is still hot and therefore used for steam generation and electricity generation in a classical steam turbine cycle, respectively. Compared to a classical power plant based on coal combustion with an efficiency of about 35%, the combined cycle power plant is more efficient (41–43%) (Moulijn, Makkee, and Van Diepen, 2004).

6.2.2.3 Case Study: Syngas and Hydrogen by Gasification of Biomass

As an example of the design of a gasification reactor, we inspect entrained flow gasification of biomass, which was investigated by *Roll* and *Hedden* for Chinese reed (Roll, 1994; Roll and Hedden, 1994). Entrained flow gasification has the advantage of low tar and low methane contents in the product gas. Owing to the short residence time in the gasifier, it is necessary to grind the reed. After grinding and drying, the reed particles are slabs about 5 mm long and 2 mm thick. Table 6.2.3 lists some characteristics of the reed. The gross calorific value (17.8 MJ kg⁻¹) of the moist reed is about half of that of hard coal. During pyrolysis, 72% is released as volatile matter (gas, water, and tar) and 28% remains as solid char.

Table 6.2.3 Characterization of Chinese reed [data from Roll (1994); Roll and Hedden (1994)].

Component	Content (wt%)
Water content	4
Volatile matter	72
Ash content	6.9
Chemical composition (remainder ash and water)	
C	42.3
H	5.2
O	40.5
N	0.8
S	0.1
Cl	0.2

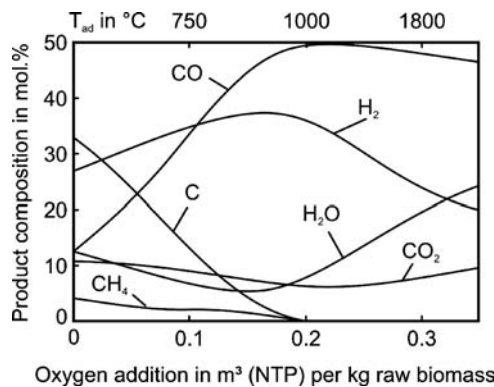


Figure 6.2.12 Equilibrium composition of syngas formed by adiabatic gasification of Chinese reed (2 bar, $T_{in} = 25^\circ\text{C}$, calculated by minimization of G_{system}). Data from Roll (1994); Roll and Hedden (1994).

The thermodynamic equilibrium composition of the syngas [including carbon formed if the O_2 addition is less than 0.2 m^3 (NTP) per kg of moist biomass] in the case of adiabatic gasification of the reed is shown in Figure 6.2.12. The enthalpy of the biomass m^3 (NTP) per kg raw biomass was calculated from the gross calorific value of the biomass (Roll, 1994).

Figure 6.2.12 indicates that an oxygen addition of around 0.2 m^3 (STP) per kg of moist reed is optimal for high yields of H_2 and CO . Side products are then practically only CO_2 and H_2O .

As shown in Figure 5.1.28, pyrolysis is the first reaction step, whereby the volatile constituents of the biomass – water, H_2 , CO , CO_2 , and hydrocarbons from CH_4 to tar – are driven off. The volatiles are combusted and the char formed by pyrolysis is partly combusted and in the main gasified with H_2O and CO_2 . These reaction steps can be described as follows.

Pyrolysis of Biomass The kinetic parameters of the pyrolysis of solid materials can be determined by means of non-isothermal thermogravimetric measurements. The rate of release of volatile matter may be described by a simple first-order expression:

$$\frac{dm_v}{dt} = k_{p0} e^{-\frac{E_{AP}}{RT}} (m_{V,\infty} - m_v) \quad (6.2.8)$$

where m_v and $m_{V,\infty}$ represent the mass of volatile matter released until time t and at the end of the pyrolysis, respectively. For a constant heating rate HR the rate of pyrolysis is given by:

$$\frac{1}{m_{V,\infty}} \frac{dm_v}{dT} = \frac{k_{p0}}{HR} \exp \left[-\frac{E_{AP}}{RT} - \frac{k_{p0} RT^2}{HR E_{AP}} \left(1 - \frac{2RT}{E_{AP}} \right) e^{-\frac{E_{AP}}{RT}} \right] \quad (6.2.9)$$

[For details on Eq. (6.2.9) see Section 4.11.5.4 for the derivation of a similar equation for the case of coke combustion. The activation energy and the frequency factor are determined by regression analysis of the measured pyrolysis rates.]

Figure 6.2.13 shows the rate of reed pyrolysis for different heating rates. The lowest one (10 K min^{-1}) is typical for thermogravimetric measurements, and the

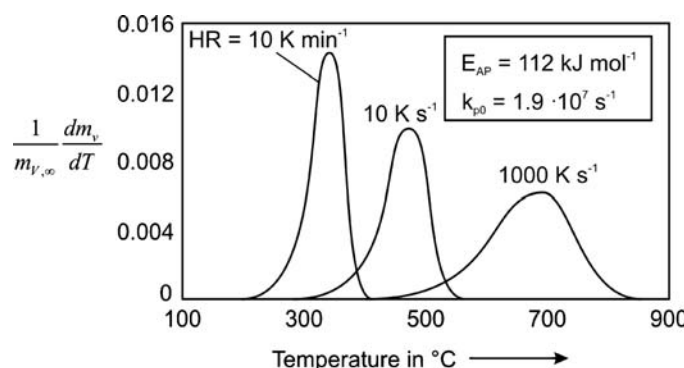


Figure 6.2.13 Rate of pyrolysis of Chinese reed (derivative thermogravimetry, DTG) at different heating rates [calculated with data given by Roll (1994); Roll and Hedden (1994)].

highest heating rate (1000 K s^{-1}) is typical for gasification and combustion processes where small particles are rapidly heated by conduction and heat transfer from the hot surrounding gas and by radiation from the hot reactor wall. The transient heating of biomass particles is inspected in Example 6.2.2.

Example 6.2.2: Transient heating of a biomass particle during pyrolysis

The equations for transient heat transfer given in Section 3.2.1.5 can be used to derive the heating rate of a biomass/char particle. The particles are heated in the gasifier by heat transfer from the hot surrounding gas and by radiation from the reactor wall. To estimate the thermal resistance by convective heat transfer to the particle compared to the resistance by heat conduction in the particle, we use the *Biot number* [Eq. (3.2.47)] for a spherical particle:

$$Bi_h = \frac{\alpha d_p}{2\lambda_{\text{char}}} \quad (6.2.10)$$

The minimal contribution of convection can be estimated by Eq. (3.2.19a):

$$\alpha_{\min} = \frac{Nu_{\min} \lambda_g}{d_p} \quad (6.2.11)$$

The thermal conductivity of the gas phase is $0.08 \text{ W m}^{-1} \text{ K}^{-1}$ (air, 1000°C), Nu_{\min} is 2 (spherical particle, stagnant gas phase, i.e., $Re \rightarrow 0$), and for the particle diameter we use 1 mm. Thus, we obtain a convective heat transfer coefficient of $160 \text{ W m}^{-2} \text{ K}^{-1}$. Radiation may also play a role, and by Eq. (3.2.35) we estimate a radiative heat transfer coefficient α_{rad} :

$$\begin{aligned} \dot{Q}_{12} &= \varepsilon_p A_p \sigma (T_{\text{wall}}^4 - T_p^4) = \left[\varepsilon_p \sigma \frac{(T_{\text{wall}}^4 - T_p^4)}{(T_{\text{wall}} - T_p)} \right] A_p (T_{\text{wall}} - T_p) \\ &= \alpha_{\text{rad}} A_p (T_{\text{wall}} - T_p) \end{aligned} \quad (6.2.12)$$

The char can be regarded as a black body ($\varepsilon_p = 1$) and for the wall and mean particle temperature we use 1473 and 873 K, respectively, which

leads to $\alpha_{\text{rad}} = 390 \text{ W m}^{-2} \text{ K}^{-1}$ and to an overall heat transfer coefficient α of $550 \text{ W m}^{-2} \text{ K}^{-1}$.

To calculate the *Biot number* by Eq. (6.2.10) we use a value of $0.4 \text{ W m}^{-1} \text{ K}^{-1}$ for the thermal conductivity (wood: $0.2 \text{ W m}^{-1} \text{ K}^{-1}$, char: $0.3\text{--}1 \text{ W m}^{-1} \text{ K}^{-1}$, Figure 6.5.6) and obtain a value for Bi_h of 0.7.

The second parameter we need to know is the *Fourier number* [Eq. (3.2.46)]:

$$Fo = \frac{ta_{\text{char}}}{r_p^2} = \frac{t\lambda_{\text{char}}}{c_{\text{char}} \rho_p r_p^2} \quad (6.2.13)$$

The progress of heating is characterized by the dimensionless temperature:

$$\theta_{\text{midpoint}} = \frac{T_{r=0}(t) - T_{\text{surr}}}{T_{r=0}(t=0) - T_{\text{surr}}} \quad (6.2.14)$$

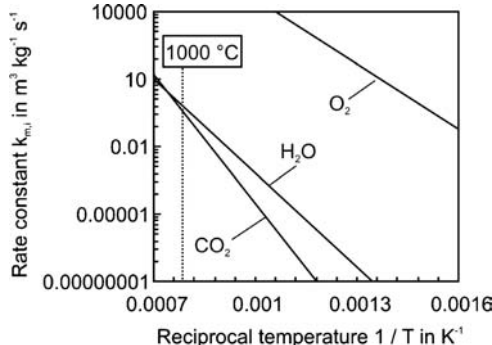
To estimate the heating time we use a value for θ_{midpoint} of 0.01, which is equivalent to the condition that the particle center has already reached 1461 K (initial particle temperature = 293 K, temperature of gas phase = 1473 K). The time is calculated by transient temperature charts as given in Figure 3.2.17 for a plane. Similar charts are given in the literature for spherical particles (Cengel, 2002). For $Bi_h = 0.7$ and $\theta_{\text{midpoint}} = 0.01$ we find $Fo = 2.6$. The mean density of the biomass/char particles is 325 kg m^{-3} (reed 500 kg m^{-3} , char 150 kg m^{-3}) and the heat capacity is $1000 \text{ J kg}^{-1} \text{ K}^{-1}$. Equation (6.2.13) finally leads to a heating time of about 0.5 s and thus to a heating rate of 2000 K s^{-1} .

Combustion and Gasification of the Coke Derived from the Reed The remaining char consists mainly of carbon and to some extent of ash, and reacts with O_2 , CO_2 , and H_2O . All three conversion rates can be expressed by a first-order expression:

$$-\frac{dm_C}{dt} = k_{m,O,i} e^{\left(\frac{-E_{A,i}}{RT}\right)} c_i m_C M_C \quad (\text{with } i = O_2, CO_2 \text{ and } H_2O) \quad (6.2.15)$$

The intrinsic rate constants are compared in Figure 6.2.14. At a typical gasification temperature of 1000°C , the reactivity of the char (derived from the reed) for

Figure 6.2.14 Intrinsic rate constants of oxidation and gasification (with H_2O and CO_2) of char derived from Chinese reed [data from Roll (1994); Roll and Hedden (1994)].



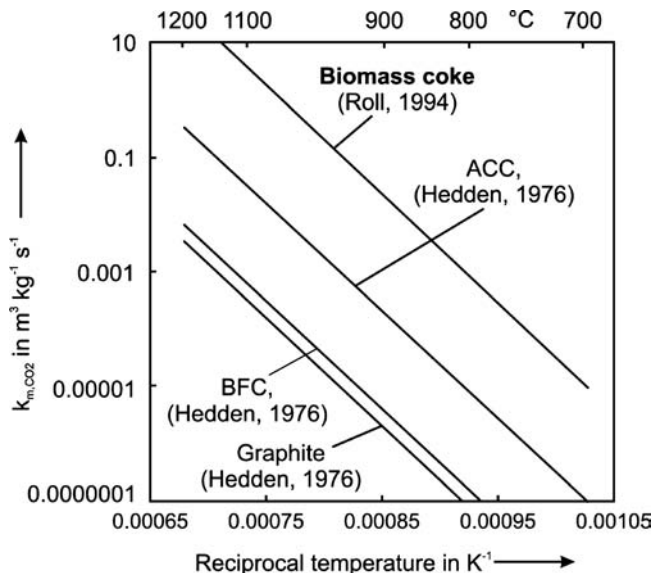


Figure 6.2.15 Reactivity of carbonaceous materials for gasification with CO_2 (BFC: blast furnace coke, ACC: active charcoal).

conversion with CO_2 and H_2O is almost similar, whereas the rate with O_2 is about seven orders of magnitude higher.

Comparison of the reactivity of different carbonaceous materials for conversion with O_2 and CO_2 (Figure 6.2.15 and Figure 6.2.16a) indicates that the char derived from the reed is much more reactive than other materials like blast furnace coke or active charcoal.

The reactivity of carbonaceous materials is not only different, if the rate constant related to the mass is used, but also if the (internal) surface area is considered (Figure 6.2.16b). Thus, the reactivity depends on the internal surface area and the chemical structure of the coke.

As examined in Section 4.6.3, the reaction of a gas with a porous solid is complicated if external mass transfer and/or pore diffusion have to be considered as we find concentration gradients of the gaseous reactants within the solid. In addition, gas–solid reactions are transient and the solid mass and sometimes also the size, surface area, porosity, and tortuosity change during the conversion of the solid. Here we only examine the influence of temperature on the initial value of the effective rate constant of char conversion, which can be calculated by the equations given in the Sections 4.5.5 and 3.2.2:

$$k_{m,i,\text{eff}} = \left(\frac{1}{\beta A_m} + \frac{1}{\eta_{\text{pore}} k_{m,i}} \right)^{-1} \quad (6.2.16)$$

$$\eta_{\text{pore},i} = \frac{\tanh \phi_i}{\phi_i} \quad (6.2.17)$$

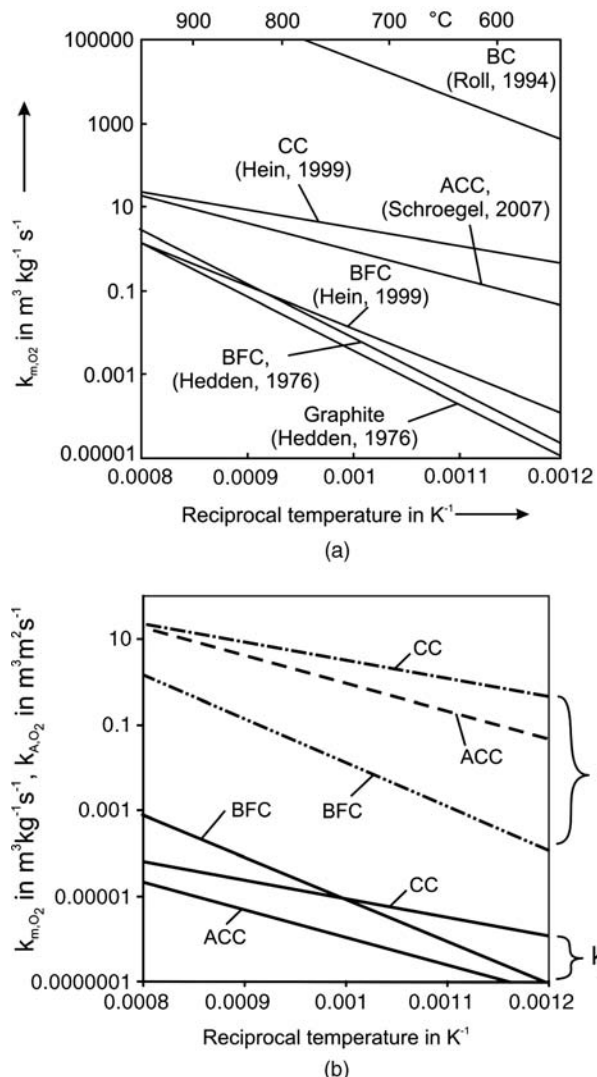
$$\phi_i = \frac{d_p}{6} \sqrt{\frac{k_{m,i} \rho_p}{D_{\text{eff}}}} \quad (6.2.18)$$

$$Sh = \frac{\beta d_{\text{charac}}}{D} \quad (6.2.19)$$

$$Sh_{\text{single particle}} \approx 2 + 0.664 \sqrt{Re_p} \sqrt[3]{Sc} \quad (\text{for gases and } Re_p < 50) \quad (6.2.20)$$

Figure 6.2.17 shows the effective rate constants of char conversion with O_2 , H_2O , and CO_2 . For the molecular and effective diffusion coefficients, the mean values at 800°C were used (2 and $0.2 \text{ cm}^2 \text{ s}^{-1}$), as the values for O_2 , H_2O , and CO_2 differ only slightly. The particle density is 500 kg m^{-3} , the diameter 1 mm , and for Sh the minimal value of two was used.

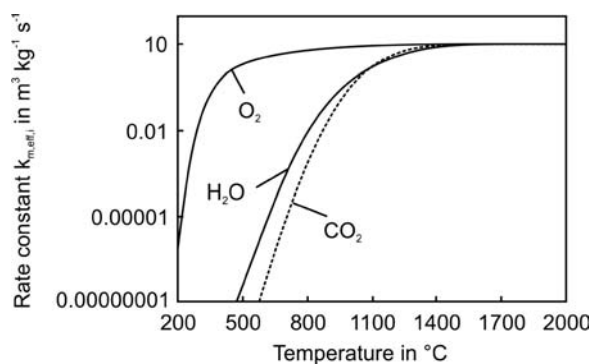
Figure 6.2.16 (a) Reactivity of carbonaceous materials (related to mass) for oxidation with O_2 (BFC: blast furnace coke, ACC: active charcoal, BC: biomass coke from Chinese reed *Misanthus*, CC: charcoal). (b) Reactivity of carbonaceous materials for oxidation related to mass as well as to surface area ($k_A = k_m/A_{BE,T}$; BFC with about $2\text{ m}^2\text{ g}^{-1}$, ACC: $900\text{ m}^2\text{ g}^{-1}$, CC: $360\text{ m}^2\text{ g}^{-1}$).



The char combustion is always controlled by external mass transfer for technically relevant temperatures ($>800^\circ\text{C}$), whereas for gasification with H_2O and CO_2 pore diffusion and the intrinsic rate of the reaction may also play an important role, until at temperatures above 1200°C the effective rate is completely determined by external mass transfer.

Figure 6.2.18 shows the content of the gaseous reactant (for the example of O_2 during combustion) at the external surface and in the center of the particle as well as the mean value within the particle (all values in dimensionless form relative to the content in the bulk phase).

Figure 6.2.17 Effective rate constants of oxidation and gasification (with H_2O and CO_2) of char derived from Chinese reed [data from Roll (1994) and Roll and Hedden (1994); parameters used for calculation: mean values at 800°C , molecular and effective diffusivity: 2 and $0.2\text{ cm}^2\text{ s}^{-1}$, particle density: $500\text{ m}^3\text{ kg}^{-1}$, $Sh=2$, particle diameter: 1 mm].



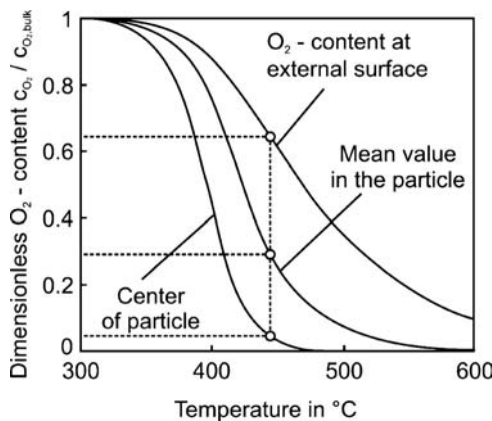


Figure 6.2.18 Oxygen content at the external surface, in the center of the particle, and mean value within the particle during oxidation of char from Chinese reed.

As expected, all values decrease with increasing temperature. For example, at 300 °C the O₂ content in the boundary layer and in the particle still equals the value in the bulk phase, whereas at 450 °C the content at the external surface is 65% of the bulk phase value and in the particle center O₂ is almost no longer present (<5%), and the mean value drops to 30%.

Equations (6.2.18) and (6.2.20) are only valid for spherical particles. Reed particles, however, have an irregular shape and for this reason an equivalent particle diameter has to be determined. For this reason, Roll and Hedden studied the hydrodynamic behavior of the reed using the apparatus shown in Figure 6.2.19 (Roll, 1994; Roll and Hedden, 1994).

The reed was fed into a cold air stream. Particles with a smaller rate of descent than the air velocity left the tube at the top. Larger particles remained in a fluidized bed. Figure 6.2.20 shows the relationship between the discharged material, air velocity in the tube, and the equivalent particle diameters.

The equivalent diameters of spheres with the same particle density (500 kg m⁻³) and with the same rates of descent as the reed particles were calculated from a balance of forces on a single particle, that is, the weight of a particle (less the almost negligible lifting force) equals the hydrodynamic resistance force (Section 3.4.1.2). The calculated equivalent sphere diameters are shown in Figure 6.2.20.

The semi-technical entrained flow reactor constructed and used by Roll (Roll, 1994) is shown in Figure 6.2.21. The reed (6 kg h⁻¹) was gasified with oxygen at around 1300 °C and a pressure of 1.4 bar. The reed was fed into the upward flowing gas stream by means of a screw feeder. To avoid blockage of the feeding device, it was purged with air.

On entering the reaction tube, the reed particles move downwards counter-currently to the gas. The particles are heated very rapidly and pyrolysis takes place immediately. Char is formed, in a quantity of 28 wt%, by the release of volatile matter. As a consequence of the weight loss, the particles change their flow direction and move upwards with the gas. On their way through the reactor the char

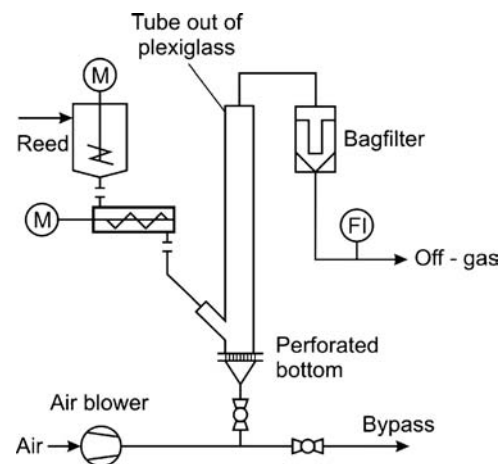


Figure 6.2.19 Apparatus used to investigate the hydrodynamic behavior of the reed (adapted from Roll, 1994; Roll and Hedden, 1994).

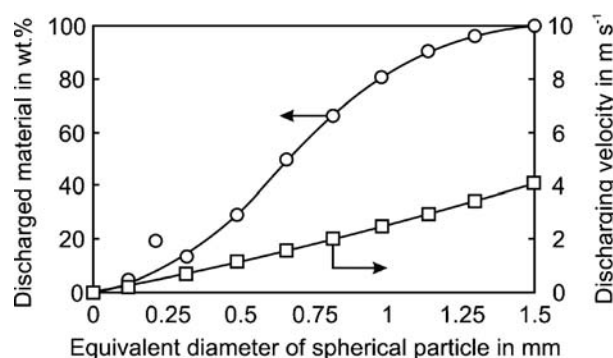
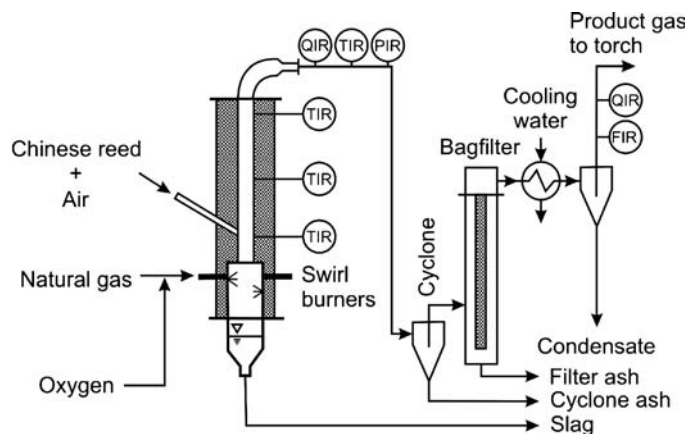


Figure 6.2.20 Relationship between air velocity and equivalent diameter of a sphere of the discharged Chinese reed. Data from Roll (1994) and Roll and Hedden (1994).

Figure 6.2.21 Scheme of the semi-technical entrained bed gasifier (adapted from Roll and Hedden, 1994).



particles are gasified and after a residence time of about 1 s the product gas and fly ash leave the reactor at the top.

Part of the mineral matter of the reed forms slag droplets in the reactor. These slag droplets hit the wall of the reactor tube; the slag then moves downwards to the bottom of the gasifier from where it is removed discontinuously. The slag removal unit of the gasifier is heated by means of two swirl burners employing natural gas burned with excess oxygen.

This excess oxygen is heated in the flames to about 1800 K and subsequently used for gasification (partial oxidation) of the reed.

The most important operating parameter is the oxygen-to-biomass ratio. As this ratio increases, the fraction of biomass burned to carbon dioxide and water increases and so does the reactor temperature. This leads to an increase in the carbon conversion. Figure 6.2.22 shows the carbon conversion and the wall temperature at a distance of 1 m below the reactor outlet as a function of the oxygen consumption (without the oxygen used for heating the slag outlet).

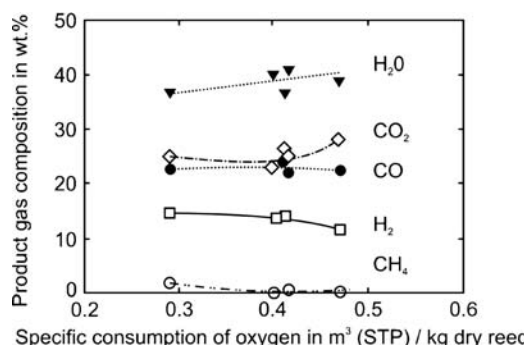
Roll and Hedden developed a one-dimensional model for the semi-technical gasifier. This model describes (i) the trajectories of the reed particles, (ii) the axial temperature profiles of the gas phase and of the reactor wall, (iii) the conversion of the reed particles by pyrolysis and gasification of the char formed, and (iv) the quantity and composition of the product gas.

To simulate the entrained flow reactor, the gasifier was divided into three sections (Figure 6.2.23; for reactor dimensions and reaction parameters see Table 6.2.4):

In zone 1, 0.1 m long, natural gas is burned with excess oxygen to heat the slag outlet. The excess oxygen is preheated and used afterwards for reed gasification. The combustion products and excess oxygen leave zone 1 and enter zone 2.

In zone 2, the reed is fed into the reactor at a height of 0.4 m. Small particles follow the gas stream immediately on entering the reactor, are heated rapidly, and pyrolysis takes place. In contrast, large particles first move downwards counter-currently to the gas. Owing to weight loss by pyrolysis, they then change their direction of flow after a finite time and move upwards. Part of the volatiles was burned

Figure 6.2.22 Influence of oxygen consumption on the product gas composition [6 kg dry reed per hour, 1.25 m³ (STP) natural gas 3 m³ (STP) air per h (Roll, 1994; Roll and Hedden, 1994)].



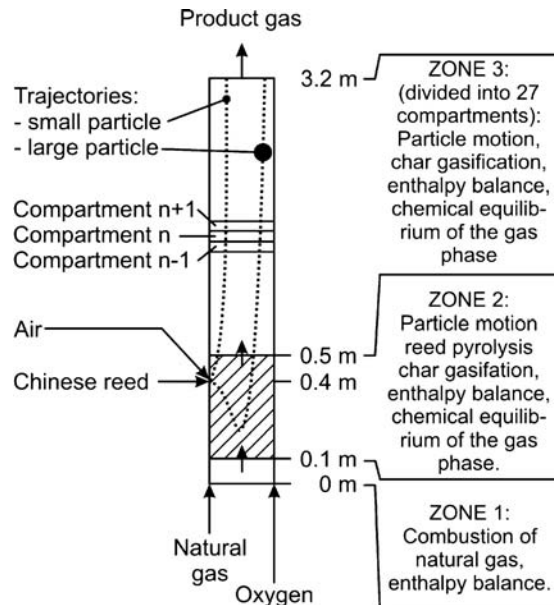


Figure 6.2.23 Zones for modeling the entrained flow gasifier (Roll and Hedden, 1994).

Table 6.2.4 Parameters for gasification computations (Roll, 1994; Roll and Hedden, 1994).

Parameter	Value
Inside diameter of reactor tube	70 mm
Reactor height	3.2 m
Reed feed rate (dry basis)	6 kg h^{-1}
Natural gas feed rate	$1.25 \text{ m}^3 (\text{STP}) \text{ h}^{-1}$
Air feed rate	$3 \text{ m}^3 (\text{STP}) \text{ h}^{-1}$
Specific O ₂ consumption (without O ₂ for natural gas combustion)	$0.4 \text{ m}^3 (\text{STP}) \text{ kg}^{-1}$ dry reed
Heat loss in zones 1, 2, and 3 (see Fig. 6.2.23)	7.5, 5.3, and 8.4 kW
Higher heating value	17.8 MJ kg^{-1} dry reed

immediately after release. The oxygen is used completely for combustion of the volatile matter. The volatile combustion provides the heat needed for the endothermic gasification of the char and for cracking the pyrolysis products. The particles leave zone 2 and enter zone 3 at a reactor height of 0.5 m.

In zone 3, all char particles move upwards and are gasified by H₂O and to a minor extent by CO₂. The product gas and unconverted char leave the reactor at a height of 3.2 m.

Figure 6.2.24 shows calculated trajectories for reed particles with two different sizes that represent the range of equivalent diameters of the reed. A small particle with an equivalent diameter of 0.12 mm follows the gas stream immediately on

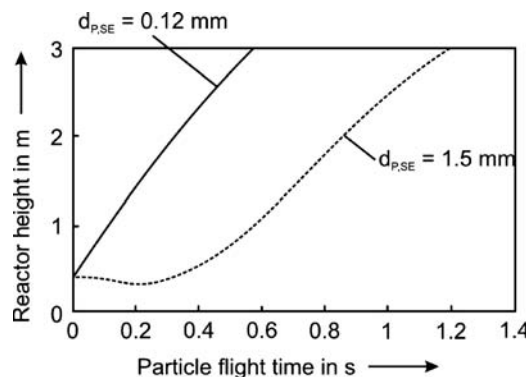
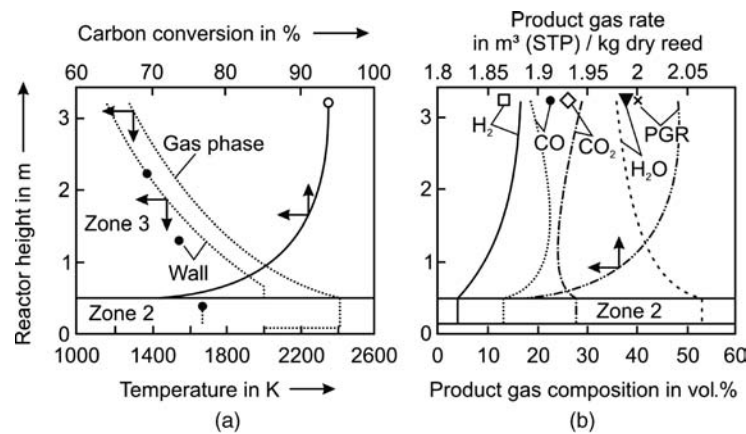


Figure 6.2.24 Calculated trajectories for reed particles with two different sizes representing the range of equivalent diameters of the reed (Figure 6.2.20) (Roll, 1994; Roll and Hedden, 1994).

Figure 6.2.25 Semi-technical gasifier of Chinese reed: calculated profiles of gas phase and wall temperature and carbon conversion (a) and profiles of the product gas composition (without nitrogen), symbols: measured values (b) (Roll, 1994; Roll and Hedden, 1994).



entering the reactor. In contrast, a large particle (diameter 1.5 mm) moves downwards on entering the reactor. After 0.2 s, the particle changes flow direction due to the weight loss arising from pyrolysis and moves upwards. Hence, large particles have a longer residence time in the reactor.

Figure 6.2.25 illustrates important measured and calculated parameters of the entrained flow gasifier like the temperature of the gas phase, degree of carbon conversion, and composition of the gas at different positions in the reactor.

The carbon conversion in zone 2 is dominated by pyrolysis, with 60% of the carbon in the reed being converted into volatile products. In the subsequent zone 3, reed pyrolysis and char gasification lead to a carbon conversion of 70%. The conversion increases further to 93% at a reactor length of 2.4 m. From this point on, no char is gasified, and only the gas composition changes by the water-gas shift reaction.

Comparison of the measured and calculated values shows that the model is well suited to describing conversion and product gas rate. Although the calculated product gas composition differs from the measured value, this can be explained by kinetic inhibition of the homogeneous CO shift reaction at temperatures below about 1200 °C. Thus, the measured gas composition corresponded to an equilibrium composition at this temperature.

By the mathematical model, Roll and Hedden also simulated a technical gasifier for about 30 000 m³ (STP) of dry syngas per hour. The data are shown in Table 6.2.26 and Figure 6.2.26.

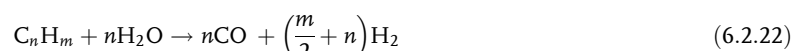
Table 6.2.5 Calculated data of a technical gasifier (Roll, 1994; Roll and Hedden, 1994).

Parameter	Value
Inside diameter of reactor tube	2.7 m
Reactor height	8.6 m
Reed feed rate (dry basis)	22.7 t h ⁻¹
Specific O ₂ consumption	0.27 m ³ (STP) kg ⁻¹
Total heat loss (1% of heating value of reed)	1 MW

6.2.3

Syngas by Partial Oxidation of Heavy Oils

Partial oxidation is the reaction of hydrocarbons with an insufficient amount of oxygen with regard to complete combustion; it is usually conducted at temperatures of up to 1600 °C and pressures up to 100 bar. The reactions of partial oxidation may be simplified as follows:



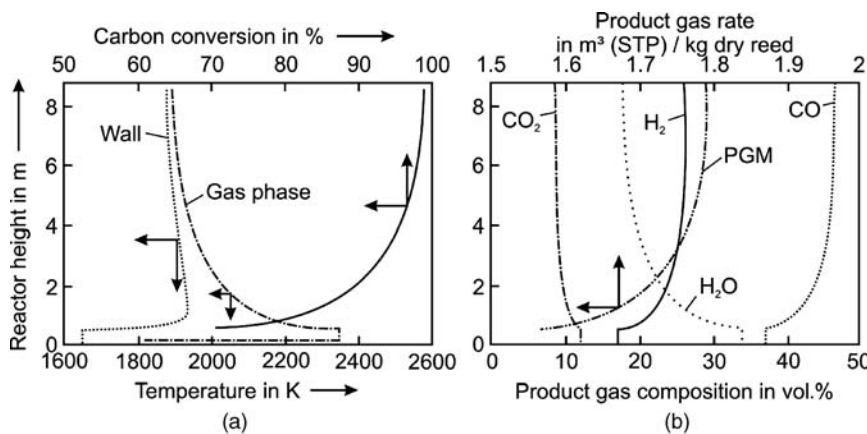


Figure 6.2.26 Technical gasifier of Chinese reed for 30 000 m³ (STP) per hour: calculated profiles of gas phase and wall temperature and carbon conversion (a) and profiles of product gas composition (b) (Roll, 1994).

CO and H₂ are the main products, but CO₂ and H₂O are also formed by combustion and the water-gas shift reaction and some CH₄ by thermal cracking. Beside oxygen, steam is added, which leads to more hydrogen [Eq. (6.2.22)] than expected according to Eq. (6.2.21) only. Sulfur, which is always present in heavy oils, is converted into H₂S (95%) and COS (5%).

Under the conditions of partial oxidation, carbon should not be present according to the Boudouard equilibrium [Eq. (6.2.6)], but nevertheless soot can be present in the raw gas. During partial oxidation of methane soot formation is practically zero, whereas in heavy-oil gasification of up to 4% by mass of feedstock is converted into soot.

Two processes are commercially established for heavy oil gasification, the *Shell* and the *Texaco* process (Figures 6.2.27 and 6.2.28) but the main steps of both processes are practically identical [see Supp (1978, 1997) for details]. Besides partial oxidation of natural gas and residue oil, this process has been developed further for coal slurries (Table 6.2.6). Oxygen, pre-heated heavy oil, and steam are fed to the refractory-lined reactor where the oil is sprayed into the reactor. The reaction starts in a water-cooled burner, which also houses the atomizing gun and the oxygen and steam inlets.

The product gas mixture leaves the reactor at about 1350 °C and is either cooled in a waste-heat boiler (WHB mode, Figure 6.2.27b) or by direct quenching with water from the soot water cycle (quench mode, Figure 6.2.27a).

The *Texaco* process with the quench mode is shown in Figure 6.2.28 (Appl, 1999). The quench is followed by two-step soot-scrubbing, a venturi-scrubber and a countercurrently operated packed scrubbing column. The soot is extracted from the water with naphtha, and the soot-naphtha suspension is

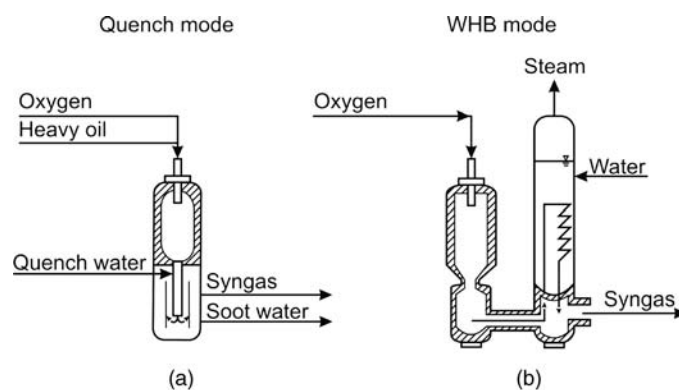


Figure 6.2.27 Gasification of heavy oil and raw gas cooling in the *Texaco* gasification process (WHB: waste-heat boiler). Adapted from Appl (1999).

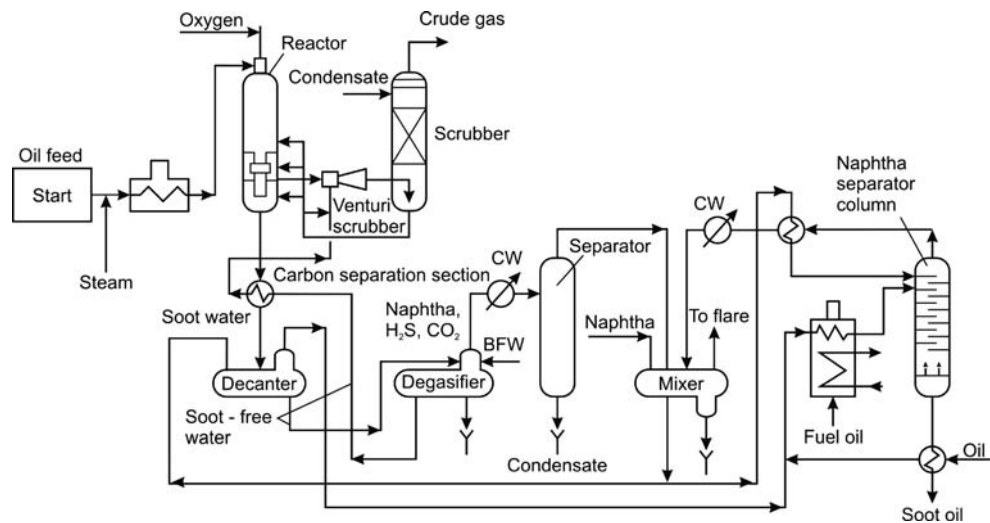


Figure 6.2.28 Gasification of heavy oil (quench mode) and soot removal in the Texaco gasification. Adapted from Appl (1999).

separated in a settler from the almost carbon-free water, which is recycled to the quench and scrubbing section. The soot–naphtha is mixed with feed oil, after which the naphtha is distilled off in a stripping column and returned to the soot extraction.

The raw syngas of partial oxidation of heavy oil contains almost equal amounts of CO and H₂, about 5% CO₂ and small amounts of CH₄, N₂, Ar, and H₂S (Table 6.2.6, second column from right). For methanol, Fischer–Tropsch, or hydrogen production part, or all, of the CO is converted with steam into CO₂ and H₂. By addition of nitrogen from the air separation unit, syngas suitable for ammonia can also be produced.

Table 6.2.6 Feedstock and raw syngas composition of Texaco process [from Appl (1999)].

	Natural gas	Naphtha	Heavy fuel oil	Tar (from coal)
Feedstock composition				
Approximate formula	CH _{3.71}	CH _{2.31}	CH _{1.28}	CH _{0.75}
C (wt%)	73.40	83.8	87.2	88.1
H (wt%)	22.76	16.2	9.9	5.7
O (wt%)	0.76	—	0.8	4.4
N (wt%)	3.08	—	0.7	0.9
S (wt%)	—	—	1.4	0.8
Ash (wt%)	—	—	—	0.1
Raw gas composition				
H ₂ (vol.%)	61.1	51.2	45.8	38.9
CO (vol.%)	35.0	45.3	47.5	54.3
CO ₂ (vol.%)	2.6	2.7	5.7	5.7
N ₂ (vol.%)	1.0	0.1	0.3	0.8
H ₂ S (vol.%)	—	—	0.3	0.2
CH ₄ (vol.%)	0.3	0.7	0.5	0.1
Soot [kg per 1000 m ³ (STP)]	—	1.8	10	6.1
Consumption for 1000 m³ (STP) syngas				
Feedstock (kg)	262	297	232	356
Oxygen [m ³ (STP)]	248	239	240	243
Steam (kg)	—	74	148	186

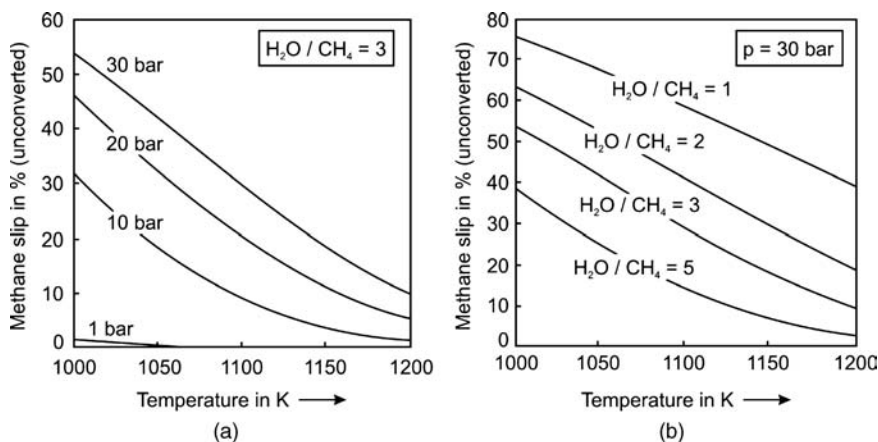
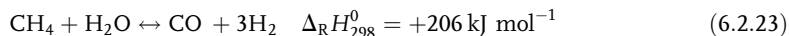


Figure 6.2.29 Equilibrium content of methane during steam reforming for different pressures, temperatures, and steam-to-carbon ratios (Moulijn, Makkee, and Van Diepen, 2004).

6.2.4

Syngas by Steam Reforming of Natural Gas

The main reaction of steam reforming of natural gas (here taken as methane) is:



As shown by Example 4.2.1 this reaction is favored by a low pressure and a high temperature. The second most important reaction is the water-gas shift reaction [Eq. (6.2.1)].

Figure 6.2.29 show the equilibrium content of methane for different pressures, temperatures, and steam-to-carbon ratios. Thermodynamically, steam reforming is hindered by elevated pressures as the number of molecules increases (Figure 6.2.29a). Nevertheless a pressure of 30 bar is adjusted as the syngas is needed in subsequent processes under pressure (*ammonia, Fischer-Tropsch, etc.*), and the energy requirement for compression of natural gas is much lower than syngas compression with a higher volume rate [factor 3, Eq. (6.2.23)]. At 30 bar, the equilibrium conversion into H_2 and CO is only complete at a temperature of over 1100°C but temperatures in excess of 900°C cannot be applied with regard to metallurgical constraints.

Although steam reforming is carried out at high temperature, a nickel catalyst is still required due to the high stability of methane. The catalyst is contained in tubes, which are placed inside a furnace that is heated by combustion of fuel (Figure 6.2.30).

The desulfurized natural gas feed is mixed with steam and preheated to 500°C before entering the reformer tubes. The heat for the reforming reaction is supplied by combustion of fuel in the furnace, which may contain up to 500 tubes with a length of 10 m and a diameter of 10 cm. Figure 6.2.31 shows axial profiles of the tube wall temperature and the heat flux.

Figure 6.2.32 shows results of simulations of the steam reforming process carried out by *Froment* and coworkers based on kinetic data and the respective heat and mass balances.

The difference between external and internal tube skin temperature is about 30 K. This is much smaller than the difference between flue gas temperature (about 1100°C) and the external tube skin temperature ($\Delta T_{\text{flue gas} - \text{external skin}}$: 200–300 K) and the difference between the internal tube skin temperature and the average process gas temperature inside the tube ($\Delta T_{\text{internal skin} - \text{process gas}}$: 120–210 K). Thus with regard to heat transfer the process is determined by the heat transfer by convection and radiation from the fire box to the tube as well as by the heat transfer from the internal tube skin to the fixed bed.

Figure 6.2.30 Primary reformer. Adapted from Appl (1999).

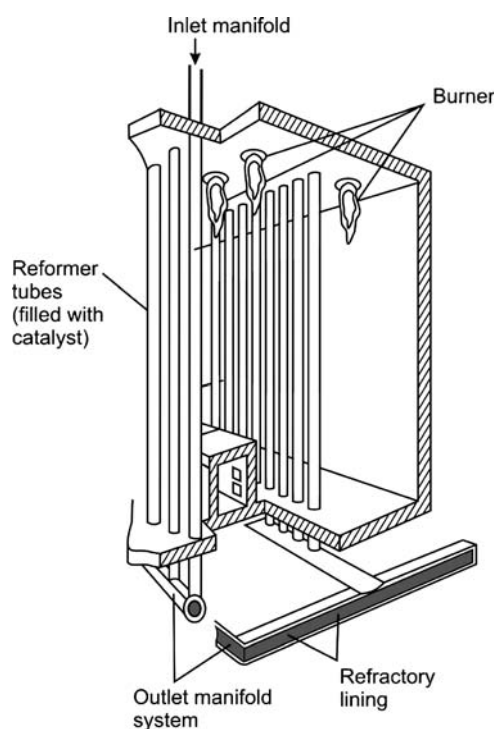


Figure 6.2.31 Temperature profile and heat fluxes in a side-fired primary reformer (adapted from Appl, 1999).

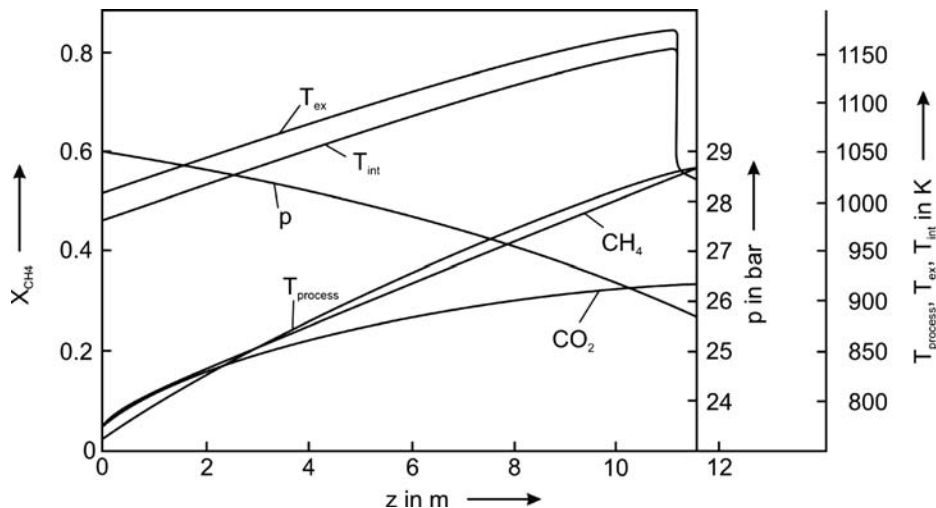
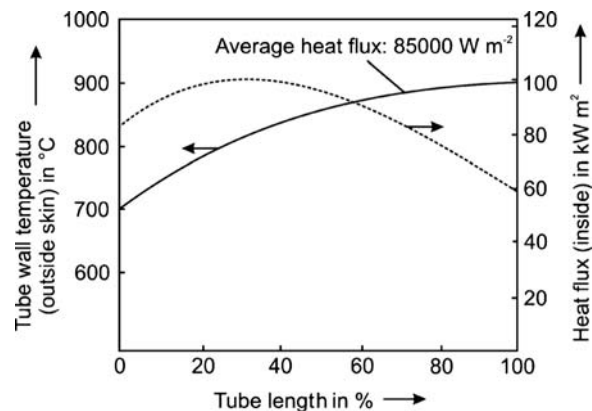


Figure 6.2.32 Evolution of methane conversion (X_{CH_4}), mean radial process gas temperature and external and internal tube skin temperatures ($T_{process}$, T_{ex} , and T_{int}), and total pressure in a tube of a steam reformer; simulations by a one-dimensional reactor model (Section 4.10.7.3), internal/external tube diameter: 10.2/13.2 cm, heated tube length: 11.1 m, ring-shaped catalyst (height: 1 cm, diameters: 0.8 and 1.7 cm), molar steam to methane ratio: 3.4, average flue gas temperature: 1100 °C [data from Xu and Froment (1989a, b); Plehiers and Froment (1989)].

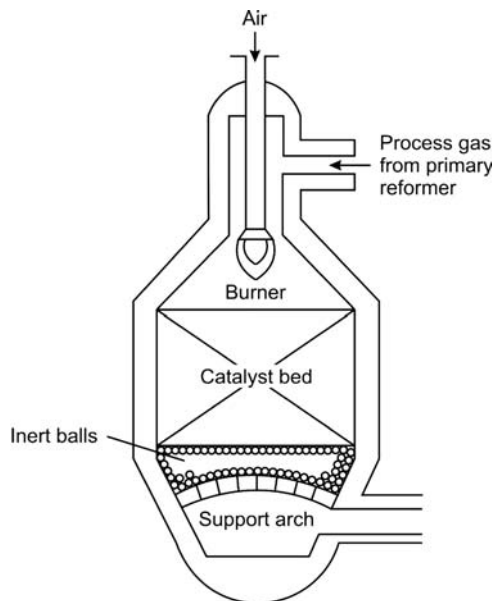


Figure 6.2.33 Secondary reformer. Adapted from Appl (1999).

The exit gas of the steam reformer may be further converted with air/oxygen by autothermic reforming in the presence of a catalyst. The reactor is a refractory lined vessel (Figure 6.2.33) and thus higher temperatures can be applied than in steam reforming.

Autothermic reforming of natural gas and light hydrocarbons is usually not applied on its own, because of the high investment and operating costs (oxygen). For ammonia synthesis, an autothermic reformer is frequently used downstream of the steam reformer where conversion of the unconverted methane with air (oxygen) takes place. The advantage of this arrangement is that the air also supplies the required nitrogen, and thus no expensive oxygen plant is needed. For syngas for methanol and *Fischer-Tropsch* plants, a combination of steam and autothermic reforming is sometimes used to adjust the required CO to H₂ ratio.

Table 6.2.7 summarizes typical process data of steam (primary) reforming and secondary reforming of natural gas for the production of ammonia syngas. The product gas of the secondary reformer is then further processed (CO-shift, CO₂ removal, methanation, see Figure 6.2.2).

Table 6.2.7 Typical process data of steam reforming and secondary reforming of natural gas [total pressure: 40 bar at exit of primary reformer, data from Appl (1999)].

Feedstreams to primary reformer	Product gas of primary reformer		Product gas of secondary reformer ^{b)}
	Natural gas ^{a)}	Steam	
CH ₄ (vol.%)	91.2	—	8.5
C _n H _m (vol.%)	5.8	—	—
N ₂ (vol.%)	1.0	—	0.2
CO ₂ (vol.%)	2.0	—	6.1
H ₂ (vol.%)	—	—	39.3
CO (vol.%)	—	—	5.9
H ₂ O (vol.%)	—	100	40.0
Ar (vol.%)	—	—	—
Total (tonnes h ⁻¹)	30.2	91.0	121.2
Total (kmol h ⁻¹)	1714	5054	8817
			199.6
			12 500

a) Natural gas as fuel for primary reformer: 9.4 tonnes h⁻¹ (24% of total natural gas). Hence, total natural gas consumption is 39.6 tonnes h⁻¹.

b) Air as feedstock for secondary reformer: 78.4 tonnes h⁻¹.

Summary of Section 6.2 (take-home messages)

- The production of **syngas**, a mixture of CO and H₂, is an important step for the manufacture of chemicals such as methanol, hydrogen, and ammonia as well as for fuels like diesel oil. Syngas may be produced from any fossil fuel and from biomass.
- Natural gas** is catalytically converted with steam, it can be easily desulfurized, and in contrast to coal and heavy oils other impurities like metal compounds or inorganic matter leading to a catalyst deactivation are not present. This process is called **steam reforming**, and is followed by **autothermal reforming** where the residual methane of the syngas is converted with air/oxygen by catalytic partial oxidation.
- Coal or biomass gasification** to syngas is commonly conducted autothermally in **fixed-bed**, **fluidized-bed**, or **entrained-flow gasifier**. Gasification is carried out with a mixture of O₂ and H₂O. The **combustion** generates the heat needed to reach the high temperatures required for the subsequent **endothermic gasification** with CO₂ and H₂O. Beside these heterogeneous reactions, homogeneous reactions like the water-gas shift reaction also occur. In addition, various gases are evolved by coal pyrolysis (H₂, CH₄, CO, aromatics, tar). Depending on the process and reactor type, the volatile compounds and the char are further converted by thermal cracking and gasification reactions.
- For syngas based on **heavy oils**, partial oxidation is used, whereby the hydrocarbons react with an insufficient amount of oxygen with regard to complete combustion; this is usually conducted at temperatures of up to 1600 °C and pressures up to 100 bar.

6.3

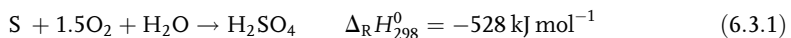
Sulfuric Acid

6.3.1

Reactions and Thermodynamics of Sulfuric Acid Production

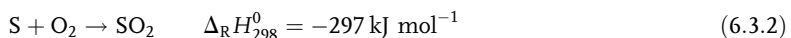
Sulfuric acid is one of the most important inorganic industrial chemicals, with a global annual production rate of 165 million tonnes (2002), and is widely used for the synthesis of fertilizers like ammonium sulfate (65%), for dissolution or beneficiation of natural deposits such as the recovery of copper, uranium, and vanadium, and for the manufacture of hydrochloric acid, sulfate salts, detergents, dyes, pigments, explosives, and drugs. It is also used in petroleum refining as an alkylation catalyst for the production of high octane gasoline from C₄-hydrocarbons, and serves as electrolyte in the lead-acid storage battery in motor vehicles.

The overall reaction of sulfuric acid production based on elementary sulfur (other feedstocks see Section 6.3.2) reads as:

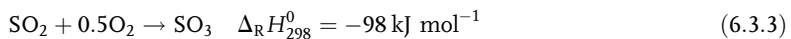


The majority of elementary sulfur is produced as a by-product of petroleum and natural gas processing and only 4% comes from native sources [mainly native mined elemental sulfur from China and extracted sulfur (Frasch process) from underground deposits in Poland].

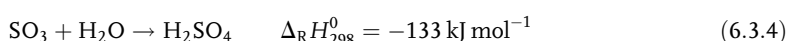
Three consecutive reactions are involved. First, sulfur is oxidized with air to SO₂:



Subsequently, SO₂ is further oxidized catalytically to sulfur trioxide:



and finally sulfuric acid is formed by absorption and reaction of SO₃ in/with water:



In contrast to sulfur oxidation to SO_2 , the oxidation to SO_3 is limited by thermodynamic constraints (Example 4.2.3), and is the crucial reaction step in H_2SO_4 production. According to Eqs. (4.2.19) and (4.2.20), the equilibrium constant K_y based on the molar fractions of SO_2 , O_2 , and SO_3 (with p as total pressure) is given by:

$$K_y = \frac{\gamma_{\text{SO}_3}}{\gamma_{\text{O}_2}^{0.5} \gamma_{\text{SO}_2}} = K_p \sqrt{\frac{p}{p_0}} = e^{-\frac{\Delta_R G_{\text{SO}_3}^0}{RT}} \sqrt{\frac{p}{p_0}} \quad (6.3.5)$$

The standard reaction Gibbs function $\Delta_R G^0$ ($= \Delta_R H^0 - T\Delta_R S^0$) is calculated by Eqs. (4.2.14)–(4.2.17) and the tabulated values of the standard enthalpies of formation $\Delta_f H^0$ and the standard entropies S^0 (Table 4.2.1). If we neglect that $\Delta_R H^0$ and $\Delta_R S^0$ depend slightly on temperature and use the values at 298 K we obtain:

$$-\frac{\Delta_R G_{\text{SO}_3}^0}{RT} \approx -\frac{\Delta_R H_{\text{SO}_3,298}^0}{RT} + \frac{\Delta_R S_{\text{SO}_3,298}^0}{R} = \ln K_p = \frac{11830 \text{ K}}{T} - 11.4 \quad (6.3.6)$$

For a feed gas free of SO_3 , the mass balance in terms of the conversion X_{SO_2} and the initial molar content of SO_2 and of O_2 (see Example 4.2.3) leads to:

$$K_y = \frac{(X_{\text{SO}_2})}{(1 - X_{\text{SO}_2})} \sqrt{\frac{1 - 0.5\gamma_{\text{SO}_2,0} X_{\text{SO}_2}}{\gamma_{\text{O}_2,0} - 0.5\gamma_{\text{SO}_2,0} X_{\text{SO}_2}}} \quad (6.3.7)$$

and thus the SO_2 conversion can be calculated for different temperatures, pressures, and feed gas compositions by Eqs. (6.3.5)–(6.3.7).

The equilibrium conversion of SO_2 is shown in Figure 6.3.1 for total pressures of 1 and 5 bar and an initial composition of 8% SO_2 and 11% O_2 (rest N_2). SO_2 oxidation is thermodynamically favored at low temperatures. The conversion is almost complete below 400 °C but – as with all reversible exothermic reactions – the real process temperature is a compromise between the achievable conversion (thermodynamics) and the rate at which this conversion can be achieved (kinetics). Thus we depend on the activity of state-of-the-art SO_2 oxidation catalysts. With current V_2O_5 catalysts, this means a minimum temperature of about 400 °C.

The reaction is thermodynamically favored by an elevated pressure (Figure 6.3.1), but this effect is rather small as with air as oxidizing agent the decrease in volume is small.

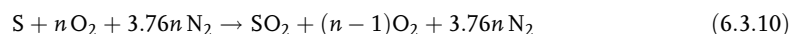
6.3.2

Production of SO_2

Sulfur dioxide can be prepared not only by burning of elementary sulfur [Eq. (6.3.1)] but also by roasting of sulfide ores such as sphalerite (zinc blende, ZnS) or iron pyrites (FeS_2):



Nowadays, most sulfuric acid processes (70%) are based on elementary sulfur, which is the result of the increasing amount of sulfur as a by-product of desulfurization of refinery products and natural gas. Oxidation of sulfur in air is represented by the following reaction:



The sulfur is preheated and delivered to a burner as a liquid at a temperature of about 145 °C. The degree of atomization and mixing are key factors for an efficient combustion. Atomization is accomplished by spray nozzles or by a mechanically driven spinning cup (Figure 6.3.2). Some burners also contain secondary air inlets to promote mixing. The atomizer breaks the liquid sulfur into microscopic droplets that burn in suspension in a refractory-lined furnace. Sulfur combustion in air is self-supporting and no supplementary fuel is required.

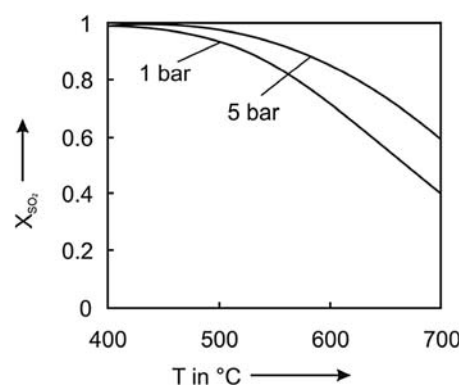
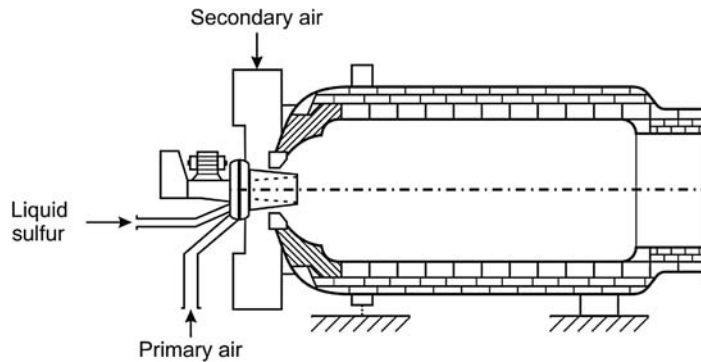


Figure 6.3.1 Equilibrium SO_2 conversion (feed gas: 8% SO_2 , 11% O_2 , rest N_2).

Figure 6.3.2 Combustion chamber for oxidation of sulfur to SO₂ (adapted from Winnacker-Küchler, 1981).



The heat balance of the adiabatic sulfur combustion reads as:

$$X_S \dot{n}_{S,in} (-\Delta_R H_{SO_2}^0) = \dot{n}_{g,out} \bar{c}_p (T - T_{in}) \quad (6.3.11)$$

if we assume that the reaction enthalpy and the mean heat capacity of the product gas (\bar{c}_p) are independent of temperature and of the conversion of sulfur (X_S).

The ratio of the molar flow of the product gas to the molar feed rate of sulfur is $4.76n$ ($= 1 + 0.79/0.21$) with n as the stoichiometric coefficient according to Eq. (6.3.10), and by introducing the adiabatic rise in temperature ΔT_{ad} ($=\Delta T$ for $X_S = 1$) we find:

$$(T - T_{in}) = X_S \frac{-\Delta_R H_{SO_2}^0}{4.76n\bar{c}_p} = X_S \Delta T_{ad} \quad (6.3.12)$$

ΔT_{ad} is here about $1890 \text{ K}/n$ ($\bar{c}_p = 33 \text{ J mol}^{-1} \text{ K}^{-1}$, $\Delta_R H_{298}^0 = -297 \text{ kJ mol}^{-1}$).

Figure 6.3.3 shows the influence of the molar O₂/S ratio (n) on the adiabatic final temperature and on the SO₂ content for complete conversion of sulfur into SO₂. Typically, a final temperature of 1000°C is reached, which corresponds to a sulfur dioxide content of about 10 vol.%.

Most of the heat of combustion is used to generate high-pressure steam in a waste heat boiler. This reduces the gas temperature to the desired inlet temperature of the subsequent catalytic converter for SO₃ production (440°C). The production rate of steam is calculated by an energy balance as follows, if we assume that overheated steam with a temperature of 450°C and a pressure of 100 bar (T_{boil} : 311°C) is produced from water at 20°C :

$$\begin{aligned} \dot{n}_s (-\Delta_R H_{SO_2}) &= \\ \underbrace{\dot{n}_s (-\Delta_R H_{SO_2})}_{\text{Heat of reaction}} &= \\ \underbrace{\dot{n}_g \bar{c}_p \Delta T_g}_{\text{Heating of gas}} &+ \underbrace{\dot{m}_{steam} [\bar{c}_{p,m,water} (T_{boil} - T_{water,in}) + \Delta_{vap} H + \bar{c}_{p,m,steam} \Delta T_{overheating}]}_{\text{Heating of water, evaporation and overheating of steam}} \end{aligned} \quad (6.3.13a)$$

Rearrangement leads to:

$$\frac{\dot{m}_{steam}}{\dot{m}_s} = \frac{1}{M_s} \frac{[-\Delta_R H_{SO_2} - 4.76n\bar{c}_p (T_{g,out} - T_{air,in})]}{[\bar{c}_{p,m,water} (T_{boil} - T_{water,in}) + \Delta_{vap} H + \bar{c}_{p,m,steam} \Delta T_{overheating}]} \quad (6.3.13b)$$

Insertion of the respective values ($\bar{c}_{p,m,steam} = 2.8 \text{ kJ kg}^{-1} \text{ K}^{-1}$, $\bar{c}_{p,m,water} = 4.6 \text{ kJ kg}^{-1} \text{ K}^{-1}$, $M_{sulfur} = 32 \text{ g mol}^{-1}$, $\Delta_R H_{SO_2}^0 = -297 \text{ kJ mol}^{-1}$, $\Delta_{vap} H_{100 \text{ bar}} = 1316 \text{ kJ kg}^{-1}$, $T_{g,out} - T_{air,in} = 420 \text{ K}$, $n = 2$, and $\Delta T_{overheating} = 139 \text{ K}$) shows that 1.7 tonnes of steam can be produced per tonne of sulfur.

6.3.3

SO₂ Conversion into SO₃

The feed gas composition of the SO₂ conversion reactor depends on the source of SO₂ (sulfur combustion or roasting of ores) and is typically in the range 7–12 vol.%

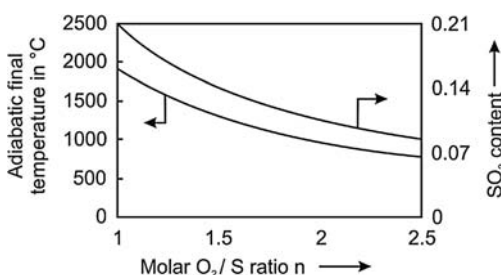


Figure 6.3.3 Influence of the molar O₂/S ratio n on the adiabatic final temperature and the SO₂ content for complete conversion of sulfur ($T_{in,air} = 25^\circ\text{C}$, oxidation with air).

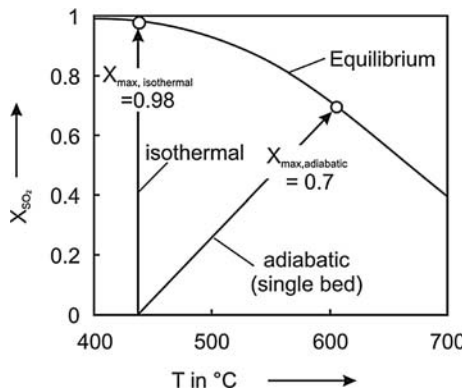


Figure 6.3.4 Conversion of SO_2 versus temperature in an adiabatic reactor for an inlet temperature of 440°C (1 bar; feed gas: 8% SO_2 , 11% O_2 , rest N_2).

SO_2 and 9–13 vol.% O_2 . In the following, we assume a gas consisting of 8% SO_2 and 11% O_2 (rest N_2).

The oxidation of SO_2 to SO_3 is a single-path reaction without side reactions. The vanadium-based catalyst is essential to accelerate the rate at the lowest possible temperature so as to “circumvent” the thermodynamic limitation (Figure 6.3.4). As already mentioned, current SO_2 oxidation catalysts still require a minimal temperature of about 440°C .

If the reactor were a single adiabatically operated fixed bed, the heat release would raise the temperature to 600°C , which corresponds to an equilibrium conversion of SO_2 of only 70% (Figure 6.3.4), but even this far from sufficient conversion would only be reached for an infinite residence time and reactor length. For isothermal operation, a conversion of about 98% would be possible, but this would require an expensive reactor (e.g., a multi-tubular reactor intensively cooled by a molten salt, Figure 4.10.7).

The thermodynamic limitation of SO_2 oxidation requires an adiabatic multibed reactor with intermittent cooling in external heat exchangers to achieve nearly full conversion. Alternatively, cooling is possible by stepwise quenching with cool air. For today’s SO_2 oxidation catalysts, typically four stages with intermittent cooling are needed to reach more than 98% conversion.

The conversion of SO_2 should be almost complete not only for economic but also for environmental reasons. For instance, in the USA SO_2 emissions are limited to 2 kg SO_2 per tonne of H_2SO_4 , which is equivalent to 99.7% SO_2 conversion (Moulijn, Makkee, and Van Diepen, 2004).

For the design of a reactor with multiple catalyst beds and intermediate cooling, knowledge of the reaction rate of SO_2 oxidation is essential. According to literature, the oxidation rate of SO_2 on a typical industrial V_2O_5 catalyst is given by (Froment and Bischoff, 1990):

$$r_{\text{SO}_2} = \frac{k_1 p_{\text{O}_2} p_{\text{SO}_2} \left(1 - \frac{p_{\text{SO}_3}}{p_{\text{SO}_2} p_{\text{O}_2}^{0.5} K_p} \right)}{\left(1 + K_2 p_{\text{SO}_2} + K_3 p_{\text{SO}_3} \right)^2} \text{ kmol } \text{SO}_2 \text{ kg}_{\text{cat}}^{-1} \text{ h}^{-1} \quad (\text{with } p_i \text{ in bar}) \quad (6.3.14)$$

This equation is based on the *Hougen-Watson* concept (Section 4.5.2) and on the observation that the reaction between adsorbed SO_2 and O_2 from the gas phase is rate controlling.

The equilibrium constant K_p is given by Eqs. (6.3.5) and (6.3.7), and according to Froment and Bischoff (1990) the rate constant k_1 and the adsorption constants K_2 and K_3 are given by:

$$k_1 = 0.0446 \exp \left(12.16 - \frac{45500}{RT} \right) \text{ kmol } \text{kg}_{\text{cat}}^{-1} \text{ h}^{-1} \text{ bar}^{-2} \quad (\text{with } T \text{ in K}) \quad (6.3.15)$$

$$K_2 = \exp\left(-9.953 + \frac{71650}{RT}\right) \text{bar}^{-1} \quad (\text{with } T \text{ in K}) \quad (6.3.16)$$

$$K_3 = \exp\left(-71.745 + \frac{437300}{RT}\right) \text{bar}^{-1} \quad (\text{with } T \text{ in K}) \quad (6.3.17)$$

The apparent activation energy of SO_2 oxidation is not constant, as we have to consider not only the “true” value of 45.5 kJ mol^{-1} [Eq. (6.3.15)] but also the influence of temperature on the rate constant k_1 and adsorption constants K_2 and K_3 . Here we only inspect the initial reaction rate, that is, without the influence of SO_3 . According to Eq. (6.3.14), the rate of the forward reaction is:

$$r_{\text{SO}_2, \text{forward}} = \frac{k_1 p_{\text{O}_2} p_{\text{SO}_2}}{(1 + K_2 p_{\text{SO}_2})^2} \text{ kmol SO}_2 \text{ kg}_{\text{cat}}^{-1} \text{ h}^{-1}$$

(for $p_{\text{SO}_3} = 0$ with p_i in bar)

and insertion of Eqs. (6.3.15) and (6.3.16) yields:

$$\begin{aligned} r_{\text{SO}_2, \text{forward}} &= \frac{0.0446 \exp\left(12.16 - \frac{45500}{RT}\right) p_{\text{O}_2} p_{\text{SO}_2}}{\left[1 + \exp\left(-9.953 + \frac{71650}{RT}\right) p_{\text{SO}_2}\right]^2} \\ &= \frac{8518 e^{-\frac{45000}{RT}} p_{\text{O}_2} p_{\text{SO}_2}}{\left(1 + 4.76 \times 10^{-5} e^{\frac{71650}{RT}} p_{\text{SO}_2}\right)^2} \end{aligned}$$

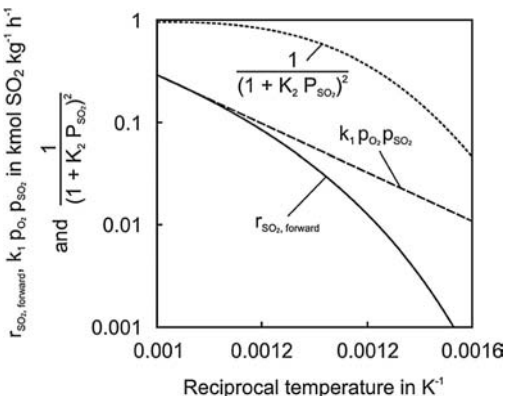


Figure 6.3.5 Arrhenius plot of the rate of the initial SO_2 conversion (forward reaction for zero conversion) for different temperatures (1 bar; feed gas: 8% SO_2 , 11% O_2 , rest N_2).

For a low temperature, $K_2 \gg 1$ and we approach:

$$\begin{aligned} r_{\text{SO}_2, \text{forward}} &\approx \frac{8518 e^{-\frac{45500}{RT}}}{\left(4.76 \times 10^{-5} e^{\frac{71650}{RT}}\right)^2} \frac{p_{\text{O}_2}}{p_{\text{SO}_2}} \\ &= 1.79 \times 10^8 e^{-\frac{188800}{RT}} \frac{p_{\text{O}_2}}{p_{\text{SO}_2}} \quad \left(\text{for } 4.76 \times 10^{-5} e^{\frac{71650}{RT}} p_{\text{SO}_2} \gg 1\right) \end{aligned}$$

that is, we have an apparent activation energy of 189 kJ mol^{-1} . For a high temperature, $K_2 \ll 1$ and we approach:

$$r_{\text{SO}_2, \text{forward}} = 8518 e^{-\frac{45500}{RT}} p_{\text{O}_2} p_{\text{SO}_2} \quad \left(\text{for } 4.76 \times 10^{-5} e^{\frac{71650}{RT}} p_{\text{SO}_2} \ll 1\right)$$

which corresponds to the “true” activation energy. The Arrhenius plot (Figure 6.3.5) indicates this change from the regime with $E_{\text{A, apparent}} = 189 \text{ kJ mol}^{-1}$ to the regime with 45 kJ mol^{-1} .

The mass balances for SO_2 , O_2 , and SO_3 in terms of conversion X_{SO_2} and the initial fractions ($\gamma_{\text{O}_2,0}$, $\gamma_{\text{SO}_2,0}$) in the feed (Example 4.2.3) lead to the molar fractions and partial pressures:

$$\gamma_{\text{SO}_2} = \frac{p_{\text{SO}_2}}{p} = \frac{\gamma_{\text{SO}_2,0}(1 - X_{\text{SO}_2})}{1 - 0.5X_{\text{SO}_2} \gamma_{\text{SO}_2,0}} \quad (6.3.18)$$

$$\gamma_{\text{O}_2} = \frac{p_{\text{O}_2}}{p} = \frac{\gamma_{\text{O}_2,0} - 0.5\gamma_{\text{SO}_2,0} X_{\text{SO}_2}}{1 - 0.5\gamma_{\text{SO}_2,0} X_{\text{SO}_2}} \quad (6.3.19)$$

$$\gamma_{\text{SO}_3} = \frac{p_{\text{SO}_3}}{p} = \frac{\gamma_{\text{SO}_3,0} X_{\text{SO}_2}}{1 - 0.5\gamma_{\text{SO}_2,0} X_{\text{SO}_2}} \quad (6.3.20)$$

Thus, for a given temperature and conversion, the rate is calculated by Eqs. (6.3.14)–(6.3.20), (6.3.5), and (6.3.7). Figure 6.3.6 shows the plot of rate versus temperature.

From Figure 6.3.6, we can now determine the optimal pathway to minimize the reactor volume by the locus of the maximum rate for a given conversion. The corresponding minimum reactor volume and minimum mass of catalyst is given by [see also Section 4.10.3.4, Eq. (4.10.85)]:

$$m_{\text{cat}} = \frac{V_{\text{R}}}{\rho_{\text{b}}} = \dot{n}_{\text{SO}_2, \text{in}} \int_0^{X_{\text{SO}_2}} \frac{dX_{\text{SO}_2}}{r_{\text{SO}_2}} = \dot{n}_{\text{SO}_2, \text{in}} X_{\text{SO}_2} \left(\frac{1}{r_{\text{SO}_2}}\right)_{\text{mean}} \quad (6.3.21)$$

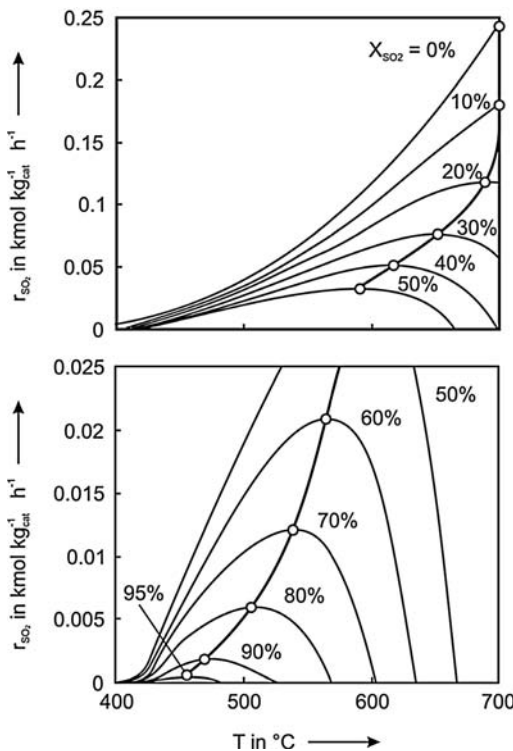


Figure 6.3.6 Rate of SO_2 conversion for different temperatures and degrees of conversion and optimal pathway to minimize the reactor volume (1 bar; feed gas: 8% SO_2 , 11% O_2 , rest N_2).

To determine the integral of Eq. (6.3.21) and the mean value of the reciprocal rate, we use the $1/r$ versus X plot (Figure 6.3.7). By graphical integration and the respective mean value of $1/r_{\text{SO}_2}$ we obtain the mass of catalyst needed for a given feed rate. For a rough estimation of the residence time τ related to the empty reactor, we use 550°C as the mean temperature T_{mean} . The bulk density ρ_B is 0.5 g cm^{-3} (Farrauto and Bartholomew, 1997), and so τ is given by:

$$\tau = \frac{V_R}{\dot{V}_{\text{in}}} \approx \frac{V_R p}{\dot{n}_{\text{total,in}} RT_{\text{mean}}} = \frac{m_{\text{cat}} \gamma_{\text{SO}_2,\text{in}} p}{\rho_B \dot{n}_{\text{SO}_2,\text{in}} RT_{\text{mean}}} = \frac{\gamma_{\text{SO}_2,\text{in}} p X_{\text{SO}_2}}{\rho_B RT_{\text{mean}}} \left(\frac{1}{r_{\text{SO}_2}} \right)_{\text{mean}} \quad (6.3.22)$$

For a feed gas with 8% SO_2 and a conversion of 95%, we find a residence time of 1.04 s for the optimal pathway shown in Fig. 6.3.6.

We now compare this limiting minimum value of the residence time with other cases. First we inspect the border case of a hypothetical isothermal operation at 440°C (Figure 6.3.4). Figure 6.3.8 shows the plot of $1/r_{\text{SO}_2}$ versus X_{SO_2} . If we again take a feed gas with 8% SO_2 and a conversion of 95% we now get a residence time of about 3.3 s [Eq. (6.3.22)], which is already about three times higher than the optimal (minimum) value of about 1 s.

The isothermal and optimal pathway (and any other pathway) can be compared descriptively by a plot of SO_2 conversion versus temperature and the curves of equal rate (Figure 6.3.9). The shape of these contours is clear: At a constant conversion, the rate first increases with temperature but then decreases as the influence of the equilibrium becomes strong. The optimal pathway to minimize the reactor size (dashed line) is the one “on top of the mountains.”

In a technical reactor, typically four beds with intermediate cooling are used. Table 6.3.1 gives typical process data.

As we can learn from the corresponding conversion versus temperature plot (Figure 6.3.10), the major part of the conversion, about 60%, is obtained in the first bed. The product gas of the first bed is cooled through a waste heat boiler (for steam generation) and passed through a second bed of catalyst at about 450°C , where the temperature rises to about 510°C , again close to the equilibrium limitation. The successive lowering of the temperature between the beds

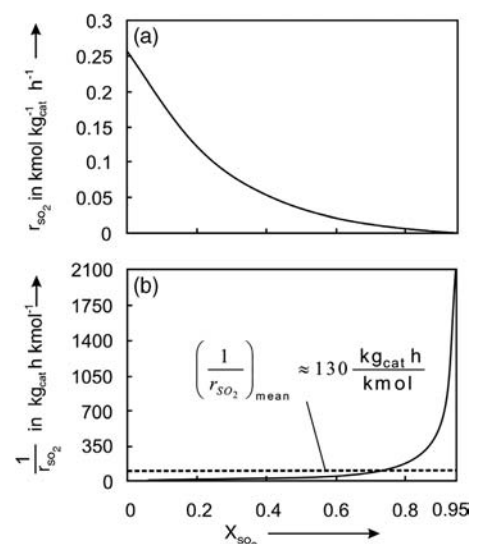


Figure 6.3.7 Reaction rate of SO_2 r_{SO_2} (a) and $1/r_{\text{SO}_2}$ (b) versus SO_2 conversion along the optimal pathway to minimize the reactor volume as given by Figure 6.3.6.

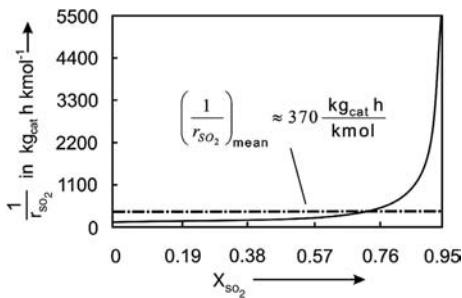


Figure 6.3.8 Plot of reciprocal reaction rate $1/r_{SO_2}$ versus SO_2 conversion for the borderline case of isothermal operation at $T = T_{in} = 440^\circ C$ (see also Figure 6.3.4).

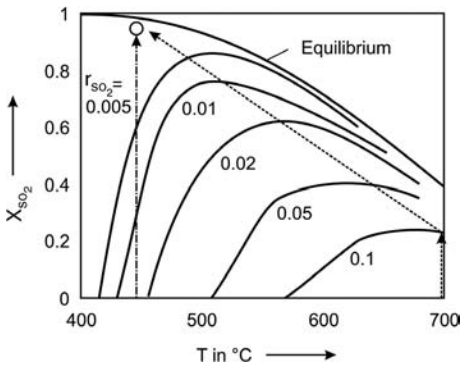


Figure 6.3.9 SO_2 conversion versus temperature plot with curves of equal reaction rate, optimal pathway (dashed line) to minimize reactor size, and isothermal pathway ($440^\circ C$) for 95% conversion (r_{SO_2} in $kmol\ kg^{-1}\ h^{-1}$, 1 bar; feed gas: 8% SO_2 , 11% O_2 , rest N_2).

Table 6.3.1 Temperatures and SO_2 conversion within the different catalyst beds for a single and a double adsorption process (Baerns *et al.*, 2006).

	Temperature ($^\circ C$)		SO_2 conversion at exit (%)
	Inlet	Exit	
Bed 1	440	600	63
Bed 2	450	510	87
Bed 3	450	470	95
Bed 4, single absorption process	425	435	98
Bed 4, double absorption process	420	435	99.6

by external heat exchange ensures an overall conversion of 98% – but this is still not sufficient to meet current environmental standards. Therefore, modern plants use intermediate SO_3 absorption after the third bed. This intermediate removal of SO_3 enables a conversion of SO_2 “beyond the thermodynamic equilibrium” by a shift of this line to a higher conversion, and a total conversion after the fourth bed of about 99.6% is reached.

As already examined for the isothermal and the optimal case (Figures 6.3.7 and 6.3.8), we now calculate the residence time for four adiabatic beds for the double absorption process with intermediate absorption after the third. The plots of $1/r_{SO_2}$ vs. X_{SO_2} are shown in Figure 6.3.11. For each bed, the residence time is given by Eq. (6.3.22), if we use $550^\circ C$ as mean temperature:

$$\tau_{bed,n} \approx \frac{p}{\rho_b R T_{mean}} \left[\gamma_{SO_2,in,n} X_{SO_2,n} \left(\frac{1}{r_{SO_2}} \right)_{mean,n} \right] \quad (6.3.23)$$

Here $X_{SO_2,n}$ is the individual conversion reached in the bed with number n and is related to the conversion of SO_2 that enters the bed and not the total conversion reached after bed n .

The SO_2 conversion reached after bed n can be expressed in terms of the conversion $X_{SO_2,n-1}$ reached after the previous bed ($n-1$) by:

$$X_{SO_2,total,n} = X_{SO_2,n-1,total} + (1 - X_{SO_2,total,n-1}) X_{SO_2,n} \quad (6.3.24)$$

and rearrangement leads to:

$$X_{SO_2,n} = \frac{(X_{SO_2,total,n} - X_{SO_2,total,n-1})}{(1 - X_{SO_2,total,n-1})} \quad (6.3.25)$$

If we neglect the small change of the volume rate, the SO_2 content reached after bed n is:

$$\gamma_{SO_2,in,n} = \gamma_{SO_2,in,1} (1 - X_{SO_2,total,n-1}) \quad (6.3.26)$$

Insertion of Eqs. (6.3.25) and (6.3.26) into Eq. (6.3.23) yields:

$$\tau_{ped,n} \approx \frac{p \gamma_{SO_2,in}}{\rho_b R T_{mean}} \left[\frac{(X_{SO_2,total,n} - X_{SO_2,total,n-1})}{r_{SO_2,mean,n}} \right] \quad \left[\text{with } X_{SO_2,total,n} = 1 - \prod_1^n (1 - X_{SO_2,n}) \right] \quad (6.3.27)$$

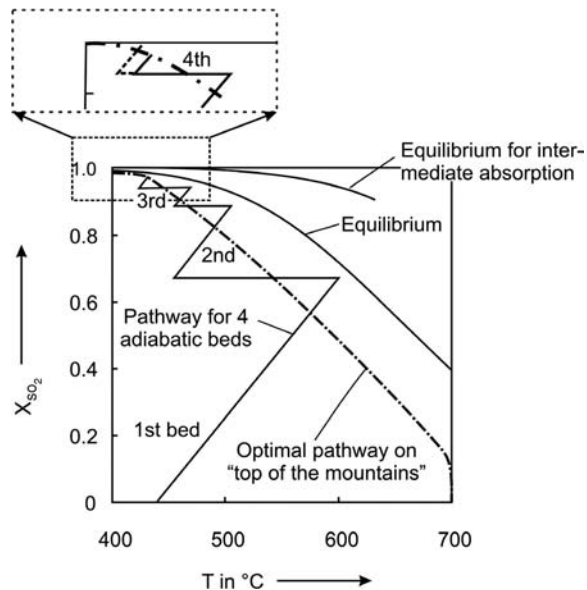


Figure 6.3.10 SO₂ conversion versus temperature plot for four adiabatic beds for single and double absorption process with intermediate absorption; for comparison, the optimal pathway (dot-dashed line) is also shown (1 bar; feed gas: 8% SO₂, 11% O₂, rest N₂).

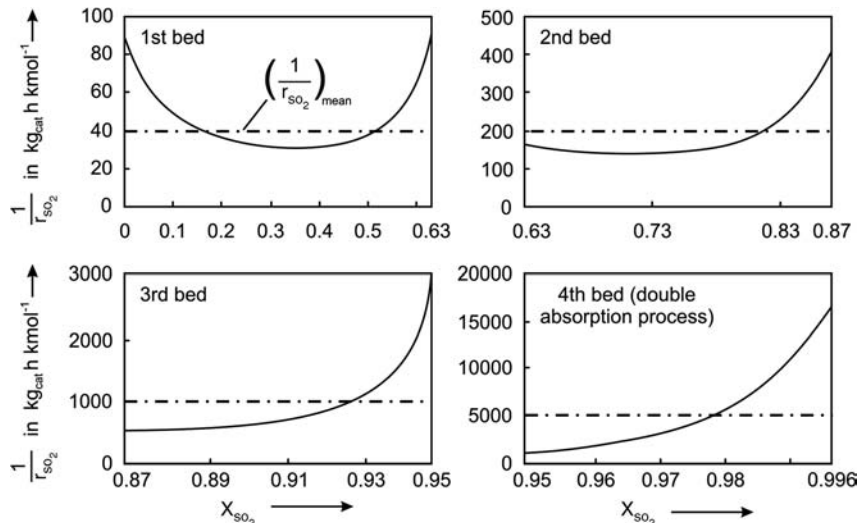


Figure 6.3.11 Plot of reciprocal reaction rate $\frac{1}{r_{SO_2}}$ versus SO₂ conversion for four adiabatic steps with intermediate absorption (1 bar; feed gas: 8% SO₂, 11% O₂, rest N₂).

Summation of the residence times of all beds leads to the residence time of the whole reactor:

$$\tau_{\text{reactor}} = \sum_1^n \tau_{\text{bed},n} = \frac{p y_{SO_2,\text{in}}}{\rho_b R T_{\text{mean}}} \sum_1^n \frac{(X_{SO_2,\text{total},n} - X_{SO_2,\text{total},n-1})}{r_{SO_2,\text{mean},n}} \quad (6.3.28)$$

Here we obtain a residence time for the double absorption process ($X_{SO_2} = 99.6\%$) of 3.4 s.

The length of each bed is proportional to the residence time. Figure 6.3.12 shows a plot of the conversion in a reactor with four stages versus the dimensionless reactor volume. After the third bed, a conversion of about 95% has been reached (residence time of 1.2 s), and about two-thirds of the total reactor volume are needed for the fourth and last catalyst bed.

Table 6.3.2 summarizes the results of the different calculations.

In industrial practice, the gas hourly space velocity (GHSV) is frequently used instead of the residence time. The GHSV is the volume rate of feed gas (NTP) per

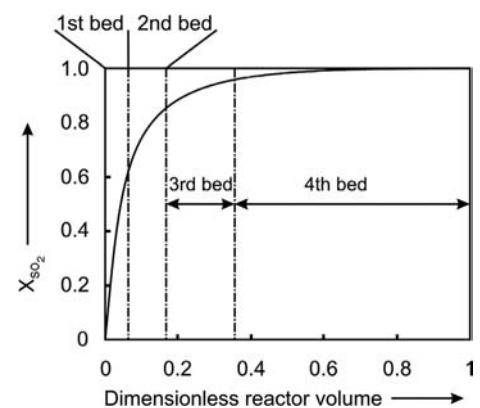


Figure 6.3.12 SO₂ conversion versus dimensionless reactor volume for four adiabatic steps with intermediate absorption after the third bed (1 bar; feed gas: 8% SO₂, 11% O₂, rest N₂).

Table 6.3.2 Residence time needed for SO₂ conversion for different modes of operation of the reactor (1 bar; feed gas: 8% SO₂, 11% O₂, rest N₂).

Operation of reactor	Residence time (s)	SO ₂ conversion (%)
Hypothetical case of optimal operation along the curve of the maximum rate for a given conversion (Figures 6.3.6, 6.3.7 and 6.3.9)	1.0	95
Isothermal operation (Figures 6.3.8 and 6.3.9)	3.3	95
Three adiabatically operated beds with intermediate cooling (single absorption process, Figures 6.3.10–6.3.12)	1.2	95
Four adiabatically operated beds with intermediate cooling (single absorption process, Figures 6.3.10, 6.3.11 and 6.3.12)	12.7	98
Four adiabatically operated beds with intermediate cooling and absorption of SO ₃ after the third bed (double absorption process, Figures 6.3.10–6.3.12)	3.4	99.6

volume of reactor (catalyst) and is a measure of the loading of the reactor. Here we would obtain:

$$GHSV = \frac{1}{\tau(T_{\text{mean}})} \frac{\dot{V}_{\text{in}}(0^\circ\text{C}, 1 \text{ bar})}{\dot{V}_{\text{in}}(500^\circ\text{C}, 1 \text{ bar})} = \frac{1}{3.4 \text{ s}} \frac{273 \text{ K}}{823 \text{ K}} \approx 350 \text{ h}^{-1} \quad (6.3.29)$$

which is of the order of magnitude of a typical value given in the literature (1000 h⁻¹, Farrauto and Bartholomew, 1997).

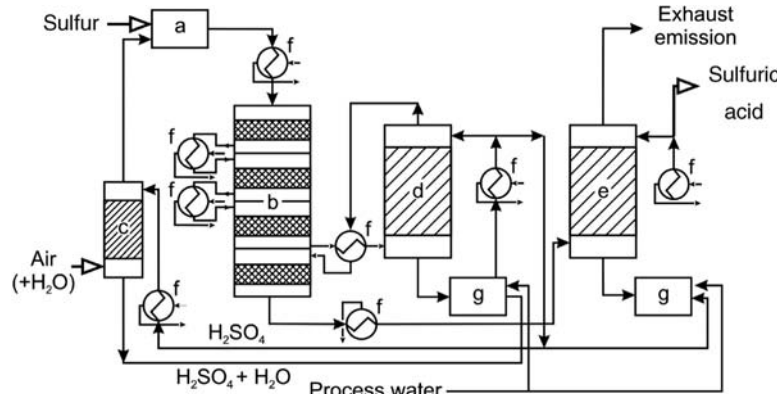
6.3.4

Sulfuric Acid Process

Figure 6.3.13 shows a modern double absorption sulfuric acid plant. Three main sections can be distinguished, sulfur combustion to produce SO₂ (burner), catalytic oxidation of SO₂ to SO₃, and absorption of SO₃ in concentrated sulfuric acid (absorption towers).

During catalytic conversion of SO₂, the hot exit gas of the first stage is cooled before entering the second bed, where further conversion takes place. The gas leaving the second bed is cooled by heat exchange with cold gas leaving the first absorption tower. Subsequently, it undergoes further conversion in the third bed, and is cooled and fed to the first absorption tower. Here, a significant portion of the SO₃,

Figure 6.3.13 Simplified flow sheet of double absorption sulfuric acid plant; (a) combustion chamber for oxidation of sulfur, (b) reactor with four adiabatic beds, (c) dryer for air, (d) intermediate absorption of SO₃, (e) final absorption of SO₃, (f) heat exchanger, and (g) tank for sulfuric acid. Adapted from Baerns *et al.*, 2006).



about 90–95% (Farrauto and Bartholomew, 1997), is absorbed in a circulating stream of sulfuric acid. The gas leaving the absorption tower is reheated by heat exchange with gas from the third and second catalytic bed and then enters the fourth and last bed, where most of the remaining SO_2 is converted into SO_3 (overall conversion >99.5%). The final absorption tower removes this SO_3 from the gas stream before release to the atmosphere. The reactor is brick lined or stainless steel to minimize the negative effects of corrosion.

Small amounts of acid aerosols are always formed if the gas is cooled or SO_3 reacts with water below the dew point of sulfuric acid. This is of course highly undesirable with regard to corrosion and emissions. Therefore, the absorbers in sulfuric acid plants are equipped with demisters, for example, consisting of beds of small-diameter glass.

Summary of Section 6.3 (take-home messages)

- **Sulfuric acid** is one of the most important inorganic industrial chemicals: It is widely used for the synthesis of fertilizers, hydrochloric acid, sulfate salts, detergents, pigments, explosives, and drugs. It is also used as an alkylation catalyst, and also serves as electrolyte in the lead–acid storage battery in motor vehicles.
- Based on **elementary sulfur**, three consecutive reactions are involved. First, sulfur is oxidized with air to SO_2 . Subsequently, SO_2 is further oxidized catalytically to sulfur trioxide, and finally sulfuric acid is formed by absorption and reaction of SO_3 in/with water. In contrast to **sulfur oxidation** to SO_2 , the oxidation to SO_3 is limited by thermodynamic constraints, and is the crucial reaction step in H_2SO_4 production. **Oxidation of sulfur** in air is carried out in a refractory-lined furnace. Sulfur dioxide is also produced as a by-product of **roasting of sulfide ores** such as ZnS or FeS_2 .
- A high equilibrium **conversion of SO_2 into SO_3** is favored at low temperatures. The conversion is almost complete below 400 °C, but – as with all reversible exothermic reactions – the real process temperature is a compromise between the achievable conversion (**thermodynamics**) and the rate at which this conversion can be achieved (**kinetics**). Thus we depend on the activity of state-of-the-art SO_2 oxidation catalysts. With current **V_2O_5 catalysts**, this means a minimum temperature of about 400 °C.
- The thermodynamic limitation of SO_2 oxidation requires an adiabatic multibed reactor (typically four beds) with intermittent cooling in external heat exchangers to achieve a high conversion. To design a reactor, knowledge of the rate of SO_2 oxidation is essential. The **optimal pathway** to minimize the mass of the catalyst and the reactor volume, respectively, is determined by the locus of the maximum rate for a given conversion. The minimal mass of catalyst is given by:

$$m_{\text{cat}} = \dot{n}_{\text{SO}_2,\text{in}} \int_0^{X_{\text{SO}_2}} \frac{dX_{\text{SO}_2}}{r_{\text{SO}_2,\text{max}}}$$

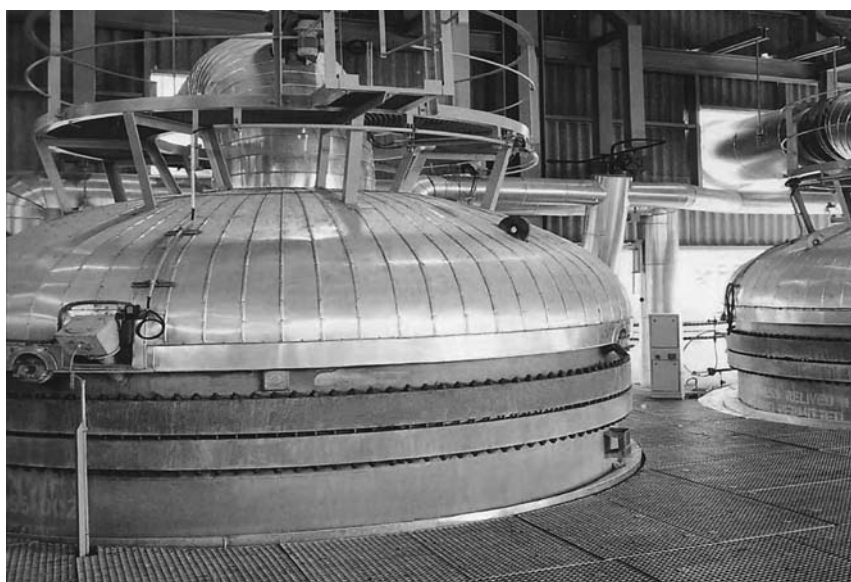
To determine this integral, we use the $1/r_{\text{max}}$ versus X plot, and by graphical integration we obtain the minimal mass of catalyst.

- Modern sulfuric acid plants use the **double absorption process** to reach a SO_2 conversion of >98%, which is needed to meet current environmental standards. The intermediate removal of SO_3 by absorption after the third bed enables a conversion of SO_2 after the fourth bed of >99%.



NH₃ burner of a nitric acid plant built in 1924 for 0.40 t HNO₃ per day. Courtesy of Uhde, Germany.

6.4 Nitric Acid



NH₃ burners of a modern dual pressure plant for 0.40 Mt HNO₃ per day. Courtesy of Uhde, Germany.

6.4.1

Reactions and Thermodynamics of Nitric Acid Production

The Persian alchemist *Jabir ibn Hayyan* is attributed as the first to synthesize nitric acid (HNO₃), in around 800 AD. Nitric acid production goes back to the Middle Ages, when it was produced from saltpeter (potassium nitrate) and sulfuric acid (Moulijn, Makkee, and Van Diepen, 2004). In the nineteenth century, Chile saltpeter (sodium nitrate) increasingly replaced saltpeter. In 1904, *Christian Birkeland*, a Norwegian industrialist and scientist, performed the first successful experiments to produce nitric oxide (NO) directly from air by passing it through an electric arc at high temperatures of around 3000 °C. Nitric acid was then produced by oxidation of NO to NO₂ and subsequent absorption in water. Together with *Sam Eyde*, *Birkeland* had developed by 1908 a commercial process for an annual production of 7000 t of fixed nitrogen, which is equivalent to 32 000 t of nitric acid. The energy consumption of the *Birkeland–Eyde* process was tremendous as 60 000 kWh electrical energy per tonne of fixed nitrogen were needed. If this electricity is generated from coal, this corresponds to 20 tonnes of coal that have to be burned in a power plant.

At about the same time, industrial ammonia production became possible by catalytic conversion of nitrogen and hydrogen (*Haber–Bosch* process, Section 6.1), at first based on coal and later on natural gas or heavy crude oil fractions. This opened up the modern route to nitric acid by catalytic oxidation of ammonia, which is examined here in detail.

Today, nitric acid is one of the 15 largest commodity chemicals with an annual world production of about 55 million tonnes (Uhde, 2005). Approximately 80% is used as an intermediate in the production of nitrogenous fertilizers, primarily ammonium nitrate (NH₄NO₃). The remainder (20%) goes into the production of various chemicals such as explosives [trinitrotoluene, C₆H₂(NO₂)₃CH₃] or of intermediates for polymers like caprolactam, adipic acid (for polyamides), or dinitrotoluene (for polyurethane).

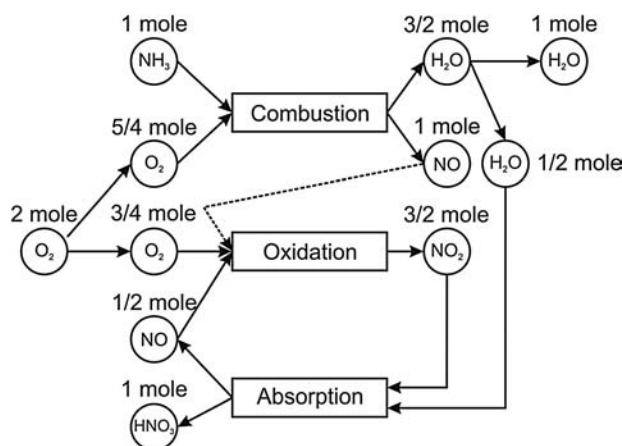
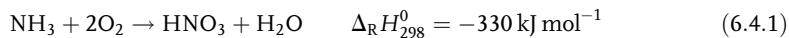


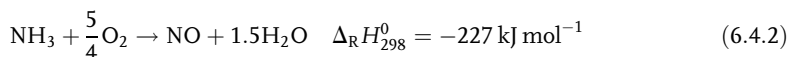
Figure 6.4.1 Reaction scheme of nitric acid process based on NH₃. Adapted from Uhde (2005).

The overall reaction of nitric acid production reads (see also the reaction scheme and the block diagram of the process in the Figures 6.4.1 and 6.4.2):



Many parallel and consecutive reactions are involved, and a simplified representation of the main reactions is the following sequence.

First, ammonia is catalytically oxidized with oxygen (air) to nitrogen monoxide:



Subsequently, NO is further oxidized non-catalytically to nitrogen dioxide:

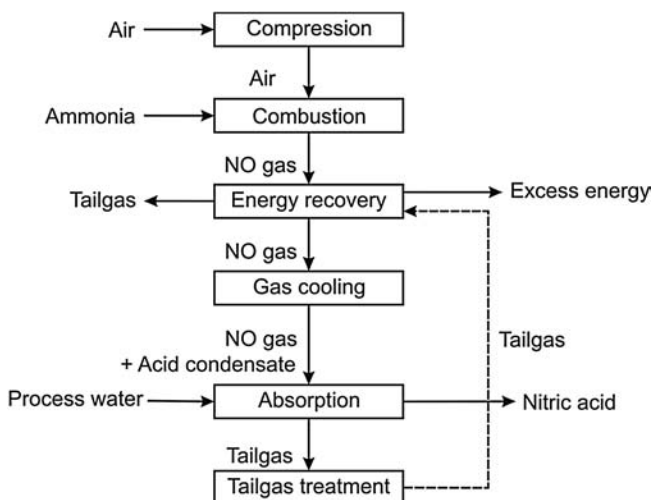
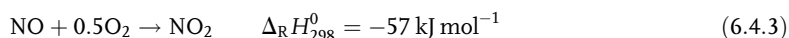


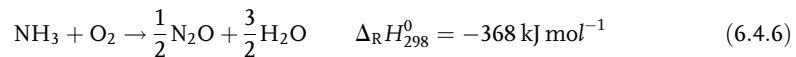
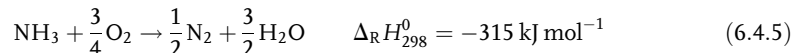
Figure 6.4.2 Block diagram of nitric acid process based on NH₃. Adapted from Uhde (2005).

and, finally, nitric acid is formed by absorption and reaction of NO_2 in water:

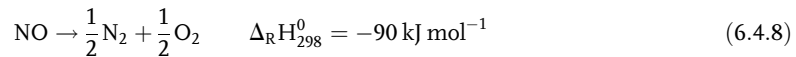


The absorption of NO_2 in water is complex; several reactions occur in the gas and liquid phase, but for practical purposes the simplified Eq. (6.4.4) represents the overall reaction.

Important (and undesirable) parallel side reactions during catalytic ammonia oxidation [Eq. (6.4.2)] lead to nitrogen and to a smaller extent also to N_2O (laughing gas):

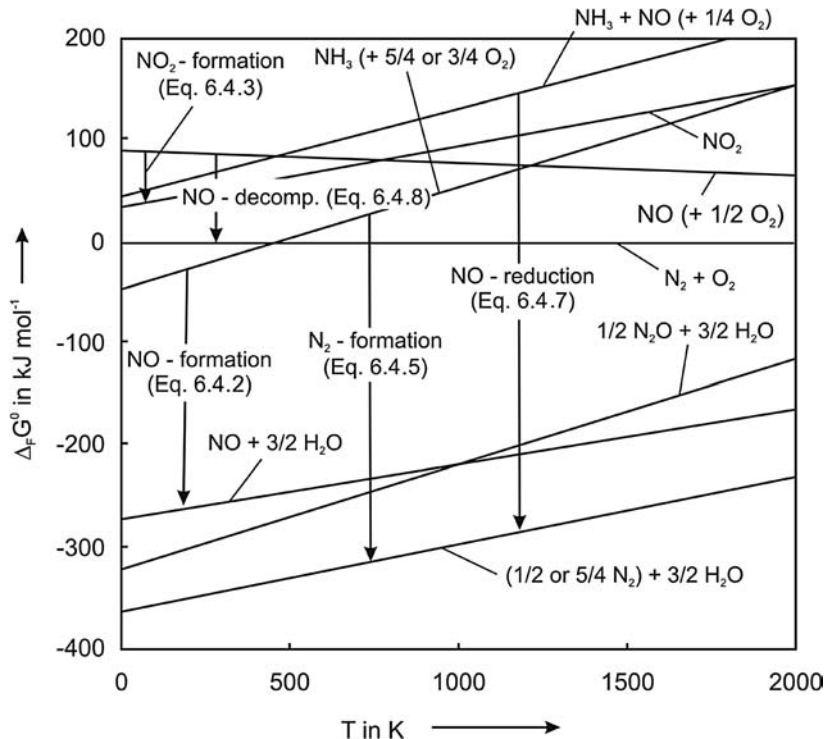


In addition, NO may be converted by unwanted consecutive reactions such as the reduction by ammonia and NO decomposition:



The thermodynamics of nitric acid production based on ammonia can be represented well by the stability diagram shown in Figure 6.4.3. If we recall Eq. (4.2.13), we know that the standard reaction Gibbs function $\Delta_{\text{R}} G^0$ corresponds to the

Figure 6.4.3 Stability diagram of main reactions of nitric acid production based on ammonia.



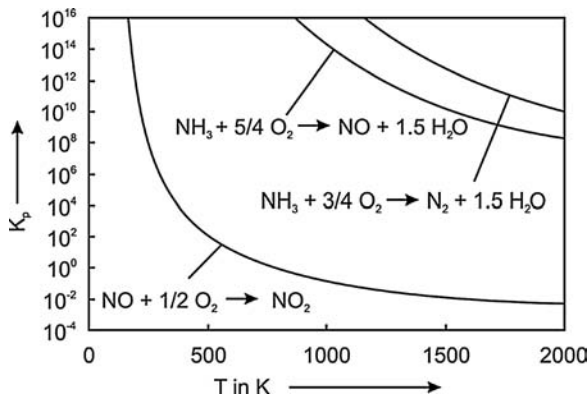


Figure 6.4.4 Equilibrium constants of NH_3 oxidation to N_2 and to NO and of NO -oxidation to NO_2 .

difference between the standard Gibbs functions of formation $\Delta_F G^0$ of all products and reactants:

$$\Delta_R G^0 = \sum v_i, \text{products} \Delta_F G_{i,\text{products}}^0 - \sum |v_i, \text{reactants}| \Delta_F G_{i,\text{reactants}}^0 \quad (6.4.9)$$

The graphical representation of $\sum v_i \Delta_F G_{\text{products}}^0$ and $\sum v_i \Delta_F G_{\text{educts}}^0$ is an easy and instructive way to see which reactions are favored and which are not. As long as the function (usually an almost straight line) representing $\sum v_i \Delta_F G_{\text{products}}^0$ is situated below the line representing $\sum v_i \Delta_F G_{\text{educts}}^0$, the reaction is thermodynamically favored $\{\Delta_R G^0 < 0$, that is, $K_p = \exp[-\Delta_R G^0/(RT)] > 1\}$. At the point of intersection, we obtain $\Delta_R G^0 = 0$ and thus $K_p = 1$.

According to Figure 6.4.3, the following trends can be identified:

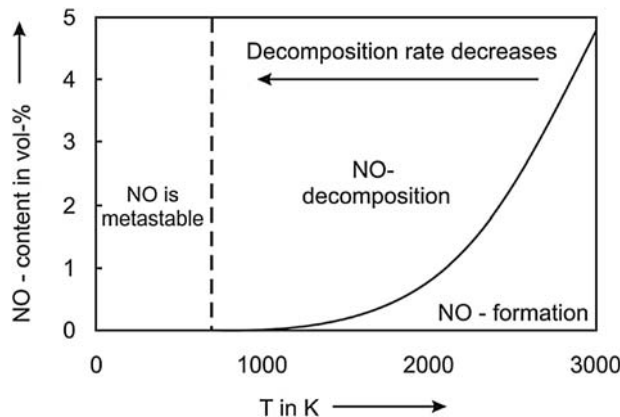
- N_2 and NO (and also N_2O) are thermodynamically favored products of ammonia oxidation as indicated by the arrows in Figure 6.4.3. $\Delta_R G^0$ is always negative and the equilibrium constants of both reactions are high (Figure 6.4.4):

$$K_{p,\text{NO},\text{Eq.(6.4.2)}} = e^{\frac{-\Delta_R G_{\text{NO}}^0}{RT}} = \frac{p_{\text{NO}} p_{\text{H}_2\text{O}}^{1.5}}{p_{\text{NH}_3} p_{\text{O}_2}^{1.25} p_0^{0.25}} \quad (\text{with } p_0 = 1.013 \text{ bar}) \quad (6.4.10)$$

$$K_{p,\text{N}_2,\text{Eq.(6.4.5)}} = e^{\frac{-\Delta_R G_{\text{N}_2}^0}{RT}} = \frac{p_{\text{N}_2}^{0.5} p_{\text{H}_2\text{O}}^{1.5}}{p_{\text{NH}_3} p_{\text{O}_2}^{0.75} p_0^{0.25}} \quad (6.4.11)$$

- The undesirable formation of N_2 by Eq. (6.4.5) is thermodynamically more favored than the desired NO formation by Eq. (6.4.2) (Figure 6.4.4). For example, at 800 °C, which is a typical temperature of catalytic ammonia oxidation, the ratio of the equilibrium constants is about 6000. The selectivity of the catalyst is therefore important in suppressing N_2 formation.
- NO may decompose [Eq. (6.4.8)]. According to Figure 6.4.5, the equilibrium NO content in air is rather small below 3000 K. This is the reason why a high temperature was needed in the electric arc of the old *Birkeland–Eyde* process. Figure 6.4.5 also indicates that during combustion processes, for example, in a coal fired power plant, a content of NO of 1000 ppmv (0.1 vol. %) or more may be reached for temperatures above about 1500 K. In the case of nitric acid production from ammonia, NO decomposition must be avoided, and the product gas of NH_3 oxidation is therefore rapidly quenched to below 700 K, where NO is metastable and decomposition is kinetically hindered.
- If NO is formed at high temperatures, it may be reduced by NH_3 to N_2 [Eq. (6.4.7)], which is thermodynamically favored (Figure 6.4.3). High gas velocities of 1 m s^{-1} are needed to reduce the residence time on the gauze to less than

Figure 6.4.5 Equilibrium content of NO in air at 1 bar.



about 1 ms to suppress NO reduction. Rapid cooling of the gas is also needed to avoid a non-catalytic thermal reduction.

- NO oxidation to NO_2 is only favored at low temperatures, for example, at 800 °C the equilibrium constant is 0.16, whereas at 25 °C we have a value of 10^6 (Figure 6.4.4). The equilibrium composition of the system NO, O_2 , NO_2 , and its dimer N_2O_4 (Figure 6.4.6) indicates that NO_2 formation is favored by higher pressures. Note that Figure 6.4.6 is only valid for the partial equilibrium of the named compounds without considering N_2 , which is thermodynamically much more stable than NO, NO_2 , and N_2O_4 ; for example, at 1000 K only 0.006% and 0.0006% of the total N would be present as NO and NO_2 , respectively (Figure 6.4.5).

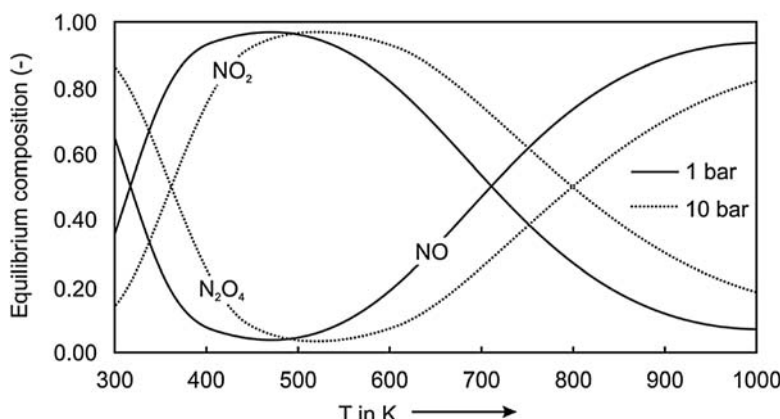
6.4.2

Kinetics of Catalytic Oxidation of Ammonia

The PtRh gauze used as catalyst for ammonia oxidation undergoes morphological changes during use (Figure 6.4.7). This surface restructuring is called “sprouting” and causes a considerable increase in roughness and surface area. A fresh gauze typically has a surface area of about $30 \text{ cm}^2 \text{ g}^{-1}$ ($= 0.003 \text{ m}^2/\text{g}$), but after some days the surface area increases by more than a factor of ten (Farrauto and Bartholomew, 1997). The ammonia conversion is completely governed by external mass transfer (examined below), and thus the increase in surface area leads to a gradual increase of conversion until a steady state is reached after a couple of days.

The platinum-rhodium gauges with a diameter of up to 5 m are nowadays produced by knitting thin wires, usually with a wire diameter of 60–80 μm . This corresponds to about 1000 knittings per cm^2 and to a mesh opening of about 0.2 mm.

Figure 6.4.6 Equilibrium composition (mol per mol total N) of the system of NO, O_2 , NO_2 , and N_2O_4 (starting with a stoichiometric NO/O_2 mixture. Partly adapted from Moulijn, Makkee, and Van Diepen (2004)).



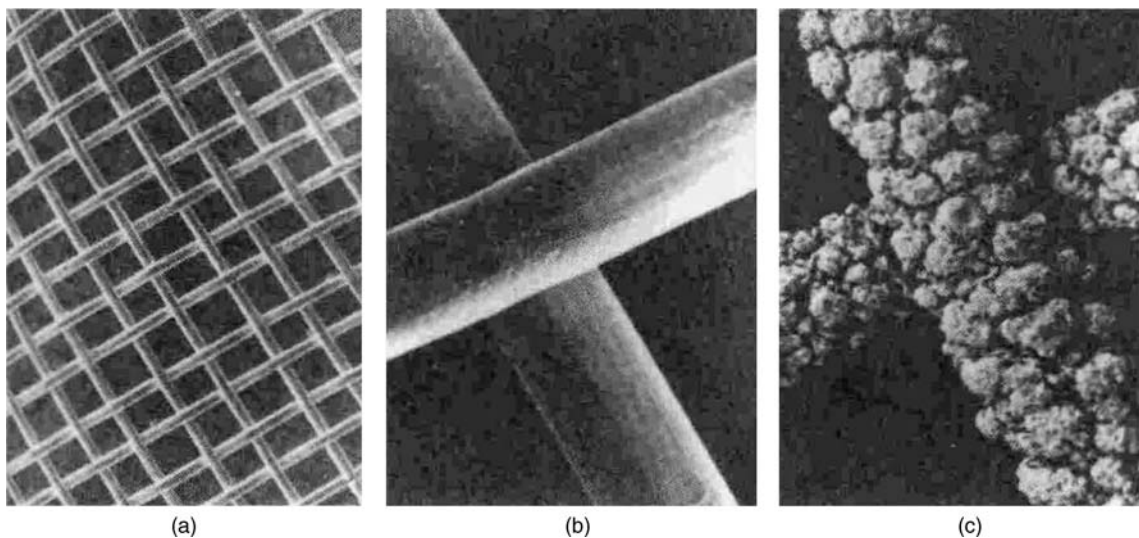


Figure 6.4.7 PtRh alloy ammonia oxidation gauze: (a) and (b) fresh at 20 \times and 300 \times magnification and (c) aged 5 days on stream at 300 \times magnification. Taken from Farrauto and Bartholomew (1997); used with permission of Blackie Academic and Professional.

The number of gauzes depends on the total pressure and varies between about 3 (1 bar) and 30 (8 bar) (Holzmann, 1967; Farrauto and Bartholomew, 1997). Woven gauzes are only used in specialized applications.

Owing to the formation of volatile platinum oxides, there is a loss of platinum from the gauze in a range of 0.05 g Pt (1 bar) to 1 g Pt per tonne of converted NH₃ (8 bar). The latter value is equivalent to a loss of 0.27 g Pt per tonne HNO₃ (100%). This has a significant impact on the costs of producing HNO₃. At today's platinum price of about €50 g⁻¹ (Sept. 2012), this corresponds to €14 per tonne HNO₃, compared to about €300 per tonne (2012) of HNO₃. The recovery of platinum by the use of a woven Pd-rich alloy gauze located immediately below the oxidation gauzes was therefore an important invention (Holzmann, 1968). The overall recovery reaction, which leads to a recovery efficiency of up to 80%, is represented by:



The feed gas of ammonia oxidation is a mixture of NH₃ with air and contains, typically, 11 vol.% NH₃ (the lower flammability limit is 15% at 20 °C). The gas velocity (empty reactor) under reaction conditions (mean gas temperature 600 °C) is in the range 0.7–1.3 m s⁻¹ for low- and medium-pressure processes (1–4 bar) and up to 3 m s⁻¹ for high-pressure processes (8–12 bar) (Holzmann, 1967). Thus, the residence time (empty reactor) is about 0.2–0.6 ms, if we take the number of gauzes N (3 for 1 bar and 30 for a high pressure of around 10 bar) and the diameter of the wire d (typically 60 μm) as basis for the reactor length $L_{\text{cat}} = Nd$ (that is, only the space taken up by the catalyst is counted).

6.4.2.1 Catalytic Oxidation of Ammonia on a Single Pt Wire for Cross-Flow of the Gas

The catalytic oxidation of ammonia is one of the rare cases where a non-porous solid catalyst is used. To calculate the ammonia conversion and the temperature of the wire we have to recall the equations for the interaction of external mass and heat transfer and a chemical reaction derived in Section 4.5.3. Initially, we consider the ammonia oxidation on a *single* Pt wire for cross-flow of the gas.

The rate of diffusion through the boundary layer of the wire (in mol m⁻² s⁻¹) is given by:

$$r_{\text{eff}} = \beta(c_{\text{NH}_3,\text{g}} - c_{\text{NH}_3,\text{s}}) \quad (6.4.13)$$

with $c_{\text{NH}_3,\text{g}}$ and $c_{\text{NH}_3,\text{s}}$ as the concentrations in the bulk phase and at the surface of the wire, respectively.

For a rough first instructive impression of the procedures that take place at an industrial gauze we consider a single cylindrical wire surrounded by a “huge” gas phase with a constant ammonia concentration (here 11 vol.% NH_3 in air).

The mass transfer coefficient β (m s^{-1}) is calculated based on the *Sherwood number*:

$$\beta = \frac{Sh D_{\text{NH}_3,\text{air}}}{d_{\text{cyl}}} \quad (6.4.14)$$

If we use the correlation given in Figure 3.2.9 (Section 3.2.1.2) for the *Nusselt number* Nu for heat transfer between a fluid and a cylinder for cross-flow of the fluid, substitution of Pr by Sc leads to the analogous correlation for the *Sherwood number* Sh (see also Topic 6.4.1):

$$Sh = 0.3 + \frac{0.62 Re^{0.5} Sc^{0.333}}{\left[1 + \left(\frac{0.4}{Sc}\right)^{0.666}\right]^{0.25}} \left[1 + \left(\frac{Re}{282000}\right)^{0.625}\right]^{0.8} \quad (6.4.15)$$

Table 6.4.1 gives typical reaction conditions and data on chemical media.

The rate of the chemical reaction (in $\text{mol m}^{-2} \text{s}^{-1}$) is given by:

$$r_{\text{chem}} = k_A c_{\text{NH}_3,\text{s}} \quad (6.4.16)$$

with k_A related to the catalyst’s surface, that is, here to the surface of a single wire ($\text{m}^3 \text{m}_{\text{cat}}^{-2} \text{s}^{-1}$). The steady-state rate of NH_3 consumption equals the flux through the film, and equating Eqs. (6.4.16) and (6.4.13) leads to the surface concentration:

$$c_{\text{NH}_3,\text{s}} = \frac{\beta}{\beta + k_A} c_{\text{NH}_3,\text{g}} \quad (6.4.17)$$

Table 6.4.1 Data on chemical media and reaction conditions used for the calculations on NH_3 oxidation on a single PtRh-wire wire [data partly from Holzmann (1967)].

Parameter	Value (4 bar, 600 °C)	Correlation for other temperatures ^{a)}
Gas velocity u_e (empty reactor)	0.75 m s^{-1}	$u_e \sim T$
Total molar gas concentration ρ_{mol}	55 mol m^{-3}	$\rho_{\text{mol}} \sim 1/T$
Total pressure	4 bar	
Diameter of PtRh-wire d_{cyl}	60 μm	
Surface area of PtRh-gauze per volume $A_{\text{cyl},V}$	20 250 $\text{m}^2 \text{m}^{-3}$	
Inlet concentration of NH_3 (gas phase)	11 vol.% (rest air)	
Feed rate of NH_3 related to cross-sectional area	4.5 $\text{mol m}^{-2} \text{s}^{-1}$	
Diffusion coefficient of NH_3 in air $D_{\text{NH}_3,\text{air}}$	$3.8 \times 10^{-5} \text{ m}^2 \text{s}^{-1}$	$D_{\text{NH}_3,\text{air}} \sim T^{1.75}$
Kinematic viscosity ν of gas mixture	$2.4 \times 10^{-5} \text{ m}^2 \text{s}^{-1}$	$\nu \sim T^{1.75}$
Thermal conductivity of gas mixture λ	0.063 $\text{W m}^{-1} \text{K}^{-1}$	$\lambda \sim T^{0.75}$
Conductibility of temperature a	$3.5 \times 10^{-5} \text{ m}^2 \text{s}^{-1}$	$a \sim T^{1.75}$
Heat capacity c_p	33 $\text{J mol}^{-1} \text{K}^{-1}$	constant ^{b)}
Schmidt number $Sc = \frac{\nu}{D_{\text{NH}_3,\text{air}}}$	0.63	constant
Reynolds number $Re = \frac{u_e d_{\text{cyl}}}{\nu}$	1.9	$Re \sim 1/T^{0.75}$
Sherwood number ^{c)} $Sh = \frac{\beta d_{\text{cyl}}}{D_{\text{NH}_3,\text{air}}} \approx Nu$	0.93	Eq. (6.4.15)
Mass transfer coefficient β	0.59 m s^{-1}	Eq. (6.4.14)
Prandtl number $Pr = \frac{\nu \rho_{\text{mol}} c_p}{\lambda}$	0.69	constant
Heat transfer coefficient α	1000 $\text{W m}^{-2} \text{K}^{-1}$	Eq. (6.4.21)
Enthalpy of reaction $\Delta_R H$ (NH_3 to NO)	227 kJ mol^{-1}	constant ^{b)}

a) All fluid properties are evaluated at the film temperature (average of bulk phase and surface).

b) Assumption to make the calculation not too complicated.

c) The simplifying (but usual) assumption of $Nu = Sh$ is discussed in more detail in Topic 6.4.1.

By combination of Eqs. (6.4.17) and (6.4.13) we find for the effective reaction rate:

$$r_{\text{eff}} = k_{\text{eff}} c_{\text{NH}_3,\text{g}} = \frac{\beta k_A}{\beta + k_A} c_{\text{NH}_3,\text{g}} \quad (6.4.18)$$

The number of publications on the (intrinsic) rate of NH_3 oxidation on platinum at conditions relevant for technical ammonia oxidation is very limited. Here we use the data given by Kraenert (2005) for NO formation at atmospheric pressure ($0.1 \text{ mol NO m}^{-2} \text{ s}^{-1}$ at 385°C , 3% NH_3 , 6% O_2). If we assume a first-order reaction ($k_A = r_{\text{NO}}/c_{\text{NH}_3}$) and activation energy of 80 kJ mol^{-1} [estimate based on the data of Kraenert (2005)] we obtain a rate constant for NH_3 conversion into NO of:

$$k_{A,\text{NO}} \approx 4 \times 10^5 e^{-\frac{80000}{RT}} \text{ m}^3 \text{ m}^{-2} \text{ s}^{-1} \quad (6.4.19)$$

Notably, NO formation is only favored at temperatures above 500°C . At lower temperatures, primarily N_2 [Eq. (6.4.5)] and also some N_2O [Eq. (6.4.6)] are formed. For example, at 385°C the selectivity to N_2 is about 85% compared to NO (10%) and N_2O (5%) [data of Kraenert (2005) for a Pt-foil, 1 bar, 3% NH_3 , 6% O_2]. Thus, Eq. (6.4.19) is not representative for the overall NH_3 conversion at low temperatures. Again estimated according to the data of Kraenert (2005), the rate constant of the overall conversion is then given by:

$$k_A \approx 1 \times 10^6 e^{-\frac{70000}{RT}} \text{ m}^3 \text{ m}^{-2} \text{ s}^{-1} \quad (6.4.20)$$

Figure 6.4.8 shows the influence of temperature on the mass transfer coefficient β , on the intrinsic rate constant of NH_3 oxidation to NO, N_2 , and N_2O [k_A , Eq. (6.4.20)], on the effective rate constant k_{eff} [Eq. (6.4.18)], and on the molar content of ammonia at the surface of a single wire surrounded by an atmosphere containing 11 vol.% NH_3 . At temperatures above 400°C the rate is completely controlled by mass transfer, and the NH_3 concentration on the wire is less than 1% (Figure 6.4.8).

For steady-state conditions, the heat produced by reaction equals the heat removed, which is governed by the heat transfer coefficient α ($\text{W m}^{-2} \text{ s}^{-1}$):

$$\dot{q}_{\text{reaction}} = k_{\text{chem}} c_{\text{NH}_3,\text{s}} (-\Delta_R H) = k_{\text{eff}} c_{\text{NH}_3,\text{g}} (-\Delta_R H) = \dot{q}_{\text{removal}} = \alpha (T_s - T_g) \quad (6.4.21)$$

To evaluate α , we use the correlation for the *Nusselt* number given in Figure 3.2.9:

$$Nu = \frac{\alpha d_{\text{cyl}}}{\lambda} = 0.3 + \frac{0.62 Re^{0.5} Pr^{0.333}}{\left[1 + \left(\frac{0.4}{Pr} \right)^{0.666} \right]^{0.25}} \left[1 + \left(\frac{Re}{282\,000} \right)^{0.625} \right]^{0.8} \quad (6.4.22)$$

For the rise in wire temperature compared to the bulk phase we obtain:

$$(T_s - T_g) = \frac{k_{\text{eff}}}{\alpha} c_{\text{NH}_3,\text{g}} (-\Delta_R H) \quad (6.4.23)$$

The adiabatic temperature rise is given by:

$$\Delta T_{\text{ad}} = \frac{c_{\text{NH}_3,\text{g}} (-\Delta_R H)}{c_p \rho_{\text{mol}}} = y_{\text{NH}_3,\text{g}} \frac{(-\Delta_R H)}{c_p} \quad (\text{here } y_{\text{NH}_3,\text{g}} = 0.11) \quad (6.4.24)$$

For the given conditions (Table 6.4.1) we obtain $\Delta T_{\text{ad}} = 757 \text{ K}$. If the reaction is controlled by external mass transfer ($k_{\text{eff}} = \beta$), Eqs. (6.4.23) and (6.4.24) and the approximation $Nu \approx Sh$ yield:

$$\begin{aligned} (T_s - T_g) &= \frac{\beta}{\alpha} \Delta T_{\text{ad}} c_p \rho_{\text{mol}} = \frac{\frac{Sh D_{\text{NH}_3,\text{air}}}{d_{\text{cyl}}}}{\frac{Nu \lambda}{d_{\text{cyl}}}} \Delta T_{\text{ad}} c_p \rho_{\text{mol}} = \frac{D_{\text{NH}_3,\text{air}}}{\frac{\lambda}{c_p \rho_{\text{mol}}}} \Delta T_{\text{ad}} \\ &= \frac{D_{\text{NH}_3,\text{air}}}{a} \Delta T_{\text{ad}} \end{aligned} \quad (6.4.25)$$

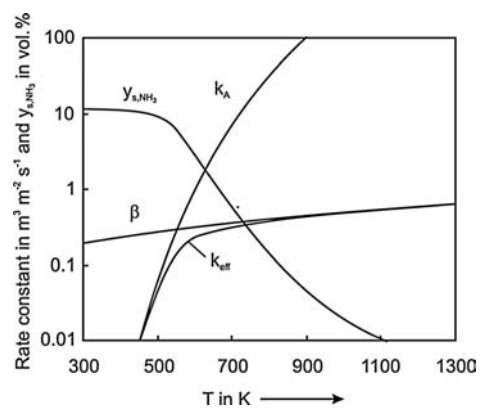


Figure 6.4.8 Influence of temperature on the mass transfer coefficient β , Eq. (6.4.14), the intrinsic rate constant of NH_3 oxidation k_A , Eq. (6.4.20), and on the effective rate constant k_{eff} , Eq. (6.4.18). The NH_3 content (vol.%) on the wire surface is also given (further data in Table 6.4.1).

The value of the conductibility of temperature α ($3.5 \times 10^{-5} \text{ m}^2 \text{ s}^{-1}$ at 600°C) has a similar value as the diffusion coefficient of NH_3 ($3.8 \times 10^{-5} \text{ m}^2 \text{ s}^{-1}$ at 600°C). Thus the difference in temperature between the wire and the bulk gas phase is according to Eq. (6.4.25) about 815 K, which is a factor of 1.1 higher than the adiabatic temperature rise. (As shown in Example 6.4.1, the heat transfer by radiation can be neglected for a thin wire; here $d_{\text{wire}} = 60 \mu\text{m}$.)

Example 6.4.1: Role of heat transfer by radiation for catalytic ammonia oxidation

The convective heat transfer coefficient α as given by Eq. (6.4.22) is (for $Nu \approx \text{constant}$) inversely proportional to the wire diameter ($\alpha = Nu \lambda / d_{\text{cyl}}$) and for NH_3 oxidation the value is about $1000 \text{ W m}^{-2} \text{ K}$ (Table 6.4.1). By contrast, heat transfer by radiation per unit surface area does not depend on the diameter. According to Eq. (3.2.35) we get for a single cylindrical wire (considered here as black body) surrounded by a cooler area (reactor wall):

$$\dot{q}_{\text{rad}} = \frac{\dot{Q}_{\text{rad}}}{A_{\text{cyl}}} = \varepsilon_{\text{Pt}} \sigma (T_{\text{cyl}}^4 - T_{\text{surrounding}}^4) \quad (6.4.26)$$

For comparison with convective heat transfer we use the heat transfer coefficient of radiation (emissivity of Pt/Rh wires ε_{Pt} is 0.17 at 900°C ,

Bradley and Entwistle, 1961):

$$\alpha_{\text{rad}} = \frac{\dot{q}_{\text{rad}}}{(T_{\text{cyl}} - T_{\text{surrounding}})} = \varepsilon_{\text{Pt}} \sigma \frac{(T_{\text{cyl}}^4 - T_{\text{surrounding}}^4)}{(T_{\text{cyl}} - T_{\text{surrounding}})} \quad (6.4.27)$$

For a wire temperature of 950°C and a gas temperature of 150°C , α_{rad} is $27 \text{ W m}^{-2} \text{ K}$. However, this estimation is only true for a single wire. In a technical reactor, the contribution of radiation is smaller as the gauzes are in radiative interchange with previous and subsequent gauzes of almost equal temperature. Thus even for the first gauze only the small part facing the direction of flow leads to a nameable contribution of radiation. If we estimate that this corresponds to 25% of the surface, we see that the contribution of radiation to the overall heat transfer is less than 1% ($7 \text{ W m}^{-2} \text{ K}$ compared to $\alpha_{\text{convective}}$ of $1000 \text{ W m}^{-2} \text{ K}$), and even for a "black body" gauze ($\varepsilon = 1$) this would only be 4%.

Figure 6.4.9 shows the sigmoidal heat production function and the line representing the heat removal when the wire just ignites. The wire ignites at a gas pre-heating temperature of around 150°C . Thus the heat production curve for NH_3 oxidation to N_2 as the preferred product at low temperatures [Eq. (6.4.5)] is relevant, and we have to use Eq. (6.4.20) for the rate constant and -315 kJ mol^{-1} for the reaction enthalpy. The calculated ignition temperature of 147°C (Fig. 6.4.9a) is in good agreement with preheating temperatures of industrial processes [130°C for 1 bar (Holzmann, 1967) and up to about 250°C for 9 bar (Farrauto and Bartholomew, 1997)], especially if we consider that the expression for the chemical kinetics [Eq. (6.4.20)] is only an estimation.

The corresponding steady-state temperature of the wire (962°C , Figure 6.4.9b) is also in good agreement with data reported for industrial gauzes, where at a pressure

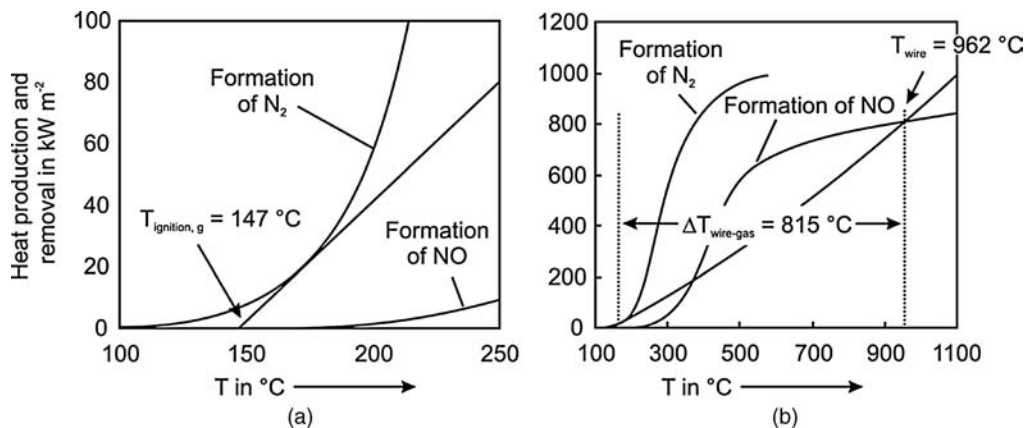


Figure 6.4.9 Ignition of a single Pt-wire during ammonia oxidation (a) and the corresponding steady-state wire temperature (b) (conditions etc. are given in Table 6.4.1).

of 4 bar 900 °C is reached (Farrauto and Bartholomew, 1997). Note that the heat production curve for NO formation is now relevant as above 500 °C NO becomes the dominant product. Thus Eq. (6.4.19) is then valid for the intrinsic rate constant and the reaction enthalpy is -227 kJ mol^{-1} .

NH₃ oxidation at a single wire can also be modeled by a computer program based on a two-dimensional finite element method to find an approximate solution of the partial differential equations. Here we used the commercial program *COMSOL PHYSICS (FEMLAB Company, Goettingen, Germany)*. The program uses a topological description of the geometric structure by a meshing procedure that breaks the system up into small elements of constant temperature, ammonia concentration, and so on (Figure 6.4.10). For NH₃ oxidation, the differential equations of mass and heat transfer (including the influence of temperature on parameters like the diffusion coefficient, gas density, thermal conductivity, NH₃ concentration, gas velocity) and the *Navier-Stokes* equations governing fluid dynamics are needed.

The result of these calculations, that is, the local temperatures and NH₃ concentrations, are shown in the Figures 6.4.11a and 6.4.12a. Comparison with the simple graphical solution given in Figure 6.4.9 reveals a very good agreement with respect to the temperature of the wire. Example 6.4.2, in which the heat and mass transfer parameters of the analytical solution and the finite element analysis are compared, also shows a good agreement. The thicknesses of the boundary layers for mass and heat transfer (position 3 o'clock, angle of 90° in Fig. 6.4.13) are shown in Figures 6.4.11b and 6.4.12b.

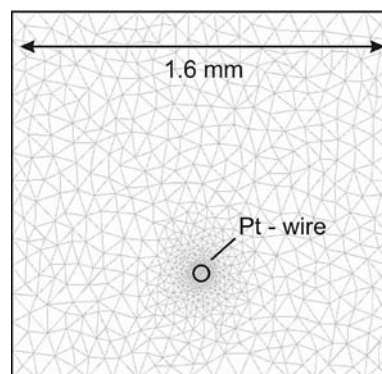


Figure 6.4.10 Two-dimensional finite element grid used to simulate NH₃ oxidation (single wire).

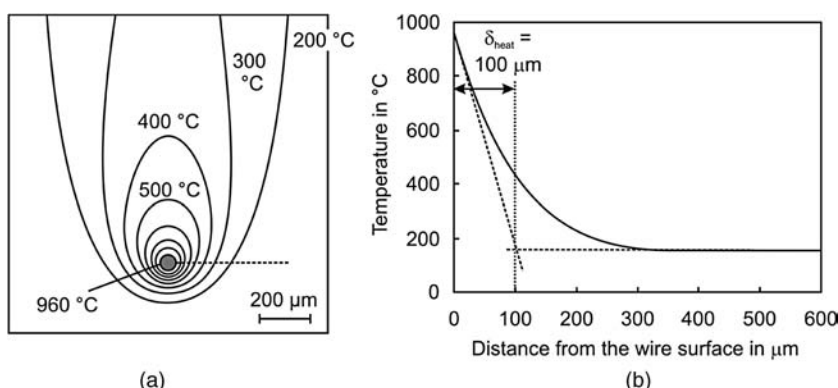


Figure 6.4.11 Temperature field around a single wire during NH₃ oxidation (a) and radial temperature profile along the dashed line (b) as indicated in (a) (conditions: see Table 6.4.1; solution by finite element method).

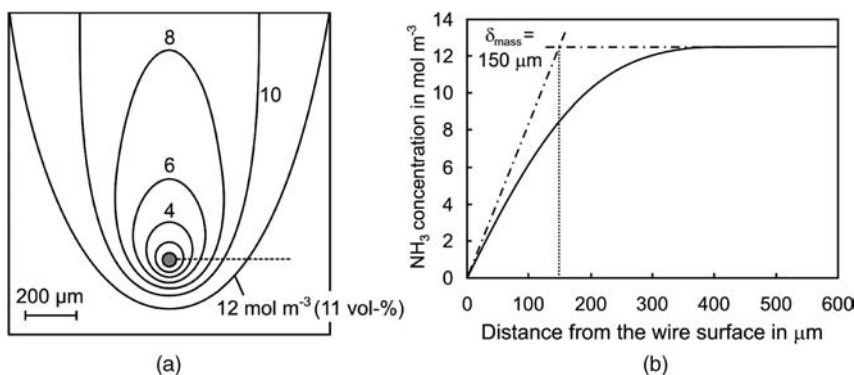
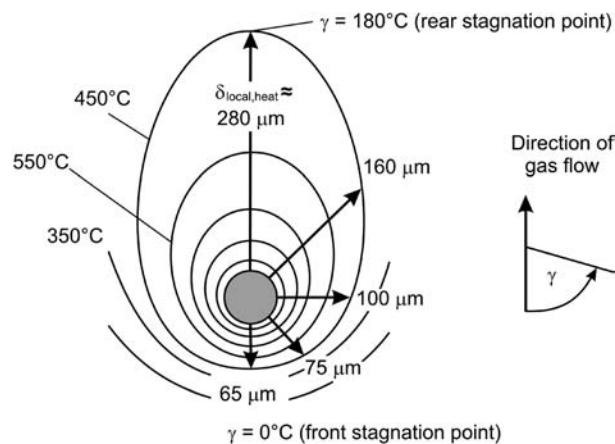


Figure 6.4.12 Ammonia concentration field around a single Pt-wire during NH₃ oxidation (a) and ammonia concentration profile along the dashed line (b) as indicated in (a) (conditions: see Table 6.4.1; solution by finite element method).

Figure 6.4.13 Isotherms around the PtRh wire (section of Figure 6.4.11) and local thickness of boundary layer (almost equivalent to the distance to reach 450 °C, see Figure 6.4.11; conditions as given in Table 6.4.1).



Example 6.4.2: Heat and mass transport during NH₃ oxidation on a single PtRh-wire calculated by the finite element method and by the classical film model

Figure 6.4.11a shows the radial temperature profile as calculated by the finite element method in the direction transverse to the flow, as indicated by the dashed line in Figure 6.4.11b. The boundary layer of the classical heat transfer approach based on a heat transfer coefficient and a *Nusselt number* is about 100 μm and can be estimated by the distance at which a temperature in the film of about 450 °C is reached (Figure 6.4.11b).

Figure 6.4.13 indicates that the size of the local boundary layer $\delta_{\text{local,heat}}$ changes along the circumference of the wire, for example, in the upstream direction we get 280 μm and at the front stagnation point we have the lowest value of 65 μm.

We can now calculate the local heat transfer coefficient α_{local} ($= \lambda_{\text{gas}}/\delta_{\text{local,heat}}$ with $\lambda_{\text{gas}} = 0.082 \text{ W m}^{-1} \text{ K}^{-1}$ at $T_s = 960 \text{ }^\circ\text{C}$) as shown in Figure 6.4.14 with the angle γ relative to the front stagnation point as parameter. The mean value α_{mean} is about $800 \text{ W m}^{-2} \text{ K}^{-1}$. The reason for the local variation of heat transfer coefficient is discussed in Section 3.2 (Example 3.2.2). For $Re < 5$, the fluid completely wraps around the cylinder, and the boundary layer increases further in the rear part. Thus, for ammonia oxidation on a Pt-wire ($Re \approx 2$), the heat transfer coefficient continuously decreases along the circumference of the wire as shown in Figure 6.4.14.

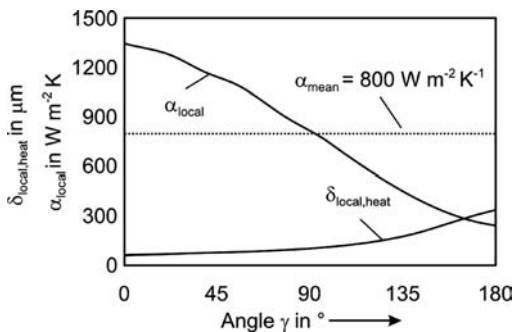


Figure 6.4.14 Variation of α_{local} and $\delta_{\text{local,heat}}$ along the circumference of the Pt wire.

Based on α_{mean} , we now finally determine the heat flux from the wire per unit surface area:

$$\dot{q} = \frac{\dot{Q}}{A_{\text{cyl}}} = \alpha_{\text{mean}} (T_s - T_{\text{gas}}) = 800 \text{ W m}^{-2} \text{ K}^{-1} (960 \text{ }^\circ\text{C} - 150 \text{ }^\circ\text{C}) \\ = 6.5 \times 10^5 \text{ W m}^{-2}$$

We can now compare this result with the classical film model with a constant value of α calculated by (semi)empirical correlations for Nu ($= \alpha d_{\text{cyl}}/\lambda_{\text{gas}}$). Here Nu is 0.93 [Eq. (6.4.22)] and for λ_{gas} we now have to use the value at the mean film temperature (555 °C). Consequently, we obtain:

$$\dot{q} = \alpha \Delta T_{\text{film}} = \frac{\lambda_{\text{gas},T_{\text{film}}} Nu}{d_{\text{cyl}}} (T_s - T_{\text{gas}}) \\ = \frac{0.06 \text{ W m}^{-1} \text{ K}^{-1} 0.93}{60 \times 10^{-6} \text{ m}} (960 - 150) \text{ K} = 7.5 \times 10^5 \text{ W m}^{-2}$$

which is in good agreement with the value of the finite element method (deviation <20%).

A similar approach can be applied for mass transfer. Figure 6.4.12a shows the radial NH₃ concentration for $\gamma = 90^\circ$. The thickness of the boundary layer by the classical mass transfer approach based on β and Sh is about 140 μm and can be estimated by the distance where we have a residual NH₃ concentration of about 8 mol m⁻³ (Figure 6.4.12b). If we apply this procedure for different angles we obtain the variation of the local boundary layer $\delta_{\text{local,mass}}$ and of the local mass transfer coefficient β_{local} ($= D_{\text{NH}_3,\text{air}}/\delta_{\text{local}}$ with $D_{\text{NH}_3,\text{air}} = 1.25 \text{ cm}^2 \text{ s}^{-1}$ at $T_s = 960 \text{ }^\circ\text{C}$) along the circumference of the wire (Figure 6.4.15). The mean value β_{mean} is 0.37 m s⁻¹.

Based on the mean value of the mass transfer coefficient, we calculate the (mean) flux of ammonia from the gas phase to the cylindrical wire surface per unit surface area:

$$\dot{n}_{\text{NH}_3} = \beta_{\text{mean}} (c_{\text{NH}_3,\text{gas}} - c_{\text{NH}_3,s}) = \beta_{\text{mean}} c_{\text{NH}_3,\text{gas}} \\ = 0.37 \text{ m s}^{-1} \cdot 12.5 \text{ mol m}^{-3} = 4.7 \text{ mol m}^{-2} \text{ s}^{-1}$$

Now we compare this result with the film model with constant β ($= Sh D_{\text{NH}_3,\text{air}}/d_{\text{cyl}}$) calculated by a (semi)empirical correlation for Sh [$= 0.93$, Eq. (6.4.15)]. For $D_{\text{NH}_3,\text{air}}$ and $c_{\text{NH}_3,\text{gas}}$ we have to use the values at the mean film temperature T_{film} (555°C , 828 K). Thus we obtain:

$$\begin{aligned}\frac{\dot{n}_{\text{NH}_3}}{A_{\text{cyl}}} &= D_{\text{NH}_3,\text{air},T_{\text{film}}} \frac{c_{\text{NH}_3,\text{gas},T_{\text{film}}}}{\frac{d_{\text{cyl}}}{Sh}} \\ &= 3.5 \times 10^{-5} \text{ m}^2 \text{ s}^{-1} \frac{6.4 \text{ mol m}^{-3}}{\frac{60 \times 10^{-6} \text{ m}}{0.93}} = 3.5 \text{ mol m}^{-2} \text{s}^{-1}\end{aligned}$$

which is – as for heat transport – in good agreement with the value of the finite element method (deviation of about 25%). Note that $c_{\text{NH}_3,\text{gas}}$ at T_{film} is here a factor of two smaller than the value at the temperature of the bulk phase ($T_{\text{gas}} = 423\text{ K}$, $T_{\text{film}} = T_{\text{mean}} = 828\text{ K}$). This is because Fick's law as represented by Eq. (3.1.56) must be used and not the “usual” form given by Eq. (3.1.54). The molar density of the fluid is, here, not constant, and changes drastically in the boundary layer as a result of the temperature gradient. Here, the general form of *Fick's law* leads to:

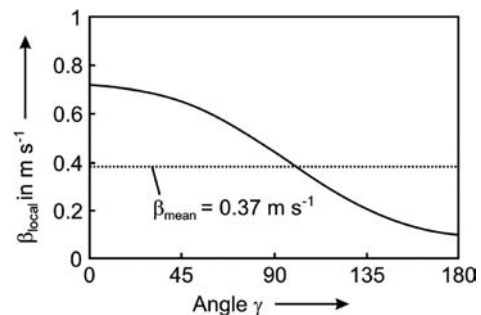


Figure 6.4.15 Variation of β_{local} along the circumference of the Pt wire.

$$\begin{aligned}\frac{\dot{n}_{\text{NH}_3}}{A_{\text{cyl}}} &= -\rho_{\text{mol},T_s} D_{\text{NH}_3,\text{air},T_s} \left(\frac{dy_{\text{NH}_3}}{dx} \right)_{\text{surface}} \\ &\approx \rho_{\text{mol},T_{\text{film}}} D_{\text{NH}_3,\text{air},T_{\text{film}}} \frac{y_{\text{NH}_3,\text{gas}}}{\frac{d_{\text{cyl}}}{Sh}} = D_{\text{NH}_3,\text{air},T_{\text{film}}} \frac{c_{\text{NH}_3,\text{gas},T_{\text{film}}}}{\frac{d_{\text{cyl}}}{Sh}}\end{aligned}$$

As a general rule, all parameters of the film model (density, diffusion coefficient, thermal conductivity) have to be used with their values at the mean (film) temperature T_{film} .

Topic 6.4.1 Analogy of heat and mass transfer correlations based on Nu and Sh

Figure 6.4.16 shows the dimensionless profiles of temperature and NH_3 concentration as calculated by the finite element method for the angle γ of 90° , as indicated by the dashed line in the Figures 6.4.11 and 6.4.12. The mean value of the thickness of the boundary layer for mass transfer (δ_{mass}) is $140\text{ }\mu\text{m}$ and that for heat transfer δ_{heat} is $100\text{ }\mu\text{m}$.

Recalling the *Sherwood* and *Nusselt numbers* (Sections 3.2.2.2 and 3.2.1.2) leads to:

$$Sh = \frac{d_{\text{cyl}}}{\delta_{\text{mass}}} \text{ and } Nu = \frac{d_{\text{cyl}}}{\delta_{\text{heat}}} \Rightarrow \frac{Sh}{Nu} = \frac{\delta_{\text{heat}}}{\delta_{\text{mass}}}$$

As already examined in Section 3.2, the equations to determine heat and mass transfer coefficients are very similar, and a frequently used correlation is:

$$\frac{Sh}{Nu} \approx C \left(\frac{Sc}{Pr} \right)^{\frac{1}{3}}$$

whereby C is usually set to unity, although according to the literature the value is reported to be in the range 0.7–1 (Emig and Klemm, 2005; Froment and Bischoff, 1990).

For NH_3 oxidation (in general for gases) the term $(Sc/Pr)^{1/3}$ is almost one (exact value 0.97, see Sc and Pr in Table 6.4.1). Thus, the ratio Sh/Nu should be unity. Based on the film thicknesses, we get a lower value of 0.7 ($= 100\text{ }\mu\text{m}/140\text{ }\mu\text{m}$, Figure 6.4.16) but with regard to the limited accuracy and number of mass transfer correlations compared to heat transfer correlations the assumption of $Sh = Nu$ (for $Sc \approx Pr$) can still be recommended.

6.4.2.2 Catalytic Oxidation of Ammonia in an Industrial Reactor, that is, on a Series of Pt Gauzes

Figures 6.4.9, 6.4.11 and 6.4.12 only represent a single wire surrounded by a gas with constant NH_3 concentration (11 vol.%). In an industrial reactor

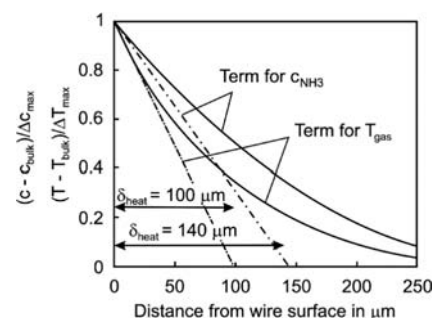


Figure 6.4.16 Comparison of film thickness for mass and heat transfer for the example of ammonia oxidation on a single PtRh wire (see text for details).

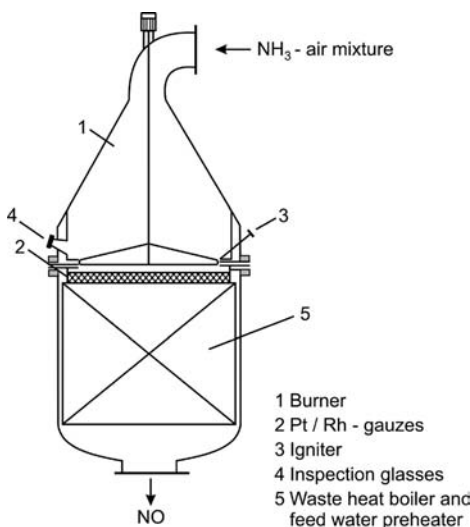


Figure 6.4.17 Technical reactor for NH_3 oxidation.
Adapted from Dittmeyer *et al.* (2006).

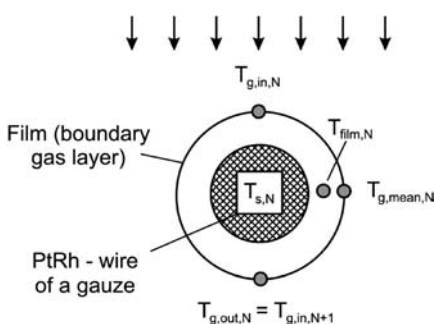


Figure 6.4.18 Description of the different temperatures used to calculate the conversion of ammonia by oxidation at gauze sheets (N = number of gauze).

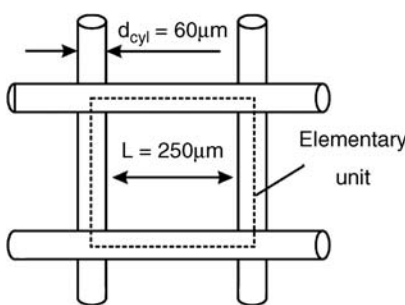


Figure 6.4.19 Simplified illustration of a typical geometry of a PtRh-gauze (data from Holzmann, 1967).

(Figure 6.4.17), the concentration changes even along a single gauze and, in addition, a series of several gauzes are used.

To calculate the conversion and temperatures at the gauzes of a technical reactor, we presume the following (see Figure 6.4.18 for description of temperatures):

- Axial and radial dispersion are negligible and, thus, we assume plug flow behavior.
- The inlet temperature (first gauze) is 150°C . This corresponds to the temperature of industrial reactors (4 bar) and to the value calculated for the ignition of a single wire (Figure 6.4.9).
- The temperature of each gauze is constant as the thermal conductivity of Pt is very high.
- For the calculations, a mean gas temperature in the free space between the gauzes ($T_{g,\text{mean}}$) is needed, which is defined as the arithmetic mean of the in- and outlet gas temperature of each gauze, $T_{g,\text{mean}} = 0.5(T_{g,\text{in}} + T_{g,\text{out}})$.
- The rate constant equals the mass transfer coefficient β as the temperature of the gauzes is higher than 900 K , and the rate is completely controlled by mass transfer (Figure 6.4.8).
- All parameters to characterize incidences in the film (Re , Sh , β , gas density, NH_3 concentration, and other fluid properties) are evaluated at the (mean) film temperature T_{film} .
- T_{film} is thereby in approximation the arithmetic mean of the mean gas-phase temperature $T_{g,\text{mean}}$ and the surface temperature of the gauze, $T_{\text{film}} = 0.5(T_{g,\text{mean}} + T_s)$.

The mass balance for a differential element of the surface of the catalyst is given by:

$$-\frac{d\dot{n}_{\text{NH}_3}}{dA_{\text{cyl}}} = \beta_{T_{\text{film}}} c_{\text{NH}_3, T_{\text{film}}} dA_{\text{cyl}} \quad (6.4.28)$$

and introduction of the volume flow (at T_{film}) and of the volume specific surface area leads to:

$$-\frac{1}{\dot{V}_{T_{\text{film}}}} \frac{d\dot{n}_{\text{NH}_3}}{d\tau} = -\frac{dc_{\text{NH}_3, T_{\text{film}}}}{d\tau_{T_{\text{film}}}} = \beta_{T_{\text{film}}} c_{\text{NH}_3, T_{\text{film}}} A_{\text{cyl}, V} \quad (6.4.29)$$

The typical surface area of a PtRh-gauze per volume of reactor $A_{\text{cyl}, V}$ is $20\,250\text{ m}^2\text{ m}^{-3}$ (Holzmann, 1967) (Figure 6.4.19).

Rearangement of Eq. (6.4.29) leads to:

$$-\frac{dc_{\text{NH}_3, T_{\text{film}}}}{c_{\text{NH}_3, T_{\text{film}}}} = \beta_{T_{\text{film}, \text{mean}}} A_{\text{cyl}, V} d\tau_{T_{\text{film}}} \quad (6.4.30)$$

and integration leads to the NH_3 conversion at the gauze N ($N=1$ for the first gauze etc.):

$$X_{\text{NH}_3, N} = 1 - e^{(-\beta_{T_{\text{film}, N}} A_{\text{cyl}, V} \tau_{T_{\text{film}, N}})} = 1 - e^{-D\alpha_{\text{NH}_3, \text{oxidation}}} \quad (6.4.31)$$

The mean temperature of the gas at the first gauze (mean value just before and after the gauze, Figure 6.4.18), can be determined by the conversion and the adiabatic temperature rise:

$$\begin{aligned} T_{g,\text{mean}, 1} &= \frac{T_{g,\text{in}, 1} + T_{g,\text{out}, 1}}{2} = \frac{T_{g,\text{in}, 1} + (T_{g,\text{in}, 1} + X_{\text{NH}_3, 1} \Delta T_{\text{ad}})}{2} \\ &= T_{g,\text{in}, 1} + \frac{X_{\text{NH}_3, 1} \Delta T_{\text{ad}}}{2} \end{aligned} \quad (6.4.32)$$

For subsequent gauzes ($N > 1$) we have (with $X_{\text{NH}_3, \text{total}, N}$ as total conversion):

$$T_{g,\text{mean}, N} = \frac{T_{g,\text{in}, N} + T_{g,\text{out}, N}}{2} = \frac{T_{g,\text{in}, N} + T_{g,\text{in}, 1} + X_{\text{NH}_3, \text{total}, N} \Delta T_{\text{ad}}}{2} \quad (6.4.33)$$

whereby the total conversion reached after the gauze with number N is given by:

$$X_{\text{NH}_3,\text{total},N} = 1 - \prod_1^N (1 - X_{\text{NH}_3,N}) \quad (6.4.34)$$

Equation (6.4.25) (with $k_{\text{eff}} = \beta$) leads to the surface temperature of the N -th gauze:

$$T_{s,N} = T_{g,\text{mean},N} + \frac{\beta_{T_{\text{film}}}}{\alpha_{T_{\text{film}}}} c_{\text{NH}_3,T_{\text{film}},N} (-\Delta_R H) \quad (6.4.35)$$

The mean concentration of ammonia (bulk phase) at the mean film temperature is given by:

$$\begin{aligned} \underbrace{c_{\text{NH}_3,T_{\text{film}},N}}_{\text{Mean concentration in the bulk phase of gauze } N} &= 0.5 \left[\underbrace{(1 - X_{\text{NH}_3,\text{total},N-1}) c_{\text{NH}_3,\text{in},T_{\text{film}},1}}_{\text{Concentration at the inlet of gauze } N \text{ (at the mean film temperature)}} + \underbrace{(1 - X_{\text{NH}_3,N}) (1 - X_{\text{NH}_3,\text{total},N-1}) c_{\text{NH}_3,\text{in},T_{\text{film}},1}}_{\text{Concentration at the outlet of gauze } N \text{ (at the mean film temperature)}} \right] \\ &= \frac{(2 - X_{\text{NH}_3,N})}{2} (1 - X_{\text{NH}_3,\text{total},N-1}) c_{\text{NH}_3,\text{in},T_{\text{film}},1}. \end{aligned} \quad (6.4.36)$$

Introduction of the adiabatic temperature rise [Eq. (6.4.24)] in terms of T_{film} leads to:

$$\Delta T_{\text{ad}} = \frac{c_{\text{NH}_3,T_{\text{film}},1} (-\Delta_R H)}{c_p \rho_{\text{mol},T_{\text{film}}}} \quad (6.4.37)$$

and insertion of Eqs. (6.4.36) and (6.4.37) and of D/a (here about 1.08) for $\beta \rho_{\text{mol}} c_p / \alpha$ [Eq. (6.4.25)] finally leads to the following term for the surface (=gauze) temperature:

$$T_{s,N} = T_{g,\text{mean},N} + 1.08 \frac{(2 - X_{\text{NH}_3,N})}{2} (1 - X_{\text{NH}_3,\text{total},N-1}) \Delta T_{\text{ad}} \quad (6.4.38)$$

Thus, for a conversion of zero (e.g., for an infinitely small residence time), the temperature of the gas phase would not change, and the temperature of the first net would be $1.08 \Delta T_{\text{ad}}$ ($= 815$ K) higher than the gas inlet temperature.

Finally, the (mean) temperature of the film (Figure 6.4.18) is given by:

$$T_{\text{film},N} = \frac{T_{g,\text{mean},N} + T_{s,N}}{2} \quad (6.4.39)$$

The system cannot be solved directly, as the values of the (mean) film and gas temperatures as well as the temperature of the gauze are initially unknown, but are needed to calculate the conversion by Eq. (6.4.31). Thus some trial and error (e.g., with the help of a spreadsheet) is needed to evaluate all values iteratively, which are summarized in Table 6.4.2.

The calculated temperature of the first gauze is 949°C . For subsequent gauzes, the temperature gradually decreases, until a final temperature of 907°C is reached. These gauze temperatures are in good agreement with those reported in the literature for industrial reactors (850 – 950°C , Holzmann, 1967; Farrauto and Bartholomew, 1997).

The conversion reached at the first gauze is 63%. In total, only four gauzes are needed to reach almost full conversion (Table 6.4.2), which is also the number of gauzes used industrially for a medium-pressure process (Holzmann, 1967). An additional verification of the calculation is the final system temperature of 907°C , which is exactly the value of ΔT_{ad} ($= 757$ K) higher than the gas inlet temperature of 150°C , as required by the overall heat balance.

The influence of the gas inlet temperature in the range 50 – 250°C is shown in Table 6.4.3 for the example of the first gauze (although for the assumed

Table 6.4.2 Ammonia conversion and characteristic temperatures during oxidation at PtRh-gauzes for a gas inlet temperature of 150 °C (other process parameters etc. in Table 6.4.1).

No of gauze	Inlet gas temperature $T_{g,in,N}$ (°C)	Outlet gas temperature $T_{g,out,N}$ (°C)	Mean film temperature $T_{film,mean,N}$ (°C)	Gauze temperature $T_{s,mean,N}$ in °C	NH ₃ -conversion $X_{NH_3,N}$ at n -th gauze (%)	Total NH ₃ -conversion $X_{NH_3,total,N}$ (%)
1	150	627	668	949	63	63
2	627	812	821	922	66	87
3	812	876	878	912	67	96
4	876	896	886	910	67	98.6
5	896	904	894	897	67	99.6
6	904	906	905	907	67	99.9
8	All temperatures are at about 907				67	99.96
9	All temperatures are at about 907				67	99.99
10	All temperatures are at about 907				67	99.999

Table 6.4.3 Ammonia conversion and characteristic temperatures during oxidation at the first PtRh-gauzes for different gas inlet temperatures (other process parameters in Table 6.4.1).

Inlet gas temperature $T_{g,in,1}$ (°C)	Outlet gas temperature $T_{g,out,1}$ (°C)	Mean film temperature $T_{film,mean,1}$ (°C)	Gauze temperature $T_{s,mean,1}$ (°C)	NH ₃ -conversion $X_{NH_3,1}$ at first gauze (%)
50	619	617	899	62
150	627	668	948	63
250	634	720	998	64

pressure of 4 bar 150 °C is the more realistic). All characteristic temperatures increase almost proportionally with increasing gas inlet temperature, but the ammonia conversion increases only to a very minor extent with increasing gas inlet temperature. The temperature of the gauze is in all three cases so high that the reaction rate is completely determined by external mass transfer, which does not depend strongly on temperature. According to Eq. (6.4.31), the *Damkohler number* Da of NH₃ oxidation and thus the NH₃ conversion depends only slightly on temperature ($\beta = Sh D_{NH_3,air}/d_{cyl}$; $Sh \approx \text{constant}$; $D_{NH_3,air} \sim T^{1.75}$; $\beta \sim T^{1.75}$, $\tau \sim 1/T$ and thus $Da \sim \beta \tau \sim T^{0.75}$).

The influence of total pressure for a constant gas velocity (0.75 m s⁻¹ at 600 °C) is shown in Table 6.4.4 for pressures of 1–12 bar, again for the example of the first gauze. An increasing pressure strongly decreases the conversion at one gauze, which reflects the dependence of external mass transfer on pressure: The diffusion coefficient $D_{NH_3,air}$ is inversely proportional to the total pressure and for the given conditions the Sherwood number Sh is only proportional to about $p^{0.4}$ ($Sh = 0.6$ for 1 bar and 1.6 for 12 bar), although Re increases with pressure because of the decreasing viscosity. Thus, the *Damkohler number* Da is proportional to $1/p^{0.6}$ ($\beta \sim Sh D_{NH_3,air}$) and the number of gauzes needed for 99% conversion increases with pressure (Table 6.4.4). On first sight, the phenomena of an increasing gauze temperature with decreasing NH₃ conversion and thus also with decreasing gas outlet and mean film temperature is astonishing, but we have to consider that the difference in gas and catalyst temperature is mainly driven by the interplay of mass and heat transfer and not by the changing gas concentration in the bulk phase [Eq. (6.4.38) and the text below]. As a consequence, the highest catalyst temperature is reached for zero conversion ($T_{s,max} = T_{g,in} + 1.08\Delta T_{ad} = 965$ °C).

Figure 6.4.20 shows a comparison of the calculated number of gauzes for 99% NH₃ conversion at different pressures and typical values of industrial processes. Two cases were considered, a gas velocity of 0.75 m s⁻¹ (at 600 °C), which is typical for low and medium pressures, and 3 m s⁻¹, which is typical for high pressures. The agreement between calculation and plant data is sufficient.

Table 6.4.4 NH₃ conversion and characteristic temperatures during oxidation at a single PtRh-gauze for different total pressures [constant gas velocity of 0.75 m s⁻¹ (at 600 °C), inlet temperature 150 °C; other process parameters etc. are given in Table 6.4.1 for a pressure of 4 bar].

Total pressure (bar)	Outlet gas temperature $T_{g,out,1}$ (°C)	Mean film temperature $T_{film,mean,1}$ (°C)	Gauze temperature $T_{s,mean,1}$ (°C)	NH ₃ -conversion $X_{NH_3,1}$ at first gauze (%)	Number of gauzes for 99% conversion ^{a)}
1	892	729	938	98	2
4	627	668	948	63	4
8	438	625	956	38	10
12	354	606	959	27	15

a) Calculated with Eq. (6.4.34) with the simplifying assumption that the conversion at each gauze equals the value reached at the first gauze (as shown in Table 6.4.2 for 4 bar and $T_{in} = 150$ °C).

6.4.3

NO Oxidation

The product gas of NH₃ oxidation is rapidly cooled from 900 °C to less than 40 °C and NO is further oxidized in a homogeneous reaction to NO₂. The oxidation of NO is strongly favored by low temperatures with regard to thermodynamics (Figure 6.4.6), as expected for an exothermic reversible reaction, but also with regard to kinetics, which is extraordinary (Figure 6.4.21).

Experiments also show that the homogeneous (thermal) NO oxidation to NO₂ [Eq. (6.4.3)] increases strongly with total pressure (Figure 6.4.21) and is third-order overall:

$$\frac{dc_{NO_2}}{dt} = k_{NO_2,apparent} c_{NO}^2 c_{O_2} \quad (6.4.40)$$

At first sight, one may think that the reaction proceeds via a simultaneous collision of three molecules (2NO + O₂), but this occurs very infrequently and cannot explain the observed rate. Furthermore, the rate decreases with temperature, which contradicts the law of Arrhenius. If we use the experimental data given in Figure 6.4.21a, and assume that the rate is inversely proportional to the reaction time, we get an apparent negative activation energy of -20 kJ mol⁻¹ by the slope = [$E_{A,apparent}/(RT)$] of the plot of ln(r_{NO}) versus 1/T.

A mechanism that accounts for these two aspects is the following. The pre-equilibrium:



is established very rapidly and thus we have:

$$c_{N_2O_2} = \frac{p_{N_2O_2}}{RT} = \frac{K_{p,N_2O_2} p_{NO}^2}{RT} \frac{p_0^2}{p_0} = \frac{K_{p,N_2O_2} RT}{p_0} c_{NO}^2 \quad (6.4.42)$$

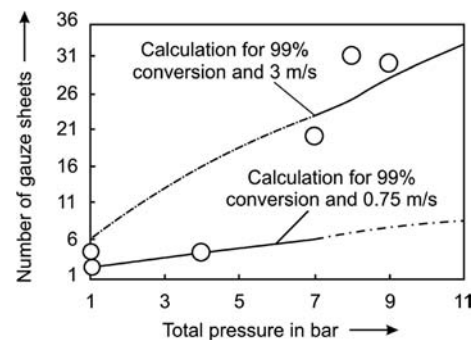
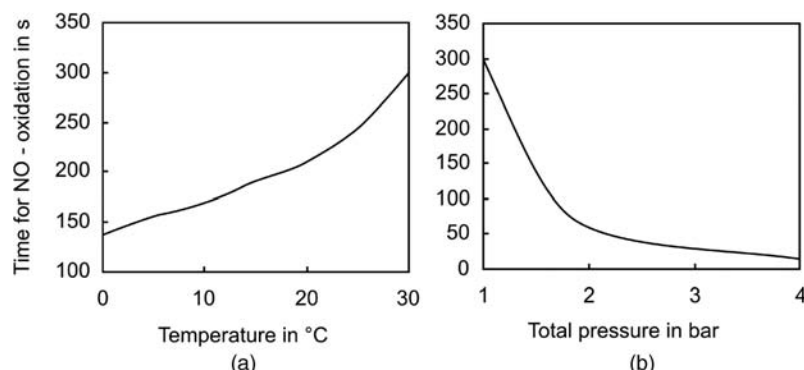


Figure 6.4.20 Number of gauzes for 99% NH₃ conversion for two gas velocities (600 °C) (symbols: data from industrial plants) (Holzmann, 1967, 1968; Farrauto and Bartholomew, 1997).

Figure 6.4.21 Influence of temperature (a) and total pressure (b) on the oxidation of NO to NO₂ [data from Dittmeyer *et al.* (2006), exact definition of the oxidation time is not given].

The rate-determining step is then the following bimolecular reaction:



and thus the “true” reaction rate is given by:

$$\frac{dc_{\text{NO}_2}}{dt} = k_{\text{NO}_2} c_{\text{N}_2\text{O}_2} c_{\text{O}_2} \quad (6.4.44)$$

Insertion of Eq. (6.4.42) into Eq. (6.4.44) leads to:

$$\frac{dc_{\text{NO}_2}}{dt} = k_{\text{NO}_2} \frac{K_{\text{p},\text{N}_2\text{O}_2} RT}{p_0} c_{\text{NO}}^2 c_{\text{O}_2} \quad (6.4.45)$$

which explains the experimentally found rate of second order with regard to NO and first order to O₂.

According to Eq. (4.2.19) the equilibrium constant of N₂O₂ formation is:

$$K_{\text{p},\text{N}_2\text{O}_2} = e^{-\frac{\Delta_R H_{\text{N}_2\text{O}_2}^0 + T\Delta_R S_{\text{N}_2\text{O}_2}^0}{RT}} = e^{\frac{\Delta_R S_{\text{N}_2\text{O}_2}^0}{R}} e^{-\frac{\Delta_R H_{\text{N}_2\text{O}_2}^0}{RT}} \quad (6.4.46)$$

and for the influence of temperature on the rate constant we have according to Arrhenius:

$$k_{\text{NO}_2} = k_{\text{NO}_2,0} e^{-\frac{E_{\text{A},\text{NO}_2}}{RT}} \quad (6.4.47)$$

Thus the overall apparent rate constant according to Eq. (6.4.45) is given by:

$$k_{\text{NO}_2} \frac{K_{\text{p},\text{N}_2\text{O}_2} RT}{p_0} = \left(\frac{k_{\text{NO}_2,0} R}{p_0} e^{\frac{\Delta_R S_{\text{N}_2\text{O}_2}^0}{R}} \right) T e^{-\frac{E_{\text{A},\text{NO}_2} - \Delta_R H_{\text{N}_2\text{O}_2}^0}{RT}} \quad (6.4.48)$$

The dimerization of NO to N₂O₂ is exothermic ($\Delta_R H < 0$), and thus the apparent activation energy is smaller than the “true” value of the rate-determining step according to Eq. (6.4.43):

$$E_{\text{A,apparent}} = E_{\text{A},\text{NO}_2} - |\Delta_R H_{\text{N}_2\text{O}_2}^0| \quad (6.4.49)$$

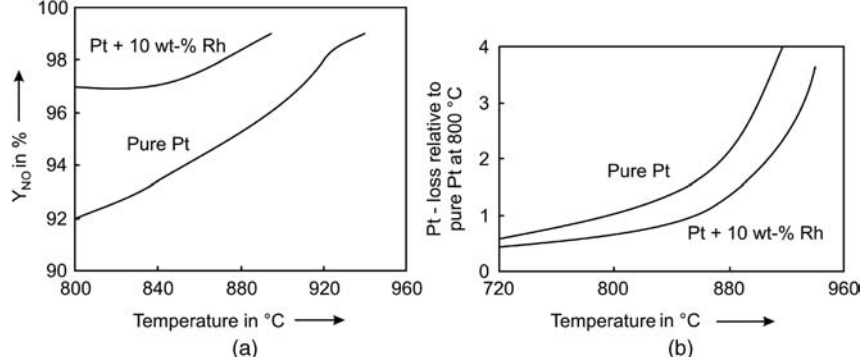
For NO oxidation, the true activation energy is coincidentally smaller than the absolute value of the reaction enthalpy of the pre-equilibrium, which leads to a negative apparent activation energy.

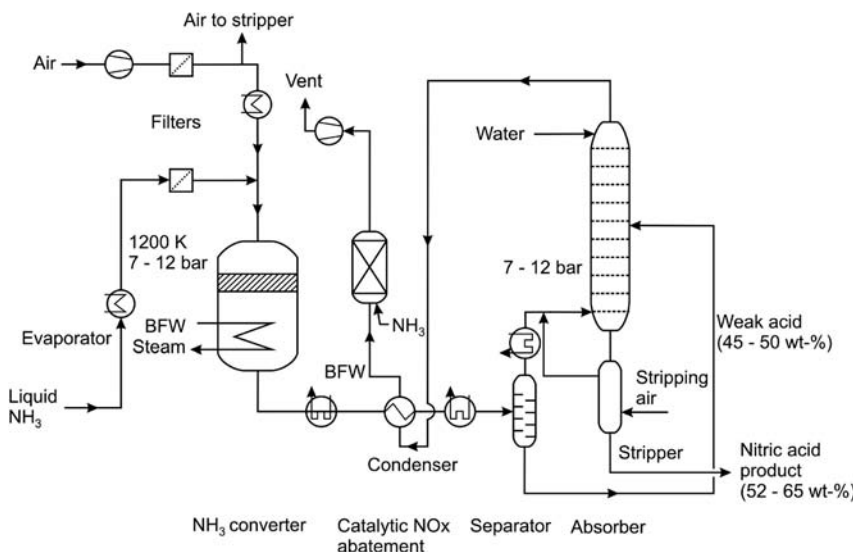
6.4.4

Nitric Acid Processes

For NH₃ oxidation, a high temperature, low pressure, short residence time, and rapid cooling of the gas minimize side and consecutive reactions and thus maximize the NO yield. In industrial reactors this is realized by a small number of gauzes. The addition of rhodium to the Pt catalyst leads to a decrease of the Pt losses and an increase of the NO yield (Figure 6.4.22). The Rh content is about

Figure 6.4.22 Influence of gauze temperature on NO yield (a) and Pt-loss (b) at atmospheric pressure with a feed gas containing 11 vol.% NH₃ [data from Handforth and Tilley (1934)].





10 wt%; a further increase of the Rh content would not lead to an additional benefit (Holzmann, 1967). Owing to surface restructuring and erosion at the high gas velocity applied (about 1 m s^{-1}) some Pt is lost but can be partly recovered by filters.

The NO yield is reduced from about 98% at 1 bar to about 95% at 10 bar. The difference in the yield would be even higher if the gauze temperatures were the same [about 5% difference in NO yield, Holzmann (1967)]. Usually, the operating temperature increases with increasing pressure, which partly compensates the negative influence of pressure on the NO yield but also leads to an increase in the losses of Pt (Figure 6.4.22).

Contrary to NH_3 oxidation, the absorption of NO_2 operates best at high pressure. Thus there is a dilemma as to whether a low or a high pressure should be used. In industrial practice, both the oxidation and the absorption are carried out at constant pressure (Figure 6.4.23) or a combination of low pressure oxidation and high-pressure absorption is applied (dual pressure process, Figure 6.4.24). Table 6.4.5 gives typical data for nitric acid plants.

The choice of process depends on site requirements and the economics of heat recovery and gas compression. Nowadays, atmospheric pressure plants have become obsolete and single-pressure plants operate at 10 bar, which reduces the equipment size and capital cost, and the higher gauze temperature and pressure lead to a more efficient energy recovery.

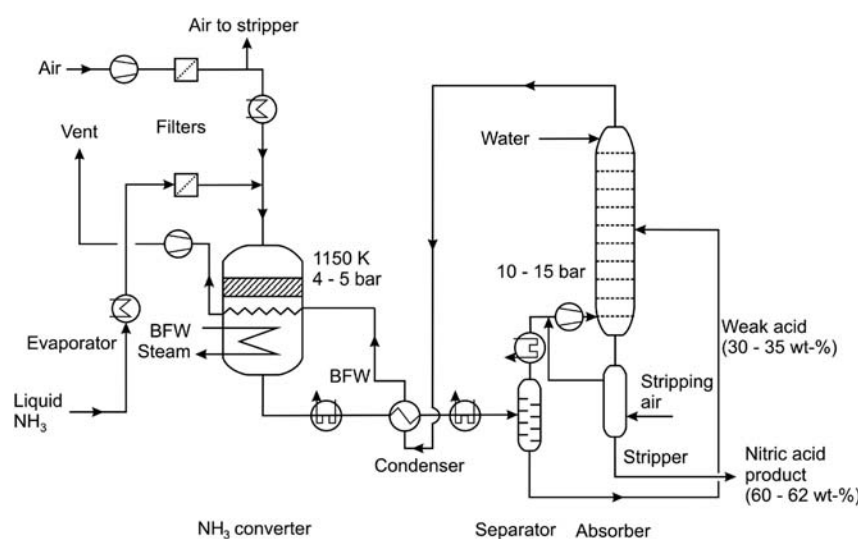


Table 6.4.5 Comparison of main process data of different nitric acid plant configurations for the production of 1 t of HNO₃ (100%) [data from Uhde (2005) and Moulijn, Makkee, and Van Diepen (2004)].

Process parameter [related to 1 t HNO ₃ (100%)]	Medium-pressure process	High-pressure process	Dual pressure process
Total pressure (NH ₃ -oxidation/NO-absorption) (bar)	5.8	10	4.6/12
NH ₃ into HNO ₃ efficiency (%)	88–95	90–94	94–96
NH ₃ into NO conversion efficiency (%)	96	95	96
Electrical power (kWh)	9	13	8.5
Pt primary losses (g)	0.15	0.26	0.13
Pt losses with recovery (g)	0.04	0.08	0.03
Cooling water ($\Delta T = 10$ K) (t)	100	130	105
Generation of high pressure excess steam (40 bar, 450 °C) (t)	0.76	0.55	0.65
Average gauze temperature (°C)	About 880	About 930	About 880
Typical gauze life (months)	4–6	1.5–3	4–6
Acid strength (wt%)	53–60	52–65	60–62
NO _x -content in untreated tail gas (ppmv)	About 500	About 200	About 150

Ammonia and air are mixed (excess of O₂ and about 10 vol.% NH₃), passed over the gauzes, and react to give NO and steam. This reaction is very exothermic, which leads to a strong increase of the gas temperature in the adiabatic system. The product gas is rapidly cooled, whereby steam is generated that can be exported or used in a steam turbine to drive the air compressor. During cooling, NO is further oxidized to NO₂ (and N₂O₄). The condensate of the condenser is a (weak) nitric acid that is fed to the absorption column. The gas that leaves the separator is mixed with secondary air to enhance the NO oxidation, and then fed to the bottom of the absorber, where NO₂ and N₂O₄ are absorbed in water and nitric acid is finally produced. In a subsequent stripper, dissolved NO_x (NO and NO₂) are stripped out of the product acid.

The gas that leaves the absorption column still contains NO, 150–500 ppm depending on the process (Table 6.4.5). For environmental reasons this has to be removed or at least reduced to less than 200 ppm before venting the tail gas to the atmosphere. This is achieved by selective catalytic reduction (SCR) with NH₃ as reducing agent or by advanced absorption, that is, by a higher pressure and/or a larger or a second absorber column.

The Figures 6.4.23 and 6.4.24 show, respectively, flow schemes of a single-pressure plant with SCR and a dual-pressure plant with extended absorption. Both NO abatement methods are interchangeable.

The emission of N₂O, a strong greenhouse gas, is nowadays also a point of concern, and novel processes for N₂O reduction are under development (Moulijn, Makkee, and Van Diepen, 2004).

Summary of Section 6.4 (take-home messages)

- **Nitric acid** is one of the 15 largest commodity chemicals with an annual world production of about 55 million tonnes. Approximately 80% is used as an intermediate in the production of nitrogenous fertilizers (NH₄NO₃). The remainder goes into the production of various chemicals such as explosives or intermediates for polymers.
- First, **ammonia** is catalytically oxidized with oxygen (air) to **nitrogen monoxide**. Subsequently, NO is further oxidized non-catalytically to **nitrogen dioxide**, and finally nitric acid is formed by absorption and reaction of NO₂ in water.
- The **thermodynamics of nitric acid production** based on ammonia can be characterized as follows: N₂ and NO (and also N₂O) are thermodynamically favored products of NH₃ oxidation. The undesirable formation of N₂ is thermodynamically more favored than the desired NO formation. The selectivity of the catalyst is therefore important in suppressing N₂ formation. NO may decompose to N₂ and O₂, but this can be avoided by quenching the product gas of

NH_3 oxidation down to below 700 K, where NO is metastable. NO oxidation to NO_2 is only favored at low temperatures.

- For **ammonia oxidation**, PtRh gauzes with a wire diameter of about 70 μm are used as catalyst. At temperatures above 400 °C the **effective rate** is completely controlled by external mass transfer, and catalytic NH_3 oxidation is one of the rare cases where a non-porous solid catalyst is used. For complete NH_3 conversion, only ten gauzes are needed, which underlines the rule of thumb that about ten characteristic lengths (here the wire diameter) are needed if the kinetics are determined by external mass transfer.
- The diagram representing the **sigmoidal heat production function** and the **line of heat removal** shows that the wire ignites at a gas preheating temperature of around 150 °C, which leads to a wire temperature of around 900 °C.
- The product gas of NH_3 oxidation is cooled to less than 40 °C and NO is further oxidized in a homogeneous reaction to NO_2 . Experiments show that this thermal reaction is third-order overall. At first sight, one may think that the reaction proceeds via a simultaneous collision of three molecules ($2\text{NO} + \text{O}_2$), but this occurs very infrequently and cannot explain the observed rate. Furthermore, the rate decreases with temperature (**negative activation energy**), which is in contradiction to the law of Arrhenius. The reason for this strange behavior is an exothermic pre-equilibrium of NO and N_2O_2 (favored at low temperatures) followed by the **rate-determining step** of the bimolecular reaction $\text{N}_2\text{O}_2 + \text{O}_2 \rightarrow 2\text{NO}_2$. The true activation energy of this reaction is smaller than the absolute value of the reaction enthalpy of the pre-equilibrium, which leads to a negative apparent activation energy.
- The NH_3 into NO conversion efficiency increases with decreasing pressure, whereas the conversion of NO into NO_2 and the subsequent absorption is favored by high pressures. Thus, **modern nitric acid plants** are **dual pressure processes**, that is, the product gas of ammonia oxidation (at 6 bar) is compressed to 12 bar and then fed to the absorption tower for NO oxidation and for NO_2 absorption.

6.5

Coke and Steel

6.5.1

Steel Production (Overview)

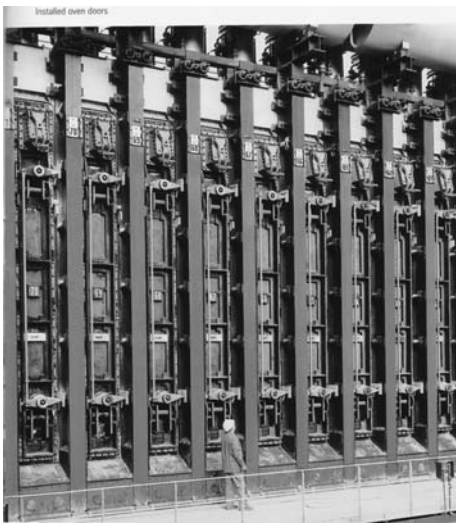
Steel is an alloy consisting of iron with a carbon content ranging from 0.02 to about 2 wt%. Carbon is the most important alloying material for iron, but for high-quality steels various other elements are also used, such as chromium, nickel, manganese, and tungsten. Carbon and other elements act as a hardening agent, and their amount control the steel qualities such as the hardness, elasticity, ductility, and tensile strength. Steel with increased carbon content is harder, but is also more brittle. The maximum solubility of carbon in iron is 2.1 wt% (at 1150 °C). Higher concentrations of carbon produce cementite, which reduces the strength.

Although steel had been produced by various inefficient methods in antiquity – for example, in China, India, the Middle East, and on the Iberian Peninsula – its use became common after efficient production methods were devised in the seventeenth century. An interesting example is *Damascus steel*, also called *Wootz steel*. *Damascus swords* were of legendary sharpness and strength. Recent studies have suggested that carbon nanotubes (Section 4.11.5.4) were included in its structure, which might explain the high quality of *Damascus steel*.

With the invention of the *Bessemer process* in the nineteenth century, steel became an inexpensive mass-produced good. Today, steel is one of the most common



Cupola furnace. Opening of the furnace with oxy lancing. Courtesy of Linde Engineering, Germany.



Section of coke oven battery. Courtesy of Uhde, Germany.



Coking plant Schwelgern in Duisburg, Germany. Courtesy of Uhde, Germany.

materials in the world and is a major component in buildings, tools, railways, and automobiles, just to name a few applications.

Figures 6.5.1 and 6.5.2 give an overview of the basic processes of steel making.

6.5.1.1 Steel Production Based on the Blast Furnace Route

The main route from iron ore to steel is via blast furnaces to produce molten iron (pig iron) from iron ore, coke and air. The coke is produced in coking plants from hard coal. Once the iron is refined in the blast furnace, the hot metal is transferred to the basic oxygen furnace, where pure oxygen is blown into the liquid pig iron through a water-cooled lance. The carbon content is reduced by oxidation to CO

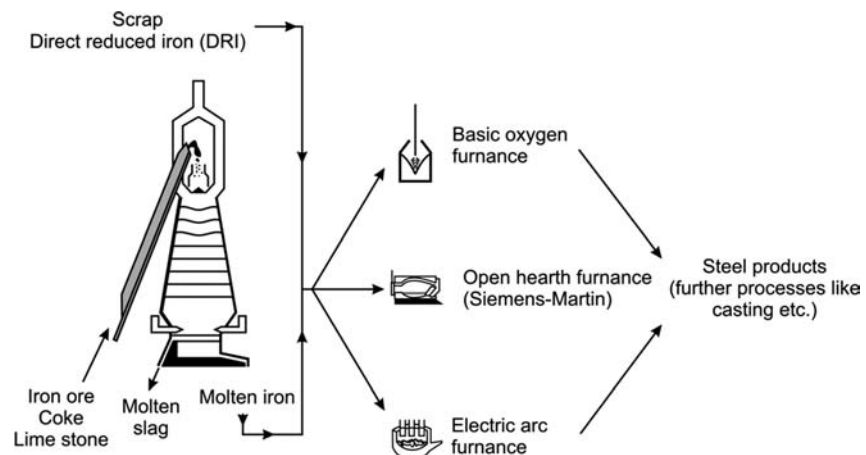


Figure 6.5.1 Basic processes for steel production from iron ore, scrap, and direct reduced iron.

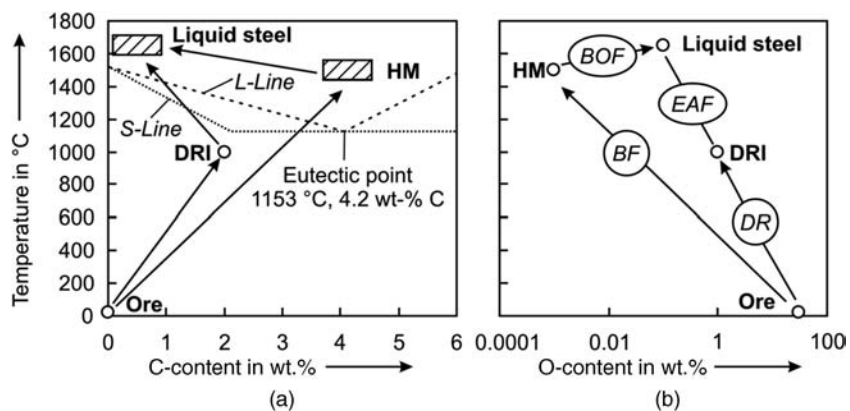


Figure 6.5.2 Routes from iron ore ($\approx \text{Fe}_2\text{O}_3$) to liquid crude steel (BF: blast furnace, BOF: basic oxygen furnace, DR: direct reduction, EAF: electric arc furnace, DRI: direct reduced iron, HM: hot metal, L-/S-line: liquidus/solidus line. Partly adapted from Schmoele and Luengen (2007).

and CO₂. Unwanted impurities such as sulfur, silicon, manganese, silica, and phosphorus are oxidized either to gaseous components such as SO₂ or to solid oxides like SiO₂ and P₂O₅ that are formed and incorporated in the generated slag. To flux the impurity oxides to form a low melting fluid slag, lime (CaO) is charged into the converter, and sulfur is then also partly incorporated into the slag as CaS. This process is also known as *LD* converter, after the two Austrian towns *Linz* and *Donawitz* near the *Voest-Alpine* steelworks where the process was developed in the beginning of the 1950s.

In former times, two other processes were also used to burn out the excess carbon and other impurities for the production of steel from pig iron. In the *Bessemer* process, air was blown through the molten iron. The bottom of the converter was perforated with a number of channels through which the air is forced into the converter. The process was rapid (about 15 min) and so there was only little time for chemical analysis and adjustment of the alloying elements in the steel. *Bessemer* converters also did not remove phosphorus efficiently, and certain grades of steel were sensitive to nitrogen, which is the major part of the air blast.

The second forerunner (and competitor for some time) of the basic oxygen furnace was the open hearth furnace [*Siemens-Martin* (SM) process], where the oxidative effect was achieved by addition of scrap, iron ore, lime, and some air, which release oxygen into the iron melt.

Bessemer processes and most open hearth furnaces were closed by the early 1970s and 1990s, respectively, not least because of their fuel inefficiency and problems with dust removal (SM process). Nowadays, they are almost completely replaced by oxygen furnaces.

6.5.1.2 Steel Production based on Scrap and Direct Reduced Iron (DRI)

The second route to steel is via an electric arc furnace, a common method of reprocessing scrap metal along with some DRI (direct reduced iron) for chemical balance to adjust the content of unwanted impurities like Cu. DRI is produced by reduction with gas (H₂, CO) or coal; 85% is based on natural gas that is converted by steam reforming into the reduction gas (Section 6.2.4).

Figure 6.5.3 indicates that about 60% of steel is produced by the blast furnace route and 35% from scrap via the electric arc furnace. DRI only contributes to about 5%.

In the following, the two main processes needed for steel production are examined in detail, namely, the production of blast furnace coke (Section 6.5.2) and the production of pig iron in the blast furnace (Section 6.5.3).

6.5.2

Production of Blast Furnace Coke

Coke is a solid carbonaceous material derived from pyrolysis (destructive “dry” distillation) of low-ash, low-sulfur coal. The volatile constituents are water, coal-gas, which consists mainly of H₂, CO, and CH₄, and coal-tar. Typical yields are 70 wt% coke and 30 wt% raw coke oven gas. Blast furnace coke is produced in coke oven batteries (see photograph on the second page of this subchapter) that consist of up to 100 slot type ovens in a side-by-side arrangement. These coking chambers are confined by brick walls, that is, the interspaces are heating chambers referred to as heating gas flues, and each chamber shares a heating flue with the adjacent oven. Typically, coking chambers are 0.35–0.6 m wide, 6–10 m high, and 8–12 m long, and thus have a volume in the range 20–70 m³.

First, selected coals are blended and pulverized. Some coal tar is added for appropriate bulk density control. The blended coal is charged into the coking chambers by a charging car, which moves on the roof of the coke oven battery in a longitudinal direction, and the chambers are filled from the top in a specific sequence via charging holes. The brick walls of each coking chamber are heated up to about 1100 °C and, in the course of time, the coal charge is heated and transformed by pyrolysis

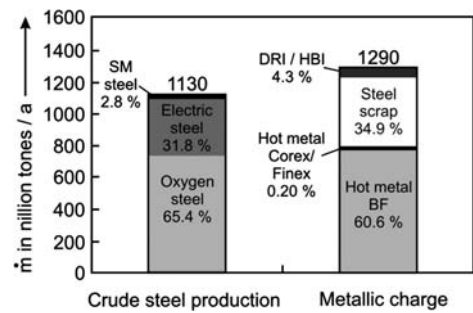


Figure 6.5.3 World steel production and metallic charge (SM: *Siemens Martin*, HBI: hot briquetted iron, BF: blast furnace. Adapted from Schmoele and Luengen (2007).

Table 6.5.1 Composition of raw coke oven gas (Jess, 1996; Benthaus *et al.*, 1978; Falbe, 1977).

Component	Content in vol.% (dry basis)
Hydrogen	59
Carbon monoxide	5
Methane	25
Carbon dioxide	1.6
Ethene	1.7
Ethane	0.9
Propene	0.5
Aromatics (benzene, toluene, xylenes)	0.9
Tar vapors (counted as naphthalene)	1.8
Hydrogen sulfide	0.9
Ammonia	0.8
Nitrogen	1.9

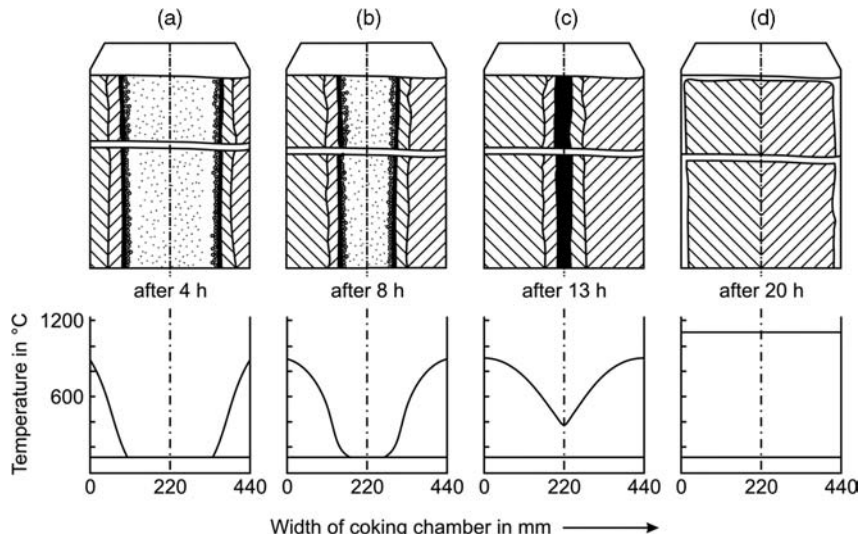
into high-temperature coke, whereas the volatile matter is driven off as hot coke oven gas. Table 6.5.1 gives the mean composition of this gas.

The heat is provided by combustion of a gas, normally either the top gas of a blast-furnace or the cleaned coke oven gas released from the coal during pyrolysis. The raw coke-oven gas is collected and sent to a by-product plant where various products are recovered (light oil, mainly aromatic C₆- to C₈-hydrocarbons, naphthalene, tar, clean coke-oven gas, sulfur, etc.). About half of the cleaned gas is reused directly in the coking plant as heating gas for the coke oven batteries. The surplus was used in former times as town gas, and careful handling was needed because of the risk of CO poisoning. Today, natural gas has almost completely replaced coal gas in urban households. At present, coke oven gas is used in the steel plant or for other industrial purposes. Non-by-product coke oven facilities are also in use to a small extent, where the off-gases are simply burnt on site to provide the heat to drive the coking process.

After a coking time of about 20 h, a pusher machine, which travels on rails alongside on one side of the battery, removes the door of the respective coking chamber while a so-called coke guide car simultaneously opens the door on the reverse side of the chamber. The hot coke is then pushed out of the oven by the coke guide car into a coke quenching car for conveyance to the quench tower where the hot coke is cooled by wet quenching with water. The cooled coke is then finally transported to a blast furnace.

The transformation of coal into coke takes place as follows (Figure 6.5.4). The heat is transferred from the heated brick walls into the coal charge. Initially, the

Figure 6.5.4 Transformation of coal into blast furnace coke in a coking chamber; (a) 600–1100 °C: coke, (b) 450–600 °C: semi coke, (c) 350–450 °C plastic stage, (d) 100–350 °C pre-degassed coal, and (e) 0–100 °C: coal and water. Adapted from Schmidt and Romey (1984).



coal charge is heated up to 100 °C and dried in the coking chamber, until the vaporization front has reached the center of the chamber. After drying and further heating to about 350 °C, the coal decomposes and forms soft plastic layers – a mixture of liquid tar compounds and dissolved coke particles. At about 450–600 °C, a marked evolution of tar and other lighter hydrocarbons takes place, followed by resolidification of the plastic mass into semi-coke. In the range 600–1100 °C, the coke stabilizes, which is characterized by contraction of the coke mass, structural development of the coke, and a final hydrogen evolution.

Because of the transient nature of coke production, these processes take place within the chamber at different horizontal positions, which feature different temperatures. For example, the center of the chamber (midplane) may still not be completely dry and thus still stays at 100 °C, whereas the coal attached to the hot wall may already be transformed into coke. The plastic layers move from each wall towards the center of the chamber, trapping the liberated gas. Once the plastic layers have met the midplane, all of the coal has been carbonized.

Figure 6.5.5 shows the influence of coking time on measured and calculated temperature profiles in a coking chamber 0.43 m wide.

6.5.2.1 Inspection of Transient Process of Coking of Coal

The coking process is complicated not only because of its transient nature; it is hard to simulate. Beside transient heat transfer, the following aspects have to be considered for an accurate description of the process:

- vaporization and recondensation take place (Hess, 1986; Sueßmeir *et al.*, 1987);
- chemical reactions occur such as pyrolysis and to a small extent gasification of coke with the deliberated steam at temperatures of more than 700 °C (Hess, 1986);
- the material parameters of the coal/coke (λ_C , a_C , ρ_C , and c_C) and of the brick wall (λ_B) depend strongly on temperature (Figure 6.5.6).

These three aspects are not considered here in order to derive simple solutions for the influence of different parameters such as the chamber width on the coking time. Subsequently, the coke formation process is simply reduced to a transient heat transport process between two plane walls (heated brick wall and coking chamber), each with constant material properties, and three different (border) cases are inspected.

6.5.2.2 Case I: Negligible Thermal Resistance of Coal/Coke Charge

For a negligible thermal resistance of the coal/coke charge compared to the resistance of the brick wall, the temperature in the chamber is constant but changes with time (Figure 6.5.7).

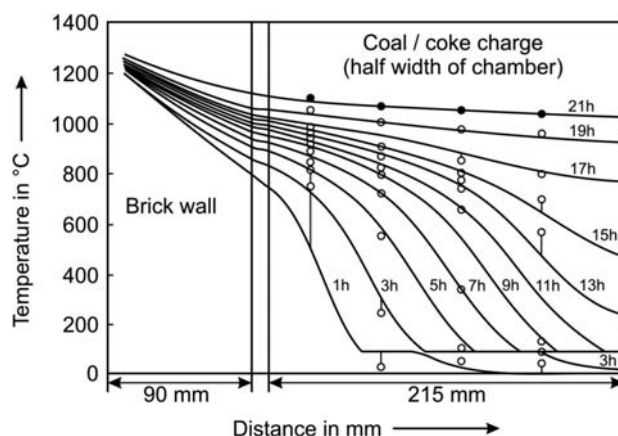
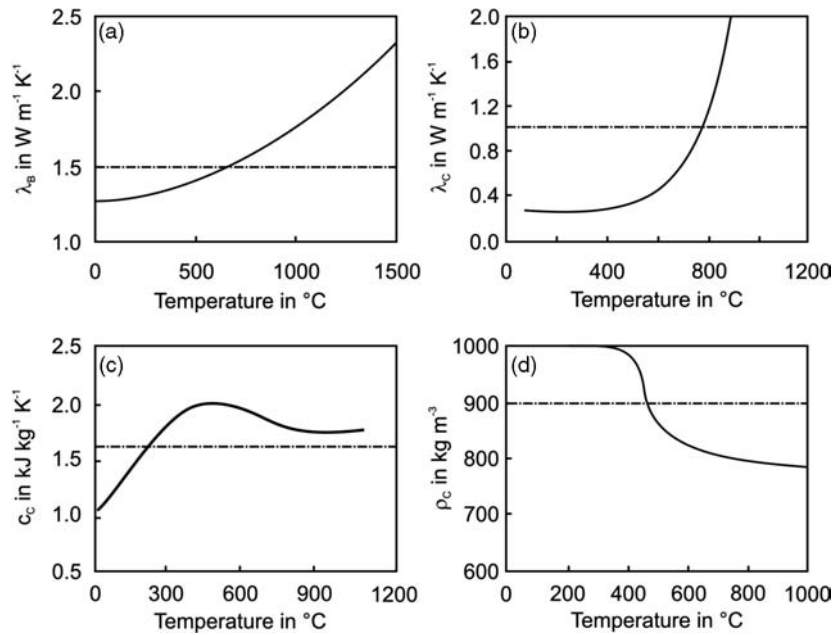


Figure 6.5.5 Influence of coking time on measured and calculated temperature profiles within a coking chamber 0.43 m wide (data from Hess, 1986).

Figure 6.5.6 Influence of temperature on parameters of heat transport during coking of coal for production of blast furnace coke: (a) thermal conductivity of the heated brick walls, (b) thermal conductivity of coal/coke, (c) heat capacity of coal/coke, (d) bulk density of coal/coke (dashed lines: mean values used for estimations given below; data from Hess, 1986).



The change of the enthalpy of the coal/coke charge is given by:

$$\frac{dH_C}{dt} = \rho_C c_C w_C A \frac{dT_C}{dt} \quad (6.5.1)$$

where w_C is the width of the coking chamber, A is the surface area, ρ_C is the bulk density of the coal/coke charge (kg m^{-3}), and c_C is the specific heat of the charge ($\text{J kg}^{-1} \text{K}^{-1}$).

The heat transfer through the two brick walls with thermal conductivity λ_B ($\text{W m}^{-1} \text{K}^{-1}$) to the charge is given by:

$$\dot{Q} = 2\lambda_B A \frac{(T_B - T_C)}{w_B} \quad (6.5.2)$$

where w_B is the width of the heated brick wall, T_B is the constant temperature on the heated side of the wall, and T_C is the temperature of the coal charge, which is assumed to be constant within the charge but not with time. Combination of Eqs. (6.5.1) and (6.5.2) leads to:

$$\frac{dH_C}{dt} = \dot{Q} \Rightarrow \frac{dT_C}{dt} = \left(\frac{2\lambda_B}{\rho_C c_C w_C w_B} \right) (T_B - T_C) \quad (6.5.3)$$

If all material properties are constant and do not depend on temperature and the changing structure of the coal/coke charge (which is in reality not true, Figure 6.5.6), Eq. (6.5.3) yields:

$$\frac{dH_C}{dt} = \dot{Q} \frac{dT_C}{T_B - T_C} = C_1 dt \quad \left(\text{with } C_1 = \frac{2\lambda_B}{\rho_C c_C w_C w_B} \right) \quad (6.5.4)$$

Integration of Eq. (6.5.4) leads to:

$$\frac{T_B - T_C}{T_B - T_{C,0}} = e^{-C_1 t} \quad (6.5.5)$$

and rearrangement with t_{coking} as final coking time and insertion of Eq. (6.5.4) leads to:

$$t_{\text{coking}} = -\frac{1}{C_1} \ln \left(\frac{T_B - T_C}{T_B - T_{C,0}} \right) = -\left[\frac{\rho_C c_C w_B}{2\lambda_B} \ln \left(\frac{T_B - T_{C,\text{final}}}{T_B - T_{C,0}} \right) \right] w_C \quad (6.5.6)$$

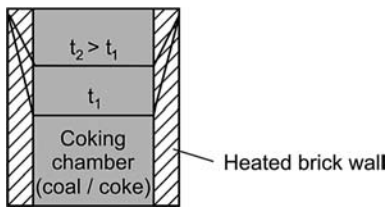


Figure 6.5.7 Border case I: negligible thermal resistance of the coal/coke charge compared to the resistance of the brick wall.

Typical (mean) values of the parameters of the coking process are (Figure 6.5.6): $w_B = 0.09 \text{ m}$, $w_C = 0.43 \text{ m}$, $\rho_C = 900 \text{ kg m}^{-3}$, $c_C = 1600 \text{ J kg}^{-1} \text{ K}^{-1}$, and $\lambda_B = 1.5 \text{ W m}^{-1} \text{ K}^{-1}$. If we take 1250°C for T_B , 20°C for the initial coal temperature $T_{C,0}$, and 1000°C for the final coke temperature $T_{C,\text{final}}$, Eq. (6.5.6) leads to a coking time of about 8 h. The real value (Figure 6.5.5) is about 20 h, which is the result of the thermal resistance of the coal charge that we have neglected.

In this (border) case, the coking time increases proportionally with the width w_C , Eq. (6.5.6), and thus the productivity of each coking chamber would be independent of chamber width:

$$\dot{m}_{\text{coke}} = \frac{\rho_C w_C A_{\text{chamber}}}{t_{\text{coking}}} = \frac{\lambda_B A_{\text{chamber}}}{0.8 c_C w_B} \quad (6.5.7)$$

(for case I, $T_B: 1250^\circ\text{C}$, $T_{C,\text{final}}: 1000^\circ\text{C}$)

Thus, if this case were true [$\dot{m}_{\text{coke}} \neq f(w_C)$], a small chamber width is favorable with regard to an increase in the production rate per unit volume ($\dot{m}_{\text{coke}}/V_{\text{chamber}} \sim 1/w_C$), but the number of chambers needed for a certain rate of coke production would be independent of w_C . Thus, the impact of a smaller width on the investment costs would be small, because the number of coking and heating chambers, brick walls, doors, and so on would remain constant. The optimum width would then almost only be determined by the operating costs, that is, by the number of working cycles N_{cycle} consisting of charging, pushing, quenching, cleaning, and sealing of coke oven openings, and so on, and N_{cycle} increases with decreasing width and coking time ($N_{\text{cycle}} \sim 1/t_{\text{coking}} \sim 1/w_C$) [Eq. (6.5.6)].

6.5.2.3 Case II: Negligible Thermal Resistance of Heated Brick Wall

The opposite to border case I is a negligible thermal resistance of the heated brick wall compared to the resistance of the coal/coke charge. Now, the temperature in the coal/coke changes not only with time but decreases in the horizontal direction towards the midplane of the charge, whereas the temperature within the brick wall is assumed to remain constant (Figure 6.5.8).

The heat balance of a differential element of the coal charge with thickness dx is given by:

$$\dot{Q}_x - \dot{Q}_{x+dx} = \frac{dH_C}{dt} \Leftrightarrow \lambda_C A \left(\frac{dT}{dx} \Big|_x - \frac{dT}{dx} \Big|_{x+dx} \right) = \rho_C c_C A dx \frac{dT}{dt} \quad (6.5.8)$$

where λ_C is the thermal conductivity of the coal charge. Rearrangement of Eq. (6.5.8) leads to the second law of Fourier [Eq. (3.2.43), Section 3.2.1.5]:

$$\frac{dT}{dt} = \frac{\lambda_C}{\rho_C c_C} \frac{d^2T}{dx^2} = a_C \frac{d^2T}{dx^2} \quad (6.5.9)$$

(with a_C as thermal conductibility of the coal charge)

As shown in Example 3.2.6 (Section 3.2.1.5), the solution of Eq. (6.5.9) depends on the *Fourier number* Fo and the *Biot number* Bi_h :

$$Fo = \frac{a_C t}{\left(\frac{w_C}{2}\right)^2} \quad (6.5.10)$$

$$Bi_h = \frac{w_C \lambda_B}{2 \lambda_C w_B} \quad (6.5.11)$$

For a negligible thermal resistance of the brick wall (as assumed for case II), Bi_h is infinite. As shown by Example 3.2.7, we can then use the following equation as a

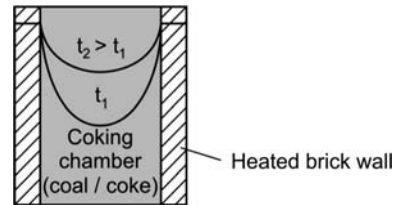


Figure 6.5.8 Border case II: negligible thermal resistance of the brick wall compared to the resistance of the coal/coke charge.

good approximation:

$$\frac{T_B - T_{C,\text{center}}}{T_B - T_{C,\text{center},0}} = 1.27 e^{-2.47 Fo} \quad (\text{for } Fo > 0.2 \text{ and } Bi_h \rightarrow \infty) \quad (6.5.12)$$

where T_B is the temperature of the heated brick wall (assumed to be constant), $T_{C,0}$ is the initial charge temperature, and $T_{C,\text{center}}$ is the midplane temperature of the coal charge at a given time t . Rearrangement of Eq. (6.5.12) and insertion of Eq. (6.5.10) lead to the coking time:

$$t_{\text{coking}} = \left(\frac{w_C}{2}\right)^2 \frac{\left[0.24 - \ln\left(\frac{T_B - T_{C,\text{center},\text{final}}}{T_B - T_{C,\text{center},0}}\right)\right]}{2.47 a_C} \quad (\text{for } Fo > 0.2 \text{ and } Bi_h \rightarrow \infty) \quad (6.5.13)$$

As in case I, we again assume $T_B = 1250^\circ\text{C}$, $T_{C,0} = 20^\circ\text{C}$, a final midplane temperature of 1000°C , and a width of the coal charge w_C of 0.43 m. For λ_C we use a mean value of $1 \text{ W m}^{-1} \text{ K}^{-1}$ (Figure 6.5.6) and a_C is then $7 \times 10^{-7} \text{ m}^2 \text{ s}^{-1}$. This leads to a coking time [Eq. (6.5.13)] of 14 h.

For this border case, the coking time increases proportionally with w_C^2 [Eq. (6.5.13)] and the productivity of each coking chamber is proportional to $1/w_C$. Thus, the number of chambers needed for a certain rate of coke production decreases in proportional to $1/w_C$, which strongly favors a small width to reduce the investment costs (number of coking/heating chambers).

A drawback of a smaller width (and shorter coking time, respectively) is that (as in case I) the number of working cycles N_{cycle} (charging, discharging, cleaning) increases with decreasing width. For example, about two cycles are needed per chamber and day for $w_C = 0.43 \text{ m}$ ($t_{\text{coking}} = 14 \text{ h}$), whereas eight cycles are needed per chamber and day for $w_C = 0.2 \text{ m}$ ($t_{\text{coking}} = 3 \text{ h}$). Thus, the total number of cycles (and thereby the operating expenses) increases with decreasing width of the coking chamber ($N_{\text{cycle, total}} \sim N_{\text{chamber}}/t_{\text{coking}} \sim 1/w_C$).

6.5.2.4 Case III: Thermal Resistances of Brick Wall and Coal Charge have to be Considered

For the values of λ_B , w_C , λ_C , and w_B as given above, Bi_h is 3.5, and the thermal resistance of the wall is not negligible. Solution by the transient temperature chart (Figure 3.2.20) leads to $Fo = 1.15$ and a coking time of 21 h, which is in agreement with measured data (Figure 6.5.5).

To estimate the influence of the chamber width on coking time, we make the same calculation for $w_C = 0.35$ and 0.51 m ($t_{\text{coking}} = 16$ and 27 h , respectively). If we use a simple power law with exponent n to describe the influence of the chamber width on the coking time, we get a good fit for $n = 1.4$ (Figure 6.5.9), a value that lies between the two border cases discussed before. Real coking plant data and accurate simulation lead to a similar value for n of about 1.3 (Hess, 1986). Consequently, t_{coking} of industrial coking chambers is proportional to about $w_C^{1.3}$, and thus the productivity of each chamber is proportional to $1/w_C^{0.3}$, which still favors a small width. Obviously, a value of around 0.5 m is optimal, if the pros and cons are balanced.

Although case III fairly represents the real coking process, all the above calculations do not consider important aspects discussed before like vaporization/recondensation, chemical reactions, and variation of material parameters of the coal/coke and the brick wall. In other words: the values chosen as mean values for λ_C , ρ_C , c_C , and λ_B coincidentally lead to a correct result.

More sophisticated models of the coking process and process simulation results are given in the literature, including the simulation with temperature-dependent values of λ_C , a_C , ρ_C , and c_C and pyrolysis and drying (Hess, 1986; Klose 1984a, 1984b; Rohde, Simonis, and Peters, 1969; Schmoele and Luengen, 2007; Sueßmeir et al., 1987).

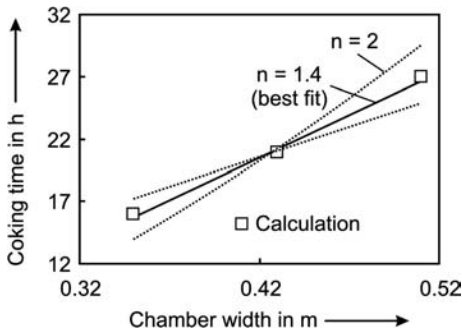


Figure 6.5.9 Influence of chamber width on coking time (simple power law, exponent n).

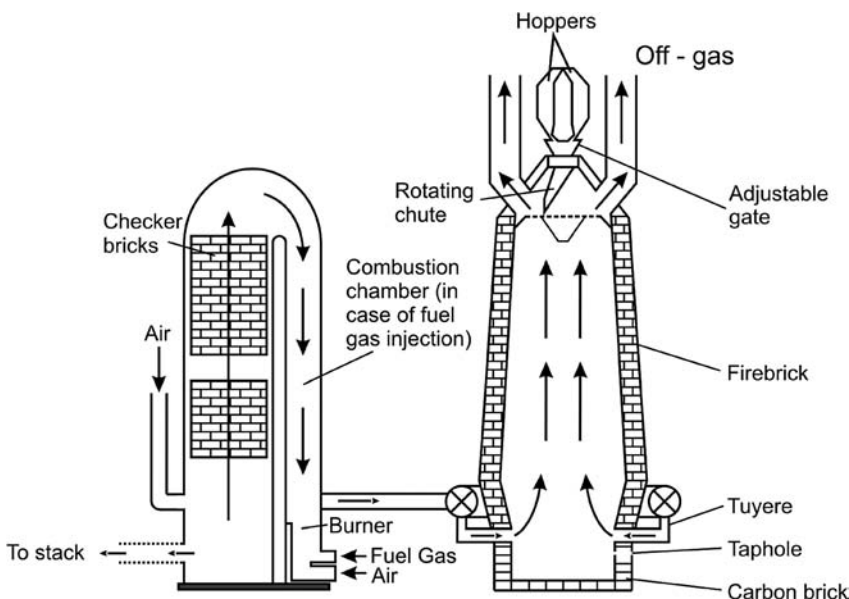


Figure 6.5.10 Configuration of a blast furnace.

6.5.3

Production of Pig Iron in a Blast Furnace

Modern blast furnaces (Figure 6.5.10) have a volume of 5000 m^3 and produce 10 000 tonnes of Fe per day. A fixed-matrix regenerator system with periodic flow – a so-called *Cowper* stove, named after *Edward A. Cowper* (see box) – is used to preheat the blast air up to 1300°C . The furnace is supplied with a constant flow of hot blast air by at least two identical regenerators operated in parallel. Usually, three are employed to reduce the temperature variations in the outlet gas. Cowper stoves are typically about 30 m high, 7 m in diameter, and are filled with refractory checker bricks. The bricks are heated by combustion of a part of the top gas produced in the furnace. Subsequently, the blast air flows through these hot bricks and is heated up. To minimize the temperature swing, part of the cold blast air is bypassed around the stove and mixed with the hot blast leaving the stove. A typical cycle time is about 2 h.

Figure 6.5.11 shows the mass and heat balance of a typical blast furnace. The furnace is operated with the injection of 160 kg pulverized coal per t of hot metal (HM). Coke consumption is 326 kg per t HM, and 43 m^3 of oxygen (as air) per t HM are added into the cold blast to achieve a sufficient temperature. The top gas leaves the blast furnace at a rate of 4.75 GJ per t HM. About two-thirds of the gas is

Edward Alfred Cowper (1819–1893), a British engineer, invented the regenerative preheating system of blast furnace air. He also invented the tangent spokes for bicycles.

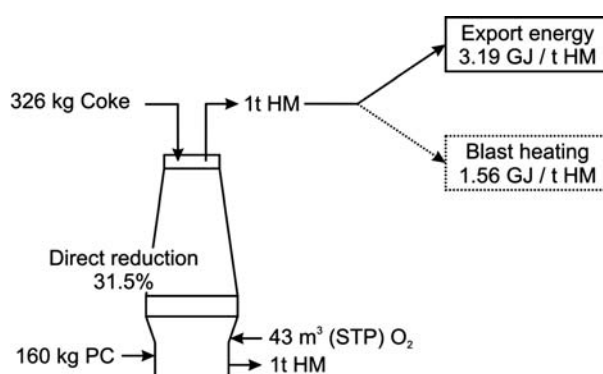
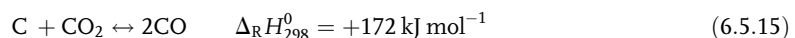
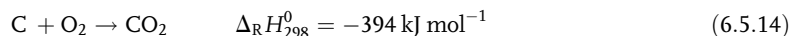


Figure 6.5.11 Mass and energy balance of a blast furnace (HM: hot metal, PC: pulverized coal). Adapted from Schmoele and Luengen (2007).

fed into the gas network of the steel work and one-third is used to preheat the blast air in the *Cowper* stoves.

The following main reactions take place in the blast furnace:

- Combustion and gasification of the coke (subsequently simply considered as "C"):



- Stepwise reduction of hematite via magnetite and wuestite to iron:

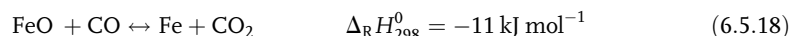
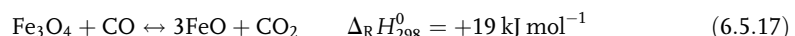
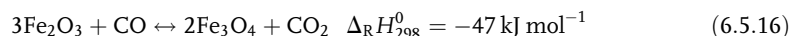
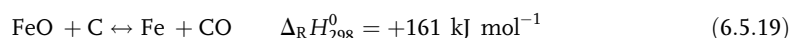


Figure 6.5.12 shows the thermodynamics of reduction of iron oxides by CO (and also by H_2 , although this is not so relevant for the blast furnace). For example, at 900°C , only traces of CO (in a mixture with CO_2) are needed to reduce Fe_2O_3 to Fe_3O_4 . The reduction of Fe_3O_4 to FeO is thermodynamically also favored as long as the CO content is above 15%. The final step of wuestite (FeO) reduction to iron is the crucial step, as we now need more than about 70% CO (and this reaction is also slow compared to reduction of hematite and magnetite).

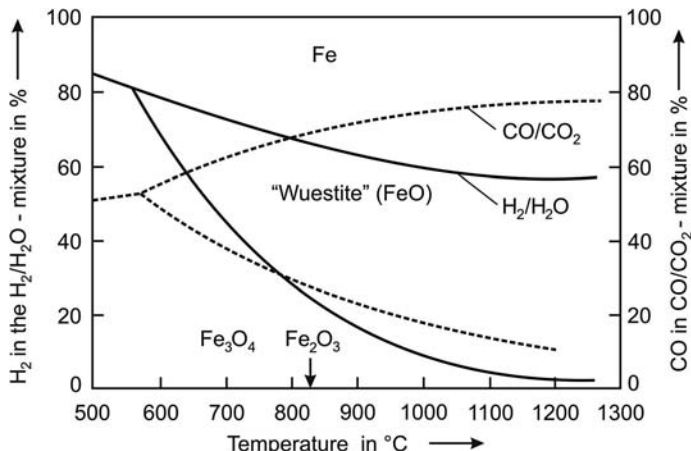
Figure 6.5.13 shows schematically the different zones of a blast furnace. At the bottom, where blast air is injected, temperatures of up to 2000°C are reached. At such high temperatures CO_2 formed by coke combustion [Eq. (6.5.14)] is instantaneously gasified to CO via the Boudouard reaction, Eq. (6.5.15). Note that the primary product of coke combustion is at temperatures above about 1000°C CO, but CO is quickly oxidized further as oxygen is present.

The CO formed in the tuyeres now reduces wuestite [Eq. (6.5.18)], which is formed in the upper part of the furnace by reduction of hematite and magnetite. As long as the temperature is high enough ($>1000^\circ\text{C}$ as shown below), the CO_2 that is formed by the reduction is "regenerated" to CO. Thus by combining Eqs. (6.5.15) and (6.5.18) we obtain:



which is called *direct reduction* although real direct reduction with carbon does not take place.

Figure 6.5.12 Thermodynamics of reduction of iron oxides by H_2 and CO.



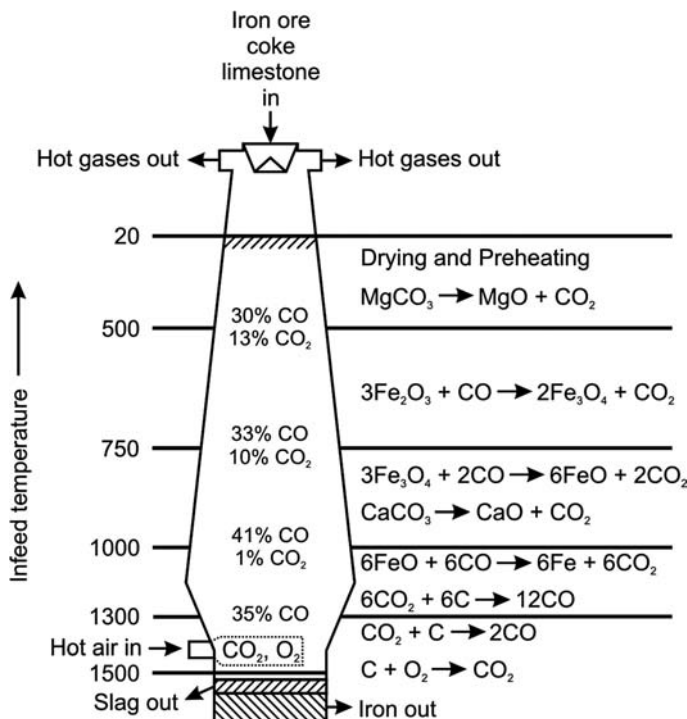


Figure 6.5.13 Reactions and reaction zones in a blast furnace.

For lower temperatures ($<1000\text{ }^{\circ}\text{C}$), CO_2 is no longer converted into CO , and thus reduction only occurs by CO [Eqs. (6.5.16)–(6.5.18)], which is called *indirect reduction*.

To prove that direct reduction, that is, the Boudouard reaction [Eq. (6.5.15)], comes to a standstill for $T < 1000\text{ }^{\circ}\text{C}$, we have to inspect the kinetics of coke gasification in more detail.

The gasification of coke with CO_2 can be regarded as a first-order reaction with regard to CO_2 . The effective reaction rate in a fixed bed reactor is given by:

$$-\frac{\dot{n}_{\text{CO}_2}}{dm_{\text{coke}}} = k_{m,\text{eff},\text{CO}_2} c_{\text{CO}_2,g} \quad (6.5.20)$$

If we do not consider the change of particle with time (solid ash layer, shrinking particle size etc., Section 4.6), we can use the equations for the influence of pore diffusion and external mass transfer that were deduced in Section 4.5 for heterogeneous catalysis. The effective rate constant $k_{m,\text{eff},\text{CO}_2}$ is given by Eq. (4.5.103), and for CO_2 gasification we have:

$$k_{m,\text{eff},\text{CO}_2} = \eta_{\text{overall}} k_m = \left(\frac{1}{\beta A_m} + \frac{1}{\eta_{\text{pore}} k_{m,\text{CO}_2}} \right)^{-1} \quad (6.5.21)$$

$$\eta_{\text{pore}} = \frac{\tanh \phi}{\phi} \quad \left(\text{with } \phi = \frac{d_p}{6} \sqrt{\frac{k_{m,\text{CO}_2} \rho_p}{D_{\text{eff},\text{CO}_2}}} \right) \quad (6.5.22)$$

The mass transfer coefficient β is calculated by Eqs. (3.2.68)–(3.2.71).

All parameters needed for the calculation are given in Table 6.5.2. The result of such a calculation for a typical blast furnace coke with a particle diameter of 4 cm is given in Figure 6.5.14. At temperatures above about $1000\text{ }^{\circ}\text{C}$, pore diffusion limits the effective rate, and for $T > 1500\text{ }^{\circ}\text{C}$ the rate is increasingly controlled by the external diffusion (film diffusion).

From the effective rate of gasification by CO_2 we can calculate the CO_2 conversion for the conditions of a blast furnace (Table 6.5.3). Assuming plug flow and a

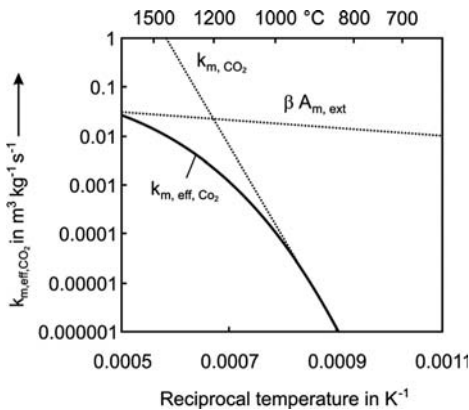


Figure 6.5.14 Effective rate of gasification of coke with CO_2 (for conditions see Table 6.5.1).

Table 6.5.2 Parameters used to calculate the effective reaction rate of coke gasification with carbon dioxide. Partly taken from Hedden (1976) and Heynert and Hedden (1961).

Parameter	Value ($p = 1 \text{ bar}$)	Comment
Rate constant k_{m,CO_2}	$10^{11} \exp[-360\ 000/(RT)] \text{ m}^3 \text{kg}^{-1} \text{s}^{-1}$	
Rate constant k_{m,O_2}	$4 \times 10^{10} \exp[-243\ 000/(RT)] \text{ m}^3 \text{kg}^{-1} \text{s}^{-1}$	
Particle diameter d_p	0.04 m	
Diffusion coefficient of $\text{CO}_2 D_{\text{CO}_2}$	0.0001 $\text{m}^2 \text{s}^{-1}$ (800 °C)	$\sim T^{1.75}$
Effective diffusion coefficient $D_{\text{eff},\text{CO}_2}$	0.1 D_{CO_2}	
Diffusion coefficient of $\text{O}_2 D_{\text{O}_2}$	0.00019 $\text{m}^2 \text{s}^{-1}$ (800 °C)	$\sim T^{1.75}$
Effective diffusion coefficient $D_{\text{eff},\text{O}_2}$	0.1 D_{O_2}	
Gas velocity (empty reactor) u_e	1 m s^{-1} (800 °C) ^{a)}	$\sim T$
Reynolds number $Re_p = u_e d_p / (\nu \rho)$	530 (800 °C)	
Bed porosity ε	0.5	
Mass transfer coefficient β	0.085 m s^{-1} (800 °C)	$\sim T^{1.75}$
Kinematic viscosity of gas ν	0.00015 $\text{m}^2 \text{s}^{-1}$ (800 °C)	$\sim T^{1.75}$
Density of coke particle ρ_p	1000 kg m^{-3}	
Bulk density of coke bed ρ_b	500 kg m^{-3}	
External surface area of coke particles A_m	0.15 $\text{m}^2 \text{kg}^{-1}$	

a) In a blast furnace, the gas flows upwards countercurrent to the solid phase (ore and coke), which slowly moves downwards with a velocity of about 2 m h^{-1} (Heynert and Hedden, 1961) compared to an interstitial gas velocity of about 2 m s^{-1} .

Table 6.5.3 Typical data of a modern blast furnace^{a)}.

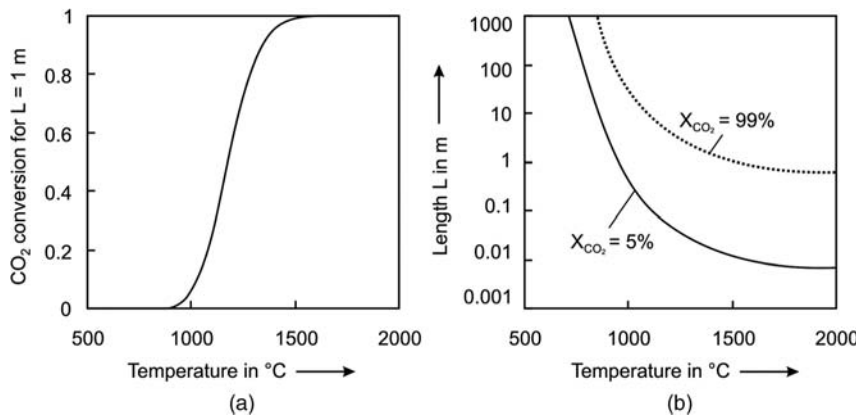
Parameter	Value
Useful volume	3125 m^3
Hearth diameter	12 m
Number of tuyeres	32
Number of tapholes	3
Pressure (tuyeres/top of blast furnace)	5/3.3 bar
Burden (pellets, sinter, lump ore, 59 wt% iron, 22.6 wt% oxygen as $\text{FeO}_{1.33}$ ^{b)}	515 t h^{-1}
Coke (including injection of heavy oil (15 wt%) and tar (1 wt%))	145 t h^{-1}
Hot blast (1217 °C) with 24.4% O_2 (96% air and 4% oxygen)	$322\ 000 \text{ m}^3 \text{h}^{-1}$ (NTP)
Hot metal (1476 °C): 94.6 wt% Fe, 4.3 wt% C, 1.1 wt% others (Si, Mn, P, S)	322 t-HM h^{-1}
Slag (wt%): 37% CaO , 39% SiO_2 , 12% Al_2O_3 , 9% MnO , 3% others	79 t h^{-1}
Top gas (128 °C): 23.2% CO, 23.3% CO_2 , 4.6% H_2 , 48.9% N_2/Ar	$498\ 000 \text{ m}^3 \text{h}^{-1}$ (NTP)
<i>Oxygen mass balance:</i>	
in as O_2 in hot blast	$7015 \text{ kmol-O h}^{-1}$
in as $\text{FeO}_{1.33}$ in burden	$7260 \text{ kmol-O h}^{-1}$
in as CO_2 in burden (MnCO_3 , CaCO_3)	$1243 \text{ kmol-O h}^{-1}$
out as CO in top gas	$5158 \text{ kmol-O h}^{-1}$
out as CO_2 in top gas	$10\ 360 \text{ kmol-O h}^{-1}$
<i>Carbon mass balance:</i>	
in as coke ^{c)}	$10\ 871 \text{ kmol-C h}^{-1}$
in as CO_2 in burden (MnCO_3 , CaCO_3)	$621 \text{ kmol-C h}^{-1}$
out as CO in top gas	$5158 \text{ kmol-C h}^{-1}$
out as CO_2 in top gas	$5180 \text{ kmol-C h}^{-1}$
out as C in hot metal	$1154 \text{ kmol-C h}^{-1}$
Contribution of indirect reduction ^{d)}	63%

a) Data from www.expeditionvoestalpine.com/hochofen.

b) According to Heynert and Hedden (1961), the O to Fe ratio is in a range of 1.31 to 1.47 mol-O mol-Fe⁻¹. The value used here (1.33) was estimated based on the mass balance of oxygen.

c) Estimation based on the carbon mass balance, that is, the carbon content of the coke (including heavy oil and tar) is 90 wt%, which is a reasonable value.

d) CO_2 formed by indirect reduction = CO_2 in top gas minus CO_2 in burden = 4559 kmol h^{-1} . The production rate of HM (with 94.6 wt% Fe) is $322 \text{ t-HM h}^{-1} = 305 \text{ t-Fe h}^{-1} = 5454 \text{ kmol-Fe h}^{-1} = 7254 \text{ kmol oxygen as } \text{FeO}_{1.33} \text{ h}^{-1}$, which leads to a contribution of the indirect reduction of 63% ($4559/7254$).



first-order reaction we have:

$$X_{\text{CO}_2} = 1 - e^{-k_{m,\text{eff},\text{CO}_2} \rho_b \tau} \quad \left(\text{with } \tau = \frac{L}{u_e} \right) \quad (6.5.23)$$

where L is the length of the reactor (here the blast furnace) and u_e the gas velocity (empty reactor). By Eq. (6.5.23) we can then calculate the conversion for a given length and temperature or the length needed to reach a certain conversion at a certain temperature (Figure 6.5.15). This leads to the following conclusions: To reach a conversion of more than 5% within a length of 1 m, a temperature of over 1000 °C is needed (Figure 6.5.15a). For lower temperatures, the length needed for 5% conversion increases exponentially (Figure 6.5.15b). Interestingly, for the high temperature regime and thus for a complete control by external mass transfer, the length needed for a high degree of conversion (in Figure 6.5.15, a conversion of 99% was assumed) is almost constant. Here we have a length of about 0.8 m, which is 20 times the particle diameter. This confirms the rule of thumb that for processes controlled by external mass transfer we only need a reactor length for complete conversion of the order of magnitude of ten particle diameters (Example 4.5.3, Section 4.5.3.1).

Similar calculations can be performed for coke combustion, if we use Eqs. (6.5.20)–(6.5.22) with the index “O₂” instead of “CO₂,” and the rate constant of combustion from Table 6.5.2.

Figure 6.5.16 shows a comparison of the effective rate constants for coke combustion and CO₂ gasification, indicating that the rate constant of the chemical reaction of combustion is by several orders of magnitude faster than the Boudouard reaction. For a particle diameter of 4 cm, the combustion rate is then already controlled by film diffusion for temperatures above about 900 °C. This confirms that at the much higher temperatures reached in the tuyeres (about 2000 °C) the combustion is almost instantaneous, that is, only a length of ten particle diameters are needed for complete oxygen conversion.

6.5.3.1 Coke Consumption of a Blast Furnace: Historical Development and Theoretical Minimum

The consumption of fuel (blast furnace coke plus powered coal or oil injected into the tuyeres) per tonne of pig iron of a blast furnace has decreased quite substantially during recent decades and has today reached a value of about 480 kg (Figure 6.5.17). Data for a modern blast furnace with oil injection are given in Table 6.5.3.

The theoretical minimum value of coke consumption (without injection of oil or pulverized coal) is 420 kg fuel per tonne Fe, as already calculated by Heynert and Heden in the early 1960s based on measured temperature and concentration profiles in a technical blast furnace (Figure 6.5.18) and by theoretical considerations (Heynert and Heden, 1961).

Figure 6.5.15 Gasification of blast furnace coke with CO₂: conversion within a fixed bed of 1 m (a) and length of fixed bed needed for 5% and 99% conversion (b) (for conditions see Table 6.5.2).

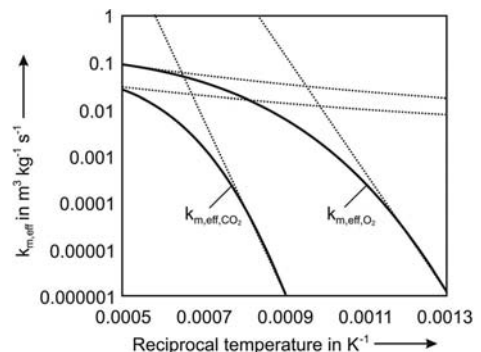


Figure 6.5.16 Effective rate constant of gasification of blast furnace coke with CO₂ and combustion with O₂ (fixed bed; data from Table 6.5.2).

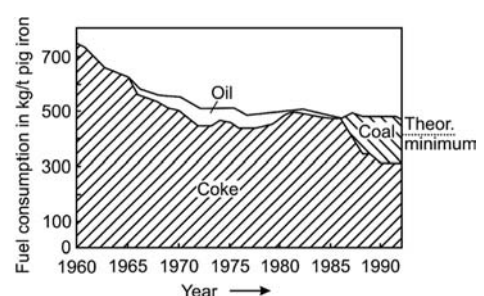


Figure 6.5.17 Historical development of specific fuel consumption (coke plus pulverized coal or oil) of a blast furnace. Data from Peters and Reinitzhuber (1994).

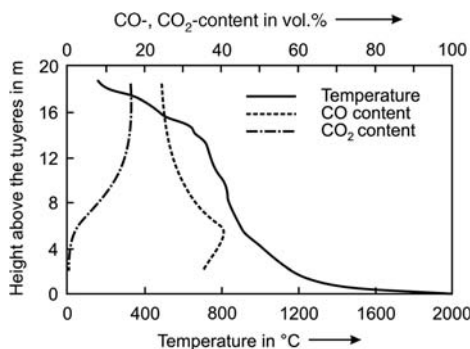


Figure 6.5.18 Temperature and CO/CO₂ content in a blast furnace (adapted from Heynert and Hedden, 1961).

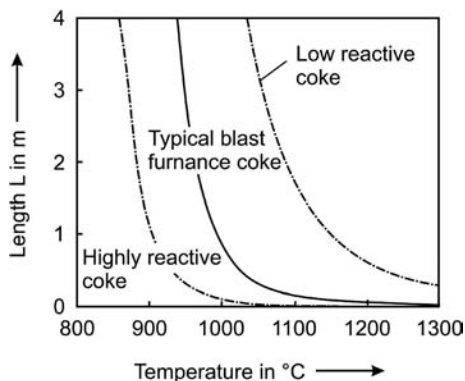
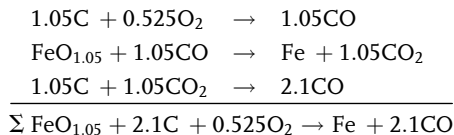


Figure 6.5.19 Conversion of coke with CO₂: length needed for 5% conversion with a very high reactive coke (factor 10 higher) and a low reactive coke (factor 10 lower).

Figure 6.5.18 indicates that at the position where 1000 °C is reached (3 m above the tuyeres), CO₂ can be detected for the first time. The reason for this is the low reactivity of blast furnace coke, which leads to a standstill of the *Boudouard* reaction at around 1000 °C (Figure 6.5.15). For very reactive blast furnace coke this may be at 900 °C and for an unreactive coke at 1100 °C. Two questions therefore arise: What is the influence of the reactivity on coke consumption? What is the minimal value of coke consumption? Both questions can be answered by the inspection of three cases, (I) a very reactive, (II) a very unreactive coke, and (III) a coke with an ideal reactivity. A furnace without coal or oil injection in the tuyeres is assumed.

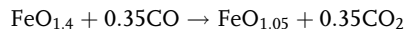
Case I: Coke with a Very High Reactivity For this case we use the following assumptions: The temperature reached when wuestite (FeO_{1.05}) is completely reduced by CO is about 900 °C. The coke is so reactive that at this temperature CO₂ is still gasified. This is only just a border case as the reactivity would then have to be several orders of magnitude higher than that of typical blast furnace coke. As shown in Figure 6.5.19, even for a reactivity that is ten times higher only 5% conversion would be reached within 1 m length at 900 °C.

For the zone of direct reduction, the mass balance for the case of a coke that is still completely gasified until 900 °C is reached reads as:



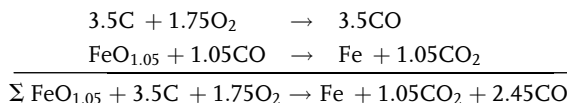
After reduction of wuestite (FeO_{1.05}), the gas only consists of CO (about 52%) and N₂ (rest) if we neglect the small amount of H₂ (1–5 vol.-%) from pyrolysis and the water-gas shift reaction (CO + H₂O → CO₂ + H₂) that may take place to a certain extent in the blast furnace.

The subsequent indirect reduction of Fe₂O₃ (via Fe₃O₄) to FeO_{1.05} takes place in the zone above the direct reduction zone. Typically, the molar ratio of oxygen to iron is not exactly 1.5 (as in Fe₂O₃), and so we use a more realistic value of 1.4 (FeO_{1.4}):



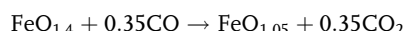
In summary, 2.1 mol of coke (C) would be consumed per mol Fe (451 kg-C per t Fe). The contribution of indirect reduction to the overall reduction would be 25% (0.35/1.4).

Case II: Coke with a Very Low Reactivity Here we assume that the coke is so unreactive that gasification only takes place in the tuyeres, that is, CO₂ formed by wuestite reduction is no longer gasified, that is, direct reduction [Eq. (6.5.18)] would not take place. The mass balances therefore read as:



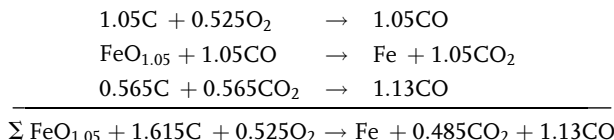
More FeO_{1.05} cannot be reduced with regard to thermodynamics as a minimum CO to CO₂ ratio (at 900 °C) of 7/3 is needed (70% CO in a CO/CO₂ mixture, Figure 6.5.12).

The mass balance of the subsequent indirect reduction of FeO_{1.4} to FeO_{1.05} reads as:

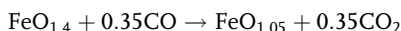


In summary, 3.5 mol of coke (C) would be consumed per mol of Fe (752 kg-C per t Fe).

Case III: Coke with Optimal Reactivity for a Blast Furnace “Ideal” coke should have a reactivity such that after reduction of $\text{FeO}_{1.05}$ the molar CO-to- CO_2 ratio is exactly 7:3, which is the ratio needed thermodynamically. The mass balance is as follows:



Thus, after $\text{FeO}_{1.05}$ reduction is finished, the CO-to- CO_2 ratio would be 7:3 (1.13/0.485) to fulfill the thermodynamics. The subsequent indirect reduction of $\text{FeO}_{1.4}$ gives:



In summary, 1.615 mol of coke (C) would be consumed per mol Fe (347 kg-C per t Fe). The contribution of the indirect reduction to the overall reduction is then about 60% ($0.485 + 0.35$ mol CO_2 formed by indirect reduction compared to 1.4 O in $\text{Fe}_{1.4}$).

To estimate the minimum coke consumption, the following aspects must be considered:

- Typically, the HM-to-Fe ratio is 1.06 t HM per t Fe, and 43 kg of carbon are dissolved per t HM.
- Blast furnace coke typically has a carbon content in a range 86–89 wt% (Ivanov, Kalchenko, and Kalach, 1975; Falbe, 1977). The remainder is mainly mineral matter (10%), moisture (1%), and some volatiles (1%) released at high temperatures (Falbe, 1977). Here we use an average value of 0.87 kg carbon per kg of coke or about 1.15 kg-coke per kg-C.

In summary, this leads to a minimum coke consumption of 420 kg per tonne of hot metal:

$$\begin{aligned} \frac{m_{\text{coke}}}{m_{\text{HM}}} &= \underbrace{\frac{347 \text{ kg C}}{\text{kg Fe}}}_{\text{Minimum consumption for reduction (case III)}} + \underbrace{43 \frac{\text{kg C}}{\text{kg HM}}}_{\text{Carbon solved in hot metal}} = \frac{399 \text{ kg coke}}{1.06 \text{ kg HM}} + 43 \frac{\text{kg C}}{\text{kg HM}} \\ &= 420 \frac{\text{kg coke}}{\text{kg HM}} \end{aligned} \quad (6.5.24)$$

The contribution of the indirect reduction and thus the influence of the coke reactivity on the coke consumption is shown in Figure 6.5.20 in comparison to process data. As we can see, modern furnaces almost operate with a fuel consumption near the theoretical optimum of 420 kg coke (including injected oil or coal) per tonne of iron, and the coke reactivity is almost at the optimum value corresponding to a contribution of the indirect reduction of about 63%. According to the data given in Figure 6.5.20, for blast furnaces at the end of the 1950s the coke reactivity was slightly too high. This was experimentally proven by *Hedden and Heynert* (1961), who tested cokes with different reactivities in an industrial blast furnace.

6.5.3.2 Residence Time Distribution of a Blast Furnace

One final reaction engineering aspect of a blast furnace that should be discussed here is the residence time distribution. The hydrodynamics and the configuration of the different phases consisting of the upflowing reduction, gas and coke, and iron ore that slowly go downwards are complicated, as shown schematically by the sectional view of the interior in Figure 6.5.21.

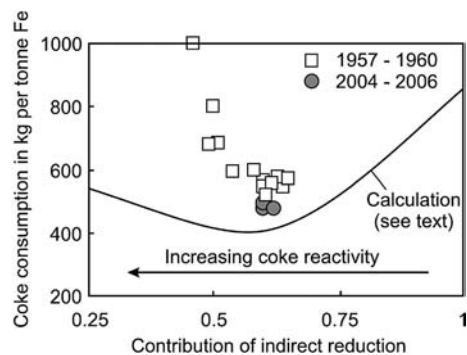
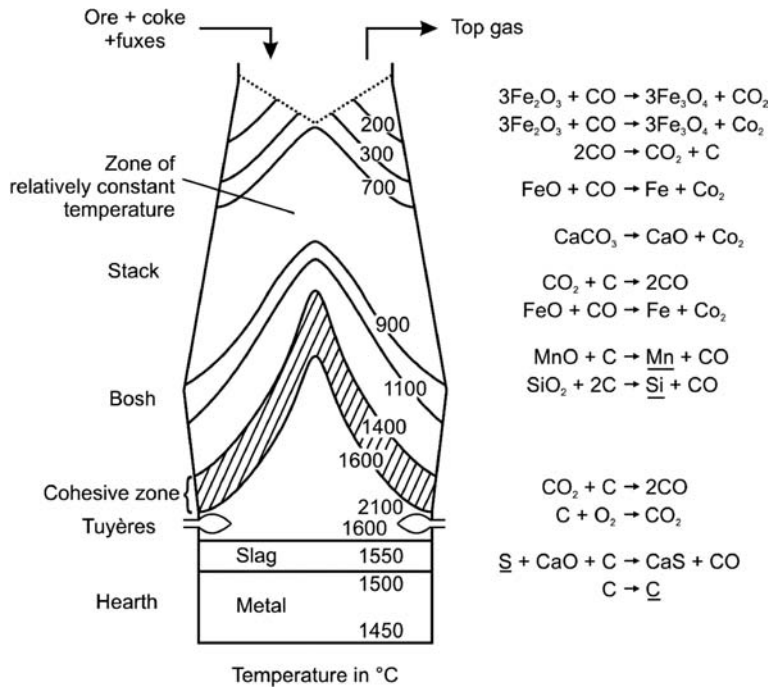


Figure 6.5.20 Contribution of indirect reduction on the coke consumption of a blast furnace [data from 1957 to 1960 from Germany, Sweden, and Japan (adapted from Heynert and Hedden, 1961), data for blast furnaces from 2004 to 2006 from [www.expeditionvoestalpine.com/hochofen](http://expeditionvoestalpine.com/hochofen)].

Figure 6.5.21 Sectional view of the interior of a blast furnace (schematically, hatched: cohesive zone, where the metallic burden loses permeability, impeding gas flow).



Nevertheless, the blast furnace is an instructive example to examine the question of to what extent this reactor can be regarded as an ideal plug reactor. As deduced in Section 4.10.5.1, we need the residence time distribution, which was measured in 1969 by a pulse experiment with the injection of ^{85}Kr into the blast air (Standish and Polthier, 1975, see also Levenspiel, 1999). Figures 6.5.22 and 6.5.23 give the dimensions of the blast furnace and the experimental results.

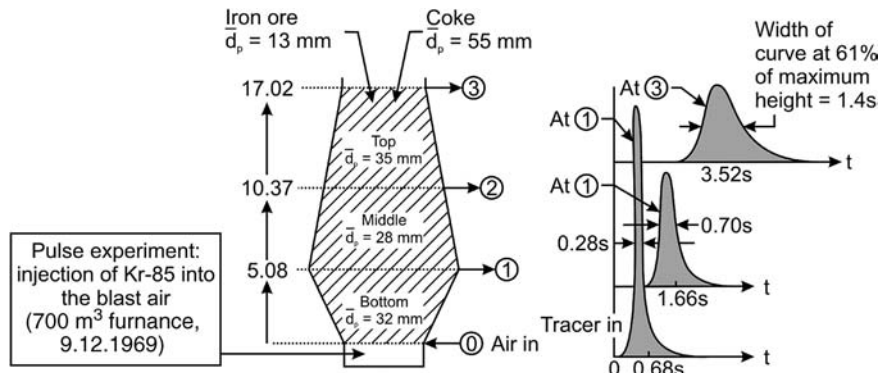
The deviation of the blast furnace from plug flow behavior can be described by the tanks-in-series model (Section 4.10.5) or by the dispersion model (Section 4.10.6).

Tanks-in-Series Model Figure 6.5.23 shows the residence time distribution of the investigated blast furnace in comparison to a cascade of stirred tanks with 20, 30, and 50 tanks. The best fit is obtained for a number N of 30. For conversion of a gaseous reactant i in a blast furnace, we therefore have according to Eq. (4.10.32) with $N = 30$:

$$X_i = \frac{\left(1 + \frac{Da}{30}\right)^{30} - 1}{\left(1 + \frac{Da}{30}\right)^{30}} \quad (6.5.25)$$

compared to an ideal plug flow reactor with $X_i = 1 - e^{-Da}$, Eq. (4.10.25).

Figure 6.5.22 Measurement of residence time distribution in a blast furnace. Standish and Polthier (1975); adapted from Levenspiel (1999).



For example, a *Damkoehler number* Da of 4 would lead to a conversion of 98.2% in a PFR. In the blast furnace [Eq. (6.5.25)], almost the same value of 97.7% is reached. Thus the blast furnace can almost be regarded as an ideal plug flow reactor.

Dispersion Model For a small extent of dispersion ($Bo > 50$), the variance σ_θ^2 characterizing the width of the residence time distribution is given by Eq. (4.10.102):

$$\sigma_\theta^2 = 2 \frac{D_{ax}}{uL} = \frac{2}{Bo} \quad (4.10.102)$$

The width of the curve at the point of inflection ($E_{\theta,\max} = 0.61 E_{\theta,\text{max}}$) equals $2\sigma_\theta$, and by Figure 6.5.23 we here obtain a value for σ_θ of 0.2. Insertion of this value into Eq. (4.10.102) leads to a high value of the *Bodenstein number* Bo of 50 and thus to a low influence of backmixing.

By Eq. (4.10.105) we can then also calculate the numbers of tanks-in-series N :

$$N = \frac{Bo}{2} \quad \text{for } Bo \geq 50 \quad (4.10.105)$$

which here leads to a value of 25, which is in good agreement with the value obtained by matching the RTD (Figure 6.5.23).

Summary of Section 6.5 (take-home messages)

- **Steel** is an alloy consisting of iron with a carbon content of up to 2 wt%. Carbon is the most important alloying material; however, for high quality steels various other elements are also used such as chromium and nickel. Carbon and other elements act as a hardening agent, and their amount control the steel qualities such as the hardness, ductility, and tensile strength. Steel with increased carbon content is harder, but is also more brittle.
- The main route from **iron ore to steel** is via blast furnaces to produce molten iron (pig iron) from iron ore, coke, and air. The coke is produced in coking plants from hard coal. Once the iron is refined in the **blast furnace**, the hot metal is transferred to the basic oxygen furnace, where the carbon content is reduced by oxidation to CO and CO₂. The second route to steel is via an **electric arc furnace**, a common method of reprocessing **scrap metal** along with some **direct reduced iron** (DRI), which is produced by reduction with gas (H₂, CO) or coal. Today, 60% of the steel is produced by the blast furnace route, and 35% from scrap. DRI only contributes about 5%.
- **Blast furnace coke** is produced in coke oven batteries that consist of up to 100 slot type ovens in a side-by-side arrangement. These **coking chambers** are confined by brick walls. The interspaces are heating gas flues, and each chamber shares a heating flue with the adjacent oven. Coking chambers are about 0.5 m wide, 8 m high, and 10 m long. First, selected coals are blended, pulverized, and charged into the coking chambers. The brick walls are heated to about 1100 °C and, in the course of time, the coal charge is heated and transformed by pyrolysis into coke, whereas the volatile matter is driven off as hot coke oven gas. After a coking time of about 1 day the hot coke is pushed out of the oven and quenched with water.
- The **coke formation process** can be simplified as a transient heat transport process between two plane walls (brick wall and coking chamber with width w_C). Two thermal resistances have to be considered, the coal/coke charge and the brick wall. Solution of Fourier's second law with the *Fourier number* Fo and *Biot number* Bi_h parameters shows that the coking time of industrial coking chambers is proportional to about $w_C^{1.4}$, which favors a small width.

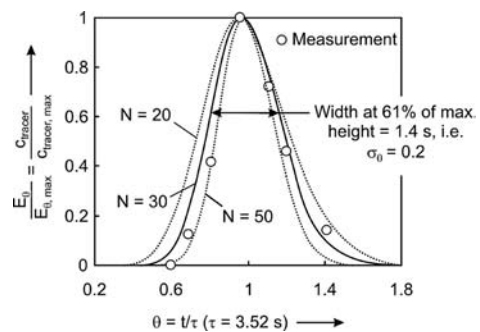


Figure 6.5.23 Residence time distribution in a blast furnace [data from Levenspiel (1999)].

- **Modern blast furnaces** have a volume of 5000 m^3 and produce 10 000 tonnes Fe per day. The following main reactions take place in the blast furnace: (i) combustion and gasification of the coke and (ii) stepwise reduction of hematite via magnetite and wuestite (FeO) to iron. The thermodynamics of reduction of iron oxides by CO show that the final step of wuestite reduction is the crucial step. Different zones of a blast furnace have to be considered. At the bottom, where the hot blast air is injected, temperatures of up to 2000°C are reached. At such high temperatures CO_2 (formed by coke combustion) is instantaneously gasified to CO via the Boudouard reaction. The CO formed in the tuyeres now reduces wuestite, which is formed in the upper part of the furnace by reduction of hematite and magnetite. As long as the temperature is high enough ($>1000^\circ\text{C}$) the CO_2 , which formed by ore reduction, is “regenerated” to CO, which is called **direct reduction** although “real” direct reduction with carbon does not take place. At temperatures below 1000°C , CO_2 is no longer converted into CO, and thus reduction only occurs by CO, which is called **indirect reduction**.
- At temperatures above about 1000°C , pore diffusion limits the **effective rate of CO_2 gasification**, and for $T > 1500^\circ\text{C}$ the rate is increasingly controlled by the external diffusion (film diffusion). Comparison of the effective rate constants for **coke combustion** and CO_2 gasification shows that the rate constant of the chemical reaction of combustion is by several orders of magnitude larger than the Boudouard reaction. For a particle diameter of 4 cm, the combustion rate is then already controlled by film diffusion for temperatures above about 900°C . This confirms that at the much higher temperatures that are reached in the tuyeres (about 2000°C), the combustion is almost instantaneous, that is, only a length of ten particle diameters is needed for complete oxygen conversion.

6.6

Basic Chemicals by Steam Cracking

Steam cracking (or “middle temperature pyrolysis”) converts alkanes and refinery cuts [e.g., ethane, light fuels (naphtha)] into a mixture of saturated and unsaturated hydrocarbons, with ethylene, propylene, butenes, butadiene, benzene, and toluene being the most valuable products.



View on the cracking furnaces of the steamcracker at the Gelsenkirchen site of BP, © BP Europa SE.

The term “steam cracking” refers to the fact that steam is added to the hydrocarbon steam cracker feed to (i) shift the reaction equilibrium to the cracking products and (ii) avoid heavy residues and coke formation.

6.6.1

General and Mechanistic Aspects

Since World War II, the chemical industry has seen a relatively rapid switch from coal to crude oil as the main basic feedstock. This development was triggered by enormous findings of new crude oil reserves in Arabian countries. Thus, the production of key organic chemicals, such as ethene and propene, became much more economic based on crude oil (via steam cracking) compared to coal-based production (via acetylene chemistry). For the development of steam cracking to the most important petrochemical process, two additional facts were essential. First, the steeply increasing production of automotive fuels and light gasoline from the late 1940s to the 1980s made refinery cuts readily available in large quantities. Second, the increasing number of applications and the steeply growing market demand for the main products of the steam cracker process, such as ethene, propene, butadiene, butenes, benzene, toluene, and xylenes.

The steam cracker process – sometimes in the literature also referred to as “middle temperature pyrolysis process” – forms the heart of modern petrochemistry. The process converts a crude oil distillation cut into a mixture of reactive small molecules that can be purified and later used to produce a wide variety of base chemicals. It is fair to state that modern petrochemistry has developed around the steam cracker process and operates today largely as a result of the characteristic product distribution provided by the steam cracker.

In the steam cracker, gaseous (such as ethane) or liquid alkanes or alkane mixtures (such as naphtha, a saturated hydrocarbon cut from the atmospheric refinery distillation with boiling points ranging from 30 to 180 °C) are cracked in a thermal process into small and partly highly reactive products. This endothermic process does not use a catalyst but operates via a radical mechanism. It is carried out at between 800 and 900 °C and uses short contact times of 0.1–0.5 s. The process name “steam cracking” originates from the fact that water vapor is added to the organic feedstock before entering the reactor. The water molecules of the steam are not cracked themselves (much higher temperatures would be necessary for the thermal decomposition of water) but serve two purposes:

- 1) The steam dilutes the hydrocarbon feedstock, thus lowering its partial pressure. Running the steam cracking process at low hydrocarbon partial pressures is important to obtain high yields in cracked products. Note that in the cracking reaction a long-chain hydrocarbon is converted into several short-chain products, thus increasing the number of moles and the hydrocarbon volume in the reactor. Therefore, the reaction equilibrium towards the cracking products is favored by low partial pressures. Steam is a suitable diluent for the cracker feed as water is cheap and chemically stable under the hot conditions in the reactor. The disadvantage of its high heat capacity (making heating water up to 800 °C quite energy intensive) is partly compensated by the recovery of a good part of this energy in the heat exchangers behind the reactor and by the ease with which water is separated from the hydrocarbon products by condensation.
- 2) As the mixture of cracking products is composed partly of highly reactive small alkenes, it is very important to prevent polymerization or reaction of these products in the cracking oven. The probability of these undesired side reactions forming polymer or coke is significantly reduced in the presence of steam.

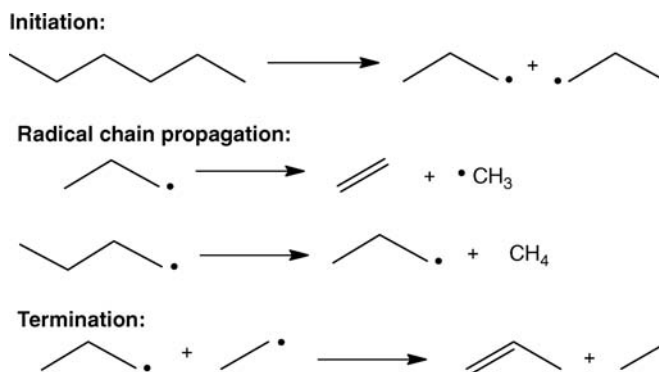
Mechanistically, long hydrocarbon molecules are converted in the steam cracker by breaking C—C and C—H bonds in a homolytic manner. Breaking C—C bonds is energetically favored over C—H bond breaking. The initial bond-breaking reactions form radicals (highly reactive molecules or atoms with unpaired electrons; see Section 2.2 for details on radical reactions) that undergo numerous consecutive reactions. Finally, they form stable molecules with paired electrons again. The radical cracking reaction can therefore be divided in (i) an initiation step in which radicals are formed, (ii) a chain propagation step in which radicals convert into other, usually smaller, radicals, and finally (iii) the chain termination step in which two radicals react to form stable molecules with paired electrons (Scheme 6.6.1).

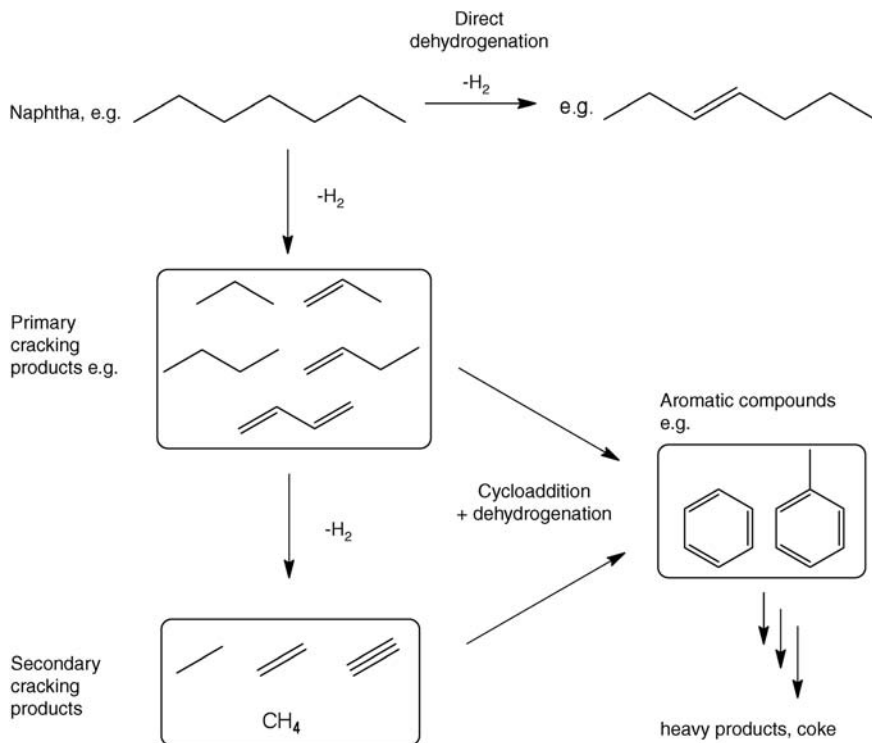
Apart from the described radical reaction pathways, there are several important side and consecutive reactions that also proceed in the cracking furnace. The higher the product concentration in the stream (i.e., at high feedstock conversion), the higher is the probability of these side and consecutive reactions. Important side and consecutive reactions include isomerization, cyclization, aromatization, alkylation, and also condensation reactions. The aromatic compounds found in the steam cracker product stream are formed, for example, by cycloaddition reactions of alkenes and dienes followed by dehydrogenation reactions. Moreover, monoaromatic compounds transform into aromatic condensates and polycyclic aromatics (see also Scheme 6.6.2) by the same reactions. Typically, more than 100 different products are found in the product mixture of a commercial steam cracker.

To predict the product distribution of a steam cracker, thermodynamics can give a first assessment. By comparing the free energies of formation for the different reaction products, some prediction of the product mixture as a function of temperature can be made. The most relevant conclusions from the thermodynamic facts illustrated in Figure 6.6.1 can be summarized as follows (Haertl *et al.*, 1996; Moulijn *et al.*, 2001):

- Over the whole temperature range that is technically reasonable, the most desired product ethene is thermodynamically unstable against decomposition to the elements C and H₂. The same is also true for other technically important alkenes and aromatics.
- Short-chain hydrocarbon molecules are more stable than long-chain representatives (compare ethane and hexane in Figure 6.6.1).
- Temperatures of over 700 °C are necessary to favor ethene formation over ethane formation. Propene/propane and isobutene/isobutane show similar behavior, although the lower reaction enthalpies of propane and isobutane dehydrogenation (124 and 118 kJ mol⁻¹, respectively, at standard conditions) versus ethane dehydrogenation (137 kJ mol⁻¹) favor the unsaturated form of longer

Scheme 6.6.1 Examples of radical reactions taking place in the hot reaction zone of the steam cracker.





Scheme 6.6.2 Set of different reactions taking place in the cracking furnace that result in more than 100 products in the steam cracker product stream. Adapted from Moulijn, 2001.

hydrocarbons already at slightly lower temperatures. In all cases, temperatures above 500 °C are necessary to obtain unsaturated products in technically interesting quantities.

- Aromatic hydrocarbons are more stable than linear, branched, and cyclic alkanes.

Owing to these thermodynamic facts, equilibrium conversions have to be avoided in the steam cracking process as under all technically realistic conditions the desired products (light alkenes, aromatics) are thermodynamically unstable. Thus, reaching the equilibrium in a steam cracker would mean that most of the valuable

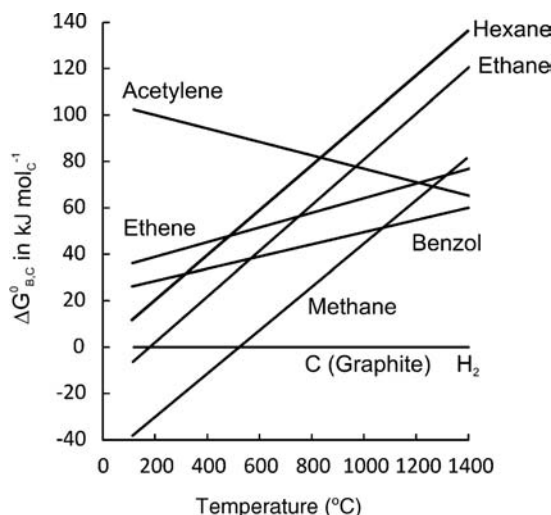


Figure 6.6.1 Free energies of formation of important products of the steam cracker process. Adapted from Baerns, 2005.

hydrocarbon feedstock is converted into the elements carbon and hydrogen. To avoid this, high reaction temperatures but very short contact times have to be realized in the steam cracker to obtain the desired light alkenes and aromatics as kinetic products in good yields.

6.6.2

Factors that Influence the Product Distribution

6.6.2.1 Influence of Applied Feedstock

The highest yield of ethene is obtained in the steam cracker process from *n*-alkanes as feedstock. For iso-alkanes the ethene yield decreases with increasing degree of branching and more hydrogen and methane is produced instead. The cracking of six-membered cycloalkanes results in more ethene and butadiene than the cracking of five-membered cycloalkanes. Aromatic compounds are converted only to a very little extent at their aromatic core, while attached alkyl groups are split off. The hydrocarbon reactivity in the cracking reaction increases with hydrocarbon chain length but the selectivity in ethene formation decreases with increasing molecular weight. The higher the molecular weight and the boiling point of the feedstock components the more likely is the formation of heavy condensation products and coke in the process. Table 6.6.1 illustrates the different product distributions obtained from different hydrocarbon feeds assuming a cracker scheme in which all C₂–C₄ alkanes are recycled back to the cracker for re-cracking.

6.6.2.2 Influence of the Temperature in the Cracking Oven

For radical cracking of longer chain saturated hydrocarbons, temperatures above 400 °C are required. Under these mild conditions the molecules are split predominantly in the middle. Only at higher temperatures the splitting moves increasingly to the ends of the longer chain feedstock with more and more short-chain alkenes and alkanes being formed. In an industrial steam cracker temperatures between 700 and 900 °C are usually applied, as the yield in ethene and propene shows a maximum in this temperature range (under otherwise identical conditions). Figure 6.6.2 illustrates the influence of the temperature in the cracking furnace on the distribution of selected products for the example of cracker 2 at BASF, Ludwigshafen.

6.6.2.3 Influence of Residence Time

The residence time of the hydrocarbon feedstock in the cracking furnace is a crucial parameter for the product distribution. For short residence times, the formation of the primary cracking dominates and this leads to the desired short-chain alkenes. At higher residence times, however, more secondary reactions occur and this

Table 6.6.1 Product yields (wt%) in the steam cracker process as a function of the feedstock applied (high severity cracking) – the figures in the table assume that all light alkanes (C₂–C₄) are recycled to the cracker (Grantom *et al.*, 1987; Haertl *et al.*, 1996).

Product	Hydrocarbon feedstock					
	Ethane	Propane	<i>n</i> -Butane	Naphtha	Light gasoline	Heavy gasoline
H ₂	3.6	1.3	1	1	0.6	0.6
CH ₄	12.4	28.7	23	16	10.4	9.4
Ethene	76	42	40	31	26	23
Propene	3	16	21	16	15	14
Total C ₄	2	5	10	9	9	8
Crack fuel (C ₅₊ liquids)	3	6	4	22	15	14
Heavy residue	0	1	1	5	24	31

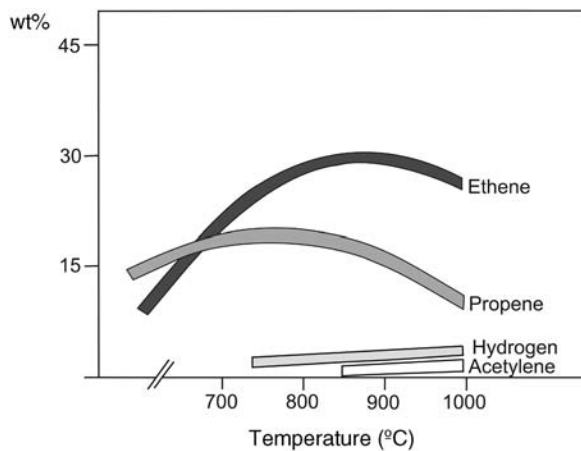


Figure 6.6.2 Influence of temperature in the crack furnace on the distribution of some selected products from a typical naphtha cracker (here cracker 2 at BASF, Ludwigshafen). Adapted from Haertl *et al.*, (1996).

causes the formation of aromatics, oligomers, and coke. Figure 6.6.3 gives as example the ethene yield as a function of the residence time for three typical reaction temperatures. It can be seen that at a cracking temperature of 800 °C the maximum ethylene yield is at higher residence times compared to cracking at 900 °C. While in principle an infinite number of furnace temperature–residence time combinations can lead to the same degree of hydrocarbon conversion, each of these combinations will come with a slightly different product distribution. This is because every product and intermediate in the steam cracker reaction mixture has a different reactivity and also the activation energies of the different side and consecutive reactions are different for each intermediate.

6.6.2.4 Influence of Hydrocarbon Partial Pressure in the Cracking Oven

Alkane cracking follows first-order kinetics. Thus, the cracking reaction rate increases with increasing hydrocarbon partial pressure as long as the composition of the reaction mixture is far from thermodynamic limitations. However, in the cracking process, 1 mol of long-chain hydrocarbon converts into two and more moles of cracking products. Thus, according to Le Chatelier's principle, a hydrocarbon partial pressure that is too high limits the equilibrium conversion into the desired short-chain cracking products. Moreover, a high partial pressure of hydrocarbons promotes unwanted secondary reactions.

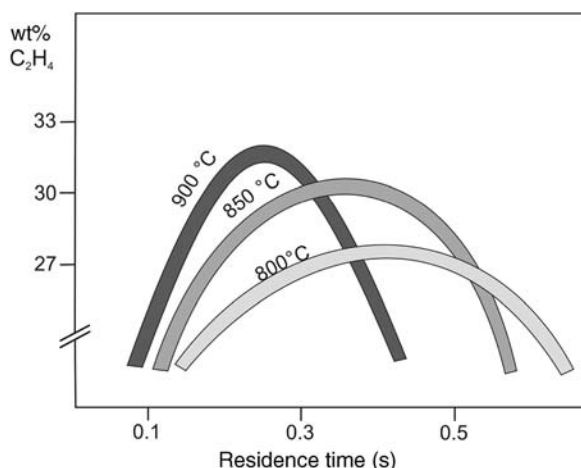


Figure 6.6.3 Influence of residence time in the crack furnace on the yield of ethene for a typical naphtha cracker (here cracker 2 at BASF, Ludwigshafen). Adapted from Haertl *et al.*, (1996).

In a commercial steam cracker slightly elevated pressures are required to convey the large volume of reaction mixture through the reactor tube at high flow rates (to realize the desired turbulent flow regime and the desired short residence times). Typically, this leads to a total pressure of 2–3 bar at the outlet of a tubular cracking reactor. As a consequence, a diluent is used to establish the pressure while keeping the hydrocarbon partial pressure sufficiently low. For this task, water is the best choice as it is inert and easily condensed. Moreover, water addition shows a beneficial reduction of coke formation in the reactor. Adjusting the right water-to-hydrocarbon ratio is a critical aspect for the process economics of a steam cracker. While increasing water content in the reactor increases the yield of valuable cracking products, it decreases the total alkene productivity (as water occupies a larger part of the reactor volume) and requires additional heating and cooling energy.

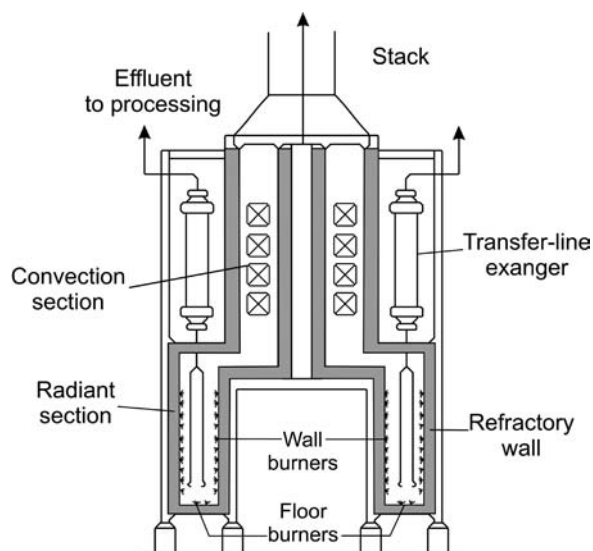
6.6.3

Industrial Steam Cracker Process

Modern steam cracker units are characterized by high temperatures and short residence times in the *cracking furnace*. This mode of operation, typically referred to as “high severity cracking”, is characterized by a temperature of up to 880 °C at the outlet of the tube reactor in the cracking furnace. The naphtha is first mixed with superheated steam and then enters a section of the reactor in the convection zone of the furnace to be preheated to 600 °C (see also Figure 6.6.4). From there, the mixture enters the radiation zone of the furnace where the cracking reaction takes place. The reactor tube in the radiation zone is typically 20–70 m long and 40–100 mm wide. Heated by gas burners (alternatively, the burners may run on LPG or fuel oils), the tube reaches up to 1200 °C, resulting in a temperature of the reaction mixture of up to 880 °C. The residence time in the radiation zone is typically 0.1–0.5 s, and typical gas velocities at the reactor outlet are 200–300 m s⁻¹. The radiation section of a typical commercial furnace contains 6–8 parallel tube reactors, each adding a capacity of 40 000–120 000 tons yr⁻¹ ethylene to the respective steam cracker unit.

The reaction mixture leaves the cracking furnace at 880 °C and should be cooled instantaneously to preserve its composition as usually all changes in composition by consecutive reactions reduce the value of the cracked gas. Industrial plants are designed to limit the residence time of the hot gas in the adiabatic section between the furnace outlet and the quench-system cooling zone to less than 10% of the residence time in the radiant zone.

Figure 6.6.4 Typical cracking furnace, showing the convection and radiation section of the furnace as well as the transfer-line exchanger. Adapted from Moulijn (2001).



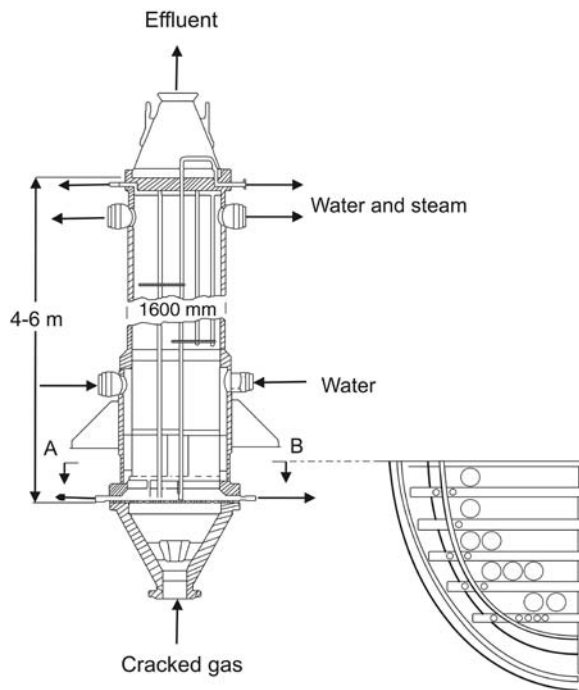


Figure 6.6.5 Scheme of a Borsig transfer-line exchanger. Adapted from Grantom *et al.* (1987).

In principle, the cracked gas can be cooled by direct or by indirect quenching. While direct quenching uses injection and evaporation of a liquid spray into the reaction mixture, indirect cooling systems transfer the heat through the wall of a heat exchanger surface to produce high-pressure steam. The latter is used to operate the gas compressor units of the steam cracker facility. Owing to this attractive option of heat and energy integration, most steam cracker units work today with indirect quenching using so-called transfer-line exchangers. Figure 6.6.5 shows a Borsig transfer-line exchanger to illustrate a typical technical realization.

Transfer-line heat exchangers are characterized by the following design objectives:

- A uniform flow to all tubes across the surface of the tube sheet to prevent eddies in the entry cone leading to longer residence times of the hot cracked gas before entering the cooling zone.
- A low pressure drop in the heat exchanger as the pressure drop in the transfer-line exchanger results in higher pressure at the outlet of the radiant coil. Higher pressure at the outlet of the radiant coil leads to a lower value of the cracking products.
- High heat recovery must be realized in the exchanger for beneficial process economics. The possibility of making use not only of high temperature heat (producing high pressure steam) but also lower temperature heat (producing in a second transfer-line exchanger low pressure steam) is influenced by the nature of the cracking feedstock. The heat exchanger outlet temperature must be higher for cracking products from naphtha and other liquid feeds as this product stream contains more heavy components. At temperatures that are too low in the heat exchangers these products would condensate and create fouling problems. In the worst case, the tubes may be blocked completely. Then the system has to be shut down and cleaned. To avoid this risk, steam cracker units operating on naphtha frequently use an indirect transfer-line heat exchanger to produce high-pressure steam followed by a direct oil quench to further lower the temperature of the cracking gas for the downstream processing. Direct cooling reduces greatly the risk of fouling.

The crack gas leaving the transfer-line exchanger runs through a sequence of cooling units operated as oil or water washing towers. Here, heavy oils and a part of the pyrolysis gasoline (a mixture of C_{5+} alkanes, alkenes, cycloalkanes, and aromatics, also called “pygas”) are condensed. The process water is cleaned of organic components in a stripper and recycled to the entry of the furnace to act again as diluent for the feedstock in the process.

The first step of *product separation by cryogenic distillation* is to compress the product gas in a multistep turbo-compressor (typically 4–6 stages) from slightly above atmospheric pressure to around 30 bar. The multistep turbo compressor operates with intermediate gas cooling to keep the temperature below 95 °C. Above this temperature polymerization reactions of the reactive gas mixture begin to occur. At each compression stage additional pygas is condensed and collected. The multistep compressor is operated using the high-pressure steam of the indirect quenching step as energy source. In-between the last compressor stages, acid gases – such as hydrogen sulfide or CO_2 – are removed by a washing step with a 1–5% NaOH solution in water. Figure 6.6.6 shows a simplified scheme of the different cooling and compression steps behind the cracking furnace.

For the subsequent cryogenic distillation, it is very important to remove everything from the gas that would solidify at the applied temperature of $-160^{\circ}C$ in the “cold box” of the separation unit. Therefore, it is essential to remove all CO_2 in the sour gas washing step (see above) and also all remaining water. Water removal takes place at $-60^{\circ}C$ over zeolites. The dry crack gas is cooled to $-160^{\circ}C$ and fractionated in a sequence of separation units to obtain the main products hydrogen, ethyne, ethene, propene, and remaining pygas components in the required purities. Figure 6.6.7 shows a simplified view of the whole product separation and purification scheme of a steam cracker operating on naphtha.

The dry products from the drying unit are first separated in the C_2/C_{3+} splitter. The C_2 -fraction contains hydrogen, acetylene, ethene, and ethane. The C_{3+} -fraction contains propyne, propene, propane, the C_4 products (butadiene, isobutene, *n*-butenes, butane), and the C_{5+} fraction, which is unified with the pygas collected from the cooling and compression units.

The production of “polymerization grade” ethene from the C_2 -fractions involves as the first step the separation of hydrogen and methane. From the remaining C_2 -stream, acetylene has to be removed completely as it has a detrimental effect on

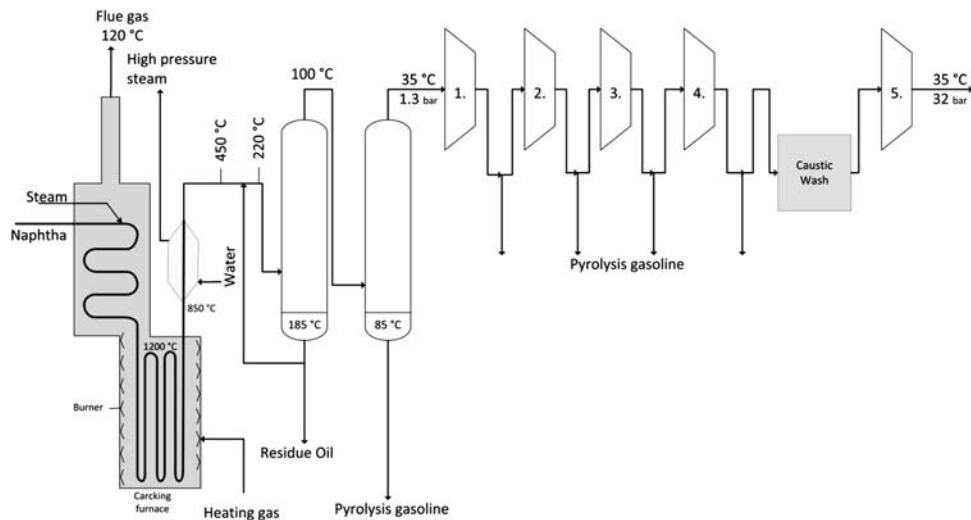


Figure 6.6.6 Simplified scheme of a steam cracker, showing the cooling and compression steps behind the cracking furnace; the gas leaving the multi-stage compression enters the separation scheme illustrated in Figure 6.6.7. Adapted from Härtl (1996).

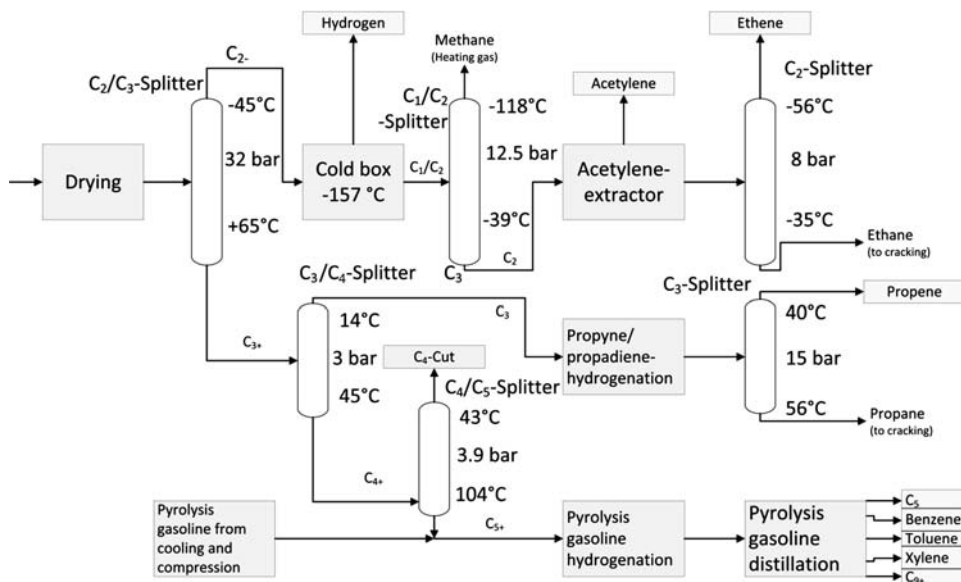


Figure 6.6.7 Simplified view of the whole product separation and purification scheme of a steam cracker operating on naphtha. Adapted from Haertl *et al.*, (1996).

most technical applications of ethene. Acetylene removal is carried out by solvent extraction or by selective hydrogenation reactions. The ethene/ethane separation is a complex separation problem as the boiling points of both components are very close. Distillation columns with more than 100 trays (often placed in two distillation towers in series) and high reflux ratios are required to meet the high quality standards for polymerization grade ethene.

The C_{3+} -fraction of the C_2-/C_{3+} splitter enters the C_3/C_{4+} splitter that separates propane, propene, propadiene, and propyne from all heavier products. The C_3 stream undergoes a selective hydrogenation step in a fixed bed reactor that converts propyne and propadiene mainly into propene. Propene and propane are separated in a very similar way as ethane/ethene. Again, distillation columns with more than 100 trays are applied, making these separation units very costly in investment and energy consumption. The bottom fraction of the C_3/C_{4+} splitter is transferred to C_4/C_{5+} splitter. The C_4 fraction leaving this column at the top contains mainly butadiene, isobutene, 1-butene, 2-butene, and butane. The further use of this crack- C_4 mixture is described in detail in Section 5.3.

The bottom fraction of the C_4/C_{5+} splitter is unified with the pyrolysis oil fractions from the compression and cooling steps. The most valuable part of this product mixture consists of the aromatic compounds benzene, toluene, and xylenes that are found in the pyrolysis oil together with saturated, mono-olefinic and di-olefinic, linear, branched, or cyclic C_{5+} compounds. In particular, the diolefinic compounds cause trouble in subsequent separation units as they tend to undergo Diels–Alder type reactions, forming solids that cause fouling in the plant. Therefore, the first step in pyrolysis oil treatment is a selective hydrogenation to remove these most reactive compounds.

The distillative pyrolysis oil fractionation produces C_5 , C_6 , C_7 , C_8 , and C_{9+} product streams. The C_5 fraction is frequently used for fuel production (Otto fuel) while the C_{9+} fraction is added to the gasoline pool. The individual C_6-C_8 fractions undergo additional steps to separate the aromatic compounds from the respective non-aromatic compounds with the same carbon number. Depending on the relative amount of aromatic compounds in each fraction these separations are carried out using extractive distillation, extraction, or adsorption processes. Note that the pygas of the naphtha steam cracker is – besides the reforming process in refineries, see

Section 6.9 – the most important source of aromatic compounds for the chemical industry. Saturated C₆–C₈ compounds separated from their aromatic counterparts are frequently recycled and undergo a second cracking together with the fresh cracker feedstock.

Example 6.6.1: Mass balance of a commercial steam cracker

The following example illustrates the dimensions of a commercial steam cracker unit. At the same time it introduces the reader to the global mass balancing of chemical plants, an important technique for dimensioning unit operations, for example, for a given production capacity.

We consider in the following a world-scale steam cracker plant with a production capacity of 125 t h⁻¹ ethene (Figure 6.6.8). The plant runs on light-run naphtha that is heated in the convection zone of the crack oven to 600°C. The naphtha is mixed with water vapor (4.5 MPa, 257.5°C) to realize a steam-to-naphtha ratio of 0.45. This mixture is introduced to the main crack oven, which is an 80 m tubular reactor at 850°C. The residence time of the feedstock in this hot section of the crack oven is 0.5 s. Following the crack oven, the product mixture is quenched to 200°C. In a first distillation column light components (C₁–C₅) are separated from the heavier pyrolysis products (C₆₊).

The stream of lights (stream 8) has the composition indicated in Table 6.6.2 (for simplification stream 8 is considered to be free of water).

The unconverted naphtha (<1%) is regarded as part of the heavy pyrolysis products. This fraction also contains the process water added as stream 3 (mass ratio process water to heavy pyrolysis products = 3 : 1).

Calculation of the light crack-fuel mass flow (flow 8):

Given:

$$\dot{m}_{\text{ethene},8} = 125 \text{ t h}^{-1} \quad \text{share}_{\text{ethene},8} = 0.3529$$

$$\dot{m}_{\text{total},8} = \frac{\dot{m}_{\text{ethene},8}}{\text{share}_{\text{ethene},8}} = \frac{125 \text{ t h}^{-1}}{0.3529} = 354.21 \text{ t h}^{-1}$$

Table 6.6.2 Composition of light crack-fuel (stream 8) in this example.

Product	Mass ratio (%)
Methane	17.65
Ethane	3.53
Ethene	35.29
Propane	2.35
Propene	17.65
C ₄ –C ₅	23.53

Calculation of the steam mass flow (flow 3) to ensure the steam to naphtha ratio at the reactor inlet:

Given:

$$\frac{\dot{m}_{\text{steam},8}}{\dot{m}_{\text{naphtha},1}} = 0.45$$

$$\frac{\dot{m}_{\text{steam},3}}{\dot{m}_{\text{crack fuel},9}} = 3$$

$$\dot{m}_{\text{naphtha},1} = \dot{m}_{\text{crack fuel},8} + \dot{m}_{\text{crack fuel},9}$$

$$\begin{aligned}\dot{m}_{\text{steam},3} &= 0.45(\dot{m}_{\text{crack fuel},8} + \dot{m}_{\text{crack fuel},9}) \\ &= 0.45\left(\dot{m}_{\text{crack fuel},8} + \frac{\dot{m}_{\text{steam},3}}{3}\right)\end{aligned}$$

$$0.85\dot{m}_{\text{steam},3} = 0.45\dot{m}_{\text{crack fuel},8}$$

$$\dot{m}_{\text{steam},3} = 187.52 \text{ t h}^{-1}$$

Calculation of the heavy crack-fuel mass flow (flow 9) and of the required flow of naphtha (flow 1):

$$\dot{m}_{\text{crack fuel},9} = \frac{\dot{m}_{\text{steam},3}}{3} = 62.51 \text{ t h}^{-1}$$

$$\begin{aligned}\dot{m}_{\text{naphtha},1} &= \dot{m}_{\text{crack fuel},8} + \dot{m}_{\text{crack fuel},9} \\ &= 354.21 \text{ t h}^{-1} + 62.51 \text{ t h}^{-1} = 416.72 \text{ t h}^{-1}\end{aligned}$$

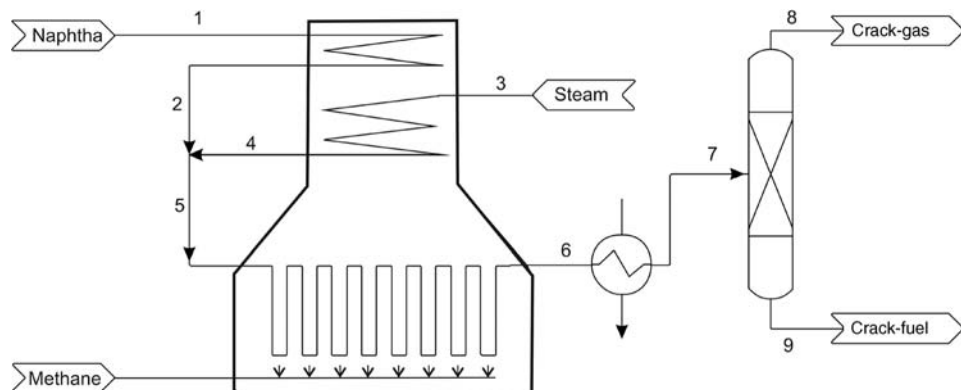


Figure 6.6.8 Simplified scheme of the steam cracker unit considered in this example.

6.6.4

Economic Aspects of the Steam Cracker Process

In the preceding sections we have seen that an industrial steam cracker operating on naphtha is characterized by a broad range of products. The most prominent product, ethylene, accounts for less than 40% of all products. It would therefore be completely uneconomic to produce only ethylene and to use all other products only as the fuel for heating the steam cracker furnace.

In contrast, it is very important for the economics of a steam cracker unit that all relevant side products can be further up-graded in production plants very close nearby. As a consequence, steam cracker units are typically surrounded by a whole network of plants that use all the different steam cracker products as their feedstock. This results in complex, integrated site structures that have to be constantly optimized to create the highest synergistic value of all downstream production sites linked to the same steam cracker unit. This includes the balancing of mass and energy streams from the different units, but also requires adoption of the whole "network" (German: "*Verbund*") to changing market conditions. Owing to the strongly coupled production sites, the cost of ethylene in such an integrated site depends not only on the actual feedstock price for naphtha and on the specific operation costs of the plant (energy cost, personal cost, capital cost) but also on the actual market value of the propylene, crack C₄ and aromatics side products. For the most important industrial uses of ethylene and all other steam cracker products see Section 5.3.

The capacity of typical steam cracker units in industry is around 1 Mio tons per year. Such world-scale capacities are beneficial due to the reduction of specific investment costs with increasing plant size. Note that this effect applies not only for the steam cracker itself but also for all the downstream production plants running on the diverse products from the cracker.

The size of the steam cracker and its central relevance as feedstock source for a large number of other plants makes the technical reliability of the steam cracker an essential aspect for the economics of whole chemical companies. If the steam cracker is having technical problems for a longer period of time there is not only a huge amount of crack-gas that has to be burned in the torch for safety reasons, in addition all other plants behind the steam cracker have to be closed down as they lack feedstock. As a consequence, existing contracts with customers on certain product quantities cannot be fulfilled, a fact that usually leads to severe contract penalties. In total, a prolonged steam cracker shut-down can cause gigantic losses for the operating company within a relatively short time.

Section 6.6 take-home-messages

- **Steam cracking** is the most important petrochemical process, producing the most relevant basic chemicals ethene, propene, benzene, and toluene from hydrocarbon feedstocks.
- Steam cracking is an endothermic, radical, high-temperature reaction that is carried out in a tubular reactor, the cracking furnace.
- All technically interesting products of the steam cracker are thermodynamically unstable under the reaction conditions. Therefore, it is important to realize short contact times in the cracking furnace and effective quenching of the product mixture behind the furnace.
- The transfer line heat exchanger behind the cracking furnace realizes fast quenching and recovers the heat energy in the form of steam. The steam is applied to operate the compressors for pygas condensation.
- Isolation of pure products in the desired quality from the crack gas mixture – for example, polymer-grade ethylene – requires a complex sequence of cryogenic and non-cryogenic distillations as well as extraction steps.

- Steam cracker units operating on naphtha produce a wide range of products. Their complete utilization is crucial to realize competitive operation of the cracker. As a consequence, steam cracker units are typically operated in networks (“Verbund”) of other plants that consume all steam cracker products on the same production site.

6.7

Liquid Fuels by Cracking of Heavy Oils

Petroleum residues such as the residues from vacuum distillation (“bottoms of the barrel”) are the least valuable products of an oil refinery, and are mainly used as fuel oils by marine vessels, power plants, and industrial facilities. The amount of these oils needed by the market has steadily decreased over recent decades. Thus, a refinery has to convert these heavy oils by cracking into higher value products such as gasoline, diesel oil, and jet fuel.

The two fractions of vacuum distillation are vacuum gas oil and vacuum residue (Section 5.1.4). The residue is cracked thermally as the content of metals (V, Ni, Fe) is too high, up to several 100 mg per liter of oil, which would lead to a rapid deactivation of catalysts. The vacuum gasoil is catalytically cracked, which has compared to thermal cracking the advantage of a higher yield and quality of valuable products like gasoline and diesel oil and lower yields of gases and coke. The two most important representatives of thermal and catalytic cracking are delayed coking (Section 6.7.1) and fluid catalytic cracking (Section 6.7.2).

6.7.1

Thermal Cracking (Delayed Coking)

The delayed coking process converts low value vacuum residues into gases, gasoline, light and heavy gas oil, and coke. The objective is to maximize the yield of liquid products (gasoline, diesel oil, etc.) and to minimize the yields of gases (methane to C₄-hydrocarbons) and of coke. The worldwide annual capacity in about 100 refineries is a throughput of about 175 million tonnes of residue oils, which corresponds to a production rate of about 50 million tonnes of coke (2002). Depending on the properties of the feedstock (sulfur and metal content), the coke may not only be used as a relatively low value fuel but also as a valuable raw material for electrodes for the aluminum and steel industry. In 2006, 58 million tonnes of aluminum and 400 million tonnes of electric steel were produced worldwide. According to Marrett, Stadelhofer, and Marsh (1983), this is equivalent to the annual consumption rate of 26 million tonnes of graphite electrodes for Al (450 kg_C kg_{Al}⁻¹) and 2.4 million tonnes for Fe (450 kg_C kg_{Fe}⁻¹).

Conversion by delayed coking is accomplished by heating the feed to a high temperature of about 500 °C and introducing the preheated oil into a large drum to provide the residence time needed for the thermal cracking reactions to take place. Figure 6.7.1 shows the flow sheet of the process. Table 6.7.1 gives data for the process.

First, the vacuum residue enters (after some preheating) the coker distillation tower, where the products of the cracker are separated into different fractions (gases, gasoline, diesel oil, etc.). The bottom product of the distillation column consists of the vacuum residue (without some lighter compounds, which may still have been present in the residue and which are now separated by distillation) and the heavy recycle oil (about 20% of the cracker products), which also remains liquid in the bottom of the column. This combined liquid heavy oil phase is then pumped through a fired heater to bring the mixture from about 350 °C to the desired heater outlet temperature of about 500 °C.

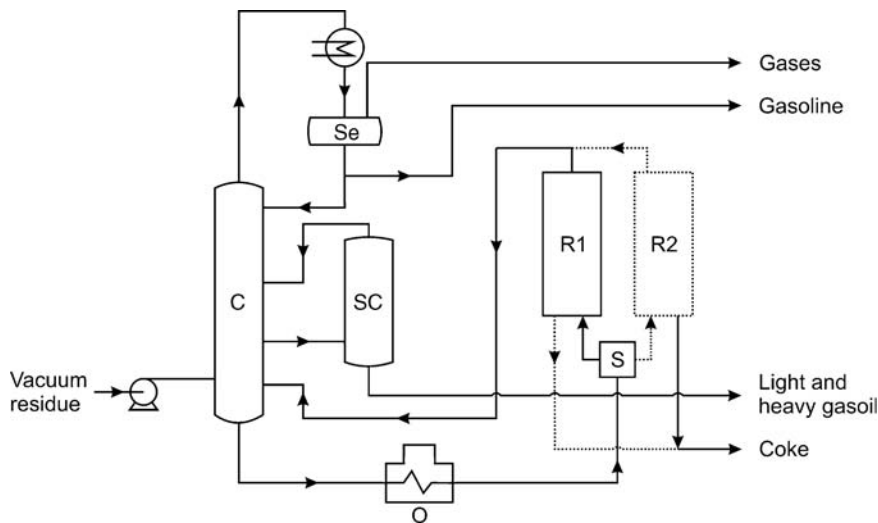


Figure 6.7.1 Delayed coking process (S: switch valve, Se: separator, C: distillation column, SC: side column, R: coking reactor).

Steam is added into the coils to increase the velocity of flow and to minimize undesired coking in the furnace. The effluent from the heaters then enters the bottom of a coking drum. The vaporized part of the heated feed oil and the gaseous products formed in the drum by cracking exit the drum at the top. The liquid remains in the drum until it cracks into lighter products or forms coke that stays in the drum and builds up from the bottom of the drum (Figure 6.7.2). Two coke drums are operated batchwise, usually in a rhythm of 24 h. One drum is “on duty.” The second drum, which was filled with coke, is cooled down first with steam to about 200 °C and then with liquid water. Then the drum is opened and coke is removed by hydraulic cutting tools and high-pressure water (200 bar). First, a hole of about 1 m in diameter is drilled from the top to the bottom of the drum, and then the rest of the coke is cut into pieces that can be handled by conveying systems. Typically, 4 h are needed for the coke removal.

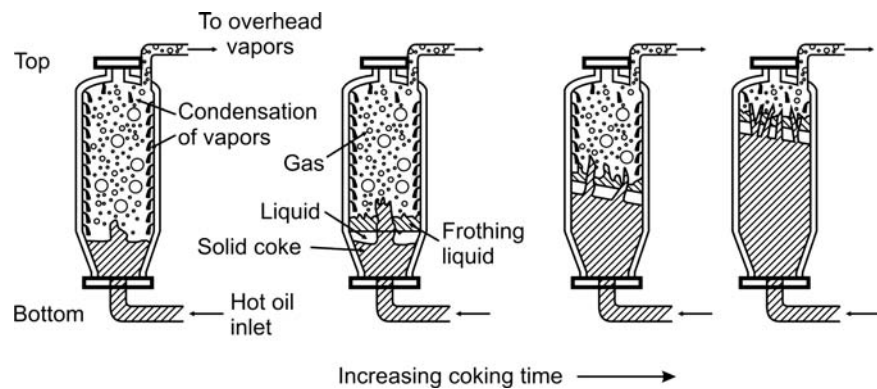
The liquid and gaseous products are separated into the desired products by fractionation in a distillation tower. Typically, 8% gases (C_1-C_4), 14% gasoline, 38% middle distillates (diesel, light fuel oil), 15% heavy gas oil, and 25% of coke are formed.

Table 6.7.1 Data and conditions of delayed coking. Data from Eckermann (1983); Rodriguez-Reinoso *et al.* (1998); Winnacker and Küchler (1971); and Agroskin *et al.* (1978).

Parameter	Value
Total pressure p	2 bar
Residence time in the tube/furnace (preheating from about 300 to 500 °C)	3 min
Temperature in the reactor (coke drum)	500–430 °C
(Mean) residence time in the reactor (coke drum)	3 h
Diameter/length of reactor	7/25 m
Total feed rate of oil \dot{V}_{oil}	320 m ³ h ⁻¹
Feed rate of oil through one coil of preheating oven \dot{V}_{oil}	80 m ³ h ⁻¹
Density of oil ρ_{oil}	1000 kg m ⁻³
Yield of coke	0.15 – 0.25 kg kg _{feed} ⁻¹
Fraction of vaporizing oil (preheating oven)	30–50 wt%
Reaction enthalpy of cracking/coking $\Delta_R H_{\text{coking}}^{\text{a)}$	≈0.6 MJ kg ⁻¹

a) The reaction enthalpy of cracking of - for example - the long-chain paraffin $C_{30}H_{62}$ into 2 $C_{10}H_{20}$, C_5H_{10} , and C_5H_{12} is 246 kJ mol⁻¹ = 584 kJ kg⁻¹. Similar values were measured by Agroskin *et al.* (1978) for different straight-run and cracked residues (430 to 780 kJ kg⁻¹). Here we use an average value of 600 kJ kg⁻¹.

Figure 6.7.2 Stages of the delayed coking process.
Adapted from Ellis and Paul (1998).



Delayed coking is a process with two major reactions, thermal cracking and oligomerization/polymerization leading to coke. The rates of the reactions are very sensitive to temperature. For example, the cracking rate roughly doubles for every 20 K increase in temperature (Figure 6.7.3). The overall reaction is endothermic and, therefore, the temperature in the coke drum is 40–70 K lower than the inlet temperature of the preheated oil (Eckermann, 1983; Winnacker and Kühler, 1971). Table 6.7.1 gives the reaction conditions.

The process name “delayed coking” is related to the fact that coking mainly occurs in the coking drums with a mean residence time of 3 h and not in the furnace during preheating within a residence time of 3 min. This effect can be examined by inspection of the kinetics. Cracking of vacuum residue can be regarded as a first-order reaction:

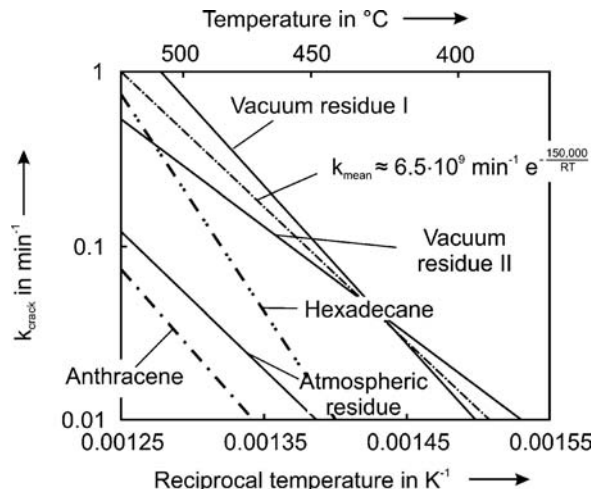
$$-\frac{dm_R}{d\tau} = km_R \quad \left[\text{with } k = k_0 e^{-\frac{E_A}{RT}} \text{ and } \tau \text{ as residence time} \right] \quad (6.7.1)$$

To start with we use the equation for an isothermal plug flow reactor (Section 4.10.2.3):

$$X_R = 1 - e^{-k\tau} \quad (6.7.2)$$

Figure 6.7.3 shows the first-order rate constants of thermal cracking of two vacuum and one atmospheric residue. The values were determined based on the

Figure 6.7.3 First-order rate constants of thermal cracking of vacuum and atmospheric residue. Data for vacuum residue from Singh *et al.* (2004), ratio of reactivity of atmospheric to vacuum residue from Eckermann (1983), and data for hexadecane from Ford (1986) and for anthracene from Scaroni, Jenkins, and Walker (1991).



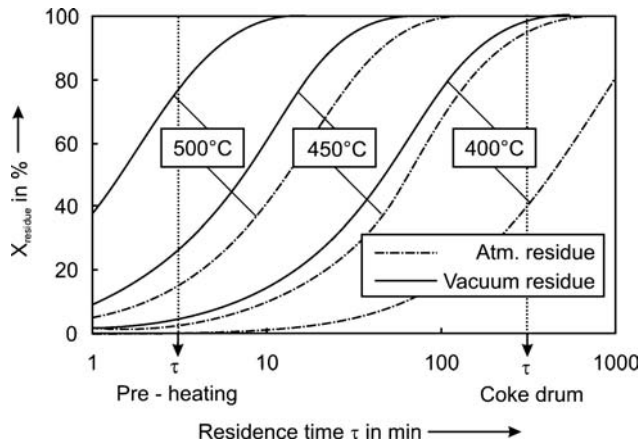


Figure 6.7.4 Influence of residence time and temperature on the conversion of atmospheric and vacuum residue (calculated with the reaction rate constants as given in Figure 6.7.3).

assumption that X_R equals the yield of all cracked products with a boiling point below 500 °C (Sing *et al.*, 2004). The reactivity increases with the chain length, and thus the reactivity of vacuum residues is by a factor of about ten higher than that of atmospheric residues. For comparison, data for the liquid phase thermal cracking of hexadecane (mainly to smaller molecules) and anthracene (mainly to coke) are also shown.

Figure 6.7.4 shows the influence of residence time on conversion at different temperatures. For a residence time in the coke drum of 3 h both residues are almost completely cracked, if we use an average drum temperature of 450 °C. For preheating in the furnace with a maximum temperature at the outlet of the coil of about 500 °C, a 3 min residence time (at this temperature) would lead to a conversion of vacuum and atmospheric residue of 75% and 15%, respectively. Thus, we have to inspect the actual case of the non-isothermal heating process in the furnace in more detail.

As examined in Section 4.11.5.4, the conversion in a non-isothermal tube with a constant heating rate $HR = dT/dt$ can be determined as follows:

$$-\frac{dm_R}{dT} = \frac{k_0}{HR} e^{-\left(\frac{E_A}{RT}\right)} m_R \quad (6.7.3)$$

Integration leads to:

$$-\int_{m_{C,o}}^{m_C} \frac{dm_R}{m_R} = \ln \frac{m_{R,0}}{m_R} = \frac{k_0}{HR} \int_{T_0}^T e^{-\left(\frac{E_A}{RT}\right)} dT \quad (6.7.4)$$

The right-hand side of Eq. (6.7.4) has no exact integral and we use a series expansion as approximation and obtain as solution (see Example 4.11.3):

$$\begin{aligned} \int_{T_0}^T e^{-\left(\frac{E_A}{RT}\right)} dT &\approx 0.92 \frac{RT^2}{E_A} e^{-\frac{E_A}{RT}} \Big|_{T_0}^T \\ &\approx 0.92 \frac{RT^2}{E_A} e^{-\frac{E_A}{RT}} \left(\text{for } T = 500 \text{ °C, i.e., here } \frac{E_A}{RT} = 23 \right) \end{aligned} \quad (6.7.5)$$

Note that the initial temperature T_0 is here low enough (300 °C) for the lower limit to be negligible. The solution of Eq. (6.7.4) in combination with Eq. (6.7.5) is shown in Figure 6.7.5 for cracking of vacuum residue during heating at rate of

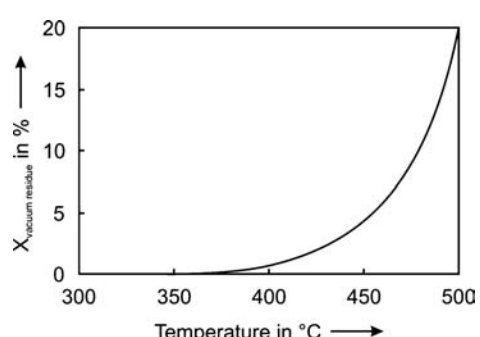
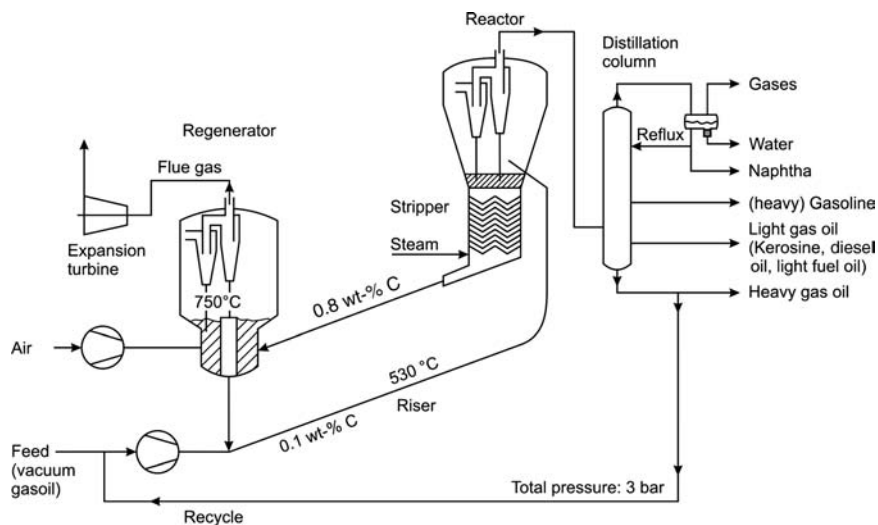


Figure 6.7.5 Cracking of vacuum residue oil during preheating in the furnace (assumptions: heating rate: 67 K min^{-1} , calculated with the average rate constant as given in Figure 6.7.3).

Figure 6.7.6 Fluid catalytic cracking (FCC) process.



67 K min^{-1} (assumption: residence time of 3 min in the preheating oven and a temperature increase from about 300 to 500 °C). Thus, thermal cracking (and coke formation) during the heating of the residue up to a final temperature of 500 °C cannot be avoided but is probably still below 20%.

6.7.2

Fluid Catalytic Cracking (FCC Process)

Fluid catalytic cracking (FCC) is one of the key processes for the production of gasoline and diesel oil in the present-day refinery. Worldwide, about 400 units are in operation with a total annual capacity of about 600 million tonnes. Commercial catalytic crackers operate at temperatures in the range 550–500 °C (decreasing from the inlet of the riser reactor to the outlet because of the endothermic cracking reaction). Total pressure is typically 3 bar and the catalyst-to-oil ratio is about 6 kg kg^{-1} . The residence time of the gas is in the range 2–8 s, and the residence time of the solid catalyst is three times higher (5–25 s, Avidan and Shinnar, 1990). The most important process variable to affect conversion and product distribution is temperature.

Since after a contact time in the cracking section of only a few seconds the cracking catalyst is largely deactivated by coke at a level of about 1 wt%, the catalyst is routed to a regenerator, where the coke is burned off, at 650–750 °C, to a level of less than 0.1 wt%. Following regeneration, the fluid catalyst is returned by gravity to the catalytic cracking section. Figure 6.7.6 shows a process flow sheet. Data are given in Table 6.7.2.

Vacuum gasoil and hot catalyst (about 650–750 °C) are mixed, and after vaporization and heating of the oil (whereby the catalyst cools down) a temperature of 550 °C is reached. Hence, FCC units operate in heat balance (Example 6.7.1), and the hot catalyst from the regenerator supplies heat for cracking, preheating, and for vaporization of the oil.

Essentially, all the cracking reactions occur in a riser reactor pipe that is about 30 m long and 0.85 m in diameter (Froment and Bischoff, 1990). The diameter increases slightly to maintain the velocity constant due to the increasing volume of the cracked products. The total residence time in the riser is about 5 s, after which about 1% by weight of the catalyst is accumulated coke. Vapor products are removed from the top of the reactor (catalyst particles are removed via a cyclone) at a temperature of about 510 °C and are separated by distillation. Typically 50% of the product (not counting the coke, which is formed with a selectivity of about 5 wt-%) is in the gasoline range, about

Table 6.7.2 Data on chemical media and reaction conditions of the fluid catalytic cracking (FCC) process.

Parameter	Value
Ratio of mass flow of catalyst to flow of oil (riser reactor)	6 kg kg^{-1}
Ratio of mass flow of catalyst to flow of air (regenerator)	10.5 kg kg^{-1}
Total pressure p	3 bar
Diameter of catalyst particle d_p	0.1 mm
Molar mass of oil (feed) M_{oil}	350 g mol^{-1}
Molar mass of air M_{air}	20 g mol^{-1}
Mean boiling temperature of oil (feed) $T_{\text{boil,oil}}$	400 °C
Density of catalyst ρ_p	1400 kg m^{-3}
Density of <i>n</i> -octane (vapor, 525 °C, 3 bar) $\rho_{n\text{-octane}}$	5.1 kg m^{-3}
Density of air/flue gas (700 °C, 3 bar) ρ_{air}	1.06 kg m^{-3}
Kinematic viscosity of <i>n</i> -octane (530 °C, 3 bar)	$2.5 \times 10^{-6} \text{ m}^2 \text{ s}^{-1}$
Kinematic viscosity of air/flue gas ν_{air} (700 °C, 3 bar)	$3.8 \times 10^{-5} \text{ m}^2 \text{ s}^{-1}$
Reaction enthalpy of combustion of coke (carbon) $\Delta_R H_C$	-33 MJ kg^{-1}
Reaction enthalpy of cracking of gasoil $\Delta_{\text{R}} H_{\text{crack}}$ (footnote of Table 6.7.1)	0.6 MJ kg^{-1}
Heat capacity of catalyst c_{cat}	$1 \text{ kJ kg}^{-1} \text{ K}^{-1}$
Heat capacity of air $c_{p,\text{air}}$	$1 \text{ kJ kg}^{-1} \text{ K}^{-1}$
Heat capacity of liquid $c_{\text{oil},l}$	$2 \text{ kJ kg}^{-1} \text{ K}^{-1}$
Heat capacity of vaporized oil $c_{\text{oil,vap}}$	$1.6 \text{ kJ kg}^{-1} \text{ K}^{-1}$
Enthalpy of vaporization ($C_{24}H_{50}$ with $T_{\text{boil,1 bar}} = 400 \text{ °C}$) $\Delta_{\text{vap}} H_{\text{oil}}$	180 kJ kg^{-1}
Carbon load of catalyst before regeneration $L_{C,\text{cat,in}}$	$0.008 \text{ kg}_C \text{ kg}_{\text{cat}}^{-1}$
Carbon load of catalyst after regeneration $L_{C,\text{cat,out}}$	$0.00045 \text{ kg}_C \text{ kg}_{\text{cat}}^{-1}$

13% are middle distillates (200–340 °C range), and about 17% gases (H_2 and C_1 – C_4). The remaining heavy oil (about 20%, boiling range >340 °C) is recycled to the feed. The FCC process operates at about 73–80% conversion since higher conversions intensify secondary cracking reactions and increase the yields of undesired low molecular weight gases and coke.

In the regenerator, the catalyst particles move by gravity towards the bottom of the reactor through a series of baffles where they are stripped of any residual oil by steam in the steam stripper. The catalyst is then fed into a stream of air that enters the bottom of the regenerator. The temperature in the regenerator rises up to 750 °C due to the exothermic nature of coke burning. This heat is recovered to preheat and vaporize the incoming heavy gas oil. The heat balance of the FCC process is inspected in more detail in Example 6.7.1. The regenerated catalyst, usually containing about 0.05% coke, is separated from the gas by cyclones and is discharged through vertical pipes, extending from the bottom of the reactor, into the stream of feed oil, completing the recycle of the catalyst.

The efficiency of catalyst regeneration by coke burn-off in the fluidized bed regenerator can be improved by operating at much higher gas velocities than the minimum discharging velocity (Example 6.7.2). Typically, the FCC regenerator operates in turbulent fluidization at a gas velocity of 1 m s^{-1} . Then about 20% of the catalyst is in the freeboard and circulates through the cyclones every 5 min (Avidan and Shinnar, 1990). Afterburning in the cyclones would be a problem, and therefore a combustion promoter (small amounts of Pt on the catalyst) is used to complete CO combustion. Figure 6.7.7 summarizes the different fluidization regimes for an FCC regenerator and riser reactor.

The FCC reactor is an upflow pipe (riser reactor). The designers of this entrained bed system soon discovered that fine powders do not seem to obey Stokes' law (Avidan and Shinnar, 1990). Even at velocities several times higher than the single particle terminal velocity in free fall (approximately 0.1 m s^{-1} , see Example 6.7.2), entrainment is not reached. The particles behave as clusters with an effectively higher terminal velocity due to interparticle forces.

Figure 6.7.7 Fluidization regimes with fine particles (a: minimum fluidization velocity; b: beginning of bubbling; c: minimum discharging velocity (terminal velocity in free fall), and d: blowout velocity. Adapted from Froment and Bischoff (1990); Squires, Kwaak, and Avidan (1985); and Avidan and Shinnar (1990).

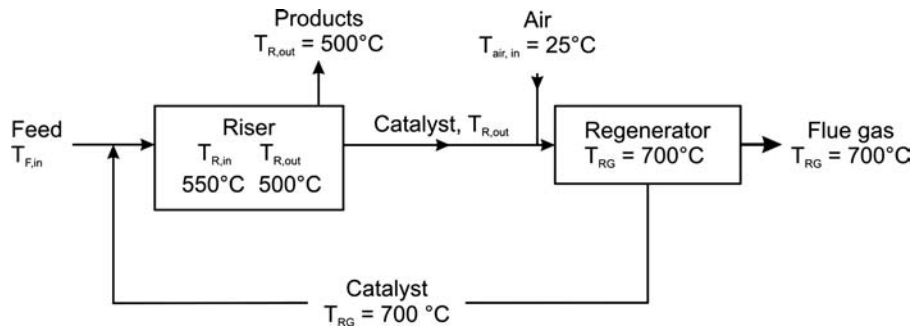
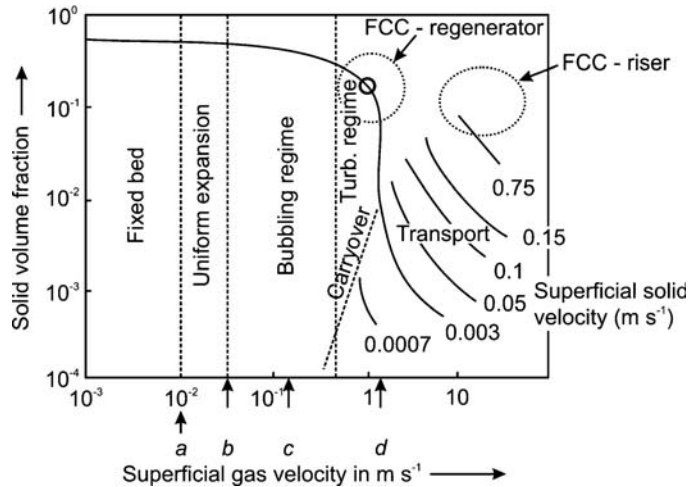


Figure 6.7.8 Block diagram of fluid catalytic cracking (FCC) process with typical values of temperatures.

Example 6.7.1 Heat balance of FCC unit

Figure 6.7.8 shows a block diagram of the FCC process with the nomenclature of the different temperatures.

Heat balances for the different sections of the FCC unit are as follows:

Mixing of hot catalyst (from regenerator) and feed (vacuum gasoil)

The hot catalyst is cooled and the oil is vaporized and preheated to $T_{R,in}$ (550°C):

$$\begin{aligned} & \dot{m}_{\text{oil}} (c_{p,\text{oil},l} [T_{\text{boil}} - T_{F,in}] + \Delta_{\text{vap}} H_{\text{oil}} + c_{p,\text{oil,vap}} [T_{R,in} - T_{\text{boil}}]) \\ &= \dot{m}_{\text{cat}} c_{\text{cat}} [T_{RG} - T_{R,in}] \end{aligned} \quad (6.7.6)$$

With the values given in Table 6.7.2 and Figure 6.7.8 we obtain an inlet temperature of the oil ($T_{F,in}$) of 160°C . For comparison, with a regeneration temperature of 650°C (instead of the assumed value of 700°C) an oil preheating temperature before mixing with the hot catalyst of 310°C would be needed.

Endothermic reaction in the (adiabatic) riser reactor

The heat balance for the riser reactor is as follows:

$$X_{\text{oil}} \dot{m}_{\text{oil}} \Delta_R H_{\text{crack}} = (\dot{m}_{\text{oil}} c_{\text{oil,vap}} + \dot{m}_{\text{cat}} c_{\text{cat}})(T_{R,in} - T_{R,out}) \quad (6.7.7)$$

If we use an average value of 70% for the conversion of oil to cracked products and the value of the reaction enthalpy of Tab. 6.7.2, this balance leads to a temperature at the outlet of the riser reactor of 495°C .

Exothermic regeneration of the catalyst in the regenerator (coke burn-off)

The heat balance for the regenerator reads as:

$$\begin{aligned} -\dot{m}_{\text{cat}} (L_{C,\text{cat,in}} - L_{C,\text{cat,out}}) \Delta_R H_C &= \dot{m}_{\text{cat}} c_{\text{cat}} (T_{RG} - T_{R,out}) \\ &+ \dot{m}_{\text{air}} c_{p,\text{air}} (T_{RG} - T_{air,in}) \end{aligned} \quad (6.7.8)$$

Solution of this balance with the values of Table 6.7.2 leads to a regeneration temperature of 690°C . The composition of the flue gas can be determined as follows: 0.0076 kg coke (counted as 0.63 mol carbon) is combusted per kg of catalyst. The ratio of air-to-catalyst is 0.095 kg air (3.3 mol air, 0.69 mol O_2) per kg catalyst. Thus, the molar ratio of O_2 to carbon is 1.1, which leads to a flue gas composition of 19% CO_2 , 2% O_2 , and 79% N_2 .

Example 6.7.2: Minimum fluidization and discharging velocity of the FCC regenerator and discharging velocity of the FCC riser

FCC regenerator (fluidized bed)

As examined in Section 3.4.1.2, the minimum fluidization velocity $u_{s,\min}$ is calculated based on a balance of forces, as the weight of the bed (less the lifting force) equals the hydrodynamic resisting force by the flow [Eq. (3.4.26)]:

$$\Delta p_b A_b = (1 - \varepsilon_{mf}) V_b (\rho_p - \rho_{air}) g \quad (6.7.9)$$

According to Eqs. (3.4.21) and (3.4.24), the pressure loss in a packed bed of spherical particles (equal diameter, porosity of fixed bed $\varepsilon = 0.4$) is given by:

$$\Delta p_b = \left(33 + \frac{1700}{Re_p} \right) \frac{L}{d_p} \frac{\rho_{air} u_s^2}{2} \quad (6.7.10)$$

where $Re_p = u_s d_p / \nu$ and u_s is the superficial velocity (empty tube) of the fluid.

If we assume that the porosity of the bed at the minimum fluidization velocity still almost equals the value of the fixed bed (0.4), insertion of Eq. (6.7.10) into Eq. (6.7.9) leads to:

$$\left(33 + \frac{1700}{Re_p} \right) \frac{\rho_{air} u_{s,\min}^2}{d_p} = 1.2 (\rho_p - \rho_{air}) g \quad (6.7.11)$$

With the data of Table 6.7.2, we obtain $u_{s,\min} = 0.0024 \text{ m s}^{-1}$ which is well within the order of magnitude as given by Figure 6.7.7. If the fluid velocity is further increased, we reach the discharging velocity, and the

fluidized bed switches over to an entrained bed. This velocity is the calculated balance of forces on a single particle [Eq. (3.4.28)]:

$$f_p \frac{\rho_{air}}{2} \left(\frac{u_{s,\text{dis}}}{\varepsilon_{\text{dis}}} \right)^2 A_{\text{proj}} = V_p (\rho_p - \rho_{air}) g \quad (6.7.12)$$

The porosity of the fluidized bed at the discharging velocity (ε_{dis}) is about 0.95. A_{proj} is the projection screen of the particle and f_p is the friction factor of a single particle, as shown in Figure 3.4.5 for a spherical particle [$A_{\text{proj}} = \pi (d_p/2)^2$] and different values of the Re number ($u_s d_p / \nu$). For $Re_p < 10^5$, Eq. (3.4.29) is valid, and Eq. (6.7.12) reads as:

$$\left(\frac{24}{Re_p} + \frac{4}{\sqrt{Re_p}} + 0.44 \right) \frac{\rho_{air}}{2} \left(\frac{u_{s,\text{dis}}}{0.95} \right)^2 A_{\text{proj}} = V_p (\rho_p - \rho_{air}) g \quad (6.7.13)$$

With the data of Table 6.7.1, we obtain $u_{s,\text{dis,regenerator}} = 0.15 \text{ m s}^{-1}$.

Riser reactor (entrained bed)

Assuming that the hydrocarbon vapor can be regarded as *n*-octane, Eq. (6.7.13) yields:

$$\begin{aligned} & \left(\frac{24}{Re_p} + \frac{4}{\sqrt{Re_p}} + 0.44 \right) \frac{\rho_{\text{octane,g}}}{2} \left(\frac{u_{s,\text{dis}}}{0.95} \right)^2 A_{\text{proj}} \\ & = V_p (\rho_p - \rho_{\text{octane,g}}) g \end{aligned} \quad (6.7.14)$$

With the data of Table 6.7.1, we find $u_{s,\text{dis,riser}} = 0.3 \text{ m s}^{-1}$.

Summary of Section 6.7 (take-home messages)

- **Petroleum residues** are the least valuable products of a refinery, and are mainly used as fuel oils by marine vessels, power plants, and industrial facilities. The amount of these oils needed by the market has decreased over recent decades. Thus, these heavy oils are converted by cracking into higher value products such as gasoline and diesel oil.
- The two fractions of vacuum distillation are **vacuum gas oil** and **vacuum residue**. The residue is cracked thermally as the content of metals (V, Ni, Fe) is too high and would lead to rapid deactivation of catalysts. The gasoil is catalytically cracked, which has the advantage of a higher yield and quality of valuable products like gasoline and diesel and lower yields of gases and coke. The two most important representatives of thermal and catalytic cracking are delayed coking and fluid catalytic cracking.
- **Delayed coking** is accomplished by heating the feed to a high temperature of about 500 °C and introducing the preheated oil into a large drum to provide the residence time needed for the thermal cracking reactions to take place.
- **Fluid catalytic cracking** is one of the key processes for the production of gasoline and diesel oil in present-day refineries. Worldwide, about 400 units are in operation with a total annual capacity of about 600 million tonnes. Commercial catalytic crackers operate at about 550 °C. Since after a contact time in the cracking section (upflow pipe, entrained bed) of only a few seconds the catalyst is largely deactivated by coke at a level of about 1 wt%, the catalyst is routed to a regenerator (fluidized bed), where the coke is burned off at temperatures of 700 °C with air to a level of less than 0.1%. The catalyst is returned pneumatically to the catalytic cracking section.

6.8

Clean Liquid Fuels by Hydrotreating

6.8.1

History, Current Status, and Perspective of Hydrotreating

The hydrotreating process for desulfurization of petroleum products was developed in the 1960s mainly to reduce the sulfur concentration in gasoline and diesel oil as the strong rise in crude oil consumption had led to a strong increase in sulfur dioxide emissions. During the last three decades this has led to a stepwise radical strengthening of the sulfur limit in Europe, North America, and Japan, as shown by the example of diesel oil in Germany in Figure 6.8.1. Some values of the statutory sulfur content in gasoline and diesel oil in the European Union and the USA are listed in Table 6.8.1.

This has led to a strong decrease in sulfur emissions caused by transportation fuels for road traffic. For example, in 1975 and 1990, respectively, 100 000 and 86 000 tonnes of SO₂ were emitted in Germany (only road traffic), whereas in 1999 the amount had fallen to 26 000 t SO₂. [For comparison: overall SO₂ emissions (Germany): 7.5 mio. t in 1975, 5.3 mio. t in 1990, and 0.8 mio. t in 1999]. Thus the share of road traffic on the overall SO₂ emissions is in many industrialized countries today much less than 10%. Today, less than 50 ppmw (mostly even < 10 ppmw) sulfur in gasoline and diesel oil is mandatory in industrialized countries, and fuels with even less sulfur are or will be on the market due to tax benefits. A similar trend can be forecast for countries in Asia such as China and India (Table 6.8.2), where until recently the sulfur limit has been much higher.

The main reasons for stringent S-limits both for gasoline and diesel oil are:

- (i) Exhaust gases that contain SO_x cause air pollution and acid rain; even in western

Figure 6.8.1 Historical development of statutory sulfur content in diesel oil (Germany).

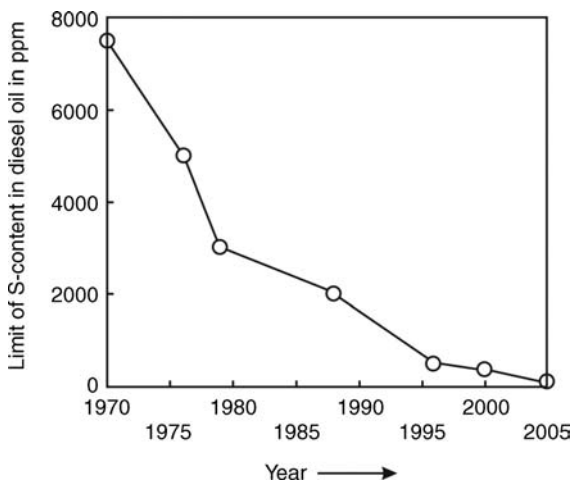


Table 6.8.1 Limit values of sulfur in gasoline and diesel oil in the European Union and in the USA (ppmw, parts per million by weight). Data from European Union (1998, 2001), US EPA (2000, 2001); Reinhardt, Balfanz, and Dimmig, (2002); and Shafi and Hutchings (2000).

	Gasoline			Diesel oil				
	2004	2005	2011	1996	2000	2005	2006	2010
EU	150	30	10	500	350	50	50	10
USA	50	30	10	500	500	500	15	15

Table 6.8.2 Gasoline and diesel oil sulfur limits (ppmw S) in selected Asian countries.

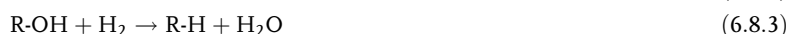
Country	Gasoline			Diesel oil		
	2000	2007	2010	2002	2007	2010
Bangladesh, Cambodia, Pakistan, Sri Lanka	No limit	No limit	No limit	No limit	No limit	500 (Sri Lanka)
China, Indonesia, India, Philippines, Thailand	1000 (India)	500	150	2500 (India) 2000 (China)	500	350
Japan	100	50	10	500	10	—

countries with a negligible contribution of transportation fuels to the total SO_x emissions ultralow sulfur fuels (<10 ppmw S) are still needed for urban areas. (ii) For gasoline, a S-content of preferably less than 10 ppmw is needed for new lean fuel engines in combination with S-sensitive DeNO_x-storage catalysts for further reduction of CO and NO_x (Section 6.18.1). (iii) The situation is similar for diesel oil with respect to new catalysts and filters to reduce particle emissions. (iv) New technologies based on fuel cells for both vehicles and stationary systems need fuels with less than at least 10 ppm S.

Desulfurization is obtained by heterogeneously catalyzed hydrodesulfurization (HDS), whereby the organic sulfur species (Figure 5.1.22) are converted into H₂S and the corresponding hydrocarbons:



H₂S is easily removed from the desulfurized oil and subsequently converted into elementary sulfur in the Claus process. Organic nitrogen and oxygen compounds (Figure 5.1.24) present in the oil are also converted, which leads to the formation of NH₃ and H₂O:



The catalysts commercially used for hydrotreating are most commonly sulfided CoMo/Al₂O₃ or sulfided NiMo/Al₂O₃, such as 3 wt.% CoO and 12–15 wt.% MoO₃ supported on γ -Al₂O₃ (Farrauto and Bartholomew, 1997).

HDS is performed in a fixed bed reactor. For gasoline, typically a total pressure of 30 bar and a reaction temperature in the range 310–370 °C is used (Moulijn, Makkee, and Van Diepen, 2004). For diesel oil and kerosene the parameters are more severe (40–100 bar, 330–400 °C) and for residues we may reach values up to 170 bar and 425 °C (Farrauto and Bartholomew, 1997).

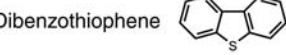
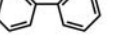
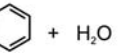
6.8.2

Thermodynamics and Kinetics of Hydrodesulfurization (HDS)

Scheme 6.8.1 shows typical reactions with different sulfur compounds that occur during hydrotreating. In general hydrotreating is exothermic, and in principle equilibrium is favored by low temperatures. Nevertheless, for typical reaction temperatures, the equilibrium is far on the side of the products (hydrogen sulfide and the corresponding hydrocarbon) as examined by the stability diagram of hydrodesulfurization of dibenzothiophene (Figure 6.8.2) and the values of the equilibrium constant of various organic sulfur components (Figure 6.8.3).

The kinetics of HDS have been studied intensively. Here, we only examine some basic principles. For details see Kabe, Ishihara, and Qian (1999), Satterfield, Modell, and Mayer (1975), McCarthy and Schrader (1987), Delmon, Froment, and Grange (1999), Givens and Venuto (1970), Gates, Katzer, and Schuit (1979), Daly (1978),

Scheme 6.8.1 Typical hydrotreating reactions.
Adapted from Mouljin, Makkee, and Van Diepen (2004).

Compound	Example		ΔH_{298}^0 (kJ/mol)
Mercaptans	RSH	+ H ₂ → RH + H ₂ S	-72 (for R = CH ₃)
Thiophenes		+ 3H ₂ →  + H ₂ S	-147
Dibenzothiophene		+ 5H ₂ →  + H ₂ S	-169
Pyridines		+ 5H ₂ →  + NH ₃	-333
Phenols		+ H ₂ →  + H ₂ O	-62

Kilanowski *et al.* (1978), Bartsch and Tanielian (1974), Kilanowski and Gates (1980), Nag *et al.* (1979), Houalla *et al.* (1978, 1980), Girgis and Gates (1991), Lamure-Meille *et al.* (1995, 1997), Meille *et al.* (1999), Farag, Mochida, and Sakanishi (2000), O'Brien *et al.* (1986), and Pecoraro and Chianelli (1981).

In recent years, kinetic studies have concentrated on the HDS of dibenzothiophene (DBT) derivatives as these species are by orders of magnitude less reactive than sulfur species such as thioles, sulfides, and thiophene, or benzothiophene (Figure 5.1.22). The reaction network of hydrodesulfurization is illustrated in Scheme 6.8.2 for the example of HDS of DBT on CoMo.

Figure 6.8.2 Stability diagram of hydrodesulfurization of dibenzothiophene (for principle aspects of a stability diagram based on the standard Gibbs functions of formation $\Delta_f G^0$ see Section 4.2.1).

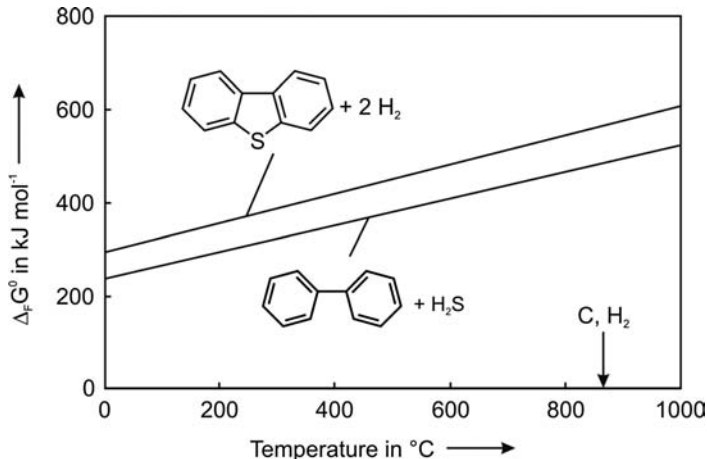
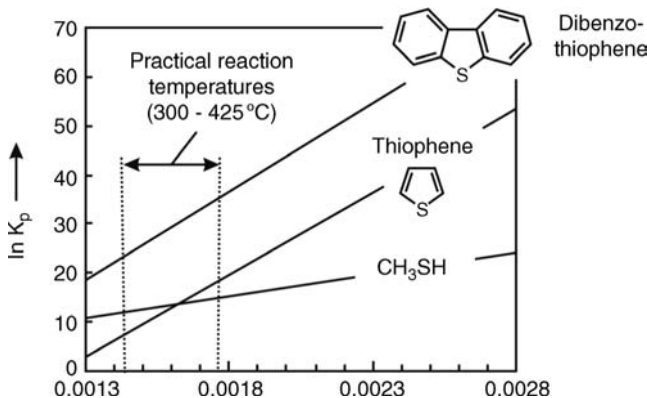
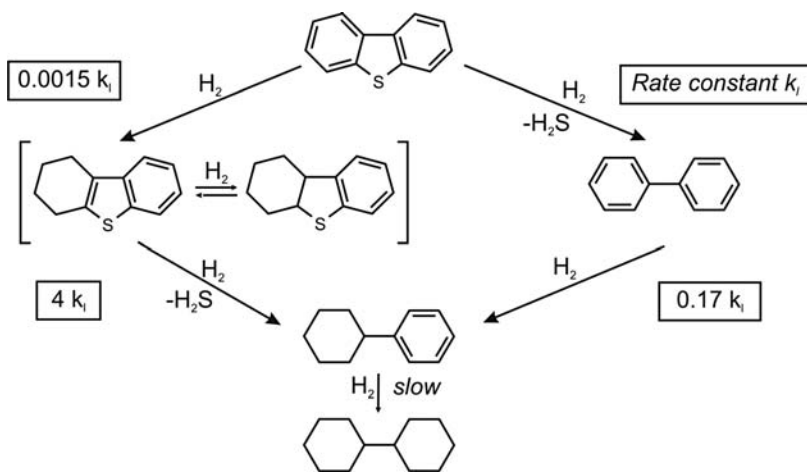


Figure 6.8.3 Equilibrium data of selected hydrotreating reactions (equilibrium constants of the three hydrodesulfurization reactions shown in Scheme 6.8.1).





Scheme 6.8.2 Reaction network of hydrodesulfurization of dibenzothiophene catalyzed by CoMo at 300 °C and 102 bar (Farrauto and Bartholomew, 1997; Houalla *et al.*, 1978).

For CoMo-catalysts direct HDS via biphenyl is preferred as the reaction of DBT to form biphenyl is by about three orders of magnitudes faster than hydrogenation to 1,2,3,4-tetrahydrodibenzothiophene and 1,2,3,4,10,11-hexahydrodibenzothiophene, respectively. For NiMo-catalysts the ratio of direct to indirect route of HDS is about two (Girgis and Gates, 1991).

A simplified intrinsic rate expression for HDS (in the liquid phase such as for diesel oil and residues, see Section 6.8.3) is for the example of DBT:

$$r_{\text{HDS}} = \frac{k_{\text{HDS}} c_{\text{DBT}}}{(1 + K_{\text{DBT}} c_{\text{DBT}} + K_{\text{H}_2\text{S}} c_{\text{H}_2\text{S},l})} \frac{c_{\text{H}_2,l}}{(1 + K_{\text{H}_2} c_{\text{H}_2,l})} \quad (\text{with } c_{\text{H}_2,l} = K_{\text{solubility}} p_{\text{H}_2}) \quad (6.8.4)$$

where k_{HDS} is the rate constant, K_i (with $i = \text{DBT}$, H_2S , and H_2) the equilibrium constant of adsorption, and c_i the concentration in the liquid phase. The concentration of H_2 in the oil is related to the partial pressure by the solubility (*Henry's law*). For high pressures of hydrogen (usually more than about 20 bar, Figure 6.8.4), the rate of HDS becomes formally zero order with respect to hydrogen, and for low concentrations of sulfur, that is, under deep desulfurization conditions ($c_s < 500 \text{ ppm}$), inhibition by H_2S is not significant. If we assume that the term $K_{\text{DBT}} c_{\text{DBT}}$ is also small ($\ll 1$) Eq. (6.8.4) simplifies to a first-order reaction rate equation:

$$r_{\text{HDS}} = k_{\text{HDS}} c_{\text{DBT}} / K_{\text{H}_2} = k_{m,1} c_{\text{DBT}} \quad (\text{for } K_{\text{H}_2} c_{\text{H}_2,l} \gg 1 \text{ and } K_{\text{DBT}} c_{\text{DBT}} + K_{\text{H}_2\text{S}} c_{\text{H}_2\text{S},l} \ll 1) \quad (6.8.5)$$

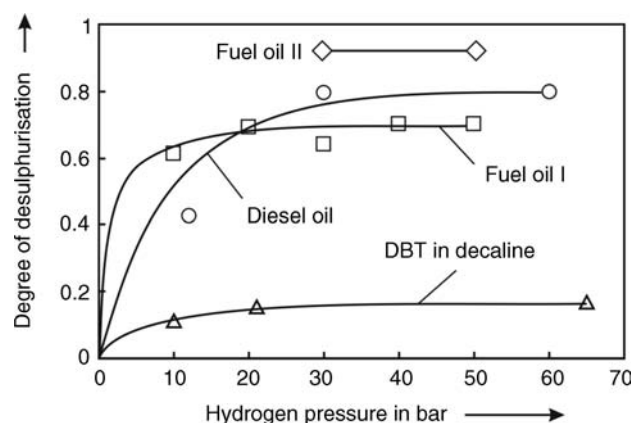
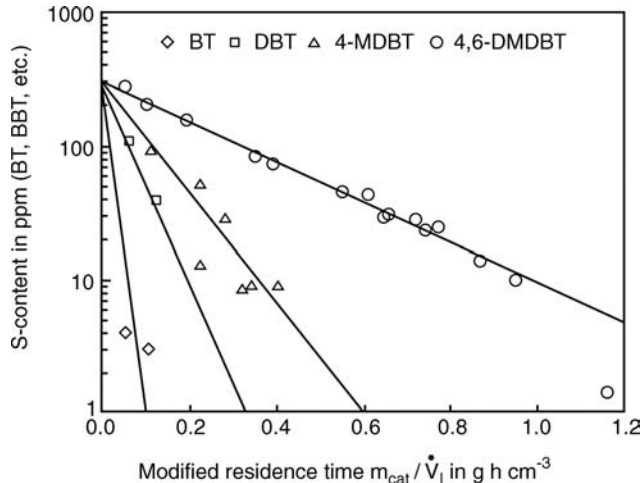


Figure 6.8.4 Influence of H_2 pressure on HDS (CoMo) of DBT, diesel, and light fuel oils (oil I: 2250 ppm S, 380 °C, $1/\text{LHSV} = 2 \text{ m}_\text{cat}^3 \text{ h m}_\text{oil}^{-3}$; oil II: 580 ppm S, 390 °C, $3.3 \text{ m}_\text{cat}^3 \text{ h m}_\text{oil}^{-3}$; diesel: 290 ppm S, 360 °C, $1.3 \text{ m}_\text{cat}^3 \text{ h m}_\text{oil}^{-3}$. Data for diesel: Schmitz, Datsevich, and Jess (2004); Schmitz (2003), fuel oil: Wache (2006), Wache *et al.* (2006), and DBT (at 250 °C): Kabe, Ishihara, and Qian (1999)).

Figure 6.8.5 HDS of single sulfur compounds [CoMo-catalyst, 360 °C, 3 MPa, feed: *n*-dodecane and single S-compound, BT: benzothiophene, DBT: dibenzothiophene, 4-MDBT: 4-methyldibenzothiophene, 4,6-DMDBT: 4,6-dimethyldibenzothiophene; lines indicate first-order reaction with regard to S-species, Eq. (6.8.6), data from Schmitz, 2003; Schmitz, Datsevich, and Jess, 2004].



For an ideal plug flow reactor we obtain [Eq. (4.10.25)]:

$$\frac{c_{\text{DBT,out}}}{c_{\text{DBT,in}}} = e^{-Da_1} \quad \left(\text{with } Da_1 = k_{m,1} \rho_b \tau = k_{m,1} \frac{m_{\text{cat}}}{V_R} \frac{V_R}{\dot{V}_l} \text{ and } k_{m,1} \text{ in } \text{m}^3 \text{ kg}^{-1} \text{ s}^{-1} \right) \quad (6.8.6)$$

The first-order rate for single S-compounds is confirmed by measurements (Figure 6.8.5).

The reactivity (rate constants) of sulfur species differs strongly (Figures 6.8.5 and 6.8.6, Table 6.8.3). The most refractory species is the sterically hindered 4,6-dimethyldibenzothiophene (4,6-DMDBT), which is about an order of magnitude less reactive than DBT.

Although HDS of S-compounds is a first-order reaction, the decrease in total sulfur content is better approximated by a second-order rate with respect to sulfur [Eq. (4.10.26)]:

$$\frac{c_{S,\text{out}}}{c_{S,\text{in}}} = \frac{1}{1 + Da_2} \quad \left(\text{with } Da_2 = k_{m,2} c_{S,\text{in}} \frac{m_{\text{cat}}}{\dot{V}_l} \text{ and } k_{m,2} \text{ in } \text{m}^6 \text{ kg}^{-1} \text{ s}^{-1} \text{ mol}^{-1} \right) \quad (6.8.7)$$

Rearrangement of Eq. (6.8.7) gives:

$$\frac{1}{c_{S,\text{out}}} = \frac{1}{c_{S,\text{in}}} + k_{m,2} \frac{m_{\text{cat}}}{\dot{V}_l} \quad (6.8.8)$$

and thus a plot of $1/c_{S,\text{out}}$ versus m_{cat}/\dot{V}_l leads to a linear relationship (Figure 6.8.7).

The reason for this, at first sight unexpected, second-order behavior is the step-wise conversion of S-compounds, which differ strongly in reactivity. As a consequence, the rate of HDS (with respect to total S) decreases

Figure 6.8.6 Reactivity (first-order rate constants) of selected organic S-species relative to DBT (dibenzothiophene) as reference species for hydrotreating on CoMo/Al₂O₃ [experiments with *n*-hexadecane as solvent, 300 °C, 72–103 bar, data from Nag *et al.* (1979) and Houalla *et al.* (1980)].

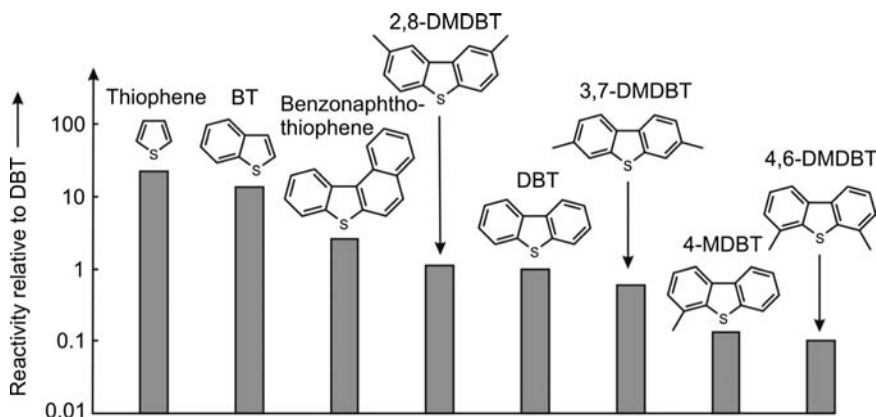


Table 6.8.3 Kinetic data of hydrodesulfurization (HDS) of individual S-compounds [340–400 °C, 10–70 bar, CoMo-catalyst (C20-6, Süd Chemie)] [Schmitz (2003), Schmitz, Datsevich, and Jess (2004)].

S-Compound and structure	E_A (kJ mol ⁻¹)	$k_{m,1,0}$ (cm ³ g ⁻¹ h ⁻¹)	$k_{m,1}$ (360 °C) (cm ³ g ⁻¹ h ⁻¹)
Dibenzothiophene (DBT)	87	2.9×10^8	19
4-Methyldibenzothiophene (4-MDBT)	117	2.3×10^{10}	5
4,6-Dimethyldibenzothiophene (4,6-DMDBT)	132	2.1×10^{11}	2.7

superproportionally with increasing degree of desulfurization through the increasing portion of the remaining, less reactive compounds like 4,6-DMDBT.

6.8.3

Hydrodesulfurization Process and Reaction Engineering Aspects

Hydrodesulfurization is technically performed either in the gas phase or in a trickle bed reactor, that is, in a three-phase system with gaseous H₂, liquid oil, and a solid catalyst. Trickle bed reactors are more complicated with respect to hydrodynamics and partial wetting of the catalyst that is unwanted but has to be considered, for example, for reactor modeling. Based on the above given reaction conditions, we can easily determine which feedstock has to be desulfurized in a trickle bed reactor and which feedstock completely forms a gas phase (vapor). The molar ratio of hydrogen (fresh and recycled) to oil (for a mean carbon number of about 20) is about two. Thus the partial pressure that the oil has to build up to be completely vaporized is about $1/3$ of the total pressure.

Based on the normal boiling point T_{boil}^0 (at 1 bar) of a hydrocarbon, we can estimate the vapor pressure at the temperature of hydrodesulfurization (T_{HDS}) by the vapor pressure equation, Eq. (3.1.44), and *Trouton's rule* [Eq. (3.1.46)]:

$$\begin{aligned} \ln \frac{p_{\text{vap}, T_{\text{HDS}}}}{p_0} &\approx - \frac{\Delta_{\text{vap}} H^0}{R} \left(\frac{1}{T_{\text{HDS}}} - \frac{1}{T_{\text{boil}, 1 \text{ bar}}} \right) \\ &\approx \frac{T_{\text{boil}}^0 \cdot 90 \text{ J mol}^{-1} \text{ K}^{-1}}{R} \left(\frac{1}{T_{\text{boil}}^0} - \frac{1}{T_{\text{HDS}}} \right) \end{aligned} \quad (6.8.9)$$

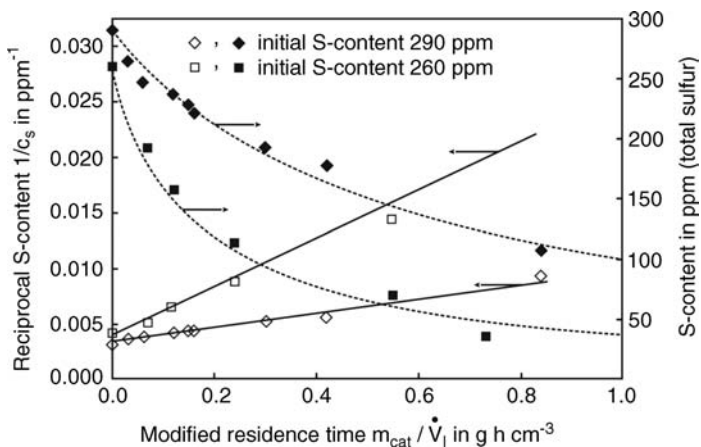
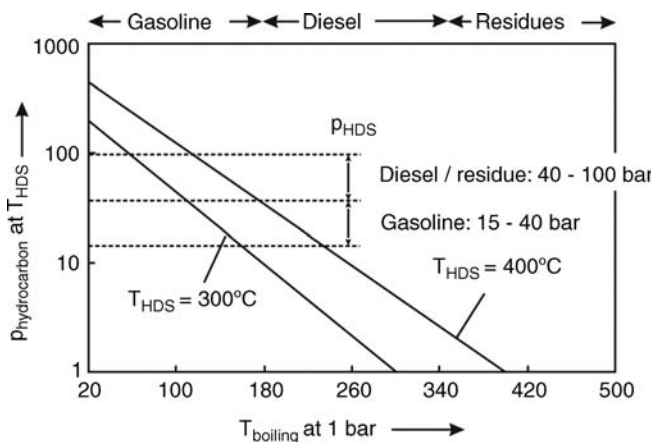


Figure 6.8.7 Deep HDS of two pre-desulfurized diesel oils [360 °C, 30 bar; lines indicate second order with respect to total S, see Eq. (6.8.8)] (Schmitz, 2003; Schmitz, Datsevich, and Jess, 2004).

Figure 6.8.8 Influence of normal boiling point on the partial pressures of hydrocarbons.



The influence of T_{boil}^0 on the partial pressure of a hydrocarbon at temperatures of 300 and 400 °C, which represent the temperature range used for HDS, is shown in Figure 6.8.8.

For gasoline with a final boiling point of about 180 °C at 1 bar, we obtain a vapor pressure of more than 10 bar at 300 °C and over 35 bar at 400 °C, and so we are working in the gas phase. For diesel oil, the vapor pressure will be much lower: If we use a temperature of 270 °C as a mean value for the normal boiling temperature of diesel oil and a relative high reaction temperature of 400 °C, the calculated vapor pressure is only 8 bar compared to an “effective” system pressure of around 13–33 bar (total pressure in a range of 40–100 bar minus partial pressure of H₂). Thus for diesel oil, and above all for residue hydrotreating, evaporation of most of the oil is not possible due to the high boiling point of the oil constituents, and a trickle-bed reactor is needed.

With respect to the increasing demand for practically S-free fuels (<10 ppm), S-species with a very low reactivity like dibenzothiophene derivatives have to be converted (Figure 6.8.6), typically in a second deep HDS step, which leads to additional high investment and operating costs. The enormous expenses needed today for such a deep HDS of already hydrotreated (pre-desulfurized) diesel oil can be illustrated by typical industrial data [MiRO-refinery 2004 (oral communication); Wache *et al.* (2006)]: Deep HDS reactors have a volume of up to 500 m³ to treat about 400 m³ of oil per h. The feed rate of fresh H₂ is about 40 m³ (NTP) per m³ oil, the recycle rate is about three, and for a typical pressure of 6 MPa the pressure drop of about 1 MPa has to be compensated by a huge recycle compressor (1 MW).

Trickle-bed reactors have the following problems: (i) In general they are complicated with respect to the mass transfer (gas–liquid and liquid–solid). In addition, proper hydrodynamic conditions (wetting of catalyst, distribution of gas and liquid phase) are hard to realize. Scale-up is therefore difficult and pilot plants are often still needed. (ii) The amount of H₂ fed to the reactor – above all in the case of a second stage deep desulfurization of an already hydrotreated fuel – is much higher than the amount chemically needed. Therefore, a costly recycle compressor for the (unconsumed) hydrogen has to be installed.

There are several options to improve (deep) desulfurization of fuels: (i) better catalysts for deep HDS based on noble metals are on the market and still the focus of research (e.g., Fujikawa *et al.*, 2001; Navarro *et al.*, 1996; Reinhardt *et al.*, 1999; Robinson *et al.*, 1999); (ii) alternative processes have been developed like the adsorption process SZorb (Sughrue, 2003); and (iii) extraction of organic S-compounds by novel extraction media like ionic liquids is now also considered (Boesmann *et al.*, 2001; Esser *et al.*, 2004).

For deep desulfurization, trickle-bed reactor technology may also be improved by using a two-phase reactor. Thereby, the oil is externally pre-saturated with H₂ and only the liquid phase is passed over the catalytic fixed bed. To discuss the

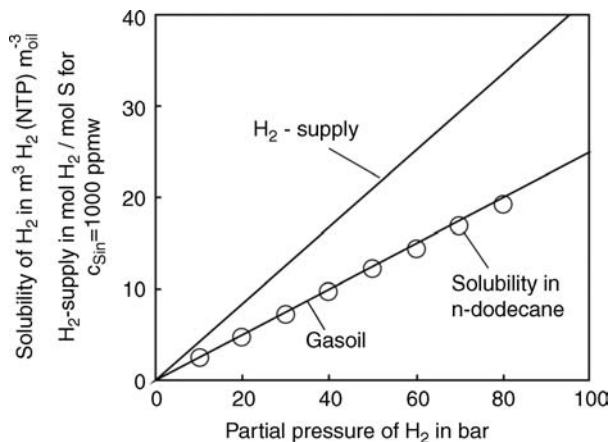


Figure 6.8.9 Solubility at 370 °C of hydrogen in *n*-dodecane (data from Schmitz, 2003) and in gasoil (data from Ronze *et al.*, 2002).

pros and cons of this concept, we inspect the solubility of H₂, which is illustrated in Figure 6.8.9 for *n*-dodecane and a gasoil at a typical HDS reaction temperature of 370 °C.

By the data given in Figure 6.8.9 we can now estimate the amount of hydrogen that needs to be solved at the reactor entrance to convert all sulfur species: For a gasoil with a sulfur content of 1000 ppmw and a density of 850 kg m⁻³, a partial pressure of hydrogen of, for example, 40 bar would lead to about 16 mol H₂ per mol of sulfur ($10 \text{ m}^3 \text{ H}_2 \text{ m}^{-3} \text{ oil} = 0.52 \text{ mol H}_2 \text{ kg}^{-1} \text{ oil} = 520 \text{ mol H}_2 \text{ kg}^{-1} \text{ sulfur} = 16.4 \text{ mol H}_2 \text{ mol}^{-1} \text{ sulfur}$, $M_s = 32 \text{ g mol}^{-1}$). Typically, 1–5 mol of hydrogen are needed per mol of sulfur species (Scheme 6.8.1), thus this estimation leads to the conclusion that the solubility of hydrogen at a pressure of 40 bar is high enough for complete desulfurization of a 1000 ppmw S oil. In other words, practically no H₂-depletion occurs along the fixed bed, even if hydrogen would not be supplied within the fixed bed reactor from the gas to the liquid phase as in a trickle-bed reactor. It should be emphasized that for an oil with a high content of sulfur or a feed rich in unsaturated hydrocarbons (like olefins in gasoils from cracking processes) this is not the case as much more H₂ is then needed and a huge amount is consumed just for the hydrogenation of unsaturated compounds. However, for deep HDS, the content of sulfur and of unsaturated components of the already hydrotreated feedstock is always so low that independent of the reactor used – trickle bed or two-phase reactor with pre-saturator – practically no H₂-depletion occurs along the fixed bed.

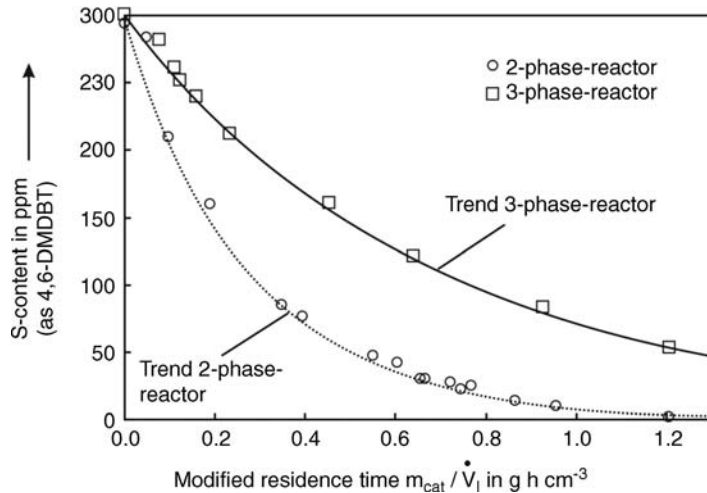
Hence, for deep desulfurization, a two-phase reactor (oil externally pre-saturated with H₂ and solid catalyst) could be an alternative to the trickle bed. The H₂-recycle is then redundant, and scale-up problems do not occur. In addition, the two-phase technology utilizes the maximum intrinsic chemical reaction rate as pore diffusion does not play a role in the slow desulfurization of refractory compounds left in pre-desulfurized feedstocks. For a trickle bed this rate is an upper limit, which cannot, or only hardly, be reached with regard to improper gas–liquid distribution and/or wetting of the catalyst. A laboratory-scale trickle-bed and two-phase reactor with pre-saturation are compared in Figure 6.8.10 for a model oil.

Compared to the respective experiment with the two-phase reactor, the reaction rate in the trickle-bed is by a factor of about two lower. Although the operation of the laboratory-scale trickle bed reactor could possibly be improved by adjusting for optimal conditions with respect to the velocity of the liquid and the gas phase, a higher reaction rate than the limiting intrinsic rate reached with the two-phase reactor is in any case not possible [details of the two-phase concept are given in Schmitz (2003); Schmitz, Datsevich, and Jess (2004); Wache *et al.* (2006); and Wache (2006)].

Figure 6.8.11 illustrates a typical HDS process configuration.

The sulfur-containing feed such as diesel oil is compressed, mixed with fresh and recycled H₂, pre-heated to about 350 °C, and then passed through the fixed-bed

Figure 6.8.10 HDS in a conventional trickle bed reactor (laboratory-scale) and in a reactor with H₂-pre-saturation of oil (model oil with 4,6-DMDBT in *n*-dodecane, 360 °C, 3 MPa, Süd-Chemie CoMo-catalyst) (data from Schmitz, 2003; Schmitz, Datsevich, and Jess, 2004).



reactor. HDS and also the hydrogenation of unsaturated compounds (aromatics and olefins) are exothermic reactions, so usually two to three beds are used for feedstocks rich in sulfur and/or unsaturated compounds. The inlet of the second and third bed is cooled by external heat exchange or by means of cold-shot cooling with H₂. For deep desulfurization a single bed is sufficient.

The products are cooled via heat exchange with the cold feed to about 200 °C and proceed through a hot high pressure (HP) separator. The liquid phase is lowered in pressure and sent to a hot low pressure (LP) separator. The vapor phase from the hot HP separator is cooled and water is injected to absorb H₂S and NH₃ (formed by hydrotreating of N-compounds) at a temperature of about 40 °C. The subsequent cold HP separator separates the hydrogen-rich gas phase, liquid sour water, and liquid oil, which mainly consists of low-molecular-weight hydrocarbons formed by unwanted cracking reactions. The remaining H₂S in the gas phase is separated by scrubbing, typically with an amine as solvent. The recovered H₂ is recycled by a compressor and is (together with make-up H₂) added to the feed.

The liquid organic phase of the cold HP separator is transferred to the LP separator where a stream rich in H₂S and light hydrocarbons is removed and sent to a gas treatment unit. The liquid stream of the LP separator is sent to a stripping column, where any remaining gases are removed.

Hydrogen sulfide from the recycle gas scrubbing and the gas treatment unit is finally transferred to a Claus process for catalytic conversion with air to elementary sulfur.

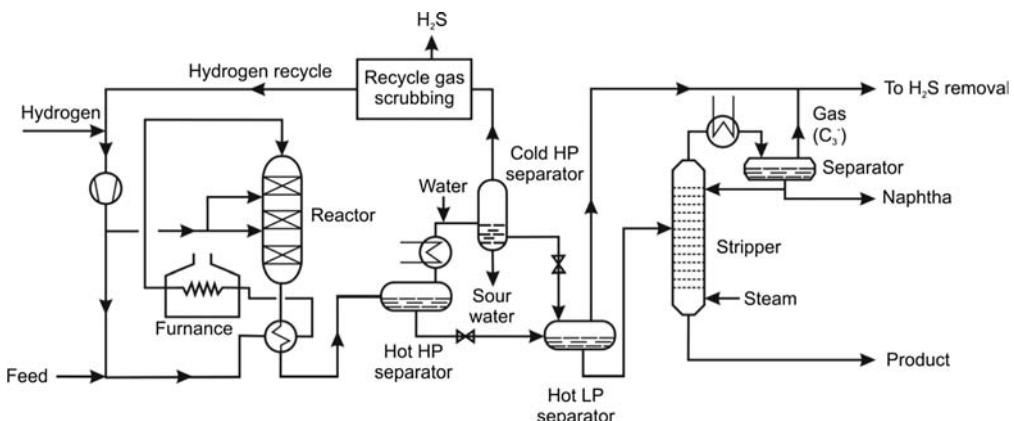


Figure 6.8.11 Typical configuration of a HDS process. Adapted from Moulijn, Makkee, and Van Diepen (2004).

Summary of Chapter 6.8 (take-home messages)

- The hydrotreating process for **desulfurization of petroleum products** was developed in the 1960s mainly to reduce the sulfur concentration in gasoline and diesel oil to reduce sulfur dioxide emissions. In Europe, North America, and Japan this has led to a strong decrease in sulfur emissions caused by transportation fuels for road traffic. A similar trend can be forecast for countries in Asia like China and India, where until recently the sulfur limit has been much higher.
- The main reasons for **stringent S-limits** both for gasoline and diesel oil are:
(i) Exhaust gases that contain SO_x cause air pollution and acid rain.
(ii) For gasoline, a S-content of preferably less than 10 ppmw is needed for new lean fuel engines in combination with S-sensitive DeNO_x-storage catalysts for further reduction of CO and NO_x.
(iii) The situation is similar for diesel oil with respect to new catalysts and filters to reduce particle emissions.
(iv) New technologies based on fuel cells both for vehicles and stationary systems need fuels with less than at least 10 ppm S.
- Desulfurization is obtained by **heterogeneously catalyzed hydrodesulfurization** (HDS), whereby the organic sulfur species are converted into H₂S and the corresponding hydrocarbons – organic nitrogen and oxygen compounds present in the oil – are also converted, leading to the formation of NH₃ and H₂O.
- The **HDS catalysts** commercially used are mostly sulfided CoMo/Al₂O₃ or NiMo/Al₂O₃,
- HDS is performed in a **fixed bed reactor** at a temperature in the range 300–400 °C at pressures of up to 100 bar.
- The **reactivity (rate constants) of sulfur species** differs strongly; the most refractory species is the sterically hindered 4,6-dimethylbenzothiophene, which is by about one order of magnitude less reactive than dibenzothiophene. Although HDS of S-compounds is a first-order reaction, the decrease of total sulfur content is better approximated by a second-order rate with respect to sulfur. The reason for this is the stepwise conversion of S-compounds that differ strongly in reactivity. As a consequence, the rate of HDS decreases superproportionally with increasing degree of desulfurization through the increasing portion of the remaining, less reactive S-compounds.
- HDS is technically performed either in the gas phase (gasoline) or in a trickle bed reactor (diesel oil or higher boiling fractions), that is, in a **three-phase system** with gaseous H₂, liquid oil, and a solid catalyst.
- **Trickle-bed reactors** have the following problems: (i) They are complicated with respect to the mass transfer (gas–liquid and liquid–solid). Proper hydrodynamic conditions (wetting of catalyst, distribution of gas, and liquid phase) are hard to realize and, therefore, **scale-up** is not an easy task. (ii) The amount of H₂ fed to the reactor is much higher than the amount chemically needed. Therefore, a costly recycle compressor for the (unconsumed) hydrogen has to be installed.

6.9**High Octane Gasoline by Catalytic Reforming****6.9.1****Reactions and Thermodynamics of Catalytic Reforming**

Modern automobiles with spark ignition engines and high compression ratios need high-octane gasoline. The octane number, which is a measure of a fuel's antiknock properties under the condition of gasoline combustion in spark ignition engines, depends on the gasoline composition. The octane number is measured in a

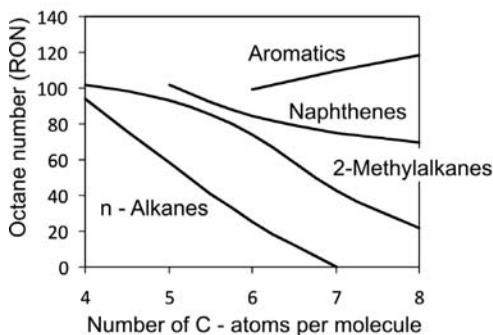


Figure 6.9.1 Research octane numbers (RONs) of hydrocarbons of different chain length and molecular structure (naphthenes: cyclopentane, cyclohexane, methylcyclohexane, 1,3-dimethylcyclohexane, and 1,3,5-trimethylcyclohexane; aromatics: benzene, toluene, and *m*-xylene).

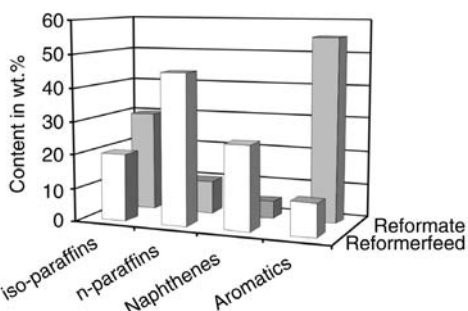


Figure 6.9.2 Typical composition of feed and product of reforming (adapted from Keim, Behr, and Schmitt, 1986).

standardized motor under standardized conditions. If the test motor rotates at 600 rpm, the octane number is called the research octane number (RON). This number corresponds to the volume percent of iso-octane (2,2,4-trimethylpentane, RON 100) that must be added to *n*-heptane (RON = 0) to match the performance of the gasoline. Figure 6.9.1 shows RON values for different hydrocarbons as a function of the carbon number. Evidently, the octane numbers of aromatics are highest followed by naphthenes and branched alkanes. With increasing carbon number, the octane numbers of alkanes and alkenes decrease whereas those for aromatics increase.

Straight-run gasoline from the crude oil distillation unit is composed primarily of alkanes and cycloalkanes (naphthenes) with only a small fraction of aromatics. The heavier end of gasoline with a boiling range of 70–180 °C has a low RON, typically 50. The octane number is therefore improved by catalytic reforming of low octane normal paraffins and cycloalkanes into high octane branched alkanes and aromatics (Figure 6.9.2). Because of the high content of aromatics in the so-called reformate, reforming is also a source of aromatics for the petrochemical industry.

Today, about 800 commercial catalytic reforming plants are in operation worldwide with a total capacity of about 0.4 billion tonnes (Farrauto and Bartholomew, 1997). The worldwide annual gasoline (petrol) consumption is about 1 billion tonnes, and reformate is a major constituent of gasoline with about 40%.

Table 6.9.1 lists the main reactions of the reforming process, relative reaction rates, and reaction conditions at which the respective reaction is favored.

It is apparent from the data in Table 6.9.1 that dehydrogenation is highly favored with regard to kinetics (highest relative activity) and also with regard to thermodynamics. Isomerization, although kinetically favored, suffer equilibrium limitations as the equilibrium constants at 500 °C are near unity. Hydrocracking is thermodynamically favored but undesirable, since low-molecular-weight gases are formed and a significant amount of H₂ is consumed by saturation of short-chain olefins formed by cracking. Fortunately, the activity is low (Table 6.9.1).

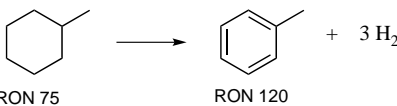
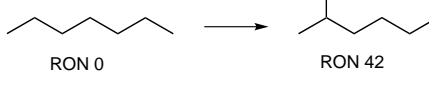
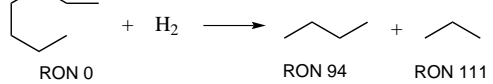
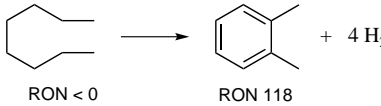
Dehydrocyclization is highly desirable but, unfortunately, is the least favorable kinetically (relative activity = 1), and thermodynamically favored at high temperatures. Because of their low relative activities, hydrocracking and dehydrocyclization do not operate near equilibrium. The equilibrium of dehydrocyclization is illustrated by the stability diagram in Figure 6.9.3 for the example of *n*-heptane conversion into toluene (+4H₂). The equilibrium constant is given by:

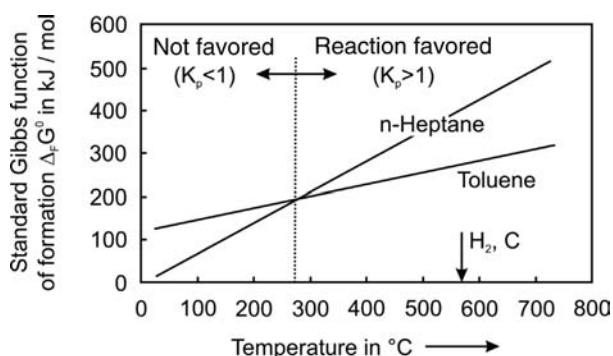
$$\ln K_p = \ln \left(\frac{p_{\text{toluene}} p_{\text{H}_2}^4}{p_{\text{n-heptane}} p_0^4} \right) = - \frac{\Delta_F G^0}{RT} = - \frac{(\Delta_F G_{\text{toluene}}^0 - \Delta_F G_{\text{n-heptane}}^0)}{RT} \quad (6.9.1)$$

Thermodynamically, coke formation is favored as the values of Δ_FG⁰ of *n*-heptane and toluene are higher than of those of hydrogen and carbon, with Δ_FG⁰ = 0 (Figure 6.9.3). Figure 6.9.4 depicts the equilibrium constants for the desired dehydrocyclization of *n*-heptane, the undesired cracking, and undesired coke formation as a function of temperature. The formation of aromatics is favored at high temperatures, but cracking and coke formation are also promoted. As a result, coking and cracking will always be a potential problem in reforming, and operating conditions must reflect a balance between desired and undesired reactions.

In the technical reforming process, hydrogen is recycled and added to the feed, although this is thermodynamically not favored, but is needed to suppress and limit coke formation. Typically, a H₂ pressure of around 15 bar is used, which limits the

Table 6.9.1 Main reforming reactions, reaction enthalpies, reaction rates (at 500 °C), and favorable reaction conditions (Farrauto and Bartholomew, 1997).

Reaction	Relative activity	$\Delta_R H_{298}^0 \text{ (kJ mol}^{-1}\text{)}$	Favorable reaction conditions	
			Thermodynamically	Kinetically
<i>Dehydrogenation</i>				
	180	+ 213	High T Low p	High T Low p
<i>Isomerisation of normal to iso paraffins</i>	12	- 9	Not strongly influenced by T and p	High T High p
				
				
<i>Hydrocracking</i>	4	- 68	Low T	High T Low p
				
<i>Dehydrocyclization</i>	1	+ 238	High T Low p	High T High p
				

Figure 6.9.3 Stability diagram of the system *n*-heptane and toluene.

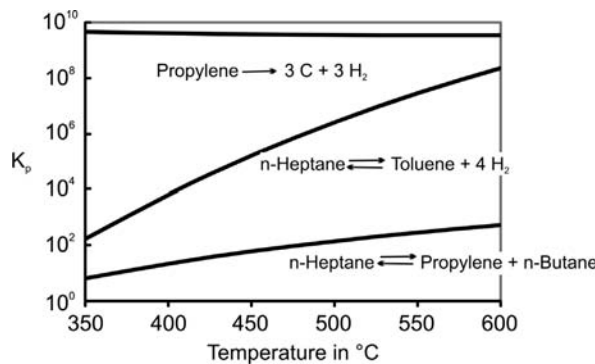
equilibrium conversion of dehydrocyclization for temperatures below 400 °C, as we can estimate by Figure 6.9.3 and the following considerations. For a constant hydrogen pressure (high excess) Eq. (6.9.1) leads to:

$$\frac{p_{\text{toluene}}}{p_{n\text{-heptane}}} = e^{-\frac{\Delta_R G^0}{RT}} \left(\frac{p_0^4}{p_{\text{H}_2}^4} \right) \quad (6.9.2)$$

and the corresponding equilibrium conversion of heptane is given by:

$$X_{n\text{-heptane}} = \frac{p_{\text{toluene}}}{p_{n\text{-heptane}} + p_{\text{toluene}}} = \frac{1}{1 + \frac{p_{n\text{-heptane}}}{p_{\text{toluene}}}} = \frac{1}{1 + e^{\frac{\Delta_R G^0}{RT}} \left(\frac{p_{\text{H}_2}^4}{p_0^4} \right)} \quad (6.9.3)$$

Figure 6.9.4 Thermodynamics of selected reactions of catalytic gasoline reforming: Equilibrium constants for the desired dehydrocyclization of *n*-heptane and the undesired cracking to propylene and butane and subsequent coke formation as a function of temperature.



At 400 °C and a hydrogen pressure of 15 bar, Eq. (6.9.3) leads to an equilibrium conversion of *n*-heptane of only 13%. At 500 °C, the equilibrium conversion is almost complete (>98%).

6.9.2

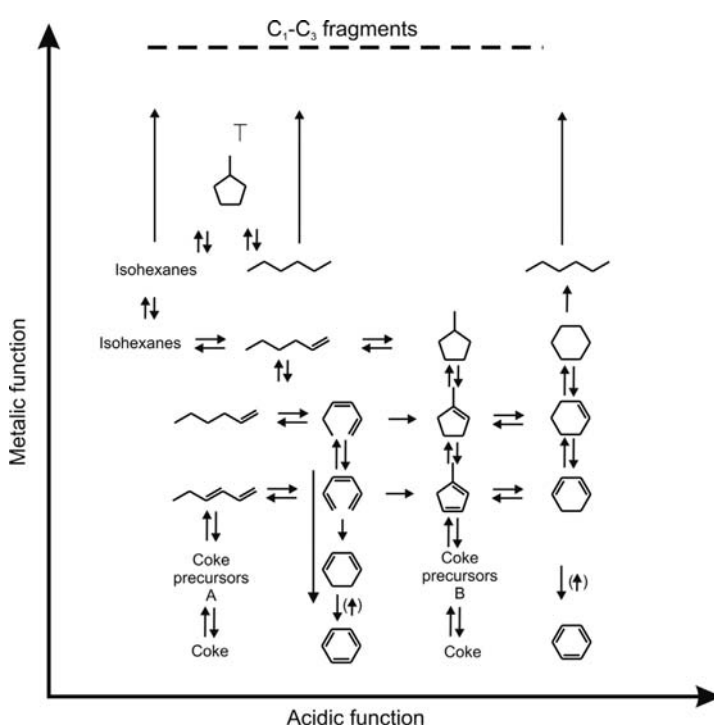
Reforming Catalyst

Reforming requires a catalyst with dual functions: an acidic function to catalyze isomerization and cyclization and a dehydrogenation function that requires an active metal site. Figure 6.9.5 illustrates a simplified reaction network for the example of C₆-hydrocarbons that also identifies the catalytic sites involved.

Typical reforming catalysts contain platinum as the metal component and modified γ-Al₂O₃ for acidity. Rhenium is used as promoter to decrease coke formation, which increases the cycle time between regenerations. The (internal) surface area of a reforming catalyst is about 200 m² g⁻¹, and commonly 1–6 mm diameter spheres or extrudates are used.

The mechanisms of reforming reactions are complex and involve adsorption on multiple sites. Kinetic models are complicated and the compounds are often combined in groups such as alkanes, naphthenes, and aromatics (Farrauto and Bartholomew, 1997; Le Page, 1978). Reforming catalysts are sensitive to poisons such as sulfur, nitrogen, oxygen, and metals (S < 5–10 ppm, N < 1 ppm, H₂O < 4 ppm, Pb + As + Cu < 20 ppb, Le Page, 1978). It is therefore necessary to hydrotreat the

Figure 6.9.5 Simplified reaction network of catalytic gasoline reforming for the example of C₆-hydrocarbons that also identifies the catalytic sites involved. Adapted from Cejka, Corma, and Zones (2010).



feed to remove unwanted components such as thiophenes and phenols to very low levels. The feed leaving the hydrotreating reactor contains H₂S, NH₃, and H₂O, which are separated by stripping. The metals are trapped on the hydrotreating catalyst, which thus acts as a filter.

6.9.3

Process of Catalytic Reforming

The reforming process consists of exothermic reactions (isomerization, hydrocracking) and endothermic reactions (dehydrogenation, dehydrocyclization). In summary the process is endothermic. Several parallel and sequential reactions with different rates and equilibrium limitations take place (Table 6.9.1). In addition, coke formation occurs, which leads to a gradual decrease of the activity of the catalyst. To minimize coke formation hydrogen is added in a large excess to the feed, that is, H₂ formed by dehydrogenation and dehydrocyclization is recycled. Nevertheless, coke must be burned off after a certain carbon load has been reached.

Depending on the type of regeneration (coke burn-off), reforming processes are classified into three types: (i) semi-regenerative, (ii) cyclic regenerative, and (iii) continuously regenerative.

In semi-regenerative processes (Figure 6.9.6), the process is shut down after some months for regeneration by coke burn-off. By the use of multimetallic catalysts (Pt, Re) with a high resistance to deactivation the period between two regenerations may last up to one year.

In cyclic processes regeneration is achieved by swinging one of several reactors (typically 4–6) off-line for coke burn-off while the others continue to operate.

In continuous regenerative processes (moving bed system, Figure 6.9.7) small quantities of the catalyst are withdrawn continuously, externally regenerated, and returned to the top of the reactor. The system consists of three to five segments stacked vertically on top of one another. The activity of the catalyst in this process is constant, whereas in the case of semi-regenerative and cyclic operation the conversion and the RON of the produced gasoline (refomate) are maintained constant by gradually increasing the reactor temperature as catalyst activity declines. The drawback of this operation mode is that cracking reactions are favored by high temperatures and thus their yield of light products increases with operation time.

In 1992, 74% of the commercial reforming plants operating in the USA, Japan, and Europe were semi-regenerative, 11% cyclic, and 15% continuous (Farrauto and Bartholomew, 1997).

The reforming reactor(s) must be designed to cope with the variety of reactions that take place. To optimize each of the different reactions, a series of separate reactors, usually three, is used. The liquid hourly space velocity (*LHSV*) is in a range of 1–3 m³ liquid feed per m³ catalyst bed volume and hour. Initially, the reactors had

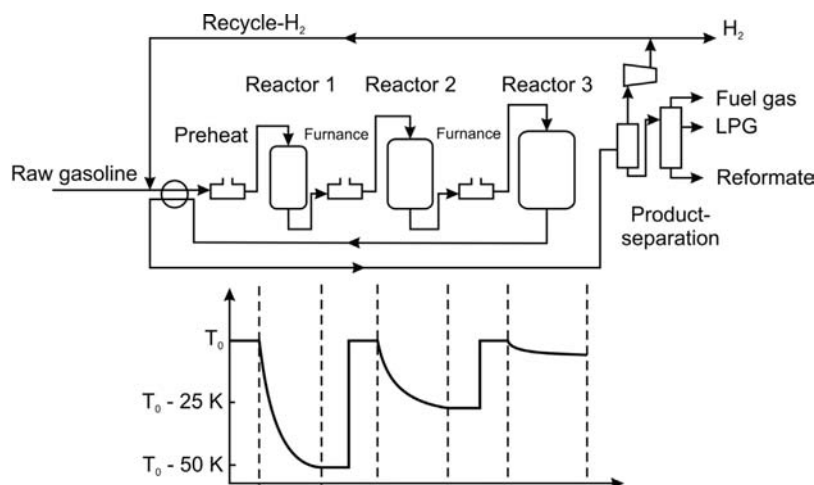


Figure 6.9.6 Flow scheme of a semi-regenerative reforming process and typical temperature profiles of the reaction mixture passing a series of reforming reactors and preheating furnaces. The initial temperature is about 470–530 °C. In order to keep a constant RON of around 100, the inlet temperature is increased gradually with time on stream. Hence, the decline in activity by deactivation (coke formation) is compensated but drawback is an increasing formation of light hydrocarbons (C₄-) by cracking. Partly adapted from Le Page (1978).

Figure 6.9.7 Scheme of a continuously regenerative moving bed catalytic reforming process.

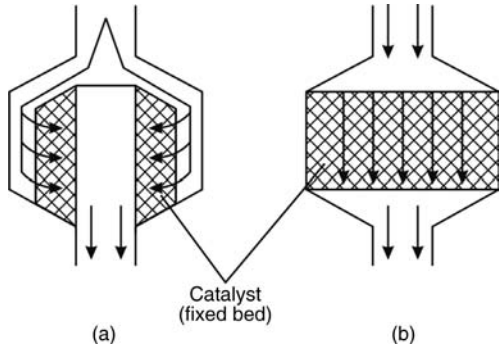
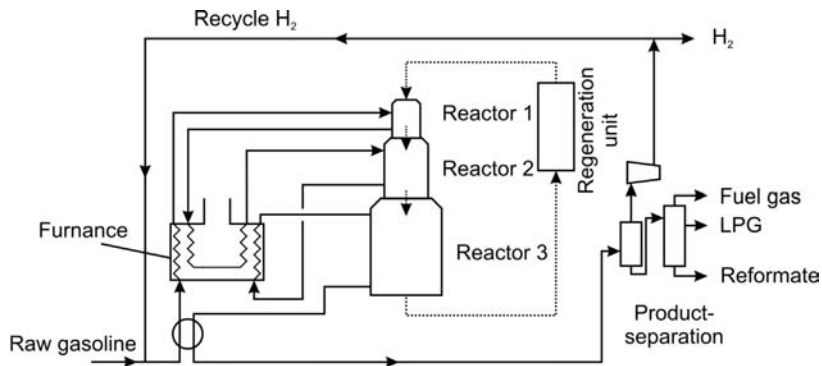


Figure 6.9.8 Flow patterns of radial flow (a) and axial flow reforming reactor (b).

axial flow, but the pressure drop was high. Modern plants operate at lower pressures (15 bar instead of up to 35 bar), and radial flow reactors, which have a lower pressure drop, are used (Figure 6.9.8).

After preheating the feed to about 500 °C, the mixture of vaporized hydrocarbons and recycled hydrogen is delivered into the first reactor, where mainly dehydrogenation of naphthenes to aromatics takes place. This is the reaction with the highest reaction rate (Table 6.9.1), and thus the first reactor contains only 5–15% of the total catalyst charge. Dehydrogenation is highly endothermic and thermodynamically favored at higher operating temperatures. The temperature in the adiabatically operated fixed bed falls rapidly from about 500 to 420 °C. At this temperature, the reaction rate is significantly decreased and dehydrogenation is limited by equilibrium. A higher initial temperature cannot be used as this would lead to a higher rate of cracking and of coke formation.

The effluent of the first reactor is reheated to 500 °C prior to entry into the second reactor (or second bed in the case of a moving bed reactor, Figure 6.9.7). There, isomerization occurs along with additional dehydrogenation. Isomerization is slower and thus the volume of the second bed/reactor is about twice that of the first one (15–30% of the total catalyst charge). Compared to the first bed, the fall in temperature is less (20–30 °C).

The effluent of the second reactor is again preheated before it enters the third bed/reactor. Here, primarily, dehydrocyclization takes place, which is kinetically the least favorable reaction. The third reactor therefore requires the largest volume, 55–65%, of the total charge. Typical temperature profiles are shown in Figure 6.9.6 for the semi-regenerative process.

The pressure, temperature, and residence time strongly influence the yield, composition, and octane rating of the gasoline (reformate) from catalytic reforming. For example, the octane number increases with increasing inlet temperature as more aromatics are formed. Conversely, the yield of reformate decreases with temperature, as more short-chain gaseous hydrocarbons are formed by hydrocracking. Increasing the H₂ pressure decreases the RON as the aromatics are saturated or formed to a lower extent by thermodynamic constraints, but the benefit is less coke formation, as the aromatics are the main coke precursors. Hence, the catalyst “life” between two cycles is longer for cyclic and semi-regenerative processes. With decreasing residence time (increasing LHSV) the RON decreases.

6.9.4

Deactivation and Regeneration of a Reforming Catalyst

Coke formation is the main reason for catalyst deactivation in catalytic reforming but also in other refinery and petrochemical processes, for example, during catalytic cracking of vacuum gasoil or hydrodesulfurization. The regeneration is conducted in fixed beds by carefully adding small amounts of O₂ in N₂ at about 400–530 °C.

Temperatures higher than 550 °C must be avoided as the reforming catalyst loses surface (sintering) and mechanical resistance above 550 °C (Le Page, 1978). The first reactor usually contains about 3 wt% coke and less than 1 wt% after regeneration. The coke content increases in the direction of flow as the content of aromatics (coke precursors) increase. In the last reactor, a content of 20% coke may be reached prior to regeneration.

In continuous reforming, only small amounts of coke accumulate and the average coke content is much lower compared to semicontinuous regeneration processes. The catalysts used in moving-bed processes are continually removed from the bottom of the reactor, regenerated, and returned to the reactor inlet (Figure 6.9.7). The regeneration of cyclic or semi-regenerative reforming processes is conducted periodically, that is, the reactor is shut down for burn-off.

Regeneration of coked particles involves both chemical reaction and transport processes, since oxygen must be transported by external mass transfer and by pore diffusion to the internal coked surface. Pore diffusion strongly influences the effective rate of burn-off, at least for particle diameters and temperatures relevant for industrial (fixed bed) processes (>1 mm, >400 °C). Consequently, radial gradients of the O₂-concentration and, with proceeding burn-off, also of the carbon content in a particle are established (Figure 6.9.9b).

Model calculations of fixed bed decoking (Westerterp, Fontein, and van Beckum, 1988) show that a moving reaction zone migrates through the reactor. Within this zone the oxygen concentration decreases steeply from the inlet value to zero (Figure 6.9.15), and the temperature increases strongly from the inlet temperature to a certain, much higher temperature. This may lead to overheating of the catalyst beyond the deactivation temperature of about 550 °C (danger of sintering), if the velocity of the zone is too fast. In practice, the process is therefore often conducted too slowly, for fear of damaging the catalyst.

In summary, we have to consider time-dependent profiles of the oxygen concentration and the carbon load both within the particles (microscopic level) and within the fixed bed (macroscopic level), as shown schematically in Figure 6.9.9. In addition, strong temperature gradients have to be considered within the fixed bed. In the next two subsections, the regeneration of a reforming catalyst is taken as a representative model system to study the regeneration by coke burn-off both on the scale of a single particle and of a technical reactor. Details are given in the literature (Kern, 2003; Kern and Jess, 2005; Tang, 2004; Tang *et al.*, 2004).

6.9.4.1 Coke Burn-Off within a Single Catalyst Particle

To understand and to model coke burn-off within a single particle the intrinsic kinetics (without any resistance by diffusion), mass transfer by pore diffusion and external diffusion, and structural parameters of the catalyst have to be taken into account.

Intrinsic Kinetics of Coke Burn-Off The intrinsic kinetics of deactivation and regeneration of a reforming catalyst have been studied by Kern *et al.* (Kern, 2003; Kern and Jess, 2005; Ren *et al.*, 2002). The main results are:

- Coke reactivity does not depend on the conditions of coke formation (H₂-pressure, feedstock), although the time needed to reach a certain carbon load may be different.
- Two sorts of coke are formed on the metal (Pt/Re) and the acidic sites (Al₂O₃), respectively, with the latter being much less reactive. At the beginning of decoking, the small amount of metal coke (e.g., 2% of the total carbon for $L_{C,0} = 0.15 \text{ g}_C \text{ g}_{\text{cat}}^{-1}$) is rapidly burned off. To model the decoking process, only the type of coke on alumina, which is dominant (with respect to the amount) and less reactive, has to be considered.

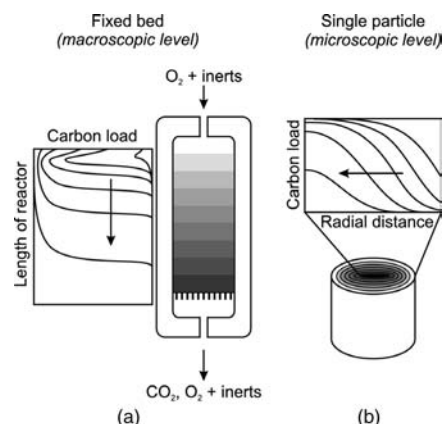


Figure 6.9.9 Schematic representation of coke burn-off during regeneration of a coked fixed bed catalyst on the level of a fixed bed reactor (a) and a single particle (b).

- The intrinsic rate of O₂-conversion (of the less reactive coke) is given by a first order reaction with regard to the carbon load and oxygen concentration by:

$$r_m = -\frac{dn_{O_2}}{dm_{cat}} = k_{m,C}(T)L_C c_{O_2}$$

$$\left(\text{with } k_{m,C} = 1.6 \times 10^6 \text{ m}^3 \text{ kg}^{-1} \text{ s}^{-1} e^{-\frac{107000}{RT}} \right) \quad (6.9.4)$$

- The reactivity of the coke is practically independent of carbon load (if the small amount on the metal sites is neglected).

Diffusional and Structural Parameters The influence of pore diffusion is considered by the effectiveness factor η_{pore} , that is, (in the case of no influence of external diffusion) by the ratio of the effective rate constant to the (maximum) intrinsic rate constant ($d_p \rightarrow 0$), and is given for a first-order reaction by (as evaluated in detail in Section 4.5.4 for heterogeneous catalysts):

$$\eta_{pore} = \frac{k_{m,C,eff}}{k_{m,C}} = \frac{\tanh \phi}{\phi} \approx \frac{1}{\phi} \quad (\text{for } \phi > 2) \quad (6.9.5)$$

The *Thiele modulus* (for a coked particle with a uniform carbon load) is given by:

$$\phi = \frac{V_p}{A_p} \sqrt{\frac{k_{m,C} L_C \rho_p}{D_{O_2,eff}}} \quad (6.9.6)$$

where V_p/A_p is the ratio of the particle volume to the external particle surface area.

Notably, ϕ depends on the carbon load L_C , which changes during burn-off with time and, in the case of a resistance of pore diffusion, also with the radial position in the particle. The *Thiele* approach as given by Eqs. (6.9.5) and (6.9.6) is then no longer exactly valid, and numerical simulations are needed. Nevertheless, the initial effectiveness factor $\eta_{pore,0}$ may be used as a descriptive measure for the pore diffusion resistance although ϕ_0 and $\eta_{pore,0}$ only refer to the start of the regeneration ($L_C = L_{C,0}$)

To describe the effective O₂ diffusion within the porous catalyst – expressed by an effective diffusion coefficient $D_{O_2,eff}$ – it has to be considered that only a portion of the particle is permeable, and that the path through the particle is random and tortuous. Both aspects are taken into account by the porosity ε_p and the tortuosity τ_p (Section 3.2.2.3), with both factors changing with the coke content. From Eqs. (3.2.75) and (3.2.76) we obtain:

$$D_{O_2,eff} = \frac{\varepsilon_p}{\tau_p} D_{O_2,pore} = \frac{\varepsilon_p}{\tau_p} \left(\frac{1}{D_{O_2,mol}} + \frac{1}{D_{O_2,Knu}} \right)^{-1} \quad (6.9.7)$$

The tortuosity τ_p of a reforming catalyst has been determined by *Ren* and *Kern* by a nuclear magnetic resonance (NMR) technique with *n*-heptane as probe molecule (Kern, 2003; Ren, 2003; Ren *et al.*, 2000). Based on these studies, the influence of carbon load on the porosity ε_p and tortuosity τ_p of the catalyst particle is approximately given by the following relationships:

$$\varepsilon_p = 0.65 - 1.3L_C \quad (6.9.8)$$

$$\tau_p = 2.59 - 5.4L_C \quad (6.9.9)$$

For a typical initial load L_C of 0.15 g_C g_{cat}⁻¹, ε_p decreases and τ_p increases by 30% compared to the fresh uncoked catalyst.

Depending on the pore diameter, the diffusivity in a pore is the combined diffusivity of the molecular and *Knudsen diffusivity* (Section 3.2.2.3):

$$D_{O_2, \text{Knu}} = \frac{d_{\text{pore}}}{3} \sqrt{\frac{8RT}{\pi M_{O_2}}} \quad (6.9.10)$$

The (mean) pore diameter (as well as the internal surface area) were measured by N₂ adsorption (BET method, see Section 3.3.5.1).

If external diffusion also has to be considered, Eq. (6.9.5) has to be extended. The overall effectiveness factor η_{overall} is then given by Eq. (4.5.103), which reads for coke burn-off as:

$$\eta_{\text{overall}} = \left(\frac{k_{m,C} L_C}{\beta A_m} + \frac{1}{\eta_{\text{pore}}} \right)^{-1} \quad (6.9.11)$$

The external mass transfer coefficient β in a packed bed of cylindrical particles (porosity of bed $\varepsilon \approx 0.4$) is calculated based on the *Sherwood number* by Eqs. (3.2.70) and (3.2.71) if we use a value of 0.3 for the minimum *Sh* number for a single cylindrical particle and the equivalent particle diameter d_p according to Eq. (3.2.23):

$$Sh_{\text{bed, cylinders}} = 1.9 \left(0.3 + 0.664 \sqrt[3]{Re_p} \sqrt[3]{Sc} \right) \quad \left(\text{for gases and } Re_p = \frac{u_s d_p}{\varepsilon \nu} < 50 \right) \quad (6.9.12)$$

Here we obtain a value for *Sh* of about 5 ($Re_p = 16$, $Sc = 0.7$). For details on external mass transfer see Section 3.2.2.2.

Table 6.9.2 summarizes the characteristic structural data of a reforming catalyst needed to use the above equations.

Figure 6.9.10 shows the influence of temperature on the overall effectiveness factor η_{overall} and on the effectiveness factor for pore diffusion η_{pore} for the initial *Thiele modulus* ϕ_0 ($L_C = L_{C,0}$), that is, for the start of regeneration. The external mass transport through the boundary gas layer has no influence on the overall effectiveness factor for temperatures below about 750 °C, which is far beyond technically relevant temperatures for the regeneration of reforming catalysts (<550 °C). For example, at 500 °C, the term βA_m is about 0.4 m³ kg⁻¹ s⁻¹, whereas the term $k_{m,C} L_C$ (for $L_C = 0.145 \text{ g}_C \text{ g}_{\text{cat}}^{-1}$) is only 0.014 m³ kg⁻¹ s⁻¹. Thus, according to Eq. (6.9.11), η_{overall} equals η_{pore} . Figure 6.9.10 also indicates that pore diffusion has an influence on the effective reaction rate at temperatures of more than about 400 °C.

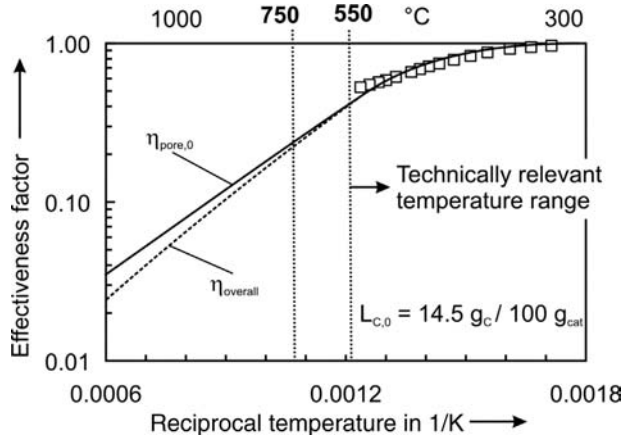
Calculation of Coke Burn-Off within a Single Catalyst Particle Coke burn-off in a catalyst particle is a specific gas–solid reaction as the particle diameter remains constant and only a small part of the solid (the coke deposits with mass $m_{\text{coke}} = m_{\text{cat}} L_C$)

Table 6.9.2 Characteristic data of a reforming catalyst (Kern, 2003; Kern and Jess, 2005).

Parameter	Data
Catalyst density ρ_{cat} (fresh catalyst)	1400 kg m ⁻³
Catalyst bulk density ρ_B	770 kg m ⁻³
Specific external surface area A_m	1.8 m ² kg ⁻¹
Geometry: length/diameter of extrudates	5 mm/1.6 mm
Equivalent particle diameter d_p [Eq. (3.2.24)]	2.6 mm
Specific internal BET surface area A_{BET} (fresh catalyst)	200 m ² g ⁻¹
Density of the catalyst ρ_{cat}	1400 kg m ⁻³
Porosity ^{a)} ε_p	0.53
Tortuosity ^{a)} τ_p	3.1
Average pore diameter d_{pore}	10 nm
Molecular diffusion coefficient ^{a)} $D_{O_2, \text{mol}}$	$1.1 \times 10^{-4} \text{ m}^2 \text{s}^{-1}$
Effective diffusion coefficient ^{a)} $D_{O_2, \text{eff}}$	$4 \times 10^{-7} \text{ m}^2 \text{s}^{-1}$

a) Typical values for a coke load of 0.1 kg_C kg_{cat}⁻¹ and for D_{O_2} for 500 °C and 1 bar.

Figure 6.9.10 Influence of temperature on the pore and overall effectiveness factor: comparison of measurement and calculation [$\mu_s = 0.2 \text{ m s}^{-1}$ (at 500 °C), $p = 1 \text{ bar}$, O₂ content = 0.5 vol.%, $\varepsilon_p = 0.46$, $\tau_p = 1.7$, $d_{\text{pore}} = 10 \text{ nm}$, η_{pore} for initial ϕ_0 ($L_C = L_{C,0}$)]. From Kern and Jess (2005).



is converted. Nevertheless, we can use the equations already examined in Section 4.6.3 for gas–solid reactions, if we use the term $m_{\text{cat}}L_C$ instead of the total mass of a solid reactant.

The thermal conductivity of the solid phase is high, and the simulation of decoking can be carried out based purely on the mass balances of O₂ and carbon without considering the heat balance (isothermal particles). Axial gradients of O₂-content and carbon load are negligible in the cylindrical particles ($L_p/d_p \approx 4$), and the mass balances for the gas and solid phase are:

$$\varepsilon_p \frac{dc_{O_2}}{dt} = \frac{d}{r dr} \left(D_{O_2,\text{eff}} r \frac{dc_{O_2}}{\delta r} \right) - r_m \rho_p \quad (6.9.13)$$

$$\frac{d L_C}{dt} = -M_C r_m \quad [\text{with the intrinsic rate } r_m \text{ as given by Eq. (6.9.4)}] \quad (6.9.14)$$

These differential equations are solved numerically for the boundary conditions:

$$\frac{dc_{O_2}}{dr} = 0 \quad (\text{for } r = 0, \text{ particle center}) \quad (6.9.15)$$

$$c_{O_2} = c_{O_2,g} \quad (\text{for } r = r_p, \text{ particle surface}) \quad (6.9.16)$$

The radial profiles of the oxygen and carbon in a particle and the time needed to reach a certain burn-off degree were simulated by the computer program *Presto* [for differential equations, details in Wulkow, Gerstlauer, and Nieken (2001)]. For comparison, the radial carbon distribution within single partly regenerated particles (50% burn-off) was measured by scanning electron microscopy. Notably, the initial radial carbon distribution was proven to be always homogeneous, which is the result of the very low rate of deactivation by coking (Kern, 2003). Figures 6.9.11–6.9.13 show calculated and experimental results.

Based on Eqs. (6.9.13)–(6.9.16), the decoking process within a single particle was numerically simulated. The essential parameters of the modeling are given in Table 6.9.2.

The calculated profiles of O₂ concentration and carbon load within a single particle during regeneration are shown in Figure 6.9.11 for two typical burn-off temperatures (450 and 550 °C). The initial effectiveness factor η_0 (calculated with the initial Thiele modulus ϕ_0 for $L_C = L_{C,0}$) as a measure for the magnitude of the pore diffusion resistance is also given.

As expected, the influence of pore diffusion on the rate of coke combustion increases with temperature, and gradients of the oxygen concentration and carbon load occur. This effect is pronounced at a very high temperature of 650 °C (Figure 6.9.12b), although 650 °C is unrealistic for a technical regeneration (T_{\max} of the catalyst is about 550 °C), but is shown here as an instructive comparison. A relatively sharp reaction front within the particle is then formed, which migrates from

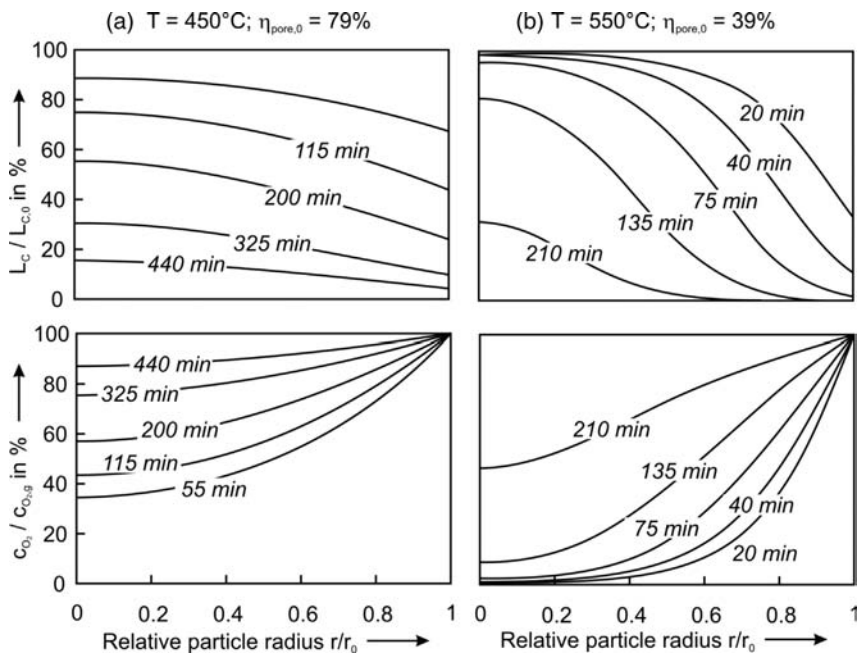


Figure 6.9.11 Radial profiles of O_2 content (relative to the gas phase) and carbon content (relative to the initial value) in a single cylindrical particle at different times [modeled results for $L_{c,0} = 10 \text{ wt.\%}$, $\gamma_{\text{O}_2} = 2 \text{ vol.\%}$, $d_p = 1.6 \text{ mm}$, $p = 1 \text{ bar}$, and $d_{\text{pore}} = 10 \text{ nm}$; ϵ_p and τ_p were calculated by Eqs. (6.9.8) and (6.9.9)]. From Kern and Jess (2005).

the outer surface to the center of the particle. For a very low temperature of 350°C (Figure 6.9.12a), diffusion limitations disappear, and the regeneration time is then very long (>4 days) compared to about 8 h in the case of a technically realistic temperature of 450°C (Figure 6.9.11a). The strong influence of pore diffusion with increasing temperature is also reflected by the (initial) effectiveness factor: at 350°C , η_0 is 98%, whereas for 450, 550, and 650°C values of 79%, 39%, and 17%, respectively, are reached.

Measured radial carbon profiles in the decoked particles are depicted in Figure 6.9.13. The experimental times to reach 50% burn-off are compared with the numerically calculated data. [Coked catalyst particles were regenerated at different temperatures up to a burn-off degree of 50% (Kern, 2003).] The calculated and

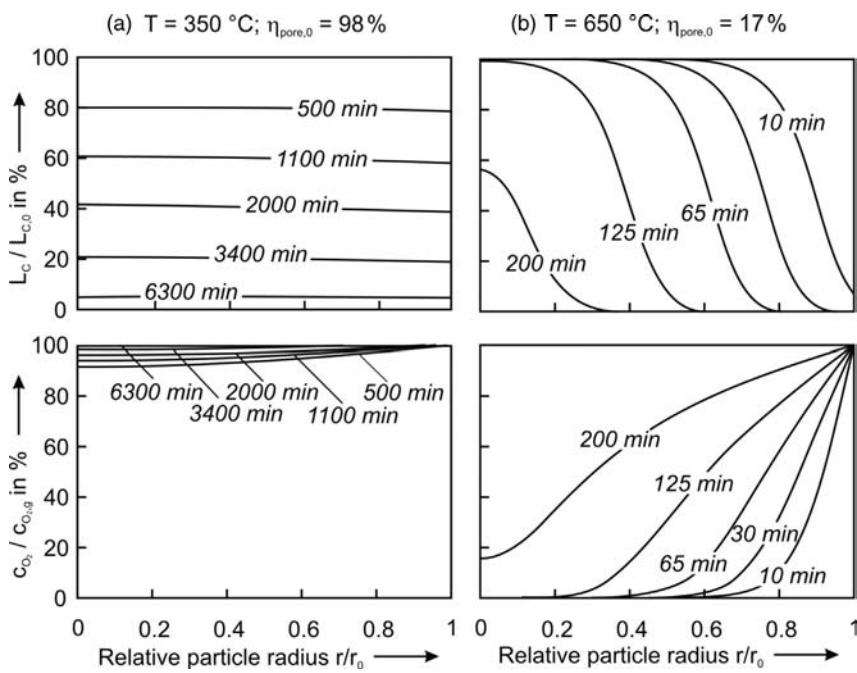
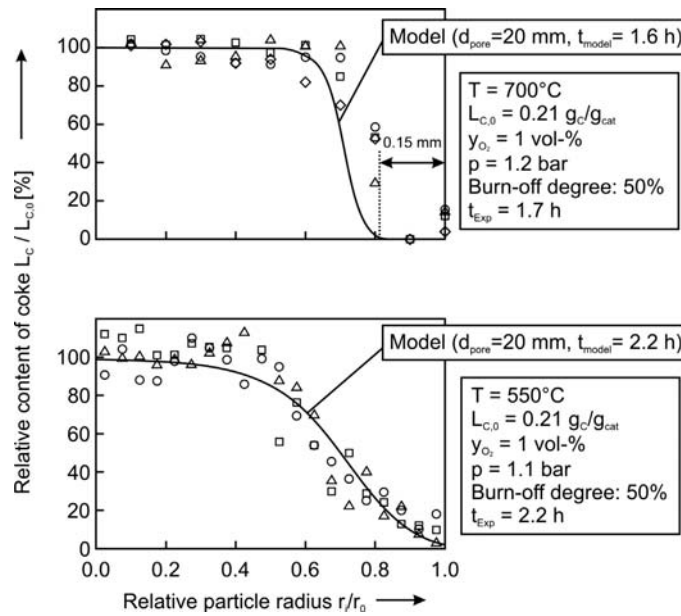


Figure 6.9.12 Radial profiles of O_2 content (relative to gas phase) and carbon content (relative to initial value) in a single cylindrical particle at different times (conditions: see Figure 6.9.10). From Kern and Jess (2005).

Figure 6.9.13 Measured and calculated radial coke profiles in a partly regenerated Pt-Al₂O₃ particle (cylinders: $d_p = 1.6$ mm, $L_p = 2-8$ mm; $\varepsilon_p = 0.5$, and $\tau_p = 3.5$). From Kern and Jess (2005).



measured values both of the C-profiles and the regeneration time are in good agreement. The scattering of the experimental data arises from the fact that three radial C-profiles were measured for each sample.

A description of the coke burn-off process in a single particle by well-known closed solutions like the homogeneous or shrinking core model (Sections 4.6.3.4 and 4.6.3.5) is only reasonable for the border cases of complete control by chemical reaction or by pore diffusion.

To describe the burn-off process without numerical methods, an advanced closed solution, the *shrinking core model with influence of the chemical reaction* (denoted as *combined model*) was developed (Kern, 2003, Kern and Jess, 2005). This model is more complicated than the homogeneous or shrinking core model, but includes pore diffusion and the intrinsic kinetics. The advantages of such a closed solution are: (i) the numerical modeling can be verified; (ii) if the combined model fits the numerical solution of single particle regeneration, it can be used for the numerical modeling of regeneration of a fixed bed. This simplifies fixed bed modeling (Section 6.9.4.2) and also bridges the coke burn-off in a particle and the regeneration of a fixed bed on the macroscopic scale.

The combined model (Section 4.6.3.3) is based on two assumptions:

- O₂-diffusion through an entirely regenerated shell of the particle ranging from the outer surface up to a defined reaction front at the radial position $r = r_C$:

$$\dot{n}_{O_2} = -2\pi r_C L_P D_{O_2,\text{eff}} \left(\frac{dc_{O_2}}{dr} \right)_{r=r_C} \quad (6.9.17)$$

- Chemical reaction without pore diffusion resistance in the remaining core ($0 < r < r_C$) with a constant carbon load of $L_{C,0}$:

$$\dot{n}_{O_2} = \pi r_C^2 L_P k_{m,C} L_{C,0} c_{O_2,g} \rho_{\text{cat}} \quad (6.9.18)$$

According to this model, the influence of pore diffusion is restricted to a coke-free shell ($r > r_C$) whereas in reality (at least for medium temperatures and not too high burn-off degrees) coke is still present in this outer zone. This leads to an underestimation of the carbon conversion by the model. Conversely, the assumption that the carbon load in the core region ($0 < r < r_C$) is still equivalent to the initial value overestimates the burn-off rate compared to reality, where both L_C and c_{O_2} decrease in the core region of the particle. As shown below, these two effects compensate each other quite well.

In Section 4.6.3.3, the solution for this model is given in detail for the reaction of a gas with a solid reactant where (almost) the whole solid (e.g., char coal) is converted. Thus we have to adapt the solution of this case, as given by Eqs. (4.6.57)–(4.6.59), to the regeneration of a coked catalyst where we finally end up with a carbon-free catalyst particle. Thus, instead of the mass of the solid (denoted in Section 4.6.3.3 as component B with an actual and initial mass m_B and $m_{B,0}$) we have to use the actual and initial mass of the carbon of the coke deposits, which are given by the terms $\bar{L}_C m_{\text{cat}}$ (with \bar{L}_C as the mean carbon load) and $L_{C,0} m_{\text{cat}}$. In addition, the density of the solid reactant (ρ_B) in the constant C_1 in Eq. (4.6.58) has to be replaced by the density of the (carbon free) catalyst ρ_{cat} . We then obtain as solution:

$$t = C_1 \left(\frac{\bar{L}_C}{L_{C,0}} \right) \ln \left(\frac{\bar{L}_C}{L_{C,0}} \right) - \frac{1}{C_2} \ln \left(\frac{\bar{L}_C}{L_{C,0}} \right) - C_1 \left(\frac{\bar{L}_C}{L_{C,0}} \right) + C_1 \quad (6.9.19)$$

with:

$$C_1 = \frac{r_p^2 k_{m,C} \rho_{\text{cat}}}{4 D_{O_2, \text{eff}}} \quad (6.9.20)$$

$$C_2 = -M_C k_{m,C} c_{O_2,g} \quad (6.9.21)$$

By Eqs. (6.9.19)–(6.9.21), the carbon conversion during coke burn-off is calculated, that is, the degree of regeneration of the catalyst $X_C = (1 - \bar{L}_C / L_{C,0})$.

Figure 6.9.14 shows the influence of regeneration time on the burn-off degree at different temperatures. The agreement between the “exact” numerical solution and the approximation by the closed solution of the *combined model* – Eqs. (6.9.19)–(6.9.21) – is very satisfying.

The effective reaction rate $r_{m,\text{eff}}$ according to the combined model is given by (see Section 4.6.3.3 for details):

$$r_{m,\text{eff}} = -\frac{1}{M_C} \frac{d\bar{L}_C}{dt} = -\frac{1}{m_{\text{cat}}} \frac{dn_C}{dt} = -\frac{dn_{O_2}}{dm_{\text{cat}}} = k_{m,C,\text{eff}} \bar{L}_C c_{O_2,g} \quad (6.9.22)$$

with:

$$k_{m,C,\text{eff}} = \frac{1}{\frac{1}{k_{m,C} \bar{L}_C} - \frac{r_p^2 \rho_{\text{cat}}}{4 D_{O_2, \text{eff}}} \ln \left(\frac{\bar{L}_C}{L_{C,0}} \right)} \quad (6.9.23)$$

This expression for the effective reaction rate can now be used to model the coke burn-off in a fixed bed reactor (next subsection) and builds the link between the microscopic and the macroscopic scale of the regeneration process.

6.9.4.2 Regeneration in a Technical Fixed Bed Reactor

To model the coke burn-off in an adiabatic technical fixed bed reactor a so-called *one dimensional pseudo-homogeneous reactor model* (Section 4.10.7.1) was

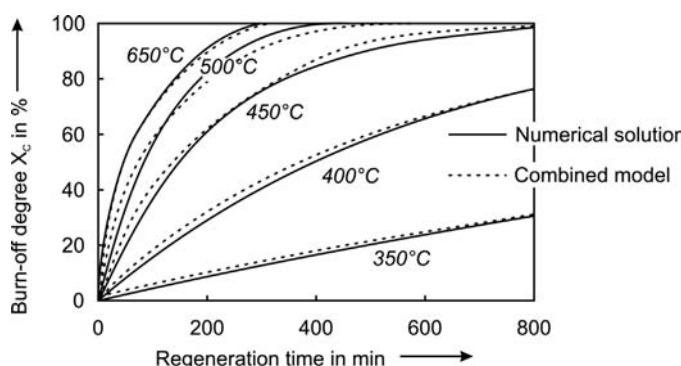


Figure 6.9.14 Comparison of the numerical and closed solution [combined model, Eqs. (6.9.19)–(6.9.21), $L_{C,0} = 0.1 \text{ kg}_C \text{ kg}_{\text{cat}}^{-1}$, $\varepsilon_p/\tau_p = 0.17$, $p = 1 \text{ bar}$, and $\gamma_{O_2} = 2 \text{ vol.\%}$]. From Kern and Jess (2005).

used, which can be characterized for the regeneration of the coked reforming catalyst as follows:

- Owing to the high ratio of the reactor-to-particle diameter in technical fixed bed reforming reactors ($\gg 100$), radial gradients of the O_2 -content and temperature are neglected.
- The reactor is regarded as an adiabatic plug flow reactor (reactor diameter $d_R \gg d_p$), and radial gradients of velocity, temperature, residence time, and concentration are negligible.
- Axial dispersion of heat and of mass are in the first instance considered, although we will learn here that both terms have no influence on the reactor behavior.
- The temperature difference between catalyst and gas phase is estimated by Eq. (4.5.30), which reads as:

$$(T_{\text{cat}} - T_g) = \frac{-\Delta_R H r_{m,\text{eff}}}{\alpha A_m} = \frac{-\Delta_R H \eta_{\text{overall}} k_{m,C,\text{eff}} L_C c_{O_2,g}}{\alpha A_m} \quad (6.9.24)$$

To estimate the maximum temperature difference we use the following values: carbon load $L_C = 0.1 \text{ kg}_C \text{ kg}_{\text{cat}}^{-1}$, $T_{\text{cat}} = 550^\circ\text{C}$, $\Delta_R H = -394 \text{ kJ mol}^{-1}$ ($C + O_2 \rightarrow CO_2$). The effectiveness factor η_{overall} is then 0.4 (Figure 6.9.10), the intrinsic rate constant $k_{m,C}$ is $0.26 \text{ m}^{-3} \text{ kg}^{-1} \text{ s}^{-1}$, Eq. (6.9.4), and $c_{O_2,g}$ is 0.29 mol m^{-3} (2%, 1 bar, 550°C). The superficial velocity is 0.5 m s^{-1} , the heat transfer coefficient α is $140 \text{ m}^{-2} \text{ K}^{-1}$ (Kern, 2003), and the external surface area A_m is $1.8 \text{ m}^2 \text{ kg}^{-1}$. Equation (6.9.24) then leads to an almost negligible temperature difference between catalyst and gas of 5 K, that is, no thermal distinction has to be made between the gas and solid phase.

Based on the aforementioned assumptions, the differential equations for the mass and heat balance of the solid and the gas phase (for the parameters see Table 6.9.3) are:

$$\frac{\rho_b}{M_C} \frac{dL_C}{dt} = -\rho_b r_{m,\text{eff}} \quad (6.9.25)$$

$$\varepsilon \frac{dc_{O_2}}{dt} = -u_s \frac{dc_{O_2}}{dz} + \varepsilon D_{ax} \frac{d^2 c_A}{dz^2} - \rho_b r_{m,\text{eff}} \quad (6.9.26)$$

$$(\rho_b c_s + \varepsilon \rho_g c_{p,g}) \frac{dT}{dt} = -u_s \rho_g c_{p,g} \frac{dT}{dz} + \lambda_{ax} \frac{dT}{dz^2} - \Delta_R H \rho_b r_{m,\text{eff}} \quad (6.9.27)$$

Equations (6.9.26) and (6.9.27) are similar to the Eqs. (4.10.125) and (4.10.126) (without the term for radial heat transfer), if we add the transient terms.

Equations (6.9.25)–(6.9.27) were solved by the above-mentioned computer program *Presto* for the following boundary conditions at $z=0$ (reactor inlet):

$$c_{O_2,g} = c_{O_2,g,\text{in}} \quad (6.9.28)$$

$$T = T_{\text{in}} \quad (6.9.29)$$

$$u_s(c_{O_2,g,\text{in}} - c_{O_2,g}) = -\varepsilon D_{ax} \frac{dc_{O_2,g}}{dz} \quad (6.9.30)$$

$$u_s \rho_g c_{p,g} (T_{\text{in}} - T) = -\lambda_{ax} \frac{dT}{dz} \quad (6.9.31)$$

The effective dispersion coefficients of heat and mass (λ_{ax} , D_{ax}) are calculated by the *Peclet numbers* [$P_{e,m,ax} = u_s d_p / (\varepsilon D_{ax})$, $P_{e,h,ax} = u_s c_p \rho_{\text{mol}} d_p / \lambda_{ax}$]. Both numbers are approximately 2 (Section 4.10.6.4). Correlations that also consider the static contribution are (VDI, 2002):

$$\lambda_{ax} = \underbrace{\lambda_{fb}}_{\substack{\text{static contribution} \\ (\text{bed without gas flow})}} + \underbrace{\frac{u_s \rho_g c_{p,g} d_p}{2}}_{\substack{\text{dynamic contribution} \\ P_{e,h,ax} = 2}} \quad (6.9.32)$$

$$D_{ax} = \frac{D_{fb}}{\varepsilon} + \frac{u_s d_p}{2\varepsilon} \quad (6.9.33)$$

The minimal values of λ_{ax} and D_{ax} without gas flow (λ_{fb} , D_{fb}) are:

$$D_{\text{fb}} = D_{\text{O}_2,\text{mol}}(1 - \sqrt{1 - \varepsilon}) \quad (6.9.34)$$

$$\lambda_{\text{fb}} = \lambda_g K \quad (6.9.35)$$

For a typical voidage of a fixed bed of 0.4, K is given by (VDI, 2002):

$$K = \frac{11k_p + 4}{2k_p + 13} \quad (\text{for } K < 20) \quad (6.9.36)$$

with k_p as the ratio of the thermal conductivity of gas and solid. For a typical value of the thermal conductivity λ_s of porous Pt/Al₂O₃ particles of 0.2 W m⁻¹ K⁻¹ (Baerns, Hofmann, and Renken, 1987), k_p is:

$$k_p = \frac{\lambda_s}{\lambda_g(500^\circ\text{C})} = \frac{0.2 \text{ W m}^{-1} \text{ K}^{-1}}{0.05 \text{ W m}^{-1} \text{ K}^{-1}} = 4 \quad (6.9.37)$$

From the result of numerical solution of Eqs. (6.9.25)–(6.9.29) (parameters in Table 6.9.3), the regeneration of a coked fixed bed was modeled. The result for an industrial fixed bed reactor is shown in Figure 6.9.15, with details of the first 6 hours in Figure 6.9.16.

After an induction period of one day, a reaction front with a constant velocity is developed. This velocity can also be deduced by a mass balance: The oxygen, which enters the volume element with length Δz in the time interval Δt , reacts with coke and fills out the void space:

$$\dot{n}_{\text{O}_2} \Delta t = u_s A_R c_{\text{O}_2,\text{in}} \Delta t = \left(\frac{\rho_b L_{\text{C},0}}{M_{\text{C}}} + \varepsilon c_{\text{O}_2,\text{in}} \right) A_R \Delta z \quad (6.9.38)$$

Thus the velocity of the reaction front u_{RF} is given by:

$$u_{\text{RF}} = \frac{\Delta z}{\Delta t} = \frac{u_s c_{\text{O}_2,\text{in}}}{\frac{\rho_b L_{\text{C},0}}{M_{\text{C}}} + \varepsilon c_{\text{O}_2,\text{in}}} \approx \frac{u_s c_{\text{O}_2,\text{in}} M_{\text{C}}}{\rho_b L_{\text{C},0}} \quad (6.9.39)$$

Also in the initial period of regeneration, a heat front moves through the bed, heating up the bed behind the moving reaction front from the initial temperature T_0 to the maximum temperature T_{max} . The velocity of the heat front (here about 1.1 m h⁻¹) is much higher than that of the reaction front (0.05 m h⁻¹), and is calculated by the heat balance:

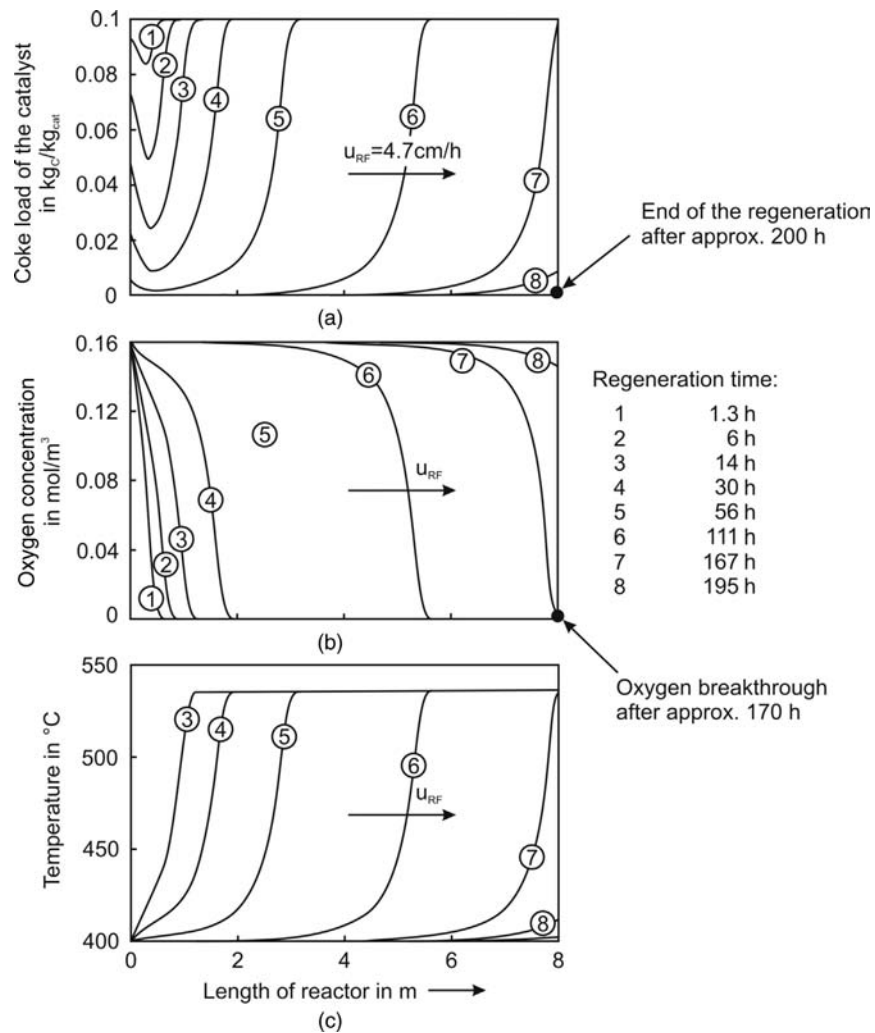
$$u_{\text{HF}} = \frac{u_s \rho_g c_{\text{p,g}}}{\rho_g c_{\text{p,g}} + \rho_b c_s} \approx \frac{u_g \rho_g c_{\text{p,g}}}{\rho_b c_s} \quad (6.9.40)$$

Figure 6.9.17 shows the influence of axial heat dispersion on the spread of the heat and reaction front. The width of the heat exchange zone is only observably altered for an unrealistic high value of the heat dispersion coefficient $\lambda_{\text{ax,eff}}$ that is ten-times higher than the value calculated by Eq. (6.9.32). If axial heat dispersion is neglected ($\lambda_{\text{ax,eff}} = 0$), the width of the heat exchange zone decreases slightly. Thus the accuracy of the calculation of the heat dispersion coefficient does not play an important role. Note that even in the case of no axial heat dispersion ($\lambda_{\text{ax,eff}} = 0$) the

Table 6.9.3 Modeling parameters for coke burn-off in a fixed bed reactor.

Parameter	Data
Bulk density of fixed bed ρ_b	770 kg m ⁻³
Porosity of fixed bed ε	0.4
Heat capacity of solid phase c_s (500 °C)	1000 J kg ⁻¹ K ⁻¹
Heat capacity of gas phase $c_{\text{p,g}}$ (500 °C, 1 bar)	30 J mol ⁻¹ K ⁻¹
Axial dispersion coefficient of heat of fixed bed λ_{ax}	0.54 W m ⁻¹
Axial dispersion coefficient of mass of fixed bed D_{ax}	7.7 × 10 ⁻⁵ m ² s ⁻¹

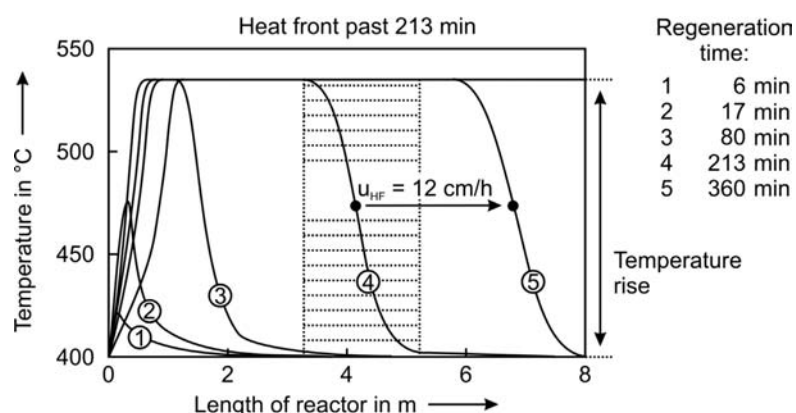
Figure 6.9.15 Modeled profiles of (a) carbon load, (b) oxygen concentration, and (c) temperature in a fixed bed reactor at different stages of regeneration (conditions: see Tables 6.9.2 and 6.9.3; $L_{C,0} = 10 \text{ g}_C$ per $100 \text{ g}_{\text{cat}}$, $p = 1 \text{ bar}$; $\gamma_{O_2} = 1 \text{ vol.\%}$, and $u_s = 0.5 \text{ m s}^{-1}$). From Kern and Jess (2005).

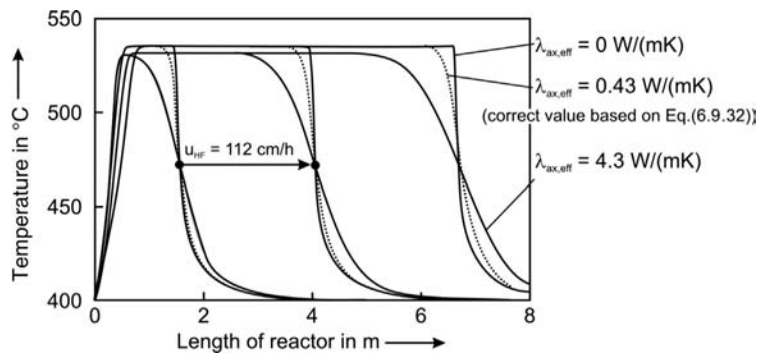


temperature decrease in the heat exchange zone is not a step function, above all in the rear part (Figure 6.9.17). This is because the input signal (T -increase in the reaction front) is not an ideal step function.

The influence of the axial dispersion coefficient of mass D_{ax} on the spread of the reaction zone is even smaller, as shown in Figure 6.9.18 [see also Kern (2003)]. Even modeling with an unrealistically high value of the effective dispersion coefficient [1000× higher than the “correct” value as calculated by Eq. (6.9.33)] does not lead to a significant enlargement of the reaction zone. [Remark: if the axial dispersion of mass is completely neglected in the model ($D_{ax}=0$), the width of the reaction zone

Figure 6.9.16 Modeled temperature profiles in the fixed bed at the beginning of regeneration (conditions: see Tables 6.9.2 and 6.9.3, $L_{C,0} = 0.1 \text{ kg}_C \text{ kg}_{\text{cat}}^{-1}$, $p = 1 \text{ bar}$, $\gamma_{O_2} = 1 \text{ vol.\%}$, and $u_s = 0.5 \text{ m s}^{-1}$).





is the same as in case of modeling with the correct value, and therefore not shown in Figure 6.9.18]. Consequently, the influence of the axial dispersion of mass can be neglected here, because the width and velocity of the reaction zone, which determine the regeneration time, are practically independent of D_{ax} .

The time of coke burn-off is 200 h compared to 179 h in the case of an infinitely high reaction rate, that is, for ideal step functions of carbon load and O₂-content ($L_R/u_{RF} = 8 \text{ m}/4.7 \text{ cm h}^{-1} = 170 \text{ h}$). In other words, the regeneration time is 15% longer than in the absence of kinetic limitations, which underlines the need for accurate modeling.

The adiabatic temperature increase (for a steady-state process) is given by:

$$\Delta T_{ad} = \frac{c_{O_{2,in}} \Delta_R H}{\rho_g c_{p,g}} \quad (6.9.41)$$

During regeneration, an unexpected overheating beyond the adiabatic end temperature may occur (Figure 6.9.19). The higher the velocity of the reaction front, that is, the lower the C-load, see Eq. (6.9.39), the higher the unwanted overheating. This “wrong way behavior” is also described in the literature (Wicke and Vortmeyer, 1959; Emig *et al.*, 1980; Eigenberger, 1983).

To quantify such behavior, the heat balance for the reaction zone is instructive, whereby the “originator” of the balance moves forward with the velocity of the reaction zone:

$$\dot{Q}_R = \dot{Q}_G - \dot{Q}_S \quad (6.9.42)$$

The heat flux produced by the coke burn-off is:

$$\dot{Q}_R = (u_g - u_{RF}) A_R \varepsilon c_{O_{2,in}} |\Delta_R H| = (u_g - u_{RF}) A_R \varepsilon \Delta T_{ad} \rho_g c_{p,g} \quad (6.9.43)$$

The heat flux needed to heat the gas from the inlet to the final temperature is given by:

$$\dot{Q}_G = (u_g - u_{RF}) A_R \varepsilon \rho_G c_{p,G} (T_{max} - T_0) \quad (6.9.44)$$

Figure 6.9.17 Influence of $\lambda_{ax,eff}$ on the modeled temperature profiles of heat and reaction front (conditions: see Tables 6.9.2 and 6.9.3, $L_{C,0} = 0.1 \text{ kg}_C \text{ kg}_{cat}^{-1}$, $p = 1 \text{ bar}$, and $\gamma_{O_2} = 1 \text{ vol.\%}$, $u_s = 0.5 \text{ m s}^{-1}$).

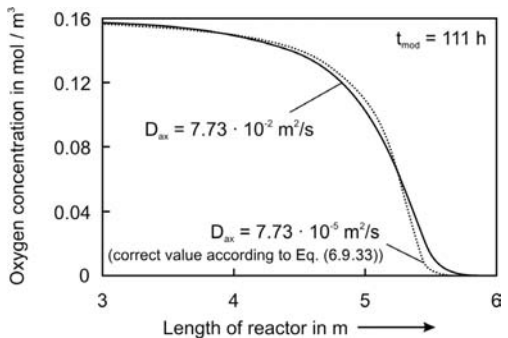


Figure 6.9.18 Influence of effective axial dispersion on the spread of the reaction zone in a fixed bed reactor during regeneration (conditions: see Tables 6.9.2 and 6.9.3, $L_{C,0} = 0.1 \text{ kg}_C \text{ kg}_{cat}^{-1}$, $p = 1 \text{ bar}$, $\gamma_{O_2} = 1 \text{ vol.\%}$, and $u_s = 0.5 \text{ m s}^{-1}$).

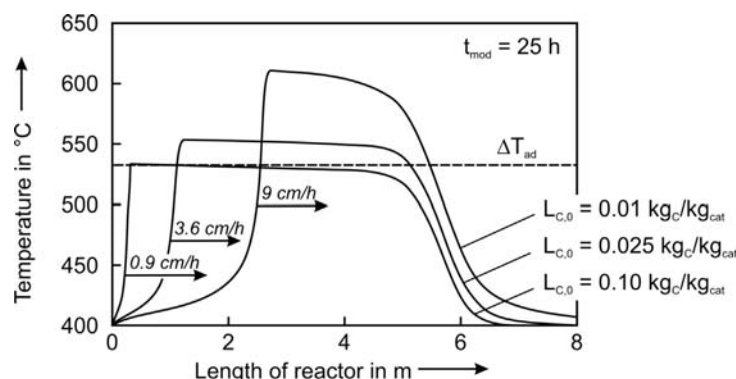


Figure 6.9.19 Influence of initial carbon load on the temperature profiles of the heat and reaction front (conditions: see Tables 6.9.2 and 6.9.3, $p = 1 \text{ bar}$, $\gamma_{O_2} = 1 \text{ vol.\%}$, and $u_s = 0.1 \text{ m s}^{-1}$).

The heat flux, which enters the reaction zone from the viewpoint of the moving observer by the already heated solid, is given by:

$$\dot{Q}_S = u_{RF} A_R \varepsilon \rho_B c_S (T_{\max} - T_0) \quad (6.9.45)$$

Equations (6.9.39) and (6.9.41)–(6.9.45) then lead to:

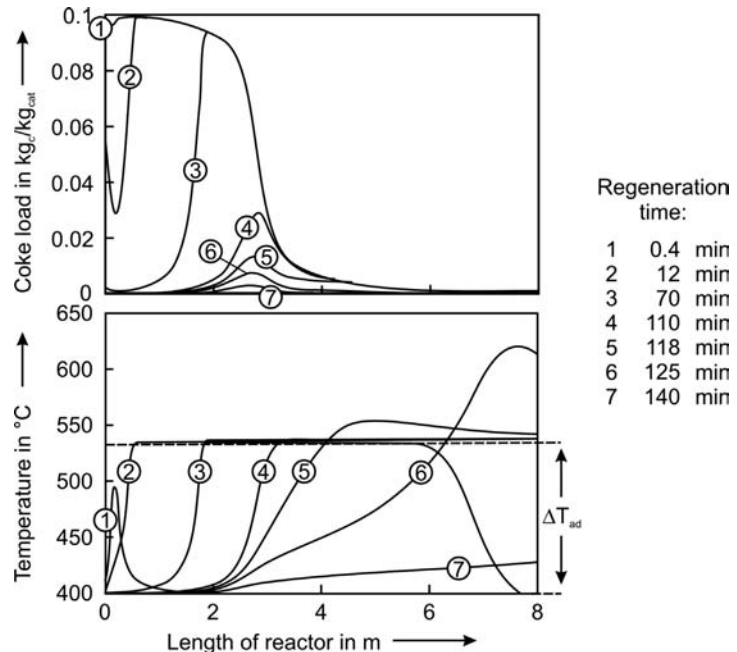
$$\frac{\Delta T_{\max}}{\Delta T_{ad}} = \frac{u_{HF} - u_{RF}}{u_{HF} - u_{RF}} \frac{\varepsilon \rho_G c_{P,G}}{(\varepsilon \rho_G c_{P,G} - \rho_B c_S)} \quad (6.9.46)$$

Therefore, the higher the velocity of the reaction front and the smaller the difference between u_{HF} and u_{RF} the higher is the overheating of the bed, as is clearly shown in Figure 6.9.19.

Such “wrong way behavior” may be also induced by a non-uniform initial axial carbon load (Figure 6.9.20), here deliberately calculated for a strong decrease of the carbon load in the second third of the bed. At first, that is, in the region with a high load of 0.1 g per g catalyst, the adiabatic “stationary” temperature increase is almost reached ($T_{\max} - T_0 = 1.015 \Delta T_{ad}$). As soon as the carbon load decreases, an overheating of the bed (wrong way behavior) is induced, and the temperature increases above the maximum allowable value of 550 °C (deactivation). Notably, this scenario is unrealistic for naphtha reforming, where carbon formation – if at all – increases in the axial direction by the formation of coke precursors. Nevertheless, Figure 6.9.20 is instructive for other decoking processes.

Performance data of the regeneration process of a technical naphtha reformer were kindly provided by the MIRO refinery (Karlsruhe, Germany). Consequently, the burn-off model could finally be tested and compared with the regeneration in a technical fixed bed reactor. The respective results are given in Figure 6.9.21, indicating that the agreement is very good. Notably, this agreement was reached although (i) not the same but a similar catalyst with the same geometry is used in the MIRO refinery and (ii) the technical

Figure 6.9.20 Modeled profiles of carbon load and temperature with non-uniform initial axial carbon distribution (conditions: see Tables 6.9.2 and 6.9.3, 1 bar, $\gamma_{O_2} = 1$ vol.%, and $u_s = 0.25 \text{ m s}^{-1}$).



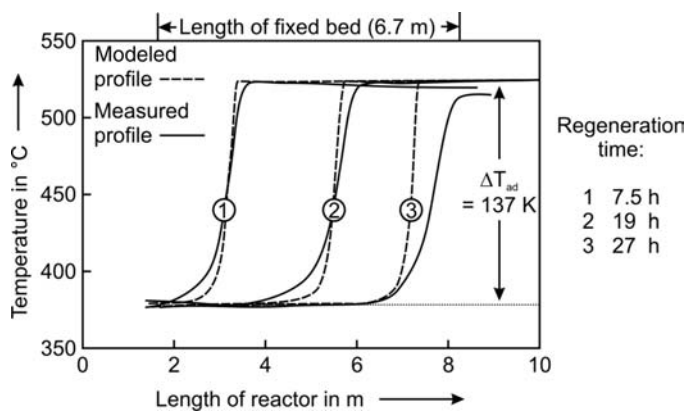


Figure 6.9.21 Comparison of measured and modeled temperature profiles in a technical fixed bed reactor (MIRO refinery, Karlsruhe, Germany) during regeneration (conditions: see Tables 6.9.2 and 6.9.3, 20 bar, $\gamma_{O_2} = 0.9$ vol.%, $u_e = 0.26 \text{ m s}^{-1}$, and $L_{C,0} = 0.21 \text{ kg}_C \text{ kg}_{\text{cat}}^{-1}$).

coke burn-off is performed at 20 bar, whereas the kinetic parameters were deduced from experiments at about 1–2 bar.

Figure 6.9.22 shows the temperature profiles in the case where the “real” values of the intrinsic rate constant (MIRO refinery) deviate by factors of 2 and 0.5 from the values obtained from laboratory-scale experiments with a different catalyst. The “real” intrinsic reactivity seems to be slightly lower (better agreement in this case by a factor of 0.5).

Summary of Section 6.9 (take-home messages)

- **Modern automobiles with spark ignition engines** need high-octane gasoline. The **octane number (ON)**, which is a measure of a fuel's antiknock properties, depends on the gasoline composition. The ONs of aromatics are highest followed by naphthenes, branched alkanes, and olefins. Normal paraffins have the lowest ON.
- **Straight-run gasoline** is composed primarily of alkanes and cycloalkanes with only a small fraction of aromatics, and has a low ON of about 50. The ON is improved by **catalytic reforming** of *n*-paraffins and cycloalkanes into branched alkanes and aromatics. The main reactions are isomerization (*n*- to iso-), cyclization, dehydrogenation, and dehydrocyclization. The **bifunctional catalyst** has an acidic function to catalyze isomerization and cyclization and a dehydrogenation function that requires an active metal site. Typically, platinum is used as the metal and Al_2O_3 for the acidity.
- **Dehydrogenation** is highly favored with regard to kinetics and thermodynamics. **Isomerization** is kinetically favored, but suffers equilibrium limitations. **Dehydrocyclization** is highly desirable but is the least favorable kinetically, while thermodynamically favored at high temperatures. Thermodynamically, **coke formation** is always favored. As a result, catalytic coking and cracking is always a problem in reforming, and operating conditions must reflect a balance between desired and undesired reactions.
- The **technical reforming process** is conducted in a fixed bed reactor, which is divided into three adiabatically operated racks. The reforming reactions are endothermic, and **interstage heating** in a furnace requires the use of exchangers. Hydrogen is recycled and added to the feed, although this is thermodynamically not favored, but is needed to suppress and limit coke formation. Typically, a H_2 pressure of around 15 bar is used, which limits the equilibrium conversion but suppresses coke formation.
- Coke formation is the main reason for **catalyst deactivation** in catalytic reforming, and also in other refinery and petrochemical processes. Catalyst

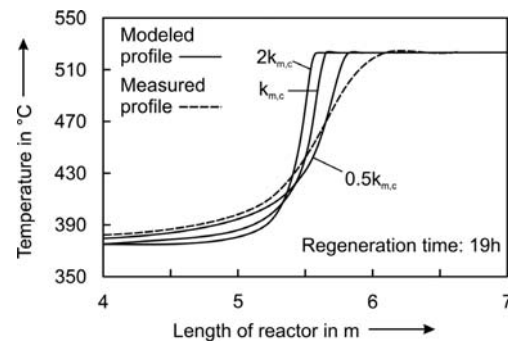
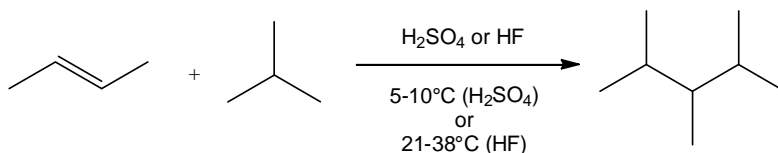


Figure 6.9.22 Influence of the intrinsic rate constant on the modeled temperature profiles and comparison with a measured profile in the technical reactor of the MIRO refinery in Karlsruhe, Germany ($p = 20$ bar; $\gamma_{O_2} = 0.9$ vol.%, $u_s = 0.26 \text{ m s}^{-1}$, and $L_{C,0} = 0.21 \text{ kg}_C \text{ kg}_{\text{cat}}^{-1}$).

regeneration is conducted by carefully adding small amounts of O₂ in N₂. Temperatures above 550 °C must be avoided as the reforming catalyst then loses surface by sintering.

- **Fixed bed decoking** involves time-dependent profiles of the oxygen concentration and the carbon load both within the particles (pore diffusion) and within the fixed bed (**moving reaction zone**). The reaction zone migrates through the reactor, which may lead to overheating of the catalyst, if the velocity of the zone is too fast. To **model** the coke burn-off process in the adiabatic fixed bed the so-called one-dimensional **pseudo-homogeneous reactor model** can be used.

6.10 Refinery Alkylation



Scheme 6.10.1: Refinery alkylation is an acid-catalyzed reaction with very high relevance for producing high quality fuels.



About 60 metres and 220 metric tons without internals: a new Iso-stripper column for an alkylation unit. The significant decrease in column diameter is a signature feature within the skyline of every alkylation unit owed to the product composition: after removal and recirculation of the surplus i-C₄ only a small amount of lights ends (C₂-C₃) remain as an overhead product. Picture courtesy of M. Wilhelm

6.10.1

Reaction and Reaction Mechanism of Refinery Alkylation

The term “refinery alkylation” is applied to the reaction of low molecular weight olefins (propene, butenes, or pentenes) with isoparaffins to form higher molecular weight isoparaffins. The latter are very important hydrocarbon compounds for the production of high-quality fuel (Scheme 6.10.1). Currently, approximately 13–15% of the gasoline pool is produced by refinery alkylation. Refinery alkylation products are characterized by high research octane numbers (RONs) (93–97) and motor octane numbers (MONs) (90–95).

Refinery alkylation takes place at high temperatures and pressures without catalysts. However, all industrially relevant processes proceed at low-temperatures in the presence of highly acidic catalysts. By appropriate choice of operating conditions, most of the alkylate can be made to fall within the gasoline boiling range with RONs of 94–99 and MONs of 88–94.

Refinery alkylation was discovered in the early 1930s when Ipatieff and Grosse reported the alkylation of hexanes with ethane using a mixture of aluminum chloride and hydrogen chloride as catalyst. The first generation of commercial units for the alkylation of olefins with isoparaffins applied sulfuric acid as catalyst. During World War II processes using sulfuric acid as well as hydrofluoric acid were installed, driven by the military demand for high octane gasoline for aircraft. With the technology changing later to jet engines the consumption of alkylates in aviation plummeted. However, the market for higher octane fuels for automotive applications increased drastically at the same time and alkylates have maintained their high relevance as premium gasoline blending stock to the present day.

Figure 6.10.1 shows the historic growth in global alkylation capacity. In the 1960s about 75% of alkylate was produced using sulfuric acid. The importance of hydrofluoric acid grew by more than 50% until two incidents in the mid-1980s made the safety risks of using hydrofluoric acid apparent. Since then, the relative importance of alkylations with sulfuric acid has increased and much effort has been put into developing process alternatives that use safer catalysts (such as solid catalysts or acidic molten salts) and into minimizing the danger in hydrofluoric acid catalyzed processes.

The alkylation of isobutane with C₃–C₅ olefins involves a series of consecutive and simultaneous reactions with carbocation species as the key intermediates. Scheme 6.10.2 shows the reaction of 2-butene and isobutane as a typical example. In the initial step, proton addition to 2-butene affords a *sec*-butyl cation. This *sec*-butyl cation can either isomerize or accept a hydride from a molecule of isobutane, giving *n*-butane and the thermodynamically more stable *tert*-butyl cation. These initiation reactions are required to generate a high level of ions in the start-up phase of alkylation but become less important under steady state conditions.

Figure 6.10.2 shows the simplified main reaction cycle in refinery alkylation. An olefin is added to the *tert*-butyl cation to give the corresponding C₈ carbocation. This C₈ carbocation may isomerize via hydride and methyl shifts to form a more stable carbenium ion and subsequently undergoes, again, hydride transfer from isobutane. This latter step forms the saturated hydrocarbon and regenerates the *tert*-butyl cation to perpetuate the catalytic cycle.

Figure 6.10.3 shows a relevant parallel reaction cycle based on the formation of acid-soluble polymers (PH), which are found in both sulfuric and hydrofluoric acid processes. However, this cycle is especially relevant in sulfuric acid systems where most of the *tert*-butyl cations are formed from the acid-soluble polymer and isobutane.

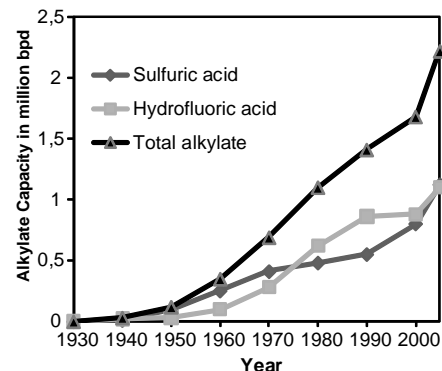
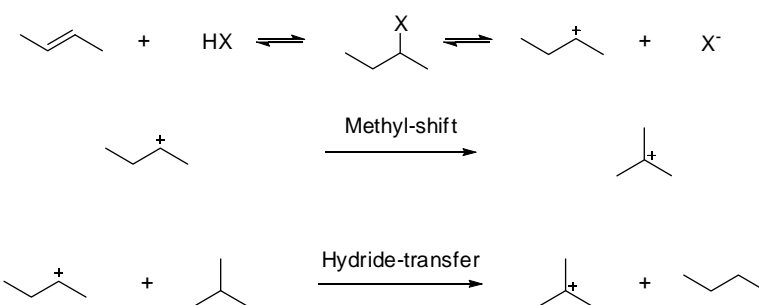
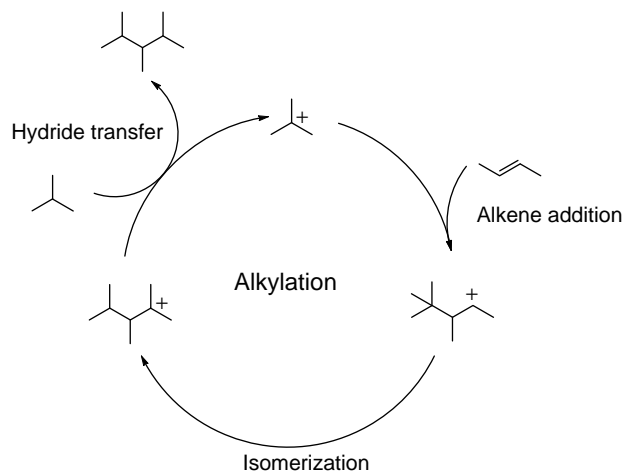


Figure 6.10.1 Historic growth in global alkylation capacity, DuPont 2010.



Scheme 6.10.2 Initial steps of the refinery alkylation reaction: proton addition to 2-butene, isomerization via methyl shift or hydride transfer with isobutane to form a *tert*-butyl cation.

Figure 6.10.2 Main catalysis cycle of the refinery alkylation of 2-butene with isobutane.

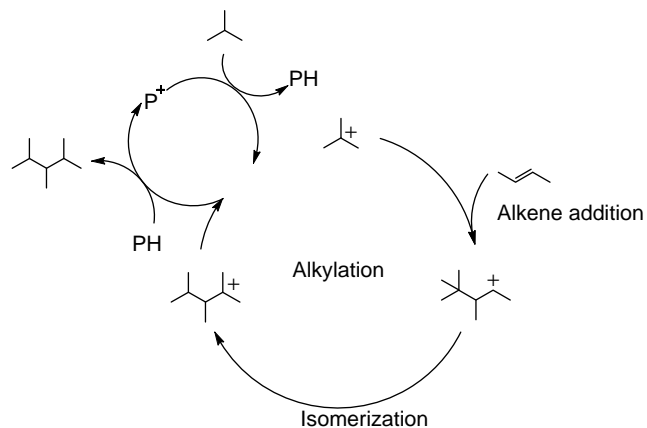


In addition to the reactions described above, several side reactions occur in the refinery alkylation process that reduce the quality of alkylate and are highly undesirable. The most important of these are polymerization, disproportionation, cracking, and self-alkylation. They are described in more detail in Example 6.10.1 [see also Corma and Martinez (1993), and Albright (2003, 2009) for further information].

6.10.2 Alkylation Feedstock and Products

To run a refinery alkylation unit isobutane and light olefins are required as feedstock. However, the composition of the olefin stream varies significantly with the local refinery situation and this requires careful adjustment of the process conditions. The most commonly used olefins are butenes and propene but sometimes the use of pentenes is also considered. New gasoline specifications and the *Clean Air Act* (a United States federal law) amendments make it necessary to remove pentenes from the gasoline pool, because of their potential for atmospheric pollution. The main sources of olefins are catalytic cracking and coking processes. The isobutane feed for alkylation units is mainly obtained from hydrocrackers, catalytic crackers, and catalytic reformers. Additional amounts of isobutane are directly available from crude distillation and natural gas processing. Moreover, *n*-butane can be

Figure 6.10.3 Additional reaction cycle for the alkylation of 2-butene with isobutane involving an acid-soluble polymer formed during the reaction.



transformed into isobutane in a catalytic isomerization step to balance shortages in the isobutane supply of refinery alkylation units.

Before entering the reactor, the alkylation feed needs to be purified from sulfur – to avoid corrosion problems of process equipment – and from all impurities that would lead to higher consumption of the acid catalyst. To illustrate this point, Table 6.10.1 gives a list of common impurities in alkylation feedstock together with the amount of acid consumption they cause.

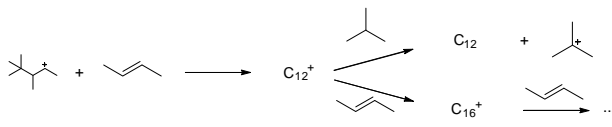
In addition to the desired isoparaffins from alkylation, the product stream leaving the reactor contains undesired lights (e.g., propane and *n*-butane), as well as certain quantities of tar produced by polymerization reactions (see also Example 6.10.1).

Table 6.10.1 Influence of feedstock impurities on sulfuric acid consumption in a refinery alkylation unit (Corma and Martinez, 1993 and Albright, 2003).

Impurity	Acid consumption (kg acid per kg impurity)
Water	10.6
Butadiene	13.4
Ethene	30.6
Mercaptan (per wt S)	17.6
Disulfide (per wt S)	12.8
Methanol	26.8
Dimethyl ether	11.1
Methyl <i>tert</i> -butyl ether (MTBE)	17.3

Example 6.10.1: Important side reactions occurring in refinery alkylations

- 1) **Oligomerization and polymerization** reactions take place through the addition of olefins to the carbocation formed in the primary reaction:



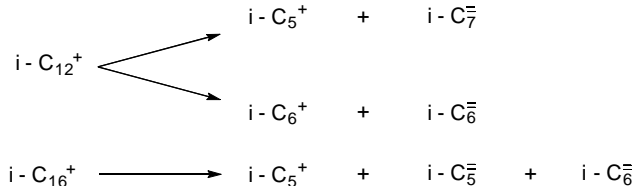
- 4) **Self-alkylation** leads to the formation of trimethylpentanes when isobutane is alkylated with *in situ* formed isobutene. Two isobutane molecules are consumed and a saturated paraffin is produced. This reaction is commercially undesired as it consumes a lot of isobutane and forms considerable amounts of light *n*-paraffins:



- 2) **Disproportionation** results in two isoparaffins formed from two alkylate molecules:



- 3) **Cracking** of isoalkyl cations forms smaller cations and olefins:



6.10.3

Process Variables

Important process variables in refinery alkylation are reaction temperature, acid strength, isobutane concentration, and mixing. When operating an alkylation unit these parameters have to be carefully controlled for optimum product quality at lowest possible operating costs. In general, the process using sulfuric acid is slightly more sensitive to parameter changes compared to its hydrofluoric acid counterpart (Albright, 2003, 2009) as described in the following.

6.10.3.1 Reaction Temperature

In sulfuric acid catalyzed alkylation, the temperature ranges between 5 and 10 °C. Higher alkylate quality is obtained at lower temperatures as oxidation reactions become important at higher temperatures, leading to higher acid consumption. However, at temperatures that are too low the acid viscosity increases so much that

good mixing of the emulsion becomes difficult. Moreover, the decreased solubility of hydrocarbons in the acid phase lowers the overall effectiveness. Owing to the relatively low temperatures, refrigeration costs have a significant effect on the operating cost of the sulfuric acid process. In contrast, in the hydrofluoric acid process, the influence of temperature is less significant and temperatures are usually in the range of 21–38 °C. This allows the use of cooling water as refrigerant. As a rule of thumb alkylate quality decreases by about 1 octane number for a temperature increase of 11 °C.

6.10.3.2 Acid Strength and Composition

In the sulfuric acid process the maximum alkylate yield is obtained at an acid phase composition of 95–97% sulfuric acid and 1% water with the remainder being hydrocarbon components. Too high and too low acidity are disfavorable. While acid concentrations that are too high (above 99% sulfuric acid) cause reaction of isobutane with sulfur trioxide combined with enhanced acid consumption, an acidity that is too low (below 85% sulfuric acid) decreases the reactivity significantly. Therefore, the concentration of acid must be maintained throughout the process by adding fresh acid of 98–100% purity. Moreover, the adjusted acidity level is a kind of compromise between the system's productivity and the catalyst lifetime. The presence of water in the acid phase influences the quality of alkylate significantly and lowers the catalytic activity about three to five times as much as the same amount of hydrocarbon diluent (see also Section 6.10.2).

The same factors also influence the hydrofluoric acid alkylation process. Special attention must be given, however, to the water content. In hydrofluoric processes the feed must be well dried before entering the alkylation section. The best quality of alkylate is obtained in the range of 86–90% acid with a water content less than 1%.

6.10.3.3 Isobutane Concentration

Isobutane concentration is generally expressed in terms of the isobutane-to-olefin ratio (I/O). This ratio is the most important process variable to control in terms of refinery alkylation productivity, yield, and quality of alkylate, as well as the acid consumption.

All alkylation processes use high I/O ratios due to the significantly higher solubility of olefins compared to isobutane in the acid phase. Using a high I/O ratio increases the concentration of isobutane in the acid phase. Thus, the formed carbocation has a higher probability of reacting with isobutane to form the desired isoparaffin while the probability for reaction with another olefin (oligomerization) is reduced. This is the reason why higher I/O ratios increase both the yield and quality (octane number) of the alkylate. The overall I/O ratios in sulfuric acid alkylation plants are usually in the range 5 : 1 to 8 : 1, while hydrofluoric acid units generally operate at even higher ratios, often in the range 10 : 1 to 15 : 1. Recycling of isobutane within the reaction zone increases the I/O ratio in the reactor even further. Especially in sulfuric acid systems, ratios in the range 100 : 1 to 1000 : 1 can be adjusted in this way at the interface between the two phases.

Unfortunately, the advantages of very high I/O ratios come at a certain price: a low olefin concentration lead to low space-time velocity in the process. Moreover, at high I/O ratios, more isobutane has to be separated from the product and its recycling requires larger volumes of equipment and higher energy consumption.

6.10.3.4 Effect of Mixing

Isobutane is almost insoluble in the liquid acid catalysts used in refinery alkylation. Therefore, intense mixing is necessary to make sure that at least this low isobutene equilibrium concentration is maintained throughout the reaction in the acid phase to allow the reaction to proceed properly. As the alkylation reaction occurs at or near

the liquid–liquid interface the amount of created interfacial area through mixing between the hydrocarbon and the acid phase affects the yield and quality of alkylate dramatically. The size of the interfacial area depends on the degree of agitation, temperature, and acid–hydrocarbon ratio, as well as on the design and operation of the reactor. The higher viscosity, surface tension, and density of sulfuric acid versus hydrofluoric acid, accompanied by its lower solubility of isobutane in the acid phase, means that much more intensive mixing is needed in the sulfuric acid process than for its hydrofluoric acid counterpart (Albright and Eckert, 2001). In fact, hydrofluoric acid alkylation reactors simply operate in some kind of heat exchangers, where rising hydrocarbon droplets cause sufficient mixing. Here, intimate contact between the hydrocarbon phase and the acid phase is provided by the use of special distribution nozzles.

6.10.4

Commercial Alkylation Processes

All refinery alkylation processes – whether based on sulfuric acid or hydrofluoric acid – are composed of a reaction part in which intense mixing of the acid phase and the hydrocarbon phase takes place followed by a separation unit. Here, the acid phase is isolated from the organic products and recycled back to the reactor while the hydrocarbons are fractionated. Excess isobutene is also recycled to the reactor. The following paragraphs give an overview of the most important process and reactor setups used today for refinery alkylation. Hydrofluoric acid based processes are offered by *ConocoPhillips Petroleum* and *UOP*. Sulfuric acid based processes have been developed by *Stratco* (now DuPont Co.), *Exxon-Mobile* as well as *M.W. Kellogg*.

6.10.4.1 Commercial Processes using Hydrofluoric Acid as Liquid Catalyst

Figure 6.10.4 shows a basic flow scheme of the *ConocoPhillips Petroleum* and *UOP* processes. First, the olefin feed as well as the isobutane feed are carefully dried to minimize corrosion problems resulting from the addition of water to hydrofluoric acid.

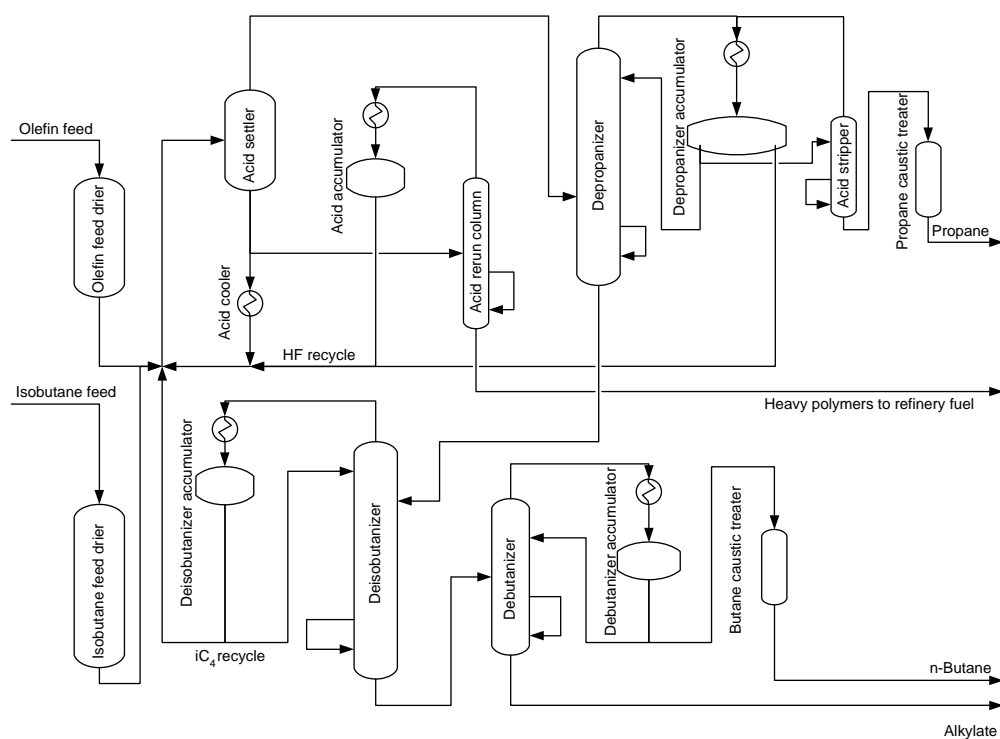


Figure 6.10.4 Basic flow scheme of the alkylation processes using hydrofluoric acid as liquid catalyst.

acid. Then the feed streams are mixed with hydrofluoric acid at sufficient pressure to maintain all components in the liquid phase. After the reactor, the acid phase is separated from the hydrocarbon phase in a settler and passed through a cooler to remove the reaction heat. The acid phase is subsequently recycled to the reactor and mixed there with fresh feed. A small amount of acid is withdrawn from the settler as a purge stream to avoid the build-up of water and polymerized hydrocarbons.

The hydrocarbon mixture from the settler is passed through a depropanizer, deisobutanizer, and debutanizer, consecutively. Usually, the propane and *n*-butane streams are processed to remove residual hydrofluoric acid and isoalkyl fluorides, while the alkylate product stream is obtained directly at the bottom of the debutanizer unit. From the deisobutanizer and the depropanizer accumulators isobutane and hydrofluoric acid are recycled back to the reactor unit, respectively. In contrast to the flow-sheet above, where three separate fractionators are shown, many alkylation plants use a single separation tower to separate the hydrocarbon mixture into propane, *n*-butane, and alkylate product fractions and isobutane for recycling.

The main difference between the *Phillips* and the *UOP* Process is a different design of the acid settler-cooler-reactor section: *The Phillips Process* uses a riser-type reactor in which the hydrocarbon mixture is introduced through nozzles. Perforated trays in the vertical reactor provide good dispersion of the hydrocarbon phase in the acid phase. In the settler the acid is separated from the hydrocarbon phase and recycled hydrofluoric acid is cooled in heat exchangers to remove the heat of reaction. As in this system acid circulation is forced by gravity – an expensive acid circulation pump is not needed.

In contrast, the *UOP Process* uses a horizontal shell reactor. The hydrocarbon mixture is introduced through nozzles while the acid is introduced at the bottom of the vessel. The heat of reaction is removed by cooling water in a cooling coil. The effluent mixture is then directed to a settler where the acid is separated and returned to the reactor. Good mixing is provided by using a recirculation pump to force the mixture through the reactor at a rate about eight to ten times the hydrocarbon feed rate to the reactor.

6.10.4.2 Commercial Processes Using Sulfuric Acid as Liquid Catalyst

There are three different designs for sulfuric acid alkylation processes: *effluent refrigeration* (*DuPont*), *cascade* or *auto-refrigeration* (*ExxonMobil Research and Engineering*), and “time-tank” processes (*M.W. Kellogg*). The major differences between the *auto-refrigeration* and *effluent refrigeration* processes are in the reactor designs and in the point of the process where propane and isobutane are evaporated to induce cooling and provide the process refrigeration required. The main characteristics of the three processes are described below.

Time-Tank Process Figure 6.10.5 shows a flow-sheet of the time-tank process. The isobutane and olefin streams are contacted with sulfuric acid in a large uncooled pipe near the entrance of a centrifugal pump, which provides mixing and emulsification. High temperatures are avoided by using high acid-to-hydrocarbon ratios. The emulsion enters the chiller where the heat of reaction is removed from the reaction mixture by the use of a refrigerant. Most of the alkylation reactions take place in a vertical column called a time-tank reactor, with an average hydrocarbon residence time between 20 and 30 min. A continuous stream is taken from the bottom of the time-tank and directed to a settler, where the hydrocarbon and acid phases are separated. The acid is returned to the centrifugal pump close to the loop with circuit times between 1 and 2 min. The hydrocarbon phase passes caustic and water scrubbers to remove acid and esters before entering the separation section, where isobutane is recycled to the reaction section and the product mixture is separated into alkylate, *n*-butane, and propane streams.

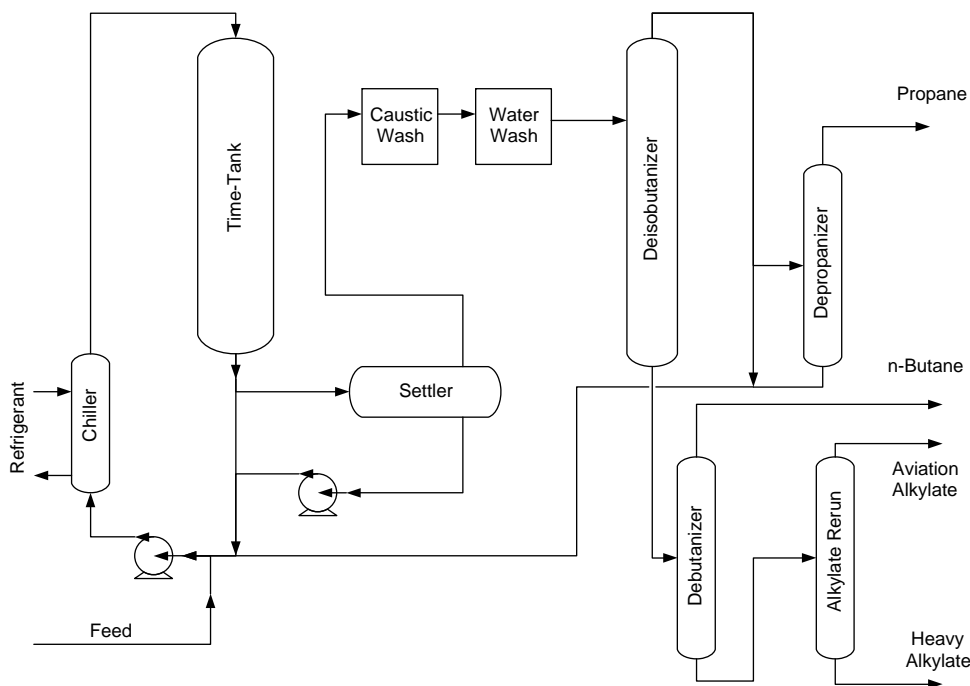


Figure 6.10.5 Scheme of the time-tank alkylation process using sulfuric acid as catalyst.

Effluent Refrigeration Process More than 60% of the worldwide alkylate production using a sulfuric acid catalyst is obtained from the effluent refrigeration process. A single-stage reactor (contactor) with an impeller in one end and cooling coils in the other is used to maintain the temperature at the desired level (Figures 6.10.6 and 6.10.7). The circulation time is around 10 s, whereas the average residence time in the reactor is around 20–25 min.

The hydrocarbon feed and the acid are introduced into the eye of the impeller and recycled through the outer shell. To remove the heat of reaction and the energy of the impeller, the mixture is pumped through a tube bundle and then sent to the settler section.

Figure 6.10.7 shows the flow-sheet of an *effluent refrigeration* alkylation unit. After passing the reaction zone, the emulsion is sent to a settler for phase separation. The acid is then recirculated and the pressure of the hydrocarbon phase is lowered to flash vaporize a portion of the stream and reduce the liquid temperature to about -1°C . The cold liquid is used as a coolant in the reactor tube bundle and is then separated into isobutane, *n*-butane, and alkylate streams in the deisobutanizer

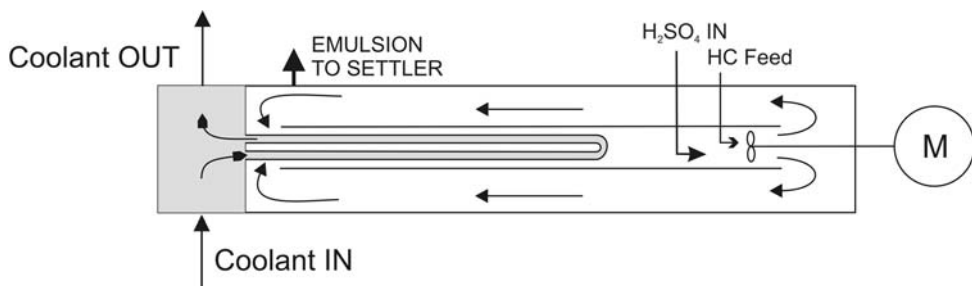


Figure 6.10.6 Schematic view of the reactor applied in the Effluent Refrigerator Process (HC = hydrocarbon). Adapted from DuPont, 2010.

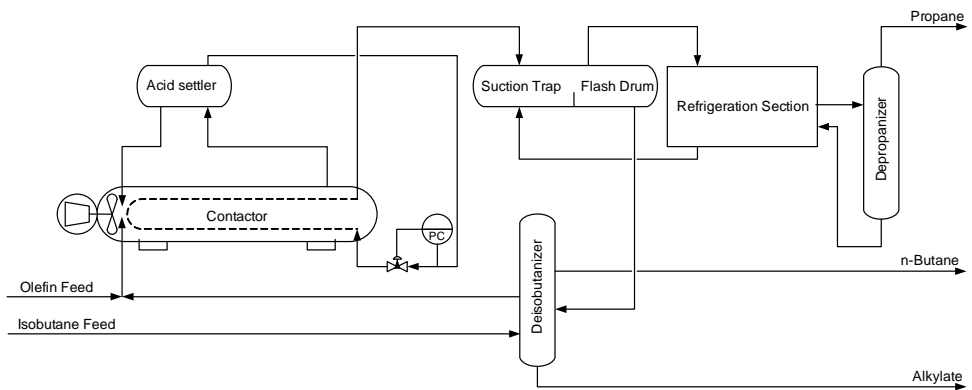


Figure 6.10.7 Flow sheet of an alkylation unit using the effluent refrigeration technique.

column. The flashed gases are compressed, liquefied, and sent to the depropanizer to separate isobutane for recycling and propane as a product stream.

Cascade Autorefrigeration Process (ExxonMobil Research and Engineering) Figure 6.10.8 shows the flow-sheet of a *cascade auto-refrigeration* refinery alkylation process. Here, a multistage cascade reactor (3–7 stages) is used. The reactors are large horizontal drums with mixers in each stage to provide enough emulsification of the acid–hydrocarbon mixture and an acid settler at the end where the acid–hydrocarbon emulsion is separated.

Acid and isobutane enter the first stage of the reactor and pass in series through the remaining stages. The fresh olefin feed is mixed with recycled isobutane and injected into the individual reactor sections to be contacted with the catalyst. Cooling is carried out by equilibrium vaporization of light hydrocarbons at the system pressure of approximately 0.69 bar to maintain the temperature at about 5 °C and hence eliminate the need for a heat-exchanger surface. The vaporized gases are compressed, liquefied, and sent to a depropanizer column, where propane is removed and liquid isobutane from the bottom of the depropanizer is pumped back to the first stage of the reactor. A portion of liquefied gas is subsequently vaporized in an economizer to cool the olefin feed before it is sent to the reactor. The resulting gas is returned for recompression. The acid in the settler is removed from

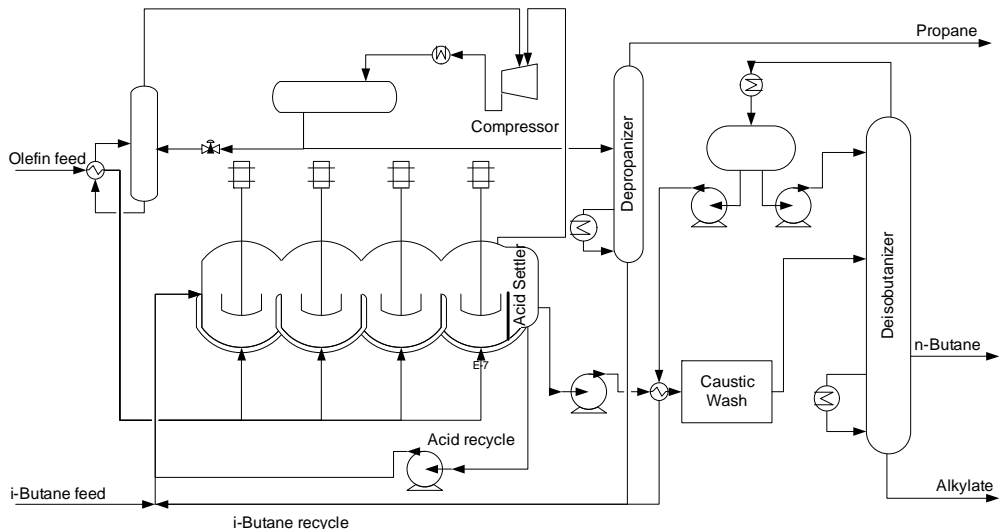


Figure 6.10.8 Flow sheet of an alkylation unit using the cascade autorefrigeration process.

the system for recycling and the hydrocarbon phase is pumped through a caustic and water wash to eliminate trace amounts of acid and sent to a deisobutanizer to separate the stream into isobutane for recycling and *n*-butane as well as alkylate as product streams.

A detailed comparison of the three sulfuric acid based alkylation processes (Corma and Martinez, 1993) reveals that the *time-tank* process produces the best alkylate quality but has higher energy consumption related to isobutene recycling and refrigeration compared to the other two. This is the reason why in the last 35 years no new *time-tank* refinery alkylation units have been installed. However, several refineries still operate older time-tank units.

6.10.4.3 Comparison of Commercially Applied Alkylation Processes

Advantages of the hydrofluoric acid based refinery alkylation processes compared to the sulfuric acid processes are mainly based on more attractive operational conditions and the related cost effects. The temperature applied in hydrofluoric acid reactors (21–38 °C) is significantly higher than that used in sulfuric acid reactors (5–10 °C). As cooling water can be used in HF alkylation units instead of special refrigeration techniques as in case of the H₂SO₄ alkylation, the cost of removing the heat of reaction is much lower in case of the HF alkylation. The kinetics of the HF-catalyzed reaction are faster than in the sulfuric acid catalyzed reaction, leading to larger and more expensive reactors in the latter case. Moreover, regeneration of HF is usually performed in the refinery by distillation, whereas spent sulfuric acid has to be transferred to a nearby sulfuric acid plant. The cost of regenerating H₂SO₄ has been reported to often account for 25–30% of the total operating costs. Finally, the energy cost related to mixing is much higher in the case of the sulfuric acid processes due to the much higher viscosity of the liquid catalyst at the very low reaction temperatures.

Advantages of the sulfuric acid processes compared to the use of HF in refinery alkylation arise from the usually better alkylate product quality and from safety aspects. Hydrofluoric acid is a very toxic chemical. Therefore, sophisticated and costly safety installations are required to operate HF-based alkylation processes in a safe manner. A particular risk is that HF leaking from the plant could lead to the formation of a toxic aerosol cloud. The latter could be carried into populated areas by the effect of wind. After two severe incidents in 1986 several methods have been implemented to reduce this risk, including additives to prevent the formation of a vapor cloud of HF, water spray systems around the hydrofluoric acid unit and installations for a rapid transfer of liquid hydrofluoric acid from a leaking tank to an alternative storage tank. Hazards originating from the operation of sulfuric acid refinery alkylation plants are minor in comparison to the risk related to the handling, use, and purification of large amounts of HF. As a further advantage of sulfuric acid alkylation, less isobutane is consumed, with relative savings of 5–10%, and the I/O ratios fed to the reactors are lower compared to hydrofluoric acid processes, leading to reduced costs for recovering and recycling of unreacted isobutane.

In conclusion, the decision of a refinery in choosing one of the established refinery alkylation processes will be governed by the economics for the specific size of the plant at the selected site. Acid supply, disposal and recycling, total operating cost, initial capital cost, required alkylate quality in the specific refinery network, required flexibility of operation, feedstock availability, required yields and conversion of reactants, maintenance and safety aspects, experience with a given process, and patents as well as licensing arrangements are all important aspects in deciding in favor or disfavor of one of the processes described above. A very detailed

comparison of alkylation processes can be found in a series of articles by *Albright* (Albright, 1966, 1990, 2003, and 2009).

Given the obvious disadvantages of the existing alkylation processes several alternative catalyst technologies have been proposed and tested but are not yet at the same mature commercial level. Solid acid catalysts (*Lummus Technology – Alky-Clean®*, *Exelus – ExSact®*, and *UOP – Alkylene®*) or acidic ionic liquid catalysts (*PetroChina – Ionikylation®*) show a lot of promise but their economics have to compete in many cases with old, fully depreciated existing plants, which prevents rapid market penetration.

Section 6.10 take-home-messages

- **Refinery alkylation** is a very important refinery process that produces high-quality fuel by the reaction of light alkenes and alkanes.
- The reaction is **acid catalyzed** and proceeds by a mechanism that involves carbocation species as the key intermediates. Two major process alternatives exists, using *sulfuric acid* and *hydrofluoric acid* as the catalyst, respectively;
- Important **undesired side reactions** of refinery alkylation are polymerization, disproportionation, cracking, and self-alkylation.
- **Acid consumption** is a **major cost driver** in refinery alkylation. Therefore, all **impurities** in the feedstock causing extra acid consumption are removed before the reactants enter the reactor.
- The **process variables** temperature, acid strength, isobutane concentration, and mixing have to be carefully optimized in refinery alkylation to obtain high fuel quality. The optimum parameters differ for the H_2SO_4 - and HF-catalyzed processes.
- Refinery alkylation suffers from the very **low isobutene solubility** in the acid phase and proceeds near or at the phase boundary between the acid phase and organic phase.
- The **refinery alkylation processes** offered commercially for licencing differ in the way the two phases are contacted in the reactor and in the heat removal.
- **Advantages of the HF technology** are faster kinetics and lower refrigeration costs due to the higher temperature level. **Advantages of the sulfuric acid technology** are higher alkylate quality, the use of a less toxic acid catalyst, and lower isobutene consumption.
- Given the disadvantages of existing alkylation processes several **alternative catalyst technologies** (solid acid catalysts, acidic ionic liquids) have been proposed and tested but are not yet at the same commercial level.

6.11

Fuels and Chemicals from Syngas: Methanol and Fischer–Tropsch Synthesis

Crude oil reserves are limited. Therefore, processes to produce fuels and chemicals from natural gas, coal, and biomass are highly important. The two main processes are Fischer–Tropsch (FT) synthesis and methanol synthesis.

Fischer–Tropsch (FT) synthesis converts syngas into higher hydrocarbons like gasoline, diesel oil, waxes, and so on, and is an important process in producing fuels and chemicals from natural gas, coal, and biomass.

In section 6.11.1, all main aspects of the FT synthesis will be covered, the reaction kinetics, history, current status, and perspectives of technical processes as well as the modeling of a multi-tubular fixed bed FT reactor.



FT plant ($6 \text{ mio. t fuels a}^{-1}$) based on coal in Secunda, South Africa.
Courtesy of Sasol, South Africa.



Fluidized bed FT reactor in Secunda. Courtesy of Sasol.



FT plant based on natural gas in Qatar. Courtesy of Sasol.

Methanol synthesis is also based on syngas.

Methanol is an important intermediate for the production of chemicals and fuels (gasoline, olefins, and aromatic hydrocarbons), and can also be used directly as an alternative fuel.

6.11.1

Fischer–Tropsch Synthesis

Production of synthetic fuels via *Fischer–Tropsch* synthesis (FTS) has the potential to produce fuels like gasoline and diesel oil and petrochemicals from fossil and renewable sources. The availability of cheap natural gas and solid raw materials like coal and biomass has given momentum to this synthesis technology, which already developed in the 1920s, and thus the worldwide FT plant capacities will increase significantly in the future, with natural gas favored as feedstock. It is, therefore, worth looking on this “old fashioned” but still important and fascinating technology. In the following two sections, we look at the main reactions and kinetics of FTS. Section 6.11.1.3 briefly summarizes the history, current status, and perspective of FTS. Processes and reactors are outlined in Section 6.11.1.4 and, finally, the modeling of a FT multi-tubular reactor is presented in Section 6.11.1.5.

Franz Fischer (1877–1947): a German chemist who together with *Hans Tropsch* discovered in the 1920 the Fischer–Tropsch synthesis. He also worked with *Wilhelm Ostwald* and *Emil Fischer*. In 1914, he became Director of the *Kaiser Wilhelm Institute for Coal Research*.

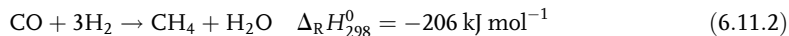
Hans Tropsch (1889–1935): A German chemist born in German Bohemia (now Czech Republic). From 1920 until 1928 he worked at the *Kaiser Wilhelm Institute for Coal Research* both with *Franz Fischer* and *Otto Roelen*. In 1928 he became professor at the *Institute for Coal Research* in Prague. From 1931 until 1935, he worked in the United States at the *Armour Institute of Technology* in Chicago. Owing to an illness he returned to Germany in 1935, where he died shortly after his arrival.

6.11.1.1 Reactions and Mechanisms of Fischer–Tropsch Synthesis

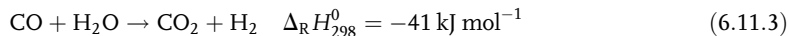
Fischer–Tropsch synthesis can be regarded as a surface polymerization reaction since monomer units are produced from the reagents hydrogen and carbon monoxide *in situ* on the surface of the catalyst (usually based on iron or cobalt). Hence, various hydrocarbons (mainly *n*-paraffins) are formed by successive addition of C₁ units to growing chains on the catalyst surface. The main reaction of *Fischer–Tropsch* synthesis is therefore represented by:



where the term ($-\text{CH}_2-$) represents a methylene group of a normal paraffin. For a kinetic description of the synthesis, methane formation is often considered as a separate reaction:



The third reaction that plays an important role – above all if iron-based catalysts are used – is the unwanted formation of carbon dioxide by the water-gas shift reaction:



Since the discovery of the synthesis at the *Kaiser Wilhelm Institute* (Germany) in 1923 by *Franz Fischer* and *Hans Tropsch*, the kinetics of the *Fischer–Tropsch* synthesis have been studied extensively and many attempts have been made to describe the rate of reaction, either by using power law rate equations or equations based on certain mechanistic assumptions. In most cases, the rate of H_2 and CO consumption is correlated with the (measurable) gas phase concentrations or partial pressures of H_2 , CO , and/or H_2O . An overview of rate equations for iron catalysts is given by Huff and Satterfield (1984a) and for cobalt catalysts by Yates and Satterfield (1991). Details on the kinetics and reaction mechanism are, for example, discussed by Donnelly and Satterfield (1989), Dry (1982), Fernandes (2005), Huff and Satterfield (1984b), Post *et al.* (1989), Riedel *et al.* (1999), Schulz and Claeys (1999), Schulz *et al.* (1999), Van Steen and Schulz (1999), and Van Steen (1993).

Three classes of reactions are distinguished in polymerization: initiation, propagation, and termination (Scheme 6.11.1). Initiation is the formation of a chain starter from the reactants H_2 and CO . From evidence in the literature it seems clear that a surface methyl species is the chain starter. The propagation step is the incorporation of monomer units into growing chains, and termination is desorption of growing chains either as a paraffin or olefin (Scheme 6.11.1, Fig. 6.11.1) from the catalyst surface.

The product distribution of the synthesis can be derived to a good approximation based on the simple kinetic scheme shown in Figure 6.11.1 for chain growth and termination.

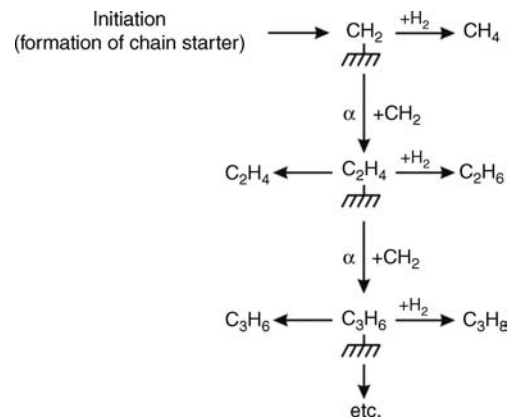
For steady state, the rate of consumption of a propagating surface species S with carbon number n by termination and chain growth equals the rate of formation by chain growth of species with carbon number $n - 1$ (Figure 6.11.1):

$$r_{g,n-1} = r_{g,n} + r_{t,n} \quad (6.11.4)$$

where r_i is the reaction rate in mol of species i per unit time and unit of catalyst (e.g., mass).

If we assume first-order reactions, we obtain:

$$k_{g,n-1} c_{S_{n-1}} = k_{g,n} c_{S_n} + k_{t,n} c_{S_n} \Rightarrow c_{S_n} = \frac{k_{g,n-1}}{k_{g,n} + k_{t,n}} c_{S_{n-1}} \quad (6.11.5)$$



Scheme 6.11.1 Simplified scheme of the mechanisms of *Fischer–Tropsch* synthesis. (S = surface species, P = desorbed product).

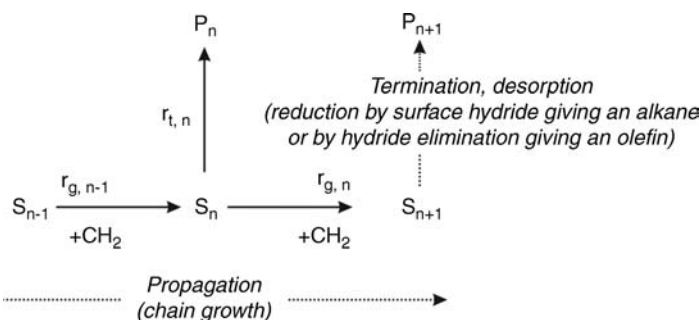


Figure 6.11.1 Kinetic scheme of chain growth and termination during *Fischer–Tropsch* synthesis (S = surface species, P = desorbed product).

The probability of chain growth $\alpha_{g,n}$ of a species with carbon number n is defined as the ratio of the rate of propagation to the overall reaction rate (propagation and termination):

$$\alpha_{g,n} = \frac{k_{g,n} c_{s_n}}{k_{g,n} c_{s_n} + k_{t,n} c_{s_n}} = \frac{k_{g,n}}{k_{g,n} + k_{t,n}} \quad (6.11.6)$$

For the probability of chain termination α_t we have:

$$\alpha_{t,n} = \frac{k_{t,n}}{k_{g,n} + k_{t,n}} \quad (6.11.7)$$

The sum of both probabilities is unity:

$$\alpha_{g,n} + \alpha_{t,n} = 1 \quad (6.11.8)$$

The rate of formation of a product P_n equals the rate of desorption of surface species S_n , and insertion of Eqs. (6.11.5) and (6.11.7) leads to:

$$r_{P,n} = k_{t,n} c_{s_n} = \alpha_{t,n} k_{g,n-1} c_{s_{n-1}} \quad (6.11.9)$$

For a surface species with carbon number $n - 1$, we find analogously to Eq. (6.11.5):

$$c_{s_{n-1}} = \frac{k_{g,n-2}}{k_{g,n-1} + k_{t,n-1}} c_{s_{n-2}} \quad (6.11.10)$$

and insertion into Eq. (6.11.9) leads to:

$$r_{P,n} = \alpha_{t,n} \frac{k_{g,n-1}}{k_{g,n-1} + k_{t,n-1}} k_{g,n-2} c_{s_{n-2}} = \alpha_{t,n} \alpha_{g,n-1} k_{g,n-2} c_{s_{n-2}} \quad (6.11.11)$$

If we repeat this procedure until surface species S_1 we obtain:

$$r_{P,n} = \alpha_{t,n} (\alpha_{g,n-1} \alpha_{g,n-2} \cdots \alpha_{g,2}) k_{g,1} c_{s_1} \quad (6.11.12)$$

All hydrocarbons are formed by chain growth starting from species S_1 and thus the rate of formation of all products equals the rate of consumption of species S_1 :

$$\sum_n r_{P,n} = (k_{t,1} + k_{g,1}) c_{s_1} = \frac{k_{g,1}}{\alpha_{g,1}} c_{s_1} \quad (6.11.13)$$

Combination of Eqs. (6.11.12) and (6.11.13) leads to the molar content γ_n of species P_n :

$$\gamma_n = \frac{r_{P,n}}{\sum_n r_{P,n}} = \alpha_{t,n} (\alpha_{g,n-1} \alpha_{g,n-2} \cdots \alpha_{g,2}) \alpha_{g,1} \quad (6.11.14)$$

If, finally, we assume that the value of the probability of chain growth α_g is independent of chain length, and thus also the probability of termination $\alpha_t (= 1 - \alpha_g)$ we have:

$$\gamma_n = (1 - \alpha_g) \alpha_g^{n-1} \quad (6.11.15)$$

The product distribution according to Eq. (6.11.15) is called the *Schulz–Flory* distribution; it was originally developed for polymerization. For *Fischer–Tropsch* synthesis, this product distribution is a good approximation for hydrocarbons with a carbon number higher than about three, whereas the formation of methane by Eq. (6.11.2) is usually underestimated. The logarithmic form of Eq. (6.11.15) is commonly used for a graphical presentation of the distribution, as shown in Figure 6.11.2 for different values of α_g and in Figure 6.11.3 for a commercial iron catalyst:

$$\log(\gamma_n) = \log(1 - \alpha_g) + (n - 1)\log(\alpha_g) \quad (6.11.16)$$

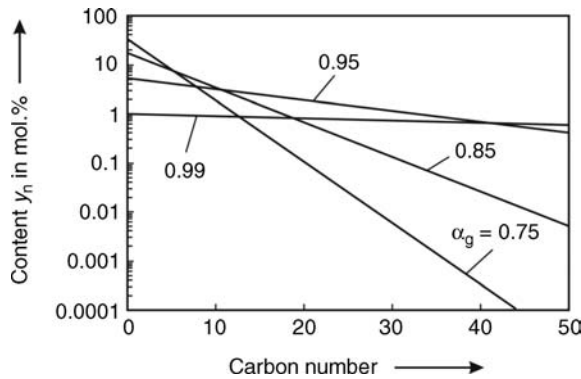


Figure 6.11.2 Product distribution of Fischer-Tropsch synthesis as calculated by Eq. (6.11.15) for different values of the probability of chain growth α_g .

The mass content of a component with carbon number n is given by:

$$w_n = \frac{m_n}{m_{\text{total}}} = \frac{M_n n_n}{\sum_1^{\infty} M_n n_n} = \frac{M_n (1 - \alpha_g) \alpha_g^{n-1}}{\sum_1^{\infty} M_n (1 - \alpha_g) \alpha_g^{n-1}} \quad (6.11.17)$$

The molar mass approximately equals nM_{CH_2} (M_{CH_2} : molar mass of the CH_2 group), which yields:

$$w_n = \frac{n_n \alpha_g^{n-1}}{\sum_1^{\infty} n_n \alpha_g^{n-1}} = \frac{n_n \alpha_g^{n-1}}{1 + 2\alpha_g + 3\alpha_g^2 + \dots + n\alpha_g^{n-1}} \quad (6.11.18)$$

The series in the denominator equals the term $(1 - \alpha_g)^{-2}$, and thus we finally obtain:

$$w_n = n_n (1 - \alpha_g)^2 \alpha_g^{n-1} \quad (6.11.19)$$

Figure 6.11.4 shows the product distribution by mass as calculated by Eq. (6.11.19) for different probabilities of chain growth, and Figure 6.11.5 gives the influence of the probability of chain growth α_g on the yield of product fractions.

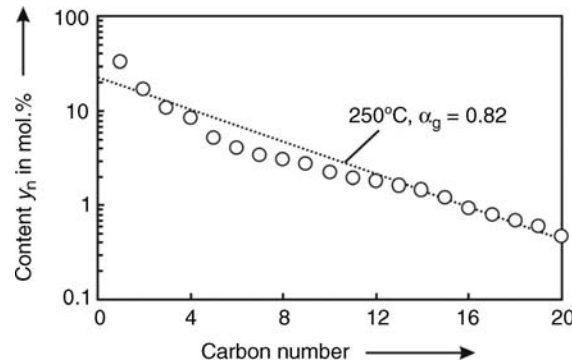


Figure 6.11.3 Typical product distribution of Fischer-Tropsch synthesis (Fe-cat., data from Raak, 1995).

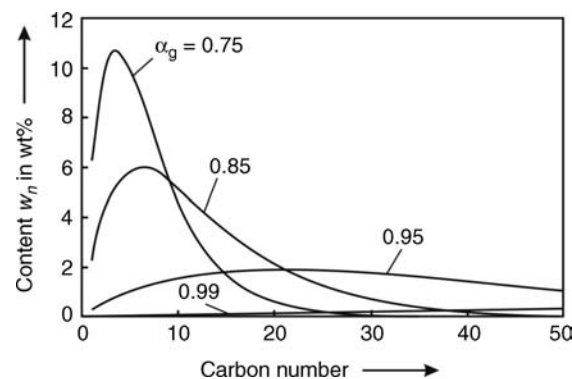
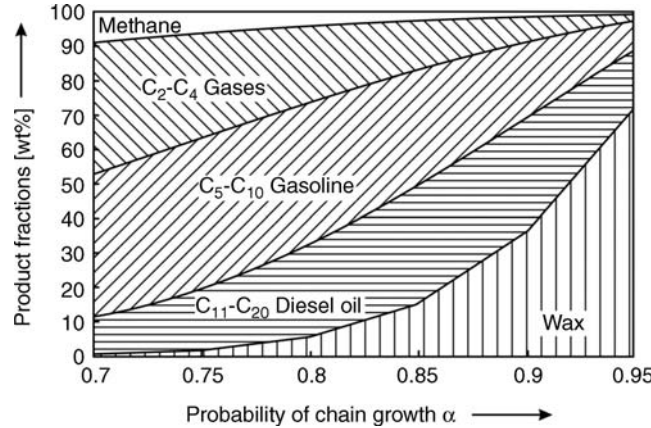


Figure 6.11.4 Product distribution by mass of Fischer-Tropsch synthesis as calculated by Eq. (6.11.19) for different values of the probability of chain growth α_g .

Figure 6.11.5 Influence of probability of chain growth α_g on the yield of product fractions as calculated by Eq. (6.11.19).



Today, cobalt and iron are considered to be the most attractive catalysts for FTS. The highest α values, beneficial for high wax selectivity, are achieved at low temperatures with cobalt. Iron is much cheaper than cobalt, but has a considerable water-gas shift activity that may be a drawback compared to cobalt since CO₂ is an unwanted by-product and less valuable hydrocarbons are formed. The water-gas shift activity is advantageous if the syngas has a low H₂/CO ratio (<2) as the conversion of CO₂ by excess H₂ into CO (and H₂O) is then a desired function in addition to FT activity.

Activation in a syngas atmosphere requires several hours or even days, during which the metal surface is rearranged or reconstructed (for cobalt) or carbided (for iron). In addition, the pores of the catalyst are filled with liquid higher hydrocarbons (wax), which leads to a decrease of the effective reaction rate by pore diffusion for particle diameters larger than about 1 mm.

6.11.1.2 Intrinsic and Effective Reaction Rate of Fischer–Tropsch Synthesis

The intrinsic rate constant of H₂ consumption on a commercial iron catalyst was calculated by Kuntze (1991) and Raak (1995) based on fixed bed experiments with small particles (<0.2 mm, no influence of pore diffusion), and is given by (see also Jess and Kern, 2009):

$$r_{m,H_2,FT} = -\frac{d\dot{n}_{H_2}}{dm_{cat}} = k_{m,H_2,HW} \frac{c_{H_2,g}}{1 + K_{HW} \frac{c_{H_2O,g}}{c_{CO,g}}} \quad (6.11.20)$$

This *Hougen–Watson* type equation considers the inhibiting influence of H₂O on the reaction rate, whereby the intrinsic reaction rate constant $k_{m,H_2,HW}$ and the coefficient K_{HW} are given by:

$$k_{m,H_2,HW} = 1.2 \times 10^7 \text{ m}^3 \text{ kg}^{-1} \text{ s}^{-1} e^{-\frac{109000}{RT}} \quad (6.11.21)$$

$$K_{HW} = 0.2e^{\frac{8800}{RT}} (1.7 > K_{HW} > 1.5 \text{ for } 220 < T < 250 \text{ }^\circ\text{C}) \quad (6.11.22)$$

For particles with diameters typically used in technical fixed bed reactors ($d_p > 1 \text{ mm}$), an effective rate considering pore diffusion has to be used:

$$r_{m,H_2,eff,FT} = \eta_{pore} \left(\frac{k_{m,H_2,HW}}{1 + K_{HW} \frac{c_{H_2O,g}}{c_{CO,g}}} \right) c_{H_2,g} = \eta_{pore} k_{m,H_2} c_{H_2,g} \quad (6.11.23)$$

The term in brackets can be regarded as a pseudo-first-order rate constant (k_{m,H_2}), and the influence of pore diffusion is considered by the effectiveness factor η_{pore} :

$$\eta_{pore} = \frac{r_{m,H_2,eff}}{k_{m,H_2} c_{H_2,g}} = \frac{\tanh \phi}{\phi} \approx \frac{1}{\phi} \quad (\text{for } \phi \geq 2) \quad (6.11.24)$$

For the *Thiele modulus* we have in case of FTS:

$$\phi = \frac{V_p}{A_{p,\text{ext}}} \sqrt{\frac{k_{m,H_2} \rho_p c_{H_2,g}}{D_{\text{eff},H_2,l} c_{H_2,l}}} \quad (6.11.25)$$

where $V_p/A_{p,\text{ext}}$ is the ratio of particle volume to external surface area.

The concentration of hydrogen in liquid wax, $c_{H_2,l}$, is calculated by the *Henry coefficient* ($H_{H_2,c} \approx 20\,000 \text{ Pa m}^3 \text{ mol}^{-1}$):

$$c_{H_2,l} = \frac{p_{H_2,g}}{H_{H_2,c}} = \frac{RT}{H_{H_2,c}} c_{H_2,g} \quad (6.11.26)$$

and thus we finally obtain for the *Thiele modulus*:

$$\phi = \frac{V_p}{A_{p,\text{ext}}} \sqrt{\frac{k_{m,H_2} \rho_p}{D_{\text{eff},H_2,l} \frac{RT}{H_{H_2,c}}}} \quad (6.11.27)$$

The effective diffusion of dissolved hydrogen in the liquid filled porous catalyst is described by an effective diffusion coefficient $D_{\text{eff},H_2,l}$. Thereby, one has to consider that only a portion of the particle is permeable, and that the path through the particle is random and tortuous. Both aspects are taken into account by the porosity ε_p and tortuosity τ_p (Section 3.2.2.3):

$$D_{\text{eff},H_2,l} = \frac{\varepsilon_p}{\tau_p} D_{\text{mol},H_2,l} \quad (6.11.28)$$

The molecular diffusivity of H_2 in liquid *Fischer-Tropsch* products is calculated by the *Wilke-Chang* equation [Eq. (3.1.90)]. For temperatures from 200 to 260 °C, $D_{\text{mol},H_2,l}$ is about $4 \times 10^{-8} \text{ m}^2 \text{ s}^{-1}$ (Raak, 1995), and for ε_p/τ_p we use a value of 0.3 (0.76/3, Kuntze, 1991; Raak, 1995). Figure 6.11.6 shows the effective rate constant of H_2 consumption for a value of $V_p/A_{p,\text{ext}}$ of 0.5 mm (cylindrical particles, 5 mm long, 2.7 mm in diameter). Pore diffusion strongly affects the effective rate constant for temperatures above 180 °C. The reason for this strong influence is the slow diffusion of the dissolved H_2 in the liquid filled pores of the catalyst. Hence for a technical particle size in the range of millimeters, only 20% of the particle (at 240 °C) is utilized, which has to be accepted to limit the pressure loss in fixed bed reactors (Figure 6.11.7).

For an accurate modeling of a *Fischer-Tropsch* fixed bed reactor (Section 6.11.1.5), not only the main reaction (the *Fischer-Tropsch* reaction, index FT) leading to the formation of higher hydrocarbons [Eq. (6.11.1)] but also methane formation [Eq. (6.11.2), index M] and the water-gas shift reaction [Eq. (6.11.3), index S] must be considered. The rate equations for these three reactions on a commercial Fe

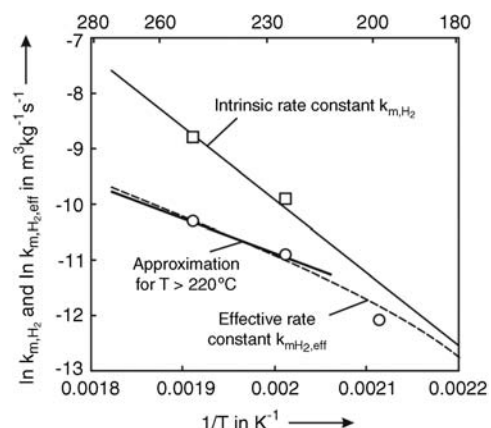


Figure 6.11.6 Intrinsic and effective rate constant of H_2 -consumption during FTS for $c_{H_2O} = 0$ (iron cat., effective value for cylinders, 2.7 mm in diameter and 5 mm long) (Jess and Kern, 2009).

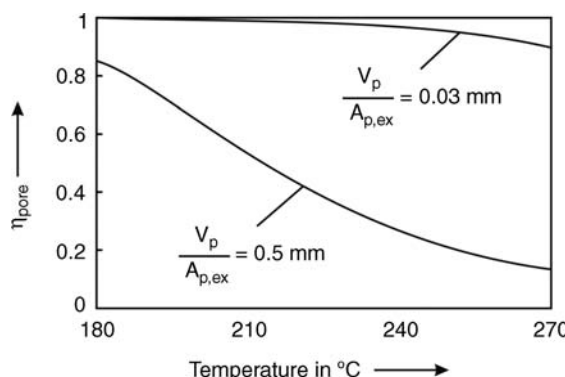


Figure 6.11.7 Influence of temperature and particle size on the effectiveness factor with regard to pore diffusion of *Fischer-Tropsch synthesis* [according to Eqs. (6.11.20)–(6.11.28)] (Jess and Kern, 2009).

catalyst (cylinders, 2.7 mm diameter, 5 mm long) were determined by Popp (1996) [see also Jess, Popp, and Hedden (1999) and Jess and Kern (2009)] as:

$$r_{m,H_2,FT} = -\frac{d\dot{n}_{H_2}}{dm_{cat}} = \frac{k_{m,H_2,eff,FT} c_{H_2,g}}{1 + 1.6 \frac{c_{H_2O,g}}{c_{CO,g}}} \\ \left(\text{with } k_{m,H_2,eff,FT} = 5.1 \text{ m}^3 \text{ kg}^{-1} \text{ s}^{-1} e^{-\frac{52000}{RT}} \right) \quad (6.11.29)$$

$$r_{m,H_2,M} = -\frac{d\dot{n}_{H_2}}{dm_{cat}} = k_{m,H_2,eff,M} c_{H_2,g} \\ \left(\text{with } k_{m,H_2,eff,S} = 155 \text{ m}^3 \text{ kg}^{-1} \text{ s}^{-1} e^{-\frac{70000}{RT}} \right) \quad (6.11.30)$$

$$r_{m,H_2,S} = \frac{d\dot{n}_{H_2}}{dm_{cat}} = k_{m,H_2,eff,S} c_{H_2O,g} \\ \left(\text{with } k_{m,H_2,eff,S} = 155 \text{ m}^3 \text{ kg}^{-1} \text{ s}^{-1} e^{-\frac{70000}{RT}} \right) \quad (6.11.31)$$

The effective rate constant $k_{m,H_2,eff,FT}$ depicted in Figure 6.11.6 as an “approximation for $T > 230^\circ\text{C}$ ” is only valid for $c_{H_2O}/c_{CO} \approx 0$. The apparent activation energy of 52 kJ mol⁻¹ is about half of the intrinsic value (109 kJ mol⁻¹) according to Eq. (6.11.21), as expected for a strong limitation by pore diffusion (Figure 6.11.6, see also Section 4.5.4.1).

Note that under the conditions of the *Fischer–Tropsch* reaction (about 250 °C) with a syngas free of CO₂, the reverse reaction of the shift reaction, that is, the formation of CO and H₂O from H₂ and CO₂ is negligible as the equilibrium is on the side of H₂ and CO₂.

Equations (6.11.29)–(6.11.31) refer only to the temperatures where the influence of pore diffusion is fully developed, that is, for $T > 220^\circ\text{C}$ and a particle diameter of 3 mm ($V_p/A_{p,ex} = 0.5 \text{ mm}$). Figure 6.11.7 shows for comparison that very small particles would be needed to exclude the influence of pore diffusion (particle diameter <0.2 mm, that is, $V_p/A_{p,ex} < 0.03 \text{ mm}$).

6.11.1.3 History, Current Status, and Perspectives of Fischer–Tropsch Synthesis

In the past, only particular geopolitical situations have favored the realization of industrial plants for synthetic production of fuels and chemicals from coal, natural gas, or biomass. For example, this was the case in Germany during World War II and for South Africa during the period of embargo over Apartheid (Table 6.11.1). Because of the historical significance, the production of synthetic fuels in Germany during World War II by *Fischer–Tropsch* and by the alternative process of direct coal hydrogenation are examined in Topic 6.11.1.

From the end of WWII until the 1990, South Africa was the only producer of liquid fuels from coal (and also from natural gas), and only plants based on *Fischer–Tropsch* were and are used. Today, FT plants provide one-third of South Africa's liquid fuel requirement.

With regard to FTS, this situation has changed significantly in recent years (Table 6.11.1). Several companies have developed their own gas-to-liquid (GTL) FTS technology. In 1992, the first commercial FT plant based on natural gas went on stream at Mossel Bay in South Africa. In 1993, Shell started up a FT GTL plant in Malaysia for the production of diesel fuel and other specialty products and, recently, huge FTS plants have started operation in Qatar.

There are also several commercial GTL projects at various stages of planning and development, initiated by companies operating in gas-rich countries such as Qatar, Iran, Russia, Nigeria, Australia, and Algeria (Table 6.11.1). Nevertheless, even the

Table 6.11.1 Commercial Fischer–Tropsch plants.

Company	Location	Startup (and shut-down)	Capacity (in 10^6 t a^{-1}) (oil equivalent)	Feedstock
Ruhrchemie and others	Germany	1935–1945 (nine plants)	0.5 (average production 1939–1945)	Coal
SASOL	South Africa	1955		
		1980	About 6 in total (3 plants)	Coal
		1982		
PetroSA	South Africa	1992	1.1	Natural gas
Shell	Malaysia	1993	0.7	Natural gas
SASOL, Qatar Petroleum	Qatar	2006	1.7	Natural gas
SASOL, Qatar Petroleum	Qatar	2009	1.7	Natural gas
Shell	Qatar	2011	6	Natural gas
Exxon Mobil	Qatar	Planned	7.5	Natural gas
ConocoPhillips	Qatar	Planned	8	Natural gas
Chevron SASOL	Nigeria	Planned	1.7	Natural gas
Tinrhert	Algeria	Planned	1.7	Natural gas
BP	Columbia	Planned	1.7	Natural gas
World GTL	Trinidad	Planned	0.2	Natural gas

total capacity of FT plants of 40 Mt a^{-1} in 2011 (including all announced plants) is still only about 1% of current global petroleum consumption.

The main driving forces for the commercial production of synthetic hydrocarbons via *Fischer–Tropsch synthesis* or methanol synthesis are (Schaub, Rohde, and Subirana, 2006):

- The availability of cheap natural gas and solid raw materials like coal and biomass may already lead to an economic profitability based on high petroleum prices. Drivers for a shift from oil to other resources are the increase in known reserves of natural gas, and the need to monetize stranded gas reserves (40% of the proven gas reserves).
- Climate change concerns will probably lead to a ban on flaring of natural (associated) gas, and to a substitution of fossil fuels by renewable feedstocks (biomass) to avoid fossil CO₂ emissions. In some regions like Western Europe and North America, political aims are already defined regarding the use of biofuels in the transportation sector.
- Production of synthetic hydrocarbons via *Fischer–Tropsch synthesis*, for example, has the potential to produce high-value automotive fuels and petrochemicals from fossil and renewable sources. The demand for liquid transportation fuels and petrochemicals worldwide is set to rise significantly in the next 50 years. Today's demand for automotive fuels is met nearly completely by petroleum-based fuels (>97%, IEA, 2004), but this share of petroleum-based fuels can be decreased by applying synthetic hydrocarbon processes. In the petrochemical industry, present day petroleum-based production of base chemicals could be replaced by synthetic hydrocarbon routes.

A significant aspect of FTS for fuel production is the energy loss of the overall conversion process in terms of chemical energy efficiency, as described for example by Schaub (Schaub, Rohde, and Subirana, 2006; Schaub, 2006). When starting with a solid feedstock (coal, biomass), hydrocarbon synthesis leads to overall efficiencies of about 30–50%, whereas with natural gas the values are 55–63%. As a reference case, gasoline or diesel from petroleum refining achieves values above 90%. This considerable energy loss during the manufacture of synthetic fuels is owing to the overall exothermicity, the internal energy requirements/heat losses of the processes involved, and to the hydrogen deficiency (in coal and biomass). The high efficiency in petroleum refining reflects the advantage that the raw material petroleum already contains hydrocarbon molecules similar to molecules desired in the fuel products.

Synfuels may substitute crude oil, but limitations have to be considered (Schaub, 2006):

- Consumption of natural gas is also limited, although the reserves are presently higher than for petroleum. In recent decades and probably also in future, gas has and will become increasingly attractive for electricity production and heat supply. Natural gas could therefore not replace petroleum products but only add to the total liquid fuel supply. In addition, conversion into liquid fuels leads to a considerable energy loss as stated above.
- Coal reserves are higher but energy loss and additional CO₂ emissions are a problem.
- The obvious limitation of biofuels is the availability of cultivated land areas. In addition, conversion into synthetic hydrocarbons competes with other biomass applications like generation of electricity and heat.
- Oil price increases and global conflicts may favor natural gas, coal, and biomass, but the prices for these feedstocks are not independent of petroleum. For cheap natural gas (stranded, associate gas) the economics are probably favorable. With coal, the costs for conversion into liquid hydrocarbons are higher than with natural gas, but if oil prices are high then competitive production costs can also be achieved with (cheap) coal. Tax policies in several countries presently help to promote biomass conversion, but the economics of biomass to liquid (BTL) processes remain to be demonstrated on a larger scale.

Topic 6.11.1: Role of synthetic fuels in Germany during World War II (WWII)

At the onset of WWII in 1939, the total fuel consumption in Germany was 6 million tonnes oil equivalent. Imports from overseas accounted for 60% of the total supply, 10% were imported overland from European sources (mainly Romania), and 10% were based on domestic oil production. Only the remaining 20% was produced synthetically from coal. This high proportion of imports indicates how precarious the fuel situation was as Germany was cut off from them by the blockade that began at the beginning of World War II. At that time (and still today), four methods of synthetic fuel production from coal were available:

- Aromatic hydrocarbons, mainly benzene, were produced as a by-product of coking. The drawback to increased production of benzene was the fact that it was tied to the quantities of coke that were determined by the production limits of crude iron.
- The second method produced a distillate from lignite coal. Brown coal was heated, and the tars and oil were extracted and distilled into fuel. Only 10% could be used as gasoline, the remaining portion 90% was only useful as heating or diesel oil.
- The third method was the *Fischer–Tropsch* process, which had been developed in the 1930s to an industrial stage operation (first plant in 1936).
- The fourth and at that time most important process was high-pressure hydrogenation, also called the *Bergius–Pier* process (see also Section 5.1.5.2), named after Friedrich Bergius and Matthias Pier (see box), which changes coal directly into liquid fuels like gasoline (first plant in 1927).

Between 1938 and the beginning of 1944, synthetic fuel production by the last two methods grew from 1 million tonnes oil equivalent to about 4 million tonnes (Becker, 1981; Stranges, 2003) (Figure 6.11.8). In spring 1944, 63% of Germany's liquid fuel availability was covered by processes based on coal (hydrogenation, FTS, coking plants, brown coal tar), 22% were refined from German and Austrian petroleum, and only the remainder of 15% still had to be covered by imports of crude oil (Table 6.11.2). Thus, Germany was almost energy independent at the end of 1943/beginning of 1944. It is the dark side of the coin of chemical technology but probably true to state that WWII and the Nazi reign of terror would have ended long before 1945 without these technologies, that is, millions of military and civilian casualties would have been avoided. Only the massive Allied air attacks on the hydrogenation and FTS plants that started in May 1944 and continued into the spring of 1945 sounded the death knell for the German war machine.

Friedrich Bergius (1877–1949): a German chemist, known for the *Bergius–Pier process* for producing synthetic fuel from coal. In 1931 he won the Nobel Prize in Chemistry (together with *Carl Bosch*) in recognition of his contributions to the development of chemical high-pressure methods. He started to study chemistry at the University of Breslau in 1903 and got a PhD at the University of Leipzig in 1907. In 1909 *Bergius* along with *Fritz Haber* and *Carl Bosch* at the University of Karlsruhe worked on the development of the *Haber–Bosch* process. He then worked with *Max Bodenstein*, a major contributor to the field of chemical kinetics, at the University of Hannover. During his tenure, *Bergius* developed methods for high-pressure chemistry of carbon-containing substrates, yielding a patent on the *Bergius* process in 1913. He developed this process well before the *Fischer–Tropsch* process. In 1914, *Karl Goldschmidt* invited him to build an industrial demonstration plant at his factory in Mannheim, but because of technical problems the first successful experiments with a reactor of industrial size began only in 1919, just after WWI when interest in synthetic fuel production decreased. During the post-war period, the reactor was run with some interruptions until 1925. The throughput was disappointing, and financial problems and inflation made progress slow. Thus, *Bergius* finally sold his patent to the *BASF*. Shortly after that, several plants (the first in 1927) were built (Table 6.11.2, Figure 6.11.8). After *Bergius* had stopped working on coal liquefaction, he investigated the hydrolysis of wood to produce sugar. The high costs and technical problems nearly led him to bankruptcy, and a bailiff followed him to Stockholm to obtain the money from his Nobel Prize in 1931. After WWII he worked as an advisor in Italy, Turkey, and Spain. Finally, he emigrated to Argentina, where he died in 1949. Details of the development of the *Bergius* process and a biography of *Bergius* can be found in the literature (Stolzenberg, 1999; Haul, 1985).

Matthias Pier (1882–1965), a German chemist, worked with *Emil Fischer* and *Walter Nernst* during his studies. After WWI, he joined *BASF* and worked on ammonia and methanol synthesis. After *BASF* had purchased the patent on coal liquefaction from *Bergius* in 1925, he developed this process further. He found better and sulfur-resistant catalysts and increased the yield of fuels by arranging the process in two steps, liquid-phase hydrogenation and gas-phase hydrotreating of the intermediate product. Thus, the process is therefore mostly known as the *Bergius–Pier* process.

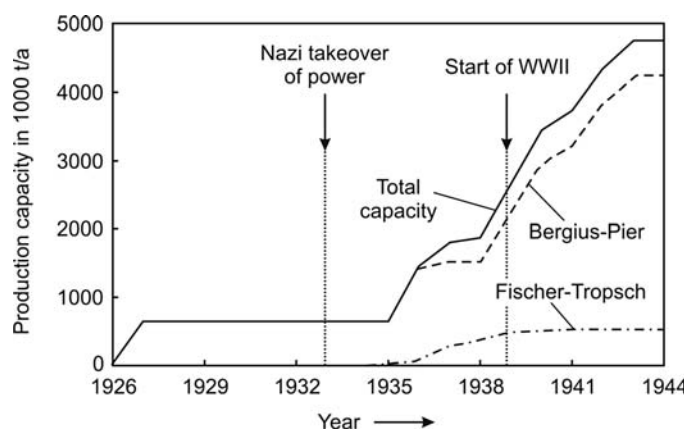


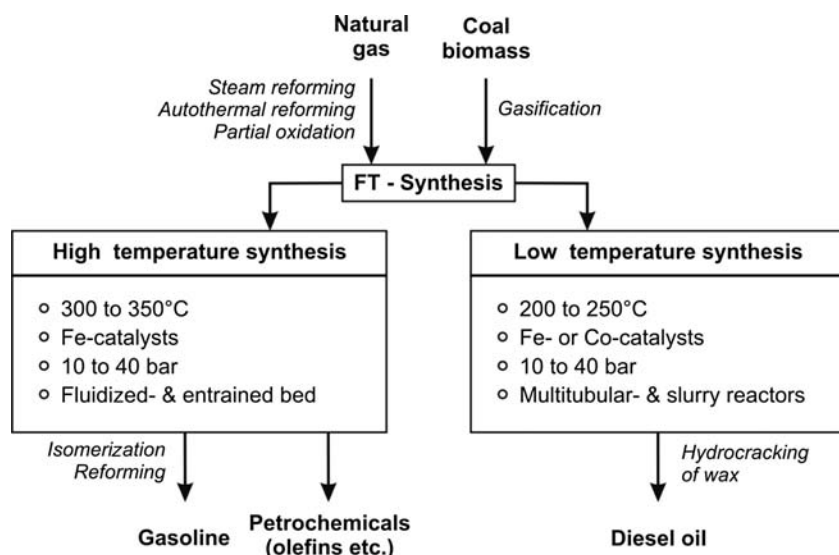
Figure 6.11.8 Development of production capacity of liquid fuels from coal in Germany by the *Bergius–Pier* and *Fischer–Tropsch* processes. [data from Haul (1985); Stranges, (2003)].

Table 6.11.2 German oil and fuel availability in spring 1944. Data from Stranges (2003).

Process	Production rate (in 10^6 t a^{-1}) (oil equivalent)	Share of total availability (%)
Domestic production of liquid fuels from coal in Germany		
• Hydrogenation of coal (<i>Bergius–Pier</i> process)	3.5 (13 plants)	40
• <i>Fischer–Tropsch</i> synthesis (based on coal)	0.6 (9 plants ^{a)})	7
• Aromatics (mainly benzene as by-product of coking plants)	0.4	5
• Brown and bituminous coal tar distillation	1.0	11
Refining of German and Austrian crude oil		
Crude oil/fuel imports of Germany (Rumania, Hungary)	1.8	22
	1.2	15

a) The total number of FT reactors was huge. According to Tijm, (2008), 994 reactors were operated. The maximum capacity of a single reactor was only 3 tonnes per day (compared to today's value of 300 t d^{-1}), requiring substantial materials and manpower, about ten workers per reactor.

Figure 6.11.9 XTL plant (X to liquid with X as natural gas, coal, biomass) with low or high temperature Fischer–Tropsch synthesis.



6.11.1.4 Fischer–Tropsch Processes and Reactors

General aspects of the synthesis and of different processes are discussed in the literature, for example, by Anderson (1984), Dry (2002, 1981), Eilers, Postuma, and Sie (1990), Falbe (1977), Haenel (2006), Schulz (1999), Zennaro, Hugues, and Caprani (2006), and Schaub, Rohde, and Subiranas (2006). For further details on different reactor types used for FT-synthesis we refer to Dry (2002), Jess, Popp, and Hedden (1999), Sie and Krishna (1999, 2000), Sie, Senden, and Van Wechem (1991), Zennaro, Hugues, and Caprani (2006), and Schaub, Rohde, and Subiranas (2006). Here we can only point out some main aspects of reactor technology and process design.

XTL technology (X to liquids with X as coal, biomass, or natural gas etc.) based on Fischer–Tropsch consists of three major parts, syngas generation, FTS, and product upgrading. Figure 6.11.9 shows different configurations of an XTL plant with low or high temperature FTS.

FTS uses syngas (CO/H_2) generated from coal, biomass, or natural gas (Figure 6.11.9). Syngas is produced via oxygen/steam gasification or steam reforming/partial oxidation. For coal and also for biomass, the syngas has to be cleaned from impurities such as H_2S and NH_3 and adjusted to the needs of the subsequent synthesis step.

Two temperature ranges are applied: high temperature (300–350 °C), leading mainly to short-chain alkenes and gasoline, and low temperature (200–250 °C), leading mainly to wax and diesel oil. Upgrading of FT products most commonly includes reforming and isomerization to improve the low octane number and hydrocracking of wax to produce more diesel oil.

Among the different products, diesel oil in particular is highly valuable because of its excellent properties. It has a high cetane number of 70 compared to the standard value of 50, and it contains near zero sulfur and aromatics, which reduces the emissions relative to conventional diesel oil. Figure 6.11.10 depicts a GTL plant with low temperature FTS and hydrocracking.

The most difficult problem to solve in the design of FT reactors is the high exothermicity combined with a high sensitivity of product selectivity to temperature. Hence, the reactor must have provisions for efficient heat removal. Four reactor types are used commercially today. For low temperature synthesis (<250 °C), multitubular fixed bed and slurry bubble column reactors are used (Figure 6.11.11a and c). For high temperature ($T > 300$ °C), the circulating fluidized bed (Figure 6.11.11b) and the bubbling fluid bed are used.

Reactor capacities are in the range of 300 (fixed bed) to 1200 tonnes (slurry bubble column) of liquid hydrocarbons per day (Schaub, Rohde, and Subiranas, 2006). Low-temperature reactors have to cope with a three-phase reaction system (gas, liquid,

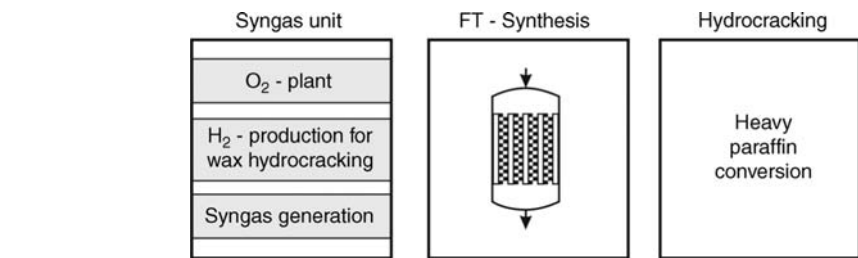


Figure 6.11.10 Main parts of a FT GTL plant (low temperature FTS). Adapted from Eilers, Postuma, and Sie, (1990).

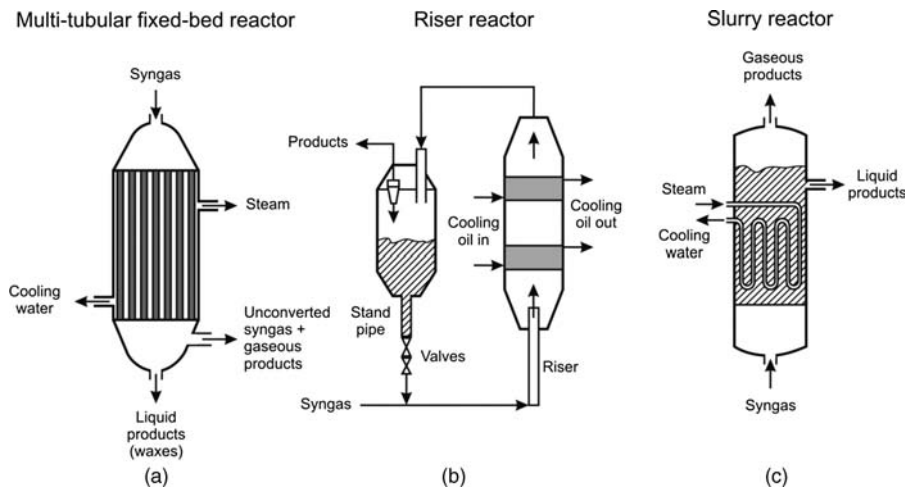


Figure 6.11.11 Reactors used for Fischer-Tropsch processes. Adapted from Moulijn, Makkee, and Van Diepen (2004).

solid catalyst), whereas high-temperature reactors work in a two-phase regime (syngas and gaseous hydrocarbons, solid catalyst). Heat is transferred via heat transfer surfaces inside the reactor or by using a multi-tubular reactor cooled by boiling water. In a slurry bubble column reactor, small catalyst particles (<200 µm) are suspended in the product, which is liquid at the reaction conditions of 20–30 bar and 200–250 °C. The syngas is fed into the bottom of the column. Such conditions enable optimum control of the heat and material exchange rate on the catalyst surface. A drawback is the fact that the fine catalyst has to be separated from the liquid products, which is not needed in fixed bed reactors.

Figure 6.11.12 shows a classical commercial Fischer-Tropsch plant, the so-called ARGE fixed bed process [ARGE = Arbeitsgemeinschaft (consortium) Ruhrchemie/

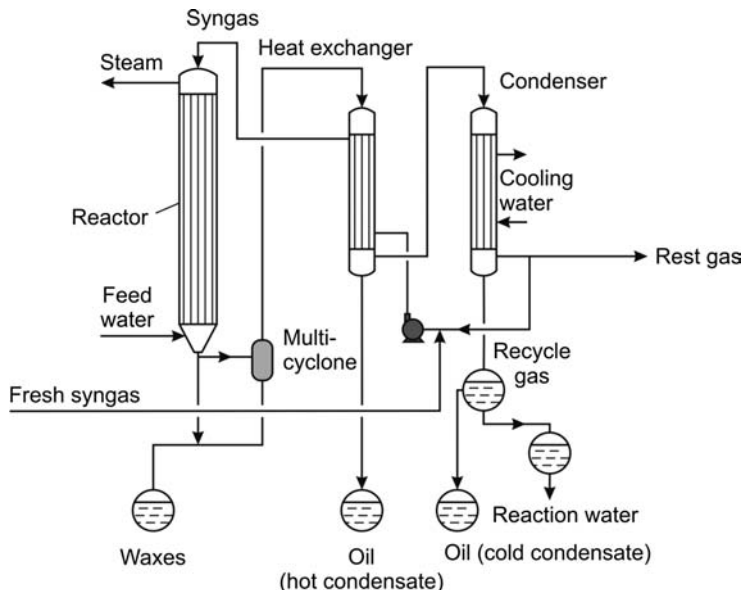


Figure 6.11.12 Classical commercial Fischer-Tropsch plant (ARGE fixed bed process) (Jesch and Kern, 2009).

[Lurgi]. The conversion of syngas per pass is only about 30%, but by the installation of a gas recycle, usually with a recycle ratio of two to three, the overall conversion is in the range 70–80%. The limited conversion per pass helps to remove the reaction heat and by this means a temperature runaway can be avoided. Example 6.11.1 (adapted from Jess and Kern, 2009) examines some general aspects of the influence of the recycle ratio on reactor behavior.

Example 6.11.1: Influence of recycle ratio on the behavior of a FT reactor

Figure 6.11.13 shows a flow sheet of a FT fixed bed reactor with recycle of unconverted syngas. To simplify the subsequent calculations, we assume that the recycle gas only consists of unconverted CO and H₂. In reality, it also contains other gases like CH₄ and CO₂ and a purge stream is needed to limit the concentration of inerts. We also assume that the temperature is constant, which is not true, as examined in Section 6.11.1.5.

In contrast to the recycle reactor examined in Section 4.10.2.6, only the unconverted syngas is returned to the reactor entrance after separation of the products (here liquid hydrocarbons and water). Hence, the concentration of CO and H₂ remains unchanged.

The recycle ratio R is defined as:

$$R = \frac{\dot{V}_{\text{recycle}}}{\dot{V}_{\text{in}}} \quad (6.11.32)$$

If we consider plug flow behavior, a first-order reaction with respect to hydrogen, and use the simplification of a constant volume reaction, the conversion of H₂ per pass is given by:

$$X_{\text{H}_2,\text{per pass}} = 1 - e^{-k_{m,\text{H}_2} \tau_{\text{per pass}}} \\ \left(\text{with } \tau_{\text{per pass}} = \frac{m_{\text{cat}}}{\dot{V}_{\text{in}}(1+R)} = \frac{\tau}{(1+R)} \right) \quad (6.11.33)$$

For total conversion of hydrogen related to the hydrogen in the fresh feed we have:

$$X_{\text{H}_2,\text{total}} \dot{n}_{\text{H}_2,\text{in}} = X_{\text{H}_2,\text{per pass}} (\dot{n}_{\text{H}_2,\text{in}} + \dot{n}_{\text{H}_2,\text{recycle}}) \Rightarrow X_{\text{H}_2,\text{total}} \\ = X_{\text{H}_2,\text{per pass}} (1+R) \quad (6.11.34)$$

Hence for $R = 1$, a conversion per pass of 50% is needed for complete conversion. Equation (6.11.34), that is, $\dot{n}_{\text{H}_2,\text{recycle}}/\dot{n}_{\text{H}_2,\text{in}} = R$, is only valid if no inerts are in the recycle, and if X_{CO} equals X_{H_2} . Hence, the syngas only consists of H₂ and CO with a molar ratio of two. In this case, the H₂ content in the recycle gas equals the content in the feed.

Insertion of Eq. (6.11.33) into Eq. (6.11.34) and substitution of the residence time per pass by the residence time related to the fresh feed leads to:

$$X_{\text{H}_2,\text{total}} = (1+R) \left(1 - e^{-\frac{k_{m,\text{H}_2} \tau}{1+R}} \right) \\ = (1+R) \left(1 - e^{-\frac{Da}{1+R}} \right) \quad \left(\text{with } \tau = \frac{m_{\text{cat}}}{\dot{V}_{\text{in}}} \right) \quad (6.11.35)$$

Figure 6.11.14 shows that for a given *Damkoehler number* Da (defined based on the residence time related to the fresh feed), the total hydrogen conversion increases with the recycle ratio R . For high values of R , Eq. (6.11.35) can be simplified further:

$$X_{\text{H}_2,\text{total}} = (1+R) \left(1 - e^{-\frac{k_{m,\text{H}_2} \tau}{1+R}} \right) \approx (1+R) \left(\frac{k_{m,\text{H}_2} \tau}{1+R} \right) \\ = k_{m,\text{H}_2} \tau \quad (\text{for } R \rightarrow \infty) \quad (6.11.36)$$

Hence, for $Da = 1$ (and $R \rightarrow \infty$) the conversion is 100%.

The total H₂ conversion and the conversion per pass for the example of a typical recycle ratio for a FT fixed bed, single bed synthesis of 2.5 is given by Figure 6.11.15. For comparison, conversion without recycle is also shown. As indicated by the dashed lines, a conversion per pass of 25% ($Da = 1$) would be sufficient for a total H₂ conversion of 87%.

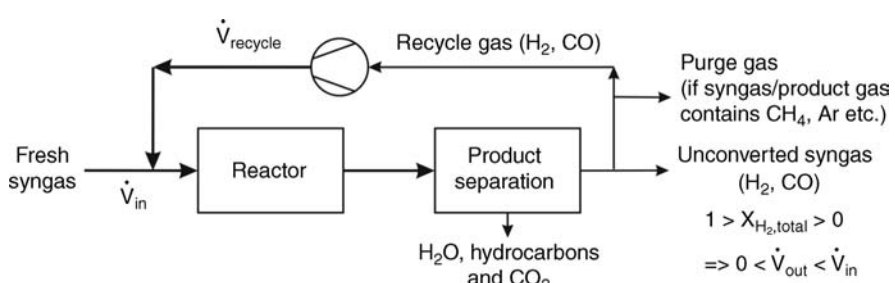


Figure 6.11.13 Simplified flow sheet of a FT fixed-bed reactor with recycling of unconverted syngas (for assumptions see text) (Jess and Kern, 2009).

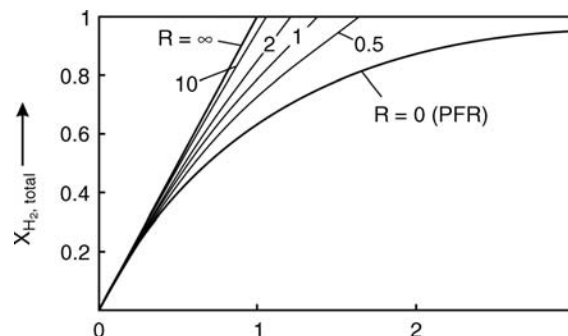


Figure 6.11.14 Influence of recycle ratio on the total H_2 conversion (for conditions see text) (Jesch and Kern, 2009).

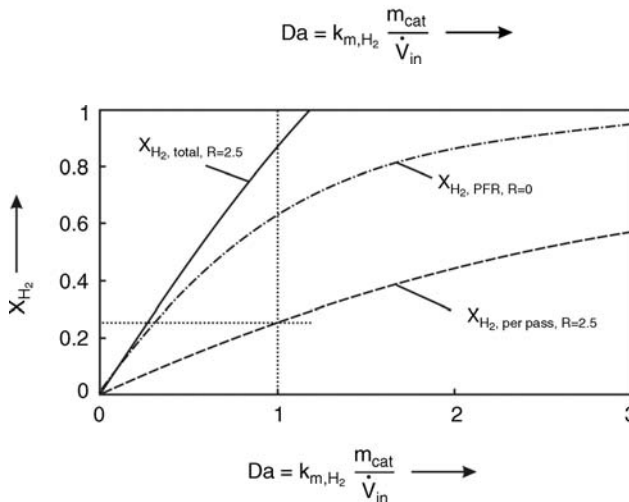


Figure 6.11.15 Total H_2 conversion and conversion per pass for a recycle ratio of 2.5; for comparison, conversion without recycle is also shown (for conditions see text).

6.11.1.5 Modeling of a Multi-tubular Fixed Bed Fischer-Tropsch Reactor

For modeling and simulation of a *Fischer-Tropsch* reactor we use the classical *ARGE* fixed bed process with Fe as catalyst. The recycle ratio is 2.5. Table 6.11.3 lists the other reaction conditions. Although the *ARGE* FT process may not be the most modern FT process it is the only one for which reliable data on the process as well

Table 6.11.3 Data on chemical media and reaction conditions of Fischer-Tropsch synthesis.

Parameter	Value (24 bar, 240 °C)
Superficial gas velocity u_s (empty reactor)	0.55 m s ⁻¹
Total molar gas concentration (feed) ρ_{mol}	563 mol m ⁻³
Total pressure p	24 bar
(Equivalent) diameter of catalyst particle ^{a)} d_p	3.8 mm
Length of tubes	12 m
Internal diameter of single tube $d_{\text{R,int}}$ (total number of tubes 2052)	4.6 cm
External diameter of single tube $d_{\text{R,ex}}$	5.6 cm
Bulk density of catalyst bed ρ_b	790 kg m ⁻³
Inlet concentration of hydrogen	66.6 vol.% (rest CO)
Kinematic viscosity ν of gas mixture (feed)	$4 \times 10^{-6} \text{ m}^2 \text{s}^{-1}$
Thermal conductivity of gas mixture (feed) λ_{gas}	$0.16 \text{ W m}^{-1} \text{ K}^{-1}$
Effective radial thermal conductivity λ_{rad}	$6.3 \text{ W m}^{-1} \text{ K}^{-1}$
Heat capacity of gas mixture (feed) c_p	$30 \text{ J mol}^{-1} \text{ K}^{-1}$
Heat transfer coefficient (bed to internal tube wall) $\alpha_{\text{W,int}}$	$900 \text{ W m}^{-2} \text{ K}^{-1}$
Thermal conductivity of wall material (steel) λ_{wall}	$50 \text{ W m}^{-1} \text{ K}^{-1}$
Heat transfer coefficient (external tube wall to boiling water, 25 bar) $\alpha_{\text{W,ex}}$	$1600 \text{ W m}^{-2} \text{ K}^{-1}$
Thermal transmittance U_{wall}	$1380 \text{ W m}^{-2} \text{ K}^{-1}$
Overall thermal transmittance U_{overall}	$364 \text{ W m}^{-2} \text{ K}^{-1}$

a) Cylinders with 2.7 mm diameter and 5 mm length. From Eqs. (4.10.199) and (4.10.200) we get an equivalent particle diameter d_p of 3.8 mm. The value of d_p is used to determine λ_{rad} and $\alpha_{\text{W,int}}$.

as on the kinetics with an Fe catalyst are available and published in the open literature (Falbe, 1977; Jess, Popp, and Hedden, 1999; Kuntze, 1991; Popp, 1996; Raak, 1995; Jess and Kern, 2009). Hence, this process is used for subsequent inspection of main aspects of modeling multi-tubular FT reactors. (Results of the modeling of a multi-tubular reactor with a Co catalyst can be found in Jess and Kern, 2009.)

If we neglect dispersion of mass, the mass balance for hydrogen yields:

$$-u_s \frac{dc_{H_2}}{dz} = r_{m,H_2} \rho_b \quad (6.11.37)$$

The total rate of H_2 consumption by the FT reaction, methane formation, and the gas shift reaction [Eqs. (6.11.29)–(6.11.31)] is given by:

$$r_{m,H_2} = r_{m,H_2,FT} + r_{m,H_2,M} - r_{m,H_2,S} \quad (6.11.38)$$

Note that the parameters given in Eqs. (6.11.29)–(6.11.31) refer to the temperature where the influence of pore diffusion is fully developed ($T > 220^\circ\text{C}$).

The boundary condition of the mass balance [Eq. (6.11.37)] is:

$$c_{H_2} = c_{H_2,in} \quad (\text{for } z = 0) \quad (6.11.39)$$

As inspected in the following, we may model the cooled tubular reactor by the so-called one- or two-dimensional fixed bed reactor model.

Two-Dimensional Fixed Bed Reactor Model If we neglect axial dispersion of heat, the heat balance according to the two-dimensional reactor model is as follows [Eq. (4.10.126), Section 4.10.7.1]:

$$\rho_{\text{mol}} c_p u_s \frac{dT}{dz} = \lambda_{\text{rad}} \left(\frac{d^2 T}{dr^2} + \frac{dT}{r dr} \right) - \rho_b \sum \Delta_R H_i r_{m,H_2,i} \quad (6.11.40)$$

with:

$$\sum \Delta_R H_i r_{m,H_2,i} = \Delta_R H_{\text{FT}} r_{m,H_2,FT} + \Delta_R H_M r_{m,H_2,M} + \Delta_R H_S r_{m,H_2,S}$$

The boundary conditions are:

$$T = T_{\text{in}} \quad (\text{for } z = 0) \quad (6.11.41)$$

$$\frac{dT}{dr} = 0 \quad (\text{for } r = 0 \text{ and all } z) \quad (6.11.42)$$

$$-\lambda_{\text{rad}} \frac{dT}{dr} = \alpha_{w,int} (T_{w,int,1} - T_{w,int,2}) \quad \left(\text{for } r = \frac{d_R}{2} \text{ at the wall} \right) \quad (6.11.43)$$

Equation (6.11.43) considers the bed and the fluid as a pseudo-homogeneous medium, and the heat transfer within the bed up to the wall is represented by the radial effective thermal conductivity λ_{rad} and the internal wall heat transfer coefficient $\alpha_{w,int}$. The model assumes a jump in temperature directly at the wall from $T_{w,int,1}$ to $T_{w,int,2}$. The values of λ_{rad} and $\alpha_{w,int}$ were calculated by Eqs. (4.10.195) and (4.10.197) (Section 4.10.7.3).

The fourth boundary condition is related to the heat transfer from an external tube side to the heat transfer medium (here boiling water at 25 bar) [Section 4.10.7.3, Eqs. (4.10.178) and (4.10.179)]:

$$\begin{aligned} \dot{q} &= \alpha_{w,int} (T_{w,int,1} - T_{w,int,2}) \\ &= U_{\text{wall}} (T_{w,int,2} - T_{\text{cool}}) \quad \left[\text{with } U_{\text{wall}} = \left(\frac{d_{\text{wall}}}{\lambda_{\text{wall}}} + \frac{1}{\alpha_{w,ex}} \right)^{-1} \right] \end{aligned} \quad (6.11.44)$$

where U_{wall} summarizes the (small) thermal resistance of heat conduction by the wall [with thickness $d_{\text{wall}} = (d_{R,\text{ex}} - d_{R,\text{int}})/2$] and the heat transfer from the external tube surface to the cooling medium, that is, to the boiling water phase.

The external heat transfer coefficient $\alpha_{w,ex}$ from the external side of the tube to the boiling water depends on the vapor pressure and on the temperature difference

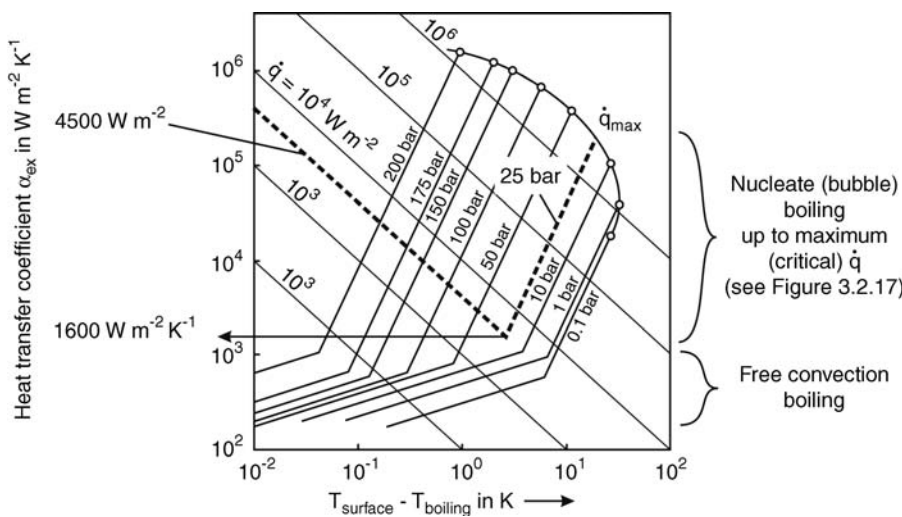


Figure 6.11.16 Heat transfer coefficient from a hot surface to boiling water [excess temperature $T_{\text{surface}} - T_{\text{boiling}}$; data from Schluender (1986)].

between the surface temperature and the boiling temperature as shown in Figure 3.2.17 (Section 3.2.1.3) for a pressure of 1 bar. Figure 6.11.16 shows an extension of Figure 3.2.17 for pressures of up to 200 bar. If the pressure and the heat flux per unit surface are known, the value of $\alpha_{w,\text{ex}}$ can be determined by this graph. For *Fischer-Tropsch synthesis* the average heat flux can be estimated based on the reaction enthalpy [Eq. (6.11.1)] and the H₂ conversion by:

$$\begin{aligned} \dot{q} &= \frac{X_{\text{H}_2} \dot{n}_{\text{H}_2,\text{in}} (-0.5 \Delta_R H_{\text{FT}})}{\pi d_{R,\text{int}} L} \\ &= \frac{X_{\text{H}_2} \gamma_{\text{H}_2,\text{in}} \nu_{s,240^\circ\text{C},24\text{ bar}} \pi \frac{d_{R,\text{int}}^2}{4} \rho_{\text{mol},240^\circ\text{C},24\text{ bar}} (-0.5 \Delta_R H_{\text{FT}})}{\pi d_{R,\text{int}} L} \end{aligned} \quad (6.11.45)$$

If we use a value of 30% as typical for the H₂ conversion per pass and the values of the geometry and data on chemical media in Table 6.11.3, we obtain a mean value for \dot{q} of 4500 W m⁻². The cooling temperature is typically 224 °C (see below), which corresponds to a vapor pressure of 25 bar. Hence, by Figure 6.11.16, we find a value for $\alpha_{w,\text{ex}}$ of 1600 W m⁻² K⁻¹. We also learn from Figure 6.11.16 that operation is far from the maximum heat flux where we approach film boiling (Figure 3.2.17). Thus for an increasing heat flux – by fluctuations of pressure, volume rate, and hence by changes of heat production – the heat transfer coefficient $\alpha_{w,\text{ex}}$ would increase almost exponentially, which helps in controlling the reaction temperature.

All heat transfer parameters and the reaction conditions are summarized in Table 6.11.3.

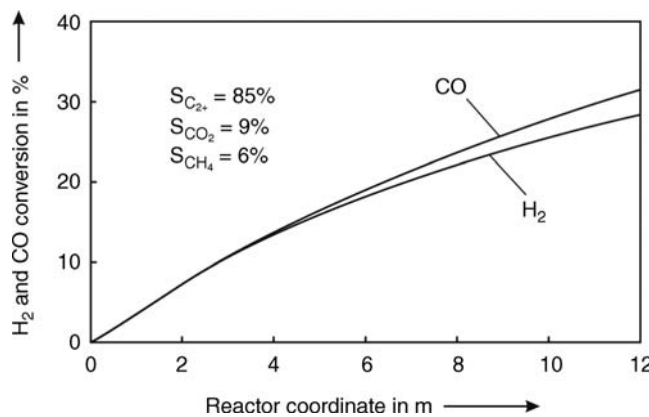
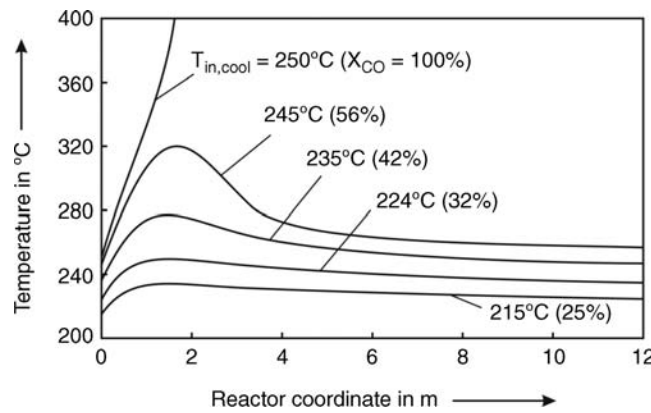


Figure 6.11.17 Profiles of H₂ and CO conversion in a multi-tubular FT reactor [tube diameter 4.6 cm, $T_{\text{in}} = T_{\text{cool}} = 224^\circ\text{C}$, $T_{\text{max}} = 250^\circ\text{C}$, two-dimensional model according to Eq. (6.11.40); for parameters see Table 6.11.3, for axial temperature profile see Figure 6.11.18] (Jess and Kern, 2009).

Figure 6.11.18 Influence of cooling temperature on the axial temperature profiles (4.6 cm tube diameter, $T_{in} = T_{cool}$, two-dimensional reactor model; for parameters see Table 6.11.3) (Jess and Kern, 2009).



The results presented in Figures 6.11.17–6.11.21 were calculated with the commercial program *Presto-Kinetics* (solver for differential equations, www.cit-wulkow.de). The maximum temperature of the ARGE catalyst is about 260 °C as the Fe catalyst then starts to deactivate by sintering, which substantially lowers the internal surface area (Kuntze, 1991). Hence, to be on the safe side, 250 °C was chosen as the maximum allowable temperature.

For an industrially used internal tube diameter of 4.6 cm and a maximum temperature of 250 °C we obtain a CO conversion per pass of around 30% (Figure 6.11.17), and thus the total CO conversion with regard to feed would be about 90% for a recycle ratio of about 2 [Eq. (6.11.34)], which is in fairly good agreement with data given in the literature (conversion of 73% for $R = 2.5$, Falbe, 1977). The selectivity to methane (6% based on carbon) is also in agreement with data from the literature (5% according to Franck and Knop, 1979). The conversion of hydrogen (28%) is slightly lower than that of CO, which reflects the influence of the shift reaction, which consumes CO and forms H₂ and unwanted CO₂.

Figure 6.11.18 shows the influence of cooling temperature on the axial temperature profiles in the multi-tubular FT reactor. We see that for a cooling temperature of more than about 245 °C the reactor is very sensitive and temperature runaway becomes likely. (Note that $X_{CO} > 30\%$ per pass is not possible because a recycle ratio of 2.5 was assumed, which is then no longer possible as the amount of unconverted syngas would be too small. Hence cases for $T_{cool} > 230\text{ }^{\circ}\text{C}$ should only show the principle of the effect of an increasing cooling temperature on the reactor behavior.)

One-Dimensional Fixed Bed Reactor Model It may be convenient to use a one-dimensional model, where only axial gradients of temperature and concentration are considered. We now compare how accurate this approach is. Like the two-dimensional model, the one-dimensional model also takes into account λ_{rad} , $\alpha_{w,int}$, λ_{wall} , and $\alpha_{w,ex}$, but now we assume a constant bed temperature and an overall thermal transmittance $U_{overall}$ that combines conduction in the bed, heat transfer at the wall, through the wall, and to the cooling medium by:

$$U_{overall} = \left(\frac{d_R}{8\lambda_{rad}} + \frac{1}{\alpha_{w,int}} + \frac{d_{wall}}{\lambda_{wall}} + \frac{1}{\alpha_{w,ex}} \right)^{-1} \quad (6.11.46)$$

where the difference between $d_{R,ex}$ and $d_{R,int}$ is neglected and thus we subsequently simply use $d_R \approx d_{R,int}$. By Eq. (6.11.46), the heat balance of the one-dimensional model is given by:

$$\rho_{mol} c_p u_s \frac{dT}{dz} = \frac{U_{overall} 4(T_{cool} - T)}{d_R} - \rho_b \sum \Delta_R H_i r_{m,H_2,i} \quad (6.11.47)$$

In Figure 6.11.19, the axial temperature profiles of the two- and one-dimensional models are compared for a cooling temperature of 224 °C. For the two-dimensional model, two profiles are given, the temperature exactly in the tube center and at the radial position 0.35 d_R . Figure 6.11.19 indicates that the axial mean bed

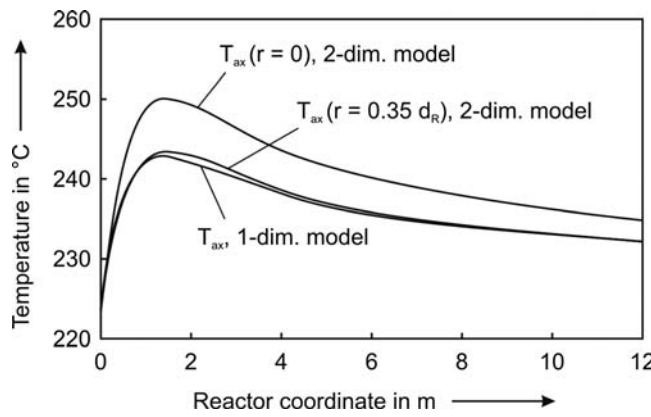


Figure 6.11.19 Axial temperature profiles in a multi-tubular FT reactor: comparison with two-dimensional model [Eq. (6.11.40)] and one-dimensional model [Eq. (6.11.47)] (tube diameter 4.6 cm, $T_{in} = T_{cool} = 224^\circ\text{C}$; for parameters see Table 6.11.3) (Jess and Kern, 2009).

temperature profile of the one-dimensional model almost exactly equals the profile of the two-dimensional model at $r = 0.35d_R$. This is in agreement with theory (Section 4.10.7.3) as for the mean temperature of the one-dimensional model this radial position was chosen to divide the bed in a radial direction into two parts with equal volume [Eq. (4.10.185)]. The good agreement of both models is underlined by the almost equal values of CO conversion (31.4% for one-dimensional and 31.5% for two-dimensional).

The radial profiles at a distance from the reactor entrance of $z = 1.5 \text{ m}$ are shown in Figure 6.11.20 for both the two- and one-dimensional model. At this axial position we have the maximum axial temperature (Figures 6.11.18 and 6.11.19) and the most pronounced radial gradients in temperature.

The good agreement of both models with respect to heat transfer can be shown with the help of the radial profiles by comparison of the heat fluxes as follows.

According to the two-dimensional model, the heat flux from the bed to the wall is given by the temperature gradient in the fixed bed directly at the wall:

$$\dot{q}_{2\text{-dim.}} = \lambda_{\text{rad}} \frac{dT}{dr} \Big|_{r=\frac{d_R}{2}} \quad (6.11.48)$$

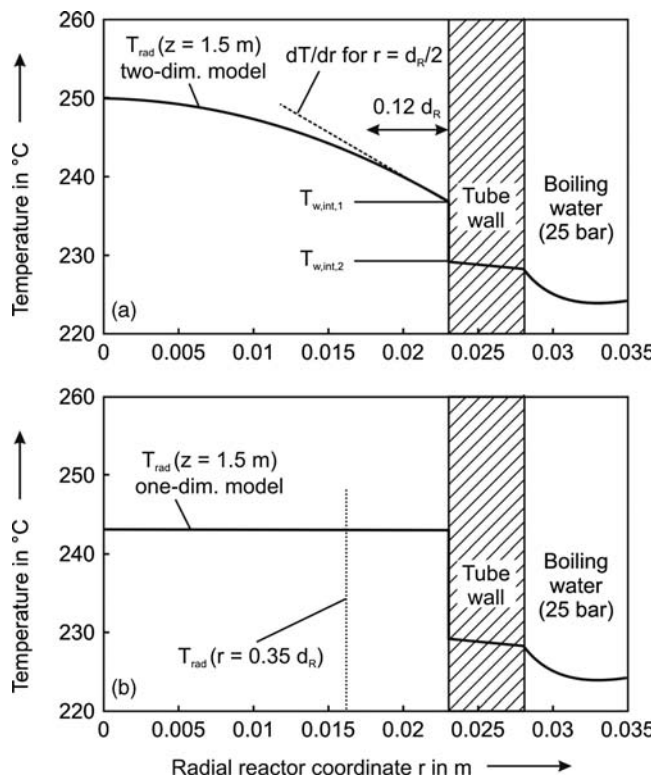


Figure 6.11.20 Radial temperature profiles in the single tube: comparison of two-dimensional (a) and one-dimensional model (b) ($T_{in} = T_{cool} = 224^\circ\text{C}$, 1.5 m from the inlet) (Jess and Kern, 2009).

According to the temperature profile shown in Figure 6.11.20, the heat flux is given by:

$$\dot{q}_{2\text{-dim.}} = \lambda_{\text{rad}} \frac{(T_{\text{rad},1\text{-dim}} - T_{w,\text{int},1})}{0.12d_R} = \lambda_{\text{rad}} \frac{(T_{\text{rad},1\text{-dim}} - T_{w,\text{int},1})}{\frac{d_R}{8.3}} \quad (6.11.49)$$

if we use the (mean) bed temperature of the one-dimensional model as reference value. This is almost exactly equivalent to the equation used for the one-dimensional model, where we have used the approximation [see Eq. (6.11.46)]:

$$\dot{q}_{1\text{-dim.}} = \lambda_{\text{rad}} \frac{(T_{\text{rad},1\text{-dim}} - T_{w,\text{int},1})}{\frac{d_R}{8}} \quad (6.11.50)$$

The runaway behavior is shown in Figure 6.11.21 by a plot of the axial maximum temperature versus the cooling temperature. The two-dimensional model leads to a critical cooling temperature of 247 °C whereas the one-dimensional model leads to 255 °C. Hence if all heat transfer data are available, the more accurate two-dimensional model should be preferred.

The runaway behavior shown in Figure 6.11.21 can also be estimated by the criteria derived in Section 4.10.3. The two characteristic parameters are N_C and N_{ad} [Eq. (4.10.83)]. If we only consider the main reaction of FT synthesis [Eq. (6.11.1)] we have:

$$N_C = \frac{U_{\text{overall}} \frac{4}{d_R} \Delta T_{\text{ad}}}{\rho_b k_{m,H_2,FT,T_{\text{cool}}} - \left(\frac{\Delta_R H_{\text{FT}}}{2} \right) c_{H_2,\text{in}}} \quad (6.11.51)$$

$$N_{\text{ad}} = \frac{\Delta T_{\text{ad}} E_{A,FT}}{RT_{\text{cool}}^2} \quad (6.11.52)$$

The critical conditions in terms of N_C and N_{ad} are given in Section 4.10.3.1. For a first-order reaction we have (Figure 4.10.25):

$$\left(\frac{N_C}{N_{\text{ad}}} \right)_{\text{crit}} = 2.72 - \frac{3.37}{\sqrt{N_{\text{ad}}}} \pm 0.15 \quad (6.11.53)$$

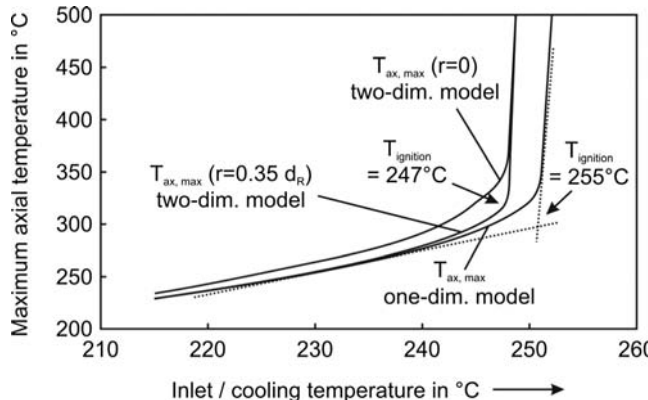
With an adiabatic temperature rise of 1700 K, the critical conditions of a 4.6 cm tube are reached for $T_{\text{cool}} = 240$ °C ($N_C/N_{\text{ad}} = 2.2$, $N_{\text{ad}} = 40$), if only the main reaction is considered. This is in agreement with the computed solution (247 °C, two-dimensional model, Figure 6.11.21) where CH₄ formation and the water-gas shift were included.

Figure 6.11.22 shows the runaway diagram for different tube diameters. The reactor operates on the safe side for a diameter of 4.6 cm but is sensitive for values higher than 5.6 cm.

The maximum allowable temperature difference between bed and cooling temperature can be determined by rearranging Eq. (4.10.82) (Section 4.10.3.3):

$$\Delta T_{\text{max}} = T_{\text{crit}} - T_{\text{cool}} = \frac{R}{E_A} (T_{\text{crit}} - T_{\text{cool}}) \approx \frac{R}{E_A} T_{\text{cool}}^2 \quad (6.11.54)$$

Figure 6.11.21 Influence of cooling temperature on the maximum axial temperature in a multi-tubular FT reactor: comparison of two-dimensional model [Eq. (6.11.40)] and one-dimensional model [Eq. (6.11.47)] ($T_{\text{in}} = T_{\text{cool}}$; for parameters see Table 6.11.3) (Jess and Kern, 2009).



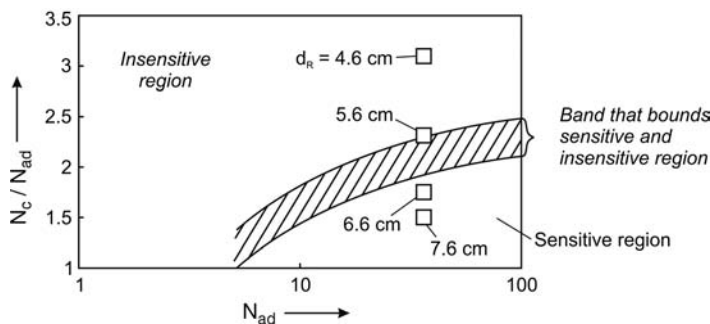


Figure 6.11.22 Runaway diagram of a multi-tubular reactor for different tube diameters according to Figure 4.10.24 and Eqs. (4.10.47)–(4.10.49), $T_{in} = T_{cool} = 224^\circ\text{C}$ (for parameters in Table 6.11.3).

If we use this rule of thumb, we here obtain a value for ΔT_{max} of 40 K, which also confirms that a diameter of 4.6 cm is small enough to avoid a runaway as we then have a value of $\Delta T_{bed,max}$ of only 26 K (Figure 6.11.21). An alternative, although very rough estimation of the maximum allowable tube diameter to avoid a temperature runaway, is given in Example 6.11.2.

Example 6.11.2: Rough estimation of maximum tube diameter to avoid temperature runaway

At the axial position in the tubes where we reach the maximum temperature, the axial temperature gradient dT/dz vanishes, and Eq. (6.11.47) reads as:

$$\frac{U_{overall} 4(T - T_{cool})}{d_R} = \rho_b \Delta_R H_{FT} r_{m,H_2,FT}$$

$$(\text{for } T_{ax} = T_{max,ax}, \text{i.e. } dT/dz = 0) \quad (6.11.55)$$

if for simplicity we only consider the main FT reaction and not methane formation and water-gas shift. The left-hand side of Eq. (6.11.55) represents the cooling term ($\dot{q}_{cooling}$, radial heat flux from bed to cooling medium) and the right-hand side represents the heat production ($\dot{q}_{reaction}$).

To estimate the maximum diameter to avoid a runaway, we use the following assumptions:

- The H_2 content at the position of $T_{max,axial}$ still equals the inlet value. Thus, we are on the safe side as the real value is smaller as a certain conversion has already taken place.
- $T_{max,axial}$ is 250°C , and we assume that the bed temperature is constant in the radial direction. Again we are on the safe side as the mean value is lower (Figure 6.11.20).

- The maximum allowable temperature difference is estimated by Eq. (6.11.54), which yields 40 K, if we estimate a cooling temperature of around 210°C .

With these assumptions and the values given in Table 6.11.3, the cooling term is given by:

$$\begin{aligned} \dot{q}_{cooling} &= \frac{4\Delta T_{max}}{d_R} \left(\frac{d_R}{8\lambda_{rad}} + \frac{1}{\alpha_{W,int}} + \frac{d_{wall}}{\lambda_{wall}} + \frac{1}{\alpha_{W,ex}} \right)^{-1} \\ &\approx \frac{160 \text{ K}}{d_R} (d_R 0.0195 \text{ m KW}^{-1} + 0.00194 \text{ m}^2 \text{ KW}^{-1})^{-1} \end{aligned}$$

For the heat produced by the reaction we obtain:

$$\dot{q}_{reaction} \approx \rho_b \Delta_R H_{FT} k_{m,H_2,eff,FT,250^\circ\text{C}} c_{H_2,in} = 1425 \text{ kW/m}^3$$

The condition to avoid thermal runaway is $\dot{q}_{cooling} > \dot{q}_{reaction}$. Figure 6.11.23 indicates that a tube diameter of more than 4.1 cm is critical. This is a smaller than the value determined by the Barkelew diagram (5.6 cm, Figure 6.11.22), but still a reasonable estimation.

One final aspect should also be discussed. For the simulation we have assumed that the syngas only consists of CO and H_2 . In reality inerts such as CH_4 are present. In addition, CO_2 and CH_4 are formed and the conversion of CO and H_2 may differ (Figure 6.11.17). Even if CO_2 is completely removed from the off-gas before recycling, CH_4 will be present in the recycle, and a purge gas stream is needed to avoid accumulation. Figures 6.11.24 and 6.11.25 show the results of a respective mass balance for a recycle ratio of 2.5. It was, thereby, assumed that the selectivities (based on carbon in CO) are 86% for the C_{2+} -hydrocarbons, 6% for CH_4 , and 8% for CO_2 . The composition of the fresh syngas is 64% H_2 , 32% CO, and 4% CH_4 . The CO conversion is then lower than for the ideal case with no inerts in the recycle. Figure 6.11.24 also shows that depending on the conversion a significant amount of the product gas has to be purged.

Figure 6.11.23 Influence of internal tube diameter on the radial heat flux from the bed to cooling medium per unit volume (\dot{q}_{cooling}), and heat produced by the FT reaction (per unit volume).

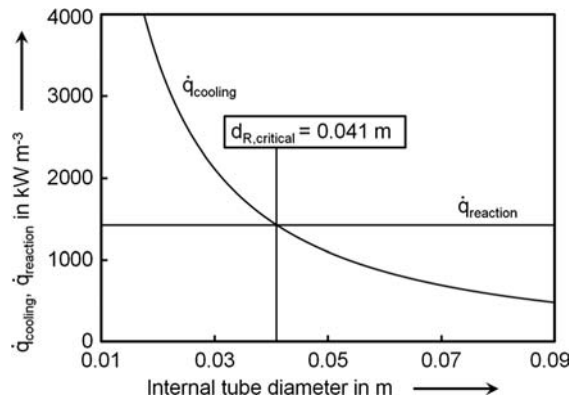


Figure 6.11.24 Influence of CO conversion per pass on total conversion and purge gas stream for a recycle ratio of 2.5 (conditions/assumptions: selectivities based on C in CO: 86% to C_{2+} -hydrocarbons, 6% to CH_4 , and 8% to CO_2 ; composition of fresh syngas: 64% H_2 , 32% CO, and 4% CH_4) (Jess and Kern, 2009).

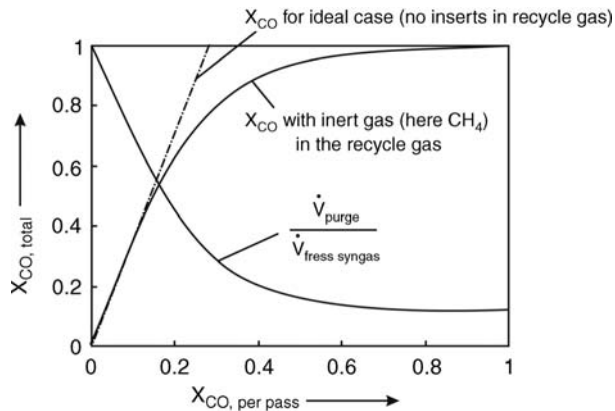
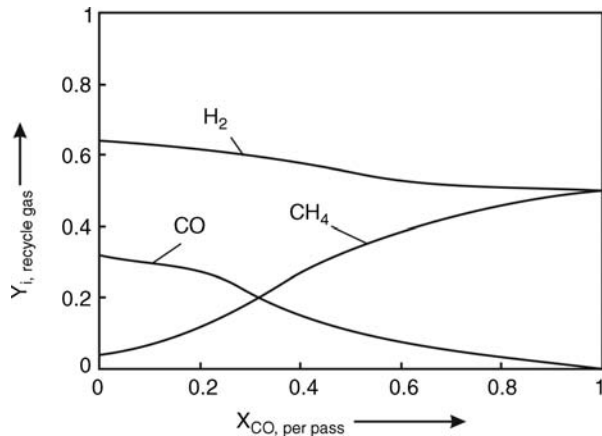


Figure 6.11.25 Composition of recycle gas for different values of CO conversion per pass (for conditions and assumptions see Figure 6.11.24) (Jess and Kern, 2009).



Summary of Section 6.11.1 (take-home messages)

- Production of synthetic fuels via Fischer-Tropsch synthesis (FTS) has the potential to produce fuels like gasoline and diesel oil and petrochemicals from fossil and renewable sources. The availability of cheap natural gas and of coal and biomass has given momentum to this synthesis technology which was already developed in the 1920. The global FTS capacities have increased

significantly in the last ten years, with natural gas favored as feedstock. Nevertheless, even the total capacity of FT plants of 40 Mt a^{-1} reached in 2011 is still only about 1% of current global crude oil consumption.

- FTS can be regarded as a **surface polymerization reaction** since monomer units are produced from the reagents hydrogen and carbon monoxide *in situ* on the surface of the catalyst (usually Fe or Co). Hence, various hydrocarbons (mainly *n*-paraffins) are formed by successive addition of C_1 units to growing chains on the catalyst surface. The main reaction of FTS is represented by $\text{CO} + 2\text{H}_2 \rightarrow (\text{---CH}_2\text{---}) + \text{H}_2\text{O}$, where $(\text{---CH}_2\text{---})$ represents a methylene group of a normal paraffin.
- The FTS **product distribution** is determined by the **probability of chain growth**, which is the ratio of the rate of propagation to the overall reaction rate.
- For particles with diameters typically used in technical fixed bed FT reactors ($>1 \text{ mm}$), the effective rate is limited by **pore diffusion**. The main reason for this is the slow effective diffusivity of the dissolved hydrogen and CO in the **liquid filled porous catalyst**.
- Two temperature ranges are applied: High-temperature FTS at about 320°C , which leads mainly to short-chain alkenes and gasoline, and low-temperature FTS at 220°C , which leads mainly to wax and diesel oil. **Upgrading of FT products** includes reforming and isomerization to improve the low octane number and hydrocracking of wax to produce more diesel oil.
- The most difficult problem to solve in the design of FT reactors is the **high exothermicity** combined with a high sensitivity of product selectivity to temperature. Hence, the reactor must have provisions for efficient heat removal. Four **reactor types** are considered today, namely, multi-tubular fixed bed reactors, slurry bubble column reactors, circulating fluidized bed reactors, and bubbling fluid bed reactors.
- For accurate **modeling of a FTS multi-tubular reactor**, the **two-dimensional fixed bed reactor model** should be used, which considers the bed and the fluid as a pseudo-homogeneous medium. Heat transfer within the bed is represented by the radial effective thermal conductivity and the internal wall heat transfer coefficient.
- To estimate the runaway behavior, the **runaway diagram** according to Barkelew is useful, for example, to determine the allowable tube diameter by just two dimensionless numbers, N_c (cooling capacity relative to heat production) and N_{ad} (accounting for the heat generation). This diagram is based on a one-dimensional model, where only axial gradients of concentration and temperature are considered, and the **overall thermal transmittance** (needed to estimate N_c) combines heat conduction in the bed, heat transfer at the wall, through the wall, and to the cooling medium.

6.11.2

Methanol Synthesis

Methanol is one of the most important bulk chemicals. In 2007, the total annual capacity for methanol production was $52.1 \times 10^6 \text{ t}$ (Figure 6.11.26).

About 90% of industrially produced methanol is converted in the chemical industry or used as solvent for synthetic applications. In addition, methanol has gained increasing importance as energy equivalent and fuel in recent decades. In 2012 the estimated annual world supply and demand of methanol is expected to rise to $62.1 \times 10^6 \text{ t}$.

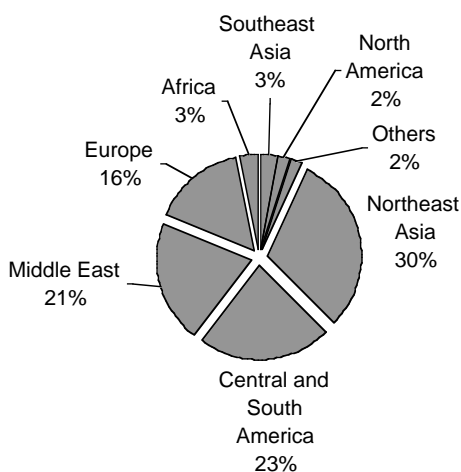
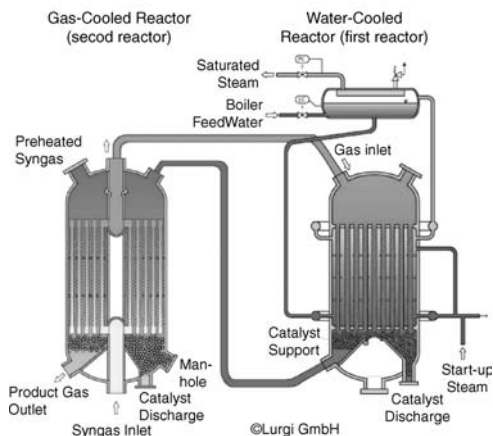


Figure 6.11.26 World capacity for methanol by regions in 2007, with a global annual capacity of $52.1 \times 10^6 \text{ t}$ [data from Saade (2009)].

The Lurgi MegaMethanol® Process



View of a MegaMethanol plant constructed by Lurgi in Trinidad to convert natural gas into methanol. The insert depicts the function of the two reactor units shown in the center of the photograph; note that the boiler is shown in the photograph on the top of the water-cooled reactor (right reactor) from the side (© Lurgi GmbH).

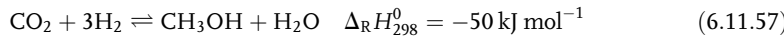
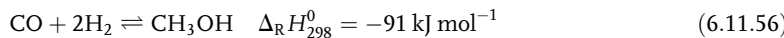
Pure methanol was first isolated by Sir Robert Boyle in 1661. He produced methanol by rectification of crude wood vinegar. Later, in 1834, its elemental composition was determined by the two French chemists *Jean-Baptiste Dumas* and *Eugene Peligot*. They introduced the name “methylene” for the “alcohol made from wood” (combination of the Greek words “methyl” = wine and “hylé” = wood). Around 1840 the term “methyl alcohol” was created and later in 1892 this was shortened to “methanol” by an International Conference on Chemical Nomenclature.

Between 1830 and 1930 “wood alcohol” was synthesized on a large scale by dry distillation of wood. A fundamental and disruptive change in methanol production technologies occurred in 1913, when *Alwin Mittasch* and coworkers at BASF successfully produced methanol from carbon monoxide and hydrogen in the presence of an iron oxide catalyst. They discovered this form of CO hydrogenation during research focused on ammonia synthesis. In the early 1920s, the decisive step towards the large-scale industrial production of methanol was made by *Matthias Pier* (for biographical information see Section 6.11.1.3) who developed a sulfur-resistant zinc oxide–chromium oxide catalyst. In 1923 the first industrial methanol production went on stream at the BASF Leuna site. Methanol synthesis using Zn/Cr-oxide catalysts has been successfully carried out for more than 40 years. But this catalyst system has the clear drawback that very high synthesis gas pressures (250–350 bar) and high temperatures (300–450 °C) have to be applied. Therefore, ICI's development of a highly selective methanol catalyst operating at much milder conditions (50–100 bar, 200–300 °C) in the 1960s was remarkable progress. Nowadays it is possible to produce methanol in low-pressure processes much more economically using state-of-the art catalysts such as Clariant's MegaMax catalyst, which is a Cu-ZnO on aluminum oxide system.

6.11.2.1 Thermodynamics of Methanol Synthesis

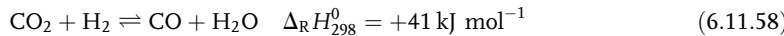
Methanol is synthesized in a catalytic gas-phase reaction from synthesis gas, which is a mixture of hydrogen and carbon monoxide. In addition, some carbon dioxide is

also present in most synthesis gas mixtures. Equations (6.11.54) and (6.11.55) describe the methanol formation reactions from CO and CO₂:



Both reactions are exothermic and exhibit a decrease in volume (reduction in moles as the reaction proceeds to the right). Therefore, methanol formation is favored by increasing pressure and decreasing temperature.

In addition to the two methanol-forming reactions, the reverse endothermic water-gas shift reaction proceeds over the methanol catalyst and must also be taken into consideration:



Formalistically, Eq. (6.11.57) is the sum of Eqs. (6.11.56) and (6.11.58). Thus, combination of these two equations completely describes the system from a thermodynamic point of view, whereas all three equations are generally considered for a kinetic description of methanol synthesis. In the following, we will deal with thermodynamic aspects of methanol synthesis and therefore only the reactions according to Eqs. (6.11.56) and (6.11.58) will be discussed in this context.

Methanol synthesis is an exothermic equilibrium reaction. The maximum conversion of syngas is given by the equilibrium composition. The latter can be calculated by the equilibrium constants of the two above-mentioned reactions:

$$K_{f,1} = \left(\frac{f_{\text{CH}_3\text{OH}} p_0^2}{f_{\text{CO}} f_{\text{H}_2}^2} \right) = \left(\frac{\varphi_{\text{CH}_3\text{OH}}}{\varphi_{\text{CO}} \varphi_{\text{H}_2}^2} \right) \left(\frac{p_{\text{CH}_3\text{OH}} p_0^2}{p_{\text{CO}} p_{\text{H}_2}^2} \right) \quad (6.11.59)$$

$$K_{f,3} = \left(\frac{f_{\text{CO}} f_{\text{H}_2\text{O}}}{f_{\text{CO}_2} f_{\text{H}_2}} \right) = \left(\frac{\varphi_{\text{CO}} \varphi_{\text{H}_2\text{O}}}{\varphi_{\text{CO}_2} \varphi_{\text{H}_2}} \right) \left(\frac{p_{\text{CO}} p_{\text{H}_2\text{O}}}{p_{\text{CO}_2} p_{\text{H}_2}} \right) \quad (6.11.60)$$

where f_i is the fugacity, φ_i is the fugacity coefficient, and p_i is the partial pressure of component i . As shown by Example 6.11.3, real gas behavior has a strong influence on the calculated equilibrium of methanol synthesis and thus needs to be considered.

Fugacity coefficients define the deviation from non-ideal to ideal gas behavior and can be determined from generalized compressibility charts or from suitable equations of state [e.g., Soave–Redlich–Kwong, Eq. (6.11.61); for details see Soave (1972)]:

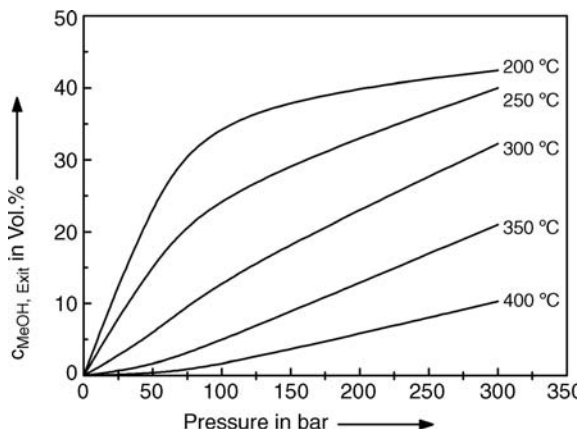
$$\begin{aligned} p &= \frac{RT}{v_m - b} - \frac{a\alpha}{v_m(v_m + b)} \\ a &= \frac{0.42747 R^2 T_{\text{crit}}^2}{p_{\text{crit}}} ; \quad b = \frac{0.08664 RT_{\text{crit}}}{p_{\text{crit}}} \\ \alpha &= [1 + (0.48508 + 1.55171\omega - 0.17613\omega^2)(1 - T_r^{0.5})]^2; \\ T_r &= \frac{T}{T_{\text{crit}}}; \quad \omega = -\log\left(\frac{p_s}{p_{\text{crit}}}\right)_{T_r=0.7} - 1 \end{aligned} \quad (6.11.61)$$

where v_m is the molar volume, T_{crit} is the critical temperature, p_{crit} is the critical pressure, R is the universal gas constant, a is the cohesion pressure, b is the co-volume, and ω is the acentric factor.

The temperature dependent equilibrium constants can be calculated, for example, by the functions derived by Cherednichenko (1953) and Bissett (1977) (with T in K):

$$\begin{aligned} K_{f,1} &= e^{\left(-\frac{\Delta_{\text{R}} G_{\text{R}1}^0}{RT} \right)} = 0.974 \exp\left(21.225 + \frac{9143.6}{T} - 7.492 \ln T + 4.076 \right. \\ &\quad \times 10^{-3} T - 7.161 \times 10^{-8} T^2 \left. \right) \end{aligned} \quad (6.11.62)$$

Figure 6.11.27 Thermodynamic equilibrium methanol concentration (feed: 15 mol.% CO, 8 mol.% CO₂, 74 mol.% H₂, and 3 mol.% CH₄) at different reaction temperatures (Chang, 1986).



$$K_{f,3} = e^{\left(-\frac{\Delta_R G_{R2}^0}{RT}\right)} = \exp\left(13.148 - \frac{5639.5}{T} - 1.077 \ln T - 5.44 \times 10^{-4} T + 1.125 \times 10^{-7} T^2 + \frac{49170}{T^2}\right) \quad (6.11.63)$$

With the calculated equilibrium constants $K_{f,1}$ and $K_{f,3}$ and the fugacity coefficients the maximum thermodynamic equilibrium concentration of methanol can be calculated by solving Eq. (6.11.60) for p_{CO} , and entering the solution into Eq. (6.11.61). This leads to:

$$p_{CH_3OH} = K_{f,1} \left(\frac{\varphi_{CO} \varphi_{H_2}^2}{\varphi_{CH_3OH}} \right) p_{H_2}^2 K_{f,3} \left(\frac{\varphi_{CO_2} \varphi_{H_2}}{\varphi_{CO} \varphi_{H_2O}} \right) \left(\frac{p_{CO_2} p_{H_2}}{p_{H_2O}} \right) \quad (6.11.64)$$

Figure 6.11.27 shows the equilibrium methanol content for a typical feed with 15 mol.% CO, 8 mol.% CO₂, 74 mol.% H₂, and 3 mol.% CH₄ at different temperatures in the pressure range 0–300 bar calculated with Eqs. (6.11.62)–(6.11.64) (Chang *et al.*, 1986).

To achieve high syngas conversion it is necessary, in terms of thermodynamics, to operate the process at high pressure and low temperature. Therefore, the chemical industry demands catalysts that work efficiently under these specific reaction conditions.

Example 6.11.3: Influence of real gas behavior on the calculated equilibrium of methanol synthesis.

The equilibrium constant of the main reaction of methanol synthesis is given by Eq. (6.11.59), and rearrangement (with x as molar content and p as total pressure) leads to:

$$K_{f,1} = \left(\frac{\varphi_{CH_3OH}}{\varphi_{CO} \varphi_{H_2}^2} \right) \left(\frac{p_{CH_3OH} p_0^2}{p_{CO} p_{H_2}^2} \right) = \left(\frac{\varphi_{CH_3OH}}{\varphi_{CO} \varphi_{H_2}^2} \right) \left(\frac{x_{CH_3OH}}{x_{CO} x_{H_2}^2} \right) \left(\frac{p_0^2}{p^2} \right) \\ = K_\varphi K_x \left(\frac{p_0}{p} \right)^2$$

The equilibrium constant $K_{f,1}$ only depends on temperature [Eq. (6.11.62), for example, for 300 °C we have a value of 2.32×10^{-4}]. The higher the value of K_x , the higher the equilibrium content of methanol and thus the conversion of the syngas:

$$K_x = \frac{K_{f,1}}{K_\varphi} \left(\frac{p}{p_0} \right)^2$$

The parameters describing the equilibrium are given in Table 6.11.4 as a function of the total pressure p . The value of K_φ strongly decreases and

deviates from unity (i.e., from ideal gas behavior). Thus, in case of methanol synthesis, real gas behavior obviously has to be considered. This can be shown for the example of a total pressure of 300 bar. The CO conversion (for a molar ratio of H₂ to CO of 2) can be calculated by the following equations:

$$x_{CO} + x_{H_2} + x_{methanol} = 3x_{CO} + x_{methanol} = 1$$

$$K_x = \frac{x_{methanol}}{x_{CO} x_{H_2}^2} = \frac{x_{methanol}}{x_{H_2}^3}$$

$$x_{CO} = 1 - \frac{x_{CO}}{(x_{CO} + K_x x_{methanol})}$$

For an ideal gas, $K_\varphi = 1$, and thus $K_x = K_1(p/p_0)^2$. For 300 °C and a total pressure of 300 bar, this would lead to a value of K_x of 0.0696, and the equilibrium conversion of CO and H₂ would then be 54% compared to the real value of about 83% (Table 6.11.4). This again underlines that in case of methanol synthesis we have to consider real gas behavior.

Table 6.11.4 Influence of pressure p on equilibrium of methanol synthesis [Eq. (6.11.59)] ($H_2/CO = 2 \text{ mol mol}^{-1}$, 300°C , $K_{f,1} = 2.3 \times 10^{-4}$). Data from Winnacker and Kuechler (1971); value of $K_{f,1}$ deviates slightly from that calculated by Eq. (6.11.62), which is 3×10^{-4} .

Pressure p (bar)	K_φ	K_x	p_{CO} (bar)	p_{H_2} (bar)	$p_{methanol}$ (bar)	Equilibrium conversion of syngas (CO or H ₂) (%)
10	0.96	0.024	3.32	6.65	0.036	1
51	0.80	0.725	15.3	30.6	4.1	21
101	0.61	3.8	25.2	50.5	34.3	58
203	0.38	24.4	34.2	68.4	97.4	74
304	0.27	77.4	37.7	75.4	186.9	83

6.11.2.2 Catalysts for Methanol Synthesis

The first catalyst for the industrial production of methanol from synthesis gas (Leuna, BASF, 1923) consisted of zinc oxide and chromium oxide (Zn : Cr ratio = 70 : 30). This catalyst worked efficiently for activity and selectivity at 250–350 bar and 300–450 °C and was highly resistant to catalyst poisons, for example, sulfur and chlorine compounds, present in the syngas feed. The catalyst was stable up to the limit of 30 ppm hydrogen sulfide. The oxides, added to the catalytic active ZnO, served as activators or promoters and as recrystallization inhibitors. These additives extended the catalyst lifetime and stability, but reduced the selectivity and increased by-product formation. The use of the zinc oxide-chromium oxide catalyst for the commercial synthesis of methanol in high-pressure processes is no longer economical, because of the high investment costs for high-pressure plants. The last high-pressure plant for methanol production was closed in the 1980s.

It was long known in research that catalysts containing copper were more active and selective in methanol production than ZnO/Cr-oxide catalysts. For this reason a more economical methanol production at lower pressures and temperatures was possible with copper-containing catalyst. However, their industrial use was not possible for a long time because of the high sensitivity and rapid deactivation by impurities in the syngas such as, for example, hydrogen sulfide or chlorine. As the quality of the synthesis gas increased over time by more efficient desulfurization units and by the change from coal to naptha as feedstock for syngas production, a reasonably sulfur tolerant catalytic mixture of CuO, ZnO, and Al₂O₃ was developed (H₂S < 0.1 ppm) and this copper catalysts found its way into industrial methanol production. The first industrial use of a copper catalyst for methanol synthesis in a low-pressure process came in 1966 at the company ICI. Because of the high activity of the catalyst the methanol synthesis could be carried out at much milder conditions (220–250 °C and 50–100 bar) than with the former ZnO/Cr-oxide systems. The second advantage of the new catalyst was the high selectivity (methanol purity >99.5%) and as a result the reduction of by-product formation (typical by-products of MeOH plants are methane, ethanol, hydrocarbons, waxes, and dimethyl ether; see also Example 6.11.4).

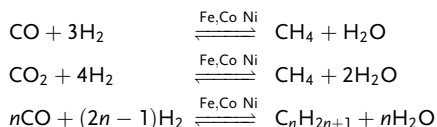
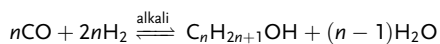
The new copper catalysts were also characterized by high space-time yields and long stabilities. For example, the fresh BASF catalyst S-3-85 shows a space-time yield of 1500 kg_{methanol} m_{catalyst}⁻³ h⁻¹ and after 4000 h on-stream this value is only reduced to 1250 kg_{methanol} m_{catalyst}⁻³ h⁻¹. The ratio of copper, zinc, and alumina varies from one manufacturer to the other. As a rule, the proportion of CuO is in the range 40–80%, ZnO 10–30%, and Al₂O₃ 5–10%. Methanol catalysts are manufactured by *Synetix* (ICI Katalco), *Clariant*, *BASF*, *Haldor Topsøe*, and *Mitsubishi Gas Chemical*.

These copper-based catalysts are synthesized by co-precipitation of metal salt solution (e.g., copper and zinc nitrates) with alkali carbonate solution. The precipitant can be sodium aluminate, if the final catalyst should contain Al₂O₃. During co-precipitation the catalyst precursor is formed. The catalyst precursor consists of

various crystal structures like hydrozincite $(\text{Zn})_5(\text{CO}_3)_2(\text{OH})_6$, aurichalcite $(\text{Cu}_x\text{Zn}_{1-x})_5(\text{CO}_3)_2(\text{OH})_6$, malachite $\text{Cu}_2\text{CO}_3(\text{OH})_2$, rosasite $(\text{Cu}_x,\text{Zn}_{1-x})_2(\text{CO}_3)_2(\text{OH})_2$, or their mixtures. The crystal structure of the precursor is very important for the final catalyst, because methanol catalysts are structurally very sensitive (e.g., catalysts based on the aurichalcite precursor are more active to CO hydrogenation). Thus, small differences in the preparation method or in the pretreatment can affect the structure of the catalyst and hence the catalytic performance quite significantly. For example, the structure of the precursor varies with different Cu : Zn ratios (a ratio of 3 : 7 results in aurichalcite structures, higher ratios result in mixtures). During co-precipitation the pH plays also an important role. At pH 7 the precipitate consists mainly of the malachite structure and the resulting catalyst is more active. In addition, the temperature plays a key factor during preparation (T should be less than 313 K). In addition, solvent effects during co-precipitation have been observed. Ethanol as solvent was found to be the most effective route for preparation of very active and selective catalysts. After co-precipitation the precursor is filtered off, washed until free of ions, and dried. In the subsequent calcination step the precursor is transformed into metal oxides. Lower heating rates in calcination favor the formation of fine catalytic particles. After preparation of catalyst pellets, the catalyst is activated by reduction with hydrogen at around 200 °C. The reduction is needed to achieve an optimal catalytic performance but, unfortunately, the exothermic reaction can lead to agglomeration of surface active sites. Thus, lower reduction temperatures and methanol as reducing agent have been shown to be beneficial for the activity of the final methanol catalyst.

Example 6.11.4: By-product reactions in the methanol production by use of a copper–zinc–alumina catalyst:

- 1) Formation of higher alcohols (in particular ethanol) catalyzed by traces of alkaline impurities in Cu catalyst (Liu *et al.*, 2003; Twigg and Spencer 2001):



- 2) Formation of methane and longer chain alkanes catalyzed by traces of iron, cobalt, and nickel or by acidic impurities (see Fischer–Tropsch process, Section 6.11.1) (Liu, 2003; Twigg, 2001):

- 3) Formation of dimethyl ether by catalyst acidity (Spencer, 1999):



Since its discovery, the mechanism of catalytic methanol formation and the exact nature of the active catalytic sites have been important research topics and many questions are still open. Many studies have been directed to elucidating the carbon source in methanol formation catalyzed by copper–zinc–aluminum systems. At the end of the 1970s Rozovskii *et al.* concluded from kinetic investigations and experiments with isotope-marked carbon oxides that methanol is formed exclusively from CO_2 (Rozovskii *et al.*, 1975, 1977). In contrast to this theory the group of Klier assumed from extensive experiments with different synthesis gas mixtures that methanol derives mainly from CO (Klier, 1982, 1984). They found that the fastest methanol formation was observed with a syngas mixtures of $\text{CO}_2 : \text{CO} : \text{H}_2 = 2 : 28 : 70$ and that high CO_2 concentrations block the adsorption of CO at the active sites. This theory was accepted in Europe and America for a long time. However, Kung and Chinchen *et al.*, both using isotope-labeled carbon dioxide ($^{14}\text{CO}_2$ or C^{18}O) in their studies, observed the main formation of methanol from CO_2 (Kung, 1980, 1984). Other groups [Liu *et al.* 1984, 2003, Denise and Sneeden (1982), and Klier *et al.* (1982)] assumed the simultaneous formation of methanol from CO and CO_2 . Nowadays, most scientists assume that both CO and CO_2 can be

Table 6.11.5 Reaction steps of methanol synthesis (RDS: rate-determining step).

Reaction step	Elementary steps
Adsorption	$\text{CO} + \Theta_1 \leftrightarrow \text{CO}-\Theta_1$ $\text{CO}_2 + \Theta_3 \leftrightarrow \text{CO}_2-\Theta_3$ $\text{H}_2 + 2\Theta_2 \leftrightarrow 2\text{H}-\Theta_2$ $\text{H}_2\text{O} + \Theta_2 \leftrightarrow \text{H}_2\text{O}-\Theta_2$
Surface reactions	
CO hydrogenation [Eq. (6.11.56)]	$\text{CO}-\Theta_1 + \text{H}-\Theta_2 \leftrightarrow \text{HCO}-\Theta_1 + \Theta_2$ $\text{HCO}-\Theta_1 + \text{H}-\Theta_2 \leftrightarrow \text{H}_2\text{CO}-\Theta_1 + \Theta_2$ $\text{H}_2\text{CO}-\Theta_1 + \text{H}-\Theta_2 \leftrightarrow \text{H}_3\text{CO}-\Theta_1 + \Theta_2$ $\text{H}_3\text{CO}-\Theta_1 + \text{H}-\Theta_2 \leftrightarrow \text{CH}_3\text{OH} + \Theta_1 + \Theta_2$ (RDS)
Water-gas shift reaction [Eq. (6.11.58)]	$\text{CO}_2-\Theta_3 + \text{H}-\Theta_2 \leftrightarrow \text{HCO}_2-\Theta_3 + \Theta_2$ (RDS) $\text{HCO}_2-\Theta_3 + \text{H}-\Theta_2 \leftrightarrow \text{CO}-\Theta_3 + \text{H}_2\text{O}-\Theta_2$ $\text{CO}_2-\Theta_3 + \text{H}-\Theta_2 \leftrightarrow \text{HCO}_2-\Theta_3 + \Theta_2$ $\text{HCO}_2-\Theta_3 + \text{H}-\Theta_2 \leftrightarrow \text{H}_2\text{CO}_2-\Theta_3 + \Theta_2$ (RDS) $\text{H}_2\text{CO}_2-\Theta_3 + \text{H}-\Theta_2 \leftrightarrow \text{H}_3\text{CO}_2-\Theta_3 + \Theta_2$ $\text{H}_3\text{CO}_2-\Theta_3 + \text{H}-\Theta_2 \leftrightarrow \text{H}_2\text{CO}-\Theta_3 + \text{H}_2\text{O}-\Theta_2$ $\text{H}_2\text{CO}-\Theta_3 + \text{H}-\Theta_2 \leftrightarrow \text{H}_3\text{CO}-\Theta_3 + \Theta_2$ $\text{H}_3\text{CO}-\Theta_3 + \text{H}-\Theta_2 \leftrightarrow \text{CH}_3\text{OH} + \Theta_3 + \Theta_2$
CO ₂ hydrogenation [Eq. (6.11.57)]	

hydrogenated to methanol and that the predominant methanol formation pathway depends on the operating conditions.

Another interesting topic in heterogeneous catalysis is the nature of the active sites of a catalyst. On the basis of studies from Klier and Sheffer the active species of a copper–zinc–alumina catalyst in the low-pressure methanol synthesis are active Cu⁺ ions embedded in a ZnO matrix (Klier, 1982; Sheffer, King, and King, 1989a, 1989b). In contrast, Waugh postulated Cu⁰ as active center of the catalyst (Waugh, 1992). Herman *et al.* proposed a bifunctional mechanism whereby the Cu⁺ sites chemisorb and activate the CO and, meanwhile, H₂ is activated on the ZnO surface (Herman *et al.*, 1979). After research on methanol synthesis for many years it seems that various routes for its formation exist and that different catalytic sites are involved. Example 6.11.5 shows the elementary reactions steps for the methanol synthesis developed by Lim *et al.* (2009).

Example 6.11.5: Kinetic mechanism of the methanol synthesis reaction catalyzed with Cu/ZnO/Al₂O₃/ZrO₂ (developed by Lim *et al.*, 2009)

The reaction mechanism of heterogeneous catalyzed methanol formation is assumed to follow the Langmuir–Hinshelwood model (Section 4.5.2.2). There are two different active sites on the copper surfaces for the adsorption of CO and CO₂. The symbol Θ₁ represents Cu⁺ (adsorption of CO) and Cu⁰ is labeled with the symbol Θ₃ (CO₂ adsorption). The adsorption of hydrogen and water occurs on Zn sites Θ₂ (Table 6.11.5). Since H₂ adsorbs very rapidly, it is assumed that the concentration of ZnO sites and adsorbed hydrogen remains constant during synthesis. For the CO hydrogenation reaction the most strongly supported mechanism consists of successive addition of adsorbed hydrogen atoms to an adsorbed CO molecule. Methanol synthesis from CO₂ occurs via formate species adsorbed on copper. The nature of active sites and the elementary steps are based on experimental observation in the literature (Herman *et al.*, 1979; McNeil, Schack, and Rinker, 1989; Chinchen *et al.*, 1987a, 1987b; Tagawa, Plerzier, and Amenomiya,

1985; Bowker *et al.*, 1988; Dennison, Packer, and Spencer, 1989, and Kung 1980).

By comparing experimental and estimated parameters three elementary reactions have been identified to be the rate-determining steps (RDSs) for methanol synthesis. For the three RDS the rate equations [according to the general Langmuir–Hinshelwood–Hougen–Watson rate equation, Eq. (4.5.8)] have been derived:

$$\text{rds CO hydrogenation} \Rightarrow r_{A1} = \frac{k_{s1} K_{\text{CO}} K_{\text{H}_2}^2 K_{\text{CH}_3\text{CO}} (p_{\text{CO}} p_{\text{H}_2}^2 - p_{\text{CH}_3\text{OH}} / K_{P1})}{(1 + K_{\text{CO}} p_{\text{CO}})(1 + K_{\text{H}_2}^{0.5} p_{\text{H}_2}^{0.5} + K_{\text{H}_2\text{O}} p_{\text{H}_2\text{O}})}$$

$$\text{rds water-gas shift} \Rightarrow r_{A2} = \frac{k_{s2} K_{\text{CO}_2} K_{\text{H}_2}^{0.5} (p_{\text{CO}} p_{\text{H}_2} - p_{\text{CO}} p_{\text{H}_2\text{O}} / K_{P2}) / p_{\text{H}_2}^{0.5}}{(1 + K_{\text{CO}} p_{\text{CO}})(1 + K_{\text{H}_2}^{0.5} p_{\text{H}_2}^{0.5} + K_{\text{H}_2\text{O}} p_{\text{H}_2\text{O}})(1 + K_{\text{CO}_2} p_{\text{CO}_2})}$$

$$\text{rds CO}_2 \text{ hydrogenation} \Rightarrow r_{A3} = \frac{k_{s3} K_{\text{CO}_2} K_{\text{H}_2} K_{\text{CH}_3\text{CO}} (p_{\text{CO}} p_{\text{H}_2}^3 - p_{\text{CH}_3\text{OH}} p_{\text{H}_2\text{O}} / K_{P3}) / p_{\text{H}_2}^2}{(1 + K_{\text{H}_2}^{0.5} p_{\text{H}_2}^{0.5} + K_{\text{H}_2\text{O}} p_{\text{H}_2\text{O}})(1 + K_{\text{CO}_2} p_{\text{CO}_2})}$$

The cost-effectiveness of an industrial catalytic process is strongly influenced by the stability, long-term activity, and life time of the catalyst. The two main causes of life-time reduction of a Cu/Zn-methanol catalyst are catalyst poisoning and thermal deactivation.

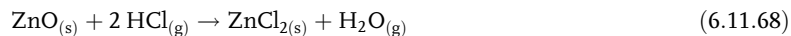
Copper catalysts are very sensitive to poisonous compounds, especially when they are used in low-temperature processes, because adsorption of poison is thermodynamically favored. The significant poisons for copper catalysts in methanol production are sulfur and chlorine. Sulfur compounds – for example, H₂S – form copper sulfides:



The structural promoter zinc oxide, which in most cases is added to commercial catalysts for methanol synthesis, is very effective in reducing the sulfur poisoning by the removal of H₂S from gas stream and the formation of zinc sulfide. The additive ZnO offers therefore a certain degree of protection against poisoning with sulfur compounds:



The chloride poisoning of copper catalyst results in blocked or modified catalytic sites. Additionally, the formed Cu(I) chloride has a very low melting point and high surface mobility and, consequently, accelerates the sintering of Cu catalysts:



In contrast to sulfur poisoning, ZnO gives no protection against chloride compounds. Zinc oxide reacts to form Zn chloride, which also has a low melting point and cause further poisoning and sintering problems. Chloride compounds in the feedstock can be reduced by guard beds of either alkalinized alumina or extra, sacrificial catalyst. Today catalyst deactivation caused by poison (sulfur and chlorine) is rarely a problem in methanol synthesis, because poisonous compounds are effectively removed in the feedstock pretreatments.

A more serious problem in catalyst deactivation in commercial methanol production is the thermal stability of copper catalysts. Copper-based catalysts are more susceptible to thermal sintering and agglomeration than other commonly used metallic catalyst such as nickel, iron, and palladium, because of the low thermal stability of Cu (Hüttig temperature Cu: 1063 °C and Fe: 1535 °C). Therefore, commercial copper-based catalysts should be operated at low temperatures (not higher than 300 °C). To improve the life-time of copper catalysts, it is essential to add suitable promoters. All modern copper-based catalysts contain therefore one or several oxides (e.g., Cr₂O₃ or Al₂O₃) to minimize thermal sintering and to improve their mechanical stability and catalyst life-time. Alumina particles, forming spinel structures with zinc, prevent the sintering of the fine copper particles and stabilize highly disperse copper-zinc oxide. Thermal damage can occur during catalyst preparation (e.g., reduction process) or during operating (e.g., non-optimal gas composition, incorrect temperature control, and insufficient heat removal and hence formation of hot spots). Therefore, it is very important to design methanol synthesis reactors with efficient cooling to prevent local overheating.

6.11.2.3 Processes and Synthesis Reactors

Processes for catalytic conversion of syngas into methanol can be divided into three classes according to reaction pressure, temperature, and catalyst composition. Today, high-pressure processes (250–350 bar, 300–450 °C, Cr/Zn) are no longer economic. Medium-pressure (100–250 bar, 220–300 °C, Cu/Zn) and low-pressure (50–100 bar, 200–300 °C, Cu/Zn) processes are operated, with the latter being much more attractive owing lower investment and operating cost.

An essential issue for methanol plants is removal of the reaction heat ($8 \cdot 10^6 \text{ kJ m}^{-3}_{\text{catalyst}} \text{ h}^{-1}$), resulting from the two exothermic hydrogenation steps, and prevention of local overheating and thus catalyst deactivation. Therefore, the most important section of the methanol synthesis process – the reactor – is designed primarily for high cooling duty and optimal temperature control. Another important issue is to limit the pressure drop and thus save energy. Reactor technologies that are used in commercial plants can be divided into two categories: (i) adiabatic reactors with multiple catalyst beds and (ii) quasi-isothermal converters with a single catalyst bed. Multiple catalyst bed reactors control the reaction temperature by separating the catalyst into several sections and by applying efficient cooling between the sections. The catalyst beds are designed to reach the equilibrium conversion of syngas. Heat removal is realized by either direct heat exchange or by injection of cool synthesis gas.

In an isothermal single bed reactor the developed heat is removed from the reactor by transfer to a heat removing medium (e.g., water).

The following subsection briefly describes current industrial processes for methanol production with adiabatic multi-bed and isothermal single-bed reactor design. We will refer to the ICI (adiabatic multiple-bed reactor) and to the Lurgi process (isothermal single-bed reactor), which are important representatives of the different ways of producing methanol commercially nowadays.

The ICI low-pressure process (50–100 bar, 230–265 °C) operates with a shot-cooled single- or multi-bed converter filled with a highly selective copper/zinc alumina catalyst. The reaction is quenched by the injection of cold syngas onto the bed or between the beds. In reactors, where heat removal results from quenching with cold syngas, the temperature profile along the axis of the reactor has a saw-tooth shape (Figure 6.11.28).

Only around 50% of the syngas is converted in one pass (owing to the thermodynamic equilibrium) and therefore the unreacted syngas has to be recycled back to the reactor after its separation from methanol and water in the separator. Parts of the recycle gas flow are released (purge gas flow) to reduce the ratio of inert gas (e.g., methane). The purge gas can be used for heating or it is separated at a later stage of the process. The heat exchanger transfers energy from the hot reactor outlet gas to the cold reactor inlet gas. A single reactor in the ICI process can produce around 2600 tonnes of methanol per day.

Other examples of methanol production processes using adiabatic multiple-bed reactor concepts are the Haldor Topsoe process and the Kellogg process.

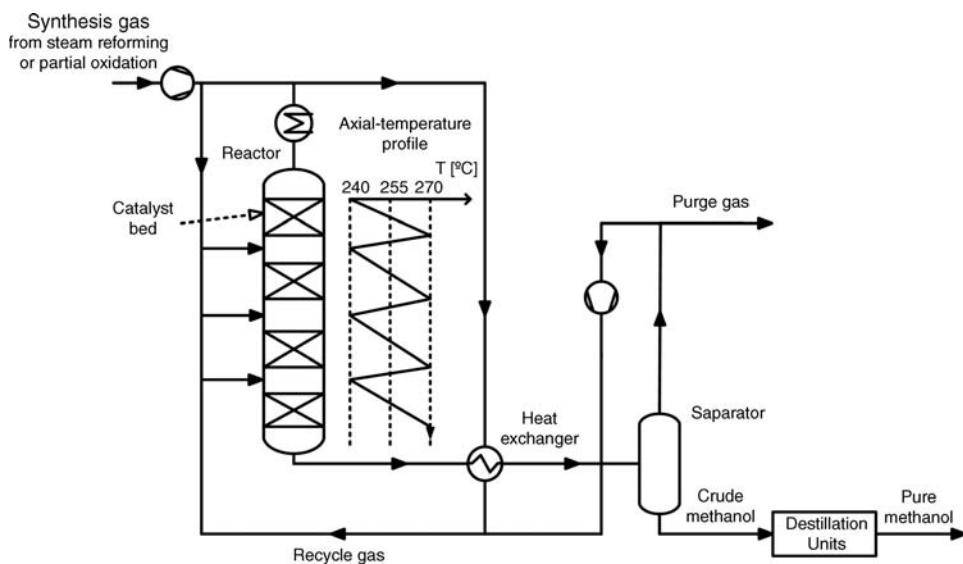


Figure 6.11.28 Flow sheet of methanol synthesis in an adiabatic quench reactor with multiple catalyst beds.
Figure adapted from (Baerns *et al.* 2006).

The Lurgi process is a famous example of a process operating with an isothermal single-bed reactor (50–100 bar, 230–265 °C, copper catalyst). The catalyst is contained in fixed tubes and the tubes are cooled by a continuous boiling water flow. The temperature of the water is controlled by a steam pressure control valve that is adjusted to the pressure corresponding to the set-point temperature in the reactor. The reactor can achieve high syngas conversions and, therefore, the recycle ratio is low.

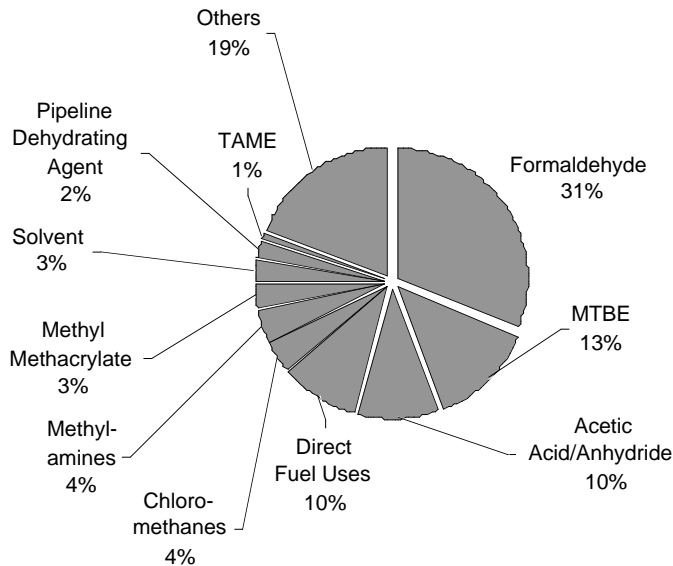
Lurgi has also developed a two-stage converter (see start of this section, Section 6.11.2) for high methanol production capacities. The first reactor (right-hand reactor in the picture) can be operated at higher space velocities and temperatures, because only partial conversion of syngas is needed. Therefore, the first reactor is small and high-pressure steam can be produced (saving energy costs). The first reactor is cooled with water/steam and shows an isothermal profile. In the second reaction stage the temperature is reduced to obtain higher equilibrium conversions (left-hand reactor in the picture). The second reactor is cooled by the feed gas before entering the first converter. The advantages of this process are the high conversion rates at low recycling ratios, superb energy efficiency, and low sensitiveness against catalyst aging (the second reaction stages can compensate for the conversion loss). This technology offers plant capacities up to 5000 t methanol per day.

In recent years the focus on methanol production has been on raising production capacities by the design and construction of “mega-methanol” plants (capacities of $1\text{--}5 \times 10^6 \text{ t a}^{-1}$). These “mega methanol” plants are frequently located at or near large supplies of stranded gas (e.g., Middle East, Trinidad and Tobago). The plants are able to produce methanol at such low cost that alkenes produced from this methanol in so-called methanol-to-olefin (MTO) plants is competitive against naphtha derived olefins produced in conventional steam crackers. In these cases, the disadvantage of not being located close to the market is compensated by extremely cheap natural gas. Furthermore, liquid methanol can be stored and transported in pipelines or tankers much easier than the “stranded gas” itself. Additionally, these mega plants have the competitive advantage of “economy of scale,” that is, they benefit from the fact that the investment cost for the plant per ton of methanol produced is significantly lower compared to smaller plants.

In recent years alternative methanol synthesis technologies have been tested in research and development, for example, methanol synthesis in liquid-phase reactions or the direct oxidation of methane to methanol.

Today most of the methanol produced worldwide is used in chemical synthesis. The most important product based on methanol is formaldehyde (31% of methanol produced in 2007). In addition methyl *tert*-butyl ether (MTBE) and acetic acid (Section 6.15) are important outlets for methanol production (Figure 6.11.29).

Figure 6.11.29 World demand for methanol by end use in 2007 [data from Saade (2009)]; TAME = *tert*-amyl methyl ether, MTBE = methyl *tert*-butyl ether.



Some 10% of the world's demand for methanol is used as fuel for direct combustion. Since the first oil crisis in the 1970s methanol has been claimed as a potential substitute for fuel. Although this promise has not turned to reality yet, methanol has been studied intensively as energy carrier for on-board hydrogen production in mobile applications using fuel cell powered electrical vehicles.

Summary of Section 6.11.2 (take-home messages)

- **Methanol** is one of the most important bulk chemicals with an annual production capacity of about 50 million tonnes. About 90% is further converted in the chemical industry or used as solvent. Methanol has also gained increasing importance as fuel.
- Methanol is synthesized in a catalytic gas-phase reaction from syngas. Thermodynamically, the exothermic formation of methanol favors high pressures and low temperatures. To calculate the equilibrium conversion of syngas, **real gas behavior** has to be considered by **fugacity coefficients**.
- The first **catalyst** for industrial methanol production (1923) consisted of zinc oxide and chromium oxide. This catalyst worked efficiently concerning activity at around 350 °C. Today, methanol production at lower pressures and temperatures (about 250 °C) is possible with copper-containing catalysts (mixture of CuO, ZnO, and Al₂O₃). Their industrial use was not possible for a long time because of the rapid deactivation by syngas impurities such as H₂S. As the quality of the syngas increased over time by more efficient desulfurization and by the change from coal to natural gas as feedstock for syngas, copper catalysts found their way into industrial methanol production.
- An essential issue is the removal of reaction heat. The reactor is therefore designed primarily for high cooling duty and optimal temperature control, which can be achieved by two types of reactors: The **multiple catalyst bed reactor** controls the temperature by separating the catalyst into several adiabatic sections with efficient cooling between the sections, for example, by injection of cold syngas. In the almost isothermal **multi-tubular reactor**, heat is removed by transfer to a cooling heat medium (boiling water).

6.12

Ethylene and Propylene Oxide

6.12.1

Commercial Production of Ethylene Oxide

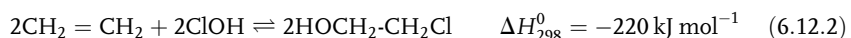
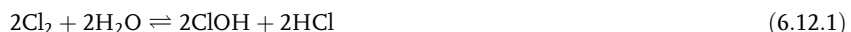
Ethylene oxide (EO) – also termed oxirane – is the simplest cyclic ether and ranks together with acetaldehyde among the most important partial oxidation products of ethylene. EO is a very reactive chemical compound (the strained ring can be easily opened). Its high reactivity provides it with an important role as raw material for the production of a wide range of intermediates and consumer products. For the same reason, EO is also a hazardous material, being toxic (irritant to humans and a suspected carcinogen) and highly flammable (extreme risk of fire and explosions). The flash point is less than –18 °C and the vapor has a low ignition energy in air ($E_{\text{ignition}} = 0.06 \text{ mJ}$, explosion limits from 2.6 to 100%). EO is heavier than air and can diffuse over a long distance to a possible ignition source. It can decompose explosively in the presence of certain metals, acids/bases, and many other chemicals (e.g., water, alcohols, amines and even rust), and careful operation of all plants producing or using EO is essential to avoid serious accidents.

EO was first mentioned in 1859 by the French chemist *Charles Adolphe Wurtz* (1817–1884), who prepared EO by the reaction of ethylene chlorohydrin with a potassium hydroxide solution. After its discovery, EO became increasingly attractive to the chemical industry (during the First World War as precursor for the coolant

ethylene glycol and the chemical weapon mustard gas). The first industrial production started in 1914. EO can be manufactured by two different routes, the chlorohydrin process or the direct oxidation of ethylene.

6.12.1.1 Chlorohydrin Process

The first industrial process for the production of ethylene oxide was based on the chlorohydrin reaction (indirect oxidation of ethylene), discovered by *Wurtz*. In the chlorohydrin process ethylene reacts with hypochlorous acid (chlorine dissolved in water) to give ethylene chlorohydrin [Eqs. (6.12.1) and (6.12.2)]. In the second step ethylene chlorohydrin is converted with hydrated lime or caustic soda to form the final product ethylene oxide [Eq. (6.12.3)]:



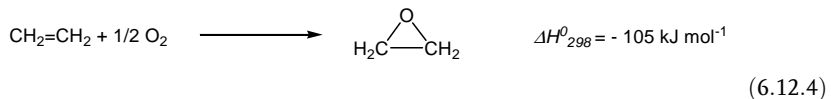
Unfortunately, useless inorganic salts (calcium chloride) as coupling product and unwanted chlorinated organic by-products are also generated. Although the process provides good yields of EO (80%), the overall process economics are not favorable. The process wastes chlorine and produces a high amount of calcium chloride combined with disposal problems and wastewater contamination and pollution. Note that the production of 100 kg EO using the chlorohydrin process creates 300–350 kg CaCl₂, 10–15 kg dichloroethane, and 7–9 kg dichlorodiethyl ether. Not surprisingly, the traditional chlorohydrin route was largely replaced for EO production by the direct oxidation of ethylene. Chlorohydrin plants have been reconstructed though for the production of propylene oxide.

6.12.1.2 Direct Oxidation of Ethylene

In 1931 the basis for another, more economical ethylene oxide manufacturing process was laid by the French chemist *Lefort*. He discovered the formation of ethylene oxide from ethylene and oxygen over a metallic silver catalyst. Only six years later, in 1937, the first process based on this reaction was commercialized by UCC (Union Carbide Corporation).

The main reaction involved in this process is the partial oxidation of ethylene [Eq. (6.12.4)]. Two side reactions, which form the major by-products carbon dioxide and water, can occur: the total oxidation of ethylene [Eq. (6.12.5)] or the consecutive oxidation of ethylene oxide to the same products [Eq. (6.12.6)].

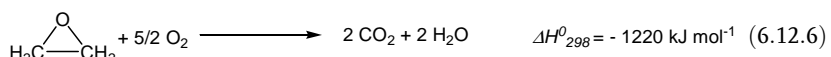
1) Partial oxidation:



2) Total oxidation:



3) Consecutive oxidation:



All three reactions are highly exothermic (especially the two side reactions) and the activation energies of the undesired side reactions are higher than that of the desired main reaction. This effect causes a high temperature sensitivity of the ethylene oxide selectivity (even at small temperature changes). Therefore precise temperature control of the reactor is necessary.

In the literature numerous studies exist on the kinetics and reaction network of the direct ethylene oxidation to ethylene oxide catalyzed by silver (see Example 6.12.1). The surface reaction is considered to proceed via the Langmuir–Hinshelwood mechanism (adsorption of ethylene and oxygen → surface reaction → desorption of ethylene oxide, see Section 4.5.2). The rate expression for the selective oxidation can be expressed in the following equation:

$$r_{\text{ethylene oxide}} = \frac{k K_{\text{oxygen}} p_{\text{oxygen}} K_{\text{ethylene}} p_{\text{ethylene}}}{(1 + K_{\text{oxygen}} p_{\text{oxygen}} + K_{\text{ethylene}} p_{\text{ethylene}})^2} \quad (6.12.7)$$

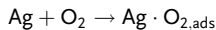
The surface reaction of ethylene and oxygen is thought to be the rate-determining step (only if the reaction takes place in the kinetic regime). The consecutive oxidation of ethylene oxide only becomes insignificant if reaction temperatures do not exceed a critical value and the reaction takes place in the kinetic regime. To avoid mass transport limitation, catalysts with high pore diameters are used in the direct oxidation.

All processes based on the direct oxidation of ethylene use a supported silver catalyst, as silver is known to be the only metal that catalyzes ethylene oxidation in a selective manner. The selectivity and activity of the supported silver catalyst is influenced by many parameters, for example, impregnation methods, promoters, supporting materials, and support characteristics. Generally, the silver concentration on a porous support is between 7 and 20 wt% and aluminum oxides/silicates are preferred supporting materials. The porous supports have defined pore structures (0.5–50 μm) and a relatively low surface area to avoid mass transport limitations. Some functional surface groups, for example, hydroxyl groups, catalyze the isomerization of ethylene oxide to acetaldehyde. Therefore, silane treatment of the supporting materials can significantly improve catalytic performance. The addition of promoters (salts/compounds containing alkali metals) increases the selectivity, for example, a chlorine layer at the silver surface suppresses the total oxidation to CO₂ and H₂O (promoters: ethyl chloride and vinyl chloride).

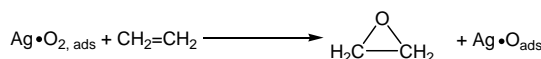
Example 6.12.1: Reaction mechanism of silver-catalyzed direct oxidation of ethylene (Rebsdat and Mayer, 2001 and Arpe, 2007).

Silver can adsorb oxygen in different forms, for example, as atomic, molecular, and subsurface oxygen. Different theories exist about the reactivity of adsorbed oxygen in the silver-catalyzed oxidation of ethylene. In one theory, only molecular oxygen reacts with ethylene, in another theory only atomic oxygen is converted with ethylene. In this example, the reaction via molecular oxygen is presented in detail.

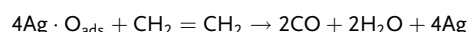
The first step is the adsorption of molecular oxygen at the silver surface:



Subsequently, ethylene is adsorbed and reacts with molecular oxygen to give ethylene oxide:



Ethylene is not adsorbed on oxygen-free silver surfaces – a pre-adsorption of oxygen is necessary. In this theory, atomic oxygen is responsible for the undesired side reaction in converting ethylene into carbon monoxide/water and carbon monoxide to carbon dioxide:



Inhibitors (e.g., chlorine) can block the adsorption of atomic oxygen and reduce the total oxidation of ethylene.

Since the original discovery by Lefort, selectivity in the direct oxidation of ethylene has improved from 50 to 90% for modern silver catalyst systems. However, these highly selective modern catalysts are prone to aging processes. The main reason for aging is the agglomeration of silver surface particles (Figure 6.12.1).

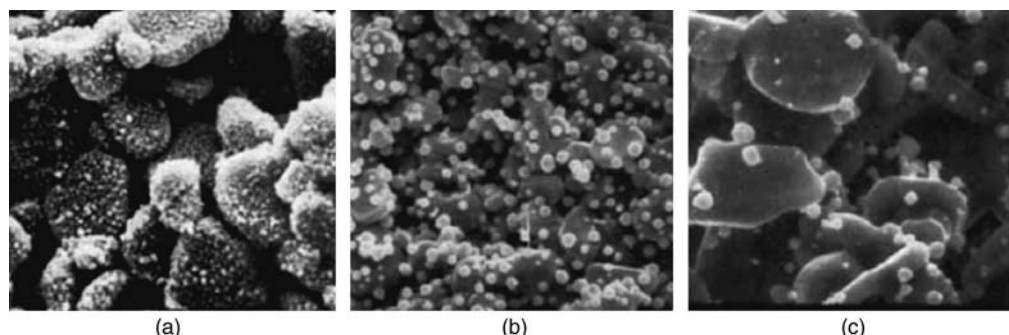


Figure 6.12.1 REM pictures of supported Ag particles after different operation times: (a) fresh catalyst, (b) after three days, and (c) after two years. Adapted from Schwarzmann *et al.* (1988).

Additional reasons for aging are abrasion, dust formation, pore blocking, and accumulation of impurities from reaction gases (e.g., sulfur).

The reduction of the catalytic active silver surface during times of operation can be compensated to a certain degree by high reaction temperatures. It is possible to regenerate aged silver catalysts by an *in situ* impregnation with a methanolic cesium salt solution (selectivity increase up to 8%). Life-times for modern Ag-catalysts vary from two to five years.

The reactor and process design in technical ethylene oxide production is dominated by the demand for exact temperature and selectivity control. The conversion must be reduced to 7–15% per pass to avoid the consecutive oxidation of ethylene oxide. A multi-tubular reactor type guarantees efficient heat transfer, avoids hot spots, and consequently minimizes undesired parallel and consecutive reactions. To reach plant capacities of up to $150\,000\text{ t a}^{-1}$ several thousand tubes (6–12 m long, 2–5 cm internal diameter) are combined in parallel in one reactor. The tubes are filled with catalyst in the form of spheres or rings (diameter 3–10 mm). The cooling agent can be high-boiling hydrocarbons (e.g., kerosene, tetralin) or water under pressure. An alternative reactor type, the fluidized-bed reactor with internal heat transfer, has not yet been commercialized due to abrasion problems of the catalyst. Two options exist to operate the direct oxidation of ethylene, which differ in the applied oxidant, air or pure oxygen. The use of air is cheaper in investment as no additional air separation unit is needed. The nitrogen in the air acts in the process as inert diluent to establish the desired reactant concentrations needed for full temperature control in the reactor. However, if air is used as oxidant, large amounts of nitrogen must be recycled and a significant gas purge is necessary to avoid the build-up of inert gas in the reactor. This purge causes a loss of unreacted ethylene feedstock. Thus, although the use of oxygen requires an extra air separation step, a higher production rate per volume of catalyst, smaller gas purge, constant inert-gas content, and less costly gas recycle often more than compensate the air separation effort. Today, nearly all modern plants apply oxygen as oxidizing agent (Figure 6.12.2).

Characteristic reaction conditions applied in the oxygen process are 10–20 bar and 250–300 °C. For safety reasons, a reaction mixture (6–8 vol.% oxygen and 20–30 vol.% ethylene) outside of the explosive range of oxygen/ethylene-mixtures is applied. Usually, the ethylene oxide selectivities are between 70 and 90% and the ethylene conversion is 8–10%.

In the process the preheated reactants, inerts (diluent methane and recycled CO₂), and promoters are fed into the multi-tubular reactor. The gas stream leaving the reactor is cooled by an external heat exchanger and sent to the ethylene oxide absorber column. In this column the relatively small amounts of ethylene oxide (concentration 1–2 mol.%) are absorbed in water. A minor part of the gas leaving the top of the absorber is purged to reduce the inerts concentration (mainly CO₂, argon, and methane). The rest of the gas stream is sent to the CO₂ absorber unit,

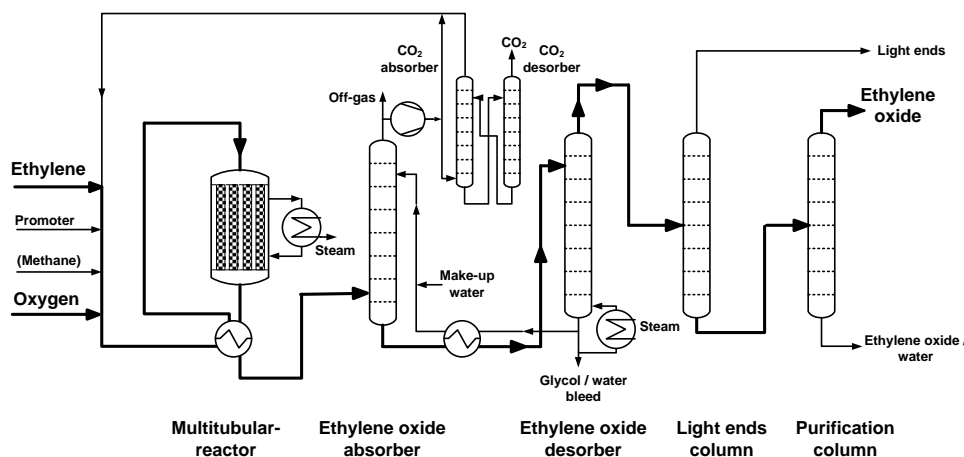


Figure 6.12.2 Flow sheet of an ethylene oxide plant. Adapted from Moulijn *et al.* (2004).

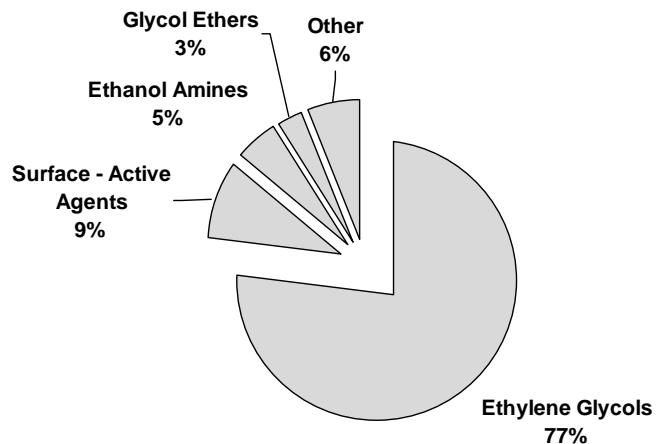
where CO₂ is removed by aqueous potassium carbonate solution or alkanolamines. The CO₂-reduced gas stream is recycled to the reactor. The water–ethylene oxide solution leaves the bottom of the ethylene oxide absorber column and is sent to the desorber column, where ethylene oxide is separated from the solution at the top. The bottom stream (water and glycol) is recycled to the ethylene oxide absorber unit. Finally, two distillation columns separate light ends (e.g., CO₂, acetaldehyde, and hydrocarbon traces) and water from the product ethylene oxide.

During the whole process, it is important to control carefully the composition of the reaction mixture to avoid the explosive range. The presence of CO₂ (formed by the total oxidation) and the diluent methane helps to reduce the flammability limit by decreasing the oxygen concentration. The produced (extremely hazardous) ethylene oxide has to be handled and stored with reasonable care. Potentially dangerous situations, for example, leakage of ethylene oxide, entry of air, oxygen, and reactive impurities into the containment, ignition sources near ethylene oxide tanks, and overheating of ethylene oxide, have to be prevented. Especially, the highly exothermic reactions of ethylene oxide present a serious hazard. Serious problems can arise if traces of polymerization initiators, such as, for example, amines and even rust, find their way into an ethylene oxide tank. These initiators may start a relative slow polymerization reaction initially. However, this reaction accelerates as the reaction exotherm leads to an increasing temperature. With increasing temperature the reaction rate increases combined with a further temperature increase. As the final result self-ignition of ethylene oxide and explosion of the tank is a serious risk.

6.12.1.3 Products Made of Ethylene Oxide

Ethylene oxide is a bulk intermediate product and feedstock for a wide range of other products. The global demand for ethylene oxide in 2006 was around $18.1 \times 10^6 \text{ t a}^{-1}$. The largest end use is in the production of ethylene glycols, representing 77% of total ethylene oxide consumption (including mono-, di- and triethylene glycols) (Figure 6.12.3). Monoethylene glycol (in short “glycol”) is used as antifreeze for engines, for the production of poly(ethylene terephthalate) (polyester fibers, films and plastic bottles), and as heat transfer liquids. Diethylene glycol is applied in the production of polyurethanes, polyesters, softeners, and plasticizers. Moreover, it is used as solvent and de-icing compound for aircrafts. Triethylene glycol is used as solvent, for gas drying, and for producing lacquers and plasticizers.

Figure 6.12.3 World consumption of ethylene oxide by end use in 2006. Data from Devanney (2007).



The second-largest end use of ethylene oxide (9%) is the production of surface-active agents (e.g., nonionic alkylphenol ethoxylates and detergent alcohol ethoxylates). These biodegradable surface-active agents are used for home laundry and dishwashing formulations. Further products manufactured from ethylene oxide are ethanol amines (for textile finishing, cosmetics, gas cleaning, or detergents) and glycol ethers (brake fluids, detergents, solvents, and extractants for sulfur compounds). Pure ethylene oxide is also used as a disinfectant, sterilizing agent, and fumigant in the medical and food industry.

Figure 6.12.4 shows the ten largest ethylene oxide producers in the world. The largest producer Dow Chemicals (including Union Carbide Corporation) accounts for 16% of the world capacity, followed by SABIC (10%), Shell (7%), and BASF (6%).

6.12.2

Commercial Production of Propylene Oxide

In comparison to ethylene oxide, propylene oxide – also known as 1,2-epoxypropane and methyloxirane – is less reactive and less hazardous. However, propylene oxide is also an important raw material for a wide range of intermediates. Propylene oxide is a chiral epoxide, but is commonly used as its racemic mixture.

Table 6.12.1 gives an overview of the world capacity of PO production by processes in 2005. The two major processes are the chlorohydrin process (which accounts for 46% of the world capacity, 2005) and indirect oxidation of propylene oxide (51%).

Figure 6.12.4 Ten largest producers of ethylene oxide in 2006. Data from Devanney (2007).

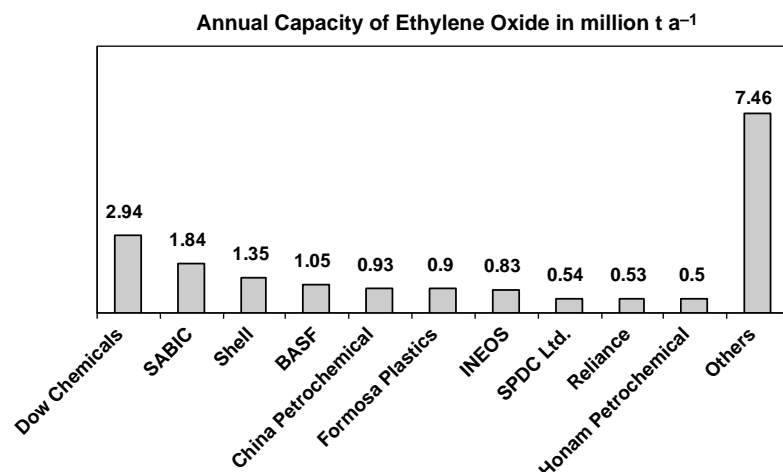


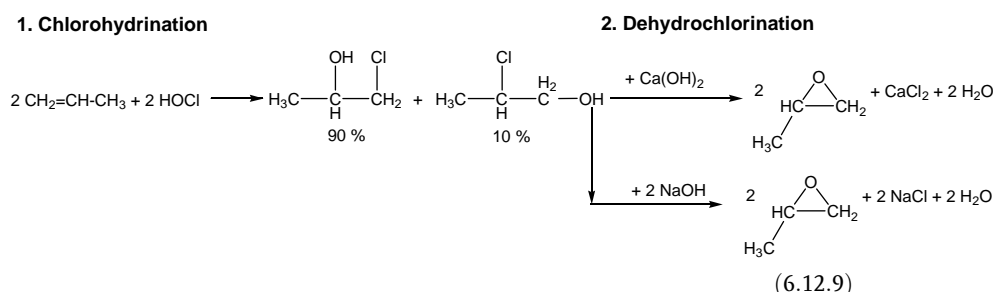
Table 6.12.1 World capacity of PO by processes in 2005 (Devaney, 2006).

Process	World capacity (million t a ⁻¹)	Share (%)
Chlorohydrin route	3.346	46
Indirect oxidation of propylene (total)	3.630	51
thereof by isobutane oxidation	1.268	18
thereof by ethylbenzene oxidation	2.362	33
Other processes	0.180	3

Direct oxidation of propylene with air or pure oxygen (equivalent to ethylene oxide manufacturing) is not efficient, since the silver catalysts used in the direct ethylene oxidation are not suitable for the reaction of alkenes with allylic hydrogen atoms (like propylene). Direct oxidation of propylene results mainly in acrolein formation and total oxidation. Some 3% of the world capacity of PO is produced by very recently developed processes, for example, hydroperoxidation of cumene and propylene and catalytic epoxidation of propylene using H_2O_2 .

6.12.2.1 Chlorohydrin Process

The chlorohydrin process for the manufacture of propylene oxide is similar to the process used for many years for the production of ethylene oxide. The chlorohydrin process is divided into two reaction steps: the chlorohydration and the dehydrochlorination:



In the chlorohydration step, the reactants propylene and hypochlorous acid (chlorine and water) are converted into two propylene chlorohydrin isomers (90% 1-chloro-2-propanol and 10% 2-chloro-1-propanol). Yields of up to 94% can be achieved in modern commercial plants. The main by-products formed in this reaction step are dichloropropane (3–10%), dichloropropanol (0.3–1.2%), and dichlorodiisopropyl ether (0.2–1.7%). In the second step (dehydrochlorination, also called “epoxidation” or “saponification”) the aqueous propylene chlorohydrin solution is treated with slaked lime or caustic soda. Propylene oxide and calcium or sodium chloride are formed. In a commercial process 1.4–1.5 units of chlorine are consumed to produce one unit of propylene oxide. Typical by-products are mono-propylene glycol, epichlorohydrin, glycerol monochlorohydrin, glycerol, propanal, and acetone. In dehydrochlorination, propylene oxide yields of up to 96% can be obtained.

Figure 6.12.5 shows a typical design for a PO plant using the chlorohydrin process.

In the chlorohydrin reactor, gaseous propylene and chlorine (equimolar amount) are mixed with an excess of water. Propylene chlorohydrin is formed at 35–50 °C and 2–3 bar. The water plays an important role in this reaction step. The reaction products remain in aqueous solution and water, acting as diluent, minimizes the formation of by-products. Water is also a reactant [Eq. (6.12.8)] and direct cooling medium. In the separator the vent gas (mixture of propane, propylene, Cl₂, O₂, N₂, H₂, and CO₂) is removed from the propylene chlorohydrin solution and sent to the

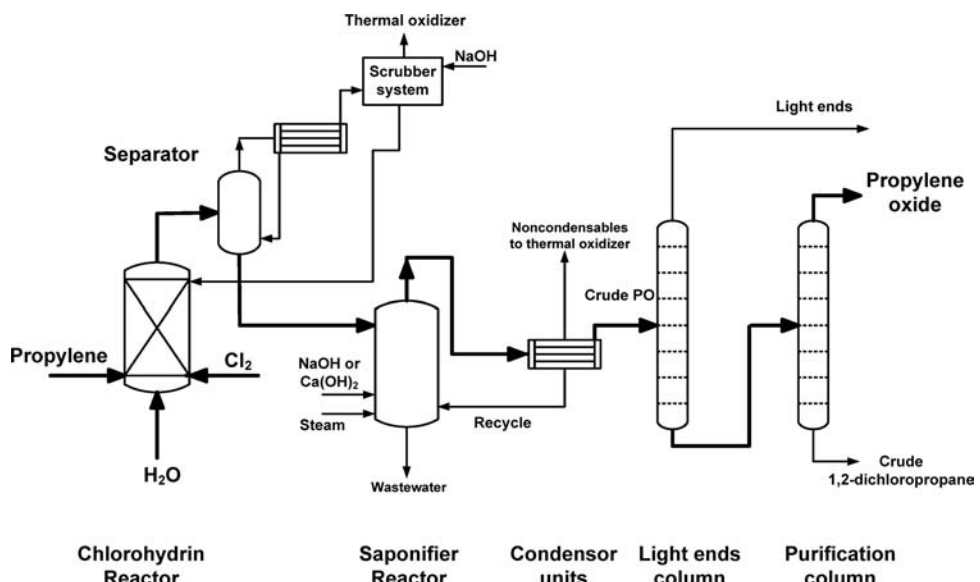


Figure 6.12.5 Flow sheet of a propylene oxide plant using the chlorhydrin process. Adapted from Kahlich *et al.* (2000) and Fedtke *et al.* (1992).

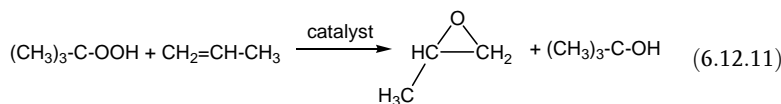
scrubber unit. The aqueous reaction solution from the separator is sent to a saponifier and lime or caustic soda is added. The dehydrochlorination is fast and optimal conversion is obtained with a slight excess of alkalinity. To neutralize HCl produced in the chlorhydrin reaction step a double excess of base is required. To avoid a hydration reaction, PO is quickly removed from the reaction mixture by stripping with steam. The overhead steam also contains, beside propylene oxide, organic by-products and water. After condensation, the crude PO solution is distilled in the light end column and the final purification column. All plant units consist of corrosion-resistant materials (e.g., Hastelloy, Monel) to cope with the highly corrosive chlorine. The wastewater contains about 4 wt% calcium chloride (use of lime) or 8 wt% sodium chloride (use of caustic soda).

Only industrial producers (e.g. Dow) with a highly integrated and cost competitive supply chain of chlorine–caustic soda (through production from caustic soda by NaCl electrolysis) to provide chlorine for the chlorhydrin reactor and sodium hydroxide for the dehydrochlorination step can operate chlorhydrin units for propylene oxide production competitively with indirect oxidation units.

6.12.2.2 Indirect Oxidation of Propylene

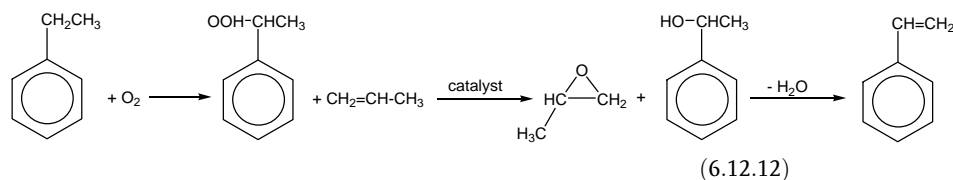
Indirect oxidation of propylene is an important route for propylene oxide production that proceeds in two reaction steps. The first step is the formation of a peroxide from alkanes, aldehydes, or acids by oxidation with air or oxygen. The second reaction step is the epoxidation of propylene to PO by oxygen transfer from the peroxide with formation of water, alcohol, or acid. The catalytic oxidation of propylene with organic hydroperoxides is nowadays a successful commercial production route (51% of world capacity). Two organic hydroperoxides dominate the processes: (i) a process using isobutane (peroxide: *tert*-butyl hydroperoxide, co-product: *tert*-butyl alcohol), which accounts for 15% of the world capacity and (ii) a process using ethylbenzene (peroxide: ethylbenzene hydroperoxide, co-product: styrene) that accounts for 33% of the world capacity. The process via isobutane is presented by:





The yield of propylene oxide is about 94% and approximately 2.2 mol of the co-product *tert*-butanol is produced per mol of propylene oxide. From this ratio it becomes immediately understandable that it is essential for an economic indirect propylene oxidation process to find a good market for the coupling product, here *tert*-butanol. For the isobutane hydroperoxidation reaction propylene is converted with pure oxygen at 120–140 °C, applying pressures of 25–35 bar. The non-catalyzed reaction takes place in the liquid-phase and acetone is formed as a minor by-product. The subsequent epoxidation is carried out in the liquid phase at 110–135 °C under 40–50 bar pressure in five consecutive reactors. The reaction is catalyzed by a homogeneous molybdenum naphthenate catalyst. The co-product *tert*-butanol can be dehydrated and is afterwards converted into methyl *tert*-butyl ether (MTBE), an important fuel additive for lead-free gasoline.

The indirect propylene oxidation process via ethylbenzene hydroperoxide (Halcon process) is displayed in Eq. (6.12.12). Ethylbenzene, obtained by the acid-catalyzed Friedel–Crafts alkylation of benzene with ethylene, is converted with air into ethylbenzene hydroperoxide. The hydroperoxide epoxidizes propylene and generates the co-product α-phenylethanol that is later dehydrated to styrene. Styrene is a major industrial chemical used mainly as monomer for polymers such as polystyrene or styrene-containing copolymers:



The yield of PO in the Halcon process is in the range 87–91% and more than 2 t of the co-product styrene are generated for each produced ton of propylene oxide. The investment costs for the ethylbenzene process are higher than for the *tert*-butanol process, because of the isolation and purification demands for polymer-grade styrene. Figure 6.12.6 shows the plant design for an indirect propylene oxidation process via ethylbenzene hydroperoxide.

In the peroxidation reactor ethylbenzene is converted with air at 146 °C and 2 bar to form a 12–14 wt% solution of ethylbenzene hydroperoxide in ethylbenzene. The reaction takes place in the liquid phase and conversion is limited to 10% for safety reasons. The reactor is a bubble tray reactor with nine separate reaction zones. To avoid decomposition of the formed peroxide the temperature is reduced from 146 °C to 132 °C over the trays. In the epoxidation reactor the reaction solution is mixed with a homogeneous molybdenum naphthenate catalyst. Epoxidation of propylene in the liquid phase is carried out at 100–130 °C and 1–35 bar. The crude product stream (containing PO, unreacted propylene, α-phenylethanol, acetophenone, and other impurities) is sent to the recycle column to remove propylene. The catalyst can be removed by an aqueous alkali wash and phase separation. The crude PO, obtained as head stream in the crude PO column, is purified by distillations. The unconverted reactant ethylbenzene can be recycled in the second recycle column. The bottom stream containing α-phenylethanol is sent to the dehydration reactor. The vapor-phase dehydration of α-phenylethanol to styrene takes place over a titanium/alumina oxide catalyst at 200–280 °C and 0.35 bar (conversion 85%, selectivity 95%).

Direct comparison of the two main PO production routes – chlorohydrin process and indirect oxidation with organic hydroperoxides – is difficult because the technologies are very different and the portfolio and the back integration of the

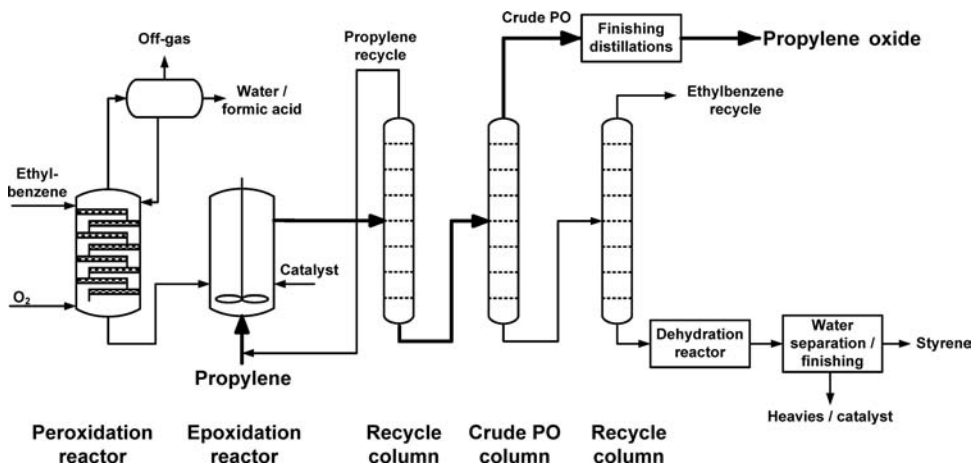
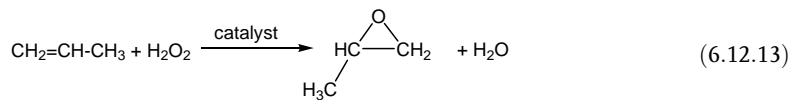


Figure 6.12.6 Flow sheet of the Halcon process for propylene oxide production. Adapted from Kahlich *et al.* (2000) and Fedtke *et al.* (1992).

respective companies play a key role in the evaluation. For a producer with a strong market position in MTBE or polystyrene, indirect oxidation is certainly the best option, even so running a co-production of two products is always a bet on simultaneous market developments for both products. For a producer with a cheap electricity supply, located near a salt deposit and close to the sea (wastewater with high salt loads) the chlorohydrin process is still a reasonable choice.

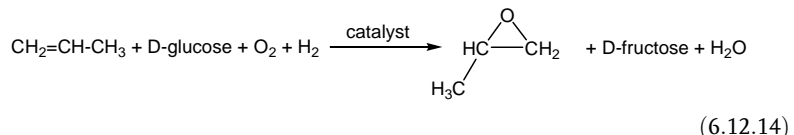
Owing to the realistic chance of unpleasant incompatible market developments for propylene oxide and the co-product in the case of indirect propylene oxidation, a lot of effort has been made in recent years to commercialize indirect propylene oxidation processes based on H₂O₂ as oxidant and water as co-product:



In 2008, BASF and Dow Chemical successfully started the first commercial production plant based on the novel “hydrogen peroxide to propylene oxide” (HPPO) process. The plant is located in Antwerp, Belgium and the initial annual capacity is around 300 000 tons. A second plant based on this technology will start production in 2011 in Map Ta Phut, Thailand.

Evonik and Uhde have also developed a HPPO process, which was commercialized in 2008 in Ulsan, South Korea (100 000 t a⁻¹). The indirect oxidation takes place at increased pressure and temperatures below 100 °C with the solvent methanol. The reaction is catalyzed by a titanium-silicate catalyst in a solid-bed reactor that is special due to its μ -reactor characteristic in one dimension. Using this new reactor type it is possible to improve isothermicity and to avoid disadvantageous concentration profiles. Figure 6.12.7 shows the pilot plant reactor of this new propylene oxidation process. Yields of 95% (relating to propylene) and 90% (relating to H₂O₂) are obtained in the Evonik/Uhde process.

An interesting future alternative for propylene oxide production is the so-called Cetus process:



The process is divided into different chemically and enzymatically catalyzed steps. Currently, it is not yet efficient enough to be economically viable.

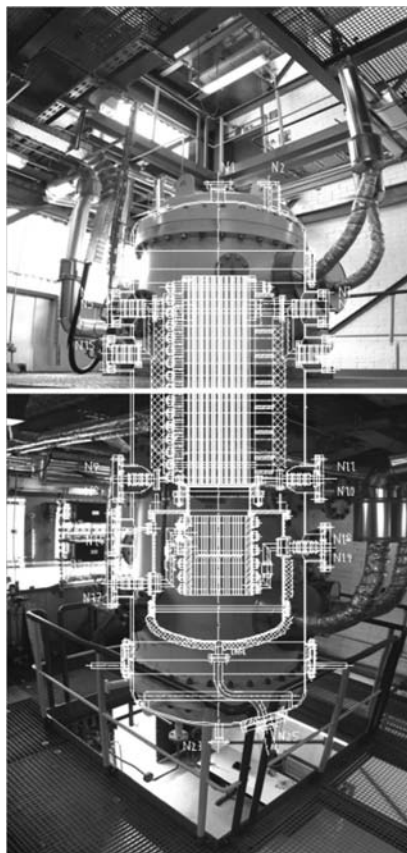


Figure 6.12.7 Pilot plant reactor for propylene oxidation with H₂O₂ according to the Evonik-Uhde process. The μ -reactor characteristics are realized in one dimension to improve heat and concentration profiles. Picture courtesy of Evonik.

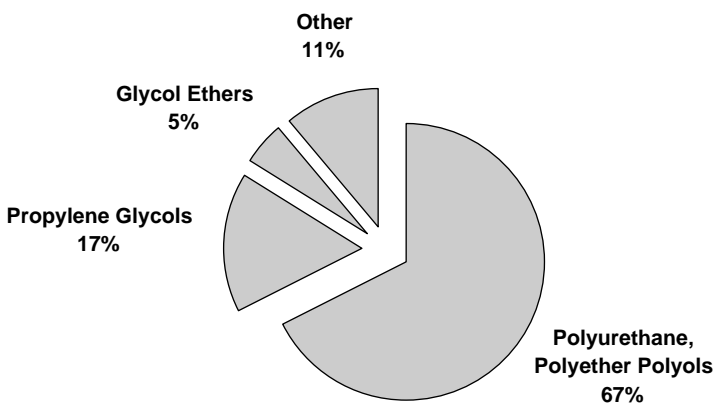


Figure 6.12.8 World consumption of propylene oxide by end use in 2005. Data from Devaney (2006).

6.12.2.3 Products Made of Propylene Oxide

In 2005, the world production of propylene oxide reached $6.2 \times 10^6 \text{ t a}^{-1}$. The main producers are located in the USA (33% of world capacity) and Western Europe (34%). Japan, China, and the Republic of Korea accounted for 20% and Brazil, Singapore, and Eastern Europe for 13%. In 2005, the five major producers were Dow ($1.9 \times 10^6 \text{ t a}^{-1}$), Lyondell ($1.8 \times 10^6 \text{ t a}^{-1}$), Shell ($0.8 \times 10^6 \text{ t a}^{-1}$), BASF ($0.3 \times 10^6 \text{ t a}^{-1}$), and Sumitomo ($0.3 \times 10^6 \text{ t a}^{-1}$).

Figure 6.12.8 gives an overview of the most relevant products based on propylene oxide.

The majority of the produced propylene oxide (67%) is converted into polyether polyols, which are consumed for manufacturing polyurethane. Polyurethane foams are used for automobile seating, furniture, bedding, carpet underlay, and thermal insulation. Polyethers from propylene oxide are also used in the production of detergents, textiles, defoamers, hair-care preparations, brake fluids, and lubricants. Propylene glycols are the second largest end use of propylene oxide (17%). They are applied as raw material for unsaturated polyester resins in the textile and construction industry. Further applications of the propylene glycols are plasticizers, solvents, heat transfer media, and antifreezes. The main advantage of propylene glycol compared to ethylene glycol is its lower toxicity. The third largest application for propylene oxide is the production of glycol ethers that are used as solvents for coatings, paints, inks, and cleaners and also as heat-transfer fluids and anti-icing agents.

Section 6.12 (take-home messages)

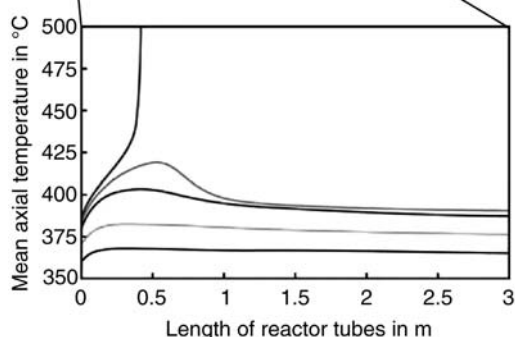
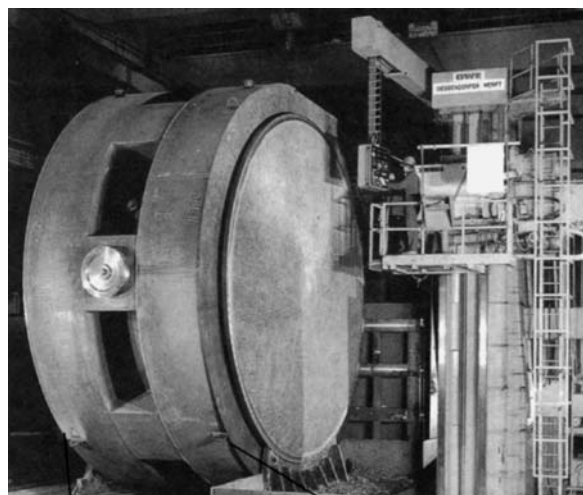
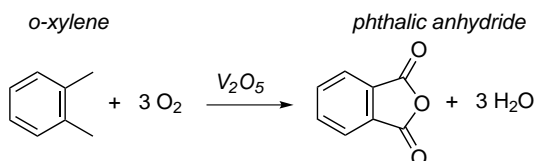
- **Ethylene oxide (EO)** is produced by partial oxidation of ethylene. EO is very reactive, because the strained ring can be easily opened, and is therefore used as raw material for the production of many intermediates and consumer products such as ethylene glycols, surface-active agents, amines, and glycol ethers.
- EO is **toxic, highly flammable**, and can **decompose explosively**. EO is manufactured by two different routes, the chlorohydrin process and by direct oxidation of ethylene.
- In the **chlorohydrin process** ethylene is converted with hypochlorous acid into ethylene chlorohydrin, which is further converted with hydrated lime or caustic soda into EO. Unfortunately, unwanted salts as coupling products and chlorinated organic by-products are generated.
- The chlorohydrin process has largely been replaced by the **direct oxidation of ethylene** with silver as catalyst. By-products are CO_2 and water, formed by total oxidation of ethylene or EO. The reactor design is dominated by the demand for an exact temperature and selectivity control. The conversion per pass is low (about 10%) to avoid the consecutive oxidation of EO, and the unconverted ethylene is recycled. A multi-tubular reactor guarantees efficient heat transfer,

avoids hot spots, and minimizes total oxidation. Usually, the EO selectivity is in the range 70–90%.

- Compared to EO, **propylene oxide** (PO) is less reactive and less hazardous. PO is mainly used for the production of polyether, polyols, polyurethane, glycols, and ethers. Direct oxidation of propylene with air or pure oxygen is not efficient, and PO is produced either by the **chlorohydrin process** (46% share) or by indirect oxidation.
- **Indirect oxidation of propylene** proceeds in two steps. The first step is the formation of a peroxide from iso-butane or ethylbenzene by oxidation with air/oxygen (peroxides: *tert*-butyl hydroperoxide and ethylbenzene hydroperoxide, respectively). The second step is the catalytic epoxidation of propylene to propylene oxide by oxygen transfer from the peroxide. In future, oxidation processes based on H_2O_2 will probably also play an important role. In 2008, the first commercial plant of this kind went on stream.

6.13

Catalytic Oxidation of *o*-Xylene to Phthalic Acid Anhydride



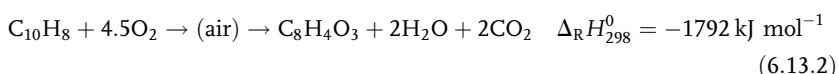
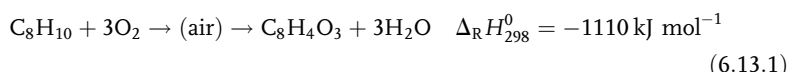
Multi-tubular reactor for *o*-xylene oxidation to phthalic anhydride. Deggendorfer Werft, from Gmehling and Brehm (1996).

6.13.1

Production and Use of Phthalic Anhydride (Overview)

Phthalic anhydride (PA, $C_8H_4O_3$), the anhydride of phthalic acid, is widely used in the chemical industry as an important organic intermediate for the production of plasticisers ($\approx 60\%$), unsaturated polyester resins (19%), and alkyd resins (14%), and also for fine chemicals ($\approx 7\%$) such as dyes, insecticides, and pharmaceuticals. The values given in brackets are the mean values of Japan, USA, and Western Europe use in 1997 (Weissermel and Arpe, 2003). The current worldwide PA production is 4.5 million tonnes (2005).

PA is produced by catalytic oxidation either of *ortho*-xylene (C_8H_{10}) or of naphthalene ($C_{10}H_8$):

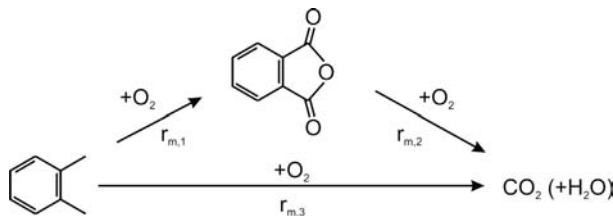


Up to the beginning of the 1960s PA was mainly produced from naphthalene, that is, on the basis of tar from coke making. In the 1970s, the demand for PA increased. Simultaneously, blast furnace coke production decreased due to a reduction of steel production and increased efficiency of the blast furnace process. In 1960, 750 kg coke was needed per tonne of pig iron compared to 500 kg since 1970 (Peters and Reinitzhuber, 1994, see Fig. 6.5.17). This led to *o*-xylene becoming an economically attractive alternative feedstock, and to a shift from coal to crude oil based PA synthesis. Today, more than 85% of PA production worldwide is based on *o*-xylene.

Unwanted by-products of PA production by catalytic oxidation of these two hydrocarbons (HCs) are CO_2 and water. For naphthalene, a minimum of two mol of CO_2 per mol PA is already formed according to the stoichiometry [Eq. (6.13.2)] whereas for *o*-xylene CO_2 formation is only the result of the unwanted catalytic combustion of *o*-xylene and PA (Section 6.13.2). The effect of stoichiometry and combustion to CO_2 (which is higher for *o*-xylene) leads in total to a phthalic anhydride yield related to the mass of the feed (naphthalene or *o*-xylene, O_2 and N_2 not counted) of 100–110 wt% compared to the theoretical maximum values according to the stoichiometries of 116 wt% (naphthalene) and 140 wt% (*o*-xylene).

Catalytic partial oxidation of *o*-xylene and naphthalene is performed mostly in intensively cooled multi-tubular fixed bed reactors, but systems with a fluidized bed were also developed. Typically, V_2O_5/TiO_2 catalysts with K_2SO_4 or Al phosphates as promoter are used. In fixed bed reactors, the conversion of both feedstocks per pass is around 90%, and the selectivity is in the range 0.86–0.91 mol PA per mol naphthalene and 0.78 mol per mol *o*-xylene. (Note that the selectivity would be 100%, if only the reactions according to Eqs. (6.13.1) and (6.13.2), respectively, would take place.) The active compounds are distributed on spheres of porcelain, quartz, or silicon carbide (shell catalyst). The thickness of the shell is only around 0.2 mm, and the diffusion paths for the reactants are short. By this means, the influence of pore diffusion is small, and the unwanted oxidation of phthalic acid anhydride to CO_2 is suppressed compared to a catalyst with an even distribution of active compounds where the influence of pore diffusion would be much stronger (see Section 4.5.6.3 “Influence of Pore Diffusion on the Selectivity of Reactions in Series”). Thus the intrinsic reaction rates are utilized for the modeling of a technical reactor (next Section 6.13.2).

Scheme 6.13.1 Simplified reaction scheme of catalytic *o*-xylene oxidation to phthalic acid anhydride. [A more complex network with *o*-tolualdehyde and phthalide anhydride as intermediates is proposed by Calderbank, Chandrasekharan, and Fumagalli (1977), Anastasov (2002, 2003) and Fiebig and Kuchling (2009)].



Subsequently, only fixed bed PA production by oxidation of *o*-xylene is examined; for further details on PA production and use, for example, on PA production based on naphthalene, see Arpe (2007), Weissermel and Arpe (2003), Baerns *et al.* (2006), and Haase (1972).

Reaction engineering aspects of cooled multi-tubular reactors have already been examined in Section 6.11 for *Fischer-Tropsch synthesis*, which can be simply described by a single reaction of syngas to higher hydrocarbons (at least for Co as catalyst; for Fe as catalyst, this main reaction can also be used to inspect the thermal behaviour of the reactor in good approximation, see Section 6.11.1). For PA production, at least three reactions are involved (Scheme 6.13.1), and this process is a good example by which to illustrate yield and selectivity problems, which are frequently encountered in industrial practice.

6.13.2

Design and Simulation of a Multi-tubular Reactor for Oxidation of *o*-Xylene to PA

The strongly exothermic partial oxidation of *o*-xylene is carried out in multi-tubular reactors with 10 000 tubes cooled by molten salt that circulates around the tubes and exchanges heat in an external heat exchanger for high-pressure steam production. Typically, a tube is 2.5 cm in diameter and 3–4 m long. The inlet content of *o*-xylene is about 1 vol.%, so as to stay below the explosion limit, and the pressure is nearly atmospheric.

To simulate such a multi-tubular reactor we use the reaction scheme given by Scheme 6.13.1, which is fairly representative for the catalytic gas-phase air oxidation of *o*-xylene to phthalic anhydride (Froment and Bischoff, 1990). For simplification, we assume that only CO_2 (and steam) and not CO (and hydrogen) are formed as unwanted by-products.

In Section 6.11, *Fischer-Tropsch synthesis* in a multtube reactor was used as an example to illustrate the differences between the one- and two-dimensional approaches for the simulation of cooled fixed bed reactors. For *o*-xylene oxidation to phthalic anhydride, only the two-dimensional reactor model is considered.

If we neglect axial and radial dispersion of mass (Example 6.13.1) the mass balances for *o*-xylene (*o*-X) and phthalic anhydride (PA) read as [see Eq. (4.10.125), Section 4.10.7.1]:

$$-u_s \frac{dc_{o-X}}{dz} = \rho_b (r_{m,1} + r_{m,3}) \quad (6.13.3)$$

$$u_s \frac{dc_{PA}}{dz} = (r_{m,1} - r_{m,2}) \rho_b \quad (6.13.4)$$

The reaction rates related to the partial pressures are given by Froment and Bischoff (1990):

$$r_{m,1} = k_{m,1} p_{O_2} p_{o-X} \quad (6.13.5)$$

$$r_{m,2} = k_{m,2} p_{O_2} p_{PA} \quad (6.13.6)$$

$$r_{m,3} = k_{m,3} p_{O_2} p_{o-X} \quad (6.13.7)$$

with the following values for the rate constants:

$$k_{m,1} = 0.0115 \text{ mol kg}^{-1} \text{ s}^{-1} \text{ Pa}^{-2} e^{-\frac{E_{A,1}}{RT}} \quad (\text{with } E_{A,1} = 113 \text{ kJ mol}^{-1}) \quad (6.13.8)$$

$$k_{m,2} = 0.0318 \text{ mol kg}^{-1} \text{ s}^{-1} \text{ Pa}^{-2} e^{-\frac{E_{A,2}}{RT}} \quad (\text{with } E_{A,2} = 131 \text{ kJ mol}^{-1}) \quad (6.13.9)$$

$$k_{m,3} = 0.0048 \text{ mol kg}^{-1} \text{ s}^{-1} \text{ Pa}^{-2} e^{-\frac{E_{A,3}}{RT}} \quad (\text{with } E_{A,3} = 120 \text{ kJ mol}^{-1}) \quad (6.13.10)$$

Note that the activation energy is different if the rate is defined based on partial pressures and not on molar concentrations (Topic 6.13.1). Also note that we have assumed that the reaction rates are not influence by external or internal diffusion (Example 6.13.2).

The axial and radial temperatures in the tubes are not constant and typically vary by up to 40 K. If we use the molar fractions ($\gamma_{o\text{-X}}$, γ_{PA}), which depend only on the degree of reaction progress (and not on T), and take the inlet temperature as reference value the change in concentrations in axial direction [left-hand sides of Eqs. (6.13.3) and (6.13.4)] can be written as:

$$-u_s \frac{dc_{o\text{-X}}}{dz} = -u_{s,T_{in}} \rho_{\text{mol},T_{in}} \frac{dy_{o\text{-X}}}{dz} = -u_{s,T_{in}} \frac{p}{RT_{in}} \frac{dy_{o\text{-X}}}{dz} \quad (6.13.11)$$

$$u_s \frac{dc_{PA}}{dz} = u_{s,T_{in}} \frac{p}{RT_{in}} \frac{dy_{PA}}{dz} \quad (6.13.12)$$

and for the reaction rates $r_{m,i}$ (in $\text{mol kg}^{-1} \text{ s}^{-1}$) we get with p as total pressure instead of Eqs. (6.13.5)–(6.13.7):

$$r_{m,1} = k_{m,1} p^2 \gamma_{O_2} \gamma_{o\text{-X}} \quad (6.13.13)$$

$$r_{m,2} = k_{m,2} p^2 \gamma_{O_2} \gamma_{PA} \quad (6.13.14)$$

$$r_{m,3} = k_{m,3} p^2 \gamma_{O_2} \gamma_{o\text{-X}} \quad (6.13.15)$$

Combination of Eqs. (6.13.11)–(6.13.15) yields:

$$-u_{s,T_{in}} \frac{dy_{o\text{-X}}}{dz} = (\rho_b RT_{in} p)(k_{m,1} + k_{m,3}) \gamma_{O_2} \gamma_{o\text{-X}} \quad (6.13.16)$$

$$u_{s,T_{in}} \frac{dy_{PA}}{dz} = (\rho_b RT_{in} p)(k_{m,1} \gamma_{O_2} \gamma_{o\text{-X}} - k_{m,2} \gamma_{O_2} \gamma_{PA}) \quad (6.13.17)$$

with the boundary conditions:

$$\gamma_{O_2} = \text{const.} \quad (\text{for large excess of oxygen}) \quad (6.13.18)$$

and:

$$\gamma_{o\text{-X}} = \gamma_{o\text{-X,in}} \quad (\text{at } z = 0) \quad (6.13.19)$$

If we neglect axial dispersion of heat (Example 6.13.1), the heat balance according to the so-called two-dimensional fixed bed reactor model is as follows [Eq. (4.10.126), Section 4.10.7.1]:

$$\rho_{\text{mol},T_{in}} c_p u_{s,T_{in}} \frac{dT}{dz} = \lambda_{\text{rad}} \left(\frac{d^2 T}{dr^2} + \frac{dT}{r dr} \right) - \rho_b (\Delta_R H_1 r_{m,1} + \Delta_R H_2 r_{m,2} + \Delta_R H_3 r_{m,3}) \quad (6.13.20)$$

where $\Delta_R H_1 = -1110 \text{ kJ mol}^{-1}$, $\Delta_R H_3 = -4360 \text{ kJ mol}^{-1}$, and $\Delta_R H_2 = -3250 \text{ kJ mol}^{-1}$ ($= \Delta_R H_3 - \Delta_R H_1$).

The first two boundary conditions are:

$$T = T_{in} \quad (\text{for } z = 0) \quad (6.13.21)$$

$$\frac{dT}{dr} = 0 \quad (\text{for } r = 0, \text{ all } z) \quad (6.13.22)$$

Example 6.13.1: Influence of axial and radial dispersion of mass and heat

The oxidation of *o*-xylene to PA is first order both with regard to O₂ and to xylene. The O₂ excess is high and thus we can regard the reaction rate as formally a first-order reaction overall. The criteria used to exclude dispersion of mass and heat in a fixed bed (first-order reaction), which are summarized in Table 4.10.8 (Section 4.10.7.2), are as follows:

$$\text{Axial dispersion of mass } \frac{L}{d_p} \geq 10 Da \quad (6.13.23)$$

$$\text{Radial dispersion of mass } \frac{d_R}{d_p} \leq 2.5 \frac{L}{Da d_R} \quad (6.13.24)$$

$$\text{Axial dispersion of heat } \frac{L}{d_p} \geq 10 Da \frac{E_A \Delta T_{ad}}{RT_w^2} \quad (6.13.25)$$

$$\text{Radial dispersion of heat } \frac{d_R}{d_p} \leq \frac{0.16 L}{Da d_R E_A \Delta T_{ad}} \quad (6.13.26)$$

Typical values of *o*-xylene oxidation are a temperature of the reactor wall T_w (= T_{cool}) of 370 °C, an activation energy (main reaction) of 113 kJ

mol⁻¹, particle diameter d_p of 3 mm, tube diameter d_R of 2.5 cm, tube length L of 3 m, and an adiabatic rise in temperature ΔT_{ad} of 358 K. For the *Damkoehler number* Da we use a value of 3, which corresponds to a conversion in a plug flow reactor of 95%. Thus we obtain as criteria:

$$\text{Axial dispersion of mass } \frac{L}{d_p} \geq 30 \quad (6.13.27)$$

$$\text{Radial dispersion of mass } \frac{d_R}{d_p} \leq 100 \quad (6.13.28)$$

$$\text{Axial dispersion of heat } \frac{L}{d_p} \geq 353 \quad (6.13.29)$$

$$\text{Radial dispersion of heat } \frac{d_R}{d_p} \leq 0.5 \quad (6.13.30)$$

The ratios L/d_p and d_R/d_p are 1000 and 8, respectively, and the influence of axial and radial dispersion of mass and of axial dispersion of heat is negligible but the radial dispersion of heat is not.

As explained in Section 4.10.7.3, Eq. (6.13.20) considers the bed and the fluid as a pseudo-homogeneous medium, and the heat transfer in the bed up to the internal side of the wall is represented by a constant radial effective conductivity λ_{rad} and the internal wall heat transfer coefficient α_{w,int}. This model assumes a jump in temperature directly at the bed side of the tube wall from T_{w,int,1} to T_{w,int,2} (Figure 4.10.67). This leads to the third boundary condition:

$$-\lambda_{\text{rad}} \frac{dT}{dr} = \alpha_{w,\text{int}} (T_{w,\text{int},1} - T_{w,\text{int},2}) \quad [\text{for } r = d_R/2 \text{ (at the wall)}] \quad (6.13.31)$$

In the following, we assume that the thermal resistances of heat transport by conduction through the tube wall and by heat transfer from the external tube wall to the cooling medium (molten salt) are negligible compared to heat transfer within the packed bed. Thus, the fourth and last boundary condition is:

$$T_{w,\text{int},2} = T_{\text{cool}} \quad (\text{for all } z) \quad (6.13.32)$$

Table 6.13.1 gives data on chemical media and reaction conditions. The parameters λ_{rad} and α_{w,int} were calculated using Eqs. (4.10.195) and (4.10.197), respectively.

Table 6.13.1 Data on chemical media and conditions of catalytic *o*-xylene oxidation. Data partly from Baerns, Hofmann, and Renken (2002), Froment and Bischoff (1990), and Papageorgiou and Froment (1996).

Parameter	Value (1 bar, 370 °C)
Superficial gas velocity u _s (empty reactor)	2.35 m s ⁻¹
Total molar gas concentration ρ _{mol}	18.6 mol m ⁻³
Total pressure p	1 bar
Diameter of catalyst particle d _p	3 mm
Diameter of single tube d _R (total number of tubes about 2500)	2.5 cm
Bulk density of catalyst bed ρ _b	1300 kg m ⁻³
Inlet concentration of <i>o</i> -xylene y _{o-x}	1 vol.-% (rest air)
Kinematic viscosity ν of gas mixture	2.3 × 10 ⁻⁶ m ² s ⁻¹
Thermal conductivity of gas mixture λ _{gas}	0.048 W m ⁻¹ K ⁻¹
Effective radial thermal conductivity λ _{rad}	1.2 W m ⁻¹ K ⁻¹
Heat capacity of gas mixture c _p	31 J mol ⁻¹ K ⁻¹
Heat transfer coefficient (bed to wall) α _{w,int}	318 W m ⁻² K
Thermal transmittance U _{h, bed}	174 W m ⁻² K
Adiabatic rise in temperature (if only main reaction 1 is considered)	358 K
Adiabatic rise in temperature (for complete conversion to carbon oxides)	1400 K

Topic 6.13.1: Influence of the choice of reaction rate (based on molar concentration or partial pressure) on the value of the activation energy

The oxidation of *o*-xylene to PA is represented based on partial pressures by:

$$r_{m,1} = k_{m,0,1} e^{-\frac{E_{A,1,p}}{RT}} p_{O_2} p_{o-X} \quad \left(\text{with } E_{A,1,p} = 113 \frac{\text{kJ}}{\text{mol}} \text{ and } k_{m,0,p} = 0.0115 \frac{\text{mol}}{\text{kg s Pa}^2} \right) \quad (6.13.33)$$

The activation energy is different if the rate is defined based on molar concentrations and not on partial pressures. Here we use the index p for the activation energy if the rate is defined based on partial pressure and the index c if molar concentrations are used, and omit for clarity the index 1 (which stands for the main reaction of *o*-xylene to PA).

For ideal gases, Eq. (6.13.33) can be rewritten based on molar concentrations as:

$$r_m = k_{m,0,p} e^{-\frac{E_{A,p}}{RT}} c_{O_2} c_{o-X} (RT)^2 \quad (6.13.34)$$

If we were to determine the activation energy based on experimental data (X_{o-X} versus T) and the definition of the rate based on molar concentrations, we would just have used:

$$r_m = k_{m,0,c} e^{-\frac{E_{A,c}}{RT}} c_{O_2} c_{o-X} \quad (6.13.35)$$

Comparison of Eqs. (6.13.34) and (6.13.35) leads to:

$$k_{m,0,c} e^{-\frac{E_{A,c}}{RT}} = k_{m,0,p} R^2 T^2 e^{-\frac{E_{A,p}}{RT}} \quad (6.13.36)$$

The activation energy $E_{A,p}$ is usually calculated based on experiments in a certain temperature range. If we use the mean value $T_{\text{mean}} = 0.5(T_{\text{max}} + T_{\text{min}})$ as a reference, we obtain:

$$k_{m,0,c} e^{-\frac{E_{A,c}}{RT}} = k_{m,0,p} (RT_{\text{mean}})^2 \left(\frac{T}{T_{\text{mean}}} \right)^2 e^{-\frac{E_{A,p}}{RT}} \quad (6.13.37)$$

The term $(T/T_{\text{mean}})^2$ can be approximated by an exponential attempt analogous to the Arrhenius function:

$$\left(\frac{T}{T_{\text{mean}}} \right)^2 \approx e^{-\frac{Q}{R} \left(\frac{1}{T} - \frac{1}{T_{\text{mean}}} \right)} = e^{\frac{Q}{RT_{\text{mean}}}} e^{-\frac{Q}{RT}} \quad (6.13.38)$$

For *o*-xylene oxidation the typical temperature range is 340–420 °C (613–693 K), and for a mean temperature of 653 K we obtain a value of Q of about 11 kJ mol⁻¹ by, for example, some trial and error with the help of a spreadsheet. The parameter Q reflects the difference between the two activation energies $E_{A,c}$ and $E_{A,p}$. Insertion of Eq. (6.13.38) into Eq. (6.13.37) and combination with Eq. (6.13.35) finally leads to:

$$r_m = k_{m,0,c} e^{-\frac{E_{A,c}}{RT}} c_{O_2} c_{o-X} \left(\text{with } E_{A,c} = 124 \frac{\text{kJ}}{\text{mol}} \text{ and } k_{m,0,c} = 2.57 \times 10^6 \frac{\text{m}^6}{\text{kg s}} \right) \quad (6.13.39)$$

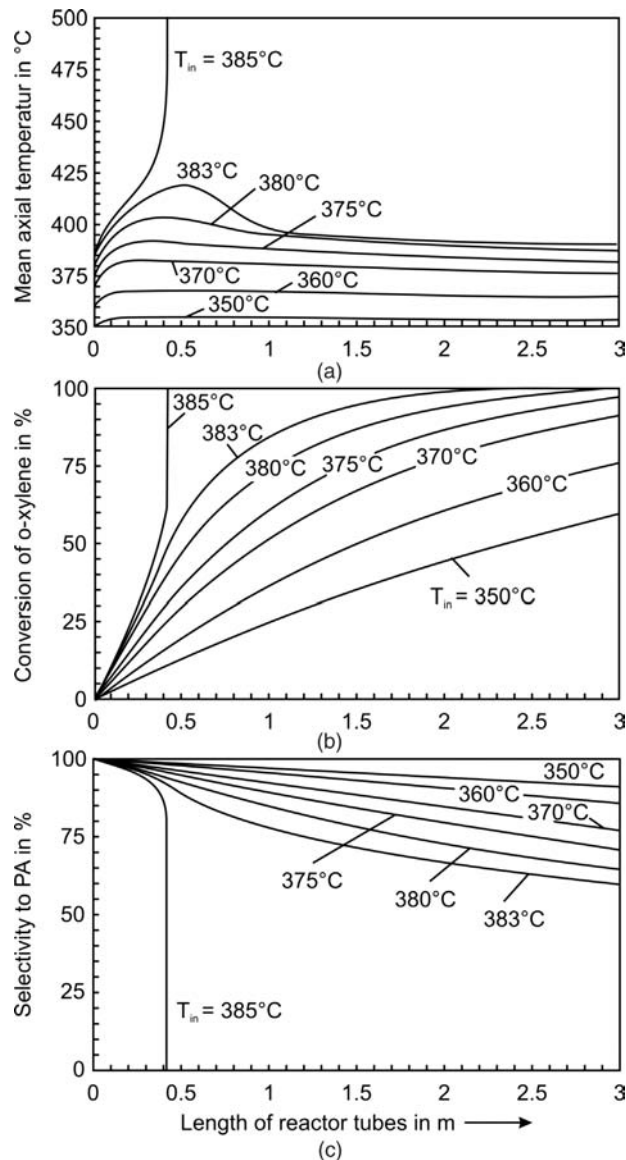
Thus for the given example the activation energy $E_{A,c}$ is by 11 kJ mol⁻¹ higher than $E_{A,p}$. (For a first order reaction this would have been about half (5.5 kJ mol⁻¹.)

If the parameters of the kinetics and heat transfer are known, the PA synthesis can be simulated by modern computers and programs to solve differential equations. Here this was carried out by the commercial program *Presto-Kinetics* (www.cit-wulkow.de), which is frequently used in this book. The results are given in Figure 6.13.1 by the axial profiles of temperature (tube axis), o-xylene conversion, and selectivity to phthalic anhydride for a tube length of 3 m.

Figure 6.13.1 shows that an inlet temperature of 370°C is almost optimal as we get a conversion of about 91% and still a relatively high selectivity to phthalic anhydride of 77%. These values are also given in the literature for industrial processes (Weisermel and Arpe, 2003). For higher temperatures, the selectivity steadily goes down. Even more important, for $T > 383^\circ\text{C}$, the danger of a temperature runaway is high (Figures 6.13.1a and 6.13.2).

The pronounced radial temperature profile within the bed is shown in Figure 6.13.3 for the example of the critical cooling inlet temperature of 383°C at the axial position of 0.5 m, where the maximum axial temperature appears (Figure 6.13.1a). As we can see, the temperature difference within the bed is about 48 K (center to wall) compared to the jump in temperature directly at the wall of about 18 K. In reality, we do not have such a “jump,” but the weaker heat transport

Figure 6.13.1 Axial profiles of temperature (tube axis) (a), o-xylene conversion (b), and selectivity to PA (c) in the multi-tubular reactor for catalytic o-xylene oxidation with different inlet temperatures [$T_{\text{in}} = T_{\text{cool}}$, two-dimensional model, Eqs. (6.13.3), (6.13.15)–(6.13.22); parameters see Table 6.13.1].



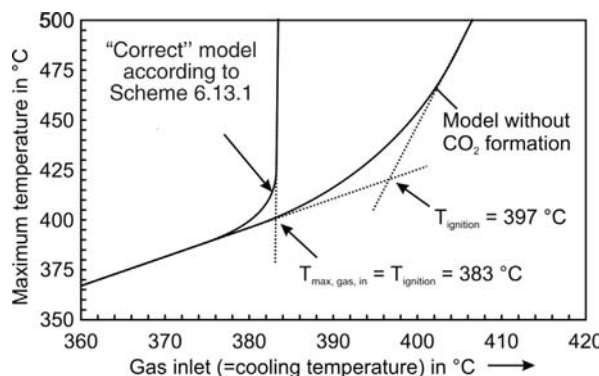


Figure 6.13.2 Influence of cooling temperature on maximum axial temperature in a multi-tubular PA production [two-dimensional model, Eqs. (6.13.14)–(6.13.22), parameters as given by Table 6.13.1].

close to the wall due to less mixing and the higher void fraction of the bed leads to a steep decrease of the temperature in a small region near the wall. Thus the jump in temperature as shown in Figure 6.13.3 is the result of the model that was used, which combines the interplay of convective flow at the wall and the conduction by contact between the bed and the internal surface of the cooled wall by the introduction of $\alpha_{w,int}$ (see Section 4.10.7.3 for details).

The temperature differences within the bed and directly at the internal wall can also be estimated by the overall heat transfer coefficient $U_{h,bed}$ by Eqs. (4.10.179) and (4.10.180):

$$\Delta T_{\text{overall}} = \frac{\dot{q}}{U_{h,bed}} = \Delta T_{\text{bed}} + \Delta T_{\text{wall}} = \dot{q} \left(\frac{d_R}{8\lambda_{\text{rad}}} + \frac{1}{\alpha_{w,int}} \right) \quad (6.13.40)$$

$U_{h,bed}$ combines the two parameters λ_{rad} and $\alpha_{w,int}$ of the two-dimensional model and can be regarded as the sum of two thermal resistances (Section 4.10.7.3).

The individual temperature differences, ΔT_{bed} and ΔT_{wall} , are proportional to the respective resistances $d_R/(8\lambda_{\text{rad}})$ and $1/\alpha_{w,int}$, Eq. (6.13.40). With the data of Table 6.13.1, we here obtain values of $0.0026 \text{ m}^2 \text{ K W}^{-1}$ for $d_R/(8\lambda_{\text{rad}})$ and of $0.0031 \text{ m}^2 \text{ K W}^{-1}$ for $1/\alpha_{w,int}$. Thus, for $\Delta T_{\text{overall}} = 35 \text{ K}$, we find a temperature difference in the fixed bed of 16 K (compared to 17 K of the simulation, Figure 6.13.3) and a jump in temperature directly at the wall of 19 K (compared to 18 K , Figure 6.13.3). The agreement is very good.

The runaway behavior as shown in Figure 6.13.2 can also be inspected and estimated by the criteria derived in Section 4.10.3. According to Eq. (4.10.83), the two critical parameters used to estimate the danger of a thermal runaway are N_C , which is a measure of the cooling capacity relative to heat release, and N_{ad} , which combines the dimensionless adiabatic temperature rise, $\Delta T_{ad}/T_{cool}$, and the temperature sensitivity, $E_A/(RT_{cool})$ (details in Section 4.10.3). If we only consider the main

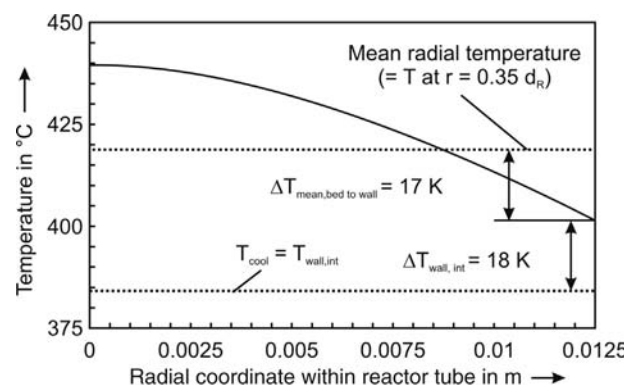


Figure 6.13.3 Radial temperature profile at the axial position of 0.5 m for the critical cooling temperature ($=$ critical gas inlet temperature) of 383 °C (for axial profile see Figure 6.13.1a).

reaction of o-xylene to phthalic anhydride we have:

$$N_C = \frac{U_{h,bed} \frac{4}{d_R} \Delta T_{ad}}{\rho_b k_{m,1,T_{cool}} (-\Delta_R H_1) p^2 \gamma_{O_2,in} \gamma_{o-X,in}} \quad (6.13.41)$$

$$N_{ad} = \frac{\Delta T_{ad} E_{A,1}}{R T_{cool}^2} \quad (6.13.42)$$

The critical conditions in terms of N_C and N_{ad} are given in Section 4.10.3.1. For a first-order reaction (here a high surplus of oxygen) we have (Figure 4.10.25):

$$\left(\frac{N_C}{N_{ad}} \right)_{crit} = 2.72 - \frac{3.37}{\sqrt{N_{ad}}} \quad (6.13.43)$$

With the values of the reaction conditions and so on listed in Table 6.13.1 and Eq. (6.13.43), the critical conditions are reached (single tube diameter of 2.5 cm) for a gas inlet temperature of 397 °C ($N_C/N_{ad} = 1.8$ and $N_{ad} = 13.7$), if the main reaction only is considered. This is almost exactly the value derived for the “exact” computed solution if we neglect CO₂ production (two-dimensional model, Figure 6.13.2). Nevertheless, we can only use Eq. (6.13.43) and the Barkelaw diagram (Figure 4.10.25) for simple reactions and not for a reaction network. For the given example of o-xylene oxidation to phthalic anhydride with CO₂ as by-product, the critical temperature would be by about 15 K lower (Figure 6.13.2). Thus, with modern techniques of solving differential equations and so on by computer it is possible to determine solutions for complicated reaction systems.

Nevertheless, the classical approaches of the “old days” of chemical engineering are still very helpful as we can also see by inspection of the maximum allowable temperature difference between the temperature of the bed and the cooling temperature. Recalling and rearrangement of Eq. (4.10.82) from Section 4.10.3.3 gives:

$$\Delta T_{bed,max} = T_{crit} - T_{cool} = \frac{R}{E_A} (T_{crit} - T_{cool}) \quad (6.13.44)$$

If we use this simple “rule of thumb,” we get a value for $\Delta T_{bed,max}$ of 33 K ($E_A = 113 \text{ kJ mol}^{-1}$, and according to Figure 6.13.1 and 6.13.2 $T_{crit} = T_{max}$ at the point of ignition = 419 °C = 692 K and $T_{cool,max} = T_{ignition} = 383 \text{ }^\circ\text{C} = 656 \text{ K}$). This is in good agreement with the value of the accurate reactor simulation of $\Delta T_{bed,max} = 36 \text{ K}$.

Figure 6.13.4 shows the strong influence of the diameter of the tubes on the maximum allowable cooling (= inlet) temperature. An internal diameter of more than 2.5 cm (standard value used in industrial reactors) would lead to a strong decrease of the maximum allowable gas inlet temperature with the result of a strong decrease in the o-xylene conversion for a tube length of 3 m (Figure 6.13.1). Conversely, smaller tubes (<2.5 cm) would also allow a safe operation for inlet temperatures of more than 400 °C but then the selectivity to phthalic anhydride would strongly decrease (Figure 6.13.1) and so also would the number of tubes needed (investment costs).

Figure 6.13.4 Influence of internal diameter on the maximum allowable gas inlet (= wall) temperature with regard to a runaway in a multi-tubular reactor of catalytic o-xylene oxidation [determined by Eqs. (6.13.41)–(6.13.43), parameters as given by Table 6.13.1].

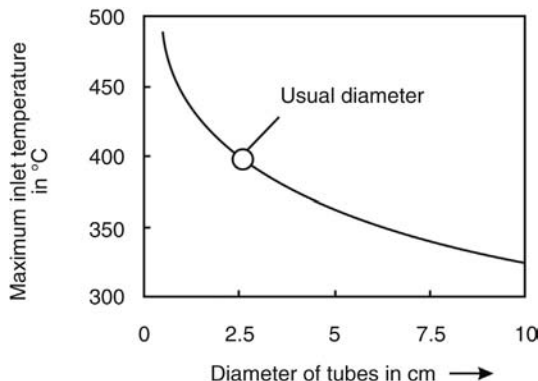


Table 6.13.2 Data on chemical media and parameters of mass transfer needed to estimate the influence of internal and external diffusion on the effective rate.

Parameter	Value (1 bar, 400 °C)
Superficial gas velocity u_s (empty reactor)	2.46 m s ⁻¹
Partial pressure of oxygen (assumed to be constant) p_{O_2}	0.21 bar
Diameter of catalyst particle d_p	3 mm
Density of catalyst particle ρ_p	1800 kg m ⁻³
External surface area of catalyst particle A_m	1.1 m ² kg ⁻¹
Kinematic viscosity of gas mixture ν	5.5 × 10 ⁻⁵ m ² s ⁻¹
Molecular diffusion coefficient of o-xylene in air D_{o-X}	2.5 × 10 ⁻⁵ m ² s ⁻¹
Effective diffusion coefficient of o-xylene in the catalyst $D_{eff,o-X}$	2.5 × 10 ⁻⁶ m ² s ⁻¹
Pseudo-first-order rate constant $k^*_{m,o-X} = (k_{m,1} + k_{m,3})RT p_{O_2}$	2.5 × 10 ⁻³ m ³ kg ⁻¹ s ⁻¹
Reynolds number $Re_p = \frac{u_s d_p}{\nu}$	134
Schmidt number $Sc_{o-X} = \frac{\nu}{D_{o-X}}$	2
Sherwood number $Sh_{o-X} = \frac{\beta d_p}{D_{o-X}}$ [by Eqs. (3.2.70) and (3.2.71)]	22

Example 6.13.2: Influence of mass transfer on the effective rate of o-xylene oxidation

To estimate the influence of external and internal diffusion on the effective rate of oxidation of o-xylene to PA we use 400 °C as reference temperature, which is the maximum temperature that we reach in a technical reactor under safe conditions (Figures 6.13.1 and 6.13.2). Table 6.13.2 gives the data on chemical media and the parameters of mass transfer needed to estimate the influence of diffusion on the rate.

The O₂ excess is high and we can regard the rate of conversion of o-xylene as first order:

$$r_m = (k_{m,1} + k_{m,3})p_{O_2} p_{o-X} \approx k_{m,o-X} p_{o-X} \quad (6.13.45)$$

In terms of concentration we get:

$$r_m = (k_{m,o-X} RT) c_{o-X} = k^*_{m,o-X} c_{o-X} \quad (6.13.46)$$

Influence of Internal Diffusion

For the *Thiele modulus*, for a spherical particle with uniform distribution of the active compounds, we have according to Eq. (4.5.77):

$$\phi = \frac{d_p}{6} \sqrt{\frac{k^*_{m,o-X} \rho_p}{D_{o-X,eff}}} = 0.7 \quad (6.13.47)$$

and for the effectiveness factor of pore diffusion [$\eta_{pore} = \tanh(\phi/\phi)$] we obtain a value of 86%. In reality, we have a shell catalyst and the characteristic length for pore diffusion is much smaller than $d_p/6$. For a catalyst (shell thickness of the shell, s_{shell} , is here about 0.2 mm), we can consider the system as a plate with thickness $2s_{shell}$, as there is no contribution of the inert core (with diameter $d_p - 2s_{shell}$) to the reaction rate. The rate constant within the shell is then higher than the average value and we obtain:

$$k^*_{m,o-X,shell} = k^*_{m,o-X} \frac{V_p}{V_{shell}} \approx k^*_{m,o-X} \frac{\frac{1}{6}\pi d_p^3}{\pi d_p^2 2s_{shell}} = k^*_{m,o-X} \frac{d_p}{12s_{shell}} \quad (6.13.48)$$

So the *Thiele modulus* for a shell catalyst is given by:

$$\phi = \frac{s_{shell}}{6} \sqrt{\frac{k^*_{m,o-X} \rho_p}{D_{o-X,eff}}} \left(\frac{d_p}{12s_{shell}} \right) = \frac{\sqrt{\frac{s_{shell} d_p}{12}}}{6} \sqrt{\frac{k^*_{m,o-X} \rho_p}{D_{o-X,eff}}} = 0.07 \quad (6.13.49)$$

So the characteristic length is here ($s_{shell} = 0.2$ mm, $d_p = 3$ mm) 0.04 mm instead of 0.5 mm ($= d_p/6$), which leads to a value for η_{pore} of 99.8%. Therefore, the influence of pore diffusion is negligible.

Influence of External Mass Transfer

The rate of the chemical reaction always equals the rate of external mass transfer:

$$r_m = k^*_{m,o-X} c_{o-X,s} = \beta A_m (c_{o-X,b} - c_{o-X,s}) \quad (6.13.50)$$

with $c_{o-X,s}$ and $c_{o-X,b}$ as the concentrations at the surface and in the bulk phase.

Rewriting Eq. (6.13.50) and introduction of the Sherwood number Sh leads to:

$$c_{o-X,s} = \left(\frac{\frac{Sh D_{o-X}}{d_p} A_m}{k^*_{m,o-X} + \frac{Sh D_{o-X}}{d_p} A_m} \right) c_{o-X,b} = \left(\frac{0.2}{0.0025 + 0.2} \right) c_{o-X,b} = 0.99 c_{o-X,b} \quad (6.13.51)$$

Therefore, the concentration at the external surface of the catalyst almost equals the concentration in the bulk phase, and the influence of external diffusion is also negligible.

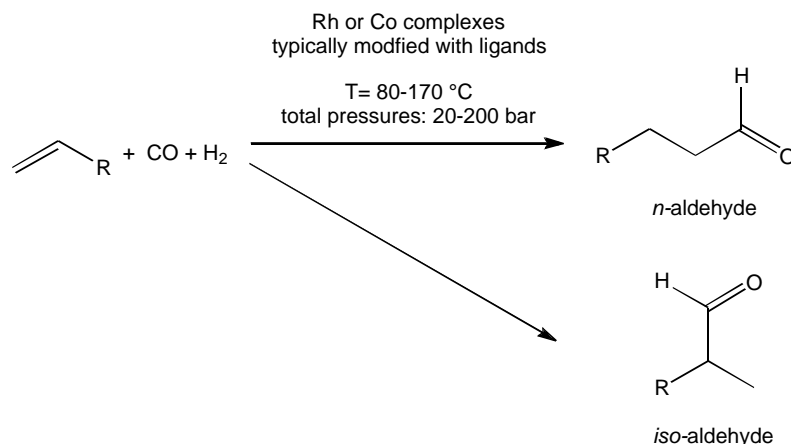
Section 6.13 (take-home messages)

- **Phthalic anhydride** (PA) is an important intermediate for the production of plasticizers and resins, and is produced by **catalytic oxidation of *ortho*-xylene or naphthalene**. Unwanted by-products of PA production by catalytic oxidation of these two hydrocarbons are CO₂ and water. Typically, V₂O₅/TiO₂ based catalysts are used.
- The strongly exothermic partial oxidation of *o*-xylene (and also of naphthalene) is carried out in **multi-tubular reactors** (with about 10 000 tubes) cooled by a molten salt. To simulate the multi-tubular reactor, the two-dimensional reactor model is appropriate in order to account for the radial temperature gradient in the catalyst bed.

6.14

Hydroformylation (Oxosynthesis)

Scheme 6.14.1 General reaction scheme of the hydroformylation reaction.



Hydroformylation, also referred to as oxosynthesis, is one of the most important applications of homogeneous catalysis in chemical technology.

The reaction converts the petrochemical basic chemicals, olefin and syngas, into aldehydes that are attractive intermediates for the production of acids, alcohols, and amines.



View of the Oberhausen propene hydroformylation plants of OXEA; the units produce 650 kt of butyraldehydes per year with a Rh-catalyst system immobilized in an aqueous reaction phase (© Oxea).

6.14.1

Industrial Relevance of Hydroformylation

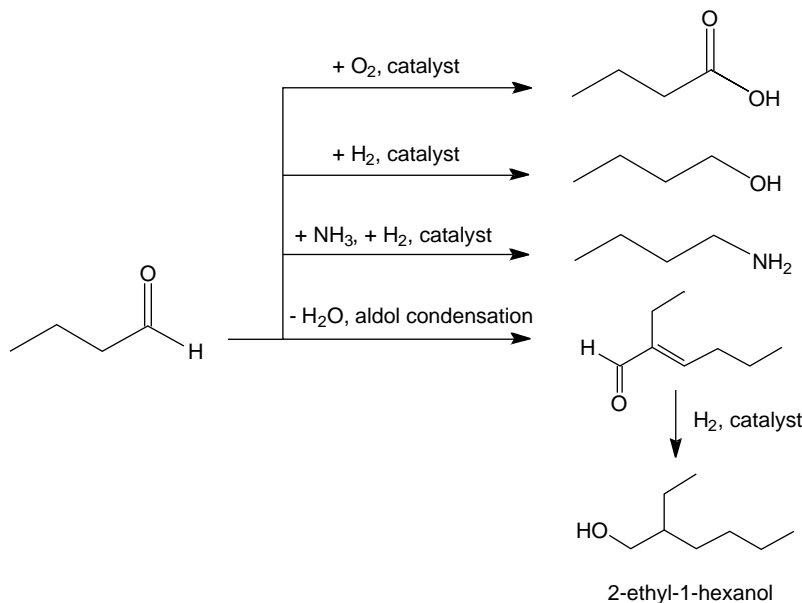
Hydroformylation was discovered in 1938 at the company *Ruhrchemie* in Oberhausen, Germany by *Otto Roelen* (1897–1993) in the context of investigations to optimize the Fischer–Tropsch synthesis (FT synthesis) for fuel production from coal based syngas (Section 6.11.1). *Otto Roelen* realized at the time that the formation of C₃-oxoproducts in the FT synthesis was due to the reaction of ethylene with syngas.

Only after the World War II was the economic value of the hydroformylation reaction fully recognized and explored. As illustrated in Scheme 6.14.2, hydroformylation converts the petrochemical basic chemicals, olefin, and syngas, in a two-step sequence into several very valuable organic intermediates. Thus, alcohols, aldol products, polyols, amines, and carboxylic acids can be produced at very attractive raw material costs using the corresponding aldehyde formed primarily by hydroformylation as common intermediate.

Today the installed hydroformylation capacity worldwide is more than 7.5 Mio tons per year (Baerns *et al.*, 2006). The most important feedstock is propene, with the products *n*-butyraldehyde and iso-butyraldehyde (Scheme 6.14.3). The most important single product from propene hydroformylation is 2-ethyl-1-hexanol (>50% of the *n*-butyraldehyde production), the aldol condensation product obtained from *n*-butanal, which is an important plasticizer alcohol. After esterification with phthalic anhydride, dioctyl phthalates plasticizers are obtained that are used mainly in poly(vinyl chloride) plastics.

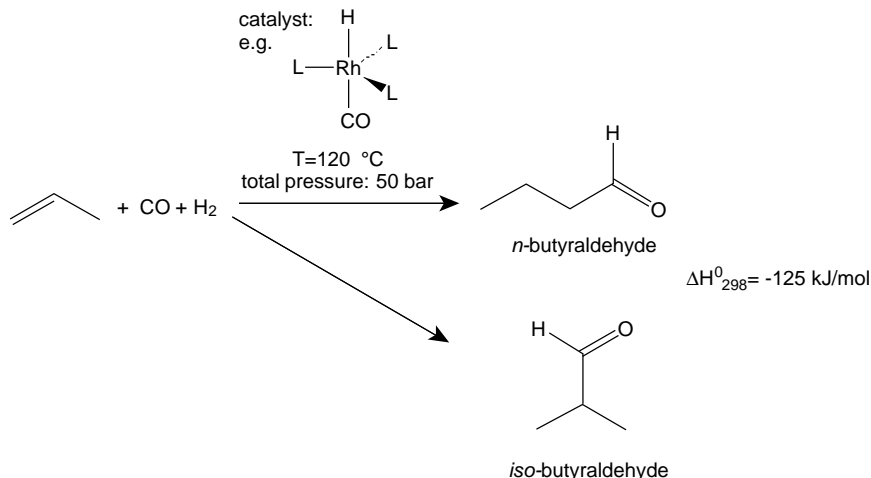
Apart from propene, a large number of C₂–C₁₇ olefins (including branched and internal ones) are applied industrially as hydroformylation feedstock depending on the market needs for the respective aldehydes and their subsequent product chains.

A very important general aspect of hydroformylation catalysis is the fact that the regioselectivity of the reaction is usually of great importance for the economic value of the generated products. Typically, the linear product enjoys a much higher market value than the branched one. This point can be exemplified for both the hydroformylation of propene and that of 1-dodecene. While the lower vapor pressure of the resulting plasticizer alcohol defines the higher



Scheme 6.14.2 Valuable organic intermediates and products obtained from *n*-butyraldehyde, the major product of propylene hydroformylation.

Scheme 6.14.3 Rh-catalyzed hydroformylation of propylene.



market value of *n*-butylaldehyde versus *iso*-butylaldehyde, the higher biodegradability of the linear C₁₃-alcohol is the key argument that requires high product selectivity to the linear aldehyde in the case of 1-dodecene hydroformylation as the product is usually further converted into the corresponding detergent alcohol. The homogeneous nature of hydroformylation catalysis allows optimization of the regioselectivity of the hydroformylation reaction by proper choice of ligands and reaction parameters. Other selectivity issues in hydroformylation catalysis arise from competing olefin hydrogenation and olefin isomerization reactions.

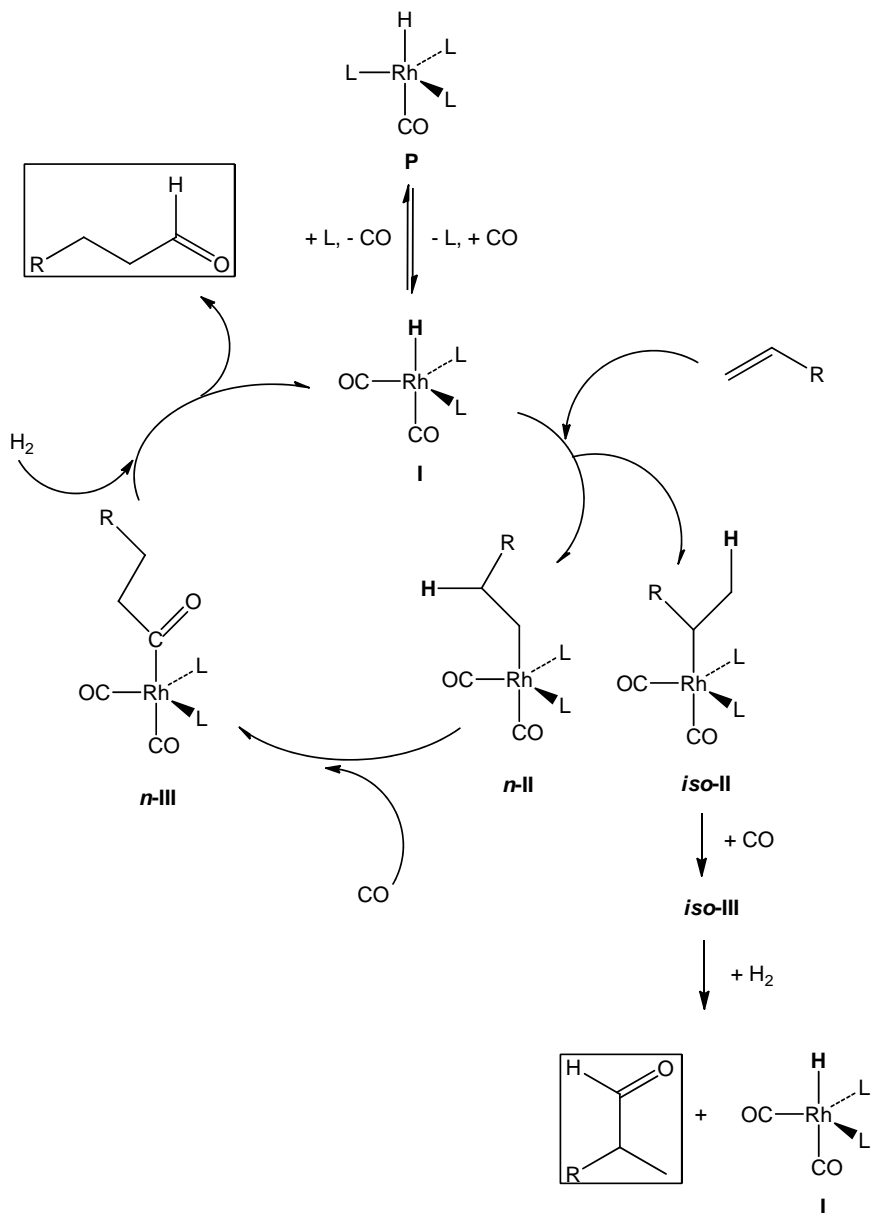
6.14.2 Hydroformylation Catalysis

Thermodynamically, hydroformylation requires low temperature and elevated pressure. For the aldehyde formation, the *iso*-isomer is thermodynamically favored and in a broader sense the hydrogenation of propene to propane is the preferred reaction.

Thus the catalyst has to favor first of all CO insertion over pure hydrogenation. This selectivity issue is mainly addressed by the choice of central transition metal for the hydroformylation catalysis. Obviously, all metals active in hydroformylation show a pronounced tendency to form metal carbonyl complexes. However, only Rh and Co complexes show sufficiently high hydroformylation activity for commercial applications, with rhodium being 1000–10 000-fold more active, but also about 1000-fold more expensive, than cobalt (Moulijn, Makkee, and van Diepen, 2001).

As the second selectivity issue, the catalyst should usually favor *n*-aldehyde over *iso*-aldehyde formation. This task is mainly addressed by the right choice of ligand. The ligand influences both the electronics and sterics of the catalyst in the step of the catalytic cycle that determines regioselectivity (see ***n*-II** versus ***iso*-II** in Scheme 6.14.4). Note that the transition state leading to the linear hydroformylation product involves a linear alkyl chain attached to the metal center that requires less space compared to the branched counterpart. Moreover, the electronic properties of the ligand influence the hydride transfer from the metal complex to C1 versus C2 during formation of the metal–carbon bond.

The hydroformylation catalyst cycle is initiated by a catalyst precursor (**P**) that is a ligand stabilized form of the active catalyst. In presence of syngas, the active catalyst



Scheme 6.14.4 Catalytic cycle in hydroformylation, highlighting the formation of the two regioisomeric products; for propene hydroformylation R = CH₃ and the two products formed are *n*-butyraldehyde and iso-butyraldehyde.

(I), a hydridorhodiumcarbonyl complex, forms by dissociation of the stabilizing ligand and by association of CO. The alkene associates first as a π -complex (not shown in Scheme 6.14.4 for clarity) followed by insertion of the olefin into the Rh—H bond to form the Rh-alkyl complexes *n*-II or *iso*-II. Note that in the insertion step the oxidation state of the central metal does not change. It is this insertion reaction that determines the regioisomer formed in the catalytic cycle as the later CO insertion can only happen at the Rh—carbon bond formed in the olefin insertion step. For CO insertion, CO adds first to the complex and is inserted into the Rh—carbon bond from the ligand sphere to form complexes *n*-III and *iso*-III, respectively. The catalytic cycle is closed for both regioisomers by an oxidative addition of hydrogen to the complex (Rh changes the oxidation state from +1 to +3) and reductive elimination of the product. This last step also involves dissociation and association of CO

at the complex to accommodate the two hydrogen ligands in the intermediate state of this step.

The competing side reactions, olefin hydrogenation, olefin isomerization (in case of higher olefins than propylene), and aldehyde hydrogenation to the corresponding alcohol, can also be explained based on this mechanism:

In the case of *olefin hydrogenation* the oxidative addition of hydrogen happens directly to the Rh-alkyl complexes **n-II** or **iso-II**. Hydrogen transfer and reductive elimination results in the same saturated alkane product from both regioisomers of the catalyst. Thus, olefin hydrogenation is a favored side reaction for all catalyst complexes that favor the kinetics of oxidative hydrogen addition over CO association and insertion. Olefin hydrogenation is, for example, much more relevant for Co hydroformylation catalysts compared to their Rh counterparts.

Olefin isomerization is a side reaction that only becomes relevant with olefin feeds higher than C₃ (R = ethyl and longer – note that the olefin isomerization product of propylene is propylene again). In 1-hexene hydroformylation (R = butyl), for example, the olefin isomerization side reaction leads to the formation of *cis/trans*-2-hexene and *cis/trans*-3-hexene and these intermediate products can also undergo hydroformylation and thus form different hydroformylation products compared to 1-hexene. Mechanistically, olefin isomerization proceeds by the catalyst intermediate **iso-II**. Immediate β -H-elimination (the reverse reaction of the insertion) leads mainly to the formation of *cis/trans*-2-hexene in a process that is driven by the higher thermodynamic stability of the internal olefin. A subsequent isomerization cycle using 2-hexene as substrate is responsible for the *cis/trans*-3-hexene formation observed in the reaction mixture of an isomerization-active 1-hexene hydroformylation catalyst. Olefin isomerization is a much undesired side reaction in the technical hydroformylation of 1-olefins as the internal olefins are less reactive and thus the kinetics of the overall hydroformylation slows down considerably. Moreover, the hydroformylation of internal olefins produces iso-aldehydes in the same undesired way as if the wrong regioisomer was formed from 1-hexene hydroformylation. There are technical scenarios, however, where the isomerization activity of a hydroformylation catalyst is highly desired. This is the case if the industrial feedstock that should be used in hydroformylation is a mixture of 1-olefins and internal olefins. Such mixed feeds are industrially available from, for example, steam cracking (raffinate II: mixture of 1-butene and *cis/trans*-2-butenes diluted with butanes, see Section 6.6) or from C₄-dimerization (linear, internal C₈-olefins) and are usually much cheaper than pure 1-olefin feeds. To convert these internal olefin feeds into the most valuable linear aldehyde a catalyst is required that isomerizes the olefins quickly into the thermodynamic equilibrium and takes from there only the most reactive minority part of the 1-olefin to convert the latter into the corresponding linear aldehyde (for details see Example 6.14.1).

Aldehyde hydrogenation is the side reaction of hydroformylation catalysis that leads directly to the formation of alcohols with one carbon atom more than the initial olefin substrate. This reaction is not always undesired as alcohol production is a major end-use of the aldehydes produced by hydroformylation. Mechanistically, a second equivalent of hydrogen is transferred to the carbonyl carbon atom and to the carbonyl oxygen via the same oxidative addition/reductive elimination mechanism. In particular, co-catalysts are known to produce alcohols directly due to their generally higher hydrogenation activity compared to the corresponding Rh complexes.

Example 6.14.1: Isomerization and hydroformylation of internal olefins to linear aldehydes

The transformation of an internal olefin (e.g., obtained from the linear dimerization of 1-butene) into a linear aldehyde requires a catalyst system that combines a high double bond isomerization activity (providing always the thermodynamic distribution of the linear double bond isomers) with a hydroformylation activity that converts the small amount of equilibrium 1-olefin with a strong kinetic preference into the desired linear aldehyde (Scheme 6.14.5).

Such catalyst systems have been developed in recent decades. They are often bidentate phosphine (Klein *et al.*, 2001) or phosphite (Behr *et al.*, 2003) ligand structures characterized by a specific ligand back bone that defines a certain “bite angle” (the ligand–metal–ligand angle of a bidentate ligand – see Figure 6.14.1) (van Leeuwen *et al.*, 2000). By its bite angle the ligand favors certain coordination spheres around the active metal. While a bite angle of 90° stabilizes octahedral or square planar coordination, a bite angle of 109° favors tetrahedral structure, and an angle of 120° trigonal bipyramidal structures. Note that during the catalytic cycle transitions between different coordination modes may be required. Therefore, flexibility of the bidentate ligand may be important to accelerate these transitions. The preference of a ligand for a certain coordination mode influences the catalytic cycle by stabilizing or

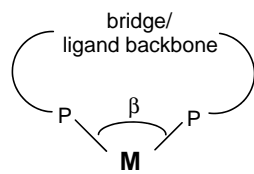
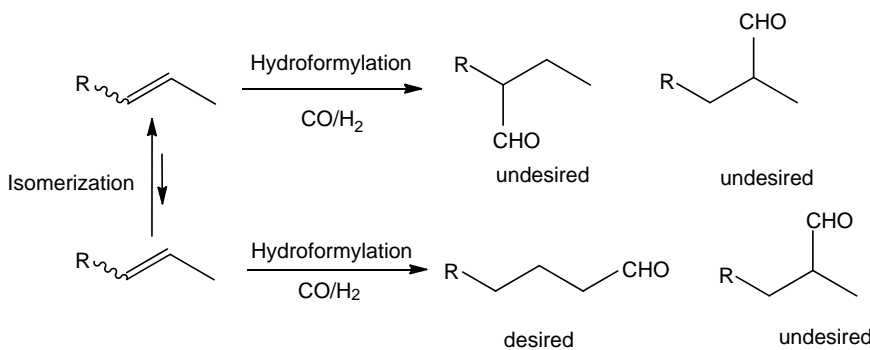


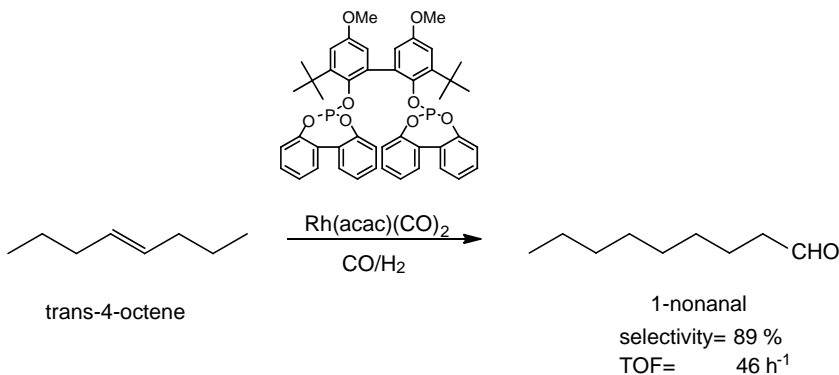
Figure 6.14.1 Ligand bite angle: the ligand–metal–ligand angle of bis-dentate ligands.

destabilizing the different states of the cycle, with severe consequences for the rate-determining step, selectivity, and overall reaction rate.

A famous example of a ligand structure that promotes the isomerization–hydroformylation reaction sequence in a highly selective manner is the BIPHEPHOS ligand (Scheme 6.14.6). BIPHEPHOS has been demonstrated to convert *trans*-4-octene into 1-nonalan with a remarkably high selectivity of 89% (given the complex reaction scheme) (Behr *et al.*, 2003). However, the Rh-BIPHEPHOS hydroformylation system for *trans*-4-octene is relatively slow ($\text{TOF} = 46 \text{ h}^{-1}$), leaving room for further ligand optimization to make combined isomerization/hydroformylation processes more efficient.



Scheme 6.14.5 Selective hydroformylation of internal olefins to *n*-aldehydes. Adapted from Klein *et al.* (2001).



6.14.3

Current Hydroformylation Catalyst and Process Technologies

Catalyst development in hydroformylation started with the discovery of the reaction in 1938 and has led to several major new developments during intensive industrial application of the reaction. Thereby, innovations in catalyst and process technologies went hand-in-hand. The introduction of Rh-based hydroformylation required, for example, much stricter requirements with regard to catalyst separation, recovery, and recycle compared to Co-based technologies due to the much higher price of the catalytic metal (by about a factor of 1000).

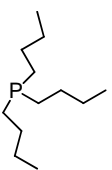
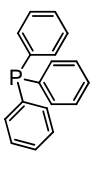
Very efficient and sophisticated catalyst recovery technologies paved not only the way for the application of the more expensive metal rhodium but also allowed the use of more sophisticated and expensive ligand systems that have to be recycled in the same way.

In general, catalyst and process technology in hydroformylation is optimized to allow transformation of the olefin feedstock into the most valuable hydroformylation products (high regioselectivity, high chemoselectivity) using the cheapest process conditions and applying process equipment installed with the lowest capital investment. To fulfill this goal, a large variety of aspects has to be taken into consideration, including, for example, protection of the active catalyst from catalyst poisons entering the reactor, stabilization of the catalyst in the reactor by the right metal/ligand ratio, separation of catalyst and product under mild conditions (avoiding too much thermal stress on the homogeneous catalyst), or proper heat integration in the process, which allows the reaction exotherm to be used for the energy-consuming steps of the process (such as distillation of crude aldehyde products).

In the following, the most important catalyst and process technologies for industrial olefin hydroformylation are presented and their specific advantages and disadvantages are discussed. Table 6.14.1 gives an overview of the different processes described in more detail throughout this subchapter.

The first generation of hydroformylation technologies used Co catalysts without modification by ligands. In these systems, which are still in use today for the production of plasticizer range (C_4 – C_{10}) or detergent range (C_{12} – C_{18}) alcohols from internal olefins, $HCo(CO)_4$ acts as the active catalyst. Note that this unmodified Co catalyst requires very harsh reaction conditions with respect to syngas pressure and shows a relatively modest regioselectivity. After the homogeneous reaction in the hydroformylation reactor it is very important to prevent dissolved cobalt carbonyls

Table 6.14.1 Comparison of different catalyst and process technologies for industrial olefin hydroformylation. Adapted from Moulijn, Makkee, and van Diepen (2001) and Baerns *et al.* (2006).

Parameter	Technology			
	Ruhrchemie, Kuhlmann	Shell	Union Carbide, Davy Powergas, Johnson Matthey	Ruhrchemie/Rhône-Poulenc
Typical feed	Internal C_4 – C_{17}	Internal C_4 – C_{17}	Propylene	Propylene
Catalyst	$HCo(CO)_4$	$HCO(CO)_3L$	$HRh(CO)L_3$	$HRh(CO)L_3$
Ligand	None			
				
Temperature (°C)	110–180	160–200	85–115	110–140
Pressure (bar)	200–300	50–100	15–20	40–50
Linearity (%) (<i>n</i> to iso ratio)	80 (4.0)	88 (7.3)	92 (11.5)	95 (19.0)
Alkane formation (%)	2	10–15	0	0

entering the downstream distillation columns. Here cobalt would precipitate out in the absence of syngas pressure (i.e., in the internals, trays, packings of the distillation equipment), which would cause severe fouling problems and frequent shutdowns. Two different techniques are applied to prevent this problem. The first is to precipitate the homogeneous catalyst in a special unit that is installed before the distillation columns. Here, cobalt precipitates in a controlled manner and this process is induced by heating after depressurization. A second, more elegant method (Kuhlmann, BASF process) adds Na_2CO_3 to the homogeneous catalyst solution after the reactor. The fast reaction of the strongly acidic $\text{HCo}(\text{CO})_4$ catalyst with the carbonate base converts the active catalyst into the water-soluble Co-salt $\text{Na}[\text{Co}(\text{CO})_4]$. The latter can be isolated by an aqueous scrubber system to obtain a virtually Co-free hydroformylation product stream (usually not water-soluble) that is sent to the distillation units. To recycle the aqueous solution of $\text{Na}[\text{Co}(\text{CO})_4]$ to the process, sulfuric acid is added and the re-formed, olefin-soluble active catalyst, $\text{HCo}(\text{CO})_4$, is extracted by fresh olefin feed back into the reactor. The remaining aqueous phase contains Na_2SO_4 in a stoichiometric amount to the treated Co-catalyst and ends up in the site's wastewater treatment system.

From 1960 on, Shell introduced phosphine modified Co catalyst systems for direct alcohol production via a hydroformylation/hydrogenation reaction sequence from $\text{C}_3\text{-C}_{17}$ olefins. The process is realized in two stages as the high hydrogen pressures required for aldehyde hydrogenation would cause too much olefin hydrogenation in a single step process. The Shell catalyst system works at significantly lower syngas pressure compared to the unmodified Co-system and displays a high activity for double bond isomerization and aldehyde hydrogenation, allowing the production of linear alcohols from 1-olefins and internal olefins (Bryant, 2006). A particular advantage of the Shell catalyst system over the unmodified Co-carbonyl catalyst system is a strong stabilizing effect of the phosphine ligands that allows direct distillation of the product alcohols from the catalyst solution. After distillation the Co-complexes remain dissolved in heavy by-products of the hydroformylation process without Co precipitation. The successful catalyst separation by distillation greatly simplifies the whole process scheme and reduces significantly the number of unit operations compared to the Kuhlmann process. However, these advantages come with two distinct disadvantages of the phosphine modified Co-catalysis in hydroformylation: (i) the basic phosphine ligands applied in the Shell system are highly sensitive to oxidation and thus thorough (and costly) purification of the syngas is required; (ii) the catalytic activity of the modified Co catalyst is much lower than that of its unmodified counterpart. The latter fact results in a reactor volume that is five to six times larger in the Shell process than for the unmodified Co-catalysis for the same productivity.

From 1974 onwards, Rh-based hydroformylation became industrial. The use of a catalyst metal that is about 1000-times more expensive than cobalt was driven by several reasons. First, Rh-hydroformylation is more active and thus requires much lower process pressures (lower energy consumption in compression units) and smaller reactors. Second, Rh-hydroformylation shows a very high selectivity to the aldehyde product with only minimal hydrogenation activity being observed. This is of particular importance for propylene hydroformylation where butyl alcohol is not the principle market use. In contrast, for the desired end-use of *n*-butyraldehyde in the form of its aldol condensation product 2-ethylhexanol a pure aldehyde feed is required as hemiacetals (formed by reaction of aldehyde and alcohol) complicate product purification and add to operating costs.

Obviously, in Rh-catalyzed hydroformylation extreme care has to be taken to avoid all loss of the precious metal compound from the process. This requires keeping the metal in its most stable active form in the process and avoiding any process conditions that would harm the catalyst's life-time. This is the reason why no industrial process is known that uses non-ligand-modified Rh-catalysis even though pure Rh-carbonyl is an active hydroformylation catalyst. The breakthrough in industrial Rh-catalyzed hydroformylation came with the discovery of triarylphosphine-

modified rhodium catalysts, which allow a simultaneous improvement in catalyst stability, reaction rate, and process selectivity compared to the unmodified Rh catalysis. The fundamental difference between unmodified Rh-catalyzed hydroformylation and triphenylphosphine ligand modified Rh-catalyzed hydroformylation catalysis also becomes obvious by comparing the reaction kinetics. For the Rh-catalyst system where all ligands are CO the rate expression is given by (Moulijn, Makkee, and van Diepen, 2001):

$$r_{\text{hydroformylation}} = k \frac{c_{\text{Rh}} c_{\text{H}_2}}{c_{\text{CO}}} = k \frac{H_{\text{c}, \text{H}_2} c_{\text{Rh}} p_{\text{H}_2}}{H_{\text{c}, \text{CO}} p_{\text{CO}}} \quad (6.14.1)$$

where c_i ($i = \text{Rh}$, H_2 or CO) is the molar concentration (mol m^{-3}), p_i is the partial pressure (Pa), and H_c is *Henry's constant* – for details see Section 3.3.3.1 – related to the concentration of H_2 or CO in the liquid organic phase ($H_{i,c} = p_i/c_i$, $\text{Pa m}^3 \text{ mol}^{-1}$).

In contrast, for hydroformylation reactions with a Rh-catalyst containing triphenylphosphine ligands a modified rate expression has been determined:

$$r_{\text{hydroformylation}} = k \frac{c_{\text{Rh}} c_{\text{H}_2}^{0.05}}{c_{\text{PPh}_3}^{0.7} c_{\text{CO}}^{0.1} c_{\text{olefin}}^{0.6}} = k \frac{H_{\text{c}, \text{H}_2}^{0.05} c'_{\text{Rh}} p_{\text{H}_2}^{0.05}}{H_{\text{c}, \text{CO}}^{0.1} c_{\text{PPh}_3}^{0.7} p_{\text{CO}}^{0.1} c_{\text{olefin}}^{0.6}} \quad (6.14.2)$$

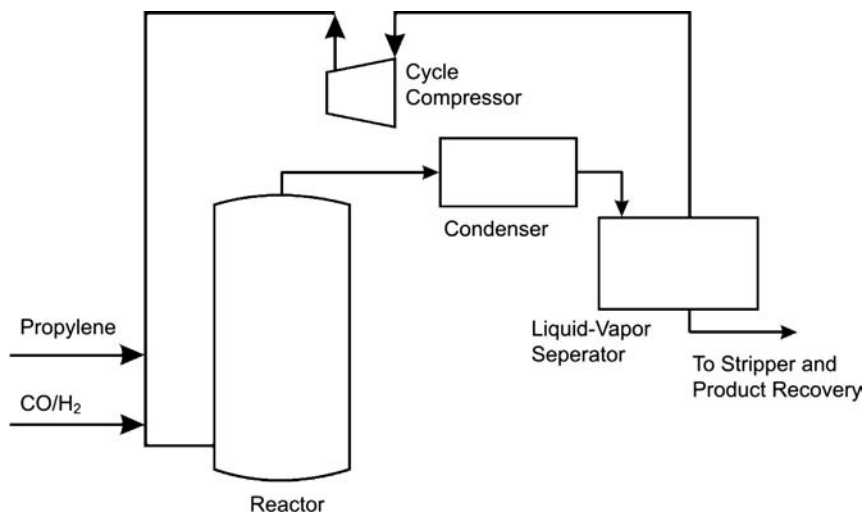
To stabilize the working Rh catalyst in the most effective manner many industrial hydroformylation processes apply the triarylphosphine ligand in high excess (i.e., a molar ligand-to-Rh ratio of 75 is common).

Rhodium-catalyzed hydroformylation of propene is industrially realized in three process variations that differ in the way the products are separated from the Rh-catalyst after or during the homogeneous catalyzed reaction.

The Union Carbide/Davy Powergas *gas recycle process* isolates the hydroformylation products by vaporization with a huge recycle of the reactant gases. The reactor contains the rhodium complex and the excess triphenylphosphine ligand dissolved in a suitable solvent at 85–115 °C. It is pressurized with the feedstock mixture in the right stoichiometry to 15–20 bar total pressure [due to its low operational pressure the process is also referred to as low-pressure oxo process (LPO)]. The entering gas mixture (propene and syngas) passes through the catalyst solution and saturates with the butyraldehyde products. A chiller behind the reactor condenses the components of lowest volatility, the butyraldehyde products, out of the gas stream. The latter are transferred to a stripper unit and from there to the crude aldehyde distillation column. The gas stream leaving the chiller over the top is compressed and returned to the reactor (Figure 6.14.2).

One important advantage of the gas recycle process is that all the catalyst always remains in the reactor and, thus, all the catalyst works under identical process

Figure 6.14.2 Schematic view of the reactor section of the Union Carbide/Davy Powergas gas recycling process for propylene hydroformylation. Adapted from Bryant (2006).



conditions all the time. This leads to a more efficient catalyst use and reduces the amount of precious Rh required for a certain level of productivity. Another advantage is that the reactor concept makes use of the reaction heat of hydroformylation to vaporize the aldehyde product. This saves energy and solves effectively all problems related to reactor cooling. Disadvantages of the gas recycle arise from the energy consumption of the recycle compressor and the chiller unit. Moreover, the large gas flow through the reactor requires a large reactor volume compared to a liquid process. Complications in the gas recycle arise from the production of “heavies,” that is, any kind of low volatile condensation, dimerization, or trimerization products. Therefore, successful operation of a gas recycle requires keeping the liquid level in the reactor as constant as possible.

Note that the process offers no independent way to remove heavies (too high boiling to be vaporized from the reactor into the chiller) independent of the dissolved catalyst. This explains why it is difficult to recover the process from disruptions in operation.

Gas recycle hydroformylation processes have been licensed worldwide and operate for ethylene and propylene hydroformylation. Butene hydroformylation has been demonstrated in a pilot plant but it was found that problems linked to the formation and removal of heavies make the process in fact technically unfeasible for all olefins heavier than propylene.

In the *liquid recycle process* product separation from the catalyst solution takes place outside of the reactor and independently of reaction conditions (Frohning *et al.*, 2002). Figure 6.14.3 shows the process scheme.

Propene and syngas are fed to the reactor, where the gases are intimately contacted with the ligand-modified rhodium catalyst in solution. The reaction exotherm is removed by a dedicated heat exchanger. The liquid effluent from the reactor passes to a degassing column where unreacted propylene and syngas is evaporated from the catalyst/product solution and recycled back to the reactor. In the fourth column the hydroformylation products are separated from the Rh-catalyst by distillation. While butyraldehydes leave the column over the top the catalyst remains at the bottom of the column dissolved in liquid heavy products of the process to be recycled back to the reactor. The crude aldehyde products undergo a further purification step in the crude aldehyde column prior to their transfer to the *n*/iso-butyaldehyde splitter column.

An important advantage of the liquid recycle process over the gas recycle process is that the product can be removed from the catalyst solution using vaporization parameters independent of the reaction parameters. This additional degree of

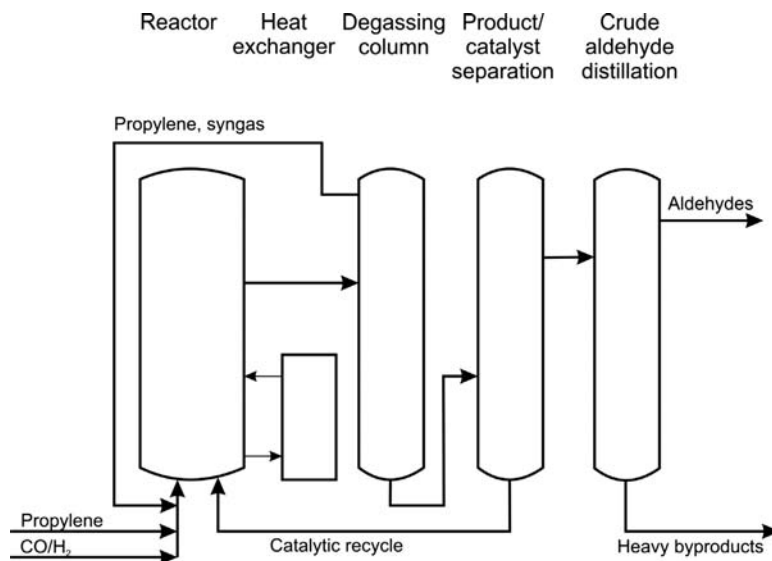


Figure 6.14.3 Schematic view of a liquid recycling process for propylene hydroformylation.

operational freedom leads to the advantage that process conditions in the reactor can be optimized for the reaction only, for example, reactor temperature and feedstock concentrations can be adjusted for optimum reaction rate and selectivity. Likewise, conditions in the product/catalyst solution distillation column (Figure 6.14.3) can be chosen independent of the reaction conditions. This allows, for example, control of the amount of heavies recycled from the product/catalyst separation back to the reactor. Here a careful optimization process is required. On the one hand side, a higher concentration of the catalyst exiting the separation system and entering the reactor (i.e., more severe distillation conditions) will ultimately lead to a higher product concentration in the effluent of the reactor. This is important as a higher product concentration means fewer passes of the catalyst solution through the vaporizer for a given aldehyde production. On the other hand, more severe separation conditions in the product/catalyst separation step can lead to faster thermal degradation of the Rh-catalyst (Garrou, 1985). Note that the catalyst experiences low propylene and syngas concentrations in the vaporizer. Therefore, apart from the distillation parameters, Rh and ligand concentration are also important parameters for the thermal stability of the catalyst solution. Thermal degradation may include significant reduction of catalyst activity or solubility by thermal ligand degradation, metal plating, or nanoparticle formation. All these potential complications underline the fact that the successful operation and optimization of a liquid recycle hydroformylation process requires a reasonable trade-off between process productivity and catalyst lifetime. Finding optimal operation conditions thus requires an intimate collaboration of process chemists and engineers. Moreover, many of the named problems become more severe if olefins higher than propylene are used as feedstock as the isolation of heavies from the process becomes increasingly difficult the less volatile they are.

An alternative process concept that realizes the task of catalyst/product separation under much milder conditions is the *water–organic, liquid–liquid biphasic reaction system*, as realized in the Ruhrchemie/Rhône-Poulenc process. The first commercial plant using this technology went on stream in 1984 and to date about 650 kton of yearly capacity has been installed. The process makes use of the fact that butyraldehydes and heavy by-products of the propylene hydroformylation are characterized by a very low solubility in water and thus can be isolated from the Rh catalyst by a liquid–liquid phase separation if the catalyst is quantitatively immobilized in an aqueous phase. Therefore, a major breakthrough in the development of the Ruhrchemie/Rhône-Poulenc process was the development of an extremely water-soluble analog of the triphenylphosphine ligand, namely, the sodium salt of tris(*m*-sulfonatophenyl)phosphine (Na-TPPTS) (Kuntz, 1987; Drießen-Hölscher, Wasserscheid, and Keim, 1998). Using this ligand in excess compared to rhodium, Rh-leaching from water into the organic phase can be minimized into the lower ppb ranges, making the process and catalyst recycling concept technically feasible. An additional advantage arises from the fact that the sulfonated ligand TPPTS provides high hydroformylation activity and a very attractive regioselectivity of the aldehyde products with an *n*/iso-ratio of 19 (*n*-butyraldehyde selectivity of 95%). Note that the Ruhrchemie/Rhône-Poulenc process operates a reactor that contains two immiscible liquid phases, of which only one contains the catalyst and, consequently, the catalytic reaction only takes place in that phase. Therefore, hydroformylation in the aqueous phase requires mass transfer of the olefin from the liquid organic into the aqueous phase and mass transfer of the syngas from the gas phase into the aqueous phase (see Section 4.4 for the reaction engineering fundamentals of fluid-fluid multiphase reactions). Figure 6.14.4 gives a schematic view of the Ruhrchemie/Rhône-Poulenc process.

The reactor is a continuous stirred tank reactor that provides intense mixing of the excess aqueous phase, the organic phase (ratio aqueous/organic phase = 6), and syngas to create enough interphase for effective mass transfer. The reaction exotherm is applied in a falling film evaporator to produce *n*-butyraldehyde vapor to

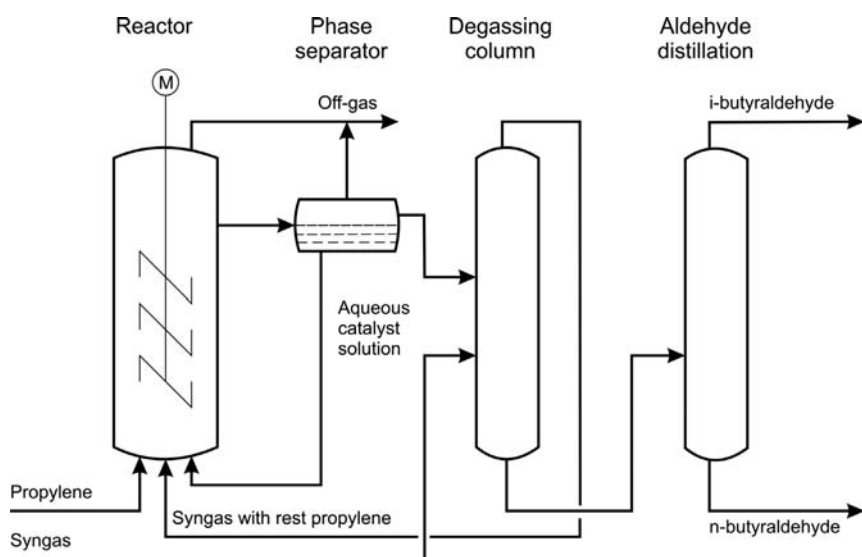


Figure 6.14.4 Process scheme of the Ruhrchemie/Rhône-Poulenc process. Adapted from Baerns *et al.* (2006).

realize heat integration with the product distillation unit (not shown in Figure 6.14.4 for clarity). In this way, the heat of the hydroformylation reaction is used to operate the crude aldehyde distillation. A liquid emulsion with dissolved syngas leaves the reactor and phase separation of the aqueous and the organic phase takes place in a liquid–liquid phase separator that requires no additional energy input. The aqueous catalyst solution is directly returned to the reactor while the organic mixture passes through a degassing unit. In this column syngas feed is used as stripping gas to remove unconverted propylene from the organic crude product. The stripping gas stream is passed directly to the reactor. The aldehyde crude product obtained from the bottom of the degassing column is passed to the crude aldehyde column where iso- and *n*-butyraldehydes are separated. Heavy products are obtained in the bottom stream of the crude aldehyde distillation column. Table 6.14.2 summarizes the average performance data of an industrial Ruhrchemie/Rhône-Poulenc process unit during 15 years of operation time.

Obvious advantages of the Ruhrchemie/Rhône-Poulenc process originate from the very mild catalyst/product separation conditions and the straightforward way of dealing with heavies. The latter are easily separated from the catalyst due to their even lower water-soluble nature. Less obvious, but very important advantages of the process arise from the attractive heat integration options offered by the favorable temperature levels of all unit operations and the unique heat transfer and heat storage properties of the reaction solvent water.

A severe drawback of the process arises from the limited solubility of olefins in water, which restricts the process to propylene and butylenes hydroformylation. Figure 6.14.5 shows the dependence of olefin solubility in water as a function of the number of carbon atoms.

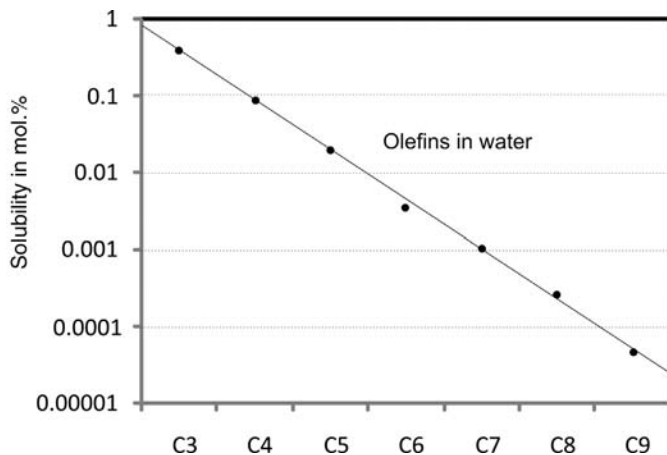
Note that for a low olefin concentration in the catalyst phase the reaction rate is first order in olefin – thus the reaction rate in the Ruhrchemie/Rhône-Poulenc process is severely limited by the low olefin concentration. As a consequence, even for propylene hydroformylation the Ruhrchemie/Rhône-Poulenc process requires a relatively large reactor and a relatively high rhodium inventory. For butylene hydroformylation, the process approaches the margin of economic operability, and for the hydroformylation of even higher olefins it becomes unfeasible because of the limited olefin solubility. Note that a significant amount of mechanical (in fact electrical) energy has to be invested in the Ruhrchemie/Rhône-Poulenc process for intense stirring to provide the necessary interphase in the biphasic system so as to operate the system free of mass transfer limitations.

Fundamental research and process optimization studies in the last 25 years have tried to overcome the above-mentioned limitations. Interesting results for the

Table 6.14.2 Conditions and performance of an industrial Ruhrchemie/Rhône-Poulenc process (15 year average). Adapted from Frohning *et al.* (2002).

Parameter	Value
Conversion	95%
Selectivities	
<i>n</i> -Butyraldehyde	94.5%
<i>iso</i> -Butyraldehyde	4.5%
<i>n</i> -to- <i>iso</i> ratio	95 : 5 = 19
Butanols	<0.5%
Butyl formates	Traces
Heavy ends	0.4% (mainly 2-ethyl-3-hydroxyhexan-1-al)
Typical process conditions	Reaction temperature: 120 °C, total pressure: 50 bar, CO to H ₂ ratio: 1.01, water to organic phase ratio: 6.

Figure 6.14.5 Solubility of 1-olefins in water as a function of their number of carbon atoms. Adapted from Frohning *et al.* (2002).



liquid–liquid multiphasic hydroformylation of higher olefins have been obtained by the addition of ethylene glycol to the aqueous catalyst phase (Wiese *et al.*, 2003). However, in pilot plant studies problems with the chemical stability of the ethylene glycol and issues with the separation of side-products formed from the additive occurred. Therefore, the technology has not been commercialized yet. Another highly interesting development is the replacement of the stirred tank reactor by a loop reactor design with internals that enable the formation of emulsion with very small droplets simply by the pressure drop over a static mixture. This design allows rational optimization of the catalyst phase droplet size to maximize the productivity of the hydroformylation reactor (Wiese *et al.*, 2003).

To conclude on the different process technologies for Rh-catalyzed propene hydroformylation, Table 6.14.3 compares the above-mentioned alternatives with respect to parameters relevant to calculating the capital investment for the process, such as reactor volume, Rh inventory, and ligand inventory. From the fact that all three technologies are operated nowadays we can conclude that none of the three alternatives is so superior that it would be economically attractive to shut a fully depreciated plant down and to install the same capacity with another technology. All three process alternatives have their specific strengths and weaknesses and a decision for one or the other process option has to be taken according to the capacity, intended further use of the aldehyde product, site infrastructure, and licensing conditions.

None of the above-described process options using rhodium as catalyst metal is suitable for the industrial hydroformylation of C_{5+} olefins. The induced phase separation process proposed by Union Carbide in the mid-1990s overcomes the problems of low heavy by-product volatility and low olefin solubility in water by a technology that avoids two separate phases in the reactor but uses nevertheless an extraction step for catalyst separation. Owing to the homogeneous monophasic nature of the reaction mixture, limited olefin solubility and mass transport issues no longer restrict the reaction rate, which results in high hydroformylation rates. The preferred option to realize the induced phase separation process is to use a monosulfonated triphenylphosphine ligand dissolved in the polar solvent *N*-methylpyrrolidone (NMP).

Table 6.14.3 Comparison of the three industrially practiced, Rh-catalyzed hydroformylation processes for propylene based on a $400\,000\,\text{t}\,\text{a}^{-1}$ plant capacity scenario. Adapted from Wiese *et al.* (2003).

Gas recycle process	Liquid recycle process	Ruhrchemie/Rhône-Poulenc process
Reactor volume (m^3)	400	300
Rh inventory (kg)	50	15
Ligand inventory (kg)	15 000	4 000
		100 000

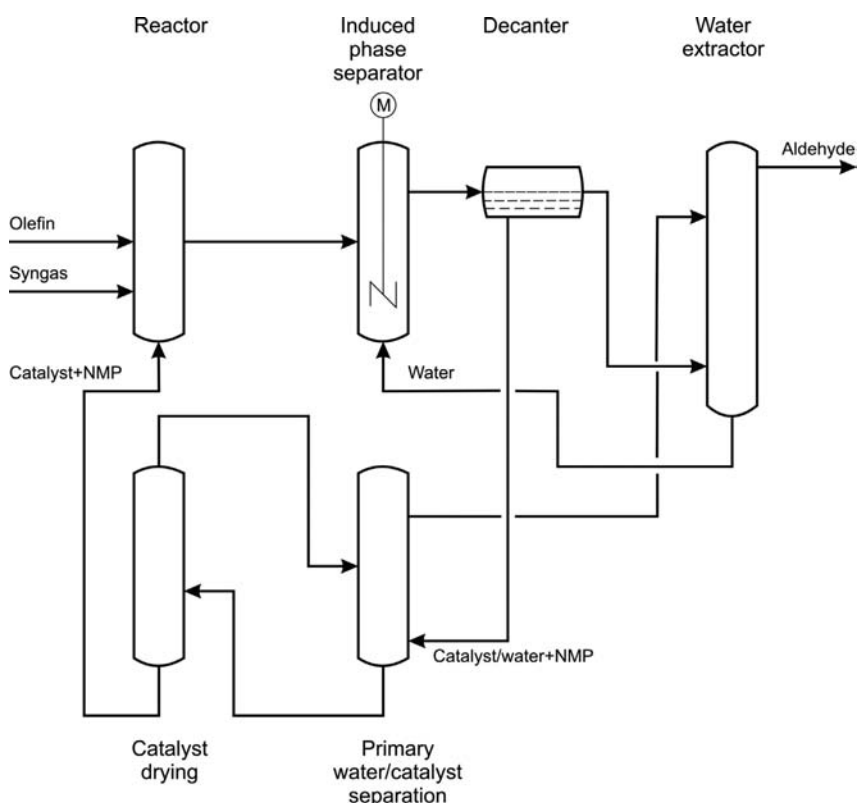


Figure 6.14.6 Schematic view of Union Carbide's Induced Phase Separation Process for the hydroformylation of C₅₊ olefins. Adapted from Bryant (2006).

(Bryant, 2006). The process scheme is displayed in Figure 6.14.6. Olefin and syngas are added to the reactor, where the modified Rh catalyst promotes hydroformylation in a monophasic reaction system. After venting the syngas, the reactor effluent contains the dissolved Rh-catalyst, aldehyde products, unconverted olefin, and heavy side products dissolved in NMP. In the induced phase separator, a small amount of water is added and phase separation occurs with the rhodium catalyst being extracted into the aqueous phase, NMP partitioning over the two phases, and all organic reaction products and unconverted olefins forming the water-immiscible organic phase. The two phases are separated in a decanter. To complete NMP and water (containing also some of the precious Rh catalyst) removal from the organic phase, a second water-extraction step is carried out using freshly distilled water from the water removal section of the catalyst phase. The crude aldehydes obtained from there are sent to the product distillation columns. The aqueous phase from the water extraction step containing NMP and water/catalyst is sent directly back to the induced phase separator. The main fraction of water/NMP/catalyst that has been separated in the decanter passes through two drying stages. The first stage produces the distilled water that is fed to the water extractor, while the second stage completes the drying of the catalyst, which is then returned to the reactor. Note that the catalyst solution in NMP must be dry enough before entering the reactor to avoid any liquid–liquid phase separation in the reactor that would greatly reduce the reaction rate due to the solubility limitation of the applied higher olefin feedstock.

The induced phase separation technology offers the great advantage that very high molecular weight olefins can also be hydroformylated effectively and the catalyst can be separated without suffering the “thermal stress” that would be unavoidable in the case of distillative product removal from the catalyst solution. Disadvantages arise from the removal of water from the catalyst solution during recycling, which is energy intensive due to water’s high heat of vaporization. In addition, the selection of ligands and solvents is very limited due to the complex

solubility and miscibility requirements of the process. These restrictions have led to the additional development of a *non-aqueous phase separation technology* where a combination of a non-aqueous polar solvent and a very nonpolar solvents form the required liquid–liquid biphasic system for extractive catalyst separation. In all cases the applied ligand must have an extremely high preference for one of the two phases and, thus, the applied ligands are usually very polar (as the product is usually highly nonpolar and the catalyst solvent is therefore polar to form the miscibility gap). The non-aqueous phase separation technology offers more flexibility with respect to hydroformylation substrate and ligand classes and avoids the vaporization of water. However, cross-solubility effects of immiscible organic solvents can mean that the polar and the nonpolar phase of the reaction system become too similar in their solubility properties to provide the necessary extreme partitioning of the catalyst complex into only one of the two phases.

In conclusion, it has to be clearly stated that for all Rh-based hydroformylation technologies the very challenging key criterion is a minimum loss of the precious metal into the organic product phase. Acceptable losses are in the lower ppb ranges (a 10 ppb Rh-loss with respect to the aldehyde product corresponds roughly to a Rh loss of 1 kg in a 100 000-ton hydroformylation plant per year). Only high value specialty hydroformylation products may permit significantly higher metal losses in economic operation. This makes metal recovery a critical aspect for the process economics. Note that in the real life operation of a hydroformylation plant product/catalyst separation is a much more complex task than in the laboratory. In real life application, the nature of the catalyst will vary over time. It may become poisoned by impurities in the feed to form inhibited or less active species that also show different solubility or stability properties in the separation and recycling step. Organophosphorous ligands undergo in real life long-term application several degradation reactions that are difficult to observe in the development laboratory. These are phosphine ligand oxidation, ligand substituent scrambling, and phosphorous ligand reaction with the olefin feed under hydroformylation conditions. In cases where phosphite ligands are applied (Example 6.14.1) the ligand can also oxidize and undergoes rapid hydrolysis in contact with water to form phosphoric acid, which itself promotes further ligand degradation (Sakakura *et al.*, 1984). Some of these ligand degradation products are relatively inert in the process and may only require addition of fresh ligand after a certain operation time. Others alter the reaction rate or catalyst selectivity significantly and this can pose a real threat to process stability. Moreover, the conversion of feedstock into the desired products is never perfect and may be seriously imperfect in the case of a process disruption or in the case of any unusual process conditions. For example, alkenes may oligomerize in the presence of acids. Under the same conditions aldehydes undergo various condensation reactions and all these products may react again with the ligand and the catalyst.

In a real life hydroformylation plant all the above-mentioned complications have to be mastered to operate the plant at the economically acceptable level of Rh loss. This requires a very robust process technology and experienced and skilled personal operating the respective hydroformylation process.

6.14.4

Advanced Catalyst Immobilization Technologies for Hydroformylation Catalysis

Over the last 40 years the economic importance of industrial aldehyde production has led chemists and engineers to propose new and alternative ways to further optimize hydroformylation technologies. Particular attention in these attempts was always given to new concepts by which to combine the molecular defined, homogeneous nature of hydroformylation catalysis with cleverer ways to separate products and catalyst after reaction. Many of the reported strategies have focused on the

separation of higher aldehydes (C_{5+}) from homogeneous or pseudo-homogeneous Rh-catalysts, as this particular topic still offers a lot of room for more efficient process technologies.

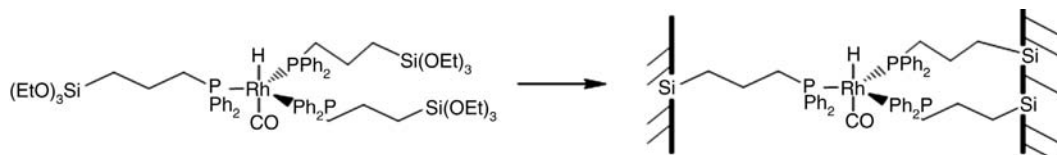
The following concepts are still under intense academic and industrial development and it is not yet clear which concept will make it to an industrial process. However, all these attempts are not only relevant for industrial hydroformylation catalysis but of very fundamental relevance to applying homogeneous catalysts in ways that allow facile product/catalyst separation. Thus, their success will be important for the extent of homogeneous catalysis application in future bulk chemicals production. The fact that hydroformylation has become over the years *the* benchmark reaction for all catalyst immobilization strategies and all new concepts for product/catalyst separation and catalyst recycling in homogeneous catalysis facilitates their direct comparison. Of course, the restricted scope of this textbook will not allow in-depth treatment of each approach. But the short descriptions given below provide an overview of the respective concepts, a flavor of the future, and an appetizer to taking a deeper look into specific ideas related to your particular interest using the specialized references given for each approach.

6.14.4.1 Immobilization of Homogeneous Hydroformylation Catalysts on Solid Surfaces by Covalent Anchoring

An obvious way to combine the advantages of homogeneous and heterogeneous catalysis for optimized hydroformylation catalysis is to covalently anchor the molecular catalyst complex to a solid surface. Such an immobilized catalyst could be used in fixed bed or slurry type reactors and product separation would be as straightforward as for any heterogeneous catalyst. Indeed, this approach has been most widely studied as evidenced by numerous academic papers and patents, reviews, and books (Keim and Driessens-Hoelscher, 1999 and Reek *et al.*, 2006).

All attempts to covalently bind homogeneous catalysts to surfaces follow similar strategies: In a first step an organic linker is attached covalently to a reactive solid surface. At one or several free ends of the linker the ligand functionality (e.g., a phosphorous or nitrogen donor atom) is attached to coordinate, finally, the active Rh catalyst. Spacer and ligand functionality are typically selected in a way that keeps the metal away from the surface (which itself would exert in direct contact a usually unfavorable ligand effect) and creates around the metal an electronic and steric environment mimicking the successful homogeneous hydroformylation catalysts in the closest possible manner. Prominent examples of reactive supports are polystyrene polymers (Leadbeater and Marco, 2002) or silica surfaces (Deschler, Kleinschmit, and Panster, 1986 and Reek *et al.*, 2006). Scheme 6.14.7 shows the example of rhodium hydroformylation catalyst attached to a silica surface by a condensation reaction that liberates ethanol (Lindner *et al.*, 1994).

Despite the obvious beauty of this approach and the enormous research work dedicated to its technical realization there is no example of a covalently surface bonded hydroformylation catalyst in industry so far. The main difficulty that has been encountered is unacceptably high metal leaching from the support, mainly due to unfavorable ligand–metal complexation equilibria. Therefore, the best results have been reported for bidentate, covalently anchored ligands, with Rh leaching in the range 100–1000 ppb. Other drawbacks of the approach in



Scheme 6.14.7 Rhodium catalyst for hydroformylation linked to a silica surface via an alkyl-triethoxysilane modified diphenylphosphine ligand. Adapted from Bryant (2006).

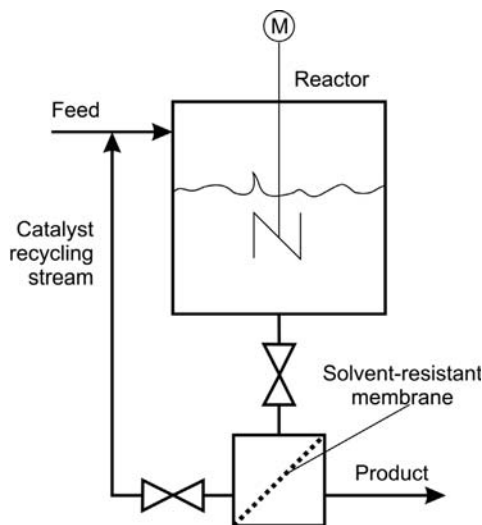


Figure 6.14.7 Cross-flow filtration reactor for the separation of a size enlarged homogeneous catalyst from its reaction products. Adapted from Nair *et al.* (2002).

hydroformylation catalysis include reduced activity and selectivity upon catalyst immobilization, limited mechanical strength and swelling properties of the resulting solid catalyst, and non-innocence of the support. If future research can solve some of the above-mentioned problems, a first application of covalently anchored hydroformylation catalysis is most likely for specialty applications (e.g., enantioselective hydroformylation) where somewhat higher Rh-leaching can be tolerated.

6.14.4.2 Catalyst Separation by Size Exclusion Membranes

An interesting alternative for the immobilization and recovery of homogeneous catalysts that follows a very different concept than anchoring on solid surfaces is catalyst separation using advanced filtration techniques. The concept builds on recent advances in the design, synthesis, and characterization of ultra- and nanofiltration membranes (Ulbricht, 2006) and offers several attractive features. Figure 6.14.7 shows a schematic view of a catalytic reactor using a membrane catalyst/product separation. The catalyst is homogeneously dissolved in the reaction mixture and remains always active in the reactor. Thus, the reaction proceeds free of mass transfer limitations due to the homogeneous nature of the reaction mixtures (membrane transport resistance is usually negligible). The separation step of filtration can be realized with low energy consumption and is combined with a minimum of thermal stress for the catalyst (Ronde and Vogt, 2006).

Note that the concept of homogeneous filtration requires a significant difference in molecular size between the catalyst complex to be retained by the membrane and the components of the reaction mixture that should pass the membrane. Therefore, molecular enlargement of the catalyst complex is a synthetic prerequisite for successful application of this strategy. Such enlargement can be realized by binding the homogeneous catalyst to large, soluble molecular entities such as dendrimers, hyper-branched polymers, or polysiloxanes. Figure 6.14.8

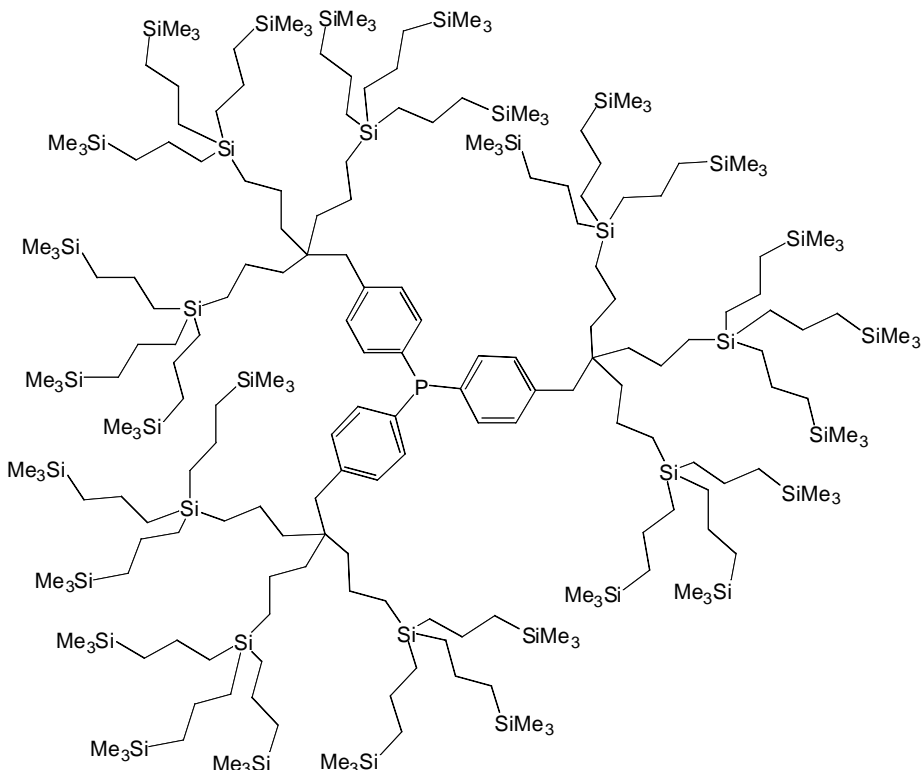


Figure 6.14.8 Example of a molecularly enlarged triphenylphosphine-type ligand obtained by core functionalization of a carbosilane dendrimer with triphenylphosphine; ligands of this type have been used for the immobilization of a Rh-hydroformylation catalyst in membrane reactors. Adapted from Oosterom *et al.* (2002).

shows a dendritic ligand that has been used instead of triphenylphosphine in the hydroformylation of 1-octene to immobilize the catalyst in a membrane reactor (Oosterom *et al.*, 2002).

The main problem that has prevented so far the industrial realization of hydroformylation catalysis in membrane reactors is, obviously, the restricted availability of suitable and cost-efficient nano- and ultrafiltration membranes that show real long-term stability in the presence of organic solvents under the reaction conditions. However, scientific progress in membrane development is dynamic. Very recently, *Evonik* has announced the successful pilot plant operation of a membrane reactor for Rh-catalyzed hydroformylation using an industrial octene feed (Franke, Rudek, and Baumgarten, 2010). Undoubtedly, once cheap and resistant membrane materials are available in sufficiently large quantities to operate a large-scale industrial hydroformylation plant this immobilization concept will also be of great interest for other industrial homogeneous catalytic reactions.

6.14.4.3 Catalyst Immobilization in Liquid–Liquid Biphasic Reaction Systems using Fluorous Phases, Supercritical CO₂ or Ionic Liquids

Liquid–liquid biphasic systems where the catalyst is designed to stay immobilized in one of the two immiscible phases is obviously a very elegant solution to the problem of product separation in homogeneous catalysis. Moreover, the concept has been demonstrated to work on an industrial scale in the aqueous hydroformylation Ruhrchemie/Rhône-Poulenc process as described in detail above.

However, the application of water as catalyst phase has – apart from many strong points such as, for example, price, availability, non-toxicity, heat transfer, and storage properties – several serious limitations. For hydroformylation catalysts that show good catalytic activity in water the main limitation is the very low solubility of C₄₊ olefins in water (see above). Moreover, the hydrolytic lability of some interesting ligand classes (e.g., phosphites) and the high water solubility of some interesting hydroformylation products (e.g., 4-hydroxybutanals obtained from allyl alcohol hydroformylation) can impose severe restrictions.

In answer to these limitations, research and development efforts of the last 20 years have tried to develop advanced liquid–liquid biphasic hydroformylation catalysis by replacing water by another catalyst solvent. As the number of organic–organic, biphasic systems with a sufficient miscibility gap in the presence of hydroformylation products is very limited, these efforts led to the application of so-called “advanced fluids” or “green solvents” in hydroformylation catalysis. Given the restricted scope of this textbook, it will be only possible to describe briefly the most important approaches and their scopes and limitations. The reader interested in the details of these dynamic research fields is referred to a series of recently published monographs (Mathison *et al.*, 2006; Leitner and Jessop, 2010, and Stark and Wasserscheid, 2010).

The first report of *fluorous phases* (organic solvents in which most or all of the hydrogen atoms have been replaced by fluorine atoms, e.g., perfluorohexane) as catalytic solvent in liquid–liquid biphasic hydroformylation catalysis was published by Horváth and Rabai in 1994 (Horvath and Rabai, 1994). Fluorous phases show – besides their very high oxygen solubility, which is less relevant for hydroformylation catalysis – the very interesting property of thermomorphic miscibility behavior. This means that at the temperature of hydroformylation catalysis (80–120 °C) the fluorous phase and the reactants mix completely, while clean separation into two liquid phases is observed at temperatures near ambient. This behavior is attractive for catalysis as the homogenous nature during reaction conditions avoids all mass transfer problems while catalyst separation can be readily achieved after cooling the reactor effluent (Pozzi and Shepperson, 2003, and Mathison and Cole-Hamilton, 2006).

Unfortunately, detailed investigation of this concept has revealed several serious drawbacks that so far could not be solved in a way that would allow commercial

application in hydroformylation catalysis. First of all, fluorous solvents are quite expensive. Even more problematic is their volatility and their persistence in the environment. To dissolve a Rh-catalyst in fluorous phases a special ligand design is necessary. This typically includes the attachment of long fluorinated alkyl groups, so-called “pony-tails,” to the ligand core, a step that requires additional synthetic effort and limits structural flexibility. Another serious process issue results from the fact that the liquid–liquid phase separation at ambient temperature suffers from cross-solubility issues. For example, the product phase of a typical 1-octene hydroformylation using perfluorohexane as fluorous phase would contain about 0.2% of the fluorous solvent in the product phase (Mathison and Cole-Hamilton, 2006). Perfluorohexane has been shown to cause problems of azeotrope formation during the product distillation process.

Supercritical carbon dioxide (scCO₂) is CO₂ that has been heated above its critical temperature T_{crit} ($T_{\text{crit},\text{CO}_2} = 31^\circ\text{C}$) and compressed above its critical pressure p_{crit} ($p_{\text{crit},\text{CO}_2} = 74$ bar). At temperatures above T_{crit} , isothermic compression of CO₂ results in a continuous increase in fluid density ($\rho_{\text{crit}} = 0.437 \text{ g ml}^{-1}$) but no condensation to liquid CO₂ occurs. Thus, the solvent properties of scCO₂ can be adjusted over a certain range by altering the density of the medium by the temperature or pressure. Moreover, scCO₂ offers a unique combination of gas-like and liquid-like properties. Thus, scCO₂ fills the entire space available like gases but at the same time shows typical liquid properties such as solubility for solids. This special nature offers – apart from attractive applications in natural product extraction technologies (Zosel, 1978) – new options for the immobilization of organometallic catalyst complexes. Three different techniques can be distinguished for catalyst immobilization using scCO₂ (Figure 6.14.9).

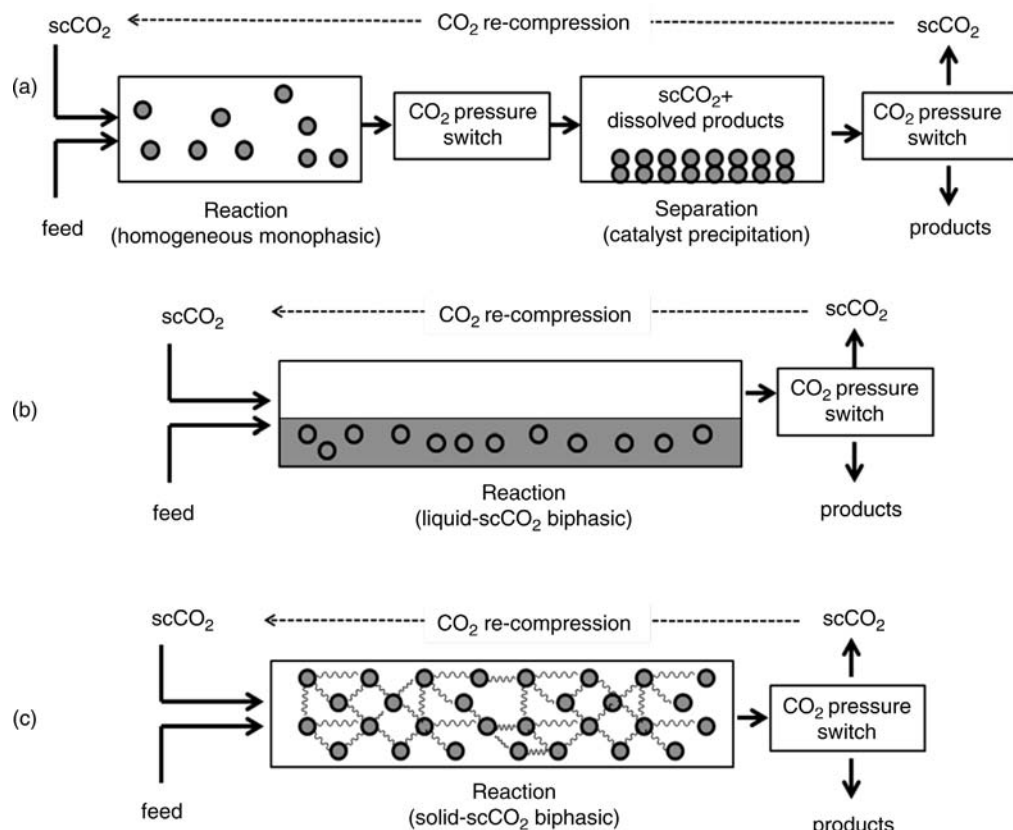


Figure 6.14.9 Schematic representation of three different techniques for applying scCO₂ for the immobilization of organometallic catalysts. Adapted from Gordon and Leitner (2006).

In the first case (Figure 6.14.9a), the pressure dependent solvent properties of scCO₂ are used to solubilize the organometallic catalyst under reaction conditions so as to work there under truly homogeneous conditions. For product/catalyst separation, the pressure is reduced and with that the solvation of the organometallic catalyst reduces drastically. Thus, the catalyst complex precipitates, while the product remains dissolved in the scCO₂ phase even at the lower density. No additional solvent is required in this approach.

In an alternative approach (Figure 6.14.9b) the catalyst is dissolved in a solvent other than scCO₂ and forms a liquid–liquid biphasic reaction system with the supercritical fluid. Here, the scCO₂ serves as mobile phase to transport the reactants and products through the reactor. In this case, the catalyst phase should stay in the reactor at all times during operation to avoid entrainment of the catalyst from the reactor.

A third approach (Figure 6.14.9c) uses organometallic catalysts in solid modifications, for example, covalently bonded (see above) or immobilized in supported liquid form (see below). Here the reaction remains a solid/supercritical fluid biphasic system during reaction and again the scCO₂ is used as the mobile phase to contact the reactant intimately with the immobilized organometallic complex.

All three techniques have been applied successfully in research laboratories for hydroformylation catalysis and these efforts have been extensively reviewed (Cole-Hamilton and Tooze, 2006; Gordon and Leitner, 2006, and Leitner and Jessop, 2010). However, no industrial application of hydroformylation catalysis using scCO₂ has been implemented so far. Critical aspects discussed in the literature concern, for example, the relatively poor solvation power of scCO₂ for most organometallic compounds. Therefore, specific ligand modifications (again using fluorous “pony-tails”) are required to homogeneously dissolve a transition metal catalyst in scCO₂ (Figure 6.14.9a). The same approach needs in addition a pressure and temperature swing for catalyst separation, which can cause catalyst stability problems and is difficult to operate fully continuously. All techniques involving scCO₂ require high-pressure equipment (which is less of a problem for hydroformylation as it is a high-pressure reaction anyway) and some energy consumption for the compression of CO₂ (even though in some cases operation of continuous processes with small pressure differences between reaction and separation steps has been demonstrated). However, given the relative recent development of homogeneous catalysis in the presence of scCO₂ there are certainly still unexplored possibilities for further innovation and approaches. A particularly interesting approach combines a mobile scCO₂ with a liquid catalyst phase of low or even negligible vapor pressure for the development of new industrial hydroformylation processes (Hintermair *et al.*, 2007).

Ionic liquids (ILs) are salts that are characterized – due to their special distribution of charges and due to their special shape of ions – by melting points below 100 °C. Many ILs have even much lower melting points (some down to –96 °C), making them an interesting class of solvents for catalytic reactions even at ambient conditions. Figure 6.14.10 displays typical cations and anions that form ionic liquids.

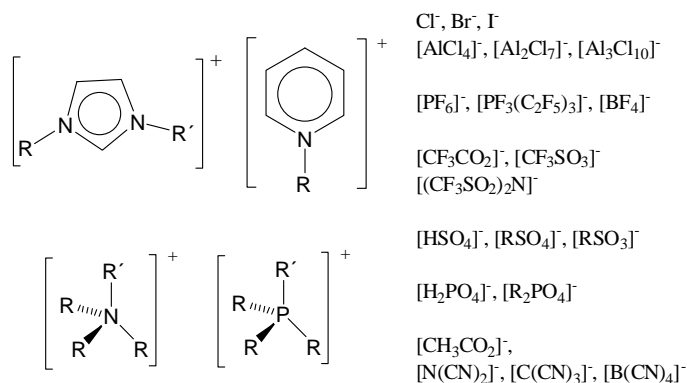


Figure 6.14.10 Typical cations and anions forming ionic liquids (ILs).

Many ILs are characterized by a unique set of properties originating from a complex interplay of coulombic, hydrogen bonding and van der Waals interactions of their ions. Understanding and utilizing these interactions to design an optimized ionic liquid structure for a specific application is the heart of IL science. All ILs are characterized by a very low, in most applications negligibly small, vapor pressure (in the range of liquid metals). This solid-like property comes together with typical liquid-like properties of high relevance for homogeneous catalysis, such as, for example, good solubility for many transition metal complexes and pronounced miscibility gaps with many unpolar products. Very important for catalytic applications is their unique combination of high solvent polarity and low solvent nucleophilicity, which allows many electrophilic catalyst complexes to show very high activity when dissolved in ILs (Wasserscheid and Schulz, 2007 and Stark and Wasserscheid, 2010).

The first application of ionic liquids in Rh-catalyzed hydroformylation was published in 1995 (Chauvin, Mussmann, and Olivier, 1995). In the following years numerous papers appeared on the same topic, describing in detail the development of specific IL-compatible ligand families, process options, and IL/catalyst combinations. Details have been reviewed extensively (Haumann and Riisager, 2008). Here Table 6.14.4 summarizes the most relevant findings by giving an overview of specific strong and weak points of ionic liquid–organic biphasic hydroformylation catalysis with respect to potential future industrial applicability of the technology.

Given the fact that IL research in general – and catalysis in ILs in particular – is a very young research field it is too early to conclude from the list in Table 6.14.4 whether IL based, liquid–liquid biphasic hydroformylation technologies will make their way into industrial practice. However, every new development that helps to overcome one of the “weak points” will help to make industrial success more likely.

6.14.4.4 Supported Liquid Hydroformylation Catalysis

The concept of supported liquid catalysis deals with the heterogenization of a homogeneous catalyst system by dispersing a homogeneous catalyst solution onto a high-surface area solid support (e.g., zeolites, silica, TiO_2). In comparison to conventional liquid–liquid biphasic catalysis the concept offers very efficient use of the catalyst solution, short diffusion lengths, and high interfacial area between the catalyst solution and the reacting fluid. The latter is created without applying stirring or any other form of mechanical energy input. In contrast to the covalent anchoring of organometallic complexes to solid surfaces with its known limitations (see above), the concept of supported liquid catalysis retains the homogeneous solvent

Table 6.14.4 Strong and weak points of ionic liquid–organic biphasic catalysis with respect to potential future industrial application of the technology.

Strong points	Weak points
Tunable and sufficiently high solubility of different olefin substrates in ILs	Relatively large quantities of IL are needed
Suitable miscibility gaps between IL and hydroformylation products	High IL viscosity can cause limitation of the overall reaction rate by mass transfer
Sufficiently high solubility of most hydroformylation-relevant Rh-complexes in ILs	For excellent catalyst immobilization (Rh-leaching down to 10 ppb) ionic modification of the ligand is required
IL does not harm ligand-influenced regioselectivity	
IL medium is compatible with phosphite ligands	
Hydroformylation catalysis works very well in halogen-free, relatively cheap ILs, such as, for example, imidazolium alkylsulfonates	
ILs can be combined in a very attractive manner with scCO_2 as mobile phase (see also Figure 6.14.9b)	

environment around the active catalyst complex and avoids in this way the negative effects of restricted complex mobility. First attempts to develop supported liquid hydroformylation catalysts date from the late 1970s (Hjortkjaer, Scurrell, and Simonsen, 1979 and Gerritsen *et al.*, 1980) when high boiling organic liquids, such as, for example, molten triphenylphosphine, were used as solvents to create a catalytically active liquid film on porous supports. Some years later, supported aqueous phase (SAP) catalysts were also intensively studied (Arhancet *et al.*, 1989). None of these early examples made their way into a technical process. Obviously, the process stability of the liquid catalytic film was not sufficient. In cases where the supported liquid catalyst was contacted with a liquid flow of reactants, removal of the active liquid by the mechanical forces of convection and cross-solubility problems were encountered. In gas contact, the significant vapor pressure of all supported liquids applied at these early times caused the problem of solvent loss by evaporation during operation. As a consequence, the homogeneous character of the surface reaction was lost over time.

In 2002, the first example of a supported liquid catalyst for hydroformylation was reported that used an ionic liquid to solubilize the homogeneous Rh-catalyst on a support (Mehnert *et al.*, 2002). This first work employed the supported ionic liquid phase (SILP) catalyst in a slurry-mode hydroformylation of 1-hexene and, disappointingly, encountered the same problems of Rh- and ionic liquid leaching as experienced before with other solvents. In 2003, however, a breakthrough was achieved by applying very similar Rh-based SILP catalyst materials for the first time in the continuous gas-phase hydroformylation of propene using a conventional fixed bed reactor (Riisager *et al.*, 2003). It was quickly realized that the particular ionic liquid properties – first of all, their negligibly small vapor pressure – provide new ground for exploring molecular defined, supported liquid catalysts in continuous gas-phase reactions with an unprecedented level of stability and versatility. Figure 6.14.11 shows a schematic representation of a SILP catalyst material for hydroformylation catalysis.

Note that all the “weak points” related to liquid–liquid biphasic catalysis with ionic liquids are effectively addressed by continuous gas-phase catalysis with SILP materials. The amount of ionic liquid used in SILP materials is much smaller than in liquid–liquid biphasic systems (referenced by the productivity of the catalyst system). This is due to the much better IL utilization in the SILP system, which is a direct consequence of the very short diffusion lengths

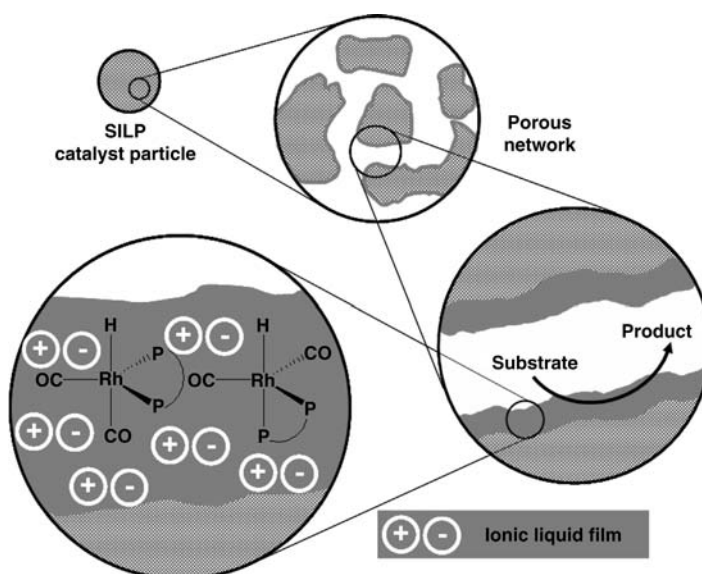


Figure 6.14.11 Schematic representation of a supported ionic liquid phase (SILP) catalyst material for continuous gas-phase hydroformylation catalysis.

through the very thin IL film (usually less than 10 nm thick). Finally, no ligand modification is necessary to apply a Rh-catalyst in SILP materials for continuous gas-phase catalysis. As all Rh or ligand leaching would necessarily involve vaporization of the respective component, the ligand solubility becomes less relevant in these systems compared to its thermal stability and its vapor pressure (Haumann and Riisager, 2008 and Gu and Li, 2009).

All these results, findings, and conclusions lead to the expectation that SILP technology offers indeed a very promising way to realize some industrial hydroformylation processes in the future. This optimistic view is supported by the fact that several companies are already operating today large laboratory plants or even pilot plants to explore the economic potential of the technology in much more detail.

Summary of Section 6.14 (take-home messages)

- **Hydroformylation** (discovered 1938 by Otto Roelen) is a homogeneous catalyzed reaction that converts an olefin and syngas into valuable intermediates. The **most important feedstock** is propene, with *n*-butyraldehyde and iso-butyraldehyde as products.
- The **regioselectivity** of the reaction is of great importance for the economic value of the products. The linear product typically enjoys a higher market value than the branched one.
- The **catalyst** has to favor CO insertion over pure hydrogenation, which is addressed by selection of the central transition metal for the hydroformylation catalysis. Only Rh and Co complexes show sufficiently high hydroformylation activity for commercial applications.
- Very efficient catalyst recovery technologies paved the way for the application of the metal rhodium, which is 1000-times more expensive than cobalt. From 1974 onwards, **Rh-based hydroformylation** became industrial. The use of rhodium was driven by two factors: (i) rhodium is up to 10 000-times more active than cobalt and (ii) Rh-hydroformylation shows a very high selectivity for the aldehyde product, with only minimal hydrogenation activity being observed. The key criterion is a minimum loss of Rh into the organic product phase. Acceptable losses are in the lower ppb range.
- Rhodium hydroformylation of propene is realized industrially in three **process variations** that differ in the way the products are separated from the catalyst:
 - (i) The **gas recycle process** isolates the hydroformylation products by vaporization with a huge gas recycle.
 - (ii) In the **liquid recycle process** product separation from the catalyst solution takes place outside of the reactor.
 - (iii) The **water-organic, liquid–liquid biphasic reaction system** makes use of the fact that butyraldehydes and heavy by-products of propylene hydroformylation are characterized by a very low solubility in water and thus can be isolated from the catalyst by liquid–liquid phase separation if the catalyst is quantitatively immobilized in an aqueous phase. The major breakthrough was the development of the extremely water-soluble ligand tris(*m*-sulfonatophenyl)phosphine.
- **New concepts** are under intense academic and industrial development that allow facile product/catalyst separation: (i) immobilization of homogeneous hydroformylation catalysts on solid surfaces by covalent anchoring; (ii) catalyst separation by size exclusion membranes; (iii) catalyst immobilization in liquid–liquid biphasic reaction systems using fluororous phases, supercritical CO₂ or ionic liquids, and supported liquid hydroformylation catalysis.

6.15

Acetic Acid



Picture of the Celanese acetic acid plant in Nanjing, China. By courtesy of Celanese Corporation

Acetic acid became known to mankind when vinegar, an aqueous solution of acetic acid, was discovered around 5000 BC by the Babylonians. Today, the major process of production of table vinegar is still the age-old aerobic fermentation of ethanol:



For the commercial production of acetic acid on an industrial scale the fermentation process is far too slow and, thus, too expensive.

In 1916 the first industrial process for synthetic production of acetic acid was commercialized. The process is based on the liquid phase oxidation of acetaldehyde. In the 1950s the petrochemical industry developed rapidly and the costs for refinery hydrocarbon cuts were very low. Therefore, the direct liquid-phase oxidation of butane and naphtha became the preferred synthetic route to producing acetic acid. However, the major disadvantage of this process is the significant amount of by-products (up to 50% of the feed is converted into by-products). Hence direct hydrocarbon oxidation to acetic acid requires complex purification units with high investment and operating costs. Today, only small amounts of acetic acid are still manufactured by this process.

The basic principle for the dominant manufacturing process for acetic acid goes back to 1913, when scientists at BASF observed that methanol can be converted into acetic acid by direct catalytic carbonylation. It was not until 1963, though, that the first commercial methanol carbonylation plant using a cobalt iodide catalyst went on stream. Severe corrosion problems had to be overcome to realize the process and new construction materials had to be identified. In 1970 Monsanto introduced a new carbonylation technology applying a highly selective rhodium-catalyst. Later, in 1996, BP commercialized an even more efficient iridium-based methanol carbonylation technology, the so-called Cativa process. These modern methanol carbonylation processes started to replace all other methods for manufacturing acetic acid. In 2006 the share of methanol carbonylation in the global capacity of acetic acid production was 78%. Figure 6.15.1 displays the development of global acetic acid production capacity by process technologies from 1988 to 2006.

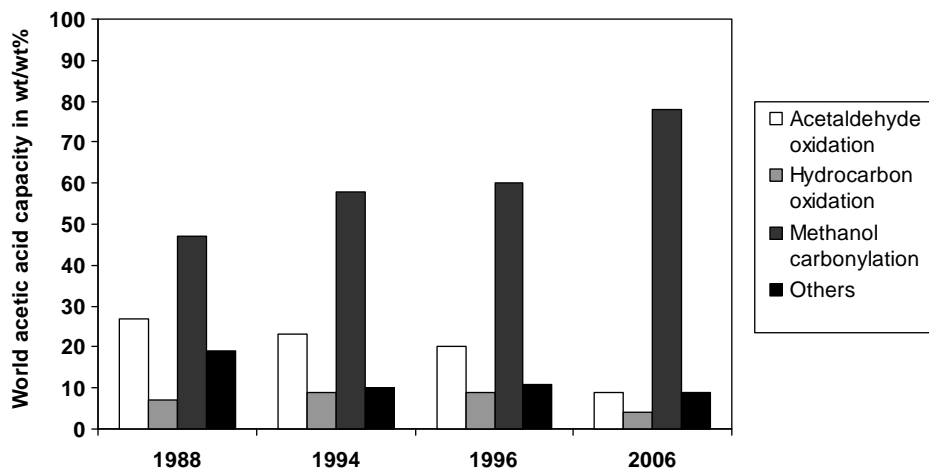


Figure 6.15.1 Global acetic acid production capacities by process technologies from 1988 to 2006. Data from Arpe (2007) and Malveda (2007).

A direct ethylene oxidation process for the acetic acid production was commercialized by Denko in 1997. This process is only competitive for small- or medium-scale plants. The raw material ethylene is more expensive than methanol and carbon monoxide, but the investment costs of these plants are much lower. Table 6.15.1 gives an overview of the catalysts, reaction conditions, yield, and by-products for the major acetic acid processes. The different processes are discussed in more detail in Sections 6.15.1–6.15.4.

Acetic acid is a bulk chemical that is used in a broad range of applications. Its global consumption was $10.9 \times 10^6 \text{ ta}^{-1}$ in 2006 and was expected to increase to approximately $13.2 \times 10^6 \text{ ta}^{-1}$ in 2011. Figure 6.15.2 gives an overview, based on a worldwide analysis, of the different applications and products that consumed acetic acid in 2008.

A large proportion of acetic acid is used as feedstock for the production of vinyl acetate and as solvent for the production of terephthalic acid (Amoco process). Vinyl acetate (VAM) is the monomer used to produce poly(vinyl acetate) (PVA), an important polymer applied in adhesives for porous materials (e.g., wood glue), textile treatment (e.g., production of viscose silk), paper coating, paint, and other industrial coatings. Terephthalic acid (PTA) is used as feedstock for polyester production [e.g., PET, poly(ethylene terephthalate) for plastic bottles]. Especially in Southeast Asia the demand for acetic acid has increased, because the region has become the major producer of polyester fibers for making clothes and consumer plastics. Acetic acid is also a raw material for acetate esters and acetic anhydride. Acetic anhydride is used, for example, as derivatizing agent in cellulose acetate production (thermoplastic/fiber constituent, membranes and paint) or as reactant in the pharmaceutical industry (e.g., aspirin synthesis).

Table 6.15.1 Acetic acid processes. Data from Yoneda *et al.* (2001); Moulijn, Makkee, and van Diepen (2004); Baerns *et al.* (2006).

Process	Catalyst	Conditions		Yield (%)	Major by-products (% yield)
		T (°C)	p (bar)		
Acetaldehyde oxidation	Mn-/Co-acetate	50–70	1	CH ₃ CHO: 95	Formic acid (2)
Hydrocarbon oxidation, for example, butane, butene, naphtha	None/Co-acetate	150–230	50	n-Butane: 50, naphtha: 40	Propanoic acid, formic acid (15–30)
Methanol carbonylation					
BASF process	Co-I ₂	200–240	700	MeOH: 90, CO: 90	Propanoic acid (4)
Monsanto process	Rh-I ₂	175	30	MeOH: 99, CO: 90	Propanoic acid (1)
BP-Cativa process	Ru-Ir-I ₂	190	30	MeOH: 99, CO: 90	Propanoic acid (<1)
Ethylene oxidation	Pd	150–160	8	Ethylene: 97	Acetaldehyde, CO ₂

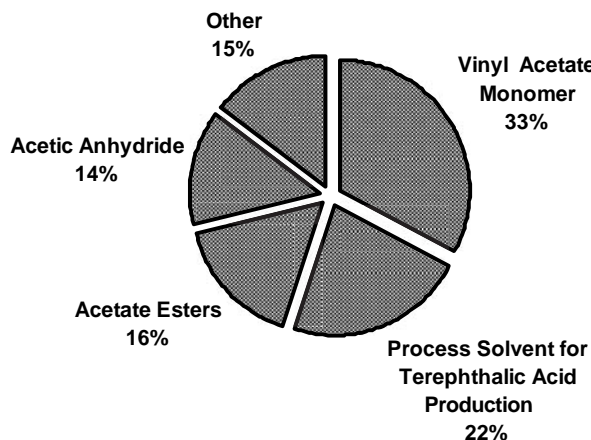


Figure 6.15.2 World consumption of acetic acid by applications and products in 2008. Data from Malveda (2009).

6.15.1

Acetic Acid Synthesis via Acetaldehyde Oxidation

The oxidation of acetaldehyde for the commercial production of acetic acid can be accomplished with pure oxygen or air in the presence of manganese or cobalt-acetate catalyst solutions [Eq. (6.15.2)]. The use of air saves the air separation unit but has the disadvantage that its high N₂ content requires extensive purging to avoid build-up of inert gases in the process:

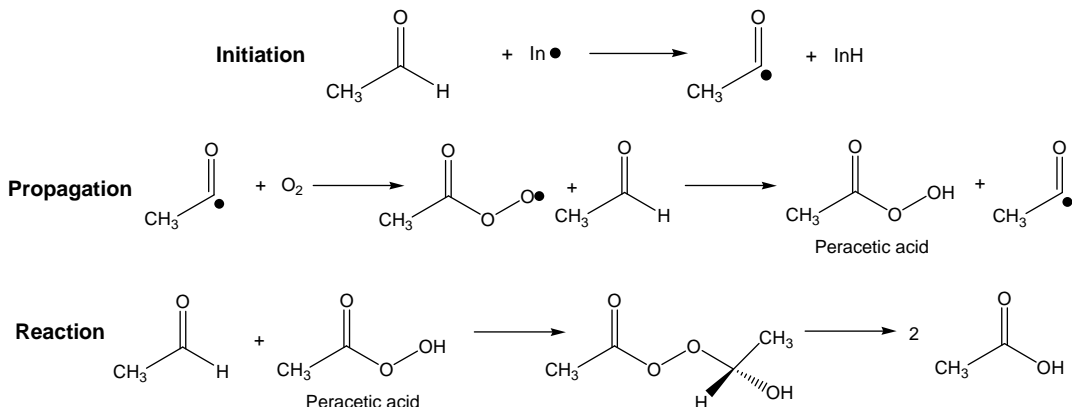


Typically, the catalyst concentration is low (maximal concentration 0.5 wt%). The reaction proceeds via a radical mechanism in which peracetic acid plays an important role as intermediate compound (for details of the mechanism, see Example 6.15.1). Under modified reaction conditions (no catalyst, solvent: ethyl acetate, $T = -15\text{--}40^\circ\text{C}$, 25–40 bar) it is possible to obtain peracetic acid as the desired main product.

Example 6.15.1: Radical mechanism of the acetaldehyde oxidation

The reaction starts with formation of an acetyl radical (**initiation**). This reaction step can be accelerated by addition of a redox catalyst (e.g., Co- or Mn-acetate). The acetyl radical reacts with oxygen and forms an acetylperoxy radical. This radical is transformed with an additional aldehyde to give the peracetic acid and a new acetyl radical (**propagation**). The **reaction** that forms acetic acid includes one molecule of peracetic acid

and one molecule of acetaldehyde reacting to give α -hydroxyethyl-peracetate, which finally dissociates to two molecules of acetic acid. A manganese-based catalyst system can enhance the reaction rate of this step. Additionally, redox catalysts decompose peroxides and, therefore, minimize the risk of explosion. Chain termination occurs by a bimolecular reaction of the acetylperoxy radicals:



In general, acetic acid production via acetaldehyde oxidation takes place continuously in a bubble column at 50–80 °C with pressures of 1–10 bar. The construction material of choice for the reactor is austenitic Cr-Ni-steel. The acetic acid product serves as process solvent and the concentration of acetaldehyde is kept at 3%. It is necessary to keep the temperature over 50 °C to obtain a sufficient peroxide decomposition and oxidation rate. To remove the heat of the exothermic reaction, the reaction mixture is circulated through an external heat exchanger. Accurate temperature control is important to decrease oxidative degradation of acetic acid to formic acid, CO₂, and water. The reaction mixture is separated by several distillation units. The process yields are typically in the range of 90–97% and the purity of acetic acid is higher than 99%. Typical by-products are CO₂, formic acid, methyl acetate, methanol, methyl formate, and formaldehyde.

It is also possible to produce acetic acid anhydride (up to 75%) by changing the reaction conditions and the catalyst system (Cu/Co-acetate) in the oxidation process. The ratio of acetic acid and acetic anhydride can be varied over a rather wide range depending on the acetaldehyde concentration and the employed entrainer (e.g., methyl or ethyl acetate).

The production capacity of acetic acid by acetaldehyde oxidation is shrinking as the process became less economic with increasing ethylene prices. Ethylene is needed as the starting material to produce the acetaldehyde applied in the oxidation process.

6.15.2

Acetic Acid Synthesis via Butane or Naphtha Oxidation

The oxidation of butane or naphtha is also used for the commercial production of acetic acid. The relevant processes were developed in the 1950s and 1960s, when increasing refinery capacities led to attractive prices for light hydrocarbon cuts. Not all mixtures of hydrocarbons are good feedstock for this process. The desirable ratio of methyl to methylene groups is 1 : 1 and the alkene content must be very low.

Two main feedstocks have been established for the commercial production of acetic acid, butane in the United States and Canada (e.g., Celanese) and light naphtha (called primary flash distillate) in the United Kingdom (e.g., BP).

The oxidation of hydrocarbons follows a radical chain reaction. Hydroperoxide radicals are formed and these radicals react to give various oxygenated products [for the detailed mechanism see Cheung, Tanke, and Torrence (2000)]. The oxidation of hydrocarbons can be non-catalytic. For catalytic processes metal ions, for example, Mn, Co, Ni, and Cr, are used as catalysts.

In the Celanese-LPO-process (liquid-phase oxidation) the catalytic oxidation of *n*-butane with cobalt acetate takes place at 175 °C and 54 bar. Many by-products are formed in this process (main by-product: methyl ethyl ketone; other by-products: butanoic acid, propionic acid, formic acid, acetaldehyde, acetone, ethyl acetate, and methanol). These by-products are recycled to the reactor where they convert into acetic acid again or oxidize totally.

The oxidation of naphtha in the BP liquid phase process takes place at 70–90 °C under 40–50 bar of oxygen pressure without a catalyst. As the process starts from a mixture of hydrocarbons, it produces even more by-products than the oxidation process of butane. The major by-products are propionic and formic acid.

In comparison to other acetic acid manufacturing processes, hydrocarbon oxidation uses very cheap raw materials, but isolation of the product is complicated and expensive. Apart from dealing with the large number of by-products, the separation of acetic acid from the water formed during oxidation is a major task that requires azeotropic distillation with entrainment agents.

Today, the production of acetic acid by butane or naphta oxidation is only economic if the by-products contribute significantly to the process economics. In comparison to methanol carbonylation, butane and naphta oxidation is less favorable and this fact has caused shrinking capacities over the last 15 years (see also Figure 6.15.1).

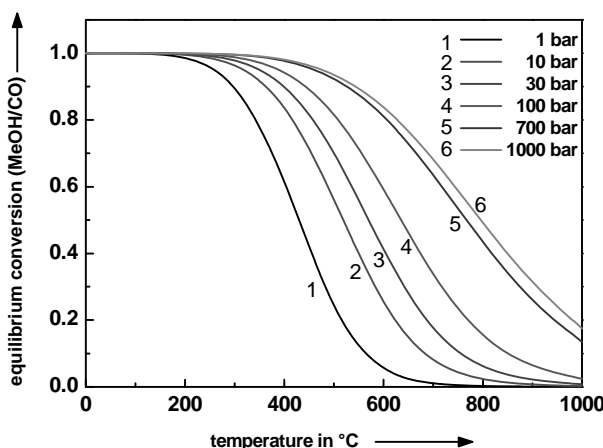


Figure 6.15.3 Equilibrium conversion of methanol carbonylation; assumptions: reaction mixture: $n_{\text{MeOH}}/n_{\text{CO}} = 1$, no by-products. Data from Aspen Plus®-Simulation, Version 2006.

6.15.3

Acetic Acid Synthesis via Methanol Carbonylation

Today, methanol carbonylation is the favored way for manufacturing acetic acid. The route is claimed to have the lowest production costs, especially for large-scale production. In general, the production costs of commodity chemicals are dominated by the raw material costs. In fact, methanol produced from synthesis gas (mainly from natural gas) is nowadays a cheap starting material. In 2006, processes based on methanol carbonylation accounted for about 78% of the world capacity for acetic acid.

Methanol carbonylation is an exothermic reaction and shows a volume decrease. Thus, the reaction is favored by low temperatures and high pressures [Eq. (6.15.3)]:



Figure 6.15.3 illustrates the effect of temperature and pressure on the equilibrium conversion of methanol carbonylation.

There are two general technologies for methanol carbonylation, high-pressure carbonylation (BASF process: 700 bar, 200–240 °C) or low-pressure carbonylation (Monsanto process: 30 bar, 175 °C; or Cativa process: 30 bar, 190 °C). Theoretically, high conversion can be reached at the reaction conditions for both pressure levels. Indeed, the yield based on methanol ranges from 90% for high-pressure carbonylation to 99.5% for low-pressure carbonylation.

However, the yield based on CO is usually much lower in carbonylation processes, due to a competing water gas shift reaction that converts CO and water into CO_2 and hydrogen:



Water is added to the reaction system to suppress the undesired formation of methyl acetate [Eq. (6.15.5)] and dimethyl ether [Eq. (6.15.6)] during the reaction. In this way the acetic acid yield with respect to methanol is increased:



The following subsections discuss the three most important carbonylation processes in more detail.

6.15.3.1 BASF High-Pressure Process

As early as 1913, scientists from BASF pioneered a new route for acetic acid production by discovering the catalytic conversion of methanol and CO. The route became of economic interest in the 1920s, when methanol became available on a technical

scale. In 1941, it was demonstrated that group VIII metal carbonyls are efficient catalyst for carbonylation reactions (including hydroformylation). In subsequent years, overcoming heavy corrosion problems caused by the highly corrosive catalyst solution was a major problem. At the end of the 1950s, BASF scientists finally found a new suitable construction material (a resistant Mo-Ni-alloy that became known as Hastelloy) to solve all corrosion problems and this opened the way to commercializing the process. In 1960 the first carbonylation plant based on a homogeneously dissolved cobalt iodide catalyst went on stream. For the first time a commercial route for the manufacture of acetic acid was developed that was not dependent on petroleum-based feedstock (as both methanol and CO can be made from natural gas or coal).

In the BASF carbonylation process, methanol and CO are converted in the liquid phase (solvent: dimethyl ether, water) at 250 °C and 700 bar. The reaction rate depends strongly on the concentration of methanol and the partial pressure of CO. The proposed mechanism for the Co-catalyzed carbonylation of methanol is presented in detail in Example 16.6.2. Acetic acid yields are typically 90% (based on methanol) and 70% (based on carbon monoxide). Selectivities are high, with the production of 100 kg of acetic acid affording 4 kg by-products (mainly CO₂, CH₄, ethanol, acetaldehyde, and propionic acid).

The reaction takes place in a high-pressure Hastelloy reactor, which is filled with the reactants, dimethyl ether, catalyst recycle, and methyl iodide recycle from the washing column. The product stream is expanded step-wise by a sequence of a high-pressure separator, a low-pressure separator, and an expansion chamber. The gas stream from the separator goes to a washing column and from the expansion chamber to a scrubber. Both scrubber and washing column recover methyl iodide and other volatile iodine compounds by a methanol washing. The obtained methanolic solution is recycled back to the reactor. The raw acetic acid from the expansion chamber (45 wt% acetic acid, 35 wt% water, and 20 wt% esters) is purified in five distillation columns to a purity of 98.8% acetic acid. In the drying column the acid is dried by azeotropic distillation (Section 3.3.2.3), because acetic acid, formic acid, and other by-products form an azeotrope with water. The azeotroping agents are ester compounds, formed as by-products in the carbonylation reaction. The water phase and catalyst solution separated in the columns are recycled to the reactor and, thus, close the production cycle.

6.15.3.2 Monsanto Low-Pressure Process

In recent decades the high-pressure BASF carbonylation process has been increasingly replaced by low-pressure alternatives mainly due to lower investment and operating costs. The starting point for the low-pressure methanol carbonylation processes was in the mid-1960s when scientists of Monsanto discovered that rhodium in combination with iodide is a far more active methanol carbonylation catalyst than CoI₂. In the following years Monsanto developed a low-pressure carbonylation process using a rhodium iodide catalyst complex. The first commercial plant using this reaction system was put on stream in 1970 at Texas City. Even at atmospheric pressure the Monsanto process yields 99% acetic acid based on methanol and 90% yield based on carbon monoxide. Owing to the much milder operating conditions (lower pressure results in lower investment costs) and the higher yields, the Monsanto process has significant economic advantages over the older BASF process.

In the Monsanto process methanol and CO react continuously in the liquid phase at 180 °C and 30 bar in the presence of a RhI₂ catalyst. Since the intermediates are anionic complexes and the reaction rate is enhanced by protic solvents, the reaction is carried out in polar solvents (e.g., acetic acid/water medium). The main by-products are CO₂ and H₂ formed with water [(6.15.4), water-gas-shift-reaction].

Example 16.6.2 shows the detailed catalytic cycle of the RhI₂-catalyzed carbonylation.

Example 6.15.2: Catalytic cycle and mechanism for the methanol carbonylation.

The mechanism of the cobalt- (BASF), rhodium- (Monsanto), and iridium- (Cativa) catalyzed reaction is similar but the rate-determining steps differ and different intermediate catalyst complexes are involved. In all three processes two catalytic cycles occur. One cycle involves the metal carbonyl catalyst (II) and the other the iodide promoter (I). For a better overview only the catalytic cycle of the rhodium-catalyzed Monsanto process is presented in detail (Figure 6.15.4). Initially the rhodium iodide complex is activated with carbon monoxide by forming the catalytic active $[\text{RhI}_2(\text{CO})_2]$ complex 4. Further the four-coordinated 16-electron complex 4 reacts in the rate-determining step with methyl iodide by oxidative addition to form the six-coordinated 18-electron transition methylrhodium(III) complex 1. This step is followed by CO insertion to give the pentacoordinated 16-electron acyl complex 2. Coordination of CO to the metal center leads to the six-coordinated 18-electron complex 3. The active catalyst complex 4 is re-formed by a reductive elimination of acetyl iodide. This acetyl iodide is then hydrolyzed by water to acetic acid and HI (see catalytic cycle I). The strong acid HI reacts with methanol to form methyl iodide, which enters the catalytic cycle II again. In this way the original rhodium complex and the methyl iodide promoter are regenerated.

For the cobalt- and iridium-catalyzed processes the intermediate catalyst complexes are shown in Figures 6.15.5 and 6.15.6, respectively.

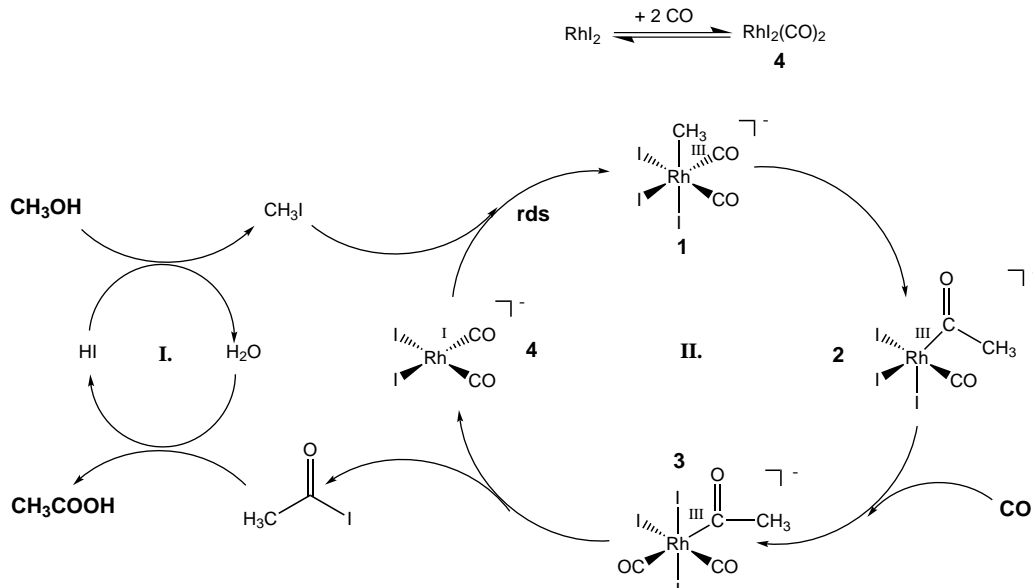


Figure 6.15.4 Catalytic cycle for the Rh-catalyzed carbonylation of methanol used in the Monsanto process. Adapted from Behr (2008).

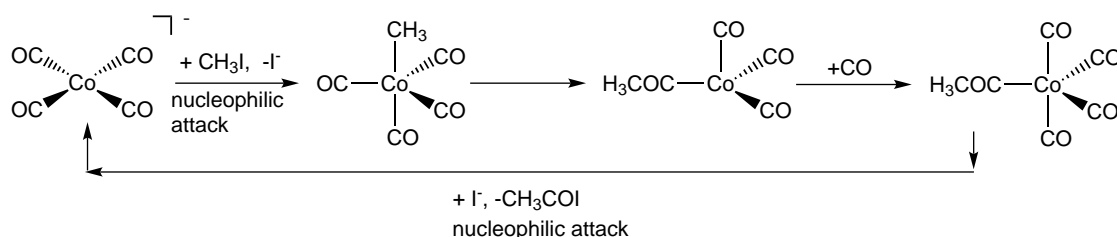


Figure 6.15.5 Catalyst intermediate complexes for the Co-catalyzed carbonylation of methanol used in the BASF process.

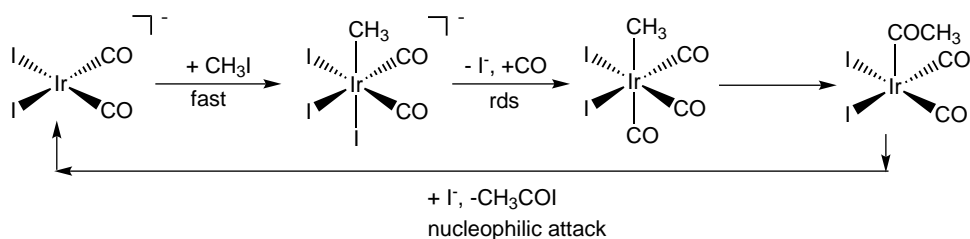


Figure 6.15.6 Catalyst intermediate complexes for the Ir-catalyzed carbonylation of methanol used in the Cativa process.

The rate-determining step is the oxidative addition of methyl iodide to the rhodium complex. The reaction rate is, therefore, independent of the two reactants methanol and carbon monoxide (6.15.7):

$$r_{\text{CH}_3\text{COOH}} = k c_{\text{Rh}} c_{\text{CH}_3\text{I}} \quad (6.15.7)$$

Since the reaction is zero order with respect to the reactants, stirred tank reactors have no disadvantage compared to tubular reactors and high conversions can be obtained even in a small volume CSTR (continuous stirring tank reactor). In fact, the use of a stirred tank reactor often guarantees a better heat and mass transfer in the gas–liquid reaction. Figure 6.15.7 shows the flow scheme of the Monsanto acetic acid process.

Carbon monoxide and methanol from the scrubber unit are fed to the reactor containing the catalyst and the solvent. The liquid product stream is depressurized in a flash vessel and divided in a gas and liquid phase. In this step the rhodium catalyst is separated from the crude acetic acid and is recycled to the reactor. It is critical for the process economics to avoid any rhodium metal loss in this step that could occur by precipitation and vaporization. The gas stream is scrubbed with methanol to recover the toxic and volatile methyl iodide and the off-gas of the scrubber system is flared. The liquid phase is sent to the light ends column (separation of light compounds, e.g., methyl iodide and methyl acetate). The bottom of this column (catalyst, water, and acetic acid) is recycled to the reactor. Wet acetic acid is sent to the drying column and dried acetic acid is obtained as bottom product. The overhead (mixture of acetic acid and water) is recycled back to the reactor. In the product column heavy by-products (major liquid by-product: propionic acid) are removed from the dried acetic acid. The overhead is sent to the finishing column, where ultrapure acetic acid is obtained as a side-stream.

In the 1980s Celanese commercialized an improved Monsanto “low-water process” that uses an additional group I metal iodide that effects an increase in the reaction rate of the rate-determining insertion of CH_3I . In the original Monsanto process relatively high water concentrations have to be applied in the reactor (15 wt%). However, the separation of water and acetic acid is a major energy consumer and limits the unit capacity. Moreover, excess of water causes additional

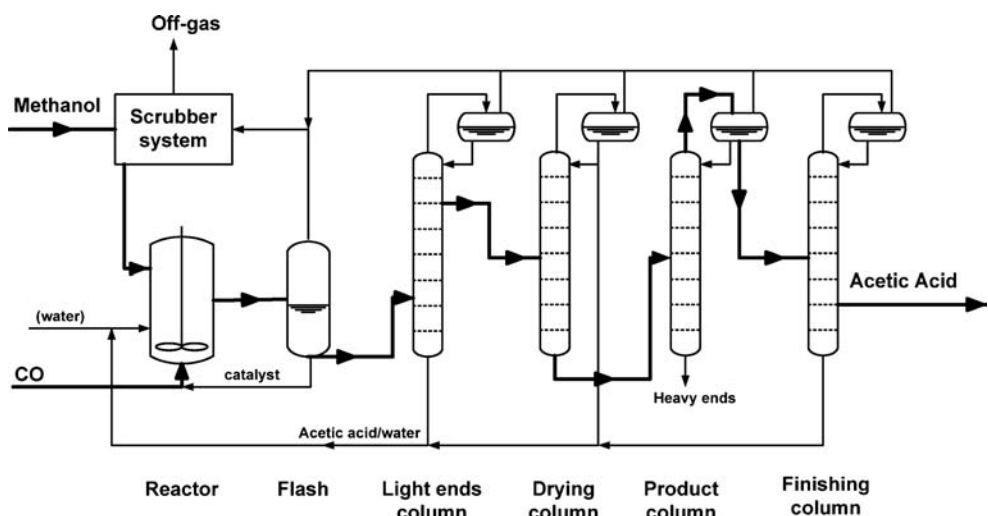


Figure 6.15.7 Flow scheme of the Monsanto process. Adapted from Moulijn, Makkee, and van Diepen (2004) and Yoneda *et al.* (2001).

CO loss due to the water-gas shift reaction. Thus, advantages of the more recent Celanese process compared to the conventional Monsanto process are lower raw material consumption, an increase in productivity, and lower capital costs per ton of product.

As yet another variation of Rh-based methanol carbonylation processes BP commercialized in 1989 a plant producing both acetic acid and acetic anhydride. The ratios are variable depending on market need, between 40:60 and 60:40 acetic acid/anhydride.

6.15.3.3 Cativa Process

For a long time it was known that group VIII metal carbonyls are efficient catalysts for carbonylation reactions. In 1996, BP developed a new catalyst system for methanol carbonylation based on iridium (additionally promoted by iodine and Ru-salts), called the “Cativa process.” Fundamental studies had shown before that the oxidative addition of methyl iodide to iridium is 150-times faster than to rhodium. Thus, in the Cativa process this step is no longer rate determining (as in the case of Rh-based methanol carbonylation). The slowest step in the iridium-cycle is the insertion of CO. This step involves the elimination of iodide and coordination of an additional CO ligand to iridium (Figure 6.15.6). Accordingly, the reaction rate can be described by Eq. (6.15.8):

$$r_{\text{CH}_3\text{COOH}} = k \frac{c_{\text{Ir}} \cdot c_{\text{CO}}}{c_{\text{I}^-}} \quad (6.15.8)$$

To achieve a high reaction rate at low concentrations of ionic iodide, promoters assisting the removal of free iodide are applied in the process. Possible promoters are simple iodide complexes of zinc, cadmium, and gallium or carbonyl-iodide complexes of osmium, tungsten, and ruthenium (the latter being used preferably).

The Cativa process employs relatively mild reaction conditions ($T=150\text{--}250^\circ\text{C}$, $p=30\text{ bar}$), comparable to the Monsanto process. The main advantages of the Cativa process are the much higher productivity ($\text{STY}_{\text{Cativa process}}=45\text{ mol l}^{-1}\text{ h}^{-1}$ versus $\text{STY}_{\text{Monsanto process}}=10\text{--}15\text{ mol l}^{-1}\text{ h}^{-1}$), and the lower water content combined with lower energy requirements for the purification of the pure product. Additionally, the iridium catalysts are more stable than their rhodium counterparts under the low-water conditions [water content: 0.5 wt% (Cativa) versus 15 wt% (Monsanto)]. The lower production rates of higher acids in the Cativa process compared to the Monsanto process allows a reduction in the number of distillation columns. Therefore, a relatively small plant set-up is appropriate for the Cativa process (one reactor, one flash, and two distillation columns).

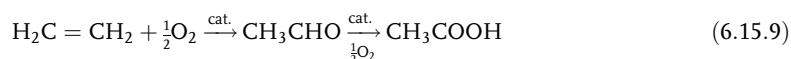
Interestingly, the Cativa process can be realized as a drop-in replacement in plants that have been used beforehand for the rhodium-based Monsanto process, a fact that makes the technology change very attractive for the plant owner. Today, very efficient high capacity production plants based on the Cativa process with capacities of up to $500\,000\text{ t a}^{-1}$ are in commercial operation worldwide.

6.15.4

Other Technologies for the Commercial Production of Acetic Acid

6.15.4.1 Direct Ethylene Oxidation

For many years the development of a direct ethylene oxidation process to manufacture acetic acid (without acetaldehyde isolation) has attracted scientific and commercial interest:



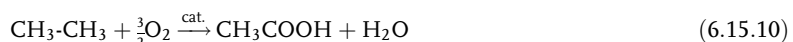
Showa Denko has developed such a direct oxidation process and commercialized the technology in 1997 ($100\,000\,\text{t}\,\text{a}^{-1}$). The catalyst consists of three components: (i) palladium supported on a carrier (0.1–2 wt%); (ii) a heteropoly acid (e.g., phosphotungstic acid or silicotungstic acid) or its related lithium, sodium and copper salts; (iii) selenium, tellurium, copper, silver, tin, lead, antimony, or bismuth. The process is operated in a fixed bed reactor at $150\text{--}160\,\text{°C}$ and up to 8 bar. The gas stream entering the reactor consists of the reactants ethylene and oxygen, steam, and nitrogen as diluent. Water/steam is needed because it enhances the activity and selectivity of the reaction. The selectivity to acetic acid is 86%. The main by-products are carbon dioxide and not fully converted acetaldehyde.

Owing to the high price of ethylene, direct ethylene oxidation is only attractive today for local small-scale acetic acid production.

6.15.4.2 Acetic Acid Production by Ethane and Methane Oxidation

The search for acetic acid production processes with even lower raw material costs has led to attempts to produce it by methane and ethane oxidation processes.

Direct oxidation from ethane [Eq. (6.15.10)] was intensively studied in the 1980s:



The work was strongly inspired by Union Carbide's Ethoxene process, a route for manufacturing ethylene from ethane and oxygen by oxidative dehydrogenation. The first catalysts consisted of molybdenum, vanadium, and niobium oxides. The selectivity for ethylene was very high but, unfortunately, the conversion of ethane was low ($\sim 10\%$). Therefore, scientists at the time focused on the co-production of ethylene and acetic acid. A catalyst consisting of molybdenum, vanadium, niobium, calcium, and antimony supported on a molecular sieve was developed (63% selectivity to acetic acid, 14% selectivity to ethylene, and 3% conversion of ethane). In addition, Rhône-Poulenc (catalyst: vanadium oxide or vanadyl pyrophosphate) and BP (catalyst: combination of rhenium and tungsten) patented processes for the production of acetic acid from ethane. Very efficient catalysts were also disclosed by Hoechst (molybdenum vanadate, promoted with Nb, Sb, Ca, and Pd, $250\text{--}280\,\text{°C}$, 15 bar, 86% selectivity to acetic acid at 11% conversion of ethane per pass) and Sabic (phosphorus-modified molybdenum-niobium vanadate, $260\,\text{°C}$, 14 bar, 50% selectivity to acetic acid at 53% conversion of ethane).

In the near future ethane oxidation will most likely not compete with methanol carbonylation (even though ethane is a very cheap and attractive raw material) because of the low ethane conversions and product inhibition problems. In addition, the large variety of by-products and the need to work with water as additive (resulting again in high costs for the purification of the acetic acid) still prevent the commercialization of this route.

An even cheaper feedstock than ethane is methane. A direct reaction from methane to acetic acid requires first methane oxidation to methanol followed by a carbonylation step. Catalyst systems based on Pd/Cu or RhCl_3 have been reported to show good acetic acid yields in academic work, but for a commercial process the reaction rates are still too slow. Nevertheless, due to the very attractive feedstock basis this route may become a threat to methanol carbonylation in the future if this problem can be convincingly overcome by further process and catalyst development.

Section 6.15 (take-home messages)

- **Acetic acid** is a bulk chemical that is used in a broad range of applications. A large proportion of acetic acid produced is used as feedstock for the production of vinyl acetate and as solvent for the production of terephthalic acid.

- The production of **acetic acid** by a **fermentation process** is far too slow and thus too expensive. The first industrial process for synthetic production of acetic acid was based on the liquid-phase **oxidation of acetaldehyde**. In the 1950s, as the petrochemical industry developed rapidly, the direct liquid phase **oxidation of butane and naphtha** became the preferred route to acetic acid. Significant amounts of by-products are formed, and complex purification units were needed. Today, the industrially preferred process is the **conversion of methanol** with CO (catalytic carbonylation). The reaction is exothermic and shows a volume decrease, and thus the equilibrium is favored by low temperatures and high pressures. There are **two general technologies for methanol carbonylation**, high-pressure carbonylation at 700 bar (BASF) or low-pressure carbonylation at 30 bar (Monsanto, BP).
 - In the **BASF process**, methanol and CO are converted in the liquid phase by a homogeneous Co-based catalyst. The reaction takes place in a high-pressure Hastelloy reactor. In recent decades the BASF process has been increasingly replaced by low-pressure alternatives mainly due to lower investment and operating costs. In the low-pressure **Monsanto process** methanol and CO react continuously in liquid phase in the presence of a RhI_2 catalyst. In 1996, BP developed a new attractive catalyst based on iridium (**Cativa process**); the oxidative addition of methyl iodide to iridium is 150-times faster than to rhodium.
 - The search for acetic acid production **processes with even lower raw material costs** has led to attempts to produce acetic acid by ethane oxidation. In the near future ethane oxidation will most likely not compete with methanol carbonylation (even though ethane is a very cheap and attractive raw material) because of the low ethane conversions, product inhibition problems, and a large variety of by-products.

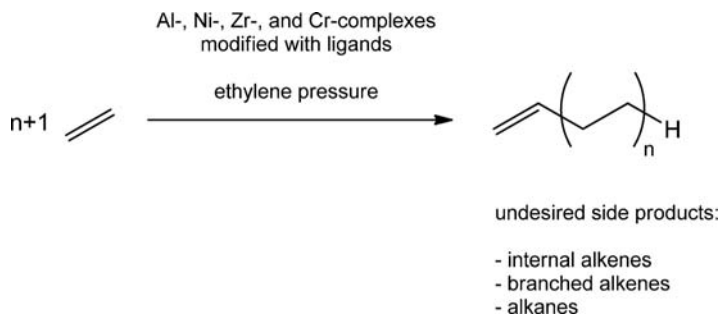
6.16

Ethylene Oligomerization Processes for Linear 1-Alkene Production

6.16.1

Industrial Relevance of 1-Olefins

1-Olefins (LAOs – linear alpha olefins) are useful and versatile intermediates for the synthesis of many industrially relevant substances. Examples include co-monomers for polyethylene production, alcohols, aldehydes, carboxylic acids, or sulfonates (Dixon *et al.*, 2004). Table 6.16.1 gives an overview of the most important applications and demonstrates that the applications of the different 1-olefins depend strongly on their chain lengths.



Scheme 6.16.1 Ethylene oligomerization is the method of choice to produce 1-alkenes (= linear α -olefins). The worldwide capacity for 1-alkene production was above 3 Mio tons in 2010.

Table 6.16.1 Industrial applications of 1-alkenes.

Chain length	Final products
C ₄ –C ₈	Copolymers (HDPE, LLDPE), Lubricant additives (oxo-alcohols)
C ₄ –C ₈	Plasticizer alcohols
C ₆ –C ₁₀	Synthetic lubricants (PAO, SHC)
C ₁₂ –C ₁₈	Detergent alcohols
C ₁₂ –C ₁₈	Alkyl and aryl sulfonates (LAS, LABS, AOS)
C ₁₆ –C ₁₈	Amines
C ₃₀₊	Lubricants



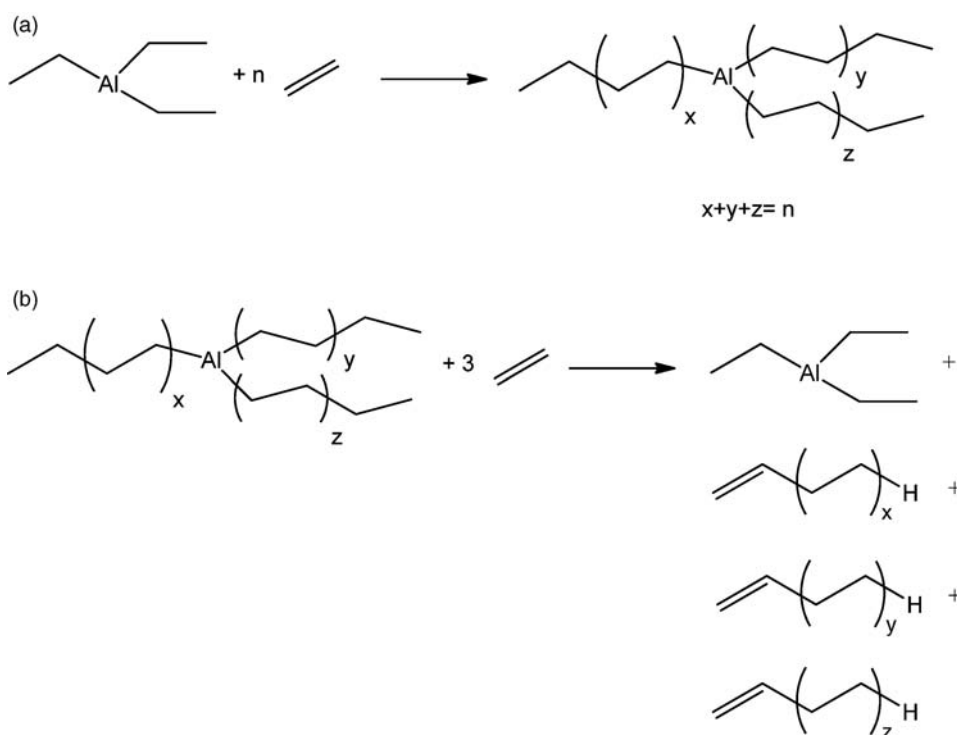
The Shell higher olefins plant at Stanlow in the UK, © Shell Chemicals

The lower C₄–C₈ 1-alkenes are mainly used as co-monomers for the polymerization of ethylene. In the production of linear low density polyethylene (LLDPE), for example, ethylene is copolymerized together with 1-hexene (gas-phase process) or 1-octene (liquid-phase process) with typically 8–10 wt% of the higher α-olefins being applied. The C₆–C₈ olefins are also hydrocarboxylated to give acids and esters that become part of lubricants. Hydroformylation of C₆–C₁₀ 1-alkenes followed by hydrogenation deliver linear primary alcohols that are used as PVC plasticisers in the form of their phthalic acid esters. Synthetic lubricants (poly α-olefins – PAO or synthetic hydrocarbons – SHC) are produced by oligomerization of 1-decene. Epoxidation of C₁₀–C₁₂ 1-alkenes leads to non-ionic surfactants. 1-Alkenes with 12–18 carbon atoms are mainly used for producing biodegradable detergents, such as linear alkyl-benzene sulfonates (LAS or LABS) or α-olefin sulfonates (AOS). Long-chain 1-alkenes in the wax region serve as ingredients in special lubricants, for example, for oil-drilling applications.

6.16.2

Aluminum-alkyl-based “Aufbaureaktion” (Growth Reaction)

The first process to oligomerize ethylene to 1-alkenes was invented in the early 1950s by *Ziegler* (see box). The original process uses triethylaluminum as the starting material, which reacts with ethylene at a pressure of 100 bar at 100 °C in a growing reaction to give aluminium-alkyl compounds with longer alkyl chains (Scheme 6.16.2a). This growing step is followed by an elimination step (Scheme 6.16.2b). The latter requires temperatures of 300 °C and is carried out at 10 bar ethylene pressure. In the elimination step, three incoming ethylene molecules replace the three grown alkyl chains which are eliminated from the Al-center in form of 1-alkenes. This elimination step requires coordination of ethylene to the aluminum center combined with the transfer of the β-hydride from the grown alkyl chain to the incoming ethylenes to allow re-formation of triethylaluminum.



Scheme 6.16.2 Growth and elimination step in the Ziegler “Aufbaureaktion.”

■ **Karl Ziegler** (1898–1973): a German chemist who won the Nobel Prize in Chemistry in 1963 (together with Giulio Natta) for his “excellent work on organometallic compounds [which] . . . led to new polymerization reactions and . . . paved the way for new and highly useful industrial processes.” Ziegler obtained his doctorate from the University of Marburg in 1920 and became professor at the University of Heidelberg in 1926. His early work on the stability of radicals led him to organometallic studies. From 1943 until 1969 Ziegler was the Director of the Max-Planck-Institute for Coal Research in Mülheim/Ruhr. During his time at Mülheim, Ziegler worked intensively with ethylene as the latter became readily available at the time from coal gas. Ziegler and his student H. Breil discovered that by passing ethylene at low pressure through a solution of TiCl_3 and Et_2AlCl in alkanes high molecular weight polyethylene was formed. Apart from this major achievement, Ziegler pioneered ethylene oligomerization processes both using aluminum- and nickel-based catalysts.

The chain length distribution in the original Ziegler “Aufbaureaktion” is adjusted by the ratio of ethylene to aluminum in the growth reaction in which the provided ethylene competes for the available Al-centers. After elimination in the second step this results in a Poisson-type distribution (Figure 6.16.1) that has the highest probability at the chain length that corresponds to an even distribution of all ethylene to the coordination sites at the aluminum.

The Poisson-type distribution and the flexibility of the “Aufbaureaktion” with respect to chain length by stoichiometry adjustment are interesting features. However, this comes with the great disadvantage of large amounts of highly reactive, flammable, and volatile AlEt_3 that have to be handled in the reactor in order to produce the technically most interesting 1-alkenes with chain lengths between C_6 and C_{18} . To avoid these safety and handling problems, modifications of the process have been developed by Gulf (today these processes are operated by Chevron Phillips) and the Ethyl Corporation (today operated by Ineos, formerly BP-Amoco).

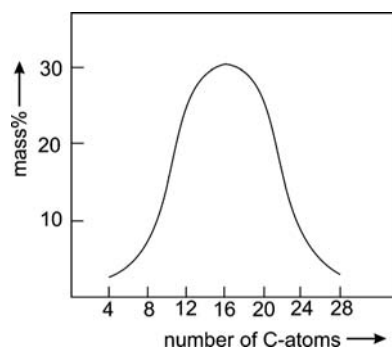


Figure 6.16.1 Poisson distribution of 1-alkenes produced by the original Ziegler “Aufbaureaktion.” Adapted from Keim (1984).

In the Gulf process, AlEt_3 is used in catalytic amounts. The reaction conditions (200°C , 250 bar) allow the coexistence of growth and elimination reactions in the same reactor. Under these conditions, each growing Al-alkyl chain has a certain probability of ethylene insertion (and growth) versus chain elimination. Assuming that this probability is independent of the length of the growing chain, and assuming further that all higher oligomers are formed by ethylene oligomerization and not by re-insertion of shorter-chain 1-alkenes into the Al—alkyl bonds, a mathematical product distribution results – the so-called *Schulz–Flory-distribution*.

To calculate the product distribution of ethylene oligomerization, the reaction orders for the insertion and the elimination steps with respect to ethylene are highly relevant. For most ethylene oligomerization processes, it is reasonable to assume that ethylene insertion is first order with respect to ethylene concentration while elimination is zero order with respect to ethylene. Under these preconditions, Eq. (6.16.1) describes the so-called β coefficient that gives the ratio of the rates of elimination over insertion (Onken and Behr 1996):

$$\beta = \frac{k_{\text{elimination}}}{k_{\text{insertion}} c_{\text{ethylene}}} \quad (6.16.1)$$

The product distribution of ethylene oligomerization with respect to chain length is a function of the β coefficient as shown in Figure 6.16.2. High values of β represent a product distribution with a high share of short oligomers, while low β values represent a distribution with higher shares of longer 1-alkenes.

Note that, from a mechanistic point of view, the molar product distribution of 1-alkenes in a Schulz–Flory distribution always gives a maximum for 1-butene. This is because the fixed ratio of chain growth and elimination works out first for the C_4 -chain attached to the aluminum center. Only a certain part grows to the aluminum-hexyl species and a fixed share eliminates here as 1-hexene. Thus, the molar amount of longer chains attached to aluminum decreases with each ethylene insertion. Note, further, that the molar mass of the oligomers increases with increasing chain length. Therefore, the mass distribution of products (as shown in Figure

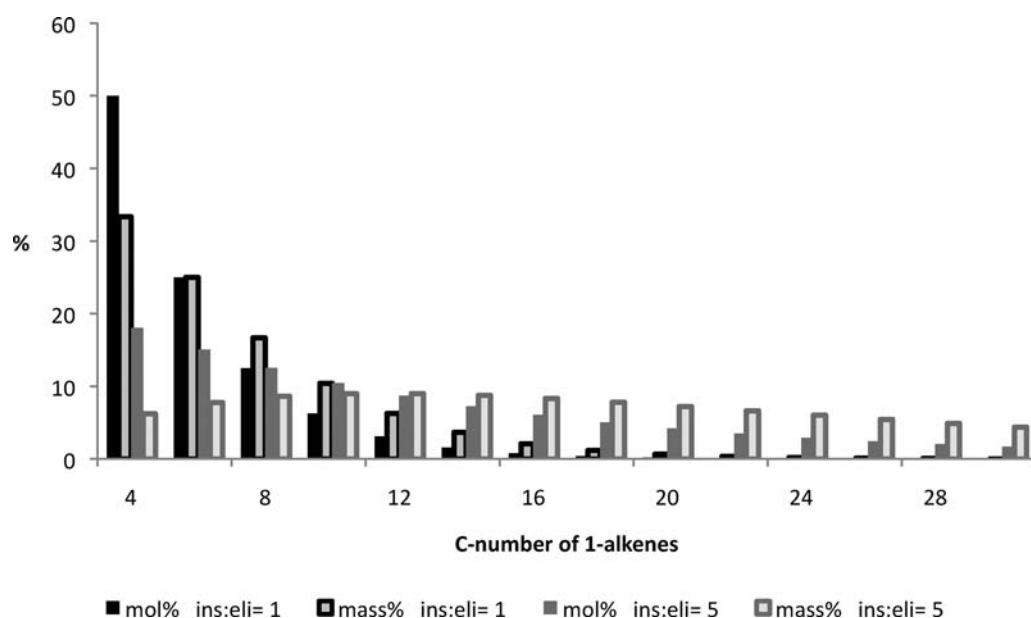


Figure 6.16.2 Schulz–Flory distribution of ethylene oligomers. Mass and mol fractions are given as a function of the ratio of rate of insertion (ins) and rate of elimination (eli) (ins:eli is equal to $1/\beta$).

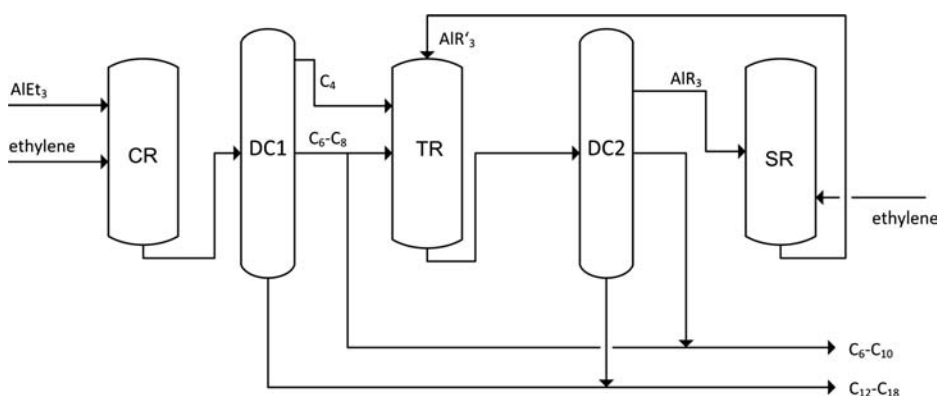


Figure 6.16.3 Flow scheme of ethylene oligomerization by the Ethyl-Corporation process (Vogt, 2002).

6.16.2) shows a different picture with maxima of mass share for certain higher 1-alkene fractions depending on the β coefficient.

From a technical point of view, a Schulz–Flory type distribution of 1-olefins is problematic as 1-butene, which is always produced in the highest molar amount, is less desired for industrial applications compared to, for example, 1-C₆, 1-C₈, or the detergent range 1-alkenes.

The second modification to the original Ziegler “Aufbaureaktion,” the Ethyl Corporation process, addresses this disadvantage and combines catalytic and stoichiometric ethylene oligomerization in a way that allows more flexibility with respect to the overall chain length distribution of the products. Figure 6.16.3 shows a scheme of the Ethyl Corporation process.

Ethylene is first oligomerized using catalytic amounts of AlEt₃ in the catalytic reactor (CR). This step works in the same way as the Gulf process at high temperatures and pressures. The obtained product mixture, with a Schulz–Flory distribution, is transferred to a first distillation column (DC1) where 1-butene, C₆–C₁₀ alkenes, and C₁₂–C₁₈ alkenes are isolated in three individual distillation cuts. While the longer chain cuts are used directly as co-monomers, lubricant monomer, or detergent feedstock, the large amount of 1-butene is transferred into a transalkylation reactor (TR). In the transalkylation reactor the 1-butene reacts with long-chain aluminum alkyls that have been produced beforehand in a separate stoichiometric reactor (SR) using typical Ziegler “Aufbaureaktion” conditions. In the transalkylation reactor the conditions are adjusted in such a way that the 1-butene substitutes the long alkyl chains at the aluminum. AlBu₃ is formed and C₁₂–C₁₈ alkenes are eliminated.

These two components are separated in a second distillation column (DC2) with AlBu₃ being transferred over-head back to the stoichiometric reactor to serve as reaction partner for chain growth while the longer chain products are isolated as commercial products.

6.16.3

Nickel-Catalyzed Oligomerization – Shell Higher Olefins Process (SHOP)

In 1964 Keim (see box) invented the Ni-catalyzed oligomerization of ethylene at the Shell research laboratories in Emeryville, California. The great advantage of the Ni-catalyzed reaction is its significantly better selectivity towards 1-alkenes in each product fraction of identical chain length (Table 6.16.2). The higher yield of the most valuable product in each fraction saves much effort in the product purification and reduces feedstock costs. However, the advantage comes with a higher catalyst

price of nickel compared to aluminum. Therefore, a suitable way had to be found to recover the Ni-catalyst from the products and to recycle it back into the reactor. Keim and his research team solved this problem by inventing the first industrial liquid–liquid biphasic catalytic reaction (see Section 2.3 for fundamentals and Section 6.14 for other important applications of this technology). Finally, the Ni-catalyst was applied in 1,4-butanediol, a solvent that forms a miscibility gap with the organic product phase in the reactor. After reaction the biphasic reaction mixture is transferred into a settler where phase separation occurs. While the butanediol–catalyst phase is recycled back to the reactor, the products are transferred to the distillative downstream processing (Figure 6.16.5). The first SHOP plant went on stream in Geismar, Louisiana, in 1977. A second plant in Stanlow, UK, followed, giving a total capacity of SHOP-made alkenes of roughly $1\,200\,000\,\text{ta}^{-1}$ (Vogt, 2005).

Wilhelm Keim (born 1934) performed his PhD thesis with Günther Wilke at the Max-Planck-Institut für Kohlenforschung, Mülheim, Germany. After post-doctoral work with Professor Katz at the University of Colombia he joined the Shell research laboratories in Emeryville in 1964. He quickly became a group leader and, later, head of petrochemical research and manager of oil refining. In 1972 he moved to the University of Technology Aachen, Germany, where he headed the Chair of Technical Chemistry until 2001.

The mechanism of Ni-catalyzed ethylene oligomerization involves both nickel hydride and nickel alkyl species. The mechanism is known in the literature as the “metal-hydride mechanism,” “Cossee–Arlman mechanism,” or “ethylene insertion – β -hydride elimination mechanism” and results in a Schulz–Flory distribution of the oligomerization products. The mechanism is depicted in Figure 6.16.4. Note that two other coordination sites at the nickel are occupied by one bidentate ligand or two monodentate ligands (see Section 2.4 for details) that have been omitted in Figure 6.16.4 for clarity.

Prior to reaction with ethylene, the active metal hydride species is formed, for example, by the reaction of a nickel salt precursor and a reducing activator (e.g., AlEtCl_2 , $\text{Na[BH}_4]$). The metal hydride species generated in this way coordinates ethylene in a ligand association reaction (for details of the elementary steps in catalysis see Topic 6.16.1). The formed metal π -complex inserts ethylene in the subsequent step into the metal–hydride bond to form a metal alkyl species. In this step a metal–carbon bond is formed and the hydrogen atom is transferred to the β -carbon atom of the alkyl chain. As this insertion step vacates one coordination site at the metal, further ethylene can coordinate and insert again. By repeated insertion of ethylene into the Ni–C bond, longer metal alkyl species are generated.

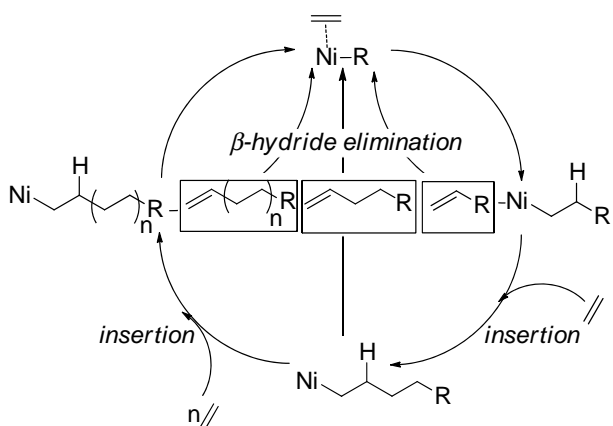


Figure 6.16.4 Formation of linear α -olefins according to the metal hydride mechanism.

Product elimination from the catalytic cycle happens in a β -hydride elimination step in which hydrogen from the β -position of the Ni-bonded alkyl chain is transferred back to the metal (hydrogens in the β position are explicitly shown in Figure 6.16.4). This step releases the respective 1-alkene. A metal butyl species thus liberates 1-butene, a metal hexyl species liberates 1-hexene, and so forth. In the same step, the Ni-hydride species is regenerated to coordinate immediately fresh ethylene to start a new catalytic cycle.

The selectivity of the process towards the product fractions of different chain-lengths depends on the ratio of the rate of ethylene insertion versus the rate of alkene elimination. In a scenario where insertion is strongly favored over elimination (low β coefficient), long-chain polymers represent the main mass share of the formed products. In a scenario where elimination is strongly favored over insertion (high β coefficient), only the shortest 1-alkene, 1-butene, is formed in high selectivity. In all cases, Schulz–Flory product distributions are obtained. The latter results from the fact that the ratio of chain growth to elimination is independent of the length of the alkyl chain bonded to the metal center. This means, for example, that the ratio of chain growth to elimination is for a given set of reaction conditions and for a given metal complex the same for a metal hexyl complex as it is for a metal dodecyl complex. To optimize the rates of elimination and insertion according to the alkene distribution technically needed, the reaction temperature and the ethylene concentration in the solvent (which is a function of the applied ethylene pressure) can be modified. Alternatively, the insertion/elimination ratio can also be influenced by the choice of ligand at the Ni center.

To allow more flexibility in adapting the obtained product distribution to market needs the Shell development team invented an overall process scheme that combines the oligomerization reactor with additional isomerization and metathesis units. All three reactions together form the so-called Shell higher olefins process (SHOP). In the isomerization reactor, 1-alkenes with less attractive chain lengths are converted into internal alkenes of the same chain lengths with the help of a heterogeneous isomerization catalyst (e.g., Na/K on Al_2O_3 catalyst). In the metathesis reactor, two internal alkenes undergo a catalytic (catalyst: Co and Re on support) alkyl group exchange reaction according to Scheme 6.16.3.

In the metathesis step, internal alkenes that are too short for the ideal technical product mix are reacted with internal olefins that are too long for the ideal technical product distribution. Thus, the combination of isomerization and metathesis converts undesired chain lengths of 1-olefins into internal olefins of the desired chain lengths. Figure 6.16.5 depicts a detailed flow scheme of the SHOP.

After the oligomerization reactor and the liquid–liquid separator, the organic product has to undergo an intensive product wash to make sure that no catalyst enters the distillation columns. In the following series of distillations, the technically desired 1-alkene cut $\text{C}_6\text{--C}_{18}$ is separated and the too light C_4 and the too heavy C_{18+} cuts are combined and isomerized to internal linear olefins in the isomerization reactor. These internal alkenes are then converted in the metathesis reactor to form internal alkenes. The desired $\text{C}_6\text{--C}_{18}$ fraction is isolated, whereas the lights and the heavies are again recycled into the isomerization reaction.

On the one hand, the possibility of controlling the chain length distribution by the process conditions in the catalytic and in the distillative process units makes the SHOP a very flexible process. On the other hand, it can be seen that many unit operations (reactors, settler, and distillation columns) are necessary to realize this flexibility and to finally convert the feedstock ethylene into the most suitable product mix according to market needs. All these investments are necessary as the Ni-catalyzed oligomerization is (as the Al-catalyzed reaction) not selective with regard to specific product chain lengths needed for the most attractive markets. Instead, product mixtures of desired and less desired products are always formed. The effort of installing a large number of unit operations to adjust the right product mix can be understood by taking into account the fact that for large-scale processes (like ethylene

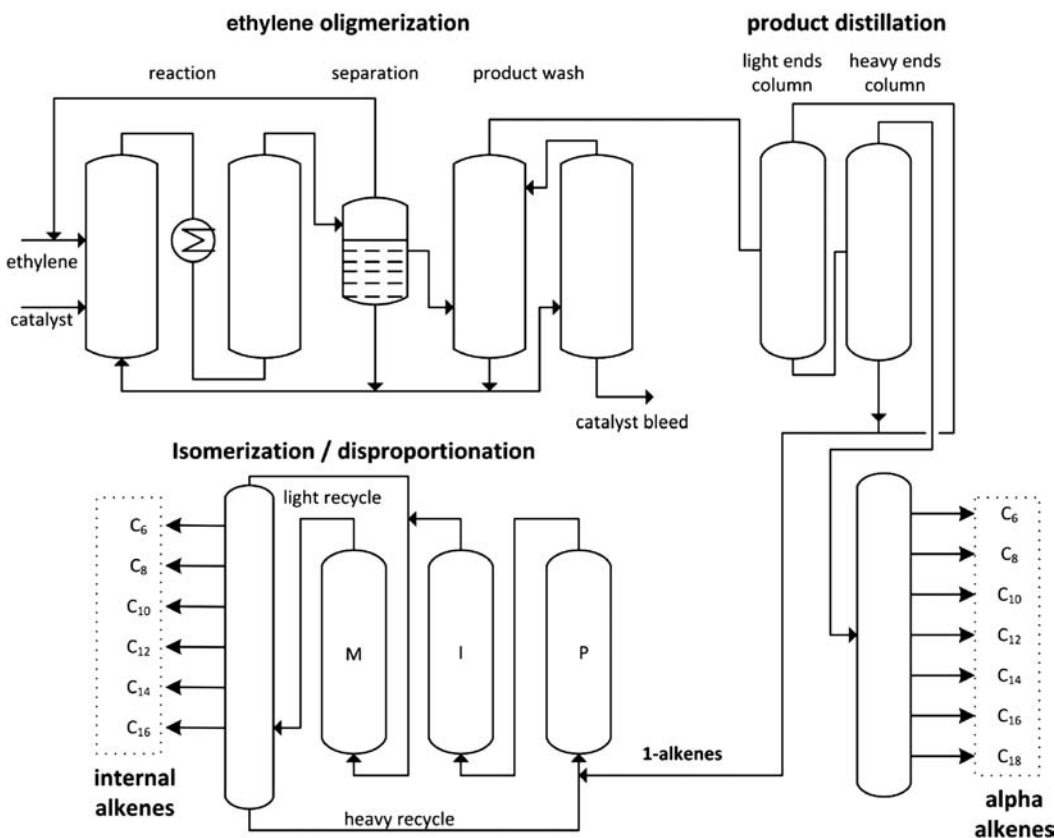
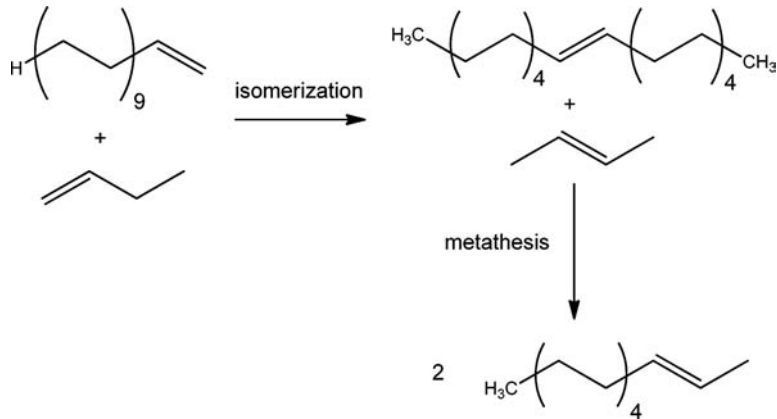


Figure 6.16.5 Flow scheme of the Shell higher olefins process (SHOP) – P = purification; I = isomerization; M = metathesis. Adapted from Vogt (2005).

Scheme 6.16.3 Isomerization and alkene metathesis steps in the SHOP employed to convert 1-alkenes with chains that are too long (here 1-C₂₀) or too short (here 1-butene) into internal alkenes of the desired chain length (here 2-dodecene).



oligomerization) the investment cost can be charged to many tons of products, so that finally the feedstock cost dominates to a very large extent the overall production cost. Consequently, making the right products from the valuable ethylene feedstock is more important than saving investment with a less sophisticated process scheme.

To conclude the presentation of the ethylene oligomerization processes described above, which are also summarized in the literature under the term “full range 1-alkene production processes” (Dixon, 2004), Table 6.16.2 shows a comparison of

their specific selectivities within each chain length. From this comparison, the Ni-catalyzed system of the SHOP obviously provides significant selectivity advantages over the aluminum-based oligomerization processes as very little internal and branched alkenes are produced in this process.

Very recently, Linde Engineering together with the Saudi-Arabian company SABIC have announced the commercialization of their α -SABLIN technology on a 150 000 t a⁻¹ scale at its Jubail plant on the Gulf coast of Saudi Arabia. In this process C₄–C₂₀₊ 1-alkenes are formed in a single stage, homogeneous catalytic process using Zr-complexes in a bubble phase reactor. Compared to alternative processes α -SABLIN is characterized by a simple process design and moderate conditions (low pressure, low temperature) (Linde, 2010).

6.16.4

Metallacycle Mechanism for Selective Ethylene Oligomerization

Companies using the Ziegler *Aufbaureaktion*, the SHOP technology, or the α -SABLIN process for the production of 1-alkenes get into trouble if the market for one specific 1-alkene grows very much faster than the market for all other chain lengths (Wass, 2007). Therefore, it is of obvious interest to develop alternative catalyst systems for the selective synthesis of a specific 1-alkene from ethylene.

Although the selective trimerization of ethylene with homogeneous Cr-catalysts was discovered as early as the late-1960s by Manyik *et al.* at Union Carbide Corporation (Manyik *et al.*, 1977), it was only in the late-1980s that Chevron Phillips picked up the discovery to develop a selective ethylene trimerization process that was later commercialized in 2003 in Qatar. Since the discovery of selective ethylene trimerization was in stark contrast to any previously reported chain-length distribution in ethylene oligomerization, Manyik proposed a novel mechanistic pathway involving metallacycle intermediates that was later refined by Briggs (see Figure 6.16.6; note that additional ligands are omitted for clarity). After generating the chromium catalytic center by reaction of a chromium(III) precursor with a reducing and alkylating co-catalyst [such as, for example, methylaluminoxane (MAO) or trialkylaluminium], it is proposed that two ethylene molecules coordinate to the chromium metal in a ligand association step. In a subsequent oxidative coupling step a chromacyclopentane species forms (for details on the elementary catalytic steps see Topic 6.16.1). This species coordinates and inserts ethylene to form the chromacycloheptane species. The latter can (dependent on the ligand) eliminate 1-hexene in a very selective manner – in many cases 1-hexene selectivities of >98% were reported. In the elimination step, one β -hydride of the metallacycle is transferred to the chromium and a chromium-bonded alkene species forms as an intermediate that is eliminated after hydride transfer to the chromium connected carbon.

Why is the metallacycle mechanism able to give selective trimerization while the insertion/elimination mechanism found for Al-, Zr-, or Ni-catalyzed ethylene

Table 6.16.2 Overview of selectivity pattern (%) of industrial ethylene oligomerization processes with mathematical product distributions. Adapted from Vogt (2002).

	Chevron/ Phillips	Ineos/Ethyl	SHOP
1-Olefins	91–97	63–98	96–98
Branched olefins	2–8	2–29	1–3
Paraffins	1.4	0.1–0.8	0.1
Monoolefins	99	>99	99.9

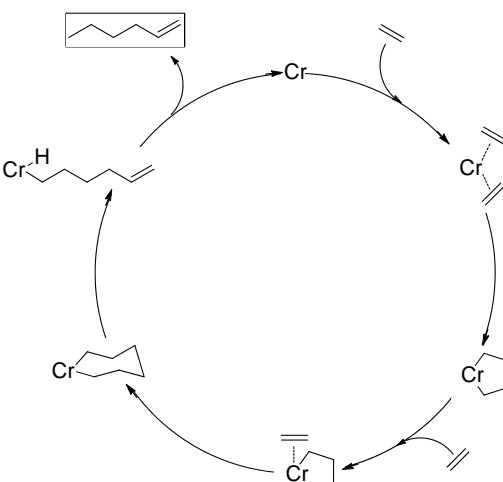


Figure 6.16.6 Generally accepted metallacycle mechanism for the selective ethylene trimerization as first proposed by Briggs (Briggs, 1989).

oligomerization results in broad product distributions? The reason is that for the metallacycle mechanism the probability of elimination changes dramatically with the ring size, while the probability of elimination is constant for different alkyl chain lengths in the insertion/elimination mechanism. This leads to the fact that chromium trimerization catalysts show no tendency to eliminate 1-butene from the metallacyclopentane intermediate, while eliminating almost completely from the chromacycloheptane. As confirmed by DFT calculations (Rensburg *et al.*, 2007), the reason for this dramatic difference is found in the steric restrictions of the hydride transfer in the metallacycles of different sizes.

In 2004 researchers from the South African company Sasol discovered a class of ligands that allows a chromium-catalyzed ethylene oligomerization forming 1-octene as the main product (up to 70% selectivity, Bollmann *et al.*, 2004). The rest of the product mixture consists mainly of 1-hexene (about 20%) together with small amounts of higher alkenes that form in a co-trimerization reaction between the alkene product and additional ethylene. The new catalyst system was found at the time by serendipity during a joint research project between the RWTH Aachen (Keim, Wasserscheid) and Sasol looking for more efficient trimerization catalysts. Mechanistic studies with deuterium labeled ethylene have provided strong hints that the 1-octene also forms by a metallacycle and suggest that additional ethylene inserts into the chromacycloheptane to form chromacyclononane from which, with high selectivity, 1-octene eliminates (Overett *et al.*, 2005). The Cr-complexes used in ethylene tetramerization are extremely reactive when properly activated with the methylaluminoxane co-catalyst. Catalyst productivities of more than 2 000 000 g olefin product/[g(Cr) h] have been reported (Kuhlmann *et al.*, 2009). Given the increasing relevance of 1-octene for co-monomer applications this technology has been further developed with great effort and very recently SASOL has announced the construction of a 100 000 t a⁻¹ plant at Lake Charles, Louisiana, that is scheduled to start beneficial operation in 2013 (Price, 2010).

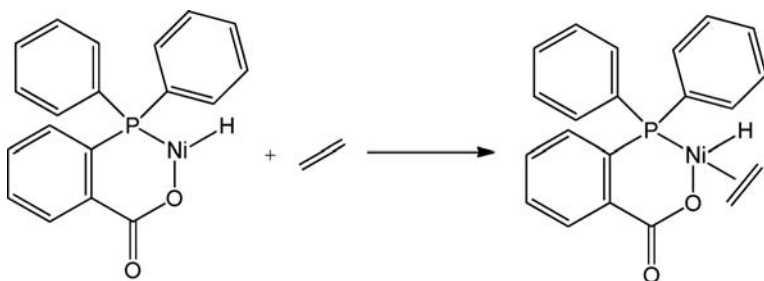
At the end of this subchapter it should be briefly noted that ethylene oligomerization is not the only way to produce 1-alkenes.

SASOL commercially extracts 1-alkenes from their high temperature Fischer-Tropsch product streams (Section 6.11.1). To produce polymer-grade 1-alkenes in this way, the 1-alkenes have to be separated from vinylidenes, linear and branched internal olefins, linear and branched paraffins, alcohols, aldehydes, carboxylic acids, and aromatic compounds. Thus, the 1-alkene extraction process operates from a very attractive feedstock basis (syngas from natural gas or coal) but comes with a significant investment in separation technology. Alternatively, 1-alkenes can be obtained by passing 1-alcohols in a vapor phase over acidic alumina catalyst. This process has been practiced by several companies in the past but it is only economic for special cases where an attractive access to the respective alcohol feedstock exists. SASOL has reported a process in which they produce 1-octanol by hydroformylation/hydrogenation of their exclusive 1-heptene feedstock extracted from Fischer-Tropsch product streams. Attractive feedstocks of the future may also be fatty alcohols from biogenic resources.

Dow Chemical Company operates a 1-octene plant in Tarragona, Spain, in which butadiene is reacted with methanol (2:1 molar ratio) in a homogeneous, Pd-catalyzed telomerization reaction. 1-Octene is formed after hydrogenation of the initial telomerization product by abstraction of methanol (van Leeuwen *et al.*, 2010).

Topic 6.16.1 Elementary steps of catalytic cycles

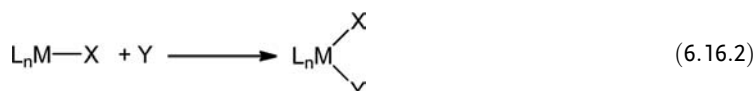
Section 2.3 introduced the fundamentals of catalysis. There, the fact that both homogeneous and heterogeneous catalysts follow a similar type of catalytic cycle has been highlighted. Indeed, substrates coordination/adsorption, reaction at the catalytic active center and, finally, product elimination/desorption are common features for all catalytic processes. However, a closer look reveals that different metals can react in the cycle in a very different manner with the same substrate. An illustrative example for this fact is the ethylene oligomerization discussed here.



Scheme 6.16.4 Ligand association reaction as initial step of ethylene oligomerization in the SHOP using a Ni-complex with a P,O-chelating ligand.

While Al-, Ni-, and Zr-complexes act by an insertion/elimination mechanism with a metal hydride as the active catalytic species, the unusual selectivity of Cr-complexes stems from the metallacycle mechanism as explained above. This different behavior originates from differences in the electronic properties of the active metal resulting in a different set and order of elementary steps forming the catalytic cycle. For a deeper understanding of the underlying principles, it is important to introduce first the most important elementary steps that typically form each catalytic cycle (Elschenbroich, 2003). We will discuss these steps with a strong focus on ethylene oligomerization to link this important extension of Section 2.3 directly to the examples provided in the rest of this subchapter:

1) Ligand (Lewis base) association



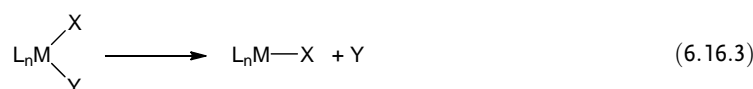
In Equation 6.16.2 M represents a catalytic metal center and X and Y are two ligands.

In this step, the coordination number (CN) of the complex increases by one, the number of valence electrons (VE) increases by two (as the ligand is a substance that brings two electrons for coordination with it), but the oxidation number (ON) stays the same (the addition of the neutral ligand does not change the oxidation state of the metal).

The example in Scheme 6.16.4 shows the association of the neutral ligand ethylene to the Ni-hydride catalyst applied in the SHOP process, which carries an *o*-diphenylphosphinebenzoic acid ligand (Vogt, 2002). In addition, the first step in the Cr-metallacycle mechanism, the addition of two neutral ethylene molecules to the Cr prior to the oxidative coupling step, is a ligand association step.

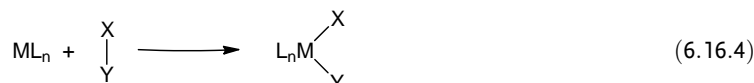
Apart from examples in ethylene oligomerization, other ligand association reactions of great importance in homogeneous catalysis are the addition of phosphine, amine, or CO ligands to metal complexes.

2) Ligand dissociation



Ligand dissociation is the reverse reaction of ligand association. Consequently, the CN of the complex reduces by one, the VE by two, and the ON stays constant. As ligand association is usually a reversible step, all reverse reactions of the examples given above for the association step represent suitable examples for ligand dissociation. In ethylene oligomerization, the dissociation step plays a role in the release of the finally formed 1-alkene from the catalyst (after β -H-elimination). An example for the case of 1-octene liberation from a Cr(I) complex is given below in Scheme 6.16.8.

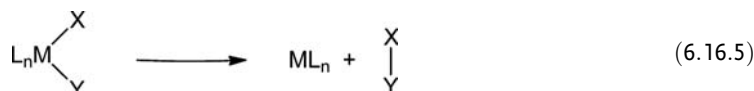
3) Oxidative addition



In oxidative addition, the CN of the complex increases by two, the VE increases by two (formally each of the ligands X and Y comes with one electron), and also the ON increases by two (as both ligands, X and Y, are ligands of higher electronegativity than M). The archetypal example of oxidative addition is the dissociative addition of hydrogen to a metal complex ($X, Y = H$). The resulting dihydride complex plays a very important role in all hydrogenation reactions.

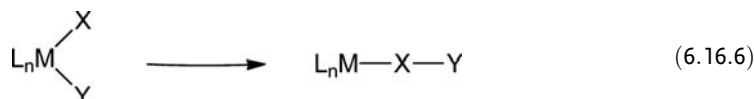
In ethylene oligomerization, oxidative addition plays no role. In the “insertion–elimination mechanism,” the metal oxidation state is constant throughout the catalytic cycle. In the metallacycle mechanism, the oxidative step is an oxidative coupling reaction (see below).

4) Reductive elimination

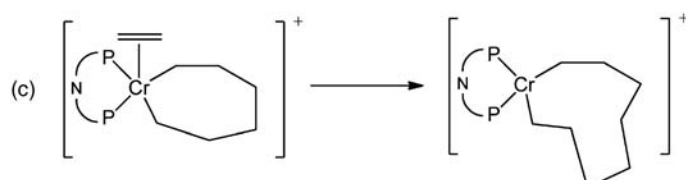
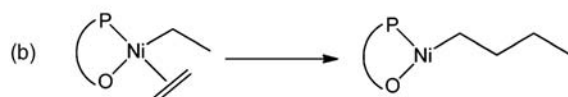


Reductive elimination is the reverse reaction of oxidative addition (CN, VE, and ON reduce by two). A practical, most important example of the reductive elimination step is the elimination of alkane product from the catalyst in alkene hydrogenation ($X = \text{alkyl}$, $Y = H$). In ethylene oligomerization, reductive elimination plays an important role in the liberation of the 1-alkene product from the chromium metallacyclic intermediate. As this process combines several elementary steps, it is shown in Scheme 6.16.8 below to sum up this topic.

5) Insertion



In the insertion step, a ligand X inserts into an existing bond between the metal and another ligand. The step reduces the CN by one and the VE by two while the oxidation state stays constant (as the inserting ligand is usually a neutral one). Insertion is a key step in the “insertion/elimination” mechanism for ethylene oligomerization ($X = \text{ethylene}$, $Y = H$). Here, the neutral ligand ethylene inserts into the nickel hydride bond to form a Ni–ethyl complex (Scheme 6.16.5a; for clarity, the P,O-chelating ligand is only schematically shown). Chain growth at the Ni-center proceeds via an insertion step as well. Here, a further ethylene unit



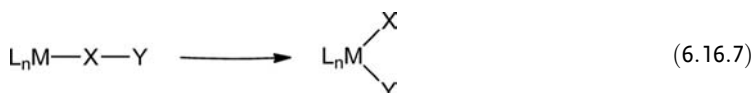
Scheme 6.16.5 Relevance of the insertion step for the different ethylene oligomerization mechanisms: (a) and (b) showing ethylene insertion into a Ni–hydride and a Ni–alkyl bond respectively; (c) showing ethylene insertion into the metal–C bond to enlarge the metallacycle in case of Cr-catalyzed ethylene oligomerization.



inserts into the already existing Ni—alkyl bond ($X = \text{ethylene}$, $Y = \text{alkyl}$) (Scheme 6.16.5b). In Cr-catalyzed oligomerization, the enlarging of the metallacycle ring is also an insertion reaction. Scheme 6.16.5c shows the step that transforms the seven-membered ring (that would eliminate 1-hexene) into the nine-membered ring (that would eliminate 1-octene). For this example, the PNP ligand of the SASOL tetramerization system is schematically indicated and the system is given as a Cr(III) complex, as indicated by the literature (McGuinness, 2010; van Leeuwen, 2010).

Apart from ethylene oligomerization, another prominent and very important example of an insertion step in catalysis is the insertion of CO into a Rh—alkyl bond in olefin hydroformylation (see Section 6.14; here $X = \text{CO}$, $Y = \text{alkyl}$).

6) Extrusion



Extrusion is the reverse reaction of insertion (CN: +1, VE: +2, ON: unchanged). The reaction plays a very important role in ethylene oligomerization according to the insertion/elimination mechanism as the so-called “ β -H-elimination.” Scheme 6.16.6 illustrates this elementary step for the extrusion of a 1-hexene product from a Ni-hexyl complex. The extrusion step is followed by 1-hexene dissociation from the complex (see above) to finally liberate the 1-hexene product. Below, in Scheme 6.16.8, the extrusion step is shown as part of a more complex reaction sequence for the liberation of a 1-alkene product from a chromium metallacyclic intermediate.

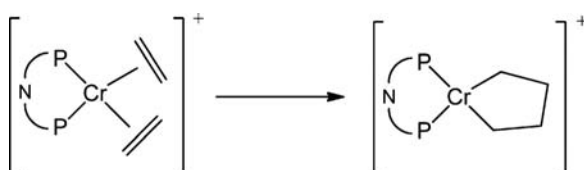
7) Oxidative coupling



Oxidative coupling involves two neutral ligands that interlink by forming a metallacycle. In this step the oxidation state of the metal increases by two as the ligand becomes formally anionic (due to the higher electronegativity of X and Y in comparison to the metal).

Oxidative coupling is the decisive step in the Cr-based ethylene oligomerization according to the metallacycle mechanism. As shown in Scheme 6.16.7, two ethylene units of the ligand sphere of the Cr-complex interlink and transform their associative π -bonds into σ -bonds to form the Cr metallacyclic intermediate. Assuming a cationic Cr-complex in the first place (with the MAO anion as very weakly coordinating counter-ion), the oxidation state of chromium increases in the process from +I to +III.

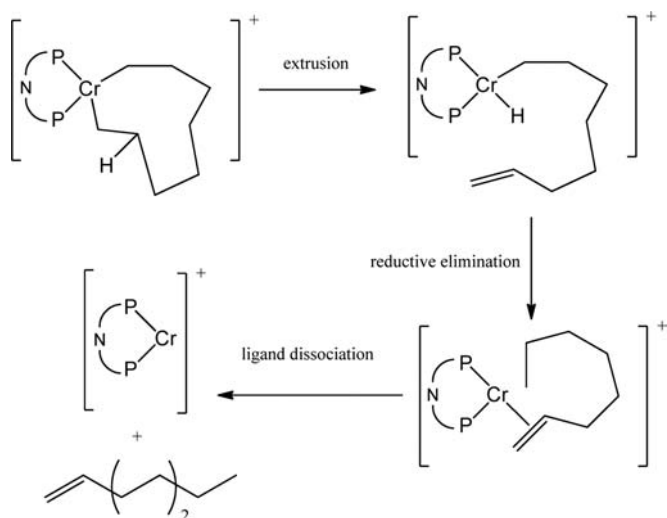
8) Reductive cleavage



Scheme 6.16.6 Extrusion of 1-hexene from a Ni-hexyl complex; the hydrogen at the β -position is shown explicitly as this is transferred in this extrusion step to the metal to form the Ni hydride.

Scheme 6.16.7 Oxidative coupling of ethylene ligands at a cationic chromium complex to form the respective Cr(III)-metallacycle that later inserts ethylene.

Scheme 6.16.8 Liberation of 1-octene from the nine-membered Cr-metallacycle by combination of the elementary steps extrusion, reductive elimination, and ligand dissociation.



Reductive cleavage is the reverse reaction of oxidative coupling. CN stays constant, ON decreases by two, and VE increases by two. The reverse reaction of metallacycle formation in Cr-catalyzed ethylene oligomerization would be in theory a suitable example of reductive cleavage; however, this reaction does not play a productive role in the cycle.

Finally, to sum up this topic on catalytic elementary steps, we have a closer look at the mechanism of 1-alkene liberation from the Cr-metallacyclic intermediate. This process requires the interplay of three elementary steps, namely, extrusion to form an intermediate Cr-hydride species, reductive elimination to form the alkene complex of Cr(I), and, finally, dissociation of the alkene product. Scheme 6.16.8 illustrates these three steps for the example of 1-octene liberation from the nine-membered Cr-metallacycle.

Summary of Section 6.16 (take-home messages)

- **Ethylene oligomerization** is a homogeneous catalyzed reaction that converts ethylene into 1-alkenes. Commercial ethylene oligomerization processes are catalyzed by Al-, Ti-, Zr-, Ni-, and Cr-complexes. 1-Alkenes find major industrial applications as co-monomers in polyethylene manufacturing or as intermediates for the production of plasticizer alcohols, detergents, or lubricants.
- Ethylene oligomerization catalyzed by Al-, Zr-, and Ni-complexes follows a so-called “**insertion/elimination** mechanism” that results in the production of 1-alkene mixtures of different chain lengths. The mechanistic reason for this product distribution is the fact that each metal-alkyl complex shows the same probability of chain growth independent of the chain length of the attached alkyl group.
- Ethylene oligomerization catalyzed by Cr-complexes follows a so-called “**metallacycle** mechanism”. This allows the selective production of 1-hexene and of 1-octene/1-hexene mixtures. Mechanistically, metallacycles of different ring size show very different rates of elimination. By clever ligand selection, selective elimination from one specific ring size is possible and leads to selective 1-alkene formation. In particular, the undesired production of large amounts of undesired 1-butene can be avoided by using Cr-complexes in ethylene oligomerization.

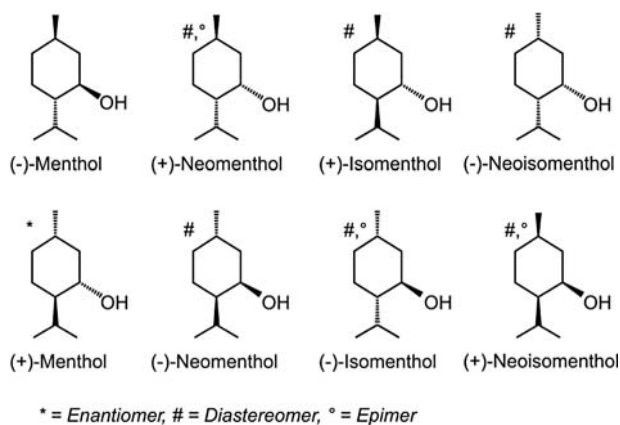


Figure 6.17.1 Structure of the eight menthol diastereomers.

6.17

Production of Fine Chemicals (Example Menthol)

6.17.1

Menthol and Menthol Production (Overview)

The terpene alcohol $(-)$ -menthol is an important flavoring substance because of its unique cooling effect and flavor. $(-)$ -Menthol is used in toothpastes, cosmetics, and in pharmacy and medicine because of its anesthetic properties, for example, for contact urticaria and treatment of headache or bronchitis. Another major user is the tobacco industry with a share of 25%.

Worldwide, 12 000 tonnes of $(-)$ -menthol are produced per year (1998). The majority is natural menthol from *Mentha arvensis* or *Mentha piperita* and only a quarter is produced synthetically. Nevertheless, the synthetic route is important as the price from natural resources fluctuates if the availability is limited due to bad harvests, that is, synthetic menthol stabilizes the price.

Stereochemical aspects have to be taken into account for the synthetic route to $(-)$ -menthol. The core of menthol is a nonplanar cyclohexane ring with a methyl, hydroxyl, and isopropyl substituents. Menthol has three chiral centers and, thus, eight different conformers are possible. These are $(+)$ - and $(-)$ -menthol, $(+)$ - and $(-)$ -neomenthol, $(+)$ - and $(-)$ -isomenthol, and $(+)$ - and $(-)$ -neoisomenthol (Figure 6.17.1). Owing to the above-mentioned properties of $(-)$ -menthol, where all substituents are in the equatorial position, this isomer is the by far most desired product.

Two routes are used for industrial synthesis of $(-)$ -menthol. One option is to achieve a chiral precursor early in the process and retain the chiral information during the process to gain only $(-)$ -menthol in the end (*Takasago process*). Alternatively, a racemic mixture of (\pm) -menthol is synthesized by heterogeneously catalyzed hydrogenation of thymol, followed by separation of the target molecule $(-)$ -menthol by distillation and crystallization. This is achieved in the *Symrise process* (formerly known

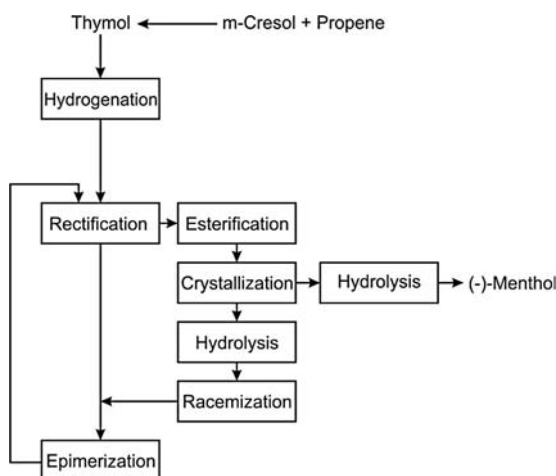
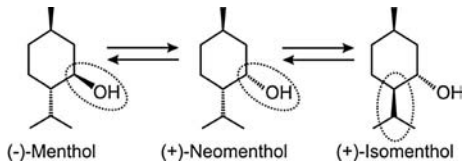
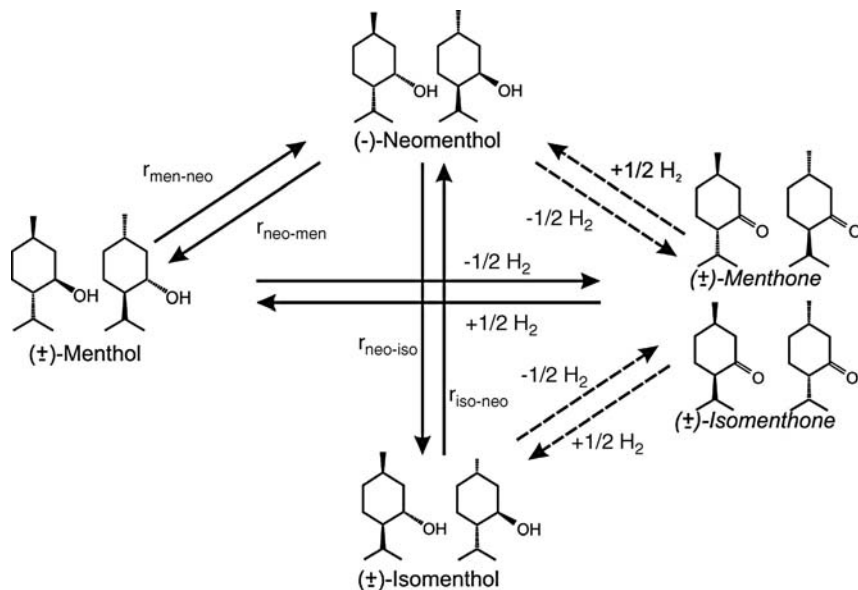


Figure 6.17.2 *Symrise* process for menthol production: Hydrogenation of thymol leads to a mixture of (\pm) -menthol, (\pm) -isomenthol, and (\pm) -neomenthol. Thereafter, (\pm) -menthol is separated by rectification and converted by esterification with methyl benzoate ($C_6H_5COOCH_3$) into (\pm) -menthyl benzoate and methanol. Finally, $(-)$ -menthyl benzoate is separated by crystallization, and the final product $(-)$ -menthol is obtained by the reverse reaction, that is, by hydrolysis with methanol. The $(+)$ -menthol benzoate is also hydrolyzed, and the resulting $(+)$ -menthol is converted into a racemic mixture of all menthol isomers. This mixture is combined with the iso- and neomenthol separated by rectification and used as feed for the epimerization.

Scheme 6.17.1 Reaction scheme of epimerization of menthol diastereomers (Etzold, 2007; Etzold and Jess, 2008 and 2009).



Scheme 6.17.2 Reaction mechanisms of epimerization of menthol diastereomers (Etzold, 2007).
Reaction mechanisms of epimerization of menthol diastereomers (Etzold, 2007).

as Haarmann & Reimer process, Figure 6.17.2). Details are given by Hopp (1996), Clark (1998), Emberger and Hopp (1987), Surburg and Panten (2006), Walker (1967), Kuhn *et al.* (2004), Lawrence (2007), and Leffingwell and Shackelford (1974).

The hydrogenation of thymol leads to an equilibrium mixture of 60% (\pm)-menthol, 30% (\pm)-neomenthol, and 10% (\pm)-isomenthol. (\pm)-Neoisomenthol is formed to a negligible extent. Thus, 40% of undesired racemic stereoisomers have to be separated by distillation and are then converted on a Ni-catalyst by epimerization in the presence of about 10 MPa H_2 ; hydrogen is not needed according to the stoichiometry, but suppresses dehydrogenation to menthone (Scheme 6.17.1). The resulting menthol rich mixture is recycled to the distillation. Subsequently, only the epimerization as a central part of the process is discussed.

According to the reaction mechanism (Scheme 6.17.1) menthol is only formed via neomenthol and not directly from isomenthol. This can be explained by Scheme 6.17.2. In each reaction step, either the isopropyl group or the alcohol group changes the orientation, and thus (+)-isomenthol reacts to give (+)-neomenthol and then to (-)-menthol. Similarly, (-)-isomenthol reacts to give (-)-neomenthol and then to (+)-menthol. The position of the methyl group is not changed during epimerization, as shown by experiments using pure substances.

6.17.2

Thermodynamics and Kinetics of Epimerization of Menthol Isomers

Kinetic studies on the epimerization of menthol diastereomers have been conducted in a laboratory-scale semi-batch reactor (Figure 6.17.3) as well as in a continuous fixed bed reactor (Figure 6.17.4). In the latter case, the liquid feed was externally saturated with H_2 to suppress dehydrogenation to menthone [presaturated one-liquid flow (POLF) reactor].

Figure 6.17.5 shows typical experimental results obtained with both reactors. The agreement between the results in both reactors is quite satisfactory. For a well-defined direct comparison, the modified residence time catalyst (in $kg\ s\ m^{-3}$) is used, which is defined as the ratio of the mass of catalyst to the feed rate in the case of the continuous fixed bed reactor, and as the product of reaction time and volumetric concentration of the catalyst for the batch reactor.

Figure 6.17.5 indicates that the epimerization reactions are limited by thermodynamic constraints. By experiments and literature data (Figure 6.17.6), Etzold determined the equilibrium constants K_i , which are given by:

$$K_i = e^{-\frac{\Delta_R H_f^0}{RT} + \frac{\Delta_R S_f^0}{R}} \quad (6.17.1)$$

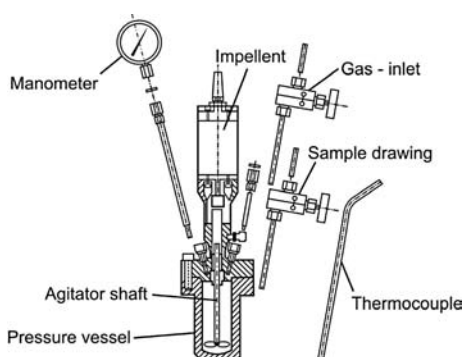


Figure 6.17.3 Semi-batch stirred tank reactor for kinetic studies on epimerization. The catalyst is fixed in a basket inside the autoclave. The H_2 pressure is kept constant.

Semi-batch stirred tank reactor for kinetic studies on epimerization. The catalyst is fixed in a basket inside the autoclave. The H_2 pressure is kept constant.

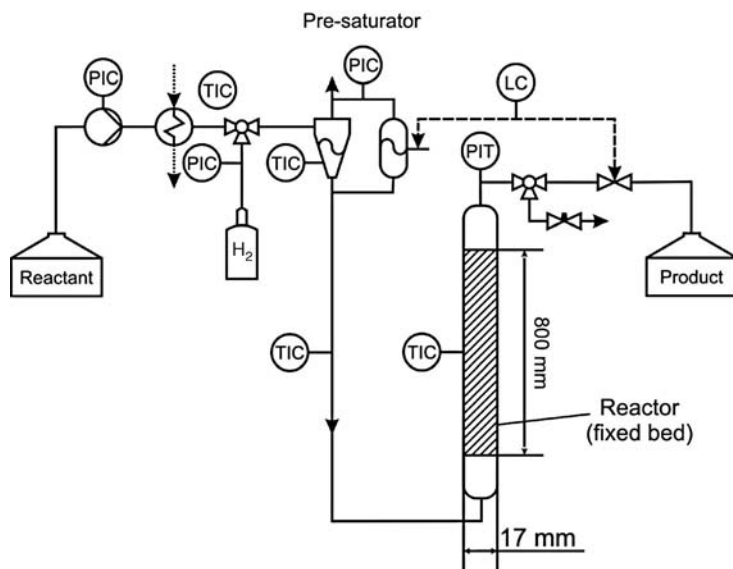


Figure 6.17.4 Laboratory-scale continuous fixed bed reactor (liquid phase externally saturated with H_2 to suppress dehydrogenation to menthone) used for kinetic studies on the epimerization of menthol isomers (P: pressure, T: temperature, L: level, I: indication, C: control).

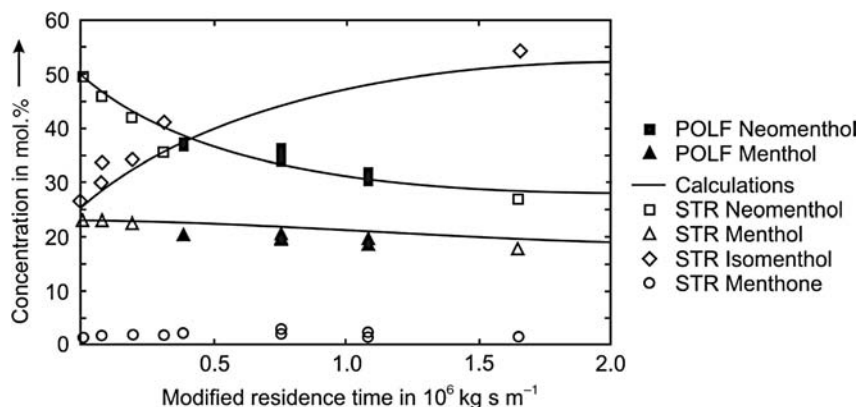


Figure 6.17.5 Experimental results of epimerization in a fixed bed reactor [presaturated one-liquid flow (POLF) reactor] and in a well-mixed semi-batch stirred tank reactor (STR) [feed: 50 mol.% (\pm) -neomenthol, 26% (\pm) -menthol, and 23% (\pm) -isomenthol, 1% menthone, 180 °C, $p_{\text{H}_2} = 2 \text{ MPa}$, $d_{\text{cat}} = 250\text{--}500 \mu\text{m}$]. Data from Etzold (2007) and Etzold and Jess (2009).

The agreement between the calculations and the experimental data (for a very long reaction time to reach the equilibrium) over a wide range of temperature is very satisfactory (Figure 6.17.6).

Kinetic and thermodynamic studies showed that the epimerization can be described by the scheme depicted in Scheme 6.17.1. Thus, the formation of neomenthol is given by:

$$\frac{1}{m_{\text{cat}}} \frac{dn_{\text{neo}}}{dt} = \frac{V_R}{m_{\text{cat}}} \frac{dc_{\text{neo}}}{dt} = \frac{dc_{\text{neo}}}{d\tau_m} = r_{\text{men-geo}} - r_{\text{geo-men}} + r_{\text{iso-geo}} - r_{\text{geo-iso}} \quad (6.17.2)$$

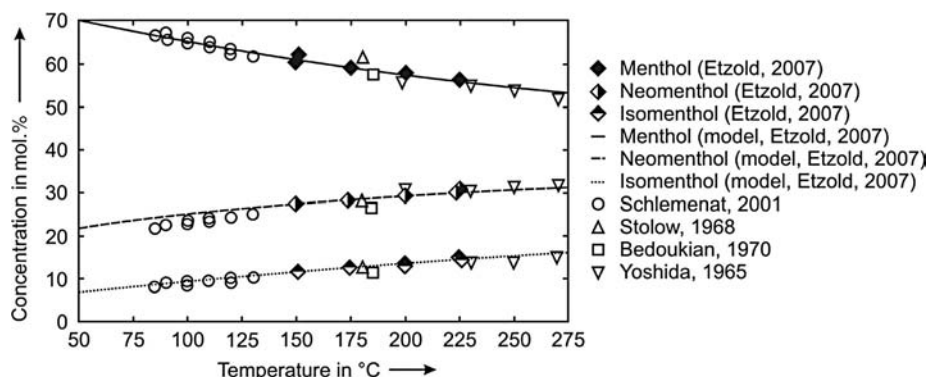


Figure 6.17.6 Equilibrium concentrations of menthol diastereomers. Data from Etzold (2007); Etzold and Jess (2008); Bedoukian (1970); Yoshida, Komatsu, and Indo (1966); Schlememat *et al.* (2001); and Stolow and Groom (1968).

where τ_m as the modified residence time (in kg s m^{-3}). The respective differential equations for the change of concentrations of menthol (index men) and isomenthol (index iso) are:

$$\frac{dc_{\text{men}}}{d\tau_m} = r_{\text{neo-men}} - r_{\text{men-neo}} \quad (6.17.3)$$

$$\frac{dc_{\text{iso}}}{d\tau_m} = r_{\text{neo-iso}} - r_{\text{iso-neo}} \quad (6.17.4)$$

For reversible reactions, the reverse reaction rate (constant) can be expressed by the forward reaction rate (constant), if the equilibrium constant is known (Section 4.3.3). Here we obtain:

$$r_{\text{neo-men}} = k_{\text{neo-men}} c_{\text{neo}} \quad (6.17.5)$$

$$r_{\text{men-neo}} = \frac{k_{\text{neo-men}}}{K_{\text{neo-men}}} c_{\text{men}} \quad \left(\text{with } K_{\text{neo-men}} = \frac{c^*_{\text{men}}}{c^*_{\text{neo}}} = e^{-\frac{\Delta_R H^0_{\text{neo-men}}}{RT} + \frac{\Delta_R S^0_{\text{neo-men}}}{R}} \right) \quad (6.17.6)$$

$$r_{\text{iso-neo}} = k_{\text{iso-neo}} c_{\text{iso}} \quad (6.17.7)$$

$$r_{\text{neo-iso}} = \frac{k_{\text{iso-neo}}}{K_{\text{iso-neo}}} c_{\text{men}} \quad \left(\text{with } K_{\text{iso-neo}} = \frac{c^*_{\text{neo}}}{c^*_{\text{iso}}} = e^{-\frac{\Delta_R H^0_{\text{neo-iso}}}{RT} + \frac{\Delta_R S^0_{\text{neo-iso}}}{R}} \right) \quad (6.17.8)$$

Although hydrogen is not needed for the epimerization, the reaction rates depend on the H_2 pressure, which indicates that hydrogenation and dehydrogenation steps are probably involved in the overall mechanism of epimerization (Etzold, 2007; Etzold and Jess, 2008 and 2009).

The reaction rate increases almost linearly with pressure, and without H_2 the reaction does come to a complete standstill. Thus, the two rate constants used in the above equations ($k_{\text{neo-men}}$ and $k_{\text{iso-neo}}$ in $\text{kg s}^{-1} \text{m}^{-3}$) are apparent rate constants, which still depend on the H_2 pressure. This can formally be described by the following equations:

$$k_{\text{neo-men}} = (p_{0,\text{neo-men}} + p_{\text{H}_2}) k_{0,\text{neo-men}} e^{-\frac{E_{\text{A},\text{neo-men}}}{RT}} \quad (6.17.9)$$

$$k_{\text{iso-neo}} = (p_{0,\text{iso-neo}} + p_{\text{H}_2}) k_{0,\text{iso-neo}} e^{-\frac{E_{\text{A},\text{iso-neo}}}{RT}} \quad (6.17.10)$$

For the reaction model, it is assumed that the influence of pressure as described by Eqs. (6.17.9) and (6.17.10) does not depend on temperature. Consequently, the two reversible reactions of menthol formation can be described by the rate constants of the forward reactions and the two equilibrium constants. Table 6.17.1 gives the values of the respective parameters.

6.17.3

Influence of Mass Transfer on the Epimerization of Menthol Isomers

For an accurate design of a technical reactor, not only the thermodynamic and intrinsic kinetic data but also the influence of pore diffusion has to be taken into account. This mass transfer limitation may occur due to a relatively high catalytic activity and a limitation of the minimum particle size with regard to the pressure drop of a fixed bed reactor and/or a filtration process in case of a slurry reactor. As a consequence, the effective rates of epimerization are lower than the intrinsic rates, which may also have a negative impact on the selectivity.

The common and classical approach to considering pore diffusion limitations is the utilization of an effectiveness factor as a single parameter, which was developed by Damkoehler, Thiele and Zeldovich in the 1930s (Damkoehler, 1936, 1937a, 1937b, 1939; Thiele, 1939; Zeldowitsch, 1939). However, an exact calculation of the effectiveness factor is only possible for simple power law kinetics, isothermal particles, or simple reaction networks, for example, for two parallel or serial reactions, as described in many textbooks (e.g., Froment and Bischoff, 1990 or Levenspiel, 1996,

Table 6.17.1 Kinetic and thermodynamic parameters of the epimerization. Data from Etzold and Jess (2008).

Parameter	Value
$k_{0,\text{neo-men}}$	$750 \text{ m}^3 \text{ kg}^{-1} \text{ s}^{-1} \text{ Pa}^{-1}$
$E_{\text{A},\text{neo-men}}$	133 kJ mol^{-1}
$p_{0,\text{neo-men}}$	10^6 Pa
$k_{0,\text{iso-men}}$	$1.2 \times 10^4 \text{ m}^3 \text{ kg}^{-1} \text{ s}^{-1} \text{ Pa}^{-1}$
$E_{\text{A},\text{iso-neo}}$	150 kJ mol^{-1}
$p_{0,\text{iso-neo}}$	$4 \times 10^6 \text{ Pa}$
$\Delta_R H^0_{\text{neo-men}}$	-4 kJ mol^{-1}
$\Delta_R S^0_{\text{neo-men}}$	$-2.8 \text{ J mol}^{-1} \text{ K}^{-1}$
$\Delta_R H^0_{\text{iso-neo}}$	-3.2 kJ mol^{-1}
$\Delta_R S^0_{\text{iso-neo}}$	$-0.4 \text{ J mol}^{-1} \text{ K}^{-1}$

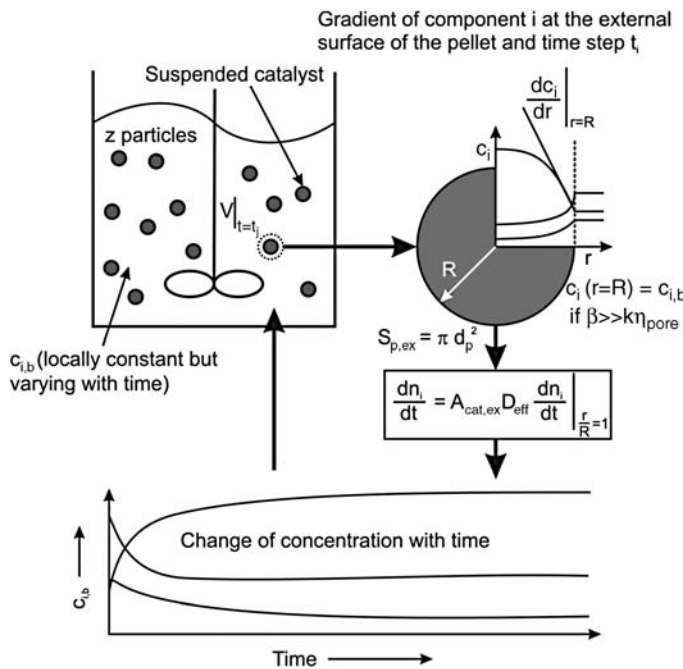


Figure 6.17.7 Scheme of numerical calculation procedure for a batch reactor. Adapted from Etzold and Jess (2008).

1999); see also Section 4.5.4. For more complex kinetics like *Langmuir–Hinshelwood* type of reactions only approximate solutions can be derived (Strieder and Aris, 1973).

For several combined reversible reactions, as in the case of the epimerization (Scheme 6.17.1), we have an analytically unsolvable reaction network with respect to the influence of internal mass transfer. In the following, a numerical method developed by *Etzold* (Etzold, 2007) is presented, which allows the fast and accurate simultaneous calculation of the change of the concentrations in the bulk phase as well as within the porous particles with time (batch reactor) or local position (tubular fixed bed reactor). This method may also be used for other reaction systems beyond the special case of epimerization of menthol diastereomers.

The modeling methodology is shown in Figure 6.17.7 for the example of a discontinuous slurry reactor. First, the concentration profiles within the catalyst particles are calculated. This information is then coupled (for each time step) with the change of concentrations in the bulk phase ($c_{i,b}$). The link between both procedures, that is, between the bulk phase and the porous catalyst particles, is the concentration gradient of each reactant at the external particle surface. Note that this calculation is also applicable for a continuous plug flow reactor simply by using the residence time τ ($= x/u$) instead of the reaction time, whereby x represents the axial coordinate x in a tubular reactor and u the fluid velocity.

The differential mass balance for spherical particles yields:

$$\frac{dc_i}{dt} = D_{eff} \left(\frac{d^2 c_i}{dr^2} + \frac{2}{r} \frac{dc_i}{dr} \right) - \rho_p r_i \quad (6.17.11)$$

Calculation of effective diffusion coefficient D_{eff} is examined in detail in Example 6.17.1.

As boundary conditions we have:

$$c_i \Big|_{r=R} = c_{i,b} \quad (\text{external surface and negligible influence of external mass transfer}) \quad (6.17.12)$$

$$\frac{dc_i}{dr} \Big|_{r=0} = 0 \quad (\text{center of particle}) \quad (6.17.13)$$

Consideration of external mass transfer is possible by the implementation of the film theory, but here is not needed as the external mass transfer resistance is

negligible for the epimerization ($c_{i,\text{surface}} = c_{i,\text{b}}$). The differential equations are then solved by a numerical solver.

The heat balance is not considered here as the epimerization is only slightly exothermic ($\Delta_R H_i^0 \approx -4 \text{ kJ mol}^{-1}$, Table 6.17.1) and the reaction system is almost isothermal.

With the above given equations, the concentration profiles in a particle can be calculated but it has to be considered that the bulk phase concentrations ($c_{i,\text{b}}$) change with time. The link between the changing bulk concentrations and the intra-particle concentrations gradients is derived from *Fick's law* for the position of the external particle surface ($r = R$):

$$\frac{dn_{i,\text{b}}}{dt} = V_l \frac{dc_{i,\text{b}}}{dt} = -A_{\text{cat,ex}} D_{\text{eff}} \left. \frac{dc_i}{dr} \right|_{r=R} \quad (\text{external surface of catalyst particles}) \quad (6.17.14)$$

The concentration gradients at the external surface are calculated by the radial concentration profiles of each component in the pellet at $r = R$. Equation. (6.17.14) then yields the rate of consumption/formation of each compound, which equals the mass transfer by diffusion to/from the outer surface of the catalyst from/into the bulk phase. $A_{\text{cat,ex}}$ represents the overall external surface of all particles, and is calculated by the mean particle diameter and the number of particles z , which can be expressed by the particle density and total mass of catalyst:

$$A_{\text{cat,ex}} = z\pi d_p^2 = \frac{m_{\text{cat}}}{V_p \rho_p} \pi d_p^2 = \frac{6m_{\text{cat}}}{d_p \rho_p} \quad (6.17.15)$$

Numerical programs use small time steps, and the change of the concentrations in the bulk phase is computed before the concentration profiles inside the catalyst are calculated for the next step. The change in bulk phase concentrations ($c_{i,\text{b}}$) within a step $\Delta t = t_j - t_{j-1}$ is:

$$\frac{dc_{i,\text{b}}}{dt} = \frac{1}{V_l} \frac{dn_{i,\text{b}}}{dt} \approx \frac{1}{V_l} \frac{\Delta n_{i,\text{b}}}{\Delta t} \quad (6.17.16)$$

Insertion of Eqs. (6.17.14) and (6.17.15) into Eq. (6.17.16) yields:

$$\frac{dc_{i,\text{b}}}{dt} = - \frac{6m_{\text{cat}}}{V_l d_p \rho_p} D_{\text{eff}} \left. \frac{dc_i}{dr} \right|_{r=R} \quad (6.17.17)$$

By Eq. (6.17.17), the change in bulk phase concentration is determined and thus we get the boundary condition (bulk phase concentration) to calculate the intraparticle concentration profiles for the next time step and so forth. For implementation of the presented numerical method the commercial software *Presto* (CiT, Rastede, Germany) was used.

Example 6.17.1: Molecular and effective diffusion coefficients of menthol isomers

Molecular diffusion coefficient in liquids

Molecular diffusion coefficients in liquids may be measured by use of the so-called Jost pot (Figure 6.17.8), which consists of two well-mixed reservoirs separated by a frit (Jost, 1960). First, both reservoirs are filled with the same amount of reaction mixture (denoted here as solvent B). Then a small amount of solute A is poured into one reservoir (here the left-hand one). Subsequently, samples are taken to track the decrease in concentration of A that diffuses between both reservoirs until the concentration is balanced.

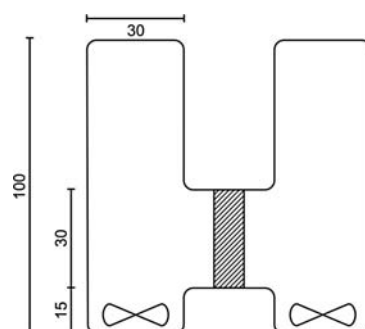


Figure 6.17.8 Jost pot used to measure the diffusion coefficient of menthol (Etzold, 2007).

The equation describing the decrease in concentration of component A with time is:

$$\begin{aligned} -\frac{dc_{A,\text{left}}}{dt} &= D_{AB,\text{eff}} \frac{A_{\text{frit}} c_{A,\text{left}} - c_{A,\text{right}}}{V_l} = \frac{\varepsilon_{\text{frit}}}{\tau_{\text{frit}}} D_{\text{mol},AB} \frac{A_{\text{frit}} \Delta c_A}{V_l} \\ &= C_{\text{frit}} \frac{D_{\text{mol},AB}}{V_l} \Delta c_A \end{aligned} \quad (6.17.18)$$

Here A_{frit} and d_{frit} are the cross-sectional area and thickness of the frit, respectively, and $\varepsilon_{\text{frit}}$ and τ_{frit} the porosity and tortuosity of the frit that separates both reservoirs with equal liquid volume V_l . Integration for the initial concentration in the left-hand reservoir ($c_{A,\text{left},0}$) and $c_{A,\text{right},0}=0$ yields:

$$c_{A,\text{left}} = \frac{c_{A,\text{left},0}}{2} \left(1 + e^{-\frac{2D_{\text{mol},AB} C_{\text{frit}}}{V_l} t} \right) \quad (6.17.19)$$

The unknown diffusion coefficient of the menthol stereoisomers can be determined if the liquid volume V_l (here 40 cm^3) and the constant $C_{\text{frit}} = \varepsilon_{\text{frit}} A_{\text{frit}} / (\tau_{\text{frit}} d_{\text{frit}})$ are known. Therefore, the diffusion of 1-octene in octane, for which the molecular diffusion coefficient is known, was measured first, which leads to a value of C_{frit} of 3.74 m . Two typical experimental results obtained with the Jost pot are shown in Figure 6.17.9. By Eq. (6.17.19), the diffusion coefficient is determined with the value of D_{mol} as the single remaining fitting parameter. Alternatively, we may also calculate D_{mol} by Eq. (6.17.18) and the initial slope as for $t=0$ we have $\Delta c_A = c_{A,\text{left},0}$ and thus $D_{\text{mol}} = [dc_A/dt]_{\text{initial}} V_l / (c_{A,\text{left},0} C_{\text{frit}})$.

Figure 6.17.10 shows experimentally determined diffusion coefficients of (+)-menthol in (-)-menthol and of menthone in the reaction mixture at different temperatures.

The influence of temperature on the diffusion coefficient is given by:

$$D_{\text{mol}} = D_0 e^{-\frac{E_A}{RT}} \quad (\text{with the values of } D_0 \text{ and } E_A \text{ as given in Figure 6.17.10}) \quad (6.17.20)$$

For comparison, the diffusion coefficient of menthol in the reaction mixture can also be calculated by the Wilke-Chang equation for diffusion in liquids:

$$D_{\text{mol}} = 5.88 \times 10^{-17} \frac{T \sqrt{\chi M}}{\eta (\nu_{\text{mol,cp}})^{0.6}} \quad (3.1.90)$$

where χ is the association parameter (here a value of one as used for nonpolar liquids), M is the molar mass of the menthol isomers (156 kg mol^{-1}), and is $\nu_{\text{mol,cp}}$ the molar volume ($2.1 \times 10^{-4} \text{ m}^3 \text{ mol}^{-1}$). The

experimentally determined viscosity η in $\text{kg m}^{-1} \text{ s}^{-1}$ is given by (Etzold, 2007):

$$\eta = 2 \times 10^{-5} e^{\frac{681}{T-203}} \quad (6.17.21)$$

The comparison of the calculation by the Wilke-Chang equation with the measured values shows a good agreement (Fig. 6.17.10).

Effective diffusion coefficient in the porous catalyst particles

To calculate the effective diffusion coefficients in the catalyst particles [$D_{\text{eff}} = D_{\text{mol}} \varepsilon_p / \tau_p$, Eq. (3.2.85)], the values of porosity of the particle and of the tortuosity are needed. The porosity was measured by mercury intrusion porosimetry ($\varepsilon_p = 0.56$) and the tortuosity was estimated based on the kinetic data at different particle sizes by comparison of calculated and measured effective reaction rates with τ_p as the only remaining fitting parameter, which yields a value of $\tau_p = 1.7$ (Etzold, 2007). For modeling the epimerization, a mean value of the diffusion coefficient representing all stereoisomers was used (Figure 6.17.10).

Figure 6.17.11 shows experimental results of the epimerization at three different temperatures for a small particle size ($0.5\text{--}1 \text{ mm}$), which represent the intrinsic kinetics, and for the original $6 \times 6 \text{ mm}$ cylindrical catalyst pellets, where pore diffusion limitations lead to a decrease of the effective reaction rate. The experiments were conducted in the well-mixed batch reactor. As expected, the influence of mass transfer increases with increasing temperature and becomes strong at 200°C . Note that for clarity Figure 6.17.11 only shows the change of menthol concentration and not of the other two stereoisomers (as in Figure 6.17.5). In addition, note that the initial menthol concentration is not zero as an industrially relevant feed was used. The dashed and solid lines in Figure 6.17.11 represent the results of the calculation by the method described before, showing a good agreement with the experimental data.

Figure 6.17.12 shows snapshots of the calculated concentration profiles inside a single pellet at three different modified residence times (corresponding to the gray symbols in Figure 6.17.11). For the calculation, a temperature of 200°C was chosen as an example for a strong limitation by pore diffusion, and thus the equilibrium concentrations are reached within a small distance from the external particle surface. The corresponding concentration gradients of all three isomers at the surface of the catalyst are also indicated. These gradients are needed as boundary conditions to solve the differential Eq. (6.17.11) for every time step.

The good fit of calculated and experimental data at different temperatures shows that the method can be used for complex kinetic systems with internal mass transport limitations.

It has to be pointed out that the model in the presented form is strictly speaking only correct for a homogeneous distribution of the catalytic activity and a constant diffusion coefficient within the particle, that is, for the ideal case of a material with one size of pore. For pellets with a pore size distribution the selectivities are not calculated accurately. Such a situation is quite common, for example, a pellet may contain macro- and micropores if it has been shaped from microparticles (with micropores) by compression (see Example 4.5.11 in Section 4.5.6.3).

Figure 6.17.9 Typical experimental results obtained by means of the Jost pot to determine the diffusion coefficient of menthol isomers at 423 K (150 °C) (Etzold, 2007).

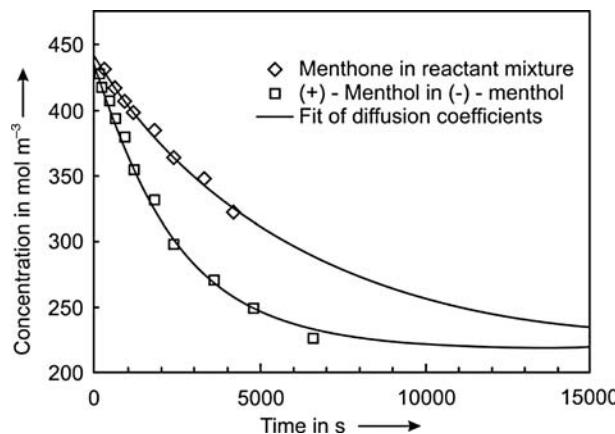


Figure 6.17.10 Experimentally determined diffusion coefficients (Etzold, 2007; Etzold and Jess, 2008) and estimations by Eq. (6.17.20) and by Wilke-Chang equation [Eq. (3.1.90)] in combination with Eq. (6.17.21).

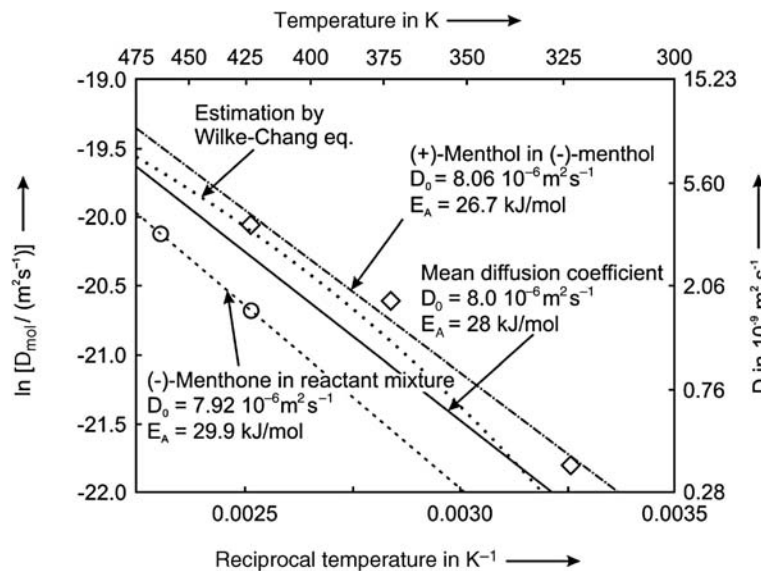
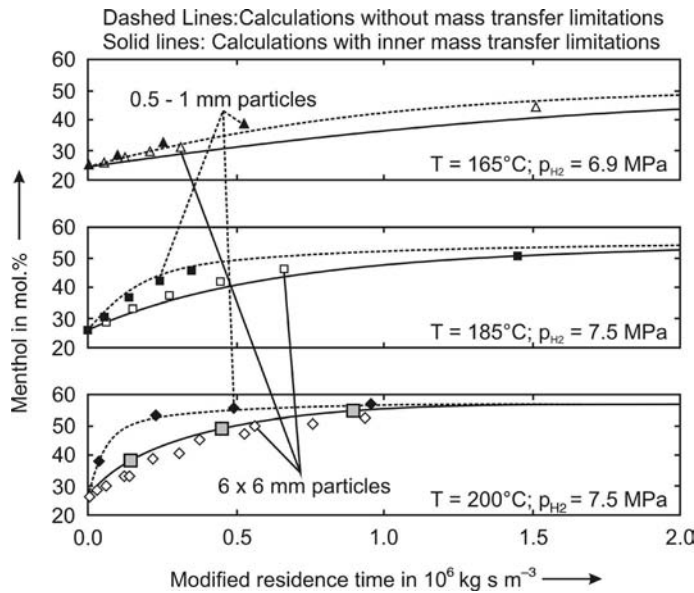


Figure 6.17.11 Experimental and calculated data of the epimerization of menthol diastereomers for small particles (intrinsic kinetics) and large particles (pore diffusion). The gray symbols represent three reference values that are also used and indicated in Figure 6.17.12. Adapted from Etzold and Jess (2008).



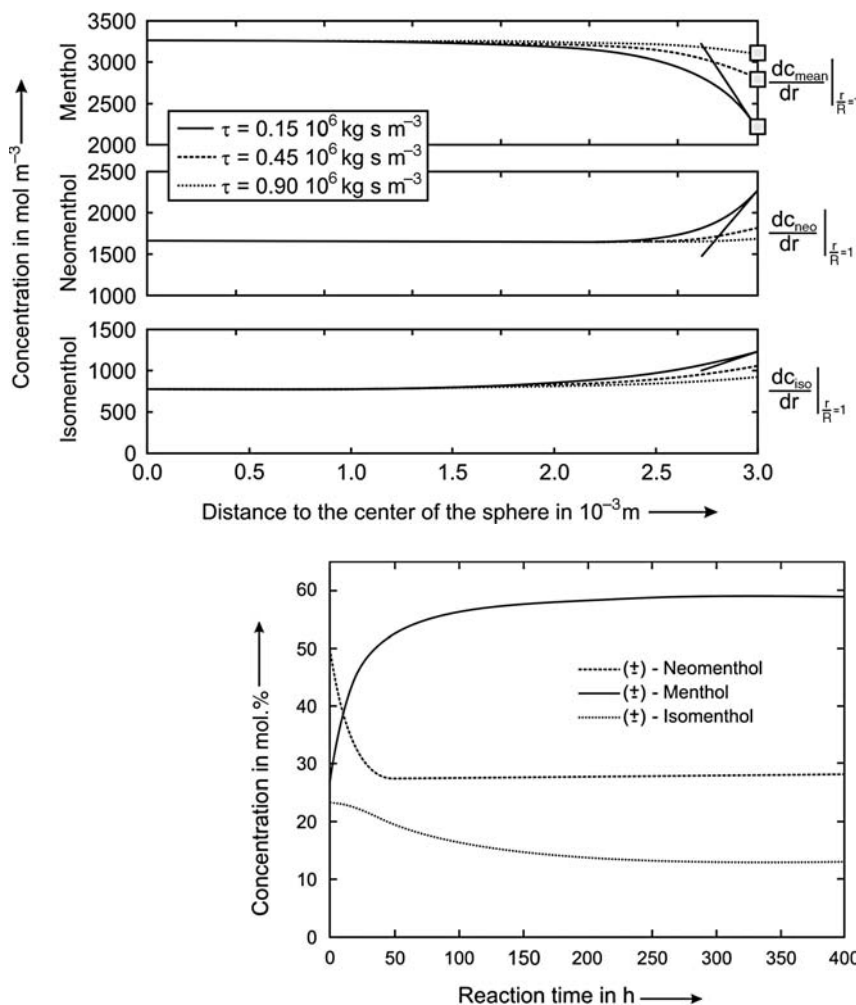


Figure 6.17.12 Calculated concentration profiles of the menthol stereoisomers inside the catalyst particles ($200\text{ }^\circ\text{C}$, 7.5 MPa H_2) at three different modified residence times. The gray symbols represent three reference values as also indicated in Figure 6.17.11. Adapted from Etzold and Jess (2008).

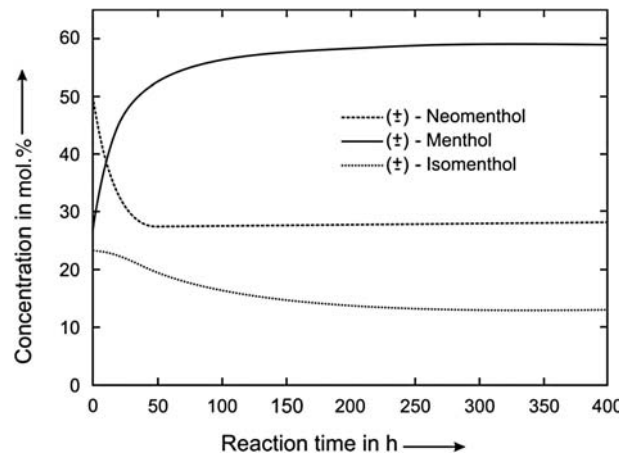


Figure 6.17.13 Simulation of a batch reactor for the epimerization of menthol isomers (catalyst particles $100\text{ }\mu\text{m}$ in diameter, $175\text{ }^\circ\text{C}$, 50 bar hydrogen, concentration of catalyst: 1 wt%, typical industrial feed mixture). Data from Etzold (2007).

6.17.4

Epimerization of Menthol Isomers in Technical Reactors

The numerical calculation based on the thermodynamic and kinetic data can be used to simulate and to compare different reactors, namely, a batch reactor and a continuous fixed bed reactor.

Figure 6.17.13 shows the results of the simulation of a batch reactor. About 215 h are needed to reach 99% of the equilibrium concentration of menthol.

For an annual production rate of 500 tonnes of $(-)$ -menthol, 1665 tonnes of feed must be converted as the equilibrium content of $(-)$ -menthol is only about 30%. If we assume 8000 operating hours per year (although this is rather optimistic for a batch process with time consuming shut-down, discharging, charging, and start-up procedures), 37 batches would be needed ($= 8000\text{ h}/215\text{ h}$). The size of the reactor with regard to the liquid volume would then be quite large at about 50 m^3 (1665 t feed with density of $890\text{ kg m}^{-3} = 1870\text{ m}^3$, thus the reactor volume is $1870\text{ m}^3/37$ batches $= 50\text{ m}^3$).

For the calculations of a continuous fixed bed reactor, a presaturated one-liquid flow (POLF) is assumed. Figure 6.17.14 compares the results of calculations for 2 and 6 mm spherical particles for $175\text{ }^\circ\text{C}$, 5 MPa hydrogen pressure, and a typical industrial feed mixture.

Without any pore diffusion limitations (thus the maximum intrinsic kinetics are used), a modified residence time of about $7 \times 10^6\text{ kg s m}^{-3}$ is needed to reach 99% of the equilibrium concentration of menthol. For 2 mm particles, the modified residence time increases only marginally to $7.6 \times 10^6\text{ kg s m}^{-3}$, and for 6 mm particles

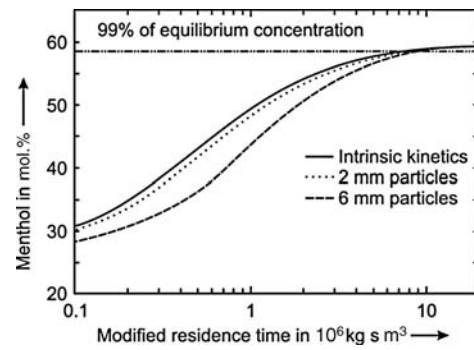


Figure 6.17.14 Calculated influence of modified residence time on the concentration of menthol in the absence of pore diffusion (intrinsic kinetics) and for two industrially relevant particle sizes ($175\text{ }^\circ\text{C}$, 5 MPa hydrogen pressure, typical industrial feed for the epimerization with 51% neomenthol, 26% menthol, and 23% isomenthol). Adapted from Etzold and Jess (2008).

a residence time of about $9 \times 10^6 \text{ kg s m}^{-3}$ is needed. Thus, by using the larger original catalyst particles 26% more catalyst is needed compared to the smaller particles due to pore diffusional limitations.

For the assumed annual production of 500 tonnes of (–)-menthol, we have a feed rate of 1665 tonnes per year, which is equivalent to a volumetric rate of $1870 \text{ m}^3/8000 \text{ h} = 6.5 \times 10^{-5} \text{ m}^3 \text{ s}^{-1}$. Thus for a modified residence time of $7.6 \times 10^6 \text{ kg s m}^{-3}$ (2 mm particles), a fixed bed with 494 kg of catalyst is needed ($m_{\text{cat}} = \text{modified residence time} \times \text{feed rate}$). The resulting reactor volume is only 0.33 m^3 (494 kg divided by bulk density of 1500 kg m^{-3}), which is about 150-fold smaller than the batch reactor. The reason for this effect is the much higher catalyst density in a fixed bed compared to a batch reactor where the catalyst density is limited by the viscosity of the slurry (here to an assumed value of $1 \text{ wt\%} = 9 \text{ kg m}^{-3}$, which is 170-fold smaller compared to the fixed bed). This clearly shows the advantage of the continuous fixed bed reactor, even if we do not count the general disadvantages of a batch process of time and labor intensive discharging and re-filling processes.

In an industrial fixed bed process, a small particle size may lead to an unwanted high pressure drop. According to Eqs. (3.4.21) and (3.4.22), the pressure drop is given by:

$$\Delta p_b = \frac{(1 - \varepsilon)}{\varepsilon^3} \left[3.5 + (1 - \varepsilon) \frac{300}{Re_p} \right] \frac{L \rho_f u_s^2}{d_p} \quad (6.17.22)$$

where Re_p is the particle Reynolds number ($u_s d_p / \nu$), ε is the porosity of the bed (here 0.37), ρ_f the fluid density (890 kg m^{-3}), d_p the particle diameter, and L the reactor length. For a reactor diameter of, for example, 0.5 m, L would be only 1.7 m. The term u_s is the superficial fluid velocity ($3.3 \times 10^{-4} \text{ m s}^{-1}$ = volume rate of $6.5 \times 10^{-5} \text{ m}^3 \text{ s}^{-1}$ divided by the cross-sectional area of the tube of 0.2 m^2). According to Eq. (6.17.19), the dynamic viscosity η (at 175°C) is $3.2 \times 10^{-4} \text{ kg m}^{-1} \text{ s}^{-1}$, and thus the kinematic viscosity $\nu (= \eta / \rho_f)$ is $3.6 \times 10^{-7} \text{ m}^2 \text{ s}^{-1}$.

Based on these data, calculation of the pressure drop by Eq. (6.17.22) for 2 mm particles leads to the very low value of 0.6 mbar, and only for much small particles would appreciable values of the pressure drop be reached; for example, 290 mbar for 0.1 mm particles. Thus, 2 mm particles are suitable for an industrial process as the intrinsic kinetics are then almost utilized.

Section 6.17 (take-home messages)

- The **terpene alcohol (–)-menthol** is an important flavoring substance because of its cooling effect and flavor, and is used in toothpastes, cosmetics, pharmaceuticals, and also by the tobacco industry. Worldwide, 12 000 tonnes are produced per year. The majority is natural menthol from plants but the synthetic route is still important as the price from natural resources fluctuates if availability is limited due to bad harvests.
- **Stereochemical aspects** have to be taken into account for synthetic production of (–)-menthol. Menthol has three chiral centers. Thus, eight conformers are possible, namely, (+)- and (–)-menthol, (+/–)-neomenthol, (+/–)-isomenthol, and (+/–)-neoisomenthol.
- Two routes are used for industrial synthesis of (–)-menthol. One option is to achieve a chiral precursor early in the process and retain the chiral information during the process to gain only (–)-menthol at the end (**Takasago process**). Alternatively, a racemic mixture of (±)-menthol is synthesized by heterogeneously catalyzed hydrogenation of thymol, followed by a separation of the target molecule (–)-menthol by distillation and crystallization (**Haarmann & Reimer process**). The hydrogenation of thymol leads to an equilibrium mixture of all menthol conformers; the undesired racemic stereoisomers have to be separated by distillation and are then converted on a Ni-catalyst by

epimerization in the presence of H₂. Hydrogen is not needed according to the stoichiometry, but suppresses the dehydrogenation to menthone.

- **Epimerization** is one central part of the Haarmann & Reimer process and proceeds via a stepwise change of either the isopropyl group or the alcohol group [isomenthol → neomenthol → menthol (and vice versa)]. The epimerization to menthol only is limited by thermodynamic constraints.
- For the **design of a technical epimerization reactor**, not only the thermodynamic and intrinsic kinetic data but also the influence of pore diffusion has to be taken into account. This **mass transfer limitation** may occur due to a relatively high catalytic activity and a limitation of the minimum particle size with regard to the pressure drop of a fixed bed reactor and/or a filtration process in the case of a slurry reactor. Numerical simulation and comparison of a batch reactor and a continuous fixed bed reactor shows the advantage of the fixed bed reactor, even if we do not count the general disadvantages of a batch process of time and labor intensive discharging and re-filling processes.

6.18

Treatment of Exhaust Gases from Mobile and Stationary Sources

Air pollution by emissions of SO_x and NO_x but also of hydrocarbons (HCs), CO, and particulate matter (PM) from combustion systems are hazards to human and animal health, and cause acid rain and smog (Section 5.4.1). In the following, two major environmental processes for the treatment of exhaust gases are discussed in detail, automotive emission control (Section 6.18.1) and the removal of NO_x from flue gases of power plants by selective catalytic reduction (Section 6.18.2). Further details on exhaust gas cleaning are given in the literature, for example, by Collins and Twigg (2007), Elvers (2008), Ertl, Knoetzinger, and Weitkamp (1999), Farrauto and Bartholomew (1997), Forzzatti (2001), Moulijn, Makkee, and Van Diepen (2004), Van Basshuysen and Schaefer (2007), Armor (1992), Schmidt *et al.* (2003), Kohl and Nielsen (1997), Chorkendorff and Niemantsverdriet (2003), Taylor (1993), Heck and Farrauto (2001), and Kaspar, Fornasiero, and Hickey (2003).

6.18.1

Automotive Emission Control

6.18.1.1 Emission Standards and Primary Measures for Reduction of Engine Emissions

Table 6.18.1 shows a typical composition of an untreated exhaust gas of a gasoline powered engine. CO₂ and H₂O are the main products resulting from complete combustion. CO is formed by incomplete combustion, and hydrocarbons (HCs) mainly originate from regions in the combustion chamber that are not reached by the flame, for example, near the chamber wall. Nitrogen oxides (NO, NO₂, N₂O) are formed by reaction of N₂ and O₂, if the temperature is high (>1400 °C). They are denoted as NO_x and consist mainly of NO. The NO_x is not only formed from atmospheric N₂ but also from fuel-bound nitrogen (Section 6.18.2.2), but this is more relevant for coal or

Table 6.18.1 Composition of an exhaust gas of a gasoline powered combustion engine *without* treatment by a catalyst (Ertl, Knoetzinger, and Weitkamp, 1999; Farrauto and Bartholomew, 1997; Moulijn *et al.*, 2001 and 2004).

Component	CO	O ₂	NO _x	HC	SO ₂	Rest (N ₂ , H ₂ O, CO ₂)
Vol.%	0.6–1.1	0.4–1.2	0.02–0.3	0.04–0.07	0–0.006	about 98% ^{a)}

a) ca. 73% N₂, 13% CO₂, and 12% H₂O, if we assume a one-to-one mixture of toluene and heptane as representative for gasoline.

Table 6.18.2 Emission standards for passenger cars in the EU, Japan, and the USA (g km^{-1}) (Collins and Twigg, 2007; Van Basshuysen and Schaefer, 2007).

Country	Engine	Emission standard (g km^{-1})			
		HC	CO	NO_x	PM
Europe 2000, China 2007, India 2005 (main cities)	Diesel	0.56 ^{a)}	0.64	0.50	0.050
	Otto	0.20	2.3	0.15	—
Europe 2005, China 2010, India 2010 (main cities)	Diesel	0.30 ^{a)}	0.50	0.25	0.025
	Otto	0.10	1.00	0.08	—
Europe 2009	Diesel	0.23 ^{a)}	0.50	0.18	0.005
	Otto	0.10	1.00	0.06	0.005
Europe 2014	Diesel	0.17 ^{a)}	0.50	0.08	0.005
	Otto	0.10	1.00	0.06	0.005
Japan 2005	Diesel	0.024 ^{b)}	0.63	0.14	0.013
	Otto	0.05 ^{b)}	1.15	0.05	—
USA 2006 ^{c)}	Otto	0.04	1.70	0.20	0.04

a) HC + NO_x .

b) Non-methane HC (hydrocarbons).

c) Ultra-low emission vehicles.

heavy oil combustion in power plants and negligible for diesel oil or gasoline powered engines as the nitrogen content of these fuels is usually small. Sulfur present in gasoline or diesel oil as organic sulfur is oxidized to SO_2 . In Europe, USA, and Japan fuels for cars are almost free of sulfur (<10 ppmw), and thus the main pollutants from cars are HCs, CO, and NO_x and for diesel oil powered engines also particulate matter.

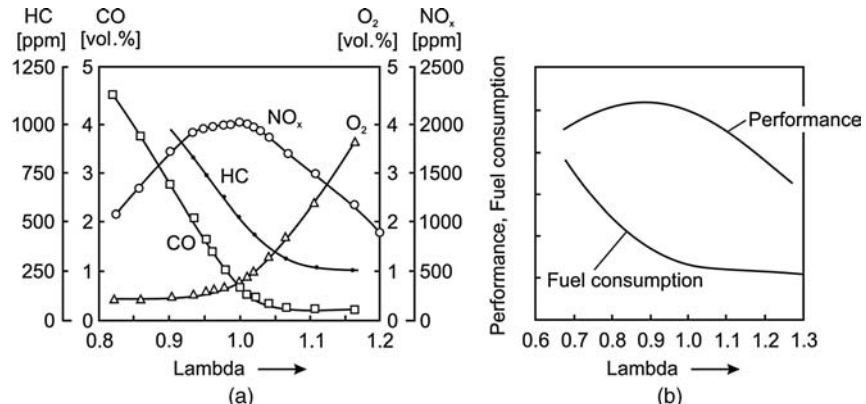
During recent years, emission legislation has tightened significantly in Europe, the USA and in Japan (Table 6.18.2). Other countries have already adopted these regulations, for example, India and China follow European regulations with a certain time delay.

Figure 6.18.1 shows a typical exhaust gas composition of a gasoline powered engine as well as the fuel consumption and engine output as a function of the lambda value λ , which is defined as the actual air-to-fuel ratio to the ratio at stoichiometric conditions, that is, if the fuel is combined with all free oxygen to form CO_2 , H_2O , and SO_2 without any excess O_2 in the flue gas:

$$\lambda = \frac{(m_{\text{air}}/m_{\text{fuel}})_{\text{actual}}}{(m_{\text{air}}/m_{\text{fuel}})_{\text{stoich}}} \quad (6.18.1)$$

Thus λ is a measure of how far from stoichiometry a mixture is. For $\lambda > 1$, we have a fuel lean (oxidizing) atmosphere, and for $\lambda < 1$ a fuel rich (reducing) atmosphere. With increasing λ , the CO and HC emissions decrease as more O_2 is present for combustion. For NO, the emissions go through a maximum for a λ -value of about 1. Under fuel-rich conditions ($\lambda < 1$), the amount of O_2 is low and NO formation decreases, and under fuel-lean conditions the temperature drops, which also leads to decreased NO formation although O_2 is present in excess.

Figure 6.18.1 Emissions of CO, HCs, and NO_x (without catalyst) (a), and fuel consumption and engine output of a gasoline spark ignition engine (b) as a function of λ . Adapted from Ertl, Knoetzinger, and Weitkamp (1999).

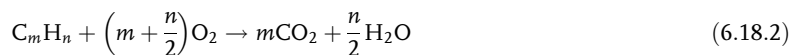


Primary methods to reduce the emissions from cars are (Moulijn, Makkee, and Van Diepen, 2001 and 2004):

- **Speed limitations:** the emission of NO_x increases with driving speed due to a higher combustion temperature and due to operation with a relative fuel lean mixture.
- **Fuel purification:** Hydrotreating reduces the content of organic sulfur and nitrogen. This has a favorable effect on the SO_2 and NO_x emissions, although nowadays the amount of N- and S-species in diesel oil or gasoline is in many countries very small. Thus NO_x formation is mainly the result of radical processes involving N_2 from air (Section 6.18.2.2).
- **Engine modifications:** A gasoline powered engine that operates at $\lambda > 1$ leads to a decrease in fuel consumption of up to 15%. During the last decade, modern high compression engines have been developed that overcome the problem of ignition due to dilution of the fuel. The first commercial engines have now being introduced into the market place. A further advantage in addition to a lower fuel consumption is the significant decrease in emissions of CO and HCs (Figure 6.18.1), but then sophisticated catalytic systems are needed to cope with the problem of how to reduce NO_x under lean fuel conditions.

6.18.1.2 Catalytic Converters for Reduction of Car Engine Emissions

Secondary measures to reduce exhaust emissions of cars, so-called end-of-pipe solutions, are based on the catalytic conversion of all three harmful emissions:



About 500 mio. cars (out of about 1 billion in total in 2011) are worldwide equipped with such a catalytic converter. Although the concentrations of CO, HCs, and of NO are small (Table 6.18.1), the overall consumption rates are high: 40 mio. tonnes CO, 10 mio. tonnes HCs, and 15 mio. tonnes NO (Votsmeier, 2012).

The success of the catalytic converter is up to now mainly limited to gasoline powered engines. However, in recent years progress has also been made in the development of catalytic filters for the cleaning of exhaust gas (e.g., particulate matter) from diesel engines.

Obviously, one reactor for the treatment of all three pollutants is preferable, but the oxidation of HCs and CO requires an oxidizing atmosphere and the conversion of NO_x a reducing one. Thus in a simple one-reactor approach only CO and HC or NO_x are converted almost completely or a compromise has to be found to convert at least a main proportion of all three pollutants simultaneously.

Figure 6.18.2 shows the development of emission control technologies until the end of the 1990s. This development can be described as follows (Moulijn, Makkee, and Van Diepen, 2001 and 2004):

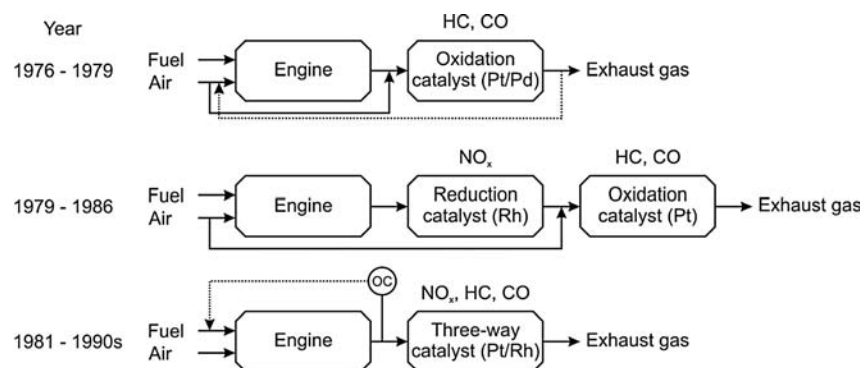


Figure 6.18.2 Development of emission control technologies for gasoline spark ignition engines until the end of the 1990s (OC: oxygen control). Adapted from Moulijn, Makkee, and Van Diepen (2001 and 2004).

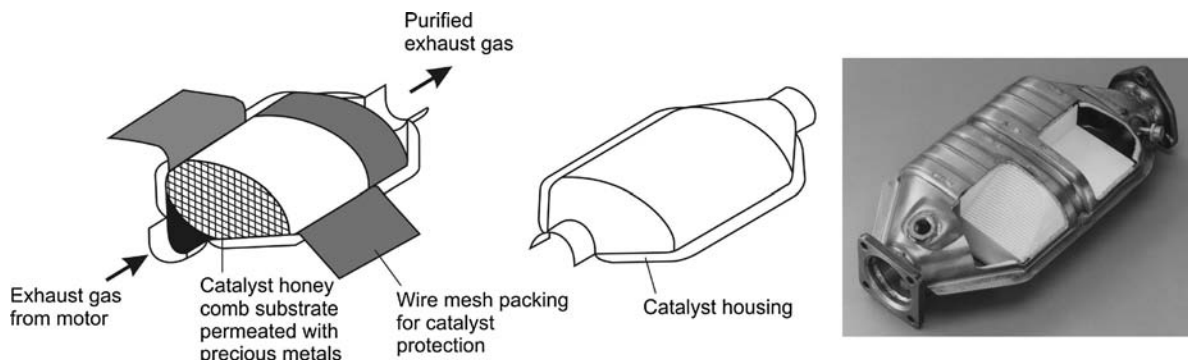


Figure 6.18.3 Design of a ceramic monolith based converter for the catalytic after treatment of exhaust gases from passenger cars.
Adapted from Ertl, Knoetzinger, and Weitkamp, 1999; photograph by courtesy of Umicore, Germany.

- Initially (1976–1979), NO_x control was not attempted as the regulations were not very strict, and only CO and hydrocarbons were converted by an oxidation catalyst.
- In later years (1979–1986) a dual catalyst system was launched. In the first reactor NO_x is reduced by CO and the HCs, and in the second reactor CO and the HCs are oxidized by a secondary supply with air. To establish a reducing atmosphere in the first reactor, the engine must operate under fuel-rich conditions.
- In the 1980s, emission standards became more stringent and the so-called three-way catalyst was applied. The name originates from the fact that all three pollutants (CO, HCs, and NO_x) are removed simultaneously in one reactor, which was achieved by improved catalysts and fuel-to-air ratio control techniques.

The first catalytic converters were conventional fixed bed reactors. Today, the majority are monoliths that combine a low pressure drop with a small size and weight, and thus provide better fuel economy than fixed-bed reactors. The catalyst is mounted in a stainless-steel container with a packing wrapped around for resistance to vibration (Figure 6.18.3).

Table 6.18.3 summarizes the composition, performance, and operating conditions of a typical three-way catalyst. Dimensional relationships of a washcoat are given in Figure 6.18.4. Figure 6.18.5 shows close-up views of a monolith and of a single channel.

Figure 6.18.6 shows the influence of the lambda value on the conversion of CO, hydrocarbons (HCs), and NO_x on a three-way catalyst. The window of optimal operation is narrow and close to $\lambda = 1$. Thus, a measurement of the O_2 -content is needed, and the signal of this so-called lambda sensor is fed back to the fuel injection system, which adjusts the air-to-fuel ratio.

At the end of the 1990s, the newest generation of automotive exhaust catalysts was developed, the NO_x storage (adsorber) catalyst that is needed for lean burn engines (Figures 6.18.7 and 6.18.8, Elvers, 2008; Van Basshuysen and Schaefer, 2007; Boegner *et al.*, 1995). These engines run under excess oxygen, which reduces fuel consumption. Thus, the three-way catalyst, which works at almost stoichiometric conditions, cannot be used.

The NO_x absorber consists of a metal oxide like BaO or carbonates like BaCO_3 that form stable nitrates with NO_2 at temperatures below 600 °C. In a NO_x adsorber/converter NO is oxidized by platinum to NO_2 , and then reacts with BaO/ BaCO_3 to the corresponding nitrate (Figure 6.18.7). The following three equations describe the system behavior during NO storage, if CO is considered as representative for a mixture of reducing agents (CO, HCs, and H_2) and BaCO_3 as representative for a mixture of storage components ($\text{BaCO}_3 + \text{BaO}$) (Tuttlies, Schmeisser, and Eigenberger, 2004):



Table 6.18.3 Composition, performance, and conditions in a three-way catalyst (Moulijn, Makkee, and Van Diepen, 2004).

Composition	
Carrier	Monolith: cordierite with 62 cells cm^{-2}
Washcoat	$\gamma\text{-Al}_2\text{O}_3$, CeO_2 (10–20%), La_2O_3 , and/or BaO (1–2%)
Active phase	Pt and Rh: 1.2–1.4 g/l
Performance	
Controlled	$\lambda = 0.99 \pm 0.06$, $X_{\text{HC}} > 80\%$, $X_{\text{CO}} > 70\%$, $X_{\text{NO}} > 70\%$
Uncontrolled (average values of conversion X)	$\lambda = 1.05 \pm 0.2$, $X_{\text{HC}} > 70\%$, $X_{\text{CO}} > 55\%$, $X_{\text{NO}} > 50\%$
Operating conditions	
Temperature	300–900 °C
Space velocity	$1\text{--}2 \times 10^5 \text{ m}^3 \text{ m}^{-3} \text{ h}^{-1}$

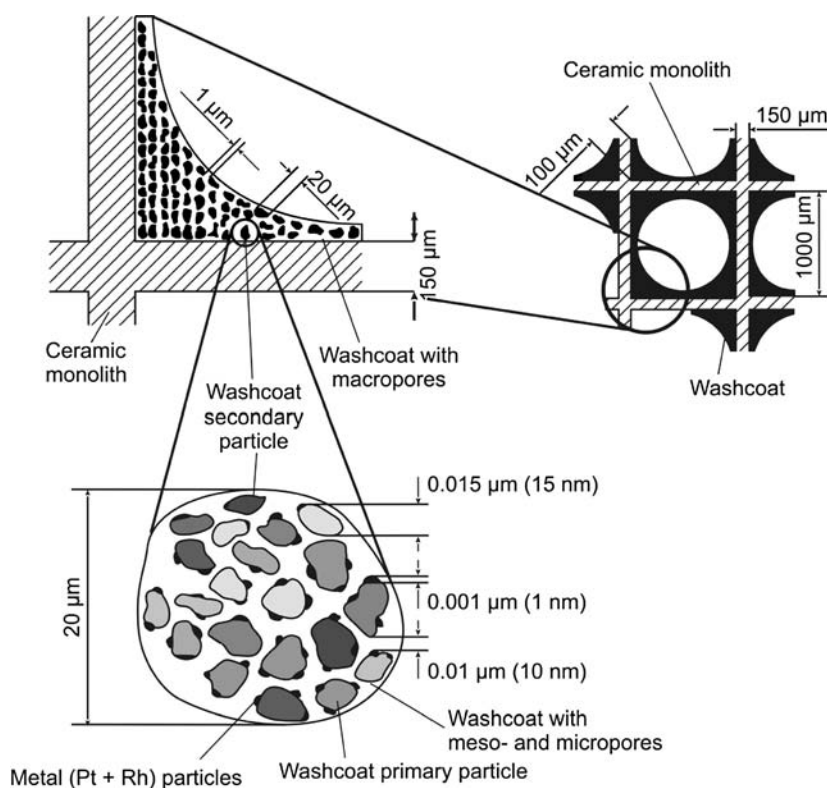


Figure 6.18.4 Dimensional relationships of washcoat on a ceramic monolith. Partly adapted from Ertl, Knoetzinger, and Weitkamp (1999).

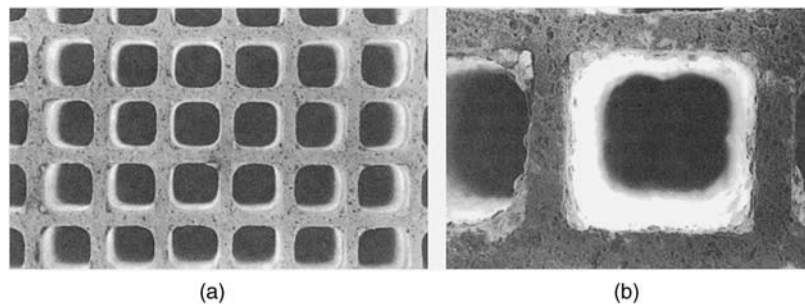


Figure 6.18.5 Ceramic monolith for the catalytic treatment of exhaust gases from cars, with $62 \text{ cells } \text{cm}^{-2}$ (a) and a single channel of a washcoated monolith (b) (Ertl, Knoetzinger, and Weitkamp, 1999).

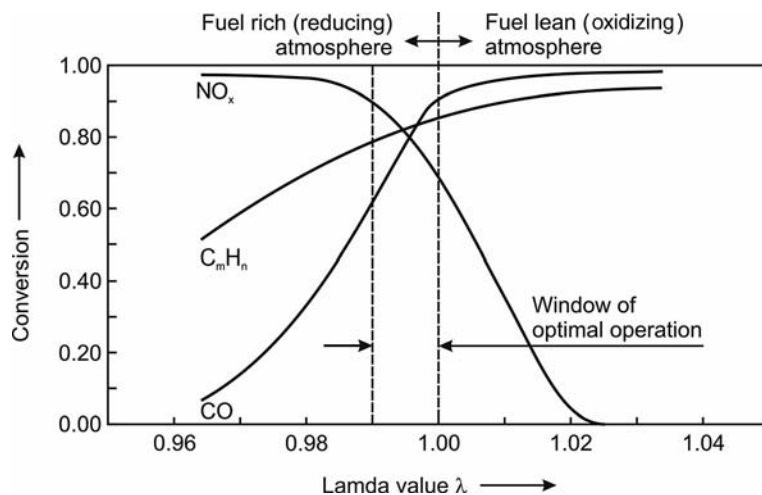


Figure 6.18.6 Influence of lambda value on the conversion of CO, hydrocarbons (HCs), and NO_x reached with a typical three-way catalyst.

Figure 6.18.7 Principle of NO_x storage catalysts developed for lean burn engines.

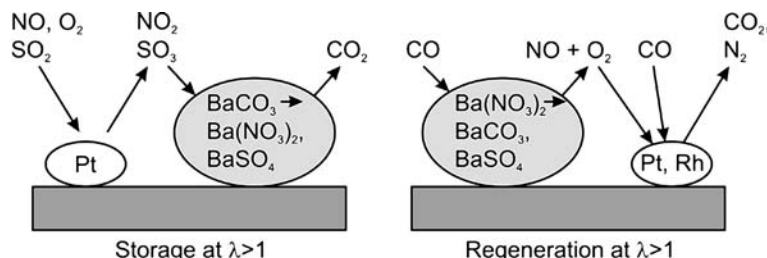
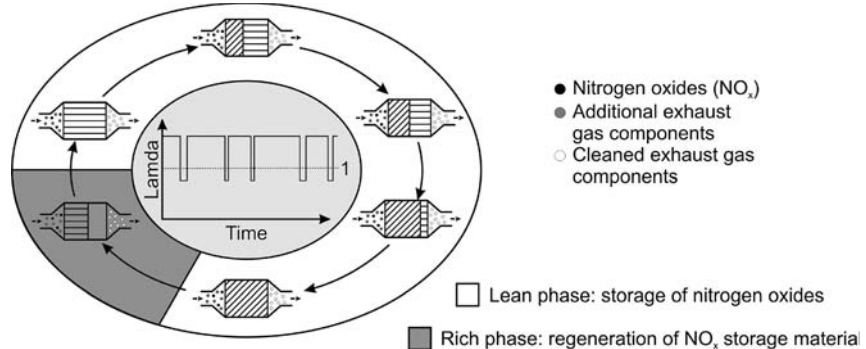
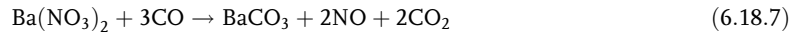


Figure 6.18.8 NO_x adsorber catalyst for lean burn engines: NO_x storage cycle (Adapted from Elvers, 2008).



As soon as the storage capacity is exhausted, the catalyst must be regenerated by switching to fuel-rich operation for a few seconds. Then barium nitrate decomposes and reacts with CO:



The released NO is then further converted with CO into N_2 and CO_2 by the Pt/Rh catalyst according to Eq. (6.18.4). By this means, BaCO_3 can again serve as a NO_x adsorber during the next cycle of lean operation (Figures 6.18.7 and 6.18.8). The regeneration cycle is triggered by a computer system that monitors the NO_x level by a sensor downstream of the adsorber.

A problem of NO_x storage catalysts is the adsorption of SO_2 by the same mechanism as NO_2 . Sulfates have a higher stability than nitrates and accumulate on the catalyst as they are not easily destroyed during regeneration, which lowers the NO_x adsorption capacity. The catalyst must therefore be regenerated from sulfur from time to time by running the engine fuel rich at elevated temperatures for several minutes. This regeneration is fuel-expensive, and the frequency of this procedure depends on the S-content of the fuel. Thus, fuels with less than 10 ppmw sulfur should be used.

6.18.2

Selective Catalytic Reduction (SCR) of NO_x from Flue Gas from Power Plants

6.18.2.1 Treatment of Flue Gas from Power Plants (Overview)

Table 6.18.4 shows the composition of a flue gas produced by a coal-fired power plant before and after modern flue gas treatment. Figure 6.18.9 shows typical steps of flue gas cleaning.

The catalytic reduction of NO_x is usually placed between the economizer of the boiler and the air preheater (Figure 6.18.9). The SCR catalyst used in this way is in the so-called high dust mode and the resistance of the catalyst against attrition by ash particles should be high. Downstream of the air preheater fly ash is collected by an electrostatic precipitator. By way of a heat exchanger and flue gas desulfurization (e.g., SO_2 separation by scrubbing using a slurry of a sorbent, usually limestone or lime) the flue gas is passed to the stack.

Table 6.18.4 Typical composition of flue gas from a coal-fired power plant before and after treatment of the flue gas by desulfurization, selective catalytic reduction of NO_x , and electrostatic precipitation for reduction of particulate matter (ash).

Component	Without flue gas cleaning ^{a)} (mg m^{-3})	With flue gas cleaning (typical emission limits) (mg m^{-3})
$\text{NO}_x^{\text{b)}$	1200	200
SO_2	1800	200
Particulate matter	200	10

a) For other fuels and power plant technologies, the NO_x content in the untreated flue gas may be different. For example, for a combined cycle gas turbine plant (CCGT), where the hot exhaust of the gas turbine powers a conventional steam power plant, the NO_x concentrations (as NO_2) are as follows for natural gas as fuel: 200–800 mg m^{-3} for conventional combustion, 50–80 mg m^{-3} with water/steam injection into the flame, which lowers the temperature and thus thermal NO_x , and 10–20 mg m^{-3} with additional SCR (Ertl, Knoetzinger, and Weitkamp, 1999). The emission limit for CCGT (Germany) is 50 mg m^{-3} .
b) Calculated as NO_2 (100 ppmv = 200 mg m^{-3}).

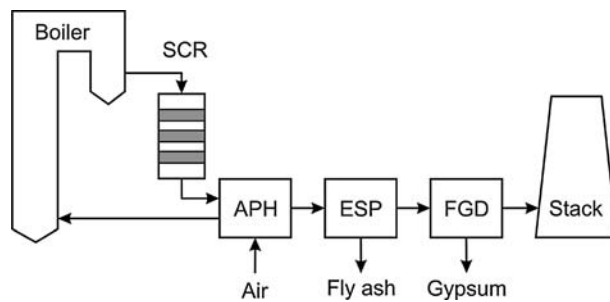


Figure 6.18.9 Power plant with selective catalytic reduction (SCR) and flue gas desulfurization (FGD) (APH: air preheater, ESP: electrostatic precipitator). From Ertl, Knoetzinger, and Weitkamp (1999).

Here, only NO_x formation and removal by SCR are discussed. Information on the separation of ash and of SO_2 is given by Schmidt *et al.* (2003) and Kohl and Nielsen (1997).

6.18.2.2 Formation of Nitrogen Oxides during Fuel Combustion in Power Plants

NO and NO_2 are undesirable by-products of the combustion of fuels such as coal, natural gas, and fuel oil in boilers of power plants (Table 6.18.5). Nitrogen oxides are formed during combustion by three different kinds of reactions:

- **Thermal NO_x** is formed by the reaction of atmospheric nitrogen and oxygen at temperatures of more than about 1200°C (Figure 6.18.10). Such high temperatures are needed with regard to the kinetics of thermal NO_x formation, as NO is already thermodynamically favored ($>1000 \text{ ppmv}$) above about 1000°C (see Figure 6.4.5).
- **Fuel NO_x** is produced by the combustion of fuel-bound nitrogen, if nitrogen-containing fuels such as coal and heavy oils are burned.
- **Prompt NO_x** is the third, but usually small, source and is attributed to the reaction of atmospheric N_2 with radicals such as CH_2 fragments derived from the fuel. This results in the formation of nitrogen species such as HCN that can be further oxidized to NO .

The major source of NO production from combustion of coal and heavy oil is fuel-bound nitrogen (Figure 6.18.10, Table 6.18.5), and can contribute to 50% of the total NO_x emissions for heavy oil and to 90% for coal. For natural gas (and also for diesel oil and gasoline combustion in engines) the majority is thermal NO , and the contribution of fuel NO is negligible.

Although boiler manufacturers have successfully reduced NO_x emissions by about 50% through modifications of the combustion process (less excess air, two-stage combustion in order to decrease the combustion temperature), a further reduction is in most cases still needed to meet the emission reduction targets (Table 6.18.4).

Table 6.18.5 Contributions of thermal, fuel, and prompt NO to the total NO emissions. The values given for natural gas, heavy oil, and coal are related to combustion in power plants; values for diesel oil and gasoline (road traffic) are given for comparison.

Fuel	Thermal NO_x (%)	Fuel NO_x (%)	Prompt NO_x (%)
Natural gas	100	—	—
Heavy oil	40–60	60–40	—
Coal	10–30	90–70	<5
Diesel oil/ gasoline in engines	90–95	—	10–5%

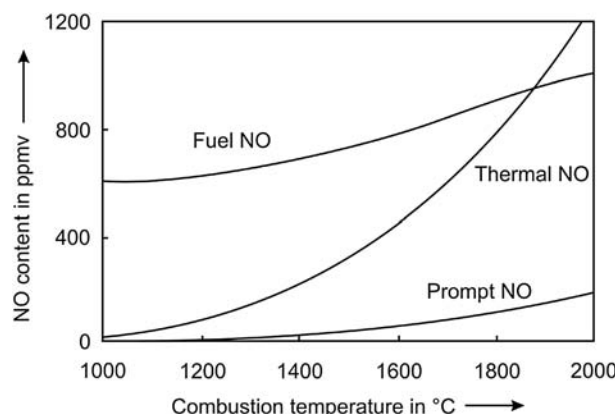
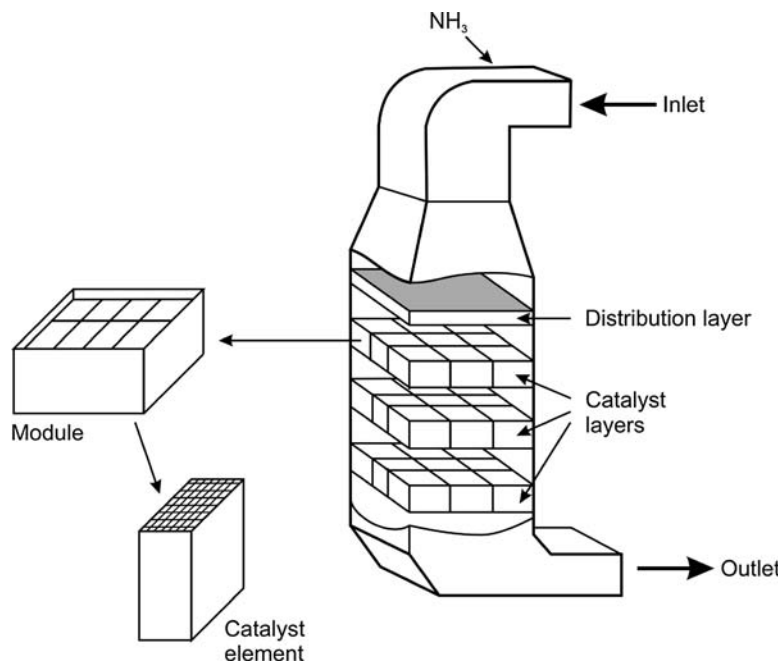


Figure 6.18.10 Typical values of the content of thermal, fuel, and prompt NO_x during combustion of coal and influence of combustion temperature. Adapted from Schrod, Semel, and Steiner (1985).

Figure 6.18.11 De- NO_x reactor for selective catalytic reduction (SCR).



6.18.2.3 Catalysts and Reactors for Selective Catalytic Reduction of NO_x

The flue gas produced in the boiler of a power plant is passed to the SCR reactor together with ammonia as reducing agent (Figure 6.18.11). The main reactions of catalytic NO_x reduction are described by:

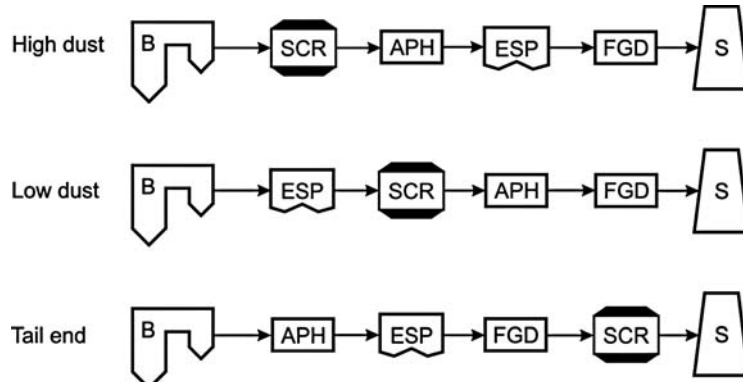


Mixing of ammonia with flue gas should be carried out with care because only a low slip (exit of unreacted ammonia) is allowed, typically less than 5 ppmv ammonia.

SCR catalysts are Pt, CuSO_4 , Fe_2O_3 , Cr_2O_3 , NiO , Co_2O_3 , WO_3 , V_2O_5 , MoO_3 , and zeolites. In power plants, WO_3 , V_2O_5 , and MoO_3 are mostly used; Pt is poisoned by SO_2 and Fe catalyzes the oxidation of SO_2 to SO_3 and iron sulfates are formed. In most cases, monoliths are used as the pressure drop is only in the range 2–10 mbar.

The type of catalyst depends on the location and the sulfur content of the fuel. The minimum temperature is about 200°C and the maximum 400°C . At higher temperatures ammonia is oxidized into undesirable by-products (N_2 , NO) and the catalyst is deactivated by sintering. Figure 6.18.12 shows different locations of the SCR unit. In the first option, the flue gas leaving the boiler is cleaned directly by SCR (high-dust system). In the low-dust system, the SCR unit is located between

Figure 6.18.12 Three locations for SCR in a power plant (B: boiler, APH: air preheater, ESP: electrostatic precipitator, FGD: flue gas desulfurization, S: stack. Adapted from Ertl, Knoetzinger, and Weitkamp (1999)).



the electrostatic precipitator (ESP) and the flue gas desulfurization (FGD) unit. A third location is between the FGD and the stack. In the high-dust system, soot blowers are needed to remove the fly ash from the catalyst. For low-dust applications high temperature electric precipitators are required, or the flue gas from the precipitator has to be reheated. Table 6.18.6 gives the major parameters of high and low dust SCR catalysts.

6.18.2.4 Reaction Chemistry of Selective Catalytic Reduction of NO_x

During SCR, NH_3 should react selectively with NO_x to N_2 [Eqs. (6.18.8) and (6.18.9)]. If the temperature is too high, undesirable oxidation of ammonia to either NO or N_2O may also occur:



Figure 6.18.13b illustrates how the reduction of NO_x to N_2 by reaction with NH_3 increases with increasing temperature for a typical SCR (vanadium) catalyst.

Compared to reduction, NH_3 conversion by oxidation, Eqs. (6.18.10) and (6.18.11), increases sharply at high reaction temperatures (Figure 6.18.13a). Thus with increasing temperature the competition between the reaction of NH_3 with NO_x and with O_2 decreases the NO_x removal efficiency. Accordingly, there is a window for a high conversion of NO_x (Figure 6.18.13c).

The conversion of NO into N_2 reaches a maximum at about 400°C . At higher temperatures, the catalyst also produces a small but significant amount of N_2O , which is a very strong greenhouse gas with 310 times the global warming potential of CO_2 .

6.18.2.5 Reaction Kinetics and Design of SCR Reactor

For the design of a SCR reactor, we need an appropriate reactor model, and the differential equations have to be solved based on the parameters of the intrinsic and effective kinetics.

The SCR reactor can be regarded as almost isothermal. For a typical inlet content of NO of 1000 ppmv, we get a rather small value of the adiabatic rise in temperature (ΔT_{ad}): if we assume a heat capacity of the flue gas of $32 \text{ J mol}^{-1} \text{ K}^{-1}$ and a reaction enthalpy of -406 kJ mol^{-1} [Eq. (6.18.8)], the heat balance leads to a relatively small value of ΔT_{ad} of 13 K:

$$\Delta T_{\text{ad}} = \frac{\dot{n}_{\text{NO,in}} \Delta_R H_{\text{NO} \rightarrow \text{N}_2}}{\dot{n}_{\text{flue gas}} c_{p,\text{flue gas}}} = \frac{y_{\text{NO,in}} \Delta_R H_{\text{NO} \rightarrow \text{N}_2}}{c_{p,\text{flue gas}}} = \frac{0.001 \times 406\,000 \text{ J mol}^{-1}}{32 \text{ J mol}^{-1} \text{ K}^{-1}} \approx 13 \text{ K}$$

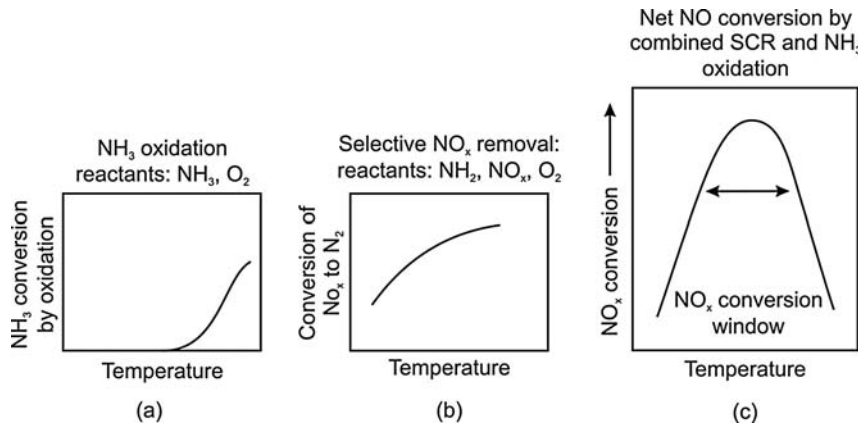


Table 6.18.6 Important parameters of high- and low-dust SCR catalysts (Ertl, Knoetzinger, and Weitkamp, 1999).

Parameter	High dust		Low dust	
Length (mm)	1000	1000	800	800
Diameter of cell (mm)	6.0	6.25	3.45	3.0
Wall thickness (mm)	1.4	1.15	0.8	0.7
Surface area ($\text{m}^2 \text{ m}^{-3}$)	2.0	1.8	1.35	1.35
Porosity (%)	64	70	64	64

Figure 6.18.13 Role of competing reactions in SCR with increasing temperature on a V-catalyst. Adapted from Farrauto and Bartholomew (1997).

This value is considerably less than in automotive converters of about 150 °C, as we then also have to consider the oxidation of CO and of HC (Hegedus, 1975). Subsequently, we assume an isothermal monolith and hence only the mass balance has to be considered.

For plug flow behavior, the differential mass balance for NO reads as:

$$u_s \frac{dc_{NO}}{dz} = -r_{m,eff} \rho_b \quad (6.18.12)$$

Intrinsic Kinetics and Influence of Pore Diffusion The effective rate based on the NO concentration at the surface of the channels of the monolith and of the effectiveness factor for pore diffusion is given by:

$$r_{m,eff} = \eta_{pore} k_{m,1} c_{NO,s} \quad (6.18.13)$$

with (Section 4.5.4):

$$\eta_{pore} = \frac{\tanh \phi}{\phi} \quad (6.18.14)$$

and:

$$\phi = \frac{d_{wall}}{2} \sqrt{\frac{k_{m,1} \rho_{cat}}{D_{NO,eff}}} \quad (6.18.15)$$

For the following calculations, we assume for a first rough estimation that the whole wall acts as a catalyst, although in most cases of SCR in power plants the internal diffusion may be restricted to the washcoat with a thickness of about 50 µm (compared to the wall thickness of about 1 mm); see Chen *et al.* (2008).

Equations (6.18.13)–(6.18.15) are only valid for a first-order reaction. In case of the SCR reaction, the rate depends on the concentration of NO, NH₃, and O₂, for example, according to Santos *et al.* (1998) the intrinsic rate of NO conversion on a Ti-V-W catalyst is given by:

$$r_m = k_m c_{NO} \frac{c_{NH_3} c_{O_2} K_{NH_3} K_{O_2}}{(1 + c_{NH_3} K_{NH_3})(1 + c_{O_2} K_{O_2})} \quad (6.18.16)$$

Comparison of Eq. (6.18.13) with Eq. (6.18.16) leads to a pseudo-first-order rate constant ($r_m = k_{m,1} c_{NO}$):

$$k_{m,1} = k_m \frac{c_{NH_3} c_{O_2} K_{NH_3} K_{O_2}}{(1 + c_{NH_3} K_{NH_3})(1 + c_{O_2} K_{O_2})} \quad (6.18.17)$$

which is now used to determine the effectiveness factor for pore diffusion by Eqs. (6.18.13)–(6.18.17). As inspected below, this apparent (pseudo-first-order) rate constant $k_{m,1}$ and thus also the effectiveness factor for pore diffusion η_{pore} depends on the degree of NO conversion.

Table 6.18.7 gives material properties, kinetic parameters, and typical reaction conditions of catalytic NO reduction with ammonia on a monolithic Ti-V-W catalyst.

Figure 6.18.14 shows the influence of NO conversion on the pseudo-first-order intrinsic rate constant and on the effectiveness factor for pore diffusion.

The O₂-concentration can be regarded as constant as O₂ is present in excess compared to NO and NH₃ (Table 6.18.7). At the entrance of the reactor, where the terms $c_{NH_3} K_{NH_3}$ and $c_{O_2} K_{O_2}$ in the denominator of Eq. (6.18.17) are still high (>1), $k_{m,1}$ is almost constant:

$$k_{m,1} \approx k_m \frac{c_{NH_3} c_{O_2,in} K_{NH_3} K_{O_2}}{(1 + c_{NH_3} K_{NH_3})(1 + c_{O_2,in} K_{O_2})}$$

$$\approx k_m \quad (\text{for } X_{NO} \ll 1, \text{ i.e., } c_{NH_3} K_{NH_3} \text{ and } c_{O_2} K_{O_2} \gg 1)$$

Table 6.18.7 Material properties, kinetic parameters, and conditions of SCR in a monolithic Ti-V-W catalyst [kinetic data from Santos *et al.* (1998), all data for 350 °C and 1 bar].

Parameter	Value
Bulk density ρ_b of monolith	396 kg m ⁻³
Porosity ε of monolith	0.62
Catalyst density ρ_{cat}	1100 kg m ⁻³
Specific surface area of the channels A_m	1.6 m ² kg ⁻¹
Wall thickness d_{wall}	1 mm
Diameter of circular channels d_t	4 mm
Molecular diffusion coefficient D_{NO}	5.9×10^{-5} m ² s ⁻¹
Effective diffusion coefficient $D_{NO,eff}$	9.6×10^{-7} m ² s ⁻¹
Linear (interstitial) gas velocity in the channels u_i	10 m s ⁻¹
Superficial velocity related to volume of monolith u_e	6.4 m s ⁻¹
NO inlet concentration (1000 ppm)	0.023 mol m ⁻³
NH ₃ inlet concentration (1000 ppm)	0.023 mol m ⁻³
O ₂ inlet concentration (3 vol.%)	0.695 mol m ⁻³
k_m in Eq. (6.18.17)	$1.19 \text{ m}^3 \text{ kg}^{-1} \text{ s}^{-1}$
K_{NH_3} in Eq. (6.18.17)	$182.1 \text{ m}^3 \text{ mol}^{-1}$
K_{O_2} in Eq. (6.18.17)	$12.4 \text{ m}^3 \text{ mol}^{-1}$
$Re Sc d_t/L$ (for $L = 3$ m, $Re = 730$)	About 1
Sh in Eq. (6.18.19)	3.6

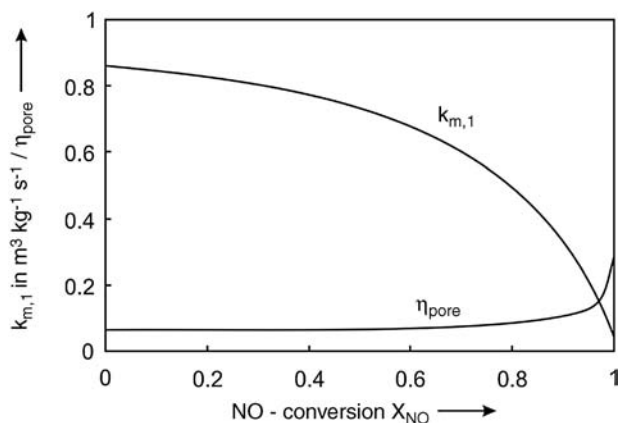


Figure 6.18.14 Influence of NO conversion on the intrinsic pseudo-first-order rate constant and on the effectiveness factor for pore diffusion.

With increasing conversion of NO (and of NH₃), the pseudo-first-order rate constant decreases and we finally get a rate constant that is proportional to the concentration of NH₃:

$$k_{m,1} \approx k_m c_{\text{NH}_3} K_{\text{NH}_3} \quad (\text{for } X_{\text{NO}} \rightarrow 1, \text{ i.e., } c_{\text{NH}_3} K_{\text{NH}_3} \ll 1 \text{ and } c_{\text{O}_2} K_{\text{O}_2} \gg 1)$$

which leads to an increase of η_{pore} with increasing conversion.

Influence of External Mass Transfer The rate of diffusion through the boundary layer of a solid catalyst and hence the effective reaction rate (in mol kg_{cat}⁻¹ s⁻¹) is given by:

$$r_{\text{m,eff}} = \beta A_m (c_{\text{NO,g}} - c_{\text{NO,s}}) \quad (6.18.18)$$

where $c_{\text{NO,g}}$ and $c_{\text{NO,s}}$ are the NO concentrations in the bulk phase and at the external surface of the monolithic. The mass transfer coefficient β can be determined by the *Sherwood number* Sh ; if we use the approximation that the *Nusselt number* equals Sh , Eq. (3.2.12) leads to the correlation for laminar flow in circular channels of a monolith with channel diameter d_t :

$$Sh = \frac{\beta d_t}{D} = \left\{ 3.66^3 + 0.7^3 + \left[1.615 \left(\frac{Re Sc d_t}{L} \right)^{\frac{1}{3}} - 0.7 \right]^3 \right\}^{0.33} \quad (6.18.19)$$

$(Re = u_t d_t / \nu < 2300)$

Several other correlations for monoliths are given in the literature, for example, Hawthorn (1974) and Tronconi and Forzatti (1992) proposed the following correlations for circular channels:

$$Sh = 3.66 \left[1 + 0.095 \left(\frac{Re Sc d_t}{L} \right) \right]^{0.45} \quad (\text{for } Re < 2300, \text{ Hawthorn, 1974}) \quad (6.18.20)$$

$$Sh = 2.977 + 0.205 \left(\frac{Re Sc d_t}{L} \right)^{0.545} e^{-\frac{48.2 L}{Re Sc d_t}} \quad (6.18.21)$$

(for $Re < 2300$, Tronconi, Forzatti, 1992)

These two equations were derived by fitting a limited number of direct measurements in monolith reactors under chemical reaction conditions.

Figure 6.18.15 compares all three correlations, indicating that the results vary. Here we have used Eq. (6.18.19), which is in our opinion the most reliable one if

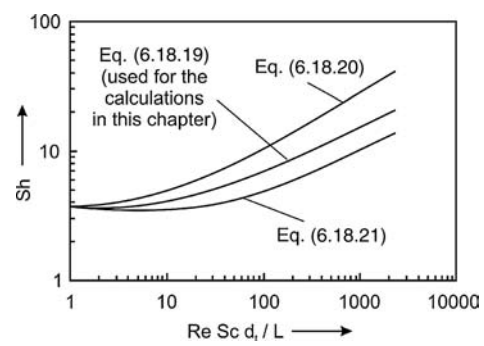
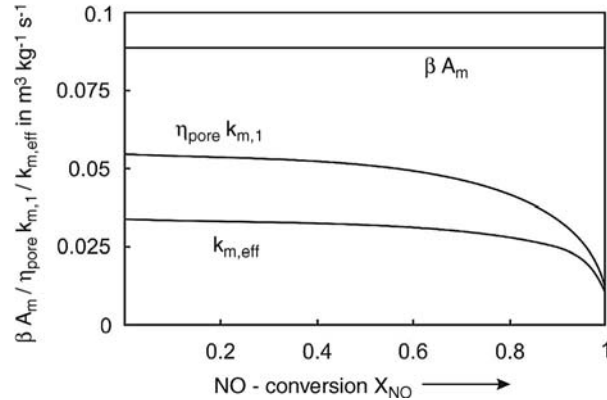


Figure 6.18.15 Different correlations for Sh in a monolith with circular channels.

Figure 6.18.16 Influence of NO-conversion on the parameter for external diffusion (βA_m), the parameter for the effective rate of reaction in the porous wall ($\eta_{\text{pore}} k_{m,1}$), and on the (overall) effective rate constant of NO conversion in a catalytic monolith ($k_{m,\text{eff}}$).



we rely on the *Nu-Sh* analogy, which was derived based on numerous heat transfer measurements and which also represents a mean value of the other two equations fairly well.

For steady-state, the rate of reactant consumption, $r_{m,\text{eff}}$, equals the flux through the boundary layer, and Eq. (4.5.14) leads to the NO concentration at the surface of the channel:

$$c_{\text{NO},s} = \frac{\beta A_m}{\beta A_m + \eta_{\text{pore}} k_{m,1}} c_{\text{NO},g} = k_{m,\text{eff}} c_{\text{NO},g} \quad (6.18.22)$$

Figure 6.18.16 depicts the influence of the NO conversion on the parameter for external diffusion (βA_m), the parameter for the effective rate of reaction in the porous wall ($\eta_{\text{pore}} k_{m,1}$), and on the (overall) effective rate constant of NO conversion in a catalytic monolith ($k_{m,\text{eff}}$).

At the entrance of the channel, the ratio of the surface concentration to that in the bulk phase of 61%, that is, the NO content decreases in the boundary layer by 39% (Figure 6.18.17).

To determine the radial NO concentration profile in the wall, which is also shown in Figure 6.18.17 (with the half-thickness of the wall as characteristic length), we use Eq. (4.5.58) and obtain:

$$\frac{c_{\text{NO}}(z)}{c_{\text{NO},s}(z=0)} = \frac{\cosh[\phi(1-2z/d_{\text{wall}})]}{\cosh \phi} \quad (6.18.23)$$

Figure 6.18.17 indicates a strong influence of pore diffusion if the whole wall acts as catalyst as assumed here. Conversely, if pore diffusion is restricted to the wash-coat with a thickness of, for example, 50 μm ($z = 0.1$ in Figure 6.18.17) the influence of pore diffusion should be small.

As explained in Section 4.10 [Eq. (4.10.15)], the following equation can be used to determine the residence time for a complex reaction such as the NO reduction:

$$\tau_m = \frac{m_{\text{cat}}}{\dot{V}} = c_{\text{NO,in}} \int_0^{X_{\text{NO}}} \frac{dX_{\text{NO}}}{r_{m,\text{eff}}} \quad (6.18.24)$$

Thus, by a plot of $c_{\text{NO,in}}/r_{m,\text{eff}}$ versus X_{NO} , the (modified) residence time is determined by graphical integration (area below the curve) as depicted in Figure 6.18.18 for a conversion of 90%.

For the assumed conditions (Table 6.18.7), we obtain a residence time related to the volume of the monolith of 0.21 s, and thus with the superficial velocity related to the monolith volume of 6.4 m s^{-1} we get a length of the monolith needed for a NO conversion of 90% of 1.34 m.

Finally, we have to consider that we have a laminar flow through the channels of the monolith (Re is about 700). Thus the assumption of plug flow is not correct and

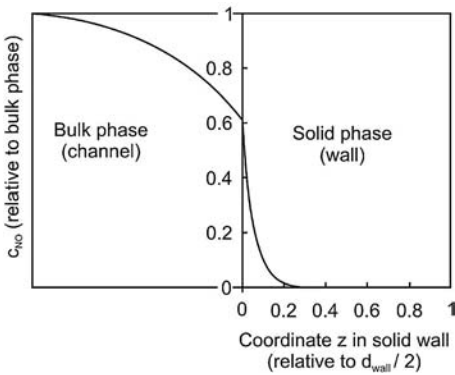


Figure 6.18.17 Interphase and intraphase gradients of NO ($c_{\text{NO}}/c_{\text{NO},g}$) under the reaction conditions at the entrance of the channel of the monolith (i.e., for zero conversion of NO); the concentration gradient in the bulk phase is only given schematically ($d_{\text{wall}} = 1 \text{ mm}$).

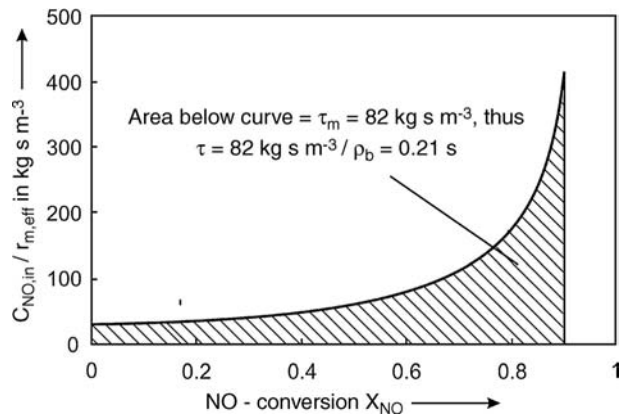


Figure 6.18.18 Plot of $c_{\text{NO,in}}/r_{m,\text{eff}}$ versus NO-conversion used to determine the (modified) residence time by graphical integration (area below the curve).

we have to account for this to obtain a better estimation of the reactor length. For a conversion of 95%, (Section 4.10.2.4), the residence time needed in a tubular reactor with laminar flow is a factor of about 1.4 higher than with a plug flow reactor [see Eq. (4.10.31)], which leads here to a length of the monolith of about 1.9 m (usually divided into three segments).

Pressure Drop of an SCR Reactor For the design of an SCR reactor, the pressure drop is also an important factor. The pressure drop of the monolith can be determined by Eqs. (3.4.6) and (3.4.11):

$$\Delta p_{\text{monolith}} = \frac{64}{Re_t} \frac{L}{d_t} \frac{\rho_g}{2} u_i^2 \left(\text{for } Re_t = \frac{u_i d_t}{\nu} < 2300 \right) \quad (6.18.25)$$

Here we find a value of 1200 Pa [$Re_t = 730$, $L = 1.9$ m, ρ_g (air, 350 °C) = 0.57 kg m⁻³, $u_i = 10$ m s⁻¹, $d_t = 4$ mm]. For comparison: according to Eqs. (3.4.21) and (3.4.24), the pressure loss in a packed bed of spherical particles is given by:

$$\Delta p_{\text{fixed bed}} = \left(33 + \frac{1700}{Re_p} \right) \frac{L}{d_p} \frac{\rho_g}{2} u_s^2 \quad \left(\text{with } Re_p = \frac{u_s d_p}{\nu} \right) \quad (6.18.26)$$

Figure 6.18.19 shows the influence of gas velocity on the pressure drop in a monolith and in a fixed bed (per length of monolith and fixed bed). It was thereby assumed that the particle diameter equals the channel diameter and that the superficial velocity in the bed equals the velocity in the channel. As expected, the pressure drop in the fixed bed is much higher.

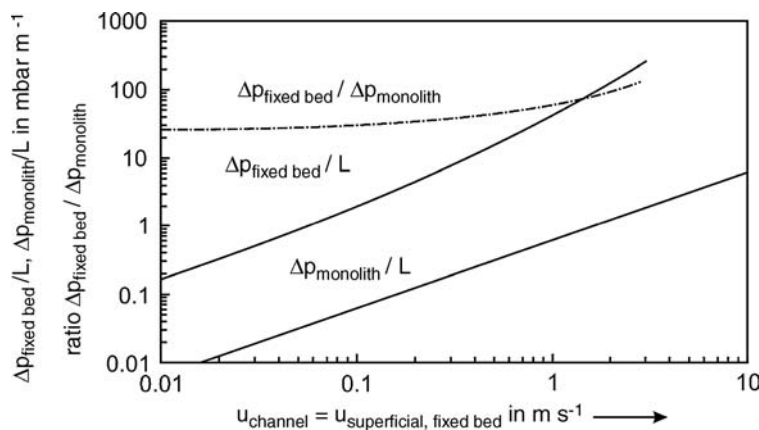
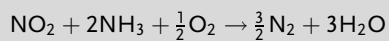
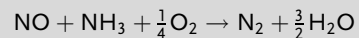


Figure 6.18.19 Comparison of pressure drop in a monolith and a fixed bed and the ratio of both values [total pressure: 1 bar, $d_p = d_t$; $u_{\text{channel}} = u_{\text{superficial, fixed bed}}$, ρ_g (air, 350 °C) = 0.57 kg m⁻³, ν_g (air, 350 °C) = 5.5×10^{-5} m² s⁻¹, $Re_p = Re_t < 2300$; unrealistically high values of $\Delta p > 100$ mbar are not given as the assumption of constant gas velocity is then no longer valid].

Section 6.18 (take-home messages)

- **Automotive emissions** [unburned hydrocarbons (HCs), NO_x, CO, and SO₂ and for diesel oil powered engines also particulate matter] can be reduced partly by **primary methods** such as speed limitations, fuel purification (hydrodesulfurization), and by engine modifications (high compression engines).
- Nevertheless, **secondary measures** are mostly still needed to reduce exhaust emissions of cars to meet current emission standard in most countries. These so-called end-of-pipe solutions are based on the catalytic conversion of all HC_s, CO and NO (**three-way catalyst**). The success of the **monolithic catalytic converter** (which has a lower pressure drop than a fixed bed) is up to now limited to gasoline powered engines. However, in recent years progress has been made in the development of catalytic filters for the cleaning of exhaust gas (e.g., particulate matter) from diesel engines.
- The oxidation of HC_s and CO requires an oxidizing atmosphere and the conversion of NO_x requires a reducing atmosphere. Thus a compromise has to be found to convert at least a main proportion of all three pollutants. The window of optimal operation is narrow and close to a **lambda value** of unity. At the end of the 1990s a new generation of automotive exhaust catalysts was developed, the **NO_x storage catalyst** needed for lean burn engines.
- **Treatment of flue gas from power plants** involves three steps: separation of fly ash, which is collected by an electrostatic precipitator, catalytic reduction of NO_x, and SO₂ separation by scrubbing using a slurry of a sorbent, usually limestone or lime.
- NO and NO₂ are undesirable by-products of the combustion of coal, natural gas, or fuel oil in boilers of power plants. Nitrogen oxides are formed during combustion by the reaction of atmospheric N₂ and O₂ at temperatures > 1200 °C (**thermal NO_x**). If nitrogen-containing fuels such as coal and heavy oils are burned, **fuel NO_x** is produced by the combustion of the fuel-bound nitrogen. The third, usually small, source is **prompt NO_x**, which is attributed to the reaction of N₂ with radicals derived from the fuel.
- The **selective catalytic NO_x reduction (SCR)** by ammonia can be described by:



The mixing of ammonia with flue gas should be carried out with care to avoid ammonia slip (exit of unreacted ammonia). The active compounds of **SCR catalysts** in power plants are mostly WO₃, V₂O₅, and MoO₃. For SCR, the pressure drop is also an important factor, and monoliths are used because of the much lower pressure drop compared to a fixed bed. Mass transfer from the bulk phase of channels of the monolith to the external surface as well as pore diffusion may influence the **effective rate of NO conversion**.

6.19

Industrial Electrolysis

6.19.1

Electrochemical Kinetics and Thermodynamics

6.19.1.1 Faraday's Law and Current Efficiency

Electrochemical reactions are characterized by at least one electron charge transfer step taking place at the electrode or electrolyte interface, for example:



The reaction rate normalized to the electrode surface area (A_e in m^2) is defined as:

$$r = \frac{1}{A_e \nu_A} \frac{dn_A}{dt} = \frac{1}{A_e \nu_e} \frac{dn_e}{dt} = \frac{1}{A_e \nu_B} \frac{dn_B}{dt} \quad (6.19.2)$$

The stoichiometric coefficient ν is by definition negative for educts and positive for products. The number of moles of electrons, n_e , transferred in time t for a given current density i (A m^{-2}) can be expressed as:

$$n_e = \frac{A_e i t}{F} \quad (6.19.3)$$

where F is the *Faraday constant* ($96\,485 \text{ A s mol}^{-1}$), named after *Michael Faraday* (see box), and represents the charge per 1 mole electrons.

Combination of Eqs. (6.19.2) and (6.19.3) yields the differential form of *Faraday's law*:

$$r = \frac{i}{\nu_e F} \quad (6.19.4)$$

For product component B, insertion of Eq. (6.19.4) into Eq. (6.19.2) and integration yields the more common form of *Faraday's law*:

$$n_B = \frac{m_B}{M_B} = \frac{\nu_B}{|\nu_e|} \frac{i A_e t}{F} = \frac{It}{zF} \quad (6.19.5)$$

where I is the current (in A) and z the number of electrons transferred in the overall process to maintain electroneutrality (electron transfer number).

For the masses of educt A (with molar mass M_A) and product B (molar mass M_B) we obtain:

$$m_i = \eta_{\text{current}} \frac{M_i A_e i t}{zF} \quad (\text{with } i \text{ as educt A or product B}) \quad (6.19.6)$$

where η_{current} is the current efficiency and yield of charge. Hence, η_{current} relates the number of moles of a reactant to the number of electrons consumed by the electrochemical reaction.

Rewriting Eq. (6.19.6) leads to the specific energy consumption (in J kg^{-1}) of an electrolytic process with voltage U :

$$q_i = \frac{U A_e i t}{m_i} = \frac{zFU}{\eta_{\text{current}} M_i} \quad (6.19.7)$$

6.19.1.2 Electrochemical Potentials

The electrochemical potential at the electrode/solution interface, $\Delta\varphi$, depends on the standard potential ($\Delta\varphi^0$), temperature, the electron transfer number (z), and on the activities (a_i) of the reactants [oxidants (Ox) = oxidizing agent or reductants (Red) = reducing agents] according to the Nernst equation:

$$\Delta\varphi = \Delta\varphi^0 + \frac{RT}{zF} \ln \frac{\prod_i a_i^{\nu_{i,\text{Ox}}}}{\prod_i a_i^{\nu_{i,\text{Red}}}} \quad (6.19.8)$$

where $\Delta\varphi^0$ is the standard potential at the standard pressure p_0 of 1.013 bar and at $a_i=1$, usually tabulated for 25 °C. For pure solids and the pure solvent (mostly water) a_i is by definition 1.

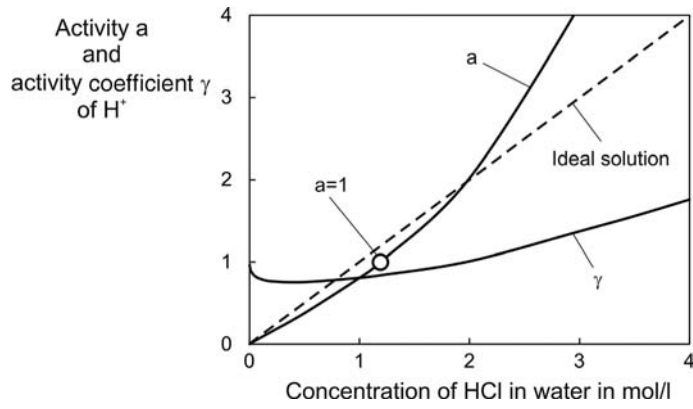
For gases, the activity is defined as:

$$a_{i,g} = \varphi_i \frac{p_i}{p_0} \quad (6.19.9)$$

The fugacity coefficients φ_i are usually close to one for electrochemical applications. Thus, in the following, we simply use the partial pressure relative to p_0 instead of $a_{i,g}$.

Michael Faraday (1791–1867): an English chemist and physicist famous for his works in the field of electromagnetism and electrochemistry. Faraday, a son of a blacksmith, had only a very basic school education and mainly educated himself. Nevertheless, he is one of the most influential scientists and one of the best experimentalists in the history of science. At the age of 14 he became the apprentice of a bookbinder and bookseller. During his seven-year apprenticeship he read many books and developed an interest in science. In 1812, he became secretary and in 1813 scientific assistant of the famous chemist Humphry Davy. In 1825, he was appointed director of the laboratory of the Royal Institution of Great Britain, and in 1833 he became the first Fullerian professor of Chemistry, named after *John Fuller* (1757–1834), better known as "Mad Jack" Fuller, an English businessman, politician, and patron of science and arts. Faraday established the basis for the concept of the electromagnetic field, and discovered the interaction between light and a magnetic field (Faraday effect). He also discovered electromagnetic induction, diamagnetism, and the laws of electrolysis [see Eqs. (6.19.4) and (6.19.5)]. He demonstrated that the charge resided only on the exterior of a charged conductor (Faraday effect). As a chemist, he discovered benzene and butene. It is said that *Albert Einstein* kept a picture of Faraday on his study wall, alongside of pictures of *Isaac Newton* and *James Clerk Maxwell*.

Figure 6.19.1 Activity a and activity coefficient γ of H^+ in a solution of HCl in water.



For components such as ions present in the liquid (mostly aqueous) state, the activities a_i are calculated based on the activity coefficients γ_i and the ratio of the concentration to a standard value of $c_0 = 1 \text{ mol l}^{-1}$:

$$a_{i,\text{liq}} = \gamma_i \frac{c_i}{c_0} \quad (6.19.10)$$

Figure 6.19.1 shows the activity (a) and the activity coefficient (γ) of H^+ as a function of concentration for the example of the system HCl and water. The activity coefficient is close to one for dilute solutions, but may deviate strongly from ideality ($\gamma = 1$) for higher concentrations. For the given example, the activity of H^+ of 1 is reached for a concentration of $1.18 \text{ mol HCl liter}^{-1}$ ($\gamma = 0.85$).

Examples of how to calculate the electrochemical potential $\Delta\varphi$ are:

- 1) Metal ion/metal electrode ($a_{\text{metal}} = 1$), for example, $\text{Cu}^{2+} + 2\text{e}^- \leftrightarrow \text{Cu}$:

$$\Delta\varphi = \Delta\varphi^0 + \frac{RT}{2F} \ln a_{\text{Cu}^{2+}} \quad (6.19.11)$$

- 2) Gas/inert metal electrode, for example, $\text{Cl}_2 + 2\text{e}^- \leftrightarrow 2\text{Cl}^-$:

$$\Delta\varphi = \Delta\varphi^0 + \frac{RT}{2F} \ln \frac{a_{\text{Cl}_2}}{a_{\text{Cl}^-}^2} \approx \Delta\varphi^0 + \frac{RT}{2F} \ln \frac{p_{\text{Cl}_2}}{a_{\text{Cl}^-}^2 p_0} \quad (6.19.12)$$

- 3) Ion/salt/metal electrode, for example, $\text{AgCl(s)} + \text{e}^- \leftrightarrow \text{Ag(s)} + \text{Cl}^-$:

$$\Delta\varphi = \Delta\varphi^0 + \frac{RT}{F} \ln \frac{1}{a_{\text{Cl}^-}} = \Delta\varphi^0 - \frac{RT}{F} \ln a_{\text{Cl}^-} \quad (6.19.13)$$

6.19.1.3 Galvanic and Electrolysis Cells, Nernst's Law

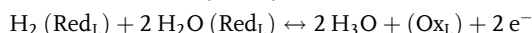
An electrochemical cell consists of two electrodes. If the cell produces electricity, it is called a galvanic cell, and if the reaction is driven by an external source of current it is called an electrolysis cell. The electromotive force E is the potential difference of an electrochemical cell (electrode potential, cell voltage). If the right-hand electrode has a higher potential than the left-hand one, electrons flow from left (anode) to the right (cathode) in a closed circuit. Consequently, for $E > 0$, reduction occurs at the right-hand electrode ($\text{Ox}_R + \text{e}^- \rightarrow \text{Red}_R$) and oxidation takes place at the left ($\text{Red}_L \rightarrow \text{Ox}_L + \text{e}^-$). The overall cell reaction is $\text{Red}_L + \text{Ox}_R \rightarrow \text{Red}_R + \text{Ox}_L$. The corresponding Nernst equation is:

$$\begin{aligned} E &= \Delta\varphi_R - \Delta\varphi_L = \Delta\varphi_R^0 + \frac{RT}{zF} \ln \frac{a_{\text{Ox},R}^{v_{i,\text{Ox}}}}{a_{\text{Red},L}^{v_{i,\text{Red}}}} - \Delta\varphi_L^0 - \frac{RT}{zF} \ln \frac{a_{\text{Ox},L}^{v_{i,\text{Ox}}}}{a_{\text{Red},L}^{v_{i,\text{Red}}}} \\ &= \Delta\varphi_R^0 - \Delta\varphi_L^0 - \frac{RT}{zF} \ln \frac{a_{\text{Red},R}^{v_{i,\text{Red}}} a_{\text{Ox},L}^{v_{i,\text{Ox}}}}{a_{\text{Red},L}^{v_{i,\text{Red}}} a_{\text{Ox},R}^{v_{i,\text{Ox}}}} = E^0 - \frac{RT}{zF} \ln \frac{a_{\text{Red},R}^{v_{i,\text{Red}}} a_{\text{Ox},L}^{v_{i,\text{Ox}}}}{a_{\text{Red},L}^{v_{i,\text{Red}}} a_{\text{Ox},R}^{v_{i,\text{Ox}}}} \end{aligned} \quad (6.19.14)$$

An example is the reaction of chlorine with hydrogen to give an aqueous solution of HCl. The reactions proceeding in the two half-cells are:



Left-hand electrode (anode):



Overall cell reaction:



and Eq. (6.19.13) yields (with $a_{\text{H}_2\text{O}} = 1$ by definition):

$$\begin{aligned} E &= E^0 - \frac{RT}{2F} \ln \frac{a_{\text{Cl}^-}^2 a_{\text{H}_3\text{O}^+}^2}{a_{\text{H}_2} a_{\text{Cl}_2}} = E^0 - \frac{RT}{F} \ln \frac{a_{\text{Cl}^-} a_{\text{H}_3\text{O}^+}}{\sqrt{a_{\text{H}_2} a_{\text{Cl}_2}}} \\ &\approx E^0 - \frac{RT}{F} \ln \frac{a_{\text{Cl}^-} a_{\text{H}_3\text{O}^+} p_0}{\sqrt{p_{\text{H}_2} p_{\text{Cl}_2}}} \end{aligned} \quad (6.19.15)$$

6.19.1.4 Standard Electrode Potentials

To normalize standard electrode potentials, differences of potentials are used. The one chosen to have zero potential is the standard hydrogen electrode: The inert metal is platinum, and the hydrogen ion and the gas are in their standard states, that is, the hydrogen pressure is 1.013 bar and the H^+ activity is 1, which is adjusted by the concentration of HCl (1.19 mol HCl per liter H_2O , Figure 6.19.1). Table 6.19.1 lists selected values of standard potentials.

6.19.1.5 Electrical Work and Thermoneutral Enthalpy Voltage

The standard electrical work, zFE^0 , is related to the standard Gibbs free enthalpy by:

$$\Delta_R G_{298}^0 = -zFE^0 \quad (6.19.16)$$

Usually, the standard Gibbs free enthalpy is calculated by the stoichiometric sums of the standard enthalpies of formation and the standard entropies:

$$\Delta_R G_{298}^0 = \Delta_R H_{298}^0 - T\Delta_R S_{298}^0 = \sum \nu_i \Delta_F H_{i,298}^0 - T \sum \nu_i S_{i,298}^0 \quad (4.2.14)$$

Table 6.19.2 lists selected values of thermodynamic data of electrochemical reactants.

For example, the values of $\Delta_R H_{298}^0$ and $\Delta_R S_{298}^0$ are -335 kJ mol^{-1} and $-243.5 \text{ J mol}^{-1} \text{ K}^{-1}$, respectively, for the cell reaction $\text{H}_2 + \text{Cl}_2 \leftrightarrow 2\text{H}^+ + 2\text{Cl}^-$. Hence,

Table 6.19.1 Electrode reactions and standard potentials [data of Hamann and Vielstich (2005)].

Oxidant(s) + $e^- \leftrightarrow$ reductant(s)	Standard potential E^0 versus standard H_2 electrode (V)
$\text{Li}^+ + e^- \leftrightarrow \text{Li}$	-3.045
$\text{Na}^+ + e^- \leftrightarrow \text{Na}$	-2.711
$\text{Al}^{3+} + 3e^- \leftrightarrow \text{Al}$	-1.706
$2\text{H}_2\text{O} + 2e^- \leftrightarrow \text{H}_2 + 2\text{OH}^-$	-0.828
$\text{Zn}^{2+} + 2e^- \leftrightarrow \text{Zn}$	-0.763
$\text{Fe}^{2+} + 2e^- \leftrightarrow \text{Fe}$	-0.409
$\text{Ni}^{2+} + 2e^- \text{H}^+ \leftrightarrow \text{Ni}$	-0.230
$\text{Pb}^{2+} + 2e^- \leftrightarrow \text{Pb}$	-0.126
$2\text{H}^+ + 2e^- \leftrightarrow \text{H}_2$	0
$\text{Cu}^{2+} + 2e^- \leftrightarrow \text{Cu}$	+0.340
$\text{Fe}^{3+} + e^- \leftrightarrow \text{Fe}^{2+}$	+0.771
$\text{Ag}^+ + e^- \leftrightarrow \text{Ag}$	+0.799
$\text{Cl}_2 + 2e^- \leftrightarrow 2\text{Cl}^-$	+1.358
$0.5\text{O}_2 + 2\text{H}^+ + 2e^- \leftrightarrow \text{H}_2\text{O}$	+1.229
$0.5\text{O}_2 + \text{H}_2\text{O} + 2e^- \leftrightarrow 2\text{OH}^-$	+0.401
$\text{F}_2 + 2e^- \leftrightarrow 2\text{F}^-$	+2.85

Table 6.19.2 Thermodynamic data of typical electrochemical reactants (at 298.15 K, 1.013 bar) [data from Hamann and Vielstich (2005)].

Substance and state (g: gas; l: liquid; s: solid, aq: aqueous solution of activity one)	$\Delta_F H_{298}^0$ (kJ mol ⁻¹)	S_{298}^0 (J mol ⁻¹ K ⁻¹)
H ₂	g	0
O ₂	g	0
C	s	0
CO	g	-110.6
H ₂ O	l	-285.9
H ⁺ (H ₃ O ⁺)	aq	0
Cl ⁻	aq	-167.5
HCl	g	-92.4
Cl ₂	g	0
Zn ⁰	s	0
Zn ²⁺	aq	-152.5

$\Delta_R G_{298}^0$ is -262.5 kJ mol⁻¹, and Eq. (6.19.16) leads to $E^0 = 1.36$ V. The same result is obtained if we use the difference between the standard potential of the half-cell $\text{Cl}_2 + 2e^- \leftrightarrow 2\text{Cl}^-$ and the standard hydrogen cell ($2\text{H}^+ + 2e^- \leftrightarrow \text{H}_2$), which has by definition a potential of zero (Table 6.19.2).

For $E > 0$, that is, $\Delta_R G < 0$, the cell reaction occurs spontaneously and the cell delivers electrical energy. This is utilized in H₂/O₂ fuel cells:

O₂ electrode (cathode):

0.5 O₂ + 2 H⁺ + 2 e⁻ \leftrightarrow H₂O; $E_{\text{O}_2/\text{H}_2\text{O}}^0 = 1.229$ V vs standard H₂ cell

H₂ electrode (anode): $\text{H}_2 \leftrightarrow 2\text{H}^+ + 2e^-$; $E_{\text{H}^+/\text{H}_2}^0 = 0$ V

Overall cell reaction: $\text{H}_2 + 0.5 \text{O}_2 \leftrightarrow \text{H}_2\text{O}$

Calculation of $\Delta_R G_{298}^0$ by Eq. (6.19.16) yields -237.2 kJ mol⁻¹ (= 2×-1.23 V $\times 96\ 485$ A s mol⁻¹). The term $T\Delta_R S_{298}^0$ has a negative value of -48.7 kJ mol⁻¹ and represents the heat released by the system, which cannot be exploited as electrical work (details in Juettnner, 2007).

If the two half-cells are arranged oppositely, the reactions are reversed and the process refers to water electrolysis. The electrode potential at equilibrium E^0 is then negative and $\Delta_R G_{298}^0$ is positive. Now $T\Delta_R S_{298}^0$ is positive (48.7 kJ mol⁻¹) and is taken up from the environment or the electrolysis cell cools down. This effect can be compensated if the cell operates at a higher cell voltage to permit isothermal operation, and is denoted as the thermoneutral voltage:

$$E_{\text{th}}^0 = -\frac{\Delta_R H_{298}^0}{zF} = -\frac{(\Delta_R G_{298}^0 - T\Delta_R S_{298}^0)}{zF} \quad (6.19.17)$$

For water electrolysis, the thermoneutral enthalpy voltage E_{th}^0 is -1.48 V compared to the electrolysis voltage E^0 with a value of -1.23 V. Note that electrochemical cells can operate against a positive ΔG if an outer source is applied that drives the electrons in the opposite direction (Juettnner, 2007).

According to the Nernst equation [Eqs. (6.19.8), (6.19.9), (6.19.10), and (6.19.14)], the electrical potential also depends on the concentration and pressure of the reactants. This is illustrated in Figure 6.19.2 for the influence of pH [= -log $a_{\text{H}^+} \approx \log c_{\text{H}^+}/(1 \text{ mol l}^{-1})$] on the electrode potential of the half-cell reaction $0.5\text{H}_2 \leftrightarrow \text{H}^+ + e^-$, where E is given by ($E^0 = 0$ by definition):

$$E_{\text{H}_2/\text{H}^+} = \frac{RT}{F} \ln \frac{a_{\text{H}^+}}{\sqrt{a_{\text{H}_2}}} = \frac{RT}{F} \ln \left(\frac{c_{\text{H}^+}}{c_0} \sqrt{\frac{p_0}{p_{\text{H}_2}}} \right) = \frac{RT}{F} \ln \left(10^{-\text{pH}} \sqrt{\frac{p_0}{p_{\text{H}_2}}} \right) \quad (6.19.18)$$

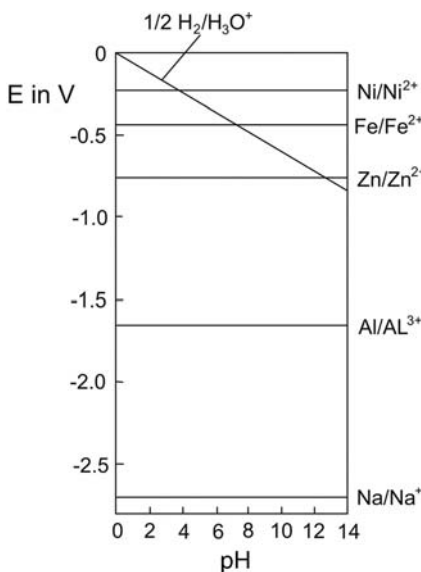


Figure 6.19.2 Influence of pH on the electrical potential of H₂ evolution for a pressure of 1.013 bar and 298 K.

Hence, for a neutral solution ($\text{pH } 7$) we get $E = -0.41 \text{ V}$ (at 1.013 bar, 25°C). Figure 6.19.2 also shows selected values of the standard potential of some metals. If E is higher than the standard potential of a metal it will dissolve in water. For aluminum and zinc, this is only prevented by a dense oxide coating. For sodium, such a coating is not formed. As a result, an intense reaction with water leading to evolution of hydrogen takes place in the whole pH range.

6.19.1.6 Overpotentials

An important factor in electrochemical processes, for example, for chlor-alkali electrolysis, is the phenomenon of an overpotential, that is, the difference between a half-reaction's thermodynamically determined equilibrium potential and the observed potential when a current is flowing. An overpotential represents the extra energy required for electrolysis at a certain current density to force the electrode reaction to proceed. In a galvanic cell overpotential means less energy is recovered than thermodynamics predict. Consequently, energy is lost as heat. Overpotentials are specific to each cell and operational conditions. Figure 6.19.3 shows this for the electrolysis of a neutral NaCl solution with iron as cathode material and graphite as anode. The operating potential of the anode is always more positive than its equilibrium potential, while the operating potential of the cathode is always more negative than its equilibrium potential.

The reduction of Na^+ ions is thermodynamically difficult ($E^0 = -2.71 \text{ V}$, Figure 6.19.3) and water is reduced, evolving H_2 and leaving OH^- ions in solution [$E = -0.41 \text{ V}$ in neutral solution, Eq. (6.19.24)]. At the anode, oxidation of chloride to chlorine is observed but not water oxidation since the overpotential is lower for chloride than for water. However, if OH^- ions reach the anode an unwanted chemical reaction with the dissolved chlorine gas takes place:



The formation of hypochlorous acid is thermodynamically highly favored, for example, at 20°C the equilibrium constant is 1.2×10^{17} (Hamann and Vielstich, 2005). This leads to a high concentration of hypochlorite ions at the anode and in a subsequent reaction oxygen is formed, which contaminates the sodium hydroxide solution with chlorate ions and chloride:



It is essential for all technical chlor-alkali electrolysis processes – as subsequently discussed in Section 6.19.2.2 – that the transport of hydroxide ions formed at the cathode into the anode compartment is excluded (membrane process) or at least largely suppressed (diaphragm process). In the mercury cell process, OH^- ions are not formed in the entire process.

6.19.2

Chlorine and Sodium Hydroxide

6.19.2.1 Applications of Chlorine and Sodium Hydroxide

Chlorine is a fundamental building block of the chemical industry (Tables 6.19.3 and 6.19.4) and is used in over 50% of all industrial chemical processes, including 85% of pharmaceuticals and 96% of crop protection chemicals. The intermediates produced from chlorine mostly contain the element chlorine, but most end products do not (Table 6.19.3).

Chlorine's co-product, sodium hydroxide (NaOH), also has a wide variety of applications (Table 6.19.5) and is used for production of pulp and paper, aluminum, and for petroleum and natural gas refining. It is also needed for pollution control to

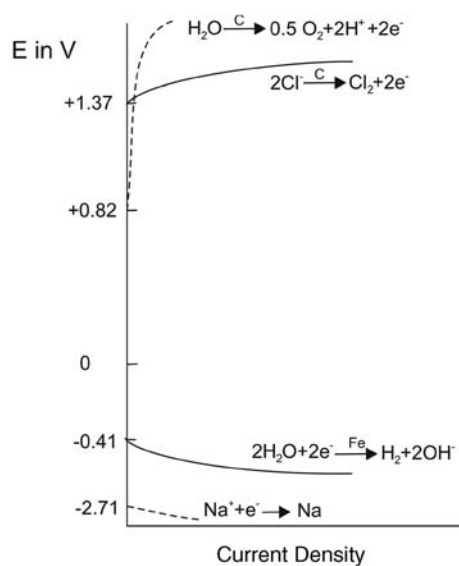


Figure 6.19.3 Scheme of electrolysis of a neutral NaCl solution (Fe cathode, graphite anode). Adapted from Hamann and Vielstich (2005).

Table 6.19.3 Important chlorine applications for intermediates and end products (Schmittinger, 2000).

Cl-compound	Intermediate		End use	
	Contains Cl	Contains no Cl	Contains Cl	Contains no Cl
Elemental chlorine	HCl		Water treatment HCl	
C ₁ -derivatives	Trichloromethane		Hydrochloro-fluorocarbons	Polytetrafluoroethylene (PTFE)
	Monochloromethane			Silicones, methylcellulose
	Tetrachloromethane			Industrial processes
	Phosgene			Polycarbonates, diisocyanates, polyurethanes
C ₂ -derivatives	Trichloroacetic acid			Pharmaceuticals
	Dichloroethane, vinyl chloride		Poly(vinyl chloride) (PVC)	
	Ethyl chloride			Ethyl-cellulose
C ₃ -derivatives		Propylene oxide	Flocculants	Propylene glycol Epoxy resins, glycerols
C ₄ -derivatives	Allyl chloride			Polychloroprene
	Dichlorobutene chloroprene			Nylon
1,4-Dichlorobutane				Dyestuffs, health, crop protection, and aramid fibers
Aromatic derivatives				
Inorganic derivatives			Fe and Al-chloride	
	Sulfur chlorides			Resins, health crop protection
	Ti-tetrachloride			Titanium oxide
	Silicon tetrachloride			Silicon dioxide, silicon

remove acid contaminants from gases prior to discharge to the atmosphere. Like chlorine, sodium hydroxide is an intermediate for the production of other products, such as sodium phenolate used in antiseptics and in producing aspirin and amyl alcohol used in the production of pharmaceuticals. NaOH also plays a significant role in the textile industry as well as in the manufacture of soaps and detergents.

6.19.2.2 Processes of Chlor-Alkali Electrolysis

In the chlor-alkali electrolysis process, an aqueous solution of sodium chloride is decomposed by direct current into chlorine, hydrogen, and a sodium hydroxide solution:



Three processes are used, the mercury process (invented in the 1880s), the diaphragm process (1890s), and the membrane process (1970). In all three cases nearly

Table 6.19.4 European chlorine production and applications in 2009 (Euro Chlor, 2011). The global production was about 57 million tonnes in 2008 (<https://www.vci.de/Themen/Umwelt-Sicherheit/Chlorchemie/Seiten/Positionen-zur-Chemie-mit-Chlor.aspx>, accessed 08.09.2012; see also Table 6.19.7).

Application	Amount (Mio. Cl ₂ t a ⁻¹)
Poly(vinyl chloride) (doors and window frames, pipes, medical supplies, clothing)	3.21
Isocyanates and oxygenates (insulation, footwear, plastics, pesticides, car paints)	2.48
Inorganics (disinfectants, water treatment, paint pigments)	1.27
Epichlorohydrin (pesticides, epoxy resins, sports boats, fishing rods)	0.51
Chloromethanes (silicon rubbers, decaffeinators, Teflon, paint strippers, cosmetics)	0.52
Solvents (metal degreasing, adhesives, dry cleaning plastics)	0.28
Other organics (detergents, ship and bridge paints, lubricants, herbicides, insecticides)	0.84
Total	9.11

Table 6.19.5 European NaOH production and applications in 2009 (Euro Chlor, 2011).

Application	Amount (Mio. t-NaOH a ⁻¹)
Organics (artificial arteries, parachutes, pen tips, telephones)	2.63
Pulp, paper, cellulose (adhesives, printing, newspapers, books)	1.21
Food industries (fruit and vegetable peelings, ice cream, thickeners, wrappings)	0.41
Water treatment (flocculation of waste, acidity control)	0.40
Bleach (textiles, disinfectants)	0.37
Aluminum and metals (greenhouses, car and airplane panels, steel hardening)	0.35
Soaps (shampoos, cosmetics, cleaning agents)	0.26
Mineral oils (greases, fuel additives)	0.17
Phosphates (detergents)	0.13
Rayon (bedspreads, surgical dressing)	0.12
Other inorganics (paints, glass, ceramics, fuel cells, perfumes)	1.17
Miscellaneous (neutralization of acids, gas scrubbing, pharmaceuticals)	1.50
Total	8.7

saturated and purified brine is fed into the electrolysis cell, and chlorine is formed at the anode:



The cathode reaction depends on the specific process and different methods are utilized to separate chlorine from sodium hydroxide and hydrogen [details in Schmittinger (2000)].

6.19.2.3 Diaphragm Process

The reaction at the cathode (iron) of the diaphragm process is:



The theoretical electrochemical potentials for production of Cl_2 and H_2 in a neutral 1 M NaOH solution (1 mol $\text{Cl}^- \text{l}^{-1}$ and 10^{-7} mol l^{-1} for OH^- and H^+), at 25 °C and at a pressure of 1.013 bar, are -0.41 V and $+1.36$ V, as we can easily calculate by the Nernst equation [Eqs. (6.19.8), (6.19.9), (6.19.10), and (6.19.14)]:

$$E_{\text{H}_2/\text{H}^+} = E_0 + \frac{RT}{F} \ln \frac{c_0}{c_{\text{OH}^-}} = -0.828 \text{ V} + 0.0257 \text{ V ln } 10^7 = -0.41 \text{ V} \quad (6.19.24)$$

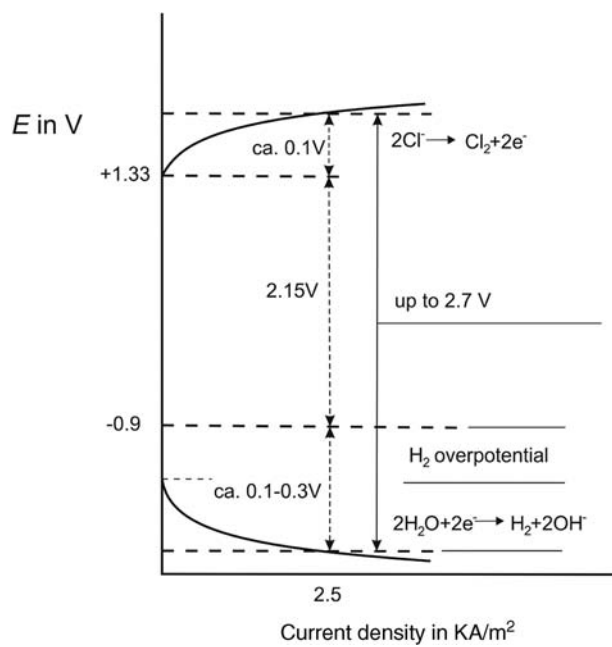
$$E_{\text{Cl}_2/\text{Cl}^-} = E_0 + \frac{RT}{F} \ln \frac{c_0}{c_{\text{Cl}^-}} \sqrt{\frac{p_{\text{Cl}_2}}{p_0}} = 1.36 \text{ V} + 0.0257 \text{ V ln } 1 = 1.36 \text{ V} \quad (6.19.25)$$

Typically, the cathode works with 3 mol NaOH l^{-1} (3 mol $\text{OH}^+ \text{l}^{-1}$), which alters the potential from -0.41 to -0.86 V and the one of the anode (titanium) to 1.34 V (3 mol $\text{Cl}^- \text{l}^{-1}$). Hence the voltage needed for the process is 2.2 V, which corresponds to a theoretical (minimum) energy consumption q_{Cl_2} of around 1700 kWh t^{-1} chlorine if we use Eq. (6.19.7):

$$q_{\text{Cl}_2} = \frac{FU}{M_{\text{Cl}_2}} = \frac{2.2 \text{ V} \times 96485 \text{ A s mol}^{-1}}{0.0355 \text{ kg mol}^{-1}} = 5.98 \text{ MJ kg}^{-1} = 1660 \text{ kWh t}^{-1} \quad (6.19.26)$$

The current density is 2.5 A m^{-2} and the corresponding overpotentials have to be considered, as depicted by the potential–current curves in Figure 6.19.4, which leads to a voltage of 2.7 V. The practical voltage is even higher (3.5 V) to overcome

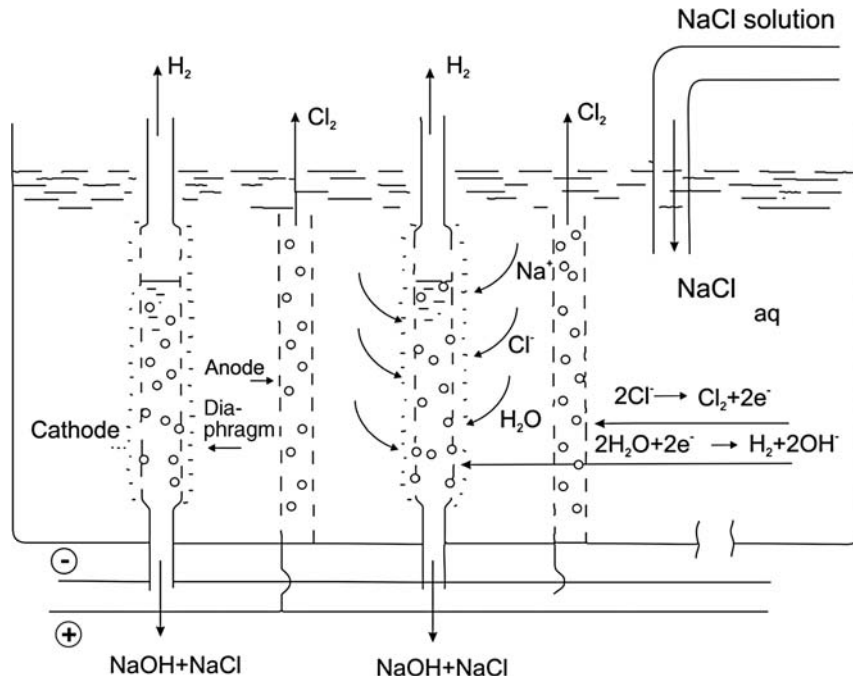
Figure 6.19.4 Potential–current curves of electrolysis of a solution of NaCl by the diaphragm process with a 3 M NaOH solution at the cathode. Adapted from Hamann and Vielstich (2005).



the additional voltage drops of the diaphragm, electrodes, and of the electrolyte, and for a typical current efficiency of 96% this leads to practical electrical energy consumption of around 2800 kWh t⁻¹ chlorine.

In the diaphragm process (Figure 6.19.5) the anode area is separated from the cathode area by a permeable asbestos based diaphragm, which separates hydrogen and chlorine (but not Cl⁻ ions) formed at the cathode and anode, respectively. The liquid level in the anode compartment is higher, which leads to a flow of the liquid through the diaphragm into the cathode compartment. The liquid NaOH solution leaving the anode compartment consists of 11 wt% NaOH and 15 wt% NaCl (Behr, Agar, and Joerissen, 2010). The caustic brine has to be separated from the salt by evaporation, but even then the resultant 50% NaOH solution still contains 1% NaCl. The salt, which is separated by filtration, is reused to saturate the diluted brine.

Figure 6.19.5 Schematic of the diaphragm process. Adapted from Hamann and Vielstich (2005).



The formation of O_2 at the anode is an unwanted side reaction: Owing to the concentration gradient against the opposing flow of brine OH^- ions migrate to a small extent through the diaphragm into the anode compartment, where they are oxidized to hypochlorous acid [Eq. (6.19.19)] and finally to oxygen [Eq. (6.19.20)]. Typically, the chlorine contains 1–2% O_2 , and separation by gas compression, liquefaction, and evaporation is needed.

6.19.2.4 Mercury Cell Process

In the mercury cell process, sodium amalgam is produced at the cathode:



The amalgam is subsequently decomposed with graphite as catalyst:



The equilibrium potential of amalgam formation at the mercury cathode is -1.78 V (Figure 6.19.6). The hydrogen overpotential at the mercury electrode is high (1.3 V). For a pressure of 1.013 bar , temperature of 25°C , and for a typical pH of 11 near the cathode, the electrode potential of hydrogen formation is given by Eqs. (6.19.9), (6.9.19), and (6.19.14):

$$\begin{aligned} E_{H_2O/OH^-} &= E_0 + \frac{RT}{2F} \ln \left[\frac{p_0}{p_{H_2}} \left(\frac{c_0}{c_{OH^-}} \right)^2 \right] \\ &= -0.828\text{ V} + 0.0129\text{ V} \ln 10^6 = -0.65\text{ V} \end{aligned} \quad (6.19.29)$$

The equilibrium potential of oxygen formation (25°C , 1.013 bar , neutral solution, pH 7) is:

$$\begin{aligned} E_{H_2O/H^+} &= E_0 + \frac{RT}{2F} \ln \left[\left(\frac{c_{H^+}}{c_0} \right)^2 \sqrt{\frac{p_0}{p_{O_2}}} \right] \\ &= 1.229\text{ V} + 0.0129\text{ V} \ln 10^{-14} = 0.81\text{ V} \end{aligned} \quad (6.19.30)$$

Hence, hydrogen formation should be favored compared to chlorine formation ($E = 1.33\text{ V}$), but compared to amalgam formation the overpotential of H_2 formation increases steeply with the current density (Figure 6.19.6).

Figure 6.19.7 depicts the mercury cell electrolysis process. A severe drawback of the process is the fact, that the chlorine and sodium hydroxide produced are contaminated with trace amounts of very poisonous mercury.

The theoretical (thermodynamically determined) voltage of the mercury process is 3.11 V (Figure 6.19.6), which corresponds to a minimum energy consumption of around 2300 kWh t^{-1} chlorine. For a typical current density of 10 A m^{-2} , the voltage and energy consumption are higher (3.5 V , 2600 kWh t^{-1} , Figure 6.19.6). The practical voltage and electrical energy consumption are even higher, about 4.1 V and about 3600 kWh t^{-1} chlorine.

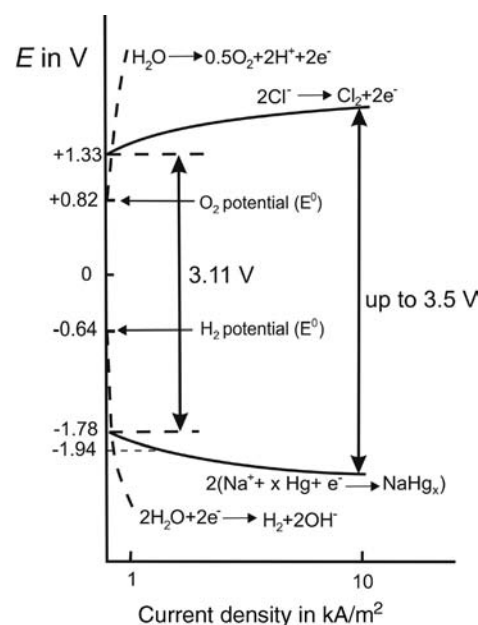


Figure 6.19.6 Potential–current curves of electrolysis by the mercury process (c of $Na^+ = 5\text{ mol l}^{-1}$, 0.2 wt% Na in Hg, Ti anode, mercury cathode). Adapted from Hamann and Vielstich (2005).

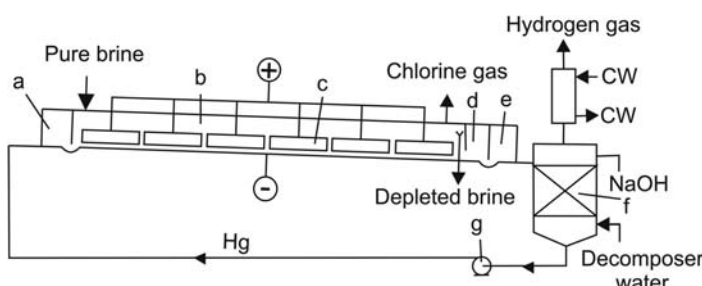


Figure 6.19.7 Mercury process (a: Hg inlet box, b: cell room, c: Ti anodes, d: end box, e: wash box, f: amalgam decomposer, g: Hg pump, and CW: cooling water). Adapted from Hamann and Vielstich (2005).

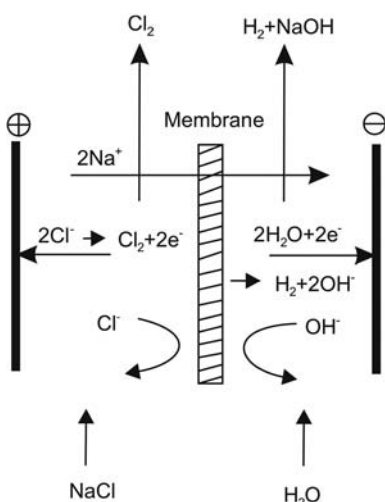


Figure 6.19.8 Membrane process.

Membrane process. Adapted from Hamann and Vielstich (2005).

6.19.2.5 Membrane Process

The advantages of the diaphragm process (low voltage) and of the mercury cell process (NaCl free NaOH solution) are combined in the membrane process (Figure 6.19.8).

In the 1970s, perfluorosulfonate membranes were developed. They have low electrical resistance, high mechanical stability, and are even stable in the presence of aggressive media such as Cl₂ and NaOH. The main difference between the membrane process and the diaphragm process is that only traces of Cl⁻ and OH⁻ ions migrate through the membrane, which leads to a NaOH solution practically free of NaCl (<100 ppm Cl⁻, Hamann and Vielstich, 2005). In addition, the chlorine only contains a small content of oxygen (0.5%, Behr, Agar, and Joerissen, 2010). The energy requirements for purification of chlorine and sodium hydroxide are therefore lower compared to the diaphragm process. The current density used in the membrane process is only about 4 A m⁻² and the voltage 3 V. The electrical energy consumption is the lowest of all three chlor-alkali processes. A comparison of the processes is given in Table 6.19.6.

The mercury process needs the most electrical energy, but no steam is required to concentrate the caustic solution. The overall primary energy needed (if a power plant efficiency of 40% is assumed) for the mercury and diaphragm process is about the same, whereas the membrane process is more efficient (Table 6.19.6). Today, 54% of all chlor-alkali plants are membrane plants (Table 6.19.7); in the last 20 years, all new plants utilize this technology (Behr, Agar, and Joerissen, 2010).

Table 6.19.6 Comparison of the three chlor-alkali electrolysis processes [estimated by data of Bergner (1994); Bergner, Hartmann, and Staab (1987); and European Commission (2001)].

	Amalgam technology	Diaphragm technology	Membrane technology
Theoretical voltage (V)	3.1	2.2	2.2
Cell voltage (V)	3.9–4.2	2.9–3.5	3.0–3.6
Current density (kA m ⁻²)	8–13	1–3	3–5
Caustic strength (wt%)	50	12	33
Theoretical consumption of electrical energy [kWh t ⁻¹ Cl ₂ (+ 1.13 t NaOH + 0.028 t H ₂)] ^{a)}	2340	1660	1660
Electrical energy (alternating current) [kWh t ⁻¹ Cl ₂ (+ 1.13 t NaOH + 0.028 t H ₂)]	3360 (at 10 kA m ⁻²)	2720 (at 1.7 kA m ⁻²)	2650 (at 5 kA m ⁻²)
Electrical energy by other equipment (pumps, compressors, etc.) (kWh t ⁻¹ Cl ₂)	200	250	140
Total electrical energy (kWh t ⁻¹ Cl ₂)	3560	2970	2790
Thermal energy (steam) to concentrate caustic to 50% (kWh t ⁻¹ Cl ₂)	0	1830	540
Thermal energy to liquefy and evaporate chlorine (kWh t ⁻¹ Cl ₂)	200	200	200
Total primary energy in toe per t-Cl ₂ ^{b)} (% share needed to produce the electrical energy)	0.77 (98)	0.83 (77)	0.67 (90)
Investment costs [\$US (t Cl ₂ a ⁻¹)] ^{c)}	735	810	650

a) Theoretical minimum value of electrical energy needed per kg of Cl₂ is given by UzF/M with $M = 0.071 \text{ kg mol}^{-1}$ for Cl₂, z (valence number, i.e., electrons transferred) = 2, and Faraday constant $F = 96\,487 \text{ A s mol}^{-1}$. Hence, for $U = 1 \text{ V}$ ($= \text{J A}^{-1} \text{ s}^{-1}$) we obtain a value of 2717 MJ per t-Cl₂ = 755 kWh per kg-Cl₂.

b) 1 kWh electrical energy is equivalent to about 2.5 kWh (9 MJ) primary energy = 0.21×10^{-3} tonnes of oil equivalent, 1 toe = 41.9 GJ. For the efficiency of steam production, a value of 90% is assumed.

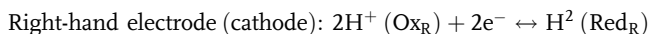
c) According to Bergner, Hartmann, and Staab (1987), the investment costs for a diaphragm plant in 1987 (in the USA) were US\$500 per tonne of Cl₂ per year. The costs for an amalgam and membrane plant were 9% and 20% lower. To calculate the actual costs for 2010, these figures were multiplied by a factor of 1.5.

6.19.3

Electrolysis of Water

Hydrogen is one option for a clean energy choice, if produced by water electrolysis and electrical energy based on renewable sources (wind, solar, etc.). Hydrogen can be used directly as fuel or can be transferred by reaction with CO/CO₂ into methanol (Section 6.11.2) or by Fischer–Tropsch synthesis into diesel oil (Section 6.11.1). Today, the production of hydrogen by water electrolysis is practically zero and H₂ production is mainly based on fossil fuels and to a small extent (about 4% of total H₂ production) hydrogen is produced as by-product of chlor-alkali electrolysis (Section 5.1.3.2). This may change in future, if alternative energy sources for electricity production like wind and solar and hence electricity storage become more important.

The following electrochemical processes take place during water electrolysis:



The electrolysis voltage depends on the activities and partial pressures of the reactants, which may differ from the standard values of 1 and 1.013 bar. By the Nernst equation [Eq. (6.19.14)], we obtain (with $a_{\text{H}_2\text{O}} = 1$, $a_{\text{H}_2} \approx p_{\text{H}_2}/p_0$, $a_{\text{O}_2} \approx p_{\text{O}_2}/p_0$):

$$\begin{aligned} E_{\text{H}_2\text{O} \text{ electrolysis}} &= E_{\text{H}_2\text{O} \text{ electrolysis}}^0 - \frac{RT}{2F} \ln \left(\frac{p_{\text{H}_2}}{p_0} \sqrt{\frac{p_{\text{O}_2}}{p_0}} \right) \\ &= -1.23 \text{ V} - \frac{RT}{2F} \ln \left(\frac{p_{\text{H}_2}}{p_0} \sqrt{\frac{p_{\text{O}_2}}{p_0}} \right) \end{aligned} \quad (6.19.31)$$

Thus, the electrolysis voltage does not depend on pH but (the absolute value) increases with pressure (Figure 6.19.9a). This is in agreement with Le Chatelier's principle: an increase in pressure encourages water formation, and more energy is needed to overcome the reverse reaction, for example, at 700 bar (25 °C), the voltage is −1.36 V compared to −1.23 V at 1 bar.

The value of the standard electrolysis voltage also depends on temperature. As a first approximation, we may assume that $\Delta_R H^0$ and $\Delta_R S^0$ are constant and use the values at 298 K ($\Delta_R H_{298}^0 = 285.9 \text{ kJ mol}^{-1}$ and $\Delta_R S_{298}^0 = 163.3 \text{ J mol}^{-1} \text{ K}^{-1}$):

$$\begin{aligned} E_{\text{H}_2\text{O} \text{ electrolysis}}^0 &\approx -\frac{\Delta_R G_{298}^0}{2F} = -\frac{(\Delta_R H_{298}^0 - T\Delta_R S_{298}^0)}{2F} \\ &= -1.482 \text{ V} + T 0.000846 \text{ V K}^{-1} \end{aligned} \quad (6.19.32)$$

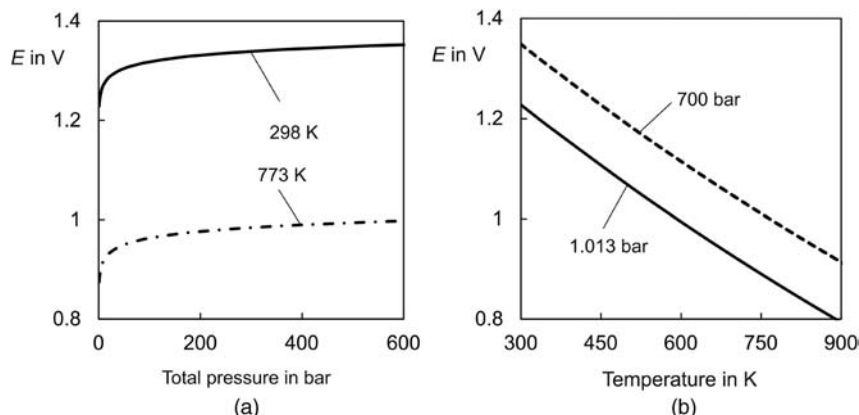


Table 6.19.7 Global Cl₂ production by different processes in 2008 (VCI, 2011).

Process of Cl ₂ production	Production (Mio. t Cl ₂ a ⁻¹)	% of total production
Membrane	31	54
Diaphragm	17	31
Mercury	6	10
Others	3	5
Total	57	100

Figure 6.19.9 (Absolute value) of the voltage for H₂O-electrolysis (zero current) at different values of T and p , calculated with Eqs. (6.19.30) and (6.19.32).

Hence, an increase in temperature leads to a lower (absolute) value of the electrolysis voltage (see also Figure 6.19.9). According to Laoun (2007), the following equation considers the influence of temperature on the standard enthalpy and entropy and is, therefore, more accurate to calculate the electrolysis voltage at 1.013 bar at different temperatures (with T in K):

$$\frac{E_{\text{H}_2\text{O electrolysis}}^0}{1 \text{ V}} = -1.5184 + 1.5421 \times 10^{-3} T - 9.523 \times 10^{-5} T \ln T - 9.84 \times 10^{-8} T^2 \quad (6.19.33)$$

For example, at 300 °C and 1.013 bar, the standard voltage is −1.01 V instead of −1.23 V at 25 °C. [If we use Eq. (6.19.30), we still obtain a very similar value at 300 °C of −1.00 V, but for higher temperatures the deviation becomes stronger and Eq. (6.19.33) should be used.]

The absolute value of the thermoneutral voltage [Eq. (6.19.17)] is higher (−1.48 V, 1.013 bar, 25 °C) than the electrolysis voltage (−1.23 V). The difference (0.25 V) reflects the energy needed to keep the temperature constant, if provided by electrical energy and not by thermal energy.

For a given cell voltage U , the (minimum) energy consumption q_{H_2} of hydrogen production by water electrolysis in W per kg hydrogen is given by Eq. (6.19.7):

$$q_{\text{H}_2} = \frac{2FU}{M_{\text{H}_2}} \quad (6.19.34)$$

To estimate the overall energy requirements, we assume that the practical cell voltage is 0.8 V higher than the ideal electrolysing energy requirement (E). This difference summarizes the hydrogen and oxygen overvoltages at current densities in the range 2–5 kA m^{−2} as well as the ohmic losses of the electrolyte (usually a 30 wt % KOH solution) and of the electrodes. For 25 °C, we then obtain values of 2.03 V for 1 bar and 2.12 V at 100 bar.

If hydrogen should be produced at higher pressures, we have two options: (i) high-pressure electrolysis and pumping of water or (ii) atmospheric electrolysis and H₂ is compressed to the desired pressure by a compressor [see Onda *et al.* (2004) and Laoun (2007)].

The minimum energy requirement (per kg hydrogen) to pump the respective amount of water from pressure p_1 (1.013 bar) to pressure p_2 can be deduced from Eq. (3.4.33):

$$q_{\text{pump}} = \frac{\dot{m}_{\text{H}_2\text{O}} P_{\text{pump}}}{\dot{m}_{\text{H}_2} \dot{m}_{\text{H}_2\text{O}}} = 9 \frac{(p_2 - p_1)}{\rho_{\text{H}_2\text{O}}} \quad (6.19.35)$$

For H₂ compression, the minimum energy requirement per kg hydrogen (ideal isothermal compression) at 25 °C can be deduced from Eq. (3.4.36):

$$q_{\text{comp, isothermal}} = \frac{P_{\text{comp, isothermal}}}{\dot{m}_{\text{H}_2}} = \frac{\dot{V}_{\text{g},1}}{\dot{m}_{\text{H}_2}} p_1 \ln \left(\frac{p_2}{p_1} \right) = \frac{RT}{M_{\text{H}_2}} \ln \left(\frac{p_2}{p_1} \right) \quad (6.19.36)$$

Table 6.19.8 gives the overall energy requirements calculated by Eqs. (6.19.34)–(6.19.36) for different pressures, assuming efficiencies of compressor and pump of 50%.

Table 6.19.8 indicates that the energy required for high-pressure electrolysis including water pumping is lower than the energy required for atmospheric electrolysis and H₂ compression, since the compression energy for water is much less than that for hydrogen as a gas.

With the current status of water alkaline electrolyzers, about 55 kWh of electrical energy is needed per kg H₂. The lower heating value of H₂ is 33 kWh kg^{−1}. Hence,

Table 6.19.8 Energy for H_2O electrolysis (25°C) for different process options [estimated by Eqs. (6.19.33)–(6.19.35) assuming isothermal compression of water and H_2 with efficiencies of 50% and practical voltages of 2.03 (1 bar), 2.12 (100 bar), and 2.15 V (500 bar)].

Electrolysis pressure (bar)	Final p_{H_2} (bar)	Electrical energy (kWh per kg H_2)			Process option
		Electrolysis	H_2O pump/ H_2 compressor	Overall	
1.013	1.013	54.38	—	54.38	Production of atmospheric pressure H_2
1.013	100	54.38	3.16	57.54	Atmospheric electrolysis and H_2 compression
100	100	56.75	0.05	56.80	High-pressure electrolysis and water pump
1.013	500	54.38	4.26	58.64	Atmospheric electrolysis and H_2 compression
500	500	57.58	0.25	57.83	High-pressure electrolysis and water pump

with regard to energy conversion (or storage of electrical energy as hydrogen) the efficiency is only 60% (or 71% if the higher heating value of hydrogen of 39 kWh kg^{-1} is used).

A future option for improved electrolytic hydrogen production from water is the use of solid oxide electrolysis cells, which are essentially solid oxide fuel cells operating in reverse. These systems work at higher temperatures and substantially replace part of the electrical energy required to split water with thermal energy (Holladay *et al.*, 2009; Hamann and Vielstich, 2005). For example, at 800°C (1.013 bar), the standard voltage is -0.69 V instead of -1.23 V at 25°C [Eq. (6.19.30), see Figure 6.19.9]. If the thermal energy is ignored, efficiencies of up to 90% may be achieved (Holladay *et al.*, 2009). In addition, the anode and cathode overpotentials decrease with increasing temperature, which (at 800°C) reduces the combined thermal and electrical energy requirements by about 35% (Holladay, 2009).

Table 6.19.9 compares the efficiency values of H_2 generation processes and other energy and fuel conversion processes. The conversion efficiency of H_2 production via electrolysis is similar to that of processes based on fossil fuels and biomass, but one has to consider that the efficiency of electricity production is not counted. If the efficiency in providing the electricity is included and produced from fossil fuels, the overall efficiency of water electrolysis would be much smaller (about 20%). Consequently, water electrolysis is today mostly only attractive for small or remote H_2 plants, but may in future be important when using electricity produced from renewable energy (hydro, solar, etc.).

Table 6.19.9 Typical characteristic efficiency values (based on lower heating values) of selected energy/fuel conversion processes [own estimations partly based on values given by Schaub and Turek (2011), Schaub (2006), and Holladay *et al.* (2009)].

Technology	Feedstock	Product	Efficiency (%)
Water alkaline electrolysis	Water	Hydrogen	60
Steam reforming	Natural gas	Hydrogen	70
Partial oxidation	Heavy oil	Hydrogen	60
Gasification	Coal or biomass	Hydrogen	50
Thermal power plant	Coal	Electricity	35
	Coal	Electricity with carbon capture and sequestration	25
	Coal or biomass	Electricity + heat	80
Petroleum refining	Natural gas	Electricity (combined cycle)	50
Tar-sand upgrading	Crude oil	Diesel oil	94
Gasification and Fischer-Tropsch synthesis	Tar sand	Diesel oil	60
Reforming/partial oxidation and Fischer-Tropsch-synthesis	Coal or biomass	Diesel oil	40
Internal combustion engine	Natural gas	Diesel oil	60
Electrical motor	Diesel oil	Mechanical energy	30
Fermentation	Electricity	Mechanical energy	90
Thermochemical conversion (gasification and methanation)	Biomass	Methane	70
	Biomass	Methane	60

Table 6.19.10 Energy requirements of different forms of passenger transport for best practice, assuming all seats are in use (MacKay, 2008).

Means of transportation	Energy requirement	
	kWh per 100 passenger-km	Diesel-oil equivalent in liter per 100 passenger-km
Electric train (160 km h ⁻¹)	2	0.2
Bicycle	2	0.2
Walking	4	0.4
Electric high-speed train (200 km h ⁻¹)	4	0.4
Underground train (50 km h ⁻¹)	4	0.4
Electric car Toyota RAV4 EV	5	0.5
Coach (100 km h ⁻¹)	5	0.5
Diesel high-speed train (200 km h ⁻¹)	9	0.9
Diesel-powered VW Polo blue motion	10	1
H ₂ fuel-cell car VW Tiguan	11	1.1
H ₂ car BMW Hydrogen 7	38	3.8
Boeing 747 (900 km h ⁻¹)	42	4.2
Cessna 310 (6 passengers)	60	6
Ocean liner	100	10

Hydrogen is sometimes also considered as an option for transportation. Table 6.19.10 summarizes the energy requirements for different means of transport. The numbers are those of best practice if all seats (four for a car) are used. The overall average requirements are higher: For example, in Japan (1999), the consumption per 100 passenger-km was 68 kWh for cars (seven times more than an efficient diesel-powered car with four seats in use!), 19 kWh for busses, 6 kWh for transport by rail, 51 kWh for air, and 57 kWh for sea (MacKay, 2008).

The values given in Table 6.19.10 for electrical vehicles (train, car) do not consider that 2.5 kWh primary energy is needed to produce 1 kWh electricity in a power plant, whereas diesel oil from crude oil is produced in a refinery with an efficiency of about 94% (Table 6.19.10).

Electrical vehicles may have a better performance than conventional fossil fuel powered cars, but the range is limited to less than 200 km. H₂ cars have no advantage compared to diesel oil or gasoline-powered cars, even if we consider that both examples given in Table 6.19.10 are prototypes and luxury cars. Further disadvantages are the problematic high-pressure storage of H₂ and the fact that the H₂ is – at least today – mainly produced from fossil fuels, which lowers the efficiency further. H₂ fuel cell cars perform better, but the energy requirement (not counting H₂ production) is today “only” similar to modern diesel-powered cars. The best option is public transport by train or coach, with roughly half of the energy requirements compared to modern diesel cars (if full), and the worst option is transport by sea or air.

6.19.4

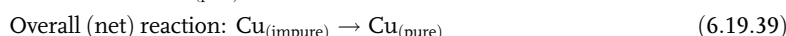
Electrometallurgy (Purification of Metals by Electrorefining)

6.19.4.1 Electrolytic Refining in Aqueous Solution

Electrorefining in aqueous solution is used for purifying metals and for electroplating, for example, for corrosion protection by zinc coating of steel. Electrorefining of metals is only possible for those metals with a positive standard potential (Ag, Au, Cu, Table 6.19.1) or if H₂ formation at the cathode (which competes with deposition of the metal) is hindered by a high overpotential (Zn, Ni). For electrochemically very non-noble metals such as aluminum with a very negative standard potential, fused salt electrolysis is needed (Section 6.19.4.2).

As an example, we inspect electrolytic copper refining, which utilizes the electrochemical dissolution of an impure copper anode in an electrolytic cell containing a

copper sulfate–sulfuric acid solution. Copper ions are transported to the cathode where they are deposited with suitable purity. The basic electrochemical reactions involved are:



As dissolution occurs, impurities are released either as solid or as aqueous species. More electrochemically noble impurities (gold, silver) will remain as solids at or near the anode (Figure 6.19.10). Elements less noble than copper (e.g., Ni, Figure 6.19.10) will dissolve along with copper into the electrolyte. At the cathode, copper, which is the most noble element in solution, will deposit preferentially.

In 2008, about 18 mio. tonnes of copper were produced by electrochemical refining (BGS, 2010). Typical cathodic current densities in commercial Cu-electrorefining are in the range $100\text{--}200 \text{ A m}^{-2}$. Theoretically, the net voltage is 0 V. In practice, overvoltages at the anode and cathode and resistance in the electrolyte and electrical system result in the need for a practical voltage of 0.25 V and a current efficiency of 95% (see Figure 6.19.10 for overpotentials). According to Eq. (6.19.7), this corresponds to a specific electrolytic energy consumption of $0.22 \text{ MWh kg}^{-1} \text{ Cu}$, which is increased to about 0.3 MWh kg^{-1} by additional power components. This value is rather low, for example, compared to electrolytic aluminum production with an energy consumption of $14 \text{ MWh t}^{-1} \text{ Al}$ (Section 6.19.4.2).

6.19.4.2 Fused Salt Electrolysis (Production of Aluminum)

Global aluminum production in 2009 was 45 Mio. tonnes. The majority (37 Mt) was primary aluminum produced by processing bauxite to alumina and smelting and reducing the alumina to aluminum; 8 Mt was secondary aluminum recovered from scrap generated in aluminum production and old or post-consumer scrap (GDA, 2011). Table 6.19.11 shows the global production of aluminum and also of some other selected metals in 2008.

Aluminum oxide, also known as alumina, is the main component of bauxite, the principal ore of aluminum. The bauxite ore is made up of impure Al_2O_3 , Fe_2O_3 , and SiO_2 . Typically, the content of Al_2O_3 in bauxite is about 40 wt%. In the Bayer process, Al_2O_3 is dissolved in sodium hydroxide, then precipitates as $\text{Al}(\text{OH})_3$.

Table 6.19.11 Global production of aluminum and other metals in 2008 (BGS, 2010).

Metal/ore	World production (2008) (tonnes)	Price (end 2011) (\$US kg ⁻¹)
Aluminum ^{a)} (primary production)	39 million	2
Iron (pig iron)	992 (1329 steel) million	0.5 (steel)
Copper (smelter/refined)	31 (18 refined) million	32
Zinc	12 million	2
Lead (mine)	4 million	2
Nickel (smelter/refined)	1.4 million	19
Tin	278 000	19
Molybdenum	223 000	29
Vanadium	67 000	12
Cobalt (metal)	56 000	32
Silver (mine)	21 565	940
Gold (mine)	2300	52 000
Mercury	1100	17 000
Platinum group metals (mainly Pt and Pd)	452 (only 25 of Rh)	46 000 Pt, 20 000 Pd, 220 000 Rh
Rhenium	50	5000

a) Produced from 212 mio. tonnes of bauxite and 82 million tonnes of alumina (Al_2O_3), respectively.

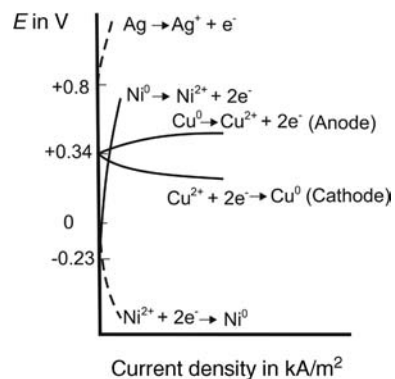


Figure 6.19.10 Aqueous electrorefining of copper. Also shown are the potential–current relationships for a more electrochemically noble impurity (Ag) and a less noble impurity (Ni). Adapted from Hamann and Vielstich (2005).

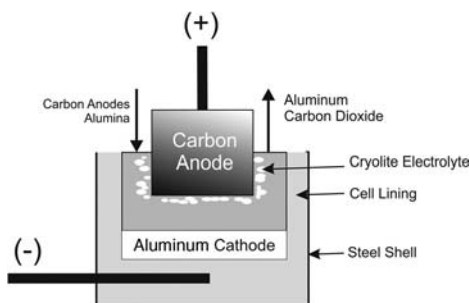


Figure 6.19.11 Schematic representation of a cell for fused salt electrolysis of aluminum.

Schematic representation of a cell for fused salt electrolysis of aluminum.

By calcination, $\text{Al}(\text{OH})_3$ decomposes to Al_2O_3 :



Alumina is then further reduced via an electrolysis process (Hall–Héroult process) to liquid Al:



About 14 MWh electrical energy is needed per tonne of Al. The annual global electrical energy consumption for aluminum production is 500×10^6 MWh ($= 14 \text{ MWh t}^{-1} \times 37 \text{ Mt Al a}^{-1}$). To produce the required electrical energy, sixty 1000 MW power plants would be needed. If we assume an efficiency of 40% for a power plant (1 kWh electrical energy = 2.5 kWh primary energy = 9 MJ), the total primary energy needed is 4.8×10^9 GJ, which equals 115 million tonnes of oil equivalent (41.9 GJ toe^{-1}). This huge amount is equivalent to about 30% of the primary energy consumption of Germany and to 1% of the global primary energy.

Figure 6.19.11 shows schematically the cell for the reduction of Al^{3+} by electrolysis of a molten aluminum salt. Al_2O_3 (alumina) is dissolved in molten cryolite, Na_3AlF_6 (sodium hexafluoroaluminate). Alumina has a melting point of 2050°C , but cryolite with a small amount of dissolved alumina has a melting point of 1000°C . The molten mixture of cryolite and alumina is electrolyzed by passing a direct electric current through it, which causes liquid aluminum to be deposited at the cathode. Oxygen from the alumina reacts with carbon (anode) to give CO_2 . The cell voltage is about 4 V compared to the theoretical value of 1.7 V (Table 6.19.1). The current density is 7 kA m^{-2} for the graphite anode and 3 kA m^{-2} for the graphite cathode.

Section 6.19 (take-home messages)

- **Electrochemical reactions** are characterized by at least one electron charge-transfer step taking place at the electrode or electrolyte interface.
- The electrochemical potential arising at the electrode/solution interface can be calculated by the **Nernst equation**.
- An **electrochemical cell** consists of two electrodes. If the cell produces electricity, it is called a galvanic cell, and if the reaction is driven by an external source of current it is called an electrolysis cell.
- To **normalize standard electrode potentials**, differences of potentials are used. The one chosen to have zero potential is the standard hydrogen electrode.
- **Chlorine**, which is produced by chlor-alkali electrolysis, is a fundamental building block of the chemical industry and is used in over 50% of all industrial chemical processes.
- Three **processes of chlor-alkali electrolysis** are currently used, namely, the mercury process, diaphragm process, and membrane process. With regard to energy consumption and environmental concerns, the membrane process is the most efficient.
- One option of a clean energy choice is **hydrogen** if it is produced by water electrolysis and electrical energy based on renewable sources (wind, solar, etc.), although today production based on fossil fuels is still dominant compared to water electrolysis.
- **Electrorefining of metals in aqueous solution** for purifying metals and for electroplating is only possible for those metals with a positive standard potential (Ag , Au , Cu) or if H_2 formation at the cathode is hindered by a high overpotential (Zn , Ni).
- For electrochemically very non-noble metals such as aluminum, with a very negative standard potential, **fused salt electrolysis** is needed.

6.20

Polyethene Production



View of the PE manufacturing plant of LyondellBasell in Wesseling, Germany. The plant produces high-performance, multi-modal HDPE grades applying the low-pressure slurry process technology "Hostalen ACP." Reproduced with permission of LyondellBasell, Wesseling.

6.20.1

Polyethene Classification and Industrial Use

In terms of production volume, polyethene (PE) is the most important polymer. The production capacity for PE was 94 mio. tons in 2008 and is expected to rise to 128 mio. tons in 2015 (Plastemart, 2010). Despite the simple structure of the ethene monomer, many different polyethene production processes are in operation, leading to different classes of products with specific physicochemical properties and application fields.

The main three polyethene classes are low-density polyethene (LDPE), high-density polyethene (HDPE), and linear low-density polyethene (LLDPE) (Scheme 6.20.1). Table 6.20.1 gives an overview of these classes and indicates the differences in density, production processes, and chemical structure.

Scheme 6.20.1 Depending on the process conditions the polymerization of ethylene leads to three different classes of materials that differ in the polymer density and find different applications.

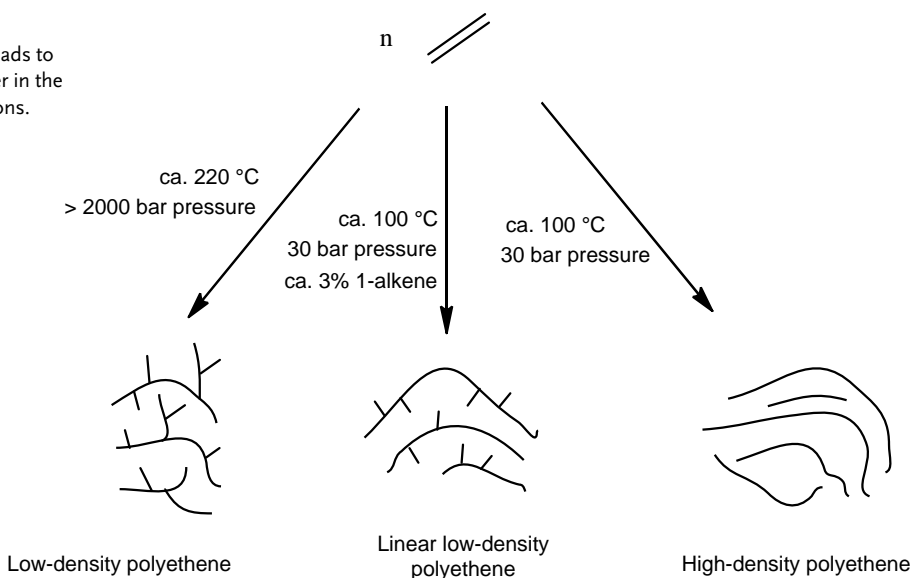
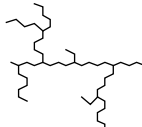
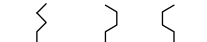
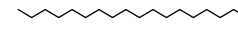


Table 6.20.1 Different classes of polyethene in overview – compiled from Whiteley (2012); data are representative for typical technical qualities.

PE type	Low-density polyethene (LDPE)	Linear low-density polyethene (LLDPE)	High density polyethene (HDPE)
Process of PE formation	Radical reaction at very high pressures (>2000 bar)	Metal catalyzed, medium pressures (30 bar), ca 3 mol.% co-monomer	Metal catalyzed, medium pressures (30 bar)
Simplified representation of backbone structure			
Density (kg m^{-3})	924	922	960
Crystallinity (%)	40	40	67
Temperature of fusion ($^{\circ}\text{C}$)	110	122	131
Short branches ^{a)}	23	26	1.2
M_w ^{b)}	200 000	158 000	136 000

a) Number of methyl groups per 1000 C-atoms.

b) M_w = Weight-average molar mass.

In LDPE synthesis, the radical high-pressure reaction leads to a PE structure containing random long branches with short-chain branches on long-chain branches. In contrast to LDPE, the branches in LLDPE are all the same length as they are produced by incorporation of a defined 1-alkene co-monomer (typically 1-butene, 1-hexene, or 1-octene) in the polymer chain. The branches in LLDPE are found in different concentrations on different chains, with shorter chains typically displaying a higher degree of branching. Typical HDPE is essentially free of any branching.

The type and degree of branching in the PE material has a direct influence on the density, crystallinity, and melting point of the resulting polymer material. As PE tends to crystallize in lamellar crystals consisting of folded PE chains, the side branches are excluded from the crystalline regions of the PE for thermodynamic reasons. Their geometry does not fit the crystalline lamellae formed by the main chains. Consequently, branching results in the formation of thinner lamellae with the branches located mainly on the chain folds in the lamellae surface. For PE structure formation the rate of cooling is also very important. If the kinetics of structure formation are slower than the cooling rate then the energetically most favorable placements are not reached and branches become incorporated into the crystalline regions as crystal defects. Under slow cooling conditions, the crystallization of PE is often nucleated at a small number of sites. At some point the growing spheres meet, resulting in a spherulitic structure of the material. The typical milkiness of PE is a result of light scattering by these spherulites and other PE aggregates. Transparent material is obtained by carefully adjusting crystallization conditions and PE structure.

PE is a viscoelastic polymer in the solid state that does not dissolve in any solvent at temperatures below its melting point. However, some solvents can swell the material. Above the melting point, PE is soluble in many aromatic and chlorinated organic solvents. The branched PE classes, LDPE and LLDPE, are fairly flexible, translucent, whitish solids. The deployment of these materials as films is most relevant. PE films include food and non-food packaging, bags, and liners. Injection and sheathing for wires and cables are other important applications. LLDPE is less suitable than LDPE for applications requiring high lubricity, flexibility, and clarity. HDPE, in contrast, is a more rigid white solid that is

mainly applied in blow molding, injection molding, and pipe manufacturing. Typical products from HDPE are milk bottles, containers, drums, fuel tanks for automobiles, toys, and extruded pipes.

Historically, LDPE was invented first. In 1935, a research team at ICI found by accident that a mixture of ethylene and benzaldehyde formed a white solid when subjected to 1900 bar pressure at 170 °C. This discovery led to the first PE production plant in 1939.

Technologies to produce HDPE were found in the 1950s by different research groups. Among these developments, the achievements of Phillips Petroleum (Cr-catalyzed ethylene oligomerization) and Karl Ziegler at the Max-Planck-Institut für Kohlenforschung, Germany (Ti/Al-alkyl catalyzed ethylene oligomerization) were later extensively commercialized.

Ethene polymerization by coordination chemistry also allowed the defined incorporation of 1-alkenes into the polymer chain, leading to production of LLDPE. The term "LLDPE" was coined together with the first large-volume production process by Union Carbide in 1978.

6.20.2

General Characteristics of PE Production Processes

Some general aspects of technical PE production should be discussed before entering the detailed discussion of the individual processes.

6.20.2.1 Exothermicity of the Reaction and Thermal Stability of Ethene

The heat of polymerization of ethylene is 93.6 kJ mol⁻¹ (3.34 kJ g⁻¹). As the specific heat capacity of ethylene is 2.08 J °C⁻¹ g⁻¹, the temperature rise in the gas phase is 16 °C per 1% conversion ($\Delta T_{\text{adiabatic}} = 1600 \text{ }^{\circ}\text{C}$). If the temperature in the reactor exceeds 300 °C, ethene decomposition to carbon, hydrogen, and methane starts. This decomposition is even more exothermic ($\Delta H_{298}^0 = -120 \text{ kJ mol}^{-1}$) and is very difficult to control.

For all these reasons heat removal and reliable temperature control are key factors in all technical ethylene polymerization processes to ensure an economical and safe process. The different processes may choose different ways to limit or remove the reaction heat (e.g., by limited conversion per reactor pass, cooling of unreacted monomer, large surface area for heat exchange); in all concepts heat management is a key aspect of the reactor design.

Apart from limiting the reaction heat that is liberated care must be taken to maintain the heat transfer from the reactor to the cooling agent during operation. This is not always trivial as, for example, high-pressure ethylene polymerization in tube reactors can suffer from severe reactor fouling problems. PE that deposits onto the heat exchange surface decreases the heat transfer rate, causing a rise in the local reactor temperature. Even small temperature peaks can trigger ethylene decomposition reactions.

6.20.2.2 Purity of Ethene

Ethylene polymerization is very demanding with respect to the required ethylene quality. The detrimental effects of the various impurities that may be found in technical ethene qualities can be grouped into four main categories:

- 1) Inert impurities (CH₄, C₂H₆, N₂): These substances do not react and do not interact with the catalyst. However, in the efficient recycling systems of a technical PE plant these inert would accumulate and dilute the process stream. Such dilution would lead to reduced reaction rates and to a less effective usage of the reactor volume.

- 2) Impurities that interact with radicals (O_2 , H_2O): these substances can cause inhibition of low-temperature initiators or can cause uncontrolled initiation reactions at higher temperatures.
- 3) Impurities that interact with transition metal catalysts (S-compounds, CS_2 , alkenes, dienes, CO , CO_2 , H_2 – only poison for the Cr-based Phillips catalyst): These substances coordinate strongly enough to the transition metal complex to block coordination sites required for ethylene polymerization. This coordination may be irreversible or reversible. In both cases the number of available catalytic sites is reduced, slowing down PE formation.
- 4) Impurities that undergo exothermic decomposition reactions (ethyne): Some impurities undergo exothermic decomposition reactions that can trigger thermal runaway reactions. This issue is particularly critical in high-pressure polyethylene reactors for the synthesis of LDPE that operate close to $300^\circ C$ and, thus, close to the thermal stability of ethene.

In Europe and North America most polyethylene plants take their feedstock from a common ethylene pipeline system that provides ethylene of a quality that is sufficient for all different polymerization processes. Table 6.20.2 gives the specification for such polymerization-grade ethene.

6.20.3

Reaction Meachanism and Process Equipment for the Production of LDPE

LDPE production takes place in a single-phase ethylene/PE mixture that allows the reaction to proceed as a free-radical-initiated solution polymerization. This particular reaction mode leads inevitably to a high-pressure process. Pressures of 2000 bar and temperatures above $160^\circ C$ are required to dissolve the already formed PE in the unreacted ethylene.

Initiation of the free-radical process of LDPE formation has been historically achieved by the addition of oxygen to the reaction mixture. Modern autoclave processes prefer the use of alkane-soluble organic peroxides as initiators, which offer the advantage of a very controlled formation of alkyl or alkoxy radicals.

Under the applied temperature and pressure conditions the formed radicals lead to very fast ethylene polymerization (typically 20% ethylene conversion in 40 s). The concentration of ethene and the reaction pressure both affect the rate of ethene polymerization. This pressure effect is generally treated in terms of a volume of activation, similar to the energy of activation. On a molecular level one can understand this pronounced pressure effect on the reaction rate in the sense that the pressure promotes the configuration change necessary for the reactants to reach the transition state. The contribution of pressure to the reaction rate of PE

Table 6.20.2 Specification of polymerization grade ethene – adapted from Whiteley, 2012.

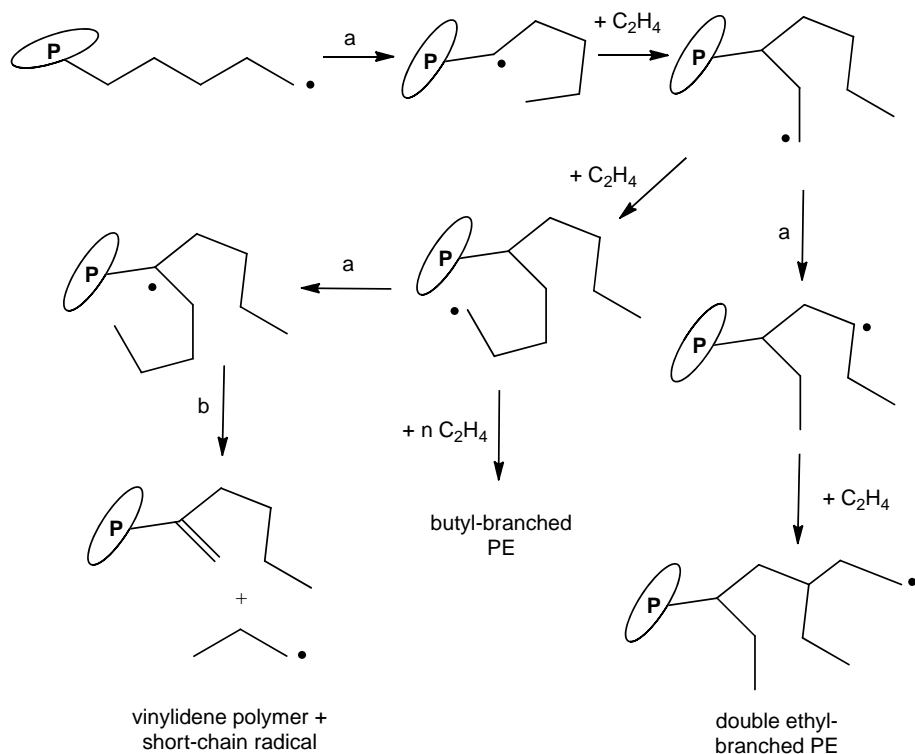
Substance/impurity	Specified content
Ethene	>99.9 vol. %
Inerts (CH_4 , C_2H_6 , N_2)	<1000 vol. ppm
Impurities interacting with free radicals	O_2 <5 vol. ppm H_2O <2.5 vol. ppm
Impurities acting as catalyst poison	Alkenes + dienes <10 vol. ppm CO <1 vol. ppm S-compounds <1 vol. ppm CS_2 <1 vol. ppm H_2 <1 vol. ppm Ethyne <2 vol. ppm
Impurities causing exothermic decomposition reactions	

formation has been reported to be a factor of 12 on going from 0 to 2000 bar reaction pressure (Lim and Luft, 1983). The temperature in LDPE varies in the reaction system between 140 and 300 °C, with 300 °C being the upper limit if exothermic ethene decomposition to carbon and methane is to be avoided. The activation energy of the radical ethylene polymerization is 32 kJ mol⁻¹.

Alkyl radicals, which represent the active species in LDPE formation, are very reactive not only in incorporating ethylene into the growing PE chain but also in abstracting hydrogen from other saturated carbon atoms to transform themselves into saturated hydrocarbons.

If the carbon atom from which the hydrogen radical is abstracted belongs to a different PE molecule, a new radical at this other molecule forms. This intermolecular process is called "chain transfer". Intermolecular chain transfer leads to a broadening of the molecular mass distribution. The longer the chains, the more likely are branching and branch formation on branches.

If the carbon atom belongs to the same PE chain, the intramolecular process is called "back-biting". Scheme 6.20.2 shows typical intramolecular radical reactions. It can be demonstrated by models that the most probable "back-biting" occurs at the carbon atom situated four carbon atoms down the chain (a in Scheme 6.20.2). If after addition of one ethene another back-biting of the same type occurs, pairs of ethyl branches or 2-ethylhexyl branches are formed that are very typical features of the LDPE structure. Vinylidene end-groups form by back-biting to a branch point of the chain. The so-formed tertiary radical is unstable and decomposes into a short radical and a PE chain with the vinylidene end-group (b in Scheme 6.20.2). The probability of back-biting and vinylidene formation increases with higher reaction temperature and with decreasing reaction pressure as the activation energy for



Scheme 6.20.2 Back-biting mechanism and vinylidene formation in the free-radical ethene polymerization process leading to the characteristic structural features of LDPE.

chain transfer is higher than for polymerization and the activation volume is smaller.

LDPE is produced either in a tubular reactor (PFTR, LDPE tubular process) or in a high-pressure, continuous stirred tank reactor (CSTR, LDPE autoclave process). In both process designs the very high pressures require very special, thick-walled equipment and fatigue is a major design aspect for the applied pumps and compressors.

Figure 6.20.1 shows a schematic representation of a *LDPE tubular process*. The main elements of the process include the two ethylene compressors, the reactor line, and the two ethylene separators. Unreacted ethylene from the flash separators (typical ethylene conversions range from 15% to 35% depending on the number of initiator injection ports) is mixed with fresh ethylene and recompressed. The reaction pressure in a typical tubular reactor for LDPE production is 2000–3500 bar and the reactor temperatures are between 100 and 300 °C. The applied reactor typically consists of a spiral-wrapped metallic pipe with 500–1500 m lengths, 70–80 mm in diameter. The tubular reactor is divided into preheating, reaction, and cooling zones. The heat of reaction is partly removed (ca. 50% of the formed heat) through the reactor wall by cooling with a heat transfer fluid, typically water. Along the tubular reactor there are a number of injection points to introduce monomer, initiator, or chain transfer agent for better control of polymer quality and polymer production rate.

In the *LDPE autoclave process*, the general process design (e.g., ethylene compression, high and low pressure product separation and ethylene recycling) is very similar to the LDPE tubular process. Instead of the jacketed tube reactor, however, the autoclave process employs a high-pressure stirred tank reactor. The reactor is designed to allow a residence time of 30–60 s (typical reactor volumes are around 1 m³ for large plants). The autoclave is usually operated in an adiabatic manner; the reaction heat is removed by the fresh ethylene

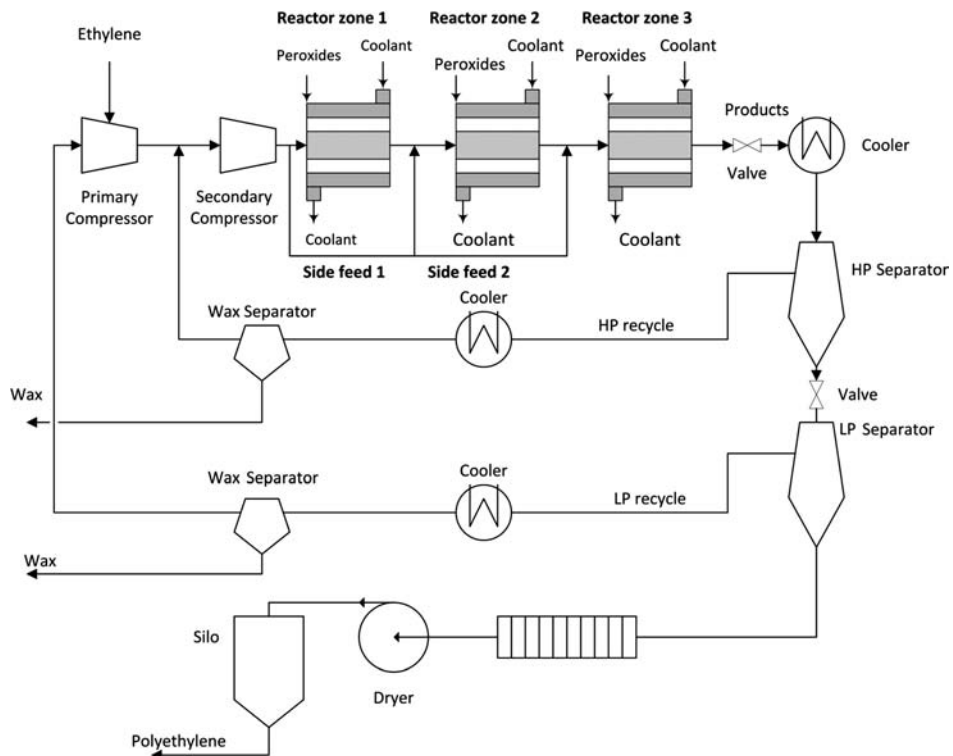


Figure 6.20.1 Schematic view of a LDPE tubular reactor process. Three reaction zones are shown to represent the reaction unit. Adapted from Kiparissides (2010).

entering the reactor. Typical reaction conditions in the LDPE autoclave process are 1500–2000 bar and 180–290 °C.

6.20.4

Catalysts for the Production of HDPE and LLDPE

Three different kinds of catalysts are relevant for the technical production of HDPE and LLDPE:

- 1) so-called “Ziegler catalyst”, Ti-complexes activated by Al-alkyl compounds,
- 2) so-called “Phillips catalysts”, Cr-oxide supported on silica,
- 3) single-site metallocene catalysts.

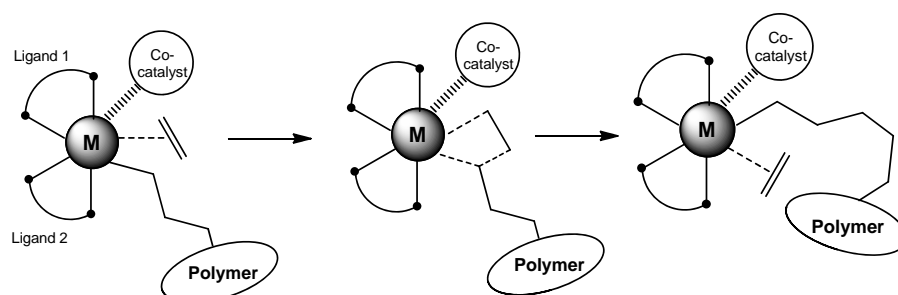
All three types have in common that a transition metal center carries – besides some stabilizing and activating ligands – one σ -bonded alkyl group (or polymer chain) and one free coordination site. Ethene coordinates first to the metal by forming a π -bond. This arrangement facilitates insertion of the ethene molecule into the existing metal–alkyl σ -bond, producing a longer alkyl (or polymer) chain and a new free coordination site (Scheme 6.20.3).

The chain-growth mechanism leads in every ethene insertion step to the addition of two CH_2 units into the linear polymer chain so that the resulting polymer is essentially free of branching (HDPE). However, chain branching can be introduced by the copolymerization of ethene and 1-alkenes. Here, incorporation of the 1-alkene leads to branches with defined side-chain lengths, reducing the density of the resulting polymer (LDPE).

Most commercial catalysts for ethylene polymerization are heterogeneous solids. The shape and size of the particles carrying the active catalytic species is important for the process as the shape of the catalyst particle determines largely the shape of the formed polymer particle, that is, spherical catalyst particles produce spherical polymer beads. Note that the polymerization rate does not decrease with growing size of the polymer bead. The active catalyst fragments (ranging from 4 nm in the case of TiCl_3 to 100 nm for oxide-supported catalyst) is embedded in the growing end of the polymer chain, keeping the monomer diffusion path short despite the growing amount of polymer product.

6.20.4.1 Ziegler Catalyst Systems

The class of catalysts that is currently called “Ziegler” or “Ziegler-Natta catalysts” was invented by *Karl Ziegler* (Section 6.16) in 1953. Using $\text{TiCl}_4/\text{Al}(\text{C}_2\text{H}_5)_3$ as organometallic catalyst system, Ziegler was able to polymerize ethylene for the first time at low temperatures and pressures (e.g., 10 bar, 50–150 °C). Shortly after this, in 1954, Natta applied a further developed version of the Ziegler catalyst to produce crystalline, isotactic polypropene.



Scheme 6.20.3 Schematic representation of ethylene polymerization by coordination catalysis.
Adapted from Matsugi (2008).

Since the development of the Ziegler catalyst based on crystalline TiCl_4 , many more catalyst systems have been found that can be activated in a similar manner by alkylaluminium compounds to promote the coordination polymerization of ethene. Therefore, the definition of a Ziegler catalyst refers to a system that combines:

- a transition metal compound from group 4–8 of the d-block elements, such as, for example, TiCl_3 , TiCl_4 , CoCl_2 , or vanadyl acetylacetone;
- an alkyl, hydride, or aryl compound of a metal of groups 1, 2, and 13 such as for example, trialkylaluminium (e.g., AlEt_3), aluminium-chloroalkyl compounds (e.g., Et_2AlCl , EtAlCl_2), magnesium dialkyl (MgEt_2), or lithium alkyl (BuLi) compounds.

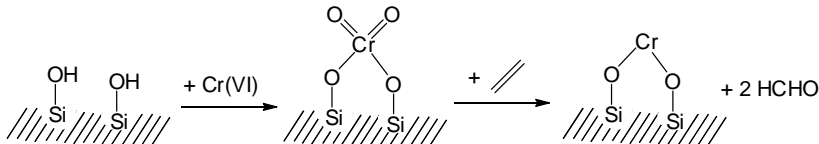
Ziegler catalysts can be applied in homogeneous or heterogeneous form, with the latter dominating industrial use in PE synthesis by far. A typical heterogeneous Ziegler catalyst is obtained by taking an amorphous silica particle, loading this particle with titanium chloride and MgCl_2 followed by activation of the loaded particle with an organoaluminium compound. The function of the added MgCl_2 is to improve the dispersion of the Ti-compound on the silica particle and by this an increase in the percentage of supported titanium atoms that form active polymerization sites. Characteristically, heterogeneous Ziegler systems obtained in this or a similar way have at least two – but probably more – distinct types of active sites. The presence of these different sites becomes relevant in the copolymerization of ethene and 1-alkene to produce LLDPE. Here, the obtained distribution of molecular weight and chemical composition result from the interplay of one type of active site that produces polymer with a low content of alkyl branching and another type more active in 1-alkene incorporation.

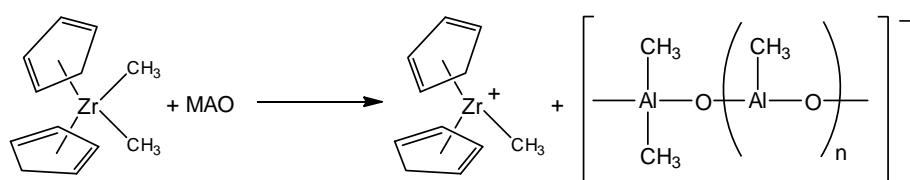
6.20.4.2 Phillips Catalyst Systems

Around the same time as Ziegler made his groundbreaking discoveries in the $\text{TiCl}_4/\text{Al}(\text{C}_2\text{H}_5)_3$ system, Phillips discovered that chromate compounds impregnated onto silica can also result in active catalysts for low-pressure coordination polymerization. Typically, the resulting catalyst contains 1% of the chromate compound. After impregnation of the silica with the chromate solution, the material is dried and calcined under air at between 500 and 1000 °C. During calcination the surface silanol groups react with the chromate groups to form a dispersed monolayer of chromate and dichromate esters. It is assumed that in the presence of ethene this chromate species is reduced to coordinatively unsaturated Cr(II) or Cr(III) species that are the active species in the polymerization reaction (Scheme 6.20.4). Alternatively, reduction of the supported Cr(VI) precursor can take place using CO as reducing agent. In addition, preparation routes for the active Phillips catalyst starting from low-valent Cr-precursors, such as chromocene, are known.

The Phillips catalyst promotes ethylene polymerization only after an induction period. Obviously, the first step in the activation of a freshly prepared Phillips catalyst is ethylene coordination to chromium. After activation, Cr-H is assumed to act as active catalyst species. However, the presence and relevance of Cr-metallacycle species in the active polymerization systems cannot be ruled out. Productivities of the Phillips catalyst are in the range of 5 kg PE per g of catalyst, resulting in a Cr-content of about 2 ppm in the polymer.

Scheme 6.20.4 Formation of the active Phillips catalyst on a silica surface via reduction of the chromate ester with ethene. Adapted from Hagen (2006).





Scheme 6.20.5 Formation of the single site Kaminsky-catalyst from ZrCp_2Me_2 and a large excess of MAO. Adapted from Whiteley (2012).

6.20.4.3 Single-Site Metallocene Catalyst Systems

The development of a single-site catalyst was triggered by the demand for LLDPE and LDPE qualities with a narrow distribution of mass and chemical composition. In 1983, Kaminsky described the first catalyst that combined ideal molecular mass distribution and high yield. A basic version of the catalyst, bis(cyclopentadienyl) dimethylzirconium, is shown in Scheme 6.20.5. This kind of zirconium complex is activated with up to 10000 equivalents of methylaluminoxane (MAO) to form the active catalyst for PE formation. MAO is made by controlled hydrolysis of trimethylaluminium and the use of MAO in metallocene activation was in fact the core of the discovery made by the Kaminsky group as metallocene complexes activated with traditional trialkylaluminium are much less productive. It is generally accepted today that the active species in metallocene single-site catalysis is a transition metal cation associated with a MAO anion. The role of MAO in catalyst activation is to transfer alkyl groups onto the catalyst (essential if the catalyst precursor is a halide complex) and to provide an extremely weakly coordinating anion once the highly electrophilic cationic catalyst complex is formed.

The active site in single-site metallocene catalysts is tetrahedrally coordinated while the active sites in heterogenous Ziegler type systems are octahedrally coordinated in the TiCl_3 or MgCl_2 lattice. This difference leads to a greater openness of the active site, facilitating incorporation of higher alkenes in the production of LLDPE.

Since this discovery, many research groups in industry and academia have worked on these “metallocene catalysts” to improve their stability, reduce the concentration of co-catalyst, increase productivity, and realize supported versions. Attempts to modify the stereochemical environment at the catalyst include catalyst structures where the two cyclopentadienyl groups are replaced by indenyl, fluorenyl, alkyl-substituted cyclopentadienyl or bridged, versions of these ligands (see Figure 6.20.2 for examples). It is known that “constrained catalyst geometries” created by bridged ligands with bond angles of less than 109° are especially favorable for the incorporation of higher alkenes as more space is available in these systems around the growing chain to accommodate short-chain branches. Many companies have developed supported versions of single-site metallocene catalysts for the use in fluidized bed or slurry phase reactors. These heterogeneous systems are usually

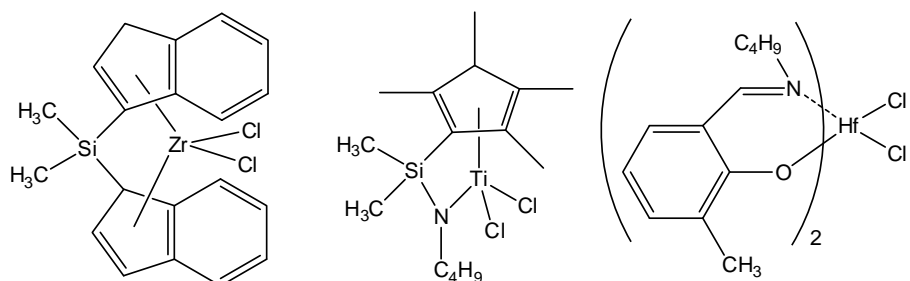


Figure 6.20.2 Examples of different forms of single-site catalysts for ethene polymerization.

obtained by treating a silica particle with MAO followed by impregnation of the metallocene complex.

While the application of multisite, heterogeneous Ziegler catalysts still dominates the mass market of PE production, single-site catalysts have enjoyed increasing market success, in particular for the production of PE with enhanced performance qualities (e.g., for the production of amorphous ethene/1-butene copolymers). Technical advantages of the single-site catalysts include the ability to produce PE with controlled molecular weight, specific tacticity (relevant for propene polymerization), improved molecular weight distribution, and better co-monomer content and distribution.

Research efforts focus on the development of single-site catalysts with ever-higher productivity or with the ability to produce very special PE qualities (e.g., hyperbranched PE). A very broad number of highly potent single-site catalyst structures have been described, including complexes of both early and late transition metals. In many of these more recent structures the cyclopentadienyl ligand motif has been replaced by groups with other steric and electronic properties, such as pyrrolide-imine, phenoxy-imine, or phenoxy-ether ligands.

6.20.5

Production Processes for HDPE and LLDPE

For PE production by coordination polymerization, various polymerization processes are used that can be classified roughly into slurry, solution, and gas-phase processes.

The *slurry process* (suspension process) for ethene polymerization was already proposed in the earliest patents of Ziegler as most Ziegler catalysts give their best yields at temperatures where the PE is insoluble in the reaction mixture. Slurry processes use a diluent and the selection of diluent affects both the process and the obtained product. While the use of high-boiling diluent (such as, for example, high-boiling alkane cuts) requires energy intensive stripping with steam to free the final polymer from traces of the diluent, low-boiling diluents (such as, for example, hexane) cause additional safety issues due to their low flash points. The slurry process is extensively applied to manufacture HDPE. It is less favorable for LLDPE synthesis as the formed polymer dissolves to a significant fraction in the diluent.

Two versions of the slurry process are most frequently applied. In the autoclave or Hoechst process (named after the former company Hoechst that introduced this version of the slurry process) the reaction temperature is 80–90 °C. Typical ethene pressures in the polymerization reactor are 5–10 bar, allowing the application of very large reactors (typically 100 m³). The catalyst compound and the aluminum alkyl activator are premixed in the catalyst preparation vessel with the diluent hexane. This mixture is fed to the polymerization reactor. Figure 6.20.3 shows a schematic view of the process with one polymerization reactor, but cascades of two or more polymerization reactors are also frequently found (allowing additional freedom in achieving specific molecular mass distributions of the PE product – see also picture at the beginning of the section, Hostalen ACP technology).

The product leaving the polymerization reactor enters the run-down reactor where all dissolved ethene is consumed to avoid the need for ethene recycling. The product obtained after reaction contains typically 15–45 wt.% PE. While an even higher value would increase the reactor output per volume, at too high PE contents heat removal and stirring becomes difficult. The slurry from the run-down reactor is treated in a centrifuge to remove the main part of the diluent. The latter is directly recycled to the reactor. The remaining diluent is removed in a continuous fluidized bed drier operated with hot nitrogen. Before extrusion into pellets, stabilizers (e.g., to neutralize the remaining catalyst in the PE) and additives (e.g., antioxidants) are added to give the final PE product. The second, technically important version of PE production by suspension polymerization is the so-called “loop

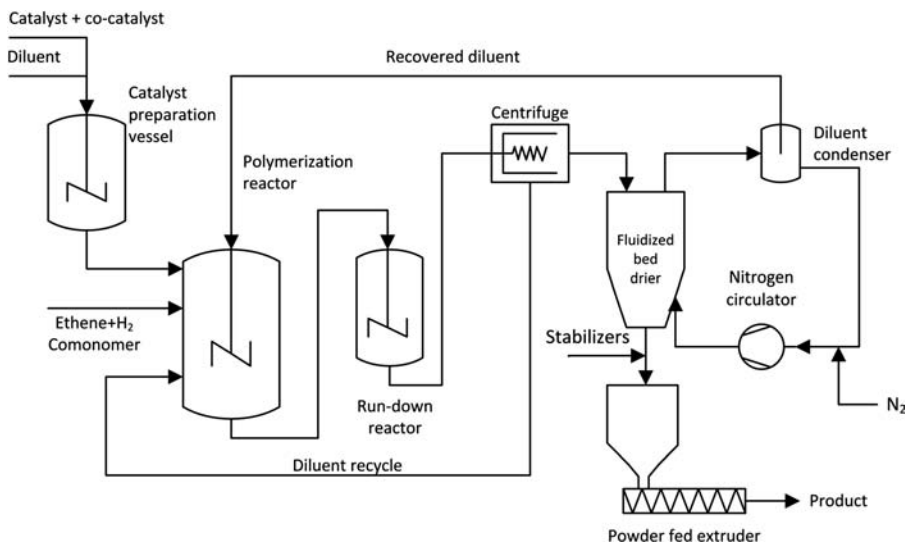
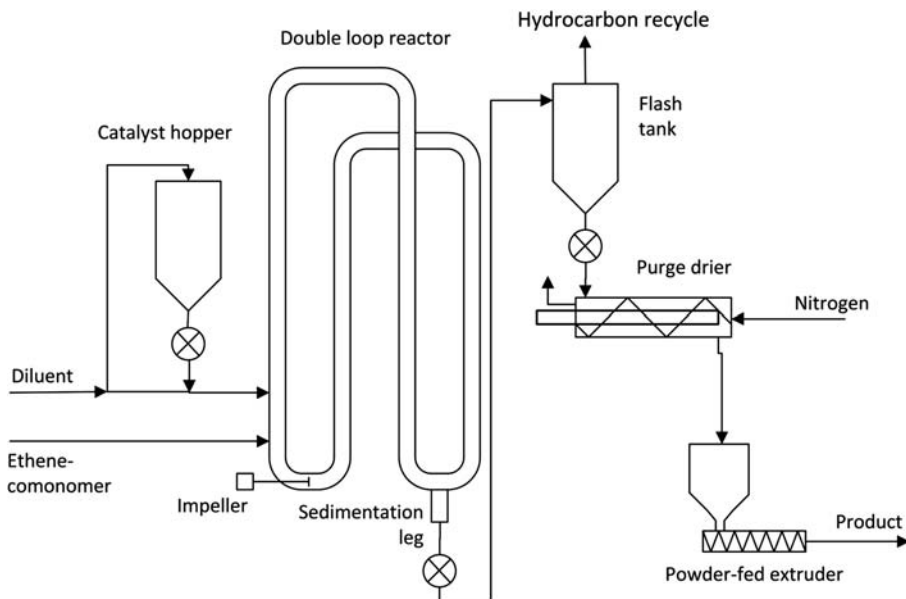


Figure 6.20.3 Schematic view of the autoclave process for the suspension polymerization of ethene.
Adapted from Whiteley (2012).

reactor process" that is realized, for example, in the Phillips Particle Form Process (Figure 6.20.4).

The driving force for developing ethylene polymerization in a loop reactor was problems encountered in the autoclave process with fouling and related problems with heat removal. In the loop process two important features support effective heat removal: the high surface-to-volume ratio offered by the pipe and the turbulent flow regime in the reactor that is caused by an impeller (typical flow velocities in the loop are $5\text{--}10\text{ m s}^{-1}$). The applied reaction conditions (100°C , 30–40 bar) correspond to the parameters in which the Phillips catalyst operates most effectively. The diluent in the Phillips Particle Form process is isobutane, which shows a remarkably low solubility for PE, a fact that facilitates the subsequent flash separation. The loop reactor has a sedimentation leg that allows the slurry to pass in higher concentration to the flash tank than present in the loop reactor (55–65% vs. 30–35% in the loop reactor). The isobutane that evaporates from the flash tank and from the hot

Figure 6.20.4 Schematic view of the loop reactor process (Phillips Particle Form process) for the suspension polymerization of ethene. Adapted from Whiteley (2012).



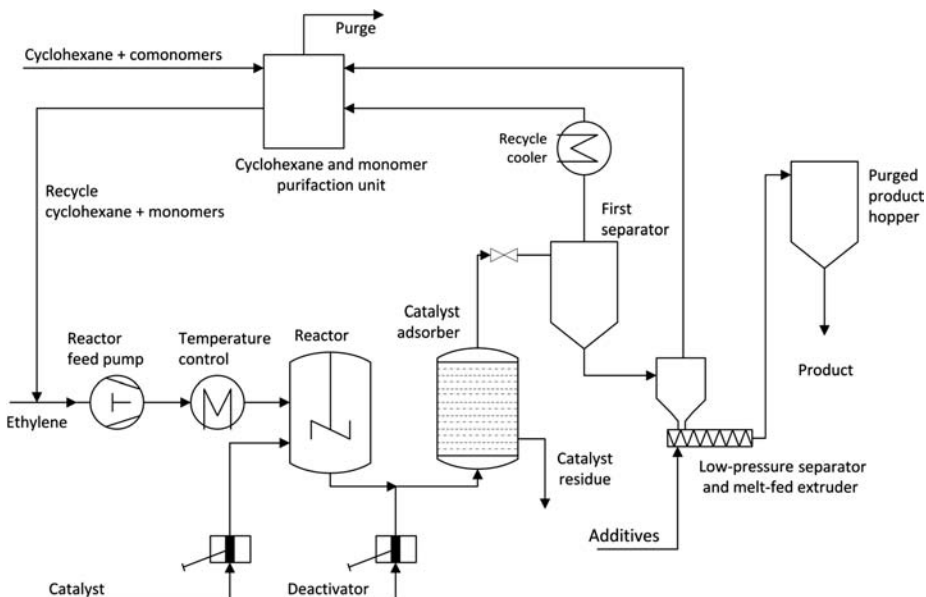


Figure 6.20.5 Schematic view of a process for solution polymerization of ethene. Adapted from Whiteley (2012).

nitrogen drying step is condensed and recycled. Pelletization of the final PE forms the last step in the production scheme as in the case of the autoclave process. The term *solution process* for ethene polymerization implies that PE is fully dissolved in the process mixture during the polymerization process. Note that the technically practiced solution processes still apply solid, heterogeneous catalysts in the form of powder or small particles. To keep the PE product in solution the reaction temperatures in the solution process are significantly higher than in the slurry processes (typically 200–300 °C). The higher reaction temperature results in much faster reaction rates, allowing 95% ethene conversion in around 2 min residence time. The main advantage of the solution process compared to the slurry process is that it can handle a wide range of LLDPE qualities and polymer densities. Depending on the applied catalyst, the solution process also supports the production of PE qualities with a narrow molecular mass distribution. However, the solution process is unable to handle highly viscous reaction mixtures. Therefore, a typical feed for the process contains only 25 mass% ethene. As shown in Figure 6.20.5, the ethene is dissolved in the solvent cyclohexane and pumped to the reactor at around 100 bar pressure. To the reaction mixture leaving the reactor a catalyst deactivator is added and the resulting mixture passes through an alumina adsorption column for catalyst removal. Solvent and residual ethene are separated in two different depressurization steps and are then recycled. The solid PE precipitated in the low-pressure separator is transformed into pellets in a melt-fed extruder.

The *gas-phase PE-process* is carried out in a fluidized bed reactor. The process is economically particularly attractive for LLDPE production if the customers of the PE production plant can directly use the PE granules leaving the reactor. In the process (Figure 6.20.6) ethene, hydrogen, and co-monomer (1-butene or 1-hexene) are fed to the reactor through a distribution plate that provides an even distribution of the gas mixture. Moreover, the plate keeps the PE powder in the reactor in the event that the gaseous feedstock is stopped. The gas entering the reactor fluidizes the heterogeneous catalyst powder (typical diameter of the spherical catalyst particles is 50 µm). The recirculating gas mixture provides very efficient mass and heat transfer. The reactor (about 4 m in diameter, 10 m working out of 30 m total height) is constructed to allow entrained particles to fall back into the bed. The gas leaving the reactor is treated in a cyclone and all PE particles separated in the cyclone are fed back to the reactor. To grow the desired size of PE-catalyst particles of about

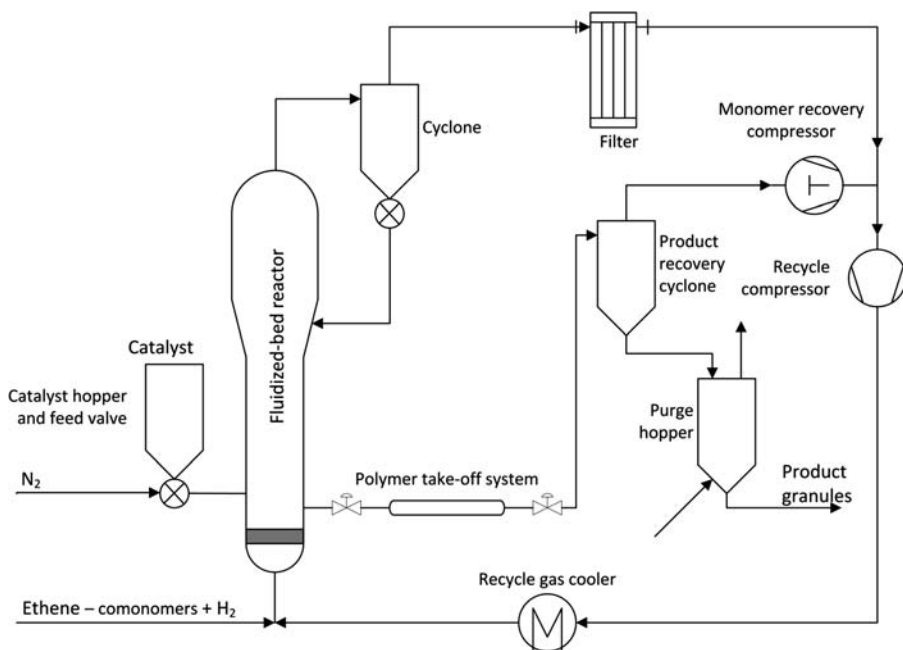


Figure 6.20.6 Schematic view of a process for gas-phase polymerization of ethene in a fluidized bed reactor (Union Carbide Unipol process). Adapted from Whiteley (2012).

500 µm, the residence time of the PE-catalyst particles is between 3 and 5 h at 80–100 °C. The product powder (containing a small amount of the initial catalyst that remains in the product) is taken from the reactor through a sequenced valve system located near the bottom of the reactor. The PE powder contains significant amounts of dissolved ethene, a fact that questions scientifically the term “gas-phase process” as the PE polymer grows mainly from ethene dissolved in the growing polymer bead. The dissolved ethene is removed from the product that left the reactor by a product recovery cyclone. The remaining ethene is purged from the polymer with a stream of nitrogen to give the final PE product.

A major aspect in the process is the control of exothermicity to avoid melting of the polymer product. Product melting points are between 100 (LLDPE) and 125 °C (HDPE). From the polymerization exothermicity and the typical temperature of the cooling water it can be calculated that the single pass conversion of ethene is around 2% in the reactor to maintain the temperature below the product melting point. In the case of thermal runaway, CO₂ is injected into the reactor to deactivate the catalyst.

6.20.6

PE Production Economics and Modern Developments in PE Production

The production costs for PE manufacturing differ from process to process but depend also on the plant capacity. The larger the plant, the lower is the specific investment per ton of PE and year. Despite this variability in the scenarios, several general points can be derived from the available data [for details see Whiteley (2012) that deserve attention:

- In all technical PE production processes, the cost for the ethylene feedstock accounts by far for the largest share, typically 70% (for the LDPE autoclave process) to 78% (for the HDPE fluid bed process). Therefore, PE production costs depend heavily on the ethene price, which means, today, on the crude oil price. In the light of this dependency, attempts to produce PE from bioethanol-derived or for coal-derived ethene become understandable.

- The share of catalyst/chemicals, manpower, maintenance, and overheads is very similar for all relevant technical PE production processes if the production capacity is comparable.
- For the high-pressure LDPE processes the share of depreciation on the invested capital and of the electric power is significantly higher than for the low-pressure processes. This is understandable considering the required high-pressure equipment and the energy demand for gas compression. Despite this less favorable process economics, the high-pressure process for LDPE production is still in operation as LDPE is still the best and most suitable material for some applications (e.g., PE extrusion). Understandably, however, much research effort is being dedicated to mimicking the special branching patterns of LDPE in alternative low-pressure PE production processes using specific molecular catalysts or suitable co-monomers.

Summary of Section 6.20 (take-home messages)

- Technical ethylene polymerization leads to three major classes of PE materials: low-density polyethene (LDPE), linear low-density polyethene (LLDPE), and high-density polyethene (HDPE). The three classes of PE material differ in the degree and type of branching in the polymer. These differences lead to different physicochemical properties of the polymer, resulting in different application areas of the PE material.
- The high exothermicity of ethene polymerization combined with the thermal instability of ethene makes efficient and robust heat removal a critical aspect in reactor design.
- LDPE production is a radical high-pressure process. Despite the high investment and higher operation cost related to this process, LDPE processes are still in use as the special branching pattern of the product cannot be achieved with low-pressure techniques. Some applications, for example, PE extrusion, require the properties of LDPE.
- Most catalysts for industrial HDPE and LLDPE manufacturing processes are heterogeneous solids and belong to the Ziegler (e.g., titanium chloride on $MgCl_2$ activated by aluminium alkyls), Phillips (chromate on silica), or single-site (e.g., metallocene complexes) type. All catalysts effective in HDPE and LLDPE production are very sensitive to impurities in the ethene feedstock and, therefore, require polymerization-grade ethene feedstock qualities.
- Processes for HDPE and LLDPE production include slurry, solution, and gas-phase processes. The choice of process depends on the specific PE quality that is desired. Slurry processes are more suitable for the production of HDPE as high degrees of branching increases the PE solubility in the diluent.

References

Note that as throughout this book, mutated German vowels ("umlaut" ä, ö, ü) are written as ae, oe, and ue, even for proper names, for example, *Damkoehler* instead of the original *Damköhler*.

Chapter 1

- Baerns, M., Behr, A., Brehm, A., Gmehling, J., Hofmann, H., Onken, U., and Renken, A. (2006) *Technische Chemie*, Wiley-VCH Verlag GmbH, Weinheim.
 Behr, A., Agar, D.W., and Joerissen, J. (2010) *Einführung in die Technische Chemie*, Spektrum Akademischer Verlag, Heidelberg.

Chapter 2

- Behr, A. (2008) *Angewandte Homogene Katalyse*, Wiley-VCH Verlag GmbH, Weinheim.
 Beller, M. et al. (2010) CT Roadmap of German catalysis research, *43rd Annual Meeting of German Catalysis Research, May 2010*, supported by DECHEMA, GDCh, DBG, DGMK, VDI, German Catalysis Society, pp. 1–43.
 Blaser, H.U. and Schmidt, E. (2004) *Asymmetric Catalysis on Industrial Scale*, Wiley-VCH Verlag GmbH, Weinheim.
 Cahn, R.S., Ingold, C.K., and Prelog, V. (1966) Spezifikation der molekularen Chiralität. *Angew. Chem.*, **78**, 413.
 Carreira, E.M. and Kvaerno, L. (2009) *Classics in Stereoselective Synthesis*, Wiley-VCH Verlag GmbH.
 Drießen-Hoelscher, B., Wasserscheid, P., and Keim, W. (1998) Recycle of homogeneous transition metal catalysts in two liquid phases. *CATTECH*, **3**, 47–52.
 Ertl, G., Knoetzinger, H., Schueth, F., and Weitkamp, J. (eds) (2008) *Handbook of Heterogeneous Catalysis*, Wiley-VCH Verlag GmbH, Weinheim.
 Fanghaenel, E. (ed.) (2004) *Organikum*, 22nd edn, Wiley-VCH Verlag GmbH.
 Forzatti, P. and Lietti, L. (1999) Catalyst deactivation. *Catal. Today*, **52** (2–3), P 165–181.
 Hagen, J. (1999) *Industrial Catalysis*, Wiley-VCH Verlag GmbH, Weinheim.
 Kern, C. and Jess, A. (2006) Verkokung und Koksabbrand in heterogenen Katalysatoren. *Chem. -Ing. Techn.*, **78**, 1033–1048.

- Klemm, E. and Emig, G. (2005) *Technische Chemie*, Springer, Berlin.
 March, J. (1992) *Advanced Organic Chemistry*, 4th edn, Wiley-Interscience.
 Moulijn, J.A., van Diepen, A.E., and Kapteijn, F. (2001) Catalyst deactivation: Is it predictable? What to do? *Appl. Catal. A: Gen.*, **212**, 3–16.
 Prelog, V. and Helmchen, G. (1982) Grundlagen des CIP-systems und Vorschlaege fuer eine Revision. *Angew. Chem.*, **94**, 614.
 Sykes, P. (1988) *Reaktionsmechanismen der Organischen Chemie*, 9th edn, Wiley-VCH Verlag GmbH.
 Sykes, P. (1996) *Guidebook to Mechanism in Organic Chemistry*, 6th edn, Prentice Hall.
 Walter, W. and Francke, W. (1998) *Beyer, Walter: Lehrbuch der Organischen Chemie*, 23th edn, Hirzel Verlag, Stuttgart.
 Weitkamp, J. and Glaeser, R. (2003) in Winnacker, Kuechler, *Chemische Technik*, vol. 1, Wiley-VCH Verlag GmbH, Weinheim, ch. 5, pp. 1–74.
 woven wire cloths versus electroformed sieves. *Part. Syst. Charact.*, **10**, 222–225.
 Bridgman, P.W. (1923) The thermal conductivity of liquids under pressure. *Proc. Am. Acad. Arts. Sci.*, **59**, 141–169.
 Broetz, W. and Schoenbucher, A. (1982) *Technische Chemie I*, Verlag Chemie, Weinheim.
 Brueschke, H. and Melin, T. (2006) CT Membranotechnik, in *Fluidverfahrenstechnik* (ed. R. Goedecke), Wiley-VCH Verlag GmbH, Weinheim, ch 6.
 Brunauer, S., Emmett, P.H., and Teller, E. (1938) Adsorption of gases in multilayers. *J. Am. Chem. Soc.*, **60**, 309–319.
 Cengel, Y.A. (2002) *Heat Transfer*, McGraw-Hill College, Boston.
 Cheng, K.C. (1999) *Some Observations on the Historical Development of Conduction Heat Transfer, Lecture Notes in Physics*, vol. 533, Springer, Berlin, pp. 1–22.
 Collis, D.C. and Williams, M.J. (1959) Two-dimensional convection from heated wires at low Reynolds numbers. *J. Fluid Mech.*, **6**, 357–384.
 Crank, J. (2003) *Mathematics of Diffusion*, Oxford Science Publications.
 Cussler, E.L. (2009) *Diffusion*, Cambridge University Press.
 Dittmeyer, R., Keim, W., Kreysa, G., and Oberholz, A. (eds) (2003) Winnacker-Kuechler. *Chemische Technik*, Wiley-VCH Verlag GmbH, Weinheim.
 Drioli, E. and Giorno, L. (2009) *Membrane Operations*, Wiley-VCH Verlag GmbH, Weinheim.
 Eckert, E.R.G. and Soehngen, E. (1952) Distribution of heat-transfer coefficients around circular cylinders in crossflow at Reynolds numbers from 20 to 500. *Trans. Am. Soc. Mech. Eng.*, **74**, 343–347.
 Einstein, A. (1905) Ueber die von der molekularkinetischen Theorie der Waerme geforderte Bewegung von in ruhenden Fluessigkeiten suspendierten Teilchen. *Ann. Phys.*, **325**, 549–560.
 Emig, G. and Klemm, E. (2005) *Technische Chemie*, Springer, Berlin.

- Emons, H.-H. (ed.) (1974) *Lehrbuch der Technischen Chemie, Grundoperationen chemischer Verfahrenstechnik*, VEB Verlag fuer Grundstoffindustrie, Leipzig.
- Ergun, S. (1952) Fluid flow through packed beds. *Chem. Eng. Prog.*, **48**, 89–94.
- Fand, R.M. and Keswani, K.K. (1972) A continuous correlation equation for heat transfer from cylinders to air in crossflow for Reynolds numbers from 10^{-2} to 2×10^5 . *Int. J. Heat Mass Transfer*, **15**, 559–562.
- Fritzmann, C., Loewenberg, J., Wintgens, T., and Melkin, T. (2007) State-of-the-art of reverse osmosis desalination. *Desalination*, **213**, 1–76.
- Froment, G.F. and Bischoff, K.B. (1990) *Chemical Reactor Analysis and Design*, John Wiley & Sons, Inc., New York.
- Fuller, E.N., Scheffler, P.D., and Giddings, J.C. (1966) A new method for prediction of binary gas-phase diffusion coefficients. *Ind. Eng. Chem.*, **58**, 19–27.
- Giedt, W.H. (1949) Investigation of variation of point unit heat transfer coefficient around a cylinder normal to an air stream. *Transactions of the ASME* **71**, 375–381.
- Gmehling, J. and Brehm, A. (1996) *Grundoperationen. Lehrbuch der Technischen Chemie Band II*, Georg Thieme Verlag, Stuttgart.
- Goedecke, R. (ed.) (2006) *Fluidverfahrenstechnik*, Wiley-VCH Verlag GmbH, Weinheim.
- Groninger, G., Hedden, K., and Rao, B.R. (1987) Kinetics of removal of impurities by high pressure adsorption. *Chem. Eng. Technol.*, **10**, 63–72.
- Harmsen, G.J. (2007) Reactive distillation: The front runner of industrial process intensification. A full review of commercial applications, research, scale-up, design and operation. *Chem. Eng. & Proc.*, **46**, 774–780.
- Hemming, W. (2008) *Verfahrenstechnik*, Vogel Verlag, Wuerzburg.
- Hirschfelder, J.O., Curtiss, C.F., and Bird, R.B. (1967) *Molecular Theory of Gases*, John Wiley & Sons, Inc., New York.
- Hugo, P. (1974) Der Einfluss der Porenvernetzung auf den Labyrinthfaktor von Presslingen und Sinterkoerpern. *Chem.-Ing.-Techn.* **46**, 266ff.
- Jakubith, M. (1992) *Memofix Chemie und Chemietechnik*, VCH, Weinheim.
- Jakubith, M. (1998) *Grundoperationen und chemische Reaktionstechnik*, Wiley-VCH Verlag GmbH, Weinheim.
- Kast, W. (1981) Adsorption aus der Gasphase. Grundlagen und verfahren. *Chem. Ing. Tech.*, **53**, 160–172.
- Kast, W. (1988) *Adsorption aus der Gasphase*, VCH-Verlagsgesellschaft, Weinheim.
- Khan, W.A., Culham, J.R., and Yovanovich, M. M. (2005) Fluid flow around and heat transfer from an infinite circular cylinder. *J. Heat Transfer*, **127**, 785–790.
- Konstantin, P. (2007) *Praxishandbuch Energiewirtschaft*, Springer Verlag, Berlin.
- Krall, K.M. (1969) Local heat transfer around a transverse circular cylinder in slip flow. Doctoral thesis, University of Minnesota, USA.
- Krall, K.M. and Eckert, E.R.G. (1966) Heat transfer to a transverse circular cylinder at low Reynolds numbers including rarefraction effects. Presented at the 3rd International Heat Transfer Conference, Chicago, USA.
- Krall, K.M. and Eckert, E.R.G. (1970) Heat transfer to a transverse circular cylinder at low Reynolds numbers including rarefaction effects. *Heat Transfer Sov. Res.*, **3**, 225–232.
- Krishna, R. (2002) Reactive separations: more ways to skin a cat. *Chem. Eng. Sci.*, **57**, 1491–1504.
- Krypilo, P. and Vogt, F. (1993) *Praktikum der Technischen Chemie*, Deutscher Verlag der Grundstoffindustrie, Leipzig, Stuttgart.
- Lide, D.R. (ed.) (2004) *CRC Handbook of Chemistry and Physics*, CRC Press, Boca Raton.
- Lohrengel, B. (2007) *Einfuehrung in die Thermischen Trennverfahren*, Oldenbourg Verlag, Munich.
- Lowell, S., Shields, J.E., Thomas, M.A., and Thommes, M. (2004) *Characterization of Porous Solids and Powders: Surface Area, Pore Size and Density*, Kluwer Academic Publishers.
- Marrero, T.R. and Mason, E.A. (1972) Gaseous diffusion coefficients. *J. Phys. Chem. Data*, **1**, 3–118.
- Martienssen, W., Landolt, H., and Boernstein, R. (eds) (1976–1997) *Numerical Data and Functional Relationships in Science and Technology - New Series*, Springer.
- McCabe, W.L. and Thiele, E.W. (1925) Graphical design of fractionating columns. *Ind. Eng. Chem.*, **17**, 605–612.
- McKellar, B.H.J. (2005) The Sutherland-Einstein equation. *AAPPS Bull.* (Association of Asia Pacific Physical Societies), February.
- Missal, P. and Hedden, K. (1990) Extraktion von Kohle und von Oelschiefer mit Wasser in unter- und ueberkritischer Phase. *Erdoel Erdgas Kohle*, **106**, 75–81.
- National Institute of Standards & Technology (2007) *NIST Chemistry Web Book* <http://webbook.nist.gov/chemistry/fluid>.
- Nunes, S.P. and Peinemann, K.V. (eds) (2001) *Membrane Technology in the Chemical Industry*, Wiley-VCH Verlag GmbH, Weinheim.
- Nusselt, W. (1915) Das Grundgesetz des Waermeuebergangs. *Gesundheits-Ing.*, **38**, 55–66.
- Paul, E.L., Atiemo-Obeng, V.A., and Kresta, S.M. (2004) *Handbook of Industrial Mixing*, Wiley-Interscience, Hoboken.
- Perry, R.H. and Chilton, C.H. (1984) *Chemical Engineer's Handbook*, 6th edn, McGraw-Hill, New York.
- Petukhov, B.S. (1970) CT Heat transfer and friction in turbulent pipe flow with variable physical properties, in *Advances in Heat Transfer*, vol. 6 (eds T.F. Irvine and J.P. Hartnett), Academic Press, New York.
- Polifke, W. and Kopitz, J. (2009) *Waermeuebertragung - Grundlagen, Analytische und Numerische Methoden*, Pearson Studium, Muenchen.
- Probst, K. and Wohlfahrt, K. (1979) Empirische Abschaetzung effektiver Diffusionskoeffizienten in poroessen Systemen. *Chem.-Ing.-Techn.* **51**, 737ff.
- Rosin, E. and Rammmer, E. (1933) The laws governing the fineness of powdered coal. *J. Inst. Fuel*, **7**, 29–36.
- Rosin, E., Rammmer, E., and Sperling, U. (1933) Korngroessenprobleme des Kohlenstaubs, Bericht C 52 des Reichskohlenrates, Berlin, pp. 1–33.
- Ruthven, D.M. (ed.) (1997) *Encyclopedia of Separation Technology*, Wiley-Interscience.
- Sattler, K. (2001) *Thermische Trennverfahren: Grundlagen, Auslegung, Apparate*, Wiley-VCH Verlag GmbH, Weinheim.
- Schluender, E.-U. (1986) *Einfuehrung in die Waermeuebertragung*, Vieweg & Sohn, Braunschweig.
- Schluender, E.-U. and Martin, H. (1995) Einfuehrung in die Waermeuebertragung, Vieweg & Sohn, Braunschweig.
- Schmidt, J. (1970) *Verfahren der Gasaufbereitung*, VEB Deutscher Verlag fuer Grundstoffchemie, Leipzig.
- Schubert, H. and Waechtler, E. (1987) Erich Rammmer - a pioneer of particle technology. *Part. Charact.*, **4**, 45–48.
- Simecek, A., Michalek, J., Kadlec, B., and Vosolsobe, J. (1969) Loeslichkeit von Schweißdioxid in Schwefelsaeure. *Chem. Ing. Tech.*, **41**, 1077–1078.
- Slattery, J.C. and Bird, R.B. (1958) Calculation of the diffusion coefficient of dilute gases and of the self-diffusion coefficient of dense gases. *Am. Inst. Chem. Eng. J.*, **4**, 137–142.
- Stankiewicz, A. (2003) Reactive separations for process intensification: an industrial view. *Chem. Eng. & Proc.*, **42**, 137–144.
- Stichlmair, J.G. and Fair, J.R. (1998) *Distillation, Principles and Practices*, Wiley-VCH Verlag GmbH, Weinheim.
- Sucker, D. and Brauer, H. (1976) Stationarer Stoff- und Waermeuebergang an stationaer quer angestromten Zylindern. *Waerme Stof-fuebertragung*, **9**, 1–12.
- Sundmacher, K. and Kienle, A. (eds) (2002) *Reactive Distillation*, Wiley-VCH Verlag GmbH, Weinheim.
- Sutherland, W. (1905) A dynamical theory of diffusion for non-electrolytes and the molecular mass of albumin. *Philos. Mag.*, **9**, 781–785.
- Sutherland, W. (1904) The measurement of large molecular masses, Australasian Association for the Advancement of Science. Report of Meeting, 10 11 (Dunedin).
- Taylor, R. and Krishna, R. (2000) Modelling reactive distillation. *Chem. Eng. Sci.*, **55**, 5183–5229.
- Van Brakel, J. (2000) Modelling in chemical engineering. *HYLE - Int. J. Philos. Chem.*, **6**, 101–116.

- VDI (Verein Deutscher Ingenieure) (2002) *VDI-Waermeatlas. Berechnungsblaetter fuer den Waermeuebergang*, VDI Verlag.
- Vianni, R. and Petracco, M. (2007) Coffee. In *Ullmann's Encyclopedia of Industrial Chemistry*, VCH-Verlagsgesellschaft, Weinheim, CD-ROM.
- Weisz, P.B. and Schwartz, A.B. (1962) Diffusivity of porous-oxide-gel-derived catalyst particles. *J. Catal.*, **1**, 399–406.
- Westerterp, K.R., van Swaaij, W.P.M., and Beecknackers, A.A.C.M. (1998) *Chemical Reactor Design and Operation*, John Wiley & Sons, Inc., New York.
- Wheeler, A. (1955) in *Catalysis*, vol. 2 (ed. P.H. Emmett), Reinhold, New York.
- Wicke, E. (1980) *Einfuehrung in die Physikalische Chemie*, Akad. Verlagsgesellschaft, Wiesbaden.
- Wilhelm, A. and Hedden, K. (1986) A non-isothermal experimental technique to study coal extraction with solvents in liquid and supercritical state. *Fuel*, **65**, 1209–1215.
- Wilke, C.R. (1950) Diffusional properties of multicomponent gases. *Chem. Eng. Prog.*, **46**, 95–104.
- Wilke, C.R. and Chang, P. (1955) Correlation of diffusion coefficients in dilute solution. *AIChE J.*, **1**, 264.
- Wisniak, J. (2001) Frederick Thomas Trouton: The man, the rule, and the ratio. *Chem. Educator*, **6**, 55–61.
- Xu, G., Scurto, A.M., Castier, M., Brennecke, J.F., and Stadtherr, M.A. (2000) Reliable computation of high pressure solid-fluid equilibrium. *Ind. Eng. Chem. Res.*, **39**, 1624–1636.
- Xu, G.-W., Zhang, C.-F., Qin, S.-J., Gao, W.-H., and Liu, H.-B. (1998) Gas-liquid equilibrium in a CO₂-MDEA-H₂O system and the effect of piperazine on it. *Ind. Eng. Chem. Res.*, **37**, 1473–1477.
- Zhang, M. (2006) Thermal diffusion in liquid mixtures and polymer solutions by molecular dynamics simulation. Doctoral thesis, University of Technology Darmstadt.
- Zlokarnik, M. (2001) *Stirring - Theory and Practice*, Wiley-VCH Verlag GmbH, Weinheim.
- Zosel, K. (1973) Patent DE-AS 2 322 038.
- Chapter 4**
- Ahn, B.-J., Zoulian, A., and Smith, J.M. (1986) Axial dispersion in packed beds with large wall effect. *AIChE J.*, **32**, 170–174.
- Appl, M. (1999) *Ammonia*, Wiley-VCH Verlag GmbH, Weinheim.
- Aris, R. (1956) On the dispersion of a solute in a fluid flowing through a tube. *Proc. R. Soc. London, Ser. A*, **235**, 66–67.
- Arrhenius, S. (1889) Ueber die Reaktionsgeschwindigkeit bei der Inversion von Rohrzucker durch Saeuren (On the reaction velocity of the inversion of cane sugar by acids). *Z. Phys. Chem.*, **4**, 226–248.
- Atkins, P.W. and de Paula, J. (2002) *Physical Chemistry*, Oxford University Press, Oxford.
- Atkins, P.W. (2002) *Physikalische Chemie*, Wiley-VCH Verlag GmbH, Weinheim.
- Baerns, M., Behr, A., Brehm, A., Gmehling, J., Hofmann, H., Onken, U., and Renken, A. (2006) *Technische Chemie*, Wiley-VCH Verlag GmbH, Weinheim.
- Baerns, M., Hofmann, H., and Renken, A. (1999) *Chemische Reaktionstechnik. Lehrbuch der Technischen Chemie*, Wiley-VCH Verlag GmbH, Weinheim.
- Barkelew, C.H. (1959) Stability of chemical reactors. *Chem. Eng. Prog. Symp. Ser.*, **55**, 37–46.
- Battsengel, B. (2002) Zur Mikro- und Makrokinetik mehrphasiger heterogen-katalysierter Reaktionssysteme - Untersuchungen am Modellsystem der Ni-katalysierten Hydrierung von 1-Octen. Doctoral thesis, University of Technology Aachen, Germany.
- Battsengel, B., Datsevitch, L., and Jess, A. (2002) Experimental and theoretical studies on hydrogenation in multiphase fixed bed reactors. *Chem. Eng. Techn.*, **25**, 621–626.
- Behr, A. (2008) *Angewandte Homogene Katalyse*, Wiley-VCH Verlag GmbH, Weinheim.
- Benenati, R.F. and Brosilow, G.B. (1962) Void fraction in beds of spheres. *AIChE J.*, **8**, 359–361.
- Berger, R.J., Stitt, E.H., Marin, G.B., Kapteijn, F., and Moulijn, J.A. (2001) Chemical reaction kinetics in practice. *CATTECH*, **5**, 30–60.
- Bey, O. and Eigenberger, G. (2001) Gas flow and heat transfer through catalyst filled tubes. *Int. J. Thermal Sci.*, **40**, 152–184.
- Bhaduri, S. and Mukesh, D. (2000) *Homogeneous Catalysis, Mechanisms and Industrial Applications*, Wiley-VCH Verlag GmbH, Weinheim.
- Bhushan, B. (2004) *Handbook of Nanotechnology*, Springer, Berlin.
- Bischoff, K.B. (1965) Effectiveness factors for general reaction rate forms. *AIChE J.*, **11**, 351–355.
- Bommarius, A.S. and Riebel-Bommarius, B. R. (2004) *Biocatalysis, Fundamentals and Applications*, Wiley-VCH Verlag GmbH, Weinheim.
- Borekov, G.K., Matros, Y.S., and Kiselev, O.V. (1979) Catalytic processes carried out under nonstationary conditions. *Kinet. Katal.*, **20**, 773–780.
- Broetz, W. and Schoenbacher, A. (1982) *Technische Chemie I*, Verlag Chemie, Weinheim.
- Calderbank, P.H. and Pogorski, L.A. (1957) Heat transfer in packed beds. *Trans Inst. Chem. Eng.*, **35**, 195–207.
- Carberry, J.J. (1961) The catalytic effectiveness factor under nonisothermal conditions. *AIChE J.*, **7**, 350–351.
- Carberry, J.J. (1962) Mass diffusion and isothermal catalytic selectivity. *Chem. Eng. Sci.*, **9**, 675–681.
- Carberry, J.J. and White, D. (1969) On the role of transport phenomena in catalytic reactor behaviour. *Ind. & Eng. Chem.*, **61**, 27–35.
- Carbonell, R.G. (1980) Flow non-uniformities in packed beds: Effect on dispersion. *Chem. Eng. Sci.*, **35**, 1347–1356.
- Cengel, Y.A. (2002) *Heat Transfer*, McGraw-Hill College, Boston.
- Chao, R.E., Caban, R.A., and Irizarry, M.M. (1973) Wall heat transfer to chemical reactors. *Can. J. Chem. Eng.*, **51**, 67–70.
- Champagnie, A.M., Tsotsis, T.T., and Minet, R.G. (1990) A high temperature catalytic membrane reactor for ethane dehydrogenation. *Chem. Eng. Sci.*, **45**, 2423–2429.
- Chmiel, H. (2006) *Bioprozesstechnik*, Spektrum Akademischer Verlag, Munich.
- Chu, C.F. and Ng, K.M. (1989) Flow in packed beds with a small tube to particle diameter. *AIChE J.*, **35**, 148.
- Cornils, B. and Herrmann, W. (eds) (2002) *Applied Homogeneous Catalysis with Organometallic Compounds*, Wiley-VCH Verlag GmbH, Weinheim.
- Cornils, B., Herrmann, W., Horvath, I.T., Leitner, W., Mecking, S., Olivier-Bourbigou, H., and Vogt, D. (eds) (2005) *Multiphase Homogeneous Catalysis*, Wiley-VCH Verlag GmbH, Weinheim.
- Crider, J.E. and Foss, A.S. (1965) Effective wall heat transfer coefficients and thermal resistances in mathematical models of packed beds. *AIChE J.*, **11**, 1012.
- Cybulski, A. and Moulijn, J.A. (eds) (1997) *Structured Catalysts and Reactors*, Dekker, New York.
- Damkoehler, G. (1936) Einfluesse der Stroemung, Diffusion und des Waermeueberganges auf die Leistung von Reaktionsoefen. I. Allgemeine Gesichtspunkte fuer die Uebertragung eines chemischen Prozesses aus dem Kleinen ins Große. *Z. Elektrochem.*, **42**, 846–862.
- Damkoehler, G. (1937a) Einfluesse der Stroemung, Diffusion und des Waermeueberganges auf die Leistung von Reaktionsoefen. III. Zur Frage der maximalen Uebertemperatur in einem rohrfoermigen Kontaktrohre bei exothermer Uebertemperatur. *Z. Elektrochem.*, **43**, 8–13.
- Damkoehler, G. (1937b) Einfluesse der Stroemung, Diffusion und des Waermeueberganges auf die Leistung von Reaktionsoefen. III. Zur Frage der maximalen Uebertemperatur in einem rohrfoermigen Kontaktrohre bei exothermer Uebertemperatur. *Z. Elektrochem.*, **43**, 8–13.
- Damkoehler, G. (1939) Stroemungs- und Waermeuebergangsprobleme in chemischer Technik und Forschung. *Chem. Ing. Tech.*, **12**, 469.
- Daszkowski, T. and Eigenberger, G. (1992) A reevaluation of fluid flow, heat transfer and chemical reaction in catalyst filled tubes. *Chem. Eng. Sci.*, **47**, 2245.

- DeGarmo, J.L., Parulekar, V.N., and Pinjala, V. (1992) Consider reactive distillation. *Chem. Eng. Prog.*, March, 43–50.
- Delgado, J.M.P.Q. (2006) A critical review of dispersion in packed beds. *Heat Mass Transfer*, **42**, 279–310.
- Delmas, H. and Froment, G.F. (1988) A simulation model accounting for structural radial non-uniformities in fixed bed reactors. *Chem. Eng. Sci.*, **43**, 2281.
- Demirel, Y., Sharma, R.N., and Al-Ali, H.H. (2000) On the effective heat transfer in a packed bed. *Int. J. Heat Mass Transfer*, **43**, 327–332.
- Dittmeyer, R., Keim, W., Kreysa, G., and Oberholz, A. (eds) (2003) *Winnacker-Kuechler. Chemische Technik*, Wiley-VCH Verlag GmbH, Weinheim.
- Dixon, A.G. (1985) The length effect on packed bed effective heat transfer parameters. *Chem. Eng. J.*, **31**, 163–173.
- Eadie, G.S. (1942) The inhibition of cholinesterase by physostigmine and prostigmine. *J. Biol. Chem.*, **146**, 85–93.
- Eichmann, M. (1999) Zweiphasige Dimerisierung von Propen und 1-Buten mit ionischen Fluessigkeiten. Doctoral thesis, University of Technology Aachen, Germany.
- Emig, G. and Klemm, E. (2005) *Technische Chemie*, Springer, Berlin.
- Ertl, G., Knoezinger, H., and Weitkamp, J. (eds) (1997) *Handbook of Heterogeneous Catalysis*, Wiley-VCH Verlag GmbH, Weinheim.
- Farrauto, R.J. and Bartholomew, C.H. (1997) *Fundamentals of Industrial Catalytic Processes*, Blackie Academic & Professional, Weinheim.
- Foersterling, H.D. and Kuhn, H. (1983) *Molekulare und Molekuelanhaeufungen*, Springer, Berlin.
- Freiwald, M.G. and Paterson, W.R. (1992) Accuracy of model predictions and reliability of experimental data for heat transfer in packed beds. *Chem. Eng. Sci.*, **47**, 1545–1560.
- Froment, G.F. and Bischoff, K.B. (1990) *Chemical Reactor Analysis and Design*, John Wiley & Sons, Inc., New York.
- Garcia-Junceda, E. (ed.) (2008) *Multi-Step Enzyme Catalysis, Biotransformations and Chemoenzymatic Synthesis*, Wiley-VCH Verlag GmbH, Weinheim.
- Gmehling, J. and Kolbe, B. (1992) *Thermodynamik*, Georg Thieme Verlag, Stuttgart.
- Gmehling, J. and Brehm, A. (1996) *Grundoperationen. Lehrbuch der Technischen Chemie Band II*, Georg Thieme Verlag, Stuttgart.
- Gunn, D.J. and Price, C. (1969) Theory of axial and radial dispersion in packed beds. *Trans. Inst. Chem. Eng.*, **47**, 351–359.
- Hagen, J. (1999) *Industrial Catalysis*, Wiley-VCH Verlag GmbH, Weinheim.
- Hagen, J. (2005) *Industrial Catalysis, A Practical Approach*, Wiley-VCH Verlag GmbH, Weinheim.
- Hayes, B. (2005) Rumours and errors. *Am. Sci.*, 5/6, 207–211.
- Hein, O. (1999) Zur Messung und Berechnung der Zuendtemperatur fester Brennstoffe. Diploma thesis, Engler-Bunte-Institute, University Karlsruhe, Germany.
- Hessel, V., Hardt, S., and Loewe, H. (2004) *Chemical Micro Process Engineering – Fundamentals, Modelling and Reactions*, Wiley-VCH Verlag GmbH, Weinheim.
- Hlavacek, V., Kubicek, M., and Marek, M. (1969) Analysis of nonstationary heat and mass transfer in a porous catalyst particle I and II. *J. Chem. Catal.*, **15**, 17–30; 31–42.
- Hofmann, H. (1979) VDI-Bericht 349 (see also Westerterp et al. 1998).
- Hoffmann, U. and Hofmann, H. (1971) *Einführung in die Optimierung*, Verlag Chemie, Weinheim.
- Hofstee, B.H. (1959) Non-inversed versus inversed plots in enzyme kinetics. *Nature*, **184**, 1296–1298.
- Hong, J., Hecker, W.C., and Fletcher, T.H. (2000) Improving the accuracy of predicting effectiveness factors for nth order and Langmuir rate equations in spherical coordinates. *Energy & Fuels*, **14**, 663–670.
- Hou, C.T. and Shaw, J.-F. (2008) *Biocatalysis and Bioenergy*, Wiley-VCH Verlag GmbH, Weinheim.
- Hsiang, T.C. and Haynes, H.W. (1977) Axial dispersion in small diameter beds of large, spherical particles. *Chem. Eng. Sci.*, **32**, 678–681.
- Hugo, P. (1974) Der Einfluß der Porenvernetzung auf den Labyrinthfaktor von Presslingen und Sinterkoerpern. *Chem. Ing. Tech.*, **46**, 645.
- Jeschar, R. (1964) Druckverlust in mehrkornschaetten aus Kugeln. *Archiv. Eisenhuettenwesen*, **35**, 91–108.
- Jess, A. (1995) Reaktionskinetische Untersuchungen zur thermischen Zersetzung von Modellkohlenwasserstoffen. *Erdoel-Erdgas-Kohle*, **111**, 479–484.
- Jess, A. (1996a) Mechanisms and kinetics of thermal reactions of aromatic hydrocarbons from pyrolysis of solid fuels. *Fuel*, **75**, 1441–1448.
- Jess, A. (1996b) Thermische und katalytische Spaltung von Kohlenwasserstoffen in wasserstoff- und wasserdampfreicher Atmosphaere - eine Modelluntersuchung zur Erzeugung von Reduktionsgas aus Koksofenrohgas. Habilitation thesis, University Karlsruhe, Germany.
- Jess, A., Kern, C., Schroegel, K., Jung, A., and Schuetz, W. (2006) Herstellung von Kohlenstoff-Nanotubes und -Fasern durch Gasphasenabscheidung. *Chem. Ing. Tech.*, **78**, 94–100.
- Jung, A. (2005) Reaktionskinetische Untersuchungen zur kontinuierlichen Wirbelschichtsynthese von Herringbone-Nanofasern. Diploma thesis, Department of Chemical Engineering, University Bayreuth, Germany.
- Kapteijn, F., Heiszwolf, J.J., Nijhuis, T.A., and Moulijn, J.A. (1999) Monoliths in multiphase catalytic processes - aspects and prospects. *CATTECH*, **3**, 24–41.
- Kapteijn, F. and Moulijn, J.A. (1999) Laboratory reactors, in *Handbook of Heterogeneous Catalysis*, vol. 3 (eds G. Ertl, H. Knoetzinger, and J. Weitkamp), Wiley-VCH Verlag GmbH, Weinheim.
- Kern, C. (1998) Einfluss des Stofftransports auf die katalytische Umsetzung von Koksofenrohgas an einem kommerziellen Nickelkatalysator. Diploma thesis, University of Karlsruhe, Germany.
- Kern, C. (2003) Regeneration eines Koksbeladenen Katalysators zur Benzinreformierung. Doctoral thesis, University of Technology Aachen, Germany.
- Kern, C. and Jess, A. (2005) Regeneration of coked catalysts - modelling and verification of coke burn-off in single particles and fixed bed reactors. *Chem. Eng. Sci.*, **60**, 4249–4264.
- Kern, C. and Jess, A. (2006) Verkokung und Koksabbrand in heterogenen Katalysatoren. *Chem. -Ing. Techn.*, **78**, 1033–1048.
- Levenspiel, O. (1996) *The Chemical Reactor Omnibook*, OSU Book Stores, Corvallis, Oregon.
- Levenspiel, O. (1999) *Chemical Reaction Engineering*, Wiley-VCH Verlag GmbH, Weinheim.
- Levenspiel, O. (2000) Catalytic kinetics and elephant curves. *Chem. Innovation*, March, IBC, 30.
- Li, C.H. and Finlayson, B.A. (1977) Heat transfer in packed beds - a reevaluation. *Chem. Eng. Sci.*, **32**, 1055–1066.
- Liese, A., Seelbach, K., and Wandrey, C. (2006) *Industrial Biotransformations*, Wiley-VCH Verlag GmbH, Weinheim.
- Lineweaver, H. and Burk, D. (1934) Determination of enzyme dissociation constant. *J. Am. Chem. Soc.*, **56**, 658–666.
- Martin, H. (1978) Low Peclet number particle-to-fluid heat and mass transfer in packed beds. *Chem. Eng. Sci.*, **33**, 913.
- Matros, Y.S. (1985) *Unsteady-State Processes in Catalytic Reactors*, Elsevier, Amsterdam.
- Matros, Y.S. (1989) *Catalytic Processes Under Unsteady-State Conditions*, Elsevier, Amsterdam.
- Matros, Y.S. and Bunimovich, G.A. (1996) Reverse-flow operation in fixed bed catalytic reactors. *Catal. Rev. Sci. Eng.*, **38**, 1–68.
- Mears, D.E. (1971) Test of transport limitations in experimental catalytic reactors. *Ind. Eng. Chem. Proc. Des. Dev.*, **10**, 541–547.
- Mears, D.E. (1976) On criteria for axial dispersion in nonisothermal packed-bed catalytic reactors. *Ind. Eng. Chem. Fundam.*, **15**, 20–23.
- Michaelis, L. and Menten, M.L. (1913) Die Kinetik der Invertinwirkung. *Biochem. Z.*, **49**, 333–369.
- Moulijn, J.A., Makkee, M., and Van Diepen, A. (2004) *Chemical Process Technology*, Wiley-VCH Verlag GmbH, Weinheim.

- Murray, J.D. (1989) *Mathematical Biology*. Springer, Berlin.
- Murzin, D. and Salmi, T. (2005) *Catalytic Kinetics*, Wiley-VCH Verlag GmbH, Weinheim.
- Pachow, J. (2005) Reaktionskinetische Untersuchung der katalytischen Hydrierung von 1-Hexen an einem Nickelkatalysator. Diploma thesis, Department of Chemical Engineering, University Bayreuth, Germany.
- Papageorgiou, I.N. and Froment, G.F. (1995) Simulation models accounting for radial voidage profiles in fixed-bed reactors. *Chem. Eng. Sci.*, **50**, 3043–3056.
- Parshall, G.W. and Ittel, S.D. (1992) *Homogeneous Catalysis, the Applications and Chemistry of Catalysis by Soluble Transition Metal Complexes*, Wiley-VCH Verlag GmbH, Weinheim.
- Petersen, E.E. (1962) Non-isothermal chemical reaction in porous catalysts. *Chem. Eng. Sci.*, **17**, 987–995.
- Podrebarac, G.G., Ng, F.T., and Rempel, G.L. (1997) More uses for catalytic distillation. *CHEMTECH*, **37**–45.
- Praeve, P., Faust, U., Sittig, W., and Sukatsch, D.A. (1987) *Handbuch der Biotechnologie*, R. Oldenburg Verlag, Munich.
- Probst, K. and Wohlfahrt, K. (1979) Empirische Abschaetzung effektiver Diffusionskoeffizienten in poroesen Systemen. *Chem. Ing. Tech.*, **51**, 737–739.
- Reich, S., Thomsen, C., and Maultzsch, J. (2004) *Carbon Nanotubes. Basic Concepts and Physical Properties*, Wiley-VCH Verlag GmbH, Weinheim.
- Retzlaff, G., Rust, G., and Waibel, J. (1978) *Statistische Versuchsplanung*, Verlag Chemie, Weinheim.
- Ridgway, K. and Tarbuck, K.J. (1968) Voids fluctuations in randomly-packed beds of spheres adjacent to a containing wall. *Chem. Eng. Sci.*, **23**, 1147–1155.
- Roberts, G.W. (1972) The selectivity of porous catalysts: parallel reactions. *Chem. Eng. Sci.*, **27**, 1409–1420.
- Roberts, G.W. and Satterfield, C.N. (1965) Effectiveness factor for porous catalyst. *Ind. Eng. Chem. Fundam.*, **4**, 288.
- Roberts, G.W. and Satterfield, C.N. (1966) Effectiveness factor for porous catalyst. *Ind. Eng. Chem. Fundam.*, **5**, 317.
- Roblee, L.H.S., Baird, R.M., and Tierney, J.W. (1958) Radial porosity variations in packed beds. *AIChe J.*, **4**, 460–464.
- Romey, I. (1981) *Kohle-Erdoel-Erdgas, Chemie und Technik*, Vogel-Verlag, Wuerzburg.
- Rothenberg, G. (2008) *Catalysis: Concepts and Green Application*, Wiley-VCH Verlag GmbH, Weinheim.
- Schlunder, E.U. and Martin, H. (1995) *Einfuehrung in die Waermeuebertragung*, Vieweg Verlag, Braunschweig.
- Schroegel, K. (2004) Synthese von Kohlenstoff-nanofasern in der Wirbelschicht. Diploma thesis, Department of Chemical Engineering, University Bayreuth, Germany.
- Schroegel, K. (2007) Reaktionskinetische und verfahrenstechnische Aspekte der Synthese von Kohlenstoff-Nanotubes und -Nanofasern. Doctoral thesis, University Bayreuth, Germany.
- Steinbach, J. (1999) *Safety Assesment for Chemical Processes*, Wiley-VCH Verlag GmbH, Weinheim.
- Tang, D., Kern, C., and Jess, A. (2004) Influence of chemical reaction rate, diffusion and pore structure on the regeneration of a coked Al₂O₃-catalyst. *Appl. Catal. A: Gen.*, **272**, 187–199.
- Taylor, G.J. (1954) The dispersion of matter in turbulent flow through a pipe. *Proc. R. Soc. London*, **223**, 446.
- Thiele, E.W. (1939) Relation between the catalytic activity and size of particle. *Ind. Eng. Chem.*, **31**, 916–920.
- Tinkler, J.D. and Metzner, A.B. (1961) Reaction rates in nonisothermal catalysts. *Ind. Eng. Chem.*, **53**, 663–668.
- Tinkler, J.D. and Pigford, R.L. (1961) The influence of heat generation on the catalyst effectiveness factor. *Chem. Eng. Sci.*, **15** (3–4), 326–328.
- Tyson, R., Haines, S., and Hodges, K.E. (2010) Modelling the Canada lynx and snowshoe hare population cycle: the role of specialist predators. *Theor. Ecol.*, **3**, 97–111 (published online: 21 August 2009).
- Valdman, B. and Hughes, R. (1976) A simple method of calculating effectiveness factors for heterogeneous catalytic gas-solid reactions. *AIChe J.*, **22**, 192–194.
- Van Den Bleek, C.M., Van Der Wiele, K., and Van Den Berg, P.J. (1969) The effect of dilution on the degree of conversion in fixed bed catalytic reactors. *Chem. Eng. Sci.*, **24**, 681–694.
- VDI (Verein Deutscher Ingenieure) (2002) *VDI-Waermealts. Berechnungsblaetter fuer den Waermeuebergang*, VDI-Verlag.
- Wasserscheid, P. and Welton, T. (eds) (2007) *Ionic Liquids in Synthesis*, Wiley-VCH Verlag GmbH, Weinheim.
- Weisz, P.B. (1982) The science of the possible. *CHEMTECH*, **7**, 424–425.
- Weisz, P.B. and Hicks, J.S. (1962) The behaviour of porous catalyst particles in view of internal mass and heat diffusion effects. *Chem. Eng. Sci.*, **17**, 265–275.
- Weisz, P.B. and Schwartz, A.B. (1962) Diffusivity of porous-oxide-gel-derived catalyst particles. *J. Catal.*, **1**, 399–406.
- Wen, C.Y. and Fan, L.T. (1975) Models for flow systems and chemical reactors, in *Chemical Processing and Engineering*, vol. 3 (eds L.F. Albright R.N. Maddox, and J.J. McKetta), Marcel Dekker, New York.
- Wen, D. and Ding, Y. (2006) Heat transfer of gas flow through a packed bed. *Chem. Eng. Sci.*, **61**, 3532–3542.
- Westerterp, K.R., Bodewes, T.N., Vrijland, M.S. A., and Kuczynski, M. (1988) Two new methanol converters. *Hydrocarb. Process.*, **67**, 69–73.
- Westerterp, K.R., van Swaaij, W.P.M., and Beeckackers, A.A.C.M. (1998) *Chemical Reactor Design and Operation*, John Wiley & Sons, Inc., New York.
- Westerterp, K.R. (1992) Multifunctional reactors. *Chem. Eng. Sci.*, **47**, 2195–2206.
- Wheeler, A. (1955) in *Catalysis*, vol. 2 (ed. P.H. Emmett), Reinhold, New York.
- Wittmer, P., Ankel, T., Gerrens, H., and Romeis, H. (1965) Zum dynamischen Verhalten von Polymerisationsreaktoren. *Chem. Ing. Tech.*, **37**, 392–399.
- Yagi, S. and Kunii, D. (1960) Studies on heat transfer near wall surface in packed beds. *AIChe J.*, **6**, 97–104.
- Yagi, S. and Wakao, N. (1959) Heat and mass transfer from wall to fluids in packed beds. *AIChe J.*, **5**, 79–85.
- Young, L.C. and Finlayson, B.A. (1973) Axial dispersion in nonisothermal packed bed chemical reactors. *Ind. Eng. Chem. Fundam.*, **12**, 412.
- Zeldowitch, Y.B. (1939) On the theory of reactions on powders and porous substances. *Acta Physicochem. URSS*, **10**, 583–592.
- Zhang, Z., Tao, Y., and Li, Z. (2007) Factors affecting hare–lynx dynamics in the classic time series of the Hudson Bay Company. *Can. Climate Res.*, **34**, 83–89.

Chapter 5

- Alldinger, F. and Weberruss, V.A. (2010) *Advanced Ceramics and Future Materials*, Wiley-VCH Verlag GmbH, Weinheim.
- Anastas, P.T. and Warner, J. (2000) *Green Chemistry: Today (and Tomorrow)*, Oxford University Press.
- Archer, D. and Rahmstorf, S. (2010) *The climate crisis*. Cambridge University Press, Cambridge.
- Arpe, H.-J. (2010) *Industrial Organic Chemistry*, 5th edn, Wiley-VCH, p. 504.
- Arpe, H.-J. (ed.) (1986) *Ullmann's Encyclopedia of Industrial Chemistry*, vol. 12, VCH Verlags-gesellschaft, Weinheim.
- Baerns, M., Behr, A., Brehm, A., Gmehling, J., Hofmann, H., Onken, U., and Renken, A. (2006) *Technische Chemie*, Wiley-VCH Verlag GmbH, Weinheim.
- Behr, A., Agar, D.W., and Joerissen, J. (2010) *Einfuehrung in die Technische Chemie*, Spektrum Akademischer Verlag, Heidelberg.
- Behr, A., Vorholt, A., and Johnen, L. (2009) Aus der Natur fuer die Chemie. *Nachrichten Chem.*, **57**, 757–761.
- BGR (Federal German Institute for Geosciences and Natural Resources) (2009) Energierohstoffe 2009 (<http://www.bgr.bund.de>).

- BMWi (Bundesministerium fuer Wirtschaft und Technologie, German Federal Ministry of Economics and Technology) (2006) Energiедaten - Nationale und Internationale Entwicklung (<http://www.bmwi.de>).
- Benthaus, F. et al. (1978) *Rohstoff Kohle*, Verlag Chemie, Weinheim.
- Boynton, R.S. (1980) *Chemistry and Technology of Lime and Limestone*, 2nd edn, John Wiley & Sons, Inc., New York.
- BP (2009) Statistical review of world energy 2009 at <http://www.bp.com>.
- Brazel, C.S. and Rosen, S.L. (2012) *Fundamental Principles of Polymeric Materials*, John Wiley & Sons, Inc., Hoboken.
- British Geological Survey (2010) World mineral production 2004–2008, Nottingham (<http://www.bgs.ac.uk>).
- Buechel, K.H., Moretto, H.-H., and Woditsch, P. (2000) *Industrial Inorganic Chemistry*, Wiley-VCH Verlag GmbH, Weinheim.
- Burkhardt, H. (2007) Physical limits to large scale global biomass generation for replacing fossil fuels. *Physics in Canada*, **63** (3), P 113.
- Centi, G. and Perathoner, S. (2009) Opportunities and prospects in the chemical recycling of carbon dioxide to fuels. *Catal. Today*, **148**, 191–205.
- Chauvel, A. and Lefebvre, G. (1989) *Petrochemical Processes: 1. Synthesis-Gas Derivatives and Major Hydrocarbons, Petrochemical Processes: 2. Major Oxygenated, Chlorinated and Nitrated Derivatives*, Editions Technip, Paris.
- CIA (Central Intelligence Agency) (2009) The World Factbook. <http://www.cia.gov>.
- DOE (US department of energy) (2005) Gasification, world survey results. <http://www.netl.doe.gov>.
- Dueker, A. (2010) Hydrogen: production and application in industry, in *Proceedings of the DGMK Conference: The Future Role of Hydrogen in Petrochemistry and Energy Supply*, ISBN 978-3-941721-07-4, DGMK, p. 39.
- Easterlin, R.A. (2001) Income and happiness: towards a unified theory. *The Econom. J.*, **111**, 465–484.
- EIA (Energy Information Administration, energy statistics from US government) (2009) Refinery Net Production at http://tonto.eia.doe.gov/dnav/pet/pet_pnp_refp2_dc_nus_mbbl_m.htm.
- Emig, G. and Klemm, E. (2005) *Technische Chemie*, Springer, Berlin.
- Euro Chlor (2011) Chlorine industry review. www.eurochlor.org.
- Falbe, J. (ed.) (1977) *Chemierohstoffe aus Kohle*, Georg Thieme Verlag, Stuttgart.
- FAO (2007) Food and Agriculture Organization of the United Nations. State of the World's forests 2007. Available at <http://www.fao.org/forestry/sofo/en/> (accessed 26 June 2012).
- FAO (2009) Food and Agricultural Organization of the United Nations. Statistical Yearbook 2007/08 (www.fao.org).
- FAO (2011) Food and Agriculture Organization of the United Nations.
- Farrauto, R.J. and Bartholomew, C.H. (1997) *Fundamentals of Industrial Catalytic Processes*, Blackie Academic & Professional, Weinheim.
- Felix, F. (1974) Energy independence: Goal for the '80s. *Electrical World* March 1, 1–4.
- Food and Agriculture Organization of the United Nations (FAO) (2008) The State of Food Insecurity in the World 2008. Available at <http://www.fao.org/docrep/011/i0291e/i0291e00.htm> (accessed 26 June 2012).
- Gerke, H., Ruthardt, K., Mathiak, J., and Roosen, C. (2010) Hydrogen: a small molecule with large impact, in *Proceedings of the DGMK Conference: The Future Role of Hydrogen in Petrochemistry and Energy Supply*, ISBN 978-3-941721-07-4, DGMK, p. 7.
- Gleick, P.H. (1996) *Water Resources. Encyclopedia of Climate and Weather*, Oxford University Press, New York, pp. 817–823.
- Global footprint network (2009) Living Planet Report 2008. Available at <http://www.footprintnetwork.org/en/index.php/GFN/page/publications/#Reports>. (accessed 26 June 2012).
- Guenther, R. (1984) *Verbrennung und Feuerungen*, Springer, Berlin.
- Gunstone, F.D. (ed.) (2011) *Vegetable Oil in Food Technology. Composition, Properties and Use*, Wiley Blackwell, Chichester.
- Hauthal, H.G. (2005) Tenside, Wasch- und Reinigungsmittel, in *Winnacker, Kuechler – Chemische Technik* (eds. R. Dittmeyer, W. Keim, G. Kreysa, and A. Oberholz), Wiley-VCH Verlag GmbH, Weinheim, pp. 795–936.
- Hillring, B. (2006) World trade in forest products and wood fuel. *Biomass Bioenergy*, **30**, 815–825.
- Hoekstra, A.Y. and Chapagain, A.K. (2007) Water footprints of nations: water use by people as a function of their consumption pattern. *Water Res. Manage.*, **21**, 35–48.
- Hoekstra, A.Y. and Hung, P.Q. (2002) Virtual water trade: A quantification of virtual water flows between nations in relation to international crop trade. Value of Water Research Report Series No. 11, UNESCO-IHE, Delft, Netherlands.
- IEA (International Energy Agency) (2006) Key world energy statistics 2006 (<http://www.iea.org>).
- IEA (International Energy Agency) (2007) Renewables in global energy supply (<http://www.iea.org>).
- IEA (International Energy Agency) (2009) Key world energy statistics 2009 (<http://www.iea.org>).
- IEA (International Energy Agency) (2009) Chemical and Petrochemical Sector. Potential of best practise technology and other measures for improving energy efficiency. (<http://www.iea.org>).
- Inglehart, R., Foa, R., Peterson, C., and Welzel, C. (2008) Development, freedom, and rising happiness a global perspective. *Perspect. Psychol. Sci.*, **3**, 264–285.
- IPCC (2007) *Climate Change 2007: The Physical Science Basis. Contribution of Working Group I to the Fourth Assessment Report of the Intergovernmental Panel on Climate Change*, Cambridge University Press, Cambridge.
- Jess, A. (2010) What might be the energy demand and energy mix to reconcile the world's pursuit of welfare and happiness with the necessity to preserve the integrity of the biosphere? *Energy Policy*, **38**, 4663–4678.
- Keim, W., Behr, A., and Schmidt, G. (1986) *Grundlagen der industriellen Chemie*, Otto Salle Verlag, Frankfurt.
- Klimont, Z., Streets, D.G., Gupta, S., Cofala, J., Lixin, F., and Yoichi Ichikawa, Y. (2002) Anthropogenic emissions of non-methane volatile organic compounds in China. *Atmos. Environ.*, **36**, 1309–1322.
- Lang, H.J. (1948) Simplified approach to preliminary capital cost estimating. *Chem. Eng.*, **74**, 112–113.
- Lange, J.-P. (2001) Fuels and chemicals manufacturing. *Cattech*, **5**, 82–96.
- Lange, J.P. and Tijm, P.J.A. (1996) Process for converting methane to liquid fuels: Economic screening through energy management. *Chem. Eng. Sci.*, **51**, 237–2387.
- Lauritzen, S.-E. (2005) Highly variable northern hemisphere temperatures reconstructed from low- and high-resolution proxy data. *Nature*, **433**, 613–617.
- Layard, R. (2003) Happiness: Has social science a clue? Lionel Robbins memorial lectures 2002/03 delivered on 3 to 5.03.2003 at the London School of Economics.
- Liu, Z., Shi, S., and Li, Y. (2010) Coal liquefaction technologies – development in China and challenges in chemical reaction engineering. *Chem. Eng. Sci.*, **65**, 12–17.
- Lucarelli, C. and Vaccari, A. (2011) Examples of heterogeneous catalytic processes for fine chemistry. *Green Chem.*, **13** (8), P 1941–1949.
- MacKay, D.J.C. (2008) Sustainable Energy - without the hot air. UIT Cambridge (available online from www.withouthotair.com, accessed 05.09.2012).
- Mann, M.E., Bradley, R.S., and Hughes, M.K. (1999) Northern hemisphere temperatures during the past millennium: Inferences, uncertainties, and limitations. *Geophys. Res. Lett.*, **26**, 759–762.
- Meyer, T. and Keurentjes, J. (eds.) (2005) *Handbook of Polymer Reaction Engineering*, Wiley-VCH Verlag GmbH, Weinheim.
- Moberg, A., Sonechkin, D.M., Holmgren, K., Datsenko, N.M., Karlen, W., and Lauritzen, S.E. (2005) Highly variable northern hemisphere temperatures reconstructed from low- and high-resolution proxy data. *Nature*, **433**, 613–617.
- Moulijn, J.A., Makkee, M., and Van Diepen, A. (2004) *Chemical Process Technology*, Wiley-VCH Verlag GmbH, Weinheim.
- Mueller, F. (ed.) (1999) *Agrochemicals – Composition, Production, Toxicology, Applications*, Wiley-VCH Verlag GmbH, Weinheim.
- MWV (Mineraloelwirtschaftsverband) (2009) Jahresbericht. Mineraloelzahlen 2008 (www.mwv.de).

- Nashawi, I.S., Malallah, A., and Al-Bisharah, M. (2010) Forecasting world crude oil production using multicyclic Hubbert model. *Energy Fuels*, **24**, 1788–1800.
- NORC (2012) National Opinion Research Center/University Chicago. http://www.norc.org/PDFs/publications/GSSTrendsinWellbeing_March2011.pdf (accessed 07.09.2012)
- OECD-FAO (2011) Food and Agriculture Organization of the United Nations. Agricultural outlook 2011–2020.
- Oerlemans, J. (2005) Extracting a climate signal from 169 glacier records. *Science*, **308**, 675–677.
- Ohara, T., Akimoto, H., Kurokawa, J., Horii, N., Yamaji, K., Yan, X., and Hayasaka, T. (2007) An Asian emission inventory of anthropogenic emission sources for the period 1980–2002. *Atmos. Chem. Phys.*, **7**, 4419–4444.
- Olivier, J.G.J., Bouwman, A.F., Van der Hoek, K.W., and Berdowski, J.J.M. (1998) Global air emission inventories for anthropogenic sources of NO_x, NH₃ and N₂O in 1990. *Environ. Pollut.*, **102**, 135–148.
- Onken, U. and Behr, A. (1996) *Chemische Prozes-skunde*, Wiley-VCH Verlag GmbH, Weinheim.
- Pfennig, A. (2007) Supporting debottlenecking of global processes by applying appropriate balances. *Biotechnol. J.*, **2**, 1485–1496.
- Riedel, E. and Janiak, C. (2011) *Anorganische Chemie*, De Gruyter, Berlin/New York.
- Rosillo-Calle, F., Pelkmans, L., and Walter, A. (2009) A global overview of vegetable oils, with reference to biodiesel. IEA Bioenergy report. Available at <http://www.globalbioenergy.org/bioenergyinfo/bioenergy-and-trade/detail/pt/news/40140/icode/4/> (accessed 26 June 2012).
- Rothenberg, G. (2008) *Catalysis: Concepts and Green Application*, Wiley-VCH, Weinheim.
- Ruckriegel, K. (2007) Erforschung von Glueck und Mitmenschlichkeit. *Orientierungen Wirtschafts-Gesellschaft*, **113**, 75–78.
- RWE (2005) World energy report 2005, World market for hard coal, 2005 edition (www.euracoal.be).
- Saade, G.A. (2009) Chemical Economics Handbook-SRI Consulting. <http://www.sriconsulting.com/CEH/Public/Reports/674.5000/Methanol, 20.10.09>.
- Saito, M., Takeuchi, M., Fujitani, T., Toyir, J., Luo, S., Wu, J., Mabuse, H., Ushikoshi, K., Mori, K., and Watanabe, T. (2000) Advances in joint research between NIRE and RITE for developing a novel technology for methanol synthesis from CO₂ and H₂. *Appl. Organomet. Chem.*, **14**, 763–772.
- Saudan, L.A. (2007) Hydrogenation processes in the synthesis of perfumery ingredients. *Acc. Chem. Res.*, **40** (12), P 1309–1319.
- Schollnberger, W.E. (2006) From scarcity to plenty. Who shapes the future mix of primary energy? What might it be? *Erdoel Erdgas Kohle*, **122**, 8–20.
- Sedriks, W. (1995) Petrochemical industry drivers. *Chemtech.*, **25**, 56–60.
- Sheldon, R. (1994) Consider the environmental quotient. *Chemtech.*, **24**, 38–47.
- Shiklomanov, I.A. (2000) Appraisal and assessment of world water resources. *Water Int.*, **25**, 11–32.
- Smil, V. (2003) *Energy at the Crossroads: Global Perspectives and Uncertainties*, MIT Press, Cambridge.
- Smith, R. (2005) *Chemical Process Design and Integration*, John Wiley & Sons, Ltd, Chichester.
- Smith, S.J., Pitcher, H., and Wigley, T.M.L. (2001) Global and regional anthropogenic sulfur dioxide emissions. *Global Planet. Change*, **29**, 99–119.
- Sophocleus, M. (2004) Global and regional water availability and demand: prospects for the future. *Nat. Resour. Res.*, **13**, 61–75.
- Stern, D.I. (2005) Global sulfur emissions from 1850 to 2000. *Chemosphere*, **58**, 163–175.
- Talbiersky, J. (2006) Der Chemierohstoff Kohle: gestern, heute und morgen. *Erdoel Erdgas Kohle*, **123**, 32–37.
- Trost, B.M. (1991) The atom economy - a search for synthetic efficiency. *Science*, **254**, 1471–1477.
- Ulber, R., Sell, D., and Hirth, T. (eds) (2011) *Renewable Raw Materials*, Wiley-VCH Verlag GmbH, Weinheim.
- Vestreng, V., Ntziachristos, L., Semb, A., Reis, S., Isaksen, I.S.A., and Tarrason, L. (2008) Evolution of NO_x emissions in Europe with focus on road transport control measures. *Atmos. Chem. Phys. Discuss.*, **8**, 10697–10747.
- Vogel, W. (2006) *Chemistry of Glass*, John Wiley & Sons.
- Wang, X., Mauzerall, D.L., Hu, Y., Russell, A. G., Larson, E.D., Woo, J.H., Streets, D.G., and Guenther, A. (2005) A high-resolution emission inventory for eastern China in 2000 and three scenarios for 2020. *Atmos. Environ.*, **39**, 5917–5933.
- Weissermel, K.K. and Arpe, H.-J. (2003) *Industrial Organic Chemistry*, Wiley-VCH Verlag GmbH, Weinheim.
- WHO/UNICEF (2008) *Progress on Drinking Water and Sanitation*, WHO Press, Geneva.
- Wiley-VCH (eds.) (2005) *Ullmann's Encyclopedia of Industrial Chemistry*, Wiley-VCH Verlag GmbH, Weinheim.
- Wiley-VCH (eds.) (2012) *Ullmann's Encyclopedia of Industrial Chemistry*, Electronic Release 2012, Wiley-VCH Verlag GmbH, Weinheim.
- Winnacker-Kuechler (1970) *Chemische Technologie*, vol. 2, Carl Hanser Verlag, Muenchen.
- Wolf, B. and Scheer, H. (2005) *Öl aus Sonne. Die Brennstoffformel der Erde*, Ponte Press, Bochum, Germany.
- World bank (2010) World Development Indicators Online. www.worldbank.org.
- World Resources Institute (2010) Industrial roundwood. www.wri.org/publication/pilot-analysis-global-ecosystems-forest-ecosystems.
- WRI (2010) World Resources Institute. www.earthtrends.wri.org.

Chapter 6

- Agroskin, A.A., Artamonova, E.V., Goncharov, E.I., Tyagunov, V.M., and Valyavin, G.G. (1978) Thermochemical characteristics of petroleum residue coking. *Chem. Techn. Fuels Oils*, **14**, 412–415.
- Akehata, T., Namkoong, S., Kubota, H., and Shindo, M. (1961) The effect of intraparticle temperature distribution on the catalytic effectiveness factor. *Can. J. Chem. Eng.*, **39**, 127–129.
- Albright, L.F. (1966) Modern chemical technology. VI. Alkylation processes using hydrogen fluoride as catalyst. *Chem. Eng.*, **73**, 205–210.
- Albright, L.F. (1966) Modern chemical technology. VII. Comparisons of alkylation processes. *Chem. Eng.*, **73**, 211–215.
- Albright, L.F. (1990) Modern alkylation - 1. Alkylation will be key process in reformulated gasoline era. *Oil Gas J.*, **88**, 79–92.
- Albright, L.F. (1990) Modern alkylation. 2. Sulfuric acid and hydrogen fluoride processes compared, and new technologies revealed. *Oil Gas J.*, **88**, 72–77.
- Albright, L.F. (2003) Alkylation of isobutane with C3-C5 olefins to produce high-quality gasolines: physicochemical sequence of events. *Ind. & Eng. Chem. Res.*, **42**, 4283–4289.
- Albright, L.F. (2009) Present and future alkylation processes in refineries. *Ind. & Eng. Chem. Res.*, **48**, 1409–1413.
- Albright, L.F. and Eckert, R.E. (2001) Formation and separation of sulfuric acid/n-heptane dispersions: applications to alkylation. *Ind. & Eng. Chem. Res.*, **40**, 4032–4039.
- Anastasov, A.I. (2002) A study of the influence of the operating parameters on the temperature of the hot spot in a fixed bed reactor. *Chem. Eng. J.*, **86**, 287–297.
- Anastasov, A.I. (2003) An investigation of the kinetic parameters of the o-xylene oxidation process carried out in a fixed bed of high-productive vanadia-titania catalyst. *Chem. Eng. Sci.*, **58**, 89–98.
- Anderson, R.B. (1984) *The Fischer-Tropsch Synthesis*, Academic Press, Orlando.
- Aparicio, L.M. and Dumesic, J.A. (1994) Ammonia synthesis kinetics: surface chemistry, rate expressions, and kinetic analysis. *Top. Catal.*, **1**, 233–252.
- Appl, M. (1999) *Ammonia*, Wiley-VCH Verlag GmbH, Weinheim.
- Arhancet, J.P., Davis, M.E., Merola, J.S., and Hanson, B.E. (1989) Hydroformylation by supported aqueous-phase catalysis: a new class of heterogeneous catalysts. *Nature*, **339**, 454–455.
- Armor, J.N. (1992) Review: environmental catalysis. *Appl. Catal. B*, **1**, 221–256.
- Arpe, H.-J. (2007) *Industrielle Organische Chemie*, Wiley-VCH Verlag GmbH, Weinheim.

- Arthur, J.R. (1951) Reactions between carbon and oxygen. *Trans. Faraday Soc.*, **47**, 164–178.
- Asinger, F. (1968) *Methanol - Chemie- und Energierohstoff: Die Mobilisation der Kohle*, Springer Verlag, Berlin.
- Atkins, P.W. and de Paula, J. (2002) *Physical Chemistry*, Oxford University Press, Oxford.
- Avidan, A.A. and Shinnar, R. (1990) Development of catalytic cracking technology. A lesson in chemical engineering. *Ind. Eng. Chem. Res.*, **29**, 931–942.
- Baerns, M., Behr, A., Brehm, A., Gmehlung, J., Hofmann, H., Onken, U., and Renken, A. (2006) *Technische Chemie*, Wiley-VCH Verlag GmbH, Weinheim.
- Baerns, M., Behr, A., Brehm, A., Gmehlung, J., Hofmann, H., Onken, U., and Renken, A. (2006) *Technische Chemie*, Wiley-VCH, Weinheim, pp. 617–629.
- Baerns, M., Hofmann, H., and Renken, A. (1987) *Chemische Reaktionstechnik. Lehrbuch der Technischen Chemie*, Band I, Georg Thieme Verlag, Stuttgart.
- Baerns, M., Hofmann, H., and Renken, A. (2002) *Chemische Reaktionstechnik. Lehrbuch der Technischen Chemie*, Wiley-VCH Verlag GmbH, Weinheim.
- Bakemeier, H., Huberich, T., Krabetz, R., Liebe, W., Schunck, M., and Mayer, D. (1997) Ammonia, in *Ullmann's Encyclopedia of Industrial Chemistry, Fifth Edition on, CD-ROM*, Wiley-VCH Verlag GmbH, Weinheim.
- Bartsch, R. and Tanielian, C. (1974) Hydrodesulfurization. I. hydrogenolysis of benzothiophene and dibenzothiophene over $\text{CoO}-\text{MoO}_3-\text{Al}_2\text{O}_3$ catalyst. *J. Catal.*, **35**, 353 ff.
- Bathen, D. (2009) Adsorption: neues auf der ACHEMA 2009. *Chem. Ing. Tech.*, **81**, 1503–1549.
- Becker, P.W. (1981) The role of synthetic fuel in world war II Germany. *Air & Space Power J.* (July/August).
- Bedoukian, P.Z. (1970) Progress in perfume materials. *Am. Perfumer Cosmetics*, **85**, 25–35.
- Behr, A. (2008) *Angewandte homogene Katalyse*, Wiley-VCH Verlag GmbH, Weinheim.
- Behr, A., Agar, D.W., and Joerissen, J. (2010) *Einführung in die Technische Chemie*, Spektrum Akademischer Verlag, Heidelberg.
- Behr, A., Obst, D., Schulte, C., and Schosser, T. (2003) Highly selective tandem isomerization-hydroformylation reaction of trans-4-octene to n-nonanal with rhodium-BIPHEPHOS catalyst. *J. Mol. Catal. A-Chem.*, **206**, 179–184.
- Benthaus, F. et al. (1978) *Rohstoff Kohle: Eigenschaften, Gewinnung, Veredelung*, Verlag Chemie, Weinheim.
- Bergner, D. (1994) Entwicklungsstand der Alkalichlorid-Elektrolyse. Teil 2: Elektrochemische Großen, wirtschaftliche Fragen. *Chem. Ing. Techn.*, **66**, 1026–1033.
- Bergner, D., Hartmann, M., and Staab, R. (1987) Fortschritte auf dem Gebiet der Alkalichlorid-Elektrolyse. *Chem. Ing. Techn.*, **59**, 271–280.
- BGS (2010) British Geological Survey. World mineral production 2004 – 2008, Nottingham. www.bgs.ac.uk.
- Bhaduri, S. and Mukesh, D. (2000) *Homogeneous Catalysis: Mechanisms and Industrial Applications*, John Wiley & Sons, Ltd, Chichester.
- Birtill, J.J. (2009) Some experiences in industrial catalysis. *J. Mol. Catal. A: Chem.*, **305**, 183–189.
- Bissett, L. (1977) Equilibrium constants for shift reactions. *Chem. Eng.*, **84**, 155–156.
- Boegner, W., Kraemer, M., Krutzsch, B., Pischinger, S., Voigtlaender, D., Wenninger, G., Wirbeleit, F., Brogan, M.S., Brisley, R.J., and Webster, D.E. (1995) Removal of nitrogen oxides from the exhaust of a lean-tune gasoline engine. *Appl. Catal. B: Environ.*, **7**, 153–171.
- Boesmann, A., Datsevitch, L., Jess, A., Lauter, A., Schmitz, C., and Wasserscheid, P. (2001) Deep desulfurization of diesel fuel by extraction with ionic liquids. *Chem. Commun.*, **23**, 2494–2495.
- Bokhoven, C. and van Raayen, W. (1954) Diffusion and reaction rate in porous synthetic ammonia catalysts. *J. Phys. Chem.*, **58**, 471–476.
- Bollmann, A., Blann, K., Dixon, J.T., Hess, F., Killian, E., Maumela, H., McGuinness, D.S., Morgan, D.H., Neveling, A., Otto, S., Overett, M., Slawin, A.M.Z., Wasserscheid, P., and Kuhlmann, S. (2004) Ethylene tetramerization: a new route to produce 1-octene in exceptionally high selectivities. *J. Am. Chem. Soc.*, **126** (45), P 14712–14713.
- Bolton, D.H. (1969) Methanol production by the ICI [Imperial Chemical Industry, Ltd.] low-pressure process. *Chem. Ing. Tech.*, **41**, 129–134.
- Bowker, M., Hadden, R.A., Houghton, H., Hyland, J.N.K., and Waugh, C.J. (1988) Mechanism of methanol synthesis on copper/zinc oxide/alumina catalysts. *J. Catal.*, **109**, 263–273.
- Bradley, D. and Entwistle, A.G. (1961) Determination of the emissivity, for total radiation, of small platinum-10% rhodium wires in the temperature range 600–1450 °C. *Br. J. Appl. Phys.*, **12**, 708–711.
- Briggs, J.R. (1989) The selective trimerization of ethylene to hex-1-ene. *J. Chem. Soc., Chem. Commun.*, 674–675.
- Broecker, F.J., Gruendler, K.H., Marosi, L., Schwarzmüller, M., Triebskorn, B., and Zirker, G. (1980) DE 2846614, BASF.
- Bryant, D.R. (2006) Classical homogeneous catalyst separation technology, in *Catalyst Separation, Recovery and Recycling – Chemistry and Process Design* (eds D.-J. Cole-Hamilton and R.P. Tooze), Springer, Dordrecht, pp. 9–37.
- Buzanowski, M.A. and Yang, R.T. (1990) Simple design of monolith reactor for selective catalytic reduction of NO for power plant emission control. *Ind. Eng. Chem. Res.*, **29**, 2074–2078.
- Calderbank, P.H., Chandrasekharan, K., and Fumagalli, C. (1977) The prediction of the performance of packed-bed catalytic reactors in the air-oxidation of o-xylene. *Chem. Eng. Sci.*, **32**, 1435–1443.
- Cejka, J., Corma, A., and Zones, S. (2010) *Zeolites and Catalysis, Synthesis, Reactions and Applications*, Wiley-VCH Verlag GmbH, Weinheim.
- Cengel, Y.A. (2002) *Heat Transfer*, McGraw-Hill College, Boston.
- Chang, T., Rousseau, R.W., and Klipatrick, P.K. (1986) Methanol synthesis reactions: calculation of equilibrium conversions using equations of state. *Ind. Eng. Chem. Proc. Des. Dev.*, **25**, 477–481.
- Chauvin, Y., Mussmann, L., and Olivier, H. (1995) A novel class of versatile solvents for two-phase catalysis: hydrogenation, isomerization, and hydroformylation of alkenes catalyzed by rhodium complexes in liquid 1,3-dialkylimidazolium salts. *Angew. Chem. Int. Ed.*, **34**, 2698–2700.
- Chen, J., Yang, H., Wang, N., Ring, Z., and Dabros, T. (2008) Mathematical modeling of monolith catalysts and reactors for gas phase reactions. *Appl. Catal. A: Gen.*, **345**, 1–11.
- Cheng, W.-H. and Kung, H.H. (1994) *Methanol Production and Use, Chemical Industries*, vol. 57, Marcel Dekker, New York.
- Cherednichenko, V.M. (1953) Doctoral thesis. Karpova, Physico Chemical Institute, Moscow, Russia.
- Cheung, H., Tanke, R.S., and Torrence, G. P. (2000) Acetic acid in *Ullmann's Encyclopaedia*, 7th edn, Wiley-VCH Verlag GmbH.
- Chinchen, G.C., Denny, P.J., Parker, D.G., Short, G.D., Spencer, M.S., Waugh, K.C., and Whan, D.A. (1984) The activity of copper-zinc oxide-aluminum oxide methanol synthesis catalysts. *Am. Chem. Soc. Div. Fuel Chem.*, **29**, 178–188.
- Chinchen, G.C., Denny, P.J., Parker, D.G., Spencer, M.S., and Whan, D.A. (1987a) Mechanism of methanol synthesis from carbon dioxide/carbon monoxide/hydrogen mixtures over copper/zinc oxide/alumina catalysts: use of carbon-14-labeled reactants. *Appl. Catal.*, **30**, 333–338.
- Chinchen, G.C., Hay, C.M., Vandervell, H. D., and Waugh, K.C.J. (1987b) The measurement of copper surface areas by reactive frontal chromatography. *J. Catal.*, **103**, 79–86.
- Chinchen, G.C., Waugh, K.C., and Whan, D.A. (1986) The activity and state of the copper surface in methanol synthesis catalysts. *Appl. Catal.*, **25**, 101–107.
- Chorkendorff, I. and Niemantsverdriet, J.W. (2003) *Concepts of Modern Catalysis and Kinetics*, Wiley-VCH Verlag GmbH, Weinheim, pp. 377–400.
- Clark, G.S. (1998) Menthol. *Perfumer Flavorist*, **23**, 33–46.

- Cole-Hamilton, D.-J. and Tooze, R.P. (eds) (2006) *Catalyst Separation, Recovery and Recycling – Chemistry and Process Design*, Springer, Dordrecht.
- Collins, N.R. and Twigg, M.V. (2007) Three-way catalyst emissions control technologies for spark-ignition engines - recent trends and future developments. *Top. Catal.*, **42/43**, 323–332.
- Corma, A. and Martinez, A. (1993) Chemistry, catalysts, and processes for isoparaffin-olefin alkylation: actual situation and future trends. *Catal. Rev. Sci. Eng.*, **35**, 483–570.
- Daly, F.P. (1978) Hydrodesulfurization of benzothiophene over CoO–MoO₃–Al₂O₃ catalyst. *J. Catal.*, **51**, 221.
- Damkoehler, G. (1936) Einflusse der Stroemung, Diffusion und des Waermeueberganges auf die Leistung von Reaktionsoefen. I. Allgemeine Gesichtspunkte fuer die Uebertragung eines chemischen Prozesses aus dem Kleinen ins Große. *Z. Elektrochem.*, **42**, 846–862.
- Damkoehler, G. (1937a) Einflusse der Stroemung, Diffusion und des Waermeueberganges auf die Leistung von Reaktionsoefen. II. Die isotherme, raumbestaendige, homogene Reaktion erster Ordnung. *Z. Elektrochem.*, **43**, 1–8.
- Damkoehler, G. (1937b) Einflusse der Stroemung, Diffusion und des Waermeueberganges auf die Leistung von Reaktionsoefen. III. Zur Frage der maximalen Uebertemperatur in einem rohrfoermigen Kontaktlofen bei exothermer Uebertemperatur. *Z. Elektrochem.*, **43**, 8–13.
- Damkoehler, G. (1939) Stroemungs- und Waermeuebergangsprobleme in chemischer Technik und Forschung. *Chem. Ing. Tech.*, **12**, 469.
- Delmon, B., Froment, G.F., and Grange, P. (eds) (1999) *Hydrotreatment and Hydro-cracking of Oil Fractions*, Elsevier, Amsterdam.
- Denise, B. and Sneeden, R.P.A. (1982) Hydrogenate CO₂. *CHEMTECH*, 108–112.
- Dennison, P.R., Packer, K.J., and Spencer, M.S.J. (1989) Proton and carbon-13 nuclear magnetic resonance investigations of the copper/zinc/aluminum oxide methanol-synthesis catalyst. *J. Chem. Soc., Faraday Trans. 1*, **85**, 3537–3560.
- Deschler, U., Kleinschmit, P., and Panster, P. (1986) 3-Chloropropyltrialkoxysilane - a key component for the industrial preparation of organofunctional silane and polysiloxane. *Angew. Chem.*, **98** (3), 237–253.
- Devanney, M.T. (2006) Propylene oxide, in *Chemical Economics Handbook*, SRI Consulting.
- Devanney, M.T. (2007) Ethylene oxide, in *Chemical Economics Handbook*, SRI Consulting.
- Dittmeyer, R., Keim, W., Kreysa, G., and Oberholz, A. (eds) (2006) *Winnacker-Kuechler: Chemische Technik, Prozesse und Produkte*, Wiley-VCH Verlag GmbH, Weinheim.
- Dixon, J.T., Green, M.J., Hess, F.M., and Morgan, D.H. (2004) Advances in selective ethylene trimerisation. *J. Organomet. Chem.*, **689**, 3641–3668.
- Donnelly, T.J. and Satterfield, C.N. (1989) Product distributions of the Fischer-Tropsch synthesis on precipitated iron catalysts. *Appl. Catal. A Gen.*, **52**, 93–114.
- Drießen-Hoelscher, B., Wasserscheid, P., and Keim, W. (1998) Recycle of homogeneous transition metal catalysts in two liquid phases. *CATTECH*, **3**, 47–52.
- Dry, M.E. (1981) The Fischer-Tropsch synthesis. *Catal. Sci. Technol.*, **1**, 159–255.
- Dry, M.E. (1982) Catalytic aspects of industrial Fischer-Tropsch synthesis. *J. Mol. Catal.*, **17**, 133–144.
- Dry, M.E. (2002) The Fischer-Tropsch process: 1950–2000. *Catal. Today*, **71**, 227–241.
- DuPont (2010) Alkylation: Introduction. http://www2.dupont.com/Clean_Technologies/en_US/assets/downloads/Alkylation.pdf.
- Dybkjaer, I. (1995) in *Ammonia, Catalysis and Manufacture* (ed. A. Nielsen), Springer, Heidelberg, pp. 199–308.
- Eckermann, R. (1983) Thermische crackverfahren. *Chem. Ing. Tech.*, **55**, 134–137.
- Eigenberger, G. (1983) Dynamik und Stabilitaet verfahrenstechnischer Prozesse. *Chem. Ing. Tech.*, **55**, 503.
- Eilers, J., Postuma, S.A., and Sie, S.T. (1990) The Shell middle distillate synthesis process (SMDS). *Catal. Lett.*, **7**, 253–270.
- Ellis, P.J. and Paul, C.A. (1998) Tutorial: Delayed coking. Great Lakes Carbon Corporation, Port Arthur, USA (unpublished), see www.coking.com/DECOKTUT.pdf, accessed 05.09.2012.
- Elschenbroich, C. (2003) *Organometallchemie*, Teubner Verlag, Stuttgart, pp. 263–268.
- Elvers, B. (ed.) (2008) *Handbook of Fuels*, Wiley-VCH Verlag GmbH, Weinheim.
- Emberger, R. and Hopp, R. (1987) Synthesis and sensory characterization of menthol enantiomers and their derivatives for the use in nature identical peppermint oils. *Speciality Chem. Mag.*, **7**, 193–201.
- Emig, G. and Klemm, E. (2005) *Technische Chemie*, Springer, Berlin.
- Emig, G., Hofmann, H., Hoffmann, U., and Fiand, U. (1980) Experimental studies on runaway of catalytic fixed-bed reactors. *Chem. Eng. Sci.*, **35**, 249.
- Ertl, G. (1991) in *Elementary Steps in Ammonia Synthesis: The Surface Science Approach. Catalytic Ammonia Synthesis* (ed. J.R. Jennings), Plenum Press, New York, pp. 109–131.
- Ertl, G., Knoetzinger, H., and Weitkamp, J. (1999) *Environmental Catalysis*, Wiley-VCH Verlag GmbH, Weinheim.
- Esser, J., Wasserscheid, P., and Jess, A. (2004) Deep desulphurization of oil refinery streams by extraction with ionic liquids. *Green Chem.*, **6**, 316–322.
- Etzold, B. (2007) Epimerisierung der Menthol-Diastereomere: kinetische und reaktionstechnische Studien fuer die heterogen katalysierte Mentholsynthese Doctoral thesis, University of Bayreuth, Germany.
- Etzold, B. and Jess, A. (2008) Heterogeneously catalysed epimerisation of menthol stereoisomers – an instructive example to account for diffusion limitations in complex reaction networks. *Chem. Eng. Techn.*, **31**, 1282–1289.
- Etzold, B. and Jess, A. (2009) Epimerisation of menthol stereoisomers: kinetic studies of the heterogeneously catalysed menthol production. *Catal. Today*, **130**, 30–36.
- Euro Chlor (2011) Chlorine industry review. www.eurochlor.org.
- European Commission (2001) Integrated pollution prevention and control (IPPC). Reference document on best available techniques in the chlor-alkali manufacturing industry.
- European Union (1998) EU-Directive 98/70/EG.
- European Union (2001) Amtsblatt der Europaeischen Gemeinschaft (2001/C 213 E/13).
- Evonik Industries (2009) Wachstumstreiber im Portfolio: Wasserstoffperoxid. http://corporate.evonik.com/sites/dc/Downloadcenter/Evonik/Corporate/de/Investor-Relations/Portrait/Portrait_Wasserstoffperoxid_-_deutsch.pdf.
- Falbe, J. (ed.) (1977) *Chemierohstoffe aus Kohle*, G. Thieme, Stuttgart.
- Farag, H., Mochida, I., and Sakanishi, K. (2000) Fundamental comparison studies on hydrodesulfurization of dibenzothiophenes over CoMo-based carbon and alumina catalysts. *Appl. Catal. A: Gen.*, **194/195**, 147–157.
- Farrauto, R.J. and Bartholomew, C.H. (1997) *Fundamentals of Industrial Catalytic Processes*, Blackie Academic & Professional., Weinheim.
- Fedtke, M., Pritzkow, W., and Zimmermann, G. (1992) *Technische Organische Chemie – Grundstoffe, Zwischenprodukte, Finalprodukte, Polymere*, Deutscher Verlag fuer Grundstoffindustrie GmbH, Leipzig.
- Fernandes, F.A.N. (2005) Polymerisation kinetics of Fischer-Tropsch reaction on iron based catalysts and product optimisation. *Chem. Eng. Technol.*, **28**, 930–938.
- Fiebig, B. and Kuchling, T. (2009) Oxidation von o-Xylool zur Herstellung von Phthalsaeure-anhydrid Teil 1: Prozesssimulation der heterogen katalysierten Gasphasenoxidation. *Chem. Ing. Tech.*, **81**, 1467–1472.
- Fiedler, E., Grossmann, G., Kersebohm, D.B., Weiss, G., and Witte, C. (2000) Methanol, in *Ullmann's Encyclopaedia*, 7th edn, Wiley-VCH Verlag GmbH.
- Ford, T.J. (1986) Liquid-phase thermal decomposition of hexadecane: reaction mechanisms. *Ind. Eng. Chem. Fundam.*, **25**, 240–243.
- Forzatti, P. (2001) Present status and perspectives in de-NO_x SCR catalysis. *Appl. Catal. A: Gen.*, **222**, 221–236.

- Forzatti, P. and Tronconi, E. (1992) Adequacy of lumped parameter models for SCR reactors with monolith structure. *AICHE J.*, **38**, 201–210.
- Franck, H.G. and Knop, A. (1979) *Kohleveredlung*. Springer, Berlin.
- Franke, R., Rudek, M., and Baumgarten, G. (2010) Nanofiltration developed to application readiness. *Elements – Sci. Newsletter*, **30**, 6–11.
- Frohning, C.D., Kohlpaintner, C.W., and Bohnen, H.-W. (2002) Hydroformylation, in *Applied Homogeneous Catalysis with Organometallic Compounds* (eds B. Cornils and W.A. Herrmann), Wiley-VCH Verlag GmbH, Weinheim, pp. 31–103.
- Froment, G.F. and Bischoff, K.B. (1990) *Chemical Reactor Analysis and Design*, John Wiley & Sons, Inc., New York.
- Fujikawa, T., Idei, K., Ohki, K., Mizuguchi, H., and Usui, K. (2001) Kinetic behaviour of hydrogenation of aromatics in diesel fuel over silica-alumina-supported bimetallic Pt-Pd catalyst. *Appl. Catal. A Gen.*, **205**, 271–277.
- Garrou, P.E. (1985) Transition-metal-mediated phosphorus-carbon bond cleavage and its relevance to homogeneous catalyst deactivation. *Chem. Rev.*, **85** (3), P 171–185.
- Gary, J.H. (ed.) (2007) *Petroleum Refining - Technology and Economics*, 5th edn, CRC Press, Boca Raton.
- Gates, B.C., Katzer, J.R., and Schuit, G.C.A. (1979) *Chemistry of Catalytic Processes*, McGraw-Hill, New York.
- GDA (2011) Gesamtverband der Aluminium Industrie. www.aluinfo.de.
- Gerritsen, L.A., Herman, J.M., Klut, W., and Scholten, J.J.F. (1980) Hydroformylation with supported liquid phase rhodium catalysts. Part II. The location of the catalytic sites. *J. Mol. Catal.*, **9** (2), P 157–168.
- Gillespie, L.J. and Beattie, J.A. (1930) The thermodynamic treatment of chemical equilibria in systems composed of real gases. I. An approximate equation for the mass action function applied to the existing data on the Haber equilibrium. *Phys. Rev.*, **36**, 743–753.
- Girgis, M.J. and Gates, B.C. (1991) Reactivities, reaction networks, and kinetics in high-pressure catalytic hydroprocessing. *Ind. Eng. Chem. Res.*, **30**, 2021.
- Givens, E.N. and Venuto, P.B. (1970) Hydrogenolysis of benzo[b]thiophenes and related intermediates over cobalt molybdena catalyst. *Prepr. Am. Chem. Soc., Div. Fuel Chem.*, **14**, 135.
- Gladysz, J.A. (2009) Catalysis involving fluorous phases: fundamentals and directions for greener methodologies, in *Handbook of Green Chemistry* (ed. P. Anastas and R.H. Crabtree), Wiley-VCH Verlag GmbH, Weinheim, vol. 1, pp. 17–38.
- Gmehling, J. and Brehm, A. (1996) *Grundoperationen, Lehrbuch der Technischen Chemie*, Georg Thieme, Stuttgart.
- Gordon, C.M. and Leitner, W. (2006) Supercritical fluids – compressed gases as mobile phase and catalyst support, in *Catalyst Separation, Recovery and Recycling – Chemistry and Process Design* (eds D.-J. Cole-Hamilton and R. P. Tooze), Springer, Dordrecht, pp. 214–236.
- Graaf, G.H., Stamhuis, E.J., and Beenackers, A. A.C.M. (1988) Kinetics of low-pressure methanol synthesis. *Chem. Eng. Sci.*, **43**, 3185–3195.
- Grantom, R.L. and Royer, D.J. (1987) Ethylene, in *Ullmann's Encyclopedia of Industrial Chemistry A10*, 5th edn (eds W. Gerhartz *et al.*), VCH, Weinheim, pp. 45–93.
- Gu, Y. and Li, G. (2009) Ionic liquids-based catalysis with solids. State of the art. *Adv. Synth. Catal.*, **351**, 817–847.
- Haase, H. (1972) Markt und Verfahrensuebersicht fuer Phthalsaeureanhydrid (PSA). *Chem. Ing. Tech.*, **44**, 987–994.
- Haber, F. and Le Rossignol, R. (1907) Ueber das Ammoniakgleichgewicht. *Ber. Dtsch. Chem. Ges.*, **40**, 2144–2154.
- Haenel, M.W. (2006) 80 Jahre Fischer-Tropsch-Synthese - Renaissance eines Klassikers der Kohleverflüssigung. *Erdoel Erdgas Kohle*, **122**, 78–80.
- Haeusinger, P., Leitgeb, P., and Rueckborn, G. (1997) Nitrogen, in: *Ullmann's Encyclopedia of Industrial Chemistry, 5th Edition on CD-ROM*, Wiley-VCH Verlag GmbH, Weinheim.
- Hagen, J. (2006) *Industrial Catalysis*, Wiley-VCH Verlag GmbH, Weinheim.
- Hamann, C.H. and Vielstich, W. (2005) *Elektrochemie*, Wiley-VCH Verlag GmbH, Weinheim.
- Handforth, S.L. and Tilley, J.N. (1934) Catalysts for oxidation of ammonia to oxides of nitrogen. *Ind. Eng. Chem.*, **26**, 1287–1292.
- Haertl, C., Heners, J., and Herion, C. (1996) *Der Steamcracker 2*, BASF AG, Ludwigshafen.
- Haul, R. (1985) Das Portrait: Friedrich Bergius (1884–1949). *Chem. Z.*, **19**, 59–67.
- Haumann, M. and Riisager, A. (2008) Hydroformylation in room temperature ionic liquids (RTILs): catalyst and process developments. *Chem. Rev.*, **108**, 1474–1497.
- Hawthorn, R.D. (1974) Afterburner catalysts - effects of heat and mass transfer between gas and catalyst surface. *AICHE Symp. Ser.*, **137**, 428–438.
- Heck, R.M. and Farrauto, R.J. (2001) Automobile exhaust catalysts. *Appl. Catal. A: Gen.*, **221**, 443–457.
- Hedden, K. (1976) Coal gasification, in *Alternative Energy Sources* (ed. J.P. Hartnett), Academic Press, New York.
- Hegedus, L.L. (1975) Temperature excursions in catalytic monoliths. *AICHE J.*, **21**, 849–853.
- Hein, O. (1999) Zur Messung und Berechnung der Zuendtemperatur fester Brennstoffe, Diploma thesis, Engler-Bunte-Institute, University Karlsruhe, Germany.
- Heinloth, K. (2003) *Die Energiefrage*, Vieweg & Sohn Verlag, Wiesbaden.
- Herman, R.G., Klier, K., Simmons, G.W., Finn, B.P., and Bulko, J.B. (1979) Catalytic synthesis of methanol from CO/H₂. *J. Catal.*, **56**, 407–429.
- Hess, J.C. (1986) Untersuchungen zur Prozessfuehrung bei der Hochtemperaturverkokung von Steinkohlen im Stampfbetrieb. Doctoral thesis, University Karlsruhe, Germany.
- Heynert, G. and Hedden, K. (1961) Temperaturprofil und Kinetik der Umsetzungen im Hochofen. *Chem. Ing. Tech.*, **33**, 469–478.
- Hintermair, U., Zhao, G., Santini, C.C., Muldoon, M.J., and Cole-Hamilton, D.J. (2007) Supported ionic liquid phase catalysis with supercritical flow. *Chem. Commun.*, (14), 1462–1464.
- Hirano, T. (2001) *Advances in Diesel fuel Production in Japan*, Idemitsu Kosan Co. Ltd, Tokyo.
- Hjortkjaer, J., Scurrell, M.S., and Simonsen, P. (1979) Supported liquid-phase hydroformylation catalysts containing rhodium and triphenylphosphine. *J. Mol. Catal.*, **6** (6), 405–420.
- Holladay, J.D., Hu, J., King, D.L., and Wang, Y. (2009) An overview of hydrogen production technologies. *Catal. Today*, **139**, 244–260.
- Holleman, A.F. and Wiberg, E. (1995) *Lehrbuch der Anorganischen Chemie*, De Gruyter, Berlin.
- Holzmann, H. (1967) Ueber die katalytische Oxidation von Ammoniak bei der industriellen Salpetersaeure-Herstellung. *Chem. Ing. Tech.*, **39**, 89–95.
- Holzmann, H. (1968) Platin-Rueckgewinnung bei der NH₃-Verbrennung an Platin/Rhodiumnetzkatalysatoren. *Chem. Ing. Tech.*, **40**, 1229–1237.
- Hoogschagen, J. (1955) Diffusion in porous catalysts and adsorbents. *Ind. Eng. Chem.*, **47**, 906–912.
- Hopp, R. (1996) (–)-Menthol: an example of the various methodologies applied in the production of enantiomers. *Riv. Ital.*, **7**, 111–130.
- Horvath, I.T. and Rabai, J. (1994) Facile catalyst separation without water: fluorous biphasic hydroformylation of olefins. *Science*, **266**, 72–75.
- Houalla, M., Broderick, D.H., Sapre, A.V., Nag, N.K., de Beer, V.H.J., Gates, B.C., and Kwart, H. (1980) Hydrodesulfurization of methyl-substituted dibenzothiophenes catalyzed by sulfided Co-Mo/γ-Al₂O₃. *J. Catal.*, **61**, 523.
- Houalla, M., Nag, N.K., Sapre, A.V., Broderick, D.H., and Gates, B.C. (1978) Hydrodesulfurization of dibenzothiophene catalyzed by sulfided cobalt oxide-molybdenum trioxide/γ-alumina: the reaction network. *AICHE J.*, **24**, 1015 ff.
- Huff, G.A. and Satterfield, C.N. (1984a) Intrinsic kinetics of the Fischer-Tropsch synthesis on a reduced fused-magnetite catalyst. *Ind. Eng. Chem. Proc. Des. Dev.*, **23**, 696.
- Huff, G.A. and Satterfield, C.N. (1984b) Evidence for two chain growth probabilities on iron catalysts in the Fischer-Tropsch synthesis. *J. Catal.*, **85**, 370–379.

- IEA (International Energy Agency) (2004) *Bio-fuels for Transport – An International Perspective*, IEA Publication, Paris.
- IEA (International Energy Agency) (2009) Chemical and Petrochemical Sector. Potential of best practise technology and other measures for improving energy efficiency. Available at http://www.iea.org/papers/2009/chemical_petrochemical_sector.pdf.
- IFA (2007) International Fertilizer Industry Association. /HomePage/STATISTICS/Production-and-trade (2010_ammonia_public.xls), accessed 05.09.2012).
- Ivanov, E.B., Kalchenko, V.I., and Kalach, N.I. (1975) Determination of the carbon content in blast-furnace coke. *Metallurgist*, **19**, 253.
- Jennings, J.R. and Ward, S.A. (1989) Ammonia synthesis, in *Catalyst Handbook* (ed. M.W. Twigg). Wolfe Publishing Ltd, London, pp. 384–439.
- Jentsch, C. (1990) *Angewandte Chemie fuer Ingenieure*, BI-Wissenschaftsverlag, Mannheim.
- Jess, A. (1996) Thermische und katalytische Spaltung von Kohlenwasserstoffen in wasserstoff- und wasserdampfreicher Atmosphaere - eine Modelluntersuchung zur Erzeugung von Reduktionsgas aus Koksofenrohgas. Habilitation thesis, University Karlsruhe, Germany.
- Jess, A. and Kern, C. (2009) Modeling of multi-tubular reactors for Fischer-Tropsch synthesis. *Chem. Eng. Techn.*, **32**, 1164–1175
- Jess, A., Popp, R., and Hedden, K. (1999) Fischer-Tropsch-synthesis with nitrogen-rich syngas - fundamentals and reactor design aspects. *Appl. Catal. A Gen.*, **186**, 321–342.
- Jones, J.H. (2000) The Cativa process for the manufacture of acetic acid iridium catalyst improves productivity in an established industrial process. *Platinum Met. Rev.*, **44**, 94–105.
- Jost, F. (1908) Ueber das Ammoniakgleichgewicht. *Z. Anorg. Chem.*, **57**, 414–430.
- Jost, W. (1960) *Diffusion in Solids, Liquids, Gases*, Academic Press, New York.
- Juettner, K. (2007) Technical scale of electrochemistry, in *Encyclopedia of Electrochemistry*, (editors in chief A.J. Bard and M. Stratmann) vol. 5: *Electrochemical Engineering* (ed. D.D. Macdonald and P. Schmuki), Wiley-VCH Verlag GmbH, Weinheim.
- Kabe, T., Ishihara, A., and Qian, W. (1999) *Hydrodesulfurization and Hydrodenitrogenation – Chemistry and Engineering*, Wiley-VCH Verlag GmbH, Weinheim.
- Kahlisch, D., Wiechern, U., and Lindner, J. (2000) Propylene oxide, in *Ullmann's Encyclopaedia*, 7th edn, Wiley-VCH Verlag GmbH.
- Kaspar, J., Fornasiero, P., and Hickey, N. (2003) Automotive catalytic converters: current status and some perspectives. *Catal. Today*, **77**, 419–449.
- Keim, W. (1990) Nickel – an element with wide application in industrial homogeneous catalysis. *Angew. Chem. Int. Ed.*, **29**, 235–244.
- Keim, W. and Driessen-Hoelscher, B. (1999) Heterogenization of complexes and enzymes, in *Preparation of Solid Catalysts* (eds G. Ertl, H. Knoezinger, and J. Weitkamp), Wiley-VCH Verlag GmbH, Weinheim, pp. 355–371.
- Keim, W., Behr, A., and Schmitt, G. (1986) *Grundlagen der industriellen Chemie*, Salle & Sauerlaender, Frankfurt/Berlin/Munich.
- Keim, W., Behr, A., and Schmitt, G. (1986) *Grundlagen der Industriellen Chemie*, Varlag Sauerlaender, Aarau.
- Kern, C. (2003) Regeneration eines koksbeladenen Katalysators zur Benzinreformierung. Doctoral thesis, University of Technology Aachen, Germany.
- Kern, C. and Jess, A. (2005) Regeneration of coked catalysts - modelling and verification of coke burn-off in single particles and fixed bed reactors. *Chem. Eng. Sci.*, **60**, 4249–4264.
- Khan, F.I. and Haddara, M.R. (2004) Risk-based maintenance of ethylene oxide production facilities. *J. Hazardous Mater. A*, **108**, 147–159.
- Kilanowski, D.R. and Gates, B.C. (1980) Kinetics of hydrodesulfurization of benzothiophene catalyzed by sulfided cobalt-molybdenum/alumina. *J. Catal.*, **62**, 70.
- Kilanowski, D.R., Teeuwen, H., de Beer, V.H.J., Gates, B.C., Schuit, G.C.A., and Kwart, H. (1978) Hydrodesulfurization of thiophene, benzothiophene, dibenzothiophene, and related compounds catalyzed by sulfided $\text{CoO}\text{-}\text{MoO}_3\text{-}\gamma\text{-Al}_2\text{O}_3$: low-pressure reactivity studies. *J. Catal.*, **55**, 129.
- Kiparissides, C., Krallis, A., and Meimargolou, D. (2010) From molecular to plant-scale modeling of polymerization processes: A digital high-pressure low-density polyethylene production paradigm. *Chem. Eng. & Techn.*, **33**, 1754–1766.
- Klein, H., Jackstell, R., Wiese, K.-D., Borgmann, C., and Beller, M. (2001) Highly selective catalyst systems for the hydroformylation of internal olefins to linear aldehydes. *Angew. Chem. Int. Ed.*, **40** (18), 3408–3411.
- Klier, K. (1982) Methanol synthesis. *Adv. Catal.*, **31**, 243–313.
- Klier, K. (1984) Structure and function of real catalysts. *Appl. Surf. Sci.*, **19**, 267–297.
- Klier, K., Chatikavanij, V., Hermann, R.G., and Simmons, G.W. (1982) Catalytic synthesis of methanol from CO/H_2 - IV. The effects of carbon dioxide. *J. Catal.*, **74**, 343–360.
- Klose, W. (1984a) Ueberblick ueber Waermetransport- und Stoffwertmodelle bei der Verkokung. *Glueckauf Forsch.*, **45**, 35–44.
- Klose, W. (1984b) Ueberblick ueber physiko-chemische Verkokungsmodelle. *Glueckauf Forsch.*, **45**, 91–997.
- Klugherz, P.D. and Harriott, P. (1971) Kinetics of ethylene oxidation on a supported silver catalyst. *AIChE J.*, **17**, 856–866.
- Kohl, A.L. and Nielsen, R.B. (1997) *Gas Purification*, 5th edn, Gulf Publishing Company, Houston, Texas.
- Kraenert, R. (2005) Ammonia Oxidation over polycrystalline platinum: surface morphology and kinetics at atmospheric pressure. Doctoral thesis, University of Technology Berlin.
- Kuhlmann, S., Paetz, C., Haegele, C., Blann, K., Walsh, R., Dixon, J.T., Scholz, J., Haumann, M., and Wasserscheid, P. (2009) Chromium catalyzed tetramerization of ethylene in a continuous tube reactor - proof of concept and kinetic aspects. *J. Catal.*, **262**, 83–91.
- Kuhn, W., Funk, H.-U., Senft, G., and Koerber, K.A. (2004) Procedure for the production of menthol, DE 10239274.
- Kung, H.H. (1980) Methanol synthesis. *Catal. Rev. Sci. Eng.*, **22**, 235–259.
- Kung, H.H. (1984) Mechanistic studies of catalytic methanol synthesis. Report, DOE/PC/30239-T4 (Order No. DE84008380) 30.
- Kuntz, E.G. (1987) Homogeneous catalysis in water. *CHEMTECH*, **17** (9), 570–575.
- Kuntze, T. (1991) Kinetik der Fischer-Tropsch-synthese unter Druck an einem Eisenfaelungskatalysator bei Einsatz eines stickstoffreichen Synthesegases. Doctoral thesis, University Karlsruhe, Germany.
- Lamure-Meille, V., Schulz, E., Lemaire, M., and Vrinat, M. (1995) Effect of experimental parameters on the relative reactivity of dibenzothiophene and 4-methylbenzothiophene. *Appl. Catal. A: Gen.*, **131**, 143.
- Lamure-Meille, V., Schulz, E., Lemaire, M., and Vrinat, M. (1997) Hydrodesulfurization of alkylbenzothiophenes over a $\text{NiMo}/\text{Al}_2\text{O}_3$ catalyst: kinetics and mechanism. *J. Catal.*, **170**, 29.
- Lange, J.P. (2001) Methanol synthesis: a short review of technology improvements. *Catal. Today*, **64**, 3–8.
- Laoun, B. (2007) Thermodynamics aspect of high pressure hydrogen production by water electrolysis. *Rev. Energ. Renouvelables*, **10**, 435–444.
- Lawrence, B.M. (2007) *Mint: The Genus Mentha*, CRC Press, Boca Raton.
- Le Page, J.-F. (1978) *Applied Heterogeneous Catalysis: Design, Manufacture and Use of Solid Catalysts*, Éd. Technip, Paris.
- Le Rossignol, R. (1928) Zur Geschichte der Herstellung des synthetischen Ammoniaks. *Naturwissenschaften*, **16**, 1070–1071.
- Leadbeater, N.E. and Marco, M. (2002) Preparation of polymer-supported ligands and metal complexes for use in catalysis. *Chem. Rev.*, **102**, 3217–3273.
- Leffingwell, J.C. and Shackelford, R.E. (1974) Laeo-menthol. Syntheses and organoleptic properties. *Cosmetics Perfumery*, **89**, 69–78.
- Leitner, W. and Jessop, P.G. (eds) (2010) *Green Solvents – Supercritical Solvents*, Wiley-VCH Verlag GmbH, Weinheim, pp. 1–475.
- Levenspiel, O. (1996) *The Chemical Reactor Omnibook*, OSU Book Stores, Corvallis, Oregon.
- Levenspiel, O. (1999) *Chemical Reaction Engineering*, Wiley-VCH Verlag GmbH, Weinheim.
- Lim, P.-C. and Luft, G. (1983) Individual steps in the high-pressure polymerization of

- ethylene. 2. Dependence of the individual rate constants on pressure and temperature. *Makromol. Chem.*, **184**, 849–859.
- Lim, H.W., Park, M.J., Kang, S.H., Chae, H.J., Bae, J.W., and Jun, K.W. (2009) Modeling of the kinetics for methanol synthesis using Cu/ZnO/Al₂O₃/ZrO₂ catalyst: influence of carbon dioxide during hydrogenation. *Ind. Eng. Chem. Res.*, **48**, 10448–10455.
- Linde, A.G. (2010) α-Sablin Process. http://www.linde-anlagenbau.de/alpha_sablin_process.php.
- Lindner, E., Kemmler, M., Mayer, H.A., and Wegner, P. (1994) Supported organometallic complexes. 5. Polysiloxane-bound ether-phosphines and ruthenium complexes. A characterization by solid-state NMR spectroscopy and catalysis. *J. Am. Chem. Soc.*, **116**, 348–361.
- Liu, G., Willcox, D., Garland, M., and Kung, H. H. (1984) The rate of methanol production on a copper-zinc oxide catalyst: the dependence on the feed composition. *J. Catal.*, **90**, 139–146.
- Liu, X.-M., Lu, G.Q., Yan, Z.-F., and Beltrami, J. (2003) Recent advances in catalysts for methanol synthesis via hydrogenation of CO and CO₂. *Ind. Eng. Chem. Res.*, **42**, 6518–6530.
- MacKay, D.J.C. (2008) Sustainable Energy - without the hot air. UIT Cambridge (available free online from www.withouthotair.com).
- Malveda, M.P. (2007) *Chemical Economics Handbook*, SRI Consulting.
- Manyik, R.M., Walker, W.E., and Wilson, T.P. (1977) Soluble chromium-based catalyst for ethylene trimerization and polymerization. *J. Catal.*, **47**, 197–209.
- Maples, R.E. (2000) *Petroleum Refinery Process Economics*, 2nd edn PennWell, Tulsa.
- Marrett, R., Stadelhofer, J.W., and Marsh, H. (1983) Die Verkokung von fluessigen Kohlenwasserstoffen zur Herstellung von Kohlenstoff-Produkten. *Chem. Ing. Tech.*, **55**, 1–7.
- Mathison, C.R. and Cole-Hamilton, D.J. (2006) Fluorous biphasic catalysis, in *Catalyst Separation, Recovery and Recycling – Chemistry and Process Design* (eds D.-J. Cole-Hamilton and R.P. Tooze), Springer, Dordrecht, pp. 144–181.
- Matsugi, T. and Fujita, T. (2008) High-performance olefin polymerization catalysts discovered on the basis of a new catalyst design concept. *Chemical Society Reviews*, **37** (6), 1264–1277.
- Maurer, E. (1919) Berechnungen zum Ammoniakgasgleichgewicht. *Z. Anorg. Chem.*, **108**, 273–302.
- McCarthy, K.F. and Schrader, G.L. (1987) Deuterodesulfurization of thiophene: an investigation of the reaction mechanism. *J. Catal.*, **103**, 261.
- McGuinness, D.S. (2011) Olefin oligomerization via metallacycles: dimerization, trimerization, tetramerization, and beyond. *Chem. Rev.*, **111**, 2321–2341.
- McNeil, M.A., Schack, C.J., and Rinker, R.G. (1989) Methanol synthesis from hydrogen, carbon monoxide and carbon dioxide over a copper oxide/zinc oxide/alumina catalyst. II. Development of a phenomenological rate expression. *Appl. Catal.*, **50**, 265–285.
- Mehnert, C.P., Cook, R.A., Dispenziere, N.C., and Afeworki, M. (2002) Supported ionic liquid catalysis - a new concept for homogeneous hydroformylation catalysis. *J. Am. Chem. Soc.*, **124**, 12932–12933.
- Meille, V., Schulz, E., Lemaire, M., and Vrinat, M. (1999) Hydrodesulfurization of 4-methyl-dibenzothiophene: a detailed mechanistic study. *Appl. Catal. A: Gen.*, **187**, 179.
- Meyers, R.A. (ed.) (2003) *Handbook of Petroleum Refining Processes*, 3rd edn, McGraw-Hill, New York.
- Mittasch, A. (1930) Einiges ueber Mehrstoffkatalysatoren. *Z. Elektrochem. Angew. Phys. Chem.*, **36**, 569–580.
- Mittasch, A. (1951) *Geschichte der Ammoniaksynthese*, Verlag Chemie, Weinheim.
- Mittasch, A., Prier, M., and Winkler, K. (1923) DE 441433, BASF.
- Moulijn, J.A., Makkee, M., and van Diepen, A. (2001) *Chemical Process Technology*, John Wiley & Sons, Ltd, Chichester.
- Moulijn, J.A., Makkee, M., and Van Diepen, A. (2004) *Chemical Process Technology*, Wiley-VCH Verlag GmbH, Weinheim.
- Nag, N.K., Sapre, A.V., Broderick, D.H., and Gates, B.C. (1979) Hydrodesulfurization of polycyclic aromatics catalyzed by sulfided CoO-MoO₃/γ-Al₂O₃: the relative reactivities. *J. Catal.*, **57**, 509.
- Nair, D., Scarpello, J.T., Vankelecom, I.F.J., Freitas Dos Santos, L.M., White, L.S., Kloeting, R.J., Welton, T., and Livingston, A.G. (2002) Increased catalytic productivity for nanofiltration-coupled Heck reactions using highly stable catalyst systems. *Green Chem.*, **4**, 319–324.
- Navarro, R., Pawelec, B., Fierro, J.L.G., Vasudevan, P.T., Cambra, J.F., Guemez, M.B., and Arias, P.L. (1996) Deep hydrodesulfurization of DBT and diesel fuel on supported Pt and Ir catalysts. *Appl. Catal. A: Gen.*, **137**, 269–286.
- Nielsen, A. (1971) Review of ammonia catalysis. *Catal. Rev.*, **4**, 1–26.
- O'Brien, W.S., Chen, J.W., Nayak, R.V., and Carr, G.S. (1986) Catalytic hydrodesulfurization of dibenzothiophene and a coal-derived liquid. *Ind. Eng. Chem. Proc. Des. Dev.*, **25**, 221.
- Onda, K., Kyakuno, T., Hattori, K., and Ito, K. (2004) Prediction of production power for high-pressure hydrogen by high-pressure water electrolysis. *J. Power Sources*, **132**, 64–70.
- Onken, U. and Behr, A. (1996) *Chemische Prozesskunde*, Georg Thieme Verlag, Stuttgart.
- Oosterom, G.E., Steffens, S., Reek, J.N.H., Kamer, P.C.J., and Van Leeuwen, P.W.N. M. (2002) Core-functionalized dendrimeric mono- and diphosphine rhodium complexes; application in hydroformylation and hydrogenation. *Top. Catal.*, **19** (1), 61–73.
- Overett, M.J., Blann, K., Bollmann, A., Dixon, J.T., Haasbroek, D., Kilian, E., Maumela, H., McGuinness, D.S., and Morgan, D.H. (2005) Mechanistic investigations of the ethylene tetramerisation reaction. *J. Am. Chem. Soc.*, **127**, 10723–10730.
- Papageorgiou, J.N. and Froment, G.F. (1996) Phthalic anhydride synthesis. Reactor optimization aspects. *Chem. Eng. Sci.*, **10**, 2091–2098.
- Park, D.W. and Gau, G. (1987) Ethylene epoxidation on a silver catalyst: unsteady and steady state kinetics. *J. Catal.*, **105**, 81–94.
- Pecoraro, T.A. and Chianelli, R.R. (1981) Hydrodesulfurization catalysis by transition metal sulfides. *J. Catal.*, **67**, 430.
- Peters, K.H. and Reinitzuber, F. (1994) Energiewirtschaftliche Auswirkungen einer optimierten Roheisenerzeugung. *Stahl Eisen*, **114**, 61–68.
- Plass, L. *et al.* (1990) Emissionen koennen um 20% sinken. *Chem. Ind.*, Nr. 3, S. 38.
- [Plastemart.com](http://www.plastemart.com/Plastic-Technical-Article.asp?LiteratureID=1407&Paper=Global_Polyethylene-consumption-demand-2008-decline-4percent) (2010) Global Polyethylene consumption in 2008 declined by almost 4%. http://www.plastemart.com/Plastic-Technical-Article.asp?LiteratureID=1407&Paper=Global_Polyethylene-consumption-demand-2008-decline-4percent.
- Plehiers, P.M. and Froment, G.F. (1989) Coupled simulation of heat transfer and reaction in a steam reforming furnace. *Chem. Eng. Techn.*, **12**, 20–26.
- Popp, R. (1996) Ergebnisse halbtechnischer Untersuchungen zur Fischer-Tropsch-Synthese mit stickstoffreichem Synthesegas. Doctoral thesis, University Karlsruhe, Germany.
- Post, M.F.M., Van't Hoog, J.K., Minderhoud, J.K., and Sie, S.T. (1989) Diffusion limitations in Fischer-Tropsch catalysts. *AIChE J.*, **35**, 1107–1114.
- Pozzi, G. and Shepperson, I. (2003) Fluorous chiral ligands for novel catalytic systems. *Coord. Chem. Rev.*, **242** (1–2), 115–124.
- Price, C. (2010) Plans underway for new petrochemical plant. <http://www.kplctv.com/Global/story.asp?S=13603718>.
- Pryor, P., Peterson, R., Gody, T., and Lin, Y. (2002) STRATCO Contactor reactor performance upgrade – alkylation tube insert technology. Available at http://www2.dupont.com/Clean_Technologies/es_MX/assets/downloads/2002_STRATCO_NPRA_AM_Paper.pdf.
- Raak, H. (1995) Reaktionskinetische Untersuchungen in der Anfangsphase der Fischer-Tropsch-Synthese an einem technischen Eisenfaellungskatalysator. Doctoral thesis, University Karlsruhe, Germany.
- Rebsdat, S. and Mayer, D. (2001) Ethylene oxide in *Ullmann's Encyclopaedia*, 7th edn, Wiley-VCH Verlag GmbH.

- Reek, J.N.H., van Leeuwen, P.W.N.M., van der Ham, A.G.J., and de Haan, A.B. (2006) Supported catalysts - immobilization of tailor-made homogeneous catalysts, in *Catalyst Separation, Recovery and Recycling – Chemistry and Process Design* (eds D.-J. Cole-Hamilton and R.P. Tooze), Springer, Dordrecht, pp. 39–72.
- Reinhardt, J., Balfanz, U., and Dommig, T. (2002) Sulfur-free diesel fuel. Modifications and operating experience using a middle-distillates hydrodesulfurization unit. *Erdöl Erdgas Kohle*, **118**, 456.
- Reinhoudt, H.R., Troost, R., van Langveld, A.D., Sie, S.T., van Veen, J.A.R., and Moulijn, J.A. (1999) Catalysts for second-stage deep hydrodesulfurisation of gas oil. *Fuel Proc. Techn.*, **61**, 133–147.
- Ren, X.H. (2003) NMR studies of molecular transport in model fixed-bed reactors. Doctoral thesis, University of Technology Aachen.
- Ren, X.H., Bartusseck, I., Demco, D., Staf, S., Bluemich, B., Kern, C., and Jess, A. (2000) NMR study of changing pore size and tortuosity during deactivation and decoking of a naphtha reforming catalyst, in *Proceedings of the Conference on Magnetic Resonance Applications to Porous Media. Bologna, October 2000*, p. 47.
- Ren, X.H., Bertmer, M., Staf, S., Demco, D., Bluemich, B., Kern, C., and Jess, A. (2002) Deactivation and regeneration of a naphtha reforming catalyst. *Appl. Catal. A: Gen.*, **228**, 39–52.
- Riedel, T., Claeys, M., Schulz, H., Schaub, G., Nam, S.-S., Jun, K.W., Choi, M.-J., Kishan, G., and Lee, K.-W. (1999) Comparative study of Fischer-Tropsch synthesis with H₂/CO and H₂/CO₂ syngas using Fe- and Co-based catalysts. *Appl. Catal. A: Gen.*, **186**, 201–213.
- Riisager, A., Wasserscheid, P., van Hal, R., and Fehrmann, R. (2003) Continuous fixed-bed gas-phase hydroformylation using supported ionic liquid-phase (SILP) Rh catalysts. *J. Catal.*, **219** (2), 452–455.
- Rizkalla, N. (2004) US 6846774B2 Scientific Design Co., Inc.
- Robinson, W.R.A.M., von Veen, J.A.R., de Beer, V.H.J., and Moulijn, J.A. (1999) Development of deep hydrodesulfurization catalysts II. NiW, Pt and Pd catalysts tested with (substituted) dibenzothiophene. *Fuel Proc. Techn.*, **61**, 103–116.
- Rodriguez-Reinoso, F., Santana, P., Romero Palazon, E., and Diez, M.A. (1998) Delayed coking: industrial and laboratory aspects. *Carbon*, **36**, 105–116.
- Rohde, W., Simonis, W., and Peters, W. (1969) Berechnung und Messung des instationären Temperaturfeldes bei der Steinkohlenpyrolyse im Koksofen. *Brennstoff-Chem.*, **50**, 1–8.
- Roll, H.J. (1994) Vergasung von grob gemahlennem Schilfgras (*Miscanthus sinensis giganteus*) im Flugstrom. Doctoral thesis, University Karlsruhe, Germany.
- Roll, H.J. and Hedden, K. (1994) Entrained flow gasification of coarsely ground Chinese reed. *Chem. Eng. Proc.*, **33**, 353–361.
- Ronde, N.J. and Vogt, D. (2006) Separation by size-exclusion filtration – homogeneous catalysts applied in membrane reactors, in *Catalyst Separation, Recovery and Recycling – Chemistry and Process Design* (eds D.-J. Cole-Hamilton and R.P. Tooze), Springer, Dordrecht, pp. 73–104.
- Ronze, D., Fongarland, P., Pitault, I., and Forissier, M. (2002) Hydrogen solubility in straight run gasoil. *Chem. Eng. Sci.*, **57**, 547–553.
- Rozovskii, A.Y., Kagan, Y.B., Lin, G.I., Slivinskii, E.V., Loktev, S., Liberov, L.G., and Bashkirov, A.N. (1975) Mechanism of methanol synthesis from carbon monoxide and hydrogen. *Kinet. Katal.*, **16**, 810.
- Rozovskii, A.Y., Lin, G.I., Liberov, L.G., Slivinskii, E.V., Loktev, S.M., Kagan, Y.B., and Bashkirov, A.N. (1977) Mechanism of methanol synthesis from carbon dioxide and hydrogen, III. Determination of rates of individual stages using ¹⁴CO. *Kinet. Catal.*, **18**, 691–699.
- Saade, G.A. (2009) Chemical Economics Handbook-SRI Consulting. <http://www.sriconsulting.com/CEH/Public/Reports/674.5000/Methanol>, 20.10.09.
- Sakakura, T., Kobayashi, T., Hayashi, T., Kawabata, Y., Tanaka, M., and Ogata, I. (1984) Stability of phosphines under hydroformylation conditions. *J. Organomet. Chem.*, **267** (2), 171–177.
- Santos, A., Bahamonde, A., Schmid, M., Avila, P., and Garcia-Ochoa, F. (1998) Mass transfer influences on the design of selective catalytic reduction (SCR) monolithic reactors. *Chem. Eng. Proc.*, **37**, 117–124.
- Satterfield, C.N., Modell, M., and Mayer, J.F. (1975) Interactions between catalytic hydrodesulfurization of thiophene and hydrodenitrogenation of pyridine. *AIChE J.*, **21**, 1100.
- Scaroni, A.W., Jenkins, R.G., and Walker, P.L. (1991) Carbonization of anthracene in a batch reactor. *Caron*, **29**, 969–980.
- Schaub, G. (2006) Neue Kraftstoffe fuer Klimaschutz und Rohstoffwandel? *Chem. Ing. Techn.*, **78**, 389–396.
- Schaub, G. (2006) Synthetic fuels and biofuels for the transportation sector - principles and perspectives. *Oil Gas Eur. Mag.*, **32**, 34–38.
- Schaub, G. and Turek, T. (2011) *Energy Flows, Material Cycles and Global Development*, Springer, Heidelberg.
- Schaub, G., Rohde, R., and Subirana, A.M. (2006) Fischer-Tropsch synthesis - development and perspectives. Presented at DGMK/SCI-Conference Synthesis Gas Chemistry, Dresden, Germany, 4–6 October 2006.
- Schindevol, U. (2000) 100 Jahre Institut fuer Physikalische Chemie an der Universitaet Karlsruhe. *Bunsen Mag.*, **2**, 138–147.
- Schlatterer, R. (1951) Wirkung von Rektifizierboeden in Luftzerlegungsanlagen nach der Theorie von Kirschbaum. *Chem. Ing. Tech.*, **23**, 470–472.
- Schlemenat, A., Langer, R., Dreisbach, C., Gross, H.-J., Prinz, T., Schulze-Tilling, A., Friederich, M., Jentsch, J.D., and John, G. (2001) Isomerization process and supported ruthenium catalysts for the preparation of D, L-menthol from menthol stereoisomers. DE10023283.
- Schloegl, R. (2003) Catalytic synthesis of ammonia - a “never-ending story”. *Angew. Chem. Int.*, **42**, 2004–2008.
- Schluender, E.U. (1986) *Einführung in die Waermeuebertragung*, Vieweg & Sohn, Braunschweig.
- Schmidt, E., Schmidt, T., Pilhofer, T., and Krill, H. (2003) Air - separation and purification, in *Ullmann's Encyclopedia of Industrial Chemistry*, 6th edn, Wiley-VCH Verlag GmbH, Weinheim, vol. 1, pp. 692–732.
- Schmidt, K.H. and Romey, J. (1984) *Kohle, Erdöl, Erdgas*, Vogel Verlag, Wuerzburg, Germany.
- Schmidt, L.D. (1998) *The Engineering of Chemical Reactions*, Oxford University Press, New York.
- Schmittinger, P. (ed.) (2000) *Chlorine - Principles and Industrial Practise*, Wiley-VCH Verlag GmbH, Weinheim.
- Schmitz, C. (2003) Zur Kinetik und zur verbesserten Reaktionsfuehrung der hydrierenden Tiefentschwefelung von Dieseloel. Doctoral thesis, University of Bayreuth, Germany.
- Schmitz, C., Datsevich, L., and Jess, A. (2004) Deep desulfurization of diesel oil: kinetic studies and use of a two-phase reactor with pre-saturator. *Chem. Eng. Sci.*, **59**, 2821–2829.
- Schmoele, P. and Luengen, H.B. (2007) Use of pre-reduced material in the blast-furnace: metallurgical, ecological and economic aspects. *Stahl Eisen*, **127**, 47–54.
- Schouten, E.P.S., Borman, P.C., and Westerterp, K.R. (1996) Determination of the kinetics of ethene epoxidation. *Chem. Eng. Proc.*, **35**, 43–55.
- Schrod, M., Semel, J., and Steiner, R. (1985) Verfahren zur Minderung von NO_x-Emissionen in Rauchgasen. *Chem. Ing. Tech.*, **57**, 717–727.
- Schroegel, K. (2007) Reaktionskinetische und verfahrenstechnische Aspekte der Synthese von Kohlenstoff-Nanotubes und -Nanofasern. Doctoral thesis, University Bayreuth, Germany.
- Schulz, H. (1999) Short history and present trends of Fischer-Tropsch synthesis. *Appl. Catal. A Gen.*, **186**, 3–12.
- Schulz, H. and Claeys, M. (1999) Kinetic modelling of Fischer-Tropsch product distributions. *Appl. Catal. A Gen.*, **186**, 91–107.
- Schulz, H., Schaub, G., Claeys, M., and Riedel, T. (1999) Transient initial kinetic regimes of Fischer-Tropsch synthesis. *Appl. Catal. A Gen.*, **186**, 215–227.
- Schwarzmann, M., Mroß, W.-D., and Bohning, K.-H. (1988) Desaktivierung von technischen Silbertraegerkatalysatoren fuer die

- Herstellung von Ethylenoxid. *Chem. Ing. Tech.*, **60**, 657–661.
- Shafi, R. and Hutchings, G.B. (2000) Hydrodesulfurization of hindered dibenzothiophenes: an overview. *Catal. Today*, **59**, 423.
- Sheffer, G.R. and King, T.S. (1989a) Potassium's promotional effect of unsupported copper catalysts for methanol synthesis. *J. Catal.*, **115**, 376–387.
- Sheffer, G.R. and King, T.S. (1989b) Differences in the promotional effect of the group IA elements on unsupported copper catalysts for carbon monoxide hydrogenation. *J. Catal.*, **116**, 488–497.
- Sie, S.T. and Krishna, R. (1999) Fundamentals and selection of advanced Fischer-Tropsch reactors. *Appl. Catal. A Gen.*, **186**, 55–70.
- Sie, S.T. and Krishna, R. (2000) Design and scale-up of the Fischer-Tropsch bubble column slurry reactor. *Fuel Proc. Techn.*, **64**, 73–105.
- Sie, S.T., Senden, M.M.G., and Van Wechem, H.M.H. (1991) Conversion of natural gas to transportation fuels via the shell middle distillate synthesis process (SMDS). *Catal. Today*, **8**, 371–394.
- Singh, J., Kumar, M.M., Saxena, A.K., and Kumar, S. (2004) Studies on thermal behavior of residual feedstocks in a batch reactor. *Chem. Eng. Sci.*, **59**, 4505–4515.
- Soares, J.B.P., Simon, L.C. Meyer, T., and Keurentjes, J. (2005) *Handbook of Polymer Reaction Engineering*, Wiley-VCH, Weinheim, 365–430.
- Soave, G. (1972) Equilibrium constants from a modified Redlich-Kwong equation of state. *Chem. Eng. Sci.*, **27**, 1197–1203.
- Spencer, M. S. (1999) The role of zinc oxide in Cu ZnO catalysts for methanol synthesis and the water-gas shift reaction. *Topics in Catalysis*, **8**, 259–266.
- Squires, A.M., Kwaik, M., and Avidan, A.A. (1985) Fluid beds: At last, challenging two entrenched practices. *Science*, **230**, 1329–1337.
- SRI Consulting (2009) Chemical Economics Handbook. http://www.sriconsulting.com/WP/Public/Reports/acetic_acid/ 3.11.09.
- Standish, N. and Polthier, K. (1975) An interpretation of tracer results from an operating blast furnace by a dispersion model, in *Blast Furnace Aerodynamics*, Australian Institute of Mining & Metallurgy, Melbourne, p. 99.
- Stark, A. and Wasserscheid, P. (eds) (2010) *Green Chemistry – Ionic Liquids*, Wiley-VCH Verlag GmbH, Weinheim, pp. 3–340.
- Stichlmair, J.G. and Fair, J.R. (1998) *Distillation, Principles and Practices*, Wiley-VCH Verlag GmbH, Weinheim.
- Stolow, R.D. and Groom, T. (1968) Equilibration of cis- and trans-2-tert-butyl-4-hydroxycyclohexanone. *Tetrahedron Lett.*, **9**, 4069–4072.
- Stolzenberg, D. (1999) Fritz Haber, Carl Bosch und Friedrich Bergius - Protagonisten der Hochdrucksynthese. *Chem. Z.*, **33**, 359–364.
- Stranges, A.N. (2003) Germany's Synthetic Fuel Industry 1927–45. Presented at the AIChE 2003 Spring National Meeting, 3rd Topical Conference on Natural Gas Utilization, New Orleans, 30 March to 3 April 2003.
- Strieder, W. and Aris, R. (1973) *Variational Methods Applied to Problems of Diffusion and Reaction*, Springer, Berlin.
- Sueßmeir, T., Jeschar, R., Beck, K.G., Poetke, W., and Eisenhut, W. (1987) Theoretische und experimentelle Untersuchung zum Waermetransport bei der Verkokung. *Glueckauf Forsch.*, **48**, 152–157.
- Sughrue, E.L. (2003) Chemistry added design of future clean fuels. Presented at the 226th American Chemical Society (ACS) National Meeting, New York, 7/11 Sept. 2003.
- Sundaram, K.M., Van Damme, P.S., and Fronment, G.F. (1994) Ethylene, in *Kirk-Othmer Encyclopedia of Chemical Technology*, 4th edn, vol. **9** (eds J.I. Kroschwitz and M. Howe-Grant), John Wiley & Sons, Inc., New York, pp. 877–915.
- Sunley, G.J. and Watson, D.J. (2000) High productivity methanol carbonylation catalysis using iridium. The Cativa process for the manufacture of acetic acid. *Catal. Today*, **58**, 293–307.
- Supp, E. (1978) *Gaserzeugung aus Schweröl*. In: *Ullmanns Enzyklopädie der technischen Chemie*, Verlag Chemie, Weinheim.
- Supp, E. (1997) Noncatalytic partial oxidation and special gasification processes for higher-boiling hydrocarbons, in *Ullmann's Encyclopedia of Industrial Chemistry, Fifth Edition on CD-ROM*, Wiley-VCH Verlag GmbH, Weinheim.
- Surburg, H. and Panten, J. (2006) *Common Fragrance and Flavor Materials Preparation, Properties and Uses*, Wiley-VCH Verlag GmbH, Weinheim.
- Tagawa, T., Plerzier, G., and Amenomiya, Y. (1985) Methanol synthesis from carbon dioxide + hydrogen. I. Characterization of catalysts by TPD. *Appl. Cat.*, **18**, 285–293.
- Tang, D. (2004) Investigations on diffusion and dispersion in reacting gas/solid-systems - combined use of reaction engineering methods and NMR-techniques. Doctoral thesis, University of Technology Aachen, Germany.
- Tang, D., Kern, C., and Jess, A. (2004) Influence of chemical reaction rate, diffusion and pore structure on the regeneration of a coked Al₂O₃-catalyst. *Appl. Catal. A: Gen.*, **272**, 187–199.
- Taylor, K.C. (1993) Nitric-oxide catalysis in automotive exhaust systems. *Cat. Rev. - Sci. Eng.*, **35**, 457–481.
- Teles, J.H., Rehfinger, A., Berg, A., Rudolf, P., Rieber, N., and Bassler, P. (2003) WO 2003011845 BASF.
- Temkin, M.I. and Pyzhev, V. (1940) Kinetics of ammonia synthesis on promoted iron catalysts. *Acta Physicochim. URSS*, **12**, 327–356.
- Thiele, E.W. (1939) Relation between the catalytic activity and size of particle. *Ind. Eng. Chem.*, **31**, 916–920.
- Tijm, P.J.A. (2008) *Gas to Liquids, Fischer-Tropsch Catalysis, Reactors Advanced Energy Technology, Future's Pathway*, booklanddirect (www.booklanddirect.com).
- Tijm, P.J.A., Waller, F.J., and Brown, D.M. (2001) Methanol technology developments for the new millennium. *Appl. Catal. A Gen.*, **221**, 275–282.
- Timm, B. (1963) 50 Jahre Ammoniaksynthese. *Chem. Ing. Tech.*, **35**, 817–880.
- Tronconi, E. and Forzatti, P. (1992) Adequacy of lumped parameter models for SCR reactors with monolith structure. *AIChE J.*, **38**, 201–210.
- Tullo, A. (2004) Diw, BASF to build a propylene oxide, companies mark success in process with plans for plant in Belgium. *Chem. Eng. News*, **82**, 3615.
- Tuttles, U., Schmeisser, V., and Eigenberger, G. (2004) A mechanistic simulation model for NO_x storage catalyst dynamics. *Chem. Eng. Sci.*, **59**, 4731–4738.
- Twigg, M.V. and Spencer, M.S. (2001) Deactivation of supported copper metal catalysts for hydrogenation reactions. *Appl. Catal. A Gen.*, **212**, 161–174.
- Twigg, M.V. and Spencer, M.S. (2003) Deactivation of copper metal catalysts for methanol decomposition, methanol steam reforming and methanol synthesis. *Top. Cat.*, **22** (3–4), 191–203.
- Uhde (2005) Brochure of nitric acid, Uhde Company, Dortmund, Germany.
- Ulbricht, M. (2006) Advanced functional polymer membranes. *Polymer*, **47** (7), 2217–2262.
- Ullmanns, E. (1976) *Ullmanns Encyklopädie der technischen Chemie*, Verlag Chemie, Weinheim.
- US EPA (2000) Gasoline sulfur regulations. *Federal Regist.*, **65**, 6698.
- US EPA (2001) Clean air act. *Federal Regist.*, **66**, 5001.
- Van Basshuysen, R. and Schaefer, F. (2007) *Handbuch Verbrennungsmotor*, Vieweg, Wiesbaden.
- Van Leeuwen, P.W.N.M. (2004) *Homogeneous Catalysis*, Kluwer Academic Publishers, Dordrecht.
- Van Leeuwen, P.W.N.M., Clement, N.D., and Tschan, M.J.-L. (2010) New processes for the selective production of 1-octene. *Coord. Chem. Rev.*, **255**, 1499–1517.
- Van Leeuwen, P.W.N.M., Kamer, P.C., Reek, J.N.H., and Dierkes, P. (2000) Ligand bite angle effects in metal-catalyzed C-C bond formation. *Chem. Rev.*, **100**, 2741–2769.
- van Rensburg, W.J., van den Berg, J.A., and Steynberg, P.J. (2007) Role of MAO in chromium-catalyzed ethylene tri- and tetramerization: A DFT study. *Organometallics*, **26** (4), 1000–1013.
- Van Steen, E. (1993) Elementarschritte der Fischer-Tropsch CO-Hydrierung mit Eisen- und Kobaltkatalysatoren. Doctoral thesis, University Karlsruhe, Germany.
- Van Steen, E. and Schulz, H. (1999) Polymerisation kinetics of the Fischer-Tropsch CO

- hydrogenation using iron and cobalt based catalysts. *Appl. Catal. A Gen.*, **186**, 309–320.
- VCI (2011) Verband der Chemischen Industrie. Positionen zur Chemie mit Chlor. www.vci.de.
- VDI (Verein Deutscher Ingenieure, ed.) (2002) VDI-Waermeatlas. Berechnungsblaetter fuer den Waermeuebergang. VDI-Verlag, 9. ed., Mh 5, Dee 3, Dee 4.
- Vogt, D. (2002) Oligomerization of ethylene to higher linear α -olefins, in *Applied Homogeneous Catalysis with Organometallic Compounds* (eds B. Cornils and W.A. Herrmann), Wiley-VCH Verlag GmbH, Weinheim, pp. 240–253.
- Vogt, D. (2005) Organic-organic biphasic catalysis – economic applications (SHOP) process, in *Multiphase Homogeneous Catalysis* (eds B. Cornils, W.A. Herrmann, I. Horwath, W. Leitner, S. Mecking, H. Olivier-Bourbigou, and D. Vogt), Wiley-VCH Verlag GmbH, Weinheim, pp. 330–337.
- Votsmeier, M. (2012) Autoabgaskatalyse im Wandel der Zeiten. Lecture at the Faculty of Applied Science, University Bayreuth, 11 January 2012.
- Wache, W. (2006) Zur verbesserten Reaktionstechnik von Mehrphasensystemen durch Einsatz einer gasgesättigten Flüssigkeit - Untersuchungen am Beispiel der Fischer-Tropsch Synthese und der hydrierenden Tieftentschwefelung von leichtem Heizoel. Doctoral thesis, University Bayreuth. Germany.
- Wache, W., Datsevich, L., Jess, A., and Neumann, G. (2006) Improved deep desulfurisation of middle distillates by a two-phase reactor with pre-saturator. *Fuel*, **85**, 1483–1493.
- Walker, G.T. (1967) Menthol. Properties, uses, and some methods of manufacture. *Manuf. Chem. Aerosol News*, **38**, 51–53.
- Wass, D.F. (2007) Chromium-catalyzed ethene trimerisation and tetramerisation – breaking the rules in olefin oligomerisation. *Dalton Trans.*, 816–819.
- Wasserscheid, P. and Schulz, P.S. (2007) Transition metal catalysis in ionic liquids, in *Ionic Liquids in Synthesis* (eds P. Wasserscheid and T. Welton), 2nd edn, Wiley-VCH Verlag GmbH, Weinheim, pp. 369–463.
- Waugh, K.C. (1992) Methanol synthesis. *Catal. Today*, **15**, 51–75.
- Weissermel, K. and Arpe, H.-J. (2003) *Industrial Organic Chemistry*, Wiley-VCH Verlag GmbH, Weinheim.
- Westterp, K.R., Fontein, H.J., and van Beckum, F.P.H. (1988) Decoking of fixed-bed catalytic reactors. *Chem. Eng. Technol.*, **11**, 367.
- Whiteley, K.S. (2012) *Polyethylene. Ullmann's Encyclopedia of Industrial Chemistry*, Wiley-VCH, Weinheim, DOI: 10.1002/14356007.a21_487.pub2.
- Wicke, E. and Vortmeyer, D. (1959) Zuendzonen heterogener Reaktionen in gasdurchstroemten Koernerschichten. *Ber. Bunsenges. Phys. Chem.*, **63**, 145.
- Wiese, K.-D., Moeller, O., Protzmann, G., and Trocha, M. (2003) A new reactor design for catalytic fluid-fluid multiphase reactions. *Catal. Today*, **79–80**, 97–103.
- Winnacker, K. and Kuechler, L. (1971) *Chemische Technologie, Band 3 Organische Technologie*, Carl Hanser, Munich.
- Winnacker, K. and Kuechler, L. (1991) *Chemische Technologie. Organische Technologie I*, Carl Hanser Verlag, Munich.
- Winnacker-Kuechler (1981) *Chem. Technologie*, Carl Hanser Verlag, Munich.
- Wittcoff, H.A. and Reuben, B.G. (1996) *Industrial Organic Chemicals*, John Wiley & Sons, Inc., New York.
- Wulkow, M., Gerstlauer, A., and Nieken, U. (2001) Modeling and simulation of crystallization processes using Parsival. *Chem. -Eng. Sci.*, **56**, 2575.
- Xu, J. and Froment, G.F. (1989a) Methane steam reforming, methanation and water-gas shift: a. intrinsic kinetics. *AIChE J.*, **35**, 88.
- Xu, J. and Froment, G.F. (1989b) Methane steam reforming, methanation and water-gas shift: a. diffusional limitations and reactor simulation. *AIChE J.*, **35**, 97.
- Yates, I.C. and Satterfield, C.N. (1991) Intrinsic kinetics of the Fischer-Tropsch synthesis on a cobalt catalyst. *Energy Fuels*, **5**, 158–173.
- Yoneda, N., Kusano, S., Yasui, M., Pujado, P., and Wilcher, S. (2001) Recent advances in processes and catalysts for the production of acetic acid. *Appl. Catal. A Gen.*, **221**, 253–265.
- Yoshida, T., Komatsu, A., and Indo, M. (1966) Isomerization and racemization of menthols. III. A new isolation procedure of (+)-menthol from isomeric mixture. *Agric. Biol. Chem.*, **30**, 68–72.
- Zeldowitsch, Y.B. (1939) On the theory of reactions on powders and porous substances. *Acta Physicochem. URSS*, **10**, 583–592.
- Zennaro, R., Hugues, F., and Caprani, E. (2006) The Eni-IFP/Axens GTL technology: from R&D to a successful scale-up. Presented at the DGMK/SCI-Conference Synthesis Gas Chemistry, Dresden, Germany, 4–6 October 2006.
- Zoeller, J.R. (2009) Eastman chemical company's "Chemicals from Coal" program: The first quarter century. *Catal. Today*, **140**, 118–126.
- Zosel, K. (1978) Practical applications of material separation with supercritical gases. *Angew. Chem.*, **90** (10), 748–755.

Index

a

- absorption 108
 - activity and activity coefficients, in chloroform 111
 - basic design data, of column for absorption of CO₂ in water 116
 - Bunsen absorption coefficient 110
 - chemical absorption of CO₂ in *N*-methyl diethanolamine 112, 113
 - CO₂ in water, and subsequent bicarbonate formation 110
 - design of columns 113–116
 - equilibria of chemical absorption 108
 - equilibria of physical absorption, comparison 109
 - gas velocity and flooding of absorption column 115
 - height equivalent of one theoretical stage (HETS) 115
 - Henry coefficients for different gases 109
 - McCabe-Thiele diagram, for absorption process 114–116
 - operation conditions of sieve tray 115
 - packed columns 115
 - principles of chemical and physical absorption 108
 - Raoult's law 110
 - solvent, and solute activity 111, 112
 - technical absorption processes 113
- acetaldehyde 464, 480, 695
 - liquid phase oxidation of 739
 - oxidation 740, 741
 - acetic acid synthesis via 741
 - radical mechanism 741
 - production 464, 480
 - anhydride 28
 - commercial production technologies
 - direct ethylene oxidation 747
 - by ethane and methane oxidation 748, 749
 - consumption 740
 - dominant manufacturing process 739, 740
 - production capacities 482, 740, 741
 - synthesis 739, 740
 - via acetaldehyde oxidation 741, 742
 - via butane or naphtha oxidation 742
 - via methanol carbonylation 743–747
 - acetone 481
 - acetylene 189, 198, 211, 437, 441, 461, 465, 470, 476, 478, 605
 - from CaC₂ 470
 - industrial products from 471

- acetyl radical 741
- acid aerosols 567
- acid-base catalyzed reactions 11
- acid catalyst 11
- acidity 10
- acid-catalyzed reaction 652
- acid-soluble polymers 653
- acrolein 30, 476, 476, 479, 481, 483, 701
- acrylamide 28, 29, 487
- acrylic acid 140, 466, 467, 479, 481–483
- acrylonitrile 462, 466, 467, 486–487
- activation energy 24, 34, 201, 203, 215, 711
 - apparent activation energy of diffusion processes 229, 230, 232
 - for chain transfer 807
 - correlation between activation energy and reaction enthalpy for a reversible reaction 212
 - influence on reaction rate constant 203
 - negative 584, 587
- active Phillips catalyst 810
- active polymerization systems 810
- activity coefficient 111, 140, 193, 194, 788
- addition reactions 10
- adhesives 506
- adiabatic beds 564–566
- adiabatic compression 160, 161, 172
- adiabatic expansion 40, 65, 154
 - total work 46
- adiabatic fixed-bed reactors 539
- adiabatic multiple-bed reactor 693
- adiabatic operation 301, 317, 319, 329
 - of a batch reactor 317, 318
 - choice of best reactor type for adiabatic operation 335
 - of a CSTR 323, 333, 334
 - of a PFR 329, 333, 334
- adiabatic reactors with periodic flow reversal 376, 377
 - commercial applications 377
 - temperature profiles 377
- adipinic acid 10, 461, 464, 473, 482, 483, 491, 498
- adipodinitrile 461, 462, 464
- adiponitrile 461, 472, 485, 487
- adsorption 120, 458
 - adsorption bed zones 131
 - application areas, liquid and gaseous components 131
 - BET isotherm 124–126
 - BET theory, originators 127
- breakthrough curves for H₂S adsorption on a molecular sieve 132, 133
- calculation of $l_{ads,ideal}$, HTZ, and LUB based on breakthrough curves 135
- capillary condensation
 - and adsorption/desorption hysteresis 126
- competitive 128
- design of a fixed-bed adsorption process 131
- design of processes 130–135
- desorption 131
- dissociative 128
- equilibrium of a binary system on zeolite 128
- estimation of slope of breakthrough curve 132
- height of mass transfer zone HTZ 132
- hysteresis loop during
 - adsorption and desorption of N₂ in a cylindrical pore 127
- kinetics (influence of pore diffusion) 129, 130
- length of unused bed of an adsorber 134
- minimal ideal length of adsorber 133
- principles 120–124
- total design length of an adsorber 134
- advanced solvents 36
- after co-precipitation 690
- Ag-catalysts 698
- air pollutants, global emissions 510
- air separation processes 458
- air velocity 549
- Al-catalyzed reaction 755
- AlCl₃ 11
- alcohol synthesis
 - by cycloalkane oxidation 475
 - by ethylene oligomerization and Al-complex hydrolysis 475
 - by fatty ester hydrogenation 475
 - global production 473
 - from olefin and syngas 474
 - by olefin hydration 475
 - by sugar fermentation 475
 - from syngas 474
- alcohohates 496
- aldehydes 17
 - distillation column 724
 - hydrogenation 475, 720, 723
 - industrial production 479
 - linear 721
 - oxidation 481
 - Rh-hydroformylation, selectivity for 738
 - Rh-loss 730
 - selectivity to linear aldehyde 718
- Alfol process 475
- aliphatic isocyanates 487

- alkanes 460, 463
 – applications 461
 – chlorination 12
 – from crude oil distillation 463
 – dehydrogenation 36, 462
 – industrial processes for 463
 – oxidation of 464
 – sulfoxidation 12
n-alkanes
 – boiling and melting point 440
 – as feedstock 608
 – important industrial processes for conversion of 463
 alkenes 14, 17
 1-alkenes
 – with chain lengths between C₆ and C₁₈ 751
 – ethene polymerization 805
 – industrial applications 465, 750
 – Poisson distribution 751
 – polymerization to 464
 – production 749, 756
 – SASOL commercially extract 758
 – SHOP technology 756
 alkylsulfonates 504
 alkylate quality 661
 alkylation processes 26, 216, 444, 456, 463, 501, 503, 606, 656, 658, 661
 – of 2-butene with isobutane 654
 – commercially applied 661, 662
 – of fatty amines 501
 – of hexanes with ethane 653
 – HF alkylation 661
 – isobutane, with C₃–C₅ olefins 653
 – of olefins with isoparaffins 653
 – with sulfuric acid as catalyst 655, 661
 – using hydrofluoric acid as catalyst 657
 alkylbenzene sulfonates 502, 503
 alkyl cations 14
 alkyl chlorides 501
 alkyl cyanates 488
 alkyl groups 8, 14, 469, 501, 608, 734, 750, 755, 761, 809, 810
 alkylolithiums 493
 alkylphenol 504
 alkylphenyl polyether glycols 504
 alkylpolyglycosides 504, 505
 alkylsulfonates 464, 503, 504, 736
 alkynes 17, 441, 464
 – industrially important 465
 allyl chloride 466, 490
 allylic alcohol (2-propen-1-ol) 476
 aluminium-alkyl compounds 750
 aluminum 457
 – aluminum-alkyl-based “Aufbaureaktion” 750
 – based oligomerization processes 756
 – cell for fused salt electrolysis of aluminum 802
 – electrical energy consumption for production 802
 – production by electrolysis 801–802
 amination 485
 amines
 – absorption 149
 – amine as solvent 632
 – industrially relevant amine compounds 484
 – industrial routes for 486
 amino acids 462
 ammonia 20, 457
 – catalytic oxidation 26, 573
 – concentration and temperature field 577
 – conversion and characteristic temperatures 582
 – technical reactor for 580
 ammonia reactor
 – inert gas, influence 532
 – pressure drop 531
 ammonia synthesis 525–536
 – annual worldwide production, evolution 527, 528
 – flow sheet
 – historical development 525–528
 – Haber–Bosch process 29, 673
 – kinetics and mechanism 529–531
 – reaction scheme 529
 – schematic energy profile 529
 – syngas composition 538
 – technical ammonia process and synthesis reactors 531–536
 – thermodynamics 527–529
 – pressure and temperature influence 528
 6-aminopenicillanic acid 29
 Amoco process 484, 740
 Andrussow process 462
 aniline 10, 484
 aniline-based herbicide (S)-metolachlor 508
 aniline hydrogenation 485
 anionic detergents 502
 anionic polymerization 496
 annual consumption, of crude oil 21
 annual global production, of chemicals 2
 anthropogenic global warming 425
 anthropogenic NO_x emissions 511
 anti-graying agents 501
 anti-icing agents 705
 Antoine equation 50
 apparent activation energy
 – diffusion processes 229, 230
 – solid catalyzed reaction 255
 – influence of reaction temperature on effective rate constant 255, 256
 aqueous electrorefining, of copper 801
 ARGE catalyst 680
 ARGE fixed bed process 675
 aromatic compounds, industrially important 15, 465
 aromatic hydrocarbons 672
 aromatization 606
 Arrhenius equation 61, 203, 212, 250, 286, 323, 382
 Arrhenius law 24, 201, 215, 583
 Arrhenius number 245, 253, 254, 285, 320, 361
 Arrhenius plot 62, 201, 256, 403, 562
 Arrhenius, Svante August 201
 asphalt 443
 Aspirin® 505
 asymmetric carbon atom 18
 – priority rule for substituents 18
 asymmetric catalysis 508
 asymmetric synthesis 18, 508, 654
 atomic absorption spectroscopy (AAS) 31
 Aufbaureaktion 750
 autoclave process 806, 808, 809, 813–815
 automotive emissions 786
 automotive fuels 605
 auto-refrigeration processes 658
 auxiliary induction 19
 Avogadro, Amedeo Carlo 41
 axial dispersion coefficient 648
 – influence 648
 axial temperature profiles 681
 azeotropic distillation 742, 744
 – heterogeneous 107
 – homogeneous 106
 azeotroping agents 744
N,N-azobisisobutyronitrile 496
- b**
 back-biting process 807
 bacteria 474
 Barkelew diagram 320, 714
 base chemicals 460
 BASF company
 – annual capacity of ethylene oxide 700
 – carbonylation process for acetic acid production 743, 744
 – sales in 2007 and 2009 2, 3
 basicity 10
 batch reactor 213–215, 298–299, 306–307
 Béchamp process 485
 Beckmann rearrangement reaction 486
 bentonite 474
 benzene 11, 16, 463
 – with ammonia, direct amination of 485
 – chlorination 458, 490
 – Friedel–Crafts alkylation 502, 703
 – important industrial products from 470
 – nitration of 16
 – produced together with toluene and xylenes 468
 Bergius, Friedrich 673
 Bergius–Pier process 431, 449, 672, 673
 Bernoulli, Daniel 152
 Bernoulli equation 154
 Berzelius 21
 Bessemer process 587, 589
 BET-equation 124/125
 biocatalysis 19, 20, 28, 29, 474
 – in chemical industry 29
 biodegradable detergents 750
 biogas 460
 biomass
 – chemis-tree, illustration 460
 – to energy supply, global contribution 432
 – gasification 558
 – to liquid (BTL) processes 672
 – particle transient heating, during pyrolysis 546
 – pyrolysis 545
 – renewable energy 421
 Biot, Jean Baptiste 81
 Biot number 82, 546, 593
 biotransformation 28
 biphasic system 290, 291, 499, 727, 730, 733, 735, 737
 BIPHEPHOS ligand 721

- Birkeland–Eyde process 571
 bisphenol A 481, 498
 bisulfite 17
 bite angle 721
 Blasius, Paul Richard Heinrich 155
 Blasius's law 153
 blast furnace coke production 589–595
 – brick wall and coal charge, thermal resistances 594
 – coal coking, transient process 591
 blast furnaces 588, 595–603
 – configuration and air preheating 595
 – gasification of blast furnace coke 599
 – reactions and reaction zones 597
 – residence time distribution in 603
 – temperature and CO/CO₂ content 600
 bleaching activators 501
 blow molding 805
 BMA process 461
 Bodenstein, Max 209
 Bodenstein number 209, 603
 Bodenstein principle 209
 Boltzmann, Ludwig 41, 57
 bomb calorimeter 187, 188
 Borsig transfer-line exchanger 611
 Bosch, Carl 527
 Boudouard reaction 542, 596, 597, 600, 604
 – equilibrium of 197
 Boyle, Robert 41
 Bridgman equation 61
 bromination 16
 2-bromopropane 17
 Brønsted acid 11, 496
 Brunauer, Stephen 127
 bubble column 742
 bubble column reactor 474
 builders 501
 butadiene 8, 466, 477
 butanal 466
 1,4-butandiol 437, 465, 476–479, 482
 butane 461, 462
 – acetic acid synthesis via 742
 – boiling and melting point 440
 – dehydrogenation 462
 – Gibbs enthalpy of system n-butane/i-butane 199
 – major applications 461
 – oxidation 462, 463, 481, 742
 butanoic acid 742
 butanols 475, 727
 – enantiomers 18
 – global production 473
 – isomers 475
 – recycle 505
 – *tert*-butanol 475, 703
 1-butanol 472
 2-butanol 17, 475
tert-butanol 465, 475
 2-butene 462, 463, 466, 653
 – alkylation 654
n-butenes, important industrial products 468
tert-butyl alcohol 702
tert-butylamine 484
tert-butyl cation 14, 653
 butylene hydroformylation 727
 butyllithium 496
 1,4-butyne diol 476
 1,4-butyne diol formation 476
 butyraldehyde 472, 481
 butyraldehyde production 481
c
 calcination of Al(OH)₃ 802
 calcium chloride 696
 capillary condensation 126/127
 capillary method (diffusion) 63
 ϵ -caprolactam 11, 461, 464, 486
 carbanions 7
 carbenium ions 496
 carboanions 7, 8, 12
 carbocations 7, 8, 11, 12, 14, 15, 653, 655, 656, 662
 carbohydrates 28, 451, 453–455, 472, 504
 – starch 454
 – sugar 455
 – wood and cellulose 453–454
 carbonaceous materials, reactivity 547, 548
 carbon/coke
 – gasification 546–549
 – oxidation 546, 548, 549
 carbon dioxide 42, 136, 137, 183, 421, 458, 550, 665, 686, 696, 697, 748
 – chemical absorption 112
 – design data of a column for absorption 116
 – diffusivity 63
 – formation by water gas shift reaction 537, 665
 – real gas factor and phase behaviour 43, 44
 – supercritical carbon dioxide (scCO₂) 734
 carbonization 446, 447
 carbon load 637, 639, 640, 642, 644–646, 648, 649, 650, 652
 carbon nanotubes 400–402
 – Arrhenius plot of oxidation
 -- based on isothermal and TG/DTG-measurements 403
 -- best fit of measurement and simulation 402
 -- comparison of kinetic data 403
 – energy-dispersive X-ray image 401
 – equation for TG analysis 401
 – evaluation of kinetic parameters based on DTG data 402
 – measured and simulated TG and DTG curves 402
 carbon number 15, 469, 475, 613, 629, 634, 665–666
 carbonyl group 17
 carbonylation 739, 743, 744
 – alcohol 482
 – BASF 743, 744
 – methanol 480, 481, 739, 742, 746
 cascade autorefrigeration process, alkylation unit, flow sheet 660
 cascade auto-refrigeration refinery alkylation process 660
 catalysts 19–37, 738
 – classification of pores of solid catalysts 228
 – deactivation 32–35, 638, 651, 692
 -- deposition of residues 33, 34
 -- loss via gas phase 34
 -- poisoning 33
 -- rate of deactivation 34, 35
 -- sintering 34
 – for HDPE and LDPE 809
 – homogeneous *versus* heterogeneous catalysis 27
 – immobilization 28, 716, 730, 733, 736
 – market 20
 – major applications 27–29
 – Nobel prizes in research 21
 – recovery 26
 – for refinery applications 20
 – and support materials 29
 – specific surface areas of 227
 catalytic ammonia oxidation, heat transfer role 576
 catalytic cracking 32, 620–623
 catalytic cycles 20, 22, 718
 cationic detergents 501
 catalytic gasoline reforming
 – high octane gasoline by 633–652
 – plants 634
 – process 637, 638
 – reactions and thermodynamics 633–636
 – reforming catalyst 636, 637
 – reforming catalyst, deactivation and regeneration 638, 639
 -- coke burn-off within single catalyst particle 639–645
 -- regeneration in technical fixed bed reactor 645–651
 catalytic o-xylene oxidation
 – data on chemical media and conditions of catalytic o-xylene oxidation 710
 – simplified reaction scheme 708
 cationic polymerization 14, 15, 17, 496
 Cativa process 739, 743, 747
 – for acetic acid 743
 caustic soda 696
 C-C-coupling reactions 20
 C₄-dimerization 720
 Celanese-LPO-process 742
 cellulose 491
 centrifuges
 – centrifugational number 171
 – hydro- or aerocyclones 167
 – sedimentation in 171
 ceramic monolith 776
 – design 776
 Cetus process 704
 C₁₈ fatty acids 451
 C–H bond breaking 606
 chain-growth
 – mechanism 807, 808
 – polymerization reactions 494, 495
 chain length distribution 755
 chain propagation 12
 chain termination 495, 496, 606
 chain transfer process 807
 char combustion 546–549
 char gasification
 – intrinsic and effective rate constants 546–549
 chemical conversion
 – terms used to quantify result 179, 180
 chemical equilibrium 20, 108, 122, 184, 188, 189

- chemical industry 2
 – annual global production of chemicals 2
 – biggest “chemical nations” 3
 – largest chemical companies by sales 3
 – pharmaceutical companies 3
 – products of German chemical industry 4
 – raw materials of 408
 – sales of the oil & gas industry 4
 – world production of important chemicals 4
- chemical process structure 176
- chemicals production 18
- chemical reaction engineering 1
 – aspects 176
 – basic definitions 176
- chemical reactors 296
 – ideal and real reactors 296–298
 – real reactors according to phases 299
 – fluid–fluid reactions 303, 304
 – gas–solid reactions 301–303
 – heterogeneously catalyzed gas–liquid reactions 304, 305
 – heterogeneously catalyzed single-phase reactions 300, 301
 – non-catalytic single-phase systems 299, 300
 – three-phase reactors 304
 – real reactors based on mode of operation 298
 – batch reactor systems 299
 – continuous mode of operation 299
 – discontinuous and semicontinuous mode of operation 298, 299
 – types and their characteristics (overview) 296
- chemicals manufacturing/fuels
 – investment costs 518–520
 – operating costs 522–524
 – price of 517–518
 – production costs of 517
 – variable costs 521, 522
 – catalyst costs 521
 – energy costs 521
 – feedstock 521
- chemical thermodynamics 182
- chemisorption 231
- chiller 658
- Chinese reed
 – biomass coke from 548
 – characterization 544
 – rate of pyrolysis 545
 – semi-technical gasifier of 552
 – technical gasifier 553
- chiral alcohols 28
- chiral compound 18
- chiral induction 19
- chiral products 18
- chiral synthons 28
- chlor-alkali electrolysis 791–797
- chlorination 16, 458
- chlorine 457
 chlorine applications 792
- chlorobenzene 458, 469, 470, 489, 490
- chloroform 110, 111, 461, 488, 489
- chlorohydrin process 696, 700, 701, 702, 703, 705, 706
 – ethylene 695, 696
 – propylene 701
- chlorohydrin reactor 701
- chloromethane 461, 488, 489
- chloroprene 465
- 1-chloro-2,2,2-trifluoroethane 490
- chromacycloheptane 757
- chromium-catalyzed ethylene oligomerization 749
- chromophores 506
- CIP system 18
- Citronellal 28
- citronellol 506
- Clapeyron, Benoit Paul Émile 50
- Clapeyron equation 51
- Clausius–Clapeyron equation 49, 50
- Clausius inequality 183
- Clausius, Rudolf Julius Emanuel 49
- Claus process 30, 625
- coal
 – from acetylene 470
 – chemis-tree, illustration 460
 – combustion 448
 – chemical reactions 448
 – and electricity production 448
 – fired power plant 571
 – gasification 449, 542, 558
 – in iron and steel production 448–449
 – liquefaction 449–450
 – processes and products 445–450
 – properties 445–447
 – pyrolysis 447–448
 – regional distribution of worldwide production 446
- cobalt/iridium-catalyzed processes 745
- C–O bond 8
- Co catalysts 722, 723
- cocurrent-flow tube-cooled ammonia reactor 534
- coke
 – combustion and gasification 546–549, 604
 – consumption in blast furnace 601
- coked reforming catalyst
 – regeneration 638–651
- coke-oven gas 434
- coking process 30, 590–594
- coking time 590–594, 603
- Colebrook, Cyril Frank 155
- Colebrook’s law 154
- colorants 506
- combined cycle power plant 544
- combined gross enrollment ratio (CGER) 415
- combustion of ammonia 567, 779
 – engines 437
 – of hot blast furnace coke, in contact with air 276
 – promoter 621
- CoMo-catalysts 627
- composition of a reaction mixture, terms used to characterize 179
- compressed natural gas (CNG) 436
- compressors 159
 – conveyance of gases by 160
- condensation 606
- conduction (heat transfer) 80
- confidence limits XIX, XXXI
- conjugative effects 8
 – stabilization of phenolate ion 9
- conjugative stabilization 16
- constant volume bomb
 – calorimeter 188
- constrained catalyst geometries 811
- continuous ideal non-isothermal reactors
 – optimum operation line for adiabatic operation 332, 334, 335
- continuous stirring tank reactor (CSTR) 297, 305, 307, 309, 311, 313, 315, 316, 323, 326, 336, 356, 543, 726, 746, 808
- convection (heat transfer) 80
- convective heat transfer coefficient 576
- conversion, definition 179, 180
- cooled multi-tubular reactors 708
- coordination number 759
- copolymerization 468
- copper catalysts 457, 689, 692
- copper–zinc–aluminum systems 690
- co-precipitation 29
- corrosion inhibitors 501
- Cossee–Arlman mechanism 754
- cost optimum reflux ratio 540
- covalent anchoring 731
- covalent bonds 7, 9, 11
- Cowper, Edward Alfred 595
- Cowper stoves 595, 596
- crack gas 612
- cracking 12, 20, 35, 441, 655
 – alkane 609
 – catalysts 20
 – furnace 606, 607, 610
 – steam 463, 465, 604, 605, 720
 – thermal 443, 444, 553, 616, 618, 620
- critical micelle concentration (CMC) 501
- cross-flow filtration reactor 732
- crude oil 438, 459, 464, 517
 – distillation fractions, yields of 441
 – fractions, composition 440
 – in OPEC countries/non-OPEC countries 439
 – paraffins/aromatics/naphthenes, typical contents 441
 – price in 1865–2009 439
 – production, reserves, and price of 437–440
 – properties of 440–442
 – refinery, flow-sheet of 445
 – regional distribution of worldwide production 438
 – sulfur content of 442
 – typical nitrogen compounds 442
 – typical sulfur compounds 441
- crushers 164
 – types 163
- cryogenic air separation process. *see* Linde process
- cryogenic distillation, product separation 458, 612
- crystallization 140
 – ideal binary eutectic phase system 140, 141
 – system p- and m-xylene
 – ideal binary phase system (both solids soluble in one another) 141–143
 – system anthracene and phenanthrene 142
- CSTR. *see* cooling stirred tank reactors
- Cu-catalyzed reaction 476
- cumene hydroperoxide 496
- Cu/Zn-methanol catalyst 692
- cyanohydrin reaction 17
- cyclization 606
- cycloaddition 606
- cycloalkanes 608

cyclododecanol 475, 476
 cyclohexane 10, 106, 107, 461, 464, 469, 483, 486, 763
 – oxidation of 475
 – solvent 814
 cyclohexanol 12, 464, 475
 cyclohexanone 464, 476
 cyclohexanone oxime 11, 486
 – production route to ϵ -caprolactam 487
 cyclone 171
 cyclopentadienyl groups 811
 cylindrical mills 163

d

Dalton, John 99
 Dalton's law 179
 Damascus steel 587
 Damascus swords 587
 Damkoehler number 215, 582, 603, 676, 710
 Darcy's law 146
 deactivation mechanism 32
 decaffeination 139
 – with supercritical CO₂ 139
 defoamers 705
 dehalogenation 10
 dehydration 10
 dehydrochlorination 11, 701
 dehydrocyclization 634, 651
 dehydrogenation 10, 20, 30, 371, 462, 478, 481, 606, 636, 651, 748, 765
 – alkane 462
 – catalysts 20
 – oxidative 478, 481, 748
 dehydrohalogenation 10
 dehydrosulfurization 30, 35
 deisobutanizer 657, 658
 delayed coking 617, 623
 – data and conditions 617
 – stages 618
 dendrimers 732
 dendritic ligand 733
 depolymerization of cellulose 36
 depolymerization of lignin 36
 desulfurization 624–632
 desulfurization catalysts 20
 detergents 500
 – anionic 502–503
 – cationic 501–502
 – enzymes 501
 – molecules
 – applications 501
 – schematic representation 500
 – neutral 504
 – non-ionic 504–505
 – structure and properties 500–501
 DFT calculations 758
 1,4-diacetoxy-2-butene 477
 diamines 495, 498
 diaphragm process 791, 792, 793
 – advantages 796
 – schematic 794
 diastereomers 18, 19, 763–765, 767, 770
 dibenzothiophene 441, 626, 628–629
 – hydrodesulfurization 625
 dibenzothiophene (DBT) derivatives
 – HDS 626
 – stability diagram 626

dibenzoyl peroxide 496
 dicarbonic acids 495, 498
 dichlorobenzenes 489, 490
 dichloroethane 11, 490
 1,2-dichloroethane 464
 dichloromethane 461, 488, 489
 dielectric permittivity 13
 Diels–Alder type reactions 17, 613
 dienes 606
 diesel 430, 436, 463
 – fuel 443
 – oil, statutory sulfur content, historical development 624
 diethylene glycol 476
 diethyl ether 474, 477
 diethyl sulfate 501
 diffusion coefficient 56, 58, 64, 129, 248, 261, 395, 577, 582, 598, 768, 769
 diffusion of liquids 230
 diffusivity 40, 52
 – of CO₂ in N₂ 63
 – Knudsen 89, 641
 – longitudinal 343, 378
 – molecular 249, 255
 diisobutene 465
 diisocyanates 498
 dimerization 466, 468
 Dimersol-process 468
 dimethylamine 484
 4,6-dimethylbibenzothiophene (4,6-DMDBT) 628
 dimethyl ether 477
 dimethylformamide (DMF) 467
 dimethyl sulfate 501
 dimethyl sulfoxide 469
 dinitrogen oxide 483
 dioctyl phthalates plasticizers 493, 717
 diolefins 441
 diols 472, 495
 1,4-dioxane 478
 diphenyl carbonate
 dipole moment 8
 direct ethylene oxidation process 740, 747
 direct reduced iron (DRI) 589
 direct reduction 303, 596, 600, 604
 dispersion 30
 dispersion model 343, 603
 – axial dispersion and residence time distribution 343, 344
 – axial dispersion model, for turbulent flow in round tubes 352
 – dispersion of mass, and heat in fixed bed reactors 352–354
 – radial variations, in bed structure 354
 – calculation of conversion by 348
 – dispersion and conversion, in empty pipes 349
 – axial dispersion model for laminar flow in round tubes 349–351
 – determination of diffusion coefficients of fluids 352
 – and flow of two liquids in a pipeline 346
 – large deviation from plug flow 346–348
 – residence time distribution 349
 – prediction of conversion based on 349
 – small deviation from plug flow 344–346
 disproportionation 469, 655
 – alkylate molecules 655
 – of carbenium ions 496
 distearyl (dimethyl)ammonium chloride 502
 distillation 97, 98, 467, 474, 755
 – azeotropic 106
 – heterogeneous 107
 – homogeneous 106
 – design of column 101–104
 – extractive 107
 – number of theoretical stages 104, 105
 – pressure swing 107, 108
 – principles 98–100
 – reactive 108
 – reflux ratio 104, 105
 – theoretical stages 104–106
 – stages of industrially important distillation processes 106
 distillation column (DC) 753
 Döbereiner 21
 1-dodecene 717
 double absorption sulfuric acid process 566
 drinking water 144, 147, 148
 – global drinking water coverage 515
 dual-pressure HNO₃ plant 585
 dyes 506

e

Eadie–Hofstee plot 289
 Earth's ecosystems 425
 ecological footprint 427, 428
 economy of scale 694
 E-factor 516
 effective diffusion coefficient 89, 129, 294, 640, 669, 767, 768
 effective dispersion coefficients 356, 646, 648
 effectiveness factor 250, 640, 642, 646, 766
 – for pore diffusion for macro- and micropores 266
 – for reversible first-order reaction 251, 252
 effective rate constants 240, 255, 286, 398, 548, 597, 599, 669, 670, 784
 effective reaction rate 247
 effluent refrigeration 658, 659
 – alkylation unit, flow sheet 660
 Einstein, Albert 248
 elastomers 455, 491, 497
 electrochemical cell 801
 electrochemical reactants 789, 790
 electrochemical reactions 786, 787, 801, 802
 electrode reactions 789, 791
 electrolysis 786, 801
 – potential–current curves 793, 794
 – voltage 796
 electrolytic copper refining 800
 electromagnetic spectrum 79
 electrometallurgy 800–802
 electron density 8, 9, 15
 electronic nature of bonds and atoms, factors influencing 7–8
 – conjugative effects 8
 – inductive effects 8
 – mesomeric effects 8
 – steric effect 8
 π -electron systems 8, 15, 17, 506
 electrophiles 9
 electrophilic reagents 9
 electrophilic substitution reaction 15

- electrorefining 800
 electrostatic precipitator (ESP) 780
 elephant function 234, 235
 elimination reactions 10
 emissions, by mobile sources 510
 emissivity 79
 Emmett, Paul Hugh 127
 emulsion 499, 500, 656, 659
 – formation 728
 – liquid 727
 – polymerization 499
 enantiomers 18, 19
 – 2-butanol 17
 – nomenclature 19
 – (*R*)- and (*S*)-enantiomers 18, 19
 enantioselective hydrogenation 25
 enantiotopic halves 18
 energy barrier 23, 24
 energy consumption 411, 422–425, 521, 522
 enthalpy 45, 184–188
 entrained-flow gasifier 552. *see also*
 Koppers-Totzek process
 – zones for modeling 551
 entrained flow reactor 550
 entropy 48–51, 183, 186
 environmental aspects 509
 – air pollution 510–512
 – green chemistry 515–516
 – water consumption and pollution 512–515
 environmental catalysts 20
 enzyme 19
 epichlorohydrin 701
 epimerization 763–771, 773
 epoxidation 701–703, 706, 750
 1,2-epoxypropane 700
 equilibrium by minimization of G of reaction system, calculation 198
 equilibrium composition 572
 – of SO₂ oxidation 190
 equilibrium of gas reaction, influence of pressure 189
 equilibrium of NH₃ synthesis, influence of real gas behavior on 191
 ethane 461, 462
 – dehydrogenation 189, 606
 – oxidation processes 747
 ethanol 474
 – age-old aerobic fermentation 739
 – alcoholic beverages 472
 – chemical production routes 474
 – isolation proceeds, via distillative processes 474
 – as solvent 690
 ethene 11
 – decomposition 805
 – oligomerization 28, 288
 – process for solution polymerization of 814
 – single-site catalysts for ethene polymerization 811
 ethene/propene/diene copolymerizations (EPDM) 499
 ethene-vinyl acetate copolymers 499
 ether, industrially importance 477
 ethylbenzene 11, 703
 ethylbenzene hydroperoxide 702
 ethyl chloride 481
 Ethyl Corporation process 753
 – ethylene oligomerization schematic 753
 ethylene 461, 462, 480
 – acetaldehyde, production of 480
 – direct oxidation 705 (*see also* ethylene oxidation)
 – ligands, oxidative coupling 759
 – oligomerization 759, 761 (*see also* ethylene oligomerization)
 – partial oxidation 696
 – pipeline system 806
 – polymerization 805
 – schematic representation 808
 – production 462
 – silver-catalyzed direct oxidation 697
 – steam-cracking process 465
 ethylene chlorohydrin 695
 ethylenediamine 484, 485
 ethylene dichloride, via ethylene oxy-chlorination 407
 ethylene hydratization 474
 ethylene oligomerization 751, 756, 758
 – aluminum-alkyl-based “Aufbaureaktion” 750–753
 – linear 1-alkene production 749–762
 – nickel-catalyzed oligomerization, shell higher olefins process (SHOP) 753–756
 – 1-olefins, industrial relevance 749
 – selective, metallacycle mechanism 757–762
 – catalytic cycles, elementary steps 758–759
 ethylene oxidation
 – on Pt wire 242
 – Wacker-Hoechst process 480
 ethylene oxide 464, 472, 476, 478, 695, 705
 – application 478
 – commercial production 695–700
 – chlorohydrin process 695, 696
 – ethylene, direct oxidation 696–699
 – ethylene oxide, products made 699, 700
 – consumption 699, 700
 – industrial epoxides 478
 – producer 700
 – production 696
 ethylene oxide plant
 – degree of utilization 523, 524
 – fixed and variable costs 523
 – flow sheet 699
 ethylene trimerization 757
 eutectic phase system 140
 exhaust gas cleaning 20
 exhaust gases treatment
 – automotive emission control 773–778
 – car engine emissions reduction, catalytic converters 775–778
 – engine emissions reduction and emission standards 773–775
 – catalytic treatment, ceramic monolith 777
 – composition of exhaust gas without treatment 773, 774
 – from mobile and stationary sources 773–786
 – NO_x, selective catalytic reduction (SCR) from 778–785
 – catalysts and reactors 779, 786
 – flue gas treatment from power plants 778, 779
 – nitrogen oxides formation during fuel combustion in power plants 778
 -- reaction chemistry of SCR 781
 -- SCR reactor, reaction kinetics and design 781–785
 experimental reaction orders, differ from stoichiometric coefficients 212, 213
 external effectiveness factor 244
 – Arrhenius number 245
 – for exothermic heterogeneously catalyzed gas reaction 244–246
 – Prater number 245
 – Sherwood number 244
 external heat transfer 283, 284
 – coefficient 329, 678
 external mass transfer
 – coefficient 641
 – estimation of required length of fixed bed reactor for gas phase reaction controlled by external mass transfer 239
 – external effectiveness factor η_{ex} 237
 – for Langmuir-Hinshelwood kinetics 237, 238
 – for negative reaction order 237, 238
 – influence of external mass, and heat transfer on effective rate 239, 240
 – interaction with chemical reaction 235–237
 – through boundary layer 282, 283
 extractive distillation 469, 474
 extra- and intraparticle mass and heat transfer limitations, criteria for 286
 extrusion 761

f

- falling film evaporator 726
 Faraday constant 787, 796
 Faraday's law 786, 787
 Faraday, Michael 786
 fats and oils
 – composition and production 451
 – industrial routes to convert 452
 fatty acid esters, hydrolysis 451
 fatty acid methyl esters 11, 452
 fatty alcohol ether sulfates 504
 fatty alcohol polyether glycols 504
 fatty alcohols 452, 473, 475, 504, 505
 – non-ionic surfactants based on 455
 fatty alcohol sulfates 504
 fatty amines 484, 485
 fatty carboxylates 502
 fatty nitrile 485
 FCC. *see* fluid catalytic cracking (FCC)
 FCC-process. *see* fluid catalytic cracking
 Fe-Cr catalyst 539
 Fe-modified bismuth-phosphorous molybdate contact 486
 fermentation processes 28, 474, 739
 fertilizers 20, 558
 – applications 459
 Fick, Adolf Eugen 54
 Fick's law 54, 218, 579, 768
 Fick's law, second 85
 film diffusion 229
 filtration
 – cake filtration 168
 – pressure 168
 – of a suspension of CaCO₃ 168
 fine chemicals 28, 505, 763–772
 – adhesives 506

- fragrance and flavor chemicals 506
 - menthol and menthol production 763–764
 - menthol isomers epimerization
 - mass transfer influence 766–771
 - thermodynamics and kinetics 764–766
 - pesticides 506–508
 - pharmaceutical 508, 509
 - vitamins, food, and animal feed additives 508
 - vs. petrochemicals, characteristic differences 505
 - fine particles, fluidization regimes**
 - with 622
 - finite element method** 578
 - first law of thermodynamics** 45
 - first-order rate constants** 618
 - first-order reaction** 204
 - Fischer, Franz** 664
 - Fischer-Tropsch synthesis** 29, 437, 449, 662, 664–685, 665, 666, 670, 673, 679, 708, 717, 797
 - chemical media and reaction conditions 677
 - commercial plants 671
 - GTL plant, main parts 675
 - history, current status, and perspectives 670–674
 - intrinsic and effective reaction rate 668–670
 - kinetic scheme 665
 - mechanisms scheme 665
 - multi-tubular fixed bed Fischer-Tropsch reactor modeling 677–684
 - processes and reactors 674–677
 - product distribution 667
 - product streams 758
 - reactions and mechanisms 664–668
 - reactors used 675
 - fission power** 421
 - fixed bed gasifier.** *see* Lurgi reactor
 - fixed-bed reactor** 300, 301
 - fixed bed reactors, modeling** 355
 - criteria used to exclude a significant influence of dispersion 357
 - axial dispersion of heat 360, 361
 - axial dispersion of mass 357, 358
 - radial dispersion of heat 361, 362
 - radial dispersion of mass 358–360
 - radial variations in bed structure 363
 - dispersion processes 356, 357
 - fundamental balance equations 355–357
 - fixed-matrix regenerator system** 595
 - flame velocity** 435
 - flavor chemicals** 506
 - flow-sheet** 658
 - flue gas** 778
 - treatment 786
 - flue gas desulfurization (FGD)** 778
 - unit 780
 - fluid catalyst** 620
 - fluid catalytic cracking (FCC)** 463, 620, 621, 623.
 - see also* cracking
 - block diagram 622
 - chemical media and reaction conditions, data on 621
 - heat balance 622
 - regenerator, minimum fluidization and discharging velocity 623
 - fluid–fluid reactions** 292
 - industrial reactions 216
 - kinetics of 216, 217
 - fluidization velocity** 157
 - fluidized bed Fischer–Tropsch (FT)**
 - reactor 663
 - fluidized-bed gasifier.** *see* Winkler process
 - fluid–solid extraction** 136
 - design 139
 - effective extraction rate, factors influencing 136
 - ideal solvent, requirements 136, 137
 - influence of particle size on rate of external mass transfer 138, 139
 - principles 136
 - solubility of caffeine in CO₂ 138
 - fluoropolymer** 493
 - fluorous phases** 733
 - food additives** 508
 - food grade phosphoric acid** 458
 - food industry** 139
 - food ingredients** 28
 - formaldehyde** 106, 254, 285, 476, 478, 479, 496, 694, 742
 - formic acid**
 - methanol, carbonylation 481
 - production capacities 482
 - N-formylmorpholine** 467
 - fossil fuels**
 - CHO content 433
 - consumption 446
 - crude oil 408
 - reserves, and resources 408, 419, 420
 - conventional and non-conventional fossil fuels 418–420
 - fouling** 723
 - Fourier, Jean Baptiste Joseph** 53
 - Fourier number** 82, 593
 - Fourier's law, first** 52, 66
 - Fourier's law, second** 81
 - fragrances, role** 501, 506
 - Frasch process** 458
 - friction factor** 153, 154
 - Friedel–Crafts acylation reactions** 14
 - Friedel–Crafts alkylation** 469, 703
 - Fritz Haber** 526
 - FT GTL plant, main parts** 675
 - FT multi-tubular reactor** 664
 - FT reactors, design** 674
 - FTS.** *see* Fischer-Tropsch synthesis
 - fuels**
 - average price and world demand 518
 - consumption 599
 - equipment costs 518
 - production costs of 517
 - purification 775
 - solid, typical composition 447
 - fugacity coefficients** 687, 695, 787
 - fugacity, influence of pressure on** 191, 687
 - functionalizations** 20, 36
 - fungicides** 506, 507, 508
 - fusion power** 421
- g**
- galvanic cell** 788, 791
 - gas compressor** 611
 - gas hourly space velocity (GHSV)** 565
- gasification**
 - chemical reactions 448
 - computations 551
 - reactors 302
 - gas–liquid interface**
 - mass transfer 217, 218
 - gas–liquid reactions**
 - equations according to two-film theory 225
 - influence of *Ha* on enhancement factor *E* 224
 - kinetics, on solid catalysts 291
 - reactor types 293, 304
 - gasoline** 430, 442, 443
 - limit values of sulfur in 624
 - production of 437
 - gasoline spark ignition engines** 775
 - gas-phase PE-process** 814
 - gas recycle hydroformylation processes** 725
 - gas recycle process** 724, 738
 - gas–solid reactions** 157, 172, 175, 181, 195, 196, 203, 547, 641, 642
 - equilibrium of 195–197
 - kinetics 268
 - reactors for 301, 302
 - spectrum of factors influencing rate of 269
 - influence of external and internal mass transfer 269
 - gas-to-liquid (GTL) FTS technology** 670
 - Gay-Lussac, Joseph Louis** 4
 - Gibbs enthalpy, of gas phase system** 199
 - Gibbs free enthalpy** 789
 - Gibbs functions** 184, 185, 559, 570, 571
 - Gibbs, Josiah Willard** 184
 - Gini coefficient** 413
 - global anthropogenic sulfur emissions** 510
 - Global Footprint Network** 426, 427
 - global warming** 424, 425, 483, 781
 - glucose** 453, 454, 505, 704
 - non-ionic surfactants based 455
 - glutaminic acid** 508
 - glycerol** 451, 452, 473, 477, 701, 792
 - glycidol** 28
 - glycol ethers** 705
 - greenhouse gas producers** 35, 425
 - Grignard reagents** 8
 - gross domestic product (GDP)** 410
 - gross national product (GNP)** 410
 - per capita (pc) vs. primary energy consumption (pc) 412
 - GTL plant** 674
 - guano, fertilizer and gunpowder ingredient** 525
 - Gulf process** 752
 - gutta-percha (*trans*-1,4-polyisoprene)** 456
 - gypsum, applications** 459
- h**
- Haarmann & Reimer process** 764, 772
 - Haber–Bosch process** 29, 525, 568, 673
 - Haber, Fritz** 526, 527
 - Hagen, Gotthilf Heinrich Ludwig** 155
 - Hagen-Poiseulle's law** 153
 - Halcon process** 703
 - haloalkane** 13

- Haldor Topsoe process for methanol production 693
half-cell reaction 790
Hall-Héroult process 802
halogenated compounds 490
– applications 489
happiness and life satisfaction of nations 416
hard coal, liquefaction 450
hardening agent 587
Hastelloy C 484, 744
Hatta number 226
HDPE fluid bed process 815
HDS process, configuration 632
heat 235
– dispersion coefficient 647
– loss estimation
-- hot wire by radiation and convection 80
-- human body 80
heat capacities 45, 434, 805
heat conduction 52
– Fourier's first law 66
– in spherical shell 67
– through wall of tube with externally cooled surface 66
heat exchangers 93, 94–97
– counter-flow and parallel-flow heat exchangers, comparison 96
– logarithmic mean temperature difference in a heat exchanger 95–97
heat of polymerization 805
heat transfer
– analogy to mass transfer 579
– boiling 78, 79
– coefficient 546, 575, 679, 710
– fluid and external surface of tube (cylinder) 73
– fluid and internal surface of empty tube 71, 72
– fluid and particles of packed bed 77
– fluid and single particle 75, 76
– local, for flow of fluid across cylinder 73, 74
– plane walls and cylindrical shells surrounded by fluids 77, 78
– by radiation 79, 80
heat transfer by convection
– contribution of free convection to overall heat transfer 76
– estimations of heat transfer coefficients (α) 67
-- Nusselt number 68, 69
– from a stagnant or a flowing fluid to a solid 67
heat transport, in chemical engineering 66
heavy oils 139, 304, 434, 444, 449, 543, 612
– cracking
-- fluid catalytic cracking (FCC) 620–623
-- thermal cracking (delayed coking) 616–620
– gasification 553, 554
height of transfer zone (HTZ) 134/135
hemicellulose 453
Henry coefficient 64, 109, 110, 116, 146, 293, 669
Henry's law 109, 217, 627
Henry, William 109
herbicides 506, 508
heterogeneous catalysis. *see* heterogeneously catalyzed process
heterogeneous catalysts 19, 20, 23, 27, 29, 269, 485, 758
– production, and characterization 29–32
– properties 27
– role in chemical technology 26
– typical conditions, and catalyst lifetimes 32
heterogeneously catalyzed hydrodesulfurization (HDS) 626, 627, 631, 633
heterogeneously catalyzed reaction
– kinetics of 226
– reactors used for 300
– spectrum of factors influencing 227
– steps of gas catalyzed reaction 229
heterogeneously catalyzed surface reactions
– Eley–Rideal mechanism 233
– Langmuir–Hinshelwood–Hougen–Watson rate equations 233, 234
– Langmuir–Hinshelwood mechanism 232, 233
– monomolecular mechanism 232
– rate equations for 231, 232
heteropoly acid 748
hexamethylenediamine 461, 464, 484, 485, 487
hexamethylene diisocyanate 461, 464
1-hexene
– extrusion 761
– heterogeneously catalyzed gas phase hydrogenation 394
– hydroformylation 720
– selectivities 757
cis/trans-3-hexene formation 720
HF-catalyzed reaction 661
high-density polyethylene 803, 816
high density polyethylen 499, 521, 522
high-dust system (in SCR) 780
high fructose corn syrup 29
higher olefins 25, 720, 727–729
– liquid–liquid multiphasic hydroformylation 728
– Shell higher olefins process (SHOP) 753–757
– solubility limitation 729
high-pressure Hastelloy reactor 744
high-pressure LDPE processes 816
high-pressure methanol synthesis 527
high-pressure steam 611
high-throughput experimentation 36
Hinterland ratio 226
Hirschfelder equation 58
Hock process, for phenol production 481
Hoechst process 812
H₂O electrolysis 797
– efficiency 799
– energy demand 799
homogeneous catalysis 19, 287, 731, 736
– advantages 731
– applications 716
homogeneous catalysts 20, 26, 722, 723
– advantages 27, 28
– catalyst deactivation 34, 35
-- rate 35
– chemical industry, examples 28
– filtration 732
– properties 26
– transition metal complex 28
homogeneous reactions
– kinetics of 21, 200
– vs. heterogeneous catalysis 27
homogeneous two-phase catalysis 290
Hougen–Watson type equation 561, 668
human development index (HDI) 413, 414
– happiness and life satisfaction of nations 416
– purchasing power parity (PPP) 415
– subjective well-being index (SWB) 416, 417, 418
– vs. energy consumption per capita 413
– vs. gross national product (GNP) 415
Hüttig temperature 692
hydrated lime 696
hydratization 17
β-hydride elimination 754
hydroamination 485
hydrochloric acid 457, 458
hydrochlorination 458
hydrocyanation 28, 29
hydrodealkylation 469
hydrodesulfurization 291, 625
– and reaction engineering aspects 629–633
– reaction network 627
– thermodynamics and kinetics 625–629
hydrodynamic entrance region 84
hydroelectricity 421
hydrofluoric acid 653
hydrofluoric acid alkylation process 656, 657
hydroformylation 25, 28, 464, 472, 474, 475, 480, 716–738
– advanced catalyst immobilization technologies for 730–738
– catalyst separation by size exclusion membranes 732, 733
-- homogeneous catalysts immobilization on solid surfaces by 731–732
– liquid–liquid biphasic reaction systems using 733–736
-- supported liquid hydroformylation catalysis 736–738
– allyl alcohol 476
– catalytic cycle 719
– current catalyst
-- and process technologies 722–730
– 1-dodecene 718
– ethylene 475
– homogeneous nature 718
– industrial relevance 717, 718
– of internal olefins to linear aldehydes 721
– plant 716, 730, 733
– propene 475, 716, 717, 718
– propylene 481, 717
– supported liquid catalyst for 737
hydrogen 457, 536–558
– hydrogen by gasification of biomass 544–552
– production
-- and application 437
-- options to produce 536–541
– syngas and 536
hydrogenations 16, 17, 20, 21, 29, 30, 35, 205, 291, 292, 394–396, 475
– aldehyde 720, 723
– catalysts 20
– fatty ester 475
– nitrobenzene 485
– olefin 720
– rate of octene 397, 398

- selective 613
- hydrogen bonding 736
- hydrogen cyanide 461, 462
- hydrogen–nitrogen–ammonia equilibrium 527
- hydrogen peroxide to propylene oxide (HPPO) process 704
- hydrogen sulfide 612
- hydrogen transfer 720
- hydroperoxidation reaction 701, 703
- hydroperoxides 702
- hydrophilicity 500
- hydrophobicity 500
- hydrothermal synthesis 29
- hydrotreating
 - clean liquid fuels by 624–633
 - history, current status, and perspective 624, 625
 - hydrodesulfurization (*see* hydrodesulfurization)
- hydrotreating reactions 624, 626
- equilibrium data 626
- hydrotreating reactor 637
- hydroxide 13
- hyper-branched polymers 732
- hypochlorous acid 791

- i**
- ICI low-pressure process 693
- ideal gas behavior
 - compressibility factor 42, 44
 - magnitude of deviation 42
 - effect of temperature 43
 - influence of pressure 42
- ideal gas constant 40
- ideal gas law 40, 41
 - originators 41
- ideal isothermal reactors 305, 306
 - comparison of ideal reactors 314
 - continuously operated
 - cascade of tank reactors 311
 - ideal tank reactor 307, 308
 - ideal tubular reactor 308, 309
 - tubular reactor with laminar flow 309–311
 - conversion for a given *Da* number 313
 - equations for conversion of reactant in ideal reactors 314
 - influence of changing volume on performance 315
 - mixed flow reactor 315
 - plug flow reactor 315
 - influence of reactor type on product yields and selectivity 316
 - tubular recycle reactor 311–313
 - well-mixed (discontinuous) isothermal batch reactor 306, 307
- I-effect 8
- ignition–extinction behavior 240, 268
- ignition of Pt-wire during oxidation of ethylene 242, 243
- ignition temperature 435
- impregnation 30
- indenoxide 28
- indirect oxidation of propylene 702
- inductive effects 8
- industrial catalysts 20
 - application areas 35
 - chemical synthesis 36
 - environmental catalysis 35
 - production of polymers and materials 36
 - refinery and energy applications 35–36
 - importance for development of efficient processes 36
 - industrial coal liquefaction processes 450
 - industrial electrolysis 786–802
 - chlorine and sodium hydroxide 791–802
 - applications 791, 792
 - chlor-alkali electrolysis processes 792, 793
 - diaphragm process 793–795
 - electrolysis of water 797–800
 - membrane process 796
 - mercury cell process 795
 - electrochemical kinetics, and thermodynamics 786–791
 - electrical work and thermoneutral enthalpy voltage 789–791
 - electrochemical potentials 787, 788
 - Faraday's law and current efficiency 786, 787
 - galvanic and electrolysis cells, Nernst's law 788, 789
 - overpotentials 791
 - standard electrode potentials 789
 - electrometallurgy 800–802
 - electrolytic refining in aqueous solution 800, 801
 - fused salt electrolysis 801, 802
 - industrial organic chemistry 459, 460
 - alkanes and syngas 460–464
 - alkenes, alkynes, and aromatic hydrocarbons 464–471
 - organic compounds containing oxygen, nitrogen, halogens 472
 - acids 481–484
 - alcohols 472–477
 - aldehydes 478–481
 - amines and nitrogen-containing intermediates 484–486
 - epoxides 478
 - ether syntheses 477–478
 - halogenated organic intermediates 488–491
 - ketones 481
 - lactams, nitriles, and isocyanates 486–488
 - polymers 491
 - polyesters, polyamides, and polyurethanes 497–500
 - polyolefins and polydienes 492–493
 - vinyl-polymers and polyacrylates 493–497
 - industrial processes
 - acetic acid 739–749
 - ammonia synthesis 525–536
 - catalytic reforming, high octane gasoline by 633–652
 - coke and steel 587–604
 - ethylene and propylene oxide 695–706
 - exhaust gases treatment from 773–786
 - fine chemicals production 763
 - fuels and chemicals from syngas, methanol and Fischer–Tropsch synthesis 662–695
 - heavy oils cracking, liquid fuels by 616–624
 - hydroformylation (oxosynthesis) 716–738
 - hydrotreating, clean liquid fuels by 624–636
 - industrial electrolysis 786–802
 - isenthalpic expansion 47
 - isobutane 463, 467, 468, 653–657, 660, 703, 813
 - isobutane-to-olefin ratio (I/O) 656
 - isobutanol 475, 478
 - isobutene 465, 466
 - isocyanates 486, 487
 - iso-hexane 11
 - isomerizations 20, 35, 469, 606, 721
 - isooctene 468
 - isophthalic acid 465
 - isopropanol 7, 475
 - isotacticity 492
 - isothermal compression 160
 - isothermal plug flow reactor 618
 - isotope-labeled carbon dioxide 690

j

- jet fuel 444
- Jost pot 768, 769
- Joule, James Prescott 46
- Joule–Thomson coefficient 45, 47
 - calculation 47
 - liquids 48
 - sign 48
- Joule–Thomson effect 45, 435, 458, 540
- Joule–Thomson throttling process 46, 47

k

- Kármán's law 154
- Kármán, Theodore von 155
- Katzschmann process 483
- Keim, Wilhelm 753
- Kellogg process 693
- Kelvin, Lord 46
- kerosene 443
- ketone 14
- kieselguhr 474
- kinetic data 379
 - case studies 392
 - heterogeneously catalyzed hydrogenation of hexene 394, 395
 - heterogeneously catalyzed multiphase reaction 395–400
 - non-isothermal oxidation of carbon nanotubes and fibers 400
 - thermal conversion of naphthalene 392–394
 - evaluation of 382–385
 - laboratory-scale reactors for kinetic measurements 385–388
 - measurement and evaluation 379, 380
 - principal methods for determining 379, 380
 - laboratory reactors 380–382
 - macrokinetics 380
 - microkinetics 380
 - pros and cons of integral and differential method 382
- kinetic energy 56, 60, 62, 152, 155, 201
- kinetic racemic resolution 19
- kinetic resolution 29
- kinetics 22
 - of biochemical reactions 177
 - birth and death of a rumor 209, 210
- kinetic theory of gases 57
- Kirchhoff's law 79
- Knudsen diffusivity 90–93, 249, 641
- Koppers-Totzek process 543
- Kuhlmann process 723

l

- laboratory-scale continuous fixed bed reactor 765
- laboratory-scale reactors for kinetic measurements 380, 385, 404
 - batchwise operated stirred tank reactor 387
 - classification of laboratory reactors 386
 - fixed bed reactor with taps 387
 - gradientless reactor 380
 - with internal recycle 388
 - integral reactors 381
 - differential evaluation of data 381, 382
 - laboratory-scale semi-batch reactor 764
 - laboratory-scale trickle bed reactor 631

lactams 486

- lambda value 776
- laminar flow 783
- Langmuir–Hinshelwood–Hougen–Watson (LHHW) model 234
- Langmuir–Hinshelwood mechanism 697, 767
- Langmuir, Irving 122
- Langmuir's adsorption isotherm 231
- L-asparaginic acid 508
- LD converter 589
- LDPE autoclave process 808
- LDPE tubular process 808
- leaving group 14
- Le Chatelier, Henry Louis 189
- Le Chatelier's principle 189, 609
- length of unused bed (LUB) 134
- Lewis acids 11, 496
- Liebig 21
- life expectancy index (LEI) 415
- ligand association 759
 - reaction 754, 759
- ligand back bone 721
- ligand bite angle 721
- ligand dissociation 759
- ligand effect 27
- ligand–metal complexation equilibria 731
- light crack-fuel, composition 614
- light heating oil 443
- light hydrocarbons
 - autothermic reforming 557
- lignin 453, 454, 456
- lignite, liquefaction 450
- limestone, applications 459
- limit cycle (oscillation) 326, 327
- Linde process for air separation 540, 541
- linear alkylbenzene sulfonates (LABS) 503, 750
- linear low-density polyethylene 750, 803
- Lineweaver–Burk plot 289
- liquefied natural gas (LNG) 419, 436
- liquefied petroleum gas (LPG) 2, 443
- liquid acid catalysts 656
- liquid catalysis 736
- liquid filled porous catalyst 669, 685
- liquid fuels 670, 672
 - production capacity 673
- liquid hourly space velocity (LHSV) 637
- liquid–liquid biphasic catalytic reaction 27, 29, 485, 730, 733, 735, 737, 738, , 753
- liquid–liquid equilibrium
 - calculation based on Gibb's enthalpy 195
 - and link to gas-phase reaction 194
- liquid–liquid extraction 116
 - design 118, 119
 - number of theoretical separation stages of extraction 120
 - principles 116–118
- liquid–liquid phase separator 727, 734
- liquid–liquid reactions
 - equilibrium of 193, 194
 - industrial reactions 216
- liquid phase esterification, equilibrium of 195
- liquid recycle process 725, 738
 - advantage 725
 - schematic view 725
- liquid–vapor equilibrium 541
- living polymerization 496
- L-methionine 462

logarithmic mean temperature 94, 95

- “loop reactor process” 489, 813
 - schematic view 813
- Loschmidt, Johann Joseph 41
- Lotka–Volterra model
 - for cyclic oscillations 327, 328
- low-density polyethylene 803, 804
- autoclave process 806
- formation, free-radical process 806
- tubular reactor process
 - schematic view 807
- low density polyethylene 498
- lower heating values (LHV) 520, 532, 798, 799
- ethylene oxide (EO) plant 520
- low-pressure methanol carbonylation 744
- low-pressure oxo process (LPO) 724
- lubricants 443, 493, 705, 750, 753, 762, 792
- Lurgi process for methanol production 694
- Lurgi reactor for coal gasification 543
- lynx-hare cycle 326, 327

m

- macropores 31
- macroradical 495
- magnetic suspension balance 63
- maleic acid 483
- maleic acid anhydride 30, 461, 464, 468, 469, 470, 482, 483
- maleic anhydride 476
- Mariotte, Edme 41
- Markovnikov's rule 17
- mass transfer
 - analogy to heat transfer 579
 - by diffusion 53–57
 - with fast/instantaneous reaction near/at gas/liquid interface 220–225
 - with (slow) homogeneous gas/liquid reaction in bulk phase 219, 220
- mass transfer coefficient 86, 294, 574, 578, 597
 - influence of temperature 575
- mass transfer resistance
 - heterogeneously catalyzed gas–liquid reaction 293
 - heterogeneously catalyzed gas or liquid reaction 229
- mass transport 84
 - diffusion in porous solids 89, 90
 - forced flow in empty tubes 84, 85
 - hydrodynamic entrance region 84, 85
 - interrelation of diffusion and convection 87, 88
 - Knudsen diffusion, and related phenomena 90–92
 - limitation 697
 - steady-state and transient diffusive mass transfer 85, 86
- Maxwell–Boltzmann distribution 60
- McCabe–Thiele approach 101–105
- mechanical unit operations
 - compressors and pumps 159
 - conveyance of gases by compressors 160, 161
 - conveyance of liquids by pumps 159
 - estimation of energy requirement for the conveyance of fluids 161
 - contacting and mixing of fluids 161, 162
 - conveyance of fluids 152

- pressure loss in empty tubes 152–156
 - pressure loss in fixed, fluidized, and entrained beds 156–159
 - crushing and screening of solids
 - particle size analysis 164, 165
 - particle size reduction 163, 164
 - sieve analysis and particle size distribution, granular material 165
 - sieve analysis of sand 166
 - cyclone for separation of solid particles from gases or liquids 171
 - plate-type electrostatic precipitator 172
 - screening and classification of particles 166, 171
 - sedimentation in centrifuges 171
 - sedimentation in electrical fields 171, 172
 - separation of solids from fluids 168
 - filtration 168
 - sedimentation 168–172
 - solid-solid separation (sorting of different solids) 167
 - tubular electrostatic precipitator 172
 - mega methanol 694
 - melting enthalpy 51
 - melting point of selected liquids 51
 - melting temperature 50
 - membrane process 792, 796
 - membrane reactors 305, 370, 371, 372, 732, 733
 - hydroformylation catalysis 733
 - membrane separation 458
 - principles 144–146
 - menthol diastereomers 770
 - epimerization, reaction scheme 764
 - equilibrium concentrations 765
 - structure 763
 - menthol isomers, diffusion coefficients 768
 - menthol stereoisomers 769
 - Menton, Maud Leonora 288
 - mercury cell process for chlor-alkali electrolysis 791, 795
 - mercury porosimetry 32
 - mesomeric effects 8
 - mesopores 31
 - metabolism 21
 - metal atoms 8
 - metal carbonyls 34
 - metal hydrides 17
 - metallacycle mechanism 757–762
 - metallocene catalysts 20, 811
 - metal–organic vapor deposition 30
 - metal oxide 776
 - metal plating 726
 - metathesis 755
 - methacrylic esters 462
 - methane 8, 460–461
 - chemical products from 461, 489
 - chlorination 7, 458
 - coal mining 446
 - equilibrium content during steam reforming 555
 - equilibrium of methane pyrolysis 197
 - formation in Fischer-Tropsch synthesis 665
 - hydrogen cyanide production 461
 - natural gas 433, 434
 - syngas production 462
 - methanol 8, 63, 100, 104, 108, 377, 449, 472, 477, 483, 662, 685, 689, 692, 695, 743, 749
 - carbonylation 742, 743
 - carbonylation, catalytic cycle and mechanism 745
 - Co-catalyzed carbonylation 745
 - industrial production 686
 - Ir-catalyzed carbonylation 745
 - oxidation 478
 - production
 - copper–zinc–alumina catalyst 690
 - high-pressure plant 689
 - Rh-catalyzed carbonylation, catalytic cycle for 745
 - synthesis 24, 664, 671, 685–695
 - catalysts for 689–692
 - equilibrium 688, 689
 - flow sheet 693
 - kinetic mechanism 691
 - processes and synthesis reactors 692–695
 - reaction steps 691
 - thermodynamics 686–689
 - methanol-to-olefin (MTO) 694
 - methylaluminoxane (MAO) 492, 496, 757, 811
 - methylaluminoxane co-catalyst 758
 - methylamine 484
 - methyl *tert*-butyl ether (MTBE) 465, 478, 694, 703
 - methyl carbocation 14
 - methyl chloride 481
 - N-methyldiethanolamine 113
 - methylene diphenyl diisocyanate (MDI) 498
 - methyl ethyl ketone 481, 742
 - methyl iodide 744
 - N-methylpyrrolidone (NMP) 728
 - N-methylpyrrolidone/water mixtures 469
 - methyl *tert*-butyl ether (MTBE) 478
 - metolachlor 28
 - (*S*)-metolachlor stereoisomer 508
 - Michaelis, Leonor 288
 - Michaelis–Menten equation 288–290
 - Michaelis–Menten kinetics 29
 - microorganisms 28
 - micropores 31
 - microreactor technology 36
 - middle temperature pyrolysis 604, 605
 - mixing 162
 - dynamic/static mixers 162
 - fluids 161
 - modified Thiele modulus 251
 - molar heat capacity 45, 317
 - molecular interaction forces 42
 - molecular speeds in gas, distribution 60
 - molybdenum naphthenate 703
 - monoethylene glycol 699
 - monomers 12, 491
 - monophasic reaction system 729
 - monopropylene glycol 701
 - Monsanto low-pressure process, for acetic acid 744–747
 - Monsanto process 743, 744, 747, 749
 - flow scheme 746
 - montmorillonite 474
 - motor octane numbers 652
 - moving-bed process 639
 - multibed ammonia reactor 533
 - with indirect cooling 533
 - with quench cooling 533
 - multifunctional reactors 36
 - multiphase catalytic processes 28
 - multiple-bed reactor 693
 - multiple catalyst bed reactors 693
 - multiple catalyst beds 561
 - multi-purpose plant (MPP) 505
 - multi-scale modeling 36
 - multistage cascade reactor 660
 - multi-tubular reactors 695, 698, 708, 716
 - cooling temperature, influence 682
 - FT reactor 680, 681
 - modeling and simulation 677
 - runaway diagram 683
- n**
- nanofiltration 732
 - naphtha 443, 463, 613–615, 739, 740, 742, 749
 - cracking 463
 - naphtha oxidation 742
 - naphthalenes 140, 359, 379, 392–394, 441, 707, 716
 - naphthalenes 189, 441, 634, 636, 638, 651
 - natural dyes 455
 - natural gas 464
 - autothermic reforming 557
 - based plant for ammonia 532
 - composition 434
 - conditioning 435–437
 - conversion 435
 - overview of processes based on natural gas 435
 - properties of 433–435
 - reforming 555–557
 - used for heating and electricity 436
 - natural gas production 434. *see also* methane
 - safety parameters 434
 - worldwide production, regional distribution of 434
 - natural oils 11
 - natural rubber (*cis*-1,4-polyisoprene) 455, 491
 - molecular structure of 456
 - n-butanol 475
 - n-butenes 465
 - Nernst equation 787, 788, 790, 793, 797
 - Nernst's partition coefficient 117
 - Nernst, Walther Hermann 117
 - neutral NaCl solution, scheme of electrolysis 791
 - Newton, Isaac 54
 - Newton number 162
 - Newton's law 53
 - NH₃ combustion 32
 - n-hexane 11
 - NH₃ synthesis 32
 - from natural gas 457
 - nickel alkyl 754
 - nickel catalyst 288, 394, 395, 398, 468, 481, 555, 753, 762
 - ethylene oligomerization mechanism 753
 - nickel hydride 754
 - nitration 464
 - nitration reaction 16

nitric acid 457, 568–586
 – ammonia, catalytic oxidation kinetics 572–583
 -- in industrial reactor, on series of Pt gauzes 579–583
 -- on single Pt wire for cross-flow of gas 573–579
 – NO oxidation 583, 583, 584
 – plant 567, 587
 – processes 584–586
 -- block diagram 569
 -- reaction scheme 569
 – production
 -- stability diagram 570
 -- thermodynamics 570
 – production, reactions and thermodynamics 568–572
 nitric oxide (NO) 568
 – equilibrium content in air 572
 nitriles 486, 487
 nitrobenzene 10, 15, 469, 485
 nitrobenzene hydrogenation 16
 nitrogen by air separation 540, 541
 nitrogenous fertilizers 568
 – production 569
 nitrogen fertilizers 525
 nitrogen oxides 779
N-methylpyrrolidone (NMP) 467
N,N-azobisisobutyronitrile 496
 non-ideal flow, and residence time distribution 336, 337
 – pulse experiment 338
 – step experiment 339, 340
 nonionic alkylphenol ethoxylates 700
 non-ionic surfactants
 – based on fatty alcohols and glucose 455
 non-isothermal ideal reactors 316
 – adiabatic operation of a batch reactor 317, 318
 – choice of best reactor type, for adiabatic operation 335
 – continuous ideal non-isothermal reactors
 -- optimum operation line for adiabatic operation 332, 334, 335
 – continuous ideal non-isothermal reactors, optimum operating lines 332
 – continuously operated non-isothermal ideal tank reactor 322, 323
 – continuously operated non-isothermal ideal tubular reactor 328, 329
 -- adiabatic operation of PFR 329, 330
 – cooled batch reactor, with exothermic reaction 318–322
 – cooling stirred tank reactors (*see* cooling stirred tank reactors)
 – and criteria for prevention of thermal runaway 316, 317
 – critical condition for thermal runaway, for a zero-order reaction 322
 – decomposition of H₂O₂ in adiabatic batch reactor 318
 – evolution of reactor temperature, in cooled batch reactor 319
 – optimum operation line for non-adiabatic operation of PFR 335
 – optimum path to minimize volume of PFR 335, 336
 – wall-cooled ideal tubular reactor 330, 331

– well-mixed (discontinuously operated) non-isothermal batch reactor 317
 non-solar renewables 429
 normalize standard electrode potentials 802
 northern hemisphere (NH), temperature deviation 426
 NO_x adsorber catalyst 778
 NO_x emissions 511
 NO_x storage catalysts, principle 778
 NTP (normal temperature and pressure) 185
 nuclear power 420–421
 nucleophiles 9
 nucleophilic additions 17, 18
 – prochiral carbonyl compound 18
 nucleophilic reagents 9
 nucleophilic substitution reactions 15
 Nusselt number 68, 575, 578, 579
 – for cross flow over a long cylinder 76, 77
 – and heat transfer through fluid between two parallel plates 68
 – local and average Nu number for laminar flow in a circular tube 72, 73
 – variation, along circumference of a cylinder for 74
 Nusselt, Wilhelm 66

o

octane number (ON) 14, 440, 443, 634, 651, 656, 674, 685
 1-octene
 – hydroformylation 733, 734
 – hydrogenation 395, 398
 – liberation 759, 762
 – liberation from 759
 – selectivity 758
trans-4-octene, isomerization/hydroformylation of 721
 Octol process 468
 olefins 441
 – hydroformylation 721, 722
 – hydrogenation 720
 – isomerization 720, 721
 – sources 654
 1-olefins 472
 – Schulz–Flory type distribution 753
 – solubility 728
 α -olefin sulfonates (AOS) 750
 oligomerization 655, 805
 – aluminum-based 757
 – catalytic cycle of ethene 288
 – 1-decene 750
 – ethylene oligomerization for linear 1-alkene production 749
 – Ni-catalyzed 753–755
 – reactor 755
 oligomers 504, 504, 609, 752
 – Schulz–Flory distribution 752
 one-dimensional fixed bed reactor model 680
 one dimensional pseudo-homogeneous reactor model 645
 optical brighteners 501
 optimum operation line (of reactor) 332–336
 organic acids, production capacities. 482
 organic S-species, reactivity 628
 organic sulfur compounds 537
 organic transformations 7
 organocatalyst 19

p

paraffins 131, 433, 440, 443–445, 651, 655
 paraformaldehyde 479
 parallel reactions 206
 – cycle 653
 particle size
 – analysis 164, 165
 – distribution curve 166
 -- Rosin–Rammler–Sperling–Bennett (RRSB) function 165
 – distribution of a granular material 165
 – influence on pressure drop of fixed bed 157

- reduction 163, 164
- reduction ratios
- and maximum sizes (charge) of crushers and millers 163
- particle temperature 240
- maximum temperature difference between center and outer surface 252
- maximum temperature difference between particle and surrounding fluid 240
- Peclet number 350–353
- perfect gas equilibria 183
- perfluorohexane 733
- peroxidation reactor of propylene oxide process 703, 704
- peroxide 702
- pesticides 506
- petrochemical base chemicals, global production 450
- petrochemicals vs. fine chemicals production 505
- petrochemistry 605
- petroleum industry 437
- petroleum residues 623
- Petukhov's law 154
- PFR. *see* plug flow reactor
- pharmaceutical 508
- phenol 8, 472
- phenol production 477
 - Hock process 481
 - α -phenylethanol 703
 - Phillips catalyst 809, 810, 813
 - Phillips Particle Form Process 813
 - phosgene 487, 498
 - phosphates 457
 - phosphite ligands 730
 - phosphoric acids 457
 - phosphoryl chloride (POCl_3) 542
 - phototungstic acid 748
 - photosynthesis 21
 - phthalic acid 484
 - anhydride 472, 521
 - esters 493
 - production capacities. 482, 484
 - phthalic anhydride 707, 708, 712, 717
 - cooling temperature influence 713
 - production 706
 - physical transformations, of pure substances 48
 - change of entropy 48
 - Clausius inequality 48
 - influence of pressure on phase transition process 51
 - Clapeyron equation 51
 - melting enthalpy 51
 - melting point of selected liquids 51
 - phase boundaries 50, 51
 - critical values 50, 51
 - supercritical state 50, 51
 - work done by system 48
 - physisorption 31, 231
 - Pier, Matthias 673
 - pig iron production, in blast furnace 595–603
 - coke consumption 599–601
 - residence time distribution 601–603
 - Planck, Max 41
 - plants, extracts/excreta 455–457, 508
 - natural dyes 455–456
 - natural resins 456
 - natural rubber 455
 - plasticizer alcohol 717
 - plastics 21
 - platinum-rhodium gauzes 572
 - alloy ammonia oxidation gauze 573
 - platinum-rhodium wire 578
 - plug flow behavior 602, 782
 - plug flow reactor 215, 262, 264, 297, 305, 308–310, 312, 315, 353, 355, 360, 381, 388, 628, 646, 710, 767, 784
 - adiabatic 646
 - continuous 767
 - ideal 297, 308, 311, 314, 353, 357, 360, 388, 603, 628
 - Poiseulle, Jean Louis Marie 155
 - poisoning 32
 - Poisson-type distribution 751
 - polarization 14
 - of bonds 8
 - polyacrylates 493, 496, 506
 - applications 494
 - polyacrylonitrile 496
 - polyaddition 494, 495
 - polyamide 6 495, 498
 - polyamide 6.6 495
 - polyamides 486, 495, 498
 - applications 497
 - formation, from diamines and dicarboxylic acids 495
 - polyarylate 495
 - polybutadienes 465, 492, 493, 496
 - polycarbonate 495, 498
 - polycondensation 494
 - polydienes 492, 493, 496, 506
 - applications 493
 - polyesters 495
 - applications 497
 - fibers 740
 - formation, from diols and dicarboxylic acids 495
 - polyethene (PE) production 803–816
 - classification and industrial use 803–805
 - HDPE and LLDPE, catalysts for production 809–812
 - Phillips catalyst systems 810–811
 - single-site metallocene catalyst systems 811, 812
 - Ziegler catalyst systems 809, 810
 - HDPE and LLDPE, production processes 812–815
 - LDPE production, reaction mechanism
 - and process equipment 806–809
 - production economics, and modern developments 815, 816
 - production processes, characteristics
 - purity 805
 - reaction exothermicity and thermal stability 805
 - polyether polyols 705
 - polyethylene (PE) 20, 491, 492, 521, 751
 - poly(ethylene terephthalate) (PET) 495, 497, 740
 - polyisobutene 465
 - polyisoprenes (IR) 493, 496
 - polymer 460
 - polymerization 7, 17, 498, 655, 699
 - cationic 15, 17, 496
 - emulsion 499, 500
 - exothermicity 815
 - grade 612
 - grade ethene, specification 806
 - in solution 498
 - in-substance 498
 - mechanism 492
 - precipitation 499
 - reaction mixture vs. monomer conversion, viscosity 500
 - reactor 812
 - slurry-phase 499
 - suspension 499
 - polymers 12, 491
 - polymer process technologies 492
 - polymethacrylate 12
 - poly(methyl methacrylate) (PMMA) 493, 496
 - polyolefins, applications 492
 - polyols 472
 - polypropylene (PP) 492
 - polysiloxanes 732
 - polystyrene (PS) 12, 493, 496
 - acrylonitrile (SAN) 493
 - butadiene-acrylonitrile (ABS) copolymers 493
 - butadiene rubber (SBR) 493
 - polysulfide 495
 - polytetrafluoroethylene (PTFE) 493
 - polyurea 494
 - polyurethanes 494, 498
 - applications 497
 - poly(vinyl acetate) 496, 740
 - poly(vinyl chloride) (PVC) 493, 496, 717
 - hard 493
 - soft 493
 - pony-tails 734
 - pore diffusion 530, 685, 782
 - and intraparticle heat transport 252, 253
 - limitations 264, 265
 - pore diffusion resistance 229, 247
 - pore effectiveness factor 530, 531
 - temperature and particle size influence 530
 - pores, of catalyst 228
 - overall pore length 228
 - pore diameter 228
 - pore dimensions 228
 - porosity 158
 - of membrane 145
 - porous catalyst
 - particles 249
 - with slab geometry in case of consecutive first-order reactions
 - pore diffusional limitations 264, 265
 - potassium nitrate (KNO_3) 525
 - potential energy surface, for reaction 202
 - practical cell voltage 798
 - Prandtl, Ludwig 71
 - Prandtl number 71
 - Prandtl's law 153
 - Prater number 254, 285
 - precipitation 29
 - pre-desulfurized diesel oil 629
 - pre-exponential factor 201

presaturated one-liquid flow (POLF)
 reactor 764, 765, 771
 – epimerization in 764
 pressure drop 536
 – comparison in a fixed bed and in a monolith 785
 – empty tube 152–154
 – entrained bed 158, 159
 – fixed (packed) bed 156, 157
 – fluidized bed 157, 158
 Presto program 646
 primary amines 484
 primary cracking 608
 primary energy consumption
 – global 423
 – forecast 424
 – regional distribution of 409
 – shares 408, 423
 – world 429
 probability, of chain growth 666
 prochiral compounds 18, 19
 products extracted, using supercritical CO₂ 137
 propagation 606
 propane 461, 462
 1,3-propanediol 476
 propanols 475
 propene 17
 – gas-phase hydroformylation 737
 – rhodium-catalyzed hydroformylation 724
 2-propen-1-ol. *see* allylic alcohol
 propionic acid 742
 propylene 461
 – direct oxidation 701
 – indirect oxidation 702
 – indirect propylene oxidation 704
 – oxidation, pilot plant reactor 704
 – Rh-catalyzed hydroformylation processes 728
 – Wacker-Hoechst oxidation of 481
 propylene glycol ether 478
 propylene oxide 466, 472, 478, 706
 – application 478
 – chlorohydrin process, flow sheet 702
 – commercial production 700–706
 -- chlorohydrin process 701, 702
 -- propylene, indirect oxidation 702–705
 -- propylene oxide, products made 705, 706
 – Halcon process, flow sheet 704
 – industrial epoxides 478
 – polyethers from 705
 – world consumption 705
 PS-butadiene-acrylonitrile (ABS) copolymer 493
 PS-butadiene rubber 493
 pseudo-first-order rate constant 668
 PtRh-gauze 583
 – geometry 580
 pumps, conveyance of liquids by 159
 purchasing power parity (PPP) 410, 415
 purified enzymes 28
 pygas 613
 pyrolysis gasoline 612
 pyrolysis oil 613
 pyrolysis of solid fuels (coal, biomass) 544
 – chemical reactions 448
 – kinetic parameters for biomass 545

q
 quenching 611
 quench-system 610

r
 racemic mixture 19
 racemic resolution processes 19
 racemization processes 19
 radial carbon profiles 643
 radial dispersion 710
 radial effective thermal conductivity 678
 radial heat dispersion 389
 radial heat flux 683, 684
 radial heat transfer in packed bed reactors.
see also fixed bed reactors, modeling
 – effective radial conductivity λ_{rad} of a packed bed 368, 369
 – heat transfer coefficient and Nu number 369, 370
 – and methods to account 363
 – one-dimensional model of a wall-cooled reactor 365–368
 – two-dimensional model of a wall-cooled reactor 363–365
 radial temperature profiles (Fischer-Tropsch reactor, o-xylene oxidation) 681, 713
 radiation 79
 radiation zone 610
 radical chain propagation 12
 radical chlorination 461, 488
 radical cracking taking place in a steam cracker 606
 radical mechanism of acetaldehyde oxidation 740, 741
 radical polymerization reactions 495
 radical reactions 11
 – steam cracking 605
 radicals 7, 490
 radicals I 495
 Raffinate 1 467, 468
 Raffinate 2 468
 Raffinate 3 468
 Raney-copper 29
 Raney-nickel 29
 Raoult, François-Marie 99
 Raoult's law 99
 rate equation 200
 – influence of temperature and reaction order 200
 rates of reactions 178
 – windows of rates, biochemical and chemical processes 177
 raw coke oven gas, composition 590
 reaction energy 187
 – calorimetric measurements 187
 reaction mechanism 200, 201
 – view of chemist and chemical engineer 200
 reaction of gases
 – with a non-porous solid 270
 -- border cases and models 270
 -- chemical reaction determines effective rate 274
 -- conversion different cases 275
 -- effective rate limited by external diffusion 274
 -- equations 275

-- rate limited by film diffusion and internal diffusion 272, 273
 -- reaction and external mass transfer 273
 -- shrinking non-porous unreacted core 270–272
 -- shrinking non-porous unreacted core and gaseous product(s) 273, 274
 -- slow chemical reaction 272
 -- solid product layer 270–272
 – with a porous solid 276
 -- basic equations for conversion 277
 -- border cases and general situation 277
 -- border cases and models 276
 -- chemical reaction, rate-determining step 281
 -- equations for conversion 281
 -- general closed solution by combined model 277–279
 -- homogeneous uniform conversion model 280
 -- rate controlled by diffusion through solid product layer 281
 -- reaction and diffusion in product layer determine rate 281
 -- shrinking unreacted core model 280
 reaction of *n*-th order 204, 205
 reaction quotient (Q_R) 185
 reaction rates 23, 24
 – different forms and units 230, 231
 reactions, general classification 10
 – acid-base catalyzed reactions 11
 – addition reactions 10
 – electrophilic addition reactions 17
 – electrophilic substitution reactions at aromatic compounds 15–17
 – elimination reactions 11
 – nucleophilic addition reactions 17, 18
 – nucleophilic substitution reactions 13
 -- choice of solvent: 13
 -- groups surrounding carbon atom 13
 -- nature of incoming group 13–14
 -- nature of leaving group 14
 – reactions via carbocations 14, 15
 – reactions via free radicals 11, 12
 – rearrangement/isomerization reactions 11
 – substitution reactions 10
 reactions in series 206
 reactions with varying volume 213–215
 reaction time 180, 181
 reactors. *See also* chemical reactors
 – batch 181
 – catalytic 23
 – chemical reactor
 -- disciplines needed for design 176
 -- scale-up dimensions 177
 – influence of mixing on the reactor size 178
 – influence of reactor type on productivity 178
 – tube 35
 reactor technology, novel developments 370
 – adiabatic reactors, with periodic flow reversal 376, 377
 – hybrid (multifunctional) reactors 370
 -- catalytic distillation 372
 -- coupling membranes and reaction 370, 371
 -- coupling reaction and adsorption 371, 372
 – microreactors 373

- advantages 373
- drawbacks 373, 374
- heat transport 375, 376
- mass transport, and residence time distribution 374
- typical values of characteristic parameters 374
- monolithic reactors 372, 373
- reagent induction 19
- reagents classification 9, 10
- real gas
 - adiabatically expansion 46
 - properties 40
- real gas equilibria 190, 191
- rearrangement or isomerization reactions 10
- reciprocal reaction rate 564, 565
- recycle compressor 630
- recycle gas, composition 684
- recycle ratio
 - definiion 676
 - influence 677
- recycle reactor 676
- recycling 27
- Redlich-Kwong equation 44
- reduce CO₂ emissions 426
- reducing agent 780
- reductive cleavage 761
- reductive elimination 720, 760
- refineries
 - flow-sheet of crude oil refinery 445
 - processes 443–445
 - products, properties of 442–443
- refinery alkylation 463, 652–662
 - alkylation feedstock and products 654, 655
 - commercial alkylation processes 657–662
 - commercially applied alkylation processes comparison 661, 662
 - using hydrofluoric acid as liquid catalyst 657, 658
 - using sulfuric acid as liquid catalyst 658–661
 - process variables 655–657
 - acid strength and composition 656
 - effect of mixing 656, 657
 - isobutane concentration 656
 - reaction temperature 655, 656
 - reaction and reaction mechanism 652–654
- reforming catalysts (reforming of gasoline) 636, 639
 - characteristic data 641
 - deactivation and regeneration 639
 - mechanisms 636
- refractory-lined furnace for sulfur combustion 559, 560
- regeneration process (decoking of reforming catalyst) 645
- regioisomers 16
- regioselectivity 738
- regulators 501
- renewable energy 421–422, 424, 430
- renewable raw materials
 - base chemicals 450–451
 - carbohydrates 453–455
 - extracts and excreta from plants 455–457
 - fats and vegetable oils 451–453
- research octane numbers (RONs) 652, 634
- reserves of fossil fuels 418–420, 423
- residence time 180, 181, 608
 - distribution 336–343
- resources of fossil fuels 418–420, 423
- reverse osmosis 147
 - basic principle 147
 - reversible reactions 210–212
 - activation energies 212
 - first-order reaction
 - effectiveness factor (pore diffusion) 251, 252
 - exothermic 258
 - with influence of external and internal mass transfer 256–259
 - ratio of rate constants 212
 - relation between equilibrium -- and rate of forward and reverse reaction 213
 - standard reaction enthalpy and entropy 212
- Reynolds number 70, 71
- Reynolds, Osborne 71
- Rh-based hydroformylation 722–724, 730, 738
- Rh-BIPHEPHOS 721
- Rh catalyst 729
- Rh-catalyzed propene hydroformylation 728
- rhodium catalyst 731
- riboflavin 508
- risertype reactor 658
- Roelen, Otto 717
- Rosin–Rammler–Sperling–Bennett (RRSB) function 165
- Ruhrchemie/Rhône-Poulenc process 726, 727, 733
- S**
- α-SABLIN technology 757
- saccharose (α -D-glucopyranosyl- β -D-fructofuranoside) 455
- Sachsse–Bartholomé process 461, 470
- sanitation, global 514
- saponification 503, 701
- SASOL tetramerization system 761
- SATP (standard ambient temperature and pressure) 185
- saturated fatty acids 451
- saturated monoalcohols, industrial production 474
- Schmidt, Ernst 86
- Schmidt number 86
- Schulz–Flory product distributions 752, 755
- SCR reactor 781
 - pressure drop 785
 - scrubbers 658
 - secondary amines 484
 - second law of thermodynamics 48
 - second-order reaction 205
 - sedimentation 168, 169
 - estimation of size of sand trap of sewage plant 170
 - in gravitational field 169
 - separation of solids from fluids 168
 - single sand particles in water 170
 - selective catalytic reduction (SCR) 586, 778
 - selectivity 25
 - definition 179, 180
 - selective hydrogenation reactions 613
 - selectivity of reactions 259
 - influence of external mass transfer on -- selectivity of parallel reactions 262, 263
- selectivity of reactions in series 259–262
- influence of pore diffusion
- on selectivity of parallel reactions 267
- on selectivity of reactions in series 263, 264
- self-alkylation 655
- self-ignition 699
- semi-batch stirred tank reactor 764
- semi-regenerative reforming process, flow scheme 637
- separation by membranes 144
 - applications of technology 144
 - basic principle of reverse osmosis 146
 - mass transport through
 - non-porous membrane 146
 - porous membrane 145, 146
 - membrane separation processes, applications 147
 - desalination of sea water 147
 - gas separation 147–149
 - principles of membrane separation 144, 145
 - dense (non-porous) membranes 144
 - porous membranes 144
 - seawater desalination process 147
 - spiral-wound membrane element 147
- separation processes, based on the wettability 167
- sequestrants 501
- Shell catalyst system 707, 715, 723
- Shell higher olefins process (SHOP) 25, 750, 753–757
 - flow scheme 753
- Sherwood numbers 86, 138, 239, 574, 579, 582, 641, 783
- Sherwood, Thomas Kilgore 86
- shrinking core model 644
- side-fired primary reformer 556
- Siemens-Martin (SM) process 589
- sieve analysis, of sand 166
- sigmoidal heat production function 587
- silicates 459
- silicones 459
- silicotungstic acid 748
- SILP catalyst 737
- SILP materials 737
- simultaneous equilibria, calculation 197
- single-phase system 287
 - homogeneous and enzyme catalysis 287
 - mechanism of homogeneous catalysis 288
 - turn over number 287
- single-pressure nitric acid plant 585
- single-site catalysts 811
 - development 811
 - Kaminsky-catalyst, formation 811
 - metallocene catalysts 809
- single-stage reactor 659
- sintering 34
- size exclusion membranes 732
- slurry-phase polymerization 499
- slurry process 812
- Smochulowski, Marian 248
- Snia-Viscosa process 486
- S_N1 reaction 13
- S_N2 reaction 13
- SO₂
 - catalytic conversion into SO₃ 560–566

- selectivity conversion *vs.* dimensionless reactor volume 565
 - selectivity of reactions conversion *vs.* temperature plot 564, 565
 - production routes 559
 - emissions
 - soap formation 503
 - Soave–Redlich–Kwong equation 44, 687
 - soda ash 457
 - sodium carbonate. *see* industrial soda ash
 - sodium hexafluoroaluminate 802
 - sodium hydroxide 457
 - sodium nitrate (NaNO_3) 525
 - sodium salt of tris(*m*-sulfonatophenyl) phosphine (Na-TPPTS) 726
 - Sohio process 462, 486
 - solar energy 430
 - sol–gel processes 29
 - solid catalysts
 - individual steps of catalysis 292
 - kinetics of gas–liquid reactions on 291–294
 - reaction and interfacial transport of mass and heat 235
 - sorption on surface of 231
 - solidification temperature curves 140
 - solvation 13
 - Solvay process 458
 - process scheme of 459
 - solid–fluid separation 168
 - solid–solid separation processes 167
 - soot-naphtha suspension 553
 - sorting of solids 167
 - sour gases 435
 - space–time yield 23, 181, 499
 - space velocity 181
 - spectrum of factors, influencing rate of reaction 227, 228
 - speed of reactions 177
 - sprouting of PtRh catalyst for ammonia oxidation 572
 - S-sensitive DeNO_x -storage catalysts 625
 - standard Gibbs function of reaction 189
 - standard of living 415
 - standard potentials 787, 789, 790, 800, 802
 - standard reaction enthalpy 186, 187
 - calorimetric measurements 187
 - standard reaction entropy 186, 187
 - standard reference conditions 184
 - starch 454, 491
 - molecular segments 455
 - starch-containing substrates 472
 - steam cracker/cracking 10, 464, 604, 605, 607
 - basic chemicals by 604–616
 - benzene 468
 - butadiene, isobutene, and butenes 466
 - C_4 -cut, technical processing 466
 - economics 615
 - ethylene 464
 - general and mechanistic aspects 605–608
 - industrial steam cracker process 610–615
 - product distribution, influencing factors 608–610
 - applied feedstock 608
 - hydrocarbon partial pressure in cracking oven 609, 610
 - residence time 608, 609
 - temperature in cracking oven 608
 - product separation and purification 613
 - propylene 465
 - simplified scheme 612
 - steam cracker process, economic aspects 615
 - steam cracker unit
 - mass balance 614
 - simplified scheme 614
 - steam reforming process 32, 536
 - ammonia plant, block diagram and temperature profile 538
 - feed for 537
 - steel 603
 - iron ore to 603
 - production processes 588
 - steel production 587–589
 - based on blast furnace route 588, 589
 - based on scrap and direct reduced iron (DRI) 589
 - coal and coke in steel production 449, 587
 - Stefan-Boltzmann law 79
 - Stefan flow 87
 - Stefan, Joseph 79
 - step-growth polymerization 494
 - stereochemical environment 811
 - stereoisomers 18
 - steric demand 13
 - steric effects 8
 - reactivity of two triyl radicals 9
 - stirred tank reactor 746
 - stirred tank reactors
 - adiabatic operation 323
 - derivation of E_θ - and F -function 340
 - dynamic behavior and oscillations 326
 - dynamic stability 325
 - equations 324, 326
 - heat production function, and heat removal lines 324
 - parameters of styrene polymerization 325
 - static stability 325
 - typical devices for 319
 - stoichiometric coefficient 560, 787
 - Stokes' law 169, 170
 - STP (standard temperature and pressure) 185
 - straight-run gasoline 651
 - stranded gas 694
 - STRATCO[®]Contactor[™] reactor 657
 - setup 659
 - stripper 612
 - styrene 464, 469, 702
 - copolymers 703
 - subjective well-being index (SWB) 416, 417, 418
 - substitution reactions 10
 - substrate induction 19
 - sugar 454
 - based surfactants 454
 - sulfochlorination 12, 463, 504
 - sulfolene 465
 - sulfonation 16
 - sulfoxidation 504
 - route 464
 - sulfur 457
 - emissions 624
 - sulfuric acid 457, 474, 558–567
 - processes for production 566
 - production, reactions and thermodynamics 558, 559
 - sulfur dioxide conversion into SO_3 560–566
 - sulfur dioxide production 559, 560
 - use as catalyst for alkylation 658
 - supercritical carbon dioxide (scCO_2) 734
 - immobilization, schematic representation 734
 - supercritical fluids 93, 136, 137, 139, 150, 485, 735
 - solvation properties 137
 - supercritical hydrocarbons 139
 - superheated steam 610
 - supported Ag particles, REM pictures 698
 - supported aqueous phase (SAP) catalysts 737
 - supported ionic liquid phase (SILP) catalyst 737
 - surface kinetics 231
 - surface renewal theory for gas–liquid mass transfer 217
 - surfactants 500
 - applications 502, 503
 - molecules
 - application field 501
 - schematic representation 500
 - neutral, applications 504
 - structure and properties 500–501
 - suspension polymerization 499
 - suspension process. *see* slurry process
 - sustained strong economic growth 423
 - Sutherland constant 58
 - Sutherland, William 58
 - SWB 416–418
 - Symrise process 763
 - syndiotacticity 492
 - synfuels, limitations 672
 - syngas 460, 464, 536–558, 716
 - by partial oxidation of heavy oils 552–555
 - from solid fuels (coal, biomass) 542–552
 - basic principles and reactions 542
 - by gasification 543, 544
 - by gasification of biomass 544–552
 - by steam reforming of natural gas 555–558
 - treatment 537
 - synthesis gas. *see* syngas
 - synthetic ammonia 525
 - synthetic fuels
 - Fischer–Tropsch synthesis (FTS) 684
 - production 664, 672
 - synthetic hydrocarbons (SHC) 750
 - synthetic lubricants 750
 - synthetic rubber. *see* elastomers
- t**
- Takasago process 763, 772
 - tanks-in-series model 340, 602, 603
 - calculation of conversion by tanks-in-series model 342, 343
 - derivation of number of tanks-in-series by E_θ function 342
 - residence time distribution of cascade of 340–342

- Teller, Edward 127
 tensides 453, 478, 504
 terephthalic acid 465, 483, 740
 – production capacities 482, 483
 terephthalic dimethyl ester 483
 tert-butylamine, production 485
 tertiary amines 484
 tetrachloromethane 488
 1,1,2-tetrafluoroethane 490
 tetrahydrofuran (THF) 478
 Texaco process for heavy oil gasification 553
 – feedstock and raw syngas
 composition 554
 thermal conductivity 69, 229, 546, 580, 592, 593, 647
 thermal conductivity 81
 thermal cracking of heavy oils 616
 thermal diffusion 56
 thermal entrance region 71
 thermal runaway during PE production 806
 thermodynamic data
 – NH_3 synthesis 192
 – selected species 185
 thermogravimetry (TG) 92, 400, 404
 thermoplastic polymers 491
 thermoset resins 491
 thickness δ of thermal boundary layer 68
 – definitions 68
 Thiele modulus 252, 254, 640, 641, 642, 669, 715
 Thomson, William 46
 three-phase system 629, 633
 three-way catalyst 776, 786
 tidal power 422
 time-tank process for alkylation 658, 661
 – scheme 659
 titanium-silicate catalyst 703
 Ti-V-W catalyst 782
 toluene 463
 toluene diisocyanate 498
 2,4-toluene diisocyanate 488
 toluene diisocyanate (TDI) 498
 total oxidation 701
 TPPTS 726
 transalkylation reactor (TR) 469, 753
 transfer-line heat exchangers, design
 objectives 611
 transient heat
 – coke production from coal 591
 – of plate for $B_i h$ 82–84
 – transfer by conduction and convection 80–82
 transition states 23, 24
 transport coefficients of gases 57
 – binary gas mixtures 58
 –– binary gas diffusion coefficients 59
 –– calculation of binary diffusion
 coefficients 58
 –– experimental values, correlation 59
 –– Hirschfelder equation 58
 –– special diffusion volumes derived 59
 – experimental values deviation 57
 – gas mixture, more than three components 59
 – for ideal gases 57
 – influence of T and p 57
 – mean free path 57
 – mean velocity of molecules 57
 – Sutherland constant 58
 transport coefficients of liquids 61–63
 – Bridgman equation 61
 – diffusion coefficient, calculation 62
 –– Wilke–Chang equation 62
 – influence of temperature on viscosity 62
 – methods to measure diffusion coefficient in
 liquids 63
 –– capillary method 63
 –– magnetic suspension balance 63, 64
 – thermal conductivity 61
 transport limitations, in experimental catalytic
 reactors
 – criterion to exclude influence of dilution of
 catalytic fixed bed 392
 – gradientless ideal particle behavior
 389, 390
 –– interfacial heat transfer 391
 –– interfacial mass transfer 390
 –– internal heat effects 391
 –– internal mass transfer 391
 – ideal plug flow behavior 388–390
 transport properties 52
 – and density of selected gases 53
 – equations for transport of mass, heat, and
 momentum 52, 53
 – in liquids and solids 53
 trays 723
 trickle bed reactor 629–632, 633
 triethylene glycol 476
 triglycerides 451
 trimethylamine 484
 trioxane 479
 triphenylphosphine 737
 – ligand 732
 trityl radicals 9
 Tropsch, Hans 664
 Trouton, Frederik Thomas 50
 Trouton's rule 50, 629
 turnover frequency (TOF) 23
 turnover number (TON) 20, 22, 23
 two-dimensional finite element method 577
 two-dimensional fixed bed reactor model 678,
 685, 709
 two-film theory 217
 – equations 218, 219
 two first-order reactions in series 207–209
 two parallel first-order reactions 206, 207
 two-phase reactor 631
- u**
- Union Carbide Corporation (UCC) 696
 Union Carbide/Davy Powergas gas recycle
 process 724
 – disadvantages 725
 – schematic view 724
 Union Carbide's Ethoxene process 748
 Union Carbide's induced phase separation
 process
 – schematic view 729
 unsaturated fatty acids 451
 UOP process 657, 658
 urea 457
 UV-irradiation 490
- v**
- vacuum distillation 616
 vacuum residue oil 618, 619
 valence electrons (VE) 759
 valuable organic intermediates 717
 vanadium-based catalyst 561
 Van der Waals constants, of selected
 gases 42
 van der Waals equation 42
 – estimation of critical data based
 on 44
 van der Waals interactions 736
 Van der Waals, Johannes Diderik 42
 van't Hoff equation 188
 van't Hoff, Jacobus Henricus 188
 vaporization 49
 – change of entropy 49
 – enthalpy 49, 50
 – Trouton's constant 50
 – vapor pressure equation 49
 vapor pressures 50, 51, 541
 – for curved systems 51, 52
 variable costs 521–524
 vegetable oils 452
 Verbund 615
 vibration mills 163
 vinyl acetate (VAM) 467, 740
 vinyl chloride 11, 465, 472, 490
 vinyl ester 465
 vinyl ether 465
 vinylidenes 758
 vinyl-polymers 496
 – applications 494
 viscoelastic polymer 804
 viscosity of gases and liquids 52, 53
 vitamin B2. *see* riboflavin
 vitamin B₃ 508
 vitamin C 508
 vitamin E 508
 vitamins 508
 V₂O₅ catalyst 561
 volatile platinum oxides 573
 volatility, relative 99
- w**
- Wacker–Hoechst process 480
 – ethylene oxidation 480
 washing machine powder 501
 washing powders 28, 504
 washing towers 612
 waste-heat boiler (WHB) 553
 water alkaline electrolyzers 798
 water consumption, domestic 513, 514
 water content/consumption,
 virtual 514
 water electrolysis 797
 water footprint 513, 514
 water-gas shift reaction 24, 539, 555, 600, 669,
 682, 687
 – equilibrium constant, influence of temperature
 on 539
 water/NMP/catalyst 729
 water resources
 – global 512
 – renewable 513
 Weisz modulus 252
 whole cell 26
 Wilke–Chang equation 62, 669, 769
 wind turbines 422
 Winkler process 543

wood
– to cellulose 454
– constituents of 454
– production of forest products 454

x

xenon 457
X-ray diffraction 31
X-ray photoelectron spectroscopy 32
XTL plant 674
xylenes 463
o-xylene 469
– oxidation

-- effective rate 715
-- multi-tubular reactor 706
– to phthalic acid anhydride
-- catalytic oxidation 706–716
-- multi-tubular reactor, design and
simulation 708–716
– phthalic anhydride, production and use 707,
708
p-xylene 465, 483, 484
y
yeasts 474
yield, definition 179, 180

z

Zeldovich, Yakov Borisovich 248
zeolites 26
– adsorbents 121
– role in refinery, and petrochemical
processes 26
Ziegler Aufbaureaktion 751, 753, 757
Ziegler, Karl 751
Ziegler–Natta catalysts 21, 492, 493, 496, 750,
809, 810, 811
Ziegler–Natta polymerization 492
ZnO/Cr-oxide catalysts 689